Ibrahim Dincer · Adnan Midilli · Haydar Kucuk   *Editors*

Progress in Exergy, Energy, and the Environment

Springer

Progress in Exergy, Energy, and the Environment

Ibrahim Dincer • Adnan Midilli • Haydar Kucuk
Editors

Progress in Exergy, Energy, and the Environment

Springer

Editors
Ibrahim Dincer
Faculty of Engineering
   and Applied Science
University of Ontario
Oshawa, ON, Canada

Adnan Midilli
Department of Mechanical Engineering
Recep Tayyip Erdoğan University
Rize, Turkey

Haydar Kucuk
Department of Mechanical Engineering
Recep Tayyip Erdoğan University
Rize, Turkey

Preface

Exergy appears to be a well-established and distinct discipline which has come out of the second law of thermodynamics and gone beyond thermodynamics to be used in many other disciplines, such as chemical, biotechnology, civil, environmental, architectural, industrial, electrical, geology, and topography in engineering and chemistry, biology, physics, mathematics, business, information technology, economy, and medicine in non-engineering areas.

At present, humanity faces great challenges about energy, economy and environment, and there is a strong need to better design, analyze, assess and improve energy processes, systems and applications. This can only be done by exergy method, rather than energy method. This is why we use exergy analysis in addition to energy analysis. The exergy method of analysis overcomes the limitations of the first law of thermodynamics. The concept of exergy is based on both first law of thermodynamics and second law of thermodynamics. Exergy analysis clearly indicates the locations of energy degradation in a process and can therefore lead to improved operation or technology. Exergy analysis can also quantify the quality of heat in a waste stream. One of the main goals for exergy analysis is to identify meaningful exergy efficiencies and the causes and true magnitudes of exergy losses.

The emphasis is now on system analysis and thermodynamic optimization, not only in the mainstream of engineering but also in physics, biology, economics, and management. As a result of these recent changes and advances, exergy has gone beyond thermodynamics and become a new distinct discipline because of its interdisciplinary character as the confluence of energy and environment. It was a prime motive to initiate a conference series on Exergy, Energy and Environment in 2003. The conference, since then, has been running successfully under the title of "International Exergy, Energy and Environment Symposium (IEEES)." The conference has a multidisciplinary nature, covering three main areas of exergy, energy and the environment and aims to provide a forum for researchers, scientists, engineers and practitioners from all over the world to exchange information, to present high-quality research results and new developments in the wide domain covered by exergy, energy, and the environment, and discuss the future direction and priorities in the field.

This unique book contains, in addition to some invited contributions, the selected papers from the latest, the Sixth International Exergy, Energy and Environment Symposium (IEEES-6), which was held in Recep Tayyip Erdogan University in Rize, Turkey. It covers a broad range of topics on energy conservation and management; energy and exergy analyses; entropy generation minimization; exergy, energy and environmental modeling; exergoeconomics and thermoeconomics; hydrogen energy technologies; fuels and alternatives; heat and mass transfer; renewable energies; new and clean energy technologies; refrigeration and heat pump systems; combustion technologies; thermal systems and applications; air-conditioning systems; thermodynamic optimization; modeling of energy systems; combustion/gasification; process optimization; sectoral energy and exergy utilization; waste exergy emissions, etc.

Oshawa, Ontario, Canada	Ibrahim Dincer
Rize, Turkey	Adnan Midilli
Rize, Turkey	Haydar Kucuk

Contents

Part IV Renewable Energy

Exergy Analysis of a Hybrid Solar–Wind–Biomass System with Thermal and Electrical Energy Storage for a Community

Kevork Hacatoglu, Ibrahim Dincer, and Marc A. Rosen

Abstract

Sustainable community energy systems often require integration of renewable energy systems with energy storages. Here, a hybrid solar–wind–biomass system with thermal and electrical storages is proposed to supply continuous and reliable energy to a typical Ontario community. Exergy analysis is applied and indicates that a 1,800 m^2 parabolic trough collector with a wind turbine (16 m rotor radius) and anaerobic digestion can meet the energy needs of a community of 50 households when thermal and electrical storages are utilized and that the steam turbine and space heating components offer the best potential for improving the overall efficiency.

Keywords

Anaeorbic digestion • Community • Energy • Exergy • Hybrid • Solar • Storage • Sustainability • Wind

Introduction

Although energy fuels the development and prosperity of billions of people around the world, concerns exist regarding access to adequate, affordable, and reliable energy supplies and accelerated rates of climate change caused by greenhouse gas emissions from fossil fuel combustion. The twin threats of energy security and climate change are driving interest in renewable energy sources such as solar, wind, biomass, and geothermal.

A key technical challenge associated with renewable energy is intermittency. The availability of solar and wind energy fluctuates, but integration with storage technologies diminishes variability and improves the reliability of supply. Another method of improving the reliability of renewable energy systems is through hybridization. Combining several technologies into a hybrid system improves the chances that at least one of the energy sources will be available at a given time.

Unlike photovoltaic-based technologies, which directly convert sunlight to electricity, solar thermal approaches heat a working fluid that drives a power conversion unit similar to conventional power plants. A number of commercial solar thermal power plants were built from 1984 to 1991 in the Mojave Desert in California [1]. The most commercialized solar thermal technology is parabolic trough collectors that concentrate direct radiation 30–80 times [2]. Other promising technologies include central receiver or dish/Stirling systems.

Thermal storage technologies such as two- and single-tank systems can improve the reliability of solar thermal systems. In the two-tank system, fluid is divided into hot and cold tanks. The direct system uses the same fluid in the solar circuit and storage, whereas the two-tank indirect system uses different fluids. Single-tank systems have a temperature gradient from hot to cold that can cool a hot fluid (charging) or heat a cold fluid (discharging).

Efficient use of energy resources requires a clear understanding of not just quantity but also quality of energy. Traditional energy analysis based on the first law of thermodynamics should be augmented by a second law-based exergy approach that

K. Hacatoglu (✉) • I. Dincer • M.A. Rosen
Faculty of Engineering and Applied Science, University of Ontario Institute of Technology,
2000 Simcoe Street North, Oshawa, ON, Canada L1H 7K4
e-mail: Kevork.Hacatoglu@uoit.ca; Ibrahim.Dincer@uoit.ca; Marc.Rosen@uoit.ca

also considers quality [3]. Linkages between exergy and increasingly important areas such as the environment and sustainable development have expanded the potential benefits of exergy analysis [4].

Sustainable communities of the future will likely need to be powered by adequate and reliable flows of renewable energy. The objective of this research is to conduct an exergy analysis and efficiency assessment of a hybrid renewable energy system using actual energy-use data and environment conditions and to investigate the sources of exergy destruction and the dependence of the system on its parameters. This system utilizes solar thermal, wind, and bioenergy technologies, along with thermal and electrical energy storages.

System Description and Component Exergy Destruction Rates

Many components comprise the considered solar–wind–biomass system (Fig. 1.1). Solar and wind energy are converted to heat, cold, and electricity to meet the energy demands of the community. Municipal solid waste (MSW) from local households is converted to a methane-rich biogas through anaerobic digestion. Variability is managed using thermal and electrical storage technologies. The system will be in either charging or discharging modes depending on the balance between demand and supply. Excess supply from the solar thermal system will charge thermal storage tanks, while surplus electricity will charge electrical storages.

Solar Thermal Subsystem

The solar thermal component is responsible for meeting space heating, cooling, and some of the electricity demand (Fig. 1.2). Integrating the solar thermal system with thermal storage ensures reliability and continued production during periods of solar unavailability.

Direct solar radiation is reflected by parabolic trough collectors to a heat transfer fluid (HTF) circulating through a receiver. The HTF is modeled as Therminol, which is also used in the aforementioned solar plants in the Mojave Desert. The HTF in a solar thermal system should be kept in a liquid state, and pressurization is required for temperatures above Therminol's normal boiling point of 257 °C. Concentration of radiation allows for the temperature of the HTF to increase up to approximately 350 °C. The hot HTF can then be used in four ways: (1) space heating, (2) absorption refrigeration, (3) electricity generation, or (4) storage.

The solar thermal system is the primary source of space heating and cooling for the community. Hot HTF from the receiver or the hot storage tank passes through heat exchangers to directly provide domestic space heating in the winter or to vaporize and separate the refrigerant (ammonia or NH_3) from the transport medium (water or H_2O) in the generator of an
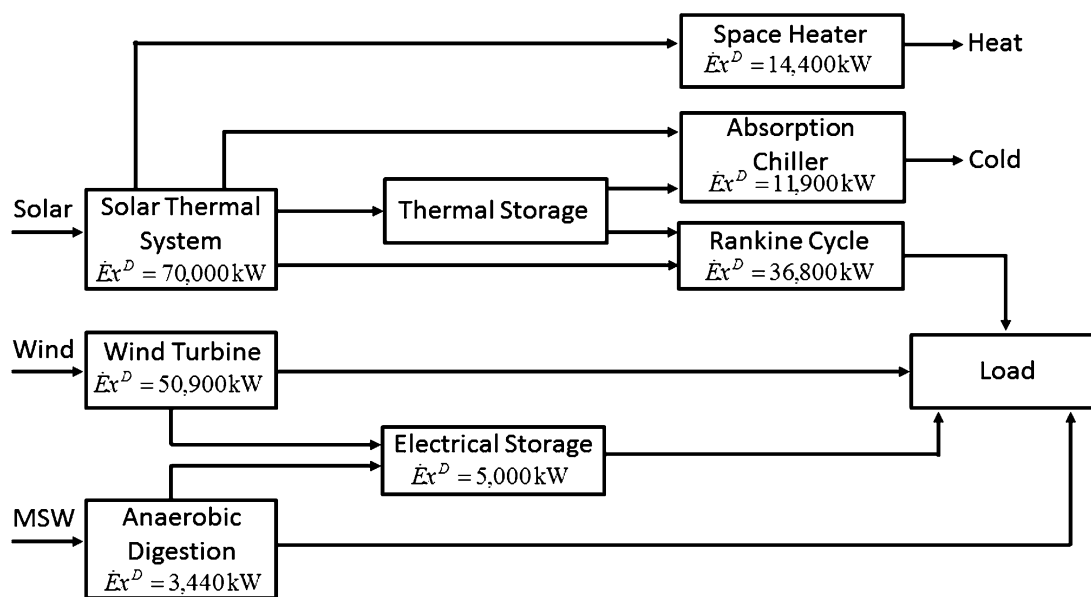
Fig. 1.1 Schematic of the hybrid solar–wind–biomass community energy system with exergy destruction rates ($\dot{E}x^D$) for each component
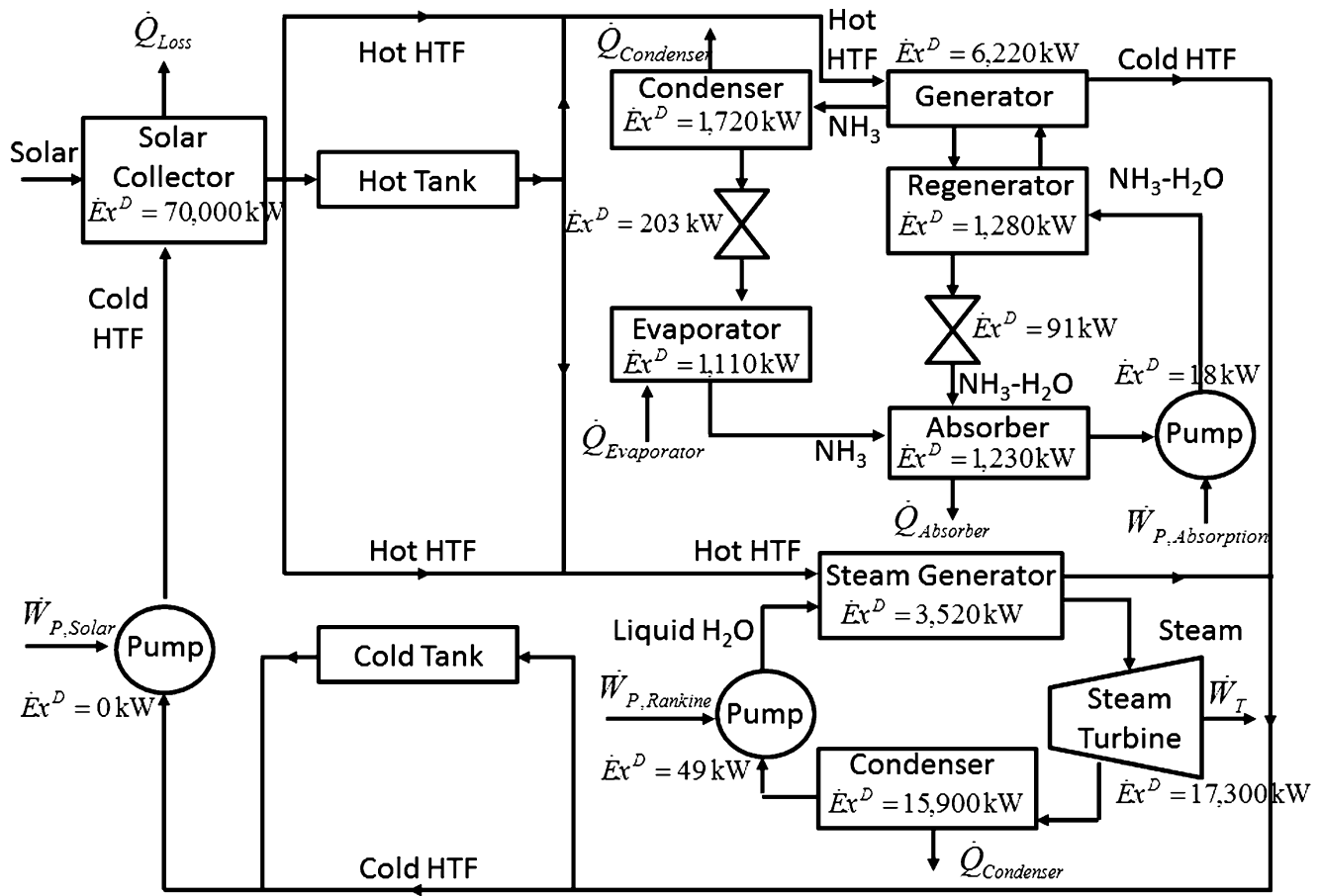
Fig. 1.2 Solar and thermal storage subsystems of the overall community energy system with exergy destruction rates

absorption refrigeration cycle in the summer. The NH_3-rich vapor then condenses and flashes via a thermal expansion valve and then evaporates due to the heat collected from households in the community. The weak solution (low in NH_3) leaving the generator preheats the incoming strong solution and flashes via a thermal expansion valve. The NH_3-rich vapor and weak solution recombine to form a strong solution that is pumped and preheated in a heat exchanger.

A power-generating Rankine cycle is only activated when the supply of electricity is insufficient. Hot HTF enters the subsystem through a steam-generating heat exchanger. The superheated steam drives a turbine that produces mechanical work followed by electricity via an electric generator. The low-pressure steam is condensed and pumped back into the steam generator.

A two-tank direct thermal storage system manages the effects of fluctuations in solar availability. When solar thermal energy is plentiful, a portion of the circulating HTF is diverted to charge a high-temperature storage tank maintained at 350 °C. Charging the hot tank simultaneously discharges the low-temperature tank (250 °C). During periods of high demand or low solar and wind availability, hot HTF is discharged from storage, which in turn charges the cold tank.

Wind and Anaerobic Digestion Subsystem

The wind and anaerobic digestion components of the hybrid system are responsible for meeting most of the electricity demand of the community (Fig. 1.3). Integrating these components with electrical storage improves reliability by providing a backup during periods of low wind speeds.

The kinetic energy in wind is converted to rotational mechanical work by a wind turbine. We assume a rotor radius of 16 m and cut-in and cut-out speeds of 5 and 23 m/s, respectively. Surplus power production charges a battery that can be discharged during periods of high demand or low wind availability.
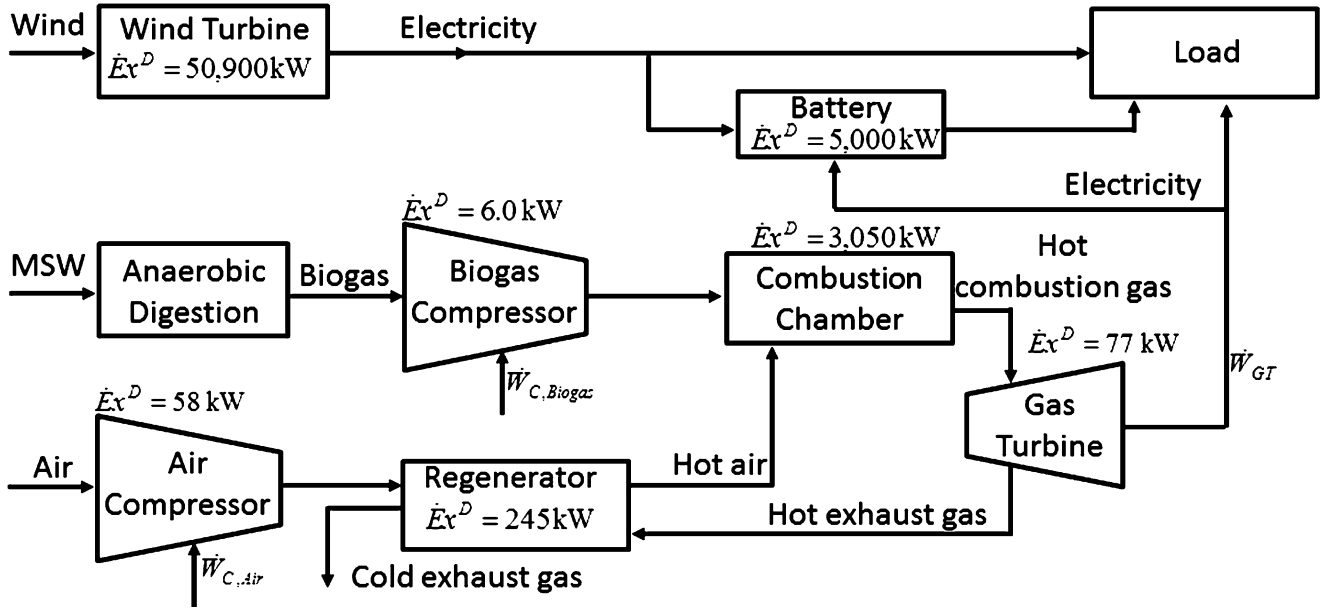
Fig. 1.3 Wind, anaerobic digestion, and electrical energy storage subsystems of the overall community energy system with exergy destruction rates

Waste biomass is consistently available throughout the year locally as the average person in Ontario produces approximately 1 kg day^{-1} of MSW [5]. Anaerobic digestion of MSW generates a methane-rich biogas and digestate that can be converted to a marketable high-quality humus material via aerobic composting [6]. The biogas can generate power in an open Brayton cycle with air/exhaust gas as the working fluid. Combustion of biogas generates hot exhaust gases that expand in a gas turbine producing mechanical work. The temperature of the gas at the outlet of the turbine is high enough to preheat fresh incoming compressed air in a regenerator.

Analysis

A thermodynamic model of the hybrid system was developed using the Engineering Equation Solver (EES) software. The model was run for 365 days with five different input variables: (1) electricity demand per household (excluding air conditioning), (2) air conditioning demand per household, (3) direct solar irradiance, (4) wind speed, and (5) ambient temperature.

Electricity demand is separated from air conditioning because the proposed model supplies cooling through an absorption refrigeration cycle driven by thermal energy. We can calculate the required heat removal rate from air conditioning data [7] using an average coefficient of performance (COP) of 4 for central air conditioners. The daily electricity needs of a typical household in Ontario are illustrated in Fig. 1.4.

Solar and wind are intermittent energy sources that exhibit variable availability over the year. The direct solar irradiance available to Toronto, Ontario, Canada, can be approximated by a semiempirical model presented in [1]. The direct solar irradiance $\left(\dot{Q}_{Solar}\right)$ on a tilted plane is a function of the extraterrestrial solar irradiance $\left(\dot{Q}_{ETR}\right)$, clearness number ($C_n$), local extinction coefficient (k_C), elevation angle (α), and angle of incidence (i):

$$\dot{Q}_{Solar} = \dot{Q}_{ETR} C_n \exp(-k_c \sin \alpha) \cos i \tag{1.1}$$

The angle of incidence is a function of the elevation angle, solar azimuth angle (a_s), collector azimuth angle (a_w), and collector tilt angle (β):

$$\cos i = \cos \alpha \cos (a_s - a_w) \sin \beta + \sin \alpha \cos \beta \tag{1.2}$$
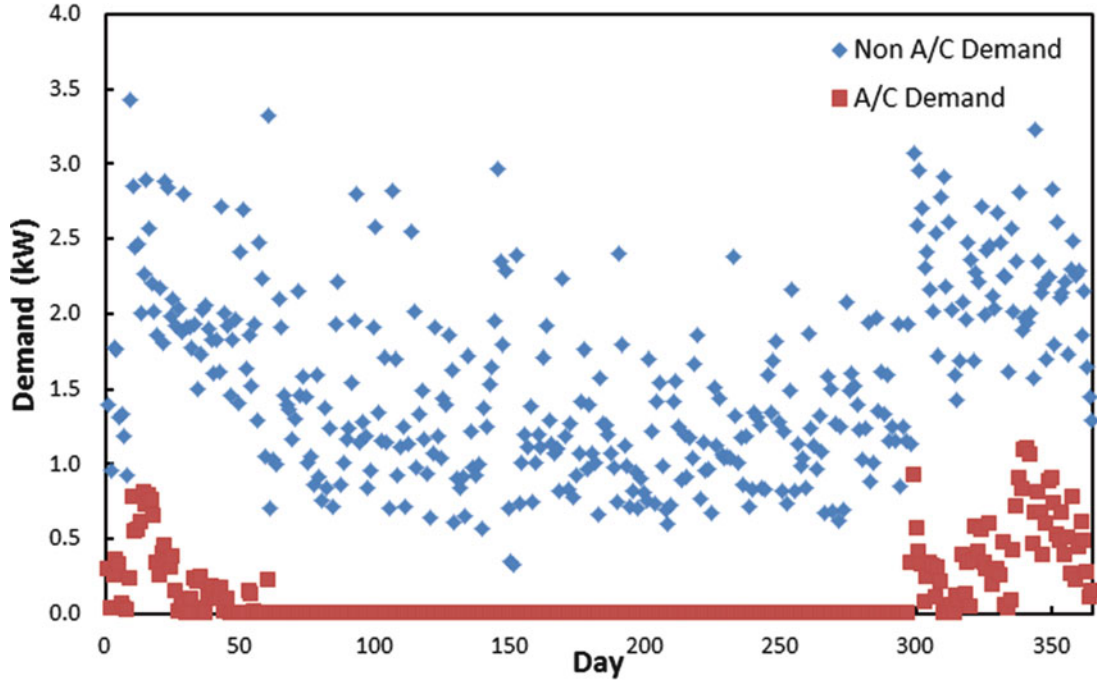
Fig. 1.4 Daily power needs over 1 year for a typical household in Ontario, excluding air conditioning (A/C) and only for air conditioning (day "0" corresponds to August 1, 2009)

Table 1.1 Direct solar irradiance parameters k_C (dimensionless), C_n (dimensionless), β (degrees), and a_w (degrees) and T_0 (°C) for Toronto, Ontario, Canada

	Jan	Feb	Mar	Apr	May	Jun	Jul	Aug	Sep	Oct	Nov	Dec
k_C	0.142	0.144	0.156	0.180	0.196	0.205	0.207	0.201	0.177	0.160	0.149	0.142
C_n	0.85	0.85	0.85	0.85	0.85	0.85	0.85	0.85	0.85	0.85	0.85	0.85
β	70	60	50	30	20	20	20	30	40	60	70	70
a_w	0	0	0	0	0	0	0	0	0	0	0	0
T_0	−6	−5	0	6	12	17	20	19	15	9	3	−3

Elevation and solar azimuth angles can be determined from the day of the year, latitude, and longitude of the location. The parameters used to calculate direct solar irradiance and the average monthly ambient temperature (T_0) in Toronto can be found in Table 1.1.

The wind speed (*WS*) profile of an average site can be modeled based on a Weibull probability density function with a shape parameter (k) ranging between 1.5 and 2.5 (dimensionless) and a scale parameter (c) between 5 and 10 m s^{-1} [8]:

$$f(WS) = \frac{k}{c}\left(\frac{WS}{c}\right)^{k-1}\exp\left[-\left(\frac{WS}{c}\right)^k\right] \tag{1.3}$$

Solar irradiance and wind speed profiles for Toronto (Fig. 1.5) were constructed based on the solar parameters in Table 1.1 and shape and scale parameters of 2.0 and 8 m s^{-1}, respectively.

The thermal exergy rate ($\dot{Ex}^Q$) of a thermal energy flow ($\dot{Q}$) at a temperature T is usually defined as the heat flow multiplied by the Carnot factor:

$$\dot{Ex}^Q = \dot{Q}\left(1 - \frac{T_0}{T}\right) \tag{1.4}$$
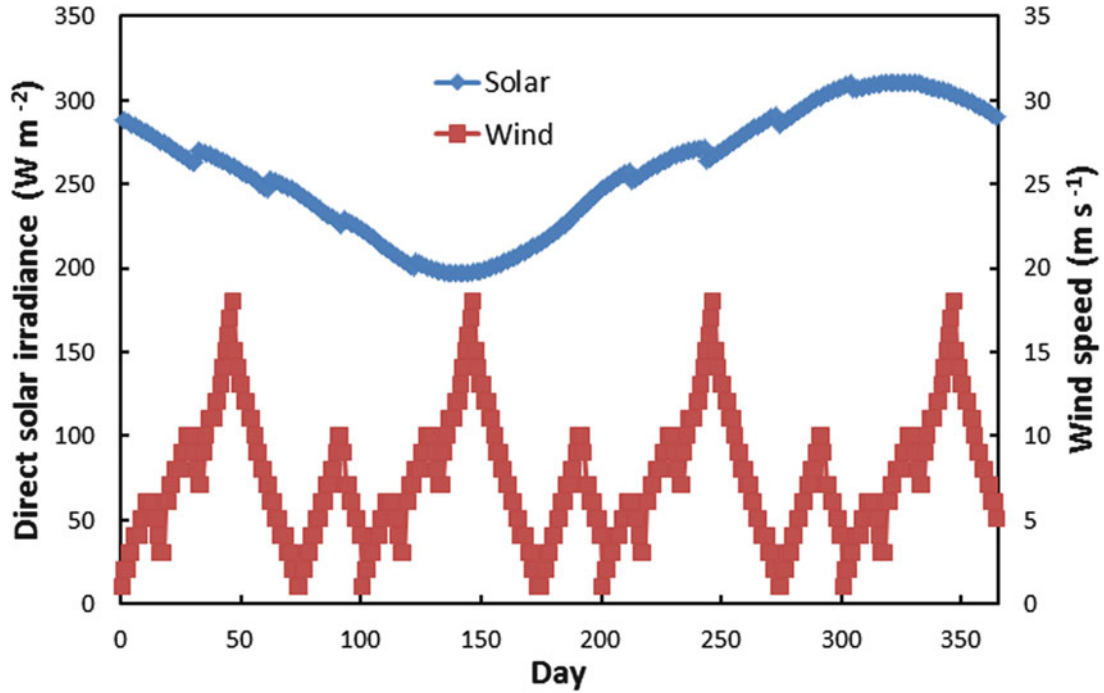
Fig. 1.5 Average daily direct solar irradiance and wind speeds over a year for Toronto, Ontario, Canada (day "0" corresponds to August 1, 2009)

An alternative method of calculating the exergy rate of solar radiation $\left(\dot{E}x_{Solar}^{Q}\right)$ is by multiplying the product of $\dot{Q}_{Solar}$ and solar collector area (A_C) by the Petela–Landsberg–Press factor, which is considered to be a more accurate measure of the exergy of blackbody radiation [9]:

$$\dot{E}x_{Solar}^{Q} = \dot{Q}_{Solar}A_C\left(1 - \frac{4}{3}\frac{T_0}{T_{Sun}} + \frac{1}{3}\left(\frac{T_0}{T_{Sun}}\right)^3\right) \tag{1.5}$$

The kinetic energy of wind is directly proportional to the swept area of the turbine blades and to the cube of wind speed:

$$KE_{Wind} = \frac{1}{2}\rho\pi R^2 (WS)^3 \tag{1.6}$$

where ρ is the density of air and R is the rotor radius. The actual power generated by the wind turbine ($\dot{P}_{Wind}$) depends on the power coefficient (C_P), mechanical efficiency (η_{Mech}), and efficiency of the electric generator (η_{Gen}):

$$\dot{P}_{Wind} = C_P\eta_{Mech}\eta_{Gen}\frac{1}{2}\rho\pi R^2 (WS)^3 \tag{1.7}$$

Most of the materials in MSW cannot be converted to biogas. Only the organic fraction of MSW (*OFMSW*) can be converted, exclusive of moisture content (*MC*). Furthermore, it is the biodegradable volatile solids (*BVS*) component of the volatile solid fraction (*VS*) of the dry organic material that can be converted to biogas. A biogas conversion factor (*BGCF*) represents the fraction of biodegradable organic material that forms biogas ($\dot{m}_{BOM}$):

$$\dot{m}_{BOM} = \dot{m}_{MSW} \times OFMSW \times (1 - MC) \times VS \times BVS \times BGCF \tag{1.8}$$

Biodegradable organic material can be represented chemically by $C_{60}H_{95}O_{38}N$, which can be used to calculate the amount of methane and carbon dioxide produced by anaerobic digestion:

$$C_{60}H_{95}O_{38}N + 18H_2O \rightarrow 32CH_4 + 28CO_2 + NH_3 \tag{1.9}$$
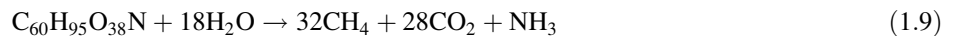
Table 1.2 Hybrid solar–wind–biomass model parameters

Parameter	Value	Units
Area of solar collector	1,800	m^2
Biodegradable volatile solid (BVS) content	0.75	–
Biogas conversion factor (BGCF)	0.90	–
Concentration ratio	30	–
Efficiency of electric generator	0.92	–
Livable floor space	195	m^2
Moisture content of MSW (MC)	0.20	–
Mechanical efficiency (wind turbine)	0.60	–
MSW production rate	1	kg person^{-1} day^{-1}
Number of households	50	–
Number of people per household	4	–
Organic fraction of MSW (OFMSW)	0.78	–
Power coefficient (wind turbine)	0.45	–
Rotor radius	16	m
Space temperature of a household	20	°C
Temperature of cold tank	250	°C
Temperature of hot tank	350	°C
Volatile solid fraction of dry organic solids (VS)	0.835	–

The above equations combined with mass, energy, and entropy balances determine mass, heat, and work flow rates through all the system components. An exergy analysis determines the exergy destruction within each component and calculates the system exergy efficiency. The overall specific exergy (ex) of a substance is the sum of its physical (ex^{ph}) and chemical (ex^{ch}) specific exergies, while the specific physical exergy of a flowing material is based on its specific enthalpy and specific entropy and the reference environment conditions:

$$ex = ex^{ph} + ex^{ch} \tag{1.10}$$

$$ex^{ph} = h - h_0 - T_0(s - s_0) \tag{1.11}$$

The chemical exergy of a substance needs to be considered when calculating exergy changes of chemical reactions. The chemical exergy for various molecules is available in [10]. The exergy reference environment of 25 °C and 101.325 kPa presented in [10] is used in the analysis. System exergy efficiency (ψ) is the ratio of total exergy outputs to total exergy inputs:

$$\psi = \frac{\dot{W}_{Load} + \dot{Ex}^Q_{Evap} + \dot{Ex}^Q_{SH} + \dot{m}^{HT}_{In} ex_{HT} + \dot{m}^{CT}_{In} ex_{CT}}{\dot{Ex}^Q_{Solar} + \dot{Ex}_{Wind} + \dot{m}^{HT}_{Out} ex_{HT} + \dot{m}^{CT}_{Out} ex_{CT} + \dot{m}_{MSW} ex_{MSW}} \tag{1.12}$$

where $\dot{W}_{Load}$ denotes the community electrical power demand, $\dot{Ex}^Q_{Evap}$ the rate at which thermal exergy needs to be removed from community households, $\dot{Ex}^Q_{SH}$ the thermal exergy rate of space heating, $\dot{m}^{HT}_{In}$ the mass flow rate into the hot tank, ex_{HT} the specific physical exergy of high-temperature heat transfer fluid, $\dot{m}^{CT}_{In}$ the mass flow rate into the cold tank, and ex_{CT} the specific physical exergy of low-temperature heat transfer fluid.

Values for several parameters are defined for the model (see Table 1.2).

Results and Discussion

The solar–wind–biomass model was run for 365 days with input variables of household electricity demand, air conditioning demand, direct solar irradiance, wind speed, and ambient temperature. The daily change in the amount of HTF in the hot tank is a function of all of the above input variables and is illustrated in Fig. 1.6.

The highest demand for hot HTF (411 kg) occurs on day 299 (May 26, 2010). The electrical demand per household that day is also very high (3.07 kW) as is the demand for air conditioning (0.93 or 3.72 kW of heat removal based on an average
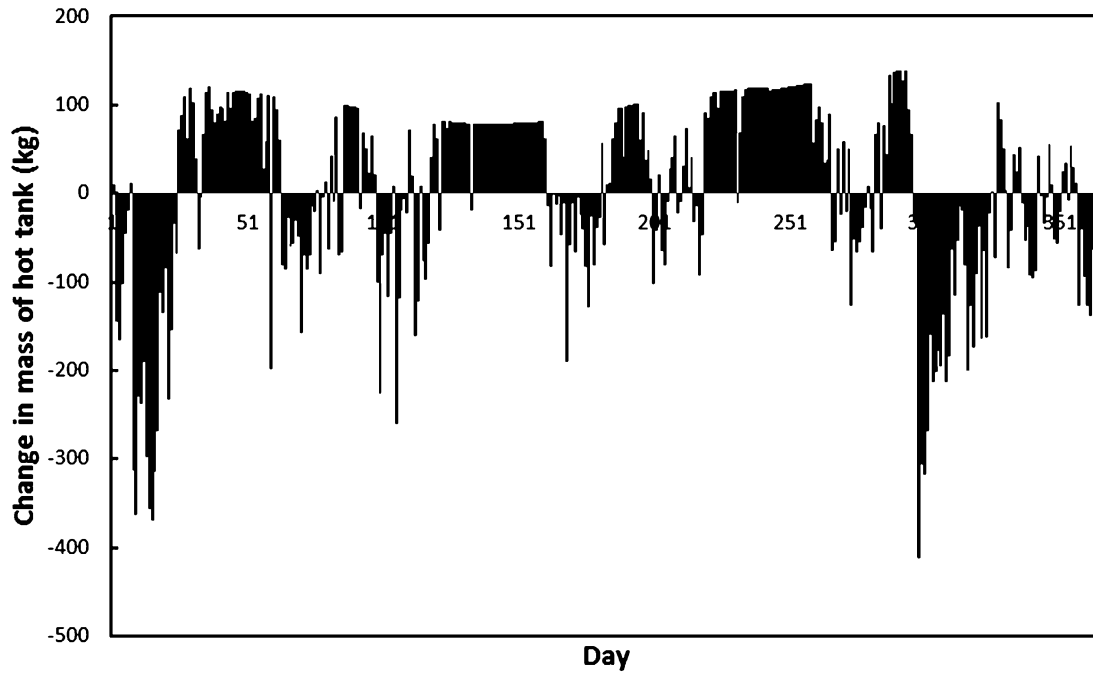
Fig. 1.6 Change in the mass of HTF in the high-temperature storage tank over time (day "0" corresponds to August 1, 2009)
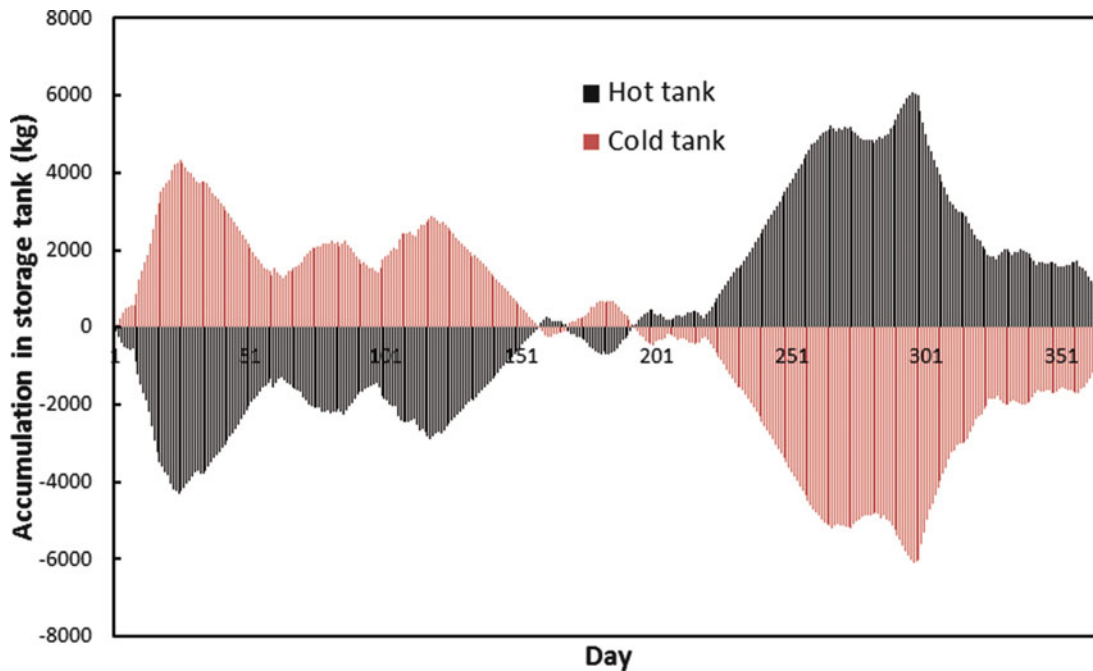
Fig. 1.7 Overall accumulation of HTF in each storage tank over time (day "0" corresponds to August 1, 2009)

COP of 4). The hot tank is charged with the most HTF (339 kg) on day 294 (May 21, 2010), when demand per household is only 0.85 kW with no air conditioning and high wind speeds (12 m/s). However, the size of the storage tank is based on the maximum HTF accumulation (positive or negative) (see Fig. 1.7).

On day 25 (August 25, 2009) the hot tank has accumulated −4,320 kg of hot HTF, whereas on day 296 (May 23, 2010) the accumulation is 6,080 kg. At year end, the net accumulation is greater than zero (1,108 kg). Conversely, the cold tank
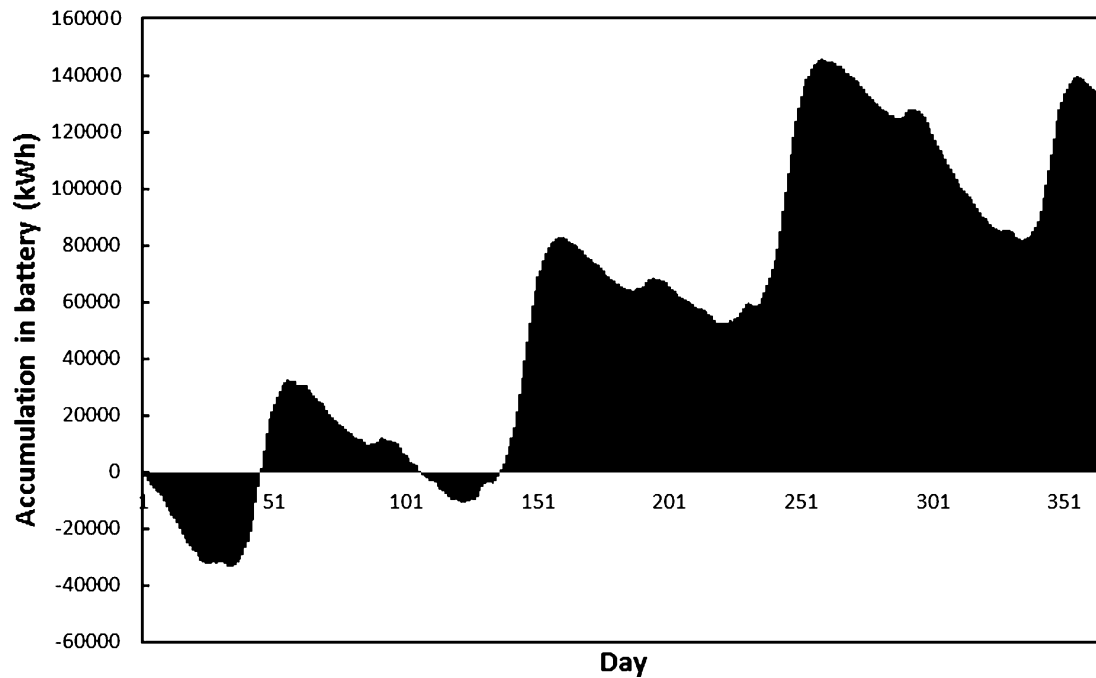
Fig. 1.8 Overall accumulation of electrical energy in the battery over time (day "0" corresponds to August 1, 2009)

accumulates $-6,080$ kg by day 296. To ensure a reliable supply of heat, cold, and electricity, each tank requires a capacity of at least 6,080 kg or 7.5 m^3 (based on a Therminol-specific volume of 0.001232 m^3 kg^{-1}).

Component exergy destruction rates are shown in Figs. 1.1, 1.2, and 1.3, and the total exergy destruction rate of the system over 1 year is found to be 192,000 kW. Of the various subsystems shown in Fig. 1.1, the solar thermal system has the most exergy destruction (70,000 kW or 36 % of the total) followed by the wind turbine (50,900 kW or 26 %). Of the various individual components, the steam turbine exhibited a high destruction rate (17,300 kW or 9.0 %). Multistage expansion with reheating could significantly reduce exergy destruction and improve the overall efficiency of the system. Another large source of exergy destruction is space heating (14,400 kW or 7.5 %), which requires low-grade thermal energy. The exergy efficiency of the system could be improved by using HTF from the cold tank instead of the hot tank to provide space heating.

The accumulation of electrical energy in the battery occurs rapidly and builds until year end (Fig. 1.8). This becomes a significant source of exergy destruction as battery charging or discharging is approximately 80 % efficient [8]. The battery reaches its maximum charge of 146,000 kWh on day 259 (April 16, 2010) and has a net charge of 133,000 kWh after 1 year. A combined energy and economic analysis could reveal the ideal size of the battery to ensure continuous and reliable operation while minimizing cost.

A parametric study was conducted to ascertain the impact on overall exergy efficiency of several key parameters: (1) ambient temperature (Fig. 1.9), (2) collector area (Fig. 1.10), and (3) hot tank temperature (Fig. 1.11). The parametric study is performed for input variable values of 1.39 kW, 0.29 kW, 288 W m^{-2}, and 19 °C for household electrical power demand, air conditioning demand, direct irradiance, and ambient temperature, respectively.

The effect of increasing the ambient temperature is a decrease in the exergy efficiency of the system for all wind speeds, although the descent is steepest at 8 m/s. The thermal exergy of heat flows and the physical exergy of a substance both decrease as ambient temperature increases.

Increasing the solar collector area gradually pushes the system towards a permanent thermal storage charging state depending on the wind speed (faster wind speeds enter a charging state at a lower collector area). The exergy efficiency increases because the system is charging the hot and discharging the cold storage tank.

Increasing the upper limit of the hot HTF is observed in Fig. 1.11 to increase exergy efficiency. As the temperature of the HTF rises, the temperature of the working fluid of the Rankine cycle also rises, which raises the electrical power that can be generated. However, beyond a certain temperature, which is dependent on wind speed, the rate of heat loss from receiver tubes and the exergy destruction in components operating at lower temperatures (e.g., space heater and the generator) exceed the gains from higher Rankine cycle efficiencies.
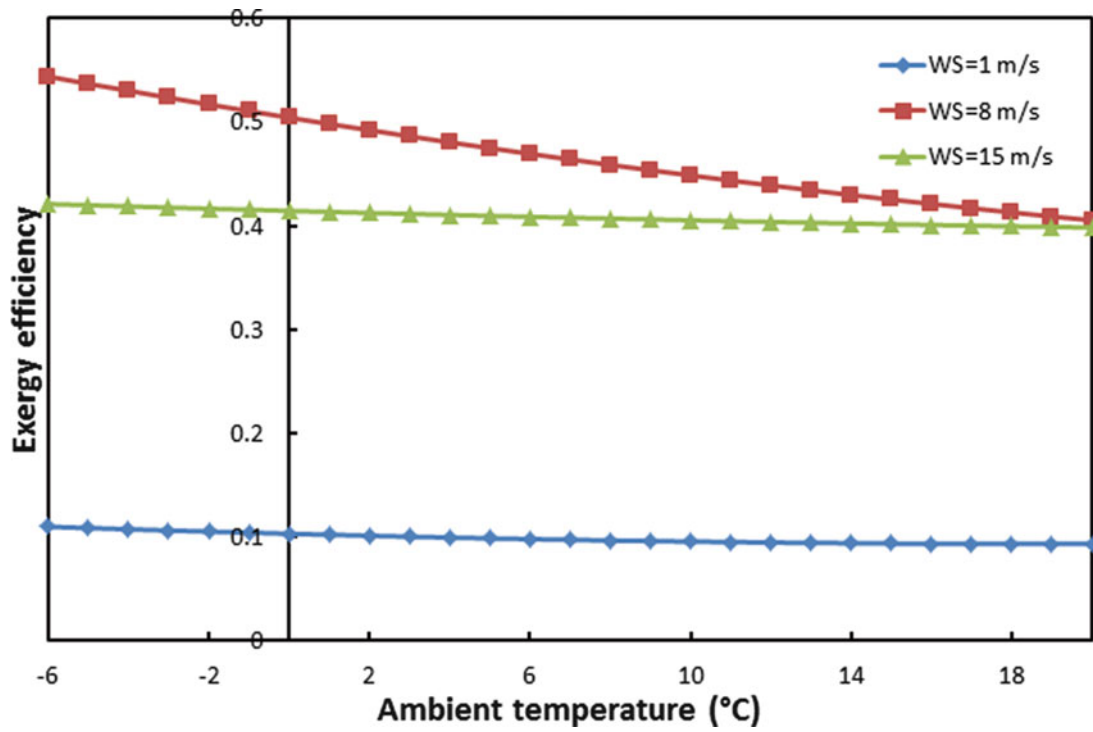
Fig. 1.9 Effect of ambient temperature on system exergy efficiency at various wind speeds
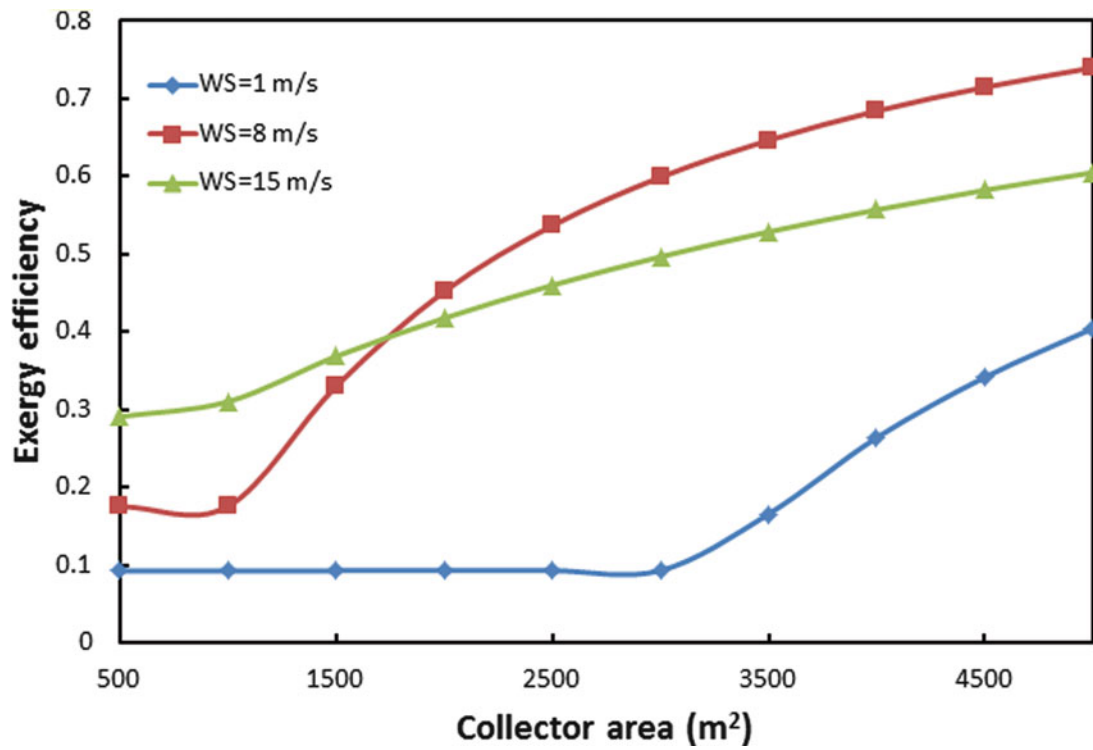
Fig. 1.10 Effect of solar collector area on system exergy efficiency at various wind speeds
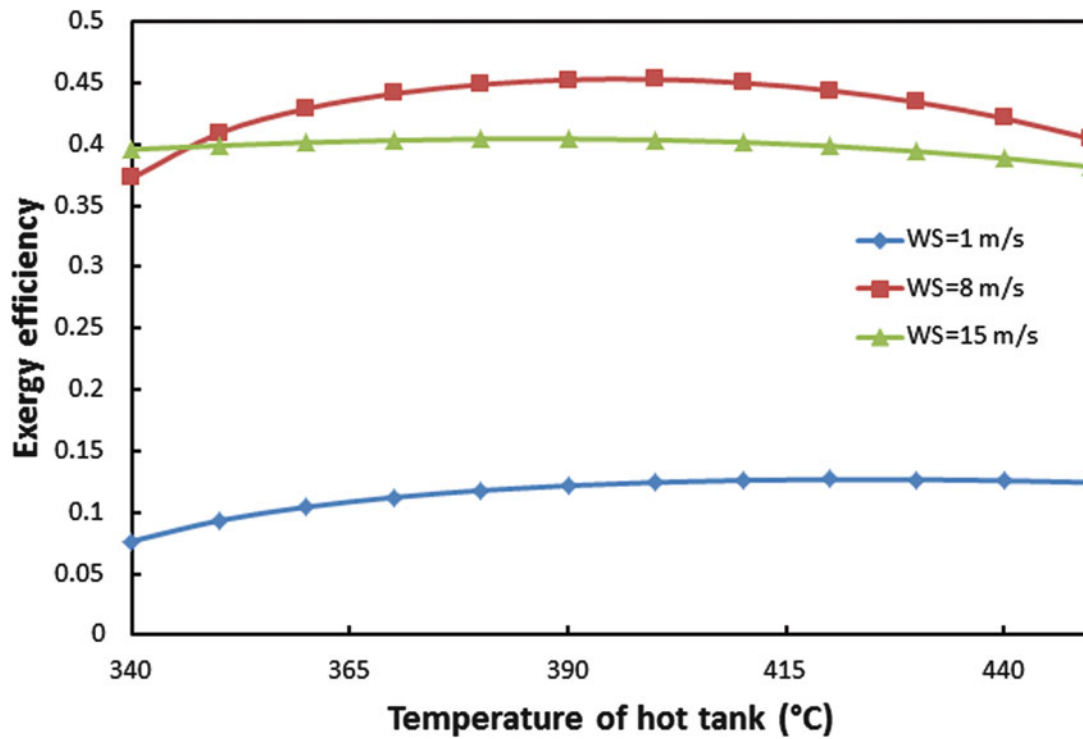
Fig. 1.11 Effect of temperature of hot storage tank on system exergy efficiency at various wind speeds

Conclusions

The hybrid solar–wind–biomass system is able to meet the energy needs of a typical community in Ontario of 50 households. Approximately 1,800 m^2 of parabolic trough collectors, a wind turbine with a rotor radius of 16 m, and anaerobic digestion of MSW generate a net amount of hot HTF after 365 days. The size of each tank should be at least 7.5 m^3 to accommodate solar and wind fluctuations and balance energy demand with supply. The exergy analysis revealed that there are significant efficiency improvements to be made especially with respect to the steam turbine and space heating, which can both be enhanced through better design.

Nomenclature

A_C	Solar collector area, m^2	k	Shape parameter dimensionless
a_s	Solar azimuth angle degrees	k_C	Local extinction coefficient dimensionless
a_w	Collector azimuth angle degrees	KE	Kinetic energy, kW
c	Scale parameter, m s^{-1}	$\dot{m}$	Mass flow rate, kW
C_n	Clearness number dimensionless	$\dot{Q}$	Thermal energy rate, kW
C_P	Power coefficient dimensionless	R	Rotor radius, m
ex	Specific exergy, kJ kg^{-1}	s	Specific entropy, kJ kg^{-1} K^{-1}
$\dot{Ex}$	Exergy rate, kW	T	Temperature, K
h	Specific enthalpy, kJ kg^{-1}	$\dot{W}$	Work rate, kW
i	Incidence angle degrees	WS	Wind speed, m s^{-1}

Greek Letters

α Elevation angle degrees
β Collector tilt angle degrees
η Energy efficiency %

ψ Exergy efficiency %
ρ Density, kg m^{-3}

Subscripts

0   Ambient conditions
BOM   Biodegradable organic matter
CT   Cold tank
ETR   Extraterrestrial radiation
Evap   Evaporator

Gen   Generator
HT   Hot tank
Mech   Mechanical
MSW   Municipal solid waste
SH   Space heating

Superscripts

ch   Chemical
D   Destruction

ph   Physical
Q   Thermal

References

1. Kreith F, Kreider JF (2011) Principles of sustainable energy. CRC Press, Boca Raton
2. Romero-Alvarez M, Zarza E (2007) Concentrating solar thermal power. In: Kreith F, Goswami DY (eds) Handbook of energy efficiency and renewable energy. CRC Press, Boca Raton
3. Rosen MA, Dincer I (1997) On exergy and environmental impact. Int J Energy Res 21:643–654
4. Dincer I, Rosen MA (2012) Exergy: energy, environment and sustainable development, 2nd edn. Elsevier, Boston, MA
5. Jackson J (1999) Resources—not garbage. The Environmental Agenda for Ontario Project
6. Kayhanian M, Tchobanoglous G, Brown RC (2007) Biomass conversion processes for energy recovery. In: Kreith F, Goswami DY (eds) Handbook of energy efficiency and renewable energy. CRC Press, Boca Raton
7. Saldanha N, Beausoleil-Morrison I (2012) Measured end-use electric load profiles for 12 Canadian houses at high temporal resolution. Energy Buildings 49:519–530
8. Zini G, Tartarini P (2010) Wind-hydrogen energy stand-alone system with carbon storage: modeling and simulation. Renew Energy 35:2461–2467
9. Badescu V (2008) Exact and approximate statistical approaches for the exergy of blackbody radiation. Central Eur J Phys 6:344–350
10. Morris DR, Szargut J (1986) Standard chemical exergy of some elements and compounds on the planet Earth. Energy 11:733–755

Exergetic Evaluation of a High-Pressure Hydrogen Production System

2

Selcuk Inac, Adnan Midilli, and Ibrahim Dincer

Abstract

This study presents exergetic assessment of a high-pressure hydrogen production system (HPS). The system considered in this study includes a high-pressure proton exchange membrane (PEM) electrolyzer, two heat exchangers, a motor pump system, a circulation pump, and a hot water tank. In order to perform the main objective of this study, the following important parameters are taken into consideration: (1) the operating pressure (ranging from 1 to 200 bar), (2) the operating temperature (ranging from 70 to 80 °C), (3) dead-state temperature (assumed to be 25 °C), (4) the energy efficiency of the PEM electrolyzer (ranging from 0.5 to 1), (5) the pump efficiency (assumed to be 0.8), (6) mass flow rate of hydrogen from PEM electrolyzer (3 kg per hour), and (7) mass flow rate of pure water supplied to the PEM electrolysis (27 per hour). Considering all these parameters, exergy analysis is performed for the HPS. The results show that exergy efficiency of HPS increases with the rise of the operating pressure and temperature. It thus requires a higher amount of energy input. In this regard, there is a strong need to optimize the process.

Keywords

Hydrogen • Energy • Exergy • High-pressure PEM electrolyzer

Introduction

Energy is a key factor in social, economic, and sustainable development of countries [1–4]. However, many environmental issues causing global climate change are originated of energy production, consumption, and conversion [5]. Today, fossil fuels (i.e., petroleum, natural gas, and coal) are quickly consumed to provide the world energy demand. Particularly, utilization of the nonrenewable fuels has caused global warming due to the carbon dioxide, methane, and nitrous oxide and chlorofluorocarbon emissions. In this regard, hydrogen seen as an energy source of sustainability, unlimited clean energy, zero emission of greenhouse gases, and high energy efficiency has been accepted to be leader energy supply for the energy industry in future [6–9].

One of the most effective methods of hydrogen production from water is electrolysis method. In this method, electrolyzer is a unique instrument for pure hydrogen and oxygen production from the water. There are many electrolyzer types, but

S. Inac (✉)
Energy Technologies, Marine Engineering, Turgut Kiran Maritime College, Recep Tayyip Erdogan University, 53900 Rize, Turkey
e-mail: selcukinac@gmail.com

A. Midilli
Mechanical Engineering Department, Faculty of Engineering, Recep Tayyip Erdogan University, 53900 Rize, Turkey
e-mail: amidilli@gmail.com

I. Dincer
Faculty of Engineering and Applied Science, University of Ontario Institute of Technology, 2000 Simcoe Street North, Oshawa, ON, Canada L1H 7K4
e-mail: Ibrahim.Dincer@uoit.ca

proton exchange membrane (PEM) electrolyzer is very simple and compact among these electrolyzers [10]. PEM electrolyzer is a promising important technology. However, PEM electrolyzer is an effective and safe technology for hydrogen production [11].

Under these considerations, a detailed literature review is performed, based on some studies over high-pressure hydrogen production technologies available in the open literature (e.g., [12–20]). In this study, a parametric study on high-pressure hydrogen production is conducted to investigate how the exergy efficiency changes with system operating conditions such as temperature and pressure.

System Description

The following system is designed for high-pressure hydrogen production and analyzed in this regard for practical applications. The working principle of the hydrogen production system (HPS) can be explained as follows (Fig. 2.1).

Exergy Analysis

In order to perform the parametric study, the following assumptions are made for the exergy analysis:
- Inlet temperature and pressure of pure water are 20 °C and 1 atm, respectively.
- Hydrogen gas production flow rate is 3 kg/h.
- Operating temperatures of PEM electrolyzer are taken as 70, 75, and 80 °C.
- Operating pressures of PEM electrolyzer are taken as 1, 10, 20, 30, 40, 50, 100, 150, and 200 bar.
- Energy efficiencies of PEM electrolyzer are taken as 0.5, 0.6, 0.7, 0.8, 0.9, and 1.
- Mass flow rate of pure water provided in system is 27 kg per hour.
- The plate heat exchangers in the system operate on an adiabatic process.
- Hydrogen and oxygen gases in system are real gas.
- Energy efficiency of the pumps is 0.8.
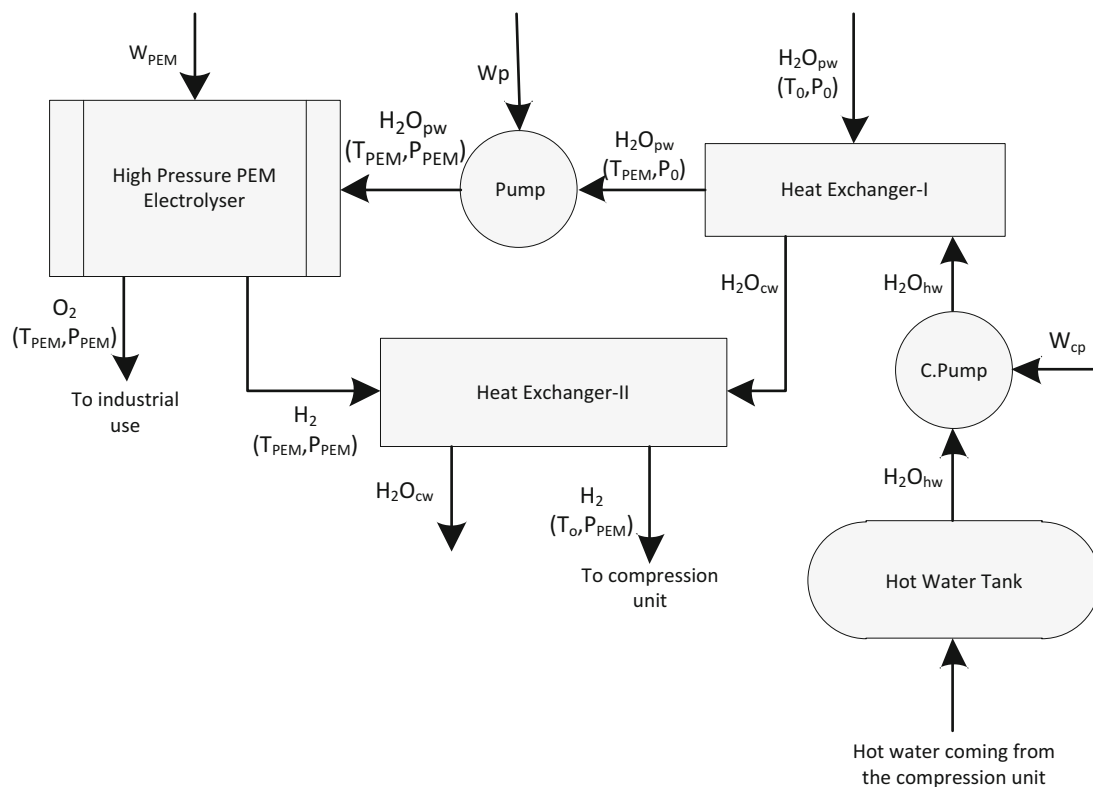
Fig. 2.1 Schematic representation of the HPS (modified from [17, 28])
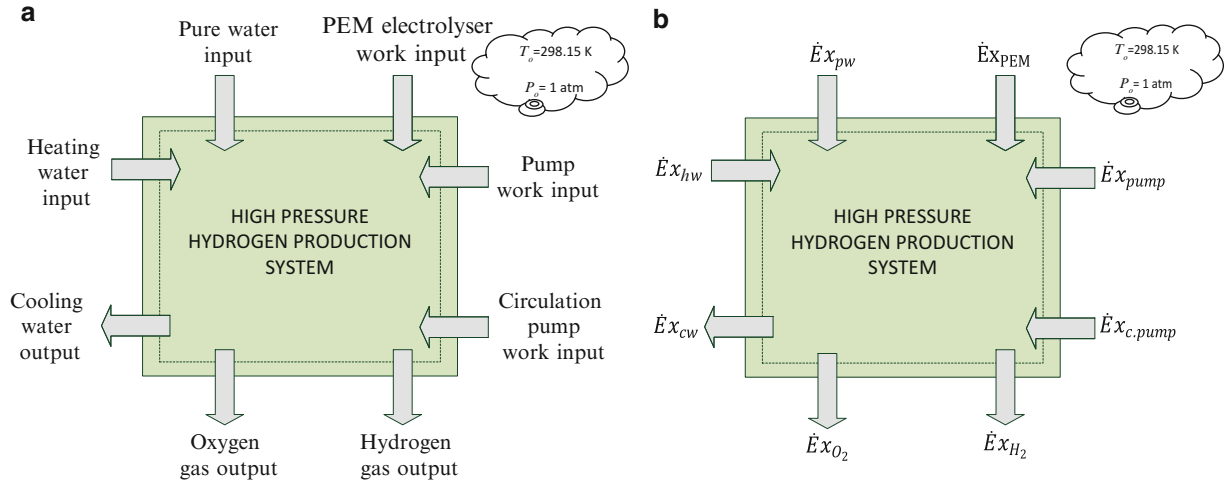
Fig. 2.2 Energy and exergy flow diagram of the HPS

- Thermodynamic properties corresponding to operating temperature and pressure in system are taken from the NIST [21]. Depending on the values taken from other sources results may vary. In this study, NIST has been selected as the data source.
- Ambient temperature and pressure in system are taken to be 25 °C and 1 atm, respectively.
- Temperature of heating water is assumed to be 90 °C.
- Temperature of cooling water is assumed to be 20 °C.
- The chemical exergy values are taken from the literature [22].

In this regard, the energy and exergy balances of the HPS are shown as in Fig. 2.2 by considering a key literature work [23]. Thus, the exergy balance for a system can be written as follows:

$$\sum \dot{E}x_{in} - \sum \dot{E}x_{out} - \dot{E}x_d = \Delta \dot{E}x_s \tag{2.1}$$

where for a steady-state system, $\Delta \dot{E}x_s$ is zero; $\dot{E}x_{in}$ and $\dot{E}x_{out}$ are the amount of total exergy input and output, respectively; and $\dot{E}x_d$ is the total irreversibility of a system.

Here, the total irreversibility for a system can be expressed as

$$\dot{E}x_d = \dot{I} = \sum \dot{E}x_{in} - \sum \dot{E}x_{out} \tag{2.2}$$

which is used for each of the main components in the HPS. However, total exergy (ex) can be calculated from

$$ex = ex^{ph} + ex^{ch} \tag{2.3}$$

where ex^{ph} and ex^{ch} are the physical and chemical exergy, respectively:

$$ex^{ph} = (h - h_o) - T_o(s - s_o) + \frac{V^2}{2} + gz \tag{2.4}$$

where changes of specific kinetic energy and specific potential energy are assumed to be zero in this study.

The physical exergy can be written as below:

$$ex^{ph} = (h - h_o) - T_o(s - s_o) \tag{2.5}$$

where h and s are enthalpy and entropy and h_o and s_o are enthalpy and entropy at the reference (dead) state of P_o and T_o, respectively.

The exergy flow rate can be calculated from

$$\dot{Ex} = \dot{m}ex \tag{2.6}$$

The total exergy balance of a system can be obtained by

$$\dot{E} = \sum \dot{m}_{in}\left[ex^{ph} + ex^{ch}\right]_{in} - \sum \dot{m}_{out}\left[ex^{ph} + ex^{ch}\right]_{out} + \sum \dot{Ex}_Q - \dot{Ex}_W - \dot{I} = 0 \tag{2.7}$$

where $\dot{m}_{in}$ and $\dot{m}_{out}$ are inlet and outlet mass flow rate, $\dot{Ex}_Q$ is the exergy transfer by heat, and $\dot{Ex}_W$ is the exergy transfer by work.

Exergy transfer by heat and work can be expressed as

$$\dot{Ex}_Q = \left(1 - \frac{T_o}{T_r}\right)\dot{Q}_r \tag{2.8}$$

and

$$\dot{Ex}_W = \dot{W} \tag{2.9}$$

The exergy efficiency of a system can be written as [24]

$$\psi = 1 - \frac{\sum \dot{I}}{\sum \dot{Ex}_{in}} \tag{2.10}$$

where $\sum \dot{I}$ is the total irreversibility in a system and $\sum \dot{Ex}_{in}$ is the total exergy input to a system.

Firstly, the energy requirement of high-pressure PEM electrolyzer must be theoretically determined for high-pressure hydrogen production. Requirement of energy necessary for high-pressure hydrogen production is calculated as [17]

$$\Delta H = \Delta G + T\Delta S \tag{2.11}$$

where ΔG is the electricity requirement of PEM electrolyzer and $T\Delta S$ is the requirement of thermal energy of PEM electrolyzer. Chemical reaction in PEM electrolyzer can be written as below [25]:

$$H_2O + \Delta G + T\Delta S \rightarrow 1/2O_2 + H_2 \tag{2.12}$$

The electricity and heat requirement of PEM electrolyzer can be defined as [26]

$$\begin{aligned}
\dot{W}_{PEM} = &\ \dot{m}_o^{H_2}\left[T_{H_2}\left(s_{H_2}^o + c_{H_2}\ln\left(\frac{T_{H_2}}{298}\right) - Z_{H_2}R\ln\left(\frac{P_{H_2}}{1atm}\right)\right) - c_{H_2}(T_{H_2} - 298)\right]_{H_2,o} \\
&+ \dot{m}_o^{O_2}\left[T_{O_2}\left(s_{O_2}^o + c_{O_2}\ln\left(\frac{T_{O_2}}{298}\right) - Z_{O_2}R\ln\left(\frac{P_{O_2}}{1atm}\right)\right) - c_{O_2}(T_{O_2} - 298)\right]_{O_2,o} \\
&- \dot{m}_i^{H_2O}\left[T_{H_2O}\left(s_{H_2O}^o + c_{H_2O}\ln\left(\frac{T_{H_2O}}{298}\right)\right) - \left(h_{H_2O}^o + c_{H_2O}(T_{H_2O} - 298)\right)\right]_{H_2O,i}
\end{aligned} \tag{2.13}$$

$$\begin{aligned}
\dot{Q}_{PEM} = &\ \dot{m}_i^{H_2O}\left(-h_{H_2O}^o - c_{H_2O}(T_{H_2O} - 298)\right)_{H_2O,i} + \dot{m}_o^{H_2}\left(c_{H_2}(T_{H_2} - 298)\right)_{H_2,o} \\
&+ \dot{m}_o^{O_2}\left(0,5c_{O_2}(T_{O_2} - 298)\right)_{O_2,o} + \dot{W}_{PEM}
\end{aligned} \tag{2.14}$$

The total energy requirement of PEM electrolyzer $\left(\dot{E}^{PEM}\right)$ can be defined as follows:

$$\dot{E}_{PEM} = \dot{Q}_{PEM} + \dot{W}_{PEM} \tag{2.15}$$

where

$$\dot{E}x_{PEM} = \dot{E}_{PEM} \tag{2.16}$$

where $\dot{Q}_{PEM}$ is the amount of total heat requirement in order to realize the chemical reaction and $\dot{E}x_{PEM}$ is the total exergy input as heat and work to PEM electrolyzer.

Exergy efficiency of PEM electrolyzer has been calculated by using Eq. (2.13) [24]:

$$\psi_{PEM} = 1 - \left(\frac{\dot{I}_{PEM}}{\dot{E}x_{PEM} + \dot{E}x_{in}^{pw}} \right) \tag{2.17}$$

where $\dot{E}x_{PEM}$ is the total exergy input to PEM electrolyzer and $\dot{E}x_{in}^{pw}$ is the pure water exergy input to PEM electrolyzer.

The total irreversibility of PEM electrolyzer can be defined as follows:

$$
\begin{aligned}
\dot{I}_{PEM} = \dot{m}_{in}^{H_2O} \left[((h - h_o) - T_o(s - s_o))_{H_2O} + ex_{H_2O}^{ch} \right] + \dot{E}x_{PEM} \\
- \dot{m}_{out}^{O_2} \left[((h - h_o) - T_o(s - s_o))_{O_2} + ex_{O_2}^{ch} \right] - \dot{m}_{out}^{H_2} \left[((h - h_o) - T_o(s - s_o))_{H_2} + ex_{H_2}^{ch} \right]
\end{aligned}
\tag{2.18}
$$

The theoretic work of pump $\left(\dot{W}_t^p \right)$ can be calculated from [27]

$$\dot{W}_t^p = \dot{m}_{pw,i}^p v_{f\,pw,i} \left(P_{pw,o}^p - P_{pw,i}^p \right) \tag{2.19}$$

where $v_{fpw,i}$ is the specific volume of pure water.

The real work of pump $\left(\dot{W}_R^p \right)$ can be written as

$$\dot{W}_R^p = \frac{\dot{W}_t^p}{\eta} \tag{2.20}$$

and

$$\dot{E}x_{pump} = \dot{W}_R^p \text{ and } \dot{E}x_{cp} = \dot{W}_R^{cp} \tag{2.21}$$

where η is the electrical efficiency of pump and $\dot{E}x_{pump}$ and $\dot{E}x_{cp}$ are the total exergy input to pump and circulation pump, respectively.

Under these considerations, the exergy efficiency of the HPS can be calculated by

$$\psi_{HPS} = 1 - \left(\frac{\dot{I}_{HPS}}{\dot{E}x^{HPS}} \right) \tag{2.22}$$

where η_{ex}^{HPS} is the exergy efficiency of system, $\dot{E}x^{HPS}$ is the total exergy input to the HPS (kW), and $\dot{I}_{HPS}$ is the total irreversibility of all components in the HPS (kW):

$$\dot{E}x^{HPS} = \dot{E}x_{pw} + \dot{E}x_{hw} + \dot{E}x_{pump} + \dot{E}x_{cp} + \dot{E}x_{PEM} \tag{2.23}$$

The total irreversibility of system is calculated by

$$\dot{I}_{HPS} = \dot{I}_{cp} + \dot{I}_p + \dot{I}_{PEM} + \dot{I}_{hex-I} + \dot{I}_{hex-II} \tag{2.24}$$

The exergy balances of other main components in the HPS are showed in Table 2.1. As a result, the exergy efficiency of the HPS can be written as follows:

$$\psi_{HPS} = 1 - \frac{I_{cp} + I_p + I_{PEM} + I_{hex-I} + I_{hex-II}}{\dot{E}x_{pw} + \dot{E}x_{hw} + \dot{E}x_{pump} + \dot{E}x_{cp} + \dot{E}x_{PEM}} \tag{2.25}$$

Table 2.1 The exergy balance for main components

System components	Irreversibility
Pump	$\dot{I}_p = \dot{m}_{pw,i}^{p}\left((h-h_o)-T_o(s-s_o)+ex_{H_2O}^{ch}\right)+\dot{W}_R^{p}-\dot{m}_{pw,o}^{p}\left((h-h_o)-T_o(s-s_o)+ex_{H_2O}^{ch}\right)$
Circulation pump	$\dot{I}_{cp} = \dot{m}_{hw,i}^{cp}\left((h-h_o)-T_o(s-s_o)+Ex_{H_2O}^{ch}\right)_{hw,i}+\dot{W}_R^{cp}-\dot{m}_{hw,o}^{cp}\left((h-h_o)-T_o(s-s_o)+Ex_{H_2O}^{ch}\right)_{hw,o}$
Heat exchanger-I	$\dot{I}_{hex-I} = \dot{m}_{pw,i}^{hex-I}\left((h-h_o)-T_o(s-s_o)+ex_{H_2O}^{ch}\right)_{pw,i}+\dot{m}_{hw,i}^{hex-I}\left((h-h_o)-T_o(s-s_o)+ex_{H_2O}^{ch}\right)_{hw,i}$ $-\dot{m}_{pw,o}^{hex-I}\left((h-h_o)-T_o(s-s_o)+ex_{H_2O}^{ch}\right)_{pw,o}-\dot{m}_{hw,o}^{hex-I}\left((h-h_o)-T_o(s-s_o)+ex_{H_2O}^{ch}\right)_{hw,o}$
Heat exchanger-I	$\dot{I}_{hex-II} = \dot{m}_{cw,i}^{hex-I}\left((h-h_o)-T_o(s-s_o)+ex_{H_2O}^{ch}\right)_{cw,i}+\dot{m}_{H_2,i}^{hex-II}\left((h-h_o)-T_o(s-s_o)+ex_{H_2}^{ch}\right)_{H_2,i}$ $-\dot{m}_{cw,o}^{hex-I}\left((h-h_o)-T_o(s-s_o)+ex_{H_2O}^{ch}\right)_{cw,o}-\dot{m}_{H_2,o}^{hex-II}\left((h-h_o)-T_o(s-s_o)+ex_{H_2}^{ch}\right)_{H_2,o}$
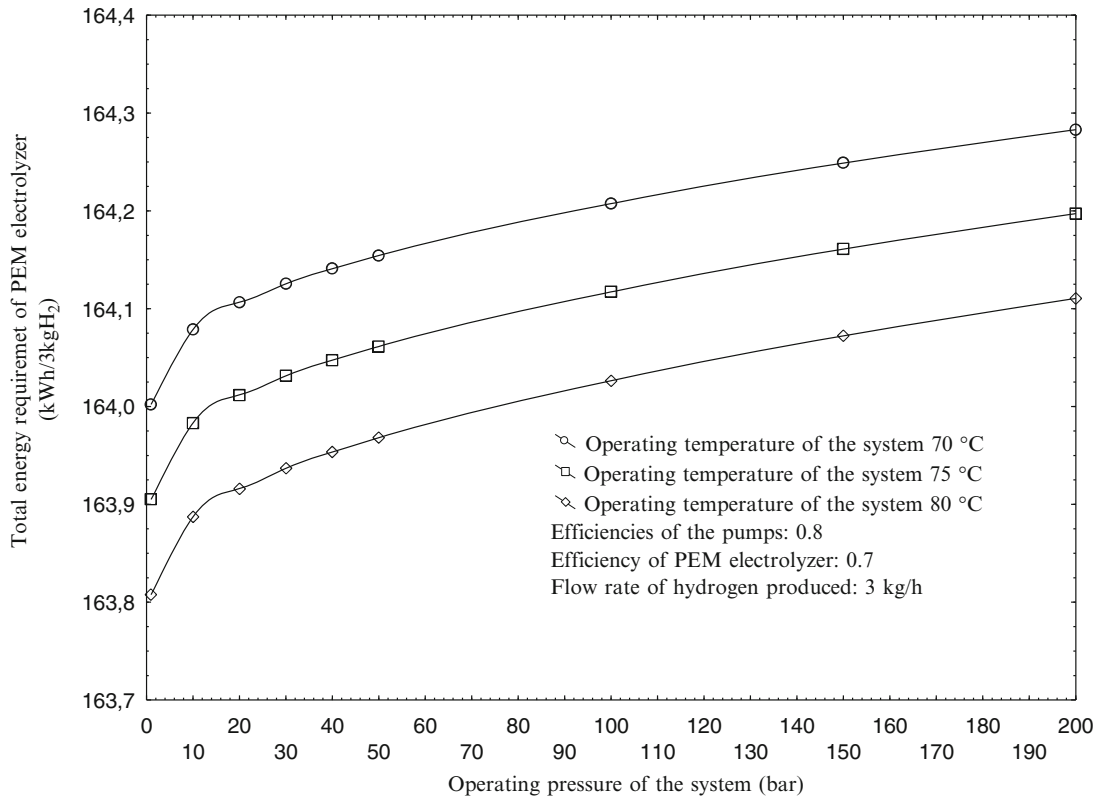
Fig. 2.3 Variation of total energy requirement of PEM electrolyzer depending on the operating pressure and temperature of the system

Results and Discussion

In this study, an exergetic assessment of the newly developed HPS is performed. Figure 2.3 shows the energy consumption amount of PEM electrolyzer as a function of the operating temperature and pressure of system. In this study, the flow rate of hydrogen production is taken to be 3 kg/h. As shown in Fig. 2.3, the energy requirement of PEM electrolyzer increases with the rise of operating pressure and decreases with the increase of operating temperature of the system.

Furthermore, Fig. 2.4 illustrates the exergy efficiency of PEM electrolyzer as a function of the operating temperature and pressure of system. As shown in Fig. 2.4, the exergy efficiency of PEM electrolyzer goes up with the increase of the operating temperature and pressure of the system.

Figure 2.5 indicates the exergy efficiency and total irreversibility of the HPS based on the operating temperature and pressure of the system. As shown in Fig. 2.5, the exergy efficiency of the HPS increases with the rise of the operating temperature and pressure of the system. However, the total irreversibility of the HPS decreases with the increase of the operating pressure and temperature of the system.
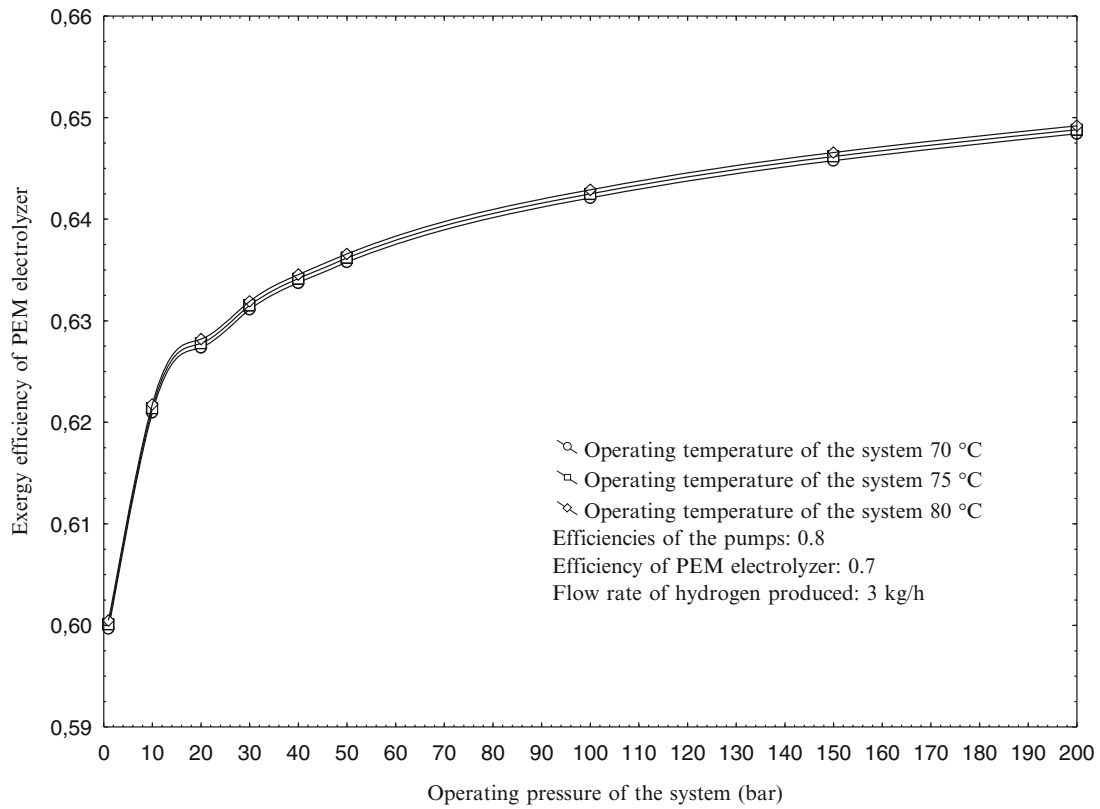
Fig. 2.4 The variation of the exergy efficiency of PEM electrolyzer depending on the operating pressure and temperature of the system
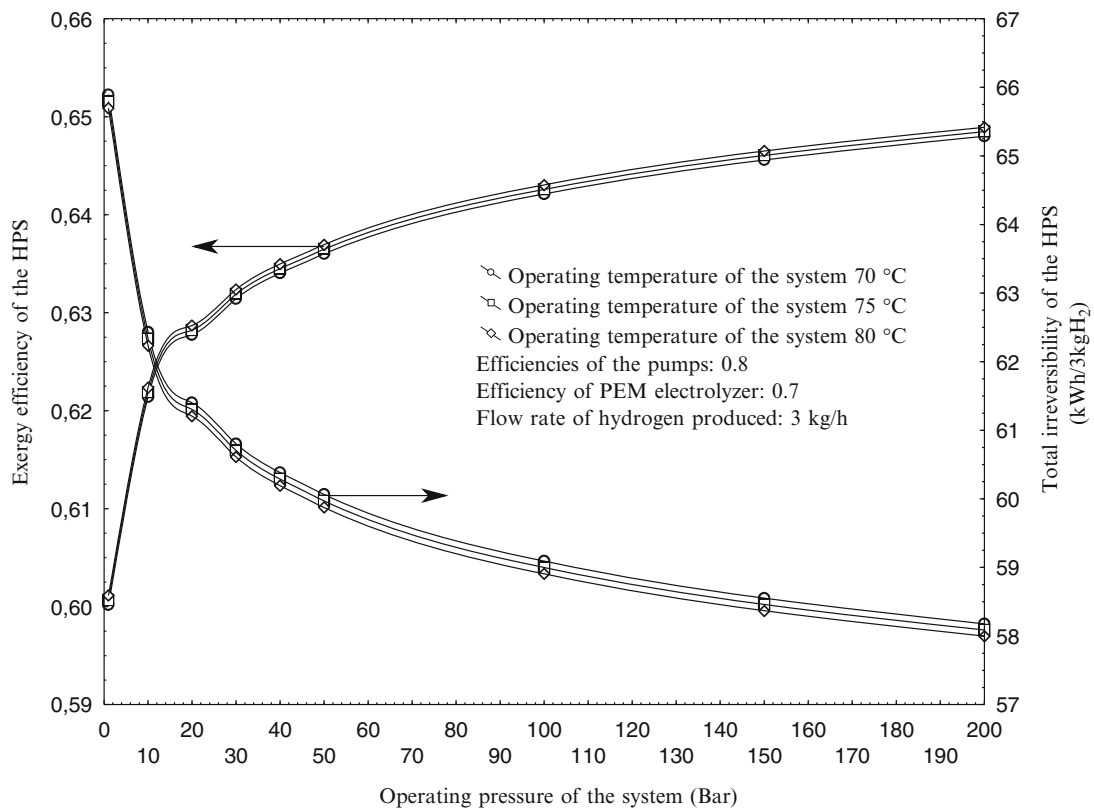
Fig. 2.5 The variation of the exergy efficiency and total irreversibility of the HPS depending on the operating pressure and temperature of the system

Conclusions

In this study, a parametric study on the exergetic evaluation of the high-pressure hydrogen production has been presented. In this regard, exergy analyses of both the HPS and PEM electrolyzer are discussed according to operating temperature and pressure of the system. The following two concluding remarks are made.

- Total energy requirement of the HPS system and PEM electrolyzer increases with the rise of operating pressure of the system. In this regard, PEM electrolyzer has maximum power consumption in the HPS.
- The overall system exergy efficiency increases and the total irreversibility of the HPS decreases with an increase in operating pressure and temperature of the system, respectively.

Note that in order to find out the optimum operating pressure and temperature and to determine the optimum exergetic efficiency and irreversibility of the system, the exergetic optimization should be performed as to be done in the future.

References

1. Ay M, Midilli A, Dincer I (2006) Investigation of hydrogen production from boron compounds for PEM fuel cells. J Power Sources 157:104–113
2. Dincer I (1999) Environmental impacts of energy. Energy Policy 27:845–854
3. Midilli A, Dincer I (2008) Hydrogen as a renewable and sustainable solution in reducing global fossil fuel consumption. Int J Hydrog Energy 33:4209–4222
4. Ozsaban M, Midilli A, Dincer I (2011) Exergy analysis of a high pressure multistage hydrogen gas storage system. Int J Hydrog Energy 36:11440–11450
5. Midilli A, Ay M, Dincer I, Rosen MA (2005) On hydrogen and hydrogen energy strategies II: future projections affecting global stability and unrest. Renew Sust Energ Rev 9:273–287
6. Dincer I (2012) Green methods for hydrogen production. Int J Hydrog Energy 37:1954–1971
7. Kalinci Y, Hepbasli A, Dincer I (2009) Biomass-based hydrogen production: a review and analysis. Int J Hydrog Energy 34:8799–8817
8. Tolga Balta M, Dincer I, Hepbasli A (2010) Energy and exergy analyses of a new four-step copper–chlorine cycle for geothermal-based hydrogen production. Energy 35:3263–3272
9. Zheng J, Liu X, Xu P, Liu P, Zhao Y, Yang J (2012) Development of high pressure gaseous hydrogen storage technologies. Int J Hydrog Energy 37:1048–1057
10. Gorgun H (2006) Dynamic modelling of a proton exchange membrane (PEM) electrolyzer. Int J Hydrog Energy 31:29–38
11. Biaku C, Dale N, Mann M, Salehfar H, Peters A, Han T (2008) A semiempirical study of the temperature dependence of the anode charge transfer coefficient of a 6kW PEM electrolyzer. Int J Hydrog Energy 33:4247–4254
12. Armandi M, Drago D, Pagani M, Bonelli B, Santarelli M (2012) Direct coupling of H2 production through a high pressure PEM electrolyzer and its storage by physisorption on microporous materials. Int J Hydrog Energy 37:1292–1300
13. Kim H, Park M, Lee KS (2013) One-dimensional dynamic modeling of a high-pressure water electrolysis system for hydrogen production. Int J Hydrog Energy 38:2596–2609
14. Laoun B (2007) Thermodynamics aspect of high pressure hydrogen production by water electrolysis. Rev Energ Renouv 10:435–444
15. Marangio F, Pagani M, Santarelli M, Calì M (2011) Concept of a high pressure PEM electrolyser prototype. Int J Hydrog Energy 36:7807–7815
16. Marangio F, Santarelli M, Cali M (2009) Theoretical model and experimental analysis of a high pressure PEM water electrolyser for hydrogen production. Int J Hydrog Energy 34:1143–1158
17. Ni M, Leung MKH, Leung DYC (2008) Energy and exergy analysis of hydrogen production by a proton exchange membrane (PEM) electrolyzer plant. Energy Convers Manag 49:2748–2756
18. Nieminen J, Dincer I, Naterer G (2010) Comparative performance analysis of PEM and solid oxide steam electrolysers. Int J Hydrog Energy 35:10842–10850
19. Pérez-Herranz V, Pérez-Page M, Beneito R (2010) Monitoring and control of a hydrogen production and storage system consisting of water electrolysis and metal hydrides. Int J Hydrog Energy 35:912–919
20. Santarelli M, Medina P, Calì M (2009) Fitting regression model and experimental validation for a high-pressure PEM electrolyzer. Int J Hydrog Energy 34:2519–2530
21. NIST (2013) Nist Web Sitesi<http://webbook.nist.gov/chemistry/fluid/>Last. Accessed Jan 2013
22. Kotas TJ (1985) The exergy method of thermal plant analysis. Butterworth Publishers, Stoneham, MA
23. Dincer I, Rosen MA (2007) Exergy, environment and sustainable development. Exergy 36–59
24. Baniasadi E, Dincer I (2011) Energy and exergy analyses of a combined ammonia-fed solid oxide fuel cell system for vehicular applications. Int J Hydrog Energy 36:11128–11136
25. Ni M, Leung M, Leung D (2007) Parametric study of solid oxide steam electrolyzer for hydrogen production. Int J Hydrog Energy 32:2305–2313
26. Newell TA (2000) Thermodynamic analysis of an electrochemical refrigeration cycle. Int J Energy Res 24:443–453
27. Cengel YA, Boles MA (2006) Thermodynamics an engineering approach. McGraw-Hill, New York
28. Oi T, Sakaki Y (2004) Optimum hydrogen generation capacity and current density of the PEM-type water electrolyzer operated only during the off-peak period of electricity demand. J Power Sources 129:229–237
29. Degiorgis L, Santarelli M, Calì M (2007) Hydrogen from renewable energy: A pilot plant for thermal production and mobility. J Power Sources 171:237–246
30. Dincer I, Hussain MM, Al-Zaharnah I (2005) Energy and exergy utilization in agricultural sector of Saudi Arabia. Energy Policy 33:1461–1467

Exergetic Performance Assessment of a Binary Geothermal Power Plant

3

Yildiz Kalinci, Arif Hepbasli, and Ibrahim Dincer

Abstract

Electricity generation is achieved by means of the medium-temperature geothermal water in the range of 90–140 ºC in binary plants with the organic Rankine cycle. So, we investigate a binary geothermal power plant as a case study, from the energy and exergy point of view. Also, exergy destruction rates throughout the plant are quantified and illustrated for comparison purposes. In the plant considered, the brine injection and reinjection temperatures are 140 and 80 ºC, with a mass flow rate of 64.87 kg/s, respectively. The energy and exergy efficiencies are calculated as 5.34 and 30.84 %, respectively, based on the heat and exergy input rates to the system at the net power. Furthermore, we examine the effects of some parameters on energy and exergy efficiencies and net power output (e.g., brine injection temperature, brine mass flow rates, turbine inlet temperature and inlet pressure).

Keywords

Energy • Exergy • Efficiency • Geothermal power plant • ORC

Introduction

"Geothermal" comes from the Greek words geo (earth) and therme (heat). So, geothermal means earth heat. Our earth's interior—like the sun—provides heat energy from nature. This heat—geothermal energy—yields warmth and power that we can use without polluting the environment [7].

The utilization of geothermal source for power generation, cooling, or heating applications depends mainly on the source temperature. High-temperature geothermal resources above 150 ºC are generally used for power generation. Moderate-temperature (between 90 and 150 ºC) and low-temperature (below 90 ºC) geothermal resources are best suited for direct applications, such as space and process heating, cooling, aquaculture, and fish farming [8, 12, 14].

Basic use of geothermal source at higher temperature is that of power production. Today, world installed electrical generation capacity is more than 10 GW [4]. High-temperature geothermal resources, such as dry steam and hot water, as well as medium-temperature geothermal resources such as water of moderate temperature can be profitably used to generate electricity using three types of geothermal power plants (GPPs): dry steam, flash, and binary power plants. Dry steam

Y. Kalinci (✉)

Department of Technical Programs, Izmir Vocational School, Dokuz Eylul University, Education Campus Buca, Izmir, Turkey
e-mail: yildiz.kalinci@deu.edu.tr

A. Hepbasli

Department of Energy Systems Engineering, Faculty of Engineering, Yasar University, 35100 Bornova, Izmir, Turkey
e-mail: arif.hepbasli@yasar.edu.tr

I. Dincer

Faculty of Engineering and Applied Science, University of Ontario Institute of Technology (UOIT), 2000 Simcoe Street North, Oshawa, ON, Canada L1H 7K4
e-mail: Ibrahim.Dincer@uoit.ca
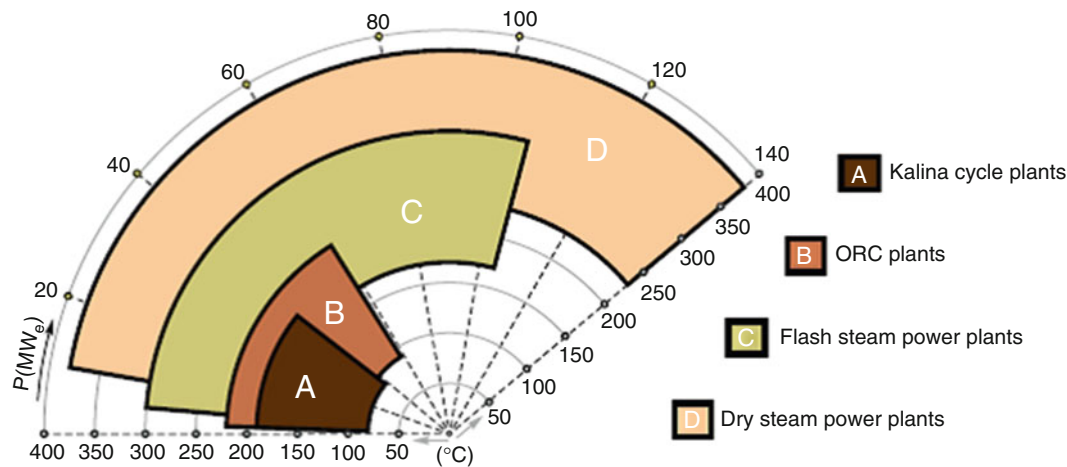
Fig. 3.1 Application ranges of various types of geothermal power plants [1, 9]

geothermal power plants use very hot steam (>235 ℃) and limited amounts of water from the geothermal resources. Flash steam power plants (single or double) use hot water (>180 ℃), while binary cycle system uses water at moderate temperatures (100–180 ℃) coming from geothermal resources [5]. An application range of various types of geothermal power plants can be seen in Fig. 3.1.

Note that binary plants convert medium-temperature resources into electricity more efficiently than other technologies. In binary plants a heat exchanger transfers heat from the produced hot geofluid in a primary loop to a low-boiling-point working fluid in a secondary loop, such as propane, isobutene, pentane, and isopentane. This thermodynamic cycle is known as organic Rankine cycle (ORC) because initially organic compounds are used as the working fluid. The working fluid in the secondary loop is evaporated in the vaporizer by the geothermal heat provided in the primary loop. The vapor expands as it passes through the organic vapor turbine which is coupled to the generator. The exhaust vapor is condensed in a water-cooled condenser or an air cooler and is recycled to the vaporizer by the feed pump. The cooled geofluid can be discharged or reinjected into the reservoir without flashing, which minimizes scaling problems. It makes decentralized geothermal production feasible and economically attractive in many remote or less developed regions of the world, where financial incentives promote low CO_2 emission energy production technologies [8].

There are some studies about geothermal binary power plants in the literature as follows: DiPippo [9] discussed the Carnot and the triangular efficiencies for geothermal binary power plants. He said that a more useful model was the triangular (or trilateral) cycle because binary plants operating on geothermal hot water used a non-isothermal heat source. The triangular cycle imposed a lower upper bound on the thermal efficiency and served as a more meaningful ideal cycle against which to measure the performance of real binary cycles.

Kose [10] examined the potential and utilization of the existing geothermal energy resources in Kutahya–Simav region. The temperature of the geothermal fluid in the Simav–Eynal field was too high for the district heating system. Therefore, the possibility of electrical energy generation by a binary cycle was researched and the preliminary feasibility studies were conducted in the field. For the environmental reasons, the working fluid used in this binary power plant was chosen as HCFC-124. It was concluded that the Kutahya–Simav geothermal power plant had the potential to produce an installed capacity of 2.9 MW_e and a minimum of 17,020 MWh/year electrical energy could be produced from this plant.

Kanoglu and Bolatturk [11] studied exergy analysis of a binary geothermal power plant using actual plant data to assess the plant performance and pinpoint sites of primary exergy destruction. Exergy destruction throughout the plant was quantified and illustrated using an exergy diagram and compared to the energy diagram. The sites with greater exergy destructions included brine reinjection, heat exchanger, and condenser losses. The energy and exergy efficiencies of the plant were 4.5 and 21.7 %, respectively, based on the energy and exergy of geothermal water at the heat exchanger inlet. The energy and exergy efficiencies were 10.2 and 33.5 %, respectively, based on the heat input and exergy input to the binary Rankine cycle.

Yari [12] presented a comparative study of the different geothermal power plant concepts, based on the exergy analysis for high-temperature geothermal resources. The considered cycles for this study were a binary geothermal power plant using a simple ORC, a binary geothermal power plant using an ORC with an internal heat exchanger (IHE), a binary cycle with a regenerative ORC, a binary cycle with a regenerative ORC with an IHE, a single-flash geothermal power plant, a double-flash geothermal power plant, and a combined flash-binary power plant. The maximum first-law efficiency was found to be

related to the ORC with an IHE with R123 as the working fluid and was calculated to be 7.65 %. In contrast, the first-law efficiency based on the energy input into the ORC revealed that the binary cycle with the regenerative ORC with an IHE and R123 as the working fluid has the highest efficiency (15.35 %). Also, the maximum first-law efficiency was shown to be given by the flash binary with R123 as the working fluid and was calculated to be 11.81 %.

A modified exergoeconomic model was proposed for geothermal power plants using exergy- and cost-accounting analyses, and a case study was in this regard presented for the Tuzla geothermal power plant system (Tuzla GPPS) in Turkey to illustrate an application of the currently modified exergoeconomic model by Coskun et al. [5]. Tuzla GPPS had a total installed capacity of 7.5 MW, and electricity was generated using a binary cycle. Exergy efficiency values varied between 35 and 49 % with an average exergy efficiency of 45.2 %.

Ganjehsarabi et al. [13] performed an exergy analysis of the Dora II geothermal power plant with 9.5 MW net power output by using actual plant data to evaluate plant performance and pinpoint the locations of exergy destructions/losses. The overall energetic and exergetic efficiencies of the plant were calculated to be 10.7 and 29.6 %, respectively. The largest exergy destruction rate took place in brine reinjection as 10.3 MW. The second and third highest exergy destruction rates occurred in cooling tower and turbine with 4.7 and 3.4 MW, respectively.

This study aims at contributing to the area of binary geothermal power plant through energy and exergy analyses. In this regard, the main objectives of this study are to (1) calculate the energy and exergy efficiencies for both the entire plant and the individual plant components, (2) identify exergy destruction rates, and (3) investigate the parameters affecting energy and exergy efficiencies.

System Description

There are several sources of medium-temperature geothermal water in the range of 90–140 ºC which is suitable to produce electricity by binary plants using ORC. In this study, the data were taken from the literature [7] on a case study using a binary power plant as apparently modified for analysis. The geothermal fluid is taken as 1,600 kPa, 140 ºC, and 64.87 kg/s from production well, and then it is injected at 1,600 kPa and 80 ºC, respectively.

The geothermal fluid transfers its heat to the working fluid—isopentane—inside the evaporator and the preheater. In the preheater, the condensed isopentane is heated to the boiling point and transforms into dry saturated steam within the evaporator. The dry saturated steam expands in the turbine, providing mechanical work to drive the electric generator. After expansion in the steam turbine, the steam is fed to the air-cooled condenser. The condensation heat is transferred to the environment by the forced convection of the air. The condensate is brought to the initial pressure by the feed pump and returns to the preheater and the evaporator. Isentropic efficiencies for the turbine and the feed pump are given as 0.85 and 0.8, respectively. Also, average annual air temperature is 15 °C. Isopentane operates between 700 and 95 kPa with a mass flow rate of 36.04 kg/s.

Analysis

The following assumptions are made in this study [11, 12].
- The operation of the geothermal power plant is considered in steady state.
- The pressure drops throughout the heat exchangers, and pipelines are considered negligible.
- The turbines and pumps have isentropic efficiencies.
- The changes in kinetic and potential energies are considered negligible.
- The geothermal fluid is treated as water.

The mass, energy, and exergy balances for any control volume at steady state with negligible kinetic and potential energy changes can be expressed, respectively, by

$$\sum \dot{m}_{in} = \sum \dot{m}_{0ut} \tag{3.1}$$

$$\sum \dot{E}_{in} = \sum \dot{E}_{0ut} \tag{3.2}$$

$$\dot{Q} + \dot{W} = \sum \dot{m}_{0ut} h_{out} - \sum \dot{m}_{in} h_{in} \tag{3.3}$$

Table 3.1 Energetic and exergetic relations for the subsystems

Subsystem	Energy relations	Exergy relations
Preheater	$\dot{m}_{geo}(h_2 - h_3) = \dot{m}_{wf}(h_6 - h_5)$	$\dot{I}_{PH} = (\dot{E}x_2 - \dot{E}x_3) - (\dot{E}x_6 - \dot{E}x_5)$
Evaporation	$\dot{m}_{geo}(h_1 - h_2) = \dot{m}_{wf}(h_7 - h_6)$	$\dot{I}_{EV} = (\dot{E}x_1 - \dot{E}x_2) - (\dot{E}x_7 - \dot{E}x_6)$
Feed pump	$\dot{W}_p = \dot{m}_{wf}(h_5 - h_4) = \dot{m}_{wf}(h_{5s} - h_4)/\eta_{ps}$	$\dot{I}_P = \dot{W}_p - (\dot{E}x_5 - \dot{E}x_4)$
Turbine	$\dot{W}_T = \dot{m}_{wf}(h_7 - h_8) = \dot{m}_{wf}(h_7 - h_{8s})\eta_{Ts}$	$\dot{I}_T = (\dot{E}x_7 - \dot{E}x_8) - \dot{W}_T$
Condenser	$\dot{Q} = \dot{m}_{wf}(h_8 - h_4) = \dot{m}_{air}(h_{10} - h_9)$	$\dot{I}_C = \dot{E}x_8 - \dot{E}x_4$
Cycle	$\eta_{cycle} = \dfrac{\dot{W}_{net}}{\dot{m}_{geo}(h_1 - h_3)}$	$\varepsilon_{cycle} = \dfrac{\dot{W}_{net}}{\dot{E}x_1 - \dot{E}x_3}$
System	$\eta_{sys} = \dfrac{\dot{W}_{net}}{\dot{m}_{geo}(h_1 - h_0)}$	$\varepsilon_{sys} = \dfrac{\dot{W}_{net}}{\dot{E}x_1}$

And exergetically, it becomes

$$\dot{E}x_{heat} + \dot{W} = \sum \dot{E}x_{in} - \sum \dot{E}x_{out} + \dot{I} \tag{3.4}$$

where the subscriptions *in* and *out* represent the inlet and exit states; $\dot{E}, \dot{Q}$, and $\dot{W}$ are the energy rate, heat rate, and work input rate; $\dot{m}$ is the mass flow rate; and h is the specific enthalpy. Also, $\dot{E}x$ and $\dot{I}$ are the exergy rate and the irreversibility (or exergy destruction) rate. $\dot{E}x_{heat}$ is the net exergy transfer by heat at the temperature T, and the subscript 0 stands for the restricted dead state, which is given by

$$\dot{E}x_{heat} = \sum \left(1 - \frac{T_0}{T}\right)\dot{Q} \tag{3.5}$$

The specific flow exergy is given by

$$ex = (h - h_0) - T_0(s - s_0) \tag{3.6}$$

where s is the specific entropy. Multiplying the specific exergy by the mass flow rate of the fluid gives the exergy rate:

$$\dot{E}x = \dot{m}\,ex \tag{3.7}$$

The energy and exergy efficiencies are generally defined as

$$\eta = \frac{\dot{E}_{out}}{\dot{E}_{in}} \tag{3.8}$$

$$\varepsilon = \frac{\dot{E}x_{out}}{\dot{E}x_{in}} \tag{3.9}$$

To determine the exergetic availability of a geothermal resource, the following equation can be used [14]:

$$\frac{\dot{E}x}{\dot{E}x_0} = \frac{(T_{geo} - T_{rej}) - T_0 \ \ln(T_{geo}/T_{rej})}{(T_{geo} - T_0) - T_0 \ \ln(T_{geo}/T_0)} \tag{3.10}$$

To compare geothermal plants, another parameter is the specific brine consumption, which is given by

$$\beta = \frac{\dot{m}_{geo}}{\dot{W}_{net}} \tag{3.11}$$

In addition, energetic and exergetic relations for components are given in Table 3.1.

Results and Discussion

In this study, the brine has a mass flow rate of 64.87 kg/s at 1,600 kPa and 140 °C. Due to the medium temperature, binary geothermal power plant is feasible to produce electricity. The rejection temperature is selected based mainly on the chemical composition of the geothermal fluid; in particular, it is necessary that the rejection temperature should be high enough to avoid silica oversaturation, which could lead to silica scaling and serious fouling problems in recovery heat exchangers and in mineral deposition in pipes and valves. It seems difficult to lower the rejection temperature below 70 °C, considering low enthalpy geothermal fields have temperatures in the 110–160 °C range [14]. So, the rejection temperature is 80 °C.

Isopentane is recommended as the working fluid in the ORC for the medium-temperature geothermal resources because among all the refrigerants and the hydrocarbons that come into consideration, it shows the best properties: low specific volumes, high efficiency (net power), moderate pressures in the heat exchangers, low cost, low toxicity, low ozone depletion potential, low global warming potential, and a low pinch-point temperature [7].

In the study, upper cycle pressure is defined according to the pinch-point temperature difference, which is a difference between the brine pinch point and the vaporization temperatures of isopentane. In the thermodynamic calculations, a special attention is given to the values of the pinch points that are not below 5 °C. In this study, the upper pressure is 700 kPa and its saturated temperature is 98.62 °C. Using Table 3.1 for evaporation, the temperature of state 2 is defined as 104 °C. According to this, the pinch-point temperature difference is calculated as 5.41 °C. A process flow chart is given in Fig. 3.2 where the main devices are preheater, evaporation, turbine, condenser with air-cooled condenser, and feed pump. According to this figure, energy analysis of each point can be made using Eqs. (3.1)–(3.3) and the relations given in Table 3.1. Here, the thermodynamic properties of the working fluid are determined using the EES software package and geothermal fluid is considered as water. While the binary cycle is considered as only cycle, geothermal energy and binary cycle are considered as a system.

Thermodynamic properties of the fluids are calculated and are given in Table 3.2 for all the points. According to these data, the turbine produces 2,229 kW and the feed pump consumes 44.34 kW. The net power is 2,184 kW. Also, it is estimated that the parasitic power is about 16.6 % of the net power generated in the cycle [11]. The parasitic power includes the brine production pumps, the condenser fans, and other auxiliaries. Subtracting the parasitic power, 362.6 kW, from the net power generated in the cycle, the net power output becomes 1,822 kW. The input energy rates to the cycle and the system
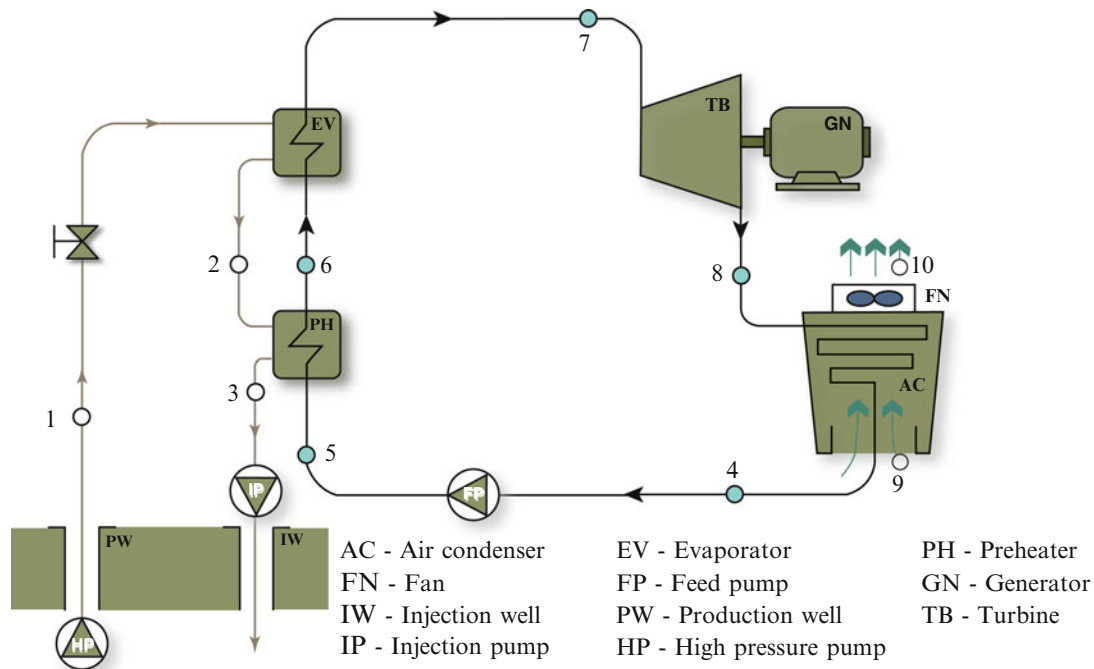
Fig. 3.2 Process flow chart (modified from Guzović et al. [7])

Table 3.2 Thermodynamic properties of fluids and exergy rates of the system

State no.	Fluid	$\dot{m}$ (kg/s)	P (kPa)	T (°C)	h (kJ/kg)	s (kJ/kg)	ex (kJ/kg)	$\dot{Ex}$ (kW)
0	Geothermal		101.325	15	63.01	0.2242		
0'	Isopentane		101.325	15	−372.4	−1.766		
1	Geothermal	64.87	1,600	140	590	1.738	91.05	5,906
2	Geothermal	64.87	1,600	104	437.2	1.351	49.66	3,221
3	Geothermal	64.87	1,600	80	336.6	1.074	28.33	1,838
4	Isopentane	36.04	95	25	−350	−1.69	0.382	13.77
5	Isopentane	36.04	700	25.32	−348.8	−1.689	1.375	49.55
6	Isopentane	36.04	700	98.62	−167	−1.146	26.86	968.1
7	Isopentane	36.04	700	98.62	108.1	−0.406	88.85	3,202
8	Isopentane	36.04	95	54.33	46.3	−0.373	17.33	624.7
9	Air	1414.12	101.325	15	288.5	5.661		0
10	Air	1414.12	101.325	25	298.6	5.695	0.308	435.55

Table 3.3 Exergetic investigation of the subsystems

Component	$\dot{Ex}_{in}$ (kW)	$\dot{Ex}_{out}$ (kW)	$\dot{I}$ (kW)	ε (%)
Feed pump	44.34	35.78	8.56	80.69
Preheater	1,383	918.55	464.45	66.42
Evaporator	2,685	2223.90	461.10	82.83
Turbine	2577.30	2229.00	348.30	86.49
Condenser	610.93	435.55	610.93	71.29
ε_{cycle} (%)				44.78
ε_{sys} (%)				30.84

are calculated as 16,470 and 34,189 kW. Using Eq. (3.8) and the data in Table 3.1 for the cycle and the system, the energy efficiencies are calculated as 11.06 and 5.34 %, respectively.

In the analysis of such systems, energy analysis has generally been a common tool for analysis. The first law of thermodynamics provides energy analysis, which identifies only externally energy wastes and losses. In this regard, exergy comes out of the second law to be a powerful and effective tool for (1) designing and analyzing energy systems by combining the conservation of mass and energy principles with the second law of thermodynamics; (2) furthering the goal of more efficient energy resource use by assessing meaningful efficiencies and enabling the locations, types, and true magnitudes of wastes and losses to be determined; (3) revealing whether or not, and by how much, it is possible to design more efficient energy systems by reducing the inefficiencies in existing systems; (4) addressing the impact on the environment of energy resource utilization; and (5) helping to achieve sustainable development (see [15] for details).

The specific exergy values and exergy rates of all the points are calculated using Eqs. (3.4)–(3.7) and the values given in Table 3.2. While the input exergy rate to the system is 5,906 kW, the rate is 4,068 kW for the cycle at 1,822 kW power output. According to this, the exergy efficiencies of the cycle and the system are defined as 44.78 and 30.84 %, respectively. After a general investigation, it can be focused on the subsystems and the defined exergy destruction rates. According to the input and output exergy rates of the equipment, the exergy destruction rates are calculated using Table 3.1 and the results obtained are listed in Table 3.3. The maximum exergy destruction rate is due to the air-cooled condenser as 610.93 kW. In this study, th exergy destruction rate of the air-cooled condenser is calculated according to the difference between states 8 and 4 because the waste heat rate cannot be transformed to the useful work by air. The exergy efficiencies vary between 66.42 and 86.49 %, which belong to the preheater and the turbine, respectively. In addition, the energy and exergy losses of the system based on the brine energy and exergy input rates are shown in Fig. 3.3. The energy input rate to the system is 34,189 kW. While 51.83 % of the energy is reinjected, 41.78 % of it is lost in the air-cooled condenser, so the net power is only 5.33 %. This is an important argument subject whether geothermal resources should be used in power generation. From the exergetic point of view, the results are similar to the energy analysis results. The biggest exergy loss is 31.12 %, which belongs to the brine reinjection. Other exergy losses can be seen in the same figure.

a

1.06%
362.60 kW

5.33%
1822 kW

51.83%
17719 kW

41.78%
14282.65 kW

- Condenser
- Parasitic
- Brine reinjection
- Net power

b

0.14%
8.56 kW

7.86%
464.45 kW

7.81%
461.10 kW

30.85%
1822 kW

5.90%
348.3 kW

10.34%
610.93 kW

31.12%
1838 kW

6.14%
362.6 kW

- Feed pump
- Turbine
- Parasitic
- Preheater
- Condenser
- Net power
- Vaporator
- Brine reinjection
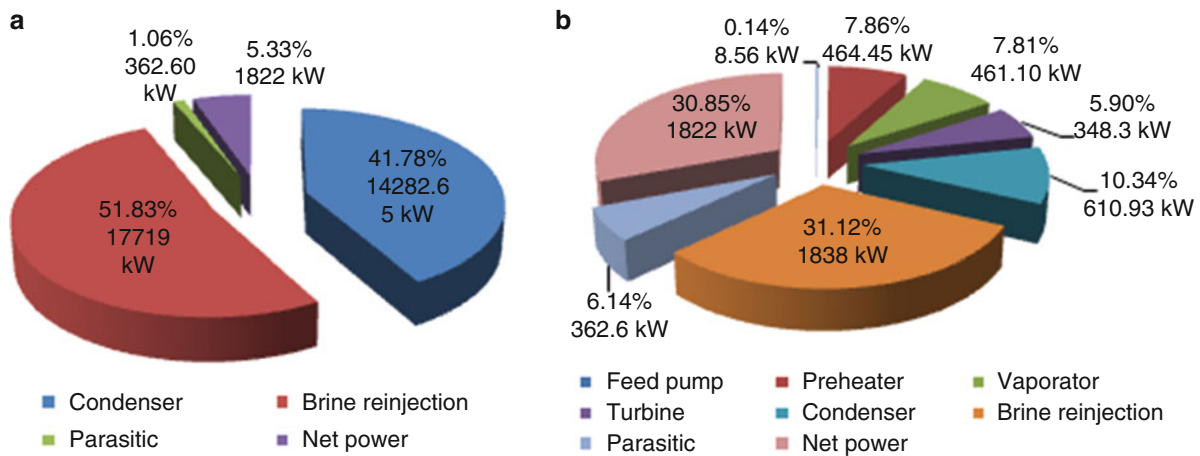
Fig. 3.3 Energy and exergy loss diagrams of the system based on (**a**) brine energy input rate (34,189 kW) and (**b**) brine exergy input rate (5,906 kW)

Fig. 3.4 Reference values for exergy efficiency

$\dot{E}x / \dot{E}x_0$

T_{rej} °(C)

- Tgeo=110 °C
- Tgeo=120 °C
- Tgeo=130 °C
- Tgeo=140 °C
- Tgeo=150 °C
- Tgeo=160 °C
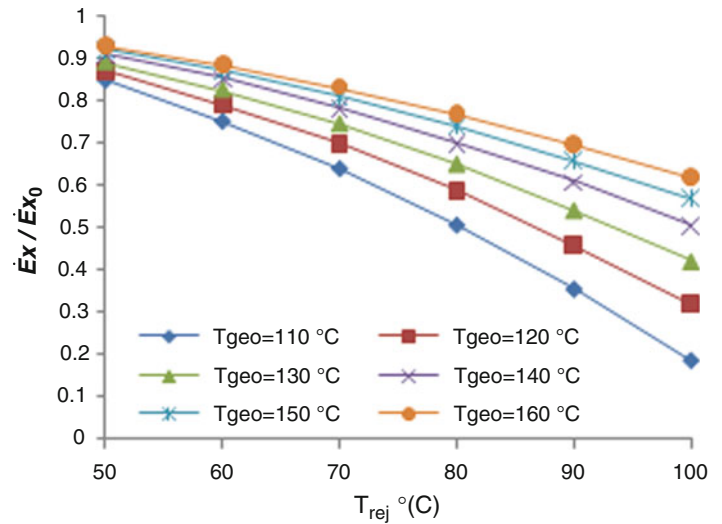
The Results of Parametric Study

A large number of design variables and operation parameters should be considered in geothermal power plants as temperature, pressure, chemical composition of brine, rejection temperature, ambient temperature, and maximum rate of energy extraction.

The inlet and rejection temperatures of the brine affect geothermal plants. Equation (3.10) represents the ratio of the theoretical work that can be extracted from the geofluid for given inlet geofluid temperatures and assumed rejection temperatures and the maximum theoretical work that can be extracted for given inlet geofluid and dead-state temperatures. It provides an upper limit to the exergy efficiency. Figure 3.4 shows the dependence of the $\dot{E}x / \dot{E}x_0$ ratio on the temperature of the source (T_{geo}) and the rejection temperature of the brine (T_{rej}). The ratio is defined as 0.698 for T_0, T_{geo}, and T_{rej} as 15, 140, and 80 °C, respectively. In addition, using Eq. (3.11), the specific brine consumption is calculated as 35.64 kg/MJ. The value is used as a comparative parameter for geothermal power plants, generally.

While the data for the brine are taken to be constant, other parameters can be investigated. At this point, the cycle upper pressure and turbine inlet temperature are important. As can be seen in Fig. 3.5a, more power is generated by higher pressure in spite of decreasing the working fluid mass flow rate. A limit to the pressure increase is represented by the minimal temperature difference between the geothermal fluid and the isopentane at the heat exchanger pinch point. The optimum pressure is considered to be the maximum pressure, at which the pinch-point difference reaches an agreed
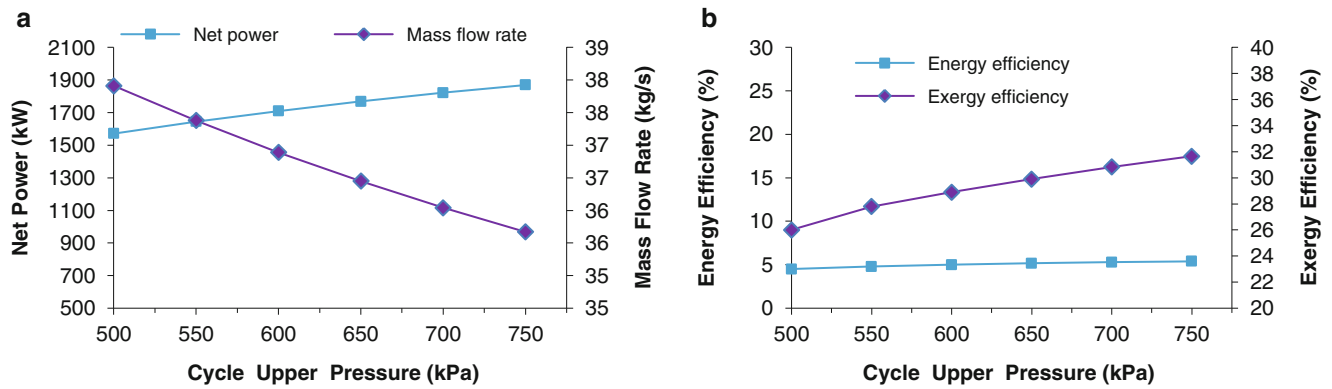
Fig. 3.5 Comparison of the system according to the cycle upper pressure ($T_{rej} = 80$ °C): (**a**) variation of net power and mass flow rate, (**b**) variation energy and exergy efficiencies
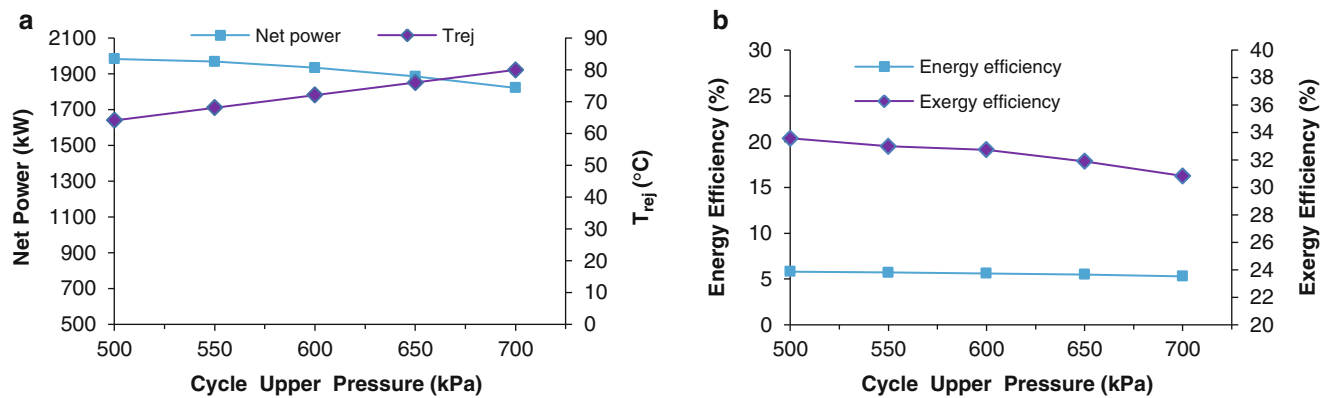
Fig. 3.6 Comparison of the system according to the cycle upper pressure ($\Delta T_{pp} = 5.41$ °C): (**a**) variation of net power and T_{rej}, (**b**) variation of energy and exergy efficiencies

minimum of 5 °C [7]. While the temperature difference is 5.41 °C for 700 kPa, it is 3.09 °C for 750 kPa. So, 750 kPa and more pressures are not convenient. Figure 3.5b gives a variation of energy and exergy efficiencies. Both of them increase with a higher pressure due to more turbine power.

Also, the heat exchanger pinch point can be taken as 5.41 °C as constant. To ensure this, the mass flow rate of the working fluid and the rejection temperature of the brine are considered as unknown parameters. As can be seen in Fig. 3.6, more pressure means more rejection temperature of the brine. That is, less heat is picked up from geothermal brine to isopentane. At this point, it can be considered that the waste heat of the brine can be used at low-temperature applications (e.g., district heating, industrial heating, greenhouse). With decreasing the mass flow rate and the net power, both energy and exergy efficiencies decrease.

Generally, in power plants, the superheated steam enters to turbine to take more power and avoid erosion of the turbine blades. If the working fluid is heated to the superheated region in the evaporation equipment, its mass flow rate decreases from 35.63 kg/s at 100 °C to 23.77 kg/s at 160 °C. The situation brings less net power and less energy and exergy efficiencies, as can be seen in Fig. 3.7. Dry fluids, such as isopentane, are characterized by a positive slope of the saturated vapor curve in the T–s diagram. Because of this characteristic, dry fluids do not need to be superheated. The reason for this is that after expansion, the saturated vapor remains in the superheated region. Additionally, problems related to the flow of wet steam through a turbine are excluded. Thus, preventing problems, such as erosion of the turbine blades, droplet separation, condensate draining, and similar problems, is not necessary, which simplifies the turbine design [7, 16–18]. While the situation is good for the turbine, the heat content of the superheated vapor is dissipated in the condenser. Therefore, a regenerator can be used to increase the cycle efficiency.
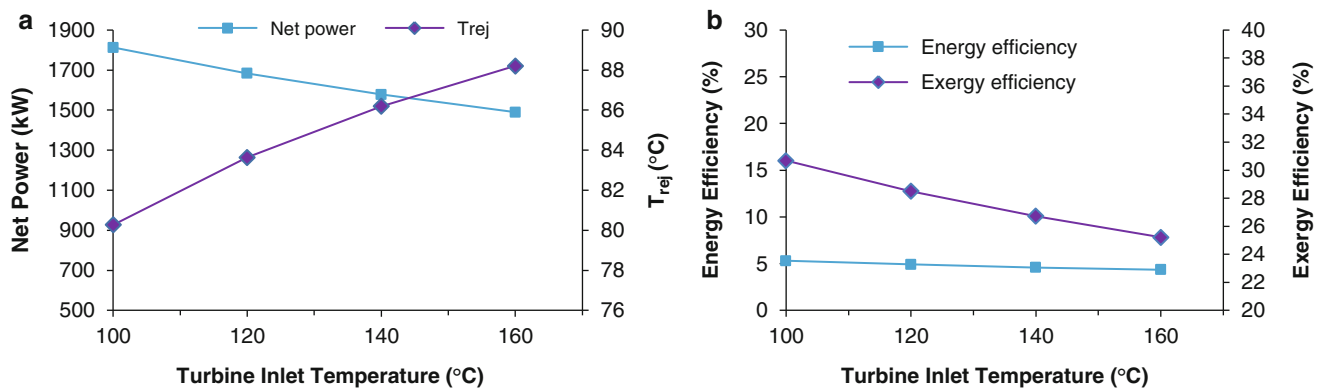
Fig. 3.7 Comparison of the system according to the turbine inlet temperature ($\Delta T_{pp} = 5.41\ °C$): (**a**) variation of net power and T_{rej}, (**b**) variation of energy and exergy efficiencies

Conclusions

We have investigated a binary geothermal power plant using the data taken from the literature through energy and exergy efficiencies in this study. We have also calculated exergy destruction rates for main components of the system. Furthermore, we have studied the effects of some important parameters (e.g., the inlet/rejection temperature of the brine, the cycle upper pressure, the turbine inlet temperature) on the energy and exergy efficiencies and indicated in figures.

We can extract some concluding remarks from this study as follows:

- The system generates a net power of 2,184 kW for energy and exergy input rates of 34,189 and 5,906 kW, respectively.
- Due to the big energy input rate, the system has a less energy efficiency of 5.34 %. Also, exergy efficiency is calculated as 30.84 %. There is still an argument at this point that geothermal sources should be used in power generation. In addition, 51.83 % of the brine energy is rejected. To increase the energy/exergy efficiencies, the waste heat can be used for lower temperature applications.
- Operation parameters affect the net power seriously. Some of them can be taken as constant for the plant (e.g., brine inlet temperature, brine mass flow rate, maybe rejection temperature). According to the decision, other ones (e.g., turbine inlet temperature, cycle upper pressure, working fluid mass flow rate) are investigated to increase the efficiencies and the net power. It is important that dry fluids, as isopentane, do not need to be superheated. Also, after the turbine, a regenerator can be considered.
- Another advantage of the binary technology is that the geothermal fluids (or brines) do not contact the moving mechanical components of the plant (e.g., the turbine), assuring a longer life for the equipment.

The results are expected to be beneficial to the researchers, government administration, and engineers working in the area of the geothermal power plants.

Nomenclature

ex	Specific exergy, kJ/kg	P	Pressure, kPa
$\dot{E}$	Energy rate, kW	$\dot{Q}$	Heat rate, kW
$\dot{E}x$	Exergy rate, kW	s	Specific entropy, kJ/kg K
h	Specific enthalpy, kJ/kg	T	Temperature, ºC or K
$\dot{I}$	Irreversibility or exergy destruction rate, kW	$\dot{W}$	Work rate or power, kW
$\dot{m}$	Mass flow rate, kg/s		

Greek Letters

ε Exergy or second-law efficiency, % Δ Interval $(-)$
η Energy or first-law efficiency, % β Specific brine consumption, kg/MJ

Subscripts

C   Condenser pp Pinch point
EV   Evaporator rej Rejection
geo Geothermal s Isentropic
in   Inlet sys System
out Outlet T Turbine
P   Pump wf Working fluid
PH   Preheater   0   Reference index

Superscripts

Over dot   Quantity per unit time

Abbreviations

AC   Air condenser   IHE   Internal heat exchanger
EES   Engineering equation solver   IP   Injection pump
EV   Evaporator   IW   Injection well
FN   Fan   ORC   Organic Rankine cycle
FP   Feed pump   P   Power
GN   Generator   PH   Preheater
GPPS Geothermal power plant system   PW   Production well
GPPs Geothermal power plants   TB   Turbine
HP   High-pressure pump

References

1. Geothermal energy facts (2012) http://geothermal.marin.org/pwrheat.html#Q1. Accessed 12 Nov 2012
2. Ghafghazi S, Sowlati T, Sokhansanj S, Melin S (2010) Techno-economic analysis of renewable energy source options for a district heating project. Int J Energy Res 34:1109–1120
3. Kilkis BA (2011) Lignite-geothermal hybrid power and hydrogen production plant for green cities and sustainable buildings. Int J Energy Res 35:138–145
4. Ratlamwala TAH, Dincer I, Gadalla MA (2012) Performance analysis of a novel integrated geothermal-based system for multi-generation applications. Appl Therm Eng 40:71–79
5. Coskun C, Oktay Z, Dincer I (2011) Modified exergoeconomic modeling of geothermal power plants. Energy 36:6358–6366
6. Guzović Z, Loncar D, Ferdelji N (2010) Possibilities of electricity generation in the Republic of Croatia by means of geothermal energy. Energy 35:3429–3440
7. DiPippo R (2007) Ideal thermal efficiency for geothermal binary plants. Geothermics 36:276–285
8. Kose R (2007) Geothermal energy potential for power generation in Turkey: a case study in Simav, Kutahya. Renew Sust Energ Rev 11:497–511
9. Kanoglu M, Bolatturk A (2008) Performance and parametric investigation of a binary geothermal power plant by exergy. Renew Energy 33:2366–2374
10. Yari M (2010) Exergetic analysis of various types of geothermal power plants. Renew Energy 35:112–121
11. Ganjehsarabi H, Gungor A, Dincer I (2012) Exergetic performance analysis of Dora II geothermal power plant in Turkey. Energy 46:101–108
12. Guzović Z, Majcen B, Cvetkovic S (2012) Possibilities of electricity generation in the Republic of Croatia from medium-temperature geothermal sources. Appl Energy 98:404–414
13. Franco A, Villani M (2009) Optimal design of binary cycle power plants for water-dominated, medium-temperature geothermal fields. Geothermics 38:379–391
14. Rosen MA, Dincer I (2003) Exergy-cost-energy-mass analysis of thermal systems and processes. Energy Convers Manag 44:1633–1651
15. Desai NB, Bandyopadhyay S (2009) Process integration of organic Rankine cycle. Energy 34:1674–1686
16. Shengjun Z, Huaixin W, Tao G (2011) Performance comparison and parametric optimization of subcritical organic Rankine cycle (ORC) and transcritical power cycle system for low-temperature geothermal power generation. Appl Energy 88:2740–2754
17. Vanslambrouck B, Vankeirsbilck I, Gusev S, De Paepe M (2011) Turn waste heat into electricity by using an organic Rankine cycle. In: Proceedings of 2nd European conference on polygeneration, Tarragona, Spain, pp 1–14
18. Clauser C (2006) Geothermal energy. In: Heinloth K (ed) Landolt-Bornstein. Group VIII: advanced materials and technologies, vol. 3: Energy technologies, Subvol. C: renewable energies. Springer Verlag, Heidelberg-Berlin p. 493–604. www.geophysik.rwth-aachen.de/IHFC/books.html. Accessed 15 Sep 2009

Exergetic Assessment of a Hybrid Steam Biomass Gasification and SOFC System for Hydrogen, Power, and Heat Production

4

Abdussalam Abuadala and Ibrahim Dincer

Abstract

In this chapter, an integrated process of steam biomass gasification and a solid oxide fuel cell (SOFC) for multi-generation purposes (hydrogen, power, and heat) is thermodynamically studied, and its performance is assessed through exergy efficiency. The scheme combines SOFC at 1,000 K and 1.2 bar and a gasifier which is used to gasify saw dust with a steam–biomass ratio of 0.8 kmol/kmol and a gasification temperature range of 1,023–1,423 K at an atmospheric pressure. A parametric study is performed to assess exergetic efficiency and investigate the effect of various parameters related to the different system components such as airflow rate and preheating temperature on the efficiency. The results show that SOFC is a major source of the system destruction exergy. For the gasification temperature range studied here, the system exergetic efficiency increases with hydrogen yield from about 22 to 32 % and the overall exergy efficiency, which considers electricity production, decreases from 57.5 to 51 %, respectively.

Introduction

Conventional energy conversion systems fed by fossil fuels are known by their negative impact on the environment through greenhouse gas emissions and air pollution, and these impacts will increase as energy demand increases by this rhythm worldwide. These impacts can be reduced or eliminated by using alternative resources that are environmentally friendly to produce fuels and use alternative energy conversion technologies, such as solid oxide fuel cell (SOFC), to generate heat and power that are required for different applications.

There is a growing, worldwide interest in the development of technologies allowing the exploitation of renewable energy sources, for both environmental and economical reasons [1]. To avoid the limitations on the use and applicability of biomass in producing energy, it must compete with other renewable energy sources as well as fossil fuels [2]. Energy systems based on the use of hydrogen offer a great promise for the future [3].

Biomass gasification-derived hydrogen is a renewable and sustainable fuel, which can be used as an alternative fuel and to fuel SOFC for various applications. It was reported that the highest yield of hydrogen from lignocellulosic biomass is from steam gasification [4].

The interest for future energy studies and solutions lies in hybrid systems to increase efficiency, reduce cost, and mitigate greenhouse gas emissions. Such hybrid systems effectively show interaction between each other, which enables one system to utilize products from other systems. The hybrid systems can differ from each other by including different numbers of components or by way of interaction between them, which enables the system to perform different duties. The most typical

A. Abuadala (✉) • I. Dincer
Faculty of Engineering and Applied Science, University of Ontario Institute of Technology (UOIT),
2000 Simcoe Street North, Oshawa, ON, Canada L1H 7K4
e-mail: Abdussalam.Abuadala@uoit.ca; Ibrahim.Dincer@uoit.ca

hybrid configuration suggested in the literature is a recuperated gas turbine process with an SOFC as the core unit of the system [5]. Barvarsad [5] reported that electrical efficiency predictions for the system that combines the two units in a range of 58–65 %. Costamagna et al. [6] energetically investigated a small-size hybrid system, combining a gas turbine that produces about 50 kWe and a tubular SOFC. Costamagna et al. [6] found that the thermal efficiency of the system was always higher than 50 %. Balli et al. [7] studied the exergetic performance assessment of a combined heat and power (CHP) system installed in the Turkish city of Eskisehir. The system did not include a gasifier or an SOFC. They found from the performed exergy analysis, along with system essential components, that the highest exergy consumption between the components occurs in the combustion chamber.

Many researchers (e.g., Barvarsad [5]; Calise et al. [8]; Akkaya et al. [9]) indicated that limited studies have been conducted on the exergetic performance of hybrid SOFC/GT systems and the effects of design and operating parameters on the exergetic system efficiencies and destructions.

Fryda et al. [10] investigated a combination of an air-blown fluidized bed biomass gasifier with a high-temperature SOFC and/or a gas micro-turbine in a CHP system of less than 1 MWe, which could operate at two pressure levels, near atmospheric and about 4 bar, respectively. They used Aspen Plus software to simulate the integrated system. They found that the pressurized SOFC operation is greatly improved and with power from a gas micro-turbine achieves efficiencies of $\geq 35\%$ when the current density value was 400 mA m^{-2}.

Akkaya et al. [9] analyzed exergy performance by an exergetic performance coefficient which would give maximum total exergy output possible for a given entropy generation rate. They used lumped control volumes to thermodynamically study the system components. The analysis was conducted on a combination of a methane-fed SOFC and gas turbine in a CHP system. They found that for a given total exergy output the maximum exergetic performance coefficient is achieved at the least entropy generation rate.

Baravsad [5] analyzed a methane-fed internal reforming SOFC–gas turbine power generation system, based on the first and the second law of thermodynamics. They found that increasing the fuel flow rate does not have a satisfactory effect on system performance. Also they found that cycle efficiency increased when fuel or air flow rates decreased.

In the present study, exergetic assessment of a hybrid system is performed, and an influence of various operating parameters of the system components on the performance is investigated. The system was proposed, and its energy efficiency was studied in a previous work [11]. In order to improve this system, it is essential to understand parametric impacts on the exergetic efficiency and hence enhanced evaluation of the system. This applies in particular to those parameters which are related to different components like SOFC preheated airflow rate, burner preheated airflow rate, and SOFC preheated air temperature. A comprehensive EES code is developed for system simulation. It is also designed to calculate destroyed exergy as a result of exchanging energy in the steam-reforming reactor, water gas shift reactor, SOFC stack, burner, gas turbine, air compressors, and heat exchangers. An assessment of the system via exergy analysis confirms an ability of the system to competitively stand against other systems. Accordingly, this study investigates an exergetic assessment of the system. Also, a parametric investigation is conducted to study the effect of single components through the impact of their related parameters on exergy efficiencies.

System Description

We know that combining/hybridizing systems results in a better efficiency and effectiveness. This study includes an exergy assessment to show how efficiently and effectively the system produces hydrogen, heat, and power. The main components of the system are gasifier, SOFC, compressors, turbine, and heat exchangers (Fig. 4.1i). The performed analysis contains the application of mass conservation, energy conservation, and entropy balance for the system components. The analysis is performed under some general assumptions: steady state with negligible kinetic and potential energies and the gases obey the ideal gas relations.

Analysis

The mass, energy, entropy, and exergy analyses of the system components are performed where the outlet stream from a component considers the input stream for the next neighbor component. Each stream may constitute a single element or a sum of elements. Separation of hydrogen from the produced gas is typically based on the separation by filters.
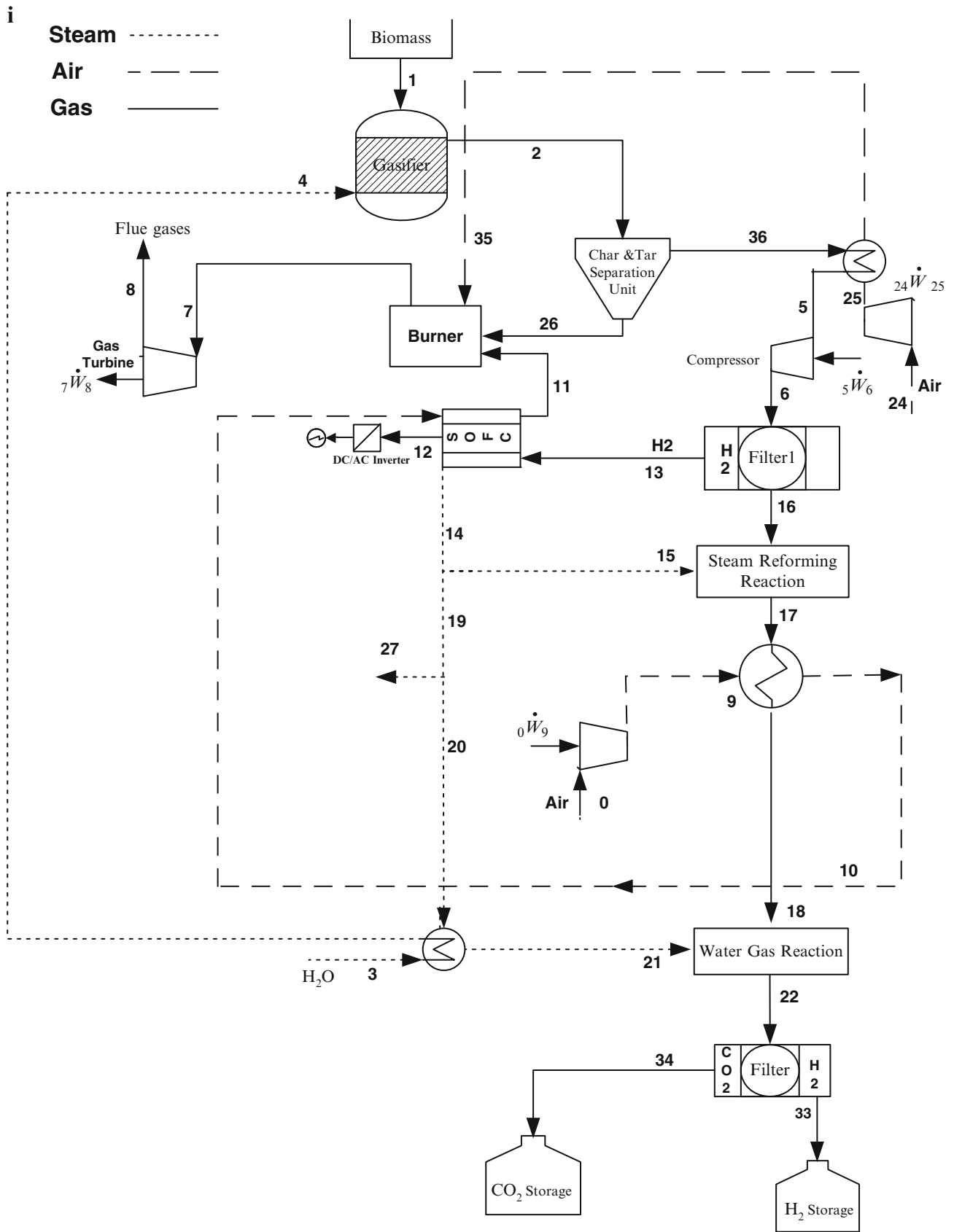
Fig. 4.1 (*i*) System layout and (*ii*) schematic diagram of system components: (**a**) Compressor 5-6. (**b**) Turbine 7-8. (**c**) Heat exchanger 17-18-9-10. (**d**) The steam-reforming reactor. (**e**) The water gas shift reactor. (**f**) The SOFC. (**g**) The burner

ii

a

$T=T_5$
$P=P_5$
$\dot{m}_5$

$_5\dot{W}_6$

Compressor

T_6
P_6
$\dot{m}_6$

b

P_7
T_7
$\dot{m}_7$

$_7\dot{W}_8$

Turbine
7-8

P_8
T_8
$\dot{m}_8$

c

$\dot{m}_{18}$

P_{18}
$T_{18}=300K$

18

Air 9   **10**

$\dot{m}_9$ $\dot{m}_{10}$

T_9 $\dot{m}_{17}$ T_{10}

P_9 T_{17} P_{10}

17 P_{17}

Gas

d

P_{16}
T_{16}
$\dot{m}_{16}$

P_{15}
T_{15}
$\dot{m}_{15}$

Steam Reforming Reactor

P_{17}
T_{17}
$\dot{m}_{17}$

e

P_{18}
$T_{18}=300\ K$
$\dot{m}_{18}$

$\dot{m}_{21}$

P_{21}
T_{21}

Water Gas Shift Reactor

P_{22}
T_{22}
$\dot{m}_{22}$

f

Cathode Channel

$\dot{m}_{10}$ $\dot{m}_{11}$

CATHODE

$\dot{W}_{ac}$ $\dot{W}_{dc}$

ELECTROLYTE

ANODE

$\dot{m}_{14}$ $\dot{m}_{13}$

Anode Channel

g

T_{35}
$\dot{m}_{35}$ 35

7

$\dot{m}_7$
T_7

Burner

$\dot{m}_{11}$ 11
T_{11}

26

$\dot{m}_{26}$
T_{26}
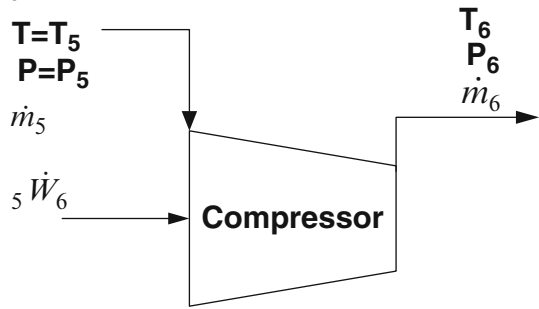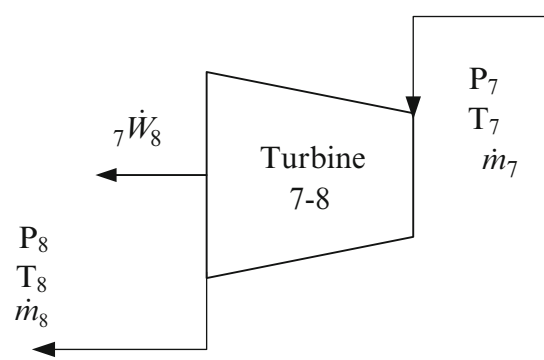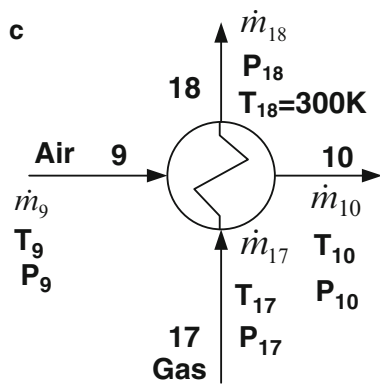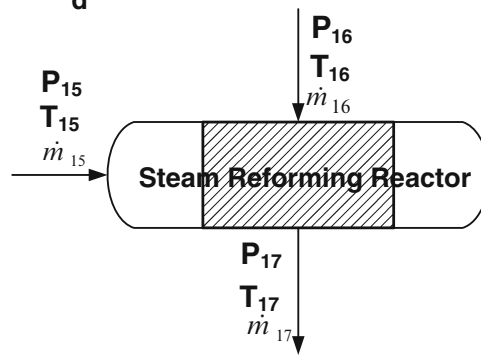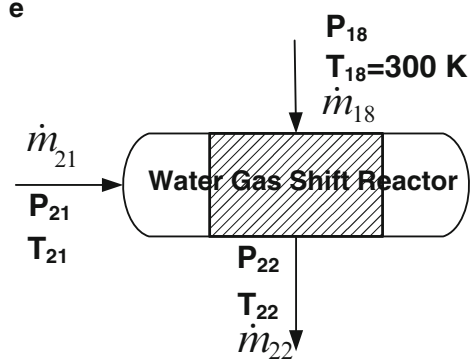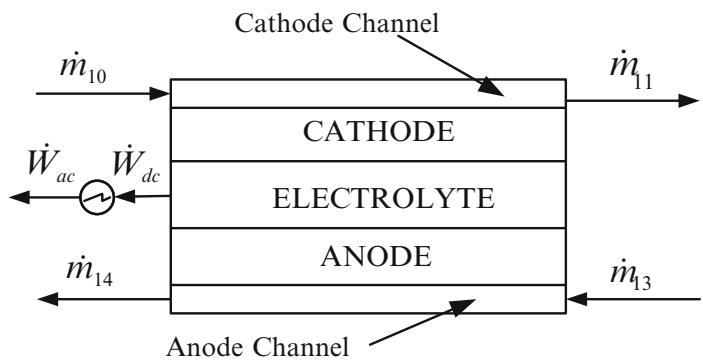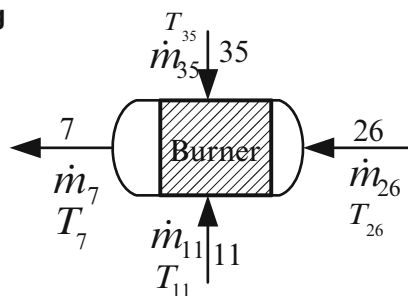
Fig. 4.1 (continued)

Table 4.1 Ultimate and proximate analysis of sawdust wood

Element	Weight on dry basis (%)
C	48.01
H	6.04
O	45.43
N	0.15
S	0.05
Ash	0.32
HHV (MJ/kg)	18.4
Volatile matter	76.78
Fixed carbon	18.7
Ash	0.32

Source: Turn et al. [16]

These devices are assumed to have a neutral effect regarding energy: i.e., they do not destroy a significant amount of exergy; and hence, their effect on the destroyed exergy is neglected. The processes taking place in the different components are assumed to be of steady state, and the change in potential and kinetic forms of energy is neglected. Also, the energy losses from a body of component to the environment are considered negligible by assuming the process adiabatic.

Energy and Exergy Balance Equations

The biomass feedstock is sawdust wood and is totally gasified to H_2, CO, and CO_2 (char represents 5 % [10] of the biomass carbon content; C_6H_6 [12, 13] represents the tar; and methane represents the other hydrocarbons). Hydrogen is oxidized in the SOFC to water (steam), and methane is gasified in reforming reaction to CO and H_2. CO is completely oxidized to CO_2 in water gas shift reaction. The remaining products (tar and char) are further processed to combust in the burner. Only hydrogen from gasification is used in the SOFC, and therefore all SOFC calculations are based on these conditions. However, the secondary hydrogen derived from downstream processing is stored.

In this study, the exergy of the used biomass is calculated by the method of Szargut et al. [14] as follows:

$$Ex_{biomass} = \beta LHV_{biomass} \tag{4.1}$$

where the biomass lower heating value is given by Shieh et al. [15]:

$$LHV_{biomass} = 0.0041868(1 + 0.15[O])(7837.667[C] + 33888.889[H] - [O]/8) \tag{4.2}$$

Here, C, H, and O are, respectively, carbon, oxygen, and hydrogen elements in sawdust wood, and they are obtained from the sawdust ultimate analysis. The ultimate and proximate analysis data of the used wood are given in Table 4.1. The quality coefficient β is given in terms of oxygen–carbon and hydrogen–carbon ratios, and according to the following equation:

$$\beta = \frac{1.0414 + 0.0177[H/C] - 0.3328[O/C]\{1 + 0.0537[H/C]\}}{1 - 0.4021[O/C]} \tag{4.3}$$

The exergy flow rate is primarily calculated from the following equation:

$$\dot{E}x_i = \dot{m}_i Ex_i \tag{4.4}$$

where the subscript i represents fuel (reactant) or agent or product and Ex is exergy. One part of the exergy depends on matter composition which is known as chemical exergy, Ex_{ch}, and for a mixture is given by

$$Ex_{ch} = \sum_i X_i Ex_{O,i} + RT_O \sum_i X_i \ln X_i \tag{4.5}$$

where X_i is the mole fraction of component i and Ex_o is standard exergy. The other part of exergy depends on the matter temperature and matter pressure. It is known as physical exergy, Ex_{ph}, and is given by

$$Ex_{ph} = (h - h_O) - T_O(s - s_O) \tag{4.6}$$

where h and s are enthalpy and entropy at T and P and h_0 and s_0 are enthalpy and entropy at standard operating state ($T_0 = 298.15$ K and $P_0 = 1$ atm). The total exergy, Ex, is the sum of the two above exergy parts.

Enthalpy and entropy data are necessary to perform both energy and exergy analyses. Gases are assumed to obey the ideal gas behavior, and their enthalpies and entropies, respectively, are

$$h = h_f^O + \Delta h \quad \text{and} \quad s = s^O + \Delta s$$

The properties of enthalpy and entropy change as a function of temperature, and they obey the ideal gas laws. To find enthalpy and entropy values, the constant pressure-specific heat in kJ/(kmol k), $\overline{C}_p$, is utilized as a third-degree polynomial equation [17]. The enthalpy of formation, h_f^O, and entropy at standard state, s^O, are obtained from thermodynamic tables. Entropy of the gases changes as a function of temperature and pressure.

The specific heat of tar in coal gasification was developed by Li et al. [18, 19] and modified by Hyman et al. [20]. The same equation is used for derived tar from biomass gasification in kJ/kg$_{tar}$ K:

$$Cp_{tar} = 0.00422T \tag{4.7}$$

The enthalpy and entropy values of tar are calculated in the same way as described above. However, its enthalpy of formation and standard entropy are calculated from the following equations [20]. The enthalpy of formation, h_{tar}^o, in kJ/kmol is given by

$$h_{tar}^o = -30.980 + X_{CO_2}\, h_{CO_2}^o + X_{H_2O}\, h_{H_2O}^o \tag{4.8}$$

where X_i is the mole fraction and h_i^O is the standard enthalpy of formation for specie i. The term related to sulphur is omitted since the used biomass has negligible sulphur content. The standard tar entropy, s_{tar}^o, in kJ/(kmol K) is given by

$$s_{tar}^o = a_1 + a_2\exp\left[-a_3\left(\frac{H}{C} + N\right)\right] + a_4\left(\frac{O}{C + N}\right) + a_5\left(\frac{N}{C + N}\right) + a_6\left(\frac{S}{C + N}\right) \tag{4.9}$$

where a_1–a_6 coefficients are $a_1 = 37.1635$, $a_2 = -31.4767$, $a_3 = 0.564682$, $a_4 = 20.1145$, $a_5 = 54.3111$, and $a_6 = 44.6712$. C, H, N, O, and S are, respectively, carbon, hydrogen, nitrogen, oxygen, and sulphur weight fractions in the sawdust.

Energy analysis is done in terms of the enthalpy. Processes in the system components are steady-state steady-flow processes. Therefore, energy conservation for the adiabatic process takes place in the system component and is found from the first law of thermodynamics as follows: rate of energy at the inlet state(s) is equal to rate of energy at the exit state(s). Mathematically, on molar basis, it can be expressed by the following equation:

$$\sum_i \dot{N}_i \overline{h}_i = \sum_e \dot{N}_e \overline{h}_e + {}_i\dot{W} \tag{4.10}$$

The continuity equation becomes

$$\sum_i \dot{N}_i MW_i = \sum_e \dot{N}_e MW_e \tag{4.11}$$

where i and e refer to inlet and exit state point(s) of the system component under the study, h is the specific enthalpy, $\dot{N}$ is the molar flow rate, and MW is the molecular weight. The term ${}_i\dot{W}$ is less than zero when the system component consumes power, greater than zero when the system component produces power, and greater zero when the system component does not produce or consume power.

The exergy destruction in a system component is calculated from the following equation:

$$\dot{Ex}_{des} = T_0 \dot{S}_{gen} \tag{4.12}$$

For each system component, the entropy generation, $\dot{S}_{gen}$, term is calculated from the entropy balance. The entropy balance for the process takes place in the system component that is written through the second law of thermodynamics as follows: rate of entropy at the inlet state(s) plus rate of the entropy generation in the system component is equal to rate of entropy at the exit state(s). Thus, it can be expressed in a molar basis by the following equation:

$$\sum_i \dot{N}_i \bar{s}_i + \dot{S}_{gen} = \sum_e \dot{N}_e \bar{s}_e \tag{4.13}$$

Compression Processes

The compressor 5–6 is used to increase the pressure needs in a filtration process and to increase the gas temperature to the temperature that is preferred for the reformation reaction to occur as well as to protect the gasifier from the backflow that can happen (Fig. 4.1ii.a). The species, namely, H_2, CO, CO_2, and CH_4, are compressed here. The temperatures of the gases at the compressor exit and inlet are related to the corresponding pressures and compressor isentropic efficiency. The compression process is also needed to compress the air as required for electrochemical reaction that takes place in the SOFC. The amount of air is that air necessary for the electrochemical reaction to take place in the SOFC which is related to fuel with a hydrogen–air ratio of 2. The pressure and the temperature of air at the compressor upstream are given at atmospheric conditions. The temperature after the preheating process is calculated from the energy balance that is conducted on the former SOFC heat exchanger. The temperature and pressure of the other streams are known. Streams which exit the SOFC have the same temperature and pressure of the SOFC; the fuel (H_2) stream has properties after filtration process where pressure exceeds by 5 % of the SOFC operating pressure. The preheated air temperature is found based on the required temperature delivered at the SOFC and the energy balance of the SOFC.

The compression process needs to compress air to the burner. The amount of air that will compress is that amount used to control the burner temperature on the one hand and on the other hand to make sure that there is a sufficient amount of air to completely burn the residuals that are sent to the burner from the SOFC and the gasifier. The power that drives this compressor is calculated through energy analysis. The temperature after the preheating process is assumed to be 430 K and a pressure which equals an operating pressure of the SOFC. The preheated air temperature is found based on a sufficient amount of air and reasonable temperature needed at the burner. The energy required for the preheating process is extracted from by-product gases when they pass through the heat exchanger that is located after the separation process.

Gas Turbine

The flue gas leaves the burner and gets expanded in the turbine to extract its energy content for power output (Fig. 4.1ii.b). The stream properties at the turbine inlet are the same as those of the burner exit. According to the analysis done for the burner, the gas consists of steam, carbon dioxide, air, and nitrogen. The properties of the stream at the turbine exit (state 8) are given at the surrounding conditions (P_0 and T_0). The species that undergo expansion are water, air, nitrogen, and carbon dioxide. One can look to the expansion process that takes place in the turbine and describe it as an opposite process to the compression process that happens in the compressor. The produced power, when flue gases expand in the turbine, is found by applying energy analysis. All species behave like an ideal gas at both states, and therefore their enthalpies become a function of temperature only, and they are given in terms of constant pressure-specific heat. The temperature of the flue gas at the turbine exit is assumed such that it obeys the environmental restrains.

Heat Exchangers

In heat exchangers 17-18-9-10, the 17-18 shows the hot stream, while the second one 9-10 indicates the cold line (Fig. 4.1ii.c). The presence of this heat exchanger aims to extract heat from the gasification product gases to preheat air that passes through the heat exchanger and utilizes in the SOFC. Three species constitute the hot stream H_2, CO, and CO_2, while the cold stream is air. The temperature of the hot stream at state 17 is obtained from the energy balance of the steam-reforming reactor, while the temperature at state 18 is assumed equal to the ambient and the pressure is decreased by about 5 % at state 17. Therefore, the parameters of the hot line are known. Also, the properties of air at the heat exchanger inlet are known from the compressor 0-9 analysis. Air properties at the heat exchanger outlet are known from the energy balance of the heat exchanger. Accordingly, a number of cells in the SOFC stack are known from the SOFC analyses. The same principles are applied to heat exchanger 36-5-25-35.

In heat exchangers 20-21-3-4, the 20-21 shows the states on the hot stream, while the second one 3-4 indicates the states on the cold stream. The presence of this heat exchanger aims to extract heat from the high-temperature steam, 20-21, to produce steam and use it as the gasification agent in the gasification process. In the present study, the amount of steam $\dot{m}_4$ delivered to the gasifier is known. Also, the amount of steam flow in the hot stream and its inlet temperature (temperature at state 20) are known from the SOFC analysis. Only the temperature of the hot stream at state 21 is unknown and is calculated from the performed energy balance. The energy balance of the heat exchanging process simply says that energy removed from the hot streamline is absorbed by the steam flow in the cold line.

Steam-Reforming Reactor

As a potential method to increase hydrogen yield from the system, the gas produced from the gasification process is further processed to the steam-reforming reactor (Fig. 4.1ii.d). The reaction in the reactor is governed by the following reaction equation:

$$CH_4 + H_2O \rightarrow 3H_2 + CO \tag{4.14}$$

According to this reaction, H_2–CO ratio of three is used in the analyses. A part of the steam of the SOFC electrochemical reaction by-product is used as a reaction medium. The amount of steam that is required for the steam-reforming reaction is calculated based on the molar balance of the reaction equation. It is clear from the reaction equation that a ratio of the number of methane moles to that of the used steam is one. The molar flow rate of methane is known from the gasification process analyses, while the molar flow rate of both the needed steam by the reaction and that of the reaction products are known from the molar balance equation of the reaction.

The steam-reforming reaction is endothermic. The reactants of the steam-reforming reactor are H_2O, CH_4, CO, and CO_2, and its product gases are H_2, CO, and CO_2. The molar rates of carbon monoxide, methane, and carbon dioxide in the steam-reforming reactor are known from the gasification analysis, while the steam is used according to the steam-reforming reaction equation. Thermodynamic properties at the steam-reforming reactor inlet states are known, and the mole flow rates at the steam-reforming reactor exit are known. Only the temperature of the exiting stream is unknown, and this can be calculated from the energy balance of the steam-reforming reactor.

Water Gas Shift Reactor

Processing the gases further to the water gas shift reactor also aims to increase a hydrogen yield of the system. In this process, the carbon monoxide from the gasification process as well as that from the steam-reforming reactor will shift by steam to hydrogen and carbon dioxide according to the following reaction:

$$CO + H_2O \rightarrow H_2 + CO_2 \tag{4.15}$$

Here, the properties at state point 21 are known from the performed analysis on the SOFC while properties of state 18 are known from the performed analysis on the heat exchanger 17-18-9-10 (Fig. 4.1ii.e). From the thermodynamic point of view, the water gas shift reactor will be treated in a manner similar to that of the steam-reforming reactor. However, in this case, the reaction is exothermic and takes place at lower temperatures. The process is assumed to take place adiabatically, and the reactants of the water gas shift reactor are H_2O, CO, and CO_2 and the products of the water gas shift reactor are H_2 and CO_2. The molar flow rate of the carbon monoxide will be the sum of the one from the gasification process and that from the steam-reforming reaction. The other species molar flows are known from the mole balance of the reaction equation. The hydrogen in this case is called secondary hydrogen and is stored after the filtration process, while the hydrogen from the gasification process is called primary hydrogen and is used to fuel the SOFC after it is purified from the contaminants.

Solid Oxide Fuel Cell

A fuel cell is a device that converts the energy released from a reaction of matter, in this case, hydrogen with oxygen, directly into electricity without the intermediate step that is seen in conventional thermal cycles where the chemical energy converts first into thermal and then into electricity. The most common classification of fuel cells is by the used electrolyte type, operating temperatures, and the mechanism by which charge is conducted in the cells and the SOFC operates in a temperature range of 650–1,000 °C [21]. Because inherent properties tolerate well with contaminants from the gasification process and operate in a temperature range similar to that of biomass gasification, the SOFC is used in the system. The depleted air at the SOFC temperature from the SOFC's cathode chamber is fed directly to the burner.

Table 4.2 Cell material resistivity and its dependence on temperature

Cell material (carrier type)	Resistivity formula Ω-cm
Air electrode (electronic)	$0.008114\exp{(600/T_{SOFC})}$
Electrolyte (ionic)	$0.00294\exp{(10{,}350/T_{SOFC})}$
Fuel electrode (electronic)	$0.00298\exp{(-1{,}392/T_{SOFC})}$
Interconnection (electronic)	$0.1256\exp{(4{,}690/T_{SOFC})}$

Source: Bessette II et al. [24]

The SOFC is the device that converts chemical energy available in matter to electricity, and the process produces electricity (and some heat) and water via the reaction that happens between oxygen from air and hydrogen from gasification according to the following reaction:

$$H_2 + \frac{1}{2}O_2 \rightarrow H_2O \tag{4.16}$$

The open-circuit voltage is calculated at an average temperature between the mixed anode and cathode inlet flow and the outlet of the SOFC from Nernst's equation as follows:

$$V_{SOFC} = -\frac{\Delta G^0}{2F} - \frac{RT_{SOFC}}{2F}\ln\left(\frac{P_{H_2O}^{SOFC}}{P_{H_2}^{SOFC}\sqrt{P_{O_2}^{SOFC}}}\right) \tag{4.17}$$

where ΔG^0 is the standard Gibbs free energy change per mole, R is the universal gas constant (8.314 kJ/kmol K), and F is the Faraday constant (96,485 C/g mol). $P_{H_2O}^{SOFC}$, $P_{H_2}^{SOFC}$, and $P_{O_2}^{SOFC}$ are, respectively, the partial pressure of H_2O and H_2 at the cathode and of O_2 at the anode. The voltage is obtained by subtracting the overpotential voltages from the above voltage. The overpotential losses are originated from three sources: concentration, V_{con}; ohmic, V_{ohm}; and activation, V_{act}:

$$V = V_{SOFC} - V_{con} - V_{ohm} - V_{act} \tag{4.18}$$

The overpotentials due to activation, V_{act}, is calculated from the Butler–Volmer equation with a reaction rate constant of 0.5 [22]:

$$V_{act} = \frac{2RT_{SOFC}}{n_{H2}F}\sinh^{-1}\left(\frac{i}{2i_o}\right) \tag{4.19}$$

This equation is applied for the electrodes, cathode and anode, where i is the current density and i_o is the apparent exchange current density. The ohmic overpotential, V_{ohm}, obeys ohm's law and is given by

$$V_{ohm} = iR_{res} \tag{4.20}$$

The resistance of all materials, R_{res}, and those used in SOFC components can be obtained from Costamagna et al. [23], and the respective resistivity is a function of temperature and is calculated by Bessette II et al. [24] from the following equation:

$$\rho = a\exp\left(\frac{b}{T_{SOFC}}\right) \tag{4.21}$$

where a and b are constants depending on cell material, see Table 4.2.

The polarization or the concentration overpotential, V_{pol}, is a summation of polarization over potential from anode, $V_{pol,a}$, and that from cathode, $V_{pol,c}$, and can be obtained from Costamagna et al. [23].

The electric power produced by the SOFC is

$$\dot{W}_{SOFC,dc} = VI \tag{4.22}$$

Table 4.3 SOFC geometries and material-related data

Parameter	Value	Reference
Utilization factor, U_f	0.95	Bessette II et al. [24]
DC/AC inverter efficiency	0.95	Bessette II et al. [24]
Temperature of SOFC, T_{SOFC}	1,000 K	Bessette II et al. [24]
Active surface area, A_{SOFC}	100 cm^2	Colpan et al. [25]
Effective gaseous diffusivity through the anode, D_{aeff}	0.2 cm^2 s^{-1}	Colpan et al. [25]
Effective gaseous diffusivity through the cathode, D_{ceff}	0.05 cm^2 s^{-1}	Colpan et al. [25]
Thickness of the anode, t_a	0.05 cm	Colpan et al. [25]
Thickness of the cathode, t_c	0.005 cm	Colpan et al. [25]
Thickness of the electrolyte, t_e	0.001 cm	Colpan et al. [25]
Thickness of the interconnect, t_{int}	0.3 cm	Colpan et al. [25]
Pre-exponential factor, γ_a	5.5×10^4 A/cm^2	Costamagnaet al. [13]
Pre-exponential factor, γ_c	7×10^4 A/cm^2	Costamagna et al. [13]
$E_{act,a}$	100×10^3 J/mol	Costamagna et al. [13]
$E_{act,c}$	120×10^3 J/mol	Costamagna et al. [13]

For H$_2$ fuel, the current I is calculated by

$$I = 2F\dot{n}_{H_2}{}^2 \tag{4.23}$$

where 2 is a number of electrons transferred per molecule of fuel and $\dot{n}_{H_2}^2$ is the H$_2$ (mol/s) that reacts in the hydrogen electrochemical reaction which was solely considered. $\dot{n}_{H_2}^2$ is the utilized part from the hydrogen that is supplied to the SOFC.

The fuel cell model developed in this study is based on a planar geometry in which its dimensions and material-related data are given according to the data listed in Table 4.3. The preheating air is fed into the cathode inlet (state 10), and excess depleted air and nitrogen flow out from the cathode exit (state 11). On the anode side from the cell, hydrogen is fed into the anode inlet (state 13) and steam and excess depleted hydrogen flow out from the anode exit (state 14). If the fuel cell utilizes fuel by a factor of U_F, the depleted hydrogen that flows out will be $\dot{n}_{H_2}^2 (1 - U_F)$. One mole from water contains a H$_2$–O$_2$ mole ratio of 2. Therefore, a molar flow rate of hydrogen, $\dot{N}_{H_2,13}$, that is used from the gasification process is twice the molar flow rate of oxygen that is used from the supplied air. It means that the consumed oxygen will change according to the utilized hydrogen and both of them will depend on the assumed utilization factor. It is well known that air has a N$_2$–O$_2$ ratio of 79-21 and the nitrogen is treated as an inert substance. Therefore, from the molar flow rate of the utilized oxygen, the total amount of air that is needed to supply to the SOFC can be calculated.

The energy balance for the adiabatic SOFC is obtained by applying the first law of thermodynamics for the states shown on the schematic diagram of the SOFC (Fig. 4.1ii.f), where the reactants of the SOFC are H$_2$ that flows at state point 13 and air that flows at state point 10. The products of the SOFC are H$_2$, N$_2$, and O$_2$ that flow at state point 11 and H$_2$O (g) that flows at state point 14.

Burner

A burner is used to convert the chemical energy of the unutilized fuel in the SOFC stack to heat. In this process, more chemical energy is converted to thermal energy. After the SOFC stack, the excess depleted fuel and air, and the separated char and tar from the gasification product, are sent to the burner (Fig. 4.1ii.g). An extra amount of preheated air via the stream 36 is fed to the burner to make sure that all materials are completely burnt. The products of the burning process contain mainly steam, carbon dioxide, and nitrogen according to the following reactions:

$$char_{26}C + char_{26}O_2 \rightarrow char_{26}CO_2 \tag{4.24}$$

$$tar_{26}C_6H_6 + 7.5tar_{26}O_2 \rightarrow 3tar_{26}H_2O + 6tar_{26}CO_2 \tag{4.25}$$

$$H_{2,11}H_2 + \frac{H_{2,11}}{2}O_2 \rightarrow H_{2,11}H_2O \tag{4.26}$$

The excess depleted oxygen from the former combustion process is the oxygen that flows at state 11, $O_{2,11}$, and is known from the SOFC analysis. Therefore, the minimum oxygen that is needed to feed to the burner becomes

$$O_{2,\min} = O_{2,consumed} - O_{2,11} \qquad (4.27)$$

where $O_{2,consumed}$ is the oxygen that the above reactions need. The oxygen supplied to the burner has to satisfy at least the minimum amount of oxygen and results in a reasonable temperature in the burner. Therefore, the preheated burner air, air_{35}, that flows at state 35 on the system flow diagram is greater than 4.762 times $O_{2,\min}$.

The molar flow rates of char and tar are known from the gasification process, while the molar flow rates of unutilized hydrogen, $H_{2,11}$; unutilized oxygen, $O_{2,11}$; and nitrogen, $N_{2,11}$, are known from the SOFC analyses. The properties of states 11, 35 (air), and 26 (char and tar) and the molar flow rate at state 7 are known. The only unknown is the temperature at the burner exit which can be determined from the energy balance equation for the adiabatic burner.

Exergy Efficiencies

A study of the system exergetic efficiency (or second-law efficiency) shows how efficiently the system works to increase the secondary hydrogen yield from gasification via downstream processes, from external steam reforming and external water gas shift reactions, and to utilize the primary hydrogen in producing electricity and heat. Four exergy efficiencies are defined for this system based on the exergy of the fed sawdust: the exergy efficiency for producing power from the SOFC, exergy efficiency for producing power from the gas turbine, exergy efficiency that considers producing secondary hydrogen from gasification downstream processes, and exergy efficiency that considers all power from the system:

$$\eta_{EX,SOFC} = \frac{\dot{Ex}_{SOFC}}{\dot{Ex}_{biomass}} \qquad (4.28)$$

The exergy efficiency that considers a production of electricity and accompanies an expansion process of gases in the gas turbine is

$$\eta_{EX,t} = \frac{\dot{Ex}_{t,net}}{\dot{Ex}_{biomass}} \qquad (4.29)$$

The third exergy efficiency that considers the hydrogen derived from gasification downstream reactions is defined as

$$\eta_{EX,H_2} = \frac{\dot{Ex}_{H_2}}{\dot{Ex}_{biomass}} \qquad (4.30)$$

The system exergetic efficiency for electricity production is calculated from the exergetic efficiency that considers producing electricity from the gas turbine and the SOFC. $\dot{Ex}_{H_2}$ is the exergy flow rate of the secondary hydrogen, $\dot{Ex}_{biomass}$ is the exergy flow rate with biomass, and the subscript t stands for turbine. The exergy that flows with species at different states is calculated in a way similar to that discussed above. The exergy of power is equal to the power itself.

Results and Discussion

Exergy Destructions

The rates of exergy destruction are calculated for the system components at the gasification temperature. Figure 4.2 shows the exergy destructions of the system components at a gasification temperature of 1,023 K. It is clear from the figure that a major part of the exergy destruction occurs in the SOFC stack followed by the turbine and the burner. Also, it is found that the total exergy destruction in the system components has minimum value when the gasification temperature is 1,175 K (Fig. 4.3).

Fig. 4.2 Exergy destruction
rates in the system at gasification
temperature of 1,023 K
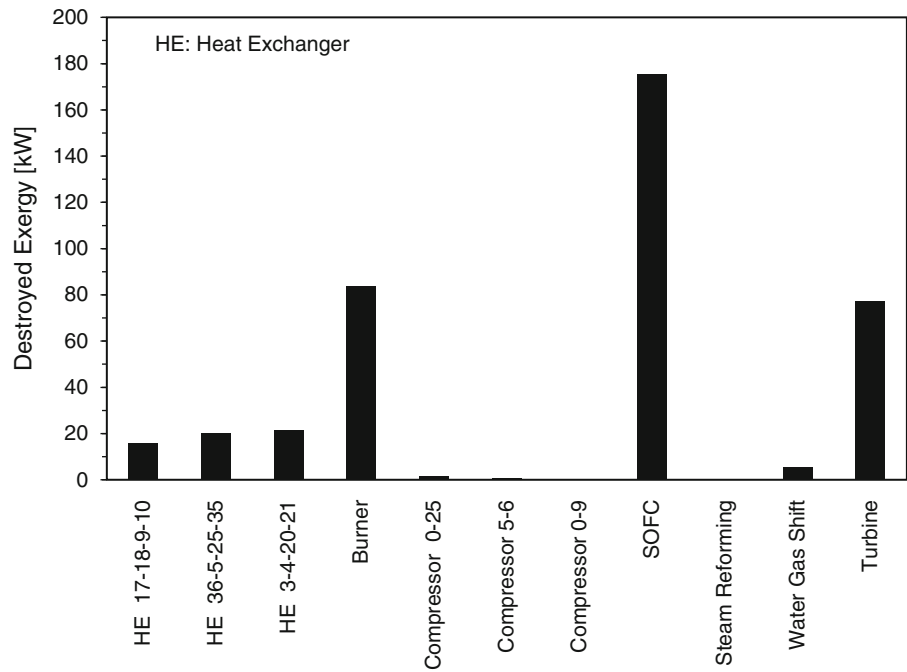
Fig. 4.3 Exergy destruction
in system components versus
gasification temperature
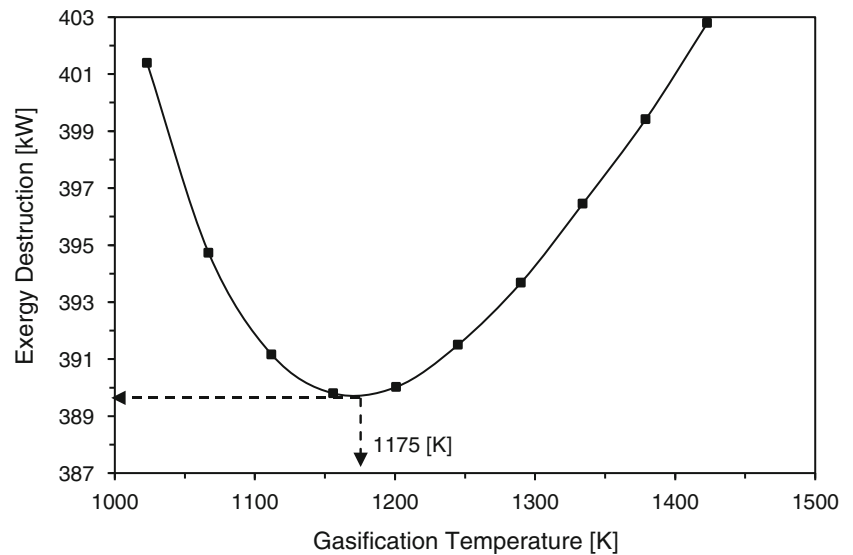
Exergy Efficiencies

In the gasification temperature range considered, and for a given utilization factor and steam–biomass ratio, the overall exergy efficiencies for electricity production, based on the exergy content of biomass, are shown in Fig. 4.4a. The efficiency decreases from 57.5 to 51 % in the studied gasification temperature range because of decrease in the exergy efficiency of turbine. From the exergy destruction results, it is found that a major part of exergy destruction occurred in the SOFC. Also, its exergy destruction increased with an increase in the gasification temperature. The results show that secondary hydrogen yield increases and hence its exergy increases. Thus, the exergy efficiency with the hydrogen production increases from about 22 % to about 32 %.

Fig. 4.4 Variations of exergy efficiencies with (**a**) gasification temperature, (**b**) burner temperature, and (**c**) burner preheated airflow–biomass ratio
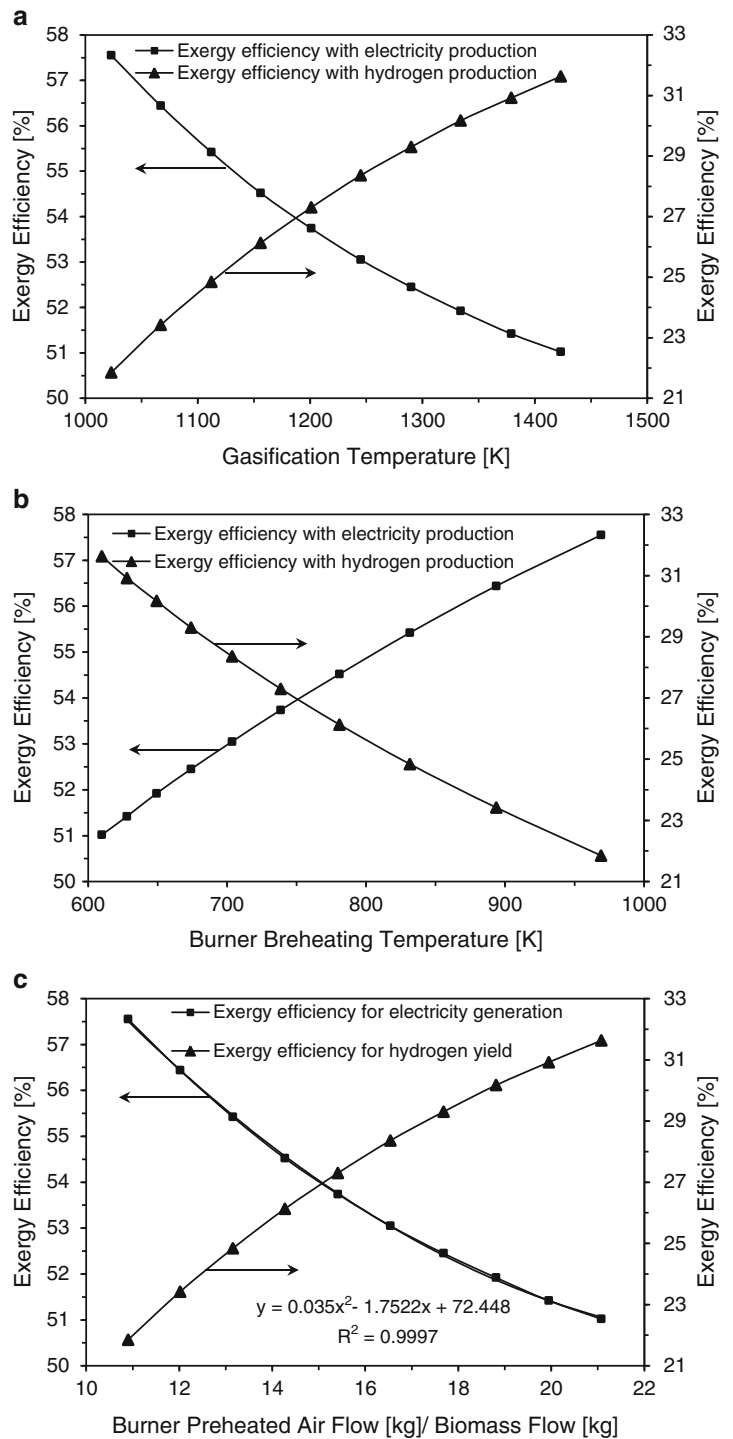
Effect of Burner Exit Temperature

The overall exergy efficiency of the system increases as the burner temperature increases (Fig. 4.4b). Increasing the burner preheated air enhances the energy available in the burner and thus its exit temperature which is the same as the turbine inlet temperature. Higher inlet turbine temperature means higher power or exergy, and thus it improves the turbine exergy efficiency which leads to improvement of the overall electrical exergy efficiency. Higher preheated burner temperature means a reduction in the gases' energy content which in turn decreases the exergy flow with product gas streams and among them hydrogen.

Fig. 4.5 Variations of exergy
efficiencies with (**a**) SOFC
preheated air temperature
and (**b**) mass ratios of SOFC
preheated airflow
and biomass flow
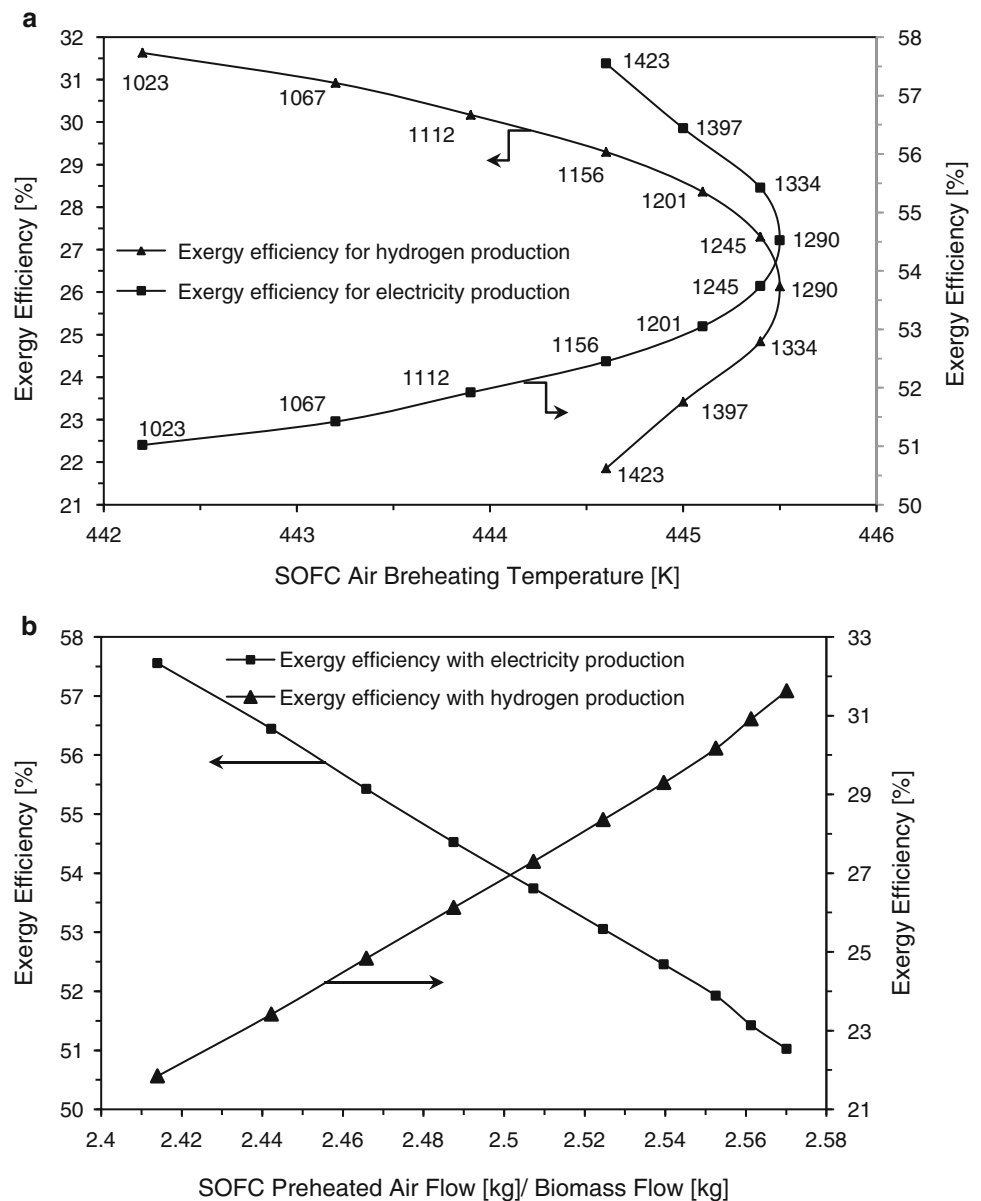
Burner Preheated Airflow

The air supplied to the burner mainly aims to provide the oxygen and the energy needed for the burning process. In the studied temperature range, an increase of preheated air per biomass throughput leads to a decrease in the overall exergy efficiency of the system. This decrease is in good fitting with second-degree polynomial (Fig. 4.4c). Also, more gasification by-products are sent to the burner at a higher gasification temperature. This will increase the burner temperature which in turn increases the turbine inlet temperature.

SOFC Preheated Air Temperature

The temperature is found to be based on the amount of air needed for the combustion of hydrogen to take place via the electrochemical reaction for the specific SOFC. The system has an exergy efficiency of 55 % when the preheated air has the highest temperature of 445.5 K. In the studied gasification temperature range, the exergetic efficiency for electricity production reaches a value of 57.5 % and that is when the preheated air temperature is 444.5 K (Fig. 4.5a). In the same gasification temperature range, the system has the potential to increase hydrogen yield from about 22 % to about 32 %.

Fig. 4.6 Variation of destroyed exergy with preheated air fed to the system in the gasification temperature range
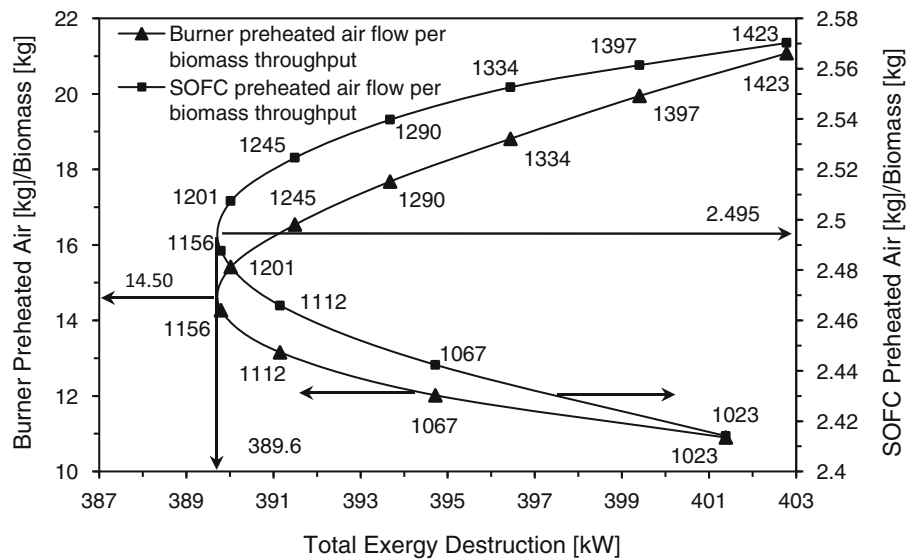
The maximum preheated temperature reaches its maximum value when the exergy efficiency of hydrogen yield is 26 % (Fig. 4.5i). After that a steep decrease in preheating temperature is observed. This is attributed to the fact that at a higher gasification temperature, more gases are produced, which results in a higher hydrogen concentration from the side reactions that take place in the steam-reforming and water gas shift reactors, which in turn increases the energy content of the product gases. After this temperature, the product gas energy content is dominant compared to the energy content of the air sent to the SOFC.

Effect of SOFC Preheated Air Flow

It is found that increasing airflow per biomass throughput results in a reduction in the system overall exergy efficiency (Fig. 4.5b). More preheated airflows increase the energy supplied to the SOFC which results in an increase in the destroyed exergy. Also, an increase in the airflow results in a decrease of its temperature; therefore, more heat content is available with product gas flow, which results in more hydrogen yield and thus higher exergy efficiency that considers hydrogen. Figure 4.6 shows that the preheated air fed to the SOFC and that fed to the burner affect the destroyed exergy in the system components and both show a similar trend. The exergy destruction has the lowest value when the SOFC preheated airflow–biomass ratio is 2.495, while the exergy destruction has the lowest value when the burner preheated air–biomass ratio has a value of 14.50.

Conclusions

The present study performed through exergy analysis investigates and assesses the potential of a new hybrid system which combines both steam biomass gasification and SOFC with external water gas shift and steam-reforming reactions for multi-generation purposes, including power, heat, and hydrogen. This chapter further studies the exergy efficiency of the system that considers the hydrogen yield and the electricity production. It is found that the system efficiency with secondary hydrogen yield increases from about 22 to 32 %, and this is attributed to the increase of hydrogen yield from the side reactions that take place in the steam-reforming and water gas shift reactors. Also, for the same gasification temperature range, the system exergy efficiency that considers electricity production decreases from 57.5 to 51 %. The SOFC has a major contribution in the system exergy destruction, and any reduction in its exergy destruction results in an improvement in electrical efficiency. The effects of the preheated air in the system on exergy efficiency were also studied. It was found that the system's electrical exergy efficiency increases, and that efficiency with hydrogen production decreases, when both preheated airflows per biomass throughput decrease.

Nomenclature

C	Carbon content in biomass (w %)	N	Nitrogen content in biomass (w %)
D_{aeff}	Effective gaseous diffusivity through the anode (cm^2/s)	$\dot{N}$	Molar flow rate (kmol/s)
		$\dot{n}_{H2}$	Hydrogen fed to SOFC (kmol/s)
D_{ceff}	Effective gaseous diffusivity through the cathode (cm^2/s)	O	Oxygen content in biomass (w %)
		P	Pressure (pa or atm)
E	Ohmic symmetry factor	R	Universal gas constant (8.314 kJ $kmol^{-1}$ K^{-1})
Ex	Exergy (kJ/kg or kJ/kmol)	S	Total entropy (kJ/K)
Ex_o	Standard exergy (kJ/kmol)	s	Specific entropy (kJ/kg K or kJ/kmol K)
F	Faraday constant (96,485 coulombs/g mol)	T	Temperature (K)
H	Hydrogen content in biomass (w %)	t	Thickness (cm)
h	Specific enthalpy (kJ/kg or kJ/kmol)	U_F	Utilization factor (−)
I	Circuit current (A)	V	Circuit or overpotential volt (volts)
i	Current density (mA/cm^2)	$\dot{W}$	Power (W or kW)
i_o	Apparent exchange current density (A/cm^2)	X	Mole fraction (−)
LHV	Lower heating value (kJ/kg)		
$\dot{m}$	Mass flow rate (kg/s)		

Subscripts

a	Anode	H_2	Hydrogen
act	Activation	H_2O	Water
$biomass$	Biomass	i	Inlet
c	Cathode	o	Reference or ambient
ch	Chemical	O_2	Oxygen
con	Concentration	ohm	Ohmic
dc	Power from DC	ph	Physical
des	Destroyed	pol	Polarization
e	Exit	res	Resistance
el	Electrical	$SOFC$	Solid oxide fuel cell
gen	Generation	t	Turbine
		tar	Tar

Superscript

Over dot	Quantity per time	*Over bar*	Quantity per kmol
		SOFC	Solid oxide fuel cell

Greek Letters

β	Quality coefficient (−)	η	Efficiency (−)
ΔG	Standard Gibbs function of reaction (kJ/kg)	ρ	Resistivity (Ω-cm)

References

1. Baratieri M, Baggio P, Fiori L, Grigiante M (2008) Biomass as an energy source: thermodynamic constraints on the performance of the conversion process. Bioresour Technol 99:7063–7073
2. McKendry P (2002) Energy production from biomass (part 2): conversion technologies. Bioresour Technol 83:47–54
3. Fermoso J, Arias B, Gil MV, Plaza MG, Pevida C, Pis JJ, Rubiera F (2010) Co-gasification of different rank coals with biomass and petroleum coke in a high-pressure reactor for H2-rich gas production. Bioresour Technol 101:3230–3235
4. Turner J, Sverdrup G, Mann MK, Maness P, Kroposki B, Ghirardi M, Evans RJ, Blake D (2008) Renewable hydrogen production. Int J Energy Res 32:379–407
5. Bavarsad PG (2007) Energy and exergy analysis of internal reforming solid oxide fuel cell–gas turbine hybrid system. Int J Hydrog Energy 32:4591–4599
6. Costamagna P, Magistri L, Massardo AF (2001) Design and part-load performance of a hybrid system based on a solid oxide fuel cell reactor and a micro gas turbine. J Power Sources 96:352–368
7. Balli O, Aras H, Hepbasli A (2007) Exergetic performance evaluation of a combined heat and power (CHP) system in Turkey. Int J Energy Res 31:849–866

8. Calise F, Palombo A, Vanoli L (2006) Design and partial load exergy analysis of a hybrid SOFC-GT power plant. In: Akkaya AV, Sahin B, Erdem HH (eds) An analysis of SOFC/GT CHP system based on exergetic performance criteria. Int J Hydrogen Energy 33 (2008) 2566–2577

9. Akkaya AV, Sahin B, Erdem HH (2008) An analysis of SOFC/GT CHP system based on exergetic performance criteria. Int J Hydrog Energy 33:2566–2577

10. Fryda L, Panopoulos K, Karl D, Kakaras JE (2008) Exergetic analysis of solid oxide fuel cell and biomass gasification integration with heat pipes. Energy 33:292–299

11. Abuadala A, Dincer I (2010) Investigation of a multi-generation system using hybrid steam biomass gasification for hydrogen, power and heat. Int J Hydrog Energy 35:13146–13157

12. Hulteberg PC, Karlsson HT (2009) A study of combined biomass gasification and electrolysis for hydrogen production. Int J Hydrog Energy 34:772–782

13. Simell PA, Hirvensalo EK, Smolander ST, Krause AO (1999) Steam reforming of gasification gas tar over dolomite with benzene as a model compound. Ind Eng Chem Res 38:1250–1257

14. Szargut J, Morris DR, Steward FR (2007) Exergy analysis of thermal, chemical and metallurgical processes, 1988. In: Pellegrini LF, Oliveira S Jr (eds.) Exergy analysis of sugarcane bagasse gasification. Energy 32 314–327

15. Shieh JH, Fan LT (1982) Estimation of energy (enthalpy) and exergy (availability) contents in structurally complicated materials. Energy Sources 6:1–46

16. Turn S, Kinoshita C, Zhang Z, Ishimura D, Zhou J (1998) An experimental investigation of hydrogen production from biomass gasification. Int J Hydrog Energy 23:641–648

17. Cengel YA, Boles MA (2008) Thermodynamics: an engineering approach, 6th edn. Mc Graw Hill Companies Inc., New York

18. Li C, Suzuki K (2009) Tar property, analysis, reforming mechanism and model for biomass gasification — An overview. Renewable and Sustainable Energy Reviews 13:594–604

19. Hyman D, Kay WB (1949) Heat capacity and content of tars and pitches. Ind Eng Chem 41:1764–1768

20. Eisermann W, Johnson P, Conger WL (1979) Estimating thermodynamic properties of coal, char, tar and ash. Fuel Process Technol 3:39–53

21. Kakaça S, Pramuanjaroenkij A, Zhou XY (2007) A review of numerical modeling of solid oxide fuel cells. Int J Hydrog Energy 32:761–786

22. Chan SH, Low CF, Ding OL (2002) Energy and exergy analysis of simple solid-oxide-fuel-cell power systems. J Power Sources 103:188–200

23. Costamagna P, Selimovic A, Borghi MD, Agnewc G (2004) Electrochemical model of the integrated planar solid oxide fuel cell (IP-SOFC). Chem Eng J 102:61–69

24. Bessette NF II, Wepfer WJ, Winnick J (1995) A mathematical model of a solid oxide fuel cell. J Electrochem Soc 142:3792–3800

25. Colpan CO, Dincer I, Hamdullahpur F (2007) Thermodynamic modeling of direct internal reforming solid oxide fuel cells operating with syngas. Int J Hydrog Energy 32:787–795

Exergoeconomic Analysis of a Hybrid Steam Biomass Gasification-Based Tri-Generation System

Abdussalam Abuadala and Ibrahim Dincer

Abstract

In this chapter, exergoeconomic analysis is performed for a hybrid system combining gasifier and solid oxide fuel cell (SOFC) as the core units. The pressurised SOFC considered is a planar type in geometry, operating at 1,000 K, and the gasifier gasifies biomass (sawdust) in a media of steam and operates near atmospheric pressure and at a range of operating temperature of 1,023–1,423 K. The analysis is conducted at steam–biomass ratio of 0.8 kmol-steam per kmol-biomass. The gasification system has a capacity of 8.1–8.6 kg h^{-1} from the steam gasification-derived hydrogen, and the SOFC has an efficiency of 50.3 % and utilises the hydrogen produced from gasifier to generate power. Exergoeconomic analyses are performed to investigate and describe the exergetic and economic interaction between the system components through calculating the exergy costs of the streams for each component of this hybrid system. In the studied gasification temperature range and on the basis of electricity cost of 0.1046 \$/kWh, it is found that both primary and secondary hydrogen costs decrease. The unit of exergy from primary hydrogen costs 0.103–0.045 \$/kWh, while the unit of exergy from secondary hydrogen costs 0.064–0.039 \$/kWh.

Keywords

Gasification • Biomass • Hydrogen • Thermodynamics • SOFC • Exergoeconomics • Cost

Introduction

Conventional energy conversion systems that used fossil fuel are known by having negative impact regarding greenhouse gas emissions and air pollution, and these impacts will increase as an energy demand increases by this rhythm worldwide. Those impacts can be reduced or eliminated by using alternative resources that are environmentally friendly to produce fuel like biomass and using an alternative conversion technology from consuming derived products to generate heat and power that are needed for different applications like solid oxide fuel cell (SOFC).

Biomass gasification-derived hydrogen is a renewable and sustainable fuel, which can be used as an alternative fuel and to fuel SOFC in its different applications and among them a hybrid system. At present, researchers put tremendous effort to develop hybrid systems, rather than single systems, and multi-generation, rather than single- and co-generation. As an example [1], a hybrid system, co-generating heat and power, increases the energy efficiency from a conventional range of 53–55 % to over 90 % for power production.

Omosun et al. [2] developed steady-state model in gPROMS modelling tool to investigate integrated system by energetic economic analysis. The system combines SOFC with air biomass gasification. They energetically found that the system using hot cleaning process efficiency is more efficient than the system using cold cleaning process. On the other hand,

A. Abuadala (✉) • I. Dincer
Faculty of Engineering and Applied Science, University of Ontario Institute of Technology (UOIT), 2000 Simcoe Street North, Oshawa, ON, Canada L1H 7K4
e-mail: Abdussalam.Abuadala@uoit.ca; Ibrahim.Dincer@uoit.ca

economically, they found that the capital cost of the system using hot cleaning is higher than the system using cold cleaning process. From the literature search, it was noticed that an evaluation of the thermodynamic performance of system using exergy analysis was recommended, e.g., Dincer et al. [1]. This also was observed by Balli et al. [3].

Economic study of exergy with flow material stream is performed by exergoeconomic analysis. The term exergoeconomic analysis is used to describe a combination of exergetic and economic analyses and has been proposed for a precise characterisation of this combination. The results obtained from such analysis can provide extra information than one can obtain from exergy or economic analysis alone.

Tsatsaronis et al. [4] presented an exergoeconomic analysis methodology and evaluation of energy conversion plants. Tsatsaronis et al. [5] applied that methodology to coal-fired steam power plant. Kim et al. [6] applied exergy costing method to 1-MW gas turbine cogeneration with a west-heat boiler. They found that the unit exergy costs increase as the production process continues. Also, they found that electricity cost increases with the input cost. Balli et al. [3] performed exergoeconomic analysis for combined heat and power (CHP) system that was installed in Eskisehir City of Turkey. The obtained results indicated that the produced electrical power cost was 18.51 US\$/GW. Colpan et al. [7] investigated thermo-economic aspects of the Bilkent combined cycle co-generation plant in Turkey. Cost balances and auxiliary equations are applied to different components that are used in the plant; the accounted cost of exergy unit from electrical power was nearly the same (18.89 US\$/GW). The hydrogen fueling infrastructure cost published in the literature [8–11] is used to validate the results of this study. In this study, exergoeconomic analyses are performed on the developed system, which constitutes two core components, SOFC and gasifier, and they operate in narrow temperature range. The SOFC unit consumes the hydrogen produced by the gasifier after cleaning and separation.

In the earlier studies [12, 13], the gasifier module had been energetically and exergetically addressed and evaluated to ward safe operating gasifier for derived steam biomass gasification hydrogen. More recently, Abuadala and Dincer [14] have studied the gasifier module as emerged in a hybrid system that utilises the biomass steam gasification products in multi-duties: heat, power and hydrogen. In the present study, we go beyond and study this hybrid system exergoeconomically and assess it through exergy and cost accounting.

The primary objectives of this study are to conduct an exergoeconomic analysis of the proposed hybrid system for tri-generation purposes as power, heat and hydrogen. The analysis includes a calculation of the exergy flows with streams of system components, determines the exergetic costs of products, and evaluates the cost formations within the system. This study is unique for its application of all of these analyses to a complex energy system. The system produces different amounts from steam depending on the internal use and external demand. Additionally, the performing of the exergoeconomic analysis gives a chance to apply the SPECO method for a system with multi-duties. The cost balance and its auxiliary equations derived for the system components give the reader a chance to better understand the theoretical basis for calculations. In this regard, the present system is analyzed for different cases and scenarios.

System Description and Analysis

This study proposed that the system constitutes different components. The main components are gasifier, SOFC unit, compressors, heat exchangers and turbine. The analysis is conducted on the system components to investigate how competitively the system is able to produce hydrogen, heat and power. The analysis is performed by application of mass conservation, energy conservation, exergy balance and cost balance on the system components with some general assumptions: steady state with negligible kinetic and potential energies and the gases obey the ideal gas relations. The specific cost of water from the main supply (state 3), air at reference state (state 0 and state 24), and exhaust gas (state 8) are negligible. Figure 5.1 shows a flow diagram of the proposed system.

Energetic and Exergetic Biomass Equations

The biomass (sawdust) is fed to the gasifier and is totally gasified to gases and char and tar. The main by-product gasification gases are H_2, CO and CO_2. A 5 % [15] of the biomass carbon content represents the char, C_6H_6 [16, 17] represents the tar and methane represents the other by-product gasification hydrocarbons. Hydrogen is oxidised in the SOFC to water (steam), and methane is gasified in reforming reaction to carbon monoxide and hydrogen. Next, CO is completely oxidised to CO_2 in water gas shift reaction. The remaining products (tar and char) are further processed to burn in the burner. Only primarily
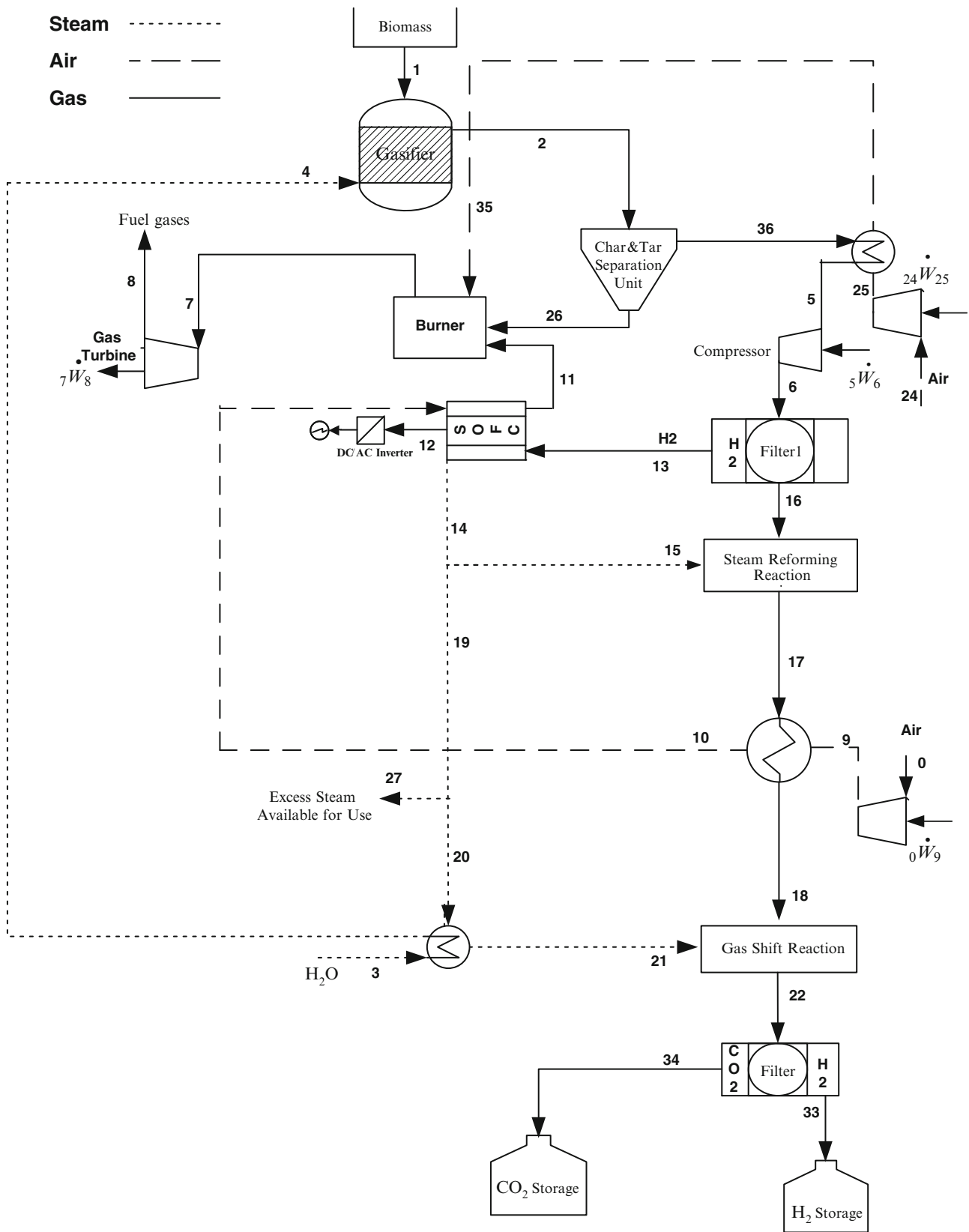
Fig. 5.1 System layout

Table 5.1 Ultimate analysis of sawdust wood

Element	Weight on dry basis (%)
C	48.01
H	6.04
O	45.43
N	0.15
S	0.05
Ash	0.32

Source: Turn et al. [20]

hydrogen from gasification was used in SOFC, and therefore all calculations regarding SOFC are done based on it. However, the secondary hydrogen which was derived from downstream processing was stored.

In this work, exergy of the used biomass was calculated using a method of Szargut et al. [18] as follows:

$$Ex_{biomass} = \beta LHV_{biomass} \qquad (5.1)$$

where the biomass lower heating value is given by Shieh et al. [19]:

$$LHV_{biomass} = 0.0041868(1 + 0.15[O])(7837.667[C] + 33888.889[H] - [O]/8) \qquad (5.2)$$

Here, C, H and O are, respectively, carbon, oxygen and hydrogen elements in sawdust wood and they are obtained from the sawdust ultimate analysis, Table 5.1. The quality coefficient β is given in terms of oxygen–carbon and hydrogen–carbon ratios and according to the following equation:

$$\beta = \frac{1.0414 + 0.0177[H/C] - 0.3328[O/C]\{1 + 0.0537[H/C]\}}{1 - 0.4021[O/C]} \qquad (5.3)$$

The exergy rate flows with fed biomass is given by

$$\dot{E}x_{biomass} = \dot{m}_{biomass}Ex_{biomass} \qquad (5.4)$$

The exergy flow rate is primarily calculated from the following equation:

$$\dot{E}x_i = \dot{m}_i Ex_i \qquad (5.5)$$

where the subscript i represents fuel or agent or product, and Ex is specific exergy. The exergy depends on matter composition which is known as chemical exergy, Ex_{ch}, and for a mixture is given by

$$Ex_{ch} = \sum_i X_i Ex_{O,i} + RT_O \sum_i X_i \ln X_i \qquad (5.6)$$

Here, X_i is the mole fraction of component i and Ex_o is standard exergy. The other part of exergy depends on the matter temperature and matter pressure. It is known as physical exergy, Ex_{ph}, and is given by

$$Ex_{ph} = (h - h_O) - T_O(s - s_O) \qquad (5.7)$$

where h and s are enthalpy and entropy of a species at T and P and h_0 and s_0 are enthalpy and entropy at standard operating state ($T_0 = 289$ K and $P_0 = 1$ atm). The total specific exergy, Ex, becomes

$$Ex = Ex_{ch} + Ex_{ph} \qquad (5.8)$$

Enthalpy and entropy values are necessary to perform thermodynamic and exergoeconomic analyses. Gases are assumed to obey the ideal gas behaviour, and their respective enthalpies and entropies are as follows:

$$\overline{h} = h_f^O + \Delta\overline{h} \qquad (5.9)$$

$$\overline{s} = s^o + \Delta\overline{s} \qquad (5.10)$$

The enthalpy rise and the entropy rise due to temperature are function of temperature, and they obey the ideal gas laws and the enthalpy of formation, h_f^O, and entropy at standard state, s^O, are known from the thermodynamic tables. Entropy for gases is normally a function of temperature and pressure. At super-atmospheric pressures, the effect of deviation from the reference state pressure should be taken into account in Eq. (5.10). The rise in enthalpy and entropy for the ideal gas are calculated in kJ/kmol and kJ/kmol K, respectively, from

$$\Delta \bar{h} = \int_{T_0}^{T} \overline{C}p \, dT \tag{5.11}$$

$$\Delta \bar{s} = \int_{T_0}^{T} \frac{\overline{C}p}{T} dT \tag{5.12}$$

where $\overline{C}p$ is constant pressure-specific heat in kJ/(kmol k), and it is a function of temperature and is given by the following empirical equation:

$$\overline{C}p = a' + b'T + c'T^2 + dT^3 \tag{5.13}$$

The coefficients, a', b', c' and d', of different gases are adopted from Cengel et al. [21]. The specific heat of tar in coal gasification was developed by Hyman et al. [22] and modified by Lowry [23]. The same equation will be used for derived tar from biomass gasification and in kJ/kg$_{tar}$ K:

$$Cp_{tar} = 0.00422T \tag{5.14}$$

Eisermann et al. [24] proposed the following equation to calculate the enthalpy and the entropy of tar. The term related to sulphur is omitted where the used biomass has negligible sulphur content:

$$h_{tar} = h_{tar}^o + \int_{T_o}^{T} Cp_{tar} \, dT \tag{5.15}$$

$$h_{tar}^o = -30.980 + X_{CO_2} h_{CO_2}^o + X_{H_2O} h_{H_2O}^o \tag{5.16}$$

where X_i is the mole fraction and h_i^O is the standard enthalpy of formation for species i. Entropy is given by

$$\bar{s} = s_{tar}^0 + \int_{T_o}^{T} \frac{\overline{C}_P}{T} dT \tag{5.17}$$

The standard tar entropy, s_{tar}^o, in kJ/kmol K is given by

$$s_{tar}^o = a_1 + a_2 \exp\left[-a_3\left(\frac{H}{C} + N\right)\right] + a_4\left(\frac{O}{C+N}\right) + a_5\left(\frac{N}{C+N}\right) + a_6\left(\frac{S}{C+N}\right) \tag{5.18}$$

The a_1–a_6 coefficients are $a_1 = 37.1635$, $a_2 = -31.4767$, $a_3 = 0.564682$, $a_4 = 20.1145$, $a_5 = 54.3111$ and $a_6 = 44.6712$. C, H, N, O and S are, respectively, carbon, hydrogen, nitrogen, oxygen and sulphur weight fractions in the sawdust.

Exergoeconomic Analysis

This type of exergoeconomic analysis combines both exergy analysis and cost accounting as a powerful tool for the systematic study and optimisation of energy systems [25]. Application of second-law costing methods is carried by assigning costs to exergy. Knowing the cost of the exergy supplied to a component allows an economic analysis of that component, and accordingly design, maintenance and operation decisions can be made without contending with the whole system [26].

Exergoeconomic is a precise characterisation of exergy-aided cost reduction approach, and many names were given to the proposed exergoeconomic approaches including [27] exergy economics approach (EEA), first exergoeconomic approach (FEA), and specific exergy costing method (SPECO). It is reported that the main differences among the approaches refer to the definition of exergetic efficiencies, the development of auxiliary costing equations and the productive structure.

If a system component has an inlet stream i and or an exit stream e, its exergy cost is

$$\dot{C} = c\dot{E}x \tag{5.19}$$

where c is the cost per exergy unit in \$/kwh and $\dot{E}x$ is the exergy rate with the flowing stream. The concept of exergy is also called available energy, availability or useful energy, which is the resource of value or the commodity of value, and it provides the key to cost accounting [26]. Part of exergy is converted to desired product(s), part is consumed by the process and known as internal lost and part is lost and known as external lost. Exergy analysis aims to identify the sources of thermodynamic inefficiencies (consumptions and losses) to make design changes that lead to improvement of overall system efficiency [5]. The equations describe the balance of exergy of the different components constituting the system and in terms of its cost are given in Table 5.2. Based on the number of unknowns, the number of extra equation(s) is decided by applying the principle of fuel and product rules. In addition to the principal equations, the extra equations are also developed and included in the same table.

In this study, SPECO approach for calculating costs in thermal systems will follow and it is based on three steps [28]: in the first step, exergy streams are identified by analyzing the system components and their contributions to the total exergy. In the second step define the fuel and the products from each component. In the last step, cost equations are built based on exergy by assigning a system of experiences with its surroundings and the sources of inefficiencies within it. A cost balance applies to any component, k, in the system stated as follows: the sum of cost rates of entering exergy stream(s), i, plus the cost rate due to expenses of investment and operating and maintenance, $\dot{Z}$, equals a sum of the cost rates of exiting stream(s), j. The above expression is mathematically expressed by the following equation [29]:
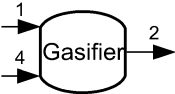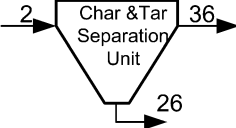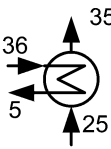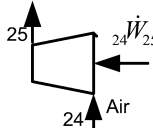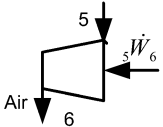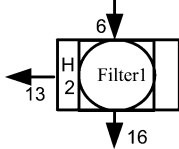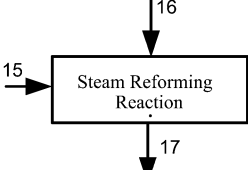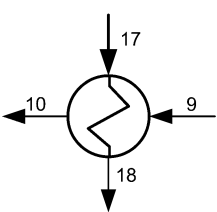
$$\sum_i \dot{C}_{i,k} + \dot{Z}_k = \sum_j \dot{C}_{j,k} \tag{5.20}$$

where $\dot{C}$ is exergy costing, and c denotes average cost per unit of exergy. For N exiting streams from a component, there will be N unknowns, and when K components constitute the system, there will be k times N equations or unknowns. To solve the obtained system of equations, N − 1 extra or auxiliary equations are obtained by applying F (fuel) and P (product) principles [27]. The formal principle refers to the removal of exergy from an exergy stream within the component under the study. It states that the average specific cost or cost per exergy unit associated with this removal of exergy must be equal to the average specific cost at which the removed exergy has been supplied to the same stream in upstream components, while the latter principle refers to the supplied exergy stream within the component under study. It states that each exergy unit is supplied to any stream associated with the exergetic product of the component at the same cost. By solving the derived equations, exergy costing of the different streams can be defined. Cost of owning and operating the component is [6]

$$\dot{Z}_k = \left[\frac{\varphi \cdot \dot{C}_o}{\tau}\right]_k \tag{5.21}$$

where φ is operating and maintenance factor excluding fuel, $\dot{C}_o$ is the annualised cost of the component and τ is the annual operation time of the component k at the nominal capacity. The operating and maintenance cost will be taken in

Table 5.2 Cost balance equations

Component name	Component control volume	Cost balance and auxiliary equations
Gasifier		$\dot{C}_1 + \dot{C}_4 + \dot{Z}_{Gasifier} = \dot{C}_2$
Separator		$\dot{C}_2 + \dot{Z}_{Sep} = \dot{C}_{26} + \dot{C}_{36}$ $$\frac{\dot{C}_2}{\dot{Ex}_2} = \frac{\dot{C}_{26}}{\dot{Ex}_{26}}$$
Heat exchanger I		$\dot{C}_{36} + \dot{C}_{25} + \dot{Z}_{HEI} = \dot{C}_5 + \dot{C}_{35}$ $$\frac{\dot{C}_{36}}{\dot{Ex}_{36}} = \frac{\dot{C}_5}{\dot{Ex}_5}$$
Compressor 24-25		$\dot{C}_{24} + \dot{C}_{W24,25} + \dot{Z}_{Comp24,25} = \dot{C}_{25}$ $$\dot{C}_{24} = 0$$
Compressor 5-6		$\dot{C}_5 + \dot{C}_{W5,6} + \dot{Z}_{Comp5,6} = \dot{C}_6$
Filter 1		$\dot{C}_6 + \dot{Z}_{F1} = \dot{C}_{16} + \dot{C}_{13}$ $$\frac{\dot{C}_6}{\dot{Ex}_6} = \frac{\dot{C}_{13}}{\dot{Ex}_{13}}$$
Steam reforming reactor		$\dot{C}_{16} + \dot{C}_{15} + \dot{Z}_{SRR} = \dot{C}_{17}$ $$\frac{\dot{C}_{15}}{\dot{Ex}_{15}} = \frac{\dot{C}_{14}}{\dot{Ex}_{14}}$$
Heat exchanger II		$\dot{C}_9 + \dot{C}_{17} + \dot{Z}_{HE,II} = \dot{C}_{10} + \dot{C}_{18}$ $$\frac{\dot{C}_{17}}{\dot{Ex}_{17}} = \frac{\dot{C}_{18}}{\dot{Ex}_{18}}$$

(continued)

Table 5.2 (continued)

Component name	Component control volume	Cost balance and auxiliary equations
Compressor 0-9		$$\dot{C}_0 + \dot{C}_{W,0,9} + \dot{Z}_{Comp0,9} = \dot{C}_9$$ $$\dot{C}_0 = 0$$
Steam shift reactor		$$\dot{C}_{18} + \dot{C}_{21} + \dot{Z}_{SSR} = \dot{C}_{22}$$
Heat exchanger III		$$\dot{C}_3 + \dot{C}_{20} + \dot{Z}_{HE,III} = \dot{C}_{21} + \dot{C}_4$$ $$\frac{\dot{C}_{20}}{\dot{E}x_{20}} = \frac{\dot{C}_{14}}{\dot{E}x_{14}}$$ $$\dot{C}_3 = 0$$
Filter II		$$\dot{C}_{22} + \dot{Z}_{F,II} = \dot{C}_{33} + \dot{C}_{34}$$ $$\frac{\dot{C}_{22}}{\dot{E}x_{22}} = \frac{\dot{C}_{33}}{\dot{E}x_{33}} + \frac{\dot{C}_{34}}{\dot{E}x_{34}}$$
Solid oxide fuel cell		$$\dot{C}_{10} + \dot{C}_{13} + \dot{Z}_{SOFC} = \dot{C}_{11} + \dot{C}_{14} + \dot{C}_{W,SOFC}$$ $$\frac{\dot{C}_{14}}{\dot{E}x_{14}} = \frac{\dot{C}_{11}}{\dot{E}x_{11}}$$
Burner		$$\dot{C}_{11} + \dot{C}_{35} + \dot{C}_{26} + \dot{Z}_{Burner} = \dot{C}_7$$
Gas turbine		$$\dot{C}_7 + \dot{Z}_{7,8} = \dot{C}_8 + \dot{C}_{W7,8}$$ $$\dot{C}_8 = 0$$

consideration through $\varphi = 1.06$ [6]. The annualised cost is calculated by converting the present worth of the component by using the capital recovery factor, *CRF*, as follows:

$$\dot{C}_o = PW \cdot CRF \tag{5.22}$$

The present worth of a system component can be calculated from initial investment, C_0, present worth factor, *PWF*, and the salvage value at the end of component life n, S_n, as follows:

$$PW = C_0 - S_n \cdot PWF \tag{5.23}$$

Table 5.3 Annualised costs of system components

Component (k)	C (k) [$]	Reference	S [$]	$\dot{C}_o$ [$/h]	$\dot{Z}_k$ [$/h]
Air compressor I	173,600	[6]	17,360	18,948.66	2.511
Air compressor II	173,600	[6]	17,360	18,928.03	2.511
Burner	92,600	[6]	9,260	10,107.41	1.339
Gas turbine	405,100	[6]	40,510	44,217.18	5.859
Gas compressor	110,000	[6]	11,000	12,006.64	1.591
Heat exchanger I	51,717	[2]	5171.7	5,644.976	0.748
Heat exchanger II	51,717	[2]	5171.7	5,644.976	0.748
Heat exchanger III	51,717	[2]	5171.7	5,644.976	0.748
SOFC stack	169,905	[28]	16990.5	18,545.35	2.457
SSR	92,600	[6]	9,260	10,107.41	1.339
SRR	92,600	[6]	9,260	10,107.41	1.339
Filter I	17,731	[2]	1,773.1	1,935.361	0.256
Filter II	17,731	[2]	1,773.1	1,935.361	0.256
Gasifier	72,403	[2]	7,240.3	7,902.879	1.047
Separator	5,726	[2]	572.6	625.0001	0.083
Total	1,578,747	Calculated	15,7874.7	172,322.2	22.833

The initial investment cost, C_0, for the components is adopted under the criteria such that its operating condition does not go beyond the maximum value obtained by applying the equations of cost model that is presented in Calise et al. [30] for turbine, compressor and heat exchanger, respectively, and they are as follows:

$$\frac{C_0}{\dot{W}_{t,\max}} = 1318.5 - 98.328\ln\left(\dot{W}_{\max}\right), \dot{W}_{t,\max} < 585, \text{kW} \tag{5.24}$$

$$\dot{W}_{c,\max} = 445\left(\frac{C_0}{91562}\right)^{\frac{1}{0.67}}, \dot{W}_{c,\max} < 1156, \text{kW} \tag{5.25}$$

$$A_{HE} = 0.093\left(\frac{C_0}{130}\right)^{\frac{1}{0.75}}, A_{HE} < 272\,\text{m}^2 \tag{5.26}$$

where $\dot{W}_{t,\max}$ is the maximum power that can be achieved by the turbine, $\dot{W}_{c,\max}$ is the maximum power that can be applied to the compressor and A_{HE} is the maximum permissible heat transfer area that can be used in the heat exchanger. The restrictions used with the above equations are based on the values used in Table 5.3. The initial cost of the system components is given in Table 5.3.

The CRF is calculated in terms of the interest rate, i, and the expected life of the component, n, from

$$CRF = \frac{i(i+1)^n}{(1+i)^n - 1} \tag{5.27}$$

The salvage factor is taken as 10 % of the initial investment [6]. The PWF simply is calculated from

$$PWF = (i+1)^{-n} \tag{5.28}$$

The data related to economic analysis are given in Table 5.4. The exergetic sawdust cost rate $\dot{C}_f$ is calculated in terms of its energetic cost rate, $\dot{C}e$, time of operation, τ, and the quality coefficient as follows:

$$\dot{C}_f = \frac{\dot{C}e}{\tau \cdot \beta} \tag{5.29}$$

Table 5.4 Economic analysis-related data

Parameter	Value	Reference
Interest rate, i	10 %	[6]
Salvage value, S_n	10 %	[6]
Lifetime, n	25 years	Assumed
Exchange rate, ER	1	Assumed
Maintenance factor, Ø	1.06	[6]
Cost of electricity	0.1046 \$/kWh	[32]
Cost of biomass, Pr	2 \$/GJ	[33]

The energetic cost rate is given by [3]

$$\dot{C}e = \frac{Pr \cdot LHV \cdot \tau}{ER} \tag{5.30}$$

where Pr is the sawdust price, ER is the exchange rate in $CA\$/US\$$ and LHV and τ are as defined above. The purchasing cost of the system components is adopted such that the initial investment of the burner, the steam-reforming reactor and the steam-shifting reactor are assumed to have the same purchasing cost as the combustion chamber. Also, the gas compressor is assumed to have the same initial investment as the fuel compressor. Cost of owning and operating for the system components is given in Table 5.3.

Energetic and Exergetic Analyses of SOFC

The SOFC model used in this study is based on planar design. The preheating air is fed in at cathode inlet (state 10), and excess depleted air and nitrogen flow out the cell at cathode exit (11). On the anode side from the cell, hydrogen is fed in at anode inlet (state 13) and steam and excess depleted hydrogen flow out at anode exit (state 14). The SOFC operates in a temperature range near to that of the steam–biomass gasification as it helps to use both of them in the hybrid system. It utilises by-product gasification hydrogen to produce heat, water (steam) and power. The mass balance equation for SOFC is

$$\dot{m}_{10} - \dot{m}_{11} + \dot{m}_{13} - \dot{m}_{14} = 0 \tag{5.31}$$

If the fuel cell utilises fuel by a factor of U_f, the mass flow rates $\dot{m}_{13}$ and $\dot{m}_{14}$ at states of 13 and 14, respectively, are related by the following equation:

$$\dot{m}_{14} = \left(1 - U_f\right)\dot{m}_{13} \tag{5.32}$$

One mole from water contains a H_2–O_2 mole ratio of 2. Therefore, it is possible to write a relation between a molar flow rate of oxygen, $\dot{N}_{O_2,13}$ that is used from the supplied air and a molar flow rate of hydrogen that is used from the gasification process as follows:

$$\dot{N}_{13} = 2\dot{N}_{O_2,10} \tag{5.33}$$

That means the consumed oxygen will change according to the utilised hydrogen and both of them will depend on the assumed utilisation factor. Approximately, it is well known that air has a N_2–O_2 ratio of 79–21 and the nitrogen is treated as an inert substance. Therefore, from the molar flow rate of the utilised oxygen, the total amount of air that is supplied to the SOFC can be calculated from

$$\dot{N}_{air,10} = 4.762\dot{N}_{O_2,10} \tag{5.34}$$

The energy balance for the adiabatic SOFC and for the states shown on the schematic diagram of the SOFC is

$$\sum_i \dot{N}_{i,SOFC}h_{i,SOFC} = \sum_e \dot{N}_{e,SOFC}h_{e,SOFC} + \dot{W}_{SOFC,dc} \tag{5.35}$$

where the subscript i refers to H_2 and airflow at inlet states of the SOFC and e refers to O_2, N_2, H_2O and H_2 flow at exit states of the SOFC. On mole basis, the entropy generation for a process that takes place in the SOFC is calculated from

$$\dot{S}_{gen,SOFC} = \sum_e \dot{N}_{e,SOFC}\bar{s}_{e,SOFC} - \sum_i \dot{N}_{i,SOFC}\bar{s}_{i,SOFC} \tag{5.36}$$

and the exergy destruction in the SOFC is calculated from the following equation:

$$\dot{Ex}_{des,SOFC} = T_0\dot{S}_{gen,SOFC} \tag{5.37}$$

The annualised cost of the SOFC is calculated by the costing model that was given in Plazzi et al. [31]. According to this model the cost of SOFC stack is given by the following equation:

$$C_{Stack} = (2.7C_{SOFC}N_{SOFC} + 2.507N_{Stack}A_{SOFC}) \tag{5.38}$$

where the cost of one cell, C_{SOFC}, is calculated in terms of its area from the following equation:

$$C_{SOFC} = 0.1442A_{SOFC} \tag{5.39}$$

And a number of the used stacks is given by

$$N_{Stack} = \frac{Total\ active\ surface\ area}{Active\ area\ of\ one\ stack} \tag{5.40}$$

Results and Discussion

It is expected that any practical system has to satisfy the thermodynamic laws. Energy and exergy analyses are thus first conducted to find the properties of the state points, and the results are then used in the exergoeconomic analysis. In the economic analysis, the system costs are levelised for 25 years. The study at different gasification temperatures should be conducted according to the used exergoeconomic model for the SOFC to find its owning and operating cost for each gasification temperature where the number of SOFC that utilises the hydrogen derived by gasification process is varied.

The results from exergoeconomic analysis by applying SPECO method and within the studied gasification temperature range of 1,023–1,423 K show how much hydrogen yield influences the cost of its exergy unit upon product gasification. It is found that within the studied gasification temperature range, the primary or by-product steam gasification hydrogen increases with increase in gasification temperature (Fig. 5.2).

The gasification temperature has a similar effect on the primary hydrogen yield and its temperature (Fig. 5.3), within the given gasification temperature range, the hydrogen temperature increases by 4 °C as the gasification temperature is increased by about 400 °C. As a result of this increase, the exergy of the hydrogen output increases and cost per unit exergy decreases (Fig. 5.4).
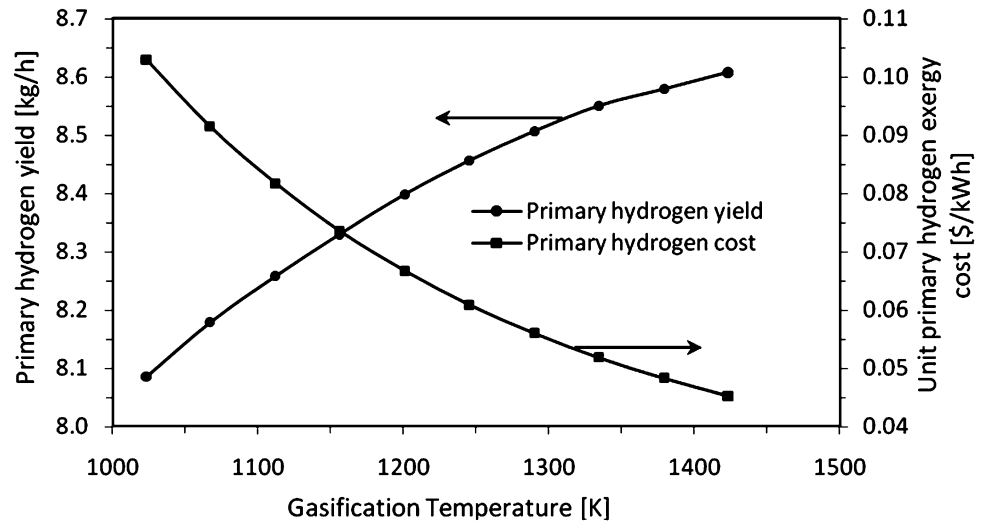
Fig. 5.2 Yield and cost of primary hydrogen at different gasification temperatures

Fig. 5.3 Yield and temperature of primary hydrogen at different gasification temperatures
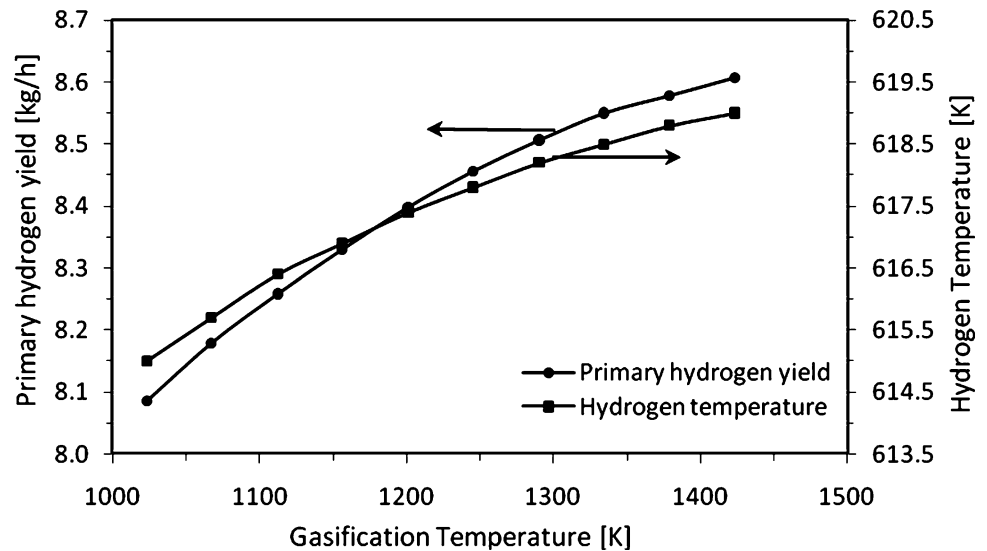
Fig. 5.4 Cost and temperature of primary hydrogen at different gasification temperatures
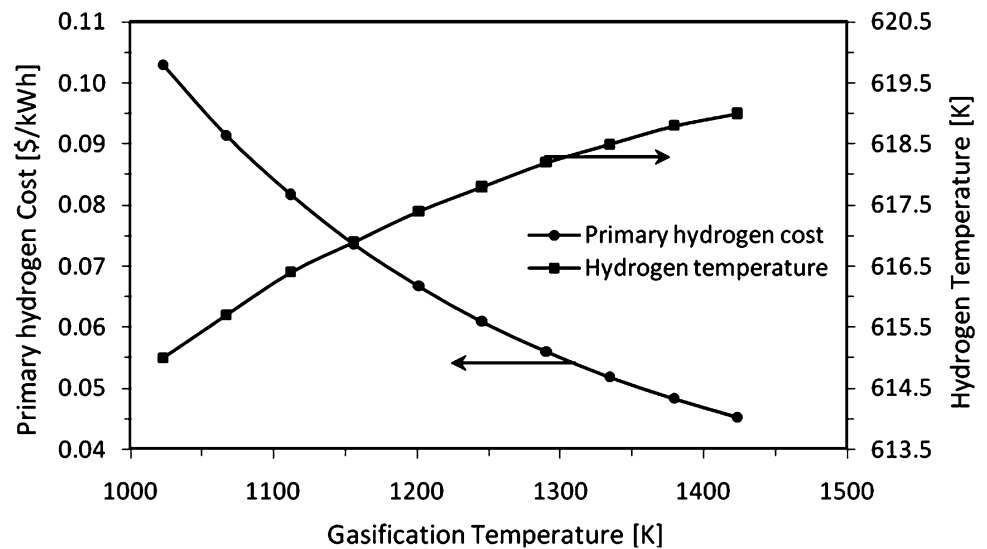
The secondary hydrogen yield or the hydrogen derived from the further processing of the gas products in the gasifier bottom processes increases within the studied gasification temperature range. It is observed at higher gasification temperature that there is a drastic decrease in the cost per unit exergy from the secondary hydrogen. This can be attributed to the hydrogen yield increase with the operating temperature of the gasifier increase which results in a reduction in specific cost by 0.025 \$/kWh (Fig. 5.5). This hydrogen has a temperature variation in a trend similar to that of its yield; however, its temperature is less sensitive at higher gasification temperature (Fig. 5.6). Although there is an increase in hydrogen yield, its temperature continuously increases, and this could be due to the increasing of hydrogen contribution from side reactions that take place in the bottom processes (Fig. 5.7).

In this study, the SOFC stack totally consumes the primary hydrogen. It is found that the primary hydrogen yield increases with increasing of the gasification temperature. According to the reaction equation that governs the reaction in the SOFC the steam will increase as more primary hydrogen is fed (Fig. 5.8).

On the other hand, more steam is needed to perform the water gas shift and steam-reforming reactions which makes less excess steam available for use (Fig. 5.9). The decreasing of the specific cost at this state point is attributed to the fact that the steam exergy cost is affected by the cost of the SOFC product steam where in the exergoeconomic model it is assumed that both have the same cost. Therefore, its cost will decrease as the cost of the total steam decreases and vice versa.

At a gasification temperature of 1,023 K, the specific cost of the other flow material streams can be found from Table 5.5. The unit hydrogen cost from this study is compared with the hydrogen fuelling infrastructure cost of the one produced from biomass as given in Table 5.6.

Fig. 5.5 Yield and cost of secondary hydrogen at different gasification temperatures
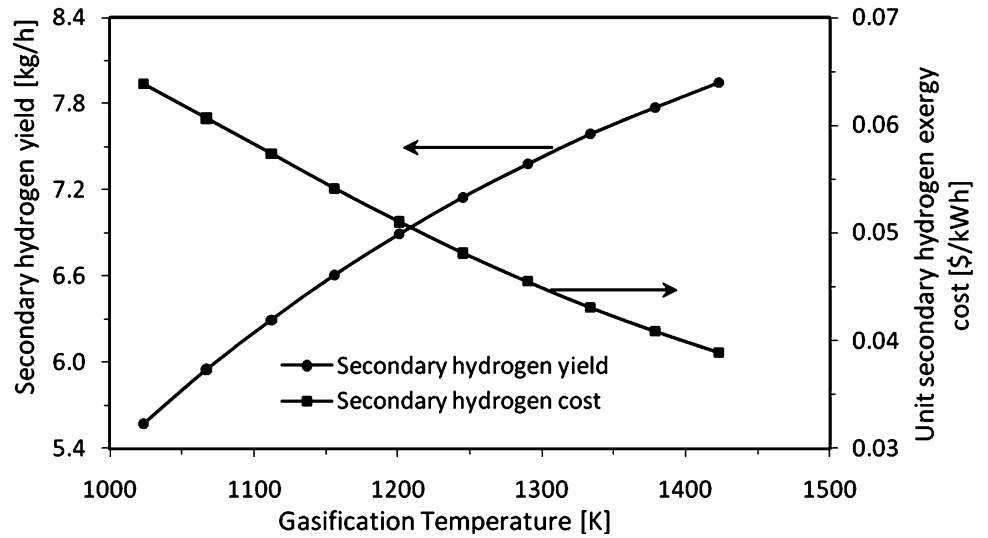
Fig. 5.6 Yield and temperature of secondary hydrogen at different gasification temperatures
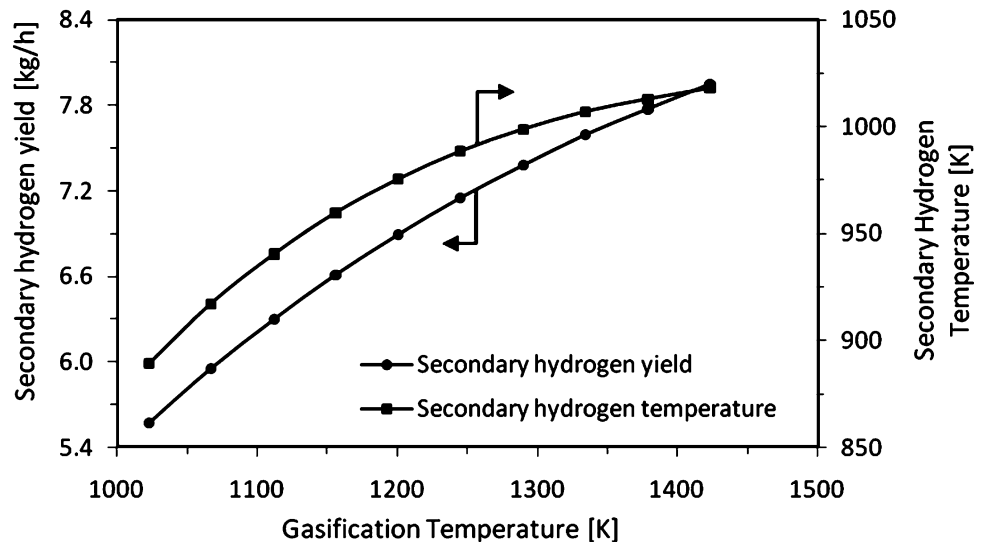
Fig. 5.7 Cost and temperature of secondary hydrogen at different gasification temperatures
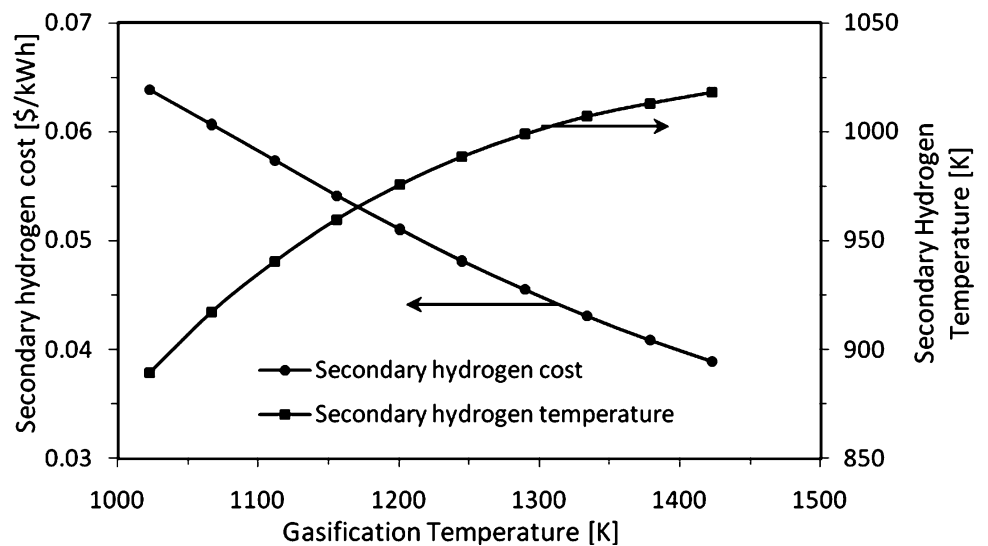
Fig. 5.8 Produced steam and its cost at different gasification temperatures
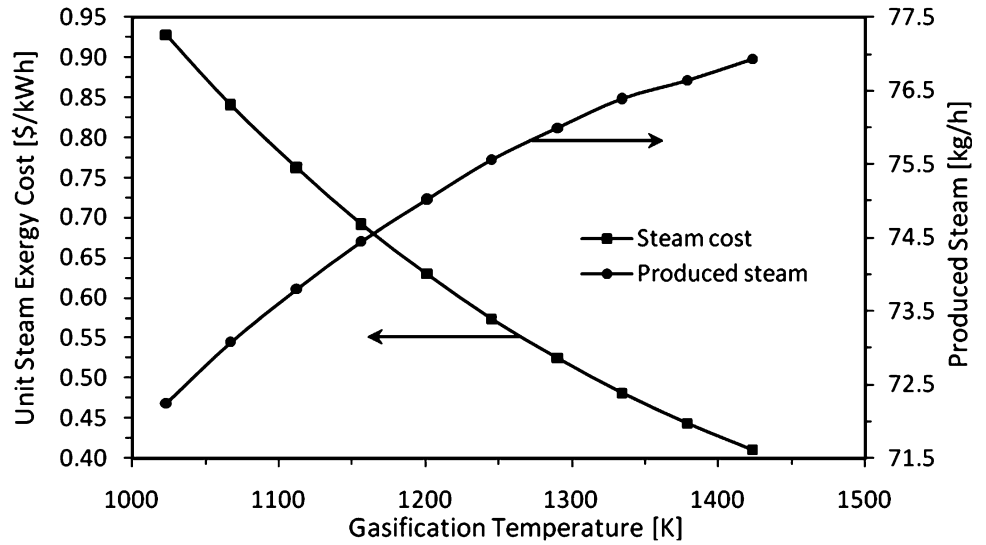
Fig. 5.9 Excess steam and its cost at different gasification temperatures
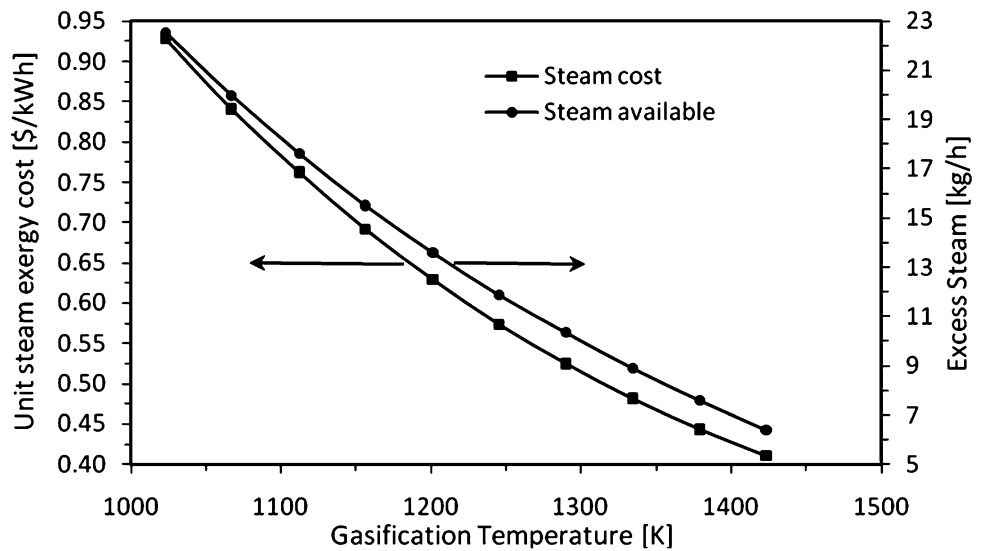
Table 5.5 Unit exergy cost and cost rate for flow material streams

State no.	C [$/kWh]		State no.	C [$/kWh]	[$/h]
0	0.000	0.000	16	0.103	17.390
1	5.2E–06	3.714	17	0.111	18.740
2	0.105	25.170	18	0.111	10.020
3	0.000	0.000	20	0.928	22.300
4	3.769	20.410	21	0.928	2.646
5	0.105	22.720	22	0.135	14.000
6	0.113	25.100	24	0.000	0.000
7	0.161	19.040	25	0.155	3.304
8	0.000	0.000	26	0.137	0.361
9	0.546	2.660	27	0.928	10.100
10	6.175	12.130	33	0.064	11.810
11	0.928	11.120	34	0.071	2.447
13	0.103	7.966	35	0.005	6.220
14	0.928	13.350	36	0.105	24.890
15	0.928	0.004			

Table 5.6 Unit hydrogen cost from different studies

Unit H_2 cost [$/kg]	Unit H_2 cost [$/kWh]	
2.76[a]	0.067	Ogden [9]
3.70[a]	0.094	Richards et al. [10]
10[b]	0.254	Georgi [11]
4.28[c]	0.108	Iwasaki [8]
4.06	0.103	This study

[a]Forming a hydrogen-based fuelling infrastructure depends on vehicular fuel cell and fuelling infrastructure
[b]Electrolysed hydrogen includes capital and operation cost
[c]Hydrogen from wood biomass pyrolysis

Conclusions

The unit cost of exergy streams is calculated regardless of the exergy type, and the results are obtained by considering the total exergy. In addition such a step does not come under the purpose of this study. This study points out the exergy inefficiencies (high exergy destruction), cost formation and cost rate of the system products. By knowing how much a product will cost (according to the desired profit that is planned to achieve), the results of this study can be beneficial to change the sale price of the products and review the system's economic policy. Also, this gives an indication about the cost levels of the components.

Both primary and secondary hydrogen yields increase, and both primary and secondary temperatures increase with increasing of the gasification temperature, while both primary and secondary hydrogen costs decrease, with increasing of the gasification temperature, from 0.103 to 0.045 $/kWh for the primary hydrogen and from 0.064 to 0.039 $/kWh for the secondary hydrogen. Both the steam production from the system and the steam demand in the secondary hydrogen path reactions are increased versus the gasification temperature, while the excess steam is decreased with increasing of the gasification temperature. The steam production increase results in the steam unit cost decrease from 0.928 to 0.410 $/kWh.

The results of this study are validated by such a way that unit exergy cost from primary hydrogen and secondary hydrogen is compared with hydrogen cost from different studies in literature. The results give the indication that the unit cost of hydrogen from this study is reasonable and falls in the acceptable margin, and therefore the system has the potential to compete practically for hydrogen production purposes. The cost calculated in this study is less than those given in other literature studies. This study also has a potential to be used when there is a lack of information to calculate the cost of delivery of hydrogen. For future improvements of the system, a reduction in the exergy destruction needs to be considered especially the components where major exergy destructions take place.

Nomenclature

A	Area (m^2)	Ex_o	Standard exergy (kJ/kmol)
C	Carbon content in biomass (wt %)	h	Specific enthalpy (kJ/kg or kJ/kmol)
c	Cost per unit of exergy ($/kWh)	h_f^O	Standard enthalpy of formation (kJ/kmol)
$\dot{C}$	Exergy cost rate ($/h)	H	Hydrogen content in biomass (wt %)
$\dot{C}_o$	Annualised cost of a component ($/y)	i	Interest rate (%)
C_0	Initial investment cost of a component ($)	j	Salvage ratio (%)
CRF	Capital recovery factor (–)	LHV	Lower heating value (kJ/kg)
Cp	Constant pressure-specific heat (kJ/kg K)	$\dot{m}$	Mass flow rate (kg/s)
$\overline{Cp}$	Constant pressure-specific heat (kJ/kmol K)	N	Nitrogen content in biomass (wt %)
ER	Exchange rate (CA$/US$)	n	Number of moles (kmol) or lifetime of components (years)
Ex	Specific exergy (kJ/kg or kJ/kmol)		
$\dot{Ex}$	Exergy rate (kW)	$\dot{N}$	Molar flow rate (kmol/s)

O	Oxygen content in biomass (wt %)	S_n	Salvage value ($)
P_0	Reference pressure (101.325 kPa)	$\dot{S}$	Entropy generation (kW/K)
Pr	Biomass cost ($/GJ)	T	Temperature (K)
PW	Present worth ($)	T_0	Reference temperature (298 K)
PWF	Present worth factor (–)	U_f	Utilisation factor (–)
R	Universal gas constant (8.314 kJ kmol^{-1} K^{-1})	$\dot{W}$	Power (kW)
s	Specific entropy (kJ/kg K)	X	Mole fraction (–)
$\bar{s}$	Specific entropy (kJ/kmol K)	$\dot{Z}$	Cost of owning and operating a component ($/h)
S	Sulphur content in biomass (wt %)		

Greek Letters

$\emptyset$	Maintenance factor (–)	β	Quality coefficient (–)
τ	Annual component operation time at the nominal capacity (h)		

Subscripts

air	Air	O_2	Related to oxygen
$biomass$	Biomass	ph	Related to physical exergy
ch	Related to chemical exergy	des	Destruction
CO_2	Related to carbon dioxide	Sep	Separator
e	Exit	$SOFC$	Solid oxide fuel cell
f	Fuel	SRR	Steam-reforming reactor
F	Filter	SSR	Steam shift reactor
HE	Heat exchanger	$STACK$	Stack
H_2	Related to hydrogen	t	Turbine
H_2O	Related to water	tar	Related to tar
i	Inlet	W	Power or electricity
o	At reference or ambient or initial		

Superscript

Over dot	Quantity per time	*Over bar*	Quantity per kmol

References

1. Dincer I, Rosen MA (2005) Thermodynamic aspects of renewable and sustainable. Dev Renew Sust Energ Rev 9:169–189
2. Omosun O, Bauen A, Brandon NP, Adjiman CS, Hart D (2004) Modelling system efficiencies and costs of two biomass-fuelled SOFC systems. J Power Sources 131(1–2):96–106
3. Balli O, Aras H, Hepbasli A (2008) Exergoeconomic analysis of a combined heat and power (CHP) system. Int J Energy Res 32:273–289
4. Tsatsaronis G, Winhold M (1985) Exergoeconomic analysis and evaluation of energy-conversion plants-I. A new general methodology. Energy 10:69–80
5. Tsatsaronis G, Pisa J (1994) Exergoeconomic evaluation and optimization of energy systems application to the CGAM problem. Energy 19(3):287–321
6. Kim SM, Doek S, Kwon YH, Kwak HY (1998) Exergoeconomic analysis of thermal systems. Energy 23:393–406
7. Colpan CO, Yesin T (2006) Energetic, exergetic and thermoeconomic analysis of Bilkent combined cycle cogeneration plant. Int J Energy Res 30:875–894
8. Iwasaki W (2003) A consideration of the economic efficiency of hydrogen production from biomass. Int J Hydrog Energy 28:939–944
9. Ogden JM (1999) Developing an infrastructure for hydrogen vehicles: a South California case study. Int J Hydrog Energy 24:709–730
10. Richards M, Liss M (2003) Reformer-based hydrogen fueling station economics. July 2002. In: Iwasaki, W., A consideration of the economic efficiency of hydrogen production from biomass. Int J Hydrog Energy 28:939–944
11. Georgi D (2002) Hydrogen extraction, more than one way to skin the cat. In: Iwasaki W. A consideration of the economic efficiency of hydrogen production from biomass. Int J Hydrogen Energy 2003;28:939–944
12. Abuadala A, Dincer I, Naterer GF (2010) Exergy analysis of hydrogen production from biomass gasification. Int J Hydrog Energy 35:4981–4990
13. Abuadala A, Dincer I (2010) Efficiency evaluation of dry hydrogen production from biomass gasification. Thermochim Acta 507–508:127–134
14. Abuadala A, Dincer I (2012) Investigation of a multi-generation system using hybrid steam biomass gasification for hydrogen, power and heat. Int J Hydrog Energy 35:13146–13157. doi:10.1016/j.ijhydene.2010.08.012

15. Fryda L, Panopoulos KD, Karl J, Kakaras E (2008) Exergetic analysis of solid oxide fuel cell and biomass gasification integration with heat pipes. Energy 33:292–299
16. Hulteberg PC, Karlsson HT (2009) A study of combined biomass gasification and electrolysis for hydrogen production. Int J Hydrog Energy 34:772–782
17. Simell PA, Hirvensalo EK, Smolander ST, Krause AO (1999) Steam reforming of gasification gas tar over dolomite with benzene as a model compound. Ind Eng Chem Res 38:1250–1257
18. Szargut J Morris DR, Steward FR (2007) Exergy analysis of thermal, chemical and metallurgical processes. In: Pellegrini LF, Jr, Oliveira S. Exergy analysis of sugarcane bagasse gasification. Energy 32:314–327
19. Shieh JH, Fan LT (1982) Estimation of energy (enthalpy) and exergy (availability) contents in structurally complicated materials. Energy Sources 6:1–46
20. Turn S, Kinoshita C, Zhang Z, Ishimura D, Zhou J (1998) An experimental investigation of hydrogen production from biomass gasification. Int J Hydrog Energy 23:641–648
21. Cengel YA, Boles MA (2008) Thermodynamics: an engineering approach, 6th edn. Mc Graw Hill Companies, Inc, New York
22. Hyman D, Kay WB (1949) In: Li C, Suzuki K (2009) Tar property, analysis, reforming mechanism and model for biomass gasification-An overview 13:594–604
23. Lowry HH (1963) In: Eisermann W, Johnson P, Conger WL (1979) Estimating thermodynamic properties of coal, char, tar and ash. Fuel Process Technol 3:39–53
24. Eisermann W, Johnson P, Conger WL (1979) Estimating thermodynamic properties of coal, char, tar and ash. Fuel Process Technol 3:39–53
25. Valero A, Lozano MA, Serra L (1994) CGAM problem: definition and conventional solution. Energy 19(3):279–286
26. Gaggioli RA, Wepfer WJ (1960) Exergy economics. Energy 5:823–837
27. Tsatsaronis, G. Application of thermoeconomics to the design and synthesis of energy plants, energy, energy system analysis, and optimization. http://www.eolss.net/ebooks/Sample%20Chapters/C08/E3-19-02-07.pdf
28. Lazzaretto A, Tsatsaronis G (2006) SPECO: a systematic and general methodology for calculating efficiencies and costs in thermal systems. Energy 31:1257–1289
29. Moran MJ, Shapiro HN (2007) Fundamentals of engineering thermodynamics. John Wiley, Inc., New York
30. Calise F, d'Accadia MD, Vanoli L, Von Spakovsky MR (2007) Full load synthesis/design optimization of a hybrid SOFC–GT power plant. Energy 32:446–458
31. Palazzi F, Autissier N, Marechal F, Favrat D (2007) A methodology for thermo-economic modeling and optimization of solid oxide fuel cell systems. Appl Therm Eng 27:2703–2712
32. Penniall CL, Williamson CL (2009) Feasibility study into the potential for gasification plant in the New Zealand wood processing industry. Energy Policy 37:3377–3386
33. Ogden JM (1999) Prospects for building a hydrogen energy infrastructure. Ann Rev Energy Envision 24:227–279

Exergoeconomic Analysis of a Cascade Active Magnetic Regenerative Refrigeration System

6

Hadi Ganjehsarabi, Ibrahim Dincer, and Ali Gungor

Abstract

In this paper, an exergoeconomic analysis of a cascade active magnetic regenerative (AMR) refrigeration system operating on a regenerative Brayton cycle is conducted with respect to various system design parameters. The finite difference method is used in order to solve the set of governing equations, which are highly nonlinear and coupled. In exergy analysis, a thermodynamic model is developed in order to determine exergy destruction rates and calculate the exergy efficiency of the system. In the economic analysis, investment cost rates are calculated with respect to equipment costs, which are determined by cost correlations for each system component, and capital recovery factors. Thus, by combining the two analyses, an exergoeconomic model is created whereby the exergy streams are identified and cost equations are allocated for each component. The results of both exergetic and exergoeconomic analyses show that increasing the fluid mass flow rate decreases the exergy efficiency, and increasing the specific exergetic cooling rate decreases the cost per unit of cooling.

Introduction

Active magnetic regenerative (AMR) refrigeration systems are considered an environmentally benign solution that could be used as an attractive alternative to vapor compression refrigeration systems [1–3]. AMR system utilizes a varying magnetic field, magnetocaloric material (MCM), and heat transfer fluid to facilitate heat transfer between reservoirs.

Barclay et al. [4] presented and patented the active magnetic regenerator refrigeration (AMRR) system in 1982. Barclay [5] showed the possibility of achieving significantly larger temperature spans than the adiabatic temperature rise of the magnetic material by using the magnetic material simultaneously as a heat regenerating medium and as a refrigerating medium. Engelbrecht et al. [1, 2] developed a 1-D transient model of a single regenerator sphere undergoing an idealized passive and active regenerative process and evaluated the impact of the internal temperature gradients and their effect on the performance of the sphere in the context of a regenerative cycle. Aprea et al. [6] have studied the effects of the secondary fluid properties, magnetic material particle diameter, heat transfer fluid blow time, secondary fluid mass flow rate,

H. Ganjehsarabi (✉) • A. Gungor
Faculty of Engineering, Department of Mechanical Engineering, Ege University, 35100 Bornova, Izmir, Turkey
e-mail: hadi.ganjehsarabi@gmail.com; ali.gungor@ege.edu.tr

I. Dincer
Faculty of Engineering and Applied Science, University of Ontario Institute of Technology, 2000 Simcoe Street North, Oshawa, ON, Canada L1H 7K4
e-mail: ibrahim.dincer@uoit.ca

regenerator geometry and axial thermal conduction on the AMRR performance. Their results can be used for the design of new experimental prototypes. Tura et al. [7] evaluated the performance of a permanent magnet magnetic refrigerator (PMMR) with gadolinium parallel plates. Their results show that, in order to obtain both temperature spans and cooling capacities comparable to those obtained with packed spheres, significantly thinner plates and channels are needed. Li et al. [8] studied the impact of the physical properties of heat transfer fluids and operating frequency on the AMRR performance. They determined that a liquid is more favorable than a gas for being used as heat transfer fluid in AMRR systems. Nellis and Klein [9] developed a method in order to examine the effect of the entrained fluid heat capacity in the passive regenerator. They found out that the entrained fluid heat capacity has a significant impact on the performance of a passive regenerator. Rowe [10, 11] derived expressions which describe the thermodynamic quantities of an idealized AMR cycle in steady state. Aprea et al. [12] carried out a comparison between three different models in order to simulate the thermal behavior of an AMR cycle. They found that for all the three models the COP increases with the regenerator's volume. Kitanovski and Egolf [13] suggested that for having high temperature differences cascade or regeneration stages have to be considered. Bjørk et al. [14] proposed an experimental data-based correlation for the total mass and the cost of magnet and MCMs needed to construct a magnetic refrigerator.

The primary objective of this study is to develop a practical model in order to perform both energy and exergy analyses of a cascade AMR cycle. The specific objectives are given as follows:

- To simulate a cascade AMR refrigeration system in order to predict the performance of the overall system.
- To perform energy and exergy analyses of the system, including calculations of the exergy efficiency and exergy destruction of the system.
- To conduct a parametric study of the effects of various selected design parameters on the COP and overall exergy efficiency of the system.
- To develop an exergoeconomic model which determines the cost per unit of cooling with respect to specific exergetic cooling rate.

System Description

The schematic of a cascade AMR system is shown in Fig. 6.1, which consists of two Brayton cycles: (I) the higher-temperature cycle and (II) the lower-temperature cycle. During adiabatic magnetization, the two stages are moved into a magnetic field, where the temperature of the MCMs increases as a result of adiabatic magnetization. In the isofield cooling process, the heat transfer fluid is blown into the second stage from the cold end to the hot end. Subsequently, the fluid flows from the cold end of the first stage to the hot end, while maintaining the magnetic field, absorbs the heat from the both stages and rejects the heat to the surrounding in the hot heat exchanger. In the adiabatic demagnetization process, both stages are cooled by the demagnetization effect. Finally, the fluid moves from the hot end of second stage to the cold end and travels from the hot end of the second stage to the cold end, where it exits at a temperature lower than the cold heat exchanger and produces the cooling power of the system.

The T-s diagram of idealized cascade AMR cycle is shown in Fig. 6.2. The first and second stage materials are $Gd_x Tb_{1-x}$ alloys. The thermo-magnetic properties of the regenerator's compositions are calculated by using the molecular field theory and the Debye approximation. The heat transfer fluid in the simulation is the water–glycol mixture (50 % by weight) (for details see [15]).
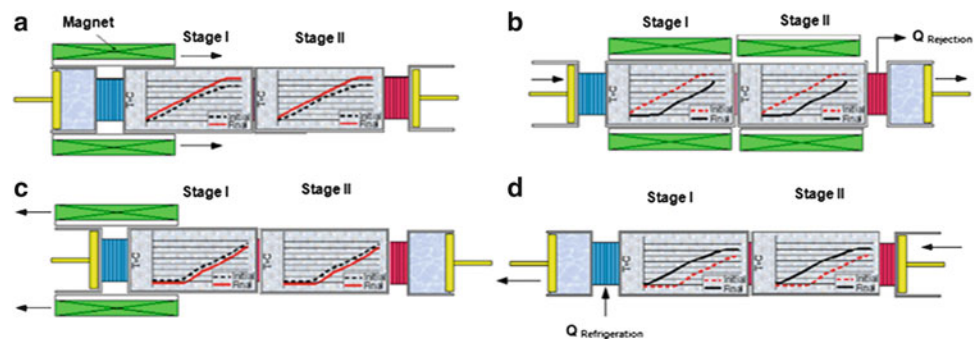
Fig. 6.1 Schematic of a cascade AMR system (**a**) magnetization; (**b**) isofield heating; (**c**) demagnetization; and (**d**) isofield cooling

Fig. 6.2 T-s diagram of the theoretical (ideal) cascade AMR refrigeration system
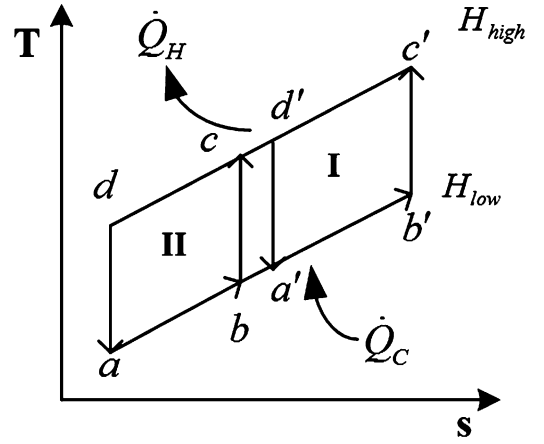
Heat Transfer Modeling

Modeling of Magnetization and Demagnetization Processes

A homogeneous ferromagnetic material model has been used in order to characterize the thermal and magnetic behaviors. The entropy balance equation for the magnetocaloric solid refrigerant and the entrained fluid in the porous matrix is given as follow:

$$ds = m_s \frac{c_s}{T_s} dT_s + \nu_s m_s \left(\frac{\partial M}{\partial T_s} \right)_H dH + m_f ds_f \tag{6.1}$$

In order to study the transient behavior, the mass of the entrapped fluid compared with the mass of the magnetic material is ignored. Therefore, the bed temperature distribution can be calculated by integrating the following differential equation:

$$\left(\frac{\partial T_s}{\partial t} \right) = -\frac{T_s}{c_s} \nu_s \left(\frac{\partial M}{\partial T_s} \right)_H \frac{dH}{dt} \tag{6.2}$$

Modeling of the Isofield Cooling and Isofield Heating Processes

Governing Equations

The mechanism of heat and mass transfer in an AMR bed is complicated; hence, some assumptions must be made in order to establish the governing equations. The several assumptions made in this study are (1) the effect of viscous dissipation on the energy balance of the fluid flow throughout the bed is neglected; (2) the heat transfer fluid is incompressible (ρ_f = constant); (3) the temperature and velocity profile of heat transfer fluid are uniform during the period of flow blowing; (4) the axial heat conduction in the regenerator is neglected; (5) heat loss to the environment in the regenerator is negligible; (6) the properties of magnetic material (except for the specific heat) are constant in the regenerator.

Based on the above assumptions, the energy-balance expression of the heat transfer fluid (f) and the magnetic material (s) can be written as

$$\varepsilon \rho_f c_f A_c \frac{\partial T_f}{\partial t} + \rho_f c_f u A_c \frac{\partial T_f}{\partial x} = h a_{sf} A_c \left(T_s - T_f \right) \tag{6.3}$$

$$(1 - \varepsilon) \rho_s c_s A_c \frac{\partial T_s}{\partial t} = h A_c a_{sf} \left(T_f - T_s \right) \tag{6.4}$$

where the subscripts f and s refer to fluid and solid, respectively. Here, ε is prosity, A_c is the cross-sectional area of the regenerator, c is the specific heat, and a_{sf} is the specific surface area.

Table 6.1 Initial and boundary conditions for the problem

	Magnetization process	Isofield cooling process	Demagnetization process	Isofield heating process
Boundary conditions		$\dot{m}(t) = \dot{m}(0)$		$\dot{m}(t) = -\dot{m}(0)$
		$T_{f_I}(t,0) = T_c$		$T_{f_{II}}(t,L) = T_H$
		$\dfrac{\partial T_f}{\partial x}(t,0) = 0$		$\dfrac{\partial T_f}{\partial x}(t,0) = 0$
		$\dfrac{\partial T_s}{\partial x}(t,0) = 0$		$\dfrac{\partial T_f}{\partial x}(t,L) = 0$
		$\dfrac{\partial T_s}{\partial x}(t,L) = 0$		$\dfrac{\partial T_s}{\partial x}(t,0) = 0$
				$\dfrac{\partial T_s}{\partial x}(t,L) = 0$
Initial conditions	$T_{s_I}(0,x) = T_{s_{I,t_4}}(x)$	$T_{s_I}(t_1,x) = T_{s_{I,t_1}}(x)$	$T_{s_I}(t_1+t_2,x) = T_{s_{I,t_2}}(x)$	$T_{s_I}(t_1+t_2+t_3,x) = T_{s_{I,t_3}}(x)$
	$T_{s_{II}}(0,x) = T_{s_{II,t_4}}(x)$	$T_{s_{II}}(t_1,x) = T_{s_{II,t_1}}(x)$	$T_{s_{II}}(t_1+t_2,x) = T_{s_{II,t_2}}(x)$	$T_{s_{II}}(t_1+t_2+t_3,x) = T_{s_{II,t_3}}(x)$
		$T_{f_I}(t_1,x) = T_{f_{I,t_4}}(x)$		$T_{f_{II}}(t_1+t_2+t_3,x) = T_{f_{II,t_2}}(x)$

The heat transfer coefficient is calculated by using a correlation given by Rohsenow et al. [16]:

$$Nu_f = 2 + 1.1Re_p^{0.6}Pr_f^{1/3} \tag{6.5}$$

where Re_p is the particle Reynolds number for a packed sphere regenerator calculated using particle diameter in a packed sphere and the free flow velocity and Pr is the Prandtl number of the heat transfer fluid.

The cycle of a cascade AMR involves four processes, namely magnetization, isofield cooling, demagnetization, and isofield heating. The initial and boundary conditions for each process are presented in Table 6.1. The cycle begins with magnetization and continues onto the next process. The final values of the dependent variables at the end of each process are the initial conditions for the following process.

Solution Procedure

The set of equations governing the four processes in the regenerator are highly nonlinear and coupled. To solve the governing equations, the equations are discretized in time and the space. An iterative resolution of the Eqs. (6.2)–(6.4) provides the regime solution utilizing a tentative profile temperature of the bed. Before the time step was increased, an inner iteration was performed until the following convergence criterion was satisfied:

$$\delta = Max\left\{ \begin{array}{l} |T_{s_I}(0,x) - T_{s_I}(t_1+t_2+t_3+t_4,x)|, \\ |T_{s_{II}}(0,x) - T_{s_{II}}(t_1+t_2+t_3+t_4,x)| \end{array} \right\} < 10^{-6} \tag{6.6}$$

Thermodynamic Analyses

In this study, the main aim is to address the thermodynamic performance of the cascade AMR refrigeration system and to compare these results in terms of magnetic field and heat transfer fluid mass flow rate. In order to accomplish this, the governing equations and numerical procedures used by Matlab must be outlined in order to obtain sufficient data for the thermodynamic assessment. Finally, these procedures are used to gain insights on the effectiveness of the cascade AMR refrigeration system through energy and exergy analyses.

Energy Analysis

The variations of the fluid and regenerator temperature, cooling capacity, heat rejection, and the rate of magnetic work performed on the regenerator during cyclic steady-state operation are the basic outputs of this model. The cooling capacity and heat rejection to the environment are calculated numerically through the integrals as follows:

$$\dot{Q}_c = \int_{t_1+t_2+t_3}^{t_1+t_2+t_3+t_4} \dot{m}(t)c_f(T_C - T_{f_I}(t,0))dt \tag{6.7}$$

$$\dot{Q}_H = \int_{t_1}^{t_1+t_2} \dot{m}_f(t)c_f(T_{f_{II}}(t,L) - T_H)dt \tag{6.8}$$

where t_1, t_2, t_3 and t_4 are the magnetization time step, cold to hot fluid flow time step, demagnetization time step and hot to cold fluid flow time step. The pressure drop in the heat transfer fluid flow can be obtained by using the Ergun correlation [17]:

$$\frac{dP}{dx} = 180\left(\frac{1-\varepsilon}{\varepsilon}\right)^2 \frac{\mu_f}{d_p}u + 1.8\left(\frac{1-\varepsilon}{\varepsilon}\right)\frac{\rho_f}{d_p}u^2 \tag{6.9}$$

where μ_f and d_P are are the dynamic viscosity of a heat transfer fluid and the particle diameter in a packed sphere. The power required for moving the heat transfer fluid through the regenerator is written as

$$\dot{W}_p = \frac{\dot{m}(t)(\Delta P_{t_2} + \Delta P_{t_4})}{\eta_p \rho_f}(t_2 + t_4) \tag{6.10}$$

The coefficient of performance (COP) of the system can be found as

$$COP = \frac{\dot{Q}c}{\dot{W}_P + \dot{Q}_H - \dot{Q}_c} \tag{6.11}$$

Exergy Analysis

The exergy analysis of the process determines the exergetic variables such as exergy destruction rate and exergy efficiency for a thermodynamic evaluation. The irreversibility in the cascade AMR cycle can be calculated through the exergy destruction rate as follows:

$$\dot{E}x_{des} = \dot{E}x_{in} - \dot{E}x_{out} + \dot{W}_M + \dot{W}_P - \dot{E}x_q \tag{6.12}$$

where $\dot{E}x_q$ is the exergetic cooling power as

$$\dot{E}x_q = \dot{Q}_c\left(\frac{T_H}{T_c} - 1\right) \tag{6.13}$$

The specific exergy cooling of the system can be defined as the ratio of exergetic cooling power to the multiplication of the applied magnetic field, H, and the total volume of refrigerant used, V_{MCM} [18].

$$\mu = \frac{\dot{E}x_q}{HV_{MCM}} \tag{6.14}$$

The exergy efficiency for the cascade AMR refrigeration system can be calculated as follows:

$$\eta_{ex} = \frac{\dot{Q}c}{\dot{W}_P + (\dot{Q}_H - \dot{Q}_c)} \left[\frac{T_H}{T_c} - 1 \right] \tag{6.15}$$

Exergoeconomic Analysis

Economic Model

Exergoeconomics is an exergy-based method that identifies and calculates the location, magnitude, causes, and costs of thermodynamic inefficiencies in an energy conversion system. The real inefficiencies in such a system are the exergy destruction (associated with the entropy generation within a system or a component) and the exergy loss (associated with the transfer to the environment of exergy that is not further being used in this or another system) [19, 20]. The cost balances are generally formulated for each component separately as

$$\sum_e \dot{C}_{e,k} + \dot{C}_{w,k} = \dot{C}_{q,k} + \sum_{in} \dot{C}_{in,k} + \dot{Z}_k \tag{6.16}$$

where

$$\dot{C}_{in} = c_{in}\dot{E}x_{in} \tag{6.17}$$

$$\dot{C}_w = c_w\dot{W} \tag{6.18}$$

$$\dot{C}_q = c_q\dot{E}x_q \tag{6.19}$$

Here, c_i, c_e, c_w, and c_q donate average costs per unit of exergy in dollars per kW ($/kW).

The cost rate expression of Eq. (6.16) can be written as

$$\sum_e \left(c_e\dot{E}x_e \right)_k + c_w\dot{W}_k = c_q\dot{E}x_{q,k} + \sum_{in} \left(c_{in}\dot{E}x_{in} \right)_k + \dot{Z}_k \tag{6.20}$$

where $\dot{Z}_k$ is obtained by first calculating the capital investment and O&M costs associated with the k_{th} component and then calculating these costs per unit of time of system operation.

In the cost balance formulation Eq. (6.16), there is no cost term directly associated with the exergy destruction of each component. Accordingly, the cost associated with the exergy destruction in a component or process is a hidden cost. If one combines the exergy and exergoeconomic balances, one can obtain the following:

$$\dot{E}x_{F,k} = \dot{E}x_{P,k} + \dot{E}x_{D,k} \tag{6.21}$$

The cost rate associated with the exergy destruction within the component is defined as

$$\dot{C}_{D,k} = c_{F,k}\dot{E}x_{D,k} \tag{6.22}$$

where $\dot{E}x_{D,k}$ is the exergy destruction of the component which is evaluated by using exergy balances.

A cost balance applied to the entire system shows that the sum of cost rates associated with all existing exergy stream equals the sum of cost rates of all entering exergy streams plus the appropriate charges due to capital investment and operating and maintenance expenses.

$$c_q\dot{E}x_q = c_{elect}\dot{W}_M + c_{elect}\dot{W}_P + \dot{Z} \tag{6.23}$$

Here C_q, cost per unit of cooling, C_{elect}, is the unit cost of electricity, which is taken as 0.075 \$ kWh^{-1}.

On the economic side, the capital investment can be calculated with respect to the purchase cost of equipment and capital recovery as well as the maintenance factor over the number of operation hours per year as shown below;

$$\dot{Z}_k = \frac{Z_k \cdot \text{CRF} \cdot \varphi}{N \cdot 3600} \tag{6.24}$$

where Z_k is the purchase equipment cost of the magnetic refrigerator components, N is the annual number of operation hours for the unit, and φ is the maintenance factor, which generally taken as 1.06. CRF is the capital recovery factor which depends on the interest rate (i) and equipment life time (n), and is determined here as follows:

$$\text{CRF} = \frac{i \times (1 + i)^n}{(1 + i)^n - 1} \tag{6.25}$$

Results and Discussion

In this study, numerical modeling and a thermodynamic analysis of cascade AMR refrigeration system through energy and exergy is conducted. In this regard, COP and exergy efficiency are examined for performance assessment. The parametric studies considering variation of various design parameter and some performance results are presented accordingly.

The parameters for model inputs that were used in order to carry out the analysis are summarized in Table 6.2. In order to investigate the influence of magnetic field on the cascade AMR cycle, three various magnetic fields (1.5, 1.75 and 2 T) were chosen. The impact of the magnetic field on AMR cycle is investigated in more detail in Bjørk et al. [21]. The temperature distribution along the length of the regenerator during the four processes of the cycle is shown in Figure 6.3. As shown in Figure 6.3 (a), each part of the AMR is magnetized during magnetization process and the temperature of magnetocaloric material increases in proportion to the MCE. During the isofield cooling process, which is illustrated in Figure 6.3 (b), the heat transfer fluid is blown from the cold to the hot heat exchanger, heating up while cooling down the magnetocaloric material in the AMR. In the demagnetization process, which is illustrated in Figure 6.3 (c), every part of the regenerator is demagnetized and the temperature of magnetocaloric material decreases, again in proportion to the MCE. During the isofield heating process, the heat transfer fluid is blown from the hot to the cold heat exchanger, cooling down while heating up the magnetocaloric material in the AMR. Figure 6.4 shows the refrigeration capacity as a function of the fluid mass flow rate for a AMR cascade system. As the fluid mass flow rate increases, the system is capable of producing refrigeration in direct proportion to the mass flow rate, and so the refrigeration capacity increases.

It can be seen that an increase of the mass flow rate increases the refrigeration capacity of the system until a certain value of mass flow rate, after where the cooling capacity of the system decreases. It is because of the mass flow rate becoming too large

Table 6.2 Parameters of the simulation used for numerical analysis

Parameters	Values	Dimensions
d_p	600	μm
L	0.1	m
ε	0.25	–
D	0.01	m
x_1	0.72	–
m_{bd_I}	41.8	g
x_{11}	0.92	–
$m_{bd_{II}}$	41.5	g
$\dot{m}_{wg}$	0.025	kg s^{-1}
H_{low}	0	T
H_{high}	1.5	T
$t_1 = t_3$	0.2	s
$t_2 = t_4$	0.5	s
T_H	293	K
T_C	255	K
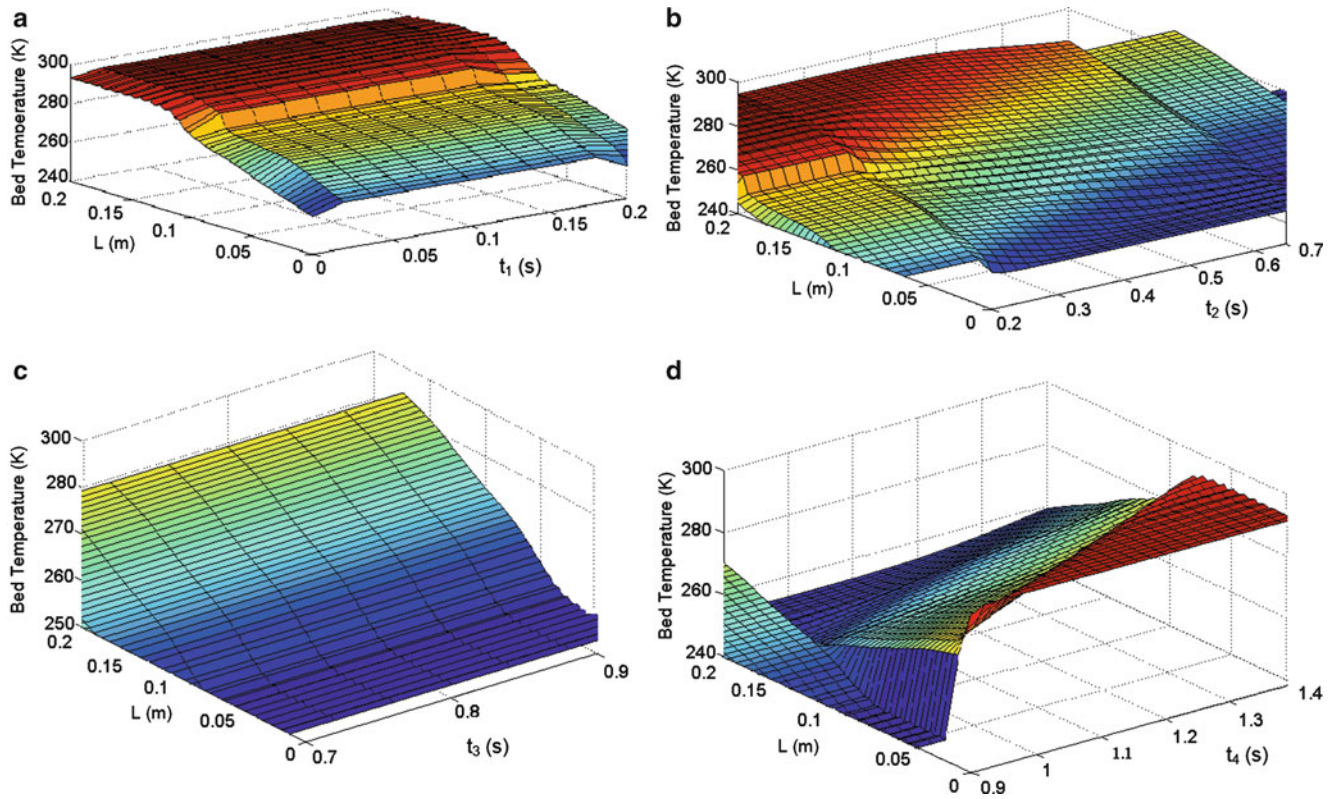
Fig. 6.3 Variation in bed temperature along the length of the regenerator; (**a**) magnetization, (**b**) isofield cooling, (**c**) demagnetization, (**d**) isofield heating

Fig. 6.4 Cooling capacity as functions of fluid mass flow rate at different magnetic field values
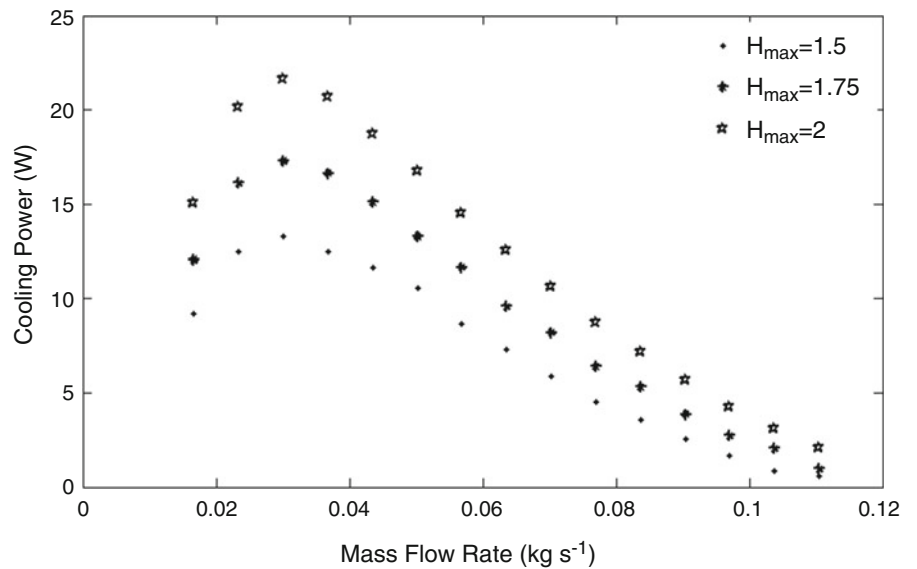
that it overwhelms the magnetocaloric effect exhibited by the bed and, thereafter, the refrigeration capacity is decreased. For cases of H = 1.5, 1.75, 2 T when the increment of magnetic field is $\Delta H = 0.25$ T, the increasing degree of refrigeration capacity is 30.1 and 69.2 %, respectively. The higher the magnetic field strength is, the greater the refrigeration capacity is.

Figure 6.5 shows the general behavior of the COP as a function of the fluid mass flow rate. Figure 6.4 shows that an increase of the fluid mass flow rate decreases the COP due to fluid mass flow rate becoming too large for the regenerator.

Fig. 6.5 COP as functions of fluid mass flow rate at different magnetic field valuesExergy efficiency against fluid mass flow rate at different magnetic field values
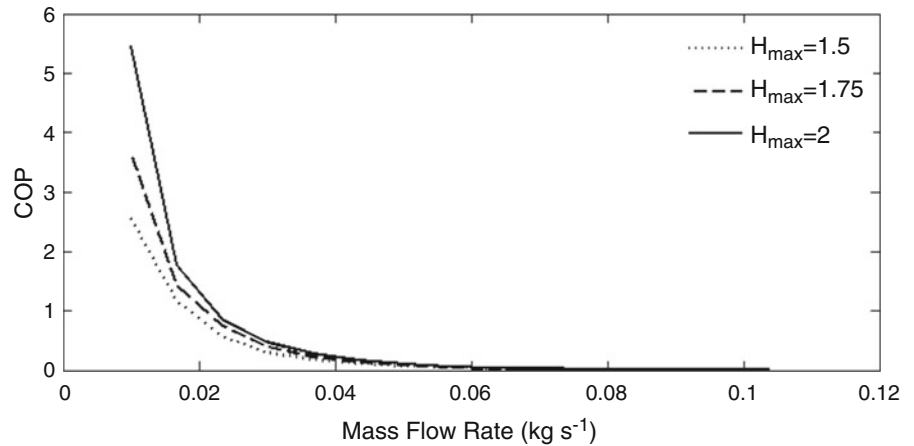
Fig. 6.6 Exergy efficiency against fluid mass flow rate at different magnetic field values
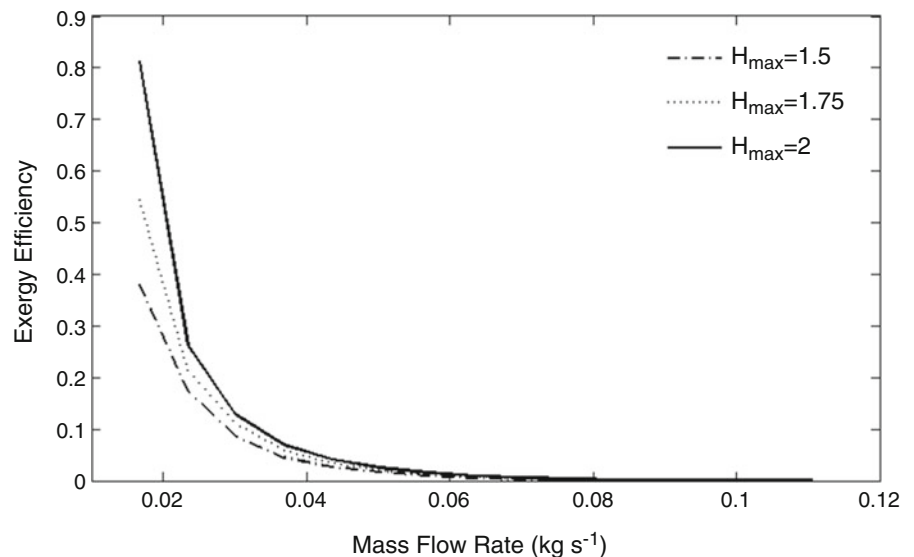
The variations in exergy efficiency with changes in the mass flow rate of heat transfer fluid are presented in Fig. 6.6. According to figure, exergy efficiency drops as the mass flow rate of heat transfer fluid increases for all applying magnetic field. In addition, as magnetic field increases the exergy efficiency increases at any chosen value of mass flow rate.

Figure 6.7 depicts the effect of rising in fluid mass flow rate on the exergy destruction rate inside the regenerator. It is found that when fluid mass flow rate increases, all curves reach their maximum values and then decrease slightly with increasing fluid mass flow rate. On the other hand, excessive mass flow causes to decrease in cooling power and due to increase in work pump resulting in decrease in the cascade AMR performance. Figure 6.8 illustrates the total exergy destruction cost of the system as a function of the fluid mass flow rate. It can be observed that the total exergy destruction cost increases with the increase of the fluid mass flow rate as a result of required pumping power. The analytical results show that in order to reach optimal performance, mass flow rate should be designed carefully regarding various operating conditions.

In this study, an exergoeconomic analysis is also conducted where the cost formation can be determined for the cascade AMR refrigeration system. The cost for the MCM and magnet material is taken to be 20 and 40 $ kg^{-1}, respectively [14]. The variation of cost per unit of cooling with respect to the specific exergetic cooling power at various magnetic fields is shown in Fig. 6.9. It can be observed that an increase in the specific exergetic cooling power causes a decrease in the cost per unit of cooling.

Fig. 6.7 Exergy destruction of regenerator as functions of fluid mass flow rate at different magnetic field values
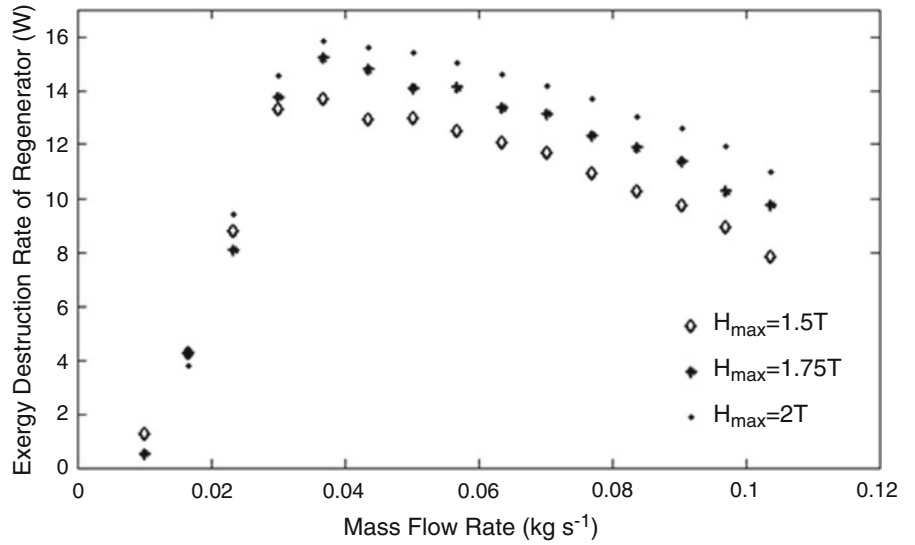
Fig. 6.8 Total exergy destruction cost of the system versus the fluid mass flow rate at different magnetic field values
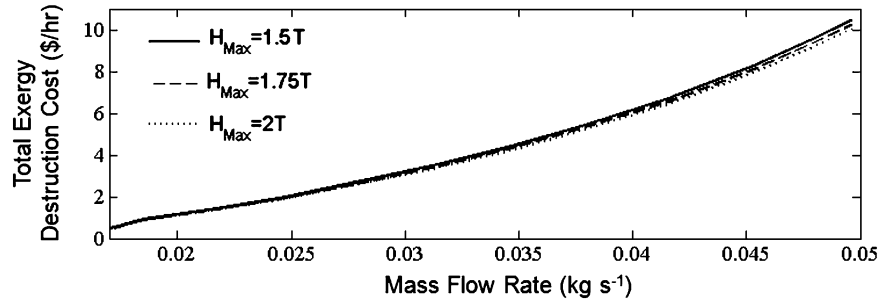
Fig. 6.9 Cost per unit of cooling as functions of the specific exergetic cooling power at different magnetic field values
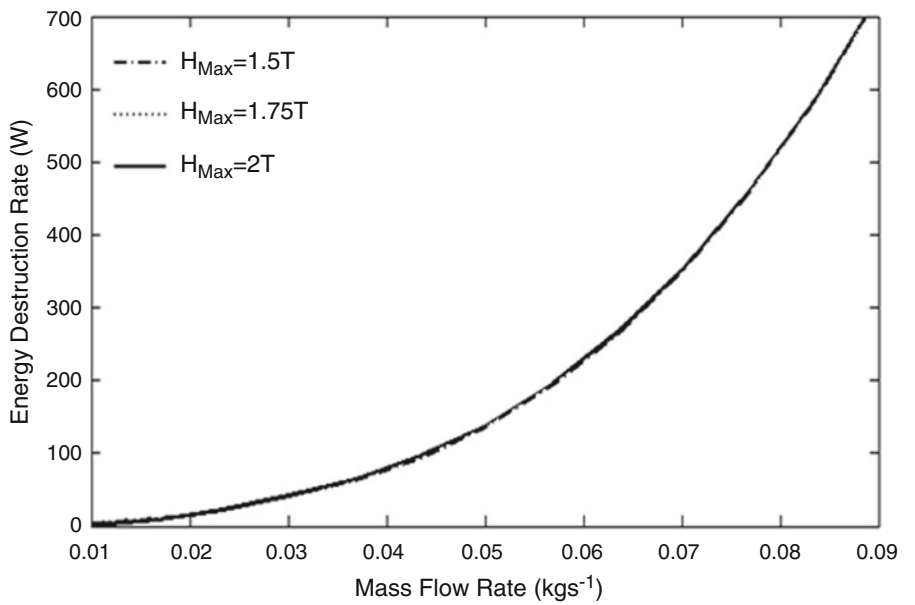
Conclusions

In this study, a mathematical model is developed to investigate the performance characteristics of a cascade AMR refrigeration system. Also, the model was applied in order to predict the cascade AMR performance characteristics at various selected design parameters. The main findings of this study are summarized as follows:

- The refrigeration capacity initially raise at lower mass flow rate up to the point that it attains its maximum value and eventually decrease with the increase of fluid mass flow rate.
- An increase in the magnetic field from 1.5 to 2 T, the COP, and exergy efficiency of the cascade AMR refrigeration increases.
- Both COP and exergy efficiency decreases as the mass flow rate increases.
- An increase in fluid mass flow rate increases the overall exergy destruction cost of the system as a result of pumping power requirements.
- An increase in the specific exergetic cooling decreases the cost per unit of cooling.

Nomenclature

A_c	Cross-sectional area, m^2	Nu	Nusselt number
a_{sf}	Specific surface area, m²/m³	Pr	Prandtl number
c	Specific heat capacity, J kg K^{-1}	$\dot{Q}$	Heat transfer rate, W
COP	Coefficient of performance	Re	Reynolds number
D	Diameter of the regenerator section, m	s	Specific entropy (J kg^{-1} K^{-1})
d_P	Diameter of the particles, μm	t	Time coordinate, s
$\dot{Ex}$	Exergy flow rate (W)	T	Temperature, K
h	Convection coefficient (W m^{-2} K^{-1})	t_1	Magnetization time step (s)
H	Magnetic field, A m^{-1}	t_2	Isofield cooling time step (s)
H_{max}	Maximum magnetic field, A m^{-1}	t_3	Demagnetization time step (s)
k	Thermal conductivity, W m^{-1} K^{-1}	t_4	Isofield heating time step (s)
L	Length of the regenerator, m	V	Volume, L
m	Mass, kg	x	Axial position, m
$\dot{m}$	Mass flow rate, kg s^{-1}	x	Mass fraction
M	Magnetic intensity, A m^{-1}	$\dot{W}$	Work, kJ s^{-1}
MCE	Magnetocaloric effect	ΔP	Pressure drop, Pa
MCM	Magnetocaloric material		

Greek Letters

ε	Porosity of the regenerator bed	η	Efficiency (-)
μ_0	Permeability of free space (m kg s^{-2} A^{-2})	μ	The specific exergy cooling of the system (W T^{-1} L^{-1})
ρ	Density kg m^{-3}		

Subscripts

ad	Adiabatic	M	Magnetization
C	Cold or refrigeration temperature	P	Pump
D	Demagnetization	s	Solid
des	Destruction	t_1	Magnetization process
ex	Exergy	t_2	Isofield cooling process
f	Fluid	t_3	Demagnetization process
H	Hot or heat rejection temperature	t_4	Isofield heating process
I	First stage of the cascade system	wg	Water–glycol mixture
II	Second stage of the cascade system		

References

1. Engelbrecht K, Bahl CRH (2010) Evaluating the effect of magnetocaloric properties on magnetic refrigeration performance. J Appl Phys 108:123918
2. Engelbrecht K, Nellis GF, Klein SA (2006) Predicting the performance of an active magnetic regenerator refrigerator used for space cooling and refrigeration. HVAC&R Res 12:1077–1095
3. Engelbrecht KL, Nellis GF, Klein SA (2006) The effect of internal temperature gradients on regenerator matrix performance. J Heat Transfer 128(10):1060–1069
4. Barclay JA, Steyert WA (1982) Active magnetic regenerator. US Patent No. 4,332,135
5. Barclay JA (1983) Wheel-type magnetic refrigerator. US Patent No. 4,408,463
6. Aprea C, Greco A, Maiorino A (2012) A dimensionless numerical analysis for the optimization of an active magnetic regenerative refrigerant cycle. Int J Energ Res 37:1475–1487
7. Tura A, Nielsen KK, Rowe A (2012) Experimental and modeling results of a parallel plate-based active magnetic regenerator. Int J Refrigeration 35 (6):1518–1527
8. Li P, Gong M, Yao G, Wu J (2006) A practical model for analysis of active magnetic regenerative refrigerators for room temperature applications. Int J Refrigeration 29:1259–1266
9. Nellis GF, Klein SA (2006) Regenerative heat exchangers with significant entrained fluid heat capacity. Int J Heat Mass Transfer 49:329–340
10. Rowe A (2011) Thermodynamics of active magnetic regenerators: part I. Cryogenics 52:111–118
11. Rowe A (2011) Thermodynamics of active magnetic regenerators: part II. Cryogenics 52:119–128
12. Aprea C, Greco A, Maiorino A (2012) Modelling an active magnetic refrigeration system: a comparison with different models of incompressible flow through a packed bed. Appl Thermal Eng 36:296–306
13. Kitanovski A, Egolf PW (2009) Application of magnetic refrigeration and its assessment. J Magn Magn Mater 321:777–781
14. Bjørk R, Smith A, Bahl CRH, Pryds N (2011) Determining the minimum mass and cost of a magnetic refrigerator. Int J Refrigeration 34:1805–1816
15. Aprea C, Greco A, Maiorino A (2011) A numerical analysis of an active magnetic regenerative cascade system. Int J Energy Res 35:177–188
16. Rohsenow WM, Hartnett JP, Ganic ENI (1985) Handbook of heat transfer, vol 6. McGraw-Hill, New York, pp 10–11
17. Kaviany M (1995) Principles of heat transfer in porous media. Springer, New York, 33, 46–47, 130, 228–229
18. Rowe A (2011) Configuration and performance analysis of magnetic refrigerators. Int J Refrigeration 34:168–177
19. Bejan A, Tsatsaronis G, Moran M (1996) Thermal design and optimization. Wiley, New York
20. Dobrovicescu A, Tsatsaronis G, Stanciu D, Apostol V (2011) Consideration upon exergy destruction and exergoeconomic analysis of a refrigerating system. Revista de Chimie 62(12):1168–1174
21. Bjørk R, Engelbrecht K (2011) The influence of the magnetic field on the performance of an active magnetic regenerator (AMR). Int J Refrigeration 34:192–203

Energy and Exergy Analyses of Solar-Driven ORC Integrated with Fuel Cells and Electrolyser for Hydrogen and Power Production

7

Md. Ali Tarique, I. Dincer, and C. Zamfirescu

Abstract

Hydrogen as an energy carrier is an excellent storage medium for harvesting renewable energies which are characterized by hourly fluctuations and intermittence. In this paper a system that integrates an organic Rankine cycle (ORC), electrolyser, hydrogen storage in metal hydrides, and a fuel cell is analyzed thermodynamically for on-demand power generation from solar energy. The system is destined to small-scale applications such as roof-top solar power at low concentration and total collector area of the order of 100 m^2. This will ensure the heating and power needs of an average residence throughout the year. Compound parabolic concentrators are used as vapor generator integrated with an ORC heat engine with cyclohexane working fluid. A small capacity thermal energy storage system is used to keep the working fluid hot during nighttime and eliminate the need of system warm-up in the mornings. The ORC is made to operate continuously and steadily during the daylight to produce power with a solar multiplicity factor of 3. A fuel cell system is used to generate power on-demand from the stored hydrogen. A part of the rejected heat is recovered and used for cogeneration. The system efficiency is determined based on thermodynamic analysis and proved to be attractive.

Introduction

Recent advancement of hydrogen technology forms a promising base for green energy use in many power demanding sectors. Hydrogen being a good energy carrier can be produced by different methods; one of them is the electrolysis of water. Once produced and stored, hydrogen can supply fuel cell systems to generate power on-demand. This infers that the power generation and demand can be decoupled through hydrogen as an energy buffer. Decoupling the generation and demand is especially relevant with renewable energies such as wind and solar which are intermittent and fluctuating.

Solar energy is available everywhere on the earth surface. Depending on the geographic and climacteric conditions the incident solar radiation on the earth surface is typically in the range of approx. 1,600–2,100 MWh/m^2 year. This energy can be converted to approx. 180 MWh/m^2 year electric power available on-demand using electrolysis-fuel cell tandem and hydrogen storage in metal hydrides. Yilanci et al. [1] constructed a small-scale residential system with PEM electrolyser and PEM fuel cell where solar energy is converted using commercially available PV-arrays and showed that the overall efficiency is of the order of 6 %.

One important issue with solar driven power generation is their bad return of investment. The system hardware is in general too costly as compared with the revenues obtained from power generation.

M. Ali Tarique • I. Dincer • C. Zamfirescu (✉)
Faculty of Engineering and Applied Science, University of Ontario Institute of Technology (UOIT),
2000 Simcoe Street North, Oshawa, ON, Canada L1H 7K4
e-mail: calin.zamfirescu@uoit.ca

On the other hand an integration of organic Rankine cycle (ORC), electrolyser, and hydrogen fuel appears to be suitable option to produce electric power on-demand at hundreds of kW generation scale using solar concentrators such as solar through. Again, hydrogen plays the role of an energy buffer which allows for satisfying the nighttime power demand. Because the scale of power generation is larger the initial costs of the hardware which must include single axis solar tracking systems can be reduced and the system made economically viable. This fact is demonstrated by the remarkable worldwide experience gained with solar through technology, see Kearney and Miller [2].

Another competitive system is the solar tower technology which is at the verge of commercialization and—according to Romero et al. [3]—is the most promising for hund reds of MW power generation at sites with annual insolation of around 2,000 MWh/m^2 year.

On the other hand the application of ORC-based concentrated solar power to individual residences imposes that the important simplification of the hardware is made in order to gain market competitiveness. Some encouragement for this green technology application can be provided by the governments through incentives. As shown in Zamfirescu et al. [4] if the government subsidy is 25 % and a feed-in-tariff program is applied then the payback period can be reduced to below 10 year for a small solar dish-based system with 9 m^2 aperture. The ORC system has the ability to provide heating which is an additional benefit as compared to photovoltaic systems.

In this study, a new integrated system with ORC, PEM fuel cell, PEM electrolyser, and metal hydride hydrogen storage which uses compound parabolic concentrator (CPC) with no sun tracking and a thermo-mechanical energy storage to cope with solar radiation fluctuation is investigated. The envisaged application is for residential on-demand power and heating with 100 m^2 roof-top solar collector.

Background

ORC integrated systems with electrolyser and fuel cells have found excellent application for power and heating generation of single residential units when solar radiation is used as an energy input. A simplified diagram showing the integration of ORC with eletrolyser and fuel cell systems is given in Fig. 7.1. The ORC is the system that generates power from a fluctuating source (solar).

Solar energy resource does have some characteristics that lead to technical and economic challenges: generally diffuse, not fully accessible, sometimes fluctuating, intermittent, and regionally variable. The solar radiation is very diffuse with sometimes less radiative power than 500 W/m^2.

For this reason, concentration is required. Imaging concentrators are in general easy to fabricate in the form of heliostat mirrors, solar dishes, solar through, or Fresnel mirrors. They have however the lack of ability of concentrating diffuse radiation and also they require non-cheap sun tracking systems. Compound parabolic concentrators are a non-imaging
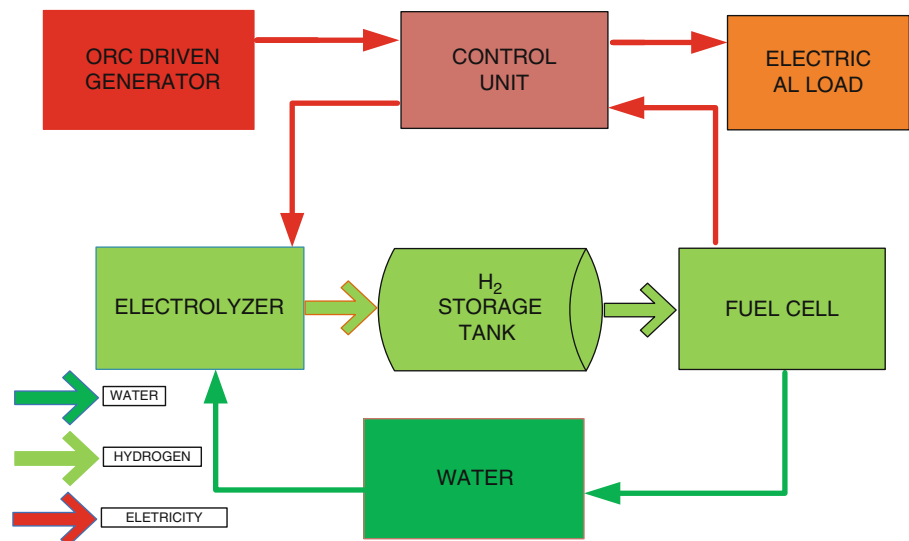
Fig. 7.1 ORC integrated with electrolyser and hydrogen fuel cell

alternative to the common imaging concentrators. These do not require sun tracking and can concentrate on diffuse radiation in addition to the direct beam radiation, but their concentration ratio is limited to 3–5 due to manufacturing considerations.

Rabl [5] compares various types of concentrators for photothermal solar energy conversion with a focus on compound parabolic concentrator (CPC) type. These concentrators act as a radiation funnel and do not have focus. The most important parameters of CPC are the acceptance angle and the average number of reflections. No radiation that enters within the acceptance angle can leave the CPC. The second law of thermodynamics imposes that the maximum possible concentration for a given acceptance half-angle ($\theta_{0.5}$) for line-focus concentrators is given by $n \sin^{-1}\theta_{0.5}$ where n is the index of refraction of the medium surrounding the concentrator. Based on Rabl [5] the heat losses through radiation and convection from CPC are related firmly to the concentration ratio: for $C = 3 \rightarrow U = 3$ W/m^2 K, for $C = 10 \rightarrow U = 1.4$ W/m^2 K.

The manufacture of the reflective area can be made on metal sheets formed parabolically and coated with aluminum or silver. The spectral reflectance becomes important because the concentrator is of non-imaging one. The spectrum of the incident radiation can be taken from the standard ASTM G 173-03 [6] for an air mass 1.5. Once the spectrum and the acceptance angle are specified the incident photon rate and associated energy and exergy rates can be easily calculated.

Small-scale ORCs driven thermally from solar concentrators have been studied in the past in many papers as summarized here based on Zamfirescu et al. [7]. The OMNIUM-G concentrator has a 6 m diameter paneled dish which provided 7–12 kW to a Rankine engine under 1 kW/m^2 insolation. The Test Bed concentrator had an 11 m paneled dish and provided 76 kW to its heat engine under the same conditions. Again, normalized to 1 kW/m^2 insolation, General Electric's Parabolic Dish Concentrator 1 used a 12 m paneled dish to provide 72.5 kW to a heat engine. Power Kinetics had a 9 m square shaped paneled concentrator that delivered 28 kW to a boiler under 0.88–0.94 kW/m^2 insolation. The Acurex Parabolic Dish Concentrator 2 used an 11 m paneled dish and was shown to have an optical efficiency of 0.88 even at concentration ratios as high as 1,300. Boeing decided to create reflector panels and test them using the Test Bed concentrator. These panels were 0.6×0.7 m and provided an optical efficiency of 0.8 up to concentration ratios of 3,000. By comparison, the ENTCH Fresnel Concentrator Lens Panel had dimensions of 0.67×1.2 m^2 and could only provide an optical efficiency of 0.68 at a concentration ratio of 1,500. A small-scale ORC solar dish has been studied based on thermodynamic, ecologic, and economic analyses in Zamfirescu et al. [4].

A single-stage expansion device of positive displacement type can be used instead of an ORC turbine. Scroll expander is a newer promising technology to work as a prime mover in ORC engine for renewable electricity generation. Because of its reliability, compactness, and suitability to work with refrigerant ORC heat engine coupled with scroll expander may be considered a cost effective, environment friendly prime mover for renewable electricity generation. Some recent experimental research and numerical simulation with scroll-based ORC is reported in Hogerwaard et al. [11] and Tarique et al. [8].

System Description and Modeling

The system under study is presented in Fig. 7.2, and its main parts are the ORC heat and engine, electrolyser and fuel cell, the hydrogen storage, and the solar radiation harvesting system. Solar light incident (#1) on the aperture of a number of CPC throughs working in parallel is concentrated (#2) with associated losses (#3).

The thermal receiver is a vacuumed double shell tube that circulates the boiling working fluid cyclohexane through the inner tube. A thermosiphon arrangement with self-regulation of mass flow rate is used in order to cope with fluctuation of solar radiation. The hot working fluid is accumulated in a high temperature liquid–vapor separator. The fluid is retrograde, and thus when saturated vapors are expanded they superheat. A regenerative ORC is used to generate power in (#9) and heating (#21). Power is only generated during the daytime. The system is set such that during the day time at most one-third of the generated power can be consumed whereas two-thirds or more are diverted toward the electrolyser (#10) to generate hydrogen (#14) which is stored in metal hydrides.

During nighttime, hydrogen is consumed (#16) and converted to power (#17) by the PEM fuel cell. The system includes a water treatment unit for makeup water (#12) and a water recycling subsystem that recovers water (#18) from the PEM fuel cell while warming-up (#19) the metal hydride tank for hydrogen release. It is assumed that the system is cooled with water circulated through a ground loop that acts as heat sink.

The thermodynamic modeling of the system is done based on balance equations which are written for each of the subsystems. The exergy and energy flows are evaluated at each state point indicated in the diagram from Fig. 7.2. The AM 1.5 solar spectrum is assumed for incident light based on ASTM G 173-03 [6] for tilted surface at 37°. The global radiation is
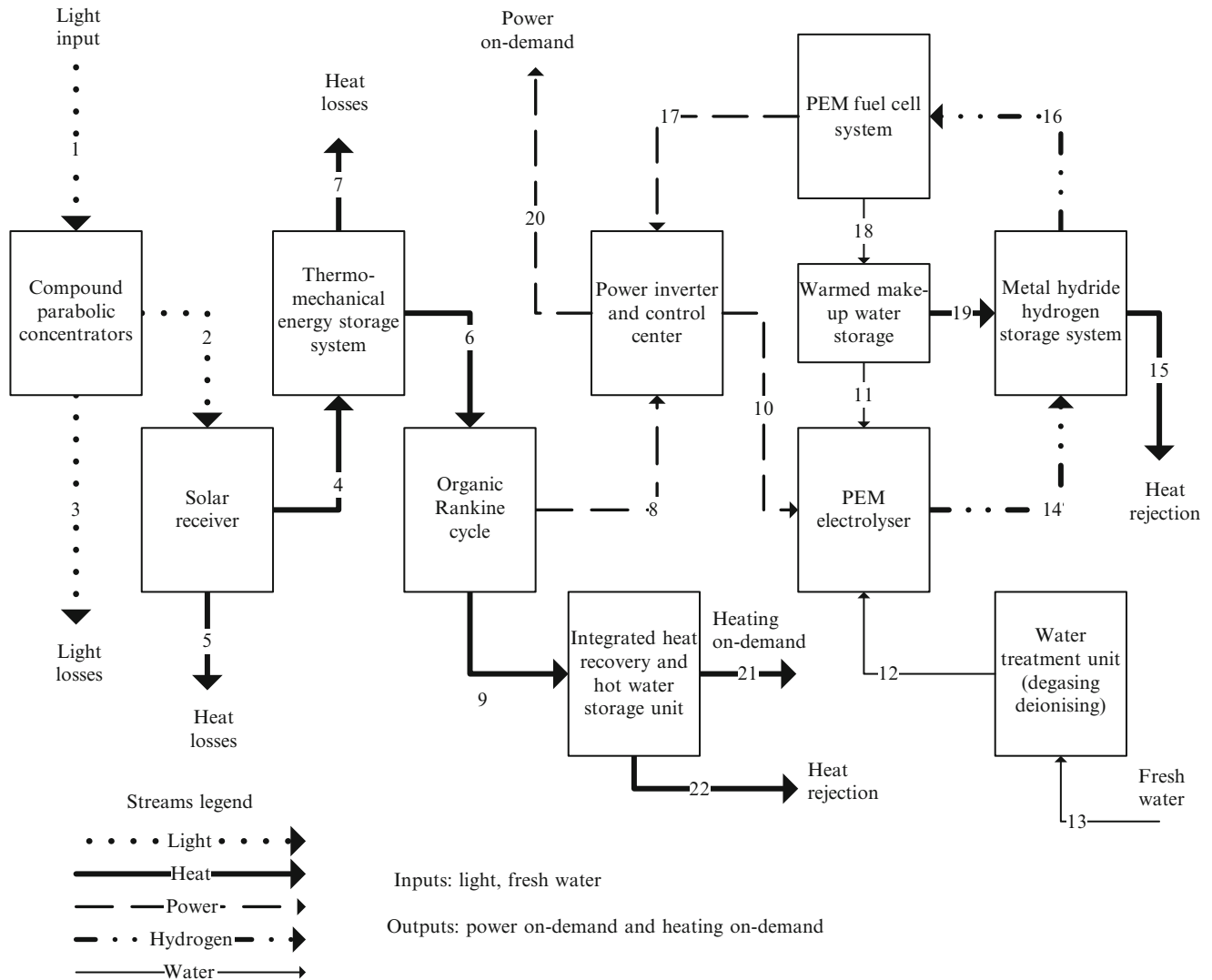
Fig. 7.2 Detailed block diagram representation of the integrated ORC/electrolyser/fuel cell system with hydrogen generation

taken 1,800 MWh/m^2 year which is representative for many locations where single house residences with sufficient roof surface (100 m^2) may exist; the roof must be southward oriented.

Note that the modeling here is made for annual averaged values. If one denotes I_T the incident global irradiation (annual average) on tilt surface, then the incident light is $\dot{E}_1 = I_T A$, where A is the total surface of solar collectors. Table 7.1 gives the energy balance equations for each of the subsystems.

The ORC system is described in Fig. 7.3. A thermally insulated vessel is used to keep the working fluid as saturated liquid–vapor mixture with high temperature. Liquid (#1), which is heavier, flows downwards and reached the solar collector. Since the liquid is hot and close to saturation it boils (#2) in the evacuated tube placed at the CPC aiming spot according to the fluctuating intensity of solar radiation. The generated vapor separates from the liquid and flows (#3) and expands in the turbine. The superheated vapors (#4) of the retrograde working fluid cool and start to condense (#6) reaching liquid in (#9). Some vapor is extracted in (#5) for cogeneration where they condensate according to the heat demand in (#8). The cycle is modeled based on balance equations written for steady operation.

Table 7.1 Energy balance equations, efficiency definition, and description

Component	Energy balance equation and description	Efficiency
CPC	$\dot{E}_1 = \dot{E}_2 + \dot{E}_3$ where $\dot{E}_2 = \frac{\theta_{0,s}}{2\pi}\dot{E}_1$, only a fraction of the incident light is harvested depending on the acceptance angle	$\eta_{CPC} = \dfrac{\dot{E}_2}{\dot{E}_1}$
SR (solar receiver)	$\dot{E}_2 = \dot{E}_4 + \dot{E}_5$ where $\dot{E}_5 = U\frac{A}{C}(T_{SR}\text{-}T_0)$, with U being the heat loss coefficient, T_{SR} receiver temperature, C concentration	$\eta_{SR} = \dfrac{\dot{E}_4}{\dot{E}_2}$
TMS (thermo-mechanical energy storage)	$\dot{E}_4 = \dot{E}_6 + \dot{E}_7$ where $\dot{E}_6 = \dot{m}_{TMS} \times \Delta h_{lv}$ with $\dot{m}_{TMS}$ the mass flow rate of working fluid through thermosiphon loop, x vapor quality at receiver exit, Δh_{lv} the latent heat of boiling. Heat loss $\dot{E}_7 = (UA)_{loss}(T_6\text{-}T_0)$	$\eta_{TMS} = \dfrac{\dot{E}_6}{\dot{E}_4}$
ORC	$\dot{E}_6 = \dot{E}_8 + \dot{E}_9$ the ORC is described separately in Fig. 7.3. The pump and turbine isentropic efficiency is assumed 0.8	$\eta_{ORC} = \dfrac{\dot{E}_8}{\dot{E}_6}$
PIC (power inverter and control)	$\dot{E}_8 + \dot{E}_{17} = \dot{E}_{10} + \dot{E}_{20}$ the inverter produces a.c. current in #20 to supply the local grid, whereas it processes d.c. current at #8, #10, #17. When demand is high, fuel call and ORC can work together during the day. ORC never operates nighttime	$\eta_{PIC} = \dfrac{\dot{E}_{10}}{\dot{E}_8} = \dfrac{\dot{E}_{20}}{\dot{E}_8 + \dot{E}_{17}}$
PEME (electrolyser)	$\dot{E}_{10} = \dot{E}_{14} + \dot{Q}_{loss}$ heat loss is released into the environment	$\eta_{PEME} = \dfrac{\dot{E}_{14}}{\dot{E}_{10}}$
FC (fuel cell)	$\dot{E}_{16} = \dot{E}_{17} + \dot{E}_{loss}$ where $\dot{E}_{loss} = \dot{Q}_{19}$ heat released through the water is recovered and used to heat the hydride tank	$\eta_{FC} = \dfrac{\dot{E}_{17}}{\dot{E}_{16}}$
HR (heat recovery)	$\dot{E}_9 = \dot{E}_{21} + \dot{E}_{22}$ a part of the heat rejected by the ORC is recovered and used for water (or space) heating	$\eta_{HR} = \dfrac{\dot{E}_{21}}{\dot{E}_9}$
SYS (overall)	$\dot{E}_1 = \dot{E}_{20} + \dot{E}_{21} + \dot{E}_{loss}$	$\eta = \dfrac{\dot{E}_{20} + \dot{E}_{21}}{\dot{E}_1}$

Fig. 7.3 The ORC system and the thermosiphon configuration of solar collector
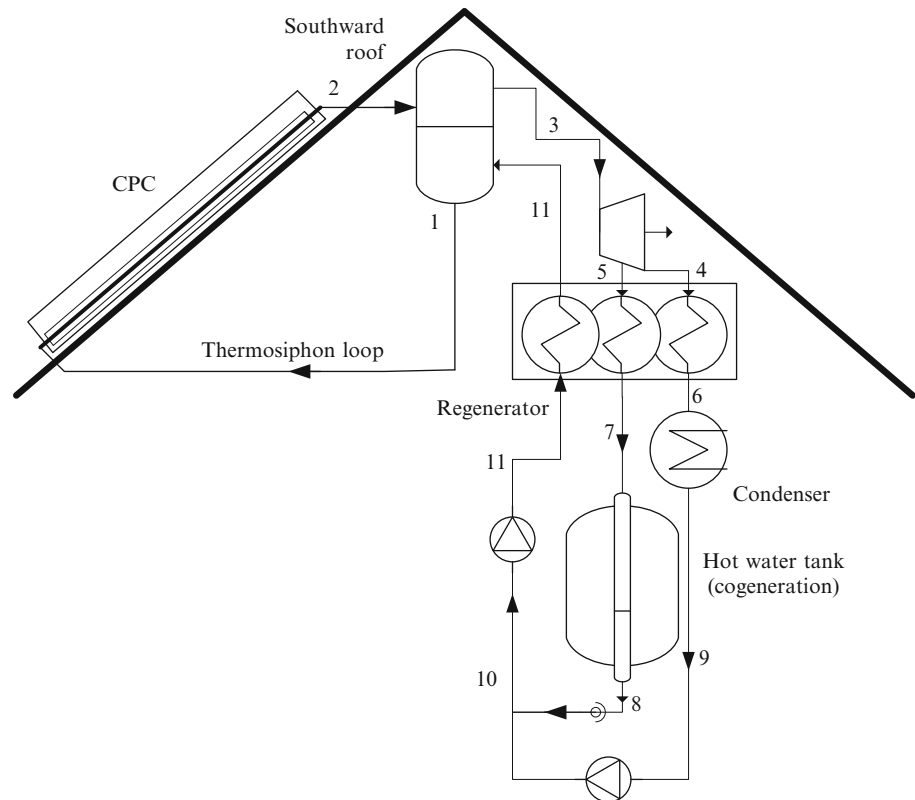
Results and Discussion

For a case study with the ORC/electrolyser/fuel cell system described in Figs. 7.2 and 7.3 a set of reasonable values for modeling parameters is assumed as given in Table 7.2. The core of the system is formed by the ORC and its thermosiphon look. Henceforth, the ORC is calculated first and the thermodynamic cycle is determined. This cycle operates between the ground loop temperature and the solar collector temperature. This imposes a condensation at $T_6 = T_9 = 20\,°C$ and a boiling temperature $T_1 = T_2 = T_3 = 120\,°C$ (see Table 7.2).

The thermodynamic cycle is illustrated in Fig. 7.4. The cycle efficiency is $\eta_{ORC} = 28\,\%$ if no heat is cogenerated. The ORC efficiency depends on the amount of cogenerated heat (the heat demand). Note that the ORC self-regulates according to the heat demand. When there is no heat demand there is no cooling in the branch 7–8 of the system (Fig. 7.3). Vapor accumulates and the extracted fraction must reduce because the pressure on the branch tends to increase. When there is heat demand, then there is also good condensation and the extraction fraction tends to increase.

We introduce the parameter *HWR*—heat to work ratio—which represents the ratio between heat cogenerated and the work generated. When this parameter is varied from 0 to 3 the ORC power efficiency degrades but more heat is recovered and delivered as useful product. Therefore the cogeneration efficiency increases. Figure 7.5 shows this parametric study. In addition is indicated the variation of extraction fraction f. When there is no extraction, then there is no cogeneration. If extraction fraction is ~0.5 then the cogeneration efficiency becomes more than 80 % even though the ORC efficiency for power generation degrades to 22 %.

As mentioned in a previous study by Zamfirescu et al. [4] the power demand in a typical residence in Ontario is of the order of 22 kWh/day whereas the annually averaged heating demand is of 53 kWh/day. Therefore, if one assumes $HWR \cong 2$ we have according to Fig. 7.4 that $\eta_{ORC} = 25\,\%$, $\eta_{HR} = 70\,\%$, and the vapor extraction fraction is $f = 38\,\%$.

Table 7.2 System parameters assumed for a case study

Half acceptance angle of CPC	$\theta_{0.5} = 60°$
Average reflections number	$n_r = 1.1$
Concentration ratio CPC	$C = 5$
Total aperture area	$A = 100\ \mathrm{m}^2$
Annual irradiation amount	$I_T = 1,800\ \mathrm{MWh/m}^2$ year
Water heating temperature	$T_8 = 60\,°C$ (Fig. 7.3)
Collector temperature	$T_1 = T_2 = T_3 = 120\,°C$
Condensation temperature	$T_6 = T_9 = 20\,°C$
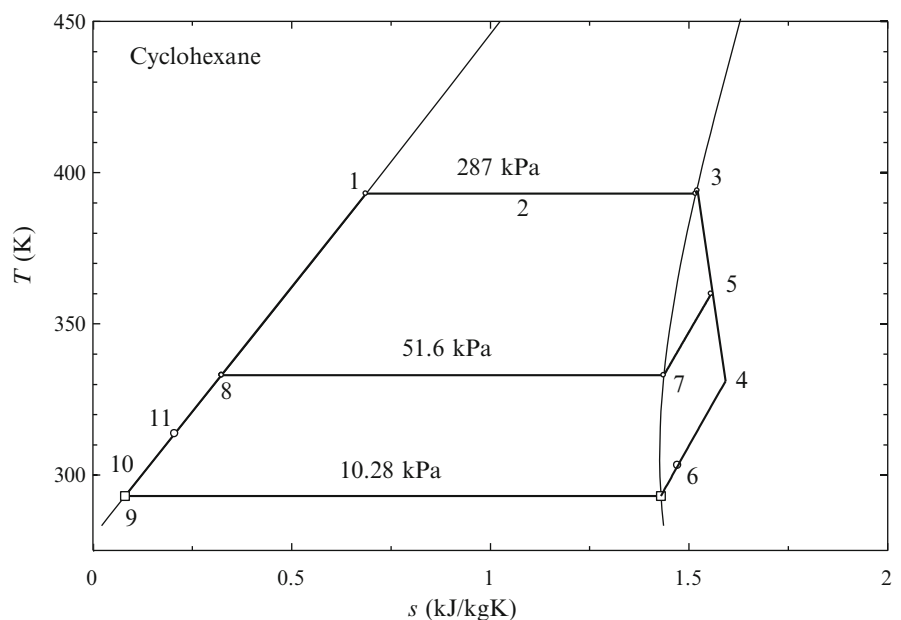
Fig. 7.4 Thermodynamic cycle of the cyclohexane-based ORC with cogeneration

Fig. 7.5 Energy efficiency of ORC, heat recovery, and cogeneration and the vapor extraction fraction vs the heat to work ratio
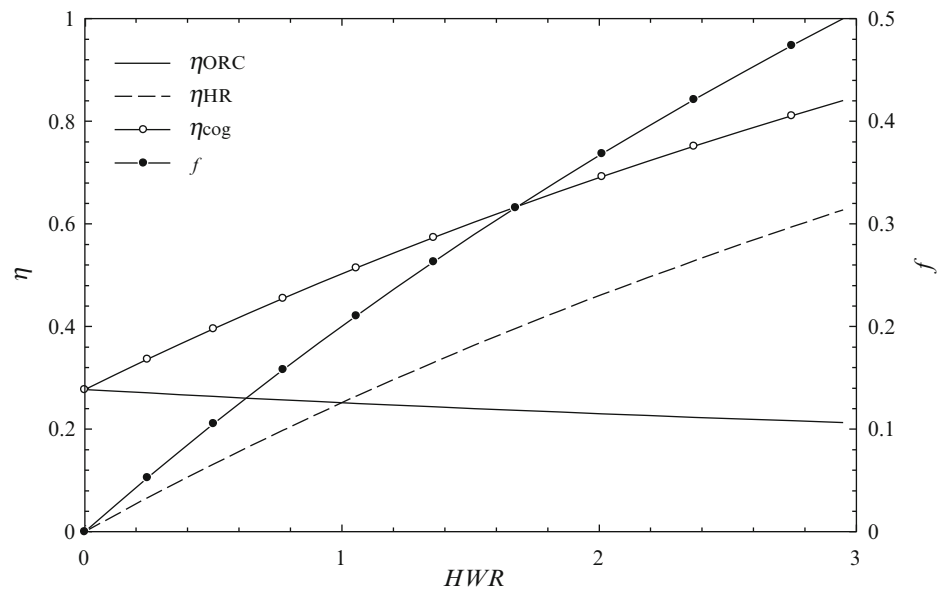
Table 7.3 The calculated geometrical parameters for the required three-stage scroll expander

Parameter	Stage 1	Stage 2	Stage 3
$\varphi_{o,0}$ (rad)	0.1	0.1	0.2
$\varphi_{i,0}$ (rad)	1.3	1.4	1.5
φ_e (rad)	$18\,\pi$	$18\,\pi$	$18\,\pi$
h_{vane} (mm)	20	40	40
r_b (mm)	2	5	10
r_o (mm)	4	10	20

Due to the high expansion ratio a three-stage scroll expander is necessary. The expansion ration is simple to calculate from the thermodynamic cycle analysis; it is of five per stage. The first stage corresponds exactly to the vapor extraction point and the other two stages are cascaded. The built-in-volume ratio of the scroll expander can be estimated as indicated in Oralli et al. [9]. The BVR depends on the rolling angle of the scroll φ_e and the initial angles for the inner φ_{i0} and outer φ_{o0} involute, respectively. The built-in-volume ratio is given by:

$$BVR = \frac{2\varphi_e - \varphi_{i0} + \varphi_{o0} - 3\pi}{5\pi - \varphi_{i0} + \varphi_{o0}}$$

The calculated parameters that define the scroll geometry for each stage are shown in Table 7.3. In the table the initial involute angles, the rolling angle, the vane height, the base (r_b), and the orbiting (r_o) radii are given.

For estimation of the overall system efficiency, the required balance equations are solved for each system component. In Table 7.4 the efficiency results are given. For the CPC the required half acceptance angle has been taken as 60°. Henceforth, one-third of the diffuse radiation is accepted by the CPC. Since the global radiation is assumed to 1,800 MWh/m^2 year and for AM 1.5 the direct beam radiation is 90 % of the global radiation, it results that the CPC will accept 180 MWh/m^2 year diffuse radiation. The CPC orientation is toward equator in tilt position. Since the average daylight is from 6 am to 6 pm it means that the CPC sees the sun from 8 am to 4 pm, therefore it accepts two-thirds of the direct beam radiation. Therefore, 1,200 MWh/m^2 year are received from direct beam and 1,380 MWh/m^2 year is the total accepted radiation. Henceforth, the CPC efficiency is 1,200/1,800 = 66.6 %.

On the basis of 1,800 MWh/m^2 year the generated power can be calculated if one assumes that one-third of it is produced during daylight with an efficiency of $\eta_{PG} = 14.9$ % while two-thirds are generated with an efficiency of $\eta_{ODPG} = 3.7$ %. Therefore, one calculates for 10 m^2 collector area $0.149 \times 0.667 \times 1,800 \times 10 = 1,790$ MWh power generation. For heat generation one obtains 5,652 MWh/ year. Therefore the system efficiency that use both direct power production during daylight and fuel cell power generation at nighttime is 41.3 %, whereas the power only efficiency of the system calculated in similar way is 9.94 %.

Table 7.4 Energy efficiencies of the system and its components

Component	Assumptions and remarks	Efficiency
CPC	AM 1.5 spectrum at 120° acceptance angle	$\eta_{CPC} = 66.7\ \%$
SR	Heat loss coefficient $U = 3\ \text{W/m}^2\ \text{K}$	$\eta_{SR} = 95\ \%$
TMS	Assume 1 % heat loss	$\eta_{TMS} = 99\ \%$
ORC	Determined according to Fig. 7.5	$\eta_{ORC} = 25\ \%$
PIC	Assume electrical losses of 5 % as shown in Yilanci et al. [1]	$\eta_{PIC} = 95\ \%$
PEME	Assume practical value at optimal current density as in Yilanci et al. [1]	$\eta_{PEME} = 50\ \%$
FC	Assume practical value at optimal current density as in Naterer et al. [12]	$\eta_{FC} = 50\ \%$
HR	Determined according to Fig. 7.5	$\eta_{HR} = 50\ \%$
SYS	The following system efficiencies are calculated: • Power generation efficiency $\eta_{PG} = \eta_{CPC}\eta_{SR}\eta_{TMS}\eta_{ORC}\eta_{PIC}$ • Hydrogen generation efficiency $\eta_{H_2} = \eta_{PG}\eta_{PEME}$ • On-demand power generation efficiency $\eta_{ODPG} = \eta_{H_2}\eta_{FC}$ • Heat generating efficiency $\eta_{HG} = \eta_{CPC}\eta_{SR}\eta_{TMS}\eta_{HR}$ • Cogeneration efficiency $\eta_{SYS} = \eta_{ODPG} + \eta_{HG}$	$\eta_{PG} = 14.9\ \%$ $\eta_{H_2} = 7.5\ \%$ $\eta_{ODPG} = 3.7\ \%$ $\eta_{HG} = 31.4\ \%$ $\eta_{SYS} = 35\ \%$

Concluding Remarks

In this chapter an integrated system that combines ORC, electrolyser, and fuel cell technology is investigated for energy harvesting from a fluctuating renewable source—the solar energy. The preferred choice of solar collector is CPC because it does not require solar tracking, it is of non-imaging type, and therefore it is able to harvest a good amount of diffuse radiation. The calculations for the system have been done for 1 year average, rather than hourly. It results that the combined efficiency of power and heat production is 41.3 % whereas the power only efficiency is approx. 10 %. In conclusion, as compared to other systems, the proposed integration scheme is promising and it is worth further investigation.

Nomenclature

A	Area, m^2	n	Refraction index
BVR	Built-in volume ratio	r	Radius, m
C	Concentration ratio	T	Temperature, K
$\dot{E}$	Energy rate, kW	U	Overall heat transfer coefficient, $\text{W/m}^2\ \text{K}$
I	Irradiance, W/m^2		

Acronyms

CPC	Compound parabolic concentrator	PIC	Power inverter and control center
FC	Fuel cell	SR	Solar receiver
HR	Heat recovery	SYS	Overall system
ORC	Organic Rankine cycle	TMS	Thermo-mechanical storage
PEME	Proton exchange membrane electrolyser		

Greek Letters

θ	Half acceptance angle	ϕ	Rolling or involute angle
η	Energy efficiency		

Subscripts

0	Reference state	loss	Losses
1	Initial	o	Outer, orbiting
b	Base	T	Tilt surface
i	Inner		

References

1. Yilanci A, Dincer I, Ozturk HK (2008) Performance analysis of a PEM fuel cell system. Int J Hydrogen Energy 33:7538–7552
2. Kearney D, Miller C (1988) Solar electric generating system VI – technical evaluation of project feasibility. LUZ Partnership Management, Inc.: January 15
3. Romero M, Buck R, Pacheco JE (2002) An update on solar central receiver systems, projects, and technologies. ASME J Solar Energy Eng 124:98–108
4. Zamfirescu C, Dincer I, Verrelli T, Wagar WR (2012) Exergetic, environmental and economic analyses of small-capacity concentrated solar driven heat engines for power and heat cogeneration. Int J Energy Res 36:397–408
5. Rabl A (1976) Comparison of solar concentrators. Solar Energy 18:93–111
6. ASTM G 173-03 (2012) Standard tables for reference solar spectral irradiances: direct normal and hemispherical on 37° tilted surface. http://rredc.nrel.gov/solar/spectra/am1.5/. Accessed May 2013
7. Zamfirescu C, Dincer I, Verrelli T, Wagar WR (2008) Residential solar power generation systems for better environment. In: Global conference on global warming, Istanbul, July 6–10, paper #805
8. Tarique Md A, Dincer I, Zamfirescu C (2014) Experimental investigation of a scroll expander for an organic Rankine cycle. Int J Energy Res (in press)
9. Oralli E, Tarique Md A, Zamfirescu C, Dincer I (2010) Modeling and analysis of a scroll compressor conversion into expander for Rankine cycle. In: Second international conference on nuclear and renewable energy resources, Ankara, 4–7 July
10. Zamfirescu C, Dincer I (2014) Performance assessment of a new integrated solar energy system for hydrogen production. Solar Energy (in press)
11. Hogerwaard J, Dincer I, Zamfirescu C (2012) Analysis and assessment of a new organic Rankine cycle with/without cogeneration. Energy the International Journal 62:300–310
12. Naterer GF, Dincer I, Zamfirescu C (2013) Hydrogen production from nuclear energy. Springer, New York, NY, p 504

Application of Scroll Expander in Cryogenic Process of Hydrogen Liquefaction

Md. Ali Tarique, I. Dincer, and C. Zamfirescu

Abstract

Hydrogen is a clean energy carrier and can be a potential alternative of fossil fuels. Its use in energy systems needs efficient storage for on-demand distribution to the facilities. However, storage of hydrogen as a gas needs large storage tank which is not feasible due to a high volume to energy ratio. By liquefying hydrogen this barrier of storing can be solved. In this paper, a modification to Claude liquefaction process of hydrogen is proposed for increased efficiency. More specifically, the Joule–Thompson valve of the typical Claude cycle is replaced with an expander for work recovery. In addition, the integration of an additional expander is found suitable to recover more work from the expanding hydrogen. However, consideration was made in selecting expanders as it involves two-phase flow. Scroll expander being capable of operating with two-phase fluid is suitable to use in this cycle for cryogenic hydrogen liquefaction. This paper presents an analytical feasibility study of the scroll expanders integration with a modified Claude cycle. The result shows that a 2–3 % work recovery is possible with the integration of the expanders which justifies further study on the process with more detailed analysis and optimization methods. The expansion power that is recoverable is of the order of 1–5 kW. The paper concludes that the scroll expander can be used for work recovery in other cryogenic applications which becomes increasingly more important.

Keywords

Liquefied hydrogen • Modified Claude cycle • Scroll expander • System integration

Introduction

Hydrogen being a promising energy carrier of the future requires suitable methods of storage which have to be as compact form as possible. Due to its large specific volume, either very high pressures or cryogenic temperatures are required for hydrogen storage as compressed gas or as liquid, respectively.

The gas liquefaction technology emerged in the last decades of the nineteenth century and became mature at the beginning of the twentieth century. According to Nandi and Sarangi [1] the followings are the main industrial processes to obtain liquefied hydrogen: (1) the Precooled Linde–Hampson process; (2) the Claude process; and (3) the helium–hydrogen cycle.

Hydrogen has its normal boiling point at 20.3 K with the density of the saturated liquid of 70.77 kg/m^3. Some peculiar problems occur in the liquefaction process, namely: (1) hydrogen has a positive Joule–Thompson coefficient at temperature higher than 190 K, (2) there is an *ortho–para* hydrogen conversion process that happens at 20 K and adds to the latent heat of 450 kJ/kg, an amount of 530 kJ/kg, (3) the latent heat of boiling of para hydrogen at 20 K is relatively very low; therefore, any small heat penetration can generate important amounts of hydrogen vapor.

M. Ali Tarique • I. Dincer • C. Zamfirescu (✉)
Faculty of Engineering and Applied Science, University of Ontario Institute of Technology (UOIT),
2000 Simcoe Street North, Oshawa, ON, Canada L1H 74K
e-mail: calin.zamfirescu@uoit.ca

In a typical process hydrogen is cooled to 80 K with the help of liquid nitrogen. For further cooling hydrogen itself is used as working fluid in a cryogenic refrigerator. Due to the auxiliary systems and irreversibility the energy required to liquefy hydrogen is as high as approx. 50 MJ/kg which represents about a third of the higher heating value.

It is becoming increasingly important to devise methods and technologies for hydrogen liquefaction from small to large scale with improved efficiency and less energy consumption. Some recent efforts of development of large-scale liquid hydrogen production and long-term storage are presented by Domashenko et al. [2]. An innovative method which uses the latent heat of natural gas for hydrogen liquefaction is disclosed in Ogawa et al. [3]. Kanoglu et al. [4] studied the ways of using geothermal energy for hydrogen liquefaction. It is suggested that the best way of doing this is by using a part of the geothermal energy to drive an absorption cycle which pre-cools the hydrogen gas, and a second part of the geothermal energy to generate electricity which drives the liquefaction plant.

The use of renewable energy to drive the process brings definitely substantial environmental advantages. The renewable energy is most relevant at small and intermediate scale of hydrogen liquefaction. In such system, 1–5 kW of recovery of compression work may be very beneficial as it enhances the system efficiency while reducing the cryogenic hydrogen cost. The selection of the thermodynamic cycle is based on the size of the plant, the available technology, the cost of the equipments, and above all the efficiency of the cycle.

Recent advancement on prime movers brings to attention the scroll expanders which have the ability to efficiently expand two-phase flows and produce net power in a range from few hundreds watts to few kW. As argued in Quoilin et al. [5] the use of scroll expanders in this power range is more advantageous than the use of turboexpander especially when the expansion occurs well in the two-phase region. Hung [6] showed that the positive displacement expanders could be built with high pressure ratio per stage. Scroll machine, a form of positive displacement machine is widely used in refrigeration industry mainly as a compressor. However, with a little modification it can easily work in reverse as an expander. Oralli et al. [7] performed an analysis on conversion of refrigeration scroll compressor to work as an expander for power generation. They demonstrated that scroll expander converted from refrigeration compressor is quite suitable to work as an expander.

Scroll machine consists of two identical intermeshing spiral elements placed in a drum-like, air-tight chamber with a phase difference of 180°. One of the scrolls is rigidly attached to the drum, while the other one orbits within it during the operation. A rotor shaft is attached to the moving scroll and may be coupled to the load (compressor/generator). The set orbiting position of the moving scroll is maintained by a special device known as "Oldham coupling." With the movement of the moving scroll, the outer periphery forms a line of contact with the fixed scroll forming a crescent shaped pocket. This pocket acts as the cavity of the gas.

The high pressure gas enters through a port in the scroll center. This high pressure gas generates forces on the scroll vanes which translates into torque and produces an orbiting movement. The orbiting movement of the scroll transfers the gas to two adjacent vanes and forms two symmetrical pockets. The trapped gas pockets further expand, forcing the orbiting scroll to move around the center of the fixed scroll thus transmitting the rotating motion to an eccentric shaft. The pockets finally break up at the periphery of the scroll and discharge through the exhaust port. Several pairs of symmetrical pockets of increasing volumes co-exist at any time during the expander operation. Advantage of scroll expander over turbine is that the scroll machine is compact, with less rotating parts and at single stage, the volume ratio is higher.

The efficiency of the whole hydrogen liquefaction process is determined by the thermodynamic efficiency of the cycle and the performance of the equipments used. The selection of the equipments, their cost, influence highly the system performance and viability of the system. In this paper, analysis has been made on the use of scroll expander as an expansion device instead of a Joule–Thompson valve for work recovery integrated with Claude liquefaction process.

System Description and Modeling

In Fig. 8.1 the modified Claude cycle which includes two-scroll expanders for work recovery is shown. The first expander is positioned between states #3 and #4 in the diagram and the second expander replaces the typical Joule–Thompson valve of the basic Claude, process 6–7. The expansion processes in this way can recover maximum work but has more chances to face two-phase expansion or in extreme cases wet expansion in the second expander.

The process starts with precooled hydrogen at 190 K (1 bar) which is obtained using the cooling effect of liquid nitrogen. As it results from the schematics hydrogen is compressed to 40 bar in #2, then cooled in subsequent processes #3 → #5

Fig. 8.1 Modified Claude process for hydrogen liquefaction with work recovery
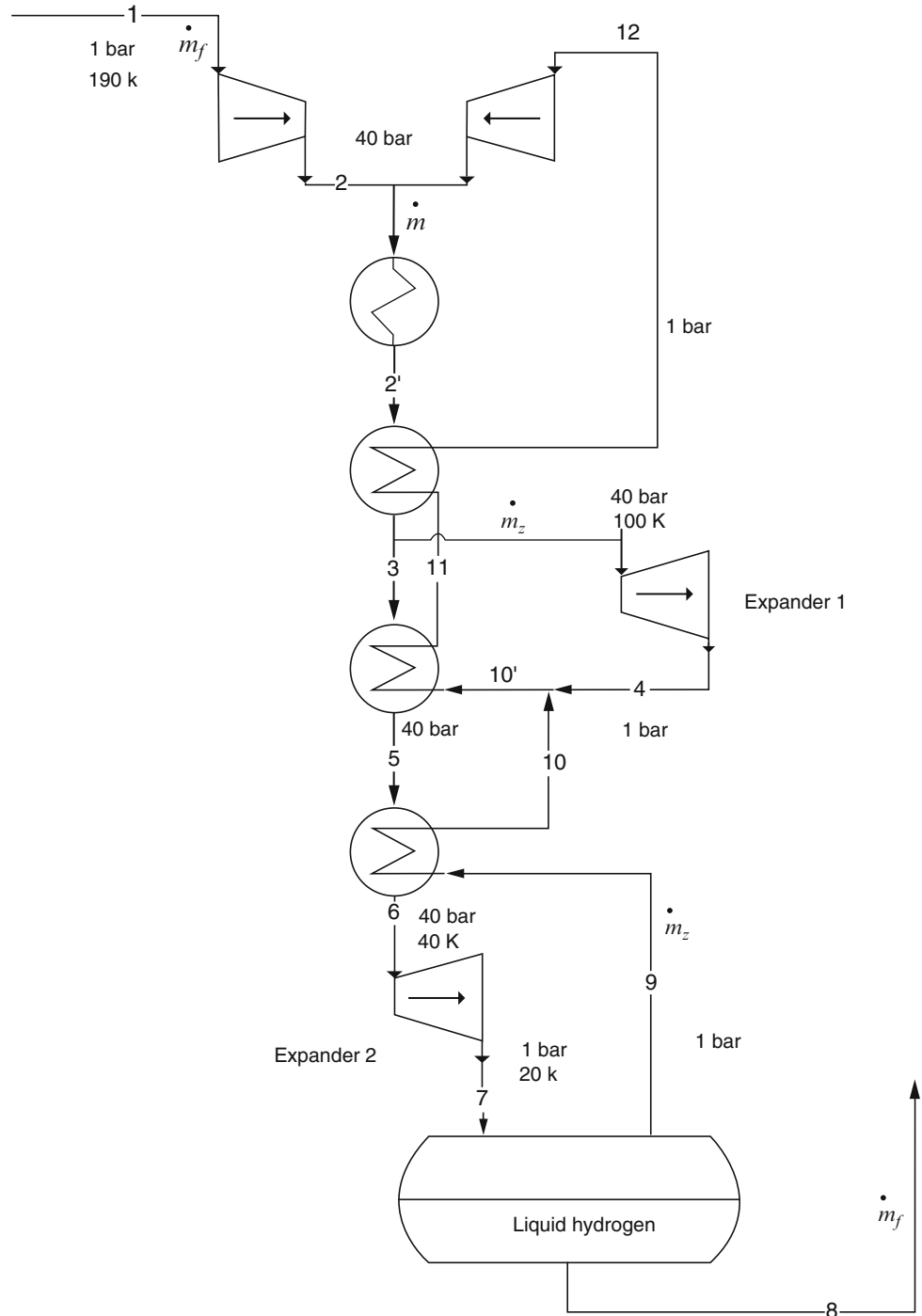
$\rightarrow$ #6 $\rightarrow$ #7 until it reaches 1 bar and 20 K, and is in the two-phase region. The cryogenic liquid separates gravitationally (#8) while the cold vapors are extracted and used to cool the liquid in the process #9 $\rightarrow$ #10.

Some vapors are extracted from high pressure stream #3 at 100 K and expanded to 1 bar to generate cooling effect in #4 and power. The cold stream resulted from mixing #4 and #10 is further used for a cooling effect in process #10′ $\rightarrow$ #11 $\rightarrow$ #12. The vapors are recycled by recompressing and mixing with makeup stream #2.

For process modeling the heat exchangers inlet and outlet temperatures are assumed to comply with the original Claude process. Therefore, the temperature in state #7 is set to 20.24 K while the temperature at state #3 is 100 K and the

Table 8.1 Modeling assumptions and equations for system components

Component	Assumptions	Equations
Makeup compressor (process 1–2)	Ideal gas behavior. Above the *ortho–para* transition $T_1 = 190$ K, $P_1 = 1$ bar, $PR = 40$	$\dot{m}_1 h_1 + \dot{W}_{1.2} = \dot{m}_1 h_2$ $\dot{W}_{1.2} = \dfrac{k}{k-1} R\, T_1 \ln\left(PR^{\frac{k-1}{k}} - 1\right) = C_p(T_2 - T_1)$
Recycle compressor (12-2′)	Ideal gas behavior. Above the *ortho–para* transition $T_{12} = 190$ K, $P_{12} = 1$ bar, $PR = 40$ Operates under similar states as makeup	$\dot{m}_1 h_1 + \dot{W}_{1.2} = \dot{m}_1 h_2$ $\dot{W}_{12.2} = \dfrac{k}{k-1} R\, T_{12} \ln\left(PR^{\frac{k-1}{k}} - 1\right) = C_p(T_2 - T_{12})$
Cooler (process 2-2′)	Heat exchanger network cooled with air and water sequentially; $T_{2'} = 400$ K	$\dot{m}_2 h_2 = Q_{2'.2} + \dot{m}_{2'} h_{2'}$ $\dot{m}_{2'} = \dot{m}_2 + \dot{m}_{12}$
Cryo-cooler (process 2′-3-11-12)	Cooling with liquid nitrogen; $T_3 = 100$ K	$\dot{m}_2 h_{2'} + \dot{m}_{11} h_{11} = (\dot{m}_3 + \dot{m}_3) h_3 + \dot{m}_{12} h_{12}$
Cryo-regenerator (process 3-5-10′-11)	Regenerative heat exchanger. Isobaric processes.	$\dot{m}_3 h_3 + \dot{m}_{10'} h_{10'} = \dot{m}_5 h_5 + \dot{m}_{11} h_{11}$
Cryo-regenerator (process 5-6-9-10)	Regenerative heat exchanger. Isobaric processes. $T_6 = 40$ K	$\dot{m}_5 h_5 + \dot{m}_9 h_9 = \dot{m}_6 h_6 + \dot{m}_{10} h_{10}$
Expander 1 (process 4′-4)	Isentropic efficiency of 0.7	$\dot{m}_{4'} h_{4'} = \dot{W}_{e.1} + \dot{m}_4 h_4$
Expander 2 (process 6–7)	Isentropic efficiency of 0.7	$\dot{m}_6 h_6 = \dot{W}_{e.2} + \dot{m}_7 h_7$

compression/expansion ratio is $PR = 40$. Table 8.1 gives the balance equation for each system components which are used for modeling.

Results and Discussion

First we determined the thermodynamic cycle of the modified liquefaction process aiming at finding the required built-in volume ratio for the expanders and implicitly the number of expansion stages. Figure 8.2 shows the thermodynamic cycle with state points in the *T-s* diagram. The volume ratios must be around 16 for both expanders. Therefore two-cascaded expanders can be used with built-in volume ratio of 4 each.

A parameter of interest is the specific work required by the compressors to liquefy 1 kg of hydrogen, net. This is of order of 8 kJ/kg and decreases to 4.5 kJ/kg if the inlet pressure could be increased eight times by external means. The exergy and energy efficiencies of the system are also dependent of makeup gas parameters. As seen in Fig. 8.3 the efficiencies increase if the temperature of the makeup gas could be reduced. In Fig. 8.4 exergy efficiency and reversible work input are plotted against inlet temperature of hydrogen. There is a clear trade-off between the exergy efficiency and the work input which have the opposite trends with the makeup gas temperature.

Figure 8.5 illustrates the variation of energy and exergy efficiency with compressor inlet pressure. Both the efficiencies increase with inlet pressure. If pressurized hydrogen is available from the generation plant, the cycle efficiency of this system can be improved. Note that hydrogen generation by some methods of electrolysis has higher output pressure.

Figure 8.6 depicts the scroll expander work output at varying inlet temperature. The optimum work output is noticed at around inlet temperature of 58 k. This supports the scroll expander's capability to work efficiently at low inlet temperature. However the work output drops sharply above this temperature. This is because of the reduction of mass flow rate due to higher temperature.

Figure 8.7 represents the variation of the specific work developed by the two expanders with respect to pressure P_3. Expander's inlet pressure is an important parameter to optimize the expander work output. Up to 40 bar the work increases steadily and after that the curve flattens as shown in Fig. 8.7.

Variation of work recovery by the expanders is proportional to mass flow rate through expanders. It is noted that expander 1 recovers higher work output, and sharing mass flow to expander 2 does not generate equivalent amount of work. This is because of the fact that expander 2 is located at the downstream of the fluid flow. Expander works are generated within 3–4 and 6–7. Expansion process 3–4 occurs in the gaseous phase region while in the second expander the exhaust gas converts to a mixture of liquid and vapor. This liquid–vapor mixture generates relatively less work.

Fig. 8.2 Modified Claude cycle
representation in *T*-*s* diagram
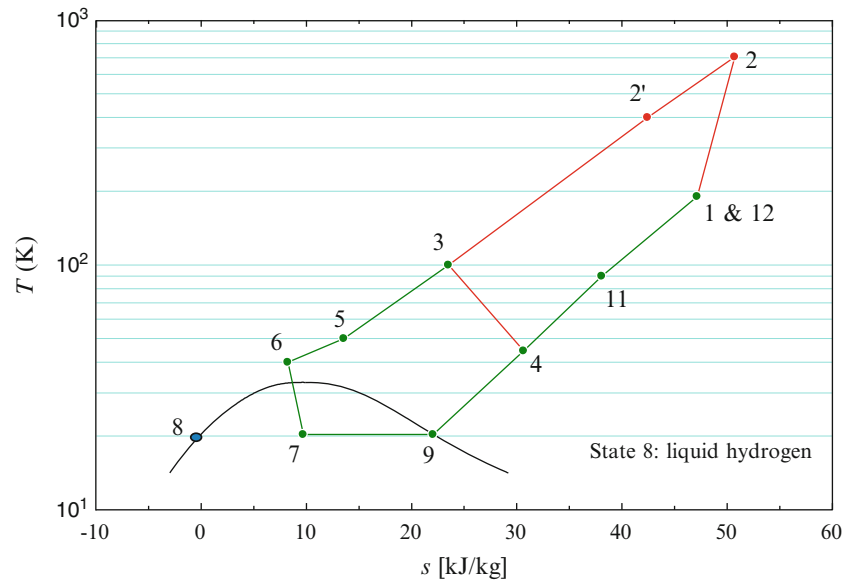
Fig. 8.3 Energy and exergy
efficiencies of the modified
Claude process in function
of makeup gas temperature
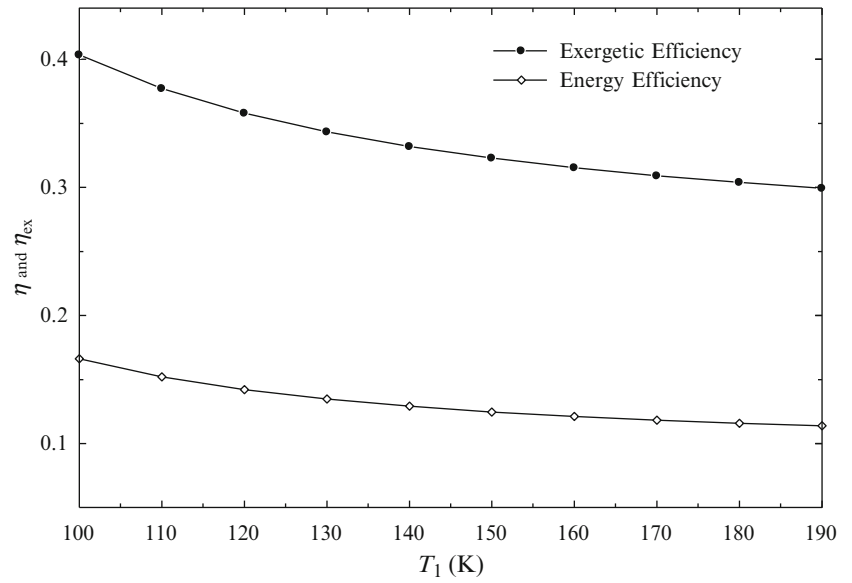
Fig. 8.4 Exergy efficiency and
the net specific reversible work
input vs makeup gas temperature
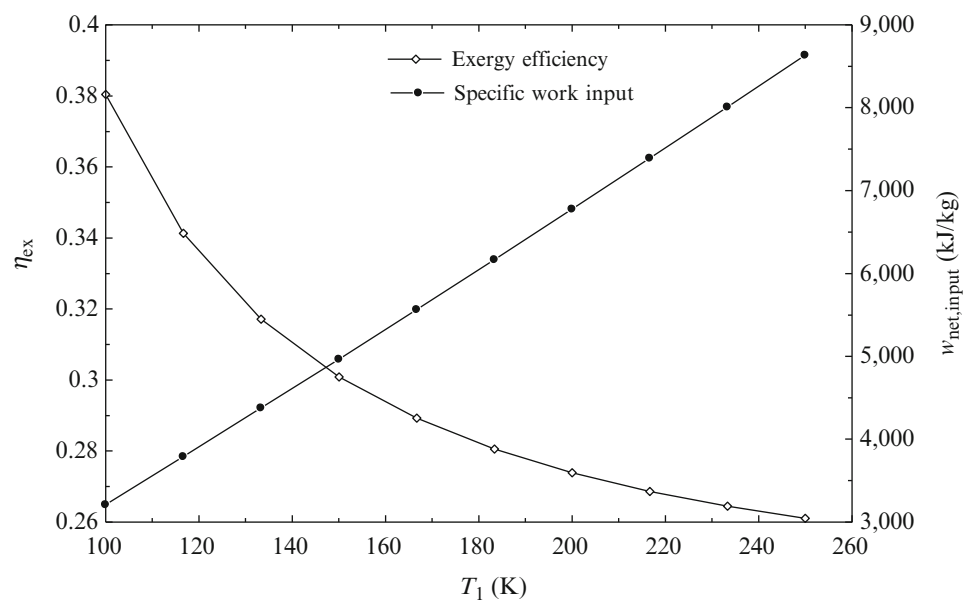
Fig. 8.5 Energy and exergy efficiencies vs compressor inlet pressure
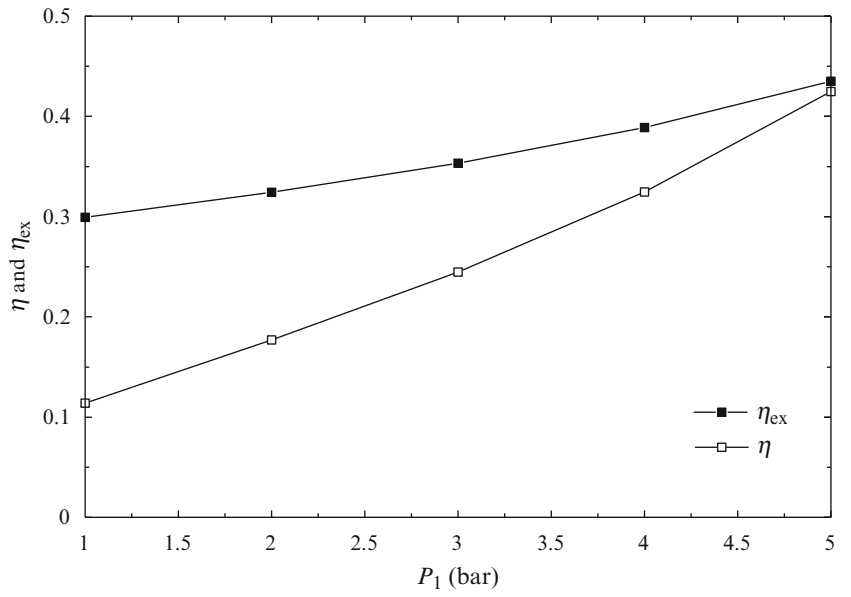
Fig. 8.6 Expander inlet temperature vs. expander work output
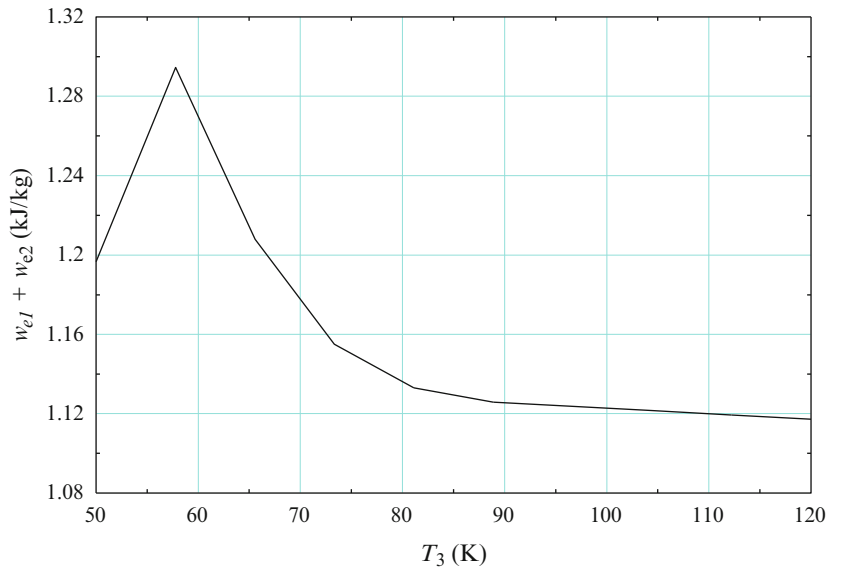
Fig. 8.7 Expander inlet pressure vs. expander work output
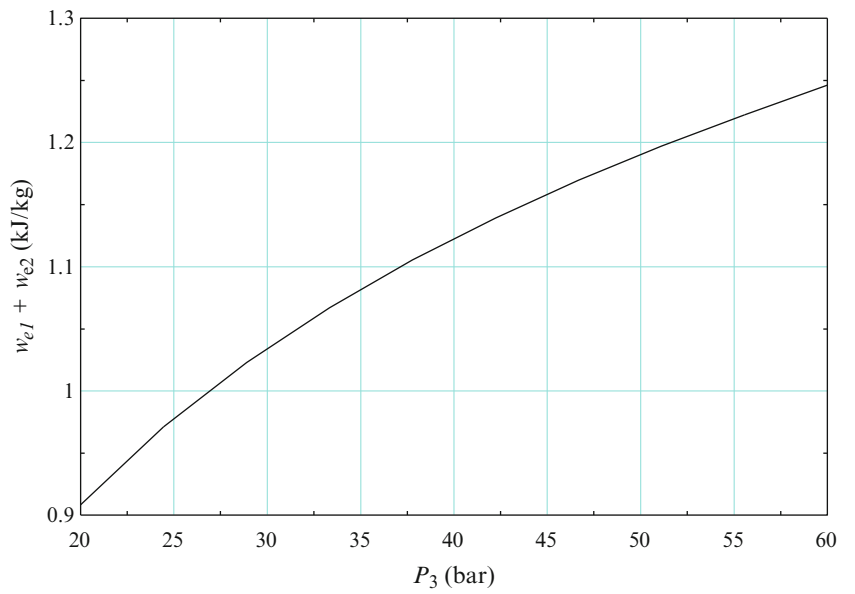
Concluding Remarks

In this study, thermodynamic analysis is used to analyze the modified Claude cycle for hydrogen liquefaction. The analysis of the expanders is performed on the basis of assumed process parameters. The heat exchangers, compressors, and the expander performance are considered ideal and the losses are not determined. The work recovery in both the expanders depends on the inlet temperature, mass flow rate, and the inlet pressure. The overall investigation validates the use of scroll expanders as a suitable expansion device and justifies the use of second expander in the two-phase region for work extraction. However, an experimental analysis with precisely designed heat exchangers and selected scroll expanders of the compatible sizes can be conducted in future. The experimental data may be used to optimize the work extraction and maximize the hydrogen liquefaction performance by adjusting the system parameters.

Nomenclature

C_p	Specific heat, kJ/kg K	PR	Pressure ratio
k	Adiabatic exponent	T	Temperature, K
h	Specific enthalpy	w	Specific work, kJ/kg
$\dot{m}$	Mass flow rate, kg/s	$\dot{W}$	Work rate, W
P	Pressure, bar		

Greek Letter

η Efficiency

Subscripts

e	Expander	ex	Exergetic
en	Energetic		

References

1. Nandi TK, Sarangi S (1993) Performance and optimization of hydrogen liquefaction systems. Int J Hydrogen Energy 18:131–139
2. Domashenko A, Gorbatsky Y, Nelidov V, Skorodumov B (2002) Production, storage and transportation of liquid hydrogen. Experience of infrastructure development and operation. Int J Hydrogen Energy 27:753–755
3. Ogawa M, Seki T, Honda H, Nakamura M, Takatani Y (2004) A hydrogen production method using latent heat of liquefied natural gas. Electrical Eng Jpn 147:32–42
4. Kanoglu M, Dincer I, Rosen MA (2007) Geothermal energy use in hydrogen liquefaction. Int J Hydrogen Energy 32:4250–4257
5. Quoilin S, Lemort V, Lebrun J (2010) Experimental study and modeling of an organic Rankine cycle using scroll expander. Appl Energy 87:1260–1268
6. Hung TC (2001) Waste heat recovery of organic Rankine cycle using dry fluids. Energy Conversion Manage 42:539–553
7. Oralli E, Ali Tarique M, Zamfirescu C, Dincer I (2011) A study on scroll compressor conversion into expander for Rankine cycle. Int J Low Carbon Tech 6:200–206

Energy and Exergy Analyses of an Integrated Solar Based Hydrogen Production and Liquefaction System

Tahir A.H. Ratlamwala and Ibrahim Dincer

Abstract

The present paper concerns studies on energy and exergy analyses of a new integrated system with heliostat field, Cu–Cl cycle, Isobutane cycle, and Linde–Hampson system. The present system is capable of producing liquefied hydrogen for easier storage than hydrogen gas. A parametric study is conducted to investigate the effects of variation in solar light intensity, ambient temperature, and flow rate of makeup water required by the Cu–Cl cycle on hydrogen production rate, hydrogen liquefaction rate, and overall energy and exergy efficiencies. The results show that an increase in solar light intensity has positive effect on hydrogen production rate and hydrogen liquefaction rate as they increase from 205 to 492.5 L/s, and 43 to 103 L/s, respectively. The overall energy and exergy efficiencies are observed to be increasing from 4.1 % to 7.3 %, and 4.9 % to 8.2 %, respectively with increase in solar light intensity from 600 to 750 W/m^2. The rise in ambient temperature from 290 to 330 K affects the performance of the system in the positive manner. The increase in supplied rate of makeup water to the Cu–Cl cycle from 0.05 to 0.15 L/s results in increase in the overall exergy efficiency of the integrated system from 8.2 % to 9.6 %.

Keywords

Energy • Exergy • Hydrogen • Cu-Cl • Liquefaction

Introduction

Increased emissions of harmful greenhouse gasses due to the extensive use of fossil fuels have made researchers and organizations around the world re-think about potential solutions for a major energy carrier. These fossil fuels have caused some critical local and global issues through increased CO_2, NOx, and SO_2 emissions. In this regard, the world has started alarming "accelerated global warming," while the need for the clean and renewable energy has become inevitable [1]. One alternative to present energy carrier is hydrogen. Hydrogen offers great advantages as a fuel and working fuel over the conventional ones. In the future, the role of hydrogen may become more important, as some researchers suggest that the world's energy systems may undergo a transition to an era in which the main energy carrier will be hydrogen [2–5]. At present, the use of hydrogen as a fuel is limited to the transportation due to the lack of proper

T.A.H. Ratlamwala (✉)
Shaheed ZUlfiqar Ali Bhutto Institute of Science and Technology, 90 & 100 Clifton Campus, Karachi, Sindh, Pakistan 75600

Faculty of Engineering and Applied Science, University of Ontario Institute of Technology, 2000 Simcoe Street North, Oshawa, ON, Canada L1H 7K4
e-mail: tahir.ratlamwala@uoit.ca

I. Dincer
Faculty of Engineering and Applied Science, University of Ontario Institute of Technology, 2000 Simcoe Street North, Oshawa, ON, Canada L1H 7K4
e-mail: ibrahim.dincer@uoit.ca

infrastructure for supply or production of hydrogen. Dufour et al. [6] mentioned that presently 96 % of the hydrogen is produced using the steam methane reforming (SMR) technology. The other major technologies which are being currently used or developed for production of hydrogen are (a) the water electrolysis, (b) the coal gasification, and (c) the thermochemical water splitting cycles (TWSCs). Among all the above mentioned technologies which are being studied for hydrogen production, TWSCs have an edge.

The study conducted by Giaconia et al. [7] concluded that TWSCs represent an appealing carbon-free option for hydrogen production powered by alternative (carbon-free) energy sources. Aghahosseinin et al. [8] explained that a thermochemical cycle is a process consisting of a closed loop of thermally driven chemical reactions, where all intermediate compounds are recycled, while water is decomposed into the hydrogen and the oxygen. Among the TWSCs, Cu–Cl cycle holds an edge because of its lower operating temperatures (around 530 °C) which results in reduced material and maintenance cost as mentioned by [9, 10]. Another benefit associated with Cu–Cl cycle is that it has one of the highest energy efficiencies among other TWSCs as studied by [11–13].

The heat required by TWSCs can be supplied by the use of advanced solar energy systems. The use of solar energy systems will ensure that the overall hydrogen production process is environmentally benign as energy is generated using renewable energy source and hydrogen is produced using TWSCs which are environmentally benign systems, as they recycle all the chemicals within the process. The use of high temperature solar technologies is governed by the temperature which they can generate. In a study, Kalogirou [14] presented the working temperature range of different solar thermal technologies which are parabolic trough collector (60–300 °C), solar dish (100–500 °C), and heliostat field (150–2,000 °C). Studies conducted by several researchers [15–17] concluded that using high temperature solar thermal collectors are beneficial from both heat production and efficiency perspectives. Within the high temperature solar technologies, the heliostat field system has an advantage of catering to wide temperature range which can be useful for operating the integrated system that requires multiple operating temperatures.

In this paper, we study a novel system integrated with heliostat field, Cu–Cl cycle, isobutane cycle, and Linde–Hampson cycle. The system presented is capable of producing hydrogen and later liquefying it for better storage and handling. A parametric study is carried out to investigate the effects of varying the operating conditions such as solar light intensity, ambient temperature, and flow rate of makeup water required by the Cu–Cl cycle on hydrogen production rate, hydrogen liquefaction rate, and overall energy and exergy efficiencies.

System Description

The integrated system presented in this paper is shown in Fig. 9.1. The system utilizes the solar energy to produce hydrogen using the Cu–Cl cycle (Fig. 9.2) and later liquefy it using the Linde–Hampson cycle (LH). The solar energy is harnessed with the help of Heliostat field system. The molten salt passes through the receiver of the Heliostat system to
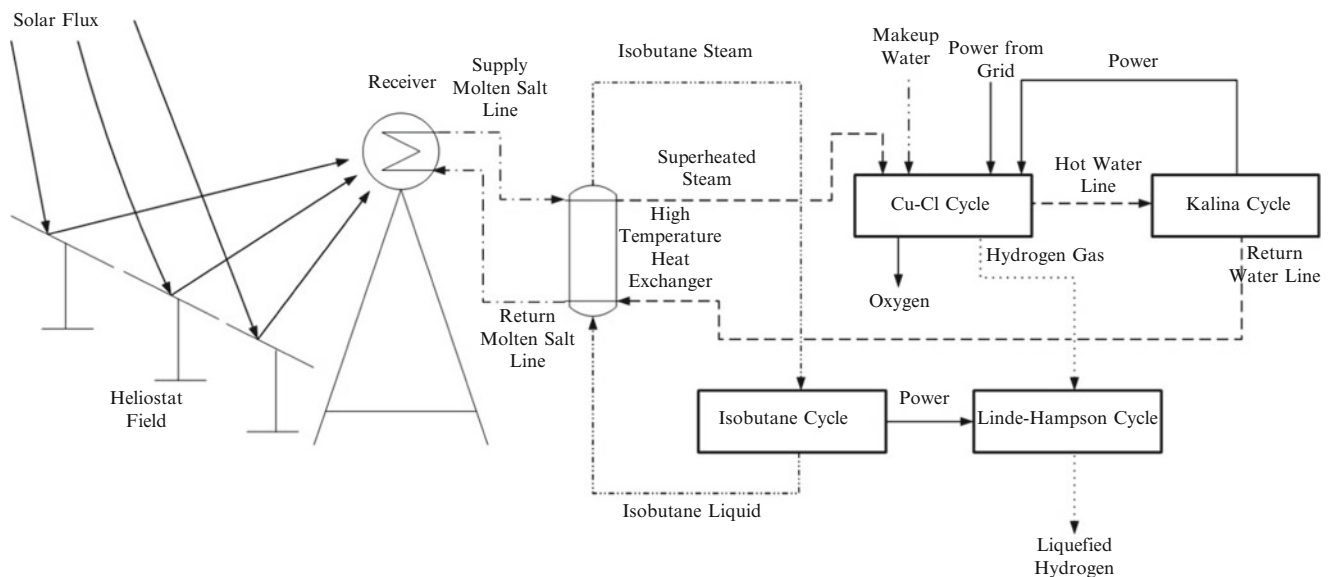
Fig. 9.1 Schematic of an integrated system
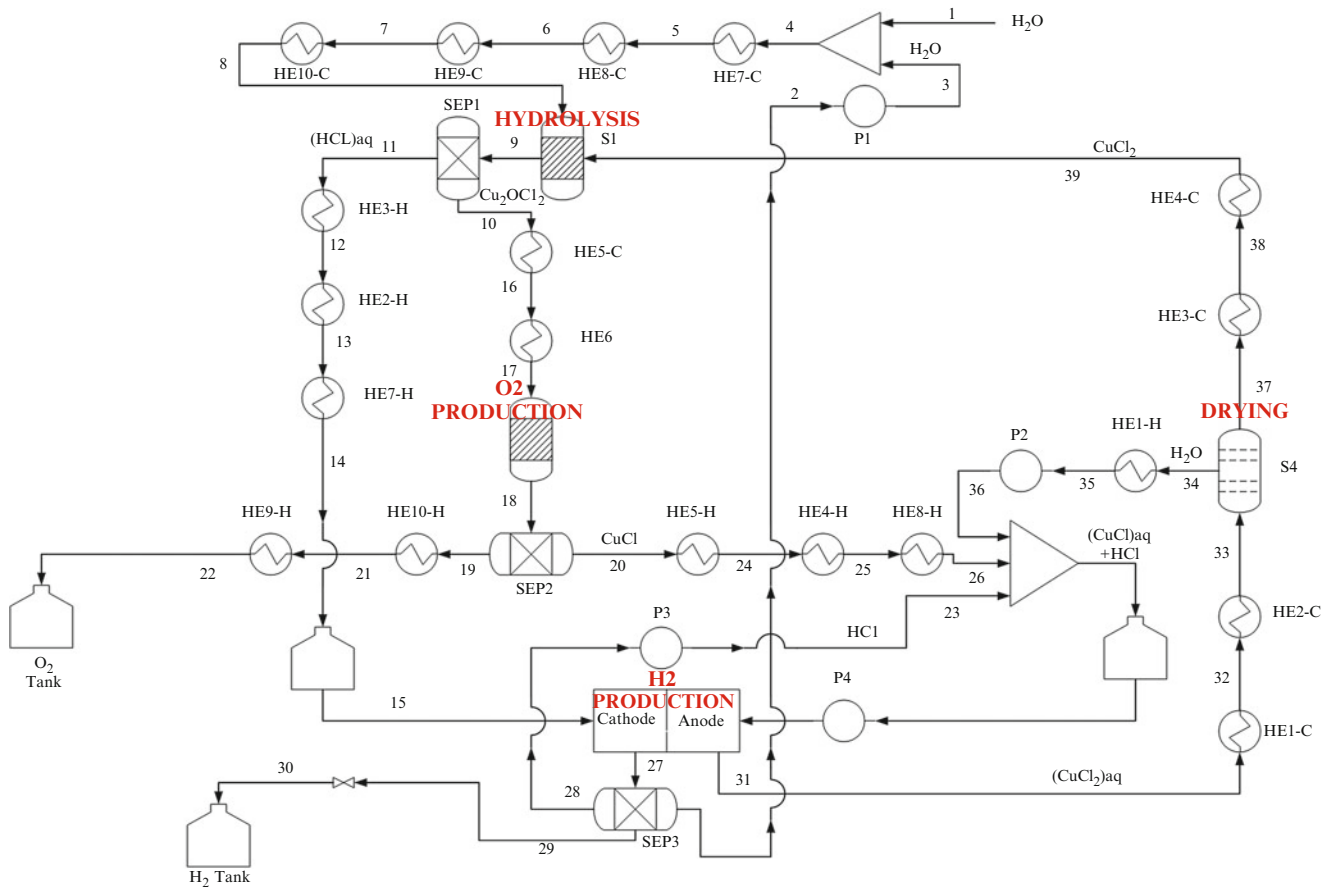
Fig. 9.2 Schematic of the Cu–Cl cycle
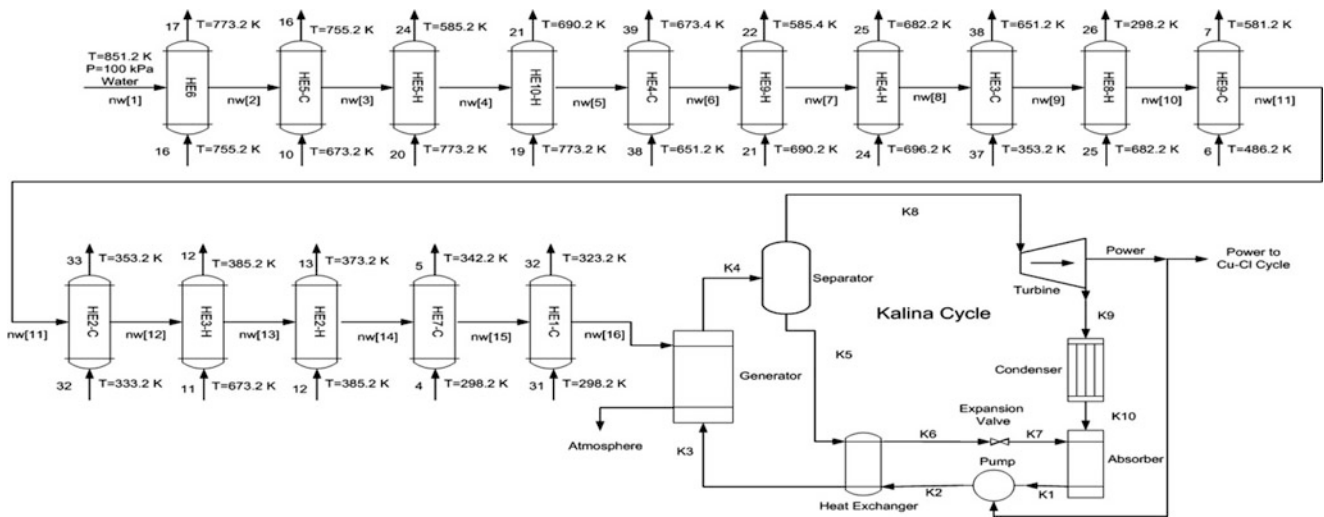
Fig. 9.3 Schematic of the heat exchanger network for the Cu–Cl cycle

carry energy extracted from the solar light in the form of heat. The high temperature molten salt then enters the high temperature heat exchanger where it releases heat to the water coming from the Cu–Cl cycle and isobutane liquid coming from the binary power plant. The heat carried by the water coming from the Cu–Cl cycle is supplied to the heat exchanger network of the Cu–Cl cycle as shown in Fig. 9.3. The water stream leaving the heat exchanger network of the Cu–Cl cycle is later supplied to the Kalina cycle to recover excess heat in the form of power. The power produced is supplied to the Cu–Cl cycle in order to decrease its energy demand from the grid. The high temperature isobutane steam leaving the high

Fig. 9.4 Schematic
of the isobutane cycle
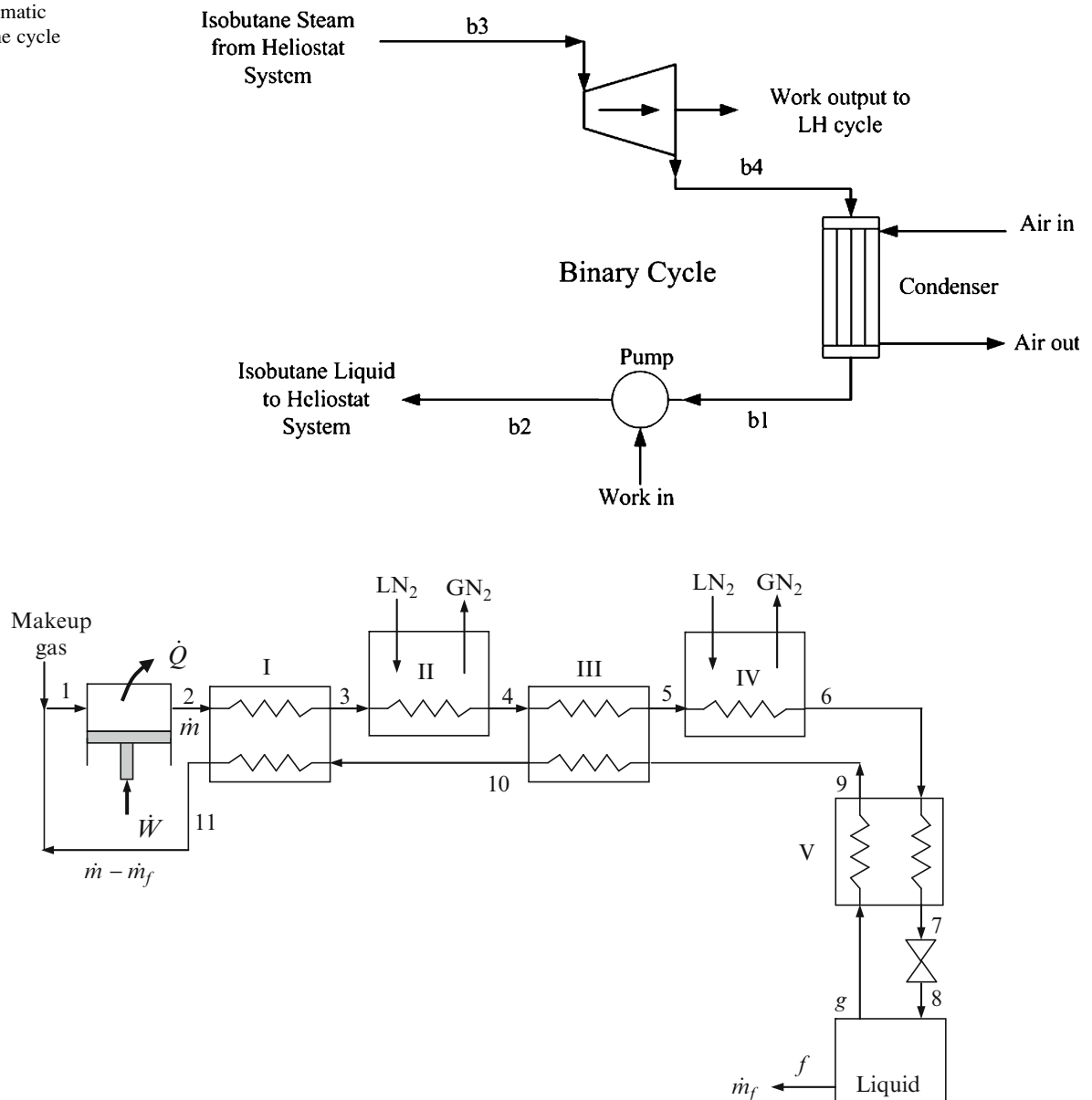
Fig. 9.5 Schematic of the Linde–Hampson cycle

temperature heat exchanger is supplied to the turbine of the isobutane cycle (Fig. 9.4) in order to produce power. The power produced by the isobutane cycle is supplied to the Linde–Hampson (LH) cycle (Fig. 9.5) for liquefying hydrogen produced by the Cu–Cl cycle. In the LH system, makeup gas is mixed with the hydrogen gas coming from the Cu–Cl cycle, and the mixture at state 1 is compressed to state 2 from 101 kPa to 10 MPa. Heat is rejected from compressed gas to a coolant. The high pressure gas is cooled to state 3 in a regenerative counter flow heat exchanger (I) by the uncondensed gas, and is cooled further by flowing through two nitrogen baths (II and IV) and two regenerative heat exchanger (III and V) before being throttled to state 8, where it is a saturate liquid–vapor mixture. The liquid is collected as the desired output for further usage and the vapor is routed through the bottom half of the cycle. The detailed system description of the Cu–Cl cycle can be found elsewhere [12].

Energy and Exergy Analyses

This section provides energy and exergy analyses of the integrated system studied in this paper.

Heliostat System

The heliostat field energy model is taken from the study conducted by Xu et al. [17]. The rate of heat received by the solar light intensity is calculated as

$$\dot{Q}_s = I \times A_{field} \tag{9.1}$$

The total rate of heat received by the receiver is defined as

$$\dot{Q}_{rec} = \dot{Q}_{rec,abs} + \dot{Q}_{rec,em} + \dot{Q}_{rec,ref} + \dot{Q}_{rec,conv} + \dot{Q}_{rec,cond} \tag{9.2}$$

where

$$\dot{Q}_{rec,em} = \frac{\varepsilon_{avg} \times \sigma \left(T_{rec,surf}^4 - T_0^4\right) A_{field}}{C}$$

$$\dot{Q}_{rec,ref} = \dot{Q}_{rec} \times \rho \times \frac{F_r}{A_{field}}$$

$$\dot{Q}_{rec,conv} = \frac{\left(h_{air,fc,insi} \times \left(T_{rec,surf} - T_0\right) + h_{air,nc,insi} \times \left(T_{rec,surf} - T_0\right)\right) A_{field}}{C \times F_r}$$

$$\dot{Q}_{rec,cond} = \frac{\left(T_{rec,surf} - T_0\right) A_{field}}{\left(\frac{\partial_{insu}}{\lambda_{insu}} + \frac{1}{h_{air,o}}\right) C \times F_r}$$

The rate of heat absorbed by the molten salt passing through the receiver is found using

$$\dot{Q}_{rec,abs} = \dot{m}_{ms} c_p (T_{ms,o} - T_{ms,in}) \tag{9.3}$$

The exergy rate carried by the solar light is calculated as

$$\dot{Ex}_s = \left(1 - \frac{T_0}{T_{sun}}\right) \dot{Q}_s \tag{9.4}$$

Cu–Cl Cycle

The specific enthalpy at any given state in the Cu–Cl cycle is calculated as

$$h_i = \sum_{m=1}^{k} mf_m h_m \tag{9.5}$$

The specific entropy at any given state in the Cu–Cl cycle is calculated as

$$s_i = \sum_{m=1}^{k} mf_m s_m \tag{9.6}$$

The exergy rate at any given state in the Cu–Cl cycle is

$$\dot{Ex}_i = \dot{m}_i((h_i - h_0) - T_0(s_i - s_0)) \tag{9.7}$$

The thermal exergy rate in each heat exchanger is defined as

$$\dot{Ex}_{th_i} = \left(1 - \frac{T_0}{T_i}\right) \dot{Q}_i \tag{9.8}$$

The heat supplied to the generator of the Kalina cycle is defined as

$$\dot{Q}_g = \dot{m}_{nw}\left(h_{nw[16]} - h_{nw[0]}\right) \tag{9.9}$$

The net power output that can be obtained from the Kalina cycle is

$$\dot{W}_{net_k} = \dot{W}_{turb} - \dot{W}_{p_k} - \dot{W}_{parasitic}$$

where

$$\dot{W}_{turb} = \dot{m}_{k8}(h_{k8} - h_{k9})$$

$$\dot{W}_{p_k} = \dot{m}_{k1}(h_{k2} - h_{k1})$$

$$\dot{W}_{parasitic} = 0.2\left(\dot{W}_{turb} - \dot{W}_{p_k}\right)$$

Isobutane Cycle

The net power that can be obtained from the binary isobutane plant is expressed as

$$\dot{W}_{net_{geo}} = \dot{W}_{turb} - \dot{W}_{p_{iso}} - \dot{W}_{parasitic} \tag{9.10}$$

where

$$\dot{W}_{turb} = \dot{m}_{iso}(h_3 - h_4)$$

$$\dot{W}_{p_{iso}} = \dot{m}_{iso}(h_2 - h_1)$$

$$\dot{W}_{parasitic} = 0.2\left(\dot{W}_{turb} - \dot{W}_{p_{iso}}\right)$$

Linde–Hampson Cycle

The ideal specific work required to compress the hydrogen from 101 kPa to 10 MPa is given as

$$w_{comp_{ideal}} = R \times T_0 \times \ln\frac{P_2}{P_1} \tag{9.11}$$

The actual specific work input to the liquefaction cycle per unit mass of the hydrogen is stated as

$$w_{comp_{actual}} = \frac{w_{comp_{ideal}}}{\eta_{comp}} \tag{9.12}$$

The total specific power required by the LH cycle is calculate as

$$w_{total_{Linde-Hampson}} = \frac{w_{comp_{actual}} + w_{Nitrogen}}{f_{liq}} \tag{9.13}$$

where

$$f_{liq} = \frac{h_9 - h_6}{h_9 - h_f} \qquad (9.14)$$

where f_{liq} represents the fraction of liquefied hydrogen which is taken out of the cycle.

The amount of hydrogen liquefied is then calculated using

$$\dot{m}_{H_{2liquefied}} = f_{liq} \times \dot{m}_{H_2} \qquad (9.15)$$

Efficiencies

The overall energy and exergy efficiencies are defined as

$$\eta_{ov_{en}} = \left(\frac{(\dot{m}_{H_2} HHV_{H_2})_{liq} + \dot{m}_{22} h_{22}}{\dot{Q}_{in} + \dot{m}_1 h_1 + \frac{(\dot{W}_{elec} - \dot{W}_{net_k} + \dot{W}_{p1} + \dot{W}_{p2} + \dot{W}_{p3} + \dot{W}_{p4} + \dot{W}_{LH})}{\eta_{convr}}} \right) \qquad (9.16)$$

where $\dot{Q}_{in} = \dot{Q}_{HE8-C} + \dot{Q}_{HE10-C} + \dot{Q}_{S1} + \dot{Q}_{S2} + \dot{Q}_{S4} + \dot{Q}_S$.

$$\eta_{ex_{ov}} = \left(\frac{(\dot{Ex}_{H_2})_{liq} + \dot{Ex}_{22}}{\dot{Ex}_{in} + \frac{(\dot{W}_{elec} - \dot{W}_{net_k} + \dot{W}_{p1} + \dot{W}_{p2} + \dot{W}_{p3} + \dot{W}_{p4} + \dot{W}_{LH})}{\eta_{convr}}} \right) \qquad (9.17)$$

where $\dot{Ex}_{in} = \dot{Ex}_{HE8-C} + \dot{Ex}_{HE10-C} + \dot{Ex}_{S1} + \dot{Ex}_{S2} + \dot{Ex}_{S4} + \dot{Ex}_1 + \dot{Ex}_S$.

Results and Discussion

This paper presents an integrated system capable of producing and liquefying hydrogen using solar energy source. The integrated system studied consists of Heliostat field system, Cu–Cl cycle, Kalina cycle, Isobutane cycle, and Linde–Hampson cycle. The heliostat field system modeled introduced by Xu et al. [17] is used in the present study. The energy efficiency of the heliostat field system obtained by Xu et al. [17] was 75 % as compared to 80 % in the present study. The efficiency of the Cu–Cl cycle in this study is found to be 52 % as compared to 55 % reported by Lewis et al. [11].

Effect of Solar Light Intensity

The continuous variation in solar light intensity throughout the day makes it very important to study the effect of variation in solar light intensity on the performance of the system. The effect of rise in solar light intensity on the hydrogen production and liquefaction rate is studied and is shown in Fig. 9.6. The hydrogen production rate and hydrogen liquefaction rate are observed to be increasing from 205.3 to 492.5 L/s, and 42.84 to 102.8 L/s, respectively with rise in solar light intensity from 600 to 750 W/m^2. Such behavior is observed because increase in solar light intensity results in the higher rate of heat production by the Heliostat field system. As the rate of heat generated by the Heliostat system increases, the hydrogen production capability of the Cu–Cl cycle and the power generating capability of the isobutane system increase. The Cu–Cl cycle is mostly heat dependent and with the increase in the rate of heat supplied, the hydrogen production capacity of the Cu–Cl cycle increases for the constant operating temperatures. The increase in the rate of heat supplied to the isobutane system results in higher temperature of isobutane fluid entering the turbine. As the temperature of the fluid entering the turbine increases, the power produced by the turbine increases. The increase in hydrogen liquefaction is directly related to the increase in power supplied to the LH cycle and as a result of increase in power produced by the isobutane system due to rise in solar light intensity, the hydrogen liquefaction rate increases. The overall energy and exergy efficiencies are found to be increasing from 4.1 % to 7.3 % and 4.9 % to 8.2 %, respectively, with rise in solar light intensity as shown in Fig. 9.7.

Fig. 9.6 Effect of rise
in solar light intensity
on the rate of hydrogen
production and liquefaction
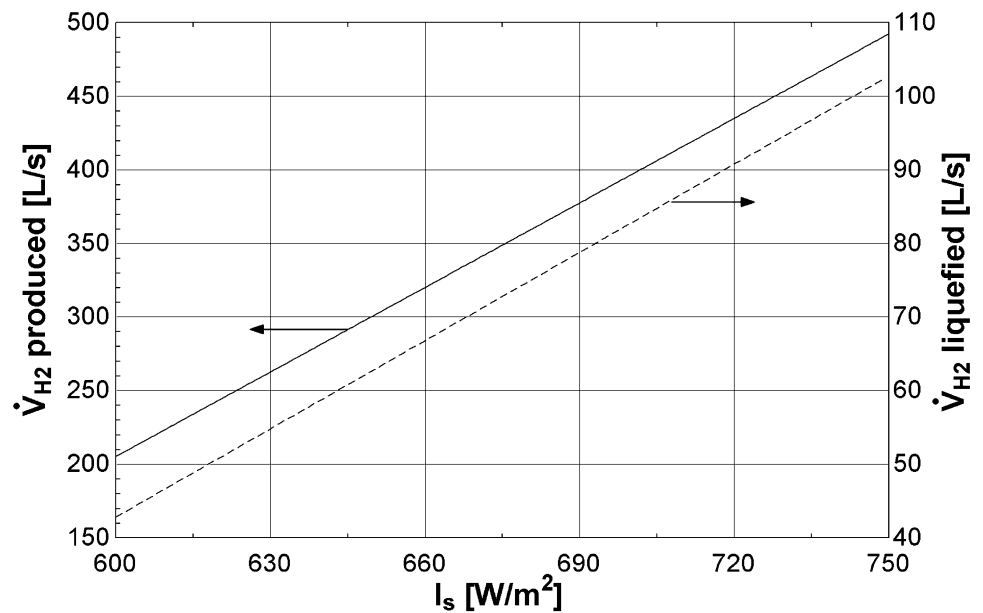
Fig. 9.7 Effect of rise
in solar light intensity
on the overall energy
and exergy efficiencies
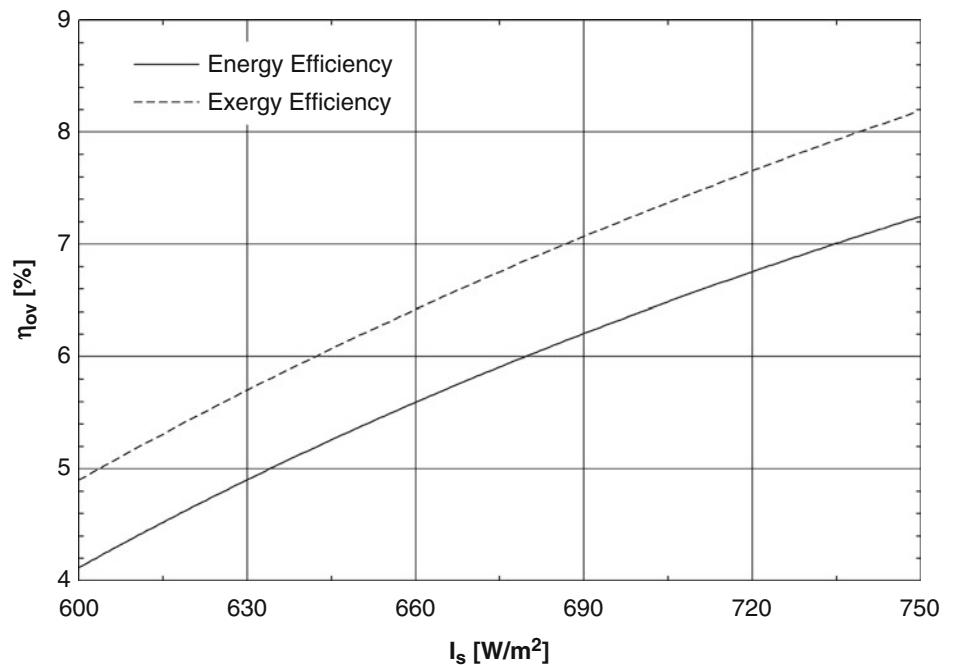
The increase in the overall energy and exergy efficiencies is directly associated with the increase in the hydrogen liquefaction capability of the integrated system. These results show that the performance of the integrated system studied in this paper enhances with the rise in solar light intensity for the given operating conditions.

Effect of Makeup Water Supplied to the Cu–Cl Cycle

The makeup water supplied to the Cu–Cl is an important parameter to study because the supplied makeup water helps in achieving the desired concentration of different chemicals circulating in the Cu–Cl cycle. The hydrogen production and liquefaction rate are observed to be increasing from 492.1 to 503 L/s and 102.7 to 105 L/s, respectively with increase in water flow rate at state cc[1] from 0.05 to 0.15 L/s as shown in Fig. 9.8. The increase in makeup water helps achieving

Fig. 9.8 Effect of increase in makeup water flow rate on the rate of hydrogen production and liquefaction
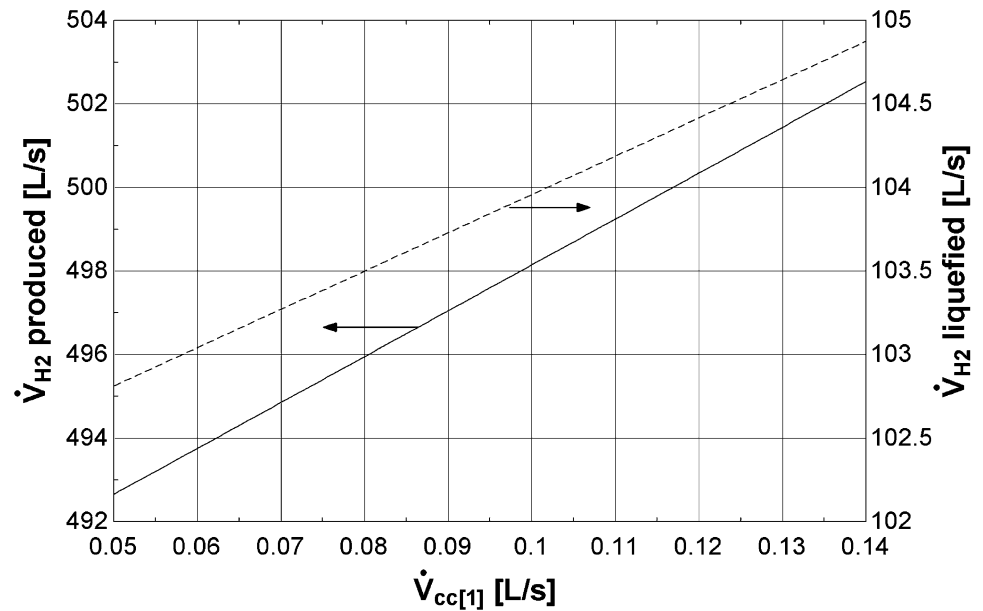
Fig. 9.9 Effect of increase in makeup water flow rate on the overall energy and exergy efficiencies
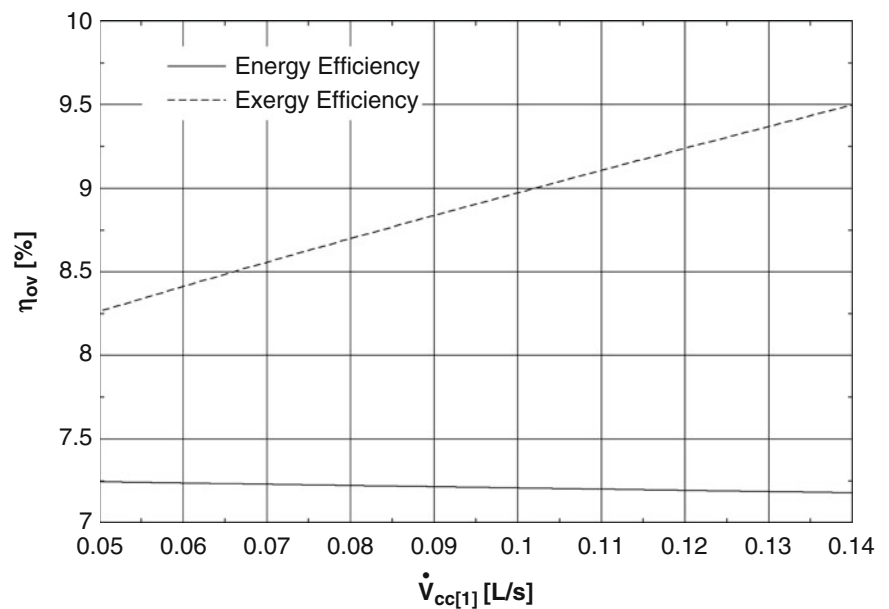
the desired concentration of aqueous HCl based on the chemical balance. This aqueous HCl then enters the electrolyzer where it reacts with Cu–Cl to produce hydrogen and $CuCl_2$. As the availability of the hydrogen ions in the HCl solution entering the electrolyzer increases with increase in the makeup water supplied, the hydrogen production rate also increases. The overall energy and exergy efficiencies of the integrated system are found to be increasing from 7.2 % to 7.3 % and 8.2 % to 9.6 %, respectively with increase in supplied makeup water rate at state cc[1] as shown in Fig. 9.9. It is noticed that the overall energy efficiency hardly changes with increase in makeup water flow rate but the overall exergy efficiency increases by almost 1.5 %. Such behavior is noticed because energy analysis doesn't take into consideration the gains or losses occurring in the system due to the interactions between the chemicals whereas, exergy analysis does take into consideration all the gains or losses happening due to the interactions of the chemical compounds. This difference between energy analysis and exergy analysis makes it essential to study system from exergy perspectives as it provides with better picture with regards to real life operation of the system in comparison to the energy analysis.

Fig. 9.10 Effect of rise in ambient temperature on the rate of hydrogen production and liquefaction
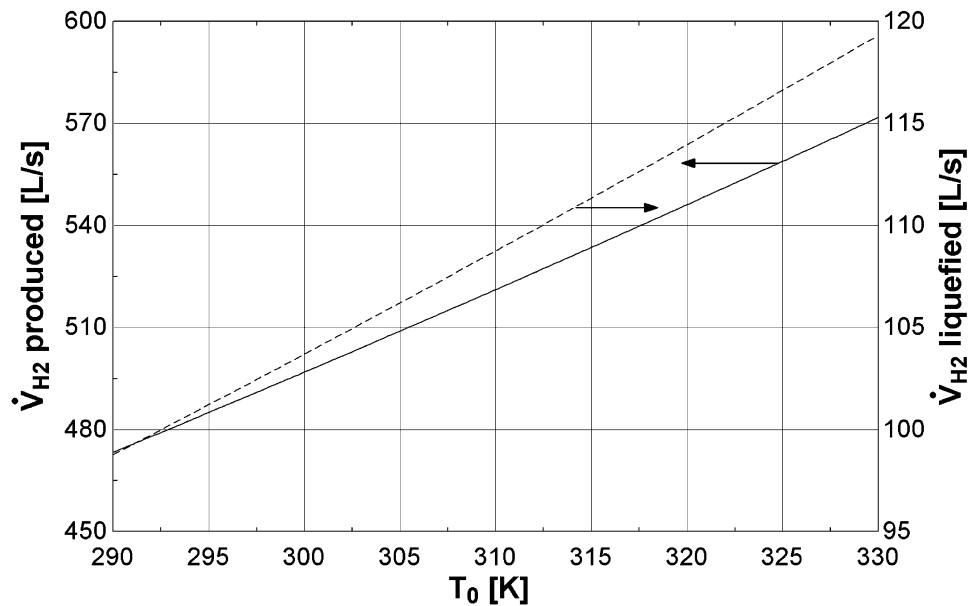
Fig. 9.11 Effect of rise in ambient temperature on the overall energy and exergy efficiencies
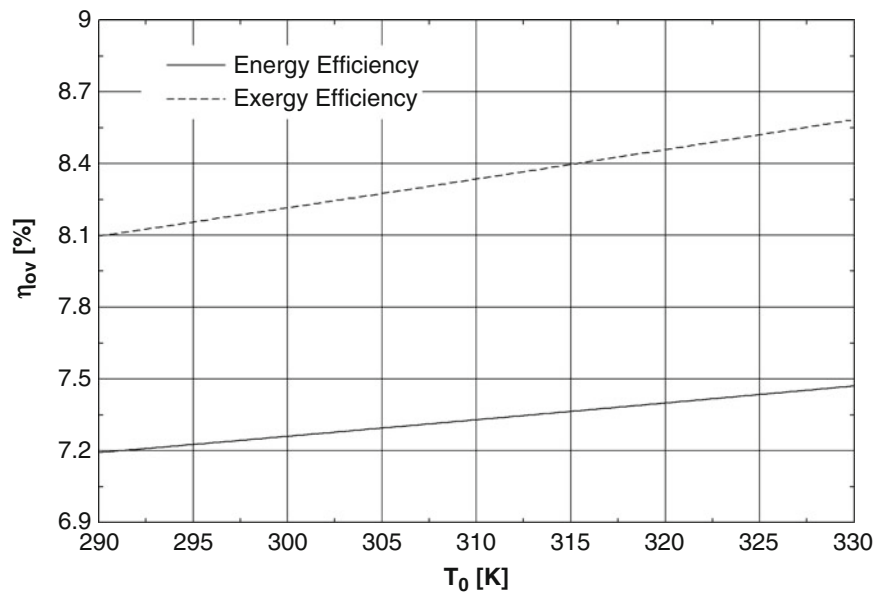
Effect of Ambient Temperature

The ambient temperature plays a major role in the performance of any system which interacts with the environment due to the temperature difference between the system and the surroundings. The temperature difference between the system and the surrounding can either lead to better performance of the system or degrading performance of the system based on the system being used. For the systems which require high temperatures to achieve its output, the increase in ambient temperature is beneficial as it results in lower heat loss from the system to the environment. The hydrogen production and liquefaction rate are seen to be increasing from 473.3 to 571.8 L/s, and 98.7 to 119.3 L/s, respectively with the rise in ambient temperature from 290 to 330 K as shown in Fig. 9.10. The integrated system studied in this paper is highly dependent on the temperature for the production of hydrogen and power. The rise in ambient temperature helps to facilitate the performance of the system because of the lower temperature differences between the system boundary and the environment. This decrease in the temperature difference leads to lower losses from the system to the surrounding in the form of heat. The effect of rise in ambient temperature on the overall energy and exergy efficiencies is displayed in Fig. 9.11.

The overall energy and exergy efficiencies are observed to be increasing from 7.2 % to 7.5 % and 8.1 % to 8.6 %, respectively with the rise in ambient temperature. This increase in energy and exergy efficiencies is directly related to the higher rate of hydrogen liquefaction and lower heat loses due to the lower temperature difference between the system boundary and surrounding with rising ambient temperature.

Conclusions

In this paper, we have presented an integrated system consisting of heliostat field system, Cu–Cl cycle, Kalina cycle, Isobutane cycle, and Linde–Hampson cycle for hydrogen production and liquefaction. Parametric studies are carried out to see the effect of variation in solar light intensity, makeup water flow rate and ambient temperature on hydrogen production rate, hydrogen liquefaction rate, and overall energy and exergy efficiencies. The results obtained show that the hydrogen production and liquefaction rate are found to be increasing from 205 to 492.5 L/s, and 43 to 103 L/s, respectively with the increase in solar light intensity from 600 to 750 W/m^2. The overall energy and exergy efficiencies are observed to be increasing from 4.1 % to 7.3 %, and 4.9 % to 8.2 %, respectively with the increase in solar light intensity. The increase in supplied rate of makeup water to the Cu–Cl cycle from 0.05 to 0.15 L/s results in the increase in overall exergy efficiency of the integrated system from 8.2 % to 9.6 %. Also, the overall exergy efficiency increases from 8.1 % to 8.6 %, respectively, with rise in ambient temperature.

Nomenclature

A	Area	I	Solar light intensity, W/m^2
C	Concentration ratio	$\dot{m}$	Mass flow rate, kg/s
d	Diameter, m	M	Molecular weight, kg/mol
$\dot{Ex}$	Exergy destruction rate, kW	mf	Mass fraction
f	Fraction	P	Pressure, kPa
Fr	View factor	$\dot{Q}$	Heat flow rate, kW
h	Specific enthalpy, kJ/kg; Heat transfer coefficient, W/m^2 K	T	Temperature, K
		s	Specific entropy, kJ/kg K
hw	Hot water	w	Specific work, kJ/kg
HHV	Higher heating value	$\dot{W}$	Work rate, kW

Greek Letters

η	Efficiency	ρ	Density, kg/m^3
ε	Receiver surface emissivity	∂	Thickness, m
σ	Stefan-Boltzmann constant, W/m^2 K^4	λ	Thermal conductivity, W/m K

Subscripts

abs	Absorbed	en	Energy
avg	Average	ex	Exergy
ch	Chemical	fc	Forced convection
cond	Conduction	H	Heliostat
conv	Convection	H$_2$	Hydrogen
convr	Conversion	HE	Heat exchanger
comp	Compressor	i	Inner
elec	Electrolyzer	iso	Isobutane
em	Emissive	insi	Inner side of receiver

insu	Insulation	ph	Physical
i	i^{th} state	rec	Receiver
k	k^{th} state	ref	Reflection
liq	Liquid	S	Solar
m	m^{th} state	surf	Surface
ms	Molten salt	sys	System
nc	Natural convection	th	Thermal
o	Outer	turb	Turbine
ov	Overall	w	Wall surface
p	Pump	0	Ambient state

References

1. Ratlamwala TAH, El-Sinawi AH, Gadalla MA, Ahmad A (2012) Performance analysis of a new designed PEM fuel cell. Int J Energy Res 36:1121–1132
2. Dincer I (2006) Environmental and sustainability aspects of hydrogen and fuel cell systems. Int J Energy Res 31:29–55
3. Muradov NZ, Veziroglu TN (2008) "Green" path from fossil-based to hydrogen economy: an overview of carbon-neutral technologies. Int J Hydrogen Energy 33:6804–6839
4. Midilli A, Dincer I (2009) Development of some exergetic parameters for PEM fuel cells for measuring environmental impact and sustainability. Int J Hydrogen Energy 34:3858–3872
5. Ratlamwala TAH, Gadalla MA, Dincer I (2010) Energy and exergy analysis of an integrated fuel cell and absorption cooling system. Int J Exergy 7:731–754
6. Dufour J, Serrano DP, Galvez JL, Moreno J, Garcia C (2009) Life cycle assessment of processes for hydrogen production: environmental feasibility and reduction of greenhouse gases emissions. Int J Hydrogen Energy 34:1370–1376
7. Giaconia A, Sau S, Felici C, Tarquini P, Karaginnakis G, Pagkoura C et al (2011) Hydrogen production via sulfur-based thermochemical cycles: Part 2: performance evaluation of Fe_2O_3-based catalysts for the sulfuric acid decomposition step. Int J Hydrogen Energy 36:6496–6509
8. Aghahosseinin S, Dincer I, Naterer G (2011) Integrated gasification and Cu-Cl cycle for trigeneration of hydrogen, steam and electricity. Int J Hydrogen Energy 36:2845–2854
9. Dincer I, Balta MT (2011) Potential thermochemical and hybrid cycles for nuclear-based hydrogen production. Int J Energy Res 35:123–137
10. Orhan MF, Dincer I, Rosen MA (2009) Energy and exergy analyses of the drying step of a copper-chlorine thermochemical cycle for hydrogen production. Int J Exergy 6:793–808
11. Lewis MA, Masin JG, Vilim RB (2010) Development of the low temperature Cu–Cl thermochemical cycle. International congress on advances in nuclear power plants
12. Ratlamwala TAH, Dincer I (2012) Energy and exergy analyses of a Cu–Cl cycle based integrated system for hydrogen production. Chem Eng Sci 84:564–573
13. Zamfirescu C, Dincer I, Naterer G (2010) Thermophysical properties of copper compounds in copper–chlorine thermochemical water splitting cycles. Int J Hydrogen Energy 35:4839–4852
14. Kalogirou SA (2004) Solar thermal collectors and applications. Prog Energy Combustion Sci 30:231–295
15. Barigozzi G, Bonetti G, Perdichizzi FA, Ravelli S (2012) Thermal performance prediction of a solar hybrid gas turbine. Solar Energy 86:2116–2127
16. Huang W, Hu P, Chen Z (2012) Performance simulation of a parabolic trough solar collector. Solar Energy 86:746–755
17. Xu C, Wang Z, Li X, Sun F (2011) Energy and exergy analysis of solar power tower plants. Appl Thermal Eng 31:3904–3913

Energy and Exergy Analyses of Copper–Chlorine (Cu–Cl) Based Integrated Systems for Hydrogen Production

10

Ahmet Ozbilen, Ibrahim Dincer, and Marc A. Rosen

Abstract

Hydrogen production via thermochemical water splitting using the Cu–Cl cycle is a promising alternative to conventional hydrogen production methods. Multi-generation systems are often attractive due to their higher energy and exergy efficiencies than individual cycles (e.g. steam or gas turbine cycles). An increase in efficiency often allows, for the same output, less resources (or exergy) to be used. This, in return, reduces the extraction from the environment of energy resources (e.g. fossil fuels), and decreases the associated environmental impacts. In this study, comprehensive thermodynamic analyses of two Cu–Cl based integrated systems for hydrogen production are reported. The systems considered here are developed to produce hydrogen and provide cooling. Hot water, drying air and oxygen are also by-products of the system. The first system also has the capability of generating electricity using a two-stage steam turbine cycle. The main sub-units of the system are the Cu–Cl thermochemical water splitting cycle and a LiBr–H_2O absorption cooling system. Solar energy drives the first system using a heliostat solar tower, whereas waste/process heat from a Generation IV nuclear supercritical water cooled reactor (SCWR) is the energy source of the second system. The energy efficiency of the first system is found to be approximately 70 %, while the exergy efficiency is approximately 58 %. The second system, on the other hand, has an energy efficiency of 63 % and an exergy efficiency of 41 %.

Keywords

Hydrogen production • Thermochemical water splitting • Cu–Cl cycle • Exergy • Multi-generation

Introduction

Global energy demand tends to increase due to the increasing living standards and a growing world population. Concerns about the energy supply security are increasing due to the reductions in supplies of fossil fuel resources which increase energy carrier prices. These resources contribute to air pollution and global climate change. Petroleum is a central concern, with a share of more than one third of global primary energy consumption and more than 95 % of the energy consumption in the transport sector. The negative environmental impact of coal mining and use combined with the large contribution of coal usage to global carbon dioxide emissions, as well as potential future risks of the declining reserves of natural gas, are other factors of concern [1].

Hence, alternatives to fossil fuels have been sought. Increases in energy demand will likely lead to a growth in nuclear and renewable energy utilization, partly to meet the objective of sustainability. The shift from fossil fuels to nuclear and renewable resources is expected due to the increase in energy demand as well as concerns over environmental issues such as

A. Ozbilen (✉) • I. Dincer • M.A. Rosen
Faculty of Engineering and Applied Science, University of Ontario Institute of Technology,
2000 Simcoe Street North, Oshawa, ON, Canada L1H 7K4
e-mail: Ahmet.Ozbilen@uoit.ca; Ibrahim.Dincer@uoit.ca; Marc.Rosen@uoit.ca

global warming. In the future, energy systems are expected to be hybrid systems when it is economically feasible. Hybrid systems combine various energy resources and energy conversion methods to help increase efficiency while reducing wastes and associated environmental impact. Hydrogen is a promising candidate as an energy carrier that helps expand markets for renewable and nuclear energy resources and contributes to sustainability and environmental stewardship, and that can act as a link between these technologies when they are utilized in hybrid systems [2, 3]. Integrated energy conversion systems can help fulfill the increasing need for energy sustainability.

Hydrogen exists in abundance in nature in the form of water. However, pure hydrogen needs to be produced and there are several methods of achieving this including steam reforming of natural gas, coal gasification, water electrolysis and thermochemical water decomposition. Dufour et al. [4] indicate that 96 % of world's hydrogen is produced using fossil fuels, and steam reforming of natural gas is the most commonly used method.

Hydrogen production using thermochemical water splitting cycles has the potential to be cleaner and more cost-effective than other production methods. Although hydrogen production systems using thermochemical cycles have not yet been commercialized, studies have shown that such systems can be expected to compete with conventional H_2 production methods including steam methane reforming [5, 6]. Due to its lower temperature requirements (around 530 °C), the Cu–Cl thermochemical water decomposition cycle has some advantages over other cycles [7].

Multi-generation systems are often attractive due to their higher energy and exergy efficiencies than individual cycles (e. g. steam or gas turbine cycles). An increase in efficiency often allows, for the same output, less resources (or exergy) to be used. This, in return, reduces the extraction from the environment of energy resources (e.g. fossil fuels), and decreases the associated environmental impacts. The objective of this study is to conduct a comprehensive thermodynamic analysis of a novel Cu–Cl based integrated system for multi-generation, to improve understanding of the system and its potential applications.

System Description

The systems discussed here produce hydrogen as the main output. Product hydrogen is considered to be exported as a commodity for industry and/or as a fuel. All systems also have the capability of hydrogen storage for energy management. Thus, the produced hydrogen is always a product; and when energy management is needed, some of the hydrogen will be stored and converted to electricity using fuel cells. Oxygen as an output of the Cu–Cl cycle is also treated as byproduct which is sufficiently pure for use or sale [8]. All the systems also have the capability of providing cooling, hot water and drying air. A LiBr–H$_2$O absorption refrigeration system is considered in the study for both systems which uses the excess energy of solar/nuclear heat transfer fluid (HTF) to obtain cooling effect. The absorption cooling system (ACS) is used instead of a conventional cooling system to utilize surplus heat. A steam turbine cycle (STC) is included in System I to generate power. Further details on the ACS and STC are presented elsewhere [9, 10]. Hot water at 42 °C is supplied to a community by the integrated system. Also, drying air is obtained by heating ambient air to drying temperature (50 °C) using excess heat of the exhaust gases. Drying air can be used in many applications, mainly drying fruits and vegetables.

System I: Cu–Cl Based Multi-Generation System Using Solar Energy

Solar thermal energy, concentrated using a heliostat solar tower, is the energy source of System I (Fig. 10.1). Molten salt (which has composition of 60 % NaNO$_3$ and 40 % KNO$_3$, on a mass basis) is considered as the HTF to supply heat to the Cu–Cl cycle. Molten salt has an advantage in that the solar heat can be stored for tens of hours for use at night, or when sunlight is not available [11]. First, heat is supplied to the copper oxychloride decomposition step (step 4) since this step has the highest temperature heat requirement (530 °C) in the cycle. Second, the heat is transferred to the hydrolysis step (step 3) of the Cu–Cl cycle and then hydrogen production (step 1) and drying (step 2). The temperature of the molten salt is increased to 650 °C, so as to match the heat requirements of the Cu–Cl cycle [11]. The temperature of the molten salt in a low temperature storage tank is higher than 250 °C which is about 30 °C higher than the melting point of the molten salt. A hydrogen storage tank and fuel cell unit are also integrated to the Cu–Cl cycle for energy management. Energy management with a hydrogen storage option is promising, since hydrogen can be converted to electricity efficiently via fuel cells during peak hours. System I also comprises a STC, which has a low pressure and a high pressure steam turbine, and
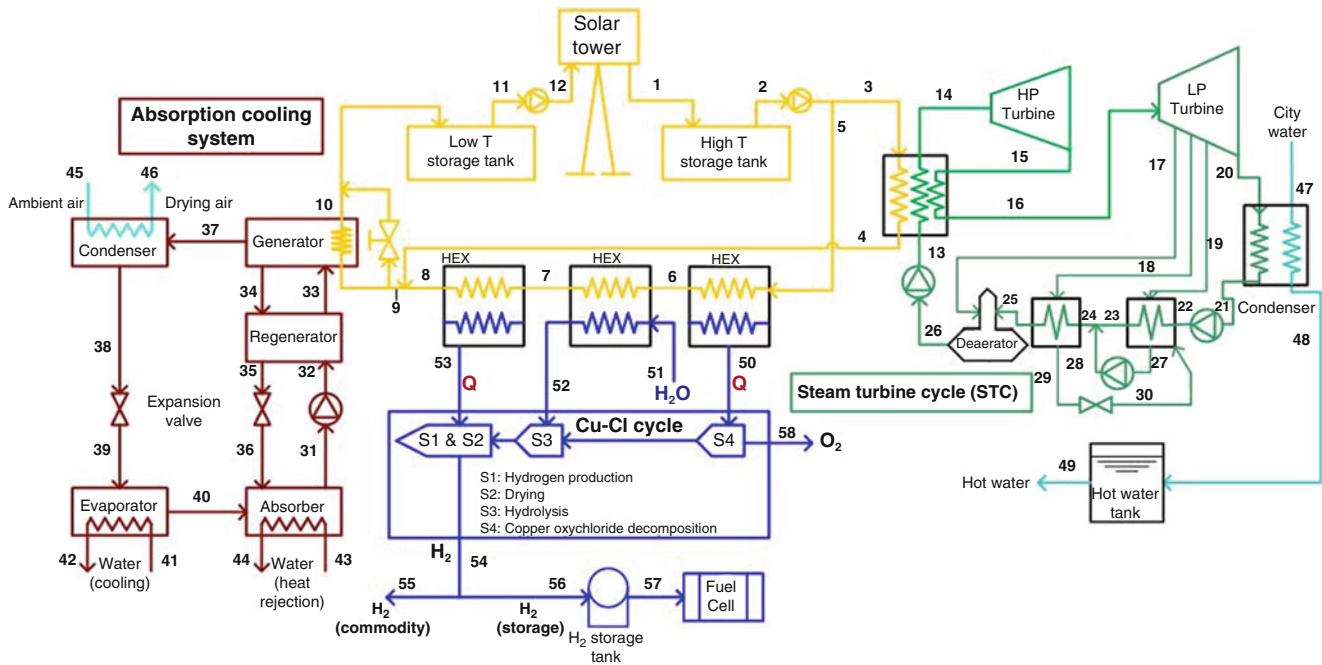
Fig. 10.1 Schematic diagram of System I

Table 10.1 Flows in System I

Sub-unit	Solar tower	Steam turbine cycle (STC)	Absorption cooling system (ACS)			Drying air	Hot water	Cu–Cl cycle		
Stream number	1–12	13–30	31–36	37–40	41–44	45–46	47–49	51, 52	54–57	58
Stream material	Molten salt	H_2O	LiBr–H_2O	H_2O	H_2O	Air	H_2O	H_2O	H_2	O_2

a LiBr–H_2O ACS. The STC and absorption system also use the solar energy, while the ORC utilizes waste heat from the STC. Figure 10.1 shows the system diagram, and Table 10.1 identifies the flows in the system. Water streams in Table 10.1 are differentiated in terms of its use:

- 13–30: H_2O is working fluid of the STC.
- 37–40: H_2O is working fluid of the ACS.
- 41–44: H_2O is for heat rejection from ACS.
- 47–49: H_2O is used in hot water production.
- 51–52: H_2O is feed to the Cu–Cl cycle.

System II: Cu–Cl Based Multi-Generation System Using Nuclear Energy

The second Cu–Cl based integrated system considered here utilizes nuclear power. A Generation IV supercritical water cooled reactor (SCWR) is a suitable match for the Cu–Cl cycle. The HTF can be both water and molten salt in this case. Unlike solar based systems, nuclear power does not have intermittent characteristics. The nuclear plant can continuously supply heat to the Cu–Cl cycle using water as the HTF. The coolant (water) inlet and exit temperatures are defined as 350 and 625 °C, respectively. Also, the coolant pressure and mass flow rate are 25 MPa and 1,320 kg/s [12]. Thus, water is selected as HTF for System II. The LiBr–H_2O ACS is also introduced to provide cooling, so there are multiple outputs in System II.
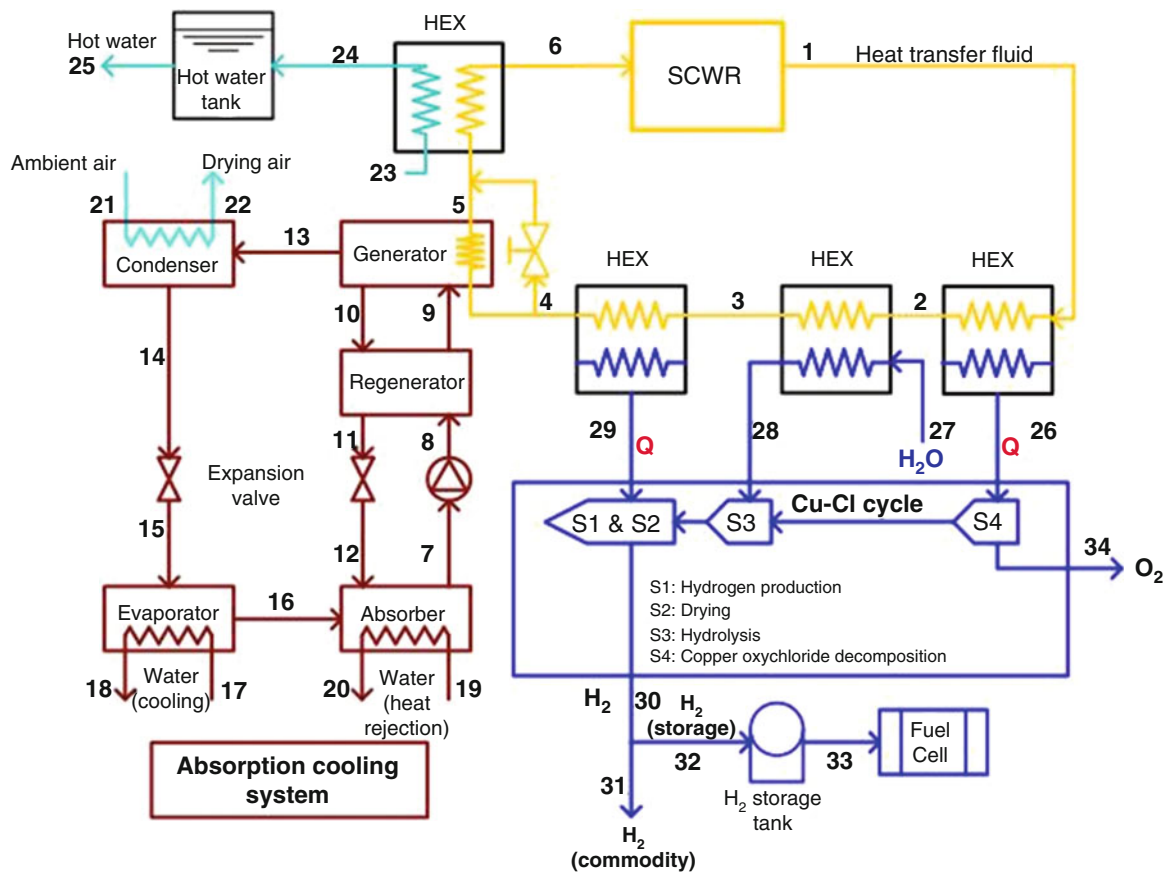
Fig. 10.2 Schematic diagram of System II

Table 10.2 Flows in System II

Sub-unit	Nuclear HTF	Absorption cooling system (ACS)			Drying air	Hot water	Cu–Cl cycle		
Stream number	1–6	7–12	13–16	17–20	21–22	23–25	27, 28	30, 33	34
Stream material	H_2O	LiBr–H_2O	H_2O	H_2O	Air	H_2O	H_2O	H_2	O_2

A hydrogen storage and fuel cell unit are also used in System II. Figure 10.2 shows the system diagram, and Table 10.2 identifies the flows in the system. Similarly, water streams in Table 10.2 are differentiated in terms of its use:

- 1–6: H_2O is HTF.
- 13–16: H_2O is working fluid of the ACS.
- 17–20: H_2O is for heat rejection from ACS.
- 23–25: H_2O is used in hot water production.
- 27–28: H_2O is fed to the Cu–Cl cycle.

Analysis

Analyses of the components in the systems (Figs. 10.1 and 10.2) are conducted using mass, energy, entropy and exergy balances. The assumptions considered throughout the analysis are as follows:

- Constant ambient temperature and pressure.
- Steady-state operation.

- Adiabatic compressors, turbines and heat exchangers.
- Isentropic efficiency for turbines and compressors of 0.9.
- Heat exchanger effectiveness of 0.85 for all heat exchangers.
- Hydrogen storage and fuel cell unit are not included to the thermodynamic calculations. Since, only steady-state operations are considered.
- Efficiency values of heliostat solar tower and SCWR are not taken into account. Hence, inputs for both systems are considered to be the energy content of the HTF.

The energy balance used in the analysis considering each component is given as follows:

$$\dot{Q}_{cv} - \dot{W}_{cv} = \sum\nolimits_{in} \dot{m}_i h_i - \sum\nolimits_{out} \dot{m}_i h_i \tag{10.1}$$

where $\dot{m}_i$ and h_i represent the mass flow rate and specific enthalpy of the flow stream into and out from each component in the system.

Exergy is defined as the maximum amount of work which can be produced by a system or a flow of matter or energy as it comes to equilibrium with a reference environment. Exergy is a measure of the potential of the system or flow to cause change as a consequence of not being in stable equilibrium with the reference environment [13, 14]. The exergy balance used in the analysis follows:

$$0 = \dot{Ex}_{Q,cv} - \dot{W}_{cv} + \sum\nolimits_{in} \dot{m}_i ex_i - \sum\nolimits_{out} \dot{m}_i ex_i - \dot{Ex}_{di} \tag{10.2}$$

The exergy quantities in an exergy balance are described below by Dincer and Rosen [13]:

Exergy of thermal energy (Ex_Q): The exergy associated with a thermal energy transfer Q can be expressed as:

$$Ex_Q = \sum\nolimits_{i=1}^{n} \left[Q_i \times \left(1 - \frac{T_0}{T_i} \right) \right] \tag{10.3}$$

Specific exergy of a matter flow (ex_i): The exergy of flow can be expressed in terms of physical, chemical, kinetic and potential components. Neglecting the kinetic and potential energy changes in the components considered in this study, ex_i of flow streams can be defined as

$$ex_i = (h_i - h_o) - T_o(s_i - s_o) + ex_{ch,i} \tag{10.4}$$

where $ex_{ch,i}$ is the specific chemical exergy of flow stream i.

Exergy destruction (Ex_d): Exergy destruction in a component is proportional to the entropy generation due to irreversibilities and can be written as

$$Ex_{di} = T_o \times S_{gen,i} \tag{10.5}$$

where $S_{gen,i}$ denotes the entropy generation in each component.

The energy efficiency of System I can be expressed as follows:

$$\eta_{en} = \frac{\dot{m}_{H_2} \times LHV_{H_2} + \dot{W}_{net} + \dot{Q}_{cooling} + \dot{m}_{air} \times (h_{air} - h_{air,0}) + \dot{m}_{hotwater} \times (h_{hotwater} - h_{hotwater,0})}{\dot{m}_{htf} \times (h_1 - h_{12})} \tag{10.6}$$

where $\dot{W}_{net} = \dot{W}_{net,STC} - \dot{W}_{in,CuCl}$

The exergy efficiency of System I can be expressed as follows:

$$\eta_{ex} = \frac{\dot{Ex}_{H_2} + \dot{W}_{net} + \dot{Ex}_{Q_{cooling}} + \dot{m}_{air} \times (ex_{air} - ex_{air,0}) + \dot{m}_{hotwater} \times (ex_{hotwater} - ex_{hotwater,0})}{\dot{m}_{htf} \times (ex_1 - ex_{12})} \tag{10.7}$$

Fig. 10.3 Energy and exergy efficiency of System I and its sub-units
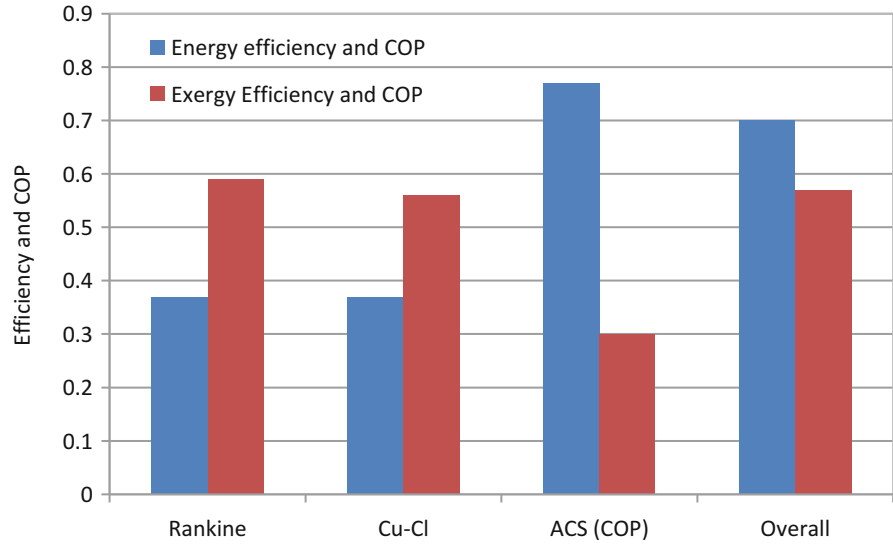
Similarly, the energy and exergy efficiencies respectively of System II follow:

$$\eta_{en} = \frac{\dot{m}_{H_2} \times LHV_{H_2} + \dot{Q}_{cooling} + \dot{m}_{air} \times (h_{air} - h_{air,0}) + \dot{m}_{hotwater} \times (h_{hotwater} - h_{hotwater,0})}{\dot{m}_{htf} \times (h_1 - h_{12}) + \dot{W}_{in,CuCl}} \tag{10.8}$$

$$\eta_{ex} = \frac{\dot{Ex}_{H_2} + \dot{Ex}_{Q_{cooling}} + \dot{m}_{air} \times (ex_{air} - ex_{air,0}) + \dot{m}_{hotwater} \times (ex_{hotwater} - ex_{hotwater,0})}{\dot{m}_{htf} \times (ex_1 - ex_{12}) + \dot{W}_{in,CuCl}} \tag{10.9}$$

Results and Discussion

The results of the comprehensive thermodynamic analysis of the Cu–Cl based integrated multi-generation system are presented in this section. Engineering Equation Solver (EES) software is used to study the performance of the system and its components. The parametric studies are carried out by varying some of the system parameters.

Figure 10.3 shows the energy and exergy efficiencies of System I and its sub-units. The energy efficiency of the overall system is 70 % whereas the exergy efficiency is 57 %. However, if the heat released by the condenser of the STC is not utilized as hot water, the energy efficiency value would be 51 %. The COP of the ACS is 0.77 and the exergetic COP is 0.30. The exergy efficiency of the STC is greater than its energy efficiency, since the exergy of output power is the power itself although exergy of input heat is lower than the energy of the heat input.

The energy and exergy efficiencies of the System II and its sub-units are shown in Fig. 10.4. The overall energy efficiency of System II is 51 % and the exergy efficiency is 41 %. The ACS and the Cu–Cl cycle used in System II have similar efficiency values as the ones in System I.

Figures 10.5 and 10.6 show the percentage contributions of System I and System II outputs to flows of (a) total energy and (b) total exergy. The energy percentages of all outputs for both systems are close to each other. The exergies of power and hydrogen dominate the System I exergy share, whereas the exergy of the output is 94 % of total exergy output for System II. Energy of cooling is defined as the amount of heat extracted from the cooling HTF (water for both systems).

Figure 10.7a and 10.7b show the impact of heat exchanger effectiveness on energy and exergy efficiencies. In both figures variation of efficiencies with 'no hot water' cases is also presented. Both energy and exergy efficiencies increase with increasing effectiveness due to reduction in lost energy to the environment. Figure 10.7a and 10.7b also show that utilizing the rejected heat out of the system as a system product, hot water significantly increases the energy efficiencies of the systems. Exergy efficiency results, however, are very close for the both 'utilized hot water' and 'no hot water' cases in Systems I and II.

Fig. 10.4 Energy and exergy efficiency of System II and its sub-units
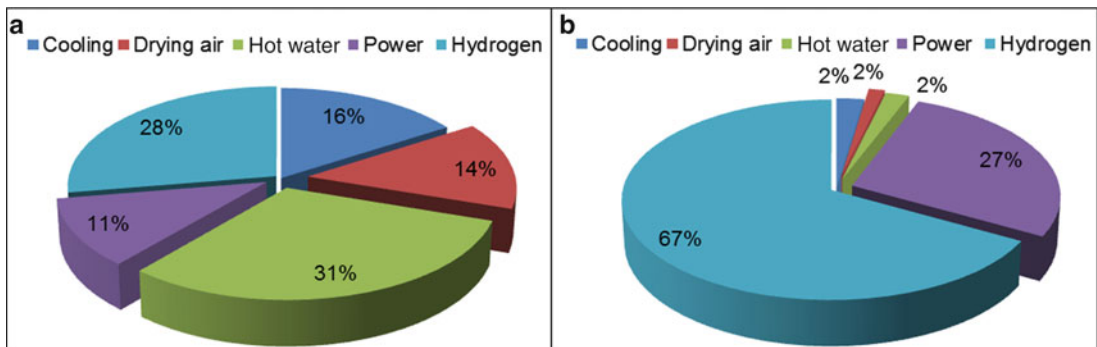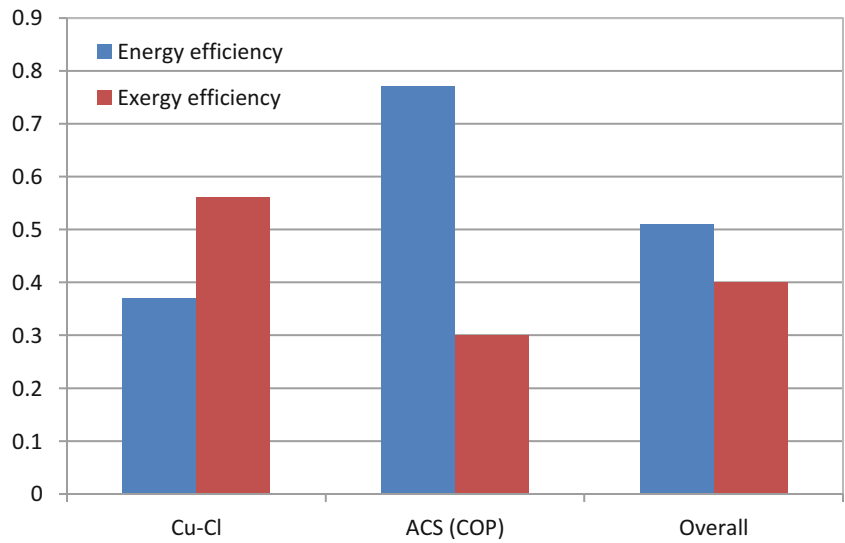
Fig. 10.5 Percentage contributions of System I outputs to (**a**) total energy and (**b**) total exergy flow
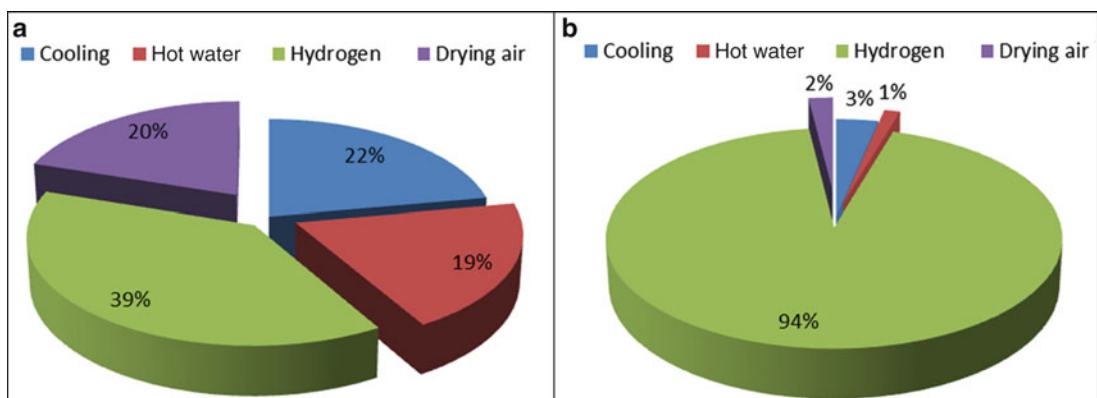
Fig. 10.6 Percentage contributions of System II outputs to (**a**) total energy and (**b**) total exergy flow

Fig. 10.7 Variation of energy and exergy efficiencies with heat exchanger effectiveness for (**a**) System I and (**b**) System II
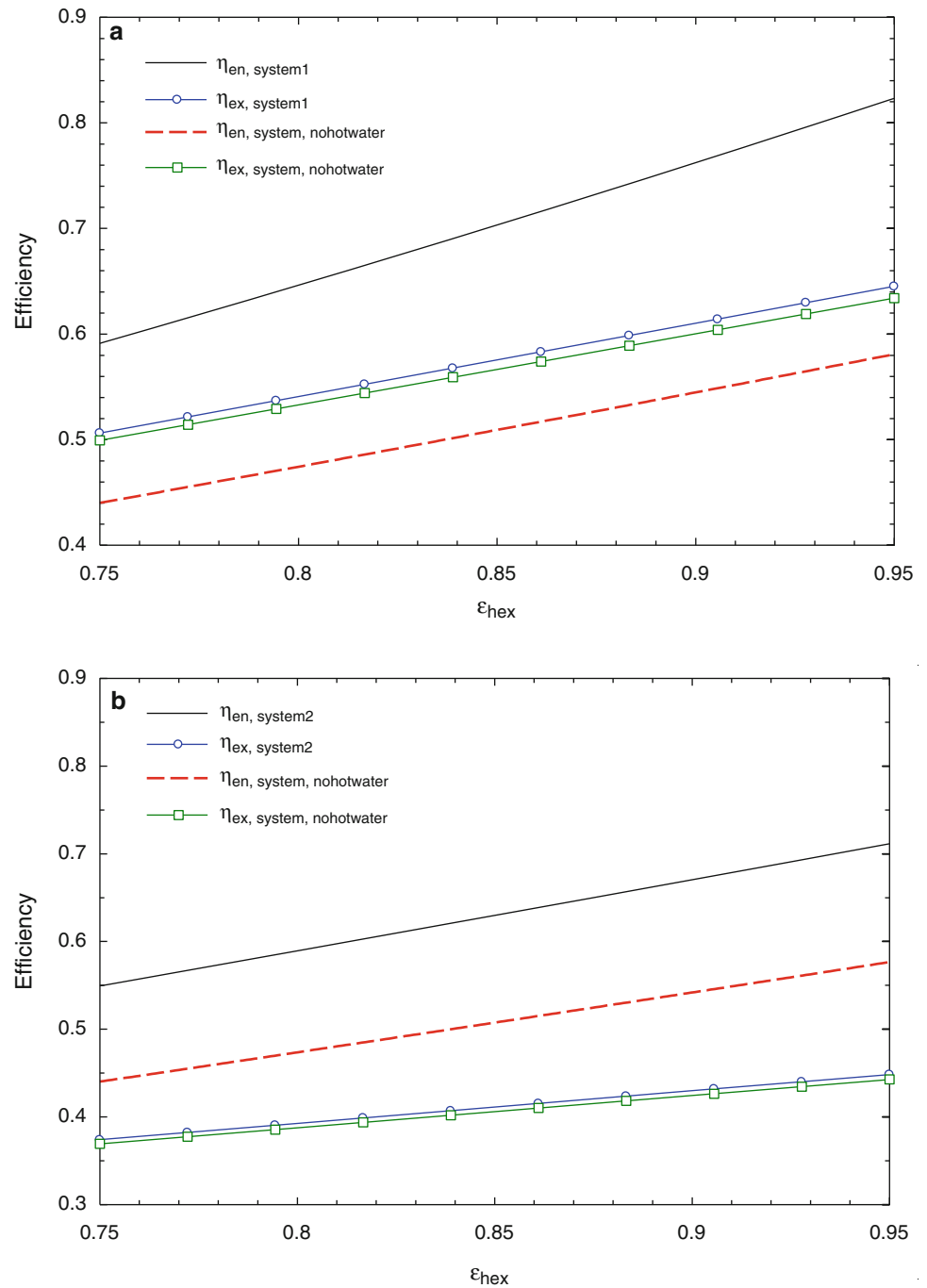
Conclusions

Thermodynamic analyses based on energy and exergy are successfully performed to investigate the performance of the Cu–Cl based, integrated multi-generation systems. The overall energy efficiency of System I is 70 % whereas the exergy efficiency is 57 %. The overall energy efficiency of System II is 51 % and its exergy efficiency is 41 %. The produced hydrogen is the main contributor to the exergy output flows of both systems. It is concluded that utilizing rejected heat as hot water to the utilities significantly increases the energy efficiency, but does not have a major impact on exergy efficiency, mainly since the temperature of the hot water is close to reference-environment temperature.

Nomenclature

ex	Specific exergy, MJ/kg	η_{ex}	Exergy efficiency
Ex_d	Exergy destruction, MJ	Q	Heat, MJ
ex_{ch}	Specific chemical exergy, MJ/kg	S_{gen}	Entropy generation, MJ/K
Ex_Q	Exergy of thermal energy, MJ	T_i	System temperature, K
h	Specific enthalpy, kJ/kg	T_0	Reference-environment temperature, K
LHV	Lower heating value, MJ	W	Work, MJ
$\dot{m}$	Mass flow rate, kg/s	$\dot{W}_{net}$	Net power output, MW
η_{en}	Energy efficiency		

Acronyms

ACS	Absorption cooling system	LP	Low pressure
EES	Engineering equation solver	SCWR	Supercritical water cooled reactor
HP	High pressure	STC	Steam turbine cycle
HTF	Heat transfer fluid		

References

1. Urbaniec K, Friedl A, Huisingh D, Claassen P (2010) Hydrogen for a sustainable global economy. J Cleaner Prod 18:S1–S3
2. Dincer I (2012) Green methods for hydrogen production. Int J Hydrogen Energy 37:1954–1971
3. Rosen MA (2010) Advances in hydrogen production by thermochemical water decomposition: a review. Energy 35:1068–1076
4. Dufour J, Serrano DP, Galvez JL, Moreno J, Garcia C (2009) Life cycle assessment of processes for hydrogen production: environmental feasibility and reduction of greenhouse gases emissions. Int J Hydrogen Energy 34:1370–1376
5. Lewis MA, Masin JG, O'Hare PA (2009) Evaluation of alternative thermochemical cycles. Part I: the methodology. Int J Hydrogen Energy 34:4115–4124
6. Pilavachi PA, Chatzinapagi AI, Spyropoulou AI (2009) Evaluation of hydrogen production methods using the analytic hierarchy process. Int J Hydrogen Energy 34:5294–5303
7. Naterer GF, Suppiah S, Stolberg L, Lewis M, Wang Z, Dincer I, Rosen MA, Gabriel K, Secnik E, Easton EB, Pioro I, Lvov S, Jiang J, Mostaghimi J, Ikeda BM, Rizvi G, Lu L, Oduyaka A, Spekkens P, Fowler M, Avsec J (2013) Progress of international hydrogen production network for the thermochemical Cu–Cl cycle. Int J Hydrogen Energy 38:740–759
8. Naterer GF, Fowler M, Cotton J, Gabriel K (2008) Synergistic roles of off-peak electrolysis and thermochemical production of hydrogen from nuclear energy in Canada. Int J Hydrogen Energy 33:6849–6857
9. Gebreslassie BH, Medrano M, Boer D (2010) Exergy analysis of multi-effect water–LiBr absorption systems: from half to triple effect. Renew Energy 35:1773–1782
10. Nezammahalleh H, Farhadi F, Tanhaemami M (2010) Conceptual design and techno-economic assessment of integrated solar combined cycle system with DSG technology. Solar Energy 84:1696–1705
11. Wang ZL, Naterer GF, Gabriel KS, Secnik E, Gravelsins R, Daggupati VN (2011) Thermal design of a solar hydrogen plant with a copper–chlorine cycle and molten salt energy storage. Int J Hydrogen Energy 36:11258–11272
12. Pioro IL, Duffey RB (2007) Heat transfer and hydraulic resistance at supercritical pressures in power engineering applications. ASME, New York
13. Dincer I, Rosen MA (2013) Exergy: energy, environment and sustainable development, 2nd edn. Elsevier, Oxford
14. Rosen MA, Dincer I (2001) Exergy as the confluence of energy, environment and sustainable development. Exergy Int J 1:3–13
15. Kotas TJ (1995) The exergy method of thermal plant analysis. Krieger, Malabar
16. Moran MJ (1989) Availability analysis: a guide to efficient energy use. ASME, New York

Simulation and Exergy Analysis of a Copper–Chlorine Thermochemical Water Decomposition Cycle for Hydrogen Production

Mehmet F. Orhan, Ibrahim Dincer, and Marc A. Rosen

Abstract

In this study, a simulation model is developed to design and analyze a five-step Cu–Cl cycle using the Aspen Plus^{TM} chemical process simulation package. Based on the developed simulation results, an exergy analysis is conducted of a Cu–Cl cycle and its relevant chemical reactions. The reaction heat, exergy destruction, and efficiencies for each chemical reaction vary with the reaction temperature and reference-environment temperature. Energy and exergy parameters and the yield effectiveness are examined for the process, based on five-step cycle. The overall energy efficiency of the cycle varies from 42 to 44 % and exergy efficiency from 72 to 75 %. Sensitivity analyses are performed to determine the effects of various operating parameters on the efficiencies and yields. A parametric study is conducted and possible efficiency improvements are discussed.

Keywords

Hydrogen production • Thermochemical water decomposition • Nuclear • Thermoeconomic analysis • Copper–chlorine cycle • Simulation • Aspen Plus • Design

Introduction

The world faces problems with depleting energy resources and the harmful impact of present energy consumption patterns on the environment, and consequently on the global climate and humanity. The concerns regarding global climate change have led to extensive research and development on clean energy sources and technologies. While many of the available natural energy resources are limited due to their reliability, quality, quantity, and density, nuclear energy has the potential to contribute a significant share of large-scale energy supply with little contributions to climate change. Hydrogen production via thermochemical water decomposition is a potentially important process for direct utilization of nuclear thermal energy.

Thermochemical water splitting with a copper–chlorine (Cu–Cl) cycle is a promising process that could be linked with nuclear reactors to decompose water into its constituents, oxygen, and hydrogen, through intermediate copper and chlorine compounds; the net inputs are water and heat. The process involves a series of closed-loop chemical reactions that do not produce or emit to environment any greenhouse gases.

M.F. Orhan (✉)
Department of Mechanical Engineering, College of Engineering, American University of Sharjah,
PO Box 26666, Sharjah, United Arab Emirates
e-mail: morhan@aus.edu

I. Dincer • M.A. Rosen
Faculty of Engineering and Applied Science, University of Ontario Institute of Technology,
2000 Simcoe Street North, Oshawa, ON, Canada L1H 7K4
e-mail: Ibrahim.Dincer@uoit.ca; Marc.Rosen@uoit.ca

The Cu–Cl cycle is a hypothetical process that has not yet been constructed. However, many studies of the Cu–Cl cycle are available in the literature. For example, Lewis et al. [1, 2] have indicated that the Cu–Cl cycle is chemically viable, feasible with respect to engineering, and energy-efficient. A conceptual process incorporating the Aspen Plus mass and energy flows has been developed and the hydrogen production cost has been estimated as \$3.30 per kg hydrogen.

Naterer et al. [3, 4] have reported recent Canadian advances in nuclear-based hydrogen production and the thermochemical Cu–Cl cycle. Developments have been described of relevant process and reactors, thermochemical properties, materials, controls, safety, and reliability for the Cu–Cl cycle. Further, the economics of electrolysis at off-peak hours and the integration of hydrogen plants with Canada's nuclear plants have been explained.

One of the most challenging steps in the thermochemical Cu–Cl cycle is the hydrolysis of $CuCl_2$ into Cu_2OCl_2 and HCl while avoiding the need for excess water and the undesired thermolysis reaction, which yields CuCl and Cl_2. Argonne National Laboratory has designed a spray reactor where an aqueous solution of $CuCl_2$ is atomized into a heated zone, in which a steam/Ar flow is injected in co- or counter-current flow [5]. Also, an experimental study using a spray reactor with an ultrasonic atomizer has been carried out [6].

Although some preliminary technical studies of the Cu–Cl cycle have been reported and some small lab scale experiments of individual reactions in the cycle carried out, there is still a need to link all the sub-steps of the cycle and build a pilot plant, to facilitate eventual commercialization. Such an experimental set up of overall cycle is lacking, especially to evaluate the behavior of the complete cycle such as energy and exergy parameters and cost effectiveness. Simulation packages, such as Aspen Plus, are useful tools to provide system designer and operators with design, optimization, and operation information that can assist in designing and building a pilot plant.

The objective of this study is to develop a simulation model to design and analyze a five-step Cu–Cl cycle using the Aspen Plus™ chemical process simulation package. An exergy analysis is conducted based on the simulation that developed the cycle and its relevant chemical reactions. Energy and exergy parameters and the yield effectiveness are examined. Sensitivity analyses are performed to study the effects of various operating parameters on the efficiencies and yields. A parametric study is conducted and possible efficiency improvements are discussed.

System Description

The Cu–Cl cycle consists of a set of reactions with the net result of splitting of water into its constituents, hydrogen, and oxygen: H_2O (g) $\longrightarrow H_2$ (g) + $1/2O_2$ (g). The Cu–Cl cycle uses a series of intermediate copper and chloride compounds. These chemical reactions form a closed internal loop that recycles all chemicals on a continuous basis, without emitting greenhouse gases.

The Cu–Cl cycle has been shown [1-9] to be a potentially attractive option for generating hydrogen from nuclear energy. Compared with other hydrogen production options, the thermochemical Cu–Cl cycle is expected to have a higher efficiency, to produce hydrogen at a lower cost, and to have a smaller impact on the environment by reducing airborne emissions, solid wastes, and energy requirements.

The five-step Cu–Cl cycle (Fig. 11.1) is the first and main conceptual design developed. All the other configurations (such as four- and three-step Cu–Cl cycles) are obtained by combining one or more steps in the five-step cycle. The five-step Cu–Cl cycle has three thermochemical reactions and one electrochemical reaction (see Table 11.1), and involves five steps:
1. HCl(g) production, using such equipment as a fluidized bed,
2. Oxygen production,
3. Copper (Cu) production,
4. Drying, and
5. Hydrogen production.

As illustrated in Fig. 11.1, only water and nuclear-derived heat enter the cycle and only H_2 and O_2 are produced. There are no greenhouse gas emissions. Liquid water at ambient temperature enters the cycle and passes through several heat exchangers where it evaporates and increases in temperature to 400 °C. Heat for this process is obtained from cooling the hydrogen and oxygen gases before they exit the cycle. Steam at 400 °C and solid copper chloride ($CuCl_2$) at 400 °C from the dryer enter the fluidized bed (S1), where the following chemical reaction occurs:

$$2CuCl_2(s) + H_2O(g) \longrightarrow CuO^*CuCl_2(s) + 2HCl(g) \tag{11.1}$$
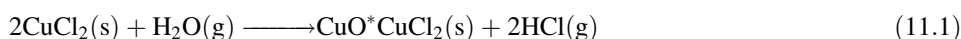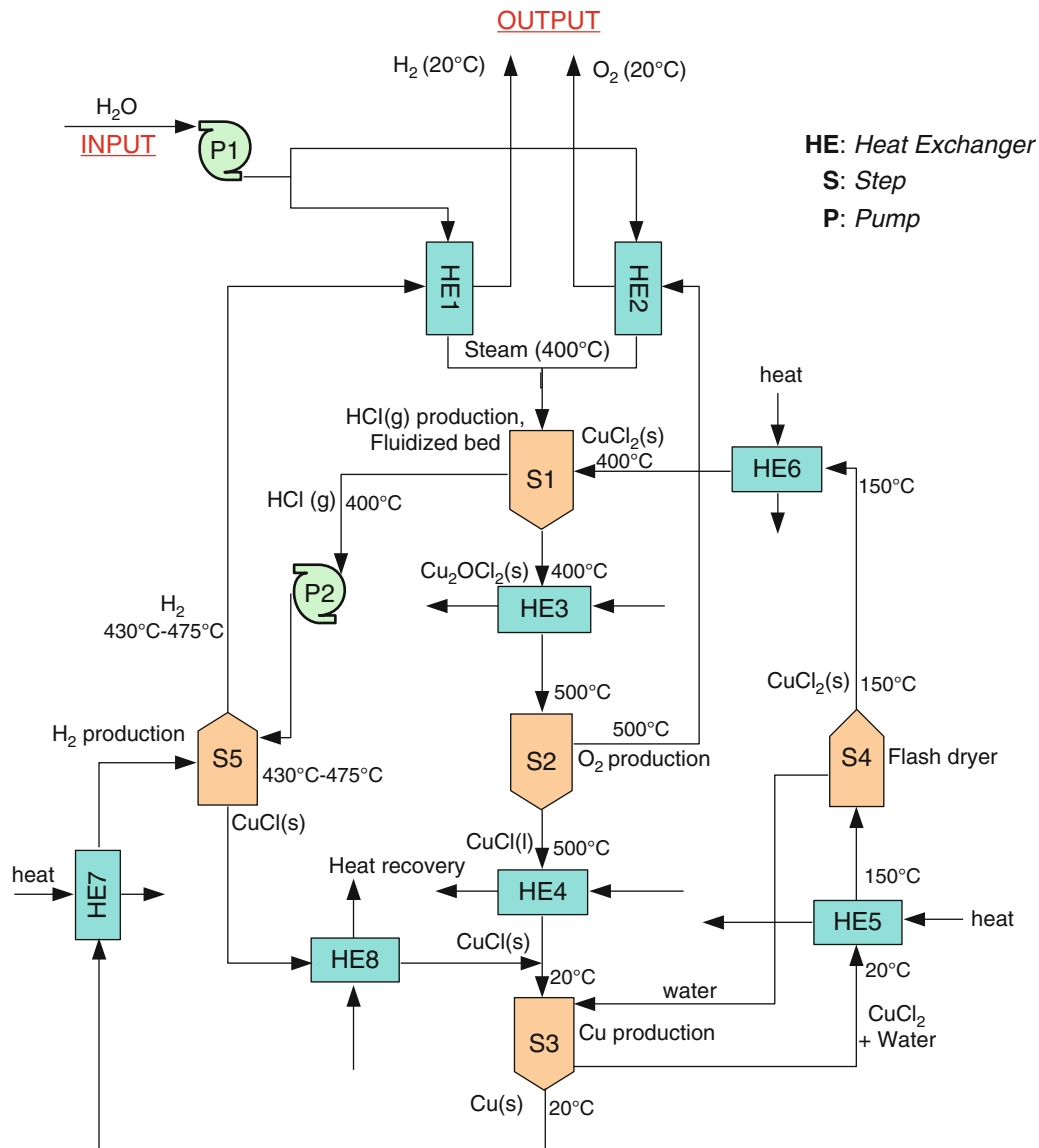
Fig. 11.1 Conceptual flow chart of the five-step Cu–Cl cycle

Table 11.1 The main steps in the five-step Cu–Cl cycle with their corresponding reactions

Step	Name	Reaction	Temperature (°C)
1	Hydrolysis	$2CuCl_2(s) + H_2O(g) \longrightarrow Cu_2OCl_2(s) + 2HCl(g)$	400
2	O_2 production	$Cu_2OCl_2(s) \longrightarrow 2CuCl(l) + 1/2O_2(g)$	500
3	Electrolyzer	$4CuCl(s) + H_2O \longrightarrow 2CuCl_2(aq) + 2Cu(s)$	25
4	Dryer	$CuCl_2(aq) \longrightarrow CuCl_2(s)$	80
5	H_2 production	$2Cu(s) + 2HCl(g) \longrightarrow 2CuCl(l) + H_2(g)$	450

This reaction is endothermic and yields hydrochloric acid gas (HCl) and Cu_2OCl_2. The hydrochloric acid gas is compressed and the Cu_2OCl_2 is transferred to another process step after its temperature is increased to the oxygen production reaction temperature of 500 °C.

In the oxygen production step (S2), an endothermic chemical reaction takes place:

$$CuO^*CuCl_2(s) \longrightarrow 2CuCl(l) + 1/2O_2(g) \tag{11.2}$$
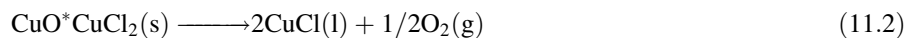
in which Cu_2OCl_2 is heated, and O_2 and copper monochloride (CuCl) are produced. Liquid copper monochloride is solidified by cooling it to 25 °C, after which it enters the copper production step (S3) together with the solid copper monochloride from the fifth step. In the third process step solid copper monochloride and water react endothermically at 25 °C as follows:

$$4CuCl(s) + H_2O \longrightarrow 2CuCl_2(aq) + 2Cu(s) \tag{11.3}$$
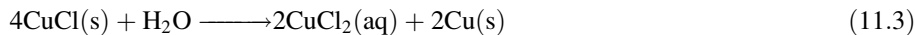
However in this reaction water acts as a catalyst and does not react with the other elements or compounds. Another specification for this third reaction that differentiates this step from others and makes it the most expensive, based on the price of electricity, is that electrolysis occurs. In this reaction, solid copper and a copper–chloride–water solution are produced. A mixture of copper–chloride and water is transferred to the dryer (S4), and solid copper enters the fifth step after its temperature is increased to that step's operating temperature. A physical reaction takes place in the dryer as follows:

$$CuCl_2(aq) \longrightarrow CuCl_2(s) + H_2O(l) \tag{11.4}$$

In the hydrogen production step (S5), hydrochloric gas and copper enter and are converted to gaseous hydrogen (H_2) and solid copper monochloride (CuCl). The reaction takes place at 450 °C at steady state as follows:

$$2Cu(s) + 2HCl(g) \longrightarrow 2CuCl(l) + H_2(g) \tag{11.5}$$
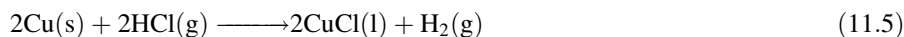
Process Design of the Five-Step Cu–Cl Cycle

In order to determine the potential of the Cu–Cl cycles, an Aspen Plus flowsheet is developed for this process design and the cycle's efficiency is calculated. Energy and mass balances, stream flows and properties, heat exchanger duties, and shaft work requirements are calculated, and heat recovery is optimized using a sensitivity analysis. An integrated heat exchange network is designed to use heat from the process streams efficiently and decrease the external heat demand.

To assist the simulation of the Cu–Cl cycles, the thermodynamic database in Aspen Plus is updated. To develop realistic simulations, values of the enthalpy of formation, the free energy of formation, and the heat capacity as a function of temperature for Cu_2OCl_2 are needed. Since Cu_2OCl_2 is not commercially available, a new experimental method for synthesizing it was developed by Lewis et al. [1, 2]. The enthalpy of formation at 25 °C was measured using two different methods and compared with data in the literature. A value of 380 ± 3 kJ/mol was determined to be the most reliable. The heat capacity was measured over three temperature regions: (1) from about 4 (liquid He temperature) to 64 K (liquid N_2 temperature), (2) from 64 to 360 K, and (3) from 298 to 700 K. The low temperature heat capacities are used to calculate the entropy. The free energy of formation is then derived from the experimental values for the enthalpy of formation and entropy values. Also, CuCl undergoes a solid–solid transition and then a solid–liquid transition. The specific enthalpy and Gibbs energy of formation of CuCl(s) at the standard temperature of 298.15 K are −37.0 and −120.0 kJ/mol, respectively. The Gibbs energy of formation of CuCl(s) is obtained by subtracting the product of the entropy of formation of CuCl at 298.15 K and the absolute temperature, 298.15 K, from the enthalpy of formation of CuCl at 298.15 K.

In this study, all thermodynamic data for the various chemical species are drawn from the literature and included in the physical property database of Aspen Plus (see Table 11.2). The reliability of the data for the other compounds is also verified by comparing data in various sources such as HSC Chemistry software.

An Aspen Plus simulation of the five-step Cu–Cl cycle is developed for the conditions discussed. Based on the five main reactions in Table 11.1 and the conceptual flow diagram in Fig. 11.1, an Aspen Plus flowsheet of the Cu–Cl cycle is

Table 11.2 Thermodynamic data used in the Aspen Plus database

Compound	DHSFRM (kJ/mol)	DGSFRM (kJ/mol)
$CuCl_2$(s)	−217.4	−173.6
CuO(s)	−162.0	−129.4
CuCl(s)	−137.0	−120.0
Cu(s)	0	0
Cu_2OCl_2(s)	−381.3	−310.45

Source: [9]

DHSFRM Enthalpy of formation at 298.15 K and 1 bar, *DGSFRM* Gibbs free energy of formation at 298.15 K and 1 bar
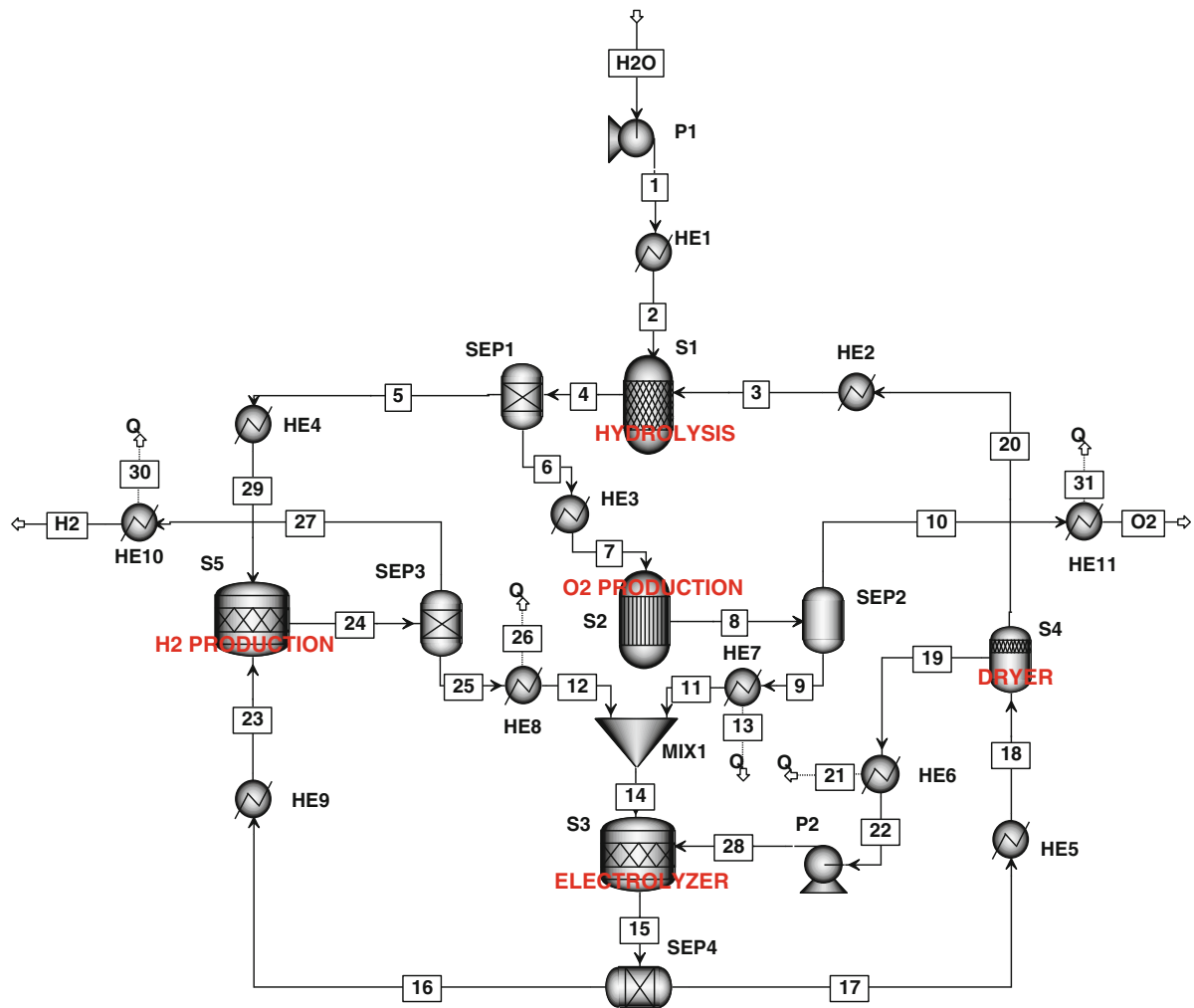
Fig. 11.2 Simplified Aspen Plus process flowsheet of the five-step Cu–Cl cycle

developed (see Fig. 11.2). This work represents one of the first completed and closed-loop flowsheet simulations of the Cu–Cl cycle.

In the process flow diagram in Fig. 11.2, hydrolysis occurs in the S1 block at 400 °C based on the equation given in Table 11.1. The products of reactor S1 are transferred to SEP1 where HCl is separated from Cu_2OCl_2. Reactor S2 is used to simulate the oxy-decomposition reaction, where oxygen gas is released and separated using the SEP2 block. The electrolysis step (block S3 in Fig. 11.2) is carried out independently and the results are linked back to the entire cycle, to avoid the problem of recycling in the electrolyzer. The drying step of the cycle is performed in unit operation S4. Finally, reactor S5 performs the hydrogen generation process through the reaction of Cu and HCl. The hydrogen gas generated is separated by unit operation SEP3, and other products are recycled.

Heaters, coolers, and heat exchangers are used to supply or recover heat for each process in the cycle. Mixers and splitters are used to combine and split the streams. Pumps are used to pressurize flows and transfer them among blocks, and to supply the required water to and within the cycle. Using the thermodynamic methods and specifying the operating conditions from experimental data in literature, the Cu–Cl cycle is simulated successfully. The reactors calculate the heat of reactions at the specified conditions. The results are presented per mol of hydrogen in this study. The corresponding heat requirements, recovered heat, work requirements, and other data for the processes at various transfer points are shown in Table 11.3. Based on data given in this table, an energy balance of the cycle and the corresponding efficiency are evaluated. Note that all the exothermic heats are denoted by a negative sign.

From Table 11.3, the total heat requirement for the endothermic processes is 501.9 kJ, and the heat recovery from the exothermic processes is 210.8 kJ per mol of hydrogen. Using the recovered heat within the cycle to meet the thermal needs of endothermic processes, the net heat requirement is 291.1 kJ.

Table 11.3 Energy balance of the five-step Cu–Cl cycle process simulation

Block	Description	Process	ΔH Endothermic (kJ/mol H$_2$)	ΔH Exothermic (kJ/mol H$_2$)	W (kJ/mol H$_2$)
S1	Step 1	$2CuCl_2(s) + H_2O(g) \xrightarrow{400°C} Cu_2OCl_2(s) + 2HCl(g)$	120.2	–	–
S2	Step 2	$Cu_2OCl_2(s) \xrightarrow{500°C} 2CuCl(l) + 1/2O_2(g)$	125.5	–	–
S3	Step 3	$4CuCl(s) + H_2O \xrightarrow{25°C} 2CuCl_2(aq) + 2Cu(s)$	–	–	53.2
S4	Step 4	$CuCl_2(aq) \xrightarrow{80°C} CuCl_2(s)$	–	–	33.2
S5	Step 5	$2Cu(s) + 2HCl(g) \xrightarrow{450°C} 2CuCl(l) + H_2(g)$	–	−41.6	–
HE1	Heat exchanger	H_2O (25 °C) $\longrightarrow H_2O$ (400 °C)	80	–	–
HE2	Heat exchanger	$CuCl_2$ (80 °C) $\longrightarrow CuCl_2$ (400 °C)	61.3	–	–
HE3	Heat exchanger	Cu_2OCl_2 (400 °C) $\longrightarrow Cu_2OCl_2$ (500 °C)	20.8	–	–
HE4	Heat exchanger	HCl (400 °C) $\longrightarrow$ HCl (450 °C)	4.0	–	–
HE5	Heat exchanger	$CuCl_2/H_2O$ (25 °C) $\longrightarrow CuCl_2/H_2O$ (80 °C)	57.6	–	–
HE6	Heat exchanger	H_2O (80 °C) $\longrightarrow H_2O$ (25 °C)	–	−30	–
HE7	Heat exchanger	CuCl (500 °C) $\longrightarrow$ CuCl (25 °C)	–	−64	–
HE8	Heat exchanger	CuCl (450 °C) $\longrightarrow$ CuCl (25 °C)	–	−60.6	–
HE9	Heat exchanger	Cu (25 °C) $\longrightarrow$ Cu (450 °C)	32.5	–	–
HE10	Heat exchanger	H_2 (450 °C) $\longrightarrow H_2$ (25 °C)	–	−9	–
HE11	Heat exchanger	O_2 (500 °C) $\longrightarrow O_2$ (25 °C)	–	−5.6	–
SEP 1	Separator	$(Cu_2OCl_2, HCl)_{mix} \xrightarrow{400°C} (Cu_2OCl_2) + (HCl)$	–	–	0.87
SEP 2	Separator	$(CuCl, O_2)_{mix} \xrightarrow{500°C} (CuCl) + (O_2)$	–	–	1.2
SEP 3	Separator	$(CuCl, H_2)_{mix} \xrightarrow{450°C} (CuCl) + (H_2)$	–	–	1.8
SEP 4	Separator	$(Cu, CuCl_2(aq))_{mix} \xrightarrow{25°C} (Cu) + (CuCl_2(aq))$	–	–	2
P1	Pump	Water feed to the cycle	–	–	3
P2	Pump	Water handling within the cycle	–	–	1.93
MIX 1	Mixer	Mixing CuCl from stream 11 and 12	–	–	0.4
Total			501.9	−210.8	97.6

The electrical energy requirement for the electrolysis step is calculated, as is the auxiliary work to operate pumps, compressors, and other electrical devices. Assuming a 40 % conversion efficiency from heat to electricity, 97.6 kJ of work in Table 11.3 accounts for 244 kJ heat per mol of hydrogen produced.

Analysis

The overall energy efficiency of the Cu–Cl cycle, η_e, indicates the fraction of energy supplied that is converted to the energy content of H$_2$ based on its lower heating value:

$$\eta_e = \frac{\overline{E}_{out}}{\overline{E}_{in}} = \frac{\overline{LHV}_{H_2}}{\left(\overline{Q}_{net} + \overline{W}\right)_{in}} \tag{11.6}$$

where $\overline{LHV}_{H_2}$ is the lower heating value of hydrogen (240 kJ/mol H$_2$), $\overline{W}$ is the electrical work required for electrolyzer and auxiliary work required for pumps, compressors, etc., and $\overline{Q}_{net}$ is the net heat (after subtracting the recovered heat) used by the process to produce a unit amount of product hydrogen, all per mole of hydrogen produced. Equation (11.6) can be rewritten as follows to evaluate the effect of the effectiveness of the heat exchangers (ε) on the overall efficiency of the cycle (η_e):

$$\eta_e = \frac{\overline{LHV}_{H_2}}{\left(\frac{\overline{Q}_{required}}{\varepsilon} - \varepsilon\overline{Q}_{recovered}\right) + \overline{W}} \tag{11.7}$$

The overall exergy efficiency of the Cu–Cl cycle can be expressed as

$$\eta_{ex} = \frac{\overline{ex}_{out}}{\overline{ex}_{in}}$$

(11.8)

where $\overline{ex}_{out}$ and $\overline{ex}_{in}$ are output and input molar exergies. Using an exergy balance for the Cu–Cl cycle, the exergy efficiency in Eq. (11.8) can be written alternatively as

$$\eta_{ex} = \frac{\overline{ex}_{H_2}}{\overline{W} + \sum_i \left(1 - \frac{T_0}{T_i}\right)\overline{Q}_i}$$

(11.9)

where $\overline{ex}_{H_2}$ is the molar exergy of the hydrogen produced, which is given as 236.12 kJ/mol [10]. The reference environment is taken to be at a temperature of 298.15 K and atmospheric pressure (1 atm). For the overall cycle, we obtain the total input exergy of the cycle by adding the total work requirement and the exergy content of net heat input to the cycle. In the summation of the input exergies, the exothermic reaction (i.e., the hydrogen production reaction of five-step Cu–Cl cycle) is taken as negative, assuming this energy can be used for other endothermic reactions.

Results and Discussion

Figure 11.3 shows the variations of energy (η_e) and exergy (η_{ex}) efficiencies of the Cu–Cl cycle with the temperature of the hydrolysis reactor, based on Aspen Plus simulation results. The expected values of temperatures of the steps of the cycle are given in Table 11.1. When we vary a step temperature in the analysis, the other steps temperatures remain constant, at the value in Table 11.1. For example, to investigate the relation between T_1 (reaction temperature of step 1) and efficiencies, T_2, T_3, T_4, and T_5 (reaction temperatures of steps 2, 3, 4, and 5, respectively) are fixed at the values in Table 11.1.

Figure 11.4 shows the variations of energy and exergy efficiencies of the five-step Cu–Cl cycle with the temperature of the oxy-decomposition reactor. The overall energy efficiency of the cycle varies from 42 to 44 % and exergy efficiency from 72 to 75 %.

Figure 11.5 shows the variations of energy and exergy efficiencies of the Cu–Cl cycle with the temperature of the electrolysis process. The overall energy efficiency of the cycle varies from 42 to 44 % and exergy efficiency from 71 to 75 %
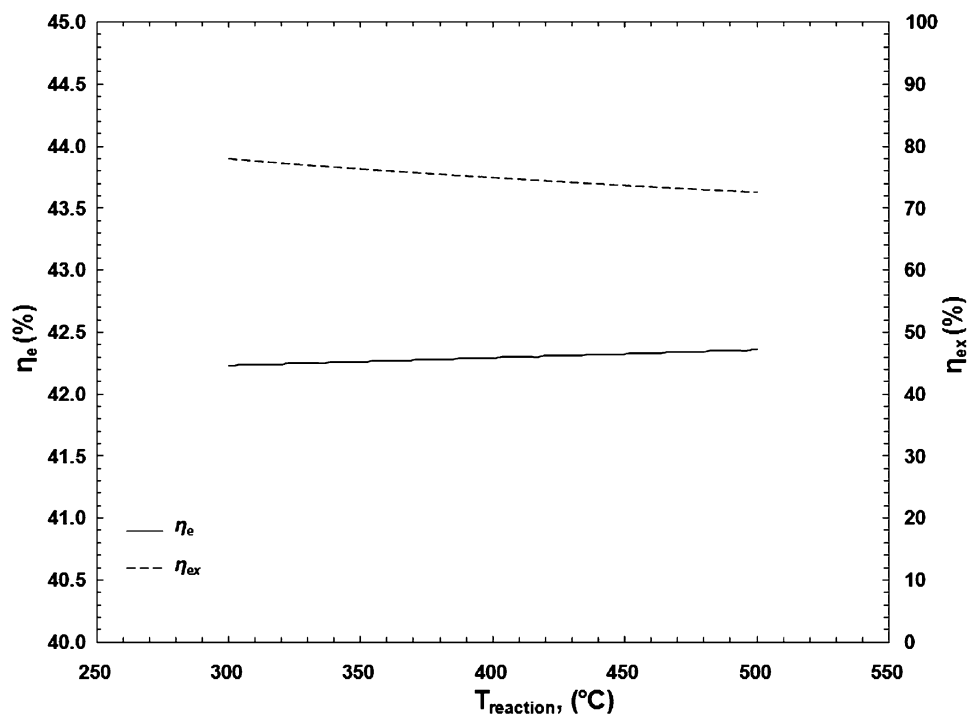
Fig. 11.3 Variation of efficiencies of the Cu–Cl cycle with the reaction temperature of step 1 (hydrolysis reactor)

Fig. 11.4 Variation of efficiencies of the Cu–Cl cycle with the reaction temperature of step 2 (oxy-decomposition reactor)
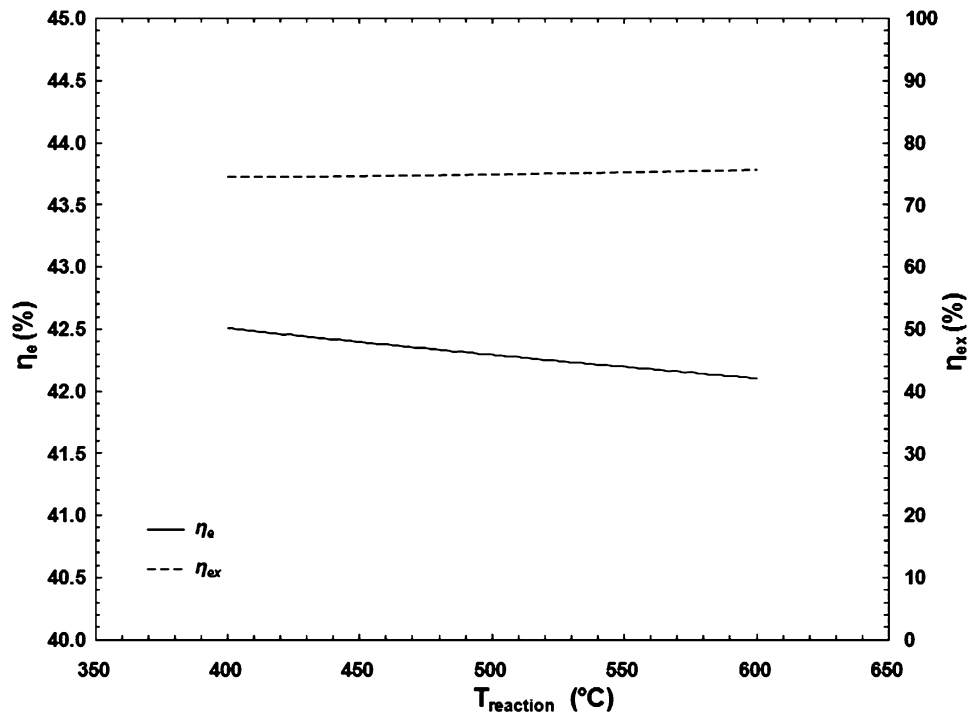
Fig. 11.5 Variation of efficiencies of the Cu–Cl cycle with the reaction temperature of step 3 (electrolysis reactor)
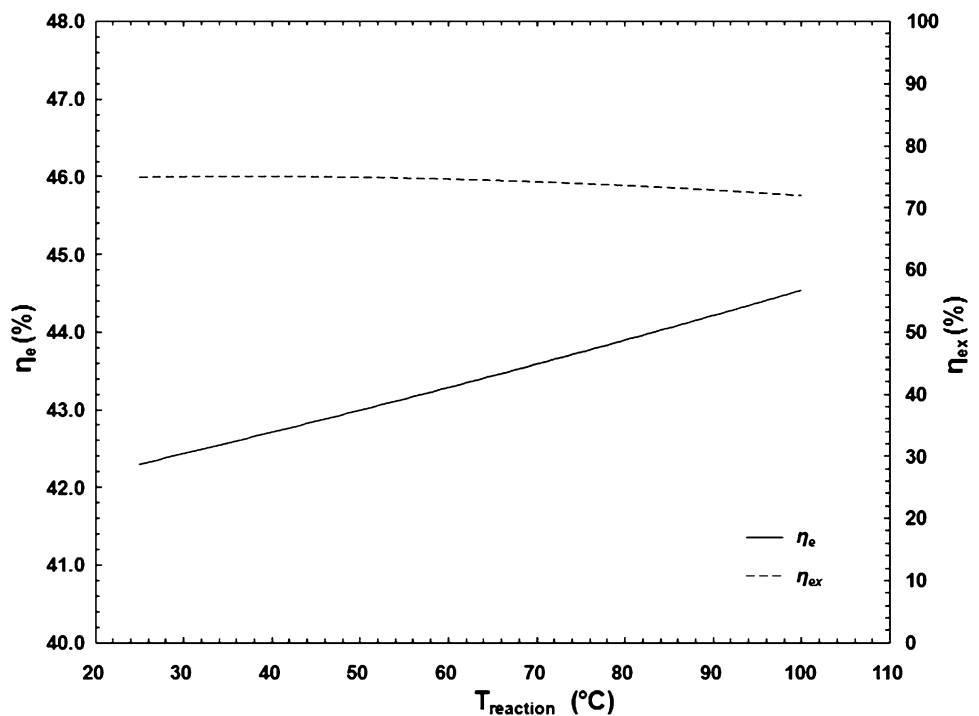
(see Fig. 11.5). The effect of the reaction temperature of step 3 on the energy and exergy efficiencies is significant. The energy efficiency of the cycle increases with increasing reaction temperature for step 3, and the overall exergy efficiency of the cycle increases with decreasing reaction temperature for step 3. Figure 11.6 shows the variations of energy (η_e) and exergy (η_{ex}) efficiencies of the Cu–Cl cycle with the temperature of the dryer.

Figure 11.7 shows the variations of energy and exergy efficiencies of the Cu–Cl cycle with the temperatures of the H$_2$ Production reactor. In all cases presented, the energy efficiency of the cycle increases with increasing reaction temperature for steps 1 and 3, and decreasing reaction temperature for steps 2, 4, and 5. Also, the overall exergy efficiency of the cycle

Fig. 11.6 Variation of efficiencies of the Cu–Cl cycle with the process temperature of step 4 (dryer)
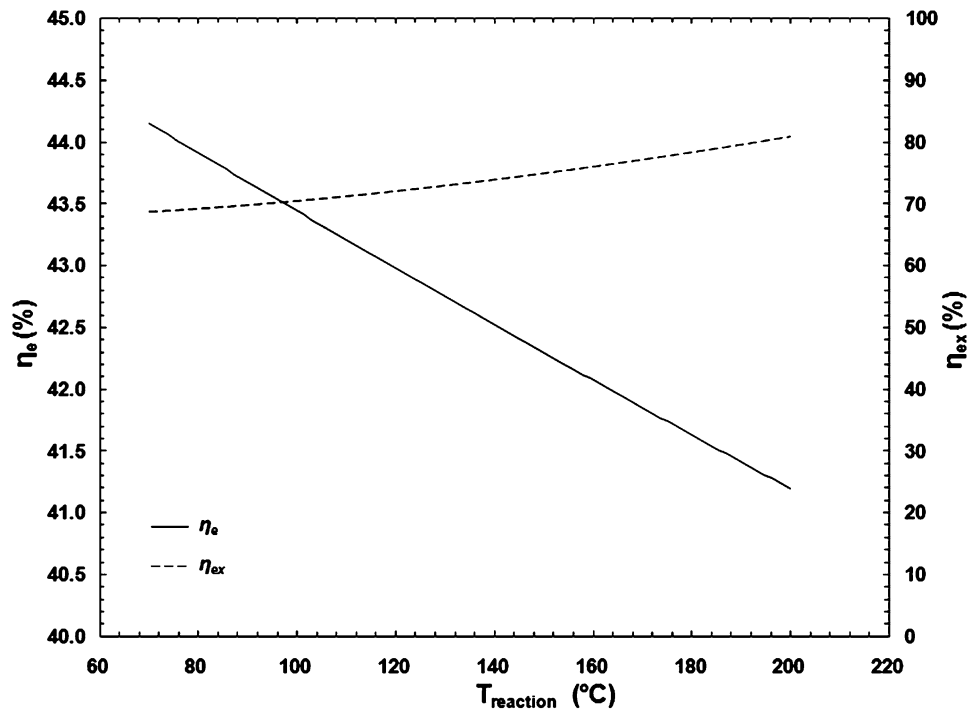
Fig. 11.7 Variation of efficiencies of the Cu–Cl cycle with the reaction temperature of step 5 (H$_2$ production)
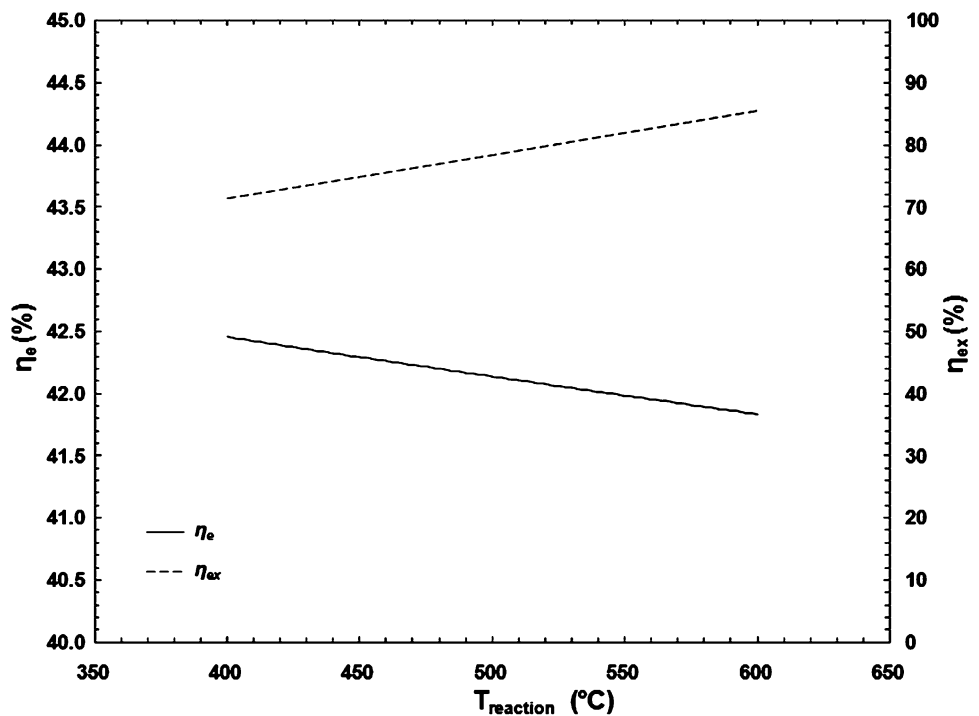
increases with increasing reaction temperature for steps 2, 4, and 5, and decreasing reaction temperature for steps 1 and 3. The effect of reaction temperature of steps 3 and 4 on the energy and exergy efficiencies is significant while the effect of reaction temperature of other steps is minor.

The variation of the overall efficiencies of the Cu–Cl cycle with heat exchangers effectiveness is shown in Fig. 11.8. Both energy and exergy efficiencies of the cycle increase using more effective heat exchangers in the cycle. This is because heat exchangers with higher effectiveness enhance heat recovery within the cycle and thus decrease the external heat requirements.

Fig. 11.8 Variation of the Cu–Cl cycle overall efficiencies with the effectiveness of the heat exchangers
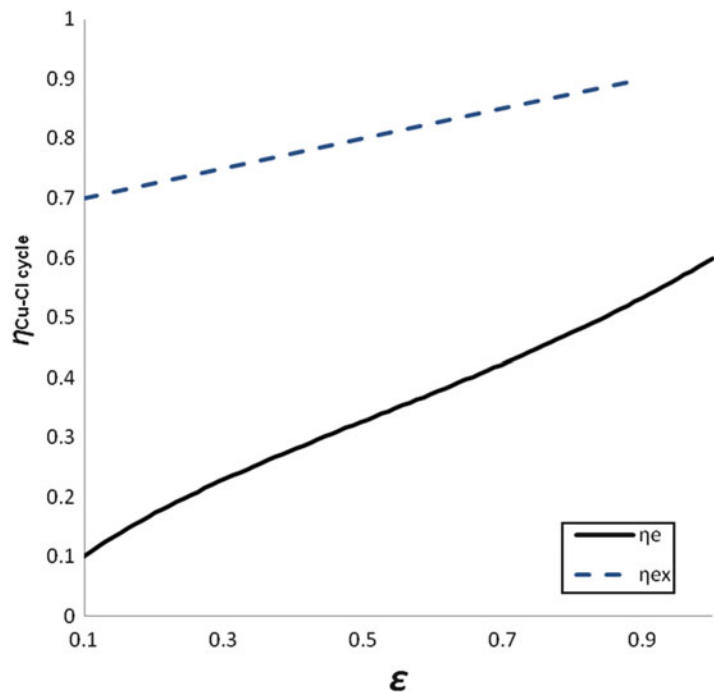
Table 11.4 Temperature profiles of heat exchangers in the five-step Cu–Cl cycle

Exothermic heat exchangers				Endothermic heat exchangers			
Block	ΔH (kJ/mol H_2)	T_{in} (°C)	T_{out} (°C)	Block	ΔH (kJ/mol H_2)	T_{in} (°C)	T_{out} (°C)
HE6	−30	80	25	HE1	80	25	400
HE7	−64	500	25	HE2	61.3	80	400
HE8	−60.6	450	25	HE3	20.8	400	500
HE10	−9	450	25	HE4	4.0	400	450
HE11	−5.6	500	25	HE5	57.6	25	80
				HE9	32.5	25	450

Fig. 11.9 Variation of the Cu–Cl cycle overall efficiencies with the recycling ratio of recovered energy
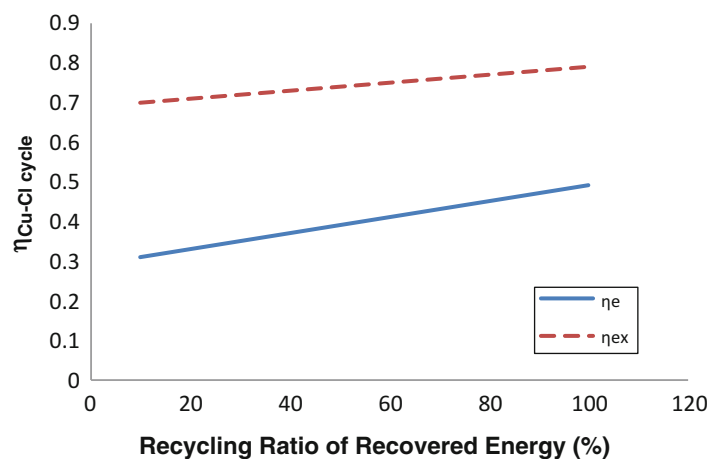
The results given here presume that all recovered heat could be used within the Cu–Cl cycle for endothermic processes. However, as can be seen in Table 11.4, most of the endothermic heat exchangers require high grade energy (above 400 °C) while most of the exothermic heat exchangers produce heat below 400 °C. Figure 11.9 shows the variation of the Cu–Cl cycle overall efficiencies with the recycling ratio of recovered energy, which is defined as the ratio of the recovered energy to the total energy from the exothermic processes within the cycle.

Conclusions

A design scheme for the overall Cu–Cl cycle and its components are investigated, which should allow the identification of potential performance improvements. The implications of these configurations are described in detail. The process simulation models are developed using the Aspen Plus simulation package and are being used in conjunction with experimental work carried out at the University of Ontario Institute of Technology and elsewhere. Energy and mass balances, stream flows and properties, the heat exchanger duties and shaft work needs are considered. The design and analysis results suggest that the Cu–Cl thermochemical water decomposition cycle is a potentially attractive option for hydrogen production.

References

1. Lewis MA, Ferrandon MS, Tatterson DF, Mathias P (2009) Evaluation of alternative thermochemical cycles – part III further development of the Cu-Cl cycle. Int J Hydrogen Energy 34:4136–4145
2. Lewis MA, Masin JG (2009) The evaluation of alternative thermochemical cycles – part II: the down-selection process. Int J Hydrogen Energy 34:4125–4135
3. Naterer GF, Suppiah S, Stolberg L, Lewis MA, Wang Z, Daggupati V, Gabriel K, Dincer I, Rosen MA, Spekkens P, Lvov SN, Fowler M, Tremaine P, Mostaghimi J, Easton EB, Trevani L, Rizvi G, Ikeda BM, Kaye MH, Lu L et al (2010) Canada's program on nuclear hydrogen production and the thermochemical Cu–Cl cycle. Int J Hydrogen Energy 35:10905–10926
4. Naterer GF, Suppiah S, Lewis MA, Gabriel K, Dincer I, Rosen MA, Fowler M, Rizvi G, Easton EB, Ikeda BM, Kaye MH, Lu L, Pioro I, Spekkens P, Tremaine P, Mostaghimi J, Avsec J, Jiang J (2009) Recent Canadian advances in nuclear-based hydrogen production and the thermochemical Cu-Cl cycle. Int J Hydrogen Energy 34:2901–2917
5. Ferrandon MS, Lewis MA, Alvarez F, Shafirovich E (2010) Hydrolysis of $CuCl_2$ in the Cu-Cl thermochemical cycle for hydrogen production: experimental studies using a spray reactor with an ultrasonic atomizer. Int J Hydrogen Energy 35:1895–1904
6. Ferrandon MS, Lewis MA, Tatterson DF, Doizi D, Croize L, Dauvois V, Roujou JL, Zanella Y, Gross A, Carles P (2010) Hydrogen production by the Cu-Cl thermochemical cycle: investigation of the key step of hydrolysing $CuCl_2$ to Cu_2OCl_2 and HCl using a spray reactor. Int J Hydrogen Energy 35:992–1000
7. Orhan MF, Dincer I, Rosen MA (2011) Exergy analysis of heat exchangers in the copper-chlorine thermochemical cycle to enhance thermal effectiveness and cycle efficiency. Int J Low Carbon Technol 6:156–164
8. Orhan MF, Dincer I, Rosen MA (2011) Design of systems for hydrogen production based on the Cu-Cl thermochemical water decomposition cycle: configurations and performance. Int J Hydrogen Energy 36:11309–11320
9. Ferrandon MS, Lewis MA, Tatterson DF, Nankanic RV, Kumarc M, Wedgewood LE et al. The hybrid Cu–Cl thermochemical cycle. I. Conceptual process design and H2A cost analysis. II. Limiting the formation of CuCl during hydrolysis. NHA Annual Hydrogen Conference, Sacramento Convention Center, CA; March 30-April 3, 2008.
10. Rivero R, Garfias M (2006) Standard chemical exergy of elements updated. Energy 31:3310–3326

Energy and Exergy Analyses of a Combined Multigeneration System

12

Janette Hogerwaard and Ibrahim Dincer

Abstract

A renewable energy-based system is proposed in the present study which will produce electricity, hot water, space heating and cooling, fresh water, and hydrogen. Thermodynamic modeling including energy and exergy analyses is performed to evaluate the feasibility of the system under the proposed operating conditions, and parametric study is performed to assess the system performance for varying conditions. The performance of the baseline system results in energy and exergy efficiencies of 0.28 and 0.25, and for the multigeneration system, efficiency values of 0.69 and 0.54 are achieved. In an additional study using actual Canadian offshore wind speed data and ocean current conditions, the multigeneration efficiencies for the present system range between the values of 0.32–0.48 energetically and 0.22–0.35 exergetically.

Introduction

Renewable energy systems are a necessary part of the solution to reducing dependence on fossil fuels. Resources such as solar, wind, biomass/biofuel, and ocean are widely available worldwide as clean energy (fuel) suitable for various systems. There are many challenges that must be addressed in order to make renewable energy systems comparable to fossil fuel-based systems in terms of providing consistent, reliable power production, and economic feasibility. To maintain the necessary power demand, renewable energy systems are often arranged in combination with fossil fuel systems to either augment or offset production by the fossil fuel-based system.

One such system is proposed by Mousavi [1], combining an offshore wind turbine, ocean tidal turbine, and a natural gas fuelled Micro gas turbine for electricity production and battery storage. The study performed in the research focuses primarily on the power management and control aspects of the combined system and addresses generation of electricity only. The system offers a good platform for integrating additional processes to produce valuable commodities from the waste heat produced by the Micro gas turbine. Multigeneration of both power and commodities through system integration is an effective method of meeting demands and can improve resource utilization efficiency when compared to simpler, stand-alone systems.

Mini- and micro gas turbine units offer a great deal of flexibility in design, with a wide range of generation capacities [2] and fuel/heat source flexibility. Various fuel combinations are possible, such as combined gas and concentrated solar heating, and various alternate fuels, such as biofuel(s) or landfill gas [3–5] reduce the overall consumption of the primary fuel. Exhaust heat from these turbines may be utilized in many different applications, depending on the quality of the waste

J. Hogerwaard (✉) • I. Dincer

Faculty of Engineering and Applied Science, University of Ontario Institute of Technology (UOIT),
2000 Simcoe Street North, Oshawa, ON, Canada L1H 7K4
e-mail: janette.hogerwaard@uoit.ca; ibrahim.dincer@uoit.ca

heat. Most gas turbine units incorporate preheating of air, precombustion, from recuperated heat of the turbine exhaust gases. If this heat is not used, it represents a major exergy—and energy—loss for the system. The exhaust gas heat energy can also be applied as process heat for multigeneration processes—for example, low-to-mid temperature organic Rankine cycles, or to direct heating processes such as desalination, or space heating and cooling systems [6–8].

Wind turbines installed in offshore locations have certain advantages over inland installations. First, offshore wind velocity tends to be higher than inland wind velocities. The relationship between the electricity produced is proportional to the cube of the velocity—that is, $\dot{W}_{WT} \propto V_W^3$—thus, a small increase in the velocity can have a large effect on the amount of electricity generated. Second, the wind velocity over the ocean tends to be more constant than that of inland winds. Tidal stream turbines generate electricity from the kinetic energy of the tidal currents. These types of turbines generate power from streams at much lower velocities—in the range of 0.8–3 m/s [9].

In this study, the system will be adapted to include multigeneration of several commodities, specifically: electricity, hot water, space heating and cooling, fresh water, and hydrogen. An adapted system is proposed and objectively assessed in the following sections through the application of energy and exergy analyses. A parametric study of the system and subsystems is conducted to observe the performance under varying conditions, based on Canadian resource data.

Systems Description

The Reference System

The investigated system is based on the renewable energy system described by Mousavi [1] (Fig. 12.1). There are three main subsystems considered: an offshore wind turbine, a tidal turbine, and a micro gas turbine. In the reference case, all of the turbines are assumed to operate at rated capacity. The turbines are connected to a main AC bus where the converted power can be distributed to consumers or to a specific application. The various control systems of the reference system are not described but can be found in the reference work.

The Adapted Multigeneration System

For this work, the addition of subsystems for hot water, space heating and cooling, fresh water, and hydrogen production are considered as shown in Fig. 12.2, which provide multigeneration of power and heat for the required commodity production. Power generated from the system is shared between direct electricity conversion and electricity provided to the electrolysis of water for hydrogen (H_2) production. Hot exhaust gases from the micro gas turbine pass through a heat exchanger, transferring heat to incoming salt water for a single stage flash desalination process for fresh water production. The heated salt water is then flashed to a pressure at or just below the saturation pressure of water at the inlet temperature and passed into a chamber at the same pressure. Water vapor and brine mist rise in the chamber, where demister baffles remove any salt water droplets suspended in the rising vapor. Pure water vapor ($\dot{m}_s$) is condensed on cooling tubes and collected for both fresh water storage and hot water production. The water for hot water production is heated in the secondary exhaust gas heat exchanger and stored in an insulated tank. Warm waste brine leaves the desalination unit, where it is then coupled in a heat exchanger with the condenser and evaporator of vapor-compression units for cooling and heating, respectively.

Analysis

The thermodynamic analysis; energy, entropy, and exergy balance equations; and efficiency definitions are described in this section. The analysis of auxiliary components (pumps, valves, etc.) is not included in the analysis.

Offshore Wind Turbine

The optimum power output and torque are defined by Mousavi [1] by the following, with the variable *CP* as the power coefficient of the turbine, which is the overall efficiency of the turbine, product of the mechanical and energetic efficiencies of the turbine:
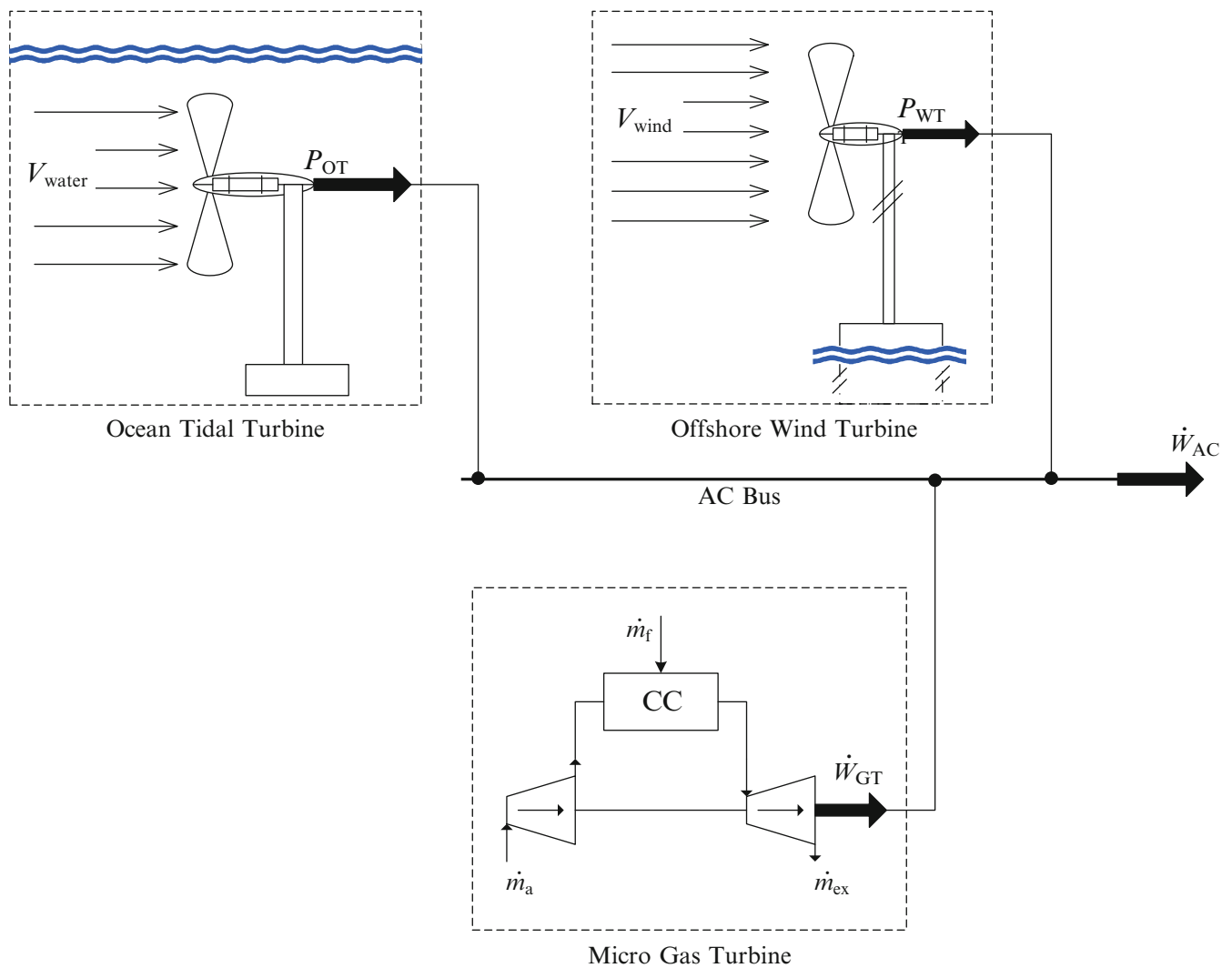
Fig. 12.1 Original system (adapted from [1])

$$P_{WT} = \frac{1}{2} \rho \cdot A \cdot CP \cdot \left(\frac{r \cdot \omega_{opt}}{\lambda_{opt}} \right)^3 \tag{12.1}$$

where the ratio of the optimal rotational velocity, ω_{opt}, to the tip-speed ratio, λ_{opt}, is equal to the ratio of the wind velocity, V_w, to the radius of the turbine blade.

$$V_W = \frac{r \cdot \omega_{opt}}{\lambda_{opt}} \tag{12.2}$$

The relationship for power is given by Mousavi [1] as a function of the wind velocities by

$$P_{WT}(V_W) = \begin{cases} \left(V_W^2 - V_{cin}^2 / V_{ra}^2 - V_{cin}^2 \right) \cdot P_{ra}; & V_{c.in} \leq V_W \leq V_{ra} \\ P_{ra}; & V_{ra} \leq V_W \leq V_{c.off} \\ 0; & V_{c.in} \geq V_W \geq V_{c.off} \end{cases} \tag{12.3}$$

where the subscripts *ra*, *c.in*, and *c.off* refer to rated, cut-in, and cutoff velocities of the turbine. The energy and exergy balances for the wind turbine are given by Dincer and Rosen [10] in the following set of equations, where the subscripts
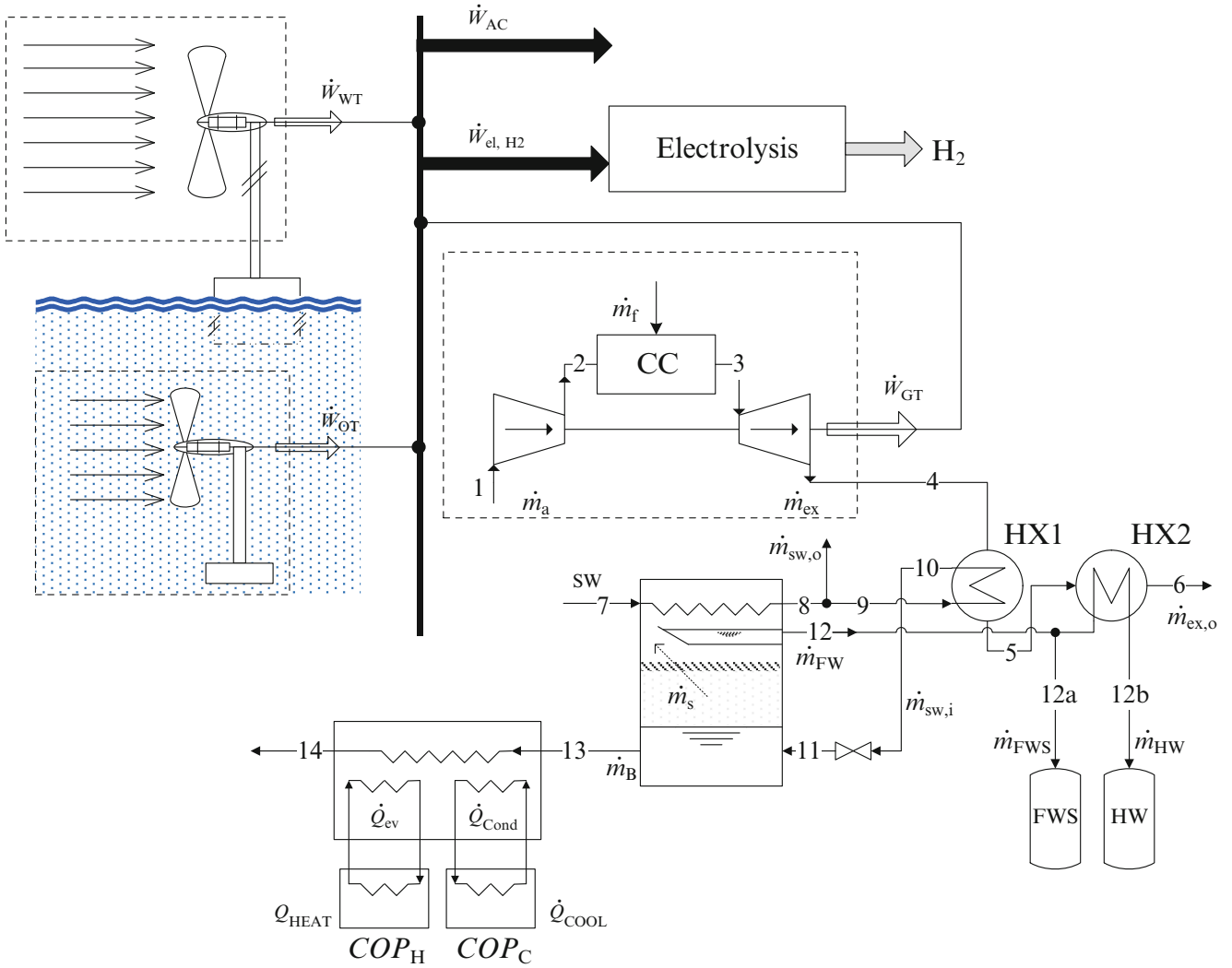
Fig. 12.2 Proposed integrated multigeneration system

1 and 2 refer to the inlet and outlet sides of the wind turbine.

$$\Delta \dot{E}_{WT} = \dot{m}\left(c_p(T_2 - T_1) + \frac{1}{2}\left(V_2^2 - V_1^2\right)\right) \tag{12.4a}$$

$$\Delta \dot{E}x_{WT} = \Delta KE + \dot{m}\cdot\left(c_p(T_2 - T_1) - T_o\left(c_p\cdot\ln\left(\frac{T_2}{T_1}\right) - R\cdot\ln\left(\frac{p_2}{p_1}\right)\right)\right) + \dot{E}x_{WT}^{\dot{Q}_L} + \dot{E}x_{d,WT} \tag{12.4b}$$

In the energy equation, $\dot{W}_{WT}$ is equal to the change in the kinetic energy due to the change in the wind velocity across the turbine, defined as $\dot{W}_{WT} = \frac{1}{2}\dot{m}_W\left(V_2^2 - V_1^2\right)$. The exit velocity, V_2, and pressure on either side of the wind turbine, p_i, are equal to

$$V_2 = \sqrt[3]{\frac{2\left(E_{potential} - \Delta ke\right)}{\dot{m}}} \tag{12.5}$$

$$p_i = p_o \pm \frac{\rho}{2}\cdot V_i^2 \tag{12.6}$$

The energy and exergy efficiencies of the wind turbine are defined based on the useful output—in both efficiencies, this is the power generated—over the total change in energy or exergy across the unit.

$$CP_{WT} = \eta_{WT} \cdot \eta_{m} \tag{12.7}$$

$$\psi_{WT} = P_{WT}/\Delta \dot{E}x_{W} \tag{12.8}$$

From the equations, it is clear that the way in which the reference state is defined is important in assessing the performance of the turbine, since this is a main source of loss in the efficiency of the turbine. The efficiency of the conversion process from generated power to user-ready electricity, η_{el}, is addressed in the efficiency of the overall system.

Tidal Turbine

The balances for the tidal turbine are much the same as those of the wind turbine, replacing the properties such as density, ρ, and specific heat, c_{p}, with those for water and defining the velocity of the flow through the turbine as the velocity of the tidal current, V_{t}.

$$P_{OT} = \frac{1}{2}\rho_{w} \cdot A \cdot CP \cdot V_{t}^{3} \tag{12.9}$$

Typical values of CP for tidal turbines are in the range of 0.35–0.5, which are higher than the typical values for wind turbines, which range from 0.25 to 3 [11]. The balances for energy, entropy, and exergy are given by the same equations for the wind turbine, using the appropriate fluid properties of water in place of air properties. The energy and exergy efficiencies of the tidal turbine are similar to those for the wind turbine and for the associated tidal turbine values.

Micro Gas Turbine

The energy balances for the main components of the Micro gas turbine system, compressor, combustion chamber, and gas turbine, are given by the following set of equations, for which the mass balance $\dot{m}_{ex} = \dot{m}_{a} + \dot{m}_{f}$ applies. No heat losses are considered in the analysis but should be included in practical applications:

$$\dot{W}_{C} = \dot{m}_{a}(h_{2} - h_{1}) \tag{12.10a}$$

$$\dot{Q}_{CC} = \dot{m}_{f} \cdot LHV_{f} = \dot{m}_{ex}h_{3} - \dot{m}_{a}h_{2} \tag{12.10b}$$

$$\dot{W}_{GT} = \dot{m}_{ex}(h_{3} - h_{4}) \tag{12.10c}$$

The entropy and exergy balances for the Micro gas turbine system are defined for each component by the equations for exergy destruction, which account for internal and external losses of the components.

$$\dot{E}x_{d,C} = \dot{W}_{C} + \dot{m}_{a}(ex_{1} - ex_{2}) \tag{12.11a}$$

$$\dot{E}x_{d,CC} = \dot{E}x_{CC}^{\dot{Q}} + \dot{m}_{a}ex_{2} - \dot{m}_{ex}ex_{3} \tag{12.11b}$$

$$\dot{E}x_{d,GT} = \dot{m}_{ex}(h_{3} - h_{4}) - \dot{W}_{GT} \tag{12.11c}$$

The energy and exergy for the Micro gas turbine system are defined below for the initial case of single generation. It will be redefined for multigeneration in a later equation to include the various additional outputs:

$$\eta_{GT} = \dot{W}_{GT}/\dot{Q}_{CC} \tag{12.12}$$

$$\psi_{GT} = \dot{W}_{GT} / \dot{Ex}_{CC}^{\dot{Q}} \tag{12.13}$$

Energy and exergy efficiencies of any individual component are defined as the ratio of the rates of change in useful energy for that component (i.e., heat, work) to that of the input energy.

Electrolysis

The hydrogen production process is based on the process defined by Levene et al. [12] for hydrogen production from wind-source electricity as input for an electrolyser. According to the authors, the process requires 53 kWh/kg of hydrogen (H_2) produced and has a specific (per kg) energy efficiency of 0.74, based on a higher heating value for H_2 of 141.8 MJ/kg (39.3 kWh/kg) [13]. Therefore, the equation for the production of H_2 ($\dot{m}_{H2}$) is defined for this system by the specified efficiency of $\eta_{H2} = 0.74$ as

$$\eta_{H_2} = \frac{\dot{m}_{H2} \cdot \mathrm{HHV}_{H2}}{\dot{W}_{el}} \tag{12.14}$$

where $\dot{W}_{el}$ refers to the portion of the electricity produced by the turbines (wind, tidal, and/or gas) directed to the electrolysis process.

Desalination Process

Fresh water produced from desalination of sea water is used for both fresh water storage and hot water production. The overall energy and exergy balance equations are given for the desalination process, with the boundary defined as the low-pressure chamber, by Eq. (12.16), and mass balance defined for fresh water production rate, $\dot{m}_{FW}$.

$$\dot{m}_{FW} = \dot{m}_{SW} - \dot{m}_{B} \tag{12.15}$$

$$\dot{m}_{FW} h_{12} = \dot{m}_{SW}(h_7 - h_8) + \dot{m}_{sw,i} h_{11} - \dot{m}_{B} h_{13} \tag{12.16a}$$

$$\dot{Ex}_{d,FW} = \dot{m}_{FW} h_{12} + \dot{m}_{SW}(ex_7 - ex_8) + \dot{m}_{sw,i} ex_{11} - \dot{m}_{B} ex_{13} \tag{12.16b}$$

Heat is transferred to the portion of the salt water stream to be flashed, $\dot{m}_{sw,i}$, in the exhaust gas heat exchanger. The process is described by the following equations for energy and exergy:

$$\Delta \dot{Q}_{HX1} = \dot{m}_{sw,i}(h_9 - h_{10}) + \dot{m}_{ex}(h_4 - h_5) \tag{12.17a}$$

$$\dot{Ex}_{d,HX1} = \dot{m}_{sw,i}(ex_9 - ex_{10}) + \dot{m}_{ex}(ex_4 - ex_5) - \dot{Ex}_{HX1}^{\Delta \dot{Q}} \tag{12.17b}$$

The rates of production of fresh water for storage, and for hot water production, are defined by the mass balance of the total fresh water production rate:

$$\dot{m}_{FW} = \dot{m}_{HW} - \dot{m}_{FWS} \tag{12.18a}$$

$$\dot{m}_{FW} = \alpha \cdot \dot{m}_{FW} + (1 - \alpha)\dot{m}_{FW} \tag{12.18b}$$

From the equation, water for storage collects at a rate of $(1-\alpha)\dot{m}_{FW}$ in the storage tank, and the mass fraction of fresh water for hot water production ($\dot{m}_{HW}$) is defined as $\alpha \dot{m}_{FW}$, which passes through the second exhaust gas heat exchanger.

$$\Delta \dot{Q}_{HX2} = \dot{m}_{HW}(h_{12} - h_{12b}) + \dot{m}_{ex}(h_5 - h_6) \tag{12.19a}$$

$$\dot{Ex}_{d,HX2} = \dot{m}_{HW}(ex_{12} - ex_{12b}) + \dot{m}_{ex}(ex_5 - ex_6) - \dot{Ex}_{HX2}^{\Delta \dot{Q}} \tag{12.19b}$$

Space Cooling and Heating

The condenser of the cooling cycle is defined by energy balance of with the exiting waste brine stream from the desalination process by the equation:

$$\Delta \dot{Q}_{Cond} = \dot{m}_B(h_{13} - h_{13a}) + \dot{m}_c(h_{c,i} - h_{c,o}) \tag{12.20a}$$

$$\dot{Ex}_{d,Cond} = \dot{m}_B(ex_{13} - ex_{13a}) + \dot{m}_c(ex_{c,i} - ex_{c,o}) - \dot{Ex}_{Cond}^{\Delta\dot{Q}} \tag{12.20b}$$

The evaporator of the heat pump is similarly defined by the following:

$$\Delta \dot{Q}_{ev} = \dot{m}_B(h_{13a} - h_{14}) + \dot{m}_h(h_{h,i} - h_{h,o}) \tag{12.21a}$$

$$\dot{Ex}_{d,ev} = \dot{m}_B(ex_{13a} - ex_{14}) + \dot{m}_h(ex_{h,i} - ex_{h,o}) - \dot{Ex}_{ev}^{\Delta\dot{Q}} \tag{12.21b}$$

For the system both the cooling cycle and the heat pump are designed for a specified coefficient of performance (*COP*), where the useful energy for the cooling cycle and heat pump are the evaporator and condenser quantities for the refrigerant, respectively.

$$COP_i = \frac{\dot{Q}_{Useful}}{\dot{W}_{C,i}} \tag{12.22}$$

The overall efficiency for the entire system is given based on the same principle of a ratio of useful outputs to total inputs. Net electrical output for the system is given by the following equation, which includes a term for the conversion from DC to AC, η_{em}, which is an assumed value of 0.95.

$$\eta_{Overall} = \frac{\dot{W}_{AC} + \dot{H}_{H2} + \dot{H}_{FWS} + \dot{H}_{HW} + \dot{Q}_{Heat} + \dot{Q}_{Cool}}{\Delta \dot{H}_{WT} + \Delta \dot{H}_{OT} + \dot{Q}_{CC} + \dot{H}_{SW}} \tag{12.23}$$

$$\psi_{Overall} = \frac{\dot{W}_{AC} + \dot{Ex}_{H2} + \dot{Ex}_{FW} + \dot{Ex}_{HW} + \dot{Ex}_{Heat}^{Q} + \dot{Ex}_{Cool}^{Q}}{\Delta \dot{Ex}_{W} + \Delta \dot{Ex}_{w} + \dot{Ex}_{CC}^{Q} + \dot{Ex}_{SW}} \tag{12.24}$$

Results and Discussion

The characteristics of the wind turbine, tidal turbine, and micro gas turbine are given in the following tables (Tables 12.1, 12.2, and 12.3). These data are used in the modeling of the system as described in the Analysis section. The fuel used in the micro gas turbine is assumed to be CH_4, with a lower heating value of 50 MJ/kg, but could be any gaseous fuel for an internal combustion or solid fuel for an external combustion application.

Baseline Model Results

The wind and tidal turbines are assumed to operate under the defined rated conditions. The rated values are used to determine characteristic values for the energy efficiency, η_i, and mechanical efficiency, η_m. The product of these two efficiencies is the ratio of the converted power (P_{iT}) to the total change in energy (or exergy) for that stream across the turbine blades and equal to the power coefficient, *CP*.

The power generated is plotted as a function of velocity, giving the characteristic curve for the turbines. The velocity ranges are from the cut-in to the cutoff velocity for the wind turbine (Fig. 12.3), and for the tidal turbine, from the cut-in velocity to a reasonable high-end velocity of 5 m/s (Fig. 12.4).

The energy and exergy efficiencies, using the captured wind energy as the useful output, is equal to the ratio of power [calculated from the velocity relationships given in Eq. (12.3)] to the change in energy of the air passing through the turbine

Table 12.1 Wind and tidal turbine characteristics[a]

	Wind turbine	Tidal turbine
Model	VestasWT Generator Type V-25-200	Verdant power KHPS
Rotor diameter, d (m)	21	5.0
Swept area, A (m^2)	415.5	19.6
RPM (rated)	14	~35
Tip speed, V_{tip} (m/s)	16.75	9
Cut in speed, $V_{c.in}$ (m/s)	3.8	0.8
Cut off speed, $V_{c.off}$ (m/s)	25	–
Rated velocity, V_i (m/s)	13.8	2.1
Rated power, P_{ra} (kW)	200	35
Drive train (mechanical) eff., η_m	–	0.86
Total height, H_t (m)	41.5	6
Total length[b], L_t (m)	–	4.82
System mass (in air), (kg)	–	3,629

[a]Turbine data obtained from Mousavi [1], Kalantar and Mousavi [14] for wind, Natural Resources Canada [9] for tidal
[b]Total length refers to the distance from inlet to outlet across the turbine blades

Table 12.2 Micro gas turbine characteristics[a]

	Micro gas turbine
Rated power, P_{ra} (kW)	250
Rated voltage, V (V)	660
Frequency, f (Hz)	60
Friction factor	0

[a]Turbine data obtained from Mousavi [1], Kalantar and Mousavi [14]

Table 12.3 Characteristic efficiency values for wind and tidal turbines

	Wind turbine (WT)	Tidal turbine (OT)
Energy efficiency η_i	0.33	0.45
Drive train (mechanical) efficiency η_m	0.91	0.86
Power coefficient, CP_i	0.30	0.39
Exergy efficiency ψ_i (rated conditions)	0.15	0.33
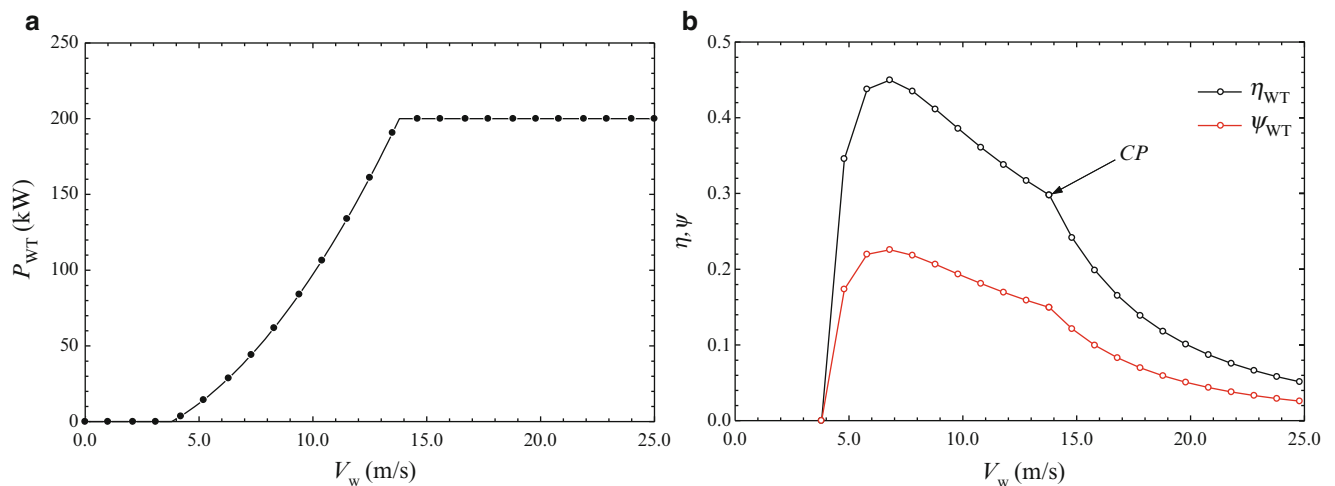
Fig. 12.3 (**a**) Turbine power and (**b**) energy and exergy efficiencies of offshore wind turbine power generation as a function of wind velocity
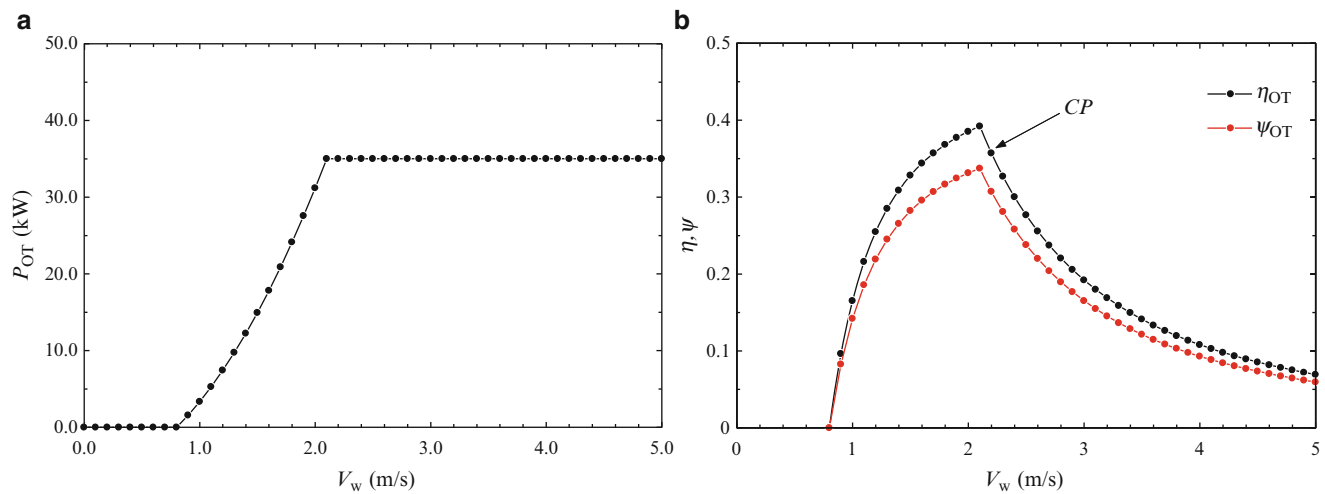
Fig. 12.4 (**a**) Turbine power and (**b**) energy and exergy efficiencies of ocean tidal turbine power generation as a function of water current velocity

Table 12.4 Fresh water production and sensible heating and cooling load data

Fresh water production (desalination)			Space heating and cooling		
	HW	FWS		Heating	Cooling
Temperature, T (°C)	>70 °C	T_0	COP	2.5	2.5
Total daily prod.	5,000 L/day (5 m³/day)		Volume (m³); ACH	200; 6	50; 0.5
HW volume Fr., α_{HW}	0.75		ΔT (supply air)	$T_0 - 40$ °C	$T_0 - 0$ °C

sweep. The efficiencies in both turbines drop off drastically after the rated conditions are surpassed, since the operational characteristics do not allow the turbines to generate more than the specified capacity (for mechanical/functional reasons), while the kinetic energy available in the flow continues to increase.

Micro Gas Turbine and Subsystems

In order to determine the required state conditions for the micro gas turbine system, the loads to be met are defined. These details are provided in Table 12.4 and include required fresh water and hot water supply rates, hot water storage temperature, heat required for desalination of seawater (to meet required total fresh water production), and the space heating and cooling requirements. For the analysis, auxiliary components of the subsystems (such as pumps, vapor-compression cycle expansion valves, and fans) are not included and are considered in terms of the major heat loads and major work quantities (i.e., compressors, turbines). Furthermore, heat losses are limited to those associated with the streams leaving the system—that is, the subsystems are assumed to have no external heat loss.

The required loads for the water and sensible heating and cooling applications are determined from basic thermodynamic analyses, based on the assumed fresh water production requirements and space (room) conditions for the heating and cooling applications. These loads are used to determine minimum performance characteristics for the micro gas turbine system, which operates at the rated output of 250 kW (Table 12.5).

Hydrogen is produced by the electrolysis of steam, requiring heat input to produce saturated steam and electricity input (supplied from wind or tidal power, as mentioned). These loads are determined based on the hypothetical hydrogen electrolysis process discussed in the analysis section. The resulting output loads (heat, energy, and net power) are shown with the flow paths for the systems in Fig. 12.5 for the rated cases of the wind, tidal, and micro gas turbine.

In both cases, the fuel is considered the only external input, since the potential power of the wind and tidal currents not captured by the turbines. Thus, for the initial case, the three systems are given their own efficiency values. For the rated case, these are the CP values for the wind and tidal turbines. The efficiencies for single and multigeneration cases are shown graphically in Fig. 12.6.

An overall energetic and exergetic efficiency for the initial case is given as the total power generated divided by the fuel input; however, this value is more of an evaluation of valuable outputs to valuable (in terms of cost, environmental, and exergetic value) input. These values are $\eta = 0.28$ and $\psi = 0.25$.

Table 12.5 Operating conditions, micro gas turbine system

Parameter	Value
Fuel (gas)	Methane, CH_4
Micro gas turbine, $\dot{W}_{GT}$ (kW)	250
Air flow rate, $\dot{m}_a$ (kg/s)	0.985
Fuel flow rate, $\dot{m}_f$ (kg/s)	0.015
Exhaust flow rate, $\dot{m}_{ex}$ (kg/s)	1.0
Exhaust temperature, T_4 (°C)	800
Lower heating value, LHV (MJ/kg)	50
Higher heating value, HHV (MJ/kg)	55.4
Isentropic efficiency ($\eta_{s,C} = \eta_{s,T}$)	0.85
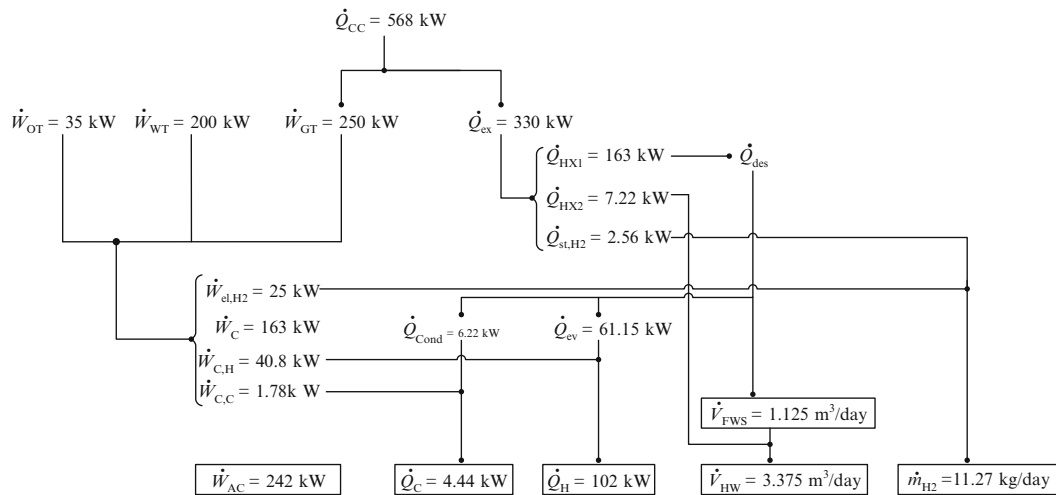
Fig. 12.5 Flow path of energy with rated case values

Fig. 12.6 System efficiencies and multigeneration efficiencies (rated case)
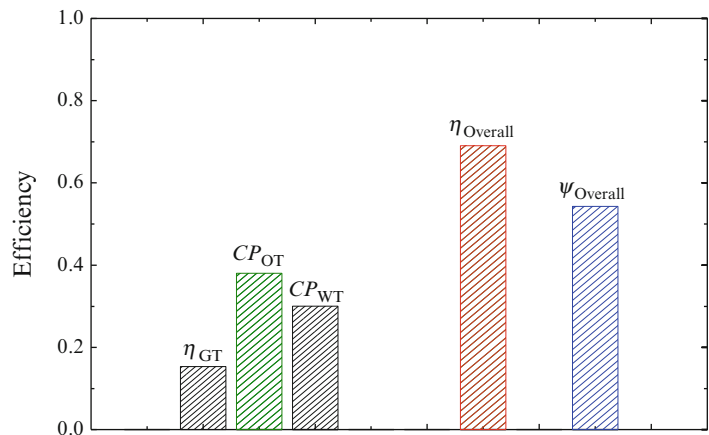
Parametric Study

Performance of the system is tested under Canadian environmental conditions. Typical values are used as inputs to the model, and the system performance is observed. Offshore wind speed and wind energy data are generated using the Canadian Wind Energy Atlas tool [15] for 30 m elevation. The data for wind speed for the offshore region of eastern Canada show speeds ranging from 7 to 10 m/s. Ocean current velocities are obtained from [16]. Surface currents are considered, since the depth is not specified. The data of interest is for the northwest region of the Atlantic, around the Canadian east coast. For the same geographical region as that used for the wind values, the surface ocean current ranges from
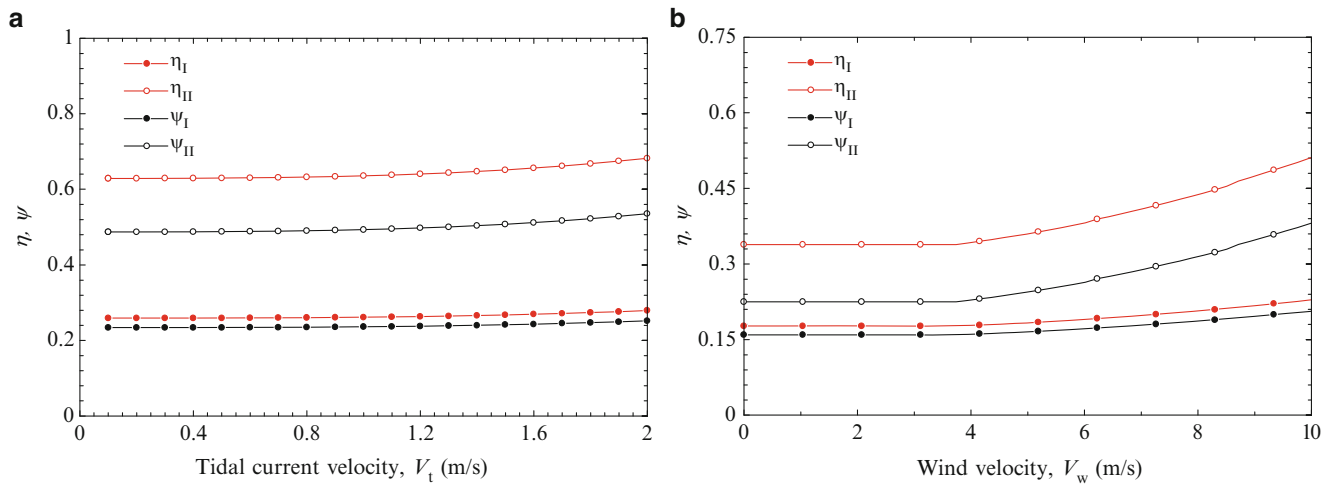
Fig. 12.7 System energy and exergy efficiencies vs. (**a**) tidal current, (**b**) wind velocity

0.3 to 1.0 m/s; however, mean current velocities at maximum passage depth(s) for high tidal power density regions such as the Bay of Fundy are reported in the range of <1.0–5.25 m/s [17].

The efficiencies of the tidal and wind turbines are plotted against varying tidal current up and wind speeds and shown graphically in Fig. 12.7. The tidal current speed is considered up to the rated value for the turbine. The plot shows, as expected, that the performance of the wind turbine at varying velocities has a more significant impact on the system performance due to its capacity within the system. Because the wind speeds encountered in the considered region are generally below the rated wind speed for the turbine considered, the efficiency is lower for both the single and multigeneration cases.

Concluding Remarks

In this chapter, a renewable energy power generation system using offshore wind and ocean tidal turbines integrated with a micro gas turbine system is proposed and investigated. The system provides sensible heating and cooling, desalination of seawater for fresh water storage and hot water, and hydrogen. The baseline system, operating at full rated capacity, results in energetic and exergetic efficiencies of 0.28 and 0.25. For the multigeneration case with commodity production, the efficiency values of 0.69 and 0.54 are achieved.

Nomenclature

A	Area, m^2	$\dot{H}$	Enthalpy rate, kW
ACH	Air changes per hour	$\dot{KE}$	Kinetic energy, kW
c_p	Specific heat, kJ/kg·K	$\dot{m}$	Mass flow rate, kg/s
COP$_i$	Coefficient of performance (i = H for space heating, i = C for cooling)	p	Pressure, kPa
		P	Power, kW
CP	Power coefficient	$\dot{Q}$	Heat rate, kW
d	Rotor diameter, m	T	Temperature, K
ex	Specific exergy, kJ/kg	V	Velocity, m/s; voltage, V
$\dot{Ex}$	Exergy rate, kW	$\dot{W}$	Shaft work rate, kW
h	Specific enthalpy, kJ/kg		

Greek Letters

α	Mass fraction	ρ	Density, kg/m^3
η	Energy efficiency	ψ	Exergy efficiency
λ	Tip-speed-ratio	ω	Rotational speed, rad/s

Subscripts

a	Air	FWS	Fresh water storage
C	Compressor	GT	Micro gas turbine
CC	Combustion chamber	H2	Hydrogen
C,C	Cooling cycle compressor	HW	Hot water
C,H	Heat pump compressor	$i\{i = 1,2,3,\ldots,n\}$	State points (or inlet)
Cond	Condenser	opt	Optimal
d	Destruction	OT	Ocean tidal turbine
des	Desalination	st	Steam
el	Electric	SW	Salt water
em	Electromechanical	sw	Fraction salt water
ev	Evaporator	t	Tidal
ex	Exhaust	WT	Wind turbine
f	Fuel	W	Wind
FW	Fresh water	w	Water

Superscripts

a	Air

References

1. Mousavi G (2012) An autonomous hybrid energy system of wind/tidal/microturbine/battery storage. Int J Electr Power Energy Syst 43(1):1144–1154
2. Pilavachi PA (2002) Mini-and micro-gas turbines for combined heat and power. Appl Ther Eng 22(18):2003–2014
3. Siva Reddy V, Kaushik SC, Tyagi SK (2012) Exergetic analysis of solar concentrator aided natural gas fired combined cycle power plant. Renew Energy 39(1):114–125
4. Poullikkas A (2005) An overview of current and future sustainable gas turbine technologies. Renew Sustain Energy Rev 9(5):409–443
5. Muis ZA, Hashim H, Manan ZA, Taha FM, Douglas PL (2010) Optimal planning of renewable energy-integrated electricity generation schemes with CO_2 reduction target. Renew Energy 35(11):2562–2570
6. Dincer I, Zamfirescu C (2012) Renewable-energy-based multigeneration systems. Int J Energy Res 36(15):1403–1415
7. Rubio-Maya C, Uche-Marcuello J, Martínez-Gracia A, Bayod-Rújula AA (2011) Design optimization of a polygeneration plant fuelled by natural gas and renewable energy sources. Appl Energy 88(2):449–457
8. Chicco G (2010) Sustainability challenges for future energy systems. J Sustain Energy 1(March):6–16
9. Natural Resources Canada (2010) Marine renewable energy – wave, tidal, and water current: Canadian Technology Status Report. CanmetENERGY, Ottawa. ISBN M154-40/2010E-PDF 978-1-100-17618-5
10. Dincer I, Rosen M (2007) Exergy, environment, and sustainable development. Elsevier, Oxford
11. Ben Elghali SE, Benbouzid MEH, Charpentier JF (2007) Marine tidal current electric power generation technology: state of the art and current status. In: Electric machines and drives conference, 2007. IEMDC'07. IEEE International, vol 2, pp 1407–1412
12. Levene JI, Mann MK, Margolis RM, Milbrandt A (2007) An analysis of hydrogen production from renewable electricity sources. Sol Energy 81(6):773–780
13. Cengel YA, Boles MA (2006) Thermodynamics: an engineering approach. McGraw-Hill Higher Education
14. Kalantar M, Mousavi SM (2010) Dynamic behavior of a stand-alone hybrid power generation system of wind turbine, microturbine, solar array and battery storage. Appl Energy 87(10):3051–3064
15. Environment Canada (2008) Canadian wind energy atlas (web). windatlas.ca. 21 August 2008. http://www.windatlas.ca/en/maps.php. Accessed 5 Nov 2012
16. NASA (2012) Ocean motion and surface currents: drift model (web). oceanmotion.org. N.D. http://oceanmotion.org/html/resources/drifter.htm. Accessed 12 Nov 2012
17. Tarbotton M, Larson M (2006) Canada ocean energy atlas (phase 1) potential tidal current energy resources analysis background. Report to Canadian Hydraulics Centre, Ottawa, Ontario

Energy and Exergy Analyses of a Zero Emission Power Plant for Coproduction of Electricity and Methanol

Canan Acar and Ibrahim Dincer

Abstract

In this study, we study and evaluate a zero emission integrated system, as taken from the literature, for coproduction of electricity and methanol. The investigated integrated system has three subsystems: water electrolysis, Matiant power plant (oxy-fuel combustion of pure methane), and methanol production unit. The system and its components are analyzed energetically and exergetically. The rates of exergy destructions, relative irreversibilities, and sustainability indexes of each subunit of each subsystem, as well as the overall system are analyzed to identify the greatest exergy losses and possible future research directions. The total rate of exergy destruction of the overall system is calculated to be around 280 MW. The greatest rate of exergy destruction, therefore the greatest irreversibility, occurs within the power plant unit (about 60 % of the total rate of exergy destruction). The energy efficiencies of electrolysis, power plant, and methanol synthesis unit are found to be 30 %, 76 %, and 41 %, respectively. The exergy efficiencies of electrolysis, power plant, and methanol synthesis unit are found to be 30 %, 64 %, and 41 %, respectively. Depending on the utilization of the heat rejected from the different units of each subsystem, the overall system could have energy and exergy efficiencies up to 68 % and 47 %, respectively.

Keywords

Methanol • Carbon capture • Cogeneration • Electricity • Energy • Exergy • Efficiency

Introduction

During the twentieth and the beginning of the twenty-first century, world's energy consumption has increased steadily due to global rise in population and standards of living. The increasing trend in world's energy need is expected to continue in the future. As a result, a growth in energy generation capacity will be needed [1]. One of the main sources of CO_2 emissions is power generation [2]. Therefore, reduction of fossil fuel utilization by increasing efficiency and decreasing emissions by converting CO_2 into valuable products offer some potential solutions to world's current energy-related problems.

There have been several studies focusing on coproduction of fossil fuels with CO_2 utilization. A comparative study of electricity and hydrogen production systems by CO_2 capture and storage has been presented by Damen et al. [3]. Minutillo and Perna [4] studied a tri-reforming process in fossil fired power plants to generate a synthesis gas for production of chemicals including methanol. Energy analysis, economy, and policy scenarios of electricity/methanol synthesis coproduction systems' are taken into account in Guang-jian et al. and Chen et al.'s [5, 6] work. Katayama and Tamaura [7] and Takeuchi et al. [8]

C. Acar (✉) • I. Dincer

Faculty of Engineering and Applied Science, University of Ontario Institute of Technology,
2000 Simcoe Street North, Oshawa, ON, Canada L1H 7K4
e-mail: canan.acar@uoit.ca; ibrahim.dincer@uoit.ca

considered methanol synthesis via CO_2 recovery and renewable hydrogen from water electrolysis unit by renewable energy sources as a zero emission integrated system. Mignard et al. [9] proposed an integrated system for coproduction of electricity and methanol in small scale/partial carbon capture in common fossil fuel power plants. The utilization of renewable hydrogen for methanol production is investigated by Cifre and Badr [10].

This chapter aims to study and evaluate a zero emission integrated system for coproduction of electricity and methanol as originally proposed and studied by Soltanieh et al. [11]. The characteristics and performance of electricity–methanol cogeneration system with water electrolysis, Matiant power cycle, and methanol synthesis unit are energetically and exergetically evaluated. Energy, exergy, and sustainability analyses of every component of the system as well as the overall system are performed. The performance of the system is assessed for various environmental parameters such as relative irreversibility and sustainability index. In the end, recommendations for better performance in terms of environmental and sustainability issues are provided.

System Description

Overall System

The integrated system, as originally developed and published by Soltanieh et al. [11], is presented in Fig. 13.1. It has three subsystems: water electrolysis for H_2 and O_2 production, the matiant-cycle power plant to produce electricity via oxy-combustion, and methanol synthesis unit fed by the CO_2 from power plant and renewable H_2. In this study, all processes are assumed to be steady state and steady flow (SSSF), where potential and kinetic energy changes are neglected. It is also assumed that no chemical reactions occur except the water electrolysis modules, combustion chambers, and methanol reactor. Heat loss and pressure drop in tubing, valves, and connections are ignored. All equipments except the heat exchangers are assumed to be adiabatic. Compressors and turbines are assumed to operate at an isentropic efficiency of 85 %, and the efficiency of heat exchangers is assumed to be 90 %.

Water Electrolysis Unit

Figure 13.2 shows the water electrolysis unit. The electrolysis unit uses wind (renewable) energy to provide the necessary energy for the electrolysis reaction is $3H_2O \rightarrow 3/2O_2 + 3H_2$ ($\Delta H = 286\,kJ/mol\ H_2$) [12]. The technical criteria used for the unit is selected based on Soltanieh et al.'s [11] study. The water feed (stream 1) is assumed to undergo complete electrolysis. The product H_2 (streams 2–10) is either stored or sent to the methanol synthesis unit. The product O_2 (streams 11–19) is either stored or sent to the matiant power plant. The inlet molar flow rate of water to the electrolysis unit is 1.4 kmol/s at
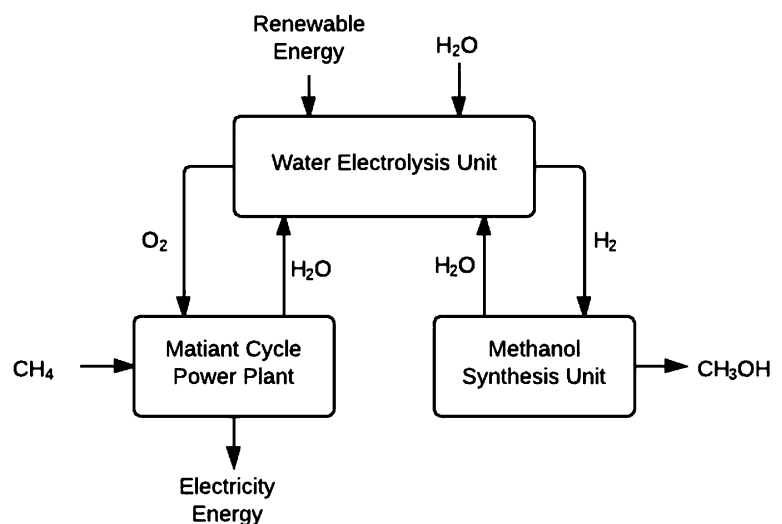
Fig. 13.1 Integrated system block diagram (modified from [11])
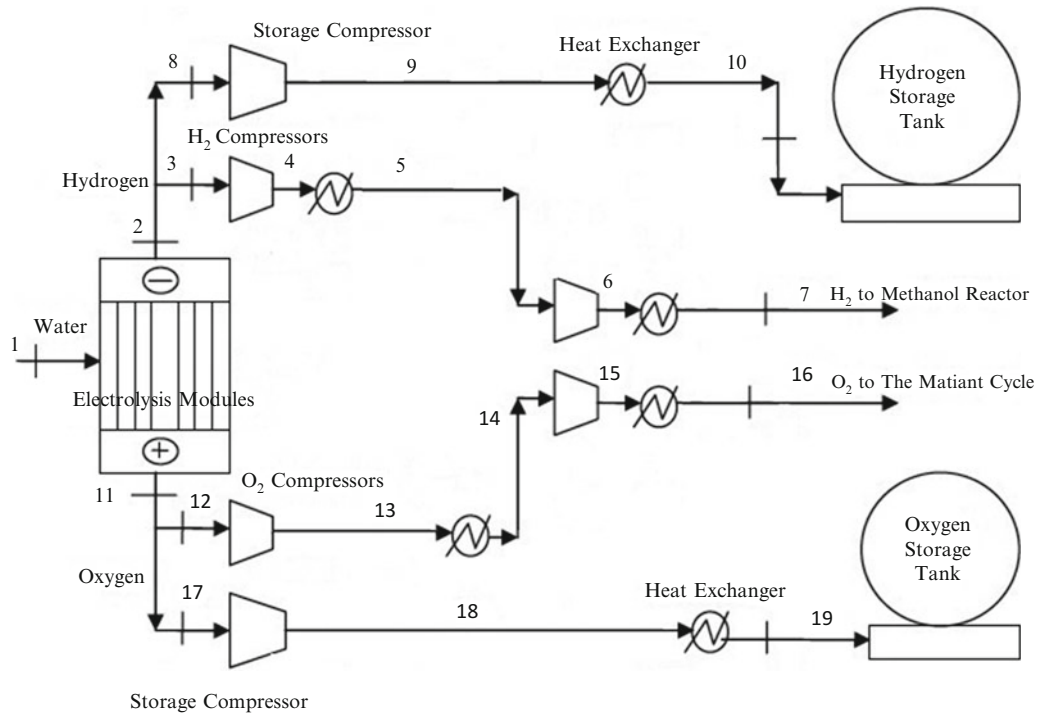
Fig. 13.2 Process flow diagram of the water electrolysis unit (modified from [11])

80 °C and 1 bar. 0.75 kmol/s of this amount comes from the power plant and methanol synthesis units while 0.65 kmol/s is the fresh feed. H_2 and O_2 are desired to be stored at 140 °C and 10 bar. O_2 is sent to the power plant at 160 °C and 40 bar. Then, H_2 is sent to the methanol synthesis at 180 °C and 50 bar.

Matiant-Cycle Power Plant

The Matiant-cycle power plant is presented in Fig. 13.3. In this subsystem, the fuel (pure methane) is burned with pure oxygen from the electrolysis unit and undergoes complete combustion. The combustion reaction is $CH_4 + 2O_2 \rightarrow CO_2 + 2H_2O$ ($\Delta H = -800$ kJ/mol CH_4) [12]. The technical criteria used for the plant is selected based on Soltanieh et al.'s [11] study. The products of two combustion chambers (CO_2 and H_2O) are separated; the H_2O is sent back to the electrolysis unit, and about 92 % of the CO_2 is used as a thermodynamic fluid within the Matiant cycle while the remaining part is sent to the methanol synthesis unit. 70 % of the O_2 from the electrolysis unit is sent to the combustion chamber H, and the remaining is sent to the combustion chamber K. The CH_4 inlet temperature and pressure are 30 °C and 2 bar, respectively. The output temperature and pressure of water from the flash drum are 80 °C and 2 bar. CO_2 is sent to the methanol synthesis unit at 180 °C and 50 bar.

Methanol Synthesis Unit

Figure 13.4 presents the methanol synthesis unit. The methanol reactor converts CO_2 to CH_3OH according to the following reaction: $CO_2 + 3H_2 \rightarrow CH_3OH + H_2O$ ($\Delta H = -49.51$ kJ/mol CH_3OH). The technical criteria used for the unit are selected based on Soltanieh et al.'s [11] study. 0.25 kmol/s CO_2 is fed to the unit from the power plant. The CO_2 to CH_3OH conversion ratio in the methanol reactor is 20 %. Methanol and water are leaving the distillation column at 1 bar and 40 °C and 80 °C, respectively.
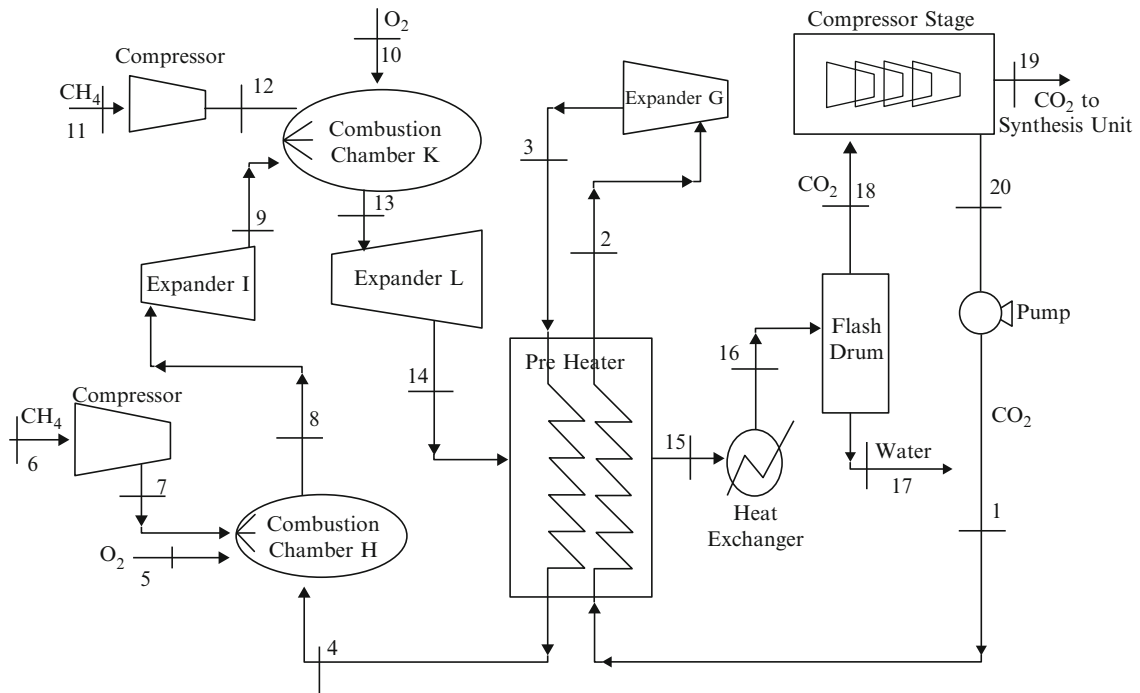
Fig. 13.3 Process flow diagram of the matiant-cycle power plant (modified from [11])
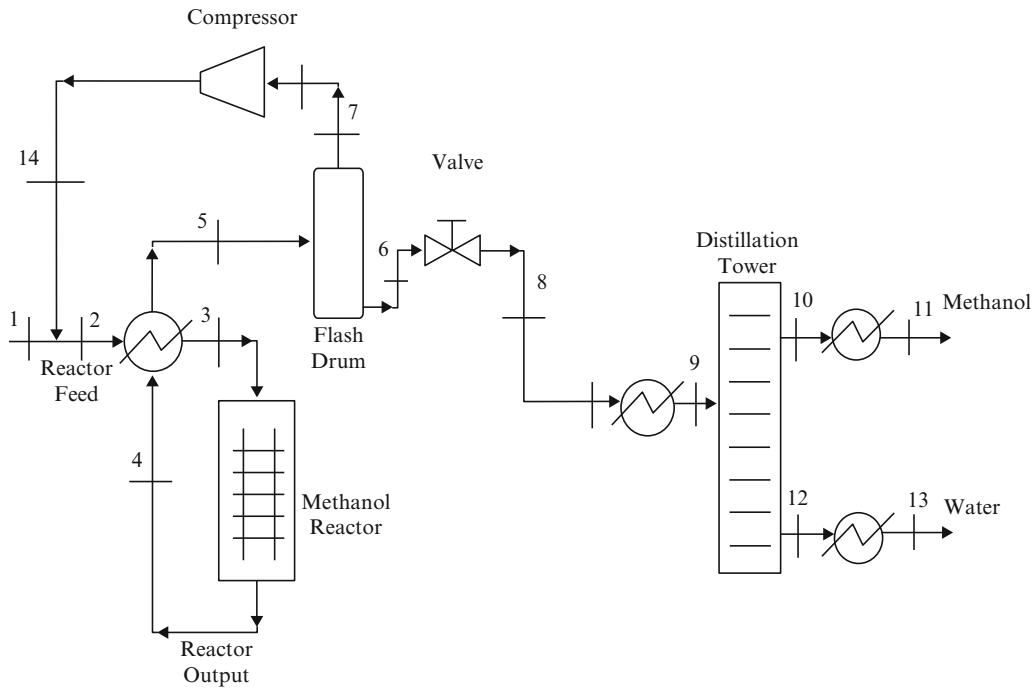
Fig. 13.4 Process flow diagram of the methanol synthesis unit (modified from [11])

Analysis

The operating conditions and production capacities of each subsystem as well as the overall system are selected based on the literature work [11]. The general mass, energy, entropy, and exergy balance equations can be summarized as:

Mass Balance Equation (MBE):

$$\sum \dot{m}_{in} = \sum \dot{m}_{out} \tag{13.1}$$

Energy Balance Equation (EBE):

$$\sum \dot{E}_{in} = \sum \dot{E}_{out} \tag{13.2}$$

Entropy Balance Equation (EnBE):

$$\sum \dot{S}_{in} + \dot{S}_{gen} = \sum \dot{S}_{out} \tag{13.3}$$

Exergy Balance Equation (ExBE):

$$\sum \dot{Ex}_{in} = \sum \dot{Ex}_{out} + \dot{Ex}_{dest} \tag{13.4}$$

Specific exergy of a stream is comprised of two components, namely physical and chemical exergy, and defined as follows [13, 14]:

$$ex = ex_{ph} + ex_{ch} \tag{13.5}$$

$$ex_{ph} = (h - h_o) - T_0 \cdot (s - s_o) \tag{13.6}$$

$$ex_{ch} = \sum x_i \, \overline{ex}_{ch}{}^0 - RT_0 \cdot \sum x_i ln(x_i) \tag{13.7}$$

$$\dot{Ex} = \dot{m} \cdot ex \tag{13.8}$$

where T_0 is the ambient temperature, R is the specific gas constant, h/h_0 and s/s_0 are the specific enthalpy and entropy of a stream at a given state/at ambient state, and x_i is the mol fraction of component i. Relative irreversibilities (RI) and sustainability indexes (SI) of each unit of each subsystem as well as the subsystems themselves and the overall system are calculated based on the following equations:

$$RI_i = \frac{\dot{Ex}_i^{dest}}{\dot{Ex}_{total}^{dest}} \tag{13.9}$$

$$SI_i = \frac{1}{1 - \Psi_i} \tag{13.10}$$

In order to study the system energetically and exergetically, each stream is defined by its state, components, temperature, and pressure. After the states were defined, the specific enthalpy, entropy, exergy, and energy and exergy flow rates of each stream is calculated based on the specified inlet data given elsewhere [11] mentioned in section "System Description" or via balance equations. Ambient state is taken to be 20 °C and 1 bar, respectively. The thermodynamic properties of H_2O, H_2, O_2, CH_4, CO_2, and CH_3OH are found using the Engineering Equation Solver (EES) software package.

Results and Discussion

Water Electrolysis Unit

Overall, the electrolysis unit needs 1.4 kmol/s of water (in total 0.75 kmol/s of this water comes from the matiant power cycle and methanol production units). After the complete electrolysis, 0.75 kmol/s of H_2 is sent to the methanol production unit while 0.65 kmol/s of H_2 is sent to the storage tank. Similarly, 0.35 kmol/s of O_2 is sent to the matiant power cycle unit while 0.35 kmol/s of O_2 is sent to the storage tank.

Table 13.1 summarizes the energy and exergy efficiencies as well as the energy input/output (either work or heat) of electrolysis modules and compressors and heat exchangers and the overall subsystem itself. The empty cells can be assumed to be 0 or "not applicable."

The electrolysis unit's total work input is around 46 MW; this amount is required to drive the electrolysis reaction and compress the products H_2/O_2. Heat exchangers' load indicates the total amount of cooling required following the compression processes. The system has an energy and exergy efficiency of 30 %. The overall sustainability index of the water electrolysis subsystem is 1.43. These energy and exergy efficiencies are calculated by the following equations:

$$\eta = \frac{\dot{E}_{O_2} + \dot{E}_{H_2}}{\dot{E}_{water} + \dot{W}_{electrolysis} + \dot{W}_{compressors}} \tag{13.11}$$

$$\Psi = \frac{\dot{Ex}_{O_2} + \dot{Ex}_{H_2}}{\dot{Ex}_{water} + \dot{W}_{electrolysis} + \dot{W}_{compressors}} \tag{13.12}$$

Figure 13.5 shows that 49 % of the system irreversibility, therefore the exergy destruction, occurs in the electrolysis modules. This means when the heat exchangers and compressors are combined together, they have about the same exergy destruction rates with the electrolysis modules alone. When compared, the total exergy destruction rate in compressors is very close to the one of heat exchangers in total. However, on average, compressors are exergetically more efficient than the heat exchangers. This might be due to the high temperature differences between the inlet and outlet of heat exchangers.

Initially, the ambient state is taken to be 20 °C and 1 bar, respectively. In order to find how the electrolysis unit performs exergetically under different ambient conditions, the system is run under various ambient temperatures. The exergy efficiency and exergy destruction rate of the electrolysis modules, compressors, and heat exchangers as well as the overall electrolysis unit at different ambient temperatures are shown in Fig. 13.6.

Table 13.1 Summary of the major components and the overall electrolysis unit

Description	η	Ψ	$\dot{Q}$(kW)	$\dot{W}$(kW)
Electrolysis modules	51%	38%		7,514
Heat exchangers	90%	64%	27,904	
Compressors	85%	80%		38,652
Overall electrolysis unit	30%	30%	27,904	46,166
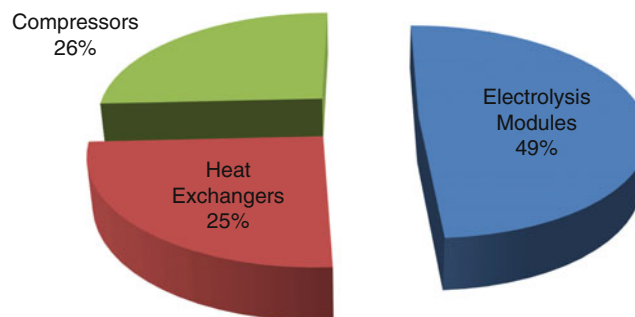
Fig. 13.5 Relative irreversibilities of the major components of the electrolysis subsystem

Fig. 13.6 The effect of ambient temperature on exergy destruction rates and exergy efficiencies of major components of the electrolysis unit

Table 13.2 Summary of the major components and the overall matiant-cycle power plant

Description	η	Ψ	$\dot{Q}$(kW)	$\dot{W}$(kW)
Heat exchangers	95%	78%	35,579	
Expanders (turbines)	85%	80%		132,588
Combustion chambers	79%	69%		
Compressors and pumps	85%	75%	11,426	16,710
Flash drum	95%	78%		
Overall unit	76%	64%	47,005	115,878

Figure 13.6 shows that, with increasing ambient temperature, a slight increase is observed in the exergy destruction rate of heat exchangers and compressors. This increase is less than 6 % when the ambient temperature is increased from 2 to 28 °C. However, there is a slight decrease in the exergy destruction rate of electrolysis modules. This decrease is less than 2 % when the ambient temperature is increased from 2 to 28 °C. The overall system's exergy destruction rate increases with increasing ambient temperature. This increase is less than 2 % as the ambient temperature is increased from 2 to 28 °C.

Furthermore, it can be seen from Fig. 13.6 that an increase in the ambient temperature has a negligible effect on the exergy efficiencies of the electrolysis modules and the compressors (1 % change as the ambient temperature increased from 2 to 28 °C). However, the exergy efficiency of the heat exchangers decreases with increasing ambient temperature (3 % decrease as the ambient temperature increased from 2 to 28 °C), and the exergy efficiency of the overall electrolysis unit increases with increasing ambient temperature (2 % increase as the ambient temperature increased from 2 to 28 °C). Taking the small percentage of the change of rate of exergy destructions and the exergy efficiencies, it can be concluded that the ambient temperature doesn't have a dramatic effect on exergetic performance of the system within the studied temperature interval.

Matiant-Cycle Power Plant

In power plant, 0.5 kmol/s of the O_2 from the electrolysis unit is used for complete combustion of 0.25 kmol/s of natural gas (pure methane). As a result, 0.50 kmol/s of H_2O is produced and sent back to the electrolysis unit. About 0.25 kmol/s of the CO_2 is sent to the methanol synthesis unit while about 3 kmol/s of CO_2 is used as thermodynamic working fluid in the system.

Table 13.2 summarizes the energy and exergy efficiencies, as well as the energy input/output (either work or heat) of the major components and the overall system itself. The empty cells can be assumed to be 0 or "not applicable." From

Fig. 13.7 Relative
irreversibilities of the major
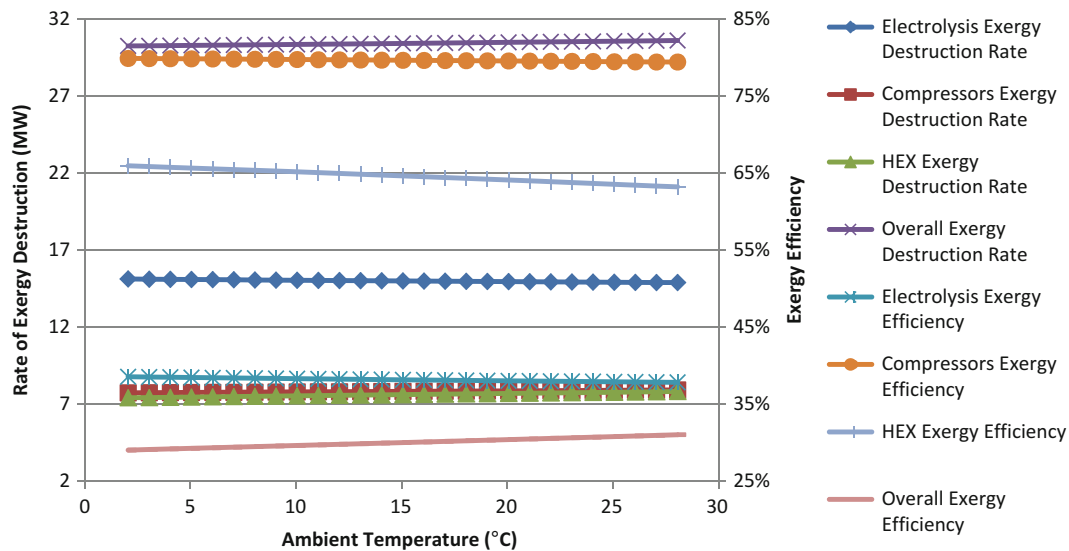components of the matiant-cycle
power plant

Fig. 13.8 The effect of ambient temperature on exergy destruction rates and exergy efficiencies of major components of the power plant

Table 13.2, it can be seen that the matiant-cycle power plant has an overall energy efficiency of 76 % and an exergy efficiency of 64 %. The sustainability index of the overall power plant is around 2.76. The total heat removal (from the heat exchanger used before the flash drum and the compressor stage) is about 47 MW, and the network output (the work output of the turbines—the work required by compressor and pumps) is around 115 MW. The total exergy destruction rate is about 168 MW. The energy and exergy efficiency of the matiant-cycle power plant unit is calculated based on the following equations:

$$\eta = \frac{\dot{W}_{turbines}}{\dot{E}_{methane} + \dot{W}_{compressors,pumps}} \tag{13.13}$$

$$\Psi = \frac{\dot{W}_{turbines}}{\dot{Ex}_{methane} + \dot{W}_{compressors,pumps}} \tag{13.14}$$

Figure 13.7 shows that the greatest irreversibilities occur at combustion chambers (combined together, 58 % of the exergy destruction happens at the combustion chambers). The temperature and pressure difference in combustion chambers is significant; also the chemical exergy destruction has a considerable effect on the irreversibility at the combustion chambers. Following the combustion chambers, turbines, compressors and pumps, and heat exchangers have similar relative irreversibilities, between 11 and 15 %. Flash drum has a small effect on the system's irreversibility. One of the reasons of this result might be because almost no temperature/pressure change is observed between the inlet/outlet streams of the flash drum.

From Fig. 13.8, it can be seen that as ambient temperature is increased from 2 to 28 °C, the total exergy destruction rate of the turbines increases by 2.7 %. Combustion chambers' total exergy destruction rate also increases by 5.9 %. Overall, the

Table 13.3 Summary of the major subunits and the overall methanol synthesis unit

Description	η	Ψ	$\dot{Q}$(kW)	$\dot{W}$(kW)
Heat exchangers	87%	78%	1,934	
Methanol reactor	68%	68%		
Flash drum	90%	82%		
Compressor	85%	76%		2,284
Distillation tower	89%	90%		
Overall synthesis unit	41%	41%	1,934	2,284

total exergy destruction rate of the power plant system increases by 1.6 %. The different effect of the ambient temperature on exergy destruction rates of various major components can be explained by the different temperature and pressures of inlet/outlet streams of each component. Since each stream's exergetic potential depends on how close/far they are to/from the ambient (dead) state, some streams' exergetic potential increases as the ambient temperature is increases, while some of them decrease. A decrease in exergy efficiency with increasing ambient temperature occurs in combustion chambers. Within the defined temperature range, the decrease in exergy efficiency of combustion chambers is about 1 %. The turbines' exergy efficiency decreases by about 0.4 % as the temperature increased within the defined range. Overall, the power plant's exergy efficiency decreases by 2 % within the defined ambient temperature range.

Methanol Synthesis Unit

The methanol synthesis unit uses the H_2 from the water electrolysis unit and the CO_2 from the power plant. Overall, the methanol synthesis unit needs 0.25 kmol/s of CO_2 (from power plant unit) and 0.75 kmol/s H_2 (from electrolysis unit). As a result, 0.25 kmol/s of H_2O is produced and sent back to the electrolysis unit. The methanol synthesis unit produces 0.25 kmol/s of CH_3OH.

Table 13.3 summarizes the energy and exergy efficiencies, as well as the energy input/output (either work or heat) of the major components and the overall system itself. The empty cells can be assumed to be 0 or "not applicable."

Overall, the methanol synthesis unit requires about 2 MW of heat and about 2.2 MW of work input. At given ambient conditions (20 °C and 1 bar), the synthesis unit has an energy and exergy efficiency of around 41 %. As a result, the sustainability index of the methanol synthesis unit is 1.7. The energy and exergy efficiency of methanol synthesis unit is calculated based on the following equations:

$$\eta = \frac{\dot{E}_{methanol} + \dot{E}_{water}}{\dot{E}_{CO_2} + \dot{E}_{H_2} + \dot{W}_{compressor} + \dot{Q}_{input}} \tag{13.15}$$

$$\Psi = \frac{\dot{Ex}_{methanol} + \dot{Ex}_{water}}{\dot{Ex}_{CO_2} + \dot{Ex}_{H_2} + \dot{W}_{compressor} + \dot{Q}_{input}\left(1 - \frac{T_0}{T_{avg}}\right)} \tag{13.16}$$

During the process, the rate of exergy destruction is about 80 MW, and Fig. 13.9 shows that 25 % of the irreversibility occurs at the methanol reactor. However, combined together, heat exchangers have a significant effect on exergy destruction rate of the overall system, which means the greatest irreversibility occurs at heat exchangers, combined. Following the heat exchangers, methanol reactor has the second highest irreversibility. Compressors, distillation tower, and the flash drum have similar relative irreversibilities, around 12–14 %. One of the reasons of the low irreversibility at flash drum and distillation column is almost no temperature/pressure change is observed between the inlet/outlet streams of the flash drum and distillation tower. The compressor's pressure difference is not significant either. The overall system requires additional heat, which is provided by the rejected heat and is not mentioned here.

Figure 13.10 shows that ambient temperature has different effects on different major units of the methanol synthesis unit. For instance, as ambient temperature is increased from 2 to 28 °C, the exergy destruction rate of heat exchangers (combined) decreases by about 6 %. The exergy destruction of the reactor increases by 12 %. Overall, the exergy destruction rate of the methanol synthesis unit increases by about 1 % within the given ambient temperature range. The different effect of the ambient temperature on exergy destruction rates of various major components can be explained by the different temperature and pressures of inlet/outlet streams of each component. Since each stream's exergetic potential depends on how close/far

Fig. 13.9 Relative irreversibilities of the major components of the methanol synthesis unit

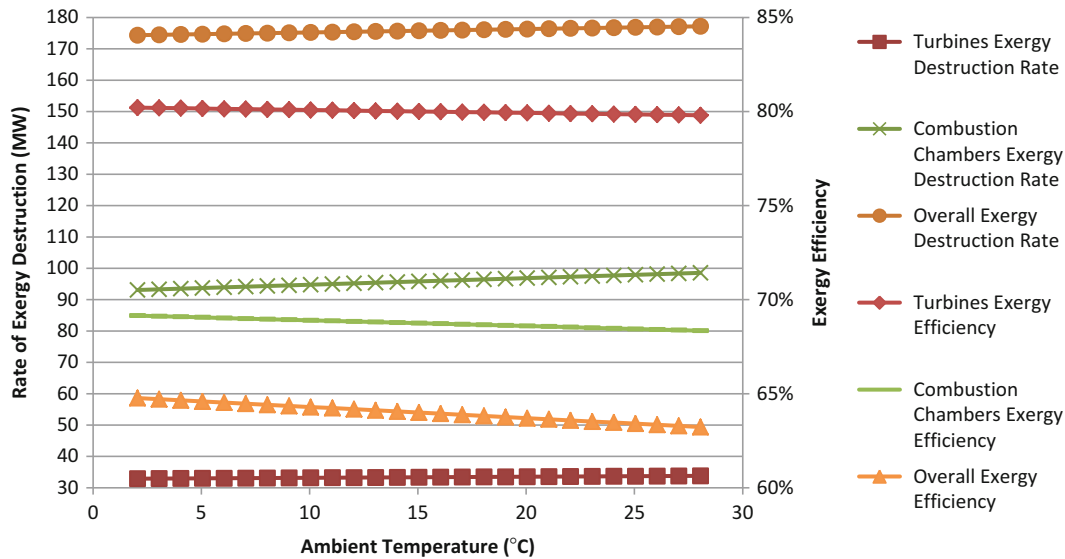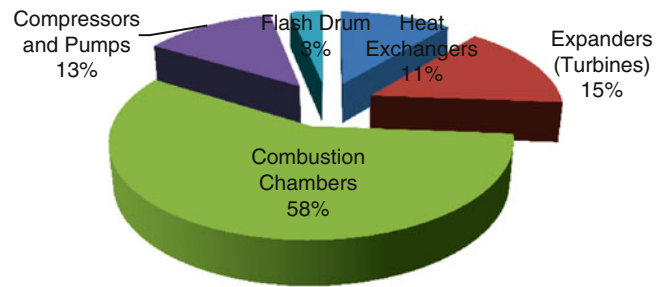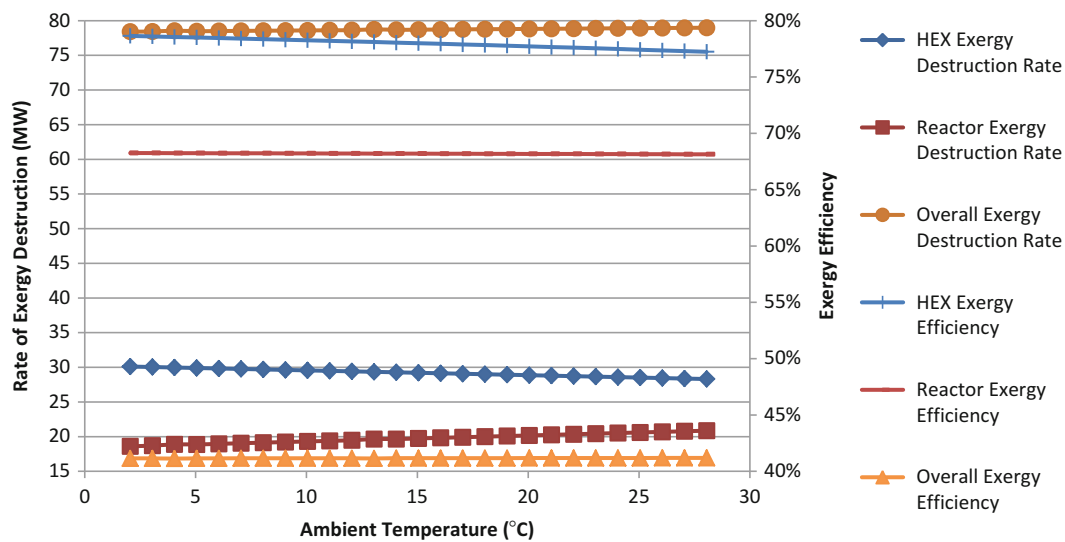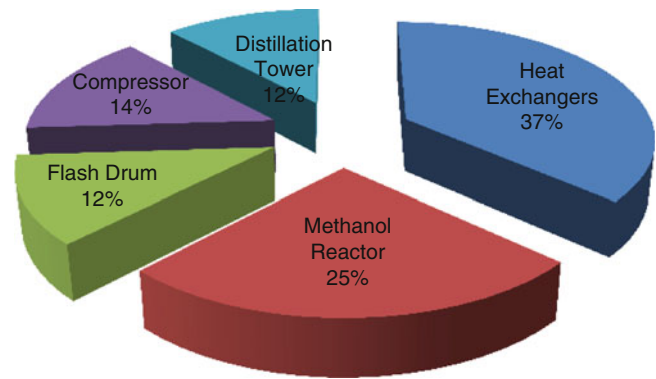**Fig. 13.10** The effect of ambient temperature on exergy destruction rates and exergy efficiencies of major components of the methanol synthesis unit

they are to/from the ambient (dead) state, some streams' exergetic potential increases as the ambient temperature increases, whereas some of them decrease. From Fig. 13.10, it can be seen that the decrease in exergy efficiency of heat exchangers is about 2 %. The reactor's exergy efficiency decreases by about 0.11 % as the temperature increased within the defined range. Overall, the methanol synthesis unit's exergy efficiency increases by about 0.2 % within the defined ambient temperature range.

Overall System Analysis

Overall, the integrated system has three major units: the electrolysis, the matiant-cycle power plant, and methanol synthesis units. In Soltanieh et al.'s [11] study wind energy is proposed as the required power input required for water electrolysis, and the work required by compressors is provided by the output of the power plant unit. The system has ten compressors, nine heat exchangers that require heat removal by a different process, three turbines, two heat exchangers that use different streams of the same unit to provide heat/cold to one another, two combustion chambers, two flash drums, two storage tanks (one for H_2 and one for O_2), one electrolysis unit, one heat exchanger that requires heat input from a different process, one methanol reactor, one distillation tower, and one pump. In this study, each unit is examined within its boundary limits, in

Fig. 13.11 Relative irreversibilities of the electrolysis, power plant, and methanol synthesis unit
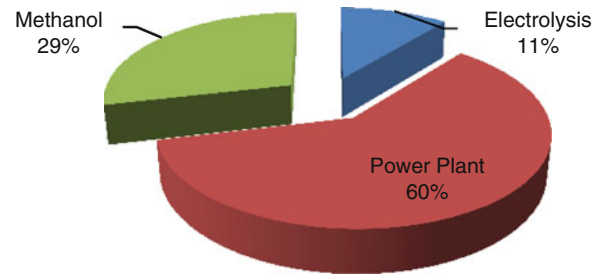
Table 13.4 Summary of different scenarios with corresponding energy and exergy efficiencies

Case	η	Ψ
1	35%	42%
2	64%	46%
3	68%	47%

order to see where the greatest irreversibilities occur and how the ambient temperature affects the system exergetically; the overall system is also investigated.

Figure 13.11 shows that the greatest irreversibility in the overall system occurs at the power plant; this is mainly because of the effect of two combustion chambers in the power plant. The combustion chambers' effect on exergy destruction rates is discussed earlier in section "Matiant-Cycle Power Plant". Temperature difference has an important effect on exergy destruction rates; therefore, any improvement to reduce the temperature difference between inlet and outlet streams would improve the system's overall performance by reducing the exergy destruction rates, therefore irreversibilities.

The energy and exergy efficiencies of the system can be defined in several ways. Table 13.4 summarizes the results based on the three different methods mentioned below:

1. Heat rejected from the system is not considered as a useful output, but some of this heat is used to provide the necessary input required for the distillation column input of the methanol synthesis unit. The work input required for the compressors and pumps are provided by the work output of turbines. The work input required for the electrolysis modules is provided externally:

$$\eta_1 = \frac{\dot{E}_{H_2,stored} + \dot{E}_{O_2,stored} + \dot{E}_{Methanol} + \dot{W}_{turbines} - \dot{W}_{compressors,pumps}}{\dot{E}_{water} + \dot{E}_{Methane} + \dot{W}_{electrolysis}} \qquad (13.17)$$

$$\Psi_1 = \frac{Ex_{H_2,stored} + \dot{E}x_{O_2,stored} + \dot{E}x_{Methanol} + \dot{W}_{turbines} - \dot{W}_{compressors,pumps}}{\dot{E}x_{water} + \dot{E}x_{Methane} + \dot{W}_{electrolysis}} \qquad (13.18)$$

2. Heat rejected from the system is considered as a useful output; some of this output is used to provide the necessary input required for the distillation column input of the methanol synthesis unit. The work input required for the compressors and pumps are provided by the work output of turbines. The work input required for the electrolysis modules is provided externally:

$$\eta_2 = \frac{\dot{E}_{H_2,stored} + \dot{E}_{O_2,stored} + \dot{E}_{Methanol} + \dot{W}_{turbines-compressors,pumps} + \dot{Q}_{rejected} - \dot{Q}_{input}}{\dot{E}_{water} + \dot{E}_{Methane} + \dot{W}_{electrolysis}} \qquad (13.19)$$

$$\Psi_2 = \frac{\dot{E}x_{H_2,stored} + \dot{E}x_{O_2,stored} + \dot{E}x_M + \dot{W}_{turbines-compressors,pumps} + \dot{E}x_{(Q,rejected-Q,input)}}{\dot{E}x_{water} + \dot{E}x_{Methane} + \dot{W}_{electrolysis}} \qquad (13.20)$$

Case Study Soltanieh et al. [11] propose to use the work output of the turbines for the work required in compressors and pumps. The paper uses wind energy to run the electrolysis unit. If electrolysis unit also used the work output of the turbines, the energy and exergy efficiencies become

$$\eta_3 = \frac{\dot{E}_{H_2,stored} + \dot{E}_{O_2,stored} + \dot{E}_{Methanol} + \dot{W}_{turbines-compressors,pumps-electrolysis} + \dot{Q}_{rejected-input}}{\dot{E}_{water} + \dot{E}_{Methane}} \tag{13.21}$$

$$\Psi_3 = \frac{\dot{Ex}_{H_2} + \dot{Ex}_{O_2} + \dot{Ex}_{Methanol} + \dot{W}_{turbines-comp,pumps-electrolysis} + \dot{Ex}_{(Q,rejected-Q,input)}}{\dot{Ex}_{water} + \dot{Ex}_{Methane}} \tag{13.22}$$

Conclusions

The integrated system, as modified from a literature work, electrolyzes water using wind energy and stores 46 % of the produced H_2 and 28 % of the produced O_2. The remaining O_2 is sent from the electrolysis unit to the Matiant-cycle power plant and goes into complete combustion with natural gas (pure methane). The combustion product water is sent back to the electrolysis unit, and CO_2 is sent to the methanol synthesis unit. In the methanol synthesis unit, CO_2 reacts with the H_2 coming from the electrolysis unit and produces methanol. The overall system does not release CO_2 to the environment, and the heating requirement of the system is met by the rejected heat within the integrated system. Exergy efficiency of the overall system increases by 2 % if the rejected heat is used as a product, such as water or space heating. This amount increases by 1 % if the work requirements of not only the compressor and pumps but also the electrolysis modules are met by the work output of the turbines. The integrated system's outputs are about 133 MW of electricity energy (60 MW, if the pumps, compressors, and electrolysis modules' input is provided) and 0.25 kmol/s methanol. By converting the CO_2 to methanol, the methanol synthesis unit avoids the release of 0.25 kmol/s CO_2 into the atmosphere. If the system is assumed to work 8,000 h, the avoided CO_2 emissions could reach around 160 tons.

References

1. International Energy Agency Technical Report (2012) Key world energy statistics. Website: http://www.iea.org/publications/freepublications/publication/kwes.pdf. Accessed 10 Jan 2013
2. Davison J (2007) Performance and costs of power plants with capture and storage of CO_2. Energy 32:1163–1176
3. Damen K, Troost T, Faaij A, Turkenburg W (2006) A comparison of electricity and hydrogen production systems with CO_2 capture and storage, Part A: Review and selection of promising conversion and capture technologies. Prog Energy Combust Sci 32:215–246
4. Minutillo M, Perna A (2010) A novel approach for treatment of CO_2 from fossil fired power plants, Part B: The energy suitability of integrated tri-reforming power plants (ITRPPs) for methanol production. Int J Hydrogen Energy 35:7012–7020
5. Guang-jian L, Zheng L, Ming-hua W, Wei-dou N (2010) Energy savings by coproduction: a methanol/electricity case study. Appl Energy 87:2854–2859
6. Chen Y, Adams TA II, Barton PI (2011) Optimal design and operation of static energy polygeneration systems. Indus Eng Chem Res 50:5099–5113
7. Katayama Y, Tamaura Y (2005) Development of new green-fuel production technology by combination of fossil fuel and renewable energy. Energy 30:2179–2185
8. Takeuchi M, Sakamoto Y, Niwa S et al (2001) Study on CO_2 global recycling system. Sci Total Environ 277:15–19
9. Mignard D, Sahibzada M, Duthie JM, Whittington HW (2003) Methanol synthesis from flue-gas CO_2 and renewable electricity: a feasibility study. Int J Hydrogen Energy 28:455–464
10. Cifre PG, Badr O (2007) Renewable hydrogen utilization for the production of methanol. Energy Convers Manage 48:519–527
11. Soltanieh M, Azar KM, Saber M (2012) Development of a zero emission integrated system for co-production of electricity and methanol through renewable hydrogen and CO_2 capture. Int J Greenh Gas Control 7:145–152
12. Perry RH, Green DW (2000) Perry's chemical engineering handbook, 7th edn. McGraw-Hill, New York, NY
13. Dincer I, Rosen MA (2007) Exergy: energy, environment and sustainable development. Elsevier, Oxford
14. Kotas TJ (1995) The exergy method of thermal plant analysis. Krieger, London

Thermodynamic Analysis of Geothermally Driven High-Temperature Steam Electrolysis System for Hydrogen Production

Mustafa Tolga Balta, Ibrahim Dincer, and Arif Hepbasli

Abstract

Hydrogen production by high-temperature steam electrolysis (HTSE) has been receiving increasing attention worldwide due to its high efficiency and carbon-free operation. Although it is still considered in its early developmental stage, it offers a promising solution for highly efficient hydrogen production. From the thermodynamic viewpoint of water decomposition, it is more advantageous to electrolyse water at high temperatures because the energy is supplied in mixed form of electricity and heat. In this study, a HTSE process coupled with and powered by a geothermal power plant is considered for analysis and assessment and as a case study. In this regard, its thermodynamic analysis through energy and exergy is conducted for performance evaluation and comparison purposes. As a result, compared to conventional water electrolysis, the operation at high temperatures reduces the electrical energy requirement for the electrolysis and also increases the efficiency.

Keywords

Energy • Exergy • Efficiency • Geothermal • Hydrogen • High-temperature steam electrolysis

Introduction

Increasing population, rapid urbanization, and development lead to high and continuous increase in energy demand. Nowadays world's energy demands are almost supplied by carbon-containing fossil sources such as natural gas, oil, and coal, which have been formed during many millions of years from plant biomass. Global consumption of these nonrenewable resources for energy demand is resulting in critical environmental issues, such as greenhouse effect, climate change, ozone depletion, and global warming. In addition to these environmental issues, there are other critical concerns, such as energy, economic, and political crises. New and more efficient energy conversion systems are required in the near future, due to the increase in oil prices and demand as well as global warming [1].

Primary energy resources, such as fossil fuels, are diminishing and must be regarded as a finite resource. Therefore, water may be considered to be the cleanest fuel source instead of fossil fuels. By developing hydrogen energy system, one can transfer energy consumption to the water cycle rather than the hydrocarbon-based cycle. It is important to highlight that hydrogen has substantial environmental benefits if it is produced through renewable energy sources.

M.T. Balta (✉)
Department of Mechanical Engineering, Aksaray University, 68100 Aksaray, Turkey
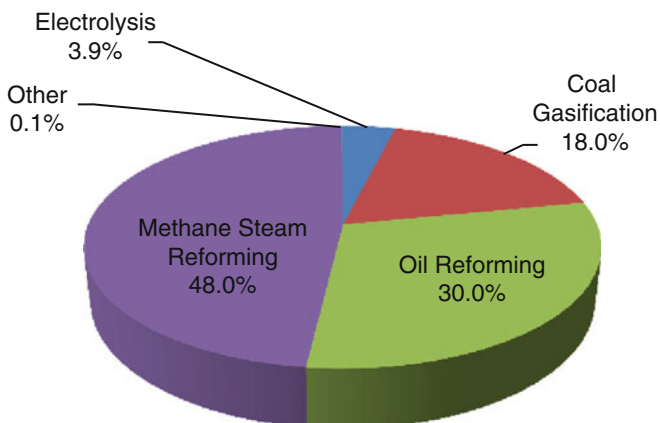e-mail: mustafatolgabalta@aksaray.edu.tr

I. Dincer
Faculty of Engineering and Applied Science, University of Ontario Institute of Technology (UOIT),
2000 Simcoe Street North, Oshawa, ON, Canada L1H 7K4

A. Hepbasli
Department of Energy Systems Engineering, Yaşar University, 35100 Bornova, Izmir, Turkey

Although many scientists propose a large variety of solutions, one of the important solutions is implementing the hydrogen economy. Hydrogen is probably the preferred energy carrier for a future zero-carbon economy, but several research efforts are required in order to supply inexpensive and plentiful amounts of fuel. Hydrogen economy offers a compelling vision of an energy future for the nation and the world that is at once abundant, clean, flexible, and secure [2].

Hydrogen is usually found as a compound combined with other elements, and thus, the production of hydrogen always requires energy [1]. Currently, the most mature and inexpensive way to produce hydrogen is through steam reforming, partial oxidation of heavy hydrocarbons, gasification, and conventional alkaline water electrolysis. Figure 14.1 illustrates that 96 % hydrogen is produced directly from fossil fuels, while about 4 % is produced indirectly by electricity utilization.

The conventional hydrogen production methods are not considered renewable since these processes consume natural resources and also release high levels of CO_2. Therefore, it will not be a potential solution to combat with environmental issues [4, 5]. Clearly, we urgently need to find alternative, eco-friendly ways for hydrogen production technologies to ensure the future generations receive a cleaner and sustainable energy-based economy and society. Several researchers have been investigating a wide range of technologies to produce hydrogen economically from a variety of resources in environmentally friendly ways [6]. In this regard, renewable energy resources have attracted great interest in recent years. Alternative clean and efficient pathways for the production of pure hydrogen are water electrolysis and thermochemical water-splitting cycles with renewable energy sources.

Hydrogen can be produced from water or steam electrolysis using much simpler technology through the following reaction:

$$H_2O + Energy \Rightarrow H_2 + \tfrac{1}{2} O_2 \tag{14.1}$$

Water electrolysis process is one of the environmentally benign hydrogen and oxygen production methods without emitting greenhouse gases if the required electricity is supplied from renewable energy sources. Electrolytic hydrogen production has many advantages such as it yields the highest-purity hydrogen (up to 99.999 %). This technology is well developed, but overall system efficiency is too low, about 27 %. The main disadvantage of water electrolysis is that electricity is an expensive "fuel". The concept of integrating renewable energy with hydrogen production systems was given some serious consideration in the 1970s [7, 8]. The aim of the above-mentioned concept was not only to improve the performance of existing hydrogen production systems but also to integrate the hydrogen production systems effectively with renewable energy sources. When considering the use of renewable energy for hydrogen production, geothermal resources seem to be an important option [9].

Geothermal energy is treated as a reliable and promising renewable energy. The use of geothermal energy through hybrid or integrated systems for sustainable hydrogen production appears to be an environmentally benign and sustainable option for the countries having abundant geothermal energy resources. In this study, a HTSE process coupled with and powered by a geothermal power plant is considered for analysis and assessment and as a case study. In this regard, its thermodynamic analysis through energy and exergy is performed for performance evaluation and comparison purposes.

High-Temperature Steam Electrolysis

High-temperature steam electrolysis (HTSE) is still considered in the early developmental stage. The HTSE offers a promising method for highly efficient hydrogen production. From the thermodynamic viewpoint of water decomposition, it is more advantageous over electrolyse water at high temperature (800–1,000 °C) because the energy is supplied in a mixed form of electricity and heat. The steam to be dissociated enters on the cathode side. After the steam has been divided into hydrogen gas and oxygen ions, the oxygen ions are transported through the ceramic material to the anode where they discharge and form oxygen gas. The most common ceramic material is zirconia, ZrO_2 [10]. Compared to conventional water electrolysis, operation at high temperatures reduces the electrical energy requirement for the electrolysis and also increases the efficiency. The effect of temperature on the energy requirement for HTSE is shown in Fig. 14.2, as related to the enthalpy of the water splitting process. The enthalpy is given as the sum of the minimum work needed and the temperature–entropy term:

$$\Delta H = \Delta G + T\Delta S \tag{14.2}$$

where ΔH is the enthalpy change or total energy demand, ΔG is the Gibbs free energy or the minimum work, T is the absolute temperature, and ΔS is the entropy change. The term $T\Delta S$ can be considered as the total amount of thermal energy needed to split water [10]. The electrical energy demand decreases with increasing temperature leading to increased direct heat requirements, the decrease in electrical energy demand drives to thermal to hydrogen energy conversion efficiency to higher values. This is one of the advantages of HTSE. The temperature dependence of the thermodynamic functions for splitting of the fluid is shown in Fig. 14.2.

The energy and exergy efficiencies of the overall system are generally defined as follows:

$$\eta_{overall} = \left(\frac{\text{energy in products}}{\text{total energy input}}\right) \tag{14.3a}$$

$$\psi_{overall} = \left(\frac{\text{exergy in products}}{\text{total exergy input}}\right) \tag{14.3b}$$

Here, the overall efficiencies of the HTSE system were analyzed by Mingyi et al. [11]. A thermodynamic model of the HTSE system efficiency was well established, and the effects of electrical, thermal, and overall efficiencies of the HTSE system were investigated. The overall efficiencies of the HTSE system under different conditions ranged from 33 % to a maximum of 59 % at a temperature of 1,000 °C, which was over two times higher than that of the conventional alkaline water electrolysis.

Note that analyses of experimental and computational model of high-temperature steam electrolysis were presented by Herring et al. [12]. Computational model and experimental results were compared favorably. Hydrogen production efficiency of high-temperature electrolysis coupling with high-temperature gas cooled reactor was evaluated by Fujiwara et al. [13]. Hydrogen production efficiency at high-temperature electrolysis for operating temperature of 800 °C was
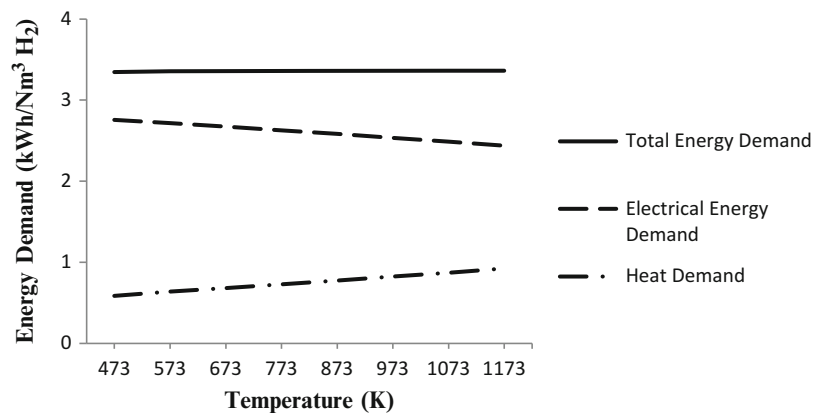
Fig. 14.2 Energy demand for high-temperature steam electrolysis (adapted from [9])

calculated over 53 %. A research and development program has been underway at the Idaho National Laboratory (INL) on high-temperature electrolysis for hydrogen production from steam [14]. The electrolysis was coupled with an advanced reactor and power cycle, and the efficiency of the system was calculated 45–50 %, respectively.

Energy and exergy analyses of a water-electrolysis process for producing hydrogen were investigated by Rosen and Scott [15] and Rosen [16]. Three driving energy inputs were considered: (1) electricity, (2) the high-temperature heat used to generate the electricity, and (3) the heat source used to produce the high-temperature heat. The analyses indicated where the losses were occurred.

Electrolysis currently accounts for a very small portion of the hydrogen generated in developed countries that have a commercial hydrogen infrastructure. However, electrolysis can be economic for small-scale generation in areas with inexpensive electricity which was generated by renewable such as geothermal resources.

System Description

Many studies have recently appeared concerning future hydrogen demand; for example, one was presented by Sigurvinsson et al. [17], considering a HTSE process coupled with a geothermal source at Nasjavellir site in Iceland. The geothermal source was about at 230 °C and 15 bar. In this section, energy and exergy analyses of a high-temperature electrolysis are performed for comparison purposes, of which detailed description is given in Sigurvinsson et al. [17]. The schematic flow diagram of the HTSE process along with its main components is shown in Fig. 14.3, while their thermodynamic properties are listed in Table 14.1.

Fig. 14.3 A schematic of the HTSE system studied, as proposed by Sigurvinsson et al. [17]

Table 14.1 The HTSE system data, thermodynamic properties, and energy and exergy values

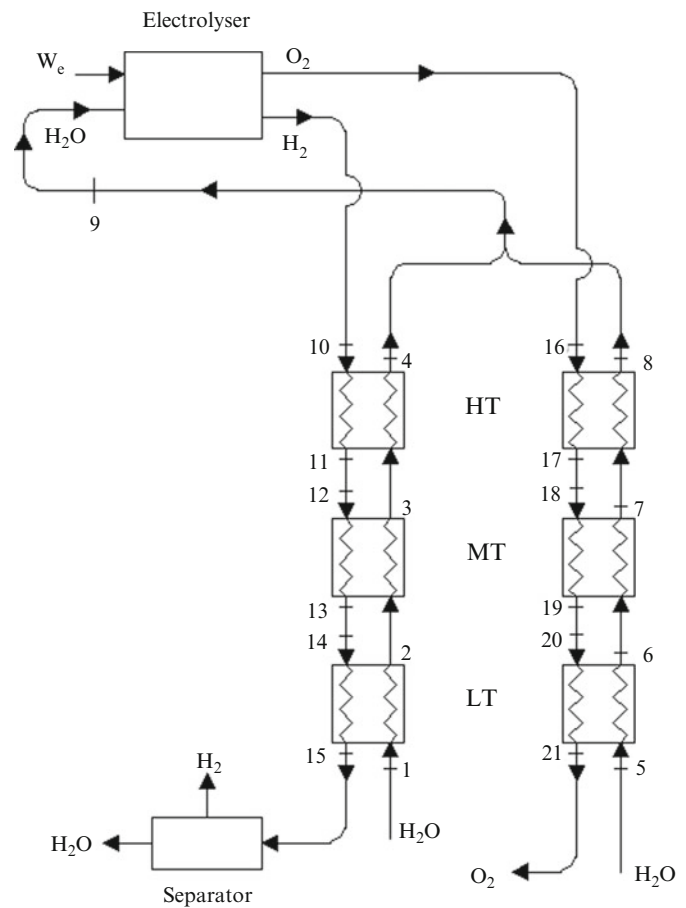| State no.	Substance	Description	T (K)	P (kPa)	$\dot{m}$ (kg/s)	h (kJ/kg)	s (kJ/kg K)	ex^{ph} (kJ/kg)	$\dot{E}x^{ph}$ (kW)	$\dot{E}$ (kW)
0	H_2O	Reference state	298	101.325	–	104.8	0.3669	–	–	–
0′	H_2	Reference state	298	101.325	–	0	64.82	–	–	–
0″	O_2	Reference state	298	101.325	–	0	6.407	–	–	–
1	H_2O	H_2O inlet LT-H_2	503	1,500	11.400	2,874	6.613	908	10,350	32,764
2	H_2O	H_2O outlet LT-H_2/H_2O inlet MT-H_2	753	1,500	11.400	3,429	7.513	1,195	13,619	39,091
3	H_2O	H_2O outlet MT-H_2/H_2O inlet HT-H_2	978	1,500	11.400	3,932	8.096	1,524	17,373	44,825
4	H_2O	H_2O outlet HT-H_2	1,185	1,500	11.400	4,421	8.549	1,878	21,408	50,399
5	H_2O	H_2O inlet LT-O_2	503	1,500	4.000	2,874	6.613	908	3,631	11,496
6	H_2O	H_2O outlet LT-O_2/H_2O inlet MT-O_2	693	1,500	4.000	3,299	7.332	1,119	4,474	13,196
7	H_2O	H_2O outlet MT-O_2/H_2O inlet HT-O_2	983	1,500	4.000	3,944	8.108	1,532	6,129	15,776
8	H_2O	H_2O outlet HT-O_2	1,185	1,500	4.000	4,421	8.549	1,878	7,512	17,684
9	H_2O	Electrolyser inlet	1,185	1,500	15.400	4,421	8.549	1,878	28,920	68,083
10	H_2	H2 inlet HT-H_2	1,223	10,000	1.147	13,653	66.51	13,149	15,076	15,653
10′	H_2O	H_2O inlet HT-H_2	1,223	10,000	5.082	4,486	7.731	2,187	11,113	22,798
11	H_2	H2 outlet HT-H_2	987	10,000	1.147	10,056	63.24	10,527	12,069	11,529
11′	H_2O	H_2O outlet HT-H_2	987	10,000	5.082	3,903	7.202	1,761	8,951	19,835
12	H_2	H2 inlet MT-H_2	987	2,000	1.147	10,056	69.88	8,548	9,800	11,529
12′	H_2O	H_2O inlet MT-H_2	987	2,000	5.082	3,950	7.982	1,576	8,009	20,074
13	H_2	H2 outlet MT-H_2	782	2,000	1.147	7,016	66.43	6,536	7,494	8,044
13′	H_2O	H_2O outlet MT-H_2	782	2,000	5.082	3,488	7.457	1,270	6,456	17,726
14	H_2	H2 inlet LT-H_2	782	7,000	1.147	7,016	61.27	8,074	9,257	8,044
14′	H_2O	H_2O inlet LT-H_2	782	7,000	5.082	3,432	6.826	1,402	7,127	17,441
15	H_2	H2 outlet LT-H_2	577	7,000	1.147	4,030	56.84	6,408	7,347	4,620
15′	H_2O	H_2O outlet LT-H_2	577	7,000	5.082	2,854	5.958	1,083	5,504	14,504
16	O_2	O_2 inlet HT-O_2	1,223	10,000	9.200	955.3	6.634	888	8,166	8,789
17	O_2	O_2 outlet HT-O_2	987	10,000	9.200	725.9	6.428	720	6,621	6,678
18	O_2	O_2 inlet MT-O_2	987	2,000	9.200	725.9	6.816	604	5,557	6,678
19	O_2	O_2 outlet MT-O_2	782	2,000	9.200	406.6	6.474	387	3,557	3,741
20	O_2	O_2 inlet LT-O_2	782	7,000	9.200	406.6	6.149	483	4,448	3,741
21	O_2	O_2 outlet LT-O_2	569	7,000	9.200	258.2	5.917	404	3,719	2,375

State numbers refer to Fig. 14.3

Analysis

Before conducting energy and exergy analyses, the following assumptions are made:

- The values for the reference environment (dead state) temperature (T_0) and pressure (P_0) are 25 °C and 100 kPa, respectively.
- All processes are considered steady state and steady flow with negligible potential and kinetic energy effects in an adiabatic form.

For a general steady state, steady flow process, the three balance equations, namely mass, energy, and exergy balance equations, are employed to find the work input, the rate of exergy destruction, and overall energy and exergy efficiencies.

Since mass is conserved in chemical reactions, the mass of products and reactants are equal and in general, the mass balance equation can be expressed in the rate form as

$$\sum \dot{m}_{in} = \sum \dot{m}_{out} \quad \text{or} \quad \sum \dot{m}_R = \sum \dot{m}_P \tag{14.4}$$

where $\dot{m}$ is the mass flow rate and the subscript *in* stands for inlet and *out* for outlet.

The general energy balance is written as

$$\dot{E}_{in} - \dot{E}_{out} = \Delta \dot{E}_s \tag{14.5}$$

Table 14.2 Enthalpy of formation and Shomate constants for H_2, O_2, and H_2O

Compound	$\overline{h}_f^o$ (kJ/kmol)	A	B	C	D	E	F	G	H
H_2O (g)	−241,830	30.0920	6.832514	6.793435	−2.534480	0.082139	−250.881	223.3967	−241.8264
O_2 (g)	0	29.6590	6.137261	−1.186521	0.095780	−0.219663	−9.861391	237.9480	0
H_2 (g)	0	33.0661	−11.36340	11.432816	−2.772874	−0.158558	−9.980797	172.7079	0

Source: Adopted from NIST [18]

Table 14.3 Gibbs free energy and standard chemical exergy of H_2, O_2, and H_2O

Compound	Specific Gibbs free energy of formation $\overline{g}_f^o$ (kJ/kmol)	Standard chemical exergy $\overline{ex}^{ch}$ (kJ/kmol)
H_2O (g)	−228,638	9,437
H_2 (g)	0	236,090
O_2 (g)	0	3,970

which becomes

$$Q + W = \sum n_P \left(\overline{h}_f^o + \overline{h} - \overline{h}^o \right)_P - \sum n_R \left(\overline{h}_f^o + \overline{h} - \overline{h}^o \right)_R \tag{14.6}$$

and the exergy balance for the process, involving chemical reactions, becomes

$$\sum \dot{E}x_{in} - \sum \dot{E}x_{out} - \dot{E}x_d = \Delta \dot{E}x_s \tag{14.7}$$

For a steady state system, $\Delta \dot{E}x_s$ is zero. The exergy associated with a process at a specified state is the sum of two contributions: physical and chemical.

Thus, the specific exergy of the process is calculated by

$$ex = (h - h_0) - T_0(s - s_0) + ex^{ch} \tag{14.8}$$

where h is enthalpy, s is entropy, and the subscript zero indicates properties at the reference (dead) state of P_0 and T_0.

The exergy rate is then calculated by

$$\dot{E}x = \dot{m}ex \tag{14.9}$$

Combining Eqs. (14.7) and (14.8) yields

$$ex_d = \sum \left[(h - h_0) - T_0(s - s_0) + ex^{ch} \right] - \sum \left[(h - h_0) - T_0(s - s_0) + ex^{ch} \right]_{out} + W_{e,in} \tag{14.10}$$

After writing mass, energy, and exergy balances for the system, enthalpy values of H_2, O_2, and H_2O are evaluated with Shomate equations as follows:

$$\overline{h} - \overline{h}_0 = A * T + B * \frac{T^2}{2} + C * \frac{T^3}{3} + D * \frac{T^4}{4} - E * \frac{1}{T} + F - H \tag{14.11}$$

where T is 1/1,000 of the specified temperature (in K) of compound and A, B, C, D, E, F, G, and H are constants, as given in Table 14.2 for H_2, O_2, and H_2O.

The chemical exergy based on a typical exergy reference environment exhibiting standard values of the environmental temperature T_0 and pressure P_0 such as 298 K and 100 kPa is called standard chemical exergy. The values of the chemical exergies for the reactants and products are taken from the literature [19], as listed in Table 14.3.

The exergy destructions in the heat exchangers and electrolyses are calculated as

$$\dot{E}x_{d,\ HE} = \dot{E}x_{in} - \dot{E}x_{out} \tag{14.12}$$

Table 14.4 The assumed typical values

Parameter	η_{el} (%)	η_{es} (%)	η_{th} (%)
Typical values	10–20	80–100	80–100

Adopted from Zhang et al. [20]

$$\dot{Ex}_{d,el} = \dot{W}_e - \left(\dot{Ex}_{out} - \dot{Ex}_{in} \right) \tag{14.13}$$

The exergy efficiency of the heat exchanger is determined by the increase in the exergy of the cold stream divided by the decrease in the exergy of the hot stream on a rate basis as follows:

$$\psi_{HE} = \frac{\dot{Ex}_{cold,out} - \dot{Ex}_{cold,in}}{\dot{Ex}_{hot,in} - \dot{Ex}_{hot,out}} = \frac{\dot{m}_{cold}(ex_{cold,out} - ex_{cold,in})}{\dot{m}_{hot}(ex_{hot,in} - ex_{hot,out})} \tag{14.14}$$

The expressions of energy and exergy efficiencies for the geothermal assisted HTSE system are based on the above definitions. The theoretical overall energy and exergy efficiencies of the system can be expressed as

$$\eta_{overall} = \frac{HHV}{\Delta G/\eta_{el}\eta_{es} + Q/\eta_{th}} \tag{14.15}$$

$$\psi_{overall} = \frac{Ex_{H_2}}{\Delta G/\eta_{el}\eta_{es} + Ex_Q} \tag{14.16}$$

$$Ex_Q = \left(1 - \frac{T_0}{T} \right) \frac{Q}{\eta_{th}} \tag{14.17}$$

Here, the theoretical overall efficiency can be affected by three key parameters. These parameters are the efficiency of the high-temperature steam electrolysis cell (η_{es}), the electricity generation efficiency by the geothermal power plant (η_{el}), and thermal efficiency (η_{th}) and also these parameters are closely related to the temperature.

Heat Exchanger Networks

In the study of Sigurvinsson et al. [17, 21], counter current heat exchangers were used while the inlet temperature of the electrolyses was kept as 950 °C. The temperatures in the geothermal case ranged from 200 to 950 °C. The heat exchangers were classified into three groups according to the ranges of the temperatures since this temperature range could not be covered with one type of heat exchangers. Therefore,

- Low temperature (LT): stainless heat exchanger, T < 600 °C and 7 MPa,
- Medium temperature (MT): nickel-based heat exchanger, 600 °C < T < 850 °C and 7 MPa,
- High temperature (HT): ceramic-based heat exchanger, T > 850 °C and 10–50 MPa.

The fluid in the first heat exchanger network is only oxygen. In the second heat exchanger, the fluid is a steam and hydrogen mixture. This mixture depends on the recycling ratio, which is taken to be 0.33 in these analyses. The mass flow rates of hydrogen and oxygen are calculated by

$$\dot{m}_{out,H_2} = (1-r) \cdot \dot{m}_{H_2O} \cdot \frac{M_{H_2}}{M_{H_2O}} + r \cdot \dot{m}_{H_2O} \tag{14.18}$$

$$\dot{m}_{out,O_2} = \frac{(1-r)}{2} \cdot \dot{m}_{H_2O} \cdot \frac{M_{O_2}}{M_{H_2O}} \tag{14.19}$$

Results and Discussion

The temperature, pressure, and mass flow rate data on water, hydrogen, and oxygen are given in Table 14.1 according to their state numbers specified in Fig. 14.3. The specific physical exergy and energy rates are calculated for each state, as presented in Table 14.1. In this study, the reference state is taken to be 25 °C at the pressure of 100 kPa. The thermodynamic properties of water, hydrogen, and oxygen are obtained using Engineering Equation Solver (EES) software package program. Note that state 0 indicates the restricted dead state for the water, hydrogen, and oxygen.

The chemical exergy is associated with the departure of the chemical composition of a system from that of the environment. For the simplicity, the chemical exergy considered in the analysis is rather a standard chemical exergy, based on the standard values of the dead state temperature of 25 °C and pressure of 100 kPa. Generally, these values are in a good agreement with the calculated chemical exergy, relative to alternative specifications of the environment. In the analyses, the values of the chemical exergies of the reactants and products for electrolyser are taken from Orhan et al. [22, 23].

The energy and exergy efficiencies of the high-temperature steam electrolyser unit are also calculated, depending on the given parameters. It is found that energy and exergy efficiencies of the HTSE are 87 % and 86 %, respectively. These are considerably consistent with the practical efficiencies. One of the main factors affecting the hydrogen production cost is the temperature of electrolyser. Figure 14.4 illustrates the effects of the electrolyse temperature on the energy and exergy efficiencies.

The energy efficiency values for the HTSE unit vary between 80 % and 87 % while exergy efficiency values for that range from 79 to 86 %. Also, it is clear from this figure that energy and exergy efficiencies increase with the electrolysis temperatures ranging from 473 to 1,173 K. The details about the system studied here for the performance analysis may be obtained from Sigurvinsson et al. [17, 21].

The overall theoretical energy and exergy efficiencies of the HTSE system are calculated and given in Tables 14.5 and 14.6.
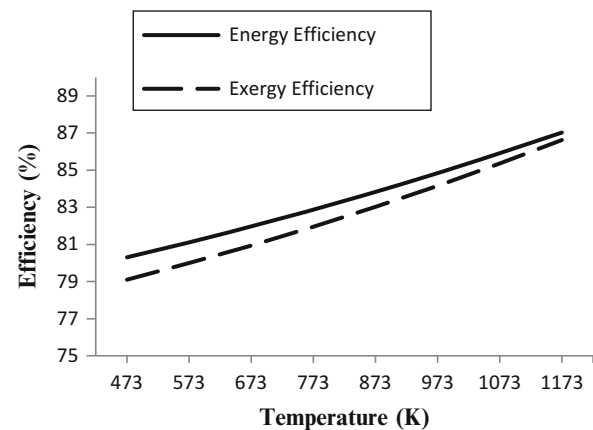
Fig. 14.4 Energy and exergy efficiencies of the HTSE unit

Table 14.5 The overall theoretical energy efficiency values of various conditions for HTSE

η_{el} (%)	η_{es} (%)			η_{th} (%)		
	80	90	100	80	90	100
10	14.10	15.82	17.53	17.41	17.48	17.53
11	15.48	17.36	19.23	19.09	19.17	19.23
12	16.85	18.89	20.92	20.76	20.85	20.92
13	18.21	20.42	22.61	22.41	22.52	22.61
14	19.57	21.94	24.28	24.05	24.18	24.28
15	20.92	23.44	25.95	25.69	25.83	25.95
16	22.27	24.95	27.60	27.31	27.47	27.60
17	23.61	26.44	29.25	28.92	29.10	29.25
18	24.95	27.93	30.89	30.52	30.72	30.89
19	26.28	29.41	32.51	32.11	32.33	32.51
20	27.60	30.89	34.14	33.69	33.94	34.14

Table 14.6 The overall theoretical exergy efficiency values of various conditions for HTSE

η_{el} (%)	η_{es} (%)			η_{th} (%)		
	80	90	100	80	90	100
10	11.87	13.34	14.82	14.79	14.80	14.82
11	13.05	14.67	16.29	16.26	16.27	16.29
12	14.23	15.99	17.76	17.72	17.74	17.76
13	15.40	17.32	19.22	19.18	19.21	19.22
14	16.58	18.64	20.69	20.64	20.67	20.69
15	17.76	19.96	22.15	22.10	22.13	22.15
16	18.93	21.27	23.61	23.56	23.59	23.61
17	20.10	22.59	25.07	25.01	25.05	25.07
18	21.27	23.91	26.53	26.46	26.50	26.53
19	22.45	25.22	27.99	27.91	27.95	27.99
20	23.61	26.53	29.44	29.35	29.40	29.44

Table 14.7 Exergy efficiency and exergy destruction rate values of heat exchangers

Heat exchanger	$\dot{Ex}_{dest, \ Hex}$ (kW)	η_{Hex} (%)
LT-H_2	263	92.55
MT-H_2	106	97.26
HT-H_2	1,133	78.08
LT-O_2	114	86.51
MT-O_2	345	82.75
HT-O_2	163	89.43

Fig. 14.5 Thermal and electricity supply to the studied system
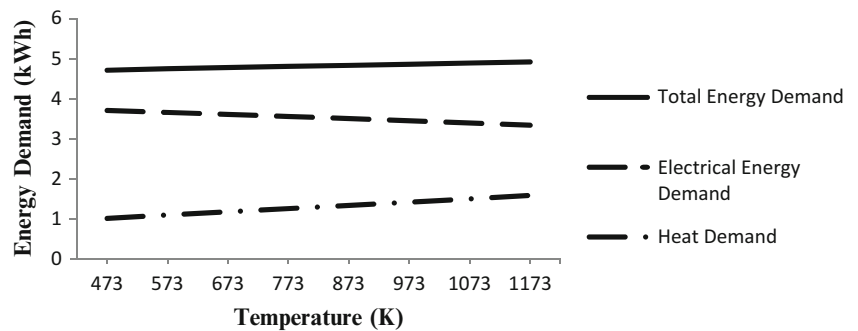
Tables 14.5 and 14.6 show the calculation results of the $\eta_{overall}$ and $\psi_{overall}$ of different η_{el}, η_{es}, and η_{th}. As given in this table, the $\eta_{overall}$ and $\psi_{overall}$ are increased by increasing η_{el}, η_{es}, and η_{th}. The overall theoretical energy and exergy efficiencies of the system are calculated as 14.10–34.14 %, and 11.87–29.44 % respectively, compared to the energy efficiency of the well-developed conventional alkaline water electrolysis, which is about 27 %. In the system studied, exergy destruction and exergy efficiency of heat exchangers were also calculated. The values for exergy destruction and exergy efficiency of heat exchangers are given in Table 14.7. The results in this table indicate that heat exchangers operate at relatively high exergy efficiencies and that most exergy destructions in the overall system are due to heat exchanger network. It is seen from this table that the maximum exergy destructions in the heat exchanger system occur at HT-H exchanger as 1,133 kW.

Table 14.2 lists the enthalpy of formation values and the Shomate constants while Table 14.3 shows the Gibbs free energy and standard chemical exergy of H_2, O_2, and H_2O. The thermodynamic parameters in the range of 473–1,173 K were basically calculated using Eq. (14.2), as shown in Fig. 14.5.

Here, the results show that the total energy demand increases slightly with the increase in temperatures while electrical energy demand decreases due to the increasing heat demand. The decrease in the demand of electrical energy increases the thermal to hydrogen energy conversion efficiency. The exergy demand of the system is illustrated in Fig. 14.6.

Fig. 14.6 Exergy demand of the studied system
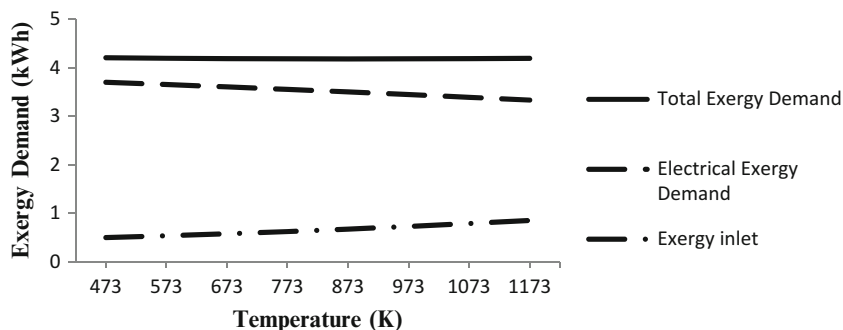
The total exergy demand of the system is constant with an increase in the temperature while electrical demand decreases due to the exergy inlet of the steam. The decrease in the electrical demand increases the thermal to hydrogen exergy conversion efficiency, as illustrated in Fig. 14.6.

Conclusions

We have evaluated the overall theoretical energy and exergy efficiencies of the HTES process coupled to the geothermal power plants to produce hydrogen in this study. We can expect a higher hydrogen production yield at the high operation temperature. The promising research results of HTSE in developed countries highlight the fact that it can be a suitable process for the next decades to consider massive production of hydrogen. A well-developed HTSE might also be a promising potential technology to resolve the long-term energy requirements in developed countries.

From this study, we can extract the following concluding remarks:

- Geothermal steam-assisted high-temperature electrolysis in countries, which are abundant due to geothermal sources, could possibly reduce the hydrogen production cost.
- The energetic and exergetic efficiencies of the overall system are obtained to be 87 % and 86 %, respectively.
- The overall theoretical energy and exergy efficiencies of the system are calculated as 14.10–34.14 % and 11.87–29.44 % respectively, compared to the energy efficiency of the well-developed conventional alkaline water electrolysis, which is about 27 %.
- The maximum exergy destruction rate occurs within the HT-H_2 exchanger with 1,133 kW.
- The overall system exergy destruction rate is found as 9,008 kW.
- For a geothermal temperature range of 500–600 °C, the system consumes less electricity.
- It is confirmed from the exergetic point of view that the electrolyse temperature is one of the basic parameters that affects the efficiency. Increase in the electrolyse temperature leads to an increase in the exergy efficiency and a decrease in the exergy destruction rate.

References

1. Laguna-Bercero MA (2012) Recent advances in high temperature electrolysis using solid oxide fuel cells: a review. J Power Sources 203:4–16
2. ANL (2004) Basic research needs for the hydrogen economy, report of the basic energy sciences workshop on hydrogen production, storage and use. 13–15 May 2003, p 3
3. Ewan BCR, Allen RWK (2005) A figure of merit assessment of the routes to hydrogen. Int J Hydrogen Energy 30:809–819
4. Balta MT, Dincer I, Hepbasli A (2010) Thermodynamic performance comparison of some renewable and non-renewable hydrogen production processes. 18th world hydrogen energy conference 2010-WHEC 2010, parallel sessions book 2: hydrogen production technologies-Part 1, proceedings of the WHEC, Essen, 16–21 May, pp 331–341
5. Balta MT, Dincer I, Hepbasli A (2011) Energy and exergy analyses of Mg-Cl thermochemical cycle. International conference on hydrogen production, Thessaloniki, Greece, 19–22 June 2011
6. Kanoğlu M, Ayanoğlu A, Abusoğlu A (2011) Exergoeconomic assessment of a geothermal assisted high temperature steam electrolysis system. Energy 36:4422–4433
7. Eisenstadt MM, Cox KE (1975) Hydrogen production from solar energy. Sol Energy 17:59–65
8. Costogue EN, Yasui RK (1977) Performance data for a terrestrial solar photovoltaic/water electrolysis experiment. Sol Energy 19:205–210
9. Balta MT, Dincer I, Hepbasli A (2009) Thermodynamic assessment of geothermal energy use in hydrogen production. Int J Hydrogen Prod 34:2925–2939
10. Arnason B, Sigfusson TI (2003) Application of geothermal energy to hydrogen production and storage. 2nd German hydrogen congress, Essen, Feb 2003, published in proceedings

11. Mingyi L, Bo Y, Jingming X, Jing C (2008) Thermodynamic analysis of the efficiency of high-temperature steam electrolysis system for hydrogen production. J Power Sources 177:493–499
12. Herring JS, O'Brien JE, Stoots CM, Hawkes GL, Hartvigsen JJ, Shahnam M (2007) Progress in high-temperature electrolysis for hydrogen production using planar SOFC technology. Int J Hydrogen Energy 32:440–450
13. Fujiwara S, Kasai S, Yamauchi H, Yamada K, Makino S, Matsunaga K, Yoshino M, Kameda T, Ogawa T, Momma S, Hoashi E (2008) Hydrogen production by high temperature electrolysis with nuclear reactor. Prog Nucl Energy 50:422–426
14. O'Brien JE, Stoots CM, Herring JS (2005) High-temperature electrolysis for hydrogen production from nuclear energy. INL research and development, 05-GA50193-19, http://www.inl.gov/technicalpublications/Documents/3394826.pdf. Accessed 14 May 2013
15. Rosen MA, Scott DS (1992) Exergy analysis of hydrogen production from heat and water by electrolysis. Int J Hydrogen Energy 17(3):199–204
16. Rosen MA (1995) Energy and exergy analyses of electrolytic hydrogen production. Int J Hydrogen Energy 20(7):547–553
17. Sigurvinsson J, Mansilla C, Arnason B, Bontemps A, Maréchal A, Sigfusson TI, Werkoff F (2006) Heat transfer problems for the production of hydrogen from geothermal energy. Energy Convers Manage 47:3543–3551
18. NIST (2013) National institute of standards and technology. http://webbook.nist.gov/chemistry/. Accessed 14 May 2013
19. EP (2013) The exergoecology portal. http://www.exergoecology.com/excalc/. Accessed 14 May 2013
20. Zhang W, Yu B, Xu J (2012) Efficiency evaluation of high temperature steam electrolytic systems coupled with different nuclear reactors. Int J Hydrogen Energy 37:12060–12068
21. Sigurvinsson J, Mansilla C, Lovera P, Werkoff F (2007) Can high temperature steam electrolysis function with geothermal heat? Int J Hydrogen Energy 32:1174–1182
22. Orhan MF, Dincer I, Naterer GF (2008) Cost analysis of a thermochemical Cu–Cl pilot plant for nuclear-based hydrogen production. Int J Hydrogen Energy 33:6006–6020
23. Orhan MF, Dincer I, Rosen MA (2008) Energy and exergy assessments of the hydrogen production step of a copper–chlorine thermochemical water splitting cycle driven by nuclear-based heat. Int J Hydrogen Energy 33:6456–6466

Thermodynamic Analysis of a Solar Driven Tri-generation System for Building Applications

15

Hasan Ozcan and Ibrahim Dincer

Abstract

Energy and exergy analyses and sustainability assessment of a conceptual solar driven tri-generation system with thermal energy storage option for power, water heating and air cooling are performed. The present tri-generation system includes parabolic trough solar collectors (PTC), an organic Rankine cycle for power generation (ORC), an absorption chiller for cooling (AC) and a thermal energy storage system (TES). The effects of solar collector dimension variations, system parameters, environmental conditions and system integration on system energy and exergy efficiencies are parametrically studied. The largest irreversibility occurs in solar collectors due to very high exergy input to solar panels and less conversion of exergy to working fluid. Energy and exergy efficiencies of the present system become 77.1 % and 27 % during day time and 37.6 % and 18.7 % during night time, respectively. The proposed system performs better performance at lower ambient temperature and higher solar radiation and PTC concentration ratio.

Keywords

Solar energy • Tri-generation • Storage • Energy • Exergy • Efficiency

Introduction

Environmental problems associated with energy use span a growing spectrum of pollutants, hazards, and accidents and degradation of environmental quality and natural ecosystems. Over the past few decades, the increasing use of energy has expanded our concerns from what were once primarily local or regional issues to a growing awareness of the international and global nature of major energy-related environmental problems [1]. Economic and environmental problems related to unsustainable energy systems have been a growing concern particularly after Kyoto Protocol in 1997 and Stern Review in 2006. Hence, relationship between the energy demands and environmental impacts should be carefully analysed [2]. It is reported by International Energy Agency [3] that global energy supply by fossil fuels is 81.3 % by 2010.

Renewable energy technologies have become increasingly important as environmental concerns increase. Development of advanced renewable energy technologies can serve as cost-effective and environmentally responsible alternatives to conventional energy generation [4]. There are many alternative energy sources that can be used instead of fossil fuels. The decision as to what type of energy source should be utilised must, in each case, be made on the basis of economic, environmental and safety considerations. Because of the desirable environmental and safety aspects, it is widely believed that solar energy should be utilised instead of other alternative energy forms, even when the costs involved are slightly higher [5].

In order to deliver high temperatures with good efficiency, high-performance solar collectors are required. Systems with light structures and low-cost technology for process heat applications up to 400 °C could be obtained with parabolic trough collectors (PTCs) [5, 6]. Tyagi et al. [7] performed a comprehensive exergy analysis and parametric study on PTCs and

H. Ozcan (✉) • I. Dincer
Faculty of Engineering and Applied Science, University of Ontario Institute of Technology,
2000 Simcoe St. N., Oshawa, ON, Canada L1H 7K4
e-mail: hasan.ozcan@uoit.ca; ibrahim.dincer@uoit.ca

investigated effect of PTC design and environmental conditions and specified optimal value for concentration ratio of PTCs. Other parametric studies to optimise PTCs can be found in Manikandan et al. [8] and Huang et al. [9]. Garcia et al. [10] investigated a new performance model for PTC-based power plants with thermal energy storage. Giostri et al. [11] compared various solar plants driven by PTCs.

Tri-generation usually refers to the simultaneous production of cooling, heating and power from a single energy source. It is known as combined cooling, heating and power (CCHP). Sometimes combined heating and power (CHP) refers to tri-generation. In other words, if the heat produced from CHP is used for cooling as well as heating, the plant is called a tri-generation plant. CHP could refer to a cogeneration plant if it produced heat and power only [12]. Zhai et al. [13] proposed a novel tri-generation system to be used in remote areas producing power, heating and cooling and carried out a comprehensive thermodynamic and economic analysis to validate applicability of such system. Marques et al. [14] presented a generic tri-generation scheme for office building and carried out first law analysis. Al-Suleiman et al. [15, 16] performed a thermodynamic assessment of solar driven tri-generation system with thermal energy storage and specified best system efficiencies considering system and environmental parameters.

The main objective of this study is to perform a comprehensive thermodynamic analysis of a solar driven tri-generation plant for power, cooling and heating. Energy and exergy analysis and irreversibilities of each sub-unit and components are evaluated; best system efficiencies are determined by parametric studies. PTC, ORC and AC parameters and environmental conditions are considered to optimise the proposed plant. A comparative study is performed for solar mode and TES mode. Detailed explanation and discussion of thermodynamic analysis are presented in next sections.

System Description

Proposed tri-generation plant is represented in Fig. 15.1. Therminol-66 that is suitable to work up to 345 °C at liquid phase is used as the working fluid for the solar cycle [17]. Working fluid is heated up to 250 °C through the PTCs and release its heat to TES heat exchanger, ORC evaporator and AC heat exchanger. To provide a steady-state working condition for the plant, heat is stored at TES to be utilised when the sun is out. Heat is initially stored in hot storage tank, and after utilisation of stored heat, it is stored in the cold storage tank. However, the performance assessment is performed for solar system only to evaluate TES integration.

Transport fluid is pumped at 28–30 bar at ORC pump and gains heat at ORC evaporator from solar cycle. Evaporated and superheated fluid expands at ORC turbine, and the power production is achieved. After condensing at ORC condensing the ORC loop is completed [18]. Here, we consider residential water at 20 °C as heat sink for the ORC plant. Heat rejected from
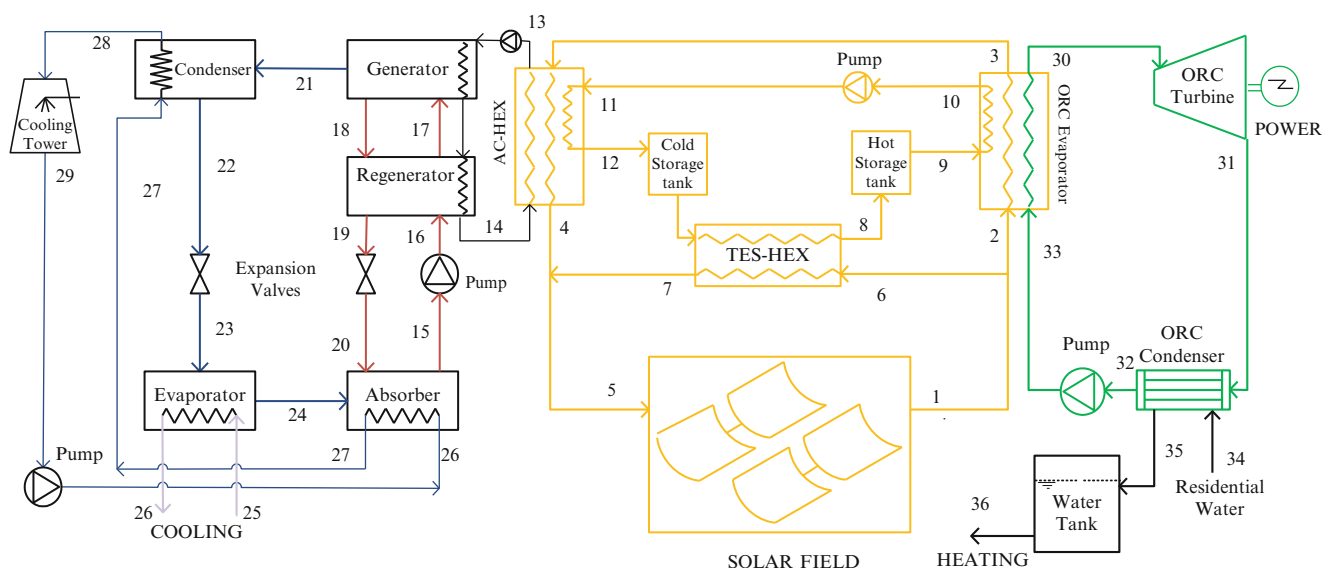

Fig. 15.1 Schematic of the tri-generation plant

Table 15.1 Some properties of R123 and R245fa (modified from [19])

Working fluid	Critical temperature (°C)	Critical pressure (Bar)	Molecular weight (kg/mol)	ODP[a]	GWP (for 500 years)[b]	Ashrae 34 safety group[c]
R123	183.7	36.6	152.9	0.02	36	B1
R245fa	157.6	36.4	134.05	0	300	A1

[a]ODP: ozone depletion potential, expresses the contribution to ozone depletion, based upon R11 = 1
[b]GWP: global warming potential, potential to warm to planet related to CO_2 emission during production
[c]ASHRAE 34: (A) means low toxicity, (B) means high toxicity, (1) means no flammability propagation

ORC condenser heats residential water up to 50 °C, and water is stored in a water tank for later use. R245fa is selected as the transport fluid for the ORC plant. R245fa has a satisfactory thermal efficiency and production of mechanical work and most important of all is ozone safe as well as follows all the environmental regulations and commercially produced [19]. However, R123 is also considered as an optional working fluid for a comparative assessment. Some thermophysical, thermodynamic and environmental properties of R123 and R245fa is given in Table 15.1. Considering environmental indicators given in Table 15.1, R245fa is considered as the working fluid for the baseline model, and R123 is used for comparison only.

The weak Li–Br water solution is first heated up to desired temperature with the heat provided by water cycle and higher temperature strong solution Li–Br water. The strong solution rejects its heat to weak solution in regenerator, expands to low pressure side and turns back to absorber. Some of the water content evaporates in the generator and condenses in the AC condenser. The heat rejected in the condenser and absorber is transmitted to cooling tower water cycle [20, 21]. The condensed water is than expanded into a lower pressure with expansion valve and its temperature decreases up to 4 °C. The performance investigation of the absorption chiller model is performed with mass, energy, exergy and entropy balances and defined in the next subsection.

System Analysis

In order to thermodynamically model the present tri-generation system, mass, energy and exergy balance equations for analysis and performance evaluation are presented in this section. The following assumptions are made for system analysis and assessment:

- Steady-state steady-flow conditions are considered for overall system except for TES and water tank.
- Pressure drops through piping are negligible.
- System components work adiabatically.
- Changes in kinetic and potential energies and the pressure drops in the piping and components of the system are negligible.
- Input parameters for the overall system and range of variations are given in detail in Table 15.2.

Energy and Exergy Analyses

The performance evaluation of all subunits and the overall system is performed using mass, energy, exergy, and entropy balances. The generalised balance equations for the system are defined with the following definitions [22]:

$$\text{Mass}: \sum \dot{m}_i - \sum \dot{m}_o = \Delta m_{sys} \tag{15.1}$$

$$\text{Energy}: \sum \dot{m}_i h_i - \sum \dot{m}_o h_o = \Delta E_{sys} \tag{15.2}$$

$$\text{Exergy}: \sum \dot{m}_i ex_i - \sum \dot{m}_o ex_o - \dot{E}x_{des} - \dot{E}x^Q = \Delta Ex_{sys} \tag{15.3}$$

$$\text{Entropy}: \sum \dot{m}_i s_i - \sum \dot{m}_o s_o + \dot{S}_{gen} + \sum \left(\frac{\dot{Q}}{T}\right)_r = \Delta s_{sys} \tag{15.4}$$

Here, indices *i, o, des, gen, sys* and *r* represent inlet, outlet, destruction, generation, system and control region. *ex* represents specific exergy and s represents entropy. Ex_{des} and $Ex^{\cdot Q}$ are destructed exergy rate and exergy due to heat

Table 15.2 System operating conditions and parameters

	Unit	Value
Parameter		
Dead state temperature (T_0)	°C	20–30
Dead state pressure (P_0)	bar	1
Heat exchanger efficiencies (η_{hex})	%	85
PTC		
Global solar radiation (S_t)	kW/m^2	0.4–0.8
Heat loss coefficient (U_L)	W/m^{2}K	8
Concentration ratio	–	30–50
Absorptivity, reflectivity and emissivity	–	0.9
Receiver effectiveness (η_r)	%	90
Collector efficiency	%	90
Sun temperature	K	5,700
Stephan Boltzmann constant	W/m^{2}K^4	5.67×10^{-8}
ORC		
Pressure ratio (PR)	–	4.2
Working fluid	–	R245fa
Condensing temperature	°C	68
Turbine isentropic efficiency (η_s)	%	90
Turbine mechanical efficiency (η_m)	%	90
Turbine electrical efficiency (η_{el})	%	95
AC		
Chilled air inlet/outlet temp.	°C	18/7
Cooling water inlet/outlet temp.	°C	32/35
Condenser temp.	°C	40
Evaporator temp.	°C	7

transfer. Since the system is assumed as steady state and steady flow, mass, energy, entropy and exergy of control volume of the components are equal to zero.

The specific exergy of a stream is comprised of two components, namely physical and chemical exergy, and defined as follows:

$$ex = ex_{ph} + ex_{ch} \tag{15.5}$$

$$ex_{ph} = (h - h_0) - T_0 \cdot (s - s_0) \tag{15.6}$$

$$ex_{ch} = \sum x_i \overline{ex}_{ch}^{0} - RT_0 \cdot \sum x_i \ln(x_i) \tag{15.7}$$

$$\dot{Ex} = \dot{m} \cdot ex \tag{15.8}$$

$$\dot{Ex}^Q = Q \cdot \left(1 - \frac{T_L}{T_H}\right) \tag{15.9}$$

$$\dot{Ex}_{des} = \dot{I} = T_0 \cdot \dot{S}_{gen} \tag{15.10}$$

where indices *0*, *ch* and *ph* represent ambient conditions, chemical and physical, respectively. Further details on system analysis through energy and exergy can be found elsewhere [22, 23].

Thermal Energy Storage

Thermal energy storage (TES) generally involves the temporary storage of high- or low-temperature thermal energy for later use. TES systems achieve benefits by fulfilling one or more of the following purposes: Increasing generation capacity, enable better operation of cogeneration plants, shift energy purchases to low-cost periods, increase system reliability and integration with other functions [22]. Energy balance for overall storage process considering Fig. 15.1 is given as follows:

$$(H_6 - H_7) - \left[(H_9 - H_{12}) + Q_l\right] = \Delta E \tag{15.11}$$

$$\Delta E = E_f - E_i \tag{15.12}$$

$$Q_l = \sum\nolimits_{j=1}^{3} Q_{l,j} \tag{15.13}$$

where Q_l represents total heat loss during charging, storage and discharging process and $j = 1,2$ and 3 indicate charging, storage and discharging processes. Energy balance for overall storage process considering Fig. 15.1 is given as follows:

$$(Ex_6 - Ex_7) - \left[(Ex_9 - Ex_{12}) + Ex_l^Q \right] - I = \Delta Ex \tag{15.14}$$

$$\Delta Ex = Ex_f - Ex_i \tag{15.15}$$

$$Ex_l^Q = \sum\nolimits_{j=1}^{3} Ex_j^Q \tag{15.16}$$

$$I = \sum\nolimits_{j=1}^{3} I_j \tag{15.17}$$

where Ex_l^Q is exergy loss associated with heat transfer for all three processes and I_j donate irreversibilities during charging, storage and discharging processes.

Parabolic Trough Collectors

Actual useful heat gain from PTCs is defined with Hottel–Whillier equation considering radiation loses as follows [5, 7]:

$$\dot{Q}_u = F_r \cdot A_a \left[C(\rho\alpha)S_t - U_L(T_{col} - T_o) - \varepsilon\sigma\left(T_{col}^4 - T_o^{\ 4}\right) \right] \tag{15.18}$$

Here, F_r is collector heat removal factor, A_a is absorber area, C is concentration ratio, ρ, α, ε and σ are reflectivity, absorptivity and emissivity and Stephan Boltzmann constant, U_L is overall heat loss coefficient, S_t is global solar radiation and T_{col} is collector temperature. The collector temperature can be determined using numerical solutions proposed in [7]. Heat removal factor of the collectors and concentration ratio can be defined through Eqs. (15.19) and (15.20):

$$F_r = \frac{\dot{m} \cdot C_p}{A_r \cdot U_L} \cdot \left[1 - exp^{-\frac{A_r \cdot U_L \cdot F}{\dot{m} \cdot C_p}} \right] \tag{15.19}$$

$$C = \frac{(w - D_c) \cdot L}{A_a} \tag{15.20}$$

where $F, \dot{m}, C_p$ and A_r are collector efficiency, working fluid mass flow rate and specific heat and reflector area, respectively. L is collector length; w is collector width and D_c is collector cover diameter. Actual heat gain can also be determined as follows:

$$\dot{Q}_u = mCp(T_{out} - T_{in}) \tag{15.21}$$

For desired outlet temperature, solar parameters can be specified using Eqs. (15.18) and (15.21). Exergy gain from PTCs and collector exergy associated with sun temperature is given as in [24] as

$$\dot{Ex}_{i-o} = mCp\left[T_{out} - T_{in} - \ln\frac{T_{out}}{T_{in}} \right] \tag{15.22}$$

$$\dot{Ex}_{PTC} = A_r S_t \left[1 - \frac{1}{3}\left(\frac{T_o}{T_{sun}}\right)^4 - \frac{4}{3}\left(\frac{T_o}{T_{sun}}\right) \right] \tag{15.23}$$

System Performance

Considering efficiencies of all subunits and overall system, a general definition of rate of useful energy/exergy to inlet energy/exergy can be used for determination of system performances. Energy and Exergy efficiencies for the subunits shown in Fig. 15.1 are written as

$$\eta_{en,ORC} = \frac{\dot{W}_{net,ORC}}{\dot{Q}_{evap,ORC}} \tag{15.24}$$

$$\eta_{ex,ORC} = \frac{\dot{W}_{net,ORC}}{\dot{Ex}_{30} - \dot{Ex}_{33}} \tag{15.25}$$

$$COP_{en,AC} = \frac{\dot{Q}_{evap,AC}}{\dot{Q}_{gen,AC}} \tag{15.26}$$

$$COP_{ex,AC} = \frac{\dot{Ex}_{25} - \dot{Ex}_{26}}{\dot{Ex}_{30} - \dot{Ex}_{33}} \tag{15.27}$$

$$\eta_{en,TES} = \frac{H_9 - H_{12}}{H_6 - H_7} \tag{15.28}$$

$$\eta_{ex,TES} = \frac{Ex_9 - Ex_{12}}{Ex_6 - Ex_7} \tag{15.29}$$

$$\eta_{en,PTC} = \frac{\dot{Q}_u}{A_r S_t} \tag{15.30}$$

$$\eta_{ex,PTC} = \frac{\dot{Ex}_{i-o}}{\dot{Ex}_{PTC}} \tag{15.31}$$

where $\dot{W}_{net,ORC}$ is net power produced in ORC plant and $\dot{Q}_{evap,AC}$ and $\dot{Q}_{gen,AC}$ are heat loads in AC evaporator and generator, respectively. Subscripts *en* and *ex* are defined as energy and exergy. Finally, overall energy and exergy efficiencies of the plant can be defined as follows:

$$\eta_{en,ov} = \frac{\dot{W}_{net,ORC} + \left(\dot{Ex}_{25} - \dot{Ex}_{26}\right) + \frac{(H_9 - H_{12})}{\Delta t} + \left(\dot{E}_{35} - \dot{E}_{34}\right)}{A_r S_t} \tag{15.32}$$

$$\eta_{ex,ov} = \frac{\dot{W}_{net,ORC} + \dot{Q}_{evap,AC} + \frac{Ex_9 - Ex_{12}}{\Delta t} + \left(\dot{Ex}_{35} - \dot{Ex}_{34}\right)}{\dot{Ex}_{PTC}} \tag{15.33}$$

Results and Discussion

The results of the thermodynamic analysis of the proposed tri-generation plant are presented and discussed in this section. EES (Engineering Equation Solver) software is used to study the performance of the system and its components.

Energy and exergy efficiencies, as well as irreversibility rates of plant sub-units and overall plant are represented in Fig. 15.2a. The energy and exergy efficiencies of ORC are 12.27 % and 52 %, respectively. The energetic and exergetic COPs of AC are 77.07 % and 30.06 %. The energy and exergy efficiencies for water heating are 86 % and 24 %. Also, the energy and exergy efficiencies for TES are 60.1 % and 35.2 % and PTC are 6.7 % and 29.4 %. The PTC energy and exergy
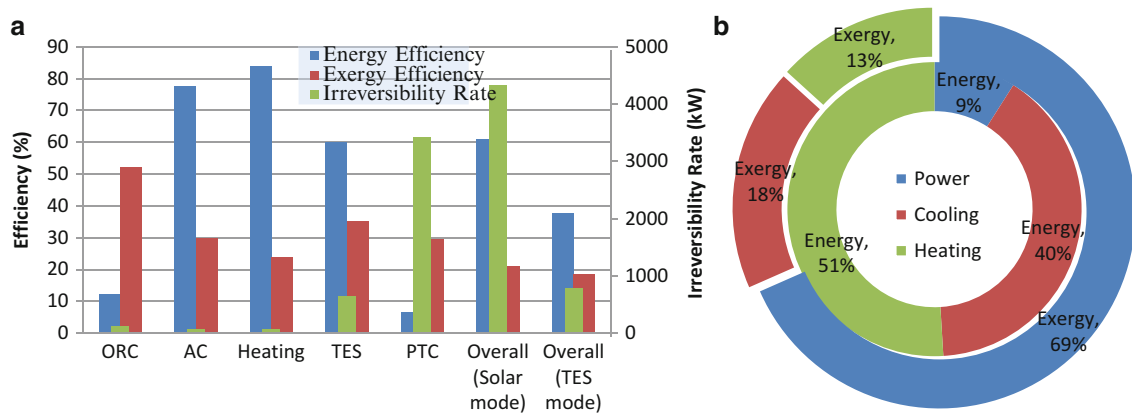
Fig. 15.2 (**a**) Energy, exergy efficiencies and irreversibility rates of the plant sub-units and overall plant. (**b**) Energy and exergy output ratios

efficiencies are in agreement with works in the literature. Low-energy efficiency is due to very high reflector area requirement in order to provide tri-generation and thermal energy storage for continuous production. 11,812 m^2 of reflector area is needed to provide tri-generation and TES with a concentration ratio of 40. When no TES is considered, the reflector area needed is 3,726 m^2. When determining overall efficiencies, night time plant performance is also considered by using TES energy as plant input. Overall energy and exergy efficiencies of solar mode and TES mode are 61–21.2 % and 37.6–18.7 %, respectively. The energy storage option through a TES system is considered as useful output for the solar mode.

The largest irreversibility occurs in PTC due to very high input exergy associated with sun temperature as defined in Eq. (15.23). Irreversibility rates of ORC, AC, water heating, TES, PTC, solar mode and TES mode are 119, 78, 79, 639, 3,420, 4,335 and 796 kW, respectively. Energy stored during the day time in TES is considered as the energy input for the tri-generation plant at night time. Thus, irreversibility of TES mode is considerably lower than that of Solar Mode as exergy of PTC associated with sun temperature is not used for TES mode.

Energy and exergy output ratios are represented in Fig. 15.2b. Tri-generation plant produces 125.4 kW power, 557 kW cooling load and 709 kW of residential water heating. As exergy of power is same as its energy, it remains the same in exergy basis; however, cooling and heating exergy corresponds to 33.6 and 24.3 kW. Considering energy output ratios, power production generates only 9 % of total production, and it increases up to 69 % by considering exergy outputs.

A comparative energy, exergy and exergy destruction variations considering ORC parameters and ambient temperature are represented in Fig. 15.3a–c. A pressure ratio increment slightly increases exergetic and energetic efficiencies and has an influential effect on specific work of turbine. A 20 °C change in assumed pump inlet temperature decreases exergy efficiency by 25 % and brings a 6 kJ/kg increase in irreversibility, whereas no considerable change occurs in energy efficiency. Ambient temperature increase also slightly increases exergy efficiency of ORC plant and decreases total irreversibility. ORC plant working with R123 shows slightly better energy and exergy performance and lower irreversibilities than that of R245fa. However, R245fa is the most promising working fluid considering environmental and safety challenges. R245fa is selected as the transport fluid for the ORC plant.

Absorption chiller condensing temperature effect on energetic and exergetic COP for various evaporator temperatures are illustrated in Fig. 15.4. Since the solution fractions of Li–Br water are strongly dependent on saturation pressures for condensing and evaporating temperatures of AC, a more careful investigation should be performed to optimise the AC performance. Energetic COP is higher at higher evaporating temperatures, and exergetic COP is higher at lower evaporating temperatures. Both energy and exergy COPs decrease at higher condensing temperatures.

Global solar radiation is a strong influential environmental parameter on solar plants. Solar radiation effect on collector and overall efficiencies are represented in Fig. 15.5. Solar global radiation changes in a sunny day from 0.4 to 0.8 kW/m^2. In this study, instead of considering the solar data from a specific region, we parametrically illustrated the effect of solar radiation on system performance. PTC energy efficiency increases up to 10 %, even if solar global radiation is used as a denominator for PTC energy performance.

Ambient temperature effect on exergy efficiencies and irreversibility rates of generated energy products are illustrated in Fig. 15.6. Exergy efficiencies of ORC and AC plant increases with ambient temperature increase whereas water heating exergy efficiency decrease by almost 40 %. Irreversibility rates of ORC and AC decrease proportional to their exergy efficiencies with increasing ambient temperatures. Irreversibility rate of water heating increase at higher ambient

Fig. 15.3 ORC pump pressure
ratio (**a**), ORC pump inlet
temperature (**b**) and ambient
temperature (**c**) effect on
efficiencies, irreversibilities
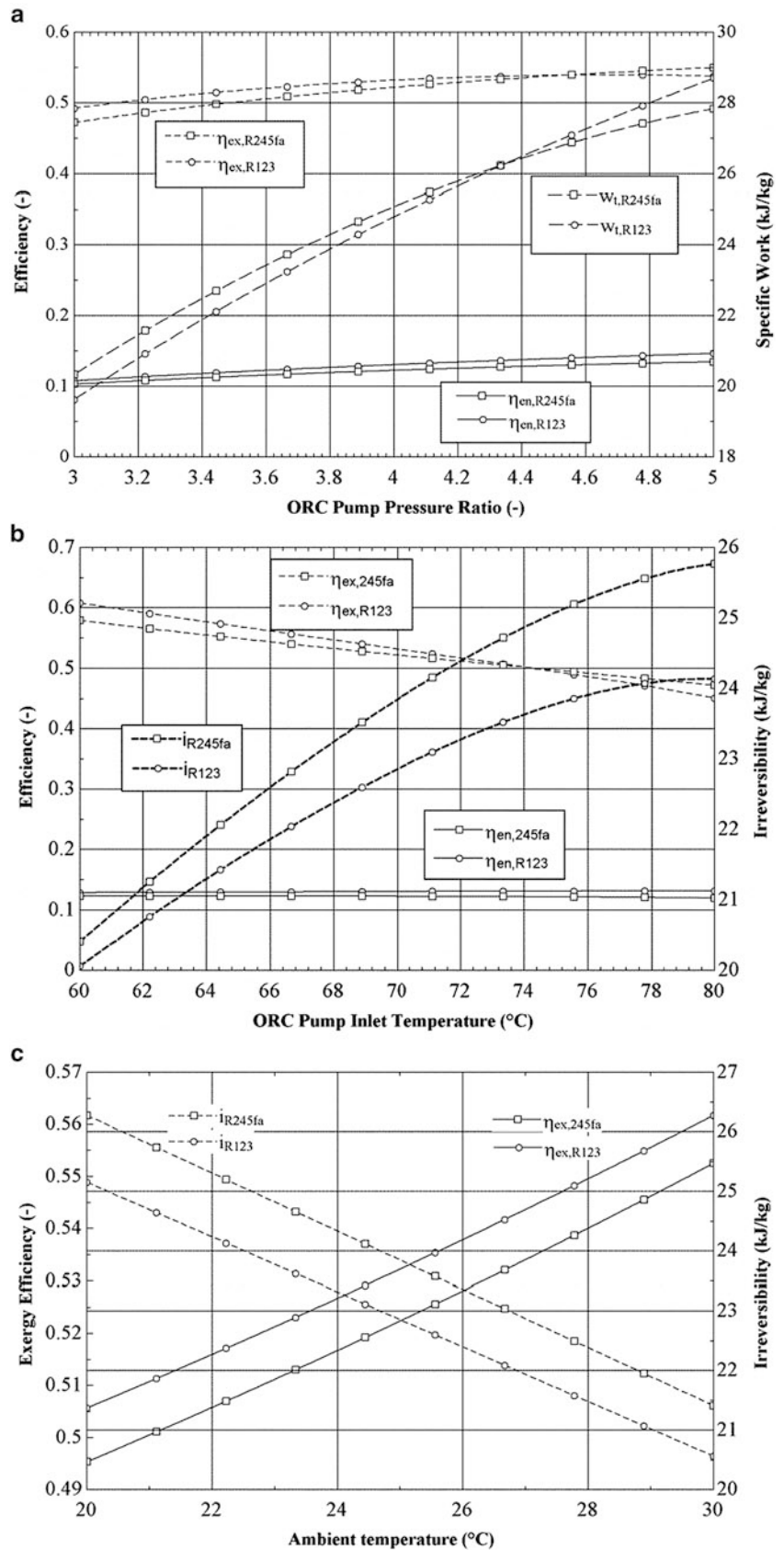and specific work output of
ORC plant

Fig. 15.4 Condensing and evaporation temperature effect on COP performance of absorption chiller
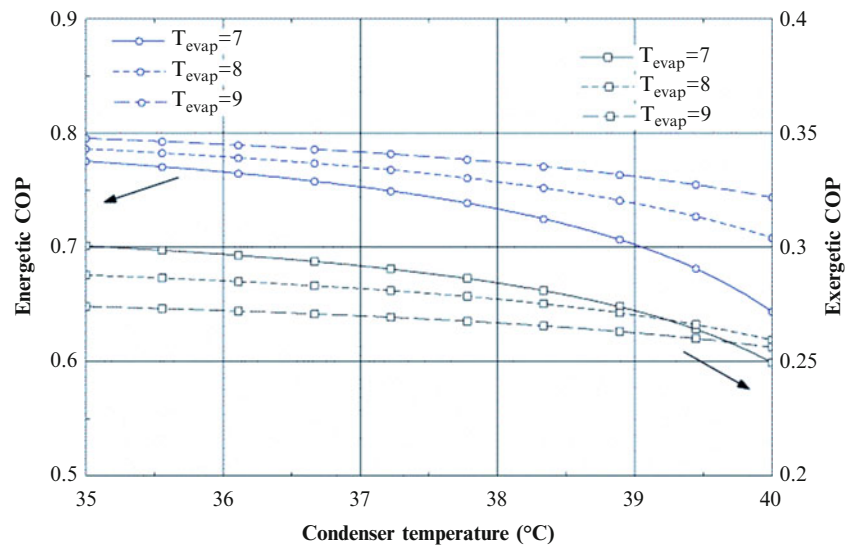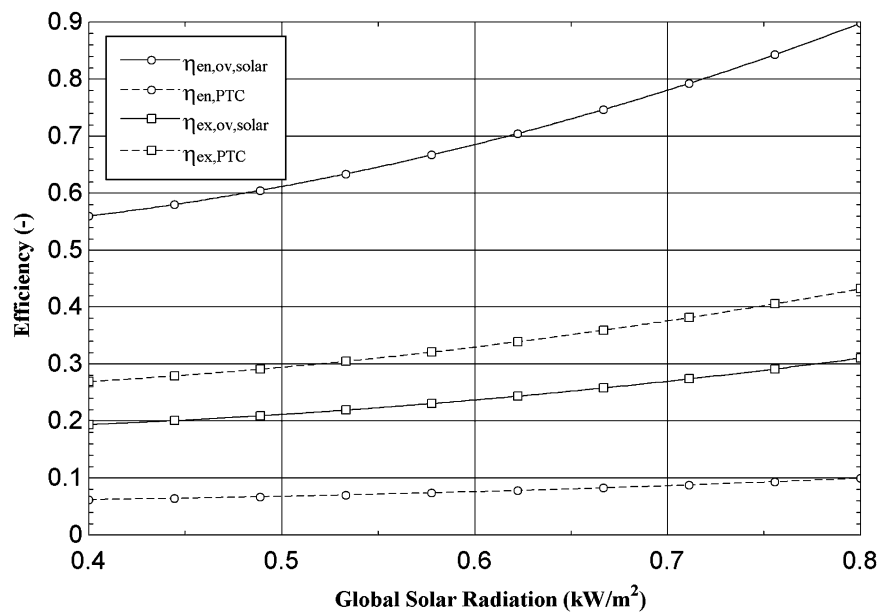

Fig. 15.5 Solar radiation effect on PTC and overall energy and exergy efficiencies

temperatures due to higher condensing energy input to residential water as mentioned in Fig. 15.1. Considering exergy output ratios of energy forms, power ratio will increase among other forms of energy at higher ambient temperatures. It can be concluded from the figure that proposed system would show better performance with power and cooling production especially in summer seasons.

Finally, exergy efficiency and sustainability index comparison of overall system considering solar and TES mode at varying ambient temperature and global solar radiation conditions are illustrated in Fig. 15.7. As known, sustainable development requires not just that sustainable energy resources be used but that the resources to be used efficiently. Exergy methods are essential in improving efficiency, which allows society to maximise the benefits it derives from its resources while minimising the negative impacts. By noting that energy can never be "lost" as it is conserved according to the first law of thermodynamics, while exergy can be lost due to internal irreversibilities, the study suggests that exergy losses, particularly due to the use of non-renewable energy forms, should be minimised to obtain sustainable development. Thus, sustainability should be considered together with exergy analysis. Overall system shows better sustainability and efficiency at higher solar radiation and lower environmental temperature. However, these conditions cannot be optimised, and this illustration is to show the impact of environmental conditions on system performances.

Fig. 15.6 Ambient temperature effect on efficiencies and irreversibilities
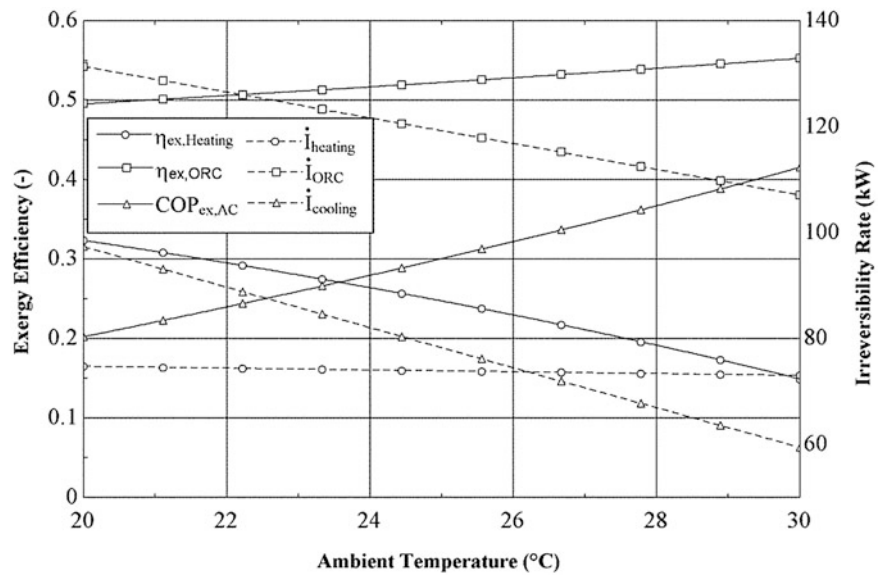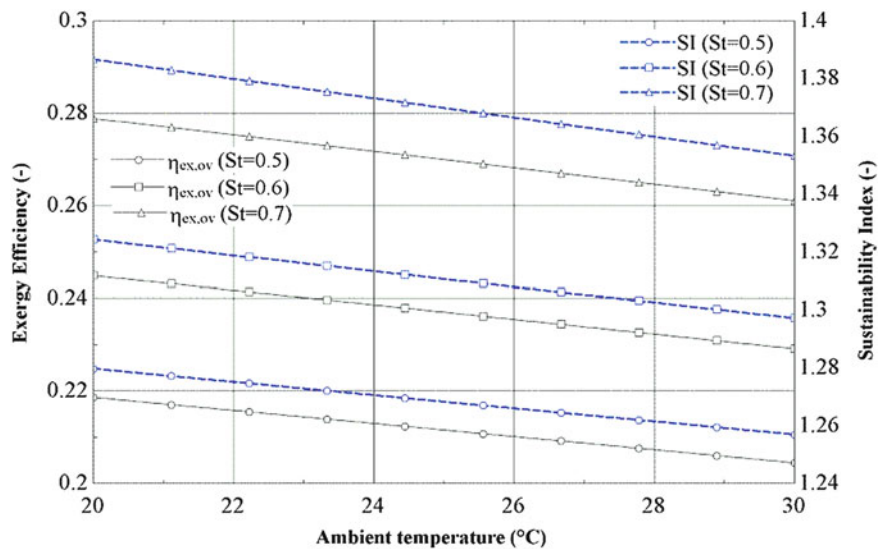

Fig. 15.7 Effect of environmental parameters on plant exergy efficiency and sustainability

Thermodynamic analysis results show that plant performance is strongly dependent on environmental conditions and collector design conditions as well as plant parameters such as mass flow rate, pressure ratios and specified temperature ranges.

Conclusions

Energy and exergy analyses and sustainability assessment of a conceptual solar driven tri-generation system for power, water heating, air cooling and thermal energy storage are performed. The following findings are obtained from the present study:

- Highest irreversibility occurs at solar collectors due to very high exergy input considering solar temperature.
- AC energy efficiency and ORC exergy efficiency appear to be highest among other system sub-units.
- Exergy output ratios of cooling and heating are considerably lower than that of energy output ratios due to low exergy quality of corresponding energy forms.
- Energy and exergy performance of ORC plant using R123 as working fluid is slightly higher than that of R245fa. However R245fa is selected for the baseline model due to toxicity and ozone depleting potential of R123.

- It is of importance to select proper condensing and evaporation temperatures for absorption chiller, since these values are strongly influencing fraction of Li–Br in water and effecting system performance.
- Environmental parameters such as ambient temperature and solar global radiation strongly influence system performances and exergetic sustainability.
- Exergy efficiency of TES mode at night time is better than that of solar mode at day time.
- Energy stored at TES during day time is considered as useful energy output; thus, energy efficiency of overall system is comparatively higher than that of TES mode.
- TES integration brings around 8,000 m^2 additional solar panel installation to provide a steady-state tri-generation; thus, a thermo-economic optimisation may be performed for the proposed system to find out flow and investment costs. However, TES option integration is inevitable to provide steady-state operation of the plant.
- Higher collector concentration ratio, ORC pump pressure ratio and pump inlet temperature, and lower absorption chiller evaporating and condensing temperatures are recommended to provide better energetic and exergetic performance and lower plant irreversibility.

Nomenclature

$\dot{Ex}$	Exergy rate, kJ/s	A_r	Reflector area, m^2
$\dot{I}$	Irreversibility rate, kJ/s	C	Concentration ratio
$\dot{Q}$	Heat transfer rate, kJ/s	ex	Specific exergy, kJ/kg
$\dot{W}$	Work rate, kJ/s	F_r	Collector heat removal factor
$\dot{m}$	Mass flow rate, kg/s	SI	Sustainability index
A_a	Absorber area, m^2	St	Global solar radiation, kW/m^2

Greek Letters

α	Absoptivity	ρ	Reflectivity
ε	Emissivity	σ	Boltzmann's constant, 5.67×10^{-8}, W/m^2K^4
η	Efficiency	ω	Collector width, m

Subscripts

ch	Chemical	i	Inlet
col	Collector	o	Outlet
des	Destruction	ph	Physical

Acronyms

AC	Absorption chiller	PTC	Parabolic trough collectors
ORC	Organic rankine cycle	TES	Thermal energy storage

References

1. Dincer I (1998) Energy and environmental impacts: present and future perspectives. Energy Sources 20:427–453
2. Ozbilen A, Dincer I, Naterer GF, Aydin M (2012) Role of hydrogen storage in renewable energy management for Ontario. Int J Hydrgen Energy 37:7343–7354
3. International Energy Agency (IEA) (2012) World energy outlook. http://www.worldenergyoutlook.org/
4. Dincer I (2000) Renewable energy and sustainable development: a crucial review. Renew Sustain Energy Rev 4:157–175
5. Kalagirou S (2004) Solar thermal collectors and applications. Prog Energy Combust Sci 30:231–295
6. Kalagirou S, Lloyd S, Ward J (1997) Modelling, optimization and performance evaluation of a parabolic trough solar collector steam generation system. Sol Energy 60:49–59
7. Tyagi SK, Wang S, Singhal MK, Kaushik SC, Park SR (2007) Exergy analysis and parametric study of concentrating type solar collectors. Int J Ther Sci 46:1304–1310
8. Manikandan KS, Kumaresan G, Velraj J, Inıyan S (2012) Parametric study of solar parabolic trough collector system. Asian J Appl Sci 5(6):384–393
9. Huang W, Hu P, Zeshao C (2012) Performance simulation of a parabolic trough solar collector. Sol Energy 86:746–755

10. Garcia IL, Alvarez JL, Blanco D (2011) Performance model for parabolic trough solar thermal power plants with thermal storage: comparison to operation plant data. Sol Energy 85:2443–2460
11. Giostri A, Binotti M, Astolfi M, Silva P, Macchi E, Manzolini G (2012) Comparison of different solar plants based on parabolic trough technology. Sol Energy 86:1208–1221
12. Al-Suleiman F, Hamdullahpur F, Dincer I (2011) Exergy modeling of a new solar driven trigeneration system. Sol Energy 85:2228–2243
13. Zhai H, Dai YJ, Wu JY, Wang RZ (2009) Energy and exergy analyses on a novel hybrid solar heating, cooling and power generation system for remote areas. Appl Energy 86:1395–1404
14. Marques RP, Hacon D, Tessarollo A, Parise JAS (2010) Thermodynamic analysis of tri-generation systems taking into account refrigeration, heating and electricity load demands. Energy Build 42:2323–2330
15. Al-Suleiman F, Hamdullahpur F, Dincer I (2011) Trigeneration: a comprehensive review based on prime movers. Int J Energy Res 35:233–258
16. Al-Suleiman F, Hamdullahpur F, Dincer I (2012) Performance assessment of a novel system using parabolic trough solar collectors for combined cooling, heating, and power production. Renew Energy 48:161–172
17. Eastman Chemical Company (2013) http://www.therminol.com/pages/products/66.asp
18. Liu B, Riviere P, Coquelet C, Gicquel R, David F (2012) Investigation of a two stage rankine cycle for electric power plants. Appl Energy 100:285–294
19. Kosmadakis G, Manolakos D, Kyritsis S, Papadakis G (2009) Comparative thermodynamic study of refrigerants to select the best use in the high-temperature stage of a two-stage organic Rankine cycle for RO desalination. Desalination 243:74–94
20. Sencan A, Yakut KA, Kalagirou S (2005) Exergy analysis of lithium bromide/water absorption systems. Renew Energy 30:645–657
21. Gebreslassie BH, Medrano M, Boer D (2010) Exergy analysis of multi-effect water-LiBr systems: from half to triple effect. Renew Energy 35:1773–1782
22. Dincer I, Rosen MA (2007) Exergy: energy, environment and sustainable development. Elsevier, Oxford
23. Kotas TJ (1995) The exergy method of thermal plant analysis. Krieger, London
24. Petela R (2005) Exergy analysis of the solar cylindrical-parabolic cooker. Sol Energy 79(3):221–233

Thermodynamic and Cost Analyses of a Residential Hybrid PV–Fuel Cell–Battery System for a Canadian House

Mehdi Hosseini, Ibrahim Dincer, and Marc A. Rosen

Abstract

A residential photovoltaic (PV)-based hydrogen fuel cell system is analyzed using energy and exergy methods, and its monthly performance is investigated. The PV system is accompanied by a water electrolyser for hydrogen production, a lead acid battery pack, and a solid oxide fuel cell (SOFC) for reconverting the hydrogen produced to electricity during periods of solar unavailability. The solar irradiance is based on a monthly average in Toronto in 2011. The energy and exergy analysis results reported include the PV power output and the shares attributable to the battery and the SOFC in meeting the electrical demand. The exergy destructions of the main components and the overall efficiencies are presented. A cost analysis is performed to determine the electricity unit cost over the system lifetime.

Keywords

Photovoltaic • Hydrogen • Fuel cell • Energy • Exergy

Introduction

Solar photovoltaic (PV) systems are capable of converting 10–20 % of solar energy into electricity with zero greenhouse gas emissions during their operation. These systems can be implemented in residential applications for electricity generation. However, solar radiation is intermittent, and supplying the electricity of a house requires the use of some energy storage options. While the PV system supplies the electricity demand of the house, the surplus electricity generated can be used in a water electrolyser for hydrogen production. Hydrogen is stored in compressed hydrogen tanks, to be fed to a fuel cell later in the night or during periods of solar unavailability. With this hybrid system, not only the power demand is supplied, but a certain amount of the thermal demand is also met.

This type of hybrid PV–fuel cell–battery system is the focus of several studies [1–4]. The use of solar energy in a renewable electricity generation system for a residential area in Italy is studied by Santarelli et al. [5], with solar energy being one of three main renewable energy resources considered. The result revealed that wind energy is not capable of meeting the demand, for that specific area. Since solar availability is more constant rather than micro-hydro energy throughout the year, smaller hydrogen storage capacity is required. Uzunoglu et al. [6] investigate a renewable energy power generation system which utilizes hydrogen and ultra-capacitors as energy storage options. The power generation system provides the electricity demand of a house based on the solar irradiance data in Turkey. The main contribution is the modeling and analysis of a renewable-based energy resource in a residential fuel cell hybrid system with short- and long-term storage options. The parametric design and dynamic behavior of the hybrid system are examined.

M. Hosseini (✉) • I. Dincer • M.A. Rosen
Faculty of Engineering and Applied Science, University of Ontario Institute of Technology,
2000 Simcoe St North, Oshawa, ON, Canada L1H 7K4
e-mail: mehdi.hosseini@uoit.ca

The components of the PV–fuel cell–battery system have been modeled separately by researchers. Sukamongkol et al. [7] study the performance of a PV system with simulation. Chenni et al. [8] and Nordin and Omar [9] validate the results of detailed mathematical models with I–V characteristic and maximum power point of real PV modules. A direct coupling of photovoltaic systems to water electrolysers for hydrogen production is the main focus of the study by Clarke et al. [10], who found that the system cost and therefore hydrogen production cost decrease with their proposed configuration. This is achieved while retaining minimum energy loss and maximum safety for the system. Solid oxide fuel cells (SOFC) are increasingly being applied in stationary power generation, especially in combined heat and power (CHP) systems and in remote areas. These systems have been studied comprehensively, in terms of experimentation, modeling, thermodynamic analysis, and implementation [11–14].

The performance of the PV–fuel cell system depends on weather conditions; here, the system is analyzed for a Canadian house with relevant solar data. The investigation of the hybrid PV–fuel cell system based on energy and exergy (quality of energy) determines the rates of energy and exergy flows in each component. The results of the analyses are used for calculating system outputs, efficiencies, and exergy destruction rates. The main contribution of the present research is the analysis of the hybrid PV–fuel cell system on a monthly basis. The daily average solar irradiance during each month of operation is taken as the input to the PV modules. The total daily average outputs of the system components are reported, along with system efficiencies. The annual total exergy destructions of the system's main components are presented, and the electricity unit cost is calculated for the system lifetime.

System Description

The configuration of the hybrid PV–fuel cell–battery system, shown in Fig. 16.1, is selected to meet the electricity requirement of a Canadian house. Solar energy is converted to electricity by the PV modules. The electricity generated is directed to a load controller, which makes the decision of energy distribution within the system components and the house. The load controller directs a part of the electricity generated to meet the power demand. The electrolyser converts the surplus electricity to hydrogen, which is stored in a pressurized hydrogen tank. During periods of solar unavailability, the fuel cell and battery cover the load. The operation of the battery is limited to the conditions where the electric load exceeds the solid oxide fuel cell (SOFC) nominal power.

The SOFC is fed with the hydrogen (the fuel, which is stored in the storage tank) and ambient air as the oxidant. Hydrogen is preheated via heat transfer from an external source, while air preheating is performed utilizing the heat from the SOFC
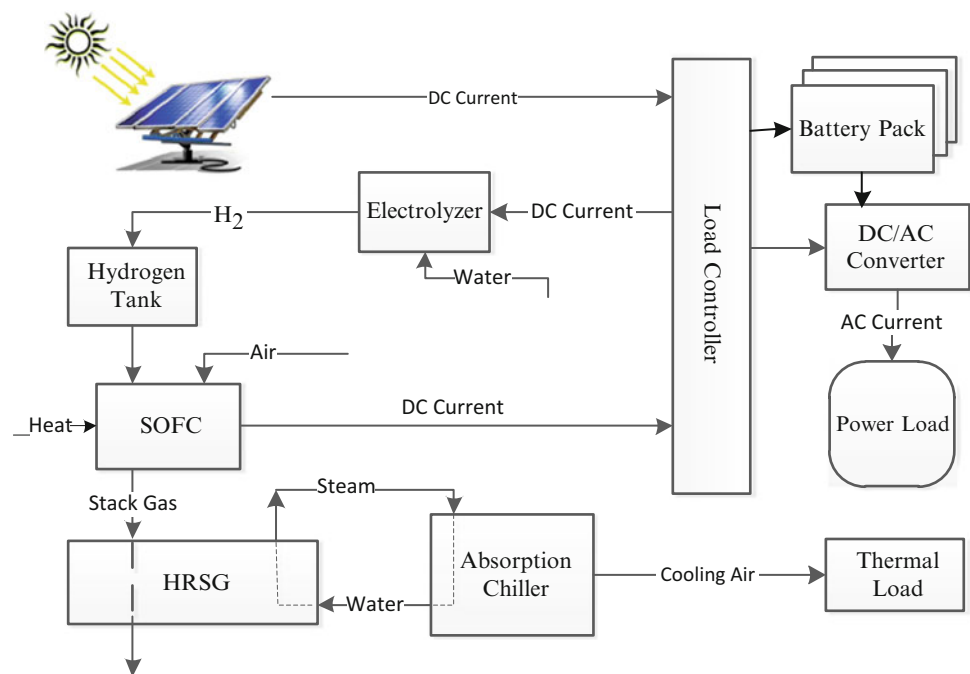

Fig. 16.1 Schematic of the residential PV–hydrogen–fuel cell CHP system
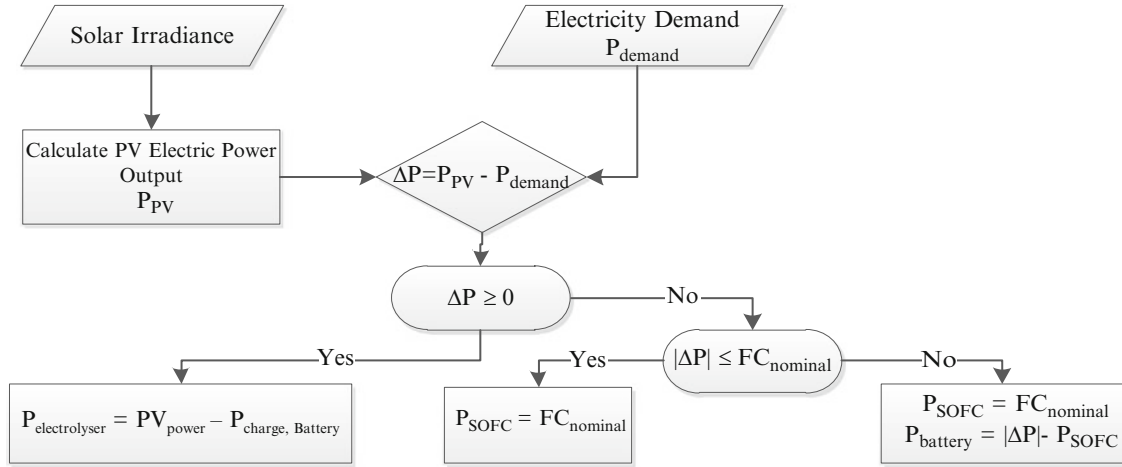
Fig. 16.2 Solving algorithm for providing the detached house with electricity

stack gases, which have adequate energy for recovery for heating or hot water production. This is accomplished using a heat recovery steam generator (HRSG), which generates low pressure saturated steam. As shown in Fig. 16.1, the steam generated in the HRSG can be used in an absorption chiller for cooling purposes, or it can be used for hot water production.

The operational algorithm is simplified and illustrated in Fig. 16.2. Once the PV output power and the load demand are calculated, the control system decides on the operation of the system components. A lower demand than the PV output results in the operation of the electrolyser or the charging of the battery pack. If the demand is higher than the electric power of the photovoltaic system, the fuel cell and the battery will be in operation.

Energy and Exergy Analyses

The modeling and energy and exergy analyses of the hybrid PV–fuel cell–battery system are briefly presented in this section.

Photovoltaic System

A previous paper [4] reported energy and exergy analyses of a residential PV–fuel cell–battery for a Canadian detached house. That analysis is used in this work. The current–voltage characteristics are calculated as a function of light current and reverse saturation current. The cell temperature and series resistance affect the I–V characteristics, as well. The general equation to obtain the I–V characteristics of the PV modules can be expressed as [8]

$$I = \left(\frac{G}{G_{\text{ref}}}\right)(I_{\text{L,ref}} + \text{k}_\text{t}(T_{\text{cell}} - T_{\text{ref}})) - I_0\left[\exp\left(\frac{\text{q}(V + IR_\text{s})}{\gamma \text{k} T_{\text{cell}}}\right) - 1\right] \tag{16.1}$$

where G is solar insolation W/m^2, G_{ref} is the solar insolation at the design condition, $I_{\text{L,ref}}$ is calculated based on the manufacturer data for short circuit and maximum point currents, and k_t is the manufacturer supplied temperature coefficient of short-circuit current (A/°C). The maximum power output of the PV modules is at a point where voltage and current have their maximum values. The control system for the PV system is designed so that the system operates at the maximum power point. The energy and exergy efficiencies of the PV cell at maximum power point are given by

$$\eta_{\text{PV, mp}} = \frac{P_{\text{mp}}}{\dot{En}_{\text{solar}}} = \frac{I_{\text{mp}} \times V_{\text{mp}}}{G \times A_{\text{cell}}} \tag{16.2}$$

$$\psi_{\text{Pv, mp}} = \frac{P_{\text{mp}}}{\dot{Ex}_{\text{solar}}} = \frac{I_{\text{mp}} \times V_{\text{mp}}}{G \times A_{\text{cell}} \times \left(1 - \frac{4}{3}\frac{T_0}{T_{\text{sun}}} + \frac{1}{3}\left(\frac{T_0}{T_{\text{sun}}}\right)^4\right)} \tag{16.3}$$

Water Electrolyser

For surplus electricity from the PV system, $P_{\text{in,el}}$, the energy efficiency relation of the electrolyser is used to calculate the produced hydrogen flow rate:

$$\eta_{\text{el}} = \frac{\dot{m}_{\text{H}_2}\text{LHV}_{\text{H}_2}}{P_{\text{in,el}}} \tag{16.4}$$

Solid Oxide Fuel Cell

The Butler–Volmer equation is used to relate the current and voltage output of the solid oxide fuel cell. Relevant voltage drops due to ohmic, activation, and concentration losses are considered in the calculation of SOFC electric power output according to Colpan et al. [12] and Motahar and Alemrajabi [13]. The energy and exergy efficiencies for the fuel cell system are

$$\eta_{\text{SOFC}} = \frac{\dot{W}_{\text{net}-\text{SOFC}}}{\dot{m}_{\text{H}_2,\text{SOFC}}\,\text{LHV}_{\text{H}_2} + \dot{Q}_{\text{H}_2-\text{preheat}}} \tag{16.5}$$

$$\psi_{\text{SOFC}} = \frac{\dot{W}_{\text{net}-\text{SOFC}}}{\dot{m}_{\text{H}_2,\text{SOFC}}\,ex_{\text{H}_2} + \dot{Ex}_{\text{H}_2-\text{preheat}}} \tag{16.6}$$

The purpose of the hybrid system is to provide a detached house with zero-emission electricity. The system also provides a part of the heating/cooling demand. This is performed through heat recovery from the fuel cell stack gases.

Heat Recovery Steam Generator

The HRSG is treated as a heat exchanger. Subcooled water enters the economizer section and receives heat from the gases leaving the HRSG. After it heats up to the saturation temperature at the boiler pressure, water vapor is formed inside the pipes. The saturated steam generated in the HRSG leaves the unit for hot water production or cooling purposes.

Hybrid PV–Fuel Cell–Battery System

The overall efficiencies of the hybrid system consider all the useful outputs and the inputs to the system. The electric power demand of the house and the heat recovered from the fuel cell exhaust gases are considered as outputs. The inlets to the overall hybrid PV–Fuel Cell–Battery system are solar irradiance and the heat required to preheat the fuel feed to the SOFC. Both enenrgy and exergy efficiencies of the overall system are then defined as follows:

$$\eta_{\text{total}} = \frac{P_{\text{demand}} + \dot{m}_{\text{H}_2}\text{LHV} + \dot{Q}_{\text{s,HRSG}}}{\dot{En}_{\text{solar}} + \dot{Q}_{\text{H}_2-\text{preheat}}} \tag{16.7}$$

$$\psi_{\text{total}} = \frac{P_{\text{demand}} + \dot{m}_{\text{H}_2}ex_{\text{H}_2} + \dot{Ex}_{\text{s,HRSG}}}{\dot{Ex}_{\text{solar}} + \dot{Ex}_{\text{H}_2-\text{preheat}}} \tag{16.8}$$

Assumption and Data

The thermodynamic and cost analyses are based on the following assumptions and data:
- The average daily demand is used of a 140 m^2 detached house (22.2 kWh/day).
- The solar irradiance is based on a monthly average in Toronto in 2011. The calculations are for each month, separately.
- The Proton Exchange Membrane (PEM) electrolyser is selected to operate at 30 bar and 65 % efficiency.
- The hydrogen generated by the electrolyser process is stored at 25 bar on a seasonal storage basis. The size of the storage tank is determined based on the seasonal need for hydrogen.

Fig. 16.3 Hourly electric power demand of the detached house broken down by hour of the day [14]
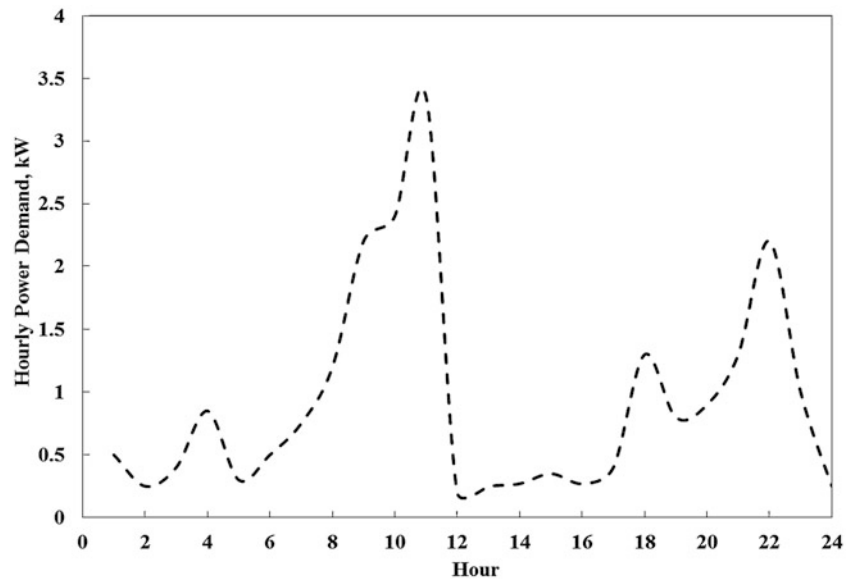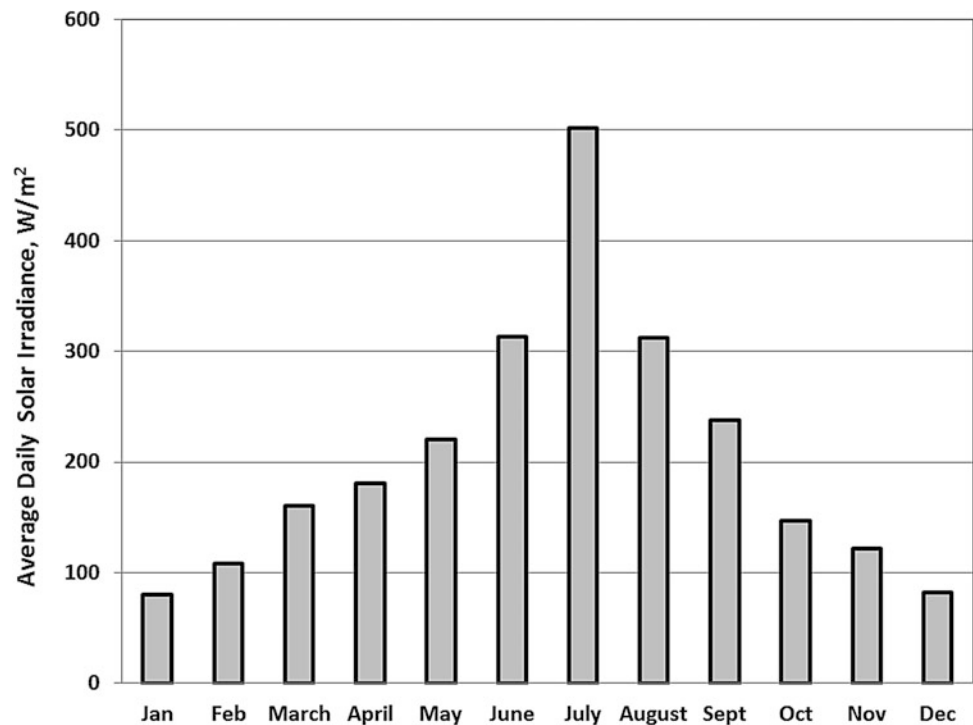

Fig. 16.4 Average daily solar irradiance over each month of 2011 (adapted from [15])

- The fuel cell is an atmospheric SOFC.
- The fuel cell nominal power is 1 kW (after accounting for 4 % internal consumption). The size of the fuel cell determines the size of the PV array, the hydrogen storage tank, and the battery.
- The annual amount of the stored hydrogen must be positive; therefore, a PV panel with 86 modules is selected. The nominal power output of each module is 210 W [at standard test conditions (STC)].

Figure 16.3 shows the daily electricity demand of the house. These sets of data are used in the previous work of the authors [4] for comparison of the performance of the system in summer and winter of 2011. Here, the data, which are adopted from the study for International Energy Agency [14], are used to perform the thermodynamic analysis and cost evaluation of the system for each month of operation.

The University of Toronto publishes solar irradiance data in Toronto over the past 6 years. Here, the 2011 solar irradiance presented in Fig. 16.4 is used [15]. Although the average monthly solar radiation on 24 h basis is used in the analyses,

Fig. 16.5 Electric power output of the PV–fuel cell system component on a daily basis as a monthly average
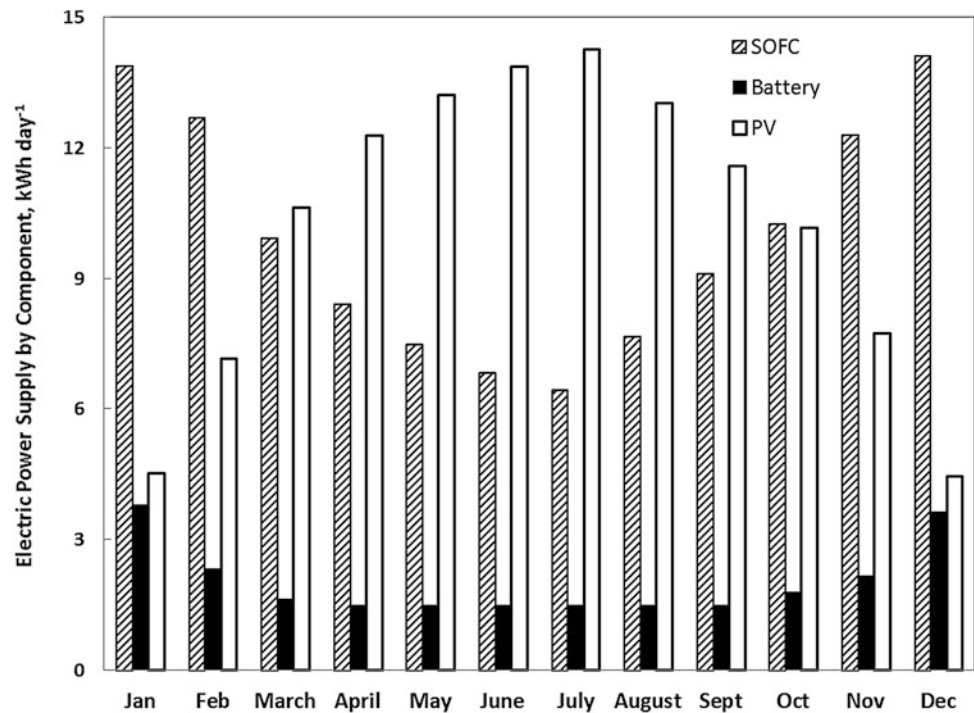

**Table 16.1** Equipment purchase and operation and maintenance costs

System and component	Nominal size	Unit cost	Cost
PV system [16]			
PV system	18.06 kW	5,156 $/kW	US$ 93,113.66
O&M [17]		47 $/kW/year	US$/year 848.82
Fuel cell system [18]			
SOFC, balance of plant (BOP)	1 kW	2,296.73 $/kW	US$ 2,296.73
O&M		5 % of purchase	US$/year 114.84
Stored hydrogen	117.29 kg (3,909.28 kWh)		
Hydrogen storage tank	58.12 m^3 at 25 bar, 300 K	4 $/kWh	US$ 15,636.73
O&M		3 % of purchase	US$/year 469.10
Electrolyser			
PEM electrolyser, BOP, installation	14.45 kW	586.5 $/kW	US$ 8,474.93
O&M		5 % of purchase	US$/year 423.75
Battery, BOP, installation	5 kWh	185 $/kWh	US$ 937.50
O&M		3 % of purchase	US$/year 28.12
Total hybrid system capital cost			US$ 120,459.55
Operation and maintenance			US$/year 1,888.63
Total O&M cost over the system lifetime (25 years)			US$ 47,115.75
Total estimated system cost over 25 years			US$ 167,575.30

Fig. 16.5 is presented to illustrate the significant difference between the summer and winter solar availability. The performance of the PV modules, and as a result the hybrid system components, are strongly dependent on the solar irradiance, as discussed further in section "Results and Discussion". The cost model considers only the purchase, installation labor, and operation and maintenance of the system components. The details are provided in Table 16.1.

Results and Discussion

The load profile depends on the instantaneous demand, which requires precise measurement of electricity consumption. However, the thermodynamic analyses can be performed based on average values to determine the initial sizes of the system components, the pattern of energy flow in the electricity generation system, and the sources of losses. The results can also help developing a control strategy and dynamic model for further investigations.

Fig. 16.6 PV and SOFC–battery power penetration
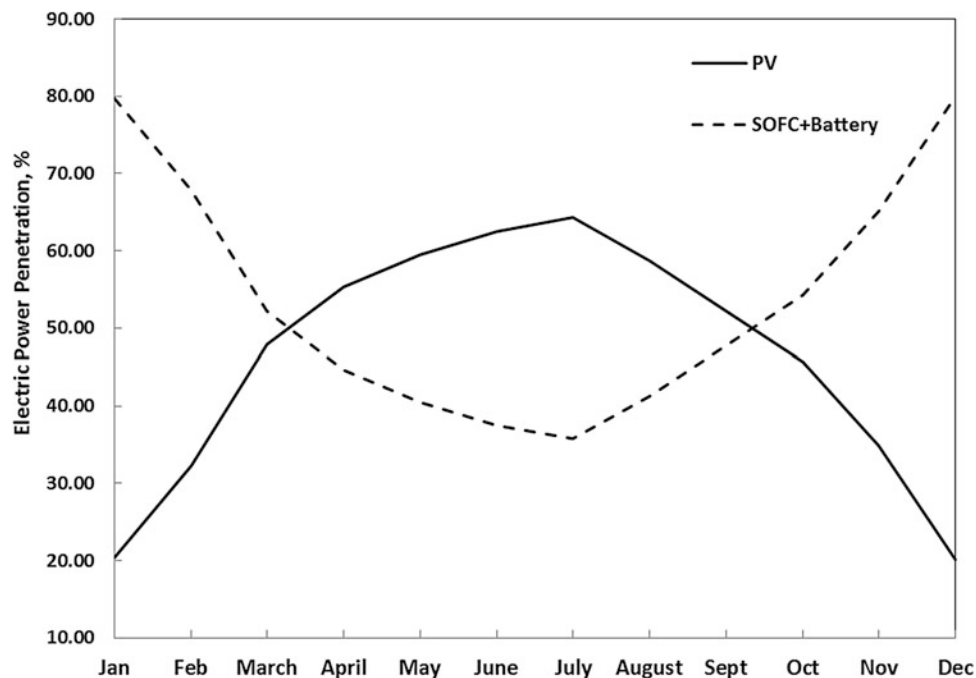
In this study, the hourly solar irradiance and load demand are considered in the analyses. The data for solar irradiance are derived from the average values over each month of the year 2011. However, the presented results only show the total daily generation/consumption of each system component. The system is considered to perform the same throughout the month.

The electric power supply by each component of the hybrid PV–fuel cell–battery system (in kWh per day) is presented in Fig. 16.5. The results are reported for each month, considering average values of solar irradiance in each month. Figure 16.5 presents the daily share of power supply of the PV modules, fuel cell, and batteries in each month. With the increase in solar irradiance in the summer months (Fig. 16.4), the PV electric power output increases significantly. Therefore, most of the electricity demand is directly met by the PV output, and the fuel cell has its minimum share in supplying the demand. To quantify this significant difference, the power penetrations of the PV system and the fuel cell–battery are shown in Fig. 16.6. Due to less solar irradiance in Fall-Winter months, the fuel cell–battery penetration in demand is as high as 80 % in January and December. The supply share of the fuel cell–battery of the demand decreases with the rise in solar availability in summer months.

The surplus electricity generated by the PV modules is directed to the electrolyser. The daily hydrogen production rate is shown in Fig. 16.7, with July having the maximum production rate as 2.33 kg/day. The fuel cell hydrogen consumption is related to its power output rate; therefore, more hydrogen is consumed by the SOFC during winter days. The difference between the electrolyser hydrogen production rate and the SOFC fuel consumption rate is taken as the amount of the hydrogen which needs to be stored in or provided by the hydrogen storage tank. The positive values for hydrogen storage in Fig. 16.5 illustrate more production than what is consumed by the fuel cell. The negative values mean that the electrolyser is not capable of producing enough hydrogen for the SOFC, and hydrogen is supplied by the storage tank. The hydrogen storage tank must be large enough to cover the total consumption during the months with more consumption than production.

The annual exergy destructions in the hybrid PV–fuel cell–battery system are given in Table 16.2, which shows that the PV modules are the main source of exergy destruction in the system. Improving the efficiency of the PV cells leads to a lower exergy destruction. Exergy destruction in the fuel cell is caused by several phenomena, e.g., electrochemical reactions and high temperature preheating of the air and hydrogen flows.

The efficiencies of the system components change when their operating conditions deviate from the nominal conditions. The variations of the efficiencies of the PV and fuel cell systems are presented in Fig. 16.8. In summer days, the average daily solar irradiance is closer to the standard test condition of the photovoltaic cells. However, the fuel cell appears to work at its nominal power rate throughout the year. Higher values are obtained for exergy efficiency because solar exergy, the input to the PV module, is less than solar energy. In the case of the fuel cell, the exergy of the required heat for hydrogen preheating is less than its energy content, which results in higher efficiencies based on exergy rather than energy.

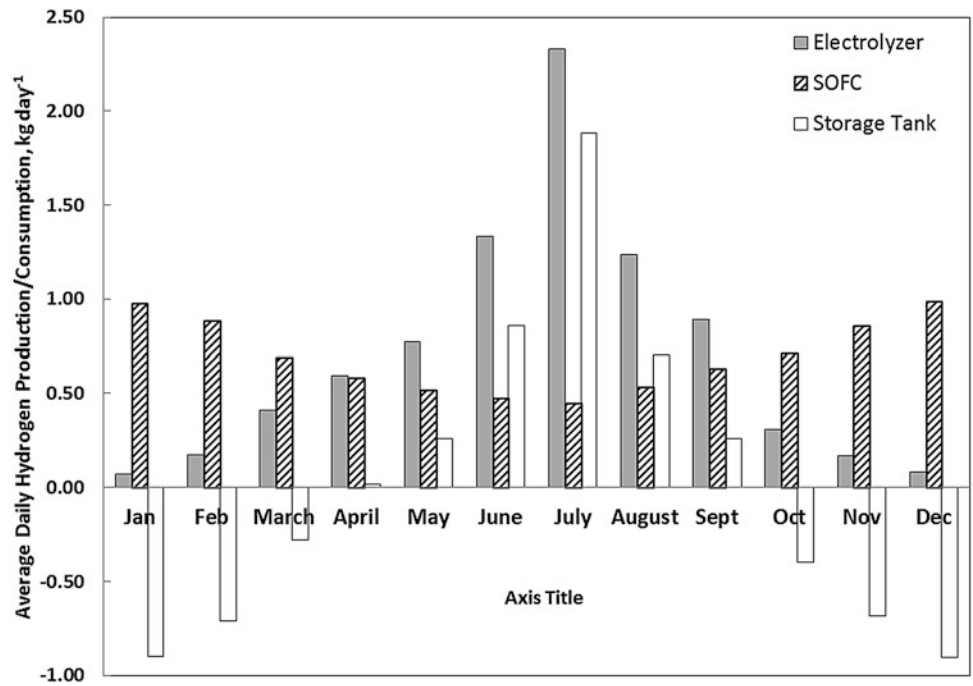**Fig. 16.7** Monthly hydrogen storage/consumption

Table 16.2 Total yearly exergy destruction in the major hybrid system components

Component	PV	Electrolyser	SOFC	HRSG
Exergy destruction, kWh/year	81,974.77	4,734.40	5,249.03	510.18

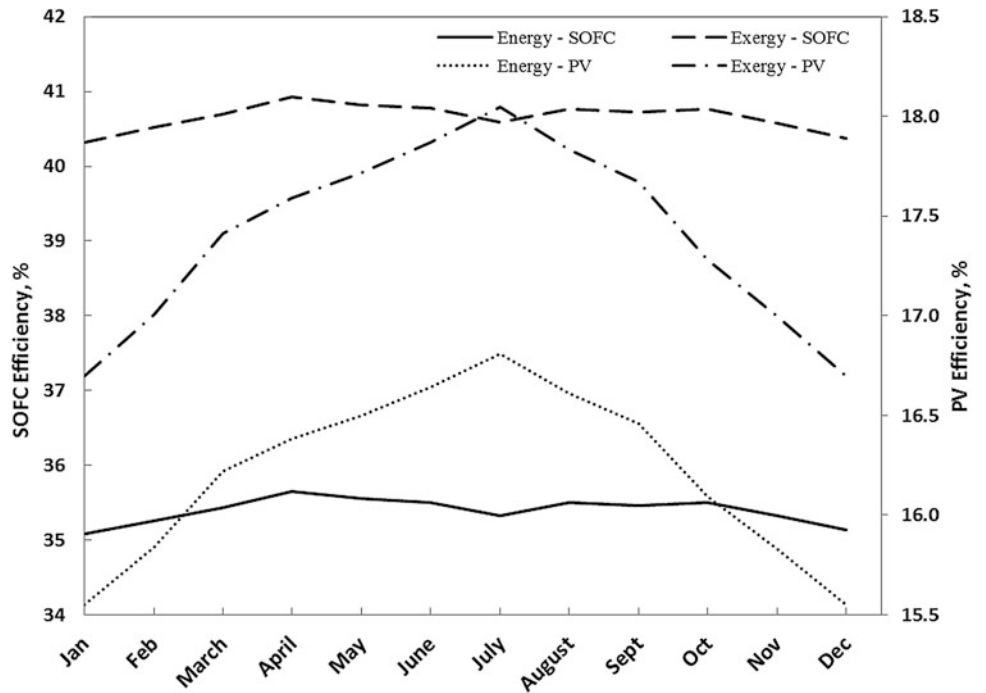**Fig. 16.8** Energy and exergy efficiencies of the PV and SOFC systems

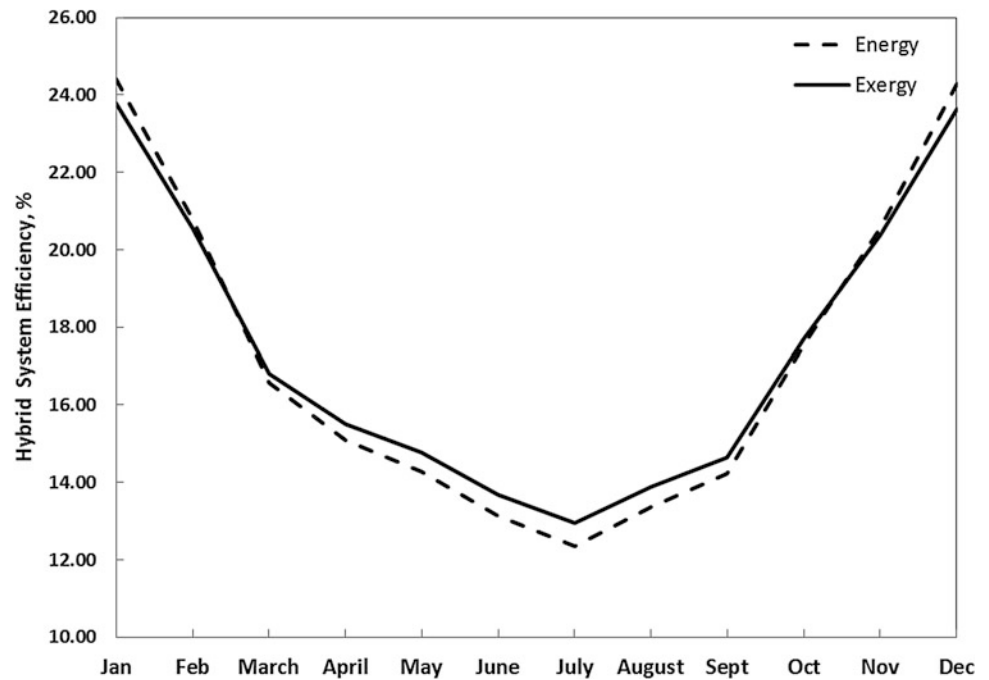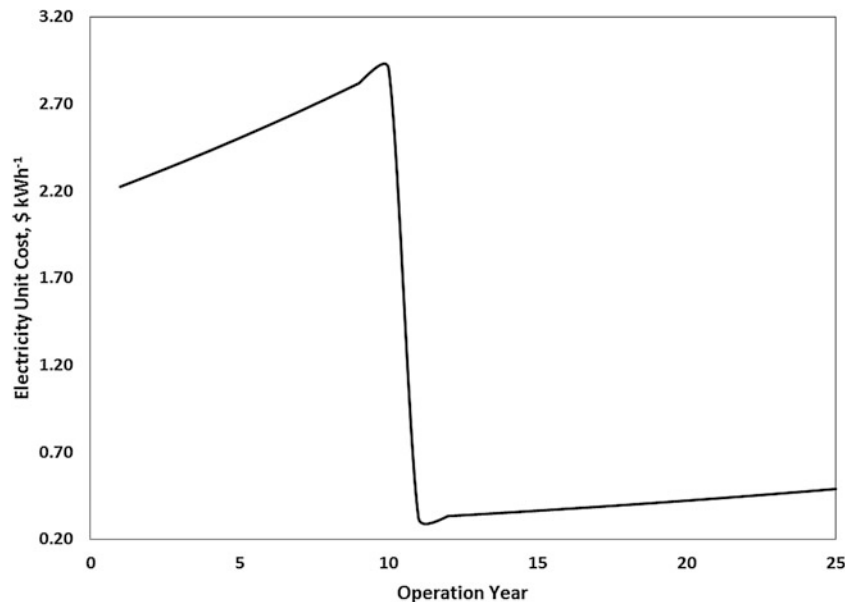**Fig. 16.9** Energy and exergy efficiencies of the hybrid PV–fuel cell–battery system

Fig. 16.10 Annual electricity unit cost during the hybrid system lifetime

However, interesting results are obtained for the overall efficiencies of the hybrid PV–fuel cell–battery system. According to Fig. 16.9, the efficiencies differ significantly with month. Higher values are reported for Fall-Winter months in which the fuel cell–battery penetration is a maximum, and lower values are reported for Spring-Summer months in which the PV modules provide a greater portion of the demand. The difference in the efficiencies of PV and fuel cell systems is the cause of such results.

The unit cost of electricity is a function of the total estimated cost and the total electricity production over 25 years of operation. The total annual electricity production is the sum of the daily production over 365 days of the year. Therefore, the electricity unit cost (EUC) is 0.83 US$/kW. However, another analysis is made to estimate the cost of electricity in each year of operation of the system. If the capital costs are assumed to be paid off in 10 years, considering the inflation rate (3 %), the electricity unit cost will follow the trend shown in Fig. 16.10. A significant drop is observed for the 11th year of operation, since the only costs of the system are associated with operation and maintenance costs.

Conclusions

Several conclusions can be drawn from the thermodynamic and cost analyses reported here of a hybrid PV–fuel cell–battery system as applied to a Canadian house. The nominal maximum power output of the PV modules is 18.06 kW, which is five times higher than the demand maximum power. The photovoltaic system is sized to meet the demand either directly or by storage of hydrogen generated in the electrolyser. Due to less solar irradiance in Fall-Winter months, the fuel cell–battery penetration in supplying of the demand is as high as 80 % in January and December. The supply share of the fuel cell–battery in meeting the demand decreases with the rise in solar availability in Summer months. The maximum H_2 production rate is in July (2.3 kg/day), and the hydrogen consumption is maximum in January (0.99 kg/day).The efficiencies differ significantly with the time of the year. Higher values are observed for fall-winter months in which the fuel cell–battery penetration is a maximum, and lower values are observed for Spring-Summer months in which the PV module provides a greater portion of the demand. The electricity unit cost is 0.83 $/kWh based on a 25-year economic evaluation period of the hybrid PV–fuel cell–battery system.

Nomenclature

ex	Specific exergy, kJ/kg	LHV	Lower heating value, kJ/kg
$\dot{En}$	Energy flow rate, kW	$\dot{m}$	Mass flow rate, kg/s
$\dot{Ex}$	Exergy flow rate, kW	P	Power, kW
G	Solar irradiance, W/m^2	$\dot{Q}$	Heat transfer rate, kW
I_L	PV light current, A	R_s	Series resistance of the PV cells, Ohm
I_0	Reverse saturation current, A	T	Temperature, K
I	PV electric current, A	V	Voltage, V
k	Boltzmann constant	$\dot{W}$	Work rate, kW
k_t	Manufacturer supplied temperature coefficient of short-circuit current, A/°C		

Greek Letters

γ	PV cell shape factor	ψ	Exergy efficiency, %
η	Energy efficiency, %		

Subscripts

0	Ambient condition	in, el	Input to the electrolyser
cell	PV cells	mp	Maximum power
H_2	Hydrogen	SOFC	Solid oxide fuel cell

Acronyms

CHP	Combined heat and power	SOFC	Solid oxide fuel cell
PV	Photovoltaic	STC	Standard test condition

References

1. Shabani B, Andrews J, Watkins S (2010) Energy and cost analysis of a solar-hydrogen combined heat and power system for remote power supply using a computer simulation. Sol Energy 84:144–155
2. Lagorse J, Simoes MG, Miraoui A, Costerg P (2008) Energy cost analysis of a solar-hydrogen hybrid energy system for stand-alone applications. Int J Hydrogen Energy 33:2871–2879

3. Morrison IB, Mottillo M, Ferguson A, Ribberink H, Yang L, Haddad K (2006) The simulation of a renewable-energy-powered hydrogen-based residential electricity system. Second national IBPSA-USA conference, Cambridge, MA, 2–4 August 2006

4. Hosseini M, Dincer I, Rosen MA (2013) Hybrid solar-fuel cell CHP Systems for residential applications: energy and exergy analyses. J Power Sources 221:372–380

5. Santarelli M, Cali M, Macagno S (2004) Design and analysis of stand-alone hydrogen energy systems with different renewable sources. Int J Hydrogen Energy 29:1571–1586

6. Uzunoglu M, Onar OC, Alam MS (2009) Modeling, control and simulation of a PV/FC/UC based hybrid power generation system for stand-alone applications. Renew Energy 34:509–520

7. Sukamongkol Y, Chungpaibulpatana S, Ongsakul W (2002) A simulation model for predicting the performance of a solar photovoltaic system with alternating current loads. Renew Energy 27:237–258

8. Chenni R, Makhlouf M, Kerbache T, Bouzid A (2007) A detailed modeling method for photovoltaic cells. Energy 32:1724–1730

9. Nordin A, Omar A (2011) Modeling and simulation of photovoltaic (PV) array and maximum power point tracker (MPPT) for grid-connected PV system. 3rd international symposium and exhibition in sustainable energy and environment, Melaka, Malaysia, 1–3 June 2011

10. Clarke RE, Giddey S, Ciacchi FT, Badwal SPS, Paul B, Andrews J (2009) Direct coupling of an electrolyser to a solar PV system for generating hydrogen. Int J Hydrogen Energy 34:2531–2542

11. La O' GJ, In HJ, Crumlin E, Barbastathis G, Horn YSh (2007) Recent advances in microdevices for electrochemical energy conversion and storage. Int J Energy Res 31:548–575

12. Colpan CO, Dincer I, Hamdullahpur F (2007) Thermodynamic modeling of direct internal reforming solid oxide fuel cells operating with syngas. Int J Hydrogen Energy 32:787–795

13. Motahar S, Alemrajabi AA (2009) Exergy based performance analysis of a solid oxide fuel cell and steam injected gas turbine hybrid power system. Int J Hydrogen Energy 34:2396–2407

14. Knight I, Kreutzer N, Manning M, Swinton M, Ribberink H (2007) European and Canadian non-HVAC electric demand and DHW load profiles for use in simulating the performance of residential cogeneration systems. Annex 42, International Energy Agency, Energy Conversions in Buildings and Community System Programme, May 2007

15. Weather Data, Department of Geography, University of Toronto Mississauga (2012) http://www.utm.utoronto.ca/geography/resources/meteorological-station/weather-data. Accessed 26 June 2012

16. Sun Power Corporation (2012) Document #001-42023, 210 solar panel. http://www.prevailingwindpower.com/sunpower.pdf. Accessed 26 June 2012

17. Enbar N (2010) PV O&M best practices. Utility/lab workshop on PV technology and systems. National Renewable Energy Laboratory, 8–9 November 2010

18. Braun RJ, Klein SA, Reindl DT (2011) Assessment of solid oxide fuel cells in building applications, phase 1: modeling and preliminary analyses. Prepared for Energy Center of Wisconsin, Report 207-R, November 2011

19. Zhang X, Chan SH, Li G, Ho HK, Li J, Feng Z (2010) A review of integration strategies for solid oxide fuel cells. J Power Sources 195:685–702

Thermodynamic Assessment of Waste Heat Operated Combined Compression–Absorption Refrigeration System

17

Abdul Khaliq and Ibrahim Dincer

Abstract

An industrial waste heat operated combined refrigeration cycle is proposed, which integrates the Rankine cycle and compression–absorption refrigeration cycle. This combined cycle produces higher coefficient of performance than the conventional refrigeration cycle. An analysis through energy and exergy is performed to guide the thermodynamic improvement for this cycle, and a comprehensive parametric study is conducted to investigate the effects of exhaust gas inlet temperature, pinch point, and gas composition on energetic and exergetic COP and exergy destruction in each component of the combined refrigeration cycle. The results show that the exhaust gas inlet temperature and pinch point have significant effects on exergy destruction in most of the components of the cycle. Effects of increasing the exhaust gas temperature and pinch point were found negligible for exergy destruction in solution pump and throttling valve. Both energetic and exergetic COPs increases with the increase in exhaust gas temperature and decreases with the increase in pinch point and oxygen content of the gas. Modeling the exhaust gas as an air underestimates the energetic performance and overestimates the exergetic performance of the combined refrigeration cycle. This study contributes important information to the role of operating variables influence on the thermodynamic performance of low temperature source combined compression–absorption refrigeration system.

Keywords

Combined refrigeration system • Vapor compression • Absorption • Energetic • Exergetic • Irreversibility

Introduction

A significant amount of heat is wasted as flue gases from industries. The flue gases on the virtue of being at a higher temperature (400–500 °C) relative to the surroundings and having a higher mass flow rate possess considerable amount of available energy, which if not utilized properly will lead to huge undesirable energy loss and increase in environmental pollution. In recent years a great deal of attention is focused on to utilize the waste heat for various applications and to analyze the units which are used to absorb heat from waste flue gases [1, 2]. There is a greater scope to recover waste heat from various industries and produce power, useful heat, and refrigeration, using a HRSG [3].

Thermodynamics permits the behavior, performance, and efficiency to be described for systems for the conversion of energy from one form to another. Conventional thermodynamic analysis is based primarily on the first law of thermodynamics, which states the principle of conservation of energy. An energy analysis of an energy-conversion system is

A. Khaliq (✉)
Department of Mechanical Engineering, KFUPM, Dhahran 31261, Saudi Arabia
e-mail: khaliq.sb@gmail.com; akhaliq@kfupm.edu.sa

I. Dincer
Faculty of Engineering and Applied Science, University of Ontario Institute of Technology,
2000 Simcoe Street North, Oshawa, ON, Canada L1H 7K4
e-mail: Ibrahim.Dincer@uoit.ca

essentially an accounting of the energies entering and exiting. The exiting energy can be broken down into products and wastes. Efficiencies are often evaluated as ratios of energy quantities, and are often used to assess and compare various systems. Power plants, heaters, refrigerators, and thermal storages, for example, are often compared based on energy efficiencies or energy-based measures of merit. However, energy efficiencies or energy-based coefficient of performance values are often misleading in that they do not always provide a measure of how nearly the performance of a system approaches ideality. Further, the thermodynamic losses which occur within a system (i.e., those factors which cause performance to deviate from ideality) often are not accurately identified and assessed with energy analysis. The results of energy analysis can indicate the main inefficiencies to be within the wrong sections of the system, and a state of technological efficiency different than actually exists. Exergy analysis permits many of the shortcomings of energy analysis to be overcome. Exergy analysis, by stemming from the second law of thermodynamics, is useful in identifying the causes, locations, and magnitudes of process inefficiencies. The exergy associated with an energy quantity is a quantitative assessment of its usefulness or quality. Exergy analysis acknowledges that although energy cannot be created or destroyed, it can be degraded in quality, eventually reaching a state in which it is in complete equilibrium with the surroundings and hence of no further use for performing tasks [4].

Industrial waste heat utilization for the production of power and refrigeration and its exergy analysis has been the subject of many investigators. Butcher and Reddy [3] conducted the second law analysis of a waste heat recovery-based power generation system. Liu and Zhang [5] proposed a waste heat operated ammonia water cycle for the cogeneration of power and refrigeration. They introduced a splitting/absorption unit into the combined power and refrigeration system. Zhang and Lior [6] proposed a new ammonia water system for the cogeneration of refrigeration and power. They investigated the effects of the key thermodynamic parameters on both energy and exergy efficiencies. Khaliq et al. [7] presented the exergy analysis of cogeneration cycle for the combined production of power and refrigeration that provide effective utilization of waste heat with reduced emissions. They investigated the effects of the industrial waste heat gas composition, specific heat, pinch point, and gas inlet temperature to heat recovery steam generator (HRSG) on thermodynamic performance parameters of the cycle, and summarized some guidelines for integration of waste heat operated power and refrigeration system to for higher energy and exergy efficiencies. Khaliq et al. [7] also reported the exergy analysis of waste heat recovery-based multiple output thermodynamic system for simultaneous production of power, heat, and refrigeration.

To meet out the cooling load demand caused by high air-conditioning requirement during summer time HVAC and refrigeration industry adopted the combined compression absorption refrigeration cycles. Absorption refrigeration machines are commercially available and they exhibit continuous and stable operation under part load conditions from 0 to 100 %, but their COP values are relatively low compared with vapor compression refrigeration system. However, absorption refrigeration cycle combined with compression refrigeration cycle provide high system performance over heat engine-driven compression refrigeration cycle because it uses the waste heat from HRSG to meet the cooling load resulting in the reduction of grid peak load caused by high air-conditioning demand [8, 9].

In order to utilize the industrial waste heat for its potential in meeting the cooling load demand and alleviating environmental problems, a combined compression–absorption refrigeration cycle is proposed in which the steam generated in HRSG through waste heat runs the turbine that directly drives the vapor compression refrigeration cycle, feed water pump, and solution pump of absorption cycle. The waste heat at the exit of HRSG (stack gases) is used to drive LiBr–H$_2$O absorption refrigeration system. This combined cycle can produce two refrigeration outputs simultaneously from industrial waste heat.

In the present study, a thermodynamic analysis is conducted using combined first and second law approach to evaluate the performance of this combined refrigeration cycle, and the parametric analysis is performed to examine the effects of key thermodynamic parameters; waste heat gas composition, specific heat, pinch point temperature difference, and gas inlet temperature on the cycle performance. In addition, a ranking among the components of the cycle is achieved with exergy destruction as a function by means of irreversibility analysis. Exergy analysis usually aims to determine the maximum performance of the system and identify the component in which major exergy loss occurs and indicates the possibilities of thermodynamic improvement of the cycle under consideration.

System Description and Assumptions

The proposed cycle combines the Rankine cycle and the compression–absorption refrigeration cycle which can produce two refrigeration outputs simultaneously with single heat source. Figure 17.1 illustrates the waste heat operated combined compression–absorption refrigeration system.

The waste heat from the industry enters the HRSG in which high pressure and temperature vapor is generated by utilizing waste heat. The high pressure and temperature vapor is expanded in the turbine to produce power which is required

Fig. 17.1 Schematic of combined power and refrigeration cycle used for analysis

by compressor of vapor compression system, feed water pump, and solution pump of absorption refrigeration system. The turbine exhaust enters the condenser where it condenses from vapor to a liquid by rejecting heat to the surroundings. The liquid pressure is then increased to the HRSG pressure by pump where it is again vaporized. The high pressure refrigerant R134a at the exit of compressor enters the condenser where it rejects heat to the surroundings. The refrigerant leaving the condenser enters the evaporator after passing through the expansion valve. In evaporator, the refrigerant R134a is vaporized by absorbing heat from the cooling media where the first cooling effect is produced. The stack gases at the exit of HRSG enter the generator of vapor absorption system. The refrigerant (H_2O) is separated from LiBr–H_2O mixture in the evaporator by means of heat driven by stack gas. The solution circulation ratio $\left(f = \dot{m}_{s2}/\dot{m}_r\right)$ depends on the temperature to which the solution is heated. After reaching the desired temperature the refrigerant passes through the condenser and enters

the evaporator through the throttling valve. In evaporator the refrigerant H_2O is vaporized by absorbing heat from the cooling media and the second cooling effect is produced in the cycle. The saturated steam at the exit of the evaporator enters the absorber where it mixes with the weak solution, generating heat that has to be dissipated to increase the efficiency of the mixing process. The heat released in the condenser and in the absorber is rejected to the cooling water. The mixing process results in strong solutions that exit the absorber and is then pumped to the upper pressure of the cycle. The high pressure strong solution in the generator is again heated to high temperature.

The following assumptions are made in the analysis [7, 10]:

- The system operates at steady state.
- No pressure drops exist on the steam side.
- Pressure drop on gas side does not affect its temperature.
- Lithium bromide solution in the generator and the absorber are assumed to be in equilibrium at their respective temperatures and pressures.
- Refrigerant (water) at condenser and evaporator exit in saturated states.
- Strong solution of the refrigerant leaving the absorber and the weak solution of refrigerant leaving the generator are saturated.
- Pressure losses in all the heat exchangers and the pipelines are neglected.
- To avoid crystallization of the solution, the temperature of the solution entering the throttling valve should be at least 7–8 °C above crystallization temperature.
- The system uses waste heat of industry to generate steam and then to drive the turbine of Rankine engine.
- Refrigerant compressor (RC), feed water pump and solution pump are powered by the Rankine engine.
- All heat exchangers are assumed to be counter flow devices.
- Heat losses towards the surroundings air are not been taken into account, as they are generally a minute fraction of the other energy transfers.

Thermodynamic Analysis

Here we first need a property evaluation before getting into analysis. The exhaust gas is considered as air in one case and the actual gas composition in other cases. The specific heat of air is calculated using standard thermodynamic tables. The specific heat of the actual exhaust gas is determined using the relation [11].

$$C_P = \frac{R}{M}\left(\alpha + \beta T + \gamma T^2 + \delta T^3 + \varepsilon T^4\right) \qquad (17.1)$$

where T is the gas temperature in K, and the equation is valid from 300 to 1,000 K. R is the universal gas constant, M is the molar mass of the gas, and α, β, γ, δ, ε are gas constants for various ideal gases.

The specific heat of a mixture of gases $[C_P(T)]$ is expressed as the sum of the specific heats of each component $[C_{Pi}(T)]$ and their mass fractions y_i.

$$C_P(T) = \sum_{i=1}^{n} y_i C_{Pi}(T) \qquad (17.2)$$

The entropy change for an ideal gas mixture between states 1 and 2 is expressed as

$$s_2 - s_1 = \sum_{i=1}^{n} y_i (s_2 - s_1)_i \qquad (17.3)$$

Using the temperature profile and pinch point, the stack gas temperature of HRSG can be calculated by [12].

$$T_{g2} = (T_P + PP) - \left[T_{g1} - (T_P + PP)\right]\left(\frac{h_f - h_c}{h_g - h_f}\right) \qquad (17.4)$$

where T_P is the process heat temperature of steam leaving the HRSG and PP stands for a pinch point.

The steam generation rate in the HRSG is obtained by performing the energy balance as

$$\dot{m}_{s1} = \dot{m}_g \left(\frac{C_{P_{T_{g1}}} T_{g1} - C_{P_{T_{g2}}} T_{g2}}{h_{s4} - h_{w3}} \right) \tag{17.5}$$

where $\dot{m}_g$ is the mass flow rate of exhaust gas from industry, C_P is the specific heat of exhaust gas, h_{s4} and h_{w3} are the enthalpies of steam at the HRSG outlet and feed water at the HRSG inlet, respectively.

The rate of heat input $\dot{Q}_{in}$ to the system is given by

$$\dot{Q}_{in} = \dot{m}_g \left[C_{P_{T_{g1}}} T_{g1} - C_{P_{T_{g, leavingGEN}}} T_{g, leavingGEN} \right] \tag{17.6}$$

The power output of steam turbine is equal to the power consumed by the refrigerant compressor, feed water pump (P1), and solution pump (P2).

$$\dot{W}_{ST} = \frac{\dot{W}_{RC}}{\eta_{RC}} + \frac{\dot{W}_{P1}}{\eta_{P1}} + \frac{\dot{W}_{P2}}{\eta_{P2}} \tag{17.7}$$

where η_{RC} is the refrigerant compressor efficiency and η_{P1}, η_{P2} are the pump efficiencies.

The rate of cold production (refrigeration capacity) of vapor compression evaporator $\left(\dot{Q}_{E1} \right)$ may be obtained after applying the energy balance on the evaporator as

$$\dot{Q}_{E1} = \dot{m}_{VCR}(h_{21} - h_{20}) = \dot{m}_{E1}\left(h_j - h_k \right) \tag{17.8}$$

where $\dot{m}_{VCR}$ is the mass flow rate of the refrigerant R134a used in vapor compression refrigeration cycle.

The rate of cold production (refrigeration capacity) at the evaporator of vapor absorption refrigeration $\left(\dot{Q}_{E2} \right)$ may be obtained in the similar fashion and is given by

$$\dot{Q}_{E2} = \dot{m}_r(h_{11} - h_{10}) = \dot{m}_{E2}(h_c - h_d) \tag{17.9}$$

The enthalpy and entropy values of LiBr–H$_2$O mixture at the inlet and outlet of the evaporator of absorption refrigeration can be obtained from [13, 14].

Performance Parameters

The system performance can be evaluated by the energetic COP which may be defined as the useful energy output divided by the total energy input and is given by

$$COP_I = \frac{\dot{Q}_{E1} + \dot{Q}_{E2}}{\dot{Q}_{in}} \tag{17.10}$$

where $\dot{Q}_{E1}$ is the refrigeration output of vapor compression system, $\dot{Q}_{E2}$ is the refrigeration output of vapor absorption refrigeration system, and $\dot{Q}_{in}$ is the heat rate added to the cycle.

From the view point of first law of thermodynamics, energy conservation used to determine the overall thermal performance, quantity and quality are equivalent. On the other hand, based on the second law of thermodynamics, exergy quantifies the difference between quality and quantity in terms of irreversibility and it is defined as the maximum amount of work which can be produced by a system when it comes to equilibrium with a reference environment. Therefore, the exergetic COP evaluates the cycle performance from the energy quality and it is chosen as a criterion for the performance evaluation.

Exergetic COP is defined as the exergy output divided by exergy input to the cycle. The exergy input is taken as the available energy change of the heat source. The exergy output is the exergy of refrigeration associated with $\dot{Q}_{E1}$ and $\dot{Q}_{E2}$.

$$COP_{II} = \frac{\dot{E}_{E1} + \dot{E}_{E2}}{\dot{E}_{in}} \tag{17.11}$$

where

$$\dot{E}_{E1} = \dot{Q}_{E1}\left(\frac{T_0 - T_{E1}}{T_{E1}}\right) \tag{17.12}$$

$$\dot{E}_{E2} = \dot{Q}_{E2}\left(\frac{T_0 - T_{E2}}{T_{E2}}\right) \tag{17.13}$$

and

$$\dot{E}_{in} = \dot{m}_g\left\{\left[h(T_{g1}) - h(T_0)\right] - T_0\left[s(T_{g1}) - s(T_0)\right]\right\} \tag{17.14}$$

which is the exergy of the exhaust gas entering the HRSG with reference to the environment. T_0 is the environmental temperature and $s(T)$ is specific entropy.

Irreversibility Analysis

Irreversibility analysis of a complex system can be performed by analyzing each component of the system separately using combined first and second law approach. Identifying the equipment in which main exergy loss occurs shows the direction for potential improvement.

The general exergetic balance applied to a fixed control volume is given by

$$\sum \dot{Q}_j\left(1 - \frac{T_0}{T_j}\right) - \dot{W} + \sum_{in} \dot{m}_{in}e_{in} - \sum_{out} \dot{m}_{out}e_{out} - \dot{I}_D = 0 \tag{17.15}$$

where $\dot{Q}_j$ is the heat transfer rate to the system, $\dot{W}$ the mechanical power produced by the system, $\dot{I}_D$ the irreversibility rate, and e is the flow exergy associated with the stream of matter.

The kinetic and potential energies are usually neglected in the case of air, because the velocity of the fluid and the height changes are small, and since there is departure of chemical substances from the cycle to the environment, the chemical exergy is taken as zero if there is no change in chemical composition (e.g., for the air approximation). Therefore, the specific exergy e can be evaluated as

$$e = (h - h_0) - T_0(s - s_0) \tag{17.16}$$

The exergy destruction or irreversibility rate in each component of combined compression-absorption refrigeration system may be obtained with the application of Eq. (17.15) and appear in the form of following expressions:

- HRSG

  The stack gas temperature at the exit of the HRSG (T_{g2}) and mass flow rate of steam ($\dot{m}_{s1}$) are calculated in Eqs. (17.4) and (17.5), respectively. The irreversibility rate in the HRSG can be evaluated using exergy balance and may be reported as

$$I_{D,HRSG} = \dot{m}_g\left\{\left[h(T_{g1}) - h(T_{g2})\right] - T_0\left[s(T_{g2}) - s(T_{g1})\right]\right\} - \dot{m}_{s1}\left[(h_{s4} - h_{w3}) - T_0(s_{s4} - s_{w3})\right] \tag{17.17}$$

- Steam turbine (ST)

  The exergy destruction or irreversibility rate in the steam turbine is given by

$$\dot{I}_{D,ST} = \dot{m}_{s1}\left[(h_{s4} - h_5) - T_0(s_{s4} - s_5)\right] - \dot{W}_{ST} \tag{17.18}$$

- Condenser-1 (C1)

$$\dot{I}_{D,C1} = \dot{m}_{s1}\left[(h_5 - h_6) - T_0(s_5 - s_6)\right] \tag{17.19}$$

The exergy destruction associated with the change in state of cooling water has not been included because it has found to be negligible.

- Pump-1 (P1)

$$\dot{I}_{D,P1} = \dot{W}_{P1} - \dot{m}_w[(h_{w3} - h_6) - T_0(s_{w3} - s_6)] \tag{17.20}$$

- Refrigerant compressor (RC)
  The exergy destruction in refrigerant compressor (RC) is given by

$$\dot{I}_{D,RC} = \dot{W}_{RC} - \dot{m}_{VCR}[(h_{18} - h_{21}) - T_0(s_{18} - s_{21})] \tag{17.21}$$

- Condenser 2 (C2)
  The refrigerant vapor goes to condenser 2 (C2) from the refrigerant compressor (RC). The irreversibility rate or exergy destruction rate in the condenser 2 (C2) is given by

$$\dot{I}_{D,C2} = T_0[\dot{m}_{VCR}(s_{19} - s_{18}) + \dot{m}_{C2}(s_i - s_h)] \tag{17.22}$$

- Expansion valve (EV1)
  The condensed refrigerant from condenser (C2) goes to the expansion valve (EV1) where its pressure reduces to the evaporator (E1) pressure. The irreversibility rate is given by

$$\dot{I}_{D,EV1} = \dot{m}_{VCR} T_0(s_{20} - s_{19}) \tag{17.23}$$

- Evaporator1 (E1)
  The condensed refrigerant from the condenser goes to the expansion valve1 (EV1), and after expansion it goes to the evaporator1 (E1). Therefore, the irreversibility rate in the evaporator1 (E1) is given by

$$\dot{I}_{D,E2} = T_0\left[\dot{m}_{VCR}(s_{21} - s_{20}) + \dot{m}_{E1}(s_k - s_j)\right] \tag{17.24}$$

- Generator (GEN)
  Energy and mass balances allow us to determine the heat transferred by the external fluid to the solution within the generator. The irreversibility in the components of vapor absorption refrigeration part of the system used for cooling is evaluated starting with exergy balance on the generator.
  We obtain the exergy destruction rate because of the irreversibilities due to heat transfer between the external fluid and the solution and is given by

$$\dot{I}_{D,GEN} = T_0[\dot{m}_r(s_8 - s_{15}) + \dot{m}_{S2}(s_{15} - s_{14})] + \dot{m}_g T_0(s_7 - s_2) \tag{17.25}$$

  The first two terms are positive while the third is negative. The overall exergy destruction is positive.

- Solution heat exchanger (SHE)
  In the similar fashion, the irreversibility rate or exergy destruction rate in the SHE, solution pump (P2), condenser (C2), evaporator (E1), and expansion valve (EV2) can be obtained in the form of following equations. The irreversibility rate in the SHE is given by

$$\dot{I}_{D,SHE} = T_0[\dot{m}_{S2}(s_{14} - s_{13}) + (\dot{m}_{S2} - \dot{m}_r)(s_{16} - s_{15})] \tag{17.26}$$

- Pump-2 (P2)
  The pump transports the diluted solution in liquid state from the absorber to the generator, raising its pressure. The irreversibility rate in the pump (P2) is given by

$$\dot{I}_{D,P2} = \dot{m}_{S2} T_0(s_{13} - s_{12}) \tag{17.27}$$

- Throttling valve (TV)
  The throttling valve (TV) reduces the pressure of the concentrated solution from the high pressure in the generator to the low pressure in the suction side of the absorber. The irreversibility rate in the throttling valve (TV) may be given as

$$\dot{I}_{D,TV} = (\dot{m}_{S2} - \dot{m}_r) T_0(s_{17} - s_{16}) \tag{17.28}$$

where $\dot{I}_{D,TV}$ is higher than zero, since the difference is positive.

- Absorber (A)

  The absorber (A) absorbs the refrigerant vapor at low pressure and low temperature, which condenses in the solution. By means of mass, energy, and exergy balances, the irreversibility rate in the absorber (A) may be defined as

$$\dot{I}_{D,A} = T_0\left[\dot{m}_{S2}s_{12} - (\dot{m}_{S2} - \dot{m}_r)s_{17} - \dot{m}_r s_{11} + \dot{m}_A\left(s_f - s_e\right)\right] \tag{17.29}$$

- Condenser3 (C3)

  The refrigerant vapor goes to condenser (C3) from the generator (GEN). The irreversibility rate or exergy destruction rate in the condenser is given by

$$\dot{I}_{D,C3} = T_0[\dot{m}_r(s_9 - s_8) + \dot{m}_C(s_b - s_a)] \tag{17.30}$$

- Evaporator (E2)

  The condensed refrigerant from the condenser goes to the expansion valve, and after expansion it goes to the evaporator2 (E2). Therefore, the irreversibility rate in the evaporator is given by

$$\dot{I}_{D,E2} = T_0[\dot{m}_r(s_{11} - s_{10}) + \dot{m}_{E2}(s_d - s_c)] \tag{17.31}$$

- Expansion valve 2 (EV2)

  The condensed refrigerant from condenser (C3) goes to the expansion valve (EV2) where its pressure reduces to the evaporator pressure. The irreversibility rate is given by

$$\dot{I}_{D,EV2} = \dot{m}_r T_0(s_{10} - s_9) \tag{17.32}$$

Results and Discussion

A parametric analysis is performed to assess the effect of exhaust gas inlet temperature, gas composition, and pinch point temperature difference on the combined first and second law performance of waste heat operated combined compression–absorption refrigeration system. Inclusion of exergy destruction in an irreversibility analysis approaches the performance of a real cycle. Operating conditions were individually varied in a straight forward thermodynamic analysis to study the effect of an exergy destruction and energetic and exergetic COPs of the combined refrigeration cycle. The parametric analysis gave insight into the behavior of the cycle and showed that analysis of the cycle would be adequate with the application of combined first and second law of thermodynamics.

The exhaust gas composition of the fuel i.e., natural gas and the operating details of the present analysis are listed in Tables 17.1 and 17.2, respectively. The combustion products, mass fraction of each gas, and the test parameters used in the parametric analysis of combined refrigeration cycle are also shown in above two tables.

Figure 17.2 shows the effect of change in exhaust gas inlet temperature (T_{g1}) and gas composition on energetic COP of waste heat operated combined compression–absorption refrigeration cycle for a fixed pinch point of 30 °C. It is found that as exhaust gas inlet temperature increases, the energetic COP increases correspondingly. This is because higher exhaust gas temperature boosts the power output of the Rankine engine resulting in higher referigeration capacity of the compression system. The waste heat at the exit of HRSG which increases with the increase in T_{g1} for fixed pinch point is being recovered in combined refrigeration system to produce additional cooling through vapor absorption system. Therefore, increase in

Table 17.1 Exhaust gas composition [3]

Combustion products	Mass fraction (%)		
	Gas I	Gas II	Air
CO_2	4.42	10.28	–
H_2O	3.43	8.41	–
O_2	16.55	7.48	20.95
N_2	75.6	73.82	78.08
Ar	–	–	0.93
Other	–	–	0.01

Table 17.2 System test parameters [7]

Test parameter	
Gas mass flow rate (kg s^{-1})	100.00
Gas inlet temperature (K)	723–823
Saturation temperature (K)	549.73
Steam pressure (bar)	60.00
Steam outlet temperature (K)	623.00
Pinch point (K)	10–50
Pressure loss (bar)	5.00
Steam turbine isentropic efficiency (%)	85.00
Pumps (P1, P2) isentropic efficiency (%)	85.00
Refrigerant compressor (RC) isentropic efficiency (%)	85.00
Condenser (C1) pressure (bar)	0.10
Condenser (C3) pressure (bar)	9.00
Environmental temperature (K)	293.00

Fig. 17.2 Variation of first law efficiency with gas composition and exhaust gas inlet temperature; PP = 20 °C, $\dot{m}_g = 100\,\mathrm{kg\,s}^{-1}$
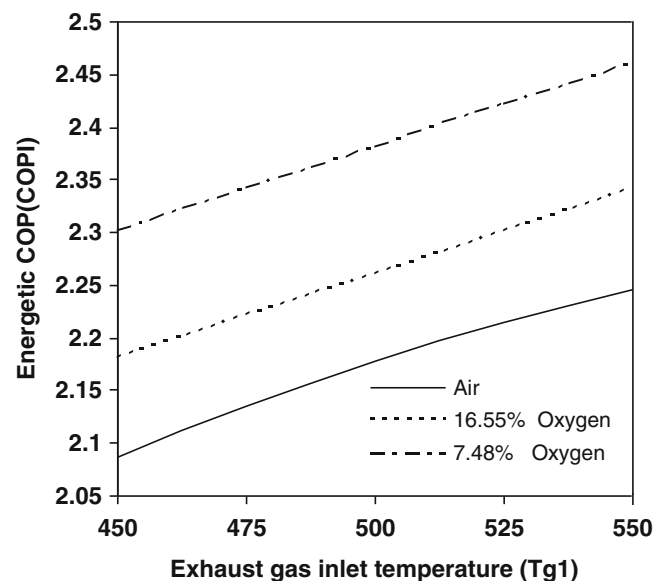
exhaust gas inlet temperature causes a significant improvement in the energetic COP of the combined refrigeration system. It is also observed that the energetic COP of combined refrigeration cycle varies with the change in gas composition and oxygen content of the exhaust gas and it is found that the energetic COP decreases with the increase in oxygen content of the exhaust gas. Figure 17.2 clearly shows that air standard approach to cycle analysis underestimates its energetic COP and hence actual gas composition needs to be considered for accurate prediction of energetic performance.

Figure 17.3 shows the effect of pinch point temperature and gas composition on energetic COP of the combined compression absorption refrigeration system for a given exhaust gas temperature $T_{g1} = 500°$C. It is found that energetic COP decreases with the increase in pinch point and oxygen content of the exhaust gas. This is because a higher pinch point causes reduced power output due to low steam generation in HRSG which results in lower cold production at the evaporator of vapor compression system and higher refrigerating effect at vapor absorption system due to large flue gas temperature. Since the contribution of vapor compression system towards total cold production of the cycle is greater, therefore, the energetic COP of the combined refrigeration cycle decreases with the increase in pinch point temperature difference of HRSG. Reduction in power to cold ratio is more pronounced at a lower pinch point as demonstrated in Fig. 17.3.

The effect of change in exhaust gas inlet temperature and gas composition on exergetic COP of the system for a fixed pinch point is shown in Fig. 17.4. It is observed that exergetic COP increases with increase in exhaust inlet temperature. This is because higher gas inlet temperature increases the steam generation rate in the HRSG which boosts the power output of the Rankine engine, resulting in higher cooling effect at vapor compression system. Increase in exhaust gas inlet

Fig. 17.3 Variation of first law efficiency with gas composition and pinch point temperature; $Tg = 500\,°C, \dot{m}_g = 100\,\mathrm{kg\,s^{-1}}$
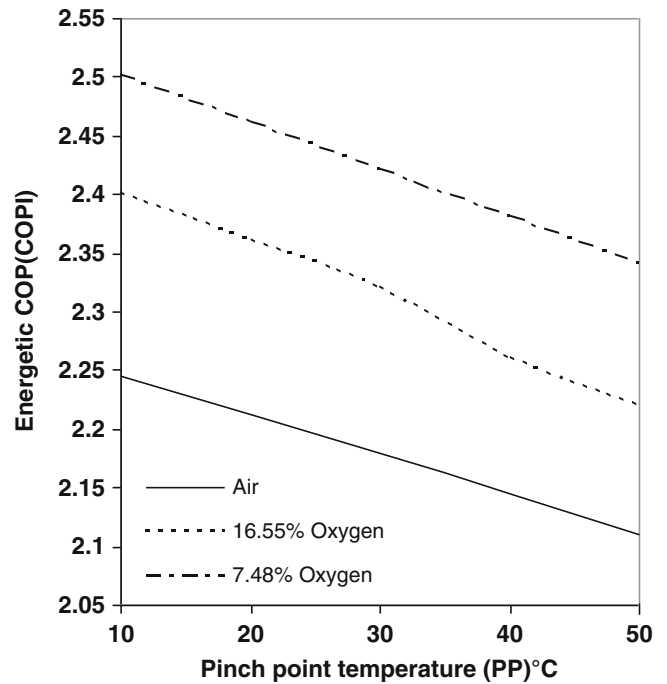
Fig. 17.4 Variation of second law efficiency (%) with gas composition and exhaust gas inlet temperature; $PP = 20\,°C$, $\dot{m}_g = 100\,\mathrm{kg\,s^{-1}}$
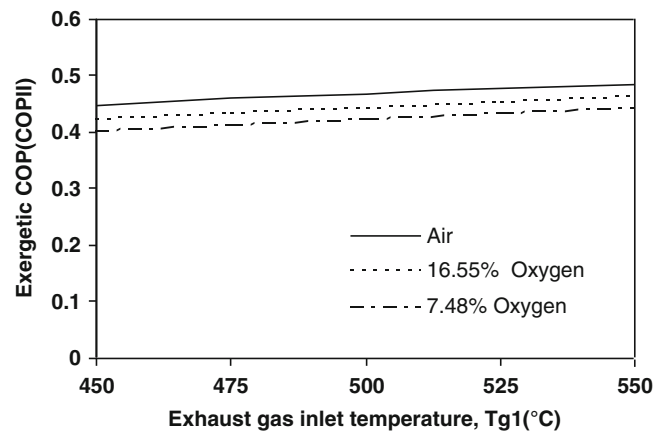
temperature for a fixed pinch point results in higher stack temperature which is utilized to produce additional cooling through vapor absorption system, resulting in increased exergetic COP with the increase in exhaust gas inlet temperature. It is known that exergy of waste heat which is heat input to the cycle is higher at higher exhaust temperature. This is why the increase in exergetic COP of the combined refrigeration cycles is not significant. The gas composition also influences exergetic COP of the combined refrigeration cycle, and hence exergetic COP is different for different gas compositions. This clearly demonstrates that treating gas as air and doing the exergy analysis based on air result is prediction of the combined refrigeration cycle performance on low or the higher side. Modeling the exhaust gas as an air can significantly overestimate the exergetic COP of combined refrigeration cycle.

The effect of variation of pinch point and gas composition on exergetic COP of the combined refrigeration cycle for a particular exhaust gas inlet temperature is shown in Fig. 17.5. It is found that as the pinch point increases, the exergetic COP decreases. It also decreases with the increase in oxygen content of the exhaust gas. This is because increase in pinch point causes reduced exergy of refrigeration at evaporator of vapor compression system due to low steam generation rate in HRSG. Larger flue gas temperature at the exit of HRSG due to increase in pinch point produce large exergy of refrigeration through vapor absorption part of the cycle. Since the exergy of cold production through vapor compression is greater than the same through vapor absorption, therefore the exergetic COP of the combined refrigeration cycle decreases with the increase in pinch point.

Fig. 17.5 Variation of second law efficiency with gas composition and pinch point temperature; Tg = 500 °C, $\dot{m}_g = 100\,\mathrm{kg\,s^{-1}}$
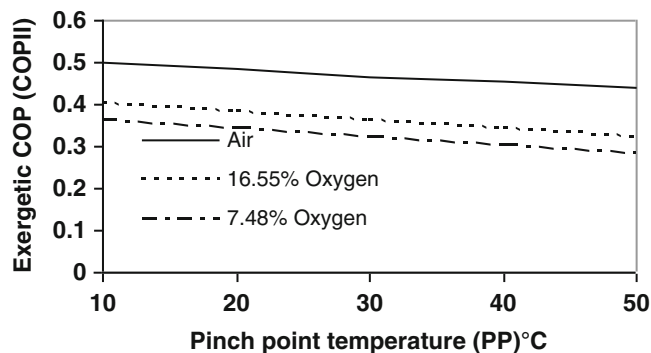
Table 17.3 Variation of exergy destruction rate (%) in each component of the combined compression-absorption refrigeration cycle with the change in exhaust gas inlet temperature at PP = 30 °C

T_{g1}	I_{HRSG}	I_{ST}	I_{C1}	I_{P1}	I_{GEN}	I_{C2}	I_{EV2}	I_{E1}	I_A	I_{P2}	I_{SHE}	I_{TV}	I_{RC}	I_{C3}	I_{EV1}	I_{E2}
450	20.88	8.89	8.53	0.08	10.97	1.94	0.12	1.50	2.92	0.01	0.58	0.01	7.28	10.13	8.72	17.44
475	22.56	9.48	9.04	0.09	7.51	1.43	0.09	1.10	2.15	0.01	0.43	0.01	7.72	10.64	9.25	18.48
500	23.91	9.89	9.44	0.10	4.90	1.01	0.06	0.77	1.51	0.01	0.30	0.01	8.05	11.13	9.64	19.27
525	24.75	10.10	9.64	0.18	2.88	0.64	0.04	0.50	0.97	0.01	0.19	0.01	9.18	11.37	9.85	19.69
550	25.25	10.20	9.74	0.27	1.35	0.34	0.02	0.32	0.54	0.01	0.10	0.01	10.2	11.81	9.95	19.89

Table 17.4 Variation of exergy destruction rate (%) in each component of the combined compression-absorption refrigeration cycle with the change in pinch point temperature (PP) at $T_{g1} = 500$ °C

PP (°C)	I_{HRSG}	I_{ST}	I_{C1}	I_{P1}	I_{GEN}	I_{C2}	I_{EV2}	I_{E1}	I_A	I_{P2}	I_{SHE}	I_{TV}	I_{RC}	I_{C3}	I_{EV1}	I_{E2}
10	22.56	10.91	10.41	0.11	1.54	0.38	0.02	0.30	0.58	0.01	0.11	0.01	8.89	12.26	10.65	21.26
20	23.35	10.40	9.93	0.10	3.10	0.69	0.04	0.54	1.04	0.01	0.20	0.01	8.47	11.72	10.14	20.26
30	23.91	9.89	9.44	0.09	4.90	1.01	0.06	0.77	1.52	0.01	0.30	0.01	8.05	11.13	9.64	19.27
40	24.25	9.37	8.95	0.08	6.94	1.32	0.08	1.01	1.98	0.01	0.39	0.01	7.63	10.54	9.14	18.30
50	24.35	8.87	8.46	0.07	9.18	1.62	0.10	1.25	2.44	0.01	0.48	0.01	7.22	9.91	8.65	17.38

Combined first and second law of thermodynamic analysis has been performed to evaluate the exergy destruction or irreversibility in each component of the waste heat operated combined refrigeration cycle. The irreversibility of each component is calculated based on the assumptions reported in Tables 17.1 and 17.2. It is found that largest irreversibility occurs in the HRSG. The major irreversibility is due to heat transfer over a finite temperature difference. Since the exergy destruction in the HRSG is largest in the combined refrigeration cycle, it influences the exergetic COP remarkably. Decreasing the exergy destruction in HRSG can increase the exergetic COP. Generator, condenser; evaporator, and absorber are exchanging heat over a finite temperature difference. The exergy destruction in the steam turbine, refrigerant compressor, and throttling valve is due to friction losses of the flow inside these components and due to non-adiabatic compression/expansion and the corresponding irreversibilities.

The parameters including exhaust gas inlet temperature (T_{g1}) and pinch point in HRSG could influence the irreversibility in each component as shown in Tables 17.3 and 17.4. The variation of exhaust gas inlet temperature influences exergy destruction in HRSG and generator significantly because the heat transfer temperature difference increases in these two heat exchangers with the increase in T_{g1}. Increase in exhaust gas inlet temperature leads to insignificant variation of exergy destruction in rest of the components of the combined refrigeration cycle. Increasing pinch point temperature difference results in sharp increase in exergy destruction in generator, absorber, condenser, and evaporator of vapor absorption system due to increase in the heat transfer temperature difference. Variation of pinch point has little effect on the exergy destruction in HRSG, steam turbine, pump, condenser, and refrigerant compressor of the cycle. There is no effect of pinch point variation on exergy destruction in throttling valve. Exergy destruction SHE increases significantly with the pinch point but decreases with the increase in exhaust gas inlet temperature.

The proposed combined cycle can be used as the refrigeration cycle to meet the cooling load demand during summer-ambient conditions using waste heat from industry, results in meeting the refrigeration and air-conditioning requirement of

the user, and hence reduces the additional load on power grid. Owing to lack of experimental data for this combined refrigeration cycle, the experimental study will be carried out to validate the feasibility of the waste heat operated combined compression–absorption refrigeration cycle in future.

Conclusions

Exergy analysis, which is a method that uses conservation of mass and conservation of energy principles together with the second law of thermodynamics, has been applied to the proposed waste heat operated combined compression–absorption refrigeration cycle. The performance was evaluated by both energetic and exergetic COPs, with the latter providing good guidance for system improvement. Parametric analysis is conducted to investigate the effects of key thermodynamic parameters on the performance and irreversibility in each component.

From the discussions above, it can be concluded that variation of exhaust gas inlet temperature influences the exergy destruction in HRSG and generator while increase in pinch point results in sharp increase of exergy destruction in the generator, absorber, condenser, and evaporator of the absorption system. Exergy destruction in SHE increases significantly with the increase in pinch point but decreases with the increase in exhaust gas temperature.

Analysis of the results further shows that exergetic COP significantly varies with the oxygen content in the exhaust gas while energetic COP shows small variation with oxygen content. Modeling the exhaust gas as an air underestimates the energetic COP and overestimates the exergetic COP of waste heat operated combined refrigeration cycle.

Nomenclature

c_p	Specific heat (kJ kg^{-1} K^{-1})	PP	Pinch point (K)
$\dot{E}$	Exergy transfer rate (kW)	$\dot{Q}$	Rate of heat transfer (kW)
h	Specific enthalpy (kJ kg^{-1})	R	Universal gas constant (kJ kmol^{-1} K^{-1})
$HRSG$	Heat recovery steam generator	s	Specific entropy (kJ kg^{-1} K^{-1})
$\dot{m}$	Mass flow rate (kg s^{-1})	ST	Steam turbine
M	Molar mass (kg kmol^{-1})	T	Temperature (K)
P	Pressure (bar)	$\dot{W}$	Rate of work output (kW)

Symbols

η_I	Energy efficiency (or first law efficiency)	η_p	Pump isentropic efficiency
η_{ex}	The second law efficiency or exergetic efficiency	η_t	Turbine isentropic efficiency

Subscript

0	Environmental	r	Refrigerant
f	Solution circulation ratio	s	Steam
g	Exhaust gas	t	Turbine
GEN	Generator	w	Water
p	Pump		

References

1. Nag PK, De S (1997) Design and operation of a heat recovery steam generation with minimum irreversibility. Appl Therm Eng 17:385–391
2. Reddy BV, Ramkiran G, Kumar KA, Nag PK (2002) Exergy analysis of a waste heat recovery steam generator. Int J Heat Mass Transf 45:1807–1814
3. Butcher CJ, Reddy BV (2007) Exergy analysis of a waste heat recovery based power generation system. Int J Heat Mass Transf 50:2355–2363
4. Dincer I, Rosen MA (2007) Exergy, 1st edn. Elsevier, New York
5. Liu M, Zhang N (2007) Proposal and analysis of novel ammonia-water cycle for power and refrigeration and cogeneration. Energy 32:961–970
6. Na Z, Lior N (2007) Development of novel combined absorption cycle for power generation and refrigeration. Trans ASME J Energy Resour Technol 129:254–265

7. Khaliq A, Kumar R, Dincer I (2009) Exergy analysis of an industrial waste heat recovery based cogeneration cycle for combined power generation and refrigeration system. Trans ASME J Energy Resour Technol 131:1–9

8. Kowlaski GJ, Zenouzi M (2006) Selection of distributed power-generating systems based on electric, heating and cooling loads. Trans ASME J Energy Resour Technol 128:168–178

9. Sun ZG (2008) Experimental investigation of integrated refrigeration system (IRS) with gas engine, compression chiller and absorption chiller. Energy 33:431–436

10. Zhao Y, Shigang Z, Haibe Z (2003) Optimization study of combined refrigeration cycles driven by an engine. Appl Energy 76:379–389

11. Moran MJ, Shapiro HN (2008) Fundamentals of engineering thermodynamics, 6th edn. Wiley, USA, 3rd Chapter

12. Khaliq A, Choudhary K (2007) Combined first and second law analysis of gas turbine cogeneration system with inlet air cooling and evaporative after cooling of the compressor discharge. ASME Trans J Eng Gas Turbines Power 129:1005–1012

13. Chua HT, Toh HK, Malek A, Ng KC, Srinivasan K (2000) Improved thermodynamic property fields of LiBr–H$_2$O solutions. Int J Refrigeration 23:412–429

14. Khaliq A, Kumar R (2008) Exergy analysis of double effect vapor absorption refrigeration system. Int J Energy Res 32:161–174

Thermoeconomic Optimization of Scroll-Based Organic Rankine Cycles with Various Working Fluids

18

Emre Oralli and Ibrahim Dincer

Abstract

In this study, thermoeconomic optimization method is applied to an organic Rankine cycle system to evaluate the cost of the system and net generated revenue as a function of exergy efficiency to be able to generate most economical electricity, depending on market conditions and fuel prices. Thermoeconomic optimization can serve as one of the most important stages in the design procedure which, for defined boundary conditions, makes it possible to find the optimal values of independent variables. The values that minimize or maximize the chosen optimization criteria are considered to be optimal in this case. It may be the annual net profit, time of return of investment, or any other economic profitability criterion. Here, the cost per unit of net electric power generated by the cycle is chosen as the primary measure of the performance of the system. It is considered to be the most universal optimization criterion since the other two mentioned are dependent on price at which electricity can be sold. This price may vary depending on the country and the type of application. It is found that best possible solutions can be obtained for the exergy efficiency of approximately 55 % in terms of cost of the system and net revenue.

Introduction

Generation of electricity from low temperature heat sources has became more popular in the last decade depending on its potential use for different types of applications such as solar thermal, waste heat and small-scale cogeneration for residential purposes. Low capacity heat engines require appropriate selection of the thermodynamic cycle and of the prime mover.

The Rankine cycle has a relatively higher efficiency by using low temperature heat sources compared to other cycles [1]. Solar energy and combustion heat can be used as a low temperature heat source for the cycle. In traditional power plants, Rankine cycle is used to produce useful work from expander mostly using water as a working fluid. The working fluid is pumped to a boiler where it is evaporated, then passes through an expander generating shaft work, and then finally condensed to be pumped again. Unlike conventional working fluids such as water, organic fluids that have lower boiling temperatures are more appropriate for low temperature Rankine cycle in terms of efficiency and environmental conditions. Water has a high vaporization because of its higher specific volume, which imposes larger installations and therefore higher cost.

E. Oralli • I. Dincer (✉)

Faculty of Engineering and Applied Science, University of Ontario Institute of Technology (UOIT), 2000 Simcoe Street North, Oshawa, ON, Canada L1H 74K

e-mail: Emre.Oralli@uoit.ca; Ibrahim.Dincer@uoit.ca

There are several kinds of prime movers namely turbomachines and positive displacement machines. However, when it is about low capacity, positive displacement machines (scroll, screw, rotary vane expanders) become more attractive than turbomachines for power cycles [2].

In this study, low temperature heat generation process is investigated for certain thermodynamic cycle and prime mover. The goal is to achieve waste heat recovery for different purposes such as residential domestic heat supply when there is an electrical breakdown, which will decrease the fragility of the centralized large-scale power generation systems. A crucial part of the system is the design of the scroll expander especially regarding the geometric and thermodynamics calculations in order to increase the efficiency to make it an alternative to conventional turbomachines.

The Rankine cycle takes advantage of the small amount of work required to pump a liquid and the amount of energy that can be extracted from latent heat. An organic Rankine cycle (ORC) differs from the basic Rankine cycle in that the working fluid is organic. Hajabdollahi et al. [3] modeled 31 different working fluids in different ORC configurations. Types of organic working fluids modeled included alkanes, fluorinated alkanes, ethers, and fluorinated ethers. These fluids can behave differently when used in an ORC and it is important to discuss the different configurations and working fluid characteristics together. Organic working fluids have performance advantages over water-steam at low power levels but these advantages disappear at 300 kW or more because of the poor heat transfer properties of organic fluids.

The irreversibilities such as friction and leakage losses in the cycle cause reduction of cycle efficiency and of net work output. Friction and leakage losses from expander contribute the highest portion of the irreversibilities with pressure drops and inefficiencies from the heat exchanger. The improvements regarding the geometry of the scroll machine will directly affect the cycle efficiency not only because of reducing the leakages but also to obtain appropriate built-in ratio for the compression/expansion process.

An ORC has inherent irreversibilities as many processes. The losses may come in the form of friction-heat loses in the expander and pump. This is accounted in the isentropic efficiencies of each device. Valves, pipes, and pressure drops are other sources of energy and exergy losses. Hung [4] stated that the largest source of irreversibility in the system is caused by the evaporator. The mismatch between the working fluid and the heat source causes this type of loss. Larjola [5] showed that the organic working fluids due to their low latent heat match the source temperature profile better than water-steam.

There are some practical solutions to reduce losses for ORC. The liquid entering the pump should be subcooled to prevent cavitations. The fluid should be superheated when using turbines with regular working fluids to prevent droplet formation during expansion. Mago et al. [6] stated that the quality at the turbine exit can be kept at 90 %. Both cavitation and high speed droplets will corrode the pump and expander.

There are a limited number of ways to improve the thermal efficiency of the cycle after the cycle configuration and fluid have been specified. Increasing the average high side temperature or decreasing the average low side temperature is one of the approaches that can be used. The high side temperature is fixed in low temperature heat recovery and decreasing the condenser temperature below atmospheric conditions is not practical. Other approaches include increasing the isentropic efficiencies of the pump and expander. The pump work is significantly less than the expander work in a Rankine cycle. Therefore improvement of the efficiency of the expander will provide the greatest degree of cycle improvement.

Badr et al. [7] modeled an ORC and performed a sensitivity study to show which of these parameters had the greatest effect on thermal efficiency. They varied the isentropic expander efficiency, evaporator temperature, and condenser temperature. They modeled both a basic and regenerative ORC with R113 as the working fluid.

In this study, the feasibility of converting a scroll compressor into an expander as to be used in heat recovery Rankine cycle of low capacity is modeled. The specific objectives of this study are given as follows:

- To characterize the scroll machine in expander mode and searching the relation between the total cost of the system and the ORC energy efficiency.
- To evaluate the cost parameters of the scroll expander powered ORC by optimization process and investigate the effect of fuel cost on total system cost for various exergy efficiencies.
- To select an appropriate organic working fluid such as R404a, Toluene, R123, R141b, R134a, and NH_3 in terms of cost which will ensure suitable temperature and pressure range to make the cycle realizable when converting scroll compressor to an expander.

System Description

Here, an exergy analysis of the ORC is conducted. The performance of an ORC will be analyzed for different working fluids under diverse working conditions using the second law of thermodynamics. There will be assumptions regarding the system as follows: steady-state conditions, no pressure drop in the evaporator, condenser and pipes, and isentropic efficiencies for the turbine and pump. The heat engine to produce electrical power with ORC is shown in Fig. 18.1a. There are four different
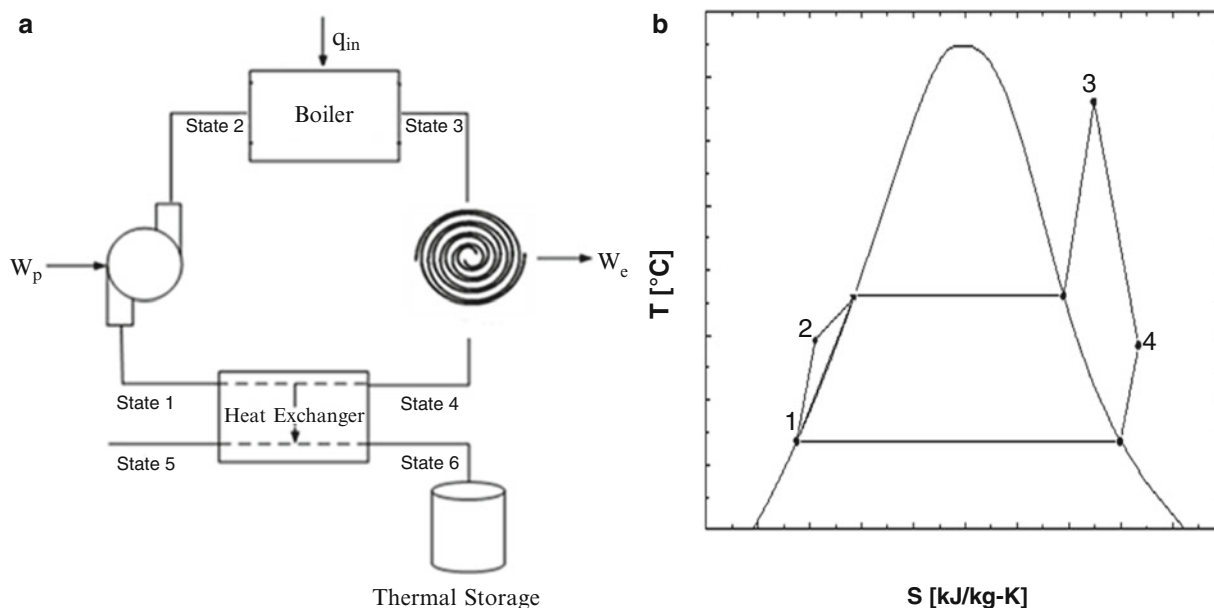
Fig. 18.1 (**a**) Rankine cycle configuration and (**b**) *T–s* diagram of a general organic Rankine cycle

processes in ORC as can be observed from Fig. 18.1b which shows a *T–s* diagram of the typical ORC: process 1–2 (constant-pressure transfer of heat), process 2–3 (expansion process), process 3–4 (constant-pressure heat transfer), and process 4–1 (pumping process).

Analysis

The capital costing equations generated in the model [8] have been used to yield approximate capital and maintenance expenditures and to reflect the consequences of changing the system's variables on these costs. The form of these equations expresses equipment costs in terms of stream and performance variables. In all cases a Capital Recovery Factor (CRF) is used to account for the cost of capital ($i = 15 \%$) and estimated useful life ($n = 40$ years). The approach taken to develop these costing equations was to single out the most important parameters that influence cost, and use them to yield a base cost, designating them with a prime. This base cost is then adjusted by multiplication factors so as to incorporate the influence of other factors. The form of these equations has been suggested in the literature [9] and by experienced engineers, then curve fit to available data. The costing equations for this system are listed in Table 18.1 [2].

Fixed Charges

The costing equations previously discussed determine the cost associated with each component of the system. The total system cost is composed of the sum of the component costs plus any other charges attributable to the system.

These other charges, called fixed charges, include such costs as the piping between components, foundation charges, building charges, operating personnel charges, etc. Fixed charges are estimated at 1.5 times the sum of the component costs. These costs are considered constant for a specified heat and work output requirement. Because the optimization scheme is at fixed product, these costs do not need to be incorporated into this part of the optimization. However, these charges must be considered in order to select the optimum exergy efficiency from the set of optimizations (each at constant product).

Comparison with Alternative System and Selection of Overall Optimum Cost

The alternative to the system is typically taken as a low pressure boiler and purchasing electricity from the utility. It is when the economy of the optimally designed system is compared to the alternative, that a system's true potential can be shown. The amortized capital cost attributable to the low pressure boiler is estimated using the relation

Table 18.1 Costing equations for the Rankine cycle

Component	Function
Boiler	CB = f(STM,P3,T3,AN,AR)
	CB = X11 × FAP × FAM × FAT × FAN × FAR
	X11 = CRF × C11
	FAP = $e^{(B11 \times P3)}$
	FAM = $e^{(B12 \times \log STM)}$
	FAT = 1.0 + C12 × $e^{[(T3-T3S)/B13]}$
	FAN = 1.0 + [(1.0 − ANS)/(1.0 − AN)]^{B14}
	FAR = 1.0 + [(1.0 − ARS)/(1.0 − AR)]^{B15}
Expander	CE = f(STM,P3,P4,T3,T4,BN)
	CE = X21 × FBW × FBT × FBN
	T3R = T3 + 460
	T4R = T4R + 460
	X21 = CRF × C21
	FB1 = B22 × BN × STM
	F2T = CPS × (T3R − T4R) − T4R × log(T3R/T4R)
	F2P = R × T4R × log(P3/P4)
	FBW = $e^{\{B21 \times \log[FB1 \times (F2T \times F2P)]\}}$
	FBT = 1.0 + (C22 × $e^{[(T3-T3S)/B23]}$)
	FBN = 1.0 + [(1.0 − BNS)/(1.0 − BN)]^{B24}
Condenser	CC = f(CA,P1,P4,PB,PC,T4,TB)
	CC = X31 × FCA1 × FCR × FCPW × FCP × FCB
	for 100 < CA < 3,000 ft^2
	CC = X31 × FCA2 × FCR × FCPW × FCP × FCB
	for CA > 3,000
	X31 = CRF
	FCA1 = CA × C31 × $e^{(B31 \times \log CA)}$
	FCA2 = CA × C36
	FCR = [(P1 × (1/CR) − 1.0)/C35]^{B32}
	FCPW = [(PC − PB)/C35]^{B33}
	FCP = C32 + C33 × P4 + C34 × (P4^2)
	FCB = exp(B34/(T4 − TB − 5))
Pump	CP = f(STM,P1,P2,DN)
	CP = X42 × FD1 × FDN
	X41 = CRF × C41
	Y2 = B42 × STM × V34 × (P2 − P1)/DN
	FD1 = exp$^{[B41 \times \log Y2]}$
	FDN = 1.0 + [(1.0 − DNS)/(1.0 − DN)]^{B43}
Fuel	CF = CF × HF

$$Z_f = CRF \times 153.964 \times 10^{0.89476 \, \log HP} \qquad (18.1)$$

where the boiler horsepower is given by

$$HP = 33500 \times Q \qquad (18.2)$$

The fixed charges for the low pressure furnace, FC_f, are estimated in the same manner as the system, at one and a half times the equipment cost. The fuel cost of producing hot fluid, $CFUEL_f$, is estimated using the unit cost of fuel, CF, the heat input to the fluid, Q, and the estimated boiler efficiency:

$$CFUEL_f = CF \times Q/\eta_b \qquad (18.3)$$

where the boiler efficiency, η_b is taken to be 0.80. The total cost of producing the hot fluid by the low pressure furnace, $CT0T_f$, is estimated by

$$CTOT_f = CFUEL_f + FC_f + Z_f \qquad (18.4)$$

The cost per unit of electricity produced, CE, can be calculated as the difference of the total cost of the system and the cost allocated to the hot fluid, all divided by the amount of electricity produced:

$$CE = \left(ZTOT + FC - ZTOT_f\right)/E \tag{18.5}$$

In order to select the electricity production that maximizes the profit returned from its sale, the market price of electricity, MPE, must be known. The net revenue generated by the sale of the generated electricity, NRG, is then expressed as

$$NRG = (MPE - CF) \times E \tag{18.6}$$

For a particular hot water requirement the optimal work output will correspond to the point where net revenue generated is a maximum.

Multi-objective Optimization

A multi-objective problem consists of optimizing (i.e., minimizing or maximizing) several objectives simultaneously, with a number of inequality or equality constraints. Hajabdollahi et al. [3] mentioned that the problem can be formally written as follows:

Find $x = x_i$,

$$\forall i = 1, 2, \ldots, N_{param} \text{ such as } f_i(x) \text{ is a minimum (respectively maximum)} \tag{18.7}$$

$$\forall_i = 1, 2, \ldots, N_{obj} \text{ subject to :} \tag{18.8}$$

$$g_j(x) = 0, \forall j = 1, 2, \ldots, M, \tag{18.9}$$

$$h_k(x) < 0, \forall k = 1, 2, \ldots, K, \tag{18.10}$$

where x is a vector containing the N_{param} design parameters, $(f_i)_{i=1,\ldots,Nobj}$ the objective functions, and N_{obj} the number of objectives. The objective function $(f_i)_{i=1,\ldots,Nobj}$ returns a vector containing the set of N_{obj} values associated with the elementary objectives to be optimized simultaneously.

Schuster et al. [10] gave the definition that an individual $X^{(a)}$ is said to constrain-dominate an individual $X^{(b)}$, if any of the following conditions are true,
1. $X^{(a)}$ and $X^{(b)}$ are feasible with
   (a) $X^{(a)}$ is no worse than $X^{(b)}$ in all objective and
   (b) $X^{(a)}$ is strictly better than $X^{(b)}$ in at least one objective
2. $X^{(a)}$ is feasible while individual $X^{(b)}$ is not.
3. $X^{(a)}$ and $X^{(b)}$ are both infeasible, but $X^{(b)}$ has a smaller constraint violation.

Objective Functions

The aim of the optimization is to minimize the total cost of owning and operating the system (at fixed product output) while maximizing the exergy efficiency of the system. Two objective functions including exergy efficiency (to be maximized), the total cost rate of product (to be minimized) are considered for multi-objective optimization. The objective function for this analysis is considered as:

Exergy efficiency of the expander:

$$\eta_{ex} = \frac{(h_3 - h_4) \times \left\{ \frac{n_e}{n_e - 1} \times \left(\frac{P_4}{\rho_4}\right) \times \left[\left(\frac{2\varphi_e - \varphi_i + \varphi_0 - 3\pi}{5\pi - \varphi_i + \varphi_0}\right)^{\frac{n_e}{n_e - 1}} - 1 \right] \right\}}{(h_3 - h_2) \times \left(1 - \frac{T_0}{T_3}\right)} \tag{18.11}$$

Table 18.2 Fixed parameters and decision variables for a cogeneration system

Code	Fixed parameters (y_f)
TB	Condenser hot water outlet temperature
TC	Condenser hot water inlet temperature
PB	Condenser hot water outlet pressure
PC	Condenser hot water inlet pressure
HWM	Required hot water mass flow rate
WA	Net turbine shaft work output
CR	Condenser shell-side pressure loss coefficient
X2	Expander exit quality
U	Condenser overall heat transfer coefficient
CPW	Specific heat of water at constant pressure
CN	Condenser first law efficiency
	Decision variables (y_k)
AN	Boiler efficiency
AR	Boiler pressure drop coefficient
P3	Expander inlet pressure
P4	Condenser inlet pressure
DN	Pump isentropic efficiency

where

- $h_1 = f(T_1, P_1)$
- $h_2 = f(T_2, P_2)$
- $h_3 = f(T_3, P_3)$
- $h_4 = f(T_4, P_4)$

  Total cost of the Rankine cycle system

$$C_{total} = C_{boiler} + C_{expander} + C_{condenser} + C_{pump} + C_{fluid} \tag{18.12}$$

where

$$C_{boiler} = f(STM, P3, T3, AN, AR)$$

$$C_{expander} = f(STM, P3, P4, T3, T4, BN)$$

$$C_{condenser} = f(CA, P1, P4, PB, PC, T4, TB)$$

$$C_{pump} = f(STM, P1, P2, DN)$$

$$C_{fluid} = f(HF)$$

Constraint Equations

The selection of fixed parameters and decision variables is given in Table 18.2. The equations of constraint link the cost estimate through the system's thermodynamic performance to fuel costs. The thermodynamic analysis must relate the variables used to describe the system's performance to those used in the cost estimate. In this problem, costing equations are used which are generally in terms of stream and performance variables. Thus the thermodynamic analysis need only to be in terms of these variables. Sixteen equations of constraint have been developed from a thermodynamic analysis of the cycle, and are given in Table 18.3. Some constraints use stream variables to describe the thermodynamic state of the working fluid.

The problem has now been reduced to five independent variables. The form of the constraint equations has been arranged such that each state variable can be obtained explicitly and the order selected such that the resulting matrix is diagonalized. In order to obtain equations for the solution of the shadow and marginal prices, various derivatives of the constraint equation

Table 18.3 Equations of constraint for the cogeneration system

State variable (x_i)	Thermodynamic constraint defining relation (Φ_i)
H4	f(P4,X4)
T4	f(P4,quality)
P1	P4 × CR
H1	f(P1,SAT,LIQ)
P2	P3/AR
H2	H1 + CF3 × V34 × (P2 − P1)/DN
STM	HWM × CPW × (TB − TC)/[CN × (H4 − H1)]
WP	STM × (H2 − H1)
H3	(WA + WP)/(STM + H4)
T3	f(H3,T3)
H4S	f(P3,P4,T3)
BN	(WA + WP)/[STM × (H3 − H4S)]
HF	STM × (H3 − H2)/AN
T1	f(P1,SAT,LIQ)
TM	[(T1 − TC) − (T4 − TB)]/log[(T1 − TC)/(T4 − TB)]
CA	HWM × CPW × (TB − TC)/(TM × U)

matrix should be evaluated. However, because not all the constraints are in algebraic form (those constraints that are functions of steam table properties) numerical derivatives must be evaluated. One other note, there are two condenser costing equations. This means that two separate derivatives must be taken and the derivative corresponding to whichever costing equation is valid for that value of condenser area, is the one that should be used.

The solution procedure requires the designer to select a feasible set of decision variables (y_k) for the first iteration. Once this initial set of five decision variables has been chosen, entire design (for that iteration) is fixed and the set of state variables (x_i) and cost estimates are determined.

Results and Discussion

The procedure generated by [8] used to optimize the Rankine cycle operating in one of the two modes. When a particular set of decision variables is far from the optimal set, there will be a large difference in the total operating cost between two successive iterations. This difference can be used as a measure of the distance from the optimum. When the difference is large, the entire set of decision variables is changed based on the input set of marginal prices. When the difference is smaller than some predetermined value, only one decision variable is changed and a new set of state variables, shadow prices, and marginal prices are evaluated. Using this new set of marginal prices, another decision variable is changed and a new set of marginal prices is computed. This is automatically repeated until all the decision variables have been changed. Each time a complete set of new decision variables is generated, the program displays the parameters necessary to evaluate the system design. This procedure can be used to generate a variety of data. It is possible to parametrically vary any or all of the fixed decision variables. The parameters that were varied (Table 18.4) included fuel cost, exergy efficiency, and boiler temperature. The stratagem was to monitor the change in the optimal design by changing fuel cost and work output for several hot water requirements.

The trends in stream and performance variables associated with increasing fuel costs are that of increasing the system's performance. As the cost of fuel increases, the boiler efficiency, pump isentropic efficiency, as well as the expander isentropic efficiency also increases. The condenser's thermodynamic performance increases because the steam's condensing temperature (or pressure as can be seen in Fig. 18.2) decreases, approaching to the required hot water temperature. This general increase in performance allows the steam mass flow rate, boiler pressure, and expander work to decrease. As an example of this increase in the system's performance, Figs. 18.3 and 18.4 clearly show the increase in boiler efficiency and expander isentropic efficiency associated with the increasing fuel costs for different values of the work/heat ratio. Figure 18.5 shows the cost per unit electricity produced by the Rankine cycle as a function of exergy efficiency for various fluids.

Figures 18.6, 18.7, and 18.8 illustrate net revenue curves as a function of the exergy efficiency for a required hot fluid temperature of 250 °F and for various market conditions. Examination of these curves shows an increase in the optimal amount of electricity as the MPE increases. Also, as fuel costs rise, the optimal amount of electricity production decreases.

Table 18.4 Parametrically varied fixed system parameters of the Rankine cycle

Parameter varied	Range varied	Increment
Specific fuel cost ($/MJ)	2–4	1
Exergy efficiency (%)	0.4–0.6	0.1
Boiler temperature (K)	380–421	14

Fig. 18.2 Optimum condenser inlet pressure as a function of exergy efficiency for various fuel prices
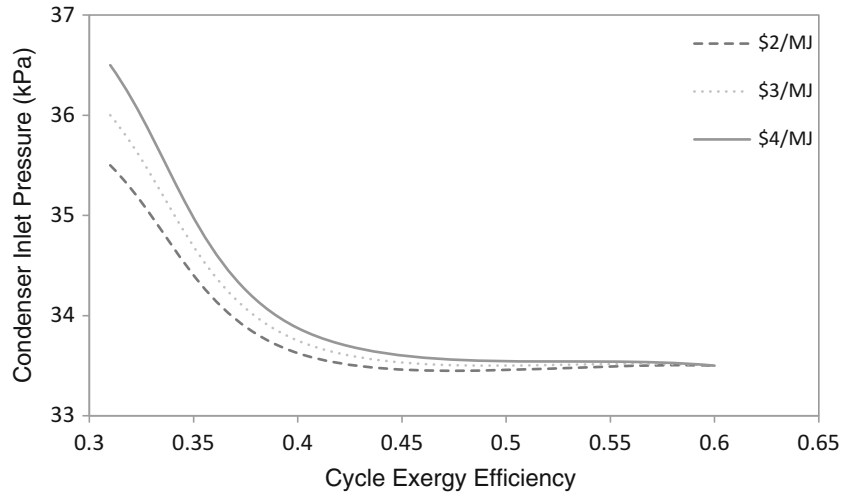
Fig. 18.3 Optimum boiler efficiency as a function of exergy efficiency for various fuel prices
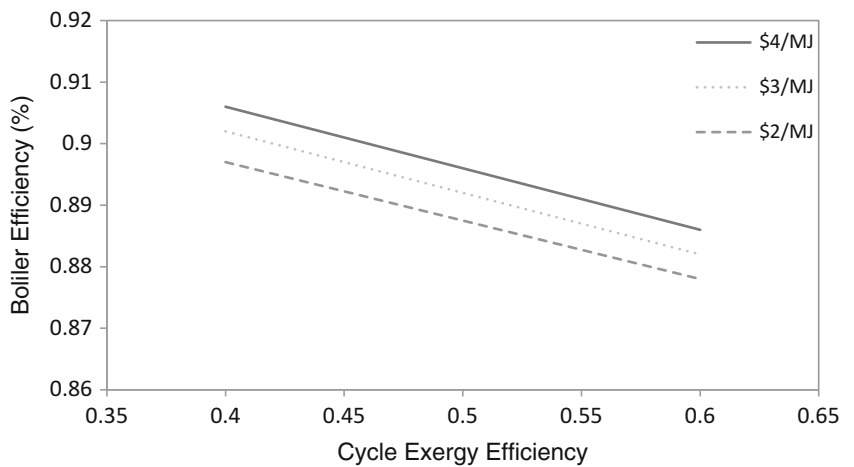
Fig. 18.4 Optimum expander efficiency as a function of exergy efficiency for various fuel prices and boiler temperatures
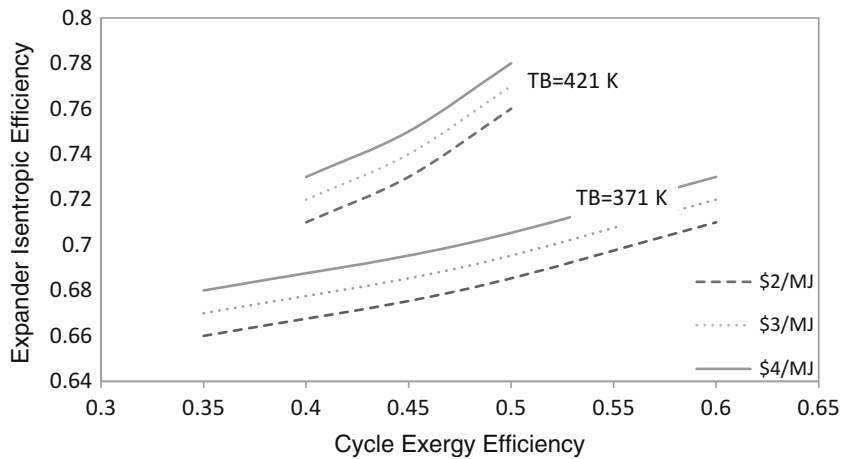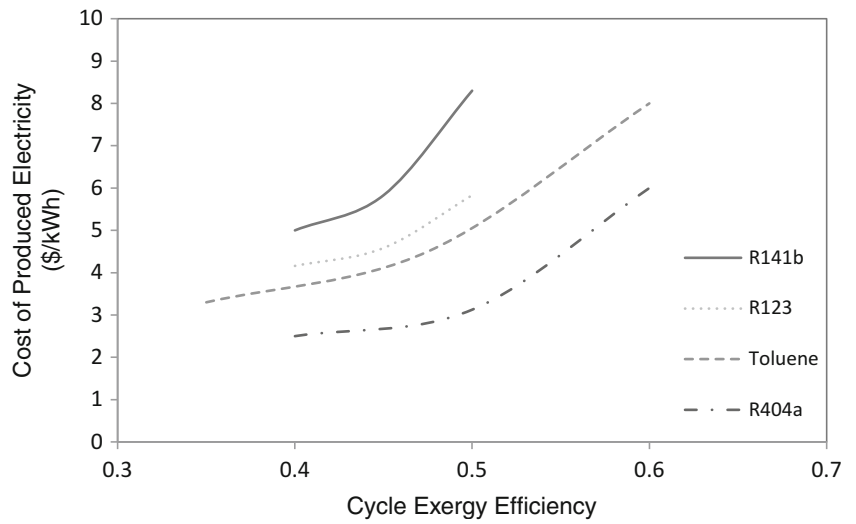
Fig. 18.8 Net revenue generated
as a function of exergy efficiency
for various market prices
of electricity and a fuel cost
of $4/MJ
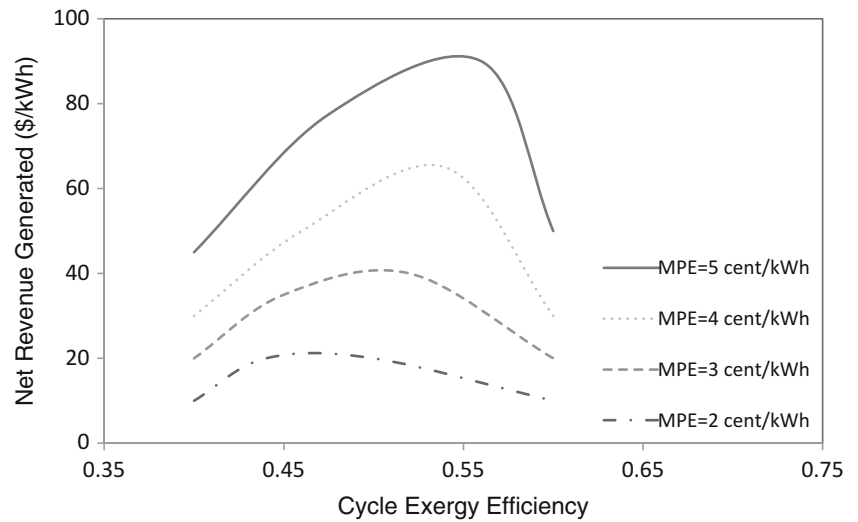
Conclusions

In this paper, thermoeconomic optimization of an ORC system has been performed to evaluate the cost of the system and net generated revenue as a function of exergy efficiency to be able to generate most economical electricity, depending on market conditions and fuel prices. The findings show that it is possible to improve the efficiency of the cycle by adjusting the scroll geometry for all fluids. R404a clearly gives the best results for a modified geometry, and the energy efficiency increases to 25 % from 19 % while the exergy efficiency increases to 61 % from 50 %, respectively. It can be said that the rolling angle should be reduced to have an optimum built-in volume ratio for the cycle in terms of appropriate temperature and pressure range that will ensure higher energy and exergy efficiency. It is found that best possible solutions can be obtained for the exergy efficiency of approximately 55 % in terms of cost of the system and net revenue.

Nomenclature

Ex	Exergy, J	s	Specific entropy, J/kg K
$\dot{Ex}$	Exergy rate, J/s	T	Temperature, °C
h	Specific enthalpy, J/kg	V_{ee}	Expander expansion chamber volume, m^3
P	Pressure, Pa	V_{ei}	Expander intake chamber volume, m^3
Q	Heat, J	W	Work, J
$\dot{Q}$	Heat rate, J/s	$\dot{W}$	Work rate, J/s

Greek Letters

η	Efficiency	$\varphi_{i,s}$	Starting angle of the inner involute, rad
θ	Orbiting angle, rad	φ_{i0}	Initial angle of the inner involute, rad
ρ	Density, kg/m^3	$\varphi_{o,s}$	Starting angle of the outer involute, rad
φ	Involute angle, rad	φ_{o0}	Initial angle of the outer involute, rad
φ_e	Rolling angle (involute ending angle), rad		

Subscripts

CB	Cost of boiler	ex	Exergy
CC	Cost of condenser	exp	Expander
CE	Cost per unit of electricity produced	FC_f	Fixed charges for the low pressure furnace
CF	Cost of fuel	fix	Fixed
$CFUEL_f$	Fuel cost of producing hot fluid	MPE	Market price of electricity
cp	Compressor	N_{obj}	Number of objectives
$CT0T_f$	Cost of producing the hot fluid by the low pressure furnace	N_{param}	Number of parameters
		NRG	Net revenue generated by the sale of the generated electricity
CV	Control volume		

References

1. Harada J (2010) Development of a small scale scroll expander. Master thesis, Oregon State University
2. Quoilin S (2007) Experimental study and modeling of a low temperature Rankine cycle for small scale cogeneration. Master thesis, University of Liege, Belgium
3. Hajabdollahi H, Ahmadi P, Dincer I (2011) An exergy-based multi-objective optimization of a heat recovery steam generator (HRSG) in a combined cycle power plant (CCPP) using evolutionary algorithm. Int J Green Energy 8(1):44–64
4. Hung T (2001) Waste heat recovery of organic Rankine cycle using dry fluids. Energy Convers Manag 42(5):539–553
5. Larjola J (1995) Electricity from industrial waste heat using high-speed organic Rankine cycle (ORC). Int J Prod Econ 41(1):227–235
6. Mago PJ, Chamra LM, Somayaji C (2007) Performance analysis of different working fluids for use in organic Rankine cycles. Proc Inst Mech Eng A J Power Energy 221(3):255–263
7. Badr O, Ocallaghan P, Probert S (1984) Performances of Rankine-cycle engines as functions of their expanders' efficiencies. Appl Energy 18(1):15–27
8. Guangbin L, Yuanyang Z, Liansheng L, Pengcheng S (2010) Simulation and experiment research on wide ranging working process of scroll expander driven by compressed air. Appl Therm Eng 30:2073–2079
9. Ingley HA, Reed R, Goswami DY (2005) Optimization of a scroll expander applied to an ammonia/water combined cycle system for hydrogen production. In: Proceedings of the solar world congress, Orlando, Florida, paper 1545, 2–12 Aug
10. Schuster A, Karellas S, Aumann R (2010) Efficiency optimization potential in supercritical organic Rankine cycles. Energy 35(2):1033–1039

Efficiency Assessment of Crude Oil Distillation Systems

19

Sayem Zafar and Ibrahim Dincer

Abstract

The assessment of energy and exergy efficiencies is conducted on a crude oil distillation system for three different cases. Each case defines efficiency in a unique way with different inputs and outputs. First case treats the heat transfer rate as useful output and the heat gained from the heaters as input. For the second case, we consider the heat provided by the heaters as input and the heat transfer rate in the distillation system as output. The third case treats the heat provided by the heaters as input and heat transfer rate along with the heat of exhaust gases as useful output. The system efficiencies are studied parametrically by changing the amount of heat transfer rate and the ambient temperatures. The results show that case 1 has the baseline energy and exergy efficiencies at 53 % and 25.3 % respectively. Case 2 has the efficiencies at 40 % for energy and 23.3 % for exergy efficiency. Case 3 efficiencies are at 72 % for energy while exergy efficiency is at 65 %. Case 1 has the highest efficiencies, followed by case 3 then the least efficient is case 2. Utilizing the unused energy, as a useful input to some other system, improves the overall efficiency of the plant and saves operating cost while making the system more environmentally friendly.

Introduction

Energy is defined as the maximum work producing ability by a system or a flow of matter as it comes to equilibrium. The exergy of an energy form or a substance is a measure of its usefulness or quality or potential to cause change [1]. Exergy analysis is an effective thermodynamic method for design and analysis of thermal systems while it is an efficient technique for revealing the improvement capacity of thermal systems [2]. With energy and exergy precisely known, it becomes easier to evaluate their efficiency for any given system.

In thermodynamics, efficiency is a concept utilized to specify the effectiveness of the energy conversion process. Efficiency is often misused and is a cause of confusion [3]. This confusion exists because efficiency is often used without being properly defined first [4]. Basically, efficiency can be described as the ratio of output against the input. This definition of efficiency holds true for all thermodynamic systems and is clearly understood. However the output and input parameters are specific to a system or a component which needs to be specified clearly for efficiency assessment.

Although, efficiencies change with the operating and environmental conditions, the overall efficiency can also be improved if the exhaust energy is used as an input to some other system. For large plants and systems, the recovered energy can add up to large values and can cause significant increase in the system's overall efficiency [5]. Even economically, it is feasible to recover a large proportion of the waste heat generated, rather than reject it to the atmosphere [6].

S. Zafar (✉) • I. Dincer
Faculty of Engineering and Applied Science, University of Ontario Institute of Technology,
2000 Simcoe Street North, Oshawa, ON, Canada L1H 7K4
e-mail: sayem.zafar@uoit.ca; ibrahim.dincer@uoit.ca

Improving the energy efficiency of crude oil distillation plant is of great interest since they consume almost 2 % of the total crude processed energy [7, 8]. Crude oil distillation system is a part of crude oil refining process where crude oil compounds convert to gases when heated at high temperature. These gases become cooler as they move along the vertical column. When gaseous compounds cool below their boiling point, they condense to be drawn off the distillation column at various heights [9]. The crude oil is processed in two towers for which the atmospheric tower separates the light hydrocarbons while the vacuum tower separates the heavier hydrocarbons. The products of the crude oil distillation plant can be either final products or feedstock to other plants for further processing [10].

Numerous researchers have studied the efficiencies of crude oil distillation systems. Al-Muslim et al. [2] have conducted an energy and exergy study to precisely evaluate the exergy losses in a one-stage and a two-stage crude oil distillation unit. The energy and exergy efficiencies are studied for the units composed of a heating furnace and atmospheric distillation column. The crude oil distillation system was further evaluated to see the effects of reference states on exergy and energy efficiencies [10].

The present paper conducts a combined energy and exergy study to propose three different efficiencies at different case scenarios and make evaluations and comparisons. Each case represents the possibility of using the input and output in different perspectives. Anything exiting or entering the distillation system cannot be treated as useful output or input, respectively, without proper assessment. Efficiency is seen through usefulness-perspective. Multiple exergy and energy definitions, for the overall distillation system, is described in the paper and evaluated for a range of surrounding conditions. Exergy destruction for each component in each case is also presented.

System Description

The crude oil distillation system, considered for a comprehensive efficiency assessment, is taken from Al-Muslim et al., as a part of the petroleum refining process [2, 10]. The system taken from this literature has two columns, namely, atmospheric distillation unit (ADU) and vacuum distillation unit (VDU). ADU separates the lighter hydrocarbons under atmospheric pressure. Before being fed to ADU, crude passes through heater 1 (stations 1 and 2) where its temperature increases. Superheated steam enters from the bottom of the column (station 18) to reduce the partial pressure in the column and thus enhancing vaporization and separation of the crude oil. The gaseous hydrocarbons get extracted at their corresponding trays while the heavier hydrocarbons get collected at the bottom of the column as residue. The atmospheric residue (station 10) passes through heater 2 before entering the VDU (station 11). Steam is also added in the VDU (station 20) for the same purpose as in ADU. Figure 19.1 shows the schematic of the studied system. Further details are available elsewhere [2, 10].

Analysis

A study is conducted to assess the efficiencies of overall crude oil distillation system by considering different scenarios as input and output. The first case represents the heated crude oil as input while the heat consumed in the distillation process, to convert the compounds to gases, as output. It is assumed that the unabsorbed heat from the heater is used as an input to some other system hence does not get wasted. The heat transfer rate, in the distillation system, is considered useful output whereas the heat from exhaust gases is considered useless. The energy efficiency for case 1 can be defined as follows:

$$\eta_{C1} = \frac{\dot{Q}_{cv}}{\dot{E}_2 + \dot{E}_{11} - \dot{E}_1 - \dot{E}_{10}} \tag{19.1}$$

where $\dot{E}$ is the energy rate which is the total enthalpy rate and the numbers in subscript correspond to the station numbers shown in Fig. 19.1 and it values tabulated in Table 19.1. The heat transfer rate, $\dot{Q}_{cv}$, represents the heat rate utilized in the distillation process to convert the compounds to gases.

The equation describing the exergy efficiency is given as follows:

$$\Psi_{C1} = \frac{\left(1 - \frac{T_0}{T}\right)\dot{Q}_{cv}}{\dot{E}x_2 + \dot{E}x_{11} - \dot{E}x_1 - \dot{E}x_{10}} \tag{19.2}$$
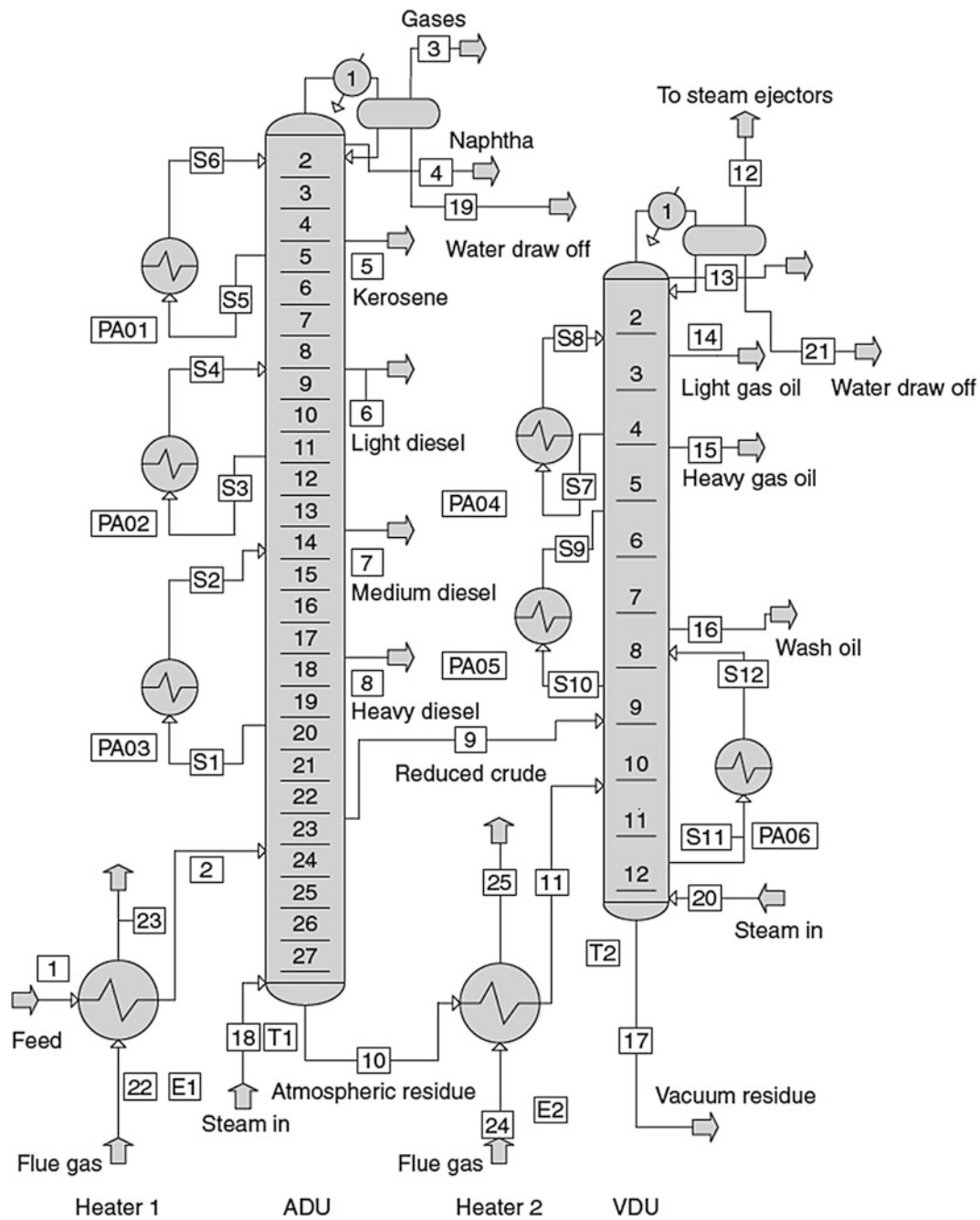
Fig. 19.1 A schematic diagram of the two-stage crude oil distillation system (crude heating furnace, E1, is heater 1 and E2 is heater 2. Atmospheric distillation unit (ADU) is shown as T1 and vapor distillation unit (VDU) is shown as T2. PA is pump-around circuits which are used to control the temperature profile) [10]

where the exergy rate is denoted by $\dot{E}x$ and the total exergy destruction, in the system, is denoted by $\dot{I}_{total}$. The surface mean temperature is defined as T while T_0 is the ambient temperature.

The second case treats heat provided by the heaters as input while the heat transfer rate in the distillation process as output. This case assumes the unabsorbed heater heat gets wasted hence not considered as a useful output. The energy efficiency of case 2 can be written as follows:

$$\eta_{C2} = \frac{\dot{Q}_{cv}}{\dot{E}_{H1} + \dot{E}_{H2}} \tag{19.3}$$

Table 19.1 Operating condition parameters at different stations [2, 10]

#	T (°C)	P (kPa)	m (kg/s)	s (kJ/kg K)	h (kJ/kg)
1	25	102	507.6221	4.440448	34.39055
2	352.3746	102	507.6221	6.615505	1,040.125
3	68.00522	206.6044	1.09E−12	4.216201	760.3895
4	68.00522	206.8148	0.566983	2.509089	164.5537
5	68.91907	208.4696	15.56693	3.039461	348.8646
6	68.86612	211.7791	32.14957	2.323762	182.8285
7	91.4	215.91	75.812	4.2661	186.98
8	157.1815	219.2254	53.9682	5.015905	323.7495
9	261.4419	223.3622	58.0393	5.878275	555.9205
10	342.2222	228.8781	260.1879	6.557474	750.3401
11	408.8889	228.8781	260.1879	6.858651	945.6614
12	203.2595	11.10056	10.21269	6.830466	1,125.868
13	203.2595	11.10056	0.834219	5.768256	398.4854
14	219.95	11.1	22.617	5.8602	438.4
15	286.3149	11.92794	39.7135	6.238811	602.1979
16	312.649	13.16899	46.74861	6.426736	666.1357
17	299.5011	15.23742	142.2034	6.386489	628.2944
18	353.3333	515.0106	5.415384	7.651651	3,172.316
19	68.00522	206.8148	0.517354	0.96201	284.4449
20	768	413.6856	2.141962	8.831165	4,075.276
21	0	0	0	0	0
22	1,100	102	600	7.986952	1,180.016
23	353.3333	102	600	7.100531	329.1276
24	1,100	102	60	7.986952	1,180.016
25	357	102	60	7.106715	333.0128

where the subscripts ADU stands for atmospheric distillation unit and VDU for vacuum distillation. The subscripts H1 and H2 represent the heater before ADU and heater before VDU, respectively. The exergy efficiency equation can be described as follows:

$$\Psi_{C2} = \frac{\left(1 - \frac{T_0}{T}\right)\dot{Q}_{cv}}{\dot{Ex}_{H1} + \dot{Ex}_{H2}} \tag{19.4}$$

The third case presents in which all the exhaust is considered as useful output while heater heat is assumed to be the input. This case treats the exhaust gases as well as the unused heat from the heaters as a useful input to some other system. The energy efficiency equation for case 3 is described as:

$$\eta_{C3} = \frac{\dot{Q}_{cv} + \dot{E}_{out}}{\dot{E}_{H1} + \dot{E}_{H2}} \tag{19.5}$$

where $\dot{E}_{out}$ represents the sum of energy from all the exiting gases, defined as follows:

$$\dot{E}_{out} = \dot{E}_3 + \dot{E}_4 + \dot{E}_5 + \dot{E}_6 + \dot{E}_7 + \dot{E}_8 + \dot{E}_{12} + \dot{E}_{13} + \dot{E}_{14} + \dot{E}_{15} + \dot{E}_{16} + \dot{E}_{17} \tag{19.6}$$

The exergy of exhaust gases, Ex_{out}, is the defined as the sum of exergy of all exhaust gases below:

$$\dot{Ex}_{out} = \dot{Ex}_3 + \dot{Ex}_4 + \dot{Ex}_5\ \dot{Ex}_6 + \dot{Ex}_7 + \dot{Ex}_8 + \dot{Ex}_{12} + \dot{Ex}_{13} + \dot{Ex}_{14} + \dot{Ex}_{15}\ \dot{Ex}_{16} + \dot{Ex}_{17} \tag{19.7}$$

Hence, the exergy efficiency equation becomes

$$\Psi_{C3} = \frac{\left[\left(1 - \frac{T_0}{T}\right)\dot{Q}_{cv}\right] + \dot{Ex}_{out}}{\dot{Ex}_{H1} + \dot{Ex}_{H2}} \tag{19.8}$$

Table 19.2 The baseline values used in the study [2, 10]

	Heater 1	ADU	Heater 2	VDU
$\sum \dot{H}_{in}$ (kW)	725,467	545,170	266,030	287,044
$\sum \dot{H}_{out}$ (kW)	725,467	270,692	266,030	166,148
$\dot{Q}_{cv}$ (kW)	0	274,478	0	120,896
$\sum \dot{Ex}_{in}$ (kW)	589,496	500,365	223,817	248,621
$\sum \dot{Ex}_{out}$ (kW)	484,221	216,749	213,858	124,560.5
$\dot{I}$ (kW)	105,275	366,121	9,960	167,033

The corresponding thermodynamic properties of each station in the distillation system are tabulated in Table 19.1. The ambient conditions for pressure and temperature are 102 kPa and 298 K respectively.

Table 19.2 shows the baseline values for enthalpy, $\dot{H}$, heat transfer rate in the distillation columns, $\dot{Q}_{cv}$, exergy, $\dot{Ex}$, and exergy destruction, $\dot{I}$. Heater 1 is the heater that provides the heat to the crude feed entering the ADU while heater 2 heats the crude entering the VDU. These values are used as baseline figures to conduct the parametric studies on the system.

Results and Discussion

The exergy and energy efficiency assessment is conducted on crude oil distillation system. The efficiency assessment is conducted on the overall system which consists of ADU and VDU together. The crude oil distillation system is assessed based on the model presented by Al-Muslim et al. [2, 10]. Throughout the process, the crude oil feed gets heated twice by two heaters. During the process, some heat is utilized to produce desired compounds and when the crude exits, it exits with high temperature and pressure. The study is conducted to assess the efficiencies by comparing different energy utilization scenarios.

Figure 19.2 shows the change in exergy and energy efficiency for case 1. This case treats the heat transfer rate in the distillation column as useful output and the heated incoming crude feed as input. Heated crude feed included the absorbed heat from the heaters. As the heat transfer rate, in the distillation column increases, the efficiency increases. Heat transfer rate can increase if distillation involves higher amount of compounds that require higher heat for distillation. For the baseline conditions, as shown in Table 19.2, the energy and exergy efficiency comes out to be 53 % and 25.3 % respectively. More heat transfer rate in the distillation plant means more heat is being used to separate compounds. The trend shows the linear increase in the efficiencies with energy efficiency increases faster than exergy efficiency. Exergy efficiency change is slower than energy efficiency since consumed exergetic heat rate is compared with the ambient temperature.

Exergy and energy efficiency for case 2 are shown in Fig. 19.3. In this case, the heat transfer rate in the distillation column is considered as useful output. The heat, provided by the two heaters, is treated as input. The input is higher in this case as compared to case 1 since in this case, the provided heat is considered as input whereas in the case 1, just the absorbed heat is input. As the system heat rate consumption increases, the efficiency increases. More heat transfer rate in the distillation plant means more heat is being used to separate compounds. For the baseline conditions, energy efficiency is 40 % while exergy efficiency is 23.3 %. Case 2 has lower efficiencies as compared to case 1 since case 2 assumes heaters' input unlike case 1 which assumes only the absorbed heat from heaters as input. The trend shows the linear increase in the efficiencies with energy efficiency increases faster than exergy efficiency.

Exergy and energy efficiencies for case 3 are shown in Fig. 19.4. In this case, the heat provided by the two heaters is treated as input. The heat transfer rate in the distillation column and heat from exhaust gases is considered as useful output. The graph in Fig. 19.4 shows that as the heat transfer rate increases, the efficiency increases. For the baseline conditions, energy efficiency is 72 % while exergy efficiency is 65 %. The trend shows the linear increase in the efficiencies with energy efficiency increase faster than exergy efficiency. Case 3 has highest efficiencies as compared to all the other cases. The efficiencies are higher because the useful output is not just the heat transfer rate but it also includes the exhaust gas heat.

Figure 19.5 shows the energy and exergy efficiency for all three cases when ambient temperature changes. The ambient temperature changes with respect to season, time of day, and location of the distillation plant. Ambient temperature does not have a direct effect on the energy efficiency hence the energy efficiencies remain constant at 53 %, 40 %, and 72 % for case 1, case 2, and case 3 respectively. Ambient temperature directly affects the exergy efficiency because exergetic heat is related to ambient temperature as exergy efficiency is defined. The baseline exergy efficiencies are 25.3 %, 23.3 %, and 65 %

Fig. 19.2 The changes of energy and exergy efficiencies with respect to consumed heat rate for case 1
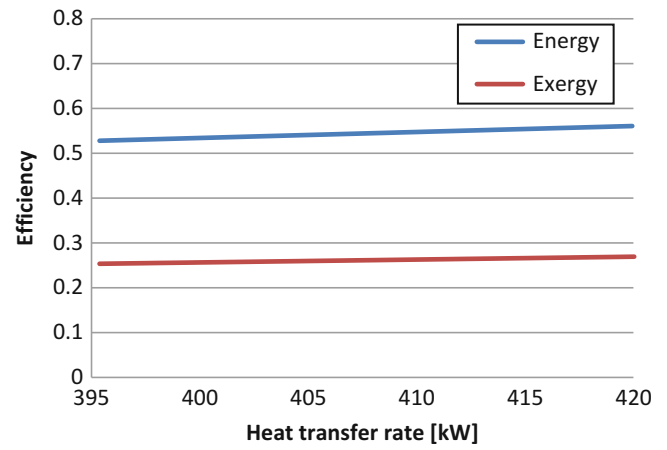
Fig. 19.3 The changes of energy and exergy efficiencies with respect to consumed heat rate for case 2
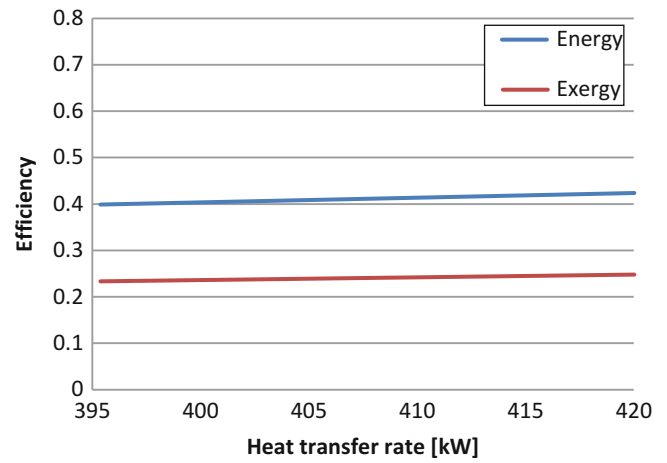
Fig. 19.4 The changes of energy and exergy efficiencies with respect to consumed heat rate for case 3
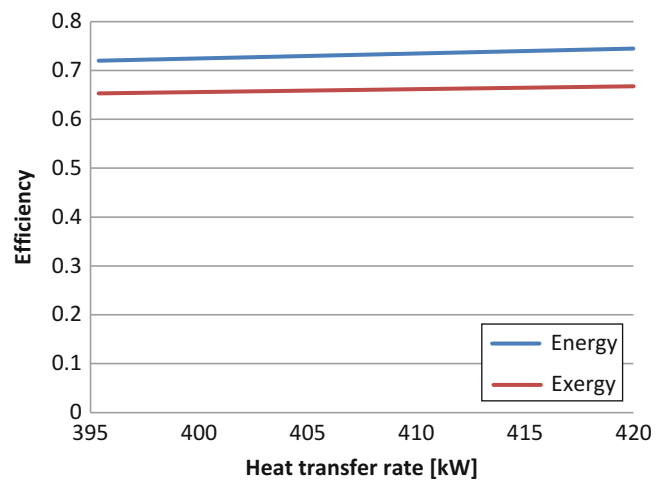
Fig. 19.5 The changes of energy and exergy efficiencies with ambient temperature
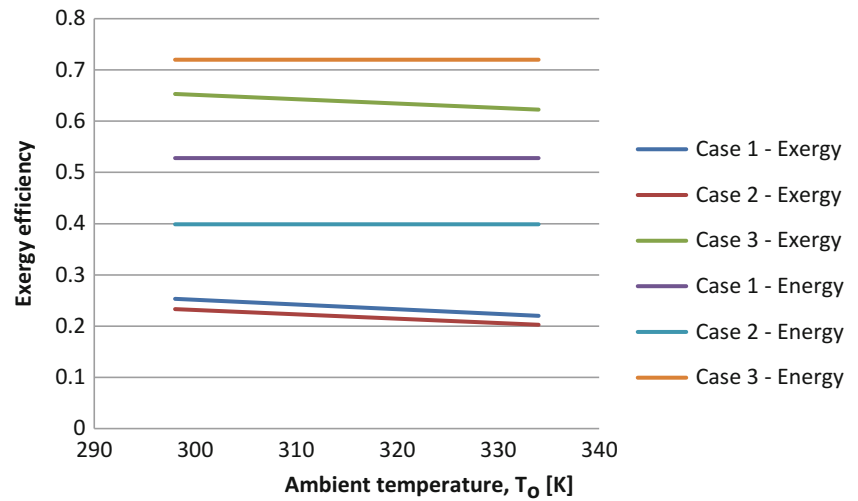
Fig. 19.6 Exergy destruction of the crude oil distillation system
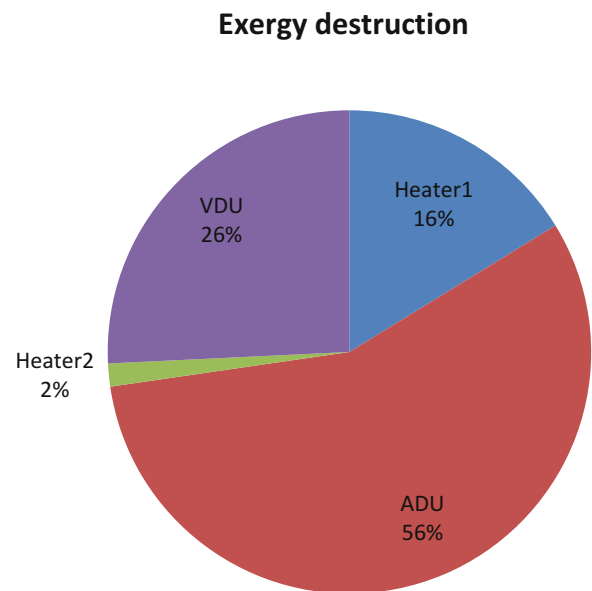
for case 1, case 2, and case 3 respectively. When compared with energy efficiencies, case 1 has the highest difference whereas case 3 has the lowest. As the ambient temperature increases, the exergy efficiency decreases linearly. This decrease in exergy efficiency is understandable since higher ambient temperature means lower amount of useful heat can be extracted from the output. The ambient temperature affects the case 1 efficiency the most as it has the highest decline for the studied temperature. Case 1 gets affected the most since its output solely relies on exergetic consumed heat in the system.

Figure 19.6 shows the exergy destruction of each component of the distillation system. ADU has the highest exergy destruction, followed by VDU, then heater 1 and heater 2. Heater 1 is the heater that heats the feed before it enters the ADU while heater 2 heats the feed before it enters the VDU. ADU has higher exergy losses since it has greater number of trays compared to VDU. Since the oil feed interacts with more number of trays and deals with heavier compounds, the exergy destruction is greater. Heater 1 has higher exergy destruction since it has higher mass flow rate to heat and secondly the feed to be heated is at a lower temperature as compared to what heater 2 secures.

Conclusions

The paper introduces three different exergy and energy efficiencies and discusses them for various inputs and outputs. For all the different cases of inputs and useful outputs, a parametric study is conducted to show the change in efficiencies when consumed heat and ambient temperature changes. Case 3 has the highest baseline energy and exergy efficiencies at 72 % and 65 %, respectively. Case 1 efficiencies are the second highest at 53 % for energy while exergy efficiency is at 25.3 %. Case 2 has the lowest baseline efficiencies at 40 % for energy and 23.5 % for exergy efficiency. Case 3 has the highest baseline efficiencies since this case treats the heat transfer rate as well as the exhaust gases as useful output. The heater heat is considered as the only input. Case 2 treats the heater heat as the input while heat transfer rate, in the distillation columns, as the output. This case has low magnitude output as the exhaust gases are not considered useful hence it has the lowest efficiency. Case 1 also treats the heat transfer rate, in the distillation columns, as the only output but it has a better efficiency compared to case 2 because it takes the absorbed heat by crude as input, not the total provided heat by the heaters. The unabsorbed heat from the heater is assumed to be utilized as a useful output. Overall, this paper concludes that by using the unabsorbed heat from the heaters, the overall plant efficiency can be improved. The paper also suggests that by utilizing the exhaust gases as useful input to some other system, the efficiencies can be further improved for the overall plant. The improvement in efficiency helps reduce the energy wastage, in turn, reduces the operational cost of the plant. The increase in efficiencies means reduction in dumped heat to the surrounding. This translates to lowered adverse effects of heat dumping to the environment and is a step towards sustainability.

Nomenclature

ADU	Atmospheric distillation unit	$\dot{Q}_{CV}$	Heat rate consumed in the distillation system, W
$\dot{E}$	Energy rate, W	T	Temperature, K
$\dot{E}x$	Exergy rate, W	T_0	Ambient temperature, K
$\dot{I}$	Exergy destruction rate	VDU	Vacuum distillation unit
PA	Pump-around circuit		

Greek Letters

η	Energy efficiency	Ψ	Exergy efficiency

Subscripts

1–17	States	H	Heater
C	Case for efficiencies		

References

1. Rosen MA, Dincer I (1997) On exergy and environmental impact. Int J Energy Res 21:643–654
2. Al-Muslim H, Dincer I, Zubair SM (2003) Exergy analysis of single and two-stage crude oil distillation units. ASME J Energy Resour Technol 12:199–207
3. Kanoglu M, Dincer I, Rosen MA (2007) Understanding energy and exergy efficiencies for improved energy management in power plants. Energy Policy 35:3967–3978
4. Cengel YA, Boles MA (2006) Thermodynamics: an engineering approach, 5th edn. New York, McGraw-Hill
5. Farooque AM et al (2008) Parametric analyses of energy consumption and losses in SWCC SWRO plants utilizing energy recovery devices. Desalination 219:137–159
6. Talbi M, Agnew B (2002) Energy recovery from diesel engine exhaust gases for performance enhancement and air conditioning. Appl Therm Eng 22:693–702
7. Bagajewicz M, Ji S (2001) Rigorous procedure for the design of conventional atmospheric crude fractionation units. Part I: targeting. Ind Eng Chem Res 40:617–626
8. Errico M, Tola G, Mascia M (2009) Energy saving in a crude distillation unit by a preflash implementation. Appl Therm Eng 29:1642–1647
9. Dincer I, Rosen M (2007) EXERGY energy, environment and sustainable development. Elsevier, London
10. Al-Muslim H, Dincer I, Zubair SM (2005) Effect of reference state on exergy efficiencies of one- and two-stage crude oil distillation plants. Int J Therm Sci 44:65–73

Performance Assessment of a Hybrid Solid Oxide Fuel Cell-Gas Turbine Combined Heat and Power System

20

Pouria Ahmadi, Mohammad Hassan Saidi, and Ibrahim Dincer

Abstract

In this chapter, a comprehensive thermodynamic modeling of a hybrid solid oxide fuel cell-gas turbine (SOFC-GT) is conducted. A heat recovery steam generator is used to produce saturated water for the heating purpose. This saturated hot water can be used in an absorption chiller system to meet the cooling load of the system. In order to model the hybrid system, chemical and electrochemical analyses of SOFCs and other components are carried out through energy and exergy analyses. The results of a hybrid system are compared to a gas turbine power generation system in order to investigate the effect of fuel cell on the system performance. Based on the model results, exergy efficiency of a hybrid SOFC-GT is higher than the one for conventional gas turbine and steam generator cycle. To enhance the understanding of the results in this study, a complete parametric study is performed and the results are presented. The results of this study, show that an increase in fuel cell stack temperature and compressor pressure ratio increases the efficiency; however an increase in fuel cell current density and gas turbine inlet temperature (GTIT) decreases the efficiency. In addition, an increase in HRSG steam pressure and a decrease in HRSG pinch point temperature results in an increase in system exergy efficiency.

Keywords

Energy • Exergy efficiency • Hybrid system • SOFC fuel cell • Combined heat and power system

Introduction

Energy is considered by many as one of the humanity's crucial problems in the next decade or so. Energy is used almost everywhere in a variety of applications, such as heating, cooling, power generation, desalination plant, and so forth. Fuel cells have been considered as relevant options for power generation, for their high efficiency and low emission. Among various types of fuel cells, solid oxide fuel cells (SOFCs) are of the greatest interest and used solely or as a part of gas turbine (GT) cycles. Solid oxide fuel cell-gas turbine (SOFC-GT) cycles have received most attention due to their high efficiency. In addition, the combinations of fuel cells and conventional cycles are used widely due to their high efficiency and low emission.

Hybridization and integration of energy system first came up with the application of cogeneration heat and power. In this simple energy system energy of waste heat is used to produce heat for heating or hot water applications. It may also be used for cooling purposes. In general, cogeneration can be said as a potential technique to produce heat and electricity in one process that can save considerable amounts of energy. It is often associated with the combustion of fossil fuels, but can also

P. Ahmadi (✉) • I. Dincer
Department of Mechanical Engineering, Faculty of Engineering and Applied Science, University of Ontario Institute of Technology (UOIT), 2000 Simcoe Street North, Oshawa, ON, Canada L1H 7K4
e-mail: Pouria.Ahmadi@uoit.ca; Ibrahim.Dincer@uoit.ca

M.H. Saidi
Center of Excellence in Energy Conversion (CEEC), School of Mechanical Engineering, Sharif University of Technology (SUT), PO Box 11155-9567, Tehran, Iran
e-mail: saman@sharif.edu

be carried out using some renewable energy sources and by utilizing waste heat. The trend recently has been to use cleaner fuels for cogeneration such as natural gas. Note that the strong long-term prospects for cogeneration in global energy markets are related to its ability to provide a multitude of operational, environmental, and financial benefits. The product thermal energy from cogeneration can be used for domestic hot water heating, pool and space heating, laundry processes, and absorption cooling. The more the product heat from cogeneration can be used year round in existing systems the more financially attractive is cogeneration. Cogeneration helps overcome the main drawback of conventional electrical and thermal systems: the significant heat losses which detract greatly from efficiency. Heat losses are reduced and efficiency is increased when cogeneration is used to supply heat to various applications and facilities. The overall energy efficiency of a cogeneration system is the percent of the fuel converted to both electricity and useful thermal energy. Typical cogeneration systems have overall efficiencies ranging between 45–60 %.

Cogeneration is a technique for producing heat and electricity in one process that can save considerable amounts of energy. Cogeneration is often associated with the combustion of fossil fuels, but can also be carried out using some renewable energy sources and by burning wastes. The trend recently has been to use cleaner fuels, such as natural gas, for cogeneration. Note that the strong long-term prospects for cogeneration in global energy markets are related to its ability to provide a multitude of operational, environmental, and financial benefits. Cogeneration often reduces energy use cost-effectively and improves security of energy supply. In addition, since cogeneration installations are usually located close to consumers, electrical grid losses are reduced when cogeneration is applied; cogeneration increases competition among producers and provides opportunities to create new enterprises; and cogeneration is often well suited for use in isolated or remote areas.

Cogeneration is treated as a very attractive option for facilities with high electric rates and buildings that consume large amounts of hot water and electricity every month. The higher the electric rates are the greater the savings with cogeneration and the faster the savings pay for the initial capital investment. The product thermal energy from cogeneration can be used for domestic hot water heating, space heating, pool and spa heating, laundry processes, and absorption cooling. The more the product heat from cogeneration can be used year round in existing systems the more financially attractive it becomes.

Cogeneration helps overcome the main drawback of conventional electrical and thermal systems: the significant heat losses that detract greatly from efficiency. Heat losses are reduced and efficiency is increased when cogeneration is used to supply heat to various applications and facilities. The overall energy efficiency of a cogeneration system is the percent of the fuel converted to both electricity and useful thermal energy. Typical cogeneration systems have overall efficiencies ranging from 65 to 90 % [1].

Cogeneration is treated as a proven technology that has been around for over 100 years. Early in the twentieth century, before there was an extensive network of power lines, many industries had cogeneration plants. In the United States, the first commercial cogeneration plant was designed and built by Thomas Edison in 1882 in New York [1]. Primary fuels commonly used in cogeneration include natural gas, oil, diesel fuel, propane, coal, wood, wood waste, and biomass. These "primary" fuels are used to make electricity a "secondary" energy form. This is why electricity, when compared on a kilowatt hour to kilowatt hour basis is typically three to four times more expensive than primary fuels such as natural gas. The thermal cogeneration product is normally in the form of steam and/or hot water and the energy source is often a fossil fuel or uranium. Cogeneration has been used, particularly in industry, for approximately a century. A cogenerator can be a utility, an industry, a government, or any other party. Cogeneration systems are often based on thermal electrical generating stations (such as fossil fuel and nuclear plants), where the energy content of a resource (normally a fossil or nuclear fuel) is converted to heat (in the form of steam or hot gases), which is then converted to mechanical energy (in the form of a rotating shaft), which in turn is converted to electricity. A portion (normally 20 and 45 %) of the heat is converted to electricity, and the remainder is rejected to the environment as waste.

Cogeneration systems are similar to thermal electricity generation systems, except that a percentage of the generated heat is delivered as a product (normally as steam or hot water) and the quantities of electricity and waste heat produced are reduced. Overall, cogeneration efficiencies of over 80 % are achievable [1]. Other advantages generally reported from cogenerating thermal and electrical energy rather than generating the same products in separate processes include reduced energy consumption, reduced environmental emissions (due to reduced energy consumption and the use of modern technologies in large central installations), and more economic operation. Most thermal systems for large-scale electricity generation are based on steam and/or gas turbine cycles and can be modified relatively straightforwardly for cogeneration. Two main categories of heat demands can normally be satisfied by cogeneration as follows:

- Residential, commercial, and institutional processes, which require large quantities of heat at relatively low temperatures (e.g., for air and water heating) and
- Industrial processes, which require heat at a wide range of temperatures (e.g., for drying, heating, boiling, chemical processing, manufacturing, metal processing, mining, and agriculture).

Many general descriptions and studies of cogeneration systems have been reported and the basic technology is well understood and proven. Numerous examples exist of large cogeneration systems: (1) a steam turbine plant in Switzerland generates 465 MW of thermal power and 135 MW of electrical power, with an overall efficiency of 75 % [2]; (2) a nuclear power plant in Michigan left incomplete due to lack of funding was eventually completed as a gas-fired, combined-cycle cogeneration plant having 12 heat recovery steam generators (HRSGs) and gas turbines and two steam turbines, producing 1400 MW of electrical power and 285,000 kg/h of steam; and (3) approximately ten plants are used to generate 240 MW of electrical power and to supply 90 % of the 1,500 MW thermal demand for the city of Malmo, Sweden (population 250,000).

The size and type of a cogeneration systems are normally selected to match as optimally as possible the thermal and electrical demands. Many matching schemes can be used. Systems can be designed to satisfy the electrical or thermal base loads or to follow the electrical or thermal loads. Storage systems for electricity (e.g., batteries) or heat (e.g., hot water or steam tanks) are often used to overcome periods when demand and supply for either electricity or heat are not coincident. Cogeneration systems are sometimes used to supply only the peak portions of the electrical or thermal demands. The thermal product of a cogeneration system often offsets the need for heating plants, where energy in the form of a fossil fuel or electricity is converted to heat (in the form of hot gases or another heated medium), often with an energy conversion efficiency of over 80 %. The practical usage of cogeneration is as old as the generation of electricity. When classification of broad areas was devised to replace gas and kerosene lighting in residences and commercial facilities the concept of central station power generation plants was born. The prime movers that drove electric generators emit waste heat that is normally blown to atmosphere. By capturing that heat and its utilization and making low pressure steam that steam could be piped throughout the district for heating homes and businesses. Thus, cogeneration on a fairly large scale was born [2]. In the past most of the generated electricity was on site in large industrial plants. After, with that generation there is no doubt that much waste heat was captured and utilized in industrial processes as a natural offshoot. Probably the word cogeneration was not even used in conjunction with those efforts.

Gas turbines are one of the most suitable prime movers for combined heating and power energy systems. A gas turbine, also called a combustion turbine, is a type of internal combustion engine which has an upstream rotating compressor coupled with a downstream turbine, and a combustion chamber in between. Energy is added to the gas stream in the combustion chamber, where fuel is mixed with hot air and then ignited. In the high pressure environment of the combustor, combustion of the fuel increases the temperature. The products of the combustion are forced into the turbine section to produce shaft work. There, the high velocity and volume of the gas flow is directed through a nozzle over the turbine blades, spinning the turbine that powers the compressor and, for some turbines, drives their mechanical output. The energy given up to the turbine comes from the reduction in the temperature and pressure of the exhaust gas. In a practical gas turbine, gases are first accelerated in either a centrifugal or radial compressor. These gases are then slowed down using a diverging nozzle known as a diffuser; these processes increase the pressure and temperature of the flow. In an ideal system this process is isentropic. However, in practice, energy is lost in the form of heat, due to friction and turbulence. Gases then pass from the diffuser to a combustion chamber or similar device, where heat is added. In an ideal system this occurs at constant pressure [3]. As there is no change in pressure, the specific volume of the gases increases. In practical situations this process is usually accompanied by a slight loss in pressure due to friction. Finally, this larger volume of gases is expanded and accelerated by nozzle guide vanes before energy is extracted by a turbine.

Micro-gas turbines are kind of gas turbine that has become widespread in distributed power generation units, combined heat and power applications and trigeneration systems. They are one of the most promising technologies for powering hybrid electric vehicles. They range from hand held units producing less than a kilowatt, to commercial sized systems that produce tens or hundreds of kilowatts. The basic principles of micro-turbines are based on micro-combustion [1]. Gas turbines have the following advantages:

- Very high power-to-weight ratio compared to reciprocating engines.
- Smaller than most reciprocating engines of the same power rating.
- Moves unidirectional, with far less vibration than a reciprocating engine.
- Fewer moving parts than reciprocating engines.
- Low operating pressures.
- High operation speeds.
- Low lubricating oil cost and consumption.
- Can run on a wide variety of fuels.
  Although gas turbines have various advantages, they have some disadvantages:
- Cost is very high.
- Less efficient than reciprocating engines at idle speed.
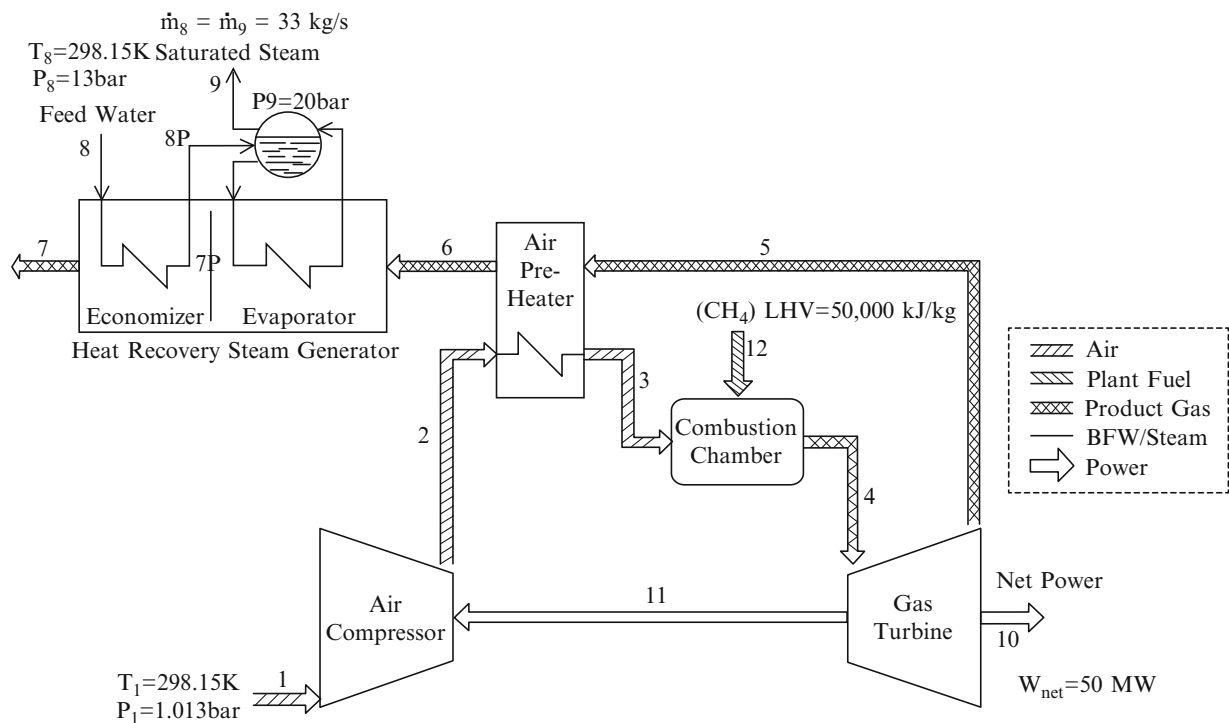
Fig. 20.1 The schematic diagram of a gas turbine prime mover used in CHP

- Longer start up than reciprocating engines.
- Less responsive to changes in power demand compared to reciprocating engines.

Figure 20.1 shows a micro-gas turbine used in a CHP system. This system has two major parts. The main part is a gas turbine Brayton cycle and the bottoming cycle is a single pressure HRSG. Hot flue gases from the gas turbine enter the HRSG to produce saturated water at $P = 20$ bar and $\dot{m} = 33$ kg/s. The net power output of this gas turbine is 50 MW. As Fig. 20.1 shows, the thermal efficiency of the CHP system is higher than in a simple gas turbine cycle because the waste energy of hot flue gases is being utilized in a heat exchanger (HRSG) to produce the heating load, which in this case is saturated water.

Selection of the HRSG is based on the size of the gas turbines; large capacity gas turbines have the ability to produce steam in double or triple pressure levels of HRSG. These gas turbines are usually used for power generation purposes. Therefore, gas turbines can be considered a good candidate for CHP energy systems according to the advantages discussed above.

Another prime mover which is used for cogeneration application is fuel cell. A fuel cell is a device that generates electricity by a chemical reaction. Every fuel cell has two electrodes, one positive and one negative called, respectively, the anode and cathode. The reactions that produce electricity take place at the electrodes. Each fuel cell also has an electrolyte, which carries electrically charged particles from one electrode to the other, and a catalyst, which speeds the reactions at the electrodes. Hydrogen is the basic fuel; however fuel cells also require oxygen. One of the greatest advantages of fuel cells is that they can generate electricity with very little pollution, since much of the hydrogen and oxygen used in generating electricity ultimately combines to form a harmless by product: water. There are various types of fuel cells:

- Alkaline
- Molten carbonate
- Phosphoric acid
- Proton exchange membrane
- Solid oxide

Thermodynamic modeling of the SOFC-GT cycles is the first step to evaluate their performance. Chan et al. [4] simply modeled a SOFC-GT cycle. They considered a fuel cell with tubular geometry which is a common case and their characteristics have been investigated extensively. For example Sanchez et al. [5] modeled thermal and electrochemical

behavior of tubular SOFCs. Various geometries and fuels are used in these fuel cells. Fuels have significant effects on the thermodynamic and environmental behavior of fuel cells and various fuel compositions are considered in literatures. As an example, Van Herle et al. [6] simulate a SOFC operated with biogas. In the case of methane or natural gas, reforming process plays a crucial role in performance of SOFCs. Various reforming models are investigated in [7] and the performance of a fuel cell which operates with a reformed natural gas based on a two-dimensional simulation method by Jafaraian et al. [8].

In addition to thermal and electrochemical modeling, the exergetic analysis is performed on single SOFCs [9] or SOFC-GT cycles [10]. Haseli et al. [11, 12] investigated the thermodynamic and exergetic performance characteristics of SOFC-GTs. To simulate the SOFC-GT hybrid cycles, a complete set of chemical and electrochemical relations and models are needed. To have such relations and models one may find elsewhere [12]. Over potential are discussed in [13, 14] and details on chemical modeling can be found in [15]. Cogeneration cycles are other options to be joined with SOFCs. CHP units as it was analyzed by Verda and Quagalia [16] can be combined with SOFCs and the result will be a significant increase in efficiency. Such cycles are so interesting and extensive works have been performed to analyze the performance of theses cycles. Cali et al. [17] investigated the SOFC-CHP 100 kW unit experimentally. Optimization of this cycle was performed based on regression models [18]. The main objective of this chapter is to see the effect of fuel cell on the performance of gas turbine hybrid system. To achieve this objective, the following steps are performed:
- To model and simulate the hybrid SOFC-GT system.
- To perform both energy and exergy analyses and assessments of the system.
- To compare the results of a conventional gas turbine power generation system with hybrid SOFC-GT system in terms of energy and exergy efficiencies.
- To conduct a comprehensive parametric study to investigate the effects of some major design parameters on the system performance.

System Description

Figure 20.2 illustrates a hybrid fuel cell-gas turbine system containing a compressor, a combustion chamber (CC), a fuel cell, a preheater, a gas turbine, a HRSG to produce superheated steam. Air at ambient conditions enters the air compressor at point 1 and exits after compression (point 2). The hot air enters the air preheater to increase the required air temperature for the fuel cell. Hot air leaves the air preheater and enters a SOFC fuel cell where both electricity and heat are produced by electrochemical reaction. Hot air with a temperature around fuel cell stack temperature leaves the fuel cell and then enters a combustion chamber (CC) at point 4 where natural gas is injected into the CC in order to increase the temperature to produce shaft work by rotating the gas turbine blades and generate power at point 8. The hot gas expands in the gas turbine to point 7. Hot flue gases enter the single pressure HRSG to provide high pressure vapor at points 17. High pressure vapor can be considered for the heating purpose later on or to be utilized in an absorption chiller to provide the cooling load of the system in summer.

Thermodynamic Modeling

In order to model the chemical reaction, equilibrium reforming and shifting processes are considered. Standard voltage is considered time dependent as the details are given in [4, 5]. Fuel utilization factor is about 0.85 %. Fuel is natural gas with 97 % methane, 1.5 % carbon dioxide, and 1.5 % nitrogen [4]. Air is considered 79 % nitrogen and 21 % oxygen [4, 15]. If air is warmed up in a single preheater with gas turbine outlet flue, temperature of gases which inter the HRSG will be low and steam generation rate will be considerably low, so air is warmed up in two preheater, as it is shown in Fig. 20.2. SOFC-GT cycle components models are discussed as follows:

Solid Oxide Fuel Cell
SOFC model is developed based on data taken from [4] which is related to a tubular geometry. Both reforming and shifting processes can be written as follows:

Reforming:

$$CH_4 + H_2O \leftrightarrow H_2 + CO \tag{20.1}$$
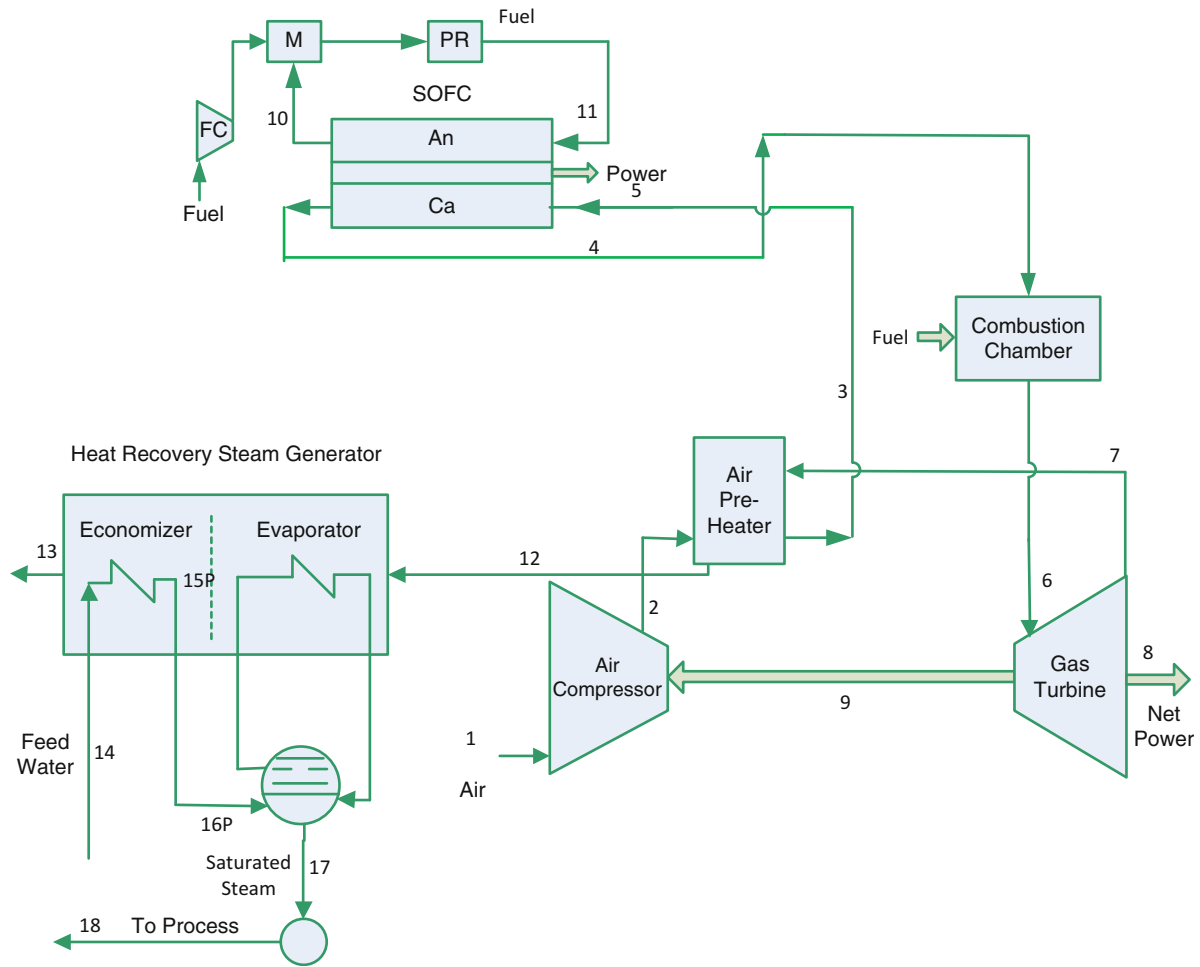
Fig. 20.2 The schematic of a hybrid SOFC-GT combined heat and power

Shifting:

$$CO + H_2O \leftrightarrow H_2 + CO_2 \qquad (20.2)$$
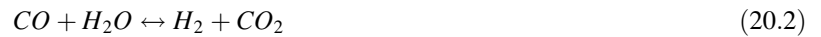
Electrochemical reaction which produces heat and work is defined as follows:

$$H_2 + \frac{1}{2}O_2 \leftrightarrow H_2O \qquad (20.3)$$

Chemical reactions are considered in equilibrium and equilibrium constants expressed by following equations [4, 5, 7, 10]:

$$K_{reforming} = \frac{x_{H_2}^3 x_{CO}}{x_{CH_4} x_{H_2O}} P^2 \qquad (20.4)$$

$$K_{shifting} = \frac{x_{H_2} x_{CO_2}}{x_{CO} x_{H_2O}} \qquad (20.5)$$

$$\ln K = AT^4 + BT^3 + CT^2 + DT + E \qquad (20.6)$$

Table 20.1 Constants for Eq. (20.6) [4, 5, 7]

Constant	Reforming	Shifting
A	−2.6312E−11	5.47E−12
B	1.2406E−07	−2.5748E−08
C	−0.00022523	0.000046374
D	0.19503	−0.03915
E	−66.1395	13.2097

The constants for this equation are listed in Table 20.1. The cell voltage can be evaluated by Nernst equation as

$$V_N = V_0 - \frac{RT}{2F} \ln\left(\frac{x_{H_2O}}{x_{H_2}\sqrt{x_{O_2}}}\right) \tag{20.7}$$

Note that due to irreversibilities, the cell voltage is less than the Nernst voltage. These irreversibilities can be summarized in three main over voltages, known as ohmic, activation, and concentration losses. Then the real cell voltage is written as follows:

$$V = V_N - V_{ohm} - V_{act} - V_{con} \tag{20.8}$$

The ohmic overvoltage can be evaluated from equation [14, 15]:

$$V_{Ohmic} = \left(R_{contact} + \sum \rho_k L_k\right) i \tag{20.9}$$

where

$$\rho_a = 8.114 \times 10^{-6} \exp\left(\frac{600}{T}\right) \tag{20.10}$$

$$\rho_e = 2.94 \times 10^{-6} \exp\left(\frac{10350}{T}\right)$$

$$\rho_c = 2.94 \times 10^{-6} \exp\left(\frac{-1392}{T}\right)$$

$$\rho_i = 125.6 \times 10^{-6} \exp\left(\frac{4690}{T}\right)$$

The activation loss can be obtained by [15]:

$$V_{act} = V_{act,a} + V_{act,c} = \frac{RT}{F} \sinh^{-1}\left(\frac{i}{2i_{o,a}}\right) + \frac{RT}{F} \sinh^{-1}\left(\frac{i}{2i_{o,c}}\right) \tag{20.11}$$

The concentration over voltage can be obtained as follows [15]:

$$V_{conc} = V_{conc}^a + V_{conc}^c = \left[-\frac{RT}{2F}\ln\left(1 - \frac{i}{i_{as}}\right) + \frac{RT}{2F}\ln\left(1 + \frac{x_{H_2} \times i}{x_{H_2O} \times i_{as}}\right)\right] + \left[\frac{RT}{4F}\ln\left(1 - \frac{i}{i_{cs}}\right)\right] \tag{20.12}$$

The anode and cathode limiting currents are discussed thoroughly in [5].
The output power of the fuel cell can be expressed as follows:

$$\dot{W}_{FC} = I.V \tag{20.13}$$

The thermodynamic model of SOFC is written as

$$\left(\sum_{anode} m_i h_i + \sum_{cathod} m_i h_i\right)_{in} = \dot{W}_{FC} + \left(\sum_{anode} m_i h_i + \sum_{cathod} m_i h_i\right)_{out} + \dot{Q}_{FC} \qquad (20.14)$$

Exergy destruction of any component can be evaluated as

$$\dot{E}_D = \dot{Q}\left(1 - \frac{T_0}{T}\right) - \dot{W} + \sum_{in} \dot{E} - \sum_{out} \dot{E} \qquad (20.15)$$

Here, the exergy rate becomes the total exergy rate as

$$\dot{E} = \dot{E}_{ch} + \dot{E}_{ph} \qquad (20.16)$$

Compressor

The thermodynamic model of air compressor is the relation based on the isentropic efficiency and pressure ratio:

$$T_{out} = T_{in}\left\{1 + \frac{1}{\eta_{AC}}\left[r_c^{\frac{\gamma_a-1}{\gamma_a}} - 1\right]\right\} \qquad (20.17)$$

Gas Turbine

The gas turbine modeling equation sets can be expressed as follows:

$$T_{out} = T_{in}\left\{1 - \eta_{GT}\left[1 - \left(\frac{p_{in}}{p_{out}}\right)^{\frac{1-\gamma_g}{\gamma_g}}\right]\right\} \qquad (20.18)$$

Combustion Chamber

In the combustion chamber the fuel cell outlet gases and natural gas react and the molar flow rate of gases at the outlet at the specific outlet temperature can be determined by using the combustion equation and energy balance. In this case outlet gases from SOFC first are cooled in secondary air preheater and then inter the combustion chamber.

Air Preheater

The air preheater thermodynamic model is written as

$$\eta_{AP}(m(h_{in} - h_{out}))_g = (m(h_{in} - h_{out}))_a \qquad (20.19)$$

Heat Recovery Steam Generator

Heat recovery steam generation produces saturated steam in a specific pressure (P_{main}). Pinch point plays a crucial role in HRSG performance. To model the HRSG the following equations are used:

Evaporator:

$$T_{out} = T_{sat} + PP \qquad (20.20)$$

$$\dot{m}_{steam}(h_{out} - h_{in})_{steam} = \dot{m}_g C_{Pg}(T_{in} - T_{out})_g \qquad (20.21)$$

Economizer:

$$\dot{m}_{steam}(h_{out} - h_{in})_{steam} = \dot{m}_g C_{Pg}(T_{in} - T_{out})_g \qquad (20.22)$$

The net output work and total exergy efficiency of the cycle can be evaluated from these equations:

$$\dot{W}_{net} = \dot{W}_{FC} + \dot{W}_{GT} - \dot{W}_{AC} - W_{Pump} \qquad (20.23)$$

$$\eta_{total} = \frac{\dot{W}_{net} + \dot{E}_{steam}}{m_{fuel} \times 1.06 \times LHV} \qquad (20.24)$$

Exergy Analysis

Exergy analysis can help develop strategies and guidelines for more effective use of energy and has been applied to various thermal processes, especially power generation, CHP, trigeneration and multigeneration. The exergy of a substance is often divided into four components. Two common ones are the physical and chemical exergy. The two others, kinetic and potential exergy, are assumed to be negligible here, as the elevation changes are small and speeds are relatively low [1, 3]. Physical exergy is defined as the maximum useful work obtainable as a system interacts with an equilibrium state [1]. Chemical exergy is associated with the departure of the chemical composition of a system from its chemical equilibrium. The chemical exergy is an important in processes involving combustion and other chemical changes [1]. Applying the first and the second laws of thermodynamics, the following exergy balance is obtained:

$$\dot{Ex}_Q + \sum_i \dot{m}_i ex_i = \sum_e \dot{m}_e ex_e + \dot{Ex}_W + \dot{Ex}_D \tag{20.25}$$

Here, subscripts i and e denote the control volume inlet and outlet flow, respectively, $\dot{Ex}_D$ is the exergy destruction, and other terms are given as follows:

$$\dot{Ex}_Q = \left(1 - \frac{T_0}{T_i}\right)\dot{Q}_i \tag{20.26}$$

$$\dot{Ex}_w = \dot{W} \tag{20.27}$$

$$ex = ex_{ph} + ex_{ch} \tag{20.28}$$

where $\dot{Ex}_Q$ and $\dot{Ex}_W$ are respectively the exergy of heat transfer and work which cross the boundaries of the control volume, T is the absolute temperature and the subscript 0 refers to the reference environment conditions respectively. In Eq. (20.28), term ex_{ph} is defined as follows:

$$ex_{ph} = (h - h_0) - T_0(s - s_0) \tag{20.29}$$

The mixture chemical exergy is defined as follows [3]:

$$ex_{mix}^{ch} = \left[\sum_{i=1}^{n} x_i ex_i^{ch} + RT_0 \sum_{i=1}^{n} x_i \ln x_i\right] \tag{20.30}$$

In this exergy analysis, the exergy of each flow is calculated at all states and the changes in exergy are determined for each major component. The cause of exergy destruction (or irreversibility) in the combustion chamber is mainly combustion or chemical reaction and thermal losses in the flow path [3]. However, the exergy destruction in the system heat exchangers (i.e., condenser and HRSG) is due to the large temperature differences between the hot and cold fluids.

Results and Discussion

Table 20.2 shows the comparative results of these two cycles. The total efficiency of the SOFC-GT-SG cycle is significantly higher than single GT-SG cycle. The SOFC hybrid cycle exergy efficiency is almost double than the efficiency of a GT cycle and this can be the reason of higher exergy efficiency of the SOFC-GT-SG cycle.

The mass flow rates in both cases are compared. For the same power output, the mass flow rates in GT compared to SOFC-GT-SG cycle are relatively higher which in turn requires more steam to be produced in HRSG. The largest exergy destruction rate takes place in HRSG, combustion chamber and SOFC. In Fig. 20.3 the effect of steam pressure on the exergy efficiency and steam mass flow rate are shown. Increase in steam pressure reduces the HRSG flue gas outlet temperature which causes exergy destruction to increase.

The pinch point effect on steam generation and exergy efficiency is shown in Fig. 20.4. Increase in pinch point temperature results in a higher flue gas outlet in HRSG, and consequently decreases in exergy efficiency and steam generation rate. The compressor pressure ratio has a strong effect on GT cycle and hence its outlet temperature. This effect

Table 20.2 Results of simulation for SOFC-GT and gas turbine cycles

SOFC-GT-SG cycle			Gas turbine cycle		
Air compressor	24.97	kW	Air compressor	133.87	kW
Combustion chamber	220.27	kW	Combustion chamber	836.45	kW
Gas turbine	24.36	kW	Gas turbine	126.47	kW
SOFC	1,004.79	kW	–	–	–
HRSG	145.24	kW	–	–	–
Total exergy efficiency	0.61		Total exergy efficiency	0.31	
CC fuel mass flow rate	0.02	kg/s	CC fuel mass flow rate	0.13	kg/s
$\dot{W}_{net}$	2,090.92	kW	$\dot{W}_{net}$	2,090.92	kW
$\dot{W}_{FC}$	1,783.34	kW	Air mass flow rate	7.28	kg/s
SOFC air mass flow rate	1.36	kg/s	–	–	–
SOFC fuel mass flow rate	0.06	kg/s	–	–	–
Steam mass flow rate	0.31	kg/s	–	–	–
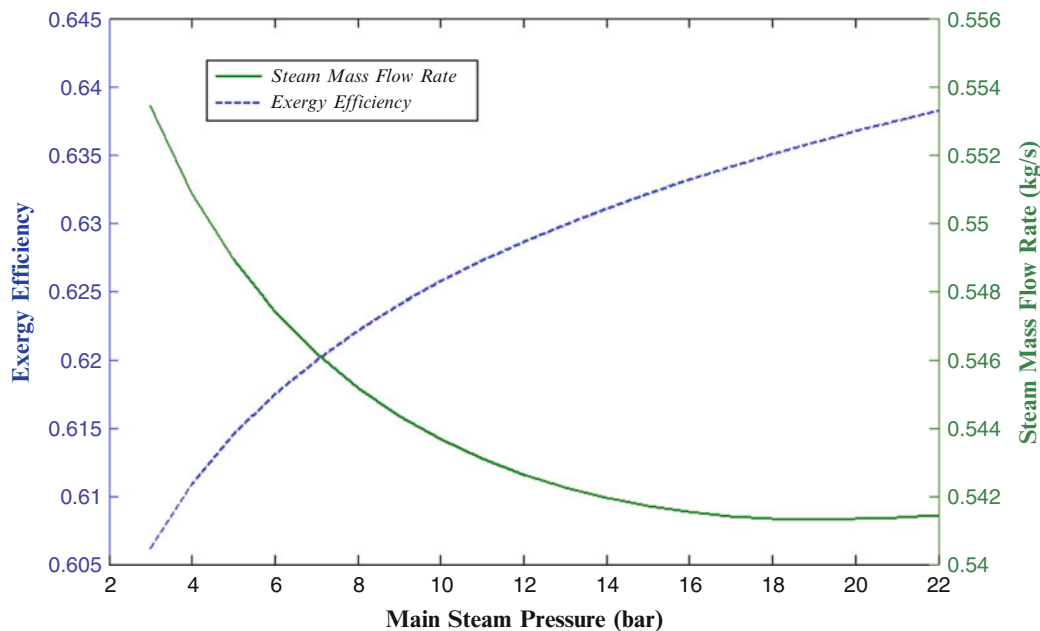
Fig. 20.3 Effect of steam pressure on exergy efficiency and steam mass flow rate

is clearly shown in Fig. 20.5. While gas turbine inlet temperature (GTIT) increases, combustion chamber fuel mass flow rate increases and GT cycle work output increases consequently.

An increase in the GT cycle output power results in an obvious decrease in exergy efficiency, for more power generation is generated by less efficient cycle. This effect is shown in Fig. 20.6.

The SOFC stack temperature is one of the main characteristics of the SOFC. Increase in SOFC stack temperature increases the irreversibility's of the SOFC. At a constant current density fuel flow rate of SOFC is constant but the air flow rate decreases which results in compressor work output decreases and total output work of the cycle decreases. In addition, increase in stack temperature reduces the fuel injected to the combustion chamber which results in a higher efficiency. When air flow rate decreases preheater flue gases temperature to the HRSG increases which reduces the exergy efficiency of the HRSG. Steam generation rate increases due to increase in inlet temperature to the HRSG. These effects are illustrated through Figs. 20.7, 20.8, 20.9, and 20.10.

An increase in the current density reduces the efficiency of SOFC significantly which result in total exergy efficiency to reduce. Furthermore, flue gases mass flow rates decrease which results in more steam generation. The effect of current density is shown in Fig. 20.11.
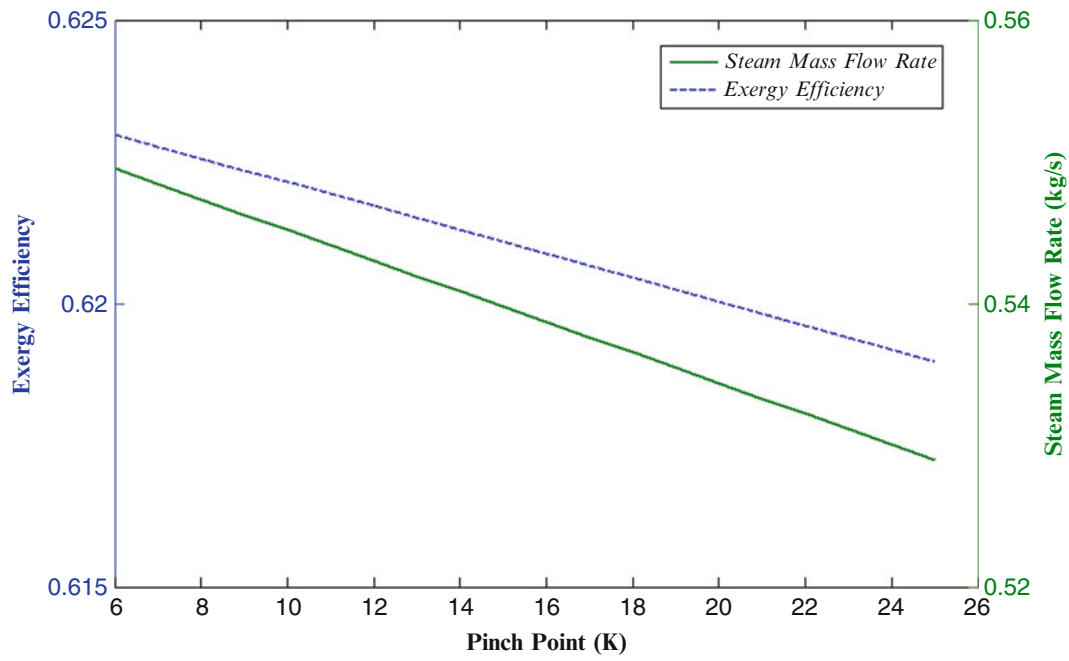
Fig. 20.4 Pinch point effect on exergy efficiency and steam generation mass flow rate
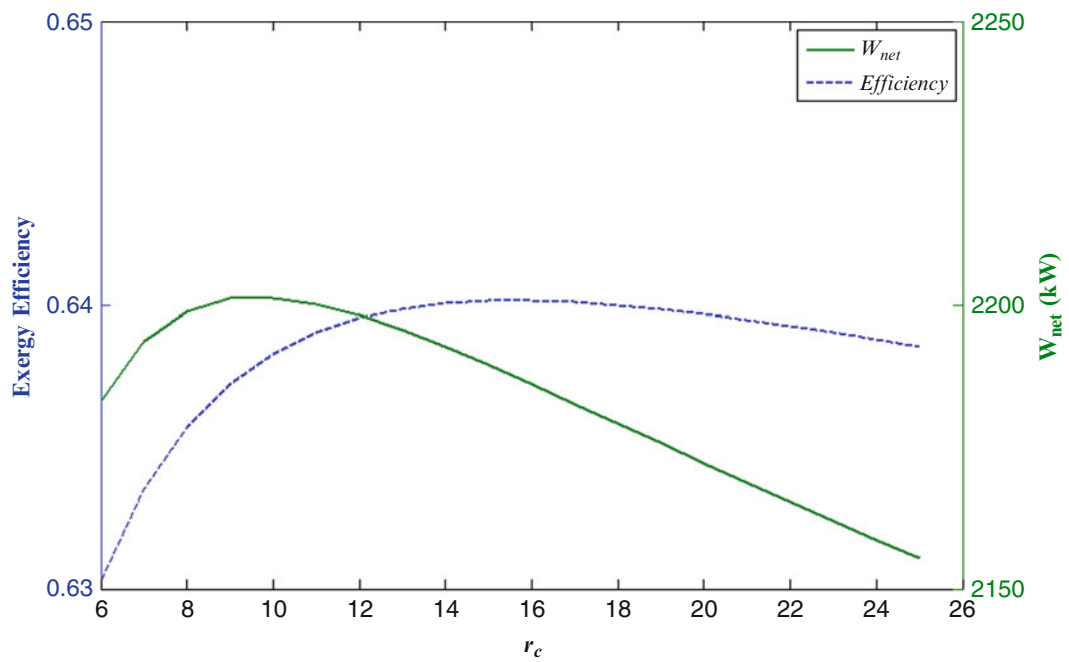
Fig. 20.5 Variation of exergy efficiency and net output power with compressor pressure ratio
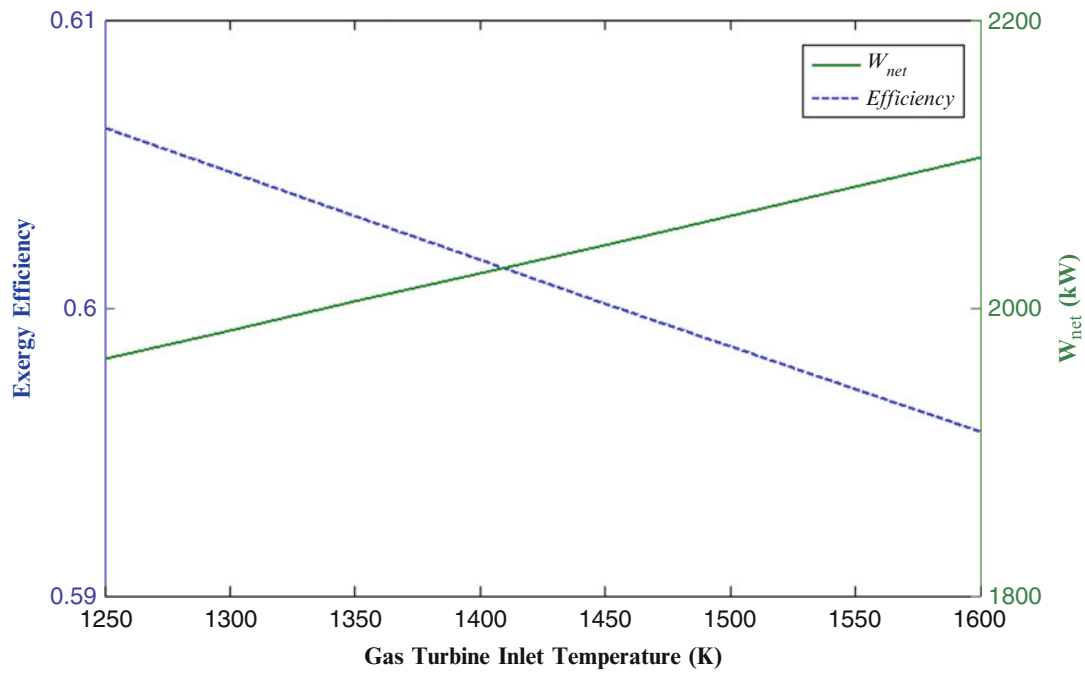
Fig. 20.6 Effect of gas turbine inlet temperature on net output power and exergy efficiency
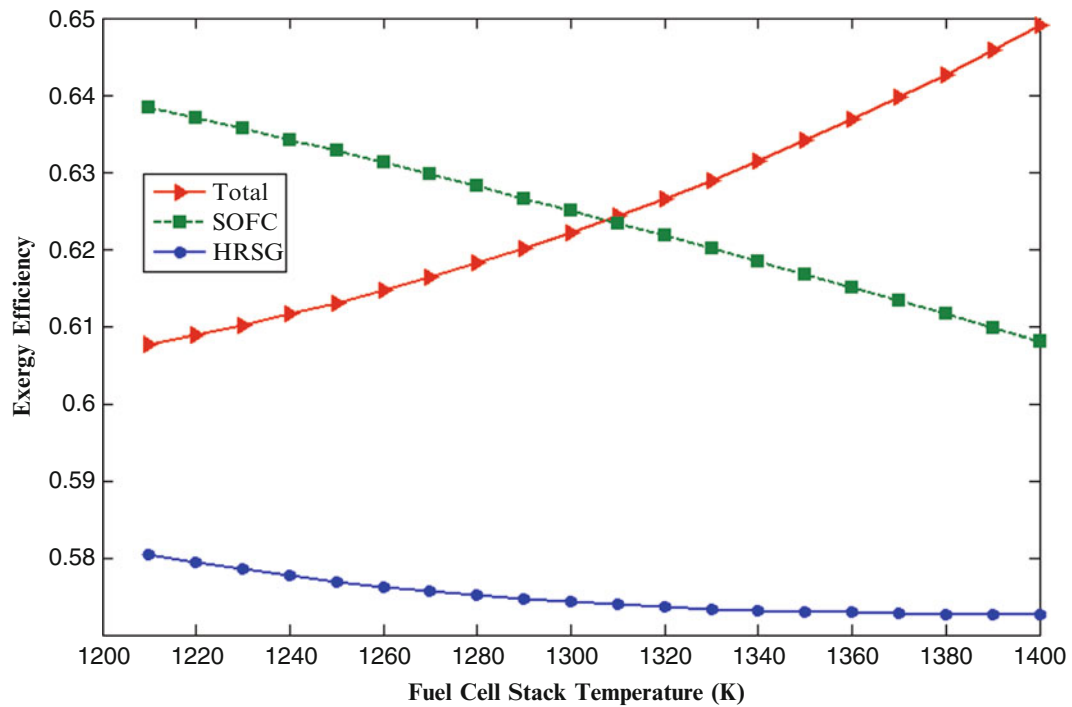
Fig. 20.7 Exergy efficiency of main exergy destructors of the cycle as functions of fuel cell stack temperature
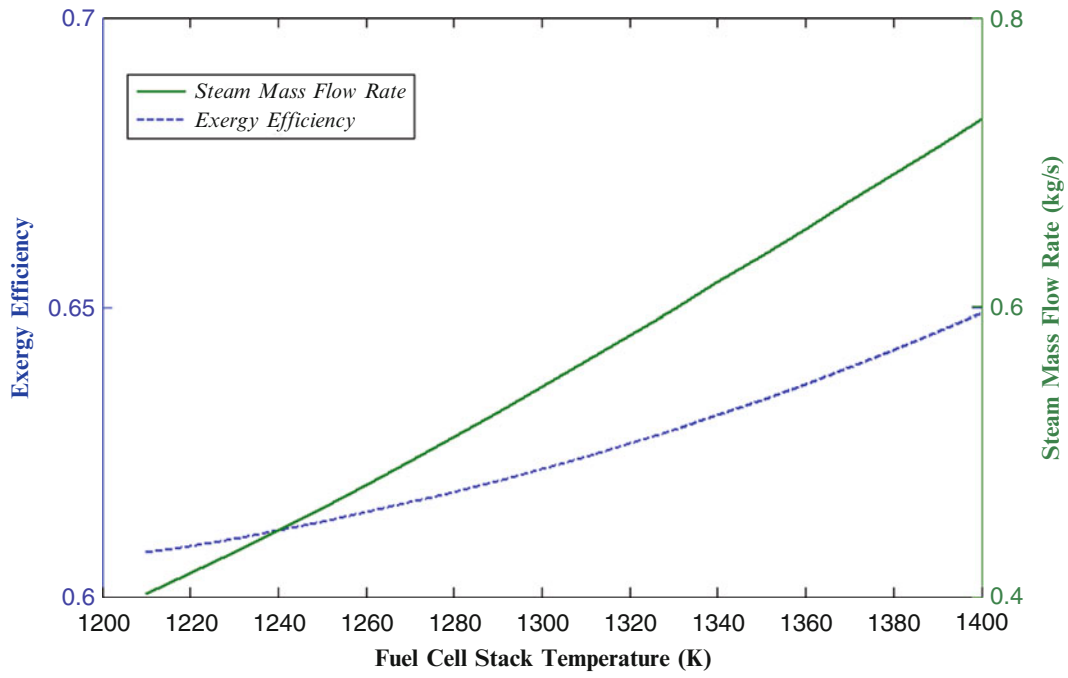
Fig. 20.8 Exergy efficiency and steam flow mass rate variations due to fuel cell stack temperature increase
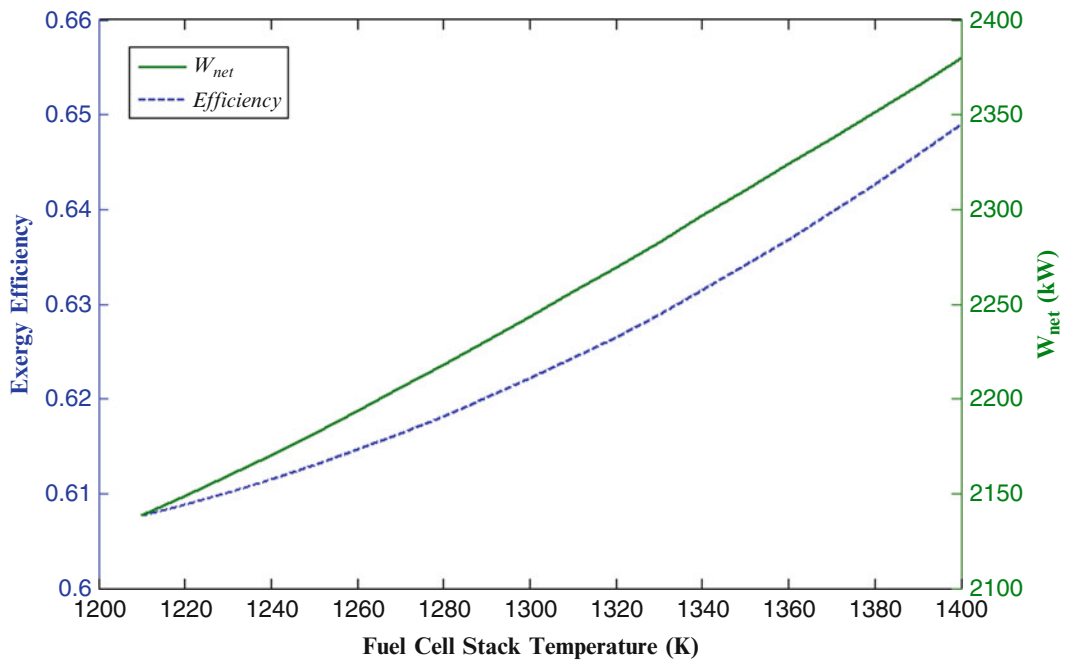
Fig. 20.9 Effect of fuel cell stack temperature on net output power and exergy efficiency
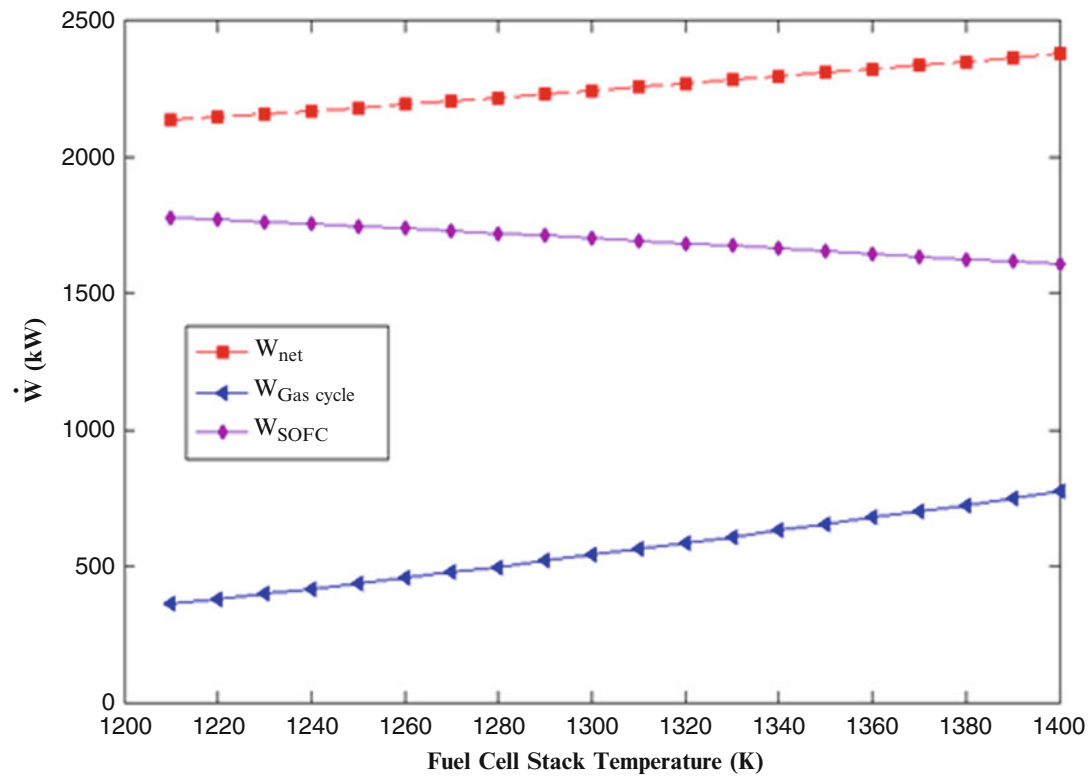
Fig. 20.10 Fuel cell stack temperature effect on the power generation
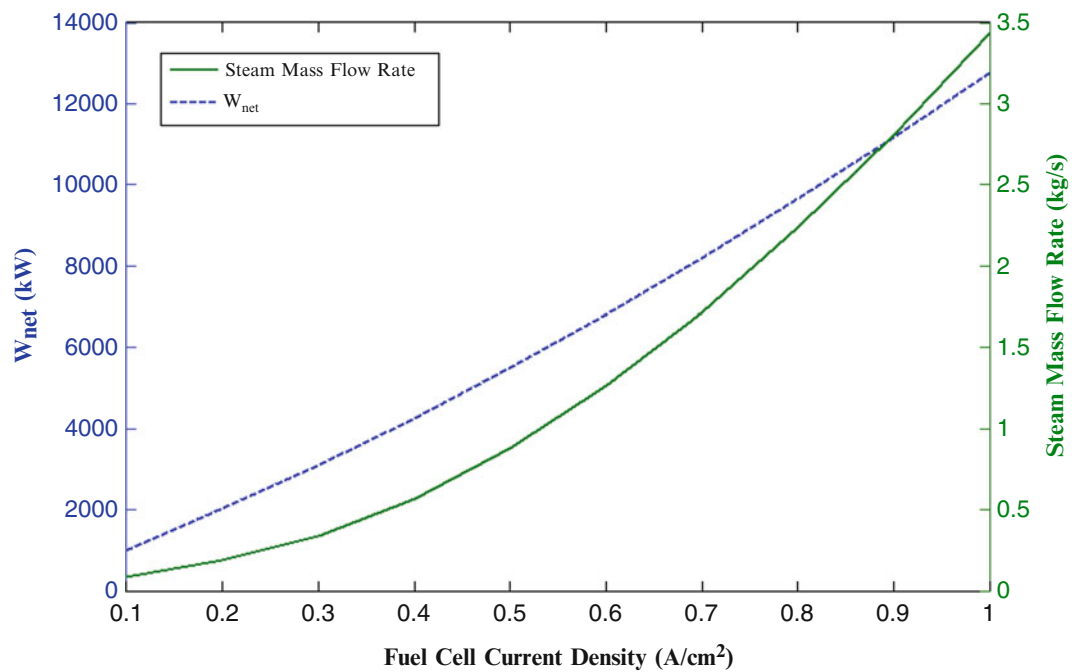
Fig. 20.11 Effect of fuel cell current density on net power output and steam mass flow rate

Conclusions

In this chapter, a comprehensive thermodynamic modeling of a hybrid SOFC fuel cell and gas turbine cycle is carried out. In this regard, an exergy analysis is performed in order to determine the exergy efficiency and exergy destruction of each component as well as the overall exergy efficiency of the system. The results show that for a fixed output power, the steam mass flow rate for gas turbine cycle is significantly higher than a hybrid cycle. However, the exergy efficiency of the hybrid SOFC cycle is higher than the conventional gas turbine cycle. This is due to a decrease in a fuel mass flow rate injected into the combustion chamber as the SOFC can increase the air temperature entering the combustion chamber. Furthermore, the present results provide a good insight for the comparison of conventional gas turbine cycle and hybrid system.

Nomenclature

A B, C, D, E	Constants in Eq. (20.6)	P_{main}	Steam pressure (bar)
$\dot{E}$	Exergy rate (kW)	$\dot{Q}$	Heat rate (kJ)
F	Faraday constant (C/kmol)	R	Universal gas constant (kJ/(kmol K))
h	Enthalpy (kJ/kg)	r_c	Compressor pressure ratio
I	Current (A)	T	Temperature (K)
i	Current density (A/cm^2)	TIT	Gas turbine inlet temperature (K)
$i_{a,s}$	Anode limiting current density (A/cm^2)	T_o	Ambient temperature (K)
i_o	Exchange current density (A/cm^2)	T_{sat}	Saturation temperature (K)
K	Equilibrium constant	V	Voltage (Volt)
L	Length (m)	V_o	Standard voltage
LHV	Lower heating value (kJ/kg)	$\dot{W}$	Power (kW)
m	Mass flow rate (kg/s)	x	Concentration
P	Pressure (bar)		

Greek Letters

γ	Specific heat ratio	ρ	Ohmic resistance per length (Ω/m)
η	Efficiency		

Subscripts

a	Air anode	FC	Fuel cell
AC	Air compressor	g	Flue gas
act	Activation	GT	Gas turbine
AP	Air preheater	i	Components index in mixture or interconnector
c	Cathode	in	Inlet
ch	Chemical	N	Nernst
conc	Concentration	Ohm	Ohmic
D	Destruction	out	Outlet
e	Electrolyte		

References

1. Dincer I, Rosen MA (2007) Exergy: energy, environment and sustainable development. Elsevier, Oxford, UK
2. Horlock JH (1987) Some practical CHP schemes. Pergamon, Oxford
3. Ahmadi P, Dincer I (2010) Exergoenvironmental analysis and optimization of a cogeneration plant system using multimodal genetic algorithm (MGA). Energy 35:5161–5172
4. Chan SH, Ho HK, Tian Y (2003) Multi-level modeling of SOFC-gas turbine hybrid system. Int J Hydrogen Energy 28:889–900
5. Sanchez D, Chacartegui R, Munoz A, Sanchez T (2006) Thermal and electrochemical model of internal reforming solid oxide fuel cells with tubular geometry. J Power Sources 160:1074–1087

6. Van Herle J, Marechal F, Leuenberger S, Favrat D (2003) Energy balance model of a SOFC cogenerator operated with biogas. J Power Sources 118:375–383
7. Sanchez D, Chacartegui R, Munoz A, Sanchez T (2008) On the effect of methane internal reforming modeling in solid oxide fuel cells. Int J Hydrogen Energy 33:1834–1844
8. Jafaraian SM, Haseli P, Karimi G (2010) Performance analysis of a solid oxide fuel cell with reformed natural gas fuel. Int J Energy Res 34(11):946–961
9. Akkaya AV, Sahin B, Erdem HH (2007) Exergetic performance coefficient analysis of a simple fuel cell system. Int J Hydrogen Energy 32:4600–4609
10. Bavarsad PG (2007) Energy and exergy analysis of internal reforming solid oxide fuel cell-gas turbine hybrid system. Int J Hydrogen Energy 32:4591–4599
11. Haseli Y, Dincer I, Naterer GF (2008) Thermodynamic modeling of a gas turbine cycle combined with a solid oxide fuel cell. Int J Hydrogen Energy 33:5811–5822
12. Haseli Y, Dincer I, Naterer GF (2008) Thermodynamic analysis of a combined gas turbine power system with a solid oxide fuel cell through exergy. Thermochim Acta 480:1–9
13. Vasquez LO (2007) Fuel cell research trends. Nova Science Publications Inc., New York
14. Motahar S, Alemrajabi AA (2009) Exergy based performance analysis of a solid oxide fuel cell and steam injected gas turbine hybrid power system. Int J Hydrogen Energy 34:2396–2407
15. Colpan CO, Dincer I, Hamdullahpur F (2007) Thermodynamic modeling of direct internal reforming solid oxide fuel cells operating with syngas. Int J Hydrogen Energy 32:787–795
16. Verda V, Quagalia MC (2008) Solid oxide fuel cell systems for distributed power generation and cogeneration. Int J Hydrogen Energy 33:2087–2096
17. Cali M, Santarelli MGL, Leone P (2007) Design of experiments for fitting regression models on the tubular SOFC CHP 100 kWe: screening test, response surface analysis and optimization. Int J Hydrogen Energy 32:343–358
18. Akkaya AV, Sahin B, Erdem HH (2008) An analysis of SOFC/GT CHP system based on exergetic performance criteria. Int J Hydrogen Energy 33:2566–2577

Performance Assessment of a Small Solar Pond Stratified with Magnesium Chloride Water

Sibel Deniz, Ismail Bozkurt, Mehmet Karakilcik, and Ibrahim Dincer

Abstract

In this study, we present an experimental investigation of energy and exergy efficiencies of a small solar pond stratified with magnesium chloride water. The solar pond system is filled with varying density magnesium chloride water in order to form layers of the respective inner zones. A data acquisition system is employed to measure the hourly temperatures at various locations in the inner zones. It is found that the gradient of the different density layers considerably affect the energy storage performance of the solar pond. Thus, the energy and exergy efficiencies of the solar pond are decreased with the increasing the erosion of layers. The efficiencies of the inner zones are defined in terms of temperatures as the average representative solar energy from August to November of the year. As a result, the maximum and the minimum energy efficiencies of the solar pond are observed in August as 27.41 % and 12.64 % in November, respectively. Also, the maximum and the minimum exergy efficiencies of the solar pond are observed in August as 26.04 % and 12.62 % in November, respectively.

Keywords

Solar energy • Solar pond • Energy and exergy efficiencies • Magnesium chloride water

Introduction

Due to a wide range of global problems, a wide range of potential energy solutions are then needed to reduce environmental impact and increase sustainable development. Many of the renewable energy resources are of limited applicability due to their reliability, quality, quantity, and density [1]. For these reasons, renewable energy sources, solar energy in particular, have gained greater importance. Solar energy has several uses like heating water, warming greenhouses, drying, water desalination, power generation, and so on. Therefore, research in the development and application of solar energy systems is essential. One of these systems is solar ponds. In this regard, a lot of studies have been undertaken on solar ponds by various

S. Deniz • M. Karakilcik (✉)
Department of Physics, Faculty of Sciences and Letters, University of Cukurova, Adana 01330, Turkey
e-mail: fzksibel.deniz@hotmail.com; kkilcik@cu.edu.tr

I. Bozkurt
Department of Mechanical Engineering, Faculty of Engineering, University of Adiyaman, Adiyaman 02040, Turkey
e-mail: ismail_bozkurt44@yahoo.com

I. Dincer
Faculty of Engineering and Applied Science, University of Ontario Institute of Technology (UOIT),
2000 Simcoe Street North, Oshawa, ON, Canada L1H 7K4
e-mail: ibrahim.dincer@uoit.ca

researchers [2–8]. Bozkurt and Karakilcik [9] investigated an integrated system that is a combination of a solar pond and collectors. Heat energy obtained from solar collector is transferred to the solar pond storage zone through a heat exchanger system that is placed in storage zone. The integrated solar pond efficiencies were calculated experimentally and theoretically according to the number of collectors. Karakilcik et al. [10] investigated a solar pond performance with and without shading effect and comparison of the energy efficiencies for the upper convective zone (UCZ), non-convective zone (NCZ), and lower convective zones, as well as determination of the shading area each zone of the experimental solar pond. Thus, the shading effect and its ratios and losses work out to determine energetic performance of system components.

Sodium chloride salt has been used in most of these studies. In few studies, however, magnesium chloride salt has been used. Subhakar and Murthy [11] constructed an experimental saturated solar pond by using magnesium chloride salt. Subhakar and Murthy [12] studied magnesium chloride and potassium nitrate salt ponds located at Madras (India) for the experimental and parametric assessment. A comparison was also made with an unsaturated solar pond. Subhakar and Murthy [13] constructed an experimental saturated solar pond by using magnesium chloride salt. The temperature and concentration gradients were developed by heating the pond from the bottom and adding finely powdered salt from the top. The development of a temperature distribution in the pond depends on the direct sunlight and its daily variation.

Many experimental and theoretical works have generally focused on to investigate the thermal efficiencies of various types of solar ponds, especially, salt gradient solar pond. The present work becomes the first work in the area dealing with the investigation of energetic and exergetic performance analyses of the magnesium chloride water solar pond and comparison with the corresponding energy efficiencies during the months (for summer season) of the year.

Experimental Apparatus and Procedure

A solar pond is stored with heat energy in salty water for a long period of time by preventing heat loss by convection. They consist of different density zones, UCZ, NCZ, and heat storage zone (HSZ). UCZ is the fresh water layer at the top of the pond. This zone is fed with fresh water to maintain its density as close as possible to the density of fresh water in the upper part and to meet the water loss due to evaporation. NCZ is composed of salty water layers whose brine density gradually increases toward bottom of the pond. The density gradient of NCZ is very important to prevent heat loss by convection. In order to maintain the density gradient of NCZ an auxiliary operating system on a feedback principle was developed. The system is first proposed by Akbarzadeh and MacDonalds [14]. HSZ is composed of salty water with highest density. The high amount of the solar energy is absorbed and stored in this zone. An experimental model solar pond with the area of 0.72 m^2 and a depth of 1.1 m was built in University of Cukurova, Turkey (i.e., $35°18'$ E longitude, $37°05'$ N latitude). The pond's bottom and side wall was insulated by using 0.10 m thick glass wool. The pond temperature was measured at seven points, starting from the bottom, at 0.25, 0.40, 0.55, 0.65, 0.75, 0.85, and 1.05 m heights by using thermocouples with an accuracy of about $\pm 1 °C$. Density distributions were also measured and analyzed by taking samples from the same point of the temperature sensors. The pond was filled in August 2012 and worked. The thicknesses of the UCZ, NCZ, and HSZ are 0.1, 0.5, 0.40 m, respectively. The range of salt gradient in the inner zones is such that the density is $1{,}000$–$1{,}020 \text{ kg/m}^3$ in UCZ, $1{,}030$–$1{,}200 \text{ kg/m}^3$ in NCZ, and $1{,}170$–$1{,}200 \text{ kg/m}^3$ in HSZ. In the present study, we report the experimental data that were measured from August to December. Figure 21.1 shows a schematic representation of the experimental solar pond system by using magnesium chloride salt.

Energy and Exergy Analyses

The energy and exergy values of the solar pond are calculated using conservation of mass and energy principles as well as second law analysis. Therefore, in this section, energy and exergy analyses of the solar pond are presented. The energy efficiency of the magnesium chloride solar pond (MCSP) can be defined as

$$\eta_{MCSP} = \frac{Q_{stored}}{Q_{solar}} = 1 - \frac{\left\{ Q_{down} + Q_{up} + Q_{side} \right\}}{Q_{solar}} \tag{21.1}$$

where Q_{stored} is stored heat energy in the HSZ of the solar pond, Q_{solar} is the amount of net solar energy which is coming from the sun, Q_{down} is the total heat loss to the down wall from HSZ, Q_{up} is the heat loss from HSZ to the above zone, and Q_{side} is the total heat loss to the side walls of the solar pond. Substituting equations for each parameter in Eq. (21.1) provides us with

Fig. 21.1 A schematic representation of the magnesium chloride layers of the solar pond
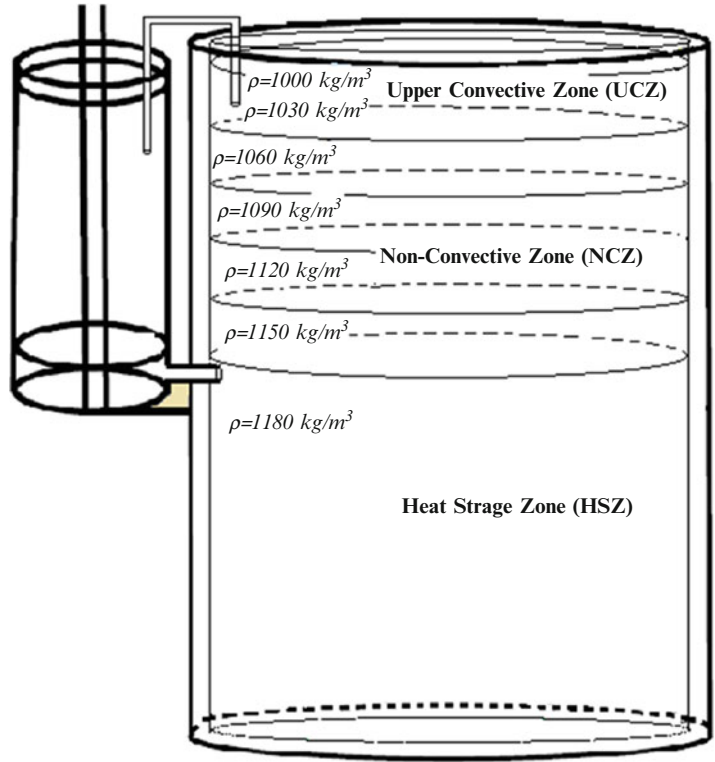
the following energy efficiency of MCSP:

$$\eta_{MCSP} = 1 - \frac{\left\{\frac{k_{sw}A}{\Delta x_{down}}(T_{down} - T_a) + \frac{k_s A}{\Delta x_{HSZ\text{-}NCZ}}(T_{HSZ} - T_{NCZ}) + \frac{k_{sw}2\,\pi\,rL_{HSZ}}{\Delta x_{side}}(T_{HSZ} - T_a)\right\}}{\beta E A_{HSZ}[(1 - F)\,h(x - \delta)]} \tag{21.2}$$

where E is the total solar energy reaching the solar pond surface, A_{HSZ} is the area of the HSZ which is subjected to solar insolation, F is the fraction of energy absorbed at a region of δ-thickness, h is solar radiation ratio, A is the surface area of the solar pond, T_a is the ambient air temperature, k_{sw} is the thermal conductivity of the side and bottom walls, k_s is the thermal conductivity of the salty water, L_{HSZ} is the thickness of the HSZ (m), r is the inner radius of the cylindrical solar pond, Δx_{down} is the thickness of the down wall, Δx_{side} is the thickness of the side wall, $\Delta x_{HSZ\text{-}NCZ}$ is the thickness of the HSZ's middle point and the NCZ's middle point, and β is the fraction of the incident solar radiation that actually enters the pond and is given by Hawlader [15] as follows:

$$\beta = 1 - 0.6\left[\frac{\sin\theta_i - \sin\theta_r}{\sin\theta_i + \sin\theta_r}\right]^2 - 0.4\left[\frac{\tan\theta_i - \tan\theta_r}{\tan\theta_i + \tan\theta_r}\right]^2 \tag{21.3}$$

Here, θ_i and θ_r are the incidence and refraction angles. h represents the ratio of the solar energy reaching the depth in the layer I to the total solar incident falling on to the surface of the pond and is given by Bryant and Colbeck [16] as $h_I = 0.727 - 0.056\ln\left[\frac{(x_I - \delta)}{\cos\theta_r}\right]$ (here x_I is the thickness of the layer, δ, thickness of the layer in the UCZ where long-wave solar energy is absorbed).

As shown in Fig. 21.2, the exergy flows in UCZ can be illustrated. We first write the exergy balance equation for HSZ as

$$Ex_{r,NCZ} - [Ex_{d,HSZ} - Ex_{l,HSZ} + Ex_{sw,HSZ} + Ex_{b,HSZ}] = \Delta E_{st} \tag{21.4}$$
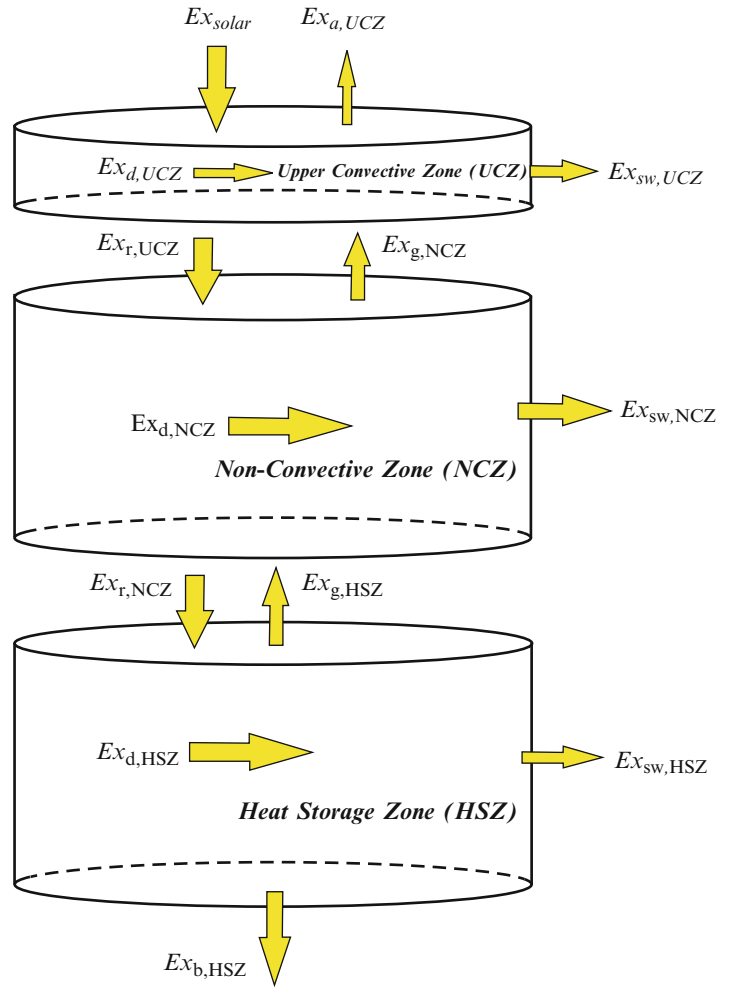
Here, $Ex_{r,NCZ}$ is the recovered exergy from NCZ for HSZ, $Ex_{d,HSZ}$ is the exergy destruction in HSZ, $Ex_{l,HSZ}$ is the exergy loss from HSZ to NCZ, $Ex_{sw,HSZ}$ is the exergy loss through side walls. $Ex_{b,HSZ}$ is the exergy loss through bottom wall and also, Ex_{st} is the exergy stored in HSZ. Here $Ex_{d,HSZ}$ is the exergy destruction in HSZ which can be written as:

$$Ex_{d,HSZ} = T_0(\Delta S_{net,HSZ}) \tag{21.5}$$

where ΔS_{net} is the net entropy change of NCZ which is defined as $\Delta S_{net} = \Delta S_{sys} + \Delta S_{surr}$. Then, the exergy losses, including exergy destructions, within NCZ can be derived as follows:

$$Ex_{d,HSZ} = T_0\left[m_{HSZ}C_{p,HSZ}\ln\frac{T_{HSZ}}{T_0} - \left(\frac{Q_{g,HSZ}}{T_{HSZ}} + \frac{Q_{sw,HSZ}}{T_0}\right) + \left(\frac{Q_b}{T_0}\right)\right] \tag{21.6}$$

$$Ex_{l,HSZ} = m_{HSZ}C_{p,HSZ}\left[(T_{HSZ} - T_{m,NCZ}) - T_0\left(\ln\frac{T_{HSZ}}{T_{m,NCZ}}\right)\right] \tag{21.7}$$

Here, $m_{HSZ} = \rho_{HSZ}V_{HSZ}$ is the mass of salty water in HSZ; ρ_{HSZ} is the averaged density as given earlier []; and V_{HSZ} is the volume of the salty water in HSZ. $C_{p,HSZ}$ is the specific heat of HSZ; T_0 is the reference environment temperature; T_{HSZ} is temperature of HSZ, and $T_{m,NCZ}$ denotes the average temperature of NCZ. We can now define the exergy efficiency for HSZ as the ratio of the exergy recovered from UCZ to the total exergy input to HSZ:

$$Ex_{sw,HSZ} = m_{HSZ}C_{p,HSZ}\left[(T_{HSZ} - T_{sw,HSZ}) - T_0\left(\ln\frac{T_{HSZ}}{T_{sw,HSZ}}\right)\right] \tag{21.8}$$

where $T_{sw,HSZ}$ denotes the side wall of the average temperature for HSZ.

Furthermore, $Ex_{b,HSZ} = Ex_{sw,HSZ}$; this is due to the fact that both side wall and bottom layer have the same insulating materials and are surrounded by the ambient air. We can now define the exergy efficiency for HSZ as the ratio of the exergy stored in HSZ to the total exergy input to HSZ which is essentially the exergy recovered from NCZ:

$$\Psi_{HSZ} = \frac{\Delta Ex_{st}}{Ex_{r,NCZ}} = 1 - \frac{Ex_{d,HSZ} + Ex_{l,HSZ} + Ex_{sw,HSZ} + Ex_{b,HSZ}}{Ex_{r,NCZ}} \tag{21.9}$$

Results and Discussion

The density gradient is an important part of the maintenance of the solar pond as it affects the heat storage performance. Figure 21.3 shows the alteration of the experimental salty solution densities with height from bottom to surface of the pond, throughout the 4 months. Here, density differences are observed between the density variation measured for these 4 different months, essentially due to increase of the inner zone's temperature and to diffusion of the salt molecules. As seen in Fig. 21.3, the density gradient in the solar pond is kept approximately stable. Some erosion is observed at the top of HSZ. The density erosion is prevented by using salt gradient protection system.

Regarding the experimental temperature distributions in Fig. 21.4, the average temperature of HSZ is observed to be a maximum of 52.42 °C in August, a minimum of 24.46 °C in November. Similarly, the average temperature of NCZ is observed to be a maximum of 44.29 °C in August, a minimum of 23.17 °C in November. The average temperature of UCZ is observed to be a maximum of 30.31 °C in August, a minimum of 15.16 °C in November.

Figure 21.5 shows both averaged energy and exergy distribution from August to November. As seen in the figure, the energy and exergy contents are determined to be a maximum of 114.77 MJ and 106.88 MJ in August, a minimum of 54.90 and 51.33 MJ in November, respectively. Difference of the energy and exergy is due to the fact that energy is conserved, but not exergy.

Figure 21.6 shows the variation of the exergy input, exergy stored, and destruction and losses from August to November. The exergy content distributions were calculated by using temperature distribution of the solar pond and the reference air temperature. As seen in Fig. 21.6, the exergy inputs are equivalent to the summation of exergy stored and exergy destruction and losses. The exergy stored appears to be a maximum of 27.84 MJ in August and a minimum of 6.48 MJ in November, respectively. The exergy destruction and losses appear to be a maximum of 79.05 MJ in August and a minimum of 44.84 MJ in November, respectively.

The energy and exergy efficiency variations are given in Fig. 21.7 for comparison purposes. As seen in the figure, the maximum and the minimum energy efficiencies of the solar pond are observed in August as 27.41 % and 12.64 % in November, respectively. Also, the maximum and the minimum exergy efficiencies of the solar pond are observed in August as 26.04 % and 12.62 % in November, respectively.
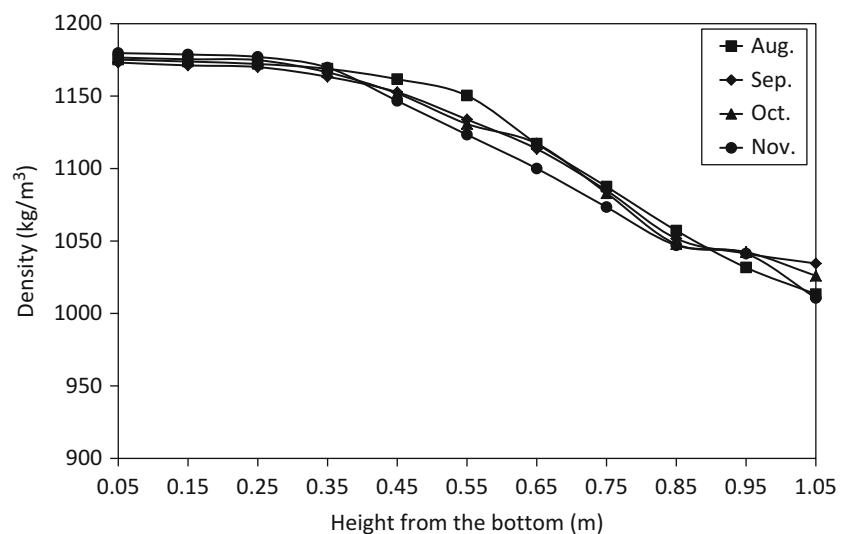
Fig. 21.3 Density distribution of MCSP

Fig. 21.4 Temperature distribution of MCSP
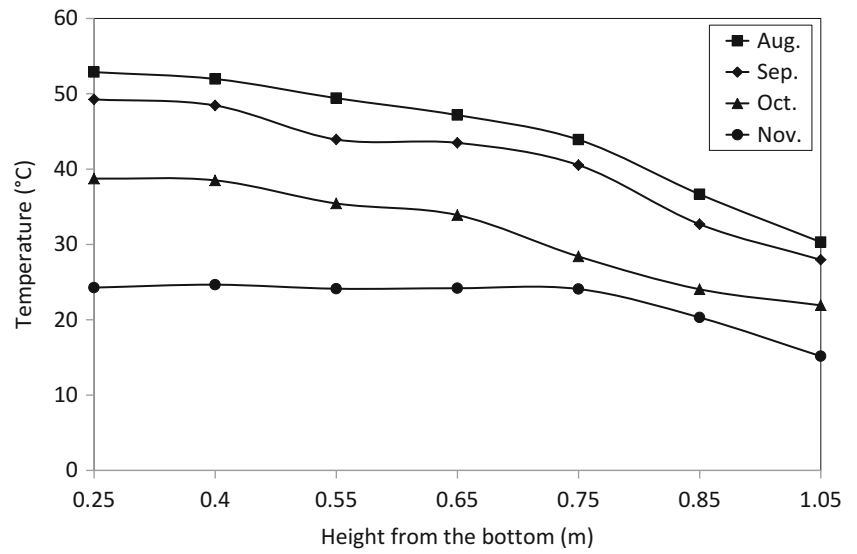
Fig. 21.5 The amount of energy and exergy input to HSZ
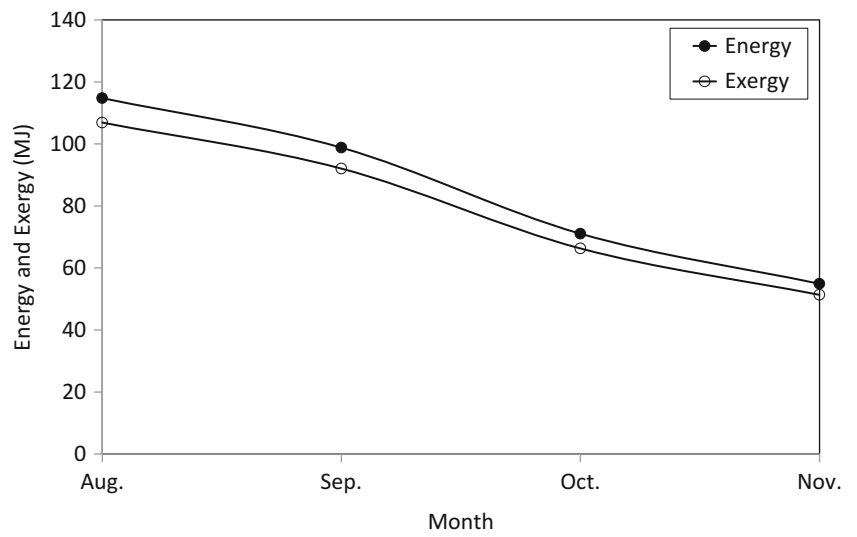
Fig. 21.6 Variations of the exergy input, stored, destruction, and losses of HSZ
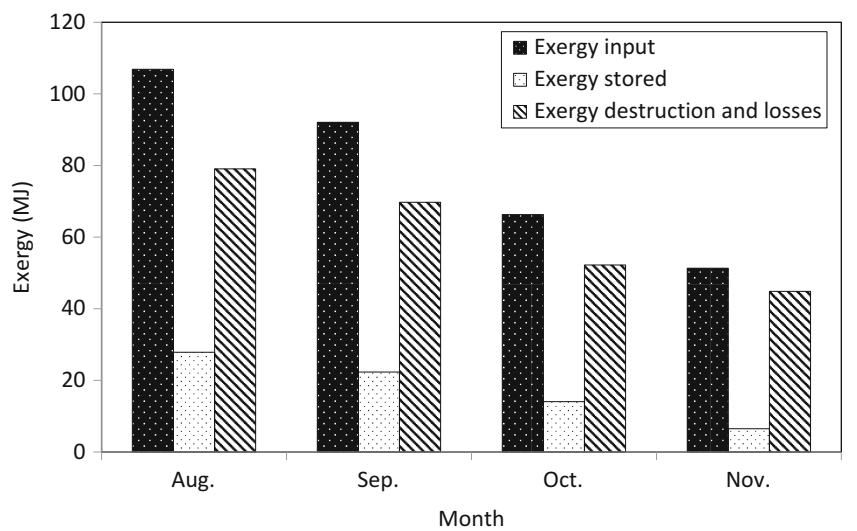
Fig. 21.7 Energy and exergy efficiency of MCSP
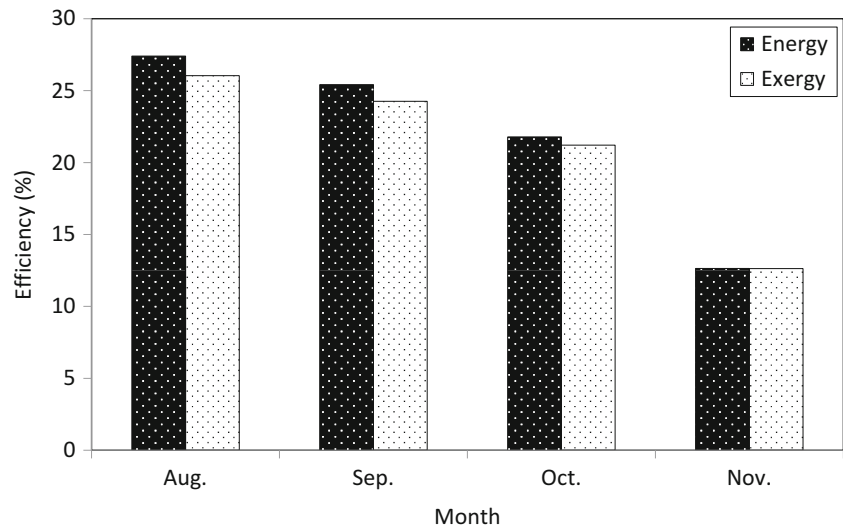
Conclusion

In this paper, we have studied both energetic and exergetic performances of a MCSP through efficiency analysis. Exergy efficiencies of a magnesium choloride water solar pond were found. The exergy efficiencies determined for storage zone using the experimental data are compared with the corresponding energy efficiencies. As expected, the exergy efficiencies appear to be little less than the energy efficiencies for storage zone of the solar pond due to the small magnitudes of exergy destructions in the storage zone and losses to surroundings. These results openly demonstrate the effect of the insulation materials and ambient temperature on the performance of the solar pond. It is important that exergy is a potential to help achieve better efficiency of the solar pond.

Nomenclature

A	Surface area, m^2	L	Thickness of the inner zones, m
C	Specific heat, J/kg K	m	Mass, kg
E	Total solar energy reaching to the pond, MJ/m^2	MCSP	Magnesium chloride solar pond
		NCZ	Non-convective zone
Ex	Exergy, J	Q	Heat, J
F	Absorbed energy fraction at a region of δ-thickness	r	Inner radius, m
		S	Entropy, J/K mol
h	Solar radiation ratio	T	Temperature, °C
HSZ	Heat storage zone	UCZ	Upper convective zone
k	Thermal conductivity, J/m °C	V	Volume, m^3

Greek Letters

η	Energy efficiency	θ	Angle, rad
δ	Thickness where long-wave solar energy is absorbed, m	ρ	Density, kg/m^3
		ψ	Exergy efficiency
β	Incident beam entering rate into water		

Subscripts

a	Ambient	NCZ	Non-convective zone
b	Bottom	net	Net irradiation
d	Destruction	out	Energy output
dw	Down wall	r	Refraction
g	Gained	rec	Recovered
HSZ	Heat storage zone	surr	Surrounding
i	Incident	sw	Side wall
in	Energy input	sys	System
m	Mean		

References

1. Orhan MF, Dincer I, Rosen MA, Kanoglu M (2012) Integrated hydrogen production options based on renewable and nuclear energy sources. Renew Sustain Energy Rev 16:6059–6082
2. Date A, Alam F, Khaghani A, Akbarzadeh A (2012) Investigate the potential of using trilateral flash cycle for combined desalination and power generation integrated with salinity gradient solar ponds. Procedia Eng 49:42–49
3. El-Sebaii AA, Aboul-Enein S, Ramadan MRI, Khallaf AM (2011) Thermal performance of an active single basin solar still (ASBS) coupled to shallow solar pond (SSP). Desalination 280:183–190
4. Karakilcik M, Dincer I (2008) Exergetic performance analysis of a solar pond. Int J Therm Sci 47:93–102
5. Karakilcik M, Dincer I, Rosen MA (2006) Performance investigation of a solar pond. Appl Therm Eng 26:727–735
6. Leblanc J, Akbarzadeh A, Andrews J, Lu H, Golding P (2011) Heat extraction methods from salinity-gradient solar ponds and introduction of a novel system of heat extraction for improved efficiency. Solar Energy 85:3103–3142
7. Nie Z, Bu L, Zheng M, Huang W (2011) Experimental study of natural brine solar ponds in Tibet. Solar Energy 85:1537–1542
8. Sakhrieh A, Al-Salaymeh A (2013) Experimental and numerical investigations of salt gradient solar pond under Jordanian climate conditions. Energy Convers Manage 65:725–728
9. Bozkurt A, Karakilcik M (2012) The daily performance of a solar pond integrated with solar collectors. Solar Energy 86:1611–1620
10. Karakilcik M, Dincer I, Bozkurt I, Atiz A (2013) Performance assessment of a solar pond with and without shading effect. Energy Convers Manage 65:98–107
11. Subhakar D, Murthy SS (1991) Experiments on a magnesium chloride saturated solar pond. Renew Energy 5–6:655–660
12. Subhakar D, Murthy SS (1993) Saturated solar ponds: 2. Parametric studies. Solar Energy 50:307–319
13. Subhakar D, Murthy SS (1994) Saturated solar ponds: 3. Experimental verification. Solar Energy 53:469–472
14. Akbarzadeh A, Macdonald RWG (1982) Introduction of a passive method for salt replenishment in the operation of solar ponds. Solar Energy 29:71–76
15. Hawlader MNA (1980) The influence of the extinction coefficient on the effectiveness of solar ponds. Solar Energy 25:461–464
16. Bryant HC, Colbeck I (1977) A solar pond for London. Solar Energy 19:321

Performance Assessment of a Recuperative Helium Gas Turbine System

22

Rami Salah El-Emam and Ibrahim Dincer

Abstract

Helium is considered an ideal working fluid for closed cycle gas turbines powered by the heat of nuclear reactors or solar concentrators. Energetic and exergetic based thermodynamic analyses are applied to an actual 120 MW recuperative closed gas turbine operating with helium with two compression stages. The maximum pressure and temperature of the plant are taken as 70 bar and 850 °C at the turbine inlet. Parametric studies are performed to investigate the effects of different parameters on the plant performance and the irreversibilities associated with the system operation. In the exergy analysis, internal and external irreversibilities are considered. At the optimal pressure ratio, the energy and exergy efficiencies obtained here are found as 45.5 and 60.5 % at the base case. Also, various exergetic parameters are calculated for the exergy assessment of the gas turbine plant. Furthermore, gas turbine exergetic performance map is introduced.

Keywords

Energy • Exergy • Efficiency • Pressure ratio • Closed cycle • Gas turbine

Introduction

Several gas turbine plants, based on the well-established closed cycle gas turbine technologies, are in operation for over hundreds of thousand hours. The main advantages of this technology is its adaptability to a wide range of fuels, e.g., gas, oil, coal, solar, and nuclear fuels and the possibility to use different working gases, e.g., air, helium, nitrogen, carbon dioxide, argon, neon, or their mixtures. Helium is the one of the most suitable working fluids for large closed cycle gas turbine plants. Helium turbines, based on a closed Brayton gas cycle, are also considered proper alternative for efficient power generation for nuclear reactors. Helium is radioactive stable, inert, and noncorrosive gas [1–3]. Helium gas offers a high thermal capacity as well.

In addition, helium gas turbine is a candidate as a multi-generation energy system for different purposes. The heat rejected from the plant is available at high temperature. It can be utilized for combined cooling and heat production, water desalination, process steam and industrial process heat in integrated chemical plants. In early 1960s, two helium closed cycle

R.S. El-Emam (✉)
Faculty of Engineering and Applied Science, University of Ontario Institute of Technology, 2000 Simcoe Street North, Oshawa, ON, Canada L1H 7K4

Faculty of Engineering, Mansoura University, Mansoura, Egypt
e-mail: rami.elemam@uoit.ca

I. Dincer
Faculty of Engineering and Applied Science, University of Ontario Institute of Technology, 2000 Simcoe Street North, Oshawa, ON, Canada L1H 7K4

gas turbines were built for power generation and air liquefaction, heat was provided to the gas at 650–660 °C and 18–23 bar through a natural gas furnace. In 1974, a helium gas turbine achieved a 30 MW of power production when the turbine was fed with helium at 750 °C and 27 bar [2]. Helium turbines are also used integrated with nuclear reactors where heat is to be provided through molten salt blanket or heat exchanger that transmits the heat from the reactor cooling system to the helium turbine plants. Conn et al. [1] studied a conceptual design of 500 MW helium gas turbine units to be utilized with a nuclear reactor. The operating turbine inlet temperature was set to 870 °C at around 68 bar. Solar energy is a good source of heat to helium turbines as well. The low density and high thermal capacity of helium facilitate a more efficient operation of the gas turbine at more compact design of the heat exchangers of the system. Heat can be provided using heliostat solar towers or parabolic dish technology and it can be concentrated to a high pressure helium heater or through a molten salt heat exchanger with storage tank.

Various studies in the literature have been undertaken to investigate the performance of helium gas turbine power plants. Some researchers [4] performed a review study on helium turbines that works with the high temperature gas cooler reactors. A model for calculating the design point performance of the gas turbine plant was developed in this study. A transient analysis software for high temperature cooled reactor helium gas turbine was developed [5]. A review on the helium gas turbine history and the operation experience from different test and power facilities was performed [6], focusing on the helium turbines powered by the nuclear heat as well. Multi-reheat helium gas turbine was investigated [7] at different turbine inlet temperature values and achieved a thermal efficiency of 39–47 %, respectively.

The thermodynamic assessment of closed cycle gas turbine plant is performed at different operating conditions at steady and transit operation. A recuperative closed cycle gas turbine of a scramjet was thermodynamically investigated [8]. They presented a thermal management system for reducing the hydrogen cooling flow and also studied the effect of different operating parameters on the system performance. A work [9] was performed to study the effects of different pressure ratios on a solar-driven closed cycle gas turbine.

The present work aims to investigate the system performance, through energetic and exergetic efficiencies, of an actual helium closed cycle recuperated gas turbine with intercooling, through energy and exergy analyses. The performance parameters are studied, and the effects of changing the operating parameters on the performance are also considered. The pressure losses on the cycle are taking into consideration in the energy and irreversibility analyses. Including the internal irreversibility calculations give a more realistic analysis of the gas turbine. The performance of the gas turbine is defined in this work in a novel representation with respect to the exergy efficiency. The exergetic performance map is introduced as a more descriptive approach with respect to the actual potential of gas turbine performance improvement at certain operating condition. Exergetic loss map is also introduced as a new exergetic assessment map. It relates the exergy destruction ratio, with respect to the total exergy of fuel streams, to the specific work or the dimensionless work parameter.

System Description

The enthalpy–entropy diagram for simple closed cycle gas turbine is shown in Fig. 22.1. The diagram shows a realistic cycle with considering the pressure losses that causes internal irreversibilities in the cycle heat exchangers. Turbine and compressor irreversibilities in form of the device adiabatic efficiency are considered in this diagram as well. P_H and P_L on this diagram represent the highest and lowest actual operating pressure in the cycle, and the pressure ratio of the gas turbine is defined in this study based on these two values.

The recuperative closed cycle helium gas turbine considered in this study is shown in Fig. 22.2. A two-stage compression with intercooling is considered for this system, while one turbine is used for power production and to drive the compressors. After being heated, helium expands through the turbine. The low pressure gas from the turbine enters a heat transfer recuperator to heat the cooler gas at the high pressure side of the cycle. The cooled helium leaving the recuperator is directed to another heat exchanger that works as a precooler before the compressor. The working fluid is further cooled in the precooler. Heat rejected from the cooler can be transferred to generator of an absorption cooling system for cogeneration. Two stage compressions with intercooler are used to raise the helium pressure to its highest value in the cycle. Then helium is heated by the turbine low pressure outlet gas through the recuperator before it goes to the main heat source.

Fig. 22.1 Enthalpy–Entropy diagram of a realistic simple closed cycle gas turbine
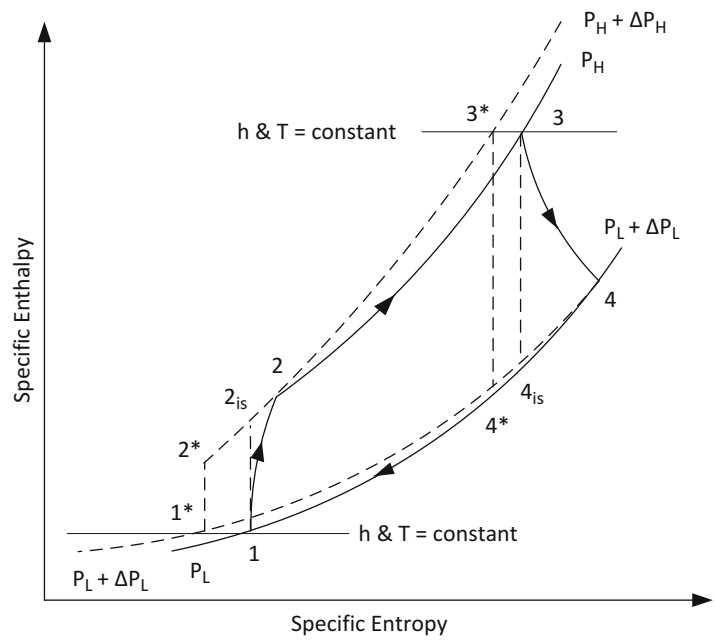
Fig. 22.2 Schematic of recuperative closed cycle gas turbine with intercooler
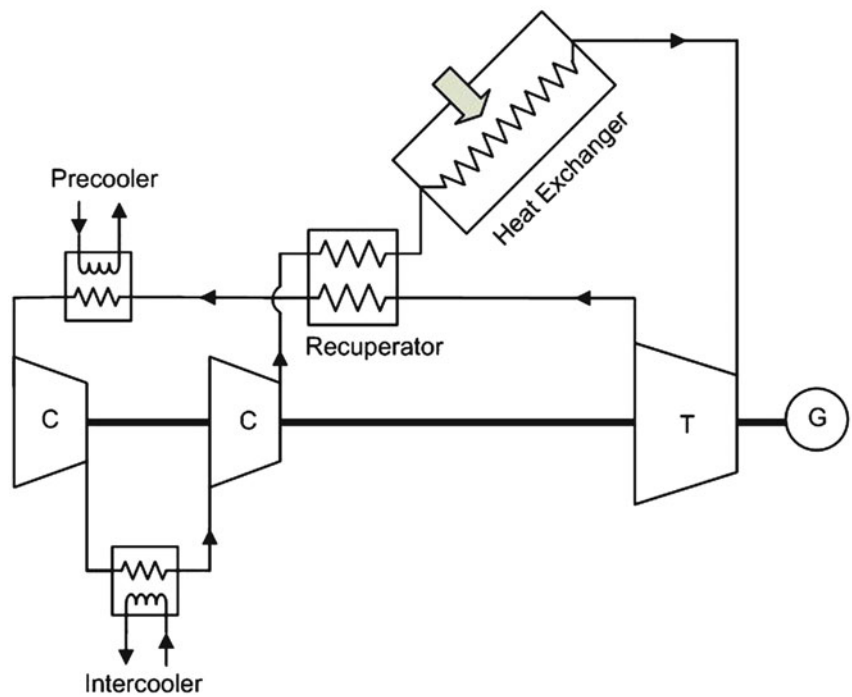
Thermodynamic Modeling

In a thermodynamic study, it is essential to make some assumptions for analysis and assessment. In this study, the following assumptions for energy and exergy analyses of the system are considered:

– Turbine and compressors are adiabatic.
– The plant operates at steady state conditions.
– Helium properties are taken for ideal gas assumption.
– Heat source is considered as molten salt at constant temperature.

– The pressure ratio is defined in terms of the higher pressure, P_H, and lower pressure, P_L, of the cycle after considering the pressure losses.
– The ambient temperature and pressure are constant.
– No cogeneration and no use of the rejected heat of the cycle are considered in the exergy assessment calculations.
– The changes in kinetic and potential energies and exergies are negligible.

Energy Analysis

The prescribed helium gas turbine energy performance is investigated and modeled in the following subsections. The energy analysis of the components is performed and the components performance is described in form of the following parameters:
– Turbine and compressor polytropic efficiency.
– Plant pressure ratio.
– Plant temperature ratio.
– Heat exchangers effectiveness.
– Heat exchangers pressure loss coefficients.

The first law of thermodynamics is applied to each of system components. The following equation represents the concept of conservation of energy for an open system:

$$dE/dt = \sum \dot{Q} - \dot{W} + \sum_{in} \dot{m}\, h - \sum_{out} \dot{m}\, h \tag{22.1}$$

where the changes in kinetic and potential energies across the system are considered negligible.

Exergy Analysis

The practical operation of any system is an irreversible operation, where work is destroyed based on the entropy generation rate that is associated with the operating process. The amount of lost available work can be defined as the difference between the reversible work when no irreversibilities are considered, i.e., entropy generation is zero, and the system actual irreversible work.

$$\dot{W}_{loss} = \dot{W}_{rev} - \dot{W} \tag{22.2}$$

The lost available work is not an actual energy loss; it represents a lost opportunity to convert part of the energy utilized into a useful work. The lost available work was defined [10] in a direct proportional relation with the entropy generation rate. This is better described by the exergy destruction term which expresses the system irreversibility as follows:

$$\dot{Ex}_d = T_o.\dot{S}_{gen} \tag{22.3}$$

The temperature T_o is the defined as the dead state temperature. It is the temperature at which the system cannot undergo any state change through any interactions with the environment [11]. The entropy generation for a general open system can be determined based on the second law of thermodynamics.

$$\dot{S}_{gen} = \frac{dS}{dt} - \sum \frac{\dot{Q}}{T} + \sum_{out} \dot{m}s - \sum_{in} \dot{m}s \tag{22.4}$$

where T is the temperature of the boundaries at which the heat transfer occurs:

$$\dot{W} = \sum \left(1 - \frac{T_o}{T}\right)\dot{Q} + \sum_{in} \dot{Ex} + \sum_{out} \dot{Ex} - \frac{d(E - T_oS)}{dt} - \dot{Ex}_d \tag{22.5}$$

The term $\dot{Ex}$ expresses the exergy flow rate or the exergy associated with the mass flow rate of the streams that enter or exit from the system. It is defined as:

$$\dot{Ex} = \dot{m}\, ex = \dot{m}(h - T_o\, s) \tag{22.6}$$

Table 22.1 The helium turbine plant operating parameters

Operating parameters for base case	
Net power output	120 MW
Turbine polytropic efficiency	92 %
Compressor polytropic efficiency	90 %
Mechanical efficiency	99 %
Recuperator effectiveness	88 %
Precooler effectiveness	90 %
Intercooler effectiveness	87 %
Pressure loss in recuperator, hot side	2.1 %
Pressure loss in recuperator, cold side	1.8 %
Pressure loss in precooler, hot side	1.2 %
Pressure loss in intercooler, hot side	1.3 %
Turbine inlet temperature	850 °C
Compressor inlet temperature	40 °C
Turbine inlet pressure	70 bar
Plant temperature ratio	313/1,123 K
Ambient temperature	25 °C
Hot source temperature	930 °C
Cooling water inlet temperature	25 °C

The exergy destruction rate is applied on the prescribed gas turbine plant components as illustrated in the following section, considering the ideal gas behavior of the working fluid.

The exergy destruction is expressed taking external and internal irreversibilities into consideration. External irreversibilities are associated with the heat transfer between the working fluid and the hot and cold reservoirs at the source and dead state temperature values, respectively. Internal irreversibilities are the mainly accompanied with the finite pressure drop across the system devices. In the following sections, energy and exergy analyses of each for system components are presented.

Compressor Modeling

The system in this study has two compression stages. The total pressure ratio is a design parameter as in Table 22.1. The compressor is considered adiabatic and its polytropic efficiency is also provided as in Table 22.1. Practically, helium compressor blades design is different than the air compressors. It has to account for the flow separation and secondary flow occurrence to achieve a better performance [4, 6]. Also, due to helium low molecular weight, a more reliable sealing mechanism needs to be integrated with the compressor and the other system components to avoid leakage [12]. Based on the defined pressure ratio and polytropic efficiency of the compressor, and the plant temperature ratio; the power required to drive the compressor can be formulated as follows:

$$\dot{W}_C = \dot{m} \, c_p \, T_H \, \beta \left(\frac{r_c^k - 1}{\eta_{C,a} \, \eta_{mech}} \right) \tag{22.7}$$

where T_H is the highest temperature at the gas turbine plant, i.e., turbine inlet condition, β is the operational temperature ratio, and is defined as follows:

$$\beta = \frac{T_L}{T_H} \tag{22.8}$$

and k is function of the heat capacity ratio:

$$k = \frac{\gamma - 1}{\gamma} \tag{22.9}$$

The pressure ratio is defined as the ratio between the higher and lower pressure across the compressor, which is defined as follows, taking into consideration the pressure losses at the high and low pressure streams of the working fluid.

$$r_c = \frac{P_H}{P_L} \tag{22.10}$$

The compressor adiabatic efficiency can be defined as a function of the polytropic efficiency as follows:

$$\eta_{C,a} = \frac{r_c^k - 1}{r_c^{k/\eta_{C,p}} - 1} \tag{22.11}$$

The temperature of the stream exits the compressor is to be estimated based on the inlet temperature of the working fluid:

$$T_{C,ex} = T_{C,in} \left(1 + \frac{r_c^k - 1}{\eta_{C,a}} \right) \tag{22.12}$$

Considering an adiabatic compression process, the exergy destruction rate associated with this process can be formulated as a function of the total pressure ratio of the gas turbine plant and the compressor adiabatic efficiency as follows:

$$\dot{Ex}_{d,C} = \dot{m}\, T_o\, c_p\, \ln\left[\left(\frac{1}{r_c^k} - 1 \right) \left(1 - \frac{1}{\eta_{C,a}} \right) + 1 \right] \tag{22.13}$$

For the calculations, identical adiabatic efficiency values are then chosen for the two operating compressors.

Intercooler Modeling

The high thermal conductivity and heat transfer coefficient of helium, compared with air, results in more compact designs of the utilized heat exchangers. The use of intercooler in between compression stages is a standard feature of efficient gas compressors. The total compression required power is formulated as a function of the total pressure ratio and the compressors stage adiabatic efficiency as follows:

$$\dot{W}_C = \frac{\dot{m}\, c_p\, T_H\, \beta}{\eta_{mech}} \left(r_c^{k/N_C} - 1 \right) \sum_{N_C} \left(\frac{1}{\eta_{C,a}} \right) \tag{22.14}$$

For two compression stages with intercooling and the same adiabatic efficiency of the two stages, the total compression work becomes

$$\dot{W}_C = 2.\dot{m}\, c_p\, T_H\, \beta \left(\frac{r_c^{k/2} - 1}{\eta_{C,a}\, \eta_{mech}} \right) \tag{22.15}$$

which does not count for the pressure loss in the intercooler. For the definition of the total pressure ratio in this study as the final pressure after second compression stage over the lowest pressure at the inlet of the first compression stage, after considering the total pressure loss in the cycle, the second stage of compression would count for the drop in the pressure at the intercooler, which means a slightly higher pressure ratio would be required for the second compression stage to achieve the design total pressure ratio of the plant. This results in more required work to drive the high pressure compressor, even if the two compressors operate at the same adiabatic efficiency.

The heat transfer rate removed from the working fluid at the intercooling stage is formulated as follows with the assumption that the flow exits the intercooler at the inlet temperature of the preceding compressor:

$$\dot{Q}_{IC} = \dot{m}\, c_p\, (T_{C,ex} - T_H\, \beta) \tag{22.16}$$

where $T_{C,ex}$ is the temperature at the exit of the preceding compression stage, at the intercooler inlet.

In the intercooler, there are irreversibilities associated with the heat transfer within the temperature difference between the stream flow and the ambient, and irreversibility associated with the flow due to the pressure drop across the device. The exergy destruction in the intercooler can be described as follows, based on the output of the energy analysis:

$$\dot{Ex}_{d,IC} = \left(\frac{\dot{Q}_{IC}}{T_{IC}/T_o}\right) - \dot{m}\,T_o\left[(s_{IC,in} - s_{IC,ex})|_{P_{IC}} - R\left(\frac{\Delta P}{P}\right)_{IC}\right] \tag{22.17}$$

Here, the destruction of exergy is expressed for an equivalent intercooler that works with no pressure loss, and hence slightly warmer, and then the entropy increase because of the pressure drop is added as it is expressed in the equation for an ideal gas assumption.

Gas Turbine Modeling

The efficiency of the helium turbine is highly affected by its design, which is a bit different from the conventional gas turbine design. It has shorter blade height and this result in an increase of the blade tip clearance leakage [4, 6, 12]. On the other hand, compared with a steam turbine, a helium gas turbine is more economic due to the less material requirements as the blades of the former are ten times larger in length [2, 13]. The power output of the gas turbine is formulated in the following form, as function of the plant pressure ratio:

$$\dot{W}_T = \dot{m}\,\eta_{T,a}c_p\,T_H\left[1 - \frac{1 + k\cdot\sum\left(\frac{\Delta P}{P}\right)}{r_c^k}\right] \tag{22.18}$$

where the turbine adiabatic efficiency is calculated as a function of the polytropic efficiency of the turbine as follows:

$$\eta_{T,a} = \frac{1 - (1/r_T)^{\frac{k}{\eta_{T,p}}}}{1 - (1/r_T)^k} \tag{22.19}$$

The turbine pressure ratio is to be determined based on the defined pressure ratio of the compression stages, considering the pressure losses in the working fluid streams across the different system components, as follows:

$$r_T = \frac{P_{T,in}}{P_{T,ex}} = r_c \cdot \left[\frac{1 - \left[\left(\frac{\Delta P}{P}\right)_{HE} + \left(\frac{\Delta P}{P}\right)_{R,c}\right]}{1 + \left[\left(\frac{\Delta P}{P}\right)_{PC} + \left(\frac{\Delta P}{P}\right)_{R,h}\right]}\right] \tag{22.20}$$

The total pressure loss effect in the turbine work equation is the summation of the pressure loss coefficients in the hot and cold streams of the recuperator, the hot streams of the precooler and intercooler, and the cold stream of the main heat exchanger.

$$\sum\left(\frac{\Delta P}{P}\right) = \left(\frac{\Delta P}{P}\right)_R + \left(\frac{\Delta P}{P}\right)_{PC} + \left(\frac{\Delta P}{P}\right)_{IC} + \left(\frac{\Delta P}{P}\right)_{HE} \tag{22.21}$$

where the recuperator pressure loss is described as the summation of its hot and cold streams pressure losses.

$$\left(\frac{\Delta P}{P}\right)_R = \left(\frac{\Delta P}{P}\right)_{R,h} + \left(\frac{\Delta P}{P}\right)_{R,c} \tag{22.22}$$

The temperature value at the exit of the turbine is to be determined as follows:

$$T_{T,ex} = T_H\left(1 - \eta_{T,a}\left(1 - \frac{1}{r_T^k}\right)\right) \tag{22.23}$$

as a function of the operating compressor pressure ratio.

The irreversibility associated with the turbine, amounts to the following form, as a function of the gas turbine operating parameters:

$$\dot{Ex}_{d,T} = \dot{m} \, T_o \, c_p \, \ln\left[1 - \left(r_T^k - 1\right)\left(\eta_{T,a} - 1\right)\right] \tag{22.24}$$

Here, the working fluid is treated as an ideal gas with constant specific heat.

Recuperator Modeling

From the defined recuperator effectiveness, the temperature at the exit of the cold stream, at the high pressure side, is determined:

$$T_{R,c,ex} = T_H \left[\beta(1 - \varepsilon_R)\left(1 + \frac{\left(\sqrt{r_c}\right)^k - 1}{\eta_{HC,a}}\right) + \varepsilon_R \left[1 - \frac{1 + k \cdot \sum\left(\frac{\Delta P}{P}\right)}{r_c^k/\eta_{T,a}}\right]\right] \tag{22.25}$$

This formula is derived based on the following recuperator effectiveness definition:

$$\varepsilon_R = \frac{T_{R,c,ex} - T_{R,c,in}}{T_{R,h,in} - T_{R,c,in}} \tag{22.26}$$

The hot stream exit temperature, on the low pressure side, is to be determined by applying the energy balance on the hot stream, at low pressure side, as follows:

$$T_{R,H,ex} = T_{R,H,in} - \dot{Q}_R/(\dot{m} \, c_p) \tag{22.27}$$

where $\dot{Q}_R$ is the heat transfer through the recuperator from the hot stream to cold stream. It is simply calculated from the energy balance of the cold stream:

$$\dot{Q}_R = \dot{m} \, c_p (T_{R,c,ex} - T_{R,c,in}) \tag{22.28}$$

By defining the exit streams of the recuperator, the analysis of the main heat exchanger and the precooler can be performed. Based on the two working fluid streams passing through the recuperator, the exergy associated with the recuperator can be formed as follows:

$$\dot{Ex}_{d,R} = \dot{m} \, T_o \left[(s_{R,c,ex} - s_{R,c,in})|_{P_H} + (s_{R,H,ex} - s_{R,H,in})|_{P_L} + R\left(\frac{\Delta P}{P}\right)_R\right] \tag{22.29}$$

Same as for the other heat exchangers in this analysis, the entropy generation analysis is performed and is formed in a no pressure loss entropy differences, and then the internal irreversibility caused by the pressure losses in hot and cold streams is added. The total pressure coefficient in the recuperator is equal to both sides' pressure losses coefficients. In the recuperator case, pressure loss at both sides need to be considered as the irreversibility analysis is performed on both flow streams considering the heat transfer effect in form of sates difference between inlet and outlet streams.

Heat Exchanger Modeling

Based on the defined highest temperature of the gas turbine plant, the heat rate required to be supplied to the working fluid through the heat exchanger can be calculated as follows:

$$\dot{Q}_{HE} = \dot{m} \, c_p \, T_H \left(1 - \frac{T_{R,c,ex}}{T_H}\right) \tag{22.30}$$

The working fluid, after being heated by the hot, low pressure stream at the recuperator, it passes through the main heat exchanger which provides the required amount of heat to reach the turbine inlet temperature with enough potential to gain the required power. The following equation expresses the destruction of exergy associated with this process:

$$\dot{Ex}_{d,HE} = \dot{m}\, T_o \left[\left(\frac{-\int_{in}^{ex} T ds \big|_{P_H}}{T_{HE}} \right) + (s_{HE,ex} - s_{HE,in})\big|_{P_H} + R\left(\frac{\Delta P}{P}\right)_{HE} \right] \tag{22.31}$$

The first term in the brackets represents the specific heat gained by the working fluid considering the heat transfer to happen at constant pressure, where:

$$\int_{in}^{ex} T ds \bigg|_{P_H} = q_{HE} \tag{22.32}$$

In the exergy destruction equation, the external irreversibility in the heat exchanger is expressed by the first two terms in the brackets. This part of irreversibility is associated with the heat transfer to the working fluid within the temperature difference between the source temperature T_{HE}, and the working fluid bulk temperature through the heat exchanger, considering no pressure loss to occur during the process. To add the effect of the pressure drop, the internal irreversibility is added in terms of pressure loss across the heat exchanger for ideal gas case as shown in the last term of the equation.

The temperature T_{HE} is the heating source temperature and is calculated, in analogous with the open gas turbine engine with combustion, based on the definition of the optimal effective flame temperature of the combustion products. It can be formulated as function of the heating molten salt temperature as follows:

$$T_{HE} = \frac{T_{s,in} - T_o}{ln(T_{s,in}/T_o)} \tag{22.33}$$

More details regarding the calculation of the optimal flame temperature can be found elsewhere [14].

Precooler Modeling

The heat released from the low pressure stream at the intercooler is determined as follows, based on the energy balance on this stream:

$$\dot{Q}_{PC} = \dot{m}\, c_p\, (T_{R,h,ex} - T_H\, \beta) \tag{22.34}$$

In the same way of calculating the exergy destruction in the intercooler, the exergy destruction in the precooler can be formed as follows:

$$\dot{Ex}_{d,PC} = \left(\frac{\dot{Q}_{PC}}{T_{PC}/T_o} \right) - \dot{m}\, T_o \left[(s_{PC,ex} - s_{PC,in})\big|_{P_L} - R\left(\frac{\Delta P}{P}\right)_{PC} \right] \tag{22.35}$$

Here, the term $(s_{PC,ex} - s_{PC,in})\big|_{Pl}$ is the entropy difference considering the process through the intercooler occurs at constant pressure with no pressure losses. $R(\Delta P/P)_{PC}$ represents the entropy change as a result of the pressure loss at the working fluid side, considering ideal gas behavior.

Energetic Assessment

The thermal energy efficiency can be formulated, based on the shown analysis, in form of the gas turbine thermal design parameters for a closed recuperative gas turbine cycle with two compression stages as follows:

$$\eta_{th} = \frac{\left[\frac{r_c^k-1-k\cdot\sum(\Delta P/P)}{r_c^k/\eta_{T,a}}\right] - \left[\frac{1}{\eta_{LC,a}}+\frac{1}{\eta_{HC,a}}\right]\left[\frac{\beta\left(\left(\sqrt{r_c}\right)^k-1\right)}{\eta_{mech}}\right]}{1-\left[\beta(1-\varepsilon_R)\left(1+\frac{\left(\sqrt{r_c}\right)^k-1}{\eta_{HC,a}}\right) + \varepsilon_R\left[1-\frac{1+k\cdot\sum(\Delta P/P)}{r_c^k/\eta_{T,a}}\right]\right]} \tag{22.36}$$

The optimal pressure ratio of the plant is determined at maximum thermal efficiency, by differentiating the previous formula with respect to pressure ratio, r_c, setting $d\eta_{th}/dr_c$ to zero for maximum efficiency. The pressure ratio for each compressor stage in this relation are assumed to be identical, however, with considering the pressure loss in the intercooler, they will be slightly different as mentioned before, based on the given definition of the higher and lower pressure values of the gas turbine cycle.

Another parameter used to describe the system performance is the dimensionless net work output of the gas turbine plant. The dimensionless work is to be calculated by relating the actual specific work output to the total potential of producing work expressed in terms of the temperature ratio and the turbine inlet temperature as follows:

$$W_{dimless} = \frac{w_{net}}{c_p T_H(1-\beta)} \tag{22.37}$$

The dimensionless work is used to express the results of the energetic performance of the system.

Exergetic Assessment

The helium turbine plant performance can be described in different exergy parameters. The exergy efficiency of the overall plant performance can be expresses in terms of the useful exergy output of the plant over the exergy of the fuel supplied in form of exergy of the heat added to the system:

$$\psi = \frac{\dot{Ex}_{output}}{\dot{Ex}_f} \tag{22.38}$$

It can be also estimated based on the exergy destruction calculation as follows:

$$\psi = 1 - \frac{\sum\dot{Ex}_d}{\dot{Ex}_f} \tag{22.39}$$

Each of the exergy destruction rates in system components is described as percentage of the total exergy destruction:

$$y_D = \frac{\dot{Ex}_d}{\sum\dot{Ex}_d} \tag{22.40}$$

The exergy destruction can be expressed by the exergy destruction ratio as it is defined by relating the exergy destruction rate in each component to the total exergy rate of the fuel to the system.

$$Ex_R = \frac{\dot{Ex}_d}{\sum\dot{Ex}_F} \tag{22.41}$$

Another parameter is the sustainability index, which helps in giving an indication of the improvement potential for more efficient use of the available resources of the system as follows:

$$SI = \frac{1}{1-\psi} \tag{22.42}$$

Table 22.2 Thermodynamic simulation model verification

Parameter	Current model	Literature data	Difference (%)
Specific heat in regenerator	1,802 kJ/kg	1,883 kJ/kg	4.30
Specific heat in intercooler	427.2 kJ/kg	428.6 kJ/kg	0.32
Specific heat in precooler	683.1 kJ/kg	685.9 kJ/kg	0.41
Overall thermal efficiency	45.68 %	46 %	0.70
Temperature after compression	127.5 °C	125.5 °C	1.59
Temperature after expansion	521.9 °C	537.7 °C	2.93

The improvement potential for each of the system components can be measured in energy units based on the following relation [15]:

$$IP = (1 - \psi)\left(\dot{Ex}_{in} - \dot{Ex}_{ex}\right) \tag{22.43}$$

And it can be also related to the plant net power output in a percentage form.

Case Study

For verifying the modeling code of the helium closed cycle gas turbine presented in this study, the results for a case study are compared in the following section with data of a helium gas turbine operating with power reactor as presented in [1]. The turbine inlet conditions are 871 °C and 69 bar. The compressor inlet temperature and pressure are 43.3 °C at 26.2 bar. This gas turbine is of 500 MW power and operates at 46 % of thermal efficiency. The adiabatic efficiency of the turbine and the high and low pressure compressors are 91, 89, and 89 %, respectively. The effectiveness of the recuperator, intercooler, and precooler are 88, 88, and 92 %, respectively. Considering the same losses in the heat exchangers streams, Table 22.2 shows the comparison of the results of thermodynamic properties and parameters of the current model compared with the data provided in the literature.

Results and Discussion

The energy and exergy analyses are performed on the prescribed system in the base case operating conditions as shown in Table 22.1. The results of the exergy analysis of the system components are given in Table 22.3. Different plant high-temperature values are studied, and the optimal operating pressure ratio is calculated based on the energy model of the system. The results in Table 22.3 show the exergy destruction rates and their ratios as percentage of the total exergy destruction of the system. The exergy efficiency calculations are also shown. Table 22.4 shows the results of the energy and exergy analyses of the overall system performance. The results show that for the same compressor inlet temperature, increasing the turbine inlet temperature results in a higher energy and exergy efficiency as a result of the higher operating optimal pressure ratio of the gas turbine plant. In the same Table, the increase of the specific work output, which reflects the enthalpy potential of producing useful work, is shown. This causes a decrease in the helium flow rate demand, for the same power output. This highly affects the economic viability of the heat exchangers and turbomachinery as the mass flow rate is to be increased by 40 % for a decrease in the temperature ratio from 2.8 to 2.4 at the same compressor inlet temperature.

Figures 22.3, 22.4, and 22.5 show the results of the parametric study of the pressure ratio effect on different performance parameters. The results in these figures are calculated at the base condition listed in Table 22.1. Figure 22.3 shows the change of the energy and exergy efficiencies with the pressure ratio; the energy efficiency shows a maximum of 45.48 % at a pressure ratio of 2.74; however, the exergy efficiency reaches a maximum of 60.6 % at pressure ratio of 2.78. It is important to note that exergy efficiency is higher than the corresponding energy efficiency due to the fact that the exergy of the heat added is considered as the exergy input in calculating the exergy efficiency. The dimensionless work is also shown in the same figure; it is as an indication of the produced power with respect to the theoretical maximum potential. It gives a peak at the pressure ratio of 6.2. At this value, the energy and exergy efficiency drops to 39.1 and 52 %, respectively.

The effects of the pressure ratio on components exergy destruction rates are shown in Figs. 22.4 and 22.5 in different representations. In Fig. 22.4, it shows the exergy destruction rate in MW. The recuperator exergy destruction rate decreases with the increase in pressure ratio. The total exergy destruction reaches a minimum at the point of maximum exergy

Table 22.3 Results of the energy and exergy analysis of the system components

	Ex_d (MW)	y_D (%)	η_{ex} (%)	Ex_d (MW)	y_D (%)	η_{ex} (%)	Ex_d (MW)	y_D (%)	η_{ex} (%)
	$\beta = 313/923$ K			$\beta = 313/1{,}023$ K			$\beta = 313/1{,}123$ K		
Gas turbine	9.067	7.56	96.8	7.535	7.91	97.1	6.467	8.23	97.3
LP compressor	7.420	6.26	90.4	6.141	6.44	90.6	5.254	6.71	90.6
HP compressor	7.644	6.39	90.5	6.308	6.63	90.5	5.386	6.87	90.6
Intercooler	12.24	10.4	97.6	10.80	11.4	97.2	9.701	12.4	96.8
Precooler	23.37	19.5	95.1	20.71	21.7	94.1	18.84	24.1	93.0
Recuperator	16.34	13.6	87.9	13.70	14.4	88.7	11.90	15.2	89.3
Heat exchanger	43.41	36.2	81.9	30.01	31.5	86.0	20.76	26.5	89.5

Table 22.4 Overall performance assessment based on the thermal analyses

Turbine inlet temperature		650 °C	750 °C	850 °C
Overall system performance	Optimal pressure ratio	2.407	2.648	2.74
	Temperature ratio	0.34	0.306	0.278
	Thermal efficiency	37.64 %	41.91 %	45.48 %
	Exergy efficiency	50.07 %	55.75 %	60.51 %
	Helium flow rate	211 kg/s	164 kg/s	128.6 kg/s
	Specific net work	545.7 kJ/kg	732 kJ/kg	933 kJ/kg
	Sustainability index	2.0	2.3	2.5
	Improvement potential	59.74 MW	42.14 MW	30.93 MW
Cooling water	Intercooler flow rate	251.0 kg/s	190.8 kg/s	152 kg/s
	Precooler flow rate	264.9 kg/s	200 kg/s	158.3 kg/s
	Intercooler exit temp	98.4 °C	105.7 °C	112.4 °C
	Precooler exit temp	133.3 °C	145 °C	156 °C

Fig. 22.3 Effect of pressure ratio on the overall system performance
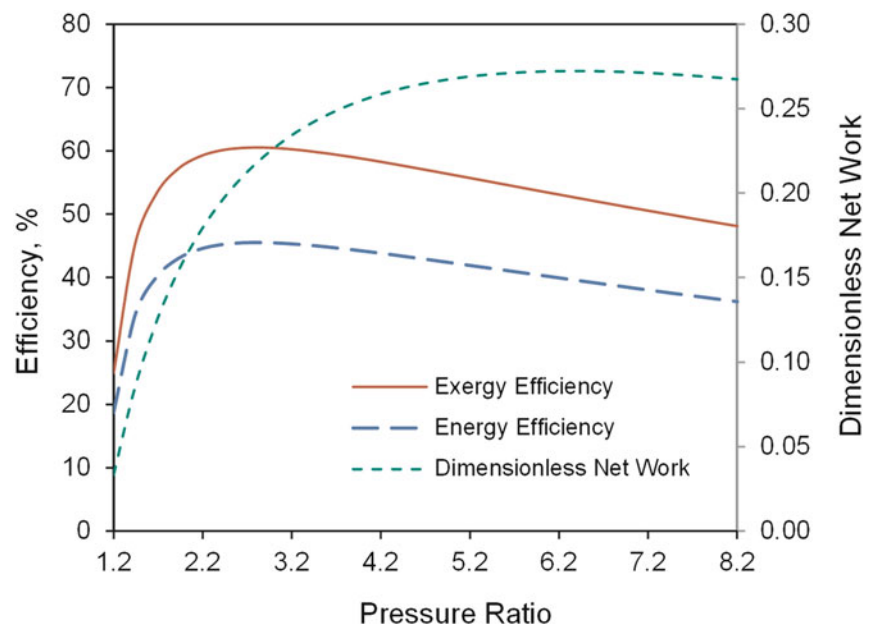
efficiency. Figure 22.5 shows the change of exergy destruction in the system components, as percentage of the total exergy destruction, with increasing the pressure ratio. For a pressure ratio more than 3.4, the changes in the percentages for the turbine, compressors, main heat exchanger, and the precooler are very small compared with the other heat exchangers of the system.

Figures 22.6, 22.7, 22.8, and 22.9 show the results of the energy and exergy analyses at different temperature ratios with respect to the turbine inlet temperature. All other operating parameters are kept constant at the base case condition shown in Table 22.1.

Fig. 22.4 Effect of pressure ratio on exergy destruction rates in the system components and the overall plant
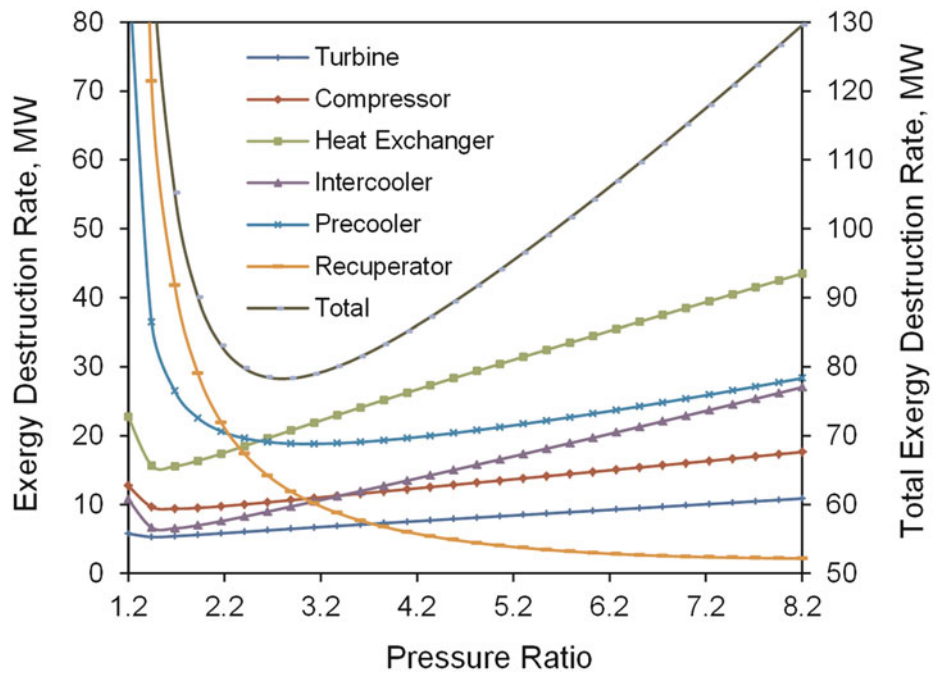
Fig. 22.5 Effect of pressure ratio on exergetic performance in form of exergy destruction rates percentage of the total exergy destruction
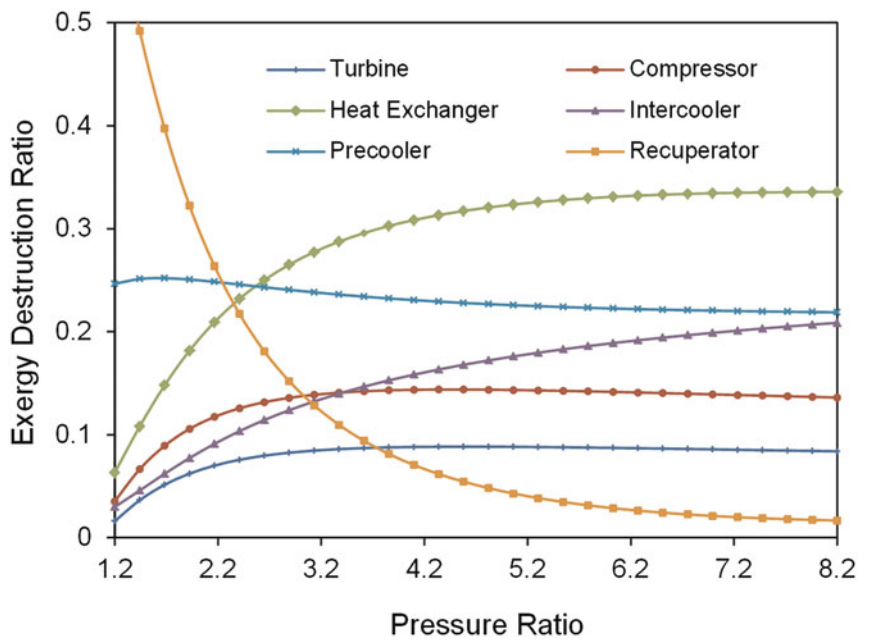
Figure 22.6 shows the effect of changing the pressure ratio on the dimensionless work and the total exergy destruction rate of the plant. Increasing the temperature ratio at constant turbine inlet temperature causes a decrease in the work output as the enthalpy difference drops. The maximum work point occurs at higher pressure ratio the higher turbine inlet temperature. The total exergy destruction rate has a fully reversed trend.

In Fig. 22.7, as a result of the increase in work output, the exergy efficiency is higher for higher turbine temperature. But with the increase of pressure ratio, even with the increase in work output, the exergy efficiency drops after the peak as a result of the increase in the exergy rate of streams provided to the system with respect to the product exergy rates. Figure 22.8 shows the exergetic performance of the studied helium turbine in a new method of performance measurement.

Fig. 22.6 Pressure ratio effect on the overall system performance at different turbine inlet temperatures
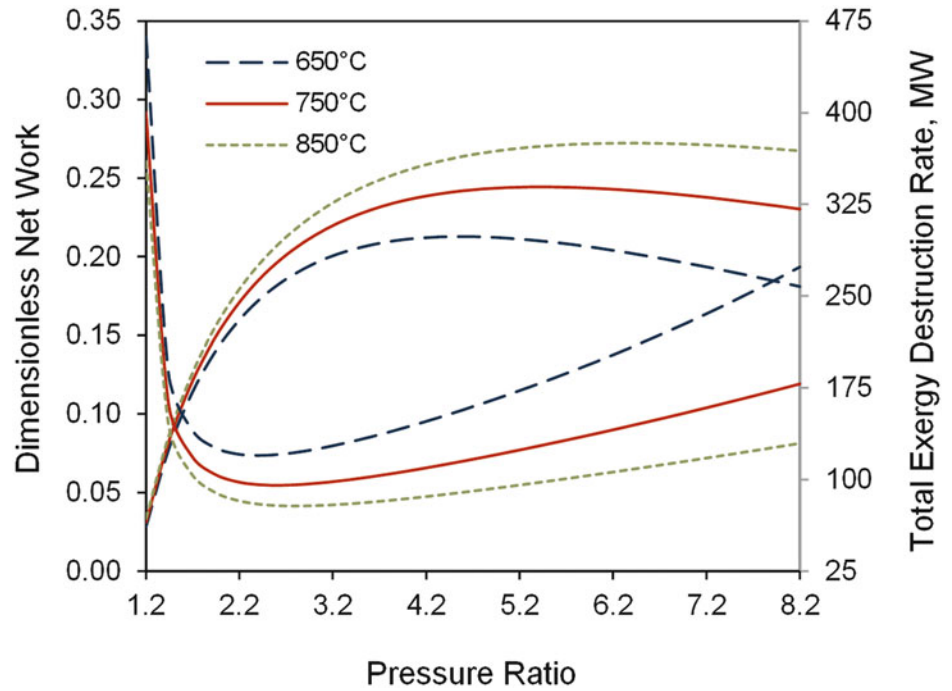
Fig. 22.7 Change in overall exergy efficiency with pressure ratio at different turbine inlet temperatures
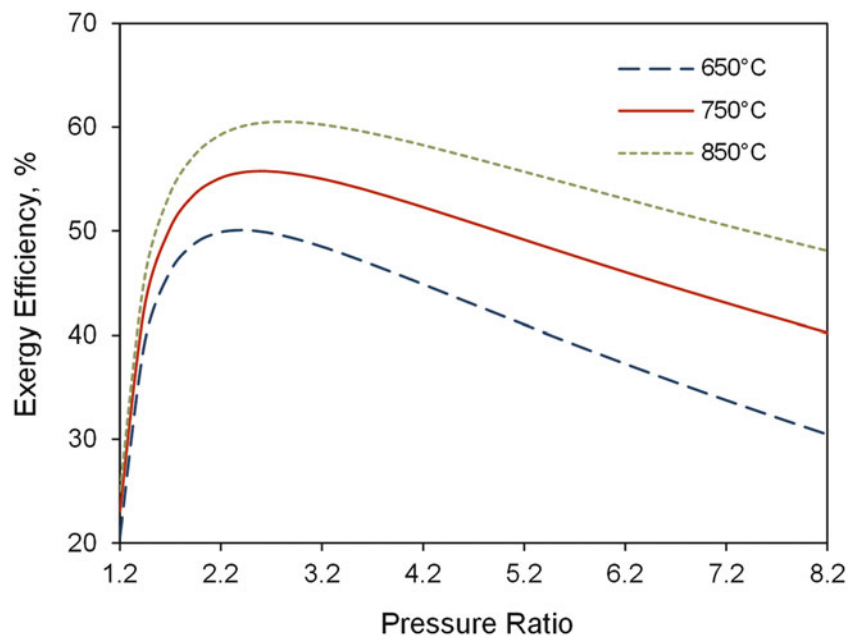
The figure is introduced as the exergetic performance map. The exergetic performance map shows the effect of pressure ratio and temperature ratio on the performance of the gas turbine and its output. This performance map measures the performance in terms of the exergy efficiency and the dimensionless work. It can be also introduced with respect to the specific work output. This map gives an idea of the potential of enhancement in the system performance. Figure 22.9 also shows a new exergetic map of the gas turbine. This map is the exergetic loss map which shows the exergy destruction ratio, with respect to the exergy of the fuel streams provided to the system components, and the specific net work output. The gas turbine operation is described on the map at constant lines of temperature or temperature ratio at different operating pressure ratios.

Fig. 22.8 Exergetic performance map at different turbine inlet temperatures
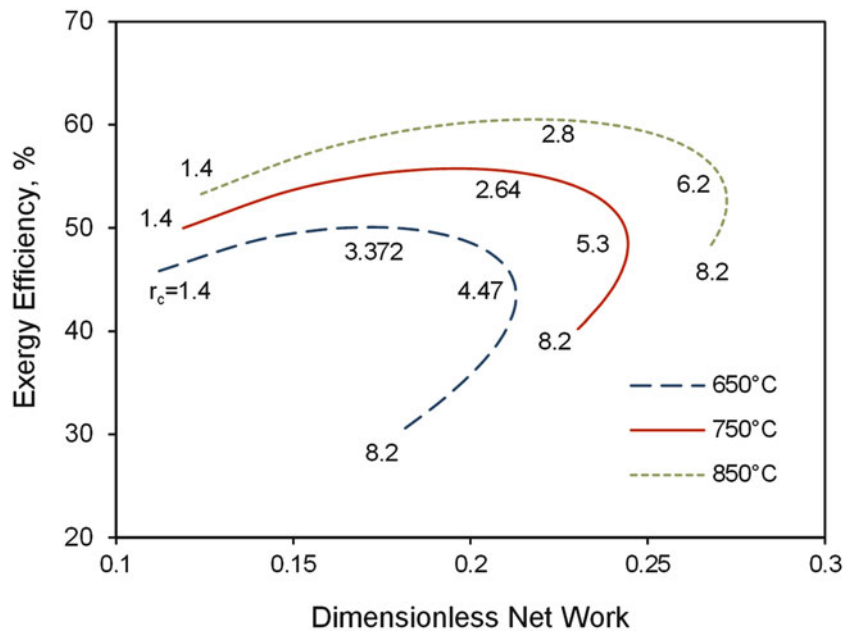
Fig. 22.9 Exergetic loss map at different turbine inlet temperatures
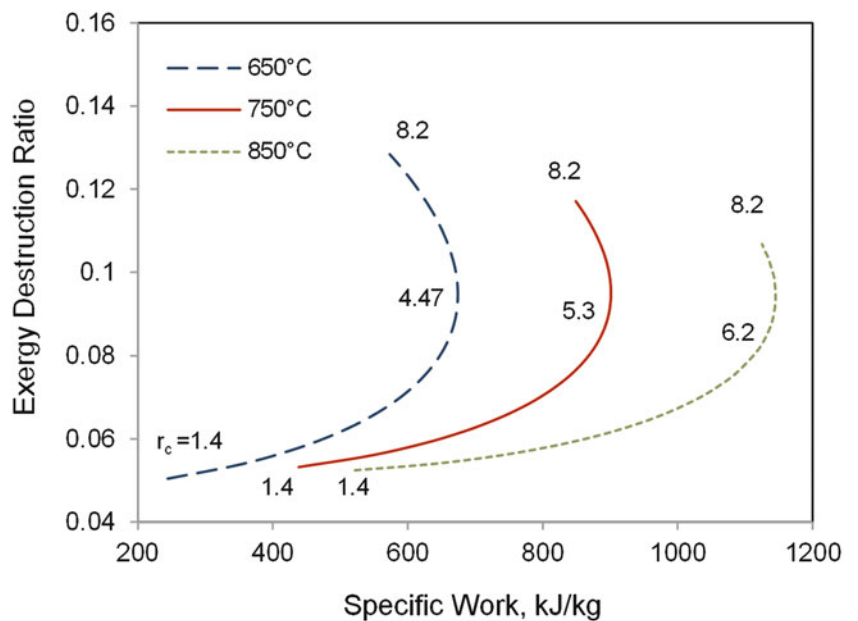
Conclusions

Energy and exergy analyses are conducted for an actual recuperated gas turbine, working on a closed cycle with helium as the working fluid. The energy and exergy efficiencies of the cycle at temperature ratio of 0.278, turbine inlet condition of 850 °C and 70 bar as a base case for a calculated optimal pressure ratio of 2.74 are found to be 45.48 and 60.51 %, respectively. Increasing the high-temperature of the cycle increases the optimal pressure ratio and also increases the plant performance.

Nomenclature

c_p	Specific heat capacity, kJ/kg K	R	Gas constant, kJ/kg K
E	Energy, kJ	s	Specific entropy, kJ/kg K
$\dot{Ex}$	Exergy rate, kW	$\dot{S}$	Entropy rate, kW/K
$\dot{Ex}_d$	Exergy destruction rate, kW	SI	Sustainability index
Ex_R	Exergy destruction ratio, %	t	Time, s
h	Specific enthalpy, kJ/kg	T	Temperature, K
IP	Improvement potential, kW	w	Specific work, kJ/kg
k	Constant	$\dot{W}$	Power, kW
$\dot{m}$	Mass flow rate, kg/s	y_D	Exergy destruction percentage, %
N_c	Number of compression stages	β	Temperature ratio
P	Pressure, kPa	ε	Heat exchanger effectiveness, %
$(\Delta P/P)$	Pressure loss coefficient	η	Energy efficiency, %
$\dot{Q}$	Heat rate, kJ/s	ψ	Exergy efficiency, %
r_c	Pressure ratio	Υ	Specific heat ratio

Subscript

a	Adiabatic	HE	Heat exchanger
c	Cold stream	in	Inlet flow
C	Compressor	IC	Intercooler
ex	Exit flow	L	Lowest
f	Fuel	p	Polytropic
gen	Generation	PC	Precooler
h	Hot stream	R	Recuperator
H	Highest	T	Turbine

References

1. Conn RW, Kuo SC (1976) An advanced conceptual tokamak fusion power reactor utilizing closed cycle helium gas turbines. Nucl Eng Des 39:45–72
2. Frutschi HU (2005) Closed-cycle gas turbines. ASME, New York
3. Horlock JH (2002) Combined power plants. Krieger, Malabar, FL
4. No HC, Kim JH, Kim HM (2007) A review of helium gas turbine technology for high-temperature gas-cooled reactors. Nucl Eng Technol 39:21–30
5. Wenlong L, Heng X, Zuoyi Z, Yujie D (2012) Development and primary verification of a transient analysis software for high temperature gas-cooled reactor helium turbine power system. Nucl Eng Des 250:219–228
6. McDonald CF (2012) Helium turbomachinery operating experience from gas turbine power plants and test facilities. Appl Therm Eng 44:108–142
7. Zhao H, Peterson PF (2008) Multiple reheat helium Brayton cycles for sodium cooled fast reactors. Nucl Eng Des 238:1535–1546
8. Qin J, Zhou W, Bao W, Yu D (2010) Thermodynamic analysis and parametric study of a closed Brayton cycle thermal management system for scramjet. Int J Hydrog Energy 35:356–364
9. Gandhidasan P (1993) Thermodynamic analysis of a closed-cycle, solar gas-turbine plant. Energ Convers Manag 34:657–661
10. Kestin J (1980) Availability, the concept and associated terminology. Energy 5:679–692
11. Moran MJ, Shapiro HN, Boettner DD, Bailey MB (2011) Fundamentals of engineering thermodynamics. Wiley, Hoboken, NJ
12. McDonald CF, Orlando RJ, Cotzas GM (eds) (1994) International joint power generation conference. Phoenix, AZ
13. Boyce MP (2006) Gas turbine engineering handbook. Gulf Professional Publishing, Burlington, MA
14. Bejan A (2006) Advanced engineering thermodynamics. Wiley, New York
15. Gool W (1997) Energy policy: fairy tales and factualities. In: Soares OD, Cruz AM, Pereira GC, Soares IRT, Reis APS (eds) Innovation and technology—strategies and policies. Springer, The Netherlands, pp 93–105

Investigation of Exergy Ratios of a Solar Pond

23

Mehmet Karakilcik and Ibrahim Dincer

Abstract

In this paper, we present an experimental and theoretical investigation for exergetic assessment of a rectangular solar pond (with dimensions of 2 m × 2 m × 1.5 m) at various reference temperatures. The experimental solar pond was designed and built at Cukurova University in Adana, Turkey. The system was filled with salty water to form three zones (namely, Upper Convective Zone (UCZ), Non-Convective Zone (NCZ), and Low Convective Zone (LCZ)) accordingly. A data acquisition device was used to measure the temperatures hourly at various locations in the pond. An exergy model was developed to study the exergetic performance of the pond for its three zones in terms of exergy efficiencies. The lowest and highest reference environment temperatures for various days in the months were considered. The results show that the efficiency ratios of the LCZ are found to be higher than the corresponding the NCZ and also the UCZ.

Keywords

Solar pond • Solar energy • Energy and exergy efficiencies • Exergy ratios

Introduction

The sun is the largest source of solar energy which is renewable, clean, abundantly and easily available everywhere in the world and also can easily be converted to thermal energy by using the renewable energy systems. These systems generally absorb the solar radiation falling on them to collect and store as thermal energy. The thermal energy is used for cooling, water and space heating, and power production using air, water, steam, or thermal fluids to transfer the heat to the location where it is used. For these reasons the renewable energy technologies are improved day by day. It is widely known that these have a significant role in reducing the energy consumption and plays an important role in energy production and saving policies. All of these are important factors to increase the use of the solar energy to reduce nonrenewable energy consumption, carbon footprints and to improve solar energy technologies. One of these is solar pond which is a large-scale energy collector with integral heat storage for supplying thermal energy and can be used for various applications (e.g., process heating, water desalination, refrigeration, drying, and power generation).

Solar ponds can suitably be constructed anywhere, regardless of the distance to the nearest power outlet, as long as there is access to direct sunlight on the site. It is economical to construct them at places where there is low-cost salt and bittern, a good supply of sea water or water for filling and flushing, high solar radiation, low cost land, etc. The maintenance of solar

M. Karakilcik (✉)
Department of Physics, Faculty of Sciences and Letters, University of Cukurova, Adana 01330, Turkey
e-mail: kkilcik@cu.edu.tr

I. Dincer
Faculty of Engineering and Applied Science, University of Ontario Institute of Technology (UOIT)
2000 Simcoe Street North, Oshawa, ON, Canada L1H 7K4
e-mail: Ibrahim.Dincer@uoit.ca

ponds is generally simple and of low cost, and does not emit greenhouse gas emissions. The solar pond works on a very simple principle. The solar radiation heats the water, and the heated water from within the pond rises and reaches the top, but loses some heat to the atmosphere. Heat is then properly stored. The solar ponds restrict this tendency of dissolving salt in the bottom layer of the pond and make it too heavy to rise [1].

The solar ponds are generally consisted of three main zones as we briefly define as follows. The upper convective zone (UCZ) is composed of low-salinity brine. This zone requires continuous flushing with freshwater or low-salinity water to compensate for evaporation and flush away the rising salt to the top surface by the natural process of salt diffusion through the non-convective zone (NCZ). Below it, the NCZ contains a salinity gradient such that the water close to the surface is always less salty than the water below it. The NCZ constitutes a thermally insulating layer since natural convection currents are suppressed. The lower convective zone (LCZ) is also called as the storage zone. This zone is where the heat is collected and stored. It is very hot and salty water, and its temperature can vary between 50 and 90 °C [2] whose density distribution is changed between 1,150 and 1,190 kg/m^3 [3]. Usage of solar energy to collect and store energy in salty water zones of solar pond becomes the heart of this study for analysis and assessment.

There have been experimental and theoretical investigations on exergetic performance analyses of integrated and non-integrated solar ponds through exergy efficiencies [4, 5]. These studies are in fact the key motivation for the present work. In this work, a detailed investigation on exergetic efficiencies is carried out through exergy analysis of the zones at higher and lower reference temperatures. Accordingly the exergy destructions and losses as well as exergy efficiency relations are determined for each of the system components and for the whole system. In this regard, exergetic efficiency ratios at lowest and highest reference temperatures are studied.

Experimental Apparatus and Procedure

Generally, solar ponds are divided into three zones as follows:

(a) The upper convective zone (UCZ) is the first zone with the freshwater layer at the top of the pond. This zone is fed with freshwater in order to maintain its density as close as to the density of freshwater in the upper part to protect the cleanness of the pond and meet the lost water due to evaporation.

(b) The second zone is non-convective zone (NCZ). It consists of several different salty water layers. The layers are heavier than freshwater and will not rise or mix by natural convection. So the body of the salty water inner zone creates a salt gradient zone. The zone permits solar radiation to pass through, but reduces the heat loss from the hot lower convective zone (LCZ) to the cold upper convective zone (UCZ). It creates a larger temperature gradient within the pond which becomes hotter with depth and also the salt content increases with its depth, hence causing a salinity or density gradient. This gradient acts as a transparent insulator permitting sunlight to reach the bottom zone but also entrapping it there. Heat transfer through this zone is by conduction only.

(c) The third zone, non-convective zone (LCZ) is also called as the heat storage zone (HSZ) which is composed of salty water with highest density. Considerable part of the solar energy is absorbed and stored by this bottom region. The LCZ has highest temperature, and hence, the strongest thermal interaction occurs between this zone and the insulated bottom and sidewalls surrounding it.

In the experimental work, a rectangular solar pond with a surface area of 4 m^2 and a depth of 1.5 m was built as shown in Fig. 23.1, and the pond was then filled with salty water to form the inner zones of UCZ, NCZ, and LCZ. A data acquisition system was used to measure the hourly temperature variations in a day in these inner zones. The bottom section and the sidewalls of the pond were insulated with a glass-wool of 50 mm thickness. The temperature measurements were taken using 16 temperature sensors, as some of which were placed into the inner zones to measure the temperature distributions of various layers. A computerized data acquisition system was used for data recording, monitoring and processing. The temperatures of inner zones of the pond were measured hourly during a day by sensors with a range of −65 to +155 °C, and with a measurement accuracy of ±0.1 °C for the temperature range of 0–120 °C. The solar energy data measured by a pyranometer and hourly average air and daily average weather temperatures taken from a local meteorological station were used as input parameters for analysis and assessment. Further information on experimental system and measurement details, as well as some thermophysical properties of materials and fluids, is available elsewhere [6, 7].
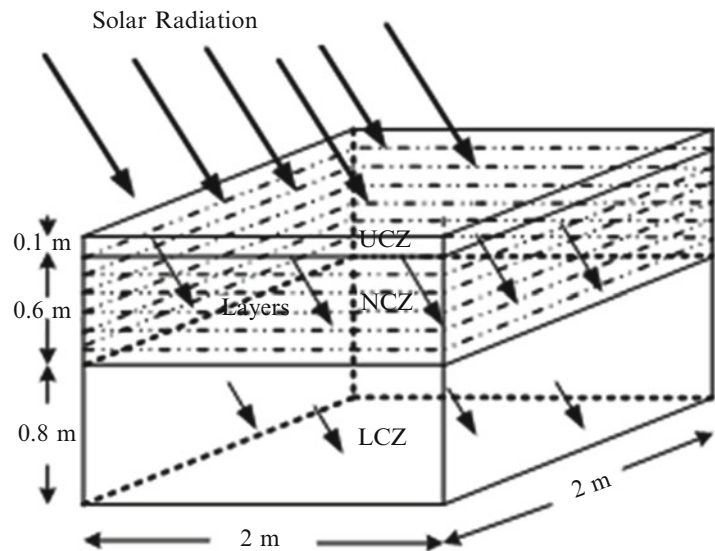
Figure 23.1 illustrates the three different zones of the solar pond as described above. The LCZ is high density salty water. Solar energy is absorbed and stored by this zone. The NCZ consists of six layers of salty water at various densities, and the last zone (UCZ) is formed by a freshwater layer. The incoming solar exergy is calculated by [8]:

$$\Xi_{so} = E_{net}\left[1 - \frac{4T_{re}}{3T_s} + \frac{1}{3}\left(\frac{T_{re}}{T_s}\right)^4\right]A_{UCZ}$$

where, Ξ_{so} is the exergy of solar radiation reaching UCZ surface; E_{net} is the net incident solar radiation reaching UCZ surface; A_{UCZ} is the net surface area of UCZ; T_{re} is the reference environment temperature; and T_s is the sun's surface temperature taken as 6,000°K. Also, A_{UCZ} is the net upper surface area of UCZ, regarded as the effective area that receives incident solar radiation and is defined as $A_{UCZ} = L_w[L_L - (\delta + (I - 1)\,\Delta x)\tan\theta]$ (here θ the angle of the refracted incidence, Δx is the thickness of each layer in UCZ and taken as 0.005 m in the calculations, and L_w and L_L are the width and length of the pond) [4].

Exergy Analysis

The energetic performance considers no effect of the environment temperature within the scope of first-law of thermodynamics. As know, the real performance is affected by many aspects of the surroundings. In this regard, the higher the emissivity of the absorbing zones inside of the pond, the higher the efficiency. The higher efficiency is for the largest absorbing surface of the pond if the zones do not losses heat from upper surface and sidewalls or if the environment temperature is equal to reference temperature, the efficiency can be high, whereas the practical value of heat absorbed at reference temperature is zero. In contrast to the work, heat is driven by the temperature difference, which makes the quality aspect of heat a critical element. Conversion of radiation energy into heat causes exergy losses during the processes.

An understanding of the relations between exergy and environment may reveal the underlying fundamental patterns and forces affecting changes in the environment, and help researchers to deal better with environmental damage. Exergy analysis permits many of the shortcomings of energy analysis to be overcome. Exergy analysis acknowledges that, although energy cannot be created or destroyed, it can be degraded in quality, eventually reaching a state in which it is in complete equilibrium with the dead state [9]. It appears to be a potential tool for design, analysis, evaluation, and performance improvement of solar pond systems. The effectiveness of conversion of the incident radiation into heat can be evaluated by the exergy conversion efficiency. Again interpreting appropriately the terms in the following exergy conservation equation can assess for a balanced system in Fig. 23.2. It is completed by exergy loss due to irreversibility of components of the inner zone. Here, Fig. 23.2 shows each of the zones and the respective exergy flows.

Fig. 23.2 Exergy flows in
the zones of the solar pond
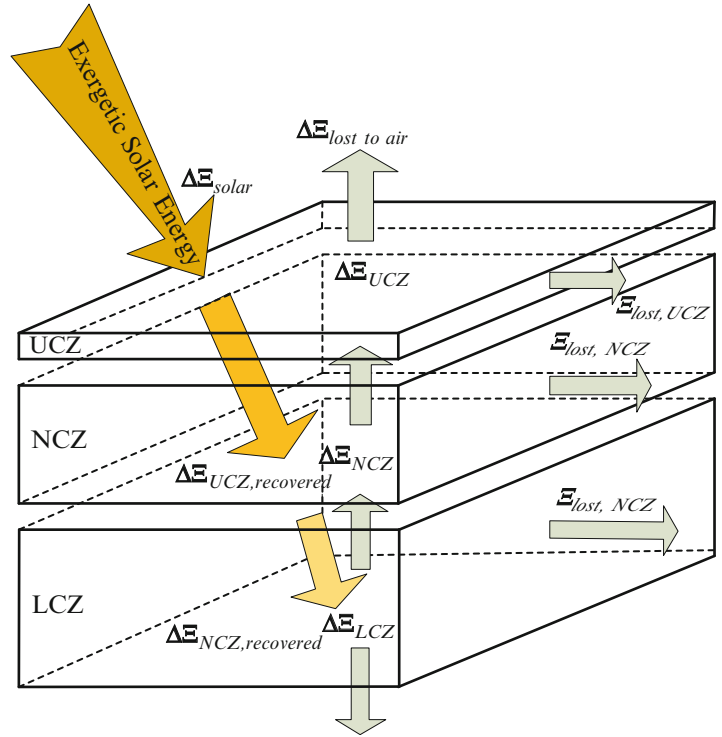
Exergy Efficiency for UCZ

As shown in Fig. 23.2, the exergy flows in UCZ can be illustrated through exergy balance equations. We first write the exergy balance equation for UCZ as

$$\Xi_{i,\text{UCZ}} = \Xi_{O,\text{UCZ}} \tag{23.1}$$

where $\Xi_{i,\text{UCZ}}$ is the total exergy input to UCZ, including the exergy of solar radiation and exergy gained by UCZ, and $\Xi_{O,\text{UCZ}}$ is the total exergy losses, including exergy recovered and destruction. So we can write the exergy efficiency equation of UCZ as

$$\psi_{\text{UCZ}} = \frac{\Xi_{r,\text{UCZ}}}{\Xi_{i,\text{UCZ}}} = 1 - \frac{\Xi_{wa,\text{UCZ}} + \Xi_{sw,\text{UCZ}} + \Xi_{dest.,\text{UCZ}}}{\Xi_{so} + \Xi_{g,\text{UCZ}}} \tag{23.2}$$

where $\Xi_{r,\text{UCZ}}$ is the recovered exergy of UCZ, Ξ_{so} is the exergy of solar radiation reaching UCZ can be expressed (as modified from [8]), $\Xi_{g,\text{UCZ}}$ is the exergy gained from NCZ, $\Xi_{wa,\text{UCZ}}$ is the exergy loss from UCZ to the ambient air and $\Xi_{sw,\text{UCZ}}$ is the exergy loss through sidewalls of UCZ, $\Xi_{dest,\text{UCZ}}$ is the exergy destruction in UCZ.

we can now define the exergy efficiency for UCZ as follows:

$$\psi_{\text{UCZ}} = 1 - \frac{\left(\begin{array}{c} m_{\text{UCZ}}C_{p,\text{UCZ}}\left[(T_{\text{L-H,UCZ}} - T_{\text{L-H,re}}) - T_{\text{L-H,re}}\left(\ln\frac{T_{\text{L-H,UCZ}}}{T_{\text{L-H,re}}} \right) \right] \\ + m_{\text{UCZ}}C_{p,sw,\text{UCZ}}\left[(T_{\text{L-H,UCZ}} - T_{\text{L-H,sw,UCZ}}) - T_{\text{L-H,re}}\left(\ln\frac{T_{\text{L-H,UCZ}}}{T_{\text{L-H,sw,UCZ}}} \right) \right] + \Xi_{dest.,\text{UCZ}} \end{array} \right)}{\left(E_{net}A_{\text{UCZ}}\left[1 - \frac{4T_{\text{L-H,re}}}{3T_{\text{L-H,re}}} + \frac{1}{3}\left(\frac{T_{\text{L-H,re}}}{T_s} \right)^4 \right] + m_{\text{UCZ}}C_{p,\text{UCZ}}\left[(T_{\text{L-H,NCZ}} - T_{\text{L-H,UCZ}}) - T_{\text{L-H,re}}\left(\ln\frac{T_{\text{L-H,NCZ}}}{T_{\text{L-H,UCZ}}} \right) \right] \right)} \tag{23.3}$$

where $m_{\text{UCZ}} = \rho_{\text{UCZ}}V_{\text{UCZ}}$ is the mass of salty water in UCZ, and is given in Table 23.1; ρ_{UCZ} is the averaged density distribution as seen in Fig. 23.3, V_{UCZ} is the average volume of the salty water in UCZ as $V_{\text{NCZ}} = 0.4 \text{ m}^3$. $C_{p,\text{UCZ}}$ is the specific heat of salty water in UCZ. $T_{\text{L-H,re}}, T_{\text{L-H,sw,UCZ}}, T_{\text{L-H,UCZ}},$ and $T_{\text{L-H,NCZ}}$ denote lowest and highest temperatures of

Table 23.1 Average mass of the salty water of the inner zones of the solar pond

Month	m_{UCZ} (kg)	m_{NCZ} (kg)	m_{LCZ} (kg)
Jan.	611.52	2,400.58	3,828.58
Feb.	619.20	2,371.65	3,819.30
Mar.	615.68	2,362.26	3,806.59
Apr.	613.70	2,350.62	3,798.80
May	618.80	2,353.17	3,784.88
Jun.	623.40	2,357.26	3,778.07
Jul.	612.24	2,342.46	3,769.62
Aug.	614.23	2,335.09	3,766.30
Sep.	619.10	2,341.85	3,776.87
Oct.	618.60	2,354.64	3,794.32
Nov.	613.65	2,354.15	3,803.03
Dec.	613.80	2,345.68	3,806.03

Fig. 23.3 The averaged density variations of the inner zones of the solar pond
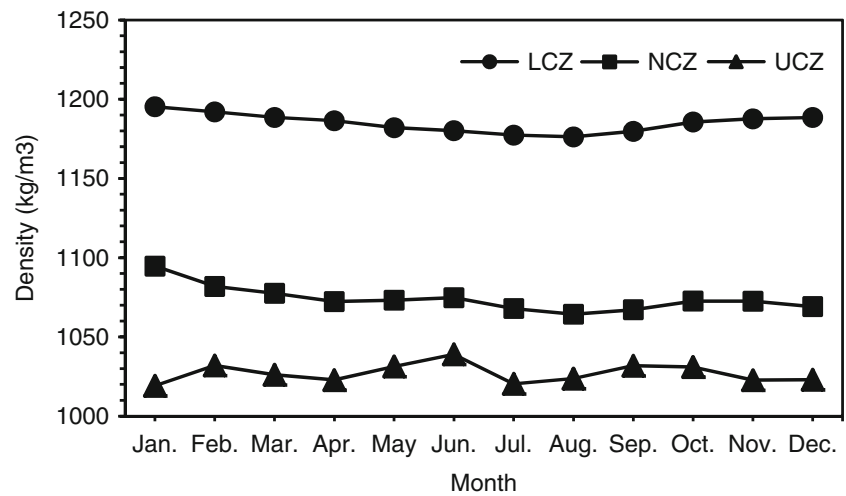
reference environment, UCZ, sidewall of the UCZ and NCZ, respectively. T_s is the sun's surface temperature taken as $6,000°K$, $C_{sw,UCZ}$ is the specific heat surrounding wall of UCZ, E_{net} is the net incident solar radiation reaching UCZ surface. Also, A_{UCZ} is the net upper surface area of UCZ that receives the solar incident.

The exergy efficiency ratio of the UCZ at the lowest and highest temperatures can be written as

$$\chi_{UCZ} = \frac{\Psi_{UCZ}}{\Psi_{T,UCZ}} \tag{23.4}$$

Exergy Efficiency Ratios for NCZ

Based on the exergy flows in NCZ as shown in Fig. 23.2, the balance equation can be written for NCZ as

$$\Xi_{i,LCZ} = \Xi_{O,LCZ} \tag{23.5}$$

where $\Xi_{i,NCZ}$ is the total exergy input to NCZ, including the recovered exergy of UCZ and the exergy gained by NCZ, and $\Xi_{O,UCZ}$ is the total exergy losses, including exergy recovered and destruction. So we can write the exergy efficiency equation of NCZ as

$$\Psi_{NCZ} = \frac{\Xi_{r,NCZ}}{\Xi_{i,LCZ}} = 1 - \frac{\Xi_{up,NCZ} + \Xi_{sw,NCZ} + \Xi_{dest.,NCZ}}{\Xi_{r,UCZ} + \Xi_{g,NCZ}} \tag{23.6}$$

where $\Xi_{r,UCZ}$ is the exergy recovered of UCZ which is given by Eq. (23.2), $\Xi_{g,NCZ}$ is the exergy gained by NCZ, $\Xi_{up,NCZ}$ is the exergy loss from NCZ, $\Xi_{sw,NCZ}$ is the exergy loss through sidewalls and $\Xi_{dest,NCZ}$ is the exergy destruction in NCZ.

We can now define the exergy efficiency for NCZ as the ratio of the exergy recovered from NCZ to the total exergy input to NCZ as follows:

$$\psi_{NCZ} = 1 - \frac{\left(\begin{array}{l} m_{NCZ}C_{p,NCZ}\left[(T_{L\text{-}H,NCZ} - T_{L\text{-}H,UCZ}) - T_{L\text{-}H,re}\left(\ln\frac{T_{L\text{-}H,NCZ}}{T_{L\text{-}H,UCZ}}\right)\right] \\ +m_{sw,NCZ}C_{p,sw,NCZ}\left[(T_{L\text{-}H,NCZ} - T_{L\text{-}H,sw,NCZ}) - T_{L\text{-}H,re}\left(\ln\frac{T_{L\text{-}H,NCZ}}{T_{L\text{-}H,sw,NCZ}}\right)\right] + \Xi_{dest.,NCZ} \end{array}\right)}{\Xi_{r,UCZ} + m_{NCZ}C_{p,NCZ}\left[(T_{L\text{-}H,LCZ} - T_{L\text{-}H,NCZ}) - T_{L\text{-}H,re}\left(\ln\frac{T_{L\text{-}H,LCZ}}{T_{L\text{-}H,NCZ}}\right)\right]} \tag{23.7}$$

where $m_{NCZ} = \rho_{NCZ}V_{NCZ}$ is the averaged mass of salty water in LCZ, and is given in Table 23.1. ρ_{NCZ} is the averaged density and V_{NCZ} is the volume of salty water in NCZ as $V_{LCZ} = 2.4$ m^3. $C_{p,NCZ}$ is the specific heat of salty water in NCZ. $T_{L\text{-}H,re}$, $T_{L\text{-}H,NCZ}$, $T_{L\text{-}H,sw,NCZ}$ and $T_{L\text{-}H,LCZ}$ denote lowest and highest temperatures of reference environment, NCZ, sidewall of the NCZ and LCZ, respectively. $C_{p,sw,NCZ}$ is the specific heat surrounding wall of NCZ.

The exergy efficiency ratio of NCZ can be written as

$$\chi_{NCZ} = \frac{\psi_{NCZ}}{\psi_{T,NCZ}} \tag{23.8}$$

Exergy Efficiency Ratios for LCZ

The exergy flows in HSZ are clearly shown in Fig. 23.2 and the stored exergy equation of LCZ can be written as

$$\Delta\Xi_{st} = \Xi_{i,LCZ} - \Xi_{O,LCZ} = \Xi_{r,NCZ} - \left(\Xi_{up,LCZ} + \Xi_{sw,LCZ} + \Xi_{dw,LCZ} + \Xi_{dest.,LCZ}\right) \tag{23.9}$$

where $\Xi_{i,LCZ}$ is the input exergy from NCZ to LCZ and is called recovered exergy ($\Xi_{r,NCZ}$) as given in Eq. (23.6), $\Xi_{o,LCZ}$ is the exergy losses from NCZ; $\Xi_{up,LCZ}$ is the exergy loss from LCZ to NCZ, $\Xi_{sw,LCZ}$ and $\Xi_{dw,LCZ}$ are the exergy losses through side and down wall and have a similar effect due to the fact that both outside walls have the same insulating materials and are surrounded by the ambient air, $\Xi_{dest.,LCZ}$ is the exergy destruction in LCZ.

Using Eq. (23.9), we can now define the exergy efficiency for LCZ as the ratio of the exergy stored in LCZ to the total exergy input to LCZ which is essentially the exergy recovered from NCZ:

$$\psi_{LCZ} = \frac{\Delta\Xi_{st}}{\Xi_{r,NCZ}} = 1 - \frac{\left(\Xi_{up,LCZ} + \Xi_{sw,LCZ} + \Xi_{dw,LCZ} + \Xi_{dest.,LCZ}\right)}{\Xi_{r,NCZ}} \tag{23.10}$$

$$\psi_{LCZ} = 1 - \frac{\left(\begin{array}{l} m_{LCZ}C_{p,LCZ}\left[(T_{L\text{-}H,LCZ} - T_{L\text{-}H,NCZ}) - T_{L\text{-}H,re}\left(\ln\frac{T_{L\text{-}H,LCZ}}{T_{L\text{-}H,NCZ}}\right)\right] \\ +m_{LCZ}C_{p,sw,LCZ}\left[(T_{L\text{-}H,LCZ} - T_{L\text{-}H,sw,LCZ}) - T_{L\text{-}H,re}\left(\ln\frac{T_{L\text{-}H,LCZ}}{T_{L\text{-}H,sw,LCZ}}\right)\right] \\ +m_{LCZ}C_{p,dw,LCZ}\left[(T_{L\text{-}H,LCZ} - T_{L\text{-}H,dw,LCZ}) - T_{L\text{-}H,re}\left(\ln\frac{T_{L\text{-}H,LCZ}}{T_{L\text{-}H,dw,LCZ}}\right)\right] + \Xi_{dest.,LCZ} \end{array}\right)}{\left(\Xi_{r,NCZ}\right)} \tag{23.11}$$

where $m_{LCZ} = \rho_{LCZ}V_{LCZ}$ is the averaged mass of salty water in LCZ, and is given in Table 23.1; ρ_{LCZ} is the averaged density and V_{LCZ} is the volume of salty water in NCZ as $V_{LCZ} = 3.2$ m^3. $C_{p,LCZ}$ is the specific heat of salty water in LCZ.

$T_{L-H,re}$, $T_{L-H,LCZ}$, $T_{L-H,sw,LCZ}$ and $T_{L-H,dw,LCZ}$ denote the lowest and highest temperatures of reference, LCZ, side and down wall of the LCZ, respectively. $C_{p,sw,LCZ}$ and $C_{p,dw,LCZ}$ is the specific heat side and down wall of LCZ, T_s is the reference environment temperature.

The exergy efficiency ratio of the NCZ can be written as

$$\chi_{LCZ} = \frac{\Psi_{LCZ}}{\Psi_{T,LCZ}} \qquad (23.12)$$

Results and Discussion

We now present the results of the present model calculations for exergy efficiencies and their ratios for each zone at lowest and highest reference environment temperatures in the experimental rectangular solar pond on various days in the year for the inner zones and also compare these results to show how exergy is crucial for determining true performance at various temperatures.

Figure 23.3 shows the averaged experimental density variations of salty water versus the height of the pond from the bottom in 12 months at different dates. One can conclude from the figure that the salt density distribution in the inner zones of the solar pond becomes nearly stable which is of great significance. It is now well known that any deterioration in salt gradient region decreases the pond's ability to store heat energy. The primary reason for differences during different months is likely the high temperatures in summer. This change is mainly attributable to the thermophysical property of the salty water, heat losses from the pond to the air, and the absorption and reflection of incident solar radiation on the surface. The reason for the fluctuations of the density in the zones is caused by the evaporation from the water surface, changes in the temperature of the zones in time, salt diffusion, insufficient protection and the deterioration of salt gradient zone. Such changes can be reduced by continuously added freshwater to the top of the pond and using a well-functioning salt gradient protection system.

There were significant differences between the density distributions measured in January and August, due to the temperature changes and evaporation of salty water from the pond. As expected, increasing temperature decreases the density more in the summer months. As further seen in Fig. 23.3, the density distribution of LCZ and NCZ are decreased due to an increase in the salt diffusion as a result of the increase in the temperature of the zones, especially in August. At same time, the density profile of UCZ fluctuates because of the salty diffusion from bottom zone to upper zone and freshwater added to the upper surface to compensate evaporation losses. The decreases in the ratio of the density distribution of the LCZ and NCZ are found to be approximately 1.6 % in January and 2.78 % in August. The maximum decrease in the density distribution of UCZ is found to be 1.94 % in June due to the salty diffusion from bottom zone and evaporation losses. Although the zone's salty water is changed with freshwater (with a density of 1,000 kg/m^3) in July, increasing the ratio of the zone density is found, to be 0.44 % in August, 1.24 % in September and 1.16 % in October. Generally, these decreases of the LCZ and NCZ can be restored by continuously injecting high density salty water and by using a well-working salt protection system. On the other hand, increases in UCZ can be eliminated by adding of freshwater to the top of the pond or changing with freshwater.

The zone temperatures of the pond were measured throughout the day and averaged to find the daily average temperature values at the respective points. It is clear that the zone temperatures vary with a day of month in the year, depending on the reference environment temperature and incoming exergetic solar energy on the surface (the useful part of solar energy). The temperatures of the zones generally increase with incident solar energy per unit area of surface. There are heat losses from each zone and this is the largest in the storage zone which affects the storage performance directly and drastically. In order to improve the performance and increase the efficiency, we should minimize the losses appropriately.

The temperature distributions are varied with time and effect on the performance of the pond. Thus, lowest and highest averaged temperature distributions of the zones were measured during day time for each month in the year. Regarding the experimental temperature distributions in Fig. 23.4, for LCZ, NCZ, and UCZ, the temperatures of LCZ, NCZ, and UCZ are observed to be a minimum of 13.06 °C, 11.27 °C, and 10.10 °C on the 1st day (in January) and a maximum of 51.92 °C, 43.76 °C, and 37.84 °C on the 243rd day of the year (in August), respectively.

Figure 23.5 shows highest temperature distributions during day time for each month in the year of the zones. The temperatures of the LCZ, NCZ, and UCZ are observed to be a minimum of 17.80 °C, 15.58 °C, and 14.37 °C on the 31st day

Fig. 23.4 Lowest temperature
distributions of the solar pond
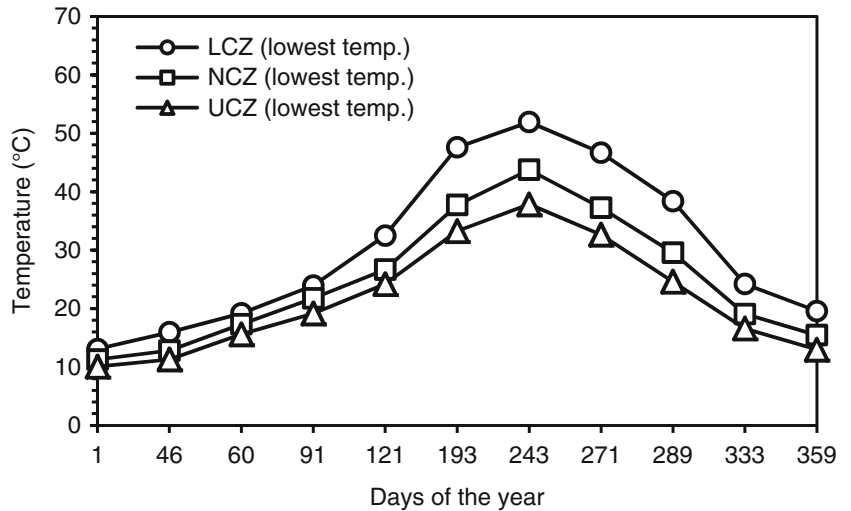
Fig. 23.5 Highest temperature
distributions of the solar pond
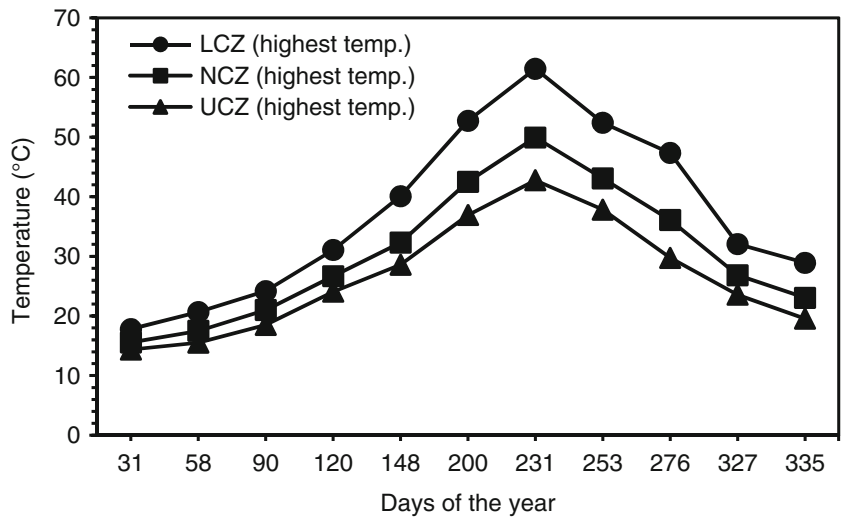
(in January) and a maximum 61.45 °C, 49.93 °C, and 42.75 °C on the 231st day of the year (in August), respectively. As seen in the figure the temperature profiles of the zones are increasing and decreasing seasonally as the same of the surrounding air of the solar pond. So the temperature profiles of the inner zones are seen to be a maximum on the 231st day of the year.

Figures 23.6 and 23.7 exhibit in a bar chart the exergetic efficiency distributions at lowest and highest temperatures taking place in the inner zones of the solar pond and their variations based on the experimental data measured during the different day of the year. Figure 23.6 shows the exergetic efficiency distributions at lowest temperature for each zone of the solar pond. The highest exergetic efficiencies of the LCZ, NCZ, and UCZ are calculated, using the experimental data, to be a maximum 22.55, 55.85, and 92.56 % at the 204th day of the year and a minimum 4.28, 10.47, and 15.85 % at the 1st day of the year, respectively.

Furthermore, Fig. 23.7 exhibits that the exergetic efficiency distributions at high temperature for each zone of the solar pond. Highest exergetic efficiencies of the LCZ, NCZ, and UCZ are calculated, using the experimental data, to be a maximum 24, 61.15, and 104.30 % at the 211st day of the year and a minimum 5.57, 13.12, and 20.97 % at the 31st day of the year, respectively.

As seen in Figs. 23.6 and 23.7, the differences in the exergetic efficiencies among the zones are smaller in cooler days than the respective warmer days of the year. As expected that the efficiencies for the LCZ are higher than the corresponding NCZ and UCZ.

We now will explain the exergetic efficiency ratios of the each zone at lowest and highest reference environment temperatures taking place in the inner zones of the solar pond and their variations based on the experimental data measured during the different months of the year.

Fig. 23.6 The exergetic efficiency distributions at lowest temperature of the solar pond
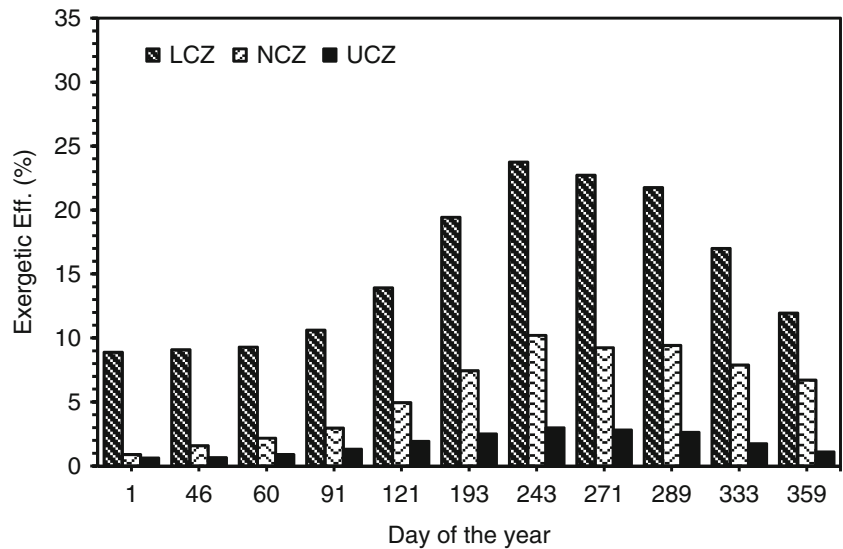
Fig. 23.7 The exergetic efficiency distributions at highest temperature of the solar pond
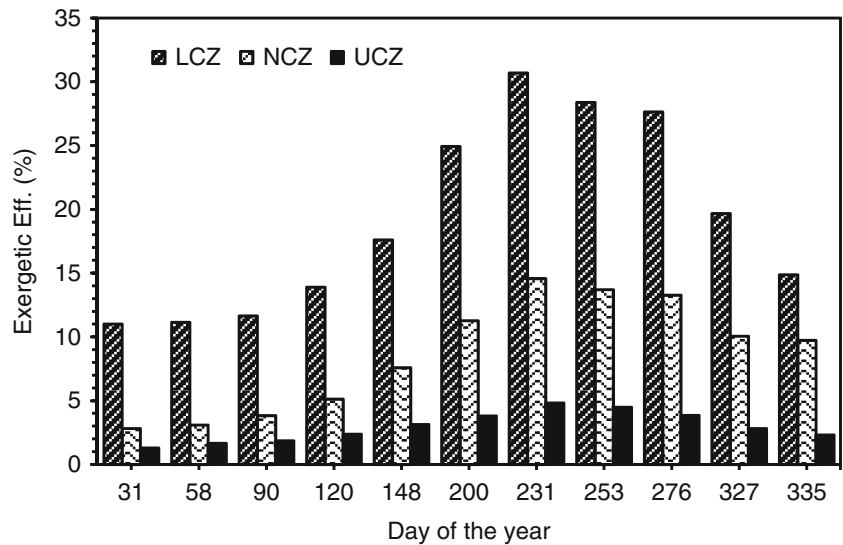
Figures 23.8, 23.9, and 23.10 show the minimum and maximum exergetic efficiency ratios at lowest and highest reference environment temperature of the LCZ, NCZ, and UCZ. As seen in Fig. 23.8, the minimum and maximum exergetic efficiency ratios of LCZ are calculated by using Eq. (23.12), using the experimental data and found to be a minimum 5.27 % at lowest and 5.20 % at highest reference environment temperatures in January, and to be a maximum 14.10 % at lowest and 14.51 % at highest reference temperatures in August, respectively. There are no significant variations between the ratios at lowest and highest references environment temperatures of LCZ. The exergy efficiency ratios are almost same in cooler months from December to March, and very small in warmer months from July to November.

Figure 23.9 shows the minimum and maximum exergetic efficiency ratios of NCZ. The ratios are calculated by using Eq. (23.8), using the experimental data and found to be minimum 1.40 % at lowest and 2.97 % at highest reference environment temperatures in January, and to be maximum 16.07 and 15.33 % at lowest and reference environment temperatures in August, respectively. As one can see the differences of the exergetic efficiency ratios are small in warmer day than cooler days of the year. Although the ratios in winter season at highest reference environment temperatures are higher than at lowest reference environment temperatures, after in summer season are lower than at lowest reference environment temperature. There are small variations between the exergetic efficiency ratios of NCZ but those are significantly effect on the performance of the solar pond.

Fig. 23.8 The exergetic efficiency ratios of LCZ
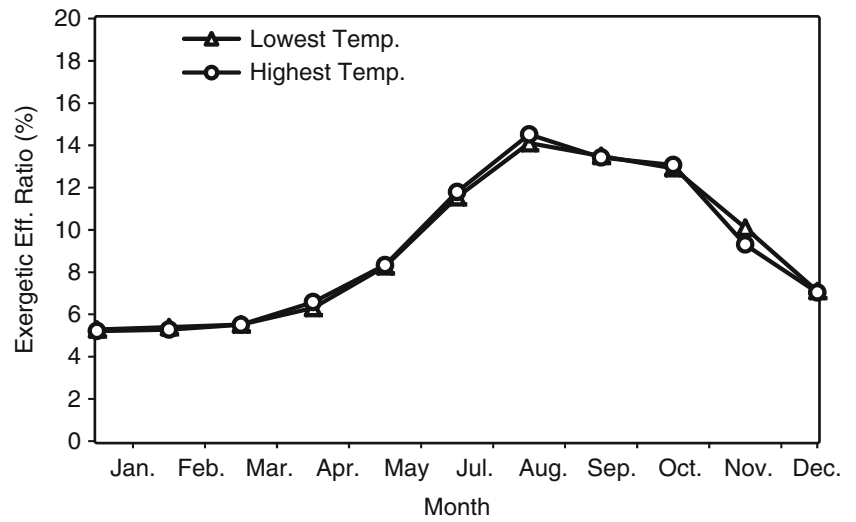
Fig. 23.9 The exergetic efficiency ratios of NCZ
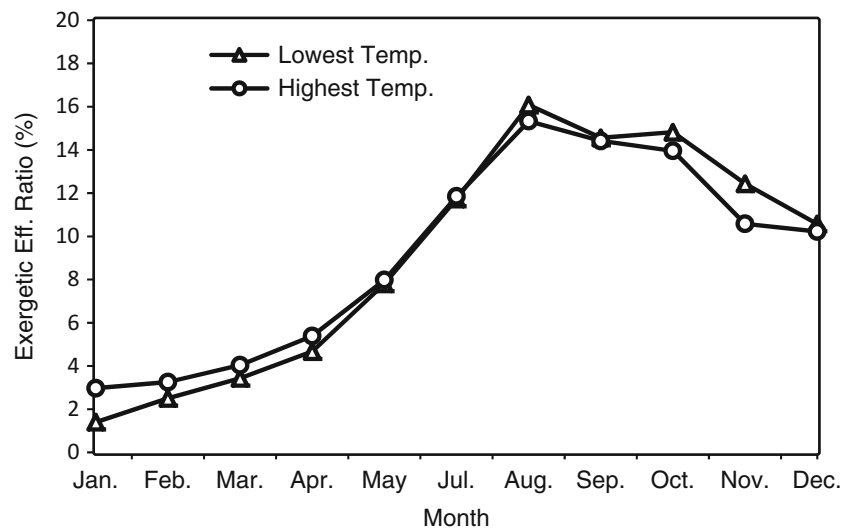
Fig. 23.10 The exergetic efficiency ratios of UCZ
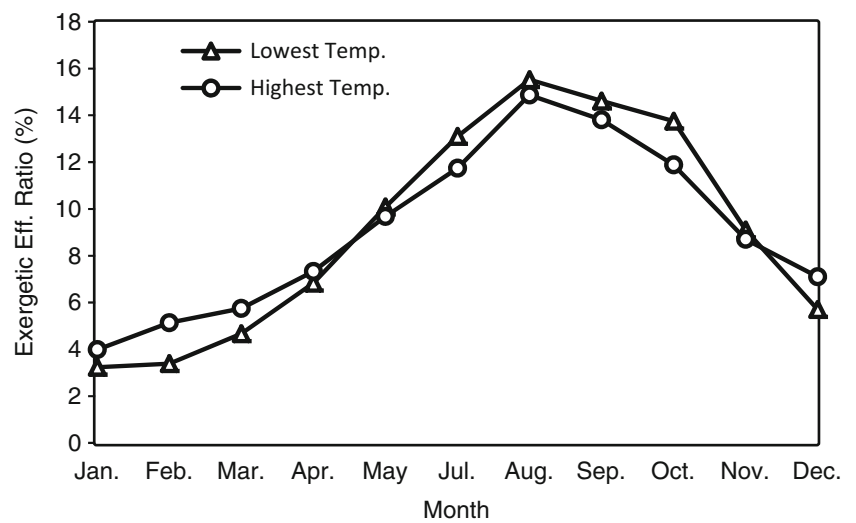
Figure 23.10 shows the minimum and maximum exergetic efficiency ratios of UCZ. The ratios are calculated by using Eq. (23.4), using the experimental data and found to be minimum 3.23 % at lowest and 3.98 % at highest reference environment temperatures in January, and to be maximum 15.52 % at lowest and 14.87 % at highest reference environment temperatures in August, respectively. There are significant variations between the exergetic efficiency ratios at lowest and highest references environment temperatures of UCZ. As one can see the differences of the exergetic efficiency ratios between winter and summer seasons are changed with at lowest and highest reference environment temperatures. The ratios at the highest reference environment temperatures of UCZ as NCZ are higher in winter season than warmer season. But the ratios at the lowest reference environment temperatures of UCZ are higher in summer season than winter season of the year. The variation of the ratios at lowest and highest reference environment temperatures between winter and summer are especially created by ambient air temperature, humidity, and salt diffusion from bottom layer to upper layer. The upper layer (UCZ) is homogeneous and convective, where the density of saline is close to freshwater. In the middle zone layers (NCZ) saline density increases in depth, thereby natural convection is stopped. In this layer, mass or thermal energy is transported only by molecular diffusion that is a very low process.

As seen in Figs. 23.8, 23.9, and 23.10, the fluctuations in the zones between of the ratios are significantly effect on the performance of the solar pond. As a result, the inner zones of the pond store more exergy in August than in January due to the considerable temperature differences between the zones. The exergy destruction and losses significantly affect the performance of the pond and should be minimized to increase the system efficiency. Furthermore, the advantages of exergy analysis of such systems for design, analysis, and performance improvement purposes are that it helps achieve the goal of more efficient energy resource utilization, enabling locations, types, and true magnitudes of wastes and losses to be determined, and revealing whether or not and how much it is possible to design more efficient energy systems by reducing the inefficiencies in the process/system.

Conclusions

In this paper, we have studied the performance analysis of a solar pond through exergy efficiency analysis. The exergy efficiencies calculated for each zone at lowest and highest temperatures using the experimental data are compared, and the corresponding minimum and maximum exergetic efficiencies and exergetic efficiency ratios are obtained. As expected, the exergy efficiencies and ratios appear to be smaller at lowest temperatures than the ones at highest temperatures. In this regard, the ratios are different at lowest and highest reference environment temperatures in the same month for each zone of the pond due to the exergy destructions in the zones and losses to the surroundings. Furthermore, the exergy analysis shows that it is important to determine the true magnitudes of the exergy efficiencies by using ratios for performance improvement studies.

Nomenclature

A	Surface area, m^2	m	Mass
C_p	Specific heat, $J\,kg^{-1}\,K^{-1}$	NCZ	Non-convective zone
E	Total solar energy reaching to the pond, J	T	Temperature, °C
HSZ	Heat storage zone	UCZ	Upper convective zone
I	Number of the layers	V	Volume, m^3
LCZ	Lower convective zone		

Greek Letters

Ξ	Exergy efficiency	θ	Angle of the refracted incidence, °
δ	Thickness where the long wave solar energy is absorbed	ρ	Density, $kg\,m^{-3}$
		ψ	Exergy efficiency
Δx	Thickness of horizontal layers, m	χ	Exergetic efficiency ratio

Subscripts

dest	Destruction	re	Reference environment
dw	Down wall	s	Sun
g	Gained	so	Solar
i	Input	st	Stored
L	Length	sw	Sidewall
L-H	Lowest and highest	T	Total
net	Net irradiation	up	Upper
o	Output	w	Width
r	Recovered	wa	Water to air

References

1. Saxena A, Goel V (2013) A technical note on fabrication and thermal performance studies of a solar pond model. J Renew Energ 2013:1–5
2. Akbarzadeh A, Andrews J (2005) Integration of solar ponds in salinity mitigation schemes to produce low grade heat for industrial process heating, desalination and power. ISES–2005 Solar World Congress, 6–12 Aug 2005, Orlando, FL, USA
3. Karakilcik M (1998) Determination of the performance of an insulated prototype solar pond, Ph.D. Thesis, University of Cukurova, Adana, Turkey (in Turkish)
4. Karakilcik M, Dincer I (2008) Exergetic performance analysis of a solar pond. Int J Therm Sci 47:93–102
5. Karakilcik M, Bozkurt I, Dincer I (2012) Dynamic exergetic performance assessment of an integrated solar pond. Int J Exergy 12:70–86
6. Karakilcik M, Dincer I, Rosen MA (2006) Performance investigation of a solar pond. Appl Therm Eng 26:727–735
7. Karakilcik M, Kıymaç K, Dincer I (2006) Experimental and theoretical distributions in a solar pond. Int J Heat Mass Transfer 49:825–835
8. Petela R (2003) Exergy of undiluted thermal radiation. Sol Energ 74:469–488
9. Dincer I, Rosen MA (2012) Exergy: energy, environment and sustainable development and energy analyses. 2nd edn. Elsevier, p 58

Assessment of Desalination Technologies Integrated with Renewable Energy Sources in Turkey

Halil S. Hamut, Ibrahim Dincer, and Marc A. Rosen

Abstract

In the past few decades, freshwater availability and quality for human consumption in the world has reduced significantly due to rapid population growth along with increasing industrial and agricultural demands, as well as uncontrolled urbanization and climate change. Even though Turkey is surrounded by water, its available freshwater per capita per year is less than the world average and much less that those for countries with developed economies [1]. Meanwhile, available freshwater sources in Turkey are diminishing rapidly due to pollution and overextraction associated with significantly increasing water demands. In order to prevent water scarcity in Turkey over the next decades, desalination is expected to be an important option. Appropriate desalination technologies need to be determined for implementation throughout the country.

In this study, potential desalination technologies, namely, multiple-effect distillation (MED), multistage flash distillation (MSF), and reverse osmosis (RO), using conventional and renewable energy sources (RESs) are evaluated, for various geographical locations and plant capacities, with respect to it overall cost and impact on the environment. Much actual plant data and results of a wide range of prior studies are used to estimate the associated costs. Airborne emissions during the operation phase are evaluated to determine the associated environmental impacts. Alternative energy sources such as waste heat from other processes and Turkey's abundant renewable energy sources (particularly wind, solar, hydro) are examined, and the integration of these sources with desalination is examined and compared to the conventional methods, using consistent criteria.

It is determined that RO is likely to be the most suitable desalination technology for Turkey, with a midsize desalination plant (around 30,000 m^3/day capacity) preferred. This result is in part due to the high cost of fossil fuels in Turkey and the low levels of the Mediterranean seawater feed, which reduce the cost of RO by 13 and 21 % with respect to MED and MSF respectively. RO can also help reduce emissions of CO_2, NO_x, NMVOC, SO_x by up to by 38, 42, 73, 60, respectively, compared to alternative technologies, even when waste heat recovery is used. Moreover, RO technology could be further improved by integrating with hydropower, the most compatible renewable energy source for Turkey, which can further reduce the emissions by 83, 82, 80, and 50 %, respectively.

Introduction

In the past century, water usage for human purposes has multiplied sixfold. Especially in the last couple of decades, due to rapid population growth along with increasing industrial and agricultural demands as well as uncontrolled urbanization and climate change, freshwater availability and quality for human consumption has declined significantly. Today, about 700 million people

H.S. Hamut (✉) • I. Dincer • M.A. Rosen
Faculty of Engineering and Applied Science, University of Ontario Institute of Technology,
2000 Simcoe St. North, Oshawa, ON, Canada L1H 7K4
e-mail: Halil.Hamut@uoit.ca; Ibrahim.Dincer@uoit.ca; Marc.Rosen@uoit.ca

in 43 countries live below the water-stress threshold and over 20 % of the world population does not have access to safe and affordable drinking water. In 2025, it is predicted that more than 3 billion people will live in water-stressed countries while 14 countries will move from water stressed to water scarcity. With 2 million annual deaths and 4 % of the global diseases attributed to unsafe water, sanitation, and hygiene, availability of freshwater remains one of the most important concerns [1–3].

Even though Turkey is surrounded by water, its available water per capita per year is only 1,586 m^3 for a population about 75 million (in 2012 statistics), which is less than the world average and 1/5 of the water use of countries with developed economies. The water needs of the country are expected to significantly increase over the next decades due to a population growth rate of 1.3 %, 69 % of the total population living in urban areas, a total final energy consumption growth rate of 9.6 % over the past three decades, and a projected primary average energy consumption growth rate of 5.9 % per year over the next decade [4]. These are some of the most reliable indicators of water demand. Meanwhile available freshwater sources in Turkey are diminishing rapidly due to pollution of freshwater supplies and overextraction. Turkey has a pollution rate of 1.1 tons of industrial organic pollutant per available km^3 of freshwater, which ranks it as 31st in the world [5]. Moreover, even though the Water Exploitation Index has decreased around 10 % in 21 European countries over the past 10–15 years, Turkey was one of the seven countries that had an increasing rate. Turkey's extraction has increased by 1/2 for public water supply and by 1/3 for irrigation (the two largest contributors of water extraction in the country) during the past decade, representing the highest upward trend among countries in Europe [6]. It is estimated that by 2023 annual freshwater per capita will decline to under 1,000 m^3 per capita, which is considered below water scarcity levels [7, 8].

The freshwater problems of Turkey can be addressed in many ways. While wastewater reclamation, urban runoff, and storm water capture can create significant impact on increasing the sustainability of available water sources, the process of desalination seems more appropriate for the country due to its geographical proximity to seawater and the negative public perception of waste water reclamation, primarily due to concerns with respect to human health [9]. Desalination is a relatively mature technology that is free from variations in rainfall. It avoids the need for dual piping networks, and has a virtually unlimited supply of the primary feedstock (seawater). Desalination is likely to play a major role in augmenting freshwater resources globally (the capacity is estimated to be in excess of 5,000 m^3/day with an annual growth rate of 12 % over the last 5 years). Growth has been notable in Mediterranean countries.

The objective is to improve understanding of desalination options for the provision of freshwater in Turkey in the future. More than 90 % of commercial desalination technology is based on multistage flash (MSF), multi-effect evaporation (MED), and reverse osmosis (RO), so these are the main technologies selected here for evaluation for utilization in Turkey. Moreover, due to Turkey's geographical proximity to three major seas, only seawater desalination is taken into consideration. The main evaluation criteria are environmental impact, cost, and compatibility (in terms of geographical, structural, and political factors) with the country.

Desalination Technologies

Industrial desalination uses seawater (as well as brackish water) and a form of energy (most commonly thermal, mechanical, or potential) to produce separate streams of nearly salt free water that can be consumed by humans (or used for irrigation). The main waste is rejected brine. Desalination processes can be phase change/thermal or membrane separation. Thermal desalination is one of the oldest ways of producing potable water and MSF accounts for over 60 % of all desalinated water, mostly in Gulf States. A majority of plant units produce over 5,000 m^3/day. Thermal desalination requires little pretreatment, is highly robust and can produce water with very low salt content (no more than 10–20 ppm). At the same time there has been a significant increase in RO plants, mostly in the USA, Spain, and Japan. RO technology consumes less energy than thermal desalination methods but usually requires more pretreatment than thermal methods (especially for seawater with high salinity) and produces water with salinities of around 200–500 ppm. In recent decades RO technology use has become significant worldwide due to its lower energy requirements, environmental compatibility, ease of control and scale-up, flexibility, and simplicity [10, 11].

Multiple-Effect Distillation

Multiple-effect distillation (MED), one of the oldest methods for desalination, involves boiling seawater in evaporators (called effects) and condensing the released steam to produce nearly pure water. The feed seawater is preheated in the evaporator tubes and to the boiling point. Tubes are heated by externally supplied steam which can be recycled as feed water and condenses at the other side of the tubes. Next the seawater is sprayed onto the surface of evaporator tubes in a thin film to

promote rapid boiling and evaporation of the portion of the seawater applied. These effects are connected together in a sequence with decreasing levels of pressure where the vapor formed in one effect is transferred to be utilized in the next to evaporate a portion of the remaining seawater. Therefore, the seawater intake is allowed to undergo multiple boiling steps without the need of adding heat after the initial effect, leading to a high thermodynamic efficiency. This system allows for low brine output and prevents rejection of large amounts of energy, which is the main drawback of the single effect distillation system [12]. MED operates at low concentration and low temperature (less than 70 °C), and can produce steadily high purity distillate (between 1 and 50 ppm total dissolved solids). The MED process usually is limited to smaller system capacities [10]. The steam economy of the system increases with increased number of effects, but is limited to the total temperature range available and minimum temperature difference between the effects. Commonly 8 or 16 effects are carried out in a typical large plant with performance ratios ranging between 10 and 18 [13, 14]. The specific electricity consumption of typical MED plants is below 1.8 kW h/m^3. However, this consumption is insignificant compared the thermal energy consumption of the process.

Multistage Flash Distillation

Unlike MED, MSF utilizes the liquid bulk as opposed to the surface of hot tubes in order to form vapor [12]. Seawater is flashed into steam in multiple stages by reducing the pressure in each stage for flashing at progressively lower temperatures (typically 2–5 °C in each stage), without the need of adding more heat. Seawater initially flows through heat exchanger tubes where it is gradually heated to the inlet temperature of the brine heater by the latent heat of seawater flashing in each chamber. Then, the seawater is further heated by the brine heater and enters the first stage of evaporator flash chambers, with high temperature and pressure, where it immediately flashes and partially vaporizes to reach the equilibrium conditions with the stage. The flashed vapor is drawn to the cooler tube bundle surfaces where it is condensed and collected as distillate. The remaining seawater is then transferred into the next stage where the same process is repeated about 19–28 times (in modern large MSF plants). The produced desalinated water contains 2–10 ppm total dissolved solids and is re-mineralized through a post-treatment process. Some portion of the cold seawater is used as a cooling medium for the heat rejection section and returned to the sea after applying scale-control measures. The plant efficiency increases with the number of stages, although this increases plant capital cost. The upper operating temperature of brine is usually 90–120 °C. Increasing the temperature increases the efficiency of the system, but also increases the probability of scale formation and accelerated corrosion of metal surfaces that are in contact with seawater [13, 15]. The specific electricity consumption of the MSF plants is typically 4 kW h/m^3, which is significantly higher than for MED plants but still low compared to thermal energy consumption.

There have been major technological advancements in MSF distillation plants over the past decades. Plants have significantly higher reliability and life expectancies at lower costs due to technical optimization (including experienced capitalization and better material alternatives) and less stringent technical restraints, mostly regarding processes, materials and plant accessories [16].

Reverse Osmosis

Reverse osmosis is one of the fastest growing desalination methods and is a good alternative to thermal desalination. It is a membrane separation process that produces a flow of near pure water by rejecting large molecules, ion and the dissolved salts from seawater, as a result of applying an external pressure higher than the osmotic pressure on the seawater (commonly with the use of high pressure stainless steel electric pumps). During the process a small percentage (1 % for new membranes) of the water leaks around the seals, but this leak is acceptable for the water quality needed for human consumption and industrial applications. Pretreatment of seawater is usually required to remove undesirable elements in the seawater and to prevent their accumulation in the membrane (membrane fouling). The latter phenomenon significant reduces the permeate flux. Post-treatment usually includes PH adjustment, addition of lime, and removal of dissolved gases and disinfection [13]. The performance of RO is characterized in terms of water flux, salt rejection, and recovery rates [10].

Since there is no heating or phase separation associated with RO, the energy input for the process is significantly less than for MED or MSF and mostly associated with pressurizing the seawater feed, which is proportional to feed water salinity. An increase of 100 ppm TDS of the input water salinity increases the feed pressure requirements by approximately 1 psi, increasing the energy requirement [17]. Operating under low ambient temperatures also reduces problems due to corrosion.

A common large seawater RO plant includes feed water pretreatment, high pressure pumping, membrane separation, and permeate post-treatment. The majority of the problems faced by the RO plants occur during pretreatment, due to the inadequacy of conventional filtration methods.

Over the past two decades, the RO process has undergone significant technological developments and cost reductions. Most of the improvements are associated with the membranes, which now have better resistance to compression, longer life, higher possible recovery, improved flux, and improved salt passages. The typical energy consumption of RO plants is 6–8 kW h/m^3 without energy recovery, but can likely be reduced significantly using current innovations in energy recovery devices.

Renewable Energy Potential of Turkey

Even though desalination can help reduce water scarcity significantly, especially in areas where other water supply alternatives are not available, it requires a great amount of energy which is mainly obtained from fossil fuels at present. This imposes problems since fossil fuels are both harmful to the environment and are costly in Turkey; therefore, alternative energy sources are worth analyzing. Turkey is a country with an abundance of many types of renewable energy sources, and the three major RESs of the country, namely, wind, solar, and hydro, are analyzed in this study. The availability, technological and economic readiness, and compatibility of RESs for use with desalination methods are examined in this section in order to provide the background, current trends and future predictions for RES utilization in Turkey, which is required before the most appropriate desalination method and energy usage can be assessed.

RESs have increased in importance with concerns over environmental and sustainability issues associated with conventional energy sources. RESs often exhibit a relation to regions where desalination is most needed, since these tend to be the regions where RESs like wind or solar are most abundant (e.g., coastal areas with warm climates and/or remote regions where connection to the electrical grid is not feasible or cost effective). However, several additional criteria, like the amount of water needed, feed-water salinity and technical infrastructure, also need be taken into account when matching RESs with desalination technologies [18].

Renewable energy sources are characterized by intermittent and variable intensity as opposed to desalination plants that require steady energy inputs. However, in many cases, a combination of multiple RESs can be used to account for the variations in energy inputs of each source if multiple sources are available. RESs can also be used for storing the excess electricity produced that is not used by desalination in the grid, for later use when the RES power decreases, if "grid-connected" systems make more economic sense [19].

Today conventional energy sources are expected to have an increasing cost trend due to ongoing depletion of available fossil fuels as well as possible introduction of fiscal penalties for power plants emitting carbon dioxide [20]. On the other hand, RESs have the opposite trend as a result of various monetary incentives (including tax cuts) and continuous advancements in technology that reduce their investment costs. The trend in low/high investment and generations costs (based on lower and upper cost estimation ranges) of RESs in the past decade are shown in Fig. 24.1.

Although all RESs account for only 12 % of the total energy consumption of Turkey, RESs in Turkey have the biggest potential in Europe, especially for hydro, wind and geothermal energy, and very good potential in terms of biomass and solar energy [21–23]. Moreover, although the current utilization of RES low, many suggest Turkey has both the potential and the political willingness to utilize RESs more in the future. The renewable energy potential of the country can be seen in Table 24.1.

In Turkey the average capital costs (the most significant costs associated with RESs) [14, 18] are even lower than the world average due to the abundance of economically exploitable sources, recent legal incentives, low construction and labor costs. Average capital costs for RESs are compared in Table 24.1.

Wind Energy

Wind-power technology has been improved significantly over the last decades and has begun to be used to supply electricity or mechanical power to small-scale desalination plants in various locations in the world. In addition to technological readiness, it is also a highly compatible method since freshwater can be produced when there is an available power supply and can be easily stored when there is not, counteracting with the fluctuations in wind speeds without the need for expensive backup systems.
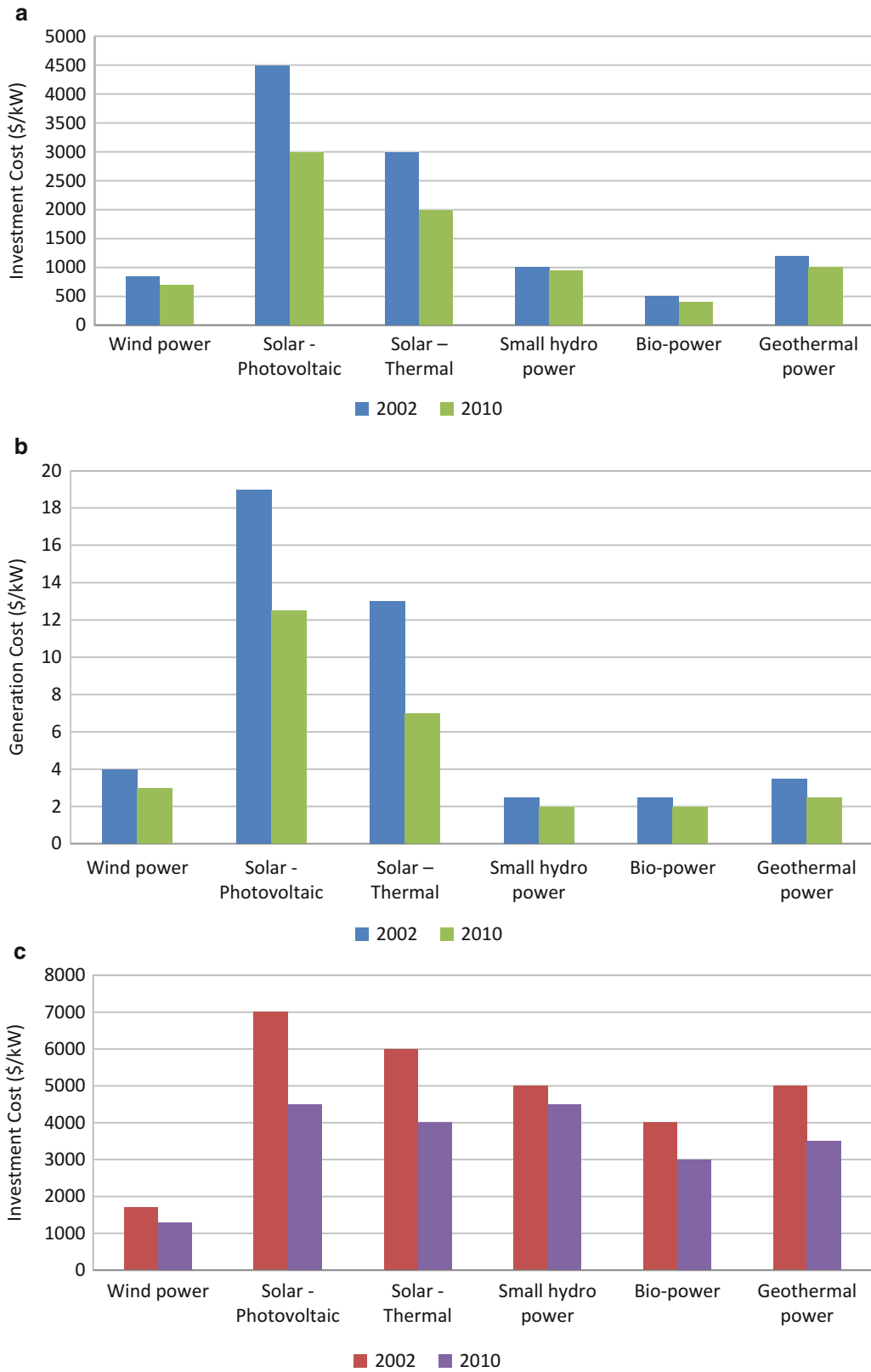
Fig. 24.1 Low scenario (**a**) investment and (**b**) generation costs (in $/kW) and high scenario (**c**) investment and (**d**) generation costs for electricity production using RESs between the years 2002 and 2010 (data obtained from [20, 21])
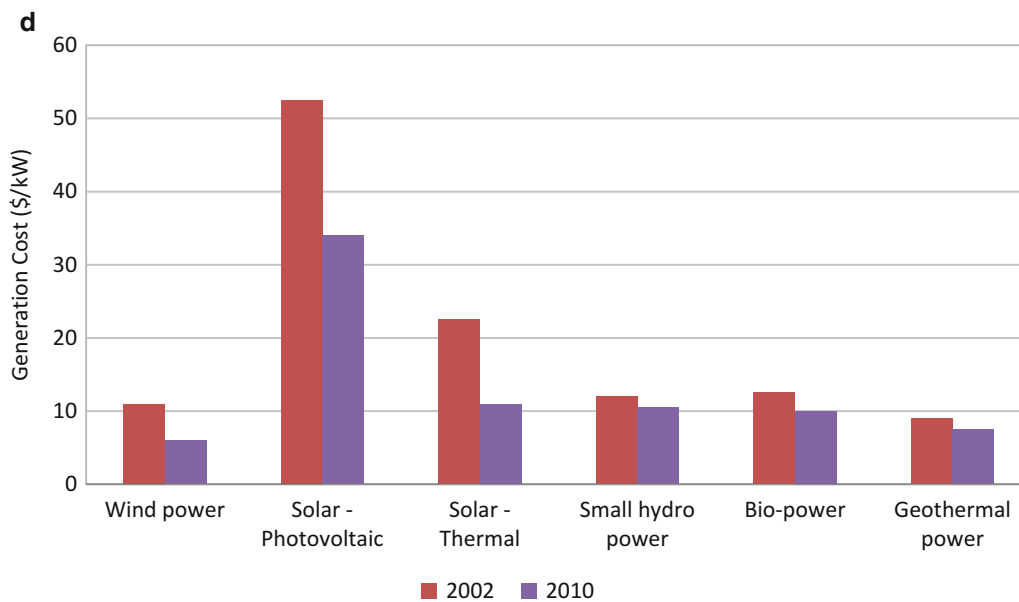
Fig. 24.1 (continued)

Table 24.1 Turkey's RES potential and share of renewable in the country's total production and consumption for major energy sources as well as capital costs associated with the RESs(data used from [20–24])

Energy type	Usage purpose[a]	Natural capacity	Technical	Economical	Share of RES in Turkey's total production (%)		Share of RES in Turkey's total consumption (%)		World capital cost (avg)[b]	Turkey's capital cost (avg)[b]
Wind energy (land)	Electric	400	110	50	Energy Exergy	0.06 0.05	Energy Exergy	0.96 0.01	920	900
Solar	Electric Thermal	977,000 80,000	6,105 500	305 25	Energy Exergy	2.41 2.42	Energy Exergy	0.32 0.31	5,400	N/A
Hydropower	Electric	430	215	124.5	Energy Exergy	22.15 23.99	Energy Exergy	2.96 3.02	1,000	650
Geothermal	Electric Thermal	109 31,500	– 7,500	1.4 2.843	Energy Exergy	14.82 4.64	Energy Exergy	1.98 0.58	1,230	1,440
Biomass	Total	120	50	32	Energy Exergy	13.00 14.77	Energy Exergy	1.74 1.86	N/A	NA

[a]The units for electricity is measured in Billion kWh and thermal energy is measured in Mtoe
[b]Capital costs are in terms of €/kW

When the desalination technologies considered in this study are examined, RO technology seems to be most compatible with wind energy due to its modular nature that allows the process to adapt to fluctuations in wind conditions and its high energy efficiency that leads to low specific energy requirements (as low as 2 kW h/m^3). The technology also has great variety of production capacities and fast start up and stop times that are compatible with wind energy [17]. Moreover, it is also possible to provide the RO system with valves that can dynamically activate/deactivate RO vessels to adjust the energy demand to the available wind energy [24].

Wind energy has the potential to be an important substitute for conventional energy sources for Turkey, since Turkey has the highest share with 166 TW/year in technical wind energy potential among European countries, enough in fact to meet all of Turkey's electricity needs. The energy costs associated with desalination plants decreases significantly with the implementation of wind energy (since there are no fuel costs), and the capital cost (about 75 % of total plant cost) is mainly associated with the wind turbines (50 % of the capital cost) [17]. Even though the cost of electricity and water produced through this technology depends significantly on plant size and location and as well as various economic, political and site-specific factors, it is estimated that the cost of electricity produced by a 500 kW wind turbine with a maximum efficiency of 30 % in a geographical location similar to Turkey would cost $0.07 per kWh [25].

Solar Energy

Solar energy is one of the most promising RESs and includes solar thermal and photovoltaics (PV) technologies. In solar thermal systems, a fluid is heated by solar radiation as it circulates along the solar collectors (flat or parabolic) through an absorber pipe. It can be stored in an insulated tank or used in the high temperature end of a standard thermal distillation process. PV technology converts solar energy directly into electricity by using sunlight to excite electrons in the cells and generate electrical charges that conducted away as direct current [26, 27]. Solar thermal energy systems are starting to be used with MED and MSF processes in large-scale applications (from 5 to 345 MW) as well as with many RO systems. PV systems are used more often with RO methods in relatively small applications (under 5 MW, corresponding to desalination plants under 15,000 m^3/day capacity).

Photovoltaic technology has many advantages such as the capability of integrating with small desalination plants, limited maintenance costs, and ease of transportation and installation [18], and is usually coupled with RO systems due to the ease of integration. The main drawback comes from storing the energy when solar energy is insufficient and sustaining the system operation using batteries. PV technology still is costly compared to other RESs. Turkey has substantial gross solar potential of 88 billion toe per year, with an average annual sunshine duration of 2,640 h and an average solar intensity of 3.6 kWh h/m^2/day [21].

In cost analyses of RO plants in the Middle East with a capacity of 10,000 m^3/day and specific electricity demand of 3 kWh/m, the price of electricity produced is calculated to be under $0.09 for solar thermal systems and $0.50 for PV [27]. Environmentally, even though solar energy has significantly less impact than conventional energy sources, there are still some potential negative effects due to the materials and chemicals utilized in the technology. Solar thermal receivers use toxic chemicals in the heat transfer system, which pose threats in cases of accidental or emergency releases to the environment. PV systems also use highly toxic chemicals that require rigorous disposal and recycling procedures.

Hydropower Energy

Hydropower contributes 20 % of the world's electricity generation, providing the majority of supply in 55 countries [28]. It is derived from the energy produced through natural flow of water, turning the blades of turbines that are connected to a generator. The energy produced is proportional to the volume of the water flow and the height from which it is falls. It can beneficially complement power sources that are more intermittent like wind and solar since the generating capacity can be reserved during peak supply periods (through regulation of water flow) and/or when the capacities of other RESs are limited [29]. Hydropower is one of the most efficient technologies for electricity production since modern turbines can convert as much as 90 % of the available energy into electricity, which is significantly higher than the 50 % efficiency of modern fossil fuel plants. During its lifetime a hydropower plant can produce 200 times the energy needed to build it [31].

Hydropower technology is more compatible with RO desalination than other renewable energy sources. Instead of converting the potential energy of water into electricity through the use of turbines and a generator (which have energy loses of 16 and 5 % of theoretical hydro-potential, respectively) and then converting the electricity to hydraulic pressure, the potential energy in the trunk main can be used to provide hydraulic pressure in the pressure pumping unit of the RO system seamlessly [32]. Since the energy requirement of the pressure pumping system is one the major costs of RO plants, removing this stage can lower initial capital costs, construction times and energy requirements and costs [30]. But hydropower systems are generally built in areas with natural waterfalls, where freshwater is usually abundant, and hence desalination may not be needed [31]. Turkey has the second largest gross hydroelectric potential in European countries after Norway, with 16 % of total theoretical hydropower potential of all Europe. It is the most important RES used for electricity production in Turkey, comprising 96 % of all electricity produced by RESs in 2008 [4].

Aside from the abundant availability of hydropower, there are also financial incentives created by the Turkish government. The May 2005 Renewable Energy Law (Law No. 5346) provides an 85 % discount on all forest land acquisition to build small hydropower, on top of other incentives created for all RESs, reducing capital costs significantly. Moreover, the operating and investment cost of small hydropower is also significantly lower in Turkey than in most of the European countries, mostly due to lower construction and labor costs. Hydroelectric plants have significantly longer economic lives (about 75 years) than most other plants, making them even more economical in the long run. The technology is highly environmentally benign (except for potential fish passage blockages and sediment transport interruption, as well as issues with dams) with additional environmental advantages from the prevention of river erosion in most areas [32].

Other Renewable Energy Sources

Biomass energy is a major renewable energy source in Turkey, especially in the rural regions, with estimated recoverable bio energy potential of 35.4 M toe [23]. In crop residues, Turkey is estimated to have the 4th highest total energy potential (9.5 M toe) among the OECD countries. However, this energy source is not considered in this study due to a significant declining trend in biomass use in Turkey, with its total energy consumption contribution reduced from 20 to 8 % between 1980 and 2005. This is primarily due to scarcity-of-supply and environmental concerns, the latter because biomass is a contributor of air pollution, e.g., biomass combustion releases over 200 chemical pollutants including 14 carcinogens and 4 co-carcinogens into the atmosphere [26] and contributes to over-timbering and deforestation. The share of biomass in RES use is expected to continue to decrease in the future [28].

Turkey also has significant geothermal energy potential and is among the top seven countries in potential, possessing 1/8th of the world's total geothermal potential [33, 34]. However, it is ranked last in installed capacity (28 MW_e) [22], and only 6 % of this potential is of suitably high temperature and enthalpy for electricity production (i.e., temperatures over 150 °C). Thus, the geothermal electricity generation potential of Turkey is estimated to be only 16 TWh/year. Few reliable studies are currently available regarding economic and environmental effects of using geothermal energy with desalination technologies.

Selection Criteria

When the global distribution of various desalination plants and their respective energy sources are examined, one of the major deciding factors in application is the availability of resources (environmental and/or technical) and cost. The majority of desalination plants in the Middle Eastern region use thermal desalination technologies, incorporating conventional energy sources (fossil fuels, natural gas, and coal), due to the lower energy costs and simpler and more reliable nature of the technologies (compared to membrane separation). Most of these countries have not implemented significant renewable energy or nuclear energy technology at large scales. Europe, on the other hand, has a significantly wider range of energy production methods (43 % thermal, 40 % nuclear, and 17 % hydropower [15]) and has started to incorporate renewable energy resources. Turkey does not seem to fit in either option. Even though geographically Turkey lies in the Middle East and like nearby countries relies mostly on conventional sources for energy production (31.8 % natural gas, 29.9 % fossil fuels, and 27.3 % coal, which makes up about 90 % of total energy consumption), the country does not have significant sources available and depends heavily on importing. Currently 97 % of Turkey's natural gas, 93 % of its oil and 20 % of its coal use is imported [4]. General trends regarding production, import and consumption suggest that Turkey will import 99 % of its oil within 20 years [25]. Therefore, the cost associated with desalination using conventional energy resources will likely be considerably higher compared to most Gulf States. Even though Turkey has the largest potential in Europe for RESs such as hydro, wind and geothermal and very good potential in terms of biomass and solar, the utilization of these resources is low (12 % of energy total energy consumption combined [21]). Here, we examine and compare desalination technologies and various energy sources with respect to its environmental impact, cost and other criteria.

Environmental Impact

Over the past century, during an era of industrialization [35], humans have left a significant footprint on the environment. With unplanned industrial growth and the false notion of unlimited resources, we have reduced many of Earth's important natural resources significantly and negatively impacted the environment. These actions have resulted in problems such as climate change and global warming, decreases of biodiversity. In past decades, people have increasingly become aware of environmental concerns across the world. Today these concerns often play a role in people's decision making and many studies are being conducted to understand the negative environmental impacts of our actions and ways to prevent them. Due to the increased complexity of today's processes and the mix of materials and energy sources utilized, understanding the exact relationship between actions and associated environmental impacts is increasingly difficulty and methods are required to analyze these relationships further to improve understanding of the technologies.

In determining the environmental impact of the studied technologies, the main focus is on the operation phase of the life cycle of the plant since many studies show that the environmental load associated with this stage is 89–99 % higher than that of assembly and final plant disposal phases [16, 18]. Since the main contributor to environmental effects in this stage is the amount and source of energy used by desalination technologies, the primary focus is the energy usage of the desalination
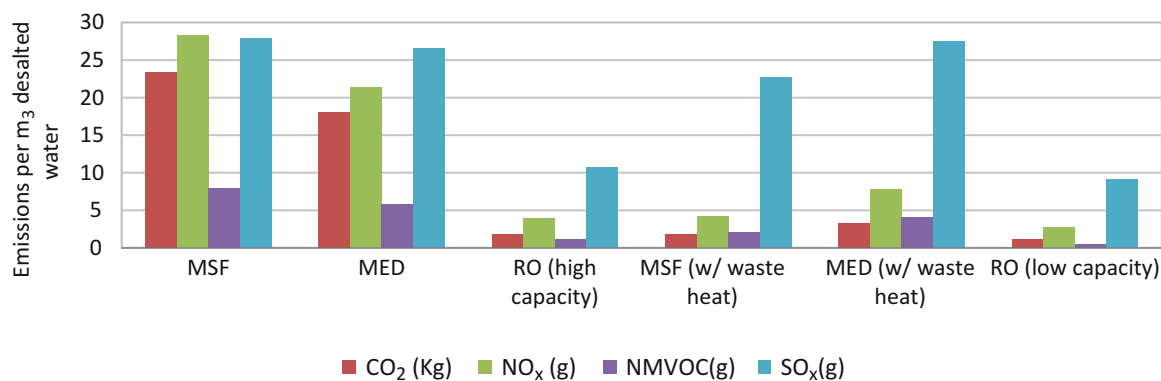
Fig. 24.2 Airborne emissions produced by MSF[1], MED[1] and RO[2] desalination systems. Data are obtained for MSF and MED from the research project REN 2001-0292 that took part in Spanish Plan for Scientific Research and Technological Development and Innovation (R & D & I) [14–16]. Values for RO are based on potential energy consumption with respect to current technological improvements [10]

technologies and the potential of alternative energy sources. The associated environmental impact for MED, MSF and RO technologies are shown in Fig. 24.2. Note that only airborne emissions are taken into consideration since these are typically associated with energy production systems, are often regulated by the each country and are emitted in higher quantities than most other substances [14].

Figure 24.2 shows that MSF desalination has the highest impact on the environment in all categories considered, followed my MED with slightly lower airborne emissions and RO with significantly less impact than the first two. A strong correlation is observed between energy consumption and airborne emissions in the first 3 columns. Thermal desalination methods usually consume 50–70 kWh/m^3 of distilled water (thermal equivalent of producing 8–12 kg of freshwater per kg of heating steam) and have an order of magnitude larger impact on airborne emissions than RO. The significantly higher energy consumption for thermal desalination technologies creates an order of magnitude larger environmental impact than RO technology.

The high energy consumption of MSF and MED plants can be reduced by utilization of waste heat from other processes, since desalination plants and production plants can often integrate in mutually beneficial ways for this purpose. Most production plants require large water intakes for cooling water and reject considerable amounts of waste heat to the atmosphere. Desalination plants can use the waste heat to provide water, some of which can be used for the production plant cooling. This can reduce the environmental impact of the thermal desalination methods significantly, often enough to make them comparable to RO technology. However, it should be noted that even though utilization of waste heat can potentially reduce the environmental effects of the desalination technologies, they require the plant to be built in the vicinity of production plants, which limits the potential locations, especially since in some cases freshwater is needed in rural regions away from industrialized areas.

Since RO plants consume almost no thermal energy (compared to MSF and MED) for desalination, waste heat utilization is not compatible with this technology to reduce the environmental effects. However, because of the latest improvements in energy consumption technology in RO plants and commercial introduction of "isobaric devices," the associated consumption can be reduced as much as 46 %, from 3.9 to 2.1 kWh/m^3 (with a 6.0 MPa feed water pressure and 50 % recovery rate) [10], reducing the overall impact on the environment.

The overall environmental impact of the desalination technologies can be reduced further by integrating them with of renewable energy sources. The extensive and increasing use of fossil fuels within the current energy infrastructure is considered the largest cause of CO_2 emissions, which are believed to be directly tied to global warming, climate change and other environmental concerns. These negative impacts can be reduced significantly through the utilization of various abundant RES in Turkey that have little negative impact compared to conventional energy sources. Due to its low energy requirement and modular nature, integration of RESs with desalination is primarily studied/used for RO since, unlike MED and MSF technologies, there exists much reliable data regarding environmental impact of the integrated technology. Therefore, integration of RES is only analyzed with respect to RO in this study. The improvements possible, for the previously discussed emissions, are shown in Fig. 24.3. It is seen that even though the environmental impact of RO technology is significantly lower with respect to thermal desalination technologies, the emissions can be reduced further, by up to 95 % in some categories, via integration of renewable energy sources. It also is observed that, among the RESs selected, hydropower provides the greatest reduction in environmental impact in every category considered, with a reduction of over 90 % on average.

Fig. 24.3 Environmental Impact of RO technology incorporating various RESs for (**a**) low and (**b**) capacity (data obtained from [14, 34]). RO data are obtained from the research project REN 2001-0292 that took part in Spanish Plan for Scientific Research and Technological Development and Innovation (R & D & I). The environmental load associated with RO technology using PV is considered based on solar radiation data extrapolated from a plant used in Spain. The minimum and maximum emission values are considered for RESs with respect to a conventional RO plant with 4 kWh/m^3 energy consumption
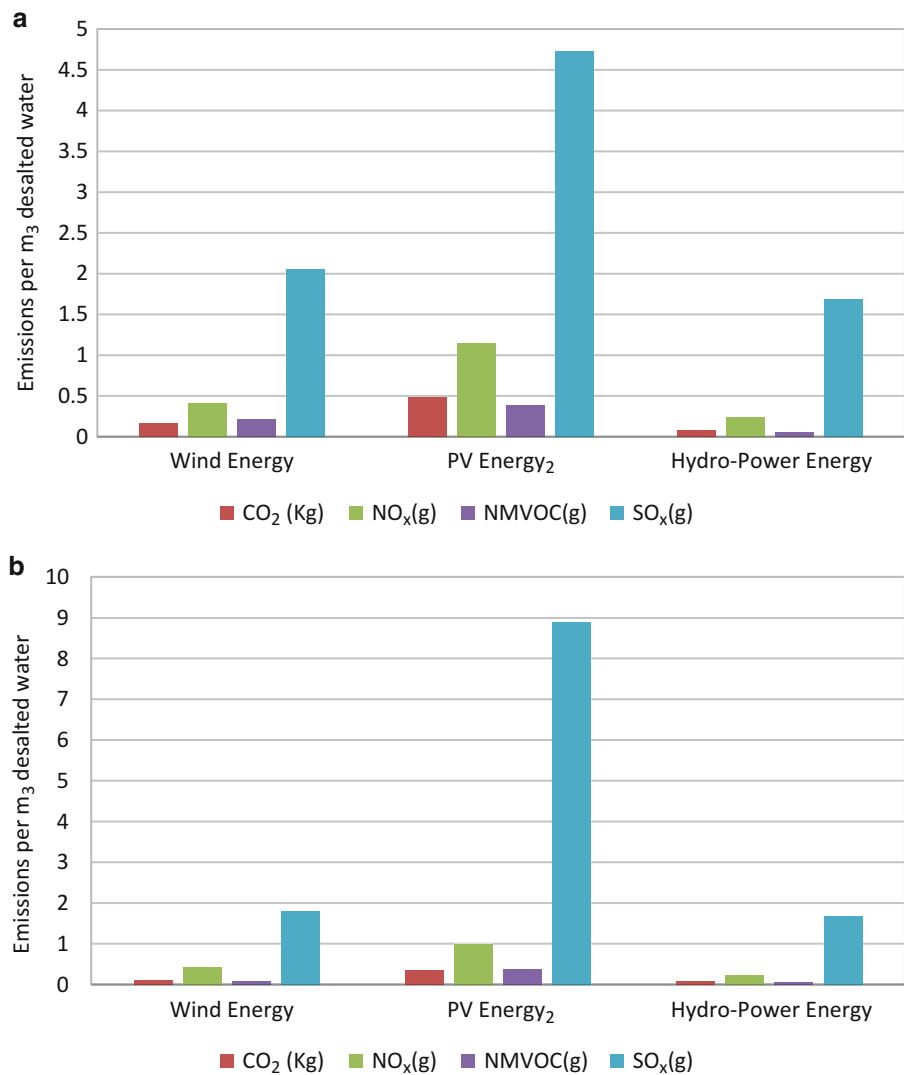
Cost

Another important criterion for determining the most suitable desalination technology (and associated energy source) is based on the cost of the overall system. Due to insufficient studies and lack of reliable data on cost estimates for MED, MSF, and RO technologies in Turkey, the analysis is based on real data for various industrial desalination plants around the world as well as studies conducted for similar geographical regions and countries that have similar energy and economic potential to Turkey. The main comparison are based on unit water production costs. Some recent estimates of water costs of various desalination technologies selected around the world are shown in Table 24.2. The unit water production cost of MED/MSF and RO technologies are seen to be very similar ($0.81/m^3 on average for MED/MSF and $0.86/m^3 for RO technologies based on plants provided in the table). The data suggests that, even though RO plant unit water costs have dropped significantly in the last decades, they still are slightly higher on average than for thermal plants on a unit water cost basis.

Note that, although unit water costs provide an important tool for comparing different technology costs, other factors should not be neglected. The majority of large capacity thermal desalination plants are in the Middle Eastern region. Thus, all MSF plants in Table 24.2 are in either the United Arabic Emirates or Saudi Arabia due to the availability of data for these plants. The primary energy sources for these plants are generally fossil fuels, which are significantly cheaper than for most other locations in the world; the unit water costs would be drastically higher if the plants were in most parts of Europe. Therefore, these costs are considerably higher in Turkey when powered by fossil fuels.

Table 24.2 Total water costs of selected industrial desalination plants (data obtained from [8, 10, 12])

Plant (location)	Technology	Water cost ($/m^3)	Plant capacity (m^3/day)
Shuweihat (UAE)	MSF	1.13	454,610
RasLaffan (UAE)	MSF	0.80	272,520
Hidd (UAE)	MSF	0.69	400,00
Tenes (Algeria)	SWRO	0.59	200,00
Taunton (Massachusetts, USA)	SWRO	1.53	18,925
Palmachim (Israel)	SWRO	0.86	83,270
OuedSebt (Algeria)	SWRO	0.68	100,00
Hadera (Israel)	SWRO	0.86	330,00
Ashkelon (Israel)	SWRO	0.78	326,144
Tianjin (China)	SWRO	0.95	150,000
Dhekelia (Cyprus)	SWRO	0.88	40,000
Carlsbad (California, USA)	SWRO	0.77	189,250
Pert (Australia)	SWRO	0.75	143,700
Marafiq (Saudi Arabia)	SWRO	0.83	758,516
Shoaiba 3 (Saudi Arabia)	MSF	0.57	881,150
Reliance refinery (India)	MED	1.53	14,400

Table 24.3 Analysis of unit production costs based on various studies in the literature

Reference	Process	Capacity (m^3/day)	Unit production cost ($/m^3)
Borsani and Rebagliati [15][a]	MED	205,000	0.52
	MSF	205,000	0.52
	RO	205,000	0.45
Karagiannis and Soldatos [39]	MED	12,000–55,000	0.95–1.95
	MSF	23,000–528,000	0.52–1.75
	RO	12,000–60,000	0.44–1.62
Wade [40][b]	MED	31,822	0.95
	MSF	31,822	1.04
	RO	31,822	0.82
Fiorenza et al. [41]	MED	10,000	0.8
	MSF	25,000	1.10
	RO	6,000	0.7
Frioui and Oumeddour[c]	MED	1,000	1.38–1.45
	MSF	1,000	1.2–1.34
	RO	1,000	1.8

[a]Cost estimates are based on a 20-year plant life, recovery ratio of 40 %, and membrane replacement of 5 years (for RO), steam factor time around 85 % (for MED and MSF), and fuel price of natural gas $4.5/MWh(th) for seawater desalination
[b]Cost estimates are based on Mediterranean seawater feed of around 37,000 mg/l total TDS
[c]Cost estimates are based on a 30-year plant life, 100 % production rate, and steam factor time around 85 %

Another factor is that, due to the nature of MED and MSF technologies, plant capacity is significantly higher than for most RO plants. Since higher capacity is associated with lower unit costs due to economies of scale, capacity should be considered when comparing unit water costs. Larger plants require significantly higher investment costs and usually pose higher initial risks than relatively smaller ones. For these reasons, the costs show a bias towards MED and MSF technologies, and therefore, the actual gap between RO and MSF/MED technologies is considerably smaller in reality when implemented in Turkey.

Beyond data from actual plants, many studies have been conducted regarding estimating the cost associated with these three desalination technologies. These studies facilitate useful comparisons based on diverse geographical locations and similar capacities, allowing fair assessments. Table 24.3 presents costs data based on combinations of several major independent studies in the literature.

It can be seen in Table 24.3 that the average unit cost estimated for MED, MSF, and RO plants are $1.03, $1.01, and $0.96/m^3 respectively, which are similar. The table also shows that, at higher capacities, RO technology can not only compete with MED and MSF technologies but also be cheaper than the same based on unit production costs.

The studies also suggest that RO technology can be economical when incorporating RESs. Based on analyses in several studies, the range of unit production costs of the examined RESs with various capacities are shown in Fig. 24.4 [18,36,37]. Note that the high end production costs refer to experimental systems.

Fig. 24.4 Unit production cost ranges for RO technology integrated with various RESs (data from [17, 39, 43])
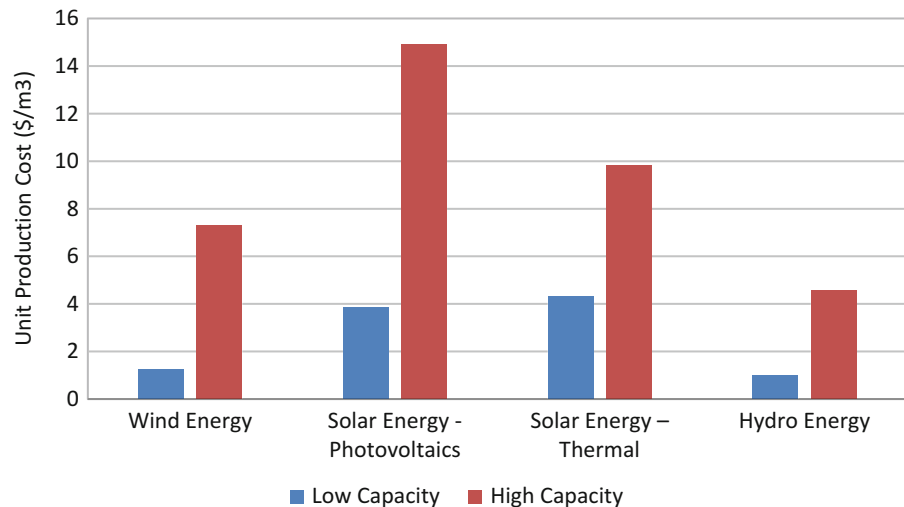
The large gap between high and low cost estimates with respect to each RES utilized with RO desalination technology is due to factors like quality of renewable energy sources, government incentives, transportation costs and production capacity. Most of these systems are built as prototypes and are hard to compare on a cost basis. Even though these costs are still higher than utilizing conventional energy source, the associated costs of using RESs have been declining significantly over the past decades and are expected to continue to do so. It can be seen that, among the RESs, RO can provide the lowest cost when integrated with hydropower. This cost average is expected to be even lower for Turkey due to the large availability of economically exploitable hydro sources, cheap labor and land costs for construction (capital cost of hydro is overwhelmingly larger than all other costs) and available technical expertise (96 % of current RES usage already comes for hydropower [14]).

Other Considerations

Through analyzing the environmental impacts and overall costs associated with building various desalination technologies in Turkey, it is seen that using RESs provides significant advantages with respect to both criteria. However, the benefits of implementing RESs for desalination technologies are far greater than the studied criteria for the country. As previously mentioned, the dependence of fossil fuels is one of the biggest concerns of Turkey, due to it comprising a considerably large portion of the country's energy use(90 %) and very small portion of its energy reserves (under 1 % of the world). This leads to importing almost all of its energy needs from outside the borders (97 % of natural gas, 93 % of oil and 20 % of coal), the majority of them being a single sources. Historically Russia has been the largest gas supplier (63 % of the total natural gas imports [38]) and Saudi Arabia has been the largest supplier for crude oil (with 110,000 b/day [39]). Dependence on a single energy resource that dominates the country's consumption is politically risky and poses national security concerns. Therefore, a transition to RESs can help reduce this threat. Meanwhile, as the country seeks energy sources within its own boundaries, such actions also help boost the local economy and create local jobs.

In the past decade, the use of RESs as an alternative to fossil fuels has been promoted and encouraged in Turkey through several legislations and such measures will be continued [40, 41]. The Electricity Market Law (EML, No. 4628, enacted in February 2001) helps legal entities applying for licenses for construction facilities based on RESs, by permitting them to pay only 1 % of the total licensing fee and avoids the requirement to pay the annual license fee for the first 8 years following the facility completion date in their licenses. In May 2005 the government passed the Renewable Energy Law No. 5346 aiming to expand the use of RESs for providing electricity by guaranteeing the purchase of the electricity produced from RESs (at a price of 7.4 cent/kWh with a 20 % price increase at the beginning of each year [32–34]) and making electricity licensees purchase at least 8 % of their annual electricity sales based on these RESs. In addition, in the case of the public land and forest use for the electricity production with RESs, the lands could be rented or awarded access by the Ministry of Environment and Forestry and/or Finance Departments. The Law also gives incentives to research and investment of energy generating facilities. Finally, Turkey is to be recipient of a US$202 million renewable energy loan by the World Bank for building renewable energy sourced electricity generation; the loan is expected to finance up to 40 % of the capital costs [42].

On the other hand, there are also certain barriers for utilizing RES in Turkey, the main one being the lack of coordination and cooperation within and between various ministries, agencies, institutes, and other stakeholders [40]. However, with the ongoing depletion of conventional energy sources and ever-rising oil prices and governments approach to increase the utilization of RES, these issues would be resolves as RES becomes a major contributor to its overall energy consumption.

Conclusions

The study analyzed various actual MED/MSF and RO desalination plants around the world as well as many studies conducted on these technologies and their integration with RESs. The evaluation was primarily based on costs and environmental impacts of the desalination technologies and associated energy sources. The analysis shows that RO technology would be the best option for Turkey for the specified plant capacity based on the following points:

- The RO method is highly competitive with MED and MSF methods, reducing the cost by 13 and 21 % for MED and MSF respectively, for the midsize plant capacity and could cost even less in high capacity plants. Moreover, continuous improvements in technology for both RO systems (especially the membranes) and integration of RES indicate that RO technology will be much more competitive with MED and MSF technologies in terms of cost.
- The cost of thermal desalination using fossil fuels in Turkey would be much more expensive than Middle Eastern regions presented due to cost of fossil fuels in Turkey being significantly higher than in the Middle East.
- The cost of RO desalination in Turkey will be significantly cheaper than in the Middle East due to Mediterranean seawater feed (around 37,000 mg/l TDS content) being considerably less than for the Arabian Gulf Region (65,000–75,000 mg/l TDS).
- RO desalination technology can reduce emissions of CO_2, NO_x, NMVOC and SO_x by as much as 38, 42, 73, 60 %, respectively compared to alternative technologies, even when waste heat recovery is used. RO is highly compatible with RESs due to its low energy consumption (5–6 times lower than other desalination methods) and modular nature.

To reduce the long term cost and environmental impact further, hydropower energy source is determined to be the best option for integrating with RO based on the following points:

- Hydropower has seamless integration with RO technology and has the lowest potential unit production cost and the least environmental impact on airborne emissions in every emission category which can further reduce the emissions of CO_2, NO_x, NMVOC, SO_x by 83, 82, 80, and 50 %, respectively.
- The actual cost of production is estimated to be even lower for Turkey due to the high number of existing economically exploitable resources, construction and labor costs that are much lower than average, experienced capitalization and various government incentives and can help reducing the country's dependency on fossil fuel imports and gain economic and political strength in the region.

Acronyms

CO_2	Carbon dioxide	PV	Photovoltaics
MED	Multiple-effect distillation	RO	Reverse osmosis
MSF	Multistage flash distillation	SO_x	Sulfur oxide
NMVOC	Non-metal volatile organic compounds	RO	Reverse osmosis

References

1. Human Development Report (2006) Beyond scarcity: power, poverty and the global water crisis. United Nations Development Programme (UNDP), New York, USA
2. WHO website. World Health Organization (2010) Facts and figures on water quality and health. www.who.int/water_sanitation_health/facts_figures/en/print.html. Accessed 18 Dec 2010
3. World Water Council (2000) World water vision, making water everybody's business. Earthscan Publications Ltd, London, UK
4. Erdem Z (2010) The contribution of renewable resources in meeting Turkey's energy-related challenges. Renew Sustain Energ Rev 14:2710–2722
5. Environmental Statistics (2001) Fresh water pollution by countries. Based on world development indicators. http://www.Nationmaster.com
6. European Environment Agency Website. Use of freshwater resources (CSI 018). Accessed 28 Jan 2009. http://www.eea.europa.eu
7. Central Intelligence Agency. The World Factbook. www.cia.gov.tr. Accessed 20 Dec 2010

8. General Directorate of State Hydraulic Works (2009) Turkey Water Report. http://www.dsi.gov.tr. Accessed 18 Dec 2010
9. Dolnicar S, Schäfer AI (2006) Public perception of desalinated versus recycled water in Australia. J Environ Manag 90:888–900
10. Cipollina A, Micale G, Rizutti L (2009) Green energy and technology. Seawater desalination. Conventional and renewable energy processes. Springer, Berlin
11. Water Desalination International website. Key desalination facts. http://www.waterdesalination.com/factssample1.htm. Accessed 25 Dec 2010
12. El-Dessouky T, Ettouney M (2002) Fundamentals of salt water desalination. Elsevier Science B.V.
13. Khawaji A, Kutubkhanah I, Wie JM (2008) Advances in seawater desalination technologies. Desalination 221:47
14. Raluy R, Uche J (2005) Life cycle assessment of water production technologies. Desalination 183:81–93
15. Raluy G, Serra L, Uche J (2006) Life cycle assessment of MSF, MED and RO desalination technologies. Energy 31:2361–2372
16. Borsani R, Rebagliati S (2005) Fundamentals and costing of MSF desalination plants and comparison with other technologies. Desalination 182:29–37
17. Koklas P, Papathanassiou S (2006) Component sizing for an autonomous wind-driven desalination plant. Renew Energ 31:2122–2139
18. Karaghouli A, Renne D, Lawrance L, Kazmerski L (2009) Solar and wind opportunities for water desalination in Arab Regions. Renew Sustain Energ Rev 13:2397–2407
19. Zejli D, Benchrifa R, Bennouna A, Zazi K (2004) Economic analysis of wind-powered desalination in the south of Morocco. Desalination 165:219–230
20. Sanden B, Azar C (2005) Near term technology policies for long term climate targets-economy wide versus technology specific approaches. Energ Policy 33:1557–1576
21. Ediger V, Kentel E (1999) Renewable energy potential as an alternative fossil fuels in Turkey. Energ Convers Manag 40:743–755
22. Ozgur M (2008) Review of Turkey's renewable energy potential. Renew Energ 33:2345–2356
23. Yuksel I (2008) Global warming and renewable energy sources for sustaining development in Turkey. Renew Sustain Energ Rev 12:372–396
24. Forstmeier M, Mannerheim F, D'Amato D, Shah M, Liu Y, Baldea M, Stella A (2007) Feasibility study on wind-powered desalination. Desalination 203:463–470
25. Evrendilek F, Ertekin C (2003) Assessing the potential of renewable energy sources in Turkey. Renew Energ 28:2303–2315
26. Garcia-Rodriguez L, Palmero-Marreroa A, Gbmez-Camachob C (2002) Comparison of solar thermal technologies for applications in seawater desalination. Desalination 142:135–142
27. Lamei A, van der Zaag P, von Munch E (2008) Impact of solar energy cost on water production cost of seawater desalination plants in Egypt. Energ Policy 36:1748–1756
28. Yuksel I (2010) Renewable energy hydropower for sustainable development in Turkey. Renew Sustain Energ Rev 14:2113–3219
29. The Pembina Institute (2010) Sustainable energy solutions. Renewable energy. Hydropower www.pembina.org/re/sources/hydro-power. Accessed 20 Nov 2010
30. Murakami M (1995) Managing water for peace in the Middle East: alternative strategies experimental seawater reverse-osmosis desalination. United Nations University Press
31. Raluy RG, Serra L, Uche J (2005) Life cycle assessment of desalination technologies integrated with renewable energies. Desalination 183:81–93
32. Kucukali S, Baris K (2009) Assessment of small hydropower (SHP) development in Turkey: laws, regulations and EU policy perspective. Energ Policy 37:3872–3879
33. Erdogdu E (2009) A snapshot of geothermal energy potential and utilization in Turkey. Renew Sustain Energ Rev 13:2535–2543
34. Erdogdu E (2009) On the wind energy in Turkey. Renew Sustain Energ Rev 13:1361–1371
35. Fiksel J (2009) Design for environment. A guide to sustainable product development. 2nd edn
36. Karagiannis IC, Soldatos P (2008) Water desalination cost literature: review and assessment. Desalination 223:448–456
37. Mohameda E, Papadakis G, Mathioulakis E, Belessiotis V (2005) The effect of hydraulic energy recovery in a small sea water reverse osmosis desalination system; experimental and economical evaluation. Desalination 184:241–246
38. Akgul D, Cakmakci M, Kayaalp N, Koyuncu I (2008) Cost analysis of seawater desalination with reverse osmosis in Turkey. Desalination 220:123–131
39. Turkish Market Case (2012) APS review oil market trends. www.AllBusiness.com
40. Kaya D (2006) Renewable energy policies in Turkey. Renew Sustain Energ Rev 10:152–163
41. Ozyurt O (2010) Energy issues and renewable for sustainable development in Turkey. Renew Sustain Energ Rev 14:2976–2985
42. Toklu E, Guney MS, Isik M, Comakli O, Kaygusuz K (2010) Energy production, consumption, policies and recent developments in Turkey. Renew Sustain Energ Rev 14:1172–1186
43. Wade NM (2001) Distillation plant development and cost update. Desalination 136:3–12
44. Fiorenza G, Sharma VK, Braccio G (2003) Techno-economic evaluation of a solar powered water desalination plant. Energ Convers Manag 44:2217–2240
45. Frioui S, Oumeddour R (2008) Investment and production costs of desalination plants by semi-empirical method. Desalination 223:457–463
46. Bilgili M, Sahin B, Kahraman A (2004) Wind energy potential in Antakya and Iskenderun regions, Turkey. Renew Energ 29:1733–1745
47. GWI Market Profile (2007) Desalination Markets Report. Accessed 12 Dec 2010
48. Khan WZ (2009) Desalination of raw water using a polyamide hollow fiber membrane. Desalination 244:59–65
49. Murakami M (2008) Hydro-powered reverse osmosis desalination for co-generation. Inaugural ceremony international seminar on efficient water use. Uruguay
50. Ozturk M, Bezir N, Ozek N (2009) Hydropower-water a renewable energy in Turkey: sources and policy. Renew Sustain Energ Rev 13:605–615
51. Somers B (2010) Energy experts say water use and energy consumption linked, urge conservation. Am Assoc Adv Sci

Exergetic Performance of a Low Bypass Turbofan Engine at Takeoff Condition

Hakan Aydın, Onder Turan, Adnan Midilli, and T. Hikmet Karakoc

Abstract

In this article, exergetic methodology is applied for a low bypass turbofan engine at maximum power setting. The engine is a low-bypass (0.96–1) turbofan engine and its variants fitted to the 737-100/200 all comprise six low-pressure compressor (LPC) stages, seven high-pressure compressor (HPC) stages, a single HP turbine (HPT), and finally three LPT stages. At the end of the analysis, the most irreversible units in the system are found to be the combustor and the fan/LPC, with exergy loss rates of 18.7 and 2.486 MW, respectively. The exergy efficiencies of the fan/LPC, the HPC, and combustor are 0.856, 0.845, and 0.744, respectively. For the HPT and LPT, the exergy efficiencies are calculated to be 0.98 and 0.963, respectively.

Keywords

Turbofan • Exergy • Aircraft • Energy • Aviation • Sustainability

Introduction

With over two billion people travelling safely around the world every year and some 23,000 aircraft in commercial service. Worldwide passenger traffic will average 5.1 % growth and cargo traffic will average 5.6 % growth 2–5 % of the world energy consumption belongs to aviation industries [1–5]. Total scheduled world revenue tonne kilometers (RTK) increased by 119 %, with scheduled passenger revenue passenger kilometers (RPK) and cargo (RTK) traffic rising by 108 and 140 %, respectively [6]. Effects of energy consumption in aviation sector give rise to potential environmental hazards. Therefore, energy consumption plays a crucial importance role to achieve sustainable development; balancing economic and social development with environmental protection. The importance of energy efficiency is also linked to environmental problems, such as global warming and atmospheric pollution [7, 8].

Energy intensity can be related to some important measures operational and technological efficiency in the aircraft and its propulsion system. An aero-engine converts the flow of chemical energy contained in the kerosene fuel and the air drawn

H. Aydın
TUSAS Engine Industries (TEI), TR-26003, Eskisehir, Turkey
e-mail: tei.hakan@gmail.com

O. Turan (✉) • T.H. Karakoc
Faculty of Aeronautics and Astronautics, Anadolu University, TR-26470, Eskisehir, Turkey
e-mail: onderturan@anadolu.edu.tr; hikmetkarakoc@gmail.com

A. Midilli
Advanced Energy Technologies, Mechanical Engineering Department, Faculty of Engineering,
Recep Tayyip Erdogan University, Rize 53000, Turkey
e-mail: adnan.midilli@erdogan.edu.tr

into the engine into propulsion power. Nearly one-fourth or one-third of fuel energy is used to propel the aircraft. The remaining energy is expelled as waste heat in the exhaust. Specific fuel consumption (SFC) is more relevant to consider propulsion power in terms of payload carried per unit range. Energy intensity (E_I) is a suitable parameter with comparing efficiency and environmental impact. It consists of two components-energy use, E_U and load factor, L_f as shown in Eq. (25.1).

$$E_I = \frac{E_U}{L_f} = \frac{MJ}{RPK} = \frac{MJ}{ASK} \Big/ \frac{RPK}{ASK} \tag{25.1}$$

Where MJ is mega joules of kerosene fuel energy, RPK is revenue passenger-kilometers, ASK is available seat-kilometers, and L_f is load factor. To have a model of aircraft, it is necessary to show E_I as a function of the engine, aerodynamic, and structural efficiency of the aircraft system as well as load factor. These parameters play important role in the energy intensity of an aircraft. Energy efficiency in commercial aircrafts is improved by averaging 1.5 % percent annually with the introduction of bypass turbofan engines. However, as the bypass ratio increased, engine diameter has also increase, leading to an increase momentum drag. Another way to propulsion system improvement is to increase turbine inlet temperature, which is limited by materials and cooling technology, and improving engine component efficiencies. Between the introduction B707 and B777, commercial aircrafts have been constructed exclusively of aluminum and are currently about 90 % metallic by weight. So improvements of structural efficiency are less evident [9].

The environmental impact of emissions can be reduced by increasing the efficiency of resource utilization [10]. Using energy with better efficiency reduces pollutant emissions. Energy and exergy concepts have been utilized in environmental sustainability, economics, and engineering. Exergy is a quantity which follows from the First and Second Laws of Thermodynamics and analyses directly impact process design and improvements because exergy methods help in understanding and improving efficiency, environmental and economic performance as well as sustainability. The potential usefulness of exergy analysis in addressing sustainability issues and solving environmental problems is substantial [11–15]. The exergy studies related to gas turbines have first been done on stationary gas turbines. In the literature, the various exergy and exergo-economic analysis of aero engines have been reported [16–30].

Through a literature review, it is noticed that there is no work to be studied about exergy analysis for a low bypass turbofan engines in the open literatures. The present assessment, therefore, aims to provide a practical framework for the use of such exergy analysis in low bypass engines. Lack of exergy analysis for low bypass turbofan engine makes the paper original and becomes main motivation.

In this paper, first the detailed exergy analysis of JT8D low bypass turbofan engine has been performed. In this analysis, exergy efficiency, exergy losses/destructions have been calculated at maximum power setting, i.e., takeoff condition. Exergy analysis of JT8D has first been studied in this paper. Moreover, there is no previous work about exergy related to low bypass turbofan engine in the aircraft engine in the literature.

System Description for Low Bypass Turbofan Engine

JT8D series engines are one of the most popular modern commercial engines ever made. More than 14,750 of them have been built, amassing more than 673 million hours of reliable service since 1964. The eight models that make up the JT8D family cover a thrust range from 62 to 76 kN. The newer JT8D-200 engine offers 18,500–21,700 pounds of thrust, and is the exclusive power for the popular MD-80 aircraft (B-1-7.pdf)

An illustrated diagram, station numbering and main component of the high bypass turbofan engine is shown in Fig. 25.1. It consist of fan (F), axial low-pressure compressor (LPC), axial high-pressure compressor (HPC), an annular combustion chamber, high-pressure turbine (HPT), and low-pressure turbine (LPT).

This engine operates according to the Brayton cycle, which includes four processes under the ideal conditions given below:

1. Isentropic compression (fan and HPC)
2. Combustion at constant pressure (CC)
3. Isentropic expansion (HPT and LPT)
4. Heat transfer at constant pressure (EN and FN).

There are two drive shafts in this engine. The first, N_2, connects the HPT and HPC and constitutes the HP system, while the second, N_1, connects the LPT to the fan and constitutes the LP system. While the HPT runs the HPC, fuel pump, starter generator, and reduction gearbox, LPT runs the fan.
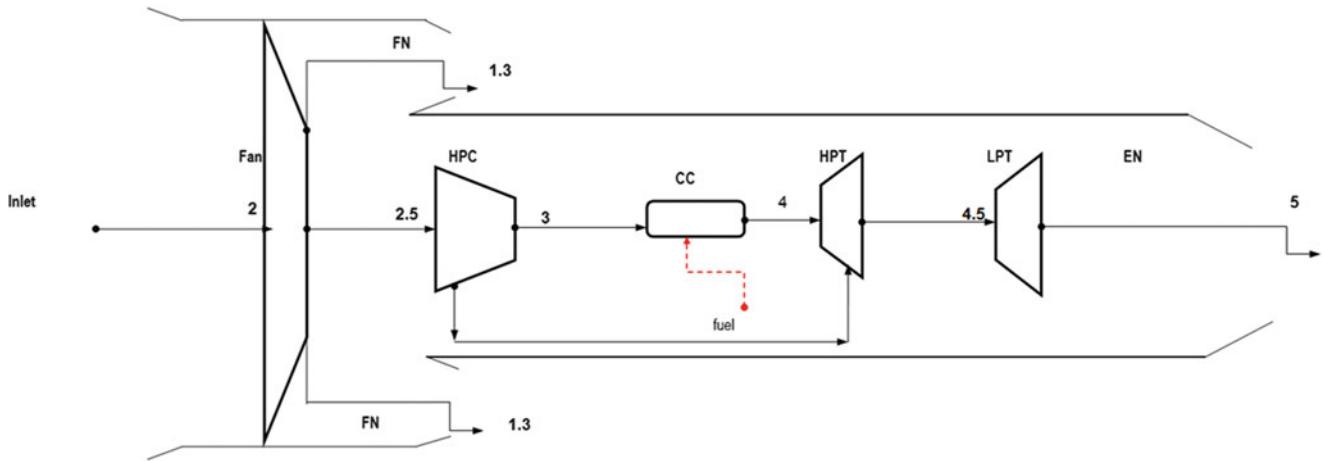
Fig. 25.1 Schematic diagram of the high bypass turbofan engine. *HPC* high-pressure compressor, CC combustion chamber, HPT high-pressure turbine, *LPT* low-pressure turbine, *EN* exhaust nozzle, *FN fan nozzle*

In the schematic diagram of the high bypass turbofan engine given in Fig. 25.1, the bypass ratio is defined as

$$\alpha = \frac{\text{Bypass airflow}}{\text{Primary airflow}} = \frac{\dot{m}_{fan}}{\dot{m}_{core}} = \frac{\dot{m}_{cold}}{\dot{m}_{hot}} \tag{25.2}$$

Thus, if the air mass through the core (HPC) is $\dot{m}_{core}$, then the bypass air mass flow rate is $(\alpha\,\dot{m}_{core})$.

Mathematical Frameworks for Thermodynamic Analysis

The Energy and Exergy Methods in Practice: Some Useful Tools and Definitions

Thermodynamic first-law analysis is energy-based approach in thermal systems. It is based on the principle of conservation of energy applied to the system. For a general steady state, steady-flow process, the four balance equations (mass, energy, entropy and exergy) are applied to find the work and heat interactions, the rate of exergy decrease, the rate of irreversibility, the energy and exergy efficiencies [31–33].

The mass balance equation can be expressed in the rate form as

$$\sum \dot{m}_{in} = \sum \dot{m}_{out}, \tag{25.3a}$$

where $\dot{m}$ is the mass flow rate, and the subscript "in" stands for inlet and "out" for outlet. The general energy balance can be expressed below as the total energy inputs equal to total energy outputs.

$$\sum \dot{E}_{in} = \sum \dot{E}_{out} \tag{25.3b}$$

Energy conservation suggests that for a steady-state process the First Law may be represented by [34]:

$$\sum (h + ke + pe)_{in} \dot{m}_{in} - \sum (h + ke + pe)_{out} \dot{m}_{out} + \sum \dot{Q} - \dot{W} = 0 \tag{25.3c}$$

where $\dot{m}_{in}$ and $\dot{m}_{out}$ denote the mass flow rate across the system inlet and outlet, respectively, $\dot{Q}$ represents the heat transfer rate across the system boundary, $\dot{W}$ is the work rate (including shaft work, electricity, and so on) transferred out of the system, and h, ke, and pe denote the specific values of enthalpy, kinetic energy, and potential energy, respectively.

This energy balance can be simplified, assuming negligibly small changes in kinetic and potential energy and no heat or work transfers, to [34]:

$$\sum H_{i,in} = \sum H_{j,out} \tag{25.3d}$$

where $H_{i,in}$ represents the various energy (or enthalpy) streams flowing into the system, and $H_{j,out}$ the different energy outputs.

First Law or "energy" analysis takes no account of the energy source in terms of its thermodynamic quality. It enables energy or heat losses to be estimated, but yields only limited information about the optimal conversion of energy. In contrast, the Second Law of Thermodynamics indicates that, whereas work input into a system can be fully converted to heat and internal energy, not all the heat input can be converted into useful work [35]. The exergy loss in a system or component is determined by multiplying the absolute temperature of the surroundings by the entropy increase [36–38]. Exergy methods also help in understanding and improving efficiency, environmental and economic performance as well as sustainability [39].

Note that, whereas energy is a conserved quantity, exergy is not and is always destroyed when entropy is produced. In the absence of electricity, magnetism, surface tension and nuclear reaction, the total exergy of a system $\dot{E}x$ can be divided into four components, namely (1) physical exergy $\dot{E}x^{PH}$, (2) kinetic exergy $\dot{E}x^{KN}$, (3) potential exergy $\dot{E}x^{PT}$, and (4) chemical exergy $\dot{E}x^{CH}$ [36].

$$\dot{E}x = \dot{E}x^{PH} + \dot{E}x^{KN} + \dot{E}x^{CH} + \dot{E}x^{PT} \tag{25.4a}$$

Although exergy is extensive property, it is often convenient to work with it on a unit of mass or molar basis. The total specific exergy on a mass basis may be written as follows [36]:

$$ex = ex^{PH} + ex^{KN} + ex^{CH} + ex^{PT} \tag{25.4b}$$

The general exergy balance can be written as follows [36]:

$$\sum \dot{E}x_{in} - \sum \dot{E}x_{out} = \sum \dot{E}x_{dest} + \sum \dot{E}x_{loss} \tag{25.5a}$$

$$\dot{E}x_{heat} - \dot{E}x_{work} + \dot{E}x_{mass,in} - \dot{E}x_{mass,out} = \dot{E}x_{dest} + \dot{E}x_{loss} \tag{25.5b}$$

$$\dot{E}x_{heat} = \sum \left(1 - \frac{T_0}{T_k}\right)\dot{Q}_k, \tag{25.5c}$$

$$\dot{E}x_{work} = \dot{W}, \tag{25.5d}$$

$$\dot{E}x_{mass,in} = \sum \dot{m}_{in}\psi_{in}, \tag{25.5e}$$

$$\dot{E}x_{mass,out} = \sum \dot{m}_{out}\psi_{out}. \tag{25.5f}$$

where $\dot{Q}$ is the heat transfer rate through the boundary at temperature T_k at location k and $\dot{W}$ is the work rate.

The flow (specific) exergy is calculated as follows:

$$ex = (h - h_0) - T_0(s - s_0) \tag{25.6}$$

where h is enthalpy, s is entropy, and the subscript zero indicates properties at the restricted dead state of P_0 and T_0.

The rate form of the entropy balance can be expressed as [36]

$$\dot{S}_{in} - \dot{S}_{out} + \dot{S}_{gen} = 0 \tag{25.7}$$

where the rates of entropy transfer by heat transferred at a rate of $\dot{Q}_k$ and mass flowing at a rate of $\dot{m}$ are $\dot{S}_{heat} = \dot{Q}_k/T_k$ and $\dot{S}_{mass} = \dot{m}s$, respectively [36].

Taking the positive direction of heat transfer to be to the system, the rate form of the general entropy relation given in Eq. (25.7) can be rearranged to give [36]

$$\dot{S}_{gen} = \sum \dot{m}_{out} s_{out} - \sum \dot{m}_{in} s_{in} - \sum \frac{\dot{Q}_k}{T_k} \tag{25.8}$$

Also, it is usually more convenient to find $\dot{S}_{gen}$ first and then to evaluate the exergy destroyed or the irreversibility rate $\dot{I}$ directly from the following equation, which is called Gouy–Stodola relation [40]:

$$\dot{I} = \dot{Ex}_{dest} = T_0 \dot{S}_{gen} \tag{25.9}$$

Assuming air to be a perfect gas, the specific physical exergy of air is calculated by the following relation [41]

$$ex_{air,per} = C_{p,a}\left(T - T_0 - T_0 \ln\frac{T}{T_0}\right) + R_a T_0 \ln\frac{P}{P_0} \tag{25.10}$$

Numerous ways of formulating exergy (or second-law) efficiency for various energy systems are given in detail elsewhere [42]. It is very useful to define efficiencies based on exergy. There is no standard set of definitions in the literature. Here, exergy efficiency is defined as the ratio of total exergy output to total exergy input, i.e.,

$$\eta_{ex} = \frac{\dot{Ex}_{out}}{\dot{Ex}_{in}} \tag{25.11}$$

Assumptions

In this study, the assumptions made are listed below
1. The air and combustion gas flows in the engine are assumed to behave ideally.
2. The combustion reaction is complete.
3. Compressors and turbines are assumed to be adiabatic.
4. Ambient temperature and pressure values are 288.15 K and 101.35 kPa, respectively.
5. The exergy analyses are performed for the lower heating value (LHV) of kerosene (JET A1) which is accepted as 42,800 kJ kg^{-1}.
6. Engine accessories, pumps (fuel, oil, and hydraulic) are not included in the analysis.
7. The kinetic and potential exergies are neglected.
8. Chemical exergy is neglected other than combustor.

Airflow

The total airflow mass is 142.7 kg s^{-1} that includes 74.74 kg s^{-1} fan air and 67.95 kg s^{-1} core air. Air is taken into LPC at ambient temperature of 288.15 K and ambient pressure of 101.35 kPa. In gas turbine engines, a part of compressed air is extracted to use for ancillary purposes, such as cooling, sealing and thrust balancing. In this study the cooling airflow is neglected since it doesn't have meaningful effect on exergy and sustainability analyses.

Combustion Balances and Emissions

As fuel the kerosene (JET A) is burned. Its chemical formula is as $C_{12}H_{23}$. The value of LHV is 42,800 kJ kg^{-1}. Fuel flow is 1.05 kg s^{-1} that results in air–fuel ratio of 64. Combustion balance equation is calculated by Eq. (25.12),

$$C_{12}H_{23} + 369 \begin{pmatrix} 0.7748N_2 \\ +0.2059O_2 \\ +0.0003CO_2 \\ +0.019H_2O \end{pmatrix} \Rightarrow \begin{pmatrix} 12.11CO_2 \\ +18.51H_2O \\ +58.22O_2 \\ +285.9N_2 \end{pmatrix} \tag{25.12}$$
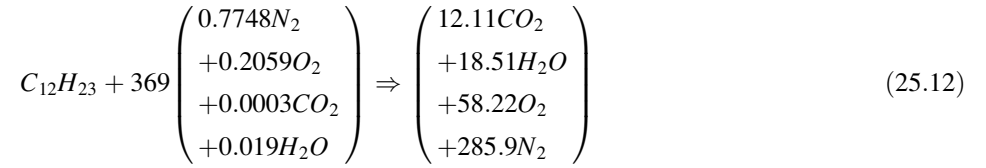
The mass of combustion gases are obtained as 3.43 kg s^{-1} for CO_2, 2.14 kg s^{-1} for H_2O, 11.98 kg s^{-1} for O_2, and 51.46 kg s^{-1} for N_2 after combustor chamber.

Specific Heat Capacities of Air and Combustion Gas

The cold air specific heat capacity is calculated by Eq. (25.2) as follows.

$$C_{P,air}(T) = 1.04841 - 0.000383719T + \frac{9.45378T^2}{10^7} - \frac{5.49031T^3}{10^{10}} + \frac{7.9298T^4}{10^{14}} \tag{25.13}$$

The specific heat capacity of the combustion gases after combustion chamber for JT8D is calculated from the composition of Eq. (25.1) of each emissions' mass percentage as follows.

$$C_{P,gas}(T) = 0.9886 + \frac{2.043T}{10^5} + \frac{1.551T^2}{10^7} + \frac{6.717T^3}{10^{11}} \tag{25.14}$$

Where the unit of temperature is K. For hot gases, R value is calculated as 0.2901 kJ kg^{-1}.

Exergy Analysis

The exergy analysis of JT8D gas turbine engine's Fan, HPC, combustor, HPT, and LPT will be performed. The exergy parameters of JT8D for two investigated operating conditions will be calculated by Eqs. (25.13–25.19a, 25.19b, 25.19c)

1. *Fan*:

$$\sum \dot{E}x_{in,fan} - \sum \dot{E}x_{out,fan} = \sum \dot{E}x_{dest,fan} \tag{25.15a}$$

$$\sum \dot{E}x_{in,fan} - \sum \dot{E}x_{out,fan} = \dot{W}_{fan} + \dot{E}x_2 - \left(\dot{E}x_{13} + \dot{E}x_{25}\right) \tag{25.15b}$$

$$\dot{W}_{fan} = \frac{\dot{m}_{fan}\left(\overline{h}_{13} - \overline{h}_2\right) + \dot{m}_A\left(\overline{h}_{25} - \overline{h}_2\right)}{M_A} \tag{25.15c}$$

$$\eta_{ex,fan} = \frac{\dot{E}x_{13} + \dot{E}x_{25} - \dot{E}x_2}{\dot{W}_{fan}} \tag{25.15d}$$

2. *HPC:*

$$\sum \dot{E}x_{in,HPC} - \sum \dot{E}x_{out,HPC} = \sum \dot{E}x_{dest,HPC} \tag{25.16a}$$

$$\sum \dot{E}x_{in,HPC} - \sum \dot{E}x_{out,HPC} = \dot{W}_{HPC} + \dot{E}x_{25} - \dot{E}x_3 \tag{25.16b}$$

$$\dot{W}_{HPC} = \frac{\dot{m}_{HPC}\left(\overline{h}_3 - \overline{h}_{25}\right)}{M_A} \tag{25.16c}$$

$$\eta_{ex,HPC} = \frac{\dot{E}x_3 - \dot{E}x_{2.5}}{\dot{W}_{HPC}} \tag{25.16d}$$

Table 25.1 JT8D Turbofan engine thermodynamic data for takeoff thrust running

Station No	Location	Mass flow (kg s^{-1})	Temperature (K)	Pressure (kPa)	Exergy flow (MW)
0	Air	677.2	288.15	101.35	0
2	FAN inlet	677.2	288.15	101.35	0
1.3	FAN bypass outlet	565.3	327.6	155.8	21.51
2.5	FAN core outlet	111.9	372	221.3	8.39
2.5	HPC inlet	111.9	372	221.3	8.39
3	HPC outlet	111.9	744.2	2178.7	50.55
3	Combustor inlet	111.9	744.2	2178.7	50.55
3	Fuel	2,110	288.15	2,000	94.37
4	Combustor outlet	114,2	1,350	2082.2	1,103
4	HPT inlet	114.2	1,350	2082.2	110.3
4.5	HPT outlet	114.2	985	535	59.43
4.5	LPT inlet	114.2	985	535	59.43
5	LPT outlet	114.2	727.6	144.1	24.51

Source: Farokhi [43]

Table 25.2 Exergy values of the JT8D turbofan engine and its components for takeoff thrust running

Component	Inlet exergy (MW)	Outlet exergy (MW)	Exergy dest (MW)	Exergy efficiency (%)
FAN	32.43	29.90	2.53	0.922
HPC	56.66	50.55	6.11	0.873
CC	144.92	110.30	34.62	0.761
HPT	110.30	108.18	2.12	0.958
LPT	59.43	57.26	2.17	0.938
JT8D	94.37	27.92		0.296

3. *Combustor (CC)*:

$$\sum \dot{E}x_{in,CC} - \sum \dot{E}x_{out,CC} = \sum \dot{E}x_{dest,CC} \qquad (25.17a)$$

$$\sum \dot{E}x_{in,CC} - \sum \dot{E}x_{out,CC} = \dot{E}x_3 + \dot{E}x_{3,fuel} - \dot{E}x_4 \qquad (25.17b)$$

$$\eta_{ex,CC} = \frac{\dot{E}x_4}{\dot{E}x_3 + \dot{E}x_{3,fuel}} \qquad (25.17c)$$

4. *HPT*:

$$\sum \dot{E}x_{in,HPT} - \sum \dot{E}x_{out,HPT} = \sum \dot{E}x_{dest,HPT} \qquad (25.18a)$$

$$\sum \dot{E}x_{in,HPT} - \sum \dot{E}x_{out,HPT} = \dot{E}x_4 - \left(\dot{W}_{HPT} + \dot{E}x_{45}\right) \qquad (25.18b)$$

$$\eta_{ex,HPT} = \frac{\dot{W}_{HPT}}{\dot{E}x_4 - \dot{E}x_{45}} \qquad (25.18c)$$

5. *LPT*:

$$\sum \dot{E}x_{in,LPT} - \sum \dot{E}x_{out,LPT} = \sum \dot{E}x_{dest,LPT} \qquad (25.19a)$$

$$\sum \dot{E}x_{in,LPT} - \sum \dot{E}x_{out,LPT} = \dot{E}x_{45} - \left(\dot{W}_{LPT} + \dot{E}x_5\right) \qquad (25.19b)$$

$$\eta_{ex,LPT} = \frac{\dot{W}_{LPT}}{\dot{E}x_{45} - \dot{E}x_5} \qquad (25.19c)$$

JT8D thermodynamic parameters are listed in Tables 25.1 and 25.2.

Results and Conclusions

In this paper, first the exergy analysis of JT8D high bypass turbofan engine at takeoff thrust power has been carried out. In this analysis main exergetic parameters are energy and exergy flows, exergy destruction and exergy efficiency. Now, it is necessary to definite the phases of flight for an aircraft. The phase of flight definitions given in Table 25.3 consist of broad operational phases. Most of them have sub-phases. Considering the flight phases as a function of engine power, the flight phases can be split into seven parts in this study: (a) landing, (b) climb, (c) maximum cruise, (d) normal takeoff, (e) maximum continuous, (f) automatic power reverse, and (g) maximum takeoff. Concerning the classification of flight phases as an engine power, it is difficult to see many examples in the literature.

Figure 25.2 demonstrates the exergy efficiencies of the fan, HPC, combustor, HPT, LPT, and JT8D turbofan engine at takeoff condition.

Table 25.3 Standard definitions the phases of a flight

Phase	Symbol	Definition	Subphases
Standing	STD	Prior to pushback or taxi, or after arrival, at the gate or parking area, while the aircraft is stationary	Engine(s) (1) not operating, (2) startup, (3) operating, (4) shutdown
Pushback/Towing	PBT	Aircraft is moving in the gate, ramp, or parking area, assisted by a tow vehicle	Engine(s) (1) not operating, (2) startup, (3) operating, (4) shutdown
Taxi	TXI	Aircraft is moving on the ground under its own power prior to takeoff and after landing	(1) Power back, (2) taxi to runway, (3) taxi to takeoff position, (4) taxi from run way
Takeoff	TOF	From the application of takeoff power through rotation and to an altitude of 35 ft above runway elevation	(1) Takeoff and (2) rejected takeoff
Initial climb	ICL	From the end of the takeoff to the first prescribed power reduction, or until reaching 1,000 ft above runway elevation	–
En Route	ENR	From completion of Initial Climb through cruise altitude and completion of controlled descent to the Initial Approach Fix	(1) Climb to cruise, (2) cruise, (3) change of cruise level, (4) descent, (5) holding
Maneuvering	MNVR	Low altitude/aerobatic flight operations	(1) Aerobatics and (2) low flying
Approach	APPR	From the Initial Approach Fix to the beginning of the landing flare	(1) Initial approach, (2) final approach, (3) missed approach/go-around
Landing	LDG	From the beginning of the landing flare until aircraft exits the landing runway, comes to a stop on the runway	(1) Flare, (2) landing roll, (3) aborted landing after touchdown
Emergency descent	EMG	A controlled descent during any airborne phase in response to a perceived emergency situation	–
Uncontrolled descent	UND	A descent during any airborne phase in which the aircraft does not sustain controlled flight	–
Post-impact	PIM	Any of that portion of the flight which occurs after impact with a person, object, obstacle	–

Source: EADS [44]
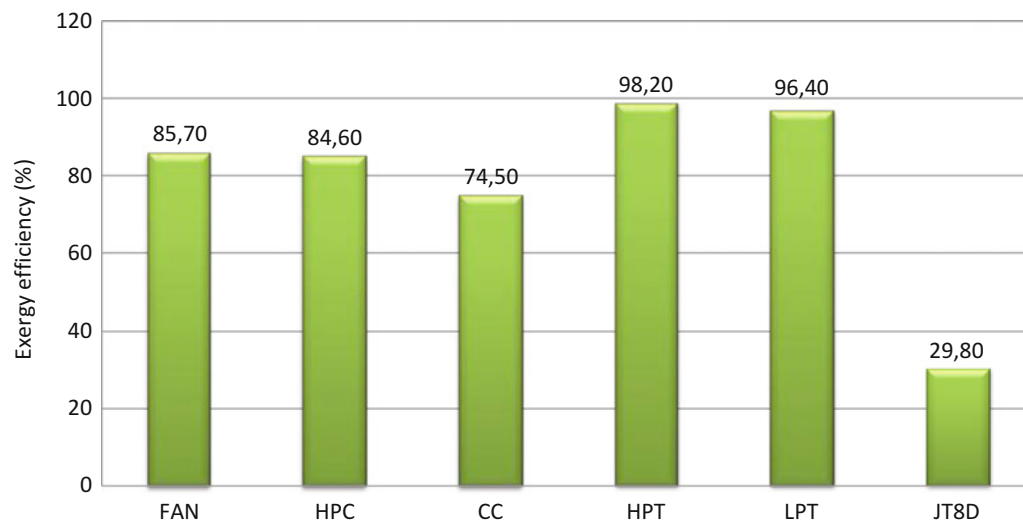
Fig. 25.2 Exergy efficiencies (%) of JT8D turbofan engine at takeoff thrust

Fig. 25.3 Exergy destruction (MW) of JT8D turbofan engine at takeoff thrust
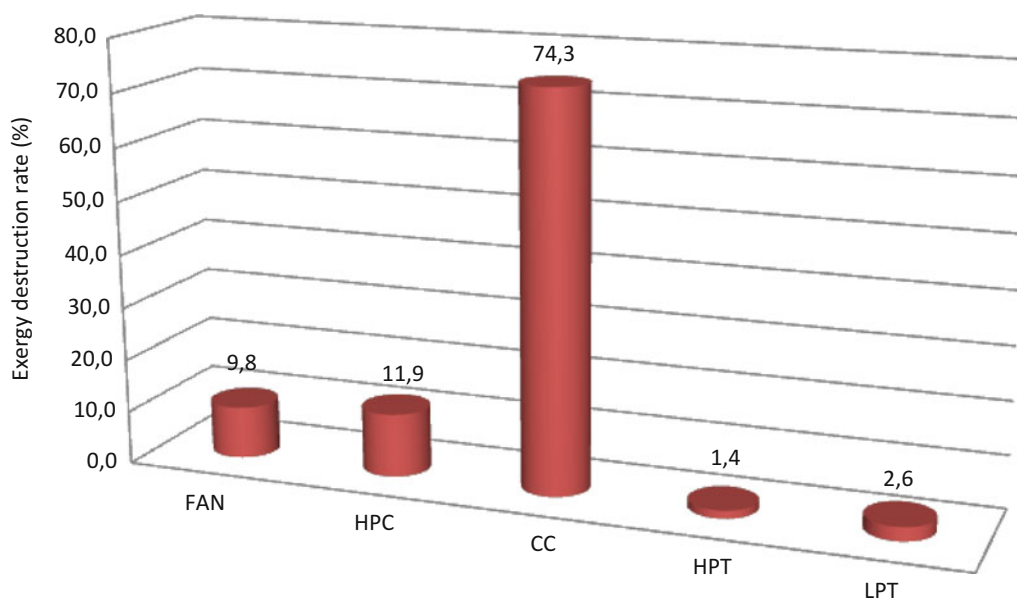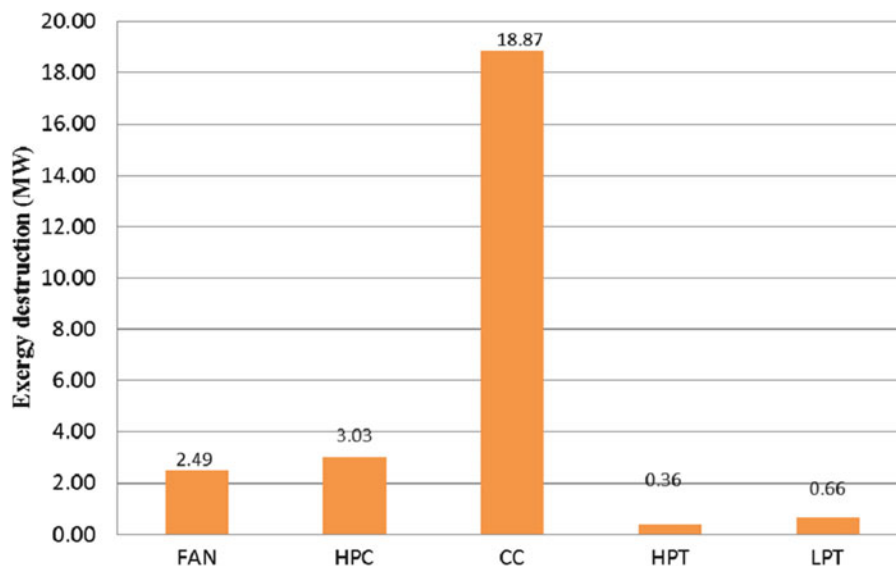
Fig. 25.4 Exergy destruction rates (%) of JT8D turbofan engine at takeoff thrust

Figures 25.3 and 25.4 presents the exergy destructions and exergy destruction rates for the fan, HPC, combustor, HPT, LPT.

The exergy efficiency, one of the most important indicators for the sustainability of the engine, is mainly based on the exergy input and the required output. It is noticed that the exergy efficiency of the turbofan engine highly affected by the input–output exergetic values of the each engine component at all phases of a flight as shown in Table 25.2. The results in Fig. 25.2 show that the exergy efficiency ranges from 0.745 to 0.982 in engine components. As can be seen in Fig. 25.2, HPT and LPT are good exergy efficiencies changes between 0.964 and 0.982 due to higher isentropic efficiencies. For the fan and HPC exergy efficiencies are found to be 0.857 and 0.846, respectively. On the other hand, minimum exergy efficiency is observed in combustor (to be 0.745) due to internal irreversibilities in CC.

The unit with greatest exergy loss is found to be CC (to be 18.87 MW) as shown in Fig. 25.3. The exergy destructions for the other units are found to be HPC (to be 3.03 MW), fan (to be 2.49 MW), LPT (to be 0.66 MW) and HPT (to be 0.36 MW). If so, greatest exergy destruction rate is calculated in the CC (to be 74.3 %) as shown in Fig. 25.4. It is clear from Fig. 25.4 that HPT has minimum exergy destruction rate with value of 1.4 %.

The results should provide a realistic and meaningful in the exergetic takeoff performance evaluation of low bypass turbofan engines, which may be useful in the analysis of similar propulsion systems. In a future study, we will focus on exergo-environmental and exergo-sustainability analysis of the low bypass turbofan engine. It is noted that, to obtain more comprehensive conclusions, exergo-economics must be considered. In particular, an exergo-economic analysis would be useful. An exergo-environmental analysis can help improve the environmental performance of the low bypass engine, and consequently should be considered in future assessments.

Nomenclature

c_p	Specific heat (kJ (kg K)$^{-1}$)	$\dot{m}$	Mass flow rate (kg s^{-1})
E	Energy rate (MW)	A	Area (m^2)
ex	Specific exergy (kJ kg^{-1})	M_A	Molecular weight
$\dot{Ex}$	Exergy rate (MW)	pe	Potential energy
f	Fuel-air ratio; fuel exergy factor	P	Pressure (bar or kPa); product exergy
h_{PR}	Fuel heating value (kJ kg^{-1})	R	Specific gas constant (kJ (kg K^{-1})), diameter (m)
H	Enthalpy (kJ)	S	Entropy (kJ K^{-1})
I	Irreversibility rate (kW)	T	Temperature (K)
ke	Kinetic energy	$\dot{W}$	Work rate (MW)

Greek letters

η	Efficiency	ρ	Air density (kg m^{-3})

Subscripts

a	Air	ke	Kinetic energy
ch	Chemical	LD	Loss and destruction
dest	Destruction	kn	Kinetic
f	Fuel	out	Outlet
gen	Generated	per	Perfect
k	kth component	ph	Physical
LPC	Low-pressure compressor	pe	Potential energy
HPC	High-pressure compressor	tot	Total
LPT	Low-pressure turbine	A	Area, m^2
HPT	High-pressure turbine	c_p	Specific heat, J kg^{-1} °C
in	Inlet	h	Heat transfer coefficient, W m^{-2} °C

References

1. Boeing (2011) See also http://www.boeing.com. Accessed 15 Aug 2011]
2. Enviro (2011) http://www.enviro.aero/Content/Upload/File/BeginnersGuide_Biofuels_Web. Accessed 5 Dec 2011
3. IATA (2011) http://www.boeing.com/commercial/cmo/forecast_summary.html. Accessed 20 Sept 2011
4. Lee J, Ian J, Waitz A, Brian Y, Kim C, Gregg G, Fleming L, Curtis M, Holsclaw A (2007) System for assessing aviation's global emissions (SAGE), part 2: uncertainty assessment. Transport Res Transport Environ 12:381–395
5. USHP (2009) http://www.house.gov/transportation/aviation/02-15-06/02-15-06memo.html. Accessed 25 Aug 2009
6. Macintosh A, Wallace L (2009) International aviation emissions to 2025: can emissions be stabilised without restricting demand? Energ Pol 37:264–273
7. Ahmadi P, Dincer I, Rosen MA (2011) Exergy, exergoeconomic and environmental analyses and evolutionary algorithm based multi-objective optimization of combined cycle power plants. Energy 36:5886–5898
8. Ptasinski KJ, Koymans MN, Verspagen HHG (2006) Performance of the Dutch energy sector based on energy, exergy and extended exergy accounting. Energy 31:3135–3144

9. Joosung IL, Stephen P. Lukachko, Ian AW (2004) Aircraft and energy use. http://web.mit.edu/aeroastro/people/waitz/publications/AircraftEnergyUse.pdf
10. Rosen MA (2002) Assessing energy technologies and environmental impacts with the principles of thermodynamics. Appl Energ 72:427–441
11. Ao Y, Gunnewiek L, Rosen MA (2008) Critical review of exergy-based indicators for the environmental impact of emissions. Int J Green Energ 5(1–2):87–104
12. Dincer I, Rosen MA (1998) Worldwide perspective on energy, environment and sustainable development. Int J Green Energ Res 22:1305–1321
13. Midilli A, Dincer I (2009) Development of some exergetic parameters for PEM fuel cells for measuring environmental impact and sustainability. Int J Hydrogen Energy 34:3858–3872
14. Midilli A, Dincer I (2010) Effects of some micro-level exergetic parameters of a PEMFC on the environment and sustainability. Int J Global Warm 2(1):65–80
15. Norberg S, Tamm G, Highley J, Rounds M, Boettner D, Arnas O (2009) Teaching thermodynamics via analysis of the west point power plant. Int J Green Energ 6 (3):230–244
16. Aydın H, Turan O, Midilli A, Karakoç TH (2012) Exergetic and exergo-economic analysis of a turboprop engine: a case study for CT7-9C. Int J Exergy 11 (1):69–88
17. Aydın H, Turan O, Midilli A, Karakoç TH (2012b) Component-based exergetic measures of an experimental turboprop/turboshaft engine for propeller aircrafts and helicopters. Int J Exergy 11(N3):322–348
18. Ballı O, Aras H, Hepbaslı A (2008) Exergetic and exergoeconomic analysis of an aircraft jet engine (AJE). Int J Exergy 5(6):567–581
19. Bejan A, Siems DL (2001) The need for exergy analysis and thermodynamic optimization in aircraft development. Int J Exergy 1(1):14–24
20. Brilliant HM (1995) Second law analysis of present and future turbine engines, AIAA Paper, 95–3030, July
21. Cesare T, Paolo AR, Luiz F, Oliveira SDJ (2010) Exergy and thermoeconomic analysis of a turbofan engine during a typical commercial flight. Energy 35:952–959
22. Diango A, Perilhon C, Descombes G, Danho E (2011) Application of exergy balances for the optimization of non-adiabatic small turbomachines operation. Energy 36:2924–2936
23. Etele J, Rosen MA (2001) Sensitivity of exergy efficiencies of aerospace engines to reference environmental selection. Int J Exergy 1(2):91–99
24. Figliola RS, Tipton R, Li H (2003) Exergy approach to decision-based design of integrated aircraft thermal systems. J Aircraft 40(1):49–55
25. Riggins DW (1996) High-speed engine/component performance assessment using exergy and thrust-based methods, NASA-CR-198271, January
26. Roth BA, Mavris DN (2000) A comparison of thermodynamic loss models applied to the J79 Turbojet Engine. Joint Propulsion Conference and Exhibit, 36th, Huntsville, July, AL, pp 16–19
27. Roth B, Mavris D (2001) A work availability perspective of turbofan engine performance. AIAA publication, No. 0391
28. Schiffmann J, Favrat D (2010) Design, experimental investigation and multi-objective optimization of a small-scale radial compressor for heat pump applications. Energy 35:436–450
29. Turan O (2012) Effect of reference altitudes for a turbofan engine with the aid of specific-exergy based method. Int J Exergy 11(2):252–270
30. Turan O (2012) Exergetic effects of some design parameters on the small turbojet engine for unmanned air vehicle applications. Energy 46:51–61
31. Balkan F, Colak N, Hepbasli A (2005) Performance evaluation of a triple effect evaporator with forward feed using exergy analysis. Int J Green Energ Res 29:455–470
32. Dincer I, Hussain MM, Al-Zaharnah I (2004) Energy and exergy use in public and private sector of Saudi Arabia. Energ Pol 32(141):1615–1624
33. Wall G (2003) Exergy tools. Proc IME J Power Energ 217:125–136
34. Hammond GP, Stapleton AJ (2001) Exergy analysis of the United Kingdom energy system. Proc IME J Power Energ 215(2):141–162
35. Hammond GP (2007) Industrial energy analysis, thermodynamics and sustainability. Appl Energ 84:675–700
36. Hepbasli A (2008) A key review on exergetic analysis and assessment of renewable energy resources for a sustainable future. Renew Sustain Energ Rev 12:593–661
37. Hermann WA (2006) Quantifying global exergy resources. Energy 31(12):1685–1702
38. Kilkis IB (1999) Utilization of wind energy in space heating and cooling with hybrid. Energ Build 30:147–153
39. Genoud S, Lesourd JB (2009) Characterization of sustainable development indicators for various power generation technologies. Int J Green Energ 6(3):257–267
40. Szargut JM, Morris DR, Steward FR (1988) Exergy analysis of thermal, chemical and metallurgical processes. Hemisphere, New York
41. Kotas TJ (1995) The exergy method of thermal plant analysis, Reprintth edn. Krieger, Malabar, FL
42. Cornelissen RL (1997) Thermodynamics and sustainable development: the use of exergy analysis and the reduction of irreversibility. Ph.D. thesis, University of Twente, The Netherlands
43. Farokhi S (2009) Aircraft propulsion. Wiley, Hoboken, NJ
44. EADS 2012. Preliminary aircraft evaluation for saseb, blm national aviation office, technical review

Exergetic Analysis of a Vertical Ground-Source Heat Pump System with Wall Heating/Cooling

Ugur Akbulut, Ozgen Acikgoz, Olcay Kincay, and T. Hikmet Karakoc

Abstract

The present study deals with an exergetic analysis and assessment of a Vertical Ground-Source Heat Pump System (VGSHP) combined with a Wall Heating System (WHCS) in a building. This study is an experimental investigation of a real building's heating system. The system is located at Yildiz Renewable Energy House (YREH) in Yildiz Technical University and fulfills the heating demand of YREH and a living room of the neighboring dormitory. In order to validate an exergetic model, the system is divided into three subsystems: (1) the ground coupling circuit, (2) the refrigerant circuit, and (3) the WHS circuit. The schematic diagram of the constructed experimental system is given in Fig. 26.1. Exergetic model is obtained by applying mass, energy, and exergy equations for each system component. YREH has four rooms, each has 8 m^2 floor area, and the neighboring dormitory has a 50 m^2 living room. In this study three rooms of YREH and the living room have been heated during heating season. The heating season was assumed to be between 1 January and 31 March. As average results on the heating season, 6.509 kW heat energy was extracted from ground and 5.799 kW was used in the WHS. In this process electrical energy consumption of system components are as follows: compressor 1.711 kW, ground heat exchanger pump 0.092 kW, accumulator tank circulation pump 0.114 kW, and WHS circulation pump 0.108 kW. For heating season, calculated overall system efficiency was 67.36 % while GSHP unit's efficiency was 85 %. In addition, overall system COP was 2.76, while GSHP unit's COP was 4.13. Total exergy destruction was found 1.759 kW and largest exergy destruction has occurred in the compressor as 0.714 kW. The exergy efficiency values for the individual components of the system have been found ranging from 58.3 to 98.4 % according to P/F concept. It is expected that the model would be beneficial for evaluating low exergy heating systems which use ground source as a renewable energy.

Introduction

Ground-source heat pump (GSHP) systems make use of renewable energy stored in the ground for building heating and cooling. They are suitable for a wide variety of building types, provide high levels of comfort, and are particularly appropriate for energy saving and environmentally attractive [1–7].

U. Akbulut (✉)
Faculty of Engineering, Recep Tayyip Erdogan University, Rize, Turkey
e-mail: ugur.akbulut@erdogan.edu.tr

O. Acikgoz • O. Kincay
Mechanical Engineering Department, Yildiz Technical University, Istanbul, Turkey
e-mail: oacikgoz@yildiz.edu.tr; okincay@yildiz.edu.tr

T.H. Karakoc
Anadolu University School of Civil Aviation, Yunusemre Kampusü, Eskisehir, Turkey
e-mail: hkarakoc@anadolu.edu.tr

Many theoretical and experimental works on GSHP systems have been accomplished, since late 1940s. GSHP systems are inherently more effective than air-source heat pumps because the ground maintains relatively stable source and sink temperatures. This situation provides a better COP for the GSHP system. For the ground heat exchangers, VGSHP systems are usually preferred over HGSHP systems. They are more efficient, and less ground area is required [8–15].

The main advantages of WHC systems are enabling better thermal comfort, providing better indoor air quality with low air velocities and homogenous heat distribution, being available to use waste heat and low-enthalpy renewable energy resources, and having low initial investment, maintenance, and operating costs [16]. WHC systems have low operation temperature benefit. This creates substantial energy savings for heating and cooling compared with conventional systems. The energy savings from a WHC system may reach more than 30 %, as demonstrated in some theoretical and experimental case studies. Researchers have mostly determined the convection heat transfer coefficient of heated and cooled walls of the WHC systems. They have solved the natural convection problems in enclosures. In these studies, heat distribution from floors, walls, and ceilings were investigated for heating and cooling situations. All studies considered in the literature about WHC systems emphasized that this system was comfortable, economical, and very suitable to use with renewable energy systems. For that reason; a real VGHP system, combined with a WHC system, has been analyzed experimentally in our previous research. Energetic aspects of the system were introduced. However, exergy analysis of the system has not been conducted yet [17–20].

Exergy analysis is widely used for scaling a process's thermodynamic ideality. This helps designing efficient and cost-effective systems that also meet environmental conditions. In addition to the energy analysis, exergy analysis must be used to identify the components where inefficiencies occur. Improvements should be done to these components to minimize the irreversibility and optimize the system [21–25]. In recent years, exergy analyses of space heating/cooling in buildings and GSHP systems have been developed [26–33]. These studies focused on the building heating mode, and few on the building cooling mode. This paper presents an exergy analysis of a real VGSHP system, combined with a WHC system. Real-time data has been obtained and used to represent destroyed exergy and exergy efficiency for both heating and cooling modes.

System Description

The investigated VGSHP system with the WHC is shown in Fig. 26.1. This system consists of a ground heat exchanger loop, heat pump unit, accumulation tank, and a WHC loop in the building. The vertical ground heat exchanger consists of two boreholes, each containing a U-tube pipe. The depth of the boreholes is 65 m, and the diameter is 0.15 m. For generating the ground-loop heat exchanger, 240 m DN40 polyethylene composite pipe was used in a vertical direction and 45 m in
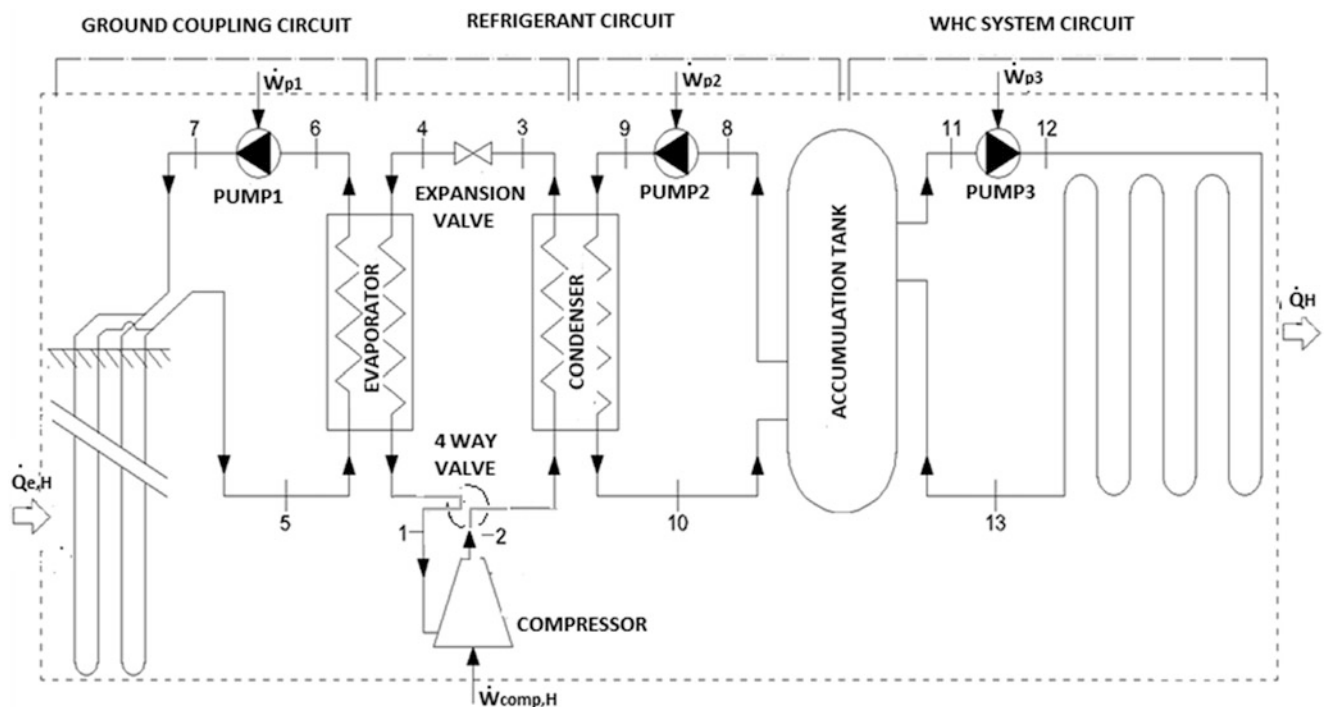
Fig. 26.1 Schematic of investigated VGSHP and WHCS systems on heating mode
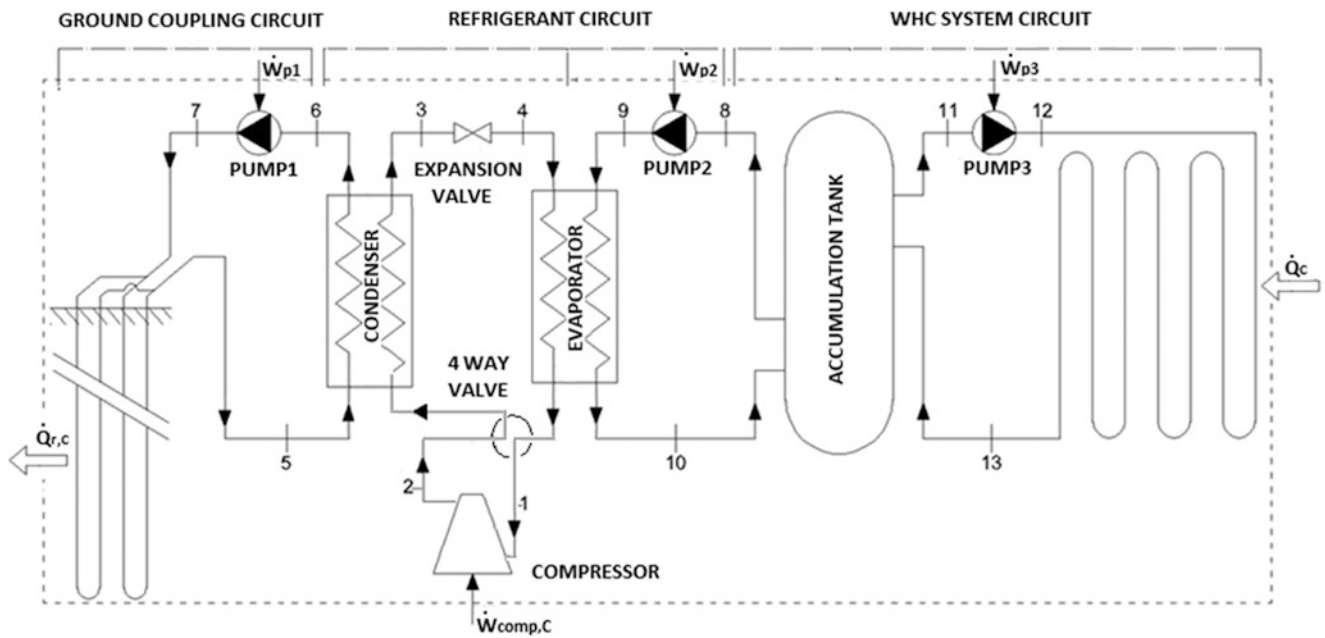
Fig. 26.2 Schematic of investigated VGSHP and WHC systems on cooling mode

horizontal. There are three circulation pumps and an isolated 500 lt accumulation tank in the system. In the WHC system, 840 m DN16 and 40 m DN20 polyethylene pipe was used. The systems were set up for holding the test room temperature at 20 °C on the heating and 24 °C on the cooling mode. For this reason, 31 °C and 18 °C V-GSHP operating temperatures were chosen especially to maintain comfort and prevent condensation on wall-mounted coils. Heating season was analyzed using data collected between Jan. 1 and March 31, 2010. In this period, the GSHP unit was online a total of 863 h for a mean of 30 %. Furthermore, cooling season was analyzed using data collected between July 1 and September 30. In this cooling period the GSHP unit was online a total 120 h for a mean of 5 %.

Schematic diagrams of the constructed experimental system on heating and cooling modes are illustrated in Figs. 26.1 and 26.2. This system mainly consists of three separate circuits as follows: (1) the ground coupling circuit, (2) the refrigerant circuit, and (3) the WHC system circuit. In the heating session, three rooms of YREH and the living room were heated; only two rooms of YREH were cooled in the cooling session. Conversion from the heating cycle to the cooling cycle is implemented by means of a four-way valve. The working fluid is R-410A. This system is installed at Yildiz Renewable Energy House (YREH) at Yildiz Technical University (latitude 41° N, longitude 29° E), Istanbul Turkey.

Exergetic Modeling

The general exergy balance can be expressed below Eq. (26.1), as the total exergy input is equal to total exergy output:

$$\sum \left(1 - \frac{T_0}{T_K}\right)\dot{Q}_k - \dot{W} + \sum \dot{m}_{in}\,\psi_{in} - \sum \dot{m}_{out}\,\psi_{out} = \dot{E}x_{dest} \qquad (26.1)$$

where $\dot{Q}_k$ is the heat transfer rate crossing the boundary at temperature T_K at location k, $\dot{W}$ the work rate, ψ the flow exergy which can be calculated by Eq. (26.2).

$$\psi = h - h_0 - T_0(s - s_0) \qquad (26.2)$$

Here h denotes the enthalpy, s the entropy, and the subscript zero indicates properties at the restricted dead state of P_0 and T_0.

The exergy rate is calculated by Eq. (26.3).

$$\dot{E}x = \dot{m}\,\psi \qquad (26.3)$$

To obtain exergy destruction, the entropy generation $\dot{S}_{gen}$ is calculated first and used in the Eq. (26.4) which is called as Stadola Law.

$$\dot{Ex}_{dest} = T_0 \dot{S}_{gen} \tag{26.4}$$

The exergy destructions in the system components are calculated as follows, respectively:
- Compressor and pumps

$$\dot{Ex}_{dest,c/p} = \dot{W}_{c/p} - \left(\dot{Ex}_{out} - \dot{Ex}_{in}\right) \tag{26.5}$$

- Heat exchangers (evaporator, condenser, and accumulator tank)

$$\dot{Ex}_{dest,HE} = \sum \dot{Ex}_{in} - \sum \dot{Ex}_{out} \tag{26.6}$$

- Expansion valve

$$\dot{Ex}_{dest,expv} = \dot{m}_{ref} \left(\psi_{in} - \psi_{out}\right) \tag{26.7}$$

- Ground heat exchanger in heating session

$$\dot{Ex}_{dest,grH} = \sum \left(1 - \frac{T_0}{T_{gr}}\right)\dot{Q}_{e,H} + \dot{m}_{in}\left(\psi_{in} - \psi_{out}\right) \tag{26.8}$$

- Ground heat exchanger in cooling session

$$\dot{Ex}_{dest,grC} = \dot{m}_{in}\left(\psi_{in} - \psi_{out}\right) - \sum \left(1 - \frac{T_0}{T_{gr}}\right)\dot{Q}_{r,C} \tag{26.9}$$

- WHCS in heating session

$$\dot{Ex}_{dest,whcs} = \dot{m}_{in}\left(\psi_{in} - \psi_{out}\right) - \sum \left(1 - \frac{T_0}{T_{room}}\right)\dot{Q}_H \tag{26.10}$$

- WHCS in cooling session

$$\dot{Ex}_{dest,whcs} = \dot{m}_{in}\left(\psi_{in} - \psi_{out}\right) + \sum \left(1 - \frac{T_0}{T_{room}}\right)\dot{Q}_C \tag{26.11}$$

System components' exergy efficiencies are calculated on product/fuel basis [21], by using Eq. (26.12)

$$\varepsilon_k = \frac{\dot{Ex}_{P,k}}{\dot{Ex}_{F,k}} \tag{26.12}$$

Results and Discussion

During the calculations for the system energy losses from the ground heat exchanger, the expansion valve and isolated pipes were neglected. The dead state temperature, which is the dry-bulb temperature and the dead state pressure were taken 0.01 °C and 101.325 kPa, respectively. After modeling the system and analysis of given data in Tables 26.1 and 26.2, exergetic results for the vertical ground-source heat pump system with wall heating and cooling were obtained by using thermodynamic equations given in the exergetic modeling section. Results are shown by Tables 26.3 and 26.4. In the year 2010, heating season was assumed to be between January 1 and March 31, and cooling season between July 1 and September 30.

Table 26.1 Measured data and calculated values of systems in the heating session

No	Name of element	ṁ [kg/s]	T [°C]	P [kPa]	h [kJ/kg]	s [kJ/kgK]	Ėx [kW]
0	Water (dead state)	–	0.01	101.325	0.1032	4.279×10^{-6}	0
0′	Refrigerant (dead state)	–	0.01	101.325	439.18	2.0982	0
1	Evaporator outlet/compressor inlet	0.035	7.97	795	429.62	1.84070	2.127
2	Compressor outlet/ condenser inlet	0.035	63.16	2,021	465.84	1.86900	3.124
3	Condenser outlet	0.035	28.37	2,021	245.49	1.15500	2.238
4	Evaporator inlet	0.035	−0.14	795	245.49	1.16670	2.127
5	Ground heat exchanger water outlet	0.44	7.48	257	31.53	0.11350	0.186
6	Ground heat exchanger water pump inlet	0.44	3.89	250	16.46	0.05945	0.052
7	Ground heat exchanger water inlet	0.44	3.94	300	16.67	0.06021	0.053
8	Water circulating pump inlet	0.57	29.65	250	124.3	0.43170	3.577
9	Water circulating pump outlet	0.57	29.70	300	124.5	0.43240	3.582
10	Heat pump outlet	0.57	32.66	293	136.9	0.47328	4.285
11	Accumulator tank outlet	0.27	30.60	250	128.3	0.44470	1.815
12	Heating water inlet	0.27	30.70	300	128.7	0.44610	1.820
13	Accumulator tank inlet	0.27	24.77	250	103.9	0.36378	1.196

Table 26.2 Measured data and calculated values of systems in the cooling session

No	Name of element	ṁ [kg/s]	T [°C]	P [kPa]	h [kJ/kg]	s [kJ/kgK]	Ėx [kW]
0	Water (dead state)	–	0.01	101.325	0.1032	4.279×10^{-6}	0
0′	Refrigerant (dead state)	–	0.01	101.325	439.18	2.0982	0
1	Evaporator outlet/compressor inlet	0.035	44.71	1,668	450.21	1.81590	2.439
2	Compressor outlet/ condenser inlet	0.035	17.71	1,113	431.75	1.83890	2.865
3	Condenser outlet	0.035	10.87	1,113	233.27	1.11490	2.194
4	Evaporator inlet	0.035	21.08	1,668	233.27	1.11680	2.176
5	Ground heat exchanger water outlet	0.44	20.80	257	87.27	0.30760	1.383
6	Ground heat exchanger water pump inlet	0.44	24.59	250	103.10	0.36110	1.918
7	Ground heat exchanger water inlet	0.44	24.63	300	103.30	0.36180	1.922
8	Water circulating pump inlet	0.57	17.66	250	74.14	0.26265	1.307
9	Water circulating pump outlet	0.57	17.70	300	74.31	0.26325	1.310
10	Heat pump outlet	0.57	14.53	293	61.05	0.21730	0.906
11	Accumulator tank outlet	0.27	17.91	250	75.19	0.26620	0.641
12	Cooling water inlet	0.27	18.00	300	75.56	0.26750	0.645
13	Accumulator tank inlet	0.27	24.26	250	101.70	0.35650	1.138

Data was recorded for each second and converted to a MySQL database. Collected data was arranged and transferred to other software for calculations and analysis. Refrigerant (R410A) properties were taken from Solkane 6.0, and water properties were taken from EES (Limited Academic version) software. Microsoft Excel pages were formed for calculations. After the calculations and analysis, for the heating and cooling seasons, average values of mass flow, temperature, pressure, enthalpy, and exergy rate are given in Tables 26.1 and 26.2, respectively. Also, the exergy rate of fuel, exergy rate of product, destroyed exergy, energy efficiency, and exergy efficiency are shown in Tables 26.3 and 26.4.

For the heating season, the exergy efficiency peak values for the expansion valve and accumulator tank were found 95 and 87.6 % respectively. During the calculations energy loss from the expansion valve was neglected. Thereby, energy and exergy efficiency values for this component are suitable for these working conditions. Also, energy and exergy efficiency values for the accumulator tank seem to be normal and prove that the tank is well isolated. On the contrary, the exergy efficiency values are lowest for the evaporator and three circulation pumps. We should consider the energy efficiency values in order to decide whether these components are inefficient and should be replaced. These components energy efficiency values are 97.63, 70.75, 87.69, and 83.01 % respectively. These values are suitable for a plate heat exchanger and small capacity circulation pumps. Thus, evaporator and pump1 have too small exergy efficiency values since their working temperatures which are too close to the dead state. Also, all three circulating pumps are not changing the temperature of water much. Whole exergy is destroyed on the pumping process. However, our overall system's energy and exergy

Table 26.3 Exergetic analysis results for representative units in the heating session

No	Name of element	$\dot{E}x_F$ [kW]	$\dot{E}x_P$ [kW]	$\dot{E}x_{dest,k}$ [kW]	η [%]	ε [%]
I	Overall system	2.254	0.496	1.759	67.36	22.0
II	GSHP unit	1.840	0.698	1.142	85.00	37.9
III	Pump1	0.092	0.001	0.091	70.75	1.1
IV	Ground heat exchanger	0.230	0.133	0.097	100.00	57.9
V	Evaporator	0.134	0.001	0.133	97.63	0.5
VI	Compressor	3.838	3.124	0.714	74.10	58.3
VII	Expansion valve	2.238	2.127	0.112	100.00	95.0
VIII	Condenser	0.886	0.703	0.183	91.65	79.3
IX	Pump 2	0.114	0.005	0.109	87.69	4.4
X	Pump 3	0.108	0.005	0.103	83.08	4.4
XI	Accumulator tank	0.708	0.620	0.088	91.73	87.6
XII	WHCS	0.625	0.496	0.129	86.61	79.4

Table 26.4 Exergetic analysis results for representative units in the cooling session

No	Name of element	$\dot{E}x_F$ [kW]	$\dot{E}x_P$ [kW]	$\dot{E}x_{dest,k}$ [kW]	η [%]	ε [%]
I	Overall system	1.892	0.567	1.325	74.85	29.9
II	GSHP unit	1.470	0.535	0.935	80.76	36.4
III	Pump1	0.130	0.004	0.126	67.69	3.0
IV	Ground heat exchanger	0.539	0.436	0.103	100.00	80.9
V	Evaporator	0.404	0.263	0.141	91.91	65.1
VI	Compressor	1.066	0.426	0.640	60.60	40.0
VII	Expansion valve	2.194	2.176	0.018	100.00	99.2
VIII	Condenser	0.671	0.535	0.136	91.73	79.7
IX	Pump 2	0.130	0.003	0.127	74.54	2.7
X	Pump 3	0.130	0.004	0.126	76.85	3.1
XI	Accumulator tank	0.498	0.400	0.098	95.93	80.4
XII	WHCS	0.567	0.494	0.073	90.29	87.2

efficiency values are 67.36 and 22.00 % respectively and definitely we should develop some system components. Main indicator for this consideration is exergy destruction rate. That is why compressor, WHCS, and the ground heat exchanger must be developed, respectively. Improvements on the compressor will positively affect the performance of the condenser if the gas temperature of compressor outlet can be reduced.

For the cooling season, the exergy efficiency peak values for the expansion valve, ground heat exchanger and accumulator tank were found 99.2, 80.9, and 80.4 % respectively. The expansion valve and accumulator tank have similar results in the heating and cooling seasons because of the reasons explained above. But the ground heat exchanger works very different. Much difference on the exergy efficiency values exist. Because the ground heat exchanger water inlet temperatures are too different, 3.94 and 24.63 °C respectively. There is a higher heat transfer coefficient due to water molecules activity at 24.63 °C temperature and also 3.94 °C is very close to dead state. However, in both cases the exergy destruction rates are similar, 0.097 and 0.103 kW respectively. The three circulating pumps have similar results working in both heating and cooling sessions. Therefore, the compressor, the WHCS and the ground heat exchanger must be developed to make the system more efficient in both sessions.

Conclusions

We have presented exergetic aspects of a vertical ground-source heat pump system combined with wall heating/cooling in general. We analyzed the overall system components such as compressor, condenser, evaporator, expansion valve, ground heat exchanger, accumulator tank and WHCS. We used energy and exergy analysis results of experimental data from our

real system which works for heating and cooling purposes. Combining this study with our previous work which presents energetic aspects of the same system [2], we can point out some concluding remarks from this study as follows:

1. In the literature, main indicator to choose system's inefficient components is exergy destruction rate. Nonetheless, exergy efficiency and exergy efficiency values must be considered too attentively if most of the components' exergy destruction rates are very similar like in our cases.
2. Technical and economical availabilities and environmental aspects must be considered much before developing the system. That's why exergy economic and exergy environmental analysis of this kind of systems are needed.
3. For the heating season, the exergy efficiency peak values for the expansion valve and accumulator tank are 95 and 87.6 % respectively. For the cooling season, the exergy efficiency peak values for the expansion valve, ground heat exchanger and accumulator tank are 99.2, 80.9, and 80.4 %.
4. Calculated exergy efficiencies of the circulation pumps seem low at first glance. Because their operating temperatures are too near to dead state. Pumps are not changing the temperature of water much and all of the exergy is destroyed on pumping process. Their energy efficiency values are within normal limits.
5. As a result of exergy analysis of this system, the order of development priority is the compressor, the WHCS and the ground heat exchanger, from much to less.
6. Heat extraction rate of 50 W/m and heat rejection rate of 54 W/m of bore depth for the heating and cooling periods, remain within the range reported in the literature. But ground heat exchanger still has a development capacity.
7. For heating season, calculated overall system efficiency was 67.36 %, while the GSHP unit's efficiency was 85 %. Adding to that, the overall system COP was 2.76, while the GSHP unit's COP was 4.13. As for the cooling season, calculated system efficiency was 74.90 %, while the GSHP unit's efficiency was 80.76 %. Furthermore, the overall system COP was 4.38 while the GSHP unit's COP was 4.78.
8. The circulator wattage for the three closed loop of the system can be categorized as efficient and excellent. However frequency converter circulation pumps can be used for energy saving.
9. The system can be improved by using a variable speed compressor. According to the literature, increase in the compressor speed lowers the heat pump COP. Optimum compressor speed is around 50 Hz [29].

Nomenclature

COP	Coefficient of performance, dimensionless	$\dot{Q}$	Heat transfer rate, kW
$\dot{Ex}$	Exergy rate, kW	T	Temperature, K
h	Specific enthalpy, kJ/kg	$\dot{W}$	Rate of work or power, kW
$\dot{m}$	Mass flow rate, kg/s	s	Specific entropy, kJ/kgK
P	Pressure, kPa	$\dot{S}$	Entropy rate, kJ/K

Greek Letters

ε	Exergy (second law) efficiency, dimensionless	ψ	Specific exergy, kJ/kg
η	Energy (first law) efficiency, dimensionless		

Subscripts

0	Reference (dead) state	HE	Heat exchanger
C	Cooling	in	Input
c/p	Compressor or pump	k	kth element
dest	Destroyed	P	Product
expv	Expansion valve	ref	Refrigerant
F	Fuel	out	Output
gr	Ground	whsc	Wall heating cooling system
H	Heating		

References

1. Agustos H, Acikgoz O, Akbulut U, Kincay O (2008) Dikey tip toprak kaynaklı ısı pompası kullanımında güneş enerji desteğinin araştırılması. TMMOB Makine Mühendisleri Odası Tesisat Mühendisliği Dergisi 106:47–53

2. Akbulut U, Acikgoz O, Kincay O, Karakoc HT (2012) Performance assessment of a vertical ground-source heat pump system with wall heating and cooling. Energ Educ Sci Technol A. Special Issue:423–428

3. Esen H, Inalli M, Esen M (2006) Technoeconomic appraisal of a ground source heat pump system for a heating season in eastern Turkey. Energ Convers Manage 47(9–10):1281–1297

4. Kavanaugh SP (1992) Field test of vertical ground-coupled heat pump in Alabama. ASHRAE Trans 98(2):607–616

5. Lund JW (2003) The USA geothermal country update. Geothermics 32(4–6):409–418

6. Ozgener L, Hepbasli A, Dincer I (2007) A key review on performance improvement aspects of geothermal district heating systems and applications. Renew Sust Energ Rev 11(8):1675–1697

7. Sanner B, Karytsas C, Mendrinos D, Rybach L (2003) Current status of ground source heat pumps and underground thermal energy storage in Europe. Geothermics 32(4–6):579–588

8. Esen H, Inalli M, Esen M (2007) Numerical and experimental analysis of a horizontal ground-coupled heat pump system. Build Environ 42(3):1126–1134

9. Grandall AC (1946) House heating with earth heat pump. Electr World 126(19):94–95

10. Hepbasli A (2002) Performance evaluation of a vertical ground source heat pump system in Izmir, Turkey. Int J Energ Res 26:121–139

11. Hepbasli A (2005) Thermodynamic analysis of a ground-source heat pump system for district heating. Int J Energ Res 7:671–687

12. Ingersoll LR, Plass HJ (1948) Theory of the ground pipe heat source for the heat pump. Heat Piping Air Cond 20(7):119–122

13. Li X, Chen Z, Zhao J (2006) Simulation and experiment on the thermal performance of U-vertical ground coupled heat exchanger. Appl Therm Eng 26(14–15):1564–1571

14. Lund JW, Freeston DH, Boyd TL (2005) Direct application of geothermal energy: 2005 worldwide review. Geothermics 34:691–727

15. Urchueguia JF, Zacares M, Corberan JM, Montero A, Martos J, Witte H (2008) Comparison between the energy performance of a ground coupled water to water heat pump system and an air to water heat pump system for heating and cooling in typical conditions of the European Mediterranean coast. Energ Convers Manage 49:2917–2923

16. ASHRAE (2004) ASHRAE handbook-HVAC systems and equipment. American Society of Heating, Refrigeration and Air-Conditioning Engineers Inc., Atlanta, GA

17. Akbulut U, Yoru Y, Kıncay O (2011) Annual investigation of ground source heat pump system performance on a wall heating system in Istanbul. The 6th International Green Energy Conference, IGEC-VI, Eskişehir, June 5–9. Anadolu University, Türkiye

18. Baskal A, Akbulut U, Kıncay O (2012) Toprak Kaynaklı Isı Pompası Destekli Duvardan Isıtma Sistemi. TMMOB Makina Mühendisleri Odası, Tesisat Mühendisliği Dergisi 128:43–50 (in Turkish)

19. Kincay O, Akbulut U, Yoru Y, Acikgoz O, Karakoc H (2010) Investigation of usage of ground source heat pump system on wall heating. AIVC International Conference, Low Energy and Sustainable Ventilation Technologies for Green Buildings, Oct 26–28. Seoul, Korea

20. Yoru Y, Akbulut U, Kıncay O, Karakoc TH (2010) Dynamic exergy analysis of a real vertical ground source heat pump system by using fast artificial neural network library (FANN). The 5th International Ege Energy Symposium and Exhibition, IEESE-5, June 27–30. Pamukkale University, Denizli, Türkiye

21. Bejan A, Tsatsaronis G, Moran M (1996) Thermal design & optimization. Wiley, New York

22. Dincer I, Cengel YA (2001) Energy, entropy and exergy concepts and their roles in thermal engineering. Entropy 3(3):116–149

23. Kotas TJ (1995) The exergy method of thermal plant analysis. Krieger, Melbourne, FL

24. Moran MJ (1989) Availability analysis: a guide to efficient energy use. ASME Press, New York

25. Rosen MA (1999) Second law analysis: approaches and implications. Int J Energ Res 23(5):415–429

26. Bejan A (2002) Fundamentals of exergy analysis, entropy generation minimization, and the generation of flow architecture. Int J Energ Res 26(7):545–565

27. Hepbasli A, Akdemir O (2004) Energy and exergy analysis of a ground source (geothermal) heat pump system. Energ Convers Manage 45:737–753

28. Kincay O, Akbulut U, Temir G (2004) İstanbul'da Bulunan Bir İş Merkezindeki Örnek Bir Katın Soğutma Sezonunda Ekserji Analizi. Tesisat Dergisi 108:68–73 (in Turkish)

29. Madani H, Ahmadi N, Claesson J, Lundqvist P (2010) Experimental analysis of a variable capacity heat pump system focusing on the compressor and inverter loss behavior. International Refrigeration and Air Conditioning Conference, Perdue University

30. Ozgener O, Hepbasli A (2007) A parametrical study on the energetic and exergetic assessment of a solar-assisted vertical ground-source heat pump system used for heating a greenhouse. Build Environ 42(1):11–24

31. Utlu Z, Hepbasli A (2007) Parametrical investigation of the effect of dead (reference) state on energy and exergy utilization efficiencies of residential–commercial sectors: a review and an application. Renew Sust Energ Rev 11:603–634

32. Yildiz A, Güngör A (2009) Energy and exergy analyses of space heating in buildings. Appl Energ 86:1939–1948

33. Bi Y, Wang X, Liu Y, Zhang H, Chen L (2009) Comprehensive exergy analysis of a ground-source heat pump system for both building heating and cooling modes. Appl Energ 86:2560–2565

34. Kavanaugh SP (1998) Development of design tools for ground-source heat pump piping. ASHRAE Trans 104(1B):932–937

Energy and Exergy Analysis of an R134A Automotive Heat Pump System for Various Heat Sources in Comparison with Baseline Heating System

Murat Hosoz, Mehmet Direk, K. Suleyman Yigit, Mustafa Canakci, Ali Turkcan, and Ertan Alptekin

Abstract

Performance of an automotive heat pump (AHP) system using R134a and driven by a diesel engine has been evaluated in this study. For this purpose, an experimental AHP system capable of providing a conditioned air stream by utilizing the heat absorbed from the ambient air, engine coolant and exhaust gas was developed. The experimental system was equipped with instruments for measuring engine torque and speed, refrigerant and coolant mass flow rates, refrigerant and air temperatures as well as refrigerant pressures. The system was tested by varying the engine speed, engine load and air temperatures at the inlets of the indoor and outdoor coils. Using experimental data, an energy analysis of the system was performed, and its performance parameters for each heat source were evaluated for transient and steady-state operations. Then, the performance of the AHP system for each source was compared with that of the system using other heat sources and with that of the baseline heating system. The investigated performance parameters include air temperature at the outlet of the indoor coil, heating capacity, coefficient of performance and exergy destruction rates in the components of the AHP system. The total exergy destruction rate in the AHP with engine coolant is higher than those in the AHP with ambient air and with exhaust gas mainly because of the greater refrigerant mass flow rate and heating capacity.

Introduction

Under cold weather conditions, comfort heating of the passenger compartment of vehicles with an internal combustion engine is usually performed by utilizing the engine waste heat. However, this coolant-based heating system cannot provide an appropriate thermal comfort in the compartment until the coolant temperature rises to a certain value. This problem is

M. Hosoz (✉) • M. Canakci • E. Alptekin
Department of Automotive Engineering, Kocaeli University, Kocaeli 41380, Turkey
e-mail: mhosoz@kocaeli.edu.tr; canakci@kocaeli.edu.tr; ertanalptekin@kocaeli.edu.tr

M. Direk
Yalova Community School, Yalova University, Yalova 77100, Turkey
e-mail: mehmetdirek@hotmail.com

K.S. Yigit
Department of Mechanical Engineering, Kocaeli University, Kocaeli 41380, Turkey
e-mail: kyigit@kocaeli.edu.tr

A. Turkcan
Department of Mechanical Education, Kocaeli University, Kocaeli 41380, Turkey
e-mail: aturkcan@kocaeli.edu.tr

more critical for the vehicles employing high-efficiency diesel engines due to the lack of sufficient waste heat within an acceptable duration of operation after the engine is started [1]. With the intention of obtaining thermal comfort rapidly, some vehicles utilize heaters using fuel or electricity. However, these systems contain several disadvantages such as high initial and operating costs, low efficiency and leading to air pollution as well as global warming. On the other hand, the problem of insufficient heating can be solved by adding some low-cost components to the present air conditioning system of the vehicle to operate it as a heat pump. The automotive heat pump (AHP) system can heat the passenger compartment individually or it can support the present heating system of the vehicle [2].

The number of the investigations on AHP systems published in open literature is limited due to its competitive nature. Domitrovic et al. [3] simulated the steady-state cooling and heating operation of an automotive air conditioning (AAC) and AHP system using R12 and R134a, and determined the change of the cooling and heating capacities, COP and power consumption with ambient temperature at a fixed compressor speed. They found that R134a and R12 yielded comparable results, while the heating capacity of the AHP system was insufficient in both refrigerant cases. Antonijevic and Heckt [4] developed and evaluated the performance of an R134a AHP system, which was employed as a supplementary heating system. They carried out the tests at very low ambient temperatures and compared the performance of the AHP system with that of the other supplemental heating systems.

Rongstam and Mingrino [5] evaluated the performance of an R134a AHP system using engine coolant as a heat source, and compared it with the performance of a coolant-based heating system operated at $-10\ °C$ ambient temperature. They found that during a drive cycle operation, the average cabin temperature provided by the heat pump system at the tenth minute of the tests was $8\ °C$ higher than those provided by the baseline heating system. Scherer et al. [6] reported an on-vehicle performance comparison of an R152a and R134a AHP system using engine coolant as a heat source. They presented the air temperatures at several locations inside the passenger compartment as a function of time, and found that both refrigerants yielded almost identical performances and heating capacities. Hosoz and Direk [7] evaluated the performance of an air-to-air R134a AHP system, and compared its performance with the performance of an air conditioning system. They observed that the AHP system using ambient air as a heat source could not meet the heating requirement of the compartment when ambient temperature was extremely low. Direk and Hosoz [8] carried out an energy and exergy analysis of an R134a AHP system using ambient air as a heat source. They observed that the heat exchangers of the system were responsible for most of the exergy destruction. Tamura et al. [9] studied on the experimental performance of an AHP system using CO_2 as a refrigerant. They found that the performance of the heat pump system using CO_2 was equal to or exceeding that of the system using R134a. Kim et al. [10] investigated the heating performance of an AHP system with CO_2. They performed transient and steady-state tests under various operating conditions finding that the use of their system improved heating capacity compared to the baseline heating system. Cho et al. [11] reported on the heating performance characteristics of a coolant source heat pump using the waste heat of electric devices for an electric bus, and suggested a heat with a heating capacity of over 23.0 kW.

In this study, the performance parameters of an experimental AHP system for the cases of using the heat from ambient air, engine coolant and exhaust gas were evaluated and compared with each other along with the performance of the baseline heating system. The investigated performance parameters are heating performance, compressor power, coefficient of performance, exergy destruction in the components and total exergy destruction in the AHP system.

Description of the Experimental Setup

As schematically shown in Fig. 27.1, the experimental AHP system is usually made from original components of a compact size AAC system. It employs a seven-cylinder fixed-capacity swash-plate compressor, a parallel-flow micro-channel outdoor coil, a laminated type indoor coil, two thermostatic expansion valves, a reversing valve to operate the system in reverse direction in the heat pump operations, a brazed plate heat exchanger between the engine coolant and the refrigerant to serve as an evaporator and another plate heat exchanger to extract heat from the exhaust gas. All lines in the refrigeration circuit of the system were made from copper tubing and insulated by elastomeric material.

The indoor and outdoor coils were inserted into separate air ducts of 1.0 m length. In order to provide the required air streams in the air ducts, a centrifugal fan and an axial fan were placed at the entrances of the indoor and outdoor air ducts, respectively. These ducts also contain electric heaters located upstream of the indoor and outdoor coils. The indoor and outdoor coil electric heaters can be controlled between 0–2 and 0–6 kW, respectively, to provide the required air temperatures at the inlets of the related coils. The refrigeration circuit was charged with 1,600 g of R134a.
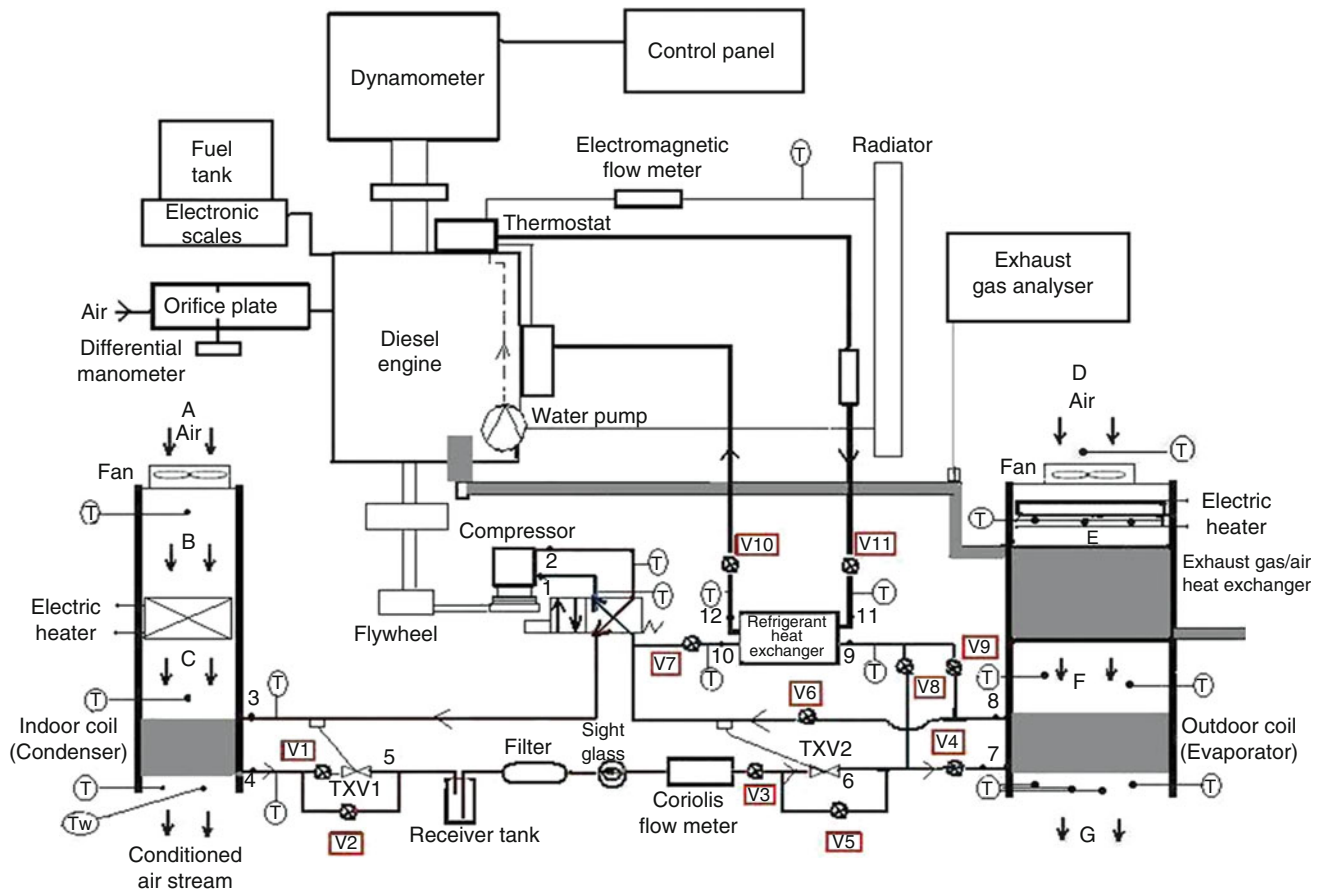
Fig. 27.1 Schematic illustration of the experimental AHP system using various heat sources

Table 27.1 Characteristics of the instrumentation

Measured variable	Instrument	Range	Uncertainty
Temperature	Type K thermocouple	−50–500 ºC	±0.3%
Pressure	Pressure transmitter	0–25 bar	±0.2%
Air flow rate	Anemometer	0.1–15 m s^{-1}	±3%
Refrigerant mass flow rate	Coriolis flow metre	0–350 kg h^{-1}	±0.1%
Compressor speed	Electromagnetic tachometer	10–100,000 rpm	±2%
Torque	Hydraulic dynamometer	5–750 N m	±2%

In order to gather data for the performance evaluation of the experimental AHP system, some mechanical measurements were conducted on the system. The employed instruments and their locations are depicted in Fig. 27.1. The characteristics of the instrumentation can be seen in Table 27.1.

The refrigerant mass flow rate was measured by a Coriolis mass flow metre. In order to ensure that the refrigerant was in a liquid phase before entering the mass flow metre, a liquid receiver with a volume of 1.1 l was placed between the condenser and filter/drier. Additionally, in order to observe if the refrigerant stream contained moisture, a sight glass was located just upstream of the mass flow metre. The temperatures of the refrigerant and air at the inlet and outlet of each component were measured by K-type thermocouples. The refrigerant pressures at the inlet and outlet of the compressor were monitored by both Bourdon gauges and pressure transmitters.

The AHP system was driven by a Fiat Doblo JTD diesel engine with a cylinder volume of 1.9 l and a maximum power of 77 kW at 4,000 rpm. The engine torque and speed were measured by means of a hydraulic dynamometer (Baturalp-Taylan

BT-190 FR) with a maximum measuring power of 100 kW, a maximum torque of 750 N m and a maximum speed of 6,000 rpm. The fuel consumption was measured using an electronic scale and a chronometer. The values of the measured variables were usually acquired through a data acquisition system and recorded on a computer. The data acquisition system has 16 bit—200 kHz frequency with a 56 channel thermocouple input module and an 8 channel transducer interface module.

Figure 27.1 also illustrates the refrigerant flow paths in the experimental heat pump system for the cases of using ambient air or exhaust gas as a heat source. In order to perform the heat pump operation, the reversing valve is energized. Then, the reversing valve directs the high temperature superheated vapour refrigerant discharged from the compressor to the indoor coil (condenser). The refrigerant passing through the indoor coil rejects heat to the indoor air stream, thus providing a warm air stream for the potential passenger compartment. After rejecting heat to the indoor air stream, the refrigerant condenses and leaves the indoor coil as subcooled liquid. In heat pump operations, thermostatic expansion valve #1 (TXV1) is bypassed. Then, the refrigerant flows through valves V1 and V2 and reaches the receiver tank, which keeps the unrequired refrigerant in it when the thermostatic expansion valve decreases the refrigerant flow rate at low evaporator loads. After passing through the filter, sight glass and Coriolis flow metre, the refrigerant reaches TXV2 located at the inlet of the outdoor coil. Since valves V5 and V8 are closed, the refrigerant passes through TXV2, which reduces the pressure, and thereby the temperature, of the liquid refrigerant. TXV2 also controls the refrigerant mass flow rate circulating through the circuit so that a constant superheat at the outlet of the outdoor coil is maintained under all operating conditions. Next, it enters the outdoor coil, where it absorbs heat taken from the outdoor air stream, and leaves the outdoor coil as low pressure superheated vapour. After leaving the outdoor coil, the refrigerant passes through valve V6 and enters the reversing valve.

The refrigerant flow paths in the experimental AHP system using exhaust gas as a heat source are the same as those shown in Fig. 27.1. In this case, the outdoor air stream is heated by the exhaust gas in a heat exchanger located upstream of the outdoor coil, and then the evaporating refrigerant absorbs its heat in the outdoor coil. Note that in this operation, the bulb of TXV2 is located at the outlet of the outdoor coil serving as an evaporator to sense the superheat of the leaving refrigerant and regulate the refrigerant mass flow rate in the circuit properly. Similar to the operations in the previous cases, in the AHP system using engine coolant, the liquid refrigerant enters TXV2 located at the inlet of the outdoor coil. Since valve V4 is closed, it flows through valve V8 and enters the heat exchanger serving as an evaporator. After absorbing heat from the engine coolant, the refrigerant evaporates and leaves the heat exchanger as superheated vapour. Then, through valve V7, the refrigerant enters the reversing valve, and the operation goes on similar to the previous cases.

Thermodynamic Analysis

The performance parameters of the experimental AHP system can be evaluated by applying the first law of thermodynamics to the system. Using this law for the indoor coil (condenser), the heating capacity of the experimental AHP system can be evaluated from

$$\dot{Q}_{cond} = \dot{m}_r \left(h_{cond,in} - h_{cond,out} \right) \tag{27.1}$$

Assuming that the compressor is adiabatic, the power absorbed by the refrigerant during the compression process can be expressed as

$$\dot{W}_{comp} = \dot{m}_r \left(h_{comp,out} - h_{comp,in} \right) \tag{27.2}$$

Coefficient of performance of the system can be defined as

$$COP = \frac{\dot{Q}_{cond}}{\dot{W}_{comp}} \tag{27.3}$$

The general form of exergy rate balance equation given below can be utilized [12].

$$\sum \left(1 - \frac{T_0}{T_j} \right) \dot{Q}_j - \dot{W}_{cv} + \sum \dot{m}_{in} \psi_{in} - \sum \dot{m}_{out} \psi_{out} = \dot{E}x_d \tag{27.4}$$

The specific flow exergy in this equation can be evaluated from [12]

$$\psi = (h - h_0) - T_0(s - s_0) \tag{27.5}$$

where subscript '0' stands for reference (dead) state.

In the adiabatic compressor, the rate of exergy destruction can be evaluated from

$$\dot{Ex}_{d,comp} = \dot{m}_r \left(\psi_{comp,in} - \psi_{comp,out} \right) \tag{27.6}$$

The rate of exergy destruction in the condenser can be determined from

$$\dot{Ex}_{d,cond} = \dot{m}_r \left(\psi_{cond,in} - \psi_{cond,out} \right) + \dot{m}_{a,cond}(\psi_B - \psi_C) \tag{27.7}$$

The total flow exergy of air to be used in Eq. (27.7) at the locations B and C can be calculated from [12]

$$\psi_a = \left(C_{p,a} + \omega C_{p,v} \right) T_0 [(T/T_0) - 1 - \ln(T/T_0)] + (1 + 6078\omega) \left(R_a T_0 \ln(P/P_0) \right. \\ + R_a T_0 \left\{ \begin{array}{l} (1 + 1.6078\omega) \ln[(1 + 1.6078\omega_0)/(1 + 1.6078\omega)] \\ +1.6078\omega \ln(\omega/\omega_0) \end{array} \right\} \tag{27.8}$$

Neglecting the heat transfer, the rate of exergy destruction in the expansion valve can be obtained from

$$\dot{Ex}_{d,valve} = \dot{m}_r \left(\psi_{valve,in} - \psi_{valve,out} \right) \tag{27.9}$$

Then, using Eq. (27.5) and considering that $h_5 = h_4$, we obtain

$$\dot{Ex}_{d,valve} = \dot{m}_r T_0 (s_{valve,in} - s_{valve,out}) \tag{27.10}$$

The rate of exergy destruction in the evaporator can be evaluated from

$$\dot{Ex}_{d,evap} = \dot{m}_r \left(\psi_{evap,in} - \psi_{evap,out} \right) + \dot{m}_{a,evap}(\psi_E - \psi_F) \tag{27.11}$$

Finally, the total rate of exergy destruction in the refrigeration circuit of the system can be determined by summing up the individual destructions, i.e.

$$\dot{Ex}_{d,total} = \dot{Ex}_{d,cond} + \dot{Ex}_{d,evap} + \dot{Ex}_{d,comp} + \dot{Ex}_{d,valve} \tag{27.12}$$

Results and Discussions

Figure 27.2 shows the variations in the heating capacity versus compressor speed at the fifth minute of the tests when the temperatures of the air streams entering the evaporator and condenser are maintained at 5 °C. The coolant based AHP system has the highest heating capacity at all compressor speeds. The heating capacity at the end of the fifth minute increases on rising the compressor speed for a fixed dynamometer load of 60 N m. In all tests performed at 60 N m, the coolant based AHP system has the highest fifth minute heating capacity, which is followed by the baseline heating system, AHP with exhaust gas and AHP with ambient air in descending order.

The effects of the compressor speed on some of the performance parameters of the AHP system at steady-state conditions are shown in Figs. 27.3, 27.4, 27.5, and 27.6. Figure 27.3 shows the variations in the heating capacity versus compressor speed for a fixed dynamometer load of 60 N m when the temperatures of the air streams entering the evaporator and condenser are maintained at 5 ºC. It is seen that the heating capacity usually gets higher on increasing the compressor speed. In the AHP system with the engine coolant, the refrigerant absorbs a greater amount of heat from the coolant heat exchanger, thereby providing considerably higher heating capacity compared with the AHP system with ambient air or exhaust gas. On the other hand, when the engine load is kept at 60 N m, the baseline heating system yields higher steady-state heating

Fig. 27.2 The change of the heating capacity as a function of the compressor speed at the end of the 5 min operation period
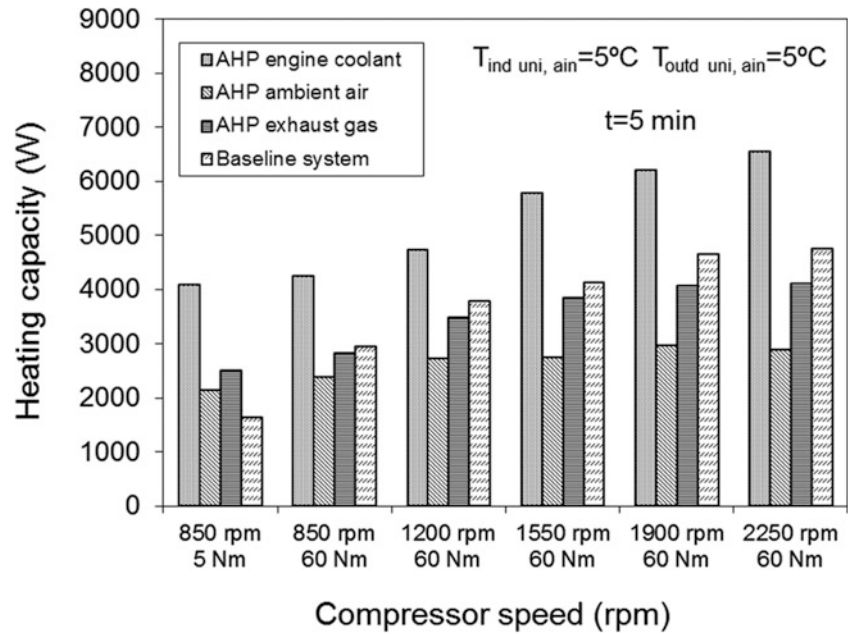
Fig. 27.3 The change of the heating capacity as a function of the compressor speed
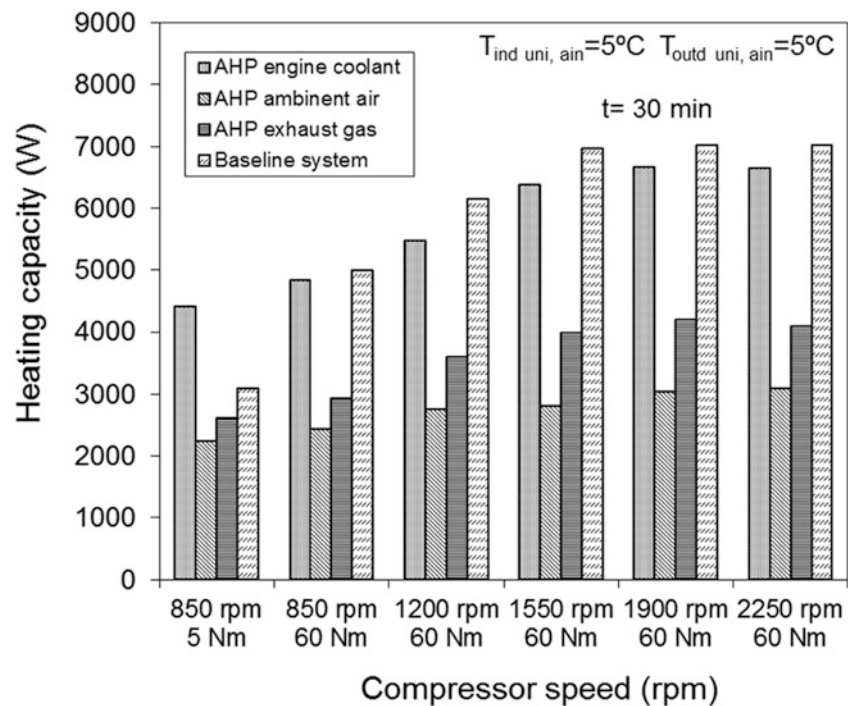
capacities than all AHP systems at all speeds. In all tests, the AHP system using exhaust gas usually results in higher heating capacities than the AHP system using ambient air as a heat source. Figure 27.4 indicates that the COP for heating decreases by increasing the compressor speed. Because the compressor power increases faster than the heating capacity does, the COP for heating decreases with increasing compressor speed. The AHP system using engine coolant provides the highest COP compared with the AHP system using ambient air and exhaust gas.

The effect of the compressor speed on the distribution of the exergy destructions in the components of the AHP system can be shown in Fig. 27.5 for the engine speed of 850 rpm when air temperatures entering indoor and outdoor coils are both 5 °C. It is seen that the indoor coil (condenser) usually causes the highest exergy destruction followed by the outdoor coil (evaporator), compressor and thermostatic expansion valve in descending order.

Fig. 27.4 The change of the coefficient of performance for heating as a function of the compressor speed
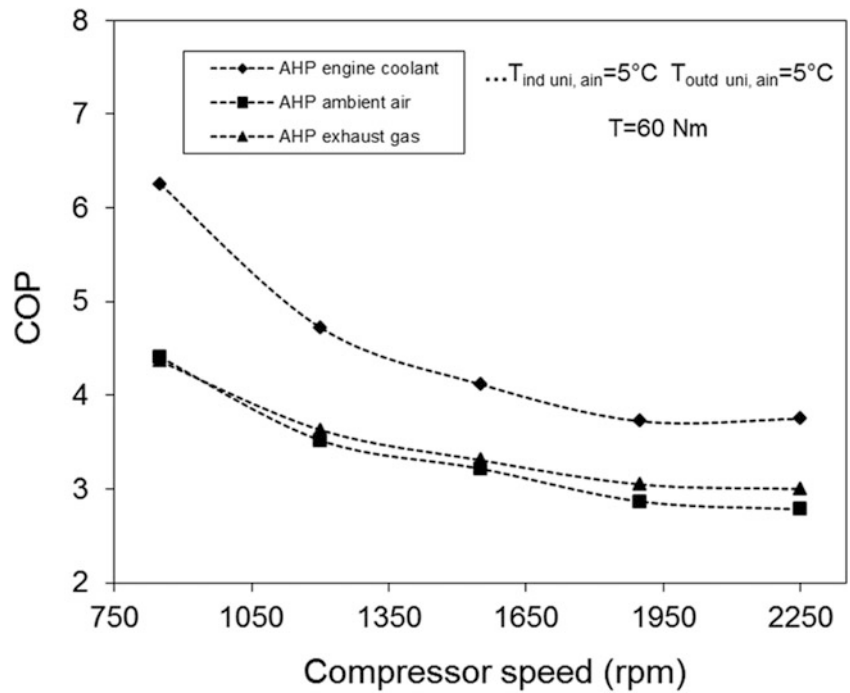
Fig. 27.5 The comparison of the exergy destructions at 850 rpm and 5 Nm
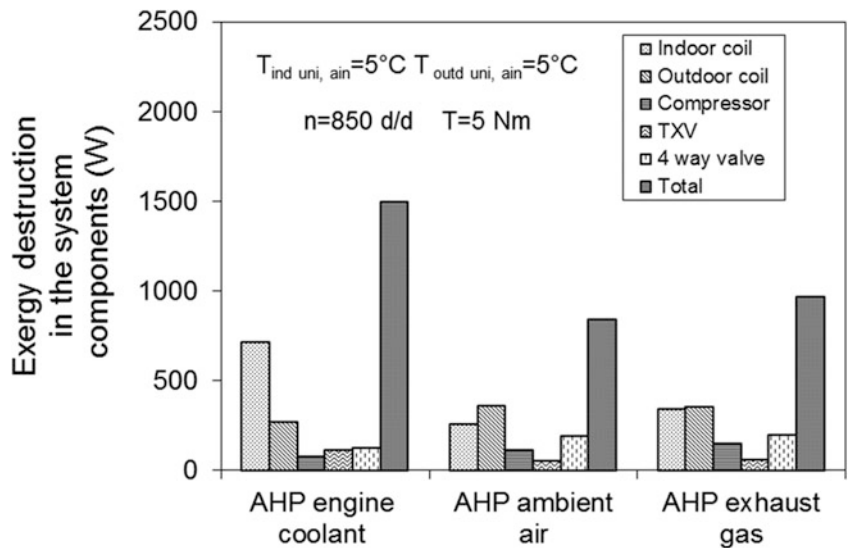
Figure 27.6 indicates that the AHP with engine coolant has the highest exergy destruction at 1,550 rpm engine speed and 60 N m dynamometer load settings. As the heat transfer in the outdoor and indoor coils takes place across a higher temperature difference, the exergy destructions in these components are higher than other components. Figure 27.7 shows the effect of the compressor speed on the rate of total exergy destruction in the AHP system. It can be seen that the rate of total exergy destruction in the AHP system increases on rising the compressor speed. This is mainly due to the increased refrigerant mass flow rate and condensing pressure together with decreased evaporating pressure with increasing compressor speed. Furthermore, as the compressor speed increases, the heat transfer in the condenser (indoor coil) and evaporator (outdoor coil) takes place across a higher temperature difference, and the exergy destructions in these components get higher. The exergy destruction rate in the AHP with coolant is higher than those in the AHP with ambient air and with exhaust gas mainly because of the greater refrigerant mass flow rate and heating capacity.

Fig. 27.6 The comparison
of the exergy destructions
at 1,550 rpm and 60 Nm
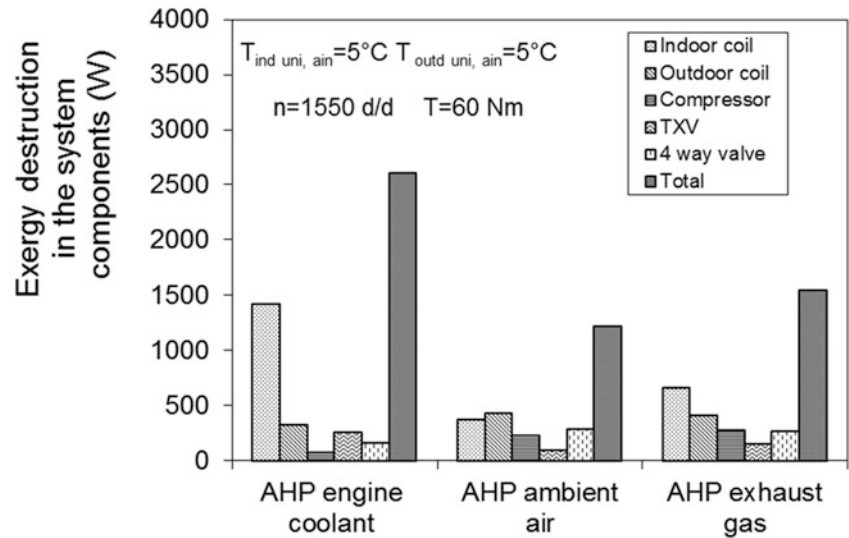
Fig. 27.7 The change of the total
exergy destruction as a function
of the compressor speed
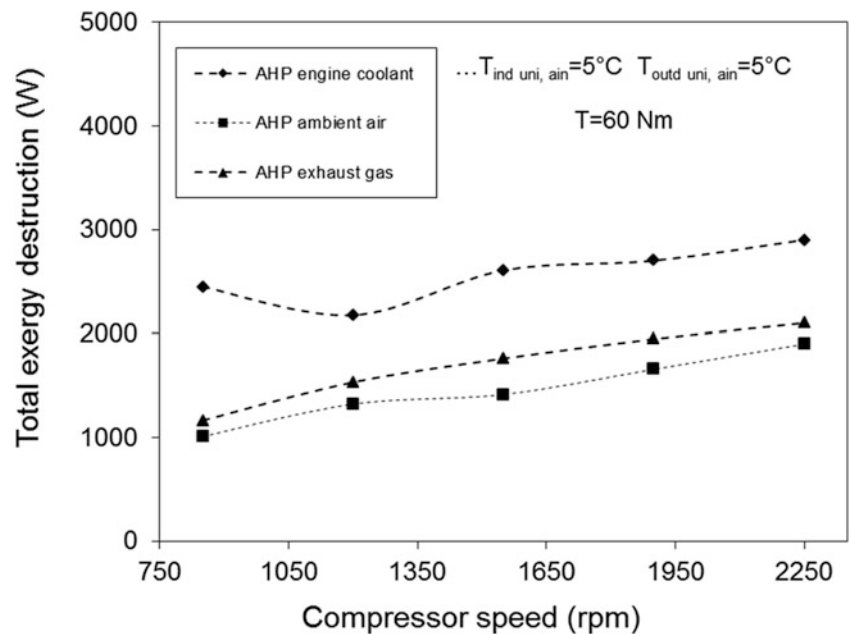
Conclusions

The performance of an experimental AHP system for the cases of using ambient air, exhaust gas and engine coolant as a heat source has been evaluated and compared with each other as well as with the performance of the baseline heating system.

AHP systems using different heat sources provided higher heating capacities than the baseline heating system at the end of 5 min operation period when the engine was operated at the idling conditions (n = 850 rpm and T = 5 N m). However, only the AHP system using engine coolant as a heat source yielded a better fifth-minute performance than the baseline heating system at higher speeds when the engine load was kept at 60 N m. On the other hand, when the engine load was 60 N m, the baseline heating system provided higher steady-state heating capacities than all AHP systems at all speeds. In all tests, the AHP system using exhaust gas usually resulted in higher heating capacities than the AHP system using ambient air as a heat source. It was determined that the AHP system with engine coolant yielded the highest COP values, while the AHP system with ambient air yielded the lowest ones.

The exergy destructions in the components of the AHP system and the total exergy destruction in the AHP system increased on rising compressor speed and temperatures of the air streams entering the evaporator and condenser. Among the AHP system components, the condenser usually caused the highest exergy destruction, followed by evaporator, compressor and expansion valve. These results reveal that the condenser has a high potential for further improvement.

Nomenclature

AAC	Automotive air conditioning	$\dot{Q}$	Heating capacity (W)
AHP	Automotive heat pump	$\dot{Q}_j$	Time rate of heat transfer (W)
COP	Coefficient of performance	R	Ideal gas constant (kJ/kg K)
$c_{p,a}$	Specific heat of air (kJ/kg K)	s	Entropy (kJ/kg K)
$c_{p,v}$	Specific heat of water vapour (kJ/kg K)	T	Temperature (°C)
$\dot{Ex}_d$	The rate of exergy destruction (W)	T_0	Environmental temperature representing the dead state (K)
h	Enthalpy (kJ/kg)		
$\dot{m}$	Mass flow rate (g/s)	T_j	Instantaneous temperature (K)
n	Engine speed (rpm)	$\dot{W}$	Power (W)
p	Pressure (Pa)	$\dot{W}_{cv}$	Power produced in the control volume (W)

Greek Symbols

ω	Humidity ratio	ψ	Specific flow exergy

Subscripts

0	Reference (dead) state	in	Inlet
a	Air	ind	Indoor
comp	Compressor	out	Outlet
cond	Condenser	outd	Outdoor
cv	Control volume	r	Refrigerant
evap	Evaporator	uni	Unit

References

1. Wienbolt HW, Augenstein CD (2003) Visco heater for low consumption vehicles. In: SAE word congress, Detroit, 2003-01-0738
2. Meyer J, Yangand G, Papoulis E (2004) R134a heat pump for improved passenger comfort. SAE paper 2004-01-1379
3. Domitrovic RE, Mei VC, Chen FC (1997) Simulation of an automotive heat pump. ASHRAE Trans 103:291–296
4. Antonijevic D, Heckt R (2004) Heat pump supplemental heating system for motor vehicles. Int J Automob Eng D 218:1111–1115
5. Rongstam J, Mingrino FA (2003) Coolant – based automotive heat pump system. In: C599/067/2003 VTMS 6 conference
6. Scherer LP, Ghodbane, M, Baker JA, Kadle PS (2003) On-vehicle performance comparison of an R-152a and R-134a HP system. In: SAE word congress, Detroit
7. Hosoz M, Direk M (2006) Performance evaluation of an integrated AAC and HP system. Energ Convers Manage 47:545–559
8. Direk M, Hosoz M (2008) Energy and exergy analysis of an automobile heat pump system. Int J Exergy 5:556–566
9. Tamura T, Yakumaru Y, Nishiwaki F (2005) Experimental study on automotive cooling and heating air conditioning system using CO_2 as a refrigerant. Int J Refrig 28:1302–1307
10. Kim SC, Kim MS, Hwang IC, Lim T (2007) Heating performance enhancement of a CO_2 heat pump system recovering stack exhaust thermal energy in fuel cell vehicles. Int J Refrig 30:1215–1226
11. Cho CW, Lee HS, Won JP, Lee MY (2012) Measurement and evaluation of heating performance of heat pump system using wasted heat of electric devices for an electric bus. Int J Energies 5:658–669
12. Ozgener O, Hepbasli A (2007) Modeling and performance evaluation of ground source (geothermal) heat pump systems. Energ Buildings 39:66–75

Energy and Exergy Analysis of a Perlite Expansion Furnace

28

Mert Gürtürk, Hakan F. Oztop, and Arif Hepbaslı

Abstract

Utilization opportunities of perlite have made the product adaptable to numerous applications in the construction, industrial, chemical, horticultural and petrochemical industries. Applications of the perlite include filler, high and low temperature insulation, concrete aggregate, textured coatings, absorbent and carrier etc. Thus, perlite seems to be a very important material. In this paper, thermodynamics analysis of a perlite expansion furnace was performed. Both energy and exergy relations were derived for the considered system. Some parameters, such as losses, irreversibility and design etc., were used for determining the energy and exergy efficiencies. Based on the results of the analysis of the system, the energy and exergy efficiencies are calculated to be 66 and 26 %, respectively. Some recommendations were also made towards increasing the efficiency in the Turkish perlite industry.

Keywords

Energy • Exergy • Perlite • Perlite expansion furnace

Introduction

Many processes in engineering applications occur under ideal conditions according to Thermodynamics Laws, but some of the processes are not efficient due to insufficient thermal design. The First Law of Thermodynamics implies the conservation of energy [1]. The energy audit and saving were applied to dry type cement rotary kiln systems consuming intensive energy. Cement production is an energy-intensive process, consuming about 4 GJ per ton of cement product. Energy loss was found from hot flue gas, kiln shell and cooler stack, and some possible ways to recover the heat losses were introduced and discussed. Finding results showed that 15.6 % of the total input energy (4 MW) could be recovered [2]. Additionally, various energy efficiency studies have been conducted at industries that consume particularly intensive energy. Liu et al. [3] studied a cement industry in China to determine the prospects renovation and they improved its energy efficiency. Various scenarios that are high-cost, state-of-the-art precalciner kilns, moderate-cost advanced vertical kilns and low-cost vertical kilns without advanced technology, were considered. They discussed the cost, energy intensities and environmental implications of these scenarios. In another study, an energy-intensive industry in Turkey was investigated [4]. Gutierrez et al. [5] studied the energy and exergy assessments of a lime shaft kiln. In their study, the energy efficiency was found to be higher than the

M. Gürtürk (✉)
Technical Education Faculty, Department of Mechanical Education, Fırat University, 23100 Elazig, Turkey
e-mail: m.gurturk@gmail.com

H.F. Oztop
Technology Faculty, Department of Mechanical Engineering, Fırat University, 23100 Elazig, Turkey
e-mail: hfoztop1@gmail.com

A. Hepbaslı
Faculty of Engineering, Department of Energy Systems Engineering, Yaşar University, 35100 Izmir, Turkey
e-mail: arifhepbasli@gmail.com

Table 28.1 Physical properties of expanded perlite [12]

Colour	White
Melting point	1,300 °C
Specific heat	0.8371 kJ/kg °C
Unit weight	2.2–2.4 g/cm^3
Rough density	30–190 kg/m^3
Heat conductivity	0.039–0.046 W/m °C
Sound insulating	18 db (125 Hz)

exergy efficiency, as 71.6 %. Their results showed that the most irreversible processes took place in the kiln. Çamdali et al. [6] performed energy and exergy analyses of a rotary burner with pre-calcination in cement production. Although the energy efficiency was found to be about 97 %, the exergy efficiency was 64.4 %. Utlu et al. [7] made energy and exergy analyses of a raw mill and raw materials preparation unit in a cement plant in Turkey using the actual operation data. Both energy and exergy efficiencies of the raw mill were investigated for the plant performance analysis and improvement, and were determined to be 84.3 and 25.2 %, respectively. Hepbasli and Ozalp [8] investigated the development of industrial energy efficiency and management studies in Turkey. They reported that the Turkish industrial sector had an annual energy saving potential of approximately 30 % and some efforts towards improving the energy efficiency in the country should be made. Jegla et al. [9] studied on a plant energy saving through efficient retrofit of the furnaces. The furnace retrofit procedure was based on an advanced furnace integration approach using some principles of pinch analysis and considering furnace limitations. This method combined principles of an effective design of both processes and equipment. They applied an efficient methodology for furnaces retrofit, using optimization of both stack temperature and air pre-heating system. They indicated that an advantage of this approach was demonstrated through a case study—retrofit of furnace in petrol hydrogenation refining plant for energy efficiency improvement. Sakamotoa et al. [10] studied on estimating the energy consumption for each process in the Japanese steel industry. Their paper exhibited that the energy consumption was estimated by a statistical process to evaluate the possibility of reducing the energy consumption. The specific energy consumption for each product was estimated and also for crude steel produced from an integrated steel plant route and an electric arc furnace route. The specific energy consumption was also compared. Madlool et al. [11] reviewed energy utilization and savings in cement industries. Their categorization for cement manufacturing included four key processes, namely dry, semi-dry, semi-wet and wet processes. Their study covered energy saving, carbon dioxide emission reductions and various technologies used to improve the energy efficiency in the cement industry. Energy efficiency measures for raw materials preparation, clinker production, products and feedstock changes, general energy efficiency measures, and finish grinding were surveyed. The largest recorded amounts of thermal energy savings, electrical energy savings and emission reductions to date were 3.4 GJ/t, 35 kWh/t and 212.54 kgCO$_2$/t, respectively.

The main objective of this study is to determine energy and exergy efficiencies of a perlite expansion furnace. The physical properties of perlite, data gathering and perlite expansion system will be described first. A thermodynamics analysis of the system considered will be then made. Finally, the results obtained will be presented in this paper.

A Brief Description of the Perlite

Perlite is a vitreous substance that contains 2–6 % water. It has gray, silver gray, dark brown and black colours. Perlite is a lightweight material because it can expand 10–30 times of its volume when heated between 800 and 1,150 °C. Density of perlite decreases as its volume increases. In Turkey, eight billion tons of perlite exist and equal to 70 % of the world reserves. This shows that the perlite is a very important material for Turkish economy, and it can be used as insulator owing to its low heat conductivity [12]. Physical properties of the expanded perlite are shown in Table 28.1. Perlite used in the furnace includes moisture less than 0.5 % and water 5 %.

Energy policy of Turkey is to improve the energy efficiency in buildings and many policies have been implemented in this context. One of these policies is to take some measures towards reducing energy losses in buildings. The insulation materials have been a very important point in insulation applications. Various particle sizes are available to meet specific customer requirements. Various utilization areas of the perlite make the product adaptable to numerous applications in the construction, industrial, chemical, horticultural and petrochemical industries. Applications of the perlite include filler, high and low temperature insulation, concrete aggregate, textured coatings, absorbent and carrier etc. The mentioned perlite
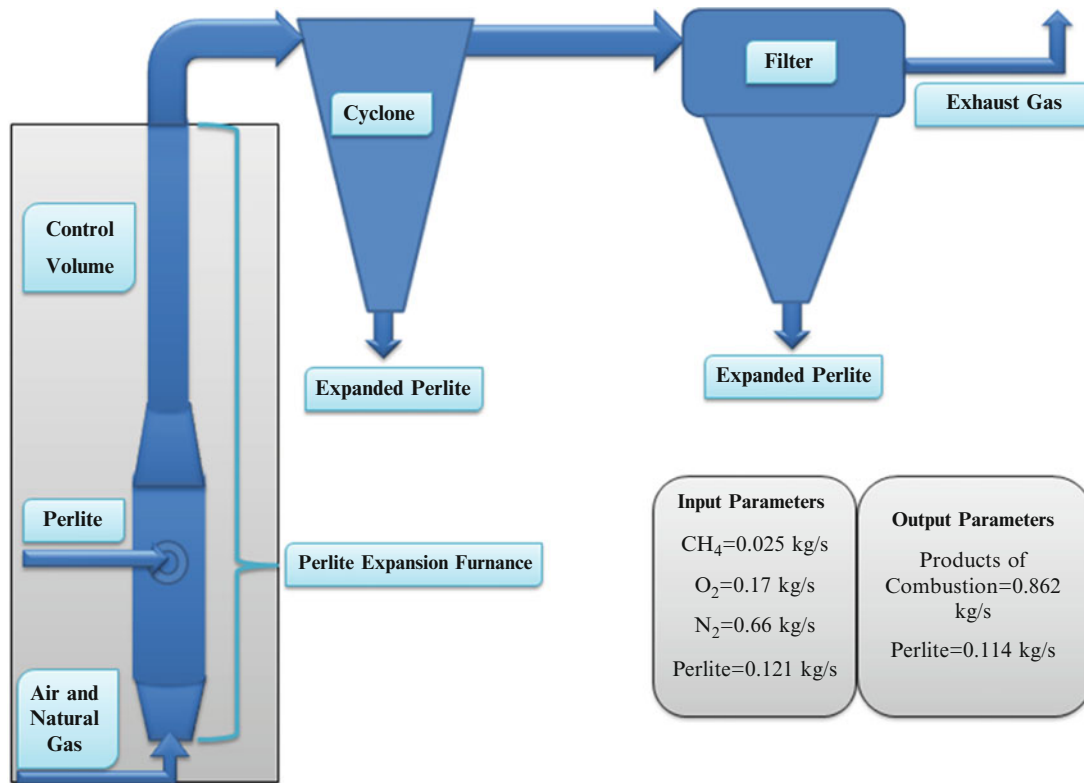
Fig. 28.1 The control volume and whole of the system

expansion furnace is used in the plaster industry for application of the plaster in this paper. The produced perlite can be used in plaster applications, so that it must be white coloured and not hold products of combustion. There are many applications of the plaster, of which one is the decoration of building in architecture. Colour quality and health are the most important parameters in applications of decoration. Therefore, in the production of the perlite and the plaster, natural gas with relatively higher combustion efficiency is used. This energy source is expensive per unit volume compared to many other countries due to its importation. Because perlite producing companies aim at a sustainable production in Turkey, they make some efforts to reduce fuel consumption and protect the environment.

Description of the Perlite Expanded Furnace and Data Gathering

Energy analysis and fuel–air ratio were determined. The gases, air and natural gas are burned in a combustor, and the occurring flame in the combustor rises up to the heating zone. The mass flow rate of the perlite is 0.121 kg/s. Four holes are placed on the cylindrical furnace. The perlite and the flame mix in the heating zone occurring expansion, so the perlite expansion process starts in the heating zone. As shown in Fig. 28.1, the heating zone consists of four parts, which are the upper and lower cones, the cylindrical body and the combustor. The upper and lower cones, which were made from the sheet metal, have the similar dimensions, with a total area of 1.24 m^2. There are four holes on the surface of the cylindrical body and its area is 2.53 m^2, also made from the sheet metal. The chimney of the furnace was considered up to the cyclone, and its length and diameter are 20 and 0.11 m, respectively. The temperature value inside the heating zone of the furnace is higher than 850 °C and the perlite expansion process starts from this section. It continues up to 850 °C in the chimney. The air, the perlite and the natural gas enter the control volume under the environmental conditions (1 atm and 0 °C) and all sections from the combustor to the cyclone are considered as a control volume, as shown in Fig. 28.1. The temperature surface of the furnace was measured as 800 °C and the temperatures of the expanded perlite and the exhaust gas were measured as 600 °C at the outlet of the control volume. This temperature value is 140 °C in the filter system, while the temperature values of the filter and the cyclone systems are not included. The temperature values for the expanded perlite, the exhaust gases, the air and the natural gas were taken from the control unit or the automatization unit of the factory, but the

Component	N_2	O_2	CO_2	H_2O
Mole fraction	0.75	0.1	0.04	0.09

surface temperatures were measured by an infrared thermometer with a range from -50 to $1,000\ ^\circ C$. The surface temperature of the chimney was taken approximately $550\ ^\circ C$. The average daily production capacity is 7 ton of expansion perlite. This value can change depending on the production capacity. Samples are taken from the cyclone tests in the laboratory of the factory to determine the rate of the expanded perlite. There is no insulation anywhere in the control volume, thus the heat losses from the control volume are very high. A flow diagram along with mass balance and control volume is also illustrated in Fig. 28.1.

The furnace is called as a vertical cylindrical furnace or named according to the intended use, which is the perlite expansion furnace. When the perlite expansion process is considered to be as a system, the main components of this system are the combustor, the heating zone, the chimney, the cyclone and the filter group. The combustor, the heating zone, the cones and the chimney were chosen as the control volume and these components of the control volume were studied using energy and exergy analysis. The flow rates of the air and the natural gas are 0.84 and 0.025 kg/s, respectively. In the analysis, the air is assumed that it consists of 79 % nitrogen (N_2) and 21 % oxygen (O_2), and the moisture in the air was neglected in the calculations. The composition of the natural gas includes methane (CH_4), ethane (C_2H_6), propane (C_3H_8), i-butane (C_4H_{10}), n-butane (C_4H_{10}), i-pentane (C_5H_{12}), n-pentane (C_5H_{12}) and hexane (C_6H_{14}), but only methane that consists of 95 % of the mass of the natural gas was considered as the combustor in the combustion equations for determining the products of the combustion. Methane is the principal component of the natural gas. The control volume operates at steady state. Combustion is complete. N_2 is inert. Kinetic and potential energy effects are ignored. For a control volume at steady state, the identity of the matter within the control volume changes continuously, but the total amount of mass remains constant. At steady state, mass balance is given by

$$\sum_i \dot{m}_i = \sum_e \dot{m}_e \qquad (28.1)$$

Air–fuel ratio is determined from Eq. (28.2) for the analysis of the combustion products [13].

$$\frac{\dot{m}_{fuel}}{M_{fuel}} \Big/ \frac{\dot{m}_{air}}{M_{air}} = \lambda \ \ or \ \ \frac{\dot{n}_p}{\dot{n}_{air}} = 1 + \lambda \qquad (28.2)$$

where λ is found as 0.05. The molar analysis of the combustion products is shown in Table 28.2, which was obtained from Eqs. (28.3) and (28.4) [13].

$$0.05 CH_4 + (0.21 O_2 + 0.79 N_2) \Rightarrow (1 + 0.05)[x_{CO_2}CO_2 + x_{H_2O}H_2O + x_{O_2}O_2 + x_{N_2}N_2] \qquad (28.3)$$

$$x_{CO_2} = \frac{\lambda}{1+\lambda}, \ \ x_{H_2O} = \frac{2\lambda}{1+\lambda}, \ \ x_{O_2} = \frac{0.21 - 2\lambda}{1+\lambda}, \ \ x_{N_2} = \frac{0.79}{1+\lambda} \qquad (28.4)$$

After applying the mass balance to the control volume, the energy balance is applied to the control volume. The energy rate balance at steady-state conditions is given by [14].

$$0 = \dot{Q}_l - \dot{W}_{cv} + \sum_i \dot{m}_i \left(h_i + \frac{1}{2}V_i^2 + gz_i\right) - \sum_e \dot{m}_e \left(h_e + \frac{1}{2}V_e^2 + gz_e\right) \qquad (28.5)$$

After rearranging Eq. (28.6), one can write

$$0 = -\dot{Q}_l + \dot{m}_a h_a + \dot{m}_f h_f + \dot{m}_{per} h_{per} - \dot{m}_p h_p - \dot{m}_{E.per} h_{E.per} \qquad (28.6)$$

The enthalpies of the air, the fuel and the products of the combustion are calculated from Eqs. (28.7) to (28.9). The values in these equations can be found in [1, 13, 14].

$$h_a = \left[0.79\frac{h_{N_2}}{M_{N_2}} + 0.21\frac{h_{O_2}}{M_{O_2}}\right] \qquad (28.7)$$

Table 28.3 Enthalpies and entropies of the components entering and leaving the control volume

Descriptions	h (kJ/kg)		s (kJ kg K)	
	273 K	873 K	273 K	873 K
Natural gas	45,000	–	0	–
N_2	280.19	925.57	6.73	7.98
O_2	245.56	840.59	6.31	7.45
CO_2	189.38	813.92	4.77	5.94
H_2O	497.41	1700.52	10.29	12.59
Perlite	226.863	725.463	$\Delta s = 0.96$	

$$h_f = LCV \tag{28.8}$$

Only methane that consists of 95 % of the mass of natural gas was considered as the combustor in the combustion equations for determining the mole fractions of the combustion products. But energy balance included the Lower Heating Value of the natural gas with 45,000 kJ/kg [1].

$$h_p = \left[0.75\frac{h_{N_2}}{M_{N_2}} + 0.1\frac{h_{O_2}}{M_{O_2}} + 0.04\frac{h_{CO_2}}{M_{CO_2}} + 0.09\frac{h_{H_2O}}{M_{H_2O}}\right] \tag{28.9}$$

The enthalpies of the air and the combustion products are determined at 273 and 873 K. The entropy and enthalpy values of O_2, CO_2, H_2O (gas) and N_2 in kJ/kmol are taken from [1]. M_k is the molar mass in kg/kmol. The Entropies, enthalpies and molar masses are used to determine the entropies and enthalpies in kJ/kg. The entropy difference of the perlite is calculated from Eq. (28.10).

$$\Delta s = C_p \ln\left(\frac{T_e}{T_i}\right) \tag{28.10}$$

The values obtained are illustrated in Table 28.3.

Heat losses occur by radiation and natural convection from the control volume while they are calculated from the following relations [1].

$$Gr = \frac{g\beta(T_s - T_\infty)L^3}{v^2} \tag{28.11}$$

$$Ra = GrPr \tag{28.12}$$

$$Nu = \left\{0.6 + \frac{0.387Ra^{1/6}}{\left[1 + (0.559/Pr)^{8/27}\right]}\right\}^2 \tag{28.13}$$

$$H = \frac{kNu}{L} \tag{28.14}$$

$$\dot{Q}_{l,c} = HA(T_s - T_\infty) \tag{28.15}$$

$$\dot{Q}_{l,r} = \varepsilon\sigma A\left(T_s^4 - T_\infty^4\right) \tag{28.16}$$

The total heat loss rate ($\dot{Q}_l$) is determined as 472.83 kW. The value of 99 kW unaccounted in the previous study of the researchers was added to the total heat loss in this study. The results of the energy balance are shown in Table 28.4.

The total energy input rate is determined as 1,396 kW, and the total energy output rate with the expanded perlite and the products of the combustion are determined as 928.3 kW. Energy analysis is concerned with the amount of energy, but does not include the quality of energy and the direction of change of state. Energy analysis is inadequate in this respect. The Second Law of Thermodynamics overcomes with the concepts of entropy and exergy. Exergy analysis of systems

Table 28.4 Energy data for the control volume

Description	Result (kW)	Description	Result (kW)
Perlite	27.45	Expanded perlite	82.70
Air	230.46	Products of combustion	840.44
Natural gas	1,125	Heat loss	472.83
Sensible heat of natural gas	13.65		
Total input	1,396	Total output	1,396

allows determining irreversibility and available energy (exergy) in the system. These analyses produce efficiency of systems in terms of First and Second Law of Thermodynamics. At steady state, the exergy balance is shown in the rate form as follows [14].

$$0 = \sum_j \left(1 - \frac{T_\infty}{T_s}\right)\dot{Q}_l - \dot{W}_{cv} + \dot{E}x_i - \dot{E}x_e - \dot{E}x_D \tag{28.17}$$

Exergy rate of heat energy is calculated by [1].

$$\left(1 - \frac{T_\infty}{T_s}\right)\dot{Q}_l = 321.88\,\text{kW} \tag{28.18}$$

Exergy of any material consists of physical and chemical exergies given by [1].

$$\dot{E}x = \dot{E}x^{ph} + \dot{E}x^{ch} \tag{28.19}$$

Natural gas, air and perlite enter into the control volume under environmental condition ($h_i = h_\infty$, $s_i = s_\infty$), so their physical exergies are zero [13]. Indeed, enthalpy consists of internal energy and flow work, which occurs with the pressure difference, which is neglected for air and natural gas because the pressure difference could not be measured in this study.

$$\dot{E}x_k^{ph} = \dot{m}((h_i - h_\infty) - T_\infty(s_i - s_\infty)) \tag{28.20}$$

$$\dot{E}x_{NG}^{ph} = 0, \dot{E}x_{N_2}^{ph} = 0, \dot{E}x_{O_2}^{ph} = 0, \dot{E}x_{per}^{ph} = 0 \tag{28.21}$$

Exergy enters into the control volume with the chemical exergy of natural gas

$$\dot{E}x_{N_2}^{ch} = 0, \dot{E}x_{O_2}^{ch} = 0 \tag{28.22}$$

The chemical exergy rate of natural gas is determined as 1,170 kW from Eqs. (28.22) and (28.23) [13, 14].

$$\dot{E}x_{NG}^{ch} = \dot{m}_f e_{NG}^{ch} \tag{28.23}$$

$$e_{NG}^{ch} = \varphi(NCV) \tag{28.24}$$

where φ is 1.04 for natural gas [14]. The chemical exergy of every component of combustion products is evaluated using Eq. (28.25) [13].

$$\sum x_k' \overline{e}_k^{ch} + \overline{R}T_\infty \sum x_k' \ln x_k' \tag{28.25}$$

Chemical and physical exergy rates of the control volume are shown in Table 28.5.

Exergy destruction rate is determined as 540.83 kW from the exergy balance rate. This value is very high due to bad working conditions. Exergy destruction is 46.22 % of the total exergy input. Energy efficiency of the control volume is calculated from

$$\eta = \frac{\dot{E}_e}{\dot{E}_i} \tag{28.26}$$

which is found as 66 %. Exergy efficiency of the control volume is obtained from

Table 28.5 Exergy data for the control volume

Description	Exergy rate (kW)				
Substance	$\dot{E}x^{ph}$		$\dot{E}x^{ch}$		
Sate	Inlet	Exit	Inlet	Exit	$\dot{E}x$
Perlite	0	26.96	0	0	26.96
Natural gas	0	–	1,170	–	1,170
N_2	0	197.3	0	1.17	198.47
O_2	0	24.54	0	−0.34	24.2
CO_2	–	10.55	–	0.39	10.94
H_2O	–	45.14	–	1.58	46.72

$$\eta_{ex} = \frac{\dot{E}_{xe}}{\dot{E}x_i} \qquad (28.27)$$

which is determined to be 26 %.

Results and Discussion

Mass and energy balance relations are applied to the control volume for energy auditing, and the results obtained are shown in Table 28.4. Heat losses are very high due to non-insulation. This value is equal to the amount of 37.46 kg of natural gas in 1 h. The system runs 16 h per day and 599.47 kg of natural gas is wasted daily. The maximum energy output from the control volume occurs with the combustion gases. These gases having energy are used for pre-heat application, namely for input parameters, which are perlite, air and natural gas. Assessment of the current situation according to energy efficiency can be evaluated from different perspectives. Perlite producer does not manufacture the perlite expansion furnaces, but the responsibility for the operation of the furnaces belongs to them. This situation shows the inadequacy of the producer according to the energy management. When the furnace manufacture is evaluated based on the obtained results, its technical infrastructure is not sufficient. Exergy rate balance is shown in Table 28.5. Exergy destruction rate is determined from the exergy rate balance as 540.83 kW. Natural gas, air and perlite are inlet parameters for the control volume under environmental conditions ($h_i = h_\infty$, $s_i = s_\infty$). Thus, their physical exergies are calculated as zero. Exergy entering the control volume are due to the chemical exergy of the natural gas. Exergy efficiency value shows that energy losses have very high values. When an insulation application is made on the control volume, it leads to increasing both energy and exergy efficiencies. Energy and exergy analyses show that this case increases the cost of production. The company should consider energy and exergy parameters in order to achieve a sustainable production.

Conclusions

In this paper, we have performed thermodynamics analysis of a perlite expansion furnace. We have derived both energy and exergy relations for the system considered. We have also included some parameters, such as losses, irreversibility and design etc., for determining the energy and exergy efficiencies.

We may list the following concluding remarks:

1. The values for energy and exergy losses are very high due to not applying insulation. Energy and exergy loss rates are 468.34 and 321.88 kW, respectively. These values showed that if the insulation would be made, a significant fuel saving could be achieved, as expected.
2. The energy and exergy efficiencies are found as 66 and 26 %, respectively. Energy efficiency can be increased by pre-heating applications of the primary air, natural gas or perlite. Energy and exergy losses must be prevented by insulation applications. Additionally, a good controlling strategy should be applied to the system.
3. Exergy analysis shows that exergy destruction rate is determined as 540.83 kW, corresponding to 46.22 % of the total exergy input. The exergy destruction is reduced by increasing the energy and exergy efficiencies.

Nomenclature

A	Area (m^2)	$\dot{m}$	Mass flow rate (kg/s)
C_p	Specific heat (kJ/kg K)	Nu	Nusselt number
$\dot{Ex}$	Exergy rate (kW)	Pr	Prandtl number
e	Specific energy (kJ/kg)	$\dot{Q}$	Heat flow rate (kW)
$\dot{E}$	Energy rate (kW)	Ra	Rayleigh number
g	Gravity (m/s^2)	$\overline{R}$	Universal gas constant (kJ/kmol K)
Gr	Grashof number	s	Specific entropy (kJ/kg K)
h	Specific enthalpy (kJ/kmol, kJ/kg)	V	Velocity (m/s)
H	Heat convection coefficient (W/m^2 K)	$\dot{W}$	Work rate (kW)
k	Thermal conductivity (W/m K)	x	Mole fraction
LCV	Low calorific value (kJ/kg)	σ	Stefan–Boltzmann (W/m^2 K^4)
L	Length (m)	ε	Thermal diffusion
M	Molar mass (kg/kmol)		

Greek Letters

λ	Air–fuel ratio	φ	Ratio for industrial fuels
β	Thermal expansion coefficient (1/K)	η	Energy efficiency
υ	Kinematic viscosity (m^2/s)	η_{ex}	Exergy efficiency

Subscripts

a	Air	k	k-th product
cv	Control volume	l	Loss
c	Convection	NG	Natural gas
D	Destruction	per	Perlite
e	Exit	p	Combustion products
e.per	Expanded perlite	r	Radiation
f	Fuel	s	Surface
i	Inlet	∞	Environment

Superscripts

ph	Physical	ch	Chemical

References

1. Cengel YA, Boles MA (2006) Thermodynamics: an engineering approach, 5th edn. McGraw-Hill, New York
2. Engin T, Ari V (2005) Energy auditing and recovery for dry type cement rotary kiln systems—a case study. Energy Convers Manag 46:551–562
3. Liu F, Ross M, Wang S (1995) Energy efficiency of Chine's cement industry. Energy 20:669–681
4. Ates SA, Durakbasa NM (2012) Evaluation of corporate energy management practices of energy intensive in Turkey. Energy 45:81–91
5. Gutierrez AS, Martinez JBC, Vandecasteel C (2013) Energy and exergy assessments of a lime shaft kiln. Appl Thermal Eng 51:273–280
6. Çamdali Ü, Erişen A, Çelen F (2004) Energy and exergy analyses in a rotary burner with pre-calcinations in cement production. Energy Convers Manag 45:3017–3031
7. Utlu Z, Sogut Z, Hepbasli A, Oktay Z (2006) Energy and exergy analyses of a raw mill in a cement production. Appl Thermal Eng 26:2479–2489
8. Hepbasli A, Ozalp N (2003) Development of energy efficiency and management implementation in the Turkish industrial sector. Energy Convers Manag 44:231–249
9. Jegla Z, Stehlik P, Kohoutek J (2000) Plant energy saving through efficient retrofit of furnaces. Appl Thermal Eng 20:1545–1560
10. Sakamotoa Y, Tonookab Y, Yanagisawa Y (1999) Estimation of energy consumption for each process in the Japanese steel industry: a process analysis. Energy Convers Manag 40:1129–1140
11. Madlool NA, Saidur R, Rahim NA, Kamalisarvestani M (2013) An overview of energy savings measures for cement industries. Renew Sustain Energy Rev 19:18–29
12. Topçu IB, Işıkdağ B (2007) Manufacture of high heat conductivity resistant clay bricks containing perlite. Build Environ 42:3540–3546
13. Bejan A, Tsatsaronis G, Moran M (1996) Thermal design and optimization. Wiley, New York
14. Kotas TJ (1995) The exergy method of thermal plant analysis. Krieger Publishing, Malabar

Hüseyin Utku Helvacı and Gülden Gökçen Akkurt

Abstract

Renewable energy sources such as geothermal energy can be used in drying processes as a heat source due to the high energy costs of fossil fuels.

In this study, geothermal cabinet type dryer was constructed and situated in Balcova-Narlidere Geothermal Field, Turkey where the clean city water of district heating system is used as an energy source for the dryer. The dryer was tested on site for drying of olive leaves and energy and exergy analyses of the drying process conducted under two cases: Case 1. Exhaust air was rejected to the environment. Case 2. A portion of exhaust air was re-circulated. Energy Utilization Ratio (EUR) was determined as 7.96 for Case 1 and 50.36 for Case 2. The highest rate of exergy destruction occurred in the fan, followed by heat exchanger and the dryer, accounting for 0.2913, 0.05663 and 0.0115 kW, respectively. Exergetic efficiency of the drying chamber was calculated as 89.66 %. Re-circulating the exhaust air decreased the exergy value at the outlet of the dryer from 0.1013 to 0.08104 kW, indicating that re-using the air increases the performance of the dyer.

Keywords

Drying • Geothermal energy • Olive leaves • Energy analysis • Exergy analysis

Introduction

Herbal, medicinal and aromatic plants have been widely used for preventing and treating specific ailments and diseases, which provide the raw material for the food, cosmetic and pharmaceutical industries to produce spice, essential oils and drugs [1]. Olive leaves have beneficial effects on human metabolism such as combating fevers and other diseases which are attributed to the phenolic compounds structure [2, 3]. Drying of olive leaves is the most important process prior to consumption and extraction by reducing moisture content and avoiding the interference of water to the process [4, 5]. Although conventional drying methods such as open air sun drying are still the most common method in the world, it is not suitable for drying of herbs and spices due to contamination with dust, soil and insects. Furthermore, unmanageable drying parameters such as temperature and velocity cause over-drying results in loss of quality of dried product. Therefore, the drying process should be undertaken in closed and controlled environment such as hot air dying in a tunnel or cabinet dryer. An improvement in the quality of dried product and decrease in time necessitates better technical drying process which results in a huge amount of thermal and electrical energy use. Thus, the use of renewable energy sources such as solar and

H.U. Helvacı (✉) • G.G. Akkurt
Energy Engineering Programme, Izmir Institute of Technology, 35430 Gulbahce Koyu, Urla-Izmir, Turkey
e-mail: huseyinhelvaci@iyte.edu.tr; guldengokcen@iyte.edu.tr

geothermal energy plays an important role in the utilization of controlled conventional drying methods [6]. The daily and seasonal changes of solar intensity in limited time that sun light is available during the day make the solar drying process intermittent. On the other hand, geothermal fluids flow at constant flowrate throughout the year which are considered as continuous resources. In drying applications, geothermal fluids can be used indirectly by a heat exchanger or heat pumps.

Numerous studies were conducted on drying where the geothermal energy was used as a heat source of the dryer. Andiritsos et al. [7] investigated a tomato drying system in Greece where the geothermal fluid enters the water–air heat exchanger to heat the drying air. Also, they discussed the possibilities of using geothermal energy for drying traditional agricultural products in the Aegean Islands. As a result of this study, such a geothermal drying unit seemed to be quite flexible regarding the product to be dried and low-temperature geothermal resources can be used efficiently to dry many agricultural products. Kumoro and Kristano [8] conducted a research on drying of tobacco leaves using geothermal steam and the effect of the steam velocity on the drying rate of tobacco leaves. Results showed that the increase of steam flow rate can improve the drying performance. Hirunlabh et al. [9] designed an industrial dryer and obtained the appropriate drying conditions and conducted cost analysis using geothermal hot water from the geothermal power plant in Thailand. Sumotarto [10] investigated a simulation study of beans and grains drying by a geothermal dryer which would be implemented and technically feasible in Kamojang geothermal field, Indonesia.

Thermodynamic analysis, mainly exergy analysis, plays an important role for system design, analysis and optimization of thermal systems [11]. Since the maximum moisture removal for desired final conditions of dried product is the main objective with the use of minimum amount of energy in drying industry, both quantity and quality of energy should be considered throughout the drying process. In other words, energy and exergy analysis of drying system should be conducted by using the first and second laws of thermodynamics [12]. Although several studies have been conducted on energy and exergy analysis of solar drying systems [13–15] very few studies have been undertaken on energy and exergy analysis of geothermal ones which were based on the geothermal heat pump drying [16, 17].

In this study, a cabinet type geothermal drier where geothermal fluid is introduced indirectly by a heat exchanger was constructed and situated in Balcova-Narlidere Geothermal Field (BNGF), Turkey. Temperature, relative humidity and velocity data of dried air are measured and evaluated the performance of the geothermal drying system by energy and exergy analysis.

Balcova-Narlidere Geothermal Field

BNGF is located 7 km west from the Izmir City Centre and 1 km south from the Izmir-Cesme highway. The Field feeds the largest district heating application in Turkey with a heating capacity of 159 MW$_t$, including 2,470,000 m^2 heating capacity and 15,660 subscribers. The system is operated by 14 heat centres and two pump stations. The geothermal fluid gathered from the 13 production wells first mixed in the mixing chamber in order to bring the temperature of mixture from 120 °C down to 99 °C. Then, the fluid is transmitted to the heat exchangers where the heat is transferred to the clean city water [18]. Figure 29.1 provides a schematic diagram for the Balcova-Narlidere District Heating System (BNDHS) (Celen Ender, May 6, 2012, personal communication).

The dryer was placed in Yenikale Heat Centre which is one of the heat centres of BNDHS. A schematic diagram of the Yenikale Heat Centre and the connection of the dryer to the circulation water line were shown in Fig. 29.2. Heat centres are the stations where geothermal fluid (1) transfers its heat by primary plate type heat exchangers (3), to the clean city water (4) which circulates through the city and provides heat to the buildings. In Yenikale Heat Centre, the clean city water returns to the heat exchanger (5) at a temperature of 62–65 °C where the dryer heat input is supplied (6). Since geothermal fluid temperature in the field (120 °C) is much higher than the temperatures for the dryer (40–60 °C), circulation water from district heating system was decided to be used.
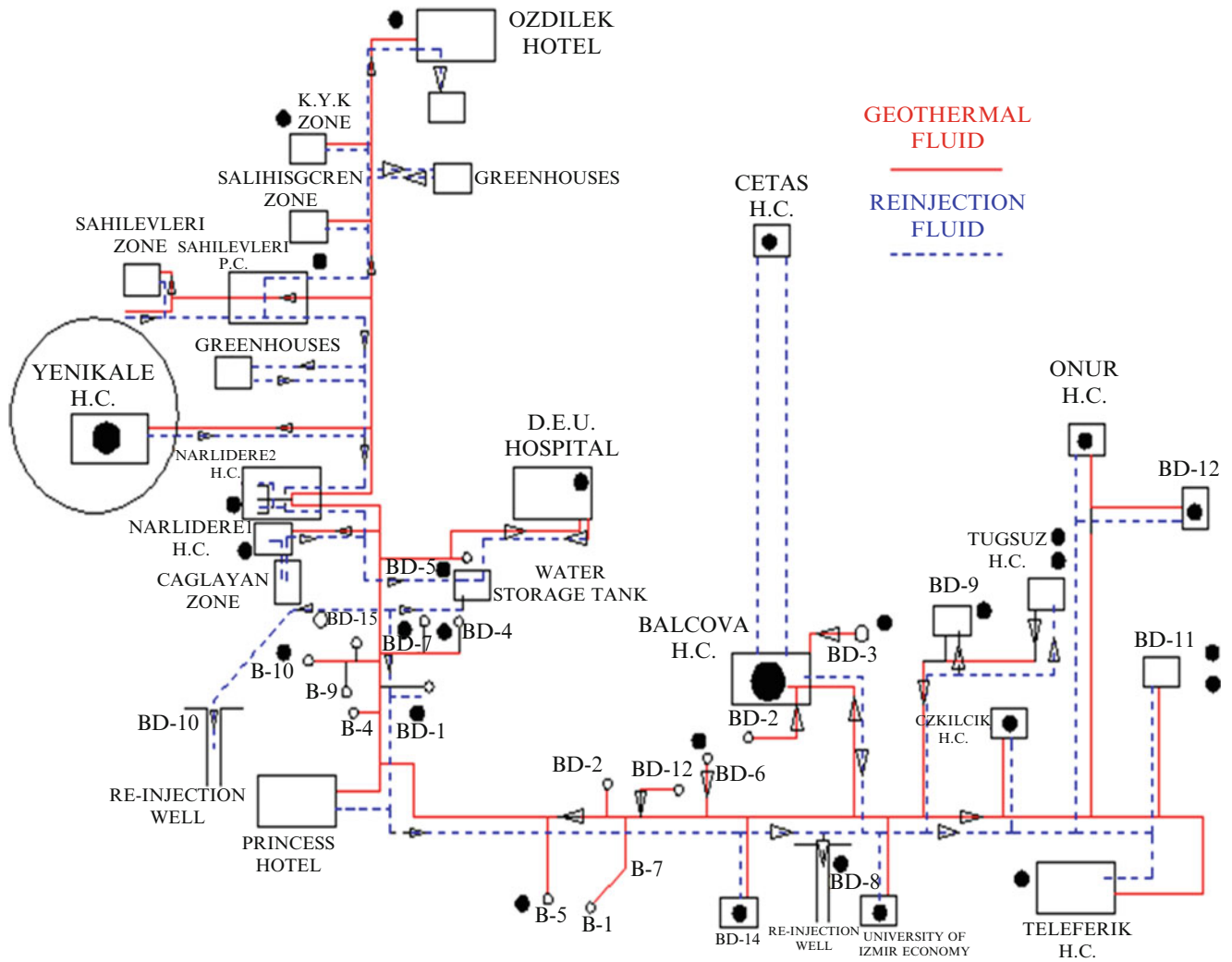
Fig. 29.1 A schematic diagram of Balcova-Narlidere geothermal district heating system (Celen Ender, May 6, 2012, personal communication)

(1) Geothermal fluid inlet
(2) Geothermal fluid outlet
(3) Heat exchanger of the heat centre
(4) Zone 1-2 circulation water inlet
(5) Zone 1-2 circulation water outlet
(6) Heat exchanger of dryer
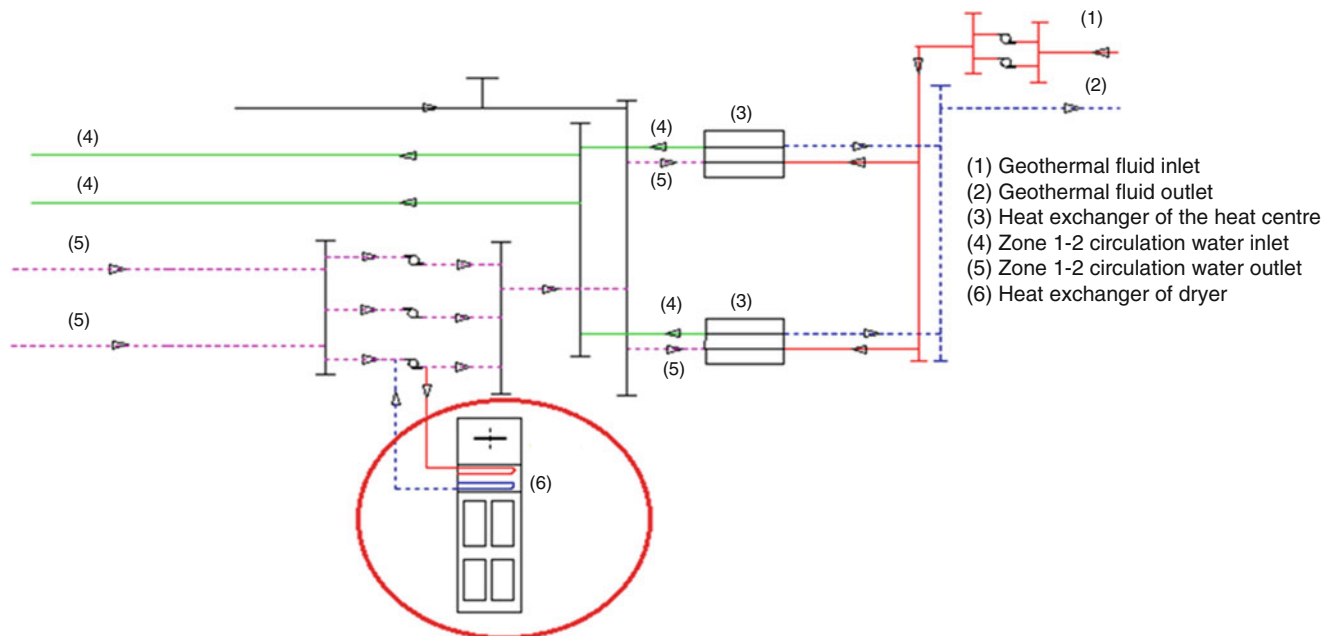
Fig. 29.2 A location of the geothermal dryer in Yenikale Heat Centre

Materials and Methods

The geothermal dryer (Figs. 29.3 and 29.4) is a cabinet type dryer, consists of three sections; fan unit, heating unit and drying tunnel sections. A schematic diagram of the dryer was given in Fig. 29.5.

As seen in Fig. 29.5, drying air is regulated by a centrifugal fan (1) which draws the fresh air into the dryer. The fresh air either is mixed with re-circulated air or directly enters to the water-to-air heat exchanger (2). The heated air leaving the water-to-air heat exchanger reaches the drying chamber (4) which was made of approximately 1″ plywood. The inner surface of the dryer was insulated by fibre glass and covered with an aluminium sheet in order to reduce heat losses. The dryer contains six trays (3) which are 600 mm in length and 500 mm in width, and there is an air re-circulating unit (5) to recover the exhaust air (Fig. 29.4). The clean water returning to the primary heat exchanger in Yenikale Heat Center is directed to the heat exchanger of the drier (Fig. 29.2) as a heat source. During the experiments, temperature [ambient (12), tray inlet (10), tray exit (11)], relative humidity [ambient (12), tray inlet (10), tray exit (11)] and velocity [tray inlet (9)] of drying air were measured and recorded by a datalogger.

Drying experiments were conducted in April, 2012 with Olive leaves (Oleaeuropaea L.) which were collected from the olive trees in the Izmir Institute of Technology Campus Area, Urla-Izmir-Turkey. The olive leaves were stored for 3 days in the air proof plastic bags at 4 °C, then were spread onto the trays as a thin layer. Approximately a mass of 150 g fresh olive
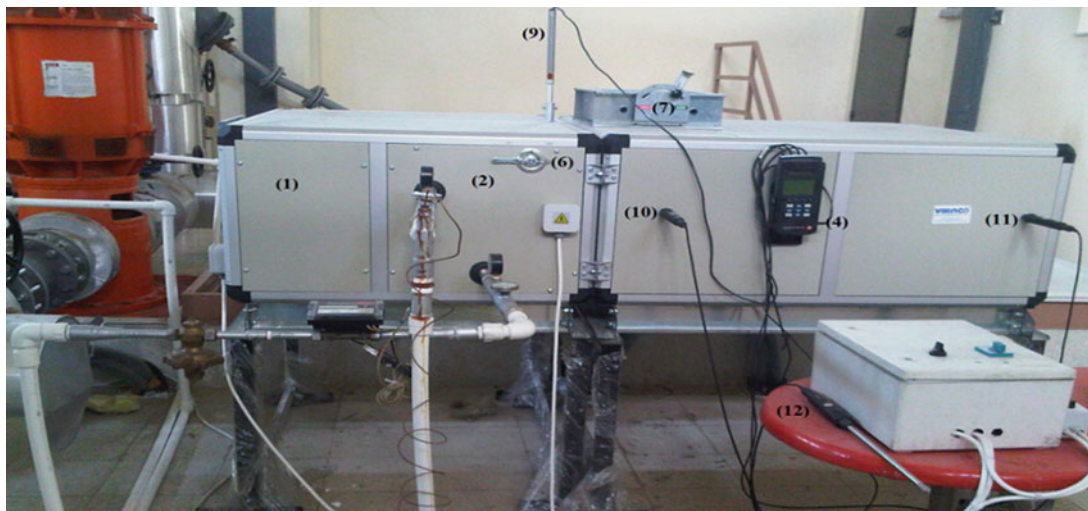
Fig. 29.3 A view of geothermal dryer

Fig. 29.4 A view of drying trays

(1) Fan, (2) Heat exchanger, (3) Trays, (4) Drying chamber, (5) Recirculation unit, (6) Discharger flap
(7) Chimney, (8) Door, (9) Velocity anemometer, (10) - (11) - (12) Thermocouples
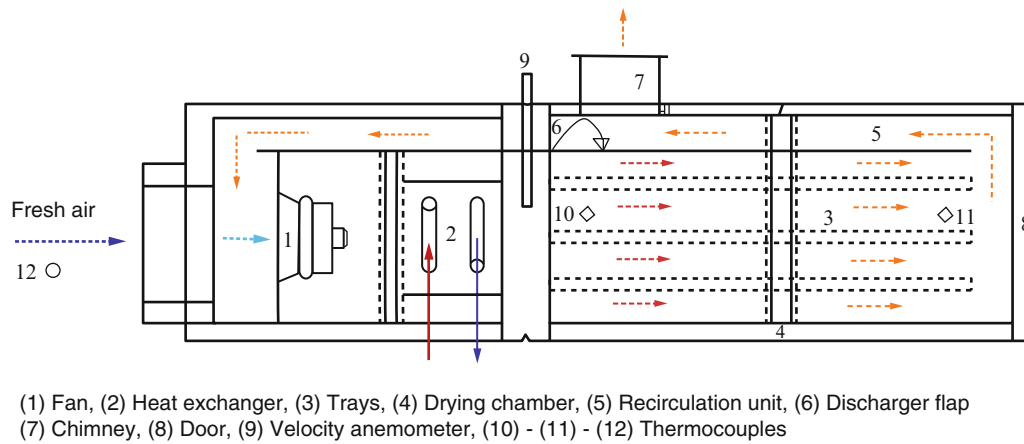
Fig. 29.5 Schematic diagram of the geothermal dryer

leaves was used for each drying experiment. The leaves were dried until the drying rate reached zero when the moisture content of the leaves was about 4–6 % (w-b). To determine the change in weight, a digital weighing apparatus (± 0.01 g) was used during the experiments.

Analysis

Using the measured temperature, relative humidity and velocity data at tray inlet, outlet and the environment, energy and exergy analysis were conducted for two cases:
- Case 1: without air re-circulation
- Case 2: with air re-circulation

Energy Analysis

Drying process was considered as a steady-state, steady-flow process in the analysis of mass (air, water) and energy balance (Figs. 29.6 and 29.7). General equations of mass conservation of drying air for drying chamber and mass conservation of moisture are given in Eqs. (29.1) and (29.2).

$$\dot{m}_{da,env} = \dot{m}_{air,(1)} \tag{29.1}$$

$$\dot{m}_{da,env} \times h_{da,env} = \dot{m}_{air,(1)} \times h_{air,(1)} \tag{29.2}$$

Equations (29.3)–(29.5) are applied to compute the mass and energy balance [15, 19].

$$\dot{m}_{da} = \dot{m}_{da,env} + \dot{m}_{re,air} \tag{29.3}$$

$$\dot{m}_{da,env} \times (1 - r) + \dot{m}_{rec,air} \times (r) = \dot{m}_{air,(1)} \tag{29.4}$$

$$\dot{m}_{da,env} \times h_{da,env} \times (1 - r) + \dot{m}_{re,air} \times h_{re,air} \times (r) = \dot{m}_{air,(1)} \times h_{air,(1)} \tag{29.5}$$

Mass and energy balance equations are applied to each component of the dryer.

Fan
Equations (29.6)–(29.8) was used to compute mass and energy balance for the fan.

$$\dot{m}_{air,(1)} = \dot{m}_{air,(2)} = \dot{m}_{da} \tag{29.6}$$

Fig. 29.6 Schematic illustration of drying system (without air re-circulation)
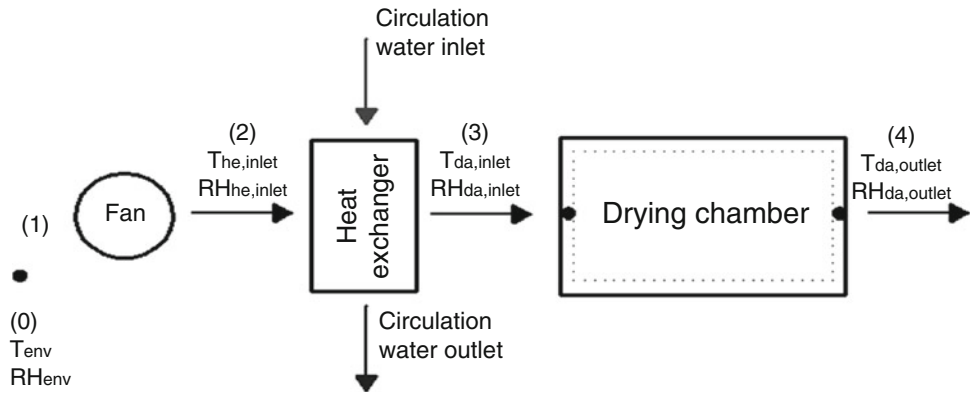
Fig. 29.7 Schematic illustration of drying system (with air re-circulation)
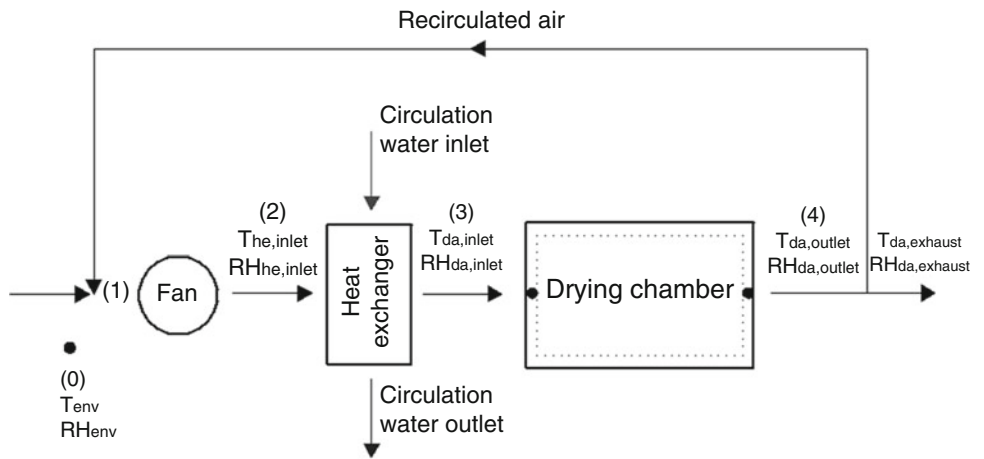
$$\dot{Q} - \dot{W} = \sum (\dot{m}_{da})_{in} \left(h_{out} + \frac{Vout^2}{2} \right) - \sum (\dot{m}_{da})_{out} \left(h_{out} + \frac{Vin^2}{2} \right) \tag{29.7}$$

$$\dot{W}_{fan} = \dot{m}_{air} \times \left(h_2 - h_1 + \frac{v_{exit}^2}{2} \right) \tag{29.8}$$

Heat Exchanger

For the water site of the heat exchanger Eqs. (29.9) and (29.10), for the air site of the heat exchanger Eqs. (29.11) and (29.12) were applied.

(a) Water

$$\dot{m}_{water,in} = \dot{m}_{water,out} \tag{29.9}$$

$$\dot{Q}_{water,in} = \dot{m}_{water} \times (h_{water,in} - h_{water,out}) \tag{29.10}$$

(b) Air

$$\dot{m}_{air,(2)} = \dot{m}_{air,(3)} = \dot{m}_{da} \tag{29.11}$$

$$\dot{Q}_{air} = \dot{m}_{da} \times (h_3 - h_2) \tag{29.12}$$

Drying Chamber

$$\sum \dot{m}_{da,(3)} = \sum \dot{m}_{da,(4)} = \dot{m}_{da} \tag{29.13}$$

General equation of mass balance of moisture can be expressed as

$$\sum (\dot{m}_{water})_{in} + (\dot{m}_{water})_{product} = \sum (\dot{m}_{water})_{out}$$

or

$$\sum (\omega_{da})_{in} \times \dot{m}_{da,(3)} + (\dot{m}_{water})_{product} = \sum (\omega_{da})_{out} \times \dot{m}_{da,(4)} \tag{29.14}$$

Equation (29.15) is used to transform the relative humidity to humidity ratio of the air at inlet and outlet of the drying chamber.

$$\omega = 0.622 \times \frac{RH\ Psat@T}{P - Psat@T} \tag{29.15}$$

Total mass flow of air required for drying process was calculated by Eq. (29.16).

$$\dot{m}_{da} = \rho_{da} \times V_{da} \times A \tag{29.16}$$

The enthalpy of drying air was obtained by Eq. (29.17).

$$h = \left(C_p\right)_{da} T_{da} + w.h_{sat@T} \tag{29.17}$$

The energy utilization (EU) which can be expressed as the amount of energy employed during moisture removal of the product was calculated using Eq. (29.18).

$$EU = \dot{m}_{da}.\left[h_{da,(3)} - h_{da,(4)}\right] \tag{29.18}$$

The energy utilization ratio (EUR) was defined as the ratio of the energy utilization to the energy given from the heat exchangers of dryer [Eq. (29.19)].

$$EUR = \frac{\dot{m}_{da}(h_{da,3} - h_{da,4})}{\dot{m}_{da}(h_3 - h_2)} \times 100 \tag{29.19}$$

Exergy Analysis

Total exergy of inlet, outlet and losses through the system components were determined in the scope of the second law analysis of thermodynamics [12, 19]. The exergy values are calculated by using the characteristics of the working fluid from an energy balance [20].

The specific exergy can be determined by Eq. (29.20).

$$\psi = (h - h_0) - T_0 \times (s - s_0) \tag{29.20}$$

Exergy rate is stated by Eq. (29.21).

$$\dot{E}x = \dot{m}\psi$$

or

$$\dot{E}x = \dot{m}_{da} C_{pda} \left[(T - T_0) - T_0 \ln \frac{T}{T_0}\right] \tag{29.21}$$

The dead state temperature (T_0) was taken as the measured environment temperature (T_{env}). Exergy destructions as well as exergetic efficiencies were obtained by exergy balances for each component [Eqs. (29.22), (29.24), (29.25), and (29.27)].

Exergetic efficiency can be defined as the ratio of exergy loss (exergy inflow–exergy outflow) to exergy inflow to the drying chamber. Equations (29.23), (29.26) and (29.28) were applied to determine exergetic efficiencies of each component.

Fan

$$Ex'_{dest,fan} = \dot{W}_{fan} + \dot{m}_{da} \times (\psi_2 - \psi_1) \tag{29.22}$$

$$\varepsilon_{fan} = \frac{\dot{m}_{da} \times (\psi_2 - \psi_1)}{\dot{W}_{fan}} \tag{29.23}$$

Heat Exchanger
(a) Water

$$Ex'_{dest,water} = \dot{m}_{water} \times \left(\psi_{water,in} - \psi_{water,out}\right) \tag{29.24}$$

(b) Air

$$Ex'_{dest,air} = \dot{m}_{da} \times (\psi_3 - \psi_2) \tag{29.25}$$

$$\varepsilon_{he} = \frac{\dot{m}_{da} \times (\psi_3 - \psi_2)}{\dot{m}_{water,in} \times \left(\psi_{water,in} - \psi_{water,out}\right)} \tag{29.26}$$

Drying Chamber

$$Ex'_{dest,dc} = \dot{m}_{da} \times (\psi_3 - \psi_4) \tag{29.27}$$

$$\varepsilon_{dc} = \frac{(Exergy\ in - Exergy\ out)}{Exergy\ in}$$

or

$$\varepsilon_{dc} = 1 - \frac{\dot{m}_{da} \times (\psi_3 - \psi_4)}{\dot{m}_{da} \times \psi_3} \tag{29.28}$$

The following assumptions were made for the analysis:
- All the process was taken as a steady-state and steady-flow.
- Heat transfer to the system and work transfer from the system are positive.
- Potential and kinetic energy effects were neglected.
- Air is an ideal gas with constant specific heat.

Results and Discussion

Energy and exergy analysis of the dryer was conducted using measured temperature, velocity and relative humidity data (Table 29.1). Mass flow rates, enthalpy values and temperature of the air at inlet of the heat exchanger and energy and exergy rates were calculated using measured data and listed in Table 29.1. The reference-dead state conditions were determined as $T_0 = T_{env}$, $RH_0 = RH_{env}$, $P_0 = 101.325$ kPa. The thermodynamic properties of air and water were obtained by using Engineering Equation Solver [21] software.

Table 29.2 presents exergy destruction and exergetic efficiencies for each component of the drying system, and EU and EUR of the drier are presented in Table 29.2.

Table 29.1 Energy and exergy analysis data

State no	Fluid	T (°C)	RH (%)	h (kJ/kg)	s (kJ/kg K)	$\dot{m}$ (kg/s)	Specific exergy (kJ/kg)	Exergy rate (kW)	Energy rate (kW)
0	Air/dead state	22	42	39.67	5.75	–	–	–	–
1	Air/fan inlet	37	19.4	56.79	5.8	0.20	0.3175	0.066	11.8
2	Air/fan outlet-HE inlet	37.9	18.5	57.67	5.81	0.20	0.3615	0.076	11.97
3	Air/HE outlet-dryer inlet	40.9	15.7	60.81	5.82	0.21	0.538	0.1128	12.78
4	Air/dryeroutlet	39.8	16.4	59.23	5.815	0.21	0.4823	0.1013	12.43
W_{in}	Water/HE inlet	62	–	259.6	0.8562	0.03	63.11	2.272	9.34
W_{out}	Water/HE outlet	56.5	–	236.5	0.7866	0.03	60.51	2.178	8.52

Table 29.2 Exergy destruction, exergetic efficiency, EU and EUR data of the dryer

Component	Rate of exergy destruction, $Ex_{destruction}$ (kW)	Exergetic efficiency, ε (%)
Fan	0.2913	3.08
Heat exchanger	0.05663	39.52
Dryer	0.0115	89.66

EU = 0.3316 kW
EUR (Case 1) = 7.96 %
EUR (Case 2) = 50.36 %

Fig. 29.8 The EUR values obtained from the experiments. (**a**) Case 1, (**b**) Case 2
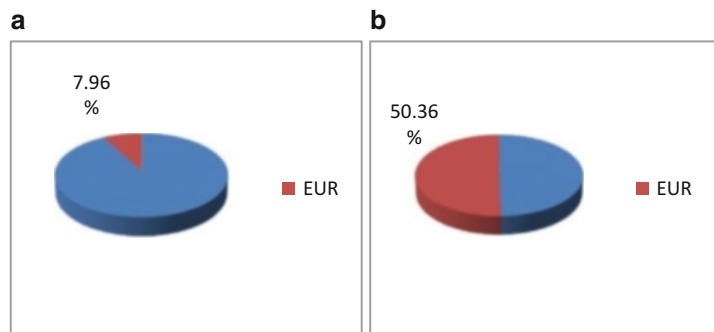
Fig. 29.9 Exergy destruction values for each component of the drying system
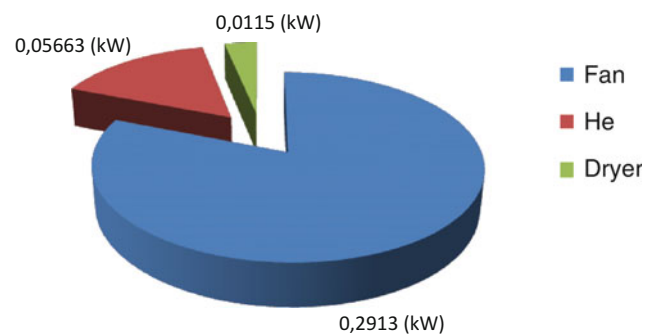
The EU, which indicates the amount of energy employed for the reduction of moisture content of the product, was calculated as 0.3316 kW. EUR values were obtained as 7.96 and 50.36 % for both Case 1 and Case 2, respectively. The EUR indicates the ratio of the energy utilization to the amount of energy given from the heat exchangers of the dryer. The lower EUR values obtained from the experiments that air was not circulated compared to the experiments with air re-circulation (Fig. 29.8). This indicates that re-cycling the exhaust air allows us to recover the energy leaving the dryer which decreases the energy input from the heat exchanger and increases the energy efficiency [22].

It is clear from Fig. 29.9 that the highest rate of exergy destruction occurs in the fan, followed by heat exchanger and the dryer, accounting for 0.2913, 0.05663, 0.0115 kW, respectively. Exergetic efficiency of the drying chamber was calculated as 89.66 % which is in a good agreement with the literature [22, 23]. According to the results, exergy value at the outlet of the dryer was decreased from 0.1013 to 0.08104 kW by re-circulating the exhaust air which still has availability.

Conclusions

Thermodynamic analysis of geothermal drying process of olive leaves in a cabinet type drier, where geothermal fluid was used indirectly by a heat exchanger, was performed in this study. The results of the energy and exergy analysis indicated that the greatest exergy destruction occurred in the fan, followed by the heat exchanger and the dryer. The re-circulation of the exhaust air increased EUR values from 7.96 to 50.36 % and decreased the exergy at the outlet of the dryer by 0.02026 kW, indicating that re-using the air enables us to increase the performance of the dryer. Besides the thermodynamic analysis, an economic analysis should be conducted to exhibit the viability of the re-circulation for commercial drying facilities.

Nomenclature

A	Area (m^2)	$\dot{Q}$	Heat rate (kW)
C_p	Specific heat (kJ/kg K)	RH	Relative humidity (%)
EU	Energy utilization (kW)	r	Re-circulation ratio (%)
EUR	Energy utilization ratio (%)	s	Specific entropy (kJ/kg K)
$\dot{Ex}$	Exergy rate (kW)	T	Temperature (°C)
h	Specific enthalpy (kJ/kg)	V	Velocity (m/s)
$\dot{m}$	Mass flow rate (kg/s)	$\dot{W}$	Work rate (kW)
P	Pressure (kPa)	ρ	Density (kg/m^3)

Greek Letters

ψ	Specific exergy (kJ/kg)	ω	Specific humidity ratio (kg water/kg air)
ε	Exergetic efficiency (%)		

Subscripts

da	Drying air	in	Inlet, inflow
dc	Drying chamber	out	Outlet, outflow
des	Destroyed	re	Re-circulated
env	Environment	sat	Saturated
He	Heat exchanger		

Superscript

0	Dead (reference) state

References

1. Oztekin S, Başçetinçelik A, Soysal Y (1999) Crop drying programme in Turkey. Renew Energy 1:789–794
2. Benavente-García O, Castillo J, Lorente J, Ortuño A, Del Rio JA (2000) Antioxidant activity of phenolics extracted from Oleaeuropaea L. leaves. Food Chem 68 (4):457–462
3. Bouaziz M, Sayadi S (2005) Isolation and evaluation of antioxidants from leaves of a Tunisian cultivar olive tree. Eur J Lipid Sci Technol 107(7–8):497–504
4. Bahloul N, Boudhrioua N, Kouhila M, Kechaou N (2009) Convective solar drying of olive leaves. J Food Process Eng 34(4):1338–1362
5. Soysal Y, Öztekin S (2001) PH—Postharvest Technology: technical and economic performance of a tray dryer for medicinal and aromatic plants. J Agric Eng Res 79(1):73–79
6. Fargali HM, Nafeh AA, Fahmy FH, Hassan MA (2008) Medicinal herb drying using a photovoltaic arrayed a solar thermal system. Solar Energy 82 (12):1154–1160
7. Andritsos N, Dalampakis P, Kolios N (2003) Use of geothermal energy for tomato drying. Geo Heat Cent Q 24(1):9–13
8. Kumoro AC, Kristanto D (2003) Preliminary study on the utilization of geothermal energy for drying of agricultural product. In: Proceedings of the international geothermal conference, September 2003, Reykjavik
9. Hirunlabh J, Thiebratand S, Khedari J (2004) Chili and garlic drying by using waste heat recovery from a geothermal power plant. GHC Bull (September)
10. Sumotarto U (2007) Design of a geothermal energy dryer for beans and grains drying in Kamojang geothermal field, Indonesia. Geo Heat Center Bull 28(1):13–18

11. Dincer I, Sahin AZ (2004) A new model for thermodynamic analysis of a drying process. Int J Heat Mass Transfer 47(4):645–652
12. Akpinar EK, Midilli A, Bicer Y (2006) The first and second law analyses of thermodynamic of pumpkin drying process. J Food Eng 72:320–331
13. Akbulut A, Durmuş A (2010) Energy and exergy analyses of thin layer drying of mulberry in a forced solar dryer. Energy 35(4):1754–1763
14. Chowdhury MMI, Bala BK, Haque MA (2011) Energy and exergy analysis of the solar drying of jackfruit leather. Biosyst Eng 110(2):222–229
15. Midilli A, Kucuk H (2003) Energy and exergy analyses of solar drying process of pistachio. Energy 28(6):539–556
16. Colak N, Kuzgunkaya E, Hepbaşlı A (2008) Exergetic assessment of drying of mint leaves in a heat pump dryer. J Food Process Eng 31(3):281–298
17. Kuzgunkaya EH, Hepbasli A (2007) Exergetic performance assessment of a ground source heat pump drying system. Int J Energy 31:760–777
18. Ozdiler U, Sayık T (2011) Balcova-Narlidere saha isletmesi. In: Jeotermal enerji semineri, Teskon, X. Ulusal Tesisat Mühendisliği Kongresi, Izmir, 13–16 April 2011
19. Cengel Y, Boles MA (2011) Thermodynamics: an engineering approach. McGraw-Hill, New York
20. Szargut J, Morris DR, Steward FR (1988) Exergy analysis of thermal, chemical and metallurgical processes. Hemisphere Publishing Corp, New York
21. Engineering Equation Solver (EES) (2012) Commercial and professional versions. F-Chart Software, Madison
22. Corzo O, Bracho N, Vasquezand A, Pereira A (2008) Energy and exergy analysis of thin layer drying of coroba slices. J Food Eng 86:151–161
23. Erbay Z, İçier F (2010) Energy and exergy analysis on drying of olive leaves (*Oleaeuropaea L.*) in tray drier. J Food Process Eng 34(6):2105–2123

Onur Uludağ and Zehra Özçelik

Abstract

In this study, performances decreasing heat losses and plant costs are compared in different stage HRSG with inlet parameters of under construction power plant. Flue gas that occurred after combustion in gas turbine was in 1–3 stage HRSG, and thermal changings, produced energies, type of equipments, and effects to environment were calculated and compared when energy and exergy analyses are applied using ASPEN Plus simulation program. Result of these calculations and comparisons has reached optimum design criteria, and 3 stage HRSG is the most effective system. Additionally, exergy analysis behind energy analysis has showed that not only the amount of heat but also the quality of heat is calculated and played important role to choose suitable type of equipment. When using these results in another process, it might not be fixed with it but used method and calculations give the optimum conditions. In conclusion, energy production in combined cycle power plant will be more effective and sensitive for environment with specified and evaluated heat recovery systems.

Keywords

Exergy analysis • Combined cycle power plant • Heat recovery steam generator • Apsen plus

Introduction

Today, rising population and developed industry in the world caused highly needed energy resource. Therefore, too many kinds of technology are improved to supply this energy. Especially, eco-friendly renewable energy plants (sun, water, wind) and power plants that have minimum effect to global warming are started to use for energy production. Waste heat and power that produced from power plants is used a certain time to gain high-yield energy. It is clear that heat recovery systems play a very important role for decreasing cost and environmental responsibility. For this reason, different types of systems are designed. And the type of using these systems depends on some different parameters. Producing electricity has been much more effective with combined cycle power plants. The most heat loss in power plants is occurred outlet of gas turbine and it is an unavoided situation.

In this study, performances decreasing heat losses and plant costs are compared in different stage HRSG with inlet parameters of under construction power plant. Ege Elektrik power plant is under construction combined cycle power plant

O. Uludağ (✉)
Ege Gaz A.Ş. Aliağa LNG Terminal, Aliağa, Izmir, Turkey

Faculty of Engineering, Department of Chemical Engineering, Ege University, Bornova, Izmir, Turkey
e-mail: onuruludag81@gmail.com

Z. Özçelik
Faculty of Engineering, Department of Chemical Engineering, Ege University, Bornova, Izmir, Turkey
e-mail: zehra.ozcelik@ege.edu.tr
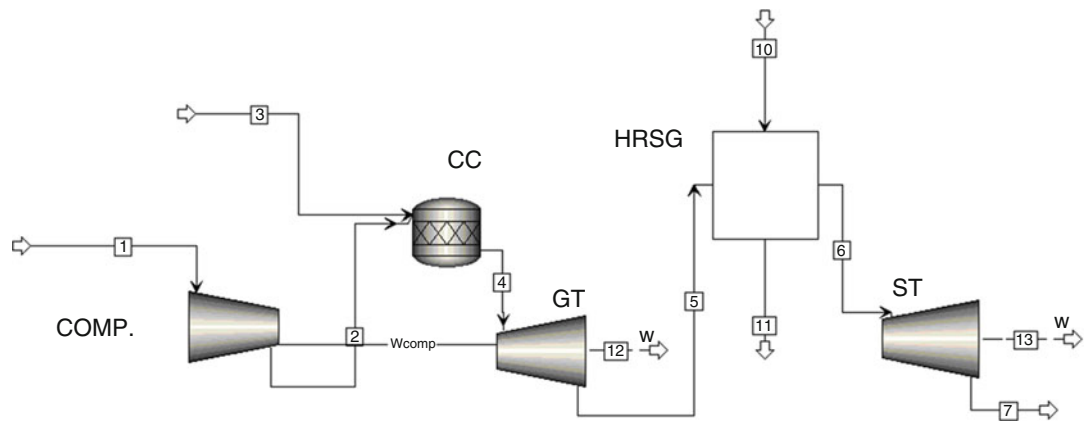
Fig. 30.1 Combined cycle power plant with 1 stage HRSG
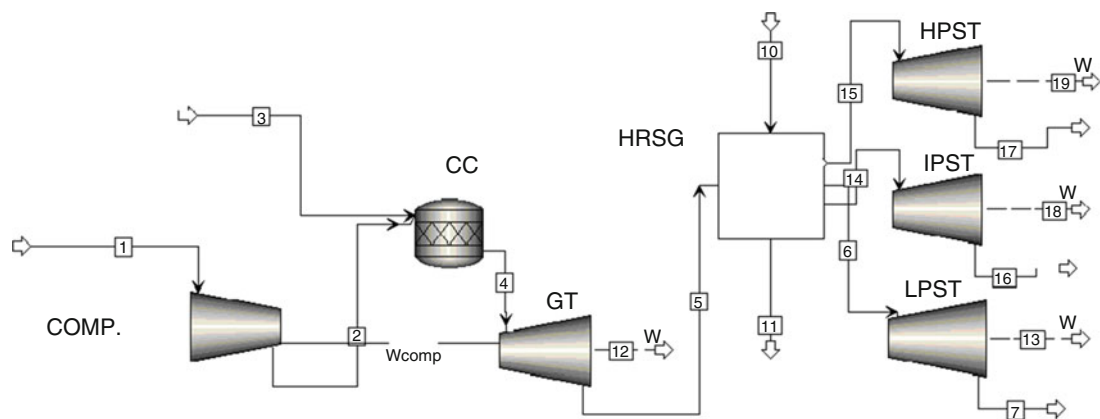
Fig. 30.2 Combined cycle power plant with 3 stage HRSG

that has 1,070 MWe capacity. One thousand seventy mega watt power is collected from two sections that include combustion gas turbine with power 378 and 296 MW each and two steam turbines with power 222 and 174 MW each. The total net production is 9,373,200 MW annually (these values are design criteria and can change during real operation). In this study, 600 MW section is considered. Power plant basic flow sheet is given as illustrated in Figs. 30.1 and 30.2.

The exergy which is the maximum available energy that a system can deliver as work from its initial state to the state of environment (dead state) is a tool of the second law analysis, which gives the quality of the energy differing from the first law analysis techniques, that gives only the quantity of the energy. The exergy concept was introduced to overcome limitations of the energy analysis. So with increasing of the energy demand and reduction in the fossil energy reserves, the best (maximum) use of energy became very important for the humankind. At this point the exergy analysis gives the view for determining the energy loss positions and the chance to improve the efficiency [1–3].

Exergetic Analysis

Exergy Analysis

The exergy which is the maximum available energy that a system can deliver as work from its initial state to the state of environment (dead state) is a tool of the second law analysis which, gives the quality of the energy differing from the first law analysis techniques, that gives only the quantity of the energy. So with increasing of the energy demand and reduction in the

Table 30.1 One stage HRSG exergy destructions

Exergy destruction	MW	%
Compressor	37.75	0.28
CC	10,093.33	74.56
GT	2,542.78	18.78
HRSG	439.00	3.24
ST	424.46	3.14
Total	13,537.32	100.00

fossil energy reserves, the best (maximum) use of energy became very important for the humankind. At this point the exergy analysis gives the wiev for the determining the energy loss positions and the chance to improve the efficiency [4, 5].

In the analysis the kinetic, potential, magnetic and nuclear exergies are neglected so that the exergy is reduced to the chemical and physical components only [1, 3, 6, 7].

$$E = E_{ph} + E_{ch} \tag{30.1}$$

A steady-state exergy balance includes;

$$E_i = E_o + W + E_d \tag{30.2}$$

E_i denotes inlet exergy to the system, E_o denotes the outlet exergy, W is the work interaction between system and environment and Ed is the exergy destructed.

With these techniques the exergy analysis is applied to the system. The reference state is chosen as 25 °C and 1 atm with basic atmospheric components.

Ege Elektirik power plant is a typical natural gas combined power plant. One thousand seventy mega watt power is collected from two combustion gas turbine with power 378 and 296 MW each and two steam turbine with power 222 and 174 MW each. The total net production is 9,373,200 MW annually.

The power plant consists of two combined cycle power blocks which are identical to each other. These power blocks use the same principle and some units are used in common. We will consider in this paper the exergy analysis of 600 MW part of plant. We will compare and discuss different HRSG configuration results.

Compressor: Air entering the compressor in atmospheric conditions. The following equations are used for exergy analysis and efficiency:

$$E_1 = E_3 + W_{comp} + E_d \tag{30.3}$$

$$\varepsilon = (E_1 - E_3)/W_{comp} \tag{30.4}$$

Combustion Chamber: It is assumed that there is a complete burning in the combustion chamber and natural gas component is 100 % methane. The following equations are used to calculate the destructed exergy in combustion chamber and the efficiency.

$$E_2 + E_3 = E_4 + E_d \tag{30.5}$$

$$\varepsilon = E_4/(E_3 + E_2) \tag{30.6}$$

Turbine: There is expansion to 1,085 bar in turbine and the outlet gas temperature is 1,001.5 K.

$$E_5 = E_4 + W + E_d \tag{30.7}$$

$$\varepsilon = W/(E_5 - E_4) \tag{30.8}$$

Heat Recovery Steam Generator: In this paper we use two different HRSG type to compare exergy destruction and yield. One of these is 1 stage HRSG and the other one is 3 stage HRSG. The results are given in Tables 30.1 and 30.2.

Table 30.2 Three stage HRSG exergy destructions

Exergy destruction	MW	%
Compressor	37.75	0.28
CC	10,093.33	73.52
GT	2,542.78	18.52
HRSG	548.41	3.99
HPTURBINE	149.84	1.09
IPTURBINE	194.33	1.42
LPTURBINE	161.87	1.18
Total	13,728.31	100.00

Table 30.3 One stage HRSG stream entering values

Stream	Molar flow rate (kmol/s)	T (K)	P (atm)
Air inlet	44.44	298.15	1.00
Natural gas	4.17	298.15	42.00
GT out	48.61	1,001.05	1.09
ST inlet	16.67	850.00	83.89

Table 30.4 Three stage HRSG stream entering values

Stream	Molar flow rate (kmol/s)	T (K)	P (atm)
Air inlet	44.44	298.15	1.00
Natural gas	4.17	298.15	42.00
GT out	48.61	1,001.05	1.09
HPST inlet	10.03	808.00	119.61
IPST inlet	12.42	748.67	25.36
LPST inlet	17.58	564.00	5.00

$$E_5 + E_{10} = E_6 + E_{11} + E_d \tag{30.9}$$

$$\varepsilon = (E_6 - E_{10})/(E_5 - E_{11}) \tag{30.10}$$

Steam Turbines: The temperature, pressure and flow rate values of stream entering turbines are given in Tables 30.3 and 30.4.

Result of Exergy Analysis

The exergy efficiency values and energy production of combined system components are given in Tables 30.5 and 30.6. The mole fraction of stack gas is calculated as 1.7 % O_2, 70.8 % N_2, 8.6 % CO_2, 18.8 % H_2O with complete burning and the gases are assumed to be ideal during the calculations. It is assumed that there is no vertical temperature difference in the HRSG.

As it is seen the largest exergy destruction occurs in the combustion turbine. So by the exergy analysis, it is seen that the exergy destruction occurs at the combustion chamber with 74 %, the GT with 19 % and from the HRSG with 4 %. So the efficiency of the power plant mostly depends on the efficiency of these equipments and so any improvement on these equipments will increase the overall efficiency of the plant noteworthy. Also chimney temperature plays important role to determine using energy efficiently. One stage HRSG chimney temperature is about 120 °C and 3 stage HRSG chimney temperature is about 100 °C.

Table 30.5 Exergetic efficiency and energy production of 1 stage HRSG

Unit	ε (%)	Energy production (MW)
Compressor	91.15	−417.35
GT	93.51	791.30
ST	85.90	169.22
HRSG	45.33	
	Total	543.17

Table 30.6 Exergetic efficiency and energy production of 3 stage HRSG

Unit	ε (%)	Energy production (MW)
Compressor	91.15	−417.35
GT	93.51	791.30
HPT	93.68	69.79
IPT	93.29	90.07
LPT	97.76	79.06
HRSG	69.47	
	Total	612.87

Conclusions

As a result, the exergy values of the streams that belong to the equipments of the combined cycle, the exergy losses and the efficiency values related with each streams and units in the power plant are listed. The highest exergy losses occur in the combustion chambers. The value is in harmony with the literature value and continues as a big problem in power plants. The improvements in this part will result as an effective increase in the overall efficiency. On the other hand when exergy destruction and energy production for two different configurated HRSGs are compared, it can be seen that 3 stage HRSG has much more efficiently energy production and lower exergy destruction than 1 stage HRSG. As an energy production, it can be observed that 3 stage HRSG has higher yield than 1 stage HRSG. Also it can be observed that 3 stage HRSGs chimney temperature is lower than 1 stage HRSGs chimney temperature. According to these results, it can be said that, if under construction power plant has 3 stage HRSG instead of 1 stage HRSG, exergy loss will be minimum and energy production will be maximum in given design criteria.

Nomenclature

E   Exergy (MW)   W   Work (MW)

Greek Letters

ε   Efficiency (%)

Subscripts

i	Inlet	ph	Physical
o	Outlet	ch	Chemical
d	Destructed	comp	Compressor

References

1. Kotas TJ (1985) The exergy method of thermal plant analysis. Anchor Brendon Ltd., Essex
2. Nag PK, De S (1998) Study of thermodynamic performance of an integrated gasification combined cycle power plant. Proc Inst Mech Eng A J Power Energy 212:89–95
3. Szargut J, Morris DR, Steward FR (1988) Exergy analysis of thermal chemical and metallurgical processes. Hemisphere Pub. Corp., New York
4. Huang Y-C, Hung C-I, Chen C-K (2000) Exergy analysis for a combined system of steam-injected gas turbine cogeneration and multiple-effect evaporation. Proc Inst Mech Eng A J Power Energy 214:61–73
5. Kakaras E, Doukelis A, Leithner R, Aronis N (2004) Combined cycle power plant with integrated low temperature heat (LOTHECO). Appl Thermal Eng 24:1677–1686
6. Bejan A, Tsatsaronis G, Moran M (1996) Thermal design and optimization. Wiley-Interscience, New York
7. Cengel YA, Boles MA (2002) Thermodynamics: an engineering approach, 4th edn. McGraw-Hill, New York

Hava Gizem Kandilci and Hanifi Saraç

Abstract

In Turkey, cement producing is one of the most important sectors in terms of energy consuming and costs. Owing to this reason, using energy efficiently and a decline in energy consumption have an importance in this sector.

This study aims to make energy and exergy analysis of a cement factory in Adana and to realize the cost of energy efficiency, by using the actual operational data. According to energy and exergy analysis, the energy efficiency value for the raw mill is obtained to be 69 % in this study, whereas the exergy efficiency value for that is found to be 11 %.

Keywords

Cement • Energy and exergy analysis • Efficiency

Introduction

By the mid 1970s, the growth in energy resource consumption that occurred in each passing year was not a source of general concern. Many researchers concern that unless corrective actions were undertaken, difficulties would be encountered in providing energy for future needs [1].

The energy and mass balances are the fundamental methods of a process analysis. They make the energy analysis possible, and points of the needs to develop the process are the key to optimization and are the main for developing the exergy balance. Analysis of the energy balance results would define the efficiency of energy utilization in particular parts of the process and enable to compare the efficiency and the process parameters with the recently feasible values in the most modern installations. They will also form the importance of the processes requiring consideration, either due to their excessive energy consumption or due to their particularly low efficiency.

The exergy analysis is the modern thermodynamic method used as an advanced tool for engineering process evaluation [2]. The exergy analysis is on the basis of both the first and the second laws of thermodynamics. Both analyses make use of also the material balance for the considered system.

Exergy analysis also brings about a better concept for the influence of thermodynamic phenomena on the process effectiveness, comparison of the priority of different thermodynamic factors, and the determination of the most effective ways of developing the process under consideration [2]. A true concept of exergy and the insights it can provide into the efficiency, environmental impact, and sustainability of energy systems are required for the engineer or scientist working in the area of energy systems and the environment [3, 4].

H.G. Kandilci (✉) • H. Saraç
Chemical Engineering Department, Yıldız Technical University, Davutpaşa, Esenler, İstanbul 34210, Turkey
e-mail: h.gizemkandilci@gmail.com; hsarac@yildiz.edu.tr

Theoretical Analysis

For a general steady-state and steady-flow process, the following balance equations are implemented to detect the work and heat interactions, the rate of exergy decline, the rate of irreversibility, and the energy and exergy efficiencies [5, 6].

The mass balance equation can be expressed in the rate form as

$$\sum \dot{m}_{in} = \sum \dot{m}_{out} \tag{31.1}$$

where $\dot{m}$ is the mass flow rate, and the subscript "in" explains inlet and "out" for outlet.

The general energy balance can be expressed as

$$\sum \dot{E}_{in} = \sum \dot{E}_{out} \tag{31.2}$$

$$\dot{Q} + \sum \dot{E}_{in} = \dot{W} + \sum \dot{E}_{out} \tag{31.3}$$

where $\dot{E}_{in}$ is the rate of net energy transfer in, $\dot{E}_{out}$ is the rate of net energy transfer out by heat, work, and mass, is the rate of net heat input, $\dot{W} = \dot{W}_{net,out} = \dot{W}_{out} - \dot{W}_{in}$ is the rate of net work output.

Presuming no changes in kinetic and potential energies with any heat or work transfers, the energy balance given in Eq. (31.3) can be simplified to flow enthalpies only:

$$\sum \dot{m}_{in} h_{in} = \sum \dot{m}_{out} h_{out} \tag{31.4}$$

where h is the specific enthalpy. The general exergy balance can be expressed in the rate form as

$$\sum \dot{E}x_{in} - \sum \dot{E}x_{out} = \sum \dot{E}x_{dest}$$

or

$$\sum \left(1 - \frac{T_0}{T_k}\right) \dot{Q}_k - \dot{W} + \sum \dot{m}_{in} \psi_{in} - \sum \dot{m}_{out} \psi_{out} = \dot{E}x_{dest} \tag{31.5}$$

with

$$\psi = (h - h_0) - T_0(s - s_0) \tag{31.6}$$

where $\dot{Q}_k$ is the heat transfer rate through the boundary at temperature T_k at location k, $\dot{W}$ is the work rate, ψ is the flow exergy, s is the specific entropy, and the subscript zero shows properties at the dead state of P_0 and T_0.

The exergy destroyed ($\dot{E}x_{dest}$) or the irreversibility ($\dot{I}$) may be expressed as follows:

$$\dot{I} = \dot{E}x_{dest} = T_0 \dot{S}_{gen} \tag{31.7}$$

where $\dot{S}_{gen}$ is the rate of entropy, while the subscript "0" means conditions of the reference environment [7, 8].

Different ways of formulating exergetic efficiency offered in the literature have been given in detail elsewhere [9]. The exergy efficiency explains all exergy input as used exergy, and all exergy output as utilized exergy.

Therefore, the exergy efficiency ε_1 becomes

$$\varepsilon_1 = \frac{\dot{E}x_{out}}{\dot{E}x_{in}}. \tag{31.8}$$

Often, there is a part of the output exergy that is out of use, i.e., an exergy wasted, $\dot{E}x_{waste}$ to the environment. In this case, exergy efficiency may be written as follows [10]:

$$\varepsilon_2 = \frac{\dot{E}x_{out} - \dot{E}x_{waste}}{\dot{E}x_{in}} \tag{31.9}$$

The rational efficiency is defined by Kotas and Cornelissen [6, 9] as the ratio of the desired exergy output to the exergy used, namely

$$\varepsilon_3 = \frac{\dot{E}x_{desired,out}}{\dot{E}x_{used}}.$$
(31.10a)

where $\dot{E}x_{desired,out}$ is all exergy transfer rate from the system, which must be regarded as forming the desired output, plus any by-product that is produced by the system, whereas $\dot{E}x_{used}$ is the required exergy input rate for the process to be performed. The exergy efficiency given in Eq. (31.10a) may also express as follows [11]:

$$\varepsilon_3 = \frac{Desired\ exergic\ effect}{Exergy\ used\ to\ drive\ the\ process} = \frac{Product}{Fuel}.$$
(31.10b)

To define the exergetic efficiency, both a product and a fuel for the system being analyzed are identified. The product stands for the desired result of the system (power, steam, some combination of power and steam, etc.). Accordingly, the definition of the product must be consistent with the purpose of purchasing and using the system. The fuel stands for the resources expended to generate the product and is not necessarily restricted to being an actual fuel such as a natural gas, oil, or coal. Both the product and the fuel are expressed in terms of exergy [12].

Description of Cement Process

The cement industry has an important role in the economy on the basis of its production. During the production of cement, natural resources are used up in large amounts. The most important raw materials for the production of cement are limestone ($CaCO_3$) and clay or calcareous clay in which both components are already naturally mixed. The components are milled and dried with flue gases from the clinker kiln. This section of the process is given in Fig. 31.1.

Depending on the type of cement to be produced, the following products may be added to the dried limestone immediately after: pyrite ash, fly ash from coal fired power plants, sandy clay, and filter ash from the electrostatic precipitator present. The mixture obtained is ground and immediately after fired in a rotary furnace to cement clinkers.
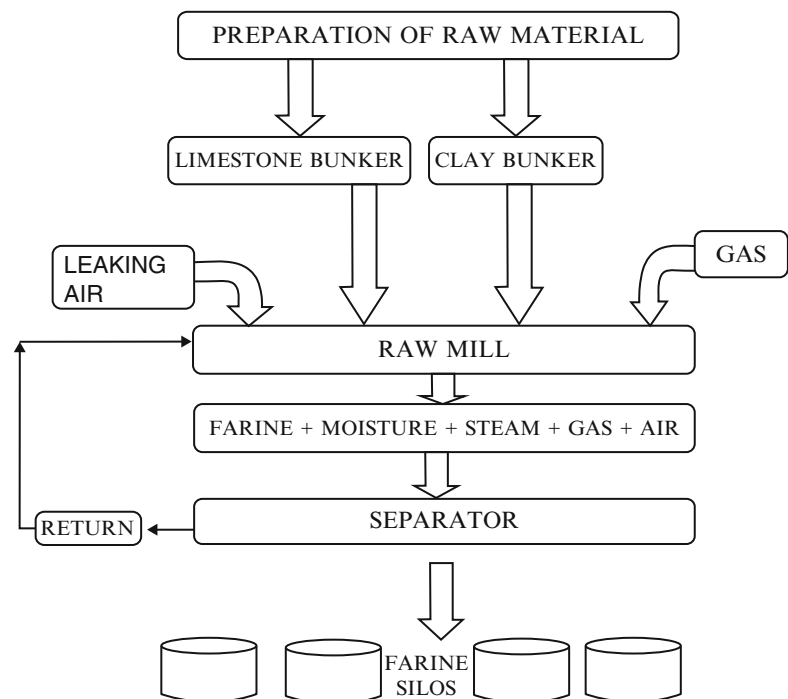
Fig. 31.1 A section of the process
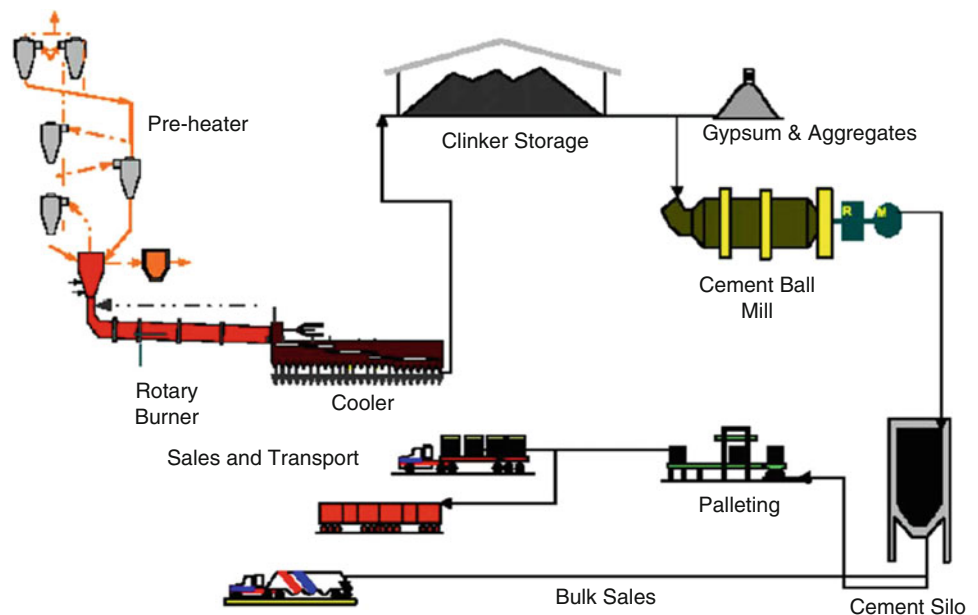
For heating, various fuels and other combustible materials, e.g., coal dust, petroleum coke, etc., are used. Depending on the type of preheating of the material, it is separated from grate and cyclone preheating, whereby the starting materials are preheated to 700–800 °C. The raw materials pass through the rotary furnace towards the flame. In the hottest zone, the material being fired reaches temperatures of around 1,450 °C. After fast cooling with ambient air, the clinkers are milled, together with gypsum, to give ready cement. A part of the process is given in Fig. 31.2 [13, 14].

Results and Discussion

Here, the energy and exergy modeling technique discussed in the previous section is applied to a raw mill in the cement factory studied using actual data.

Energy Analysis of the Raw Mill

In order to analyze the raw mill thermodynamically, the following assumptions are made:

(a) The system is assumed as a steady-state, steady-flow process.
(b) Kinetic and potential energy chances of input and output materials are ignored.
(c) No heat is transferred to the system from the outside.
(d) Electrical energy produces the shaft work in the raw mill.
(e) The change in the ambient temperature is neglected.

Under the above-mentioned conditions and using the actual operational data of the plant, an energy balance is applied to the raw mill. The references for enthalpy, entropy, and input energy are considered for the calculations. The complete energy balance for the system is shown in Table 31.1. Energy flow of the raw mill is also illustrated in Fig. 31.3.

In addition, the enthalpies of the materials going into and leaving the raw mill are given for the chemical components in Table 31.2, while the energy balance is given in Table 31.1. Relatively good consistency between the total heat input and total heat output is obtained.

Table 31.1 Mass and energy balances of the raw mill

	T (K)	m (kg/h)	ν (N m^3/h)	Cp (kJ/kg K)	Cp (kJ/N m^3 K)	Q (kJ/h)
Input material						
Limestone	T_l	m_l		Cp_l		95,962,697.60
Clay	T_c	m_c		Cp_c		14,681,654.40
Return from separator	T_r	m_r		Cp_r		59,887,878.40
Moisture in the limestone	T_{ml}	m_{ml}		Cp_{ml}		42,638,780.80
Moisture in the clay	T_{mc}	m_{mc}		Cp_{mc}		5,814,379.20
Gas	T_g		ν_g		Cp_g	521,342,976.00
Leaking air	T_{la}		ν_{la}		Cp_{la}	78,578,560.00
Dust in the gas	T_d		ν_d		Cp_d	19,272,704.00
Heat from electrical energy						28,591,088.40
					Total	866,770,718.80
Output material						
Farine	T_{out}	m_f		Cp_f		205,474,008.88
Gas	T_{out}		ν_g		Cp_g	247,582,464.00
Leaking air	T_{out}		ν_{la}		Cp_{la}	116,442,355.00
Moisture	T_{out}	m_m		Cp_m		4,050,073.44
Steam	T_{out}	m_s		Cp_s		27,051,787.70
					Total	600,600,689.02
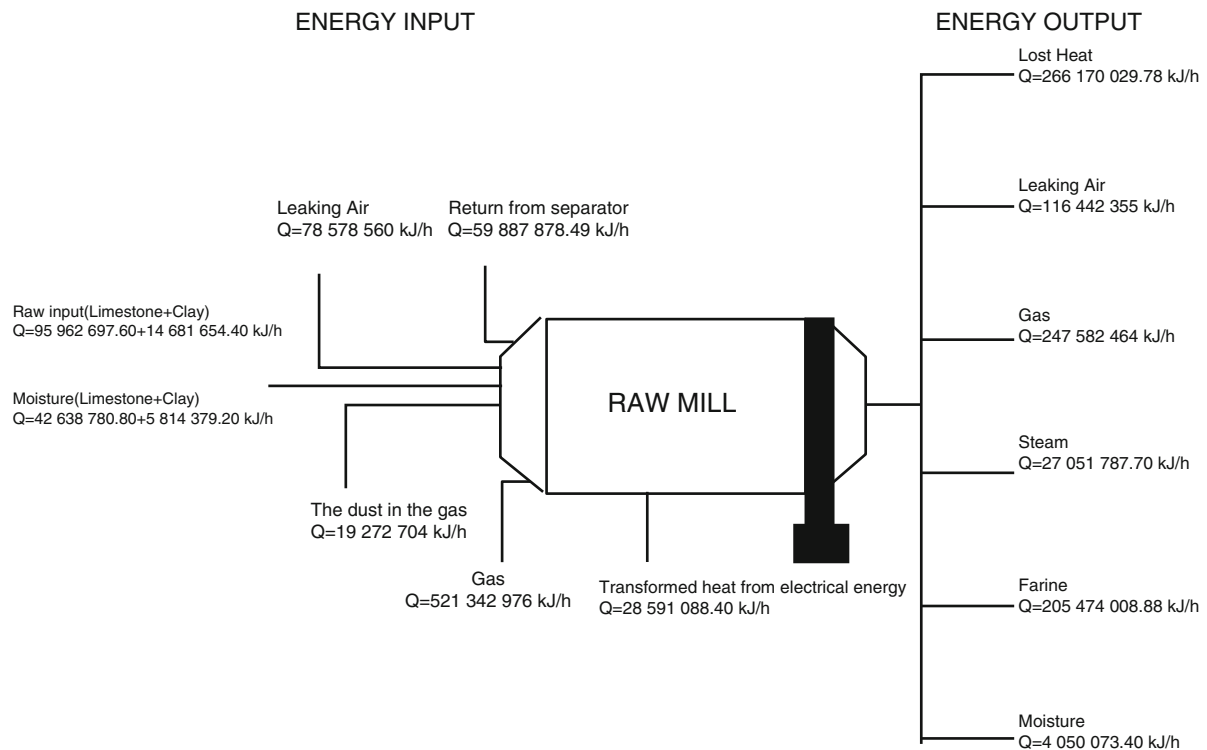
Fig. 31.3 Energy flow of the raw mill

Table 31.2 Enthalpy balance of the raw mill

	T (K)	T_0 (K)	m (kg/h)	ν (N m^3/h)	Cp (kJ/kg K)	Cp (kJ/N m^3 K)	Δh (kJ/kg)
Input material							
Limestone	T_l	T_0	m_l		Cp_l		0
Clay	T_c	T_0	m_c		Cp_c		0
Return from separator	T_r	T_0	m_r		Cp_r		10,949,030.40
Moisture in the limestone	T_{ml}	T_0	m_{ml}		Cp_{ml}		0
Moisture in the clay	T_{mc}	T_0	m_{mc}		Cp_{mc}		0
Gas	T_g	T_0		ν_g		Cp_g	280,283,136.00
Leaking air	T_{la}	T_0		ν_{la}		Cp_{la}	0
Dust in the gas	T_d	T_0		ν_d		Cp_d	10,361,344.00
Output material							
Farine	T_{out}	T_0	m_f		Cp_f		37,565,885.28
Gas	T_{out}	T_0		ν_g		Cp_g	45,264,384.00
Leaking air	T_{out}	T_0		ν_{la}		Cp_{la}	21,288,630.00
Moisture	T_{out}	T_0	m_m		Cp_m		740,456.64
Steam	T_{out}	T_0	m_s		Cp_s		4,945756.20

Energy Efficiency of the Raw Mill

Energy efficiency of the raw mill is calculated from the following relation

$$\eta = \frac{\sum \dot{m}_{out} h_{out}}{\sum \dot{m}_{in} h_{in}} \tag{31.11}$$

Using energy analysis values and Eq. (31.11), the energy efficiency of the raw mill is calculated as follows:

$$\eta = \frac{600\ 600\ 689.02}{866\ 770\ 718.80} = 0.69$$

The overall thermal efficiency of the raw mill has been found to be 69 % and is close to the best practice with the current technological limitations. The waste heat has been estimated at about 31 % of the energy input. This has represented an improvement of about 31 % in terms of primary energy efficiency of the raw mill.

Exergy Analysis of the Raw Mill

The irreversibility of each of the components is calculated from the exergy consideration, while it may also be found using the entropy balance equations. Entropy balance of the raw mill is illustrated in Table 31.3, while exergy balance of the raw mill is shown in Table 31.4. The following assumptions are made in the calculations.

Table 31.3 Entropy balance of the raw mill

	T (K)	T₀ (K)	m (kg/h)	ν (N m³/h)	Cp (kJ/kg K)	Cp (kJ/N m³ K)	ΔS (kJ/kg K)
Input material							
Limestone	T_l	T_0	m_l		Cp_l		0
Clay	T_c	T_0	m_c		Cp_c		0
Return from separator	T_r	T_0	m_r		Cp_r		33,494.51
Moisture in the limestone	T_{ml}	T_0	m_{ml}		Cp_{ml}		0
Moisture in the clay	T_{mc}	T_0	m_{mc}		Cp_{mc}		0
Gas	T_g	T_0		ν_g		Cp_g	630,320.76
Leaking air	T_{la}	T_0		ν_{la}		Cp_{la}	0
Dust in the gas	T_d	T_0		ν_d		Cp_d	23,301.33
Output material							
Farine	T_{out}	T_0	m_f		Cp_f		114,918.94
Gas	T_{out}	T_0		ν_g		Cp_g	138,469.65
Leaking air	T_{out}	T_0		ν_{la}		Cp_{la}	65,124.69
Moisture	T_{out}	T_0	m_m		Cp_m		2,265.15
Steam	T_{out}	T_0	m_s		Cp_s		15,129.71

Table 31.4 Exergy balance in the raw mill

	Δh (kJ/kg)	T₀ (K)	ΔS (kJ/kg K)	Ex (kJ/h)
Input material				
Limestone	0	T_0	0	0
Clay	0	T_0	0	0
Return from separator	10,949,030.40	T_0	33,494.51	1,068,149.65
Moisture in the limestone	0	T_0	0	0
Moisture in the clay	0	T_0	0	0
Gas	280,283,136.00	T_0	630,320.76	94,338,512.23
Leaking air	0	T_0	0	0
Dust in the gas	10,361,344.00	T_0	23,301.33	3,487,451.27
			Total	98,894,113.15
Output material				
Farine	37,565,885.28	T_0	114,918.94	3,664,798.23
Gas	45,264,384.00	T_0	138,469.65	4,415,837.22
Leaking air	21,288,630.00	T_0	65,124.69	2,076,845.33
Moisture	740,456.64	T_0	2,265.15	72,236.40
Steam	4,945,756.20	T_0	15,129.71	482,490.92
			Total	10,712,208.10

ENERGY INPUT   ENERGY OUTPUT
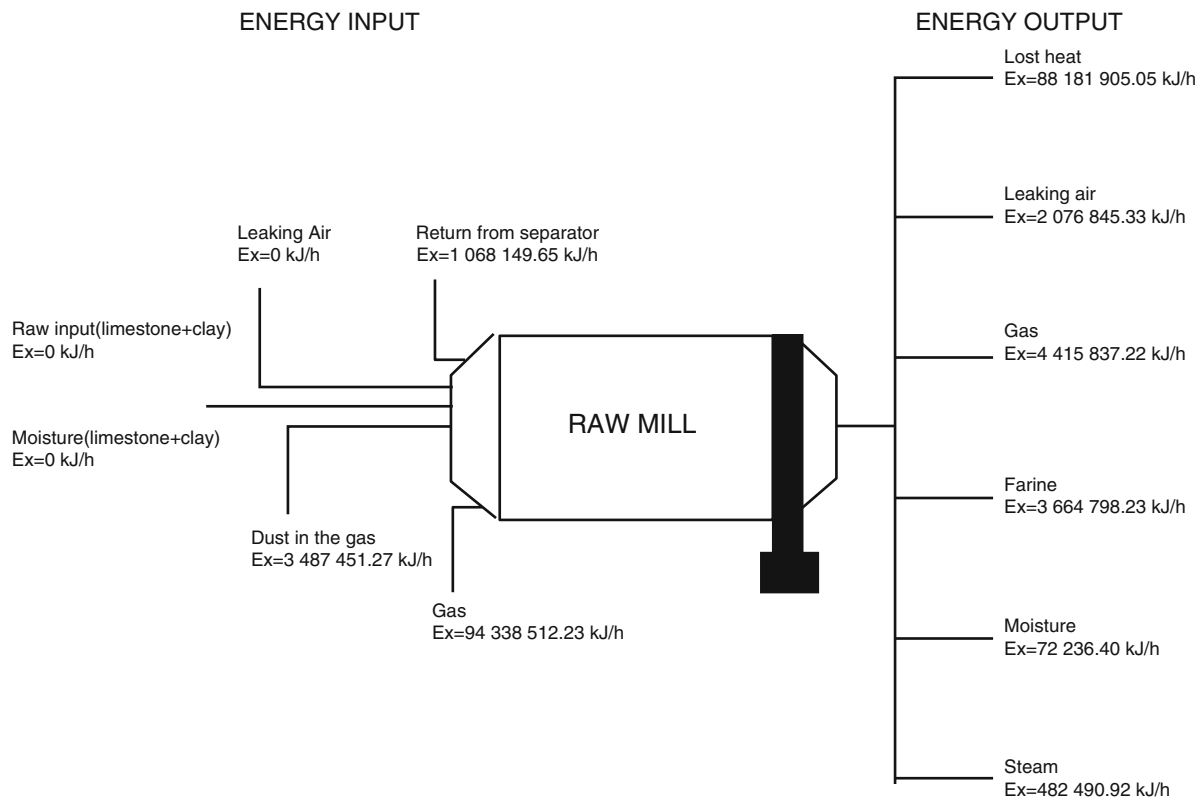
Fig. 31.4 Exergy flow of the raw mill

(a) The system is assumed as a steady-state, steady-flow process.
(b) Chemical exergies of the substances are neglected.
(c) Kinetic and potential exergies of materials are ignored.

Total exergy values of the input and output materials are calculated to be respectively 98,894,113.15 and 10,712,208.10 kJ/h. Exergy flow of the raw mill is also illustrated in Fig. 31.4. The lost heat for the raw mill in the energy flow is obtained to be 266,170,032.78 kJ/h in this study, whereas the lost heat for the raw mill in the exergy flow is found to be 88,181,905.05 kJ/h.

Exergy Efficiency of the Raw Mill

The exergy efficiency of the raw mill is calculated from

$$\varepsilon = \frac{\sum \dot{E}x_{out}}{\sum \dot{E}x_{in}}. \tag{31.12}$$

Using exergy analysis values and Eq. (31.12), the exergy efficiency of the raw mill is computed as follows:

$$\varepsilon = \frac{10\ 712\ 208.10}{98\ 894\ 113.15} = 0.11.$$

The overall exergy efficiency of the raw mill was determined as 11 %.

Conclusions

The aim of this study has been to determine energy and exergy efficiencies for a raw mill in a cement factory. Energy balance, energy, and exergy efficiencies of the raw mill have been analyzed using the actual plant operational data.

The main conclusions from this study may be summarized as follows:

(a) Exergy analysis is an advanced tool, which has been successfully and effectively used in the design and performance evaluation of energy-related systems.

(b) The energy efficiency value for the raw mill is obtained to be 69 % in this study, whereas the exergy efficiency value for that is found to be 11 %.

(c) Heat losses that show up especially at the beginning stage of the process show problem with the efficiency of the system. Heat losses will decrease if necessary precautions are taken in the raw mill. It will also cause saving of fuel at the rotary kiln.

(d) This study has indicated that exergy utilization in the raw mill has been worse than energy utilization. In other words, this process represents a big potential for increasing the exergy efficiency. Some suggestions are given below to increase the efficiency of the raw mill.

- The mixing temperatures of the materials, which constitute farine and gas coming from the preheater cyclones and being the energy source of the raw mill should be reexamined. Cement plants are designed at a full production capacity. The system productivity would be increased when the raw material input capacity would be held at the highest capacity and when the turning speed of the farine mill and the material flow rate could be decreased because the system output temperature would be raised.

- The waste energy in the raw mill and the leaving temperature of the farine could be recovered by means of a heat recovery system. Thus, the efficiency of the system would be increased.

Nomenclature

E	Energy (kJ)	P	Pressure (Pa)
$\dot{E}$	Energy rate (kW)	Q	Heat transfer (kJ)
Ex	Exergy (kJ)	$\dot{Q}$	Heat transfer rate (kW)
$\dot{Ex}$	Exergy rate (kW)	s	Specific entropy (kJ/kg K)
h	Specific enthalpy (kJ/kg)	$\dot{S}$	Entropy rate (kW)
I	Irreversibility, exergy consumption (kJ)	T	Temperature (K)
$\dot{I}$	Irreversibility rate, exergy consumption rate (kW)	W	Work (kJ)
m	Mass (kg)	$\dot{W}$	Work rate or power (kW)
$\dot{m}$	Mass flow rate (kg/s)		

Greek Letters

η	Energy (first law) efficiency (%)	ψ	Flow exergy (kJ/kg)
ε	Exergy (second law) efficiency (%)		

Indices

c	Clay	l	Limestone
dest	Destroyed	la	Leaking air
d	Gas dust	mc	Moisture clay
f	Farine	ml	Moisture limestone
gen	Generation	r	Return from separator
g	Gas	s	Steam
in	Input	out	Outlet, existing
m	Moisture	0	Dead state or reference environment

References

1. Moran MJ (1982) Availability analysis. Prentice-Hall, New Jersey
2. Szargut J, Morris DR, Steward FR (1998) Exergy analysis of thermal and metallurgical processes. Hemisphere Publishing Corporation, New York
3. Dincer I (2000) Thermodynamics, exergy and environmental impact. Energ Source 22:723–732
4. Dincer I (2002) The role of exergy in energy policy making. Energ Policy 30:137–149
5. Bejan A (1988) Advanced engineering thermodynamics. Wiley, New York
6. Kotas TJ (1985) The exergy method of thermal plant analysis. Anchor Brendon Ltd., Tiptree, Essex
7. Dincer I, Hussain MM, Al-Zaharnah I (2003) Energy and exergy use in the industrial sector of Saudi Arabia. Proc Inst Mech Eng 217:481–492
8. Dincer I, Hussain MM, Al-Zaharnah I (2004) Energy and exergy utilization in transportation sector of Saudi Arabia. Appl Thermal Eng 24:525–538
9. Cornelissen RL (1997) Thermodynamics and sustainable development: the use of exergy analysis and the reduction of irreversibility. PhD thesis, University of Twente, Twente
10. Wall G (2003) Exergy tools. In: Proceedings of the Institution of Mechanical Engineers. Wilson applied science and technology abstracts plus text, 217:125–136
11. Torres EA, Gallo WLR (1998) Exergetic evaluation of a cogeneration system in a petrochemical complex. Energy Convers Manag 16–18:1845–1852
12. Moran MJ (1999) Engineering thermodynamics. In: Kreith F (ed) Mechanical engineering handbook. CRC Press LLC, Boca Raton
13. Çelen F (1998) Exergy analysis in a rotary burner with pre-calcination in dry system cement production. MS Thesis, Kırıkkale University Institute of Science & Technology
14. Gürüz HK (1977) Mass and energy balances in cement factories. J Chamber Chem Eng (Turkish)

Energy Analysis of Scroll Compressor Conversion into Expander for Rankine Cycles with Various Working Fluids

32

Emre Oralli and Ibrahim Dincer

Abstract

In this study, a refrigeration scroll compressor as expander for power generation applications with Rankine cycle is analyzed through a mathematical model. The methodology adopted has three phases. In the first phase, a scroll compressor is selected from a refrigeration manufacturer catalog namely Copeland ZF06K4E. Based on the catalog data and thermodynamic model the specific parameters of the compressor such as built-in volume ratio and leakage coefficient are determined through mathematical regression as 7.3 and 1.36×10^{-6}, respectively. In the second phase, the scroll parameters and the efficiency of the Rankine cycle are determined, which use the selected scroll machine in reverse, namely as expander, without any geometrical modifications and keeping the range of temperatures and pressures constant as the same as that characterizing the compressor operation. An expander model is developed to predict the efficiency of the prime mover and of the Rankine cycle for the working fluids such as R404a, Toulene, R123, R141b, R134a, and NH_3. The highest energy efficiency is obtained with R404a as 18 % by applying supercritical conditions for the working fluid, and it is observed that the expander does not operate optimally when converted from a compressor without any modifications. In the third phase, the geometry of the expander is modified with respect to rolling angle in order to obtain the appropriate built-in volume ratio which assures better efficiency of the Rankine heat engine. R404a clearly gave the best results for the modified geometry and the energy efficiency is increased to 25 % from 19 %. The results show that it is possible to improve the efficiency of the cycle by adjusting the scroll geometry for the fluids used.

Keywords

Scroll compressor • Expander • Rankine cycle • Heat engine • Energy • Efficiency

Introduction

Energy demand before the industrial revolution was mostly provided by man power to meet the basic requirements of humanity. Over the last century, developments in science and concurrent technological advances helped to improve the quality of life for society. Unfortunately growing energy demand was mostly covered by fossil fuels, which caused environmental problems and forced the design of new energy conversion technologies like electricity production by sustainable sources such as solar, wind, and geothermal power to eliminate global warming and atmospheric pollution problems.

The present global yearly energy consumption is about 500 EJ, which is equivalent to about 16 TW as the average rate of world primary energy consumption [1]. It is expected that the world's demand for energy will be 60 % more than it is now, which cannot be expected to be met by fossil fuels because of the limited reservoirs of coal, oil, and gas. Based on proven reserves, the current production level of oil can be maintained for over 40 years, gas over 66 years, and coal for over 160 years. This picture requires developing production of electricity without generating environmental pollution.

E. Oralli (✉) • I. Dincer
Faculty of Engineering and Applied Science, University of Ontario Institute of Technology (UOIT),
2000 Simcoe Street North, Oshawa, ON L1H 74K, Canada
e-mail: Emre.Oralli@uoit.ca; Ibrahim.Dincer@uoit.ca

The problem regarding the environmental impact of energy use is primarily caused by high atmospheric carbon dioxide (CO_2) concentrations as a result of burning fossil fuels. Earth's long-term carbon cycle implies to keep CO_2 emissions below such a level that would cause environmental problems. The concern is the increasing temperature of the planet caused by high levels of greenhouse gases in the atmosphere by burning fossil fuels. The greenhouse effect threatens the natural life on the planet. The level of carbon dioxide in the atmosphere was more or less stable at 280 ppm over the last few thousand years up to the onset of the industrial revolution at the beginning of the nineteenth century. Current CO_2 level is 380 ppm and rising fast. Global CO_2 emissions in the alternative scenarios are 16 % less in 2030 [2] but are still more than 50 % higher than 1990.

In the present time, when there is a push toward sustainable energy-based economy, externally driven heat engines which have been used for a long time for conversion of thermal energy to work are playing a major role. There are many sources of heat that can be considered sustainable. Examples are: geothermal reservoirs, solar heat, ocean thermal energy, industrial waste heat recovery, and power cogeneration. An important segment of the abovementioned applications is covered by low power heat generation systems that can be used, for example, for small-scale residential or commercial settings. In such applications the generated power is typically below 10 kW. One common case is local generation of electricity and water/space heating from natural gas rather than only heating.

Generation of electricity from low temperature heat sources has become more popular in the last decade depending on its potential use for different types of applications such as solar thermal, waste heat, small-scale cogeneration for residential purposes, etc. Low capacity heat engines require appropriate selection of the thermodynamic cycle and of the prime mover.

The Rankine cycle has a relatively higher efficiency by using low temperature heat sources compared to other cycles [3]. Solar energy and combustion heat can be used as a low temperature heat source for the cycle. In traditional power plants, Rankine cycle is used to produce useful work from expander mostly using water as a working fluid. The working fluid is pumped to a boiler where it is evaporated then passes through an expander generating shaft work and then finally condensed to be pumped again. Unlike conventional working fluids such as water, organic fluids that have lower boiling temperatures are more appropriate for low temperature Rankine cycle in terms of efficiency and environmental conditions. Water has a high vaporization because of its higher specific volume, which imposes larger installations and therefore higher cost [4].

There are several kinds of prime movers namely turbomachines and positive displacement machines. However, when it is about low capacity, positive displacement machines (scroll, screw, rotary vane expanders) become more attractive than turbomachines because [5, 6]:

- Performance of rotary machines depends on their peripheral speed, $\vartheta = 2\pi n R$ where n is the revolution speed per second and R is the radius of the rotary machine.
- Typical peripheral speed for scroll machines is 1–10 m/s, while for turbomachines it is about 300 m/s.
- For a similar radius, the revolution speed of the turbomachine must be the order of hundreds of thousands of RPM while the one of scroll expander it is of couple of thousands RPM. Therefore using turbomachines creates problems with bearings and coupling the electric generator.
- Turbomachines have to be made with multiple expansion stages because they have low pressure ratio per stage, while a positive displacement expander would be preferred having one single expansion stage.
- Scroll or screw kind expanders are capable to expand in two phase vapor–liquid region which represents a clear advantage for Rankine cycle applications.

In this study, low temperature heat generation phenomenon is investigated for certain thermodynamic cycle and prime mover. The purpose is to achieve waste heat recovery for different purposes such as residential domestic heat supply when there is an electrical breakdown, which will decrease the fragility of the centralized large-scale power generation systems. A crucial part of the system is the design of the scroll expander especially regarding the geometric and thermodynamics calculations in order to increase the efficiency to make it an alternative to conventional turbomachines.

Rankine cycle takes advantage of the small amount of work required to pump a liquid and the amount of energy that can be extracted from the latent heat. An organic Rankine cycle (ORC) differs from the basic Rankine cycle in that the working fluid is organic. Saleh et al. [7] modeled 31 different working fluids in different ORC configurations. Types of organic working fluids modeled included alkanes, fluorinated alkanes, ethers, and fluorinated ethers. These fluids can behave differently when used in an ORC and it is important to discuss the different configurations and working fluid characteristics together. Organic working fluids have performance advantages over water-steam at low power levels but these advantages disappear at 300 kW or more because of the poor heat transfer properties of organic fluids [8].

The irreversibilities such as friction and leakage losses in the cycle cause reduction of cycle efficiency and of useful work output. Friction and leakage losses from expander contribute the highest portion of the irreversibilities with pressure drops and inefficiencies from the heat exchanger. The improvements regarding the geometry of the scroll machine will directly

affect the cycle efficiency not only because of reducing the leakages but also to obtain appropriate built-in ratio for the compression/expansion process [9–11].

ORC has inherent irreversibilities as many processes. The losses may come in the form of friction-heat loses in the expander and pump [12]. This is accounted in the isentropic efficiencies of each device. Valves, pipes, and pressure drops are other sources. Hung [13] stated that the largest source of irreversibility in the system is caused by the evaporator. The mismatch between the working fluid and the heat source causes this type of loss. Larjola [14] showed that the organic working fluids due to their low latent heat match the source temperature profile better than water-steam.

There are some practical solutions to reduce losses for ORC. The liquid entering the pump should be sub-cooled to prevent cavitations. The fluid should be superheated when using turbines with w-type working fluids to prevent droplet formation during expansion. Moran [15] stated that the quality at the turbine exit can be kept at 90 %. Both cavitation and high speed droplets will corrode the pump and expander.

There are a limited number of ways to improve the thermal efficiency of the cycle after the cycle configuration and fluid have been specified. Increasing the average high side temperature or decreasing the average low side temperature is one of the approaches that can be used. The high side temperature is fixed in low temperature heat recovery and decreasing the condenser temperature below atmospheric conditions is not practical. Other approaches include increasing the isentropic efficiencies of the pump and expander. The pump work is significantly less than the expander work in a Rankine cycle [16]. Therefore improvement of the efficiency of the expander will provide the greatest degree of cycle improvement.

Badr [17] modeled an ORC and performed a sensitivity study to show which of these parameters had the greatest effect on thermal efficiency. They varied the isentropic expander efficiency, evaporator temperature, and condenser temperature. They modeled both a basic and regenerative ORC with R113 as the working fluid.

In this study, the feasibility of converting a scroll compressor into an expander as to be used in heat recovery Rankine cycle of low capacity is modeled. The specific objectives of this work are given as follows:

- To characterize the scroll machine in expander mode and searching the effect of scroll geometry on the ORC energy efficiency.
- To evaluate the geometric parameters of the scroll expander by optimization process to reduce the leakage loss caused by the gaps between the fixed and orbiting scroll and between the scrolls and plates which will ensure appropriate built-in volume ratio for the cycle.
- To select an appropriate organic working fluid such as R404a, Toluene, R123, R141b, R134a, and NH_3 which will ensure suitable temperature and pressure range to make the cycle realizable when converting scroll compressor to an expander.

System Description

Here, an energy analysis of the ORC is conducted. The performance of an ORC will be analyzed for different working fluids under diverse working conditions using the first law of thermodynamics. There will be assumptions regarding the system as follows: steady-state conditions, no pressure drop in the evaporator, condenser and pipes, and isentropic efficiencies for the turbine and pump. The heat engine to produce electrical power with ORC is shown in Fig. 32.1a. There are four different processes in ORC as can be observed from Fig. 32.1a: process 1–2 (constant-pressure transfer of heat), process 2–3 (expansion process), process 3–4 (constant-pressure heat transfer), and process 4–1 (pumping process). A *T-s* diagram of the typical ORC is given in Fig. 32.1b.

Analysis

The geometrical model and volume expressions for the chambers will be used to model the thermodynamic process of the working fluid from the beginning of suction ($\theta = 0$) to the end of the discharge process ($\theta = 2\pi$ rad)

The first law of thermodynamics for the control volume with a mass balance can be applied to calculate the temperature, mass, and pressure in the working chambers with respect to orbiting angle.

The conservation of energy for the control volume is:

$$\frac{dE_{cv}}{dt} = \dot{Q} + \dot{W} + \sum \dot{m}_{su}\left(h + \frac{V^2}{2} + gz\right)_{su} - \sum \dot{m}_{ex}\left(h + \frac{V^2}{2} + gz\right)_{ex} \tag{32.1}$$

Fig. 32.1 (a) The organic Rankine cycle and (b) its T-s diagram
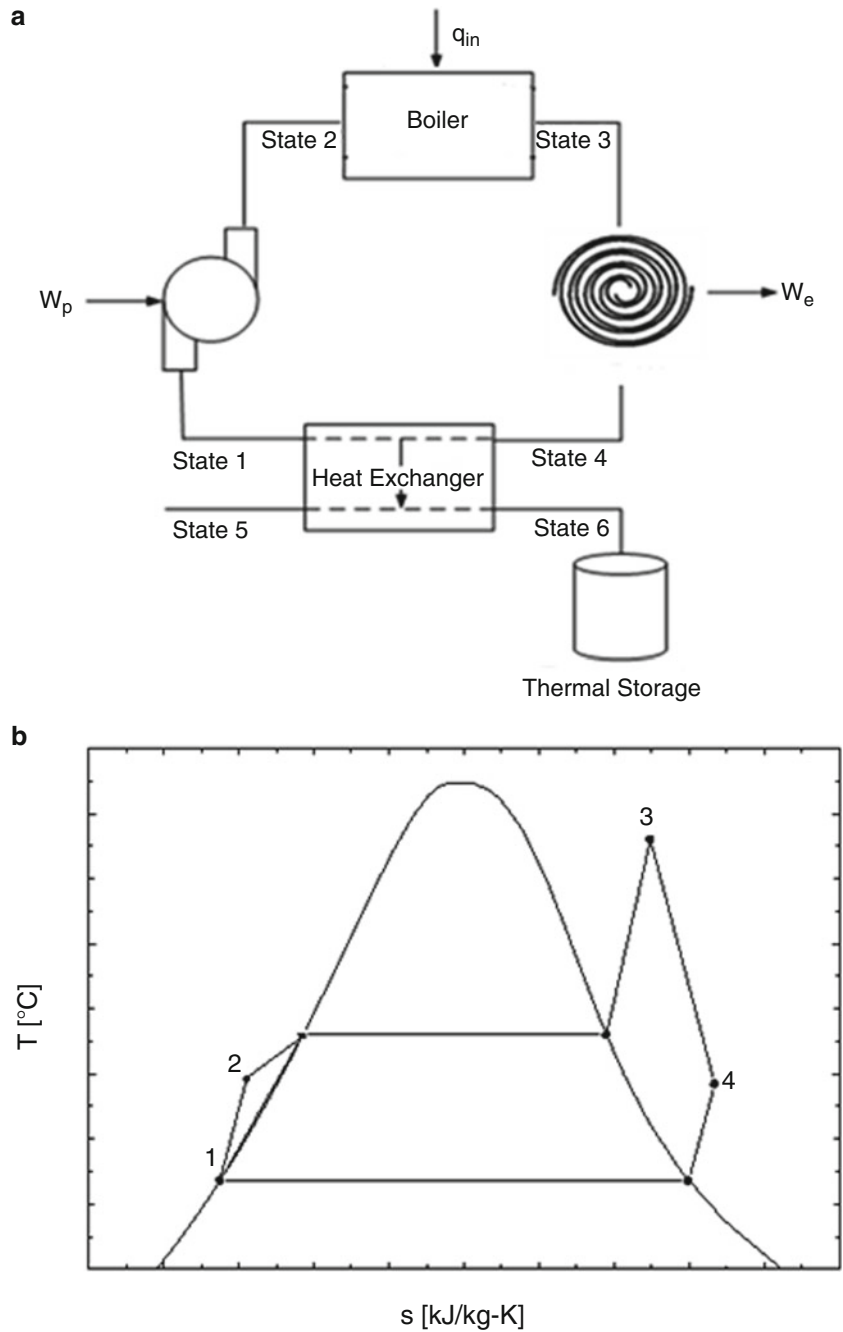
where $\frac{dE_{cv}}{dt}$ is the rate of total internal energy increase (W), $\dot{Q}$ is the heat transfer rate (W), $\dot{W}$ is the power output from expander (W), $\dot{m}$ is the inflow or outflow rate (kg/s), $h + \frac{V^2}{2} + g$ is the total enthalpy (J/kg).

The mass balance for the control volume is:

$$\frac{dM}{dt} = \sum \dot{m}_{su} - \sum \dot{m}_{ex} \tag{32.2}$$

The total energy of the control volume E_{cv} can be reduced to internal energy U_{cv} neglecting kinetic and potential energies. The left side of the conservation of energy equation can be written as

$$\frac{dE_{cv}}{dt} = \frac{dU_{cv}}{dt} = m\frac{du}{dt} + u\frac{dm}{dt} \tag{32.3}$$

The change of the specific internal energy u for the control volume is

$$du = C_v dT + \left[T \left(\frac{\partial P}{\partial T} \right)_v - P \right] dv \tag{32.4}$$

The specific internal energy u can be written as $u = h - Pv$, where h is the specific enthalpy, such that Eq. (32.3) can be written as

$$\frac{dU_{cv}}{dt} = mC_v \frac{dT}{dt} + T \left(\frac{\partial P}{\partial T} \right)_v \left(\frac{dV}{dt} - V \frac{dm}{dt} \right) - P \frac{dV}{dt} + h \frac{dm}{dt} \tag{32.5}$$

Uniform pressure and temperature can be assumed for each control volume and the work term $\dot{W} = \frac{\partial W}{\partial t}$ on the right hand side of Eq. (32.1) can be expressed as

$$\dot{W} = -P \frac{dV}{dt} \tag{32.6}$$

The first law of thermodynamics for the control volume becomes

$$mC_v \frac{dT}{dt} + T \left(\frac{\partial P}{\partial T} \right)_v \left(\frac{dV}{dt} - V \frac{dm}{dt} \right) + h \frac{dm}{dt} = \dot{Q} + \sum \dot{m}_{in} h_{in} - \sum \dot{m}_{out} h_{out} \tag{32.7}$$

Equation (32.7) can be arranged to

$$\frac{dT}{dt} = \frac{1}{mC_v} \left\{ -T \left(\frac{\partial P}{\partial T} \right)_v \left[\frac{dV}{dt} - v(\dot{m}_{in} - \dot{m}_{out}) \right] - \sum \dot{m}_{in}(h - h_{in}) + \dot{Q} \right\} \tag{32.8}$$

by applying mass balance equation (32.2) for $h = h_{out}$. The temperature change with respect to orbiting angle can be obtained from Eq. (32.8) if angular speed w is expressed as

$$w = \frac{d\theta}{dt} \tag{32.9}$$

Substituting Eq. (32.9) into Eq. (32.8) yields

$$\frac{dT}{d\theta} = \frac{1}{mC_v} \left\{ -T \left(\frac{\partial P}{\partial T} \right)_v \left[\frac{dV}{dt} - (v/w)(\dot{m}_{in} - \dot{m}_{out}) \right] - \sum (\dot{m}_{in}/w)(h - h_{in}) + (\dot{Q}/w) \right\}$$

And the mass balance equation becomes

$$\frac{dM}{d\theta} = \left(\sum \dot{m}_{in}/w \right) - \left(\sum \dot{m}_{ex}/w \right) \tag{32.10}$$

In Eq. (32.8), independent variables temperature T and mass m should be integrated for the first order differential equation. Applying the mass balance equation (32.10) and the equation of temperature distribution with respect to orbiting angle (32.9) the thermophysical properties in each chamber can be evaluated as a function of the orbiting angle (θ).

There are different types of heat transfer mechanisms in a scroll compressor including between:
1. The shell of the scroll compressor and the fluid in suction
2. The fluid and motor, oil, scrolls (electromechanical losses)
3. The shell of the scroll compressor/expansion and the fluid in discharge
4. The fluid and the ambient

It can be assumed that the wall temperature is constant at T_w The steady-state energy balance for the wall can be given as

$$\dot{Q}_{ex} - \dot{Q}_{su} - \dot{Q}_{amb} - \dot{W}_{loss} = 0 \tag{32.11}$$
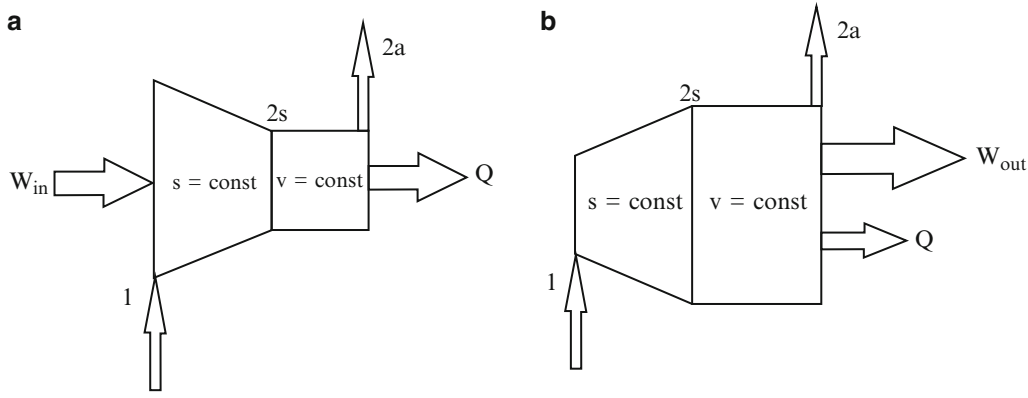
Fig. 32.2 Scroll machine models for (**a**) compressor and (**b**) expander

The suction heat transfer assuming constant envelope temperature for the isothermal heat exchanger and uniform wall temperature is

$$\dot{Q}_{su} = \dot{m}c_p(T_{su,1} - T_{su}) = \varepsilon_{su}\dot{m}c_p(T_w - T_{su}) = \left[1 - e^{\left(\frac{-AU_{su}}{Mc_p}\right)}\right]\dot{m}c_p(T_w - T_{su}) \tag{32.12}$$

The discharge heat transfer under the same conditions and assumptions [12, 18]:

$$\dot{Q}_{ex} = \dot{m}c_p(T_{ex} - T_{ex,1}) = \varepsilon_{su}\dot{m}c_p(T_{ex} - T_w) = \left[1 - e^{\left(\frac{-AU_{su}}{Mc_p}\right)}\right]\dot{m}c_p(T_{ex} - T_w) \tag{32.13}$$

where AU_{su} can be written in terms of nominal heat transfer coefficient ($AU_{su,n}$) which is given by Bergman [19] to develop the model for a turbulent flow through a pipe by the Reynolds number as follows [20]:

$$AU_{su} = AU_{su,n}(\dot{m}/\dot{m}_n)^{0.8} \tag{32.14}$$

The ambient heat transfer can be evaluated by the following equation introducing a global heat transfer coefficient (AU_{amb}):

$$\dot{Q}_{amb} = AU_{amb}(T_w - T_{amb}) \tag{32.15}$$

After defining the properties of the fluid and the volume of the chambers as a function of the orbiting angle there is a need to develop a model to analyze and describe the main features of the machine regarding the energy efficiencies and fluid flow characteristics with a limited number of parameters.

The model proposed by Winandy et al. [20] and Lemort et al. [21] was modified to be able to predict the characteristics of the flow and the thermodynamic process of the scroll machine converting from scroll compressor to scroll expander and to improve the modeling of heat pump systems.

The schematic representation of the evolution of the refrigerant through the scroll machine is given for both the compressor and expander case in Fig. 32.2. In this study the heat up in suction and cool down in discharge are not taken into account considering the compression and expansion process of the refrigerant in a scroll machine.

The compression process can be decomposed into two parts:
1. Isentropic compression (1 → 2s)
2. Isochoric pressure rising (2s → 2a)

The expansion process can be decomposed into two parts:
1. Isentropic expansion (1 → 2s)
2. Constant volume pressure rebuild (2s → 2a)

The equations describing the thermodynamic model will be given in terms of heat transfer, the internal leakage, and pressure drop to describe the compression and expansion processes separately.

Figure 32.2 introduces scroll machine models functioning as a compressor (a) and expander (b). Assume that a low pressure gas is to be compressed (Fig. 32.2a) from state 1. The compression process in positive displacement compressors implies closing the volume of gas in a compression chamber, which reduces its volume according to the built-in volume ratio. One assume that no leakages and no heat transfer occurs during the theoretical compression process represented from state 1 to state 2s as an isentropic one. The amount of work required for this part of compression process is denoted W_s.

In real compression processes the gas does not evolve isentropically and more work is consumed. The additional work is in fact transformed into heat that increases the entropy and enthalpy of the gas. Therefore, after the isentropic process 1–2s it follows an isochoric process with rising pressure driven by heat addition. The added heat originates from the input work, which is partially destroyed such that $Q = W_{in} - W_s$ (see Fig. 32.2a). After the isochoric process the working fluid achieves state 2a. Eventually a part of the discharged gas flows back to suction as leakage flow. The leakage flow rate can be estimated from energy balance applied to simplified model. The energy balance can be written it as follows, in the compressor case. The isentropic compression work is

$$\dot{W}_s = (\dot{m} + \dot{m}_{leak})(h_{2s} - h_1) \tag{32.16}$$

where $\dot{m}$ is the net mass flow rate, and $\dot{m}_{leak}$ represents the internal leakage flow rate. The summation $\dot{m} + \dot{m}_{leak}$ is the mass flow rate actually circulated through the compressor. In order to compensate the irreversibilities (leakages and heat exchange) more work input is needed to drive the compressor, such that $\dot{W}_{in} = \dot{W}_s + \dot{Q}$. Assuming that most of the irreversibilities are due to leakage flows, it becomes possible to calculate the leakage flow rate from an energy balance:

$$\dot{Q} = \dot{W}_{in} - \dot{W}_s = (\dot{m} + \dot{m}_{leak})(h_{2a} - h_{2s}) = \dot{m}_{leak}(h_{2a} - h_1). \tag{32.17}$$

Therefore, noting also that $v_{2a} = v_{2s}$ one solves for $\dot{m}_{leak}$ and obtains

$$\frac{\dot{m}_{leak}}{\dot{m}} = \frac{h_{2a} - h_{2s}}{h_{2s} - h_1}. \tag{32.18}$$

A leakage flow coefficient $\zeta = C_F A_{leak}$ can be determined if one solves volume equation for known pressure difference across the compressor

$$\dot{m}_{leak} = \zeta \sqrt{P_{2a}/v_{2a} - P_1/v_1} \tag{32.19}$$

where C_f is the specific flow coefficient per average leakage area A_{leak}.

The simplified model for the expander is introduced in Fig. 32.2b. In this case, a part of the main flow by-passes the expander and dissipates power as it flows over the expander's "flow resistance"; this is the leakage flow, $\dot{m}_{e,leak}$. The expansion process according to the simplified model, evolves first isentropically from state 1 to 2s followed by, a constant volume pressure rebuild 2s–2a. At the reverse operation—as expander—a reasonable assumption is to consider that the leakage coefficient remains the same. Therefore, denoting expander's states with index "e" one has the following equations that can be written for the expander to apply for the thermodynamic modeling [22].

$$\begin{cases} v_{e,2a} = v_{e,2s} \\ \dot{m}_{e,leak} = \zeta \sqrt{\dfrac{P_{e,1}}{v_{e,1}} - \dfrac{P_{e,2a}}{v_{e,2s}}} \\ \dot{W}_{e,s} = (\dot{m}_e - \dot{m}_{e,leak})(h_{e,1} - h_{e,2s}) \\ \dot{Q}_{e,diss} = \dot{m}_{e,leak}(h_{e,1} - h_{e,2s}) \\ \dot{W}_{e,out} = \dot{W}_{e,s} - \dot{Q}_{e,diss} = \dot{m}_e(h_{e,1} - h_{e,2a}) \end{cases} \tag{32.20}$$

From Eq.(32.20) one can determine the ratio

$$\frac{\dot{m}_e}{\dot{m}_{e,leak}} = 2 \times \frac{h_{e,1} - h_{e,2s}}{h_{e,2a} - h_{e,2s}}, \tag{32.21}$$

which is important for calculating the mass flow rate through the expander.

Pump

Process $1 \rightarrow 2$ in Fig. 32.1b implies an increase in the pressure resulting from using the pump. The driving mechanism of the ORC is the pump since it ensures the circulation.

The energy balance equation for the pump is

$$\dot{m}_1 h_1 + \dot{W}_p = \dot{m}_2 h_2 \tag{32.22}$$

The pump power can be expressed as

$$\dot{W}_p = \frac{\dot{W}_{p,ideal}}{\eta_p} = \frac{\dot{m}(h_1 - h_{2s})}{\eta_p} \tag{32.23}$$

where $\dot{W}_{p,ideal}$ is the ideal work that should be supplied for the pump, η_p is the isentropic efficiency of the pump, $\dot{m}$ is the flow rate of the working fluid, h_1 *and* h_{2s} are the inlet and outlet enthalpies of the refrigerant for the ideal case.

The actual specific enthalpy can be given as

$$h_2 = h_1 - \frac{\dot{W}_p}{\dot{m}} \tag{32.24}$$

Boiler

The pressure of the working fluid stays constant during the heat addition process in boiler. The boiler heats the working fluid at the pump outlet to the turbine inlet condition, which can be saturated or superheated vapor.

The energy balance equation for the boiler is

$$\dot{m}_2 h_2 + \dot{Q}_{in} = \dot{m}_3 h_3 \tag{32.25}$$

The heat transfer rate from the boiler into the working fluid is given by

$$\dot{Q}_b = \dot{m}(h_3 - h_2) \tag{32.26}$$

where h_3 and h_2 are the enthalpies of the working fluid at the exit and inlet of the boiler.

Expander

In the expander, the superheated or saturated vapor working fluid passes through the scrolls of the expander to rotate the shaft to generate mechanical power. The pressure decreases in the expansion process due to the volume increase of the chambers between the fixed and orbiting scroll [23].

The energy balance equation for the expander is

$$\dot{m}_3 h_3 = \dot{m}_4 h_4 + \dot{W}_e \tag{32.27}$$

The expander power can be given as

$$\dot{W}_e = \dot{W}_{e,ideal}\eta_e = \dot{m}(h_3 - h_2)\eta_e \tag{32.28}$$

where $W_{e,ideal}$ is the ideal power of the expander, η_e the expander isentropic efficiency, and h_3 and h_{4s} the enthalpies of the working fluid at the inlet and outlet of the expander for the ideal case. The actual specific enthalpy of the working fluid at the expander exit is

$$h_4 = h_3 - \frac{\dot{w}_e}{m} \tag{32.29}$$

Condenser

The low pressure and temperature working fluid leaving the expander rejects the latent heat to the environment or condenser coolant by heat exchanger through a constant-pressure phase change process.

The energy balance equation for the condenser is

$$\dot{m}_4 h_4 + = \dot{Q}_{out} + \dot{m}_1 h_1 \tag{32.30}$$

The condenser heat rate, $\dot{Q}_c$, which is the rate of latent heat rejection from the condensing working fluid, can be expressed as

$$\dot{Q}_c = \dot{m}(h_1 - h_4) \tag{32.31}$$

Cycle Energy Efficiency

The thermal efficiency is defined as the ratio between the net power output of the cycle and the boiler heat rate as follows:

$$\eta_{en} = \frac{\dot{W}_e - \dot{W}_p}{\dot{Q}_{in}} \tag{32.32}$$

Results and Discussion

Several working fluids for Rankine cycle were investigated. For each studied case the expander geometry has been adjusted with respect to the rolling angle only. The rolling angle and Rankine cycle parameters were determined by a trial and error method. The results are summarized in Table 32.1 where six working fluids were investigated. The working fluid is originally used for the scroll compressor, R404a, that gave the best performance. Two cases were analyzed with R404a. In the first case the rolling angle has been reduced to 27 rad. The corresponding built-in pressure ratio in this case becomes 3.0. In this situation, a supercritical Rankine cycle has been implemented for a maximum pressure and temperature values of 38 bar and 139 °C. The cycle is illustrated in Fig. 32.3, and the corresponding efficiency is 25 %. The cycle configuration offers a good opportunity for internal heat regeneration between streams 2–3 and 5–1. For this reason, the resulted efficiency is exceptionally high.

Table 32.1 Scroll expander and Rankine cycle parameters with various working fluids

Working fluid	φ_e (rad)	r_v	V_{suc} (ml/rev)	P_{max} (bar)	T_{max} (°C)
R404a	27	3.0	54	38	139
R404a	57[a]	7.3	128	68	264
R141b	33	3.8	68	30	178
R141b	69[a]	9.2	161	54	338
NH$_3$	57[a]	7.3	128	60	173
NH$_3$	29	3.3	61	33.5	91
R134a	57[a]	7.3	128	40	170
R134a	28	3.1	59	22.3	89.4
R123	185[a]	25	447	21	230
R123	90	10.6	206	11.7	121
Toluene	725[a]	100	1,790	20	273
Toluene	352	42.4	824	11.1	143

[a]No modification of scroll geometry

Fig. 32.3 Recommended cycle and scroll compressor modifications
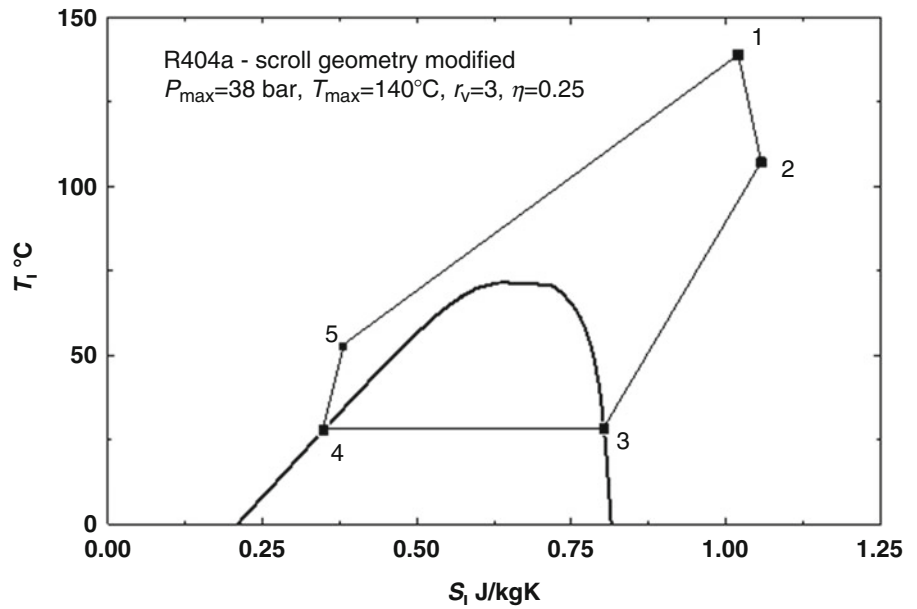
Fig. 32.4 Energy efficiency of the cycle for the modified and non-modified geometry

	R404a	R141b	NH3	R134a	R123	Toluene
■ nonmodified	19	9.8	11	12	17	18
■ modified	25	13	14.4	15.7	22.2	21
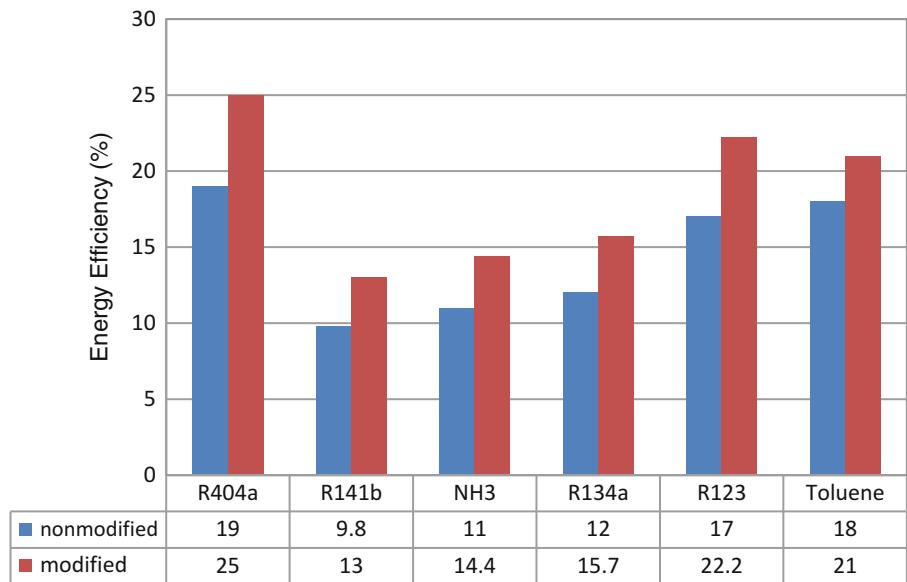
Here, the first law analysis is performed and corresponding energy efficiencies are evaluated for modified and unmodified scroll geometries with different organic fluids and the results are given in Fig. 32.4. The configuration given in Fig. 32.3 with R404a involves modifications of the scroll geometry. This configuration described above achieves 18 % efficiency. The other working fluid that shows a good performance is R123a; however, Table 32.1 shows that the rolling angle is very high which results in a less compact design with 17 % efficiency. Toluene requires an expansion ratio of 100, leading to a massive expander with 725 rad rolling angle, which is not practical. All other studied fluids show lower efficiency and therefore appear to be less attractive for implementation. Note that the efficiency listed in Fig. 32.4 is the general efficiency of Rankine cycle, defined as useful output over heat input.

Table 32.1 indicates that if no modifications are made to the scroll machine, the appropriate choice of working fluid for Rankine cycle is R134a because the resulted efficiency is good (12 %) and the maximum level of pressure and temperature in the system does not require modification of the housing. If modification of the housing is to be considered only with respect to maximum pressure and temperature but not to the scroll geometry modifications, then the original working fluid can be used. In this case, the pressure that needed to be withstood is more than triple and the temperature is 100 °C higher, while the

Fig. 32.5 Variation of the energy efficiency with the rolling angle of the scroll machine
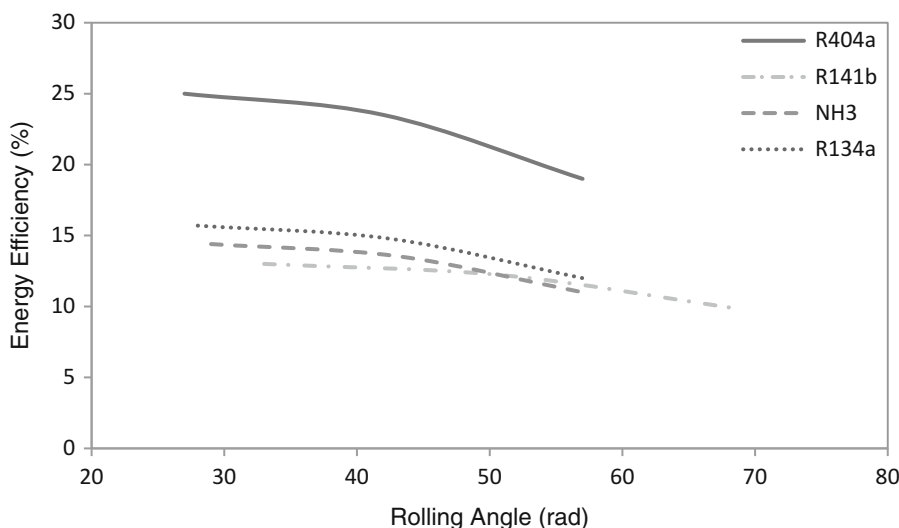
cycle efficiency is 18 %. The best results are obtained with R404a and the built-in ratio is reduced from 7.3 to 3. The scroll rolling angle is 27 rad, the temperatures and pressures in the system are reasonably low and are suitable for low temperature heat engine, and the energy efficiency will reach 25 %. The T-s diagram of the cycle for R404a with modified scroll geometry is given in Fig. 32.4. It can be observed from Fig. 32.4 that the energy efficiency of the Rankine cycle is strongly depended on the scroll expander geometry.

For all the organic working fluids, the efficiency can be improved by modifying the geometry in order to be able to calculate the most appropriate built-in volume ratio for the scroll machine. The rolling angle is the most important geometric parameter since it defines the length of the scroll and the number of loops through the expansion process [24–26]. Built-in volume ratio of the scroll expander is modified with respect to the rolling angle and influence of the modified geometry on the efficiency is evaluated for different working fluids as shown in Fig. 32.4.

The optimum rolling angle of the scroll expander for each organic fluid is evaluated and results are given in Table 32.1 to obtain an appropriate built in volume ratio for the best possible cycle efficiency. The results are provided in Fig. 32.4, and the modified geometry is shown by the columns labelled in red. R404a clearly gives the best result for the modified geometry and the energy efficiency is increased from 19 to 25 % (see Fig. 32.4). R123 and Toluene are the other working fluids which have relatively higher energy efficiencies compared to other organic fluids for the modified and unmodified cases of the scroll expander geometry as can be observed in the figures.

The effect of increased rolling angle on the energy efficiency of the cycle is shown in Fig. 32.5. Some fluids were omitted from the figure in order to analyze easily. It can be observed that the energy efficiency decrease for all the fluids with the increment of the rolling angle. In order to be able to obtain an optimum built-in volume ratio for the scroll machine, rolling angle should be decreased to the value that the rate of increase for the net work output from the scroll expander over the total heat input from the boiler has reached to the maximum value for the supercritical temperature condition at the expander inlet. The number of rotations of the orbiting scroll with respect to the fixed scroll is limited by the rolling angle. The produced shaft power will be lower for reduced rolling angles, however the efficiency will increase until the optimum built-in volume ratio is obtained for the scroll expander through the optimization process.

Figure 32.6 shows the variation of the system energy efficiency with respect to the boiler outlet temperature. The effect of superheating of the working fluid over the energy efficiency of the cycle is shown in the figure for the temperature ranges that vary from the saturation temperature to the critical temperature. The isentropic efficiencies of the expander and pump are taken to be 80 %. The condenser temperature and boiler pressure were kept constant at 25 °C and 1 MPa, respectively in order to generate the figure. It shows that the efficiency of the cycle for the organic fluids is a weak function of the boiler outlet temperature since it remains approximately constant or slightly increases with the increment of the boiler outlet temperature. It can be concluded that organic fluids do not need to be superheated to increase the energy efficiency of the cycle. It can be observed that R404a shows the best energy efficiency while NH$_3$ has the lowest efficiency for the temperature range from 300 to 500 K. The figure clearly illustrates that organic fluids can be used to produce power from low-temperature waste heat.

Figure 32.7 shows the variation of the system energy efficiency with the expander inlet pressure. Expander inlet temperature remained at saturated conditions for the constant condenser temperature of 25 °C and the maximum pressure

Fig. 32.6 Variation of the system thermal efficiency with the expander inlet temperature
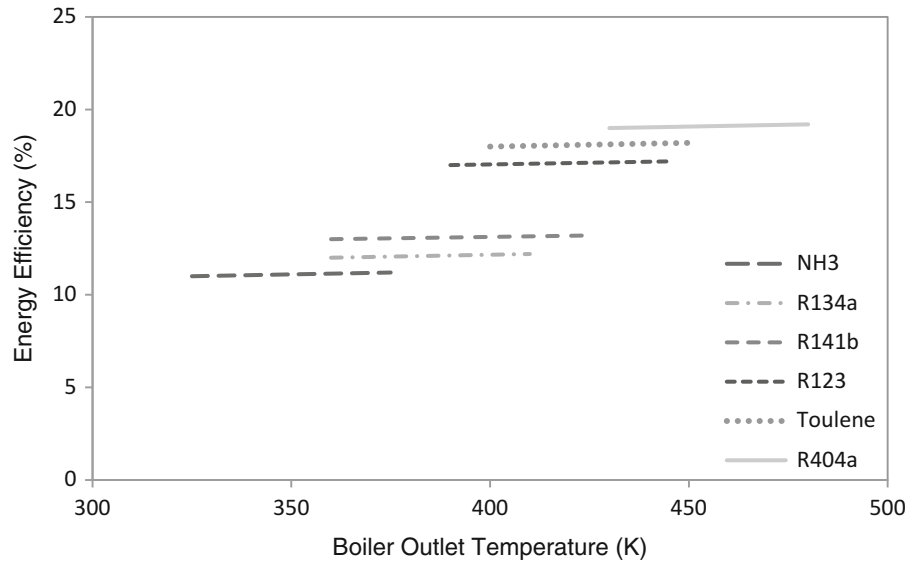
Fig. 32.7 Variation of the system energy efficiency with expander inlet pressure
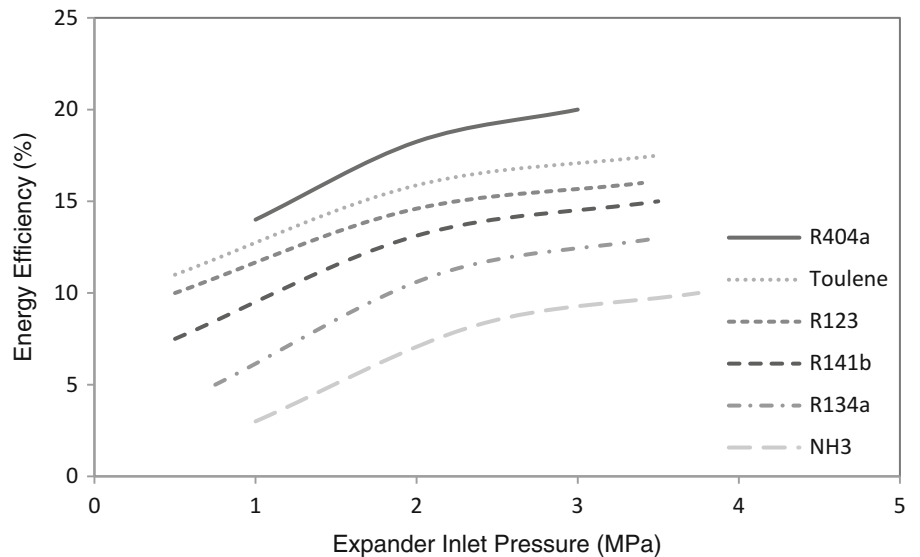
used for each fluid was the critical pressure. The isentropic efficiencies of the expander and pump were taken to be 0.80 for the analysis. It can be observed from Fig. 32.7 that the system energy efficiency increases with the increment of the expander inlet pressure for all fluids. Both the net work and the boiler heat increase with an increase in the inlet pressure. However the percentage of increase of the net work is higher than that of increase of the boiler heat. Therefore the ratio of the net work to the boiler heat increases with the expander inlet pressure. R404a shows the best energy efficiency for a range of pressure between 0.5 and 4.0 MPa.

The variation of the mass flow rate needed to generate the same power output with the expander inlet pressure is shown in Fig. 32.8. Using the same conditions given in Fig. 32.6 and a fixed power output of 1.7 kW the figure is generated. It can be observed that the mass flow rate needed decreases with the increment of an expander inlet pressure. The reason is due to the increase in the net work output of the cycle with the increment of the expander inlet pressure. These results agree well with the results obtained from Fig. 32.6, because an increment of the net work represents an increase in the cycle efficiency. R141b requires the highest mass flow rate for the pressure range from 0.5 to 4.0 MPa and R134a needs the lowest mass flow rate for the expander inlet pressure of 2 MPa and above.

Figure 32.9 shows the variation of energy efficiency with the condenser outlet temperature for the constant boiler pressure at 2.5 MPa. It can be observed form the figure that the system energy efficiency decreases linearly with the increase in the

Fig. 32.8 Variation of the mass flow rate with the expander inlet pressure
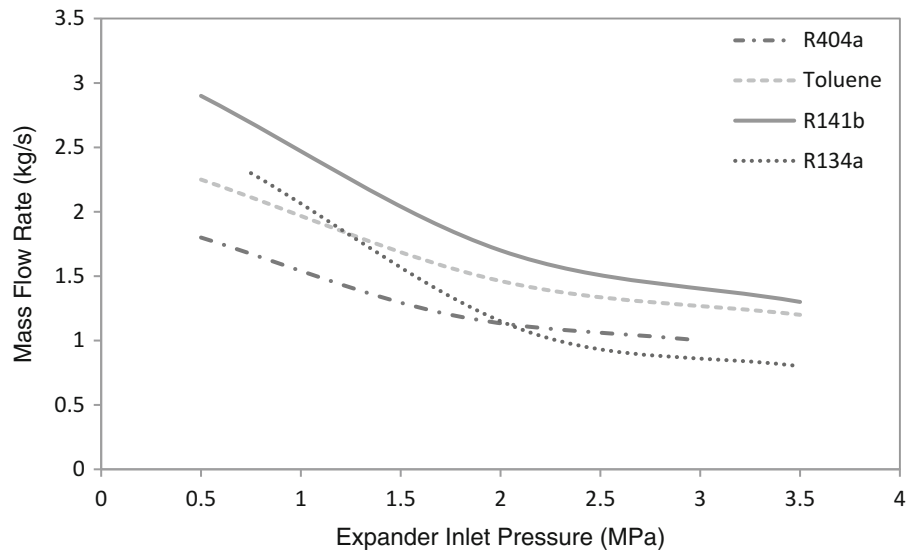
Fig. 32.9 Variation of the energy efficiency with the condenser outlet temperature
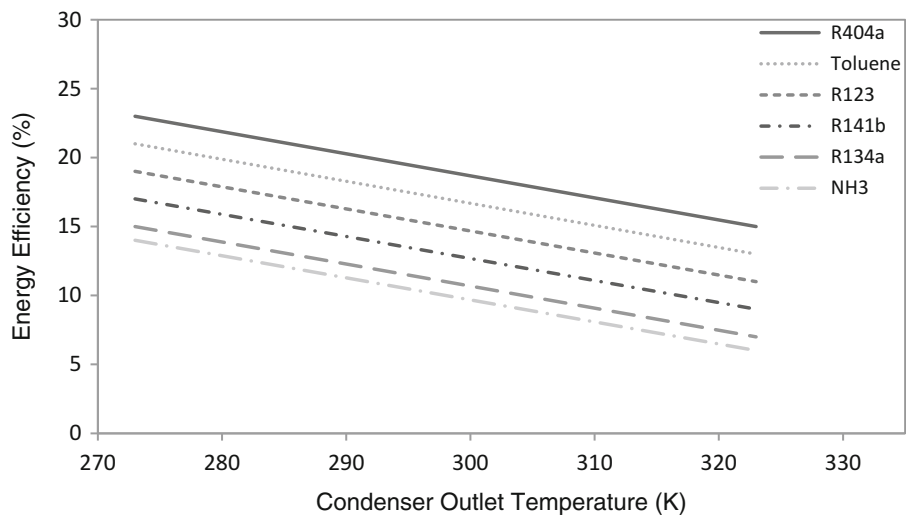
condenser outlet temperature. The isentropic efficiencies of the expander and pump were 0.85. The results obtained from Fig. 32.9 agree well with the results shown in Figs. 32.6 and 32.7 where R404a and NH$_3$ show the best and worst energy efficiencies among the evaluated working fluids.

Conclusions

The resulting ORC is non-realizable with a low efficiency of 14 % since the sink temperature for the cycle is far below the normal environmental temperature. In order to run a feasible Rankine cycle with the selected expander, without changing the scroll geometry and the working fluid, the upper pressure and temperature must be increased. It is found that by increasing the pressure and temperature at the expander intake to supercritical value, that is 68 bar and 264 °C, the cycle becomes realizable and achieves an efficiency of 18 %.

Several working fluids for Rankine cycle are investigated for the modified scroll geometry. The results showed that the rolling angle of the scroll machine should be modified in order to obtain an appropriate built-in volume ratio. First- and second-law analysis showed that energy efficiency of the Rankine cycle is strongly depended on the geometry of the scroll expander. Built-in volume ratio of the scroll expander is modified with respect to rolling angle and the influence of the modified geometry on the efficiency is evaluated for different working fluids. The results show that it is possible to improve the efficiency of the cycle by adjusting the scroll geometry for all fluids. R404a clearly gives the best results for the modified

geometry and the energy efficiency is increased to 25 % from 19 %. It can be said that the rolling angle should be reduced to have an optimum built-in volume ratio for the cycle in terms of appropriate temperature and pressure range that will ensure higher energy efficiency.

A parametric study is performed in order to evaluate the influence of the geometric and thermodynamic parameters on the cycle performance. It can be concluded that organic fluids need to be superheated as the cycle thermal efficiency remains approximately constant when the inlet temperature of the expander is increased. It can be also concluded that the thermal efficiency of ORC increases when the condenser temperature is decreased. Therefore using ORC in locations with low ambient temperature will be more effective.

Design optimization of the geometry showed that the mass flow rate can be improved when the radius increases to 1.25 time the original designed radius, but the radius of the basic circle needs to be reduced to 0.75 times the original radius in terms of achieving the best possible efficiency for the scroll expander. Therefore it can be said that the designed radius $(r_b/r_{b,design} = 1)$ is an optimum value since the mass flow rate and the expander efficiency are both close to their maximum value. The leakage rates and the rotation angles for different inlet pressures and rotating speeds of n = 956 rpm and n = 2,847 are compared, and these show that every curve has a jump at a rotation angle of 210°. The reason is that the expansion pocket opens up to the discharging region and the leakage mode changes at this angle.

The procedure can be applied for the conversion of scroll compressors use in reverse, as expanders for Rankine cycles applications. Through an appropriate modeling, scroll compressors can be used to predict the operation in reverse, as expanders. If no modifications are made to the scroll compressor, the efficiency of the Rankine cycle will result low because the built-in volume ratio is not adapted to the cycle configuration for the same pressure and temperature levels in the expanders

Nomenclature

A	Area (m^2)	r_b	Radius of the basic circle of the scroll (m)
c_p	Specific heat at constant pressure (J/kg K)	r_o	Orbiting radius of the rotating scroll (m)
c_v	Specific heat at constant volume (J/kg K)	r_v	Built-in volume ratio
C_d	Discharge coefficient	s	Specific entropy (J/kg$-$K)
C_f	Specific flow coefficient	t	Scroll thickness (m)
D	Diameter (m)	T	Temperature (°C)
E	Total internal energy (J)	u	Specific internal energy (J/kg)
g	Gravity of earth (m/s^2)	U	Internal energy (J)
h	Specific enthalpy (J/kg)	v	Velocity (m/s)
h_c	Convective heat transfer coefficient (W/m^2-K)	v	Specific volume (m^3/kg)
h_s	Scroll height (m)	V	Volume (m^3)
k	Specific heat ratio	V_{ed}	Expander discharge chamber volume (m^3)
L	Length (m)	V_{ee}	Expander expansion chamber volume (m^3)
m	Mass (kg)	V_{ei}	Expander intake chamber volume (m^3)
$\dot{m}$	Mass flow rate (kg/s)	W	Work (J)
N	Rotational speed (Hz)	$\dot{W}$	Work rate (J/s)
P	Pressure (Pa)	W_{in}	Total work input to the compressor (J)
Q	Heat (J)	W_{out}	Net work output from the expander (J)
$\dot{Q}$	Heat rate (J/s)	W_s	Total work output for the expander (J)
r	Radius (m)	z	Height (m)

Greek Letters

v	Specific volume (m^3/kg)	ρ	Density (kg/m^3)
w	Rotational speed (rad/s)	φ	Involute angle (rad)
ȝ	Leakage flow coefficient	φ_e	Rolling angle (involute ending angle) (rad)
δ	Gap (m)	$\varphi_{i,s}$	Starting angle of the inner involute (rad)
Δ	Difference	φ_{i0}	Initial angle of the inner involute (rad)
ε	Effectiveness	$\varphi_{o,s}$	Starting angle of the outer involute (rad)
η	Efficiency	φ_{o0}	Initial angle of the outer involute (rad)
θ	Orbiting angle (rad)		

Subscripts

a	Actual	fix	Fixed
amb	Ambient	i	Initial
b	Base circle	l	Low
c	Curvature	leak	Leakage
conj	Conjugate	loss	Mechanical loss
cp	Compressor	mot	Motor
CV	Control volume	o	Outer orbiting radius
d	Discharge	orb	Orbiting
diss	Dissipated	plen	Plenum
e	Expansion	rad	Radial
en	Ending	s	Isentropic
exh	Exhaust	su	Supply
exp	Expander	suc	Suction

References

1. International Energy Agency Technical Report (2006) World Energy Outlook. http://www.worldenergyoutlook.org/media/weowebsite/2008-1994/WEO2006.pdf
2. International Panel on Climate Change (2001) Third Assessment Report: Climate Change 2001. https://www.ipcc.ch/publications_and_data/publications_and_data_reports.shtml
3. Harada J (2010) Development of a small scale scroll expander. Master thesis, Oregon State University
4. Wang B, Li X, Shi W (2005) A general geometrical model of scroll compressors based on discretional initial angles of involute. Int J Refrig 28:958–966
5. Quoilin S (2007) Experimental study and modeling of a low temperature Rankine cycle for small scale cogeneration. Master thesis, University of Liege, Belgium
6. Quoilin S, Lemort V, Lebrun J (2010) Experiment study and modeling of an organic Rankine cycle using scroll expander. Appl Energy 87:1260–1268
7. Saleh B, Koglbauer G, Wendland M, Fischer J (2007) Working fluids for low-temperature organic Rankine cycles. Energy 32(7):1210–1221
8. Zhang B, Peng X, He Z, Xing Z, Shu P (2007) Development of a double acting free piston expander for power recovery in transcritical CO_2 cycle. Appl Thermal Eng 27(8):1629–1636
9. DeBlois RL, Stoeffler RC (1988) Instrumentation and data analysis techniques for scroll compressor. In: Proceedings of the international compressor engineering conference at Purdue, pp 182–188
10. Gravesen J, Henriksen C (2001) The geometry of the scroll compressor. SIAM Rev 43:113–126
11. Kim HJ, Ahn JM, Park I, Rha PC (2007) Scroll expander for power generation from a low-grade steam source. Proc Inst Mech Eng A J Power Energy 221 (5):705–711
12. Yanagisawa T, Fukuta M, Ogi Y, Hikichi T (2001) Performance of an oil-free scroll type air expander. In: Proceedings of the Institution of Mechanical Engineers conference transactions on compressors and their systems, pp 167–174
13. Hung T (2001) Waste heat recovery of organic Rankine cycle using dry fluids. Energy Convers Manag 42(5):539–553
14. Larjola J (1995) Electricity from industrial waste heat using high-speed organic Rankine cycle (ORC). Int J Prod Econ 41(1):227–235
15. Moran MJ, Shapiro HN (2004) Fundamentals of engineering thermodynamics. Wiley, New York
16. Zamfirescu C, Dincer I (2008) Thermodynamic analysis of a novel ammonia-water trilateral Rankine cycle. Themochim Acta 477:7–15
17. Badr O (1984) Multi-vane expanders as prime movers for low-grade energy organic Rankine-cycle engines. Appl Energy 16(2):129–146
18. Hirano T, Matsumura N, Takeda K (1988) Development of high efficiency scroll compressors for air conditioners. In: Proceedings of international compressor engineering conference at Purdue, pp 65–74
19. Bergman TL, Lavine AS, Incropera FP, DeWitt DP (2011) Fundamentals of heat and mass transfer. Wiley, New York
20. Winandy E, Saavedra CO, Lebrun J (2002) Experimental analysis and simplified modelling of a hermatic scroll refrigeration compressor. Appl Thermal Eng 22:107–120
21. Lemort V, Quoilin S, Cuevas C, Lebrun J (2009) Testing and modeling a scroll expander integrated into an organic Rankine cycle. Appl Thermal Eng 29 (14):3094–3102
22. Ishii N, Fukushima M, Sano K, Sawai K (1986) A study on dynamic behavior of a scroll compressor. In: Proceedings of international compressor engineering conference at Purdue, pp 901–916
23. Bush JW, Beagle WB (1992) Derivation of general relationship governing the conjugacy of scroll profiles. In: Proceedings of international compressor engineering conference at Purdue, pp 1079–1088
24. Chen Y, Halm NP, Groll EA, Braun JE (2002) Mathematical modeling of scroll compressors—part I: compression process modeling. Int J Refrig 25:731–750
25. Halm NP (1997) Mathematical modeling of scroll compressors. Master thesis, Purdue University
26. Xiaojun G, Liansheng L, Yuanyang Z, Pengcheng S (2004) Research on a Scroll expander used for recovering work in a fuel cell. Int J Thermodyn 7(1):1–8

Energy Analysis of Hydrogen Production from a Hybrid Wind Turbine-Electrolyzer System

Ersin Akyuz, Zuhal Oktay, and Ibrahim Dincer

Abstract

In this study, the energy performance of hybrid wind-hydrogen system is investigated. In addition to energy performance, a cost analysis of hydrogen production is also carried out for stand-alone system for different PEM electrolyzer capacities. Monthly efficiency variations for wind turbine operation for the total system are calculated and maximum efficiency values obtained as 22 % and 11.9 %, respectively. Energy efficiency of the PEM electrolyzer is determined for different temperature and electric current values. The results show that increasing the working temperature from 35 °C to 75 °C increases the energy efficiency of PEM electrolyzer from 62 % to 70 % at 30 A current. Hydrogen cost is calculated by economic analysis of wind-electrolysis-hydrogen production systems using the present-value method. The lowest cost at 6 m/s wind speed is calculated as 23.6 US$/kg. The size of electrolysis unit gains importance in regions with high annual average wind speed. In this regard, the optimum size is determined as 0.7 kW. The lowest cost at 6 m/s wind speed is calculated as 23.6 US$/kg. Furthermore, economics of wind-hydrogen system not only depends on the cost of wind turbine and electrolyzer but also on the configuration and resources.

Introduction

Hydrogen is proposed as one of the most promising solution as a mid- and long-term energy carrier for transport and electricity generation with regard to fossil fuels scarcity and the necessity of reducing greenhouse gas emissions. One of the main challenges is to develop a sustainable and cost-efficient process for hydrogen production. Together with electrolyzer and fuel cell technologies, hydrogen can provide a potential solution to this challenge. In addition, the use of hydrogen as a clean transportation fuel will bring a strong need for renewable hydrogen generation. Furthermore, energy available for hydrogen production is strongly dependent on the wind energy resources [1–3].

E. Akyuz (✉)
Mechanical Engineering Department, Faculty of Engineering, Balikesir University, 10110 Balikesir, Turkey
e-mail: akyuz11@gmail.com

Z. Oktay
Energy System Engineering Department, Faculty of Engineering, Recep Tayyip Erdogan University, Rize, Turkey
e-mail: zuhal.oktay@gmail.com

I. Dincer
Faculty of Engineering and Applied Science, University of Ontario Institute of Technology (UOIT),
2000 Simcoe St. N., Oshawa, ON, Canada L1H 7K4
e-mail: ibrahim.dincer@uoit.ca

Wind energy is becoming a competitive option for both small and large-scale power plant applications due to gradual reduction in its investment cost. Several wind-hydrogen hybrid energy systems have been investigated by scientists over the past decade. Both grid dependent systems and stand-alone applications have great significance in terms of performance and cost. Hydrogen can also be used to feed an energy conversion device which will act as a secondary power source during periods of high demand. Hydrogen could be produced by an electrolyzer powered by the excess electrical energy from the renewable energy source [4].

Many scientists have focused on the feasibility and system performance of hybrid renewable energy systems with a view to the production of hydrogen, mainly concentrating on solar, wind, and geothermal energy options [5–15].

The effect of operating parameters of the PEM electrolyzer, such as PEM operating temperature and current density, on PEM electrolyzer energy efficiency was studied by [16]. Parametric analyses were performed to investigate the effect of important design and operating parameters on the plant energy conversion efficiency. The results show that the energy efficiency of PEM electrolyzer increases with increasing temperature and decreases with current density.

A comprehensive mathematical model of a small wind-hydrogen stand-alone power system was investigated by Khan [17]. He focused on the dynamic and nonlinear model for a more realistic system simulation significantly affecting the system behavior. Also, control system and dynamic systems performance test were carried out.

An important experimental study was carried out by [2] on a combined wind and solar (PV) system operating at the Hydrogen Research Institute (HRI) of the Université du Quebec, Trois Rivieres. Photovoltaics and wind turbines were used to generate hydrogen in the system designed as a stand-alone for remote area applications and a wind/solar hybrid energy system working on small 5 kW electrolyzer.

Gokcek [4] studied the tecno-economic performance of stand-alone wind-hydrogen energy systems for remote areas in Turkey. Cost calculations and hydrogen generation were evaluated for different hub heights ranging from 12 m to 60 m.

The proposed study is conserned with the hybrid wind turbine electrolyzer system. It is proposed that the wind energy produced is delivered directly to the electrolyzer for hydrogen production. The aim of this study is to evaluate the energy performance of hybrid wind-hydrogen energy systems. In addition to energy performance, a cost calculation of hydrogen was also carried out for stand-alone systems of different PEM electrolyzer capacities.

Analysis

Hybrid Wind Turbine Electrolyzer

The basic components of the wind-hydrogen power system are given in Fig. 33.1. The Bergey XL-1 kW model wind turbine, at a hub height of 15 m, is used for the calculations. The wind turbine system is composed of a permanent magnet WT that can deliver a maximum output power of 1,000 W at 11 m/s of wind speed. The voltage produced by these sources is regulated and converted to 24 V on a power controlled center. The wind turbine produces DC electricity, which is transferred to DC-buck convert. In order to determine the 1 h time step of average energy flows throughout 1 year, MATLAB-Simulink was used to simulate and optimize the annual performance of the system. The commercial PEM electrolyzer system is used for the production of hydrogen. The electrolyzer consists of one cell, the water treatment unit, and the hydrogen generator at process pressure without a compressor. PEM electrolyzer has a capacity of 150 ml/min of H_2 production.

Wind Energy System

The number of studies on the application and effects of wind energy has rapidly increased in the world, so the efficiency of wind energy constructions has gained importance. Theoretically, maximum advantage an efficiency of 59.2 % from blowing wind according to the Betz Criteria. Today, wind energy ratio of around 40–45 % can be achieved by modern wind turbine types. In order to extract the maximum possible power, it is important that the blades of small wind turbines start rotating at the lowest possible wind speed. In the conventional windmill model, the wind power P_i is found as follows:

$$P_i = 0.5 \cdot \rho \cdot \pi . R^2 \cdot V_w{}^3 \tag{33.1}$$
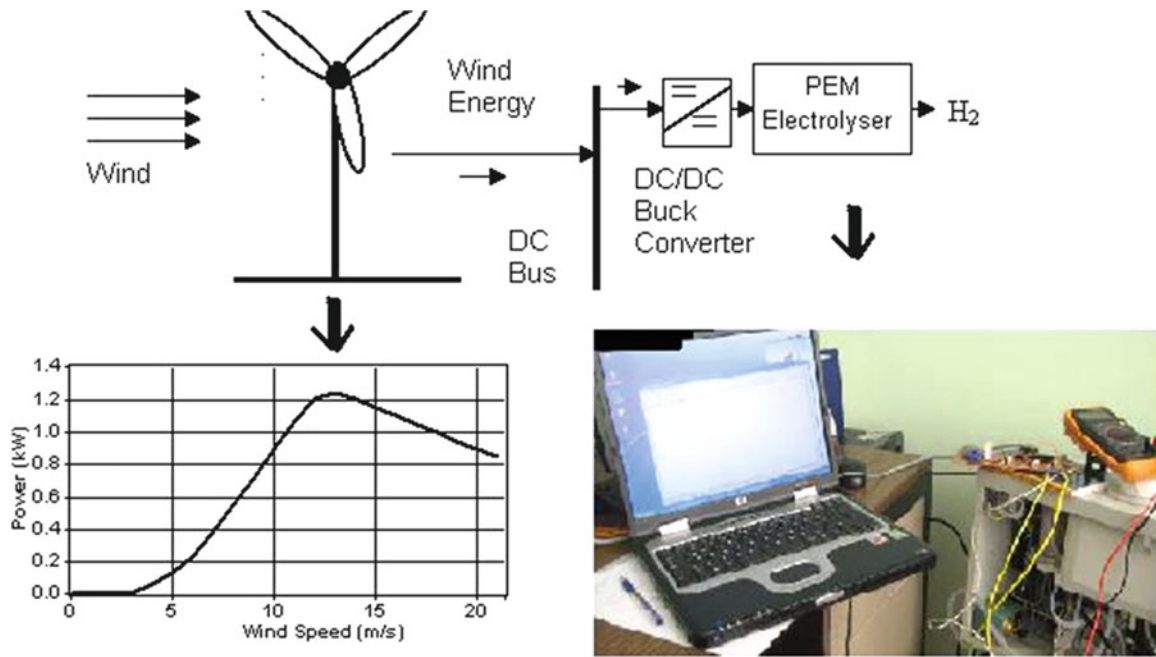
Fig. 33.1 Schematic diagram of wind-hydrogen experimental system

where ρ, R, and V_w represent the air density, rotor radius, and wind speed, respectively. The windmill power is given by

$$P_w = C_p \cdot P_i \tag{33.2}$$

For the wind turbine dynamics, Eq. (33.3) is used for the Simulink model power coefficient $[C_p(\lambda, \vartheta)]$ changing with tip speed ratio λ and blade pitch angle ϑ, which is based on the turbine model characteristics of [18], given by

$$C_p = 0.22 \cdot \left(\frac{116}{\lambda} - 0.4 \cdot \vartheta - 5 \right) \cdot e^{\frac{-12,5}{\lambda i}} \tag{33.3}$$

$$\frac{1}{\lambda i} = \frac{1}{\lambda + 00.8 \cdot \vartheta} - \frac{0.035}{\vartheta^3 + 1} \tag{33.4}$$

Figure 33.2 shows MATLAB-Simulink model. It was used to calculate energy efficiency and energy generation of wind turbine in the study.

PEM Electrolyzer

Typical industrial electrolyzers consume electricity between 4.5 and 6.0 kWh/Nm^3, corresponding to an energy efficiency of 65–80 %, and advanced electrolyzers were reported with an efficiency of 90 %. Typical industrial electrolyzers have electricity consumption between 4.5 and 6.0 kW h/Nm^3, corresponding to an efficiency of 65–80 %, and advanced electrolyzers have been reported with an efficiency of 90 % [18]. The voltage efficiency of the electrolyzer is defined by

$$\eta_v = \frac{1.48}{V_{elc}} \cdot 100\% \tag{33.5}$$

According to Faraday's law, the amount of hydrogen produced in the electrolyzer can be calculated by [19]

$$m_{elc} = \frac{i_{elc} \cdot n}{2 \cdot F} \eta_i [mol/s] \tag{33.6}$$
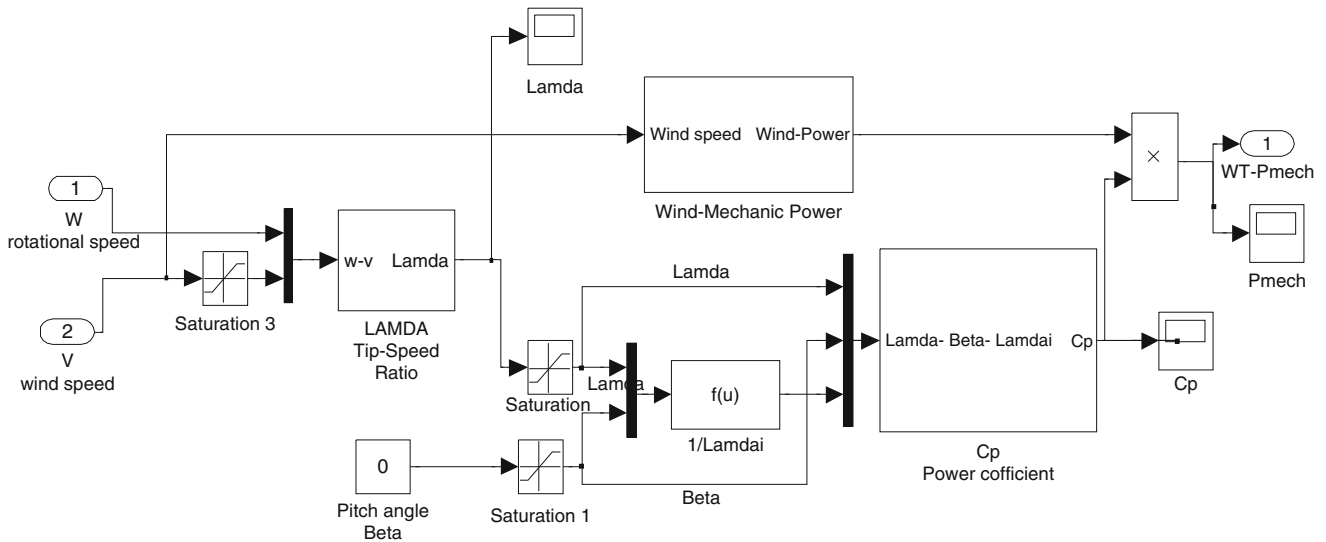
Fig. 33.2 MATLAB-Simulink model for the wind turbine

where i_{elc} is the current through the electrolyzer, n is the stack number in the electrolyzer, F is Faraday Constant, and η_i is the current efficiency of the electrolyzer [20].

The efficiency of an electrolyzer is inversely proportional to its cell potential. Electrolyzer efficiency could be determined by the current density, and it directly corresponds to the rate of hydrogen production per unit of electrode active area. The energy efficiency of the PEM electrolyzer is given as

$$\eta_{elc} = \frac{(HHV)_{H_2} \cdot n_{H2}}{\sum W_{elc}} \tag{33.7}$$

where the higher heat value (HHV) of hydrogen is used for PEM efficiency calculation as 39 kWh/kg.

Economic Evaluation

The life cycle cost (LCC) analysis is a useful tool for the comparison of the ultimate delivered costs of technologies using different cost structures. Rather than comparing only the initial capital costs or the operating costs, LCC analysis seeks to calculate the cost of delivering a service over the life of the project. The final cost per kg-H_2 is estimated to be independent of the technology that was used to produce the hydrogen. The cost of hydrogen can be given in terms of its total present value (TPV), as follows [21]:

$$TPV = Initial\ cost + \sum O\&M + \sum Replacement \tag{33.8}$$

$$Cost\ (\$/kg\,H_2) = \frac{TPV \cdot CRF}{Annual\ H_2\ production} \tag{33.9}$$

where CRF is the capital recovery factor and defined as

$$CRF = \frac{(1+R)^N \cdot R}{(1+R)^N - 1} \tag{33.10}$$

In the analysis, the following assumptions are satisfactorily made:
- The net discount rate (R) and economic evaluation period (N) are taken as 8 % and 25 years, respectively.
- The economic lifetime for the converter and PEM electrolyzer is taken as 15 years.

- The operation and maintenance costs are taken as 5 % of initial cost of the wind turbine.
- The total system cost per kW$_p$ of wind energy system is about 2,500 US$, and the DC–DC converter and electrolyzer cost about 6,000 US$.

Results and Discussion

In the study, a wind-PEM electrolyzer system is modeled, and performance evaluation is made for hydrogen production. In addition, the hourly average wind speed is used in order to obtain the electric energy output of the wind turbine. Hydrogen generation via electrolysis and electric generation from the wind turbine are shown in Fig. 33.3.

In order to determine the energy performance of PEM electrolyzer at different current densities and temperatures, the cell current, temperature, voltage, and hydrogen production rate of PEM electrolyzer are measured and recorded to data logger. As can be seen from Fig. 33.4, the energy efficiency of the PEM electrolyzer decreases with current density. The total energy input increases with current density at a rate higher than the energy output. At low current density, the electrical energy
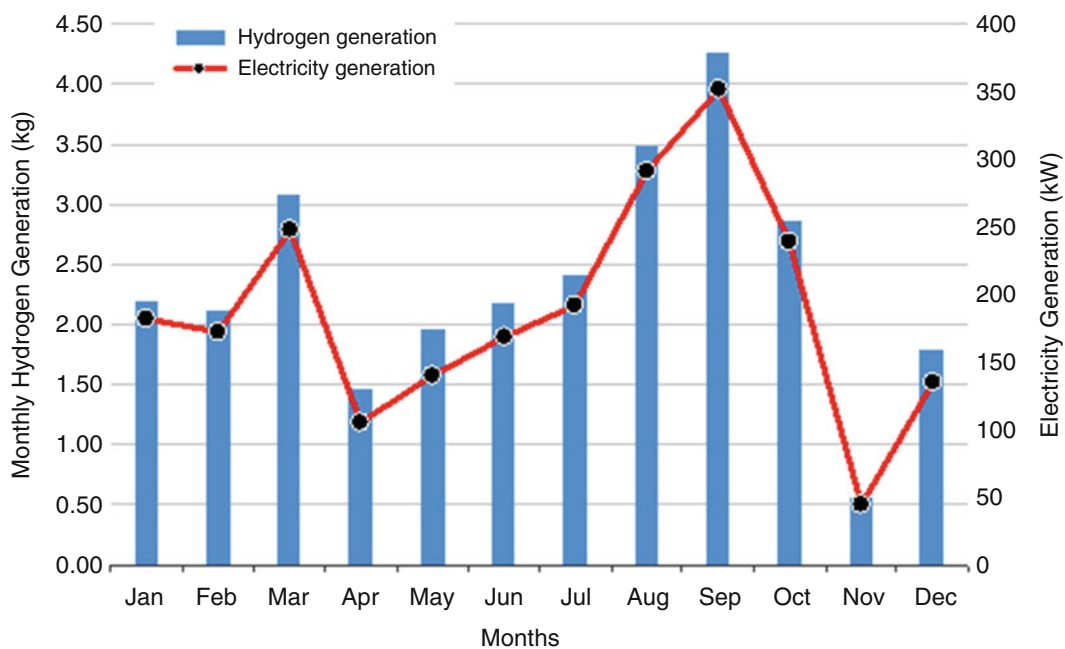
Fig. 33.3 Monthly electricity and hydrogen production from hybrid system
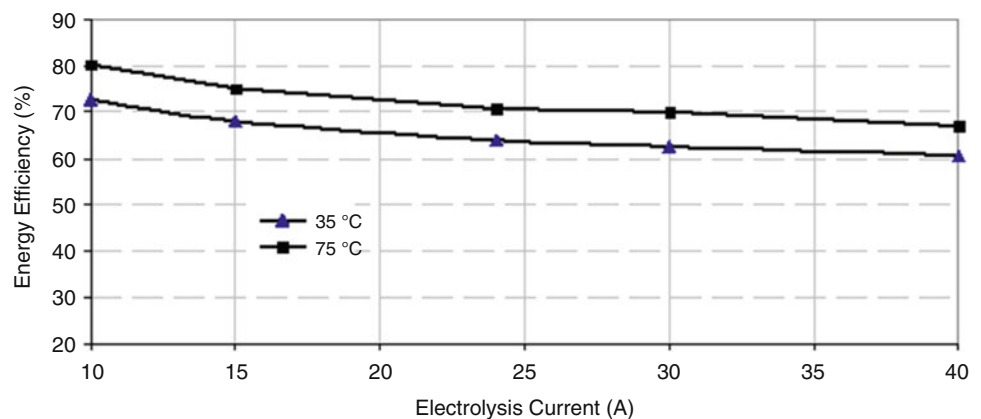
Fig. 33.4 PEM electrolyzer energy efficiency for different current at the temperatures of 35 and 75 °C
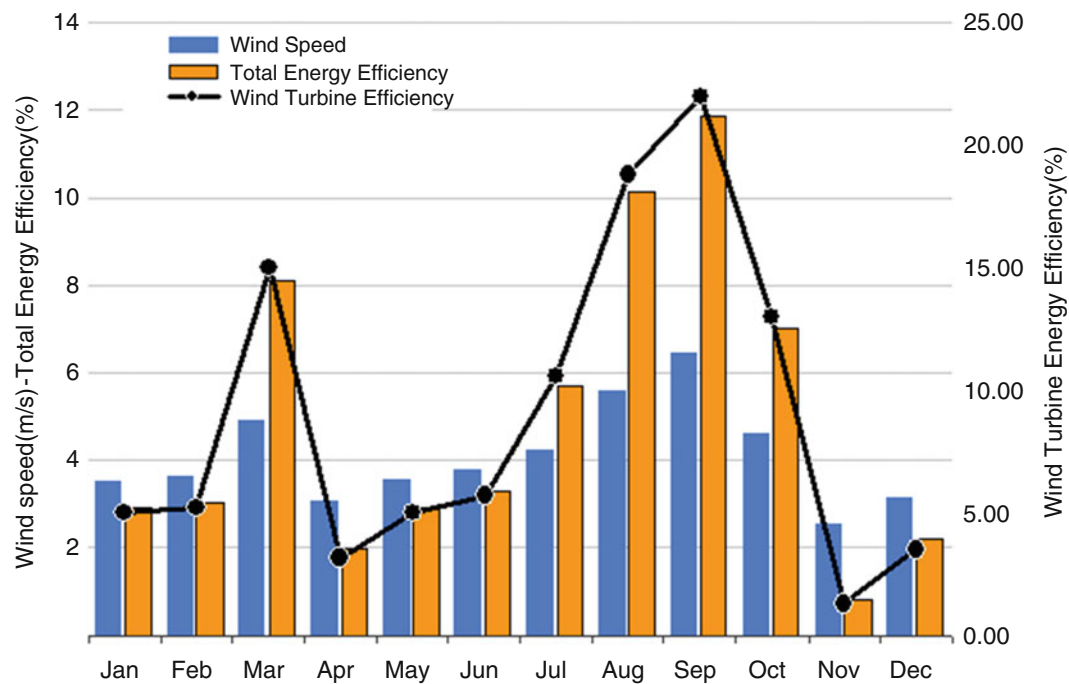
Fig. 33.5 Monthly efficiency variation for wind turbine and hybrid system

Table 33.1 Hydrogen production cost for various wind speed for 0.7 kW PEM electrolyzer

Annual wind speed (m/s)	Annual H_2 production (kg/year)	Wind turbine capacity factor (%)	Cost of H_2 (US$/kg)
4	23.5	0.28	30.8
4.5	26.1	0.31	27.7
5	28.4	0.338	25.5
5.5	29.7	0.354	24.3
6	30.7	0.366	23.6

demand increases considerably with increasing current density, while the thermal energy input and the energy output increase linearly with current density.

The energy efficiency of the PEM electrolyzer is determined for different temperature and current values. Figure 33.4 shows that energy efficiency increases with increasing temperature. But, the operating temperature generally should not exceed 373 K because liquid water is needed to sustain the high ionic conductivity of the PEM electrolyte. When the working temperature increases 35–75 °C, the energy efficiency of the electrolyzer increases 62–70 % at 30 A current.

The variation of average monthly wind speed with wind turbine and total system energy efficiency values are shown in Fig. 33.5. It is clear from the figure that the efficiency of the wind turbine increases in parallel with the wind speed. While the maximum efficiency of the system was found as 11.9 % in September, the minimum efficiency of system was found as 0.8 in November.

Hydrogen production cost is calculated by economic analysis of wind-electrolysis-hydrogen production systems using present-value method. In addition, the amounts of hydrogen which could be produced were determined annually. For a more generalized calculation, the optimum capacity value of the electrolysis unit was achieved in the cost and energy perspective.

Also, the variable annual average amount and cost of hydrogen production were calculated for electrolysis units of different capacities. Capacity usage rate and thus the amount of hydrogen production were found to increase in parallel with the wind speed. The decrease in the cost of hydrogen production was lower above 5 m/s wind speed (see Table 33.1).

Consequently, it was determined that 20.3 kg hydrogen could be produced at 30.8 US$/kg on average using an electrolysis unit of 0.56 kW with 65 % efficiency and a wind turbine of 1 kW in Balikesir region with an average wind speed of 4.09 m/s.

Fig. 33.6 Variation of the hydrogen production cost depending on electrolysis capacity at annual average wind speed values
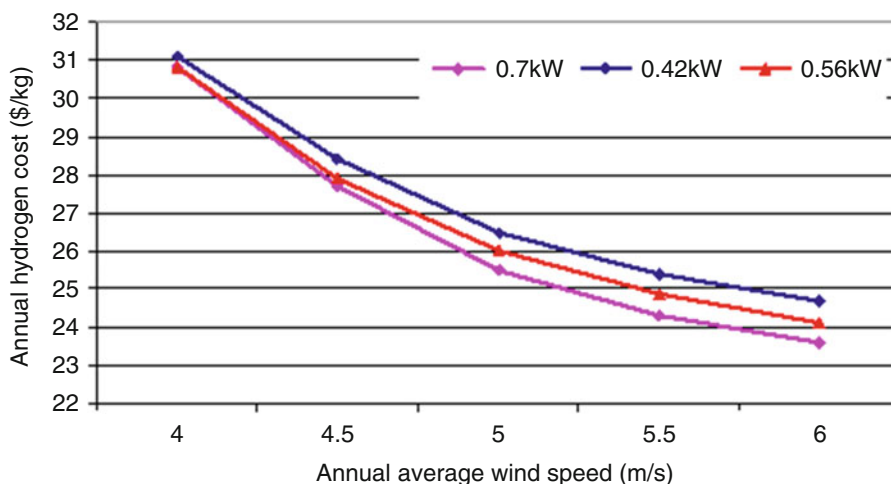
Hydrogen production cost is investigated for different annual average wind speeds and electrolysis capacities, and the calculation results are shown in Fig. 33.6. The cost of hydrogen production is found to be approximately the same at 4–4.5 m/s wind speeds using a 1 kW wind turbine. And there was found to be only a small difference in using 0.42 kW or 0.7 kW electrolysis units. The size of electrolysis unit gains importance in regions with high annual average wind speed. In this regard, the optimum size was determined as 0.7 kW. The lowest cost, at 6 m/s wind speed, was calculated as 23.6 US$/kg.

Conclusions

The purpose of this study was to carry out a techno-economic analysis of hydrogen production using the wind turbine-electrolysis hybrid system. The calculation of energy production is made by averages of the levelized cost method. The key conclusions of this study are given below:

- In order to find a feasible system option for the wind-hydrogen system, the electrolyzer has to be chosen at a power lower than the wind turbine's maximum power output. In this case some of the power from the wind would be unutilized, but the electrolyzer would operate with a higher capacity factor.
- Economics of wind hydrogen is determined by the cost of the wind turbine and the electrolyzer. Also, a feasible system greatly depends on the configuration and resources.
- Hydrogen cost is calculated by economic analysis of wind-electrolysis-hydrogen production systems using the present-value method. The lowest cost at 6 m/s wind speed is calculated as 23.6 US$/kg.
- Increasing the operating temperature from 35 °C to 75 °C increases the energy efficiency of the PEM electrolyzer from 62 % to 70 % at 30 A current.

Nomenclature

A	PV area (m^2)	R	Resistance
C_p	Power coefficient (–)	S_t	Global solar radiation (W/m^2)
n	Stack number	T	Ambient temperature (°C)
P	Power (W)	V	Voltage (V)

Greek Letters

η	Energy efficiency	λ	Tip speed ratio (–)
ϑ	Blade pitch angle (°)		

Abbreviations

AL	Annual load (kWh)	N	Economic evaluation period (year)
COE	Cost of energy (US\$/kWh)	NPC	Net present cost (US\$)
CRF	Capital recovery factor	R	Net discount rate
LEC	Levelised energy cost (US\$/kWh)	TPV	Total present value (US\$)

References

1. Agbossou K, Kolhe ML, Hamelin J, Bose TK (2004) Performance of a stand-alone renewable energy system based on energy storage as hydrogen. IEEE T Energy Conver 19(3):633–640
2. Agbossou K, Chahine R, Hamelin J, Laurencelle F, Anouar A, St-Arnaud JM, Bose TK (2001) Renewable energy systems based on hydrogen for remote application. J Power Sources 96:168–172
3. Levene JI et al (2005) An analysis of hydrogen production from renewable electricity sources. NREL Report N° CP-560-37612 USA
4. Gökcek M (2010) Hydrogen generation from small-scale wind-powered electrolysis system in different power matching modes. Int J Hydrogen Energy 35:10050–10059
5. Levin DB, Chahine R (2010) Challenges for renewable hydrogen production from biomass. Int J Hydrogen Energy 35(10):4962–4969
6. Moriarty P, Honnery D (2007) Intermittent renewable energy: the only future source of hydrogen. Int J Hydrogen Energy 32(12):1616–1624
7. Gorensek MB, Forsberg CW (2009) Relative economic incentives for hydrogen from nuclear, renewable, and fossil energy sources. Int J Hydrogen Energy 34 (9):4237–4242
8. Briguglio N, Andaloro L, Ferraro M, Di Blasi A, Dispenza G, Matteucci F et al (2010) Renewable energy for hydrogen production and sustainable urban mobility. Int J Hydrogen Energy 35(18):9996–10003
9. Greiner CJ, Korpas M, Holen AT (2007) A Norwegian case study on: the production of hydrogen from wind power. Int J Hydrogen Energy 32:1500–1507
10. Balta MT, Dincer I, Hepbasli A (2010) Potential methods for geothermal-based hydrogen production. Int J Hydrogen Energy 35(10):4949–4961
11. Turner J, Sverdrup G, Mann MK, Maness P, Kroposki B, Ghirardi M et al (2008) Renewable hydrogen production. Int J Energy Res 32(5):379–407
12. Rosen MA, Naterer GF, Chukwu CC, Sadhankar R, Suppiah S (2012) Nuclear-based hydrogen production with a thermochemical copper–chlorine cycle and supercritical water reactor: equipment scale-up and process simulation. Int J Energy Res 36(4):456–465
13. Dincer I (2007) Environmental and sustainability aspects of hydrogen and fuel cell systems. Int J Energy Res 31(1):29–55
14. Aiche-Hamanea L, Belhamela M, Benyoucef B, Hamanea M (2009) Feasibility study of hydrogen production from wind power in the region of Ghardaia. Int J Hydrogen Energy 34:4947–4952
15. Korpa SM, Greiner CJ (2007) Opportunities for hydrogen production in connection with wind power in weak grids. Renew Energy 33(9):119–208
16. Meng N, Leung MKH, Leung DYC (2008) Energy and exergy analysis of hydrogen production by a proton exchange membrane (PEM) electrolyzer plant. Energ Convers Manage 49(10):2748–2756
17. Khan MJ, Iqbal MT (2009) Analysis of a small wind-hydrogen stand-alone hybrid energy system. Appl Energy 86(11):2429–2442
18. Sherif SA, Barbir F, Veziroglu TN (2005) Wind energy and the hydrogen economy—review of the technology. Sol Energy 78(5):647–660
19. Sopian K, Ibrahim MZ, Daud WR, Othman MY, Yatim B, Amin N (2009) Performance of a PV–wind hybrid system for hydrogen production. Renew Energy 34 (8):1973–1988
20. Heier S (1998) Grid integration of wind energy conversion systems. Wiley, New York, NY
21. Lazou AA, Papatsoris AD (2000) Economics of photovoltaic stand-alone residential households: a case study for various European and Mediterranean locations. Sol Energy Sol Cells 62:411–427

Evaluation of Thermal Characteristics of a Borehole Thermal Energy Storage System

34

Önder Kizilkan and Ibrahim Dincer

Abstract

Energy storage technologies are usually a strategic and necessary component for the efficient utilization of renewable energy sources and energy conservation. Their use is important to overcome energetic and environmental issues. Thermal energy storage (TES) serves at least three different purposes: (1) energy conservation and substitution (by using natural energy sources and waste energy), (2) energy peak shifting (from more expensive daytime to less expensive nighttime rates), and (3) electricity conservation (by operating efficient devices at full load instead of part load to reduce peak power demands and increase efficiency of electricity use). Numerous TES systems have received attention for practical applications. Underground thermal energy storage systems may be divided into two groups: (1) closed storage systems, so-called borehole TES, in which a heat transport fluid (water in most cases) is pumped through heat exchangers in the ground and (2) open systems where groundwater is pumped out of the ground and then injected into the ground using wells (aquifer TES) or in underground caverns. In this study, the thermal resistance characteristics of borehole heat exchangers of borehole TES at University of Ontario Institute of Technology (UOIT) are investigated. In this regard, the ground thermal properties of Oshawa are studied, and a comparison of different methods for determining such thermal resistances is made for practical applications. Finally, a thermal response test mode for BTES is illustrated.

Introduction

Energy saving is a major task to fulfil in daily applications, due to increasing energetic and environmental issues. For energy saving and reducing the emissions, it is required to improve the energy efficiency of systems. In addition, renewable energy technologies have received an increasing interest for environmentally-benign applications. Heat pumps for space heating and cooling are considered an interesting example. To improve their performances, both low temperature in heating and high temperature in cooling operation are required. On the other hand, a suitable source or sink temperature is necessary. In general, external air is used but in this case the energy performance is affected by climatic variations. Instead of this,

Ö. Kizilkan (✉)
Department of Energy Systems Engineering, Süleyman Demirel University, Isparta, Turkey

Faculty of Engineering and Applied Science, University of Ontario Institute of Technology (UOIT), Oshawa, ON, Canada
e-mail: onderkizilkan@sdu.edu.tr

I. Dincer
Faculty of Engineering and Applied Science, University of Ontario Institute of Technology (UOIT), Oshawa, ON, Canada
e-mail: ibrahim.dincer@uoit.ca

if available and allowed, ground water use becomes a good option under constant temperature conditions. Another possibility is to use the ground as a heat source or sink, since its temperature is almost constant all over the year, thus allowing smaller temperature variations than external air during both heating and cooling seasons [1].

Borehole thermal energy storage (BTES) systems use the ground as a heat source or sink for space conditioning in residential and commercial buildings. In last decades, ground source heat pump (GSHP) systems have been used increasingly around the world, because they are among the cleanest and most energy efficient air-conditioning systems for commercial and residential buildings. A typical GSHP system mainly consists of a heat pump unit with a BTES. BTES systems are coupled with a group of borehole heat exchangers (BHEs). BHEs are devised for the extraction or injection of thermal energy from or into the ground. However, the thermal performance of BHEs is site-specific, due to the differences of the underground thermal properties, sizes and configuration of BHEs, and backfill materials of boreholes [2]. The structure and physical properties of the ground are factors affecting temperature in all zones. The temperature of the ground is a function of the thermal conductivity, geothermal gradient, water content, and water flow rate through the borehole [3].

In a vertical U-tube ground heat exchanger, a water pump circulates fluid through pipes inserted into a borehole in the ground. The borehole, after the insertion of the U-tube, is usually backfilled with grout or water in order to ensure good thermal contact with the ground [4]. In Scandinavia groundwater is often used to fill the space between borehole wall and collector wall, while otherwise it is more common to backfill with some grouting material. The advantage of using water is cheaper installations and more easy access to the collector if needed. Grouting is on the other hand required in many counties by national legislation in order to prevent groundwater contamination or is used to stabilize the borehole wall [5]. The circulating fluid is usually water or a water–antifreeze mixture. A borehole heat exchanger is usually drilled to a depth between 20 and 300 m with a diameter of 10–15 cm. A borehole system can be composed of a large number of individual boreholes [4].

In this study, a closed BTES using BHEs at University of Ontario Institute of Technology (UOIT) in Oshawa, Canada, is analyzed in terms of ground thermal characteristics. The underground BTES system considered in this chapter is installed at UOIT. The UOIT campus includes four new buildings that are designed to be heated and cooled, sometimes with renewable energy in order to minimize greenhouse gas emissions. Test drilling programs were carried out to determine the feasibility of thermal storage in the overburden and bedrock formations at the UOIT site. In situ tests were conducted to determine the groundwater and thermal characteristics. An almost impermeable limestone formation was encountered from 55 m to 200 m below surface. For meeting the required energy demand, 370 boreholes, each 200 m in depth, were used. In addition, five temperature monitoring boreholes were installed, increasing the total drilling for the project to 75 km. Some design changes were made to the borehole heat exchangers (BHEs) as a result of the lack of groundwater flow in the rock. The Swedish practice of water-filled BHEs was utilized instead of the North American practice of grouted BHEs. Waterfilled BHEs improve the efficiency of the U-tube installation and extend the life of the boreholes indefinitely (further details, see [6]).

Ground Thermal Characteristics of Oshawa

For determination of the thermal interaction of BHE with the ground, it is important to have an accurate representation of local ground temperature since it is the temperature difference between the ground and the circulating fluid that drives the heat transfer. The ground temperature near the surface cycles with the time of the year. These variations disappear at lower depths, where the ground remains at its mean temperature throughout the year. An equation for calculating the ground temperature at any time of the year was developed by Kasuda who found that the temperature of the ground is a function of the time of year and the depth below the surface [7]. The equation is used for predicting soil temperatures, $T(z, t)$, for any depth z and at any time t in the year, based on the mean ground temperature (T_{mean}), the surface amplitude (T_{amp}), and the time of the minimum surface temperature (t_0) [8]. The vertical ground temperature distribution can be theoretically modeled based on the following equation:

$$T(z,t) = \left(T_{mean} - T_{amp}\right) - exp\left(-z\sqrt{\frac{\pi}{365\alpha}}\right)cos\left(\frac{2\pi}{365}\left[t - t_0 - \frac{z}{2}\sqrt{\frac{365}{\pi\alpha}}\right]\right) \qquad (34.1)$$

Table 34.1 Earth temperature data for various Canadian locations [7]

Location	T_{mean} (°C)	T_{amp} (°C)	t_0 (days)
Calgary (AB)	6.4	11.1	22
Edmonton (AB)	7.1	14.9	11
Vancouver (BC)	11.3	12.2	7
Victoria (BC)	11.8	12.2	5
Winnipeg (MB)	6.1	14.0	36
Halifax (NS)	9.0	10.2	50
St. John's (NL)	6.7	10.0	50
Fredericton (NB)	7.7	11.6	38
Charlottetown (PE)	7.5	15.2	44
Montreal (QC)	6.4	15.1	14
Quebec City (QC)	7.4	13.5	52
Ottowa (ON)	8.9	12.6	36
Toronto (ON)	10.1	12.5	41
Oshawa[a] (ON)	10.3	12.9	44
Regina (SK)	4.8	15.9	36
Saskatoon (SK)	5.9	17.2	12

[a]Data for Oshawa was obtained from [10]

Table 34.2 Thermal and physical properties of some types of rock and soil [7]

Layer material	k (W/mK)	α (m^2/day)	ρ (kg/m^3)	C_p (kJ/kgK)
Dense rock (granite)	3.46	0.1114	3,204.0	0.8374
Average rock (limestone)	2.42	0.0891	2,803.5	0.8374
Heavy soil—damp (clay, compacted sand)	1.30	0.0557	2,098.6	0.9630
Heavy soil—dry (clay, compacted sand)	0.87	0.0445	2,002.5	0.8374
Light soil—damp (loose sand, silt)	0.87	0.0445	1,602.0	1.0468
Light soil—dry (loose sand, silt)	0.35	0.0245	1,441.8	0.8374

where T_{mean} is the mean soil temperature, T_{amp} the annual surface temperature amplitude, t the "Julian day", where t = 0 refers to January 1st and t_0 the day of minimal soil surface temperature, and α the thermal diffusivity of the soil (in m^2/day). The annual surface temperature amplitude T_{amp} can be found using the following equation [9]:

$$T_{amp} = \frac{T_{surf,\max} - T_{surf,\min}}{2} \qquad (34.2)$$

The required ground measurement data are the mean or average ground temperatures at approximately 3 m or as deep as is available. The data at which $T_{surf,\min}$ occurs (t_0) is also available. To calculate the value for t_0, it is the best way counting the number of days since January 1st, including January 1st and the day on which t_0 occurs. For groundwater systems, the entering water temperature can be approximated by the mean ground temperature. Table 34.1 contains the ground property data for 15 Canadian locations.

The thermal conductivity of the soil and the thermal diffusivity are the two soil and rock properties that most affect the design of the heat pump system. The thermal conductivity represents the ability of heat to travel through the ground. The thermal diffusivity is am measure of the ground's ability to conduct thermal energy relative to its ability to store thermal energy. Table 34.2 provides a simplified subdivision of rock and soil properties accompanied by approximate thermal and physical properties.

Calculation of Thermal Resistances

Thermal Resistance Inside the Borehole

Thermal resistance of fluid convection is defined as:

$$R_{conv} = \frac{1}{2\pi r_{in} h_{in}}$$ (34.3)

where subscript in represents inner flow. The convection heat transfer coefficient h_{in}, for inner flow is determined by using Nusselt number:

$$Nu = \frac{h_{in} d_{in}}{k_{fluid}}$$ (34.4)

For a fully developed turbulent flow in smooth tubes, a simple relation for the Nusselt number is given by Gnielinski [11]:

$$Nu = \frac{(f/8)(Re - 1000)Pr}{1 + 12.7\sqrt{f/8}\left(Pr^{\frac{2}{3}} - 1\right)} \quad \left(0.5 \leq Pr \leq 2000, \quad 3 \times 10^3 < Re < 5 \times 10^6\right)$$ (34.5)

where f is the friction factor and can be determined for smooth tubes, in turbulent flow from the first Petukhov equation [11]:

$$f = (0.790 lnRe - 1.64)^{-2} \quad \left(10^4 < Re < 10^6\right)$$ (34.6)

The fluid properties are evaluated at the bulk mean fluid temperature $T = (T_{in} + T_{out})/2$. Thermal resistance of conduction in the pipe then becomes

$$R_{cond} = \frac{ln\left(\frac{r_{p,out}}{r_{p,in}}\right)}{2\pi k_p}$$ (34.7)

where $r_{p,in}$ and $r_{p,out}$ are the inner and outer radius of the pipe and k_p is thermal conductivity of pipe. Since in most of the GSHP systems, the boreholes are usually grouted, a few of them left with groundwater to fill the space between heat exchanger pipes and borehole wall. Few models concern the convective heat transfer in the groundwater. Also it was reported by Gustafsson et al. [5] that most of them are dealing with regional groundwater flow, which is shown not to influence the system except in porous ground or high fractured bedrock. None of these models concern natural convection in groundwater filled borehole situated in solid rock without any larger fractures, which is a common situation in Sweden. In Scandinavia groundwater is often used to fill the space between borehole wall and collector wall, while otherwise it is more common to backfill with some grouting material [5]. Like in most GSHPs in Sweden, the system at UOIT was also built using water as filling material.

For UOIT, the background temperature of the geologic formations at the site is 10 °C. Considering the ground temperature, the poor quality shale groundwater, and the lack of a measurable groundwater flux in the limestone, it was concluded that the site was ideally suited for a borehole thermal energy storage (BTES) system. No water-bearing sand deposits were found in the 44 m of deposits (silt/clay overburden) [12].

Calculation of Thermal Resistances of Filling Material for Grouts

The three effective thermal resistances, R_{conv}, R_{cond}, and R_{grout} are, respectively, the convective resistance inside each tube, the conduction resistance for each tube, and the grout resistance. They are obtained using the analytical equation proposed by Hellström [13]. Thermal resistance of the grout has the following expression [14]:

$$R_{grout} = \frac{1}{4\pi k_{grout}}\left[ln\left(\frac{r_{bh}}{r_{p,out}}\right) + ln\left(\frac{r_{bh}}{L_s}\right) + \frac{k_{grout} - k_{soil}}{k_{grout} + k_{soil}} ln\left(\frac{r_{bh}^4}{r_{bh}^4 - \left(\frac{L_s}{2}\right)^4}\right)\right]$$ (34.8)

Fig. 34.1 Cross section of geothermal vertical borehole [14]
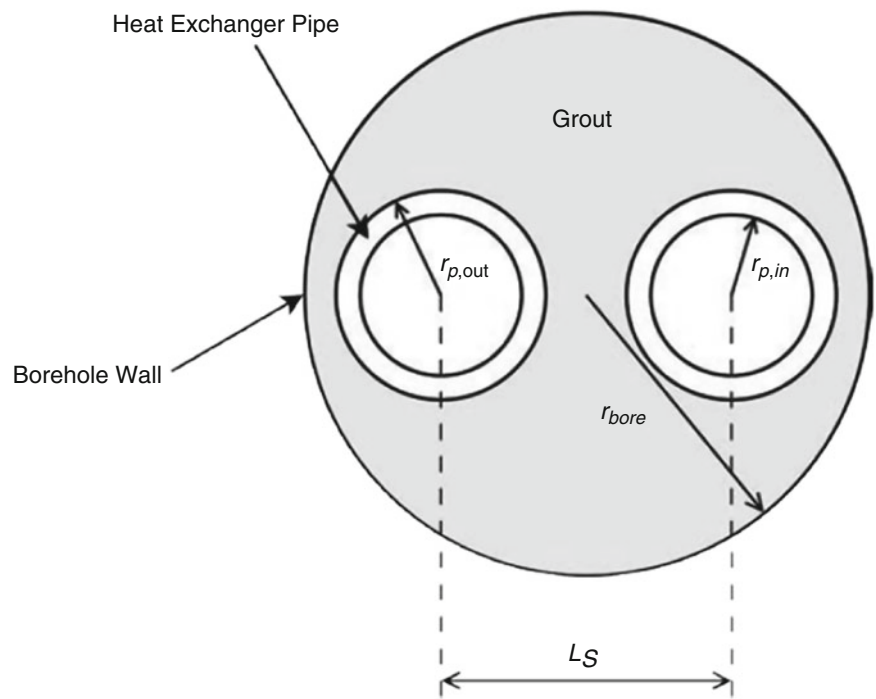
Fig. 34.2 Configurations of U-tube pipes in borehole [15]
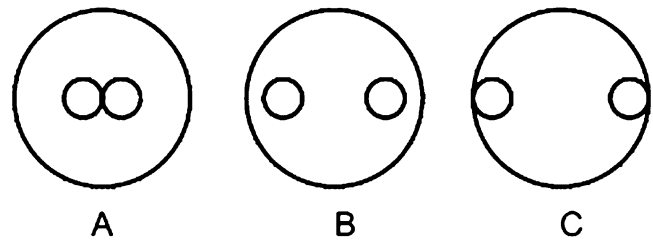
where subscript bh represents borehole, k_{grout} is the thermal conductivity of the grout, k_{soil} is the ground thermal conductivity, and L_s is the center-to-center distance between the two pipes (Fig. 34.1).

Thermal resistance of grout can be computed by shape factor method and equivalent diameter method. The shape factor method is used to describe the heat conduction characteristics of a complicated geometry [15].

$$R_{grout} = \frac{1}{k_{grout}\beta_0 \left(\frac{d_{bh}}{d_{out}}\right)^{\beta_1}} \tag{34.9}$$

where β_0 and β_1 are the shape factors of R_{grout}, whose values depend on the relative location of U-tube pipes in the borehole. Remund [16] studied three configurations as shown in Fig. 34.2; the corresponding values are provided in Table 34.3. To be mentioned, configuration B would be an appropriate design assumption in most situations, as it represents an average spacing along the entire borehole length. While configuration A is a conservative design assumption, configuration C is a risky design assumption [15].

Equivalent diameter method means the two legs in the U-tube are replaced by a single concentric cylindrical heat source (or sink); the equivalent diameter given by Claesson and Dunand [17] is given as follows:

$$d_e = \sqrt{2}d_{out} \tag{34.10}$$

The equivalent diameter given by Gu and O'Neal is as follows [15]:

$$d_e = \sqrt{2d_{out}L_s} \quad (d_{out} < L_s < d_{bh}) \tag{34.11}$$

Table 34.3 Values for β_0 and β_1 for three configurations [16]

Configuration	β_0	β_1
A	20.10	−0.9447
B	17.44	−0.6052
C	21.91	−0.3796

When equivalent diameter method is used for computing the thermal resistance inside the borehole, thermal resistance of fluid and pipe should remain constant; the mass flow rate and heat capacity of the fluid should also be constant. Application of this method is especially advantageous when an analytical solution developed for a single cylindrical source is available [15].

$$R_{grout} = \frac{1}{2\pi k_{grout}} ln\left(\frac{d_{bh}}{d_e}\right) \tag{34.12}$$

Another commonly used relation for R_{grout} is the multipole model of Bennet et al., which is an extension of the relation presented by Hellström, and is given by the following expression [18,19]:

$$R_{grout} = \frac{1}{2\pi k_{grout}} \left[ln\left(\frac{x_1 x_2^{1+4\sigma}}{2(x_2^4 - 1)^\sigma}\right) - \frac{x_3^2 \left(1 - \frac{4\sigma}{(x_2^4 - 1)}\right)^2}{1 + x_3^2 \left(1 + \frac{16\sigma}{\left(x_2^2 - \frac{1}{x_2^2}\right)^2}\right)} \right] \tag{34.13}$$

where

$$x_1 = \frac{r_{bh}}{r_{p,out}} \tag{34.14}$$

$$x_2 = \frac{2r_{bh}}{L_s} \tag{34.15}$$

$$x_3 = \frac{x_2}{2x_1} \tag{34.16}$$

$$\sigma = \frac{k_{grout} - k_{soil}}{k_{grout} + k_{soil}} \tag{34.17}$$

Using a numerical model presented Sharqawy et al. [20], the following alternate definition for R_{grout} is obtained [19]:

$$R_{grout} = \frac{1}{2\pi k_{grout}} \left(\frac{-1.49}{x_2} + 0.656ln(x_1) + 0.436\right) \tag{34.18}$$

Other definitions for R_{grout} also include as proposed by Shonder and Beck [21]:

$$R_{grout} = \frac{1}{2\pi k_{grout}} ln\left(\frac{x_1}{\sqrt{2}}\right) \tag{34.19}$$

and that of Gu and O'Neal [22].

$$R_{grout} = \frac{1}{2\pi k_{grout}} ln(x_1 \sqrt{x_2}) \tag{34.20}$$

Calculation of Thermal Resistances of Filling Material for Water

For determining the thermal resistance of filling material for water, we use the following equation [5].

$$Nu = 0.291 \, (Ra^*)^{0.244} A^{-0.238} R^{0.442} \quad \left(1.8 \times 10^4 \leq \ Ra^* \ \leq \ 4.21 \times 10^7\right) \tag{34.21}$$

where Ra* is modified Rayleigh number, A is the aspect ratio, and R is the radius ratio as given below [5]:

$$Ra^* = g \, \beta_{bw} \, q''_{p,oou} \, \frac{\left(r_{bh} - r_{p,out}\right)^4}{k_{bw} \nu_{bw} \alpha_{bw}} \tag{34.22}$$

$$A = \frac{L}{r_{bh} - r_{p,out}} \tag{34.23}$$

$$R = \frac{r_{bh}}{r_{p,out}} \tag{34.24}$$

Here, g is gravitational acceleration, β is thermal expansion coefficient, q'' is heat flux, and subscript bw is borehole water. Thermal expansion coefficient is defined as

$$\left(\rho - \rho_{ref}\right)g \approx -\rho_{ref}\beta \, \left(T - T_{ref}\right)g \tag{34.25}$$

Note that Littlefield and Desai suggest the following relationship of Nusselt's number for isothermal boundary condition [5]:

$$Nu = 0.443(Ra^*)^{(0.233-0.009R)}A^{-0.245}R^{0.44} \quad \left(1.5 \leq R \leq 5 \quad 10 \leq A \leq 50 \quad N_{hf} \leq 0.5 \quad Ra^* \leq 10^8\right) \tag{34.26}$$

where N_{hf} is heat flux number, $q''_{bw}/q''_{p,out}$.

Thermal Resistance outside the Borehole

Predicting the thermal behavior inside and in the vicinity of boreholes is important to establish the required borehole length and to determine the resulting fluid temperature. In the literature one can find several methods to calculate heat flow in the ground around vertical boreholes. These methods can be divided into three distinct categories: analytical, numerical, and semi-analytical models. The main advantage of analytical models is that they are simple to implement, and they lead to relatively fast solutions. However, they are restricted to pure conduction cases. For instance, in the presence of groundwater flow, numerical methods are necessary. A number of studies on the analytical models presented here can be found in the literature and are reviewed briefly in the following paragraphs [14].

Kelvin's Line Source Model

Ingersoll and Plass [23] first applied the Kelvin line source theory to buried pipe heat transfer problems. The theory assumes that heat is obtained from an infinitely long permanent line source of heat or a sink in an infinite medium (soil) at an initial uniform temperature T_0 [15].

$$\Delta T = T_{bh} - T_0 = \frac{\dot{q}_{bh}}{2\pi k_{soil}} \int_X^\infty \frac{e^{-\beta^2}}{\beta} d\beta = \frac{\dot{q}_{bh}}{2\pi k_{soil}} I(X) \tag{34.27}$$

$$R_{soil} = \frac{T_{bh} - T_0}{\dot{q}_{bh}} = \frac{1}{2\pi k_{soil}} I(X) \tag{34.28}$$

where

$$X = \frac{r}{2\sqrt{\alpha t}} = \frac{r}{2\sqrt{Fo}} \tag{34.29}$$

When $0 < X \leq 1$, the I-function is calculated by

$$I(X) = 0.5(-lnX^2 - 0.57721566 + 0.99999193X^2 - 0.24991055X^4 + 0.05519968X^6 \\ - 0.00976004X^8 + 0.00107857X^{10}) \tag{34.30}$$

and when x $\geq$ 1,

$$I(X) = \frac{1}{2X^2 exp(X^2)} \frac{A}{B} \tag{34.31}$$

where

$$A = X^8 + 8.5733287X^6 + 18.059017X^4 + 8.637609X^2 + 0.2677737 \tag{34.32}$$

$$B = X^8 + 9.5733223X^6 + 25.6329561X^4 + 21.0996531X^2 + 3.9684969 \tag{34.33}$$

Finite Line-Source Model

When using finite line theory, the heat conduction outside the borehole is treated as a finite line source in a semi-infinite medium, which has a constant initial and boundary temperature for field and upper surface. In the finite line source model, end effects are not negligible and the real borehole wall temperature varies along the borehole depth, especially near the end of borehole region [24]. The analytical solution of the finite line source model was derived by Eskilson [25] and Zeng et al. [26], respectively. The temperature is obtained by integrating contributions of imaginary point source distributed along the borehole [25,27].

$$T_{bh}(r,z,t) - T_0 = \frac{\dot{q}_{bh}}{4\pi k_{soil}} \int_{D}^{D+H} \left\{ \frac{1}{r_+} erfc\left(\frac{r_+}{4\alpha t}\right) - \frac{1}{r_-} erfc\left(\frac{r_-}{4\alpha t}\right) \right\} dh \tag{34.34}$$

where H stands for depth of borehole, and the other parameters are defined as

$$r_+ = \sqrt{r^2 + (z-h)^2} \quad and \quad r_- = \sqrt{r^2 + (z+h)^2} \tag{34.35}$$

Substituting Eq. (34.35) into Eq. (34.34) yields

$$T_{bh}(r,z,t) - T_0 = \frac{\dot{q}_{bh}}{4\pi k_{soil}} \int_{0}^{H} \left\{ \frac{erfc\left(\frac{\sqrt{r^2+(z-h)^2}}{2\alpha t}\right)}{\sqrt{r^2 + (z-h)^2}} - \frac{erfc\left(\frac{\sqrt{r^2+(z+h)^2}}{2\alpha t}\right)}{\sqrt{r^2 + (z+h)^2}} \right\} dh \tag{34.36}$$

Infinite Cylindrical Heat Source Model (Kavanaugh's Approach)

The cylindrical source model assumes the single borehole as a single infinite isolated pipe surrounded by an infinite solid with constant properties. With a constant heat flux at the pipe wall, the temperature of point under consideration at or near the pipe is calculated as follows [14]:

Table 34.4 Several expressions of G-Function [15]

P	$G(z,p)$	
1	$G = 10^{z1}$	$z1 = -0.89129 + 0.36081\text{Log}(z) - 0.05508\text{Log}^2(z) + 0.00359617\text{Log}^3(z)$
2	$G = 10^{z2}$	$z2 = -1.4541 + 0.89933\text{Log}(z) - 0.31193\text{Log}^2(z) + 0.061119\text{Log}^3(z)$
5	$G = 10^{z3}$	$z3 = -3.0077 + 2.25606\text{Log}(z) - 0.7928\text{Log}^2(z) + 0.134293\text{Log}^3(z)$
10	$G = 10^{z4}$	$z4 = -9.1418 + 11.7025\text{Log}(z) - 7.09574\text{Log}^2(z) + 0.269837\text{Log}^3(z)$

$$\Delta T = T_r - T_0 = \frac{\dot{q}_{bh}}{k_{soil}} G(z,p) \quad z = \frac{\alpha t}{r^2} \quad p = \frac{r}{r_{bh}} \tag{34.37}$$

where G (z,p) is commonly referred to as the cylinder source integral or function, whose values was tabulated by Ingersoll et al. [28], or can be computed by equation given below [29,30]:

$$G\left(Fo(z), \frac{r}{r_{bh}}(p)\right) = \frac{1}{\pi^2} \int_0^\infty \frac{\frac{e^{-\beta Fo} - 1}{J_1^2(\beta) + Y_1^2(\beta)} [J_0(p\beta)Y_1(\beta) - J_1(\beta)Y_0(p\beta)]}{\beta^2} d\beta \tag{34.38}$$

By solving this equation, G-factor at the borehole wall as a function of Fo, for $10^{-1} < Fo < 10^6$, is given in Table 34.4.

Eskilson's Model

The borehole wall temperature T_{bh} varies along the borehole depth, especially near the end; therefore, it is more reasonable to use the integral mean temperature of the borehole wall to represent the heat transfer between the borehole and the ground as explained by Eskilson in 1987. The borehole wall temperature for a single borehole can be calculated by [27]

$$T_{bh} - T_\infty = -\frac{\dot{q}_l}{2\pi k_{soil}} g\left(\frac{t}{t_s}, \frac{r_{bh}}{H}\right) \tag{34.39}$$

$$g\left(\frac{t}{t_s}, \frac{r_{bh}}{H}\right) \approx \begin{cases} ln\left(\frac{H}{2r_{bh}}\right) + \frac{1}{2}ln\left(\frac{t}{t_s}\right) & \frac{5r_{bh}^2}{\alpha} < t < t_s \\ \\ ln\left(\frac{H}{2r_{bh}}\right) & t > t_s \end{cases} \quad t_s = \frac{H^2}{9\alpha} \tag{34.40}$$

Thermal Response Test

Soil thermal properties, i.e., thermal conductivity and borehole thermal resistance, represent the main design data in thermo-technical applications that exploit the ground heating storage. When the heat storage system is vertically oriented, that is the case considered here, the common method to estimate the soil properties is named Thermal Response Test. An essential role in the estimation procedure is played by the choice of the reference model adopted to recover the above-stated unknown quantities; this procedure is based on the comparison of the experimental data with the solution of the equations describing the model's behavior [31].

A thermal conductivity test (Fig. 34.3) consists of a fully drilled borehole fitted with a U-tube and backfilled. This is then connected to a defined artificial load, and the resultant temperature fluctuations of the circulating fluid are measured. Data on

the energy use of the pump and inlet/outlet water temperature and flow rate can then be used to determine the thermal properties of the soil. It should be noted though that while on-site tests are accurate, they are also expensive to conduct [32].

The equation for the temperature field as a function of time (t) and radius (r) around a line source with constant heat injection rate may be used as an approximation of the heat injection from a BHE [33]:

$$T_{bh} = \frac{\dot{Q}}{4\pi k_{soil}H} \left[ln\left(\frac{4\,\alpha\,t}{r^2}\right) - \gamma \right] + \frac{\dot{Q}}{4\pi k_{soil}H} R_{bh} + T_0 \tag{34.41}$$

which can be rewritten in a linear from as

$$T_{bh} = k\,ln(t) + m \tag{34.42}$$

with

$$k = \frac{\dot{Q}}{4\pi k_{soil}H} \tag{34.43}$$

Therefore, it can be determined from the slope of the line resulting when plotting Tb against ln(t), hence the name and basis of the evaluation method [34].

Results and Discussion

For determining the daily soil temperatures at different depths of Oshawa, Eq. (34.1) is used. According to the data given in Table 34.1, the time shift is 44 days, the mean surface temperature is 10.3 °C, the amplitude of the surface temperature is 12.9 °C are taken for Oshawa, ON. The result is given in Fig. 34.4. The mean surface temperature which by definition should correspond to the temperature of the ground at an infinite depth shows a discrepancy.

In BTES systems, the shank spacing is considered an important parameter for placing the BHEs. Assuming the filling material is grout, thermal resistances are calculated using equations given in previous sections. For a comparative study, the variation of thermal resistance of grout with shank spacing is given in Fig. 34.5.
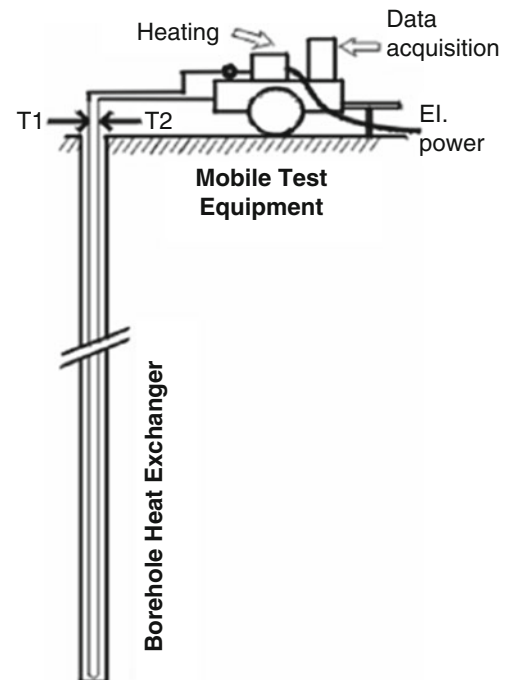
Fig. 34.3 Schematic of a thermal response test [31]

Fig. 34.4 Predicted daily soil temperatures at different soil depths for Oshawa
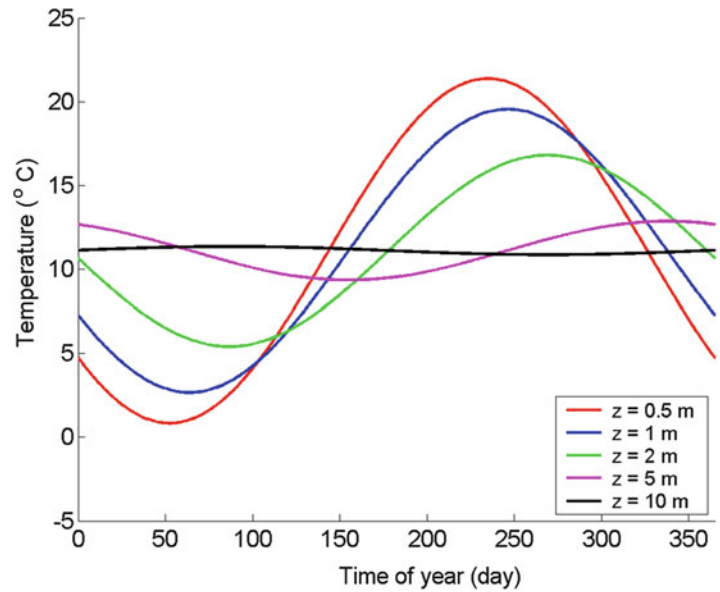
Fig. 34.5 Thermal resistance of grout calculated using different equations. R1: Hellström [13], R2: Remund [16], R3: Claesson and Dunand [17], R4: Gu and O'Neal [22], R5: Bennet et al. [35], R6: Sharqawy et al. [20], R7: Shonder and Beck [21], R8: Gu and O'Neal [36]
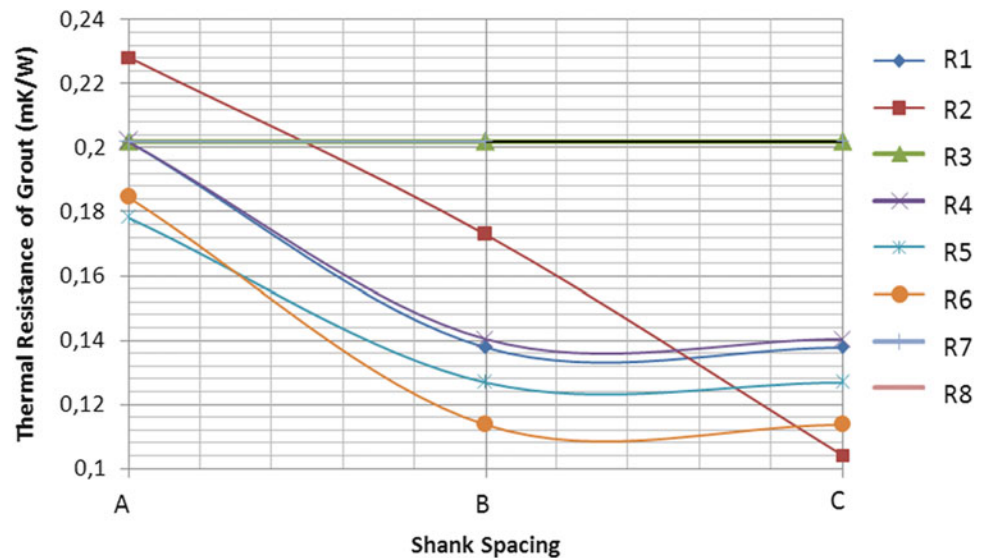
Figure 34.6 illustrates the radial temperature profile for different time periods and a given set of parameters for BTES system in UOIT in Oshawa. These curves were obtained by evaluating the Kelvin's Line Source Model integral numerically.

For the Finite Line Source the integral in Eq. (34.36) is numerically evaluated using a recursive adaptive Simpson quadrature for the parameters for the BTES system in UOIT. The results are presented in Fig. 34.7 where the temperature profile has been plotted after 6 months of operation for four radial distances from the center of the borehole.

In order to calculate the thermal resistance outside the borehole, four models are used: Kelvin's Line Source Model, Eskilson's Model, Infinite Cylindrical Heat Source Model (Kavanaugh's Approach), and Finite Line-Source Model. For comparison of four models, the parameters of GSHP system in UOIT were used, and the results are shown in Fig. 34.8. As seen from the figure, all four models are very similar.

The thermal response test (TRT) for BTES system founded in UOIT were made by Beatty and Thompson [12] who were the construction executives during the building process. TRT test results given here are calculated using the data obtained from reference. According to their data, water was circulated through the closed loop at a rate of 0.75 L/s, with a constant heat injection of 3.2 kW. The heat injection test was conducted for 72 h, followed by a 72-h recovery period. The power input, flow rate, and the loop inlet and outlet temperatures were recorded during the heat injection and recovery period.

Fig. 34.6 Temperature
distribution in the ground
determined by Kelvin's Line
Source Model
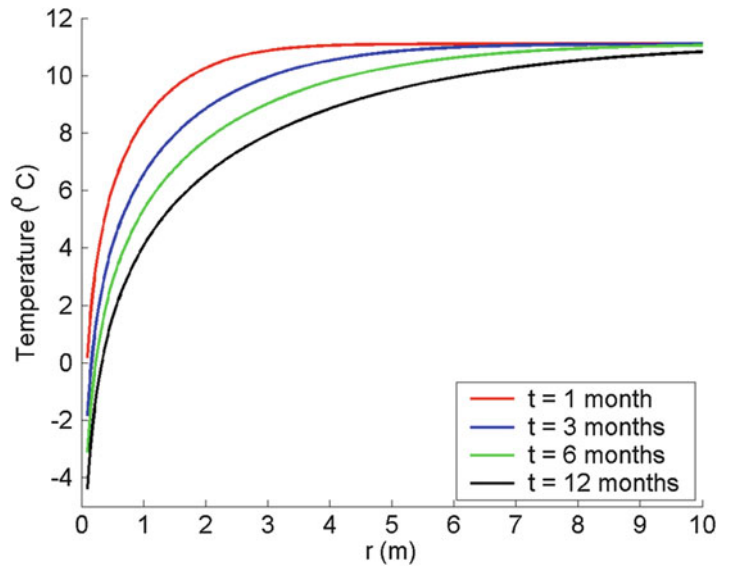
Fig. 34.7 Temperature
distribution in the ground
determined by Finite Line
Source at t = 6 months
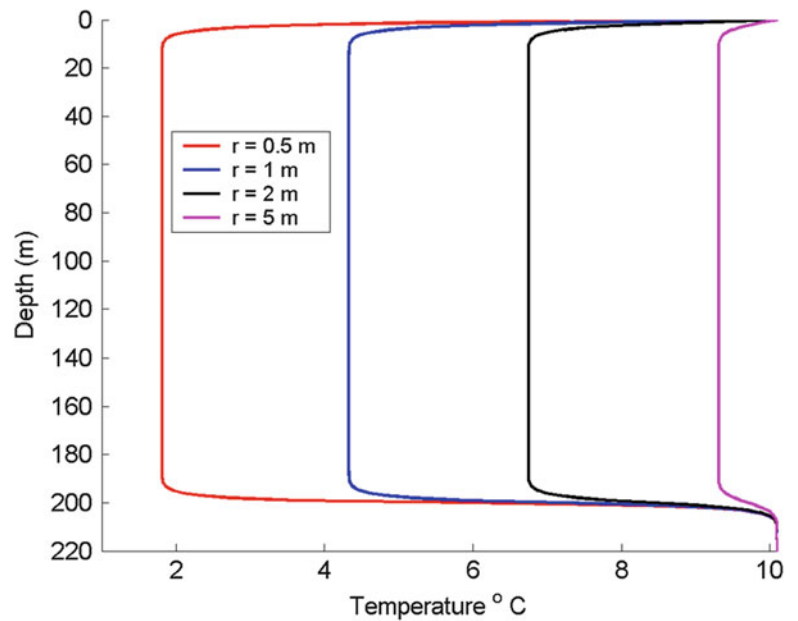
The rate of heat injection is 3,000 W, and the length of borehole is 190 m for the TRT. Figure 34.9 shows the resulting plot for the experimental data gathered from Beatty and Thompson [12] during the test.

The thermal conductivity rate was determined from the relationship between the heat rate, the test hole length, and the slope of the mean temperature data vs. the natural log of time. Using Eq. (34.41) we obtain

$$T_{bh} = k \, ln(t) + m = \frac{\dot{Q}}{4\pi k_{soil} H} n(t) + m \tag{34.44}$$

and the slope from Fig. 34.9:

$$y = 0.6493 ln(x) + 9.4286 \tag{34.45}$$

Fig. 34.8 Thermal resistance outside the borehole calculated by for different models (R1: Kelvin's Line Source Model, R2: Eskilson's Model, R3: Infinite Cylindrical Heat Source Model (Kavanaugh's Approach), R4: Finite Line-Source Model)
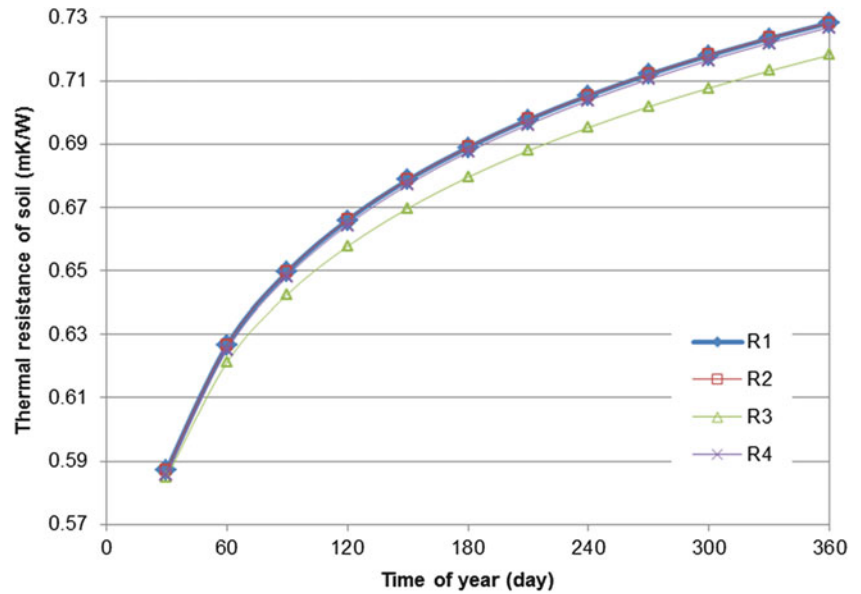
Fig. 34.9 The results of TRT (data obtained from Beatty and Thompson [12])
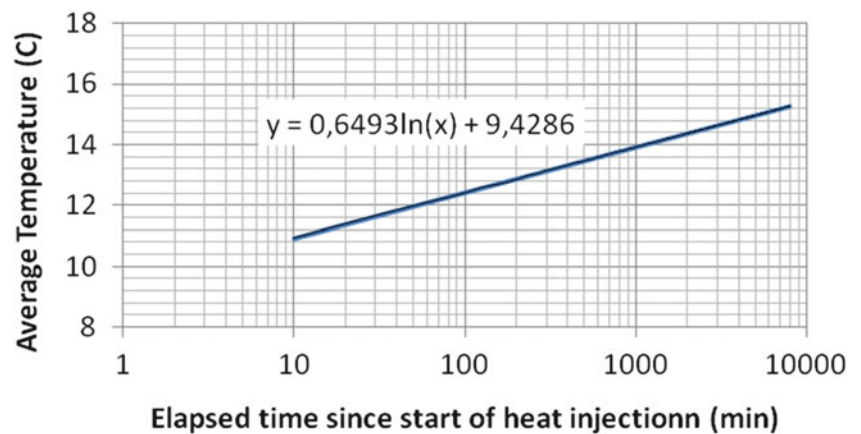
The slope of curve is

$$y' = 0.6493 = \frac{\dot{Q}}{4\pi k_{soil} H} \Rightarrow 0.6493 = \frac{3000W}{4\pi k_{soil} 190m} \Rightarrow k_{soil} = 1.93513 \, W/mK \tag{34.46}$$

The thermal conductivity was calculated to be in the order of 1.9 W/mK.

Conclusions

Borehole thermal resistance is a very important parameter that can lead to an erroneous estimate of the required borehole depth for sizing the BHEs of GSHPs. There are several methods to calculate heat flow in the ground around vertical boreholes. In this study, analyses of thermal resistance of the BTES system build at UOIT are conducted. For this aim, a ground thermal characteristics of Oshawa are calculated primarily using the climate data. For the thermal resistances inside the borehole, several suggestions from the literature are used in order to define the differences between the correlations available in the literature. For determining the thermal resistance outside the borehole, four different models were used,

namely Kelvin's Line Source Model, Eskilson's Model, Infinite Cylindrical Heat Source Model, and Finite Line-Source Model. It is seen from the results that all models' curves appear to be similar to each other. Finally, the thermal response test for the BTES system gives the thermal conductivity as 1.9 W/mK.

For energy savings and reducing the emissions, GSHP systems are more effective than conventional systems. BHEs are key parameters when designing these kinds of GSHP systems. Sizing such systems requires an extensive knowledge on ground thermal properties, building loads, climate conditions, etc. Since there are several parameters that influence the GSHP systems, it is necessary to perform detailed examinations before constructing such systems.

References

1. De Carli M, Tonon M, Zarrella A, Zecchin R (2010) A computational capacity resistance model (CaRM) for vertical ground-coupled heat exchangers. Renew Energy 35:1537–1550
2. Wang H, Qi C, Du H, Gu J (2010) Improved method and case study of thermal response test for borehole heat exchangers of ground source heat pump system. Renew Energy 35:727–733
3. Florides GA, Pouloupatis PD, Kalogirou S, Messaritis V, Panayides I, Zomeni Z, Partasides G, Lizides A, Sophocleous E, Koutsoumpas K (2010) The geothermal characteristics of the ground and the potential of using ground coupled heat pumps in Cyprus. Energy 36:5027–5036
4. Florides G, Kalogirou S (2008) First in situ determination of the thermal performance of a U-pipe borehole heat exchanger, in Cyprus. Appl Ther Eng 28:157–163
5. Gustafsson AM, Westerlund L, Hellström G (2010) CFD-modelling of natural convection in a groundwater-filled borehole heat exchanger. Appl Ther Eng 30:683–691
6. Dincer I, Rosen M.A. 2005. A Unique Borehole Thermal Storage System at University of Ontario Institute of Technology. in: Paksoy H.O. Thermal Thermal Energy Storage for Sustainable Energy Consumption Fundamentals, Case Studies and Design, Proceedings of the NATO Advanced Study Institute on Thermal Energy Storage for Sustainable Energy Consumption - Fundamentals, Case Studies and Design, Izmir, Turkey, 6-17 June, 221–228
7. Keen Engineering (2003) Rock and soil property data. UOIT/Durham College GSHP Report, March
8. Kasuda T, Archenbach PR (1965) Earth temperature and thermal diffusivity at selected stations in the United States. ASHRAE Trans 71(1):61–76
9. Jenkins DP, Tucker R, Rawlings R (2009) Modelling the carbon-saving performance of domestic ground-source heat pumps. Energy Build 41:587–595
10. Weather Canada (2011) http://www.weatheroffice.gc.ca/canada_e.html
11. Cengel AY (2002) Heat transfer: a practical approach. McGraw-Hill, New York, NY, 896 pp
12. Beatty B, Thompson J (2004) 75 Km of drilling for thermal energy storage. Technical Report for BTES system installed in UOIT/Durham College
13. Hellström G (1991) Ground heat storage-thermal analyses of duct storage systems. Ph.D. Thesis, Department of Mathematical Physics, University of Lund, Lund, Sweden, 310 pp
14. Philippe M, Bernier M, Marchio D (2010) Sizing calculation spreadsheet vertical geothermal borefields. ASHRAE J 52:20–28
15. Jun L, Xu Z, Jun G, Jie Y (2009) Evaluation of heat exchange rate of GHE in geothermal heat pump systems. Renew Energy 34:2898–2904
16. Remund CP (1999) Borehole thermal resistance: laboratory and field studies. ASHRAE Trans 105:439–445
17. Claesson J, Dunand A (1983) Heat extraction from the ground by horizontal pipes: a mathematical analysis. Swedish Council for Building Research, Stockholm
18. Lamarche L, Kajl S, Beauchamp B (2010) A review of methods to evaluate borehole thermal resistances in geothermal heat-pump systems. Geothermics 39:187–200
19. Raymond J, Therrien R, Gosselin L (2011) Borehole temperature evolution during thermal response tests. Geothermics 40:69–78
20. Sharqawy MH, Mokheimer EM, Badr HM (2009) Effective pipe-to-borehole thermal resistance for vertical ground heat exchangers. Geothermics 38:271–277
21. Shonder JA, Beck JV (2000) Field test of a new method for determining soil formation thermal conductivity and borehole resistance. ASHRAE Trans 106:843–850
22. Gu Y, O'Neal DL (1998) Development of an equivalent diameter expression for vertical U-tube used in ground-coupled heat pumps. ASHRAE Trans 104:347–355
23. Ingersoll LR, Plass HJ (1948) Theory of the ground pipe heat source for the heat pump. Heating, Piping & Air Cond. 20(7):119–122
24. Pesl M, Goricanec D, Krope J (2007) Response functions and thermal influence for various multiple borehole configurations in ground coupled heat pump systems. WSEAS Trans Heat Mass Transf 3:61–71
25. Eskilson P (1987) Thermal analysis of heat extraction boreholes. Ph.D. Thesis, University of Lund, Lund, Sweden
26. Zeng HY, Diao NR, Fang ZH (2002) A finite line-source model for boreholes in geothermal heat exchangers. Heat Transf Asian Res 31(7):558–567
27. Xu X (2007) Simulation and optimal control of hybrid ground source heat pump systems. Ph.D. Thesis, Graduate College of the Oklahoma State University
28. Ingersoll LR, Zobel OJ, Ingersoll AC (1954) Heat conduction with engineering, geological and other applications. McGraw-Hill, New York, NY
29. Chiasson AD (2007) Simulation and design of hybrid geothermal heat pump systems. Ph.D. Thesis, Department of Civil and Architectural Engineering, University of Wyoming
30. Deng Z (2004) Modeling of standing column wells in ground source heat pump systems. Ph.D. Thesis, Faculty of the Graduate College of the Oklahoma State University
31. Sanner B (2003) Current status of ground source heat pumps in Europe. 9th international conference on thermal energy storage, Warsaw, Poland, 1–4 Sept
32. Le Feuvre P (2007) An investigation into ground source heat pump technology, its UK market and best practice in system design. M.Sc. Thesis, Department of Mechanical Engineering, Strathclyde University
33. Eklöf C, Gehlin S (1996) TED – a mobile equipment for thermal response test. M.Sc. Thesis, Lulea University of Technology, Sweden
34. Georgiev A, Busso A, Roth P (2006) Shallow borehole heat exchanger: response test and charging–discharging test with solar collectors. Renew Energy 31:971–985
35. Bennet J, Claesson J, Hellstrom G (1987) Multipole method to compute the conductive heat transfer to and between pipes in a composite cylinder. Notes on Heat Transfer 3, Department of Building Physics, Lund Institute of Technology, Lund, Sweden
36. Gu Y, O'Neal DL (1998) Modeling the effect of backfills on U-tube ground coil performance. ASHRAE Trans 104:356–365

Design and Assessment of a Net Zero Energy House

Anwar Hassoun and Ibrahim Dincer

Abstract

This work presents an attempt to solve the shortage of power generation for a house in Lebanon, as a renewable energy-based case study, and aims to supply a neighborhood with electricity, hot water, and seasonal heating and cooling. The study starts by choosing the right orientation and construction materials of the house, in order to minimize energy and water usage and reduce outside noise transmission, by optimizing the thicknesses of acoustic and thermal insulation materials used to achieve the desired requirements. An exergy analysis is conducted to assess various system components and the overall system efficiency through multiparametric variables. A comprehensive economic evaluation is carried out where several techniques are utilized and the optimization of several factors achieves maximization of renewable energy usage by reducing exergy destruction and minimizing cost is carried out. The ultimate goal of the study is to produce a sustainable net zero energy house with reduced CO_2 emissions.

Keywords

Zero energy • Photovoltaic • Wind turbine • Absorption chiller electricity • Energy • Exergy • Efficiency • Exergoeconomic analysis • Optimization • Pareto front

Introduction

Energy shortages have been increasing due to population growth and increased industrial activities in especially developing countries. This makes a sustainable supply of energy critical to world development. After the maximum rate of global oil extraction is reached, a decline in the supply occurs. This will cause a significant increase in oil prices and their byproducts which will cause worldwide socioeconomic implications. Delaying the time of peak oil can be achieved by resorting to other alternatives for producing energy such as nuclear energy and renewable energy, unconventional oil resources like oil shale and oil sands, and by producing hydrogen fuel from the electrolysis of water. Moreover, fossil fuels are considered a major contributor to pollution and global warming. Hence, reducing the usage of fossil fuels is as important as achieving a sustainable energy supply. So, switching to sustainable energy options such as renewable energy and nuclear energy becomes an ultimate goal and helps reduce carbon dioxide emissions.

This present study aims to achieve the above-mentioned goal for Lebanon, in addition to the fact that Lebanon has huge big problems in electricity supply, because it has been stricken by shortages, wars, crises, etc. On average, throughout the year, a house is supplied by no more than 8 h of electricity daily. This forces the population to buy electricity from nongovernmental individuals who use generators to provide electricity at very high rates. Adding to all that are shortages in water supply during the summer season, even though Lebanon is rich in water, but the above reasons and the past occupations prevent Lebanese from using their water resources or develop projects to provide water to the country.

A. Hassoun (✉) • I. Dincer
Faculty of Engineering and Applied Science, University of Ontario Institute of Technology,
2000 Simcoe Street North, Oshawa, ON, Canada L1H 7K4
e-mail: hassounanwar@uoit.ca; ibrahimdincer@uoit.ca

These factors combined, make the need to generate electricity in Lebanon by renewable energy a must. In this regard, we select an area in South Lebanon where nearby river water is being wasted, but the water needs treatment due to negligence, to promote a community which would benefit from the natural resources and become self-sufficient if the proposed design is implemented. A net zero energy house where production of electricity is equal to consumption or greater is also targeted in this study.

Problem Statement

In this case study, a house occupied by a family of six, with a total living area of 225 m^2 located in South Lebanon near the Litani River is considered, as to be powered by maximum renewable energy with least green house gases emission and low noise pollution. An overall heat transfer coefficient for walls not exceeding 0.1 W/m$^{2\circ}$C and for ceiling 0.075 W/m$^{2\circ}$C are to be used, while for acoustic insulation the ability to attenuate a sound pressure level from 76 db outside the house to 30 db inside the house was used.

Solution Strategy

Since Lebanon has a moderate climate, where peek summer temperatures are at 32.8 $^\circ$C and winter temperatures are around 5.6 $^\circ$C in average [1]. The following approach is applied to reduce the energy requirements and noise pollution:
- Constructing a good building envelope by optimizing the sizes of thermal and acoustic insulation used.
- Choosing the right orientation of the house.
- Using energy-efficient appliances and light fixtures.
- Using efficient water fixtures.
- Using high-efficiency mechanical systems.
- Maximizing the use of solar powered cooling and heating techniques.
- Producing space and water heating by solar thermal systems, thermal storage techniques, and heat pumps.
- Producing water by systems powered by solar energy.
- Offsetting electrical use by an integrated system with grid-connected, photovoltaic, wind turbine, etc.

Fields of Study

The concept of net zero energy house is described by The U.S. Department of Energy (DOE) Building Technologies Program: "A net zero-energy building (ZEB) is a residential or commercial building with greatly reduced energy needs through efficiency gains such that the balance of energy needs can be supplied with renewable technologies" (e.g., [2]).What is important in this study is to maximize electrical power from renewable sources that would be equal to the house consumption and preferably more, to offset any governmental taxes and price variations, in order to cost the owner no additional charges and to minimize the government grid supply of electricity for sustaining a low carbon emission house, because the government supply might be through power stations running on fossil fuels.

Acoustic Insulation

Acoustic insulation of the proposed house is determined through experimental techniques.

An experimental study is in this regard carried out using Roxul fiber glass insulation and rigid expanded polystyrene foam to determine the *SPL* transmitted through the acoustic material, in order to determine the thickness to be used in the wall construction. In addition another experiment is conducted using the impedance tube to determine the coefficients of reflection of the two acoustic materials. The driving force for any heat transfer is the temperature difference while for acoustics it is the propagation of sound waves. The sound is a pressure wave that travels through an elastic medium with certain speed.

Fig. 35.1 Impedance tube
experiment setup
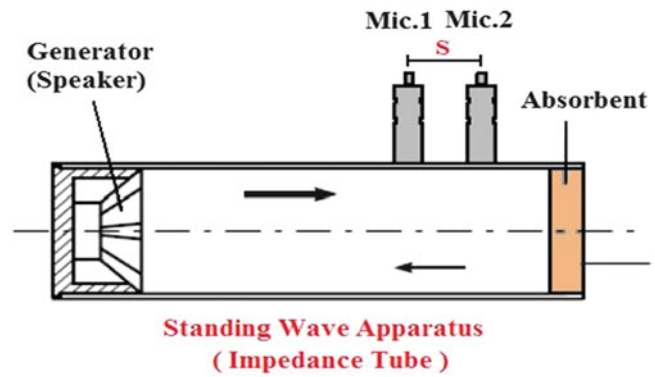
Experimental Setup

The experiment is conducted at the acoustics and noise control lab at the UOIT campus where *SPL* and reflection coefficients are measured for the following acoustical materials by two different techniques:

Impedance Tube

A speaker is placed at the face of one end of a tube and is sealed properly by using two wooden flanges to insure that there is no leakage of transmitted sound, while at the other end the tested material is fixed by two flanges to secure the test in place and to make sure that no noise is leaking. Two pressure microphones are installed at the surface of the tube as shown in the following figure. The experiment was conducted to calculate the reflection coefficients using a 100×15 cm *PVC* pipe arranged as shown in Fig. 35.1 where $S = 2$ cm. $L = 15$ cm being the distance from the face of the acoustic material to the first microphone.

In this method, a broadband stationary random acoustic wave in a tube is mathematically decomposed into its incident and reflected components using a simple transfer-function relation between the acoustic pressures at two locations on the tube wall. The wave decomposition leads to the determination of the complex reflection coefficient from which the complex acoustic impedance and the sound absorption coefficient of a material and the transmission loss of a silencer element can be determined [3]. A methodology is used as follows, based on the work done by [4]:

$$\frac{Z}{\rho c} = J \left[\frac{H_{12} sin\,(kl) - sin\,(k(l-s))}{cos\,(k(l-s) - H_{12} cos\,(kl))} \right] \tag{35.1}$$

$$\frac{Z}{\rho c} = x + ir \tag{35.2}$$

$$X = \rho c \frac{\left[R_e(H_{12}) sin\,(k(2l-s)) - \frac{1}{2} \left\{ sin\,(k(2l-s)) + |H_{12}|^2 sin\,(2kl) \right\} \right]}{H_d} \tag{35.3}$$

$$r = \rho c \frac{[-I_m(H_{12}) sin\,(ks)]}{H_d} \tag{35.4}$$

where ρc is the characteristic impudence of air.

$$H_d = cos^2[k(l-s)] + |H_{12}|^2 cos^2(kl) \tag{35.5}$$

Here, I_m, R_e represent the real and imaginary parts and l is the distance from the speaker to the first microphone. H_{12} is the transfer signal between the two microphone signals.

$$R_1(f) = \frac{H_{12}(f) - H_i(f)}{H_r(f) - H_{12}(f)} \tag{35.6}$$

$$R = R_1 e^{j2kl} \tag{35.7}$$

where R is the reflection coefficient and α is the absorption coefficient.

$$\alpha = 1 - |R_1|^2 \tag{35.8}$$

Enclosure Experiment

The enclosure is made up of the acoustic material. The enclosure is well sealed to avoid any sound leakage, and a free field microphone is installed inside the enclosure while a generated noise is built on the outside using a speaker. The microphone signal is connected to the analog instrument and then transferred to the lab view software where the FFT voltage signal is recorded at different frequencies and then transformed into pressure signal by multiplying with the voltage/pressure sensitivity factor of the microphone. After which the *SPL* is calculated and the attenuation by each material are evaluated as follows:

$$SPL = 20 \, log_{10}\left(\frac{P_{rms}}{P_0}\right) \tag{35.9}$$

$$P_0 = 20.10^{-6} \tag{35.10}$$

$$P_{rms} = \text{Value obtained from } FFT \tag{35.11}$$

Photovoltaic Systems

Photovoltaic systems used in this study produce electricity directly from sunlight and are referred to as solar energy systems. Two layers of a semi-conducting material are combined to produce electricity when exposed to sunlight. It works when one layer has a depleted number of electrons that gets excited by absorbance of sunlight photons and cause electrons to jump from one layer to the other causing electric charge. The photovoltaic material is silicon cut into very thin wafers and undergoes contamination by doping to create electron imbalance. These wafers are joined together to form a solar cell, and many cells are connected in series and laminated between clear glazing and an encapsulating substrate.

The efficiency of *PV/T* system used in this study depends on many factors, and it is described in detail by [5]:

$$\eta = \frac{h_c(T_{cell} - T_a)A_{SPVT} + Elec_{gener}}{\dot{Q}_s} \tag{35.12}$$

$$\Psi = \frac{h_c(T_{cell} - T_a)A_{SPvT}\left(1 - \frac{T_{amb}}{T_{sun}}\right) + Elec_{gener}}{\dot{Q}_s\left(1 - \frac{T_{amb}}{T_{sun}}\right)} \tag{35.13}$$

where all temperatures in exergy and energy calculations are absolute and must be in K.

Wind Turbine

Wind turbine is considered in this study to produce electricity by converting wind kinetic energy into mechanical energy. At the end of 2009, 159.2 GW [5] of wind-powered generators were produced worldwide which is about 2 % of the total electricity produced. Several countries have achieved relatively high levels of wind power penetration.

The efficiency of the wind power generators is commonly explained by [6]

$$\dot{P}_{turb} = 0.5\rho_{air}A_{swept}V_{air_{in}}^3 C_{POW} \tag{35.14}$$

where Aswept represents the area swept by tubbine blades in m^2.

$$\dot{P}_{turb\_Elec} = \dot{P}_{turb}\eta_{TRANS}\eta_{CAPAC} \tag{35.15}$$

$$\eta_{turb} = \frac{\dot{P}_{Turb,elec}}{\dot{P}_{Turb\_Nom}} \tag{35.16}$$

$$\psi_{turb} = \dot{P}_{Turb,elec} \Big/ \left(\dot{P}_{Turb,Nom} + \dot{m}_{Turb}Cp(T_{bt} - T_{at}) + \dot{m}_{Turb}T_o \left(Cp \ \mathrm{Ln} \left(\frac{T_{at}}{T_{bt}} \right) - R \ \mathrm{Ln} \left(\frac{P_{at}}{P_{bt}} \right) \right) - \frac{\dot{Q}_{Turb,loss}}{(T_{amb})} \right) \tag{35.17}$$

Batteries and Electrical Systems

Batteries and electrical systems are considered and used in this study. Batteries store DC electrical energy in chemical form for later use. The energy is used at night and during periods of emergency .The *DC* is inverted to *AC* before it is supplied to the house.

Absorption Chiller

Absorption chiller is considered and used in this study which operates as a mechanical vapor compression heat pump except that the compressor is replaced by an absorbent fluid circuit. An absorption chiller uses an aqueous solution of LiBr where the absorbent has a great affinity for the refrigerant. The refrigerant is absorbed by the absorbent solution in the absorber, releasing heat of solution. The weak solution is then pumped to the generator. In the generator, hot water is supplied to drive off the refrigerant from the absorbent solution. The refrigerant is condensed giving up its latent heat in the condenser. The strong solution is then returned to the absorber. The refrigerant from the condenser is pumped to the evaporator pressure, where air from the house causes it to evaporate. The refrigerant vapor then passes to the absorber to close the cycle. The overall system *COP* is defined by [6]:

$$\eta_{th,abs,sys} = COP_{abs,sys} = \frac{\dot{Q}_{eva}}{\dot{W}_{Pmp,1} + \dot{Q}_{gen}} \tag{35.18}$$

$$\psi_{x,abs,sys} = \frac{\dot{Q}_{eva}\left(\frac{T_0}{T_{a,in}} - 1\right)}{\dot{W}_{Pmp} + \dot{Q}_{gen}\left(1 - \frac{T_0}{T_{gen}}\right)} \tag{35.19}$$

$$\eta_{GL\_SYS} = \frac{\dot{Q}_{eva} + \dot{P}_{elec,PVT} + \dot{P}_{Turb,elec} + h_c A_{PVT}(T_{cell} - T_{amb})}{\dot{Q}_S(A_{solar} + A_{PVT}) + \dot{W}_{Pmp1} + \dot{W}_{Pmp,s} + 0.5\rho_{air}A_{Swept}V_{avg}V_{a\_in}{}^2} \tag{35.20}$$

$$\psi_{GL\_SYS} = \frac{\dot{Q}_{eva}\left(\frac{T_0}{T_{a,in}} - 1\right) + \dot{P}_{elec\ PVT} + \dot{P}_{elec_{Turb}} + h_c A_{PVT}(T_{cell} - T_{amb})\left(1 - \frac{T_0}{T_{cell}}\right)}{\dot{Q}_S(A_s + A_{PVT})\left(1 - \frac{T_0}{T_{Sun}}\right) + \dot{W}_{Pmp1} + \dot{W}_{Pmp,s} + 0.5\rho_a A_{Swept}V_{avg}V_{a,in}{}^2} \tag{35.21}$$

Heating Load Calculations

These calculations are carried out using hourly analysis program software for the proposed house. The software simulates hour-by-hour operation of all heating and air conditioning systems in the house and operation of all plant equipment and non-HVACs systems including lighting and appliances. It uses results of simulations to calculate total annual energy use and energy costs and generates tabular and graphical reports of hourly, daily, monthly, and annual data [7].

Exergoeconomic Analysis

The following methodology of exergoeconomic analysis is employed to evaluate the energetic and exergetic costs based on the studies by [6, 8]:

$$\dot{C}_i = \sum_i c_i \dot{m}_i \left[(h_i - h_0) - T_0(s_i - s_0) \right] \tag{35.22}$$

$$\dot{C}_e = \sum_e c_e \dot{m}_e \left[(h_e - h_0) - T_0(s_e - s_0) \right] \tag{35.23}$$

$$\dot{C}_w = \left(\sum_i c_{w,i} \dot{W}_i - \sum_e c_{w,e} \dot{W}_e \right) \tag{35.24}$$

$$\dot{C}_q = \sum_i c_{q,i} \frac{\dot{Q}_i (T_{source} - T_0)}{T_{source}} - \sum_e c_{q,e} \frac{\dot{Q}_e (T_{source} - T_0)}{T_{source}} \tag{35.25}$$

$$\dot{C}_{cinv} = IC \frac{(1 + ir)^n}{(1 + ir)^n - 1} \left(\frac{1}{N} \right) \tag{35.26}$$

$$\dot{C}_{o\&m} = \dot{C}_{FYM} \frac{(1 + ir)^n}{(1 + ir)^n - 1} \left(\frac{1}{N} \right) \tag{35.27}$$

where ir = interest rate, n = # of life cycle years, N = # of hours of production/year, IC = Initial cost, FYM = First year maintenance cost.

$$\dot{C}_i + \dot{C}_q + \dot{C}_{cinv} + \dot{C}_{o\&m} = \dot{C}_e + \dot{C}_w \tag{35.28}$$

$$\dot{C}_{ex\_des} = \left(\sum_k \dot{m}_k \cos t_{SFP_k} ex_k \right) \tag{35.29}$$

$$\dot{C}_{TC} = \dot{C}_{ex\_des} + \dot{C}_{cinv} + \dot{C}_{o\&m} = \dot{C}_e \tag{35.30}$$

Multi-objective Optimization

A multi-objective optimization approach is used to minimize the total cost and maximize the overall exergetic efficiency. This multi-objective optimization uses a genetic algorithm that deals with the minimization of a vector of objectives F(x) that can be the subject of a number of constraints or bounds, and when maximization is needed the F(x) is multiplied by a minus sign [9–12]:

$$G_i(x) = 0, i = 1, \ldots \ldots \ldots, k_e; G_i(x) \le 0, i = k_e + 1, \ldots k; l \le x \le u \tag{35.31}$$

Results and Discussion

The design of a zero energy house was established by following the procedure outlined in section "Solution Strategy" and all the system components needed to provide the house with electricity, hot water, and seasonal air-conditioning are shown in Fig. 35.2. First, the thermal and acoustic sizes of the material chosen for this study are determined, and the heat load calculations are carried out next. After establishing the total electrical KW needed for the house, the optimum power system, based on the system minimum net present value cost, minimum CO_2 emissions, and maximum renewable energy fraction, is selected. After which an energy and exergy analyses are conducted to assess the system performance along with an
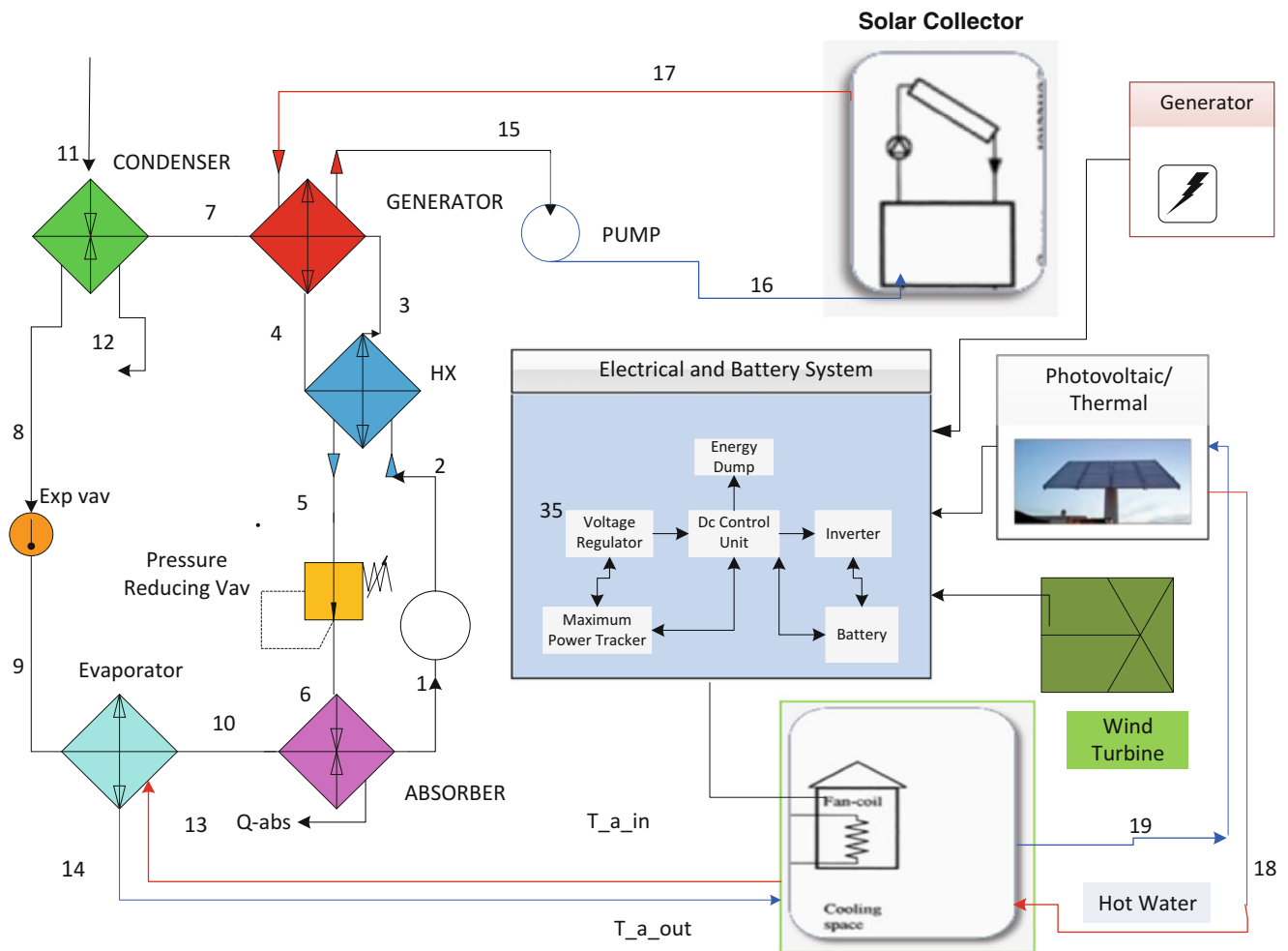
Fig. 35.2 A schematic diagram of the present system

exergoeconomic analysis to the overall system. Finally, the selected system is optimized for minimum overall cost and maximum exergetic efficiencies, and assessment for zero energy classification is investigated. Here, in the system hot water from the solar collector powers the generator of the absorption chiller while ambient air cools off the condenser and absorber. Cooled air is being provided to the house at stream 14 after being recirculated at stream 13 to the evaporator where it loses heat and moisture as explained in section "Absorption Chiller," while hot water is supplied to the house at stream 18 through the photovoltaic cum thermal system. Electricity is generated by the photovoltaic cells, wind turbine, and diesel generator.

Selecting the Thermal and Acoustic Material Sizes

After conducting the impedance tube and enclosure experiments, a Matlab code was generated to produce the results as shown in Figs. 35.3 and 35.4.

An examination of Fig. 35.3 indicates that the sound pressure level (*SPL*) of the ambient noise plus the 1,000 Hz sinusoidal noise is 75 db, while the SPL of the tested specimen of one inch rigid expanded polystyrene foam and 3 in. Roxul fiber glass insulation is 35 db, which means a reduction of 40 db was caused by using an enclosure of the $1''+3''$ combination. In the second experiment, the same ambient plus 1,000 Hz noise level was used, but this time a $2''+3''$ combination was used for the enclosure on all sides and the measured SPL as seen in Fig. 35.3 was 15 db. Therefore, the $1''$ rigid expanded polystyrene foam has the power to attenuate 20 db and is equal to that of the $3''$ fiber glass insulation. These results were verified by the impedance tube experiment that shows that the two specimens as in Fig. 35.4 have the

Fig. 35.3 Sound pressure level for ambient noise + 1,000 Hz sinusoidal wave vs. a combination of (1″ + 3″, 2″ + 3″) material measured at different frequencies (Hz)
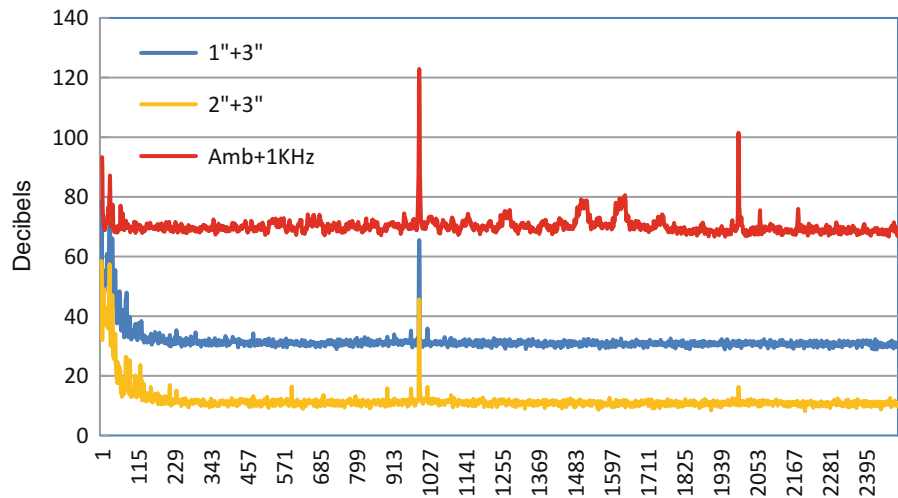
Fig. 35.4 Reflection coefficients of the 1″ and 3″ materials vs. the theoretical of open impedance tube measured at various frequencies
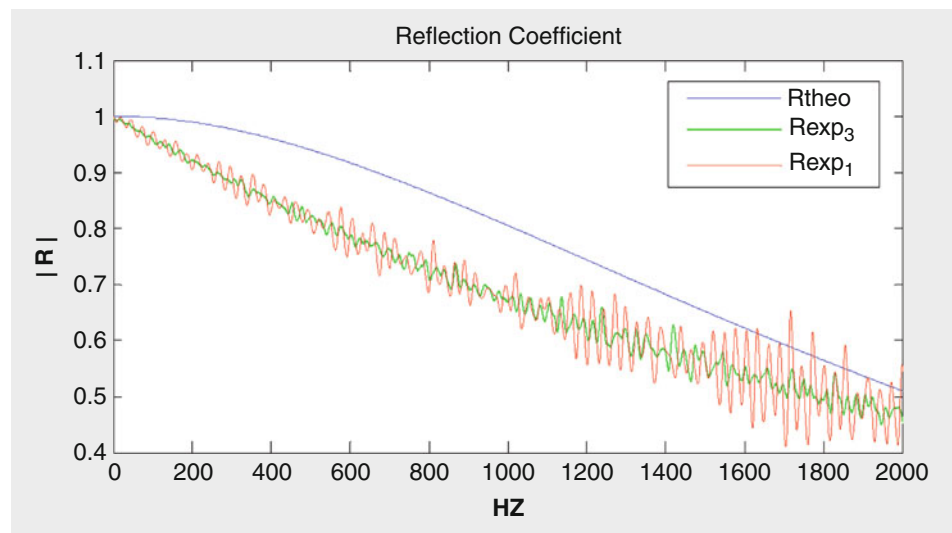
Table 35.1 Design temperature values for summer cooling and winter heating

Air temperature	Cooling	Heating
Outside dry bulb (°C)	32.8	5.6
Outside wet bulb (°C)	25.6	1.8
Inside dry bulb (°C)	23	21.1
Inside relative humidity (%)	50	50

same reflection coefficient. The thermal and acoustic insulation sizes that satisfy the problem statement were determined by a code which optimized the thicknesses to be at 4.1″ and 2.3″ for the wall and 4.72″ and 2.3″ for the roof, structures, etc.

Calculating the Seasonal Heat Loads

The building wall and roof composition were finalized by the previous step, and the rest of the design criteria were designed to enable saving in heat transfer from and to the building to reduce electricity requirements. Special care was given to the glass-to-wall ratio not to exceed 8 % and to have an air tight building. Summer and winter loads were calculated using HAP software for design temperatures as shown in Table 35.1. The building heat transfer coefficients were set low to minimize the seasonal loads, and the results obtained by the simulation software were 4,601 W for summer cooling and 1,703 W for winter heating.

Table 35.2 Optimized systems architecture for on and off grid connections

Off grid connection		On grid connection	
PV array	16 kW	PV array	2 kW
Wind turbine	1 Generic 10 kW	Wind turbine	1 Generic 10 kW
Generator 1	4 kW	Grid	1,000 kW
Battery	50 Hoppecke 24 OPzS 3000	Battery	2 Hoppecke 24 OPzS 3000
Inverter	7 kW	Inverter	10 kW
Rectifier	7 kW	Rectifier	10 kW

Fig. 35.5 Monthly electrical productions for on grid connection
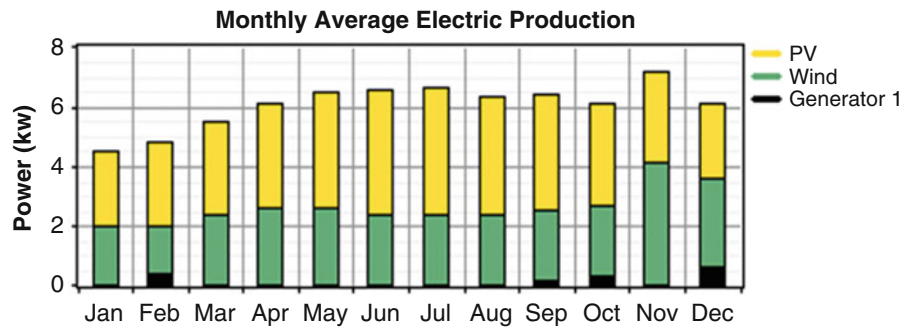
Fig. 35.6 Monthly electrical productions for off grid connection
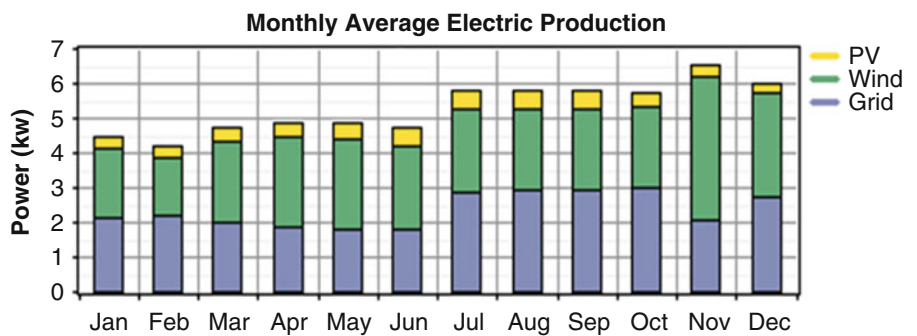
Selection of the Power System

After determining the heat loads of the house, the total peak electrical usage was calculated at 5.7 kW and the average electrical daily demand at 102 kWh/day which was the basis for our modeling and optimization. Two schemes were configured for our analysis, one was connecting to the grid while the other not. The basis for our optimization is to minimize the net present value of the power system and minimize the CO_2 emissions. Around 18,100 simulations were conducted and the following on grid and off grid systems were selected as shown in Table 35.2 and their monthly average electrical production in Figs. 35.5 and 35.6.

The net present cost of the on grid and off grid systems are $41,775 and $80,146, respectively, as seen in Figs. 35.7 and 35.8. The emissions generated by the selected optimized systems are given in Table 35.3 where the grid connected system produces carbon dioxide emissions about 10 times more than the off grid in kg/year. This is a major concern that will be considered in system evaluation further down the study.

The electrical production for the selected systems components and the renewable energy fractions are determined and listed in Table 35.4.

Exergy Analysis Results

A sensitivity analysis on the system components was carried out by varying independent parameters. EES software was used to calculate all the system properties and develop the parametric studies. The effect of keeping the dead state temperature T_o = constant and $T_{eva} = 7$, $T_{gen,} = 80$, $T_{a,in} = 20$ (°C) is shown for the overall COP for the absorption chiller and the

Fig. 35.7 Net present cost for on grid connection

Cash Flow Summary
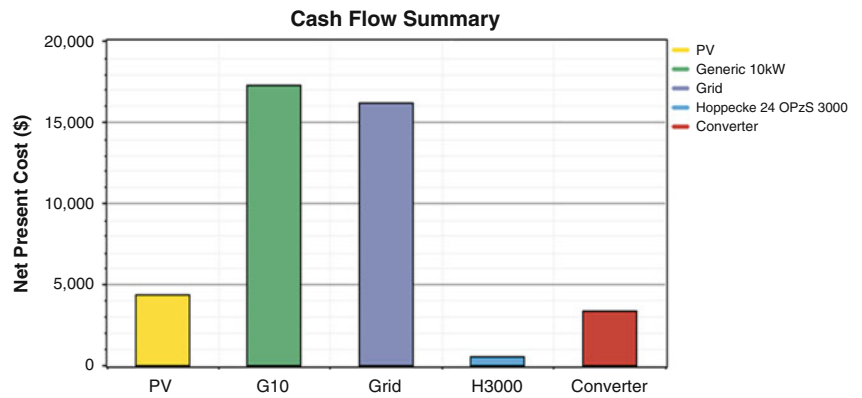
Fig. 35.8 Net present cost for off grid connection

Cash Flow Summary
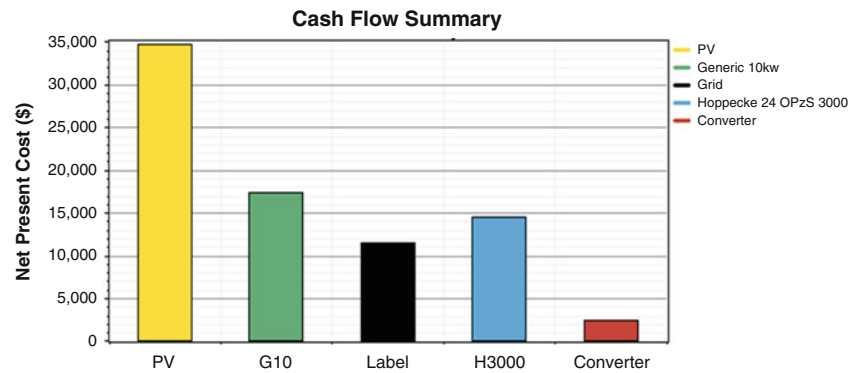
Table 35.3 Pollutants emitted by the selected optimized on grid and off grid systems

Off grid connection		On grid connection	
Pollutant	Emissions (kg/year)	Pollutant	Emissions (kg/year)
Carbon dioxide	922	Carbon dioxide	8,920
Carbon monoxide	2.28	Carbon monoxide	0
Unburned hydrocarbons	0.252	Unburned hydrocarbons	0
Particulate matter	0.172	Particulate matter	0
Sulfur dioxide	1.85	Sulfur dioxide	38.7
Nitrogen oxides	20.3	Nitrogen oxides	18.9

Table 35.4 Electrical production for off grid and on grid system components

Off grid connection			On grid connection		
Component	kWh/year	Fraction	Component	kWh/year	Fraction
PV array	29,961	57 %	PV array	3,745	8 %
Wind turbine	21,969	41 %	Wind turbine	21,969	47 %
Generator 1	1,024	2 %	Grid purchases	20,738	45 %
Renewable	–	0.972	Renewable	–	0.527

overall system efficiencies in Figs. 35.9 and 35.10. The COP varied from 0.53 to 0.28 at around 3:00 PM due to increase in generator heat as seen in Fig. 35.11 while the exergetic COP varied slightly around 0.15. The overall efficiency varied between 38 and 45 % due to solar and velocity changes while the overall system exergy efficiency varied between 6 and 10 %. These results clearly indicate that the exergetic analysis represents a better sensitivity analysis of the system performance than energy.

Figures 35.12 and 35.13 where all parameters were fixed except for reference temperature; we notice that the exergetic COP of the absorption system increased from 0.16 to about 0.22 at maximum T_0 because the factor $\dot{Q}_{gen}\left(1 - \frac{T_0}{T_{gen}}\right)$ decreases

Fig. 35.9 First and second law coefficients of performance of the absorption chiller
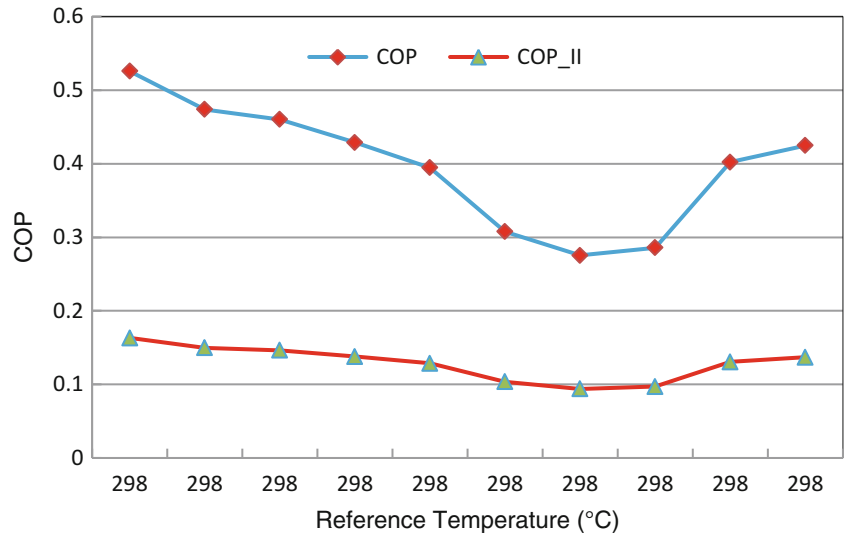
Fig. 35.10 Energy and exergy efficiencies of the overall system
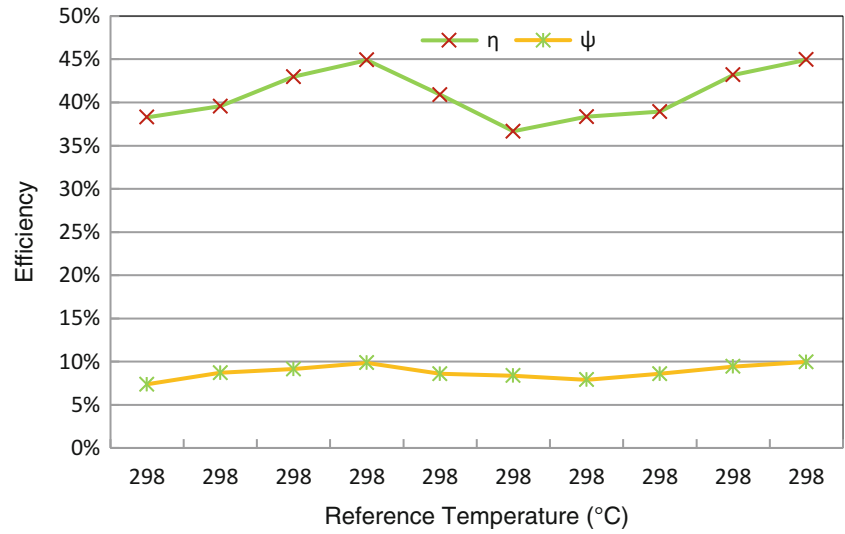
Fig. 35.11 Generator and evaporator thermal heat at different hour of the day and constant temperatures
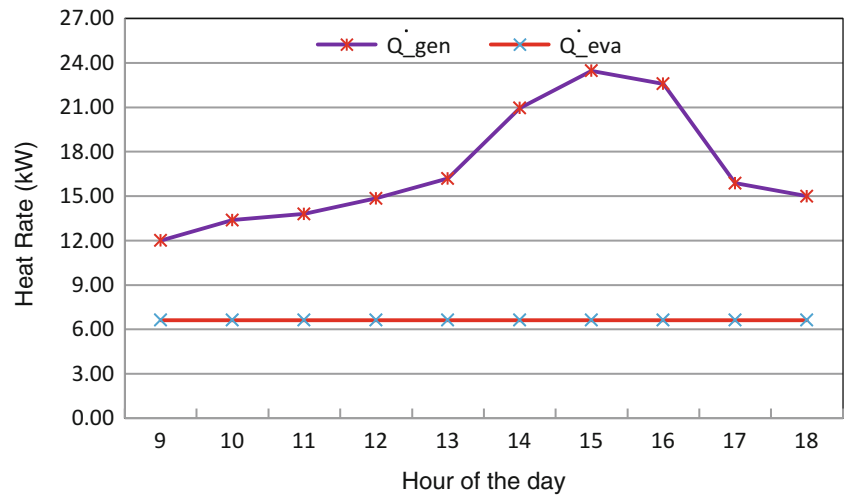
Fig. 35.12 First and second law coefficients of performance of the absorption system at variable dead state temperature and $T_{eva} = 7$, $T_{gen,} = 80$, $T_{a,in} = 20$ (°C)
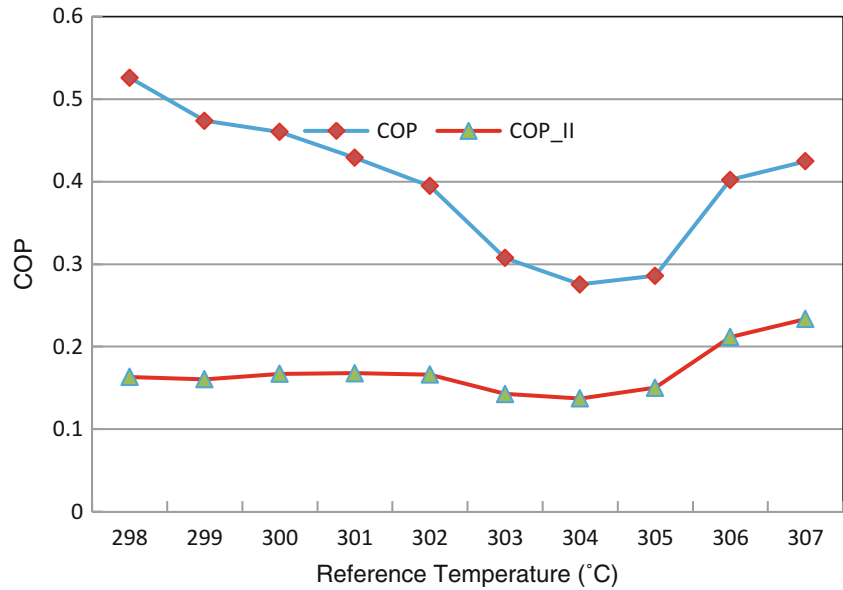
Fig. 35.13 Energy and exergy efficiencies of the overall system at variable dead state temperature and $T_{eva} = 7$, $T_{gen,} = 80$, $T_{a,in} = 20$ (°C)
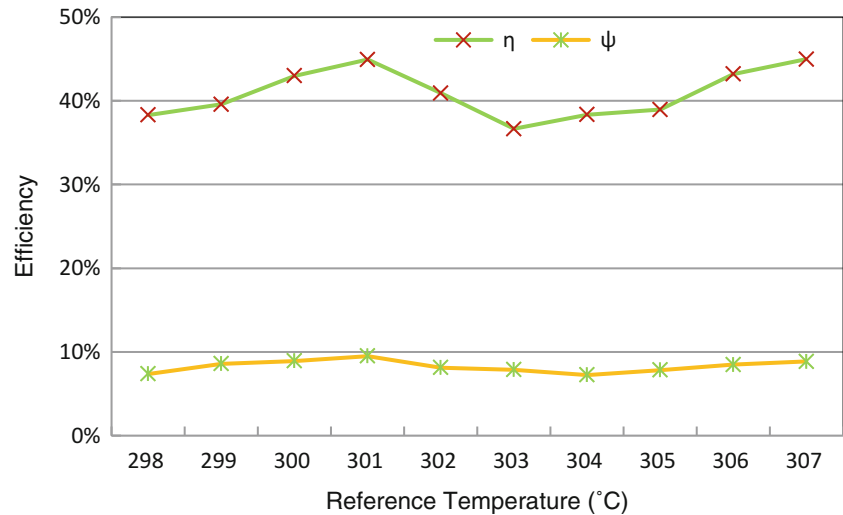
more than $\dot{Q}_{eva}\left(\frac{T_0}{T_{ev}} - 1\right)$. While the overall exergy efficiency has the factor $\left(1 - \frac{T_0}{T_{Sun}}\right)$ in the denominator which is not affected by the range of changes in T_0 since T_{Sun} is large and the numerator was affected slightly by $\left(\frac{T_0}{T_{ev}} - 1\right)$, thus causing an unnoticeable decrease.

Comparing Figs. 35.14 and 35.15 where all parameters were fixed except for temperature of air entering the evaporator, the *COP* of absorption chiller increased dramatically from 0.3 to 0.9 with temperature increase, because $\dot{Q}_{eva}$ increased. Also the overall efficiency increased slightly, while the exergetic *COP* of the absorption system increased with increased air temperature from 0.1 to 0.24. The overall system exergy efficiency was increased slightly with increased air temperature while the energy efficiency dropped slightly at higher temperature with comparison to Fig. 35.10.

In Figs. 35.16 and 35.17, the temperature of air entering the evaporator and the evaporator temperature are varying while $T_{gen} = 80$, $T_o = 25$ (°C) remains constant. We notice that the *COP* of absorption chiller increased but less than that of Fig. 35.14 due to evaporator temperature increase which countered some of the increase caused by air temperature. Also, the overall efficiency decreased from that of Fig. 35.15 due to the same reasoning, while the exergetic *COP* of the absorption system decreased with increased air and evaporator temperature due to additional decrease in Q_{eva}, caused by increase in

Fig. 35.14 First and second law coefficients of the absorption system at variable air on evaporator temperature and $T_{eva} = 7$, $T_{gen,} = 80$, $T_o = 25$ (°C)
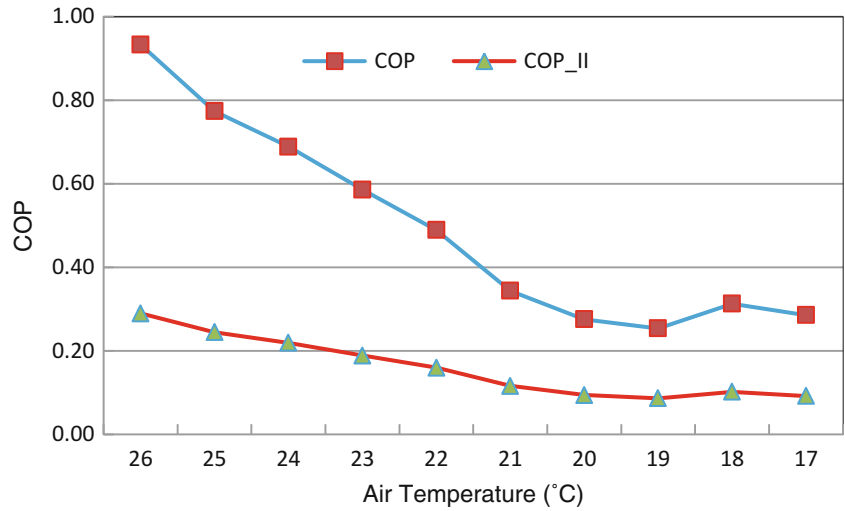
Fig. 35.15 Energy and exergy efficiencies of the overall system at variable air on evaporator temperature and $T_{eva} = 7$, $T_{gen,} = 80$, $T_o = 25$ (°C)
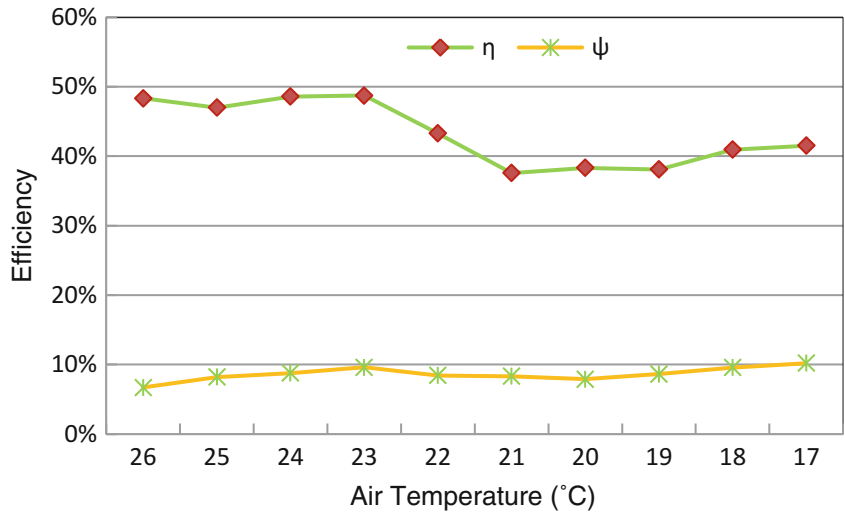
Fig. 35.16 First and second law coefficients of absorption system at variable T_{eva} and T_a (°C)
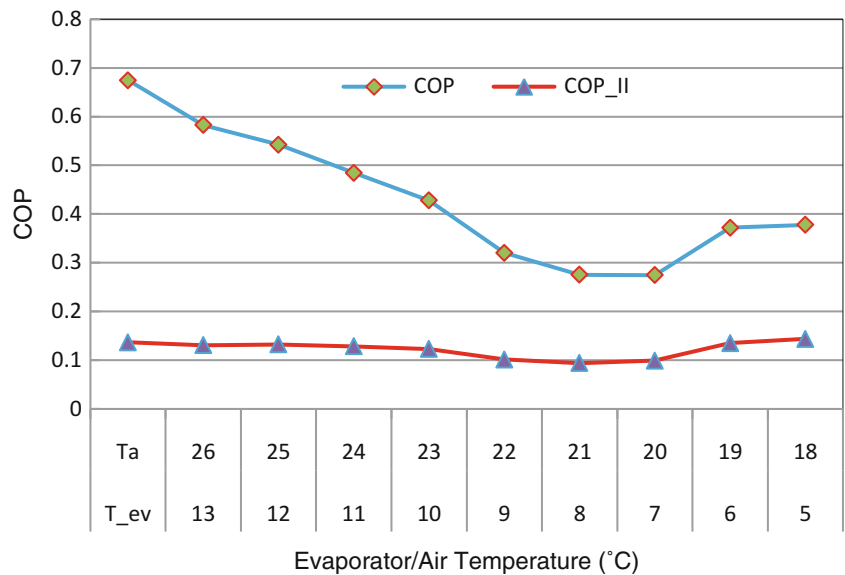
Fig. 35.17 Energy and exergy efficiencies of the overall system at variable T_{eva} and T_a (°C)
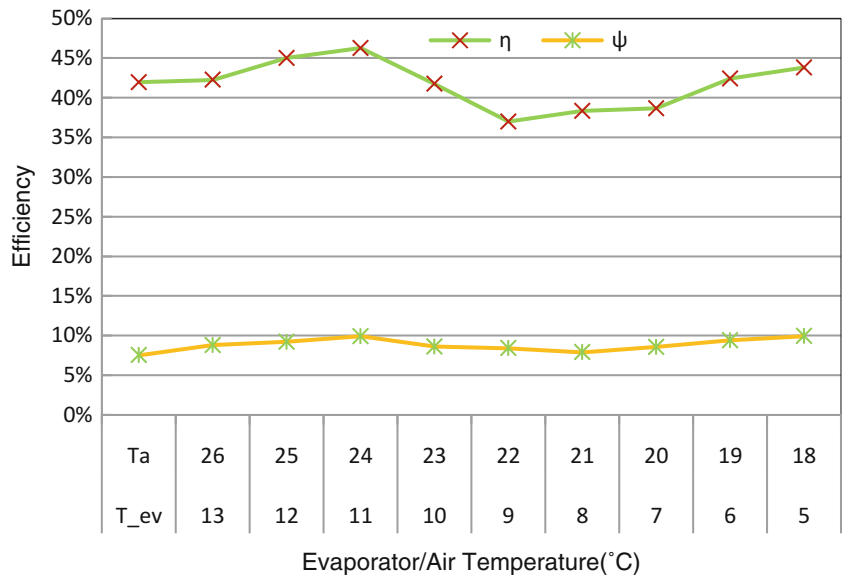
Fig. 35.18 Percentage of total exergy destructed for system components
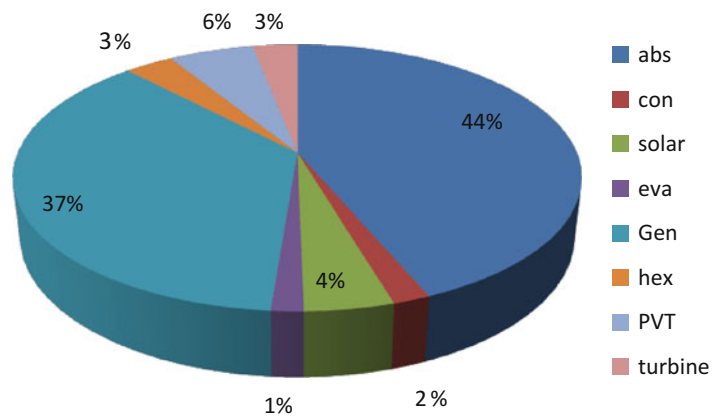
Fig. 35.19 The values of exergy destructed for system components at variable reference temperature (°C)
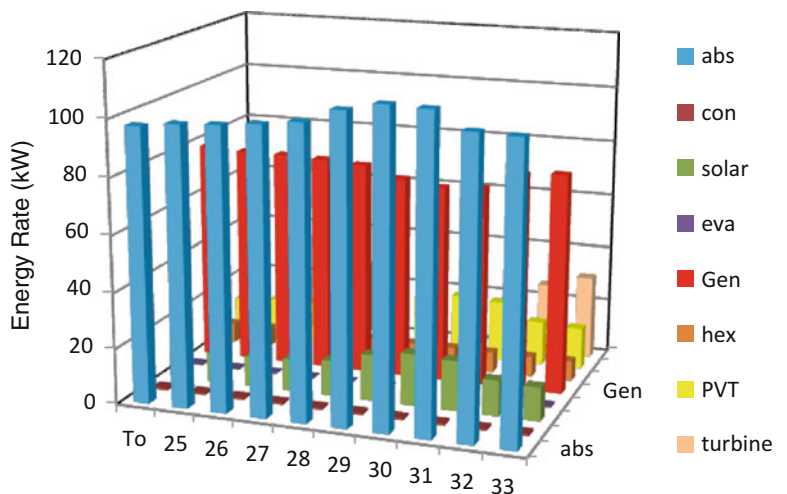
evaporator temperature. The overall system exergy decreased unnoticeably due to increase in evaporator temperature in comparison to Fig. 35.15.

The percentage and values of exergy destructed for system components are presented in Figs. 35.18 and 35.19 for variable T_0. The absorber followed by the generator has the highest exergy destruction rate because of chemical exergy losses caused by heat of solution due to absorption and desorption, respectively.

Fig. 35.20 Optimal solution curves for the overall system exergy efficiency vs. the total cost

The chart shows Total cost $/hr (y-axis, 0.785–0.82) vs Overall exergy efficiency (%) (x-axis: 19.54, 19.55, 19.66, 19.92, 19.95, 20.12, 20.19, 20.29, 20.35, 20.37, 20.41, 20.45, 20.46). Legend: Pareto Front, Curve fitting.

$$y = 2E\text{-}06x^5 - 6E\text{-}05x^4 + 0.0007x^3 - 0.0034x^2 + 0.0072x + 0.7937$$
$$R^2 = 0.9618$$
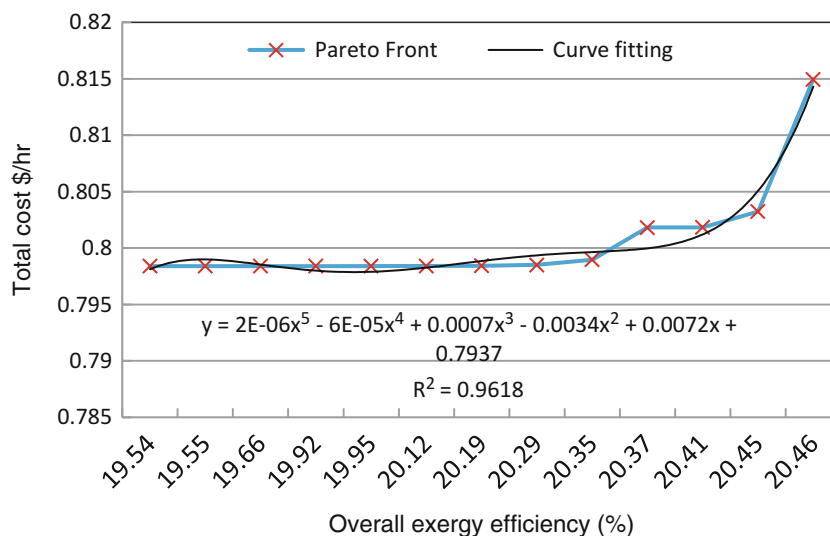
Exergo-economic Analysis and Optimization Results

The exergo-economic analysis was conducted to calculate the total cost of the system equipments, operation, maintenance, and exergy destructed. Optimization using multi-objective technique was carried out for minimum total system cost and maximum overall system exergy efficiency. The Pareto Front is plotted in Fig. 35.20 where the overall exergy efficiency ranged from 19.5 % to 20.5 % at a total cost range of 0.785–0.82 $/h.

Conclusions

The system with no grid connection was chosen, even though the net present value of the grid connected is half that of the off grid. The reason was the large undesired emissions. A sustainable environment and the objective of this study outweigh the cost.

The overall system exergy efficiency was improved from the original design, by the optimization, due to variation of 24 independent parameters through an exhaustive simulation, from 11 % to a maximum of 21 % at a total system net present cost increase of 16 %. The Pareto Front from the simulations represents all possible combinations for the system objectives at the studied parameters. It is worth noting that if one objective is enhanced the other is degraded. Even though the overall exergetic efficiency was low due to the influence of solar and wind losses, the system is recommended because it serves the objective well and cost of solar energy is free.

Exergy analysis of the system efficiencies clearly showed a lower performance of the system components in comparison to energy.

The maximum renewable energy fraction of the selected system was 0.972. In other words, we have achieved a near zero sustainable energy house.

Future study will concentrate on adding fresh water to the house and utilizing thermal ground storage with hydro and ammonia turbine generators.

Nomenclature

Cp	Specific heat (kJ/kg-K)	p	Pressure (kPa)
$\dot{C}$	Stream cost rate ($/s)	To	Reference temperature (°C)
$\dot{s}$	Entropy (kJ/kg-K)	T	Temperature (°C)
h	Enthalpy (kJ/kg)	$\dot{m}$	Mass flow rate (kg/s)
$\dot{P}$	Power (kW)	$\dot{Q}$	Heat rate (kW)
P_O	Reference pressure (kPa)	$\dot{w}$	Power rate (kW)

Subscripts

gen	Generator	h_c	Heat transfer coefficient
abs	Absorber	ir	Interest rate
eva	Evaporator	N	Yearly hours of operation
con	Condenser	R	Universal constant (kJ/kg-k)
hex	Heat exchanger	n	Life cycle in years
in	Inlet	c	Cost of stream ($/GJ)
i	Inlet stream	R_e	Real part
e	Exit stream	Turb	Turbine
PV/T	Photovoltaic/thermal	Capc	Capacitance
turbine	Wind turbine	Trans	Transmission
Ve	Wind velocity	at	After turbine
Ex	Exergy	bt	Before turbine
Cpow	Power coefficient	Pmp	Pump
ηtrans	Efficiency of transferring Dc to Ac current	k	Stream number
in	Inlet	gener	Generated
s	Solar	SFPK	Stream component fueling the product
W	Water	GL	Overall
cell	Photovoltaic cell		

Greek Letters

ψ	Exergy efficiency	x	Concentration of the desiccant by mass (%)
η	Efficiency	°	Degrees
ε	Heat exchanger effectiveness	ω	Turbine rotational speed (rpm)
λ	Turbine blade tip speed (m/s)	α	Absorption coefficient

References

1. ASHRAE (1993) Handbook of fundamentals. American Society of Heating, Refrigerating and Air-Conditioning Engineers, Atlanta, GA, Chapter 28
2. Torcellini P, Pless S, Deru M, Crawley D (2006) Zero energy buildings, a critical look at the definition. ACEEE, Pacific Grove, CA
3. Jung SS, Kim YT, Lee YB (2008) Measurement of sound transmission loss by using impedance tube. J Kor Phys Soc 53(2):596–600
4. Chung JY, Blaser DA (1980) Transfer function method of measuring in duct acoustics properties. J Acoust Soc Am 68(3):907–921
5. Wind Atlases of the World. American Wind Energy Association , "Annual Wind Industry Report, Year Ending 2008," (http://www.awea.org/publicr eports/ AWEA-Annual-Wind Report-2009.pdf) pp. 9–10
6. Dincer I, Rosen M (2007) Exergy: energy, environment and sustainable development, 2nd edn. Elsevier
7. Carrier Corporation (1999–2004) Hourly analysis program system design load software, Version: 4.2-a
8. Bejan A, Tsatsaronis G, Moran M (1996) Thermal design and optimization. Wiley
9. Censor Y (1977) Pareto optimality in multiobjective problems. Appl Math Optim 4:41–59
10. Cunha Da, Polak E (1967) Constrained minimization under vector-valued criteria in finite dimensional spaces. J Math Anal Appl 19:103–124
11. Kalyanmoy Deb (2001) Multi-objective optimization using evolutionary algorithms. Wiley
12. Zadeh LA (1963) Optimality and nonscalar-valued performance criteria. IEEE Trans Autom Control AC-8(1):59–60

A Compact Design of Water Heating–Humidification Processes for Solar HDD Systems

Maher Ghazal, Uğur Atikol, and Fuat Egelioğlu

Abstract

This work investigates the thermal performance of a solar humidification technique that is suitable to use in a Humidification Dehumidification Desalination system (HDD). Water heating and air humidification processes have been merged to take place in a direct contact water solar thermal collection unit. Experiments are conducted under the weather conditions of N. Cyprus. Air passes through brackish water in the humidifier and reaches saturation at the outlet. The difference between temperatures and relative humidity at the inlet and outlet of the humidifier were recorded for different airflow rates (8.2, 10.4, and 12.6 kg/h) between December 1 and 4, 2012. The experiment demonstrated that for an average solar radiation of 600 W/m^2 and a mass flow rate of 12.6 kg/h of air, the increase in average absolute humidity was 0.62 kg/h m^2. As the airflow rate was stepped up, the rate of vapor transfer increased but the efficiency of the humidification process slightly dropped.

Introduction

As the demand for fresh water is growing, scientists are proposing new methods for desalination. With the exponential growth in industry, techniques used in desalination have advanced too. Among all the desalination techniques known up to the present time, reverse osmosis and multistage flash systems are the most common ones in terms of large scale applications. On the other hand, medium and small scale desalination techniques are competing for the lead in terms of independency, reliability, productivity, and cost. The importance of the small scale plants manifests itself in the rural areas, countryside, and remote places.

This work focuses on one of the latest small scale desalination techniques known as humidification dehumidification desalination. HDD systems have had limited use in industry, due to their poor process efficiency caused by heat losses; however, their feasibility became more favorable with the use of solar energy.

Several works have been performed on solar HDD desalination systems, using different configurations. Prakash et al. [1] provided a comprehensive review on solar-driven humidification–dehumidification desalination. These systems varied between open and closed systems with heated air or heated water setups. The technique is versatile with the main idea being bringing dry air in contact with water to be humidified in an evaporator before passing it through a condenser in which air is dehumidified to give fresh water.

M. Ghazal (✉) • U. Atikol • F. Egelioğlu
Department of Mechanical Engineering, Eastern Mediterranean University, via Mersin 10, Gazimagusa, North Cyprus, Turkey
e-mail: maher.ghazal@emu.edu.tr; ugur.atikol@emu.edu.tr; fuat.egelioglu@emu.edu.tr

This study investigates the moisture carrying capacity of air bubbles passing through water. In general, this setup compresses air into water through a pipe, which has several holes on its immersed end. The air exits the holes in the form of bubbles and then ascends vertically under the buoyancy effect. A similar experimental investigation has been carried out by El-Agouz [2] but on a system that uses electrical energy in order to heat sea water. The present study uses solar energy as the main energy source (i.e., energy used for water and air heating). The evaporation chamber and the solar water/air heater are combined into one unit, containing a glass and inclined towards the sun, to achieve water heating, air bubbles heating, and humidification at the same time.

In fact this technique is widely used by chemists to diffuse gasses in liquids in a system known as a column reactor. But these systems have a challenging problem called the coalescence of bubbles. Bubble coalescence takes place even at the generation point or while rising to the surface. Upon coalescence of bubbles the superficial gas–liquid contact area decreases and thus mass and heat transfer to the bubble decrease (i.e., humidification decreases).

In their study of the lower region of the bubble column, Perry and Green [3] found that bubble coalescence depends on the dispersion device. They claimed that in the bubble generator design, the typical separation between orifice centers should range from 2.5 to 4 times the orifice diameter. This result has been considered in the design of the bubble generator used in this study. The coalescence process has been studied in the central region of the bubble column by Camarasa et al. [4] and Pohorecki et al. [5] where bubble break-up and coalescence processes reach equilibrium. They have determined the bubble mean diameter was responsible for the superficial area available for transport phenomena between the gas phase and the liquid phase. It is evident from these studies that the smaller the bubble diameter, the greater the heat and mass transfer to it.

Martin et al. [6] studied the effect of coalescence of bubbles at sieve plate on mass transfer revealing that the results showed that although coalescence decreases mass transfer rate from bubbles, the deformable bubble generated can, in certain cases, balance the decrease in mass transfer rate due to the reduction in superficial area.

Chen et al. [7] investigated the coalescence of bubble pairs rising in a stagnant liquid numerically and compared the results with the experimental ones. The numerical results indicated that the rising velocity of the trailing bubble was larger than that of the leading bubble. They indicated that both of the leading bubble and the trailing bubble rose faster than the single bubble. This is in fact another factor that affects the rate of heat and mass transfer to the bubbles since faster rising bubbles decrease the interaction time and thus decreases the amount of heat and mass transferred.

The main objective of the present study is to investigate experimentally the result of merging the humidification and water heating processes of the HDD in an inclined solar collector bed. The effects of different parameters (i.e., temperatures and different air mass flow rates) on the moisture carrying capacity of air bubbles are also studied.

Experimental Setup

The experimental setup presented in this study comes with a new conceptual solar humidifier by which two stages of the HDD system are accomplished, namely heating and humidification. The major components that were used in the setup are the humidifier bed, the compressor, and the data retrieving devices, see Fig. 36.1. These components are briefly explained in the following sections.

The Humidifier Bed

The humidifier bed is made using Plexiglas for framing, galvanized metal sheet is used as an absorber, and glazing from glass sheets for the aperture. The whole bed then was insulated and enclosed in a wooden box, except the aperture side was glazed allowing sunlight to penetrate through onto the 2 mm absorber plate by which the water contained in the cavity was heated by solar energy. In order to withstand the pressure of water underneath the humidifier, the aperture is double glazed with 8 mm thick inner glass and 4 mm thick outer glass having width of 50 cm and length of 100 cm. A half inch diameter and 60 cm long copper pipe was inserted all the way through a hole, which was drilled from one side of the bed to the opposite side of the bed and was fixed internally. The pipe had 2 mm diameter holes drilled apart with 10 mm center-to-center distances along 500 mm of its length, which is immersed in the bed. The purpose of this pipe is to generate air bubbles into the water. The distance between the glazing and the absorber plate was 5 mm. Air exits the system through 1 in. diameter Plexiglas pipe attached to a hole in the upper part of the frame. The whole bed was mounted on a frame and was tilted due south to face the sun.

Fig. 36.1 The humidification system

Compressor and Controllers

An electrically driven two-piston compressor was used to supply air to the system. The compressor was equipped with a 200 L of storage tank, airflow controller, and pressure controllers to control the air in the tank as well as the inlet air to the system.

Data Acquisition and Measuring Devices

The data collected in this study was airflow rate, global solar radiation, water temperature, inlet and outlet air temperatures, and relative humidity. Solar intensity on the surface of the system was measured using a Pyranometer coupled with a digital multimeter. The Eppley radiometer Pyranometer has the accuracy of ± 0.5 for the range from 0 to 2,800 W/m^2. Water temperature was snapped using two thermocouples which were connected to Xplorer GLX data logger. Inlet and outlet relative humidity and temperatures of the air were acquired using an Omega Thermo Hygrometer RH411 with measurement range of 5–98 % relative humidity and 0–49 °C temperature. The measurement accuracy of the hygrometer is ± 0.8 °C for temperature and ± 3 % for relative humidity. The airflow rate was measured using a hot wire anemometer.

Experimental Procedure and Data Processing

Procedure

The main working principle is to bring unsaturated air (i.e., air bubbles) into contact with water to saturate the air in a process called humidification. In this setup air bubbles travel freely through still water in the cavity to ensure maximum contact surface area; thus, greater mass transfer rate can be achieved.

Fig. 36.2 Working principle of
the humidifier
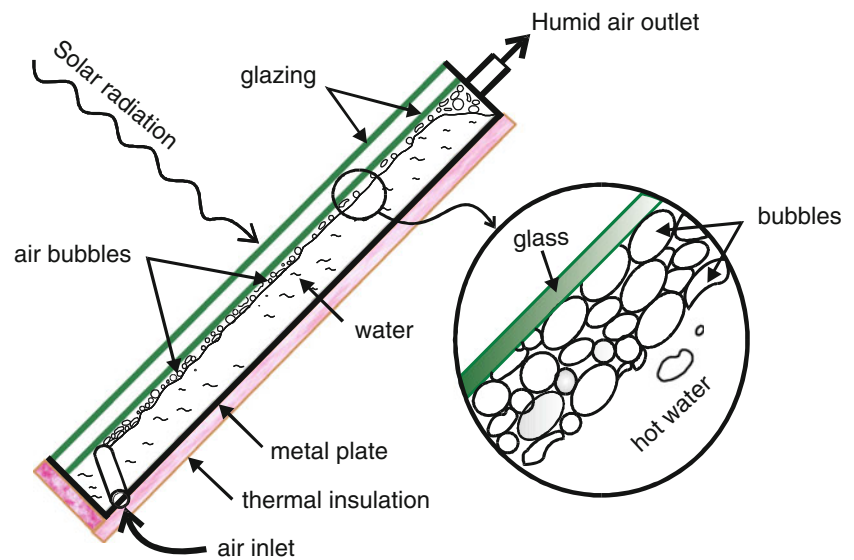
Water was filled in the cavity to about two-third in order to make room for the volume of the air bubbles. The south facing bed allowed the solar energy to penetrate through the glazing to the black painted absorber plate. The absorber in turn transferred the absorbed heat to the contained water and increased its temperature. Compressed air was directed through the copper pipe and bubbles were generated in the water. While ascending upwards, heat and mass transfer to the bubbles took place (Fig. 36.2).

Data of the solar intensity, water temperature, and air relative humidity and temperatures at the inlet and outlet of the evaporator were recorded hourly from 9:30 AM to 3:30 PM in mid-winter for three different airflow rates (8.2, 10.4, and 12.6 kg/h).

Data Processing

The absolute humidity calculation was made possible using the data snapped by the electronic Hygrometer. The inlet and outlet relative humidity and temperatures of air were inserted to a computer-aided thermodynamic table that gave all the thermodynamic properties of air including the most important of which, the absolute humidity. Then the difference between the inlet and outlet absolute humidity was calculated to determine the increase in water vapor content in air through the process. Humidification Process Efficiency η_h was determined according to the following consideration.

Humidification Process Efficiency is considered as the ratio of actual increment in humidity to the maximum possible increment in vapor content at the saturated temperature of air. Humidification Process Efficiency is given by:

$$\eta_h = 100 \, \frac{\omega_{out} - \omega_{in}}{\omega_{out@sat.air} - \omega_{in}} \tag{36.1}$$

Results and Discussion

Figure 36.3 shows the inlet and the outlet relative humidity of the air passing through the humidifier for different airflow rates (i.e., 8.2, 10.4, and 12.6 kg/h) on different days. Although the inlet relative humidity varied for each day, the outlet relative humidity was almost 100 % with slight decrease at flow rate of 12.6 kg/h.

Figure 36.4 shows the inlet and outlet temperatures of air as well as that of the water. It can be seen that there is a gap between the passing air temperature and water temperature for all of the flow rates. As the flow rate increases the difference between the inlet and outlet temperatures decreases. This behavior can be explained with two reasons: the first one is the chilling effect of air on water due to higher flow rate and thus higher heat transfer rate. The second reason is that the energy
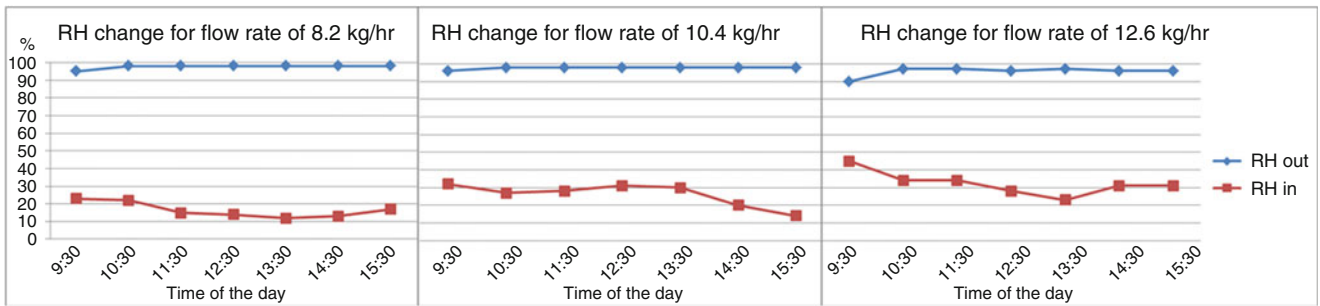
Fig. 36.3 The inlet and outlet relative humidity of air for different flow rates
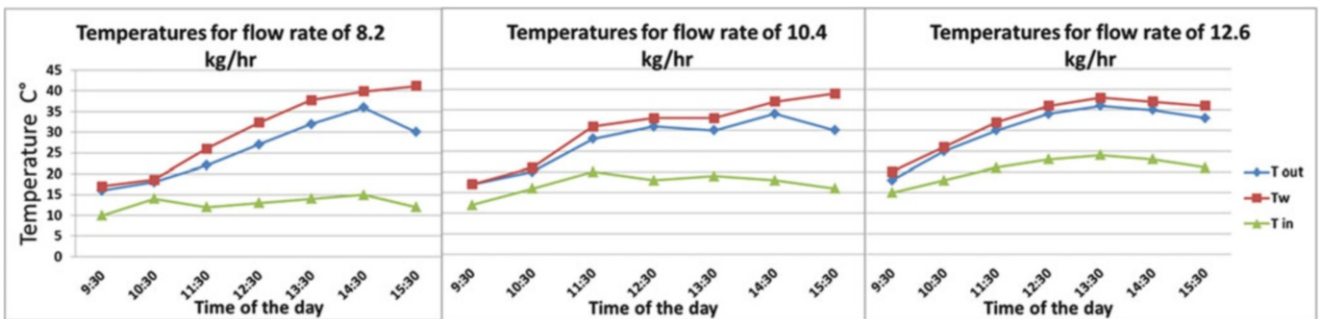
Fig. 36.4 Effect of airflow rate on the temperature differences between the air inlet and outlet
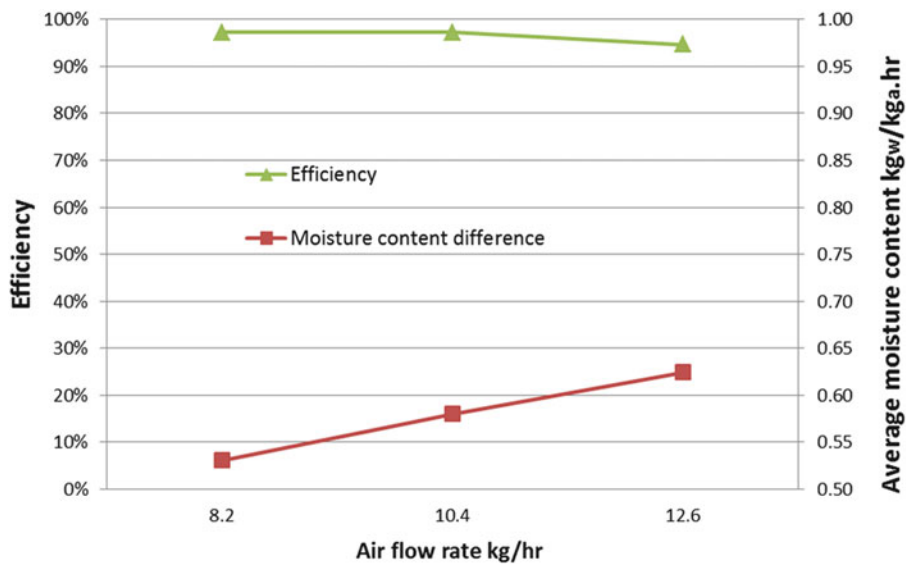
Fig. 36.5 Effect of higher flow rates on the productivity and humidification efficiency

of vaporization, which comes mainly from water, needed for phase change, increases as it is directly proportional to the amount of vaporized water which increases with the airflow rate.

Figure 36.5 illustrates the average moisture content differences between the inlet and outlet air for each flow rate (i.e., 8.2, 10.4, 12.6 kg/h) in addition to the average efficiency calculated using Eq. (36.1). It can be clearly seen that mass transferred is greater for greater flow rates whereas efficiency of the humidification process decreases slightly.

Conclusions

In the present work a novel solar humidification unit was developed for using in HDD systems. The efficiency of the system together with the effect of water temperature and flow rate on the productivity have been studied and the following points were concluded:

1. Direct contact humidification is an effective technique to be used in solar HDD systems. Merging water heating and air humidification processes in a compact design result in efficient humidification and efficient use of space for small scale HDD systems.
2. Although the system hasn't reached high temperatures, due to the mid-winter weather conditions, air comes out from the humidifier as saturated.
3. Although there was slight drop in the efficiency of the humidification process as the flow rate increases, the average increment in moisture content per hour increased and thus the productivity also increased.

Nomenclature

T	Temperature, °C	RH	Relative humidity, %

Greek Letters

η	Efficiency of the humidification process, %	ω	Absolute humidity, kg water vapor/kg dry air

Subscripts

w	Water	out	Outlet
a	Air	sat	Saturated, saturation
in	Inlet		

References

1. Prakash NG, Sharqawy MH, Summers EK, Lienhard JH, Zubair SM, Antar MA (2010) The potential of solar-driven humidification–dehumidification desalination for small-scale decentralized water production. Renew Sustain Energy Rev 14:1187–1201
2. El-Agouz SA (2010) A new process of desalination by air passing through seawater based on humidification-dehumidification process. Energy 35:5108–5114
3. Perry RH, Green DW, Maloney JO (1997) Perry's chemical engineers' handbook, 7th edn. McGraw-Hill
4. Camarasa E, Vial C, Poncin S, Wild G, Midoux N, Bouillard J (1999) Influence of coalescence behaviour of the liquid and of gas sparging on hydrodynamics and bubble characteristics in a bubble column. Chem Eng Process 38:329–344
5. Pohorecki R, Moniuk W, Zdrojkowski A, Bielski P (2001) Hydrodynamics of a pilot plant bubble column under elevated temperature and pressure. Chem Eng Sci 56:1167–1174
6. Martin M, Montes FJ, Galan MA (2007) Bubble coalescence at sieve plates: II. Effect of coalescence on mass transfer. Superficial area versus bubble oscillations. Chem Eng Sci 62:1741–1752
7. Chen RH, Tian WX, Su GH, Qiu SZ, Ishiwatari Y, Oka Y (2011) Numerical investigation on coalescence of bubble pairs rising in a stagnant liquid. Chem Eng Sci 66:5055–5063

Investigation of Humidity Effects on the Thermal Comfort and Heat Balance of the Body

Omer Kaynakli, Mustafa Mutlu, Ibrahim Atmaca, and Muhsin Kilic

Abstract

Humidity, one of the most confusing of all climatic parameters in assessing the indoor climate, affects comfort in a number of ways both directly and indirectly, and the avenues by which humidity affects comfort are not completely known. The aim of this study is to comprehend the effects of humidity on thermal interaction between the human body and its environment, and thermal sensation. In this chapter, the effect of humidity on heat and water balance of human body, and in turn on body temperatures and thermal sensation, is investigated. A mathematical model of heat and mass interaction between the human body and the surrounding environment has been established, and the effect of air humidity has been examined under various relative humidity levels by means of using the empirical relations that express thermoregulatory control mechanisms. In the numerical model, human body has been separated into 16 sedentary segments, and possible local discomforts have been taken into consideration. Using the model, changes in the sensible and latent heat losses, body temperatures, skin wettedness, and thermal comfort indices have been calculated and results have been discussed explicitly.

Keywords

Thermal comfort • Heat balance • Humidity • Body temperature

Introduction

The living body constantly produces heat, and this must be transferred to the environment. Heat balance is the balance between the rate of heat production and the rate of heat loss. Body temperature is regulated by the blood flowing from the core to the skin where the heat is dissipated by radiation, convection, and evaporation to the environment. Thermal comfort is generally associated with a neutral or near neutral whole body thermal sensation. Thermal sensation depends on body temperature, which in turn depends on thermal balance and the effects of environmental factors, as well as personal factors [1, 2]. Air temperature and humidity are two important factors affecting thermal comfort. Other factors include radiant temperature, air velocity, occupant activity levels, and clothing.

Humidity is the most confusing of all climatic parameters in assessing the indoor climate. The humidity of the ambient air has a wide range of effects on the energy and water balance of the body as well as on elasticity of the materials, air quality perception, build up of electrostatic charge and the formation of mould. The humidity of ambient air has an

O. Kaynakli (✉) • M. Mutlu • M. Kilic
Mechanical Engineering Department, Uludag University, Bursa, Turkey
e-mail: kaynakli@uludag.edu.tr; mustafamutlu@uludag.edu.tr; mkilic@uludag.edu.tr

I. Atmaca
Mechanical Engineering Department, Akdeniz University, Antalya, Turkey
e-mail: atmaca@akdeniz.edu.tr

influence on three mechanisms of water loss from the human body. These are the diffusion of water vapor through the skin, the evaporation of sweat from the skin surface, and the humidification of the respired air. In all cases, the water is lost in gaseous form, which also results in an energy loss from the body from which the relevant evaporation heat is taken [3, 4].

Relative humidity is the ratio of the water vapor content of air to the maximum possible water vapor content of air at the same temperature and air pressure. For people who perform very light or sedentary activities, the influence of humidity on personal comfort is not great. Higher humidity will make a person feel warmer particularly in a ventilated area where the air speed is low. Elevated relative humidity reduces the body's ability to lose heat through perspiration and evaporation. When this happens, individuals may perceive temperatures to be higher than they actually are. On the other hand, low relative humidity can cause discomfort due to drying of the eyes, nose, throat, mucous membranes, and skin [5, 6].

Humidity affects human comfort in heat balance and in other many ways, such as healthy thermal sensation, skin wettedness, tactile sensation of fabrics, and perception of air quality. Liviana et al. [7], which studied humidity effects on human health, found that low humidity can contribute to eye irritation. Eye discomfort increased with time in low humidity environments ($T_{dp} < 2\ °C$). Teodosiu et al. [4] described a numerical model to assess the thermal comfort taking into account the indoor air moisture and its transport by the air flow within an enclosure.

Thermal neutrality is a necessary but not sufficient condition for thermal comfort [8]. At the thermal neutrality, humidity may be a cause of discomfort for two reasons: an uncomfortably high level of skin humidity or insufficient cooling of the mucous membranes in upper respiratory tract by inhalation of humid or warm air. Toftum et al. [9] dealt with discomfort caused by skin humidity. In the companion paper of that, Toftum et al. [10], they have presented the results of the experiments on humidity and temperature of inhaled air on discomfort. de Dear et al. [11] studied the impact of humidity on thermal comfort during step changes between 20 and 80 % relative humidity. They found that thermodynamics of moisture absorption and desorption in clothing fibers during humidity transients affected the heat balance and thermal sensation of subjects. Berglund and Cain [12] showed that air freshness and acceptability perceptions decreased with increasing temperature and humidity. In particular, relative humidities above 65 % were associated with unacceptable air quality judgments. Fang et al. [13] reached to similar results from air contaminated with emissions for common building materials. The air quality was perceived to be more acceptable with decreasing temperature and humidity. Fountain et al. [14] presented a short summary of previous studies on the influence of humidity on thermal comfort. Guan et al. [15] summarized the current advances in thermal comfort modeling for both building and vehicle HVAC applications that have occurred in the literature. Fiala et al. [16] modeled the physiological mechanisms within the body, thermal exchanges between the body and its environment, and gave the detailed numerical model in their study. Each body segment was considered as five-body layers (core, muscle, fat, inner skin, and outer skin). In their model, local variations of surface convection, directional radiation exchange, evaporation and moisture collection at the skin, and the nonuniformity of the clothing ensembles were considered. Further study is warranted to better understand and quantify how humidity affects building occupants and HVAC system users.

This chapter inclines to relative humidity, one of the most complex parameter of the independent thermal comfort variables. As mentioned above, relative humidity affects comfort in a number of ways both directly and indirectly. In this study, investigation of the effects of low, intermediate, and high relative humidity values on the energy balance and the thermal comfort indices is aimed. Human body is divided into 16 sedentary segments and simulation of the heat-mass transfer between the body segments, and their environment is performed. By using the present model, variations of the core, skin, and mean body temperatures; sensible and latent heat losses from the body; and skin wettedness with the relative humidity are obtained for both whole body and body segments at different ambient temperatures. The effects of the same conditions on the thermal comfort indices, *TSENS* and *DISC*, are presented in graphical forms.

Mathematical Model

The model used in this study combines the Gagge et al. [2] and Olesen et al. [8] models and based on the same approach used in the study by McCullough et al. [17]. The fundamental equations of the model are presented in this section. Further details of the developed model can be found in references [18, 19].

A two-compartment transient energy balance model developed by Gagge et al. [2] represents the body as two concentric cylinders: the inner cylinder represents the body core (skeleton, muscle, internal organs) and the other cylinder represents the skin layer. This model, by considering instantaneous heat storage of the core and the skin compartment, assumes that

temperatures of these compartments change with time. Thermal interaction of the human body with the environment for the core and the skin compartments can be written as follows [2, 20]:

$$S_{cr} = M - W - Q_{res} - Q_{cr,sk} \tag{37.1}$$

$$S_{sk} = Q_{cr,sk} - \left(Q_{cd} + Q_{cv} + Q_{rd} + Q_{e,sk}\right) \tag{37.2}$$

where M is the rate of metabolic heat production, W is the rate of external work done by the muscles, Q_{res} is the total rate of heat loss through respiration, $Q_{cr,sk}$ is the rate of heat exchange between the core and skin, and $Q_{e,sk}$ is the total rate of evaporative heat loss from skin. The total rate of sensible heat loss from skin can be divided to three parts, namely conductive (Q_{cd}), convective (Q_{cv}), and radiative (Q_{rd}) heat loss rates. Since the conductive heat loss is a small fraction of the total heat loss from the body, generally it is neglected in the comfort calculations [21, 22]. Heat storage rate of the core and skin causes instantaneous temperature changes in each compartment. This effect may be expressed with following equations:

$$dt_{cr}/d\theta = S_{cr}A_b/\left((1-\alpha)mc_{p,b}\right) \tag{37.3}$$

$$dt_{sk}/d\theta = S_{sk}A_b/\left(\alpha mc_{p,b}\right) \tag{37.4}$$

where α is the fraction of body mass concentrated in skin compartment, m is the mass of body, $c_{p,b}$ is the specific heat of body, and t_{cr} and t_{sk} are the core and skin temperature of the body, respectively.

Heat is generated in the body by metabolism and can be lost to the environment by conduction, convection, radiation, and evaporation of moisture from the skin and respiration. Convective and radiative heat loss from clothed body to environment is calculated as

$$Q_{cv} + Q_{rd} = \frac{(t_{sk} - t_o)}{R_{cl} + \dfrac{1}{(h_{cv} + h_{rd})f_{cl}}} \tag{37.5}$$

where R_{cl} is thermal resistance of clothing, f_{cl} is the ratio of clothed to nude body area, and h_{cv} and h_{rd} are the convective and radiative heat transfer coefficients, respectively. Operative temperature (t_o) can be defined as the average of the mean radiant and ambient air temperatures, weighted by their respective heat transfer coefficients. The radiative heat transfer coefficient (h_{rd}) was assumed to be 4.7 W/m$^{2\circ}$C for typical clothing systems, and the necessary equation for calculating the convective heat transfer coefficient for seated person with moving air was taken from ASHRAE [20].

In naturally ventilated rooms with closed windows, air velocity rarely exceeds 0.1 m/s [3]. For that reason, in the present study average air velocity over the body is assumed to be 0.1 m/s. The maximum total latent heat loss from the skin ($Q_{e,max}$) is given by

$$Q_{e,\max} = \frac{\left(p_{sk,s} - p_a\right)}{\dfrac{R_{cl}}{i_{cl}LR} + \dfrac{1}{h_{cv}f_{cl}LR}} \tag{37.6}$$

where, $p_{sk,s}$ is the saturated water vapor partial pressure at the skin temperature and p_a is the water vapor partial pressure in the ambient air, i_{cl} is the permeation efficiency of the clothing, and LR is the Lewis Ratio which is the ratio of the evaporative heat transfer coefficient to the convective heat transfer coefficient. McCullough et al. [17] have found an average value of $i_{cl} = 0.34$ for common indoor clothing and LR equals approximately 16.5 °C/kPa at typical indoor conditions [20].

Total skin wettedness (w) including wettedness due to regulatory sweating (w_{rsw}) and to diffusion through the skin (w_{dif}) can be written as

$$w = w_{rsw} + w_{dif} \tag{37.7}$$

where w_{rsw} and w_{dif} are given by

$$w_{rsw} = \frac{\dot{m}_{rsw}h_{fg}}{Q_{e,\max}} \tag{37.8}$$

$$w_{dif} = 0.06(1 - w_{rsw}) \tag{37.9}$$

where $\dot{m}_{rsw}$ is the rate of sweat production and h_{fg} is the heat of vaporization of water. $\dot{m}_{rsw}$ is given by control signal equation. Evaporative heat loss from the skin $(Q_{e,sk})$ is a combination of the evaporation of sweat secreted due to thermoregulatory control mechanisms $(Q_{e,rsw})$ and the natural diffusion of water through the skin $(Q_{e,dif})$:

$$Q_{e,rsw} = w_{rsw}Q_{e,\max} \tag{37.10}$$

$$Q_{e,dif} = w_{dif}Q_{e,\max} \tag{37.11}$$

$$Q_{e,sk} = (Q_{e,rsw} + Q_{e,dif}) = w\,Q_{e,\max} \tag{37.12}$$

During respiration, the body loses both sensible and latent heat by convection and evaporation of heat on water vapor from the respiratory tract to the inhaled air. Sensible $(Q_{s,res})$ and latent $(Q_{e,res})$ heat losses due to respiration are

$$Q_{s,res} + Q_{e,res} = \dot{m}_{res}\big[c_{p,a}(t_{ex} - t_a) + h_{fg}(W_{ex} - W_a)\big]/A_b \tag{37.13}$$

where $\dot{m}_{res}$ is the mass flow rate of air inhaled and t_{ex} and t_a are the exhaled air and the ambient air temperatures, respectively. W_{ex} and W_a are the exhaled air and the ambient air humidity ratio, respectively. The heat of vaporization (h_{fg}) is 2.43×10^6 J/kg. Humidity ratio of the exhaled and ambient air can be expressed as

$$W_{ex} = 0.0277 + 0.000065T_a + 0.2W_a \tag{37.14}$$

$$W_a = \frac{\overline{R}_a}{\overline{R}_v}\frac{p_a}{(p_{atm} - p_a)} = 0.622\frac{p_a}{(p_{atm} - p_a)} \tag{37.15}$$

where $\overline{R}_a$ and $\overline{R}_v$ are gas constants of air and vapor, respectively and p_a is the water vapor partial pressure in the ambient air.

The body is divided into 16 segments which are uniformly clothed. In the model, dry and evaporative resistances are calculated for each body segments which are treated as concentric cylinders. The total thermal resistance (R_t) and the total evaporative resistance $(R_{e,t})$ for each segments are as follows [17]:

$$R_t(i) = R_a(i)\frac{r(i,0)}{r(i,nl)} + \sum_{j=1}^{nl}\left[R_{al}(i,j)\frac{r(i,0)}{r(i,j-1)} + R_f(i,j)\frac{r(i,0)}{r(i,j)}\right] \tag{37.16}$$

$$R_{e,t}(i) = R_{e,a}(i)\frac{r(i,0)}{r(i,nl)} + \sum_{j=1}^{nl}\left[R_{e,al}(i,j)\frac{r(i,0)}{r(i,j-1)} + R_{e,f}(i,j)\frac{r(i,0)}{r(i,j)}\right] \tag{37.17}$$

where R_a and $R_{e,a}$ are the thermal and evaporative resistances of the outer air layer, R_{al}, and $R_{e,al}$ are the thermal and evaporative resistances of the air layer between the clothing layers, respectively. Detailed information about these resistances may be found in McCullough et al. [17], and convective–radiative heat transfer coefficients for 16 individual body segments are reported by de Dear et al. [23].

Control Signal Equations

The parameters used in the control signals are the core, skin, and mean body temperatures. The blood flow between the core and skin per unit of skin area can be expressed mathematically as [20, 24]

$$\dot{m}_{bl} = [(6.3 + 200WSIG_{cr}/(1 + 0.5CSIG_{sk}))]/3600 \tag{37.18}$$

The heat exchange between the core and skin can be written as

$$Q_{cr,sk} = \left(K + c_{p,bl}\dot{m}_{bl}\right)(t_{cr} - t_{sk}) \tag{37.19}$$

where K is the average thermal conductance and $c_{p,bl}$ is the specific heat of blood. The rate of sweat production per unit of skin area is estimated by

$$\dot{m}_{rsw} = 4.7x10^{-5}WSIG_b \exp(WSIG_{sk}/10.7) \tag{37.20}$$

The average temperature of human body can be predicted by the weighted average of the skin and core temperatures:

$$t_b = \alpha t_{sk} + (1 - \alpha)t_{cr} \tag{37.21}$$

Prediction of Thermal Comfort

Because comfort is a "condition of mind," empirical equations must be used to relate comfort perceptions to specific physiological responses. The compartment model uses empirical expressions to predict thermal sensations (*TSENS*) and thermal discomfort (*DISC*). *TSENS* and *DISC* values can be calculated by the following equations [20]:

$$TSENS = 0.4685(t_b - t_{b,c}) \quad t_b < t_{b,c} \tag{37.22}$$

$$TSENS = 4.7\eta_e(t_b - t_{b,c})/(t_{b,h} - t_{b,c}) \quad t_{b,c} \le t_b \le t_{b,h} \tag{37.23}$$

$$TSENS = 4.7\eta_e + 0.685(t_b - t_{b,h}) \quad t_{b,h} < t_b \tag{37.24}$$

$$DISC = 0.4685(t_b - t_{b,c}) \quad t_b < t_{b,c} \tag{37.25}$$

$$DISC = \frac{4.7\left(Q_{e,rsw} - Q_{e,rsw,req}\right)}{\left(Q_{e,\max} - Q_{e,rsw,req} - Q_{e,dif}\right)} \quad t_{b,c} \le t_b \tag{37.26}$$

Validation of the Simulation

The equations, given in the mathematical model section, are solved in the computer medium, and the simulation is performed to determine the heat and mass transfer between the body and its environment, and also thermal comfort. In order to validate the present model, the simulation results have been compared with the experimental data of Werner and Reents [25], Tanabe et al. [26], and with the numerical results of Huizenga et al. [27].

In Table 37.1, sensible heat losses from a whole human body and body segments are given, and the present results are compared with the experimental measurements of Tanabe et al. [26]. In the calculations, the following values are used: $R_t = 0.205$ m^{2}K/W, $R_{e,t} = 0.0326$ m^{2}kPa/W, $RH = 50$ %, and $t_a = t_{rd} = 24.7$ °C. It can be seen that the present results are very close to the measured values.

Werner and Reents [25] and Huizenga et al. [27] investigated the effects of ambient temperatures on the body segment temperatures at 40 % relative humidity. Variation of skin temperatures with ambient temperature is comparatively given in Fig. 37.1. In this calculation, it is assumed that body is in rested position and wears only shorts. Results obtained from the present model are also in good agreement with the results of Werner and Reents [25] and Huizenga et al. [27].

Table 37.1 Comparison of heat losses from each part of the body with experimental results

| Segment number | Rate of sensible heat loss (W/m^2) | | |
	Experimental[a]	Present study	Difference (%)
1	70.00	78.90	12.7
2	70.00	78.90	12.7
3	50.00	49.48	1.0
4	51.35	50.77	1.1
5	45.57	44.40	2.6
6	48.60	47.28	2.7
7	35.00	32.44	7.3
8	44.43	43.57	1.9
9	57.00	58.68	2.9
10	60.71	65.97	8.7
11	35.57	32.44	8.8
12	40.00	37.67	5.8
13	37.30	35.17	5.7
14	41.43	39.32	5.1
15	38.86	36.49	6.1
16	43.10	41.71	3.2
Whole body	45.30	45.97	1.5

[a]Tanabe et al. [26]
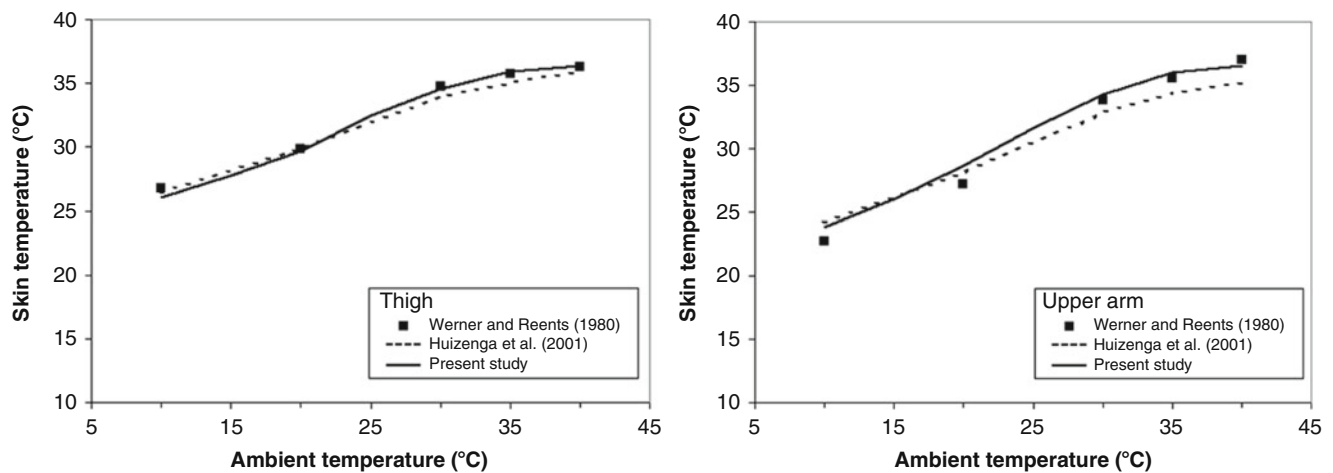
Fig. 37.1 Comparison of measured [25] and simulated ([27] and present study) skin temperatures during ambient temperatures ranging from 10 to 40 °C

Results and Discussion

After the comparisons and validation of the simulation, it can be examined the results of humidity effects. The relation among ambient temperature, clothing, humidity, and the influence of these parameters on the body temperatures and also the thermal comfort are investigated in this section.

Variations of the body temperatures with the ambient temperature at two different clothing configurations ($R_{cl} = 0.6$ and 1.0 clo) are given in Fig. 37.2. In these calculations, it is assumed as $M_{act} = 60$ W/m^2 (for seated-quiet person) and RH = 50 %, $0.05 < V < 0.10$ m/s, $t_a = t_{rd}$ (for typical indoor conditions). In figures presenting the temperatures of the body and segments, the curves are formed by referring the minimum value. So, the increasing rate of the temperature with respect to determined reference value rather than the real values is given. Since the initial temperatures of body parts are different according to experimental conditions and manikin situation in many studies, a qualitative comparison can be more accurate and rationalist approach instead of quantitative. From Fig. 37.2, the amounts of increase and decrease of body temperatures

Fig. 37.2 Increment of body temperatures vs. ambient temperature
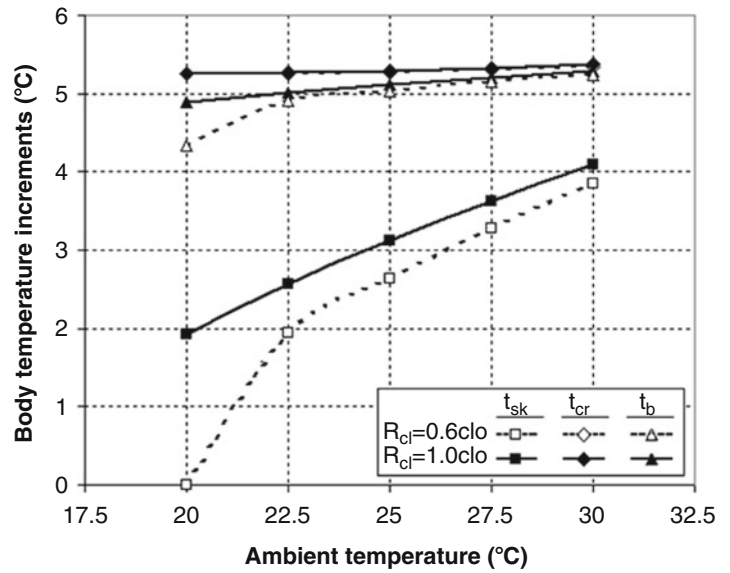
Fig. 37.3 Heat loss vs. ambient temperature
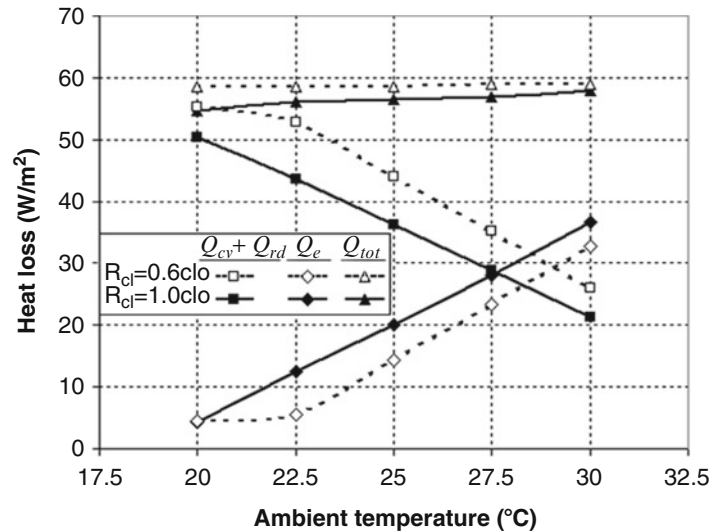
can be seen easily. In this figure, the body temperatures at $t_a = 20\ °C$ and $R_{cl} = 0.6$ clo are taken as a reference point. For other cases, increasing amounts of body temperatures in respect of the reference value are given. Because of the fact that the heat losses from the body to environment decrease with increasing ambient temperature, as expected, the body temperatures (t_{sk}, $t_{cr,}$ and t_b) increase. Moreover, variation amount in the skin temperature is higher than that in the core and the mean body temperatures. At the ambient temperature in the range of 20–30 °C, the maximum change of skin temperature is 3.8 °C while the core temperature is almost stable. This figure also shows that generally the body temperatures have smaller values for low clothing insulation, and the core temperature of the body doesn't change markedly with the clothing insulation. The core temperatures for $R_{cl} = 0.6$ and 1.0 clo are nearly coincided. In addition, the difference between skin temperatures for $R_{cl} = 0.6$ and $R_{cl} = 1.0$ clo decreases with increasing ambient temperature although it is high at the low ambient temperatures. So, the effect of clothing on the skin temperature is greater at low ambient temperatures.

Under the same conditions (environmental and personal), variation of the heat losses from the whole body is shown in Fig. 37.3. When the ambient temperature increases, temperature difference between the ambient and skin decreases; for this reason, sensible (convection + radiation) heat losses fall down but latent (evaporation + diffusion) heat losses boost. To maintain heat balance between the body and its environment depending on decreasing sensible heat losses from the body, evaporation heat losses increase with increasing sweat generation. Besides, total heat losses from the skin (sensible + latent) slightly increase as well. At low clothing insulation, the total heat loss and the sum of the convective and radiative heat losses

Fig. 37.4 Skin wettedness
vs. ambient temperature
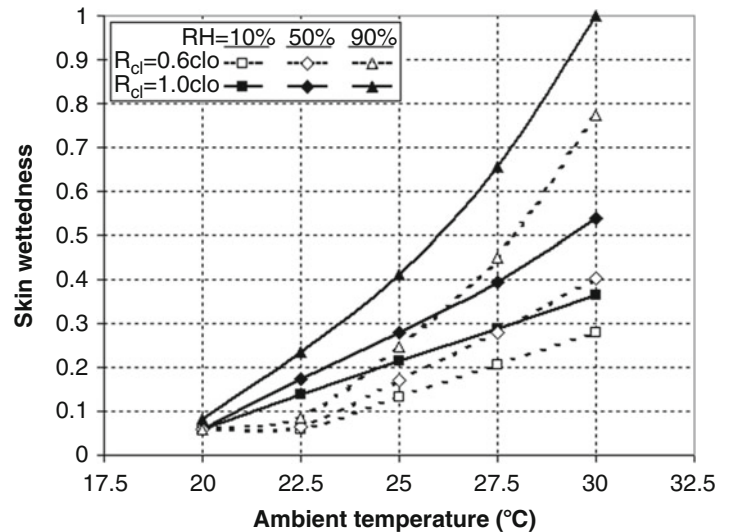
Fig. 37.5 Increment of skin
temperature vs. ambient
temperature
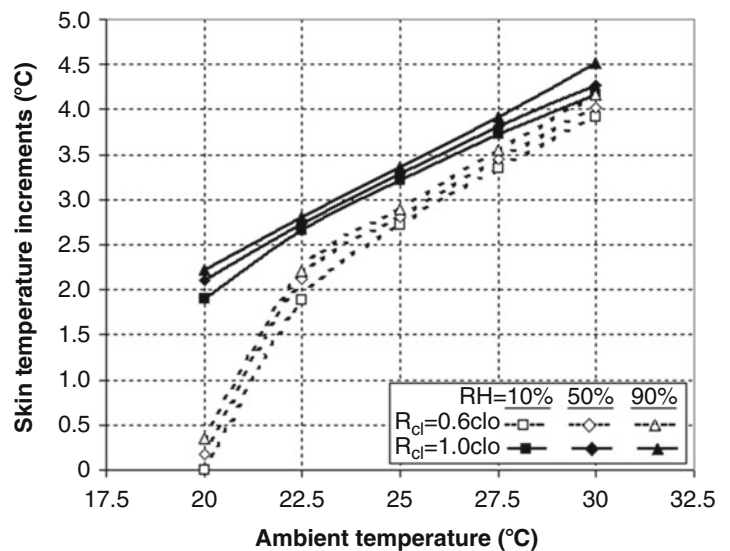
have higher values due to low thermal resistance. Meanwhile, the evaporative heat loss for R_{cl} = 0.6 clo has lower values in comparison to that for R_{cl} = 1.0 clo. Because the body can easily transmit the heat at the low clothing resistance by using sensible heat loss mechanisms, the sweat generation is lower and so the evaporative heat loss.

The effects of three different relative humidity levels as low (10 %), intermediate (50 %), and high (90 %) on the skin wettedness are given in Fig. 37.4. In these calculations, the environmental and personal conditions except for the relative humidity are assumed as the same conditions given above. As known, if the water vapor partial pressure in the ambient air boosts, the relative humidity increases. In this circumstance, skin wettedness increases as moisture on the skin does not penetrate easily into ambient air. Skin wettedness is a parameter connected with evaporative potential of the environment together with generated sweat. If the evaporative potential of the environment decreases with increasing relative humidity, skin wettedness increases. Relative humidity value is an important factor for the thermal comfort, especially in high ambient temperatures. While skin wettedness is 0.06 for each three relative humidity values (10, 50, and 90 %) at the ambient temperature of 20 °C, the difference among skin wettedness' increases with increasing of ambient temperature.

The effect of the relative humidity on the skin and core temperatures is smaller than that of the ambient temperature (Figs. 37.5 and 37.6). At the ambient temperature of 30 °C and the clothing insulation of 1 clo, when the relative humidity varies from 10 % to 90 %, variation in the skin temperature is 0.4 °C while that in the core temperature is only 0.05 °C (Fig. 37.5). Furthermore, the difference between the skin temperatures for clothing resistances 0.6 and 1 clo is high at the low ambient temperatures. The temperature difference decreases with increasing ambient temperature. So, clothing resistance

Fig. 37.6 Increment of core temperature vs. ambient temperature
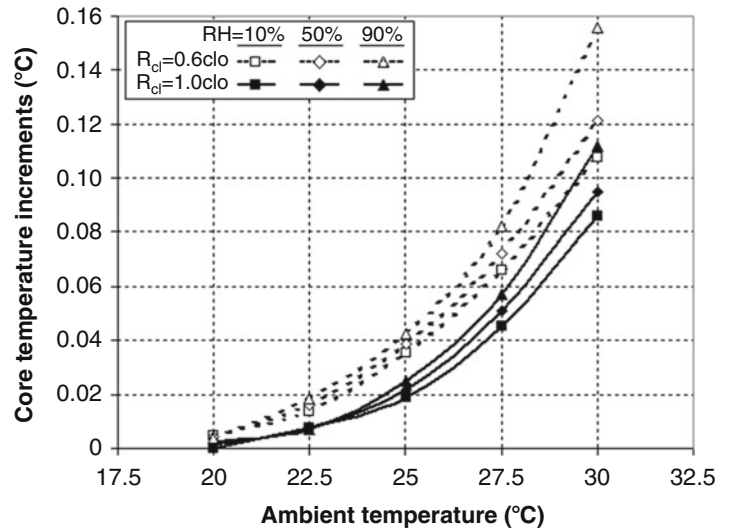
Fig. 37.7 *TSENS* vs. ambient temperature
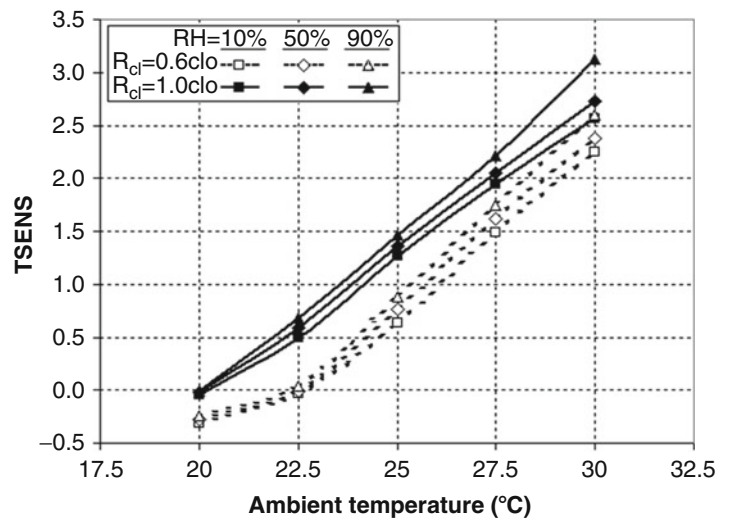
has more effect on the skin temperature at low ambient temperatures. As it can be seen from Fig. 37.6, while relative humidity has a small effect on the body core temperature at the low ambient temperatures, it has a greater effect on this temperature at the high ambient temperatures. As the ambient temperature increases, the difference among the core temperatures increases for various relative humidity values.

The effects of relative humidity on the thermal comfort perception are shown in Figs. 37.7 and 37.8. In these figures, variation of *TSENS* and *DISC* thermal comfort indices with the ambient temperature are given for different relative humidity and clothing insulation values. Since body temperatures and skin wettedness increase with increasing ambient temperature, comfort sense gets worse. While relative humidity has a small effect on the *TSENS* and *DISC* values at the low ambient temperatures, it has a greater effect on these values at the high ambient temperatures. Relative humidity has a strong influence on the *DISC* which takes into account regulation by sweating. At the ambient temperature of 30 °C and the clothing insulation of 1 clo, while *DISC* is 1.6 for the 10 % relative humidity, it is 5.3 for the 90 % relative humidity. *DISC*, which is related to skin wettedness, has a high value at the high temperature and humidity.

In the following figures, some of the body parts are investigated in detail for different humidity values at $R_{cl} = 1.0$ clo. Variations of the skin temperature and wettedness of, for example, the pelvis and fibula are shown in Figs. 37.9 and 37.10. If the ambient temperature gets high values, the body segments' temperatures increase similar to the mean body skin temperature. Since pelvis has more clothes than fibula, skin temperature and wettedness of the pelvis have higher values. Skin temperature of the pelvis rapidly increases at 30 °C ambient temperature and 50 % *RH*. Because the skin wettedness of the pelvis reaches value of 1, which is the maximum value, at a little lower than $t_a = 30$ °C, it does not increase anymore at

Fig. 37.8 *DISC* vs. ambient
temperature
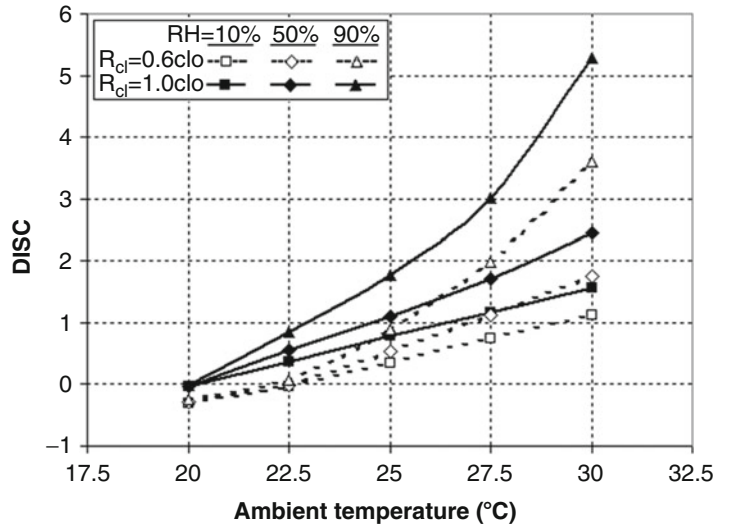
Fig. 37.9 Increment of fibula
and pelvis skin temperatures
vs. ambient temperature
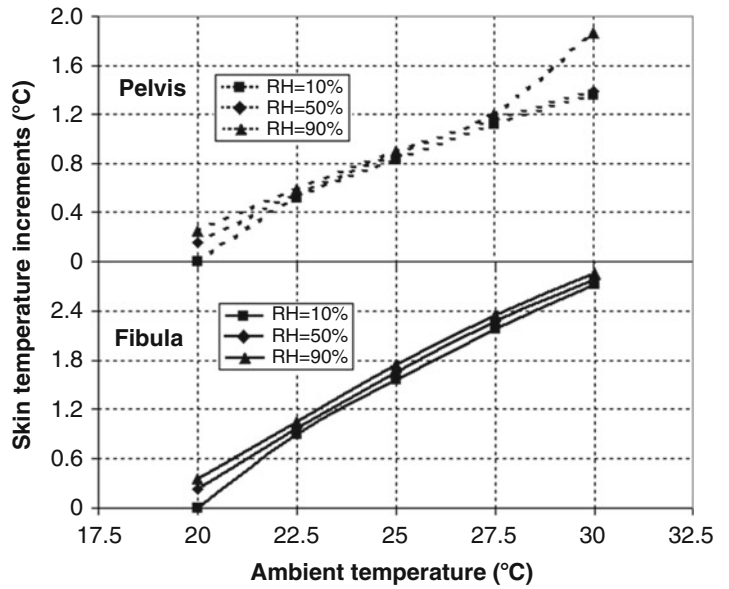
Fig. 37.10 Fibula and pelvis
skin wettedness vs. ambient
temperature
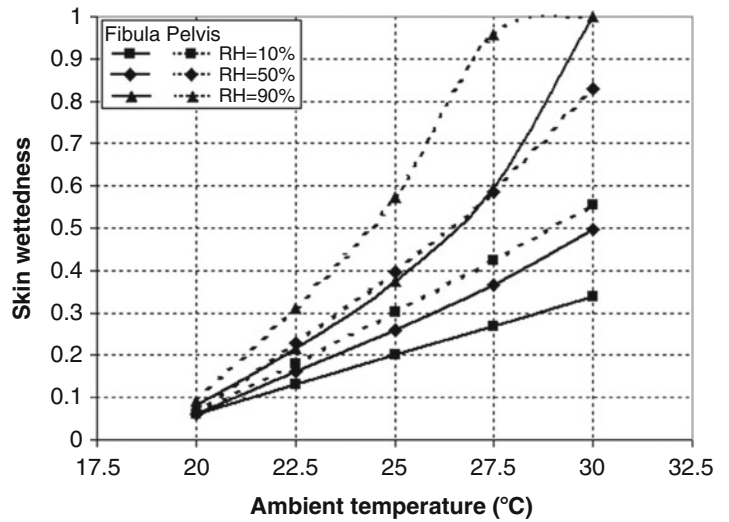
Fig. 37.11 Increment of head and back skin temperatures vs. ambient temperature
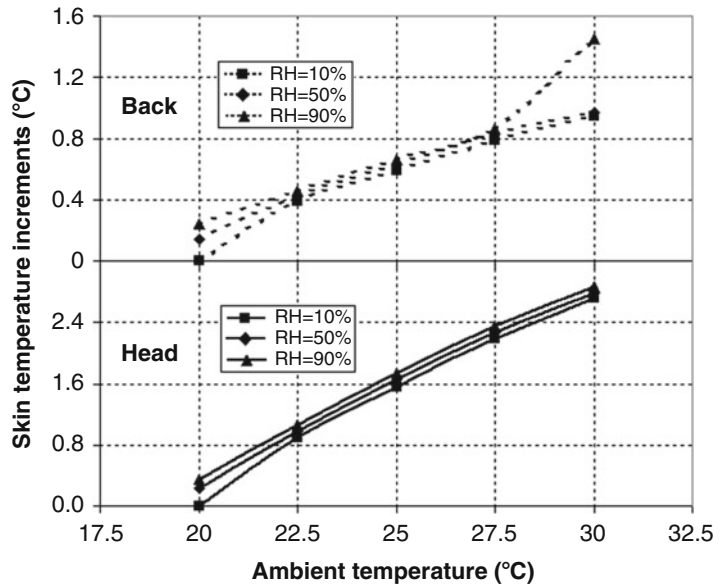
Fig. 37.12 Head and back skin wettedness vs. ambient temperature
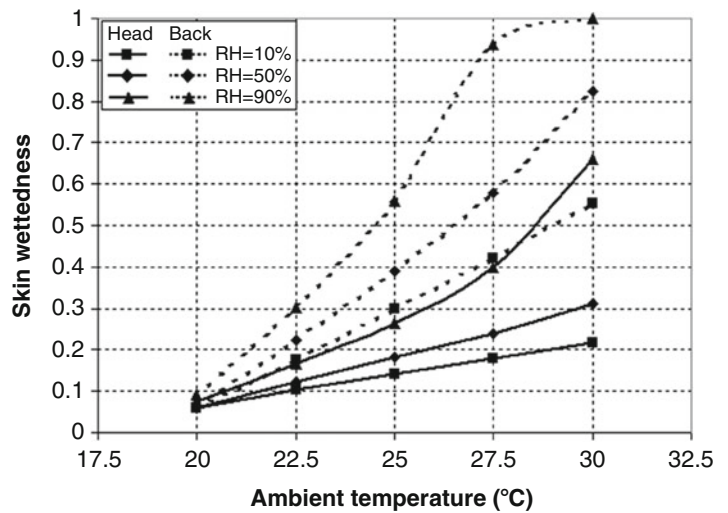
the higher ambient temperatures. As the skin wettedness reaches the maximum value, the evaporation loss remains constant, and as a result of this, skin temperature increases. A similar situation is shown in Fig. 37.11 for back segment. At the same environmental conditions (~30 °C, 90 %), skin temperature of the back suddenly increases. Because, as it can be seen from Fig. 37.12, the skin wettedness of the back reaches value of 1, which is the maximum value, at a temperature lower than 30 °C ambient temperature, and since the heat balance is not maintained at the higher ambient temperatures, the skin temperature of the back rapidly increases. When the ambient temperature increases, increasing ratio of the head skin temperature is relatively faster than that of the back skin temperature. So, the head is more affected from the environmental conditions, because it is naked.

Variation of the required ambient temperature for the thermal comfort conditions with humidity ratio in the air for two different clothing ($R_{cl} = 0.6$ and 1 clo) is given in Fig. 37.13. Values of *TSENS* and *DISC* are equal to zero on these curves presenting for $R_{cl} = 0.6$ clo and $R_{cl} = 1$ clo. As it can be seen, as the humidity ratio in the air increases, the required ambient temperature should be decreased for applying thermal comfort conditions. At $R_{cl} = 0.6$ clo, while the required ambient temperature is 23.3 °C for the relative humidity of 20 %, it is 23 °C for the relative humidity of 60 %. It is also seen in this figure that for the thermal comfort conditions, the required ambient temperature decreases with increasing clothing resistance. These temperatures are required temperatures keeping heat balance between the body and environment. But, apart from the heat balance, there are various factors affecting the thermal comfort in different ways. For instance,

Fig. 37.13 Thermal comfort conditions in psychometric chart
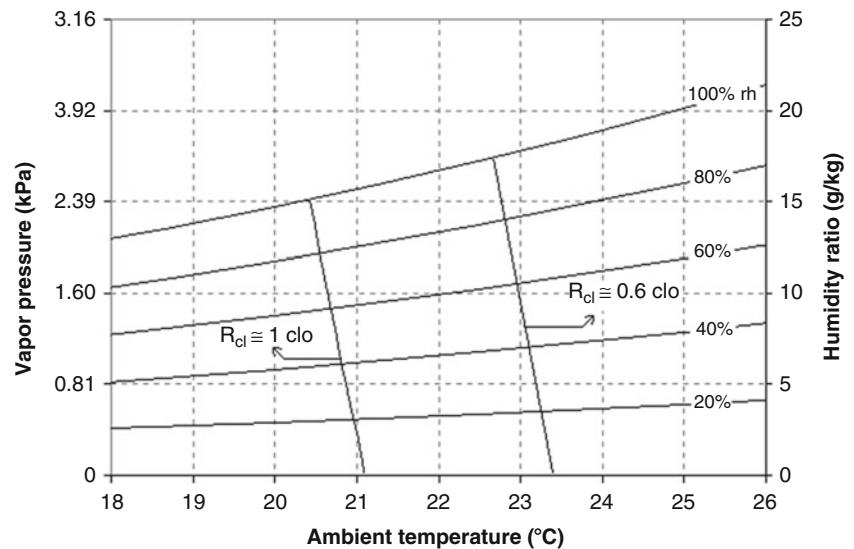
at the high and low humidity cases, human can feel uncomfortable due to respiration arduous, skin, eyes, and throat trouble. Therefore, even if energy balance is maintained, in general, the cases in which relative humidity is higher than 70 % and lower than 30 % are not considered as a thermal comfort zone.

Conclusion

The main results derived from this study are as follows:

1. Relative humidity of air affects the heat balance between the body and environment in numerous ways.
2. Relative humidity value is an important factor for the thermal comfort, especially in high ambient temperatures. The effect of this factor increases with clothing resistance.
3. Water vapor partial pressure increases with increase in relative humidity at constant temperature. As the difference between the skin and environment water vapor partial pressures decrease, total latent heat losses from the skin decreases. For that reason, the core and skin temperature of the body increase slightly with increasing the relative humidity. But, variation of the core temperature is quite lower than that of the skin temperature.
4. With increasing the relative humidity, the difference between the skin and environment water vapor partial pressures decrease, and so greater portion of the body is covered by sweat. For that reason, if the relative humidity increases, skin wettedness boosts.
5. When the clothing has lower thermal resistance values, the total heat loss and the sum of the convective and radiative heat losses rise. Meanwhile, the evaporative heat loss related to the sweat generation of the body increases with increasing clothing resistance.
6. With both the body temperatures and skin wettedness increase, thermal comfort perception is negatively influenced. As a result of this, *TSENS* and *DISC* values increase with the ambient temperature, relative humidity, and clothing resistance.
7. Increase in the *DISC*, which is parallel with the skin wettedness, is higher than that in the *TSENS*.
8. Since pelvis and back have more clothes from the other body segments, the skin temperature and wettedness of these segments is higher.
9. After the skin wettedness reaches the maximum value ($w = 1$), if the ambient temperature keeps on increasing, skin temperature increases rapidly. This effect is shown in back and pelvis at 90 % relative humidity for approximately 30 °C ambient temperature.
10. Since the head has no cloth, it is more affected from the environmental conditions than the other segments. Increasing ratio of the skin temperature in this segment is higher than that of the back segment.

　　Due to the fact that an understanding of human thermoregulatory processes and effects of humidity on the energy and water balance of the body facilitates the design and development of improved heating and cooling systems, this study can be useful for HVAC engineers and researchers.

Nomenclature

A_b	Body surface area, m^2	r	Outer radius of fabric layer, m
$c_{p,b}$	Specific heat of body, kJ/(kg K)	R_a	Thermal resistance of outer air, (m^2 K)/W
$DISC$	Discomfort	R_{al}	Thermal resistance of air layer, (m^2 K)/W
f_{cl}	Clothing area factor	R_{cl}	Thermal resistance of clothing, (m^2 K)/W
h_{cv}	Convective heat transfer coefficient, W/(m^2 K)	R_f	Thermal resistance of fabric, (m^2 K)/W
h_{rd}	Radiative heat transfer coefficient, W/(m^2 K)	R_t	Total thermal resistance of clothing, (m^2 K)/W
i	Segment number	$R_{e,a}$	Evaporative resistance of outer air, (m^2 kPa)/W
i_{cl}	Vapor permission efficiency of clothing	$R_{e,al}$	Evaporative resistance of air layer, (m^2 kPa)/W
j	Air or fabric layers number	$R_{e,cl}$	Evaporative resistance of clothing, (m^2 kPa)/W
K	Effective conductance between core and skin, W/(m^2 K)	$R_{e,f}$	Evaporative resistance of fabric, (m^2 kPa)/W
		$R_{e,t}$	Total evaporative resistance of clothing, (m^2 kPa)/W
LR	Lewis Ratio, °C/kPa		
m	Body mass, kg	$\overline{R}_a$	Gas constant of air, kJ/(kg K)
M	Rate of metabolic heat production, W/m^2	$\overline{R}_v$	Gas constant of vapor, kJ/(kg K)
M_{act}	Rate of metabolic heat production due to activity, W/m^2	RH	Relative humidity
		S_{cr}	Rate of heat storage in the core, W/m^2
$\dot{m}_{bl}$	Mass flow rate of blood, kg/(s m^2)	S_{sk}	Rate of heat storage in the skin, W/m^2
$\dot{m}_{res}$	Mass flow rate of air inhaled, kg/s	t_a	Air temperature, °C
$\dot{m}_{rsw}$	Mass flow rate of regulatory sweat generation, kg/(s m^2)	t_b	Body temperature, °C
		$t_{b,c}$	Lower limit temperature of evaporative regulation zone, °C
nl	Number of layers covering segment		
p_a	Water vapor pressure in the ambient air, kPa	$t_{b,h}$	Upper limit temperature of evaporative regulation zone, °C
$p_{a,s}$	Saturated water vapor pressure in the ambient air, kPa	t_{cr}	Core temperature, °C
p_{atm}	Atmosphere pressure, kPa	t_{ex}	Exhaled air temperature, °C
$p_{sk,s}$	Saturated water vapor pressure at the skin temperature, kPa	t_o	Operative temperature, °C
		t_{rd}	Mean radiant temperature, °C
Q_{cd}	Heat flow rate due to conduction, W/m^2	t_{sk}	Skin temperature, °C
$Q_{cr,sk}$	Heat flow rate between core and skin, W/m^2	$TSENS$	Thermal sensation
Q_{cv}	Heat flow rate due to convection, W/m^2	w	Total skin wettedness
Q_{rd}	Heat flow rate due to radiation, W/m^2	w_{dif}	Skin wettedness due to diffusion
Q_{res}	Total heat flow rate due to respiration, W/m^2	w_{rsw}	Skin wettedness due to regulatory sweating
$Q_{e,dif}$	Latent heat flow rate due to diffusion, W/m^2	W_a	Humidity ratio of ambient air, kg H$_2$O/kg dry air
$Q_{e,max}$	Maximum latent heat flow rate due to evaporation, W/m^2	W_{ex}	Humidity ratio of exhaled air, kg H$_2$O/kg dry air
$Q_{e,res}$	Latent heat flow rate due to respiration, W/m^2	W	Rate of external work accomplished, W/m^2
$Q_{e,rsw}$	Latent heat flow rate due to regulatory sweat generation, W/m^2	$WSIG_b$	Warm signal from body
		$WSIG_{cr}$	Warm signal from core
$Q_{e,rsw, req}$	Required latent heat flow rate due to regulatory sweat generation, W/m^2	$WSIG_{sk}$	Warm signal from skin
		α	Fraction of total body mass concentrated in skin compartment
$Q_{e,sk}$	Total latent heat flow rate from skin, W/m^2	θ	Time, s
$Q_{s,res}$	Sensible heat flow rate due to respiration, W/m^2	η_e	Evaporative efficiency

References

1. Fanger PO (1972) Thermal comfort. McGraw-Hill, New York, NY
2. Gagge AP, Stolwijk JAJ, Nishi Y (1971) An effective temperature scale based on a simple model of human physiological response. ASHRAE Trans 77(Part 1):247–262
3. Höppe P, Martinac I (1998) Indoor climate and air quality. Int J Biometeorol 42:1–7

4. Teodosiu C, Hohota R, Rusaouena G, Woloszyn M (2003) Numerical prediction of indoor air humidity and its effect on indoor environment. Build Environ 38:655–664
5. Berglund LG (1998) Comfort and humidity. ASHRAE J 40(8):35–41
6. Toftum J, Fanger PO (1999) Air humidity requirements for human comfort. ASHRAE Trans 105(2):81–86
7. Liviana JE, Rohles FH, Bullock OD (1988) Humidity, comfort and contact lenses. ASHRAE Trans 94(1):3–11
8. Olesen BW, Hasebe Y, de Dear RJ (1988) Clothing insulation asymmetry and thermal comfort. ASHRAE Trans 94(1):32–51
9. Toftum J, Jorgensen AS, Fanger PO (1998) Upper limits for indoor air humidity to avoid uncomfortably humid skin. Energy Build 28:1–13
10. Toftum J, Jorgensen AS, Fanger PO (1998) Upper limits of air humidity for preventing warm respiratory discomfort. Energy Build 28:15–23
11. de Dear RJ, Knudsen HN, Fanger PO (1989) Impact of air humidity on thermal comfort during step-changes. ASHRAE Trans 95(2):336–350
12. Berglund LG, Cain W (1989) Perceived air quality and the thermal environment. Proceedings of the IAQ'89, San Diego, CA, pp 93–99
13. Fang L, Clausen G, Fanger PO (1996) The impact of temperature and humidity on perception and emissions of indoor air pollutants. 7th International Conference on Indoor Air Quality and Climate, Nagoya, Japan, 1996.
14. Fountain ME, Arens EA, Xu T, Bauman FS, Oguru M (1999) An investigation of thermal comfort at high humidities. ASHRAE Trans 94:94–102
15. Guan Y, Hosni MH, Jones BW, Gielda TP (2003) Literature review of the advances in thermal comfort modeling. ASHRAE Trans 109:908–916
16. Fiala D, Lomas KJ, Stohrer M (1999) A computer model of human thermoregulation for a wide range of environmental conditions: the passive system. J Appl Physiol 87(5):1957–1972
17. McCullough EA, Jones BW, Tamura T (1989) A data base for determining the evaporative resistance of clothing. ASHRAE Trans 95(2):316–328
18. Kaynakli O, Kilic M (2005) Investigation of indoor thermal comfort under transient conditions. Build Environ 40(2):165–174
19. Kaynakli O, Pulat E, Kilic M (2005) Thermal comfort during heating and cooling periods in an automobile. Heat Mass Transfer 41:449–458
20. ASHRAE (1989) ASHRAE handbook – fundamentals, Chapter 8. American Society of Heating, Refrigeration and Air-Conditioning Engineers, Atlanta. 29 p
21. Kaynakli O, Unver U, Kilic M (2003) Evaluating thermal environments for sitting and standing posture. Int Commun Heat Mass Transfer 30(8):1179–1188
22. Burch SD, Pearson JT, Ramadhyani S (1991) Analysis of passenger thermal comfort in an automobile under severe winter conditioning. ASHRAE Trans 97:239–246
23. de Dear RJ, Arens E, Hui Z, Ogura M (1997) Convective and radiative heat transfer coefficients for individual human body segments. Int J Biometeorol 40:141–156
24. Doherty TJ, Arens E (1988) Evaluation of the physiological bases of thermal comfort models. ASHRAE Trans 94(Part 1):1371–1385
25. Werner J, Reents T (1980) A contribution to the topography of temperature regulation in man. Eur J Appl Physiol 45:87–94
26. Tanabe S, Arens EA, Bauman FS, Zang H, Madsen TL (1994) Evaluating thermal environments by using a thermal manikin with controlled skin surface temperature. ASHRAE Trans 100(1):39–48
27. Huizenga C, Hui Z, Arens E (2001) A model of human physiology and comfort for assessing complex thermal environments. Build Environ 36:691–699

Thermal Comfort Analysis of Novel Low Exergy Radiant Heating Cooling System and Energy Saving Potential Comparing to Conventional Systems

38

Aliihsan Koca, Zafer Gemici, Koray Bedir, Erhan Böke, Barış Burak Kanbur, and Yalçın Topaçoğlu

Abstract

In this study characteristics of a model room with dimensions 6 m × 4 m × 3 m has been investigated using Computational Fluid Dynamics method with regard to thermal comfort, in case of that the room is heated and cooled by the means of radiant panels. Both general thermal comfort parameters [PMV (percentage mean vote), PPD (predicted percentage of dissatisfied)] and local thermal comfort parameters (radiant temperature asymmetry, draught, vertical air temperature difference, warm and cool floors) which are described by the standards ISO 7730 and ASHRAE 55 have been taken into consideration. Radiant panels have been placed to exterior walls for heating system, and they have been put on both exte\rior walls and ceiling for cooling system. According to the TS 2164 standards, different regions are identified with regard to outdoor climate conditions for heating and cooling seasons in Turkey, and analysis of heating/cooling is done for each region. Heat fluxes from radiant panels and corresponding values of room mean temperature required in order for the conditions of thermal comfort described by the standards ISO 7730 to be met have been determined for these regions and heating/cooling system configurations. Energy saving potential of radiant system has been evaluated for these regions and heating/cooling mode.

Keywords

Energy saving • Thermal comfort • Low exergy • Heating • Cooling

Introduction

Energy saving and emission reduction are both affected by the energy efficiency of the built environment and the quality of the energy carrier in relation to the required quality of the energy. Low exergy heating and cooling systems allow to use low valued energy, which is delivered by sustainable energy sources (e.g., by using heat pumps, solar collectors, either separate or linked to waste heat, energy storage, etc.) and improve their performances.

It is vitally important to have a clear image of the exergy balance of the human body in order to understand what the low exergy systems for heating and cooling in buildings are. It is interesting that the thermal comfortable condition is provided

A. Koca (✉) • Z. Gemici • K. Bedir • B.B. Kanbur • Y. Topaçoğlu
Mir Arastirma ve Gelistirme Inc., Y.T.U. Technopark A1 Building, 34220 Istanbul, Turkey
e-mail: ihsankoca@mirholding.com.tr; zafergemici@mirholding.com.tr; koraybedir@mirholding.com.tr; burakkanbur@mirholding.com.tr; yalcintopacoglu@mirholding.com.tr

E. Böke
I.T.U. Mechanical Engineering Faculty, Istanbul Technical University, 34437 Istanbul, Turkey
e-mail: boke@itu.edu.tr

with lowest exergy consumption rate with the human body. This suggests that rational heating and cooling systems in building would go well with low exergy consumption under a condition in which we humans consume as low amount of exergy as possible. That is we may be able to establish both thermal comfort and low exergy consuming systems at the same time.

Human body doesn't sense just the temperature of the air, but also feels the operative temperature that is combination of air temperature, air humidity, air velocity, and radiant temperature. According to this relationship lowest exergy consumption rate emerges at the point where the room air temperature equals 18 °C and mean radiant temperature 25 °C [1]. This suggest that use of warm radiant energy is more effective than use of convective warm energy for a heating purpose to realise both thermal comfort and as low exergy consumption within human body as possible.

The work concerning low exergy systems (LowEx) by Virtane and Ala-Juusela [2, 3] encourages the use of low temperature heating systems for buildings. Low exergy heating systems allow the use of low valued energy sources. Such heating system operates at low temperature levels that are close to room temperature. These systems can provide the occupants with comfortable, clean, and healthy environment. In addition, low temperature systems lead to efficient use of energy and provide flexibility in the choice of the energy source. To the knowledge of the authors, there are only a few papers available about low temperature heating systems.

Low temperature heating with heat pump or other low temperature devices has several advantages. When using, for example, a heat pump in low temperature systems, energy may be saved because the thermal efficiency of the pump (COP) increases and energy loses in the distribution net decrease. Energy efficiency aside, studies show that low temperature heating may improve indoor air quality as well as the thermal comfort conditions [4–7].

Scientist and engineers are concerned about new heating and cooling systems in buildings due to conventional air conditioning systems consuming large amount of energy. As a result of their studies, radiant heating and cooling systems which can produce more comfortable conditions in occupied zone and energy saving are developed. Working principle of radiant system is based upon at least 50 % of heat transfer occurring via radiation from radiant panel placed on floor, wall, or ceiling. By the radiant panel heat transfer occurs in two ways, primarily via radiation between panel surface and occupants which constitutes 60–80 % of heat transfer and secondarily, heat transfer to indoor air by means of natural convection [8]. The intent of radiant systems is to lower thermostat set point temperature in winter and to increase it in summer, resulting in substantial energy savings for heating and cooling as compared with conventional systems [9]. A forced convection air-conditioning system creates uncomfortable environment caused by draught and air temperature differences between the human head and foot, whereas radiant air-conditioning systems can provide lower vertical air temperature differences and air velocity. At a given volume flow rate, water is about 4,000 times more efficient for heat transport than air. Therefore, water heating systems are very common in Europe, and hydronic cooling systems progressively replace air conditioning [10].

Thermal Comfort

As defined by ASHRAE Standard 55, thermal comfort is that condition of the mind that expresses satisfaction with the thermal environment. Thermal comfort is investigated considering both general and local thermal sensation of the human body.

General Thermal Comfort

General thermal comfort that is mainly related to PMV–PPD index can be expressed as mathematically and occupant's thermal sensation temperature by the whole body called as operative temperature. PMV consists of six comfort variables (metabolic rate, clothing insulation, ambient air temperature, mean radiant temperature relative humidity, and air velocity) and is expressed Eq. (38.1) [11] as

Table 38.1 General thermal comfort criteria

Parameter	Limit value	
PMV	$-0.5 < PMV < 0.5$	
PPD (%)	PPD < 10	
Operative temperature (°C)	Winter (1 clo/1.2 met)	20–24
	Summer (0.5 clo/1.2 met)	23–26

$$PMV = \left(0.303 \cdot e^{-0,036 \cdot M} + 0.028\right) \begin{bmatrix} (M - W) - 3.05 \cdot 10^{-3} \cdot \{5733 - 6.99 \cdot (M - W) - p_a\} \\ -0.42 \cdot \{(M - W) - 58.15\} - 1.7 \cdot 10^{-5} \cdot M \cdot (5867 - p_a) \\ -0.0014M(34 - T_a) - 3.96 \cdot 10^{-8} f_{cl} \left\{(T_{cl} + 273)^4 - (T_r + 273)^4\right\} \\ -f_{cl} \cdot h \cdot (T_{cl} - T_a) \end{bmatrix} \tag{38.1}$$

PPD is expressed via Eq. (38.2) using PMV index value [11]:

$$PPD = 100 - 95 \cdot \exp\left(-0.03353 \cdot PMV^4 - 0.2179 \cdot PMV^2\right) \tag{38.2}$$

Operative temperature is not equal to the ambient air temperature and is affected by surface and object temperatures of indoor environment. When mean air speed is less than 0.2 m/s, operative temperature is calculated by Eq. (38.3):

$$T_0 = \frac{T_r + T_a}{2} \tag{38.3}$$

General thermal comfort criteria which are described by the standards ISO 7730 are shown in Table 38.1.

Local Thermal Comfort

In the earlier years of thermal comfort studies, comfort was usually described as affected by the occupant's thermal sensation by the whole body. But aside from the overall thermal state of the body, an occupant may also find the thermal environment unacceptable if local influences on the body from radiant temperature asymmetry, draught, vertical air temperature differences, and cold or warm floors.

Radiant temperature asymmetry is the difference between the maximum and the minimum radiant temperature on the surfaces of a cube element located at a point in the space being conditioned [3].

Draught is the unwanted local cooling of the body caused by air movement.

Vertical air temperature difference is a high vertical air temperature difference between the ankle and the head (0.1 and 1.1 m above the floor) which usually causes discomfort. This air temperature difference should be less than 3 °C.

Floor surface temperature is especially important for thermal comfort assessment of spaces with occupants wearing light indoor shoes or in cases where occupants sit/lie on the floor or walk indoors with bare feet as common in Asia.

Room Modeling

A CFD model with dimensions 6 m × 4 m × 3 m is designed. Two single-glazed windows which are included in the CFD model have 1.4 m height and 1.2 m weight. Four different room models are obtained to be placed on wall surfaces of panels with dimensions 0.6 m × 1.2 m as shown in Fig. 38.1; panels are installed all around of the window in the first model (Fig. 38.1a), windowless exterior wall in the second model (Fig. 38.2a), either walls in the third model (Fig. 38.3a), and ceiling in the fourth model (Fig. 38.4a). The TS 2164 standards identify four different regions in Turkey with regard to outdoor climate conditions in winter used in heating systems design. Each region has been represented in numerical analysis by setting these climatological parameters as boundary conditions in heating mode (Table 38.2), where in the case of cooling, summer conditions as well as incident radiation through window are taken into account.

Fig. 38.1 (**a**) Model 1;
(**b**) Model 2; (**c**) Model 3;
(**d**) Model 4
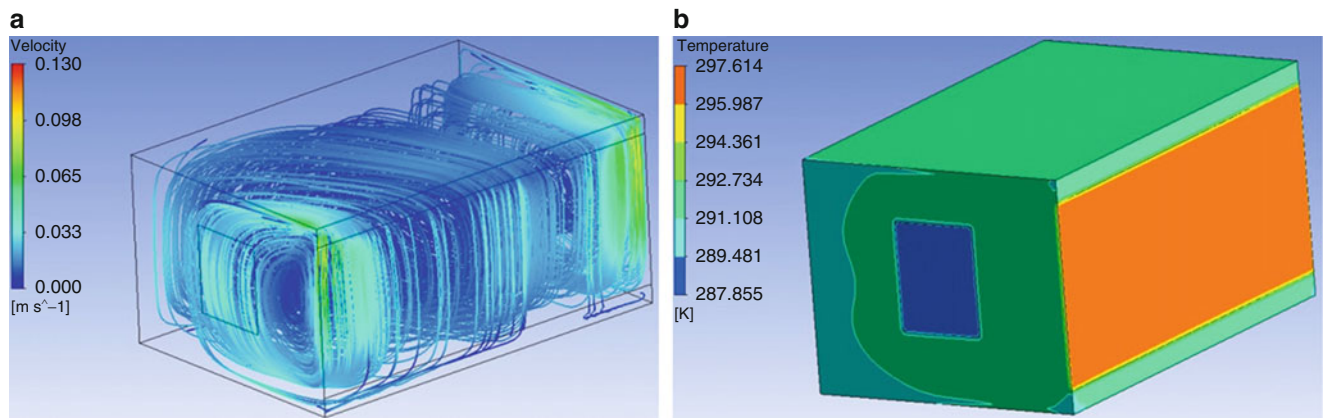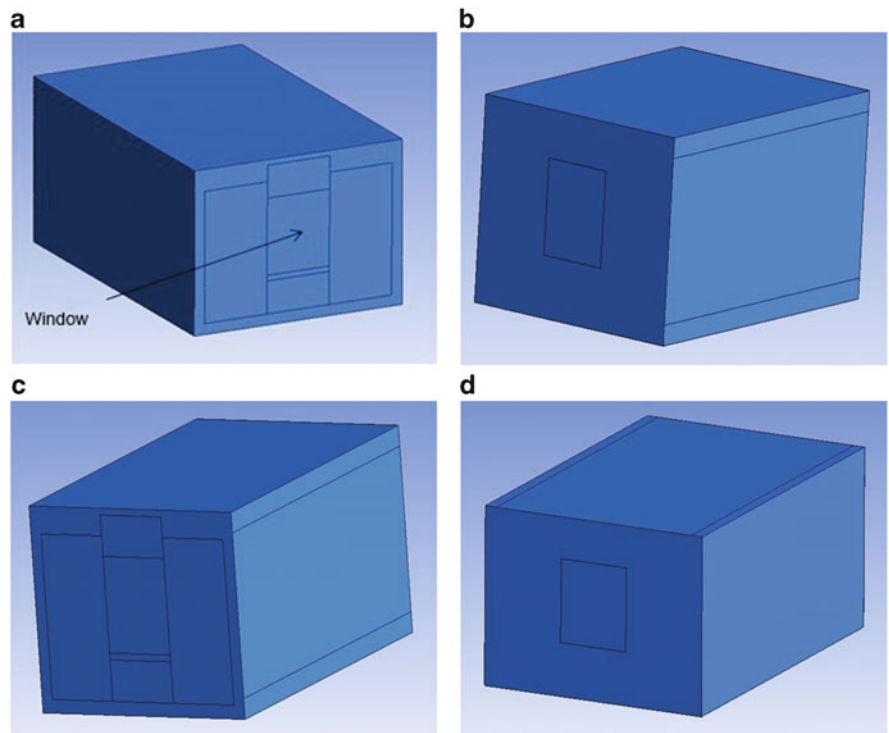
Fig. 38.2 (**a**) Streamline distribution in model 2; (**b**) Model 2 surfaces temperature distribution

Fig. 38.3 The relationship
between PMV and PPD
for model 2
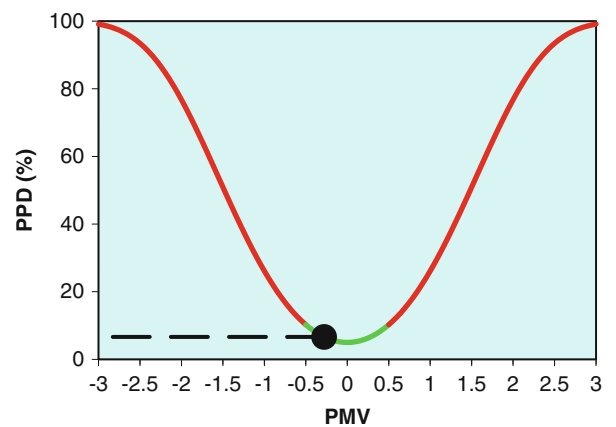
Fig. 38.4 Reference line 1, 2, 3
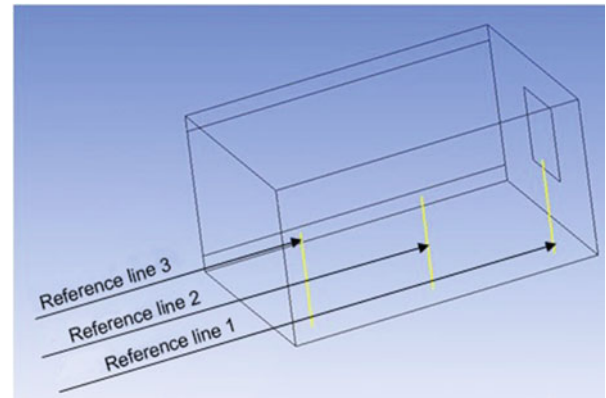
Table 38.2 Outside air temperature in different region for cooling and heating season

Region	City	Heating season outside air temperature (°C)	Cooling season outside air temperature (°C)
1	Antalya	3	39
2	Istanbul	−3	33
3	Ankara	−12	35
4	Erzurum	−21	31

Numerical Solution Method

In fluid mechanics and heat transfer, basis of conservation equations stated as mathematical treatment of fluid depends on conservation of mass, momentum, and energy. In this study, flow is steady state and three dimensional, and physical properties of the fluid such as density, viscosity, and thermal conductivity are constant. Consequently, conservation equations are obtained as below [12]:

Continuity equation,

$$\frac{\partial u}{\partial x} + \frac{\partial v}{\partial y} + \frac{\partial w}{\partial z} = 0 \tag{38.4}$$

Momentum equations of x, y, z direction can be stated, respectively:

$$u\frac{\partial u}{\partial x} + v\frac{\partial u}{\partial y} + w\frac{\partial u}{\partial z} = -\frac{1}{\rho}\frac{\partial p}{\partial x} + \nu\left(\frac{\partial^2 u}{\partial x^2} + \frac{\partial^2 u}{\partial y^2} + \frac{\partial^2 u}{\partial z^2}\right) \tag{38.5}$$

$$u\frac{\partial v}{\partial x} + v\frac{\partial v}{\partial y} + w\frac{\partial v}{\partial z} = -\frac{1}{\rho}\frac{\partial p}{\partial y} + \nu\left(\frac{\partial^2 v}{\partial x^2} + \frac{\partial^2 v}{\partial y^2} + \frac{\partial^2 v}{\partial z^2}\right) - g \tag{38.6}$$

$$u\frac{\partial w}{\partial x} + v\frac{\partial w}{\partial y} + w\frac{\partial w}{\partial z} = -\frac{1}{\rho}\frac{\partial p}{\partial z} + \nu\left(\frac{\partial^2 w}{\partial x^2} + \frac{\partial^2 w}{\partial y^2} + \frac{\partial^2 w}{\partial z^2}\right) \tag{38.7}$$

Energy equation can be stated as below:

$$u\frac{\partial T}{\partial x} + v\frac{\partial T}{\partial y} + w\frac{\partial T}{\partial z} = \alpha\left(\frac{\partial^2 T}{\partial x^2} + \frac{\partial^2 T}{\partial y^2} + \frac{\partial^2 T}{\partial z^2}\right) \tag{38.8}$$

Between radiant panels and indoor air, heat transfer occurs via natural convection which has been modeled by employing Boussinesq method that yields good results provided with small difference in extremum values of temperature within the space in question. Turbulence is simulated by the standard k-ε model which is reported to be a good approximation especially for near-wall flows. Radiation heat transfer has been represented by employing the Discrete Ordinates method which takes account scattering, semi-transparent media, reflecting surface, and wavelength-dependent transmission [13].

Results and Discussion

Heating Cases of Study

Room has two exterior and interior walls, a ceiling, and floor. This room heating analysis is done when room situate in self-contained flat. In this case, ceiling, floor, and interior walls of the room are neighbor to cockloft, ground, and unheated space, respectively. Heating analysis was made for room model 1, 2, 3.

Results of Heating Cases

Analysis results will be expressed with regard to model 2. These results were obtained when panel heating performance was 35 W/m^2, considering second region's outside air condition. Figure 38.2a shows velocity streamline in room. Natural circulation of air flow in contact with warm panel surface is obviously shown in Fig. 38.2a. On the panel, surface had air speed 0.13 m/s which is the highest air velocity in the room. Figure 38.2b represents temperature distribution on walls, window, and panels. Warmed panel, cold window, and whole wall surface mean temperatures were found to be 296.4, 288, and 292 K, respectively, in the room.

Investigation of General Thermal Conditions Comfort for Room Model 2

General thermal comfort is based on PMV and PPD indices and operative temperature. Therefore, these parameters must be calculated. The PMV value is calculated from Eq. (38.1). For the purpose of solving this equation, mean radiant temperature that must be calculated is expressed in Eq. (38.9) [14].

$$T_r = \frac{T_p + T_{aust}}{2} \tag{38.9}$$

Panel surface temperature (T_p) was found to be 296.4 K as a result of numerical analysis. Area-weighted unheated surface temperature (T_{aust}) was calculated as 292 K with Eq. (38.10) [14].

$$T_{aust} = \frac{(T_{s1} \cdot A_{s1} \cdot \varepsilon_{s1} + T_{s2} \cdot A_{s2} \cdot \varepsilon_{s2} + \ldots + T_{sn} \cdot A_{sn} \cdot \varepsilon_{sn})}{(A_{s1} \cdot \varepsilon_{s1} + A_{s2} \cdot \varepsilon_{s2} + \ldots + A_{sn} \cdot \varepsilon_{sn})} \tag{38.10}$$

Depending on these values, mean radiant temperature (T_r) was estimated to be 294.1 K using Eq. (38.9). As a result of numerical analysis, mean air temperature and air velocity were found to be 292.5 K and 0.013 m/s, respectively. Clothing in winter, metabolic rate of occupants, and relative humidity were admitted 1 clo, 1.2 met, and 50 %, respectively [11]. Values of these six comfort variables are shown in Table 38.3.

Operative temperature was computed 293.3 K with Eq. (38.3). PMV and PPD values were estimated by computer program which is written based on ASHRAE 55 and ISO 7730 standards. Values of the these parameters are shown in Table 38.4.

Table 38.3 General thermal comfort input values for model 2

Parameter	Input values
Clothing insulation (clo)	1
Mean air temperature (°C)	19.5
Mean radiant temperature (°C)	21.1
Metabolic rate (met)	1.2
Air velocity (m/s)	0.013
Relative humidity (%)	50

Table 38.4 General thermal comfort output values for model 2

Parameter	Output values
Operative temperature (°C)	20.3
PMV	−0.28
PPD (%)	6.63

Table 38.5 Vertical air temperature differences 0.1–1.1 m on reference line

Reference line	$T_{0.1}$ (K)	$T_{1.1}$ (K)	$T_{1.1}$–$T_{0.1}$ (K)	ISO 7730 (K)
1	292	292.4	0.4	<3
2	292.1	292.4	0.3	<3
3	291.8	292.3	0.5	<3

Table 38.6 Maximum air velocities on reference line

Reference line	Maximum speed (m/s)	ISO 7730 (m/s)
1	0.013	<0.18
2	0.01	<0.18
3	0.017	<0.18

Fig. 38.5 Temperature distribution in the middle plane of the room
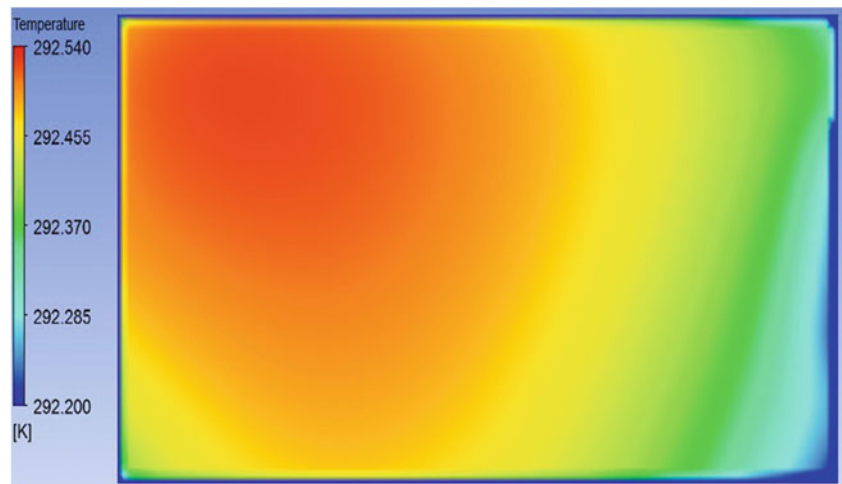
The relationship between PMV and PPD is shown in Fig. 38.3. Intersection of PMV and PPD values is within the region defined by thermal comfort

Investigation of Local Thermal Comfort Conditions for Room Model 2

The occupied zone is defined as a space 0.6 m distant from all walls and up to 1.8 m above floor level [9]. Most critical plane in the occupied zone is farthest from panels. Reference lines were all in the critical plane and the reference lines 1, 2, and 3 were 0.6, 3, and 5.4 m distant from exterior wall which has a window, respectively (Fig. 38.4).

Temperature differences between 0.1 and 1.1 m above the floor on reference line 1, 2, and 3 were found to be 0.4, 0.3, and 0.5 °C, respectively. None of the values exceed recommended limit that is given by ISO 7730 (Table 38.5).

Maximum air velocities on reference line 1, 2, and 3 were obtained as 0.013, 0.01, 0.017 m/s, respectively. These air velocities are less than 0.18 m/s described by ISO 7730 (Table 38.6).

Figure 38.5 represents temperature distribution in the middle plane of the room. The difference between highest and lowest temperature is 0.34 K, which is under the standard limitation of 23 K (radiant temperature asymmetry caused by warm vertical wall) set by ISO 7730.

Room floor surface temperature was found to be 19.2 °C which is the range of floor surface temperatures (19–29 °C) described by ISO 7730.

Fig. 38.6 The relationship between PPD and clothing insulation
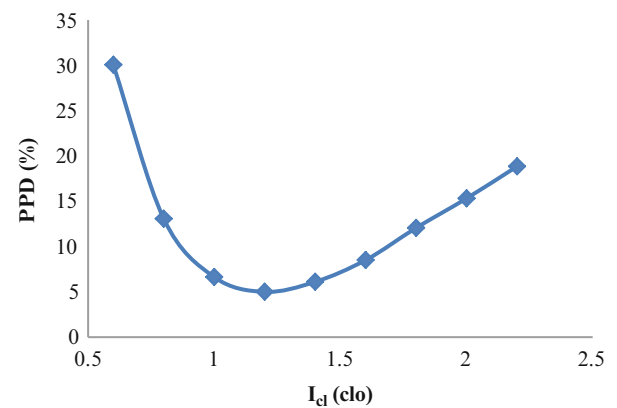
Fig. 38.7 The relationship between PPD and metabolic rate
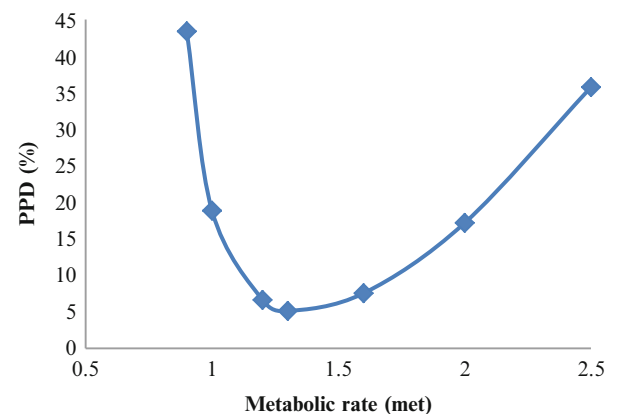
Investigation of Thermal Comfort as Regards Clothing Insulation and Metabolic Rate

The relationship between PPD and clothing insulation is shown in Fig. 38.6. Thermal comfort requirement is provided in the range of 1–1.6 clo. Clothing insulation and PPD values of the optimal thermal comfort are 1.2 clo and 5 %, respectively.

Figure 38.7 presents the relationship between PPD and metabolic rate. Thermal comfort is satisfied from 1.2 to 1.6 clo, so occupants feel comfortable themselves in this metabolic rate range in room. Clothing insulation and PPD values of the optimum thermal comfort are 1.3 met and 5.13 %, respectively.

Cooling Cases of Study

Room cooling analysis is done when room situate in mezzanine, so heat loss takes place from exterior walls and window only. Cooling analysis was made for all room models.

Results of Cooling Cases

Analysis results will be explained considering model 4. These results were obtained when panel cooling performance was 18 W/m^2, considering second region's outside air condition. Figure 38.8a represents velocity streamline in model 4, and maximum air speed was 0.111 m/s. Figure 38.8b demonstrates temperature distribution on whole room surfaces. Warm window, cooled panel, and other wall surface temperatures were found to be 302.2, 299, and 296.8 K, respectively.

Investigation of General Thermal Comfort Conditions for Room Model 4

Parameters of calculating PMV were given as follows: clothing, 0.5 clo in summer; metabolic rate of occupant, 1.2 met; relative humidity, 50 % [11]. As a result of numerical analysis, mean air temperature and air velocity were found to be 298.5 K and 0.018 m/s, respectively, and mean radiant temperature was found to be 297.9 K using with Eq. (38.9). Consequently, the values of these six comfort variables are shown in Table 38.7.

PMV, PPD, and operative temperature values are shown in Table 38.8. These values show that thermal comfort is provided.
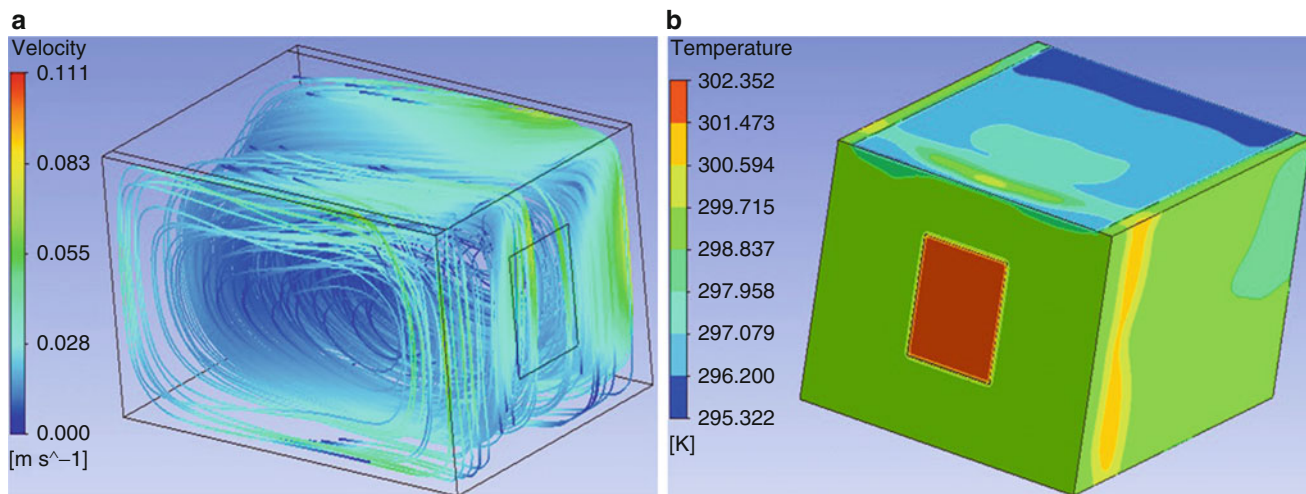
Fig. 38.8 (**a**) Streamline distribution in model 4; (**b**) Model 4 surfaces temperature distribution

Table 38.7 General thermal comfort input values for model 4

Parameter	Input values
Clothing insulation (clo)	0.5
Mean air temperature (°C)	25.5
Mean radiant temperature (°C)	24.9
Metabolic rate (met)	1.2
Air velocity (m/s)	0.018
Relative humidity (%)	50

Table 38.8 General thermal comfort output values for model 4

Parameter	Output values
Operative temperature (°C)	25.2
PMV	0.21
PPD (%)	5.91

Table 38.9 Minimum heat flux requirements from radiant panels for different regions in heating

	Model 1				Model 2				Model 3			
Region	1	2	3	4	1	2	3	4	1	2	3	4
Heat flux (W/m^2)	60	70	90	110	30	35	45	55	15	20	25	30
PMV	−0.47	−0.29	−0.32	−0.39	−0.35	−0.28	−0.29	−0.32	−0.48	−0.28	−0.37	−0.44
PPD (%)	9.61	6.75	7.13	8.17	7.55	6.63	6.75	7.1	9.81	6.63	7.85	9.04
Operative temperature (°C)	20	20.4	20.4	20.2	20	20.3	20.3	20.2	20	20.2	20	20
Mean air temperature (°C)	17.2	18.4	17.8	17	19.2	19.5	19.2	18.9	18.9	19.7	19.2	18.8

Minimum Heat Flux Requirements from Radiant Panels in the Case of Heating and Cooling

Minimum heat fluxes from radiant panels and corresponding values of PMV, PPD, and room mean temperature are shown for different region and heating/cooling in Tables 38.9 and 38.10. Mean air temperature of model 1 became lower in cooling and higher in heating than other models for different regions.

Comparison of Radiant and Conventional Systems Under Similar Thermal Conditions

Having compared radiant and conventional heating systems under similar thermal conditions, indoor air temperature was found to be 1.1 °C less in case of radiant heating than that of conventional heating because mean radiant temperature in radiant heating was 1.1 °C higher than in convective heating (Table 38.11).

Table 38.10 Minimum heat fluxes requirements from radiant panels for different regions in cooling

	Model 1				Model 2				Model 3				Model 4			
Region	1	2	3	4	1	2	3	4	1	2	3	4	1	2	3	4
Heat flux (W/m^2)	54	47	49	44	25.5	23.5	24	21	15.5	15	15	13.5	20.5	17.5	18.5	15.5
PMV	0.25	0.35	0.35	0.37	0.32	0.33	0.44	0.43	0.31	0.29	0.4	0.4	0.36	0.38	0.39	0.37
PPD (%)	6.3	7.55	7.55	7.85	7.13	7.26	9.04	8.86	7	6.75	8.33	8.33	7.7	8.01	8.17	7.85
Operative temperature (°C)	25.2	25.6	25.6	25.7	25.6	25.6	25.9	25.9	25.5	25.5	25.8	25.8	25.7	25.8	25.8	25.5
Mean air temperature (°C)	27	27	27	26.9	26.1	26.2	26.6	26.4	26	25.8	26.2	26.1	26	26.1	26.1	26

Table 38.11 Comparison of radiant and conventional systems

	Parameter	Radiant heating	Conventional heating
Input	Clothing insulation (clo)	1	1
	Mean air temperature (°C)	20.9	22
	Mean radiant temperature (°C)	22.3	21.2
	Metabolic rate (met)	1.2	1.2
	Air velocity (m/s)	0.028	0.028
	Relative humidity (%)	50	50
Output	Operative temperature (°C)	21.6	21.6
	PMV	0	0
	PPD (%)	5	5

Table 38.12 Annual energy saving use of radiant heating systems

	Energy saving (Turkish currency)		
Region	Model 1	Model 2	Model 3
1	79.0	79.0	100.7
2	143.2	143.2	179.4
3	178.5	178.5	233.8
4	268.2	268.2	333.7

Table 38.13 Annual energy saving use of radiant cooling systems

	Energy saving (Turkish currency)			
Region	Model 1	Model 2	Model 3	Model 4
1	25.7	30.0	36.4	15.1
2	15.0	15.0	16.7	10.1
3	11.9	12.5	14.5	7.6
4	1.3	1.5	1.6	1.1

Annual Energy Saving in the Case of Radiant Heating and Cooling

Table 38.12 demonstrates annual energy savings using radiant heating system for different regions. There is remarkable energy saving using radiant system for heating. Energy saving was larger at regions where heating load was higher and could reach maximum level in the coldest region. The more energy saving could be achieved using model 3.

Annual energy savings are shown for radiant cooling system in Table 38.13. Model 3 has maximum energy saving, whereas model 4 has minimum energy saving. Energy saving is larger at regions where cooling load is higher.

Conclusion

Thermal comfort and energy efficiency performance of the novel radiant heating and cooling systems were investigated with CFD method according to different building and heating/cooling system configurations in this study. The following conclusions have been reached:

- The use of radiant heating and cooling systems in a model room fulfills general and local thermal comfort requirements with lower air temperature for heating and higher air temperature for cooling than conventional system

- All investigated radiant heating and cooling systems gave an acceptable indoor environment, which has smaller vertical temperature differences and almost no air movement field
- In order to meet the conditions of thermal comfort required heat flux from radiant panels are obtained numerically for different regions
- There is remarkable energy saving using radiant system for heating, even much more in colder areas in Turkey. In cooling season energy saving associated with radiant system is lower than it is in heating season, since there is a smaller difference between values of indoor and outdoor temperature, and furthermore, cooling period is shorter than its heating counterpart.
- Both in heating and cooling cases, energy savings increase when panels are placed and heat loss occurred in either exterior walls

Nomenclature

A_s	Surface area	T_s	Surface temperature
M	Metabolic rate, W/m^2	$T_{0.1}$	Air temperature at 0.1 m above floor level, °C
W	Effective mechanical power, W/m^2	$T_{1.1}$	Air temperature at 1.1 m above floor level, °C
p_a	Water vapour partial, Pa	h	Convective heat transfer coefficient, W/m^2°C
T_a	Air temperature, °C	u	Velocity component in x direction, m/s
f_{cl}	Clothing surface area factor	v	Velocity component in y direction, m/s
T_{aust}	Area-weighted unheated surface temperature, °C	w	Velocity component in z direction, m/s
T_{cl}	Clothing surface temperature, °C	x,y,z	Cartesian coordinates
T_o	Operative temperature	p	Pressure, Pa
T_p	Panel surface temperature, °C	g	Acceleration of gravity
T_r	Mean radiant temperature, °C		

Greek Letters

ρ	Density, kg/m^3	ε	Emissivity
α	Thermal diffusivity coefficient		

References

1. Isawa K, Komizo T, Shukuya M (2002) Low exergy systems will provide us with the lowest human-body exergy consumption and thermal comfort. Lowex News, publication of IEA Annex 37, No 5, July 2002, pp 8–11
2. Virtanen M, Ala-Juusela M (2007) Increased energy efficiency and improved comfort. Paper No. 1494. 9th REHVA world congress, Clima 2007, 10–14 June, Helsinki, Finland
3. Ala-Juusela M (2003) Heating and cooling with focus on increased energy efficiency and improved comfort. Guidebook to IEA ECBCS, Annex 37, Low Exergy Systems for Heating and Cooling of Buildings, VTT Technical Research Centre of Finland. http://www.vtt.fi/inf/pdf/tiedotteet/2004/T2256.pdf
4. Olesen BW, Mortensen E, Thorshauge J (1980) Thermal comfort in a room heated by different methods. Technical Paper no. 2256, Los Angeles Meeting, ASHRAE Transactions 86
5. Nilsson PE (ed) (2003) Achieving the desired indoor climate, IMI indoor climate and studentlitteratur. ISBN 91-44-03235-8
6. Hutter E (1991) Comparison of different heat emitters in respect of thermal comfort and energy consumption. In: Proceedings of the international centre for heat and mass transfer, heat and mass transfer in building materials and structures, pp 753–769
7. Eijdems HHEW, Boerstra AC (2000) Low temperature heating systems: impact on IAQ. Thermal comfort and energy consumption, Annex 37, Newsletter 1
8. Laouadi A (2004) Development of a radiant heating and cooling model for building energy simulation software. Build Environ 39:421–431
9. Myhren JA, Holmberg S (2008) Flow patterns and thermal comfort in a room with panel, floor and wall heating. Energy Build 40:524–536
10. Okamoto S, Kitora H, Yamaguchi H, Oka T (2010) A simplified calculation method for estimating heat flux from ceiling radiant panels. Energy Build 42:29–33
11. EN ISO 7730 (2005) Ergonomics of thermal environment-analytical determination and interpretation of thermal comfort using calculation of the PMV and PPD indices and local thermal comfort criteria. International Organization for Standardization, Geneva
12. White FM (2003) Fluid mechanics. Hemisphere–McGraw-Hill, New York, NY
13. Fluent User's Guide (1998) Fluent incorporated. Centerra Resource Park, Lebanon
14. ASHRAE Standard 55 (2003) Thermal environment conditions for human occupancy. ASHRAE

Comparison of Alternating-Current Losses in Two-Layer Superconducting Cables Constructed by Shell-Type and Solid-Core Cylindrical Wires

39

Fedai Inanir and Ahmet Cicek

Abstract

Alternating-current losses in two-layer power transmission cables of type-II superconducting wires with cylindrical geometry are numerically investigated with regard to wire cross section. Losses in shell-type and solid-core superconducting wires are calculated through the Finite Element Method for an applied alternating current with 50 Hz frequency. Each cable layer is composed of 20 wires which have 1.0 mm radii, while the thickness of shell-type wires is 0.1 mm. The two wire layers are wound over a copper core such that the inner and outer layer radii are 20.0 and 25.0 mm, respectively. Alternating-current losses at small applied current amplitudes in shell-type wires are three-times smaller than in solid-core wires, where the discrepancy diminishes for high current amplitudes above 90 % of the critical current. Besides, losses in both configurations are considerably higher in outer-layer wires for current amplitudes less than half the critical current, while they converge at higher amplitudes. The reason for smaller losses in shell-type wires at low applied current amplitudes is associated to the fact that current distribution is more homogeneous, whereas magnetic field lines penetrate into the hollow core of these wires.

Introduction

A great deal of effort is concentrated on reduction of alternating-current (AC) transport losses in superconducting power transmission systems. In this respect, especially geometries of the high-temperature superconducting (HTS) wires play an important role [1–3]. Existing round-type HTS cable technologies rely on winding multiple layers of wires with rectangular cross-sections around a cylindrical conductor, such as copper (Cu) [4–6]. However, AC current losses in such cables are still considerably high. Thus, utilization of cylindrical wires, rather than rectangular ones, draws notable attention in HTS cable technologies [7–9]. In this respect, HTS cables composed of superconducting coatings over a cylindrical metallic substrate with a radius on the order of a few millimeters are devised [10, 11]. Alternatively, composite cylindrical cables obtained by winding wires around a flexible core in a helical manner are also demonstrated [12]. Besides, Odier et al. [13] achieved manufacturing shell-type (annular) cylindrical HTS wires.

F. Inanir (✉)
Department of Physics, Faculty of Arts and Sciences, Recep Tayyip Erdoğan University, 53100 Rize, Turkey
e-mail: inanir@ktu.edu.tr

A. Cicek
Department of Physics, Faculty of Arts and Sciences, Mehmet Akif Ersoy University, Campus 15100, Burdur, Turkey
e-mail: ahmetcicek@mehmetakif.edu.tr

The magnetic response of either solid-core or shell-type HTS wires with circular cross-sections is substantially different than the response of rectangular wires if they are exposed to a transport AC current or an external magnetic field. A theoretical investigation of the magnetic behavior and AC transport losses of circular HTS wires under a magnetic field is carried out by Mawatari [14]. Besides, Gömöry and Inanir [15] numerically investigated AC losses in coils composed of solid-core and shell-type HTS wires. Pi et al. [16] conducted a numerical study of AC losses in an HTS shell under an external magnetic field. The above approaches can be adopted to investigation of AC losses in multi-layer HTS cables with circular wires.

This work focuses on a numerical study of the AC transport losses in two-layer superconducting cables with either solid-core or shell-type circular HTS wires under an applied alternating current. A comparison of induced losses in the two configurations is carried out. Furthermore, the loss mechanisms are discussed with regard to distribution of current density and magnetic field in and around the wires, respectively.

Cable Geometries and Computational Methods

Cross-sections of the HTS power transmission cables on the xy plane are depicted in Fig. 39.1. Wires are composed of second-generation high-temperature superconductors. Inner sections of the shell-type wires are vacuum with relative permeability $\mu_r = 1.0$. Inner core of both cables in Fig. 39.1 are circular Cu wires with a radius of $R_i = 20.0$ mm. The space between the layers is filled with Kapton® dielectric with a thickness of 5.0 mm, such that the outer cable radius is $R_o = 25.0$ mm. The total number of wires in each layer is $N = 20$ so that the system is symmetric with respect to discrete rotations by an angle of $\theta_e = 18^\circ$ ($2\pi/N$), as depicted in Fig. 39.1a. The radius of all wires is $r_{sc} = 1.0$ mm. The thickness of shell-type wires is $t = 0.1$ mm, as depicted in the inset in Fig. 39.1. Twisting of wires around the core is ignored so that the system is assumed to extend indefinitely along the z direction and the computational problem is reduced to two dimensions (2D).

Numerical calculations are carried out through the use of the AC/DC module of COMSOL MultiPhysics® package via the Finite Element Method (FEM). Computations are based on the solution of Ampere's Law in differential form:

$$\nabla \times \left(\frac{1}{\mu} \nabla \times \mathbf{A} \right) = \mathbf{j} \tag{39.1}$$

where the magnetic flux density (**B**) is written as the rotational of the magnetic vector potential (**A**) as $\mathbf{B} = \nabla \times \mathbf{A}$. Thus, Eq. (39.1) is solved via FEM for **A**. In Eq. (39.1), μ is permeability and **j** is the applied current density. In 2D, assuming permeabilities of all elements in the problem are equal to μ_0, Eq. (39.1) can be written as

$$-\frac{1}{\mu_0} \left(\frac{\partial^2 A_z(x,y)}{\partial x^2} + \frac{\partial^2 A_z(x,y)}{\partial y^2} \right) = j_z(x,y) \tag{39.2}$$

where $j_z(x,y)$ corresponds to the current density distribution over the wires applied along the z direction.
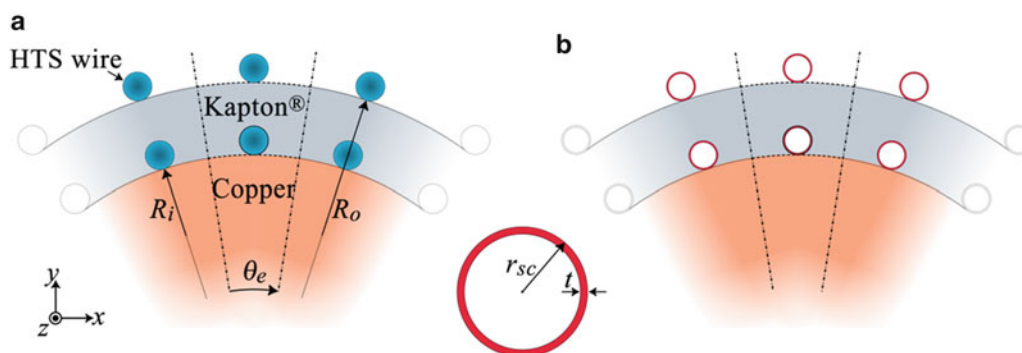
Fig. 39.1 Design of two-layer HTS cables with solid-core (**a**) and shell-type (**b**) cylindrical wires. The *dash-dotted lines* represent computational domain boundaries, where discrete rotational symmetry is exploited. The *inset* in the middle is a close-up view of a shell-type wire

According to the Critical State Model, the magnitude of the current density, j, in type-II superconductors is either zero or equal to the critical current density J_c. The current density in domains where the electric field (**E**) vanishes within the superconductor is zero. In addition, the direction of the current density is determined by the local electric field within the superconductor with non-vanishing amplitude.

Non-zero components of both **E** and **j** are those along the z axis in Fig. 39.1. The reduced dimensionality of the computational problem requires assumption of a non-linear relation between **E** and **j** in the form of [17]:

$$j_z(x, y) = J_c \cdot \tanh\left(\frac{E_z(x, y)}{E_c}\right) \tag{39.3}$$

where E_c is a scaling parameter for the electric field, whose value is taken as 10^{-4} V/m. In obtaining $E_z(x,y)$ at small frequencies through the sum of the time-derivative of **A** and the gradient of the scalar potential (φ) as $\mathbf{E} = -\partial\mathbf{A}/\partial t - \nabla\varphi$, a point collocation method (Brandt-type formulation) is utilized [18, 19]. In this case, Eq. (39.3) becomes

$$j_z(x, y) = J_c \cdot \tanh\left(\frac{\frac{\partial A_z(x,y)}{\partial t} - \nabla\varphi(x, y)}{E_c}\right) \tag{39.4}$$

where the only non-vanishing component of **A** is A_z. By obtaining $j_z(x,y)$ and $E_z(x,y)$ simultaneously, the AC losses can be calculated as will be explained below.

Due to the discrete rotational symmetry stated above, the computational domain in FEM simulations is a pie of a circle, centered on the HTS cable's center, with a radius of $R_{CD} = 100.0$ mm and a base angle of $\theta_e = 18°$. Furthermore, the influence of the core and the inter-spacing dielectric is neglected for simplicity. Thus, the computational domain comprises only two wires in each case.

The adopted boundary condition is such that the normal component of the magnetic field across the boundary of the domain along the azimuthal direction is continuous. Besides, a constraint requiring that each wire in the HTS cable carries the same current $I(t)$ is adopted. This can be accomplished by adjusting $\nabla\varphi$, for which an iterative technique was devised. Constant current in each wire requires $\int_{wire} j_z \, dA_{wire} = I$, while $\nabla\varphi$ is constant over the cross-sectional area of a wire.

The FEM elements in simulations are triangular with a total number of 75,252, for which the minimum element quality is 0.6. The critical current for each HTS wire is set as $I_c = 100$ A. The applied current is sinusoidal in the form of $I(t) = I_{max}.\cos(2\pi f t)$, where I_{max} is the current amplitude and the frequency is $f = 50$ Hz. Moreover, magnetic field, temperature and position dependence of current is ignored. I_{max} is set to nine different vales ranging between 5 A ($0.05I_c$) and 90 A ($0.9I_c$).

Results and Discussion

Variation of total AC transport loss, Q_e, which is the sum of the individual losses occurring in the inner (Q_i) and outer (Q_o) wires with the applied current amplitude is presented in Fig. 39.2. When $I_{max} < I_c/2$, both loss curves vary almost linearly in the log–log scale of Fig. 39.2. The loss for the shell-type wires is significantly smaller than that of the solid-core wires in this current range. In fact, Q_e equals 1.8×10^{-6} and 5.8×10^{-6} J/m at $I_{max} = 5.0$ A ($0.05I_c$), respectively, while it becomes 8.5×10^{-4} and 1.6×10^{-3} J/m at $I_{max} = 50.0$ A ($0.5I_c$). Thus, Q_e in the solid-core wires is approximately three-times and twice as high as that in the shell-type wires at $0.05I_c$ and $0.5I_c$, respectively. However, the increase rate of Q_e at higher current amplitudes is higher for the shell-type wires, where Q_e for the solid-core and shell-type wires becomes 1.0×10^{-2} and 1.2×10^{-2} J/m at $I_{max} = 90.0$ A ($0.9I_c$). That, is Q_e of shell-type wires is 16.7 % higher at this current amplitude.

AC losses in both cable types are not equally distributed between the inner and outer layers, as depicted in Fig. 39.3. Losses are considerably higher in the outer cable layer for $I_{max} < I_c/2$, while they are higher in the inner layer for large amplitudes. At $I_{max} = 5.0$ A ($0.05I_c$), Q_i and Q_o for the solid-core wires are calculated as 1.2×10^{-6} and 1.7×10^{-6} J/m, respectively, whereas they are 3.7×10^{-7} and 5.5×10^{-7} J/m for the shell-type wires. Discrepancy between losses in different layers at that amplitude is 46.6 % and 50.2 % for the solid-core and shell-type wires, respectively. At $I_{max} = 5.0$ A ($0.05I_c$), however, Q_i is 2.8 % and 17.5 % higher than Q_o for the solid-core and shell-type wires, respectively.

Fig. 39.2 Variation of total AC transmission losses in cylindrical cables with respect to the applied current amplitude
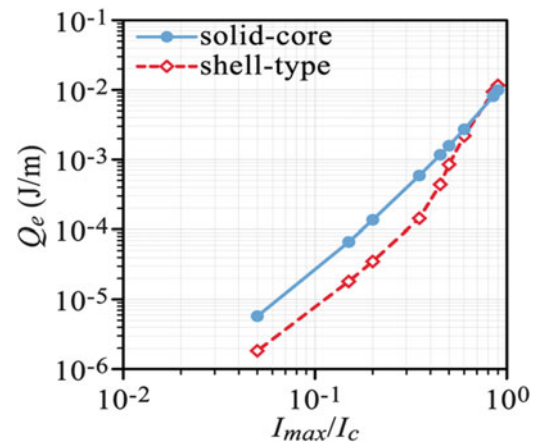
Fig. 39.3 Comparison of individual losses in the inner (Q_i) and outer (Q_o) layers of solid-core and shell-type wires
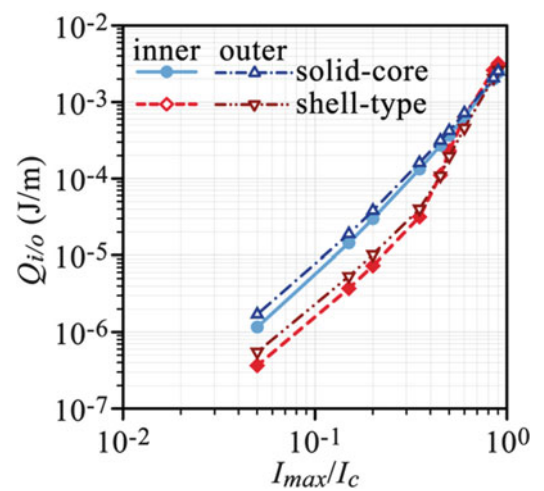
To understand the variation of AC loss curves in Figs. 39.2 and 39.3, distribution of equi-potential lines of **A** and current density around and in the wires, respectively, for a number of instantaneous values of the applied current with $I_{max} = 90.0$ A. Figure 39.4a demonstrates that current flow is almost homogeneous, except for a small circular cross-section over which current flows in the opposite direction, when the value of the instantaneous current is close to $\pm I_{max}$ (i.e. at the beginning or the end of a full-cycle of the applied sinusoidal signal). The opposite-current-flow region expands when the instantaneous current is small (or the half of the period of the applied sinusoidal current is reached), as the integral of current density over a wire's cross-sectional area approaches zero. Moreover, current flow in this region is not homogeneous and it does not appear at the center of neither the inner nor the outer wires. Figure 39.4a also indicates that the magnetic field lines are concentrated mainly around the outer wire at any moment of the applied current, whereas penetration into this wire is more significant. Besides, the outer wire is subject to the normal component of the magnetic field to a larger extent. Thus, the fact that the outer wire suffers more AC losses at moderate or small current amplitudes can be explained in terms of the responses of the HTS wires to their self-fields.

The situation is significantly different for the shell-type wires, in which the current distribution is more homogeneous when the instantaneous current is close to I_{max}, Fig. 39.4b. Towards the half of the cycle, however, almost equal amounts of current flows in opposite directions over the halves of the shells. Although magnetic field pattern of the shell-type wires is similar to that of the solid-core wires, normal components of the field are primarily trapped in the interiors of the shell (vacuum region), especially on the outer wire, at any instant of the applied current, Fig. 39.4b.

Fig. 39.4 Distribution of the equi-potential contours of the vector potential (*lines*) and the current distribution (*color shades*) in solid-core (**a**) and shell-type (**b**) wires at several instantaneous current values over a cycle of an applied current with $I_{max} = 90.0$ A (Color figure online)
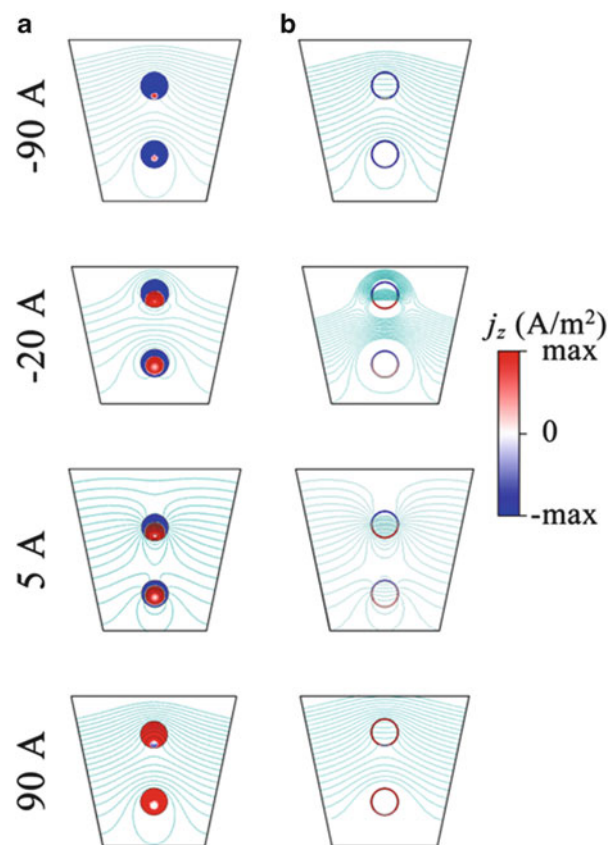
Conclusion

Alternating-current transport losses in two-layer HTS cables with circular wires is numerically investigated with respect to wire cross-section. Smaller AC losses can be obtained if the wires are in the form of annuli, rather than filled circles. Calculated losses for the former are several times smaller than those in the latter if the amplitude of the applied current with 50 Hz frequency is smaller than half the critical current in each wire. AC losses are generally higher in the outer-layer wires for such current amplitudes, while losses in the inner wires become higher at amplitudes close to the critical current. Current distribution over a cycle is more homogeneous in both wires of shell-type conductors. In addition, the self-field of the wires is concentrated more around the outer wire in both configurations, while penetration into the conductor is more pronounced in the outer layer of solid-core wires. Moreover, the boundaries of these wires are subject to the normal component of the field to a larger extent, whereas normal component is trapped in the interior space of the shell-type conductors.

References

1. Dechoux N, Jiménez C, Chaudouët P, Rapenne L, Sarigiannidou E, Robaut F, Petit S, Garaudée S, Porcar L, Soubeyroux JL, Odier P, Bruzek CE, Decroux M (2012) Textured YBCO films grown on wires: application to superconducting cables. Supercond Sci Technol 25(12):125008
2. Jiang J, Starch WL, Hannion M, Kametani F, Trociewitz UP, Hellstrom EE, Larbalestier DC (2011) Doubled critical current density in Bi-2212 round wires by reduction of the residual bubble density. Supercond Sci Technol 24(8):082001
3. Majoros M, Sumption MD, Susner MA, Kovacs C, Collings EW, Peng X, Doll D, Tomsic M, Lyons D (2012) A model superconducting helical undulator fabricated using a small filament, tube-type multifilamentary Nb₃Sn wire. Supercond Sci Technol 25(11):115006
4. Kim S-K, Ha S-K, Kim J-G, Kim S, Park M, Yu I-K, Lee S, Sim K (2013) Design and AC loss analysis of a 22.9 kV/50 MVA class triaxial HTS power cable. J Supercond Novel Magn 26(4):755–758

5. Maruyama O, Ohkuma T, Masuda T, Ashibe Y, Mukoyama S, Yagi M, Saitoh T, Hasegawa T, Amemiya N, Ishiyama A, Hayakawa N (2013) Development of 66 kV and 275 kV class REBCO HTS power cables. IEEE Trans Appl Supercond 23(3):5401405

6. Rostila L, Lehtonen J, Masti M, Lallouet N, Saugrain J-M, Allais A, Schippl K, Schmidt F, Balog G, Marot G, Ravex A, Usoskin A, Gömöry F, Klinčok B, Šouc J, Freyhardt HC (2006) Design of a 30 m long 1 kA 10 kV YBCO cable. Supercond Sci Technol 19(4):418–422

7. Allais A, Isfort D, Theune C-F, Porcher K (2008a) Method for the production of superconducting electrical conductor. Patent Number: US2008/0119365.A1

8. Allais A, Isfort D, Theune C-F, Porcher K (2008b) Method for the production of superconducting electrical conductor. Patent Number: EP1916720

9. Bruzek CE, Allais A, Morice S, Theune C-F, Petit S, Mikolajczyk M, Dechoux N, Jimenez C, Sarigiannidou E, Porcar L, Soubeyroux J-L, Odier P, Waeckerle T (2012) New HTS 2G round wires. IEEE Trans Appl Supercond 22(3):5800204

10. Ferrando V, Orgiani P, Pogrebnyakov AV, Chen J, Li Q, Redwing JM, Xi XX, Giencke JE, Eom C-B, Feng Q-R, Betts JB, Mielke CH (2005) High upper critical field and irreversibility field in MgB_2 coated-conductor fibers. Appl Phys Lett 87(25):252509

11. Ma B, Balachandran U (2006) Prospects for the fabrication of low aspect ratio coated conductors by inclined substrate deposition. Supercond Sci Technol 19 (6):497–502

12. Šouc J, Vojenčiak M, Gömöry F (2010) Experimentally determined transport and magnetization ac losses of small cable models constructed from YBCO coated conductors. Supercond Sci Technol 23(4):045029

13. Odier P, Allais A, Millon C, Morlens S, Ortega L, Jiménez C, Porcar L, Chaud X, Chaudouët P, Pairis S, Tixador P, Soubeyroux JL (2009) New YBCO superconducting wires obtained from narrow textured tubes. Supercond Sci Technol 22(12):125024

14. Mawatari Y (2011) Superconducting tabular wires in transverse magnetic fields. Phys Rev B 83(13):134512

15. Gömöry F, Inanir F (2012) AC losses in coil wound from round wire coated by a superconducting layer. IEEE Trans Appl Supercond 22(3):4701704

16. Pi W, Wang Y-S, Dong J, Chen L (2010) AC alternating-current loss analyses of a thin high-temperature superconducting tube carrying AC transport current in AC external magnetic field. Chin Phys Lett 27(3):037401

17. Gömöry F, Vojenčiak M, Pardo E, Šouc J (2009) Magnetic flux penetration and AC loss in a composite superconducting wire with ferromagnetic parts. Supercond Sci Technol 22(3):034017

18. Brandt EH (1996) Superconductors of finite thickness in a perpendicular magnetic field: strips and slabs. Phys Rev B Condens Matter 54(6):4246–4264

19. Sirois F, Roy F (2007) Computation of 2-D current distribution in superconductors of arbitrary shapes using a new semi-analytical method. IEEE Trans Appl Supercond 17(3):3836–3845

Influences of Ferromagnetic Deflectors Between Layers of Superconducting Power Transmission Cables on Transport Current Losses

40

Ahmet Cicek and Fedai Inanir

Abstract

Alternating-current losses in two-layer power transmission cables constructed by type-II superconducting strips in the presence of ferromagnetic deflectors between the layers are numerically investigated. Each layer comprises 15 wires with rectangular cross section of 4 mm width and 2 μm height, while the inner and outer layer radii are 20 and 21 mm, respectively. Deflectors are composed of either non-magnetic or strongly ferromagnetic material, where the width and height of each is 5 mm and 80 μm, respectively. Losses are obtained through Finite-Element Method simulations with respect to amplitude of the applied current with 1 Hz frequency. Use of ferromagnetic deflectors increases the total alternating-current loss in the two layers considerably for small amplitudes, while the loss approaches that in non-magnetic case at amplitudes around the critical current. Individual layer losses are such that outer-layer loss is significantly larger, 2.5-fold at 1/16 of the critical current, for ferromagnetic deflectors, whereas they are almost identical in non-magnetic case at all amplitudes. Inner and outer wires are exposed to similar self magnetic fields of wires in non-magnetic case, while ferromagnetic deflectors accumulate magnetic field lines on themselves and increase the losses in outer wires. The current profile is homogeneous except at the edges of the wires in the non-magnetic case, whereas homogeneity is disrupted for the outer wire in the case of ferromagnetic deflectors, such that current flow in the positive direction is confined to the central region.

Introduction

Among promising applications of high-temperature superconductors (HTS) is power transmission. HTS power transmission cables generally operate at temperatures between 64 and 77 K. The most important advantages of these cables on conventional ones are the ability to transport high currents and their efficiency.

In evaluation of the efficiency of HTS cables, determination of alternating-current (AC) transport losses plays a central role. Primary factors affecting AC losses include (1) the number and dimensions of the wires composing a cable, (2) geometrical alignment of wires on cables and (3) the twist-pitch length.

A. Cicek (✉)
Department of Physics, Faculty of Arts and Sciences, Mehmet Akif Ersoy University, Campus 15100, Burdur, Turkey
e-mail: ahmetcicek@mehmetakif.edu.tr

F. Inanir
Department of Physics, Faculty of Arts and Sciences, Recep Tayyip Erdoğan University, 53100 Rize, Turkey
e-mail: inanir@ktu.edu.tr

The critical current densities (J_c) of HTS cables depend heavily on the magnetic field distribution at elevated temperatures. In such power transmission cables, the total critical current density is higher than the sum of the corresponding densities of the strips forming the cable [1]. The reason for this lies in the fact that the variation in magnetic field distribution takes place in a more favorable manner, especially along the edges of an individual strip.

Ferromagnetic deflectors are successfully utilized in HTS coils and practical applications [2, 3]. It is reported that a correction in the critical current density (J_c) is required in strips coated by a ferromagnetic jacket [4]. The ferromagnetic material restrains coupling between the filaments within the superconductor [5]. This is expected to give rise to a decline in the transport AC losses in HTS cables. This is demonstrated by occupying the space between the filaments which inhibits the interaction between the filaments and facilitates decrease in AC losses [6]. Screening in HTS strips coated by ferromagnetic materials is also studied [7, 8]. Furthermore, influence of magnetization on AC transport losses in superconductors over a ferromagnetic substrate due to applied magnetic field is studied [9, 10]. It is reported that an important improvement in the performance of BiSCCO-2223 strips coated by a partially ferromagnetic material can be achieved [11]. Vojenčiak et al. [12] demonstrated both theoretically and experimentally that introduction of ferromagnetic deflectors in the space between the strips of a single-layer HTS cable gives rise to a reduction in AC losses.

Application of ferromagnetic deflectors between the layers of a two-layer HTS cable could also give rise to a reduction in AC transport losses in such cables. This work focuses on a numerical investigation on the influences of ferromagnetic deflectors introduced in the space between the HTS strips in a two-layer cable along the radial direction. The variation of transport current losses with respect to the applied current for deflectors with varying permeability is studied.

Cable Geometry and Computational Methods

The two-layer HTS cable geometry is depicted in Fig. 40.1. Each layer comprises $N = 30$ rectangular superconducting tapes with width and height as $w_{sc} = 4.0$ mm and $h_{sc} = 2.0$ μm, where the inner and outer layers are on circular arcs with $R_i = 20.0$ mm and $R_o = 21.0$ mm, respectively. The wire parameters are compatible with the standards set by American Superconductors Inc. The core of the cable is made of copper (Cu), whereas the space between the layers is filled with Kapton® dielectric. The ferromagnetic deflectors between the layers also possess a rectangular cross section with $w_T = 5.0$ mm and $h_T = 80.0$ μm, Fig. 40.1b.

The two-layer HTS cable in Fig. 40.1a possesses discrete azimuthal symmetry with respect to a unit of rotation by $\theta_C = 2\pi/30$ (12°), whereas the ferromagnetic deflectors, aligned on a circle with Radius $R_T = 20.5$ mm, are rotated by $\theta_T = \theta_C/2 = 2\pi/62$ (5.8°) with respect to the wires. Due to the above-mentioned symmetry, the problem in two dimensions
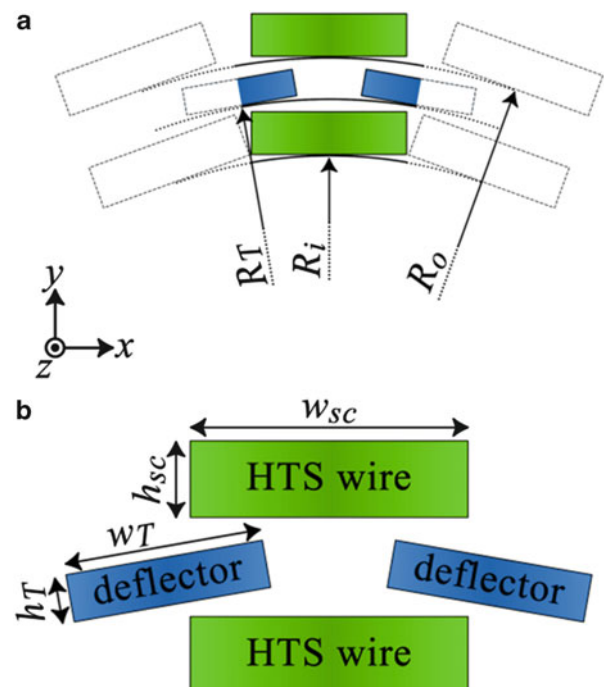
Fig. 40.1 Geometry of the two-layer HTS cable with ferromagnetic deflectors (**a**) and a close-up view of the wires and deflectors (**b**). Elements are not drawn to scale for clarity

(2D) is solved through the Comsol MultiPhysics® package with AC/DC module, which is a commercial implementation of the Finite Element Method (FEM), by only considering the periodic element in Fig. 40.1a. Thus, the two wires and halves of the deflectors, which are depicted by the filled rectangles with solid borders, are considered in computations, Fig. 40.1a.

The HTS wires are composed of second-generation yttrium barium copper oxide (YBCO) superconductors, whereas the deflectors are either non-magnetic or strongly ferromagnetic with relative permeability of $\mu_r = 1.0$ and 5,000, respectively. The magnetic flux dependence of the ferromagnetic deflectors is assumed as $B = \mu_0 \mu_r H$ and ferromagnetic losses are ignored. The influence of the substrate is neglected for simplicity, so that it is not depicted in Fig. 40.1a. Moreover, twisting of the wires along the z direction is also not taken into account. The choice of geometrical and physical parameters is to facilitate a comparison between other possible configurations of the cable with respect to the use of ferromagnetic material.

In FEM simulations, an alternating current with a frequency of f is applied along the z direction and the component of the vector potential along this direction (A_z) is treated as the independent variable. The rotational of the vector potential yields magnetic flux density. The critical current for each wire, which is calculated through an integration of the critical current density (J_c) over the cross-sectional area (A_{SC}) of the wire on the xy-plane,

$$I_c = \int_{A_{SC}} J_c \, dA_{SC} \tag{40.1}$$

is taken as $I_c = 80$ A. Dependence of I_c on magnetic flux density and position, which may be important in case of wires with circular cross-sections, is ignored. The current is sinusoidal with $I(t) = I_{max}.\sin(2\pi f t)$, where I_{max} is its amplitude with respect to I_c and $f = 1$ Hz.

The boundary condition for addressing the cable geometry in Fig. 40.1a considers the vector potential at an arbitrary position r due to an HTS wire in Fig. 40.1b as

$$A_r = -\frac{\mu_0 I}{2\pi} \left(\ln\left(\frac{r}{R_i + h_{SC}}\right) + \ln\left(\frac{r}{R_o + h_{SC}}\right) + 2 \right) \tag{40.2}$$

Besides, the azimuthal boundary condition exploits continuity of the normal component of the magnetic field. The superconducting current density in computations can be written as

$$j_{sc,z}(x,y) = J_c \tanh\left(\frac{A_p(x,y) - (A_z(x,y) + \nabla V)}{A_n}\right) \tag{40.3}$$

where $A_p(x,y)$ is the distribution of $A_z(x,y)$ in the previous step in the time march of simulations, whereas A_n is the scaling parameter which adjusts the sharpness of the translations between the region in superconductor with positive and negative current densities and ∇V is the scalar potential. By numerically solving Ampere's Law in combination with Eqs. (40.2) and (40.3), the distributions of $j_{sc,z}$ and $\mathbf{E} = -\partial \mathbf{A}/\partial t - \nabla V$ over a wire's cross-section are calculated and AC loss, Q (J/m), in each wire is obtained, in turn, by:

$$Q = \int_{A_{sc}} \mathbf{E} \cdot \mathbf{j} \, dA_{sc} \tag{40.4}$$

Results and Discussion

Variation of the total AC transport loss (Q_e) of the HTS cable on each periodic element in Fig. 40.1a with respect to the applied current amplitude is depicted in the log–log scale in Fig. 40.2. In computations I_{max} is set to eight different values ranging from 5.0 to 75.0 A ($I_c/16$ to $15I_c/16$). Q_e is calculated as the sum of the losses in inner (Q_i) and outer (Q_o) layers.

Figure 40.2 demonstrates that use of strongly ferromagnetic deflectors significantly increases Q_e, while the discrepancy between the two materials vanishes for large current amplitudes close to I_c. The losses increase almost linearly in Fig. 40.2 for $I_{max} < I_c/2$, whereas the increase is slightly steeper at higher amplitudes. The calculated losses for $\mu_r = 1.0$ are 2.98×10^{-6}, 1.74×10^{-4} and 1.91×10^{-3} J/m for $I_{max} = 5.0$ A ($I_c/16$), 35.0 A ($7I_c/16$), and 75.0 A ($15I_c/16$), respectively. Corresponding losses for $\mu_r = 5,000$ are 3.82×10^{-6}, 2.47×10^{-4} and 1.93×10^{-3} J/m, respectively. These values are 28.2, 41.4 and 0.8 % higher than the corresponding values in the $\mu_r = 1.0$ case.

Fig. 40.2 Variation of total AC transport loss on each periodic element with respect to the applied current amplitude for non-magnetic and strongly ferromagnetic deflectors
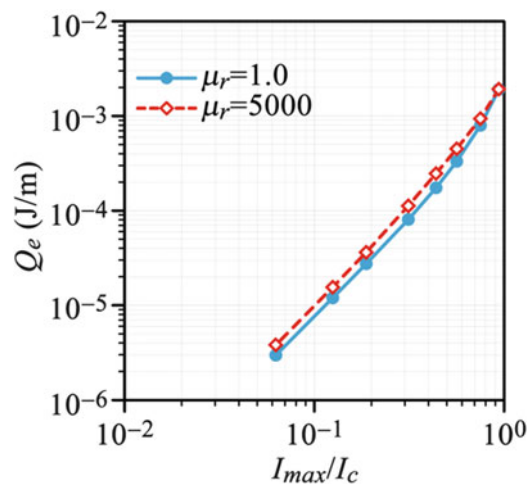
Fig. 40.3 Comparison of individual AC transport losses on the inner and outer layers of the HTS cable for non-magnetic and strongly ferromagnetic deflectors
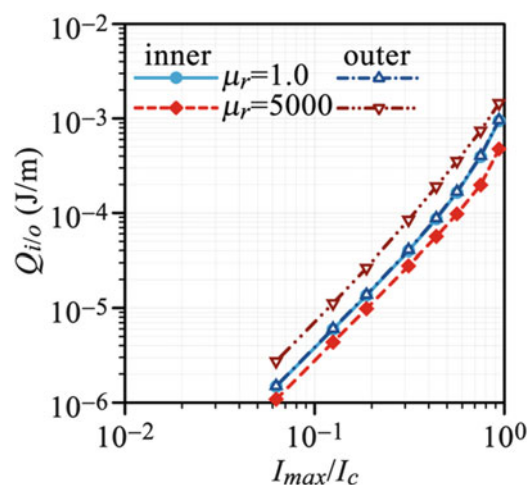
To elucidate the loss mechanism due to the presence of deflectors, individual losses on each layer should be considered. Figure 40.3 depicts the variation of Q_i and Q_o with respect to I_{max}. In case of $\mu_r = 1.0$, Q_i and Q_o are almost equal to each other (and thus to $Q_e/2$), as expected. In contrast, a significant discrepancy is observed for $\mu_r = 5,000$, where Q_i is considerably smaller at all I_{max} values. In fact, Q_i is also smaller than the corresponding value for the non-magnetic deflector case. The value of Q_i and Q_o are 1.1×10^{-6} and 2.7×10^{-6} J/m, respectively, such that Q_o is 145.4 % higher than Q_i, at $I_{max} = 5.0$ A ($I_c/16$) for the ferromagnetic deflectors. The corresponding value for non-magnetic deflectors is 1.5×10^{-6} J/m, which is 35.8 % larger than the Q_i value at the same amplitude for the ferromagnetic case. Q_i and Q_o for $\mu_r = 5,000$ becomes 5.6×10^{-5} and 1.9×10^{-4} J/m, respectively at $I_{max} = 35.0$ A ($7I_c/16$), that is Q_o is almost fourfold higher at amplitudes around $I_c/2$. At the highest amplitude ($15I_c/16$), the corresponding values are calculated as 4.7×10^{-4} and 1.5×10^{-3} J/m, respectively. Although presence of ferromagnetic deflectors increases the total AC transport loss, the loss in the inner layer of the cable can be tuned by modifying the deflector parameters. This can particularly be important in technological applications in order to reduce process and cooling-down costs [13].

How the relative permeability of deflectors influences AC losses is closely related to how they manipulate the magnetic field distribution around the HTS wires. Figure 40.4 presents distribution of the equi-potential lines of the magnetic vector potential (A_z) for non-magnetic and strongly ferromagnetic deflectors at an instant, at which the instantaneous current on a wire is $I(t) = 18.5$ A, of the sine-wave cycle of the applied current with $I_{max} = 75.0$ A.

Non-magnetic deflectors do not affect the magnetic field lines due to current distributions in the wires as expected, Fig. 40.4a. Besides, the wires on the inner and outer layers are exposed to similar self-fields. Thus, Q_i and Q_o for $\mu_r = 1.0$ in Fig. 40.3 are almost equal. On the other hand, strongly ferromagnetic deflectors both trap and concentrate field lines on themselves, Fig. 40.4b. Moreover, the inner layer is exposed to its self-field to a lesser extent in this case. This is the reason
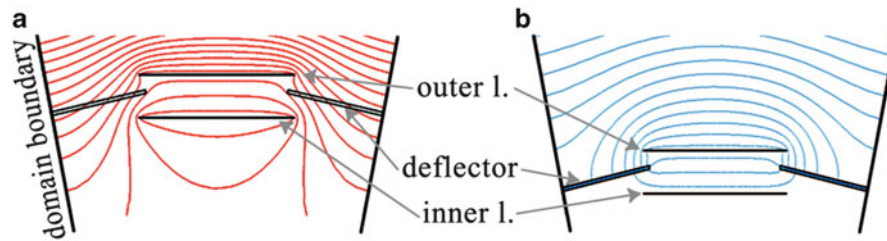
Fig. 40.4 Distribution of the equi-potential lines of the magnetic vector potential (A_z) around the wires for $\mu_r = 1.0$ (**a**) and 5,000 (**b**) at an instant of the applied sinusoidal current such that the instantaneous current takes a moderate value (18.5 A)
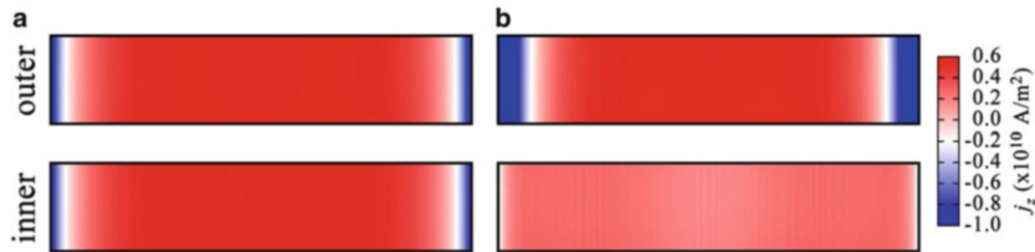
Fig. 40.5 Distribution of current amplitude over the inner (*lower*) and outer (*upper*) wires of the HTS wire for non-magnetic (**a**) and strongly ferromagnetic (**b**) deflectors at an instant of the applied sinusoidal current such that the instantaneous current takes a moderate value (18.5 A)

behind the fact that Q_i for the ferromagnetic deflectors is smaller than both Q_o in the same configuration and the corresponding Q_i for non-magnetic deflectors, as seen in Fig. 40.3. Moreover, the normal component of the magnetic field is more dominant at the edges of the outer wire for $\mu_r = 5,000$. The above facts indicate that current distributions in the wires are affected by the presence of the ferromagnetic deflectors, as depicted in Fig. 40.5.

Figure 40.5a depicts that current flow is homogeneous in the interiors of both wires, while higher current amplitudes close to I_c are confined to the edges parallel to y direction in case of $\mu_r = 1.0$. Furthermore, the current distribution is almost identical in inner and outer wires, Fig. 40.5a. On the other hand, the situation is quite different in case of $\mu_r = 5,000$, as depicted in Fig. 40.5b. The current flow is more homogeneous in the inner wire, lower part of Fig. 40.5b, than in the case of non-magnetic deflectors. For this wire, the high current flow at the edge is confined to a smaller area. However, the region expands more into the wire along x direction in the outer wire, upper part of Fig. 40.5b. This, in turn, indicates that magnetic field penetrates deeper into the outer wire in case of ferromagnetic deflectors. The current distribution patterns in Fig. 40.5 are consistent with distribution of magnetic field lines in Fig. 40.4.

Conclusion

Alternating-current transport losses in two-layer high-temperature superconducting cables accompanied by ferromagnetic deflectors are numerically studied through FEM simulations. Presence of ferromagnetic deflectors with relative permeability as high as 5,000, located in the space between the layers and rotated by half the unit angle of rotation due to discrete azimuthal symmetry of the cable, increases the total loss relative to the case of non-magnetic deflectors. The increase in the total loss is due mainly to the increased self-magnetic field around the outer-layer wires, whereas the ferromagnetic deflectors concentrating magnetic field lines on themselves lead to a reduction in the individual losses of inner-layer wires. This fact can be utilized in tuning the losses in the inner layers of multi-layer cables to reduce both operation and cooling-down costs. In consistent with the distribution of magnetic field lines due to self-fields of the wires in the existence of ferromagnetic deflectors, the current flow is largely homogeneous in the inner-layer wires, while the region of high current flow expands more into the outer-layer wires.

References

1. Rostila L, Söderlund L, Mikkonen R, Lehtonen J (2007) Modelling method for critical current of YBCO tapes in cable use. Physica C Supercond Appl 467 (1–2):91–95
2. Pardo E, Šouc J, Vojenčiak M (2009) AC loss measurement and simulation of a coated conductor pancake coil with ferromagnetic parts. Supercond Sci Technol 22(7):075007
3. Wen H, Bailey W, Goddard K, Al-Mosawi M, Beduz C, Yang Y (2009) Performance test of a 100 kW HTS generator operating at 67 K–77 K. IEEE Trans Appl Supercond 19(3):1652–1655
4. Kovác P, Hušek I, Melišek T, Ahoranta M, Šouc J, Lehtonen J, Gömöry F (2003) Magnetic interaction of an iron sheath with a superconductor. Supercond Sci Technol 16(10):1195–1201
5. Glowacki BA, Majoros M (2000) A method for decreasing transport ac losses in multifilamentary and multistrip superconductors. Supercond Sci Technol 13 (7):971–973
6. Majoros M, Sumption MD, Collings EW (2009) Transport AC loss reduction in striated YBCO coated conductors by magnetic screening. IEEE Trans Appl Supercond 19(3):3352–3355
7. Farinon S, Fabbricatore P, Gömöry F, Greco M, Seiler E (2005) Modeling of current density distributions in critical state by commercial FE codes. IEEE Trans Appl Supercond 15(2):2867–2870
8. Yampolskii SV, Genenko YA, Rauh H (2007) Penetration of an external magnetic field into a multistrip superconductor/soft-magnet heterostructure. Physica C Supercond Appl 460–462(2):1262–1263
9. Seiler E, Gömöry F (2006) Modelling of the flux penetration into a superconducting strip with magnetic sheath. J Phys Conf Ser 43:9–13
10. Suenaga M, Iwakuma M, Sueyoshi T, Izumi T, Mimura M, Takahashi Y, Aoki Y (2008) Effects of a ferromagnetic substrate on hysteresis losses of a $YBa_2Cu_3O_7$ coated conductor in perpendicular ac applied magnetic fields. J Phys Conf Ser 97:012025
11. Safran S, Vojenčiak M, Gencer A, Gömöry F (2010) Critical current and AC loss of DI-BSCCO tape modified by the deposition of ferromagnetic layer on edges. IEEE Trans Appl Supercond 20(5):2294–2300
12. Vojenčiak M, Šouc J, Gömöry F (2011) Critical current and AC loss analysis of a superconducting power transmission cable with ferromagnetic diverters. Supercond Sci Technol 24(7):075001
13. Gerhold J, Tanaka T (1998) Cryogenic electrical insulation of superconducting power transmission lines: transfer of experience learned from metal superconductors to high critical temperature superconductors. Cryogenics 38(11):1173–1188

Multimodal Structure for the Management of Energies in a Residential Home

Hadia Bouguessa, Nadia Saadia, Nadia Touileb, and Amina Makhlouf

Abstract

Buildings consume a significant fraction of the energy produced in the world (39 % in Algeria), so they are responsible for important emissions of greenhouse gases; since climate change has become an international concern, we attempt to adopt energy policies to mitigate global warming and its side effects. This is the reason for which the migration to positive energy buildings is more and more obvious for better environment protection. The aim of this paper is a conception of a home automation platform controlling energy. It consists of designing an adaptive software architecture using multiple modalities for managing two important requirements: the switch between the energy sources (wind, solar and the network) and the control of different households in a smart building to improve energy efficiency. This multimodal software architecture is modeled by colored, timed and stochastic Petri nets (CTSRP) simulated in CPN Tools.

Keywords

Multi-agent multimodal platform • Energy efficiency • Home automation • Renewable energies

Introduction

Global demand for energy keeps increasing with economic development and population growth, raising concerns about the depletion of energy resources and heavy environmental impacts (depletion of the ozone layer, global warming, etc.) during the period (1984–2004), the emission of CO_2 increased by 43 %, with an average annual rate of 1.8 % as shown in Fig. 41.1 [1]. Given that the building sector (residential and commercial) is the largest consumer of energy produced in Algeria and around the world with the rate of 39 % according to [2], exceeding the consumption of large sectors (industrial and transportation); it represents a potential research axis to respond to these energy and environmental challenges as it provides important opportunities to reduce energy consumption and CO_2 emissions by maximizing the thermal performance of the building envelope, minimizing energy demand whilst maintaining energy service levels [3] and implementing renewable energy sources.

In residential sector, several computer technologies and methodologies have been used in building energy management systems (BEMS), such as genetic algorithms, neural networks, and weighted linguistic fuzzy rules [4], to reach a better energy efficiency and make ordinary building smarter.

In this paper, we focused on multimodal multi-agent systems (SMA) that have evolved significantly over the past 20 years; they constitute a preferred approach to deal with complex systems in many fields such as image processing, robotics, eldercare, home automation . . ., due to their decentralized processing component entities and their interactions with the environment.

H. Bouguessa (✉) • N. Saadia • N. Touileb • A. Makhlouf
Laboratory of Robotics, Parallelism and Power system, Faculty of Electronics and Computer Science,
U.S.T.H.B., BP 32 El Alia, Bab Ezzouar, 16111 Algiers, Algeria
e-mail: hadia.bouguessa@gmail.com; saadia_nadia@hotmail.com; n-touileb@hotmail.fr; amina.makhlouf14@gmail.com

Fig. 41.1 Primary energy consumption, CO_2 emissions and world population. Reference year 1984. *Source*: International Energy Agency (IEA)
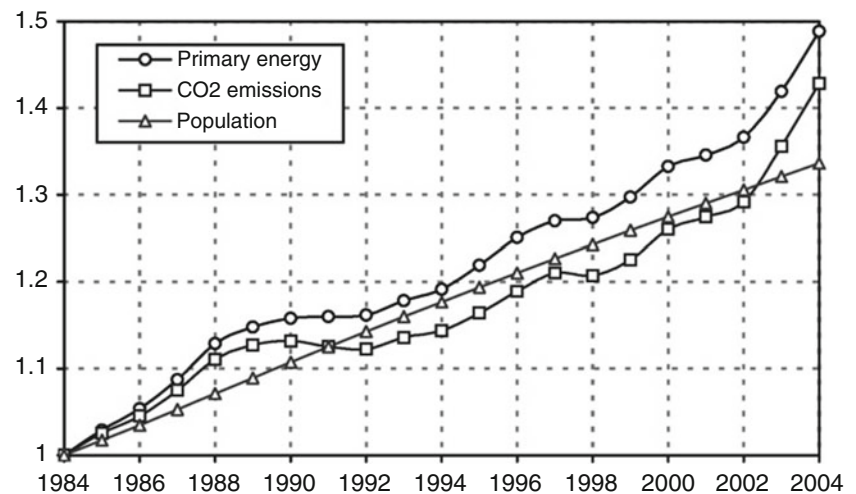
The objective is to develop a Home Automation System Controlling Energy (HASCE) based on multi-agent approach for managing several modalities such as temperature, light …, in a smart building. To evaluate and validate the proposed architecture, we modeled the HASCE using CPN Tools. The paper is organized as follows: "Intelligent Buildings" section presents the evolution of smart buildings. "Overview of Multi-agent Systems" section presents an overview of multi-agent systems in smart buildings. "Home Automation System Controlling Energy" section describes the overall multimodal system architecture. Case studies, results and discussion are presented in "Results and Discussion" section.

Intelligent Buildings

The word intelligent appeared, in the beginning of the 1970s in the United States under the name BEMS. That's a center of aggregation and data processing (dump outstation) for buildings, with the development of Information and Communication Technologies [5]. This concept is reinforced in 1980s by the increasingly sophisticated demand for "comfort living environment and requirement for increased occupant control of their local environments" [6].

Since then, the intelligent building (IB) concept converged on several meanings, according to the research conducted by Wigginton and Harris [7], there is over 30 different definitions related to intelligent building with the development of other technologies and communication protocols, the introduction of renewable energy sources and sustainable development; other terms have emerged such as low-energy building, passive building, net zero energy building, and positive energy building.

In [8], we find a definition of IB that we adopt in this article: "The building is more efficient, with integrated management equipment: equipment manufacturers and equipment storage of electricity, energy efficiency also depends on the technical construction of the building, insulation, for example, intelligent building concept is the integration of energy management solutions in the home, particularly to ensure in buildings with positive energy". From this point of view, IB should have these main characteristics:

- Exploiting and managing renewable energy on the site
- Reduce energy consumption and costs
- Improve the safety in buildings
- Improve the comfort and building

Overview of Multi-agent Systems

Researches around the smart building, home automation, and energy management reporting use of SMA appear for many years in the literature [9, 10]. The SMA approach meets the requirements of distributed systems, it allows to understand model and simulate complex systems, which consist of several entities in dynamic interaction with each other and the outside world, to collectively solve a global problem.

Fig. 41.2 The real environment of the proposed SMA

In this paper, we are interested in the SMA developed for energy management in buildings, Davidsson and Boman developed a platform for energy management for tertiary building with the establishment of three agents controlling lighting, heating, and ventilation [11]. In the approach proposed by Dujardin et al. [9], four active and three passive agents take charge of control and energy management in a room with four offices (Fig. 41.2), the active agents are defined as follows: Avatar agent representing humans, the Lamp agent for the control of office lamps, the Room agent to control temperature and finally the Energy agent to turn On/Off the halogen lamp if desk lamps consume too much energy, the passive agents are charged with the control of radiator, air conditioner, and the halogen lamp. The SMA Interactions on the environment are the ignition and extinction of electrical appliances as well as increase and decrease the level of heating appliances. The system is articulated around a software bus named WSE (Web Server Event), all messages exchanged by agents of the system, such as interactions, users or actions required of devices, transit through the bus (Fig. 41.3).

The proposed layered control system by Wang et al. [12] is made up of multiple agents, which are classified into two levels. The first level interacts with the power grid or micro source termed as the central coordinator-agent. The second level termed local controller-agents in charge of users' comfort in the smart and energy-efficient buildings mainly decided by three factors, which are environment temperature, indoor air quality (CO_2 concentration), and illumination. A similar approach is proposed by Wang et al. [13], it consists of a hierarchical multi-agent control system with an intelligent optimizer (PSO) to optimize the overall system and enhance the intelligence of the integrated building and micro grid system. Duan and Indin [14] use a pure distributed architecture to achieve a number of important environmental control parameters inside the IB, temperature control and lighting experiments are performed on a Windows CE embedded platform. Abras [11]) proposes a system composed of software agents performing each a specific task, interacting and communicating to find dynamically a production and energy consumption policy, satisfying various constraints. In this work, agents are associated with equipment and sources of energy production. The Multi-Agent System (SMA) is called MAHAS "Multi-Agent Home Automation System." The following diagram (Fig. 41.4) shows the overall structure of the MAHAS.

Fig. 41.3 Communication protocol between the SMA, peripherals, and control interfaces through WSE bus
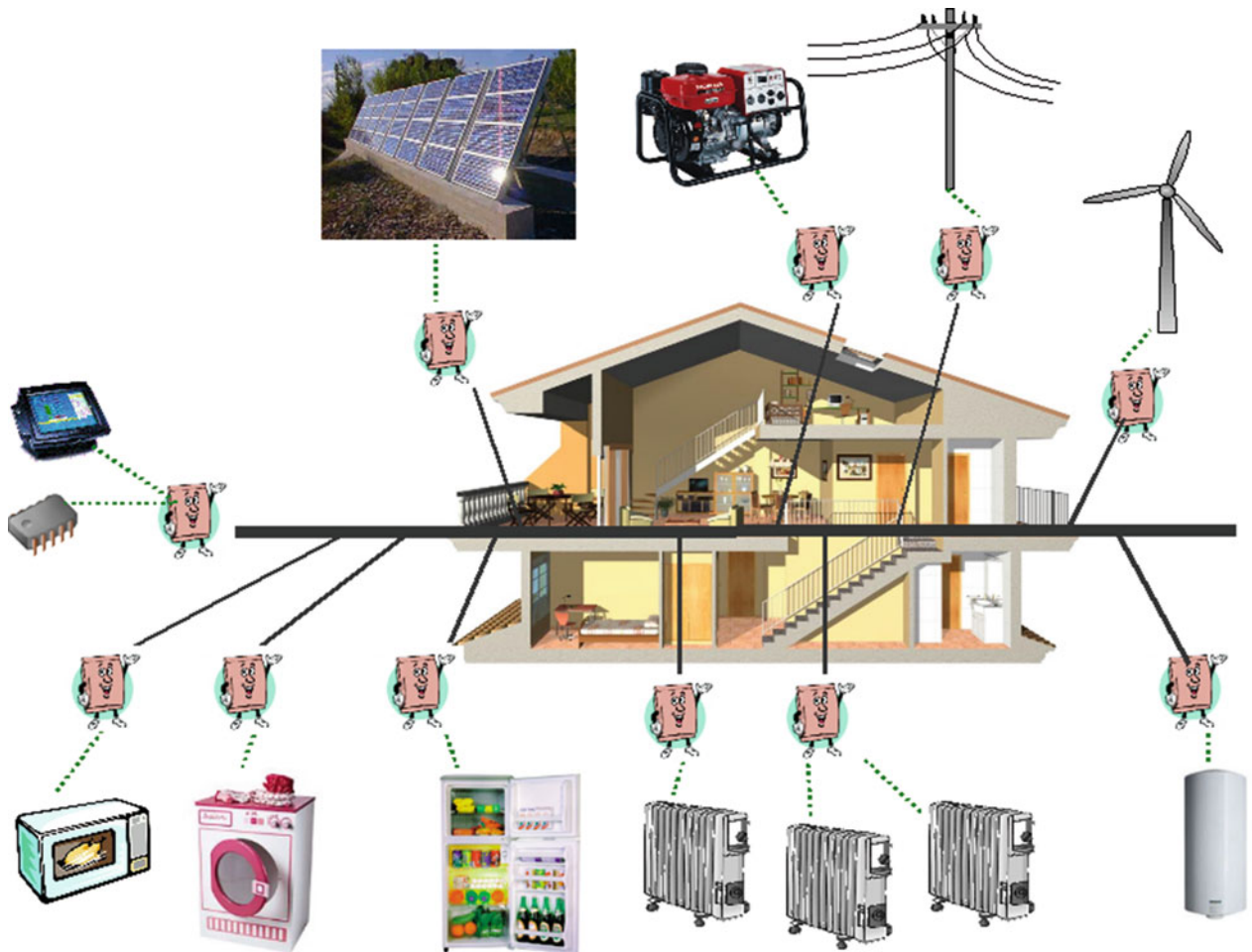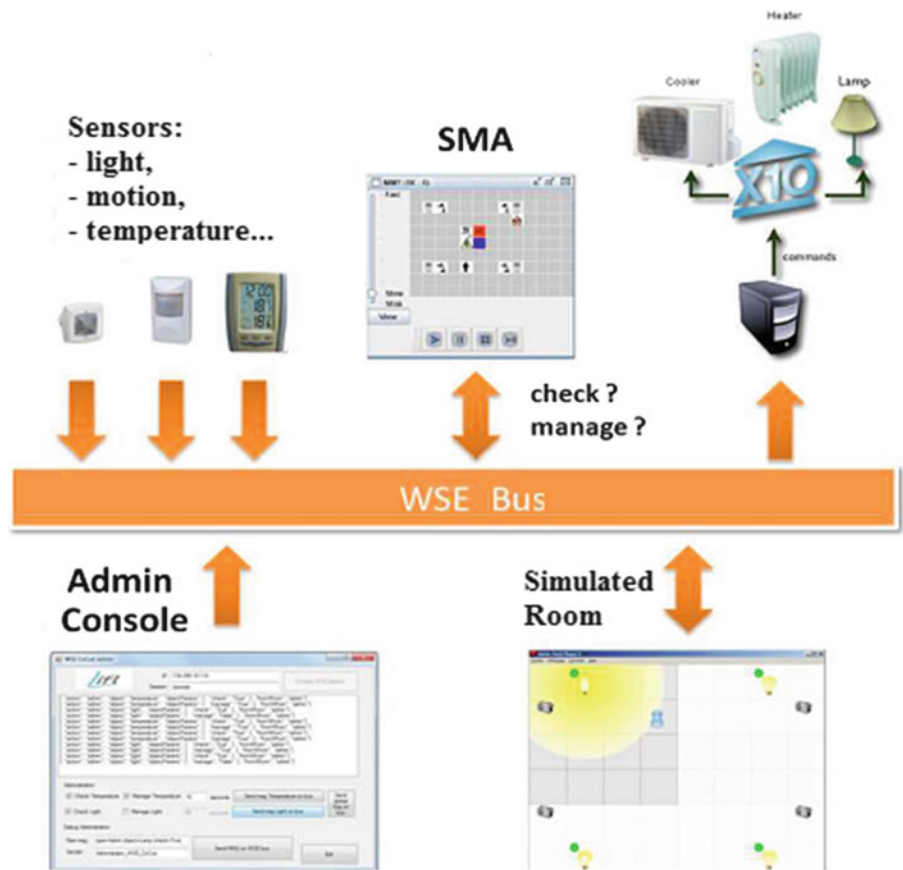
Fig. 41.4 The MAHAS structure for energy management

Home Automation System Controlling Energy

System Architecture

The objective of this work is to design a HASCE based on multi-agent approach for managing multiple modalities such as temperature, light . . . in a smart building. Indeed, the platform is constituted of an IB supplied with various sources of energy (solar, wind, and the network), light sensors placed inside and outdoors of the building, presence and temperature sensors and a switch for selecting the mode of operation (automatic or manual). The proposed interface will allow according to the input modalities to toggle between renewable energy sources and the network switch on or off the light, start or stop the air conditioner and heater, and raise or lower the roller shutters.

Fig. 41.5 illustrates the general aspect of our multimodal multi-agent architecture. Modalities ensure the communication between the environment and the IB, while SMA's role is to merge data from the sensors of the input modalities to control the actuators. Th\is merger will ensure occupant comfort and better control of the energy produced and consumed.

Modeling Architecture by Timed Petri Nets

Introduced by Carl Adam Petri in his thesis, timed petri nets (TPN) are very suitable models for representing parallel processes. They are at once a mathematical and a graphical language for modeling complex systems [15]. The most appropriate formalism tool for modeling multimodal network is timed colored Petri nets (TCPN) [16] because it can:
(a) Let us assume the temporal parameters
(b) Take into account the dynamic aspects of a dialogue
(c) Represent the data exchanged in a dialogue as well as media and data structures
(d) Have a distributed representation, graphical and hierarchical
(e) Allow agents to communicate easily with the same semantics
   The combination of SMA and TCPN will allow us to model a multimodal system through the interaction between agents. Figure 41.6 illustrates the architecture of the proposed system, it consists of four agents:
• Switch energy sources agent
• Light comfort agent
• Thermal comfort agent
• Inhabitants agent
   In order to validate the proposed multi-agent-based network petri multimodal platform, we build a model using CPN Tools software, each agent is modeled by a TCPN.

CPN Tools Software

CPN Tools is a graph editor and simulator TCPN stochastic. Developed at the University of Aarhus (Denmark), it is based on direct manipulation of menus and dialog boxes. It can produce networks with more than a thousand structured places, transitions, and arrows into a hundred modules or more. Also CPN Tools allows multiple subnets in the same window and
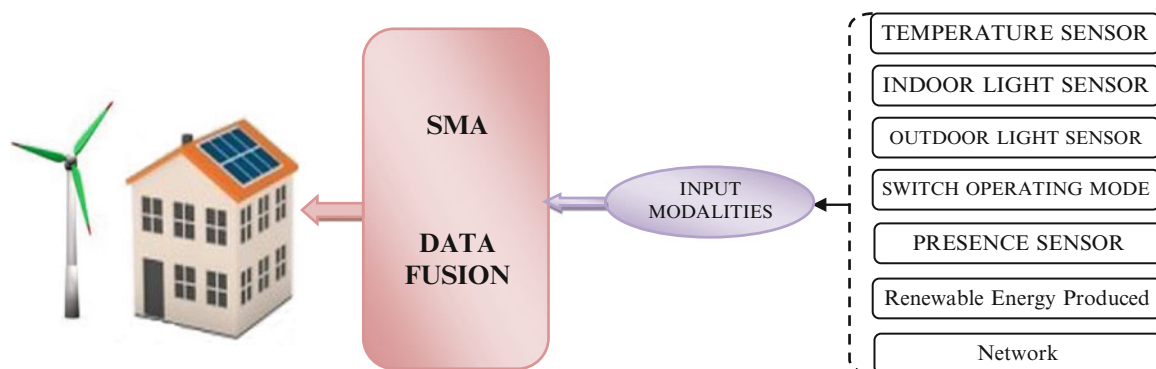
Fig. 41.5 The multimodal software architecture

Fig. 41.6 Architecture
of the proposed SMA
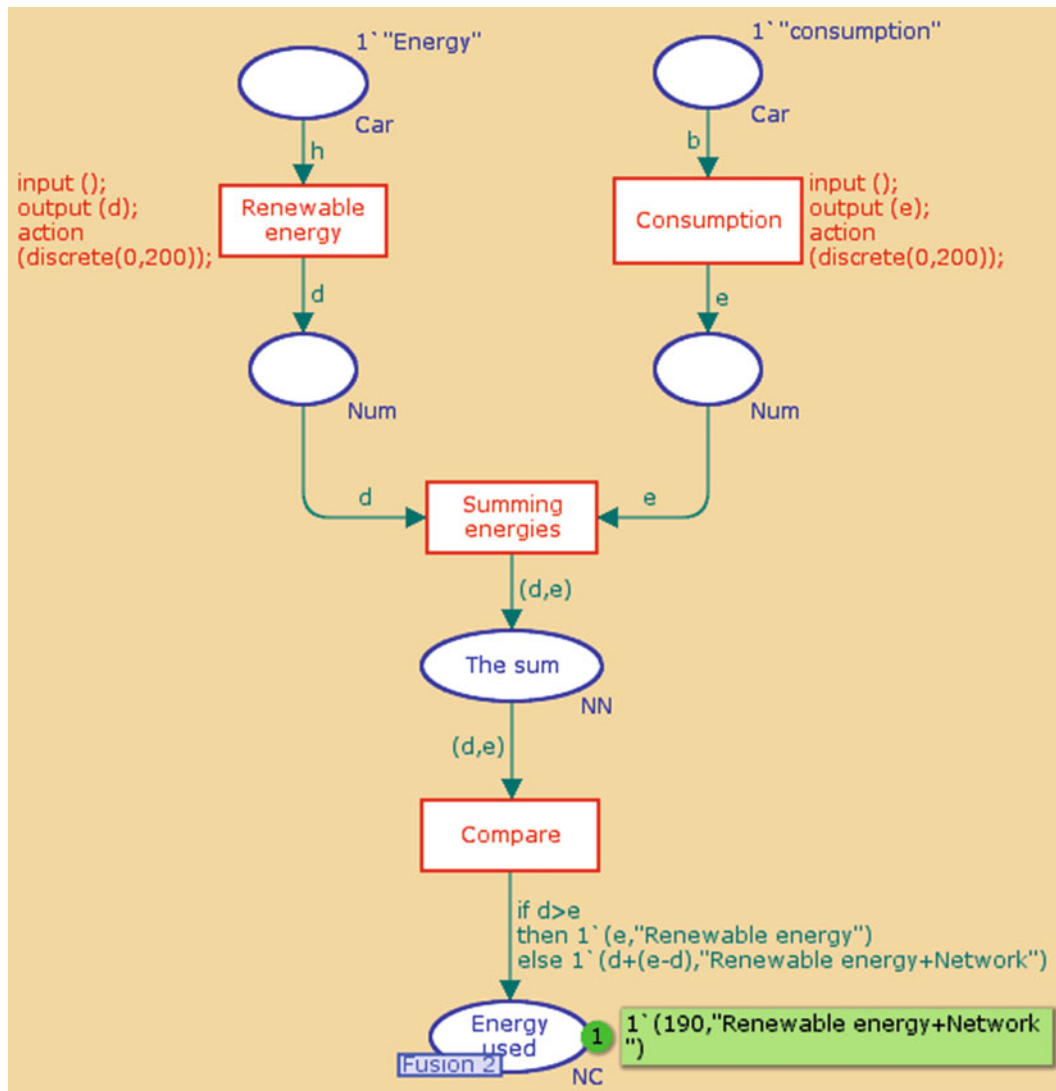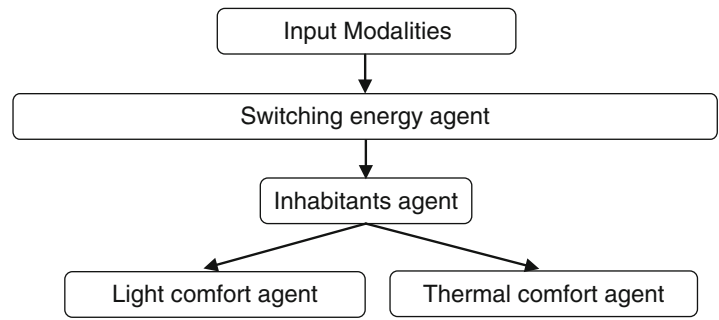
Fig. 41.7 Switching energy agent

have a link between them, with the possibility of spatially distributed places. Therefore, this feature can be used to produce structures of multi-agent systems by representing each agent separately and make a connection between them. The CPN Tools license can be obtained free of charge, also for commercial use [17].

(a) Switching energy agent

The switching energy agent (Fig. 41.7) represents the binding between the network and the IB. Considering consumer demand and the amount of energy supplied by renewable sources; if production exceeds the estimated consumer
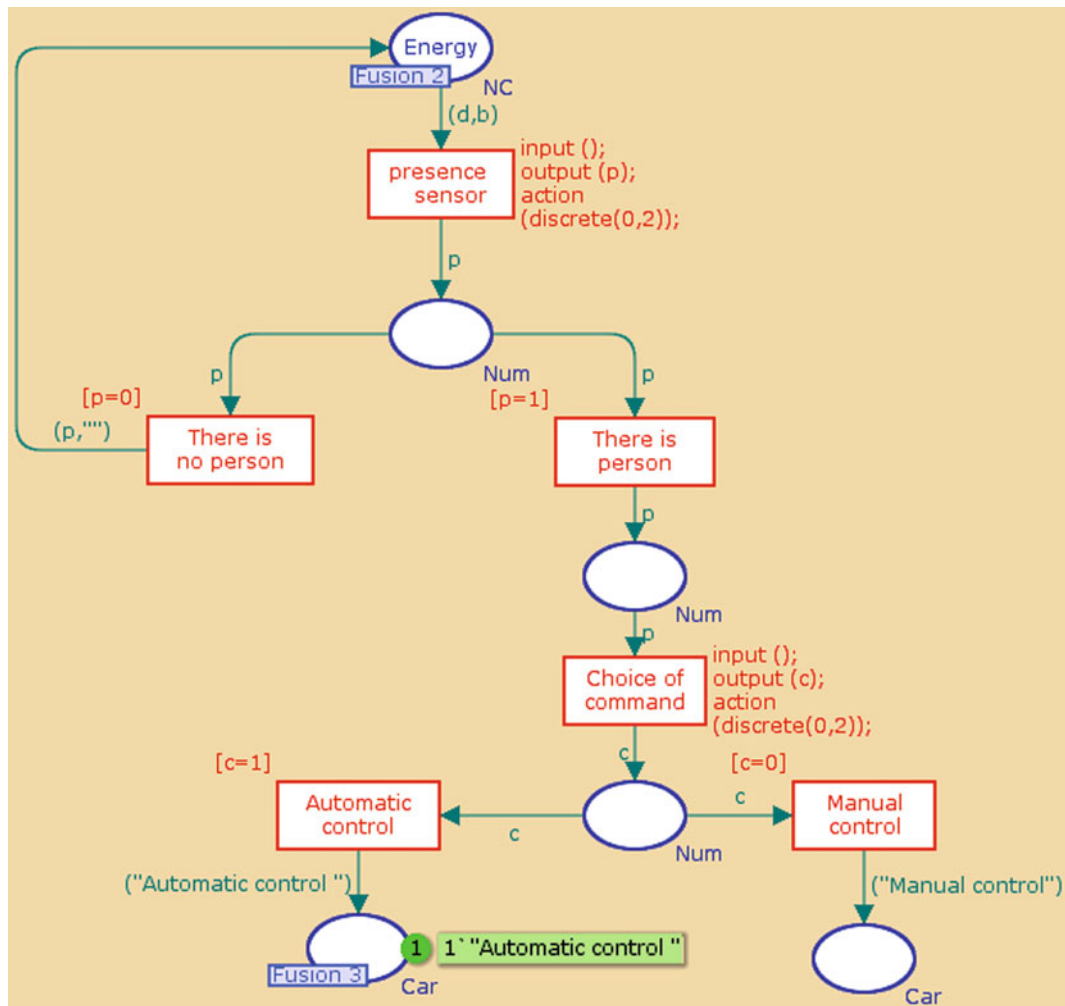
Fig. 41.8 Inhabitants agent

demand, switching agent disconnects IB from the network to power it by renewable energies. Otherwise, if production is less than consumption estimated demand or there are disruptions in the production of renewable energies, the switching agent requests relief to the network.

(b) Inhabitants agent

Inhabitants agent has two functions: people detection in the IB and the choice of the operating mode of the platform. Indeed, this function gives them the hand to switch to automatic mode if they want that HASCE pilots the IB, or they put the switch in the Manual position if they prefer control the actuators themselves. These two functions of the inhabitants agent operate in all other agents except the switching energy agent. The inhabitants agent modeling is shown in Fig. 41.8.

(c) Light comfort agent

In the case where the presence detector sends information that there's a person in the IB, taking into account the choice of the operating mode transmitted by agent population, Light comfort agent modeled (Fig. 41.9) ensures a graduated ignition and raising or lowering shutters depending on the time and intensity of the light detected by the light sensors placed respectively inside and outside the building.

(d) Thermal comfort agent

The actuation of air-conditioner and heater is ensured by the thermal comfort agent (Fig. 41.10). The agent acts according to the temperature value sent by the sensor. Considering that the ambient temperature is between 18 and 22°, the agent regulates temperature to 19° by actuating either heater or air-conditioner if temperature is below or above ambient temperature. If the temperature is within the ambient temperature interval, the agent does nothing.
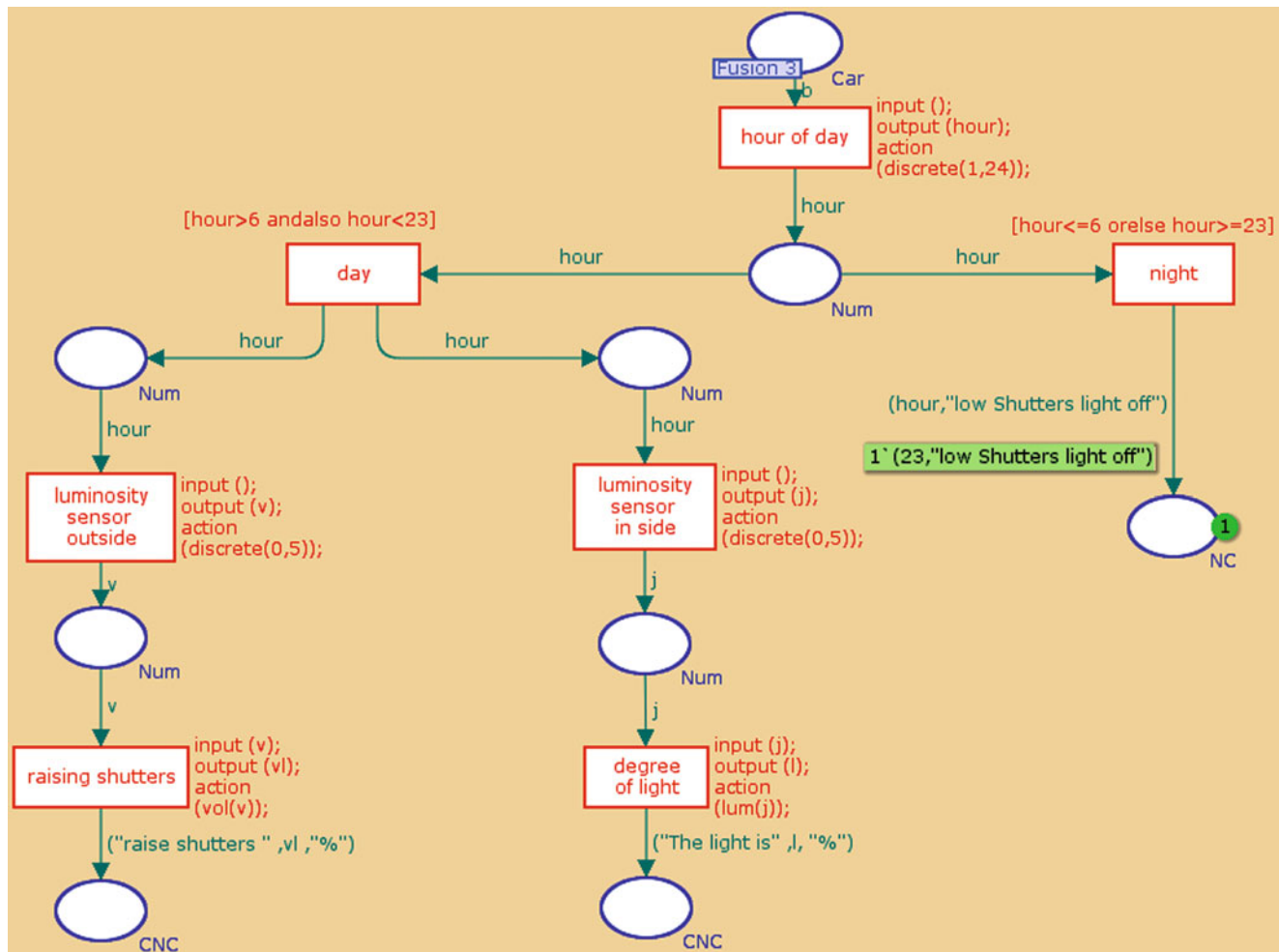
Fig. 41.9 Light comfort agent

Results and Discussion

In this section, we present first an illustrative simulation example for HASCE on CPN Tools which allows us to generate random values for the simulation, indicate the different states of each agent and display the results in comments (in green rectangles) as shown in Figs. 41.7, 41.8, 41.9, and 41.10. Then, to validate our results, we plotted system outputs by recovering 50 samples of random value modalities to visualize and simulate the behavior of the proposed SMA.

Simulation Results on CPN Tools

Indeed, as shown in Fig. 41.7, the switching energy agent perceives that energy demand is greater than the amount of renewable energy produced, so it requests relief to the network (see comment in figure).

In Fig. 41.8, the values generated randomly give that the selected mode is automatic and the presence sensor has detected the presence of a person in the intelligent building (IB). So, it sends the information to the thermal and light agents. If the inhabitant switches to the manual operating mode of HASCE, the switching energy agent still operational.

Light comfort agent acts according to the random values provided by the modeled outdoor and indoor light sensors in CPN Tools. In our example (Fig. 41.9), the shutters are down with 40 % while the graduated lamp lights by 20 %.

Thermal comfort agent is able to maintain ambient temperature in the IB. In Fig. 41.10, it detects that the temperature is equal to16°; then it turns on the heater for regulating temperature by adding 3° to achieve ambient temperature.
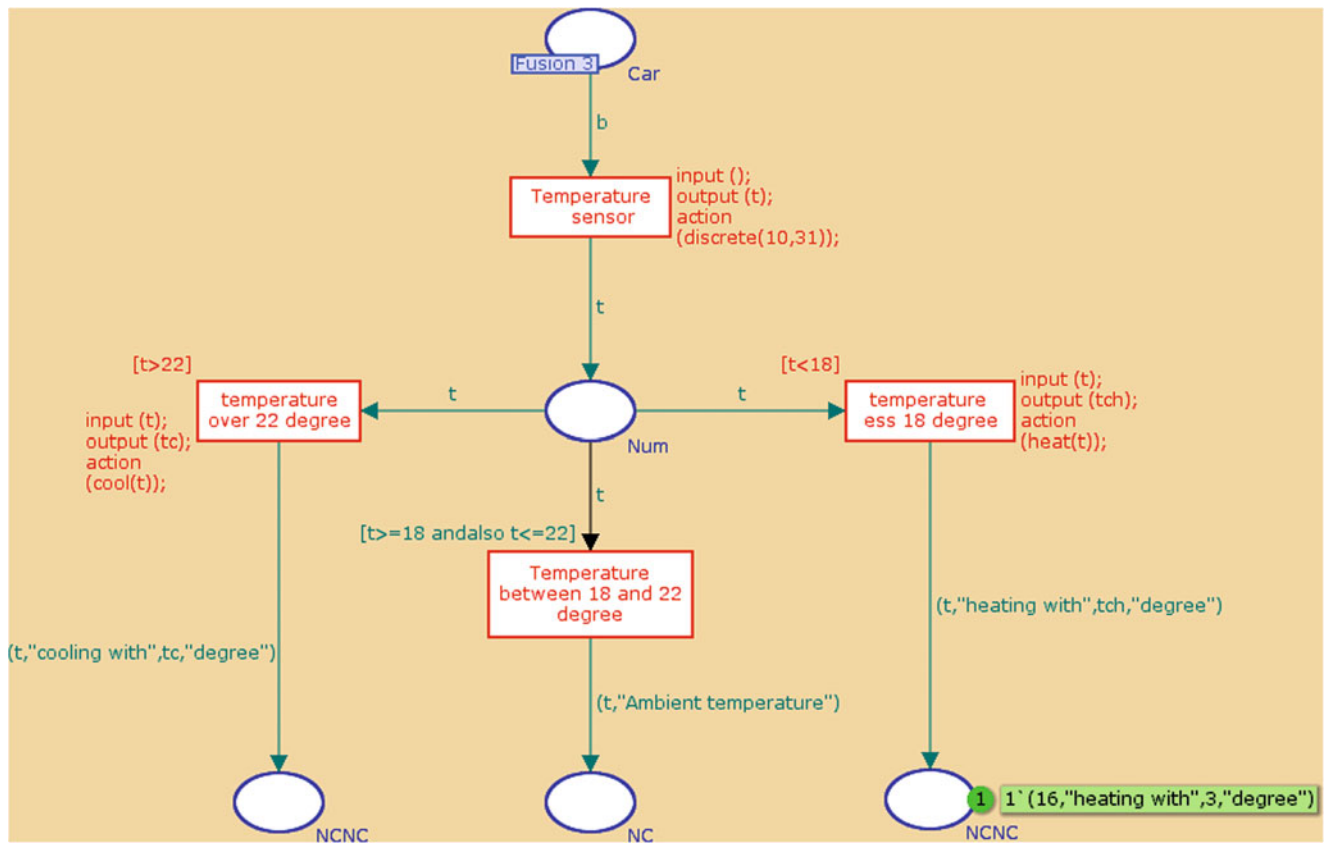
Fig. 41.10 Thermal comfort agent

Results Validation on Matlab

The Fig. 41.11 shows us 50 samples of input modalities and their respective system responses. We note for example sample 1 (indicated by a dash-dotted line in Fig. 41.11), manual operating mode is selected, thermal and light comfort agents are off service. In the second example at the sample 11, automatic operating mode is selected. The temperature is 22°, the thermal comfort agent actuates neither heater nor air-conditioner since temperature is ambient; while the lighting comfort agent downs the shutters and the graduated lamp lights by 100 % at 1 pm.

After checking all the samples, we can conclude that the system responds correctly based on criteria established in the beginning of our work. The proposed architecture displays the appropriate command considering the input modalities for better energy management in IB.

Conclusion

This paper has presented the principles of a proposed HASCE, which allows the agents to cooperate and coordinate their actions in order to find an acceptable near-optimal solution for power management. We showed why autonomous and cooperative agents are particularly well suited for power management in buildings. In our structure, we used four agents: switch energy sources agent, light comfort agent, temperature comfort agent, and inhabitant agent. A cooperation mechanism that reduces the problem complexity has been detailed.

The validation of the proposed structure is done using CPN Tools and Matlab. We used the TCPN for modeling the proposed agents and simulating the proposed structure. The obtained results show the good correlation between inputs and outputs of the system. Indeed, the proposed multimodal multi-agent architecture model acts with the expected behavior. Therefore, we can say that the results validate the proposed approach.
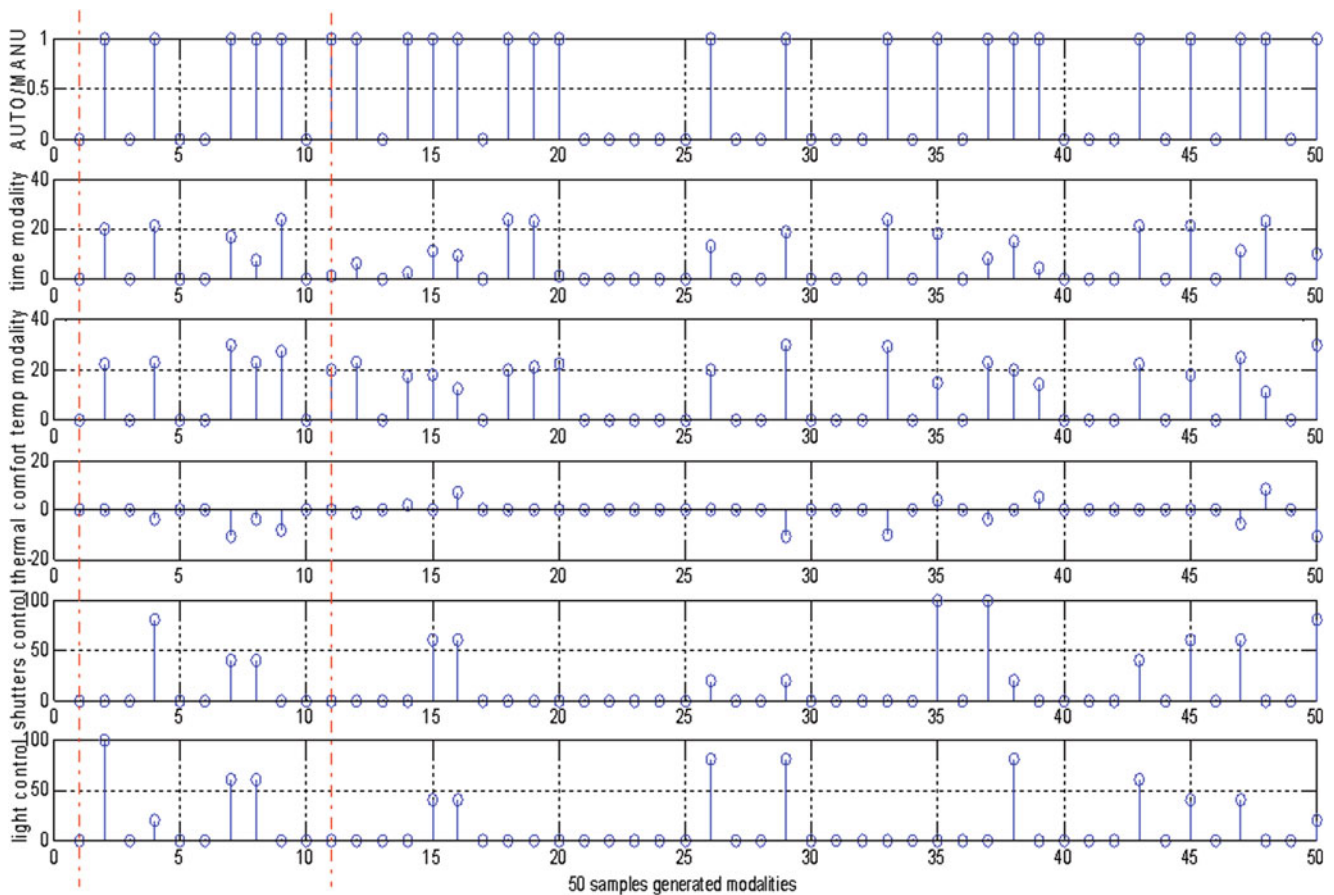
Fig. 41.11 Graphical representation of results

Subscripts

| IB | Intelligent building | TCPN | Timed colored Petri nets |
| TPN | Timed Petri nets | HASCE | Home automation system controlling energy |

References

1. Pérez-Lombard L, Ortiz J, Pout C (2008) A review on buildings energy consumption information. Energy Buildings 40(3):394–398
2. APRUE (2010) Bilan de la consommation énergie finale en Algérie. Agence de promotion et de rationalisation de l'utilisation de l'énergie, affiliée au ministère de l'énergie et des mines
3. De Silva LC, Morikawa C, Petra IM (2012) State of the art of smart homes. Eng Appl Artif Intel 25:1313–1321
4. Sierra E, Hossian A, Rodríguez D, García-Martínez M, Britos P, García-Martínez R (2008) Optimizing building's environments performance using intelligent systems. New Front Appl Artif Intell Lect Notes Comput Sci 5027:486–491
5. Missaoui Badreddine R (2012) Gestion Énergétique optimisée pour un bâtiment intelligent multi-sources multi-charges: différents principes de validations. Thèse de Doctorat—Laboratoire de Génie Électrique de Grenoble (G2eLab)—Ecole Doctorale 'Electronique, Electrotechnique, Automatique et Traitement de Signal' EEATS
6. Wong JKW, Li H, Wang SW (2005) Intelligent building research: a review. Autom Constr 14:143–159
7. Wigginton M, Harris J (2002) Intelligent skins. Intelligent building research. Architectural Press, Oxford, pp 52–175
8. http://www.smartgrids-cre.fr/index.php?rubrique=dossiers&srub=batiment&action=imprimer
9. Dujardin T, Rouillard J, Jean-Christophe R, Jean-Claude T (2011) Gestion intelligente d'un contexte domotique par un Système Multi-Agents. In: Actes Journées Francophones sur les Systèmes Multi-Agents, France
10. Clarke G, Sharples S, Callaghan V (1999) A multi-agent architecture for intelligent building sensing and control. Int Sens Rev J 19(2):135–140
11. Abras S (2009) Système domotique Multi-Agents pour la gestion de l'énergie dans l'habitat. Thèse de doctorat. Laboratoire d'Informatique de Grenoble—Imag. Ecole doctorale Mathématiques, Sciences et Technologies de l'Information, Informatique (MSTII)—Grenoble INP

12. Wang Z, Yang R, Wang L (2010) Multi-agent control system with intelligent optimization for smart and energy-efficient buildings. In: 36th Annual conference on IEEE industrial electronics society
13. Wang L, Wang Z, Yang R (2012) Intelligent multiagent control system for energy and comfort management in smart and sustainable buildings. IEEE Trans Smart Grid 3(2):605–617
14. Duan J, Indin FL (2008) Research of intelligent building control using an agent-based approach. In: The IEEE international conference on industrial informatics DCC, Daejeon
15. Boussier J-M (2007) Modélisation de comportements dans les systèmes dynamiques : Application à l'organisation et à la régulation de stationnement et de déplacement dans les Systèmes de Trafic Urbain. Thèse de doctorat—Laboratoire Informatique, image et Interaction de La Rochelle—Ecole Doctorale ED 0374
16. Djaid NT (2011) Architectures et modèles dynamiques dédiées aux applications multimodales pour renforcer l'interaction du robot-Mémoire de Magister en Electronique Spécialité contrôle de processus et robotique, USTHB
17. Djaid NT, Saadia N, Ramdane-Cherif A (2012) Multimodal architecture to strengthen the interaction of the robot in ambient intelligence environments. Multi-disciplinary workshop on smart gadgets meet ubiquitous and social robots on the Web (UbiRobs). In: 14th ACM international conference on ubiquitous, computing, Pittsburgh, PA

Quantum Dots Conjugated *E. coli* Living Cells as Fluorescent Reporters to Detect Cytotoxicity of Chemicals

Raghuraj Singh Chouhan, Javed H. Niazi, and Anjum Qureshi

Abstract

Quantum dots (QDs) have attracted much of research interest in recent years for imaging, diagnostics, and therapy due to their unique optical properties, such as broad excitation spectra and long fluorescence stability. In this study, a controlled bioconjugation using CdTe QDs with gram negative *E. coli* cells was performed to develop QD-*E. coli* bioconjugates. These bioconjugates were used as whole cell living baits to determine cytotoxicity of model toxic chemicals, such as oxidative stress inducer (H_2O_2) and a pesticide (methyl viologen or paraquat). These chemicals over a wide concentration ranges were exposed to QD-*E. coli* bioconjugates that interacted with cells and the real time fluorescence responses, with QD-*E. coli* bioconjugates, were analyzed. The results showed that the fluorescent ability of QD-*E. coli* bioconjugates tend to diminish with increasing concentration of toxic chemicals. This stress is attributed to the damages occurred as a result of interaction of toxic chemicals to the cell-wall or membrane of cells that resulted in the loss of fluorescence signal. This loss in the fluorescence (signal off phenomena) of QD-*E. coli* bioconjugates can be used as probes to develop a variety of fluorescence-based detection kits for the rapid determination of toxic drugs or food sample testing.

Keywords

E. coli • Cytotoxicity • Quantum dots • Bioconjugate • Fluorescence

Introduction

The properties and applications of fluorescent semiconductor nanocrystals stand among the most exciting research fields in chemistry, physics, and biology [1]. Quantum dots (QDs) have several advantages over traditional fluorescent dyes such as stronger luminescence, better photo-stability against bleaching and physical environments, such as pH, temperature, and optical tunability. These properties have been used in immunoassays, molecular imaging, and in vivo biological labels [2]. Optically quenched QDs have recently gained tremendous interest in environmental applications [3]. Simple assays such as by-direct visualization of luminescence from the living cells decorated with quantum dots (QDs) as labeling probes can be used as whole cell living baits. The water soluble quantum dots (QDs) are nontoxic because the polymer coatings make them a better alternative as labeling probes in biological and biomedical applications. Until now, QDs as labeling probes have been successfully used in fluorescent resonance energy transfer (FRET) [4], in vitro and in vivo imaging [5, 6], immunoassay [7, 8] and DNA hybridization [9]. Hence, bioconjugation of QDs is of great importance in developing whole-cell based biosensors.

Carboxylated QDs can be successfully conjugated to the secondary amines on biomolecules, such as proteins, enzymes, or antibodies. This linking approach is simple and rapid that has been widely used in certain biosystems. Conjugation efficiencies of QDs-biomolecules can be improved by chemically modifying surface charge states of biomolecules

R.S. Chouhan • J.H. Niazi (✉) • A. Qureshi (✉)
Sabanci University Nanotechnology Research and Application Center, Orta Mahalle, Tuzla, Istanbul, Turkey
e-mail: raghuraj@sabanciuniv.edu; javed@sabanciuniv.edu; anjum@sabanciuniv.edu

(e.g., proteins) as well as QDs surfaces [10, 11]. Repulsion of QDs and biomolecules is likely to occur mainly in proteins/whole-cells, which may prevent their conjugation processes. In such cases, a high ionic strength or higher concentration of proteins/cells can be used for conjugation, which may be accompanied by partly quenching of QDs' luminescence intensity [12].

In the present work, we have covalently attached QDs on the surface of living *E. coli* cells to give rise to QD-*E. coli* bioconjugates. These bioconjugates were used as a new molecular tool for probing cellular damages induced by model test chemicals. It required labeling of cells in order to probe their responses against the model test chemicals in the form of detectable signals. Labeling of cells was done by nontoxic chromogenic water-soluble, capped QDs that emit light or attain fluorescent abilities while cells are active and viable as well as retain their cellular integrity. This enabled monitoring the cellular interaction and behavior of cells when exposed to external perturbations, such as nanomaterials, environmental contaminants, food toxins that also find application in medical diagnostics.

Our results demonstrated that the fluorescence signal diminished in a concentration-dependent manner with known toxic chemicals, such as H_2O_2 and paraquat, which is an oxidative stressor and a pesticide, respectively. The developed method demonstrated the ability to evaluate the cellular integrity in terms of fluorescent signal generated from QDs localized on the cell-surfaces against exposure of different toxic chemicals. Thus, it was possible to probe the cellular damages occurred by the interaction of toxic chemicals using QD-*E. coli* bioconjugates developed in this study.

Materials and Methods

Chemical and Reagents

Wild-type *E. coli* DH5α strain was used as a model living bacterial cells in this study. Luria-Bertani broth (LB-broth) and Luria-Bertani agar (LB-agar) were obtained from Difco (MI, USA). *N*-hydroxysuccinimide (NHS) and *N*-ethyl-*N*′-(3-(dimethylamino) propyl) carbodiimide (EDC), Paraquat and H_2O_2 were purchased from Sigma-Aldrich. Triton-X 100 was procured from Merk, Germany. A 10-mM Phosphate Buffer Saline (PBS), pH-7.4 used in this study was prepared from a $10\times$ stock solution accordingly and prepared with deionized water (Milli Q, Millipore, Barnstead, CA, USA). Qdot® 585 carboxyl quantum dots (Invitrogen) were used as labeling probes having emission maxima at ~585 nm.

All glasswares and solutions used in these studies prior to experiment were autoclaved with HMC, Hirayama, Che Scientific Co., Hong Kong. All bioconjugation studies and related work were carried out under sterile conditions using Thermo scientific HERAsafe® KS microbiological safety cabinet. The spectral studies of QD-*E. coli* bioconjugate with Paraquat and H_2O_2 were done in a range 500–750 nm using advanced NanoDrop 3300 Fluorospectrometer (Thermo Scientific NanoDrop Products). All other reagents used were of analytical grade.

Preparation of *E. coli* Culture

Lyophilized cells of *E. coli* DH5α were precultured in LB-broth at 37 °C for 15 h and then the cells were harvested by centrifugation at 3,000 rpm for 5 min at 4 °C. The cells were subsequently washed thrice with sterile PBS followed by centrifugation for 5 min at 3,000 rpm at 4 °C. The cell pellet was resuspended in PBS and CFU were measured by serial dilution followed by plating on LB-agar plates. The cell-suspension was divided into several aliquots carrying same number of cells (~10^9 CFU/mL) for test and control experiments.

Bioconjugation of *E. coli* with QDs

Bioconjugation of *E. coli* with QD was successfully conjugated and detailed studies were done in our laboratory. Briefly, 50-mM EDC and 5-mM NHS were incubated for 5 min at 25 °C. This mixture was quickly added with 2 μL of 8 μM QD solution and the entire reaction mixture was again incubated at 25 °C for 15 min. under constant shaking at 110 rpm. The QD-conjugated cell-suspension (QD-*E. coli* bioconjugates) was centrifuged at 1,500 rpm for 3 min and the supernatant was carefully removed and washed the pellet thrice after resuspending in PBS, pH 7.4 followed by centrifugation with same buffer and stored at 4 °C until further use.

Viability Tests of Cells Before and After Treatment

About 25 μL of cell suspension from all the sample tubes (control and chemical treated samples) were spread on Luria-Bertani (LB) agar plates. CFU originating from a single living cell was counted. Images of plates with visible colonies were captured for comparison.

Results and Discussion

Response of Bioconjugates Against H_2O_2

Wild-type *E. coli* (DH5α) cells were covalently conjugated with carboxyl-QDs by EDC/NHS coupling. The QD-*E. coli* bioconjugates generated exhibited a characteristic fluorescent emission peak at 585 nm, which was derived from the cell-bound QDs (Fig. 42.1). The covalent coupling strategy was employed to immobilize QDs on the surface of the cells without affecting the cellular integrity or viability.

H_2O_2 generates hydroxyl radical ($^{\cdot}OH$) that induces oxidative toxicity in all living cells. The cellular damage or toxicity that occurred in the QD-*E. coli* bioconjugates was studied by exposing H_2O_2 and paraquat as model toxic chemicals that induce generation of $^{\cdot}OH$ and $^{\cdot}O_2^-$, respectively in cells. The cytotoxic effects of these model chemicals on QD-*E. coli* bioconjugate were determined using change in fluorescence emission spectra. The effect of various concentrations (0.5–5 mM) of these chemicals on cells was studied through changes in fluorescent characteristics of bioconjugates. Treatment of bioconjugates with initial 0.5 mM H_2O_2 concentration resulted in diminishing response of their characteristic fluorescent peak at 585 nm (Fig. 42.1). At above 0.5 mM concentrations of H_2O_2, the fluorescent peak was completely disappeared due to severe cellular toxicity. These results showed that higher concentrations of H_2O_2 severely affected the cellular integrity of *E. coli* cells as a result of change in cellular integrity of QD-*E. coli* cells and therefore, the fluorescence signal was diminished.

Response of Bioconjugates Against Methyl Viologen (Paraquat)

Paraquat is a pesticide chemical that generates superoxide radicals ($^{\cdot}O_2^-$) that are toxic to living cells. The cellular damage that occurs to cells with paraquat was studied by exposing with three different concentrations (0.5–5 mM) of paraquat (Fig. 42.2).
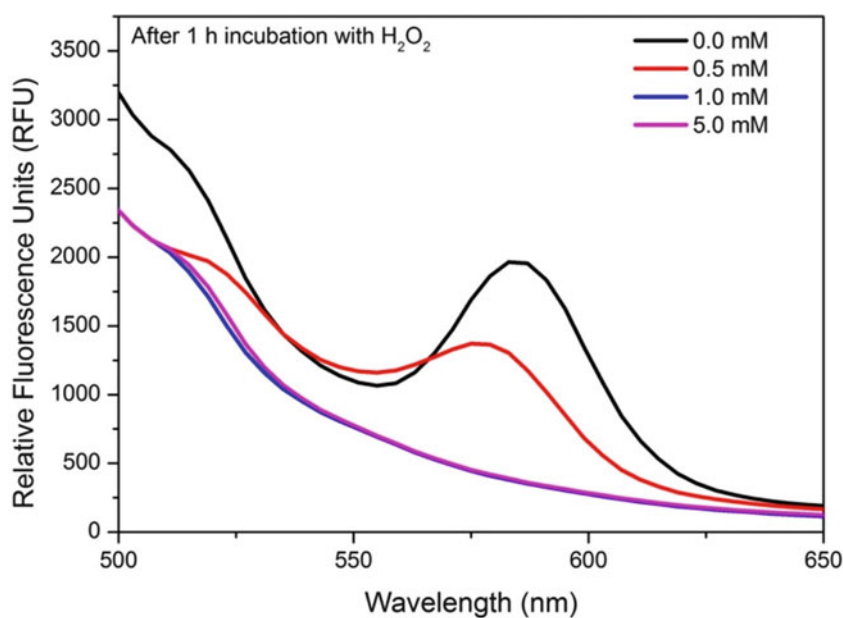
Fig. 42.1 Fluorescence emission spectra of QD-*E. coli* bioconjugates with or without H_2O_2 incubation showing complete disappearance of fluorescence emission. The fluorescent spectra shown in *black* was obtained against PBS as the blank

Fig. 42.2 Fluorescence emission spectra of QD-*E. coli* bioconjugates with or without paraquat incubation showing diminishing of fluorescence emission. The fluorescent spectra shown in *black* was obtained against PBS as the blank
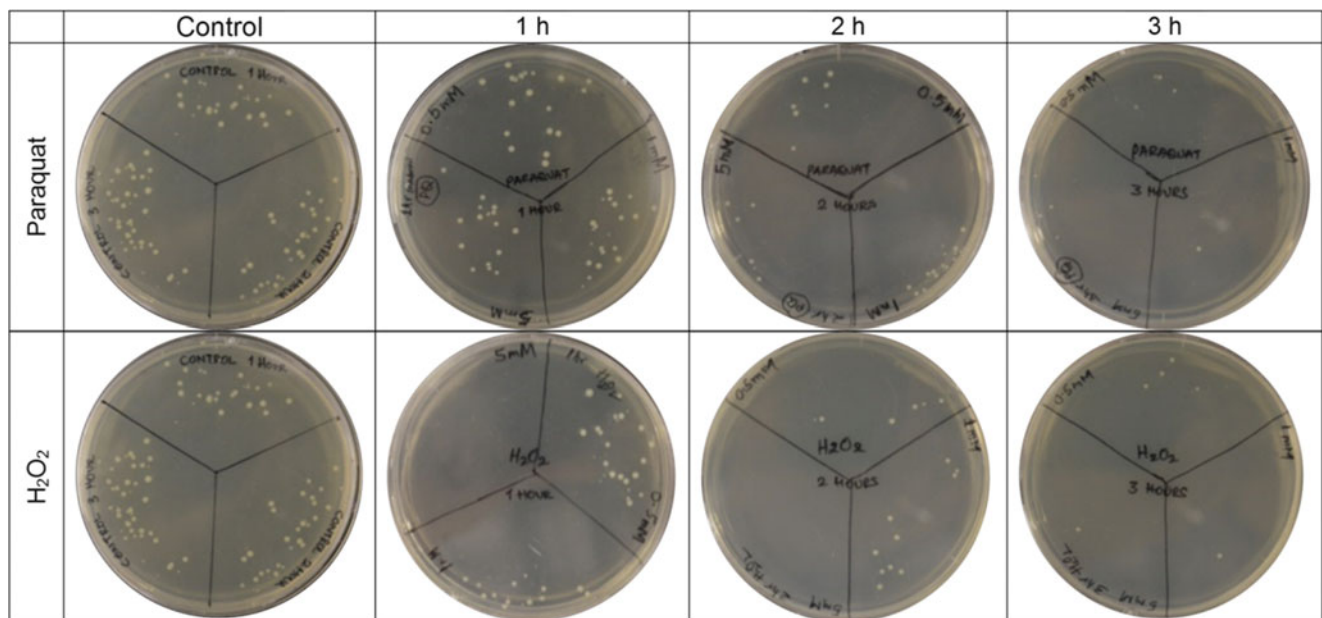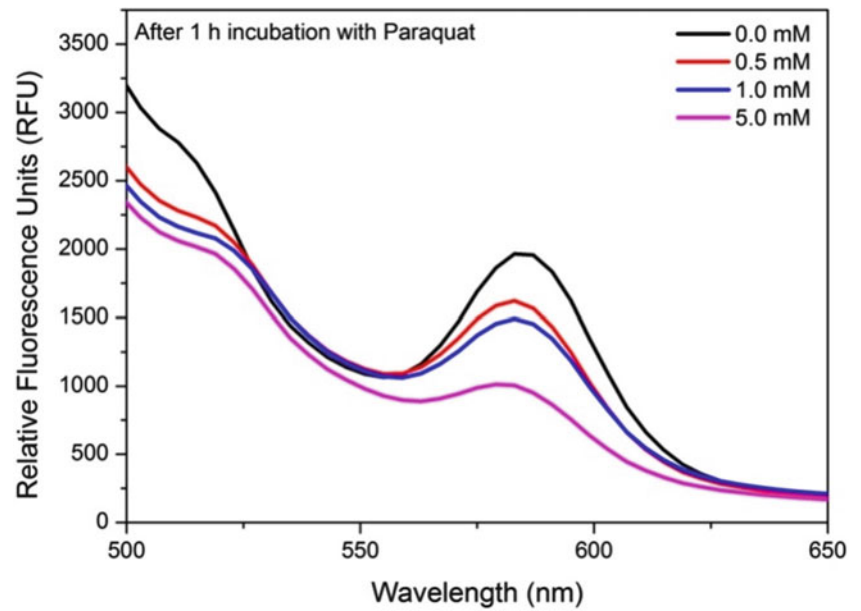
Fig. 42.3 Control and test QD-*E. coli* bioconjugate cells exposed to paraquat and H_2O_2 at different time intervals were plated on LB-agar plates. The figure shows colonies of living cells in control and test samples that formed visible colonies. Those cells that severely affected by the chemical fail to grow or form colonies

It was observed that the fluorescence emission at 585 nm gradually decreased with increasing concentration of paraquat (Fig. 42.2). Exposure of above 1 mM concentration of paraquat, the fluorescence signal dramatically dropped suggesting that the cells severely affected with paraquat above 1 mM concentration. Paraquat, however, did not have detrimental effects on cellular structure at 2 h initial exposure with lower concentrations. Elevated levels of PQ however showed destructive effects because of the significant loss of fluorescence from bioconjugates with extended incubation (3 h). The above results were also supported by the results of viability tests where H_2O_2 severely damaged the cells and therefore cells tend to lose their viability right at the initial stages compared to PQ (Fig. 42.3). The colonies of living cells in control and test samples that formed visible colonies suggest that the bioconjugated cells tend to lose their viability with increasing time of chemical exposure (from left to right in Fig. 42.3) consistent to the results of fluorescence emission measurements (Figs. 42.1 and 42.2).

Conclusions

In this work, QD-*E. coli* bioconjugate was developed to probe the cellular damages caused by model toxic chemicals, such as H_2O_2 and paraquat. To probe the cellular damages or toxic effects of model chemicals, optical properties of QD were utilized through labeling the living *E. coli* cells, which provided the cellular damage information in the form of diminishing fluorescence emission responses. The results demonstrated that the fluorescent ability of these bioconjugates diminishes if the toxic chemicals interacted with QD-*E. coli* conjugates. The strategy reported in this study may be useful for creating a novel methodology for investigating cellular interactions with toxic chemicals to determine their cytotoxicity. Our results demonstrated that QD-conjugated cells served as an important tool to monitoring the impact of chemicals has on cells. This method is robust, rapid, and easy to use that finds applicable in environmental and biomedical applications. The QD-*E. coli* bioconjugate can be directly applied in microenvironments while the strategy opens opportunities for a new class of biological and biomedical applications with high biocompatibility and biorecognition ability, offering a timeline interface between fluoro-nanosensor and biological worlds.

References

1. Stinaff EA, Scheibner M, Bracker AS, Ponomarev IV, Korenev VL, Ware ME, Doty M, Reinecke FTL, Gammon D (2006) Optical signature of coupled quantum dots. Science 311:636–639
2. So MK, Xu C, Loening AM, Gambhir SS, Rao J (2006) Self-illuminating quantum dot conjugates for in vivo imaging. Nat Biotechnol 24:339–343
3. Donald S, Marcus J, Garry R, Pingrong Y, Jovan N, Sean S (2005) Quenching of semiconductor quantum dot photoluminescence by a π-conjugated polymer. J Phys Chem B 109:15927–15932
4. Li YQ, Wang JH, Zhang HL, Yang J, Guan LY, Chen H, Luo QM, Zhao YD (2010) High-sensitivity quantum dot-based fluorescence resonance energy transfer bioanalysis by capillary electrophoresis. Biosens Bioelectron 25(6):1283–1289
5. Bae PK, Kim KN, Lee SJ, Chang HJ, Lee CK, Park JK (2009) The modification of quantum dot probes used for the targeted imaging of his-tagged fusion proteins. Biomaterials 30(5):836–842
6. He Y, Su YY, Yang XB, Kang ZH, Xu TT, Zhang RQ, Fan CH, Lee ST (2009) Photo and pH stable, highly-luminescent silicon nanospheres and their bioconjugates for immunofluorescent cell imaging. J Am Chem Soc 131(12):4434–4438
7. Chen LP, Sheng ZH, Zhang AD, Guo XB, Li JK, Han HY, Jin ML (2010) Quantum-dots-based fluoroimmunoassay for the rapid and sensitive detection of avian influenza virus subtype H5N1. Luminescence 25(6):419–423
8. Jokerst JV, Raamanathan A, Christodoulides N, Floriano PN, Pollard AA, Simmons GW, Wong J, Gage C, Furmaga WB, Redding SW, McDevitt JT (2009) Nano-bio-chips for high performance multiplexed protein detection: determinations of cancer biomarkers in serum and saliva using quantum dot bioconjugate labels. Biosens Bioelectron 24(12):3622–3629
9. Li YQ, Guan LY, Wang JH, Zhang HL, Chen J, Lin S, Chen W, Zhao YD (2011) Simultaneous detection of dual single-base mutations by capillary electrophoresis using quantum dot-molecular beacon probe. Biosens Bioelectron 26(5):2317–2322
10. Gerhards C, Schulz-Drost C, Sgobba V, Guldi DM (2008) Conjugating luminescent CdTe quantum dots with biomolecules. J Phys Chem B 112(46):14482–14491
11. Shakya AK, Sami H, Srivastava A, Kumar A (2010) Stability of responsive polymer-protein bioconjugates. Prog Polym Sci 35(4):459–486
12. Ren L, Jeung WY, Han HC, Choi HJ (2007) Optical activation of Si and Ge nanowires codoping with Er: Yb rare earth by sol-gel methods. J Nanoelectron Optoelectron 2(2):191–196

Mathematical Modeling of a Small Scale Compressed Air Energy Storage System

43

Muhsin Kiliç, Zeliha Kamiş Kocabiçak, Elif Erzan Topçu, and Mustafa Mutlu

Abstract

Using compressed air to store energy is one of the energy storage methods. In this study, a small scale compressed air energy storage (CAES) system is designed and modeled. The energy storage capacity of designed CAES system is about 2 kW. The system contains a hydraulic pump unit, expansion–compression liquid pistons, valves, a tank, and a control unit. The aim of the designed system is basically to store air under a defined pressure. The designed CAES system is modeled and simulated by MATLAB/Simulink program. Pressure changes in the tank and pistons are obtained. Besides, energy storage capacity of the system for different pressures is investigated in isothermal conditions.

Introduction

The development and use of renewable energy has shown a rapid growth over the past few years. In the next 20–30 years, all sustainable energy systems will have to be based on the rational use of traditional resources and greater use of renewable energy. Renewable energy sources are plentiful and conversion systems are becoming more and more affordable. Their significant contribution to sustainable energy use will however require considerable further development of storage methods. This will open up a new field of application, especially due to the growth of electrical production from renewable energy, along with decentralized production. Thus, the growth of this decentralized production means greater network load stability problems and requires energy storage.

There are various energy storage systems technologically. These systems are classified generally according to the technology, size of power, energy, and application area. Beside the high-capacity storage facilities based on hydro-power technologies, electrochemical solutions are the today's candidate to store for renewable energy sources. However, limited life-cycles and sustainability of batteries are often inhibiting factors. Compressed air technology is another renewable energy storage system which has many advantages. They can be summarized that air is available everywhere, compressed air can be stored for long time in a tank and pneumatic energy conversion doesn't produce waste or greenhouse emissions.

There are many studies in the literature on energy storage. Ibrahim et al. [1] comparatively investigated the basic characteristics and application areas of different energy storage techniques and analyzed to determine the most appropriate technique. Energy networks for the electrical energy storage systems are investigated by Kondoh et al. [2]. In this study, the characteristics of energy storage systems are examined and hydraulic, compressed air, secondary batteries, super-conducting magnets, flywheels

M. Kiliç (✉) • E.E. Topçu • M. Mutlu
Faculty of Engineering, Department of Mechanical Engineering, Uludağ University, Görükle, Bursa, Turkey
e-mail: mkilic@uludag.edu.tr; erzan@uludag.edu.tr; mustafamutlu@uludag.edu.tr

Z.K. Kocabiçak
Faculty of Engineering, Department of Automotive Engineering, Uludağ University, Görükle, Bursa, Turkey
e-mail: zkamis@uludag.edu.tr

or capacitors are investigated. Lund and Salgi [3] discussed the compressed air energy storage systems in their studies. Lund et al. [4] describe three different computer-aided methods to determine the optimal operating strategy for a given CAES device. Glendenning [5] examined long-term projections for compressed air storage systems. Denholm and Kulcinski [6] investigated greenhouse gas emissions of large-scale energy storage systems and the energy requirements for their life cycle. The use of compressed air energy storage systems working with wind energy was discussed in several studies [7, 8].

Grazzini and Milazzo [9] did thermodynamic analysis for a CAES system working under adiabatic condition. Baker [10] examined the developments in energy storage systems and worked on electrochemical, mechanical, and thermal energy storage systems. Milazzo [11] investigated CAES system with thermal energy storage (CAES-TES) for the compression stage. Using the second law of thermodynamics, thermodynamic analysis of a compressor unit is examined. Lemofouet and Rufer [12] study on a long-lasting, hybrid energy storage system based on compressed air energy. In the study, the general concept of the system, the power-electronic interface circuits, the maximum efficiency point tracking algorithm, and the output power strategy are described. In addition, the principles of energy storage system with hydro-pneumatic transducer are defined. Van de Ven and Li [13] are investigated liquid piston gas compression systems in detail.

In this study, a mathematical model is constructed for the designed small scale compressed air energy storage system and simulated by MATLAB/Simulink program. Pressure changes in pistons and the tank are investigated. It is assumed that air is compressed in isothermal conditions.

The Designed CAES System

The schematic view of the designed system is shown in Fig. 43.1. The system consists of two liquid pistons, four electro-pneumatic valves, a tank, a hydraulic pump, an electric motor, and a control unit basically.

In the system, the compression and expansion processes occur in reciprocating liquid piston working chambers. One liquid piston is sucking the atmospheric air while the other is sending the compressed air to the tank such as internal combustion engines. During this process, the tank pressure increases by sending the compressed air to the tank. The greater stored air in the tank means more pressure and also more energy. The amount of energy stored in the system can be improved by increasing tank pressure or tank volume.

The hydraulic pump is used to supply the flow of the liquid pistons and to set the working speed of the system. The speed of the system can be changed according to the liquid piston pressure and can be necessary to save time and to eliminate overheating. This working principle can be provided with the adjustment of the geometric displacement or speed of pump. Due to developments in electronic technology in recent years, obtaining variable flow rate by changing electric motor speed can be possible easily. In this system, a variable speed pump is selected to adjust the speed of liquid pistons and to direct hydraulic oil in both directions without using any directional control valves. Thus, partial energy loses arising from friction and throttle losses at the directional control valves are eliminated and energy recovery is increased.

The air flow in liquid pistons is controlled by electro-pneumatic valves. Two of them (B, C) are used to send the compressed air to tank, the others (A, D) are used to suck the atmospheric air. The valves are controlled by the computer control unit.

Mathematical Modeling of the System

In the designed system, the energy storage capacity of the designed CAES system is defined about 2 kW. Liquid piston diameter (D), length and dead length (L, L_{dead}) is determined, respectively, 0.2, 1.1 and 0.05 m. The air tank capacity (V_{tank}) is 0.5 m^3. The equations used in system design and modeling are given below.

Stored air energy per unit mass depending on the air pressure can be calculated from Eq. (43.1).

$$W = RT \ln \frac{P_{tank}}{P_{atm}} \tag{43.1}$$

Air mass stored in the tank can be calculated from ideal gas equation.

$$P_{tank} V_{tank} = mRT \tag{43.2}$$

Fig. 43.1 Designed CAES system
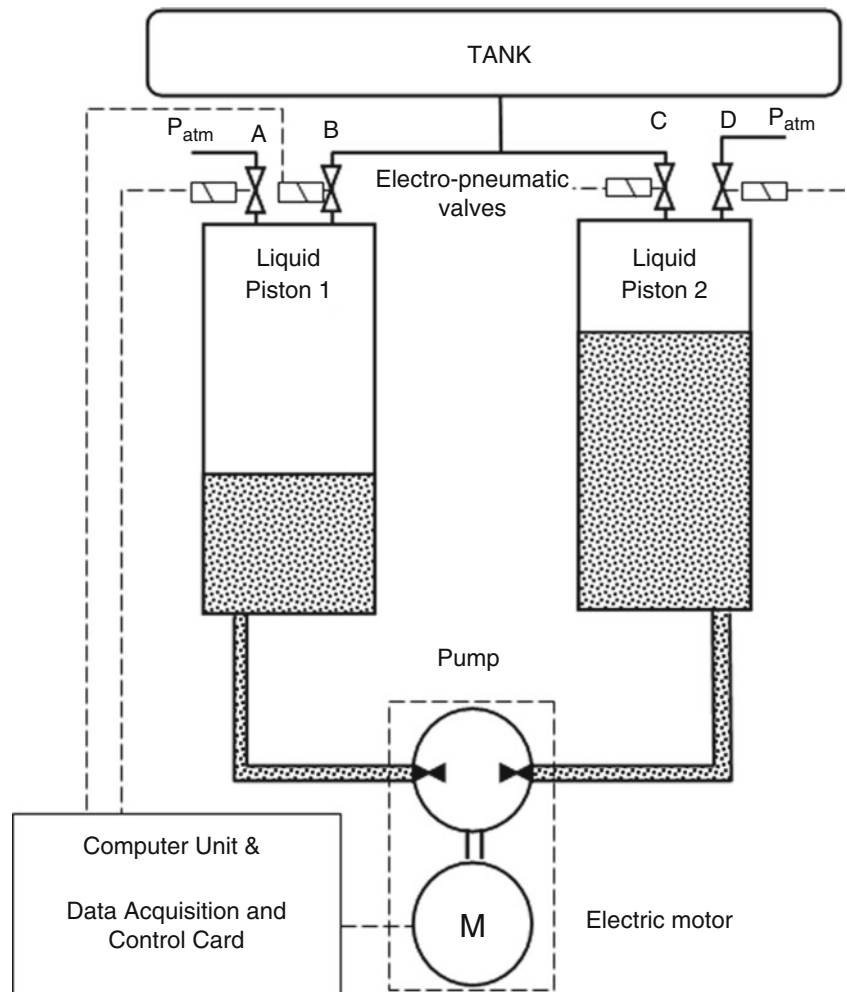
Table 43.1 Energy values stored in the tank for different pressures

Pressure in the tank, P_{tank} (bar)	Stored energy per unit mass, W (kJ/kg)	Stroke, n	Total stored energy, E (kWh)
10	193.626	148	0.32
20	251.914	290	0.83
30	286.010	442	1.40
40	310.201	595	2.04
50	328.965	738	2.70

According to Eq. (43.2), pressure change in the tank can be defined as:

$$\frac{dP_{tank}}{dt} = \frac{RT}{V_{tank}}\frac{dm}{dt} - P_{tank}\frac{dV_{tank}}{dt} \tag{43.3}$$

With the acceptance of isothermal working conditions, the relationship between pressure and volume can be given by Eq. (43.4):

$$P_1 V_1 = P_2 V_2 \tag{43.4}$$

The mean strokes of liquid pistons to generate the desired pressure in the tank can be calculated from Eq. (43.5):

$$\Sigma n = \frac{P_{tank} V_{tank}}{P_{atm}(V - V_{dead})} \tag{43.5}$$

The stroke numbers to create the desired pressure in the tank is given in Table 43.1. Energy stored in the tank per unit mass and the total stored energy for different pressures, which is calculated from above equations, is given in Table 43.1.

Table 43.2 Hydraulic pump characteristics of the system

D_p (cm^3/dev)	M (Nm)	P_{max} (bar)	n_{min} (dev/dk)	n_{max} (dev/dk)	Q_{min} (lt/dk)	Q_{max} (lt/dk)
20	50	160	150	3,200	2.8	60.8

Working speed of the pistons can be arranged by changing the flow rate of the pump as mentioned earlier. The specifications of the selected pump are given in Table 43.2. The pump flow rate is given below;

$$Q = D_p \cdot n_{pump} \cdot \eta_v \tag{43.6}$$

MATLAB/Simulink Model of the System

Compressed air storage system is modeled by MATLAB/Simulink program for isothermal condition. The flow diagram of the system is shown in Fig. 43.2.

Both of the pistons are used for compressing and expanding phases. As one of them compresses the air, the other expands and sucks the air from atmosphere. When compressing piston pressure is reached to the tank pressure, the valve (B or C) is opened, compressed air is sent to the tank and the tank pressure is increased. In the expanding piston, the valve (A or D) is opened through the stroke and liquid piston's pressure drops to atmospheric pressure.

The MATLAB/Simulink model given in Fig. 43.3 calculates the pressures in the tank and liquid pistons. Some variables such as the liquid level, the amount of mass sending to the tank, liquid piston speed, etc. can also be obtained by the model.

The liquid levels of both liquid pistons are determined by "n_x1_x2" submodel (Fig. 43.4). The air mass is calculated by the "mass_calculation" submodel (Fig. 43.5). Tank pressure and liquid piston pressures are calculated by, respectively, "tank_pressure" and "liquid pistons_pressures" submodels (Figs. 43.6 and 43.7).

Results and Discussion

Stored energy according to the tank pressure can be shown from Fig. 43.8. As shown in this figure, 2.7 kW energy can be stored in the tank at 50 bar. Pressure changes in liquid pistons and tank are given in Fig. 43.9. Compressing piston's pressure increases as the expanding piston's pressure drops to atmospheric pressure, because air is compressed and sent to the tank by compressing piston. Until the valve is opened, the compressing piston pressure increases fast. In addition, pressure increasing in the piston and the tank are the same but the rate of increasing decreases after opening the valve. Tank pressure remains constant when the valve is closed. The pressures of the tank and pistons reach to the 15 bar in 10,000 s at 3,200 rpm. If the time is extended, more air mass will be stored in the tank. Consequently, the tank and piston pressures and stored energy will be raised.

The air mass sending to the tank is shown in Fig. 43.10. Air mass sucked by expanding piston at one stroke is approximately 40 g. But the air mass changes as long as the system is running because of dead volume. As the tank pressure increases, the amount of mass in the dead volume is also increases and less mass is sent to the tank. The air mass in the tank is 9 kg in 10,000 s at 3,200 rpm (Fig. 43.10).

The tank pressure changes and energy variations for different pump speeds are given in Figs. 43.11 and 43.12. As shown in these figures, tank pressure and the stored energy values will increase faster if pump speed increases.
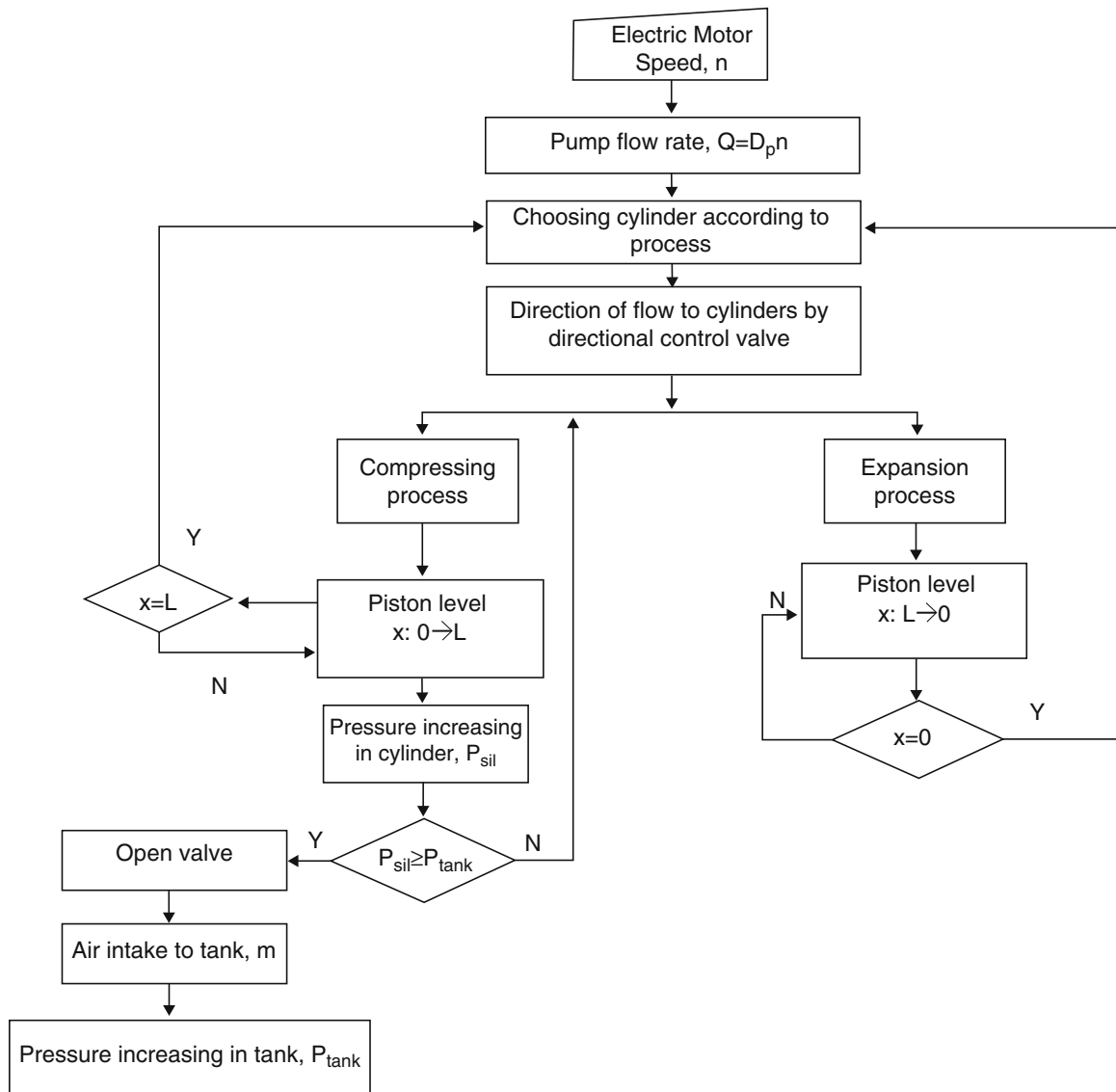
Fig. 43.2 The flow diagram of the model
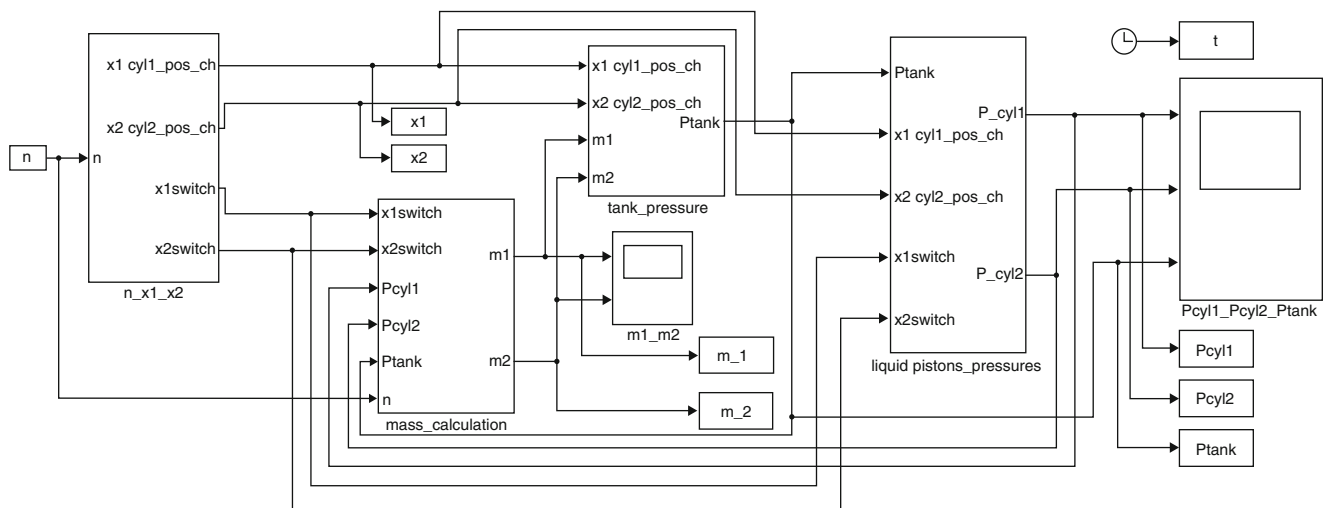
Fig. 43.3 Simulink model of the system
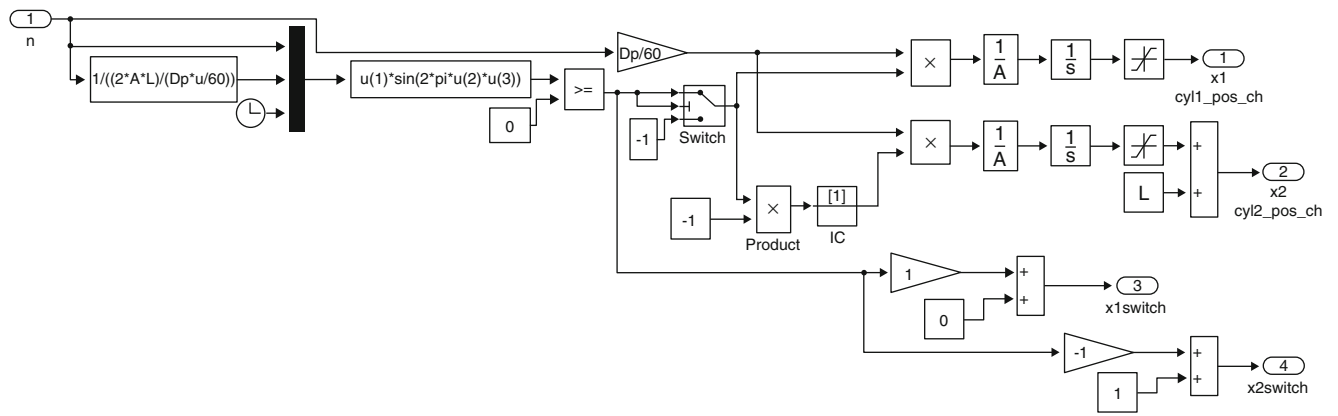
Fig. 43.4 "n_x1_x2" submodel
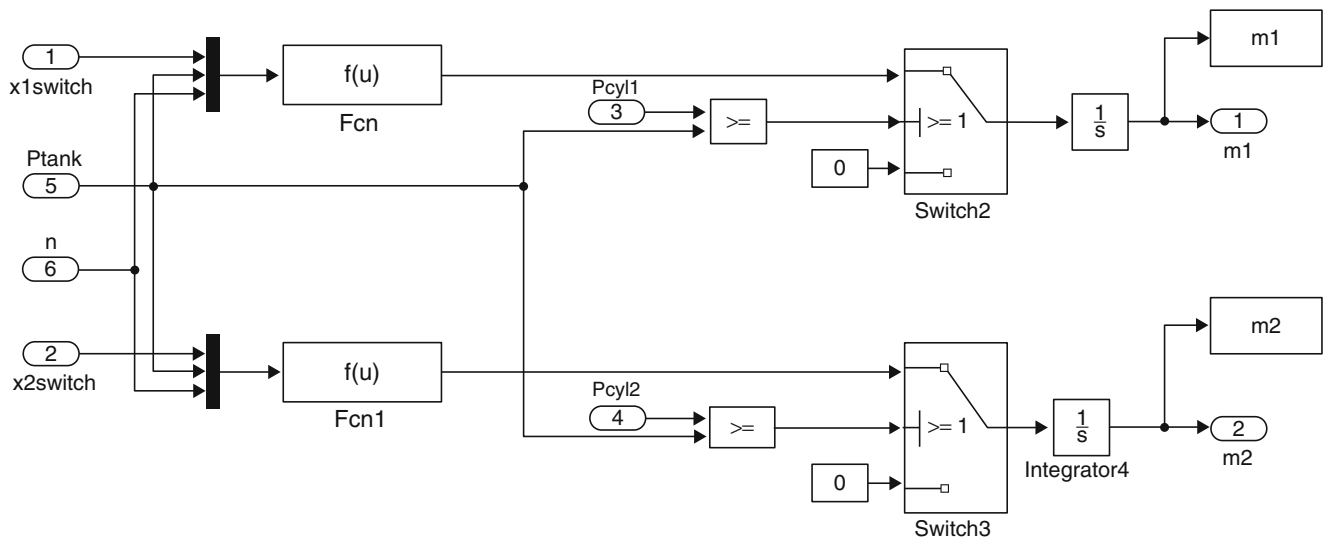
Fig. 43.5 "mass_calculation" submodel
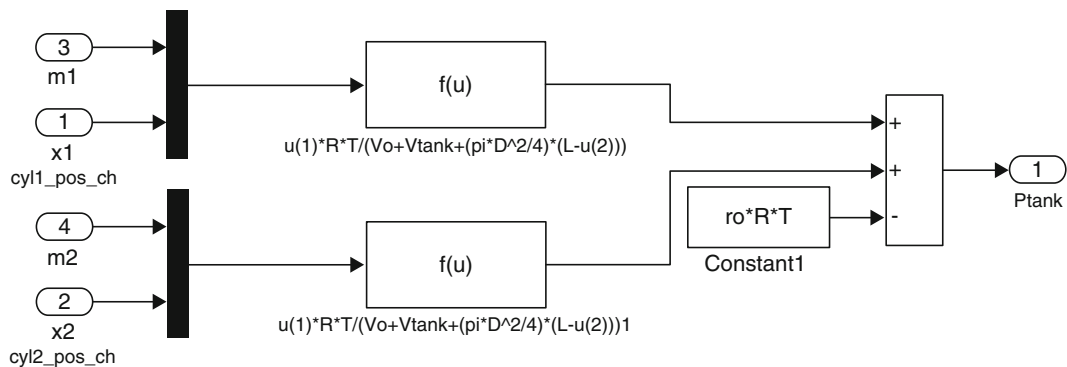
Fig. 43.6 "tank_pressure" submodel
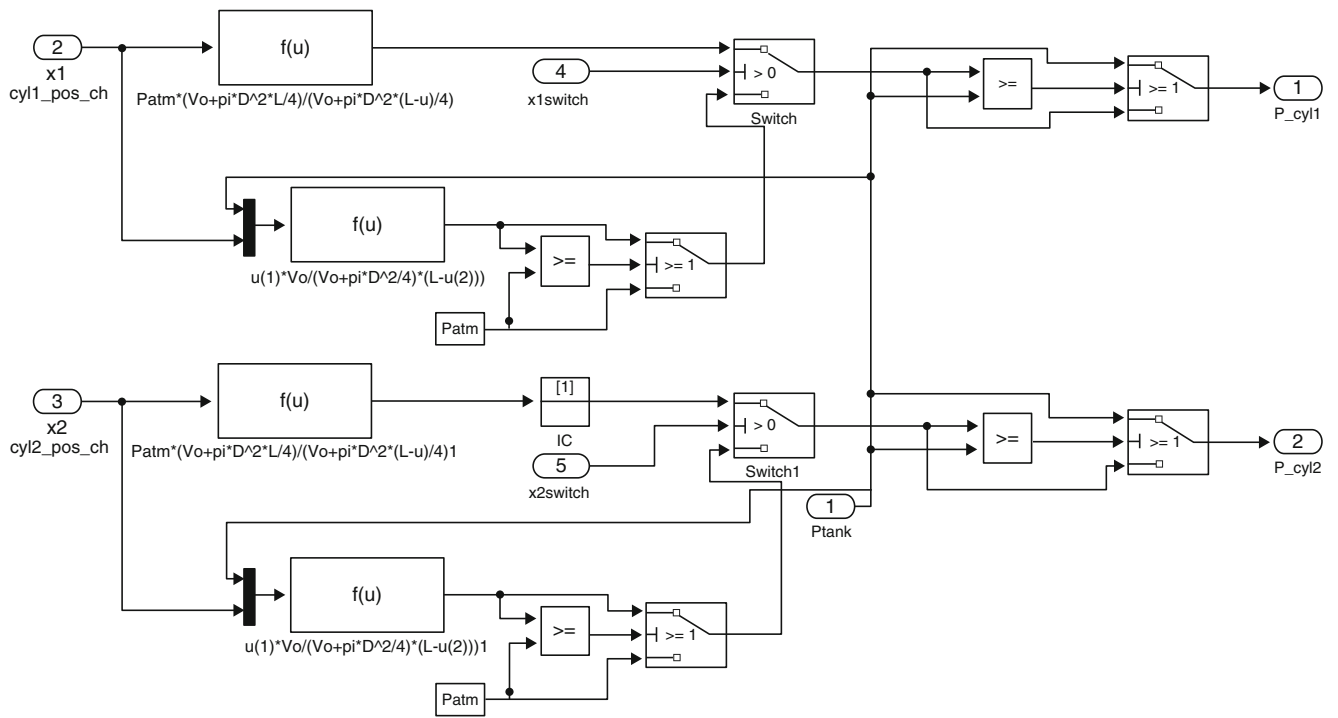
Fig. 43.7 "liquid pistons_pressures" submodel

Fig. 43.8 Tank pressure–stored energy variations
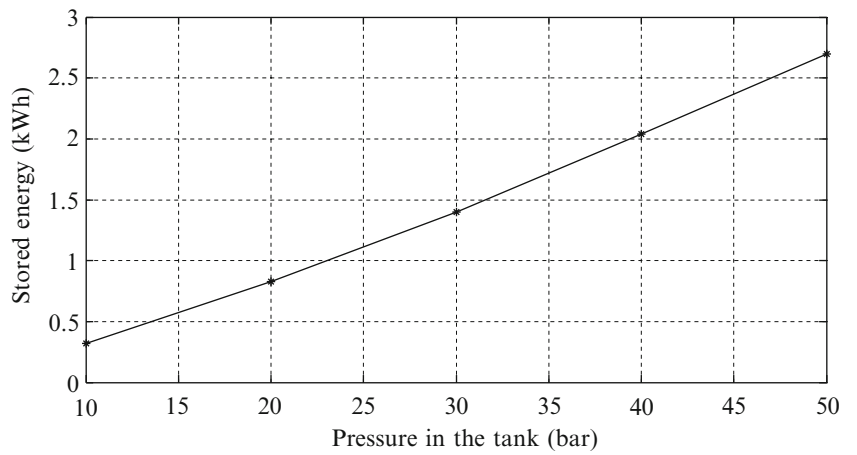
Fig. 43.9 Pressure changes in tank and pistons
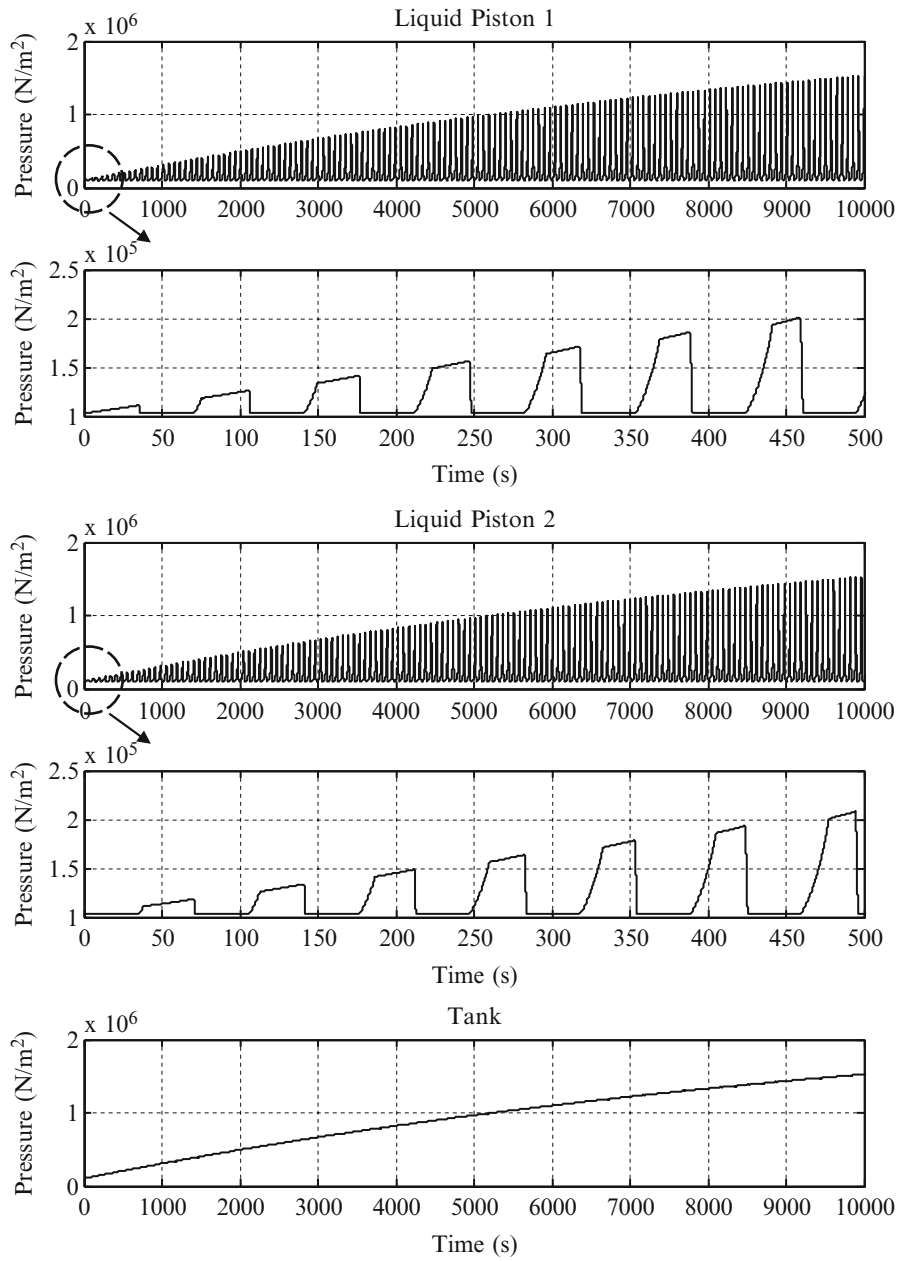
Fig. 43.10 Air mass changes in tank
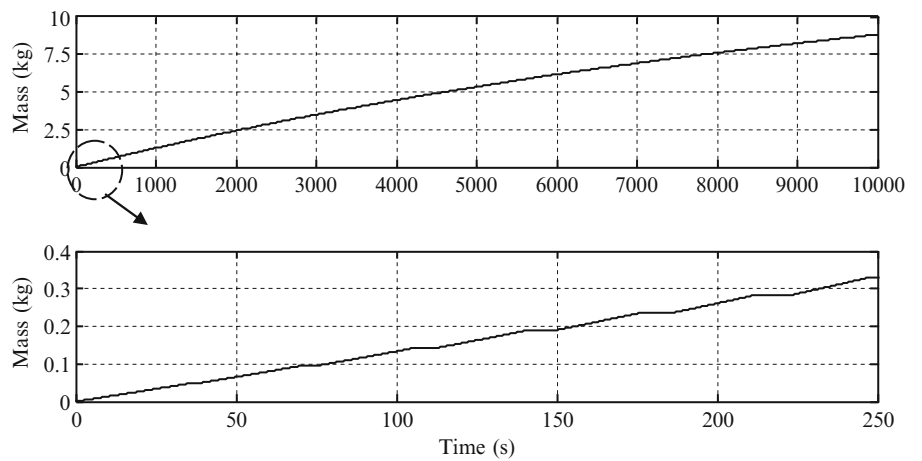
Fig. 43.11 Tank pressures
in different pump speeds
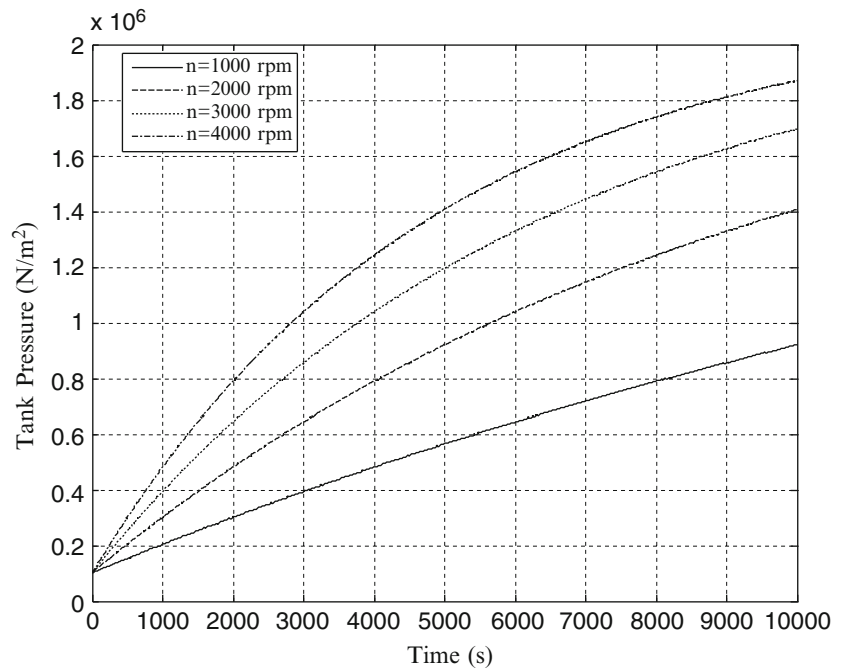
Fig. 43.12 Stored energy
in different pump speeds
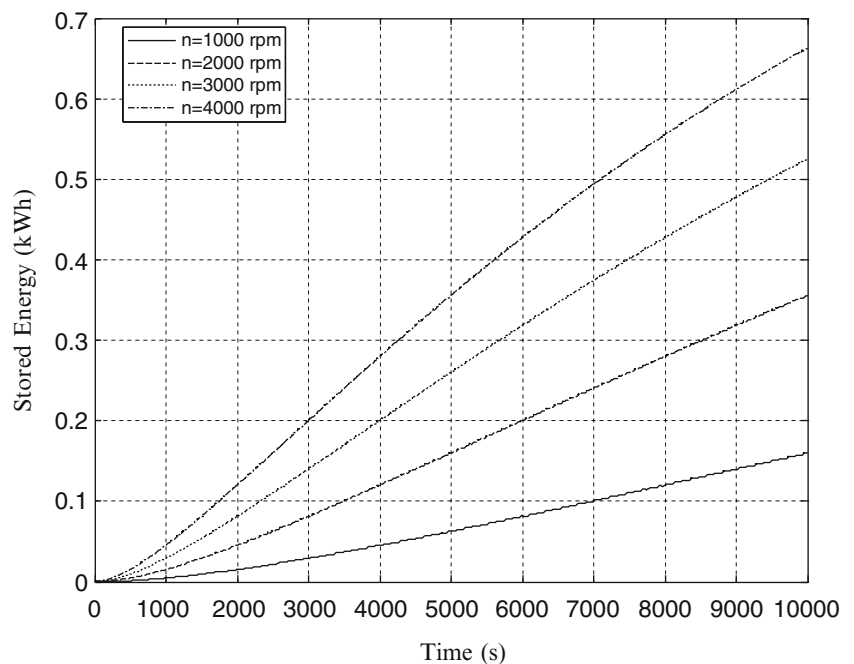
Conclusions

In this study, the design and modeling of a small scale compressed air energy storage system has been examined. The system is modeled by MATLAB/Simulink program. Isothermal conditions are taken into account in the modeling and modeling stages are given in detail. Pressure changes in the tank and pistons are obtained.

In this system, it is determined that 2.7 kW energy can be stored in the tank at 50 bar. The pressures of the tank and pistons reach to the 15 bar in 10,000 s at 3,200 rpm. The air mass and stored energy in the tank is 9 kg and 0.55 kW, respectively, at the same period and speed. If the time is extended or speed of the pump is raised, more air mass will be stored in the tank.

In the advanced stages of the study, the model will be expanded with the evaluation of feedback control system.

Nomenclature

R	Universal gas constant (J/kgK)	V	Liquid piston volume (m^3)
T	Air temperature (K)	V_{dead}	Dead volume (m^3)
P_{atm}	Atmospheric pressure (N/m^2)	D	The diameter of liquid piston (m)
P_{tank}	Tank pressure (N/m^2)	L	The length of liquid piston (m)
V_{tank}	Tank volume (m^3)	L_{dead}	The dead length of liquid piston (m)
Q	Flow rate (m^3/s)	A	Area of liquid piston ($=\frac{\pi D^2}{4}$)
D_p	Pump displacement (m^3/rev)	η_v	Volumetric efficiency
n_{pump}	Pump speed (rev/min)		

References

1. Ibrahim H, Ilinca A, Perron J (2008) Energy storage systems—characteristics and comparisons. Renew Sustain Energy Rev 12:1221–1250
2. Kondoh J, Ishii I, Yamaguchi H, Murata A, Otani K, Sakuta K, Higuchi N, Sekine S, Kamimoto M (2000) Electrical energy storage systems for energy networks. Energy Convers Manag 41:1863–1874
3. Lund H, Salgi G (2009) The role of compressed air energy storage (CAES) in future sustainable energy systems. Energy Convers Manag 50:1172–1179
4. Lund H, Salgi G, Elmegaard B, Andersen AN (2009) Optimal operation strategies of compressed air energy storage (CAES) on electricity spot markets with fluctuating prices. Appl Therm Eng 29(59):799–806
5. Glendenning I (1976) Long-term prospects for compressed air storage. Appl Energy 2(1):39–56
6. Denholm P, Kulcinski GL (2004) Life cycle energy requirements and greenhouse gas emissions from large scale energy storage systems. Convers Manag 45 (13–14):2153–2172
7. Denholm P (2006) Improving the technical, environmental and social performance of wind energy systems using biomass-based energy storage. Renew Energy 31 (9):1355–1370
8. Swider DJ (2007) Compressed air energy storage in an electricity system with significant wind power generation. IEEE Trans Energy Convers 22(1):95–102
9. Grazzini G, Milazzo A (2008) Thermodynamic analysis of CAES/TES systems for renewable energy plants. Renew Energy 33:1998–2006
10. Baker J (2008) New technology and possible advances in energy storage. Energy Policy 36:4368–4373
11. Milazzo A (2008) Optimization of the configuration in a CAES-TES system. In: Shape and thermodynamics, International Workshop Florence 2008, 25–26 September 2008, Florence
12. Lemofouet S, Rufer A (2006) Hybrid energy storage systems based on compressed air and supercapacitors with maximum efficiency point tracking. IEEE 4:1105–1115
13. Van de Ven JD, Li P (2009) Liquid piston gas compression. Appl Energy 86:2183–2191

Use of Transparent Insulation Materials as One of the Measures of Improving Energy of Structures

Mirjana Miletic

Abstract

Structures can be repaired in several ways: physically, economically or in terms of their energy consumption. When talking about energy efficiency, buildings are certainly repaired in terms of their energy saving capacity, provided that there is a need for it. The energy saving aspect of reparation is reflected in the rationalization of their energy consumption, preservation of their engineering substance, improving their thermal comfort, as well as in the use of renewable energy sources. In terms of thermal comfort, one of the traditional building reparation methods is improving the thermal properties of sheathing by using transparent insulation materials. Depending on the purpose of the structure, it is often necessary to use transparent insulation. Heat flows through these materials that are part of the structure's thermal mass are calculated specifically according to regulations on energy efficiency of structures applied in our country. These thermal insulations are belonging to the group of newer materials. This paper provides an overview of transparent insulation materials, along with the opportunities they are offering regarding the improvements of energy efficiency of heating, i.e. improvements in the buildings' thermal comfort, with the minimum use of primary energy.

Keywords

Energy efficiency • Heating • Transparent insulation materials

Introduction

Buildings, as derived based on the consumption of other resources of the earth, are the only continuously growing resources. Previously, in the developed EU countries, buildings accounted for 50 % of energy consumption, while 25 % of energy was consumed by the traffic; today, 40 % of the energy is spent on mechanical energy, 2 % on lighting, and 33 % on room heating. When talking about energy efficiency, buildings are certainly being repaired in terms of their energy saving capacity, provided that there is a need for it. The energy saving aspect of reparation is reflected in the rationalization of their energy consumption, preservation of their engineering substance, improving their thermal comfort, as well as in the use of renewable energy sources. The energy aspect of reparation is closely related to the spatial and economic aspects. In addition to the need for improving the buildings in terms of their energy-efficiency, it is necessary to expand the current space of floor areas in homes, or at least to keep the existing ones. Thermal comfort is being achieved by using proper thermal insulation materials. In Serbia, conventional materials, i.e. polystyrene and Styrodur, are commonly used materials. However, the thickness to which they are traditionally applied neither can meet the required criteria nor the conditions for achieving the specific levels of energy classes. By adopting the Regulation on Energy Efficiency ("Official Gazette of the Republic of

M. Miletic (✉)
Belgrade University, Beograd, Serbia
e-mail: p_mirjana@yahoo.com

Serbia" no. 061/2011 of 19 August 2011) and the forthcoming Law on Energy Efficiency in Buildings, the situation in the near future will certainly be changed also regarding the use of materials, particularly in the facade assembly as part of the building's thermal envelope.

This paper provides a description of a typical residential building (GF+0), along with the materials applied and the thickness of thermal envelope layers commonly used in Serbia. The aim is to present a building where thermal insulation of standard thickness fails to meet the minimum criteria to be achieved as prescribed by the Regulation on Energy Efficiency in Buildings in our country (class C), which would mean that the annual energy use for heating purposes should not exceed $Q_{H,nd} \leq 65$ kW/m^{2}a.

Regarding the layers of thermal envelope, as applied based on calculations, the present building belongs to class D. By increasing the thickness of thermal insulation in order to achieve the desired criteria, insulation layers will grow to 25 cm, reducing thereby the residential space and making the possibility of repair uncertain. Therefore, innovative approaches are being proposed using new insulating materials such as lightweight construction materials and innovative insulation materials, namely Neopor, aerogels, and coatings. The use of transparent insulations, belonging to the group of new materials, is also recommended. When it comes to transparent thermal insulation, according to the Regulation on Energy Efficiency, heat flows through these materials are calculated separately (Appendix 6, "Official Gazette of the Republic of Serbia" no. 061/2011), which is not discussed here.

Improving the Thermal Properties of Elements of the Thermal Envelope

Improving the thermal properties of elements of the thermal envelope requires treating the thermal layers of facade walls, basement structures, ceilings above open passages, roof structures, windows and window protection elements, i.e. the transparent and non-transparent positions of the external envelope.

The building we refer to is a family house of a surface area of A = 103.82 m^2 in Belgrade (Fig. 44.1).

Architectural Requirements for Achieving Energy Efficiency in Buildings

Buildings can be rehabilitated and enhanced with respect to their energy efficiency. One of the traditional methods of doing this is improving the thermal properties of thermal sheathing elements. The term "thermal sheathing" refers to structural elements by which the heated part of the building is separated from its unheated part, i.e. parts of the building with different levels of comfort (Regulations on energy efficiency in buildings, "Official Gazette of the Republic of Serbia", no. 61/2012, Art. 2). Sheathing elements consist of facade walls, basement constructions, ceilings, and roof structures. One of the measures of reducing energy consumption in buildings is to insulate the external walls and eliminate thermal bridges.
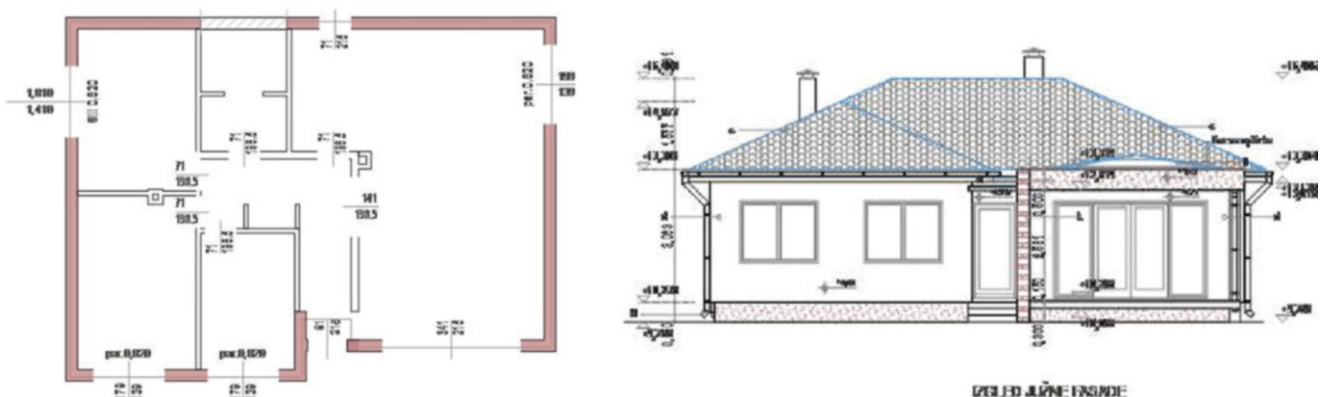
Fig. 44.1 Ground floor and south facade of the residential house: energy efficiency was elaborated based on *Methodology on heat protection and heat losses*, Appendix 6, Article 3.1, "Official Gazette of the Republic of Serbia" no. 061/2011. Author: Mirjana Miletic, November 2012

Thermal Sheathing

Achieving the Appropriate Heat Transfer Coefficients

The structure's thermal sheathing refers to its elements in contact with the external environment—these are the elements by which the heated and the unheated rooms are separated. When speaking about the façade of the building in question, we need to refer to its transparent and non-transparent positions as parts of the thermal sheathing. Transparent positions are the windows, patio doors, front doors, and storefronts, while the exterior walls are considered to be the non-transparent part of the facade assembly. The transparent positions account for the highest percentage of heat energy being lost, while 40 % of energy is being lost through standard facade doors and windows; therefore, they need to receive a special attention.

Transparent Positions of the Facade Assembly

In the context of materials that are important for the thermal insulation of buildings in addition to insulation materials, glass is treated as a specific class, because its nature makes it a poor thermal insulator. Thus, in order to achieve adequate thermal protection and energy efficiency in terms of heating, glass has to be improved.

For heat and light energy transfer, glass needs to meet the following requirements (Table 44.1):
1. Minimize heat loss (outward heat transfer)
2. Minimize heat gains (inward heat transfer)
3. Provide the optimum amount of light

Innovative Glass

For the purpose of reducing the heat transfer coefficient, thermal insulating glasses are being used. These glasses are made of two or three layers, while the space between them is completely filled with dry air or some gas.

The heat transfer coefficient can be further reduced by mounting a heat-reflecting layer on the outward face of the inner glass or the inward face of the outer glass. The disadvantage of these glasses is that their use results in a somewhat reduced light permeability, which is not suitable for working spaces, where this is one of the essential comfort-related requirements [1].

Solar radiation is controlled by adequate sheathings. The use of inorganic substances as a protection against UV rays is an innovative approach in this area. Three components are used: titanium dioxide (TiO_2—absorbing the energy along with the UV rays), zinc oxide (ZnO—protecting against UVB and UVA rays), and ceroxide (CeO—absorbing the UV rays, in addition to a small amount of light) [2].

Non-transparent Positions of the Façade Assembly

The non-transparent positions of thermal sheathing which are parts of elements in contact with the external environment are walls, roofs, and floor trusses. External walls are non-transparent facade positions.

Consider the layered external wall of an object which is made of gitter block and mortar. Its thickness is 25 cm, while its U_{max} is 0.4 W/m^2 K, complying with the new regulations. Along with the other improvement measures, the thickness of insulation is recommended to be about 15 cm, although usually it is 5 cm [1].

Hygrothermal properties of the external wall of this facade assembly are shown in Table 44.2.

Table 44.1 Requirements that glass needs to meet regarding its heat and light energy transfer properties

Type of glass	Heat transfer coefficient, U (W/m^2 K)	Total sun energy transfer, g	Light permeability, T
Duplex thermo insulation glass	≥ 1.1	0.55–0.65	0.8
Triplex thermo insulation glass	≥ 0.5	0.5	0.4–0.7
Sun radiation controlling glass	≥ 1.1	0.5–0.65	0.7–0.8

Table 44.2 Hygrothermal properties of the external wall of the residential house

Construction layer	δ (cm)	λ (W/mK)	ρ (kg/m³)
1. Composition lime mortar	3	0.85	1,700
2. Gitter block	25	0.61	1,400
3. Styrodur	15	0.038	33
4. Baumit silicate facade	1	0.70	1,600

Table 44.3 Heat transfer resistance and temperature values for the layers listed below

Description	λ (W/mK)	R (m² K/W)	$\Delta\theta$ (°C)	θ (°C)
Inside				max20
Transfer		0.13	0.97	19.3
1. Composition lime mortar	0.85	0.035	0.26	19.04
2. Gitter block	0.61	0.15	1.12	17.92
3. Styrodur	0.038	3.95	29.39	−11.47
4. Baumit silicate facade	0.70	0.01	0.07	−11.54
Heat transfer		0.04	0.3	−11.84
Outside				min−12.1
Total resistance		4.315		

Calculation from the report on the building's energy efficiency made based on the *Methodology on heat protection and heat losses*, Appendix 6, Article 3.1, "Official Gazette of the Republic of Serbia" no. 061/2011

Table 44.4 Hygrothermal properties of ceiling of the residential house

Construction layer	d (cm)	λ (W/mK)	ρ (kg/m³)
1. Gauged mortar	2	0.87	1,800
2. Ceiling	16	0.61	1,400
3. Concrete	4	2.04	2,400
4. Vapor permeable foil	0.04	0.19	215
5. Mineral wool	25	0.041	120
6. Vapor permeable foil	0.04	0.19	215

Then we have the following values for heat transfer resistance (Table 44.3):

Where the surface heat transfer coefficient is as follows:

$$U = 1/R = 1/4.315 = 0.23$$

$$U < U_{max}$$

$$0.23 \ \text{W/m}^2\text{K} < 0.3 \ \text{W/m}^2\text{K} \tag{44.1}$$

The above Eq. (44.1) shows that the assembly meets the requirements prescribed in "Official Gazette of the Republic of Serbia", Appendix 3, Art. 3.2.

Hygrothermal properties of materials used in the layers of ceiling as part of thermal sheathing of the above mentioned house are listed in Table 44.4.

Then we have the following values for heat transfer resistance (Table 44.5):

$$U = 1/R_u = 0.15 \, \text{W/m}^2\text{K}$$

$$U < Umax$$

$$0.15 \, \text{W/m}^2\text{K} < 0.3 \, \text{W/m}^2\text{K} \tag{44.2}$$

Equation (44.2) shows that in order to meet the requirements (i.e. $U < U_{max}$), we need a thermal insulation layer—in this case mineral wool—of 25 cm of thickness.

Another part of thermal sheathing of a residential house is the floor. The layers are listed below in Table 44.6.

Table 44.5 Heat transfer resistance and temperature values for the ceiling layers listed below

Description	λ (W/mK)	R (m^2 K/W)	$\Delta\theta$ (°C)	θ (°C)
Inside		0.100		20
Transfer			0.7276	19.272
1. Gauged mortar	0.87	0.023	0.167	19.105
2. Ceiling	0.61	0.262	1.906	17.199
3. Concrete	2.04	0.0196	0.1426	17.056
4. Vapor permeable foil	0.19	0.0021	0.01527	17.041
5. Mineral wool	0.041	6.098	21.296	−4.254
6. Vapor permeable foil	0.19	0.0021	0.01527	−4.269
Heat transfer			0.7276	−4.997
Outside		0.100		−5
		Ru 6.5		

Calculation from the report on the building's energy efficiency made based on the *Methodology on heat protection and heat losses*, Appendix 6, Article 3.1, "Official Gazette of the Republic of Serbia" no. 061/2011

Table 44.6 Hygrothermal properties of the floor of the residential house

Construction layer	d (cm)	λ (W/mK)	ρ (kg/m^3)
Inside			
Transfer			
1. Ceramic tiles	1	1.28	2,300
2. Cement mortar	4	1.40	2,100
3. Vapor permeable foils	0.04	0.19	215
4. Mineral wool	14	0.039	180
5. Hydro insulation	1	0.17	1,100
6. Concrete	10	2.04	2,400
7. Gravel	10	0.81	1,700
Transfer			
Outside			
Total			

Table 44.7 Heat transfer resistance and temperature values for the floor layers listed below

Construction layer	λ (W/mK)	R (m^2 K/W)	$\Delta\theta$ (°C)	θ (°C)
Inside		0.17		20
Transfer			0.590	19.41
1. Ceramic tiles	1.28	0.00781	0.027	19.383
2. Cement mortar	1.40	0.0285	0.099	19.284
3. Vapor permeable foils	0.19	0.0021	0.0073	19.2767
4. Mineral wool	0.039	3.5897	12.474	6.803
5. Hydro insulation	0.17	0.0588	0.204	6.5987
6. Concrete	2.04	0.049	0.170	6.4287
7. Gravel	0.81	0.1234	0.4288	6
Transfer			0	6
Outside		0.00		6
Total		Ru = 4.029		

Calculation from the report on the building's energy efficiency made based on the *Methodology on heat protection and heat losses*, Appendix 6, Article 3.1, "Official Gazette of the Republic of Serbia" no. 061/2011

Then we have the following values for heat transfer resistance (Table 44.7):

$$U = 1/R_u = 0.248$$

$$U < Umax$$

$$0.248\,\text{W/m}^2\text{K} < 0.3\,\text{W/m}^2\text{K} \tag{44.3}$$

Equation (44.3) shows that the assembly meets the requirements prescribed in "Official Gazette of the Republic of Serbia", Appendix 3, Art. 3.2.

Table 44.8 List of heat transfer coefficients of the facade assembly thermal sheathing

Part of thermal sheathing	U (W/m^2 K)	U_{max} (W/m^2 K)	Fulfilled criteria for class C
External walls	0.231	0.3	Yes
Ceiling	0.15	0.3	Yes
Floor	0.248	0.3	Yes

By increasing the thickness of the entire thermal sheathing on the treated house, requirements for achieving its energy efficiency have been fulfilled (Table 44.8).

The annual energy required for heating purposes according to SRPS EN ISO 13790 is $Q_{H,nd} = 6{,}142.66$ kW/a, which corresponds to class C.

The insulation thickness of the presented external wall is 15 cm, which is seldom encountered in today's objects. With the insulation on the inward face of the wall being set to a minimum of 15 cm (this is the appropriate ratio if the floor and ceiling insulation are increased to a significant degree; for this case, the above calculation shows that insulation for the ceiling has to be 25 cm of thickness, while for the floor it has to be 14 cm), the space within the building is highly reduced, while the wall thickness is increased, with deep openings appearing on the facade. In order to avoid this, using thermal insulation which belongs to the group of new and innovative insulating materials may be a good solution. There are many products that are used to a varying degree, depending mainly on their price; here, only some of them are specified.

Thermal Insulation

Thermal insulation products that are used in Serbia are mostly made of expanded polystyrene, styropor, and extruded polystyrol, styrodur. The energy consumed by conventional buildings in heating days amounts 200–300 kW/m^2. New buildings constructed based on standards of low energy consumption consume less than 100 kW/m^2. This model of constructing enables high levels of residential comfort. Since conventional styropor is not sufficient, there is a need for materials with better technical and thermal insulation properties [3].

Use of Transparent Insulation Materials

Aerogel
The Concept and Properties of Aerogel
The nickname for aerogel is "frozen smoke" [4] and currently it is the lightest known solid material. The aerogel was developed in 1931 at Stockton University, California, in the laboratory of Professor Steven Kistler. "Actually, the structure of aerogel is relatively banal: it is simply an ultra light aerated foam that consists almost 100 % of nothing else than air (the exact figure varies between 95 and 99.9 %)" ([2], p. 128). The remaining is a glass-like material—silicon dioxide, known as silica. The extremely high thermal resistance is conceived by low thermal conductivity of 0.018 W/mK. Using this nanogel, heating and cooling costs can be reduced to a significant degree. The insulation value of aerogel is extremely high. It can be used between panels of different materials, including plastics. "The insulation efficiency of a single inch[1] of Aerogel is equal to that of 32 layers of glass" ([5], p. 41). The main properties of aerogel are listed below (Table 44.9).

Use and Processing
Aerogels can be used as filtering or insulation materials. For architectural purposes, these gels are primarily used as transparent insulation panels (Fig. 44.2), additives to glass structures, as parts of the roof construction or in double-webbed panels. This material is mostly available in the form of granulates and it can be poured and used as high performance insulation material when injected into narrow, 1.5 cm thick cavity layers. It is suitable for the core insulation of dual skin external masonry and as an insulating material behind klinker brick facades. The level of heat protection provided by aerogels is high even in the case when applied in thin layers and that is why it is referred to as one of the materials of choice for improving the energy efficiency in the context of heating of all types of buildings.

In the above mentioned residential building aerogel can be applied as dual skin masonry or behind the gitter block.

---

[1] 2.5 cm.

Table 44.9 The main properties of aerogel

Material	Group of materials	Trade name	Density (g/cm²)	Thermal conductivity (W/mK)	Transparency	Sustainability aspect
Aerogel	Insulation material	Pyrogel Nanogel Okagel Makrolon ambient	0.02–0.5	0.008–0.017	High transparency	Outstanding thermal insulation properties, extremely low weight

Fig. 44.2 Transparent heat insulation for industrial buildings, aerogel structure. Source: Peters, S. 2011. p.111

Table 44.10 The main properties of ceramic foams

Material	Group of materials	Trade name	Resistance	Transparency	Sustainability aspect
Ceramic foam	Insulation material	Duocel Sic Foam Stelex Dual component	Water and steam resistant Durable at 1,000 °C	Optical	100 % Recyclable Air purifying Heat insulating

In this context, we also need to mention the translucent aerogel insulating glass, which is intended to be used mostly in museums, sports facilities, and administration buildings for the purpose of improving their energy efficiency. Using a 60 mm nanogel layer as the intermediate layer, the material's G value is lower than 0.3 W/m² K. This kind of transparent insulation panel meets the standards prescribed for passive houses.

Aerogels can also be used as a fill between two layers of polycarbonate panels (PC panels). This material provides with high heat-insulating qualities, and ensures high translucence and optimum light diffusion. While used as roof glazing, it is also worth to be mentioned in the heating context. The G value of these panels is comparable to that of triple glazing [6].

Nansulate Shield

Nansulate shield is a thin transparent insulation material with the G value many times higher than that of the current best known insulation. This new product is the first of the Industrial Nanotech's that is not a coating, while having the same core nanotechnology as the Nansulate line of thermal insulation and protective coatings [7]. This nano-composed thermal insulation consists of 70 % Hydro-NM-Oxide, 30 % acryl, as well as various other additives [4].

This is a coating-like insulation of steady appearance and thickness, with its sole drawback being in its manufacturing costs, limiting its use to a significant degree. It can be easily applied to the outward surface of construction materials.

Ceramic Foams

The Concept and Properties of Ceramic Foams

These foams are made of ceramics as silicon carbide. Given their high thermal insulating performances, these foams are used widely in construction industry, especially in heating systems. Ceramic foams can be used on temperatures up to 2,000 °C, particularly in lightweight construction systems. For application in construction industry, dual-component ceramic foams were developed. At room temperature, these foams harden within half an hour. Ceramic foams are water and steam resistant, fiber free, and contain no toxic substances [6]. These foams are mentioned here for their possibility of being used as transparent insulation systems (Table 44.10).

Results and Discussion

As indicated by the above, this housing unit cannot meet the required criteria in terms of its existing thermal layer thickness. Achieving class C, i.e. the minimum criteria for the building to become energy-efficient, requires the thickness of layers to be increased to a substantial degree. The building was initially insulated using 5 cm roof and 10 cm wall insulation (although a 5 cm Styrofoam insulation is commonly used), which makes it a class D building. If installing a thicker thermal insulation, consisting in some parts (e.g. in the ceiling structure) of a 25 cm thick stone wool, we have a problem at hand that we cannot resolve using current materials and construction techniques. Namely, due to the dimensions of roof wooden beams, this thick insulation is unsuited for mounting the roof structure. Therefore, new approaches are needed using new insulating materials. In this case, transparent insulating materials are suggested as the sole possibility. The use of these materials is limited mainly as a result of their price; nowadays, they are used mostly for non-residential buildings. They should be surely taken into account given the need for achieving the minimum criteria when it comes to use of primary energy and buildings of higher energy-efficiency.

Further researches are needed in terms of calculating the heat transfer ratio of thermal envelopes on buildings insulated using new thermal insulation materials. Figures for these materials, indicating their properties, are not provided in the new Regulations on Energy Efficiency ("Official Gazette of the Republic of Serbia" no. 061/2011). It appears that the research process of these kinds of innovations is at its very beginning.

Conclusion

Some of the measures for achieving the desired comfort and reducing the consumption of primary energy are aimed at improving the performance of the building's thermal insulation. We have proposed new and innovative insulating materials. If used properly, these materials can significantly contribute to the improvement of energy efficiency of buildings. However, what is important for all materials, including insulation, is the performance/price ratio. Namely, innovative products, including the new generation of thermal insulation materials, are characterized by the fact that they can be obtained from a number of different materials, with the choice ultimately depending on the desired quality and the price. Indeed, the price is the main limiting factor to using these materials in the construction industry both in Serbia and abroad. In Serbia, these materials are not included in the Regulations on Energy Efficiency of structures [8, 9]. It seems that we have a lot of work ahead of us to learn about these materials potentially enabling us to improve energy efficiency.

Nomenclature

A	Surface area (m^2)		θ	Temperature (°C)
U	Heat transfer coefficient ($W/m^2 K$)		λ	Thermal conductivity (W/mK)
Umax	Maximum heat transfer coefficient ($W/m^2 K$)		g	Total sun energy transfer
R	Resistance of heat transfer coefficient ($m^2 K/W$)		ρ	Density (kg/m^3)
$Q_{H, nd}$	Annual energy for heating		T	Light permeability

References

1. Radivojević A, Rajičić A (2012) Architectural structures, lecturing on energy efficiency of the buildings. Chamber of Engineers of Serbia, Belgrade
2. Laydecker S (2008) Nano materials in architecture, interior architecture and design. Birkhauser Verlag AG, Berlin
3. Polymers in structural engineering. http://static.oglasnik.hr/nekretnine/clanak/polimeri-u-graditeljstvu,428. Accessed 9 Aug 2010
4. Juran D (2012) Nanotechnology in construction, Faculty of Electrical Engineering, Aerogel, Zagreb. http://www.fer.unizg.hr/_download/repository/djuran_DS.pdf. Accessed 20 July 2012
5. Mori T (ed) (2002) Immaterial-ultramaterial, vol 1. Harvard Design School in association with George Braziller, New York, p 41
6. Peters S (2011) Material revolution, sustainable and multipurpose materials for design and architecture. Birkhauser, Munich
7. Nansulate Shield. http://www.industrialnanotech.com/INTK_press_release_11152006.htm. Accessed 25 Aug 2012
8. Regulation on energy efficiency of the buildings. "Official Gazette of RS", no. 61/2011
9. Regulation on conditions, contents and certification of energy efficiency in buildings. "Official Gazette of Republic of Serbia" no. 61/2011, from 19.08.2011

Experimental Insulation Performance Evaluation of Aerogel for Household Refrigerators

45

Gamze Gediz Iliş

Abstract

Energy saving is one of the most important topic in refrigeration technology. For this reason, insulation of a household refrigerator should be improved by innovative insulation materials. Aerogel insulation is one of the most promising high performance thermal insulation materials for different applications nowadays. Within this work, a different application area of aerogel is studied. Aerogel insulation sheets were applied to a household refrigerator as an additional insulation material. Aerogel insulation was applied on the evaporators and different surfaces of the two types of static and no frost type household refrigerators. According to the energy consumption test results, the application of 10 mm thick aerogel sheet to the outer backside surface of the refrigerator decreases the energy consumption of the refrigerator down to 5 %.

Introduction

Over the past two decades, energy and energy efficiency are the main important topics around the world and many researchers and manufacturers devote significant efforts to improve the energy efficiency of their appliances. Due to the global warming and ozone depletion, many energy efficiency procedures have been written as energy labeling of the appliances and many standards were written and have been applied to different sectors. ISO 15502 standard is one of them and used for energy labeling of household refrigerating appliances.

The consumers are interested in the energy efficient appliances and this idea forces the manufacturers to make developments and investments on energy efficient instruments. Interest in more energy efficient appliances for the household refrigerators encourage the manufacturers to focus on many applications like modern appliances with many sensors [1], new compressor designs [2], new working fluids [3], additives to the refrigerant [4], or the lubricant oil [5]. Also, the innovative insulation materials or vacuum insulation panels to decrease the energy consumption of the domestic refrigerators are the other ways to achieve more energy saving domestic refrigerator.

Polyurethane is the base insulation material of a household refrigerator. It is used not only for the insulation but also for the rigidity of the refrigerator. Due to its long reaction time, expensive application procedure, and construction constraints, manufacturers look for other insulation alternatives to achieve more energy efficient refrigerators. Vacuum insulation panels are one of the alternatives on this way [6]. Another alternative can be the Aerogel insulation sheets.

Aerogels were discovered approximately 100 years ago [7]. Its density is very low (50–200 kg m^{-3}) and they have significant thermal, acoustic, and optical properties [8–10]. Aerogels are also used in various areas of science such as vacuum insulation panels, acoustics, and have significant application area for possible building applications [11–13].

G.G. Iliş (✉)

Indesit Company R&D Center, Manisa Organize Sanayi Bölgesi, 45030 Manisa, Turkey
e-mail: gamze.gedizilis@indesit.com

Highly energy efficient windows, translucent aerogel insulation for the buildings, are one of the examples for building applications of the aerogel. Aerogel insulation has distinct advantages due to its ability with low thermal conductivity (down to 0.010 W m^{-1} K^{-1}).

Although Aerogel has such various kinds of application areas, almost no application was performed in the household refrigerator sector. In this paper, Aerogel insulation sheet was applied to the domestic refrigerator in order to decrease the energy consumption. For this purpose, 10 mm thick Aerogel insulation sheet was applied to the probable critical heat loss areas of the household refrigerator. Energy consumption tests were performed for two kinds of refrigerators: one is static type cooler refrigerator, other one is the four-door no frost type refrigerator with freezer and cooler. The energy consumptions of the refrigerators with and without Aerogel were compared and necessary discussions were performed.

The Thermophysical Properties of Aerogel Sheet

In this work, Aspen Aerogel sheet was applied. The Cryogel Z type aerogel sheets with 10 mm thickness were used. As can be seen from Fig. 45.1, the sheet is flexible with aluminum sheet cover on one side. It is hydrophobic and has a density of 128 kg/m^3. The thermal conductivity of the used aerogel varies with temperature, i.e. $\lambda = 138$ mW m^{-1} K^{-1} at 0 °C and $\lambda = 129$ mW m^{-1} K^{-1} at -50 °C. It is non-flammable and non-reactive and not hazardous to human health.

The Tested Refrigerators

The tests were performed with two types of refrigerators: one is static only with cooler (R1), other one is no frost type refrigerator both with cooler and freezer (R2). Both refrigerators work with 230 V–50 Hz and the refrigerant is R600a. The refrigerant charge of the R1 and R2 is 26 and 50 g, respectively. The R1 has 341 L cooler capacities and has no freezer. The R2 has 292 L cooler with chiller compartment and 110 L freezer capacities.

The Aerogel Application Procedure to the Refrigerators

Totally five different energy consumption tests were performed with both types of the refrigerators. Figure 45.2 illustrates the test numbers and the procedure of the experimental work of these refrigerators. For the static type refrigerator, two tests were performed:

Fig. 45.1 The Cryogel Z type aerogel (Aspen Aerogels)
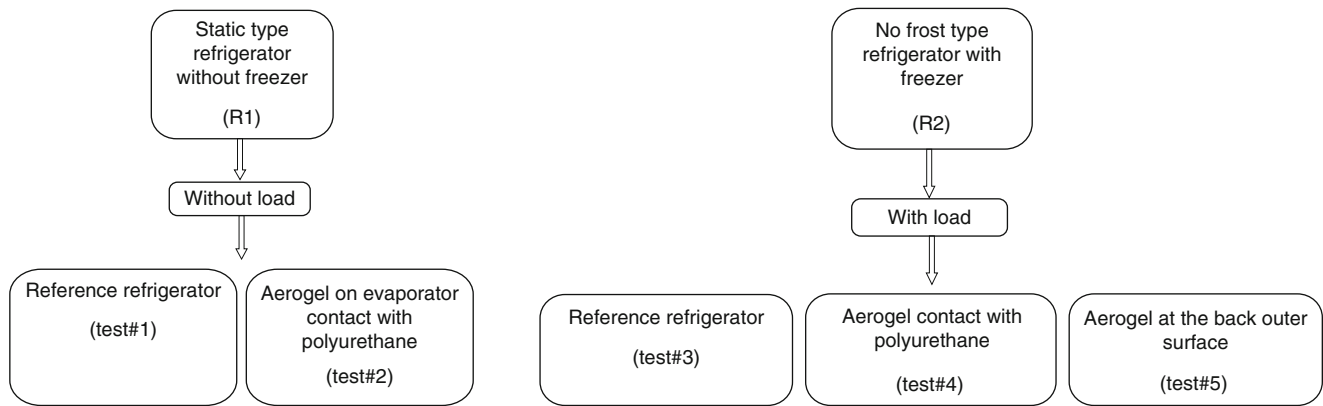
Fig. 45.2 The procedure of the experiments and the test numbers
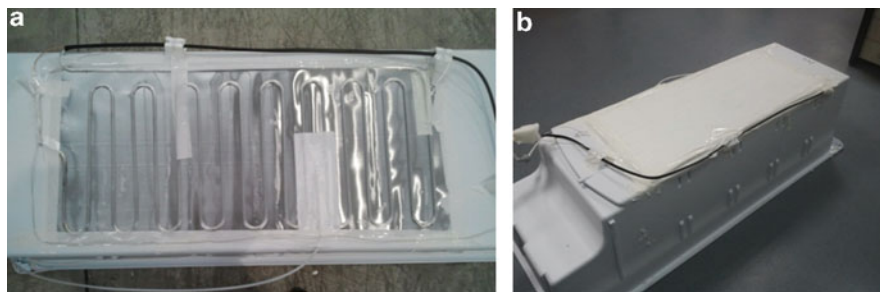
Fig. 45.3 The aerogel sheet application onto the evaporator of the static type refrigerator, (**a**) uncovered evaporator, (**b**) covered evaporator

(a) Reference refrigerator without aerogel (test#1)
(b) Aerogel located on the evaporator and the porous side contact with the polyurethane (test#2)
    For the no frost type refrigerator three different types of tests with load were performed:
(c) Reference refrigerator without aerogel (test#3)
(d) Aerogel porous side contact with the polyurethane (test#4)
(e) Aerogel porous side, no contact with the polyurethane located at the back part of the refrigerator (test#5)

As given in Fig. 45.1, aerogel sheet has two sides, one is covered with aluminum sheet and the other side has porous structure. Aerogel sheet was located to allow the polyurethane contact with the porous side of the aerogel.

Due to lack of freezer for the static type refrigerator, there is no need to load the refrigerator for the EC test (ISO 15502) [14]. The evaporator was covered with the aerogel sheet and the energy consumption test, test#2, was performed. As illustrated in Fig. 45.3, the aerogel porous side is located to allow contacting the polyurethane. The aerogel application onto the evaporator of the static type refrigerator is illustrated in Fig. 45.3.

The application of the Cryogel Z aerogel sheet to the basement and the backside of the refrigerator for test#4 is illustrated in Fig. 45.4. The porous side of the sheet is located to be able to contact with the polyurethane.

The test#5 was performed by covering the aerogel sheet between the back part of the refrigerator and the condenser. Figure 45.5 shows the application of the Cryogel sheet on the refrigerator. The application is performed by covering the aerogel sheet onto the reference refrigerator.

Experimental Procedure-Test Chamber

The refrigerators were tested according to the standard ISO 15502 [14]. The steady stated Energy Consumption (EC) test procedures were applied. M packages were used for the refrigerator with freezer. For static type refrigerator (R1) the EC tests were performed without M packages due to the existence of freezer. For this purpose, the M packages were placed into the R2. The M package storage plan was given in Fig. 45.6. The thermocouples were instrumented on the M packages and

Fig. 45.4 The aerogel sheet application to the backside and the basement of the no frost type refrigerator (test#4)

Fig. 45.5 The aerogel sheet application to the backside of the no frost type refrigerator for test#5

Fig. 45.6 No frost four-door refrigerator (R2) load plan of the M packages

1° compartment with basket

2° compartment with wireshelves

3° compartment with basket

4° compartment with basket

Freezer Load Plan

Chiller Load Plan
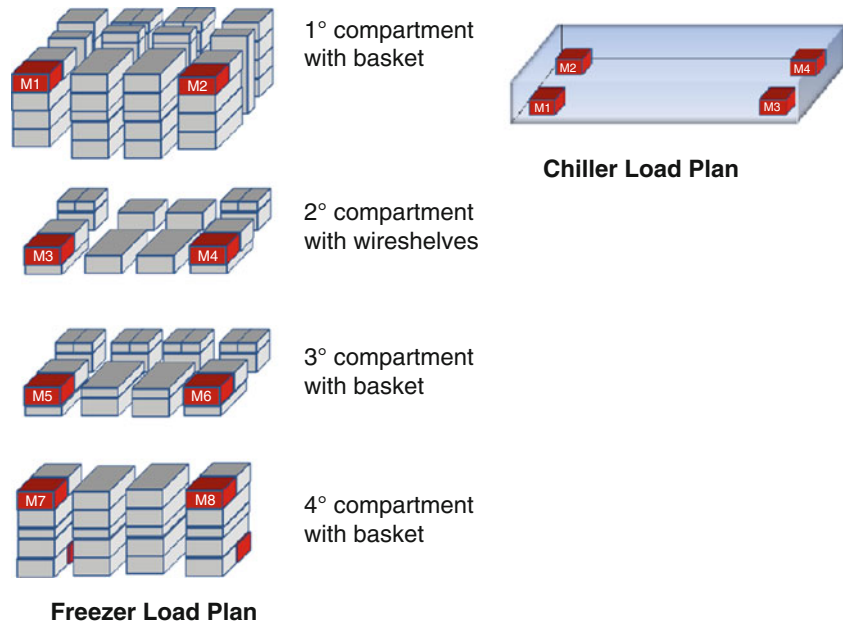
Fig. 45.7 The schematic view of the test chamber
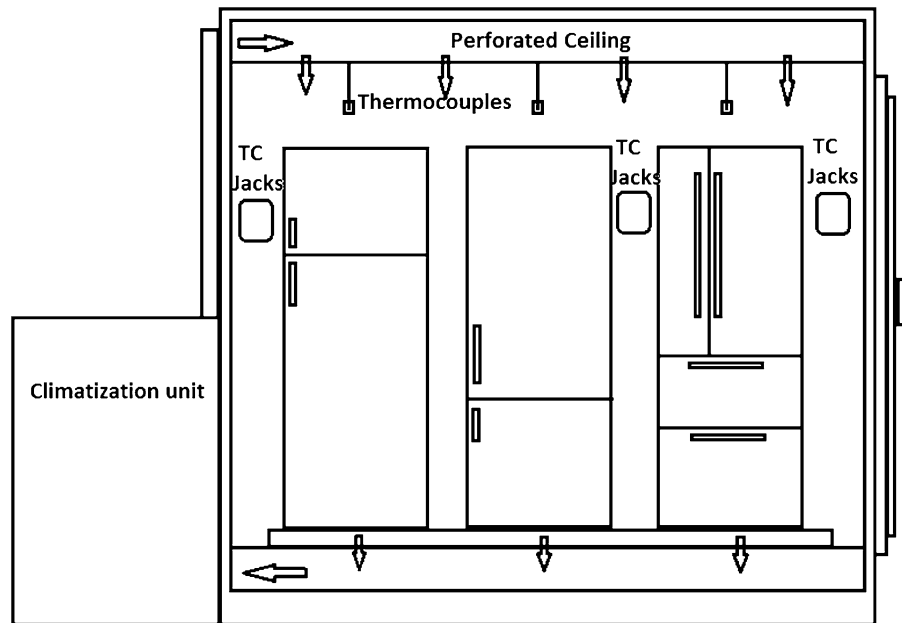
the M packages were placed both in cooler and freezer as highlighted in Fig. 45.6. The tests were held within a climate chamber. The climate chamber temperature can be varied between 10 and 48 °C with ±0.2 uncertainty band. A compressor, a condenser, an expansion device, and an evaporator control the test chamber cooling system. Fans and dampers obtain the air circulation in the chamber and an electrical heater provides the warm air. Many thermocouples were located into the chamber to provide the homogenous air temperature inside the chamber and the chamber temperature was fixed at 25 °C. The schematic view of the test chamber is given in Fig. 45.7. The air chamber velocity should not exceed 0.25 m/s according to the International standards [14].

T-type thermocouples were located in the refrigerator; ten for freezer, four for chiller, three for cooler, and one for crisper. Evaporator inlet and outlet, suction line, compressor outlet, condenser inlet and outlet and compressor top point temperatures are also measured by T-type thermocouples. The data that monitored and collected was performed with the Marel Climatic Chamber program.

Results and Discussion

In this section the temperature variation analysis of the internal volume and the temperature variation of the evaporator inlet–outlet of the refrigerator were given. The energy consumption tests and the power analysis of the refrigerators were obtained and illustrated via tables and figures. As mentioned before, two types of refrigerators were taken into consideration and five tests were performed at 25 °C.

Temperature Variation Analysis of the Inner Temperature and at the M Packages

Static Type Refrigerator

In this section the temperature variation analysis of the internal volume and the inlet and outlet temperature of the evaporator, crisper, suction line, dryer, compressor outlet, compressor shell, and space temperature variations of R1 for test#1 and test#2 were measured and the collected data were illustrated in Figs. 45.8 and 45.9.

For the R1 refrigerator, EC tests were performed (test#1–2). During these tests, the variation of temperature for different locations was also plotted. As can be seen from Fig. 45.9, the inner temperatures of the refrigerator T1, T2, T3, and crisper temperatures were at 5 °C during the EC test. The suction line temperature varies approximately between 15 and 31 °C.

The second test of the R1 was performed for the same refrigerant charge amount with the reference static type refrigerator as 26 g. The test result is illustrated in Fig. 45.9a. After a period that was needed for the stabilization of the refrigerator to a steady state condition, the test results were plotted for 300 min and five operation cycles were observed during this period. As can be seen from Fig. 45.9a, the suction line temperature starts to vary between 19 and 33 °C. The suction line temperature is higher when compared with the reference refrigerator. Also the inlet and outlet temperatures of the evaporator are lower when compared with the reference refrigerator, test#1. After this amount of refrigerator charge, the charge was increased to 29 g. As can be seen from the Fig. 45.9b, the inlet and outlet temperatures are lower and the suction line temperature is higher than the reference refrigerator temperatures. This means that the refrigerant could not be able to vaporize. The charge reduction should be done. Finally, the charge was reduced to 22 g as the temperature variation was given in Fig. 45.9c. When compared with the 26 g and 29 g tests, the 22 g gas charge has convergence with the reference refrigerator.
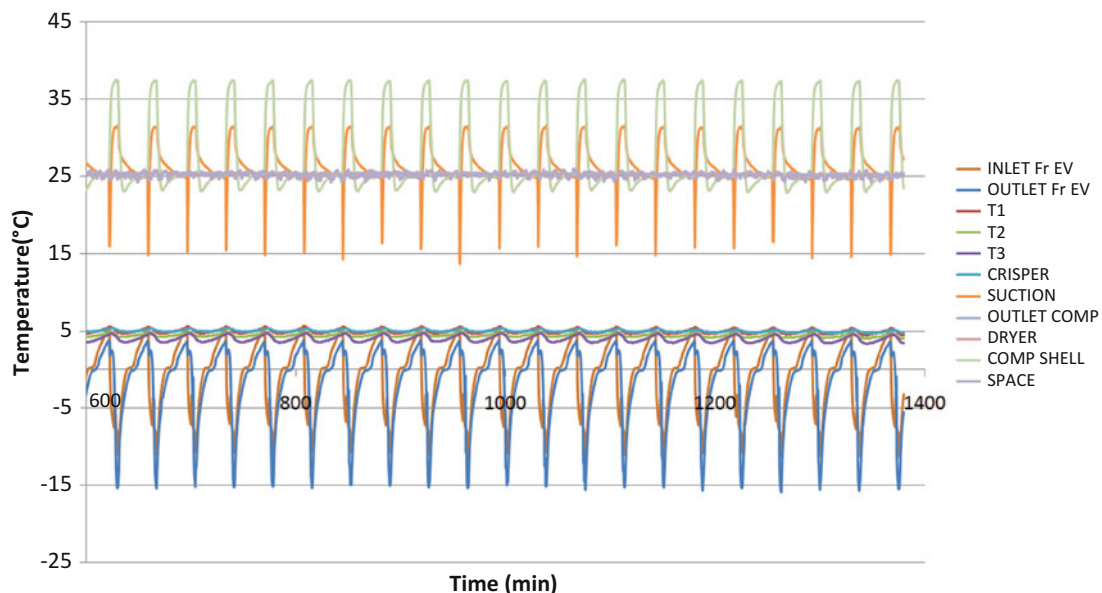
Fig. 45.8 The temperature variations inside and at the important locations of the static type reference refrigerator (test#1)
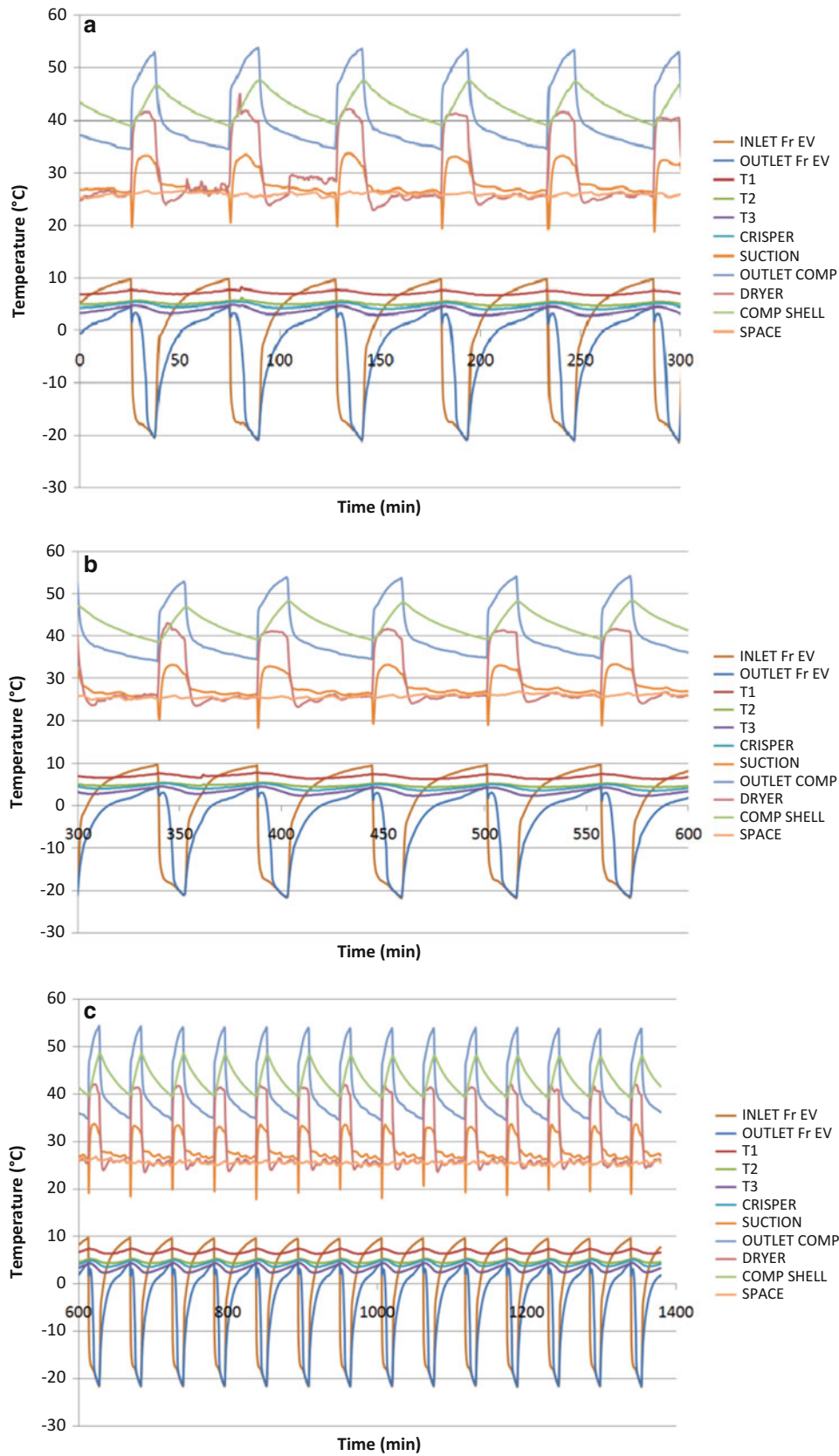
Fig. 45.9 The temperature variations inside and the important locations of the R1 refrigerator (test#2) with, (**a**)26 g, (**b**)29 g, (**c**)22 g refrigerant charge
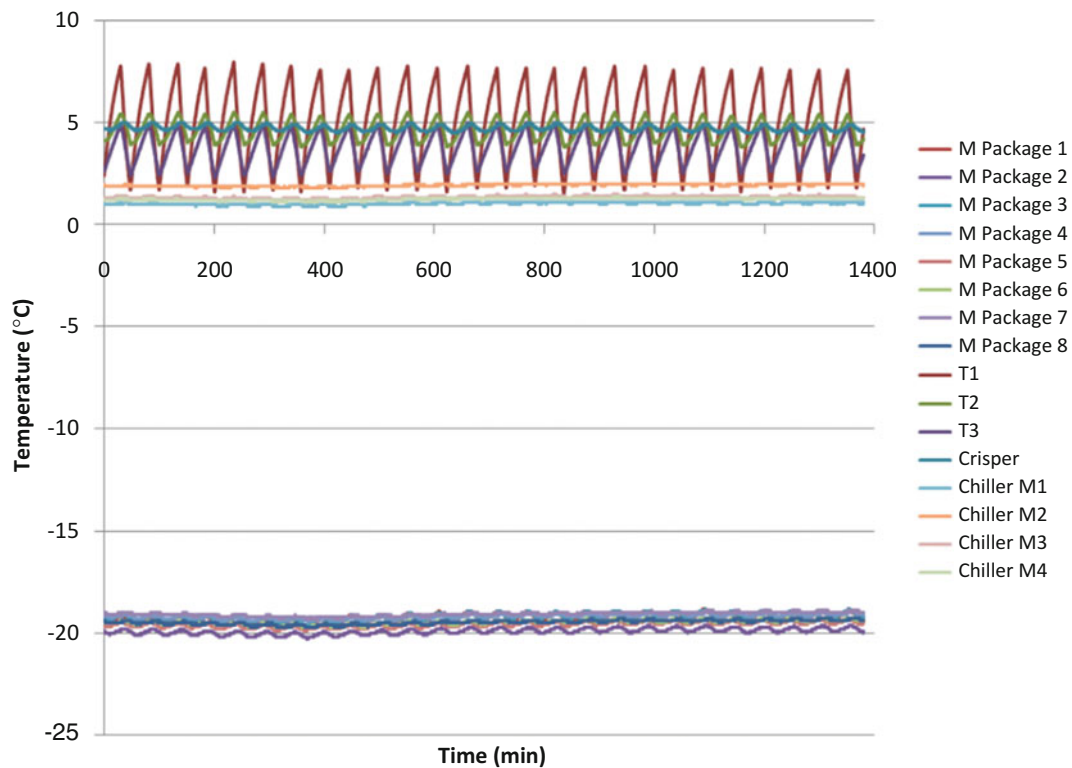
Fig. 45.10 The temperature variations inside and the important locations of the no frost type reference refrigerator (test#3)

No Frost Type Refrigerator

In this section the temperature variation analysis for the no frost type reference refrigerator (R2) was given and illustrated in Figs. 45.10 and 45.11 for the test#3 and #4, and Fig. 45.12 for the test#5. As seen from Fig. 45.10, the M package temperatures inside the freezer and the chiller, the temperature variation of the crisper, and the shelve temperature inside the cooler, during the EC test, are given. The temperature variations of the M packages inside the freezer and the chiller are around −18 °C and 0 °C, respectively. The temperature is measured in the cooler at three different locations as T1, T2, and T3 as illustrated in the figure. The temperatures of these points vary during the start/stop period of the compressor. During the whole cycle, the averages of these points are around 5 °C. The same temperature variation behavior with the reference refrigerator is seen for the test#4 in Fig. 45.11. The test#4 was performed and the temperature variations are also given when the aerogel is applied inside the polyurethane. The M package temperatures are around −18 °C and 0 °C for the freezer and chiller, respectively. The average inner temperature of the cooler is around 5 °C. The test results for the test#5 were also given in Fig. 45.12 and as expected, approximately the same temperature variations with test#3 were seen.

Energy Consumption and Power Analysis of the Refrigerator

In this section the EC test results for both static and no frost refrigerators and the power analysis of the reference refrigerators for tests 2, 4, and 5 were plotted and illustrated via figures and tables.

Static Type Refrigerator

The measured compressor power consumption of static type reference refrigerator and test#2 for the first 100 min is illustrated in Fig. 45.13. As can be seen from the figure, the compressor on and off time of the test#2 is longer than the reference test. The compressor cycle time, on-off-on period, and the compressor running time were calculated and the related results were given in Table 45.1.
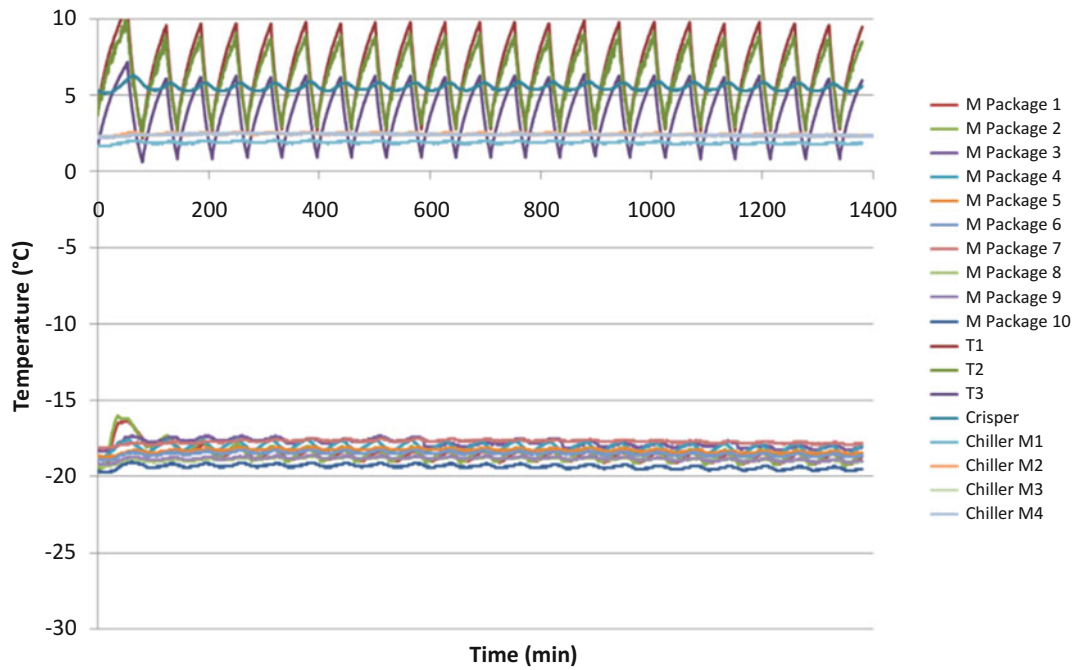
Fig. 45.11 The temperature variations inside and the important locations of the no frost type R2 refrigerator (test #4)
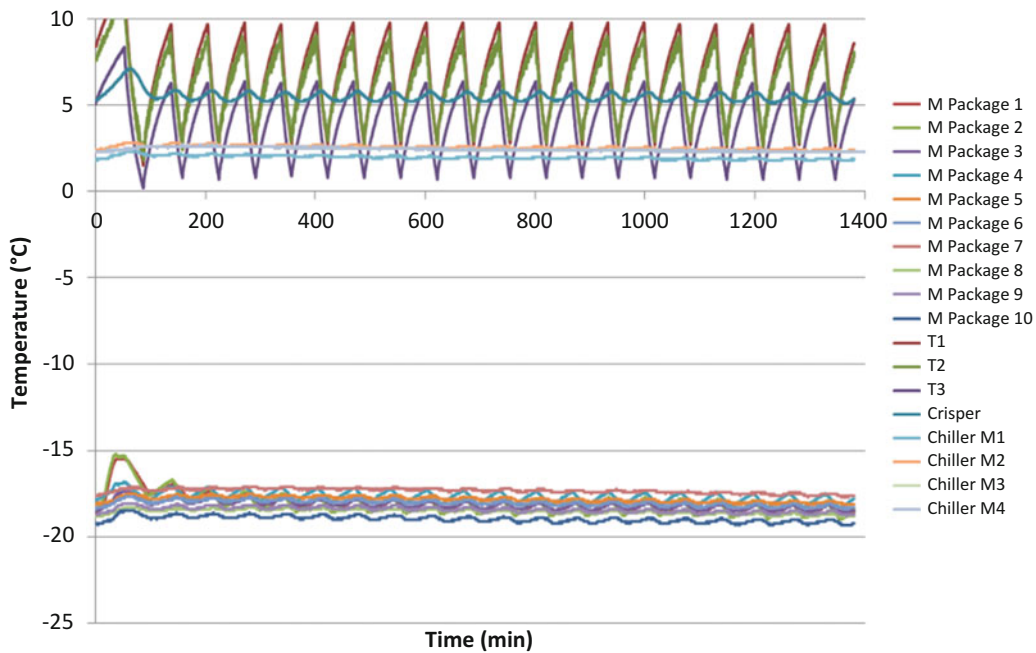
Fig. 45.12 The temperature variations inside and the important locations of the no frost type R2 refrigerator (test #5)

As mentioned before, the reference refrigerator for the static type has 26 g gas charge and the EC results showed that for the test#2, 22 g refrigerant charge is more suitable. The comparison of power, compressor on/off time and the EC result comparisons are given according to these refrigerant charges. As seen from Table 45.1, the average inner cabin temperatures for reference and test#2 refrigerators are 5 °C for both and the chamber temperatures for reference and test#2 refrigerators are 25.2 °C and 24.3 °C, respectively. Although the compressor off time of test#2 refrigerator is longer than the reference refrigerator, the on time of the compressor is longer, too. For this reason, the EC result of the aerogel applied R1 refrigerator

Fig. 45.13 The power of the static type refrigerator, reference refrigerator (test#1) and for test#2 for 100 min
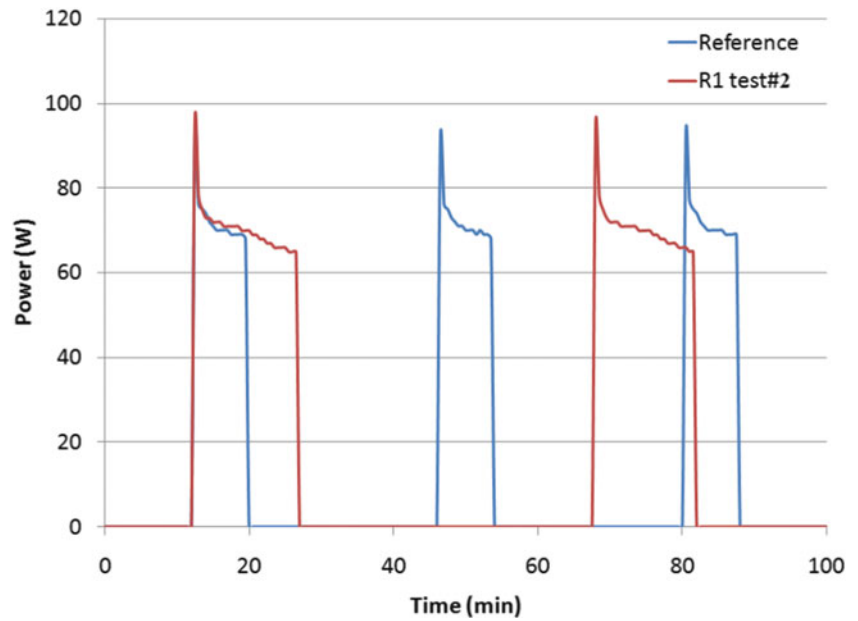
Table 45.1 The average cabin and chamber temperature, compressor on/off time, and the EC results of reference and aerogel applied R1 refrigerator

	Static type reference refrigerator	Test#2 (22 g)
T average (°C)	5.0	5.0
CPS ON time (min)	21.7	42.3
CPS OFF time (min)	79.0	123.0
(%) Running ratio	21.5	25.6
Average chamber temperature (°C)	25.2	24.3
EC result (kW/24 h)	0.38	0.43

is 5 % higher than the reference refrigerator. Although the refrigerant charge is decreased, the EC is increased. Otherwise, with 26 g charge caused liquidification at the suction line and icing problem is observed on the pipe of the compressor. That's why the reduction of charge should be necessary and it affects and reduces the EC of the refrigerator.

No Frost Type Refrigerator

Figure 45.14 shows the measured compressor power consumption of no frost refrigerator in reference tests (test#3), test#4, and test#5, for the first 200 min. By this result, the compressor cycle time, on-off period, and the compressor running time is calculated and presented in Table 45.2. As clearly seen from Fig. 45.14, the off time of the R2 for test#4 and test#5 is longer than the reference refrigerator. The EC result cannot be predicted from this figure due to the longer on times of the test#4 and test#5. As given from Table 45.2, the cabin and the chamber temperatures of all tests are around 5 and 25 °C, respectively. The hottest M packages inside the freezer are around −18 °C for all tests. The test#4 and test#5 show an increase in both compressor off and on times when compared with the reference test. If reference test is compared with test#4, it is clearly seen that, the running ratio of the compressor causes 3 % high EC result. The EC test of test#5 shows that the application of aerogel is not suitable in polyurethane. It gives good results at the outer surface of the refrigerator and 5 % decrease in EC is observed.

Fig. 45.14 The power of the no frost type refrigerator, reference refrigerator (test#3), R2 for test#4, R2 for test#5 for 200 min
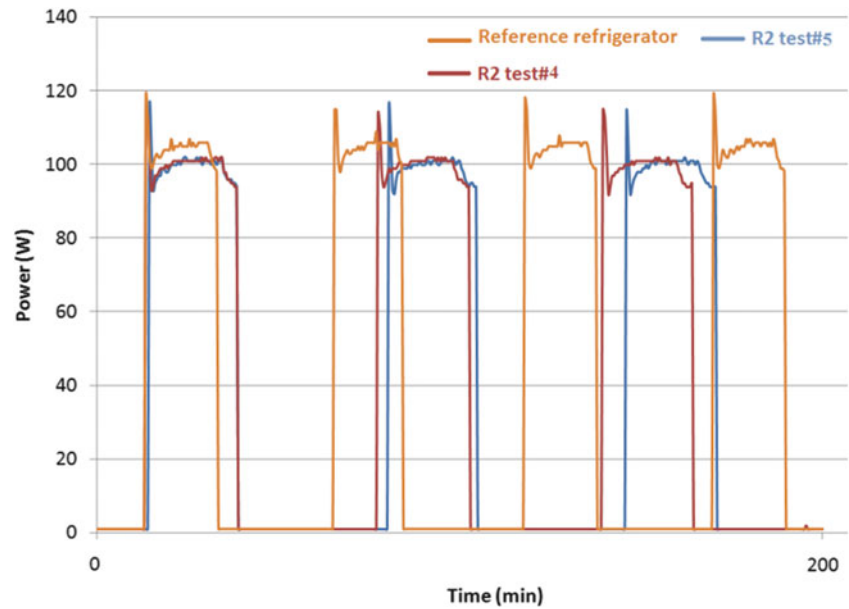
Table 45.2 The average cabin, M package, and chamber temperature, compressor on/off time, and the EC results of reference and aerogel applied refrigerators

	NF-type reference refrigerator	Test#4	Test#5
T average (°C)	5.2	5.1	5.1
Warmest M package	−18.0	−18.0	−17.8
CPS ON time (min)	14.0	19.5	20.0
CPS OFF time (min)	23.0	36.5	41.5
(%) Running ratio	37.8	40.6	36.2
Average chamber temperature (°C)	25.0	25.4	25.2
EC result (kW/24 h)	1.00	1.03	0.95

Conclusion

The application of the aerogel sheet to a household refrigerator in order to decrease the energy consumption was carried out in this study. Two types of refrigerators as static and no frost were held and with these refrigerators, totally five main energy consumption tests were performed. The cooler, chiller, M packages' temperature variations, the compressor on/off time, and the power during the EC tests were measured and collected by using ISO 15502 standard procedures. The test results performed during this study can be concluded that the application of aerogel:

- Can be suitable for the household refrigerators in order to decrease the EC where the maximum heat loss is dominant for the refrigerator.
- In contact with the polyurethane has no effect on the EC of the refrigerator. 10 mm aerogel is used instead of 10 mm polyurethane and almost no thermal conductivity was changed.
- To the static type refrigerator is not suitable thus the thermodynamic cycle cannot be controlled with an electronic code or command.
- Is suitable when applied on the outer surface of the refrigerator.
- Can be applied where polyurethane cannot flow and fill the gap due to the constructional constraints like small spaces (e.g. water dispenser backside space) that causes heat loss.
- Can be applied where the heat bridges occur (e.g. vacuum panels contact edges).

The future works can be held for the heat bridges of the refrigerators where vacuum insulated panels applied to the refrigerators.

Nomenclature

EC   Energy consumption
NF   No Frost
R1   Static type refrigerator

R2   NF-type refrigerator
T   Temperature (°C)

Greek Letter

λ   Thermal conductivity (W/mK)

References

1. Xiao J, Wang W, Guo QC, Zhao YH (2010) An experimental study of the correlation for predicting the frost height in applying the photoelectric technology. Int J Refrig 33:1006–1010
2. Lee H, Ki S, Jung S, Rhee W (2008) The innovative green technology for refrigerators development of innovative linear compressor. In: International compressor engineering conference
3. Jung D, Kim C, Song K, Park B (2000) Testing of propane/isobutane mixture in domestic refrigerators. Int J Refrig 23:517–527
4. Mahbubul IM, Fadhilah SA, Saidur R, Leong KY, Amalina MA (2013) Thermophysical properties and heat transfer performance of Al2O3/R-134a nanorefrigerants. Int J Heat Mass Transf 57:100–108
5. Bi S, Shi L, Zhang L (2008) Application of nanoparticles in domestic refrigerators. Appl Therm Eng 28:1834–1843
6. Clodic D, Zoughaib A (2000) Technical and economical evaluation of vacuum insulated panels for a European freezer. In: International refrigeration and air conditioning conference
7. Kistler SS (1931) Coherent expanded aerogels and jellies. Nature 127:741
8. Anderson AM, Wattley CW, Carroll MK (2009) Silica aerogels prepared via rapid supercritical extraction: effect of process variables on aerogel properties. J Non Cryst Solids 2:101–108
9. Reim M, Reichenauer G, Körner W, Manara J, Arduini-Schuster M, Korder S et al (2004) Silica-aerogel granulate—structural, optical and thermal properties. J Non Cryst Solids 350:358–363
10. Tajiri K, Igarashi K (1998) The effect of the preparation conditions on the optical properties of transparent silica aerogels. Sol Energy Mater Sol C 4:189–195
11. Beatens R, Jelle BP, Gustavsen A (2011) Aerogel insulation for building applications: a state of the art review. Energy Buildings 43:761–769
12. Buratti C, Moretti E (2012) Experimental performance evaluation of aerogel glazing systems. Appl Energy 97:430–437
13. Buratti C, Moretti E (2013) Glazing with silica aerogel for energy saving in buildings. Appl Energy 98:396–403
14. ISO15502 (2005) Household refrigerating appliances-characteristics and test methods. International Organization for Standardization, Geneva

Full-Scale Experimental Studies of a Passive Cooling Roof in Hot Arid Areas

Hamida Bencheikh

Abstract

A full-scale evapo-reflective roof for arid climates has been developed. The proposed roof design is composed of a concrete ceiling over which lies a bed of rocks in a water pool. Over this bed is an air gap separated from the external environment by an aluminum plate. The upper surface of this plate is painted with a white titanium-based pigment to increase reflection of a radiation to a maximum during the day. At night, the temperature of the aluminum sheet falls below the temperature of the rock bed mixed with water. Water vapor inside the roof condenses and falls by gravity. This heat pipe effect carries heat outwards and cold inwards. Heat exchange is improved by radiation between two humid internal surfaces. The efficiency of this cooling system is studied using finite difference method. Numerical calculations performed for different external temperatures and solar radiation show that the cooling produced by such a system is significant. As a result of this, the mean air temperature in the room may be kept a few degrees above the minimum nocturnal outdoor temperature throughout the day. However, the maximum indoor air temperature was observed at sunset. This could further be lowered by allowing ventilation of the building in the evening.

A full-scale experimental study of passive cooling roof was carried out for a typical summer day of June at Laghouat in Algeria. The proposed roof design is composed of a concrete ceiling over which lies a bed of rocks in a water pool. Over this bed is an air gap separated from the external environment by an aluminum plate. The upper surface of this plate is painted with a white titanium-based pigment to increase the radiation reflection process during daytime. Several passive modifications have been introduced to the roof in order to reduce indoor air temperature in hot climates. An experimental investigation, employing a passive procedure, has been carried out to study the possibility of reducing air temperature in buildings. The results show that the air temperature can decrease within a range from 6 to 10 K. This decrease can further be lowered by 2–3 °C if night natural ventilation of buildings is allowed.

Introduction

In hot climates such as southern Algeria, excessive heat is the major problem that causes human thermal discomfort. Space cooling is therefore the most desirable factor for the inhabitants. Various examples of dwellings responsive to climatic constraints were found in vernacular architecture throughout the world. Compact cellular layout with minimum external surface exposure to the sun, whitewash surfaces to reduce absorptivity, blind external facades, courtyards, vegetation to provide humidity and shade, heavy buildings with high thermal capacity materials are common passive features in most hot arid climates such as M'Zab settlements in southern Algeria, Egypt, and Iran [1, 2]. Wind towers for cooling ventilation are

H. Bencheikh (✉)
Laboratoire de génie civil Amar telidji university Laghouat Algeria, BO 7072 oasis, Nord Laghouat 03000, Algeria
e-mail: h.bencheikh@mail.lagh-univ.dz

Fig. 46.1 Room with cooling roof system
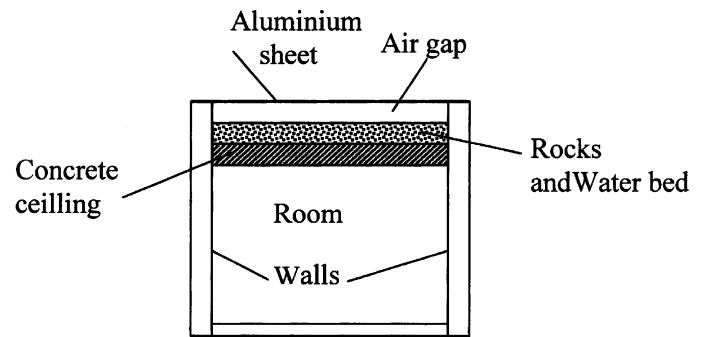
Fig. 46.2 Room without cooling roof system
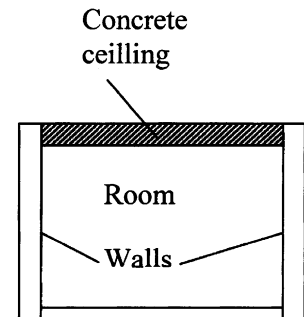
well known in Iranian and Middle East architecture, which along with cooling of the air by water evaporation kept the building comfortable during hot periods [3]. Underground Buildings have the advantage of large thermal capacity storage of the earth. They are used in Matmata in Tunisia and Cappadocia in central Turkey [4].

In recent years several investigations have been performed and have shown that there can be multiple solutions to the excessive heat problem. The popular one is cooling ventilation using a solar chimney [1, 4]. The results showed that cooling ventilation using a solar chimney can reduce internal temperatures of buildings. Shading devices (overhangs and verandas) to reduce summer solar radiation are also investigated, and useful depths of these shading elements for various orientations in continental climates were defined [5].

Space cooling can also be achieved by improving the performance of roofs. This is because the roofs are the most exposed surfaces to direct solar radiation and can cause excessive heat gain during hot periods. Some efforts were made by investigators to improve the roof thermal performance. The use of low emissive material in the attic of a roof reduced the underside ceiling surface temperature which in turn lowered the room air temperature [6]. Evaporative cooling approach for passive cooling of buildings in hot arid climates has also become an attractive subject of investigation for many researchers. The relative advantage of evaporative cooling in relation to many other approaches (cavity wall, insulation, whitewash and large exposure orientations, vegetable pergola shading, roof with removable canvas, water film, soil humid grass, and roof with white pots cover) were demonstrated by [7, 8].

The reduction of heat gain through the roofs using evaporative cooling systems was extensively investigated on open roof pond [9–11], and on water spraying over the roof, moving water layer over the roof, thin water film, and roofs with wetted gunny bags [9, 11, 12]. Chandra and Chandra have developed a periodic heat transfer model to study the effects of evaporative cooling using water spray and variable ventilation on the temperature control of a non-air-conditioned building [12]. The influence of evaporative cooling over the roof as compared to bare roof case and intermittent ventilation as compared to the continuous or no-ventilation case has been assessed for controlling the indoor air temperature. It was found that the effectiveness of the evaporative cooling can be improved by conscious choice of the rate and duration controls the inside air temperature significantly. It was concluded that a combination of evaporative cooling and variable ventilation can make the internal environment of a building more comfortable. Chandra et al. presented a theoretical assessment of three roof cooling systems for a non-air-conditioned building [5], and showed that the maximum cooling is achieved by water spray over the roof. But the roof pond system with stationary water is more effective in stabilizing the fluctuations of indoor temperature.

The present study suggests an improved roof design by combining the advantages of previous described cooling techniques (water ponds, low emissive surfaces) and inserted rocks of high thermal capacity materials. The resulting design can be more advantageous and effective than other systems for reducing heat during daytime and storing coolness at night. High thermal

Table 46.1 Material properties

Material	Density (kg/m^3)	Specific heat (j/kg°K^{-1})	Conductivity (w/m°K^{-1})
Concrete slab	2,400	1,080	1.8
Rocks	2,600	800	2.3
Water	1,000	4,175	0.613
Aluminum	1.22	1,008	0.026
Concrete slab	2,750	936	204

capacity materials (rock bed) will delay the entry of daytime heat into the building in such a way that by the time it reaches the interior during the evening it is least bothersome or often welcome. The roof is composed of a concrete ceiling and a flat aluminum plate separated with an air space partially filled with rocks inserted in a small quantity of water. The system is closed to prevent water vapor from skipping outside. A schematic diagram of the model design is shown in Fig. 46.1.

Mathematical Model

The basic configuration of the model considered here are shown in Fig. 46.1. It is a cubic room with 3 m height and 3 m width. The south wall is provided with a window and the North one is provided with a door. Physical properties of materials used for the roof are presented in Table 46.1.

The purpose of the present mathematical model is to determine the inside air temperature at each time step as a function of outside air temperature, solar radiation, and heat due to ventilation. The solution is based on the inside heat balance at each time step, and the method of lagging with zone capacitance uses information from previous time steps to predict system response and update the zone temperature at the current time. Fifteen minutes is used as a time step (the shorter the time step the smaller the error). The simulation was done for the described model for two highest-temperature summer days. The model is situated in Algeria (Laghouat, latitude +33.46°, longitude +2.56° and elevation 767 m). The simulated day was the 26 of July, and the maximum and the minimum temperature were respectively 42.7° and 24.5°.

Inside Air Heat Balance Equation

The heat balance for the inside room air may be formulated as follows:

$$C_{ai} \frac{dT_{ai}}{dt} = Q_{\text{int}} + Q_{ci} + Q_v \tag{46.1}$$

$C_{ai} \frac{dT_{ai}}{dt} =$: The heat stored in the inside air $C_{ai} = m_{ai} \cdot c_{ai}$
Q_{int}: Heat exchange by convection in the inside;

$$Q_{\text{int}} = \sum_{i=1}^{i=n} Q_{\text{int}i} \cdot (w)$$

Q_{int}: Heat exchange by convection between air and other surfaces

$$Q_{ci} = \sum_{i=1}^{i=n} h_i A_i (T_{si} - T_{ai}) (w) \tag{46.2}$$

$Q_{\text{int}}°$: Heat exchange by ventilations and infiltration

$$Q_v = m_{ae} c_{ae} (T_{ae} - T_{ai}) (w) \tag{46.3}$$

The derivative term $\frac{dT_{ai}}{dt}$ can be expressed by finite differences approximations as follows:

$$\frac{dT_{ai}}{dt} = \left(T_{ai}^t - T_{ai}^{t-\partial t}\right)\frac{1}{\partial t} \tag{46.4}$$

From the above equations the inside air temperature;

$$T_{ai}^t = \frac{\Sigma Q_i^t + \left[\frac{C_{ai}}{\partial t}T_{ai} + \Sigma A_i h_i T_{si} + m_{ae}c_{ae}T_{ae}\right]^{t-\partial t}}{\frac{C_{ai}}{\partial t} + \left[\Sigma A_i h_i + m_{ae}c_{ae}\right]} \tag{46.5}$$

Surface Temperatures

To calculate the internal surface temperatures $T_{si}{}^t$, at each time step t, as a function of outside conditions, finite deference equations based on heat balance at each node were used, which allows for temperature determination at any point of interest. The first step is to select these points, by subdividing the medium into a number of small regions represented by reference points called nodes. In our case, we considered the heat flow in one direction in plan elements (walls, roof and floor) composed of deferent materials, so each layer of these material is divided into small regions and represented by nodes. Clarke suggested that three nodes per homogeneous element and a 1 h time step, in building applications are consistent with acceptable accuracy [13]. The temperature for each single node at time t is evaluated using heat balance equations.

The heat exchange between internal slab nodes is modeled using Fourier's one-dimensional heat conduction equation (Kreith 1985).

$$\frac{dT}{dt} = \frac{d\lambda}{\rho c}\frac{d^2 T}{dx^2} \tag{46.6}$$

This equation can be solved numerically [9] by dividing the element into layers of thickness dx called nodes, making a heat balance for each node. The boundary condition for the inside surface nodes in contact with room air may be given by:

$$\frac{\lambda\partial T_{si}}{\partial x} = h_i(T_{si} - T_{ai}) \tag{46.7}$$

The boundary condition for the outside surface nodes in contact with outside air may be formulated using the following equation:

$$\frac{\lambda\partial T_{se}}{\partial x} = h_e(T_{se} - T_{ao}) \tag{46.8}$$

The upper roof surface exchanges heat with the outside air by convection and by radiation to the sky. According to [14], a horizontal surface with emissivity ε_r and absolute temperature Tr produces a net radiative cooling rate Qr, where

$$Q_r = A\sigma\varepsilon_r\left(T_r^4 - T_{sky}^4\right) \tag{46.9}$$

Where

$$T_{sky} = \varepsilon_{sky}^{1/4}T_{ae}, \varepsilon_{sky} = 0.741 + 0.0062T_{dp}$$

σ is the Stefan–Boltzman constant

Tdp is the surface dew point temperature in °C. It was computed as a function of the ambient temperature (Tae) and the relative humidity (RH), using the expression by Murray [8]:

$$T_{dp} = 237.3 \frac{\ln RH + a \cdot b}{(a - \ln RH) + a \cdot b} \tag{46.10}$$

The heat exchange by convection for outside horizontal surface is given by:

$$Q_c = A h_{ce}(T_r - T_{ae}) \tag{46.11}$$

The heat exchange between the lower aluminum surface and the upper rock bed surface is by radiation, convection and evaporation. Following equations reported in [25], we may write the following.

Heat exchange by radiation is given by:

$$Q_r = A h_r E_{wr,al}(T_{wr} - T_{al}) \tag{46.12}$$

Heat exchange by convection is given by:

$$Q_c = A h_{c,wr,al}(T_{wr} - T_{al}) \tag{46.13}$$

Heat exchange by evaporation and condensation is given by:

$$Q_{evp} = 6.3 \times 10^{-3}[P_{vs}(T_{wr}) - P_{vs}(T_{al})] \cdot L \cdot h_{c,wr,al} \tag{46.14}$$

Where L is the latent heat of evaporation at an average temperature, which is equal to 2,350 kJ/kg and Pvs is the saturated vapor pressure in kPa at temperature T in °C. For the temperature range

$$20 \leq T \leq 80\,°C$$

The following polynomial gives acceptable results [15]:

$$P_{vs}(T) = -16.037 + 1.8974T - 0.0699T^2 + 0.0012T^3 - 5.8511 \times 10^{-6}T^4 \tag{46.15}$$

In modeling the floor elements the earth temperature at 60 cm of depth below the floor is considered constant and equal to the daily average temperature of the region [4]. In the above equations the number of the unknowns is greater than the number of equations; these equations were solved by proposing the initial inside air temperature at start time t. This initial temperature Tai (t) will not be correct, and it is necessary to simulate the model with the same daily repetition of air temperature and solar radiation until the temperature of each node returns to the same value at the same time in each day simulation. At this point the building is in thermal harmony with the environment.

Experimental Measurements

The experimental setup consisted of two identical test cells (A) and (B), a cubic room with 3 m height and 3 m width. The south wall is provided with a window and the North one is provided with a door. The experimental cell (B) was the basic reference unit. The roof was constructed of simple aluminum sheet painted white.

Temperature Measurements

Air temperatures outside the room were measured using weather stations installed near the laboratory, far from the test cell by 150 m. The temperature at different positions under the roof level has been measured by copper constant thermocouples connected to digital thermometer. Thermocouples were fixed under the roof surface, and the end of the thermocouples was enveloped in thin aluminum paper to reflect the radiation from the surrounding interior surfaces. The readings of all thermocouples have been averaged to give the average temperature.

Results and Discussion

Figure 46.3 shows the calculated and measured inside and outside air temperature in test cell (A) with cooling system, without nocturnal natural ventilation. When the maximum outside temperature was 39 °C, the maximum measured and calculated temperatures were, respectively, 36 °C and 35 °C, while the minimum ones were 27 °C and 29 °C. The maximum inside air temperature of 36 °C accrued at 19.00 pm when the outside one at this time was 32 °C, and natural ventilation was allowed. Figure 46.4 shows the calculated and measured inside and outside air temperatures in cell (A) with a cooling system, with nocturnal natural ventilation. The ventilation lowered the inside air temperature by 3–4 °C.
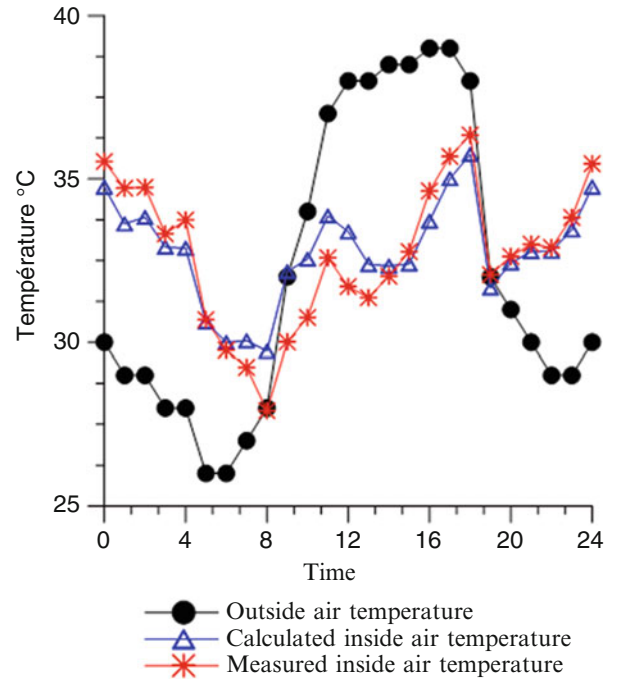
Fig. 46.3 Calculated and measured temperature in test cell (A) without night natural ventilation
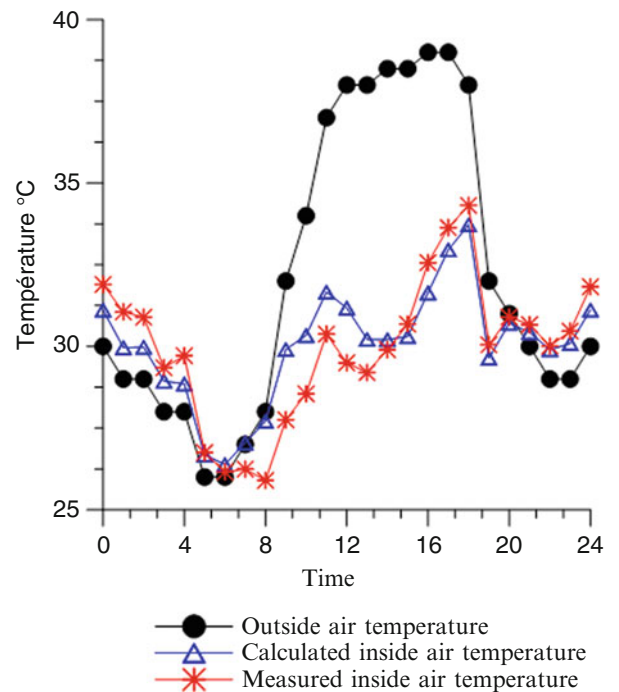
Fig. 46.4 Calculated and measured temperature in test cell (A) with night natural ventilation

Fig. 46.5 Calculated and measured temperature in test cell (B) without night natural ventilation
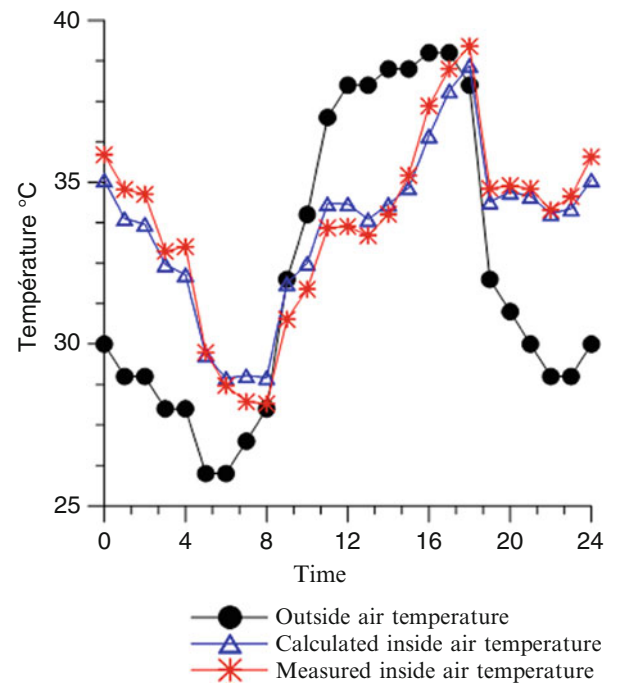
Fig. 46.6 Calculated and measured temperature in test cell (B) with night natural ventilation
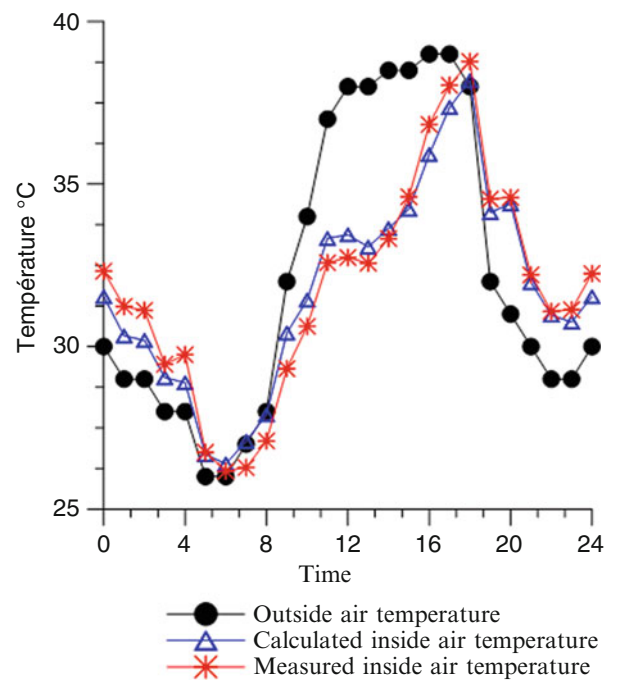
Figures 46.5 and 46.6 show the calculated and measured inside and outside air temperatures in test cell (B) without a cooling system, with and without nocturnal natural ventilation. The calculated and measured inside air temperature in Fig. 46.5 present no differences; however, in Fig. 46.6 the two graphs present small differences during ventilation period due to the uncertainty in wind speed which is variable from 1 h to another.

Figure 46.7. shows a comparison of room air temperatures with cooling roof system and with bare roof without room night natural ventilation. It can be seen from this figure that the evaporative reflective roof can reduce the internal room air

Fig. 46.7 Comparison of room air temperatures, test cell (A) and (B) without night natural ventilation
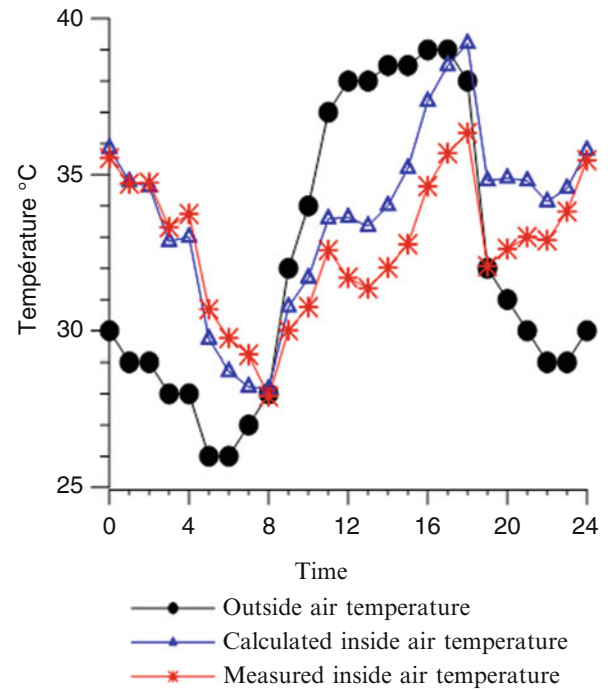
Fig. 46.8 Comparison of room air temperatures, test cell (A) and (B) with night natural ventilation
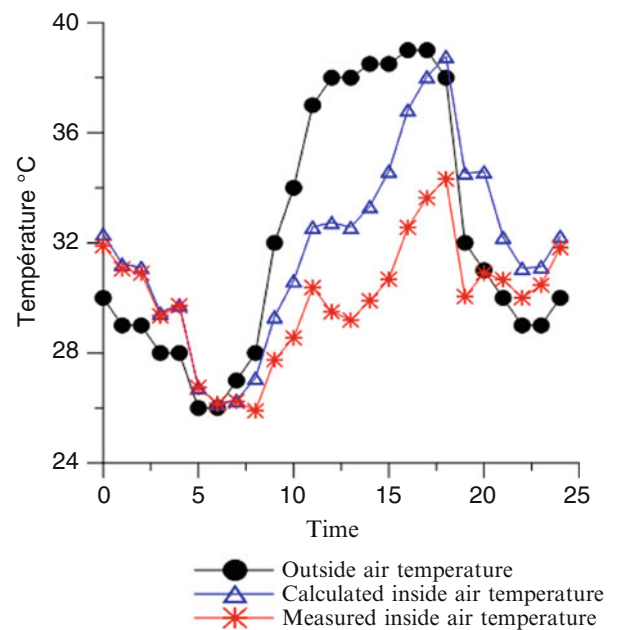
temperatures during the day up to 10 °C in comparison to the air temperatures for a bare roof over the room. Figure 46.7 is the comparison of room air temperatures with cooling roof system and with bare roof when room night natural ventilation is allowed. The ventilation was allowed from 8 pm till 9 am, a period when the outside air temperature is relatively low. This can significantly improve cooling of room air temperatures, as shown in Fig. 46.8.

Conclusion

In comparison between calculated and measured inside air temperatures in cell (B) without cooling system, without nocturnal natural ventilation, the two temperatures have almost the same values; however, the calculated and measured ones in the same cell with nocturnal natural ventilation present a small difference between calculated and measured temperatures during ventilation period as shown in Fig. 46.8, due to wind speed variations during nighttime, which was usually considered a constant value in calculations.

Measured and calculated temperatures in cell (A) with cooling system, with and without nocturnal natural ventilation, present a small difference in two time periods, from 6.00 am till 5.00 pm and from midnight till 4.00 am which correspond to the evaporation and condensation periods. The differences were due to the fact that the quantities of water vapor and condensate water were not exactly well known.

Under hot arid conditions a full-scale test cell for an evaporative reflective roof used to improve space cooling in buildings has been tested. The experimental results examined the effectiveness of such a roof cooling system in comparison to a bare roof. The results showed that cooling inside buildings can be improved by the application of such a cooling design. It was also seen that combining evaporative reflective roof with night ventilation increases such cooling more significantly.

Nomenclature

C_{ai}	Specific heat of inside air (J/kg.K)	I	Total solar radiation (W/m)
C_{ae}	Specific heat of outside air (J/kg.K)	I_j	Long wave radiation (W/m)
E	Surface emissivity	P_{vs}	Saturated vapor pressure (kPa)
$h_{c,i}$	Inside convection heat transfer coefficient (W/m^2.K)	T_{al}	Aluminum outside surface temperature (C)
		T_{ao}	Sol-air temperature
h_r	Radiation heat transfer coefficient (W/m^2.K)	T_{wr}	Rock bed upper surface temperature (C)
$h_{c, wr, al}$	Convection heat transfer coefficient between the rock bed and aluminum (W/m^2.K)		

References

1. Bouchair A (1994) Solar chimney for promoting cooling ventilation in southern Algeria. Building Serv Eng Res Technol 15(2):81–93
2. Evans M (1980) Housing, climate and comfort. The Architectural Press, London
3. Bahadori MN (1978) Passive cooling systems in Iranian architecture. Sci Am 238:144–154
4. Bouchair A (1989) Solar induced ventilation in the Algerian and similar climates. PhD thesis, University of Leeds, Leeds, UK
5. Chandra S, Kaushik SC, Bansal PK (1985) Thermal performance of a non-air-conditioned building for passive solar air-conditioning: evaluation of roof cooling systems. Energy Build 8:51–69
6. Lambert (1988) Heat transfer through roofs of low cost Brazilian houses. PhD thesis. UK: University of Leeds
7. Nayak JK, Srivastava A, Singh U, Sodha MS (1982) The relative performance of different approaches to passive cooling of roofs. Build Environ 17(2):145–161
8. Verma R, Bansal NK, Garg HP (1986) The comparative performance of different approaches to passive cooling. Build Environ 21(N2):65–69
9. Sodha MS, Srivastava A, Kumar A, Tiwari GN (1980) Heating and cooling of a building by flow of water over the roof. Appl Energy 7(1):229
10. Sodha MS, Kumar A, Singh U, Srivastava A, Tiwari GN (1981) Experimental validation of thermal model of open roof pond. Build Environ 16(2):93
11. Sodha MS, Singh U, Tiwari GN (1980) Periodic theory of an open roof pond. Appl Energy 7(4):307
12. Chandra S, Chandra S (1983) Temperature control in a building with evaporative cooling and variable ventilation. Solar Energy 30(4):381–387
13. Clarke AJ (1985) Energy simulation in building design. Adam Hilger, Bristol
14. Berdahl P, Fromberg R (1982) The thermal radiance of clear skies. Sol Energy 29(4):299–314
15. Sfeir AA, Guarracino G (1981) Ingé´nerie des systeme solaires applications a' l'habitat. Technique et documentation
16. Bouchair A, Dupagne A (2003) Building traditions of Mzab facing the challenges of re-shaping of its built form and society. Building Environ 38(1):1345–1364
17. Bouchair A, Fitzgerald D, Tinker JA (1989) Passive solar induced ventilation. Alternative energy sources VIII. Proceedings of the Miami International Conference on Alternative Energy Sources (1987: Miami Beach, Florida). Solar energy fundamental and applications, vol 1. Hemisphere Publishing Corporation, New York
18. CIBSE guide (1986) Vol. A. London: chartered institution of building services engineers
19. Deihimi S (1984) Control of sunshine in buildings by fixed shading in continental climates. PhD thesis, Leeds University
20. Golany G (1980) Housing in arid lands: design and applications. The Architectural Press, London
21. Murray FW (1967) The computation of saturated vapor pressure. J Appl Meteorol 6:203–204
22. Nahar NM, Sharma P, Purohit MM (2003) Performance of different passive techniques for cooling of buildings in arid regions. Build Environ 38:109–116
23. Runsheng T, Etzion Y, Erell E (2003) Experimental studies on a novel roof pond configuration for the cooling of buildings. Build Environ 28:1513–1522
24. Sodha MS, Kharty AK, Malik MAS (1978) Reduction of heat flux through a roof by water film. Sol Energy 20:189

Investigation of Latent-Heat Storage Systems for Green Building Applications

Devrim Aydin, Zafer Utlu, and Olcay Kincay

Abstract

In green building applications, highest energy demands are needed for air conditioning to provide comfort conditions. This study is done by using real data obtained from a prototype structure built as part of a project. The necessity of heat storage systems during the usage of solar energy and ground-sourced heat pump systems for heating is investigated in the present study. This way, various techniques used for storing heat are researched and compared. Efficiency of latent-heat storages, constituted by utilising latent heat of phase change material, is analysed. Thermodynamic analyses of the heating system combined with solar panels, ground-sourced heat pump, and latent-heat storage are conducted. Lastly for variable ground temperature and solar radiation, changes in amount of heat storage in a heat storage system are analysed. For a 6-month heating period, analyses showed that especially in winter, energy consumption in compressor shows a sharp rise. So utilising period from heat pump with low energy consumption is too short. This study focuses on energy generation from solar panels in relation to time. Thereby, supply ratios of hourly energy demand of the inspected building are investigated.

Keywords

Energy storage • Renewable energy • Green building

Introduction

Due to the technological and industrial development and the increase in human population, environmental pollution is getting even worse. This phenomenon has increased the tendency to adopt renewable energy sources. Because the public buildings and industrial corporations are generally located at city centres, migration to the city centres have been increasing, resulting in air pollution and unplanned urbanisation. The main result of unplanned urbanisation is this: structuring without any planning about energy systems. This situation ends up with sharp rises in energy consumptions. On the contrary, with the recent studies, building energy consumptions have been tried to be kept under control. Concordantly "energy performance certificate" is issued to buildings, thereby reducing energy consumption and aiming and encouraging an increase in utility of renewable energy systems.

In addition to this, rise in the amount of greenhouse gases and price of fossil fuels are the driving force to benefit from various renewable energy resources [1]. For most people all over the world, solar energy is evaluated as a primary energy source for the future. Scientists are maintaining their research about new and renewable energy resources [2]. But improving energy storage systems is as important as using new energy resources. Storage of energy in an appropriate way and

D. Aydin (✉) • O. Kincay
Yildiz Technical University, 34349 Beşiktaş, İstanbul, Turkey
e-mail: devrimayd@yahoo.com; okincay@yahoo.com

Z. Utlu
İstanbul Aydın Üniversity, Florya, İstanbul, Turkey
e-mail: zaferutlu@aydin.edu.tr

developing systems to make it available in the case of necessity are the key missions of today's researchers. Storing energy in a suitable way provides an equilibrium between supply and demand, also increases performance and utility of energy systems as well as contributes to energy conservation. Energy storage systems provide an economical usage of fuels and as a result reduce the amount of waste energy. Thus, these systems improve utility of energy systems in an economical way [3].

Nowadays fossil fuels, on which national energy systems are dependent, are limited and predicted to be an insufficient and expensive source in the future. In addition to this, common energy demand rises day by day. Beside this, depending on the rise in energy consumption, environmental impacts such as climate change and atmospherical pollution are increasing. Greenhouse emissions have attracted attention as a primary factor of climate change. Within this context, various international organisations such as Kyoto Protocol study this problem [4].

Developing heat storage systems has a vital importance in achieving advanced level and efficient energy systems.

Energy Consumption and Green Buildings

Global energy generation and consumption amounts have a vital importance in each step of economical development, for energy conservation and using it efficiently. Global energy consumption is related to economical and environmental improvement, so energy consumption factor necessitates considering design of energy-saving and efficient systems as well as environmental factors. Depending on the economical development, the main consumption fields of energy are structuring, environmental improvement, commercial establishments, industries, transportation and buildings. In recent years the demand for structuring has been heavily increased. Huge buildings constructed to meet this demand have an important effect on energy consumption. In developed countries the highest energy consumption is in the building sector with 27 % (Fig. 47.1). Also 70 % of consumption of electricity energy and atmospherical emissions including greenhouse gases sourced from the building sector. Determination of energy consumption rates and energy losses are two important necessities for designing energy-efficient buildings [5].

Green Buildings are known as sustainable buildings. Green building applications are aimed to meet the 75–80 % of thermal and electrical demand from renewable energies, whereas in classical structures only 15–20 % of energy demand is supplied from renewable energies. Recently, green building applications have been maintaining a rising trend. These applications have paid attention not only to active technologies (mechanical cycle) but also to construction architecture, solar radiation, green fields and construction materials for decreasing energy consumption and greenhouse-gas emissions. In addition to this, renewable energy sources used for supplying energy to buildings are cyclical. So these systems sometimes cannot meet the energy demand of building or sometimes provide more energy than what is needed. When all these issues are taken into consideration, it is clear that improving energy storage systems will increase the utility of renewable energy sources.

Recently, to keep energy usage efficient, smart building management systems have been developed. In addition to this, various disciplines of engineering such as lighting, air conditioning, cooling, ventilating and heating have been improved, thereby providing suitable thermal conditions, high-quality indoor air, and sufficient lighting. Thus, appropriate comfort conditions are achieved. Despite usage of energy-efficiency enhancement techniques, capital costs increase over a long
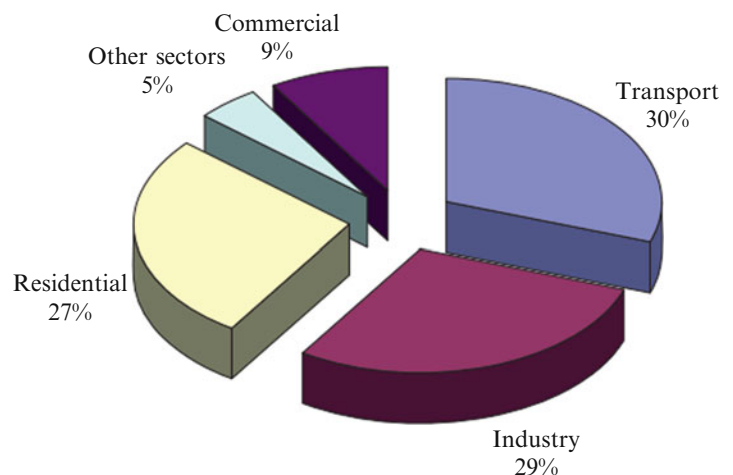
Fig. 47.1 Energy consumption breakup sector wise [5]

Fig. 47.2 Avarage breakup of energy usage and losses in buildings [8]
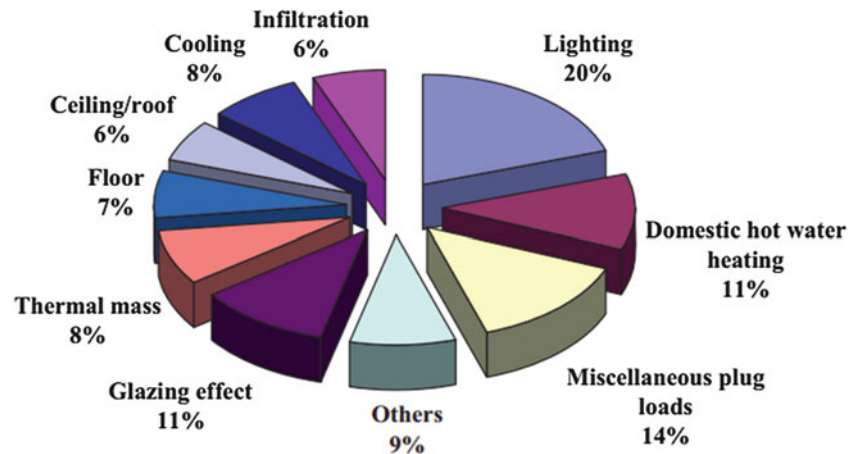
period of time with low energy consumption amounts; it meets the capital costs and provides profitability. Briefly, a well-designed building is a construction which meets the comfort demand of people living in it with minimum energy consumption (Fig. 47.2) [5].

Latent-Heat Storage Systems in Buildings

Recently, due to the increasing energy demand and environmental factors, interests on energy storage systems have been rising. As it can be seen from the diagram above, building sector is one of the leading sectors in energy consumption. Although there are several methods for decreasing energy consumption in buildings, a system which has a potential of compensating peak thermal load demand of a building is a necessity. Energy storage systems store heat in the period during which the building has a low heating or cooling energy demand, for using it during peak thermal load conditions. Heat storage systems integrated with thermal systems provide usage of thermal energy in an efficient way as well as stabilise unstable energy demands [6].

Thermal Energy Storage Methods in Buildings

Heat storage systems, depending on their dimensions, applied method and heat storage material, can be applied in low temperature for a short time or a long time period in any application. In case the difference between solar energy and energy demand of building is low, short time heat storage is applied. Long time period heat storage is used to supply seasonal energy demand with solar energy. Utilising from heat storage increases contribution of solar energy to the process of balancing overall energy demand. By considering thermal energy generation prices and utilisation from solar energy, it is decided whether short time storage or long time storage can be used [7].

The selection of heat storage method mainly depends on heat storage period, economical applicability and operating conditions. For any application, efficiency and economy of heat storage not only depends on heat storage method but also on design of the system. For a heat storage system design, the following factors must be considered [8]:
1. Heat storage capacity of unit mass and volume of heat storage material.
2. Heat storage, recovery temperature and method.
3. Temperature gradient.
4. Dimensions of system components.
5. Material, shape and dimensions of heat storage tank.
6. Properties of the environment where the stored energy is used.
7. Total cost of storage system.

Mainly there are three types of heat storage systems. These are sensible, latent and chemical energy storage systems (Fig. 47.3). Sensible heat storage systems store energy by changing the temperature of a heat storage material. In thermochemical heat storage systems, energy is stored using a fission reaction. Recovering energy from the storage takes place with an inverse reaction [9].
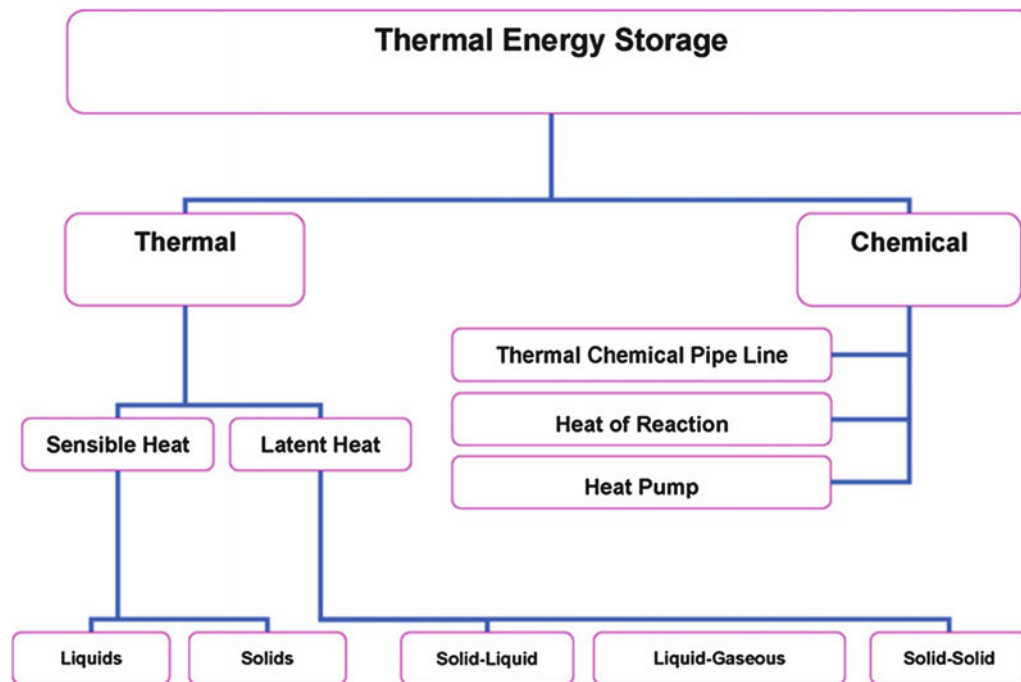
Fig. 47.3 Heat storage methods [3]

In latent-heat storage systems storage, recovery of heat takes place with a fusion reaction (melting/solidification) during phase change period. Latent-heat storage systems, in which phase change materials are used, allow for storing heat densely as well as in high amounts with low temperature and volume changes [4].

Benefiting from heat storage systems allows for usage of thermal systems efficiently and also provides conservation of energy and thermal comfort. In this study a latent-heat storage system in which paraffin is used as a heat storage material is investigated. Effect of heat storage system in regard to the energy consumption of a building was demonstrated.

Latent-Heat Storage Materials

Classification
Depending on the phase change type, phase changed materials are classified in three groups. They are solid–solid PCMs, solid–liquid PCMs and liquid–gas PCMs. The most suitable phase change materials for thermal energy storage are solid–liquid ones. Solid–liquid PCMs are investigated in three groups: organic PCMs, inorganic PCMs and eutectics [4].

PCM Selection Criteria
Although selection of PCM for any application is a complex problem, it has an importance in heat storage performance. Potential PCMs depend on the application conditions; they must have appropriate melting temperature, high fusion (phase change) heat and thermal conductivity. Expected properties of PCMs are given in the table below (Table 47.1). The most suitable PCMs used in heat storage systems in a building environment in terms of melting temperature are paraffin, fatty acids, salt hydrates and eutectic mixtures.

Experimental Study

In this study utility of thermal storage combined with solar collectors for heating of an energy building is investigated. Yildiz Energy Building is located at Davutpasa Campus of Yildiz Technical University.

Table 47.1 Expected properties of phase change materials [4]

Thermodynamic properties	Appropriate melting temperature scale
	High fusion latent heat per unit volume
	High thermal conductivity
	High specific heat and density
	For preventing storage problem, low volume changes and vapour pressure at phase change duration
	Suitable melting
Kinetic properties	High nucleation rate to prevent rapid cooling
	High crystallisation rate to meet heat demand from heat storage
Chemical properties	Inverse melting/solidification cycle
	Chemical stability
	Not to have any deterioration after a high number of phase change cycles
	Not to be corrosive
	Not to be a toxic, flammable and explosive material
Economic properties	Suitable price
	A wide range of application areas

Fig. 47.4 Heating system diagram of Yildiz renewable energy building
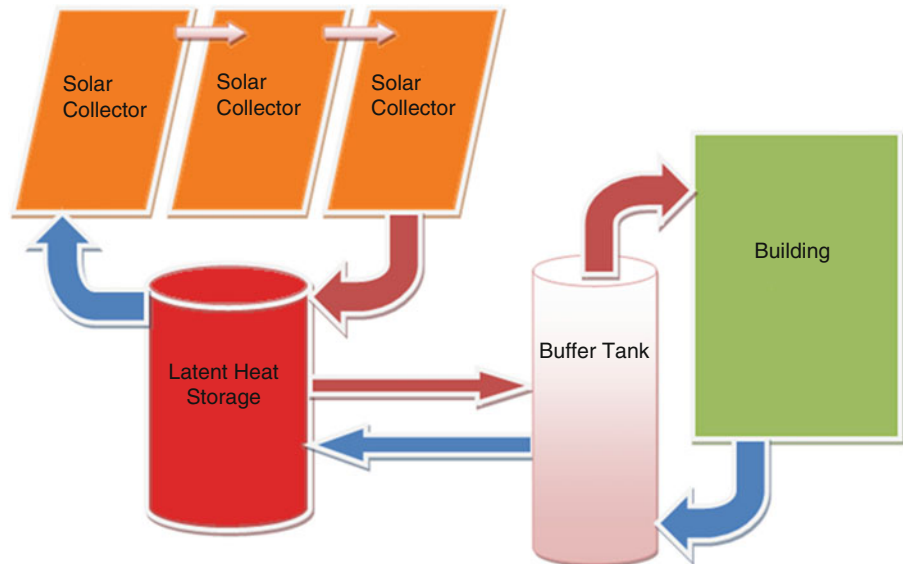
System Description

Solar energy is a cyclical energy source. So storing excess energy during daytime and using it at nighttime will increase utilisation of solar energy. The energy building is a duplex structure which has 46 m^2 floor areas [10]. The building is heated with the pipe coils furnished inside the wall. For heating purpose, three solar collectors having a 4.86 m^2 total surface area are used. The heating system diagram of the energy building is given below (Fig. 47.4). For the experiment, paraffin, which melts in the range of 42–44 °C and which is easily found in Turkey, was used. The shell that Paraffin was stored in has a volume of 0.063 m^3, and the paraffin shell is located in an outer shell which is 0. 22 m^3. Heat transfer fluid circulates in the gap between the inner and outer shell. There is also a 0. 1 m diameter gap in the middle of the inner shell to increase heat transfer surface area.

Evaluation of Experimental Measurements

Determination of Heat Losses of the Building and Heat Gain of Solar Collectors

In this study, a 6-month heating season between October and March was investigated. For analysing the system, hourly average solar irradiation and temperature for each day were used [4]. Using this data, hourly average building heat load and heat gain of solar collectors were calculated. Accumulated excess energy during daytime was analysed, and storable thermal energy for nighttime was determined (Figs. 47.5, 47.6, 47.7, 47.8, 47.9, and 47.10).

The rate of heat gain of the solar collectors was calculated by using Eq. (47.1):

$$Q_u : A_c . F_R \left[H_t . (\tau\alpha)_n U_c (T_{f,i} - T_a) \right] \tag{47.1}$$

The rate of heat loss from each surface of the experimental building was calculated by using Eq. (47.2):

$$Q_c : U.A.(T_i - T_a) \tag{47.2}$$

By collecting heat loss from each surface, overall heat loss of the building investigated depends on time. The difference between heat gain from heat collection unit and overall heat losses of the building Eq. (47.3) gives the amount of storable energy:

$$Q_s = Q_u - Q_c \tag{47.3}$$
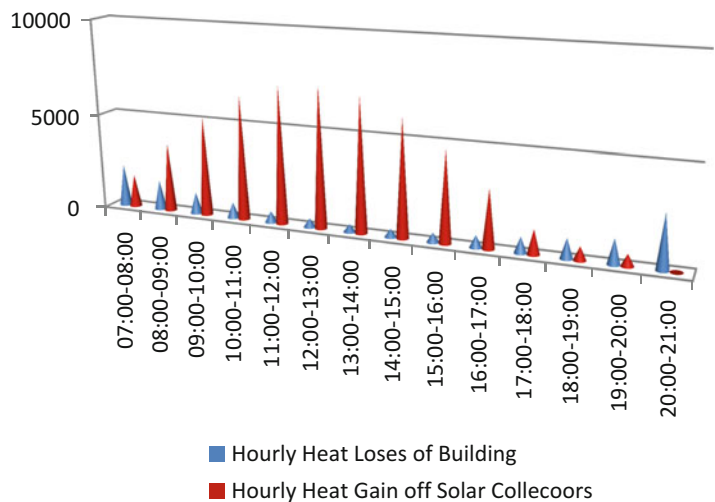
Fig. 47.5 October, building heat loss–collector heat gain diagram
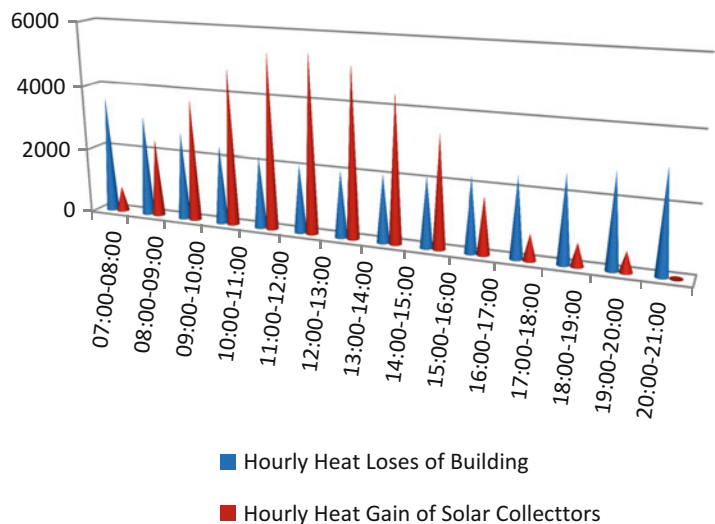
Fig. 47.6 November, building heat loss–collector heat gain diagram

Fig. 47.7 December, building heat loss–collector heat gain diagram
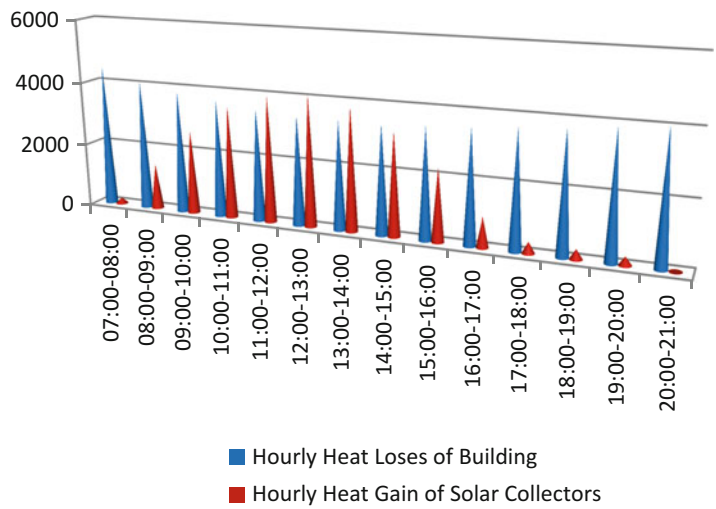
Fig. 47.8 January, building heat loss–collector heat gain diagram
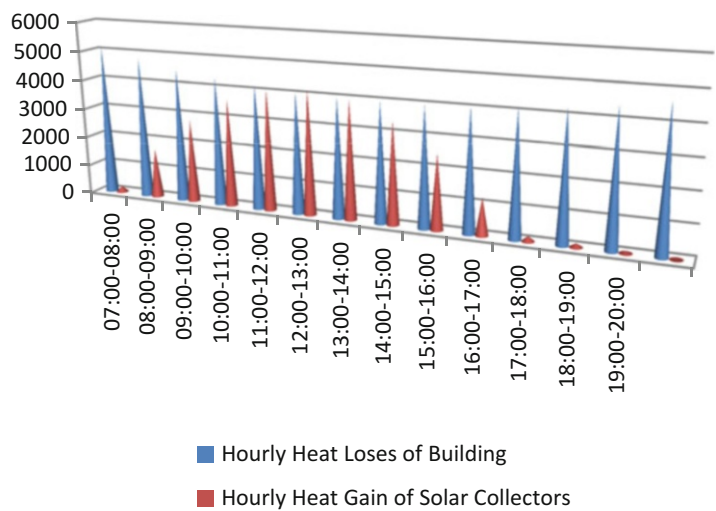
Fig. 47.9 February, building heat loss–collector heat gain diagram
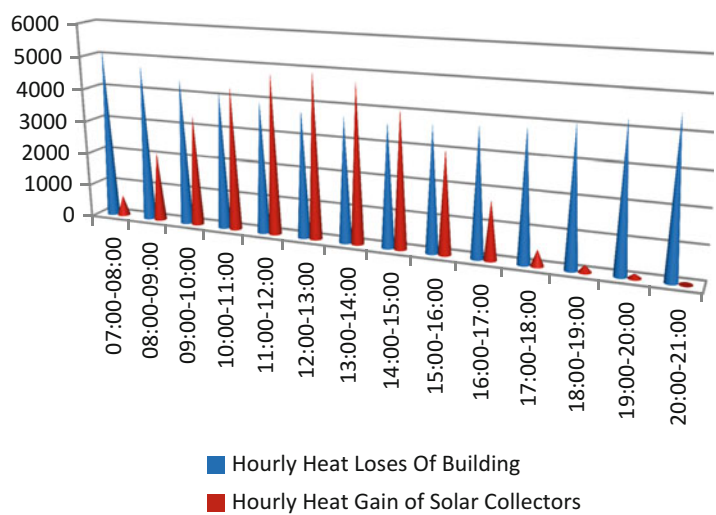
Fig. 47.10 March, building heat loss–collector heat gain diagram
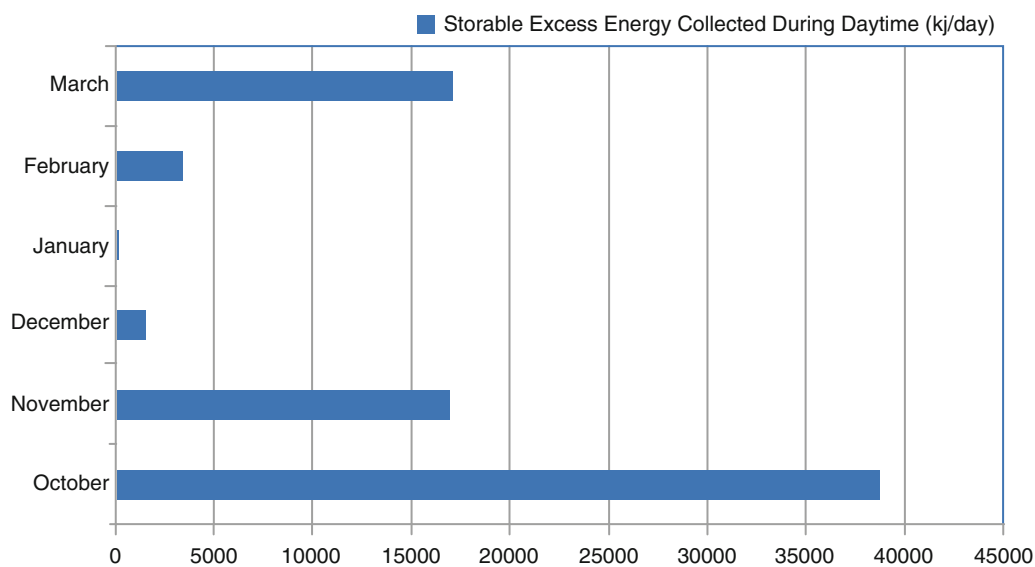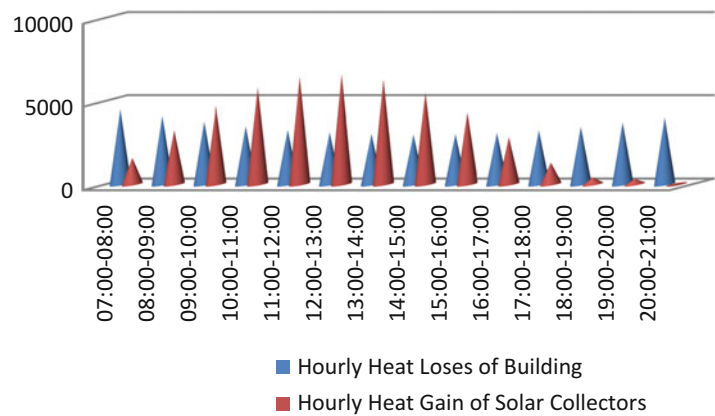
Fig. 47.11 Daily storable excess energy for a 6-month heating period

This study was carried out at Yildiz Renewable Energy Building, located at Yıldiz Technical University Davutpasa Campus. Building Heat Loss–Collector Heat Gain graphics given above shows hourly changes in heat losses of building against thermal energy absorbed by collectors. Concordant with these results, during the 3-month period from December through February, because the heat load of the building rose sharply, storing energy gained by collectors did not seem presentable. On the other hand, during spring and winter period (December, November, March) especially between the hours 10:00 and 15:00 utilising heat from thermal storage seemed possible. During this period, storable excess thermal energy was available. Stored heat could be used at nighttime while the solar energy was not available.

Determining the Amount of Excess Storable Energy

Daily amount of storable, excess energy figured out in the diagram below (Fig. 47.11). It is clearly shown from the figure that especially in December, October and March high amount of storable energy is available. In the last decade energy demand has been increasing from day to day however energy supply decrease in the similar trend. So utilising from renewable energies such as solar energy and wind energy is a necessity. Studies on the way of increasing efficiency of energy systems are important for improving utility of these sources. However, storing energy and using it in the time while energy demand increases will contribute to economy and also provide a demand–supply balance. Within this context, it seems worth to do research and development studies about heat storage systems to increase their efficiency (Fig. 47.11).

Results and Discussion

This study carried out in Yildiz Renewable Energy Building located at Davutpaşa Campus, Yıldiz Technical University. Utility of thermal storage in the process of heating the energy building was investigated. Heat storage systems; depends on their dimensions, applied storage system and heat storage material, can be applied for short time or long time. Short time storage can be applied if the difference between solar energy and energy demand is low. For meeting the seasonal energy demand, long time storage applied. This type of application allows for a rise in utility of solar energy.

The study results are as follows:

- With this system, in a 3-month period, from December through February, because the heat load of the building rose sharply, storing the energy gained by collectors did not seem presentable.
- In Spring and Autumn period (December, November and March) especially between the hours 10:00 and 15:00, utilising heat from thermal storage seemed possible. During this period storable excess thermal energy was available. Stored heat could be used at nighttime while the solar energy had run out.

Conclusions

The results of this study show that during day time, especially in Autumn and Spring, because the heat load of the building is low, most of the collected thermal energy cannot be used. Heat storage systems allow for storing this excess energy anytime while the heat loads get higher.

Research and development studies are important to increase the efficiency and utility of latent-heat storage systems. Consequently the rate of utilisation from solar energy will get higher.

Nomenclature

A	Area, m^2	H	Global radiation, w/m^2
Q	Heat, w	T	Temperature, $°C$
F_R	Exchanger heat efficiency coefficient	U heat	Transfer coefficient, $w/m^2\,°C$

Greek Letters

τ	Diffusion coefficient	α	Absorption coefficient

Subscripts

u	Useful	f, i	Fluid inlet
c	Collector	a	Ambient
t	Total	i	Indoor

References

1. Benli H, Durmuş A (2009) Performance analysis of a latent heat storage system with phase change material for new designed solar collectors in greenhouse heating, Fırat Üniversitesi. Sol Energy 83:2109–2119
2. http://re.jrc.ec.europa.eu/pvgis/
3. Sharma A, Tyagi VV, Chen RC, Buddhi D (2009) Review on thermal energy storage with phase change materials and applications. Renew Sust Energ Rev 13:318–345
4. Zhou D, Zhao YC, Tian Y (2012) Review on thermal energy storage with phase change materials in building applications. Appl Energy 92:593–605
5. Paremeshwaran R, Kalaiselvam S, Harikrishnan S, Elayaperumal A (2012) Sustainable thermal energy storage technologies for buildings; a review. Renew Sust Energ Reviews 16:2394–2433
6. Koca A, Oztop FH, Koyun T, Varol Y (2008) Energy and exergy analysis of a latent heat storage system with phase change material for a solar collector. Renew Energy 33(4):567–574
7. Koray A (2006) Güneş Enerjisinin Depolanması ve Isıl Analizi, Master's Thesis, Erciyes University
8. Öztürk H (2005) Experimental evaluation of energy and exergy efficiency of a seasonal latent heat storage system for greenhouse heating. Energy Convers Manag 46:1523–1542
9. Dincer İ (2002) Thermal energy storage systems as a key technology in energy conservation. Int J Energy Res 26:567–588
10. Kıncay O, Utlu Z, Ağustos H, Akbulut U, Açıkgöz Ö (2009) Yenilenebilir Enerji Kaynaklarında Birleşme Eğilimi. Sigma: Nat J Eng Sci 27(2):60–82

Short- and Long-Term Solar Radiation Estimation Method

48

Yavuz Selim Güçlü, İsmail Dabanlı, and Eyüp Şişman

Abstract

In this study, Angstrom equation solar radiation estimation values corresponding to the sunshine durations are achieved by a linear equation, which is an improvement over the classical model. The results turn out to be better than the classical Angstrom equation. In the suggested equation, 1–10 days' solar irradiation values are assumed to affect the present-day values as short-term estimates. The proposed model for summer months (June–July–August) has provided estimations that are in close agreement with observations. Both long- and short-term estimations have been obtained rather successfully. In the proposed methodology there are two extra factors, as dependence coefficients. Finally, the classical Angstrom equation remains as a special case of the model.

Keywords

Solar radiation • Sunshine duration • Angstrom equation • Short-term estimate • Dependence

Introduction

Especially in the twentieth Century and during its second half energy crisis has been experienced due to extreme consumption of fossil fuels. As a result, people began to search for alternative energy sources. Solar energy is one of the clean energy sources. To benefit from solar energy as the most important energy source in the future, present calculation and estimation of the radiation amounts have been a problem waiting for solution. In order to determine the potential of the solar energy for an area, solar radiation values are prerequisites. Thus, the decisions of whether or not to invest in a region should be given by the potential of solar energy plan possibilities in the area.

Angstrom [1] made the first study on this subject and proposed a linear equation that expresses the relationship between the sunshine duration and amount of solar radiation. Later, Page [2] changed the definition of an expression by using radiation on the horizontal area out of the atmosphere instead of clear day radiation. Similarly, many researchers have demonstrated studies linearly [3–12]. In addition to these studies, Şahin and Şen [13] brought dynamism to the Angstrom equation. Some of the scientists have suggested approaches by proposing the second order equations. Ögelman et al [14] stated that second order equation better expresses the relationship between solar radiation and sunshine duration. Akınoğlu and Ecevit [15], and Yıldız and Öz [16] studied the same problem by using second order equation too. Samuel [17] proposed a nonlinear equation in third order. Şen [18] contributed to the nonlinear model estimates of the solar radiation. Additionally, Şen [19] has estimated solar radiation using fuzzy logic modeling techniques. The aforementioned studies, respectively, are

Y.S. Güçlü (✉) • İ. Dabanlı
Department of Hydraulics, Faculty of Civil Engineering, Istanbul Technical University, 34469 Maslak, Istanbul, Turkey
e-mail: gucluya@itu.edu.tr; dabanli@itu.edu.tr

E. Şişman
Department of Hydraulics, Faculty of Civil Engineering, Yildiz Technical University, 34220 Davutpasa, Turkey
e-mail: esisman@erdemir.com.tr

linear and nonlinear, with no dependencies between successive values. However, the solution suggested in this article takes into consideration the linearity with dependencies.

The purpose of this article is to show the present day's solar radiation and sunshine duration depending on the previous days' values and to provide new equation that yields better results than Angstrom approach. In the equation, two important dependency coefficients are implemented. This method reduces to the classical Angstrom equation when the dependencies are equal to zero.

Methodology

The following linear Angstrom equation that estimates solar radiation is the starting point of the present study.

$$\left(\frac{H}{H_0}\right) = a + b\left(\frac{S}{S_0}\right) \tag{48.1}$$

H, Solar Radiation, H_0, Monthly Mean Solar Radiation, S, Sunshine Duration, S_0, Monthly Mean Sunshine Duration, a and b are coefficients.

To refine this equation, the time-effect is considered in other words, today's sunshine duration and solar radiation are thought of dependent on previous or earlier days' sunshine duration and solar radiation, amounts. In Eq. (48.2), additionally, t, day, c and d coefficients.

$$\left(\frac{H}{H_0}\right)_t = a + b\left[\left(\frac{S}{S_0}\right)_t - d\left(\frac{S}{S_0}\right)_{t-i}\right] + c\left(\frac{H}{H_0}\right)_{t-i} \tag{48.2}$$

Where 'i' value ranges from 1 to 10 for short-term estimates. However, for some stations, it can be further extended to include the range $(t - 1, t - 2, t - 5, t - 10, t - 15, t - 30, t - 60,$ etc.). Long-term estimates are suitable for the summer months from $t - 1$ to $t - 731$.

In the first stage of creating the equation, c and d dependency coefficients are obtained, where c is the solar radiation dependency coefficient and d is sunshine duration dependency coefficient.

To obtain the solar radiation dependency coefficient c,

$$\left(\frac{H}{H_0}\right)_{t-i}$$

is plotted against

$$\left(\frac{H}{H_0}\right)_t,$$

where the slope of the drawn regression line yields c coefficient. Similarly, to obtain the sunshine duration dependency coefficient d,

$$\left(\frac{S}{S_0}\right)_{t-i}$$

is plotted versus

$$\left(\frac{S}{S_0}\right)_t,$$

where the slope of the drawn regression line gives coefficient d.

Finally, a and b coefficients are determined similar to the Angstrom case. For this purpose, the following equations are substituted into Eq. (48.2), then into Eq. (48.5), which yields,

$$X = \left(\frac{S}{S_0}\right)_t - d\left(\frac{S}{S_0}\right)_{t-i} \tag{48.3}$$

$$Y = \left(\frac{H}{H_0}\right)_t - c\left(\frac{H}{H_0}\right)_{t-i} \tag{48.4}$$

$$Y = a + bX \tag{48.5}$$

To obtain coefficients a and b, X values are pointed on the horizontal axis and Y values on the vertical axis. The slope of the drawn regression line provides coefficient b, and the intersection point on the vertical axis gives the coefficient a. New version and the classical Angstrom equations are now available for estimating the solar radiation.

Application

Daily data used in this study are taken from DMI and measured in Antakya, Turkey from 2000 to 2010. For Antakya a, b, c, and d coefficients are obtained by using approximately half of the data and then the rest of the data are used for validation. The same procedure is applied by using Angstrom equation. In addition, for each $t - i$, Angstrom equation is redetermined. First, coefficients are determined according to $t - 1$.

In Fig. 48.1, the horizontal values are solar radiations for $t - 1$ day; the vertical values are solar radiations for t day and then regression line is drawn. Coefficient c is determined as the slope of the regression line, as 0.541.

In Fig. 48.2, the horizontal values are sunshine durations for $t - 1$ day; the vertical values are sunshine durations for t day and then regression line is drawn. Coefficient d is determined by the slope of the regression line as 0.591.

In Fig. 48.3, the horizontal values are X's, the vertical values are Y's and hence the regression line is drawn. Coefficient b is determined by the slope of the regression line as 0.321 and the intercept point on the vertical axis yields the coefficient a as 0.1.

In Fig. 48.4, the horizontal values are sunshine durations for t day, whereas the vertical values are solar radiations for t day and then the regression line can be drawn. The coefficient b is then determined by the slope of the regression line as 0.329 and the intercept point on the vertical axis gives the coefficient as 0.193.
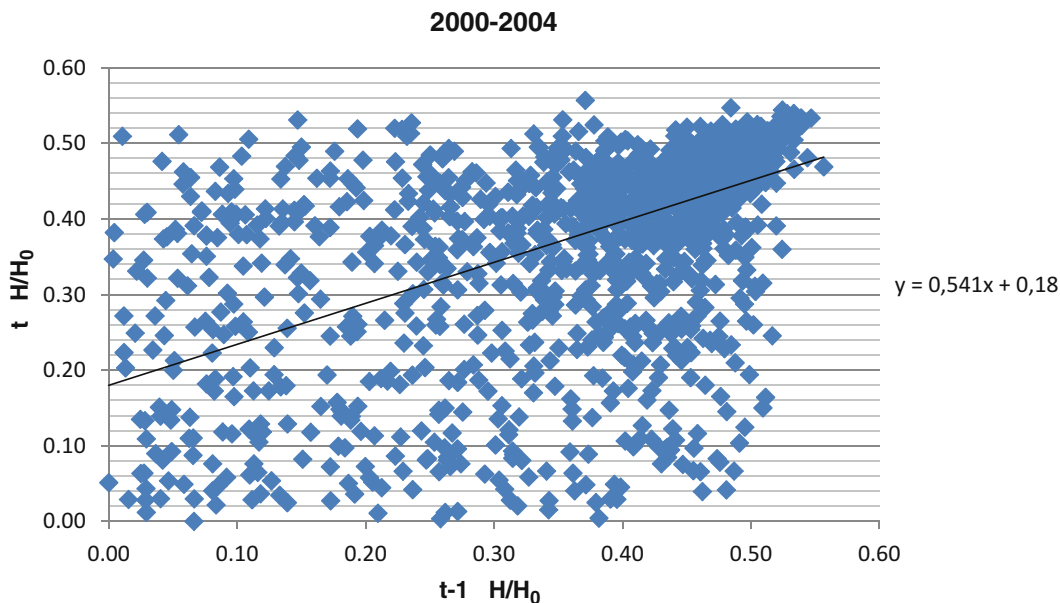
Fig. 48.1 Lag-one scatter diagram of solar radiation for c coefficient

2000-2004
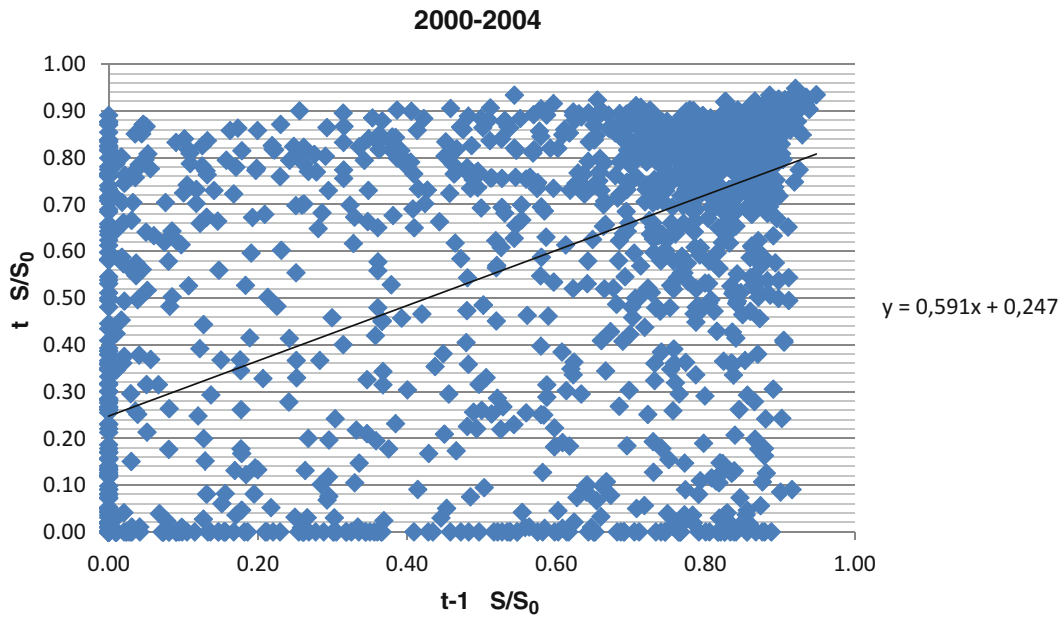
Fig. 48.2 Lag-one scatter diagram of sunshine duration for d coefficient

2000-2004
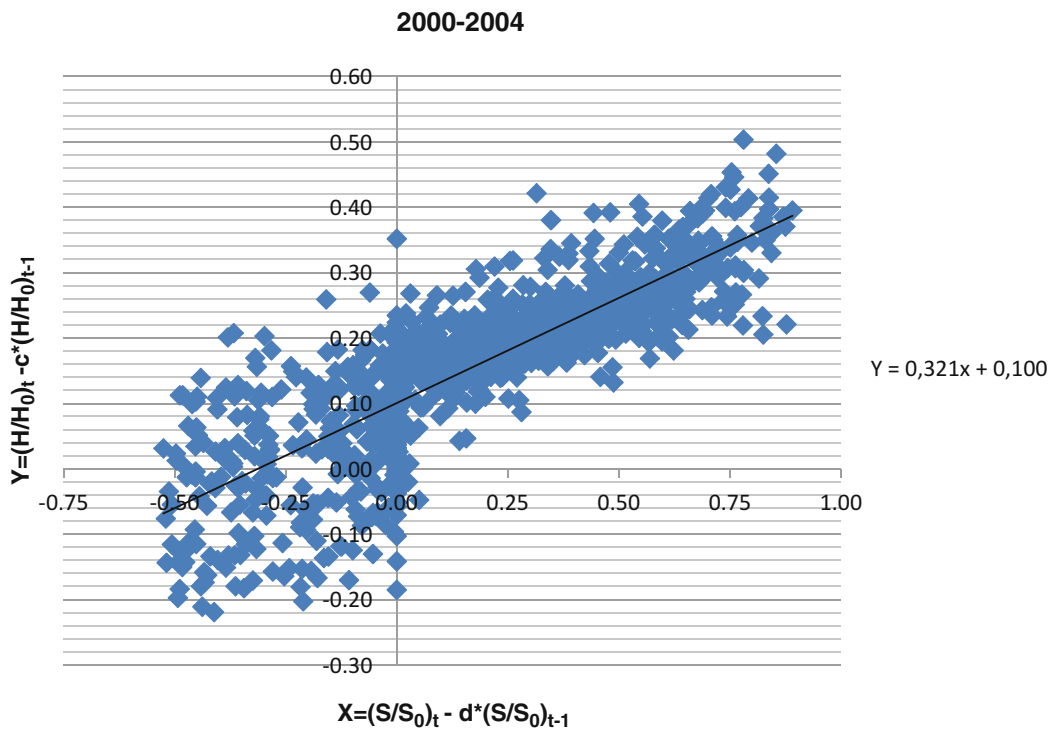
Fig. 48.3 Scatter diagram for a and b coefficients of the proposed method

After that verification process begins. In this stage, solar radiation is estimated at time t. In Fig. 48.5, the horizontal values are estimations with Angstrom (red) and the new equation (blue), whereas the vertical values are measurements. It is obvious that the new estimation straight line is closer to measurements line than Angstrom straight line.

The daily error amounts are determined as follows;

$$\text{Daily Error} = (\text{Measurement} - \text{Estimation})^2$$
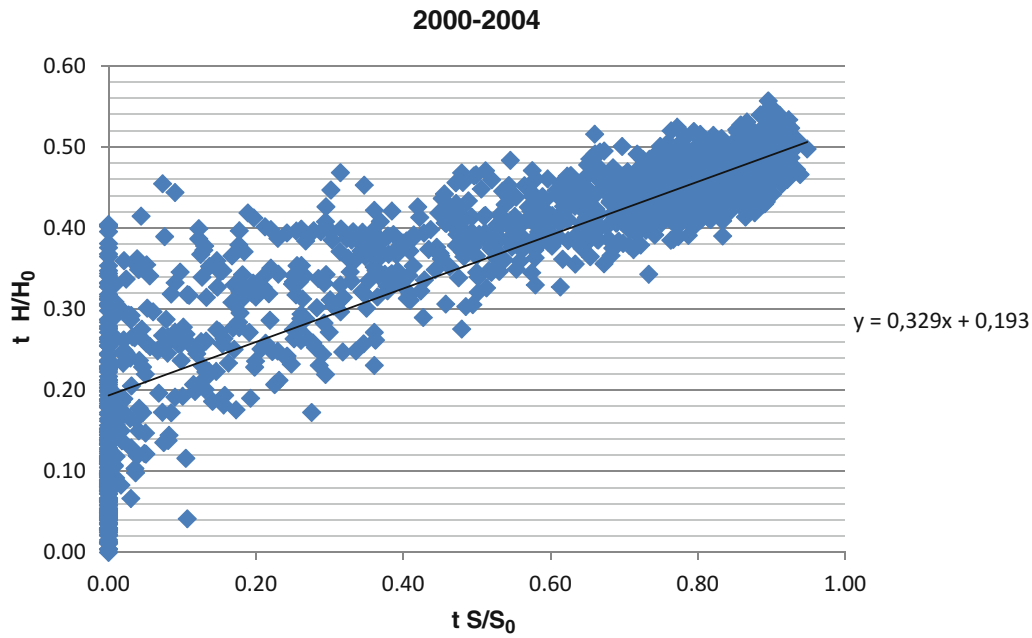
Fig. 48.4   Scatter diagram for classical Angstrom coefficients
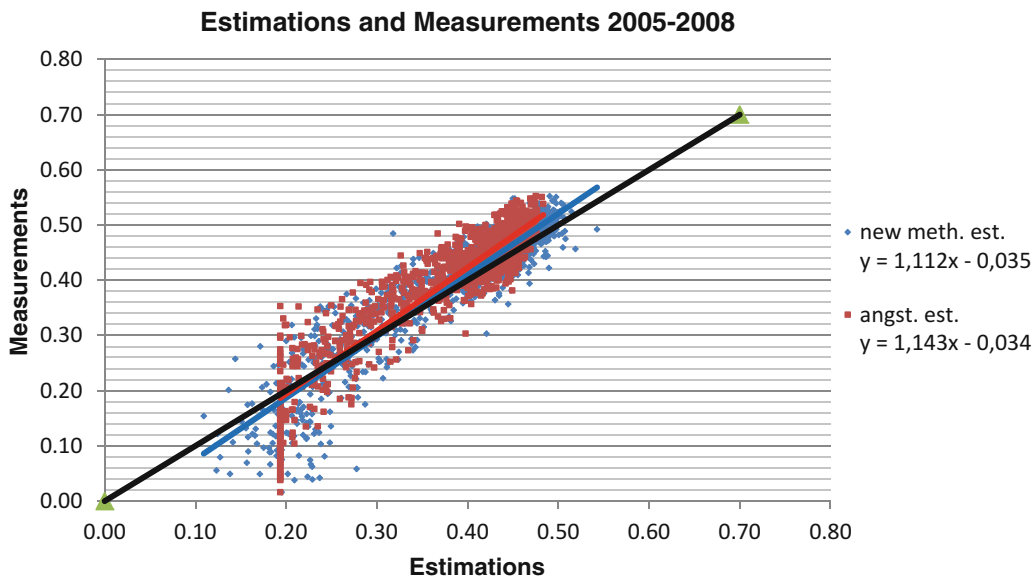
Fig. 48.5   Scatter diagram for Angstrom and comparison of the proposed methods

The total errors of the two methods are compared. After estimation of the solar radiation for all days from 2005 to 2008, the dependency model as developed in the article has a total error equal to 2.37 but the Angstrom model has a total error of 3.14 for $t - 1$. Therefore, Angstrom model has been more defective than the model of dependency as suggested in this study. The comparison of square root errors between the two methods yields as follows 13 %,

$$\left(\sqrt{3,14} - \sqrt{2,37}\right)/\sqrt{3,14} = 0,13 \ (13\%).$$

In the same way, the above steps are applied for times instances $t - 2, t - 3, t - 4, t - 5, t - 6, t - 7, t - 8, t - 9,$ and $t - 10$ but still Angstrom model appeared more defective than dependency model. Error ratios are respectively as follows; 9 %, 8 %, 7 %, 7 %, 6.5 %, 6 %, 7 %, 7 %, and 7 %. According to measuring station's compatibility, $t - i$ values can be $t - 15, t - 30,$ or $t - 60$.

Proposed new model in the article has estimates very close to the measurements in June, July, and August. However, the short-term estimation model during the summer solar energy production has very high estimates of the solar radiation with error almost zero with the highest estimation error in summer months. This is of great importance for energy planning.

In case of $t - 1$, after estimating of solar radiation for all summer days from 2005 to 2008, the dependency model has a total error of 0.2226 but the Angstrom model has a total error equal to 0.5651. Therefore, Angstrom model has been more defective with 37 % than the model of dependency. It seems that the new model has good estimation for summer days, so in the cases of t-366 and t-731 the estimates are obtained.

In case of t-366, after estimation of the solar radiation for all summer days from 2007 to 2010, the dependency model has a total error; 0.2407 but the Angstrom model has a total error of 0.3097. Therefore, the Angstrom model has been more defective with 12 % than the model of dependency. Proposed model also has the ability for the long-term estimations during the summer months. However, when the time distance increases from t onwards, then the dependence reduces.

Conclusion

In this study, the Angstrom equation is improved significantly. The new equation represents additional c and d dependency coefficients the values of which are multiplied by previous or earlier days' values of radiation as well as the time. The days before the sun are thought to be dependent due to the solar radiation and sunshine duration dependence on previous days. The new equation has estimates better than estimates of the Angstrom equation. Previous day's solar radiation and sunshine duration values enter into the calculations in the suggested method. Dependency model brings well short-term estimates, in particularly in the event of loss of short-term solar radiation values. As noted, before maximum 10 days, short-term estimate can be made because after 10 days, dependency decreases but error increases. However, as mentioned in the application part, new model has less error especially in the summer months. So that during the summer months dependency model is compared to the Angstrom model in case of short-term estimations and as a result, the Angstrom model has more error, which is almost 40 %. Additionally, during the summer months dependency model is also compared to the Angstrom model in case of long-term estimations and hence it is found that the Angstrom model has more error at about 12 %. If i values in $t - i$ increase than time error increases too, because of that dependency decrease. In summary, for 1 year difference, the new model estimations have less error during the summer months.

In the case of no dependencies, the proposed model reduces to the classical Angstrom equation.

References

1. Angström A (1924) Solar terrestrial radiation. Q J R Meteorol Soc 50:121–126
2. Page JK (1964) The estimation of monthly ea values of daily total short wave radiation on vertical and inclined surfaces from sunshine records for latitudes 40N–40S, Proceedings of the UN conference on new sources of energy, paper no. 598, 4, pp 378–390
3. Rietveld MR (1978) A new method for estimating the regression coefficients in the formula relating solar radiation to sunshine. Agric Meteorol 19:243–252
4. Gopinathan KK (1988) A general formula for computing the coefficients of the correlation connecting global solar radiation to sunshine duration. Sol Energy 41:499–502
5. Wahab AM (1993) New approach to estimate Angström coefficients. Sol Energy 51:241–245
6. Hinrichsen K (1994) The Angström formula with coefficients having a physical meaning. Sol Energy 52:491–495
7. Şen Z (2001) Angström equation parameter estimation by unrestricted method. Sol Energy 71:95–107
8. Swartman RK, Ogunlade O (1967) Solar radiation estimates from common parameters. Sol Energy 11:170–172
9. Sabbagh JA, Sayigh AAM, El-Salam EMA (1977) Estimation of the total solar radiation from meteorological data. Sol Energy 19:307–311
10. Dogniaux R, Lemoine M (1983) Classification of radiation sites in terms of different indices of atmospheric transparency. In Palz W. (éd.), *Solar Energy R&D in the European Community*, Series F, Vol. 2, Solar Energy Data. D. Reidel Publ. Co., Dordecht, 94–107
11. Lewis G (1989) The utility of the angström –type equation fort he estimation of global radiation. Sol Energy 43:5,297–299
12. Soler A (1990) Monthly specific Rietveld's correlations. Solar Wind Technol 2(3):305–306
13. Şahin AD, Şen Z (1998) Statistical analysis of the Angström formula coefficients and application for Turkey. Sol Energy 62:29–38
14. Ögelman H, Ecevit A, Taşemiroğlu E (1984) Method for estimating solar radiation from bright sunshine data. Sol Energy 33:619–625
15. Akınoğlu BG, Ecevit A (1990) Construction of a quadratic model using modified Angström coefficients to estimate global solar radiation. Sol Energy 45:85–92
16. Yıldız M, Öz S (1994) Evaluation of the solar energy potential of Turkey. In: Proceedings of the 6th National Energy Congress; pp 250–60 [in Turkish]
17. Samuel TDMA (1991) Estimation of global radiation for Sri Lanka. Sol Energy 45:333–337
18. Şen Z (2007) Simple nonlinear solar irradiation estimation model. Renew Energy 32:342–350
19. Şen Z (1998) Fuzzy algorithm for estimation of solar irradiation from sunshine duration. Sol Energy 63:39–49

Energy Saving with Double-Skin Glazed Facades in Multistorey Buildings

Esra Lakot Alemdağ and Figen Beyhan

Abstract

As a result of growing population and technological developments, increasing consumption of limited energy sources all over the world leads to environmental pollution. The rapid increase of environmental problems has required the world to revise their production and consumption patterns in every sector. Minimizing energy consumption and building design approaches which aim at using renewable energy sources in the field of architecture have come into prominence. From this point of view, the aim is to design energy-efficient buildings that can adapt to changing climatic conditions. Building skin, one of the most significant parameters, effecting the performance of energy-efficient buildings has important functions in energy conservation and providing indoor comfort conditions. Within this context, energy-efficient double-skin facade systems acting as a filter have been developed by analyzing the negative features of constantly changing outdoor environment. These facade systems frequently used in multistorey buildings in many countries offer advantages such as natural lighting, heat and solar control, noise control and natural ventilation. On the other hand, these facade systems not only reduce the need for mechanical systems but also provide user comfort requirement.

In this study, the aim is to indicate the importance of energy-efficient double-skin facade systems for today's architecture and energy performance, and to provide a better conceptual technical understanding. For this purpose, the positive and negative features of system were evaluated by giving technical information and construction details concerning energy saving double-skin facade systems from the examples of contemporary architecture around the world.

Keywords

Sustainable architecture • Energy conservation • Building skin • Double-skin glazed facades

Introduction

Regarding technological developments and changes in life conditions, the necessity of energy has reached a peak. Beside this, consuming fossil energy resources in order to meet requirements has caused huge damages to natural environment as well as its extinction. Growing environmental consciousness with awareness of this situation that endangers the continuity of life brings out new and alternative energy investigations which can reduce the damage to minimum and which have continuity in all fields of life. Depending on this fact, conceptions such as 'energy efficient' and 'sustainability' have become a current issue and also affect the design, construction and technology of buildings which life circle continues and a big percentage of energy is consumed in big proportion [1].

E.L. Alemdağ (✉)
Department of Architecture, Faculty of Architecture, Karadeniz Technical University, 61080 Trabzon, Turkey
e-mail: ela@ktu.edu.tr

F. Beyhan
Department of Architecture, Faculty of Architecture, Gazi University, 06570 Ankara, Turkey
e-mail: fbeyhan@gazi.edu.tr

One of the most important methods of saving energy in a building is by carefully designing its facade. The facade is one of the most significant contributors to the energy budget as well as the comfort parameters of a building. Because, the facade of a building can account for between 15 and 40 % of the total building budget and may be a significant contributor to the cost of up to 40 % more through its impact on the cost of building services [2]. The facade can only be described as truly "energy efficient" when it makes use of natural, renewable energy sources, such as solar radiation, air flows and ground heat sources to secure a building's needs in terms of heating, cooling, ventilation and lighting [3].

A "double-skin facade" is optimally one of the best options in managing the interaction between the outdoors and the internal spaces. "Energy-efficient double-skin facade approach", which can show best performance in accordance with summer and winter conditions and also take up the task of setting a balance between interior and exterior climate, has changed building facade into a friend to the environment and dynamic ones.

In the context, aim of this study is to make energy-efficient double-skin facade design more understandable as functional, conceptual and technical by indicating the importance of current architecture.

Double-Skin Facade Systems

Double-skin facade is composed of an external facade, an intermediate space (also called cavity or an air corridor) and an inner facade. Double-skin structures make up one of the most widely employed functional principles used to protect against exterior environmental influences through the facade envelope. Various terms are used to name these facades. Terms such as "active facades," "passive facades," "double-skin facades," "climatic facades" or "multiple-skin facades" are often used. Double-skin facades create different options, depending on layers of facades with opaque and/or transparent material. The facade that consists of two transparent skins separated by a cavity is described as "Double-Skin Glazed Facades." The layers of the double-skin facade are described below:

- Exterior Glazing: Usually it is a hardened single glazing. This exterior facade can be fully glazed.
- Interior Glazing: Insulating double glazing unit (clear, low-E coating, solar control glazing, etc. can be used). Almost always this layer is not completely glazed.
- The air cavity between the two panes. It can be totally natural, mechanically or hybrid ventilated. The width of the cavity can vary as a function of the applied concept between 200 mm and more than 2 m.
- The interior window can be opened by the user. This may allow natural ventilation of the offices.
- Automatically controlled solar shading is integrated inside the air cavity.
- As a function of the facade concept and of the glazing type, heating radiators can be installed next to the facade [4].

Five main ventilation modes for double-skin facade are described here bear on the ventilation of the facades at the component level, not at the building level (Table 49.1).

Different ways to classify Double-Skin Facade systems are mentioned in literature. Oesterle et al. [6] categorize the Double-Skin Facades mostly by considering the type of the cavity. The types are described as follows:

- Box window facades
- Corridor facades (storey-high double-skin facade)
- Shaft box facades
- Multistorey facades (building-high double-skin facade)

Box Window Facades

In this facade types horizontal partitions on each floor and vertical partitions on each window divide the facade in smaller and independent boxes. The inlet and outlet vents are placed at each floor.

The interior windows can be opened for ventilation into the gap between the two facade layers. The exterior facade comprises opening for supply and exhaust air. Horizontal as well as vertical separation from adjacent elements ensures optimum sound insulation not only from the outside but from neighbouring offices as well. Unpleasant odour and flashover can be prevented rather easily if the compartmentalization is designed correctly. Thermal shorts, meaning exhaust air from a lower element flowing into an element above, can be avoided by offsetting the supply and exhaust openings from storey to storey [7].

Table 49.1 Ventilation modes of the cavity [5]

1. Outdoor air curtain
In this ventilation mode, the air introduced into the cavity comes from the outside and is immediately rejected towards the outside.
The ventilation of the cavity therefore forms an air curtain enveloping the outside facade
2. Indoor air curtain
The air comes from the inside of the room and is returned to the inside of the room or via the ventilation system. The ventilation of the cavity therefore forms an air curtain enveloping the indoor facade
3. Air supply
The ventilation of the facade is created with outdoor air. This air is then brought to the inside of the room or into the ventilation system. The ventilation of the facade thus makes it possible to supply the building with air
4. Air exhaust
The air comes from the inside of the room and is evacuated towards the outside. The ventilation of the facade thus makes it possible to evacuate the air from the building
5. Buffer zone
This ventilation mode is distinctive in as much as each of the skins of the double facade is made airtight. The cavity thus forms a buffer zone between the inside and the outside, with no ventilation of the cavity being possible
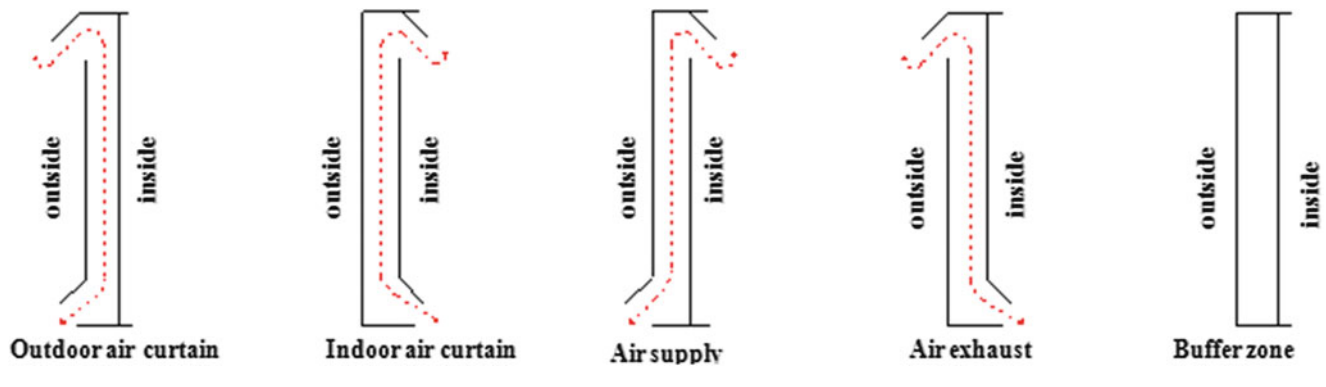
Corridor Facades

Corridor facades manage the air flow storey by storey. Air inlets are located near the floor and the ceiling. They are arranged at an offset to avoid thermal shorts by exhaust air mixing with fresh air. The corridor between the facades is accessible and is typically designed to be wide enough to be used as a service platform. This corridor is ventilated through openings at ceiling level. The airflow can be regulated by motorized flabs [7].

When inlet and outlet vents are placed at each floor, the lowest degree of air heating and therefore the most effective level of natural ventilation is to be expected [3]. The facade cavity is therefore generally divided horizontally for acoustical, fire security or ventilation reasons.

Shaft Box Facades

Shaft facade is a combination of a double-skin facade with a building-high cavity and a double-skin facade with a storey-high cavity. The full height cavity forms a central vertical shaft for exhaust air. One both sides of this vertical shaft and connected to it via overflow openings are storey-high cavities. The warmed, exhaust air flows from the storey-high cavity into the central vertical shaft. There it rises, due to the stack effect and escapes into the open at the top [4].

Even when there is a little air flow outside natural ventilation of the building is ensured by the buoyancy in the shaft. However, at a certain height the pressure situation reverses and warmed air might return in the storey-high cavities. For this reason it is necessary to limit the height of the shaft. This limitation is influenced by various factors, such as overall building height, prevailing wind etc., and it has to be calculated individually for each building [3]. Therefore, this type of facade is suitable for lower rise buildings.
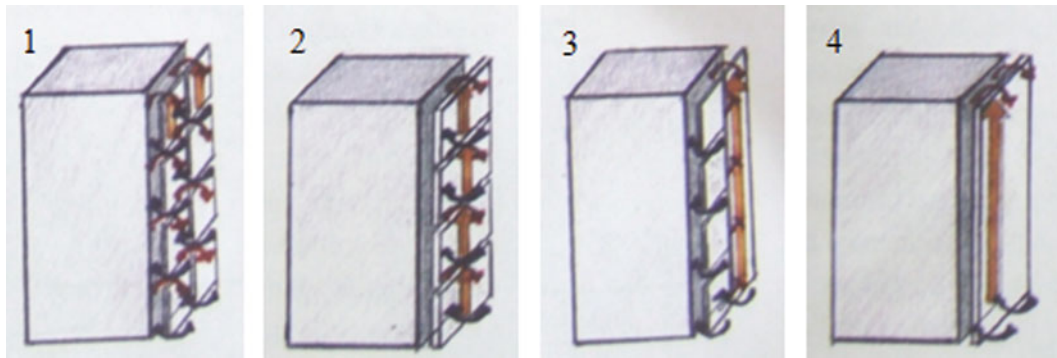
Fig. 49.1 Types of the double-skin facade systems [1]

Multistorey Facades

Multistorey facades are characterized by a cavity which is not partitioned either horizontally or vertically; the space between the two glazed facade layers therefore forming one large volume. Generally, in this type of facade, the cavity is wide enough to permit access to individuals (cleaning service, etc.) and floors which can be walked on are installed at the level of each storey in order to make it possible to access the cavity, primarily for reasons of cleaning and maintenance. In some cases, the cavity can run all around the building without any partitioning [8]. The basic idea of a building-high cavity is the following: air that accumulates at the top of the air space between the two layers is likely to get hot on sunny days. Openings in the outer skin and at the roof edge siphon out the warm air, while cooler replacement air is drawn from near the base of the building [4] (Fig. 49.1).

Double-Skin Glazed Facade Examples

In this part of the study, design criteria of four selected samples building with double-skin glazed facades have been evaluated in tables. It is aimed to examine details (facade construction, ventilation of the cavity, shading device type, HVAC system) and summarized briefly the concept of double-skin glazed facades in multistorey building project (Tables 49.2, 49.3, 49.4, 49.5 and 49.6).

Conclusions

A wide range of energy saving measures can be implemented such as natural ventilation, night-time cooling, natural lighting, the creation of buffer zone, etc. This assumes an intensive interaction between the facade and the building. In this context, energy-efficient double-skin facade systems that act as a filter of constantly changing outdoor environment are frequently used in multistorey buildings in many countries. The advantage and disadvantage of DSF system are given briefly below, very much depending on location and type of building.

Advantages

- Acoustic insulation (reduced internal noise from room to room and external noise from outdoor sources)
- Thermal insulation (during the winter, the external additional skin provides improved insulation)
- Night time ventilation (pre-cool the offices during the night using natural ventilation)
- Natural ventilation (provide fresh air before and during the working hours)
- Reduction of the wind pressure
- Thermal comfort-temperatures of the internal wall
- Better protection of the shading or lighting devices (when they are placed inside the air cavity)
- Energy saving and reduced environmental impact
- Natural daylight, transparent architectural design

Table 49.2 Building certificate of type 1

Type 1: Box window facade example—Print Media Academy building

Building certificate

Architect: Schroder Architects and Studio Architects
Location: Bechtloff, Germany
Completion: 2000
Facade Type: Box Window Facade
Building height: 50 m
Number of Floors: 12
Facade Function: Energy efficiency, Optimum air-conditioning, Daylighting
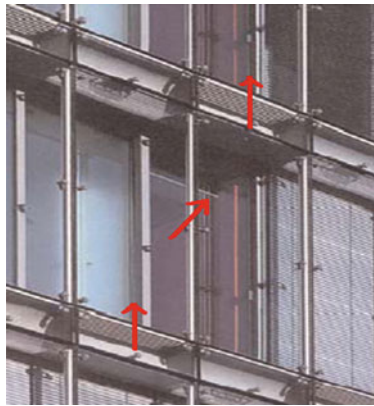
Table 49.3 Building certificate of type 2

Type 2: Corridor facade example—Galleries Lafayette building

Building certificate

Architect: Jean Nouvel
Location: Germany
Completion: 1995
Facade Type: Corridor Facade
Building height: –
Number of Floors: –
Facade Function: Energy efficiency, Optimum air-conditioning, Noise Control, Daylighting
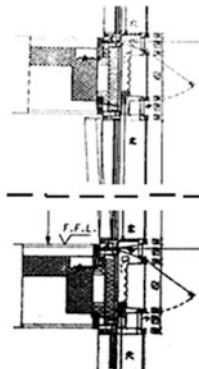
Table 49.4 Building Certificate of type 3

Type 3: Shaft box facade example—Halenseestrabe building
Building certificate

Architect: Leon-Wohlhage Architects
Location: Germany
Completion: 1996
Facade Type: Shaft box facade
Building height: –
Number of Floors: 10
Facade Function: Energy efficiency, Optimum air-conditioning, Noise Control, Daylighting
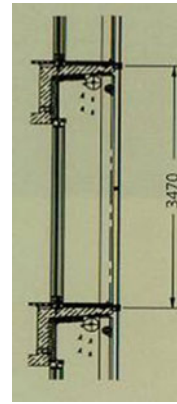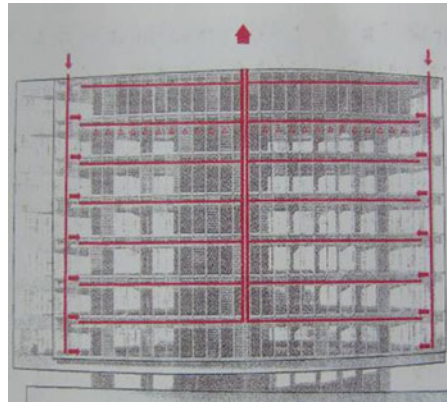
Table 49.5 Building Certificate of type 4

Type 4: Multistorey facade example—Telus/William Farrell building
Building certificate

Architect: Peter Busby
Location: 2001
Completion: Canada
Facade Type: Multistorey facade
Building height: 48 m
Number of Floors: 10
Facade Function: Energy efficiency, Optimum air-conditioning, Natural ventilation, Daylighting
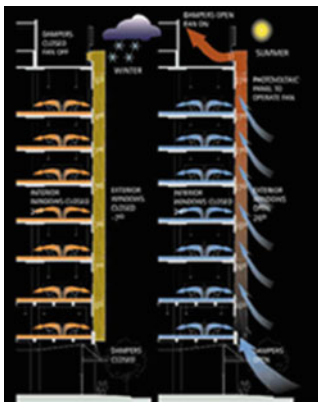
Table 49.6 Design criteria of selected four building examples with double-skin glazed facades

	Type 1	Type 2	Type 3	Type 4
Types	Box window facade	Corridor facade	Shaft box facade	Multistorey facade
Facade construction	*External skin*: Fixed single glass pane *Internal skin*: Openable sealed double glass pane *Air Cavity*: 46 cm	The 29 mm thick insulating glass unit, has a cavity filled with argon *External skin*: Fixed 8 mm single glass *Internal skin*: Openable 6 mm low-E coated glass *Air Cavity*: 20 cm	*External skin*: Fixed 12 mm single-pane *Internal skin*: Openable sliding double-pane glass doors *Air cavity*: ~20 cm	*External skin*: Openable-fixed fritted glass *Internal skin*: Openable low-E coated glass *Air cavity*: 90 cm
Ventilation of the cavity	*Type of ventilation*: Hybrid *Ventilation mode*: Outdoor air curtain, Air supply, Air exhaust, Buffer zone	*Type of ventilation*: Natural *Ventilation mode*: Outdoor air curtain, Air supply, Air exhaust, Buffer zone	*Type of ventilation*: Mechanical *Ventilation mode*: Outdoor air curtain, Air supply, Air exhaust, Buffer zone	*Type of ventilation*: Hybrid *Ventilation mode*: Outdoor air curtain, Air supply, Air exhaust, Buffer zone
Shading device type	*Shading system*: Aluminium blind system *Control System*: Mechanical *Location*: Inside of the cavity	*Shading system*: Perforated stainless steel louver blind *Control System*: Manuel *Location*: Inside of the cavity	*Shading system*: A blind (85 cm wide, one storey high) *Control System*: Manuel *Location*: Inside of the cavity	*Shading system*: Solar shade glass panel *Control System*: Manuel *Location*: External skin
HVAC	Fresh air can be gained by operating the inner window slider. The building central system then controls the rate of air flow into the cavity	The facade enables natural ventilation of the offices for most of the year. If the outside temperature is too low or too high, a mechanical ventilation system is switched on	During the summer, the blinds can be used to block solar radiation while the air space is mechanically ventilated. At night, internal heat gains are removed with mechanical ventilation. During the winter, solar gains prewarm the air in the cavity	The steam-heating system was replaced with a heat-recovery system, which uses waste heat from the cooling process of the adjacent building
Commentary	Cross ventilation control system exists that moderates the buffer space between the outer and the inner glazing. This is done by opening sets of upswing glass louvers to allow outside air flow to pass through and push the heated air in the cavity out, thus cooling the envelope	The inlet and outlet vents are placed at each floor, the lowest degree of air heating and therefore the most effective level of natural ventilation is to be expected. The openings permanently open	Fresh air is mechanically drawn from the roof, the passed down to the intermediate space of the double-skin facade through vertical channels at both ends of the corridor. Air is extracted through the horizontal ducts leading to vertical channels situated in the center of the facade	The air cavity, acts as a thermal buffer, which provides insulation during winter and allows air intake during off-peak seasons. Motorized dampers are installed at the top and bottom of the cavity. When the dampers are opened, it allows air to flow into the air space and create natural ventilation. Furthermore, PV powered fans are employed to boost the air movement. During the cold season, the dampers close and the cavity becomes an insulator

Disadvantages

- Fire Protection (is not properly designed, room to room or floor to floor smoke transmission problems can take place)
- Higher Construction costs (compared to a conventional facade)
- Reduction of rentable office space (it is quite important to find the optimum depth of the facade in order to be narrow enough so as not to lose space and deep enough so as to be able to use the space close to the facade)
- Overheating problems (if the facade is not properly designed)
- Increased air flow velocity (inside the cavity, mostly in multistorey high types)
- Acoustic insulation (sound transmission problem can take place if the facade is not designed properly)
- Additional maintenance and operational costs

Double-skin facade has to be designed for a certain building location and facade orientation otherwise the performance of the system will not be satisfactory. The constraining parameters (climate, site and obstructions of the building, use of the building, building and design regulations) have to be taken into account in the early design stage.

It is really important to understand the performance of double-skin facade by studying the physics inside the cavity. The geometry of the facade influences the air flow and thus the temperatures at different heights of the cavity. Different panes and shading devices results in different physical properties. The interior and exterior openings can influence the type of flow and the air temperatures of the cavity. All together these parameters determine the use of the double-skin facade and the HVAC strategy that has to be followed in order to succeed in improving the indoor environment and reducing the energy use [4].

References

1. Lakot E (2007) Ekolojik ve Sürdürülebilir Mimarlık Bağlamında Enerji Etkin Çift Kabuklu Bina Cephe Tasarımlarının Günümüz Mimarisindeki Yeri ve Performansı Üzerine Analiz Çalışması. KTÜ Fen Bilimleri Enstitüsü, Yüksek Lisans Tezi, Trabzon
2. Wiggington M, Harris J (2002) Intelligent skins. Architectural Press, Oxford
3. Compagno A (2002) Intelligent glass façades, material practice design. Birkhäuser Publishers, Berlin
4. Poirazis H (2004) Double skin façades for office buildings. Lund Institute of Technology Department of Construction and Architecture, Lund University, Lund
5. Loncour X, Deneyer A, Blasco M, Flamant G, Wouters P (2004) Ventilated double facades. Belgian Building Research Institute, Department of Building Physics, Indoor Climate and Building Services
6. Oesterle E, Lieb R-D, Lutz M, Heusler W (2001) Double skin facades: integrated planning. Prestel, Munich
7. Knaack U, Klein T, Bilow M, Auer T (2007) Façades: principles of construction. Birkhäuser Publishers, Berlin
8. Waldner R (2005) Best practice for double skin façades, EIE/04/135/S07.38652, WP 1 Report, State of the Art, www.bestfacade.com/pdf

Isil Yazar, Emre Kiyak, and Fikret Caliskan

Abstract

Aviation is the one of the continually developing sector in transportation area. People prefer to travel with more comfortable, more economic, time saver and safety vehicles during their travel. According to this selection, the number of passengers in civil aviation is increasing day by day. Due to this acceleration, air-lines expand their fleet and increase the number of their daily flights. Eventually, manufacturing velocity accelerates as well. Today, aircraft manufacturers focus on trying to design safer, more efficient, more environment-friendly, more economic aircraft. No doubt, it is not an easy process. Aircraft has a complex structure, and its design duration takes a very long time.

Aircraft is composed of two main parts: structural part and system part. Both of them have a critical design process. After the design level, manufacturing and test levels are followed respectively. These levels are valid for all parts in aircraft. It means that every component has a critical mission in aircraft. One of the critical sections of the aircraft is the engine part. In aircraft, different kinds of gas turbine engines are used. A typical example of a gas turbine engine is formed in five parts. These are, respectively, inlet, compressor, combustion chamber, turbine, exhaust parts. Basic operation principle of the gas turbine engine is to convert chemical energy into mechanical energy. In compressor part, the air that is taken from inlet is compressed and pressurized. In the combustion chamber, the pressurized air is burnt under the high temperature. Then the gas form is taken to the turbine part and it expands to the ambient pressure crossing through the turbine. Finally it is exhausted in the exhaust part.

In the design process of gas turbines, all parts have different design issues. Especially, compressor and turbine design models have critical points that must be considered due to their geometrical structure. When preparing models for these parts, component maps are used. Especially, for the transient conditions, maps represent the component performance very well. The maps are difficult to directly use in simulations so, different techniques are used to read data from maps. In our study, a technique based on the "Adaptive Neuro-Fuzzy Inference System (ANFIS)" is tested and proposed on MATLAB/Simulink.

Keywords

Compressor mapping • Turbine mapping • Adaptive neuro-fuzzy inference system (ANFIS) • Gas turbines • Energy • Performance maps

I. Yazar (✉)
Department of Mechatronics, Industrial Zone, Eskisehir Osmangazi University, Eskisehir, Turkey
e-mail: iyazar@ogu.edu.tr

E. Kiyak
Faculty of Aerospace Sciences, Anadolu University, 26470 Eskisehir, Turkey
e-mail: ekiyak@anadolu.edu.tr

F. Caliskan
Department of Control Engineering, Istanbul Technical University, Istanbul, Turkey
e-mail: caliskanf@itu.edu.tr

Introduction

Gas turbines are widely used in aviation sector. Different types of aircraft engines are classified in terms of range, efficiency, and thrust demands. These demands identify the design cycle of the gas turbine at the same time. Gas turbines are complex structures. In order to monitor and control the operation of these complex structures and predict the abnormal conditions in steady-state and transient operations, reliable mathematical models are needed [1]. Gas turbine nonlinear mathematical models are made up of aerothermodynamics laws, energy-mass conservation laws, and empirical formulations and so on [2]. These models are prepared for design process before manufacturing. An accurate mathematical model helps the design of the control system process, so deriving a realistic mathematical model is very important. Each component of gas turbine can be modeled by using equations and empirical solutions. The critical ones are the compressors and turbines. These components are composed of multiple individual stages and in modeling, they are assumed to be a stacked single stage structure. By this way, components dynamic behavior can be analyzed with only inlet and outlet conditions [3]. For defining the performance characteristics of these components, compressor and turbine maps are used. These maps are formed from actual rig test of the engines and then the values are plotted on the map [3]. An example of compressor map can be seen in Fig. 50.1.

Compressor maps can be determined in several ways in terms of the accuracy, complexity and processing time [5]:
- Streamline Curvature Methods
- Map Scaling Techniques
- Stage Stacking Methods
- Row-by-Row Analysis
- Two-Zone Models
- One-Dimensional Loss Models

Map scaling is one of the most used techniques in this area. Map Scaling techniques use different digitizing methods for providing data to the simulations. The following methods are the commonly used examples for the digitizing process [6]:
- Beta Line Method
- Curve Fitting Techniques
- Neural Network Techniques

In the literature, many studies have been done for making the map data comprehensible for computer simulations. Beta Line Method is used by Kurzke in describing data from maps [7]. Curve fitting techniques try to form an equation that shows the characteristic outputs of the compressors and turbines. Sieros et al. [8], Moraal and Kolmanovsky [9], Orkisz and Stawarz [10] and Ailer et al. 2001 [11] uses functions to represent the characteristics of the components. Kong et al. [12] and Kong and Ki [13] use genetic algorithm method to generate digital data from maps. In the last few years, neural network is a popular concept for preparing digitalized data from maps. Bao et al. [14], Yu et al. [15], and Ghorbanian and Gholamrezaei [16–19] based their studies on studying and comparing different types of Artificial Neural Network structures for digitizing map data.
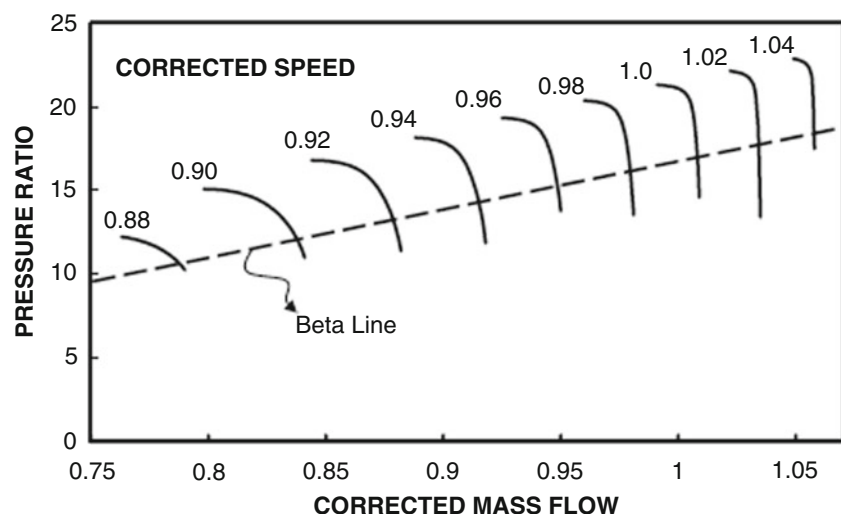
Fig. 50.1 Compressor map with one beta line [4]

In this study, the compressor and turbine components characteristic performance output parameters are calculated via Adapted Neuro-Fuzzy Inference System (ANFIS). By using test data, corrected mass flow rate and isentropic efficiency values of the components are estimated for a given input data (RPM, Pressure ratio) between idle to maximum thrust levels. As a result of training calculations, accurate output data is found at the end of the simulations in a short time. Both on design and off design values are simulated and the results are satisfactory. Fuzzy connected neural network structure is suitable for modeling output performance parameters of these components.

Compressor and Turbine Performance Maps

Fluid machines that transfer energy between a rotor and a fluid are called turbo machines. Compressors and turbines are categorized in this type of machines [20]. In the literature, there are three types of compressors that are used in gas turbines [21]. These are respectively centrifugal flow, axial flow, and centrifugal-axial flow compressors. In centrifugal flow compressor, compression is formed by accelerating the air outward perpendicular to the longitudinal axis of the compressor. In axial flow compressor, compression is formed by a series of rotating and stationary airfoils moving the air parallel to the longitudinal axis. The last type, centrifugal-axial flow compressor, uses both compression methods for achieving the desired compression [21]. In a gas turbine, compressor and turbine parts work correspondingly. In turbine part, the energy that is extracted from the expansion of the fluid is transferred into compressor part mechanically. In modeling of turbo machines, forming the accurate model is important. Especially in compressor and turbine parts, it is possible to find mutual dimensionless parameters characterizing the flow [22]. Maps are used for finding these characteristic performance parameters.

Maps are designed among corrected mass flow parameter, pressure ratio, and corrected speed lines. An example can be seen in Fig. 50.1. Characteristics are defined in corrected parameters for eliminating the dependence of the performance characteristics from temperature and pressure. Corrected mass flow rate ($\dot{m}_{corr}$) and isentropic efficiency (η) can be determined as a function of pressure ratio (π) and corrected rotational speed in Eqs. (50.2) and (50.3) [3]. To define corrected rotational speed Eq. (50.1) is used. It is the proportion of actual data over design data. Final value of mass flow rate is defined as in Eq. (50.4).

$$N_{corr} = \frac{\left(\frac{N}{\sqrt{\theta}}\right)}{\left(\frac{N}{\sqrt{\theta}}\right)_{design}} \tag{50.1}$$

$$\dot{m}_{corr} = f_a(\pi, N_{corr}) \tag{50.2}$$

$$\eta = f_b(\pi, N_{corr}) \tag{50.3}$$

$$\dot{m} = \dot{m}_{corr}\left(\frac{\delta}{\sqrt{\theta}}\right) \tag{50.4}$$

As mentioned earlier, there are many ways to calculate f_a and f_b functions in the literature. f_a and f_b are functions that digitize the map data into suitable simulation form. Instead of using 2D Look Up table, curve fitting, beta lines, or individual neural network algorithms, in our work, Adapted Neuro-Fuzzy Inference System is applied to our simulation model. Map data for two types of compressors and two types of turbines are used in different simulation models. Initially, with real test data, the system is trained and then by using the trained system, on design and off design values are tested on the system.

Adaptive Neuro-Fuzzy Inference System (ANFIS)

System modeling techniques based on mathematical formulations are sometimes not suitable for nonlinear systems. In this type of systems, input–output mapping method usage can be convenient [23]. This work is an application example of input–output mapping method in MATLAB/ANFIS structure (Fig. 50.2). ANFIS (Adaptive Neuro-Fuzzy Inference System) is a combination of Neural Network training structure and Fuzzy Logic clustering structure. It can be directly used on command window of MATLAB as ANFIS or GUI structure on MATLAB/Simulink.

ANFIS GUI structure consists of two parts: generating FIS and training FIS. In generating FIS structure, MATLAB presents two types of methods: Grid Partitioning and Sub Clustering. Furthermore, a preformed FIS structure can be used
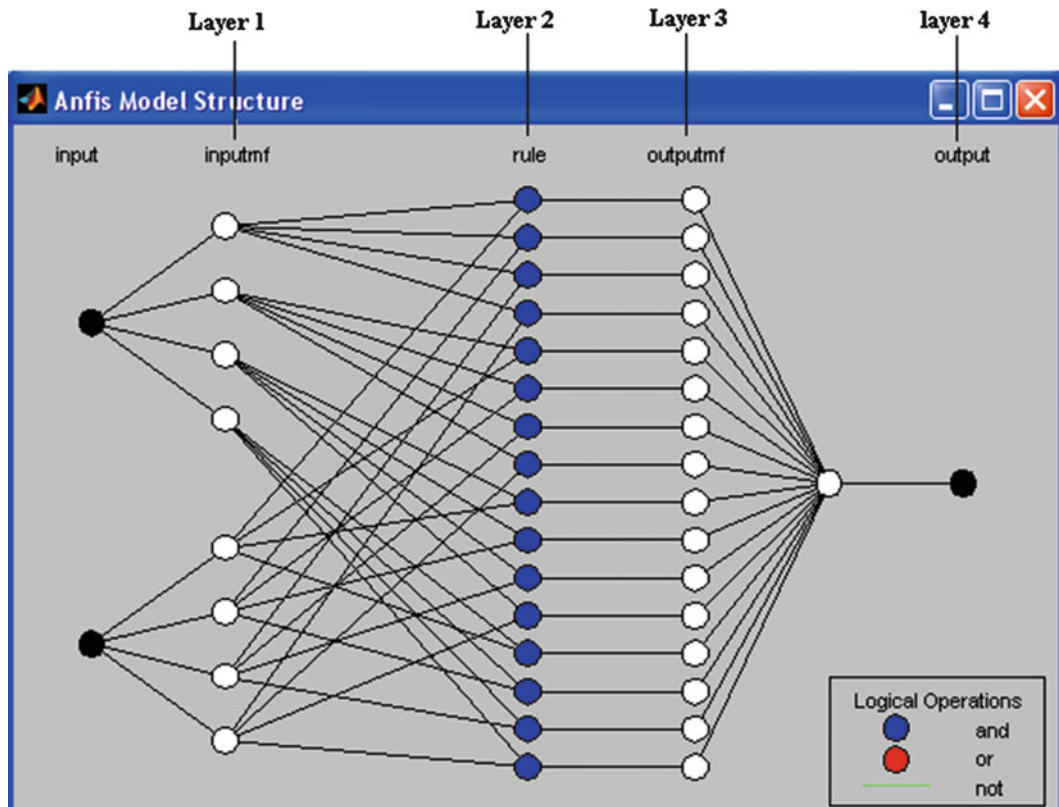
Fig. 50.2 An example of ANFIS model structure [24]

directly by loading from a file or workspace. In this study, Grid Partitioning method is adopted for generating FIS structure. Grid Partitioning is a method that generates a single-output Sugeno-type FIS structure by grid partitioning on the data [24].

Training FIS is the important part of the ANFIS structure. There exist two types of training methods in ANFIS: backpropagation training and backpropagation-least squares combination Hybrid training methods. In our work, hybrid training method is used for training the FIS structure.

The ANFIS architecture can be explained as follows [23]:

The FIS structure with two inputs x, y and one output z can be formed by describing following two fuzzy if-then rules of Takagi and Sugeno's type [25]:

Rule 1: If x is A_1 and y is B_1, then $f_1 = p_1x + q_1y + r_1$.
Rule 2: If x is A_2 and y is B_2, then $f_2 = p_2x + q_2y + r_2$.

Layer 1: Every node in this layer has a membership function as the following. This function is the output function of the node as well.

$$O_i^1 = \mu_{A_i}(x)$$

where x is the input, i is the node number, and A_i is the linguistic variable of this node function. The node function in our work is selected as a Gaussian function. Constants of the Gaussian function are labeled as premise parameters in ANFIS.

Layer 2: In this layer, incoming signals (membership functions) are multiplied. Each node output represents the firing strength of a rule.

$$w_i = \mu_{A_i}(x) \times \mu_{B_i}(y), i = 1, 2.$$

Then normalized firing strengths are calculated by taking the ratio of related node firing strength to the sum of all rule's firing strengths:

$$\overline{w}_i = \frac{w_i}{w_1 + w_2}, i = 1, 2.$$

Layer 3: Output function of this layer is described as the following. The parameters $\{p_i, q_i, r_i\}$ are called consequent parameters in ANFIS.

$$O_i^3 = \overline{w}_i f_i = \overline{w}_i(p_i x + q_i y + r_i)$$

Layer 4: The last layer is the overall output of the system. It is calculated by summing of all signals from the previous layer.

$$\text{Overall output} = O_i^4 = \sum_i \overline{w}_i f_i = \frac{\sum_i w_i f_i}{\sum_i w_i}$$

Hybrid Learning Algorithm

The algorithm of the Hybrid Learning is composed of two different procedures (Table 50.1). These are Forward Pass and Backward Pass respectively [23]:

In the forward pass, input and related functional signals go forward to layer 3 and least squares estimation method tries to estimate consequent parameters in this period. After fixing the consequent parameters, in the backward pass, the premise parameters are updated by using gradient descent method corresponding to the sum of all nodes error rates from output to the input [23]. ANFIS tries to accurate the described error value in each epoch, so the selected epoch number is important as well.

Simulations, Results and Discussions

In the simulations, different compressor and different turbine models that are created on MATLAB/Simulink are used. In training section, two different types of compressor and two different types of turbine data are used. For each engine component, different membership function test error values searched via performance parameters. According to the error values, a stable membership function number value is fixed. For generating Fuzzy Inference System (FIS), in case of small number of inputs, both Grid Partition Method and Sub Clustering Method can be used [26, 27]. In our work we prefered Grid Partition method for generating FIS structure. In the FIS training section, instead of only back propagation gradient descent method, a combination of back propagation gradient descent method and least squares estimation methods, Hybrid Optimization Method is preferred. Hybrid Optimization Method has faster and nearer results than the individual back propagation gradient descent optimization method [28, 23]. Simulink model view for compressor type 1 and an example of membership function view are shown in Figs. 50.3 and 50.4 respectively.

The average error values, epoch numbers and number of membership function values can be seen in the following tables and ANFIS figures. In Fig. 50.5, for compressor 1, corrected mass flow rate (MF = 5) and isentropic efficiency (MF = 5) training solutions are seen. In Table 50.2, the best value of average test error for corrected mass flow is found with five

Table 50.1 Hybrid learning algorithm table [23]

	Forward pass	Backward pass
Premise parameters	Fixed	Gradient descent
Consequent parameters	Least squares estimate	Fixed
Signals	Node outputs	Error rates
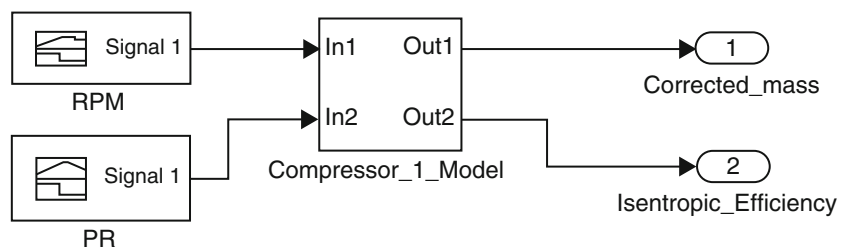
Fig. 50.3 Simulink model view

Fig. 50.4 An example of membership function view of PR
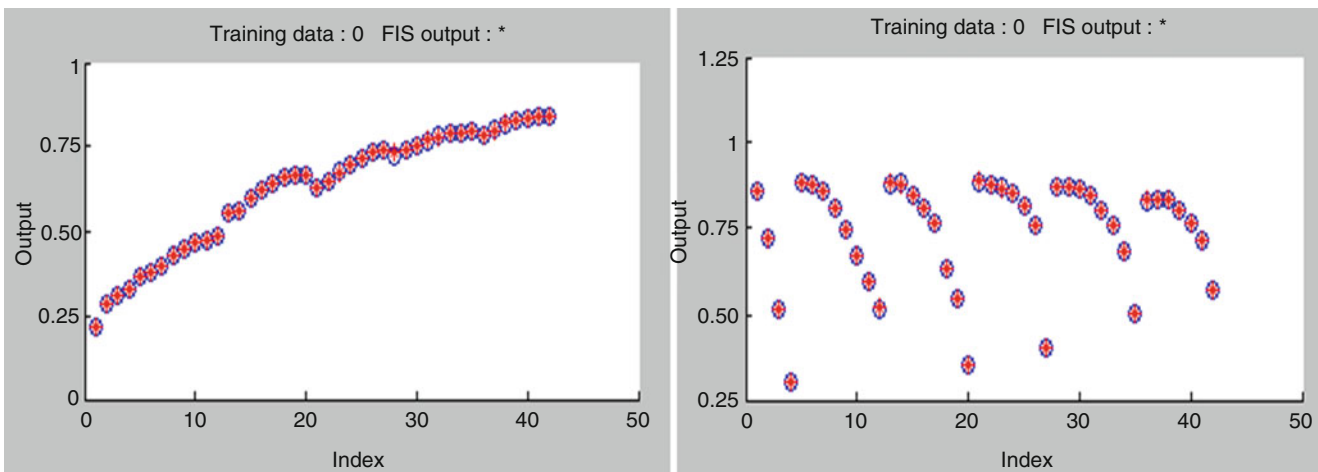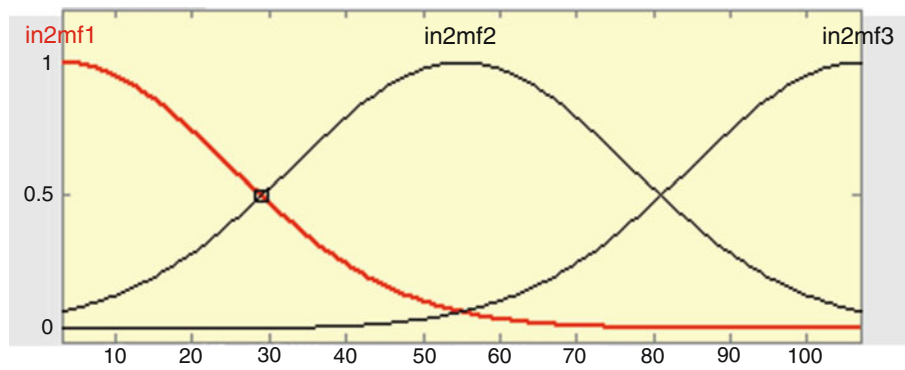
Fig. 50.5 Corrected mass flow (MF = 5) and isentropic efficiency (MF = 5) training data diagrams for compressor 1

Table 50.2 Corrected mass flow error results for compressor 1

Compressor 1-corrected mass flow		
Epoch number	Average test error	Number of membership function (MF)
5	0.0027004	2
5	0.0016331	3
5	0.0010621	4
5	0.00078742	5
5	0.0085135	6
5	0.0019336	7
5	0.011696	8
5	0.0093629	9
5	0.0095345	10

membership functions and in Table 50.3, the best value of average test error for isentropic efficiency is found with five membership functions. After these membership function values, unstability of average test error starts in the increasing direction of membership functions and so does the simulation time.

In Fig. 50.6, for compressor 2, corrected mass flow rate (MF = 5) and isentropic efficiency (MF = 5) training solutions are seen. In Table 50.4, the best value of average test error for corrected mass flow is found with five membership functions and in Table 50.5, the best value of average test error for isentropic efficiency is found with five membership functions. After these membership function values, unstability of average test error starts in the increasing direction of membership functions and so does the simulation time.

Table 50.3 Isentropic efficiency error results for compressor 1

Compressor 1-isentropic efficiency		
Epoch number	Average test error	Number of membership function (MF)
5	0.015914	2
5	0.0022847	3
5	0.001627	4
5	0.00074378	5
5	0.2824	6
5	0.0012207	7
5	0.045845	8
5	0.001561	9
5	0.016111	10
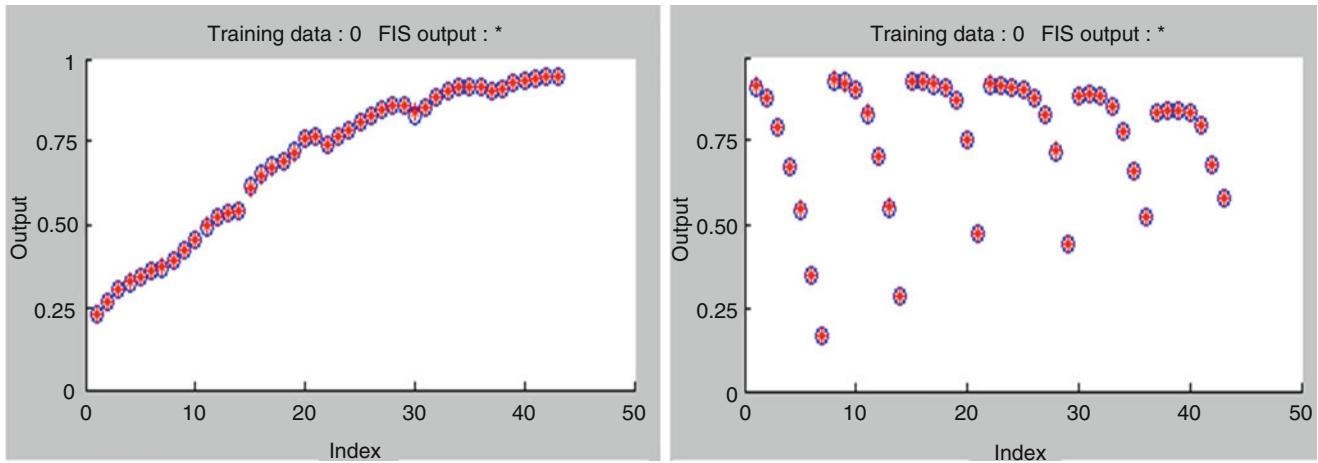
Fig. 50.6 Corrected mass flow (MF = 5) and isentropic efficiency (MF = 5) training data diagrams for compressor 2

Table 50.4 Corrected mass flow error results for compressor 2

Compressor 2-corrected mass flow		
Epoch number	Average test error	Number of membership function (MF)
5	0.0031677	2
5	0.0018184	3
5	0.0011317	4
5	0.00099039	5
5	0.055742	6
5	0.0051453	7
5	0.054999	8
5	0.0075333	9
5	0.0023086	10

Table 50.5 Isentropic efficiency error results for compressor 2

Compressor 2-isentropic efficiency		
Epoch number	Average test error	Number of membership function (MF)
5	0.026705	2
5	0.0035932	3
5	0.0024906	4
5	0.0010388	5
5	0.056028	6
5	0.006311	7
5	0.070202	8
5	0.018059	9
5	0.005396	10
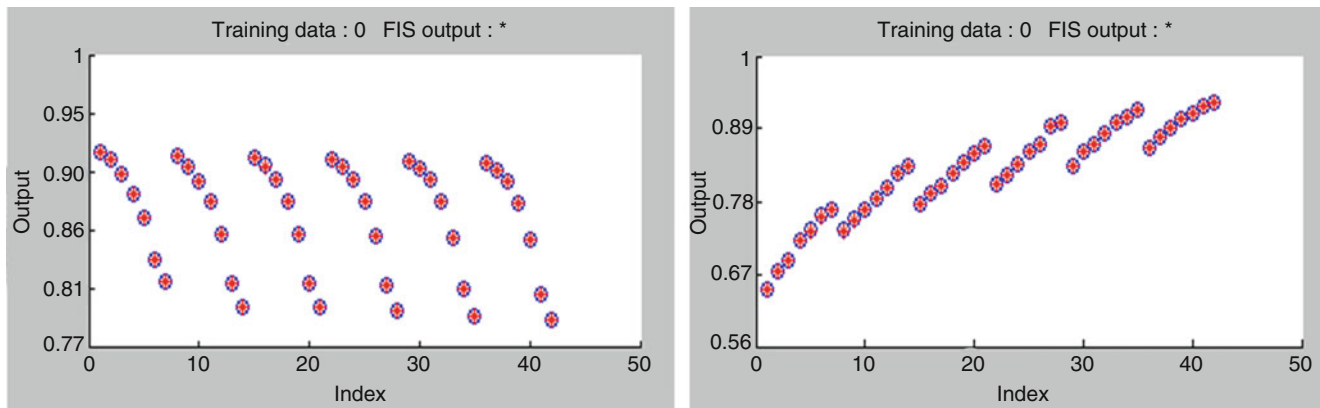
Fig. 50.7 Corrected mass flow (MF = 11) and isentropic efficiency (MF = 11) training data diagrams for turbine 1

Table 50.6 Corrected mass flow error results for turbine 1

Turbine 1-corrected mass flow

Epoch number	Average test error	Number of membership function(MF)
5	0.004068	2
5	0.0015129	3
5	0.00037277	4
5	0.00025415	5
5	0.00035519	6
5	0.000060146	7
5	0.000015917	8
5	0.00000042807	9
5	0.00000042586	10
5	0.00000042266	11
5	0.00000045725	12
5	0.00000051955	13
5	0.0000005217	14

Table 50.7 Isentropic efficiency error results for turbine 1

Turbine 1-isentropic efficiency

Epoch number	Average test error	Number of membership function (MF)
5	0.0058168	2
5	0.0027477	3
5	0.0018257	4
5	0.0015368	5
5	0.0013878	6
5	0.00040202	7
5	0.00017977	8
5	0.00000088838	9
5	0.00000079984	10
5	0.00000079876	11
5	0.00000085982	12
5	0.00000096349	13
5	0.00000096971	14

In Fig. 50.7, for turbine 1, corrected mass flow rate (MF = 11) and isentropic efficiency (MF = 11) training solutions are seen. In Table 50.6, the best value of average test error for corrected mass flow is found with 11 membership functions and in Table 50.7, the best value of average test error for isentropic efficiency is found with 11 membership functions. After these membership function values, unstability of average test error starts in the increasing direction of membership functions and so does the simulation time.
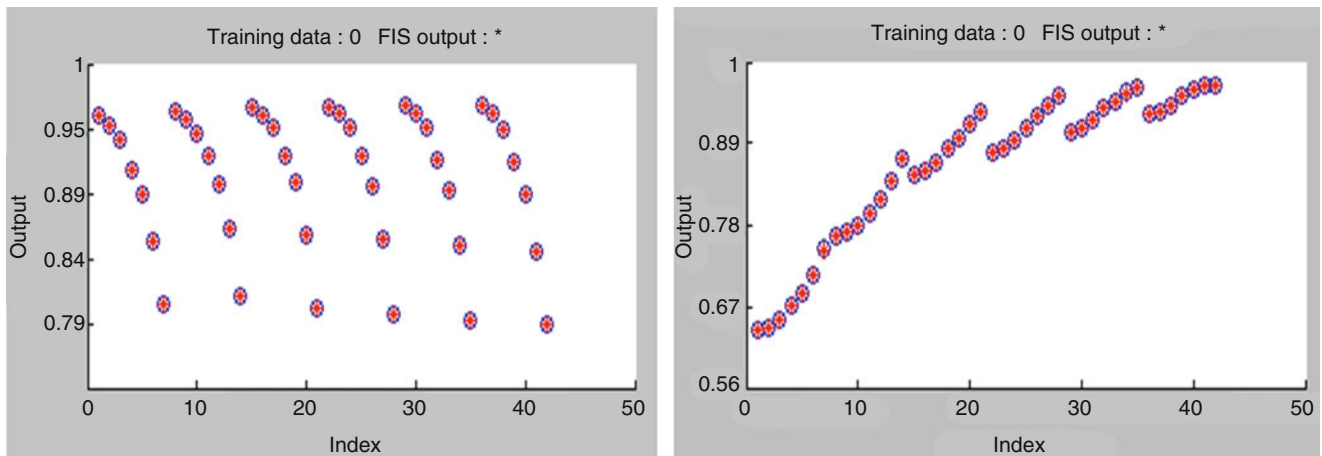
Fig. 50.8 Corrected mass flow (MF = 11) and isentropic efficiency (MF = 12) training diagrams data for turbine 2

Table 50.8 Corrected mass flow error results for turbine 2

Turbine 2-corrected mass flow		
Epoch number	Average test error	Number of membership function (MF)
5	0.0055707	2
5	0.0022691	3
5	0.0016757	4
5	0.00082476	5
5	0.00070482	6
5	0.000399	7
5	0.000041398	8
5	0.000082751	9
5	0.0000004618	10
5	0.00000038769	11
5	0.00000047972	12
5	0.00000049337	13
5	0.0000004891	14

Table 50.9 Isentropic efficiency error results for turbine 2

Turbine 2-isentropic efficiency		
Epoch number	Average test error	Number of membership function
5	0.0074187	2
5	0.0040202	3
5	0.0028297	4
5	0.0021117	5
5	0.0016568	6
5	0.00094596	7
5	0.00015175	8
5	0.00016766	9
5	0.0000041732	10
5	0.0000012372	11
5	0.0000008691	12
5	0.00000098896	13
5	0.0000010333	14

In Fig. 50.8, for turbine 2, corrected mass flow rate (MF = 11) and isentropic efficiency (MF = 12) training solutions are seen. In Table 50.8, the best value of average test error for corrected mass flow is found with 11 membership functions and in Table 50.9, the best value of average test error for isentropic efficiency is found with 12 membership functions. After these membership function values, unstability of average test error starts in the increasing direction of membership functions and so does the simulation time.

Conclusion

In this work, an approach for modeling performance parameters of gas turbine engine compressor and turbine is proposed. The proposed approach is an effective and easy-use way for modeling the performance parameters of compressors and turbines. The proposed method is tested with two different compressors and two different turbines data. The Adaptive Neuro-Fuzzy structure estimates good output values for both on-design and off-design conditions. By altering the number of membership functions, different error values are calculated and it shows that the models can be run accurately with a few number of membership functions. Additionally, this decreases the simulation time. If the selected number of membership function is over the best membership function value, unstability increases in average test error and so does the simulation time. By comparing with the previous studies declarations, this proposed approach has advantages about both accuracy and simulation time. The individual neural network method usage sometimes fails about error value, although it is short simulation time. Curve fitting and beta line methods do not work accurately. In addition, as a difference from other studies it is applied to the turbine component as well. The proposed compact fuzzy-neural network method is functional for both compressor and turbine. In the upcoming works, it is planned to study about engine start up modeling. It is very hard to model the startup operation in an engine. In the next step, this operation regime is tried to adapt this examination.

Nomenclature

$\dot{m}_{corr}$	Corrected mass flow rate, dimensionless	θ	Compressor input temperature under sea level condition, dimensionless
π	Pressure ratio, dimensionless		
N_{corr}	Corrected revolution, dimensionless	O	Output function
N	Revolution	p, q, r	Premise parameters
η	Isentropic efficiency	f	Fuzzy rule
$\dot{m}$	Mass flow rate	$\mu(x)$	Membership function
δ	Compressor input pressure under sea level condition, dimensionless	w_i	Firing strength of the rule
		$\overline{w}_i$	Normalized firing strength value

References

1. Filho FACB, Goes LCS, Boaventura A, Bosa W, Fernandes G (2012) Dynamic modelling nonlinear and control system for a turboshaft, 12th Pan-American Congress of Applied Mechanics, Port of Spain, Trinidad
2. Kulikov GG, Thompson HA (2005) Dynamic modelling of gas turbine: identification, simulation, condition monitoring and optimal control. Springer, New York
3. Yarlagadda S (2010) Performance analysis of j85 turbojet engine matching thrust with reduced inlet pressure to the compressor. Master of Science Thesis in Mechanical Engineering Graduate Faculty of University of Toledo
4. Sexton WR (2001) A method to control turbofan engine starting by varying compressor surge valve bleed. Master of Science Thesis in Mechanical Engineering Graduate Faculty of Virginia Polytechnic Institute and State University
5. Britton IAW (2008) Development of a performance estimation tool for gas turbine engine centrifugal compressors. Master of Applied Science Thesis in Mechanical Engineering, Carleton Institute for Mechanical and Aerospace Engineering, Ottawa, ON
6. Polat C (2009) An electronic control unit design for a miniature jet engine. Master of Science Thesis in Mechanical Engineering Graduate School of Natural and Applied Sciences of Middle East Technical University
7. Kurzke J (1996) How to get component maps for an aircraft gas-turbine's performance calculations. ASME paper 96-GT-164
8. Sieros G, Stamatis A, Mathioudakis K (1997) Jet engine component maps for performance modeling and diagnosis. J Propul Power 13(5):665–674
9. Moraal P, Kolmanovsky I (1999) Turbocharger modeling for automotive control application. SAE Tech Paper Ser 108:1324–1338
10. Orkisz M, Stawarz S (2000) Modeling of turbine engine axial-flow compressor and turbine characteristics. J Propul Power 16(2):336–339
11. Ailer P, Santa I, Szederkenyi G, Hangos KM (2001) Non-linear model-building of a low-power gas turbine. Period Polytech Ser Transp Eng 29:117–135
12. Kong CD, Kho S, Ki JY (2006) Component map generation of a gas turbine using genetic algorithms. J Eng Gas Turbines Power 128(1):92–96
13. Kong CD, Ki JY (2007) Components map generation of gas turbine engine using genetic algorithms and engine performance deck data. J Eng Gas Turbines Power 129(2):312–317
14. Bao C, Ouyang M, Yi B (2006) Modeling and optimization of the air system in polymer exchange membrane fuel cell system. J Power Sources 156(2):232–243
15. Yu Y, Chen L, Sun F, Wu C (2007) Neural network based analysis and prediction of a compressor's characteristic performance map. J Appl Energ 84(1):48–55
16. Ghorbanian K, Gholamrezaei M (2006) Neural network modeling of axial flow compressor off-design performance.10th Fluid Dynamic Conference Yazd, Iran
17. Ghorbanian K, Gholamrezaei M (2006) Neural network modeling of axial flow compressor performance map. 45th AIAA Aerospace Science Meeting and Exhibit Reno, USA
18. Ghorbanian K, Gholamrezaei M (2007) Axial compressor performance map prediction using artificial neural network. ASME Turbo Expo, GT2007-27165, Montreal, Canada

19. Ghorbanian K, Gholamrezaei M (2009) An artificial neural network approach to compressor performance prediction. J Appl Energ 86:1210–1221
20. Turie SE (2011) Gas turbine plant modeling for dynamic simulation. Master of Science Thesis in Industrial Engineering and Management KTH School of Industrial Engineering and Management
21. Federal Aviation Administration (FAA) (2009) Pilot's handbook of aeronautical knowledge. Skyhorse Publishing, Ventura, USA
22. Fözö L, Andoga R, Madarasz L (2010) Mathematical model of a small turbojet engine MPM-20. Comput Intell Informat 313:313–322
23. Jang JR (1993) ANFIS: adaptive-network-based fuzzy inference system. IEEE Trans Syst Man Cybern 23(3):665–685
24. http://www.mathworks.com/help/fuzzy/anfis-and-the-anfis-editor-gui.html#bq97_i_
25. Takagi T, Sugeno M (1983) Derivation of fuzzy control rules from human operator's control actions. Proceedings of IFAC Symposium on Fuzzy Information, Knowledge Representation and Decision Analysis, pp 55–60
26. Neshat M, Adeli A, Masoumi A, Sargolzae M (2011) A comparative study on ANFIS and fuzzy expert system models for concrete mix design. IJCSI 8 (3):196–210
27. Wei M, Bai B, Sung AH, Liu Q, Wang J, Cather ME (2007) Predicting injection profiles using ANFIS. J Inform Sci 177:4445–4461
28. Jang JR (1991) Fuzzy Modeling using generalized Neural Networks and Kalman Filter algorithm, AAAI-91 Proceedings, p 762–767

Performance Estimation of Gas Turbine System via Degree-Day Method

51

Umit Unver and Muhsin Kılıc

Abstract

Nowadays the focus of the power sector is on renewable energy sources. Even so, in Turkey, the most preferred power plants are still co-generation power plants. Considering installed power, gas turbine power plants are the most used type. In gas turbine power cycles, both power and efficiency are highly affected by atmospheric temperature. In this study, the degree-day method is used to expose the variation of the electric power of a gas turbine with respect to atmospheric conditions. The installed capacity of the gas turbine is 237 MW. The operating data were supplied by Ovaakça Power Plant Administration of Bursa/Turkey. In this paper it is indicated that, for a 45 °C increment of atmospheric temperature, mass flow through the compressor at a unit time decreases by about 85.2 kg. Therefore, the compression work decreased by about 11.45 %. In addition, by means of the atmospheric temperature increment, both the total energy input via natural gas and intake airflow rate were decreased by 17.1 % and this resulted in a reduction in net electric power production.

Keywords

Gas turbine • Performance analysis • Degree-day • Topping cycle

Introduction

Energy is one of the world's most important issues since the last two centuries. Until recently, energy demand was met by fossil fuels. But, due to the negative effects of fossil fuels on the environment, the release of hazardous gases came into prominence. Therefore, many countries prefer to convert their energy production systems from fuel oil to natural gas. Because natural gas is a clean source compared to fuel oil, installations are easier and have high efficiency. Also in Turkey, in the 1990s when air pollution began to threaten human health, coal and fuel oil systems were converted to natural gas, to meet domestic and industrial energy demand, and the conversion was stimulated by the government.

The use of high-tech materials and methods in natural gas-fired turbines increased the efficiency of energy production. In addition, the emissions of hazardous gases in flue gases decreased to controllable limits. However, although installing gas turbine cycles is quick and easy, there are also some disadvantages. One of the most important disadvantages is that gas turbine systems are highly affected by atmospheric conditions. It is indicated that compressors of gas turbines are designed to pass a constant volumetric flow [1]. When the atmospheric temperature rises, specific volume increases. Thus, through a constant volume, the mass flow rate decreases, and as a result both the useful power that is achieved from the gas turbine and the thermal power that is achieved from the Heat Recovery Steam Generator (HRSG) decrease. Bassily [2] studied the interaction between atmospheric temperature and compressor work, as well as their effect on system performance, and also

U. Unver (✉)
Yalova University, Kazım Karabekir Mah. Rahmi Üstel Cad. No: 1, Yalova, Turkey
e-mail: umit.unver@yalova.edu.tr

M. Kılıc
Bursa Orhangazi University, Mechanical Engineering Department, Yıldırım, Bursa, Turkey
e-mail: muhsin.kilic@bou.edu.tr

studied the efficiency improvement by cooling of inlet air via evaporative coolers. Similarly Alhazmy has addressed the issue to inlet air cooling via spray cooling and cooling coil methods [3]. Gareta and Gil also focused on cooling the inlet air by various methods [4]. Arpaci İ. ve Binark [5] examined a natural gas-fired co-generation cycle and described the algorithm of the calculation of system parameters in detail.

The studies mentioned up to here declare that the increase of the atmospheric temperature has a negative effect on gas turbine cycle performances. Thus they all agreed that the selection of the climate of the place where the power plant would be installed has significant importance. However, studies investigating the gas turbine systems have not clearly stated that how climate impact should be determined.

In this paper, we have shown the relationship between the degree-day method, which is generally used to determine the optimum insulation thickness of buildings, and net electric power produced by gas turbine cycles. In this way, first it will be possible to determine the atmospheric affect on the net electric power production, and then, comparing different climatic locations with reliable numerical data would be possible.

The degree-day method that was used in this study was described in detail in [6]. In the study, the optimum insulation thickness was determined via the degree-day method.

Material

The data were obtained from an operating 501F type gas turbine, which was produced by Mitsubishi Heavy Industries. At the topping cycle electric power is generated by natural gas combustion. Additionally, exhaust gases about 550 °C, are sent to an HRSG to obtain more electric power from the bottoming cycle.

The natural gas consumption is about 14 kg/s at full load while the atmospheric temperature is 15 °C. Annual average of Lowest Heating Value (LHV) was calculated from monthly analysis data of natural gas, which was about 45,000 kJ/kg. The combustion system of 701F consists of 20 combustion cells. Combustion cells consist of two-stage burners and a by-pass valve. The cooling cycle of turbine consists of rotor cooling cycles and four stationery cooling cycles. Cooling air is obtained from various stages of turbine blades. The compressor and turbine have a single shaft on a couple of bearings.

Characteristic data for gas turbines:

Manufacturer	Mitsubishi Heavy Industries/Japan
Type	Axial flow—701F
Gross output power/efficiency	239,000 kW/701F
NOx emission	50 mg/m^3
Number of blade stage	4
Inlet temperature	1,350 °C (ISO)
Exhaust temperature	558 °C
Revolution per minute	3,000 rev/min
Critic rev.	(1) Critic 930, (2) Critic 2550
Start up time	1,200 s
Combustion chamber type/num.	Multi cell/20
Ignition	Spark
Compressor type	Axial flow
Stage number	17
Compression ratio	16
Air flow (ISO)	580 kg/s (100 % load, 15 °C)

Method

The degree-day method is a powerful tool to calculate heating and cooling loads of buildings. First a base temperature is defined, and then from the difference of mean temperature of each day of the year and the base temperature, heating and cooling degree-days can be obtained. A wide range of information can be obtained from the recent studies [7–12]. Generally;

$$DD = \sum_{1}^{365}(T_b - T_0) \tag{51.1}$$

Equation is used to define degree-day.

Gas turbine cycles are very sensitive cycles vs. atmospheric conditions and so degree-day method. Because of this, when atmospheric temperature decreases, the mass flow rate through the cycle is expected to decrease while the volumetric flow rate remains constant, which means the power required to compress air calculated by

$$W_{comp} = \frac{\dot{m}(h_i - h_e)}{\eta_{comp}} \tag{51.2}$$

should change. The atmospheric temperature variation changes both mass flow rate of inlet air and natural gas. That means the energy that is supplied by natural gas and the net electric power production changes. The net electric power, which is produced by gas turbine cycles, can be calculated by:

$$W_e = (\dot{m} \ x \ LHV) - W_{comp} \tag{51.3}$$

Results and Discussion

As it is well known, when the air temperature increases, the specific volume of the air also increases. The volumes of the stages of a turbo compressor are constant. Thus, the amount of volumetric flow per unit time is considered to remain unchanged. In this case, for a constant rotation, an increment of volume of unit mass flow through stages means a reduction in the mass flow rate. According to this statement, the variation of specific volume and mass flow rate with respect to inlet air temperature difference are given in Fig. 51.1. As it is seen from the figure, with a 45 °C increase of temperature, the specific volume rose from 0.76518 to 0.89264 m³/kg. The increment is about 0.12746 m³/kg. For small-scale cycles, this value can be considered negligible, but this slight change affects mass flow rate dramatically. The mass flow rate was about 621.6 kg/s at −3 °C and decreased down to 536.5 kg/s with the 45 °C decrease of atmospheric temperature. In other words, for a 45 °C increment of atmospheric temperature, mass flow through the compressor for a unit time decreases by about 85.2 kg.

If the enthalpy is defined as the energy level of the fluid, we can consider that the energy level of the fluid increases with the increasing atmospheric temperature. Naturally, when the inlet air temperature increases, exit air temperature also increases. This means, the enthalpy of air at the compressor exit increases. In Fig. 51.2 the enthalpies at inlet, exit of the compressor and the difference between these are given. At first glance, the increase of the enthalpy at the exit seems to be useful but if we look into Fig. 51.2, when the atmospheric temperature is at −3 °C, the enthalpy is about 684.8 kJ/kg while with a 45 °C temperature increment it increases by about 56 kJ/kg and reaches 740.7 kJ/kg. Meanwhile inlet air enthalpy was 270.1 kJ/kg at −3 °C, and with a 45 °C increment it rises up to 425.5 kJ/kg. In other words, the enthalpy difference, which can be calculated via Eq. (51.2) goes up about 10.8 kJ/kg with the increase of atmospheric temperature of about 45 °C. The increase of difference between enthalpies, means a serious energy loss if we take such a big mass flow rate into account.
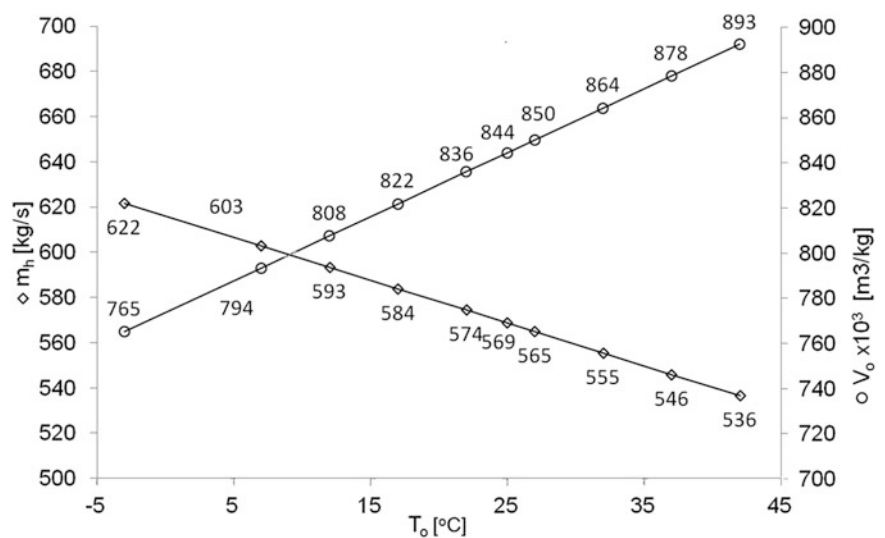
Fig. 51.1 Variation of specific volume and mass flow rate with respect to atmospheric temperature

Fig. 51.2 Inlet, exit and the difference air enthalpies at the compressor
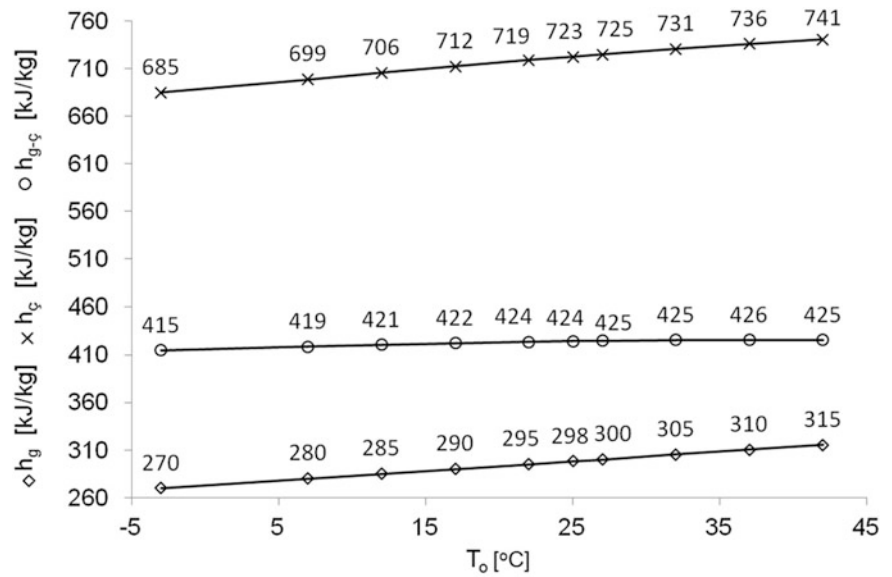
Fig. 51.3 Variation of compression work and total input energy vs. atmospheric temperature
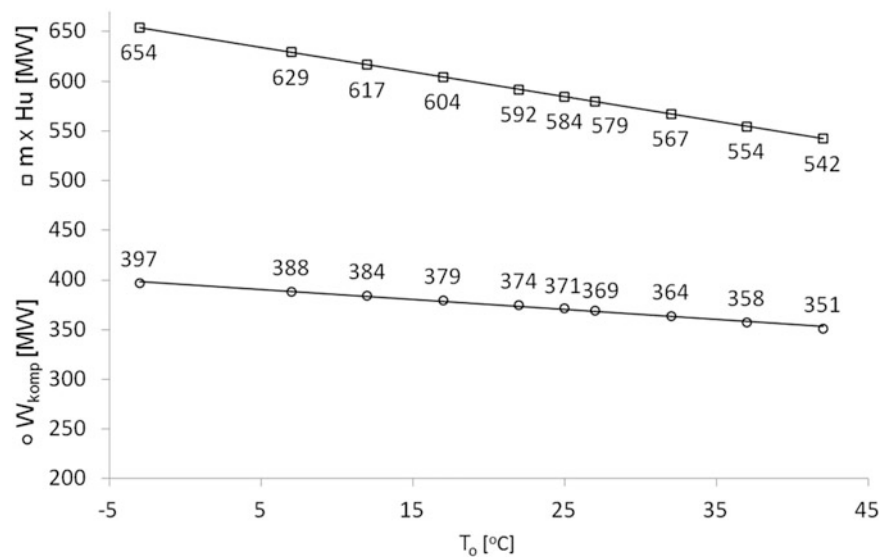
In Fig. 51.3 the variation of the energy supplied to the system with combustion and the compression work vs. atmospheric temperature are given. As it is seen in the figure, decrease of the mass flow rate of air reduces the compression work positively. In other words, with the increasing atmospheric temperature, the compression work reduces by means of decrease of mass flow rate of air. In the calculations, compressor efficiency is considered 0.65. The compression work was obtained at 396.6 MW at −3 °C. With a 45 °C increase of temperature, 45.4 MW of reduction is observed and compression work decreased to about 351.2 MWs. On the other hand, analyzing the reduction of compression work alone is specious. Because, the reduction of the energy which is supplied by natural gas is more dramatic. The energy supplied by natural gas was about 653.8 MW and with the 45 °C increase of temperature, it reduces by about 112 MW and decreases to 542 MW. That means the reduction of the natural energy gas is more than the reduction of energy that is used for compression work, which also means that, by a 45 °C increase of atmospheric temperature, the reduction of the total energy entering the system is more than the reduction of the required energy for compression work. The main cause of this is, in gas turbine cycles, that atmospheric temperature difference not only affects the inlet air mass flow rate but also affects the mass flow rate of natural gas negatively. The decrease of flow rates of fuel and air results in more reduction on the energy that is supplied by fuel than the reduction of the compression work. Consequently, the net electric power produced by the gas turbine cycle also reduces.

Fig. 51.4 Atmospheric temperature difference vs. days of the year in order
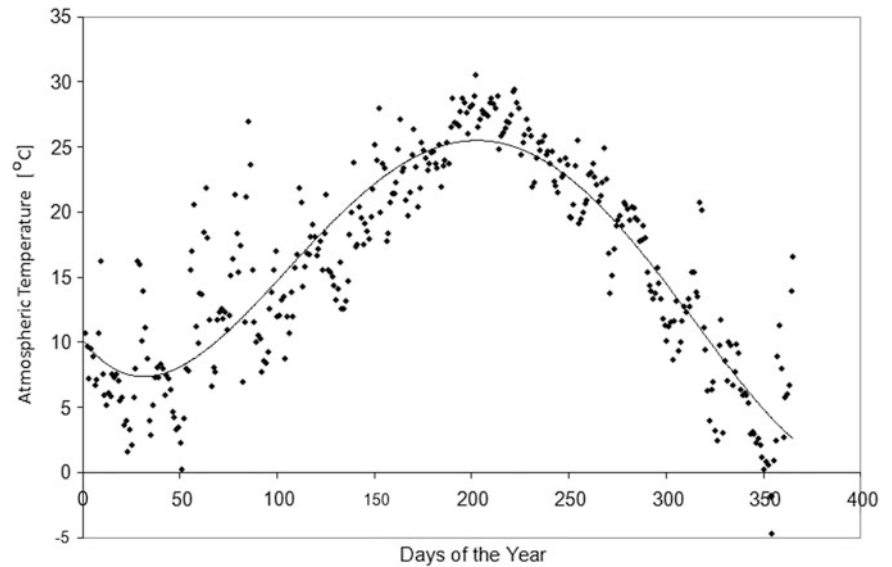
Fig. 51.5 Net electric power production vs. days of the year in order
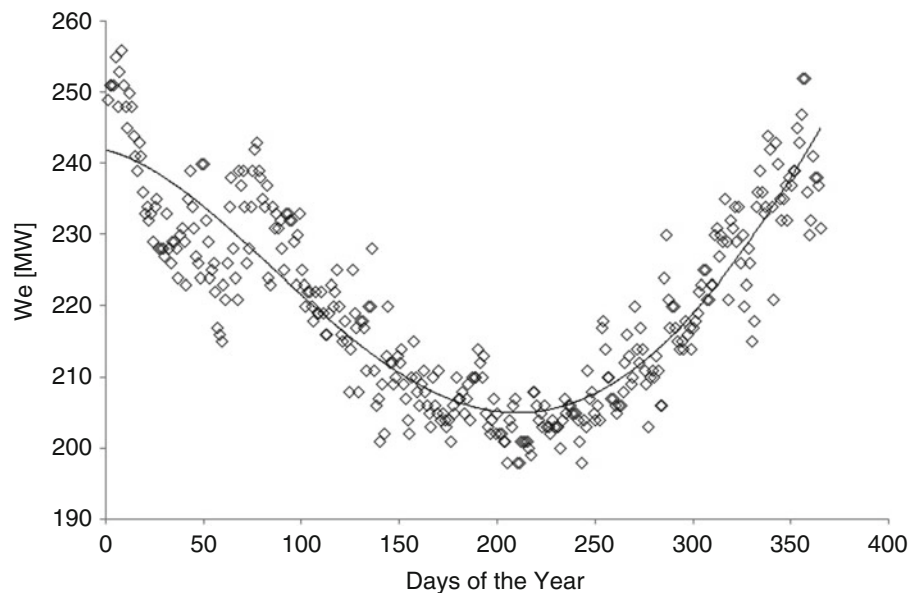
So far, the findings show us that atmospheric temperature has a direct impact on the power production of the gas turbine cycle. Recent studies note that the effect of atmospheric temperature must be taken into consideration during the selection of the power plant's location. Of course, proximity to the sources and the market are very important parameters during the selection of location of a power plant on where it would be installed. In parallel to this, with this study, the relationship between the electric power achieved from the plant and the effect of climate was given via the degree-day method.

The degree-day method is a method that may expose the impact of atmospheric temperature that can become visible. With the method, significant comparable numerical results can be obtained by using the degree-day method for different climatic zones during the selection of the location of the power plants. The degree-day curve of Bursa, where the power plant considered in this study is located, is given in Fig. 51.4. For the same time interval, the electric power produced by the power plant is given in Fig. 51.5. As it can be seen in the figures, there is a significant similarity that attracts the attention between the degree days and the produced power. The causes of similarity were examined in detail so far. The net electric power was about 240 MW during the cold days in winter. During spring season, when the atmospheric temperature begins torise, the electric power begins to decrease. When the atmospheric temperature reaches to a maximum during summer, the net electric power reaches to the minimum values—about 200 MW. It is also observed that the slopes of the curves are in counter agreement with each other.

Conclusion

In this study, the variation of net electric power achieved from gas turbine cycles was analyzed with respect to atmospheric temperature. Also a similarity between atmospheric temperature and power production were exposed. It was seen that, with the increase of atmospheric temperature, specific volume increased by 16 %; as a result, the intake air mass flow rate decreased by 13.7 %. The reduction of intake air and increment of atmospheric temperature were negatively affected the total energy input via natural gas, and intake air flow rates in parallel. Both the total energy input via natural gas and intake air flow rate were decreased by 17.1 %. The atmospheric temperature increment also caused to decrease compression work by 11.45 %. However, if we take into account that the decrease of compression work is less than the decrease of total energy input, the compression work relatively seemed to be ascending in proportion to the total energy input. As a result, the net electric power decreases with increasing temperature.

In the study, quite a significant relationship was determined between degree-day and net electric power curves. It is seen that the relation between the net electric power production and atmospheric conditions may be defined quantitatively. In this way, during the selection of location of power plants, forecasting the power production variation vs. the atmospheric conditions variation would be possible even if the power plants were not operating. By using this method, not only possible production but also unavailability may be forecasted quantitatively. Moreover, the effect of different climate zones may be compared, and an alternative and clear criterion, except from proximity to market and source parameters, may be achieved.

Nomenclature

DD	Degree day	h_i	Inlet air enthalpy (kJ/kg)
T_b	Base temperature (°C)	h_i	Exit air enthalpy (kJ/kg)
T_o	Atmospheric temperature (°C)	η_{comp}	Compressor efficiency
W_{comp}	Compression work (kW)	W_e	Net electric power (kW)
$\dot{m}$	Mass flow rate (kg/s)	LHV	Lower heating value (kJ/kg)

References

1. Arrieta FRP, Lora EES (2005) Influence of ambient temperature on combined-cycle power-plant performance. Appl Energy 80(3):261–272
2. Bassily AM (2001) Effects of evaporative inlet and after cooling on the recuperated gas turbine cycle. Appl Therm Eng 21:1875–1890
3. Alhazmy MM, Najjar YSH (2004) Augmentation of gas turbine performance using air coolers. Appl Therm Eng 24:415–429
4. Gareta R, Gil LMRA (2004) Methodology for the economic evaluation of a gas turbine air cooling systems in a combined cycle applications. Energy 29:1805–1818
5. Arpacı İ. ve Binark AK (2002) Doğal gazlı kojenerasyon sisteminde ekserji analizi. In: 7th international combustion symposium, Ankara, 17–18 July 2002, pp 368–375
6. Kaynaklı O, Özdemir S, Karamangil İM (2012) Güneş ışınımı ve duvar yönü dikkate alınarak optimum ısıl yalıtım kalınlığının belirlenmesi. J Fac Eng Archit Gazi Univ 27(2):367–374
7. Bolattürk A (2006) Determination of optimum insulation thickness for building walls with respect to various fuels and climate zones in Turkey. Appl Therm Eng 26:1301–1309
8. Bolattürk A (2008) Optimum insulation thicknesses for building walls with respect to cooling and heating degree-hours in the warmest zone of Turkey. Build Environ 43(6):1055–1064
9. Ozkahraman HT, Bolattürk A (2006) The use of tuff Stone cladding in buildings for energy conservation. Construct Build Mater 20:435–440
10. Çomaklı K, Yüksel B (2003) Optimum insulation thickness external walls for energy saving. Appl Therm Eng 23:473–479
11. Dombaycı ÖA (2007) The environmental impact of optimum insulation thickness for external walls of buildings. Build Environ 42:3855–3859
12. Dombaycı ÖA, Gölcü M, Pancar Y (2006) Optimization of insulation thickness for external walls using different energy sources. Appl Energy 83:921–928

Evaluation of Turkish Electricity Demand Projections

52

Betül Özer

Abstract

Electricity demand forecasting and energy models are required for many different utility purposes. According to the results of the large number of studies in the literature about electricity consumption forecasting and modeling, the factors affecting energy consumption may change from country to country. Accordingly energy demand models may be developed for each country basing on their own situations. Economic indicators such as population, gross domestic product (GDP), GDP per capita, imports and exports, prices, and the other socioeconomic factors such as continuous tendency for better living standards, and access to electricity are the variables that were taken into consideration for the forecast studies. There are several studies in the literature on forecasting the electricity consumption of Turkey in which various models were used with different assumption of variables, correspondingly presenting different results. The aim of this study is to overview these studies and to evaluate the different results.

Introduction

Energy is one of the most significant components in the economic development of countries. It is also certain that energy is the most important necessity of human life and, hence, there is an increasing relation between the level of development and the amount of energy consumption. Worldwide energy consumption is rising fast because of the increase of human population, continuous pressures for better living standards, emphasis on large-scale industrialization in developing countries and the need to sustain positive economic growth rates. Given this fact, a sound forecasting technique is essential for accurate investment planning of energy production, generation and distribution [1].

The estimation of electricity consumption is of great importance for effective implementation of electricity policies, such as conservation programmes, the planning of capacity expansion and the construction of nationwide interconnections of power network [2]. Therefore, studies focusing on the forecasting of electricity demand using different techniques are important for an accurate energy planning in order to avoid electricity shortage and to guarantee adequate infrastructures of the countries.

The most common difficulty for a good prediction of the electricity demand is the determination of sufficient and necessary information, and selecting the most related variables. Electricity is not demanded for its own sake; it is a derived demand that comes from the demand for lighting, heating, cooling, and it is the demand for the services it produces with the capital stock in a place at a certain time. The amount of energy consumed is therefore connected to the technological level of the energy appliances to assure the demanded level of services. Consequently there are some exogenous factors that might

B. Özer (✉)

Eurasia Institute of Earth Sciences, Istanbul Technical University, Maslak, İstanbul, Turkey
e-mail: betlozer@hotmail.com

influence electricity demand behavior, such as improved technical efficiency of the capital and appliance stock, and changes in consumer tastes, preferences, demographic parameters, social structures, environmental regulations, economic structure like gross domestic product (GDP) per capita or economic growth, business cycles etc. [3, 4].

Various studies in the literature indicate that the relationships between electricity consumption and several potentially relevant variables, like prices, consumer income, key weather parameters, number of customers and tourists, and sectoral demand trend, change from one country to another [5]. These variables can all or partially have an influence on electricity demand according to country-specific characteristics. The predictive ability of the models that are applied to energy demand forecasts depend on the variables, estimated values and the assumption of their influence factors on electricity demand.

It is obvious that consumption is related to population. As the population increases more electricity will be consumed. However, the increase ratio of the energy consumption is usually higher than the increase ratio of the population. This proves that there are some other factors affecting the electricity demand, such as gross national product (GNP), which is a measure of all economic activities, imports and exports. Increasing GNP means improved living standards that cause increase of energy use, while imports and exports are related to manufacturing processes and therefore strongly affect electricity consumption [6]. These factors are generally difficult to observe directly but arguably play an important role in determining electricity demand behavior [3]. Consequently the goal of accurate modeling of consumption requires attention to a few extremely important points. The first point is to identify all the necessary variables and parameters that contribute to electricity consumption in a given country. The second point is to choose a modeling methodology that can handle the difficulties of the consumption modeling task. One difficulty in this area, similar to many other modeling studies, is the fact that the relationship between the input variables and the output variable is nonlinear and the nature of the nonlinearity is not known very well. Therefore it is not easy to postulate the form and/or order of a mathematical function whose parameters could be estimated through regression type computations [7, 8]. Although being the most important aspect, accuracy of the model is never the only concern in any modeling analysis. Models should also be able to handle imperfections in the data such as noise, errors, missing data points, disturbances and short-term effects. Another area of concern in modeling is the so-called local minima. Most modeling techniques compute model parameters by minimizing a cost function which may not have a single local minimum that is also the global minimum. Then getting trapped in one of the local minima avoids reaching the real optimal parameters. Therefore a good modeling method should either be able to guarantee reaching global minimum or should have a single global minimum for its cost function. In summary, the models should exhibit good global optimization and robustness characteristics as well as accuracy in prediction. Furthermore, the methodology used should allow future prediction by letting the model topology cover one-step or multi-step ahead predictions. This is critical since the eventual goal here is to predict the future values of electricity production that leads to dynamic model structures. It is well-known that time series formalism using nonlinear models is very suitable for these types of problems. In addition, the methodology should allow rangeability as often the data available for modeling does not cover the ranges of data for the times the predictions need to be done [7].

Energy security is the one of the most important issues of the twenty-first century. Arguably, the policies and strategies cannot be neither assessed nor constructed without sound demand forecasts [4]. Therefore, demand forecast results of different kinds of studies have great importance when implementing future energy policies, especially for energy supply and security and when demand grows faster, as in the case of Turkey. Turkish Parliament ratified the Kyoto protocol in February 2009, which is leading to the introduction of legally compulsory commitments for the reduction of greenhouse gases (GHGs). It is therefore commonly expected there will be a change in Turkish energy policy that might include CO_2 taxes. Even there are some regulations including incentives to the use of renewable energy. Regarding this new environment in which markets will operate, determining the total and sectoral electricity demand (including industrial, residential and services etc.) function might have a significant importance on evaluating new policy implications. Sensible and reliable energy demand forecasts assist in financing and developing the necessary measures for the sustainable economic growth of Turkey [4]. According to the various studies on the forecast of the electricity demand of Turkey, the results differ from each other as they used different models, and variables with different future assumptions. Furthermore, the effects of the variables to the demand forecast mainly depend on the model setup.

From the point of view the aim of this chapter is to present an overview of the studies in literature on the electricity demand projections of Turkey. The results were evaluated by putting forward to what extent the projections can be done with various assumptions of the variables used in different methodologies. The results of this chapter can indicate the importance of using alternative forecasting methodologies to the energy planners and policy makers for building Turkey's future electricity generation scenarios.

Background: Development of Turkish Electricity Sector

Turkey's electricity demand has been growing very rapidly as a result of the rate of population growth, a rapid industrialization and economic development. It has increased from 47 TWh in 1990 to 195 TWh in 2012, with an annual average growth rate of 6.8 %. Only in the economic crisis years (2001 and 2009) the demand decreased. The installed capacity has increased from 16.3 GW in 1990 to about 57 GW in 2012 by a 5.8 % growth rate ([9]; Fig. 52.1). The electricity industry is a large, high-growth sector in the Turkish economy. The industry contributes significantly to the country's GDP and is a US$12 billion industry at current end-user prices [10]. Despite the increasing demand, Turkey's per capita gross consumption is still very low at the value of about 2,900 kWh when compared to the EU average of about 5,700 kWh.

Figure 52.2 indicates the comparison of the increase ratios of the GDP and electricity demand in the period of 1980 to 2012 for Turkey. The electricity consumption growth rate was 7.4 % which is higher than 4.4 % the average annual growth rate of GDP [9, 11, 12].
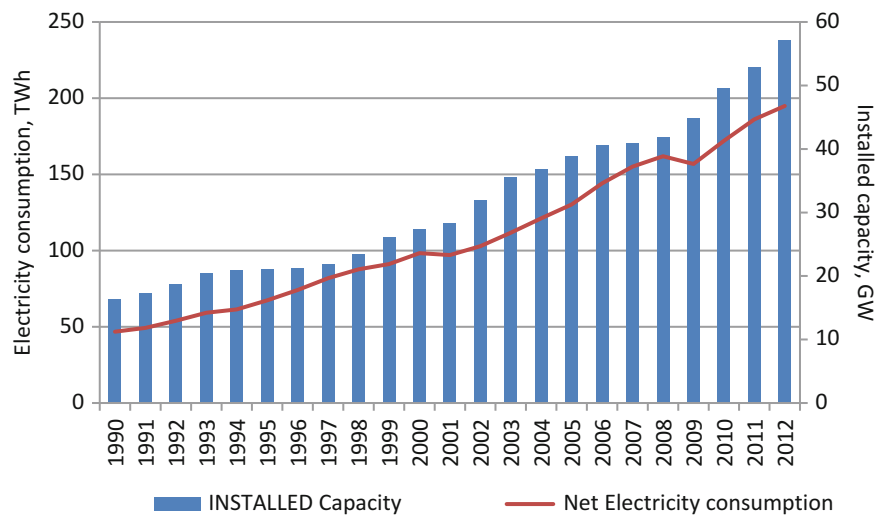
Fig. 52.1 Turkish electricity system development (1990–2011) [9]
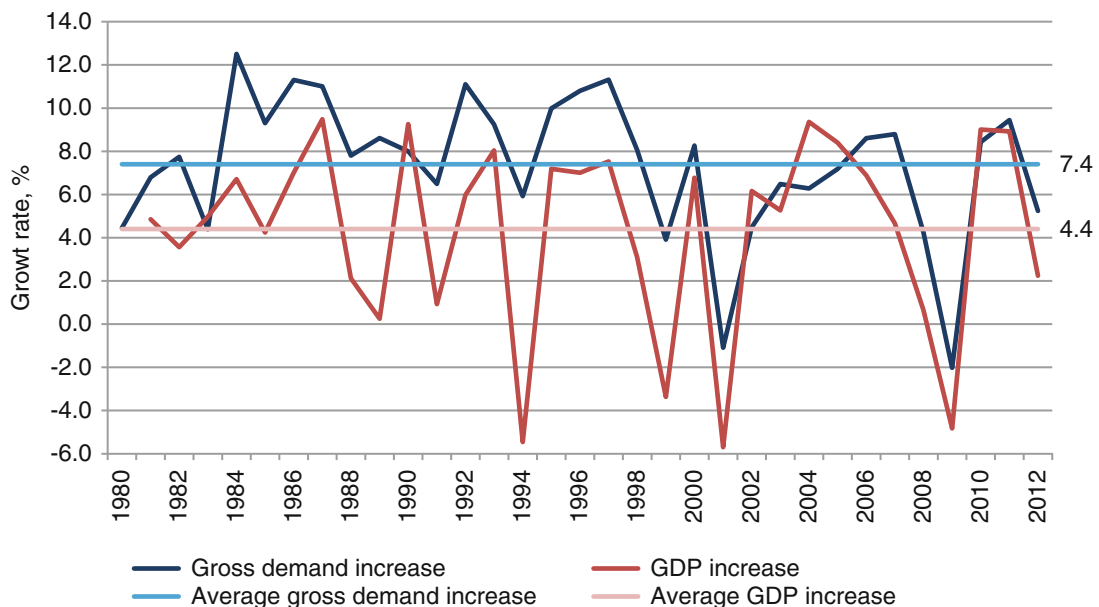
Fig. 52.2 Turkish electricity demand and GDP growth (1980–2012) [9, 11, 12]

Review of Turkish Electricity Demand Studies

In the planning of investment strategies of the electricity production, transmission and distribution systems, mid- and long-term electricity forecasting is very important.

Studies before the 1970s that directly focused on analyzing Turkish electricity demand are very limited, being generally carried out by governmental institutions with their own approaches, namely the State Planning Organization (SPO), the State Institute of Statistics (SIS) and the Ministry of Energy and Natural Resources (MENR). Although some researches in those institutions tried to apply mathematical modeling techniques to analyze energy demand in the late 1970s, these methods were not used in official energy planning until 1984. Before 1984, national energy policy was shaped by the forecasts of the SPO in which they employed various simple best-fit curves [4, 13]. The MENR utilized "balance" and "impact" models in order to determine energy demand functions and to make future projections, and also used the simulation models: Model for Analysis of Energy Demand (MAED), Wien Automatic System Planning (WASP III) and Energy Flow Optimization Model (EFOM-12C Mark). The SPO also developed its own models based on sectoral energy demand for different consumer groups and subgroups whereas the SIS explored the relationship between demographic factors and economic parameters with energy demand in its models [14]. Since 1984, the MENR is preparing Turkey's future electricity projections yearly and has carried out projections for Turkey's energy demands by using the MAED simulation technique. In the model, energy demand forecasting is realized by considering past situations of the country's economic, demographic and social structure. They also have some deviations due to the deviations of the assumed values of the variables.

There was a large increase in the number of Turkish energy modeling studies after the late 1990s and they can be divided into three main groups. In the first group, the focus is on investigating the causality between energy consumption and economic variables and can be defined as causality studies. In the second group, the focus is on identifying the relationship and the magnitude of the key relationships—mainly the elasticities between economic variables and energy consumption that can be defined as relationship studies. And in the third group, the aim is to forecast future energy demand using a number of different approaches which can be defined as forecast studies [4]. Most of the studies for Turkish electricity demand projections in the literature are overviewed in this section.

Yumurtacı and Asmaz [15] proposed an approach to calculate the future energy demand of Turkey for the period of 1980–2050, based on the population and energy consumption increase rates per capita. The multiplication of population value and the consumption per capita gives the necessary energy amount. According to the calculations for the year 2050, if an individual uses 10,197 kWh of energy in 1 year, then 115 million individuals will need an electric energy of 1,173 billion kWh.

Öztürk et al. [16] used the genetic algorithm (GA) approach to investigate the relationship between total electricity consumption, GNP, population, imports and exports for the period 1980–2001 in Turkey with annual data. The total electricity demand of Turkey was estimated 220 and 300 TWh in 2020 with exponential and quadratic forms of the genetic algorithm electricity demand (GAED) models, respectively. They mentioned that the estimation of electric energy demand, based on the socioeconomic indicators, might be estimated with various forms of mathematical expressions. These equations might be linear or nonlinear forms. The nonlinear forms of the equations could better estimate the future electricity demand of Turkey due to the fluctuations of socioeconomic indicators.

However, in the study of Öztürk and Ceylan [2], total electricity consumption was estimated based on GNP, population, and import and export figures of Turkey. Industrial sector electricity was calculated based on the GNP, import and export figures. Three forms of the GAED models for the total electricity consumption and two forms of GAED for the industrial electricity consumption were developed. The best-fit GAED model in terms of total minimum relative average errors between observed and estimated values that was GAEDquadratic (GAEDquad) was selected for future demand estimation. High- and low-growth scenarios were proposed for predicting the future electricity consumption. The electricity consumption in 2020 with the GAEDquad estimation for the low-growth scenario will be about 462 TWh while it will be about 500 TWh for the high-growth scenario. The following conclusions can be drawn from the study as the GA notion can be applied as an alternative way of electricity consumption estimation for the future by appropriately fitting the mathematical expressions to the existing data. The reason for applying the GA is that it is flexible in nature to provide many optimal, or near-optimal solutions to estimate the future trends of the electricity consumption. This advantage comes from the GA approach itself, because the GA starts the solution of the problem from a large population base. The model is actually a multi-parameter solution, which has many feasible solution points. The inclusion of the import and export figures in the electricity demand estimation improves the GAED model performance.

In the study of Tunç et al. [17] Turkey's electric energy consumption rates were predicted by regression analysis for the years of 2010 and 2020, and finally a linear mathematical optimization model was developed to predict the distribution of future electrical power supply investments in Turkey. In 2020 it was predicted that Turkey's electricity consumption will be about 322 TWh.

Erdoğdu [18] used co-integration analysis and autoregressive integrated moving average (ARIMA) modeling, for both providing an electricity demand estimation and forecast, and compared the results with official projections. The study concluded, first, that consumers' response to price and income changes is quite limited and therefore there is a need for economic regulation in the Turkish electricity market; and second, that the existing official electricity demand projections highly overestimated the electricity demand, which may endanger the development of both a coherent energy policy in general and a healthy electricity market in particular. The data used in the estimation process was quarterly time series data on real electricity prices, real GDP per capita and net electricity consumption per capita for the period 1984–2004, a total of 84 observations. The electricity demand of Turkey was predicted to be 160 TWh by the year 2014.

Hamzaçebi [19] used the artificial neural networks (ANN) model with a time series structure for the period 1970 and 2004 to analyze sectoral electricity consumption in order to forecast sectoral and aggregate electricity demand. Residential, industrial, agricultural and transportation sectors were considered. The results indicated that aggregate electricity demand would be just below 500 TWh in 2020. Although this network structure is well suited for prediction beyond an existing data set; the confidence in predictions decreases as time moves forward [6]. ANN, imitating the functioning of the human brain, is a tool of great importance in sample classification, pattern recognition, and forecasting. The most widely used ANN type for forecasting is a multi-layer perceptron (MLP). In an MLP designed for time series forecasting, determining the variables, such as number of input, hidden and output neurons, is highly important. However, these parameters are subject to change with respect to the problem at issue [19].

The grey prediction with rolling mechanism (GPRM) approach was proposed to predict Turkey's total and industrial electricity consumption in the study of Akay and Atak [20]. The GPRM approach was used because of high prediction accuracy, applicability in the case of limited data situations and requirement of little computational effort. Results showed that the proposed approach estimated more accurate results than the results of MAED, and had explicit advantages over extant studies. Grey prediction is thought to be an alternative forecasting tool for those systems whose structure is complex, uncertain and chaotic as in the case of Turkey's energy demand structure. Grey prediction has been widely used in forecasting studies due to its advantages, requiring low data items to build forecasting models and higher forecasting accuracy when compared with other forecasting techniques. The rolling mechanism is an efficient technique to increase forecasting accuracy of grey prediction in case of having exponential and chaotic data. The electricity consumption data for Turkey from 1970 to 2004 was modeled and it showed an exponential trend for the period of 1970–2004. The model was applied separately to forecast total and industrial sector electricity consumption. It was expected that industrial and total consumption would be 140.37 and 265.7 TWh in 2015, respectively. The reason for the differences with the MAED model results were mentioned as MAED uses too many indicators, and in case of the existence of a high level of variability between them, this simply brings about an error effect on the results. On the other hand, GPRM uses only the consumption data of the last 4 years. In this respect, it has both simplicity and much better prediction accuracy, and can be implemented reliably [20].

Yüksek [21] evaluated some previous demand projection studies. He evaluated nine projection results of the MAED model which were used for Turkey's long-term electricity energy demand by Turkish Electricity Transmission Company (TEIAS). According to the comparison of the projection and the observed electricity demand values for the years 2005, 2006 and 2007, only three of those studies were taken into consideration for future demand values due to very well predicted values. According to the results of comparison values for the years 2005, 2006 and 2007 Yumurtacı and Asmaz [15], Tunç et al. [17], and Hamzaçebi [19] have an average of 11.3, 3.5 and 19.6 % relative errors respectively. Thus these studies weren't taken into consideration in Yüksek's [21] study. Six new scenarios were applied in the study according to the different assumptions of the increase ratios of population, electric energy consumption per capita and total electric energy consumption values. Depending on the applied scenarios and MAED model results, Turkey's annual electric energy demand in 2010, 2015 and 2020 varied between 222 and 242 TWh; 302 and 356 TWh; and 440 and 514 TWh; with average values of 233, 334 and 476 TWh, respectively.

Kavaklıoğlu et al. [6] used ANN for predicting the electricity consumption of Turkey. They mentioned that it was better to use models those can handle nonlinearities among variables, as the expected nature of the energy consumption data is nonlinear. It is a well-known fact that ANN can model any nonlinear relationship to an arbitrary degree of accuracy by adjusting the network parameters. Electricity consumption was modeled in their study as a function of economic indicators such as population, GNP, imports and exports. Imports and exports to Turkey were related to manufacturing processes and therefore strongly affect electricity consumption. Turkey's electricity consumption was predicted to reach 240 TWh in 2020 and 279 TWh by the year 2027. From year 2010 to 2027, a slower pace growth was predicted with an average 5.6 billion kWh increase year over year. In essence, the neural network model indicated that the fast growth was not sustainable. Murat and Ceylan [22] obtained that modeling of the energy consumption may be carried out with ANN with a lack of future prediction since the ANN models they built were good at solving existing data, but were not good for prediction since they do not use any mathematical models [6].

Toksarı [23] studied models obtained by using the ant colony optimization (ACO)-based algorithm to forecast net electrical energy generation and demand. ACO is a multi-agent system in which the behavior of each unit is inspired by the foraging behavior of real ants to solve the optimization problem. The estimation of electrical energy generation and demand based on economic indicators was to be modeled by using linear and quadratic forms of equations. The economic indicators that were used during the model development were GDP, population, import and export data. Ant colony optimization electricity energy generation and demand (ACOEEGE and ACOEEDE) were developed inspired from the ACOEDE algorithm used to estimate energy demand [24]. Both models were developed by using the ACO-based algorithm and observed data between 1979 and 2006. And the linear and quadratic forms of the proposed ant colony optimization electricity energy estimation (ACOEEE) algorithm were used. The linear ACOEEGE and ACOEEDE, and quadratic ACOEEGE and ACOEEDE were obtained. Quadratic models for both generation and demand provided the better fit solution due to the fluctuations of the economic indicators. The ACOEEGE and ACOEEDE models were used under three scenarios with different assumptions of the variables for estimating Turkey's electricity generation and demand in the years 2007–2025. Electricity generation and demand estimations were thought to be separate and varied according to the forms of the equations. Consequently the electricity demand estimates varied from 125 TWh to 2,500 TWh in 2025 for three scenarios.

In Küçükali and Barış' study [25], the fuzzy logic electricity demand model was developed in Turkey. Unlike most of the other forecast models about Turkey's electricity demand, which usually use more than one parameter, GDP based on purchasing power parity was the only parameter used in the model. In the most of the previous studies the net electricity consumption of Turkey was predicted. MENR, Küçükali and Barış' [25] study have tried to forecast the gross electricity consumption of Turkey. According to this study the fuzzy model follows the general trend in the scatter more closely than the regression solutions. This was because internal uncertainties and system behavior at different time periods were not taken into account in the classical regression approach. The advantage of the fuzzy logic procedure lies in the ability to mimic human thinking and reasoning. The results indicate that the electricity demand growth mainly reflects the changing expectations of GDP. So, forecasting the Turkey's electricity consumption with the country's economic performance in the short-term will be more meaningful and will provide more reliable data for the policy makers and investors. Turkey's electricity demand was predicted to be 230 TWh in 2014.

Çunkaş and Taşkiran [26] have carried out Turkey's electric consumption forecasting by using genetic programming (GP). Unlike GA, GP is a symbolic regression tool that performs well on assigned tasks. GP does not need any functional relationship between dependent and independent variables [26, 27]. In general, Turkey's electricity consumption can be characterized as both unstable and fluctuating. Therefore, the GP method is a good forecasting tool for systems which are complex, uncertain, and unstable. The proposed model effectively predicts the future electricity demand through GP using annual data for the previous years. By using the available data, finding the function which represents the data well is called curve fitting. There are many different curve-fitting techniques like interpolation, regression, and symbolic regression. Conventional regression techniques are used to find the function and the coefficients best representing the data. Most of the time, it is very hard to find the best fit function. On the other hand, symbolic regression does not look for function coefficients; instead, it looks for the best fitting structure that represents the model. GP is known as the best symbolic regression tool [26, 28]. According to GP results in this study, the electricity consumption is predicted to be 315 TWh in 2020.

In the study of Kavaklıoğlu [7], support vector regression (SVR) methodology was used to model and predict the Turkey's electricity consumption. Electricity consumption was modeled as a function of time, and socio-economic indicators such as population, GNP, imports and exports. In order to facilitate future predictions of electricity consumption, a separate SVR model was created for each of the input variables using their current and past values; and these models were combined to yield consumption prediction values. An analysis of historical data for these four variables has shown that except for the population variance, there are no steady trends within these indicators. This is probably due to the fact that Turkey is a developing country and is very vulnerable to global influences and also has a highly dynamic internal structure. In addition, these four variables do not constitute a full list of all the variables that affect electricity consumption although they are responsible for the majority of the input–output relationship. Based on the optimal consumption model by SVR method, future electricity consumption of Turkey is predicted until 2026 using data from 1975 to 2006. The model predicts that the consumption will reach 285 TWh in the year 2026.

Dilaver and Hunt [3] investigated the relationship between Turkish aggregate electricity consumption, GDP, average real electricity prices, and an Underlying Energy Demand Trend (UEDT) in order to forecast future Turkish aggregate electricity demand. Structural Time Series Model (STSM) was the adopted methodology which allowed the estimation of a stochastic UEDT. The STSM decomposes a time series into explanatory variables, a stochastic trend and an irregular component. As Dilaver and Hunt [3] mentioned in their study arguably, some of the previous studies failed since the relative big deviations of the actual demand values. A key reason for their failure was the inability to adequately capture the impact of the main economic drivers and the UEDT for Turkish electricity demand. They argued that their results attempted to rectify

these perceived defects by using the STSM to estimate a Turkish aggregate electricity demand function and use it to produce future forecast scenarios. Turkish aggregate electricity demand was predicted to be 259, 310 and 368 TWh in 2020 in the low, reference and high case scenarios respectively according to the forecast scenarios based upon GDP, electricity price, STSM coupled with the UEDT.

In another study of Dilaver and Hunt [4] it was mentioned that technological progress of the capital stock was an important factor that influences industrial energy demand. Overall based upon the different forecast assumptions, Turkish industrial electricity demand was predicted to be between 90 and 106 TWh in 2015 and between 97 and 148 TWh in 2020. This is somewhat less than the previous forecasts for Turkish industrial electricity demand; Akay and Atak [20] suggested that demand would be 140.4 TWh in 2015 and Hamzaçebi [19] suggested demand would be 219.2 TWh in 2020—both of which are somewhat higher than the high case scenario of this study. The differences in forecasts, it is argued, being primarily due to these other studies neglecting the relationship between economic variables, underlying trend and electricity consumption.

In the study of Dilaver and Hunt [14] Turkish residential electricity demand is predicted to be 48, 64 and 80 TWh in low, reference and high case scenarios, respectively by 2020. They mentioned that although the UEDT could not anticipate how future unknown structural changes would affect the evolution of electricity demand—but this is an issue with all forecasts, whatever methodology is utilized.

TEIAS is preparing a Turkish electricity demand projection report as an affiliated foundation of MENR. In the last report it was predicted that the electricity demand will be 398 and 434 TWh in 2020 in the low and high scenario respectively according to MAED model results [9, 29].

In the study of Özer [30] electricity demand forecast is mainly based on the population, historical consumption, GDP, value added of each activity sector, the energy intensity of the different sectors with sectoral growth rates and the ratio of each sector in the total electricity demand. The gross electricity demand was predicted to be 416 TWh in 2020 and 848 TWh in 2030, whereas net electricity demand was predicted to be 341 TWh in 2020 and 696 TWh in 2030. Electricity demand per capita is calculated as 5.3 MWh in 2024 which is about the average value of EU-27 as 5.7 MWh in 2008 [31]. Annual average total electricity demand growth rate was predicted at 6.8 % (from 2006 to 2030) which is also convenient with the average growth rate of 7.3 % for the period of 1990–2006. As the predicted Turkish net electricity demand for the year 2020 is 341 TWh, it is in the range of the results of Dilaver and Hunt's [3] study. This study's results indicated that the growth rates for total, industrial and residential electricity demand were different from each other as convenient to the historical data. This was also mentioned in the study of Dilaver and Hunt's studies [3, 4, 14].

Turkish electricity demand forecast results of the researches overviewed in this section are summarized in Table 52.1. The common decision of most of the studies overviewed here is that the MAED model results used in the official reports are higher than most of the other model results in the literature and the actual demand values.

Results and Discussion

Most of the studies in the literature for Turkish electricity demand forecast have results for the year 2020. The minimum electricity demand prediction is 220 TWh in the study of Öztürk et al. [16] as a result of the GA model and the maximum prediction is 514 TWh from the study of Yüksek [21] that used the MAED model. Besides, for the year 2020 in the results of the studies such as Özer [30], Dilaver and Hunt [3], Çunkaş and Taşkiran [26], Tunç et al. [17], and Öztürk et al. [16] have demand predictions in the same range as they are 341, 310, 315, 322 and 300 TWh, respectively. In the most of these studies the previous data and the energy demand trend were taken into consideration. The results of the studies are given in Fig. 52.3.

On the other hand, actual Turkish net electricity consumption in 2010 and 2011 were 172 and 186 TWh respectively [9, 29]. Kavaklıoğlu [7] has the best forecast for the year 2010 with 1.16 % relative error, whereas for 2011 Dilaver and Hunt [3] predicted 185 TWh and Özer [30] predicted 184 TWh with 0.5 and 1.075 % relative errors, respectively. Furthermore Turkish actual gross electricity demand values were 211 and 229 TWh in 2010 and 2011, respectively. Çunkaş and Taşkiran [26] have forecast values as 216 TWh in 2010 and 227 TWh in 2011 with 2.37 and 0.87 % relative errors, respectively. Forecasting Turkey's electricity consumption with the country's economic performance in the short term will provide more reliable data for policy makers and investors [25].

Turkey's electricity consumption can be characterized as fluctuating and mostly increasing. According to the results of the studies in the literature overviewed here, and emphasized in Öztürk et al.'s study [16] the nonlinear forms of the equations can better estimate the future electricity demand of Turkey due to the fluctuations of socioeconomic indicators. Population, GDP, import and export data are the most used variables while the variables of per capita consumption, increase ratios, income elasticities, prices, previous data and sectoral demand trend could find fewer usage areas for the forecast results.

Table 52.1 Summary of Turkish electricity demand studies literature review

TWh	Projection year	TWh	Variables/assumptions	Methodology
Yumurtacı and Asmaz [15]	2010 2011 2050	~195 ~198 1,173	Population and energy consumption per capita	Increase rates
Öztürk et al. [16]	2010 2011 2020	150–180 170–190 220–300	Population, GNP, import and export	GA
Öztürk and Ceylan [2]	2010 2011 2020	270–290 290–310 462–500	Population, GNP, import and export	GAEDquad
Tunç et al. [17]	2010 2011 2020	225 270 322		Regression analysis, linear mathematical optimization model
Erdoğdu [18]	2010 2011 2014	155.6 156 160	Income elasticities, population, real electricity prices, real GDP per capita and net electricity consumption per capita	Cointegration analysis and ARIMA
Hamzaçebi [19]	2010 2011 2020	207 226 500		ANN, time series structure
Akay and Atak [20]	2010 2011 2015	180 200 266	Previous consumption data	GPRM
Yüksek [21]	2010 2015 2020	222–242 (233) 302–356 (334) 440–514 (476)	Population, electric energy consumption per capita, total electric energy consumptions	MAED and increase ratios
Kavaklıoğlu et al. [6]	2010 2011 2015 2020 2027	183 189 212 240 279	Population, GNP, imports and exports	ANN
Toksarı [23]	2010 2011 2025	175–190 160–200 125–2,500	GDP, population, import and export	ACO
Küçükali and Barış [25]	2010 2011 2014	193 206 230	GDP	Fuzzy logic method
Çunkaş and Taşkiran [26]	2010 2011 2020	216 227 315	Population, annual data of the previous years	GP
Kavaklıoğlu [7]	2010 2011 2026	170 175 285	Population, GNP, imports and exports	SVR
Dilaver and Hunt [3]	2010 2011 2020	175 185 259–310–368	GDP, average real electricity prices, and an UEDT	STSM
TEIAS [29]	2010 2011 2020	– – 398, 434	Macroeconomic targets, demand trend forecast	MAED
Özer [30]	2010 2011 2020 2030	– 184 341 696	Population, GDP, historical data, value added per sector, the energy intensity of sectors, sectoral demand trend, the ratios of the sectors in total demand	Time series approach

Turkey has an annual electricity demand growth rate of about 7 %. This will continue until the consumption per capita reaches a convenient level for Turkey. Then it will be more stable and can be expected to have a more similar growth rate of population and GDP. Besides sectoral electricity demand projections are also important in the case of aggregate electricity projections.
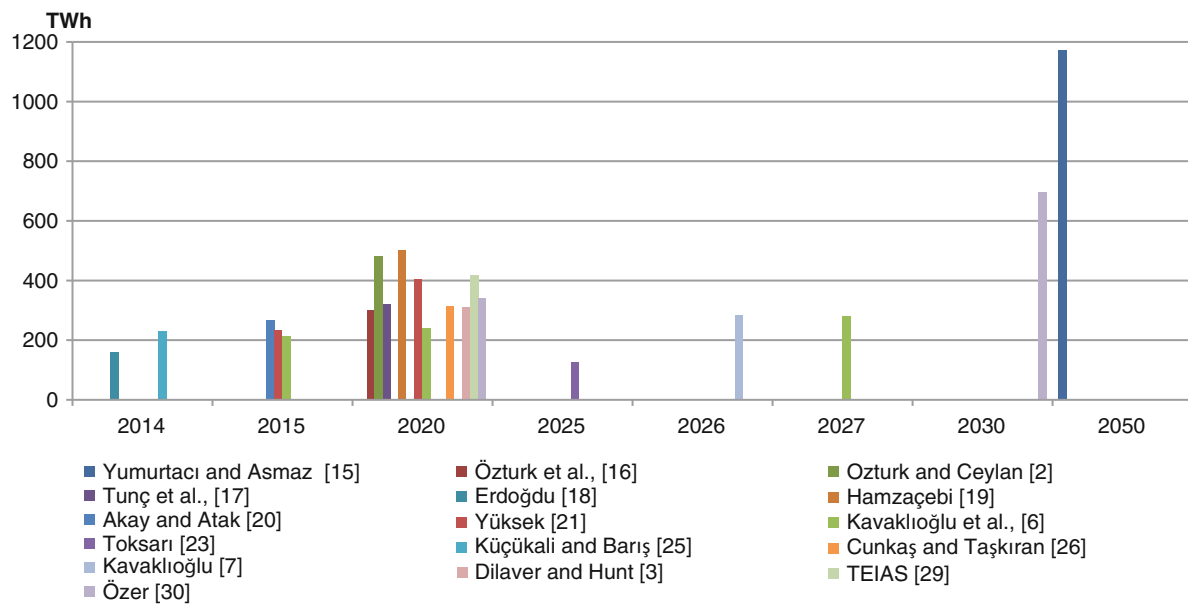
Fig. 52.3 The results of Turkish electricity demand forecast studies

According to the results of several numbers of studies in the literature about electricity consumption forecasting and modeling for Turkey, the electricity demand projections differ from each other with varying methodologies based on the different assumptions of the variables. All the researchers mentioned that the results of their own studies give better results than the results of MAED used by MENR, as the absolute relative errors of the other model results for the actual values were less than that of the MAED results. The overviewed studies in this chapter indicate that electricity demand growth mainly reflects the changing expectations of population and GDP. However, Turkish electricity demand growth rate was higher than the GDP growth rate according to the historical data, which indicates there are some other factors affecting electricity demand. Those can be prices, GDP per capita, imports and exports, sectoral demand trends and so on.

The results of different model studies used various methodologies and variables are important for energy planners and policy makers to plan Turkey's future energy investments. In Turkey, as still being a developing country, the aforementioned indicators are not stable. Thus it is rather difficult to handle uncertain factors such as socioeconomic indicators for electricity demand projections. Projection of these indicators is another significant issue which has to be studied with for electricity demand projections.

Nomenclature

Abbreviations

ARIMA	Autoregressive integrated moving average	GPRM	Grey prediction with rolling mechanism
ACOEEE	Ant colony optimization electricity energy estimation	GW	Gigawatt
		kWh	Kilowatt-hour
MAED	Model for analysis of energy demand	MENR	Ministry of energy and natural resources
ANN	Artificial neural networks	MLP	Multi layer perceptron
ACO	Ant colony optimization	SPO	State planning organization
DPT	State planning organisation	SIS	State institute of statistics
EFOM	Energy flow optimisation model	STSM	Structural time series model
GA	Genetic algorithm	SVR	Support vector regression
GDP	Gross domestic product	TEIAS	Turkish electricity transmission company
GHG	Greenhouse gas	TWh	Terawatt-hour
GNP	Gross national product	UEDT	Underlying energy demand trend
GP	Genetic programming		

References

1. Bianco V, Manca O, Nardini S (2009) Electricity forecasting regression models. Energy 34:1413–1421
2. Öztürk HK, Ceylan H (2005) Forecasting total and industrial sector electricity demand based on genetic algorithm approach: Turkey case study. Int J Energy Res 29:829–40
3. Dilaver Z, Hunt LC (2011) Turkish aggregate electricity demand: an outlook to 2020. Energy 36:6686–6696
4. Dilaver Z, Hunt LC (2011) Industrial electricity demand for Turkey: a structural time series analysis. Energy Econ 33:426–436
5. Egelioğlu F, Mohamad AA, Guven B (2001) Economic variables and electricity consumption in Northern Cyprus. Energy 26:355–362
6. Kavaklıoğlu K, Ceylan H, Ozturk HK, Canyurt OE (2009) Modeling and prediction of Turkey's electricity consumption using artificial neural networks. Energy Convers Manag 50:2719–2727
7. Kavaklıoğlu K (2011) Modeling and prediction of Turkey's electricity consumption using support vector regression. Appl Energy 88:368–375
8. Lippmann RP (1987) An introduction to computing with neural nets. IEEE ASSP Mag 4(4):4–22
9. TEIAS (2012) Turkish electricity generation-transmission statistics. http://www.teias.gov.tr/TürkiyeElektrikİstatistikleri /istatistik2012/istatistik%202012.htm. Accessed 12 Nov 2013
10. Balat M (2009) Electricity consumption and economic growth in Turkey: a case study. Energy Sources B 4:155–165
11. DPT (2010) Economic and social indicators, national income and production table 1–44, harmonized GDP By expenditures at 1998 prices (1980–2010). State Planning Organization, Ankara
12. DPT (2013) Main economic indicators, national income, table 2–8: by expenditures, at 1998 prices (2005–2012). State Planning Organization, Ankara
13. Ediger VS, Tatlidil H (2002) Forecasting the primary energy demand in Turkey and analysis of cyclic patterns. Energy Convers Manag 43:473–487
14. Dilaver Z, Hunt LC (2011) Modelling and forecasting Turkish residential electricity demand. Energy Policy. doi:10.1016/j.enpol.2011.02.059
15. Yumurtacı Z, Asmaz E (2004) Electric Energy Demand of Turkey for the year 2050. Energy Sources 26:1157–1164
16. Öztürk HK, Ceylan H, Canyurt OE, Hepbaşlı A (2005) Electricity estimation using genetic algorithm approach: a case study of Turkey. Energy 30:1003–1012
17. Tunç M, Çamdalı Ü, Parmaksızoğlu C (2006) Comparison of Turkey's electrical energy consumption and production with some European countries and optimization of future electrical power supply investments in Turkey. Energy Policy 34:50–59
18. Erdoğdu E (2007) Electricity demand analysis using cointegration and ARIMA modelling: a case study of Turkey. Energy Policy 35:1129–1146
19. Hamzaçebi C (2007) Forecasting of Turkey's net electricity energy consumption on sectoral basis. Energy Policy 35:2009–16
20. Akay D, Atak M (2007) Grey prediction with rolling mechanism for electricity demand forecasting of Turkey. Energy 32:1670–1675
21. Yüksek Ö (2008) Reevaluation of Turkey's hydropower potential and electric energy demand. Energy Policy 36:3374–3382
22. Murat YS, Ceylan H (2006) Use of artificial neural networks for transport energy demand modeling. Energy Policy 34:3165–3172
23. Toksarı MD (2009) Estimating the net electricity energy generation and demand using the ant colony optimization approach: case of Turkey. Energy Policy 37:1181–1187
24. Toksarı MD (2007) Ant colony optimization to estimate energy demand of Turkey. Energy Policy 35:3984–3990
25. Küçükali S, Barış K (2010) Turkey's short-term gross annual electricity demand forecast by fuzzy logic approach. Energy Policy 38:2438–2445
26. Çunkaş M, Taşkiran U (2011) Turkey's electricity consumption forecasting using genetic programming. Energy Sources B Econ Plan Pol 6(4):406–416
27. Lee DG, Lee BW, Chang SH (1997) Genetic programming forecasting of electric power demand. Electr Power Syst Res 40:7–22
28. Koza JR (1992) Genetic programming: on the programming of computers by means of natural selection. MIT, Cambridge
29. TEIAS (Turkish Electricity Transmission Company) (2012) Turkish electricity transmission company. Turkish electrical energy 10 year generation capacity projection 2012–2021
30. Özer B (2012) The scenario analysis of CO_2 emission mitigation potential in the Turkish electricity sector. PhD dissertation, Istanbul Technical University, Graduate School of Science Engineering and Technology, Istanbul
31. Eurostat (2010) Energy, yearly statistics 2008. Luxembourg

Optimized Analysis of Cold Energy Utilization for Cold Storage Project of Xingtan LNG Satellite Station

Wendong Xu, Zhonghao Huang, and Shuanshi Fan

Abstract

The project of cold energy utilization for cold storage of Xingtan LNG satellite station is the first cold energy utilization demonstration project of LNG satellite station in China with $(2–4) \times 10^4$ m³/day gasification rate of LNG and 10–15 tons/day supply of liquid ammonia in a temperature range of -25 to $-38\ ^\circ$C. Its innovation lies in the point of adopting two ammonia refrigeration circulation systems to recover LNG cold energy for cold storage at the same time. Although this project had operated smoothly for more than 2 years after commissioning, there still existed some problems. Such as refrigerant frozen blocking problem and undersupply of cold energy which are caused by underperformed coordination between the two ammonia refrigeration circulation systems. According to the equipment running state and automatic control system data, this article presented optimized analyses of the whole process, including using a redesigned ammonia refrigerant flow channel and achieving dynamic balance of ammonia refrigeration to relieve the refrigerant frozen blocking phenomenon, improving production process and optimizing process parameters to ameliorate the condition of the cold supply shortage problem. Combined with the above research, many new methods were proposed which can effectively solve the above problems in the utilization of LNG cold energy so as to increase the LNG cold energy utilization ratio and enhance the safety and stability of project operation. In addition, it provides a valuable reference for design, development and construction of other analogous LNG cold energy utilization projects in China.

Keywords

LNG • Cold energy • Cold storage • Optimized analysis

Introduction

With the energy security and environmental pollution problem becoming more and more serious, the liquefied natural gas (LNG) industry and energy-saving projects are developing rapidly in China. LNG needs to be heated and gasified before supplying it to downstream users with a cold energy release of 830 kJ/kg [1]. If the price of electricity is calculated as 0.85 yuan/(kWh), LNG of $-162\ ^\circ$C contains cold energy value of about 510 yuan/ton. So making full use of LNG cold energy can not only save enormous amounts of electricity for refrigeration, but also be helpful to reduce the costs of LNG gasification and expand the natural gas downstream market [2].

There are many theoretical studies on the LNG cold energy utilization technology at present, mainly including the cold energy used for power generation, air separation, cryogenic freezing (cold storage and cold water), etc. [3]. So far, the LNG cold energy utilization has successfully realized the application for power generation, air separation and the cryogenic

W. Xu • Z. Huang (✉) • S. Fan
Key Laboratory of Ministry of Education on Enhanced Heat Transfer and Energy Conservation,
School of Chemistry and Chemical Engineering, South China University of Technology, No. 381, Wushan Road,
Tianhe District, Guangzhou 510640, Guangdong Province, China
e-mail: wdxu@scut.edu.cn; hzhprince@163.com; ssfan@scut.edu.cn

freezing project abroad. But in the domestic sector, the LNG cold energy utilization projects are still in the demonstration research stage and the development of technology is relatively backward. In order to improve this actuality, we developed a technical solution with independent intellectual property rights about LNG cold energy utilization on the basis of fully absorbing domestic and foreign experience, and successfully applied it to Xingtan LNG satellite station in Shunde district, Foshan city. After having operated smoothly for more than 2 years, the cold energy utilization project of Xingtan LNG satellite station reflected its well technical feasibility and practical operability. The project can recycle LNG cold energy effectively and create economic benefits in the meantime. However, some problems still exist in the actual operation of the project reflecting some shortcomings of the technical design.

Therefore, this paper analyzed the LNG cold energy recycling system of the Xingtan LNG satellite station and put forward some constructive improvement and optimization solutions. It can not only perfect the overall scheme and solve the existing problems in the current project, but also provide a very valuable reference to the design, development and construction for similar projects of LNG cold energy utilization in our country. All in all, it is of great significance for promoting the work process of energy-saving and emission reduction in China.

The Project Overview of LNG Cold Energy Utilization for Cold Storage in Xingtan LNG Satellite Station

Project Background and Gas Station Situation

Xingtan LNG satellite station which affiliated to Hong Kong China Gas Co. Ltd. is a supplementary gas regulating station for the insufficient daily average and fluctuant flow in Shunde district, Foshan city. The current amount of LNG gasification is $(2-10) \times 10^4$ N m^3/day with a maximum supply capacity of 24×10^4 N m^3/day, the gasification pressure is 0.4–0.7 MPa and the pipeline transmission pressure is 0.3 MPa.

There are six cylindrical LNG storage tanks with 100 m^3 cubage in the station, including four tanks with storage pressure of 0.35 MPa and two tanks with storage pressure of 0.55 MPa. The station also has eight air-heated evaporators with a single gasification capacity of 2,000 N m^3/h. During daily operation, a mass of mist condensed around the evaporators, which caused a certain degree of cold pollution on the station environment.

Adjacent to the station, there is a cold storage with the total capacity of 3,000 tons. The cold storage which is divided into a freezer of $-30\,^\circ$C and a refrigerator of 15 $^\circ$C is mainly engaged in aquatic products process and storage. The cold storage has three ammonia compression refrigeration units that should be turned on selectively according to the quantity of aquatic products process and the process requirements. Generally, two refrigerating installations will be turned on and run 15–16 h/day to supply cold quantity of 4,890–5,216 kWh in summer, while one will be turned on and run 18–20 h/day to supply cold quantity about 3,100 kWh in winter, and the electricity fee is about 120×10^4 yuan all the year round [4].

Technological Process Description

In the light of the characteristics of the Xingtan LNG satellite station and the needs of downstream cold users, the scheme of LNG cold energy recovery for cold storage has been chosen for the station's cold energy utilization project. The technical solution mainly includes three parts: LNG gasification system, low pressure ammonia refrigeration circulation and ammonia electric compression refrigeration circulation. The process flow diagram is shown in Fig. 53.1.

LNG out from the storage tank (T1) will be divided into two streams, one stream will flow into the air-heated evaporator (H1) directly and evaporate into gas of 25 $^\circ$C, then it will pass through the pressure regulating valve and be regulated to 0.3–0.35 MPa. The other stream will flow into a heat exchanger (E1) first and exchange heat with ammonia gas from cold storage of $-20\,^\circ$C, 0.10 MPa, then the LNG stream will turn into gas of -25 to $-30\,^\circ$C and flow into the air-heated evaporator (H2) to evaporate to 25 $^\circ$C. After mixing with the former stream and its pressure having been regulated, the gas will enter the urban gas pipe network in the end. In the meanwhile, ammonia gas will be condensed into liquid ammonia of $-40\,^\circ$C and flow into the liquid ammonia tank (T2), then the pump will pressurize the liquid ammonia to 0.3–0.5 MPa. The stream will flow via a flow-meter to a pressure regulating valve, dropping to 0.15 MPa, and will finally flow into the cold storage for cooling supply [5].

When the cold quantity demand of cold storage is in a larger amount or the gasification quantity of LNG is in short supply, the electric compression refrigeration circulation of ammonia will be turned on and the two ammonia refrigeration circulation systems will operate together. In the electric compression ammonia refrigeration circulation system, ammonia
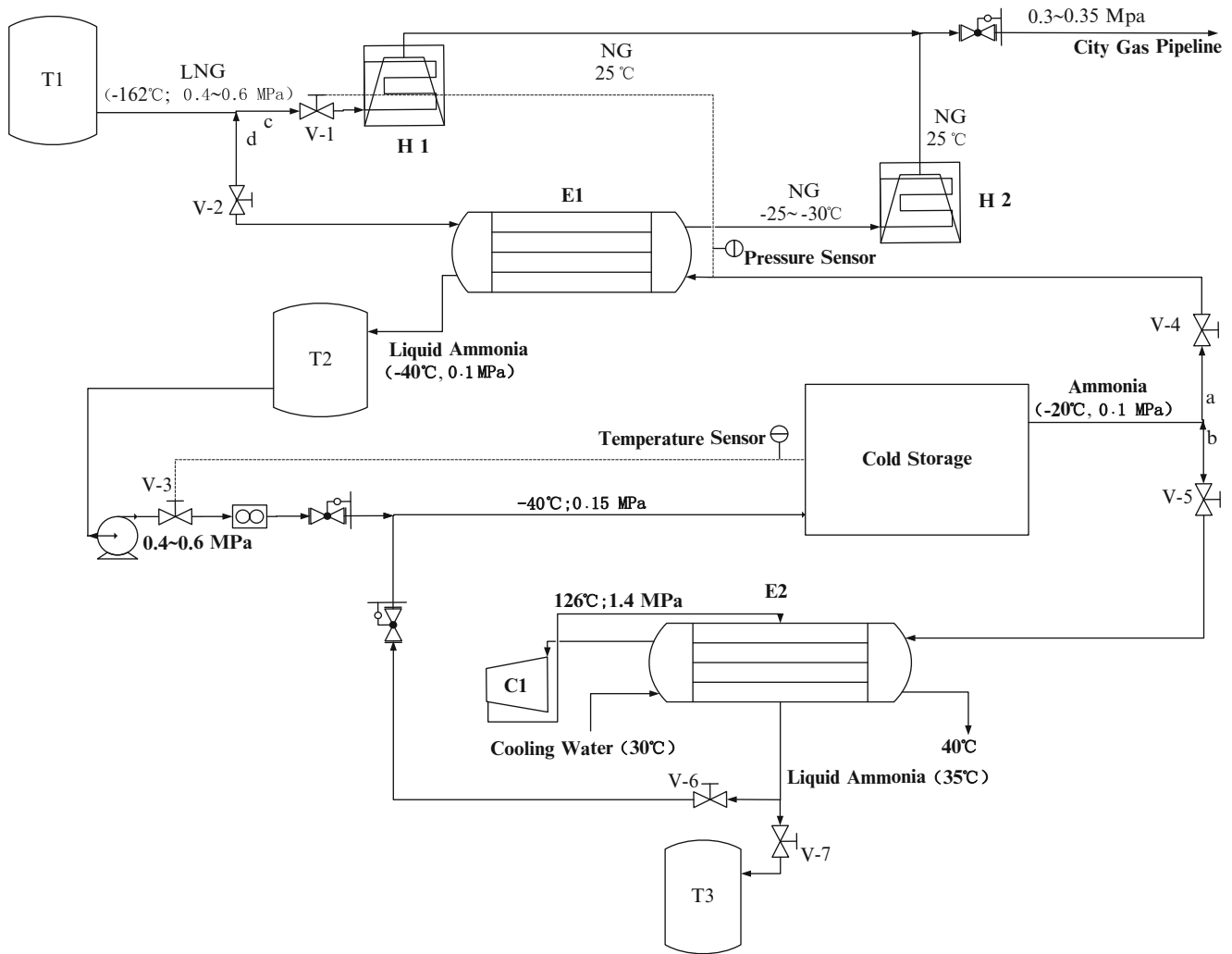
Fig. 53.1 The process flow diagram of LNG cold energy utilization technology for cold storage

gas out from cold storage will transform into liquid ammonia of 35 °C through twice compression and heat exchange with cold water in a heat exchanger (E2). Then after being regulated to 0.15 MPa by the pressure regulating valve with the temperature dropping to −40 °C, the liquid ammonia stream will mix with the stream out from low pressure ammonia refrigeration circulation and will finally flow into the cold storage for cooling supply.

Project Operation Situation

The project was completed in May 2010 and began to process debugging in June. One month later, the technology process basically achieved the design requirements with the LNG gasification rate of (2–10) × 10⁴ N m³/day, provided liquid ammonia temperature of −25 to −38 °C and liquid ammonia flow rate of 10–15 tons/day. After 3 months of commissioning, the project has been put into production officially. So far the system has been running for more than 2 years, no major accidents have occurred and equipments were all in good condition and working properly during that period. What's more, the system obviously alleviated the cold-fog phenomenon in the station and continued supplying reclaimed cold energy of LNG to cold storage for its normal operation.

The project construction was invested by Xingtan LNG satellite station, and the cold storage users bear the cost of cold supply by taking the liquid ammonia flow rate as the settlement measurement. The annual sales income of the project is 850,000 yuan/year and the average annual after-tax profit is 300,700 yuan/year, so it shows a good economy.

In addition, as the first domestic engineering example of LNG cold energy used for cold storage, the project passed the recognition of scientific and technological achievements by experts of Gas Professional Committee, Guangdong Institute of Petroleum, and won the Hang Seng Pearl River Delta Environmental Protection awards issued by the Hong Kong Industrial Association. The success of the project has attracted extensive attention within the LNG industry.

Analysis of the Existing Problems in the System

Refrigerant Frozen Blocking

From the operation report recorded by the operation department of the Xingtan LNG cold energy utilization project group, we have known that during the actual running, the system often faced the problem where part of the liquid ammonia solidified and blocked pipes in the heat exchanger. With regard to the designed process, the inlet of LNG is at the bottom of the heat exchanger and the outlet of NG is at the top, while the inlet of ammonia is at the top left of the heat exchanger and the outlet of liquid ammonia is at the bottom right so as to facilitate their counterflow heat exchange. Because the freezing point of ammonia is $-77.73\,^{\circ}\mathrm{C}$ and the inlet temperature of LNG which would exchange heat with ammonia is $-162\,^{\circ}\mathrm{C}$, especially as the inlet of LNG is located closely to the outlet of liquid ammonia, that will cause partial undercooling of the liquid ammonia by LNG in the process of heat exchange, and result in liquid ammonia freeze between the outlet at the bottom of the heat exchanger and tube plates. The frozen layer would thicken with the extension of time and eventually make the blockage in the liquid ammonia pipeline, leading to equipment damage. The problem of refrigerant frozen blocking seriously influenced the thermal efficiency in the heat transfer system, and hindered the normal operation of the system as well [6].

Cold Energy Undersupply

From the design perspective of the whole system, the cold storage refrigeration system would not affect the overall LNG gasification quantity and the control operation of gas pressure, thus the system has the advantages of more simple operation, less investment and so on. But as the project only has one heat exchange system, the refrigerant exchanges heat with LNG directly and recycles cold energy to supply for cold storage cooling capacity. The system can only adjust the flux of LNG flow based on the actual cold capacity requirement of cold storage, and it can't adapt to the volatility of the gasification quantity of the station.

Moreover, although the electric compression ammonia refrigeration system as a backup control system can replenish cold energy to cold storage with the method of electric compression refrigeration when the cooling supply is insufficient, the coordination and operation of the two ammonia refrigeration systems was not that effective in the actual operation. In addition, the cold storage continuously was expanding year by year. By the end of 2012, the capacity of cold storage has been increased to 8,000 tons, which made the problem of cold energy undersupply increasingly outstanding.

The Design Optimization of System Process

The Design Optimization of Heat Exchange System

Aiming at the problem of refrigerant frozen blocking, the following optimization measures in several aspects are put forward:

1. In the heat exchange system, LNG of $-162\,^{\circ}\mathrm{C}$ will first flow through the heat exchanger and pass cold energy to ammonia gas, then enter the evaporator and be heated up again. Under the circumstances, there is a big heat transfer temperature difference between the two heat transfer mediums in the heat exchanger, and the temperature of LNG is far below the freezing point of the refrigerant. So it is very likely to lead to the refrigerant frozen blocking phenomenon. The key to solve this problem is the optimal selection of refrigerant and redesign of pipelines. Through the comparison and analysis we found that choosing the refrigerant which can be resistant to low temperature, such as butane or R404A, can effectually avoid the solidification of refrigerant. Furthermore, the horizontal heat exchanger should be adopted in the design of the heat exchange system, and strict monitoring of the fluid pipeline should be taken to prevent the infiltration of impurities and water in the process of equipment operation.

2. Through practical observation and operation experience, we also found that when the flow rate of refrigerant (ammonia) was less than 30 % of design value, the flow velocity of refrigerant was slow and the unit heat load increased; When the flow rate of refrigerant was more than 140 % of design value, the pressure drop of the heat exchanger would increase
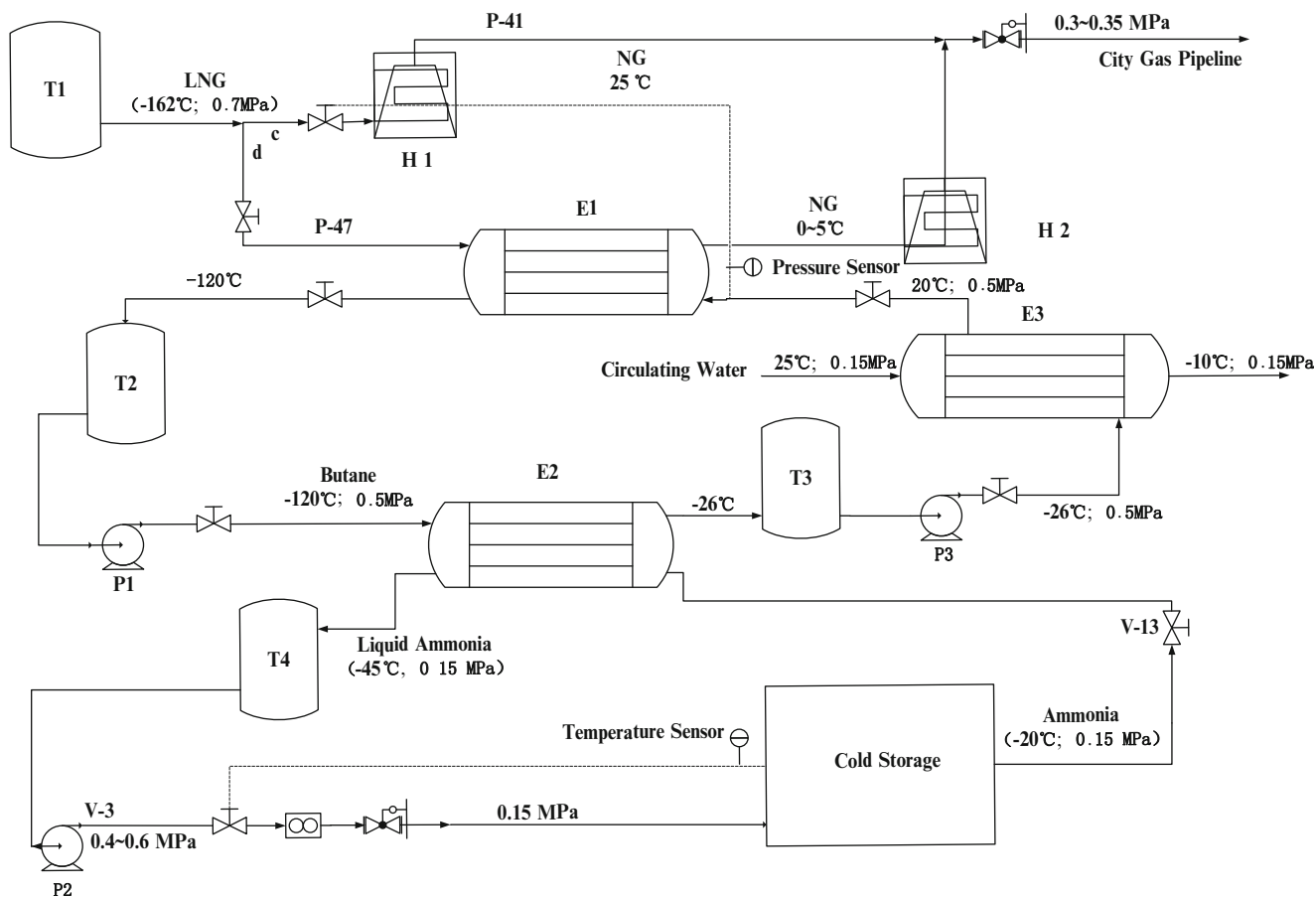
Fig. 53.2 The optimized process flow diagram of LNG cold energy utilization technology for cold storage

more than 0.05 MPa. These are most likely to cause the refrigerant to freeze. So during the running of the equipment, it is necessary to make appropriate regulation of the refrigerant flow rate and keep the fluctuation of the flow rate in the allowed range in order to avoid refrigerant frozen blocking.

3. In order to deal with the refrigerant frozen blocking problem that occurs in the actual operation process, a thaw line should be set up in the heat exchange system. When the circulating line has been blocked by the frozen refrigerant, the LNG pipe line should be shut off firstly and then switch on the thaw line, a part of natural gas of 25 °C from the original gasification process would be introduced into the LNG flow channel through this thaw line melted the frozen refrigerant by exchanging heat in the heat exchanger until the refrigerant circulation line restore clear.

The Design Optimization of Refrigerant Circulation

Aiming at the problem of cold energy undersupply, the following optimization measures in several aspects are put forward:

1. Because of a lack of the intermediate refrigerant circulation, the whole system lacks the function of cold storage and peak shaving. In the current designed system, the refrigerant storage tank is the sole equipment that can temporarily store cold energy, so we need to modify it. The transformation method is tank capacity expansion: increasing the volume of the tank from 3 to 15 m³. Using the newly designed storage tanks of large capacity can make it carry more refrigerant and ensure that there are plenty of refrigerants to transfer heat with LNG and provide cold energy to the cold storage continuously. What's more, increasing the capacity of the refrigerant tank may also avoid the liquid ammonia pump cavitation caused by the flash of internal liquid ammonia in the storage tank, to a certain extent.

2. In the long run, the better solution is adding a set of refrigerant circulation devices in the system and using the intermediate refrigerant cycle for the purpose of cold storage and peak shaving [7]. The redesign process is shown in Fig. 53.2.

Firstly, LNG of −162 °C, 0.7 MPa, 162 kg/h will exchange heat with the refrigerant (butane) of 20 °C, 0.5 MPa, 3,000 kg/h in the heat exchanger (E1). LNG will be warmed up to 2 °C after gasification and flow into the city gas pipeline network after regulating the pressure; Butane will be cooled down to −120 °C and enter the low-temperature liquid phase refrigerant tank (T2). Then, Butane will be pressurized to 0.5 MPa by the pump (P1) and exchange heat with ammonia of −20 °C, 0.15 MPa, 380 kg/h out from cold storage in the heat exchanger (E2). Butane will be warmed up to −26 °C and enter the liquid refrigerant tank (T3); Ammonia gas will be cooled into liquid ammonia of −45 °C and enter the liquid ammonia tank (T4). Finally, Butane will be pressurized to 0.5 MPa by the pump (P2) and exchange heat with circulating water of 25 °C, 0.15 MPa, 5,000 kg/h in the heat exchanger (E3). Butane will be warmed up to 20 °C and flow back to the heat exchanger (E1) to complete the intermediate refrigerant circulation; Circulating water will be cooled down to 10 °C. Meanwhile, liquid ammonia of −45 °C will be pressurized to 0.2 MPa by the pump (P2) and enter the cold storage for cooling supply.

According to the analysis computation by Aspen-plus, the above scheme can ensure the system operates well with the fluctuation of LNG gasification quantity and still meet the dynamic needs of cold storage by appropriate adjusting. The addition of intermediate refrigerant circulation will directly increase the total cost and the initial investment of the project and make the operation more complex. But for the growing amount of LNG gasification quantity and cold energy demand of cold users, this design can not only solve the imbalance problem of cold energy supply and demand, but also make the adjustment and distribution of cold energy utilization more reasonable.

Thoughts and Suggestions on the Development of Cold Energy Utilization Project in LNG Satellite Station

As for the development and construction of current domestic LNG cold energy utilization projects, both the depth and the scale of cold energy utilization still have a very big development space. Through the case study of the first LNG satellite station cold energy utilization project in China: cold energy utilization for cold storage in Xingtan LNG satellite station, we raised some thoughts and suggestions on the development of the current domestic cold energy utilization project of the LNG satellite station:

Choosing Appropriate Refrigerant to Adapt to Different Occasions

In the technical process of LNG cold energy recycling, the selection of refrigerant is one of the key technologies. The desired refrigerant not only needs to meet the requirements of some specific physical and chemical properties, but also should be high-efficiency, economical, and environmental friendly. At present, the domestic and foreign experts have done a lot of research about the circulating refrigerant, and proposed many available refrigerants which can be applied to LNG cold energy utilization technology such as ammonia, glycol aqueous solution and R404A [8], etc. But for the specific application occasions and design requirement, we should considerate comprehensively containing the function of the refrigerant circulation system, the equipment and operating cost, the control temperature and so on before choosing the optimal refrigerant. For example, R404A or butane can be a good choice used as the refrigerant in the low-temperature refrigerant circulation system, while ammonia or ethylene glycol aqueous solution can be a good choice used as the refrigerant in a high-temperature refrigerant circulation system.

Setting the Intermediate Refrigerant Heat Circulation to Realize Cold Storage and Peak Shaving

LNG satellite stations have the characteristics of wide distribution, small but wildly fluctuant flow rate and indefinite operation time [9]. So if we want to fully recover and utilize the cold energy of LNG, it needs to set up a set of devices for cold storage and peak shaving in the design of LNG cold energy utilization projects. That is, using an intermediate refrigerant circulation to store excess cold energy in the gas supply peak and provide the stored cold energy to cold users when LNG gasification quantity decreases in gas supply trough. In this way, the entire system can run smoothly and meet the demand of cold users.

The refrigerant circulation system is mainly composed of four parts: a low-temperature storage tank (containing phase change material), a high-temperature storage tank, a heat exchanger for refrigerant and LNG, a heat exchanger for low-temperature refrigerant and high-temperature refrigerant. The refrigerant circulation system can adjust the supply and demand of the recovery and utilization of LNG cold energy. Especially for the long-term development of the LNG cold energy utilization

project, the utilization of cold energy from LNG gasification and the energy matching in different temperature levels with other cold users all depend on the operation of the multi-stage refrigerant circulation to achieve. Therefore, setting intermediate refrigerant circulation in the cold energy utilization system is not only the requirement of cold storage and peak shaving of LNG cold energy, but also the needs of the further development of LNG cold energy utilization technology.

Planning Comprehensive Utilization Scheme to Promote the Cascade Utilization of LNG Cold Energy

As we know, according to the principle of refrigeration, the lower the requirement of the process temperature, the more power consumed by a conventional refrigeration method. Within a certain low-temperature region, every 1 K decrease of the evaporation temperature will increase the energy consumption by 10 %. So at that point, the energy-saving effect of LNG cold energy utilization will be more obvious and the utilization ratio of cold exergy will be higher [10]. Thus it can be seen, if we only use LNG cold energy for cold storage refrigeration—that means only the high temperature part of LNG cold energy has been recycled and the utilization of the low temperature part still has great development space, which results in the low utilization ratio of cold exergy.

Consequently, we need to design a comprehensive utilization of the LNG cold energy scheme in consideration with the characteristics of LNG satellite stations. First, establish the refrigerant circulation system to recover LNG cold energy and store it appropriately. Then, provide the stored cold energy for cold users based on the principle of "temperature counterpart and cascade utilization" by matching with their cold needs in different temperature sections. The low-temperature section of cold energy can be used for air separation or cryogenic crushing, and the high-temperature section of cold energy can be used for cold storage or cold water air conditioning [11]. Through this method, LNG cold energy can be made full use of and the cold exergy utilization ratio will be improved significantly.

Conclusions

1. The cold energy utilization for cold storage project of Xingtan LNG satellite station, which was designed by Shunde, Hong Kong China Gas Co. Ltd. and South China University of Technology, is the first LNG cold energy utilization project of LNG satellite station in China. In this project, the cold energy generated during LNG gasification would be recycled by ammonia and applied to cooling the cold storage so as to save electricity for refrigeration. The annual profit of the project is about 300,700 yuan. After over 2 years' practical running, the system has shown a pretty good result of cold energy utilization. There is no doubt that the project has great benefits of technical, economic and social.
2. According to the practical operation condition of the cold energy utilization for cold storage project of Xingtan LNG satellite station and the analysis of the equipment running state and automatic control system data, some corresponding optimization measures were proposed: redesigning the heat exchange system to ease the problem of refrigerant frozen blocking, adding an intermediate refrigerant circulation system to solve the situation of insufficient cold supply by re-matching the cold energy with the downstream cold users, which will ultimately make the device running smoothly and orderly.
3. Concerned with the characteristics of the cold energy utilization project of LNG satellite station, we put forward some suggestions on long-term development of LNG cold energy utilization: choosing the proper refrigerant and setting multistage refrigerant circulation system to establish the integrated technology of LNG cold energy comprehensive utilization. The integrated technology will recycle LNG cold energy in different temperature ranges more effectively, match the cold-requiring systems more reasonably and gain maximum economic benefits. This paper would provide a valuable reference to the similar LNG cold energy utilization projects in China.

References

1. Zhu G, Gu A (1999) The utilization of liquefied natural gas (LNG) cold energy. Energy Eng 3:1–2
2. Li J, Li Z, Hua B (2005) The current situation and development prospect of LNG cold energy utilization. Nat Gas Ind 05:103–105 + 14
3. Wang Q, Li Y, Zhang Z (2002) The recovery and utilization of liquefied natural gas (LNG) cold energy. Cryogenic Eng 128(4):38–42

4. Liu Z, Zheng H, Shang W, Xu W (2010) The project development of cold energy utilization in LNG satellite station. Gas Heat 09:1–5
5. Liu Z, Huang J, Xu W (2010) The technology development and demonstration of cold energy utilization for cold storage in LNG satellite station. Urban Gas 09:8–11
6. Tao J (2011) The technology design of LNG cold energy used for cold storage. Guangdong Chem Ind 06:179–180
7. Zhang S, Jiao L, Li X, Nie Y, Duan C (2007) The research of the cold storage system using LNG gasification cold energy of LNG station. Gas Heat 12:15–17
8. Du L, Luo D, Xu W (2007) The research of LNG cold energy utilization technology for cold storage in south China. Nat Gas Ind 06:115–117 + 160
9. Xu W, Bian H, Fan S (2009) The cold energy utilization technology of LNG station satellite. Nat Gas Ind 29(5):112–114
10. Tang X, Wang C, Yang Z (2012) The exergy analysis of Guangdong LNG cold energy and its application in cold storage. Energy and Energy Conserv 05:12–13 + 29
11. Bian H (2011) The research and process analysis of liquefied natural gas (LNG) cold energy utilization technology. South China University of Technology

Comparison of Different Turbulent Models in Turbulent-Forced Convective Flow and Heat Transfer Inside Rectangular Cross-Sectioned Duct Heating at the Bottom Wall

Kamil Arslan and Nevzat Onur

Abstract

In this study, steady-state turbulent-forced flow and heat transfer in a horizontal smooth rectangular cross-sectioned duct was numerically investigated. The study was carried out in the turbulent flow region where Reynolds number ranges from 1×10^4 to 5×10^4. The flow was developing both hydrodynamically and thermally. The bottom surface of the duct was assumed to be under constant surface temperature. A commercial CFD program Ansys Fluent 12.1 with different turbulent models was used to carry out the numerical study. Different turbulence models (k–ε Standard, k–ε Realizable, k–ε RNG, k–ω Standard and k–ω SST) were used. Based on the present numerical solutions, new engineering correlations were presented for the heat transfer and friction coefficients. The numerical results for different turbulence models were compared with each other and the experimental data available in the literature. It was observed that k–ε turbulence models represented the turbulent flow condition very well for the present study.

Keywords

Simultaneously developing flow • Forced convection • Heat transfer • Rectangular cross-sectioned duct • Turbulent flow • CFD

Introduction

Predicting the pressure drop and heat transfer under hydrodynamically and thermally developing flow conditions is quite important in many applications such as compact heat exchangers where flow passages are typically short in length. Flow and heat transfer in rectangular channels have received considerable attention due to their practical importance. Especially, turbulent-forced convection inside rectangular cross-sectioned ducts is of interest in the design of a high-Reynolds number heat exchanger apparatus. Ducts having rectangular cross-sections are widely used in industrial heat transfer equipment such as compact heat exchangers. They have been widely used in various industries because of their high heat transfer area on the basis of unit volume and good mechanical strength even with very thin foils. These devices are required to be compact as well as to transfer heat rapidly to the environment. Among the various duct cross-sections, rectangular cross-sectioned ducts are used in compact the heat exchanger extensively, because of its simplicity of construction. Compared to circular cross-sectioned ducts, heat transfer and fluid flow in rectangular cross-sectioned ducts are complicated and dependent on several parameters [1].

Several studies of flow in straight rectangular cross-sectioned ducts were presented in the past. An excellent comprehensive review of forced convection flow in rectangular ducts was presented by Shah and London [2], Kakaç et al. [3],

K. Arslan (✉)
Faculty of Engineering, Mechanical Engineering Department, Karabük University, 78050 Karabük, Turkey
e-mail: kamilarslan@karabuk.edu.tr

N. Onur
Faculty of Engineering, Mechanical Engineering Department, Çankaya University, 06810 Ankara, Turkey
e-mail: nevonur@cankaya.edu.tr

and Kakaç and Liu [4]. Zhang [1] carried on numerical study for hydrodynamically developed thermally developing forced convection heat transfer in rectangular ducts under uniform plate temperature. Bottom and top plates of the rectangular duct were kept at constant temperature, at the same time different conductance materials were chosen for side walls. Various duct aspect ratios were considered, and the side walls had different conductance parameters from zero to infinitely large. The forced convection heat transfer parameters for rectangular ducts were determined. Muzychka and Yovanovich [5] investigated laminar-combined developing flow in non-circular cross-sectioned ducts. New models were proposed which simplify the prediction of the Nusselt number for combined entry region in most non-circular duct geometries. This new model predicts both local and average Nusselt numbers and is valid for both isothermal and isoflux boundary conditions. Chung et al. [6] investigated the numerical behavior of hydrodynamically fully developed and thermally developing laminar flow of Newtonian fluids in rectangular ducts for the constant heat flux boundary condition. The developing Nusselt number was obtained for a wide range of duct aspect ratios. Aparecido and Cotta [7] analytically studied laminar-forced convection inside a rectangular duct by extending the generalized integral transform technique. Fully developed and thermally developing regions were examined. Beavers et al. [8] investigated experimentally hydrodynamic flow development in rectangular ducts for different aspect ratio. The concern of the research was the determination of the pressure field associated with the hydrodynamic development of the flow in the rectangular duct. Montgomery and Wibulswas [9] developed an alternative numerical method which was used to solve the heat transfer equations for laminar flow in ducts of rectangular cross-sectioned with simultaneously developing temperature and velocity profiles, both for constant wall temperature and for constant heat input per unit length of the duct. Comparisons were made with analytical solutions for circular ducts and parallel plates with experimental data. It was obtained that Prandtl number had a strong effect on the Nusselt number for simultaneously developing profiles. Sparrow [10] studied laminar simultaneous development of temperature and velocity profiles in the entrance region of a flat rectangular duct for different Prandtl numbers. Two temperature conditions at the duct walls were considered: both duct walls had the same uniform temperature and one of the duct walls was maintained at a uniform temperature while the other wall was insulated. The results were presented graphically for different boundary conditions, Reynolds and Prandtl numbers. Savino and Siegel [11] determined the temperature distributions analytically for fully developed heat transfer in rectangular ducts with different aspect ratios. The channel walls were uniformly heated, but the heat flux on the short sides was an arbitrary fraction of the heat flux on the broad sides. Chiu et al. [12] numerically examined the mixed convection heat transfer in rectangular cross-sectioned duct with radiation effects. The vorticity–velocity method was employed to solve the three-dimensional Navier–Stokes and energy equation simultaneously. It was obtained that radiation effects had a considerable impact on the heat transfer and would reduce the thermal buoyancy effects. Naccache and Mendes [13] examined the heat transfer to non-Newtonian fluids flowing laminarly through rectangular cross-sectioned ducts. It was observed in the numerical investigation that shear thinning yields a negligible heat transfer enhancement effect when compared with the secondary flow effect. Chong et al. [14] experimentally investigated the laminar and transition opposing mixed convection in the entrance region through a rectangular cross-sectioned duct. The friction factors were calculated and analyzed under different Reynolds numbers, Grashof numbers, and inclination angles. The results indicated that the friction factors showed different characteristics when the Reynolds numbers were larger or smaller than 1,500. Gnielinski [15] modified the widely accepted turbulent flow correlations which provide fully developed heat transfer coefficients for flows with Reynolds numbers exceeding 1×10^4. It was noted that the modified equation purported to be applicable to Reynolds numbers as low as 2,300. The vast majority of the data were mean values of the heat transfer coefficient rather than fully developed values, reflecting the early era in internal convection investigations. Kostic and Hartnett [16] reported an experimental investigation for the turbulent flow of water in a 2:1 asymmetrically heating rectangular duct. The results of the study were compared with the literature results. Abraham et al. [17] presented a predictive theory which was capable of providing quantitative results for the heat transfer coefficients in round pipes for the three possible flow regimes: laminar, transitional, and turbulent. The theory was based on a model of laminar-to-turbulent transition which was also viable for purely laminar and purely turbulent flow.

Heat and momentum transfer processes in the simultaneously developing flow of rectangular cross-sectioned channels are very complex. Basic knowledge on the flow and heat transfer of the three-dimensional turbulent forced convection in rectangular cross-sectioned duct is needed for the design of thermal equipment. However, it is seen from literature surveys that in spite of being commonly used in engineering applications, the rectangular geometry under constant bottom surface temperature and turbulent flow condition has not been adequately studied in depth despite its importance.

The present study concerns a three-dimensional numerical study of turbulent flow heat transfer in a horizontal straight rectangular cross-sectioned duct under hydrodynamically and thermally developing turbulent flow conditions. The bottom surface of the duct was isothermally heated. Air ($Pr \cong 0.7$) was used as the heat transfer medium. The momentum, continuity, energy, and turbulence equations for three-dimensional flow in a rectangular cross-sectioned duct were solved

using finite volume-based commercial software Ansys Fluent 12.1. Five turbulence models (k–ε Standard, k–ε Realizable, k–ε RNG, k–ω Standard and k–ω SST) were used in numerical calculations. Practical engineering correlations for the average Nusselt number and average Darcy friction factor were determined. Local Nusselt number and local Darcy friction factor for different Reynolds numbers along the flow direction were also obtained. Furthermore, the results of the numerical investigation with different turbulence models were compared with each other and as well as experimental data available in the literature.

Theoretical Description

A schematic diagram depicting the computational domain of the rectangular cross-sectioned duct along with the coordinate system and flow geometry is presented in Fig. 54.1a. The rectangular cross-sectioned duct was mathematically modeled for numerical computations. Since the flow field was symmetric with respect to the y–x plane, only one half of the channels was considered for the computational domain to reduce the computational time. The principle flow was in the x-direction. Turbulent flow enters the duct with a uniform velocity and temperature profile. The three-dimensional Navier–Stokes, energy, and turbulence equations were used to describe the flow and heat transfer in the computational domain. The three-dimensional incompressible Newtonian flow with negligible buoyancy effects and viscous dissipation was assumed to be turbulent and steady; the physical properties of fluid, taken at the bulk temperature were considered to be constant in the duct.

The continuity, momentum, energy, and turbulence equations were solved by Ansys Fluent 12.1 in the duct. The code provides mesh flexibility by structured and unstructured meshes. Ansys Fluent 12.1 includes several turbulence models. Turbulence intensity levels used at the inlet of the duct varied from 4 to 5 % depending on the Reynolds number. Hydraulic diameter of the duct was used as appropriate length scale at the inlet. No slip boundary conditions were employed on the duct walls. A uniform wall temperature boundary condition was employed on the bottom surface of the duct. Insulated boundary condition was applied on the sides and top surface of the duct. At the outlet of the duct, pressure outlet boundary condition of Ansys Fluent 12.1 was used. Symmetry boundary condition was employed on the symmetry planes. All the boundary conditions applied on the duct were depicted in Fig. 54.1b.

The objective of the data reduction is to calculate the average Nusselt number and Reynolds number along with average Darcy friction factor. The hydraulic diameter ($D_h = 4A_c/P$) is chosen as the characteristic length.

$$Re = U \cdot D_h / \nu \qquad (54.1)$$
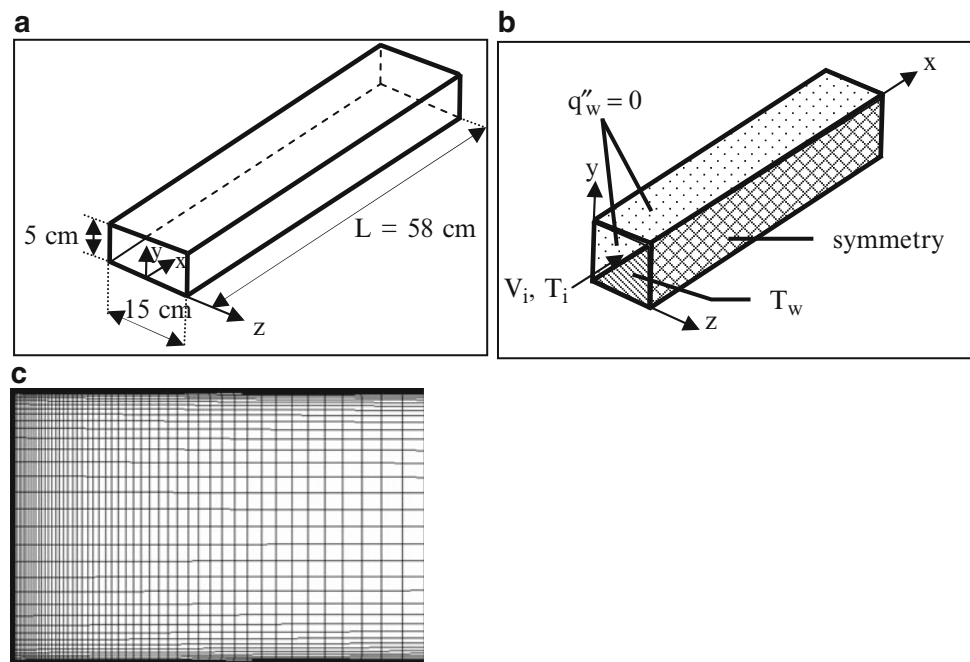
Fig. 54.1 (a) Computational domain of the rectangular cross-sectioned duct, (b) boundary condition of the duct, (c) mesh distribution in y–z plane

Table 54.1 Grid size effect for average Nusselt number and average Darcy friction factor for k–ε standard turbulence model

Grid size	Nu	f
1.80×10^5	137.7626	0.03296
2.80×10^5	138.0095	0.03293
4.00×10^5	138.1041	0.03293
6.45×10^5	138.1762	0.03296
10.50×10^5	138.2819	0.03299
17.25×10^5	138.3207	0.03302

$$Nu = h \cdot D_h/k \tag{54.2}$$

$$f = \Delta p (D_h/L) / \left[\rho U^2/2 \right] \tag{54.3}$$

In Eqs. (54.1)–(54.3), U (m s^{-1}) is the mean velocity of the air flow in the rectangular cross-sectioned duct, D_h (m) is the hydraulic diameter of the rectangular duct, ν (m^2 s^{-1}) is the kinematic viscosity of air, h (W m^{-2} K^{-1}) is the average heat transfer coefficient, and k (W m^{-1} K^{-1}) is the thermal conductivity of air. In addition, Δp (Pa) is the pressure drop along the duct, L (m) is the axial length of the duct, and ρ (kg m^{-3}) is the density of air.

Average convective heat transfer coefficient of the air flow in the rectangular cross-sectioned duct is obtained [18] as follows

$$h = \dot{Q}_c / [A(T_w - T_b)] \tag{54.4}$$

where A (m^2) is the surface area (i.e., in contact with the air) of the bottom surface of the duct and T_w (K) is the surface temperature of the bottom surface of the duct. T_b (K) is the mean bulk temperature of the air flow in the duct. $\dot{Q}_c$ (W) is the convective heat transfer from the duct's bottom surface to the air flowing through the duct under steady-state condition and is calculated as follows [18]

$$\dot{Q}_c = \rho U A_c \, c_p (T_{bo} - T_{bi}) \tag{54.5}$$

where A_c (m^2) is the cross-sectional area of the rectangular cross-sectioned duct, c_p (J kg^{-1} K^{-1}) is the specific heat of the air. T_{bi} (K) and T_{bo} (K) are bulk temperatures of the air at the inlet and outlet of the duct, respectively. All fluid properties in the duct were evaluated at the bulk temperature; $T_b = (T_{bi} + T_{bo})/2$. The air flow properties were taken from Incropera and DeWitt [19].

Computations were performed under turbulent flow conditions. The energy equation was solved neglecting radiation effects. Five different turbulence models (k–ε Standard, k–ε Realizable, k–ε RNG, k–ω Standard and k–ω SST) were used in this study for solving the flow in this study. The Reynolds averaged Navier–Stokes equations were solved numerically in conjunction with transport equations for turbulent flow. Near wall regions were fully resolved for average y^+ values between 0.5 and 1.1 in all the calculations, sufficiently resolving the laminar sub-layer (i.e., $y^+ \leq 4$–5). In the present study, hexahedral cells were created with a fine mesh near the duct walls. A non-uniform grid distribution was employed in the plane perpendicular to the main flow direction while uniform grid distribution was employed in main flow direction as shown in Fig. 54.1c. Close to each wall, the number of grid cells or control volumes was increased to enhance the resolution and accuracy. Steady segregated solver was used with a second order upwind scheme for convective terms in the mass, momentum, energy, and turbulence equations. For pressure discretization, the standard scheme was employed while the SIMPLE-algorithm [20] was used for pressure–velocity coupling discretization.

The grid independence study was performed by refining the grid size until the variation in both average Nusselt number and average Darcy friction factor are less than 0.18 and 0.09 % respectively. To obtain the optimum mesh size, a grid independence study was conducted using six different grid sizes changing from 1.8×10^5 to 17.25×10^5 for $Re = 5 \times 10^4$. Each mesh was processed using the k–ε Standard turbulence model. It was observed that a further refinement of grids from 2.8×10^5 to 4.0×10^5 did not have a significant effect on the results in terms of average Nusselt number and average Darcy friction factor as depicted in Table 54.1. Based on this observation, grid size of 2.8×10^5 was used for all of the calculations. No convergence problems were observed during the calculations. The same procedure was used for other turbulence models, and optimum grid size was obtained for each turbulence model calculations. To obtain convergence, each equation for mass, momentum, and turbulence was iterated until the residual falls below 1×10^{-5} while the energy equation was iterated until the residual falls below 1×10^{-6}.

Results and Discussion

In the study reported here, the convective heat transfer and fluid friction in an air-cooled rectangular cross-sectioned duct under uniform bottom surface temperature were numerically investigated. The investigation was carried out under hydrodynamically and thermally developing turbulent flow conditions. The results were presented in a non-dimensional Nusselt number and Darcy friction factor. After the determination of temperature fields in the fluid, the average Nusselt number was calculated. In addition, the average Darcy friction factor was estimated with the determination of a pressure drop in the duct. Numerical results obtained under steady-state conditions are presented in Figs. 54.2, 54.3, 54.4, 54.5, and 54.6 for different turbulence models. Plotted in these figures are the best-fit lines. The flow and temperature distributions,
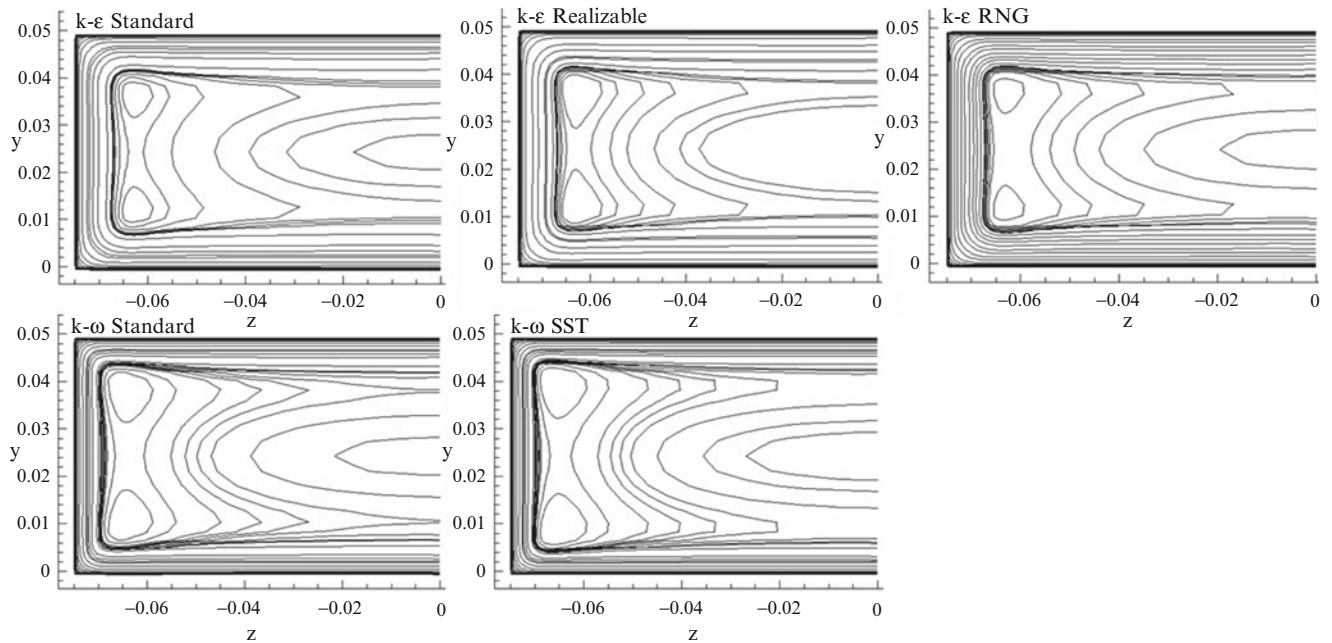
Fig. 54.2 Isovel contours of velocity magnitude for different turbulence models at the entrance region of the duct
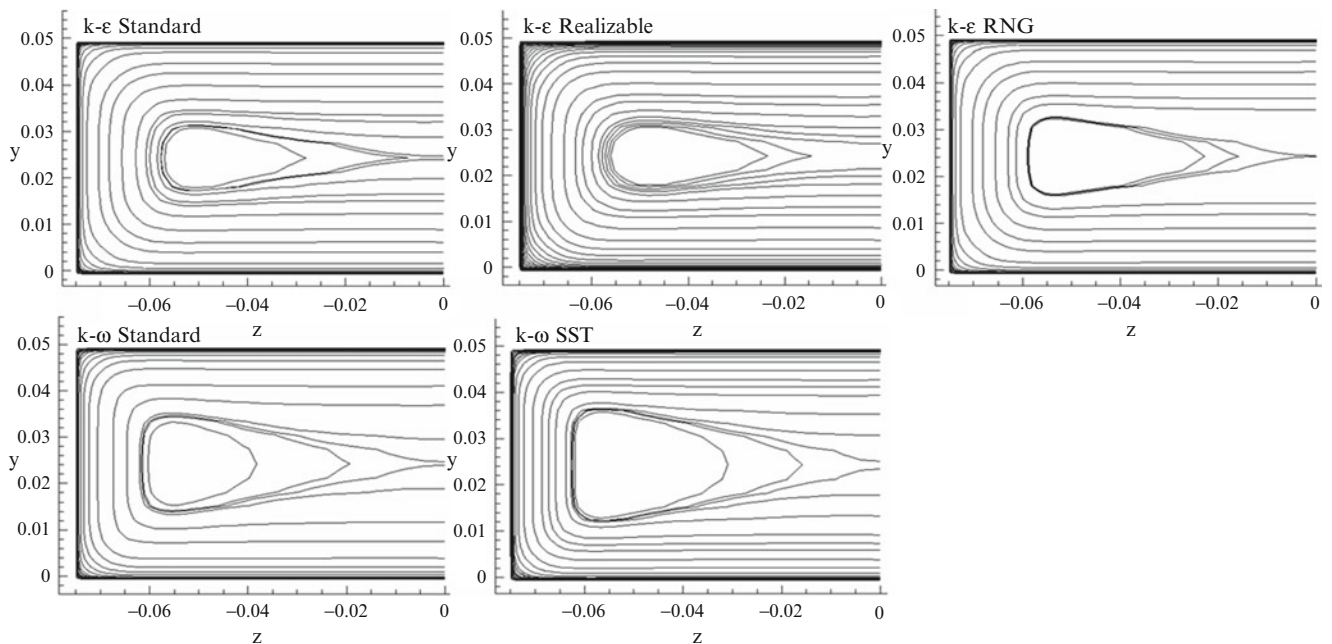
Fig. 54.3 Isovel contours of velocity magnitude at the outlet of the duct for different turbulence models
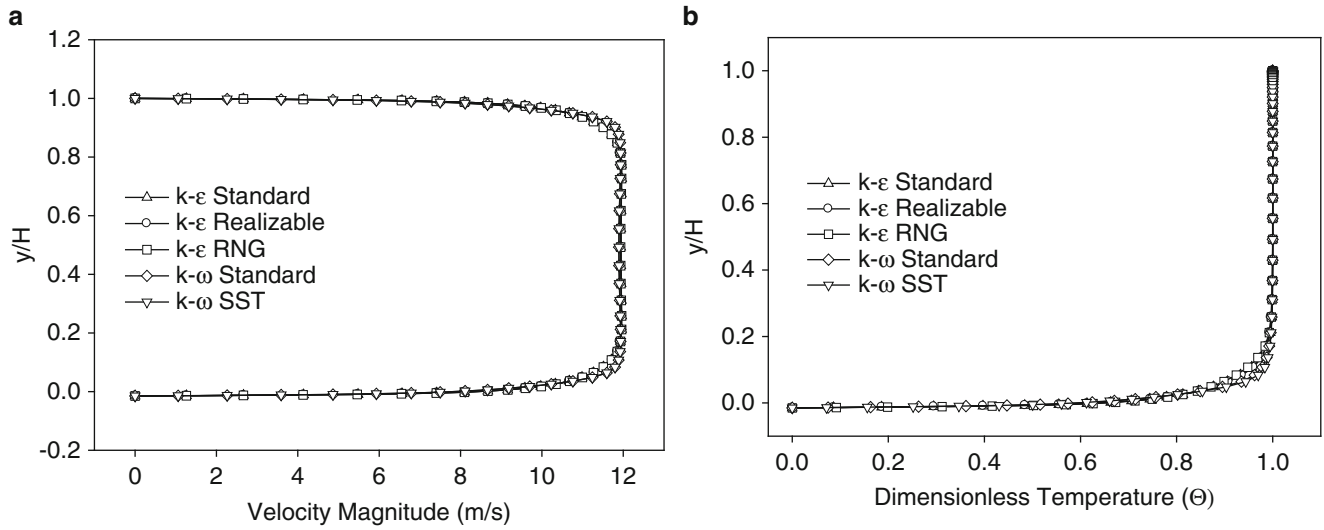
Fig. 54.4 (**a**) Velocity and (**b**) dimensionless temperature distributions along the duct on symmetry plane
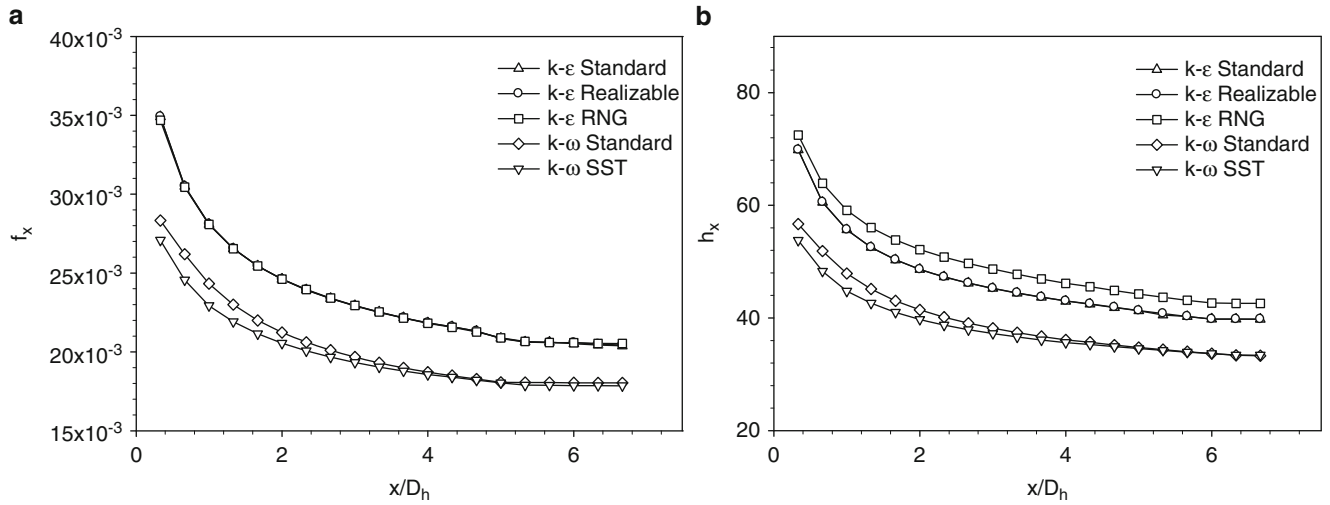
Fig. 54.5 (**a**) Local Darcy friction factor and (**b**) local heat transfer coefficient, as function of dimensionless position (x/D_h)
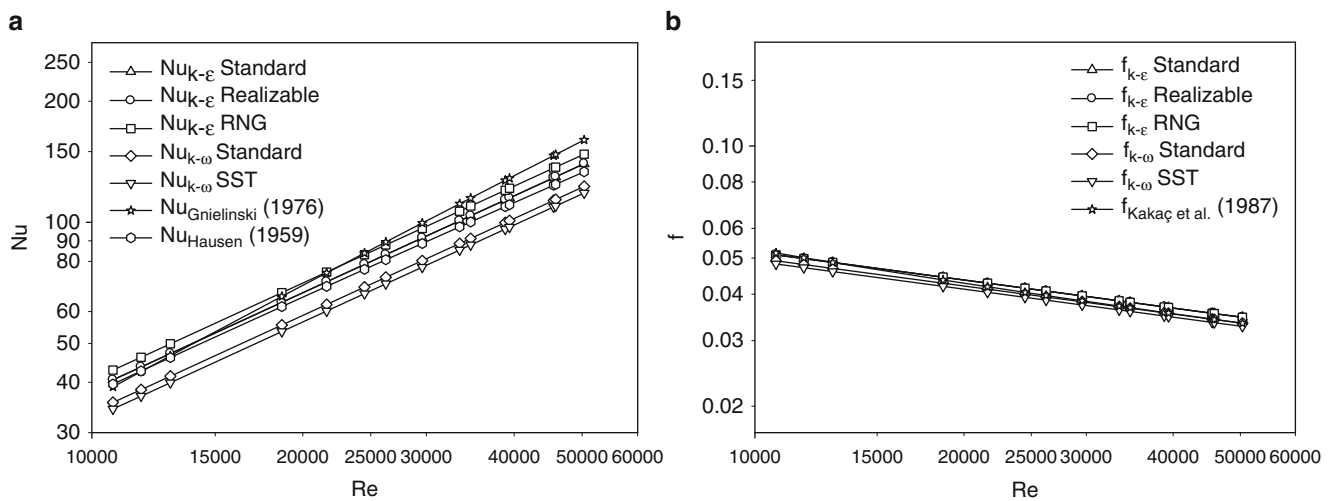
Fig. 54.6 (**a**) The changing of average Nusselt number with Reynolds number; (**b**) the changing of average Darcy friction factor with Reynolds number

numerically obtained average Nusselt numbers and average Darcy friction factors presented in this study highlight the influence of duct geometry and wall boundary conditions on the thermal performance of a rectangular cross-sectioned duct and provide additional useful design data.

Air at the ambient temperature entered the duct with a uniform velocity profile. The velocity fields for different turbulence models at $x = 0.2$ m of the duct entrance were considered first. Typical velocity magnitude contours for different turbulence models at $x = 0.2$ m are presented in Fig. 54.2 for $Re = 5 \times 10^4$. It is seen in Fig. 54.2 that there are small differences for velocity contours at the entrance region of the duct for different turbulence models.

Velocity contours at the outlet of the duct is presented in Fig. 54.3 for $Re = 5 \times 10^4$ and different turbulence models. It is obtained in the figure that velocity contours for k–ε turbulence models have almost the same profile; however, velocity profiles for k–ω turbulence models are slightly different from k–ε turbulence models.

In order to compare the velocity distributions of different turbulence models, typical velocity profiles are obtained for each turbulence model and these are plotted on a symmetry plane at the entrance region for $Re = 5 \times 10^4$. As can be seen from Fig. 54.4a, the velocity profile for different turbulence models in the rectangular duct is plotted as a function of the dimensionless height (y/H) of the duct. It is obtained in this figure that velocity magnitudes of k–ε and k–ω turbulence models have nearly the same profiles; however, velocity profiles of k–ω turbulence models are slightly different from velocity profiles of k–ε turbulence models. Dimensionless temperature distribution is plotted as a function of the dimensionless height (y/H) of the duct for various turbulence models on a symmetry plane at the entrance region as shown in Fig. 54.4b. Dimensionless temperature profile is defined as $\Theta = (T_w - T(x, y, z))/(T_w - T_i)$ where T_w (K) is the bottom wall temperature of the duct and T_i (K) is the inlet temperature [3]. It is seen in the figure that the dimensionless temperature profile of k–ε turbulence models are a bit different than the dimensionless temperature profile of k–ω turbulence models.

One of the key parameters of interest in the hydrodynamic and thermal entrance region is the variation of the numerically obtained local Darcy friction factor and the local heat transfer coefficient for different turbulence models along the axial position. Figure 54.5a, b shows the variation of the local Darcy friction factor and local heat transfer coefficient as a function of dimensionless position (x/D_h) for the channel, respectively. Figure 54.5a shows the local Darcy friction factor as a function of dimensionless position (x/D_h) for different turbulence models. An examination of Fig. 54.5a reveals that the local Darcy friction factor in the entrance is very large and decreasing along the duct for all turbulence models. An inspection of Fig. 54.5b reveals that the values of local heat transfer coefficient in the inlet of the duct is very large and is decreasing along the duct for various turbulence models. It is observed from an inspection of Fig. 54.5a that the local Darcy friction factor of each k–ε turbulence model is larger than the local Darcy friction factor of each k–ω turbulence model. The local heat transfer coefficient of each k–ε turbulence model is larger than the local heat transfer coefficient of each k–ω turbulence model. On the other hand, the k–ε RNG turbulence model predicts the largest value for local heat transfer coefficient.

Figure 54.6a, b displays the average Nusselt number and the average Darcy friction factor in the duct along with the available experimental data from the literature for Reynolds numbers ranging from 1×10^4 to 5×10^4. It is observed that as the Reynolds number increases, the average Nusselt Number increases. In addition, the average Darcy friction factor decreases with increasing the Reynolds number. It is also seen from an inspection of Fig. 54.6 that the Nusselt numbers obtained using the k–ε turbulence models are closer to each other and larger than the Nusselt numbers obtained using the k–ω turbulence models. At the same time, the average Darcy friction factors obtained using the k–ε turbulence models are slightly larger than those obtained using the k–ω turbulence models.

Average Nusselt numbers obtained with the present study are compared with the experimental correlations of the Gnielinski [15] and Hausen [21] in Fig. 54.6a.

The average Darcy friction factors obtained with the present study are compared with the experimental correlation of the smooth rectangular cross-sectioned duct given by Kakaç et al. [3] as;

$$f = [1.0875 - 0.1125(H/W)]f_c \tag{54.6}$$

where f_c is the average Darcy friction factor for the circular cross-sectioned duct, suggested by Petukhov [22] in Fig. 54.6b. H (m) and W (m) are the duct height and width, respectively.

A comparison of the average Nusselt numbers of the present study with the experimental data available in literature was carried out. It is observed that the results of the k–ε turbulence models are very close in correlation of Gnielinski [15] and Hausen [21], especially for small Reynolds numbers. On the other hand, the k–ω turbulence models predict lower Nusselt numbers compared to the experimental data available in the literature. The difference is nearly 16 %. The average Darcy friction factors obtained using the k–ε turbulence models are nearly harmonious with the experimental correlation of Kakaç et al. [3]. However, the average Darcy friction factors obtained using the k–ω turbulence models are approximately 6 % lower than experimentally obtained average Darcy friction factors.

Table 54.2 Values of a, b, c, and d for $Nu = aRe^b$ and $f = cRe^d$

		k–ε standard	k–ε realizable	k–ε RNG	k–ω standard	k–ω SST
Nu	a	0.0242	0.0243	0.0256	0.0213	0.0205
	b	0.8	0.8	0.8	0.8	0.8
f	c	0.5190	0.5192	0.5190	0.5003	0.4905
	d	−0.25	−0.25	−0.25	−0.25	−0.25

Numerically obtained average Nusselt numbers and average Darcy friction factors were expressed as a power law variation with a Reynolds number. In other words, the results were presented in the forms of $Nu = aRe^b$ and $f = cRe^d$. The average Nusselt number, average Darcy friction factor, and Reynolds numbers for flow in this duct are based on the hydraulic diameter D_h. The equations were obtained with the least-square method for the average Nusselt number and the average Darcy friction factor. The values of a, b, c, and d for $Nu = aRe^b$ and $f = cRe^d$ were given in Table 54.2.

Conclusions

In this study, hydrodynamically and thermally developing three-dimensional steady turbulent flow in a horizontal rectangular cross-sectioned duct with constant bottom surface temperature and with three insulated sides were numerically investigated for different turbulence models. A numerical study was carried out for a Reynolds number ranging from 1×10^4 to 5×10^4 with $Pr = 0.7$. The turbulence models used in numerical simulations were k–ε Standard, k–ε Realizable, k–ε RNG, k–ω Standard and k–ω SST. The results of numerical computations are presented in terms of average Nusselt numbers and average Darcy friction factors. The results are given in Table 54.2 and in Figs. 54.2, 54.3, 54.4, 54.5, and 54.6. It is shown that increasing the Reynolds number increases the average Nusselt number. On the other hand, the average Darcy friction factor decreases with increasing the Reynolds number. Based on the present numerical solutions of full 3D governing equations, new engineering correlations were obtained for the average Nusselt number and the average Darcy friction factor in the form of $Nu = aRe^b$ and $f = cRe^d$, respectively. It is obtained that k–ε turbulence models represent the turbulent region very well for the present study.

References

1. Zhang L (2007) Thermally developing forced convection and heat transfer in rectangular plate-fin passages under uniform plate temperature. Numer Heat Transf A 52:549–564
2. Shah RK, London AL (1978) Laminar flow forced convection in ducts. Academic, New York
3. Kakaç S, Shah RK, Aung W (1987) Handbook of single-phase convective heat transfer. Wiley, New York
4. Kakaç S, Liu H (2002) Heat exchangers selection, rating, and thermal design. CRC, Boca Raton
5. Muzychka YS, Yovanovich MM (2004) Laminar forced convection heat transfer in the combined entry region of non-circular ducts. J Heat Transf 126:54–61
6. Chung BTF, Zhang ZJ, Li G (1992) Thermally developing convection from Newtonian flow in rectangular ducts with uniform heating. J Thermophys Heat Transf 7(3):534–536
7. Aparecido JB, Cotta RM (1990) Thermally developing laminar flow inside rectangular ducts. Int J Heat Mass Transf 33(2):341–347
8. Beavers GS, Sparrow EM, Magnuson RA (1970) Experiments on hydrodynamically developing flow in rectangular ducts of arbitrary aspect ratio. Int J Heat Mass Transf 13:689–702
9. Montgomery SR, Wibulswas P (1967) Laminar flow heat transfer for simultaneously developing velocity and temperature profiles in ducts of rectangular cross section. Appl Sci Res 18:247–259
10. Sparrow EM (1955) Analysis of laminar forced convection heat transfer in entrance region of flat rectangular ducts. NACA Technical Note 3331
11. Savino JM, Siegel R (1964) Laminar forced convection in rectangular channels with unequal heat addition on adjacent sides. Int J Heat Mass Transf 7:733–741
12. Chiu HC, Jang JH, Yan WM (2007) Mixed convection heat transfer in horizontal rectangular ducts with radiation effects. Int J Heat Mass Transf 50 (15–16):2874–2882
13. Naccache MF, Mendes PRS (1996) Heat transfer to non-newtonian fluids in laminar flow through rectangular ducts. Int J Heat Fluid Flow 17(6):613–620
14. Chong DT, Liu J, Yan J (2011) An experimental study of pressure drop and friction factor for laminar and transition opposing mixed convection in entrance region of rectangular duct. Energy Convers Manag 52:2272–2281
15. Gnielinski V (1976) New equations for heat and mass transfer in turbulent pipe and channel flow. Int Chem Eng 16:359–368
16. Kostic M, Hartnett JP (1986) Heat transfer to water flowing turbulently through a rectangular duct with asymmetric heating. Int J Heat Mass Transf 29 (8):1283–1291
17. Abraham JP, Sparrow EM, Tong JCK (2009) Heat transfer in all pipe flow regimes: laminar, transitional/intermittent, and turbulent. Int J Heat Mass Transf 52:557–563
18. Çengel YA (1998) Heat transfer a practical approach. McGraw-Hill, Boston
19. Incropera FP, DeWitt DP (2002) Fundamentals of heat and mass transfer. Wiley, Toronto
20. Patankar SV (1980) Numerical heat transfer and fluid flow. Hemisphere Publishing Corporation, Washington, DC
21. Hausen H (1959) Neue gleichungen für die wärmeübertragung bei freier oder erzwungener stromüng (New equations for heat transfer in free or forced flow). Allg Wärmetechn 9(4/5):75–79
22. Petukhov BS (1970) Heat transfer and friction factor in turbulent pipe flow with variable physical properties. Adv Heat Transf 6:503–565

Muhsin Kılıç, Gökhan Sevilgen, and Mustafa Mutlu

Abstract

Nowadays, new developments in the properties of insulation materials used in buildings and international regulations lead to the use of more efficient heating systems. On the other hand, the increased energy efficiency of modern buildings makes necessary the use of low-temperature heating systems. Thus, we need to design a new generation of energy-efficient radiators which have a low capacity of water volume and low weight compared to conventional radiators. Moreover, the standards defined for the testing procedures of the thermal output of steel panel radiators have been changed depending on the objectives of energy efficiency. In this context, a detailed thermal analysis of a panel radiator should be performed to meet the needs for these objectives. Three-dimensional computational fluid dynamics (CFD) is a useful tool for the thermal analysis of a steel panel radiator. In this study, three-dimensional numerical calculations of the thermal output of a steel panel radiator, in accordance with TS EN442, was performed by using CFD analysis based on the finite volume method. The numerical calculations were performed under steady-state conditions. The results obtained from the numerical simulations were in good agreement with the experimental data available in the literature.

Keywords

Panel radiator • Thermal output • Computational fluid dynamics

Introduction

Steel panel radiators are the most common used elements for heating systems of indoor environments such as buildings and offices. This heating elements are chosen for energy efficiency and simple compact design to have a long-lasting effect. On the other hand, design configurations should be performed due to new developments in insulation materials, new international regulations and testing procedures and the consumer demands for thermal comfort levels. Moreover, the displacement, location, surface area and operating temperature of the panel radiator(s), heat transfer characteristics of the wall surfaces and surface area of the window(s) have a great impact on thermal comfort and energy consumption [1]. Thermal sensation of the human body is dependent on local heat transfer characteristics of the human body's surfaces [2]. For this reason, consideration of local heat transfer characteristics of a human body surface is highly important for numerical calculations with sufficient accuracy and acceptable results. A combined numerical simulation was performed modeling for airflow,

M. Kılıç (✉)
Faculty of Engineering, Department of Mechanical Engineering, Bursa Orhangazi University, Yıldırım Bursa, Turkey
e-mail: muhsin.kilic@bou.edu.tr

G. Sevilgen
Faculty of Engineering, Department of Automotive Engineering, Uludağ University, Görükle, Bursa, Turkey
e-mail: gsevilgen@uludag.edu.tr

M. Mutlu
Faculty of Engineering, Department of Mechanical Engineering, Uludağ University, Görükle, Bursa, Turkey
e-mail: mustafamutlu@uludag.edu.tr

thermal radiation, heat and moisture transfer with thermo physiological properties between a standing human body and its surroundings in an adiabatic room [3]. Considering the energy efficiency, studies show that low-temperature heating may improve indoor air quality as well as the thermal comfort conditions [4, 5]. Experimental studies show that people living in houses with low-temperature heating systems are more satisfied with the indoor climate than people living in houses with high-temperature heating systems [6, 7]. Previous researches for thermal comfort used to be carried out by means of experiments. But, performing experiments with consideration of the all parameters reveals complexity and difficulty. However, researchers have also used combined numerical simulations based on the CFD method with experimental studies [8–15]. The analysis of complex HVAC systems based on numerical calculations with sufficient accuracy and acceptable results is now possible for HVAC researchers due to improved computer technology and CFD techniques [16, 17]. All considerations described above, it can be said that the thermal output of a steel panel radiator is the main important parameter for design configurations and heating performance. For this purpose, a detailed analysis of the thermal output of a steel panel radiator should be performed to meet the needs for these objectives. In this study, three-dimensional steady-state numerical calculations of the thermal output of a steel panel radiator, in accordance with TS EN442, was performed by using the CFD method.

Method

Today there are many computer software packages for CFD analysis. In this study Ansys Fluent software is used for three-dimensional flow field and heat transfer analysis. Fluent software solves continuum, energy and transport equations numerically with natural convection effects [18]. A sectional view of steel panel radiators and the CAD Model of the steel panel radiator used in the numerical study are shown in Figs. 55.1 and 55.2. In the numerical simulations, we used original dimensions and geometry of a steel panel radiator without any simplifications in geometrical detail and we chose a type-10 steel panel radiator, according to TS EN442, and the type of fittings was a TBSE (Top–Bottom–Same–End) connection.

Constructions of steel panel radiators include panels, convectors (fins), grilles and T connections in general. In the numerical calculations, a type-10 radiator model (Fig. 55.2b) which includes one panel without any extended surfaces (convectors) was used. The dimension of a steel panel radiator is shown in Table 55.1. Water flow volume (Fig. 55.3) extraction was achieved from the original CAD data of a steel panel radiator to get precise velocity and temperature fields of a real radiator.

The boundary surfaces defined in the computational model are shown in Fig. 55.3. In numerical calculations mesh generation is very crucial for getting accurate predicted results and reducing computing time. The mesh structure of the surfaces of the radiator includes triangular elements. The computational domain consists of about 2,300,000 volume cells (Fig. 55.4, Table 55.2).

Heat is transferred from warm water inside a radiator to air and room surfaces surrounding the radiator. In the numerical simulations, we calculated the thermal output of a radiator from Eq. (55.1) and we just employed on the parameters shown on the left side of the Eq. (55.1). The parameters on the left side, $\dot{m}$(kg/s), c_p (W s kg^{-1} K^{-1}), T_{inlet} and T_{outlet} are the mass flow of water inside the radiator, specific heat capacity of water and temperature difference between inlet and outlet water, respectively.
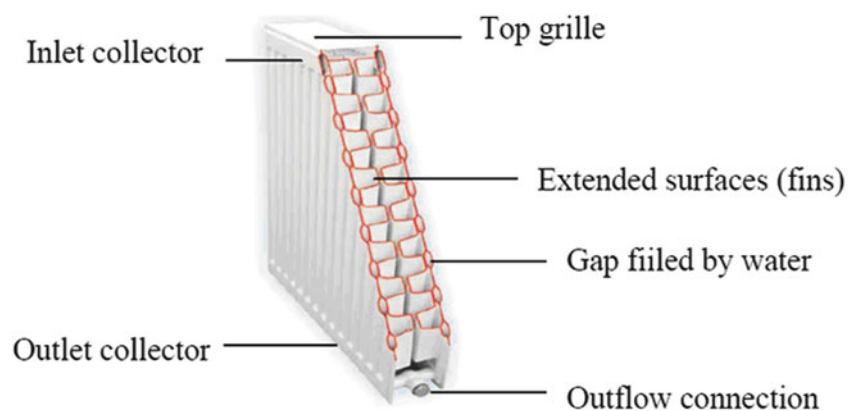
Fig. 55.1 Sectional view of steel panel radiator

Fig. 55.2 The detailed CAD model of the steel panel radiator (**a**) Type-22, (**b**) Type-10
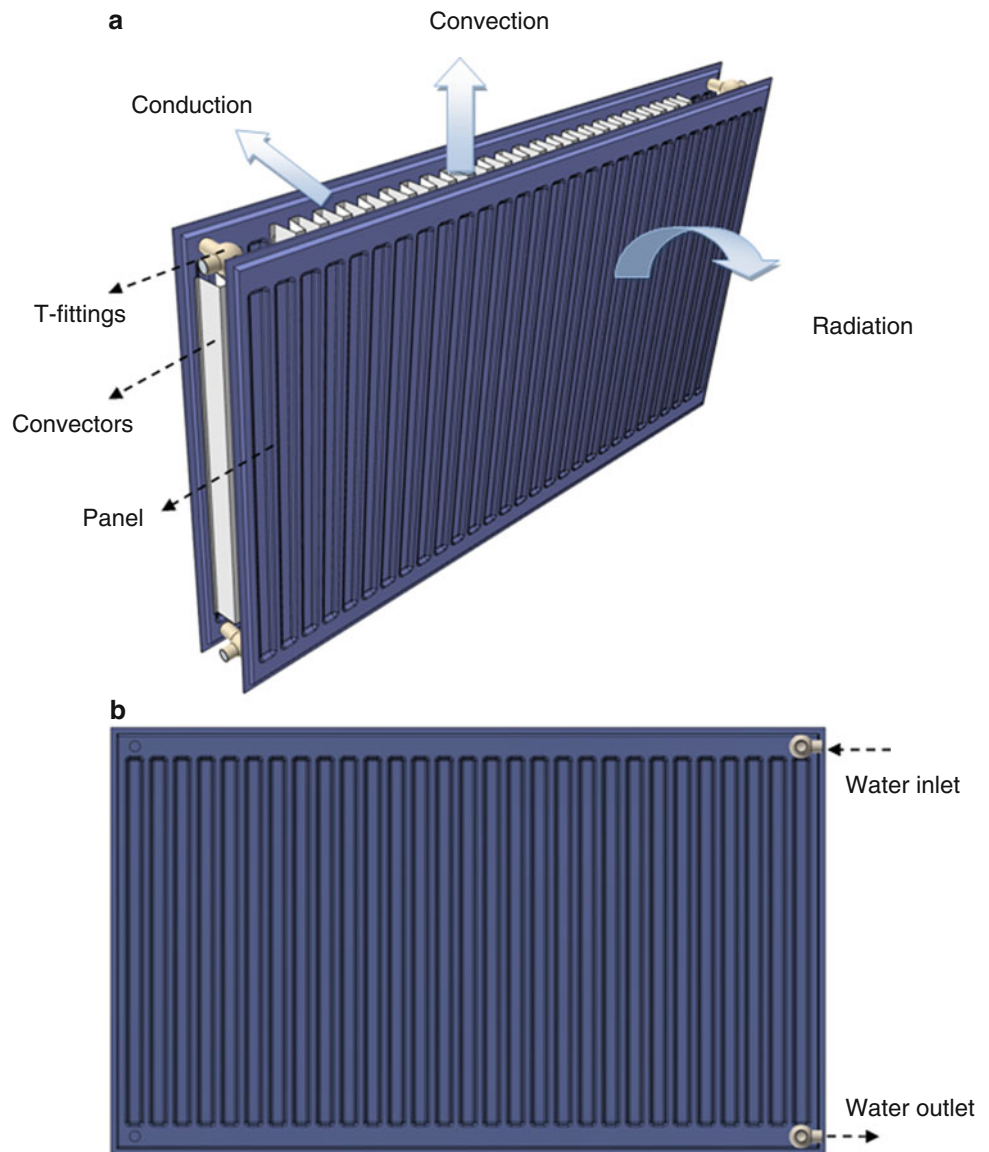
Table 55.1 The dimensions of steel panel radiator(s) used in this study

Type	Connection type	Length (mm)	Height (mm)	Width (mm)
Type-10	TBSE	2,000 mm	600 mm	13 mm

The parameters on the right side, U (W/m^2 K), A (m^2), ΔT_{ln} are the total heat transfer coefficient, total surface area of the radiator and logarithmic temperature difference between radiator surface and indoor air.

$$\theta = \dot{m}c_p(T_{inlet} - T_{outlet}) = UA\Delta T_{ln} \tag{55.1}$$

In the solution process, numerical calculations were performed under steady-state conditions. Water flow was assumed as laminar and Simple C algorithm was chosen for velocity–pressure coupling and a cell-based option was set for flow field computations (Table 55.3). The first order schemes were employed in the discretization of all the governing equations at the beginning of the numerical simulations, and then the second order scheme was chosen depending on the convergence criteria and getting precise results. The convergence criterions were assumed when the normalized residuals of flow equations are less than 10^{-4} and the energy equations are less than 10^{-6}.

Three different cases were considered according to standard test conditions of the thermal output of a steel panel radiator. In all three cases, the value of water inlet temperatures were set to 85.7, 74.9, 52.4 °C and the value of entering mass-flow

Fig. 55.3 Water flow volume extraction from the original CAD data of steel panel radiator

Water inlet

Water outlet

Wall surfaces
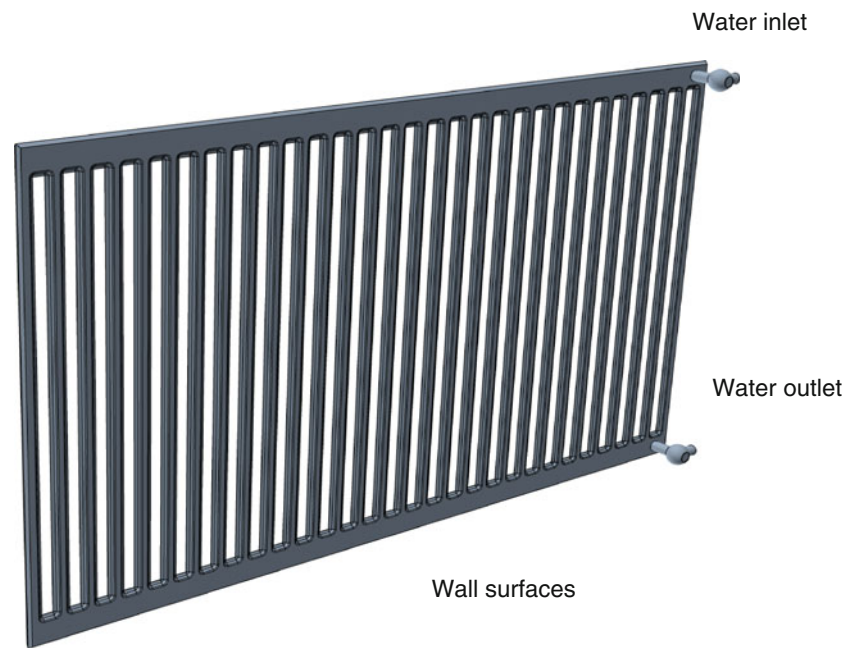
Fig. 55.4 Mesh structure of computational domain for water flow volume
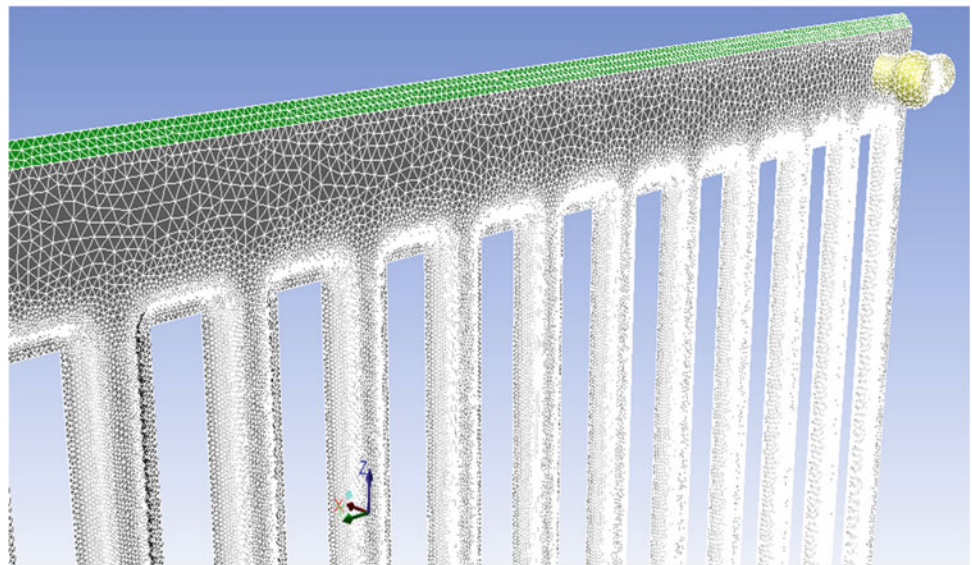
Table 55.2 Mesh structure and boundary conditions

Mesh structure	
Element type	Tetrahedral
Number of elements	2,300,000
Number of nodes	450,000

rates were set to 0.027719, 0.027822, 0.027972 kg/s, respectively. Thus, the leaving temperature of water was computed to calculate the thermal output of the radiator in all cases. The reference air temperature values were obtained from the experimental results and they were set to 20.4, 20.5, 19.8 °C, respectively (Table 55.4). The boundary conditions used for all cases in the numerical simulations were shown in Table 55.5. At the water outlet surfaces, atmospheric boundary conditions were used for calculating the leaving temperature of water. The thickness of the panel surfaces were set to 0.0012 m and the material type of the panel radiator was steel. At the panel surfaces, a boundary condition was set which includes convection,

Table 55.3 Solver settings and turbulence model used in the numerical simulations

Solver settings and turbulence model	
Time	Steady-state
Solver	Pressure-based/coupled
Gradient option	Least squares cell-based
Formulation	First-order implicit scheme
Equations	Combined simulation of flow and energy
Flow	Laminar

Table 55.4 Three different cases obtained from experimental results

Cases	T_{inlet} (°C)	Mass-flow rate (kg/s)	T_{air} (°C)
Case-I	85.7	0.027719	20.4
Case-II	74.9	0.027822	20.5
Case-II	52.4	0.027972	19.8

Table 55.5 Boundary conditions used in numerical simulations

Boundary conditions		
Surface	Boundary-type	Properties
Water inlet	Mass flow inlet	$T_{inlet} = T_{exp}$ (obtained from experiments) Mass-flow rate: (obtained from experiments)
Water outlet	Pressure outlet	Atmospheric conditions
Panel surfaces and T-fittings connections	Ambient temperature	h_m is computed from Eqs. (55.2) and (55.3), T_{air} (obtained from experiments)
	Wall thickness	0.0012 mm
	Material	Steel

and a shell conduction zone. At the outer surfaces of the panel radiator natural convection occurs thus, we used UDF (user defined function) in Fluent for the computation of the heat transfer coefficient [Eq. (55.1)] at the outer surfaces of the panel radiator surfaces. UDF is a function that you program that can be dynamically loaded with the Fluent solver to enhance the standard features of the code. More descriptions and detailed information can be obtained from [19]. We used correlation for Nu (Nusselt) number as described in Eq. (55.2) [20], where, Ra, Pr and Gr are the dimensionless numbers as the known Rayleigh, Prandtl and Grashof numbers respectively. h_m (W/m^2 K) is the mean heat transfer coefficient, k_f (W/m K) is the thermal conductivity of fluid (water) and L (m) is the length of the vertical plate.

$$\overline{Nu_L} = \frac{h_m L}{k_f} \tag{55.2}$$

$$\overline{Nu_L} = \left[0.825 + \frac{0.387 Ra_L^{1/6}}{\left[1 + (0.492/\text{Pr})^{9/16} \right]^{8/27}} \right]^2 ; \quad Ra_L = Gr_L \text{Pr} \tag{55.3}$$

Results and Discussions

The computed values of thermal output (W) and temperature (°C) of water from the radiator are shown in Table 55.6 and the temperature distributions obtained from the numerical simulations are shown in Figs. 55.5, 55.6, and 55.7.

In case-I, the thermal output was computed at about 1,500 W and the difference in percentage between the experimental and CFD data was 5 %. From the numerical results shown in Table 55.6, we can say that the predicted results of both temperature and thermal output are in good agreement with the experimental data.

The cooler and warmer area of the whole radiator surfaces were at the bottom and the top of the radiator, respectively. The maximum predicted temperature was achieved near the water inlet surfaces for all cases. A temperature field obtained by

Table 55.6 Three different cases obtained from experimental results

Cases	T_{inlet} (°C)	T_{outlet} (°C) (CFD)	T_{outlet} (°C) (Exp.)	θ (W) (CFD)	θ (W) (Exp.)	Difference (%)
Case-I	85.70	72.79	73.40	1,501.20	1,431	5
Case-II	74.90	64.68	65.20	1,191.04	1,131	5
Case-II	52.40	47.08	47.40	622.12	583	7
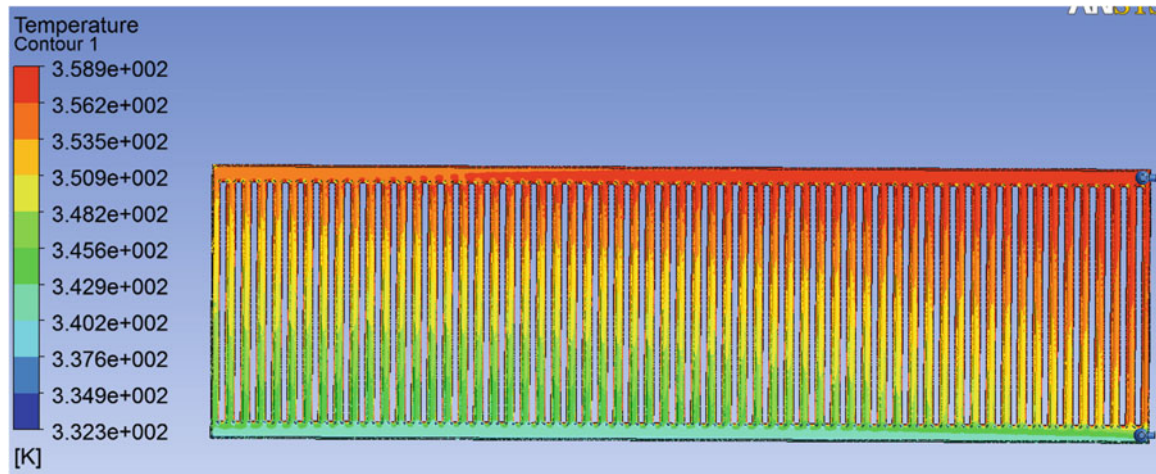
Fig. 55.5 Temperature contours of panel radiator surface (Case-I)
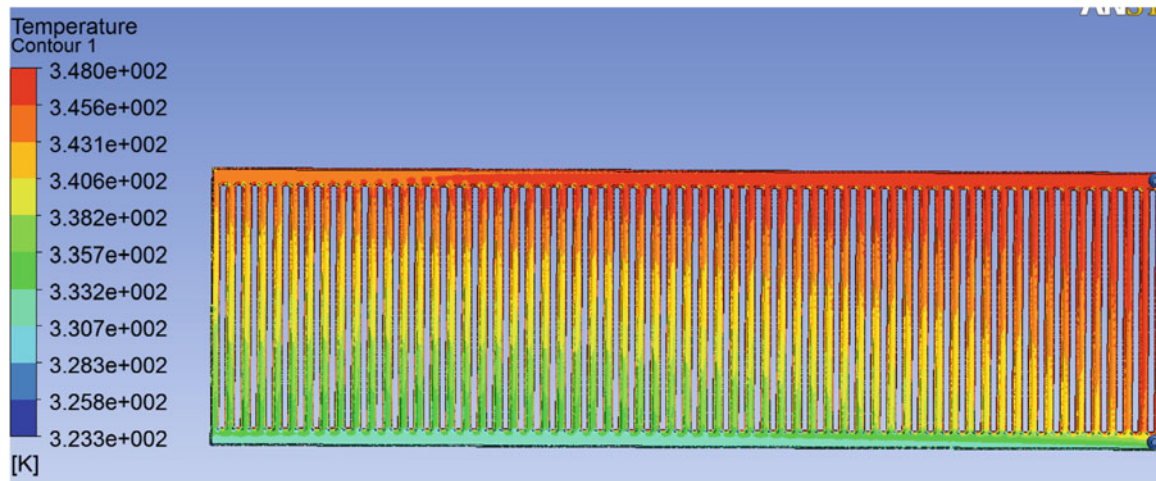
Fig. 55.6 Temperature contours of panel radiator surface (Case-II)

Vavricka and Basta is shown in Fig. 55.8. They used thermography for mapping temperature fields of radiator surfaces. This radiator used in their study was nearly about our steel panel radiator in view of dimensions and conditions. The temperature fields obtained from their experimental studies have the same trends with our numerical results shown in Figs. 55.5, 55.6, and 55.7. Three different lines were defined to get comparative results on the surface of the panel radiator (Fig. 55.9).

From the results shown in Figs. 55.10, 55.11, and 55.12, all three cases have the same trends and higher temperature gradients were computed between the bottom and top of the radiator surfaces. The maximum temperature gradients were obtained in the
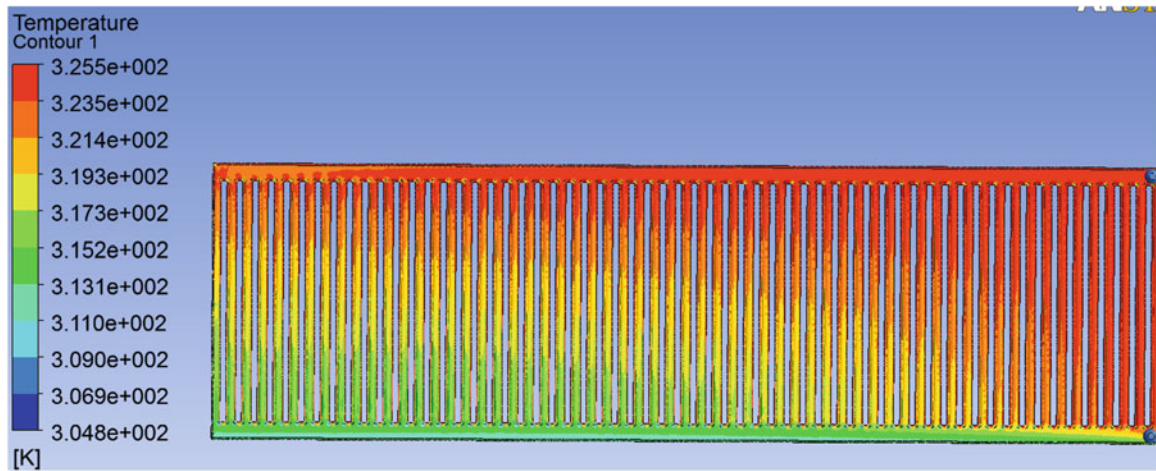
Fig. 55.7 Temperature contours of panel radiator surface (Case-III)

Fig. 55.8 Temperature fields by radiator $10 \times 500 \times 2{,}000$ mm (single-side top connection) [8]
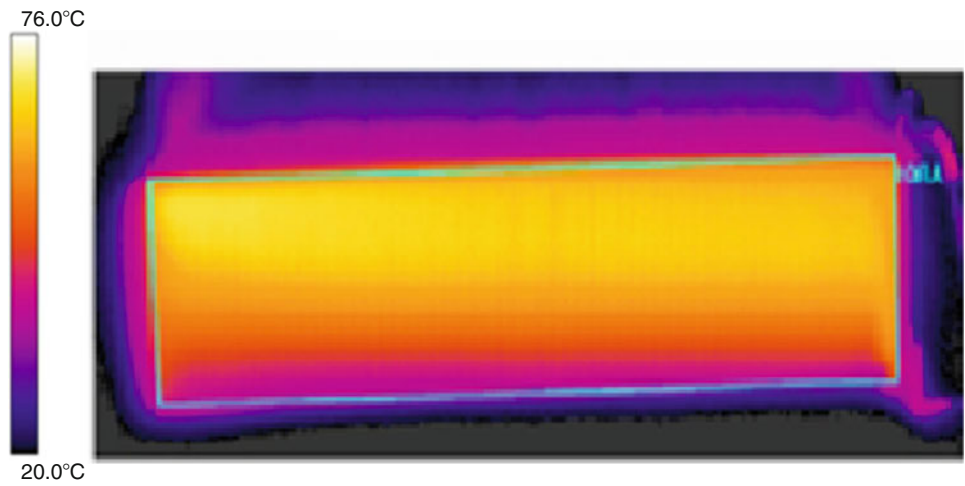
Fig. 55.9 The locations of the lines described for temperature results
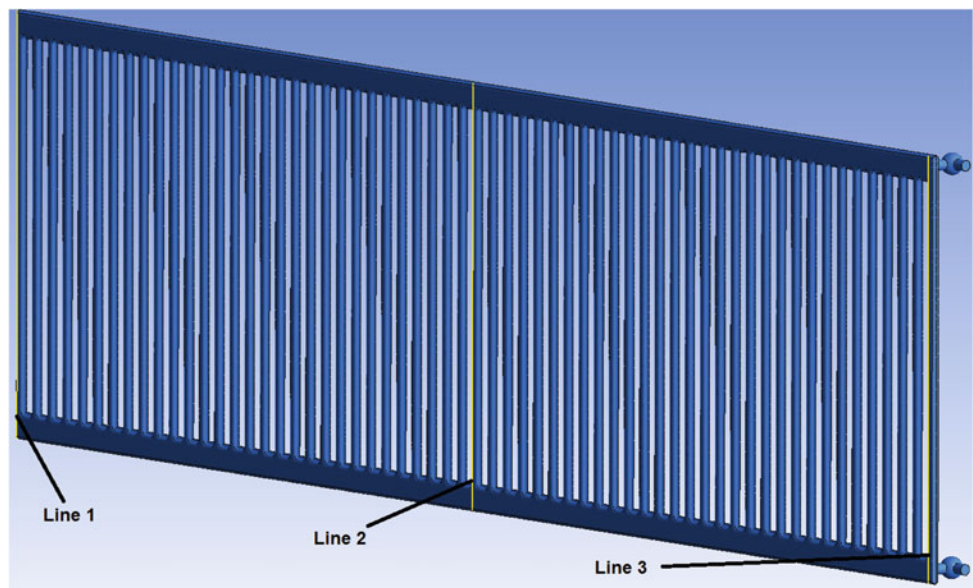
Fig. 55.10 Temperature values obtained from CFD results for Case-I
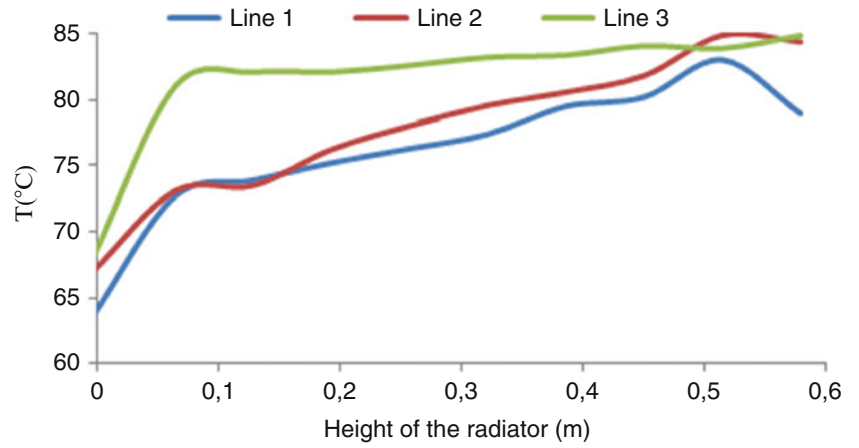
Fig. 55.11 Temperature values obtained from CFD results for Case-II
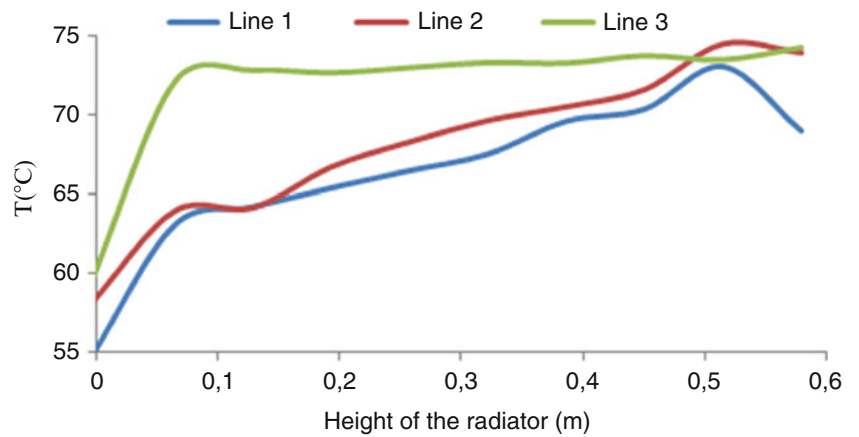
Fig. 55.12 Temperature values obtained from CFD results for Case-III
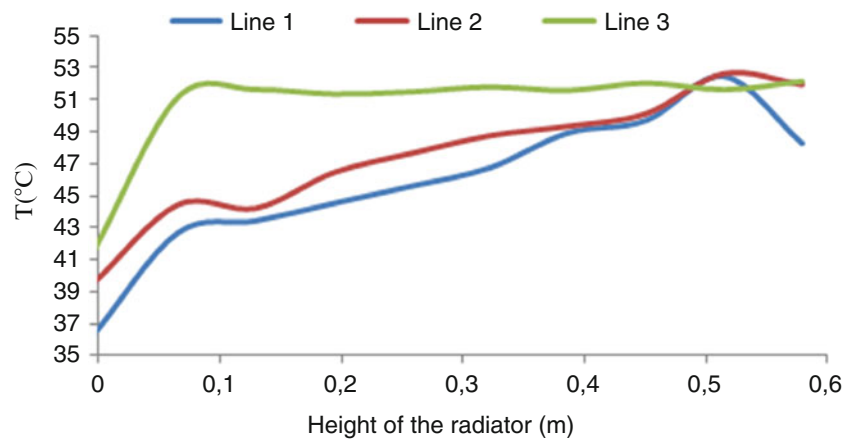
zone which has 0.1 m height from the radiator bottom. The temperature values along the radiator surface were not remarkably altered from the half part of the radiator surface in all three cases. Another important result is that the temperature difference between inlet and outlet water temperature, decreases depending on the heat transfer coefficient.

Conclusion

In this study, three-dimensional steady-state numerical calculations of the thermal output of a steel panel radiator, in accordance with TS EN442, was performed by using the CFD method. In the numerical simulations, original dimensions and geometry of a steel panel radiator was used without any simplifications in geometrical detail. Three different cases were considered according to standard test conditions of the thermal output of a steel panel radiator. The water inlet temperatures, mass flow rates and ambient temperatures were set to different values obtained from experimental results in all three cases. The results show that higher temperature gradients occurred at the radiator surface and the temperature values along the radiator surface were not remarkably altered from the half part of the radiator surface in all three cases. The lowest temperature difference between inlet and outlet surfaces was obtained for case-III. Another important result was that the convective heat transfer coefficient gets an important role in the thermal output of steel panel radiators. Numerical results show that CFD is a useful tool for predicting the thermal output of a panel radiator and temperature distributions of panel radiator surfaces. The results obtained from the numerical simulations were in good agreement with the experimental data.

References

1. Sevilgen G, Kilic M (2011) Numerical analysis of air flow, heat transfer, moisture transport and thermal comfort in a room heated by two-panel radiators. Energy Build 43(1):137–146
2. Murakami S, Kato S, Zeng J (2000) Combined simulation of airflow, radiation and moisture transport for heat release from a human body. Build Environ 35:489–500
3. Kilic M, Sevilgen G (2008) Modelling airflow, heat transfer and moisture transport around a standing human body by computational fluid dynamics. Int Commun Heat Mass Transf 35(9):1159–1164
4. Myhren JA, Holmberg S (2008) Flow patterns and thermal comfort in a room with panel, floor and wall heating. Energy Build 40:524–536
5. ASHRAE Handbook—fundamentals, chapter 8 (1997) American Society of Heating, Refrigeration and Air-Conditioning Engineers, Atlanta
6. Hutter E (1991) Comparison of different heat emitters in respect of thermal comfort and energy consumption. In: Proceedings of the international centre for heat and mass transfer, heat and mass transfer in building materials and structures, pp 753–769
7. Myhren JA, Holmberg S (2009) Design considerations with ventilation-radiators: comparisons to traditional two-panel radiators. Energy Build 41:92–100
8. Vavricka R, Basta J (2001) Temperature fields of radiators. Department of Environmental Czech Technical University in Prague, Faculty of Mechanical Engineering, Prague
9. Gritzki R, Perschk A, Rösler M, Richter W, Dresden TU (2007) Modeling of heating systems and radiators in combined simulations. In: Proceedings of Clima 2007 wellbeing indoors, Germany
10. Beck SMB, Grinsted SC, Blakey SG, Worden K (2004) A novel design for panel radiators. Appl Therm Eng 24:1291–1300
11. Akın D (November 2007) Computer aided design of thermal systems. İzmir
12. Pillutla G, Mishra R, Barrans S (2008) Determination of convective heat transfer over a standalone water filled radiator using thermal imaging. In: School of Computing and Engineering Researchers' conference, University of Huddersfield, November 2008
13. Bangert K (2010) Radiator heat transfer augmentation by changes to wall surface roughness and emissivity. Mini-project report, University of Sheffield, EPSRC Pioneering Research and Skills
14. Aydar E (2009)The estimation of the thermal efficiency of panel type radiators by CFD analysis and an alternative design research to increase efficiency. Yüksek Lisans Tezi, Marmara Üniversitesi, Makine Mühendisliği Bölümü
15. Erdoğmuş AB (2011) Simulation of the heater test room defined by EN 442 standard and virtual testing of different type of heaters. Graduate School of Engineering and Sciences of İzmir Institute of Technology, İzmir
16. Akın D (2007) Computer aided design of thermal systems. Graduate School of Natural and Applied Sciences of Dokuz Eylül University, Degree of Master of Science in Mechanical Engineering, Energy Program
17. Myhren JA (2011) Potential of ventilation radiators: performance assessment by numerical, analytical and experimental investigations. Royal Institute of Technology, Department of Civil and Architectural Engineering, School of Architecture and the Built Environment, Fluid and Climate Technology, Haninge
18. Fluent 6 (2001) User's guide. Fluent Inc, Lebanon
19. Fluent 6.2 (2003) UDF manual. Fluent Inc, Lebanon
20. Churchill SW, Chu HHS (1975) Correlating equations for laminar and turbulent free convection from a vertical plate. Int J Heat Mass Transf 18:1323–1329

Combined Effect of Viscous Dissipation on the Coupling of Conduction and Mixed Convection Along a Vertical Slender Hollow Cylinder

Ahmet Kaya and Orhan Aydin

Abstract

An analysis is presented to investigate the influences of viscous dissipation and Joule heating in the entire thermo-fluid dynamic field resulting from the coupling of bouncy forced flow with conduction along one side of a heated/cooled vertical slender hollow cylinder. The governing equations are transformed into dimensionless non-similar equations by using a set of suitable transformations. The non-similar solutions using the Keller box method are obtained. The wall conduction parameter, the buoyancy parameter, the viscous dissipation parameter and the magneto-hydrodynamic parameter are the main parameters. For various values of these parameters the local skin friction and local heat transfer parameters are determined. The validity of the methodology is checked by comparing the results with these available in the open literature and a fairly good agreement is observed.

Keywords

Vertical slender hollow cylinder • Conjugate heat transfer • Buoyancy effect • Viscous dissipation • Joule heating

Introduction

The interaction between the conduction inside and the buoyancy forced flow of fluid along a solid surface is termed as conjugate heat transfer process [1]. In many practical applications, such as heat exchangers, heaters, nuclear reactors, pipe insulation systems, etc., the effect of conduction within the solid wall is significant and must be taken into account. Hence, the analysis of this type of heat transfer mechanism possesses the necessary coupling of the conduction in the solid body and the convection in the fluid surrounding it [2, 3].

The conjugate heat transfer problem, in which the coupled heat transfer processes between the solid body (conduction mechanisms) and the fluid flow (convection mechanisms) are considered simultaneously, has been investigated by several researchers. Mamun et al. [1] investigated the heat generation effect on natural convection flow along and conduction inside a vertical flat plate. Miyamoto et al. [4] studied two-dimensional conjugate heat transfer problems of free convection from a vertical flat plate with a uniform temperature or a uniform heat flux at the outside surface of the plate. Sparrow and Chyu [5] investigated the conjugate problem for a vertical plate fin with various heat transfer coefficients under forced convection. They assumed that the heat conduction in the fin was to be one-dimensional. Hossain [6] studied the effect of viscous and Joule heating on the flow of an electrically conducting fluid past a semi-infinite plate of which temperature varies linearly with the distance from the leading edge and in the presence of a uniformly transverse magnetic field. Na [7] investigated the effect of wall conduction on the heat transfer characteristics of the natural convection over a vertical slender hollow circular cylinder. Wang [8] studied the

A. Kaya (✉)
Department of Mechanical Engineering, Kahramanmaras Sutcu Imam University, 46100 Kahramanmaras, Turkey
e-mail: kaya38@ksu.edu.tr

O. Aydin
Department of Mechanical Engineering, Karadeniz Technical University, 61080 Trabzon, Turkey
e-mail: oaydin@ktu.edu.tr

thermo-fluid-dynamic field resulting from the coupling of wall conduction with laminar mixed convection heat transfer of micropolar fluids along a vertical flat plate. Shu and Pop [9] investigated the conjugate heat transfer across a vertical finite wall separating two forced and free convection flows at different temperatures. They assumed that the heat conduction in the wall was only in the transversal direction. Pop and Na [10] reported a numerical study of the steady conjugate-free convection over a vertical slender hollow circular cylinder with the inner surface at a constant temperature and embedded in a porous medium. Vaszi et al. [11] investigated two-dimensional conjugate-free convection from an inclined flat plate in a semi-infinite porous medium under the boundary layer approximation. Jilani et al. [12] investigated the conjugate heat transfer in a heat generating vertical cylinder washed by a laminar-forced convection boundary layer. El-Amin [13] analyzed the influences of both first and second order resistance, due to the solid matrix of non-Darcy porous medium, Joule heating and viscous dissipation on forced convection flow from a horizontal circular cylinder under the action of a transverse magnetic field. Chang [2, 14] presented a numerical analysis of the flow and heat transfer characteristics of forced and natural convection in a micropolar fluid flowing along a vertical, slender, hollow, and circular cylinder with wall conduction and buoyancy effects. Chang [15] presented a numerical analysis of the flow and heat transfer characteristics of mixed convection in a micropolar fluid flowing along a vertical flat plate with conduction effects. It is assumed that the heat conduction in the wall was only in the transversal direction. Jahangeer et al. [16] investigated the conjugate heat transfer problem pertinent to the rectangular fuel element of a nuclear reactor dissipating heat into an upward moving stream of liquid sodium. Hsiao [17] studied a radiative and viscous dissipation effect conjugate heat transfer problem of a second-grade viscoelastic fluid past a stretching sheet. Alim et al. [18] investigated the influences of viscous dissipation and Joule heating in the entire thermo-fluid dynamic field resulting from the coupling of bouncy forced flow with conduction along one side of a heated flat plate. Hsiao and Hsu [19] studied a conjugate mixed convection heat transfer problem of a second-grade visco-elastic fluid past a horizontal flat-plate fin. Kaya [3, 20] studied steady laminar magneto-hydrodynamic (MHD) mixed convection heat transfer about a vertical slender hollow cylinder under the effect of wall conduction for pure and porous medium.

In the present paper, the studies of the conjugate effects of viscous dissipation and Joule heating on the coupling of conduction with mixed convection along a heated/cooled vertical slender hollow cylinder have been investigated. The boundary layer equations governing the flow are reduced to local non-similarity equations which are solved using the implicit finite difference method (Keller box). Variation in the fluid–solid interfacial temperature distribution, the local skin friction and local heat transfer parameters as well as the velocity and temperature profiles are presented to highlight the influence of the wall conduction, viscous dissipation, magneto-hydrodynamic and buoyancy parameters.

Analysis

This study considers the case of an MHD mixed convection flow past a vertical slender hollow circular cylinder of length L and outer radius r_o ($L \gg r_o$). Also, this study considered the case of a vertical slender hollow cylinder such that the heat conduction within the wall is one-dimensional [2, 15]. The physical model and coordinate system are shown in Fig. 56.1.

The gravitational acceleration, g, acts in the downward direction. The temperature and velocity of the fluid at a distance remote from the cylinder are given by T_∞ and u_∞, respectively. The temperature of the inside surface of the cylinder is maintained at a constant temperature of T_0, where $T_0 > T_\infty$. Other than the density variation, the remaining fluid properties are assumed to be constant. The temperature difference between the body surface and the surrounding fluid generates a buoyancy force, which results in an upward convective flow. A magnetic field of constant strength B_0 is applied in the negative r direction at all times. Its interaction with the electrically conducting working fluid produces a resistive force in the negative x direction. This force is called the Lorentz force. The magnetic Reynolds number is assumed to be small so that the induced magnetic field is neglected. Under foregoing assumptions and taking into account the Boussinesq approximation and the boundary layer approximation, the system of continuity, momentum and energy equations can be written [18, 21]:

$$\frac{\partial (ru)}{\partial x} + \frac{\partial (rv)}{\partial r} = 0 \tag{56.1}$$

$$u \frac{\partial u}{\partial x} + v \frac{\partial u}{\partial r} = \left(\frac{v}{r}\right) \frac{\partial}{\partial r} \left(r \frac{\partial u}{\partial r} \right) + g\beta(T - T_\infty) - \frac{\sigma B_0^2}{\rho}(u - u_\infty) \tag{56.2}$$
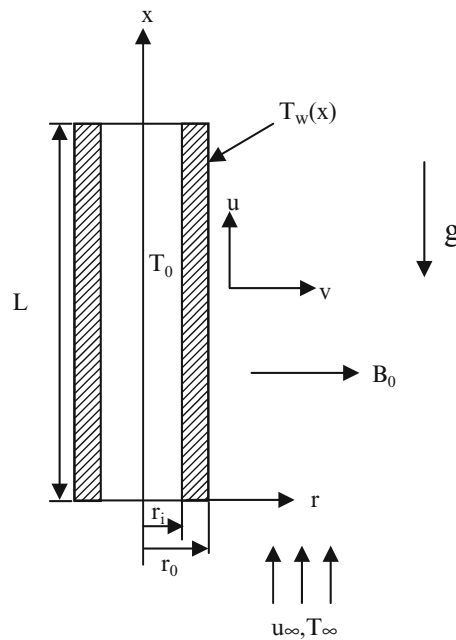
Fig. 56.1 The schematic of the problem

$$u\frac{\partial T}{\partial x} + v\frac{\partial T}{\partial r} = \frac{v}{\text{Pr}}\frac{1}{r}\frac{\partial}{\partial r}\left(r\frac{\partial T}{\partial r}\right) + \left(\frac{v}{c_p}\right)\left(\frac{\partial u}{\partial r}\right)^2 + \frac{\sigma B_0^2}{\rho c_p}\left(u^2 - u_\infty u\right) \tag{56.3}$$

The viscous dissipation and Joule heating term are included in the energy equation [Eq. (56.3)]. Here u and v are the velocity components in the x and r direction, respectively, T is the temperature of the fluid, β is the coefficient of thermal expansion, v is the kinematic viscosity, ρ is the fluid density, g is the acceleration due to gravity σ is the electrical conductivity of the fluid and B_0 is the magnetic flux density.

The boundary conditions are given by the following:

$$\begin{aligned}
r = r_0; &\quad u = v = 0, &\quad T = T_w(x) \\
r \to \infty; &\quad u \to u_\infty, &\quad T \to T_\infty
\end{aligned} \tag{56.4}$$

where subscripts w and ∞ refer to the wall and the boundary layer edge, respectively. In addition, $T_w(x)$ is the outer surface temperature of the cylinder, which is not known a priori. One of the objectives of the current study is to predict the outer surface temperature of the cylinder, $T_w(x)$. Therefore, an additional governing equation is required for the slender hollow cylinder based on the simplification that the wall of the cylinder steady transfers its heat to the surrounding fluid. Since the outer radius of the hollow cylinder, r_o, is small compared to its length, L, the axial conduction term in the heat conduction equation of the cylinder can be omitted [2, 7, 22]. The governing equation for the temperature distribution within the slender hollow circular cylinder is given by Chang [2] and Kaya [3] as follows:

$$\frac{1}{r}\frac{d}{dr}\left(r\frac{dT}{dr}\right)_s = 0; \qquad 0 \le x \le L; \qquad r_i < x \le r_0 \tag{56.5}$$

The boundary conditions for the wall of the cylinder are given:
At

$$r = r_i, \quad T_s = T_0, \tag{56.6a}$$

At the interface

$$(r = r_0), T_s = T(x, r_0): \quad -k_s \frac{dT}{dr}\bigg|_s = -k_f \frac{\partial T(x, r_0)}{\partial r}\bigg|_f \tag{56.6b}$$

where k_s and k_f are the thermal conductivity of the cylinder and the fluid, respectively. The boundary conditions given in Eq. (56.6b) state the physical requirements that the temperature and heat flux of the cylinder must be continuous across the solid–fluid interface. From Eqs. (56.5) and (56.6b), the temperature distribution T_w at the interface is derived as [2]:

$$T_w(x) = T(x, r_0) = r_0 \frac{K_f}{K_s} \ln\left(\frac{r_0}{r_i}\right) \frac{\partial T(x, r_0)}{\partial r} + T_0 \tag{56.7}$$

To seek a solution, the following dimensionless variables are introduced:

$$\xi = \frac{x}{r_0}, \quad \eta = \frac{1}{2x} \mathrm{Re}_x^{1/2} \left[\frac{r^2 - r_0^2}{r_0}\right], \quad \theta = \frac{T - T_\infty}{T_0 - T_\infty}, \quad \psi(x, r) = r_0 (vu_\infty x)^{1/2} f(\xi, \eta) \tag{56.8}$$

where $\psi(x, y)$ is the free stream function that satisfies Eq. (56.1) with $u = (1/r)(\partial\psi/\partial r)$ and $v = -(1/r)(\partial\psi/\partial x)$

In terms of these new variables, the velocity components can be expressed as

$$u = u_\infty f', \quad v = \frac{r_0}{r} \left(\frac{vu_\infty}{x}\right)^{1/2} \left[\eta f' - \frac{1}{2}f - \xi \frac{\partial f}{\partial \xi}\right] \tag{56.9}$$

The transformed momentum and energy equations together with the boundary conditions, Eqs. (56.2)–(56.4), can be written as

$$(1 + \lambda\eta)f''' + \lambda f'' + \frac{1}{2}ff'' + Ri\xi\theta - Mn\xi\left(f' - 1\right) = \xi\left[f' \frac{\partial f'}{\partial \xi} - f'' \frac{\partial f}{\partial \xi}\right] \tag{56.10}$$

$$\frac{1}{\mathrm{Pr}}(1 + \lambda\eta)\theta'' + \frac{\lambda}{\mathrm{Pr}}\theta' + \frac{1}{2}f\theta' + Ec(1 + \lambda\eta)\left(f''\right)^2$$
$$+ MnEc\,\xi f'\left(f' - 1\right) = \xi\left[f' \frac{\partial\theta}{\partial\xi} - \theta' \frac{\partial f}{\partial\xi}\right] \tag{56.11}$$

with the boundary conditions;

$$\eta = 0; \quad f + 2\xi\frac{\partial f}{\partial\xi} = 0, \quad f' = 0, \quad \theta - 1 = p\xi^{-1/2}\theta'$$

$$\eta \to \infty; \quad f' = 1, \quad \theta = 0 \tag{56.12}$$

where

$$p = \frac{k_f}{k_s} \ln\left(\frac{r_0}{r_i}\right) \mathrm{Re}^{1/2}$$

is the conjugate heat transfer parameter. It should be noticed that for the limiting case of $p = 0$, the thermal boundary condition in Eq. (56.12) on the wall becomes isothermal. Intuitively, if the heat conductivity of the hollow cylinder is very large, its temperature can be expected to be approximately uniform at T_0. Hence, the magnitude of p determines the importance of the wall heat conduction effect [2, 3].

The corresponding dimensionless groups that appeared in the governing equations were defined as:

$$\text{Pr} = \frac{\mu c_p}{k} = \frac{v}{\alpha}, \quad Ri = \frac{Gr}{\text{Re}^2}, \quad Gr = \frac{g\beta(T_0 - T_\infty)r_0^3}{v^2}, \quad \text{Re} = \frac{u_\infty r_0}{v},$$

$$Mn = Ha/\text{Re}, \quad Ha = \frac{\sigma B_0^2 r_0^2}{\mu}, \quad \lambda = 2\left(\frac{\xi}{\text{Re}}\right)^{1/2}, \quad Ec = \frac{u_\infty^2}{c_p(T_0 - T_\infty)}$$

(56.13)

where Pr is the Prandtl number, Ri is the Richardson number, Gr is the Grashof number, Re is the Reynolds number, Mn is the magnetic parameter, Ha is the Hartman number, λ is the transverse curvature parameter and Ec is the Eccert number.

The dimensionless interfacial temperature distribution θ_w, is defined as follows [14, 15].

$$\theta_w = \frac{T_w - T_\infty}{T_0 - T_\infty}$$

(56.14)

Numerical Solution

The system of transformed equations under the boundary conditions, Eqs. (56.10)–(56.12), have been solved numerically using the Keller box scheme, which is proved to be an efficient and accurate finite-difference scheme [23]. Readers are referred to Cebeci and Bradshaw [23] for the details of the numerical methods. This is a very popular implicit scheme, which demonstrates the ability to solve systems of differential equations of any order as well as featuring second-order accuracy (which can be realized with arbitrary non-uniform spacing), allowing very rapid x or ξ variations [20, 24].

A set of nonlinear finite-difference algebraic equations derived are then solved by using the Newton quasi-linearization method. The same methodology as that followed by Takhar and Beg [24] is followed. Therefore, for the finite-difference forms of the equations, the reader is referred to Takhar and Beg [24] for the brevity of the article.

In the calculations, a uniform grid of the step size 0.01 in the η-direction and a non-uniform grid in the ξ-direction with a starting step size 0.001 and an increase of 0.1 times the previous step size were found to be satisfactory in obtaining sufficient accuracy within a tolerance better than 10^{-6} in nearly all cases. The value of $\eta_\infty = 16$ is shown to satisfy the velocity to reach the relevant stream velocity [20].

In order to verify the accuracy of the present method, the present results were compared with those of Chang [2], Chen and Mucoglu [25] and Takhar et al. [26]. The comparison is found to be in good agreement, as shown in Table 56.1.

Table 56.1 Comparison of the local skin friction and local heat transfer parameters with Pr = 0.7, Ri = 0.0, Mn = 0.0, Ec = 0.0 and p = 0.0

$\xi = \frac{4}{r_0}\left(\frac{vx}{u_\infty}\right)^{1/2}$	Chen and Mucoglu [25]		Takhar et al. [26]		Chang [2]		Present study	
	$f''(\xi,0)$	$-\theta'(\xi,0)$	$f''(\xi,0)$	$-\theta'(\xi,0)$	$f'(\xi,0)$	$-\theta'(\xi,0)$	$f'(\xi,0)$	$-\theta'(\xi,0)$
0.0	1.3282	0.5854	1.3281	0.5854	1.3280	0.5852	1.3201	0.5846
1.0	1.9172	0.8669	1.9167	0.8666	1.9133	0.8658	1.8934	0.8599
2.0	2.3981	1.0986	2.3975	1.0963	2.3900	1.0940	2.3822	1.0918
3.0	2.8270	1.3021	–	–	2.8159	1.2982	2.8098	1.2902
4.0	3.2235	1.4921	–	–	3.2187	1.4925	3.2102	1.4898
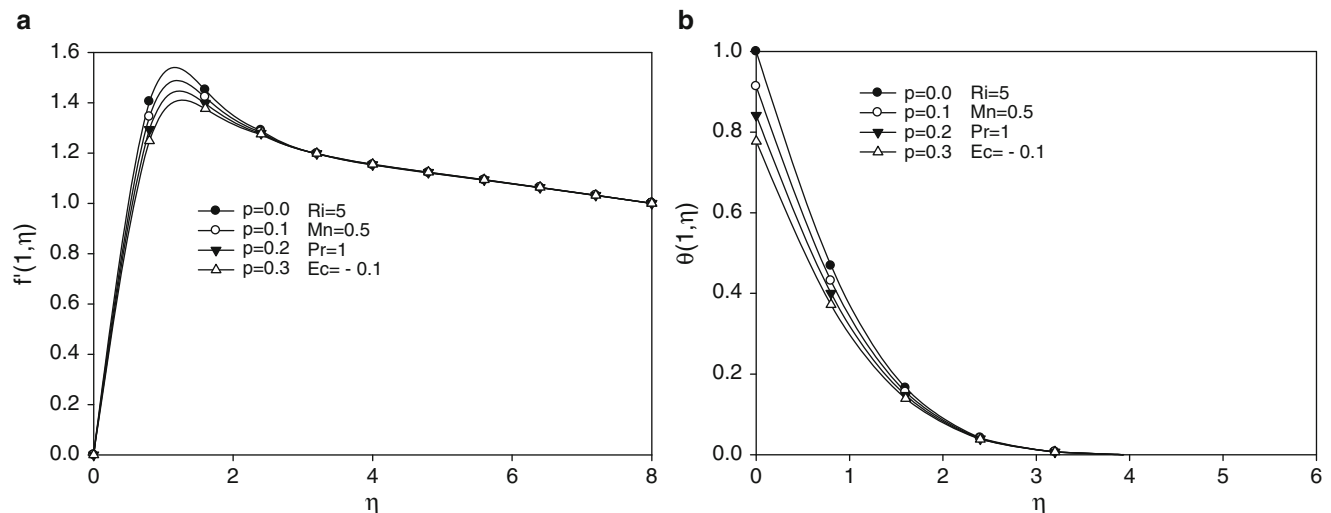
Fig. 56.2 Dimensionless velocity (**a**) and temperature (**b**) profiles for different p while Pr $= 1.0$, Ri $=5$, Mn $= 0.5$, Ec $= -0.1$ and $\xi = 1.0$

Results and Discussion

The aim of this study was to investigate the flow and heat transfer characteristics for the mixed convection flow along a vertical slender hollow cylinder with wall conduction effect, taking into account the effects of Ohmic heating and viscous dissipation. The following ranges of the main parameters are considered: Ri $= 0.0$, 1.0, 5.0 and 10.0; Ec $= -0.1$, 0.0 and 0.1; Mn $= 0.0$, 0.5, 1.0 and 2.0 and Pr $= 1.0$. Hence, the numerical computations were performed with Re $= 250$ [2, 3, 20]. The conjugate heat transfer parameter, p, is ranged 0.0–0.3 to conform to the practical cases. For example, the fluid (for water: $k_f = 0.628$ W/m K) flows along a slender stainless steel tube with $r_o = 0.03$ m, $r_i = 0.02$ m and $k_s = 15$ W/m K, we can find the conjugate heat transfer parameter p $= 0.27$ [2].

The combined effects of p, Ri, Mn and Ec on the momentum and heat transfer are analyzed. The Richardson number, Ri represents a measure of the effect of the buoyancy in comparison with that of the inertia of the external forced or free stream flow on the heat and fluid flow. Outside the mixed convection region, either the pure forced convection or the free convection analysis can be used to describe accurately the flow or the temperature field. Forced convection is the dominant mode of transport when Ri $\rightarrow 0$, whereas free convection is the dominant mode when Ri $\rightarrow \infty$. Buoyancy forces can enhance the surface heat transfer rate when they assist the forced convection [20]. Viscous dissipation, as an energy source, severely distorts the temperature profile. Remember positive values of Ec correspond to wall heating (heat is being supplied across the walls into the fluid) case ($T_0 > T_\infty$), while the opposite is true for negative values of Ec [27].

The effect of conjugate heat transfer parameter p on the velocity (a) and temperature (b) profiles within the boundary layer with Ri $= 5.0$, Ec $= -0.1$, Mn $= 0.5$ and Pr $= 1.0$ is shown in Fig. 56.2a, b, respectively. The increasing of the conjugate heat transfer parameter decreases velocity and temperature gradients at the wall. A lower wall conductance k_s or higher convective cooling effect due to greater k_f increases the value of p as well as causes greater temperature difference between the two surfaces of the cylinder. The temperature at the solid–fluid interface is reduced since the temperature at the outside surface of the cylinder is kept constant [3].

The variation of the interfacial temperature, the local skin friction and the local heat transfer parameters for different values of p with ξ are shown in Fig. 56.3a–c, respectively where Ri $= 5.0$, Mn $= 0.5$, Ec $= -0.1$ and Pr $= 1.0$. It can be seen that the temperature of the fluid on the wall increases monotonically with ξ for a given value of p (Fig. 56.3a). Comparing this with an isothermal cylinder (p $= 0$), an increase in the conjugate heat transfer parameter, p, causes a reduction in the interfacial temperature. This is because an increased value of p corresponds to a lower wall conductance, k_s, and promotes a greater surface temperature variation (Fig. 56.3a). The increased value of p increases the momentum and thermal boundary layer thickness and therefore the local skin friction and the local heat transfer parameters decrease as shown in Fig. 56.3b, c. Also, increasing the streamwise direction ξ increases the interfacial temperature, the local skin friction and the local heat transfer parameters (Fig. 56.3a–c). Similar results were found in the literature [2, 3, 15, 20].

Figure 56.4 shows the effects of *Ec* on the dimensionless velocity and temperature profiles for the cases of an isothermal cylinder (p $= 0$) and a non-isothermal cylinder (p $= 0.2$). For a positive value of *Ec*, since the temperature of the wall is greater than that of the free stream, there will be a heat transfer from the wall to the fluid. The viscous dissipation will cause
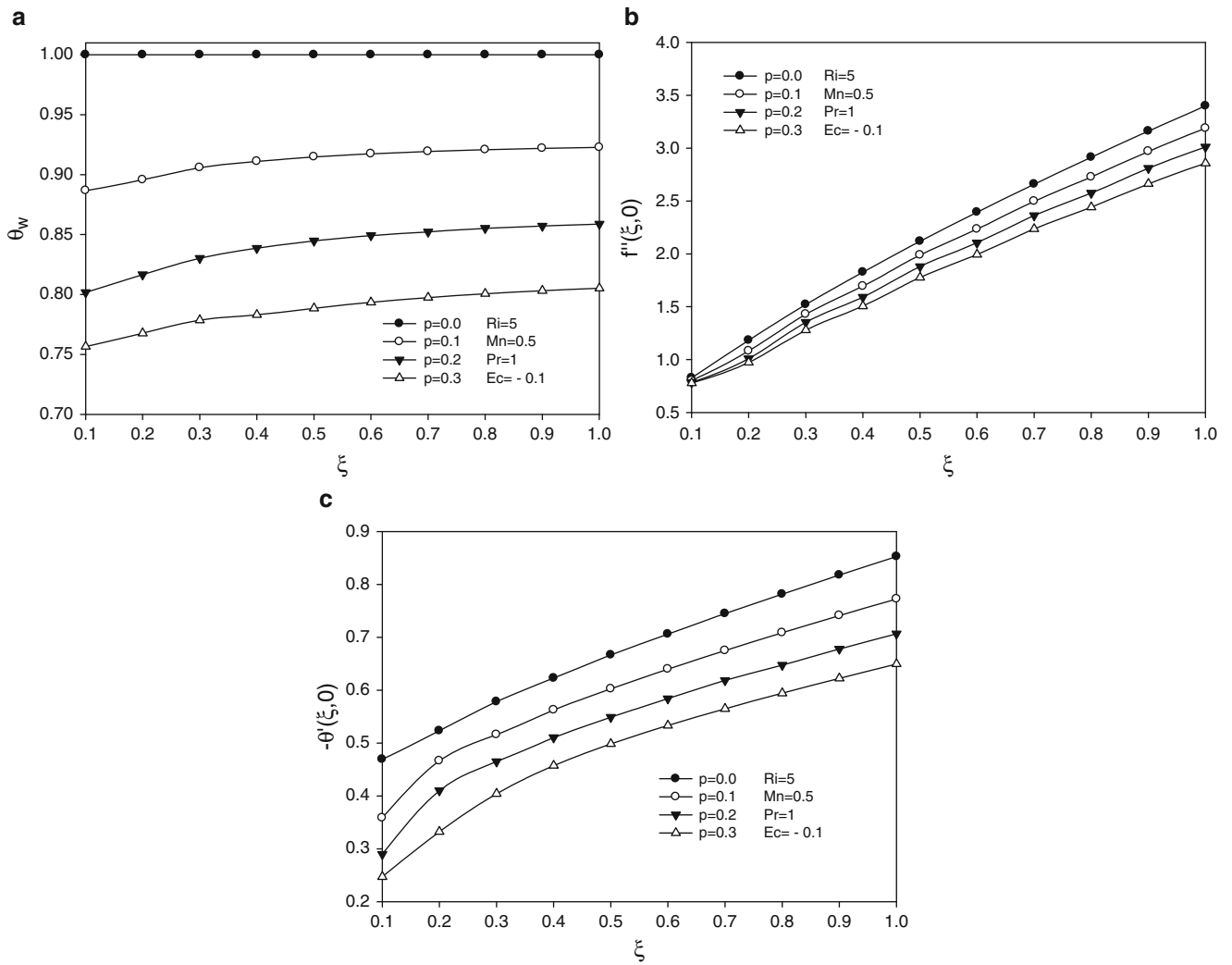
Fig. 56.3 Effect of conjugate heat transfer parameter p on the dimensionless interfacial temperature (**a**), local skin friction (**b**) and local heat transfer (**c**) parameters against the stream-wise direction ξ while Pr = 1.0, Ri = 5, Mn = 0.5 and Ec = −0.1
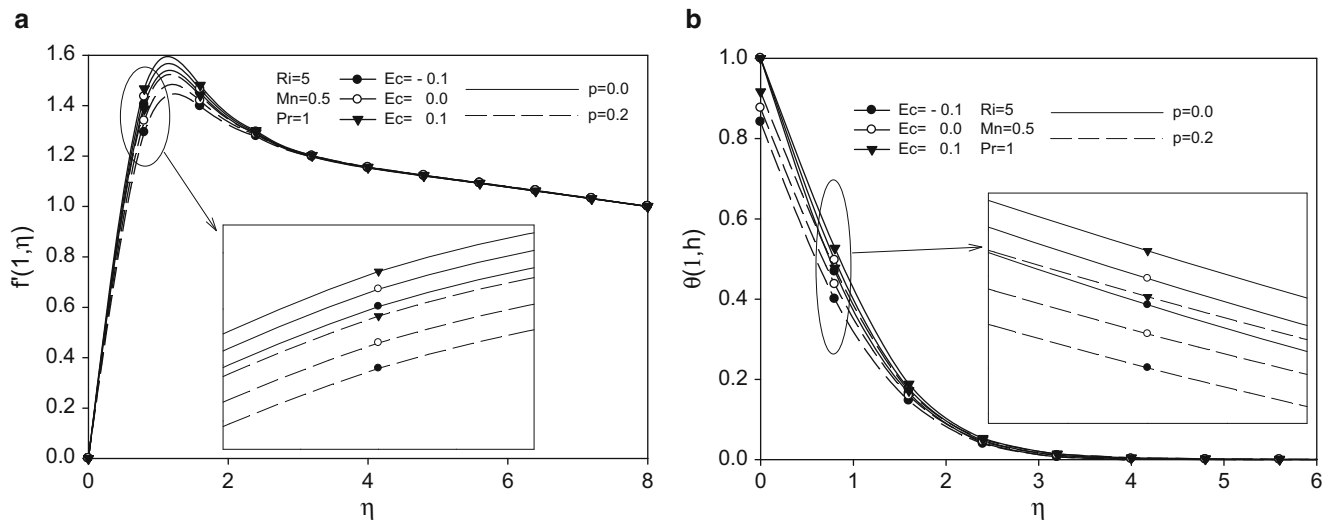
Fig. 56.4 Dimensionless velocity (**a**) and temperature (**b**) profiles for different Ec while Ri = 5, Pr = 1.0, Mn = 0.5 and ξ = 1.0 for isothermal (p = 0) and non isothermal plate (p < 0)

a

b

c
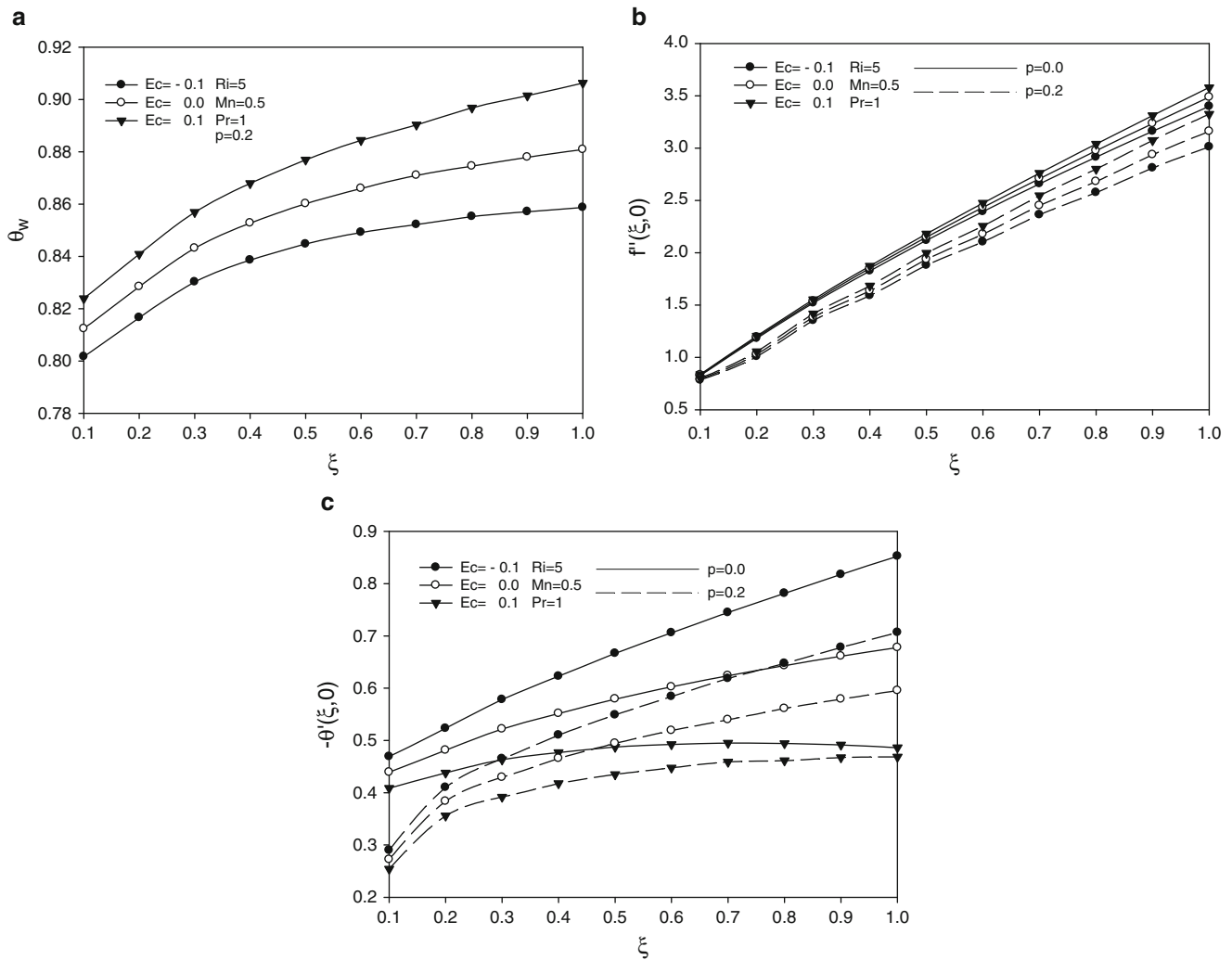
Fig. 56.5 Effect of Ec on the dimensionless interfacial temperature (**a**), local skin friction (**b**) and local heat transfer (**c**) parameters against the stream-wise direction ξ while Ri = 5, Pr = 1.0 and Mn = 0.5 for isothermal (p = 0) and non isothermal plate (p < 0)

a heat generation inside the fluid, which results in an increase in the temperature distribution and a decrease in the velocity distribution in the flow region. This is due to the fact that heat energy is stored in the fluid due to frictional heating. Due to the increased bulk fluid temperature, the temperature gradient will decrease. For a negative value of Ec, since $T_o < T_\infty$, the viscous dissipation will increase the temperature distribution in the flow region more. Finally, this leads to an increased temperature gradient, as will be shown later, which will result in increased heat transfer values. As it can be noticed from Fig. 56.4, the effect of Ec intensifies downstream [27].

Figure 56.5 shows the variation of the interfacial temperature, the local skin friction and the local heat transfer parameters for different values of Ec with ξ are shown in Fig. 56.5a–c, respectively where Ri = 5.0, Mn = 0.5 and Pr = .0 for isothermal cylinder (p = 0) and non-isothermal cylinder (p = 0.2).

Increasing the Ec decreases the interfacial temperature and the local skin friction whereas increases the local heat transfer parameter. Also, both the local skin friction and the local heat transfer parameters decrease for non-isothermal wall cases (Fig. 56.5a–c).

Figure 56.6 shows the dimensionless velocity (a) and temperature (b) profiles inside the boundary layer for different values of the buoyancy parameter Ri for the cases of an isothermal cylinder (p = 0) and a non-isothermal cylinder (p = 0.2). The increasing of Ri increases velocity and temperature gradients at the wall. And also, increasing the conjugate heat transfer parameter decreases the velocity and temperature profiles in the boundary layer.

The variation of the dimensionless interfacial temperature distributions, the local skin friction and the local heat transfer parameters as a function of ξ in the boundary layer are shown in Fig. 56.7a–c, respectively. It can be seen that as the values of
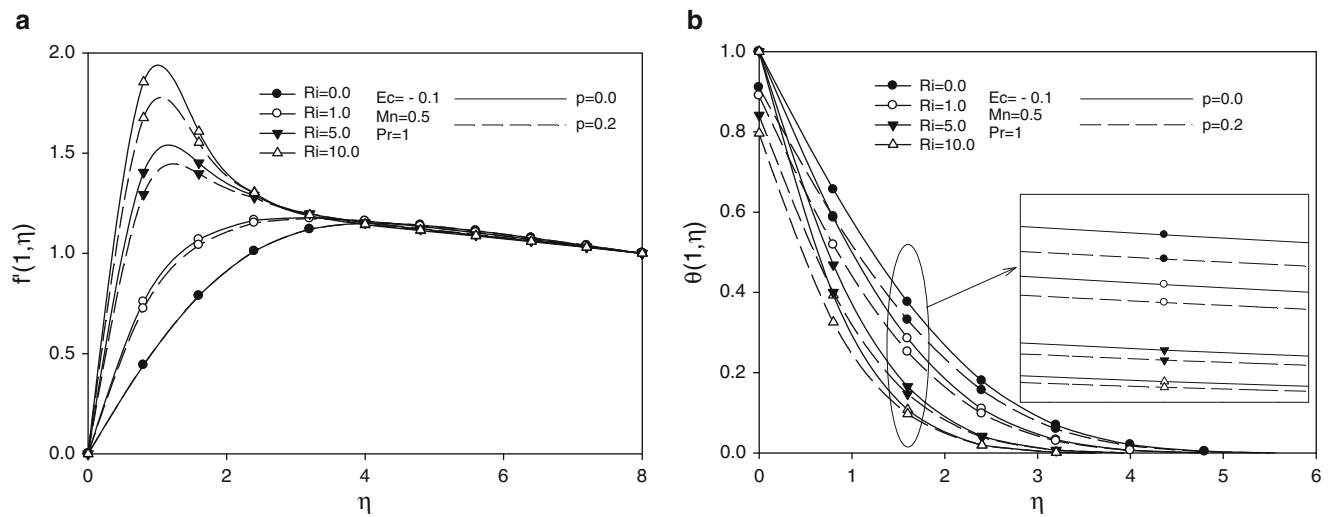
Fig. 56.6 Dimensionless velocity (**a**) and temperature (**b**) profiles for different Ri while Ec = −0.1, Pr = 1.0, Mn = 0.5 and ξ = 1.0 for isothermal (p = 0) and non-isothermal plate (p < 0)
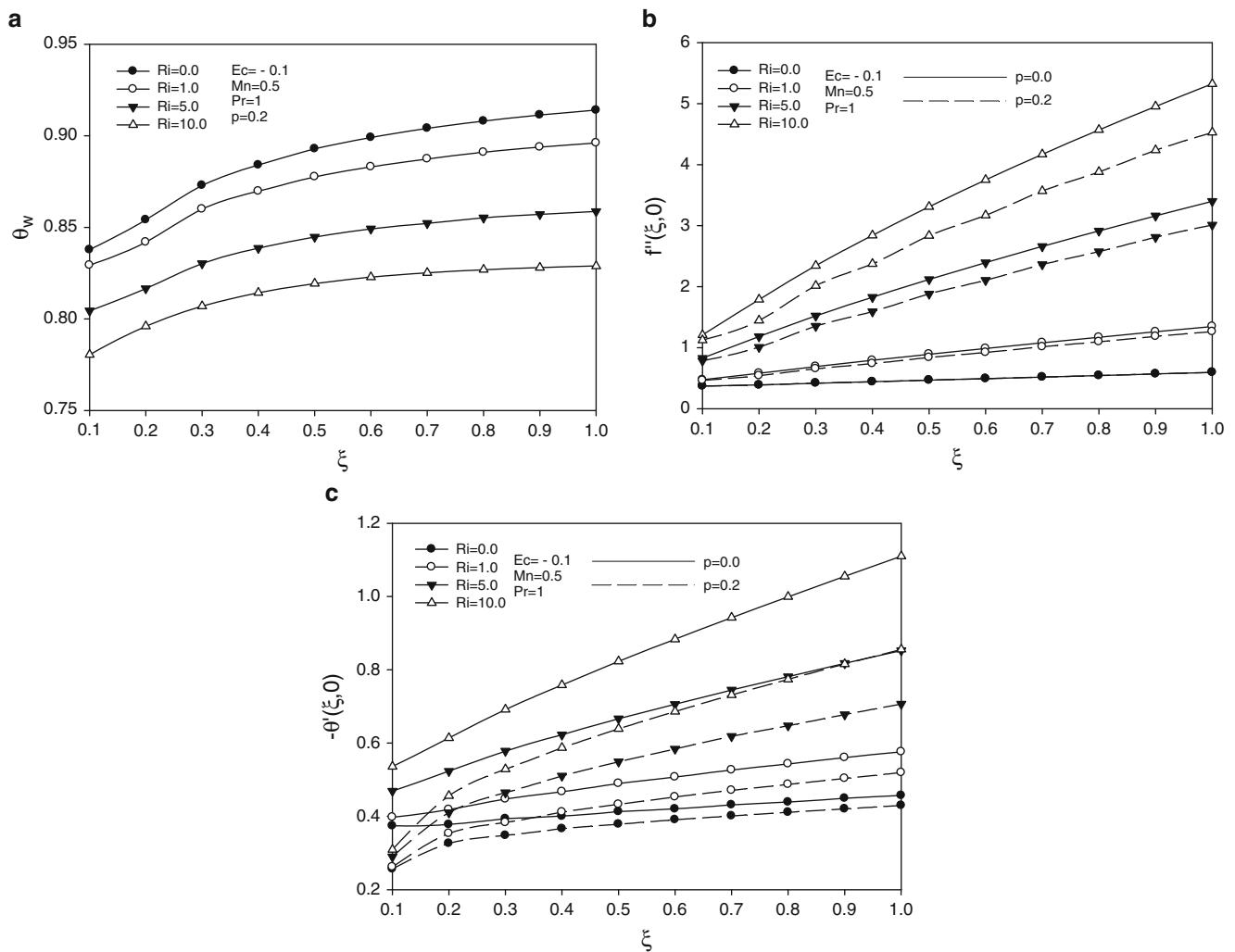
Fig. 56.7 Effect of Ri on the dimensionless interfacial temperature (**a**), local skin friction (**b**) and local heat transfer (**c**) parameters against the stream-wise direction ξ while Ec = −0.1, Pr = 1.0 and Mn = 0.5 for isothermal (p = 0) and non-isothermal plate (p < 0)
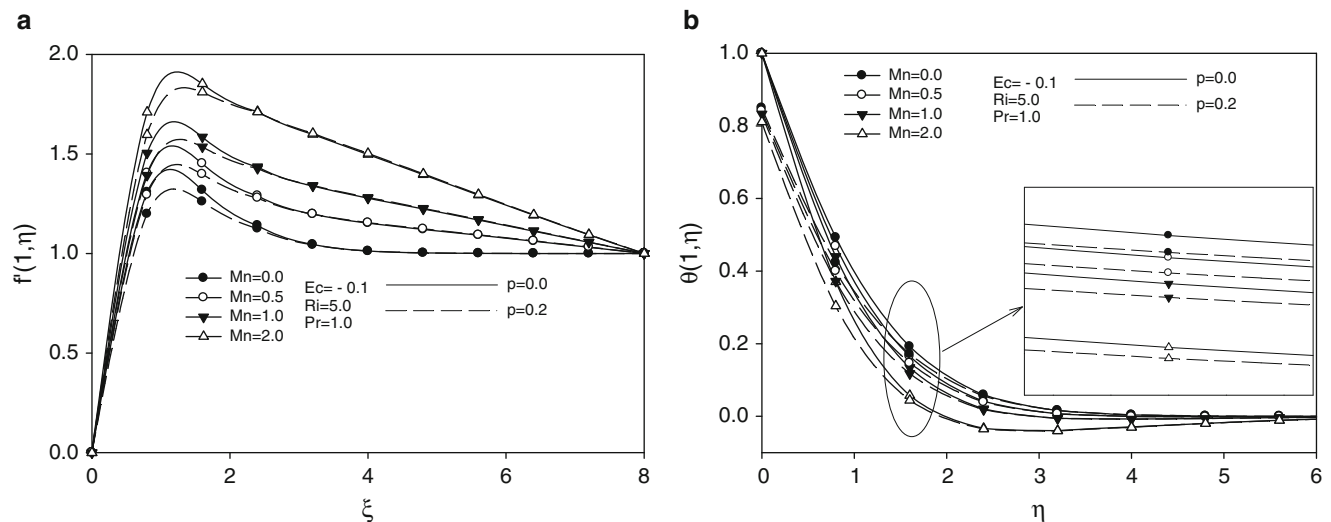
Fig. 56.8 Dimensionless velocity (**a**) and temperature (**b**) profiles for different Mn while Ec $= -0.1$, Pr $= 1.0$, Ri $= 5$ and $\xi = 1.0$ for isothermal ($p = 0$) and non-isothermal plate ($p < 0$)

ξ increases, the interfacial temperature rises, i.e., the interfacial temperature increases from the bottom of the cylinder towards the top of the cylinder. Compared with the limiting case of Ri $= 0$ (i.e., pure forced convection), an increase in the value of Ri gives rise to a reduced interfacial temperature since a greater value of Ri indicates a greater buoyancy effect, which increases the convection cooling effect and hence reduces the wall temperature (Fig. 56.7a). Figure 56.7b illustrates the effect of the buoyancy force on the local skin friction factor for $p = 0$ (dashed lines) and 0.2 (solid lines). It is observed that the local skin friction factor increases with the buoyancy effect. The reason for this is that an increase in the buoyancy effect in mixed convection flow leads to an acceleration of the fluid flow, which increases the local skin friction factor. Additionally, the higher the value of the buoyancy effect, the more the sensitivity of the wall conduction effects that influence the skin friction factor. In the limiting case of Ri $= 0$, i.e., pure forced convection with no buoyancy effects, the conjugate heat transfer parameter, p, is virtually independent of the skin friction factor because the buoyancy effect generated by the temperature difference is relatively weaker. In Fig. 56.7c, the effect of the buoyancy force on the local heat transfer parameter is illustrated. It is noted that as the value of the Ri increases, the local heat transfer parameter also increases, both for the case of an isothermal cylinder (dashed lines) and a non-isothermal cylinder (solid lines). This is because an increased buoyancy effect generates a greater buoyancy force, which increases the fluid velocity, and hence raises the local heat transfer parameter [15, 20].

Figure 56.8 shows the dimensionless velocity (a) and temperature (b) profiles inside the boundary layer for different values of the magnetic parameter Mn for the cases of isothermal cylinder ($p = 0$) and non-isothermal cylinder ($p = 0.2$). The increasing of the magnetic parameter Mn increases velocity and temperature gradients at the wall. As mentioned above, increasing the conjugate heat transfer parameter p decreases velocity and temperature gradients at the wall.

The variations of the dimensionless interfacial temperature distributions, the local skin friction and the local heat transfer parameters as a function of ξ in the boundary layer for different magnetic parameters are shown in Fig. 56.9a–c, respectively. Increasing the magnetic parameter Mn decreases the interfacial temperature (Fig. 56.9a). The local skin friction and the local heat transfer parameters with different values of Mn for an isothermal cylinder ($p = 0$) and a non-isothermal cylinder ($p = 0.2$) are illustrated in Fig. 56.9b, c. The magnetic force aids the flow and increases the local skin friction (i.e., shear stress) and the local heat transfer (i.e., heat transfer rate) parameters at the wall.
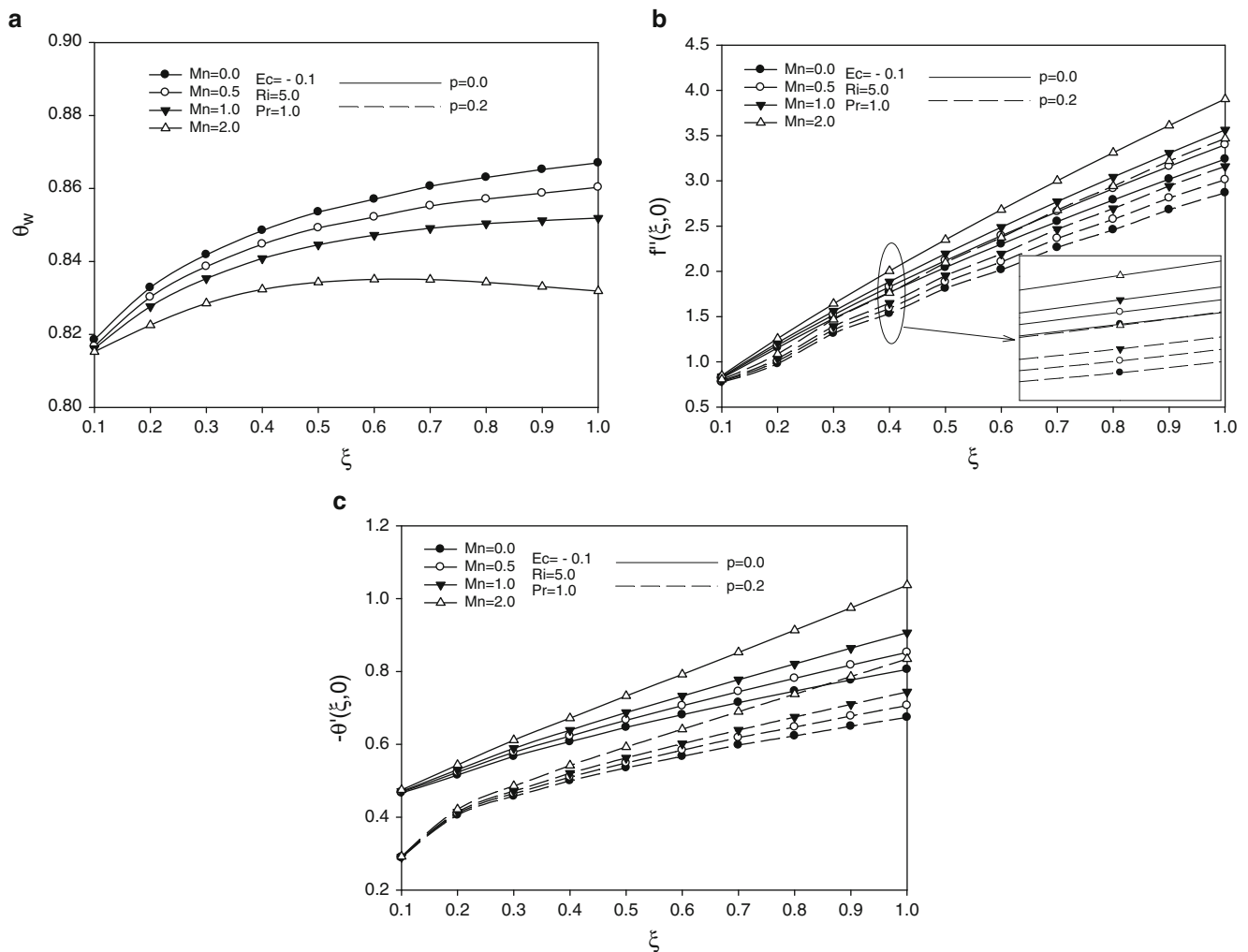
Fig. 56.9 Effect of Mn on the dimensionless interfacial temperature (**a**), local skin friction (**b**) and local heat transfer (**c**) parameters against the stream-wise direction ξ while Ec = −0.1, Pr = 1.0, Ri = 5 for isothermal (p = 0) and non-isothermal plate (p < 0)

Conclusions

This study has analyzed the influences of viscous dissipation and Joule heating in the entire thermo-fluid dynamic field resulting from the coupling of bouncy forced flow with conduction along one side of a heated/cooled vertical slender hollow cylinder. The nonlinear formulation governing equations and their associated boundary conditions have been obtained and solved using the non-similarity transform and the finite difference method (Keller box), respectively. The influences of the conjugate heat transfer parameter, the viscous dissipation parameter, the Richardson number and the magnetic parameter on the solid–liquid interfacial temperature distribution, the local skin friction and the local heat transfer parameters have been systematically examined. From the present numerical investigation, the following conclusions can be drawn:

1. An increase in the conjugate heat transfer parameter decreases the velocity and the temperature gradient and therefore decreases the dimensionless interfacial temperature distribution, the local skin friction and the local heat transfer parameters.
2. An increase in the magnetic and buoyancy parameters increases the local skin friction and local heat transfer parameters and decreases the dimensionless interfacial temperature distributions. Increasing Mn and Ri decreases the velocity and temperature gradients at the wall for a non-isothermal cylinder (i.e., p > 0).
3. An increase in the viscous dissipation parameter increases the local skin friction and the dimensionless interfacial temperature distributions and decreases the local heat transfer parameter.

Nomenclature

c_p	Specific heat of the convective fluid	p	Conjugate heat transfer parameter
Ec	Eccert number	Pr	Prandtl number
G	Gravitational acceleration	r_i r_o	Inner and outer radii of the hollow cylinder
Gr	Grashof number	Re	Reynolds number
F	Dimensionless stream function	Ri	Richardson number
Ha	Hartman number	T	Temperature
K	Thermal conductivity	T_0	Temperature of the inside surface of the cylinder
L	Length of the cylinder	u, v	Velocities in x and r directions, respectively
Mn	Magneto-hydrodynamic parameter	x, r	Coordinates in axial and radial directions respectively

Greek Symbols

η	Similarity variable	M	Dynamic viscosity
Λ	Transverse curvature	U	Kinematic viscosity
ξ	Dimensionless streamwise coordinate	Θ	Dimensionless temperature profile in Eq. (56.8)
ρ	Fluid density	θ_w	Dimensionless interface temperature in Eq. (56.14)

Subscripts

F	Condition in the fluid	W	Wall
S	Condition in the wall of cylinder	∞	Free stream

References

1. Mamun AA, Chowdhury ZR, Azim MA, Maleque MA (2008) Conjugate heat transfer for a vertical flat plate with heat generation effect. Nonlinear Anal Model Control 13(2):213–223
2. Chang L (2006) Buoyancy and wall conduction effects on forced convection of micropolar fluid flow along a vertical slender hollow circular cylinder. Int J Heat Mass Transf 49:4932–4942
3. Kaya A (2011) The effect of conjugate heat transfer on MHD mixed convection about a vertical slender hollow cylinder. Commun Nonlinear Sci Numer Simul 16:1905–1916
4. Miyamoto M, Sumikawa J, Akiyohi T, Nakamura T (1980) Effects of axial heat conduction in a vertical flat plate on free convection heat transfer. Int J Heat Mass Transf 23:1545–1553
5. Sparrow EM, Chyu MK (1982) Conjugated forced convection–conduction analysis of heat transfer in a plate fin. ASME J Heat Transf 104:204–206
6. Hossain MA (1992) Viscous and Joule heating effects on MHD-free convection flow with variable plate temperature. Int J Heat Mass Transf 35:3485–3487
7. Na TY (1995) Effect of wall conduction on natural convection over a vertical slender hollow circular cylinder. Appl Sci Resource 54:39–50
8. Wang TY (1998) The coupling of conduction with mixed convection of micropolar fluids past a vertical flat plate. Int Commun Heat Mass Transf 25(8):1075–1084
9. Shu JJ, Pop I (1999) Thermal interaction between free convection and forced convection along a vertical conducting wall. Heat Mass Transf 35:33–38
10. Pop I, Na Y (2000) Conjugate free convection over a vertical slender hollow cylinder embedded in a porous medium. Heat Mass Transf 36:375–379
11. Vaszi AZ, Ingham DB, Lesnic D, Munslow D, Pop I (2001) Conjugate free convection from a slightly inclined plate embedded in a porous medium. Z Angew Math Mech 81(7):465–479
12. Jilani G, Jayaraj S, Ahmadi MA (2002) Conjugate forced convection-conduction heat transfer analysis of a heat generating vertical cylinder. Int J Heat Mass Transf 45:331–341
13. El-Amin MF (2003) Combined effect of viscous dissipation and Joule heating on MHD forced convection over a non isothermal horizontal cylinder embedded in a fluid saturated porous medium. J Magn Magn Mater 263:337–343
14. Chang CL (2008) Numerical simulation for natural convection of micropolar fluids flow along slender hollow circular cylinder with wall conduction effect. Commun Nonlinear Sci Numer Simul 13:624–636
15. Chang CL (2006) Numerical simulation of micropolar fluid flow along a flat plate with wall conduction and buoyancy effects. J Phys D Appl Phys 39:1132–1140
16. Jahangeer S, Ramis MK, Jilani G (2007) Conjugate heat transfer analysis of a heat generating vertical plate. Int J Heat Mass Transf 50:85–93

17. Hsiao KL (2007) Conjugate heat transfer of magnetic mixed convection with radiative and viscous dissipation effects for second-grade viscoelastic fluid past a stretching sheet. Appl Therm Eng 27:1895–1903
18. Alim MA, Md Alam M, Mamun A, Hossain B (2008) Combined effect of viscous dissipation and joule heating on the coupling of conduction and free convection along a vertical flat plate. Int Commun Heat Mass Transf 35:338–346
19. Hsiao KL, Hsu CH (2009) Conjugate heat transfer of mixed convection for viscoelastic fluid past a horizontal flat-plate fin. Appl Therm Eng 29:28–36
20. Kaya A (2011) Effects of buoyancy and conjugate heat transfer on non-Darcy mixed convection about a vertical slender hollow cylinder embedded in a porous medium with high porosity. Int J Heat Mass Transf 54:818–825
21. Duwairi HM (2005) Viscous and joule heating effects on forced convection flow from radiate isothermal porous surfaces. Int J Numer Met Heat Fluid Flow 15:429–440
22. Pozzi A, Lupo M (1988) The coupling of conduction with laminar natural convection along a flat plate. Int J Heat Mass Transf 31 (9):1807–1814
23. Cebeci T, Bradshaw P (1977) Momentum transfer in boundary layers. Hemisphere, Washington, DC
24. Takhar HS, Beg OA (1997) Effects of transverse magnetic field, Prandtl number and Reynolds number on non-Darcy mixed convective flow of an incompressible viscous fluid past a porous vertical flat plate in a saturated porous medium. Int J Energy Resource 21:87–100
25. Chen TS, Mucoglu A (1975) Buoyancy effects on forced convection along a vertical cylinder. ASME J Heat Transf 97:198–203
26. Takhar HS, Chamkha AJ, Nath G (2000) Combined heat and mass transfer along a vertical moving cylinder with a free stream. Heat Mass Trans 36:237–246
27. Aydin O, Kaya A (2008) Non-Darcian forced convection flow of viscous dissipating fluid over a flat plate embedded in a porous medium. Transp Porous Med 73:173–186

Effect of Radiation–Conduction Interaction on Mixed Convection from a Slender Cylinder

Ahmet Kaya and Orhan Aydin

Abstract

The problem of steady laminar mixed convection heat transfer about a slender cylinder is studied numerically, taking into account the radiation–conduction effect. The resulting governing equations are transformed into the non-similar boundary layer equations and solved using the Keller box method. The velocity and temperature profiles as well as the local skin friction and the local heat transfer parameters are determined for different values of the governing parameters, mainly the Richardson number, the Planck number (i.e., radiation–conduction parameter), and the surface temperature ratio. For some specific values of the governing parameters, the results agree very well with those available in the literature. Generally, it is determined that the local heat transfer coefficient increase, increasing the Richardson number Ri (i.e., the mixed convection parameter) and Planck number (i.e., radiation–conduction parameter) R_d or decreasing the surface temperature ratio θ_w.

Keywords

Slender cylinder • Buoyancy effect • Radiation • Surface temperature ratio

Introduction

Mixed convection flow along vertical cylinders is important in situations encountered in the areas of geothermal power generation and drilling operation when free stream velocity and induced buoyancy velocity are of comparable order and received much less attention. Chen and Mucoglu [1] analyzed the buoyancy and transverse curvature effects on forced convection of Newtonian fluid flow along an isothermal vertical cylinder using the local non-similarity method. The same problem for a uniform surface heat flux case was conducted by Mucoglu and Chen [2]. Lee et al. [3] studied the problem of mixed convection along a vertical cylinder with uniform surface heat flux for the entire mixed convection regime, ranging from pure forced convection to pure free convection by employing the buoyancy and curvature parameters. Hossain and Alim [4] studied a free convection flow of an optically dense viscous incompressible fluid along a vertical thin circular cylinder with effect of radiation. Hossain et al. [5] studied mixed convection flow of an optically dense viscous incompressible fluid along a horizontal circular cylinder with the effect of radiation when the surface temperature is uniform. Takhar and Nath [6] studied the mixed convection flow over a continuous moving vertical slender cylinder under the combined buoyancy effect of thermal and mass diffusion. Kumari and Nath [7] studied the effects of localized cooling/heating and injection/suction on the mixed convection flow on a thin vertical cylinder. Datta et al. [8] obtained the non-similar solution of a steady laminar forced convection boundary layer flow over a horizontal slender cylinder including the effect of nonuniform

A. Kaya (✉)
Department of Mechanical Engineering, Kahramanmaras Sutcu Imam University, 46100 Kahramanmaras, Turkey
e-mail: kaya38@ksu.edu.tr

O. Aydin
Department of Mechanical Engineering, Karadeniz Technical University, 61080 Trabzon, Turkey
e-mail: oaydin@ktu.edu.tr

slot injection (suction). Roy et al. [9] developed general analysis for the influence of nonuniform double slot injection (suction) on the steady non-similar incompressible laminar boundary layer flow over a slender cylinder. Anwar et al. [10] numerically studied the steady mixed convection boundary layer flow of a viscoelastic fluid over a horizontal circular cylinder in a stream flowing vertically upwards for both cases of heated and cooled cylinders. Singh et al. [11] studied unsteady mixed convection flow over a rotating vertical slender cylinder under the combined effects of buoyancy force and thermal diffusion with injection/suction where the slender cylinder is inline with the flow. The effect of surface curvature is also taken into account, especially for the applications such as wire and fiber drawing, where accurate predictions are desired. Molla et al. [12] investigated natural convection boundary layer laminar flow from a horizontal circular cylinder with uniform heat flux in the presence of heat generation.

In this chapter the effect of radiation–conduction on mixed convection flow over a slender cylinder with uniform surface temperature has been analyzed. The boundary layer equations governing the flow are reduced to local non-similarity equations which are solved using the implicit finite difference method (Keller box). Numerical results for the velocity and temperature profiles as well as local skin friction and local heat transfer parameters are presented.

Analysis

In this analysis, a two-dimensional steady laminar mixed convective flow of a viscous incompressible fluid along a slender cylinder of length L and outer radius r_o ($L \gg r_o$) is considered. The physical model and coordinate system are shown in Fig. 57.1. The gravitational acceleration, g, acts in the downward direction. The temperature and velocity at a distance remote from the cylinder are given by T_∞ and u_∞, respectively, and the body has a uniform temperature T_w. The radiative heat flux in the x-direction is considered negligible in comparison with that in the r-direction. Under foregoing assumptions and taking into account the Boussinesq approximation and the boundary layer approximation, the system of continuity, momentum, and energy equations can be written:

$$\frac{\partial(ru)}{\partial x} + \frac{\partial(rv)}{\partial r} = 0 \tag{57.1}$$

$$u\frac{\partial u}{\partial x} + v\frac{\partial u}{\partial r} = \left(\frac{v}{r}\right)\frac{\partial}{\partial r}\left(r\frac{\partial u}{\partial r}\right) + g\beta(T - T_\infty) \tag{57.2}$$

$$u\frac{\partial T}{\partial x} + v\frac{\partial T}{\partial r} = \left(\frac{v}{\text{Pr}}\right)\frac{\partial}{\partial r}\left(r\frac{\partial T}{\partial r}\right) - \left(\frac{1}{\rho c_p}\right)\frac{1}{r}\frac{\partial}{\partial r}(q_r) \tag{57.3}$$

Here u and v are the velocity components in the x and r direction, respectively, T is the temperature of the fluid, β is the coefficient of thermal expansion, v is the kinematic viscosity, ρ is the fluid density, and g is the acceleration due to gravity.
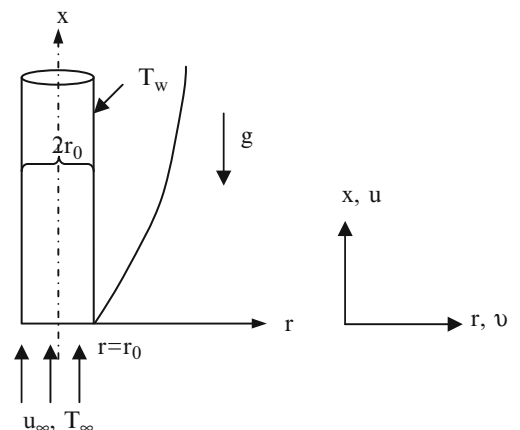
Fig. 57.1 The schematic of the problem

The quantity q_r on the right-hand side of Eq. (57.3) represents the radiative heat flux in the r direction. For simplicity and comparison, the radiative heat flux term in the energy equation is analyzed by utilizing the Rosseland diffusion approximation [13] for an optically thick boundary layer as follows:

$$q_r = -\frac{4\sigma}{3\alpha_R}\frac{\partial T^4}{\partial r} \quad \text{and} \quad \frac{\partial q_r}{\partial r} = -\frac{16\sigma}{3\alpha_R}\frac{\partial}{\partial r}\left(T^3\frac{\partial T}{\partial r}\right) \tag{57.4}$$

where σ is the Stefan–Boltzmann constant and α_R is the Rosseland mean absorption coefficient. This approximation is valid at points optically far from the bounding surface and is good only for intensive absorption, that is, for an optically thick boundary layer [14].

The appropriate boundary conditions for the velocity and temperature of this problem are

$$\begin{aligned} r = r_0; & \quad u = v = 0, \quad T = T_w \\ r \to \infty; & \quad u \to u_\infty, \quad T \to T_\infty \end{aligned} \tag{57.5}$$

To seek a solution, the following dimensionless variables are introduced

$$\xi = \left(\frac{4}{r_0}\right)\left(\frac{vx}{u_\infty}\right)^{1/2}, \quad \eta = \left[\frac{r^2 - r_0^2}{4r_0}\right]\left(\frac{u_\infty}{vx}\right)^{1/2}, \quad \theta = \frac{T - T_\infty}{T_w - T_\infty}$$

$$\psi(x,r) = r_0(vu_\infty x)^{1/2}f(\xi,\eta), \quad \frac{r^2}{r_0^2} = [1 + \xi\eta], \tag{57.6}$$

where $\psi(x, y)$ is the free stream function that satisfies Eq. (57.1) with $u = (1/r)(\partial\psi/\partial r)$ and $v = -(1/r)(\partial\psi/\partial x)$

In terms of these new variables, the velocity components can be expressed as

$$u = \frac{1}{2}u_\infty f', \quad v = \frac{r_0}{2r}\left(\frac{vu_\infty}{x}\right)^{1/2}\left[\eta f' - f - \xi\frac{\partial f}{\partial\xi}\right] \tag{57.7}$$

The transformed momentum and energy equations together with the boundary conditions, Eqs. (57.2), (57.3), and (57.4), can be written as

$$(1 + \xi\eta)f''' + \xi f'' + ff'' + Ri\xi^2\theta = \xi\left[f'\frac{\partial f'}{\partial\xi} - f''\frac{\partial f}{\partial\xi}\right] \tag{57.8}$$

$$\frac{1}{Pr}(1 + \xi\eta)\theta'' + \frac{\xi}{Pr}\theta' + f\theta' + \frac{1}{3PrR_d}\left[(1 + \xi\eta)[\theta(\theta_w - 1) + 1]^3\theta'\right]' = \left[f'\frac{\partial\theta}{\partial\xi} - \theta'\frac{\partial f}{\partial\xi}\right] \tag{57.9}$$

with the boundary conditions,

$$\begin{aligned} \eta = 0; & \quad f + \xi\frac{\partial f}{\partial\xi} = 0, \quad f' = 0, \quad \theta = 1 \\ \eta \to \infty; & \quad f' = 2, \quad \theta = 0 \end{aligned} \tag{57.10}$$

The corresponding dimensionless groups that appeared in the governing equations defined are as

$$Pr = \frac{\mu c_p}{k} = \frac{v}{\alpha}, \quad Ri = \frac{Gr}{Re}, \quad Gr = \frac{g\beta(T_w - T_\infty)r_0^3}{2v^2}, \quad Re = \frac{u_\infty r_0}{v}, \quad R_d = \frac{3\alpha_R k}{4\sigma T_\infty^3}, \quad \theta_w = \frac{T_w}{T_\infty} \tag{57.11}$$

where Pr is the Prandtl number, Ri is the Richardson number, Gr is the Grashof number, Re is the Reynolds number, R_d is the Planck number (radiation–conduction parameter), and θ_w is the surface temperature ratio to the ambient fluid.

Table 57.1 Comparison of the local heat transfer rate and local skin friction with $Pr = 0.7$, $R_d \to \infty$, $\theta_w = 0.0$, and $Ri = 0.0$

	Chen and Mucoglu [1]		Chang [17]		Present results	
ξ	$f''(\xi, 0)$	$-\theta'(\xi, 0)$	$f''(\xi, 0)$	$-\theta'(\xi, 0)$	$f''(\xi, 0)$	$-\theta'(\xi, 0)$
0.0	1.3282	0.5854	1.3280	0.5852	1.3201	0.5846
1.0	1.9172	0.8669	1.9133	0.8658	1.8934	0.8599
2.0	2.3981	1.0986	2.3900	1.0940	2.3822	1.0918
3.0	2.8270	1.3021	2.8159	1.2982	2.8098	1.2902
4.0	3.2235	1.4921	3.2187	1.4925	3.2102	1.4898
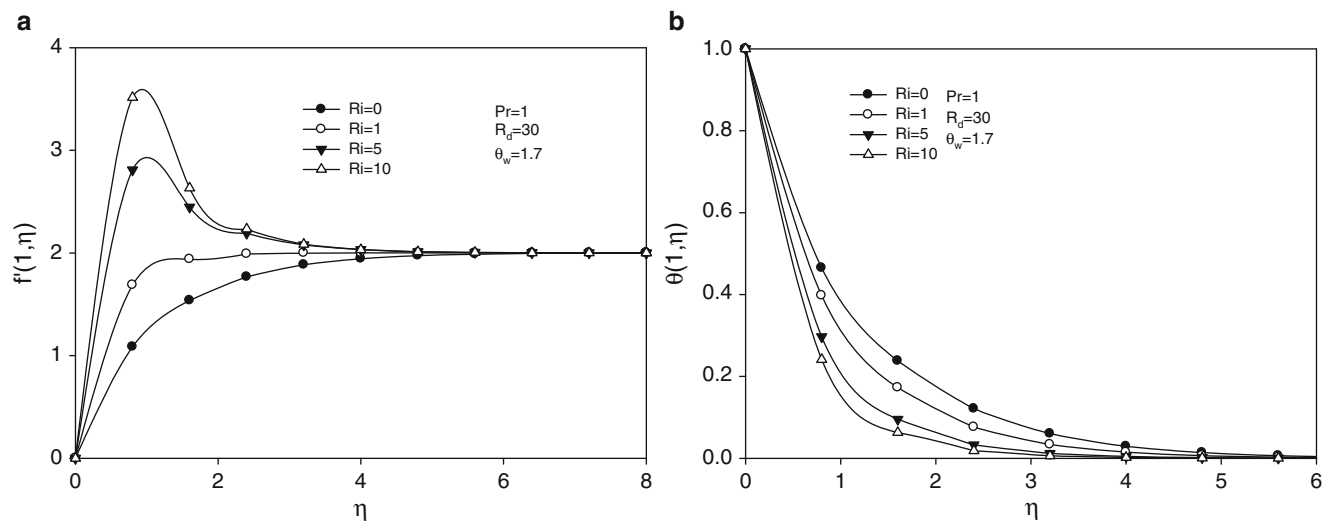
Fig. 57.2 Dimensionless velocity (**a**) and temperature (**b**) profiles for different Ri while $Pr = 1.0$, $R_d = 30$, $\theta_w = 1.7$, and $\xi = 1$

In the above system of equations, the radiation conduction parameter is absent from the mixed convection heat transfer problem when $R_d \to \infty$. It should be mentioned that the optically thick approximation should be valid for relatively low values of the radiation–conduction parameter, R_d. According to Ali et al. [15], some values of R_d for different gases are as follows: (1) $R_d = 10$–30: carbon dioxide (100–650 °F) with corresponding Prandtl number range 0.76–0.6; (2) $R_d = 30$–200: ammonia vapor (120–400 °F) with corresponding Prandtl number range 0.88–0.84; (3) $R_d = 30$–200: water vapor (220–900 °F) with corresponding Prandtl number 1.

The system of transformed equations together with the boundary conditions, Eqs. (57.8), (57.9) and (57.10), has been solved numerically using the Keller box scheme, an efficient and accurate finite-difference scheme, similar to that described in Cebeci and Bradshaw [16]. For the sake of brevity, details of the numerical method are not described, referring the reader to Cebeci and Bradshaw [16].

In order to verify the accuracy of the present method, the present results were compared with those of Chen and Mucoglu [1] and Chang [17]. The comparison is found to be in good agreement, as shown in Table 57.1.

Results and Discussion

In this study, the effect of radiation–conduction on mixed convection is examined. The following ranges of the main parameters are considered: the mixed convection parameter $Ri = 0.0$, 1, 5 and 10; $Pr = 1.0$, the radiation–conduction parameter $R_d = 30$, 50, 100, and 150, and the surface temperature ratio $\theta_w = 1.5$, 1.7, 2.0 and 2.3. The combined effects of Ri, R_d, and θ_w on the momentum and heat transfer are analyzed.

Figure 57.2 shows the effect of the buoyancy parameter Ri on the dimensionless velocity and temperature profiles while Fig. 57.3 shows the effect of the mixed convection parameter Ri on the local skin friction and the local heat transfer parameters. The Richardson number, Ri, represents a measure of the effect of the buoyancy in comparison with that of the
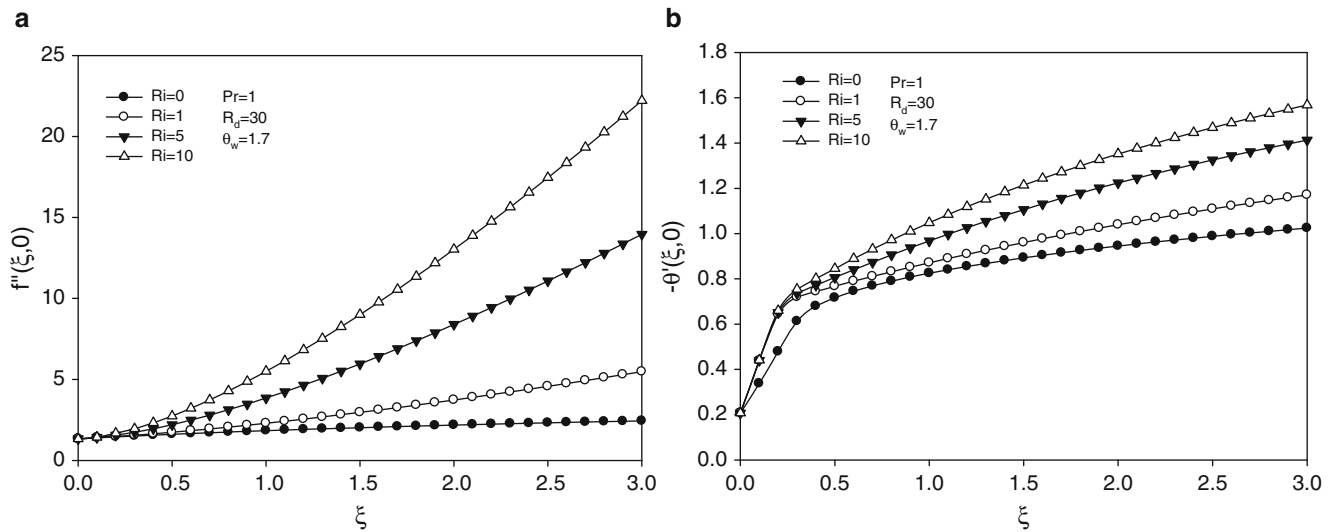
Fig. 57.3 Numerical values of local skin friction (**a**) and local heat transfer (**b**) against the streamwise distance ξ for different Ri while Pr = 1.0, R_d = 30, and θ_w = 1.7
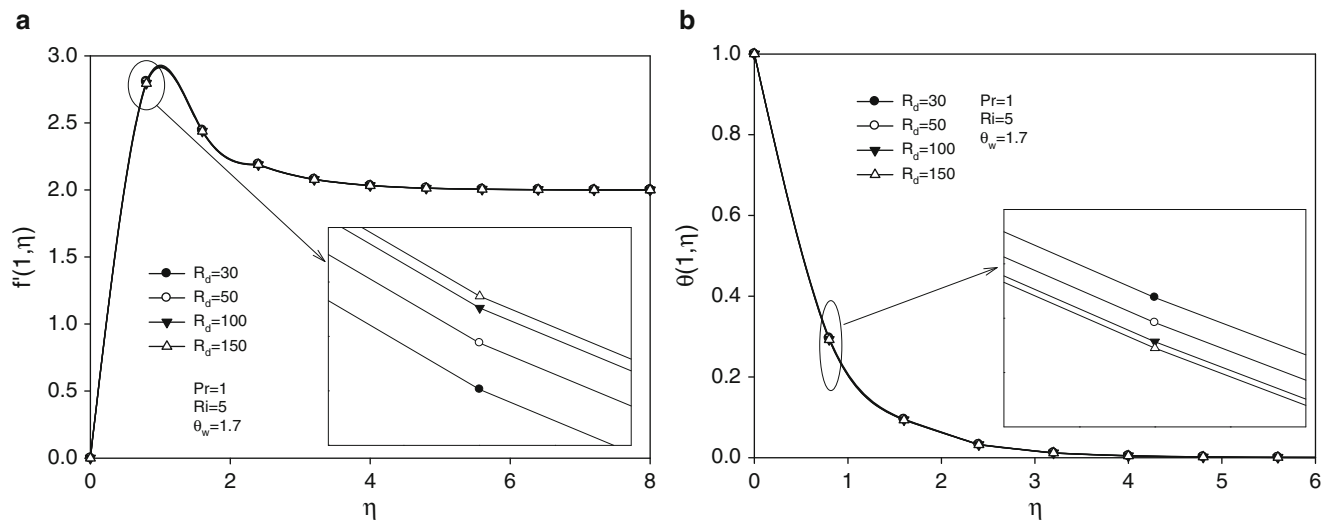
Fig. 57.4 Dimensionless velocity (**a**) and temperature (**b**) profiles for different R_d while Pr = 1.0, Ri = 5, θ_w = 1.7, and ξ = 1

inertia of the external forced or free stream flow on the heat and fluid flow. Outside the mixed convection region, either the pure forced convection or the free convection analysis can be used to describe accurately the flow or the temperature field. Forced convection is the dominant mode of transport when Ri $\rightarrow$ 0, whereas free convection is the dominant mode when Ri $\rightarrow$ ∞. Buoyancy forces can enhance the surface heat transfer rate when they assist the forced convection [18].

Figure 57.4 shows the dimensionless velocity and temperature profiles inside the boundary layer for different values of the radiation parameter R_d. The increasing of conduction–radiation parameter increases temperature gradients near the wall (Fig. 57.5a), which increases heat transfer rates; this is due to the fact that radiation effects increase temperatures of ionized gases and the absence of radiation defines small temperatures (Fig. 57.5b).

The effect of surface temperature parameter θ_w on the velocity and temperature profiles is shown in Fig. 57.6. Increasing the surface temperature ratio increases dimensionless velocity profile (Fig. 57.6a), which is shown to increase the local skin friction parameter (Fig. 57.7a). Moreover increasing the temperature ratio also increased the temperatures inside the boundary layer (Fig. 57.6b) and consequently decreases the local heat transfer parameter (Fig. 57.7b).
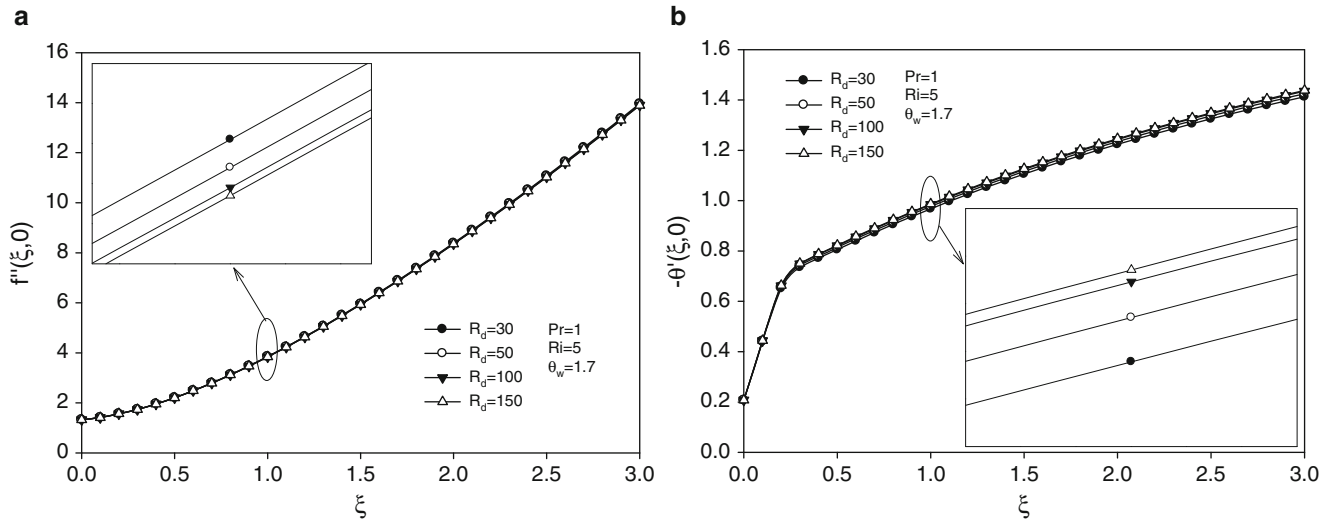
Fig. 57.5 Numerical values of local skin friction (**a**) and local heat transfer (**b**) against the streamwise distance ξ for different R_d while $Pr = 1.0$, $Ri = 5$, and $\theta_w = 1.7$
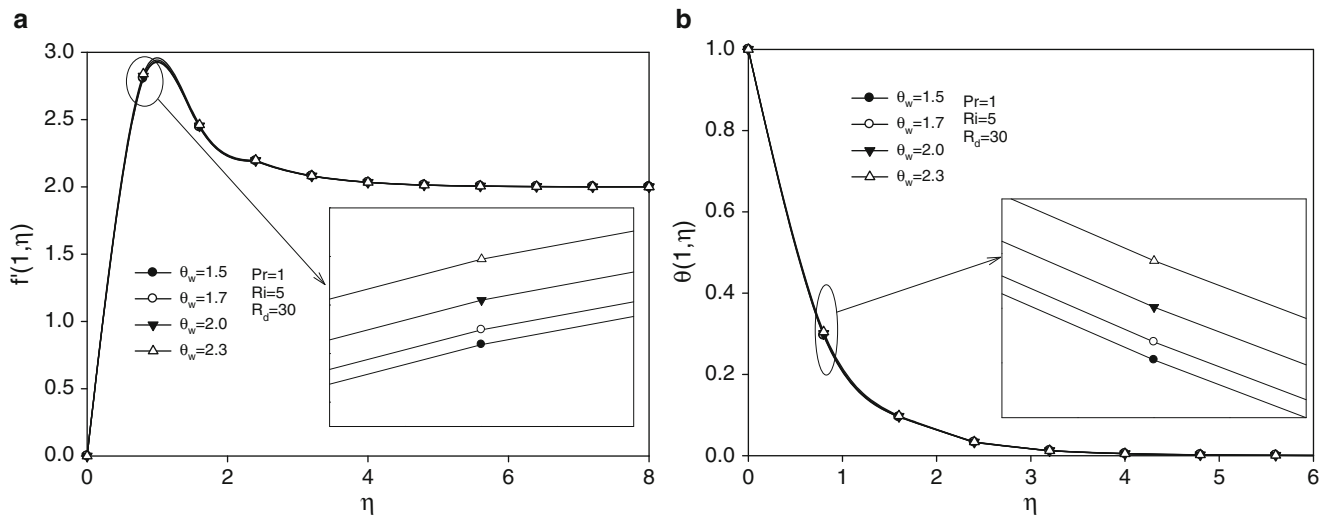
Fig. 57.6 Dimensionless velocity (**a**) and temperature (**b**) profiles for different θ_w while $Pr = 1.0$, $Ri = 5$, $R_d = 30$, and $\xi = 1$
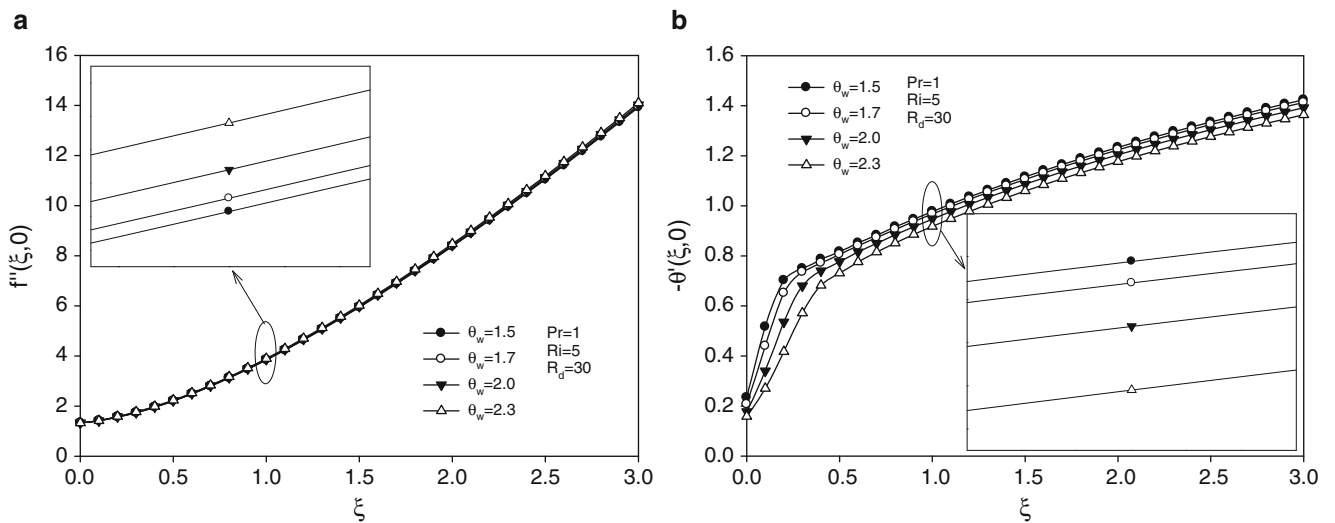
Fig. 57.7 Numerical values of local skin friction (**a**) and local heat transfer (**b**) against the streamwise distance ξ for different θ_w while $Pr = 1.0$, $Ri = 5$, and $R_d = 30$

Conclusions

In this chapter, we have studied numerically the effects mixed convection parameter Ri, radiation–conduction parameter R_d, and surface temperature ratio θ_w on a steady mixed convective flows about an inclined slender cylinder. A transformed set of non-similar equations have been solved using the Keller box scheme. From the present numerical investigation, the following conclusions can be drawn:

1. An increase in the mixed convection parameter Ri increases the local skin friction and the local heat transfer parameters.
2. An increase in the radiation parameter R_d decreases the local skin friction parameter and increases the local heat transfer parameter.
3. An increase in the surface temperature parameter θ_w increases the local skin friction parameter and decreases the local heat transfer parameter.

Nomenclature

c_p	Specific heat of the convective fluid	Ri	Richardson number
Gr	Grashof number	R_d	Planck number
f	Dimensionless stream function	T	Temperature
Pr	Prandtl number	u, v	Velocities in x and r directions, respectively
q_r	The component of radiative flux in r direction	x,r	Coordinates in axial and radial directions respectively
Re	Reynolds number		

Greek Symbols

α_R	Rosseland mean absorption coefficient	μ	Dynamic viscosity
η	Similarity variable	υ	Kinematic viscosity
ξ	Transverse curvature	θ	Dimensionless temperature profile
σ	Stefan–Boltzmann constant	θ_w	Surface temperature ratio
ρ	Fluid density		

Subscripts

w	Wall	∞	Free stream

References

1. Chen TS, Mucoglu A (1975) Buoyancy effects on forced convection along a vertical cylinder. ASME J Heat Tran 97:198–203
2. Mucoglu A, Chen TS (1976) Buoyancy effects on forced convection along a vertical cylinder with uniform surface heat flux. ASME J Heat Tran 98:523–525
3. Lee SL, Chen TS, Armaly BF (1987) Mixed convection along vertical cylinders and needles with uniform surface heat flux. ASME J Heat Tran 109:711–716
4. Hossain MA, Alim MA (1997) Natural convection-radiation interaction on boundary layer flow along a thin vertical cylinder. Heat Mass Tran 32:515–520
5. Hossain MA, Kutubuddin M, Pop I (1999) Radiation-conduction interaction on mixed convection from a horizontal circular cylinder. Heat Mass Tran 35:307–314
6. Takhar HS, Nath G (2000) Self-similar solution of the unsteady flow in the stagnation point region of a rotating sphere with a magnetic field. Heat Mass Tran 36:89–96
7. Kumari M, Nath G (2004) Mixed convection boundary layer flow over a thin vertical cylinder with localized injection/suction and cooling/heating. Int J Heat Mass Tran 47:969–976
8. Datta P, Anilkumar D, Roy S, Mahanti NC (2006) Effect of non-uniform slot injection (suction) on a forced flow over a slender cylinder. Int J Heat Mass Tran 49:2366–2371
9. Roy S, Datta P, Ravindran R, Momoniat E (2007) Non-uniform double slot injection (suction) on a forced flow over a slender cylinder. Int J Heat Mass Tran 50:3190–3194
10. Anwar I, Amin N, Pop I (2008) Mixed convection boundary layer flow of a viscoelastic fluid over a horizontal circular cylinder. Int J Nonlinear Mech 43:814–821
11. Singh PJ, Roy S, Pop I (2008) Unsteady mixed convection from a rotating vertical slender cylinder in an axial flow. Int J Heat Mass Tran 51:1423–1430
12. Molla MM, Paul SC, Hossain MA (2009) Natural convection flow from a horizontal circular cylinder with uniform heat flux in presence of heat generation. Appl Math Model 33:3226–3236
13. Sparrow EM, Cess RD (1961) Free convection with blowing or suction. ASME J Heat Tran 83:387–389

14. Hossain MA, Pop I (1997) Radiation effect on Darcy free convection flow along an inclined surface placed in porous media. Heat Mass Tran 32(4):223–227

15. Ali MM, Chen TS, Armaly BF (1984) Natural convection–radiation interaction in boundary-layer flow over horizontal surfaces. AIAA J 22:1797–1803

16. Cebeci T, Bradshaw P (1977) Momentum transfer in boundary layers. Hemisphere, Washington, DC

17. Chang CL (2006) Buoyancy and wall conduction effects on forced convection of micropolar fluid flow along a vertical slender hollow circular cylinder. Int J Heat Mass Tran 49:4932–4942

18. Aydin O, Kaya A (2008) Radiation effect on MHD mixed convection flow about a permeable vertical plate. Heat Mass Tran 45:239–246

Emir Aydar, İsmail Ekmekçi, and Yaşar Şen

Abstract

There are many panel radiator manufacturers in Turkey. Their panel radiator designs are very similar, and radiators that have been manufactured by various producers have very similar thermal efficiency values and specific heating per unit weight of the radiator. In this study, CFD analysis of existing panel radiators was made with a commercial CFD software of STAR-CCM+ with top-bottom-opposite-end connection method in three-dimensional space. Panel-convector-convector-panel, Type-22-600×500 steel panel radiator, was used in this numerical study. In the content of this analysis, new configurations at fin design were performed to increase the rate of heat transfer of the panel radiator. Four fin designs were drawn and examined. Since triangular profile fin design contains less material and has higher heat flux, it is more efficient than the other profiles, and therefore it is more suitable for applications requiring minimum weight.

Keywords

Panel radiator • Thermal efficiency • Computational fluids dynamics (CFD) • Fin design

Introduction

Panel radiators are the most widely used central-heating emitters to heat most homes and offices in Europe. There is a high demand for panel radiators due to their compact design and less place requirements. 80 % of the heat output from radiators is natural convection; 20 % of the heat output from radiators is radiation. Although radiators are known as radiator, most of their output is by natural convection [1]. Since panel radiators are elegant design, light, cheap, and occupy less place, they are in common use at homes and offices. Radiators are the combination of water circulation channels and high convectors that is directly welded onto these panels. All panel radiators release a combination of radiant and convective heat into a room as hot water flows through them.

There is insufficient 3-D numerical study about panel radiator in literature. Lu et al. [2] showed the airflow and temperature field in a heated room by using a CFD package. This study includes using CFD to predict a three-dimensional airflow field and temperature distribution in a full-scale enclosure with a radiator; the predicted airflow pattern and temperature field will be validated by the measured data carried out by Lebrun and Marret and using CFD to predict the

E. Aydar (✉)
TUBITAK Marmara Research Center Gebze Campus Energy Institute, 41470 Kocaeli, Turkey
e-mail: emir.aydar@mam.gov.tr

İ. Ekmekçi
Faculty of Applied Sciences, İstanbul Commerce University, Kucukyalı campus E-5 Kavsagi İnonu Cad. No:4 34840, Istanbul, Turkey
e-mail: iekmekci@ticaret.edu.tr

Y. Şen
Sakarya University, Sapanca Vocational School, Sapanca 54000, Sakarya, Turkey
e-mail: ysen@sakarya.edu.tr

smoke particle distribution in the room. Zhai et al. [3] are interested in coupling an energy simulation (ES) program with a computational fulid dynamics (CFD) program. Static and dynamic coupling strategies have been implemented to bridge the gap between ES and CFD programs to reduce the computing costs while achieving accurate results but conserve the accuracy and details of the computed results.

The aim of this study is that there are many panel radiator manufacturers in Turkey, but their panel radiator designs are very similar and due to this similar design, radiators that have been manufactured by various producers have very similar values of thermal efficiency and specific heating for unit weight of the radiator. In our research, CFD analysis of existing panel radiator will be made with a commercial CFD software of STAR-CCM+ with top-bottom-opposite-end connection method using forced convection model in three-dimensional space. After that, four fin designs will be created in order to obtain more efficient panel radiator with containing less material with respect to original radiator fin design.

Mathematical Modeling

When inlet water temperature and mass flow rate were fixed, optimum air-side heat transfer coefficient was obtained and used for the other numerical analysis. Mass flow rate was computed from energy balance equation as given below:

$$\dot{Q} = \dot{m} \times c_p \times \Delta T \tag{58.1}$$

$$899 = \dot{m} \times 4189.8 \times (75 - 65) \tag{58.2}$$

$$\dot{m} = 0.0214 \, \text{kg/s} \tag{58.3}$$

All conditions and properties are defined via the STAR-CCM+ GUI. This study incorporates both multi-region and conjugate heat transfer. Outlet temperature was obtained according to the fixed inlet temperature and mass flow inlet. In this numerical study, rate of heat transfer of the panel radiator was obtained by the help of the forced convection model. Rate of heat transfer of the whole panel type radiator is 899 W/m obtained from experimental result. Rate of heat transfer of the one module was calculated from the rate of heat transfer of the whole panel type radiator times the module length as follows:

$$Q' = Q \times L \tag{58.4}$$

$$Q' = 899 \times 0.0017 \tag{58.5}$$

$$Q' = 15.28 \, \text{W} \tag{58.6}$$

Mass flow rate is found from the energy balance.

$$\dot{Q} = \dot{m} \times c_p \times \Delta T \tag{58.7}$$

$$15.28 = \dot{m} \times 4189.8 \times (75 - 65) \tag{58.8}$$

$$\dot{m} = 0.00036 \, \text{kg/s} \tag{58.9}$$

Under most practical conditions, the flow in a tube is laminar for Re < 2,300, fully turbulent for Re > 10,000, and transitional in between. But it should be kept in mind that in many cases the flow becomes fully turbulent for Re > 4,000 [4]. In order to define nature of the flow in a circular tube, Reynolds number was computed as follows:

$$\text{Re} = \frac{4 \times \dot{m}}{\pi \times D \times \mu} \tag{58.10}$$

$$Re = \frac{4 \times 0.00036}{3.14 \times 0.017 \times 0.0004} \tag{58.11}$$

$$Re = 67.20 \tag{58.12}$$

which is less than the critical Reynolds number of 2,300, and the flow regime of a circular tube is laminar.

Computational Methodology

This numerical study is based on a domestic radiator which is in accordance with Standard TS EN442. Half of the geometry was used for numerical study because of the symmetrical structure of the panel radiator geometry, and then the drawn geometry was imported to STAR-CCM+.

The panel radiator has been drawn by means of CAD software according to original measurements of the PCCP (panel-convector-convector-panel) arrangement of the panel radiator. PCCP, Type-22 steel panel radiator is used in this numerical study. Heat transfer rate of the steel panel radiator has been measured according to EN 442 in an accredited laboratory [5]. Connection type of the steel panel radiator used in this study is top-bottom-opposite-end. The outer panel is made of a shaped plate with horizontal and vertical depressions. In order to increase heating performance, some types of radiators are provided with a convector plate, welded to the vertical waterways of the panel. The panel is made of two stamped steel sheets welded together with a seam weld on the perimeter and with a spot weld where the depressions are. Since the panel radiator is symmetrical, a half of the geometry can be used for numerical study. A 500-mm-long, 600-mm-high, and 105-mm-wide are the dimensions of the half of the panel radiator. A 150-mm-high and 473.5-mm-long are the dimensions of the convector. First four and last four convectors are smaller than middle ones to prevent the difficulties at the installation of T-Junctions. Panels and convectors are made of steel sheet. Water channels are 1.1 mm thick, and the panel radiator has 25 mm pitch. The convectors are 0.5 mm thick and have a height of 37 mm from the base. The width of one panel is 12 mm.

Four fin designs were performed to enhance heat transfer rate by using less material usage. It is aimed to manufacture a more efficient panel radiator. Four different fin designs were performed by the help of CAD software. Fin material, height, width, and length weren't changed. Cross-sectional area of the fin was only changed. Original and new fin designs are shown in Figs. 58.1, 58.2, and 58.3.

Fin design-3 is different from the other ones. Original design and the other fin ones have two contact faces, but Fig. 58.3 shows that fin design-3 has three contact faces between panel and convector. Mesh sizes of the panel radiator geometry are listed in Table 58.1.

The panel radiator with TBOE connection was meshed using tetrahedral volume meshing model and also surface remesher and prism layer mesher were selected. Figures 58.4, 58.5, and 58.6 show the mesh type and the mesh density of outer side of the original radiator fin design and novel fin designs.
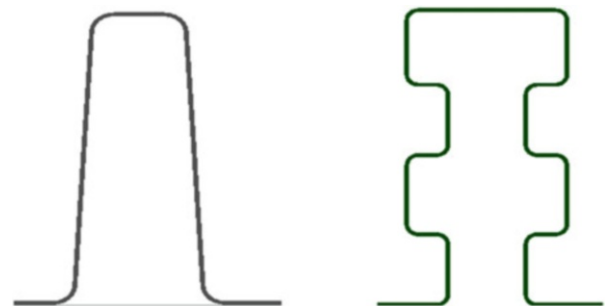
Fig. 58.1 Original fin and new fin design-1

Fig. 58.2 New fin design-2 and
triangular profile fin design
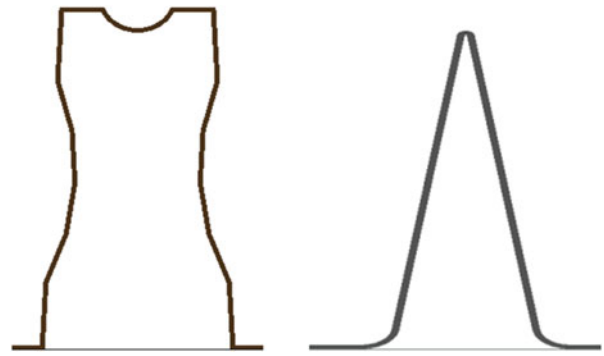
Fig. 58.3 New fin design-3
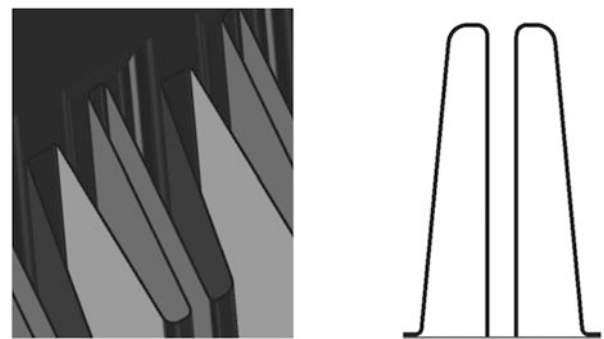
Table 58.1 Mesh sizes of the panel radiator geometry

Number of prism layers	Number of prism layers	2
Prism layer stretching	Prism layer stretching	1.2
Prism layer thickness	Absolute size	1 mm
Surface curvature	# Pts/circle	36
Surface size	Absolute size	4 mm
Surface size	Absolute size	2 mm

Fig. 58.4 Computational meshes of the panel radiator with original fin and new design-1

Fig. 58.5 Computational meshes of the panel radiator with new design-2 and triangular fin
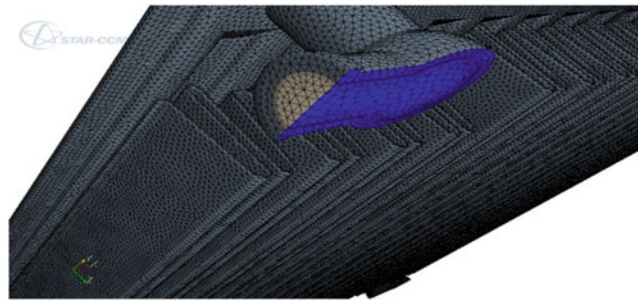
Fig. 58.6 Computational meshes of the panel radiator with new design-3

Table 58.2 Material properties

Material type	Density (kg/m^3)	Dynamic viscosity (Pa-s)	Specific heat (J/kg K)	Thermal conductivity (W/m K)
Water	977.7	0.0004	4,189.8	0.6
Stainless steel (AISI 316)	8,238		468	13.4

The computational meshes with high resolution of approximately 1,800,000–1,900,000 for fluid region and 3,000,000–4,400,000 cells for solid region were created for the flow analysis of the panel radiator. The numerical simulations were carried out using the finite volume CFD-based code STAR-CCM+ with parallel processing to accelerating the calculations. The computations were performed on a 3.00 GHz CPU and 16GB of RAM workstation.

Steel panel radiator (AISI 316) used in this study was computed at inlet and outlet temperatures respectively, 75 °C and 65 °C according to EN 442 [6]. In this numerical study, inlet temperature and mass flow rate will be determined, and outlet temperature will be computed in order to obtain optimum air-side convective heat transfer coefficient according to boundary conditions. Inlet water temperature was specified as 75 °C according to EN 442 [5].

Water was selected as liquid material. Material properties of water was computed as the average of inlet and outlet water temperatures. The tables of thermophysical properties of saturated water was used to compute material properties of water. Stainless steel (AISI 316) was selected for solid material. Material properties of stainless steel were determined according to the database of commercial CFD code of STAR-CCM+. Material properties of stainless steel (AISI 316) and water are listed in Table 58.2. Boundary conditions of the panel radiator geometry are also listed in Table 58.3.

Results and Discussion

The view of the scalar temperature distribution of fluid flow and the original radiator fin design at air-side convective heat transfer coefficient of 6.5 W/m^{2}K are given in Figs. 58.7 and 58.8.

Table 58.3 Boundary conditions of the panel radiator geometry

Boundary	Type	Physics values	Inputs
Inlet	Mass flow inlet	Mass flow rate	0.0214 kg/s
		Total temperature	75 °C
		Direction	x-direction
Outlet	Flow-split outlet	Split ratio	1
		Direction	x-direction
Four T-fittings	Wall	Thermal specification	Adiabatic
Panel surface	Wall	Thermal specification	Convection
		Ambient temperature	20 °C
		Heat transfer coefficient	6.5 W/m^{2}K
Convectors surface	Wall	Thermal specification	Convection
		Ambient temperature	20 °C
		Heat transfer coefficient	6.5 W/m^{2}K

Fig. 58.7 Scalar temperature distribution of fluid flow
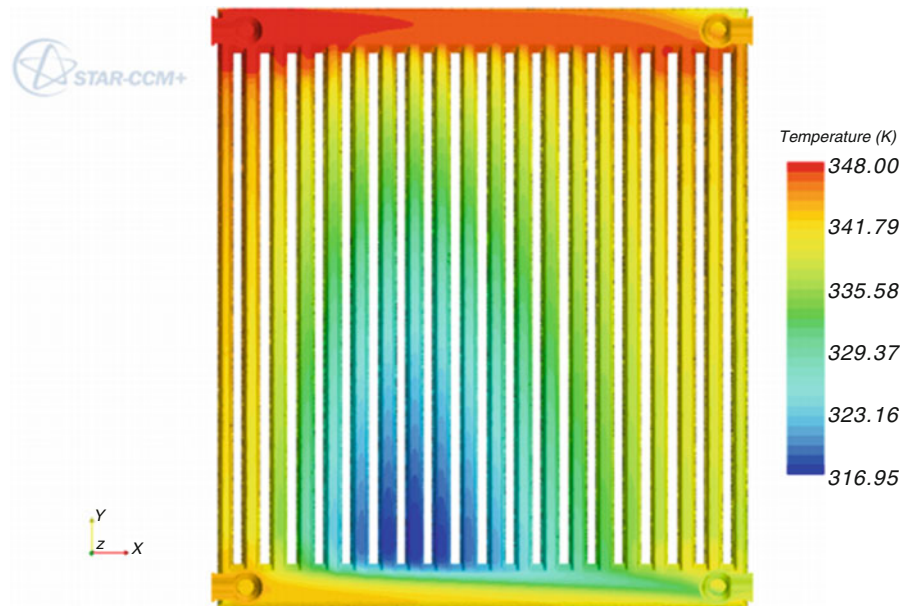
Fig. 58.8 Scalar temperature distribution of original fin design
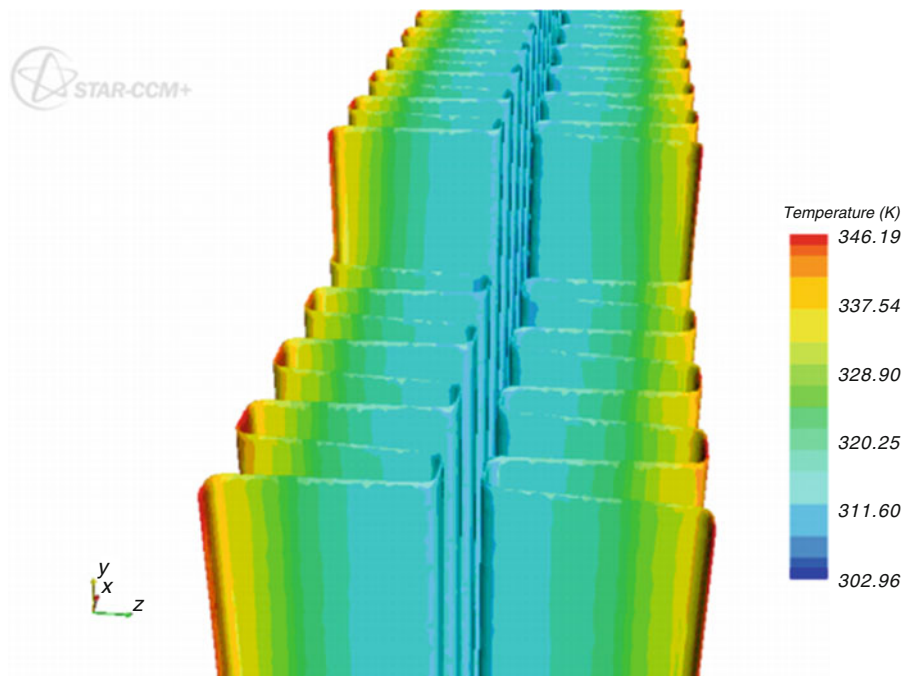
Table 58.4 Numerical results at different air-side heat transfer coefficients

Specifications	Symbol	Values			
Heat transfer coefficient (W/m^{2}K)	h	5	6.5	8	10
Mass flow inlet (kg/h)	$\dot{m}$	77.2	77.2	77.2	77.2
Inlet water temperature (°C)	T_1	75	75	75	75
Outlet water temperature (°C)	T_2	66.5	64.9	63.6	62
Room temperature (°C)	T_r	20	20	20	20
Heat transfer rate (W) (based on enthalpy)	$\dot{Q}_h$	755	894.2	1,015.8	1,157.1
Heat transfer rate (W) (the heat output from the radiator)	$\dot{Q}_{tot}$	753.7	892.1	1,015.4	1,156

Figures 58.7 and 58.8 show that there are high temperature gradients that are readily seen at the middle-bottom region of panel and fluid flow regions. This high temperature gradients are caused by distinct values of mass flow rates at vertical ducts.

Evaluation of Numerical Result

Different air-side convective heat transfer coefficients were tested so as to compute outlet water temperature of 65 °C that is related to panel radiator in accordance with TS EN442. Inlet water temperature of 75 °C is fixed for all studies. The numerical results of convective heat transfer coefficients of 5 W/m^{2}K, 6.5 W/m^{2}K, 8 W/m^{2}K, and 10 W/m^{2}K were compared to each other. Numerical results at different air-side heat transfer coefficients of the panel radiator with TBOE connection are listed in Table 58.4.

Convective heat transfer coefficient of air side is directly proportional to the thermal output of the radiator. Normally, the larger the air-side heat transfer coefficent, the higher the rate of heat transfer from the panel radiator. Table 58.4 should offer a good compromise between heat transfer rates of numerical study and experimental study whose heat transfer rate is 899 W, when the air-side heat transfer coefficent is 6.5 W/m^{2}K. Therefore, the air-side heat transfer coefficent of 6.5 W/m^{2}K was used in all numerical studies.

The heat transferred to the air by means of forced convection model, which was calculated from the difference in enthalpy times the mass flow rate between the inlet and outlet of the water within the radiator as following:

$$\dot{Q}_h = \dot{m} \times (h_1 - h_2) \tag{58.13}$$

For the fix inlet temperature of 75 °C, fix mass flow rate of 0.0107 kg/s, and convective heat transfer coefficient of 6.5 W/m^{2}K, outlet temperature of 64.9 °C was obtained.

Effects of Original Fin Design of the Panel Radiator on Fin Efficiency

In the limiting case of zero thermal resistance or infinite thermal conductivity, the temperature of the fin will be uniform at the base value of T_b. The heat transfer from the fin will be maximum in this case and can be expressed as

$$\dot{Q}_{fin,\max} = hA_{fin}(T_b - T_\infty) \tag{58.14}$$

In reality, however, the temperature of the fin will drop along the fin, and thus the heat transfer from the fin will be less. To account for the effect of this decrease in temperature on heat transfer, fin efficiency is defined as

$$\eta_{fin} = \frac{\dot{Q}_{fin}}{\dot{Q}_{fin,\max}} \tag{58.15}$$

Fig. 58.9 Split each fin of the panel radiator

Table 58.5 The values of each original radiator fin design to compute fin efficiency

Specifications	Heat transfer rate from the fin (W)	Heat transfer surface area (m^2)	Base temperature (°C)	Ideal heat transfer rate from the fin (W)
Fin 1	14.850	0.0795	69.147	25.396
Fin 2	14.312	0.0794	67.167	24.342
Fin 3	13.251	0.0795	63.559	22.509
Fin 4	12.048	0.0795	59.620	20.473
Fin 5	12.628	0.0893	56.499	21.185
Fin 6	12.012	0.0894	54.485	20.039
Fin 7	11.699	0.0893	53.843	19.644
Fin 8	11.767	0.0893	53.914	19.685
Fin 9	12.059	0.0893	54.870	20.240
Fin 10	12.527	0.0893	56.189	21.005
Fin 11	13.116	0.0892	57.951	22.003
Fin 12	13.736	0.0892	59.690	23.012
Fin 13	14.359	0.0893	61.544	24.114
Fin 14	14.915	0.0891	63.100	24.961
Fin 15	15.395	0.0890	64.679	25.846
Fin 16	14.050	0.0791	65.838	23.567
Fin 17	14.352	0.0790	66.809	24.036
Fin 18	14.537	0.0791	67.242	24.289
Fin 19	14.255	0.0784	66.847	23.873

where A_{fin} is the total surface area of the fin. $\dot{Q}_{fin}$ means the actual heat transfer rate from the fin and $\dot{Q}_{fin,max}$ the ideal heat transfer rate from the fin if the entire fin were at base temperature. Each fin was dissolved as shown in Fig. 58.9. Actual heat transfer rate from the fin and ideal heat transfer rate from the fin were computed for each fin and they are listed in Table 58.5.

After values had been computed, fin efficiency for each fin of the original radiator fin design was computed by using Eq. (58.15). Fin efficiency results of each fin of the original radiator fin design are listed in Table 58.10.

Effects of New Fin Design-1 on Fin Efficiency

The view of the scalar temperature distribution of fin design-1 at air-side convective heat transfer coefficient of 6.5 W/m^{2}K is given in Fig. 58.10.

The values used in order to compute fin efficiency by means of Eq. (58.15) are listed in Table 58.6 for design-1.

After values had been computed, fin efficiency for each fin of fin design-1 was computed by using Eq. (58.15). Fin efficiency results of each fin of fin design-1 are listed in Table 58.10.
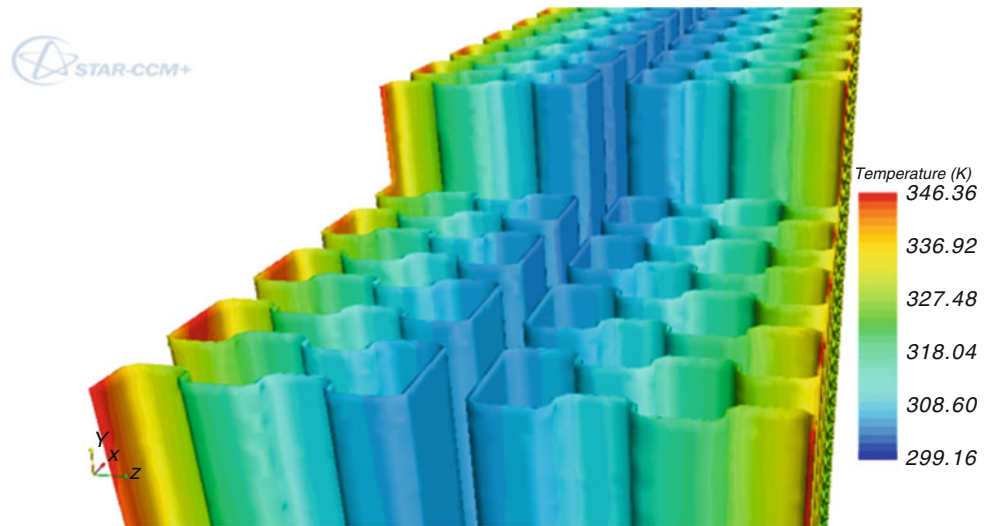
Fig. 58.10 Scalar temperature distribution of fin design-1

Table 58.6 The values of each fin design-1 to compute fin efficiency

Specifications	Heat transfer rate from the convector (W)	Heat transfer surface area (m^2)	Base temperature (°C)	Ideal heat transfer rate from the convector (W)
Fin 1	16.289	0.1083	69.016	34.504
Fin 2	15.494	0.1081	66.866	32.930
Fin 3	14.321	0.1081	63.180	30.340
Fin 4	13.155	0.1081	59.517	27.766
Fin 5	13.469	0.1194	56.292	28.166
Fin 6	12.690	0.1195	54.258	26.609
Fin 7	12.292	0.1194	53.135	25.716
Fin 8	12.287	0.1194	52.932	25.558
Fin 9	12.568	0.1194	53.853	26.273
Fin 10	13.108	0.1195	55.516	27.587
Fin 11	13.719	0.1194	57.167	28.869
Fin 12	14.384	0.1195	59.153	30.412
Fin 13	15.062	0.1194	61.114	31.908
Fin 14	15.671	0.1194	62.764	33.189
Fin 15	16.201	0.1194	64.312	34.390
Fin 16	15.085	0.1082	65.602	32.071
Fin 17	15.329	0.1081	66.527	32.692
Fin 18	15.456	0.1081	66.852	32.920
Fin 19	15.388	0.1082	66.473	32.684

Effects of New Fin Design-2 on Fin Efficiency

The view of the scalar temperature distribution of fin design-2 at air-side convective heat transfer coefficient of 6.5 W/m^{2}K is given in Fig. 58.11. The values used in order to compute fin efficieny by means of Eq. (58.15) are listed in Table 58.7 for design-2.

After values had been computed, fin efficiency for each fin of fin design-2 was computed by using Eq. (58.15). Fin efficiency results of each fin of fin design-2 are listed in Table 58.10.
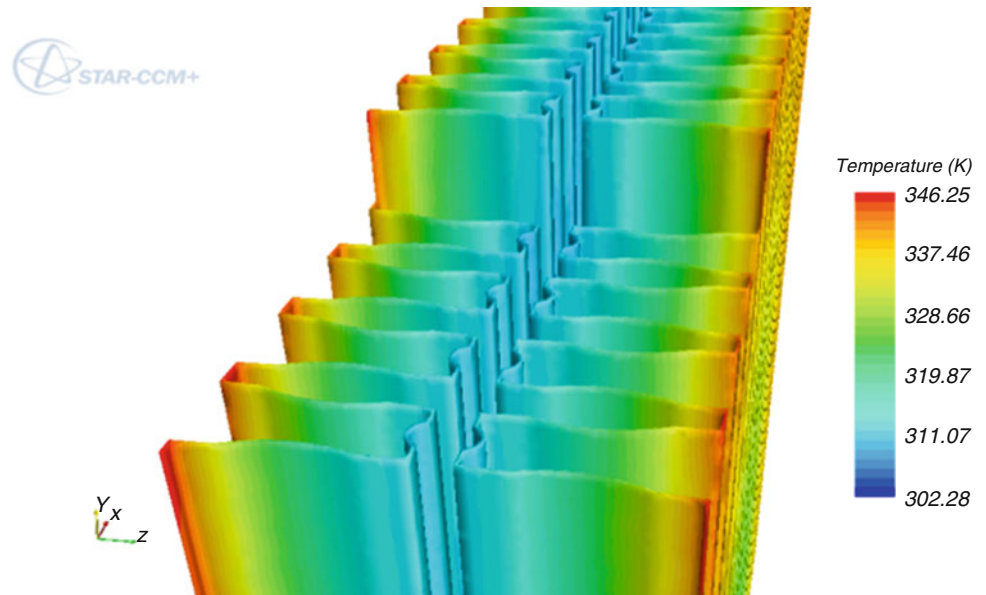
Fig. 58.11 Scalar temperature distribution of fin design-2

Table 58.7 The values of each fin design-2 to compute fin efficiency

Specifications	Heat transfer rate from the convector (W)	Heat transfer surface area (m^2)	Base temperature (°C)	Ideal heat transfer rate from the convector (W)
Fin 1	15.339	0.0853	68.933	27.130
Fin 2	14.657	0.0851	67.071	26.037
Fin 3	13.626	0.0851	63.740	24.194
Fin 4	12.591	0.0851	60.469	22.385
Fin 5	12.943	0.0939	57.422	22.840
Fin 6	12.188	0.0939	55.386	21.597
Fin 7	11.909	0.0940	54.372	21.001
Fin 8	11.926	0.0939	54.473	21.040
Fin 9	12.191	0.0939	55.275	21.530
Fin 10	12.644	0.0939	56.543	22.304
Fin 11	13.192	0.0939	58.228	23.332
Fin 12	13.797	0.0939	60.083	24.464
Fin 13	14.396	0.0939	61.802	25.513
Fin 14	14.903	0.0939	63.370	26.470
Fin 15	15.429	0.0939	64.752	27.314
Fin 16	14.296	0.0851	65.950	25.417
Fin 17	14.575	0.0851	66.827	25.902
Fin 18	14.667	0.0851	67.122	26.065
Fin 19	14.565	0.0851	66.772	25.871

Effects of Triangular Profile Fin Design on Fin Efficiency

The view of the scalar temperature distribution of triangular profile fin design at air-side convective heat transfer coefficient of 6.5 W/m²K is given in Fig. 58.12.

The values used in order to compute fin efficieny by means of Eq. (58.15) are listed in Table 58.8 for triangular profile fin design.

After values had been computed, fin efficiency for each fin of triangular profile fin design was computed by using Eq. (58.15). Fin efficiency results of each fin of triangular profile fin design are listed in Table 58.10.
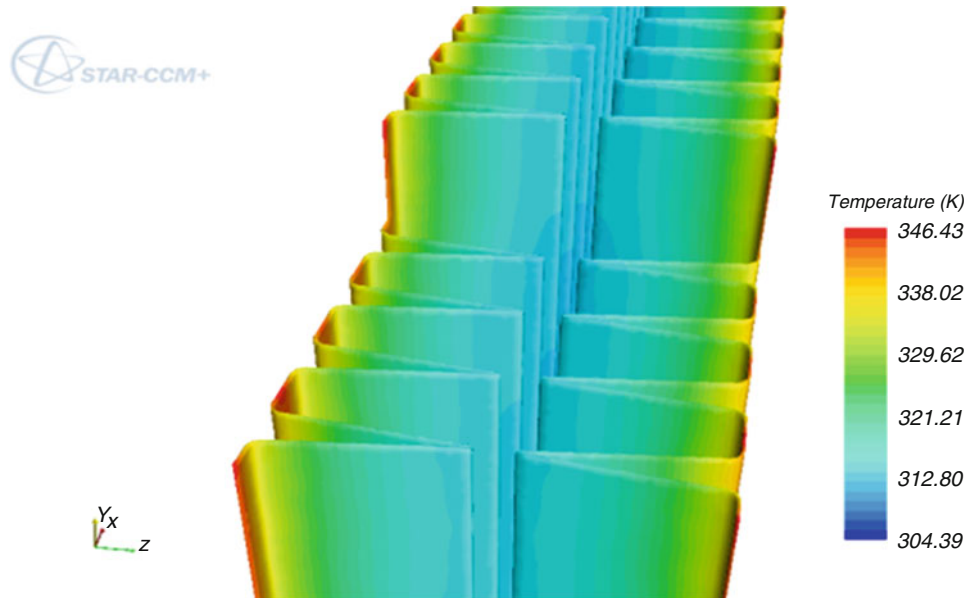
Fig. 58.12 Scalar temperature distribution of triangular profile fin design

Table 58.8 The values of each triangular profile fin design to compute fin efficiency

Specifications	Heat transfer rate from the convector (W)	Heat transfer surface area (m²)	Base temperature (°C)	Ideal heat transfer rate from the convector (W)
Fin 1	14.941	0.0767	68.874	24.366
Fin 2	14.254	0.0765	66.805	23.273
Fin 3	13.179	0.0765	63.275	21.518
Fin 4	12.274	0.0765	60.362	20.070
Fin 5	13.088	0.0861	57.811	21.160
Fin 6	12.486	0.0861	56.102	20.204
Fin 7	12.243	0.0861	55.385	19.803
Fin 8	12.243	0.0861	55.350	19.783
Fin 9	12.462	0.0861	56.166	20.240
Fin 10	12.878	0.0861	57.320	20.886
Fin 11	13.378	0.0861	58.857	21.746
Fin 12	13.933	0.0861	60.528	22.681
Fin 13	14.448	0.0861	62.086	23.553
Fin 14	14.958	0.0861	63.580	24.389
Fin 15	15.359	0.0859	64.935	25.089
Fin 16	14.047	0.0765	66.073	22.909
Fin 17	14.303	0.0765	66.985	23.363
Fin 18	14.417	0.0764	67.321	23.499
Fin 19	14.120	0.0757	67.160	23.205

Effects of New Fin Design-3 on Fin Efficiency

The view of the scalar temperature distribution of fin design-3 at air-side convective heat transfer coefficient of 6.5 W/m^{2}K is given in Fig. 58.13.The values used in order to compute fin efficieny by means of Eq. (58.15) are listed in Table 58.9 for design-3.

Fin efficiency results of new fin designs according to the Eq. (58.15) are listed in Table 58.10 for each fin. They were compared with original radiator fin design.These fin efficiency results can be easily seen in graph as shown in Fig. 58.14. In Fig. 58.14, it can be seen that arithmetic average of triangular profile fin design is 61.42 %, arithmetic average of original radiator fin design is 59.48 %, arithmetic average of design-3 is 58.44 %, arithmetic average of fin design-2 is 56.43 %,

Fig. 58.13 Scalar temperature distribution of convector for design-4

Table 58.9 The values of each fin design-3 to compute fin efficiency

Specifications	Heat transfer rate from the convector (W)	Heat transfer surface area (m^2)	Base temperature (°C)	Ideal heat transfer rate from the convector (W)
Fin 1	27.213	0.1510	67.765	46.881
Fin 2	25.585	0.1508	64.959	44.068
Fin 3	22.985	0.1508	60.328	39.529
Fin 4	20.120	0.1507	55.323	34.600
Fin 5	19.838	0.1664	51.152	33.694
Fin 6	18.344	0.1664	48.791	31.140
Fin 7	17.793	0.1665	47.868	30.160
Fin 8	17.965	0.1665	48.119	30.431
Fin 9	18.526	0.1664	49.072	31.444
Fin 10	19.508	0.1664	50.586	33.081
Fin 11	20.765	0.1665	52.736	35.428
Fin 12	22.176	0.1665	55.054	37.937
Fin 13	23.616	0.1665	57.354	40.426
Fin 14	24.915	0.1665	59.497	42.745
Fin 15	26.155	0.1664	61.423	44.803
Fin 16	24.598	0.1508	63.156	42.301
Fin 17	25.314	0.1508	64.461	43.580
Fin 18	25.648	0.1508	64.987	44.096
Fin 19	25.398	0.1508	64.729	43.843

Table 58.10 Fin efficiency comparison between original radiator fin design and new fin designs

	Fin efficiency (η_{fin}) (%)				
Specifications					
Fin 1	58.47	47.20	56.53	61.31	58.04
Fin 2	58.79	47.05	56.29	61.24	58.05
Fin 3	58.86	47.20	56.31	61.24	58.14
Fin 4	58.84	47.37	56.24	61.15	58.15
Fin 5	59.60	47.82	56.66	61.85	58.87
Fin 6	59.94	47.69	56.43	61.79	58.90
Fin 7	59.55	47.79	56.70	61.82	58.99
Fin 8	59.97	48.07	56.68	61.88	59.03
Fin 9	59.58	47.83	56.62	61.57	58.91
Fin 10	59.63	47.51	56.68	61.65	58.97
Fin 11	59.61	47.52	56.54	61.51	58.61
Fin 12	59.69	47.29	56.39	61.43	58.45
Fin 13	59.54	47.20	56.42	61.34	58.41
Fin 14	59.75	47.21	56.30	61.33	58.28
Fin 15	59.56	47.10	56.48	61.21	58.37
Fin 16	59.61	47.03	56.24	61.31	58.14
Fin 17	59.71	46.88	56.26	61.22	58.08
Fin 18	59.85	46.95	56.27	61.35	58.16
Fin 19	59.71	47.08	56.29	60.84	57.92
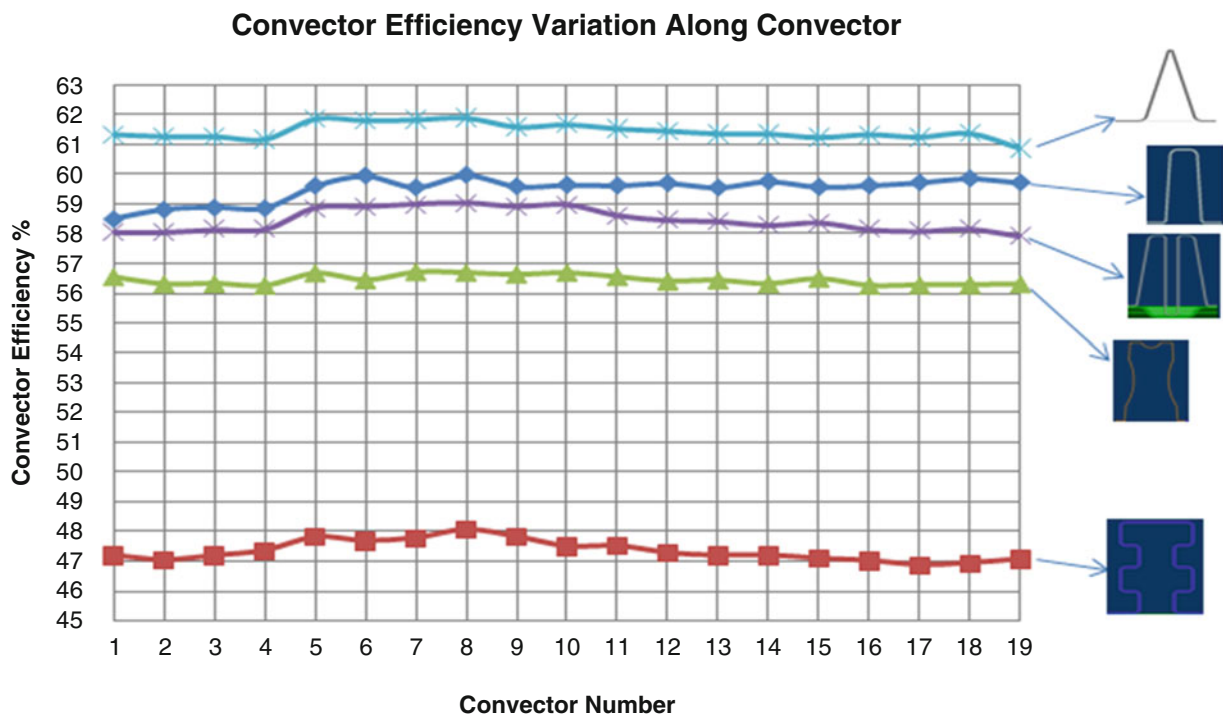
Fig. 58.14 Fin efficiency comparison between original radiator fin design and new fin designs

Table 58.11 Numerical results of new fin designs according to original radiator fin design

Specifications					
Area magnitude of fin (m^2)	1.616	2.180	1.715	1.559	3.038
Area magnitude increase ratio relative to original radiator	1	1.349	1.061	0.964	1.879
Heat transfer rate of panel (W)	190.028	187.865	189.633	190.921	174.955
Panel decrease ratio relative to original radiator fin design	1	0.988	0.997	1.004	0.920
Heat transfer rate of fin (W)	256.020	272.044	259.912	259.090	426.538
Fin increase ratio relative to original radiator fin design	1	1.0625	1.015	1.011	1.666
Outlet water temperature (°C)	64.9	64.7	64.8	64.8	61.4
Enthalpy difference (J/kg)	41,673	42,336	42,136	42,200	56,338
Heat transfer rate (W) [based on Eq. (58.13)]	894.172	908.398	904.136	905.479	1,208.837
Increase ratio for heat transfer rate relative to original radiator fin design	1	1.015	1.011	1.012	1.351
Heat flux (W/m^2)	553.324	416.696	527.193	580.807	397.905
Decrease ratio for heat flux	1	0.753	0.952	1.049	0.719

and arithmetic average of fin design-1 is 47.34 %. The most increase in the fin efficiency results was obtained for triangular profile fin design. The specifications of numerical results of original radiator fin design and new fin designs are listed together in Table 58.11.

The area magnitude of fin design-1 is 35 % greater than original radiator fin design. The increase at heat transfer rate from the radiator based on Eq. (58.13) is 1.5 %. Heat flux is 24.7 % smaller than original radiator fin design. 6.1 % increase at area magnitude of fin design-2 according to original radiator fin design was obtained but 1.1 % increase at heat transfer rate from the radiator based on Eq. (58.13) was obtained. Heat flux is 4.8 % smaller than original radiator fin design. The area magnitude of triangular profile fin design is 3.6 % smaller than original radiator fin design. The increase at heat transfer rate from the radiator based on Eq. (58.13) is 1.2 %. Heat flux is 4.9 % greater than original radiator fin design. The area magnitude of fin design-3 is 87.9 % greater than original radiator fin design. The increase at heat transfer rate from the radiator based on Eq. (58.13) is 35.1 %. Heat flux is 28.1 % smaller than original radiator fin design.

Conclusions

New fin designs were created in order to enhance the rate of heat transfer of the panel radiator with containing less material. It is aimed to manufacture a more efficient panel radiator. Different air-side convective heat transfer coefficients were tested so as to compute outlet water temperature of 65 °C that is related to panel radiator in accordance with TS EN442. 6.5 W/m^{2}K was optimum value for this panel radiator and used in these all numerical studies. The contact interface type was used to join together to permit conjugate heat transfer between a fluid and solid region. Heat transfer rate of the panel radiator was specified by the help of a commercial CFD code of STAR-CCM+ with top-bottom-opposite-end connection. Four convector designs were drawn so as to compare their fin efficiencies and heat transfer rates with respect to the original panel radiator. Since the increase at heat transfer rate from the radiator based on Eq. (58.13) is 1.2 %, in case of 3.6 % decrease at the area magnitude of convector, and heat flux is 4.9 % greater than original radiator fin design, most efficient fin among these ones is triangular profile fin design. Arithmetic average of triangular profile fin design efficiency is 3.151 % greater

than original radiator. Figure 58.14 proves that most increase in fin efficiency was obtained for triangular profile fin design, and thus triangular profile fin design is more efficient, has a higher heat transfer rate and has a lower cost material than original radiator fin design.

Nomenclature

A	Total area [mm^2]	$\dot{Q}_{fin}$	Actual heat transfer rate from the fin [W]
A$_{fin}$	Total surface area of the fin [m^2]	$\dot{Q}_{fin,max}$	Ideal heat transfer rate from the fin [W]
c_p	Specific heat [kJ/kg K]	$\dot{Q}_h$	Heat transfer based on enthalpy [W]
EN	European standard	Q'	Rate of heat transfer of the one module [W]
H	Panel radiator height [mm]	Re	Reynolds number
h_a	Air-side heat transfer coefficient [W/m^{2}K]	TBOE	Flow and return top and bottom at opposite ends
h_i	Enthalpy at inlet side [kJ/kg]	TS	Turkish standard
h_o	Enthalpy at outlet side [kJ/kg]	T_b	Base temperature [K]
k	Thermal conductivity [W/m K]	T_i	Inlet temperature [K]
L	Module length of the radiator [mm]	T_o	Outlet temperature [K]
$\dot{m}$	Mass flow rate [kg/s]	T_∞	Ambient temperature [K]
$\dot{Q}$	Heat transfer rate [W]	V	Fluid inlet velocity [m/s]

Greek Symbols

ΔT	Temperature difference between inlet and outlet side [K]	ρ	Density [kg/m^3]
μ	Dynamic viscosity [Pa s, kg/ms]	η_{fin}	fin efficiency

Subscripts

i	Inlet condition	o	Outlet condition

References

1. Beck SMB, Grinsted SC, Blakey SG et al (2004) A novel design for panel radiators. Appl Therm Eng 24:1291–1300
2. Lu W, Howarth AT, Jeary AP (1997) Prediction of airflow and temperature field in a room with convective heat source. Build Environ 32(541–550):1997
3. Zhai Z, Chen Q, Haves P et al (2002) On approaches to couple energy simulation and computational fluid dynamics programs. Build Environ 37:857–864
4. Cengel YA (2006) Heat and mass transfer, 3rd edn. Mcgraw Hill
5. EN 422–2 (1997) Radiators and convectors, part 2. BSI
6. Incropera FP, DeWitt DP (1993) Introduction to heat transfer, 3rd edn. Wiley

Hydrodynamic Aspects of Oscillating Flow Through Porous Media Consisting of Steel Spheres

Mehmet Turgay Pamuk and Mustafa Özdemir

Abstract

Hydrodynamic aspects of oscillating flow through porous media are investigated within the scope of this experimental work where water is used as the flow medium. Friction factors are found reducing the data of hydrodynamic experiments for oscillating flows. The experimentally determined maximum friction factors for oscillating flow are represented as correlations. They are then compared to those obtained by the other researchers. The results can readily be used in the design of cryogenic coolers and heat exchangers where pressure drop; thus, hydraulic losses are of primary importance.

Keywords

Porous medium • Oscillating flow • Friction factor • Permeability • Inertial coefficient

Introduction

The porous media have been used widely in many engineering fields such as cryogenic coolers, solid matrix heat exchangers, cooling of electronic equipment, and regenerators in order to enhance heat transfer. However, due to the complex structures of porous media, pressure loss and thus fluid pumping power have always been very important. Henri Darcy, a French hydrologist who designed a water filter for the city's drinking water system established the first theory on the hydrodynamic aspects of fluid flow through porous media about 150 years ago. Another historic work was accomplished by Ergun [1] who calculated experimentally the coefficients of the constitutive equations required by the continuum modeling such as permeability and inertial coefficients of porous media. These experimental coefficients can be found widely in the literature according to the types of porous media.

Özdemir [2] investigated the hydrodynamic aspects of porous media consisting of wire screen meshes under steady flow conditions. His work suggests a new method to calculate the porosity using REV. He used Ergun's equations to define the permeability and other parameters of the media used in his experiments.

Dukhan et al. [3] conducted steady-state unidirectional pressure-drop measurements in wind tunnel for airflow through nine compressed and uncompressed isotropic open-cell aluminum foam samples, having different porosities and pore densities. They found that the compressed foam produced significantly higher pressure drop, which increased with increasing Darcian velocity following the quadratic Forchheimer equation. Both compressed foam and uncompressed foam were correlated using an Ergun-like equation with the correlation.

M.T. Pamuk (✉)
Department of Marine Engineering, Piri Reis University, Postane Mahallesi,
Manastır Yolu Eflatun Sk. No:16, 34940 Tuzla/İSTANBUL, Turkey
e-mail: turgaypamuk@hotmail.com

M. Özdemir
Mechanical Engineering Faculty, Istanbul Technical University, Beyoglu, Istanbul, Turkey
e-mail: ozdemirmu4@itu.edu.tr

Riberio et al. [4] tried to establish equations to represent wall effects in densely packed porous media subjected to steady flow. According to their findings, average porosity increases as D/d_p decreases. This feature should be taken into consideration especially when particle sizes are big when compared to that of the channel through which the flow takes place.

Aside from these developments in steady fluid flow through porous media, the oscillating fluid flow also has found many engineering applications such as internal combustion engines, Stirling engines, cryogenic coolers, and other periodical processes in thermal and chemical systems.

Zhao and Cheng [5] investigated experimentally oscillatory pressure drops through a woven-screen packed column. They presented correlations for maximum pressure drop factor and cycle-averaged pressure drop factor in the kinetic Reynolds number range of 0.001–0.13 and in dimensionless fluid displacement range of 614.73–2,827.56, under the condition of sinusoidal motion of air. They found that the values of cycle-averaged pressure drop of oscillatory flow were several times higher than that of steady flow.

Ju et al. [6] conducted experiments to determine the oscillating flow characteristics for a regenerator consisting of stacks of wire meshes in a pulse tube cryogenic cooler. The oscillating flow characteristics appear not only as pressure drops but also as phase lags, as gas is used as the flow medium throughout the experiments. It is found that the value of the cycle-averaged pressure drop of the oscillating flow in the regenerator is 2–3 times higher than that of a steady flow at the same Reynolds numbers based on the cross-sectional mean velocity.

Hsu et al. [7] studied experimentally pressure–velocity correlations of steady and oscillating flows in regenerators made of wire screens. They indicate that, for oscillating flows, the velocity responses quite linearly to the pressure gradient when the piston amplitude is small. This suggests that Darcy's law is valid for small amplitude oscillating flows. When the piston amplitude becomes large, the response and therefore the correlation of pressure-drop and velocity in the regenerator become nonlinear.

Nam and Jeong [8] analyzed a regenerator under oscillating flow. In their model, they used an additional parameter named as Breathing factor for the precise estimation of the phase angle. They obtained empirical correlations of the friction factor and the Breathing factor for the screen regenerators.

Ju and Shen [9] studied comparatively the oscillating flow characteristics of cryogenic cooler regenerators at low temperatures. They proposed universal friction factors for various temperature conditions to be used in regenerator designs.

Cha [10] studied experimentally and numerically hydrodynamic parameters of microporous media for steady and oscillatory flow on oscillating flow in eight different microporous media. His findings show that pressure drop in oscillatory flow is not necessarily lower than that of steady flow which actually depends on packing material and the oscillating frequency.

Shen and Ju [11] summarized typical experimental results and correlations on the friction factor of regenerators, at different operating frequencies, at room and cryogenic temperatures. The comparison of these friction factor data was presented to clarify the reason for their difference. Finally, a new correlation of friction factor for oscillating flow regenerator, in terms of two nondimensional parameters, was presented.

Jin and Leong [12] and Leong and Jin [13] have conducted an experimental study regarding steady and oscillating flows through open cell aluminum foams. Considering various porosities and permeabilities, they conclude that flow resistance increases with form coefficient and decreases with the increasing permeability for a given porosity. Form drag is the primary reason for pressure loss by increasing flow velocity. They presented correlations of friction factors as Zhao and Cheng. They also showed that the pressure loss is increased both with increasing A_o and kinetic Reynolds number Re_ω.

Cheadle et al. [14] studied packed sphere regenerator friction factors under oscillating flow conditions using CFD Analysis. They used Valensi number which is defined as kinetic Reynolds number in other publications, to take into account the oscillation frequency. They point out that friction factor is independent of Valensi number, for Va < 10, and is therefore not effected by oscillating flow in this range. For Va > 10, however, oscillating flow effects are evident.

Pamuk and Özdemir [15] studied experimentally oscillatory and steady flows of water through two different porous media consisting of mono-sized stainless steel balls. They provided expressions for friction factors for both steady and oscillating flows.

In this chapter, findings of Pamuk and Özdemir [15] have been compared to those of Zhao and Cheng [5] and Leong and Jin [12] who used wire screen meshes and aluminum foam, respectively. It has thus been possible to assess these three most common packing materials in terms of pressure drop under oscillating flow conditions.

Experimental Setup

Water is used in this study as the working fluid unlike the majority of the experimental studies in literature. The air dissolved or encapsulated by water is a major problem when it comes to pressure and velocity measurement. The compressibility of water is considerably affected due to air content; thus, the flow rates of half cycles are different. In order to overcome this problem, the whole system was vacuumed and then filled with water.

A schematic diagram of the experimental setup is shown in Fig. 59.1. Main components of the experimental setup are an oscillation generator (a double-acting cylinder), an electrical motor reducer to drive it, and a flywheel with an adjustable crank arm. The remaining components are related to piping.

Data collected by means of Keithley 2700 data acquisition system from pressure sensors installed at the inlets of the porous medium are sent to a PC to be processed. An inductive type proximity sensor is installed to sense a metallic target mounted on the periphery of the flywheel such that the location of the target corresponds to the maximum piston movement (full stroke). Since pressure and location signals are both collected by the data acquisition system, it is possible to synchronize them due to the fact they are in the same phase, as opposed to when gas is used as the working fluid where significant phase lags may occur depending on the oscillation frequency.

The test chamber is made from a stainless steel pipe. Porous media are formed by filling the test chamber with mono-sized stainless steel balls of 1 and 3 mm in diameter. The test chamber is shaken to ensure that no excessive voids are left. Wire meshes are installed at both ends of the test chamber in order to prevent the balls from scattering.

An uncertainty analysis based on the method described by Figliola and Beasley [16] is performed. The uncertainties of angular frequency, maximum fluid displacement x_{max}, dimensions, the amplitude of area averaged fluid velocity, and pressure gradient ($\Delta P/L$) are estimated to be 0.43 %, 0.51 %, 1.95 %, 0.23 %, and 1.76 % respectively.
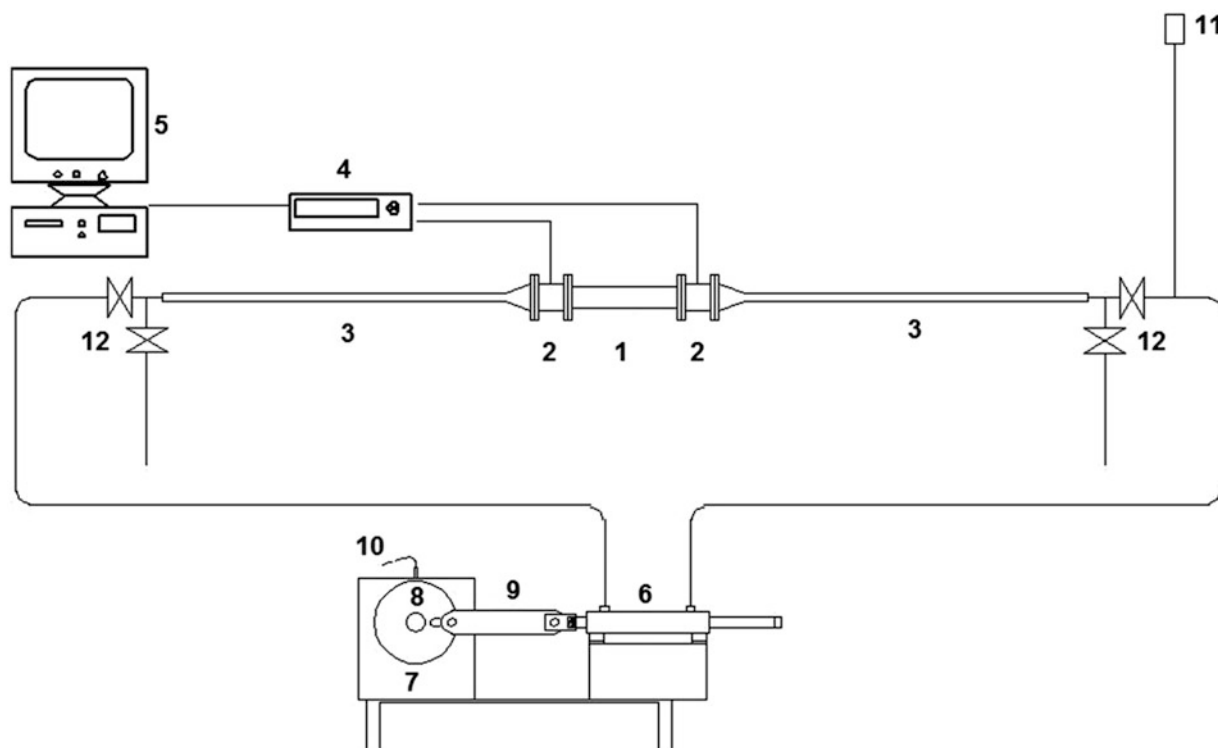
Fig. 59.1 Experimental setup: 1. test section (porous medium), 2. PE pipe, 3. pipe of 32 mm in diameter, 4. Keithley 2700, 5. PC, 6. oscillation generator, 7. motor reducer, 8. flywheel, 9. crank arm, 10. inductive proximity sensor, 11. air purger, 12. separating valves for steady and oscillating flows

Results and Discussion

Oscillating flow experiments are conducted for three different flow amplitudes and eight different flow frequencies. Maximum fluid displacements are chosen according to the displacement of the piston as 130, 170, and 195 mm. In this case, the maximum flow displacements (x_{max}) at the entrance of the porous channel are calculated from the ratio of cross-sectional areas of piston and the entrance of porous channel as 72.63, 94.97, and 108.94 mm, respectively. For each amplitude, line frequency of 50 Hz is changed from 5 Hz to 15 Hz by an A/C motor drive. As a result of this, flow frequency changes in the range of 0.115–0.345 Hz depending on the 6.9–20.7 rpm speed of motor reducer which normally operates at 69.7 rpm at 50 Hz of line frequency.

The displacement of the piston is taken as zero at the rear position inside the cylinder, and it becomes maximum value which is equal to the diameter of the flywheel at the forward position. The piston displacement will be equal to the fluid displacement due to the fact that the fluid is incompressible. Hence, at the entrance of the porous medium, the fluid displacement x_m varies with angular frequency (ω) and time (t) according to

$$x_m(t) = \frac{x_{\max}}{2}(1 - Cos\omega t) \tag{59.1}$$

where $x_{\max} = 2RA_p/A$. Here, R, A_p, and A are flywheel radius, cross-sectional areas of double acting cylinder, and test chamber, respectively. The cross-sectional mean fluid velocity in the channel is

$$u_m(t) = u_{\max}Sin\omega t \tag{59.2}$$

where $u_{\max} = \omega x_{\max}/2$

In Fig. 59.2 it is seen that the slope of the pressure gradient is subjected to an abrupt change near the oscillation axis. The rate of pressure gradient is low within this region where flow velocity is very low, but it is considerably higher for the other region. This abrupt change may mean that the flow regime inside the porous medium changes. Four distinct flow regimes for steady flow through porous medium are determined with Reynolds number defined as $Re_p = \rho(u_m/\varepsilon)d/\mu$. These regimes are Darcy flow regime ($Re_p < 1$), inertial flow regime ($1 < Re_p < 150$), unsteady laminar flow regime ($150 < Re_p < 300$), and unsteady and chaotic flow regime ($Re_p > 300$) as pointed out by Kaviany [17]. The instant average velocity of oscillating flow changes 0–0.12 m/s, so that Reynolds number increases up to approximately 300.

The temporal variation of pressure gradient with respect to cycle angle and the maximum flow displacement is given in Fig. 59.3 for a fixed frequency ($\nu = 0.233$ Hz). As seen in the figure, amplitude of the pressure gradient increases as the amplitude of the flow displacement increases. The abrupt change near the oscillation axis can be observed here also.

Because the mean velocity and pressure gradient vary with time in oscillating flows, friction factor defined above also varies with time. For this reason, friction factor is defined in the literature with amplitudes of mean velocity and pressure
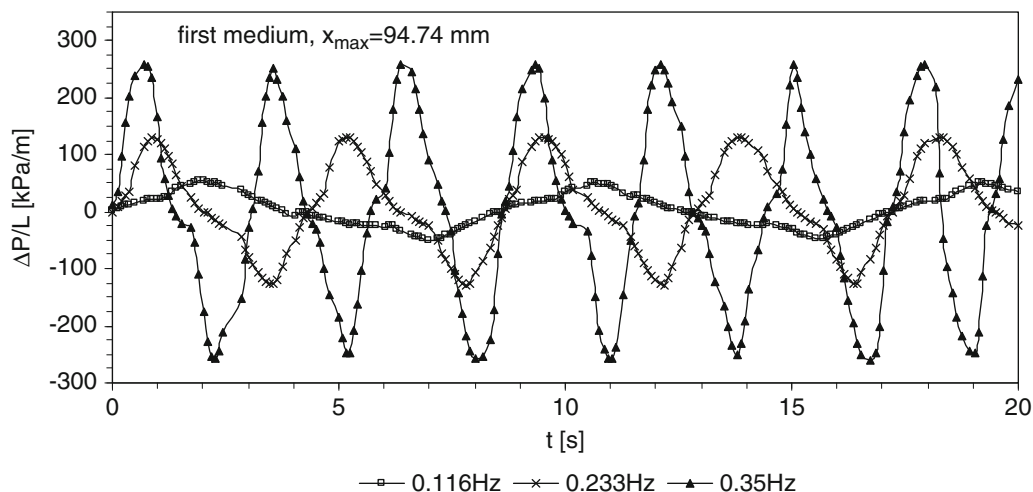
Fig. 59.2 Temporal variation of pressure gradient for various oscillation frequencies ($x_{max} = 94.97$ mm, first medium)
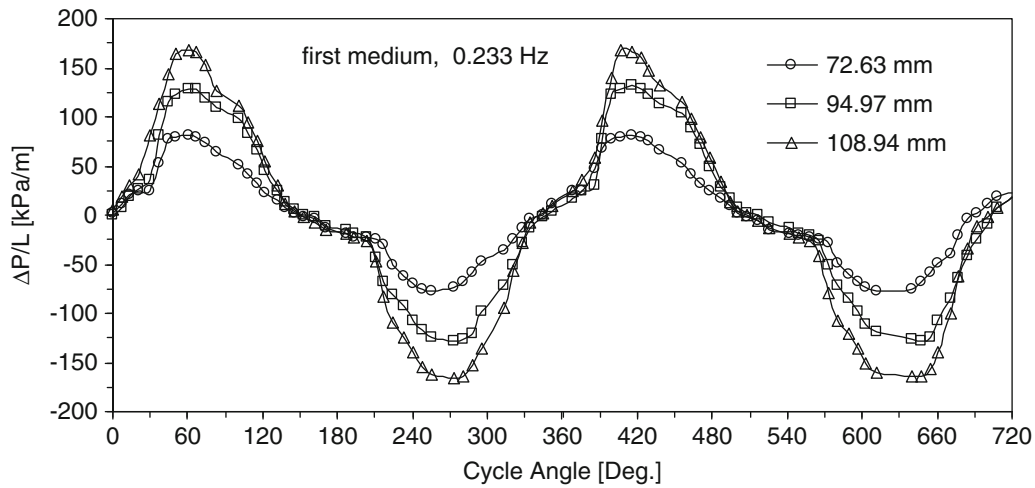
Fig. 59.3 Variation of pressure gradient with respect to various flow displacements for fixed frequency ($\nu = 0.233$ Hz, first medium)
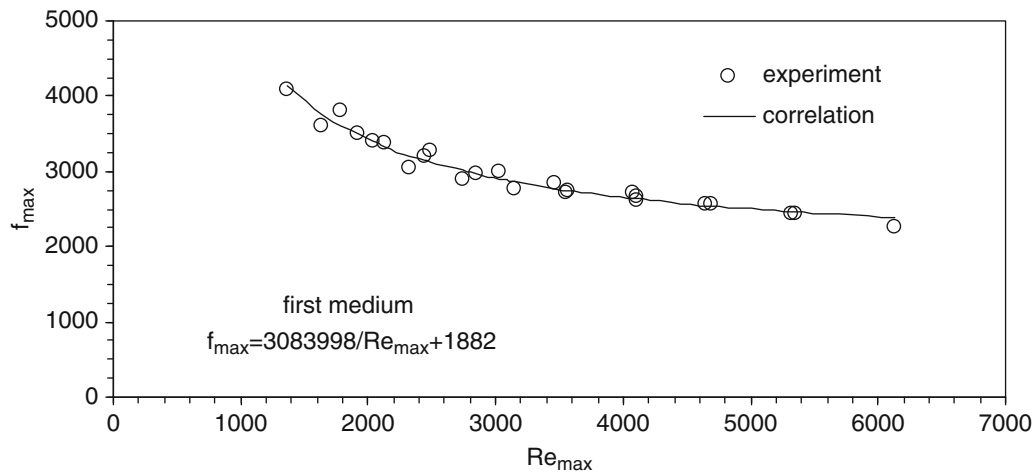
Fig. 59.4 Maximum friction factor versus Re_{max} (first medium)

gradient as shown in the following:

$$f_{max} = \frac{2D\Delta P_{max}}{\rho u_{max}^2 L} \tag{59.3}$$

Variation of friction factor obtained from the experimental data with respect to Re_{max} for the first porous medium is shown in Fig. 59.4. The correlation equation in the form of Eq. (59.4) is obtained by curve fitting of the experimental data.

$$f_{max} = \frac{3083998}{Re_{max}} + 1882 \tag{59.4}$$

It is seen that this kind of correlation equation is in reasonable agreement with experimental data. Eq. (59.5) expresses the behavior of the maximum friction factor in oscillating flow through porous medium in a good manner.

Figure 59.5 shows the variation of maximum friction factor with respect to Re_{max} for the second porous medium. And the correlation equation obtained by curve fitting of the experimental data is

$$f_{max} = \frac{532936}{Re_{max}} + 612.1 \tag{59.5}$$
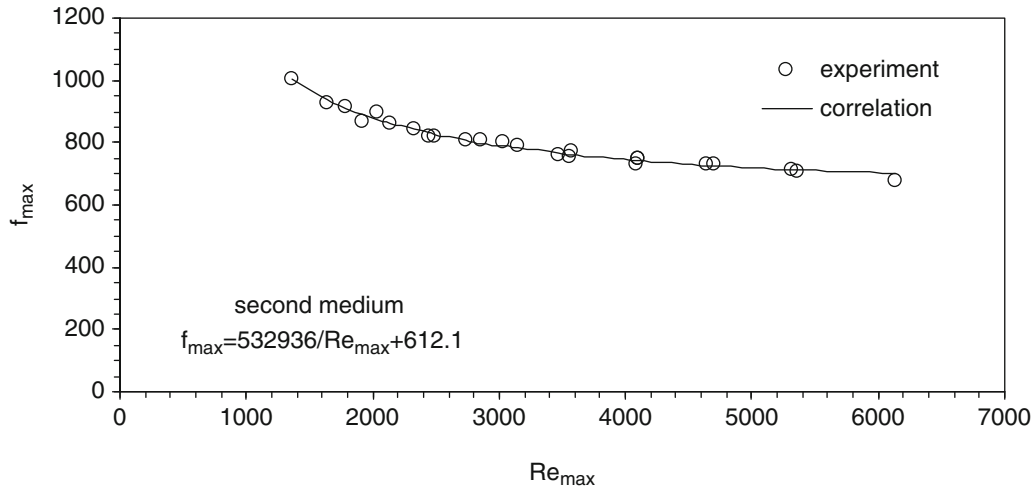
Fig. 59.5 Maximum friction factor versus Re_{max} (second medium)
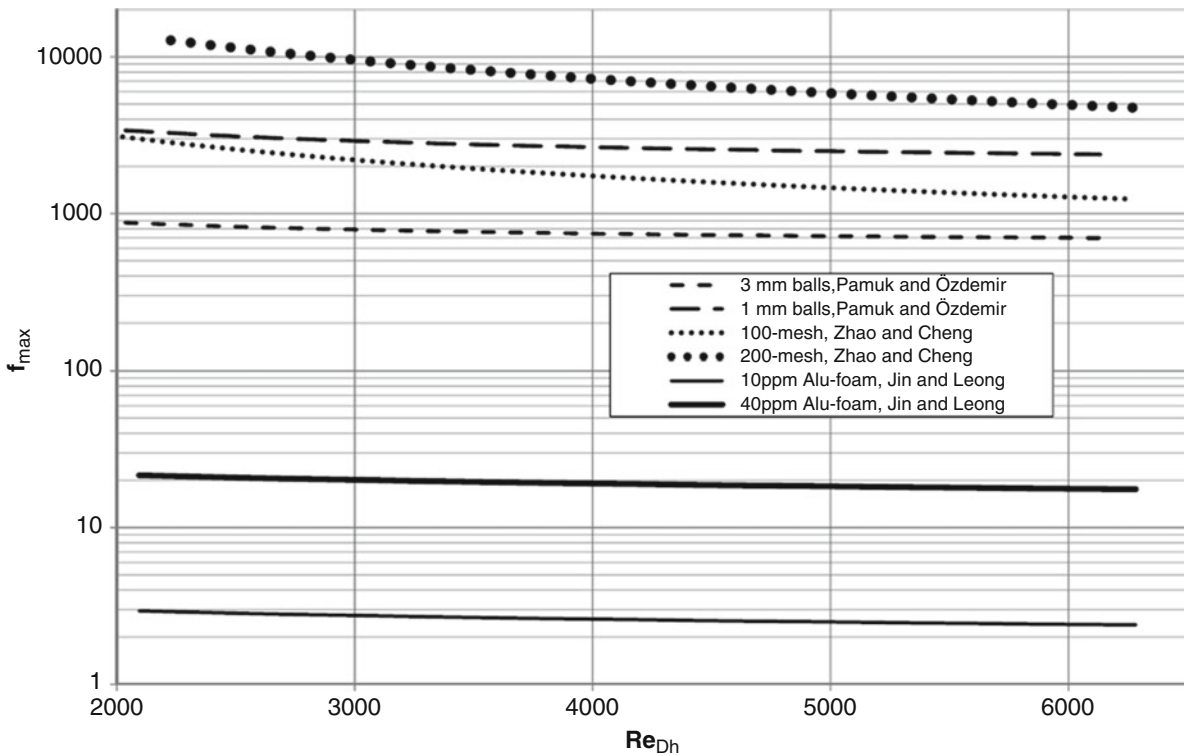
Fig. 59.6 Comparison of maximum friction factors for various packing materials

As seen in Figs. 59.4 and 59.5, the maximum friction factor for the first medium with the porosity of 0.369 is about four times higher than that of the second medium with the porosity of 0.3912. Increasing porosity reduces the maximum friction factor considerably as expected. These correlation equations of maximum friction factors for oscillating flows through porous media have a maximum relative error of 9 % in comparison with experimental data.

The above correlations have then been compared to those of Zhao and Cheng [5] and Leong and Jin [12] who used wire screen meshes and aluminum foam, respectively. Figure 59.6 shows all six correlations together. Their correlations normally given in terms of pore hydraulic diameter are here recalculated in terms of channel-diameter-based Reynolds numbers for comparison. For the selected set of porous media, it is obvious that the aluminum foams that have a porosity of 0.90 have the lowest friction factor. However, friction factors of both wire screen meshes and steel balls have the same order of magnitudes.

Conclusion

Friction factor representing the pressure drop through porous media subjected to oscillating flow decreases asymptotically independent of the porous media. However, the porosity differences and variation of permeability due to complex geometries within the porous media have key importance in terms of the magnitude of the friction factors and thus the pressure loss through these media. It is therefore important to decide the type of the medium when it comes to comparing the cost of constructing the porous medium to energy cost due to pressure loss. However, heat transfer features of these different types of media have not been mentioned here and assumed to be comparable to each other.

Nomenclature

A	Cross-sectional area of the test chamber	P'	Nondimensional pressure parameter defined in Eq. (59.1)
A_p	Cross-sectional area of double acting cylinder	R	Radius of flywheel
A_o	Nondimensional displacement defined as $A_o = x_{max}/D$	Re_D	Reynolds number defined in Eq. (59.1)
d	Ball diameter	Re_{max}	Reynolds Number defined as $Re_{max} = A_o Re_\omega/2$
D	Inner diameter of test chamber	Re_ω	Kinetic Reynolds Number ($\rho\omega D^2/\mu$)
D_h	Hydraulic diameter, same as inner diameter of test chamber	t	Time
f_{max}	Maximum friction factor defined in Eq. (59.3)	u_m	Cross-sectional mean fluid velocity
		u_{max}	Amplitude of mean fluid velocity
F	Inertial coefficient	x_m	Temporal fluid displacement at the inlet of the test chamber
K	Permeability		
L	Length of the porous medium	x_{max}	Maximum fluid displacement at the inlet of the test chamber
ΔP	Pressure difference		
ΔP_{max}	Amplitude of pressure difference	Va	Valensi Number ($\rho\omega D^2/\mu$)

Greek Letters

ε	Porosity	ν	Frequency, 1/s
ρ	Fluid density	μ	Dynamic viscosity
ω	Angular frequency, rad/s		

References

1. Ergun S (1952) Fluid flow through packed columns. Chem Eng Prog 48(2):89–94
2. Özdemir M (1996) Tel Örgü Katmanlarından Oluşan Gözenekli Ortamda Zorlanmış Isı Geçişi. Ph.D. Thesis, Istanbul Technical University, May 1996
3. Dukhan N, Feliciano R, Hernandez A (2006) Air flow through compressed and uncompressed aluminum foam: measurements and correlations. Trans ASME 128:1004–1012
4. Riberio AB, Neto P, Pinho C (2010) Mean porosity and pressure drop measurements in packed beds of mono sized spheres: side wall effects. Int Rev Chem Eng 2 (1)
5. Zhao TS, Cheng P (1996) Oscillatory pressure drops through a woven screen packed column subjected to cyclic flow. Cryogenics 36:333–341
6. Ju Y, Jiang Y, Zhou Y (1998) Experimental study of the oscillating flow characteristics for a regenerator in a pulse tube cryogenic cooler. Cryogenics 38 (6):649–656
7. Hsu C, Fu H, Cheng P (1999) On pressure-velocity correlation of steady and oscillating flows in regenerators made of wire screens. Trans ASME 121:52–56
8. Nam K, Jeong S (2005) Investigation of oscillating flow friction factor for cryocooler regenerator considering cryogenic temperature effect. Cryogenics 45:733–738
9. Ju Y, Shen Q (2009) Comparative study of oscillating flow characteristics of cryogenic cooler regenerator at low temperatures. Front Energy Power Eng China 3 (1):80–84
10. Cha JJ (2007) Hydrodynamic parameters of micro porous media for steady and oscillatory flow: application to cryogenic cooler regenerators. A dissertation presented to the Academic Faculty, Georgia Institute of Technology
11. Shen QQ, Ju YL (2008) A new correlation of friction factor for oscillating flow regenerator operating at high frequencies. CP 985, advances in cryogenic engineering, transactions of the cryogenic engineering conference-CEC, vol 53
12. Jin LW, Leong KC (2008) Pressure drop and friction factor of steady and oscillating flows in open-cell porous media. Transport Porous Media 72:37–52. doi:10.1007/s11242-007-9134-3

13. Leong KC, Jin LW (2006) Effect of oscillatory frequency on heat transfer in metal foam heat sinks of various pore densities. Int J Heat Mass Transfer 49:671–681
14. Cheadle MJ, Nellis GF, Klein SA (2011) Regenerator friction factor and Nusselt Number information derived from CFD analysis. In: Miller SD, Ross RG Jr (eds) Cryogenic coolers, vol 16. International Cryogenic Cooler Conference, Boulder, CO
15. Pamuk MT, Özdemir M (2012) Friction factor, permeability and inertial coefficient of oscillating flow through porous media of packed balls. Exp Ther Fluid Sci 38:134–139
16. Figliola RS, Beasley DE (2006) Theory and design for mechanical measurements. Wiley
17. Kaviany, M (1995) Principles of heat transfer in porous media, 2nd edn. Springer, New York, pp 48–49

Flow and Heat Transfer Characteristics of an Empty Refrigerated Container

60

Ersin Alptekin, Mehmet Akif Ezan, and Nuri Kayansayan

Abstract

To preserve the quality and the shelf life of perishable foods, it is essential to analyze the airflow distribution inside a refrigerated truck for maintaining homogeneous temperature throughout. This study is an initiation of such analysis, and air distribution patterns of ceiling-slot ventilated enclosure are numerically investigated for three different geometries. Numerical analysis is carried out by using ANSYS-FLUENT software which is based on control volume approach. In the analysis, the container's cross-sectional area is kept constant. However, by changing the container length as 6 m, 8 m, and 13.3 m, the aspect ratio of the container is varied accordingly. The air velocity at the slot exit is varied in such a way that Reynolds number of the discharge flow covers the range between 20 and 1.23×10^5.

A three-dimensional solution domain is considered in the analysis and is identified by a total number of 2.5×10^6 meshes. The Reynolds Stress Model (RSM) is applied in solving turbulent Navier–Stokes equations at each computational node. The validity of the present computational method is checked by generating and comparing the results with available work in literature. The flow distribution patterns of empty container indicate that there exist circulation zones close to the surface at the opposite of air discharged slot. In fact, two different vortices at two perpendicular planes coexist. The location of these circulation zones does not change with the discharge flow rate, but the circulation intensity increases as the flow rate increases. It is determined that variation of the container aspect ratio affects the flow behavior. For the case of container length at 13.3 m, the flow at the upper surface separates at a distance of 11.5 m from the air injection plane.

Keywords

Refrigerated vehicle • Airflow distribution • Food transportation • Cold chain

Introduction

Cold chain is generally used to define a combination of temperature-controlled supply systems in food industry. As illustrated in Fig. 60.1, from the cold storage (or *warehouse*) to the client, the food must be kept in a predefined temperature range to preserve its quality and increase the shelf life. According to Flick et al. [1] about 60 % of food products require refrigeration process in the cold chain. They also stated that inadequate storage or transport conditions cause corruption of 25–30 % of global food production. This huge amount of loss can be regained by designing each component of the cold chain properly.

As indicated by Hoang et al. [2], 120 million tons of chilled foods are transported each year in Europe. With the expansion of the urban areas, the temperature control of frozen foods in refrigerated vehicles becomes crucial. Hoang et al. also mentioned that the ATP (International Agreement for the Transport of Perishables) separates the refrigerated vehicles into

E. Alptekin (✉) • M.A. Ezan • N. Kayansayan
Department of Mechanical Engineering, Dokuz Eylül University, 35397, Tinaztepe, Buca, Izmir, Turkey
e-mail: ersin.alptekin@deu.edu.tr; mehmet.ezan@deu.edu.tr; nuri.kayansayan@deu.edu.tr
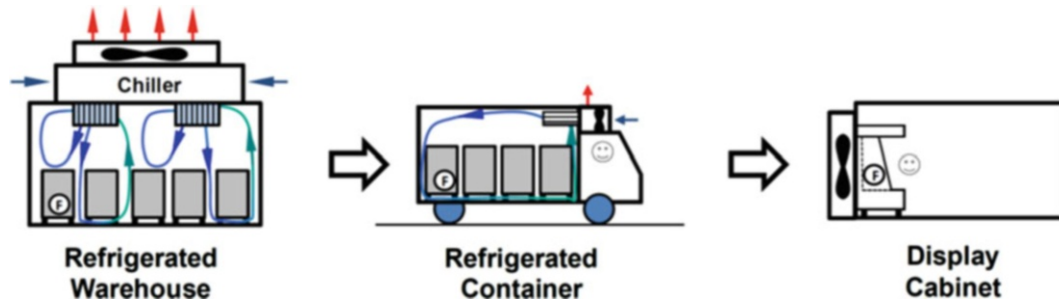
Fig. 60.1 Cold chain

two categories, which are "Normally Insulated" and "Heavily Insulated" vehicles. Heavily insulated trucks are adequate for frozen food transportation with an overall heat transfer coefficients less than 0.4 W/m^{2}K, and normally insulated trucks are considered to be proper for chilled foods ($U \leq 0.7$ W/m^{2}K). In these trucks, the main issue is to control the temperature distribution within a narrow range. To accomplish this in large volume ($V > 50$ m^3) transportation, the cooling system is usually driven by an engine separated from the vehicle's main engine. The positioning of the evaporator is a critical issue in acquiring homogeneous temperature distribution inside the container. Neglecting the small influences of radiation and natural convection, the cooling process is mainly controlled by forced convection, and the homogenous temperature distribution may be achieved by optimization of the flow distribution inside the container.

Even though numerous experimental and numerical results have been published for thermal behavior of warehouses, there are few studies conducted related with the refrigerated vehicles. As a pioneer, Moureh and his colleagues numerically and experimentally examined the flow and thermal behavior of a refrigerated container under several conditions. Moureh et al. [3] used FLUENT CFD software to obtain velocity distribution in empty and loaded containers. They compared the predicted velocity field with experimental LDA (Laser Doppler Anemometer) measurements. Two different turbulence models are implemented, k-ε and RSM. As a result, RSM turbulence model showed good agreement with the experimental data. After this pioneer study, Moureh and his colleagues conducted many other researches related with the refrigerated containers. Moureh and Flick [4] represented dimensionless temperature distribution inside container for one selected case at a single Reynolds number and a container length. In addition, Moureh and Flick [5] experimentally and numerically studied the temperature and velocity distributions inside a loaded container for two different spacings between loads, and the spacing is taken to be at 1 cm and 2 cm. Later, Moureh and Flick [6] tried to improve the performance of the container ventilation by locating the inlet section near lateral surface. They compared the ventilation efficiency for lateral and central inlet orientations. Besides, Moureh et al. [7] tried to improve the cooling effect by changing the air duct configuration. Unlike the previous numerical models, in this study, Moureh and his colleagues considered loads as porous medium to achieve more realistic velocity field.

In this study, air is discharged from the evaporator located at midsection of front surface having half width of the container. Suction, on the other hand, takes places at all surfaces except the discharge plane of the evaporator. First, the flow field is studied and the circulation zones are identified. To do this, flow Reynolds number and container aspect ratio have varied, and the local and the average heat transfer characteristics of such a flow are computed. The refrigerated truck is assumed to be moving for external flow simulations. Thus, the container's overall heat transfer coefficients and heat gains through the container surfaces are realistically evaluated.

Material and Method

Definition of the Problem

The geometry and the size of the refrigerated container are provided in Fig. 60.2. The evaporator is located at the center of the front surface, and the spacing between the ceiling and the evaporator is 4 cm. Air is supplied to the computational domain from the inlet section as represented in Fig. 60.2 and collected by the openings at the bottom, lateral, and top surfaces of the evaporator. The container cross-sectional area is kept constant, but the length is varied, so that the aspect ratio (L/H) is in the range between 2.4 and 5.32.
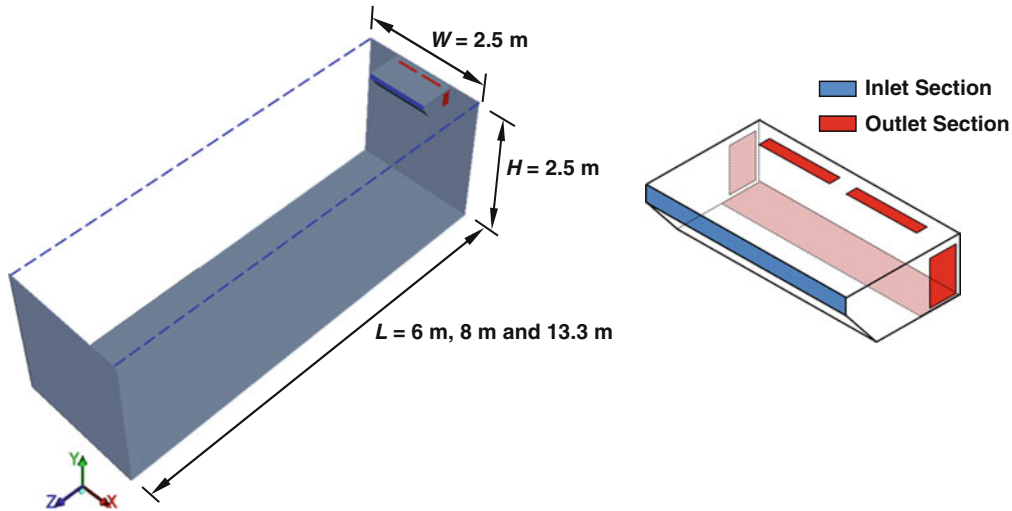
Fig. 60.2 Geometry of the container and evaporator

Governing Equations and Solution Method

To simplify the problem, instead of solving time-dependent governing equations, time averaged Reynolds-Averaged-Navier–Stokes (RANS) equations are solved. Considering steady and incompressible flow conditions, the principle of conservation of mass, momentum, and energy can be satisfied by the following equations:

Mass:

$$\frac{\partial}{\partial x_i}(u_i) = 0 \tag{60.1}$$

Momentum:

$$\frac{\partial}{\partial x_j}(\rho u_i u_j) = -\frac{\partial p}{\partial x_i} + \frac{\partial}{\partial x_j}\left[\mu\left(\frac{\partial u_i}{\partial x_j} + \frac{\partial u_j}{\partial x_i}\right) - \rho\overline{u_i' u_j'}\right] \tag{60.2}$$

Energy:

$$\frac{\partial}{\partial x_i}(\rho C_\rho u_i T) = \frac{\partial}{\partial x_j}\left[k\frac{\partial T}{\partial x_j} - \rho C_\rho \overline{u_j' T'}\right] \tag{60.3}$$

where u and u' indicate the average and fluctuating velocities, respectively. Similarly, T and T' represent the mean and instantaneous temperatures. Turbulence modeling by using RSM (Reynolds Stress Model) has been in use by many authors. Norton et al. [8] discussed the pros and cons of eddy viscosity and Reynolds stress closure models in turbulence modeling for confined rooms with adverse pressure gradients and flow separations. It is determined that RSM provided reasonable predictions for flow separations and Coanda effects. Similarly, Schälin and Nielsen [9] and Moureh and Flick [6] indicated that for three-dimensional flow in confined spaces, RSM method of calculations predicts the experimental results with a maximum of 10 % deviation. As a result, Reynolds Stress Model (RSM) is considered in this study for modeling the 3D turbulent flow.

Equations (60.1), (60.2), and (60.3) are solved with the aid of ANSYS-FLUENT software [10]. Software is based on the control volume approach of Patankar [11]. QUICK scheme [12] is applied for discretization of convective terms, and SIMPLE [13] algorithm is adapted for solution of momentum and continuity equations. For evaluating the turbulence boundary layer near the wall, "*log-law*" function is used [14]. Computational domain is divided into nonuniform quadrilateral grids. To capture the temperature, velocity, and pressure gradients close to the solid surface, fine grids are generated. Convergence criteria for all conservation equations are taken to be 10^{-5}.
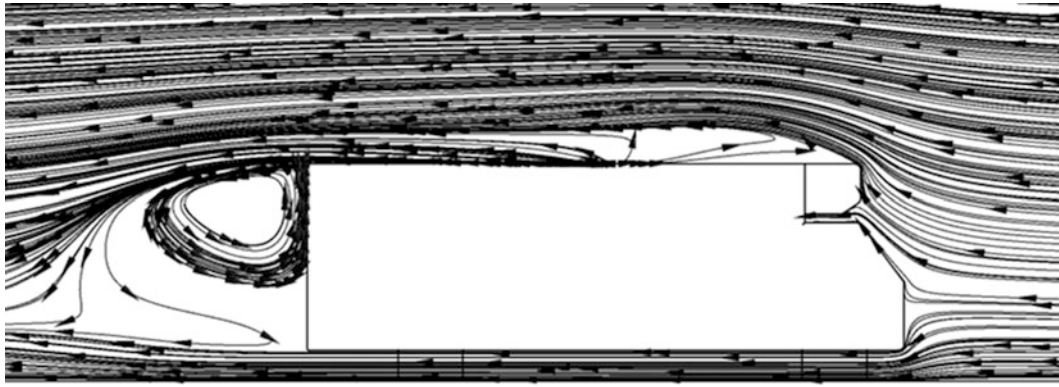
Fig. 60.3 Flow patterns around the refrigerated truck

Table 60.1 Mean heat transfer coefficients for external surfaces of container

| | Mean heat transfer coefficient, h (W/m^{2}K) | | |
| | | Theoretical | |
Surface	Predicted	Correlation	Result
Top	64.48	$\overline{Nu}_L = 0.037 Re_L^{4/5} Pr^{1/3}$	50.73
Lateral	66.18		56.4
Rear	42.05	—	—

Boundary Conditions and Mesh Independency

Because of container symmetry, half of the computational domain is taken into account, and at the symmetry plane, the boundary condition is set to be $\partial\phi/\partial x|_{x = W/2} = 0$. Uniform velocity ($w_{in}$) and temperature ($T_{in}$) profiles are assumed at the inlet section of the evaporator. On the container walls, no slip condition is sufficed by $u = v = w = 0$. Due to large insulation thickness at the bottom and front (i.e., surface with evaporator) surfaces, these surfaces are assumed to be adiabatic ($\partial T/\partial n|_{surface} = 0$). The insulation material is selected to be polyurethane, with $k = 0.02$ W/mK, and the thickness of the insulation layers are 100 cm, 85 cm, and 80 cm for the ceiling, lateral, and rear surfaces, respectively. On the top, lateral, and rear surfaces, the combine effect of solar radiation, convection, and surface emission is considered, and the following energy balance equation is defined at those surfaces:

$$-k\frac{\partial T}{\partial n}\bigg|_{surface} = \alpha I_{solar} - \sigma\varepsilon\left(T^4 - T_{sky}^4\right) - h_\infty(T - T_\infty) \tag{60.4}$$

where α and I_{solar} are the surface absorptivity and the incident solar radiation, respectively. Meteorological data of Izmir, Turkey, for June 21st at 1 PM noon are considered for solar radiation intensity (I_{solar}), the sky (T_{sky}), and atmospheric (T_{atm}) temperatures.

Average heat transfer coefficient (h) for each surface is evaluated by considering the results of a preliminary analysis. To solve 3D flow over the truck and container combination, at a velocity of 90 km/h, a total of 16 million hybrid grids are generated. The flow patterns around the truck are represented in Fig. 60.3. At the top and back sides of the container, separation of flow can easily be located. As a result of this preliminary analysis, average heat transfer coefficients for three surfaces are calculated as given in Table 60.1. The predicted heat transfer coefficients are compared with the well-known correlation over a flat plate [15]. Comparative results show that the numerical heat transfer coefficients are approximately 30 % higher than that calculated by theoretical methods.

To get numerical results free of mesh size, the same geometry at the same flow conditions is studied for three different mesh sizing which are respectively 2.5 million, 4.5 million, and 10 million. As indicated in Fig. 60.4, no remarkable change of results is detected due to change in mesh size. Therefore, 2.5 million mesh is selected for the current study.

Fig. 60.4 Influence of number of grids on the jet velocity decay
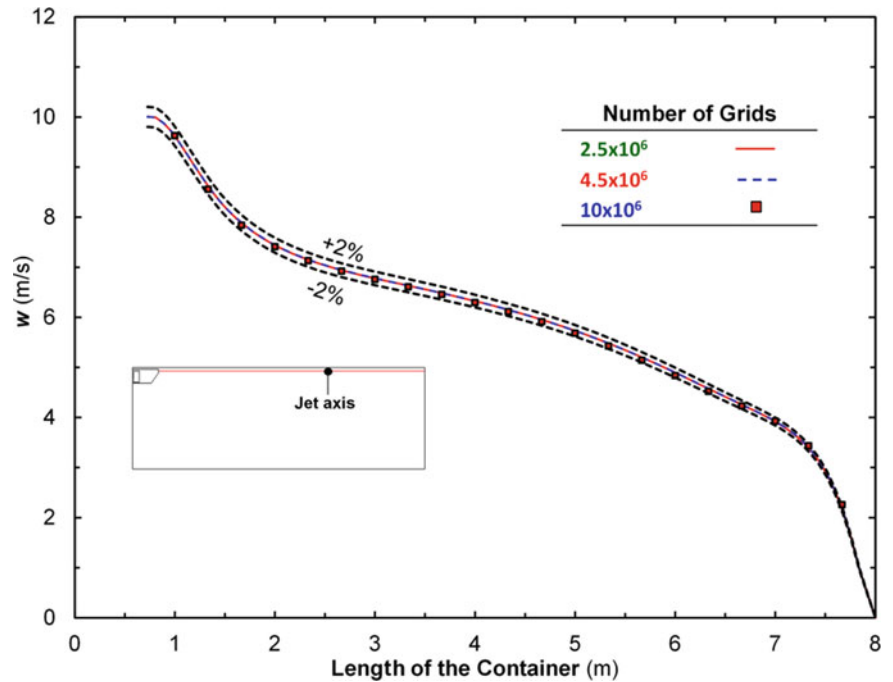
Results and Discussion

In this section, first the validity of the numerical method is discussed with regenerating the numerical data for the same geometry and flow conditions as studied experimentally by Moureh and Flick [6]. After that, the influence of selected parameters on the heat transfer inside the container is evaluated.

Validation of the Methodology

Recent experimental work of Moureh and Flick [6] that provides flow patterns inside a refrigerated vehicle is selected for comparison of present methodology. The container studied by Moureh has the same cross-sectional dimensions as $H = W = 2.5$ m with the present study, and the container length is taken to be 13.3 m. Unlike the present study geometry, the air inlet section is at the top, and the outlet is at the bottom of the front plane. Moureh and Flick studied the airflow characteristics of such a container both experimentally and numerically. In their analysis, LDA is used to capture the velocity distributions on the symmetry surface. In addition, the inlet velocity is taken to be 11 m/s, and the turbulence intensity of entering flow is defined to be 10 %. Moureh's results and the present study are compared for the same flow geometry and flow conditions.

In Fig. 60.5, airflow patterns on the symmetry plane of the container are compared with the experimental and numerical results of the reference work. On the symmetry plane of the container, two separated circulation zones are formed. Owing to the viscous effects, flow separates from the upper surface and generates a secondary circulation at the rear region of the container. As illustrated in Fig. 60.5, this study results predict the experimental results of the reference work fairly accurately. In Fig. 60.6, decay of the jet axis velocity in longitudinal direction is given and represents Moureh's experimental results within acceptable engineering accuracy.
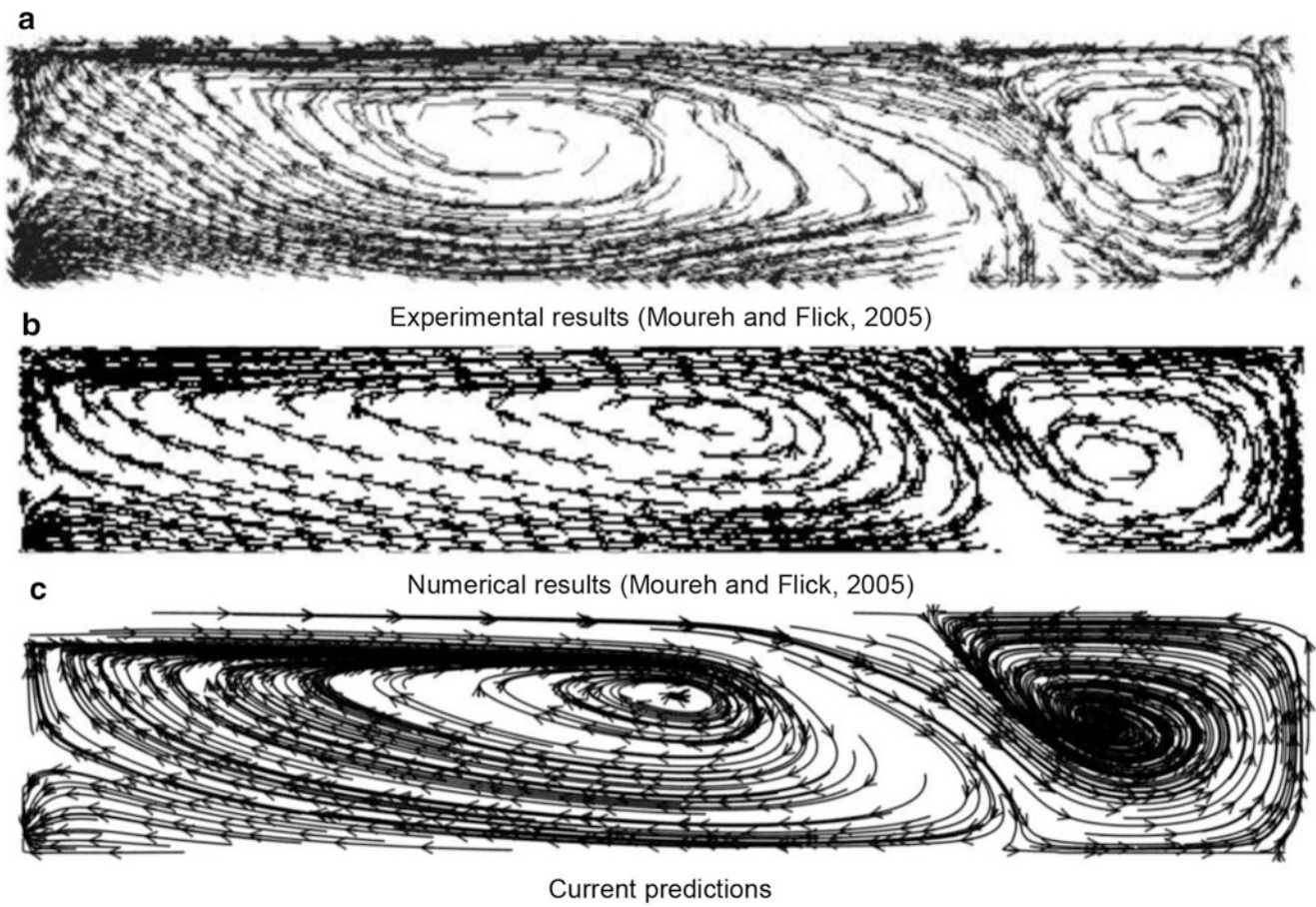
Fig. 60.5 Comparison of airflow patterns with the reference work. (**a**) Experimental results [6]. (**b**) Numerical results [6]. (**c**) Current predictions

Fig. 60.6 Comparison of velocity variation on jet axis with the reference work
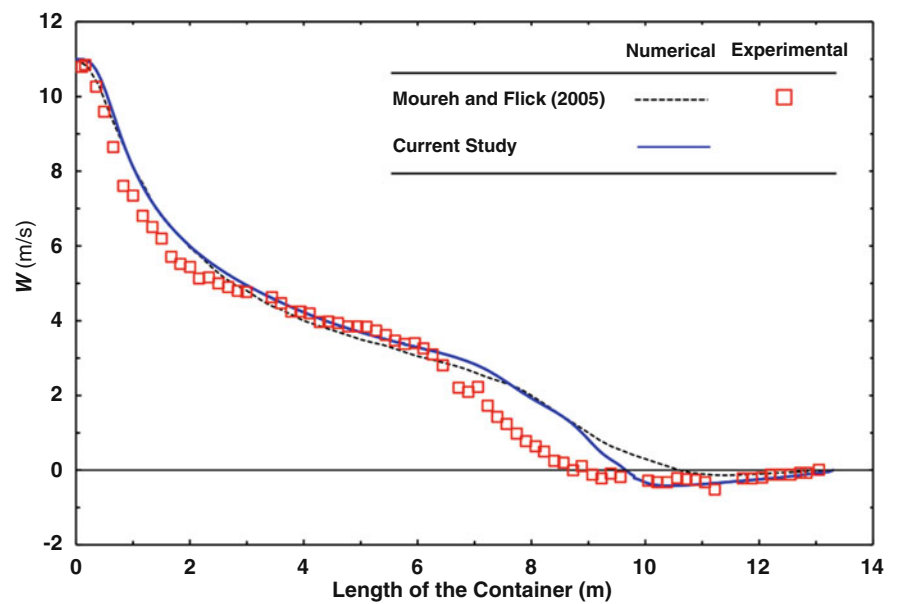
Table 60.2 Parameters that are used in the current study

Case	Reynolds number	Inlet temperature	Length of the container
#1	20		
#2	200		
#3	2,000		
#4	1.23×10^4		8 m
#5	6.23×10^4	$-10\,°C$	
#6	1.23×10^5		
#7	1.23×10^5		13.3 m
#8			6 m

Parametric Results

In order to evaluate the effect of inlet velocity on heat transfer through container surfaces, the flow Reynolds number is varied in the range of 20–1.23×10^5. In Reynolds number definition, characteristic length is taken to be hydraulic diameter of the evaporator exit section. In addition, the container length is varied so that the container aspect ratio (H/L) assumes the following values 2.4, 3.2, and 5.32. Hence, as shown in Table 60.2, a total of eight parameters are varied in the analysis.

Effect of Reynolds Number

Flow patterns and isotherms are illustrated in Fig. 60.7 for various Reynolds numbers. Temperature contours are represented in nondimensional form as $T^* = (T - T_{in})/(T_{out} - T_{in})$. As the Re number increases from 20 to 1.23×10^5, intensity of circulation increases and dominates the rear side region of the container. From Fig. 60.7, one can clearly see the Coanda effect for Re > 20. Coanda effect is defined as the tendency of the fluid jet which is attracted to a nearby surface. After leaving the inlet section, because of Coanda effect, flow becomes attached to the ceiling surface; however, depending on the Reynolds number, flow separates from the surface after travelling a certain distance. At low Re numbers (Re $\leq$ 2,000), flow separates from the ceiling and creates secondary circulation zone at the rear side of the enclosure.

The existence of reverse flow for various Reynolds numbers are revealed with representing the velocity distribution along the container length calculated at the jet axis (see Fig. 60.8). For Re = 20, almost 75 % of the enclosure is stagnant. However, for Re = 200 and 2,000, flow separation from the ceiling is observed at container lengths approximately $z/L = 0.9$ and 0.95, respectively. At higher Reynolds numbers, Re $\geq$ 12,300, there is no separation of flow and a single circulation zone forms. Increasing Reynolds number slightly changes the velocity variation especially at Reynolds numbers above 61,500.

Referring to Table 60.3, increasing the Reynolds number decreases the mean air temperature of the container. In fact, average temperature decreases from 25.47 °C to -9.68 °C by increasing the Reynolds number as indicated in the table. As shown in Fig. 60.7, container temperature distributions become more uniform at high Reynolds numbers. As seen by Fig. 60.9, average values of inner surface heat transfer coefficients assume high values as the Reynolds number increases. Due to decrease in surface thermal resistance, the surface heat gains assume asymptotic values accordingly.

Effect of the Container Length

Figure 60.10 shows the flow patterns and isotherms for three different lengths of the container. For the suction design considered in this study, a stagnant region takes place just below the evaporator suction line. As indicated in Fig. 60.10, increasing the container length increases the size of the stagnant region; this in turn deteriorates the uniformity of air temperature distribution of the container. Specifically for container length at 13.3 m, due to separation of flow from the ceiling surface at a length ratio $z/L = 0.88$ (see Fig. 60.11), the temperature distribution even becomes worse. Table 60.4 presents the average air temperatures at three different container lengths. One may conclude that the length effect on average temperature is insignificant. Besides, as in Fig. 60.12, the heat gain per unit surface area varies insignificantly at all surfaces.
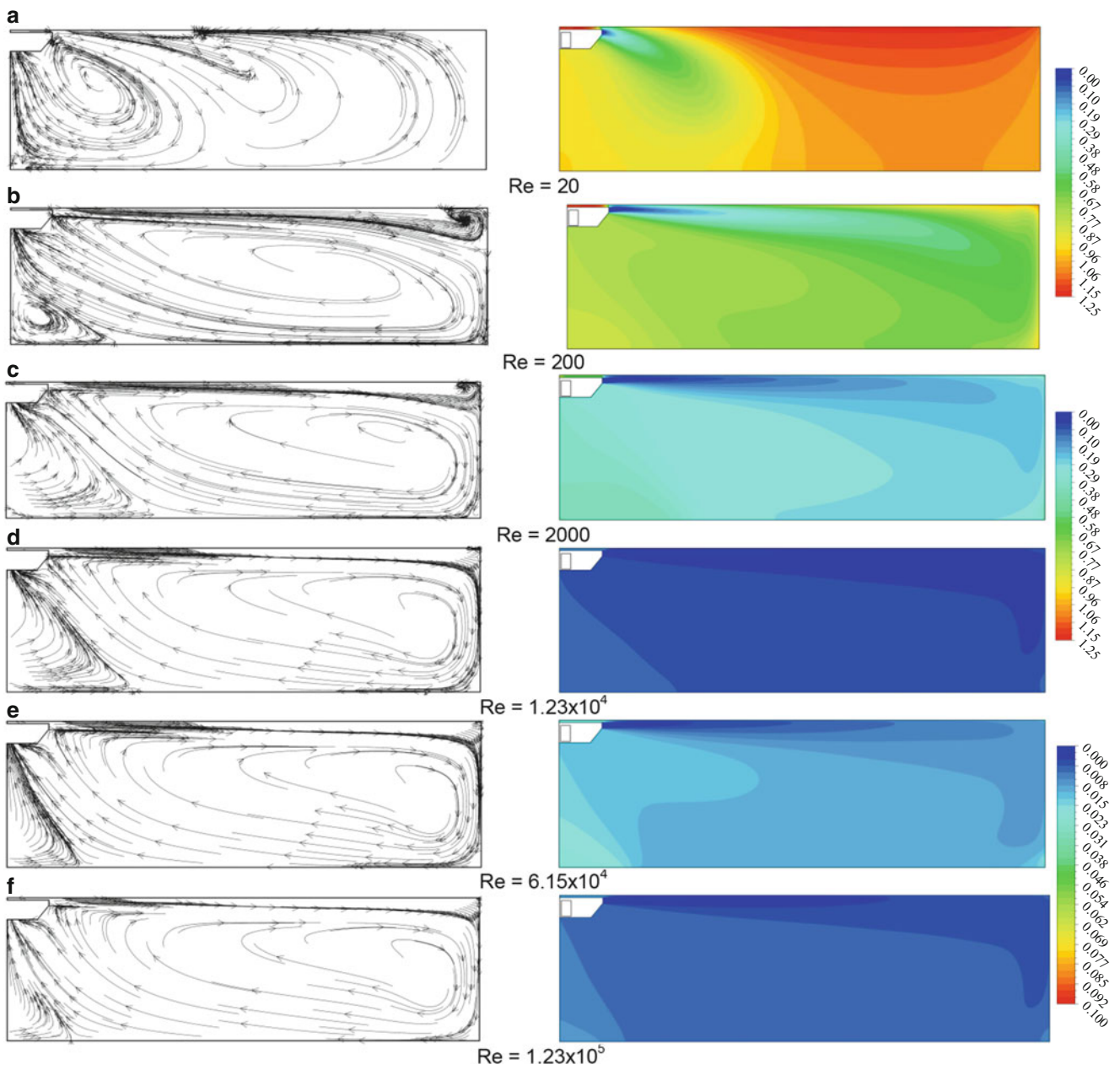
Fig. 60.7 Airflow patterns and isotherms on the symmetry surface. (**a**) Re = 20. (**b**) Re = 200. (**c**) Re = 2,000. (**d**) Re = 1.23×10^4. (**e**) Re = 6.15×10^4. (**f**) Re = 1.23×10^5

Fig. 60.8 Decay of velocity
on jet axis
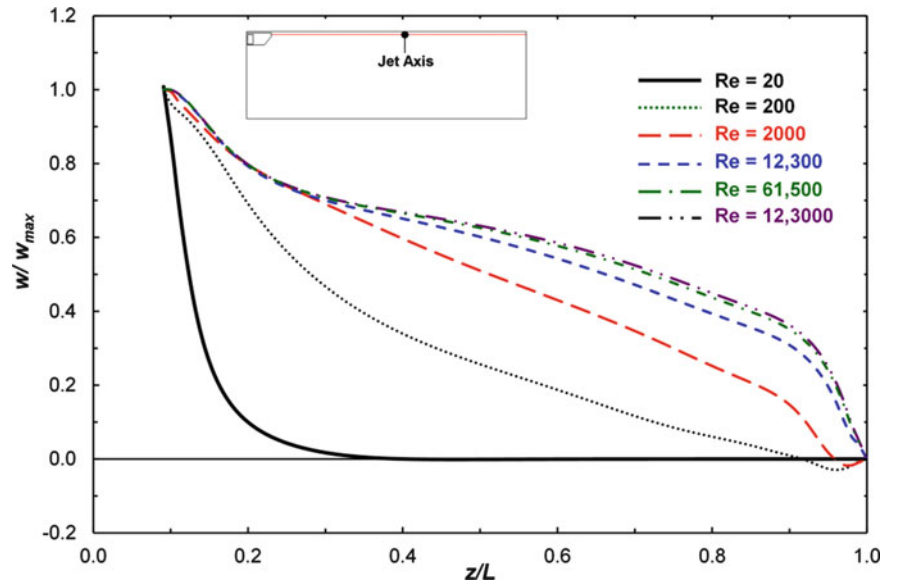
Table 60.3 Average air temperatures at various inlet conditions

Reynolds number	20	200	2,000	1.23×10^4	6.15×10^4	1.23×10^5
T_{mean}	25.47 °C	16.74 °C	1.07 °C	−7.26 °C	−9.38 °C	−9.68 °C
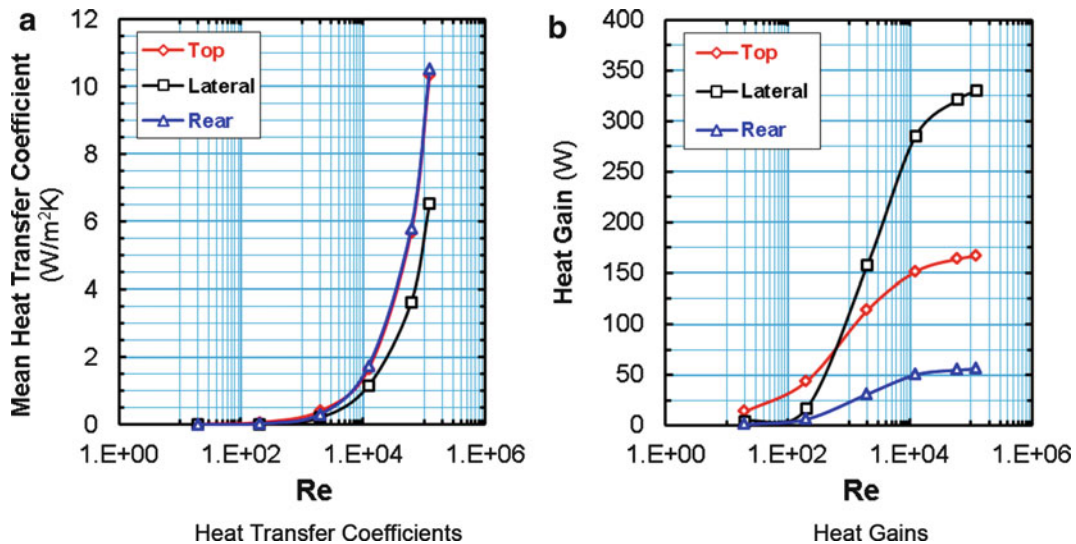
Fig. 60.9 Influence of flow Reynolds number on heat transfer. (**a**) Heat transfer coefficients. (**b**) Heat gains
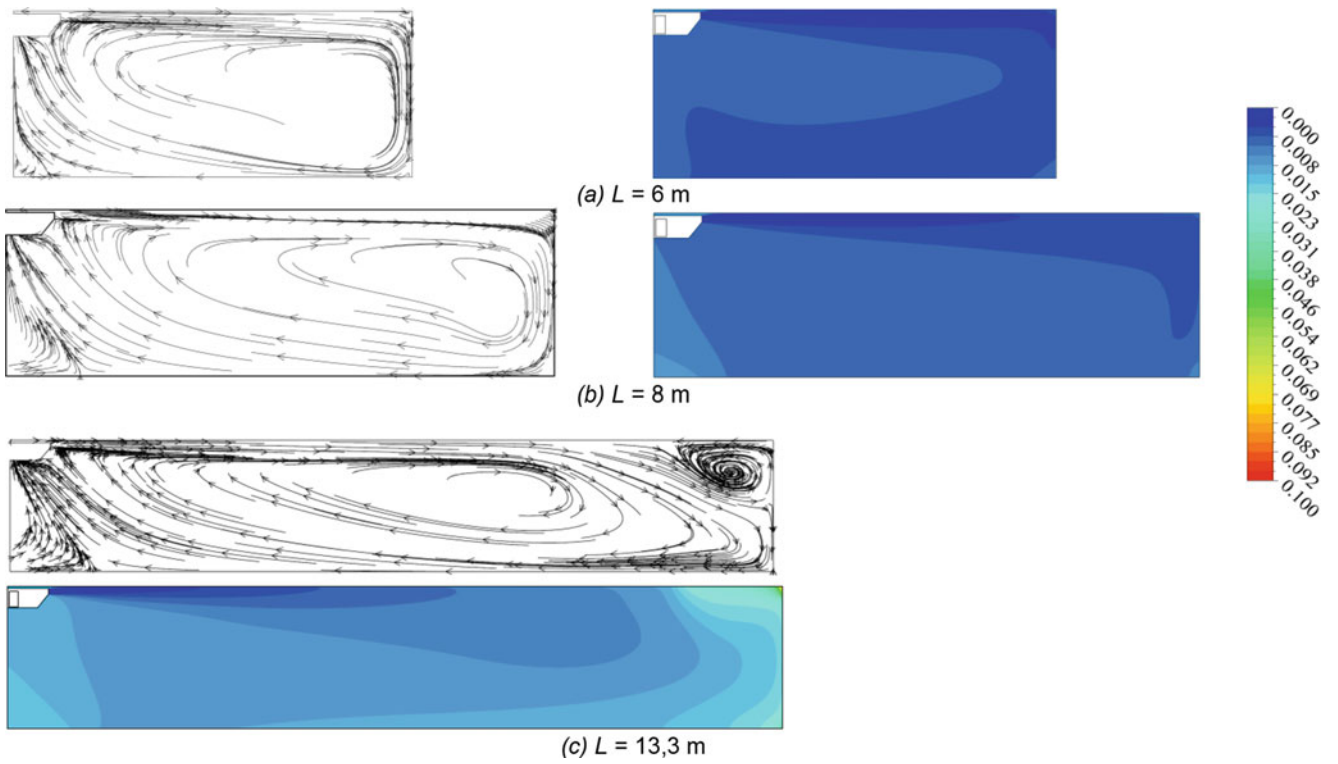
Fig. 60.10 Airflow patterns and isotherms on the symmetry surface. (**a**) $L = 6$ m. (**b**) $L = 8$ m. (**c**) $L = 13.3$ m

Fig. 60.11 Decay of velocity on jet axis
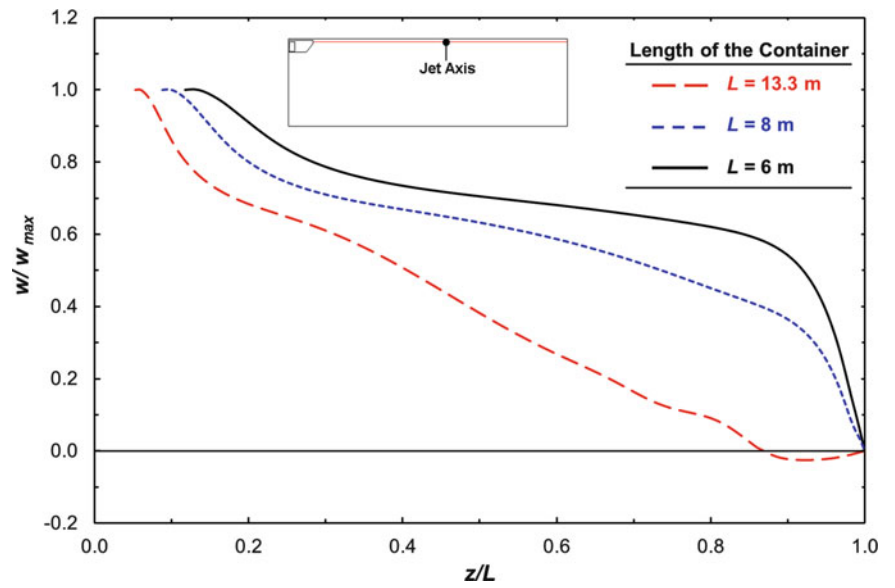
Table 60.4 Average air temperatures at various container lengths

Container length	6 m	8 m	13.3 m
T_{mean}	−9.72 °C	−9.68 °C	−9.47 °C
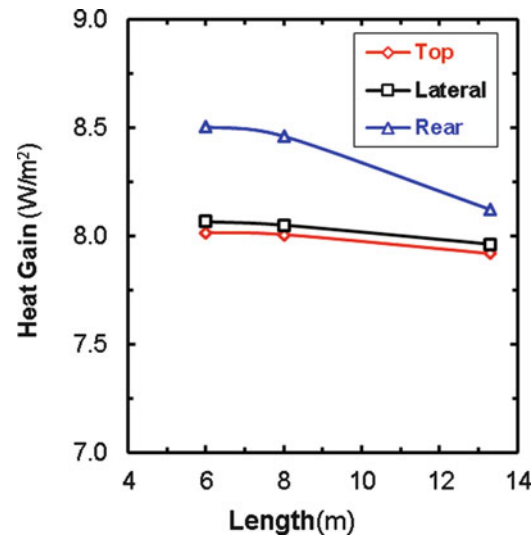
Fig. 60.12 Influence of container length on heat transfer

Conclusions

Flow and heat transfer characteristics of an empty container used for frigorific transportation is numerically studied. The container has constant cross-sectional dimensions of 2.5 m × 2.5 m, and the length is varied in such a way that the container aspect ratio takes the values of 2.4, 3.2, and 5.32. Identifying the turbulent stresses, Reynolds Stress Model is adopted. Similar studies of literature are also recalculated and compared by this method of solution. Satisfactory results indicate that RSM method of analysis is appropriate for studying the flow inside of refrigerated containers.

In the analysis, the flow Reynolds number is changed by varying the flow injection rate at the evaporator outlet. For aspect ratios between 2.4 and 3.2, no separation of flow from the upper surface is noted. However, in a region close to the rear surface of the container, two separate vorticities perpendicular to each other occur at flow Reynolds numbers greater than 200. Occurrence of these vorticities indicates that a stagnant region develops at the rear side of the container. For aspect ratio 5.32, the flow separates from the upper surface of the container at a length ratio $z/L = 0.88$. Similar to smaller aspect ratios, two distinct circulation zones occurs but their plane of occurrence is different from the cases with $H/L = 2.4$ and 3.2.

Nondimensional temperature, T^*, should vary in the range between 0 and 1. If it is greater than the unity, at a particular location, then that location would not be affected heat transfer wise by the airflow in the container. In the analysis, as the Reynolds number increases, T^* assumes less than 0.1 for the entire container region. This also indicates that at high Reynolds numbers, temperature uniformity throughout the container is satisfactorily obtained. In addition, as the Reynolds number increases, the volumetric mean temperature of air in the container drastically drops and approaches to the exit temperature at the evaporator.

Current study investigates the essential features of the flow and describes the heat transfer characteristics of an empty refrigerated container. Further studies should be conducted to evaluate the effect of loading conditions on the flow and on the heat transfer characteristics in a frigorific container.

Nomenclature

c_p	Specific heat, J/kgK	Re	Reynolds number, $\rho D_H w_{in}/\mu$
D_H	Hydraulic diameter of the inlet section, m	T	Temperature, °C
h	Convective heat transfer coefficient, W/m²K	T^*	Dimensionless temperature, $T^* = (T - T_{in})/$
H, L, W	Height, length, and width of the container, m		$(T_{out} - T_{in})$
I_{solar}	Incident solar radiation, W/m²	u, v, w	Velocity components on Cartesian geometry, m/s
k	Thermal conductivity, W/mK	U	Overall heat transfer coefficient, W/m²K
Nu	Nusselt number, hL/k	V	Volume of the container, m³
p	Pressure, Pa	x, y, z	Cartesian coordinates, m
Pr	Prandtl number		

Greek Letters

α	Surface absorptivity	μ	Viscosity, Ns/m²
ε	Surface emissivity	ρ	Density, kg/m³

References

1. Flick D, Hoang HM, Alvarez G, Laguerre O (2012) Combined deterministic and stochastic approaches for modeling the evolution of food products along the cold chain. Part I: Methodology. Int J Refrigeration 35:907–914
2. Hoang MH, Laguerre O, Moureh J, Flick D (2012) Heat transfer modelling in a ventilated cavity loaded with food product: application to a refrigerated vehicle. J Food Eng 113:389–398
3. Moureh J, Menia N, Flick D (2002) Numerical and experimental study of airflow in a typical refrigerated truck configuration loaded with pallets. Comput Electron Agric 34:25–42
4. Moureh J, Flick D (2003) Wall air–jet characteristics and airflow patterns within a slot ventilated enclosure. Int J Therm Sci 42:703–711
5. Moureh J, Flick D (2004) Airflow pattern and temperature distribution in a typical refrigerated truck configuration loaded with pallets. Int J Refrigeration 27:464–474
6. Moureh J, Flick D (2005) Airflow characteristics within a slot-ventilated enclosure. Int J Heat Fluid Flow 26:12–24
7. Moureh J, Tapsoba S, Derens E, Flick D (2009) Air velocity characteristics within vented pallets loaded in a refrigerated vehicle with and without air ducts. Int J Refrigeration 32:220–234
8. Norton T, Sun DW, Grant J, Fallon R, Dodd V (2007) Applications of computational fluid dynamics (CFD) in the modelling and design of ventilation systems in the agricultural industry: a review. Bioresour Technol 98:2386–2414
9. Schälin A, Nielsen PV (2004) Impact of turbulence anisotropy near walls in room airflow. Indoor Air 14:159–168
10. ANSYS Inc (2009) ANSYS-FLUENT 14.0 theory guide. ANSYS Inc
11. Patankar SV (1982) Numerical heat transfer and fluid flow. Taylor & Francis, New York, NY
12. Leonard BP (1979) A stable and accurate convective modelling procedure based on quadratic upstream interpolation. Comput Meth Appl Mech Eng 19:59–98
13. Patankar SV, Spalding DV (1972) A calculation procedure for heat, mass and momentum transfer in three-dimensional parabolic flows. Int J Heat Mass Transfer 15:1787–1806
14. Launder BE, Spalding DB (1974) Numerical computation of turbulent flows. Comput Meth Appl Mech Eng 3:269–289
15. Incropera FP, DeWitt DP, Bergman TL, Lavine AS (2007) Fundamentals of heat and mass transfer. Wiley, New York, NY

Numerical Simulation of 1-D Compression Stroke Using Smoothed Particle Hydrodynamics

Tarek El-Gammal, Essam Eldin Khalil, Hatem Haridy, and Essam Abo-Serie

Abstract

1-D numerical simulation is conducted for compression stroke of air inside a flat piston-cylinder pattern using Smoothed Particle Hydrodynamics (SPH) and explicit time integration methods. Flow and fluid properties are calculated and represented during the whole stroke time and at different piston positions inside the cylinder. Investigations about the value of the smoothing length (h) of minimum error and optimizing the ghost particles' position and interaction boundary conditions have been undergone. The simulation results show consistent accuracy with isentropic data in reasonable time consumption.

Keywords

Compression • Mesh-less • Smoothing length • Stroke • Virtual particles

Introduction

Smoothing Particle Hydrodynamics (SPH) is one of the recently developed mesh-less methods which have acquired the reliability in the last decade as a numerical solution approach. SPH is a Lagrangian adaptive method that does not need a mesh for solving the discretized domain. Using this method, the physical domain is divided into unrelated particles that have physical properties (i.e., volume, mass, velocity, pressure, etc.) of the domain. The field function (temperature, pressure, velocity, etc.) is calculated for a discrete particle from the field functions of the all surrounding particles weighted by the smoothing function (W_{ij}). The smoothing (weighting) kernel function takes into account the percentage effect of the neighboring particles within a predefined radius called smoothing length (h). Many common kernel functions use a dependent factor (K) to multiply with the smoothing length (h) [1].

After being developed for simulating the cosmological phenomenon [2], SPH has been used in solving fluid and solid mechanics problems. The adaptive nature of SPH makes it more suitable for simulations involving fluid free surfaces, wave discontinuity, solidification [3] multiphase flow [4], and highly deformable geometries which are difficult and require large memory and long computational time due to the continuous change in the computational mesh in space and time to fit the domain leading to inaccuracy and sometimes system collapse.

Pressure wave propagation is of great interest to be studied. High attention is directed for those which is developed by impacts and reflected by solid walls. An important example is the adiabatic compression process for a gas to increase its pressure for storage (Air compressors) of further processing (Internal combustion engines). Differential (i.e., Lagrangian) analysis is required in this case with high effect and accurate method.

T. El-Gammal (✉) • E.E. Khalil • H. Haridy
Department of Mechanical Power Engineering, Cairo University, Giza, Egypt
e-mail: tarekelgammal@eng.cu.edu.eg; khalile1@asme.org; hatem_kayed@eng.cu.edu.eg

E. Abo-Serie (✉)
Mechanical Department, Mevlana University, Konya, Turkey
e-mail: eaboserie@mevlana.edu.tr

In this chapter, a simulation is done for compression stroke inside a cylinder to track the behavior of air particles and measure the fluid and flow properties at different points during the stroke till the end. The verification is applied to the isentropic relations depending on the compression ratio and the initial and boundary conditions. The smoothing length (h) was varied to minimize the error, and the virtual particles were laid and carefully treated to optimize the solution.

Problem Definition

The case represents a compression stroke in internal combustion engine using a flat piston inside a cylinder (D = 0.1285 m, L_{stroke} = 1.2D = 0.15842 m).The stroke starts from rest (velocity u = 0) at the top dead center (TDC) to stop and finish at the bottom dead center (BDC). The other cylinder specifications were as follows: compression ratio (r_c = 6), and rotational speed (N = 1,000 rpm).

The medium under investigation is air and it's dealt as inviscid perfect gas of constant volumetric specific heat (C_v = 717.5 J/kg) and isentropic index (γ = 1.4).The initial pressure and temperature are (P_i = 10^5 Pa, T_i = 300 K).

Finally, the cylinder piston arrangement is considered adiabatic but not isentropic. It should be noted that the simulation was 1-D (the direction of piston motion).

The governing equations describing the change in density (ρ), pressure (p), horizontal velocity component (u), and temperature (T) are

Continuity equation:

$$\frac{D\rho}{Dt} = -\rho \frac{\partial u}{\partial x} \tag{61.1}$$

Linear momentum conservation:

$$\frac{Du}{Dt} = \frac{-1}{\rho} \frac{\partial p}{\partial x} \tag{61.2}$$

Energy conservation:

$$\frac{DT}{Dt} = \frac{1}{C_v} \frac{-p}{\rho} \frac{\partial u}{\partial x} \tag{61.3}$$

Equation of state:

$$P = \rho(\gamma - 1)C_v T \tag{61.4}$$

Speed of sound:

$$C = \sqrt{\gamma(\gamma - 1)C_v T} \tag{61.5}$$

Note the air is considered inviscid (i.e., no shear term in linear momentum equation). Artificial viscosity is added later to account for particle over penetration. The piston is governed by equations of motion and adiabatic boundary conditions [5], such that the properties of air particles attached to the piston are calculated by

Piston equations of motion:

$$u_p = \left(\frac{L_{stroke}}{2}\right) * \omega * \sin(\omega t) + \frac{\left(\frac{L_{stroke}}{2}\right)^2 * \omega * \sin(2\omega t)}{2 * l} \tag{61.6}$$

$$a_p = \left(\frac{L_{stroke}}{2}\right) * \omega^2 * \cos(\omega t) + \frac{\left(\frac{L_{stroke}}{2}\right)^2 * \omega^2 * \cos(2\omega t)}{l} \tag{61.7}$$

Piston momentum equation:

$$\frac{Du}{Dt}\bigg|_p = a_p = -\frac{1}{\rho}\frac{\partial P}{\partial x}\bigg|_p \tag{61.8}$$

Adiabatic density-pressure gradients:

$$\frac{\partial \rho}{\partial x}\bigg|_p = \frac{1}{C_p^2} * \frac{\partial P}{\partial x}\bigg|_p \tag{61.9}$$

where (u_p) is the piston velocity in (m/s), (a_p) is the piston acceleration (m/s^2), (C_p) is the sound speed of air particles at the piston conditions (m/s), $\left(\omega = 2\pi\frac{N}{60}\right)$ is the angular velocity of the crank shaft (rad/s), (t) is the time from the start till the required moment (s), and (l) is the connecting rod length in (m) and it is taken equal to L_{stroke}.

The cylinder head side is fixed. This applies a zero velocity particle with constant zero gradients for the other properties (density, pressure, temperature) at all times.

The validation of this case already exists in the isentropic solution for a compression process of ratio (r_c) for an air charge of initial pressure and temperature (P_i and T_i). This is shown in the following relations:

$$P_f = P_i(r_c)^{\gamma} \tag{61.10}$$

$$T_f = T_i(r_c)^{\gamma-1} \tag{61.11}$$

P_f and T_f are the final pressure and temperature after the compression stroke.

Methodology

Governing Equations Using SPH

SPH formulation starts from the integral representation of field function using a limited zone, kernel function W(x_{ij},h). Then we can write the function approximation in SPH formulation as

$$f(x_i) \approx \langle f(x_i)\rangle = \int f(x_j)W(x_{ij}, h)dx \tag{61.12}$$

where $<f(x_i)>$ is the kernel approximation of the scalar field f(x) at particle (i).

For two or three dimensions, the kernel function W (x_{ij},h) can be replaced by W (r_{ij},h) such that (r_{ij}) is the vectorial distance between (i) and (j).

The gradient ($\partial f(x_i)/\partial x$) and Laplacian ($\partial^2 f(x_i)/\partial x^2$) of the field function are evaluated in integral representation [6] to be

$$\partial f(x_i)/\partial x \approx \langle \nabla_i f(x)\rangle = \int f(x_j)\nabla_i W(r_{ij}, h)dx \tag{61.13}$$

$$\frac{\partial^2 f(x_i)}{\partial x^2} \approx \langle f_{xx_i}\rangle = 2\int \frac{[f(x_i) - f(x_j)]}{r_{ij}^2}.x_{ij}.\nabla_i W(r_{ij}, h)dx \tag{61.14}$$

The field functions in Eqs. (61.12), (61.13), and (61.14) are discretized in space, using the particles representing the domain, so the integrations are approximated by summations of functions weighted by the kernel function [6].

$$\langle f(x_i)\rangle = \sum \frac{m_j}{\rho_i}f(r_j)W(x_{ij}, h) \tag{61.15}$$

$$\langle \nabla_i f(x) \rangle = \sum \frac{m_j}{\rho_i} f(r_j) \nabla_i W(x_{ij}, h) \tag{61.16}$$

$$\langle f_{xx_i} \rangle = 2 \sum \frac{m_j}{\rho_i} \frac{[f(r_i) - f(r_j)]}{r_{ij}^2} . x_{ij} . \nabla_i W(x_{ij}, h) \tag{61.17}$$

SPH formulation mentioned above can be substituted into the governing equations (61.1, 61.2, and 61.3). Accordingly, the SPH representation of 1-D continuity, momentum, and energy can be written as follows:

$$\frac{D\rho_i}{Dt} = \Sigma_{j=1}^{N_b} m_j (u_i - u_j) \nabla_i W_{ij} \tag{61.18}$$

$$\frac{Du_i}{Dt} = -\Sigma_{j=1}^{N_b} m_j \left(\frac{p_i}{\rho_i^2} + \frac{p_j}{\rho_j^2} + \pi_{ij} \right) \nabla_i W_{ij} \tag{61.19}$$

$$\frac{DT_i}{Dt} = \frac{1}{2C_v} \Sigma_{j=1}^{N_b} m_j \left(\frac{p_i}{\rho_i^2} + \frac{p_j}{\rho_j^2} + \pi_{ij} \right) (u_i - u_j) \nabla_i W_{ij} \tag{61.20}$$

Note that (π_{ij}) is the artificial viscosity term which will be discussed later.

The compact cubic spline is kernel function that has been used in this study [7]. The formulations of the cubic spline kernel function (W_{ij}) and its spatial derivative can be shown in Eqs. (61.21) and (61.22).

$$W(x_{ij}, h) = W_{ij} = a_1 * \begin{cases} \frac{2}{3} - R^2 + \frac{1}{2}R^3 & 0 \leq R < 1 \\ \frac{1}{6}(2 - R)^3 & 1 \leq R < 2 \\ 0 & R > 2 \end{cases} \tag{61.21}$$

$$\nabla_i W_{ij} = \frac{dW_{ij}}{dR} * \frac{dR}{dr_{ij}} * \frac{(x_i - x_j)}{r_{ij}} \tag{61.22}$$

where $(R = x_{ij}/h)$ is the ratio between the magnitude of the distance between two neighboring particles (x_{ij}) and the smoothing length (h). In Eq. (61.22), the coefficient (a_1) is dependent on the smoothing length (h) and has a value of (1/h).

Numerical Analysis

Domain Particles Distribution

Using MATLAB®, the cylinder domain is discretized into (Nx) equally spaced particles which are classified into (Nx−2) interior particles with two boundary particles (one at each side).

The initial conditions of (ρ, P, T, u) are set to all the particles. Particle differential length will be calculated from its spacing in x coordinate (i.e., m/ρ = dx). The cylinder starts from rest (i.e., $u_i = 0$) at pressure and temperature mentioned above with adiabatic boundaries (q″ = 0).

Virtual (Ghost) Particles

The virtual or ghost particles [8] are generated in every time step as an image for the medium particles near the boundary (i.e., lie within the kernel domain of the wall/boundary particle) as in Fig. 61.1.

The virtual particle gains its physical properties from its real particle and the boundary condition of the wall. The existence of artificially particles plays an important role in completing the kernels to give accurate physical properties for all particles. Also they facilitate accurately representing the boundary conditions as in F.D. especially for Neumann boundary condition.

The virtual particles were applied to the two boundaries, the moving piston and the cylinder head, and they are increasing every time step due to compactness of particles.

Boundary Forces

If any fluid particle approaches the special limited zone of the boundary, it is exerted by a repulsive force from the wall particle (along the line of centers) to prevent the penetration. This force is calculated in the same way as the molecular force of Lennard-Jones form. The repulsive force on particle (i) is generated according to this relation [9]:

$$RF_i{}^k = \begin{cases} D\left[\left(\dfrac{r_0}{r_{ij}}\right)^{n_1} - \left(\dfrac{r_0}{r_{ij}}\right)^{n_2}\right]\dfrac{x_{ij}{}^k}{r_{ij}{}^z} & r_{ij} \leq r_0 \\ 0 & r_{ij} > r_0 \end{cases} \tag{61.23}$$

$(RF_i{}^k)$ is the repulsive force on particle (i) in the (k)th dimension. (r_0) is the cutoff distance which determines the effective zone of the wall repulsive force. (r_0) is usually taken as a fraction from the initial spacing. (D) is a problem-dependent factor.

Artificial Viscosity

The artificial viscosity approach [10] is proposed to prevent particles' interpenetration by adding viscous terms in the momentum and energy equations to overcome the drawbacks that arise from SPH kernel in solving the pressure waves along the particles. The proposed artificial terms are

$$\pi_{ij} = \begin{cases} \dfrac{-\alpha_\pi \bar{c}_{ij} + \beta_\pi \varnothing_{ij}^2}{\bar{\rho}_{ij}} & u_{ij}.x_{ij} < 0 \\ 0 & u_{ij}.x_{ij} \geq 0 \end{cases} \tag{61.24}$$

where $\alpha_\pi = \beta_\pi = 1$ in most reviews [1], but in this case they were taken equal to 0.1 and zero, respectively, to minimize their detrimental effect of disturbing the particles' order, while other parameters are calculated from

$$\varnothing_{ij} = \frac{h_{ij}u_{ij}.x_{ij}}{\left|x_{ij}\right|^2 + \varphi^2} \tag{61.25}$$

$$C_{ij} = \frac{(C_i + C_j)}{2} \tag{61.26}$$

$$\bar{\rho}_{ij} = \frac{\left(\rho_i + \rho_j\right)}{2} \tag{61.27}$$

$$u_{ij} = u_i - u_j \tag{61.28}$$

$$\varphi = 0.1h_{ij} \tag{61.29}$$

Time Marching

The property (i.e., density, temperature) at the current time step is calculated using the value of the previous time step and its rate of change.

At t = dt (i.e., n = 1)

$$T_1 = T_0 + (dt) * \left.\frac{\partial T}{\partial t}\right|_{n=0} \tag{61.30}$$

where $\left.\frac{\partial T}{\partial t}\right|_{n=0}$ are evaluated by initial values T_0 from the governing energy equation. For n > 1:

$$T_n = T_{(n-1)} + dt * \left.\frac{\partial T}{\partial t}\right|_{n-1/2} \tag{61.31}$$

where $\left.\frac{\partial T}{\partial t}\right|_{n-1/2}$ are evaluated by $T_{n-1/2}$ from the energy equation.

The time step has been chosen to satisfy the Courant-Levy condition for mechanisms involving thermo-fluids [11].

$$dt \leq 0.3 \frac{h}{max(c_i + u_i)} \tag{61.32}$$

In this case, time step was considered as (dt = 1×10^{-5} s) which is very convenient to the above-mentioned condition that deals with small time steps.

Results

Optimum Smoothing Length

Due to the variety of properties in this case, the optimized smoothing length (h_{opt}) was based on reducing the maximum percentage error found at the stroke end, and it was always dedicated to the pressure values. Note that the percentage error is calculated from this equation:

$$\% \text{ error} = \frac{calculated\ value - isentropic\ value}{isentropic\ value} \times 100\% \tag{61.33}$$

Figure 61.1 shows the permanent increase of h_{opt} value with the increase in number of discretizing particles (Nx). This trend is best fitted with proper linear equation. Other polynomial orders aren't better than this fit.
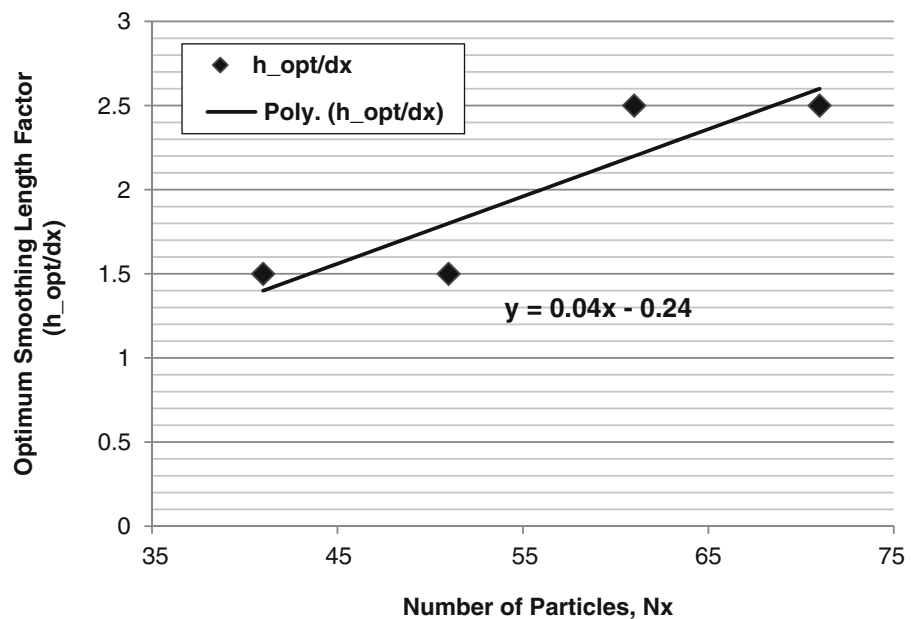
Fig. 61.1 Variation of optimized smoothing length factor with the number of discretizing particles

Other important variable to be taken into consideration was the calculation time to achieve the acceptable accuracy. This is demonstrated in Figs. 61.2 and 61.3 where the maximum percentage error and the numerical time of calculation are plotted against (Nx). It's worth noting that the plotting values were considered in case of (h_{opt}) of each (Nx).

From Figs. 61.2 and 61.3, the chosen number of particles was (Nx = 41) with optimized factor of smoothing length (h_{opt} = 1.5). This is because of the acceptable limits of error, time (0.015 % and 1.37 s, respectively), and well-organized final distribution of particles.

After the choice of (Nx) and (h_{opt}), the results produced by the code are presented for any time during the stroke to show the development of properties under effect of pressure waves and the motion of particles with their internal velocities. The plots are illustrated in lines of property variation with different air particles according to the position inside the cylinder.

Fig. 61.2 The effect of increasing of particles number to the computational percentage error
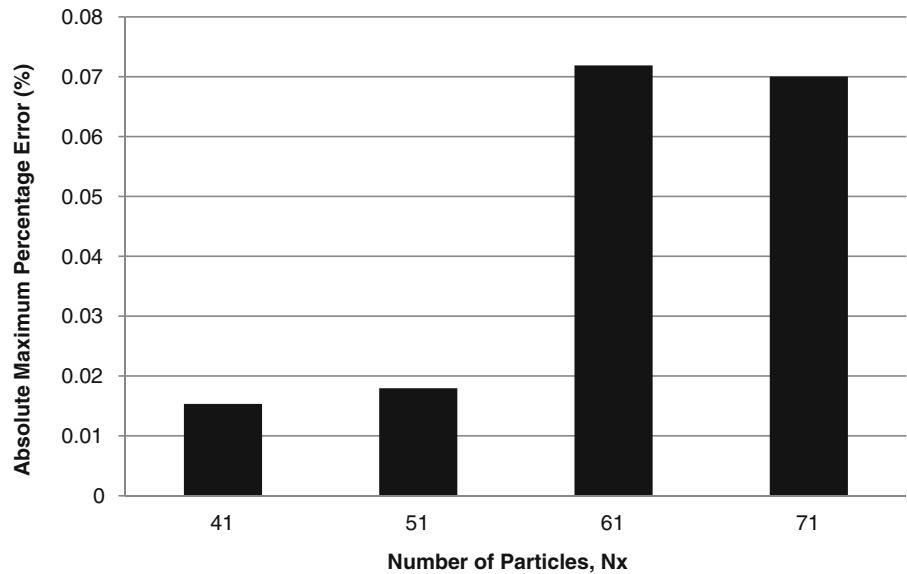
Fig. 61.3 The effect of increasing of particles number to the computational time consumed
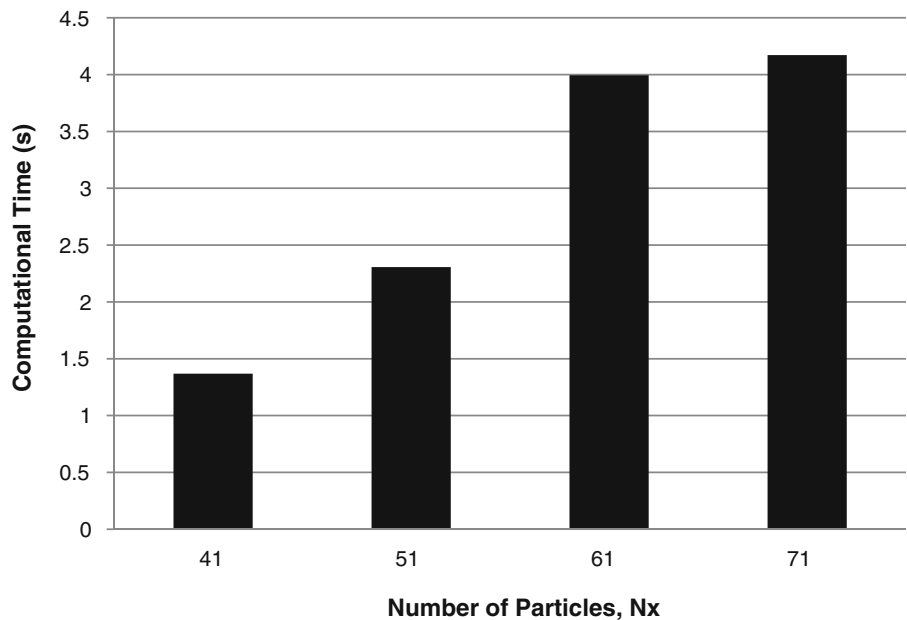
Transient Period

The following plots (Figs. 61.4, 61.5, and 61.6) are showing the percentage difference of particles' properties (pressure, density, and temperature) to the isentropic values at three times of compression (t = 0.01, 0.02, and 0.03 s). It's obvious that the properties near piston head at the first period (t = 0.01 s) are having a lower value than the isentropic. This happens due to the permanent deceleration of piston lowering the generated pressure wave every time step (i.e., concentrated rarefaction at the piston side). Meanwhile, at t = 0.02 and 0.03 s, the cylinder stroke highly decreased, so the wave is reflected between both sides in very short distance and time. Consequently, the reflected pressure wave is added with the compression applied by piston causing an exceptional rise near the piston head.

In Fig. 61.7, the particles' velocities are compared to the mean piston speed (mps) at the three different times to show the variation in place and time. The highest gradient is achieved at t = 0.02 s as the piston reaches its maximum at t = 0.015 s in half the stroke and then decreases to stop at t = 0.03 s at the end of stroke.
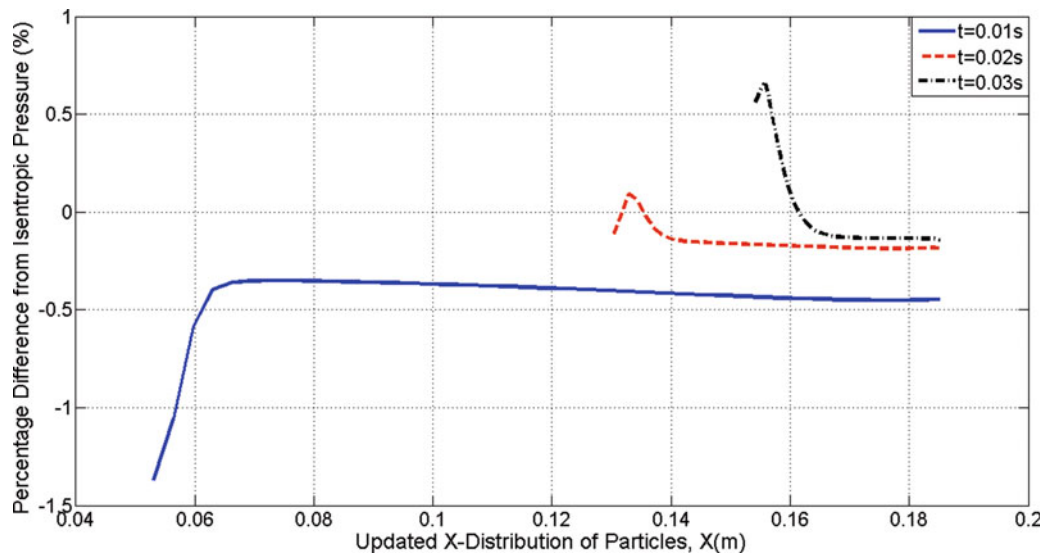
Fig. 61.4 Pressure difference from isentropic values in (%)
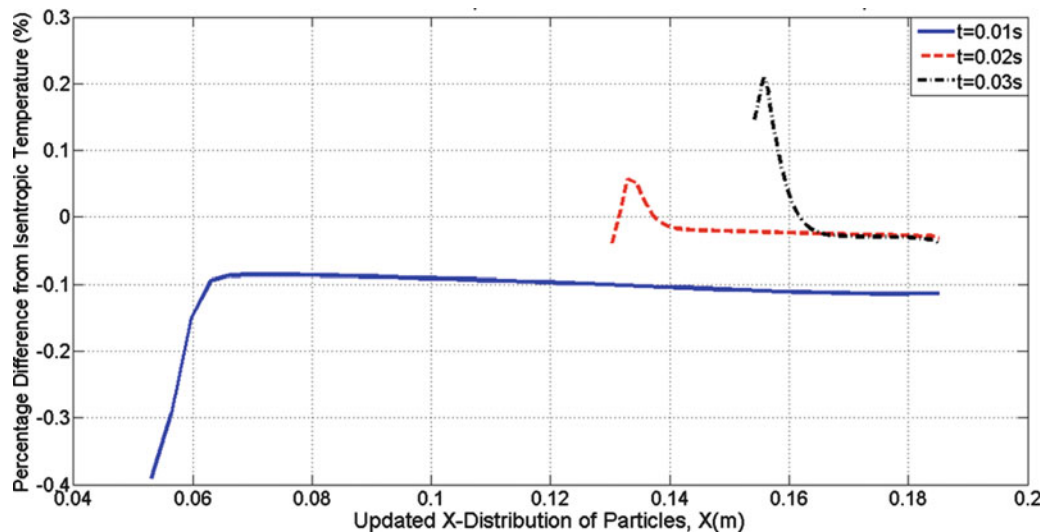
Fig. 61.5 Density difference from isentropic values in (%)
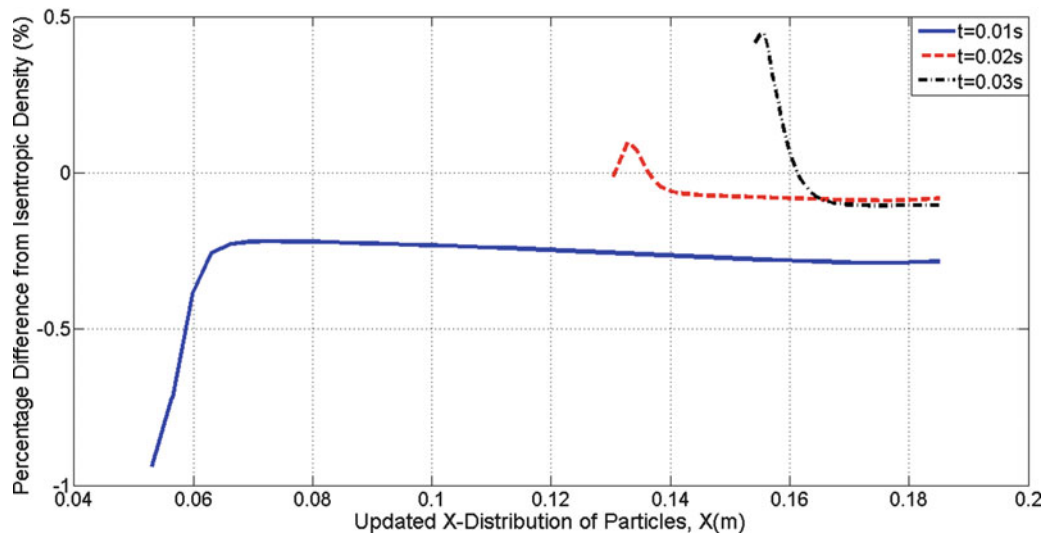
Fig. 61.6 Temperature difference from isentropic values in (%)
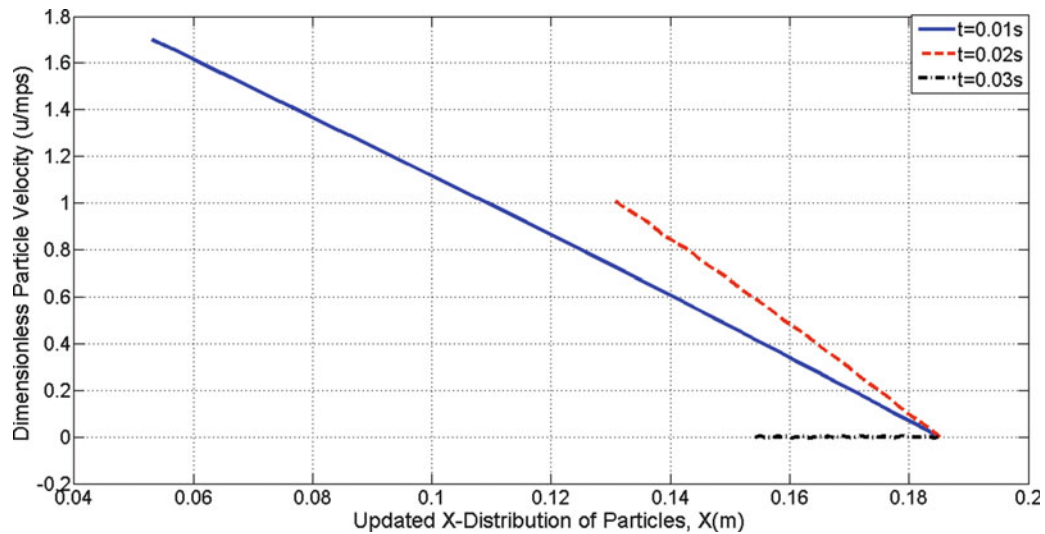
Fig. 61.7 Particles' velocities in percentage of mean piston speed

Conclusion

From the simulation, the property field evolves during compression stroke depending on the pressure waves sent by the moving piston. These waves are reflected at the boundaries with continuous shrinking in stroke length causing a high rate of properties development.

Optimizing the smoothing length in SPH achieves the merits of high accuracy and less computation time. Any increase or decrease in the smoothing length will change the kernel weighting function (W_{ij}) in shape and value and disorients it from the actual property profile.

The optimized (h) is not a constant value at every circumstance. It varies with the discretizing particles number (Nx) and other parameters like initial gradients. In this case, (h_{opt}) changes in linear relation with (Nx).

The proper choice of the number of virtual particles and the boundary treatment are very important in achieving the accuracy at the boundary and avoiding system collapse. Meanwhile the addition of artificial viscosity terms helped in preserving the motion from improper behavior of some particles due to inconvenient approximation of kernel function.

SPH ability of calculating the properties at any differential particle independent on predefined connectivity or distribution with smooth results makes it superior in applications of material deformation and the generated pressure waves with its reflections. This was well obvious in this case study of compression stroke for air charge.

Nomenclature

α_π	Shear viscosity coefficient	D	Engine Diameter, m
β_π	Bulk viscosity coefficient	L	Engine stroke length, m
ρ	Density, kg/m^3	P	Pressure, Pa
φ	Non-singularity coefficient	q	Heat rate, W
π	Artificial viscosity term	RF	Repulsive force per particle mass, m/s^2
a	Piston acceleration, m/s^2	T	Temperature, K
a_1	Dimension coefficient of smoothing kernel function	u	Velocity, m/s
C	Specific heat, kJ/kg K	X	Position

Subscript

i	Initial, interested particle	opt.	Optimum
f	Final	p	Piston
j	Neighbor particle		

Superscript

$''$	Flux

References

1. Liu GR, Liu MB (2003) Smoothed particle hydrodynamics: a meshfree particle method. World Scientific, Singapore, Chap 1, pp 18
2. Lucy LB (1977) A numerical approach to the testing of the fission hypothesis. Astro J 82:1013–1024
3. Monaghan JJ, Hupper HE, Worster MG (2005) Solidification using smoothed particle hydrodynamics. J Comput Phys 206:684–705
4. Tartakovsky AM, Ferris KF, Meakin P (2009) Lagrangian particle model for multiphase flows. Comput Phys Commun 180:1874–1881
5. Fazio R, Russo G (2010) Central schemes and second order boundary conditions for 1D interface and piston problems in Lagrangian Coordinates. Commun Comput Phys 8:797–822
6. Rook R, Yildiz M, Dost S (2007) Modeling transient heat transfer using sph and implicit time integration. Numer Heat Transfer B 51(1):1–23
7. Nayanajith PGH, Gu YT, Saha SC, Senadeera W, Oloyede A (2012) Numerical simulation of red blood cells' deformation using sph method. The 4th international conference on computational methods
8. El-Gammal T, Khalil EE, Haridy H, Abo-Serie E (2012) Influence of smoothing length and virtual particles on sph accuracy. Int J Mater Mech Manuf 1(2):166–170
9. Liu MB, Shao JR, Chang JZ (2012) On the treatment of solid boundary in smoothed particle hydrodynamics. Sci Chn Technologic Sci 55:244–254
10. Cullen L, Dehnen W (2010) Inviscid smoothed particle hydrodynamics. Mon Not R Astron Soc 408:669–683
11. Hosseini SM, Feng JJ (2011) Pressure boundary conditions for computing incompressible flows with sph. J Comput Phys 230:7473–7487

Performance Evaluation of Eco-friendly Humidifying Material Using Hwangto

Hyeon Ku Park, Seong Seok Go, and Myeong Yeol Ryu

Abstract

Indoor air in the winter season is very dry because of heating especially in Korea. When indoor air is dry, the problems arise not only in the furniture and static electricity but also in the residents' health due to contaminated indoor air. This has resulted in the use of artificial humidifier to humidify dry indoor air easily and continuously. Recently, there were accidents because of the sterilizing agent used in humidifier and it became social problem. This study aimed to develop humidifying material using Hwangto called loess to substitute the artificial humidifier. The material developed is used in the evaporating humidifier and, therefore, is effective as humidifier, and environmental performances were examined by test.

Introduction

Dry air effects on the human body are a potential health hazard, causing skin irritations, eye itching, and static electricity. These problems can be reduced by increasing the indoor humidity by humidifiers, vaporizers, steam generators, and other simple methods such as boiling water or wet towels. In the winter season the room is heated to keep the temperature warm, and the ventilation is decreased, that is why the air in the room becomes dry and gives bad effects to resident and furniture [1]. Particularly, the impacts of dry air on people are decreased immunity to the disease due to the dry respiratory organs, snivel, soar throat, and headache. Dry air also makes problem skin over sensitiveness.

To humidify room plant or small artificial water fountain is used, and the most general way of humidifying room is to use electrical device. The electrical device can add moisture in room effectively, while a side effect of using the sterilizing agent to prohibit the fungi and bacteria from growing inside the humidifier was lung disease. This put an infant to death and became social problem.

The aim of this study is to seek for the alternatives to avoid this kind of problem, thus to develop humidifying pad to be used in evaporating humidifier with eco-friendly performance and antibacterial performance. Contrary to the general electrical humidifier, the evaporating humidifier can reduce electric energy; furthermore, it can heat room while humidifying.

H.K. Park (✉)
Sustainable Building Research Center, Hanyang University, 55 Hanyangdaehak Ro, Sangnok Gu, Ansan Shi, Kyeonggi Do 426-791, Korea
e-mail: soundpark@cricmail.net

S.S. Go
School of Architecture, Chonnam National University, 300 Yongbong dong, Buk gu, Gwangju Shi 500-757, Korea

M.Y. Ryu
Jigu Co., 985-16 Jagndeok dong, Gwangsan Gu, Gwangju Shi 506-251, Korea

To develop pad material, the tests on the antibacterial performance and resistance performance to fungi were carried out to give good effect to the indoor air quality together with the performance of absorbing and evaporating moisture.

The most popular humidifying pads are of two categories depending on their behavior of flowing wind: aspen excelsior and rigid cellulose media. The aspen pad doesn't have uniform direction of wind flow, but draws the wind to every direction. On the contrary the rigid media pads are made of special wettable cellulose in corrugated sheets bonded together at opposing angles [2]. The angles of the corrugated cellulose are intended to maximize air contact and evaporation [3]. The main material used in this study is hwangto, which has never been used for the evaporative pad in the existing research or industry. The shape of the pad using hwangto is considered to be well fitted to make corrugated sheet, and the work to make the corrugated sheet will be carried out using hwangto with hardening agents and function materials.

Evaporative Humidification

Evaporation is to transmit moisture into the air invisibly by using a fan to blow air through a moistened absorbent material such as a belt, wick, or filter [4]. When the fluid turns into vapor, it needs heat from outside. The heat absorbed is called evaporative heat. In case of evaporative humidifier, it uses the heat of warm air from air conditioner; thus, no extra energy is needed. The evaporative humidifier is a humidifier applying such phenomenon that the heated air blows on the surface of wet material and the room becomes humid. The ways of wetting a material are of mainly two types: a spraying method above the material through water pipe and a capillary method that makes material absorb water from the water stored at the bottom.

Development of Humidifying Pad

The objective of this study is to develop a humidifying pad which is composed of various eco-friendly or natural materials such as Hwangto (loess), traditional paper, silica, and charcoal. The existing pads used for evaporative humidifier are made from silica-coated ceramic mixed with glass wool or rubber type for a spraying method and fiber for a capillary method to absorb water well. Hwangto, the main raw material to develop evaporating pad, is abundant in Korea and has been used in the traditional housing. Thus, the research has been done to use hwangto as pozzolanic admixtures [5, 6]. So it is expected to provide environment reservation if the development of evaporating pad is successful. Especially, the pad is wet which is likely to be contaminated by fungi or bacteria; it is very important to develop a pad free of contamination. In this point, mixed rates between natural materials like pulp, hwangto, elvan, or silica, including fiber material, were considered.

The development was proceeded in the point of getting strength of the specimen and then the attempt to make standardized size was done, and finally the representative specimen was used for the evaluation of environmental performance. Firstly to get enough strength of specimen it should act well with water. Whether it absorbs water or not, the specimen should keep its strength. Hardening agent that consists of natural material and vegetable adhesive material were applied for the test, and fiber and pulp were used for the reinforcement of the strength to prevent leakage.

Table 62.1 shows the test for the strength of pad carried out in three steps. In the first step, the pulp law material of paper was used to check if it has enough strength when mixed with hwangto. Because there is no specific standard for the test of

Table 62.1 Test for the strength of hwangto paste with adhesives

Test	Main ingredients	Process	Result
First test	Pulp	Mixing hwangto with pulp	Not good
		Examine the strength after hardening	
Second test	Starch from sea plant	Use adhesive from sea plant	Not good
		Mixing hwangto with pulp and fiber	
		Examine the strength	
Third test	Powder and fluid from MGO	Use hardening powder and fluid from MGO	Enough strength
		Mixing hwangto with pulp, fiber	

Table 62.2 The result from the test to examine the strength of hwangto mixture depending on the mixing ratio

Mixing ratio	Appearance Good—fair—bad	Crack	Hardening (bad—fair—good)	Separation of material (none—normal—severe)	Photo	Evaluation
Hwangto:hardening powder:hardening fluid:fiber:water = 1:1:1:0.01:0.6	Good	None	Good	None		Good
Hwangto:hardenign powder:hardening fluid:fiber:water = 1:0.5:0.5:0.01:0.6	Bad	Crack	Good	None		Bad

pad strength, it was observed by eye on the surface and on the resistance to water if the specimen maintains the strength without any deformation or separation. The second test was carried out using natural bondage made from sea plant which is generally used for the adhesion of wall paper. In addition, the pulp and the fiber were used to reinforce the strength. In the third step, the strength of mixed material was examined. The materials mixed were MGO powder, fluid, pulp, and fiber with activated hwangto.

The results from the tests showed that the strength of the hwangto mixture with pulp was not good. Practically, the pulp needs some specific mould with high temperature to have enough strength. In this test the mould was not applied; then it is considered not to have enough strength. The disadvantage is that the pulp can be applied only in order to improve the strength as a subsidiary material. When the adhesive from sea plant in the second test was used, the shape was good, but there was separation in the materials. The strength was judged to be good, but appeared to be contracted. In addition the specimen when absorbing water was deformed so that it can't be applied to humidifying pad. The result when powder and fluid extracted from MGO (oxygenized magnesium) were mixed with hwangto was good that the specimen has enough strength. Moreover, the pulp and fiber were shown to give additional strength to the specimen. The specimen with thin cloth was best, and there was no deformation of its shape when it absorbs water. The details about the test and result are represented in the Table 62.2.

The test result showed that the hwangto mixture mixed with hardening powder, fluid from MGO, and fiber at the same time was best in strength and had good performance of both absorbing and discharging water. The mixing ratio was when hwangto is mixed with hardening powder and fluid with same amount. Therefore, the mixing ratio which showed best result was decided to apply to the humidifying pad; then the size fit to the evaporating humidifier and the shape were taken into consideration.

The concept of shape design was based on the type of evaporating humidifier. The humidifier considered to this study is that the water is sprayed above the pad and discharged at bottom through small pipe. The types considered were (1) vertical type, (2) horizontal type, (3) bending type, and (4) sponge type. The horizontal type has some problems in keeping water balanced that the water is supplied excessively and consumed. The bending type was considered to be effective but the water flowing was not well balanced. The sponge type has limitation to compose the mould. Eventually, the vertical type was chosen to be applied to the humidifier by making specimen. The specimen would be used for the test of eco-friendly characteristics and humidifying performance.

Performance Evaluation

The performance of specimen was evaluated on the eco-friendly characteristics and humidity control performance. The test of eco-friendly performance is done for the antibacterial performance and resistance performance to fungi to provide good effect on the indoor air quality. The humidity control performance is tested on the performance of absorbing and evaporating moisture by testing the room humidity when operating evaporating humidifier practically. The test method on

Table 62.3 Mixing ratio of the specimen for the test of eco-friendly performance

No.	Hwangto	Charcoal powder	Elvan	Silica	Hardening agent (powder)	Hardening agent (fluid)	Adhesive agent (from sea plant)	Water	Remarks
1	300				300	300		180	
2	300	15			300	300		180	
3	300	15	15	15	300	300		180	
4	300	15	15	15			300	300	
5	300	15	15	15	300	300		180	PVA 5 g

Table 62.4 Test specimen for the test of eco-friendly performance

Specimen	No. 1	2	3	4	5
Antibacterial test					
Resistance to fungi					

the antibacteria was in accordance with KS J 4206:2008 [7] and that on the resistance performance was in accordance with KS J 3201:1980(2006 reexamined) [8]. The humidity control performance was tested and evaluated for the specimen manufactured with the corrugated form fit to be equipped to the evaporative humidifier in two same sized test rooms.

Eco-friendly Performance

To evaluate the eco-friendly performance, some materials known to be good in the air were used for the mixing. The ingredients were hwangto including coal powder, elvan, and silica. These materials were mixed with hardening materials from MGO with fiber reinforcing strength which was approved to give enough strength to the specimen through earlier test. Tables 62.3 and 62.4 illustrate the mixing ratio of each material and the specimen, respectively. For the test of antibacteria and resistance to fungi, the specimen no. 1 and no. 5 were used. The specimen no. 4 was excluded in the test because it took a relatively long time to dry and harden by using adhesive from sea plant, and no. 2 and no. 3 were also not used in the test but examined if the strength and shape were good because the ingredients used were included in the specimen no. 5 as well.

After hardening, the specimen's strength and shape were good except that no. 4 used sea plant adhesive. The result of antibacterial test showed that the rate of bacteria reduction was above 99.9 % and then there was no bacteria growth. The test result of the resistance to fungi showed that there was no any fungi growth until 4 weeks were passed.
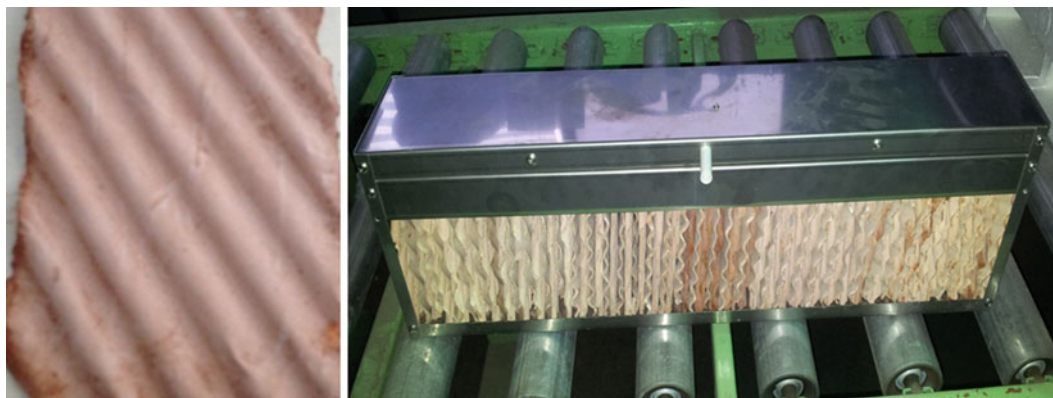
Fig. 62.1 The shape of the corrugated specimen and installation to the case fit to evaporating humidifier
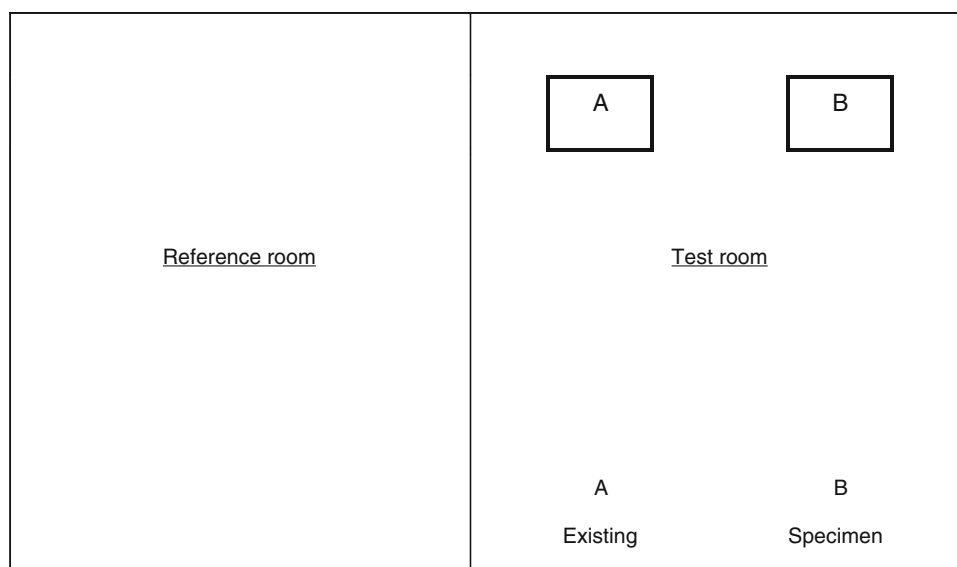
Fig. 62.2 Test room for the test of humidity control performance

Humidifying Performance

For the evaluation of humidity control performance, only specimen no. 1 was used among those specimen. The shape is corrugated like in the Fig. 62.1, which was manufactured using corrugated mould. The corrugated mould was made from the punched iron plate flexible to be bent. The easy separation between mould and specimen could be able to use oil paper between them. Finally, the specimen made one by one was installed to the frame of evaporating humidifier to measure indoor air temperature and humidity. The test rooms are composed of two same rooms that one room, the reference room, doesn't have anything in it, and in the other room, the test room, the humidifier has been installed (Fig. 62.2). The two humidifiers were tested to compare the performance of the specimen with the existing humidifier. The air temperature and the humidity were measured by self-writing thermohygrometer manufactured by SATO.

The air temperature outdoor was 22–30 °C, and the humidity was 20–70 % fluctuated by time. The air temperature in the reference room was 22–27 °C, and the humidity 45–60 % less fluctuated than that in outdoor. On the contrary while the air temperature in the test room was 22–25 °C similar to the reference room, the humidity was approached to 78 % close to the humidity which was set up to 80 % which is quite different with that in the reference room. It could be judged that the humidity control performance of the specimen is quite good, because the evaporating humidifier installed specimen set the optimized indoor humidity and kept the humidity targeted value. Figure 62.3 is showing the trend of humidity in the test room how it matches the targeted value well comparing with reference room and outdoor.
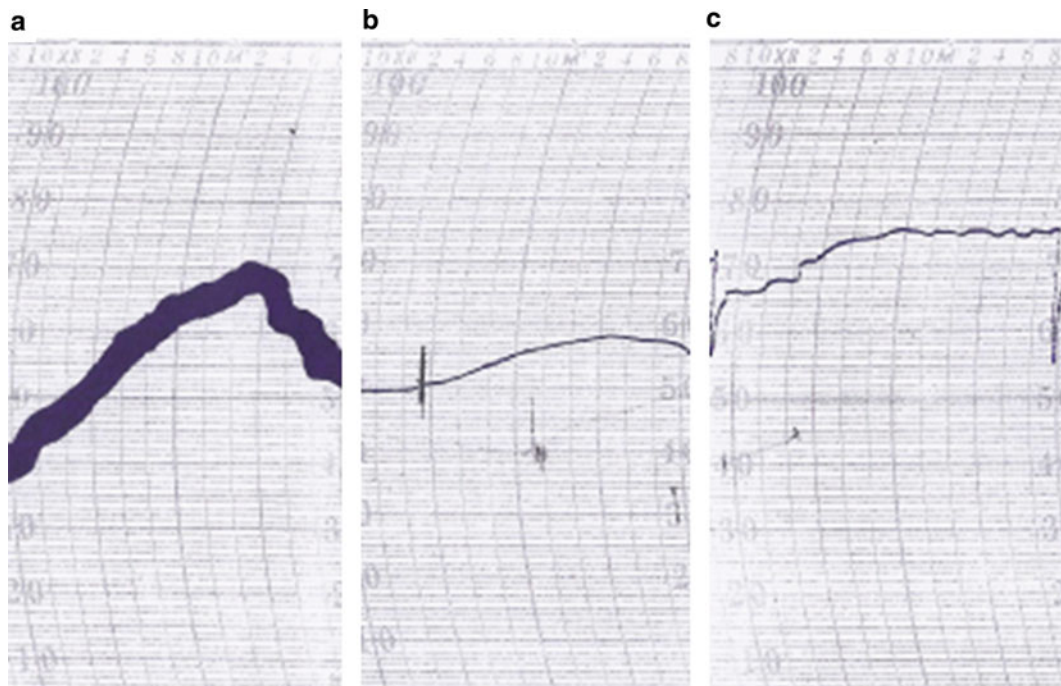
Fig. 62.3 The humidity in the test room compared with outdoor and reference room. (**a**) Outdoor. (**b**) Reference room. (**c**) Test room

Conclusions

The electrical humidifier has become a social problem due to the use of a sterilizing agent to prevent the device from contamination; the eco-friendly humidifier is necessary for the indoor air quality. In addition, the electrical devices more or less consume electrical energy to run it; then the device reducing the energy consumption is another reason of developing humidifier. In this study, focusing on the evaporating humidifier, the humidifying pad was developed and tested. Tests were carried out for the eco-friendly performance and humidity control performance. The developed pad has shown good ability for the antibacteria and resistance to fungi, which can be used for good indoor air quality. The humidity control performance was evaluated good that the humidity in the test room, where specimen was installed, meets the targeted value, even though the humidity in the reference room was very low. This result shows that the evaporating humidifier installed specimen developed can provide optimized room humidity together with good air quality, and be useful in the point of energy saving.

References

1. Aldous MB, Holberg CJ, Wright AL, Martinez FD, Taussig LM (1996) Evaporative cooling and other home factors and lower respiratory tract illness during the first year of life. Am J Epidemiol 143(5):423–430
2. Paschold H, Li WW, Morales H, Walton J (2003) Laboratory study of the impact of evaporative coolers on indoor PM concentrations. Atmos Environ 37:1075–1086
3. Watt JR, Brown WK (1997) Evaporative air conditioning handbook, 3rd edn. The Fairmont, Lilburn, GA
4. US EPA (1991) Indoor air facts. No. 8. Use and care of home humidifiers. US Environmental Protection Agency, Office of Air and Radiation, Office of Research and Development, Document Number: 402-F-91-101,Washington, DC
5. Go SS, Lee HC, Lee JY, Kim JH, Chung CW (2009) Experimental investigation of mortars using activated Hwangtoh. Construct Build Mater 23:1438–1445
6. Go SS, Chung CW, Struble LJ, Lee HC (2010) Pozzolanic activity of Hwangtoh clay. Construct Build Mater 24:2638–2645
7. KS J 4206:2008 (2008) Testing method for antibacterial activity of antibacterial functional products – Part 1: Shake flask method. Korean Standards Association
8. KS J 3201:1980(1980) Methods of test for fungus resistance. Korean Standards Association

Common Applications of Thin Layer Drying Curve Equations and Their Evaluation Criteria

Haydar Kucuk, Aydin Kilic, and Adnan Midilli

Abstract

In this study, thin layer drying curve equations commonly used in the literature between 2003 and 2013 are systematically discussed and evaluated in terms of their applications and selection for thin layer drying processes by considering the model evaluation criteria. As a result of this study, serious complications, confusions, and conflicts in the applications of thin layer drying curve equations and their evaluation criteria are noticed. Consequently, it is recommended that the drying curve equations should be applied in accordance with the forms commonly used in the literature. Also, it is determined that the following drying curve equations give the best results for thin layer drying processes which are the Midilli-Kucuk, Page, Logarithmic, Two-term, Wang and Singh, Approximation of diffusion, Modified Henderson and Pabis, Modified Page, Henderson and Pabis, Two-term exponential, and Verma et al.

Keywords

Thin layer drying curve equation • Midilli-Kucuk model • Mathematical modeling

Introduction

Thin layer equations have been used to estimate drying times of several products and to generalize drying curves. In the development of thin layer drying models for agricultural products, generally the moisture content of the material at any time after it has been subjected to a constant relative humidity and temperature conditions is measured and correlated to the drying parameters [1]. The thin layer drying models can be classified as theoretical, semi-theoretical, and empirical. The most widely used theoretical models are derived from Fick's second law of diffusion. Similarly, semi-theoretical models are generally derived from Fick's second law and modifications of its simplified forms (other semi theoretical models are derived by analogues with Newton's law of cooling) [2]. The empirical models have also similar characteristics with semi-theoretical models. They strongly depend on the experimental conditions and give limited information about the drying behaviors of the product [2]. The empirical method is based on experimental data and dimensional analysis. They are easily applied to drying simulation as they depend on experimental data [1]. The theoretical method takes into account not only the external conditions, but also the mechanism of internal movement of moisture and their consequent effects [3]. The Semi-theoretical and empirical models consider only the external resistance to moisture transfer between the product and air [4].

H. Kucuk (✉) • A. Midilli
Department of Mechanical Engineering, Faculty of Engineering, Recep Tayyip Erdoğan University, 53100 Rize, Turkey
e-mail: haydar.kucuk@erdogan.edu.tr; adnan.midilli@erdogan.edu.tr

A. Kilic
Department of Food Engineering. Faculty of Engineering, Recep Tayyip Erdoğan University, 53100 Rize, Turkey
e-mail: aydin.kilic@erdogan.edu.tr

Thin Layer Drying Curve Equations

Researchers have developed numerous thin layer models given as below for various agricultural products depending on product type, pretreatment of the product, drying parameters, and drying methods.

Newton (Lewis, Exponential, Single exponential) Model [2–44]

$$MR = \exp(-kt))\tag{63.1}$$

Page Model [2–7, 5, 9–20, 16, 22–24, 27, 26–34, 36–46]

$$MR = \exp(-kt^n)\tag{63.2}$$

Modified Page (Modified Page-I, Overhults et al.) Model [4, 6, 17, 18, 21–23, 37, 40–43]

$$MR = \exp(-(kt)^n)\tag{63.3}$$

Modified Page-II Model [58]

$$MR = \exp\left(-c\left(\frac{t}{L^2}\right)^n\right)\tag{63.4}$$

Henderson and Pabis (Single term, Generalized exponential) Model [1–3, 5, 7, 8, 10, 11, 13, 17, 19–23, 26, 28–31, 35, 37, 39, 42–44, 46–54, 56–58, 61–63]

$$MR = a\exp(-kt)\tag{63.5}$$

Logarithmic (Asymptotic, Yagcioglu et al.) Model [1–3, 5, 7, 8, 11, 14, 19, 21, 23, 26, 28, 30, 31, 34, 35, 37, 39, 42–44, 46, 47, 49, 50, 53–54, 56–58, 61–63]

$$MR = a\exp(-kt) + c\tag{63.6}$$

Midilli-Kucuk (Midilli, Midilli et al.) Model [1–3, 5, 7–11, 13, 14, 16, 19, 23, 26, 28, 30, 31, 35, 37–39, 42–44, 47, 49, 50, 52–54, 56–59, 61–63]

$$MR = a\exp(-kt^n) + bt\tag{63.7}$$

Modified Midilli et al. (Ghazanfari et al.) Model [24]

$$MR = \exp(-kt^n) + bt\tag{63.8}$$

Abbasi et al. (Modified Midilli-Kucuk) Model [1]

$$MR = a\exp(-kt^n) + b\tag{63.9}$$

Demir et al. Model [3, 21, 29]

$$MR = a\exp(-kt)^n + b\tag{63.10}$$

Modified Henderson and Perry (Agrawal and Singh) Model [45]

$$MR = a\exp(-kt^n)\tag{63.11}$$

Three Parameter Model [45]

$$MR = a \exp(-(kt)^n) \tag{63.12}$$

Two-Term Model [1–3, 5, 8, 14, 22, 26, 28, 31, 39, 42, 50, 51, 56, 57, 63]

$$MR = a \exp(-k_1 t) + b \exp(-k_2 t) \tag{63.13}$$

Two-Term Exponential Model [1–3, 5, 9, 14, 20–23, 26, 30, 31, 37, 39, 46, 49–51, 56, 57, 61–63]

$$MR = a \exp(-kt) + (1 - a) \exp(-kat) \tag{63.14}$$

Verma et al. (Modified Two-Term Exponential) Model [1, 2, 5, 9, 14, 21–23, 26, 29–31, 34, 37, 39, 46, 47, 49, 51, 53, 57, 61–62]

$$MR = a \exp(-kt) + (1 - a) \exp(-gt) \tag{63.15}$$

Approximation of Diffusion (Diffusion Approach) Model [1–3, 5, 10, 11, 13, 21, 23, 28, 30, 31, 35, 37, 39, 46, 47, 49–51, 53–54, 57, 58, 61–63]

$$MR = a \exp(-kt) + (1 - a) \exp(-kbt) \tag{63.16}$$

Modified Henderson and Pabis (Three Term Exponential) Model [1–3, 5, 9, 21, 22, 28, 30, 31, 35, 37, 39, 49–51, 57, 62]

$$MR = a \exp(-kt) + b \exp(-gt) + c \exp(-ht) \tag{63.17}$$

Thompson Model [5, 21, 22, 37, 63]

$$t = a\ln(MR) + b \left(\ln(MR)\right)^2 \tag{63.18}$$

Wang and Singh Model [1–3, 5, 7, 9, 11, 14, 16, 21–24, 26, 28, 30, 31, 35, 37, 39, 42, 43, 46, 49, 52, 56–58, 61–63]

$$MR = 1 + at + bt^2 \tag{63.19}$$

Kaleemullah Model [21]

$$MR = \exp(cT) + bt^{(pT+n)} \tag{63.20}$$

Diamente et al. Model [17]

$$\ln(-\ln(MR)) = a + b(\ln(t)) + c(\ln(t))^2 \tag{63.21}$$

Hii et al. Model [29]

$$MR = a \exp(-kt^n) + c \exp(-gt^n) \tag{63.22}$$

Simplified Fick's diffusion (SFFD) Model [22, 49, 58]

$$MR = a \exp\left(-c\left(\frac{t}{L^2}\right)\right) \tag{63.23}$$

Weibull Model [3]

$$MR = \exp\left(-\left(\frac{t}{a}\right)^b\right) \tag{63.24}$$

Modified Drying Model [27]

$$MR = a + \exp(-kt^n) \tag{63.25}$$

Aghbashlo et al. Model [3]

$$MR = \exp\left(-\frac{k_1 t}{1 + k_2 t}\right) \tag{63.26}$$

Seiiedlou and Aghbashlo Model [47]

$$MR = \exp\left(-\frac{k_1 t}{1 - k_2 t}\right) \tag{63.27}$$

Decay Model [40]

$$MR = \exp\left(\frac{k_1 \tau}{1 + k_2 \tau}\right) \tag{63.28}$$

Chavez-Mendez et al. Model [35]

$$MR = [1 - (1 - L_2)L_1 t]^{\left(\frac{1}{1-L_2}\right)} \tag{63.29}$$

Geometric Model [13]

$$MR = at^{-n} \tag{63.30}$$

Parabolic (Polynomial, Quadratic) Model [2]

$$MR = a + bt + ct^2 \tag{63.31}$$

Logistic Model (Yurtsever 2005)

$$MR = \frac{b}{(1 + a \exp(kt))} \tag{63.32}$$

Multiple Multiplicative Factor (MMF) Model [7]

$$MR = \frac{(a \times b + c \times t^d)}{(b + t^d)} \tag{63.33}$$

Noomhorn and Verma (Ranjbaran and Zare, Modified Two Term) Model [29]

$$MR = a \exp(-k_1 t) + b \exp(-k_2 t) + c \tag{63.34}$$

Akbulut and Durmuş Model [4]

$$MR = a \left[\frac{(T_{di} - T_{do})}{(T_{co} - T_{ci})}\right] \exp(-kt^n) \left[\frac{V_c}{(L_i - L_{i-1})/\Delta t}\right]^{m-1} \left[\frac{(b_w + b_d)/2}{(L_w + L_d)/2}\right]^{s-1} \tag{63.35}$$

Simplified Fick's Second Law of Diffusion Model [60]

$$MR = \frac{8}{\pi^2} \exp\left(-\frac{\pi^2 D_{eff} \tau}{4L^2}\right) \tag{63.36}$$

Exponential-hyperbolic Decay (Montazer-Rahmati and Amini-Horri) Model [40]

$$MR = \exp\left(-\frac{k_1(t/t_0)}{1 + k_2(t/t_0)}\right) \tag{63.37}$$

Third-degree Polynomial (Cubic) Model [34]

$$MR = a + bt + ct^2 + kt^3 \tag{63.38}$$

Das et al. (Jena-Das) Model [9]

$$MR = a \exp\left(-kt + b\sqrt{t}\right) + c \tag{63.39}$$

Linear Model (Sharifian et al. 2012)

$$MR = at + b \tag{63.40}$$

Quasi-stationary Model [30]

$$MR = \frac{1}{(1 + (t/x)^y)} \tag{63.41}$$

Balbay and Şahin Model [10]

$$MR = (1 - a)\exp(-kt^n) + b \tag{63.42}$$

Alibas (Modified Midilli-Kucuk) Model [6]

$$M_R = a \exp(-kt^n) + bt + g \tag{63.43}$$

Polynomial (Meda et al.) Model [36]

$$MR = (a + bt)^2 \tag{63.44}$$

Exponential (Meda et al.) Model [36]

$$MR = \exp\left(m + nt^{1.5}\right) \tag{63.45}$$

Jittanit (Modified Page) Model [33]

$$MR = \exp\left((-Kt^N)\exp\left(-\frac{A}{T_k}\right)\right) \tag{63.46}$$

Jittanit (Modified two-term) Model [33]

$$MR = A_1\exp\left((-K_1t)\exp\left(-\frac{B}{T_k}\right)\right) + A_1 \exp\left((-K_2t)\exp\left(-\frac{B}{T_k}\right)\right) \tag{63.47}$$

Regression Model [15]

$$M_R = \exp\left(-\left(at^2 + bt\right)\right) \tag{63.48}$$

Yun et al. Model [56]

$$MR = \frac{a \times bt + ct^2}{1 + dt + ft^2} \tag{63.49}$$

Kaleta et al. (Modified Verma et al.) Model [29]

$$MR = a \exp(-kt^n) + (1 - a) \exp(-gt^n) \tag{63.50}$$

Ademiluyi Model [29]

$$MR = a \exp(-(kt)^n) \tag{63.51}$$

Kaleta et al. (Modified two-term) Model [29]

$$MR = a \exp(-(kt)^n) + b \exp(-(gt)^n) \tag{63.52}$$

Jaros and Pabis-I Model [29]

$$M = M_o \left(\frac{1}{1-b} \left(1 - \frac{1-b}{NM_o} kt \right)^N - \frac{b}{1-b} \right), \quad b = \frac{0.85}{1 + M_o} \tag{63.53}$$

Jaros and Pabis-II Model [29]

$$M = M_e + (M_c - M_e) \exp\left(\frac{-k(t - t_c)}{M_c - M_e} \left(1 - \frac{1-b}{NM_o} kt_c \right)^{N-1} \right) \tag{63.54}$$

Henderson et al. Model [18]

$$X_r = c \left(\exp(-Kt) + \left(\frac{1}{9} \right) \exp(-9Kt) \right) \tag{63.55}$$

Law et al. (New Variable Diffusion Drying) Model [32]

$$X = X_{cr2} - \frac{(X_{cr2} - X_{eq})}{c} \ln\left(1 - \frac{\exp(c)bc(dX/dt)_{cr2}}{X_{cr2} - X_{eq}} t \right) \tag{63.56}$$

Zero Model [45]

$$X = X_o \exp(-Kt) \tag{63.57}$$

Motta Lima et al.-I Model [18]

$$X_r = (a + bT)^{-2} \tag{63.58}$$

Motta Lima et al.-II Model [18]

$$X_r = a + (at + ct^2 + dt^3) \exp\left(-\frac{e}{T} \right) \tag{63.59}$$

Pillai [46]

$$MR = a \exp\left(-a(IMC)^b (MWP)^c (SA)^d (DT) \right) \tag{63.60}$$

Evaluation Criteria

There are many evaluation criteria used to choose the best thin-layer drying curve equation for different products, drying methods, and drying conditions.

Correlation coefficient [12, 13, 21]

$$r = \frac{N\sum_{i=1}^{N}(MR_{pre,i})(MR_{\exp,i}) - \left(\sum_{i=1}^{N}MR_{pre,i}\right)\left(\sum_{i=1}^{N}MR_{\exp,i}\right)}{\sqrt{\left(N\sum_{i=1}^{N}MR_{pre,i}^2 - \left(\sum_{i=1}^{N}MR_{pre,i}\right)^2\right)\left(N\sum_{i=1}^{N}MR_{\exp,i}^2 - \left(\sum_{i=1}^{N}MR_{\exp,i}\right)^2\right)}} \tag{63.61}$$

The regression sum of squares [28]

$$SSR = \sum_{1}^{n}\left(MR_{cal,i} - MR_{avg}\right)^2 \tag{63.62}$$

The total sum of squares [28]

$$SST = \sum_{1}^{n}\left(MR_{\exp,i} - MR_{avg}\right)^2 \tag{63.63}$$

The error (residual) sum of squares [51]

$$SSE = \sum_{i=1}^{N}\left(MR_{\exp,i} - MR_{cal,i}\right)^2 \tag{63.64}$$

Residual sum of squares (RSS) [23, 35, 43, 46, 55]

$$RSS = \sum_{i=1}^{N}\left(MR_{\exp,i} - MR_{pre,i}\right)^2 \tag{63.65}$$

Coefficient of determination [28, 51]

$$R^2 = \frac{SSR}{SST} = 1 - \frac{SSE}{SST} = \tag{63.66}$$

The adjusted R^2 [37]

$$\overline{R}^2 = 1 - \left(1 - R^2\right)\frac{N-1}{N-k-1} \tag{63.67}$$

The reduced chi-square [9, 17, 21, 22, 31, 37, 39, 46, 50, 54, 55, 57, 58]

$$\chi^2 = \frac{\sum_{i=1}^{N}\left(MR_{\exp,i} - MR_{pre,i}\right)^2}{N-n} \tag{63.68}$$

The root mean square error [4, 9, 12, 13, 19, 21, 22, 26, 30, 37, 47, 49, 54, 56–58, 61]

$$RMSE = \sqrt{\frac{\sum_{i=1}^{N}\left(MR_{pre,i} - MR_{\exp,i}\right)^2}{N}} \tag{63.69}$$

Residuals [49]

$$residuals = \sum_{i=1}^{N} \left(MR_{\exp,i} - MR_{pre,i} \right) \tag{63.70}$$

Modeling efficiency [58]

$$EF = \frac{\sum_{i=1}^{N} \left(MR_{\exp,i} - MR_{\exp,ave} \right)^2 - \sum_{i=1}^{N} \left(MR_{pre,i} - MR_{\exp,i} \right)^2}{\sum_{i=1}^{N} \left(MR_{\exp,i} - MR_{\exp,ave} \right)^2} \tag{63.71}$$

The standard error of estimate (SEE) [51]

$$SEE = \sqrt{\frac{\sum_{i=1}^{N} \left(MR_{\exp,i} - MR_{cal,i} \right)^2}{N - n_p}} \tag{63.72}$$

Variance (s^2) (Standard error (σ^2)) [43]

$$\sigma^2 \approx s^2 = \frac{\left(\sum_{i=1}^{N} \left(MR_{\exp,i} - MR_{pre,i} \right)^2 \right)_{\min}}{N - n} \tag{63.73}$$

The reduced sum square error [51]

$$RSSE = \frac{\sum_{i=1}^{N} \left(MR_{\exp,i} - MR_{cal,i} \right)^2}{N} \tag{63.74}$$

The mean bias error [12, 26, 57, 58]

$$MBE = \frac{\sum_{i=1}^{N} \left(MR_{pre,i} - MR_{\exp,i} \right)}{N} \tag{63.75}$$

Mean relative percentage error [50]

$$P = \frac{100}{N} \sum_{i=1}^{N} \frac{\left| MR_{\exp,i} - MR_{pre,i} \right|}{MR_{\exp,i}} \tag{63.76}$$

Mean absolute error [41]

$$MAE = \frac{1}{N} \sum_{i=1}^{N} \left| x_{pi} - x_{di} \right| \tag{63.77}$$

t-value [26]

$$t - value = \sqrt{\frac{(n-1)(MBE)^2}{(RMSE)^2 - (MBE)^2}} \tag{63.78}$$

Degrees of freedom [25]

$$\nu = \frac{\left[\left(\sigma_{\exp}^2/n_{\exp}\right) + \left(\sigma_{pre}^2/n_{pre}\right)\right]^2}{\dfrac{\left[\sigma_{\exp}^2/n_{\exp}\right]^2}{n_{\exp} - 1} + \dfrac{\left[\sigma_{pre}^2/n_{pre}\right]^2}{n_{pre} - 1}} \tag{63.79}$$

F-value [55]

$$F - value = \frac{MS_{treatment}}{MS_{error}} \tag{63.80}$$

Results and Discussion

As a result of literature review, it is observed that 60 thin layer drying curve equations have been derived by researchers by taking into consideration the following parameters: (1) product type, (2) pretreatment of the product, (3) drying parameters such as temperature, air velocity, layer thickness, micro-wave power levels, amount of solar radiation, vacuum pressure, frequency of the sound wave, excitation amplitude, relative humidity, bed dept, shape of product, pH, salt content, absolute pressures (4) drying methods. On the other hand, 20 evaluation criteria have been defined to evaluate the performance of the thin layer drying curve equation. Serious complications, confusions, and conflicts in the applications of thin layer drying curve equations and their evaluation criteria such as name, equation and nomenclature are noticed. In this study, the drying curve equations have been given in accordance with the forms commonly used in the literature. It is realized that Newton (Lewis, Exponential, Single exponential) (Eq. 63.1), Page (Eq. 63.2), Henderson and Pabis (Single term, Generalized exponential) (Eq. 63.5), Logarithmic (Asymptotic, Yagcioglu et al.) (Eq. 63.6), Midilli-Kucuk (Midilli, Midilli et al.) (Eq. 63.7), Two-Term (Eq. 63.13), Two-Term Exponential (Eq. 63.14), Verma et al. (Modified Two-Term Exponential) (Eq. 63.15), Approximation of Diffusion (Diffusion Approach) (Eq. 63.16), Modified Henderson and Pabis (Three Term Exponential) (Eq. 63.17), Wang and Singh (Eq. 63.19), Modified Page (Modified Page-I, Overhults et al.) (Eq. 63.3), Thompson Model (Eq. 63.18) and SFFD (Eq. 63.23) models are commonly used in the literature. The other thin layer drying curve equations have been rarely used by the researchers. Also, It is noticed that, coefficient of determination (R^2) (Eq. 63.66), the reduced chi-square (χ^2) (Eq. 63.68), the root mean square error (RMSE) (Eq. 63.69), the mean bias error (MBE) (Eq. 63.75), mean relative percentage error (P) (Eq. 63.76), RSS (Eq. 63.65), modeling efficiency (EF) (Eq. 63.71) and the SEE (Eq. 63.72) are commonly used to evaluate thin layer drying models in the literature. However, it is determined that Midilli-Kucuk, Page, Logarithmic, Two-term, Wang and Singh, Approximation of diffusion, Modified Henderson and Pabis, Modified Page, Henderson and Pabis, Two-term exponential, Verma et al., and the others give best results, respectively, for different drying methods, drying parameters, and dried products.

Conclusions

Thin layer drying curve equations are commonly used in the literature to estimate drying behavior of the different products depending on pretreatment of the product, drying parameters, and drying methods. It is realized that there is a complexity in both drying methods and evaluation criteria such as name, equation, and nomenclature. It is clear that the standardization is necessary for thin layer drying curve equations and their evaluation criteria. The comprehensive review of thin layer drying curve models seems that, when the evaluation criteria are considered the Midilli-Kucuk, Page, Logarithmic, Two-term, Wang and Singh, Approximation of diffusion, Modified Henderson and Pabis, Modified Page, Henderson and Pabis, Two-term exponential and Verma et al., give better results respectively.

Nomenclature

A, A₁, a, B, b, c, d, e, f, g, h, K, K₁, K₂, k, k₁, k₂, L, L₁, L₂, m, n, N, p, s, x, y	Drying constants	L	Sample thickness (Eq. 63.35), half-thickness (Eq. 63.36), m
b	Sample length, m (Eq. 63.35)	N, n	Number of observations
D	Moisture diffusion coefficient, m²/s	n, nₚ	Number of constants
DT	Drying time, min	P	Mean relative percentage error
EF	Modeling efficiency	r	Correlation coefficient
IMC	Moisture content	R²	Coefficient of determination
M	Moisture content (g water/g dry solids), % dry basis	RMSE	Root mean square error
		RSS	Residual sum of squares
		RSSE	Reduced sum square error
MAE	Mean absolute error	s²	Variance
MBE	Mean bias error	SA	Surface area, m²
MR, x, Xᵣ	Moisture ratio	SEE	Standard error of estimate
MS	Mean squares	SSE	Error (residual) sum of squares
MW	Microwave	SSR	Regression sum of squares
MWP	Microwave output power, W	SST	Total sum of squares
t	Drying time, min	T	Drying air temperature, °C
		Tₖ	Drying temperature, K
		V	Drying air velocity, m/s
		X	Moisture content (g water/g dry solids), % dry basis

$A, A_1, a, B, b, c, d, e, f, g, h, K, K_1, K_2, k, k_1, k_2, L, L_1, L_2, m, n, N, p, s, x, y$ — Drying constants

b — Sample length, m (Eq. 63.35)
D — Moisture diffusion coefficient, m^2/s
DT — Drying time, min
EF — Modeling efficiency
IMC — Moisture content
M — Moisture content (g water/g dry solids), % dry basis
MAE — Mean absolute error
MBE — Mean bias error
MR, x, X_r — Moisture ratio
MS — Mean squares
MW — Microwave
MWP — Microwave output power, W
t — Drying time, min

L — Sample thickness (Eq. 63.35), half-thickness (Eq. 63.36), m
N, n — Number of observations
n, n_p — Number of constants
P — Mean relative percentage error
r — Correlation coefficient
R^2 — Coefficient of determination
$RMSE$ — Root mean square error
RSS — Residual sum of squares
$RSSE$ — Reduced sum square error
s^2 — Variance
SA — Surface area, m^2
SEE — Standard error of estimate
SSE — Error (residual) sum of squares
SSR — Regression sum of squares
SST — Total sum of squares
T — Drying air temperature, °C
T_k — Drying temperature, K
V — Drying air velocity, m/s
X — Moisture content (g water/g dry solids), % dry basis

Greek Letters

χ^2 — Reduced chi-square
ν — Degrees of freedom
σ — Standard deviation

σ^2 — Standard error
τ — Drying time, min

Subscripts

ave, avg — Average
c — Critical
cal — Calculated
cr1 — First critical
cr2 — Second critical
ci — Collector in
ci — Collector out
d — Dry
di — Dryer inlet

do — Dryer outlet
e — Equilibrium
eff — Effective
eq — Equilibrium state
exp — Experimental
0 — Initial
pre — Predicted
w — Wet

References

1. Abbasi S, Mousavi SM, Mohebbi M (2009) Propose suitable model for modeling of moisture ratio and estimation of effective moisture diffusivity of onion slices by hot air dryer. In: The 6th international chemical engineering congress and exhibition, Kish Island
2. Abano EE, Haile MA, Owusu J, Engmann FN (2013) Microwave-vacuum drying effect on drying kinetics, lycopene and ascorbic acid content of tomato slices. J Stored Prod Postharvest Res 4(1):11–22
3. Aghbashlo M, Kianmehr MH, Khani S, Ghasemi M (2009) Mathematical modelling of thin-layer drying of carrot. Int Agrophys 23(4):313–317
4. Akbulut A, Durmuş A (2009) Thin layer solar drying and mathematical modeling of mulberry. Int J Energy Res 33(7):687–695
5. Akpinar EK, Sarsılmaz C, Yildiz C (2004) Mathematical modelling of a thin layer drying of apricots in a solar energized rotary dryer. Int J Energy Res 28(8):739–752
6. Alibas I (2012) Selection of a the best suitable thin-layer drying mathematical model for vacuum dried red chilli pepper. J Biol Environ Sci 6(17):161–170

7. Amira T, Saber C, Fethi Z (2010) Modelling of the drying kinetics of opuntia ficus indica fruits and cladodes. Int J Food Eng 6(2):1–17. http://www.bepress.com/ijfe/vol6/iss2/art11

8. Arslan D, Özcan MM (2008) Evaluation of drying methods with respect to drying kinetics, mineral content and colour characteristics of rosemary leaves. Energy Convers Manag 49(5):1258–1264

9. Ashraf Z, Hamidi-Esfahani Z, Sahari MA (2012) Evaluation and characterization of vacuum drying of date paste. J Agric Sci Technol 14:565–575

10. Balbay A, Şahin Ö (2012) Microwave drying kinetics of a thin-layer liquorice root. Drying Technol 30(8):859–864

11. Bingol G, Roberts JS, Balaban MO, Devres YO (2012) Effect of dipping temperature and dipping time on drying rate and color change of grapes. Drying Technol 30(6):597–606

12. Chin SK, Law CL, Supramaniam CV, Cheng PG (2009) Thin-layer drying characteristics and quality evaluation of air-dried Ganoderma tsugae Murrill. Drying Technol 27(9):975–984

13. Cihan A, Kahveci K, Hacıhafızoğlu O (2007) Modelling of intermittent drying of thin layer rough rice. J Food Eng 78(1):293–298

14. Corzo O, Bracho N, Alvarez C (2011) Determination of suitable thin layer model for air drying of mango slices (Mangifera indica L.) at different air temperatures and velocities. J Food Process Eng 34(2):332–350

15. Costa A, Pereira H (2013) Drying kinetics of cork planks in a cork pile in the field. Food Bioprod Process 91(1):14–22

16. Demirhan E, Özbek B (2010) Drying kinetics and effective moisture diffusivity of purslane undergoing microwave heat treatment. Korean J Chem Eng 27(5):1377–1383

17. Diamante LM, Ihns R, Savage GP, Vanhanen L (2010) A new mathematical model for thin layer drying of fruits. Int J Food Sci Technol 45(9):1956–1962

18. dos Santos JAB (2007) Análise Comparativa Entre Técnicas de Processamentos Para Extração de Pigmentos nas Sementes de Urucum. Ph.D. thesis, Federal University of Campina Grande, Campina

19. Doymaz İ (2012) Evaluation of some thin-layer drying models of persimmon slices (Diospyros kaki L.). Energy Convers Manag 56:199–205

20. Duan Z, Zhang M, Hu Q, Sun J (2005) Characteristics of microwave drying of bighead carp. Drying Technol 23(3):637–643

21. Erbay Z, Icier F (2010) A review of thin layer drying of foods: theory, modeling, and experimental results. Crit Rev Food Sci Nutr 50(5):441–464

22. Evin D (2012) Thin layer drying kinetics of Gundelia tournefortii L. Food Bioprod Process 90(2):323–332

23. Ganesapillai M, Regupathi I, Murugesan T (2008) An empirical model for the estimation of moisture ratio during microwave drying of plaster of paris. Drying Technol 26(7):963–978

24. Ghazanfari A, Emami S, Tabil LG, Panigrahi S (2006) Thin-layer drying of flax fiber: II. Modeling drying process using semi-theoretical and empirical models. Drying Technol 24(12):1637–1642

25. Gunhan T, Demir V, Hancioglu E, Hepbasli A (2005) Mathematical modeling of drying of bay leaves. Energy Convers Manag 46(11–12):1667–1679

26. Hayaloglu AA, Karabulut I, Alpaslan M, Kelbaliyev G (2007) Mathematical modeling of drying characteristics of strained yoghurt in a convective type tray-dryer. J Food Eng 78(1):109–117

27. Hemis M, Singh CB, Jayas DS (2011) Microwave-assisted thin layer drying of wheat. Drying Technol 29(10):1240–1247

28. Jazini MH, Hatamipour MS (2010) A new physical pretreatment of plum for drying. Food Bioprod Process 88(2–3):133–137

29. Kaleta A, Gornicki K, Winiczenko R, Chojnacka A (2013) Evaluation of drying models of apple (var. Ligol) dried in a fluidized bed dryer. Energy Convers Manag 67:179–185

30. Khanali M, Rafiee S, Jafari A, Hashemabadi SH, Banisharif A (2012) Mathematical modeling of fluidized bed drying of rough rice (Oryza sativa L.) grain. J Agric Technol 8(3):795–810

31. Lahsasni S, Kouhila M, Mahrouz M, Idlimam A, Jamali A (2004) Thin layer convective solar drying and mathematical modeling of prickly pear peel (Opuntia ficus indica). Energy 29(2):211–224

32. Law CL, Tasirin SM, Daud WRW (2003) A new variable diffusion drying model for the second falling rate period of paddy dried in a rapid bin dryer. Drying Technol 21(9):1699–1718

33. Le TQ, Jittanit W (2011) Drying kinetics of cooked jasmine brown rice during various drying methods. In: The 22nd national graduate research conference, Bangkok

34. Liu W, Zheng Y, Huang LX, Zhang CH, Xie PJ (2011) Low-temperature vacuum drying of natural gardenia yellow pigment. Drying Technol 29(10):1132–1139

35. McMinn WAM, Farrell G, Magee TRA (2007) Prediction of microwave drying behavior of pharmaceutical powders using thin-layer models. Drying Technol 25(9):1551–1569

36. Meda V, Gupta M, Opoku A (2008) Drying kinetics and quality characteristics of microwave-vacuum dried saskatoon berries. J Microw Power Electromagn Energy 42(4):4–12

37. Menges HO, Ertekin C (2006) Modelling of air drying of Hacıhaliloglu-type apricots. J Sci Food Agric 86:279–291

38. Midilli A, Kucuk H, Yapar Z (2002) A new model for single-layer drying. Drying Technol 20(7):1503–1513

39. Mohamed LA, Kane CSE, Kouhila M, Jamali A, Mahrouz M, Kechaou N (2008) Thin layer modelling of Gelidium sesquipedale solar drying process. Energy Convers Manag 49(5):940–946

40. Montazer-Rahmati MM, Amini-Horri B (2005) From laboratory experiments to design of a conveyor-belt Drryer via mathematical modeling. Drying Technol 23(12):2389–2420

41. Nazghelichi T, Kianmehr MH, Aghbashlo M (2011) Prediction of carrot cubes drying kinetics during fluidized bed drying by artificial neural network. J Food Sci Technol 48(5):542–550

42. Ong SP, Law CL (2009) Mathematical modelling of thin layer drying of salak. J Appl Sci 9(17):3048–3054

43. Özbek B, Dadali G (2007) Thin-layer drying characteristics and modelling of mint leaves undergoing microwave treatment. J Food Eng 83(4):541–549

44. Pin KY, Chuah TG, Abdull Rashih A, Law CL, Rasadah MA, Choong TSY (2009) Drying of betel leaves (Piper betle L.): quality and drying kinetics. Drying Technol 27(1):149–155

45. Phoungchandang S, Kongpim P (2012) Modeling using a new thin-layer drying model and drying characteristics of sweet basil (Ocimum Baslicum Linn.) using tray and heat pump-assisted dehumidified drying. J Food Process Eng 35(6):851–862

46. Pillai MG (2013) Thin layer drying kinetics, characteristics and modeling of plaster of Paris. Chem Eng Res Des. http://dx.doi.org/10.1016/j.cherd.2013.01.005

47. Rasouli M, Seiiedlou S, Ghasemzadeh HR, Nalbandi H (2011) Convective drying of garlic (Allium sativum L.): part I: drying kinetics, mathematical modeling and change in color. Aust J Crop Sci 5(13):1707–1714

48. Roberts JS, Kidd DR, Padilla-Zakour O (2008) Drying kinetics of grape seeds. J Food Eng 89(4):460–465

49. Ruiz CA, Francisco C, Fernand L-R, Aida R (2013) Thin layer drying behavior of industrial tomato by-products in a convective dryer at low temperatures. Res J Biotechnol 8(2):50–60

50. Sacilik K, Elicin AK (2006) The thin layer drying characteristics of organic apple slices. J Food Eng 73(3):281–289

51. Saeed IE (2010) Solar drying of roselle (Hibiscus sabdariffa L.) Part I: mathematical modelling, drying experiments, effects of the drying conditions. Agric Eng Int CIGR J 12(3):1–13. http://www.cigrjournal.org/index.php/Ejounral/article/viewFile/1484/1366

52. Sarimeseli A (2011) Microwave drying characteristics of coriander (Coriandrum sativum L.) leaves. Energy Convers Manag 52(2):1449–1453

53. Sharifian F, Motlagh AM, Nikbakht AM (2012) Pulsed microwave drying kinetics of fig fruit (Ficuscarica L.). Aust J Crop Sci 6(10):1441–1447

54. Sobukola OP, Dairo OU, Sanni LO, Odunewu AV, Fafiolu BO (2007) Thin layer drying process of some leafy vegetables under open sun. Food Sci Technol Int 13 (1):35–40

55. Tahmasebi A, Yu J, Han Y, Zhao H, Bhattacharya S (2013) Thermogravimetric study and modeling for the drying of a Chinese lignite. Asia Pacific J Chem Eng 8:793–803. doi:10.1002/apj.1722

56. Tee YM, Ifa P, Siti TM, Meor TMZ, Wan DWR, Zahira Y (2013) Drying of oil palm frond particles in a fluidized bed dryer with inert medium. Chem Ind Chem Eng Q 19:593. doi:10.2298/CICEQ120327094Y

57. Toğrul İT, Pehlivan D (2004) Modelling of thin layer drying kinetics of some fruits under open-air sun drying process. J Food Eng 65(3):413–425

58. Toğrul H (2005) Simple modeling of infrared drying of fresh apple slices. J Food Eng 71(3):311–323

59. Vega-Gálvez A, Ayala-Aponte A, Notte E, de la Fuente L, Lemus-Mondaca R (2008) Mathematical modeling of mass transfer during convective dehydration of brown algae macrocystis pyrifera. Drying Technol 26(12):1610–1616

60. Wiktor A, Iwaniuk M, Śledź M, Nowacka M, Chudoba T, Witrowa-Rajchert D (2013) Drying kinetics of apple tissue treated by pulsed electric field. Drying Technol 31(1):112–119

61. Yurtsever S (2005) Mathematical modeling and evaluation of microwave drying kinetics of mint (Menthaspicatta L.). J Applied Sci 5(7):1266–1274

62. Yücel U (2006) Evaluation of high pressure pretreatment for enhancing the drying rate of selected fruits and vegetables. M.Sc. thesis, Middle East Technical University, Ankara.

63. Zomorodian A, Moradi M (2010) Mathematical modeling of forced convection thin layer solar drying for cuminum cyminum. J Agric Sci Technol 12(4):401–408

Experimental Study of Thin Layer Drying Behavior of a Fish

64

Murat Erdem, Yasin Varol, Hakan Fehmi Öztop, and Fethi Kamışlı

Abstract

This study covers the drying behavior of *rainbow trout* (*Oncorhynchus mykiss*) in a square cross-sectioned dryer. For this, approximately 200 g fish was used to dry at different air inlet velocities like 0.5, 1.5, and 2.5 m/s for the constant air inlet temperature at 46 °C in ranges of 28–43 % of relative humidity. In the experiments, interior temperature values and moisture loses of fish were measured as a function of the drying time. It is seen that the moisture content of the fish has decreased with time and drying procedure for inlet air velocity to be effective. And it is suggested that the fish samples should be dried as single layer at 46 ± 0.1 °C and velocity of 2.5 ms^{-1} for optimal boundary conductions.

Keywords

Drying • Fish drying • Food drying • Tray dryer

Introduction

The drying of nutrients in agriculture and animal science is a method, which has been known since ancient times. The method can be applied in many kinds of food. The process of fish drying is one of the most reliable methods that is used to storage fish such as others foods for a long time. One of the drying techniques applied in the world is the open sun technique. But nutrients dried with this technique cannot be protected from harmful matters such as dust, rain, and insects. Therefore, drying of fish and other nutritional products in closed places is healthier than in open sun. In this way, control of drying process brings benefit on behalf of healthier for human life. In this regard, works of some researches can be listed as follows: Walnut, pine, beech, and poplar which are commonly used in wood material industry in Turkey by Kamisli [1] were dried at constant temperature but different velocities of drying air in the tray dryer. It was observed that the drying rates and heat transfer coefficients decrease with the drying time. Bala et al. [2] examined the drying of pineapple by using a solar tunnel dryer. They indicated that the pineapple dried in the solar dryer is a good quality dried product for human consumption. Bala and Mondol [3] investigated experimentally the drying of fish using solar tunnel dryer. They found that moisture content

M. Erdem (✉)
Vocational School of Technical Sciences, Fırat University, Elazig, Turkey
e-mail: m.erdem82@gmail.com

Y. Varol
Department of Automotive Engineering, Technology Faculty, Fırat University, Elazig, Turkey
e-mail: yvarol@gmail.com

H.F. Öztop
Department of Mechanical Engineering, Technology Faculty, Fırat University, Elazig, Turkey
e-mail: hfoztop1@gmail.com

F. Kamışlı
Department of Chemical Engineering, Engineering Faculty, Fırat University, Elazig, Turkey
e-mail: fkamisli@firat.edu.tr

decreases with drying time and the fish dried in the solar tunnel dryer was completely protected from rain, insect, dust, and that the dried fish was a high quality product. Bellagha et al. [4] studied on salting and drying of sardine (sardinella aurita). Erdem [5] investigated experimentally the drying behavior of fish (*Oncorhynchus mykiss*) in a tray dryer under different flow velocity and air inlet temperature at different dimensions of the fish, and drying of salted fish at different temperatures and at different air flow velocities. It is observed that moisture content of either case (both fish salted and fish unsalted) dwindles with drying time. Jain and Pathare [6] investigated the drying kinetics of open sun drying of fish. The fishes used in the experiment are prawn and *chelwa* fish (Indian minor carp). They observed that the drying rate curves contained no constant and showed linear falling rate throughout the drying process. Kituu et al. [7] developed a drying model in Visual Basic 6 for simulating the drying of Tilapia fish (*Oreochromis niloticus*) in a solar tunnel dryer. They showed that the model can be used to predict the drying of Tilapia fish in a solar tunnel dryer. Oztop and Akpinar [8] examined experimentally and numerically the moisture transfer during the convective drying of the same products. Both experimental and numerical results showed that there is a good agreement between numerically and experimentally measured data and predicted values. Erdem et al. [9] investigated experimentally the behavior of drying of rainbow trout at different inlet temperatures but constant inlet velocity in a square cross-sectioned tray dryer. It is observed that the curves are decreased with drying time during the drying process. Arason and Arnason [10] carried out a study on drying of fish products using geothermal energy. They suggested that the equipment designed for drying of fish can also be used to dry the other industrial products. Koyuncu [11] actualized the performance of improvement of greenhouse-type agricultural dryers. It observed that systems improved are more efficient than open air dryer.

The main purpose of this work is to examine the thin layer drying behavior of fish (*Oncorhynchus mykiss*) in a tray dryer under different air flow velocities and at a constant inlet temperature. Because there is no sufficient data related to drying behavior of *the rainbow trout* in literature, the results obtained from the experiments are very important for the future studies.

Materials and Methods

Experimental Setup and Methods

Figure 64.1 shows the dryer setup used in this experimental work. It mainly consists of an electric fan with 375 W, heater resistance, drying chamber, air duct, and measurement instruments.

The air flow rate of the experimental setup was adjusted by the fan speed control unit. The heating system consists of an electric heater (maximum power of 800 W), which is placed into the duct. The drying chamber temperature was adjusted by the heater power control. The drying duct was constructed from st-52 steel sheet with a square section of 2,000 mm length, 300 mm width, 300 mm height, and 590 mm length in a drying chamber. In the measurements of temperature, three numbers of K type thermocouples were used with a manually controlled two-channel digital thermometer (CHY, 806AW, accuracy of ± 0.1 °C). The velocity of air passing through the system was measured by a 0.4–3 m/s range anemometer (RAM DT-619, m/s—range: 0.4~3.0 accuracy: 3 %). Moisture loss was recorded by a digital balance (Avery Berkel, Model CC061) at time interval of 10 min during the drying period to determine a removal rate of the moisture. The digital balance has the measurement range between 0 and 6,000 g with the accuracy of ± 0.1 g. For thin layer drying experiments, the fish samples were selected, carefully cleaned, washed, and rested for a while to remove the water on the samples.

Experimental Uncertainty

During experiments, some errors take place because of measuring instruments, unknown causes, and electronic oscillations. These errors are determined with the following equation [12]:

$$W_x = \left[(x_1)^2 + (x_2)^2 + \ldots\ldots\ldots\ldots\ldots + (x_\infty)^2 \right]^{1/2} \tag{64.1}$$

Total error values of measuring instruments are illustrated in Table 64.1.
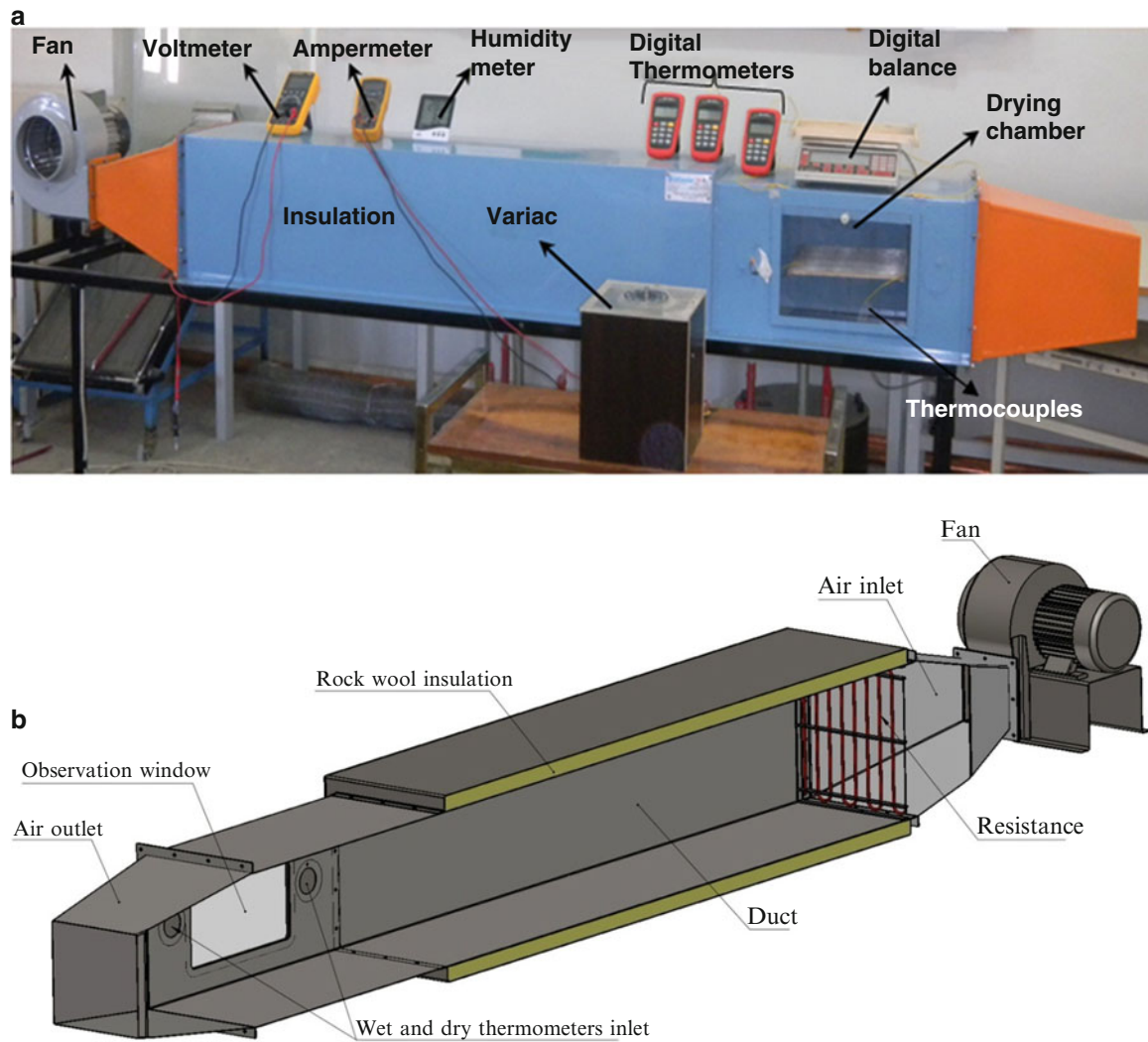
Fig. 64.1 Experimental setup; (**a**) the picture of experimental setup, (**b**) the schematic picture of experimental setup

Table 64.1 Uncertainties of the measuring parameters

Parameter	Unit	Total error
Temperature measurement	°C	±0.07
Air inlet velocity	m/s	±0.025
Mass measurement	g	±0.1
Moisture loss values	min	±0.17
Dimensionless moisture content	min	±0.2
Drying rate	g/s	±0.14

Mathematical Formulation

Dimensionless moisture content is determined by the following equation [13]:

$$M = \frac{M_t - M_e}{M_i - M_e} \tag{64.2}$$

In this equation, M explains dimensionless weight losses of the fish during drying; M_i, weight of the fish at beginning; M_t, weight of the fish at time of t; and M_e, weight of the fish in equilibrium (final weight). Moisture content wet basic (w.b.) is calculated by the following equation [14]:

$$M_{wb} = \frac{Mw}{M_i} \tag{64.3}$$

where Mwb refers to the moisture content of fish and Mw, the amount of water at time of t (g) for fish samples. The following equation is used to calculate drying rate [15]:

$$\frac{dM}{dt} = \frac{M_{t+dt} - M_t}{dt} \tag{64.4}$$

In the above equation, dM/dt is the drying rate; M_t, the weight of fish at time of t; and M_{t+dt}, the weight of fish at time of t + dt.

Results and Discussion

In this study, the effect of inlet air velocity on drying of a fish (*Oncorhynchus mykiss*) was determined experimentally in the tray dryer. In the experiments, inlet air temperature and air inlet velocities were selected as 46 °C and 0.5, 1.5, and 2.5 m/s, respectively.

Figure 64.2 refers to the variation of the interior temperature with drying time of fish at different velocities but at constant temperature of T = 46 °C in the tray dryer. As shown in the figure the interior temperature of fish increases as a function time at all velocities until first 15 h. The curve of interior temperature of the fish sample at air velocity of 0.5 and 1.5 m/s was broken due to adverse working conditions. Next day (after 7 h) is continued to working where it left off. As can be seen in the figure, the constant air velocity of 2.5 m/s the curve of sample is more irregular according to others curve. Figure 64.3 displays the variation of moisture content with time of drying fish at three different velocities but at constant temperature (T = 46 °C). After first 15 h, the curve of interior temperature of the fish sample at air velocity of 0.5 and 1.5 m/s is broken, since drying is broken for 7 h (night time), and then it is continue working. As expected, the moisture content of the sample decreases with time at each air velocity used in the experiments. As seen in the figure, increasing velocity of drying air has an important positive effect on drying time. In other words, when air inlet velocity increases, drying time decreases. At all parameters studied are seen to be the best model the sample dried at V = 2.5 m/s and T = 46 °C.

Variation of the dimensionless moisture content with drying time for the air temperature of 46 °C and at different air velocities is given in Fig. 64.4. A case similar to Fig. 64.2 is seen, where, how the velocity to be effective on drying time is showed clearly. In the figure, it is observed that moisture loss decreases with time. At study except median was worked with the time interval 7 h, and then was continued to working. Variation of drying rate with drying time at the air temperature of 46 °C is illustrated in Fig. 64.5 at different inlet velocities. As seen from the figure up to first 400 min the drying rate
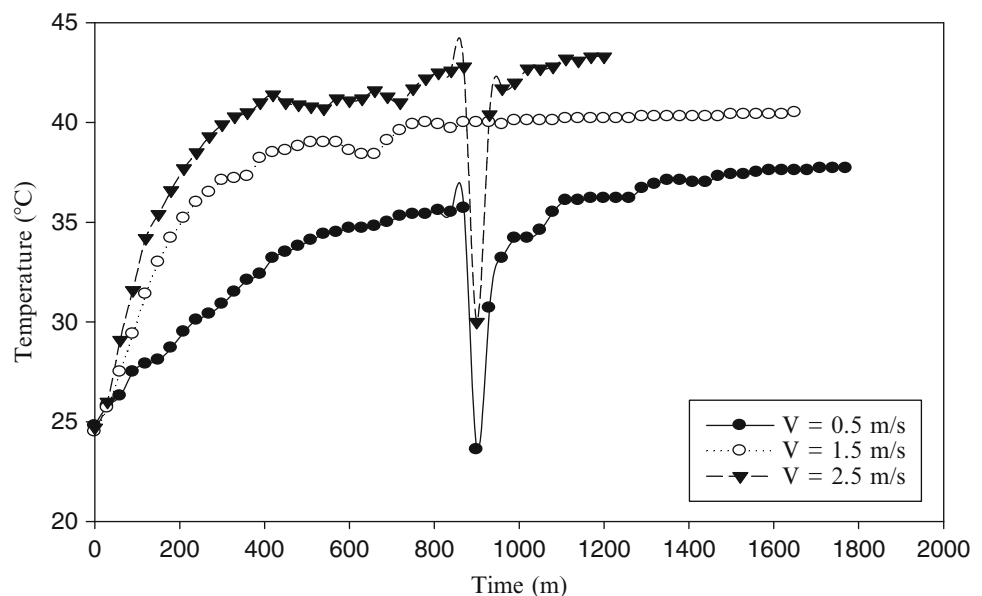
Fig. 64.2 Variation of interior temperature of fish with drying time at T = 46 °C and different inlet air velocities

Fig. 64.3 Variation of moisture content of fish with drying time at T = 46 °C and different inlet air velocities
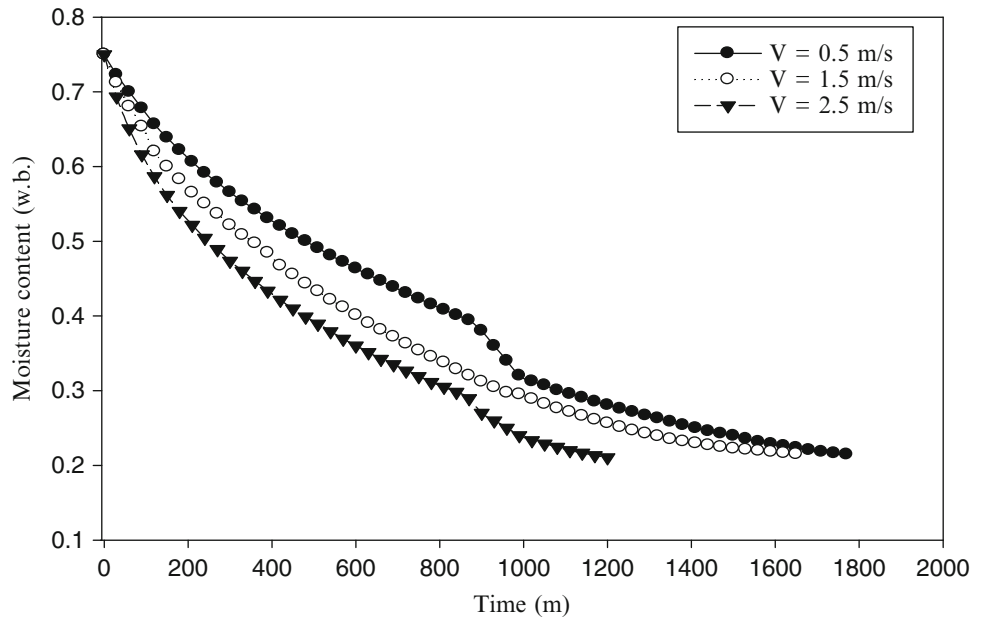
Fig. 64.4 Variation of dimensionless moisture content of fish with time at T = 46 °C and different inlet air velocities
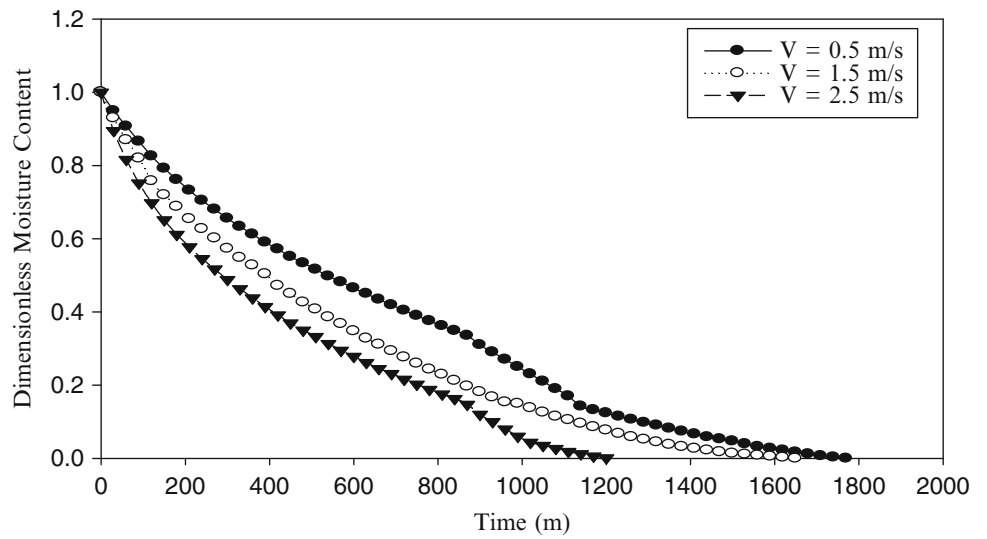
Fig. 64.5 Variation of drying rate of fish with drying time at T = 46 °C and different inlet air velocities
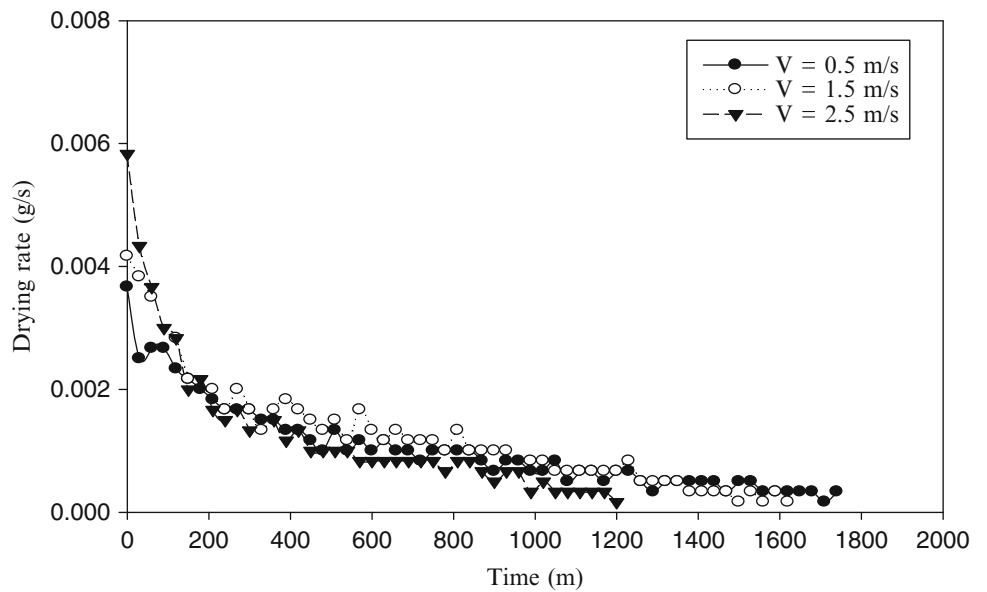
decreases very rapidly, but then this rapid decreasing varies less, later almost constants. It is observed that this case is valid for all velocities. It is seen from the figure that curve in 2.5 m/s is dried more quickly than other two curves. No change appeared on the surface of the samples dried in these velocities. Also, among the drying experiments of the *rainbow trout*, the best results were obtained in 2.5 m/s.

Conclusion

In this study, behaviors of drying of the *rainbow trout* samples were experimentally investigated in a square cross-sectioned type dryer. In the study, interior temperature, moisture content, dimension moisture content, and drying rate curves were analyzed. It is seen that when the drying time increases, the interior temperature of fish increases, but moisture content and drying rate curves decrease. It is concluded that drying procedure for inlet air velocity is effective. Also, no change appeared on the surface of the samples in these velocities, and among the drying experiments, the best results were obtained in 2.5 m/s.

Nomenclature

dM/dt	Drying rate, g/s	M_t	The weight at t, g
t	Time, min	M_{t+dt}	The weight at t + dt, g
T	Air inlet temperature, °C	Mw	The amount of water, g
M	Dimensionless moisture weight	Mwb	Moisture content, g/g
M_e	Final weight (equilibrium weight), g	V	The air inlet velocity, m/s
M_i	First weight, g	W_x	Total uncertainty in measurement

References

1. Kamisli F (2011) Dynamics of wood drying and determination of heat transfer coefficients. Turk J Sci Technol 6(1):35–45
2. Bala BK, Mondol MRA, Biswas BK, Das Chowdury BL, Janjai S (2003) Solar drying of pineapple using solar tunnel drier. Renew Energy 28:183–190
3. Bala BK, Mondol MRA (2001) Experimental investigation on solar drying of fish using solar tunnel dryer. Drying Technol 19:427–436
4. Bellagha S, Sahli A, Farhat A, Kechaou N, Glenza A (2007) Studies on salting and drying of sardine (Sardinella aurita): experimental kinetics and modelling. J Food Eng 78:947–952
5. Erdem M (2011) Experimental investigation of fish drying in a tray drier. MSc thesis, Firat University, Graduate School of Natural and Applied Sciences, Elazig, Turkey
6. Jain D, Pathare PB (2007) Study the drying kinetics of open sun drying of fish. J Food Eng 78:1315–1319
7. Kituu GM, Shitanda M, Kanali CL, Mailutha JT, Nijoroge CG, Wainaina JK, Silayo VK (2010) Thin layer drying model for simulating the drying of Tilapia fish (Oreochromis niloticus) in a solar tunnel dryer. J Food Eng 98:325–331
8. Oztop HF, Akpinar EK (2008) Numerical and experimental analysis of moisture transfer for convective drying of some products. Int Commun Heat Mass Transf 35:169–177
9. Erdem M, Varol Y, Oztop HF, Kamisli F (2013) The effect of inlet air temperature on drying of rainbow trout dried in a tray drier. 2nd Anatolian Energy Symposium, Diyarbakir, Turkey
10. Arason S, Arnason H (1992) Utilization of geothermal energy for drying fish products. Geothermics 21(5/6):745–757
11. Koyuncu T (2006) An investigation on the performance improvement of greenhouse-type agricultural dryers. Renew Energy 31:1055–1071
12. Holman J (1994) Experimental methods for engineers, 2nd edn. McGraw-Hill, New York
13. Afzal TM, Abe T (2000) Simulation of moisture changes in barley during far infrared radiation drying. Comput Electron Agric 26:137–145
14. Gokoglu N (2002) Aquatic products processing technology. Basic publications of aquatic products, Faculty of Agricultural, University of Akdeniz, Istanbul
15. Akpinar EK, Bicer Y (2003) Investigation of drying behaviour of pumpkin in a cyclone type dryer. Gazi Univ J Sci 16(1):159–169

Mert Gur and Mesut Gur

Abstract

In this study, the thin layer drying characteristics of corn were experimentally investigated in a fluidized bed dryer and a convective tray dryer. Corn with an initial moisture content of 25 % dry basis was used in the experiments. Experiments were performed at three different drying temperatures: 55, 65, and 75 °C. In each experiment one layer of corn was inserted into the dryer and then drying was performed for 90 min. The drying air velocities were set to 0.45 m/s for the convective tray dryer and 2.5 m/s for the fluidized bed dryer. Single exponential and Page models were fitted onto the measured drying data. Effective diffusivities were calculated using Fick's first law. The equilibrium moisture contents were evaluated using the Guggenheim-Andersen-de Boer model. From the experiments it was observed that drying rates in the fluidized bed dryer were considerably higher than drying rates in the convective tray dryer. Effective diffusion coefficients obtained in the fluidized bed dryer were approximately 70 % higher than those in the convective tray dryer. This increase is mainly attributed to the homogeneous mixing motions in the fluidized bed dryer, which enhances heat and mass transfer between the corn and the drying air. In addition, the temperature dependence of the effective diffusion coefficients was described by an Arrhenius-type relationship.

Keywords

Drying • Fluidized bed dryer • Corn • Thin layer drying characteristics

Introduction

Corn is one of the main agricultural products in Turkey [1] and its preservation is of great importance. As is the case for almost all agricultural products in Turkey, corn is most commonly preserved by sun-exposed drying in the open air. In sun-exposed drying, food is in continuous contact with the open air for an extended period of time. During this period, the food may easily become contaminated due to the soil transferred by the air [2]. In order to reduce contamination and drying time, the use of industrial dryers is required. Many types of industrial drying methods for food have been investigated in the literature. Among these methods fluidized bed drying stands out due to its high energy savings and short drying times which are caused by the effective contact between the drying mediums [3, 4].

In order to successfully predict drying behavior and optimize drying parameters, the drying kinetics of corn must be understood. For this aim many thin layer models have been proposed in the literature [1, 5–9]. Thin layer characteristic for foods are generally derived from conventional convective drying experiments, where food is put on a perforated tray. For corn thin layer drying characteristics were extensively investigated in convective tray dryers [1, 7, 10, 11] and corresponding

M. Gur (✉)
Department of Computational and Systems Biology, School of Medicine, University of Pittsburgh, Pittsburgh, PA 15213, USA
e-mail: meg78@pitt.edu; gurmert@gmail.com

M. Gur
Department of Mechanical Engineering, Faculty of Mechanical Engineering, Istanbul Technical University, Istanbul 34437, Turkey
e-mail: mesutgur@itu.edu.tr

effective diffusion coefficients, D_{eff}, were proposed [1]. Corn drying was also studied in batch fluidized bed dryers [12–16]. However, in none of these studies fluidized bed drying experiments were conducted under thin layer drying conditions. Thus, there is a lack of work in the literature regarding the thin layer drying of corn in the fluidized bed dryer.

Madhiyanon et al. [17] have investigated the thin layer behavior of coconut in fluidized bed dryer and have determined the effective diffusivities from the experimental results. The value of the effective diffusivities were 1–4 orders of magnitude larger than the thin layer results obtained for other food and biological materials dried in conventional convective tray dryers (no fluidization). The large discrepancy was attributed to the homogeneous mixing motions in the fluidized bed dryer, which boosts heat and mass transfer between corn and air. Consequently, from this work, it can be concluded that the thin layer kinetics distinguish significantly between the fluidized bed dryer and the convective tray dryer.

The main objective of the present study is to determine the thin layer drying characteristics of corn in the fluidized bed dryer and compare them with the drying characteristics in the convective tray dryer. Furthermore, the Page and the single exponential models are investigated on the experimental data in order to explore their validity for corn drying in the fluidized bed. The effective diffusivities of corn are determined at each drying temperature for both the fluidized bed dryer and the convective tray dryer. It is observed that M_{eq} values are widely omitted in literature due to the very small values they attain at high drying temperatures. In this work the equilibrium moisture contents M_{eq} are evaluated using the Guggenheim-Andersen-de Boer (GAB) model. The effect of the incorporation of the equilibrium moisture content in the calculations on the evaluated effective drying coefficient values is investigated. In addition, an Arrhenius type relation is used to explain the dependence of the effective diffusivities on temperature.

Materials and Methods

A special dryer, with adjustable drying air velocity, has been constructed for the corn drying experiments. Schematic diagram of the test apparatus is shown in Fig. 65.1. The drying chamber is of cylindrical shape with an inner diameter of 10 cm and a height of 50 cm. The bottom of the drying chamber is a perforated tray with holes of 2 mm in diameter. The chamber is constructed of two telescoped identical cylinders which make it possible to insert and remove the inner cylinder. The drying air which enters the cylindrical chamber through the perforated tray is provided by a centrifugal fan, the speed of which is controlled by the Siemens Micromaster 6SE92 (7.5 kW) frequency inverter. As shown in Fig. 65.1, before entering the fan (part 2), air is preheated by an electrical heater of 7.6 kW power capacity (part 1). After leaving the fan, the preheated drying air is heated to the desired temperature by the main heater, which has an 8 kW power capacity (part 3). The power settings of the heater are adjusted for each drying experiment at 55, 65, and 75 °C to attain the required drying temperatures. A pitot tube and a manometer are used (part 4) to measure the drying air velocity. The temperature and the humidity of the air are measured every 5 min. Measurements are performed with a Testo 454 multifunction instrument, Testo 905-T1 temperature measure sensor, and Testo 605-H1 humidity measure sensor (part 5). The moisture content of the corn samples is measured by gravimetric methods with Sartorius MA 30 moisture analyzer. According to the instrument
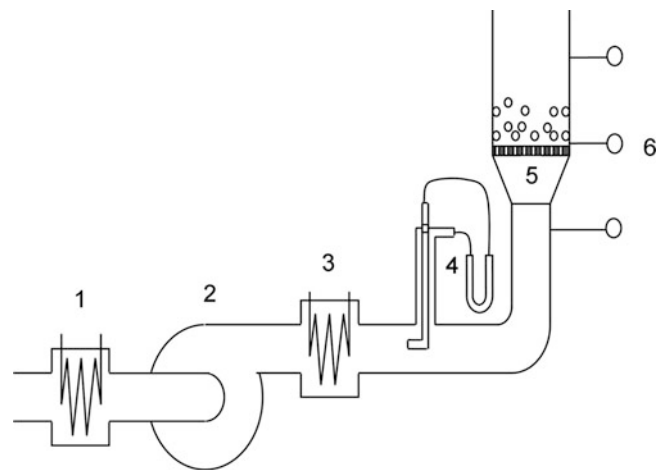
Fig. 65.1 Schematic diagram of fluidized bed dryer (FBD) (*1*: Preheater, *2*: Fan, *3*: Main-heater, *4*: Pitot tube, *5*: Perforated plate, *6*: Temperature and humidity sensors)

specification, temperature and humidity measurements were performed with an accuracy of 0.3 % for the Testo 454-P1 instrument, 0.2 % for the Testo 454-H1 instrument and with 0.05 % for the Sartorius 30 moisture analyzer.

Corn "Zea mays indentata" were provided from the Sakarya region of Turkey and were characterized as being of spherical shape with an average diameter of 6.8 mm. All experiments were conducted under thin layer drying conditions. In each experiment corn samples of 40 g in total weight were inserted into the drying chamber forming a single layer of corn on the perforated tray. Two different drying air velocities were used in the experiments: 0.45 and 2.5 m/s. For the air velocity of 0.45 m/s no fluidization was observed. Therefore, drying conditions resembled those of convective tray dryers. For the drying air velocity of 2.5 m/s, the corn was brought into fluidization state and fluidized bed drying conditions were attained. At both drying air velocities, experiments were conducted for 90 min at three different temperatures; 55, 65, and 75 °C. The initial moisture of the corn was measured by gravimetric methods with a Sartorius MA 30 moisture analyzer. The moisture contents during drying were determined every 5 min by taking the inner cylinder out of the outer cylinder and measuring its weight on a scale. The weight of the completely dried corn was determined to be 32 g on average.

Mathematical Model

The Moisture Ratio (MR), the dimensionless moisture content, can be defined as

$$MR(t) = \frac{M(t) - M_{eq}}{M_o - M_{eq}} \tag{65.1}$$

where $M(t)$ denotes the moisture content at time instant t, M_{eq} denotes the equilibrium moisture content and M_o denotes the initial moisture content of the corn.

Most of the food drying experiments performed in literature have shown that food drying occurs mainly in the falling rate period. The falling rate period is the second phase of drying, in which the moisture transfer is driven mainly by the moisture diffusion inside the corn particles. In order to model the thin layer drying kinetics in the fluidized bed dryer and the convective tray dryer, drying will be assumed to occur only in the falling rate period.

The drying process is modeled using a single spherical shaped corn particle, representing any corn particle inside the dryer. Mass diffusion inside the corn is assumed to take place only in the radial direction. Using Fick's first law defined for spherical coordinates and the mass balance Fick's second law for spherical coordinates is written as

$$\frac{\partial MR(t)}{\partial t} = \frac{1}{r}\frac{\partial}{\partial r}\left(D_{eff}r\frac{\partial MR(t)}{\partial r}\right) \tag{65.2}$$

where D_{eff} represents the effective diffusion coefficient inside the corn particle. Assuming diffusive moisture transfer, negligible volume shrinkage, constant temperature and diffusion coefficients, an analytic solution to Eq. (65.2) was proposed as follows [17]:

$$MR(t) = \frac{6}{\pi^2}\sum_{n=1}^{\infty}\frac{1}{n^2}\exp\left(-\frac{D_{eff}n^2\pi^2t}{r^2}\right) \tag{65.3}$$

Considering only the first term [18], Eq. (65.3) is simplified into the following form:

$$MR(t) = \frac{6}{\pi^2}\exp\left(-\frac{D_{eff}\pi^2}{r^2}t\right) \tag{65.4}$$

Taking the natural logarithm of both sides we end up with the linear form Eq. (65.4):

$$\ln MR(t) = \ln\frac{6}{\pi^2} + \left(-\frac{D_{eff}\pi^2}{r^2}\right)t \tag{65.5}$$

The theoretical form of Eq. (65.4) is referred to as the single exponential equation. In addition to this theoretical model, plenty of empirical and semi-empirical models can be found in the literature [19, 20]. Among these methods, the Page

equation, the two-term model, and the Henderson & Pabis model were used for thin layer drying in fluidized bed for coconut [17]. The Page model has already shown to be able to successfully determine the drying kinetics of corn in conventional tray dryer [1] and is formulated as follows [19, 20].

$$MR(t) = \exp(-xt^y) \tag{65.6}$$

Therefore, to keep the work as simple as possible and in accord with the related previous works, only the Page model and the single exponential model are used to determine the drying kinetics for both the fluidized and non-fluidized corn drying, convective tray dryer. Effective diffusivities were obtained via the single exponential model.

The equilibrium moisture content M_{eq} is defined as the average moisture content of corn at which no moisture transfer takes place between the corn particle and the drying air. This equilibrium moisture content is highly dependent upon the temperature and relative humidity of the drying air. Samapundo et al. [21] have investigated the sorption isotherms of corn at 25, 30, and 37 °C. They concluded that the equilibrium moisture content could be best estimated by the GAB model [22]

$$M_{eq} = \frac{M_m C K a_w}{[(1 - K a_w)(1 - K a_w + C K a_w)]} \tag{65.7}$$

where a_w is the water activity (equilibrium relative humidity of air), M_m is the monolayer moisture content (kg/100 kg dry matter), and C and K are constants. In their work it can be observed that their sorption isotherms tend to come very close at low water activity values. Since water activity values in our experiments were quite small, the parameters proposed by Samapundo et al. [21] for the GAB model at 37 °C were used to estimate the equilibrium moisture content at each drying temperature. Although the moisture content of the drying air is the same at each drying temperature, it was observed that the equilibrium moisture content of corn decreases with increasing drying temperatures. The reason for this decrease is the lower water activity values attained at higher drying temperatures.

The relationship between the effective diffusivities D_{eff} and the drying temperature T is provided by a simple Arrhenius equation [18, 20] as

$$D_{eff} = D_o \exp\left(\frac{E_a}{RT}\right) \tag{65.8}$$

Here E_a is the activation energy, or the energy required for drying reaction to occur at that specific drying condition. D_o is a pre-exponential factor and R is the universal gas constant.

Results and Discussion

The drying curves of corn obtained from the experiments performed in fluidized bed dryer and convective tray dryer are shown in Fig. 65.2 in terms of dry basis (db) moisture content versus time. Even a cursory comparison of the curves in Fig. 65.2 demonstrates significantly higher drying rates for the fluidized bed dryer compared to those for the convective tray dryer at each drying temperature. For example, the moisture contents after 90 min of drying at 55 °C in the fluidized bed dryer can be achieved by the convective tray dryer only if the drying temperature is increased to 75 °C. From the continuously decreasing slopes of the curves it can be inferred that falling drying rates are observed which satisfies the assumption used to develop the mathematical model in the previous section. In the falling rate phase it was concluded that drying moisture transfer is controlled by the interior resistance to moisture diffusion [23]. Therefore, Eq. (65.3), which was developed for the diffusive moisture drying, can be applied to our experimental data.

The equilibrium moisture contents were evaluated using the GAB model with the parameters provided for 37 °C by Samapundo et al. [21]. The water activity values in Eq. (65.7) correspond to the measured drying air humidity [21]. Using the water activity values measured in the experiments, the equilibrium moisture content M_{eq} was evaluated via Eq. (65.7) as 4.39 % (db) at 55 °C, as 4.13 % (db) at 65 °C and as 3.43 % for 75 °C. Using these equilibrium moisture content M_{eq} values, the moisture ratios (MR) were evaluated via Eq. (65.1) and their natural logarithms are shown in Fig. 65.3 with respect to drying time. In Fig. 65.3 it is observed that the slope of drying curves increase with elevated temperatures. A drastic increase in slope is also observed when switching from conventional tray dryers to fluidized bed dryers. Recalling Eq. (65.5), larger slopes result in higher effective diffusion coefficients and hence, in higher drying rates. The rate of drying can be directly

Fig. 65.2 Effect of fluidization on the drying curves at different temperatures
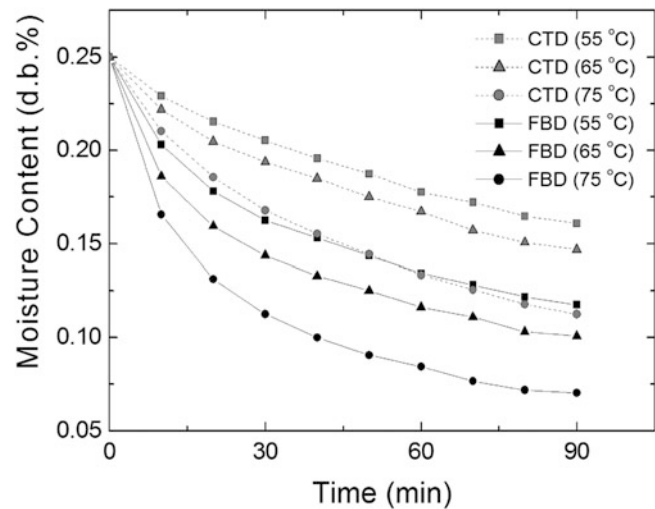
Fig. 65.3 Logarithmic drying curves for corn in conventional tray dryer (CTD) and FBD
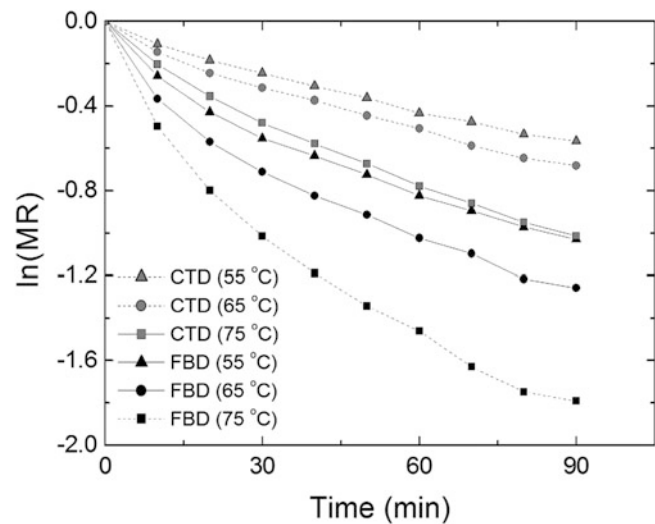
Table 65.1 Effective diffusion coefficients and relative increase in the effective diffusion coefficients evaluated with zero equilibrium moisture content assumption

Temperature (°C)	(Doymaz and Pala) $D_{eff}(m^2/s)$ $M_{eq} = 0$	$D_{eff}(m^2/s)$ $V_{air} = 0.45 m/s$ $M_{eq} = 0$	$D_{eff}(m^2/s)$ $V_{air} = 2.5 m/s$ $M_{eq} = 0$	$\Delta D_{eff}(\%)$
55	9.488×10^{-11}	9.3128×10^{-11}	1.4967×10^{-10}	61
65	1.153×10^{-10}	1.1020×10^{-10}	1.7540×10^{-10}	59
75	1.768×10^{-10}	1.6510×10^{-10}	2.4753×10^{-10}	50

linked to larger effective diffusion coefficients which result in more homogeneous temperature distribution inside the corn. Therefore, it can be concluded that the enhanced homogeneity of the corn's temperature distribution in the fluidized bed dryer induces higher drying rates than the convective tray dryer.

In accordance with the related previous work [1], the effective diffusivities M_{eq} were first assumed to be zero. Using Eq. (65.4), the effective diffusivities were evaluated from the slope of the linear portion of the logarithmic drying curves [24] at 55, 65, and 75 °C. The results are listed and compared in Table 65.1 with the D_{eff} values obtained by Doymaz and Pala [1] for untreated corn dried in cabinet dryers (convective tray dryer) at an air velocity of $V_{air} = 0.43$ m/s with zero equilibrium moisture content assumption. It was observed that our results for an air velocity of $V_{air} = 0.45$ m/s are consistent with the work of Doymaz and Pala [1] under the same assumptions. Moreover, the relative increase in the effective diffusion coefficient ΔD_{eff}, shown in Table 65.1, is defined as

Table 65.2 Effective diffusion coefficients and relative increase in the effective diffusion coefficients evaluated with the equilibrium moisture content evaluated by the Guggenheim-Andersen-de Boer model

Temperature (°C)	$D_{eff}(m^2/s)$ $V_{air} = 0.45 m/s$ $M_{eq} \neq 0$	$D_{eff}(m^2/s)$ $V_{air} = 2.5 m/s$ $M_{eq} \neq 0$	$\Delta D_{eff}(\%)$
55	1.2017×10^{-10}	2.0704×10^{-10}	72
65	1.4208×10^{-10}	2.4763×10^{-10}	74
75	2.1140×10^{-10}	3.6147×10^{-10}	71
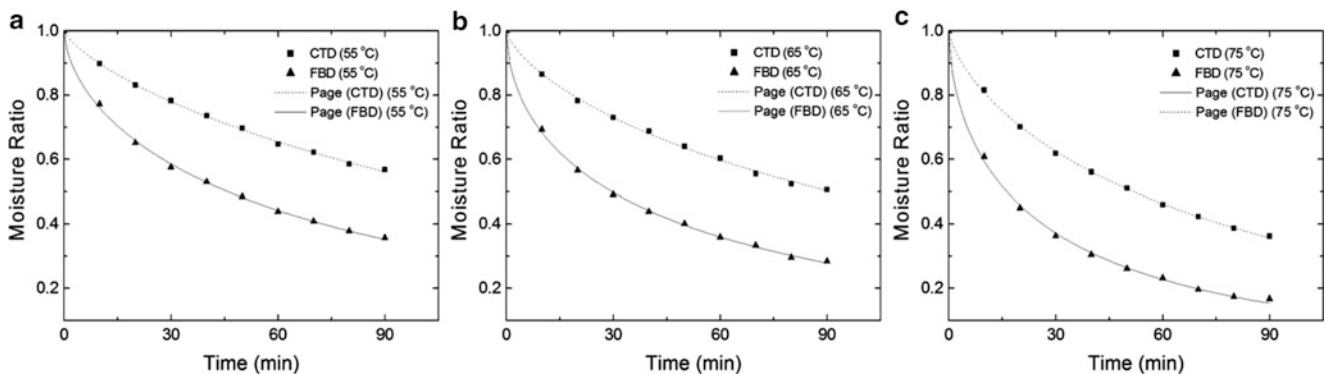
Fig. 65.4 (**a**) Comparison of the Page model fitted for CTD and FBD at 55 °C. (**b**) Comparison of the Page model fitted for CTD and FBD at 65 °C. (**c**) Comparison of the Page model fitted for CTD and FBD at 75 °C

$$\Delta D_{eff} = \frac{D_{eff}^{FBD} - D_{eff}^{CTD}}{D_{eff}^{CTD}} \tag{65.9}$$

where D_{eff}^{CTD} is the effective diffusion coefficient obtained in the conventional tray dryer and D_{eff}^{FBD} is the effective diffusion coefficient obtained in the fluidized bed dryer. Have given the results assuming M_{eq} to be zero, we will now pursue our analysis by taking M_{eq} into account. In that case, the equilibrium moisture content values are not zero and take the values evaluated by Eq. (65.7). Hence, the effective drying coefficients are evaluated from the slopes of the drying curves in Fig. 65.3 and are presented in Table 65.2. Including the nonzero equilibrium moisture contents in the calculations resulted in a substantial increase of the effective drying coefficient D_{eff} values. Furthermore, the relative increase in the effective diffusion coefficient ΔD_{eff} induced due to fluidization, has shown to rise from the range of 50–61 % to the range of 71–74 %. When the equilibrium moisture content is assumed to be non-zero, the effect of the fluidized dryer on the drying rates is more evident. In fact, the equilibrium moisture content M_{eq} is never zero and always has a specific value depending on the drying air conditions. Therefore, the correct detection of M_{eq} values shows importance in the prediction of the correct drying kinetics.

In Fig. 65.4 the moisture ratios are shown for the drying at air velocity of $V_{air} = 0.45$ m/s as squares whereas for $V_{air} = 2.5$ m/s they are shown as triangles. As shown in Fig. 65.4, Page's equation was fitted onto the drying data of the convective tray dryer (dashed line) and the data of the fluidized bed dryer (solid line). Curve fitting was utilized using the Ezyfit toolbox for Matlab to determine the constants of the best fitting Page's equation. All coefficients of determination R^2 of these fits were found to be larger than 0.99.

To describe the temperature dependence of the effective diffusion coefficients the Arrhenius type relationship indicated by Eq. (65.8) is used. For that purpose the calculated effective diffusivities were plotted in Fig. 65.5 as a function of the reciprocal of the absolute temperature. Using Eq. (65.8) and the slopes of the best fitting straight lines in Fig. 65.5, the activation energy E_A was found to be 26.7 kJ/kg mol for drying in the conventional tray dryer and 26.4 kJ/kg mol for drying in the fluidized bed dryer. Both of these values are close to $E_A = 29.56$ kJ/kg mol which was proposed previously by Doymaz and Pala [1].

Fig. 65.5 Relationship among effective diffusivity and the reciprocal of the drying temperature
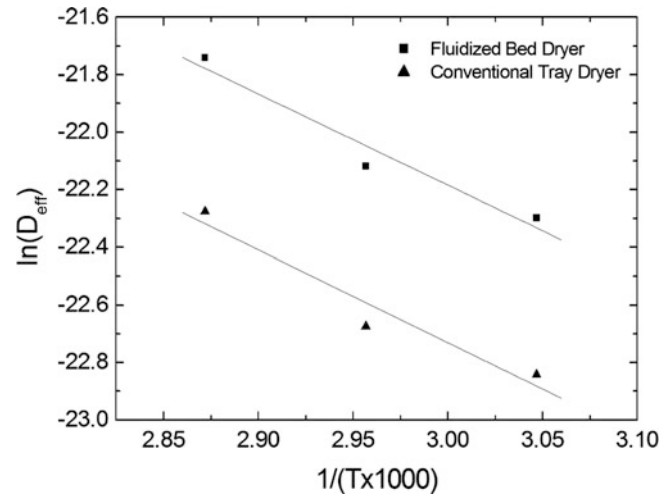
Conclusion

The experimental results have shown that corn drying proceeds only in the falling drying rate period where drying is controlled only by the moisture diffusion inside the corn particle. Moreover, from the experiments it was found that the drying rates of corn in the fluidized bed dryer are substantially higher than the convective tray dryer at all drying temperatures. The effective drying coefficients are increased by an average of 72 % by the improved drying rates. The values of effective diffusivities were found to be in the range $2.1 - 3.6 \times 10^{-10} \mathrm{m}^2/\mathrm{s}$ for the fluidized bed dryer and $1.2 - 2.1 \times 10^{-10} \mathrm{m}^2/\mathrm{s}$ for the conventional tray dryer. The main reason for this behavior is the homogeneous mixing motions in the fluidized bed dryer, which enhances heat and mass transfer between corn and air significantly. The Page model was able to fit the drying data of the conventional tray dryer and the fluidized bed dryer successfully at all drying temperatures (55, 65, and 75 °C). Calculations revealed a significant dependence of the evaluated effective drying coefficients on the equilibrium moisture contents. Setting equilibrium moisture contents to zero decreases the numerical values of the effective diffusion coefficients. Therefore, the equilibrium moisture is required to be determined correctly in order to evaluate the effective drying coefficients most accurately. Moreover, effective diffusion coefficients have been shown to increase with higher drying temperatures and pursued an Arrhenius type relationship. The activation energy E_A was found to be 26.4 kJ/kg mol for the convective tray dryer and 26.7 kJ/kg mol for the fluidized bed dryer. These values are consistent with the activation energies proposed by Doymaz and Pala [1].

References

1. Doymaz I, Pala M (2003) The thin-layer drying characteristics of corn. J Food Eng 60:125–130
2. Oztekin S, Bascetincelik A, Soysal Y (1999) Crop drying programme in Turkey. Renew Energy 16:789–794
3. Wang ZH, Chen GH (2000) Heat and mass transfer in batch fluidized-bed drying of porous particles. Chem Eng Sci 55:1857–1869
4. Tatemoto Y, Bando Y, Yasuda K, Senda Y, Nakamura M (2001) Effect of fluidizing particle on drying characteristics of porous material in fluidized bed. Drying Technol 19:1305–1318
5. Henderson SM, Pabis S (1961) Grain drying theory I. Temperature effect on drying coefficient. J Agric Eng Res 6:169–174
6. Wang CY, Singh RP (1978) Use of variable equilibrium moisture content in modelling rice drying. ASAE Paper No. 78–6505
7. Zhang Q, Litchfield JB (1991) An optimization of intermittent corn drying in a laboratory scale thin-layer dryer. Drying Technol 9:383–395
8. Liu QA, Bakker Arkema FW (1997) Stochastic modelling of grain drying. 2. Model development. J Agric Eng Res 66:275–280
9. Yaldiz O, Ertekin C, Uzun HI (2001) Mathematical modeling of thin layer solar drying of sultana grapes. Energy 26:457–465
10. Overhults DD, White GM, Hamilton ME, Ross IJ (1973) Drying soybeans with heated air. Trans ASAE 16:195–200
11. Li HZ, Morey RV (1984) Thin-layer drying of yellow dent corn. Trans ASAE 27:581–585
12. Jumah RY, Mujumdar AS, Raghavan GSV (1996) Batch drying kinetics of corn in a novel rotating jet spouted bed. Can J Chem Eng 74:479–486
13. Soponronnarit S, Pongtornkulpanich A, Prachayawarakorn S (1997) Corn quality after drying by fluidization technique at high temperature. Drying Technol 15:2577–2586
14. Soponronnarit S, Pongtornkulpanich A, Prachayawarakorn S (1997) Drying characteristics of corn in fluidized bed dryer. Drying Technol 15:1603–1615
15. Syahrul S, Dincer I, Hamdullahpur F (2003) Thermodynamic modeling of fluidized bed drying of moist particles. Int J Therm Sci 42:691–701

16. Hatamipour MS, Mowla D (2006) Drying behaviour of maize and green peas immersed in fluidized bed of inert energy carrier particles. Food Bioprod Process 84:220–226

17. Madhiyanon T, Phila A, Soponronnarit S (2009) Models of fluidized bed drying for thin-layer chopped coconut. Appl Therm Eng 29:2849–2854

18. Ramesh MN, Wolf W, Tevini D, Jung G (2001) Influence of processing parameters on the drying of spice paprika. J Food Eng 49:63–72

19. Diamante LM, Munro PA (1993) Mathematical-modeling of the thin-layer solar drying of sweet-potato slices. Solar Energy 51:271–276

20. Madamba PS, Driscoll RH, Buckle KA (1996) The thin-layer drying characteristics of garlic slices. J Food Eng 29:75–97

21. Samapundo S, Devlieghere F, De Meulenaer B, Atukwase A, Lamboni Y, Debevere JM (2007) Sorption isotherms and isosteric heats of sorption of whole yellow dent corn. J Food Eng 79:168–175

22. Berg VD (1985) Development of B.E.T.-like models for sorption of water on foods, theory and relevance. In: Simatos D, Multon JL (eds) Properties of water in foods. Springer, Netherlands, pp 119–131

23. Keey RB (1972) Drying principles and practice, 1st edn. Pergamon Press, Oxford

24. Goksu EI, Sumnu G, Esin A (2005) Effect of microwave on fluidized bed drying of macaroni beads. J Food Eng 66:463–468

Investigation of Drying Characteristics of Blueberry Using a New Solar Air Collector Design

66

Adem Acır, Mustafa Aktaş, and Fatih Danışman

Abstract

In this study, a new solar air collector design was made for drying applications. Blueberry (*Myrtus communis*) was dried in this drying process based on solar energy. The drying experiments were carried out at 0.026, 0.0325, and 0.052 kg/s mass flow rate and at variable air temperatures between 8:30 and 18:00 hours. Solar radiation, blueberry mass, collector inlet–outlet air temperatures, drying chamber inlet–outlet air temperatures, and relative humidity values were measured during the experiments. The drying air velocity was controlled by using frequency inverter according to set value. Blueberry was dried from initial moisture content (2.18 g water/g dry matter) to final moisture content (0.594, 0.540, and 0.672 g water/g dry matter) for 0.026, 0.0325, and 0.052 kg/s mass flow rates, respectively. The average solar collector efficiencies were found as 56.97 %, 63.30 %, and 71.59 % for 0.026, 0.0325, and 0.052 kg/s mass flow rates, respectively. As a result, the high efficiency solar air collector was obtained as regards thermal performance and the blueberry drying process was performed successfully.

Introduction

Drying of agricultural products has always been of great importance for the preservation of food by human beings. Drying of agricultural products provides effective and practical preservation in order to reduce the losses after harvest. Drying techniques of agricultural products is divided mainly into three parts:

- Drying with heat pump
- Drying with solar energy
- Drying with other techniques (infrared energy, etc.)

Drying with solar energy is a well-known method as preservation technique. The solar energy is a renewable energy resource. Therefore, drying with solar energy is contributed in the economic cost and utilization the renewable energy. Also, solar drying is a safer and efficient method to preserve agricultural products. Solar drying will reduce the product losses and it will improve the quality of the final product. In brief, solar drying methods have advantages in terms of cost of energy and environmental factors. In the literature, there have been many studies with drying of agricultural products using solar dryer. Different authors have performed on the drying of pistachio [1], potato [2], apple [3, 4], green chilli [5], green pepper, green bean, squash [6], and apricot [7, 8]. El-Sebaii et al. [9] dried green peas by using an indirect type natural convection solar

A. Acır (✉) • M. Aktaş
Faculty of Technology, Department of Energy Systems Engineering, Gazi University, Teknikokullar, Ankara, Turkey
e-mail: adema@gazi.edu.tr; mustafaaktas@gazi.edu.tr

F. Danışman
Gazi University Institute of Science and Technology, Ankara, Turkey
e-mail: fsmturk@gmail.com

dryer. Jadhav et al. [10] used solar cabinet dryer for drying pretreated green peas. And also, mathematical modeling of drying characteristics of tropical fruits was investigated by Ceylan et al. [11].

In this study, the drying characteristics of blueberry using a new solar air collector design are investigated at different mass flow rate and variable air temperatures. Also, efficiencies of a new type solar air collector have been determined.

Materials and Methods

Materials

Blueberry (*Myrtus communis*) was used in the drying experiments which was supplied from the markets. It grows spontaneously in the Black Sea, the Aegean and Mediterranean coasts in Turkey as shown in Fig. 66.1. Also, blueberry contains high vitamin A, and it also improves sight.

Experimental Setup

The schematic diagram of the experimental setup was shown in Fig. 66.2. An experimental setup was constructed and tested in Gazi University, Ankara, Turkey. The main components were solar collector, air channels, a fan, an air regulating damper, PLC control unit, and drying chamber.

The collector size used in the experiment was 800 mm in length, 500 mm in width, and 120 mm in height. The collector was the single-pass finned collector. The collector consists of the glass cover, the insulated container, and the black-painted copper absorber. The collector was designed as parabolic absorber plates. Also, technical properties and equipments used in drying based on solar energy are given in Table 66.1. Solar drying air experiments were carried out between 5 July and 10 July 2012 (9.00 am–18.30 pm) in Ankara, Turkey for different mass flow rates.

Uncertainty Analysis

Uncertainty analysis in the experiments is very important in order to be able to make reliable measurement. The instrument selections, conditions, calibration, environmental factors, observation, reading, and test planning can be caused some errors and uncertainties in the experiments. In drying experiments in solar dryer of blueberry, air temperature, relative humidity, weight losses, air velocity, and solar radiation were measured with appropriate instruments. During the experiments, total uncertainties of the measured parameters and calculated experimental parameters were presented as shown in Table 66.2.

Considering relative uncertainties in the individual factors denoted by x_n, uncertainty estimation was made using the following equation [12]:

$$W = \left[(x_1)^2 + (x_2)^2 + \dots (x_n)^2 \right]^{1/2} \tag{66.1}$$

Fig. 66.1 A picture of blueberries

Fig. 66.2 A schematic view of the PLC-controlled experimental setup [15]. *1*: Solar collector, *2*: Data-logger, *3*: Solarimeter, *4*: Computer, *5*: Exhaust air, *6*: Blower, *7*: Flexible air duct, *8*: PLC-controlled drying cabinet, *9*: PLC screen
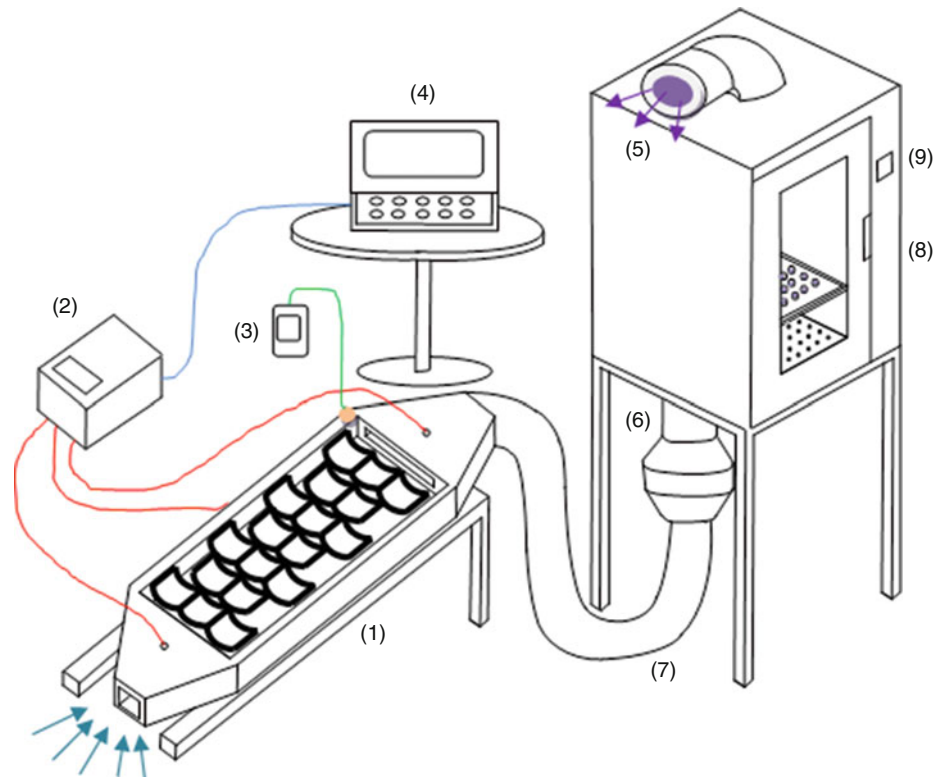
Table 66.1 Main properties of equipments used in solar dryer [15]

Equipment	Technical properties
PLC controller	Controlling of air temperature, relative humidity, air velocity, dried product mass, and LCD screen
Blower	160 W, 990 m^3/h, 2750 d/d, 50 Hz, 230 V IN:0.74A
Solarimeter	SL 100, 1 W/m^2-1300 W/m^2 measurement range
Data-logger	VCC 0,1 V, 2.7 V-5.5 V operating range, 110 dB minimum
Thermocouple	Inlet Pt-100, R/T Type Scala: 0–70 °C
Load-cell	Nominal out (mV/V) 2,0 $\pm$ 0.2, 5–12 V, Operation temperature: -35 +65 °C, Error (%FS): $\pm$ 0.02

Table 66.2 The uncertainties during the measurements of the parameters

Parameter	Unit	Comment
Uncertainty in the temperature measurement		
Collector inlet temperature	°C	$\pm$0.173
Collector outlet temperature	°C	$\pm$0.173
Absorber surface (copper plate)	°C	$\pm$0.173
Ambient air temperature	°C	$\pm$0.173 °C
Uncertainty in the time measurement		
Temperature values	Min	$\pm$0.1
Uncertainty in the air velocity measurement	m/s	$\pm$0.1446
Uncertainty in the measurement of pressure loss	Pa	$\pm$0.3
Uncertainty in reading values of table	%	$\pm$0.1–0.2

Mathematical Modeling

In this study, initial moisture content, moisture ratio, and solar thermal efficiency were investigated. Initial moisture content (dry basis) of the blueberry was calculated using the following equation [4, 11]:

$$MC = \frac{M_i - M_d}{M_d} \tag{66.2}$$

The moisture ratio of blueberry during drying experiments is calculated using the following equation [4, 11]:

$$MR = \frac{M - M_e}{M_0 - M_e} \tag{66.3}$$

where MR is the moisture ratio, M the moisture content, M_e the equilibrium moisture content, and M_o is the initial moisture content, respectively.

Also, the thermal efficiency of the solar collectors (η_I) is defined as the ratio between the energy gain and the solar radiation incident on the collector plane [13, 14]:

$$\eta_I = \frac{\dot{m} c_p (T_{a,out} - T_{a,in})}{(IA_c)} \tag{66.4}$$

Results and Discussion

The drying experiments were carried out at 0.026, 0.0325, and 0.052 kg/s mass flow rate, 40° collector angle and variable air temperatures between 8:30 and 18:00 hours. Change in mass was recorded every 30 min in the experiment. In this study, first, the dry matter amount, initial and final moisture contents for each product are determined. The initial moisture content of the Blueberry samples (50 g) was considered. Initial moisture content (dry basis) of the Blueberry was calculated from Eq. (66.1). The initial moisture content (MC) of Blueberry was calculated as 2.25 g water/g dry matter (Fig. 66.3).

The final moisture content is obtained as 0.594, 0.540, and 0.672 g water/g dry matter for 0.026, 0.0325, and 0.052 kg/s mass flow rates, respectively. Final drying levels of Blueberry are realized in 9 h in the solar dryer. In addition, the moisture
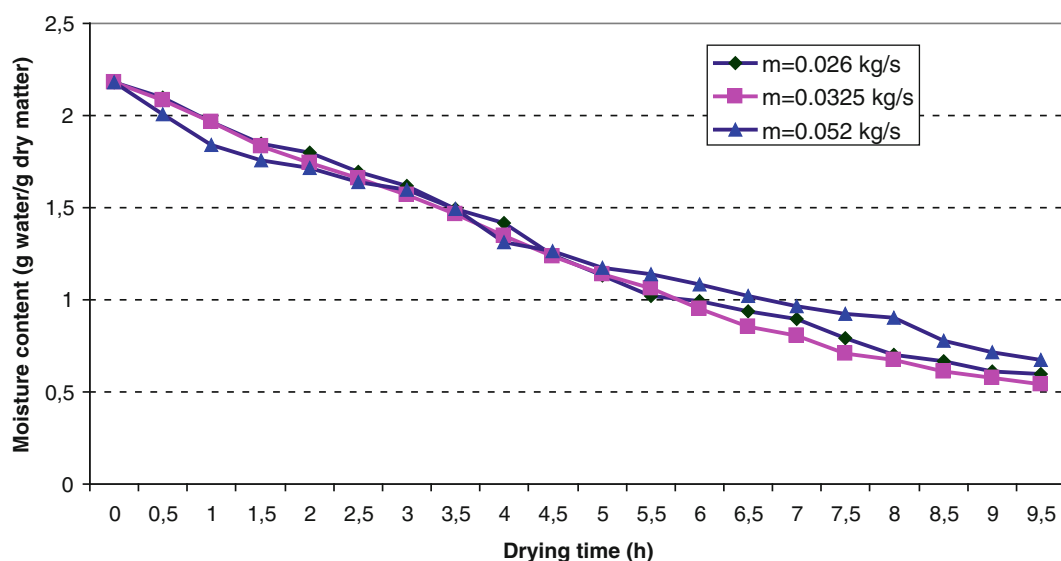
Fig. 66.3 The change of moisture content in the experiments
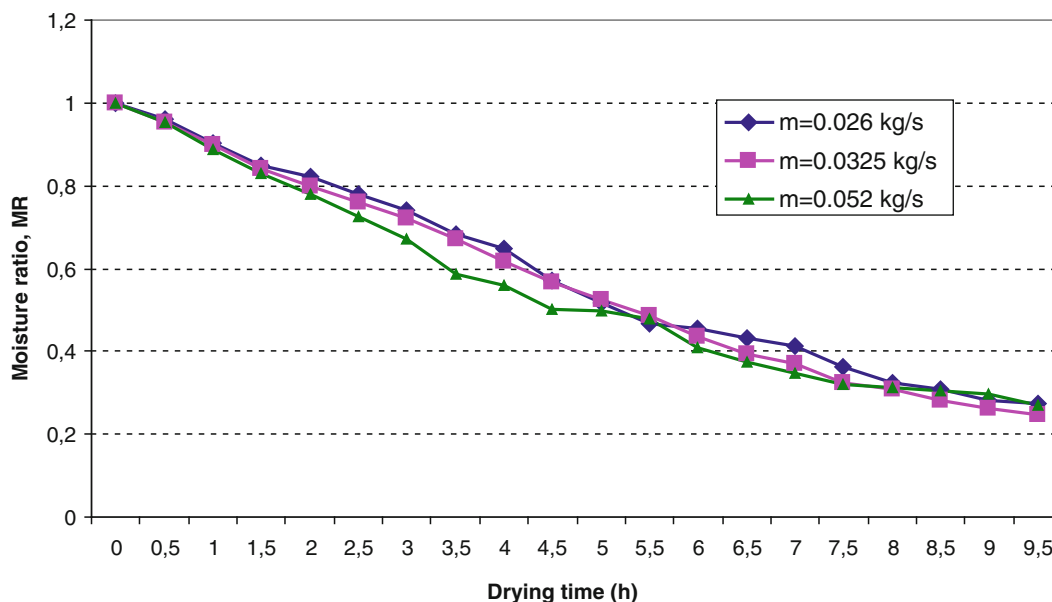
Fig. 66.4 Variation of moisture ratio in the experiments

Table 66.3 Experimental results for 40° collector angle

Mass flow rate (kg/s)	Final YA (g)	Final MC (g water/g dry matter)	Final MR (%)	I (W/m^2)	ΔT (°C)	η (%)
0.026	25.06	0.594	0.272	709.9	5.90	56.97
0.0325	24.21	0.540	0.248	764.0	5.75	63.30
0.052	26.28	0.672	0.308	688.9	3.61	71.59

ratio (MR) of Blueberry during drying experiments was calculated from Eq. (66.2). As shown in Fig. 66.4, the moisture ratio are computed as 0.272, 0.248, and 0.308 for 0.026, 0.0325, and 0.052 kg/s mass flow rates, respectively.

As a result, the optimum values as regards moisture ratio were provided in 0.0325 kg/s mass flow rate of experiments as seen in Table 66.3. Also, a picture of blueberries before drying and after drying was given Fig. 66.5.

Solar radiation values were measured between the 680 and 810 W/m^2 during the experiments. Generally, the maximum solar radiation energy was obtained at midday, whereas the minimum solar radiation energy at evening in the day was seen. The solar collector efficiencies based on the obtained solar radiation were changed during days. In this study, a new collector was designed. This solar air collector was considered as parabolic absorber plates. In this study, the average solar collector efficiencies were calculated from Eq. 66.4. The solar collector efficiency values during experiment are given in Fig. 66.6, which are plotted using Eq. (66.4). As shown in Table 66.3, the average thermal efficiency was found as 56.97 %, 63.30 %, and 71.59 % for 0.026, 0.0325, and 0.052 kg/s mass flow rates, respectively. When the thermal efficiency obtained in this present study was compared the results obtained in the previous studies given in literature, the solar collector having parabolic absorber plates showed very good performance.

Conclusions

In this study, drying characteristics of Blueberry (*Myrtus communis*) of a solar dryer controlled with PLC were investigated. The drying process can be continued with solar energy in daytime. Solar energy can provide free and renewable energy. The initial moisture content of blueberry was calculated as ~2.25 g water/g dry matter, whereas the final moisture content is obtained as 0.594, 0.540, and 0.672 g water/g dry matter for 0.026, 0.0325, and 0.052 kg/s mass flow rates, respectively. The moisture ratio was computed as 0.272, 0.248, and 0.308 for 0.026, 0.0325, and 0.052 kg/s mass flow rates, respectively.

Fig. 66.5 A picture of blueberries (**a**) before drying, (**b**) after drying
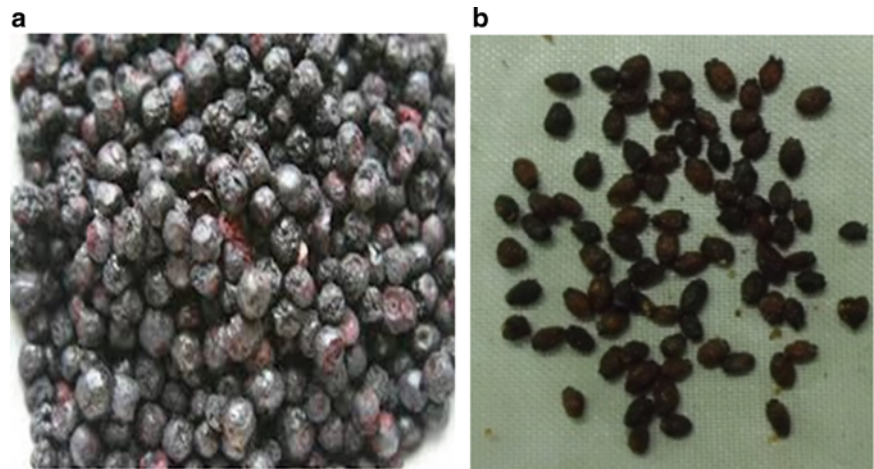
Fig. 66.6 Variation of thermal efficiency values of the collectors
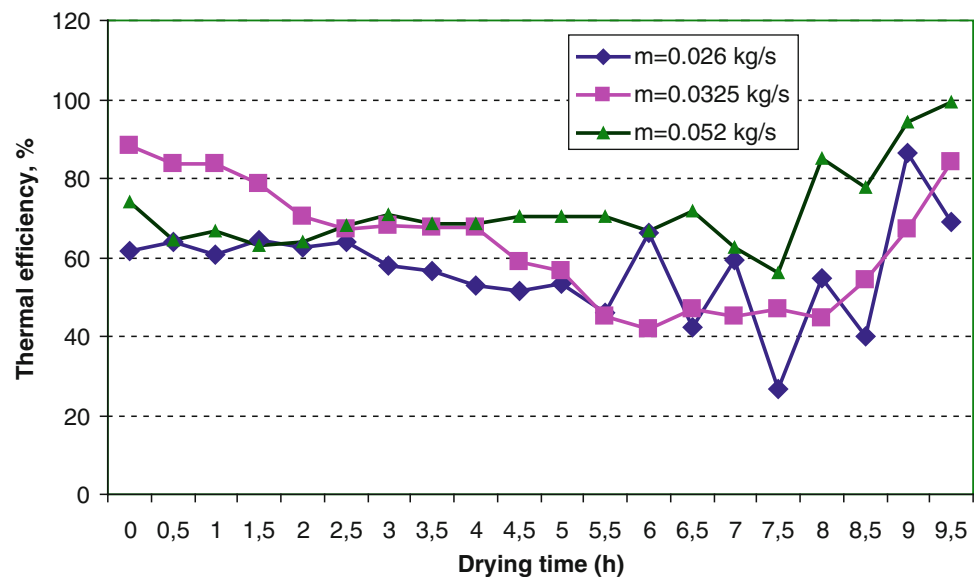
As a result, the optimum values as regards moisture ratio were provided as 0.248 in 0.0325 kg/s mass flow rate. The drying process can be expected much more quickly than according to nature drying. The quality of blueberry dried with PLC-controlled solar dryer was acceptable, drying took place in a shorter time than compared to different drying methods. In conclusion, it is expected that this system will help reduce the cost of drying and obtain more quality dried products. Also, a new design solar collector having parabolic absorber plates can be used efficiently at different thermal applications.

Nomenclature

W	Uncertainty in the measurement (%)	M_e	Equilibrium moisture content (g water/g dry matter)
η_I	Thermal efficiency	M_0	Initial moisture content (g water/g dry matter)
MC	Moisture content (g water/g dry matter)	I	Solar radiation (W/m^2)
MR	Moisture ratio	A_C	Surface area of the collector (m^2)
M_i	Initial wet weight (g)	c_p	Specific heat of air at constant pressure (kJ/kg K)
M_d	Final dry weight (g)	T_a	Air temperature (°C)

References

1. Midilli A (2001) Determination of pistachio drying behaviour and conditions in a solar drying system. Int J Energy Res 25:715–725
2. Akpinar E, Midilli A, Bicer Y (2003) Single layer drying behaviour of potato slices in a convective cyclone dryer and mathematical modeling. Energy Convers Manag 44:1689–1705
3. Aktaş M, Ceylan İ, Yılmaz S (2009) Determination of drying characteristics of apples in a heat pump and solar dryer. Desalination 239:266–275
4. Elicin AK, Sacilik K (2005) An experimental study for solar tunnel drying of apple. Tarim Bilimleri Dergisi 11:207–211
5. Hossain MA, Bala BK (2002) Thin-layer drying characteristics for green chilli. Drying Technol 20:489–505
6. Yaldiz O, Ertekin C (2001) Thin layer solar drying of some vegetables. Drying Technol 19:583–596
7. Sarsılmaz C, Yildiz C, Pehlivan D (2000) Drying of apricots in a rotary column cylindrical dryer (RCCD) supported with solar energy. Renew Energy 21:117–127
8. Togrul IT, Pehlivan D (2003) Modelling of drying kinetics of single apricot. J Food Eng 58:23–32
9. El-Sebaii AA, Aboul-Enein S, Ramadan MRI, El-Gohary HG (2002) Experimental investigation of an indirect type natural convection solar dryer. Energy Convers Manag 43:2251–2566
10. Jadhav DB, Visavale GL, Sutar N, Annapure US, Thorat BN (2010) Studies on solar cabinet drying of green peas (*Pisum sativum*). Drying Technol 28:600–607
11. Ceylan İ, Aktaş M, Doğan H (2009) Mathematical modeling of drying characteristics of tropical fruits. Appl Therm Eng 27:1931–1936
12. Holman JP (1994) Experimental methods for engineers, 6th edn. McGraw-Hill, Singapore
13. Esen H (2008) Experimental energy and exergy analysis of a double-flow solar air heater having different obstacles on absorber plates. Build Environ 43:1046–1054
14. Karsli S (2007) Performance analysis of new-design solar air collectors for drying applications. Renew Energy 32:1645–1660
15. Danışman F (Supervisor: Assoc. Prof. Dr. Adem Acır) (2013) Application of the drying blueberry and analysis of performance on solar air collector. MSc thesis, Institute of Science and Technology, Gazi University (in Turkish)

Exergy-Based Sustainability Indicators for a Single Layer Solar Drying Process

Adnan Midilli and Haydar Kucuk

Abstract

The main objective of this study is to develop the exergetic sustainability indicators for a single layer solar drying process of the shelled and unshelled pistachio samples. In this regard, the exergetic sustainability indicators such as exergetic efficiency, waste exergy ratio, exergy recoverability ratio, exergy destruction ratio, environmental impact factor, and exergetic sustainability index are defined and estimated by depending on the experimental data obtained from the single layer solar drying process. Accordingly, it is noticed that the rise of waste exergy ratio decreases the exergetic efficiency and exergetic sustainability index while increasing environmental impact factor.

Keywords

Exergetic sustainability • Single layer drying • Solar drying • Environmental impact factor • Exergetic sustainability index

Introduction

Energy is a key element in the interactions between nature and society and considered a key input for the environment and sustainable development. During the past decade, environmental and sustainability issues have become major burdens to overcome since they have caused regional and global consequences [1].

The supply and utilization of low-priced and clean fuel are particularly significant for environmental sustainability as well as social, economic, and institutional sustainability since energy plays a vital role in industrial and technological developments around the world [2–4]. Exergy analysis is considered as an essential tool to expose the impacts of a power generating and consuming devices on exergy-based sustainability. On the other hand, sustainability is necessary to overcome current ecological, economic, and developmental problems [5]. Also, sustainability concerns often lead local and national authorities to incorporate environmental considerations into energy planning. In this regard, sustainable development demands a sustainable energy source that, in the long term, is readily and sustainably available at reasonable cost and can be utilized for all required tasks without causing negative societal impacts [6].

In terms of exergy analysis of the single layer solar drying processes, Midilli and Kucuk [7] examined the energy and exergy analyses of the drying process of shelled and unshelled pistachios using a solar drying cabinet. Midilli and Dincer [6] developed some new exergy-based parameters, such as exergetic efficiency, exergetic stability factor, environmental benign index, and exergetic sustainability index for PEM fuel cells in order to study how some of their operating aspects and system characteristics affect the environment and sustainability. Also, Midilli et al. [8] presents some new exergy-based parameters

A. Midilli (✉) • H. Kucuk
Department of Mechanical Engineering, Faculty of Engineering,
Recep Tayyip Erdoğan University, 53100 Rize, Turkey
e-mail: adnan.midilli@erdogan.edu.tr; haydar.kucuk@erdogan.edu.tr

for Recirculating Aquaculture System (RAS) for Black Sea trout (Salmotruttalabrax). In this regard, the exergetic parameters, such as exergetic efficiency, waste exergy ratio, exergy recoverability ratio, exergy destruction ratio, environmental impact factor, and exergetic sustainability index are proposed and investigated. This paper presents the effects of some exergetic sustainability indicators on the performance of the single layer solar drying processes of the shelled and unshelled pistachio samples.

Analysis

To parametrically investigate the environmental and sustainability aspects of the single layer solar drying processes in terms of exergy, Solar drying process was considered to be a steady-flow process. The experimental setup, shown in Fig. 67.1, consists of a drying cabinet, solar air collector, and auxiliary heater and circulation fan. Drying cabinet is $55 \times 92 \times 117 \text{ cm}^3$ and has 16 shelves, which were made of wire-mesh-bottomed trays. The 4.5 m^2 solar air collector (collectors area $= 2 \times (1.25 \times 1.8 \text{ m}^2)$) was connected to solar drying cabinet, and was used when solar radiation was intense. The circulation fan to supply fresh air has a power of 0.37 kW [7, 9].
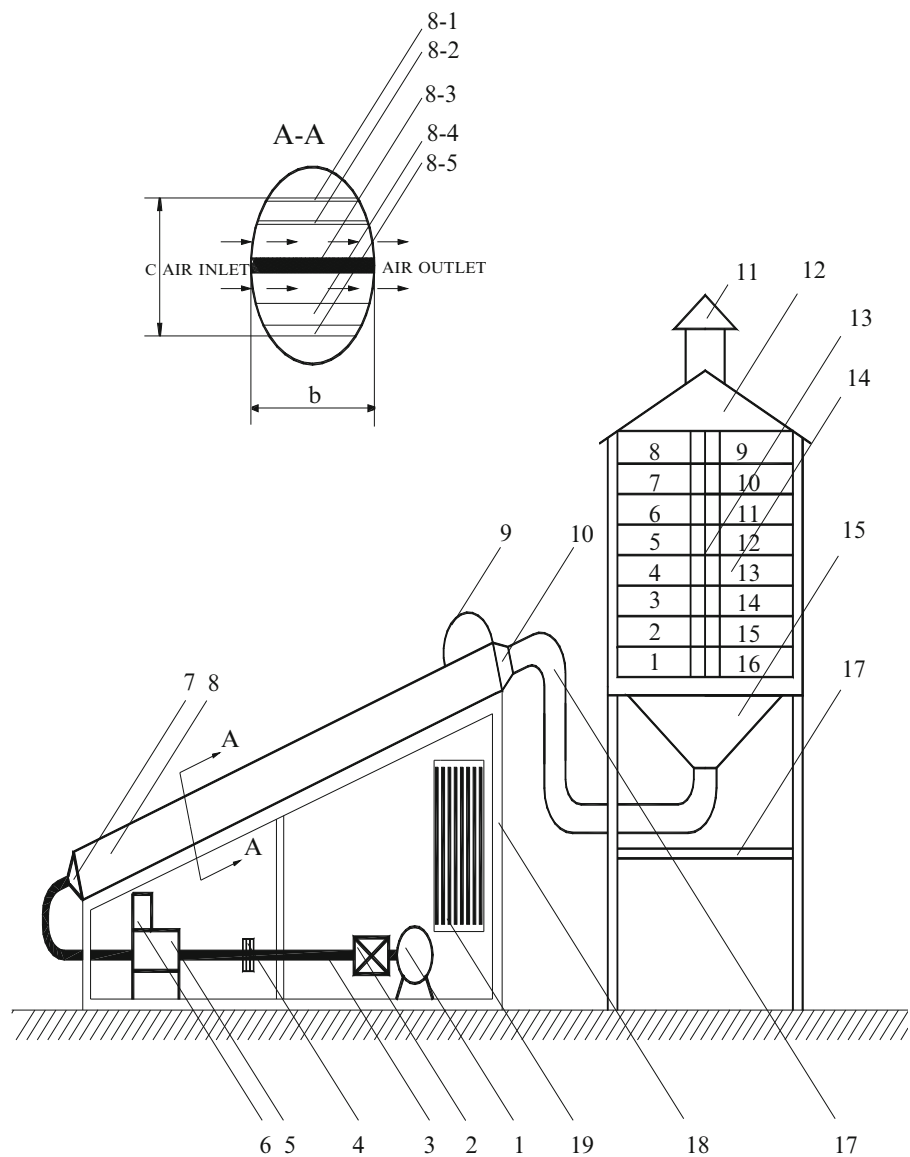
Fig. 67.1 Solar-assisted drying cupboard (*1*. Fan, *2*. Valve, *3*. Connection pipe, *4*. Orifice, *5*. Auxiliary heater, *6*. Temperature controller, *7*. Inlet of solar air collector, *8*. Solar air collector, *8-1*. Glass cover, *8-2*. Glass cover, *8-3*. Absorber plate, *8-4*. Insulation, *8-5*. Wood cover, Pyranometer, *10*. Outlet of solar air collector, *11*. Chimney, *12*. Outlet of drying cupboard, Inter section, *14*. Shelves, *15*. Inlet of drying cupboard, *16*. Support of drying cupboard, *17*. Flexible connection pipe, *18*. Support of solar air collector, *19*. Manometer) [7, 9]

Experimental Data

In order to estimate the exergetic sustainability indicators, the required experimental data have been taken from the literature [7, 9]. Moreover, all details related to the experiments can be found in the literature [7].

Parameters

General exergy balance of solar drying processes can be written as

$$(Exergy\ Input) = (Exergy\ output) + (Irreversibility) \tag{67.1}$$

However, if total exergy output and irreversibilities are clearly taken into consideration, the exergy balance for the solar drying processes can be written as

$$(Total\ exergy\ input) = (Total\ exergy\ used\ in\ shelves) + (Total\ exergy\ loss) + (Total\ exergy\ destruction) \tag{67.2}$$

which can be arranged as

$$\sum \dot{E}x_{in}^{SDP} = \sum \dot{E}x_{L}^{SDP} + \sum \dot{E}x_{d}^{SDP} + \sum \dot{E}x_{eus}^{SDP} \tag{67.3}$$

where

$$\sum \dot{E}x_{d}^{SDP} = \sum \dot{E}x_{input,f}^{SDP} + \sum \dot{E}x_{input,sol}^{SDP} - \sum \dot{E}x_{dci}^{SDP} \tag{67.4}$$

$$\sum \dot{E}x_{in}^{SDP} = \sum \dot{E}x_{input,f}^{SDP} + \sum \dot{E}x_{input,sol}^{SDP} \tag{67.5}$$

$$\sum \dot{E}x_{L}^{SDP} = \sum \dot{E}x_{dco}^{SDP} \tag{67.6}$$

where $\sum \dot{E}x_{input,f}^{SDP}$ describes inlet exergy from the fan, $\sum \dot{E}x_{input,sol}^{SDP}$, gained exergy from solar air collector.

If Eqs. (67.4–67.6) are replaced into Eq. (67.3)

$$\sum \dot{E}x_{eus}^{SDP} = \sum \dot{E}x_{dci}^{SDP} - \sum \dot{E}x_{dco}^{SDP} \tag{67.7}$$

where $\sum \dot{E}x_{dci}^{SDP}$ describes inlet exergy to the drying cabinet, $\sum \dot{E}x_{dco}^{SDP}$, outlet exergy from drying cabinet.

Under this solid theoretical background, the exergy-based environmental and sustainability parameters previously presented in the literature [6, 8] are considered and rearranged for the solar drying processes as
1. Exergetic efficiency
2. Waste exergy ratio
3. Exergy recoverability ratio
4. Exergy destruction ratio
5. Environmental impact factor
6. Exergetic sustainability index

Exergetic efficiency $\left(\eta_{ex}^{SDP}\right)$

In order to define the exergetic efficiency for solar drying processes, total exergy entering from fan and solar air collector and total exergy used in shelves should be taken into consideration. If so, the exergetic efficiency of the solar drying processes can be rearranged as in the following algebraic form, ranging from 0 to 1 theoretically [6, 8].

$$\eta_{ex}^{SDP} = \sum \dot{E}x_{eus}^{SDP} / \dot{E}x_{in}^{SDP} = \left(\sum \dot{E}x_{dci}^{SDP} - \sum \dot{E}x_{dco}^{SDP}\right) / \left(\sum \dot{E}x_{input,f}^{SDP} + \sum \dot{E}x_{input,sol}^{SDP}\right) \tag{67.8}$$

Waste exergy ratio $\left(r_{ex}^{SDP}\right)$

During the solar drying processes, exergy losses occur in the solar air collector and drying cabinet. Under these considerations, waste exergy ratio can be written as follows, ranging from 0 to 1 [6, 8].

$$
\begin{aligned}
r_{wex}^{SDP} &= \left(\sum \dot{E}x_d^{SDP} + \sum \dot{E}x_L^{SDP}\right) / \sum \dot{E}x_{in}^{SDP} \\
&= \left(\sum \dot{E}x_{input,f}^{SDP} + \sum \dot{E}x_{input,sol}^{SDP} - \sum \dot{E}x_{dci}^{SDP} + \sum \dot{E}x_{dco}^{SDP}\right) / \left(\sum \dot{E}x_{input,f}^{SDP} + \sum \dot{E}x_{input,sol}^{SDP}\right)
\end{aligned}
\tag{67.9}
$$

Exergy Recoverability Ratio $\left(r_{ex}^{SDP}\right)$

Exergy recoverability ratio indicates the exergy potential that is possible to be recovered in the system. Exergy recoverability ratio of a solar drying process can be assumed as the ratio of the exergy recovery potential for the system to total exergy input. The exergy recoverability ratio can be written as in the following form, ranging from 0 to 1 [6, 8].

$$
r_{exr}^{SDP} = \sum \dot{E}x_r^{SDP} / \sum \dot{E}x_{in}^{SDP} = \dot{E}x_{dco}^{SDP} / \left(\sum \dot{E}x_{input,f}^{SDP} + \sum \dot{E}x_{input,sol}^{SDP}\right)
\tag{67.10}
$$

where $\dot{E}x_r^{SDP}$ describes the quantity of exergy recovery potential for the system.

Exergy destruction ratio $\left(r_{ex}^{SDP}\right)$

Exergy destruction ratio is an important parameter to indicate the decrease of the positive impact of the solar drying processes on exergetic sustainability. The reference value of this factor should be "zero" for better exergyetic sustainability of the solar drying processes. Exergy destruction ratio is given in the following form, ranging from 0 to 1 [6, 8].

$$
\begin{aligned}
r_{exd}^{SDP} &= \sum \dot{E}x_d^{SDP} / \sum \dot{E}x_{in}^{SDP} \\
&= \left(\sum \dot{E}x_{input,f}^{SDP} + \sum \dot{E}x_{input,sol}^{SDP} - \sum \dot{E}x_{dci}^{SDP}\right) / \left(\sum \dot{E}x_{input,f}^{SDP} + \sum \dot{E}x_{input,sol}^{SDP}\right) \\
&= 1 - \left[\sum \dot{E}x_{dci}^{SDP} / \left(\sum \dot{E}x_{input,f}^{SDP} + \sum \dot{E}x_{input,sol}^{SDP}\right)\right]
\end{aligned}
\tag{67.11}
$$

Environmental Impact Factor $\left(f_{ex}^{SDP}\right)$

Environmental impact factor of solar drying processes is an important parameter to indicate whether or not it damages the environment because of its unusable waste exergy output and exergy destruction. Environmental impact factor [6, 8] can be rearranged as in the following form, ranging from 0 to $+\infty$ ([6, 8].)

$$
f_{envi}^{SDP} = r_{wex}^{SDP} \times \frac{1}{\eta_{ex}^{SDP}}
\tag{67.12}
$$

Exergetic sustainability index $\left(\Theta_{ex}^{SDP}\right)$

Exergetic sustainability index is an important parameter for exergetic sustainability of the solar drying processes in terms of the second-law of thermodynamics. The exergetic sustainability index can be written to be reverse of the environmental impact factor, ranging from 0 to 1 theoretically [6, 8].

$$
\Theta_{esi}^{SDP} = \frac{1}{f_{envi}^{SDP}}
\tag{67.13}
$$

Results and Discussion

This paper presents the effects of some exergetic sustainability indicators on the performance of a single layer solar drying process by using the experimental data in the literature [7]. For this purpose, the following parameters which are investigated based on the constant characteristics of a solar drying process are taken into consideration: (1) Exergetic efficiency, (2) waste exergy ratio, (3) exergy recoverability ratio, (4) exergy destruction ratio, (5) environmental impact factor, (6) exergetic sustainability index.

Fig. 67.2 Variation of exergetic efficiency and waste exergy ratio with time
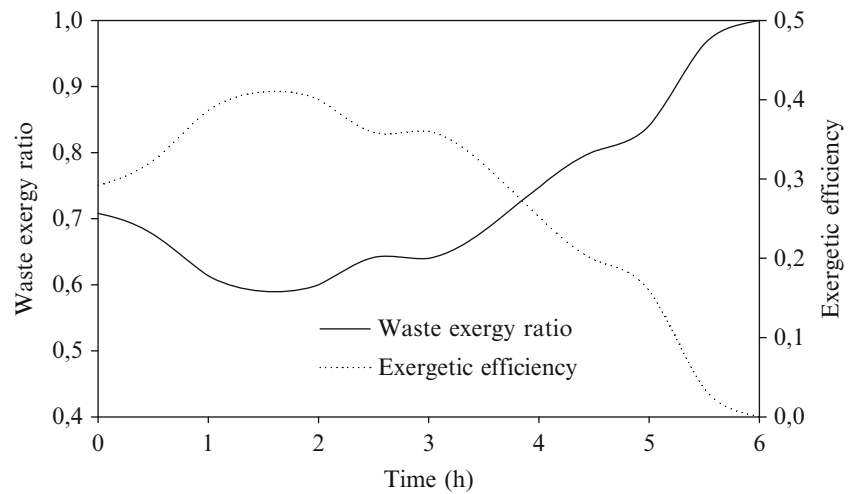
Fig. 67.3 Variation of exergetic efficiency and exergy destruction ratio with time
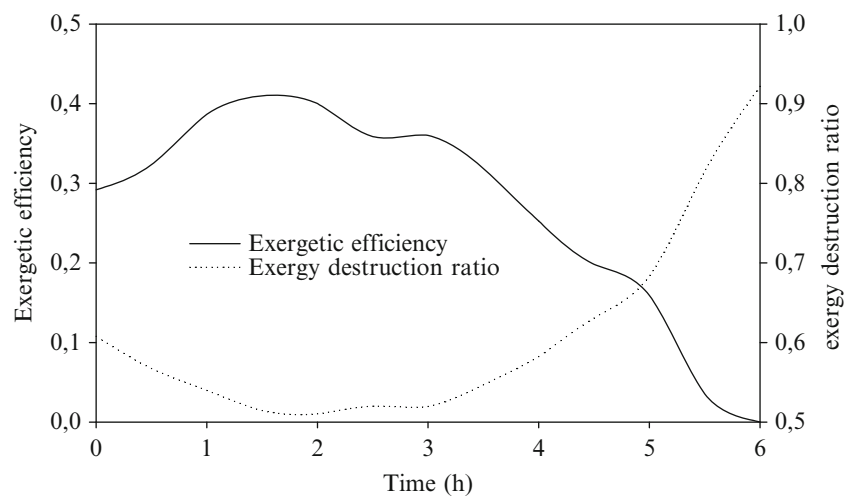
Figure 67.2 presents the variation of exergetic efficiency and waste exergy ratio as a function of time (h) based on the characteristics of a single layer solar drying process. The exergetic efficiency which is one of the most important parameters for exergetic sustainability of the solar drying process is mainly based on the total exergy input (total exergy entering from fan and solar air collector) and the total exergy used in the drying cabinet. It is noticed that the exergetic efficiency highly affected by the amount of solar radiation. When the amount of solar radiation increase, total exergy used in the drying cabinet and exergetic efficiency of the solar drying process increase. It can be assumed that waste exergy ratio is an important parameter to refer to the necessity of waste energy management of the solar drying process in order to increase its exergetic performance and its role on exergetic sustainability. As shown in Fig. 67.2, exergetic efficiency decreases while waste exergy ratio increases for single layer solar drying process. The waste exergy ratio of solar drying process is a function of exergy losses occur in the solar air collector and drying cabinet and total exergy entering from fan and solar air collector. The results show that exergetic efficiency and waste exergy ratio range from 0 to 0.410 and from 0.590 to 1, respectively (their theoretical values range from 0 to 1) [6, 8].

Figure 67.3 shows the variation of exergetic efficiency and exergy destruction ratio as a function of time based on the constant characteristics of the solar drying process. Exergy destruction ratio is an important parameter to affect the exergetic efficiency; and waste exergy ratio of the single layer solar drying process should be taken into consideration to indicate its role on exergetic sustainability. As shown in Fig. 67.3, when the exergy destruction goes up, the exergetic efficiency decreases. Therefore, in order to minimize the exergy destruction ratio and increase the contribution to exergetic sustainability of the solar drying process, exergy loses occurred in the solar air collector should be minimized. Thus, the contribution to exergetic sustainability of the solar drying process will be remarkable. In terms of the second-law of thermodynamics, all outputs become meaningful for the single layer solar drying process because they have potential to

Fig. 67.4 Variation of exergy recoverability ratio and exergy destruction ratio with time
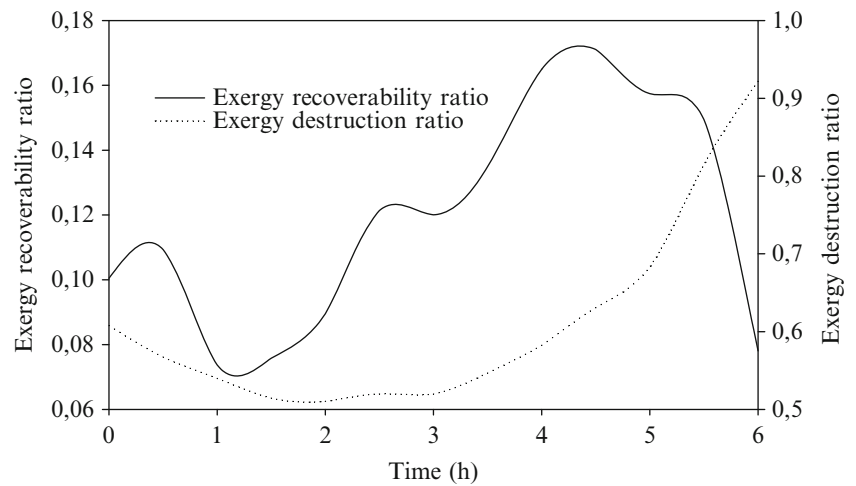
Fig. 67.5 Variation of exergetic sustainability index and environmental impact factor with time
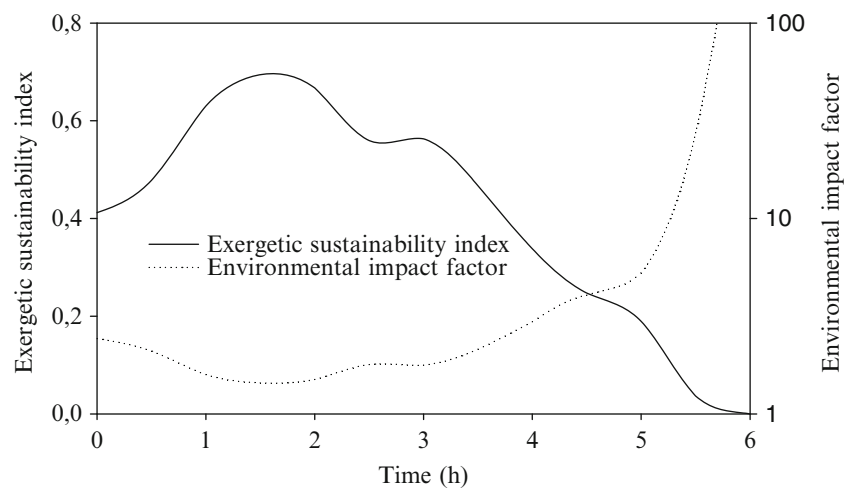
generate entropy in the environment. In terms of the first-law of thermodynamics, the environmental effect of the heat losses from solar air collector and drying cabinet outlet is not taken into account. It is estimated that exergy destruction ratio ranges from 0.510 to 0.922 (its theoretical values range from 0 to 1) [6, 8].

Figure 67.4 presents the variation of exergy recoverability and exergy destruction ratios as a function of time based on the constant characteristics of the single layer solar drying process. Exergy recoverability ratio indicates the exergy potential that is possible to be recovered in the solar drying process. Exergy recoverability ratio of a solar drying process can be assumed as the ratio of the exergy recovery potential for the system to total exergy input (total exergy entering from fan and solar air collector). Outlet exergy of the drying cabinet is a potential exergy which can be used for preheating of drying air for this system. It is determined that exergy recoverability ratio ranges from 0.074 to 0.171 (its theoretical values range from 0 to 1) [6, 8]. Exergy destruction occurs in the solar air collector which is relating with the structure of collector. It is noticed that the exergy destruction ratio highly affected by the amount of solar radiation. It is seen that, when the amount of solar radiation increases, exergy destruction ratio decreases.

Figure 67.5 presents quantitatively the relationships between exergetic sustainability index and environmental impact factor as function of time. Exergetic sustainability index and the environmental impact factor are a function of waste exergy ratio and exergetic efficiency. Environmental impact factor of single solar drying process is an important parameter to indicate whether or not it damages the environment because of its waste exergy output and exergy destruction. As seen in Fig. 67.5, the exergetic sustainability index and the environmental impact factor are highly affected by the amount of solar radiation. When the amount of solar radiation increases, exergetic sustainability index increases and environmental impact factor decreases. It is estimated that exergetic sustainability index and environmental impact factor range from 0 to 0.694 and from 1.441 to ∞, respectively (their theoretical values range from 0 to 1 and from 0 to ∞, respectively) [6, 8].

Fig. 67.6 Variation of exergetic sustainability index and environmental impact factor with exergetic efficiency
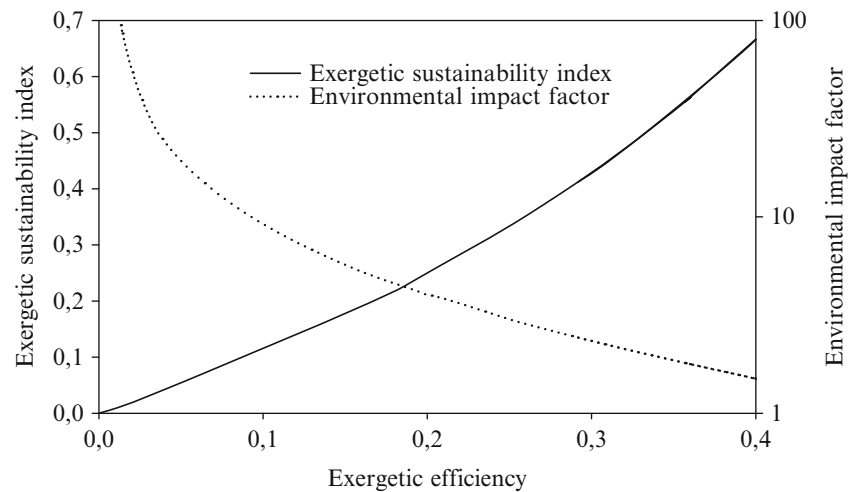
Figure 67.6 shows the variation of exergetic sustainability index and environmental impact factor as function of exergetic efficiency. As shown in Fig. 67.6, as the exergetic efficiency increases, the exergetic sustainability index increases and the environmental impact factor decreases. In other words, increased exergy efficiency reduces environmental damage for a single layer solar drying process. If total waste exergy output from the solar drying process increases, exergy-based sustainability ability of the system decreases and thus environmental impact factor goes up, whereas exergetic sustainability index decreases. As exergetic efficiency is zero value, the exergetic sustainability index has a ∞ value, whereas environmental impact factor is zero. Accordingly, it can be said that at the end of the single layer solar drying process in which the amount of solar radiation has a minimum value, this system will not be an exergetic and environmental benign system. However, since amount of solar radiation has a maximum value, environmental impact factor has a minimum value and exergetic sustainability index has a maximum value. As a result, it can be said that for higher amount of solar radiation this system is an exergetic and environmental benign system. Thus, to decrease the environmental impact factor and to increase exergetic sustainability index of the solar drying process, exergy destruction occurred in the solar air collector should be minimized and the exergy recovery potential from the system should be optimized.

Conclusions

Environmental and sustainability aspects of a single layer solar drying process have been parametrically studied based on the actual data. Some concluding remarks are given as follows:

- The exergetic efficiency and the exergy recoverability ratios range from 0 to 0.410 and from 0.074 to 0.171, respectively while exergy destruction and waste exergy ratios range from 0.510 to 0.922 and from 0.590 to 1, respectively.
- The single layer solar drying process has some high values of waste exergy ratio and exergy destruction ratio, and it needs improvement for better environment. In this regard, exergy destruction occurred in the solar air collector should be minimized and the exergy recovery potential from the system should be optimized.

Nomenclature

$\dot{Ex}$ Exergy (kW)

Greek Letters

η   Efficiency

Subscripts

d	Destruction	ex	Exergy
dci	Drying cabinet inlet	exr	Exergy recoverability
dco	Drying cabinet outlet	f	Fan
envi	Environmental	L	Loss
esd	Exergy destruction	sol	Solar
esi	Exergetic sustainability index	wex	Waste exergy
eus	Exergy used in shelves		

Superscripts

SDP   Solar drying process

References

1. Dincer I (2007) Environmental and sustainability aspects of hydrogen and fuel cell systems. Int J Energy Res 31:29–55
2. Dincer I (1999) Environmental impacts of energy. Energy Policy 27:845–854
3. Midilli A, Ay M, Dincer I, Rosen MA (2005) On hydrogen and hydrogen energy strategies: I: current status and needs. Renew Sustain Energy Rev 9(3):255–271
4. Midilli A, Ay M, Dincer I, Rosen MA (2005) On hydrogen and hydrogen energy strategies II: future projections affecting global stability and unrest. Renew Sustain Energy Rev 9(3):273–287
5. Dincer I, Rosen MA (2007) Exergy, Energy, Environment and Sustainable Development. Elsevier, Cambridge
6. Midilli A, Dincer I (2009) Development of some exergetic parameters for PEM fuel cells for measuring environmental impact and sustainability. Int J Hydrogen Energy 34(9):3858–3872
7. Midilli A, Kucuk H (2003) Energy and exergy analyses of solar drying process of pistachio. Energy 28(6):539–556
8. Midilli A, Kucuk H, Dincer I (2012) Environmental and sustainability aspects of a recirculating aquaculture system. Environ Prog Sustain Energy 31(4):604–611
9. Midilli A (2001) Determination of pistachio drying behavior and conditions in a solar drying system. Int J Energy Res 25:715–725

Investigating the Exergetic and Environmental Effects of Subcooling and Superheating Processes on the Performance of Direct Expansion Systems

M. Ziya Sogut, Hikmet Karakoç, Zuhal Oktay, and Arif Hepbasli

Abstract

Recently, subcooling and superheating applications, which are proposed as an approach for the efficient use of energy, have positive effect on the emission next to increasing the energy efficiency. This study examines energetic, exergetic, and environmental effects of subcooling and superheating processes in cooling applications separately. In this study, a direct expansion system (DX), which is used widely in supermarket cooling applications, is taken into consideration. The evaporator temperatures of $-25\,°C$ and $0\,°C$, the refrigerants of R-22, R-404A, and R-134a, which are preferred widely in DX systems, and minimum and maximum leakage rates of 3 and 30 % are taken as reference values for the analysis. According to the results, while subcooling and subheating processes increase approximately 10 % of COP and exergy efficiencies based on refrigerants and decrease CO_2 emissions for all refrigerants. The study also concluded with an emphasis on the importance of subcooling and superheating applications, especially for DX systems and the importance of the preference refrigerant.

Keywords

DX systems • COP • Refrigerants • Exergy analyses • CO_2 emission

Introduction

Negative impacts of the energy costs in recent years are an important problem before the sustainable economic development for all countries suffering difficulties in energy supply. Efficient use of energy and energy saving works is an obligation for all sectors that are subject to this impact. There are also increasing amount of works about this obligation due to the heavy energy consumption in the air conditioning and cooling sector which take around 9 % of the world energy consumption [1].

Since 1990s, refrigerant fluids have become prominent due to the environmental threats in particular due to the ozone consumption and greenhouse gas emissions. Although the ozone consumption is minimized by the processes limiting refrigerant fluid supply through the international activities of the international society like the Kyoto Protocol and London Conference, these fluids still have important effect on the climate change based on global warming. The selection of

M.Z. Sogut (✉)
Technical and Computer Applications Center, Military Academy, Ankara, Turkey
e-mail: mzsogut@yahoo.com

H. Karakoç
Faculty of Aeronautics and Astronautics, Anadolu University, Eskisehir, Turkey
e-mail: hkarakoc@anadolu.edu.tr

Z. Oktay
Department of Energy Systems Engineering, Faculty of Engineering, Recep Tayyip Erdoğan University, Rize, Turkey
e-mail: zuhal.oktay@gmail.com

A. Hepbasli
Department of Energy Systems Engineering, Faculty of Engineering, Yasar University, 35100 Bornova, Izmir, Turkey
e-mail: arif.hepbasli@yasar.edu.tr

appropriate system, conducting a configuration with high efficiency and especially the choice of appropriate fluid for all sectors using these fluids are important due to energy costs and environmental effects. However, excessive cooling and excessive heating have been a catalyst on the evaporator and condenser units for especially the DX systems in recent years.

Among the cooling applications, market applications in particular have come to the fore with their heavy use of refrigerant fluid and heavy energy consumption. Among them, supermarkets with a sales area of 3,700–5,600 m^2 are structures of heavy energy consumption in commercial applications with an annual average energy consumption of 2–3 million kW [2]. Energy consumptions of these systems used for the protection of food in supermarkets can reach approximately 50 % of the total energy consumption of a market. This ratio goes up to 65 % in low capacity market applications [3–5]. Around 60–70 % of the energy consumption in these systems is carried out in compressors and condensers [6]. These systems have gained importance because of their negative impacts on total consumption costs as well as the environmental threats caused by refrigerants and energy consumption. Work to develop refrigerant systems is based on the reduction of energy use requirements in the systems to reduce these effects and on the choice of environment-friendly refrigerant fluids with low GWP and ozone depletion potential in refrigerant systems.

With respect to the storage areas in market applications, it was observed that many refrigerant systems were used based on the commercial requirements and that the Direct Expansion (DX) system was remarkable among them with a ratio of up to 60 %. This system is followed by secondary lop systems, distributed systems, low-charge multiplex systems, and advanced self-contained systems. Supermarket systems with high energy consumption as well as high amounts of refrigerant fluids have important environmental effects in addition to the direct or indirect effects of refrigerant fluids. In addition, the leakage losses arising from the repair and maintenance processes, setbacks in operation conditions, and installation errors in this type of structure with high amounts of refrigerant fluid charge have significant impacts on their energy consumption, the efficiency performance of the systems, and the environmental effects they cause. In this type of refrigerating application, refrigerant fluid choices with less environmental effects, system choice, installation, and operation are important, in addition to the capacity of efficient energy use.

In current systems, reducing energy costs is possible only by the efficient use of energy or use of energy saving technologies. Saving works in refrigerant systems are examined in many applications from energy consuming fan and compressor choices to ambient conditions and from the flow properties of system elements like the evaporator to fluid and system control. Among them, the subcooling and superheating applications directly affect compressor efficiency due to its impact on the cooling capacity, and thus they have an indirect effect on energy consumption and provide significant savings in the systems. The subcooling application reduces the amount of energy required by minimizing the cooling requirement in the system. So it reduces operation costs in the cooling system. A temperature fall of 2 °C in subcooling applications corresponds to around 1 % savings in the operation costs of the systems. Efficiency is affected adversely by the mass loss up to 30 % because of high refrigerant fluid charge or excessive leakage for providing high pressure in the system of refrigerant applications. Superheating application ensures optimum use of energy by ensuring the refrigerant fluid control depending on the needs of the systems. Superheating can be defined as turning a refrigerant fluid which cannot be fully gasified into gas and preventing entry of the liquid refrigerant to the compressor [7].

The energy saving potential in refrigerant systems is calculated by making energy analyses in traditional applications. In this type of analysis, the coefficient of performance (COP) is calculated according to the first law of thermodynamics and the energy consumption potential caused by the systems is evaluated in comparison. These evaluations ensure the examination of the properties of the fluids used. Energy analyses in the cooling systems are not sufficient in the evaluations of the irreversibilities and saving potentials based on irreversibility, unlike other thermodynamic applications. Energy analyses are only the numeric results of energy use. Therefore analyses for defining efficiency in performance evaluations based on the quality of the system and determining the real irreversibilities should be carried out by exergy analyses according to the second law of thermodynamics.

Exergy, which is defined as the maximum work which can be produced by a process as it comes to equilibrium with a reference environment, is a measurement of the quality of the energy stream. For industrial processes, exergy analysis is a powerful concept in the modern thermodynamic method, which is used as an advanced tool [8, 9]. For refrigeration applications, exergy analysis is also a powerful concept and the modern thermodynamic method used as an advanced tool. By use of an exergy analysis, the process can be optimized into more sustainable processes. The exergy analyses depend mainly on the effects of environmental parameters such as temperature and pressure. Thus, environmental parameters affect efficiency directly. Exergy is exhausted or destroyed due to irreversibility in real processes. The basic aim of exergy analyses is determined as real potential of losses exhausted or destroyed in thermodynamic processes. Consequently, exergy analyses are an important criterion for all of the thermodynamic evaluations. Today, many science studies concerning the exergy concept for thermal processes are being made. For example, Dincer and Rosen, Kanoğlu et al., Hepbasli, Korenes et al., Wall, and Sogut have performed most extensive studies in the exergy field [10–15].

Today, improving environmental awareness requires that the CO_2 emission potential caused by this type of system be kept under control. Many scientific approaches can be seen in these scientific studies. One of them, the concept of Total Equivalent Warming Impact (TEWI), has been developed to combine the global warming effects of CO_2 released into the atmosphere due to energy used over the lifetime of a system (indirect effect) with the effects resulting from refrigerant and blowing agent emissions system (direct effect). Contrary to Life Cycle Climate Performance (LCCP) analysis, which also involves emissions from energy expenditures for production of the system and further greenhouse gas emissions caused during the production of the refrigeration system, the focus of a TEWI analyses consists of the emissions following the operation of the system [16].

In this study, the energy and exergy analyses based on different refrigerant fluids were carried out for the Direct Expansion Systems were commonly used in supermarket applications. In addition, the performance effects of the subcooling and superheating applications in the range of 0–5 K were examined in terms of energy and exergy in DX systems and reducing the environmental effects caused by the refrigerant.

Subcooling and Superheating of Direct Expansion System (DX)

Direct Expansion System (DX)

Supermarkets with increasing importance in meeting daily food requirements are commercial structures of heavy energy consumption with an annual average of 1,000 kW/m². The cooling techniques used in this type of structure spend around 50 % of the total energy consumption with the cooling and air conditioning systems of different properties. In small capacities, cooling systems spend approximately 65 % of total energy consumption. In these structures, where cooling applications of various types with large volumes are used, the charge amounts of the refrigerant fluids used in the system reached up to 2,500 kg. In the supermarket applications of cooling systems, different cooling temperatures are needed to keep different products fresh. In applications of commercial refrigeration, three different kinds of application are used: supermarkets refrigeration direct expansion system, indirect system, and decentralized system. The low and medium evaporating temperatures of these types of typical refrigeration systems are around −35 °C and −10 °C respectively [17].

Refrigeration systems used widely in supermarket applications are determined as direct systems or direct expansion (DX) systems. In these systems, the refrigerant is used to directly transport heat from the areas to be cooled to the outside areas where heat is released. DX systems have four main components: evaporator, compressor, condenser, and expansion valve, and the main work principle is they are run as a vapor expansion cooling cycle. The flow schema of a DX system is given in Fig. 68.1.
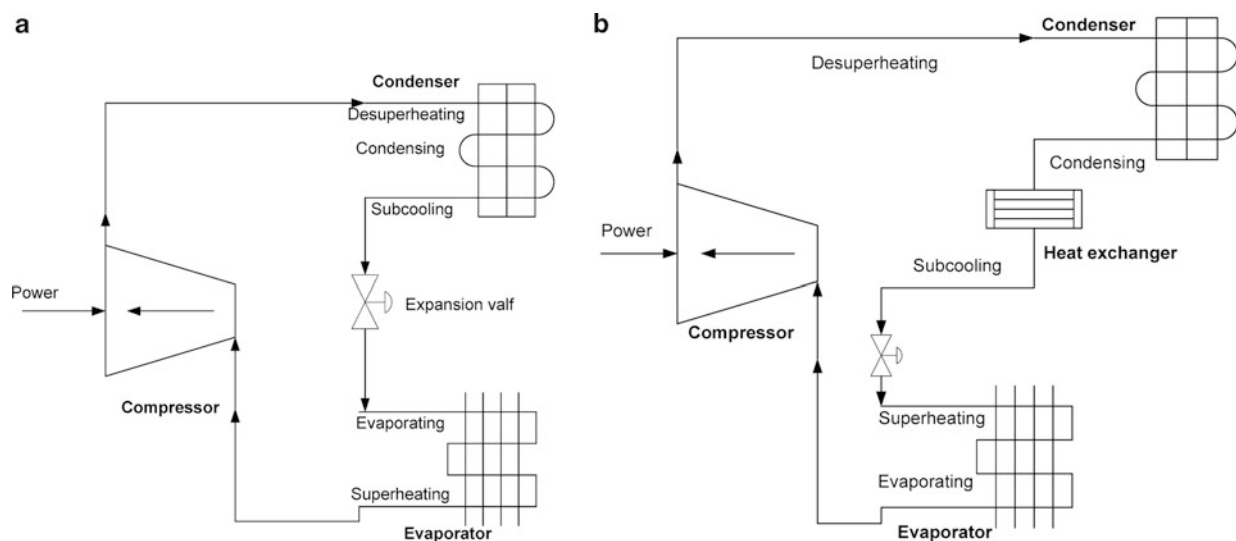
Fig. 68.1 Direct expansion system [17]. (**a**) Normal system (**b**) System with subcooler and superheating

Table 68.1 Thermodynamics and environmental parameters of refrigerants

Refrigerants	R-22	R-134a	R-404A
Thermodynamics parameters			
Chemical formula	CHC1F2	CH_2FCF_3	CHF2CF3/CH3CF3/CH2FCF3
Molecular weight (kg/kmol)	86.5	102	97.6
Boiling point at (1.013 bar)	−40.8	−26.1	−46.6
Enthalpy of evaporation (kJ/kg)	182.5	177.5	140.1
Critical temp. (°C)	96.1	101.1	72.1
Critical pressure (bar)	49.9	40.6	37.4
Cp_{likid} (kJ/kgK)	1.26	1.425	1.541
Cp_{vapor} (kJ/kgK)	0.864	1.011	1.2
Environmental parameters			
ODP	0.04	0	0
GWP	1,810	1,430	3,900
Atmospheric life (year)	12	14	16

Fig. 68.2 Subcooling and superheating in cooling cycle [28]
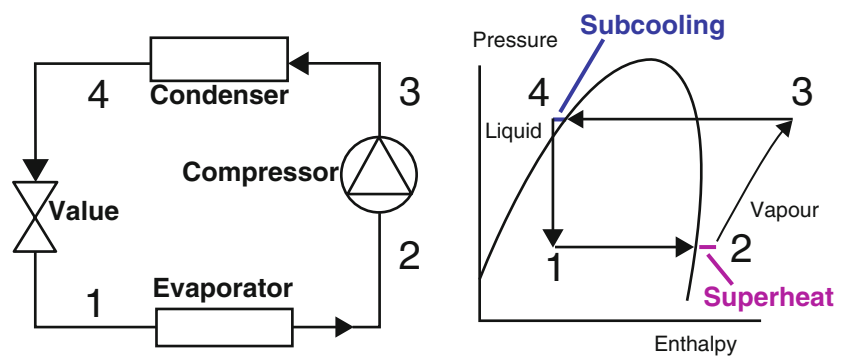
In these applications, a separate cooling machine with compressor is often used for each evaporator and cooling unit. In other cases, several or all evaporators and cooling units in a system are connected to one or more compressors placed in a central machine room. Condensers may be in an air-cooled machine room, remote outdoors, or indoors. Heat recovery from the condensers may be utilized for space or water heating. The refrigerant changes from liquid to vapor or gas in the evaporator that is placed in the space to be cooled. The pressure (and temperature) of the refrigerant gas is increased in the compressor and the gas then passes to the condenser where the refrigerant is cooled and condenses to liquid. The liquid then passes to the expansion valve, a throttling device where the pressure of the refrigerant is reduced, and then back to the evaporator and the process starts all over again (see Fig. 68.1). The refrigerant is then often transported through long tubes, requiring a relatively large refrigerant charge [18].

Direct expansion systems are the dominant technology for supermarkets worldwide. Refrigerants used include HCFC R-22 and HFCs such as R-507 and R-404A and to a smaller extent R-134a for medium temperature applications. But R-22, R-134a, and R-404A refrigerants are used commonly in DX systems. The thermodynamic and environmental parameters of these refrigerants are given in Table 68.1.

Subcooling of Refrigerants

Excessive cooling of the refrigerant fluids in cooling systems provides an indirect saving by increasing the cooling capacity of the system. It works best where year-round outdoor temperatures are high and constant. The effectiveness of the application depends mainly on the cooling fluid. Subcooling which causes increases in the cooling capacity in the system uses an external heat surface. It is not very easy to determine the subcooling temperature in a system. However the general approach in practice is accepted as the difference of the Bubble-point temperature and actual liquid temperature. Figure 68.2 illustrates the subcooling impact on systems.

Excessive cooling is used in old or new type direct expansion vapor compression as the most usable system. The subcooling system can be either a dedicated mechanical subcooling system or an integrated mechanical subcooling system.

Ambient subcooling involves the use of an oversized condenser or an additional subcooling heat exchanger to subcool the condensed high-pressure refrigerant. Subcooling reduces the enthalpy of the liquid refrigerant, which is equal to the enthalpy

of the two-phase stream of the refrigerant leaving the expansion valve and entering the evaporator. The specific capacity of the refrigerant in Btu/lb is increased, hence reducing the required mass flow rate of refrigerant to be compressed and the required compressor electric load. Ambient subcooling is effective only when the head pressure control prevents further reduction in head pressure. Otherwise, reduction in head pressure is more efficient than simply reducing the liquid temperature. Hence, the savings for ambient subcooling are generated during times of low ambient temperature, when head pressure is being maintained at a high level. This will represent a large percentage of operating hours in cooler climates.

As with ambient subcooling, mechanical subcooling involves further reduction in enthalpy of the condensed liquid refrigerant. Mechanical subcooling is provided by the expansion of part of the refrigerant liquid in a subcooling heat exchanger, as shown in the figure below. The expanded refrigerant is compressed from an intermediate pressure to the common discharge pressure. The specific refrigerant capacity of the main stream of liquid is increased, thus reducing the compressor electric load for this stream of refrigerant. The additional electric load of the subcooling compressor must be subtracted from the potential savings. However, since the subcooling compressor has a higher suction pressure, its specific work requirement in kW/kg of refrigerant is less. The result is an overall savings in electricity usage.

Superheating of Refrigerants

In a cooling cycle, a fluid entering into the evaporator units is theoretically expected to evaporate and enter into the compressor after receiving heat. However, this cannot be always achieved in evaporator units with different working zones especially in market applications. In order to prevent liquid entrance to the compressor, usually heat collectors, or driers are added. This causes performance to be affected negatively since the flow process is affected. In recent years, the superheating process in the evaporator exit in these systems increases the heat withdrawal effect from the environment to be cooled and removed of these adverse effects (see Fig. 68.2). In addition, the superheating application prevents cooling refrigerant entrance to the compressor and limits the working range and has positive effect on the system energy consumption. However, it is important to control the evaporator exit temperature in superheating application. If the temperature is lower than the expected values, this may cause the entrance of the fluid to the compressor in the evaporator exit. If this value is high, it causes insufficiency of the fluid amount and excessive work of the compressor for the desired compression work. Therefore, it is necessary to take the overheating temperature with recommended values determined through experimental data. On the other hand, superheating temperature for a system can be defined as the difference between the actual steam temperature of the fluid and dew-point temperature.

Exergy Concept in Cooling Systems

As a measure of the machine's working activities in cooling systems, the thermal efficiency and the COP have been defined. The COP for a cooling machine is

$$COP = \frac{Q_L}{W_{net}} \tag{68.1}$$

where Q_L indicates the temperature moving away from the cooled environment and W_{net} indicates the net effort input into the compressor [19]. Cooling machines are systems that work based on the cycle principle and the energy saving for the cycle may be expressed as follows:

$$W_{net} = Q_H - Q_L \tag{68.2}$$

where Q_H is the heat output from the machine. In cooling systems, COP is expressed as efficiency according to the first law of thermodynamics. In these systems, the working ability of a machine is explained by the second law of thermodynamics and this is defined as exergy. In the cooling system, exergy efficiency is compared to the possible highest COP_{tr} of the real COP in the same work parameters. In a cooling machine, COP_{tr} can be expressed as [20, 21]

$$COP_{tr} = \frac{1}{\frac{T_H}{T_L} - 1} \tag{68.3}$$

where T_H is the outside temperature and T_L is the environmental temperature removed. In this case, the exergy efficiency of the cooling machine can be expressed as

$$\eta_{II} = \frac{COP}{COP_{tr}} \qquad (68.4)$$

If Eq. (68.1) and Eq. (68.3) are united [12],

$$\eta_{II} = \frac{Q_L \frac{T_H}{T_L} - Q_L}{W_{net}} \qquad (68.5)$$

The maximum improvement in exergy efficiency for a process or system is most certainly achieved at the point where the exergy loss or irreversibility is minimized. The exergy loss or irreversibility is based on the difference between the exergy input and output [22]. The improvement potential (IP) is developed for irreversibility processes used in thermal applications [23].

$$IP = (1 - \eta_{II}) \cdot \left(\dot{E}x_{in} - \dot{E}x_{out} \right) \qquad (68.6)$$

TEWI Concept in Cooling Systems

At the meeting in Copenhagen, a concept for evaluating the total sum of global warming caused by refrigeration systems, namely through refrigerant emissions and also through CO_2 emissions from the fossil fuel power plant which produces the energy for the refrigeration system was presented; it is called the TEWI and was developed by the US Department of Energy and Oak Ridge National Laboratories [24].

An appropriate method of evaluating any refrigerant is the TEWI value as defined in EN 378:2,000. This is an internationally accepted formula that may be used to directly compare the relative effect of different systems. It represents the environmental effects, based on the global warming potential of the refrigerant, and energy consumption of the plant over its lifetime. The higher the TEWI value, the poorer the system in terms of its overall impact on the environment:

$$TEWI = \underbrace{\underbrace{[GWP.L.n]}_{Leakage\ losses} + \underbrace{[GWP.m.(1 - \alpha_{recovery})]}_{Recovery\ losses}}_{Direct\ GWP} + \underbrace{\underbrace{[n.E_{annual}.\beta]}_{Energy\ consumption}}_{Indirect\ GWP} \quad (\text{kgCO}_2/\text{year}) \qquad (68.7)$$

where TEWI is the total equivalent warming impact, GWP is the global warming potential, L is the amount of leakage, n is the system operating time, m is the refrigerant charge, $\alpha_{recovery}$ is the recovery or recycling factor, E_{annual} is the annual energy consumption, and β is the CO_2 emission produced by power generation [25].

The global warming effects of different substances are compared with carbon dioxide using an index known as the global warming potential or GWP. The GWP of a substance of the global warming impact due to the emission of 1 kg of that substance is divided by the global warming impact of 1 kg of carbon dioxide, both effects are measured over a 100-year time span [26].

The entire climatically relevant impact by the refrigeration process is composed of direct and indirect emission of greenhouse gases. The direct impact includes the emission of working substances by the greenhouse effect due to leakages, maintenance, and losses during disposal. The indirect impact is related to the CO_2 emissions, particularly due to the generation of electrical energy in power stations. But also those indirect CO_2 emissions which are created by the energy consumption needed by supplying material, material processing, maintenance, and waste disposal have been taken into consideration [27]. In TEWI analysis, the CO_2 emission per kW of generated energy is taken into consideration for the calculation of indirect TEWI contribution. The CO_2 emission for the production of electricity is dependent upon the mixture of energy carriers used in power plants. The burden on the Earth's climate resulting from the greenhouse effect is a global problem. The study is based on published data on CO_2 emissions from power plants and utilizes the average value for the regions of North America, Japan, and Europe. In this study, the average value is 0.47 kg CO_2/kW [26].

Results and Discussion

In this study, energetic, exergetic, and environmental effects of the subcooling and superheating applications of the system with different refrigerants and under adiabatic conditions by taking a DX system as the model have been examined. The subcooling and superheating temperatures in the study have been taken respectively as 0 and 5 K. The cooling capacities of DX systems vary between 20 and 1,000 kW. The study takes as reference 836 kg charge amount in the cooling system of a market with a sales area of 3,500 m^2 for the evaluation of environmental effects. When the market cooling is examined, we see that the evaporator temperature ranges between −35 and 0 °C. However, the most popular range −25 to 0 °C has been accepted as the evaporator temperature in the study. The study examines COPs to evaluate the energetic performances in the unit cooling load depending on the refrigerants taken as reference. Figure 68.3 includes the COP breakdown of the system for the subcooling and superheating application in the range of 0 and 5 K.

It has been observed that the subcooling and superheating application have direct effects on energetic performance. However, the fluid has an important part in this effect. It was observed that the COP performance of the R-22 gas restricted by the international society increased by 4.25 % in average in the range of 0–5 K. R134a gas which is used commonly in many systems from domestic applications to vehicle air conditioning has better COP performance by 6.17 %. R-404A, which is very common in commercial applications and especially in market applications, has a significant increase of 10.37 %. The exergetic performances of each gas per unit cooling load have been individually examined, and the results are given in Fig. 68.4.

Exergy analysis is an important tool in defining the irreversibilities in system as well as in defining the effects on the irreversibilities depending on subcooling and superheating applications in this type of systems. Refrigerant effects were also observed in the improvement ratios in the exergetic efficiency of the system for base cooling capacity. In current
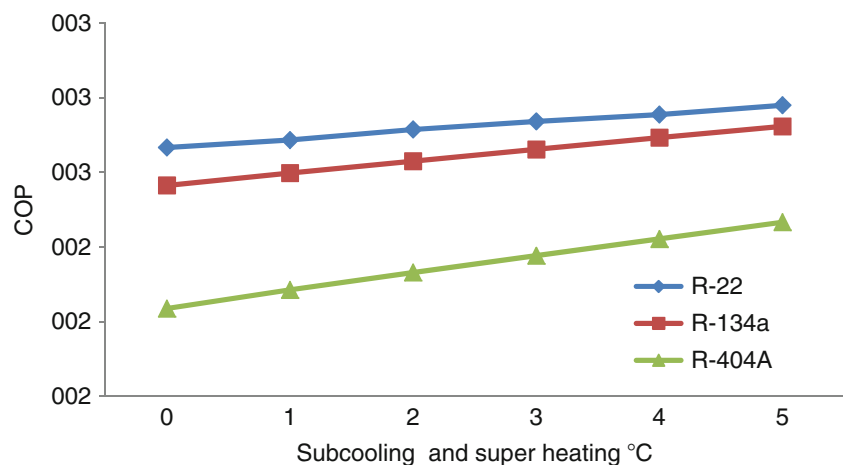
Fig. 68.3 COP distribution of refrigerants based on subcooling and superheating temperatures
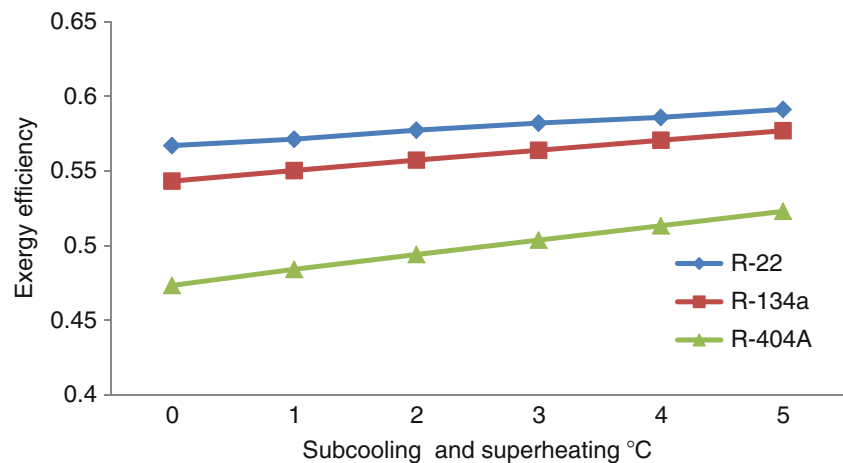
Fig. 68.4 Exergy efficiencies of refrigerants based on subcooling and superheating temperatures

Fig. 68.5 Exergy efficiencies of refrigerants based on subcooling and superheating temperatures
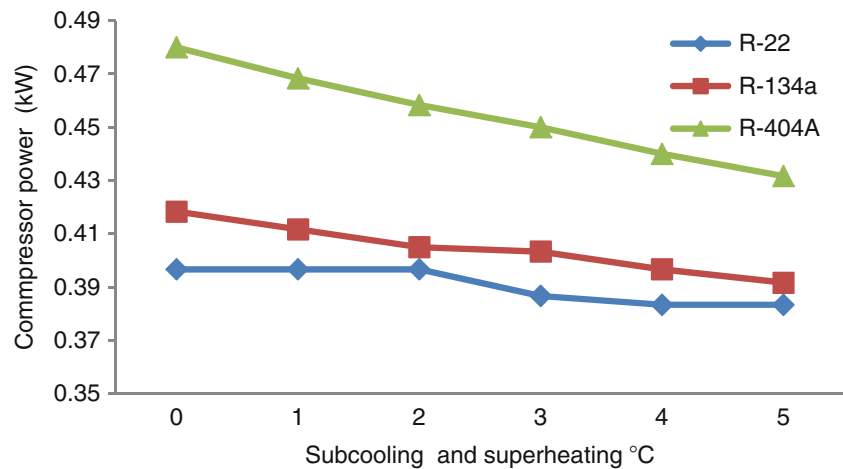
Fig. 68.6 Mass flow changes of refrigerants based on subcooling and superheating temperatures
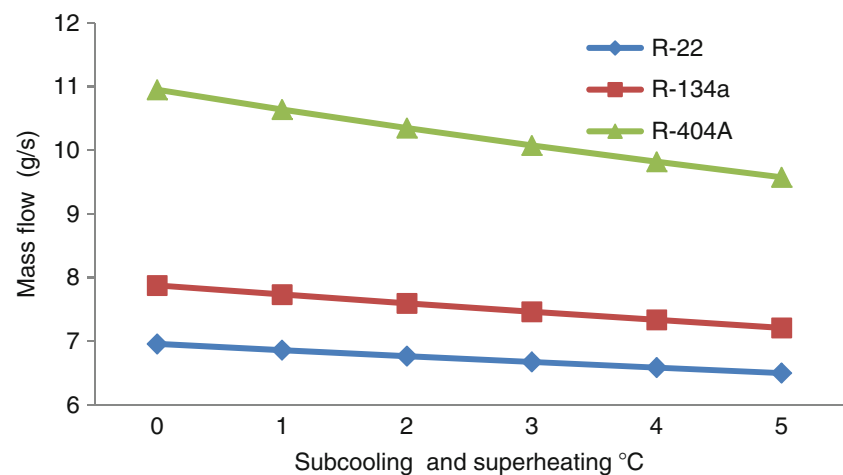
applications, the average change ratio of exergetic efficiency in systems using R-22 gas is 4.27 % for the superheating application. This effect was determined as 6.22 % in the systems using R-134a. However, the highest effect for the R-404A gas which is intensively used in market applications was found as 10.50 %. The increase ratios for both COP and exergetic efficiency are defined with the energy consumption values in the systems. Therefore, the effects of the subcooling and superheating values for each refrigerant were examined, and the results are given in Fig. 68.5.

The change in the power consumptions in the systems has different effects for each fluid. It is seen that the highest change is valid for the systems using R-404A gas. There is 10.07 % decrease in average in the energy consumption for the unit cooling capacity in the systems using this gas. In these systems, the change was found linear for each temperature increase in the subcooling and superheating application. A decrease of 6.38 % in average was determined in the energy consumption for the systems using R-134a gas. This effect has a 3.36 % degree for systems using the least R-22 gas. However, even this effect is an important potential when the full cooling loads are evaluated. In fact, the most important effect in the subcooling and superheating application can be determined as providing the sustainability of the system thermodynamic parameters by creating flow control. This effect causes a decrease in the flow rates. The change in mass flows for each refrigerant in the subcooling and superheating application was examined and the results were given in Fig. 68.6.

For the maintenance and repair process of systems and increase of efficiency, the fluid is charged usually with the pressure value taken as basis. However, due to the temperature-based change of effectiveness, optimum point is usually exceeded and high charge is perceived as an advantage. For some operation temperatures, this effect causes excessive work of the compressor and high energy consumption. In the subcooling and superheating application, it also affects the charge ratio in low flow systems due to temperature and because it controls the vapor phase into the compressor. The highest decrease in this effect has been determined as 12.55 % in systems using R-404A gas. This effect has been found to be 8.44 % for the R-134a gas and 6.57 % for the R-22 gas.

Fig. 68.7 TEWI changes of refrigerants based on 3 % leakage rate
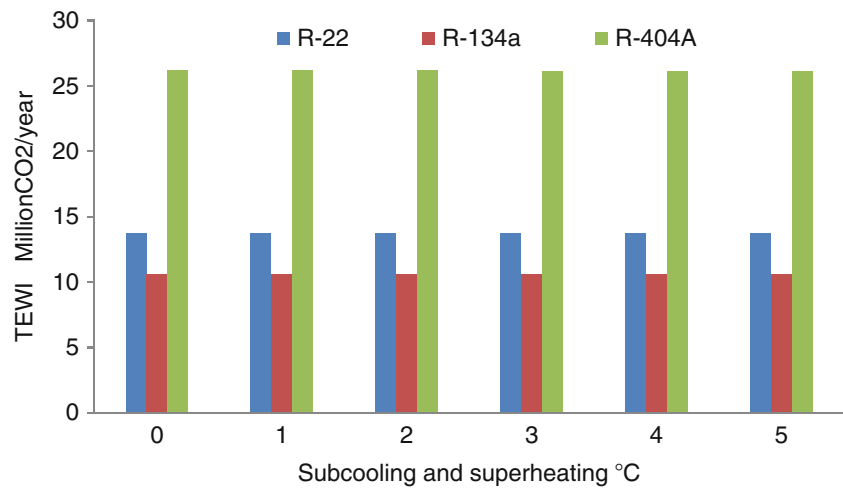
Fig. 68.8 TEWI changes of refrigerants based on 30 % leakage rate
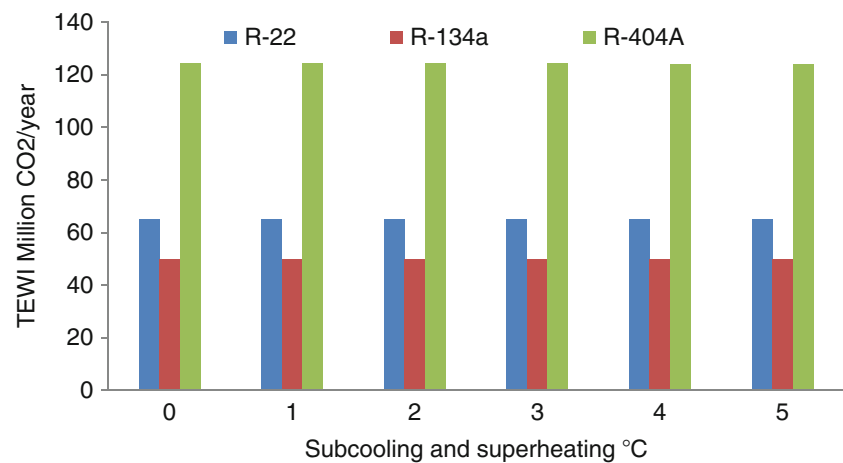
Market applications are systems with intensive refrigerant charge. The most important environmental effect in these systems is the direct effect based on the leakage ratio of the refrigerant. These effects are subject to indirect emission releases caused by the energy consumptions of the system. However, the most important actual effect in the system performances is the fluids. The GWP potentials of fluids have direct influence on the effect based on the leakage ratio in the emission releases. It is seen that the lowest and highest leakage ratio are in the range of 3–30 % in the market applications. In the study, the TEWI values have been calculated separately taking the refrigerants as reference for both peak points. Figure 68.7 includes the change of TEWI values for the subcooling and superheating applications in the 3 % leakage ratios.

When we consider the refrigerants, we noticed that the effects of the subcooling and superheating application are very limited. This effect is limited by 5.88×10^{-2} % for the R-22 gas, by 15.28×10^{-2} % for the R-134a gas, and by 11.19×10^{-2} % for the R-404A gas. This limited effect is caused by the indirect effect of the energy change on the emission potential. In this type of systems, emission potential based on the refrigerant is important. Especially the TEWI value of the R-404A gas, which is heavily used in market applications, has the highest degree as 26.17 million CO_2/year. It has a 47.50 % higher emission potential than that of R-22 gas, which is replaced in this kind of systems. Similar TEWI analyses have been conducted for the leakage ratio of 30 % and the results are given in Fig. 68.8.

The increase in the leakage ratio increases the direct effect on emission. However the emission effect of the subcooling and superheating application is a decreasing effect for all fluids. The study found the average increase for the subcooling and superheating temperatures for the R-22 gas, R-134a gas, and R404A gas to be 0.25×10^{-2} %, 3.25×10^{-2} %, and 2.36×10^{-2} %, respectively. For the 30 % leakage ratio, the R404A gas has a higher potential of 47.78 % than the R-22 gas. However, the emission potential of the R-134a gas has 30.6 % less effect than the R-22 gas and 60.04 % less effect than the R-404A gas.

Conclusions

The energetic, exergetic, and environmental effects of the subcooling and superheating applications for different refrigerants in the DX system taken as reference in this work have been examined separately. The main conclusions drawn from the results of the present study may be as follows:

- Depending on the refrigerants, the subcooling and superheating applications cause an increase of around 10 % in the energetic and exergetic performances of the systems.
- Depending on the choice of refrigerants, an effective subcooling and superheating application causes a saving of up to 10 % in the energy consumption.
- The subcooling and superheating application controls the mass flows of the systems and increases the compressor performance in particular. This prevents the unnecessarily high cooling charge.
- The subcooling and superheating application has a very limited effect in the total emission effect of the system. However, the choice of refrigerant has direct effect on the TEWI value.

In conclusion, an effective subcooling and superheating application has direct effect on the energetic and exergetic performance of the system. The choice of refrigerant also has direct effect on the energetic, exergetic, and environmental performances. Therefore, choice of correct system as well as natural fluid choice together with low GWP value will further increase these effects.

References

1. ECCJ (2002) Energy Conservation Center, Japon. http://www.eccj-or-jp/summary/local0303/eng/03-01.html, http://www.eccj-or-jp/databook/2002-2003e/03-04.html, http://www.eccj-or-jp/databook/2002-2003e/03-05.html
2. Baxter VD (2003) Advances in supermarket refrigeration systems. Oak Ridge National Laboratory, Oak Ridge, TN. www.arb.ca.gov/cc/commref/adv_supmkt_ref_syst.pdf
3. Van Baxter D, Walker DH (2003) Analysis of advanced low-charge refrigeration for supermarkets. ASHRAE Trans 109:8
4. IPCC/TEAP (2005) Refrigeration, draft of IPCC/TEAP special report on ozone and climate, Chapter 4, Intergovernmental panel on climate change/technology and economic assessment panel. Cambbridge Üniversitesi, New York, NY
5. Arthur D. Little, Inc. (ADL) (2002) Global comparative analysis of HFC and alternative technologies for refrigeration, air conditioning, foam, solvent, aerosol propellant, and fire protection applications. Final report to the alliance for responsible atmospheric policy 2002. http://www.arap.org/adlittle/HFCstudy3-22JD.pdf
6. IEA (International Energy Agency) (2003) IEA Annex 26: advanced süpermarket refrigeration/heat recovery systems. Final report, vol 1—executive summary, compiled by Van D. Baxter, Oak Ridge National Laboratory
7. Energetic (2012) The effect of sub-cooling on refrigeration processes. Energistics.biz, Carlsbad, CA. www.energistics.biz/pdf/SubCoolingEffect.pdf
8. Schijnel PPAJV, Kasteren JMN, Janssen FJJG (1998) Exergy analysis—a tool for sustainable technology—in engineering education. Eindhoven University of Technology, Eindhoven
9. Dincer I, Rosen MA (2005) Thermodynamic aspects of renewable and sustainable development. Renew Sustain Energy Rev 9:169–189
10. Dincer I, Rosen MA (2007) Exergy, energy, environment and sustainable development. Elsevier, Oxford
11. Kanoglu M, Dincer I, Rosen MA (2007) Understanding energy and exergy efficiencies for improved energy management in power plants. Energy Policy 35:3967–3978
12. Hepbasli A (2010) A review on energetic, exergetic and exergoeconomic aspects of geothermal district heating systems (GDHSs). Energy Convers Manag 51 (10):2041–2061
13. Koroneos CJ, Nanaki EA, Xydis GA (2011) Exergy analysis of energy use in Greece. Energy Policy 39(5):2475–2481
14. Wall G (2003) Exergy tools. In: Proceedings of the ınstitution of mechanical engineers. Wilson Applied Science and Technology Abstracts Plus Text, p 125–136
15. Sogut MZ (2012) A research on exergy consumption and potential of total CO_2 emission in the Turkish cement sector. Energy Convers Manag 56:37–45
16. Rhiemeier JM, Kauffeld M, Leisewitz A (2009) Comparative assessment of the climate relevance of supermarket refrigeration systems and equipment. Environmental research of the federal ministry of environment nature conservation and nuclear safety research report 206 44 300, UBA-FB 001180/e, March, Federal Environmental Agency
17. SERDP (1999) Refrigerant subcooling, technology for improving cooling system performance. U.S. Department of Energy by the Pacific Northwest National Laboratory. www.eren.doe.gov/femp/
18. Sogut MZ, Oktay Z, Karakoc H (2012) Investigation of the effects of leakage rate on exergetic and environmental performances of refrigerants in the direct expansion system. In: Global conference on global warming, İstanbul
19. Sogut Z (2011) A study on the exergetic and environmental effects of commercial cooling systems. Int J Exergy 9(4):414–434
20. Akpinar EK, Hepbasli A (2007) A comparative study on exergetic assessment of two ground-source (geothermal) heat pump systems for residential applications. Build Environ 42:2004–2013
21. Cengel Y, Boles MA (2001) Thermodynamics: an engineering approach, 4th edn. McGraw-Hill, New York, NY
22. Van Gool W (1997) Energy policy: fairly tales and factualities. In: Soares ODD, Martins da Cruz A, Costa Pereira G, Soares IMRT, Reis AJPS (eds) Innovation and technology—strategies and policies. Kluwer, Dordrecht
23. Hammond AJ (2001) Stapleton, exergy analysis of the United Kingdom energy system. Proc Inst Mech Eng 215(2):141–162
24. Horst K (2000) Refrigerant use in Europe. ASHRAE J. www.ashraejournal.org
25. DUPONT (2005) Dupont refrigerants the science of cool. Du Pont de Nemours (Deutschland) GmbH, Germany. www.refrigerants.dupont.com
26. Hellmann J, Barthélemy P (1997) AFEAS-TEWI III study: results and evaluation of alternative refrigerants. Solvay Fluor und Derivate GmbH Technical Service-product Refrigerants, Bulletin no. C/11.97/06/E, p 5
27. Eurammon (1996) Evaluation of the environmentally friendly refrigerant ammonia according to the TEWI concept, NH_3 for ecologically friendly future, Frankfurt. http://www.eurammon.com
28. Aleph Zero (2012) Refrigeration, a simple practical cycle. http://www.alephzero.co.uk/ref/practcyc.htm

Investigation of Exergetic and Environmental Performance of HFCs with 20-Year and 100-Year GWP Metric

M. Ziya Sogut

Abstract

In recent years, Hydroflourocarbons (HFCs) used instead of CFCs, which have become the dominant in the refrigeration sector, have lower ozone depletion potential (ODP) than CFCs. However, they have worse performance from CFCs considering COP, exergy efficiency and global warming potential (GWP). Besides, their CO_2 equivalent emission potentials are also higher when GWP potentials taken into consideration.

In this study, first, COP and exergy efficiencies of HFCs are examined considering unit cooling capacity and evaporator temperature −20 °C and 10 °C. Then, the total equivalent warming impact (TEWI) of each refrigerant as depending on the metric values of GWP 20 and 100 years is calculated. Besides, the changes of COP, exergy efficiency and TEWI for each refrigerant according to R-22 are examined separately. Furthermore, for each refrigerant, the changes according to R22, which are taken as reference refrigerant, are examined separately. In the end of the study, the assessments and recommendations about environmental performances of HFCs, which have higher GWP than R-22 gas, have been made.

Keywords

Refrigerants • HFCs • Exergy • Global warming potential • TEWI

Introduction

Refrigerants, solvents, foams and fire extinguishers are important substances causing ozone depletion and global warming considering effects of climate change [1]. It is noticed that PFCs (perfluorocarbons) and SF6s (sulphur hexafluorides) are used heavily in the production process of these substances with intensive use of hydrofluorocarbon (HFC). The GWPs (global warming potentials) of these gases are far more effective than their CO_2 emissions and their atmosphere life reaches to 1,000 years. Refrigerants are the ones using the HFCs most.

The air condition and cooling sector takes around 9 % of the world's energy consumption and it is a sector where its emission effects caused by refrigerants are discussed in recent years with respect to sustainable life and environment [2]. The consumption of refrigerants is increased in order to meet the comfort requirements needed in the varying environmental conditions as well as the demand increase in the air conditioning and cooling systems due to economic requirements. This increase indirectly causes an increase in the energy demand and emission potentials. Likewise, the refrigerant effects reached to around 80 % in 2010 with 94.5 MMTCE (million metric tons of carbon equivalent). Estimations indicate that this effect will continue with similar rates in 2020. These gases are followed by foams around 12.27 % with 14.44 MMTCE [3].

It has been an international concern to ensure the control of production and consumption of the refrigerants which are important catalysts in the weather change based on global warming and ozone layer depletion (ODP) with the emissions they

M.Z. Sogut (✉)
Technical and Computer Applications Center, Military Academy, Ankara, Turkey
e-mail: mzsogut@yahoo.com

caused. For decreasing this effect, Montreal Protocol and European Council Directive (3093/94) restricted the use and sales of hydrochlorofluorocarbon (HCFC) and chlorofluorocarbon (CFC) gases that were used as safe fluids instead of refrigerants like ammonium which was commonly used in cooling systems during 1930s [12]. As an alternative to them, HFCs and their mixtures like R-134a, R-404A, R-507, R-407C and R-410A started to be widely used in market applications. However, despite their low ODP potential, these gases have high GWP and this condition shows a problematic process with respect to environmental impact and global warming [4].

The air conditioning and cooling systems, thermodynamically inappropriate system choice, wrong assembly, missing and wrong capacity determination, repair and maintenance activities, uncontrolled leakages and similar irreversibilities based on many effects cause more emission release. In determining the emission effects of the system, the method of Total Equivalent Warming Impact (TEWI) developed for the objective is a methodology for evaluation of greenhouse gases especially CO_2 emissions for cooling applications [5, 6].

This study examines separately the changes for the 20 and 100 years of GWP values of the emission potentials caused by gases with their thermodynamical performances including the irreversibilities under unit cooling load of the HFC fluids used in the air conditioning and cooling applications.

Air Conditioning and Cooling Systems and HFCs

Air conditioning and cooling systems find wide application area like house type, commercial, industrial, vehicle air conditioning and transportation (land, sea, air), cooling applications. Among these application areas, refrigerant amounts vary from 50 g to several tons depending on the cooling capacities of the refrigerant systems [5].

It is observed that steam compressed cooling cycle is taken as basis throughout these cooling systems. This model operating on a cycle in thermodynamical process is taken as basis in the study. In the cooling cycle, the refrigerant having low pressure is increased to the high pressure and sent the condenser by the compressor. Condensation starts in the condenser and the refrigerant turns to liquid under low pressure through the expansion valve. Cooling takes place here with the effect of the heat from the internal environment and the fluid comes to the compressor with the steam phase [7]. Cooling performance is affected by the capacitive qualities of the mechanical system preferred in the system. However, the effect of the cooling fluid is important. Choice of refrigerant for a system should include a safe quality where the toxic and combustible effects are taken into consideration. On the other hand, performance parameters should also be taken into consideration where atmospheric life, GWP and OD qualities, exergetic efficiency, mechanical qualities and investment costs are taken into consideration.

Together with the development of the evaporation compressed cooling cycles starting from 1990s, CFCs being used to replace refrigerants like ammonium in cooling systems were replaced through the course of time by HCFC gases with higher performance than CFCs like R22. The CO_2 equivalent emissions caused by these gases became important catalyst for ODP and global warming, which affects climate change. For decreasing this effect, Montreal Protocol and European Council Directive (3093/94) restricted the use and sales of HCFC ve CFC gases that were used as safe fluids instead of refrigerants like ammonium which was commonly used in cooling systems during 1930s [4]. Nevertheless there is a tendency of decrease in recent years in the use of these gases since 1994. Figure 69.1 includes the breakdown of refrigerants between 1990 and 2006.

The refrigerant capacity consumed between 1990 and 2006 had an increase of around 120 %. In this process, it is seen that the CFC gases with rather bad environmental parameters are in a declining tendency but the use of HFC gases is becoming more and more widespread while the sector mainly prefers HCFC gases [8–10]. In this flow trend, a consumption of around 566 k tons is expected in the developed countries as at the end of 2013 with respect to the consumption of HCFC gases that are being used. This value is around 3.4 times more than the CFC gases. This effect unfortunately indicates that the use of HCFC gases will continue in the sector. However, it can be said that this effect is low especially in developed countries and that HFC gases are preferred instead.

As to the refrigerants, GWP is a valid measurement for the greenhouse gas emissions equal to the CO_2 emissions of a refrigerant for a specific time period. This measurement is usually important for the decision it makes while UNEP/IPCC (United Nations Environment Programme/Intergovernmental Panel on Climate Change) required three different time zones for the GWP values, namely 20 years, 100 years and 500 years. Among these values, GWP20 has been a reference measurement for the short evaluations and decisions. For potential analyses, usually GWP100 is used. GWP500 is a valid measurement in the assessment of long-term scenario. Table 69.1 includes the GWP20 and GWP 100 values, and distribution of HFC gases per usage areas are becoming dominant in the sector with respect to the air conditioning and cooling systems.

Fig. 69.1 Refrigerant breakdown between 1990 and 2006 [8]
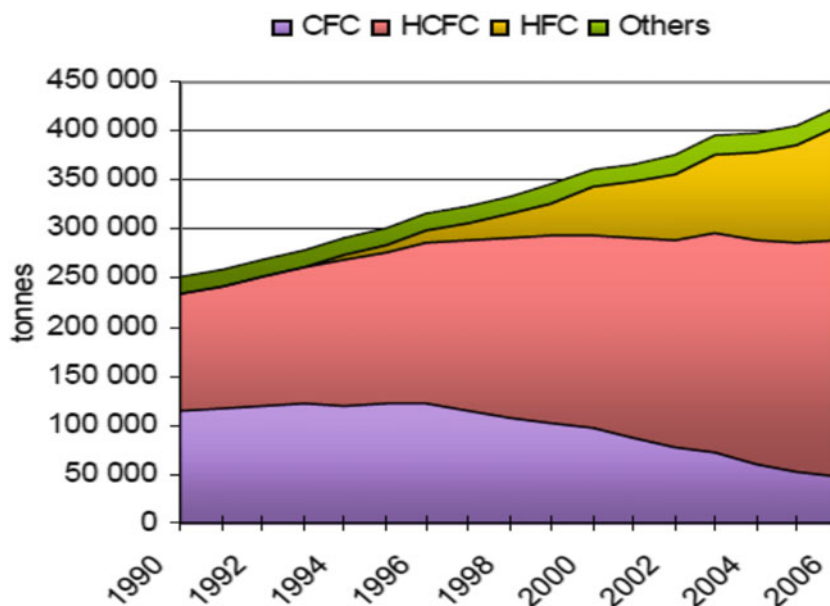
Table 69.1 The most commonly used HFCs [11]

HFC-refrigerant	Applications	20-year GWP	100-year GWP
R-23	Low temperature refrigerant	12,000	14,800
R-32	Blend component of refrigerants	2,330	675
R-125	Blend component of refrigerants	6,350	3,500
R-134a	Refrigerant in domestic refrigerators, mobile air conditioning, stationary air conditioning, blend component of refrigerants, foam blowing agent, aerosol propellant	3,830	1,430
R-143a	Blend component of refrigerants	5,890	4,470
R-152a	Blend component of refrigerants, foam blowing agent, possible future refrigerant	437	124
R-227ea	Refrigerant	5,310	3,220
R-245fa	Foam blowing agent Possible future refrigerant	3,380	1,030
R-365mfc	Foam blowing agent Possible future refrigerant	2,520	794
R-404A	Refrigerant blend: a leading alternative to HCFC-22 in air conditioning and commercial cooling	6,010	3,922
R-410A	Refrigerant blend: a leading alternative to HCFC-22 in air conditioning, transport refrigeration	4,340	2,088
R-407C	Refrigerant blend: a leading retrofit alternative to HCFC-22 in air conditioning, transport refrigeration	4,115	1,774
R-507	Refrigerant blend: a leading alternative to HCFC-22 in air conditioning and commercial cooling	5,700	3,300

Today, refrigerant solvents, foams and fire extinguishers are defined as the most important items strengthening the global warming effect and causing ozone consumption [1]. The global warming effects and distribution of these items are given in Fig. 69.2.

In the production processes of these items with heavy HFC use, PFCs and SF6s are heavily used. Mainly the GWP effects of these gases are more effective than the CO_2 effects and the atmosphere lives of these gases reach to 1,000 years. Among them, the effects of the refrigerant reached to 80 % with 94.5 MMTCE (million metric tons of carbon equivalent) in 2010. The estimates indicate that this effect will continue with the same rates also in 2020. These gases are followed by foams by around 12.27 % with 14.44 MMTCE [11].

In the sector based on emission calculation, different models are preferred in many countries. For instance, the Vintanging model developed by the energy environmental agency where data are collected from sectors based on the simulation of the ozone depletion values of the refrigerants in the USA are used is found in the European Union by dividing the gross local product cost of each country to the individual consumption of European Union member countries. In other countries, ozone consumption estimates of the countries from the UNEP are used.

In scenarios created for the projection estimates, economic growth ratio, ozone consumption ratio and sector date of the country are used together with the ozone consumption values stated in the Montreal protocol or UNEP. For the calculation of

Fig. 69.2 Items with high ozone consumption and global warming effect [1]
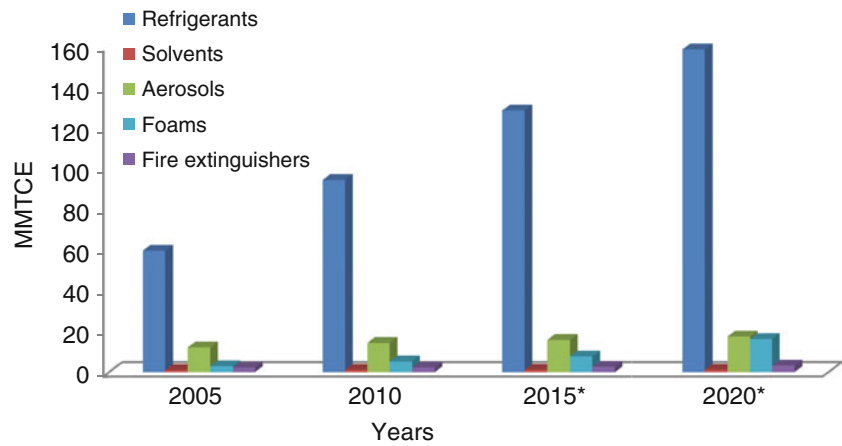
the emission effects of the cooling systems in the sector, there are two categories namely the emission during the equipment life time and emissions released in scrap status. In the first approach, the leakage ratios and service processes of the fluids are taken into consideration. In the second approach, the emissions released as a result of exposure of system equipment are calculated.

Emission Analyses for Cooling Systems

For the emission analysis of systems, usually the TEWI system where a cooling system is evaluated from an integral point of view and the *Potential Emissions of System Components* approach where each system component is evaluated from production to scrap process are taken into consideration. This process defined by IPPC is an evaluation method which is taken separately for each system component. Emission effect in the production process of this type of systems is an effect depending on the fluid transfer and has a very low direct emission effect of 5–10 %. During the life of the systems, emission effect, charge amounts, repair and maintenance processes are effective. Emission effect for each element in systems during repair, maintenance and operation process can be calculated as follows [1].

$$E_{s_J} = (I_a - I_s) \sum_{i=1}^{i=k} Q_{C_{J-i+1}} \qquad (69.1)$$

Here,
E_s: Emissions of the equipment serviced
l_a: Annual leakage ratio (normal operation process)
l_s: Service leakage ratio (service process)
Q_c: Quality of the chemical used in the new equipment (total charge amount of the specific item)
j: emission year
i: life process index
k: lifetime process

Scrap process of an element is also a cause of emission in the cooling system. Calculation of the emission defined as scrap emission is based on the assumption that the scrap element releases a certain amount of existing fluid inside to the atmosphere. Scrap emission:

$$E_{d_J} = Q_{C_{J-k+1}} [1 - (r_m * r_c)] \qquad (69.2)$$

Here
$E_d = $ *Emission of the scrap element.*
Qc $= $ Quality of the chemical used in the new equipment (total charge amount of the specific item)
$r_m = $ The remaining fluid amount (depending on the total fluid)
$r_c = $ The recycle ratio of the remaining fluid

Total emission potential for a cooling cycle is defined as the total of the scrap emission potential and emission potential during lifetime. Total emission potential:

$$E_J = E_{s_J} + E_{d_J} \tag{69.3}$$

The energy consumption of the system is also effective according to the preferred fluid. The emission effect in this process is defined as the indirect effect based on energy. It is noticed that emission effects of the refrigerant groups are evaluated in many organizations including the Montreal protocol and that the projections of these items are conducted [1]. However, there have been different approaches for the evaluation of the emission potentials of the cooling systems by taking lifetime processes into consideration. Among them the most popular one is the TEWI method.

TEWI Concept

At the meeting in Copenhagen, a concept for evaluating the total sum of global warming caused by refrigeration systems, namely through refrigerant emissions and also through CO_2 emissions from the fossil fuel power plant which produces the energy for the refrigeration system was presented. It is called the TEWI and was developed by the US Department of Energy and Oak Ridge National Laboratories [12].

An appropriate method of evaluating any refrigerant is the TEWI value, as defined in EN 378:2,000. This is an internationally accepted formula that may be used to directly compare the relative effect of different systems. It represents the environmental effects, based on the GWP of the refrigerant, and energy consumption for the plant over its lifetime. The higher the TEWI value (kgCO$_2$/year), the poorer the system in terms of its overall impact on the environment:

$$TEWI = \underbrace{\underbrace{[\,GWP.L.n\,]}_{Leakage \ losses} + \underbrace{[GWP.m.(1-\alpha_{recovery})]}_{Recovery \ losses}}_{Direct \ GWP} + \underbrace{[\,n.E_{annual}.\beta\,]}_{\substack{Energy \ consumption \\ Indirect \ GWP}} \tag{69.4}$$

where *TEWI* is the total equivalent warming impact, *GWP* is the global warming potential, *L* is the amount of leakage, n is the system operating time, m is the refrigerant charge, $\alpha_{recovery}$ is recovery or recycling factor, E_{annual} is the annual energy consumption, β is CO_2 emission produced by power generation [13].

The global warming effects of different substances are compared with carbon dioxide using an index known as the global warming potential or GWP. The GWP of a substance of the global warming impact due to the emission of 1 kg of that substance is divided by the global warming impact of 1 kg of carbon dioxide; both effects are measured over a 100-year time span [14].

The entire climatically relevant impact by the refrigeration process is composed of direct and indirect emission of greenhouse gases. The direct impact includes the emission of working substances by the greenhouse effect due to leakages, maintenance and losses during disposal. The indirect impact is related to the CO_2 emissions, particularly due to the generation of electrical energy in power stations. And also those indirect CO_2 emissions which are created by the energy consumption needed by supplying material, material processing, maintenance and waste disposal have been taken into consideration [15]. In TEWI analysis, the CO_2 emission per kW of generated energy is taken into consideration for the calculation of indirect TEWI contribution. The CO_2 emission for the production of electricity is dependent upon the mixture of energy carriers used in power plants. The burden on the Earth's climate resulting from the greenhouse effect is a global problem. The study is based on the published data on CO_2 emissions from power plants and utilizes the average value for the regions of North America, Japan and Europe. In this study, the average value is 0.47 kg CO_2/kW [16].

Results and Discussion

TEWI values for widely used HFC fluids have been taken individually in the study based on the vapour-compressed cooling cycle taken as a model. R-22 gas has been taken as a reference fluid in the performance evaluation of the HFC fluids. Basic operation parameters for a cooling system with vapour compression considered under adiabatic conditions are accepted as given in Table 69.2.

Table 69.2 Cycle parameters

Parameters	Units	Values
Evaporator temperature.	(°C)	−10/0
Evaporator superheating	(°C)	0
Condenser temperature	(°C)	45
Condenser superheating	(°C)	0
Refrigerating capacity	(kW)	1
Leakage rate	(%)	Min (%3), max. (%30)

Fig. 69.3 COP distributions of HFCs and R-22 refrigerant
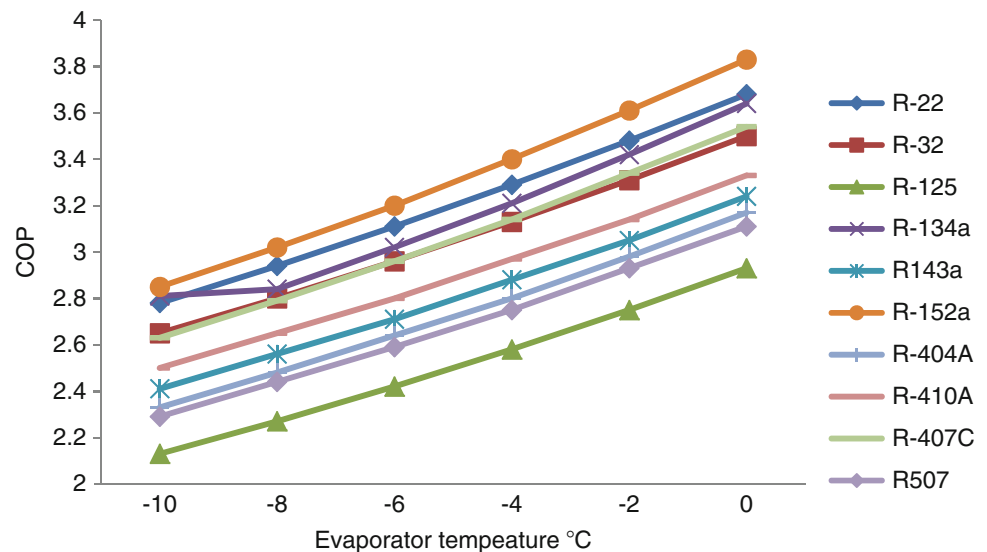
In the study, the R-227 and R-365 refrigerants have different operation parameters than the other HFC fluids. For these gases, the evaporator and condenser temperatures have been examined for the temperatures between −10 and 35 ºC. However, it is not given here considering the shortness of the work. However, the mass flow for the refrigerants is 6.678 g/s for R-22 gas for unit kW while it varies between 7 and 12 g/s. While refrigerant charge of 0.22 kg per kW cooling for R-22 gas is sufficient, these values for HFCs are not below 0.45 g/s. However, the fluid charge amount is an important parameter for the TEWI values. Determination of these values is a variant for each system. The charge amount in the system has been evaluated in proportion with the flow speed.

COP and exergy values of each refrigerant have been examined in the study for each cooling load. Then the improvement potentials of each fluid are taken into consideration and the emission analyses have been examined in detail. Figure 69.3 includes the COP distributions based on evaporator temperatures between −10/0 °C of the R-22 gas together with the HFCs examined.

COP values of the R152a are the highest among the HFCs in the study. The performances of other HFCs are below the R-22 gas. The performances of the widely used R134a, R404a and r-410a refrigerants are worse than the R-22 gas with values 1.8 %, 17.56 % and 10.87 % respectively. In addition, the R-123 and R-507 gases have the worst COP values with 2.5 and 2.91 respectively. Exergetic performances of HFCs have been examined separately and the results are given in Fig. 69.4.

R-152a gas is prominent among the exergy efficiencies of HFCs. The average exergy efficiency of 59.55 % of this gas has a 5.06 % better performance than the R-22 gas. In addition, it is seen that the R-152a gas has 5.06, 21.44 and 14.46 % better performance than the R-134a, R-404A and R-410A gases which dominate the market. R-407C gas has a high performance after the R-152a and R-134a gases among HFCs. Among them, R-125 gas has a performance of 46.53 % and R-507 gas has a performance of 49.72 %.

Like in the thermal processes, high entropy is the biggest source of irreversibility in processes. In this type of processes, energy recycle is an important factor not only in efficient operation of the processes but also in the decrease of energy costs and sera gas emissions. Therefore, improvement potentials of the HFCs were examined together with the R-22 gas. Figure 69.5 includes the compressor consumption together with the recycling potentials.

General average (0.3494 kW) of power consumption for each kW cooling capacity of HFCs has 11.53 % worse performance when compared to the R-22 gas. When we consider the dominance of HFCs in the cooling sector, general

Fig. 69.4 Exergy efficiencies of HFCs and R-22 refrigerant
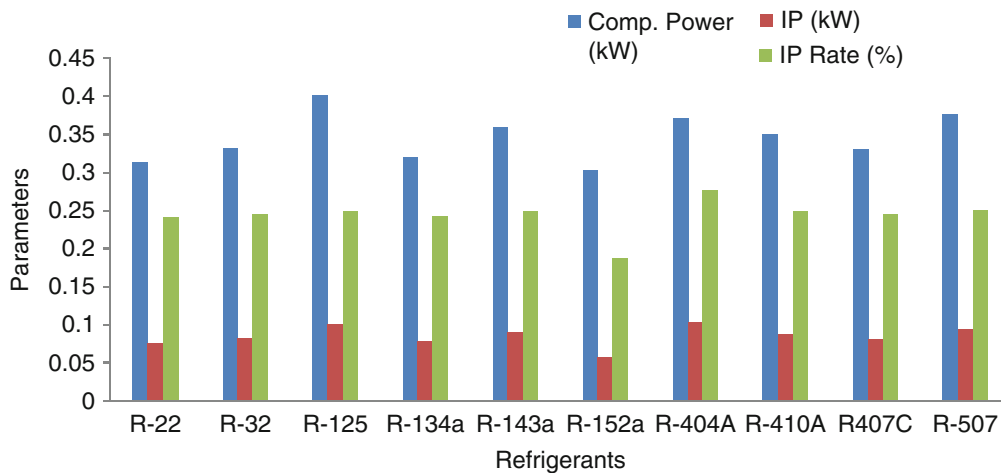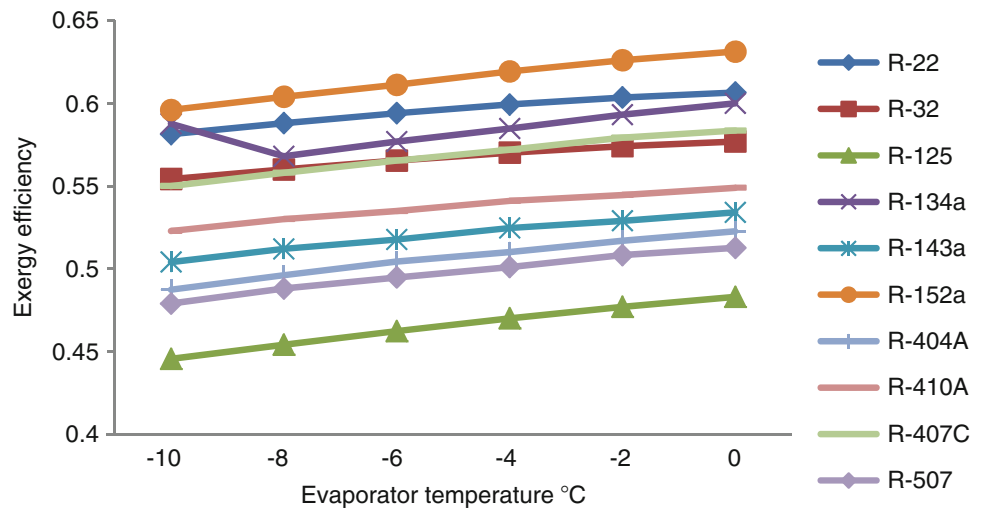
Fig. 69.5 Compressor power, improvement potential and rates of HFCs and R-22 gas

energy consumption has also increased accordingly. However, R-152a gas has the best performance with 0.3033 kW for the −10 °C/0 °C evaporator temperature with respect to power consumption among HFCs. This gas is followed by R-134a gas with 0.32 kW and R-407C gas with 0.33 kW.

Despite the ozone depletion in HFC fluids is zero, most of them have high emission potentials due to high GWP value. The TEWI effects of these gases have been examined separately according to the minimum and maximum values. The leakage ratios for the TEWI effects have been taken as 3 % and 30 % respectively according to minimum and maximum values, and the $\alpha_{recovery}$ values have been taken as 3 and 30 % respectively. Depending on these assumptions, TEWI values of the refrigerants for GWP20 have been found and the results have been given in Fig. 69.6.

The average TEWI values of HFCs for the GWP20 potentials have been found as 34,134.6 kgCO$_2$/year. When this value is considered with R-22, it is a higher value with 47.92 %. This increase is not valid for all HFCs. Among them, only R-152a gas is below R-22 with its value of 19,326.4 kgCO$_2$/year. The R-125 and R-507 gases have 1.83 and 2.31 times higher TEWI values compared to R-22. Similar analyses have been done for GWP 100 and the results are given in Fig. 69.7.

The TEWI values of HFCs according to GWP100 have been calculated as 23,063.78 kgCO$_2$/year for 3 % leakage ratio and as 28,682.76 kgCO$_2$/year for 30 % leakage ratio. However, when the R-22 TEWI values are taken into consideration, the average HFCs have 14.30 % higher value for 3 % leakage ratio and 23.12 % higher value for 30 % leakage ratio. For GWP100, only the TEWI values of R-152a gas were found to be 3.99 and 18.94 % lower for the leakage ratios of 3 and 30 %. The TEWI values of the R-404A gas which is used heavily in commercial applications have been found as 26.73 % for 3 % and 52.24 % for 30 %.
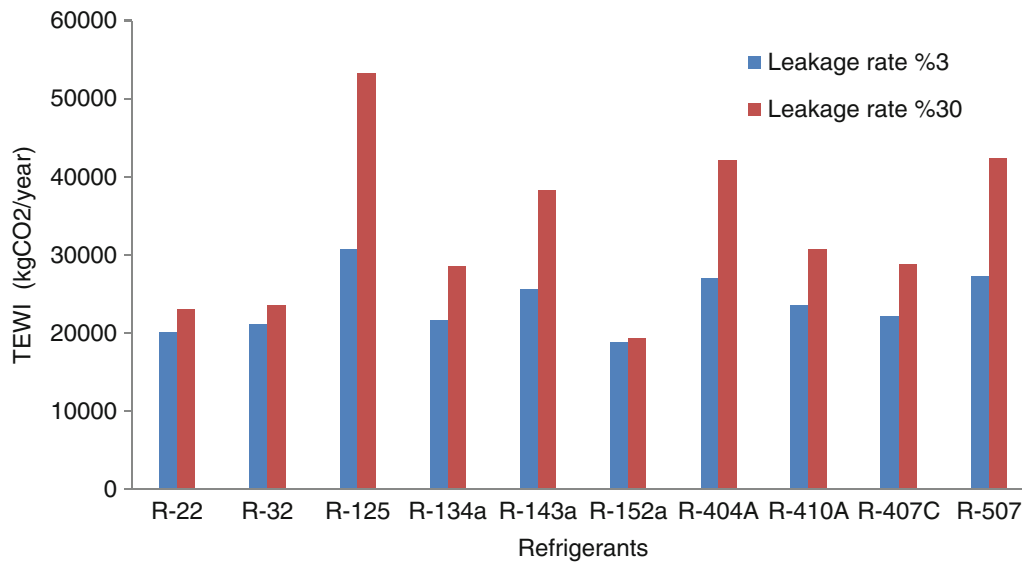
Fig. 69.6 TEWI values of HFCs refrigerants and R-22 for GWP20
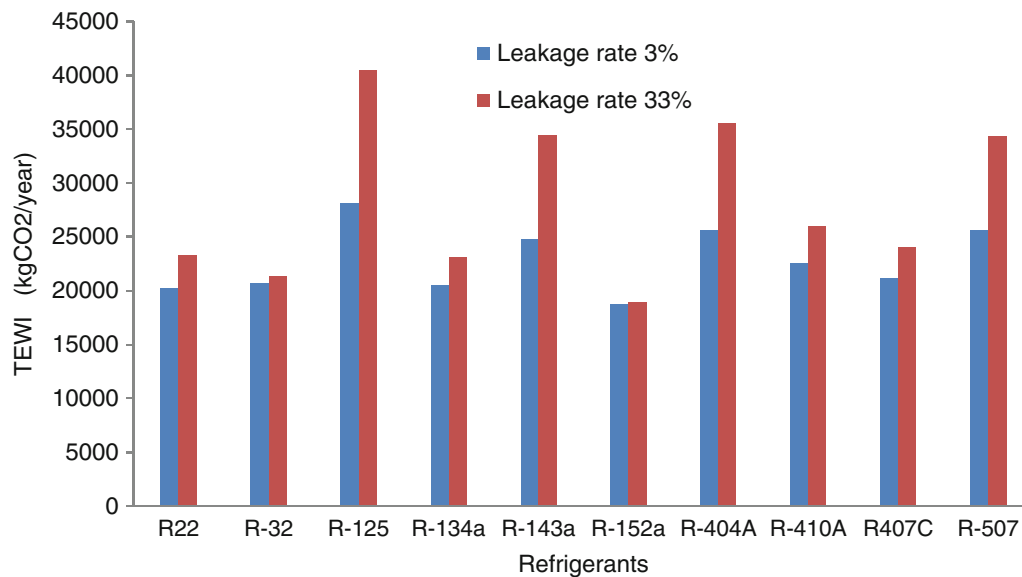
Fig. 69.7 TEWI values of HFCs refrigerants and R-22 for GWP100

Conclusions

COP and exergy efficiencies under unit cooling of the HFC refrigerants have been examined separately together with the power consumptions and irreversibility based on improvement potentials and ratios. Then the CO_2 emission equivalents based on TEWI values have been calculated. The results of the study are given below:

(a) Among HFCs, R-152a gas has the best performance with a COP value of 3.32 and exergy efficiency of 61.47. COP and exergy efficiencies of other HFCs have been below R-22.

(b) R-152a gas is more prominent with respect to compressor power consumptions and irreversibility based on improvement potentials and ratios. Among all these parameters, the worst gas was found to be R-125.

(c) For both leakage ratios, all gases except R-152a have higher TEWI values than the R-22 gas.

(d) The emission equivalent of the leakage ratio in TEWI values has been found 41.04 % higher for GWP20 and 24.36 % higher for GWP100.

Based on these results, the thermodynamic properties of HFCs except R-152a gas have higher values with respect to CO_2 emission equivalent of TEWI. In fact, these refrigerants with only low ozone depletion value should either be developed or alternative refrigerants like CO_2 should be preferred. In addition, choice of exergy analyses is important for determining borders of irreversibility in these systems and for defining the irreversibilities based on the system performances.

References

 1. EPA (2004) Determination of comparative HCFC and HFC emission profiles for the foam and refrigeration sectors until 2015 part 1—refrigerant emission profiles. Centre D'energetɪque, Paris. www.epa.gov/ozone/snap/emissions/dowloands/FoamEmissionProfiles_Part1.pdf
 2. ECCJ (2002) Energy Conservation Center, Japon. http://www.eccj-or-jp/summary/local0303/eng/03-01.html, http://www.eccj-or-jp/databook/2002-2003e/03-04.html, http://www.eccj-or-jp/databook/2002-2003e/03-05.html
 3. EPA (2004) Analysis of costs to abate international ozone-depleting substance substitute emissions, EPA 430-R-04-006. Environmental Protection Agency, Washington, DC
 4. Halozen H (2007) HFCs or the old refrigerants—what is the best choice?, XII European conference technological innovations in air conditioning and refrigeration industry, June 8–9, Politecnico of Milano, Milano. http://www.centrogalileo.net/nuovaPA/Articolitecnici/INGLESECONVEGNO/XIIConvegnoEnglish/ISESSIONE/Halozan_eng.pdf
 5. IPCC/TEAP (2005) Refrigeration, draft of IPCC/TEAP special report on ozone and climate, Chap 4, Intergovernmental panel on climate change/technology and economic assessment panel. Cambridge University, New York
 6. Arthur D. Little, Inc. (ADL) (2002) Global comparative analysis of HFC and alternative technologies for refrigeration, air conditioning, foam, solvent, aerosol propellant, and fire protection applications, Final report to the alliance for responsible atmospheric policy. http://www.arap.org/adlittle/HFCstudy3-22JD.pdf
 7. Sogut MZ, Bulgurcu H, Yalçın E (2012) Emission inventory based on refrigerants in cooling sector national air conditioning and cooling education symposium 5–7 December, Balıkesir
 8. Clodic D, Barrault S, Saba S (2010) Global inventories of the worldwide fleets of refrigerating and airconditioning equipment in order to determine refrigerant emissions. The 1990 to 2006 updating. ADEME/ARMINES Agreement 0874C0147—final report. Centre Energetɪque Et Procedes, Paris
 9. Jubb C, Bennett M, Fraser P (2002) Inventories and projections of ozone depleting and synthetic greenhouse gases used in Montreal Protocol Industries, Burnbank Consulting Pty. Ltd., Australia. www.environmental.gov.au/atmosphere/ozone/publications/pubs/burnbank-report.pdf
10. UNEP (2006) Report of the refrigeration, air conditioning and heat pumps technical options committee 2006 assessment, ISBN: 978-92-807-2822-4, Job No: OZO/0948/NA. UNEP Nairobi, Ozone Secretariat, Kenya, 2007
11. Maté J (2010) The benefits of basing policies on the 20-year GWP of HFCs, Öko-Recherche GmbH in cooperation with HEAT GmbH, Frankfurt am Main
12. Horst K (2000) Refrigerant use in Europe. ASHRAE J. www.ashraejournal.org
13. Moore D (2005) A comparative method for evaluating industrial refrigerant systems. Sabroe Ltd. (revA). www.Sabroe.org
14. DUPONT (2005) Dupont refrigerants the science of cool. Du Pont de Nemours (Deutschland) GmbH, Neu-Isenburg. www.refrigerants.dupont.com
15. Eurammon (1996) Evaluation of the environmentally friendly refrigerant ammonia according to the TEWI Concept, NH_3 for ecologically friendly future, Frankfurt. http://www.eurammon.com
16. Hellmann J, Barthélemy P (1997) AFEAS-TEWI III study: results and evaluation of alternative refrigerants. Solvay Fluor und Derivate GmbH Technical Service-product Refrigerants, Bulletin no. C/11.97/06/E, p 5

Performance Evaluation of the Bio-char Heavy Metal Removal Produced from Tomato Factory Waste

Eylem Önal, Nurgül Özbay, Adife Şeyda Yargıç, Rahmiye Zerrin Yarbay Şahin, and Özgül Gök

Abstract

Bio-char is a carbon-enriched and porous material produced from a variety of biomass. When bio-char is produced from biomass, approximately 50 % of the carbon that the plants absorbed as CO_2 from the atmosphere is "fixed" in the charcoal. Bio-char is similar in its appearance to charcoal and activated carbon.

In this study tomato factory waste has been used for the production of the bio-char. Biomass with a mean particle size was carbonized at 623 K in a furnace. Biomass and bio-char were characterized by using elemental analyses, Fourier Transform Infrared Spectroscopy (FTIR), and scanning electron microscope (SEM) analysis.

The adsorption capacity of the bio-char produced with carbonization of tomato factory waste has been evaluated with the Co(II) ion removal to investigate the effects of pH, amount of adsorbent, initial concentration of the aqueous solution, adsorption time, and solution temperature. To describe the equilibrium isotherms Langmuir and Freundlich models were applied. Pseudo-first order and pseudo-second order kinetic models were used to find out the kinetic parameters and mechanism of adsorption process with increasing adsorbent dosage from 1 to 10 g/l in the batch mode. The final heavy metal concentrations have been reduced from 59 to 8 ppm and removal efficiencies have been increased from 60 to 82 % respectively.

Experimental results showed that, tomato factory waste char seems to be an effective and alternative adsorbent precursor for the removal of heavy metal ions from aqueous solutions due to its high adsorption capacity, low cost, and availability.

Keywords

Adsorption • Bio-char • Characterization • Co(II) removal • Isotherms • Kinetics • Tomato factory waste

Introduction

The growth of human population, urbanization, and industries contribute to environmental contamination by hazardous metals, which is of very important and serious environmental concern for all living organisms. Heavy metal ions, such as cobalt, accumulated through the food chain, even at low concentrations, have damaging influences on human health. Cobalt has toxic effects as imparting neurotoxicological disorders, genotoxicity, carcinogenicity, cardiomyopathy, and bronchial asthma [1, 2].

Numerous technologies have been developed for the removal of heavy metals from wastewater such as chemical precipitation, ion exchange, liquid–liquid extraction, membrane filtration, biosorption, and electro-coagulation.

E. Önal • N. Özbay (✉) • A.Ş. Yargıç • R.Z.Y. Şahin
Chemical & Process Engineering Department, Faculty of Engineering, Bilecik Seyh Edebali University, Bilecik, Turkey
e-mail: eylem.onal@bilecik.edu.tr; nurgul.ozbay@bilecik.edu.tr; seyda.guler@bilecik.edu.tr; zerrin.yarbay@bilecik.edu.tr

Ö. Gök
Chemical Engineering Department, Hakkari University, Hakkari, Turkey
e-mail: ozgulgok@hakkari.edu.tr

The majority of salts heavy metals are soluble in water so it cannot be separate for conventional physical processes of separation [3]. Besides, the application of these conventional methods have been impeded by some inherent limitations, involving high capital and maintenance cost, expensive equipment, high sensitivity to operational conditions, significant energy consumption, incomplete metal removal or sludge generation, etc. Great interest is currently being expressed in adsorption owing to its high efficiency, cost-effectiveness, and easy handling [2]. Nut and walnut shells, tree barks, rice hulls, tea waste, sugar beet pulp, sunflower seed cake, tomato waste, fly ash, waste rubber, and animal bones are just a few examples of low-cost adsorbents used for heavy metal removal [4].

The application of various types of bio-char which is a carbon-enriched and porous material produced from a variety of biomass, as low-cost adsorbents, for the control of environmental pollution in terms of heavy metals removal from aqueous media is currently of great interest. Various adsorbents have been examined for removal of Co(II) from water, but agricultural wastes like tomato wastes, which have relatively high carbon and present porous structure, have not been explored fully. The present research is to explore an inexpensive and efficient adsorbent from agricultural waste, specifically tomato waste, to replace the existing commercial adsorbents such as activated carbon and nanosorbents. In the present study, bio-char from tomato waste was characterized using FT-IR and SEM techniques and used as an adsorbent for Co(II) ion removal. Batch mode studies were used to study the effect of pH, adsorbent dose, contact time, initial concentration of metal, and solution temperature. In addition, the adsorption mechanism was determined [5].

Material and Methods

Materials and Preparation of Bio-char

Tomato waste was collected from Marmara Region. Tomato waste first washed with distilled water to remove impurities as dust, air-dried at room temperature, ground in a ball-mill, sieved, and stored in a dark room Tomato waste with a mean particle size was carbonized at 623 K in a furnace. The bio-char was classified as BC.

Stock solution of Co(II) was prepared by dissolving a weighed amount of cobalt in distilled water. The experimental test solutions were prepared by diluting the respective stock solution of cobalt with distilled water and mixing them in the desired proportion.

Analytical Techniques

Flame atomic absorption spectrophotometer (GBC 933 AA) was used to determine the concentration of the metals. Fourier Transform Infrared (FTIR) spectroscopy (Perkin Elmer Spectrum 100) was used to identify the functional groups and functional molecules that facilitate metal ion uptake in the bio-char. Scanning electron microscopy (SEM) were performed with a Zeiss Supra 40VP microscope.

Adsorption Studies

Batch adsorption studies were performed in 50-ml conical flasks by varying 2–8 for pH, 0.05–0.5 g for adsorbent dose, contact time, 25–125 mg/l with an increase of 25 for initial concentration of metal, and solution temperature. The suspension was separated using Whatman filters, and supernatant was subject to Atomic Absorption Spectrometer (AAS) to determine the residual metal concentration. For the quantitative estimation of metals adsorbed on the surface of bio-char, the Eq. (70.1) was used:

$$q_e = (C_0 - C_1)\frac{V}{M} \tag{70.1}$$

where q_e is the metal uptake (mg g^{-1}) by bio-char, C_o and C_1 are initial and final metal concentrations (mg l^{-1}), V is the solution volume (l), and M is the mass of the adsorbent (g) [5].

Results and Discussion

Characterization of Materials

The composition of the tomato waste and bio-char are given in Table 70.1. Bio-char has higher carbon content than tomato waste which makes them more carbonaceous material. Nitrogen is increased at levels ranging from 3.776 to 5.032 wt%. Carbonization increased the nitrogen content.

Fourier transform infrared (FT-IR) technique was applied to investigate the differences on the morphology after carbonization and the FT-IR spectra of tomato waste and bio-char are shown in Fig. 70.1. The FTIR spectrum of the tomato waste shows a broad peak at 3,280 cm^{-1}. The peak is attributed to the O–H in hydroxyl functional group in alcohols, phenolic and carboxylic acids. Two peaks between 2,921 and 2,851 cm^{-1} were assigned to the asymmetric and symmetric tension modes of the aliphatic C–H. The peaks are seen at nearly 1,750–1,640 cm^{-1} indicate aromatic C=C and C=O tensions. The peak intensities of the asymmetric and symmetric tension modes of the aliphatic C–H at around between 3,000 and 2,900 cm^{-1} were decreased according to increasing temperature from 350 to 550. The peak is seen at nearly 1,600 cm^{-1} indicates aromatic ring. When FT-IR spectrum of the tomato waste and bio-char were compared, they appear to be similar however some differences were observed in the chemical structure. In addition a decrease in OH-, CH$_2$-groups, and olefinic structure were acquired.

Figure 70.2 shows surface morphology of the tomato waste and bio-char which were investigated by scanning electron microscope (SEM). Magnification used in SEM analysis for tomato waste and BC was 10,000× and 3,000×, respectively. As seen in Fig. 70.2, the absence of porosity is evident for tomato waste and displays a platelet shape. However, the surface of the BC includes some pores of varying sizes. The external surface of the BC has a little sponge-like morphology and consists of some cavities. Carbonization process caused pores to open due to a great part of the volatiles originally available in tomato waste have evolved.

Table 70.1 Characteristics of tomato waste and bio-char

	Elemental analysis (%)			
Sample code	C	H	N	O[a]
Tomato waste	49.689	7.430	3.776	39.105
BC	65.776	2.152	5.032	27.039

[a]By difference
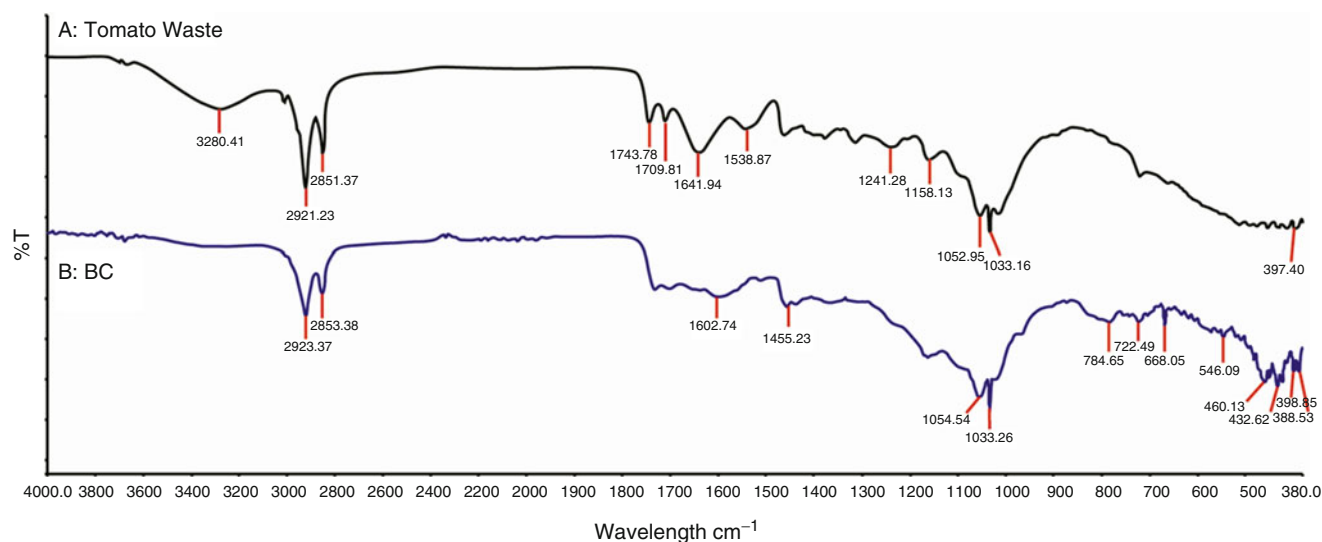
Fig. 70.1 Infrared spectra of tomato waste (**a**) and BC (**b**)
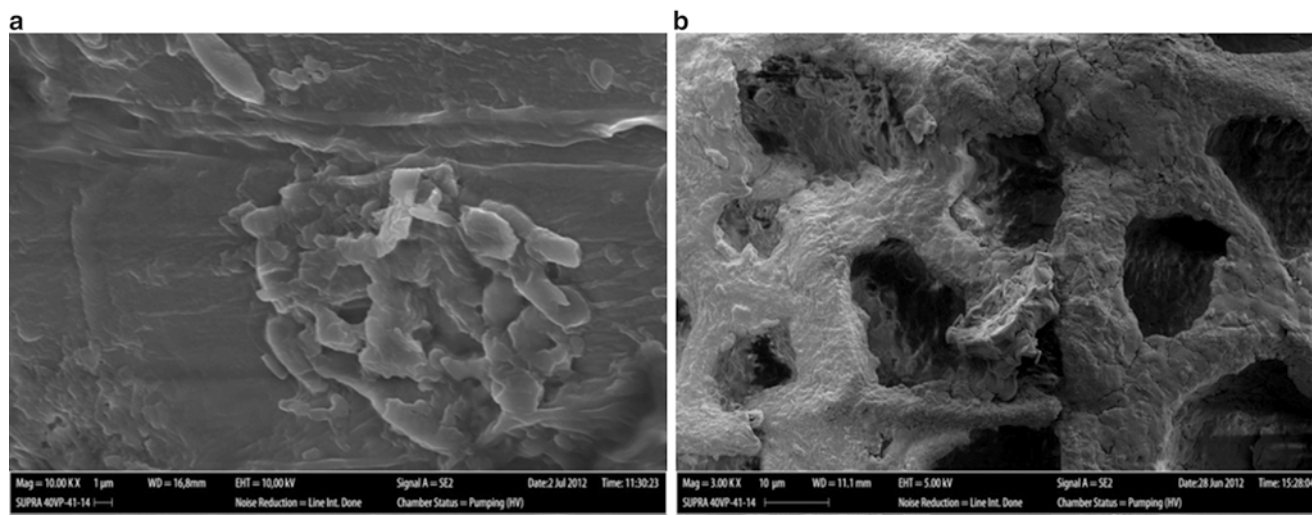
Fig. 70.2 SEM images of tomato waste (**a**) and bio-char (**b**)

Fig. 70.3 Effect of pH on cobalt (II) adsorption capacity (initial cobalt concentration: 50 mg/l, contact time: 60 min, temperature: 293 K, adsorbent dosage: 0.25 g)
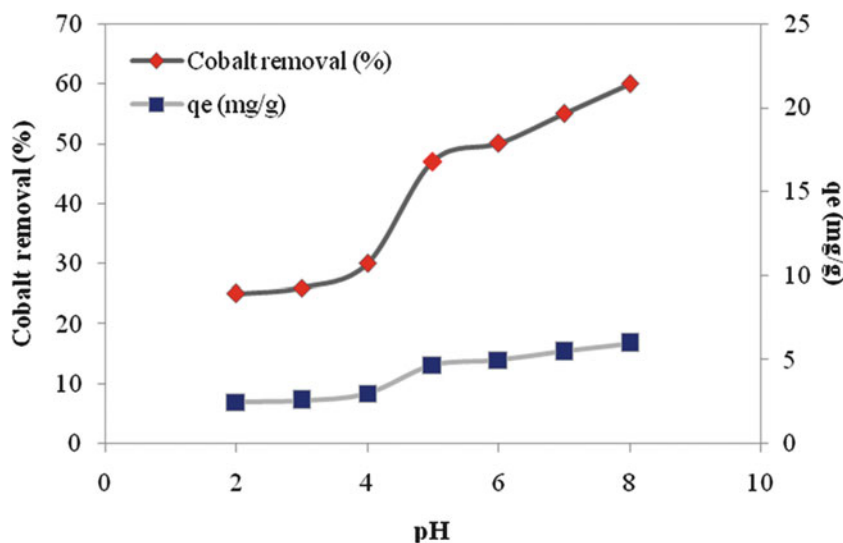
Effect of pH

Hydrogen ion concentration in the adsorption is considered as one of the most important parameters that influence the adsorption behavior of metal ions in aqueous solutions. It affects the solubility of the metal ions in the solution, replaces some of the positive ions that were found in the active sites and affects the degree of ionization of the adsorbate during the reaction. In this study, the pH of the solution was adjusted by adding 0.1 M HCl or 0.1 M NaOH and measured with a Thermo Scientific Orion 3 Star pH-meter. The effect of initial pH on the biosorption of Co(II) ions onto BC was evaluated within the pH range of 2–8 with 0.25 g/50 ml adsorbent dosage. Studies beyond pH 8 have not been done as precipitation of the ions as hydroxides would be likely [6].

It can be seen in Fig. 70.3, cobalt adsorption was increased along with the increase of pH of the adsorbate solution. This pH dependency of adsorption efficiency could be explained by the functional groups involved in metal uptake and metal chemistry. At low pH values, protons occupy most of the adsorption sites on the adsorbent surface and less cobalt ion could be sorbed because of electric repulsion with protons on adsorbent. When the pH values were increased, adsorbent surfaces were more negatively charged and the adsorption of metal ions (positive charge) was increased. Decrease in adsorption at higher pH (pH >4.0) is due to the formation of soluble hydroxylated complexes of the metal ions and their competition with the active sites, as a consequence, the retention would decrease again.

Fig. 70.4 Effect of adsorbent dosage on cobalt (II) adsorption capacity (initial cobalt concentration: 100 mg/l, contact time: 60 min, temperature: 293 K, pH: 7)
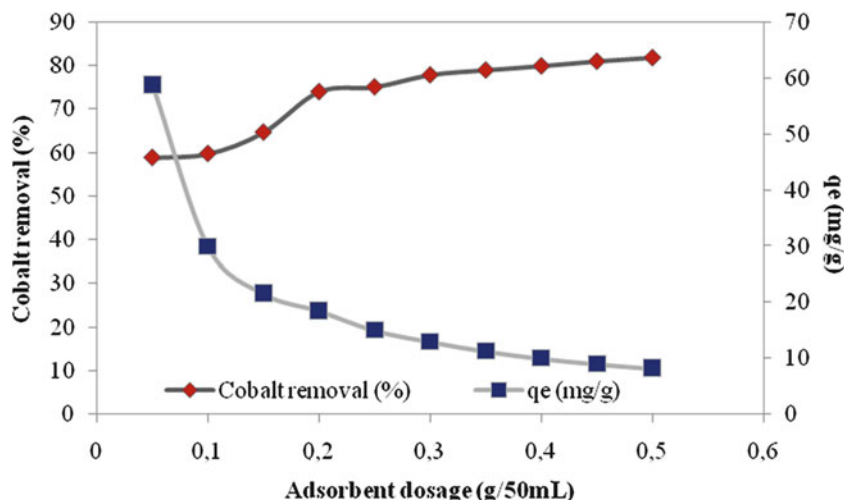
Fig. 70.5 Effect of initial cobalt concentration on cobalt (II) adsorption capacity (pH: 7, contact time: 60 min, temperature: 293 K, adsorbent dosage: 0.25 g)
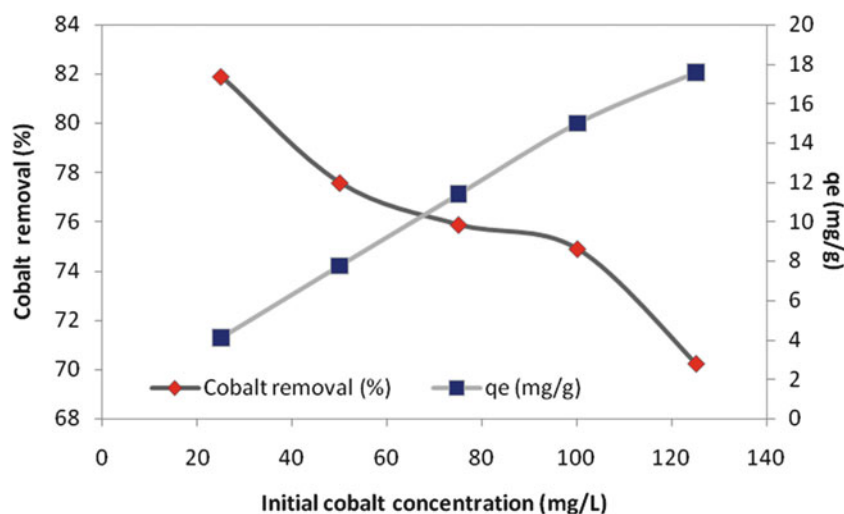
Effect of Adsorbent Dosage

The number of available sites and exchanging ions for adsorption depend upon the amount of adsorbent in the adsorption process. The effect of adsorbent concentration on the metal removal efficiency is presented in Fig. 70.4. The cobalt uptake was increased with increasing concentration of adsorbent up to an adsorbent dosage of 0.2 g/l. However, beyond this dosage the increase in removal efficiency was slightly increased. This is may be related to reduction in concentration gradient [6]. Increase in adsorption with adsorbent dosage can be attributed to increased adsorbent surface area and availability of more adsorption sites. However, the increase in the adsorbent dosage caused a remarkable decrease in the amount of metal ion uptake per gram of adsorbent. This can be related to (1) the increase in adsorbent mass at fixed metal ion concentration, and correspondingly the volume will lead to unsaturation of adsorption sites through the adsorption process; (2) the reduction in adsorbent capacity is likely to be due to particle aggregation, resulting from high adsorbent mass. Such aggregation would lead to a decrease in total surface area of the adsorbent and an increase in diffusional path length [7].

Effect of Initial Cobalt concentration

The effect of initial cobalt concentration on the metal removal efficiency is given in Fig. 70.5. The initial concentration of the cobalt in the solution was remarkably influenced the equilibrium uptake of cobalt. It was noted that the initial concentration increased the sorption of cobalt as this is generally expected due to the equilibrium process. This increase in uptake capacity

Fig. 70.6 Effect of contact time and solution temperature on cobalt (II) adsorption capacities (pH: 7, initial cobalt concentration: 50 mg/l, adsorbent dosage: 0.25 g)
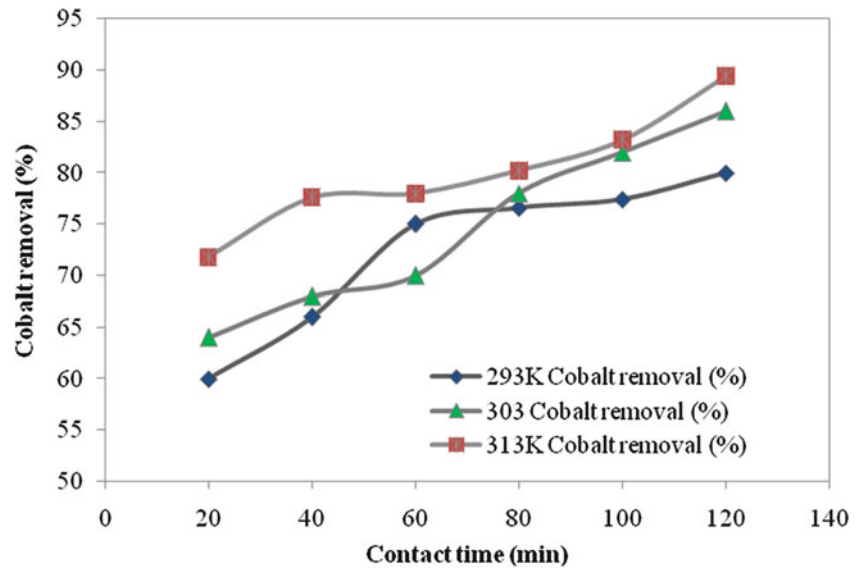
of the adsorbent with the increase in initial cobalt concentrations is due to higher availability of cobalt ions for the adsorption. Moreover, higher initial concentration provides increased driving force to overcome all mass transfer resistance of metal ions between the aqueous and solid phase resulting in higher probability of collision between metal ions and adsorbents. This also results in higher metal uptake [6].

Effect of Contact Time and Solution Temperature

In this study, the effect of temperature as a function of time was studied in an isothermal bath shaker at 293, 303, and 313 K. Adsorption of cobalt (II) by BC as a function of time is shown in Fig. 70.6. In the case of 293, 303, and 313 K solution temperature, the removal efficiency was almost increased. The highest removal efficiency was reached at 313 K solution temperature. The improvement in adsorption with temperature may be tended to increase in the number of active surface sites available for adsorption on activated carbon. In addition, the decrease in the thickness of the boundary layer surroundings with temperature would be also a reason.

Adsorption Isotherms

The analysis of equilibrium data to construct adsorption isotherms is usually important for design of adsorption systems. Adsorption isotherms express the mathematical relationship between the quantity of adsorbate and equilibrium concentration of adsorbate remaining in the solution at a constant temperature. The most common types of isotherms are Langmuir and Freundlich models. The Langmuir isotherm model is applicable to monolayer adsorptions and can be expressed as Eq. (70.2):

$$\frac{C_e}{q_e} = \frac{1}{q_m K_L} + \frac{C_e}{q_m} \tag{70.2}$$

where C_e is concentration of metal ions in solution at equilibrium (mg/l), q_e is the amount of metal ions at equilibrium in unit mass of adsorbent (mg/g), q_m and K_L are the Langmuir coefficient related to adsorption capacity (mg/g) and Langmuir adsorption constant (l/mg), respectively. The Langmuir isotherm parameters q_m and K_L were determined from slope ($1/q_m$) and intercept ($1/q_m K_L$) of the plot of C_e/q_e vs. C_e, respectively. The empirical Freundlich isotherm is based on adsorption on a heterogeneous surface and express by the Eq. (70.3):

$$ln q_e = ln K_F + \frac{1}{n} \, ln C_e \tag{70.3}$$

Table 70.2 Isotherm constants for the adsorption of cobalt onto BC

Isotherms	Parameters
Langmuir	
q_m (mg/g)	166.67
K_L (l/mg)	0.02927
R^2	0.952
Freundlich	
K_F ((mg/g) (l/mg)$^{1/n}$)	1.3647
n	1.40
R^2	0.972

Table 70.3 Kinetic parameters for the adsorption of cobalt onto BC

T (K)	Pseudo-first order kinetic model			Pseudo-second order kinetic model		
	k_1 (min^{-1})	q_e (mg/g)	R^2	k_2 [g/(mg/min)]	q_e (mg/g)	R^2
293	4.606×10^{-3}	4.8083	0.896	0.0126	8.547	0.998
303	0.0115	2.1478	0.445	0.01	8.9285	0.988
313	0.0184	1.555	0.924	0.0249	8.6206	0.998

The sorption parameters are as follows: q_m is the maximum adsorption capacity (mmol g^{-1}), K_L the Langmuir constant related to energy of sorption (dm^3 mmol^{-1}), K_F and n are the Freundlich coefficient related to adsorption capacity and intensity, respectively. The values of Freundlich constants n and K_F were obtained from the slope (1/n) and intercept (ln K_F) of the plot of ln q_e vs. ln C_e, respectively [8].

The plots give straight lines, indicating that the adsorption of Co(II) onto BC followed the Langmuir isotherm model. The Langmuir and Freundlich isotherms constants and regression coefficients are listed in Table 70.2. For Freundlich isotherm, the R^2 values were all higher than 0.97, and it indicated monolayer coverage by Co(II) ions of the BC and a homogenous distribution of the active sites on the surface of the BC.

Adsorption Kinetics

In order to investigate the mechanism of sorption, two kinetic models were used to test the experimental data: the pseudo-first-order equation proposed by Lagergren, and the pseudo-second-order kinetic model proposed by Ho and McKay. The respective linear forms of the equations are given in Eqs. (70.4) and (70.5):

$$\ln(q_e - q_t) = ln q_e - k_1 t \tag{70.4}$$

$$\frac{t}{q_t} = \frac{1}{k_2 q_e^2} + \frac{1}{q_e} t \tag{70.5}$$

where t (min) is the contact time, q_e and q_t (mmol/g) are the amounts of sorbed Co(II) at equilibrium and time t, respectively, and k_1 (min^{-1}) and k_2 (g/(mmol/min)) are the rate constants of the pseudo-first-order and pseudo-second-order model, respectively [1].

As can be seen from Table 70.3, the sorption data of Co(II) can be satisfactorily described by the pseudo-first-order equation, since values of the correlation coefficient is close to 1. Cobalt adsorption onto BC consisted of chemical adsorption due to the fact that pseudo-first order kinetic model suggested that adsorption process involved chemisorption mechanism.

Conclusions

In the present work, the cobalt adsorption characteristics of bio-char obtained from tomato waste was examined. Batch sorption experiments were conducted to examine the efficiency of the bio-char on cobalt binding. According to batch adsorption experiments, the uptake of Co(II) ion increased with the increase of pH, adsorbent dosage, contact time, and temperature; however, it decreased with the increase of initial Co(II) concentration. The maximum Co(II) removal

efficiency was found as ~90 % at 313 K. The equilibrium data were analyzed by employing Langmuir, and Freundlich isotherm models. The Freundlich model has a good agreement with the experimental data. Kinetic evaluations showed that the cobalt adsorption process follows the pseudo-first order kinetic model. Overall, this study showed that bio-char with high cobalt removal capacity could be prepared from tomato waste through simple treatment methods at low temperature such as 623 K. It may be concluded that tomato waste bio-char may be used as a low-cost, natural, and abundant source for the removal of Co(II).

Nomenclature

b	Langmuir coefficient related to adsorption energy, l/mg	M	Mass of the adsorbent, g
C_1	Final metal concentration, mg/l	q_e	Amount of metal ions at equilibrium in unit mass of adsorbent, mg/g
C_e	Concentration of metal ions in solution at equilibrium, mg/l	q_{max}	Langmuir coefficient related to adsorption capacity
C_o	Initial metal concentration, mg/l	q_t	Amounts of sorbed Co^{2+} at time t, mmol/g
FTIR	Fourier transform infrared spectroscopy	R_L	Dimensionless constant separation factor
k_1	Rate constant of the pseudo-first-order, 1/min	SEM	Scanning electron microscope analysis
k_2	Rate constant of the pseudo-second-order model, g/(mmol/min)	t	Contact time, min
		V	Solution volume, l

References

1. Lazarevica S, Jankovic-Castvana I, Potkonjak B, Janackovic D, Petrovica R (2012) Removal of Co2+ ions from aqueous solutions using iron-functionalized sepiolite. Chem Eng Process 55:40–47
2. Liu Y, Chen M, Hao Y (2013) Study on the adsorption of Cu(II) by EDTA functionalized Fe3O4 magnetic nano-particles. Chem Eng J 218:46–54
3. Fagundes-Klen MR, Ferri P, Martins TD, Tavares CRG, Silva EA (2007) Equilibrium study of the binary mixture of cadmium-zinc ions biosorption by the Sargassum filipendula species using adsorption isotherms models and neural network. Biochem Eng J 34:136–146
4. Çay S, Uyanık A, Özaşık A (2004) Single and binary component adsorption of copper (II) and cadmium (II) from aqueous solutions using tea-industry waste. Sep Purif Technol 38:273–280
5. Lakshmipathy R, Sarada NC (2013) Application of watermelon rind as sorbent for removal of nickel and cobalt from aqueous solution. Int J Miner Process 122:63–65
6. Vimala R, Das N (2009) Biosorption of cadmium (II) and lead (II) from aqueous solutions using mushrooms: a comparative study. J Hazard Mater 168:376–382
7. Özbay N, Yargıç AŞ, Yarbay-Şahin RZ, Önal E (2013) Full factorial experimental design analysis of reactive dye removal by carbon adsorption. J Chem 2013:13 pp. doi:10.1155/2013/234904, Article ID 234904
8. Gupta N, Kushwaha AK, Chattopadhyaya MC (2012) Adsorptive removal of Pb2+, Co2+ and Ni2+ by hydroxyapatite/chitosan composite from aqueous solution. J Taiwan Inst Chem Eng 43:125–131

Ecological Performance Analysis of Irreversible Brayton Cycle

71

Yusuf Yeğiner, Serkan Kenç, Güven Kömürgöz, and İbrahim Özkol

Abstract

This paper presents a performance analysis and optimization for irreversible Brayton cycle based on the Ecological Coefficient of Performance (ECOP) criterion. The ECOP objective function is defined as the ratio of power output to the loss rate of availability. The maximum of ECOP and performance parameters are derived analytically under the assumption of optimal design. The graphical representations of the developed ECOP function in terms of governing parameters are discussed in detail. The effect of dominant parameters on optimal ecological performances has been investigated. The comparisons of ECOP, dimensionless ecological function and power output with respect to the dimensionless entropy generation rate and the enthalpy ratio are presented.

Keywords

Irreversibility • Brayton cycle • Performance parameter • Ecological performance criterion • Entropy generation rate

Introduction

Finite Time Thermodynamics (FTT) Method, providing performance bounds (and extremes/boundaries) for irreversible thermodynamic processes, can be applied to various engineering fields such as refrigerators, heat pumps, engines with heat regeneration, several coupled engines, solar engines, and photovoltaic cells. The Finite Time Thermodynamics can be used to find the optimal time path of any cyclic processes with friction and heat leakage (all possible irreversibilities) by providing maximization of the work output per cycle. In irreversible thermodynamics processes, FTT modeling gives more realistic results than those provided by reversible thermodynamic. By applying FTT processes it is possible to get more physical understanding of how irreversibilities affect the performance of thermodynamic processes [1–4].

Brayton cycles have been used extensively in gas turbine power plants and aircraft propulsion systems. Detailed works on Brayton heat engines have made tremendous progress using finite-time thermodynamics as well as smaller size and higher thermal efficiency heat engine design [5–7]. Detailed information about optimization works based on different objective functions for Brayton and the other heat engine models can be found in literature by Bejan [2], Chen et al. [3] and recently by Durmayaz et al. [8]. During the last decade, some authors have studied the ecological performance of endoreversible and irreversible heat engines by considering finite-time and finite-size constraints [9–13]. The ecological performance criterion was first introduced by Angulo-Brown [9] for finite-time Carnot heat engines. In addition, it has been found that the thermal efficiency for maximum ecological function is almost equal to the average of Carnot efficiency introduced by Curzon and Ahlborn [14]. It has also been derived the general characteristics of the internal reversible thermal cycles by Angulo-Brown [9]. Later Yan has developed the ecological function found by Brown [10].

Y. Yeğiner • S. Kenç • G. Kömürgöz • İ. Özkol (✉)
Istanbul Technical University, Maslak, Istanbul, Turkey
e-mail: yeginer@itu.edu.tr; serkanc@yahoo.com; komurgoz@itu.edu.tr; ozkol@itu.edu.tr

According to the result of these studies, it is observed that the objective function can have negative values contrary to the reasonable rate of the loss term which is always possible. It can be defined that the difference between the actual and the theoretical power output is the negative reasonable rate of loss. Ust has described a new ecological function called ecological coefficient of performance (ECOP) [15]. By this definition he shows that the objective function must have positive values, as in the thermal coefficient of heat engines or performance coefficient of refrigerators and heat pumps, in order to determine the effect of the reasonable rate of loss on the power output. This objective function is called as the coefficient of ecological performance. It is expressed as power output divided by the reasonable loss rate. Ust et al. have also performed performance analysis applications for irreversible dual cycle, based on ECOP [15].

In this paper, the thermo-ecological optimization technique introduced by Ust [15] and Ust et al. [16] has been applied to an irreversible Brayton cycle. A performance analysis of Brayton cycle using a finite-time ecological optimization technique based on enthalpy approach has not been published yet, to the author's knowledge. Application of the maximum ecological objective function to a Brayton cycle gives a sense how the natural resources can effectively be used and how a sense the work output of existence system output.

The Theoretical Model

The purpose of this section is to examine a steady-flow irreversible open Brayton cycle with an external heat source. Let the heat engine cycle (1–2–3–4–1) consists of two constant-pressure processes and two non-isentropic processes (the compression 1–2 and the expansion 3–4). The temperature–entropy diagram and pressure-volume is shown in Fig. 71.1.

The cycle operates between two heat reservoirs of temperatures T_H and T_L. In the cycle, $\dot{Q}_H$ is the rate of heat transfer from the heat source at the temperature T_H to the working fluid in processes 2–3, $\dot{Q}_L$ is the rate of heat transfer from the working fluid to the heat sink at the temperature T_L in process 4–1. $\dot{Q}_H$ and $\dot{Q}_L$ can be defined as below;

$$\dot{Q}_H = \dot{m}(h_3 - h_2) \tag{71.1}$$

$$\dot{Q}_L = \dot{m}(h_3 - h_2) \tag{71.2}$$

where $\dot{m}$ is mass flow rate, and h_2 and h_3 are enthalpy values at state 2 and 3, respectively. The effectiveness of hot and cold-side heat exchangers ε_H and ε_L for counterflow heat exchangers are defined as

$$\varepsilon_H = 1 - e^{-N_H} \tag{71.3}$$

$$\varepsilon_L = 1 - e^{-N_L} \tag{71.4}$$
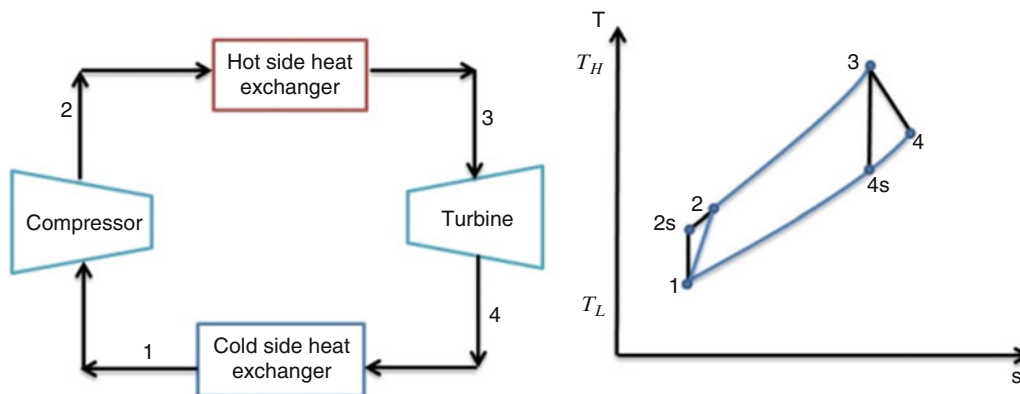
Fig. 71.1 Brayton cycle model and T-S diagrams

and the numbers of heat transfer units of hot- and cold-side heat exchangers are

$$N_H = (U_H A_H)/\dot{C}_w \tag{71.5}$$

$$N_L = (U_L A_L)/\dot{C}_w \tag{71.6}$$

where $U_H A_H$ is the hot-side heat-exchanger conductance and $U_L A_L$ is the cold-side heat-exchanger conductance, $\dot{C}_w$ is the capacity rate of the working fluid. The power produced by the Brayton heat engine according to the first law of thermodynamics can be given as

$$\dot{W} = \dot{Q}_{HT} - \dot{Q}_{LT} = \dot{m}[(h_3 - h_2) - (h_4 - h_1)] \tag{71.7}$$

The thermal efficiency becomes,

$$\eta = \frac{\dot{W}}{\dot{Q}_{HT}} = 1 - \frac{(h_4 - h_1)}{(h_3 - h_2)} \tag{71.8}$$

The entropy generation rate can be obtained as follows

$$\dot{S}_g = \frac{\dot{Q}_{LT}}{T_L} - \frac{\dot{Q}_{HT}}{T_H} = \frac{\dot{m}(h_4 - h_1)}{T_L} - \frac{\dot{m}(h_3 - h_2)}{T_H} \tag{71.9}$$

Enthalpy values at state 3, 4 can be expressed in following form

$$h_3 = \varepsilon_H T_H C_p + h_2(1 - \varepsilon_H) \tag{71.10}$$

$$h_4 = \frac{h_1 - \varepsilon_L T_L C_p}{1 - \varepsilon_L} \tag{71.11}$$

where C_p is pressure coefficient. The isentropic efficiencies of turbine and compressor are

$$\eta_c = \frac{h_{2s} - h_1}{h_2 - h_1} \tag{71.12}$$

$$\eta_T = \frac{h_3 - h_4}{h_3 - h_{4s}} \tag{71.13}$$

By using Eqs. (71.12) and (71.13)

$$h_{2S} = (1 - \eta_c)h_1 + \eta_c h_2 \tag{71.14}$$

$$h_{4S} = \frac{h_4}{\eta_T} + \left(1 - \frac{1}{\eta_T}\right)h_3 \tag{71.15}$$

$$\phi = \frac{h_{2s}}{h_1} = \frac{h_3}{h_{4s}} \tag{71.16}$$

where ϕ is the enthalpy ratio of the Brayton cycle. By using Eqs. (71.14)–(71.16), enthalpy values can be obtained as

$$h_2 = \frac{h_1[\phi - (1 - \eta_C)]}{\eta_C} \tag{71.17}$$

$$h_3 = \varepsilon_H T_H C_p + \left[\frac{h_1[\phi - (1 - \eta_c)]}{\eta_k}\right](1 - \varepsilon_H) \tag{71.18}$$

By substituting Eqs. (71.10), (71.11), (71.14), (71.15), (71.17) and (71.18) into Eq. (71.16)

$$h_1 = \frac{a_1\phi + a_2}{a_3\phi^2 + a_4\phi + a_5} \tag{71.19}$$

where the simplification parameters are defined as

$$a_1 = \eta_c C_p[\varepsilon_L T_L - (\eta_T - 1)(1 - \varepsilon_L)\varepsilon_H T_H] \tag{71.20}$$

$$a_2 = \eta_C \eta_T (1 - \varepsilon_L)\varepsilon_H T_H C_p \tag{71.21}$$

$$a_3 = (\eta_T - 1)(1 - \varepsilon_L)(1 - \varepsilon_H) \tag{71.22}$$

$$a_4 = \eta_C - (\eta_T - 1)(1 - \varepsilon_L)(1 - \varepsilon_H) \tag{71.23}$$

$$a_5 = \eta_T(\eta_T - 1)(1 - \varepsilon_L)(1 - \varepsilon_H) \tag{71.24}$$

The ECOP (ecological coefficient of performance) objective function defined as the ratio of power output to the loss rate of availability can be written as

$$\text{ECOP} = \frac{\dot{W}}{T_0 \dot{S}_g} \tag{71.25}$$

where T_0 is the environment temperature. Using Eqs. (71.7) and (71.9) in Eq. (71.25), the ECOP function is derived as

$$\text{ECOP} = \frac{\dot{W}}{T_0 \dot{S}_g} = \frac{\dot{m}[(h_3 - h_2) - (h_4 - h_1)]}{T_0\left[\frac{\dot{m}(h_4 - h_1)}{T_L} - \frac{\dot{m}(h_3 - h_2)}{T_H}\right]} \tag{71.26}$$

Finally, ECOP function can be reduced as a simple algebraic relation,

$$\text{ECOP} = \frac{b_1\phi^2 + b_2\phi + b_3}{b_4\phi^2 + b_5\phi + b_6} \tag{71.27}$$

where;

$$b_1 = a_3 a_6 + a_1 a_7 \tag{71.28}$$

$$b_2 = a_4 a_6 + a_1 a_8 + a_2 a_7 \tag{71.29}$$

$$b_3 = a_5 a_6 + a_2 a_8 \tag{71.30}$$

$$b_4 = a_3 a_9 + a_1 a_{10} \tag{71.31}$$

$$b_5 = a_4 a_9 + a_1 a_{11} + a_2 a_{10} \tag{71.32}$$

$$b_6 = a_5 a_9 + a_2 a_{11} \tag{71.33}$$

Then the defined parameters a_6 a_7 a_8 a_9 a_{10} and a_{11} for simplicity:

$$a_6 = \eta_C \left[T_H T_L \varepsilon_H T_H C_p (1 - \varepsilon_L) + T_H T_L \varepsilon_L T_L C_p \right] \tag{71.34}$$

$$a_7 = T_H T_L (-\varepsilon_H)(1 - \varepsilon_L) \tag{71.35}$$

$$a_8 = -(1 - \eta_C) T_H T_L (-\varepsilon_H)(1 - \varepsilon_L) - \eta_C T_H T_L \varepsilon_L \tag{71.36}$$

$$a_9 = -\eta_C \left[T_H T_0 \varepsilon_L T_L C_p + T_0 T_L \varepsilon_H T_H C_p (1 - \varepsilon_L) \right] \tag{71.37}$$

$$a_{10} = -T_0 T_L (-\varepsilon_H)(1 - \varepsilon_L) \tag{71.38}$$

$$a_{11} = \eta_C T_0 T_H \varepsilon_L + (1 - \eta_C) T_0 T_L (-\varepsilon_L)(1 - \varepsilon_L) \tag{71.39}$$

Results and Discussion

In this section, analytical results are presented and compared to illustrate the application of thermo-ecological optimization technique for Brayton cycle. The variation of ECOP functions with respect to the enthalpy ratio (ϕ) and the dimensionless power output ($\bar{\dot{W}} = \dot{W}/(\dot{C}_w T_L)$) for different values of isentropic efficiencies (η_C, η_T), heat sources temperature ratio ($\tau = T_H/T_L$), and the total number of heat transfer units ($N_T = N_H + N_L$) are demonstrated in Figs. 71.2 and 71.3. Variation of the ECOP function, the ecologic performance function, and work output are presented graphically and discussed in detail. All the graphs were constructed for the values of variables (T_L, T_H, ε_L, ε_H) and given in Table 71.1.

It can easily be noticed from Fig. 71.2a–c that the ECOP function has a maximum for a certain ϕ value for the chosen set of operation parameters. The maximum ECOP value is getting higher for the higher heat sources temperature ratio (τ), the total number of heat transfer units ($N_T = N_H + N_L$), and isentropic efficiencies (η_C, η_T).

The maximum ECOP with respect to ϕ can be found analytically by setting d(ECOP)/dϕ = 0. The optimum value ϕ at the maximum ECOP is found as below;

$$\phi_{opt} = \frac{b_4 b_3 - b_1 b_6}{b_1 b_5 - b_4 b_2} \times \left[1 - \sqrt{1 - \frac{(b_2 b_6 - b_5 b_3)(b_1 b_5 - b_4 b_2)}{(b_4 b_3 - b_1 b_6)^2}} \right] \tag{71.40}$$

The maximum of ECOP can be obtained by substituting Eq. (71.40) into Eq. (71.27), i.e.

$$ECOP_{max} = \frac{b_1 \phi_{opt}^2 + b_2 \phi_{opt} + b_3}{b_4 \phi_{opt}^2 + b_5 \phi_{opt} + b_6} \tag{71.41}$$

As heat sources temperature ratio (τ), the total number of heat transfer units ($N_T = N_H + N_L$), and isentropic efficiencies (η_C, η_T) increase, the performances in terms of ECOP and $\dot{W}$ increase too. The maximum power output ($\dot{W}_{max}$) is higher than the power output at the maximum ECOP conditions ($\dot{W}^*$), as expected, but the $ECOP_{max}$ is higher than the ECOP at $\dot{W}_{max}$ conditions ($ECOP_{mp}$). By taking into account the power and entropy generation rate (loss rate of availability) of the heat engine together the optimal design intervals in terms of ECOP and $\dot{W}$ yields:

$$ECOP_{max} \geq ECOP \geq ECOP_{mp} \quad \text{or} \quad \dot{W}^* \leq \dot{W} \leq \dot{W}_{max} \tag{71.42}$$

To make a correct decision that which optimal design parameters of a heat engine will be important one should take into consideration the followings; If the power is the substantial interest then the design parameters must be selected near to the W_{max} conditions or if the aim is to keep the entropy generation minimum design parameters must be chosen to make ECOP maximum. The maximum of thermal efficiency is an important parameter due to engineering viewpoint. For the given temperatures, ECOP and thermal efficiency are dependent. In addition to this, maximum of them overlaps, despite the fact
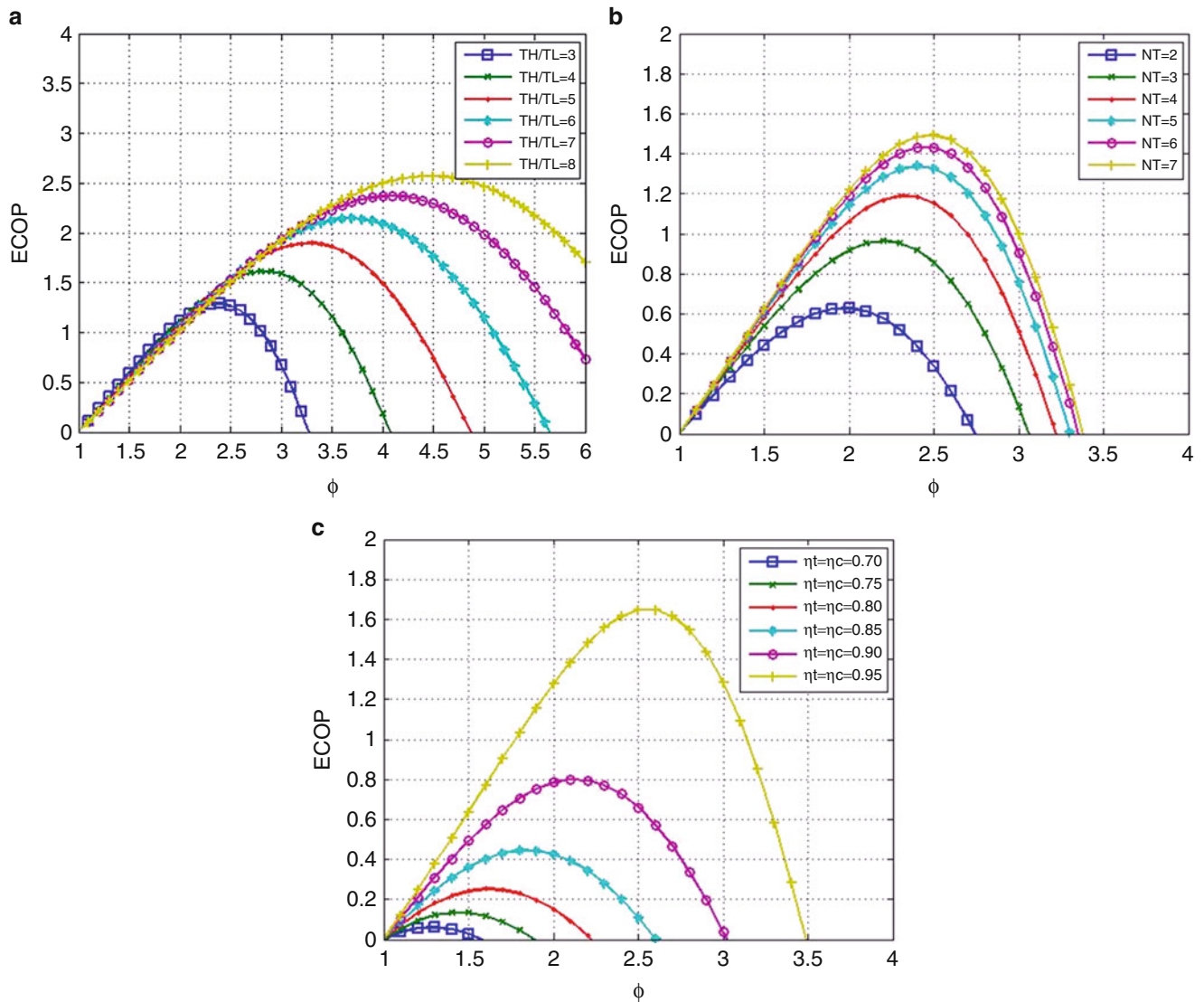
Fig. 71.2 Variation of the ECOP function with respect to the enthalpy ratio for various values (**a**) τ (**b**) N_T (**c**) $\eta_C = \eta_T$ ($T_L = 300K$, $T_H = 1200K$, $\eta_c = 0.9$, $\eta_t = 0.95$, $\varepsilon_L = \varepsilon_H = 0.9$)

that they have distinctive physical bases. Obtaining the identical performance conditions at the maximum ECOP and thermal efficiency are a foreseen and reasonable conclusion. For the reason of the fact that the maximum thermal efficiency conditions for a definite power results in minimum fuel consuming that leading to minimum environmental destruction. Consequently, the ECOP takes into account environmental influence properly. As ECOP provides knowledge about the entropy generation (the loss rate of availability), thermal efficiency provide knowledge about the essential fuel consumption to provide certain power.

Similar to Eqs. (71.40)–(71.41), it is possible to obtain the optimum value of power at the maximum ECOP,

$$\frac{\dot{W}_{opt}}{\dot{C}_w} = \frac{b_1\phi_{opt}^2 + b_2\phi_{opt} + b_3}{b_4\phi_{opt}^2 + b_5\phi_{opt} + b_6} \tag{71.43}$$

The comparisons of ECOP, dimensionless ecological function $\left(\bar{\dot{E}} = \dot{E}/\left(\dot{C}_W T_L\right)\right)$ proposed by Angulo-Brown [9] and power output ($\bar{\dot{W}}$) with respect to the dimensionless entropy generation rate ($\bar{\dot{S}}_g$), and the enthalpy ratio (ϕ), are demonstrated in Fig. 71.4a, b. The optimum enthalpy ratio (ϕ^*) at the (ECOP$_{max}$) conditions is always greater than enthalpy ratio (ϕ_{mef}) at the maximum of ecological function ($\dot{E}_{max}$) and (ϕ_{mp}) at the maximum power output ($\dot{W}_{max}$) conditions in Fig. 71.4a. Limits can be given as follows;
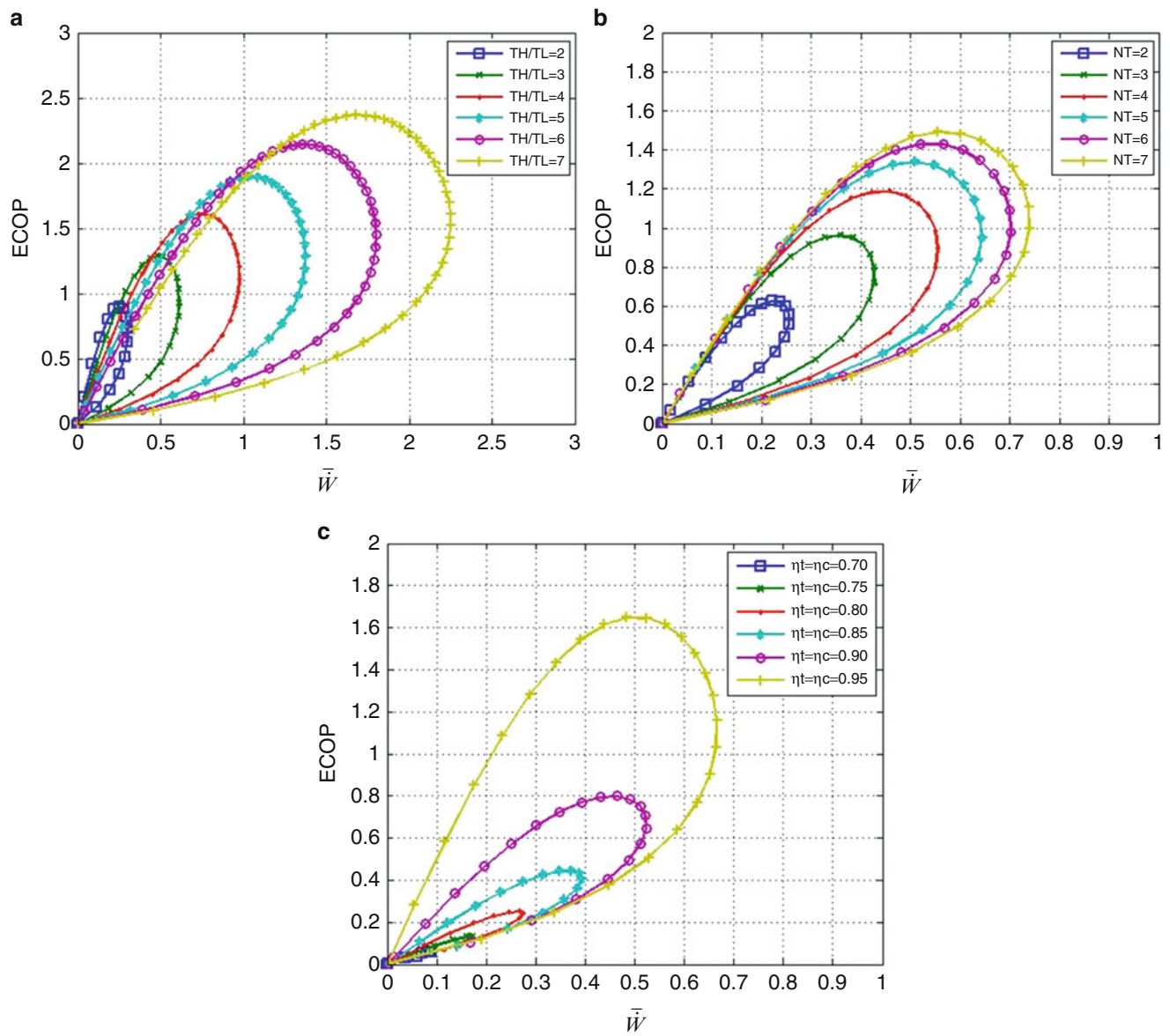
Fig. 71.3 Variation of the ECOP function with respect to the power output for various values (**a**) τ (**b**) N_T (**c**) $\eta_C = \eta_T$ ($T_L = 300K$, $T_H = 1200K$, $\eta_c = 0.9$, $\eta_t = 0.95$, $\varepsilon_L = \varepsilon_H = 0.9$)

Table. 71.1 The value of the variables

Low temperature heat source (T_L)	300 K
High temperature heat source (T_H)	1,200 K
Low temperature heat exchanger effectiveness (ε_L)	0.9
High temperature heat exchanger effectiveness (ε_H)	0.9

$$\phi^* \geq \phi_{mef} \geq \phi_{mp} \tag{71.44}$$

It can be observed from Fig. 71.4b that the entropy generation rate ($\dot{S}_g^*$) at the ECOP$_{max}$ conditions is lower than the entropy generation rate ($\dot{S}_{g,mp}$) at $\dot{W}_{max}$ conditions and ($\dot{S}_{g,mef}$) at the $\dot{E}_{max}$ conditions. In order to minimize the entropy generation rate, limits can be described as below;

$$\dot{S}_g^* < \dot{S}_{g,mef} < \dot{S}_{g,mp} \tag{71.45}$$
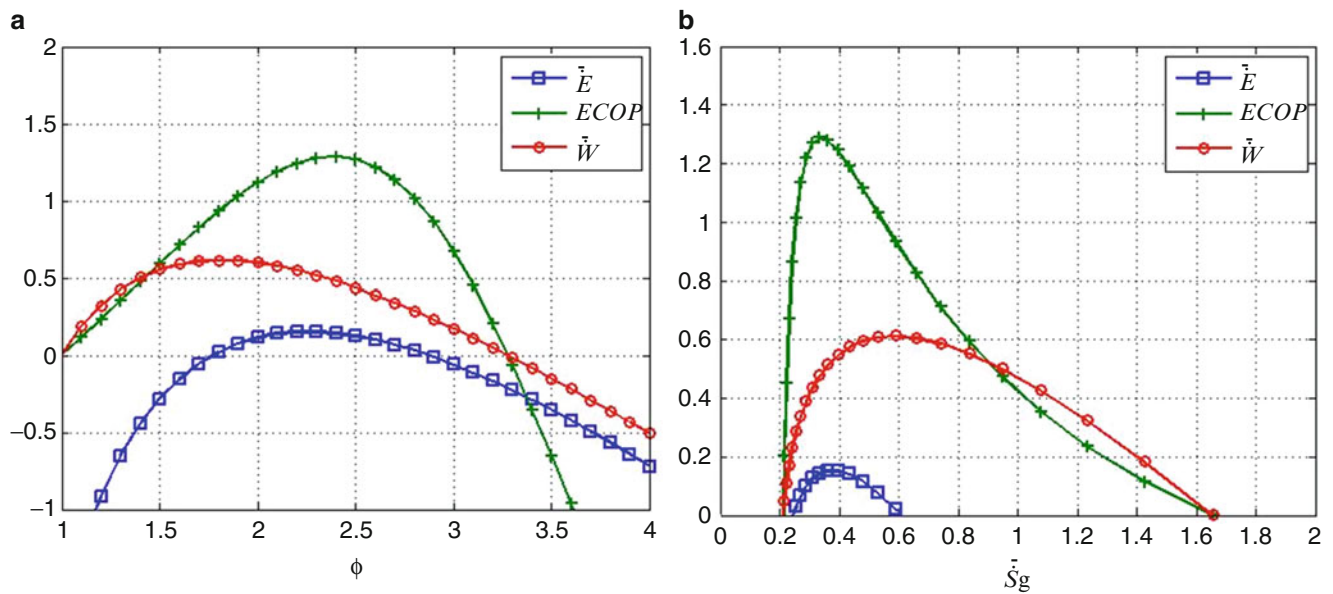
Fig. 71.4 Variations of the ECOP, dimensionless power output and the ecologic performance functions with respect to the (**a**) enthalpy ratio and (**b**) dimensionless entropy generation rate ($\eta_C = 0.9$, $\eta_T = 0.95$)

Conclusion

A performance analysis was carried out for an irreversible Brayton heat engine based on the thermo-ecological objective function, that is, the Ecological Coefficient of Performance (ECOP) is defined as the ratio of power to the loss rate of availability. In the analysis, the maximum of ECOP and performance parameters are derived analytically under the assumption of optimal design and presented graphically. For the environmental view, the design parameters based on the maximum of ECOP conditions can be used as a measure of the compromise between the power output and the entropy generation. The paramount importance of this study is to provide guidance for optimal design in terms of entropy generation rate, power, and thermal efficiency of Brayton cycles.

Nomenclature

A	Area, m^2	N_T	Total number of heat transfer units
$\dot{C}_w$	Product of mass flow rate and specific heat capacity, $= \dot{m}C_p$, kW K^{-1}	$\dot{Q}$	Rate of heat transfer, kW
$\dot{E}$	Ecological performance function	S	Entropy, kJ K^{-1}
ECOP	Ecological coefficient of performance	T	Temperature, K
h	Enthalpy, Cal	U	Overall heat transfer coefficient, kW m^{-2} K^{-1}
$\dot{m}$	Mass flow rate of the working fluid, kg s^{-1}	$\dot{W}$	Power output, kW

Greek Letters

ε	Heat exchanger effectiveness	η	Thermal efficiency
ϕ	Enthalpy ratio	τ	Heat sources temperature ratio, $= T_H/T_L$

Subscripts

c	Compressor	mef	Maximum ecological function conditions
g	Generation	mp	Maximum power conditions
H	High temperature heat source	opt	Optimum
L	Low temperature heat source	T	Turbine
max	Maximum	0	Environment conditions

Superscripts

*	Maximum ECOP conditions	−	Dimensionless

References

1. Cheng CY, Chen CK (1997) The ecological optimization of an irreversible Carnot heat engine. J Phys D Appl Phys 30:1602–1609
2. Bejan A (1996) Entropy generation minimization: the new thermodynamics of finite-size devices and finite time processes. J Appl Phys 79(3):1191–1218
3. Chen L, Wu C, Sun F (1999) Finite-time thermodynamic optimization or entropy-generation minimization of energy systems. J Non Equilib Thermodyn 24 (4):327–359
4. Chen L, Sun F (2004) Advances in finite-time thermodynamics: analysis and optimization. Nova, New York, NY
5. Chen L, Zheng J, Sun F, Wu C (2002) Performance comparison of an irreversible closed Brayton cycle under maximum power density and maximum power conditions. Exerg Int J 2:345–351
6. Kaushik SC, Tyagi SK (2002) Finite time thermodynamic analysis of a non isentropic regenerative Brayton heat engine. Int J Sol Energ 22:141–151
7. Chen L, Sun F, Wu C (1997) Theoretical analysis of the performance of a regenerated closed Brayton cycle with internal irreversibilities. Energ Convers Manag 18:871–877
8. Durmayaz A, Sogut OS, Sahin B, Yavuz H (2004) Optimization of thermal systems based on finite-time thermodynamics and thermoeconomics. Progr Energ Combust Sci 30:175–217
9. Angulo-Brown F (1991) An ecological optimization criterion for finite-time heat engines. J Appl Phys 69:7465
10. Yan Z (1993) Comment on 'An ecological optimization criterion for finite time heat engines'. J Appl Phys 73:3583
11. Angulo-Brown F, Paez-Hernandez R (1993) Endoreversible thermal cycle with a nonlinear heat transfer law. J Appl Phys 74:2216–2219
12. Cheng CY, Chen CK (1998) Ecological optimization of an endoreversible Brayton cycle. Energ Convers Manag 39:33
13. Cheng CY, Chen CK (1999) Ecological optimization of an irreversible Brayton heat engine. J Phys D Appl Phys 32:350–357
14. Curzon FL, Ahlborn B (1975) Efficiency of a Carnot engine at maximum power output. Am J Phys 43:22–24
15. Ust Y (2004) Ecological performance analysis and optimization of power generation systems. Ph.D. thesis, Progress report, Yildiz Technical University, Turkey (in Turkish)
16. Ust Y, Sahin B, Sogut OS (2005) Performance analysis and optimization of an irreversible dual cycle based on ecological coefficient of performance criterion. Appl Energ 82(1):23–29

Muharrem İmal and Çelebi Karapınar

Abstract

In this study, sulfur dioxide (SO_2) and particulate substance (PM) density rate have been measured through analyzing the various factors affecting the air quality in Kahramanmaraş. It has been aimed to point out how the air pollution could be cut down to a minimum with these parameters.

For this purpose, SO_2 and PM density rates between the years 2007 and 2012 from Provincial Environmental Directorate of Kahramanmaraş, temperature and wind range values from Provincial Meteorology Directorate of Kahramanmaraş, the increase of population from Turkish Statistical Institute, the volume of consumed natural gas, and the increase rate in the number of subscribers between the years 2007 and 2012 from ARMADAŞ (incorporation of distribution) have been obtained.

Keywords

Natural gas • Air pollution • SO_2 • PM

Introduction

Air, just like water and soil, is an environment which can be polluted. Air pollution can be described as the presence of one or more pollutants in air at a certain level and period of time that will harm human life, habitat, both articles of trade and personal belongings, and environmental quality [1].

The source of pollutants leading to pollution in the atmosphere is varied. Beyond doubt primary particles leading to air pollution are fossil fuels which are used as a source of energy. Also some particles released as gas by chemical industry, some kind of metallurgical dust, the dust emitted by cement chimneys, and other industrial activities are the causes of pollution [2].

One of the most important negative factors of modern life in human life is air pollution. Air pollution, in general environmental pollution, began to come into question as far from the nineteenth century when industrialization had started developing rapidly. A case of air pollution indicates a complex structure with its social, technical, and economical dimensions, and every country makes its legal and technical regulations in accordance with its structure. In these regulations, air pollution is tried to be controlled within the harmless limits in terms of environmental health [3].

In Turkey, depending on the meteorological conditions especially in winter in some urban areas, air pollution is observed. Main causes of air pollution resulting from heating in winter can be listed as the use of poor-quality fuels without overhauling process, wrong combusting techniques and lack of maintenance in combustion systems. But in heating, as a result of the use of natural gas and high-quality fuels, especially in big cities, air pollution has been reduced compared to the 1990s.

M. İmal (✉) • Ç. Karapınar
Mechanical Engineering Department, Faculty of Engineering, University of K. Maraş S. I., Kahramanmaraş, Turkey
e-mail: muharremimal@ksu.edu.tr; celebikarapinar@hotmail.com

While building industrial plants, inappropriate locating also increases negative effects of air pollution. Because of high sulfur content of domestic lignite used in coal based thermal power plants and lack of treatment systems in some facilities; sulfur dioxide (SO_2) emissions pose a problem.

Materials and Methods

Air pollution can be described as a mixture of pollutants, enough to harm people and the environment, into air [1]. But there are particulate substances in fresh air, named as fog, smoke, vapor, etc. Particulate emission may result from human doings (fuel combustion, grinding stones and minerals), natural resources (volcanoes, wind erosion, sea waves, natural corrosion), and atmospheric reactions (Table 72.1).

In our country, SO_2 and PM rates are measured in air pollution measurement stations. Among the gaseous pollutants sulfur oxide is the most common nonflammable and colorless air pollutant. Its retentivity in the atmosphere lasts for about 40 days. Often it arises from the combustion of fossil fuels. More than 80 % of anthropogenic sulfur oxide is estimated to have arisen from industrial resources [4]. Particulate substance is the mixture of solid particles suspended in the atmosphere with liquid droplets. Particle size is very wide in range. Some particles such as dust and smoke are big enough to be seen through naked eye. Along with this, there are also microscopic particles [5].

Effect of Topography on Air Quality

In this study, how the natural gas use and topography change the amount particulate substance SO_2 is studied.

Especially in cities where air pollution is very high, as a result of failure to take necessary measures there has been air pollution problem and in case critical meteorological conditions occur, air pollution starts to threaten the environment and human health [6].

Kahramanmaraş has been settled in around the mount of Ahir. As the population has increased, the city has expanded upward, to the foothills of the mountain. That the city has expanded in this direction has had a positive impact on the air quality of the city. Especially in winter when viewed from a vantage point, it can be seen the pit area of the city, which is called "Ancient Maraş," is under a cloud of smoke. But in newly urbanized higher part of the city, this cloud of smoke is less.

It will be helpful to study the reports of Provincial Directorate of Environment in order to more clearly observe this circumstance.

In the center of Kahramanmaraş, there is one air quality monitoring station. Until 2009 March, this station had been located in the yard of Governor's Office, which is the pit area of the city, then has been moved to the yard of City Cultural Center, which is in newly urbanized and higher part of the city (Fig. 72.1).

Based on this information, comparison between the parameters about the air quality of the periods 2007–2008 and 2009–2012 will provide us with the information about whether topography has an effect on air quality or not (Figs. 72.2 and 72.3).

When Figs. 72.4, 72.5, 72.6, and 72.7 above are analyzed, it can be seen the PM and SO_2 parameters of the periods 2007–2008 and 2008–2009 are in the same line with each other. Also, the PM and SO_2 graphs of 2009–2010 are in the same line with each other. But a significant change stands out in the graphs starting from third month of 2009. This coincides with the date of the location of air quality

In order to see this change more clearly, we have to examine the following analysis where PM and SO_2 parameters of the years from 2007 to 2011 are supplied in a single graph.

Table 72.1 Clean and polluted settlements

Pollutant	Clean air	Polluted air
PM_{10}	10–20 μg/m3	260–3,200 μg/m^3
SO_2	0.001–0.01 ppm	0.02–3.2 ppm
CO_2	300–330 ppm	350–700 ppm
CO	1 ppm	2–300 ppm
NOx	0.001–0.01 ppm	0.3–3.5 ppm
T. Hydrocarbons	1 ppm	1–20 ppm
T. Oxidants	0.01 ppm	0.01–1.0 ppm

Fig. 72.1 The SO₂ parameters measured monthly for the years 2007 and 2008

Fig. 72.2 The PM parameters measured monthly for the years 2007–2008
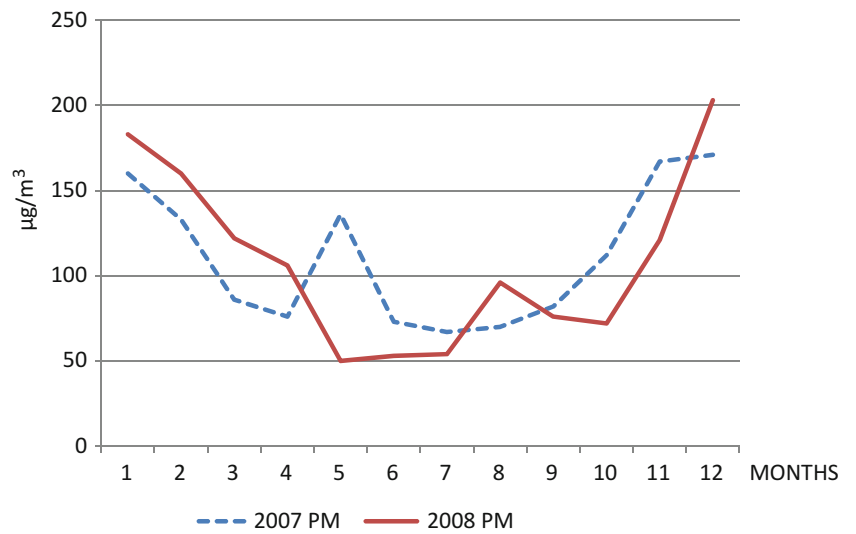
Fig. 72.3 The SO₂ parameters measured monthly for the years 2007 and 2008
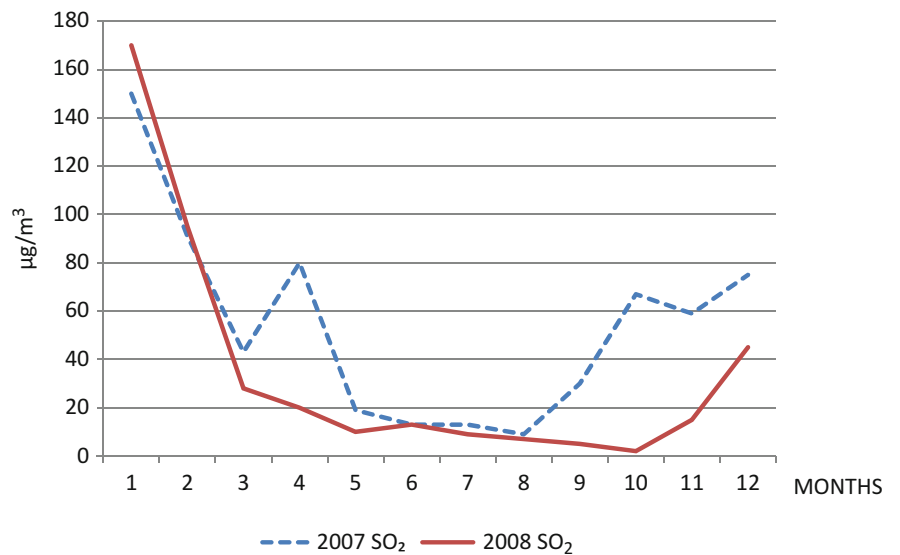
Fig. 72.4 The SO$_2$ parameters measured monthly for the years 2008 and 2009
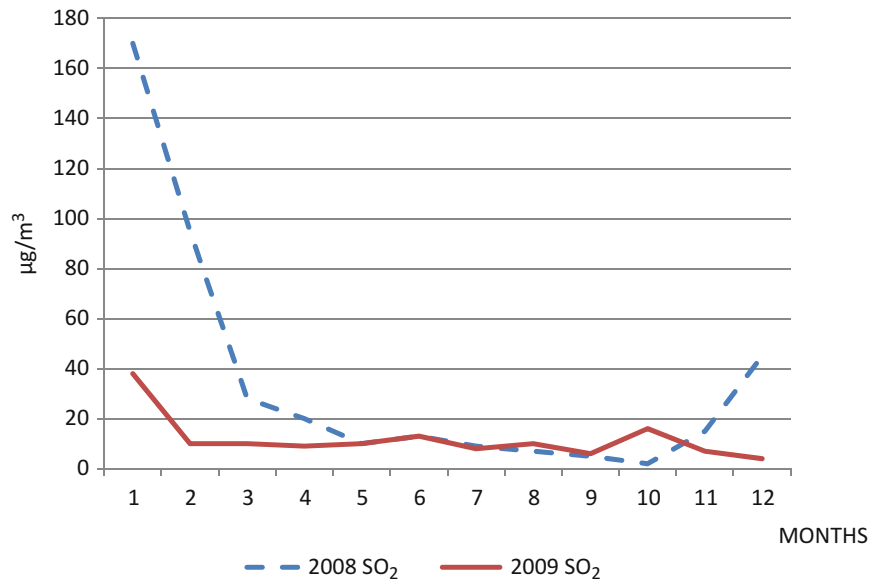
Fig. 72.5 The PM parameters measured monthly for the years 2008 and 2009
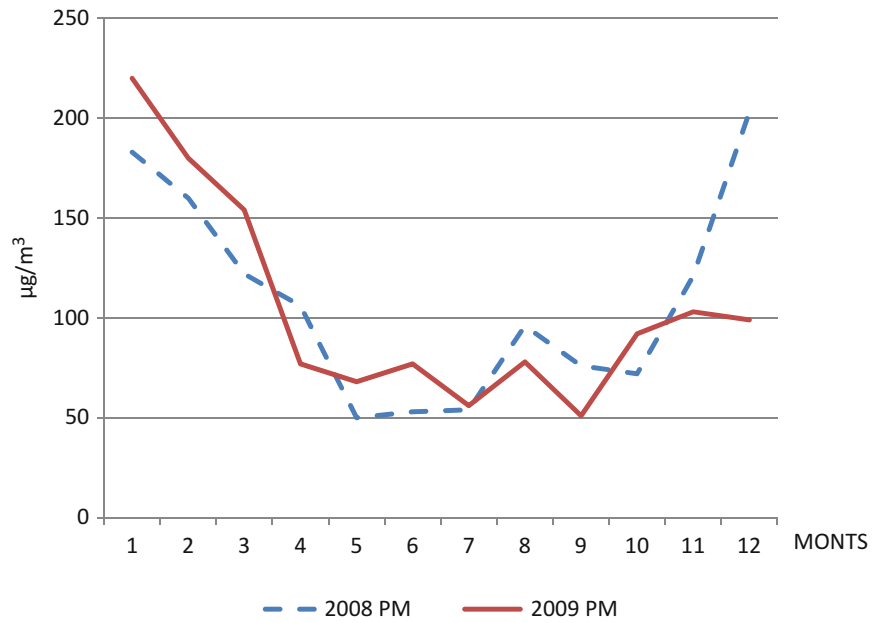
Fig. 72.6 The PM parameters measured monthly for the years 2009 and 2010
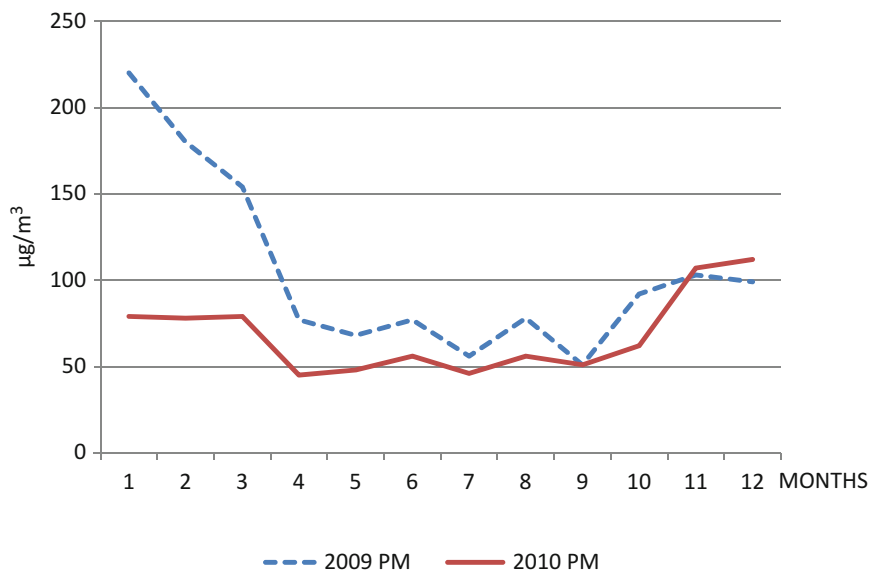
Fig. 72.7 The SO₂ parameters measured monthly for the years 2009 and 2010
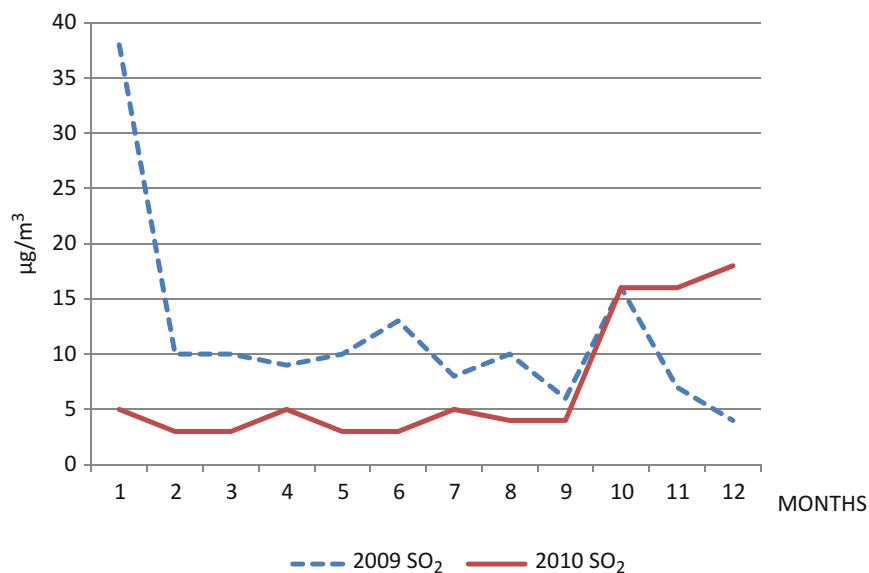
Fig. 72.8 The PM parameters measured monthly for the years 2007–2011
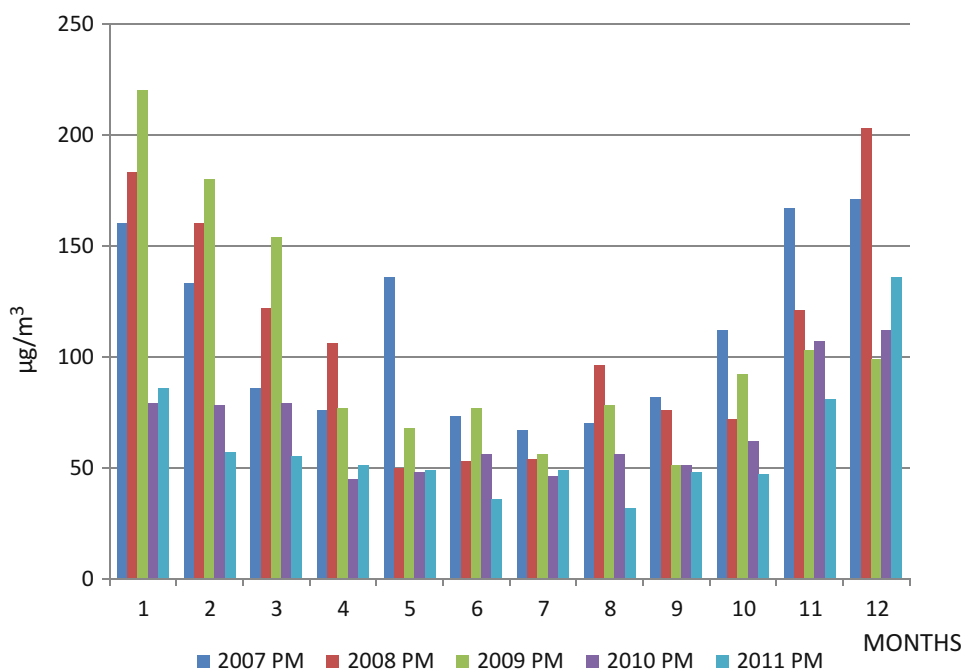
When the PM parameter of 5 years shown in Fig. 72.8 are analyzed it can be easily seen that these parameters have changed significantly, especially starting from 2009. As mentioned earlier, the location of air quality monitoring station was replaced in February 2009. As a result of this replacement, there has been a significant reduction in PM parameters.

The monthly change of SO₂ parameters in 5 years is given in the graph shown in Fig. 72.9.

When the PM parameters in this graph are analyzed, it can be seen that SO₂ change over the years is very sharp, especially in particular periods. From 2009 on SO₂ parameters have declined in comparison with those of 2008 and 2009. The reason for this decline is that the air quality monitoring station, that was earlier located in the yard of Governor's Office, the pit area of the city, was moved to the yard of City Cultural Center, the higher part of the city.

Furthermore, that the location of Governor's Office is in the pit area of the city directly affects the velocity of wind in this area. The average velocity of the wind here is about 0.6 m/s. Low velocity of the wind hampers the dispersion of pollutants collected over the city.

Fig. 72.9 The SO$_2$ parameters measured monthly for the years 2007–2011
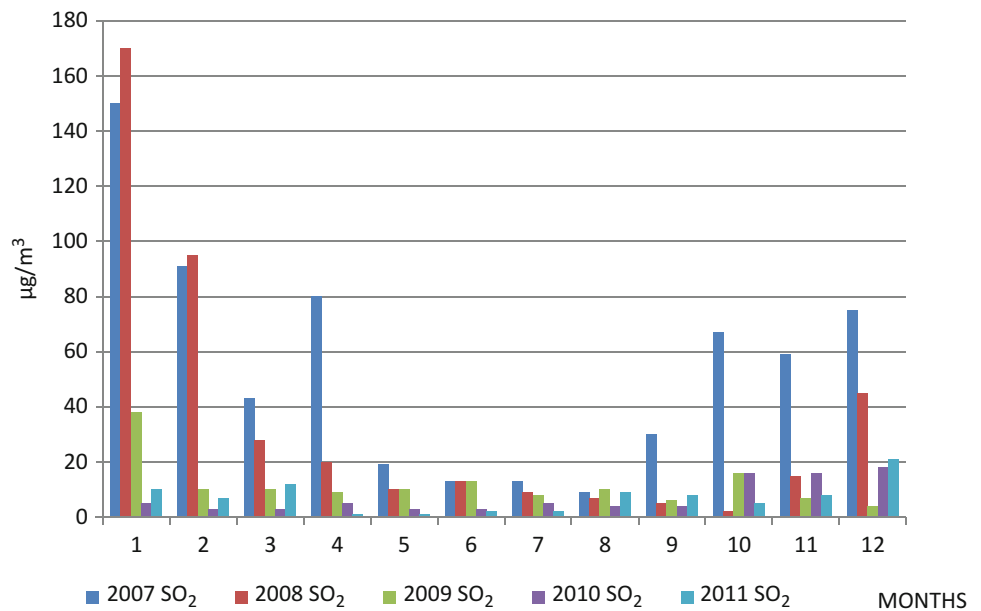
Table 72.2 Number of subscribers in Kahramanmaraş in years

The number of subscribers declared by Arsan Maraş natural gas distribution Inc.	
Date	Number of subscribers
31.12.2007	7,887
31.12.2008	14,460
31.12.2009	19,835
31.12.2010	30,545
31.12.2011	42,229
01.05.2012	43,779
Total target	100,000

Low velocity of the wind does not result only from the topography. Along with that the Governor's Office is located in the pit area of the city; this is the area where there is the highest density of buildings. In this area, the buildings are contiguous and 10-storeyed approximately. These contiguous buildings hinder the flow of wind and significantly reduce the air current. Thus, it takes a while for pollutants to disperse and move away from the area.

Based on these results, it can be said that the expansion of the city must be towards to the higher and plain part where there is fluent air current rather than the pit area where there is less air current. Furthermore, the buildings must be built in a way that they do not hamper the air current.

In the light of the data above, it is clear that the topography of the city directly affects its air quality.

The Effect of Fuels Burned for Heating

One of the main sources of air pollutants in Kahramanmaraş is the fuel used for heating. Coal and natural gas are used for heating in dwellings and workplaces for heating. In 2011, 145,000 ton of coal was sold for heating by the vendors of imported coal and 31,000 ton of domestic coal was distributed by the Social Aid Association in Kahramanmaraş. In the same period 81,650 million m^3 of natural gas was consumed in the city.

Natural gas began to be used in 2006 in Kahramanmaraş and the number of subscribers is increasing day by day. Even if it was not at desired level in 2007–2009 when the economic crisis was influential, in 2010 and 2011 the sector recovered from this recession and the number of subscribers began to increase. According to the data received from ARMADAŞ, incorporation of distribution, the number of subscribers in years 2007–2012 is as follows in Table 72.2 [7].

Table 72.3 Emission coming out as a result fuels, equivalent to 1 ton of oil

Fuel emission (kg)	Coal (% sulfur % 10 ash)	Fuel oil (%1 sulfur)	Natural gas
PM	100	1.8	0.1–0.3
Sulfur oxide	29.2	20	–
Carbon monoxide	1.5	0.7	0.3
Nitrogen oxides	11.3	8.2	2.3–4.3
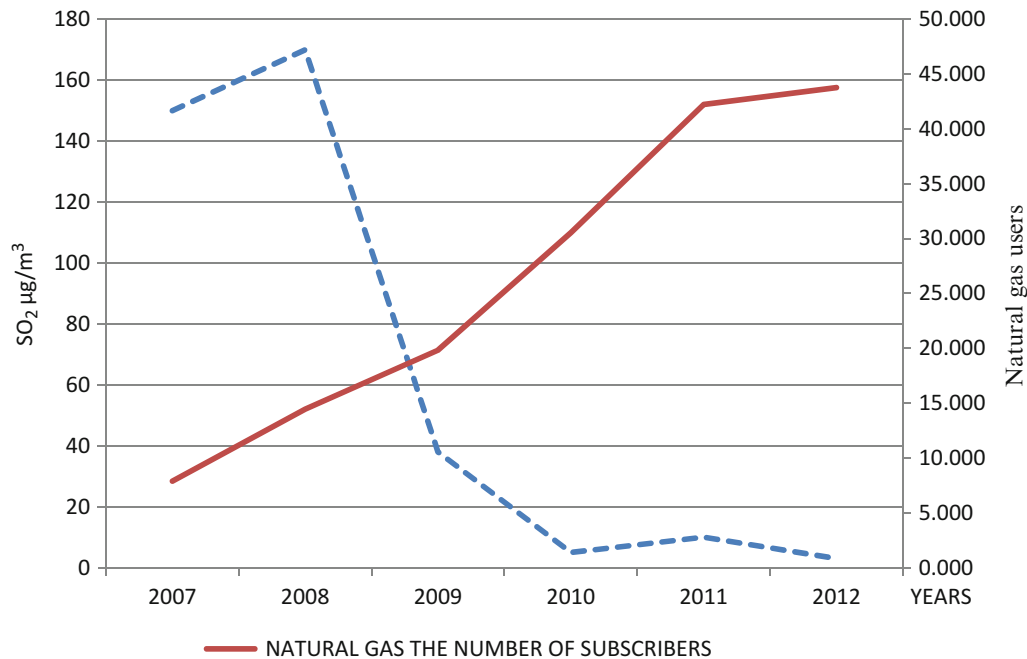
Fig. 72.10 SO_2 parameters measured monthly for the years 2009–2010

That natural gas is a clean fuel makes it advantageous in terms of boiler maintenance and performance. When fuel oil or coal is burned, ash and soot accumulated on the inner layer of boiler both corrode it and lower the efficiency hindering heat conduction. So the boiler pipes must be cleaned at least twice a week, whereas this is not the case in natural gas [8].

Furthermore, natural gas, emission standard of which is quite low in comparison with other types of fuels used, is crucial in terms of air quality. In Table 72.3 Some emission standards of coal fuel oil and natural gas, each of which is equivalent to 1 ton of oil [9].

About 40 % of objected natural gas user number has now been achieved and these subscribers have been using natural gas since April 2012. This situation is supposed to affect the air quality. In order to observe the effect of increased natural gas use, the air quality reports of Kahramanmaraş in years 2007–2011 are examined in graph.

In Fig. 72.10 the change in SO_2 parameters in February compared to the number of natural gas users in Kahramanmaraş is observed. It is observed that there is a sharp decline in the years 2008–2009. This is because the location of air quality monitoring station was replaced in 2009. Besides this, measured SO_2 parameters continued to decline in 2010, 2011, and 2012. It has been observed that the more natural gas use resulted in the less SO_2 in the air.

As seen in Table 72.3 while there is 29.2 kg sulfur ingredient in 1 TEP coal, it is about zero in natural gas. Coal use will decline in proportion to the increased use of natural gas. Therefore, the amount of SO_2 emitted into the atmosphere will decrease.

In Fig. 72.11 the change in the number of natural gas users is indicated. A sharp decline is observed in the years 2008–2009. This is because the location of air quality monitoring station was replaced in 2009. Besides this, measured PM parameters continued to decline in 2010, 2011, and 2012. It has been clearly observed that the more natural gas use resulted in the less PM in the air.
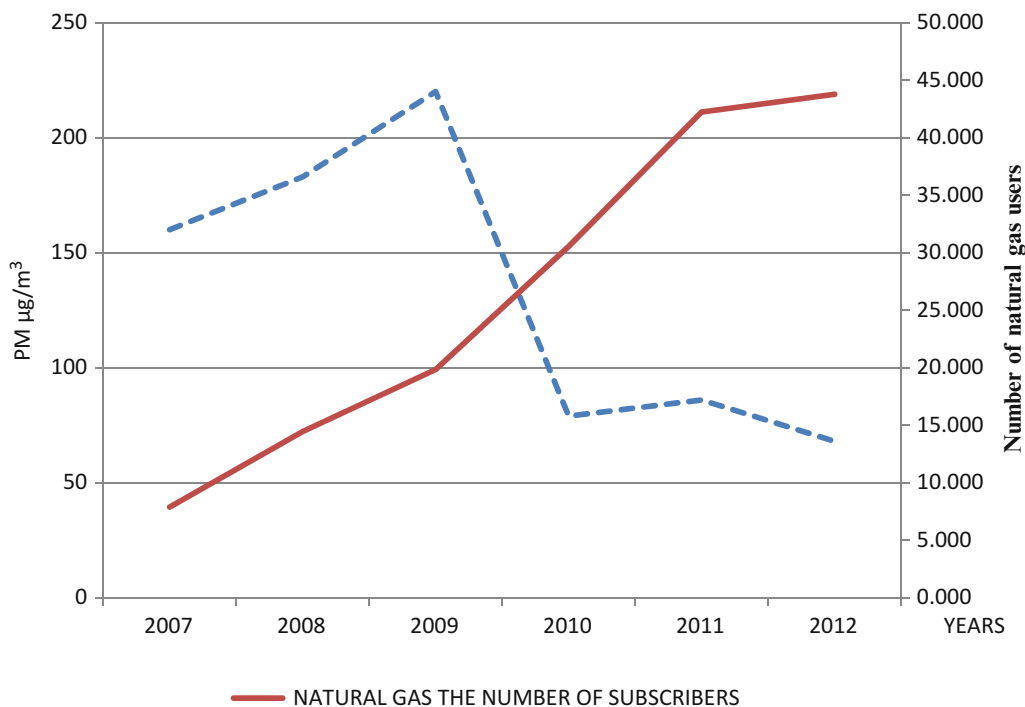
Fig. 72.11 Measured PM parameters for February in years and the change in the number of natural gas users in the city

As seen in Table 72.3 while there are 100 kg PM ingredients in 1 TEP coal, it is about 0.1–0.3 in natural gas. Coal use will decline in proportion to the increased use of natural gas. Therefore, the amount of PM emitted into the atmosphere will decrease.

Conclusion

The only air quality monitoring station in the city center of Kahramanmaraş is located in the pit area of the city, the yard of Governor's Office. In 2009, it has been moved to the yard of City Cultural Center, which is in the higher part of the city and where there is more fluent air current. It has been concluded that the topography is one of the main factors affecting the air quality of the city according to the measurements made before and after the year 2009. When constructing new neighborhoods in the city, choosing areas where there will be more air current and wind will improve the air quality. The fact that the buildings are contiguous and 10-storeyed approximately in the area of Governor's Office adversely affects the air current and hampers the dispersion of pollutants in the atmosphere. While constructing buildings in newly urbanized areas if not to cut off the air current is taken into account, the air quality improves.

Natural gas has improved the air quality in Kahramanmaraş. For this study, temperature and wind statistics over the years from the Meteorological Service, PM and SO_2 statistics from the Directorate of Environment and Urban Planning, the number of subscribers and the amount of natural gas consumed over the years from ARMADAŞ (incorporation of distribution) were collected. Using this statistics, the graphs of "SO_2—the number of natural gas users" and "PM—the number of natural gas users" were formed. It has been observed in these graphs that the more natural gas use resulted in the less SO_2 and PM in the air, especially in recent years when the number of natural gas users has increased.

The use of coal decreases in inverse proportion to the increase in the use of natural gas. This decline in the use of coal directly affects the air quality and leads to more clean air. Thus, the municipality should cooperate with the incorporations of natural gas distribution to help the natural gas be serviced to people, and the use of natural gas should be supported.

Burning equipment should be maintained regularly and renewing the economically worn-out burners will increase the efficiency. Due to the boilers running more efficiently will emit less pollutant to environment, air quality will improve. Because the boiler is renewed in the buildings that shifted to natural gas from coal, its efficiency directly increases. Besides this, the companies that take on the conversion to natural gas and boiler maintaining services inform people, and thus, the average boiler efficiency increases in proportion to the natural gas use.

References

1. Muezzinoglu A (1987) Fundamentals of air pollution and control, 0908.87.DK.006.042. Dokuz Eylul University Press, Izmir
2. Akman Y, Ketenoğlu O, Kurt L, Evren H, Düzenli S (2004) Environmental pollution. Palme Press, Ankara
3. Alp K (2010) Environmental specialist education meeting, Antalya
4. Agren C (1991) EMEP report, MCS-W 1/91 Norway
5. Ministry of Health of The Republic of Turkey (2010) General Dir. of Primary Health Care Press. No.811, Ankara
6. Ministry of Environment and Forestry of The Republic of Turkey (2004) General Dir. of Environmental Man., Circular letter of air pollution, B.18.O. ÇYG.0.02.00.02/3888, Ankara
7. Armadas (2012) The bulletin of ARMADAŞ. Arsan Maraş Natural Gas Distribution Inc, Kahramanmaras
8. (2005) http://www.cagisitmaklima.com/faydali4.htm
9. Eren Z, Turan T (2007) With the transition from fossil fuels to natural gas in the Province of Erzurum Weather Change pollution, TBMMOB 7. Chamber of Environmental Engineers, National Environmental Engineering Congress, Izmir

Soumia Zen, Fatima Zohra El Berrichi, and Ammar Maoui

Abstract

The discharge of the tanning industry constitutes enormous nuisances for the environment and exactly for the human health, in particular the various dyes which are used excessively to improve the dye industry. Therefore, the use of local clays in the treatment of the discharge has an important economic and environmental interest and with the aim for value the local's clays from Algerian East, we have selected the Djebel Debagh "DD3" and Tamazert "AT" clays which are the low-cost materials abundant in highly weathered soils. Adsorption experiments were accomplished using tannery dyes namely: Coriacide Bordeaux 3B, Derma Blue R67, and Coriacide Brown 3J, adsorbed on activated kaolin by acid treatment. The adsorption capacity of all three dyes exceeds 90 % observed after 40–80 min. Natural and treated clay samples were characterized by chemical analyses, powder X-ray diffraction, FTIR, and SEM. Finally, the obtained results confirmed the applicability of local clays as an efficient adsorbent for anionic dyes and from dyes wastewater.

Keywords

"DD3" and "AT" clays • Activation • Adsorption kinetics • Anionic dyes

Introduction

Textile and tannery effluents are two of the most polluting industrial wastes, and the problems of treatment and disposal of such wastes require much attention. The presence of dyes in aqueous effluent such as in river stream can be noticed easily because dyes are colored and highly visible. The discharge of dyes directly into aqueous effluent can endanger living organism and its aquatic ecology because most dyes are toxic. They have negative environmental effects, causing oxygen impoverishment and light transmission attenuation in aquatic ecosystems affecting both fauna and flora [1]. It is difficult to remove the dyes from the effluents, since most dyes are stable to light and heat and are not biodegradable [2]. Several conventional methods for the treatment of effluents containing dyes are available [3], and the most efficient one is the adsorption process, because it is simple in terms of operation and can remove the contaminant even at very low concentration. However, the choice of the adsorbent is based on economical and practical reasons and clay minerals are natural materials, due to their low cost and better adsorption capability, appears to be a more convenient route for removing organic pollutants and heavy metal ions [4–7]. Acid treatments of clay consist to modify its structure by changing the properties of

S. Zen
Laboratoire de chimie appliquée, Université de 8mai45, BP 401 Guelma, Algeria
e-mail: soumia.zen@yahoo.fr

F.Z. El Berrichi (✉)
Laboratoire de chimie physique, Université de 8mai45, BP 401 Guelma, Algeria
e-mail: zora172001@yahoo.fr

A. Maoui
Laboratoire de génie civil et hydraulique, Université de 8 mai 45, BP 401 Guelma, Algeria
e-mail: maoui_ammar@yahoo.fr

surface, porosity, and acidity. The results obtained through acid activation vary according to the type of clay used, its nature, the acid concentration, the temperature and the time of treatment [8]. Acid activated clay is widely used in industry as a bleaching and decontaminating agent "adsorbent" catalyst and catalyst support [9, 10]. Therefore, the aim of this study is to investigate the adsorption of specific anionic dyes, widely used in the tannery, such as Derma blue R67, Coriacide Brown 3J, and Coriacide Bordeaux 3B, on Algerian clays from Djebel Debagh "DD3" and EL Milia "AT" of which Algeria possesses millions of tons, in the East, that need to be valorized. To explore the feasibility of this clay, Bentonite was chosen to test the adsorption capacity to release the anionic dyes after treatment.

Experimental

Materials

Two commercial clays, DD3 and AT, were chosen to represent abundant raw materials without special degree of purity. The kaolin (DD3), gray in color, was obtained from the region of Guelma (Djebel Debagh) in Algeria and supplied by ETER (ceramic company in Guelma, Algeria). The type of kaolin is much rarer other clay minerals [11]. The second clay used is an Algerian kaolin "AT," type kaolinite came from EL Milia deposit "TAMAZERT" from Jijel region (Algeria), and supplied by ETER (Algeria). In order to obtain the acid-activated clays (DD3) and AT, the acid treatment was carried out with 0.1 N H_2SO_4 acid [12]. The cation-exchange capacity (CEC) was measured in order to evaluate the potential use of these clays for adsorption. The exchange was followed by the ammonium acetate method with a concentration of 2.0 mol dm^{-3} at pH 8.0, giving 15 meq g^{-1} for both clays: DD3 and AT.

The chemical composition in mass % and loss on ignition (at 1,000 °C) of natural AT and DD3 is shown in Table 73.1.

Characterisation

Mineralogical compositions of representative clays samples were determined by XRD using air-dried. XRD patterns of DD3 and AT clays (before and after activation) were collected on a X-Pert Propanalytical diffractometer using Ni filtered Cu-Kα radiation ($\lambda = 1.5406$ Å, 30 kV, 30 mA and automatic monochromator). The diffractograms were recorded in the range $2\theta = 6-65°$. The scanning speed was 1°/min. The FTIR spectra of natural and treated AT and DD3 with H_2SO_4 acid were obtained in the region 4,000–500 cm^{-1} using FT-IR spectrometer, type Perkin Elmer Spectrum one model, at room temperature dispersed in KBr disks. The morphologies of natural and activated DD3 and AT were examined using a scanning electron microscopy (Model JEOL JSM 6390 LU).

Table 73.1 Chemical analysis of natural Tamazert "AT" and DD3 clays

Component	DD3	AT
	Content mass %	
SiO_2	41.97	71.10
Al_2O_3	38.00	18.6
Fe_2O_3	0.12	0.58 to 1.22
MgO	0.07	0.39
CaO	0.20	0.02
Na_2O	–	0.22
K_2O	–	0.82
NO_2	–	0.37
TiO_2	–	–
BaO	–	0.04
SO_3	0.75	–
MnO	1.34	–
LOI	16.80	5.68

LOI loss on ignition at 1,000 °C

Dyes Solutions

The reactive dyes used as adsorbates are bifunctional dyes; they were provided by the Stahl Iberica of Spain, and they were simulated by aqueous solutions of organic anionic dyes industrially used in tanning industry, namely, Coriacide Bordeaux 3B, Derma Blue R67, and Coriacide Brown 3J. Synthetic test dye solution was prepared by dissolving an accurately weighed amount of dye (1 g/L) in distilled water and subsequently diluted to required concentrations. Their chemical formulas and complete structure diagrams are not available.

On a Photolab Spektral WTW UV–Vis spectrophotometer, the Coriacide Bordeaux 3B, Derma Blue R67, and Coriacide Brown 3J are absorbed at 510, 610 and 430 nm, respectively. Intrinsic pH values of 6.1, 5.6, and 6.3 were measured at 25 °C with a Consort C 831 potentiometer. These pH values did not vary immediately after addition of clay but only after few minutes once dye adsorption has started.

Adsorption Kinetics

In addition to Djebel Debagh "DD3" and Tamzert "AT" clays, the Bentonite was chosen to test the adsorption capacity to release the anionic dyes after treatment.

The adsorption process was conducted by adding a known amount of activated clays Tamazert "AT" or Djebel Debagh "DD3" at constant dye concentration 20mg/L and a constant stirring speed of 450 rpm. Dye adsorption kinetics was investigated at 20 °C and natural pH = 4 for 200 min.

Two milliliters of samples were drawn at suitable time intervals. The samples were then centrifuged for 15 min at 5,000 rpm and the left out concentration in the supernatant solution was analyzed through UV visible at maximum wavelength.

It was investigated the effect of the contact time, and the clay amount (2 g,6 g) on the removal rate of Coriacide Bordeaux 3B, Derma Blue R67, and Coriacide Brown 3J dyes on AT, DD3 and bentonite clays in the experiments.

The amount (mg) of dye adsorbed per unit weight of clays: Djebel Debagh "DD3," Tamazert "AT" and Bentonite at time t, Q_t (mg g^{-1}) and the percentage removal (P %) were determined by the following Eqs. (73.1) and (73.2):

$$Q_t = (C_0 - C_t)V/m \tag{73.1}$$

$$P\% = 100(C_o - C_t)/C_i \tag{73.2}$$

Where C_0 and C_t (mg/L) are the initial and liquid phase concentrations of dye adsorbed at time t respectively.

V is the volume of dye solution (L) and m is the mass of activated used (g).

Results and Discussion

Characterisation of Adsorbents

The interlayer spacing or d_{001} spacing is measured from the top of the corresponding Si tetrahedral silica sheet (T) to the top of the Si tetrahedral sheet of the following layer [13, 14]. The X-ray diffractograms of the AT and DD3 clays, before and after acid treatment, are given in Fig. 73.1. The AT and DD3 clays yielded, seven peaks in the range of 6–40° (2θ). The basal spacing is 7.26 and 7.13 Å, respectively for kaolinite (K) in DD3 and AT. The XRD pattern (Fig. 73.1a) showed sharp reflections at d = 4.42 Å; 3.62 Å (kaolinite) and the major impurities are quartz (reflection at 3.96 Å), calcite (reflection at 2.45 Å and 2.02 Å). Natural AT shows (Fig. 73.1c) reflections at 4.24 Å, 3.33 Å attributed to kaolinite and quartz, and calcite, as impurities, with reflections at 2.56 and 1.98 Å, respectively. Identical XRD patterns of activated clays (Fig. 73.1b, d) indicate the acid treatment does not affect intensely the structure of the components and shows that the d (001) band of AT and DD3 shifts to 7.23 and 7.33 Å, respectively, showing an increase of the basal distance. Furthermore, acid treatment with H_2SO_4 0.1 N, dissolves major impurities such as calcite, quartz, and dolomite for both materials.
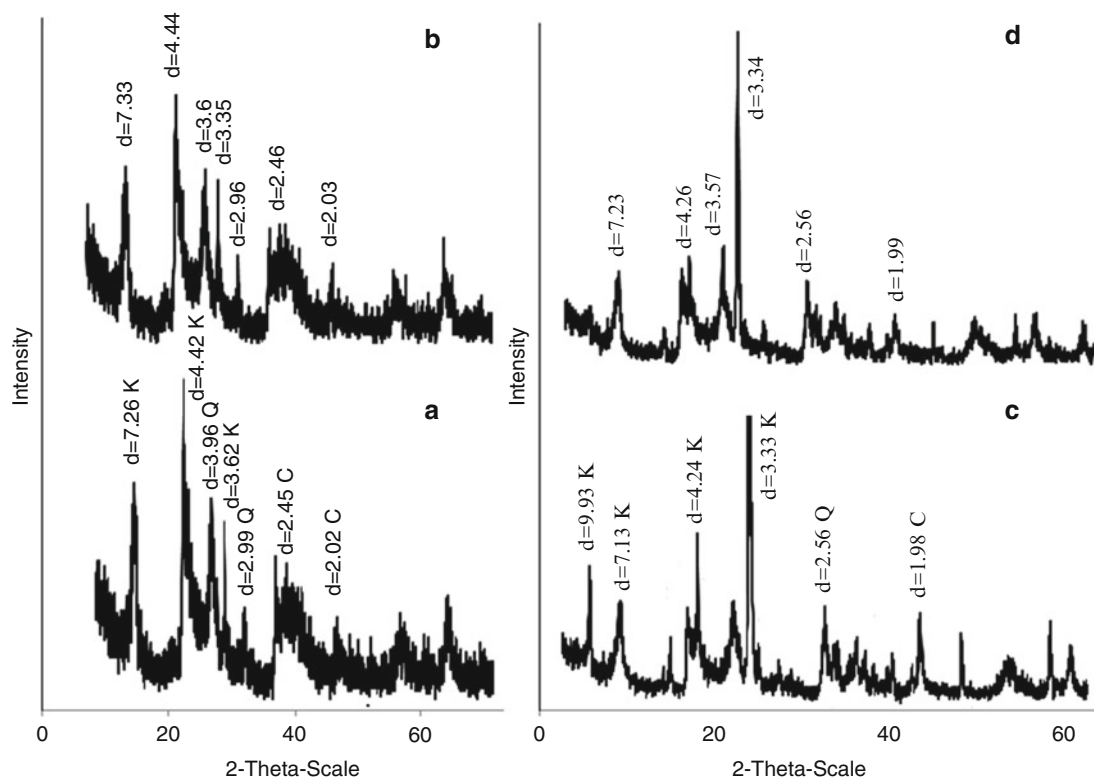
Fig. 73.1 XRD patterns of the natural and activated clays; (**a** and **c**): natural DD3 and AT; (**b** and **d**): activated DD3 and AT: K = kaolinite and impurity phases (C = Calcite, D = Dolomite, and Q = Quartz) are shown
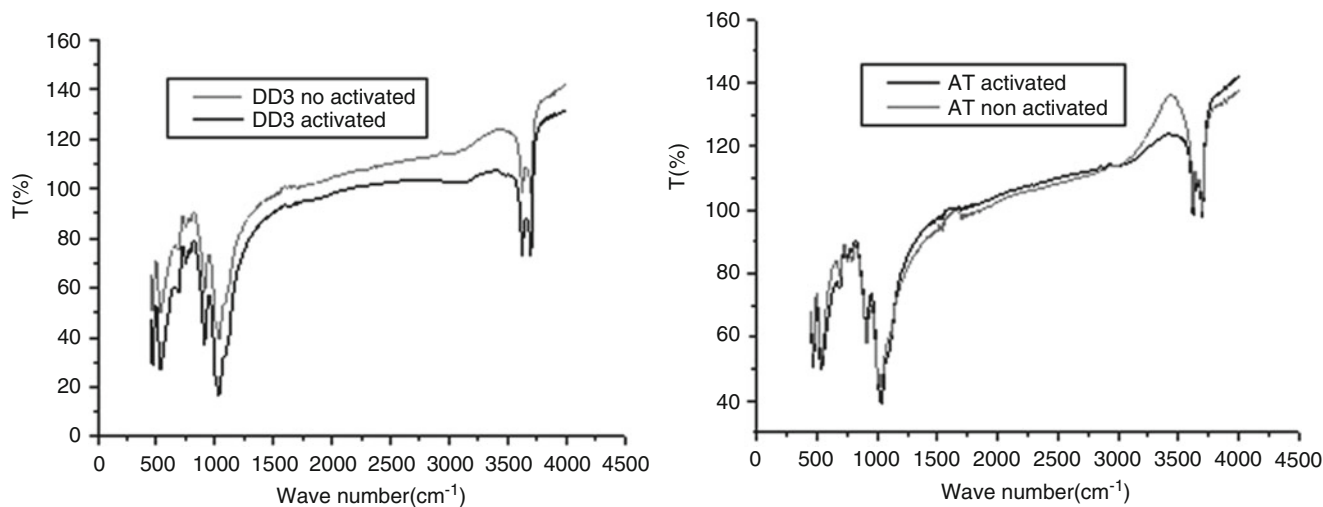
Fig. 73.2 Infrared Spectra of naturel and activated Tamazert "AT" and Djebel Debagh "DD3" clays

The Infrared Spectroscopy constitutes for the mineralogists a tool for characterization of the crystallinity of clays by the observation of the relative intensities of the bands of vibrations of hydroxyls of structure. The FTIR spectrums of natural and activated clays are shown in Fig. 73.2.

As we can see, all clays natural and activated exhibit two moderately intense bands between 3,620.64 and 3,750 cm^{-1}, which might be ascribed to the stretching frequencies of the OH functional groups of coordination water and of the hydration OH stretching. The absorption peaks between 1,620 and 1,630.53 cm^{-1} can be taken as both due to OH stretching vibration and $\delta(H_2O)$ deformation. The rest of the bands between 450 and 1,095 cm^{-1} in natural clays are due to stretching vibration of Si–O,
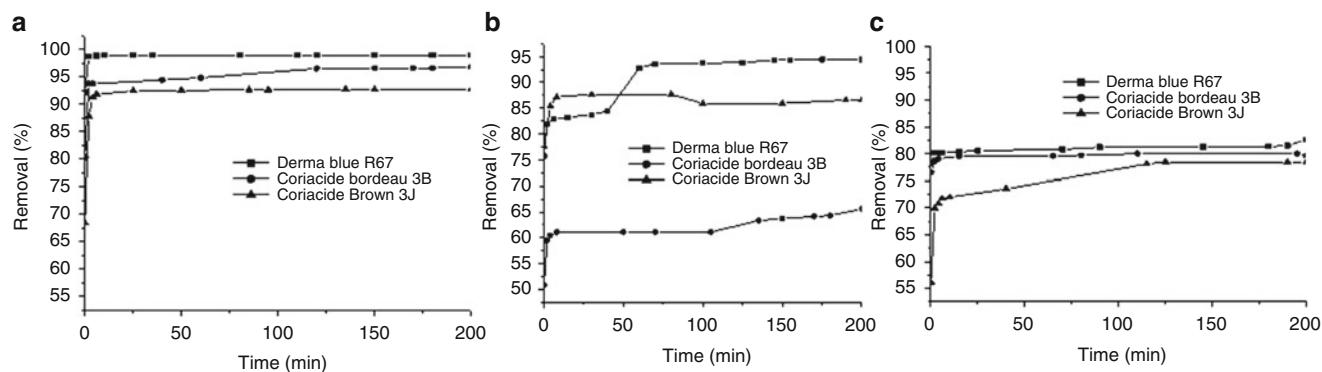
Fig. 73.3 Effect of contact time on the removal of anionic dyes on activated clays DD3 (**a**), AT (**b**), and Bentonite (**c**)

Table 73.2 Results of % removal dyes obtained at equilibrium

Anionic dyes	Activated clays	The percentage removal (P %) of anionic dye at equilibrium
Derma Blue R67	DD3	98.03
Coriacide Brown 3J		93.83
Coriacide Bordeaux 3B		96.83
Derma Blue R67	AT	94.42
Coriacide Brown 3J		89.55
Coriacide Bordeaux 3B		65.73
Derma Blue R67	Bentonite	82.70
Coriacide Brown 3J		76.0
Coriacide Bordeaux 3B		79.76

Si–O–Si, OH attached to (Al^{3+}, Fe^{3+}, and Mg^{2+}) groups, and the silica quartz impurities. After acid treatment, a significant difference is not observed between original and activated AT and DD3. Under these mild conditions, the FTIR curves showed that a weak destruction of the layers and interlayer space of activated clay was carried [15].

Kinetics of Adsorption

Effect of Contact Time

The influence of contact time on removal of Derma Blue R67, Coriacide Bordeaux 3B, and Coriacide Brown 3J by 6 g of activated Tamazert clay "AT," kaolin Djebel Debagh (DD3) or Bentonite at pH 4 and 20 °C with an initial dye concentration 20 mg/l are shown in Fig. 73.3. It is evident that all clays are efficient to adsorb dyes with different efficiencies (Fig. 73.2) and the removal of dyes was rapid and strong in the initial stages of contact time (2 min) followed by a slow increase until reaching equilibrium, due to the abundant availability of active sites on the clay surface, and with the gradual occupancy of these sites, the sorption becomes less efficient. The shape of the curves for DD3, AT, and Bentonite clays are similar. This indicates a monolayer formation of the dye on the external surface [16]. The adsorption of the activated DD3 and AT is faster than that of activated Bentonite for three dyes except the Coriacide Bordeaux 3B on activated AT. Moreover, the maximum removal percentage of three dyes adsorbed (P%) is higher for the activated DD3 (98 %) than for the activated AT (94 %) and higher than for activated Bentonite (82 %). To reach equilibrium for anionic dye as Derma Blue R67, it takes 40 min, 60 min, and 80 min for activated DD3, AT, and Bentonite, respectively. At the equilibrium, the activated DD3, AT, and bentonite fixes more Derma Blue R67 than the Coriacide Brown 3J and Coriacide Bordeaux 3B. The results of dye removal at equilibrium obtained are given in Table 73.2. Similar results have been obtained on a textile dyes adsorbed by natural and activated Bentonite [12].

Effect of Mass of DD3 Kaolin

The adsorption of three anionic dyes on the activated DD3 amount was studied on mass of kaolin of 2 g in constant dye solution of 20 mg/l at pH = 4 and 20 °C at constant stirring speed of 450 rpm. The effect of clay amount on dye removal
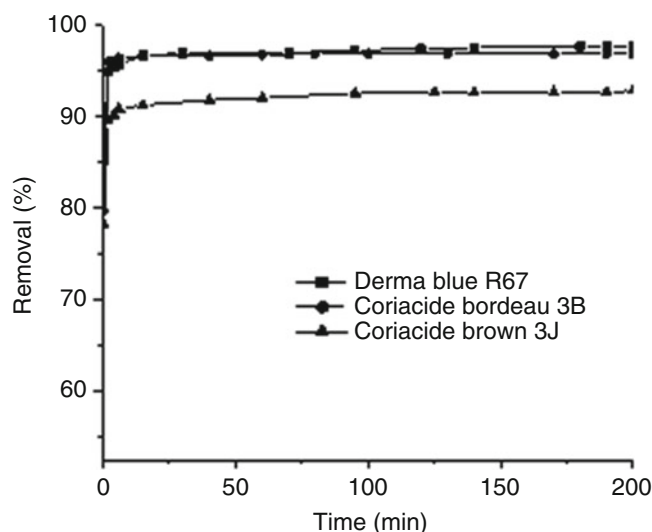
Fig. 73.4 Effect of clay amount on the removal of anionic dyes on activated kaolin "DD3"

Table 73.3 Results of % removal dyes obtained at equilibrium

Anionic dyes	Activated clays	The percentage removal (P %) of anionic dye at equilibrium
Derma Blue R67	DD3	96.81
Coriacide Bordeaux 3B		96.87
Coriacide Brown 3J		92.87

is shown in Fig. 73.4. Decreasing mass of activated DD3 induced an increasing in removal percentage of adsorbed dyes with the maximum of 97 % and it takes 40 min for Coriacide Bordeaux 3B and 75 min for Derma Blue R67 and Coriacide Brown 3J, to reach equilibrium. From Fig. 73.4 and Table 73.3, it was clear that the decrease of mass (2 g) of DD3 influences slightly the percentage removal of dyes adsorbed and its removal efficiency. This may be explained by the fact that a large adsorbent amount (6 g) reduces the saturation of the adsorption sites and correspondingly, the number of such sites per unit mass comes up resulting in comparatively more adsorption at higher adsorbent amount. Furthermore, the results obtained in dye adsorption experiments onto kaolinite showed that the adsorption capacity was higher with increasing amount clay [17, 18].

Effect of Clay Nature

Figure 73.5 shows the effect of clay nature on the anionic adsorption dye at initial dye concentrations of 20 mg/L at pH = 4 for Derma Blue as function of contact time on 6 g of activated Bentonite or DD3 or AT clays. In order to characterize the adsorption capacity on kaolin of the anionic dye "Derma Blue R67" which was fixed more than Coriacide Bordeaux 3B and Brown 3J, we have compared with activated Bentonite. The removal of Derma Blue R67 was rapid in the initial stages of contact time (Fig. 73.5) and gradually decreased with lapse of time until equilibrium. The rapid adsorption observed during the first 5 min is probably due to the abundant availability of active sites on the kaolinite surface, and with the gradual occupancy of these sites, the sorption becomes less efficient. The time required to attain this state of equilibrium was termed as the equilibrium time and the amount of dye adsorbed at the equilibrium time reflected the maximum dye adsorption capacity of the adsorbent under these particular conditions [19]. The time necessary to reach this equilibrium is about 40 min for DD3 with higher removal percentage (98 %). However, it appears from Fig. 73.5 the rapid adsorption of Derma Blue R67 on AT and Bentonite clays was observed during the first 3 min and this is followed by a strong increase of adsorption after 60 min for activated AT with higher removal percentage (94 %) than that of Bentonite (82 %) (Table 73.4). The shapes of the curves of activated DD3 and Bentonite are similar (Fig. 73.5). This indicates a monolayer formation of the dye on the

Fig. 73.5 Effect of clay nature on the removal of Derma Blue R67 on activated clays "DD3," AT, and bentonite
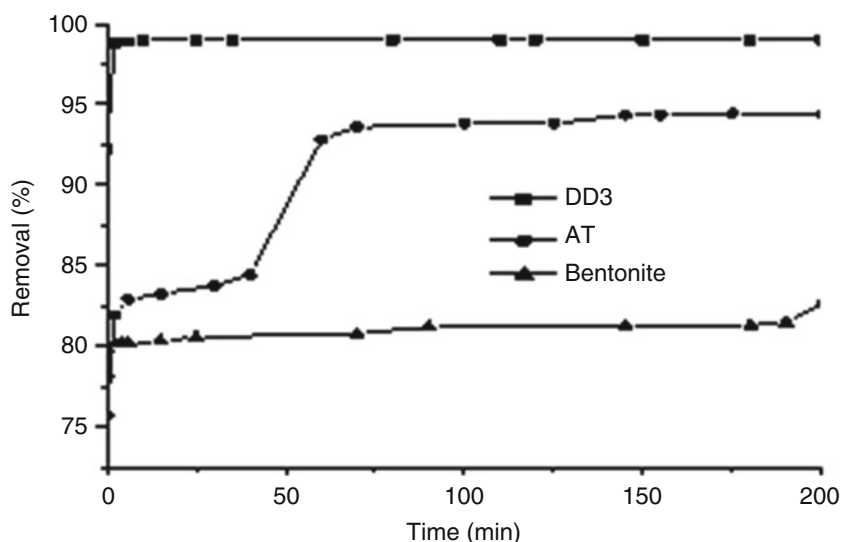
Table 73.4 Results of % removal dyes obtained at equilibrium

Anionic dyes	Activated clays	The percentage removal (P %) of anionic dye at equilibrium
Derma Blue R67	DD3	98.03
	AT	93.50
	Bentonite	82.70

external surface [16]. Thus the main process involved in anionic Derma Blue dye adsorption on activated DD3 kaolin may be the attraction on the broken edges of clay particles where charges become positive at acidic pH. That is why although acidic pH conditions were found to enhance the dye removal. On the other hand, the anionic dyes of the tannery industry used in this study are acids. The effect of clay nature on dye adsorption observed in this study was explained by electrostatic interaction between kaolinite or Bentonite and dye molecules. As the pH of the system (dye + kaolinite) is acid (pH = 4), knowing that the pH has a relatively high value for kaolinite (2–4.6) [20], the number of negatively charged sites decreases and the number of positively charged sites increases in activated DD3. Therefore, the extent of dyes adsorbed on kaolinite tended with pH system, which can be attributed to the electrostatic attraction between the positively charged surface and the negatively charged dye molecule [17]. Also, lower adsorption of anionic dyes on activated Bentonite is because of the low presence of H^+ ions competing with dye anions for the adsorption sites.

Structure of Clays After Adsorption

SEM was used to probe the change in morphological features of activated DD3 and AT before and after tanning dye adsorption (Derma Blue R67). The surface morphology of both clays before adsorption is different from that after adsorption. Activated DD3 has larger pores between particles before adsorption than activated DD3 after adsorption (Fig. 73.6a, b). The same for activated AT (Fig. 73.6c, d).

Also the micrographs presented in Fig. 73.6b, d show clearly the dye-loaded clay coated by dye molecules over the whole surface at natural pH conditions. The dye molecules seem to have formed a void-free film masking the reliefs of particles and porosity of the aggregates. On the contrary, the clay before adsorption exhibits well distinguishable particles and a porous structure (Fig. 73.6a, c).

Fig. 73.6 SEM image of DD3
and AT activated clays: (**a** and **c**):
DD3 and AT before adsorption of
Derma Blue dye; (**b** and **d**): DD3
and AT after adsorption of Derma
Blue dye
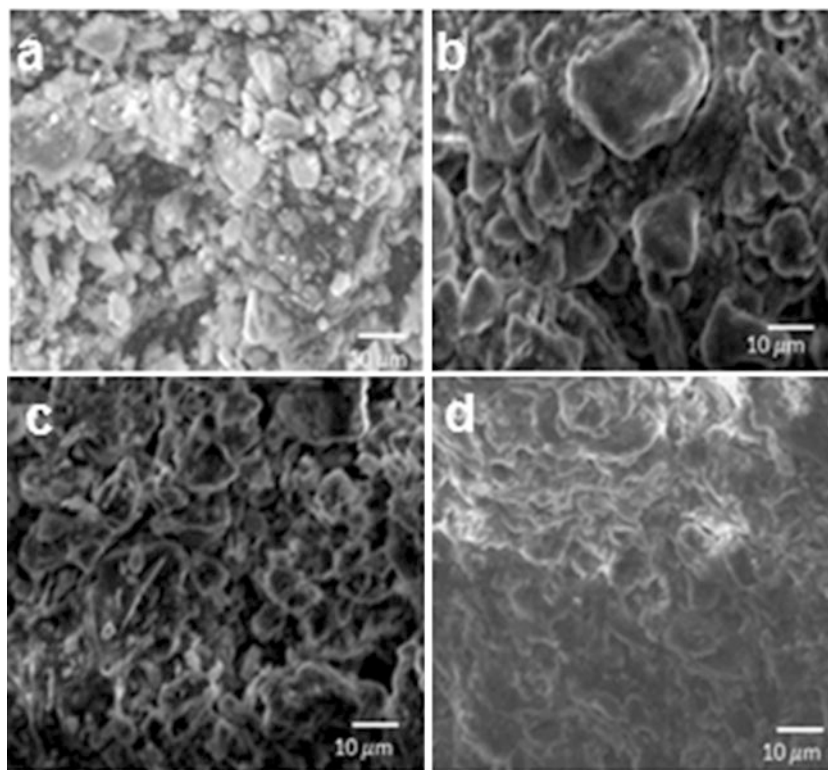
Conclusion

Algerian clay, DD3 from Djebel Debagh and AT from El Milia region, activated by acid treatment can be employed as an effective and promising low cost alternative adsorbents for the removal of anionic dyes from tannery wastewater. A comparative study of adsorption of Derma Blue R67, Coriacide Brown 3J, and Coriacide Bordeaux 3B evidences the high adsorption capacity of dye on the activated DD3 and AT than activated Bentonite. The acid activation enhances the interaction between dyes and clays "DD3 and AT," resulting in greater and fast adsorption capacity with the equilibrium was attained after 40–60 min for anionic dyes by comparison with activated bentonite, the adsorption capacity is low for all the three anionic dyes and the time to reach equilibrium was 80–140 min. The results showed that the adsorption anionic dyes on activated DD3 and AT could be explained by the electrostatic attraction between the positively charged surface and the negatively charged dye molecule in the acidic medium (natural pH = 4). Furthermore, the experiments conditions (acidic medium, activated adsorbent, low temperature) of kinetics adsorption study were found to enhance the dye removal great adsorption efficiency.

Compared to standard Bentonite clay, activated DD3 and AT have a good and high potential for adsorption removal of anionic dye from aqueous solution.

References

1. Maes M (1994) Paris. Les résidus industriels, traitement valorisation et législation. Entreprise Moderne d'Edition Technique et Documentation
2. Robinson T, McMullan G, Marchant R, Nigam P (2001) Remediation of dyes in textile effluent: a critical review on current treatment technologies with a proposed alternative. Bioresour Technol 77:247–255
3. Akar T, Demir TA, Kiran I, Ozcan A, Ozcan AS, Tunali S (2006) Biosorption potential of *Neurospora crassa* cells for decolorization of Acid Red 57 (AR57) dye. J Chem Technol Biotechnol 81:1100–1106
4. Adebowale KO, Unuabonah IE, Olu-Owolabi BI (2005) Adsorption of some heavy metal ions on sulfate- and phosphate-modified kaolin. Appl Clay Sci 29:145–148
5. Dubey SP, Gopal K, Bersillon JL (2009) Utility of absorbents in the purification of drinking water: a review of characterization, efficiency and safety evaluation of various absorbents. J Environ Biol 30:327–332
6. Gupta VK, Suha N (2009) Application of low-cost adsorbents for dye removal. Rev J Environ Manag 90:2313–2342
7. Liu P, Zhang L (2007) Adsorption of dyes from aqueous solutions or suspensions with clay nano-adsorbents. Sep Purif Technol 58:32–39

8. Srasra E (1987) Caractérisation minéralogique, propriété physico-chimique et application des argiles du gisement Haidoudi. Thèse de 3eme cycle, Fac. Sc. Tunis, p 171
9. Belver C, Angel Bañnares Munoz M, Vicente M (2002) Chemical activation of a kaolinite under acid and alkaline conditions. Chem Mater 14:2033–2204
10. Min-Yu T, Su-Hsia L (2006) Removal of basic dye from water onto pristine and HCl-activated montmorillonite in fixed beds. Desalination 194:156–165
11. Papke KG (1971) Halloysite deposits in the Terraced Hills. Washoe CT Nevada Clay Clay Min 19:71–74
12. Benguella B, Yacouta-Nour A (2009) Adsorption of bezanyl red and nylomine green from aqueous solutions by natural and acid-activated bentonite. Desalination 235:276–292
13. Güngör N, Karaoglan S (2001) Interactions of polyacrylamide polymer with bentonite in aqueous systems. Mater Lett 48:168–175
14. Majdan M, Pikus S, Rzaczynska Z, Iwan M, Maryuk O, Kwiatkowski R, Skrzypek H (2006) Characteristics of chabazite modified by hexadecyltrimethy-lammonium bromide and of its affinity toward chromates. J Mol Struct 791:53–60
15. Salem A, Karimi L (2009) Physico-chemical variation in bentonite by sulfuric acid activation. Korean J Chem Eng 26(4):980–984
16. Al-Ghouti MA, Khraisheh M, Allen SJ, Ahmad MN (2003) The removal of dyes from textile wastewater: a study of the physical characteristics and adsorption mechanisms of diatomaceous earth. J Environ Manage 69:229–235
17. Dogan M, Hamdi Karaoglu M, Alkan M (2009) Adsorption kinetics of maxilon yellow 4 GL and maxilon red GRL dyes on kaolinite. J Hazard Mater 165:1142–1151
18. Errais E (2011) Réactivité de surface d'argiles naturelles, étude de l'adsorption des colorants anioniques. Thèse de doctorat. Université de Strasbourg, p 114
19. Hameed BH (2008) Equilibrium and kinetic studies of methyl violet sorption by agricultural waste. J Hazard Mater 154:204–212
20. Schroth BK, Sposito G (1997) Surface charge properties of kaolinite. Clay Clay Min 45(1):85–91

Investigation of Turbidity Effect on Energy Transmission in a Solar Pond

Ayhan Atiz, Ismail Bozkurt, Mehmet Karakilcik, and Ibrahim Dincer

Abstract

Renewable energy sources, such as solar, play a key role due to their environmentally benign nature. There are various types of solar energy applications, including solar ponds. A solar pond consists of three different density zones: Upper Convective Zone (UCZ), Non-convective Zone (NCZ), and Heat Storage Zone (HSZ). The zones's density increases from top to bottom of the pond. Each of the zones is important and affects the performance of the pond. Because of this, many investigators aim to increase the efficiency of the pond for better performance. There are also some key parameters affecting the efficiency. One of them is turbidity, which is caused by dirt over time (e.g., insects, leaf, dust, and wind bringing parts falling down). Thus, the turbidity in the salty water decreases the heat transmission through the zones. In this study, the samples are taken from the zones of the solar pond and analyzed by using a spectrometer for one year. Furthermore, the results confirm that the performance of solar ponds is greatly affected by turbidity.

Keywords

Solar energy • Solar pond • Efficiency • Turbidity • Transmission

Introduction

Solar energy is treated as a great energy source. Turkey lies in a sunny belt between $36°$ and $42°$ N latitudes. The yearly average solar radiation is 3.6 kW h/m^2 day, and the total yearly radiation period is approximately 2,640 h which is sufficient to provide adequate energy for solar thermal applications [1].

The energy content of solar radiation can be used as light, heat, and electricity. This diversity makes solar energy an important option to power different energy systems all over the world. Indeed, the interest in solar energy systems has been increasing in recent years throughout the world. This interest has been due to several factors, such as the environmental damage, the efforts to minimize countries dependence on fossil-based and nonrenewable fuels and the international agreements demanding reduction in the greenhouse gases in the atmosphere [2]. Heat storage technologies, systems and applications are studied in the field of solar energy [3, 4]. Solar ponds and collectors are very important solar energy systems that generate heat energy from solar energy. Solar ponds are relatively simple devices that operate straightforwardly, require little maintenance (e.g., they need cleaning to maintain water transparency), and have long life times [5]. Solar ponds have been proposed and demonstrated to be simple in design, low in cost and naturally abundant for the large scale collection and

A. Atiz (✉) • M. Karakilcik
Department of Physics, Faculty of Sciences and Letters, University of Cukurova, Adana 01330, Turkey
e-mail: ayhanklicc@hotmail.com

I. Bozkurt
Department of Mechanical Engineering, Faculty of Engineering, University of Adiyaman, Adiyaman 02040, Turkey

I. Dincer
Faculty of Engineering and Applied Science, University of Ontario Institute of Technology (UOIT), 2000 Simcoe Street,
North Oshawa, ON, Canada L1H 7K4

storage of solar energy. Solar energy is received as both direct and diffuse radiation and distributed primarily over the wide range of the ultraviolet, visible and infrared spectra. A higher radiation transmission through the upper zone and gradient in a solar pond results in a higher heat collection efficiency [6]. The attenuation of light in the clearest natural waters, solar pond, and salt waters is variable. Irradiance depends not just on water and salt. There is another important impact, i.e., turbidity, and a common problem encountered in salinity-gradient solar ponds is the growth of various types of algae and bacterial populations which affects the brine clarity and hence reduces thermal performance [7].

A solar pond as a solar collector is dependent on light transmission to the storage zone. Clarity of the brine is one of the most important factors in achieving good thermal performance and stability—the higher the transparency, the better the performance [8]. Therefore, it is important to maintain the clarity of solar ponds to allow maximum possible solar radiation to reach the LCZ [9].

In the present study, we conduct an experimental investigation of a solar pond with a particular interest in the effect of turbidity on the pond efficiency and study how much effect is possible under various conditions.

Experimental Apparatus and Procedure

Solar Ponds

In general, solar ponds are composed of three zones. The first zone, so-called: upper convective zone (UCZ), is the fresh water layer at the top of the pond. This zone is fed with fresh water in order to maintain its density as close as to the density of regular fresh water. The second zone is the non-convective zone (NCZ), lying between the heat storage zone (HSZ) and UCZ. NCZ is composed of salty water layers whose brine density gradually increases towards HSZ. NCZ is the key to the working of a solar pond. The third zone is known as heat storage (HCZ). HSZ is composed of salty water with highest density. Considerable part of the solar energy is absorbed and stored by this bottom region [10].

In the present experimental work, a solar pond with a radius of 0.80 m and a depth of 2 m was built in Cukurova University in Adana, Turkey (i.e., 35°18′ E longitude, 37°05′ N latitude). The experimental temperature distributions were measured using temperature sensors, which were placed into the inner zones of the solar pond. The bottom and the side-walls of the pond were plated with the iron sheets in 0.005 m thickness and in between with a glass–wool of 0.10 m thickness as the insulating layer. Figure 74.1 illustrates the inner zones of the solar pond. The inner zones consist of the saline water layers with various densities. To measure the temperature distributions of various regions, the temperature sensors were placed into the inner zones, starting from the bottom, at 0.10, 0.30, 0.50, 0.70, 0.90, 1.10, 1.30, 1.50, 1.70, 1.90 m heights. The data acquisition system was connected to a computer for data recording monitoring. Hence, the temperature distribution profiles of these regions at any time were
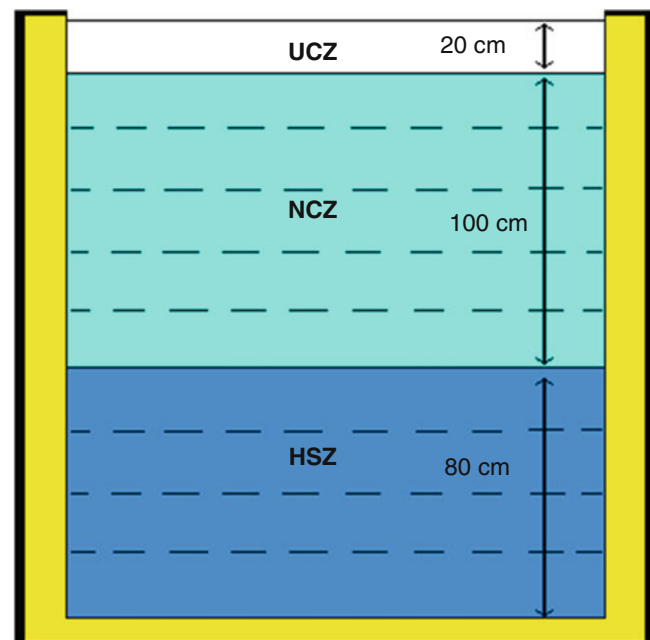
Fig. 74.1 Inner zones of the solar pond

experimentally obtained by a data acquisition system. The solar pond is filled up with salty water. HSZ is started from the bottom of the pond until 0.80 m height and its density approximately 1,180 kg/m^3 with salt water. The middle zone, NCZ, is composed of salty water layers whose brine density gradually increases towards HSZ. NCZ has five layer thicknesses, and each layer is 0.20 m thick. These layers have a density between 1,100 and 1,015 kg/m^3 decreasing as graded. The surface zone, UCZ, is the fresh water layer at the top of the pond.

The salinity gradient sustainability of the solar pond is very important for heat storage performance. Therefore, the density of the solar pond becomes critical. To measure the density distribution of the solar pond, place 5 mm diameter 10 unit transparent plastic hoses with 20 cm distance on a 2 m length board in the pond. The salinity water samples of the layers are taken from the hoses to measure density by using a hydrometer.

Salt Gradient Protection System

The density gradient in the NCZ is very important to keep the stored energy. In order to maintain the density gradient of the pond, an auxiliary operating system on a feedback principle was developed since it generates a continuous and self-regulating operation. This was a passive system based on the natural circulation of water caused by density difference as it was first proposed by Akbarzadeh and MacDonalds [11]. It was built as a cylindrical polyethylene tank having 1.20 m length and 0.30 m diameter. The tank has a connection from its bottom to the top of the HSZ. Because of the density difference between the storage zone and a higher zone, the less dense brine entered via a plastic tube to the top of the tank from the top of NCZ and diffused through a salt bed on a mesh within the tank and reached about 1,180–1,200 kg/m^3 density at the bottom. This denser brine was injected into the top level of HSZ via a distributing pipe system. The salty water distribution system was made of a circular polyethylene pipe with a diameter of 1.20 m and a thickness of 0.02 m diameter. It has several holes along them to lead the higher density brine out at the top of the HSZ [12].

Spectrometer

A spectrometer was used to measure the properties of light over a specific portion of the electromagnetic spectrum as it is used in spectroscopic analysis to identify materials [13]. The measurement samples contained a solution of distilled water and normal grade salt. The following salts were studied: $MgCl_2$, Na_2SO_4, $NaNO_3$, KNO_3, and Na_2CO_3. The transmission spectra were measured with a spectrometer in the range of 300–1,200 nm. The quartz–glass sample containers of 50 mm length were of good quality [14].

Optical Properties of Salty Water

Essentially all of the solar radiation absorption that takes place in most natural waters is attributable to three components (the water itself, dissolved organic matter, variously referred to as yellow substance gelbstoff and gilvin) Kirk [15]. In order to increase the energy input, in relation to the storage zone of the solar pond, NCZ and UCZ should be as transparent as possible because both the intensity of incident ray and the absorptance of salt-water solution depend on the wavelength to calculate the total transmittance precisely [16].

Estimation of total solar radiation available at various depths of a salt gradient solar pond is an integral part of modeling its thermal performance. The radiation flux incident at the surface of the pond gets partially reflected, and the remainder penetrates into the pond. The radiation flux as it propagates through the body of the pond gets attenuated in its path [17]. The relation among absorption, reflection and transmission coefficients is given as

$$\rho + \alpha + \tau = 1 \tag{74.1}$$

where α, ρ, and τ are the absorption, the reflection, and the transmission, respectively.

Most of the solar radiation in the near infrared spectrum is absorbed within the first few centimeters of depth. The radiation associated with wavelengths greater than 1,200 nm represented 22.4 % of the total incident radiation, and this radiation was totally absorbed in this upper water boundary layer for radiation with $\lambda < 1,200$ nm [18]. The radiation emitted by the sun travels through the vacuum of space unaltered. The percentage of energy associated with certain

bandwidths of solar radiation emitted from a blackbody at 5,800 K (the temperature of the sun) [19]. The light entering the pond is also scattered by the various suspended particles. The scattering particles however are not assumed to absorb energy [20].

Here, we note that β is the fraction of the incident solar incident that actually enters the pond [21].

$$\beta = 1 - 0.6 \left[\frac{\sin\theta_i - \sin\theta_r}{\sin\theta_i + \sin\theta_r}\right]^2 - 0.4\left[\frac{\tan\theta_i - \tan\theta_r}{\tan\theta_i + \tan\theta_r}\right]^2 \tag{74.2}$$

where θ_i and θ_r are the incidence angle and the refraction angle. The attenuation of radiation through a pure medium is described by the Bouguer–Beer Law; to measured solar energy with deep giving Lambert–Beer Law which is dependent on wavelength λ and way, ray of light intensity in the x deep as follows:

$$I_\lambda(x) = I_{0i} \exp(-\mu_\lambda x) \tag{74.3}$$

where $I_\lambda(x)$ is the wavelength λ bunch of the beam in the x depth. I_{0i} is incoming part of sun's energy and $\mu_\lambda = -1/\delta_\lambda$ is the absorption coefficient of the beam at the wavelength (λ), δ_λ is the characteristic absorption depth of the incident beam. By using Eq. (74.3) we can calculate the transmission of the incident beam at any depth to contribute of energy transmission from various portions of the beam spectrum, which is divided into several spectral bands. Then, the absorbing beam function of at any depth is given as

$$\sum_{i=1}^{n} I_i = \sum_{i=1}^{n} I_{0i} \exp(-\mu_i x) \tag{74.4}$$

which can be arranged to find the absorbing rate of function $h(x)$ as

$$h(x) = \frac{\sum_{i=1}^{n} I_{0i} \exp(-\mu_i x)}{\sum_{i=1}^{n} I_{0i}} \tag{74.5}$$

where we employ $\frac{I_{0i}}{\sum_{i=1}^{n} I_{0i}}$ as η_i and obtain the following relation:

$$h(x) = \sum_{i=1}^{n} \eta_i \exp(-\mu_i x) \tag{74.6}$$

Results and Discussion

A solar pond is an important thermal energy system to store the heat energy in the heat storage zone. The heat storage performance of the storage zone is decreased due to turbidities in the salty water layers of the inner zones of the pond. The experimental study is consist of two part to determine the effect on turbid water layers of the pond performance. The first part of the experimental investigation is carried out to determine the temperature and density distribution of the solar pond. In the second part of the experiment, some spectroscopic analyses are carried out to determine the transmission of various densities salty water of the inner zones' layers to determine the turbidity effect on the performance of the solar pond by using spectrometer. As seen in Figs. 74.2 and 74.3, the differences of the salinity gradient is kept approximately stable by using salt gradient protection system.

Figures 74.4 and 74.5 show the transmissions of the turbid water and clean water samples getting at ten different points of the ponds at different times, vertically. The characteristic transmission of ponds appears to be very different from each other. A UV–Vis spectrometer was used in order to understand the characteristic transmission of each of the samples (e.g., clear

Fig. 74.2 Variation in the density with depth in August, 2009
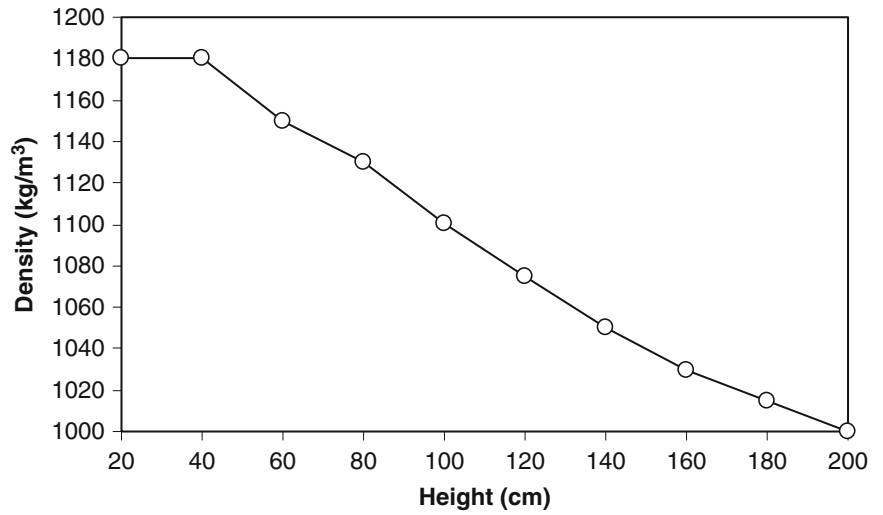
Fig. 74.3 Variations in the density with depth in August, 2010
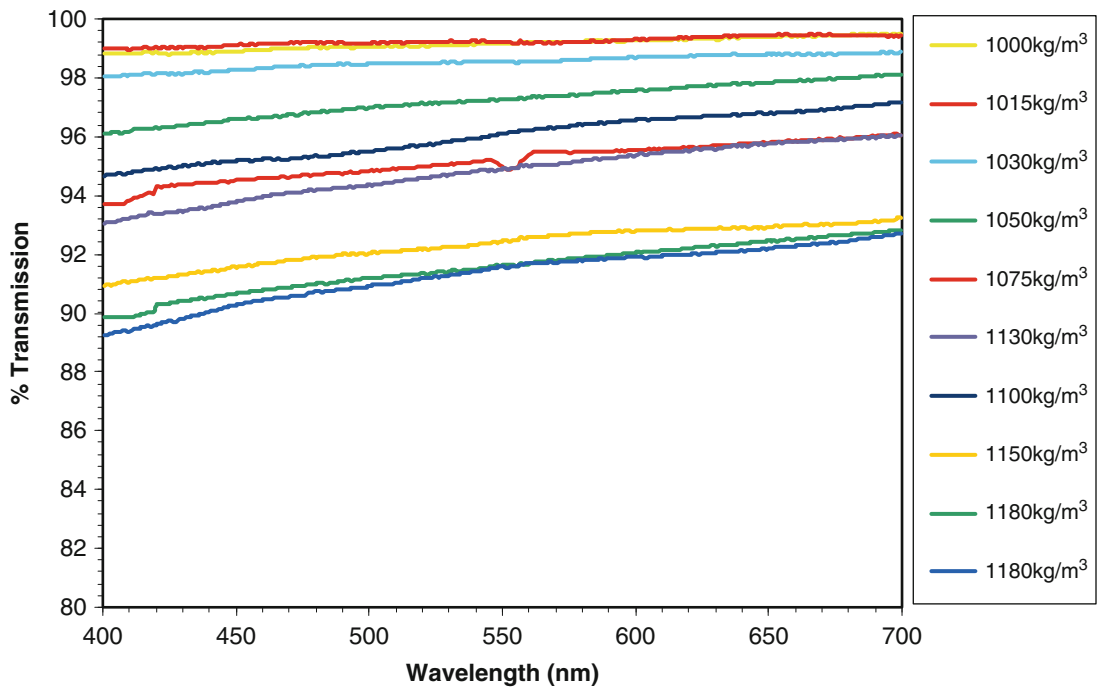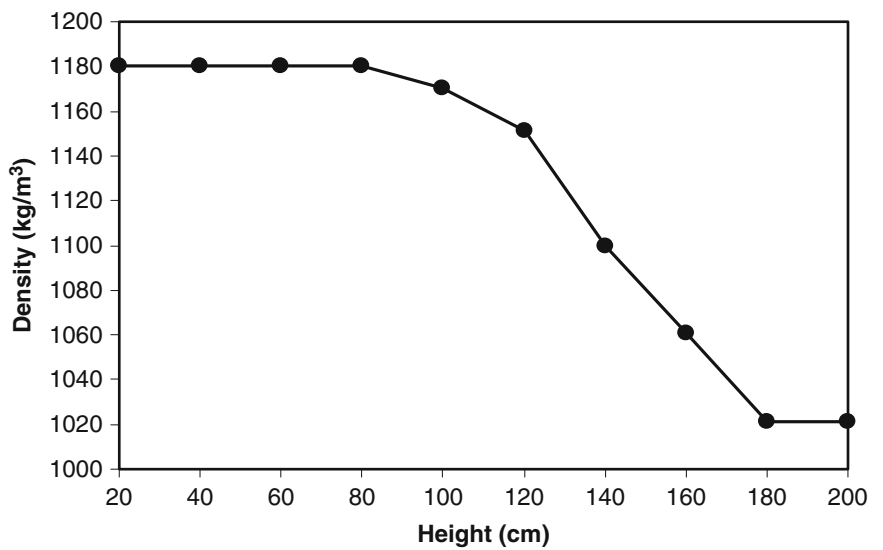
Fig. 74.4 Variation of the transmission of the wavelength for clean water of solar pond in August, 2009
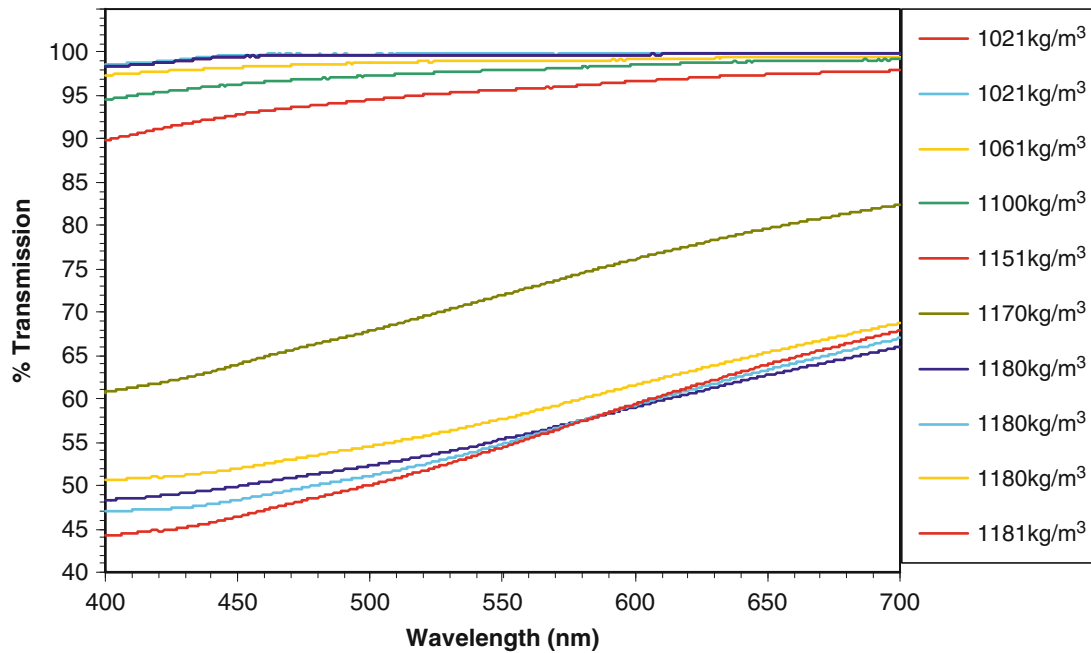
Fig. 74.5 Variation of the transmission of the wavelength for turbid pond in August, 2010

Table 74.1 Absorption coefficients with respect to transmission data for turbid solar pond

Height(cm)	Bandwidth (nm)		
	600–700	500–600	400–500
0–20	0.002	0.005	0.015
20–40	0.002	0.004	0.006
40–60	0.005	0.011	0.004
60–80	0.012	0.024	0.036
80–100	0.025	0.044	0.101
100–120	0.222	0.244	0.159
120–140	0.224	0.247	0.159
140–160	0.265	0.343	0.247
160–180	0.248	0.296	0.170
180–200	0.221	0.244	0.148

salty water and turbid salty water). UV–Vis spectrum measurements were performed in the wavelength range of 400–700 nm by a Perkin Elmer UV–Vis Lambda 2S spectrophotometer at room temperature. We used two clean quartz–glass sample containers, including the clean water and turbid salty water. The clean water in quartz–glass sample container was used as reference.

Tables 74.1 and 74.2 give the absorption coefficients of turbid and clear water in the solar pond, based on the samples taken from solar pond at ten different heights from top to bottom. The absorption coefficients of the sample were measured by using the spectrometer. The Beer–Lambert Law was used to calculate the absorption coefficients between 400 and 700 nm. In Eq. (74.3), the thickness of x was measured as 0.5 cm using the quartz–glass sample container in the spectrometer. Then, using the transmission data in Figs. 74.4 and 74.5 with Eq. (74.3), the absorption coefficients listed in Tables 74.1 and 74.2 were determined. These tables then give the transmission data of light with different depths for turbid water and clear water in the pond.

Table 74.2 Absorption coefficients with respect to transmission data for clear solar pond

Height(cm)	Bandwidth (nm)		
	600–700	500–600	400–500
0–20	0.004	0.004	0.004
20–40	0.002	0.002	0.003
40–60	0.002	0.005	0.008
60–80	0.007	0.001	0.018
80–100	0.013	0.013	0.027
100–120	0.011	0.021	0.018
120–140	0.008	0.012	0.024
140–160	0.012	0.017	0.018
160–180	0.015	0.022	0.030
180–200	0.017	0.022	0.036

Fig. 74.6 Transmission of visible spectrum for clear solar pond
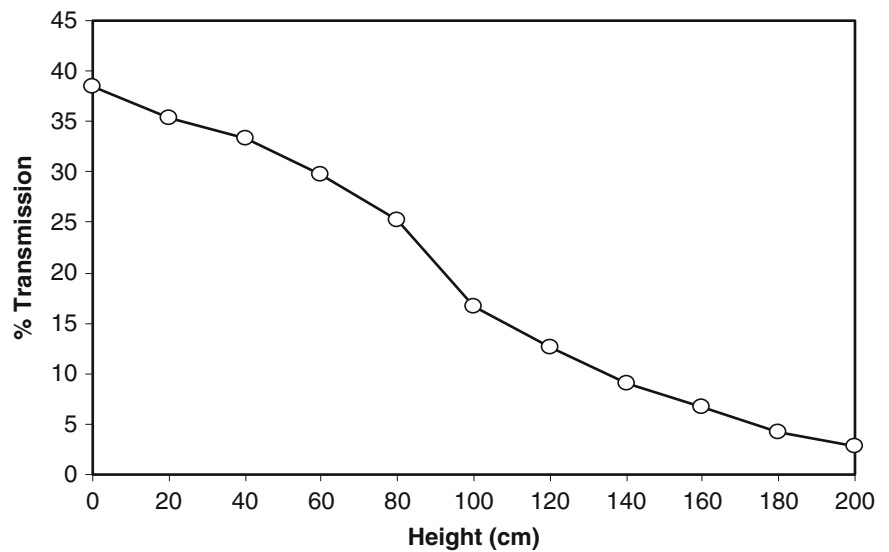
Here, we consider each layer thickness as equal to $x = 20$ cm from top to bottom in the pond and the solar radiation reaching the surface of the solar pond as 100 % visible light. We used Eq. (74.3) to calculate the transmission values of the first layer. Thus, the calculation was repeated for each layer of the inner zone down to the bottom. Note that the absorption coefficients listed in the tables are used to calculate the transmission of clear and turbid water in the pond. The transmission results were then used to obtain the transmission distributions in the salinity water to understand the entering the total visible spectrum in clear and turbid water of the solar pond. It is assumed that the sun has a surface temperature of 5,800 K. In this regard, the total emitted energy for given bandwidths was calculated to be 38.5 % of all emitted energy as associated with the visible spectrum in the atmosphere [19]. As seen in Figs. 74.6 and 74.7, we present the percentage of the entering visible light of the storage zone from 120 to 200 cm. The values of 5.39 % and 11.93 % were found for turbid and clear salinity water solar pond for the storage zone, respectively. Figure 74.8 shows the temperature distributions of clean water and turbid water. As seen here, there is some difference between these two profiles.

Fig. 74.7 Transmission of visible spectrum for turbid solar pond
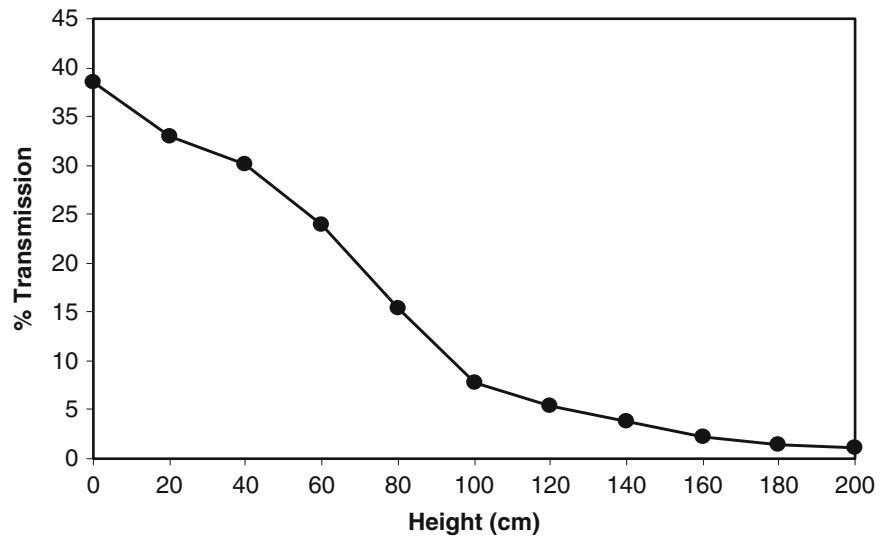
Fig. 74.8 Variations in the temperature distributions for clean and turbid saline water with depth in a 1-year period for August
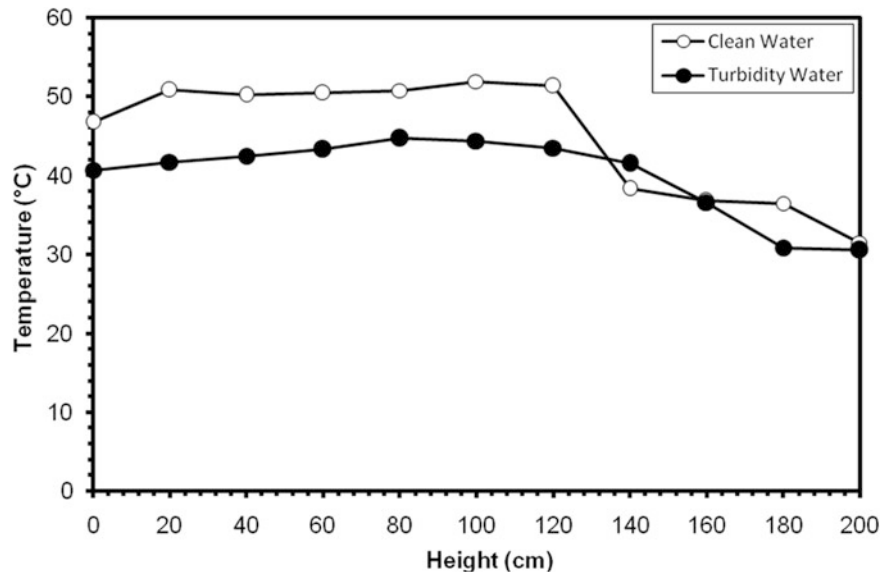
Conclusions

Transmission visible spectrum of the light has been investigated in turbid and clear saline water of a solar pond. We compare the transmission of the turbid and clean salinity water to understand both of effect on performance of the solar pond. The turbidity in saline water of the pond increased with time due to outdoor factors (e.g., insects, leaf, dust, and wind bringing parts falling down). This increasing is caused by decreasing transmission of solar pond. Therefore, especially the temperature distributions are decreased in the storage zone in time. The results show that the performance of the solar pond is affected strongly by the turbidity. The turbidity is not homogeneous in the layers which caused variations in transmission ratios. The transmission ratio of saline water is an important parameter for analyzing the performance of the storage zone.

Nomenclature

IBW	Insulated bottom wall	a	Absorption coefficient
ISW	Insulated side walls	θ_i	Incidence angle
HSZ	Heat storage zone	θ_r	Refraction angle
LCZ	Lower convective zone	$h(x)$	Transmittance of the working fluid
n	Number of the part	$I_\lambda(x)$	λ-wavelength solar beam at x depth
NCZ	Non-convective zone	x	Depth, m
T	Temperature, °C	I_{oi}	Total reaching solar energy to the surface
UCZ	Upper convective zone	μ_λ	Absorption coefficient at λ-wavelength
K	Kelvin temperature	δ_λ	Characteristic absorption coefficient at λ-wavelength

Greek Letters

ρ	Reflection coefficient	β	Incident beam entering rate into water
t	Transmission coefficient	λ	Wavelength, nm
ρ	Density, kg/m^3		

References

1. Kaygusuz K, Sarı A (2003) Renewable energy potential and utilization in Turkey. Energ Convers Manag 44:459–478
2. Khan FI, Hawboldt K, Iqbal MT (2005) Life cycle analysis of wind–fuel cell integrated system. Renew Energy 30:157–177
3. Dincer I (1999) Evaluation and selection of energy storage systems for solar thermal applications. Int J Energ Res 23:1017–1028
4. Dincer I (2002) Thermal energy storage systems as a key technology in energy conservation. Int J Energ Res 26:567–588
5. Dincer I, Rosen MA (2011) Thermal energy storage systems and applications. Wiley, New York, NY. ISBN 978-0-470-74706-3
6. Wang J, Seyed-Yagoobi J (1994) Effect of halobacteria and selected chemicals on radiation transmission in salt water. Sol Energ 52:411–418
7. Malik N, Date A, Leblanc J, Akbarzadeh A, Meehan B (2011) Monitoring and maintaining the water clarity of salinity gradient solar ponds. Sol Energ 85:2987–2996
8. Xu H, Sandoval JA, Lu H, Golding P, Swift A (1994) Operating experience with the El Paso Solar Pond. In: Joint Solar Engineering Conference ASME, pp 503–511
9. Alagao FB (1996) Simulation of the transient behavior of a closed-cycle salt-gradient solar pond. Sol Energy 56:245–260
10. Karakilcik M, Dincer I, Rosen MA (2006) Performance investigation of a solar pond. Appl Thermal Eng 26:727–735
11. Akbarzadeh A, MacDonald RWG (1982) Introduction of a passive method for salt replenishment in the operation of the solar ponds. Sol Energ 29:71–76
12. Bozkurt I, Karakilcik M (2012) The daily performance of a solar pond integrated with solar collectors. Sol Energ 86:1129–1672
13. Butler LRP, Laqua K (1996) Nomenclature, symbols, units and their usage in spectrochemical analysis-IX. Instrumentation for the spectral dispersion and isolation of optical radiation. Spectrochimica Acta B Atom Spectrosc 51:645–664
14. Lund PD, Keinonen RS (1984) Radiation transmission measurements for solar ponds. Sol Energ 33:237–240
15. Kirk J (1980) Spectral absorption properties of natural water's: contribution of the soluble and particulate fractions to light absorption in some inland waters of South Australia. Aust J Mar Freshwater Res 31:287–296
16. Li YX, Kanayama K, Baba H (2000) Spectral calculation of the thermal performance of a solar pond and comparison of the results with experiments department of mechanical engineering. Renew Energy 20:371–387
17. Husain M, Patil SR, Samdarshi SK (2004) Simple methods for estimation of radiation flux in solar ponds. Energ Convers Manag 45:303–314
18. Rabl A, Neilsen CE (1975) Solar ponds for space heating. Sol Energ 17:1–2
19. Holman JP (1997) Heat transfer, 8th edn. McGraw-Hill, New York, NY
20. Tsilingiris PT (1991) Radiation transmission through a composite pure water layer of uniform and depth-dependent extinction characteristics. Int J Energ Res 15:723–730
21. Hawlader MNA (1980) The influence of the extinction coefficient on the effectiveness of solar ponds. Sol Energ 25:461–464

Performance Analysis of a Solar Pond

Ismail Bozkurt, Ayhan Atiz, Mehmet Karakilcik, and Ibrahim Dincer

Abstract

In this contribution, we develop a theoretical solar pond in different geometries for the Adiyaman region in Turkey and analyze its performance assessment through energy efficiency. Some key parameters such as surface area, depth, densities of the layers, the thicknesses of the inner zones and the insulations of the walls to assess the solar pond are considered. In the parametric studies, the dimensions of the zones (e.g., upper convective zone, non-convective zone, and low-convective zone) are varied to investigate their effects. Although the density and temperature gradient of the inner zones are considered similar to each other, the energy efficiencies of the storage zones become different due to varying dimensions of the pond. The shading area decreases by increasing the surface area of the inner zones. The amount of incoming solar energy to the upper surface is increased with the size of the solar pond. The energy efficiency of the solar pond is determined to be maximum (31.76 %) for case4a, and to be minimum (16.80 %) for case1b in August. As a result, through careful determination of the dimensions and insulation parameters, incoming solar radiation reaching the storage zone increases the energy efficiency of the solar pond.

Keywords

Solar energy • Solar pond • Heat storage • Shading effect • Energy • Efficiency

Introduction

Solar energy appears to be an important alternative energy source that will primarily be utilized in the future. Some critical factors that limit the application of solar energy are its time-dependency and fluctuating nature. Therefore, solar energy systems require energy storage to provide energy during the night and overcast periods [1]. One of the thermal energy storage systems is solar pond. Solar pond was discovered as a natural phenomenon around the turn of the last century in the Medve Lake in Transylvania in Hungary. In this lake, temperatures up to 70 °C were recorded at a depth of 1.32 m at the end of the summer season. Nowadays, mini model solar ponds are also being constructed for various thermal applications [2]. Solar pond's energetic and exergetic performance was studied experimentally and theoretically by Karakilcik and Dincer [3], Bozkurt and Karakilcik [4], Karakilcik et al. [5]. In the literature, some studies have been undertaken on shading effect in solar ponds by various researchers [6–9]. The sunny area of the model solar ponds is affected by wall shading. So when a

I. Bozkurt (✉)
Department of Mechanical Engineering, Faculty of Engineering, University of Adiyaman, Adiyaman 02040, Turkey
e-mail: ismail_bozkurt44@yahoo.com

A. Atiz • M. Karakilcik
Department of Physics, Faculty of Sciences and Letters, University of Cukurova, Adana 01330, Turkey
e-mail: ayhanklicc@hotmail.com; kkilcik@cu.edu.tr

I. Dincer
Faculty of Engineering and Applied Science, University of Ontario Institute of Technology (UOIT), 2000 Simcoe Street, North Oshawa, ON, Canada L1H 7K4
e-mail: ibrahim.dincer@uoit.ca

model solar pond is constructed the sunny area should be considered. In this paper, we present the sunny area ratios of the inner zones of a solar pond in different dimensions for Adiyaman region in Turkey and study its performance assessment through energy efficiency. Thus, the energy efficiency of the solar pond is predicted according to its surface area and height.

System Considered

A model solar pond is described, as consisting of three layers. The top surface layer is known as upper convective zone (UCZ). UCZ is filled with fresh water but in time its density is increased slightly due to upward salt transport, surface heating and cooling, and wave action. The second layer is the non-convective zone (NCZ) acts as an insulating layer of the pond. The density in NCZ increases with increasing depth of the gradient layer. The bottom layer is a high temperature layer known as the heat storage zone (HSZ). This layer has a constant temperature and salinity. Useful heat is usually extracted from this layer; its thickness depends on the temperature and the amount of the thermal energy to be stored [2]. The vertical walls in the inner zones of the pond form a shading area. The shading area is defined as the area where solar radiation does reach or which is under shade. Thus, the incident solar energy on surface of the pond decreases the pond's efficiencies by shading from vertical side walls. Therefore, it is important to better understand the effect of shading on the performance of the solar pond [10]. So we study here the effect of shading on the efficiencies of solar pond of different dimensions for Adiyaman region in Turkey.

Analysis

Sunny Area of Inner Zones

In this section, we determine the sunny area for different surfaces and heights. The angle of refraction, which is the angle that the refracted ray makes with the normal line, is defined by the Snell law as:

$$\theta_r = \sin^{-1}(1.33 \sin(\theta_i)) \tag{75.1}$$

where θ_i is called incidence angle and is defined as:

$$\theta_i = \cos^{-1}[\cos(\delta_d)\cos(\phi)\cos(\theta_h) + \cos(\delta_d)\cos(\phi)] \tag{75.2}$$

where δ_d is declination angle which can generally be calculated by the Cooper equation as $\delta_d = 23.45 \sin[360(284 + n)/365]$. n is any day of the year, given as $(1 \leq n \leq 365)$ [11]. φ is calculated according to latitude angle. $(-90 < \varphi < +90)$ is latitude degree which is found out from solar elevation angle, and this is plus (+) for the Northern hemisphere and minus (−) for the Southern hemisphere. We use $38°23'$ East longitude and $37°75'$ North latitude for the location of Adiyaman University in Adiyaman, Turkey. θ_h is the hour angle which is equal to zero while the sun is at the highest point in the sky at 12.00 h, and its value in the morning becomes positive (+) and in the afternoon becomes negative (−). According to per $15°$ of longitude per hour, for example at 11.00 am, it is $+15°$ but $-15°$ at 13.00 pm and for a special case, $\theta_z = 90°$, hour angle is defined as $\theta_h = \cos^{-1}[-\tan(\phi)\tan(\delta_d)]$. The day length (the smallest sunshine duration) is defined as $N = (2/5)\theta_h$ as given by Karakilcik [12]. The sunny area of HSZ for model solar ponds are defined as:

$$A_{sa.} = A_{sur.} - A_{sh.} \tag{75.3}$$

where $A_{sa.}$ is the sunny area of HSZ, A_{sur} is the surface area of the model solar pond, $A_{sh.}$ is the shading area of HSZ. $A_{sh.}$ is defined as:

$$A_{sh.} = I_{wd}I_{HSZ} \tag{75.4}$$

Here, I_{wd} is the width of the model solar pond. l_{HSZ} is the length of the shading area in HSZ's middle point from the surface. l_{HSZ} is defined by Karakilcik et al. [10] as:

$$I_{HSZ} = h_{HSZ} \tan \theta_r \tag{75.5}$$

where h_{HSZ} is the height of HSZ's middle point from the surface.

Table 75.1 The thicknesses of the solar pond zones for different dimension cases

Case	Surface area (m^2)	Depth (m)	HSZ (m)	NCZ (m)	UCZ (m)
1	1 × 1	(a) 1.50	0.90	0.50	0.10
		(b) 2.00	1.40	0.50	0.10
2	2 × 2	(a) 1.50	0.90	0.50	0.10
		(b) 2.00	1.40	0.50	0.10
3	3 × 3	(a) 1.50	0.90	0.50	0.10
		(b) 2.00	1.40	0.50	0.10
4	4 × 4	(a) 1.50	0.90	0.50	0.10
		(b) 2.00	1.40	0.50	0.10

Fig. 75.1 The inner zones of the solar pond and the sunny area of its zones
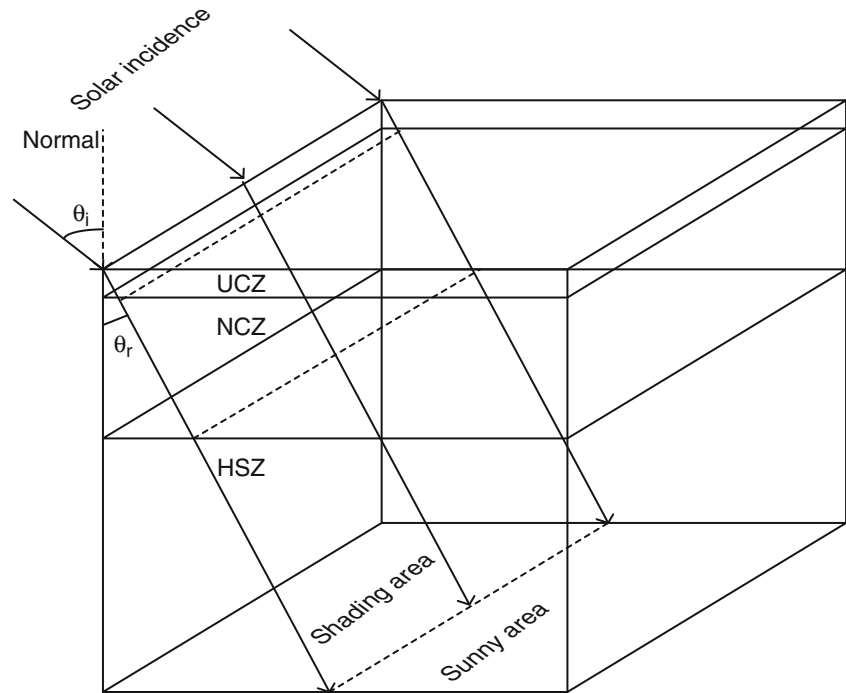
Note that $X_{sa.}$ is the ratio of the sunny area of the model solar pond and determined for NCZ and UCZ as follows:

$$X_{sa.} = \frac{A_{sa.}}{A_{sur.}} \tag{75.6}$$

The refractive indexes of the salty water and water were assumed to be about the same. The thicknesses of NCZ and UCZ were assumed to be fixed. The thicknesses of UCZ and NCZ were then taken as 0.1 and 0.5 m, respectively. HSZ's thickness varies with depth. The thicknesses of the solar pond zones for different dimension cases are given in Table 75.1.

Energy Analysis of Model Solar Pond

Figure 75.1 illustrates the inner zones of the solar pond and the sunny area of the zones. Inner zones consist of the salty water layers with various densities.

It is very important to determine the energy efficiency of the solar pond. To calculate the energy efficiency, we used the temperature distribution, the incident radiation reaching the heat storage zone, the ambient temperature, and the insulation parameters. Solar energy is transmitted through UCZ and NCZ, after attenuation, to HSZ. Part of the transmitted solar energy from NCZ to HSZ is reflected from the bottom and the majority of the solar energy is absorbed in HSZ. Therefore, the solar energy is collected and stored in HSZ. The radiation heat losses of the solar pond are neglected because solar ponds are

working at a low temperature. At the same time, the convection heat losses from the solar pond are prevented by NCZ, with no heat losses. The energy efficiency of the solar pond can be defined as

$$\eta = \frac{Q_{stored}}{Q_{in,HSZ}} = 1 - \frac{\{Q_{bottom} + Q_{up} + Q_{side}\}}{Q_{in,HSZ}} \tag{75.5}$$

where Q_{stored} is stored heat energy in HSZ of the solar pond. $Q_{in,HSZ}$ is the amount of net solar energy absorbed by HSZ. Q_{bottom} is the total heat loss to the bottom wall from HSZ. Q_{up} is the heat loss from HSZ to the above zone. Q_{side} is the total heat loss to the side walls of HSZ. Substituting equations for each parameter in Eq. (75.5) provides us with the following energy efficiency of the solar pond:

$$\eta = 1 - \frac{\left\{\dfrac{k_w A_{sur.}}{\Delta x_{bottom}}(T_{HSZ} - T_a) + \dfrac{k_s A_{sur.}}{\Delta x_{HSZ\text{-}NCZ}}(T_{HSZ} - T_{NCZ}) + \dfrac{k_w A_{HSZ}}{\Delta x_{side}}(T_{HSZ} - T_a)\right\}}{\beta E A_{sa.}[(1 - F)\, h(x - \delta)]} \tag{75.6}$$

where E is the total solar energy reaching the solar pond surface, A_{HSZ} is the side area of HSZ, F is the fraction of energy absorbed at a region of δ-thickness, h is solar radiation ratio; $A_{sa.}$ is the sunny area of HSZ, T_a is the ambient air temperature, k_w is the thermal conductivity of the side and bottom walls, k_s is the thermal conductivity of the salty water, Δx_{bottom} is the thickness of the bottom wall, Δx_{side} is the thickness of the side wall, $\Delta x_{HSZ\text{-}NCZ}$ is the thickness of HSZ's middle point and NCZ's middle point, β is the fraction of the incident solar radiation that actually enters the pond and is given by Hawlader [13].

$$\beta = 1 - 0.6\left[\frac{\sin\theta_i - \sin\theta_r}{\sin\theta_i + \sin\theta_r}\right]^2 - 0.4\left[\frac{\tan\theta_i - \tan\theta_r}{\tan\theta_i + \tan\theta_r}\right]^2 \tag{75.7}$$

where θ_i and θ_r are the incidence and refraction angles. h represents the ratio of the solar energy reaching the depth in the layer I to the total solar incident falling on to the surface of the pond and is given by Bryant and Colbeck [14] as

$$h_I = 0.727 - 0.056 \ln\left[\frac{(x_I - \delta)}{\cos\theta_r}\right] \tag{75.8}$$

Here, x_I is the thickness of the layer, δ is the thickness of the layer in the UCZ where long-wave solar energy is absorbed. The following equation is employed to estimate the temperature distributions in HSZ, theoretically as follows:

$$T_{HSZ,K+1} = T_{HSZ,K} + \frac{\Delta t}{m_{HSZ}C_{HSZ}}\left\{\begin{array}{l}[\beta E A_{sa.}(1 - F)h(x - \delta)] - \left[\dfrac{k_w A_{sur.}}{\Delta x_{bottom}}(T_{HSZ,K}\text{-}T_{a,K})\right] \\[4mm] -\left[\dfrac{k_s A_{sur.}}{\Delta x_{HSZ-NCZ}}(T_{HSZ,K}\text{-}T_{NCZ,K})\right] - \left[\dfrac{k_w A_{HSZ}}{\Delta x_{side}}(T_{HSZ,K}\text{-}T_{a,K})\right]\end{array}\right\} \tag{75.9}$$

where $T_{(HSZ,K+1)}$ is the temperature of HSZ at time (K+1). $T_{(HSZ,K)}$ is the temperature of the HSZ at time (K). $T_{(a,K)}$ is the temperature of air at time (K). $T_{(NCZ,K)}$ is the temperature of NCZ at time (K). m_{HSZ} is the mass of HSZ. C_{HSZ} is the heat capacity of HSZ.

Results and Discussion

The energy efficiency of the solar pond depends not only on thermal energy flows (e.g., heat losses and/or heat gains in the zones) but also on incoming solar radiation (e.g., accounting for reflection, transmission, and absorption). Moreover, shading decreases the performance of the solar pond [5]. In this study, we present the results of the theoretical calculations for the sunny area of the different dimensions model solar ponds. At the same time, the model solar pond energy efficiencies were determined. These results show how sunny area affects the efficiency of the solar pond. Figure 75.2 shows the variations of the sunny area according to the surface area during a year.

As seen in Fig. 75.2, the sunny area is affected by different surface area cases. As apparent, there are significant differences between sunny area. The sunny area distributions are calculated by using Eq. (75.4) during a year. In Fig. 75.2,

Fig. 75.2 Comparison
of the sunny area ratio of HSZ
for 1.50 m depth and various
surface areas
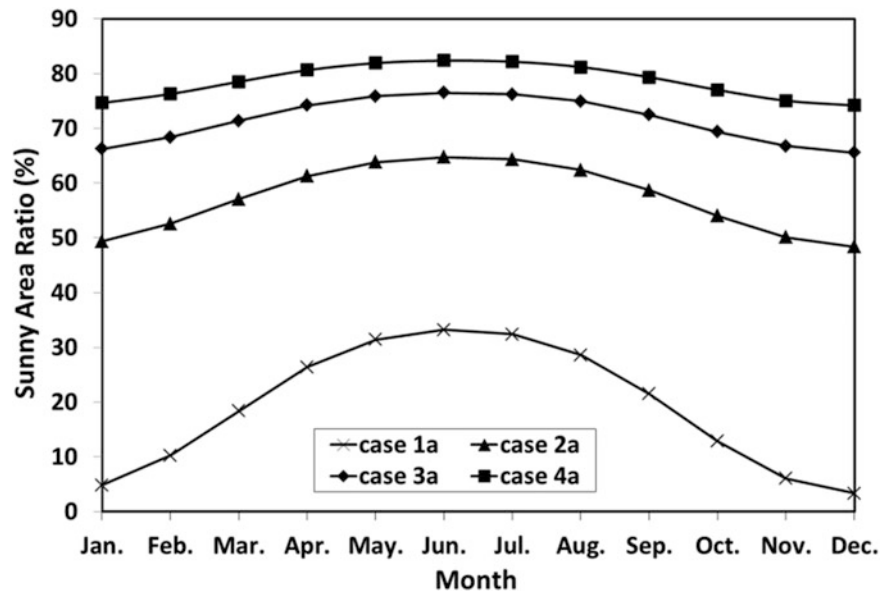
Fig. 75.3 Comparison
of the sunny area ratio of HSZ
for 2.00 m depth and various
surface areas
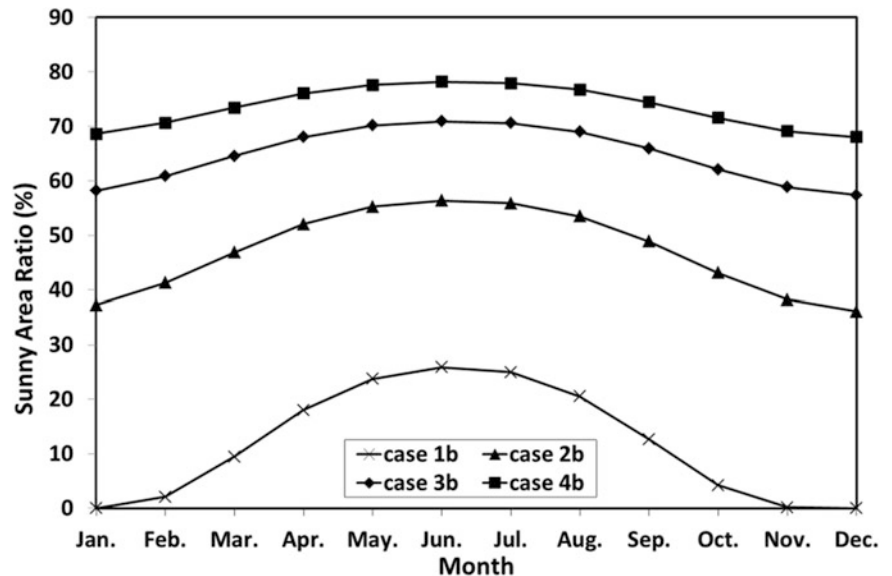
the theoretical sunny area ratio according to the surface area is observed to be maximum 33.21 %, 64.75 %, 76.50 %, and 82.37 % for case1a, case2a, case3a, and case4a in June, respectively. The amount of the sunny area for HSZ is increased with surface area of the solar pond. The highest sunny area is observed for case 4a. The sunny area of HSZ for 1.5 m depth is determined to be minimum 3.33 %, 48.38 %, 65.59 %, and 74.19 % for case1a, case2a, case3a, and case4a in December, respectively. As seen in Fig. 75.2, very little solar energy reaches to HSZ for case1a. The selection of solar pond dimensions is very important for energy efficiency. This sunny area can be used to determine of the solar pond dimensions.

Figure 75.3 shows the variations of the sunny area ratio for HSZ during a year for 2.00 m depth. As seen in Fig. 75.3, the theoretical sunny area ratio of HSZ is observed to be maximum 25.89 %, 56.35 %, 70.90 %, and 78.18 % for case1b, case2b, case3b, and case4b in June, respectively. The amount of the sunny area for HSZ is decreased with depth of the solar pond. The sunny area of HSZ is determined to be minimum 0 %, 36.09 %, 57.39 %, and 68.04 % for case1b, case2b, case3b and case4b in December, respectively. As seen in Fig. 75.3, solar energy does not reach to HSZ for case1b during 4 months (November, December, January, February) and this profile shows that the dimensions is not suitable for solar ponds. So we can select other cases according to the size of the application area.

Figure 75.4 shows the variations of the sunny area ratio for NCZ during a year for different surface area cases. As seen in Fig. 75.4, the theoretical sunny area ratios of NCZ are observed to be maximum 76.50 %, 88.25 %, 92.17 %, and 94.12 % for case1, case2, case3, and case4 in June, respectively. The amount of the sunny area for NCZ is increased with the surface area

Fig. 75.4 Comparison of the sunny area ratio of NCZ for various surface areas
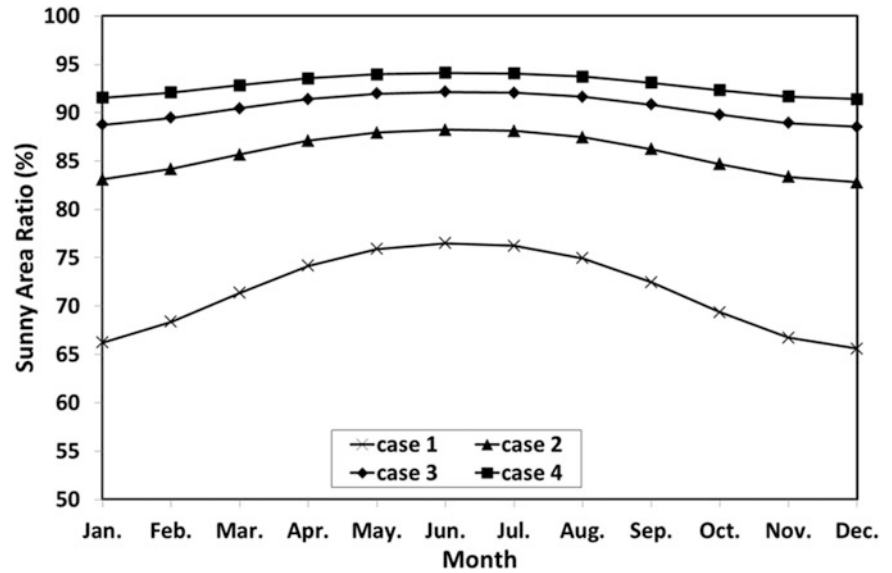
Fig. 75.5 Comparison of the sunny area ratio of UCZ for various surface areas
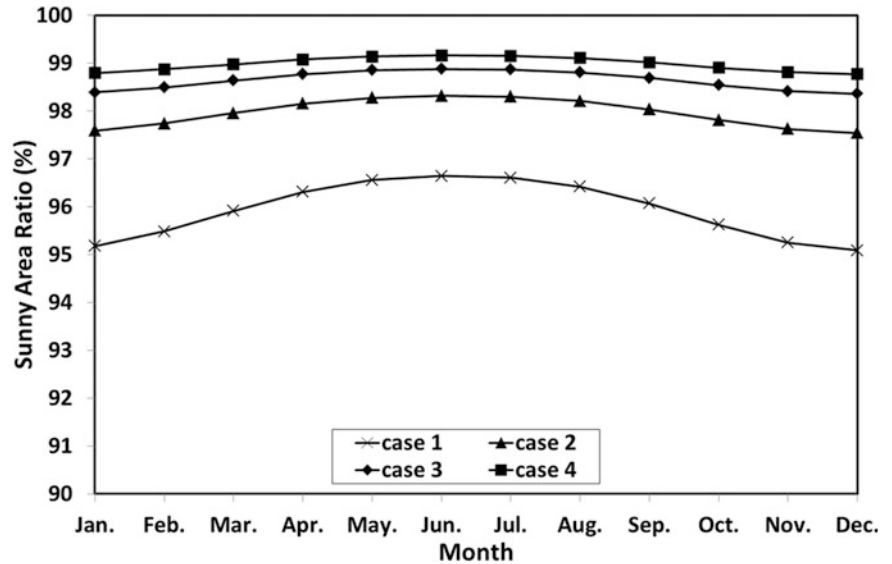
of the solar pond. The sunny area ratios of NCZ are determined to be minimum 66.23 %, 83.11 %, 88.74 %, and 91.56 % for case1, case2, case3 and case4 in December, respectively. The sunny area ratios of NCZ are changed a little during a year because NCZ is close to the surface.

Figure 75.5 shows the variations of the sunny area ratio for UCZ during a year for different surface area cases. As seen in Fig. 75.5, the theoretical sunny area ratios of UCZ are observed to be maximum 96.64 %, 98.32 %, 98.88 %, and 99.16 % for case1, case2, case3, and case4 in June, respectively. The amount of the sunny area ratio for UCZ is increased with the surface area of the solar pond. The sunny area ratios of UCZ are determined to be minimum 95.08 %, 97.54 %, 98.36 %, and 98.77 % for case1, case2, case3, and case4 in December, respectively. The sunny area of UCZ is less affected from shading area because UCZ is close top of the surface of the solar pond.

The temperatures of the model solar ponds were calculated by using Eq. (75.9). Figure 75.6 shows average temperature distributions inside the pond during the months of June, July, and August. As shown in Fig. 75.6, the maximum average temperature of HSZ is determined as 87.12 °C in August for case4a. The reasons of the low temperature in HSZ for especially case1a–1b are that small surface area, shading by the side vertical walls, high depth. So the reaching solar energy of HSZ is decreased by these negative effects.

In a solar pond, the efficiencies are low since the reaching solar energy of HSZ is much smaller than the incident solar radiation on the zone surfaces. To increase performance of the solar pond, the reaching solar energy of HSZ should be increased

Fig. 75.6 The temperatures distributions of the model solar pond for the various cases
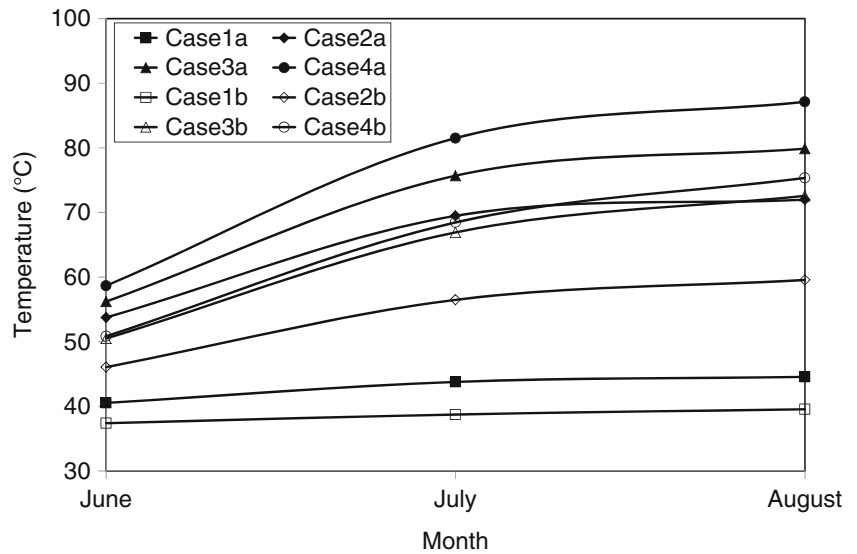
Fig. 75.7 The energy efficiencies of the model solar pond for various cases
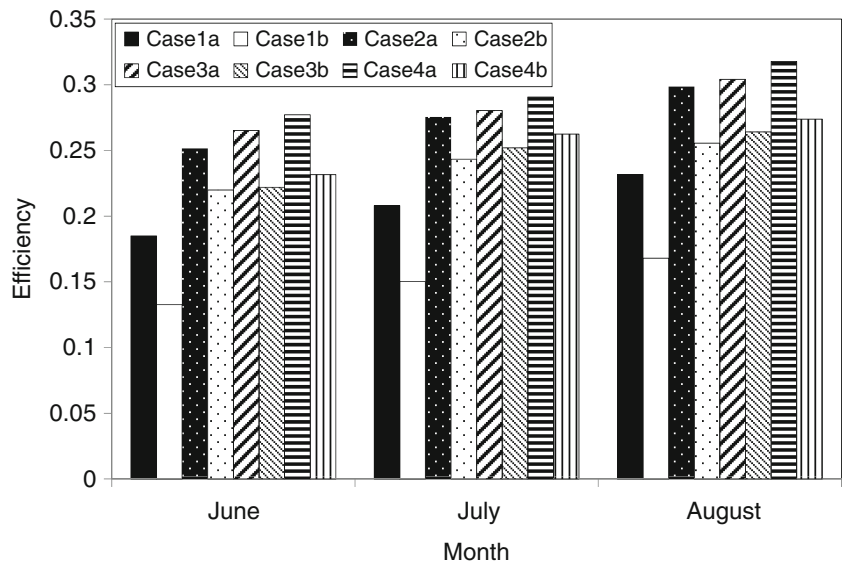
selecting the correct size of the solar pond before construction. The solar pond efficiencies are calculated by using Eq. (75.6) for different cases. As seen in Fig. 75.7, the efficiencies of the solar pond are found to be maximum (31.76 %) for case4a and to be minimum 16.80 % for case1b in August. Figure 75.7 shows that the sunny areas of the inner zones have an important effect on the performance of the solar pond. Increasing the sunny areas of the zones allow much more solar radiation to reach HSZ and increase the thermal energy potential of the pond and hence its performance. We analyze the energy efficiency of the solar pond for different cases. The maximum efficiencies of the solar pond are seen to occur for case4a.

Conclusions

In this study, we carried out energy efficiency calculations of inner zones of a model solar pond in order to demonstrate the effect of the sunny areas ratios of each zone due to different sizes of a solar pond. The solar energy reaching depends on the zone thicknesses, shading area of the solar pond. So to increase the efficiency of the solar pond, the sizes of the solar pond should be predicted to achieve higher efficiency. Meteorological data are used to determine the efficiencies for the various sizes of a model solar pond. As expected, the energy efficiencies of the solar pond are affected by the sizes of the solar pond, strongly. The results help to select the sizes of the solar pond before construction.

Nomenclature

A	Area (m^2)	m	Mass (kg)
C	Heat capacity (J/kg °C)	n	Number of days
E	Total solar energy reaching the pond (J)	N	Day length
F	Absorbed energy percentage at a region of δ-thickness	NCZ	Non-convective zone
		T	Temperature (°C)
HSZ	Heat storage zone	Q	Heat energy (MJ)
k	Thermal conductivity (J/m °C h)	UCZ	Upper convective zone
l	Length (m)		

Greek Letters

η	Thermal energy efficiency	φ	Latitude angle (rad)
δ	Thickness where the long wave solar radiation is absorbed (m)	χ	Ratio
		θ	Angle (rad)
β	Rate of incident beam entering into the water	Δx	Thickness of horizontal layers (m)

Subscripts

a	Air	side	Side wall
d	Declination	stored	Heat stored
h	Hour	sh.	Shading
i	Incident	sur.	Surface
r	Refracted	up	Just above zone
s	Salty water	w	Wall
sa.	Sunny area	wd	Width

References

1. Dincer I, Rosen MA (2003) Thermal energy storage: systems and applications. John Wiley and Sons, New York, NY
2. El-Sebaii AA, Ramadan MRI, Aboul-Enein S, Khallaf AM (2011) History of the solar ponds: a review study. Renew Sustain Energy Rev 15:3319–3325
3. Karakilcik M, Dincer I (2008) Exergetic performance analysis of a solar pond. Int J Therm Sci 47:93–102
4. Bozkurt I, Karakilcik M (2012) The daily performance of a solar pond integrated with solar collectors. Sol Energ 86:1611–1620
5. Karakilcik M, Bozkurt I, Dincer I (2013) Dynamic exergetic performance assessment of an integrated solar pond. Int J Exerg 12:70–86
6. Hassab MA, El-Masry OA (1991) Effects of edges on solar-energy collection in small solar ponds. Appl Energ 38(2):81–94
7. Jaefarzadeh MR (2004) Thermal behavior of a small salinity-gradient solar pond with wall shading effect. Sol Energ 77:281–290
8. Karakilcik M, Dincer I, Bozkurt I, Atiz A (2013) Performance assessment of a solar pond with and without shading effect. Energ Convers Manag 65:98–107
9. Mazidi M, Shojaeefard MH, Mazidi MS, Shojaeefard H (2011) Two-dimensional modeling of a salt-gradient solar pond with wall shading effect and thermo-physical properties dependent on temperature and concentration. J Therm Sci 20:362–370
10. Karakilcik M, Kıymaç K, Dincer I (2006) Experimental and theoretical distributions in a solar pond. Int J Heat Mass Tran 49:825–835
11. Duffie JA, Beckman WA (1991) Solar engineering thermal processes, 3rd edn. John Wiley and Sons, New York, NY
12. Karakilcik M (1998) Determination of the performance of an insulated prototype solar pond. Ph.D. thesis, Cukurova University, Adana, Turkey (in Turkish)
13. Hawlader MNA (1980) The influence of the extinction coefficient on the effectiveness of solar ponds. Sol Energ 25:461–464
14. Bryant HC, Colbeck I (1977) A solar pond for London. Sol Energ 19:321

Parametric Analysis of Pumped Storage Hydropower-Coupled Wind Turbine Plants

Kurtuluş Değer, Birol Kılkış, and Tahir Yavuz

Abstract

The concept of a hybrid system consisting of a wind turbine plant and a pumped storage hydropower plant is a promising idea with respect to a number of important factors. Wind turbine plant power output has a fluctuating and interrupted nature, and the penetration of the electrical energy to the grid usually poses problems to the steady operation of the system. Pumped storage hydropower is a mature technology in the energy storage sector. Pumped storage hydropower has advantages compared to other energy storage technologies such as CAES, batteries, etc. due to its short discharge time, high energy storage capacities, and high power output. The first objective of this study is to time-shift the power output of the wind turbine plant to the peak-demand periods by means of storage and thus realizing increase in the penetration level to the grid. The second objective is to obtain a more stable power output from the wind turbine plant that inevitably has a variable power output. A 1-year operation simulation of the hybrid system was carried out under peak tariff strategy within the scope of these two objectives. An operation simulation was also made covering only the wind turbine plant with same power output data and same demand strategy and the results were compared. Without storage, the wind turbine plant feeds 6,350.30 MW h of electrical energy into the grid; this value increases to 7,656.00 MW h for the hybrid system, and this means that there is 17.05 % increase in penetration and the system is technically applicable for the first objective. Annual stable power output ratio that shows the fulfillment of demand is approximately 72.49 % for wind turbine plant without storage, and this value is approximately 87.40 % for the hybrid system. This means that there is a 14.91 % increase and that the system is technically applicable for the second objective. This paper provides the details of the year-long analysis, draws generalized conclusions, and provides recommendations for future studies.

Keywords

Wind turbine plants • Pumped storage hydropower plants • Hybrid systems • Energy storage

Introduction

Energy production from renewable sources is affected by private factors such as climatic and topographical conditions of project implementation area and, as a result; energy production levels have a variable structure in time. Wind turbine plants (WTP) could not provide continuous power output due to variable wind speed and air density, and thus, energy production

K. Değer (✉)
Ankara, Turkey
e-mail: k_deger@yahoo.com.tr

B. Kılkış • T. Yavuz
Mechanical Engineering Department, Başkent University, Ankara, Turkey
e-mail: bkilkis@baskent.edu.tr; tyavuz@baskent.edu.tr

level varies with time; therefore, the produced energy level that is not harmonized with grid load level could not be recovered, if power output level is lower than the grid load, demand could not be met in full, if the power output amount is greater than the latter, some amount of excess power occurs. Also the variable power output of WTPs could cause problems on grids that have an inappropriate design; in this respect a hybrid system (HS) design of which energy storage system (ESS) is the other component could be a solution for to time-shift power output and for obtaining a more stable power output. While considering the superior factors it has, pumped storage hydropower plant (PSHP) could be opted as the component of HS among various ESSs, and PSHP is selected as the ESS component of the HS. An operation simulation numerical model is developed to investigate the technical benefits of a hypothetical HS model. The numerical model is based on power and energy units, and the results are compared with the results obtained from the simulation that was carried out for WTP without storage.

The HSs are investigated commonly for isolated grids in literature. The results of HS model's optimization for an isolated grid show that there is an increase in wind energy penetration to the grid [1]. A general model was also presented for the technical and economic sizing of HSs in another study [2], and installation of a HS for an isolated grid is proposed by same researchers with a following study, according to the results; with the application of optimum sized economic model, the renewable sourced energy penetration to the grid increases [3]. In particular, the aspects of control and operation of a variable speed PSHP for the objective of wind power integration into an isolated grid is also studied [4]. Stochastic based approach for optimization of HSs is another fact also. WTP power output amount and electricity unit selling prices vary in time; these parameters could be evaluated in scope of stochastic models [5, 6]. In various studies economic benefit based models are developed for HSs [7, 8]. In those studies objective function is derived to gain maximum profit, and linear algorithm approach is used for optimization, and the future values of variables such as power output or grid electrical energy demand were obtained by forecasting techniques.

Installation objectives directly influence the design approach of the HS model. There are two objectives of the HS model analyzed in this study. Climatic and meteorological conditions influence wind speed and air density, and consequently WTP power output fluctuates in time, and therefore, the power output level of WTP could not be harmonized with grid load or with the level of power amount committed to the transmission grid operator (TGO) in some periods. If the energy produced at WTP is higher than the level committed to TGO, then excess energy occurs, otherwise hence the produced energy level is lower than the committed level, then the commitment is not fulfilled and economic loss may occur in producer side. The first objective of the HS model is to time-shift the power output of the WTP to peak demand periods by means of storage and thus realizing increase in the penetration level to the grid. Also the fluctuation occurs in WTP power output could affect the grid. If the grid is not designed especially for such conditions, the power fed to grid can cause stability problems. With an appropriate operation approach, the power output of WTP could be smoothed by power output of PSHP and a more stable power output level could be obtained. Second objective is to obtain more stable power output from the WTP which normally has a variable power output. The penetration restrictions are not included in HS model and also it is assumed that when WTP itself feeds electrical energy to the grid, the stability of the grid is not influenced. Renewable energy time-shift and wind generation grid integration are some benefits of ESSs. Today there are various mature ESS technologies; besides this, a number of ESS technologies are in development stage. ESSs could be evaluated according to factors such as their power output capacities, cycle life, energy storage capacities. etc. PSHP, as one of the mature ESS technologies, could be opted as a component of HS in the scope of mentioned objectives while considering the superior factors such as its long cycle life, high energy storage capacity, high power output capacity, energy input and output in the form of electrical energy, and low environmental impact; they are also eligible for renewable concept. In this study an operation simulation numerical model is developed for a hypothetical HS model. Power and energy units are used for numerical model and the model is based on evaluation of technical benefits. In various studies economic benefit based models are developed for HSs and objective function is derived to gain maximum profit, linear algorithm approach is used for optimization and the future values of variables such as power output or grid electrical energy demand were obtained by forecasting techniques [7, 8]. However, in the present paper, the simulation is not based on the economic benefit and electrical energy prices are not included in the model structure. Forecasting techniques are not used for obtaining wind speed and grid demand values, instead predetermined data is used. An approach of such studies [7, 8] for power limits of WTP turbines, power limits of reversible PSHP pump-turbines, and energy capacity limits of reservoir is preferred in this paper. However, the general numerical model of the operation simulation is developed specifically in the scope of this study [9].

Hybrid System and the Model Development

Generally PSHPs are designed considering either one of the three types of operation approach. In daily operation strategy, energy is generated during peak periods; emptied reservoir is filled on the same day while the demand level is low. In weekly operation, energy is generated on the weekdays and emptied reservoir is filled on the weekends. Seasonal operation strategy is the last one. In the seasonal strategy the PSHP is designed for other purposes besides energy production. In this study the daily operation strategy is opted.

There can be one or more than one penstock in the PSHP scheme. The configuration that has more than one penstock enables pumping and energy production synchronously. Excess energy output of WTP could be stored in PSHP's upper reservoir while energy is generated at the turbines of PSHP, notwithstanding the mentioned advantages; additional penstocks increase the initial cost. In this study the PSHP model has one penstock. PSHPs could be designed in the way where the pump units and turbine units are separated units. Besides this, reversible pump-turbine and variable speed motor–generator arrangement is another option, and this option is preferred in the study. This type of arrangement has benefits such as adjustability, compensation of WTP power output fluctuation, and consequently improvement in the functionality of the grid.

Generally PSHPs consume electrical energy from the grid in low demand periods and produce electrical energy in peak periods and feed the grid. Energy consumption from grid may be considered as an option for providing electrical energy that is committed to TGO when amount of energy that could be provided by HS is insufficient and for also preventing over sizing of the reservoirs. Here the technical benefits of the HS and WTP without storage are compared under same conditions; for this type of approach HS just should consume electrical energy that is produced by WTP and so electricity consumption from grid for pumping is not allowed for HS. The HS model provides electrical energy for scheduled hours. Operation approach could be regarded as peak strategy while considering the projected period is 6 h a day. Power plants are generally classified as base-load plants, mid-merit plants, and peaking plants. WTP is not a peaking plant by itself. However, a design with storage may allow a WTP to act as a peaking plant.

The HS is a hypothetical model. Specific topographical requirements for WTP and PSHP are out of the scope of this study. HS consists of WTP, PSHP, and the system operator. The previously electrical energy production amount committed by HS is submitted to TGO at the pre-concerted time periods, while the TGO is the part of the system as the demand side component. It is assumed that WTP turbines and wind conditions are identical for each turbine. A variable speed wind turbine is selected. The power output values of the wind turbine are given in Table 76.1. Wind speeds were calculated according to the selected Weibull parameter values. The calculated wind speeds are based on hourly intervals. Therefore, there are 8,760 wind speed values for a 1-year period and this situation is harmonized with the duration of interval that is selected for the simulation. The synthesized wind speed values were originally for 10 m height, and the actual values for selected hub height were calculated with the power law method [10], (v: Wind speed, P_{wt}: Power output of wind turbine).

The technical specifications of the WTP model are given in Table 76.2 (k: Shape parameter, c: Scale parameter, α: Hellman exponent, ρ_a: Air density, v_m: Average wind speed, P_v^{max}: Maximum power output of WTP's turbines, P_v^{min}: Minimum power output of WTP's turbines).

The technical specifications of the PSHP model are given in Table 76.3 (E_1^{in}: Initial energy storage level of reservoir, E^{max}: Maximum energy storage capacity of reservoir, E^{min}: Minimum energy storage capacity of reservoir, P_h^{max}: Maximum

Table 76.1 Wind turbine power output values for different wind speeds (pc_aaer.xls, [11])

v (m/s)	P_{wt} (MW)
0–3	0
4	0.029
5	0.071
6	0.138
7	0.238
8	0.361
9	0.507
10	0.673
11	0.860
12–21.99	1.001
22	0

Table 76.2 Summary of technical specifications of the WTP model

Model specifications	Explanation/selection
k	1.73
c (m/s)	8.11
α	0.14
ρ_a (kg/m^3)	1.225
v_m (m/s)	7.23
Wind speed measurement height (m)	10
Measurement interval (h)	1
Wind turbine hub height (m)	70
Number of wind turbines	10
$P_v^{\max}$ (MW)	10.01
$P_v^{\min}$ (MW)	0.00

Table 76.3 Summary of technical specifications of the PSHP model

Model specifications	Explanation/selection
Type	Pure PSHP
Operation period	Daily basis
Number of the penstocks	1
Source of electrical energy for pumping	WTP
E_1^{in} (MW h)	1.00
$E^{\max}$ (MW h)	7.00
$E^{\min}$ (MW h)	1.00
$P_h^{\max}$ (MW)	7.00
$P_h^{\min}$ (MW)	1.00
$P_p^{\max}$ (MW)	7.00
$P_p^{\min}$ (MW)	1.00

power output of PSHP's turbines, $P_h^{\min}$: Minimum power output of PSHP's turbines, $P_p^{\max}$: Maximum power of PSHP's pumps, $P_p^{\min}$: Minimum power of PSHP's pumps).

Operation simulation strategy of the HS is explained below.

- Operation of PSHP's turbines: The potential energy stored in the upper reservoir of PSHP is converted to electrical energy via reversible pump-turbines and variable speed motor-generators. With the variable speed motor-generators the power output is adjusted between available minimum and maximum values. This operation step is applicable for the intervals that wind energy is not available.
- Operation of PSHP's pumps: Energy output of the WTP is stored as potential energy in the upper reservoir by pumping. Variable speed motor-generators are operated in motor-pump mode between the minimum and maximum power output values. As mentioned before; electrical energy from grid is not used for pumping. This operation step is applicable as there is sufficient wind energy, there is no grid demand, and also there is enough space for storage in the upper reservoir.
- Operation of WTP's turbines: As the power output values depends on the wind speed; with the selection of variable speed wind turbines the electrical power output could be adjusted between the minimum and maximum values. Energy produced at WTP is fed to grid at first.

Also there are other situations for the operation simulation strategy of the HS.

- Operation of PSHP's turbines and WTP's turbines together: Grid electrical power demand is met with the WTP and PSHP together. This operation step is applicable as if the electrical energy production level of WTP is lower than the grid demand level and there is adequate stored potential energy in the upper reservoir.
- Operation of PSHP's pumps and WTP's turbines together: If the electrical energy produced at WTP is adequate and there is enough space for storage in the upper reservoir of PSHP; power output of the WTP is fed to the grid and also it is consumed by PSHP's pumps and energy is stored in the upper reservoir.

Other details of the operation simulation are listed below.

Fig. 76.1 Representation of the HS model
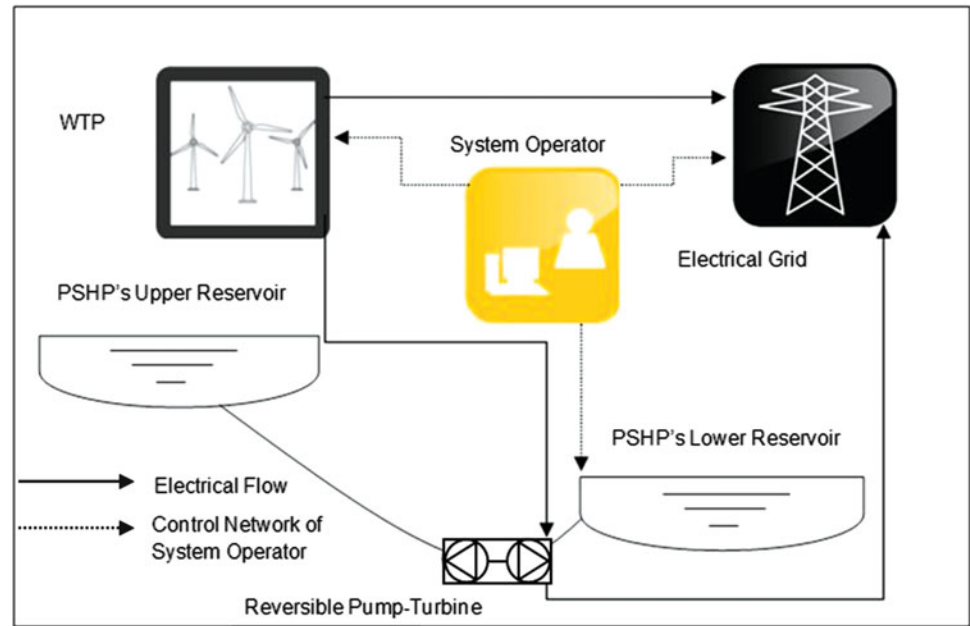
Table 76.4 Summary of technical specifications of the HS model

Model specifications	Explanation/selection
Type of power plant	Peaking plant
Daily power output period of HS (h)	6 (Maximum)
$P_d(t)$ (MW)	4
Δt (h)	1
η_c	0.86
η_d	0.88
η_t	0.76

- Grid demand: Grid demand is selected as constant 4 MW for 6 h a day. In the model, grid load is as well as equal to the electrical energy production amount that is submitted to TGO by HS.
- Duration of the interval: While taking into account the startup and shutdown periods of the components of the HS, the selected Δt value is 1 h (Δt: Duration of interval).
- Simulation period: Simulation period is determined as 1 year. Values of power output and energy production variables of the HS model are calculated on hourly basis for 1 year. This approach is opted for also WTP without storage.
- A representation of HS model is given in Fig. 76.1. The summary of the technical specifications of HS model is given in Table 76.4 ($P_d(t)$: Power demand of grid, during Δt interval, t: Time index, η_c: Isentropic charge efficiency of HS, η_d: Isentropic discharge efficiency of HS, η_t: Isentropic cycle efficiency of HS).
  Selections and constraints for system components are given by following equations.
  WTP's turbines have minimum and maximum power output limits Eq. (76.1), ($P_v(t)$: Power output of WTP's turbines, during Δt interval).

$$P_v^{\min} \leq P_v(t) \leq P_v^{\max} \tag{76.1}$$

PSHP's turbines have minimum and maximum power limits, besides them the available energy level of the upper reservoir is the other constraint Eq. (76.2), ($P_h(t)$: Power output of PSHP's turbines, during Δt interval, $E(t)$: Energy storage level in reservoir, during t interval).

$$P_h^{\min} \leq P_h(t) \leq \min\left\{ \left(\frac{E(t) - E^{\min}}{\Delta t}\right).\eta_d, \ P_h^{\max} \right\} \tag{76.2}$$

PSHP's pumps have minimum and maximum power limits, besides them the available space for of the upper reservoir to store energy is the other constraint Eq. (76.3), ($P_p(t)$: Power of PSHP's pumps, during Δt interval).

$$P_p^{\min} \leq P_p(t) \leq \min\left\{ \left(\frac{E^{\max} - E(t)}{\Delta t}\right) \cdot \frac{1}{\eta_c}, P_p^{\max} \right\} \tag{76.3}$$

Maximum power limits of PSHP's turbines and pumps are equal and also minimum power limits of PSHP's turbines and pumps are equal similarly Eqs. (76.4) and (76.5).

$$P_h^{\max} = P_p^{\max} \tag{76.4}$$

$$P_h^{\min} = P_p^{\min} \tag{76.5}$$

PSHP's upper reservoir has an initial storage value; this is equal to minimum energy level of the reservoir Eq. (76.6).

$$E_1^{in} = E^{\min} \tag{76.6}$$

PSHP's upper reservoir has minimum and maximum energy storage capacity limits Eqs. (76.7)–(76.9).

$$E(t) - \Delta t \cdot \frac{P_h(t)}{\eta_d} \geq E^{\min} \tag{76.7}$$

$$E(t) + \Delta t.\eta_c.P_p(t) \leq E^{\max} \tag{76.8}$$

$$E^{\min} \leq E(t) \leq E^{\max} \tag{76.9}$$

There are two main simulation steps according to the check of actual $P_v(t)$ and $P_d(t)$ values that is made by system operator.

First situation: Actual $P_v(t)$ and $P_d(t)$ values are controlled by system operator. If the power output of the WTP is greater than or equal to grid demand during Δt interval then grid demand is primarily met by WTP output Eqs. (76.10) and (76.11). In this case WTP output is also equal to the total delivered power to the grid, $P_{dg}(t)$, Eq. (76.12), ($P_w(t)$: Power delivered to grid from WTP, during Δt interval, $P_{dg}(t)$: Total delivered power to grid, during Δt interval).

$$P_v(t) \geq P_d(t) \tag{76.10}$$

$$P_w(t) = P_d(t) \tag{76.11}$$

$$P_w(t) = P_{dg}(t) \tag{76.12}$$

If the power output of the WTP is greater than the grid demand during Δt interval then for the difference value of the delivered grid and power output of WTP ($P_v(t) - P_d(t)$) three probable sub-situations could occur according to minimum and maximum power limits of the pumps and available storable space of the reservoir. $P_{ex}(t)$ term is defined Eq. (76.13); this term indicates the excess power occurred due to mentioned restrictions,($P_{ex}(t)$: Excess power output, during Δt interval). The equation shows energy storage level regarding the operation of PSHP's pumps during the Δt interval is given by Eq. (76.14), ($E(t + 1)$: Energy storage level in reservoir, during ($t + 1$) interval).

$$P_{ex}(t) = P_v(t) - P_d(t) - P_p(t) \tag{76.13}$$

$$E(t + 1) = E(t) + \Delta t.\eta_c.P_p(t) \tag{76.14}$$

Second situation: Actual $P_v(t)$ and $P_d(t)$ values are controlled by the system operator. If the power output of the WTP is less than the grid demand during Δt interval then Eq. (76.15), the stored energy amount in the upper reservoir is controlled and three probable sub-situations could occur according to minimum and maximum power limits of the turbines and

available energy capacity of the reservoir. Here $P_{dg}(t)$ is equal to the sum of WTP power output and PSHP's turbines power output Eq. (76.16). $P_{def}(t)$ term is defined Eq. (76.17), this term indicates the unmet energy demand level even if the WTP and the PSHP contribute to energy production together ($P_{def}(t)$: Unmet (deficient) power demand of grid, during Δt interval). The equation shows energy consumption from upper reservoir regarding operation of PSHP's turbines during the Δt interval is given by Eq. (76.18).

$$P_v(t) < P_d(t) \tag{76.15}$$

$$P_{dg}(t) = P_w(t) + P_h(t) \tag{76.16}$$

$$P_{def}(t) = P_d(t) - P_{dg}(t) \tag{76.17}$$

$$E(t+1) = E(t) - \Delta t \cdot \frac{P_h(t)}{\eta_d} \tag{76.18}$$

In order to compare with HS model and consequently to evaluate the technical benefits of the HS, an operation simulation for WTP without storage is also made under same conditions.

First situation: Actual $P_v(t)$ and $P_d(t)$ values are controlled by the system operator. If the power output of the WTP is greater than or equal to grid power demand during Δt interval then it is met by WTP output, in case of the excess energy, $P_{ex}(t)$ occurs Eqs. (76.19)–(76.21).

$$P_v(t) \geq P_d(t) \tag{76.19}$$

$$P_w(t) = P_d(t) \tag{76.20}$$

$$P_{ex}(t) = P_v(t) - P_d(t) \tag{76.21}$$

Second situation: Actual $P_v(t)$ and $P_d(t)$ values are controlled by system operator. If the power output of the WTP is less than the grid power demand during Δt interval then, the grid demand is met at the level of WTP output and $P_{def}(t)$ occurs Eqs. (76.22)–(76.24).

$$P_v(t) < P_d(t) \tag{76.22}$$

$$P_w(t) = P_v(t) \tag{76.23}$$

$$P_{def}(t) = P_d(t) - P_v(t) \tag{76.24}$$

Results and Discussion

While results are evaluated with respect to first objective of the HS; annual electrical energy demand of the grid is 8,760.00 MW h and annual electrical energy produced at WTP is 41,800.09 MW h. These values are same for HS and WTP without storage as the comparison is made under same conditions.

Without storage, the WTP feeds 6,350.30 MW h of electrical energy to the grid, this value increases to 7,656.00 MW h for the HS; this means that there is 17.05 % increase in penetration level. Without storage, annual excess electrical energy value is 35,449.79 MW h, this value decreases to 34,103.47 MW h for the HS; this means that there is 3.80 % decrease. Without storage, annual unmet (deficient) electrical energy demand of the grid is 2,409.70 MW h, this value decreases to 1,104.00 MW h for the HS; this means that there is 54.19 % decrease.

The annual energy values according to the results Eqs. (76.25)–(76.32) are given in Table 76.5 (E_d^a: Electrical energy demand of grid (annual), E_v^a: Electrical energy produced at WTP(annual), E_w^a: Electrical energy delivered to grid by WTP (annual), E_h^a: Electrical energy produced at PSHP(annual), E_{dg}^a: Total electrical energy delivered to grid (annual),

Table 76.5 Comparison of annual energy values of HS and WTP

Annual values	HS	WTP
E_d^a (MW h)	8,760.00	
E_v^a (MW h)	41,800.09	
E_w^a (MW h)	6,350.30	
E_h^a (MW h)	1,305.70	–
E_{dg}^a (MW h)	7,656.00	6,350.30
E_p^a (MW h)	1,346.32	–
E_{ex}^a (MW h)	34,103.47	35,449.79
E_{def}^a (MW h)	1,104.00	2,409.70

E_p^a: Electrical energy consumed by PSHP's pumps (annual), E_{ex}^a: Excess electrical energy (annual), E_{def}^a: Unmet (deficient) electrical energy demand of grid (annual)).

$$\sum_{t=1}^{8760} P_d(t).\Delta t = E_d^a \tag{76.25}$$

$$\sum_{t=1}^{8760} P_v(t).\Delta t = E_v^a \tag{76.26}$$

$$\sum_{t=1}^{8760} P_w(t).\Delta t = E_w^a \tag{76.27}$$

$$\sum_{t=1}^{8760} P_h(t).\Delta t = E_h^a \tag{76.28}$$

$$\sum_{t=1}^{8760} P_{dg}(t).\Delta t = E_{dg}^a \tag{76.29}$$

$$\sum_{t=1}^{8760} P_p(t).\Delta t = E_p^a \tag{76.30}$$

$$\sum_{t=1}^{8760} P_{ex}(t).\Delta t = E_{ex}^a \tag{76.31}$$

$$\sum_{t=1}^{8760} P_{def}(t).\Delta t = E_{def}^a \tag{76.32}$$

The $\overline{P_{hs}}$ term is defined, this term indicates the ratio of the fulfillment of demand for HS and $\overline{P_{ow}}$ term is defined, this term indicates the ratio of the fulfillment of demand for WTP without storage Eqs. (76.33) and (76.34), ($\overline{P_{hs}}$: Stable power output ratio of HS (annual), $\overline{P_{ow}}$: Stable power output ratio of WTP (annual)).

$$\overline{P_{hs}} = \frac{\sum\limits_{t=1}^{8760} P_{dg}(t)}{\sum\limits_{t=1}^{8760} P_d(t)}.100 \tag{76.33}$$

Table 76.6 Comparison of annual stable power output ratio values of HS and WTP

Annual values	$\overline{P_{hs}}$ (%)	$\overline{P_{ow}}$ (%)
Stable power output ratio	87.40	72.49

Fig. 76.2 $P_d(t)$-time diagram for the month of January
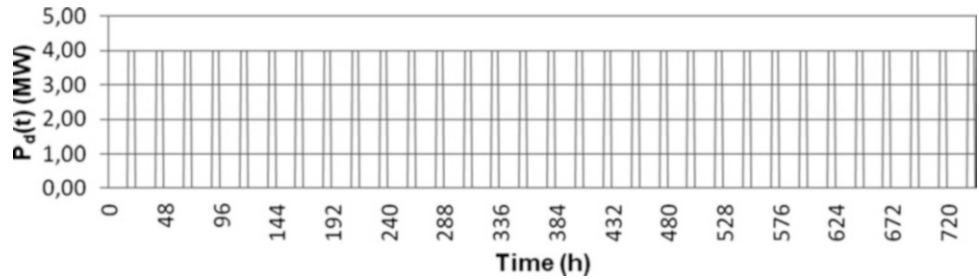
Fig. 76.3 $P_v(t)$-time diagram for the month of January
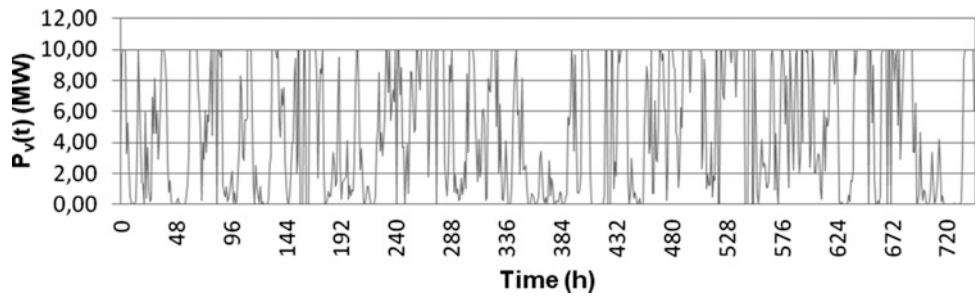
Fig. 76.4 $E(t)$-time diagram for the month of January
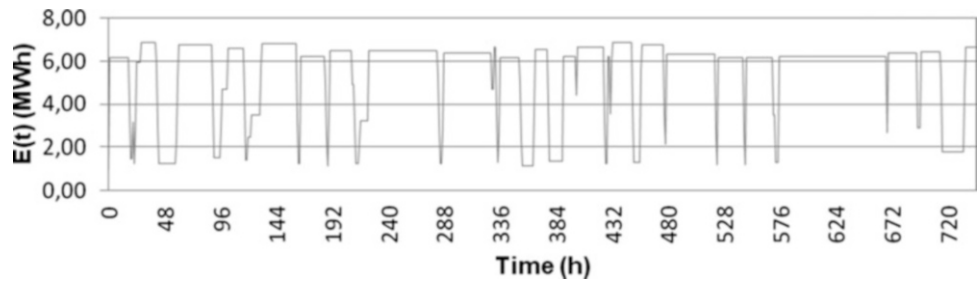
$$\overline{P_{ow}} = \frac{\sum_{t=1}^{8760} P_w(t)}{\sum_{t=1}^{8760} P_d(t)} \cdot 100 \qquad (76.34)$$

Annual stable power output ratio is approximately 72.49 % for WTP without storage and this value is approximately 87.40 % for the HS. This means that there is 14.91 % increase, Table 76.6.

The diagrams showing annual energy values for 1 year are plotted. In this paper the diagrams for 1 month (January) are presented; Figs. 76.2, 76.3, 76.4, 76.5, 76.6, 76.7, 76.8, 76.9, and 76.10. The simplified flow-chart of the operation simulation algorithm is given in Fig. 76.11.

Fig. 76.5 $P_{dg}(t)$-time diagram for the month of January
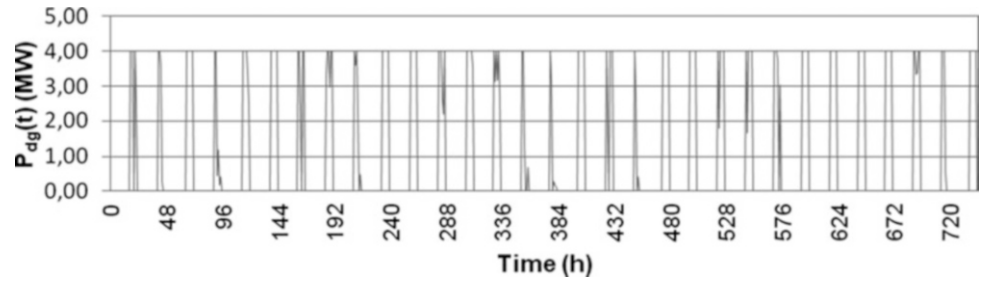
Fig. 76.6 $P_w(t)$-time diagram for the month of January
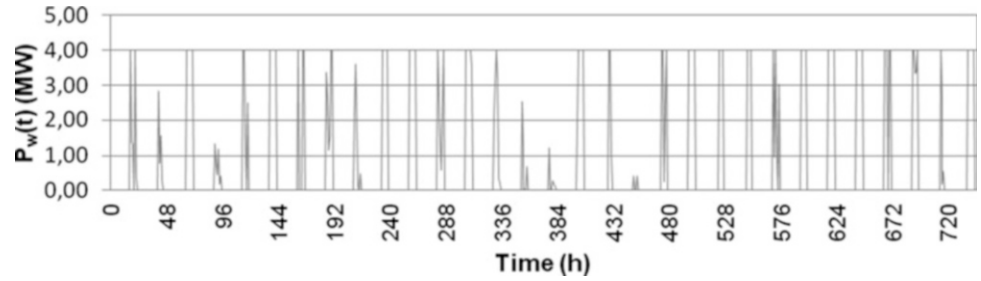
Fig. 76.7 $P_h(t)$-time diagram for the month of January
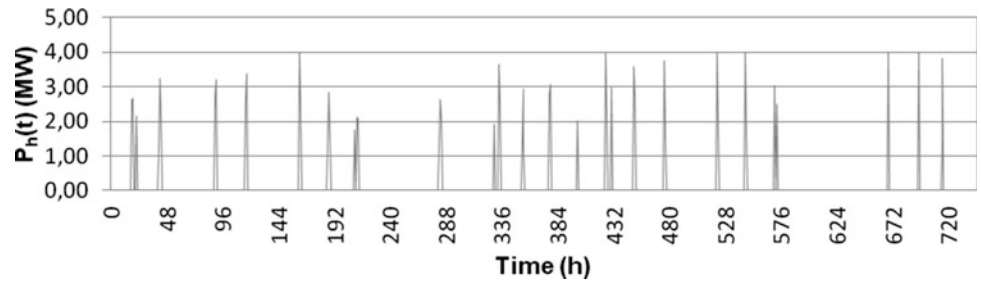
Fig. 76.8 $P_p(t)$-time diagram for the month of January
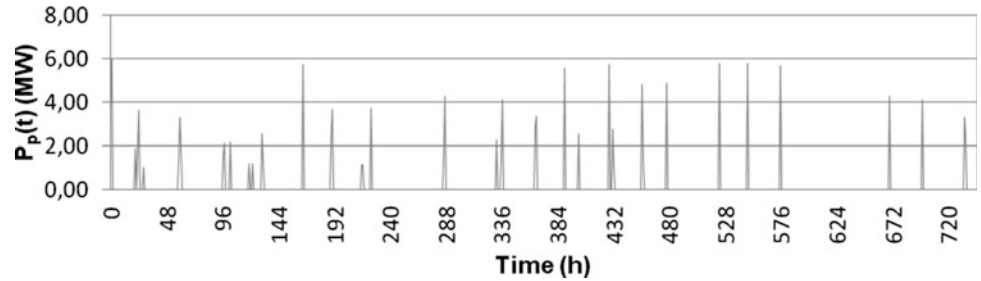
Fig. 76.9 $P_{ex}(t)$-time diagram for the month of January
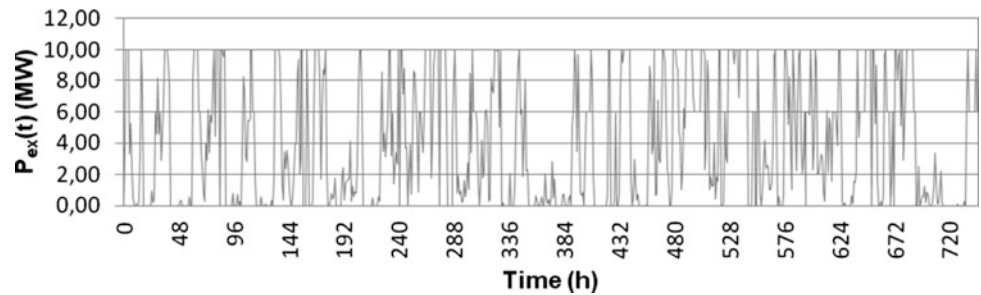
Fig. 76.10 $P_{def}(t)$-time diagram for the month of January
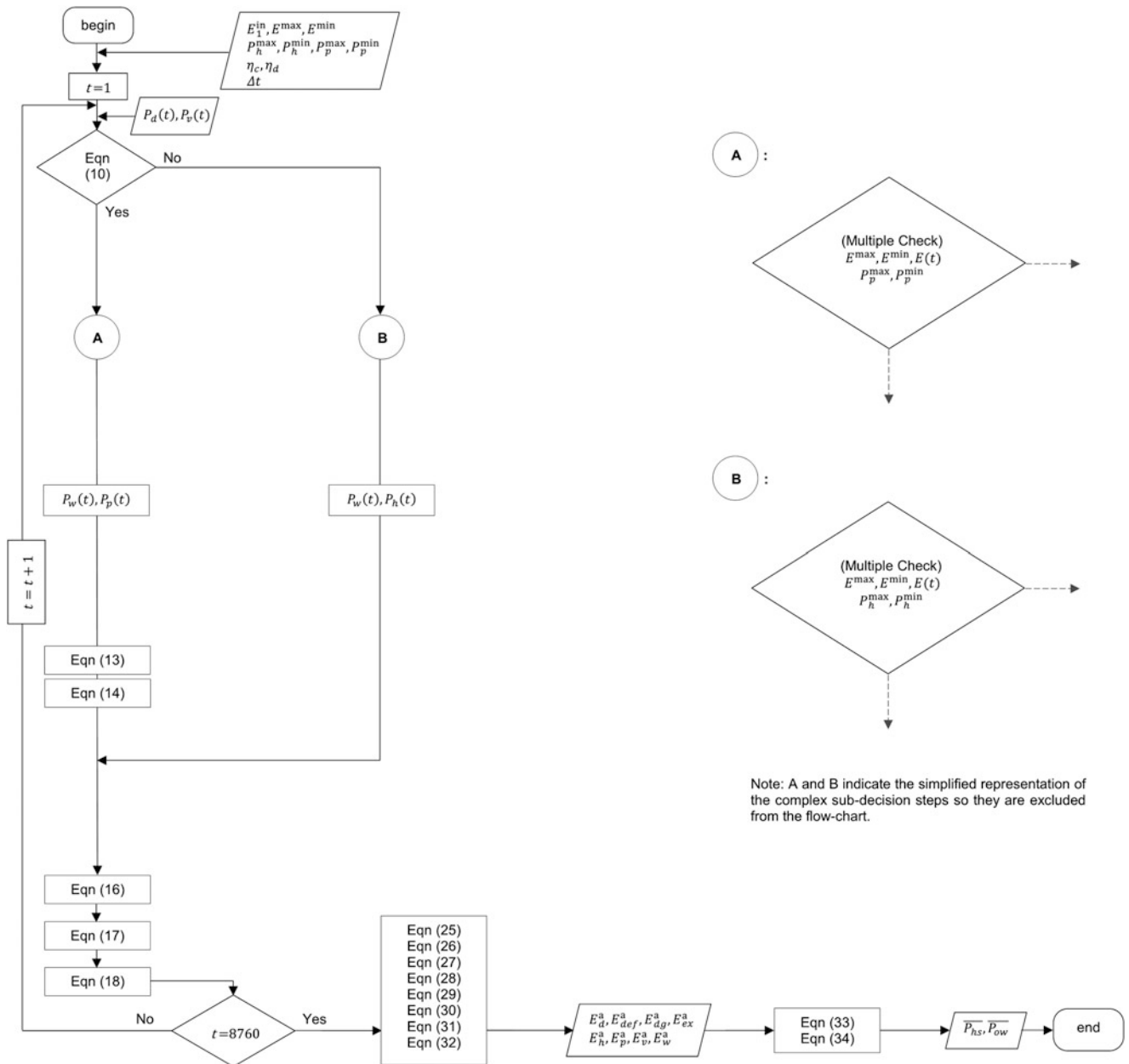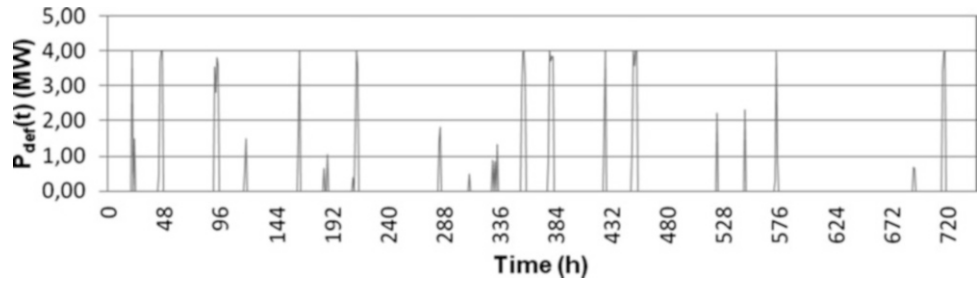
Fig. 76.11 Simplified flowchart that represents the operation simulation algorithm of HS

Conclusions

In this paper a hypothetical HS model that consists of a combination of a PSHP and a WTP is parametrically analyzed. As the installation objectives of the HS directly influence the design approach, two objectives were determined in the first place. Factors such as climatic and topographical conditions of project implementation area affect the wind speed and air density and consequently the energy production levels of WTPs have a variable structure in time. If power output level is lower than the grid load, demand could not be met properly and deficiency occurs; if the power output value is greater than the demand value, then an amount of excess power occurs. The first objective of the HS is to time-shift the power output of the WTP to peak demand periods by means of storage and thus realizing increase in the penetration level to the grid. Due to fluctuating and interrupted nature of the power output of the WTP, penetration of the electrical energy to the grid may pose problems to the steady operation of the grids that are not reliable for such conditions. The second objective is to obtain more stable power output from the WTP which inevitably has a variable power output. The technical specifications of WTP and PSHP models were determined. A general numerical model of the operation simulation is developed specifically in the scope of the mentioned two objectives. A 1-year operation simulation of the HS was carried out under peak tariff strategy, 1-year power output values of the WTP were calculated and this data was employed in the simulation. Interval time was selected to be 1 h. Also another simulation was made, results are obtained from the operation simulation that was made covering only the WTP with same power output data; annual electrical energy produced at WTP is 41,800.09 MW h, and with same demand strategy; constant 4 MW for 6 h a day, in total, annual electrical energy demand of grid is 8,760.00 MW h.

The following conclusions are drawn from the study. Annual total electrical energy amount delivered to grid for the WTP without storage is 6,350.30 MW h, and this value increases to 7,656.00 MW h for the HS; there is 17.05 % increase in the penetration level. Annual excess electrical energy value is 35,449.79 MW h for WTP without storage and 34,103.47 MW h for HS; there is 3.80 % decrease and annual unmet (deficient) electrical energy demand of the grid decreases from 2,409.70 to 1,104.00 MW h; there is 54.19 % decrease. When the results relevant to these three variables were compared, the penetration levels increase for the HS and HS is technically applicable for the first objective.

For the evaluation of the second objective of the system, stable power output ratios are considered. Annual stable power output ratio of WTP without storage is approximately 72.49 %, and annual stable power output ratio of HS is approximately 87.40 %; there is 14.91 % increase. The increase in the variable indicates that there is an improvement in stable power output in comparison with WTP without storage. According to these values, HS is technically applicable for the second objective.

In further studies, the HSs that are coupled with other types of ESSs may be investigated. Also with the selection of a solar power system instead of WTP, the HSs may be investigated. Designing a model with stochastic approach and simulation of this stochastic model is also another subject.

Nomenclature

c	Scale parameter (m/s)	E_h^a	Electrical energy produced at PSHP (annual) (MW h)
$E(t)$	Energy storage level in reservoir, during t interval (MW h)	E_p^a	Electrical energy consumed by PSHP's pumps (annual) (MW h)
$E(t+1)$	Energy storage level in reservoir, during $(t+1)$ interval (MW h)	E_v^a	Electrical energy produced at WTP (annual) (MW h)
E^{max}	Maximum energy storage capacity of reservoir (MW h)	E_w^a	Electrical energy delivered to grid by WTP (annual) (MW h)
E^{min}	Minimum energy storage capacity of reservoir (MW h)	E_1^{in}	Initial energy storage level of reservoir (MW h)
E_d^a	Electrical energy demand of grid (annual) (MW h)	k	Shape parameter
		$P_d(t)$	Power demand of grid, during Δt interval (MW)
E_{def}^a	Unmet (deficient) electrical energy demand of grid (annual) (MW h)	$P_{def}(t)$	Unmet (deficient) power demand of grid, during Δt interval (MW)
E_{dg}^a	Total electrical energy delivered to grid (annual) (MW h)	$P_{dg}(t)$	Total delivered power to grid, during Δt interval (MW)
E_{ex}^a	Excess electrical energy (annual) (MW h)	$P_{ex}(t)$	Excess power output, during Δt interval (MW)

$P_h(t)$	Power output of PSHP's turbines, during Δt interval (MW)	$P_w(t)$	Power delivered to grid from WTP, during Δt interval (MW)
P_h^{max}	Maximum power output of PSHP's turbines (MW)	P_{wt}	Power output of wind turbine (MW)
P_h^{min}	Minimum power output of PSHP's turbines (MW)	$\overline{P_{hs}}$	Stable power output ratio of HS (annual) (%)
$P_p(t)$	Power of PSHP's pumps, during Δt interval (MW)	$\overline{P_{ow}}$	Stable power output ratio of WTP (annual) (%)
		t	Time index
P_p^{max}	Maximum power of PSHP's pumps (MW)	v	Wind speed (m/s)
P_p^{min}	Minimum power of PSHP's pumps (MW)	v_m	Average wind speed (m/s)
$P_v(t)$	Power output of WTP's turbines, during Δt interval(MW)	α	Hellman exponent
		Δt	Duration of interval (h)
P_v^{max}	Maximum power output of WTP's turbines (MW)	η_c	Isentropic charge efficiency of HS
		η_d	Isentropic discharge efficiency of HS
P_v^{min}	Minimum power output of WTP's turbines (MW)	η_t	Isentropic cycle efficiency of HS
		ρ_a	Air density (kg/m^3)

Acronyms

ESS	Energy Storage System	TGO	Transmission Grid Operator
HS	Hybrid System	WTP	Wind Turbine Plant
PSHP	Pumped Storage Hydropower Plant		

References

1. Bueno C, Carta JA (2005) Technical-economic analysis of wind-powered pumped hydro storage systems. Part I: model development. Solar Energy 78(3):382–395
2. Bueno C, Carta JA (2006) Wind powered pumped hydro storage systems, a means of increasing the penetration of renewable energy in the Canary Islands. Renew Sustain Energy Rev 10(4):312–340
3. http://www.inl.gov/wind/software/powercurves/pc_aaer.xls. Accessed on 2012
4. Paul DB, Lopes JAP, Matos MA (2008) Optimization of pumped storage capacity in an isolated power system with large renewable penetration. IEEE Trans Power Syst 23(2):523–531
5. Jon AS, Uhlen K, Undeland T (2008) Wind power integration in isolated grids enabled by variable speed pumped storage hydropower plant. IEEE ICSET 2008:309–404
6. Javier G-G, de la Muela RMR, Santos LM, González AM (2008) Stochastic joint optimization of wind generation and pumped-storage units in an electricity market. IEEE Trans Power Syst 23(2):460–468
7. Feng G, Hallam A, Yu C-N (2009) Wind generation scheduling with pump storage unit by collocation method. IEEE PES General Meeting 2009:1–8
8. Edgardo DC, Lopes JAP (2004) Optimal operation and hydro storage sizing of a wind-hydro power plant. Electr Power Energ Syst 26(10):771–778
9. Phuc DNN, Pham TTH, Bacha S, Roye D (2009) Optimal operation for a wind-hydro power plant to participate to ancillary services. IEEE ICIT 2009:1–5
10. Kurtuluş D (2013) Hybrid systems of pumped storage hydropower plants and wind turbine plants, M.Sc. thesis, Başkent University, Turkey
11. Vaughn N (2009) Wind energy: renewable energy and the environment. CRC Press, New York, NY

Noorfidza Yub Harun and Muhammad T. Afzal

Abstract

The torrefaction of agriculture (switchgrass and timothy) and forestry (spruce and pine) biomass was studied using simultaneously thermogravimetric analyzer (TGA) coupled with Fourier transform infrared (FTIR), and mass spectrometer (MS). The chemical functional groups present in the gases were identified by FTIR and the quantification of gaseous products was determined using MS at different torrefaction temperatures ranging from 200 to 290 °C. TG-FTIR and TG-MS techniques are paired to refine the identification of gases. TGA results showed that the behavior of the agricultural and forestry biomass was not the same due to their composition variation. The decomposition of switchgrass took place at a lower temperature than other biomass. Both switchgrass and timothy have two peaks of degradation rate compared to only one peak present for forestry biomass. The FTIR analysis indicated that most of the chemical compositions present in the biomass are decomposed at torrefaction temperature of 290 °C. The mass spectrometric analysis at torrefaction temperature 200 and 230 °C quantified the degradation of combustible gases: CH_4, C_2H_4, CO, and O_2 around 20–30 %, whilst at torrefaction temperature 260 and 290 °C the degradation of combustible gases was more than 30 %. Moreover, all gaseous products evolved from the torrefaction of agricultural and forestry biomasses were almost similar in characteristics, but varied in proportions.

Introduction

Canada is one of the countries in the world which generates abundant amount of biomass from agriculture and forestry sector. Canada has about 42 % of forest land and 6.8 % of agricultural land from which about 42 % of residue is produced entirely from forestry and agricultural [26]. Hence, there exists large potential to convert this biomass into valuable products for various applications. Thermochemical treatment is an effective method to handle the issue of this huge biomass resource. This process has great advantages since it is flexible in feedstock, produces different fuels, and is environmental friendly.

Torrefaction is also emerging as one of thermochemical method to produce energy fuel by improving the biomass properties [1]. The biomass is heated between temperatures 200–300 °C in an inert condition. Torrefaction has been reported [1] to improve the hygroscopic behavior, decay resistivity, grindability, and higher heating value. Moreover, it can help to reduce the greenhouse gas emissions. Assuming a net calorific value of 6.2 MW h/ton, torrefied pellets (4,533,724 ton) is estimated to save CO_2 emissions of 21,081,816 ton, if the former is replaced by traditional pellets (5,736,549 ton) [12]. Despite this saving in emissions, the behavior of biomass torrefaction still needs serious research attention.

N.Y. Harun • M.T. Afzal (✉)

Department of Mechanical Engineering, University of New Brunswick, Fredericton, NB, Canada E3B 5A3

e-mail: Noorfidza.Yub_Harun@UNB.ca; mafzal@unb.ca

With regard to this, TGA–FTIR technique is the most widely used method to observe the thermal decomposition of materials under various environments. Understanding about the kinetics and an in-depth analysis of mass loss with the type of release of gas products [18] are essential for the fundamental knowledge, design, operation, and control [13] of torrefaction equipment and process. Therefore, the influence of parameters on chemical composition of the torrefied product has been extensively studied. In torrefaction, the lignin network is modified [2, 15, 23], and hemicelluloses are strongly degraded [17] leading to formation of carbonaceous material within the wood [16]. The anhydrous mass loss during torrefaction could be a reliable and accurate indicator to predict dimension stability and decay resistivity of pellet fuel [9, 25].

Some studies were found related to torrefaction of biomass using TG analysis to determine the torrefaction kinetic of cellulose, hemicellulose, lignin, and xylan [6]. The same author has also conducted torrefaction of various biomasses (bamboo, willow, coconut shell, and wood) using TG analysis [7]. Another study also reported which was focused on torrefaction of deciduous wood (beech and willow), coniferous wood (larch), and straw using TG analyzer [19]. Very recently, a study on torrefaction of wheat straw but using TGA/DSC configuration mode was performed [21]. From this and other literature survey, none has attempted to torrefy biomass using TGA coupled with FTIR. Since TGA coupled with FTIR can be advantageous for continuous online gas analysis, the torrefaction thermal decomposition can be studied in depth. It was also difficult to find torrefaction of agriculture (switchgrass and timothy) and forestry (spruce and pine) biomass using TG-FTIR-MS technology. Keeping this in view, the study contributes new knowledge about the characteristics of the gas evolved during torrefaction of various types of biomass. The main objective was to determine the torrefaction behavior as well as simultaneously investigate the chemical functional groups and quantification of the gas product. TG-FTIR-MS analyses of gas were carried out at different temperature of the torrefied biomass. Comparison of torrefaction of agriculture and forestry biomass is presented in this study.

Materials and Method

Four types of biomass were selected for torrefaction. Two were agriculture (switchgrass and timothy) and other two were forestry (spruce and pine). The agricultural biomass samples were provided by NB Department of Agriculture. The forestry biomass chips of size ranging from 10 to 50 mm were acquired from local sawmill. Prior to the analysis, biomasses were first dried in the oven at 105 °C for 24 h, and then grounded to about 500 μm particle size.

TG-FTIR Experiment

A Nicolet 6700 FTIR Thermo Scientific connected to TGA Q500 TA Instrument was used to perform torrefaction experiments. Approximately 10 mg of sample was loaded in a TGA crucible. The temperature was initially raised to 105 °C at heating rate of 20 °C/min and held for 5 min in order to remove moisture. At second stage the samples were torrefied using same heating rate to a desired temperature. The inert atmosphere was maintained using nitrogen gas at flow rate of 100 ml/min. Vapors released from biomass torrefaction were subjected to the FTIR spectrometer through a transfer tube, which is heated to about 200 °C to prevent the condensation of vapors on the tube wall. The IR spectra were recorded with a temporal resolution about 2 s. The resolution of the collected spectra was set to be 1 cm^{-1} and the spectral range was set from 4,000 to 400 cm^{-1}. At the carrier gas flow rate of 100 ml/min, it took about 50 s for the vapors to reach the FTIR cell from the thermogravimetric analyzer. Therefore, there was time delay of about 50 s.

TG-MS Experiment

The volatile products generated from TGA that was first scanned by FTIR spectrometer to detect the functional group, and then were furthered transferred to the ionization source of the mass spectrometer, SRS RGA 200, in order to determine specific chemical compound. The transfer line was heated and maintained at a temperature of 200 ºC to prevent the condensation of the volatile gases released during the torrefaction process. The mass spectrometer is operated at electron energy of 70 eV. The gases were analyzed by using the RGA software. A scan of the m/z was carried out from 1 to 100 amu to determine which m/z has to be followed during the TG experiments. The intensities of ten selected ions (m/z = 15, 16, 27, 28, 29, 32, 43, 44, 94, and 96) were monitored with the thermogravimetric parameters. An absolute quantification in this

work was performed for each monitored gases: CH_4, CO_2, CO, C_2H_4, NH_3, O_2, C_6H_6O, CH_2O, $C_2H_4O_2$, and CH_5O_3P. The concentrations of CH_4, CO_2, CO, C_2H_4, NH_3, O_2, C_6H_6O, CH_2O, $C_2H_4O_2$, and CH_5O_3P were directly deduced from the partial pressure of gases by using Eq. (77.1).

$$[A_i] = (P_i/P_T) \times 1\ 000\ 000 \tag{77.1}$$

Where, $[A_i]$ is the concentration of the gas A, Pi is the partial pressure for m/z = i representing of gas A, and P_T is the total pressure for all species i.

Results and Discussion

Proximate Analysis

Table 77.1 shows the proximate analysis of the biomass used in this study. Moisture content, volatile matter and fixed carbon were determined using TGA analysis. However, ash content was investigated as per ASTM Standard Method E1755-01. Low moisture content in the present biomass suggests them as a good candidate for torrefaction process. Switchgrass showed highest amount of volatile matter and lowest fixed carbon content compared to other biomass. Agricultural biomass showed high amount of ash content compared to forestry biomass. The same comparison in the ash content was reported for agricultural biomass and woody biomass [20].

TG-DTG Analysis

Figure 77.1 depicts the thermogravimetric curve for different biomasses. The degradation reactivity for forestry biomass (spruce and pine) was almost similar to each other. However the degradation behavior of switchgrass differed from other biomass. The initial decrease in the weight loss of biomass was attributed to removal of moisture content up to temperature 110 °C. The initial degradation temperature for spruce, pine, and timothy was about 210 °C. Whilst for switchgrass it was about 175 °C. This shows that the decomposition of switchgrass took place earlier compared to other biomass. From the TGA, the final degradation temperature for spruce, pine, switchgrass, and timothy was about 375, 375, 360, and 380 °C, respectively. Between temperatures 200 and 500 °C higher decomposition of cellulose and hemicellulose might have occurred, while small amount of lignin degradation is expected to take place. This observation was reported similarly for various woody biomasses [7]. No significant weight loss was observed after temperature of 500 °C. The residual or biochar content for spruce, pine, switchgrass, and timothy was about 16, 15, 21, and 11 wt%, respectively.

Apparently, switchgrass showed a highest total weight loss at temperature 800 °C. With respect to the torrefaction temperature of about 300 °C, switchgrass showed highest weight loss of about 30 wt% compared to spruce (17 wt%), pine (20 wt%), and timothy (20 wt%). This shows that switchgrass can be an attractive raw material for torrefaction. According to previous studies [3] and [11], the thermal decomposition of hemicellulose, cellulose and lignin occurs at temperatures ranging from 150 to 350, 275 to 350, and 250 to 500, respectively. Similarly, the decomposition of lignocellulosic materials in four biomasses is presented in Fig. 77.2.

Figure 77.2 shows that agricultural biomass has two peaks as contrast to one peak for the forestry biomass. The first peak is attributed due to degradation of hemicellulose. However, second peak represent the decomposition of cellulose. The first and the second peak for switchgrass were found at temperature of about 230 and 330 °C, respectively. In the case of timothy it was found at temperature of about 310 and 355 °C, respectively. The DTG peaks for forestry biomass (spruce and pine)

Table 77.1 Proximate analysis data of selected biomass materials (% weight dry)

	Spruce	Pine	Switchgrass	Timothy
Moisture (%)	2.92	4.63	2.23	2.82
Volatile matter (%)	73.75	73.05	68.46	79.55
Fixed carbon (%)	23.33	22.32	25.70	13.57
Ash (%)	Trace	Trace	3.61	4.06

Fig. 77.1 Thermo-diagram of biomass in nitrogen atmosphere, the loss of moisture, volatiles and char
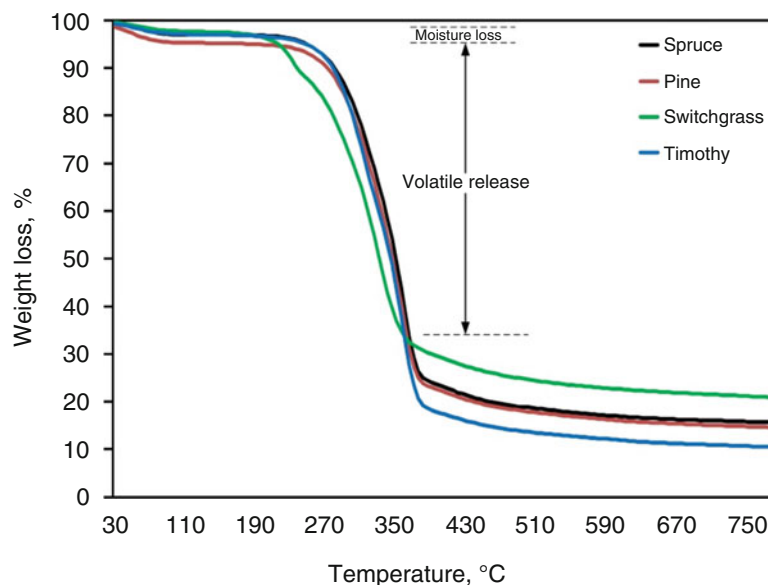
Fig. 77.2 DTG curves of biomass
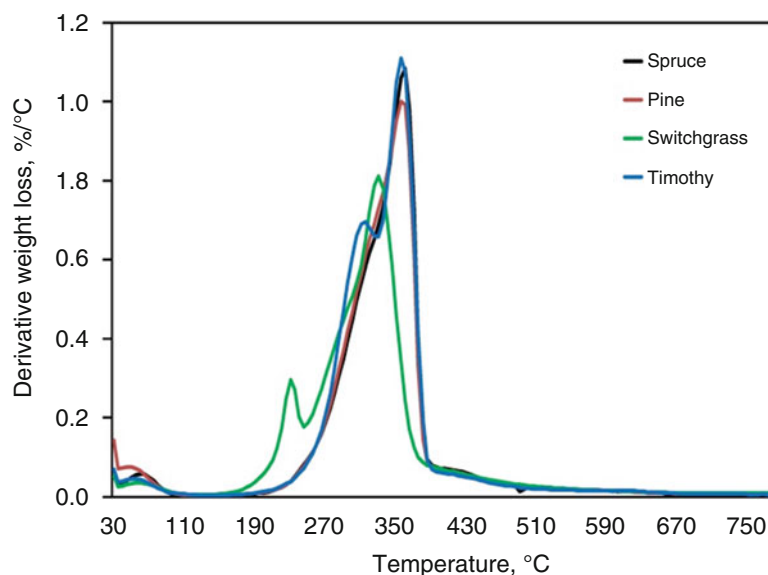
was at temperature 350 °C. From this observation, it can be concluded that the hemicellulose content in the softwood biomass is less compared to agricultural biomass. A kinetic study on willow and agricultural biomass was found that willow has less hemicellulose content compared to reed canary grass and wheat straw [5].

FTIR Analysis

Figures 77.3, 77.4, 77.5, and 77.6 illustrates the possible chemical functional groups of the torrefied biomass. The FTIR spectra shown in Figs. 77.3, 77.4, 77.5, and 77.6 correspond to the gas analyzed at different torrefaction temperature of 200, 230, 260, and 290 °C, respectively. Overall, the peaks for different functional groups became more sharp and visible when the temperature was increased from 200 to 290 °C. This shows that at higher temperature around 300 °C more degradation of biomass took place. The band around 3,600–3,400 cm^{-1} is apparently due to hydroxyl (O–H) groups, which was found in all torrefied biomass. The C–H stretch band around 2,970–2,780 cm^{-1} is the indication of an organic compound. A sharp band around 2,300–2,200 cm^{-1} wave number is due to the formation of CO_2 during torrefaction of biomass. It is observed that the

Fig. 77.3 Decomposition of functional groups at torrefaction temperature 200 °C
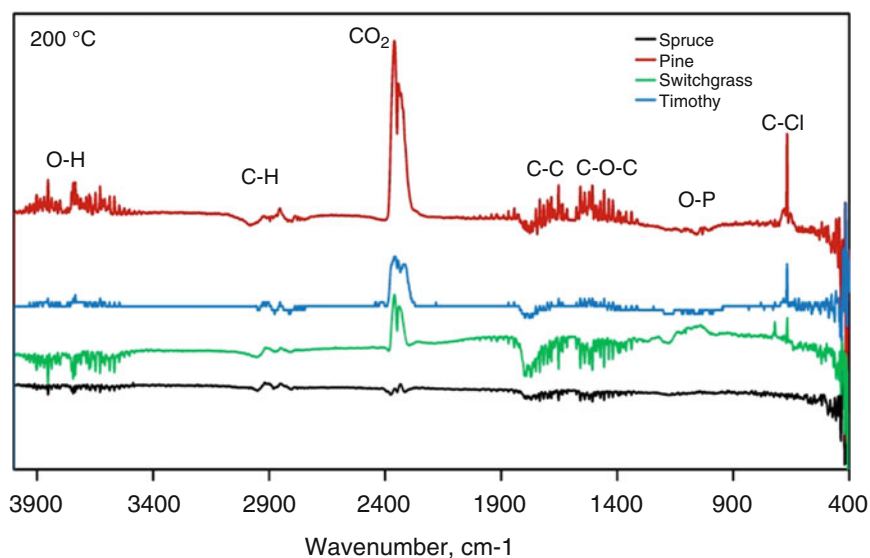
Fig. 77.4 Decomposition of functional groups at torrefaction temperature 230 °C
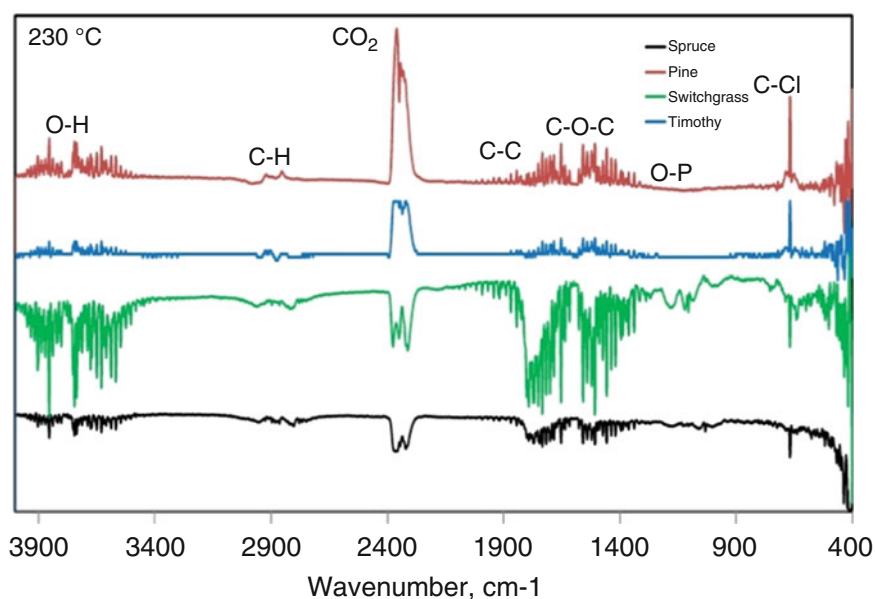
two major bands in the region of 1,740–1,710 cm^{-1} and 1,250–1,220 cm^{-1} might be because of C–O and C–O–C functional groups, respectively. Organic phosphates (P–O) functional groups can be found in range of 1,350–1,250 cm^{-1} stretch band, and the presented of aliphatic phosphates (P–O–C) functional groups is more obvious at around 1,050–990 cm^{-1} than organic phosphates (P–O) functional groups. A very sharp peak around 730–550 cm^{-1} might be due to acid chlorides (C–Cl) functional groups present [10].

Torrefaction 200 °C

Same procedure was employed for all torrefaction condition; the change of transmittance intensities indicates a variation in the gas concentration [4]. Figure 77.3 shows that pine and switchgrass are more reactive than timothy and spruce at torrefaction temperature 200 ºC, particularly for O–H, C–C, and C–O–C of functional groups. C–H and O=C=O functional groups in all biomass, which are obviously methane (CH_4), and carbon dioxide (CO_2) and carbon monoxide (CO), significantly transmit as they are reactive between 150 and 300 °C [22]. However, different biomass gives out CO_2 and CO at different concentration as shown in Figs. 77.3, 77.4, 77.5, and 77.6. CO_2 from spruce is the lowest in concentration compared to pine, switchgrass, and timothy at torrefaction temperature 200 ºC. Switchgrass shows significant C–O–P and

Fig. 77.5 Decomposition of functional groups at torrefaction temperature 260 °C
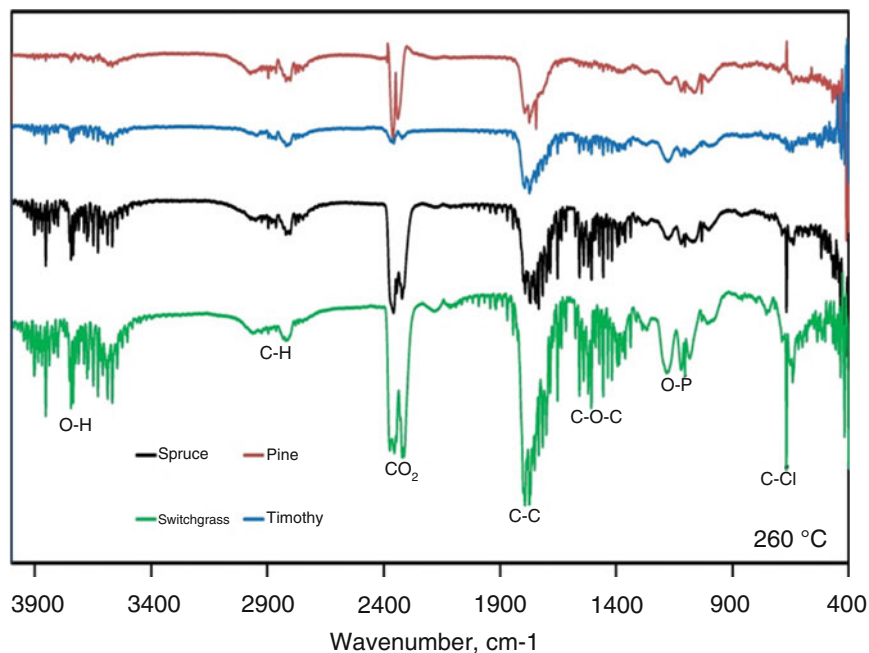
O–P groups than the others. Organochlorine compounds (C–Cl functional groups) are normally present in plants and wood. Its reactivity varies enormously, but most are relatively inert. However, this functional group has shown different concentration from different biomass. The intensity at torrefaction temperature 200 ºC is at the highest in pine compared to switchgrass and timothy, and seemingly none from spruce.

Torrefaction 230 °C

As at torrefaction temperature 200 ºC, most functional groups significantly transmitted at torrefaction 230 ºC but at different level of intensity. Figure 77.4 shows, the chemical compounds in switchgrass are the most reactive compared to the one in pine, spruce, and timothy. O–H, C–C and C–O–C of functional groups in particular, an increase in the intensity were transmitted from torrefaction temperature 230 ºC. The release of CO_2 at torrefaction temperature 230 ºC is about the same as at torrefaction temperature 200 ºC for pine, switchgrass, and timothy. However, the CO_2 release from spruce has increased at this torrefaction temperature. At torrefaction temperature 200 ºC, as well as torrefaction temperature 230 ºC, the phosphate compounds released significantly only from switchgrass, and apparently none from the other biomass. Organochlorine compounds (C–Cl functional groups) are released from all biomass at this torrefaction temperature, but the transmittance still at different intensity. Pine and switchgrass released almost of this compound at torrefaction temperature 230 ºC.

Torrefaction 260 °C

From Fig. 77.5, pine and timothy were found has less reactive as compared to spruce and switchgrass. The transmittance intensity for spruce has shown significant increased at torrefaction temperature 260 ºC from the torrefaction temperature 200 and 230 °C. The intensities of all the functional groups of chemicals for spruce were just a slight lesser than switchgrass. This can be anticipated that the degradation of spruce, pine, and timothy were engaged at later temperature than that of switchgrass. This might be almost hemicellulose and partially cellulose from switchgrass easily released at lower torrefaction temperature (200, 230 and 260 °C) due to less lignin content to bind them from devolatilization and depolymerization [8, 14, 24]. Lignin decompose from temperature 280 ºC and difficult to dehydrate. Thus it converts to more char and loose the covalent bond to cellulose or hemicelluloses [24]. The releases of CO_2 from switchgrass and spruce at torrefaction temperature 260 ºC were higher than that of lower torrefaction temperature (200 and 230 ºC). Switchgrass was also identified giving off the gases (functional groups O=C=O) the highest among the selected biomasses at torrefaction temperature 260 °C. The phosphate compounds were gradually degraded at this torrefaction temperature from torrefaction temperature 200 and 230 °C for all biomass. Organochlorine compounds (C–Cl functional groups) released from spruce and switchgrass significantly greater than that from pine and timothy.

Fig. 77.6 Decomposition of
functional groups at torrefaction
temperature 290 °C
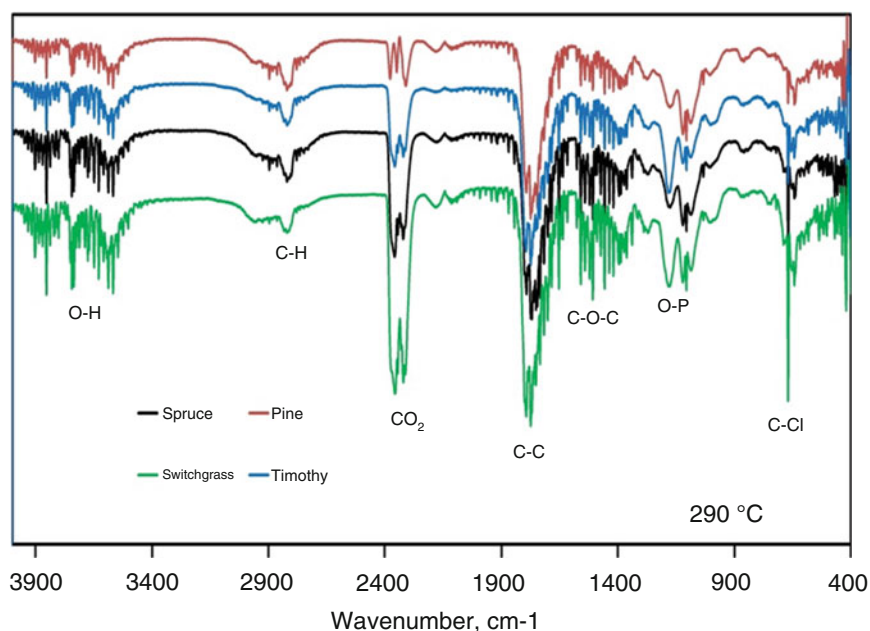
Torrefaction 290 °C

It is clearly shown from Fig. 77.6, the transmittance intensities of all the selected functional groups were significantly high which means almost gases and organic compound were degraded at torrefaction temperature 290 ºC. The released intensities of O–H, C–H, O=C=O, C–C, C–O–C, and O–P functional groups were found greater at torrefaction temperature 290 °C than that of at lower torrefaction temperature. The lignocellulosic biomass has converted to carbonaceous materials due to generous hemicellulose and cellulose was degraded at this torrefaction temperature. The organochlorine compounds (C–Cl functional groups) and gases (O=C=O functional groups) released from switchgrass were still significantly greater than that of spruce, pine, and timothy.

Gas Quantification

FTIR and mass spectrometric analyses have advantages and disadvantages. Using information provided by the FTIR spectrum is possible to have an identification of the gases emitted by each biomass. However, quantification of each emitted gases require specific tool or software to measure. TG-FTIR and TG-MS techniques are therefore complementary since they can refine the identification of gases. Table 77.2 shows the concentration of each gas during torrefaction of the selected biomass as the results from the TG-MS. To compare the evolution of gas emissions during torrefaction, the gas composition was calculated as a function of temperature. The comparison is made upon the gas concentration released by the biomass, which the yields of the gases were calculated for the four range of torrefaction temperature (Table 77.2). From the table all the four stages of temperature, the degradation of gases are mainly composed on O_2, CO_2, and CO, and then are followed by C_2H_4, NH_3, CH_2O and CH_4. Carbolic acid, acetic acid and phosphonic acid have the lowest degradation during the torrefaction. Switchgrass has degraded carbon dioxide and carbon monoxide the highest compared to spruce, pine, and timothy. These results are in agreement with the FTIR spectrum, which the functional group showed among the highest of transmittance for switchgrass. The C-H functional group in the FTIR spectrum has depicted about the same transmittance intensities for all the biomass. The mass spectrum analysis found for these same intensities was attributed due to the methane (CH_4) generated from switchgrass, timothy, and pine, and ethylene (C_2H_4) generated from spruce. Simple gas molecule O_2 does not have infrared spectra, which cannot be scanned by FTIR. MS has this advantage on O_2 that has shown in this study the amount composed in biomass is as high as other main composition such as H_2O (depicted in FTIR spectrum). The main composition of volatile products released from biomass was identified as H_2O, CO, CO_2 [22], which was found to be the same in this study including O_2. Pine has generated the oxygen at the highest concentration as compared to switchgrass, timothy, and spruce. Generally, the concentration of the selected gas degradation emitted during torrefaction is around 20–35 % of the total concentration for all biomass, but vary in the propositions when compare between biomass and stages of

Table 77.2 Concentration of selected gaseous products evolved from torrefaction of spruce, pine, switchgrass, and timothy

		Methane (mg CH_4/g biomass)				Carbon dioxide (mg CO_2/g biomass)			
	Temp. (°C)	Spruce	Pine	SW	Timothy	Spruce	Pine	SW	Timothy
Residence time 30 min	200	0.015	0.02	0.023	0.024	0.017	0.036	0.02	0.043
	230	0.018	0.023	0.027	0.028	0.019	0.042	0.028	0.05
	260	0.021	0.026	0.032	0.032	0.025	0.05	0.039	0.058
	290	0.024	0.03	0.036	0.036	0.031	0.063	0.061	0.068
Total[a] of 81 min	30–800	0.07	0.088	0.110	0.105	0.171	0.284	0.339	0.341

		Carbon monoxide ($\times 10^{-2}$ g CO/g biomass)				Ethylene (mg C_2H_4/g biomass)			
	Temp. (°C)	Spruce	Pine	SW	Timothy	Spruce	Pine	SW	Timothy
Residence time 30 min	200	0.074	0.11	0.143	0.121	0.041	0.02	0.017	0.02
	230	0.087	0.128	0.166	0.141	0.047	0.022	0.02	0.024
	260	0.098	0.146	0.189	0.16	0.054	0.025	0.023	0.028
	290	0.111	0.164	0.214	0.18	0.06	0.028	0.026	0.031
Total[a] of 81 min	30–800	0.309	0.454	0.575	0.511	0.167	0.074	0.081	0.092

		Ammonia (mg NH_3/g biomass)				Oxygen (mg O_2/g biomass)			
	Temp. (°C)	Spruce	Pine	SW	Timothy	Spruce	Pine	SW	Timothy
Residence time 30 min	200	0.035	0.041	0.04	0.042	0.181	0.324	0.258	0.231
	230	0.04	0.046	0.046	0.049	0.209	0.36	0.299	0.269
	260	0.046	0.051	0.053	0.055	0.236	0.393	0.34	0.305
	290	0.052	0.057	0.06	0.063	0.262	0.428	0.381	0.342
Total[a] of 81 min	30–800	0.152	0.16	0.18	0.183	0.589	0.916	0.896	0.854

		Phenol (mg C_6H_6O/g biomass)				Formaldehyde (mg CH_2O/g biomass)			
	Temp. (°C)	Spruce	Pine	SW	Timothy	Spruce	Pine	SW	Timothy
Residence time 30 min	200	0.006	0.007	0.007	0.009	0.034	0.026	0.027	0.027
	230	0.007	0.008	0.008	0.011	0.044	0.03	0.032	0.032
	260	0.008	0.009	0.009	0.013	0.046	0.034	0.037	0.036
	290	0.009	0.01	0.01	0.014	0.047	0.039	0.043	0.042
Total[a] of 81 min	30–800	0.023	0.028	0.029	0.035	0.155	0.125	0.135	0.135

		Acetic acid (mg $C_2H_4O_2$/g biomass)				Phosphonic acid (mg CH_5O_3P/g biomass)			
	Temp. (°C)	Spruce	Pine	SW	Timothy	Spruce	Pine	SW	Timothy
Residence time 30 min	200	0.006	0.008	0.009	0.009	0.005	0.007	0.007	0.009
	230	0.007	0.01	0.01	0.011	0.006	0.008	0.008	0.01
	260	0.008	0.011	0.012	0.013	0.007	0.009	0.009	0.012
	290	0.009	0.013	0.014	0.014	0.008	0.01	0.011	0.013
Total[a] of 81 min	30–800	0.037	0.045	0.05	0.049	0.024	0.028	0.031	0.035

[a]*Note*: The continuous torrefaction from room temperature to 800 °C

torrefaction temperatures. For the continuous torrefaction range of temperature, the degradation of combustible gases (CH_4, CO, C_2H_2, O_2) released by switchgrass (1.662 mg/g$_{switchgrass}$) is more than timothy (1.562 mg/g$_{timothy}$), pine (1.532 mg/g$_{pine}$), and spruce (1.135 mg/g$_{spruce}$). The degradation of combustible gases during torrefaction temperature 200, 230, and 260 °C by pine showed the highest (0.474, 0.533, and 0.590 mg/g$_{pine}$, respectively) as compared to switchgrass (0.441, 0.512, and 0.584 mg/g$_{switchgrass}$, respectively), timothy (0.396, 0.462, and 0.525 mg/g$_{timothy}$, respectively), and spruce (0.311, 0.361, and 0.409 mg/g$_{spruce}$, respectively). Whilst, for torrefaction temperature 290 °C, the degradation of combustible gases has similar trend as for continuous torrefaction range of temperature that is switchgrass took place the highest (0.657 mg/g$_{switchgrass}$) as compared to pine (0.650 mg/g$_{pine}$), timothy (0.587 mg/g$_{timothy}$), and spruce (0.457 mg/g$_{spruce}$). For all species, the percentages of combustible gases may increases significantly after 300 °C, and thus, loose the energetic content of the biomass.

Conclusion

Four different types of Canadian biomasses were torrefied using TGA-FTIR analyzer and TGA-Mass spectrometry. Forestry and agriculture biomass showed single and two DTG peaks respectively during torrefaction. It was observed that the species had different evolution patterns, which indicates the presence of different chemical functional groups within the biomass

samples. In general, TG-FTIR analysis showed that the torrefaction behavior of forestry (spruce and pine) biomass were similar. Of all the biomass, switchgrass experienced considerable weight loss at lower torrefaction temperature. Pine, timothy, and spruce were found to have similar degradation behavior in terms of chemical functional groups when torrefied at lower temperature (200 and 230 °C). Degradation of combustible gases: CH_4, CO, C_2H_2, and O_2, during torrefaction at lower temperature: 200 and 230 °C is around 20–30 %, whilst at temperature 260 and 290 °C is around 30–45 %. Most of the chemical compositions were decomposed at higher torrefaction temperature of 290 °C. Overall, the gaseous products evolved during torrefaction of forestry and agricultural biomass showed similar FTIR spectra patterns and in agreement with mass spectrometric, MS, with regard to the degradation of combustible gases. Torrefaction temperature played a key role in the formation of these gaseous products.

References

1. Acharya B, Sule I, Dutta A (2012) A review on advances of torrefaction technologies for biomass processing. Biomass Convers Biorefine 2:349–369
2. Alen R, Kotilainen R, Zaman A (2002) Thermochemical behavior of Norway spruce (Picea abies) at 180–225°C. Wood Sci Tech 36:163–171
3. Antal MJ (1983) Biomass pyrolysis: a review of the literature. Part I – carbohydrate pyrolysis. Adv Sol Energ 11:61–111
4. Bassilakis R, Carangelo RM, Wójtowicz MA (2001) TGFTIR analysis of biomass pyrolysis. Fuel 80:1765–1786
5. Bridgeman TG, Jones JM, Shield I, Williams PT (2008) Torrefaction of reed canary grass, wheat straw and willow to enhance solid fuel qualities and combustion properties. Fuel 87:844–856
6. Chen W-H, Kuo P-C (2012) Isothermal torrefaction kinetics of hemicellulose, cellulose, lignin and xylan using thermogravimetric analysis. Energy 36:6451–6460
7. Chen W-H, Kuo P-C (2010) A study on torrefaction of various biomass aaterials and its impact on lignocellulosic structure simulated by a thermogravimetry. Energy 35:2580–2586
8. Demirbas A (2009) Pyrolysis mechanisms of biomass materials. Energ Source A Recov Utiliz Environ Effect 31(13):1186–1193
9. Hakkou M, Pétrissans M, Gérardin P, Zoulalian A (2006) Investigations of the reasons for fungal durability of heat-treated Beech wood. Polymer Degrad Stabil 91:393–397
10. John C (2000) Interpretation of infrared spectra, a practical approach. In: Meyers RA (ed) Encyclopedia of analytical chemistry. Wiley, Chichester, pp 10815–10837
11. Mansaray KG, Ghaly AE (1998) Thermal degradation of rice husks in nitrogen atmosphere. Bioresour Technol 65:13–20
12. Melin S (2012) Development of the Canadian bulk pellet market. Wood Pellet Association of Canada REF to FII Agreement #11/12-050
13. Miranda R, Sosa-Blanco C, Bustos-Martinez D, Vasile C (2007) Pyrolysis of textile wastes. I. Kinetics and yields. J Anal Appl Pyrolysis 80:489–495
14. Mohan D, Pittman CU, Steele PH (2006) Pyrolysis of wood/biomass for bio-oil: a critical review. Energy Fuel 20(3):848–889
15. Nguila-Inari G, Pétrissans M, Gérardin P (2007) Chemical reactivity of heat treated wood. Wood Sci Tech 41:157–168
16. Nguila-Inari G, Mounguengui S, Dumarcay S, Pétrissans M, Gérardin P (2007) Evidence of char formation during wood heat treatment by mild pyrolysis. Polym Degrad Stab 92:997–1002
17. Nuopponen M, Vuorinen T, Jamsa S, Viitaniemi P (2004) Thermal modifications in softwood studied byFT-IR and UV resonance Raman spectroscopies. J Wood Chem Tech 24(1):13–26
18. Oladiran F, Littlefield B (2012) TG-FTIR analysis of Pecan shells thermal decomposition. Fuel Process Tech 102:61–66
19. Prins MJ, Ptasinski KJ, Janssen FJJG (2006) Torrefaction of wood. Part 1: weight loss kinetics. J Anal Appl Pyrolysis 77:28–34
20. Raimie H, Ibrahima H, Darvella LI, Jenny M, Jonesa M, William A (2013) Physicochemical characterisation of torrefied biomass. J Anal Appl Pyrolysis 103:21–30. doi:10.1016/j.jaap.2012.10.004
21. Shang L, Ahrenfeldt J, Holm JK, Barsberg S, Zhang R, Luo Y, Egsgaard H, Henriksen UB (2013) Intrinsic kinetics and devolatilization of wheat straw during torrefaction. J Anal Appl Pyrolysis 100:145–152
22. Tihay V, Gillard P (2010) Pyrolysis gases released during the thermal decomposition of three Mediterranean species. J Anal Appl Pyrolysis 88:168–174
23. Tjeerdsma B, Militz H (2005) Chemical changes in hydrothermal treated wood: FTIR analysis of combined hydrothermal and dry heat-treated wood. HolzalsRoh Werkstoff 63:102–111
24. Tumuluru JS, Sokhansanj S, Wright CT, Boardman RD (2010) Biomass torrefaction process review and moving bed torrefaction system model development. INL publication 08, http://www.inl.gov/technicalpublications/Documents/4737111.pdf. Accessed on March 18, 2013
25. Welzbacher C, Brischke C, Rapp A (2007) Influence of treatment temperature and duration on selected biological, mechanical, physical and optical properties of thermally modified wood. Wood Mater Sci Eng 2:66–76
26. Wood SM, Layzell DB (2003) A Canadian biomass inventory: feedstocks for a bio-based economy. BIOCAP Canada Foundation Final Report Industry Canada Contract #5006125

Model-Based Performance Analysis of a Concentrating Parabolic Trough Collector Array

İbrahim Halil Yılmaz, Mehmet Sait Söylemez, Hakan Hayta, and Recep Yumrutaş

Abstract

This study presents a comprehensive thermo-mathematical model of a parabolic trough solar collector (PTSC) array which consists of three modules connected in series. A detailed model for the absorbed solar energy falling on the array aperture, the optical efficiency changing with incidence angle, and the useful energy gained by heat transfer fluid (HTF) for a linear with a single-axis tracking motion rotating about a horizontal north–south orientation was programmed in Engineering Equation Solver (EES) based on the actual system parameters. The model comprises steady-state and one-dimensional heat transfer approach using the thermodynamics and the heat transfer relations to evaluate the thermal losses of the receiver (heat collector element) by taking into account the effects of collector dimensions, material properties, and fluid properties. In the performance analysis of the PTSC array, the effects of hourly solar radiation flux, ambient conditions, collector inlet temperature, and mass flow rate of the working fluid were investigated. Typical operating conditions on the 1st day of July at 12:00 solar time exhibited that when the HTF mass flow rate 0.3 kg/s, inlet temperature 150 °C, ambient temperature 39 °C, ambient air velocity 1 m/s and having a 10.26 m^2 PTSC aperture area, and 940 W/m^2 direct beam radiation incident with 13.98°, the estimated collector array efficiency is about 59.2 %. The model predictions are to be confirmed by the operation of PTSC being installed at Gaziantep.

Introduction

Concentrating collectors are widely used for many applications to supply thermal energy at temperatures higher than those nonimaging collectors. Not only this feature but also having relatively high thermal efficiency put them forward in usage of compact thermal systems. A typical PTSC consists of a reflector material shaped in parabola, a linear receiver to collect solar energy, and a tracking unit to configure the position of the reflector. The linear receiver is commonly composed of an absorber tube and its cover envelope. A glass cover tube is usually placed around the receiver tube to reduce the increasing convective heat loss from the receiver at higher temperatures. The receiver follows the sun path by the tracking unit on the mode of single or double-axis during its operation while concentrating direct normal irradiance (DNI) to the receiver locating at the focal line of the parabolic reflector. The concentrated radiation reaching the receiver tube heats the fluid that circulates through it. The resulting thermal energy is transferred continuously to the fluid as useful energy. In order to calculate the energy absorbed by the working fluid, thermal and optical analyses are needed. These analyses are essential to reach the thermal and optical losses from the receiver element and correspondingly to the thermal performance of the PTSC. The analyses being made serve as a thermo-mathematical modeling of the PTSC while projecting the system characteristics.

İ.H. Yılmaz (✉) • M.S. Söylemez • H. Hayta • R. Yumrutaş
Department of Mechanical Engineering, University of Gaziantep, Gaziantep 27310, Turkey
e-mail: iyilmaz@gantep.edu.tr; sait@gantep.edu.tr; hakanhyt@hotmail.com; yumrutas@gantep.edu.tr

Many researchers presented studies of energy models of parabolic trough collectors. When the recent studies conducted on the detailed modeling of PTSC are handled, the most noticeable one was established by Forristall [1] who developed both a 1-D and a 2-D heat transfer model of parabolic trough solar receiver implemented in EES. His model included input variables as collector geometry, optical properties, HTF properties, HTF inlet temperature, flow rate, solar insolation, wind speed, and ambient temperature. Corresponding model outputs were investigated to determine collector efficiency, outlet HTF temperature, heat gain, and heat and optical losses of parabolic trough collector. The other study is of Jacobson et al. [2] who developed a solar parabolic trough simulation to determine the optimum parameters to sustain a solar thermal power plant system in Thailand. Another study was applied with a comprehensive model for the tubular receiver of the PTSC to improve the PTSC design and the overall system performance [3]. The model was verified by the experimental data from the tests on the PTSC in a high temperature solar cooling and heating system.

Other models on PTCs were followed by Padilla et al. [4] who performed a 1-D numerical heat transfer analysis, and an optical analysis for the PTC to optimize and understand its performance under different operating conditions. The model was compared with experimental data of Sandia National Laboratory and other 1-D heat transfer models to validate the obtained numerical results. Huang et al. [5] proposed a new analytical model for optical performance to simulate the performance of a parabolic trough solar collector (PTSC). Kalogirou [6] presented a detailed thermal model of a parabolic trough collector considering all modes of heat transfer. The model was written in EES and validated with known performance of existing collectors to be installed at the Cyprus University of Technology.

In this study, a comprehensive thermo-mathematical model analysis of a PTSC array has been presented. Solar energy calculations for determining the optical efficiency and the useful heat gain by the HTF have been conducted for obtaining the thermal performance of the PTSC array. The heat losses from the receiver have been evaluated considering steady-state and one-dimensional heat transfer approach. In the performance analysis of the PTSC array, the effects of hourly solar radiation flux, ambient conditions, collector inlet temperature, and mass flow rate of the working fluid have been investigated.

Parabolic Trough Solar Collector

System Description

The PTSC array consists of three modules connected in series shown in Fig. 78.1. It has been supplied from the German company, Smirro and has the technical specifications as indicated in Table 78.1. Its linear receiver is considered to have oriented coincidentally with the north–south axis of the local and the HTF is circulated within it by means of a frequency-controlled gear pump. The resulting thermal energy is transferred continuously to the HTF whose technical name is Renolin Therm 320 [7].
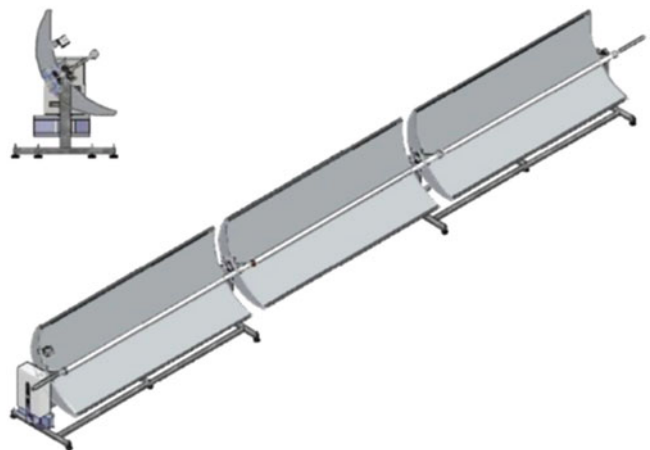
Fig. 78.1 The PTSC array

Table 78.1 Characteristics of a single PTSC module

Description	Value
Parabola length, l_a	3,000 mm
Parabola aperture, w_a	1,140 mm
Focal distance, f	358 mm
Rim angle, φ_r	77°
Outside absorber diameter, D_{oa}	35 mm
Inside absorber diameter, D_{ia}	32 mm
Outside cover diameter, D_{oc}	60 mm
Inside cover diameter, D_{ic}	54 mm
Mirror reflectance, ρ	0.90
Absorber material	Stainless steel
Cover material	DURAN glass
Mirror material	Aluminum

Solar Energy Calculations

The emitted radiation from the sun has a directional characteristic that is defined by a set of geometric relations to determine the angle of incidence of the radiation on a surface. Due to the instant change in the position of the sun, the incidence angle of the collector surface is to be calculated depending on solar time. Thus, the geometric relations between a plane moving relative to the earth and the beam radiation are to be determined during solar energy calculations. These calculations have been considered as the PTSC array installed at Gaziantep where the local geographic position is latitude N37°02′, longitude E37°19′, and the site elevation 881 m above sea level.

Solar time does not coincide with the local clock time and it is used in all of the sun-angle relationships; thus it is necessary to convert standard time to solar time. The general equation for calculating the apparent solar time is

$$AST = LST \pm 0 : 04(L_{st} - L_{loc}) + E - DST \tag{78.1}$$

where L_{st} is the standard meridian for the local time zone, L_{loc} is the longitude of the location interested. The values of the equation of time, E as a function of the day of the year can be obtained approximately from the following equation:

$$E = 9.87 \sin 2B - 7.53 \cos B - 1.5 \sin B \tag{78.2}$$

where $B = (n - 81)\frac{360}{364}$

The declination angle, denoted by δ, varies seasonally due to the tilt of the Earth on its axis of rotation at an angle of 23.45° with the ecliptic axis. This requires a coordinate transformation, i.e., the sun moves around the earth. The declination is zero at the equinoxes (March 22 and September 22), positive during the northern hemisphere summer, and negative during the northern hemisphere winter. The declination reaches a maximum of 23.45° on June 22 (summer solstice in the northern hemisphere) and a minimum of −23.45° on December 22 (winter solstice in the northern hemisphere). The declined function of the day of the year can be defined as

$$\delta = 23.45 \sin \left(360 \frac{284 + n}{365} \right) \tag{78.3}$$

Hour angle, ω determines the angular displacement of the sun from east or west of the local meridian due to the rotation of the earth on its axis at 15° per hour and takes negative values before solar noon and positive values after solar noon.

$$\omega = \pm 15°(AST - 12 : 00) \tag{78.4}$$

Zenith angle is the angle between the beam radiation and the normal of the earth surface. Thus, for the horizontal surfaces, the angle of incidence becomes the zenith angle of the sun, θ_z. In this case, the zenith angle is defined as

$$\theta_z = \cos^{-1}(\cos \phi \cos \delta \cos \omega + \sin \phi \sin \delta) \tag{78.5}$$
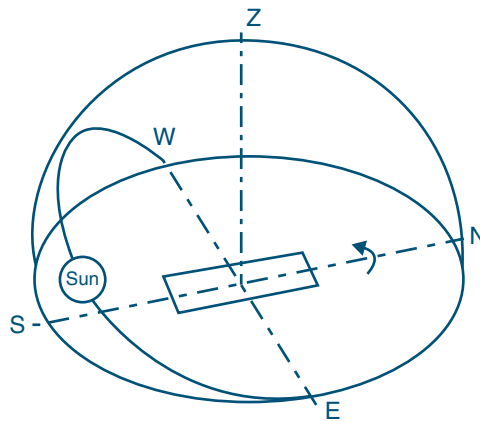
Fig. 78.2 Orientation of the PTSC array

The solar radiation received from the sun falling on a horizontal surface depends on the incidence angle. Solar tracking systems are intended to have PTSCs performed lessening the incidence angle in order to increase the beam component of the solar radiation falling on its aperture area. In addition, the orientation of the collector system with respect to a location where the PTSC system being setup is significant from the view of following the sun path as close as normal to minimize the angle of incidence and to be able to harvest much more solar energy. For a plane rotated about a horizontal north–south axis shown in Fig. 78.2 with a continuous adjustment from east to west is estimated by the relation

$$\theta = \cos^{-1}\left(\sqrt{\cos^2\theta_z + \cos^2\delta\sin^2\omega}\right) \tag{78.6}$$

Optical Efficiency Analysis of the Collector Array

Optical efficiency is defined as the ratio of the energy absorbed by the receiver to the energy incident on the collector's aperture. The optical efficiency is related with the radiative properties of optical materials, construction and operation of the collector, and the geometric factors due to the position of the collector with respect to the sun. The optical efficiency of the collector, η_o can be defined with the following terms,

$$\eta_o = \rho\tau\alpha\gamma(1 - \kappa\tan\theta)\cos\theta \tag{78.7}$$

The optical efficiency of the collector depends upon the radiative and optical properties of the receiving and the reflecting surfaces which are affected instantaneously by the variation of incidence angle. Thus the relation between the incidence angle and the radiative properties of the optical elements is demonstrated herein through the calculation of the optical efficiency.

Cover Transmittance
The cover material is made of DURAN type glass whose transmission property depends on the wavelength and the wall thickness shown in Fig. 78.3 [8]. As it is seen from the figure, its transmittance is nearly constant within the solar radiation spectrum. However, the directional surface property of the cover varies with solar incidence angle. The relationship between the normal specular transmittance and its angular dependency has been described with respect to the cover material used.

Since the receiver is composed of a single glass cover, the solar radiation is refracted from the ambient air with a refractive index, n_1, to the glass with a refractive index, n_2. The angles θ_1 and θ_2 are related to the indices of refraction by Snell's law,

$$\frac{n_1}{n_2} = \frac{\sin_1}{\sin_2} \tag{78.8}$$
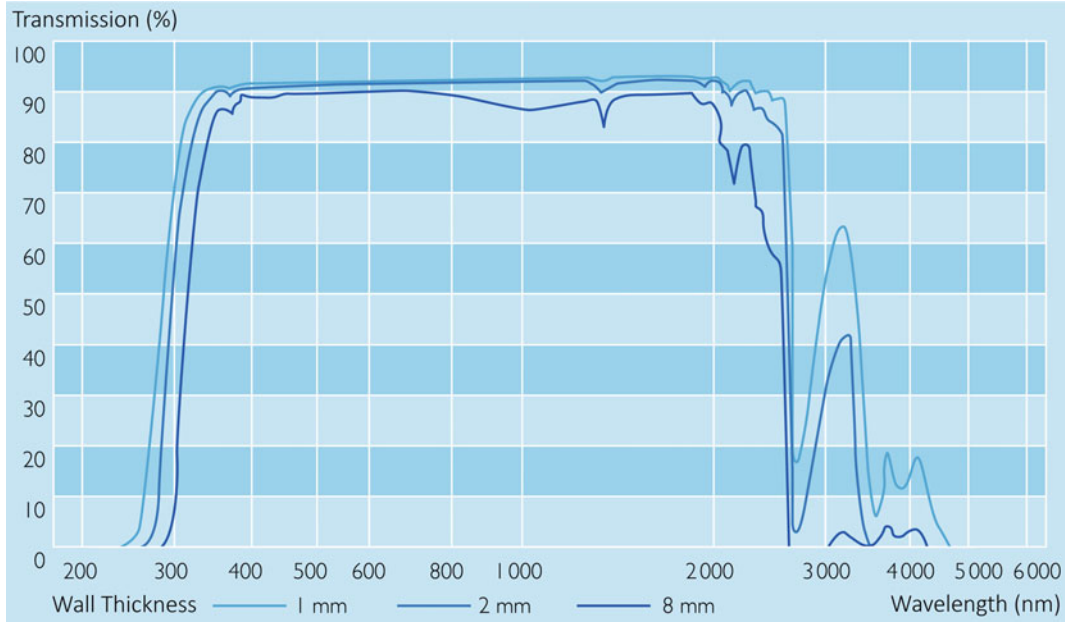
Fig. 78.3 Transmission of DURAN glass for thicknesses 1, 2, and 8 mm

The parallel and perpendicular components of unpolarized radiation for smooth surfaces can be defined using Fresnel's derivation,

$$r_\perp = \frac{\sin^2(\theta_2 - \theta_1)}{\sin^2(\theta_2 + \theta_1)}$$
$$r_\parallel = \frac{\tan^2(\theta_2 - \theta_2)}{\tan^2(\theta_2 + \theta_2)} \tag{78.9}$$

The absorption of the solar radiation in the partially transparent cover is determined according to the assumption that some portion of the incidence radiation is absorbed by the cover material.

$$\tau_a = e^{\left(\frac{-KL}{\cos\theta_2}\right)} \tag{78.10}$$

where K is called the extinction coefficient that is considered as 4 m^{-1} for "water white" glass.

For a single cover, the transmittance is defined by averaging the transmittance of the parallel and perpendicular components of polarization when only reflection losses are considered. As a result, the transmittance of the cover element is specified from Eq. (78.11) depending on incidence angle.

$$\tau = \frac{\tau_a}{2}\left[\frac{1 - r_\parallel}{1 + r_\parallel} + \frac{1 - r_\perp}{1 + r_\parallel}\right] \tag{78.11}$$

Absorptivity of the Receiver

The absorbance property of the absorber tube, which is made of stainless steel, depends also upon the incidence angle; however, there is no sufficient study in the literature for describing the relationship between the angular absorbance and the normal absorbance. Nevertheless it is estimated from the relation that provides fair results within 0 and 80° incidence angle [9].

$$\alpha = \alpha_n\left(1 + 2.0345 \times 10^{-3}\theta - 1.99 \times 10^{-4}\theta^2 + 5.324 \times 10^{-6}\theta^3 - 4.799 \times 10^{-8}\theta^4\right) \tag{78.12}$$

Intercept Factor of the PTSC

The intercept factor is an optical property which is defined as the ratio of the solar radiation intercepted by the receiver to the radiation reflected by the parabolic mirror that strikes directly to the receiver. It is affected by random and nonrandom errors [10]. Random errors are truly random in nature owing to the fact that they can be represented by normal probability distributions with zero mean. These errors originate from the misalignment of the ideal focus of the reflector depending on the energy distribution of the sun shape due to purely random tracking errors, σ_{sun}, the slope errors of the reflector surface during its manufacture, assembly and/or operation due to the surface imperfections, σ_{slope}, and the scattering effects due to the property of the optical material used, σ_{mirror}. However, random errors are modeled statistically, by determining the standard deviation of the total reflected energy distribution, at normal incidence [10], and are defined in the form of

$$\sigma = \sqrt{\sigma_{sun}^2 + 4\sigma_{slope}^2 + \sigma_{mirror}^2} \tag{78.13}$$

Nonrandom errors are generally defined with their permanent characteristics which can be related directly to anticipate errors in manufacture/assembly and/or in operation. In general these errors will cause the central ray of the reflected energy distribution (effective sunshape) to shift from the design direction of the focusing line. The value of the intercept factor is governed by random and nonrandom errors as well as the collector geometric parameters like area concentration ratio (the ratio of the area of aperture to the area of the receiver) and receiver diameter to yield universal error parameters. Using the universal error parameters, the intercept factor is defined as [11]

$$\gamma = \frac{1 + \cos\varphi_r}{2\sin\varphi_r} \int_0^{\varphi_r} \left[Erf\left[\frac{\sin\varphi_r(1 + \cos\varphi)(1 - 2d^*\sin\varphi) - \pi\beta^*(1 + \cos\varphi_r)}{\sqrt{2}\pi\sigma^*(1 + \cos\varphi_r)} \right] -Erf\left[-\frac{\sin\varphi_r(1 + \cos\varphi)(1 + 2d^*\sin\varphi) + \pi\beta^*(1 + \cos\varphi_r)}{\sqrt{2}\pi\sigma^*(1 + \cos\varphi_r)} \right] \right] \frac{d\varphi}{(1 + \cos\varphi)}. \tag{78.14}$$

where
d_r: dislocation of receiver center from ideal focus (m).
D_{oa}: outside diameter of receiver tube (m).
β: misalignment slope error (°).
C: area concentration ratio, $C = (w_a - D_{oa})/\pi D_{oa}$.
d^*: universal nonrandom error parameter due to receiver mislocation and reflector profile errors, $d^* = d_r/D_{oa}$.
β^*: universal nonrandom error parameter due to slope error, $\beta^* = \beta C$.
σ^*: universal random error parameter, $\sigma^* = \sigma C$.

For the evaluation of the intercept factor, a computer program was written in Mathematica to solve Eq. (78.14) numerically using Trapezoidal rule. The obtained numerical solutions used for different random and nonrandom collector parameters gave consistently satisfactory results compared to [10]. Based on this program, the intercept factor of the collector was calculated by considering it a carefully fabricated collector [12] so that the parameters were taken into account regarding a lower limit of 0.0025 rad, which is the standard deviation of the energy distribution of the sun's rays at solar noon on a clear day, for the random error parameter, σ_{sun}, 0.004 rad for σ_{slope}, and 0.002 rad for σ_{mirror}. When the maximum tracking error is considered as 0.0035 rad and the nonrandom slope error is used as 0.0035 rad, the intercept factor was obtained approximately 1.

End-Effect Correction

Another optical property of the PTC is the end-effect which is a measure of the reduction in aperture area due to the fact that some part of the reflected beam radiation along the end of the collector cannot be received by the absorber tube, therefore the image is formed beyond the end of it. The aperture area lost is given by end-effect correction that is expressed with Eq. (78.15).

$$\kappa = \frac{f}{l_a}\left(1 + \frac{w_a^2}{48f^2}\right) \tag{78.15}$$

Fig. 78.4 Thermal analysis
of the receiver
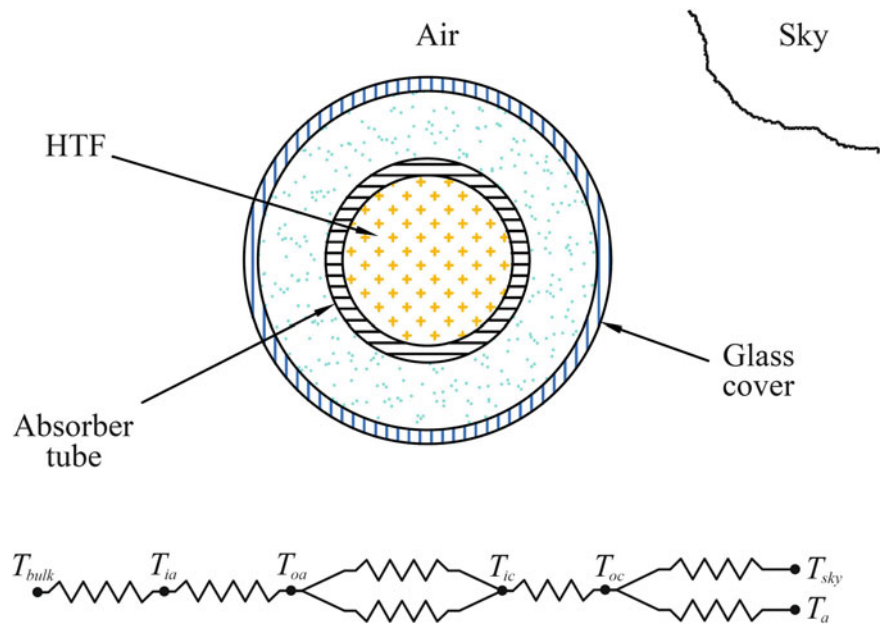
Thermal Analysis of the Collector Array

Thermal analysis of the collector system is significant to determine its thermal efficiency which means how much of the solar radiation is converted into useful gain. In this stage, the heat losses from the receiving element are to be analyzed. A comprehensive analytical analysis using thermodynamics and heat transfer relations has been made in order to establish a model that is consistently to meet the nearest actual system behavior. Thus the model study is developed on the base of a number of assumptions that give reasonable results with holding the physical nature of the system. The main characteristics of the model include the following assumptions:

- The PTSC performs under steady-state conditions since there is no change in the thermodynamic state properties with respect to time due to the constant surface temperatures.
- Heat transfer is one-dimensional since any significant temperature gradients exist in radial direction. There is a negligible temperature change along the length of the PTSC. Since the two-dimensional model provides a higher degree of accuracy relative to the one-dimensional when the length of the receiver is longer than 100 m [1]. The total length of the receiver tube existing in this model study is lower than 10 m. Hence, the one-dimensional approximation is totally valid and gives reasonable results from this view.
- Heat losses from the retainers used for absorber tube are negligible.
- The atmospheric emission is treated as a blackbody's emission at an effective sky temperature.
- Dust and dirt over the PTSC array are neglected.

During the system operation, the receiver tube gains energy from the sun and correspondingly it losses some energy as heat due to high temperature. At the beginning of the thermal analysis, the calculation of the heat losses from the receiver tube is required to reach the useful heat gain transferred to the working fluid. The cross-section of the receiver tube and its resistance network is shown in Fig. 78.4. As it is seen from the figure, the forced heat convection within the absorber is conducted through the absorber wall and then the transfer of heat flow exhibits itself as the sum of the radiation and the natural convection between the absorber and the cover. It is conducted through the cover material and equals to the sum of convection to the ambient air and radiation to the sky over the outer surface of the cover material.

The heat transfer from the HTF to the absorber pipe is stated by forced convection in the closed system due to pumping operation. The flow regime is defined according to the Reynolds number (Re) which specifies whether it is laminar or turbulent. The flow in a circular pipe is laminar when the generally accepted value of the critical Re is considered below 2,300. The total mass flow rate is specified to reach the mean velocity for determining the flow regime using the conservation of mass principle and Re of the HTF. Typical technical data of the HTF is given in Table 78.2 [7].

$$\dot{m}_{HTF} = \rho_{HTF} A_a u_{m,HTF} \tag{78.16}$$

Table 78.2 Technical specifications of Renolin Therm 320

Temperature (°C)	Density (kg/m³)	Specific heat capacity (kJ/kg °C)	Thermal conductivity (W/m °C)	Kinematic viscosity (m²/s × 10⁻⁶)	Prandtl number
0	879	1.864	0.134	535	6,543
50	848	2.078	0.131	28.6	385
100	816	2.293	0.127	6.5	96
200	750	2.721	0.120	1.5	26
300	685	3.151	0.113	0.7	13.4
320	672	3.236	0.111	0.6	11.8

It is considered that a constant heat flux occurs on the surface of the absorber tube due to the distribution of the sun's radiation. For a fully developed flow in a circular tube subjected to constant surface heat flux, the Nusselt number (Nu) is constant and its value is

$$Nu_{HTF} = 4.364 \tag{78.17}$$

When the Re is higher than 2,300, the flow turns to transition. In this case, the Nu relation for a circular smooth pipe is defined by the Gnielinski equation which covers both the transition and the turbulent regions for the fully developed turbulent flow [13].

$$Nu_{HTF} = \frac{f/8(Re_{HTF} - 1000)Pr_{HTF}}{1 + 12.7(f/2)^{1/2}\left(Pr_{HTF}^{2/3} - 1\right)} \quad (0.5 \leq Pr \leq 2000 \ and \ 2300 \leq Re \leq 5 \times 10^6) \tag{78.18}$$

where f is the friction factor, $f = (0.79 \ln(Re_{HTF} - 1.64))^{-2}$ for smooth pipes.

Thus, the convection heat transfer coefficient of the HTF is obtained by

$$h_{HTF} = Nu_{HTF} \frac{k_{HTF}}{D_{ia}} \tag{78.19}$$

Then, the convection heat transfer within the absorber tube is defined using the Newton's law of cooling,

$$\dot{Q}_{conv,HTF} = h_{HTF}A_{ia}(T_{ia} - T_{bulk}) \tag{78.20}$$

The bulk mean fluid temperature, T_{bulk} is used as the arithmetic average of the mean temperatures of the fluid at the inlet and the exit. During heating process, the mean temperature of the fluid changes so the fluid properties in internal flow are usually evaluated at this temperature.

Heat transfer through a hollow cylinder can be applied analogously using the Fourier's law of heat conduction for the absorber tube.

$$\dot{Q}_{cond,a} = \frac{2\pi k_a L_a}{\ln(D_{oa}/D_{ia})}(T_{oa} - T_{ia}) \tag{78.21}$$

The heat transfer between the absorber and the cover is equal to the sum of the convection and the radiation. The convection heat transfer within the annulus is considered to have generated naturally. Heat transfer in enclosure with an annulus type was studied by Raithby and Hollands for two long concentric horizontal cylinders with a range of $0.70 \leq Pr \leq 6000$ and $10^2 \leq F_{cyl}Ra_{an} \leq 10^7$ [14]. The rate of heat transfer through the annular space by natural convection with a characteristic length, $L_{an} = (D_{ic} - D_{ia})/2$ is expressed as

$$\dot{Q}_{conv,an} = \frac{2\pi k_{eff} L_a}{\ln(D_{ic}/D_{oa})}(T_{oa} - T_{ic}) \tag{78.22}$$

The recommended relation for effective thermal conductivity is defined by

Table 78.3 Constants for Eq. (78.27)

Range of Re	C	m
0.4–4	0.989	0.330
4–40	0.911	0.385
40–4,000	0.683	0.466
4,000–40,000	0.193	0.618
40,000–400,000	0.027	0.805

$$\frac{k_{eff}}{k} = 0.386 \left(\frac{Pr_{an}}{0.861 + Pr_{an}}\right)^{1/4} \left(F_{cyl}\text{Ra}_{an}\right)^{1/4} \tag{78.23}$$

where the geometric factor for concentric cylinders F_{cyl} is

$$F_{cyl} = \frac{[\ln(D_{ic}/D_{oa})]^4}{L_{an}\left(D_{oa}^{-3/5} + D_{ic}^{-3/5}\right)^5} \tag{78.24}$$

The radiation heat transfer within the annulus occurs due to temperature difference between the absorber and the cover even if the annulus space comprises air. Considering the enclosure consisting of two opaque surfaces at equilibrium temperatures, the radiation heat transfer is calculated by Eq. (78.25) which is applicable to two gray (independent of wavelength), diffuse (independent of direction), and opaque surfaces. These approximations are reasonable since the absorber is a diffuse emitter, and behaves almost gray characteristic in the solar spectrum. Its directional emissivity remains nearly constant for about the incidence angle lower than 40° such as metals [15]. The calculations for the incidence angle illustrate that this situation is possible when it is considered with solar tracking. The cover material behaves like an opaque material at longer-wavelength infrared regions of the electromagnetic spectrum during heat loss. When these approaches are considered, the radiation heat transfer within the annulus can be expressed by

$$\dot{Q}_{rad,a} = \frac{\sigma\left(T_{oa}^4 - T_{ic}^4\right)}{\dfrac{1 - \varepsilon_a}{A_{oa}\varepsilon_a} + \dfrac{1}{F_{ac}} + \dfrac{1 - \varepsilon_c}{A_{ic}\varepsilon_c}} \tag{78.25}$$

Heat transfer through the cylindrical layer of the cover material is described by

$$\dot{Q}_{cond,c} = \frac{2\pi k_c L_c}{\ln(D_{oc}/D_{ic})}(T_{ic} - T_{oc}) \tag{78.26}$$

Heat loss on the outer side of the cover is treated as the sum of the convection and the radiation heat transfer modes. The convection heat transfer can change depending on windy conditions of ambient air. Calculation of the heat transfer requires the average heat transfer coefficient over the entire surface although the variation of the local heat transfer coefficient along the circumference of a circular cylinder is not uniformly distributed. Supposed that the cover material is cylindrical in shape and the heat transfer over it is considered as cross-flow of air. The average Nusselt number in this case is estimated with Zhukauskas' correlation [14] when the flow is presumed external forced convection for flow across cylinders and expressed compactly as

$$\text{Nu}_{air} = \frac{h_{air}D_{oc}}{k_{air}} = C\,\text{Re}^m\text{Pr}^n \tag{78.27}$$

where $n = 1/3$ and the experimentally determined constants C and m are given in Table 78.3.

If Re is lower than 0.4, the flow is treated to turn to free convection. The relation implies that this circumstance is given in Eq. (78.28). All the fluid properties are evaluated at the film temperature $T_f = \frac{1}{2}(T_{oc} + T_a)$, which is the average of the free-stream and surface temperatures.

$$\text{Nu}_{\text{air}} = \left[0.6 + \frac{0.387 \text{Ra}_{\text{air}}^{1/6}}{\left[1 + (0.559/\text{Pr}_{\text{air}})^{9/16} \right]^{8/27}} \right]^2 \tag{78.28}$$

Then, the convection heat transfer outside of the cover can be denoted by

$$\dot{Q}_{conv,air} = h_{air} A_{oc} (T_{oc} - T_a) \tag{78.29}$$

The radiation heat transfer is caused by the temperature difference between the cover and the sky. Although the atmospheric emission character is far from a blackbody' exhibits, it is convenient to treat it as a blackbody at some lower fictitious temperature, i.e., the effective sky temperature that emits an equivalent amount of radiation energy. The simple relationship between the local air temperature and the sky temperature is expressed in [9].

$$T_{sky} = 0.0552 T_a^{1.5} \tag{78.30}$$

In this case, the radiation transfer between the glass cover and the sky is given by

$$\dot{Q}_{rad,sky} = \sigma A_{oc} \varepsilon_c \left(T_{oc}^4 - T_{sky}^4 \right) \tag{78.31}$$

The net heat loss from the receiver tube is caused by the temperature difference arising in radial direction. In order to determine the temperatures through the receiver, the steady-state energy balance relations have been written between the nodal points of the resistance network. The model algorithm makes it possible to solve the nonlinear equations for calculating the temperatures and the heat transfer coefficients through the receiver. These energy balance relations are expressed with three sets of equality as shown in Eq. (78.32).

$$\begin{aligned} \dot{Q}_{conv,HTF} &= \dot{Q}_{cond,a} \\ \dot{Q}_{cond,a} &= \dot{Q}_{conv,an} + \dot{Q}_{rad,a} \\ \dot{Q}_{cond,c} &= \dot{Q}_{conv,air} + \dot{Q}_{rad,sky} \end{aligned} \tag{78.32}$$

During the evaluation of the thermal losses, the estimation of the absorbed solar radiation, the thermal loss coefficient, and the heat removal factor are required. All these parameters are calculated subsequently to find the temperature of the surfaces until the initial iteration value for the exit temperature of the HTF converges to its ending value while satisfying the energy balance and heat transfer relations.

The thermal loss coefficient of the receiver tube is defined as below when considering the absorber tube covered and no temperature gradients around the receiver [9].

$$U_L = \left[\frac{1}{h_{an} + h_{ac}} + \frac{1}{h_{air} + h_{c,sky}} \left(\frac{A_{oa}}{A_{oc}} \right) \right]^{-1} \tag{78.33}$$

where h_{ac} and $h_{c,sky}$ is the radiation heat transfer coefficients. The radiation heat transfer coefficient enables to express conveniently radiation heat transfer in an analogous manner with convection in terms of a temperature difference. The linearized form of the radiation coefficient can be calculated from Eqs. (78.34) and (78.35) for the annulus region and the outside of cover, respectively.

$$h_{ac} = \frac{\sigma (T_{oa} + T_{ic}) \left(T_{oa}^2 + T_{ic}^2 \right)}{\frac{1 - \varepsilon_a}{A_{oa} \varepsilon_a} + \frac{1}{F_{ac}} + \frac{1 - \varepsilon_c}{A_{ic} \varepsilon_c}} \tag{78.34}$$

$$h_{c,sky} = \sigma \varepsilon_c (T_{oc} + T_{sky}) \left(T_{oc}^2 + T_{sky}^2 \right) \tag{78.35}$$

The actual useful energy gain is quantified by the collector heat removal factor, F_R which is used as the effectiveness of the receiver tube. It is related with lowering of the maximum possible useful energy gain since the whole receiver surface temperature is not at the fluid inlet temperature.

$$F_R = \frac{\dot{m}_{HTF}C_{P,HTF}(T_{ex} - T_{in})}{A_a[S - U_L(T_{in} - T_a)]} \qquad (78.36)$$

where S is the absorbed solar energy by the receiver. It is directly related to beam radiation coming from the sun and the optical efficiency of the collector as shown in Eq. (78.37).

$$S = I_b\eta_o \qquad (78.37)$$

The useful energy gain transferred to the HTF under steady-state condition can be written in the form of

$$\dot{Q}_u = F_R A_a \left[S - \frac{U_L}{C}(T_{in} - T_a) \right] \qquad (78.38)$$

where $A_a = n_{PTSC}\zeta_{sf}w_a l_a$. Here $\zeta_{sf} = 1 - D_{oa}/l_a$ is named as shading factor which is basically used as a multiplier for specifying the effective collector aperture area. It is related to what fraction of the reflector is shaded by the receiver. Since the shaded area is not effectively used due to not being subjected to the solar heat flux. After all the parameters affecting the thermal efficiency are defined, the useful energy gain absorbed by the HTF can be obtained from the energy balance. The exit temperature of the HTF whose sensible energy increases due to not undergoing in phase change is calculated from Eq. (78.39).

$$T_{ex} = T_{in} + \frac{\dot{Q}_u}{\dot{m}_{HTF}C_{P,HTF}} \qquad (78.39)$$

The thermal efficiency of the array is established maintaining the system parameters or variables stable under steady-state conditions. Hence, these variables can be regarded as constant during system operation, and the thermal efficiency of the PTSC array is associated with

$$\eta_{PTC} = \frac{\dot{Q}_u}{I_b A_a} \qquad (78.40)$$

Results and Discussion

The thermal performance of the PTSC is affected by operating conditions under where it functions. There are many system parameters which play roles over the PTSC's performance. The very dominants of them can be considered as DNI and operating temperature. The effects of the other factors were figured out from the model analysis as mass flow rate of HTF, receiver thermal properties, and ambient conditions. Figure 78.5 indicates the variation in the thermal efficiency of the PTSC array with respect to the bulk mean fluid temperature of the HTF. Typical operating condition on the 1st day of July at 12:00 solar time has been dealt when the incident angle of the direct beam radiation, 13.98°, the HTF mass flow rate 0.3 kg/s, ambient temperature 39 °C, ambient air velocity 1 m/s; the estimated efficiency of the collector array reduces due to the increasing bulk temperature and thermal losses. The model predictions are to be confirmed by the operation of PTSC being installed at Gaziantep.

Fig. 78.5 Thermal performance
of the PTSC array
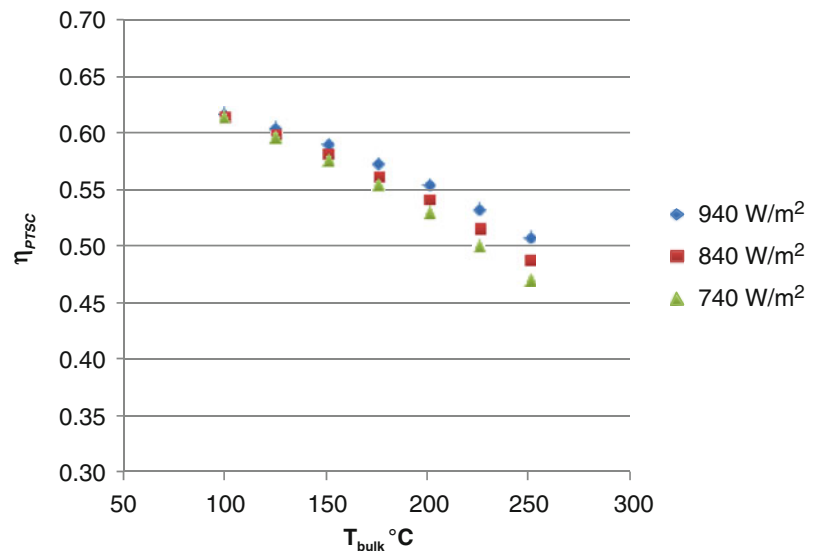
Conclusions

In this paper, a comprehensive thermo-mathematical modeling used for the analysis of a PTSC has been presented. The model is performed by developing a program in EES. The model comprises one-dimensional steady-state heat transfer approach using the thermodynamics and the heat transfer relations to evaluate the thermal analysis of the receiver by taking into account the actual system parameters. In addition that it covers the solar energy calculations and optical efficiency of the collector array. The validation of the model is in accordance with the literature. The consistency of the model is to be identified after installing the collector system in Gaziantep.

Nomenclature

A	Cross-sectional area (m^2)	LST	Local sun time (min)
AST	Apparent sun time (min)	$\dot{m}$	Mass flow rate (kg/s)
C	Concentration ratio	n	Number of day; refractive index; number of PTSC
C_p	Specific heat capacity (J/kg °C)	$\dot{Q}$	Rate of heat transfer (W)
D	Diameter (m)	$\dot{Q}_u$	Useful energy gain
DST	Daylight savings time (min)	$Wr_\perp$	Perpendicular component of unpolarized radiation
E	Equation of time (min)	$r_\parallel$	Parallel component of unpolarized radiation
f	Focal distance (m); friction factor	S	Absorbed solar energy (W/m^2)
F_R	Heat removal factor	T	Temperature (°C)
h	Convection heat transfer coefficient (W/m^2 °C)	T_a	Ambient temperature (°C)
I_b	Beam radiation (W/m^2)	T_{bulk}	Bulk mean fluid temperature (°C)
k	Thermal conductivity (W/m °C)	T_{ex}	Exit temperature (°C)
K	Extinction coefficient (m^{-1})	T_f	Film temperature (°C)
k_{eff}	Effective thermal conductivity (W/m °C)	T_{in}	Inlet temperature (°C)
L	Thickness of glass cover (m)	U_L	Thermal loss coefficient (W/m^2 °C)
l_a	Parabola length (m)	u_m	Mean velocity (m/s)
L_{loc}	Local meridian (°)	w_a	Parabola aperture (m)
L_{st}	Standard meridian (°)		

Greek Letters

α	Absorptivity	σ	Total reflected energy standard deviations at normal incidence; Stefan–Boltzmann constant (W/m^2 K^4)
α_n	Normal absorptivity		
γ	Intercept factor	σ_{sun}	Standard deviation of the energy distribution of the sun's rays at normal incidence (rad)
δ	Declination angle (°)		
ε	Emissivity	σ_{slope}	Standard deviation of the distribution of local slope errors at normal incidence (rad)
ζ_{sf}	Shading factor		
η_o	Optical efficiency	σ_{mirror}	Standard deviation of the variation in diffusivity of the reflective material at normal incidence (rad)
η_{PTSC}	Efficiency of PTSC array		
θ	Incidence angle (°)	τ	Tranmissivity
θ_z	Zenith angle (°)	φ_r	Rim angle (°)
κ	End-effect correction	ϕ	Latitude (°)
ρ	Average specular reflectance of parabolic mirror; density (kg/m^3)	ω	Hour angle (°)

Subscripts

1; 2	Medium number	HTF	Heat transfer fluid
a	Absorber	ia	Inside of absorber
ac	Gap between absorber and cover	ic	Inside of cover
air	Ambient air	oa	Outside of absorber
an	Annulus	oc	Outside of cover
c	Cover	rad	Radiation
$cond$	Conduction	sky	Sky
$conv$	Convection		

References

1. Forristall R (2003) Heat transfer analysis and modelling of a parabolic trough solar receiver implemented in engineering equation solver: NREL/TP-550e34169
2. Jacobson E, Ketjoy N, Nathakaranakule S, Rakwichian W (2006) Solar parabolic trough simulation and application for a hybrid power plant in Thailand. Sci Asia 32:187–199
3. Qu M, Yin H, Archer DH (2010) Experimental and model based performance analysis of a linear parabolic trough solar collector in a high temperature solar cooling and heating system. J Solar Energy Eng 132:1–12
4. Padilla RV, Demirkaya G, Goswami DY, Stefanakos E, Rahman MM (2011) Heat transfer analysis of parabolic trough solar receiver. Appl Energy 88:5097–5110
5. Huang W, Hu P, Chen Z (2012) Performance simulation of a parabolic trough solar collector. Solar Energy 86:746–755
6. Kalogirou SA (2012) A detailed thermal model of a parabolic trough collector receiver. Energy 48:298–306
7. Product information—Renolin Therm 320 heat transfer fluid. http://www.fuchs-oil.de
8. Technical datasheet of DURAN glass—tubing, capillary and rod of borosilicate glass 3.3. http://www.schott.com
9. Duffie JA, Beckman WA (2005) Solar engineering of thermal processes. Willey, New York
10. Guven HM, Bannerot RB (1984) Optical and thermal analysis of parabolic trough solar collectors for technically less developed countries. Technical report 1. USAID Project Grant No. 386-0465
11. Guven HM, Bannerot RB (1985) Derivation of universal error parameters for comprehensive optical analysis of parabolic troughs. In Proceedings of the ASME-ASES solar energy conference, Knoxville, pp 168–174
12. Arasu AV, Sornakumar T (2007) Design, manufacture and testing of fiberglass reinforced parabola trough for parabolic trough solar collectors. Solar Energy 81:1273–1279
13. Rohsenow WM, Hartnett JP, Cho YI (1998) Handbook of heat transfer. McGraw-Hill, New York
14. Cengel YA, Ghajar AJ (2011) Heat transfer and mass transfer: fundamentals & applications. McGraw-Hill, New York
15. Touloukian YS, DeWitt DP (1970) Thermal radiative properties, metallic elements and alloys. IFI/Plenum, New York

Wind Energy Resource Assessment of Ergan Mountain Ski Center, Erzincan, Turkey

Ahmet Tandıroğlu and Murat Çetin

Abstract

Ergan Mountain Ski Center is located in Erzincan, East Anatolian region of Turkey. It is 15 km south of the city and situated in the Mercan (Munzur) Mountain chain whose length is 200 km and width of between 15 and 45 km. Height of the Ergan is about 3,300 m. In this study, wind energy potential of Ergan Mountain Ski Center which is located in Erzincan, East Anatolian region of Turkey was investigated by analyzing wind speed data collected in ten minutes intervals by wind energy observation station situated at a height 2,350 m above sea level at 12 m above the ground. These measurements are performed from 2011 February to 2013 May. Wind energy potential of monitored area is determined by performing statistical analysis of collected data. Weibull distribution is used in the statistical analysis, and it is examined that the numerical values of shape and scale parameters for Ergan Mountain Ski Center varied over a wide range. The annual values of dimensionless Weibull shape parameter k ranged from 1.41 to 1.83 with a mean value of 1.71, while those of Weibull scale parameter c were in the range of 3.11–11.99 m/s with a yearly mean wind speed of 7.8 m/s. Results revealed that the highest and the lowest wind power potential is in March and October, respectively. Annual mean wind power density is obtained as 230.68 W/m^2 inside the observatory field. The results show that the investigated location of Erzincan Ergan Mountain Ski Center has available wind energy potential and is feasible to establish wind power generation plant in a medium scale for installed power load of Erzincan Ergan Mountain Ski Center.

Introduction

As it is known, wind power is an important source of environmental-friendly energy and has become more and more important in the recent years. A general criterion for determining the feasible site for wind energy is to know the wind speeds of a certain region that is important in the determination of characteristic speeds of the turbine, which are its cut-in velocity, rated velocity, and the cut-out velocity. Also, the effective utilization of wind energy entails a detailed knowledge of the wind characteristics at the particular location (Shata and Hanitsch).

In the last decade, a lot of studies related to the wind characteristics and wind power potential have been made in many countries worldwide. Ucar and Balo [1, 2] investigated the wind energy potential in Kartalkaya-Bolu,

A. Tandıroğlu (✉)
Department of Mechanical Engineering Technology, Erzincan University, Erzincan 24100, Turkey
e-mail: atandiroglu@erzincan.edu.tr

M. Çetin
Department of Engine Vehicles and Transportation Technologies, Vocational High School, Erzincan University, Erzincan 24100, Turkey
e-mail: mcetin@erzincan.edu.tr

Turkey and Uludağ-Bursa, Turkey, respectively. The wind speed distribution curves of the investigated location of Kartalkaya-Bolu were obtained by using the Weibull and Rayleigh probability density functions based on these data. Weibull shape parameter k and scale parameter c were found to be 1.79 and 6.64 m/s for the period from 2000 to 2006. A yearly mean wind speed of 5.90 m/s was obtained in Kartalkaya-Bolu for the 7-year period [1]. The wind speed distribution curves of Uludağ-Bursa were obtained by using the Weibull and Rayleigh probability density functions. The average Weibull shape parameter k and scale parameter c were found as 1.78 and 7.97 m/s for the period 2000–2006. The yearly mean wind speed in Uludağ-Bursa was obtained as 7.08 m/s for a period of 7 years [2]. Köse [3] evaluated wind energy potential as a power generation source in Kütahya, Turkey. Most of the wind energy potential related studies are intensively summarized by Köse [3] and Ucar and Balo [1, 2] as follows. Eskin et al. [4] estimated wind power potential of Gokceada Island in the Northern Aegean Sea, Turkey. The wind data used in this study was collected at 10 and 30 m of height above ground. This study demonstrated the presence of high wind speeds and power in Gokceada, as well as in the northern–western part of Turkey. Wind power potential of Nurdağı/Gaziantep district which is on the south of Turkey is evaluated by Karslı and Gecit [5]. They found that the observed highest value wind speed is 23.3 m/s and mean power density of the site is 222 W/m^2. Gokçek et al. [6] investigated the wind characteristics and wind potential of Kırklareli province in the Marmara Region, Turkey. It was found that annual mean power density based on the observed data and Weibull function were calculated as 142.75 and 138.85 W/m^2. The wind energy potential in the eastern Mediterranean region using hourly wind data was taken from seven stations during 1992–2001 periods investigated by Sahin et al. [7]. They determined that the mean power density is 500 W/m^2 in many areas of this region at 25 m from the ground level.

Gokçek et al. [6] investigated the wind characteristics and potential for wind power of Kırklareli province in the Marmara Region, Turkey. Annual mean power density based on the observed data and Weibull function was calculated to be 142.75 and 138.85 W/m^2, respectively. The results indicate that the investigated location has potential for wind energy utilization. Eskin et al. [4] estimated the wind power potential of Gökçeada Island in the Northern Aegean Sea, Turkey. The wind data used in this study were collected at above-ground heights of 10 and 30 m. This study demonstrated the presence of high wind speeds and power in Gökçeada, as well as in the northwestern part of Turkey. The wind power potential of the Nurdağı/Gaziantep District, which is in the south of Turkey, is evaluated by Karslı and Gecit [5]. They found that the observed highest wind speed is 23.3 m/s and the mean power density of the site is 222 W/m^2. Akpinar and Akpinar [8] used the Weibull density function to determine the wind energy potential in Maden-Elazığ, Turkey and found that the yearly mean wind speed and mean power density are 5.63 m/s and 244.65 W/m^2, respectively. Bilgili et al. [9] investigated the potential and the feasibility of wind energy resources in some locations in the eastern Mediterranean region of Turkey. They determined the dominant wind directions, the mean wind speeds, the potential for wind power, and the frequency distributions in the Antakya and Iskenderun regions and showed that at 50 m height above ground level, the mean wind speeds reach 7.5 m/s in the Antakya region and are 5–7 m/s in the south and east regions of Iskenderun. In Turkey, the Turkish State Meteorological Service conducts general wind measurements, together with other meteorological measurements [10].

The wind data that is collected from 229 meteorological stations making wind observations by anemometer do not reflect the real energy values, since these stations are in or around villages, town, or cities. Therefore, most of this type of data is of questionable use for wind power prediction, since the measurements are usually taken at a relatively low (10 m) height at airports or in urban locations where wind turbines are unlikely to be sited. In this regard, before making plans or programs related to the use of wind energy, it is necessary to discover the potential of this resource. Thus, public institutions and universities have been striving to measure the wind potential and conduct certain research projects about this resource [1, 10–18].

The main objective of the present work is to investigate the availability of the wind potential to produce electricity from wind energy for the requirements of installed power load of Erzincan Ergan Mountain Ski Center. To this end, present investigation has been undertaken and it is intended to contribute to previous and further studies.

Data Collection and Site Description

In this study, wind energy potential of Ergan Mountain Ski Center which is located in Erzincan, East Anatolian region of Turkey was investigated by analyzing wind speed data collected in 10 min intervals by wind energy observation station situated at a heights of 2,014, 2,350, 2,597, and 2,966 m above sea level. The location of Ergan Mountain Ski Center on Turkey is shown in Fig. 79.1. All measurements in the wind observation stations are recorded using the cup anemometer at a height of 12 m above the ground level by means of SCADA system. Wind speed data measurements were taken by 10 min intervals during 2011 February to 2013 May.

Fig. 79.1 Turkey map with terrains [19, 20]

A total of four wind speed measurement locations were investigated at various heights of Ergan Mountain Ski Center. It is observed from the measurement values of statistical analysis that the station at a height of 2,350 m exhibits the maximum available wind energy potential which is located at the x and y Cartesian coordinate world system of 4,386,053.727 and 542,627.750, respectively.

Ergan Mountain Ski Center is located in Erzincan, East Anatolian region of Turkey. It is 15 km south of the city and situated in the Mercan (Munzur) Mountain chain whose length is 200 km and width between 15 and 45 km. Height of the Ergan is about 3,300 m. Wind energy potential of the monitored area is determined by performing statistical analysis of collected data. Location of the site studied and topographic map of Ergan Mountain Ski Center are seen in Fig. 79.2.

Analysis

Mathematical Analysis

The wind speed distribution, one of the wind characteristics, is of great importance for not only structural and environmental design and analysis but also the assessment of the wind energy potential and the performance of wind energy conversion system. The Weibull distribution function, which is a two-parameter distribution, can be expressed as [21]:

$$f(v) = \frac{k}{c}\left(\frac{v}{c}\right)^{k-1}\exp\left[-\left(\frac{v}{c}\right)^{k}\right](k > 0, v > 0, c > 1) \tag{79.1}$$

where $f(v)$ is the probability of observing wind speed v, c is the Weibull scale parameter and k is the dimensionless Weibull shape parameter. The Weibull parameters k and c characterize the wind potential of the region under study. Basically, the

Fig. 79.2 Location and topographic map of Erzincan Ergan Mountain Ski Center [19, 20]

scale parameter c indicates how "windy" a wind location under consideration is, whereas the shape parameter, k, indicates how peaked the wind distribution is (i.e., if the wind speeds tend to be very close to a certain value, the distribution will have a high k value and is very peaked). The cumulative probability function of the Weibull distribution is:

$$F_W(v) = 1 - \exp\left[-\left(\frac{v}{c}\right)^k\right] \tag{79.2}$$

Once the mean, v, and the variance, σ^2, of the data are known, the following approximation can be used to calculate the Weibull parameters c and k.

$$k = \left(\frac{\sigma}{v}\right)^{-1.086} (1 \leq k \leq 10) \tag{79.3}$$

$$c = \frac{\overline{v}}{\Gamma\left(1 + \frac{1}{k}\right)} \tag{79.4}$$

where Γ is the gamma function and the average wind speed $\overline{v}$ is:

$$\overline{v} = \frac{1}{n}\left[\Sigma_{i=1}^n v_i\right] \tag{79.5}$$

The variance, σ^2, of wind velocity recording is:

$$\sigma^2 = \left[\frac{1}{n-1}\Sigma_{i=1}^n (v_i - \overline{v})^2\right]^{1/2} \tag{79.6}$$

where n is the number of hours in the period of considered time, such as month, season, or year. Average wind speed and the variance of wind velocity can be calculated on the basis of the Weibull parameters as given below [13]:

$$\overline{v} = c\Gamma\left(1 + \frac{1}{k}\right) \tag{79.7}$$

$$\sigma^2 = c^2\left[\Gamma\left(1 + \frac{2}{k}\right) - \Gamma^2\left(1 + \frac{2}{k}\right)\right] \tag{79.8}$$

and gamma function of (x) standard Formula is calculated as:

$$\Gamma(x) = \int_0^\infty e^{-u}u^{x-1}\,du \tag{79.9}$$

In circumstances where k is equal to 2, the Weibull distribution is referred to as Rayleigh distribution. Often wind energy conversion turbine manufacturers provide standard performance figures for their turbines using this special case of the Weibull distribution [18]. The main limitation of the Weibull density function is that it does not accurately represent the probabilities of observing zero or very low wind speeds [22]. However, for the purpose of estimating wind potential for the commercial use of wind turbines, this is usually unnecessary as the energies available at low wind speeds are negligible (i.e., wind energy is proportional to the cube of wind velocity) and below the operating range of wind turbines (i.e., the cut-in wind speed is usually between 2.5 and 3.5 m/s [23]). Probability density and cumulative function of Rayleigh distribution are calculated as:

$$f_R(v) = \frac{\pi v}{2\bar{v}^2} exp\left[-\left(\frac{\pi}{4}\right)\left(\frac{v}{\bar{v}}\right)^2\right] \tag{79.10}$$

and

$$F_R(v) = 1 - exp\left[-\left(\frac{\pi}{4}\right)\left(\frac{v}{\bar{v}}\right)^2\right] \tag{79.11}$$

The power of the wind that flows at speed v through a blade sweep area A increases with the cube of the wind speed and the area, that is:

$$P_{(v)} = \frac{1}{2}\rho A \bar{v}^3 \tag{79.12}$$

where ρ is the standard air density at sea level with a mean temperature of 15 °C and a pressure of 1 atm equal to 1.225 kg/m^2 and v is the mean wind speed. Then the corrected monthly air density ρ is calculated as follows [24]:

$$\rho = \frac{\bar{P}}{R_d\bar{\bar{T}}} \tag{79.13}$$

where $\bar{P}$ is the monthly average air pressure; T is the monthly average air temperature; R_d is the gas constant for dry air. The corrected power density available in wind at a height of 10 m can be calculated as follows [25]:

$$P_{(h=10\,m)} = \frac{1}{2}\overline{\rho v^3} \tag{79.14}$$

The average wind power density of the site based on the Weibull probability density function can be expressed as:

$$P_m = \frac{1}{2}\rho\bar{v}^3 \frac{\Gamma\left(1 + \frac{3}{k}\right)}{\left[\Gamma\left(1 + \frac{1}{k}\right)\right]^3} \tag{79.15}$$

Calculation of the monthly corrected and uncorrected wind power revealed that the corrected air density values are almost stable. Also, the shift from the standard air density ($\rho = 1.225$ kg/m^3) is very small for the selected region, consequently the latter value was considered in the present study. Wind power estimates are based on the assumption that the air density is not correlated with wind speed. The error introduced by this assumption on a constant pressure surface is less than 5 % [26, 27]. Wind power density, expressed in Watt per square meter (W/m^2), takes into account the frequency distribution of the wind speed and the dependence of wind power on air density and the cube of the wind speed. Therefore, wind power density is generally considered a better indicator of the wind resource than wind speed [28]. The average wind power density in terms of wind speed is calculated as:

$$WPD = \frac{\sum_{i=1}^{N}\frac{1}{2}\rho v_i^3}{N} \tag{79.16}$$

where i is the measured three-hourly wind speed and N is the total sample data used for each year. Besides, calculation of wind power density based on the wind speed provided by field measurements can be developed by Weibull distribution analysis using the following form:

$$\frac{P}{A} = \int_0^\infty \frac{1}{2}\rho V^3 f(V)dV = \frac{1}{2}\rho c^3 \Gamma\left(\frac{k+3}{k}\right) \tag{79.17}$$

Once wind power density of a site is given, the wind energy density for a desired duration, T, can be calculated as:

$$\frac{E}{A} = \frac{1}{2}\rho c^3 \Gamma\left(\frac{k+3}{k}\right) \tag{79.18}$$

This equation can be used to calculate the available wind energy for any defined period of time when the wind speed frequency distributions are for a different period of time. The Betz limit, which has been commonly used now for decades, gives that a wind turbine would not extract more than 59.3 % of the available wind power. Therefore, the maximum extractable power from the wind will be the product of the factor 0.593 and the calculated result from Eq. (79.17). As the scale and shape parameter are calculated, two meaningful wind speeds for wind energy estimation, the most probable wind speed, and the wind speed carrying maximum energy can be easily obtained. The most probable wind speed denotes the most frequent wind speed for a given wind probability distribution and is expressed by:

$$V_{mp} = c\left(1 + \frac{2}{k}\right)^{1/k} \tag{79.19}$$

In some references this is expressed as the optimum wind speed for a wind turbine, vop, which is the speed that produces the most energy [29]. The wind turbine should be chosen with a rated wind speed that matches this maximum energy wind speed for maximizing energy output. Once vop is obtained for one site, the optimal rated wind speed of a wind turbine can be found (the rated velocity of a turbine is the lowest wind velocity corresponding to its rated power that due to technical and economical reasons, the wind turbine is designed to produce constant power, termed as the rated power). For the annual energy output, the chosen wind turbine will have the highest capacity factor, defined by the ratio of the actual power generated to the rated power output [30].

WAsP Software Analysis

As mentioned [31] one of the commonly used softwares in wind energy potential determination is WAsP (Wind Atlas Analysis and Application Program) which was developed in Denmark National RISO Laboratory and used in the development of European wind atlas. WAsP has been used in 100 different countries and by more than 1,600 people. The software takes the effects of different roughness, curtaining effects of nearby building and obstacle effects, and the wind speed variations due to the topographic conditions into account [9]. Therefore, the modified fundamental meteorological details can be implemented through the software for better wind turbine deployment.

A local position and surface statistics at a certain elevation can be exposed by the wind atlas. Moreover, the extrapolation of the average wind statistics can be investigated according to the statistical and micro-meteorological technique with regard to the wind energy evaluations. This process helps acquire the correct information for the wind turbine sitting and estimate the wind climate for the wind energy applications. The purposes of the WAsP are analyzing the row data, developing the wind atlas, wind climate evaluation, and estimation of the wind power potential. Row data analysis collects the row data in the histogram and provides the time series of the wind measurements. Meanwhile, the Weibull parameters are calculated using this data analysis. In order to prepare the wind atlas data, wind speed histograms can be converted to the wind atlas data arrays.

For the wind climate evaluation, wind atlas data arrays calculated through the WAsP or another source can be used for a specific local position. Again using WAsP, the estimation of the wind energy potential can be extracted through the total energy content of the average wind. In addition, the annual average energy generation of a wind turbine can be obtained using the power curve of that turbine in the WAsP. WAsP assumes that the wind speed data fit the two-parameter Weibull distribution when dealing with the data analysis. Moreover, WAsP calculates the local wind atlas statistics using four different information inputs.

These four information inputs are hourly wind speed data, local roughness data, curtaining effects, and the topography of the region. WAsP uses three sub-models for processing these four inputs. These are the roughness variation mode, obstacle

curtaining model, and the topographic model. In this study, the data measured from a meteorological station between 2011 February and 2013 May have been used. During the current investigation, the information for the speed and the direction of the wind has been collected for 28 months, making use of anemometers placed at 10 m height.

The data logger recorded the parameters measured at the observation station for each second, and the average, minimum, and maximum values and their standard deviations have been measured at 10 min intervals. Weibull distribution has been developed and Weibull shape and scale parameters are calculated in WAsP software. Then, using the edited data and the maps, an average energy density map has been developed. For preparing the map, the orographic, roughness, and wind data of the region are processed through the WAsP Map Editor of the WAsP 8.0 software.

Results and Discussion

Monthly mean wind speed values, standard deviations, and Weibull parameters are presented in Table 79.1 for Erzincan Ergan Mountain Ski Center, from 2011 February to 2013 May. Monthly Weibull parameters were also calculated in this study and are presented in Table 79.2.

The results show that the parameters are distinctive for different months in a year, which means the monthly wind speed distribution differs over a whole year. The trends of the monthly mean values for the different years are similar. Most of the monthly mean speed wind values are between 8.00 and 9.00 m/s but some are over 9.00, while only a few are over 5.50 m/s and under 4.0 m/s. While March showed the highest mean wind speed value with 11.31 m/s, December and October showed the minimum mean wind speed value of 3.14 m/s.

Table 79.1 Monthly mean wind speeds, standard deviations, and Weibull parameters for Ergan Mountain Ski Center

Mean wind speed, $\bar{v}$	Standard deviation, σ	Weibull shape factor, k	Weibull scale parameter, c
8.17159409	4.92	1.734966397	9.177510229
8.17159409	4.82	1.774091788	9.188964146
11.31451489	6.85	1.724601139	12.70268303
10.68593073	6.54	1.704404933	11.98791297
8.800178251	5.33	1.723820283	9.879586740
10.05734657	6.22	1.685158022	11.27396971
9.428762412	6.18	1.582137819	10.51394939
9.428762412	5.36	1.846651038	10.62199245
5.657257447	3.44	1.716435884	6.349446481
3.142920804	2.05	1.590521046	3.506417526
3.142920804	1.93	1.698200153	3.524994904
7.80492	4.73908	1.719128799	8.760756006

Table 79.2 Monthly Weibull parameters and characteristic speeds (at 12 m height, in m/s) and wind power density and wind energy density per month for a whole year in Erzincan Ergan Mountain Ski Center

Month	Mean wind speeds, $\bar{v}$	Wind power density (W/m^2)	Wind energy density (kWh/m^2/month)
January	8.17	264.74	190.62
February	8.17	264.74	190.62
March	11.31	702.77	505.99
April	10.69	592.02	426.26
May	8.80	330.65	238.07
June	10.06	493.57	355.38
July	9.43	406.69	292.82
August	9.43	406.69	292.82
September	5.66	87.84	63.25
October	3.14	15.06	10.85
November	3.14	15.06	10.85
December	5.66	87.84	63.25
Annual	7.80	3,667.73	2,640.77

Fig. 79.3 Monthly variation
of the wind power density
for a whole year
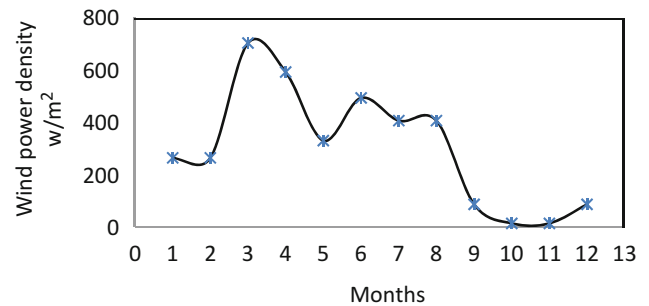
Fig. 79.4 Average annual
variation of observed and Weibull
wind speed frequencies
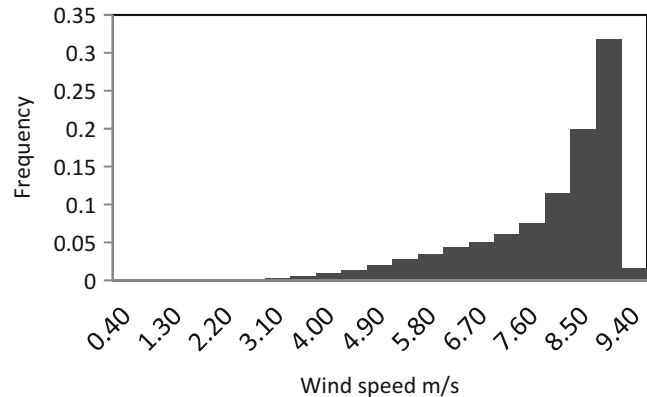
Fig. 79.5 Monthly mean wind
speed in Erzincan Ergan
Mountain Ski Center
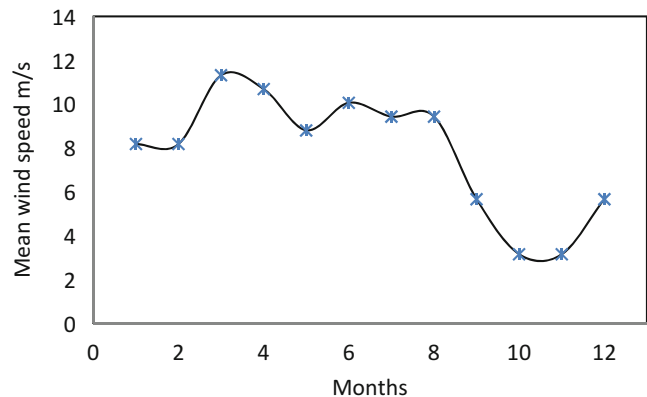
The results from Fig. 79.3 and Table 79.2 revealed some oddness about the mean wind speeds, wind power densities, and wind energy densities in Erzincan Ergan Mountain Ski Center. For example, the mean wind speed is found same both in October and November and July and August. Figure 79.4 shows the annual variation of Weibull wind speed frequencies for Erzincan Ergan Mountain Ski Center. It can be clearly seen that Weibull function fits the observed distribution reasonably well in the relevant wind range.

The mean wind speed variations are illustrated in Figs. 79.5 and 79.6. The monthly mean wind speed in Erzincan Ergan Mountain Ski Center during the period 2011 February to 2013 May. The highest monthly mean wind speed of 11.31 m/s arose in March while the lowest mean wind speed of 3.14 m/s occurred in October and November. It is found that the mean annual wind speed in the period of 2011 February to 2013 May was 7.8 m/s.

In Figs. 79.7 and 79.8, the power density vector map and observed wind data for the region of Erzincan Ergan Mountain Ski Center are presented.

The wind atlas obtained from WAsP software contains data for four reference roughness lengths (0.0, 0.03, 0.1, 0.4 m) and five reference heights (10, 25, 50, 100, 200 m) above ground level. The roses of Weibull parameters have 12 sectors each. Related regional climate data for Erzincan Ergan Mountain Ski Center will be presented in further works.

Fig. 79.6 Average annual mean wind speed variations
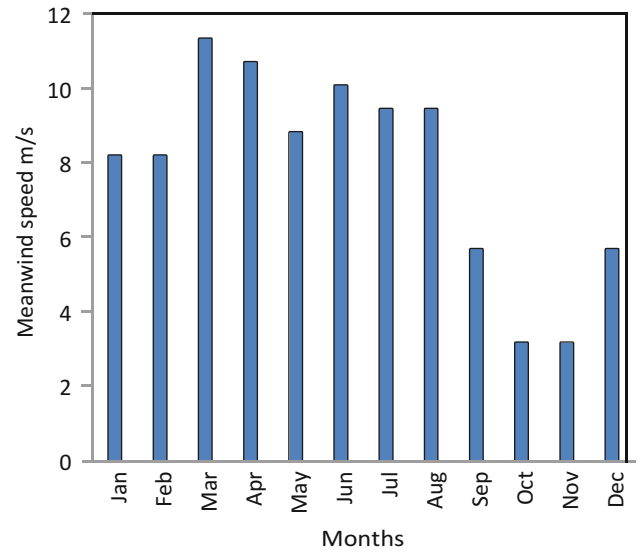
Fig. 79.7 Power density vector map of Erzincan Ergan Mountain Ski Center
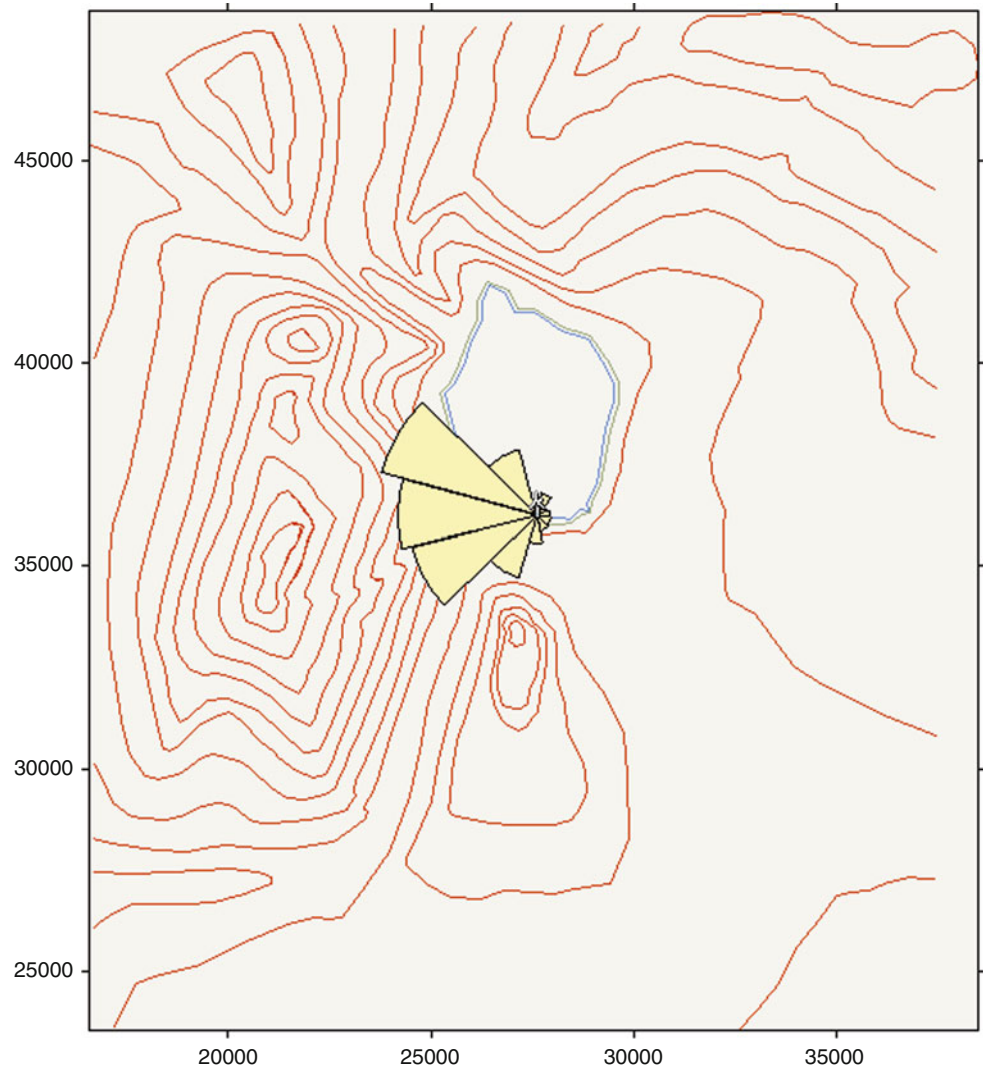
Fig. 79.8 Observed wind climate of Erzincan Ergan Mountain Ski Center
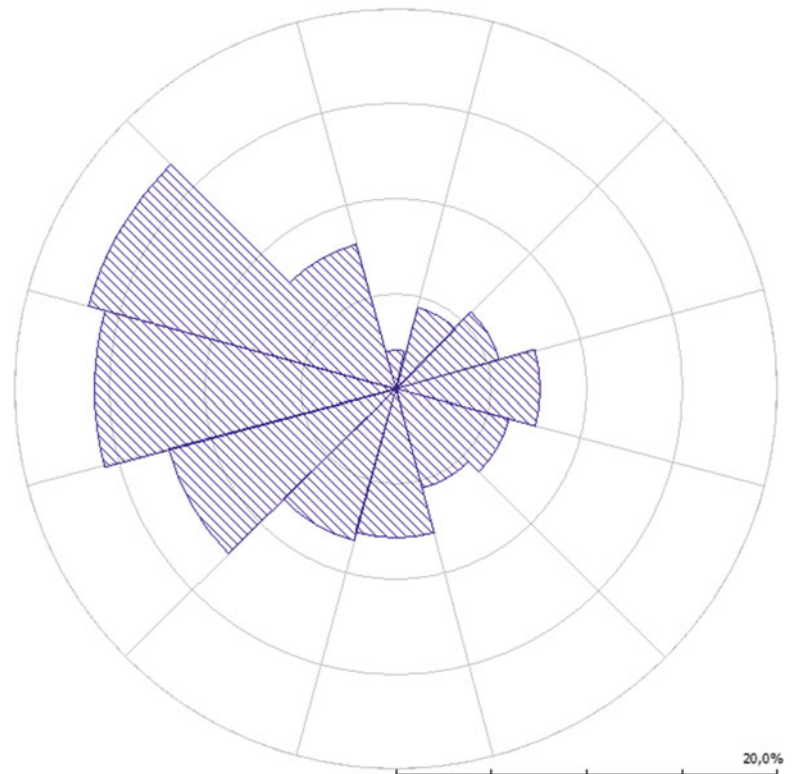
Conclusion

The result derived from this study encourages the utilization of the wind energy potential on the Erzincan Ergan Mountain Ski Center. The wind energy potential of the location has been studied based on the Weibull model. The probability density distributions were derived and the distribution parameters were identified. One of the most important outcomes of the study is; March, April, and June are the 3 months in which the average wind speeds are the highest all around the year. The yearly mean wind speeds were found to range between 8 and 10 m/s, while the maximum yearly mean wind speed was 11.31 m/s. The monthly average wind power density value was found as 305.64 W/m^2 and this level of power density may be almost enough for installed power load of Erzincan Ergan Mountain Ski Center. The data also showed that the maximum monthly wind speed occurs in the month of March, while the months of October and November have the lowest mean wind speed. At the end, it is worth mentioning that the current work is only a preliminary study in order to estimate the wind energy potential analysis of Erzincan Ergan Mountain Ski Center, to have a comprehensive wind data base and obtain good predictions prior to construction and installation of wind energy conversion systems.

Nomenclature

A	Swept area (m^2)	P_m	Weibull probability density function
c	Weibull scale parameter (m/s)	$\overline{P}$	Monthly average air pressure (Pa)
$f_R(v)$	Probability density	T	Average air temperature (K)
$F_W(v)$	Cumulative probability function	V_{mp}	Wind probability distribution (m/s)
k	Weibull shape parameter	v	Wind speed (m/s)
n	Number of hours in the period	$\overline{v}$	Mean wind speed (m/s)
N	Total sample data	WPD	Average wind power density
P	Power of wind (W)		

Greek Symbols

ρ	Standard air density (kg/m^3)	σ	Standard deviation
Γ	Gamma function	σ^2	The variance

References

 1. Ucar A, Balo F (2009) Investigation of wind characteristics and assessment of wind-generation potentiality in Uludağ-Bursa, Turkey. Appl Energy 86:333–339
 2. Ucar A, Balo F (2009) Investigation of wind energy potential in Kartalkaya-Bolu, Turkey. Int J Green Energy 401:412–416
 3. Köse R (2004) An evaluation of wind energy potential as a power generation source in Kütahya, Turkey. Energy Convers Manag 45:1631–1641
 4. Eskin N, Artar H, Tolun S (2008) Wind energy potential of Gokceada Island in Turkey. Renew Sustain Energy Rev 12:839–851
 5. Karslı VM, Gecit C (2003) An investigated on wind power potential of Nurdağı-Gaziantep, Turkey. Renew Energy 28:823–830
 6. Gokçek M, Bayülken A, Bekdemir Ş (2007) Investigation of wind characteristics and wind energy potential in Kirklareli, Turkey. Renew Energy 32:1739–1752
 7. Sahin B, Bilgili M, Akilli H (2005) The wind power potential of the eastern Mediterranean region of Turkey. J Wind Eng Ind Aerodyn 93:171–183
 8. Akpinar EK, Akpinar S (2004) Determination of the wind energy potential for Maden-Elazig, Turkey. Energy Convers Manag 45:2901–2914
 9. Bilgili M, Şahin B, Kahraman A (2004) Wind energy potential in Antakya and İskenderun regions, Turkey. Renew Energy 29:1733–1745
10. Turkish State Meteorological Service (2003) Available from http://www.meteor.gov.tr
11. Durak M, Şen Z (2002) Wind power potential in Turkey and Akhisar case study. Renew Energy 6:463–472
12. Dündar C, İnan D (1996) Investigation of wind energy application possibilities for a specific island (Bozcaada) in Turkey. Renew Energy 9:822–826
13. Jamil M, Parsa S, Majidi M (1995) Wind power statistics and evaluation of wind energy density. Renew Energy 6:623–628
14. Köse R, Işık A, Buran D, Özgür A, Erbaş O, Urtekin L (2002) Determination of the electrical energy production potential with data at a chosen place in Kütahya, Dumlupınar University Research Fund Project No. 2001/17
15. Ozerdem B, Turkeli M (2003) An investigation of wind characteristics on the campus of Izmir Institute of Technology, Turkey. Renew Energy 28:1013–1027
16. Şen Z, Şahin AD (1998) Regional wind energy evaluation in some parts of Turkey. J Wind Energy Ind Aerodyn 74:353–354
17. Türksoy F (1995) Investigation of wind power potential at Bozcaada, Turkey. Renew Energy 6(8):917–923
18. Weisser D (2003) A wind energy analysis of Grenada: an estimation using the Weibull density function. Renew Energy 28:1803–1812
19. Anonymous (2013) Available from http://tr.wikiloc.com/wikiloc/view.do?id=3046184
20. Anonymous (2013) Available from http://www.nationsonline.org/oneworld/map/google_map_turkey.htm
21. Chang TJ, Wu YT, Hsu HY, Chu CR, Liao CM (2003) Assessment of wind characteristics and wind turbine characteristics in Taiwan. Renew Energy 28:851–871
22. Persaud S, Flynn D, Fox B (1999) Potential for wind generation on the Guyana coastlands. Renew Energy 18(2):175–189
23. Anonymous (2002) VESTAS. Products. Available from http://www.vestas.com
24. Aslan Z, Mentes S, Yukselen MA, Tolun S (1994) Global wind energy assessment of Turkey and a case study in the northwest. In: International energy symposium in 21st century, Istanbul, 28–30 April 1994
25. Ahmed Shata AS, Hanitsch R (2006) Evaluation of wind energy potential and electricity generation on the coast of Mediterranean sea in Egypt. Renew Energy 31:1183–1202
26. Barber DA, Court A, Hewson EW (1977) Wind characteristics. Wind energy over the United States. Final Report, Wind Energy Mission Analysis, ERDA Contract AT (04-3)-1075. Lockheed-California Company (Chapter 3). Available from http://www.worldcat.org
27. Hennessey JP (1977) Some aspects of wind power statistics. J Appl Meteorol 16:119–128
28. Al-Nassar W, Alhajraf S, Al-Enizi A, Al-Awadhi L (2005) Potential wind power generation in the State of Kuwait. Renew Energy 30:2149–2161
29. Johnson GL (1985) Wind energy systems. Prentice-Hall, Englewood Cliffs
30. Lu L, Yang H, Burnett J (2002) Investigation on wind power potential on Hong Kong islands – an analysis of wind power and wind turbine characteristics. Renew Energy 27:1–12
31. Oner Y, Ozcira S, Bekiroglu N, Senol I (2013) A comparative analysis of wind power density prediction methods for Çanakkale, Intepe region, Turkey. Renew Sustain Energy Rev 23:491–502
32. Hanağasıoğlu M (1999) Wind energy in Turkey. Renew Energy 16:822–827
33. Kocak K (2008) Practical ways of evaluating wind speed persistence. Energy 33:65–70
34. Öztopal A, Şahin AD, Akgün N, Şen Z (2000) On the regional wind energy potential of Turkey. Energy 25:189–200
35. Tolun S, Menteş S, Aslan Z, Yükselen MA (1995) The wind energy potential of Gökçeada in the northern Aegean Sea. Renew Energy 6(7):679–685
36. Topçu S (2000) Analysis of wind energy at the Western Black Sea region. İTÜ Araştırma Fonu Projesi İstanbul

Investigation of the Use of Solar Thermal Buffer Zone in Buildings

Asad Jan, Mohamed S. Hamed, Ghani Razaqpur, and Simon Foo

Abstract

This paper presents results of a collaborative study that is being carried out by the Thermal Processing Laboratory (TPL), the Department of Civil Engineering and Public Works and Government Services Canada (PWGSC). The main objective of this study is to investigate the feasibility of passive means to achieve net-zero energy (NZE) in federal buildings in Canada.

An experimental and numerical investigation of the fluid flow and heat transfer inside a solar thermal buffer zone (TBZ) has been carried out. The numerical work has been conducted using the ANSYS-CFX commercial software package. A TBZ is an air-filled cavity that envelopes the building. It acts as an additional insulation and allows solar energy collected from the south side of the building to be distributed throughout the other sides, hence, reducing the heating load of the building. The main objective of the current study was to determine the optimum TBZ size.

Considering a one-third model of a typical floor in a building located in Ottawa, Ontario, Canada, our results obtained using an average winter day solar intensity show that the TBZ could result in a significant saving in the building heating load, which makes the TBZ an attractive passive technology to achieve significant sustainable energy savings in commercial buildings.

Introduction

One of the biggest problems our society will face in the coming years pertains to energy conservation and management. Our population is growing at an increasing rate while our planet's resources are slowly diminishing. This is creating an increase in demand for more efficient, clean and more sustainable methods of energy production, consumption and possible storage. In the past few decades we have witnessed an enormous interest in the impact of human activities on the environment. Despite the fact that fossil fuel use has an adverse effect on the environment, fossil fuels still contribute significantly towards energy production in the developed countries. As per the Natural Resources Canada's Energy Use Data Handbook [1], buildings are known to use more than 40 % of primary energy used in North America. The need for Sustainable development has been on the increase in the recent past.

A large portion of energy is spent every year on space heating and cooling. In Canada, this is of great concern due to very harsh, varying climate which often reaches extremes from year to year. Table 80.1 shows that the most amount of energy used in buildings is used for space heating.

A. Jan • M.S. Hamed (✉)
Thermal Processing Laboratory (TPL), Department of Mechanical Engineering, McMaster University, Hamilton, ON, Canada
e-mail: hamedm@mcmaster.ca

G. Razaqpur
Department of Civil Engineering, McMaster University, Hamilton, ON, Canada

S. Foo
Public Works and Government Services Canada (PWGSC), Ottawa, ON, Canada

In the 1970s and 1980s, the aim of net-zero energy buildings (NZEB) was taken into consideration earnestly due to the rise in oil prices. NZEB is the reduction of energy obtained from fossil fuels in building operations and maintenance. It can be accomplished by taking conservation measures or replacing fossil fuels with renewable energy sources. The main goal of the present study was to reduce the amount of non-renewable energy used for space heating in buildings by using a passive means utilizing naturally present solar energy; namely the thermal buffer zone (TBZ). To the best of the authors' knowledge, the present experimental approach investigating the use of TBZ in buildings is unique.

Solar Thermal Buffer Zone

Due to the orientation of the sun, a building receives an uneven amount of solar gain (solar radiation energy). The south-facing side of a building receives more energy than the north-facing side, which creates an uneven temperature distribution and significant heating and cooling loads. For example, even in the winter, sometimes the north side of the building requires heating while the south side requires cooling. A better distribution of the solar gain could eliminate such problems. This can be done by creating a TBZ around the building. A TBZ, as shown in Fig. 80.1, consists of two layers of glass separated by an air cavity. Due to the higher solar gain on the south-facing cavity, a density difference between the two columns of air causes an air flow around the building envelope. The strength of such thermally driven flow depends on the amount of solar gain, the envelope size and the material properties. The main objective of this study is to investigate the effect of the cavity size on the amount of heat that can be distributed from the south side to the north side of the building.

Literature Review

A solar thermosiphon is a differentially heated open cavity. Therefore, research related to predicting performance of solar thermosiphons can be traced back to work of natural convection over a single-heated vertical plate and flow between a differentially heated parallel plate open cavities. The air flow in solar chimneys, Trombe wall and airflow windows has often been treated as separate subjects. However, the basic assumption of modelling them as flow between parallel plates is universal in all the research done on these methods. This discussion will treat all three methods of buoyancy-induced flow under the same heading as flow between heated vertical parallel plates. Experimental and numerical modelling of the heated vertical parallel plate channel has been carried out extensively and the flow within the channel is well understood [2].

Table 80.1 Total energy use in buildings [1]

	Total energy use (%)					
	1990	2005	2006	2007	2008	2009
Space heating	61.8	61.3	60.3	62.8	63	62.8
Water heating	19.1	18.1	18.8	17.9	17.5	17.3
Appliances	14.3	13.8	14.4	13.4	13.9	14.4
Lighting	4	4.4	4.5	4.1	4.2	4.3
Space cooling	0.8	2.5	2	1.9	1.5	1.2
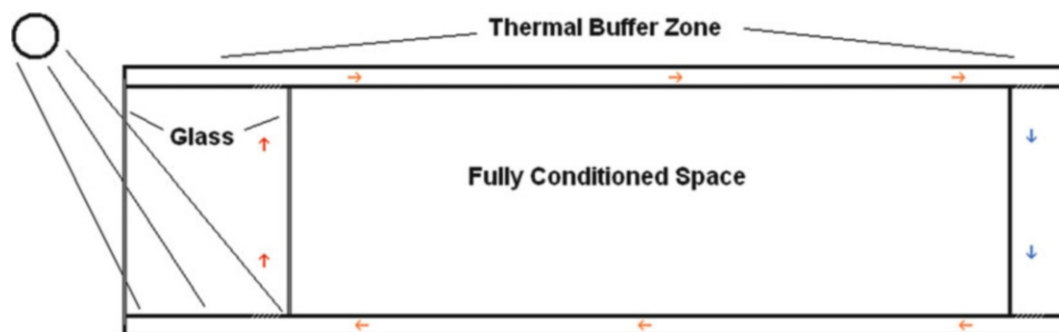
Fig. 80.1 Solar thermal buffer zone

There has been no research work done previously on a TBZ with a convection loop, i.e., the ability to move the hot air from the south side around the building, passively [3]. The closest previous work to the present configuration is the work of Richman [4] on the solar dynamic buffer zone (SDBZ). The SDBZ is a curtain wall system which 'works by ventilating a cavity within a wall with heated exterior air to control moisture migration across the assembly'. The SDBZ is also employed within the spandrel area just like the Solar Air Flow Window. During the heating season, the model used by Richman [4] predicted an average overall seasonal efficiency of 35 %. His experimental results showed that the SDBZ curtain wall is an effective means of collecting solar energy in a relatively passive manner with experimental efficiency of 25–30 % on average. However, connecting the produced air to the main air conditioning duct system is the main practical restraint, similar to the case of solar air windows.

Another research that is similar to a TBZ is the concept of double facades in a building. A double skin façade is a special type of envelope where a second skin, usually transparent glazing, is placed in front of the regular building façade. The air space in between, the channel, is ventilated (naturally or mechanically) in order to diminish overheating problems in summer and to contribute to energy saving in winter [5]. It has been installed and monitored for at least 1 year at the Siemens building in Dortmund, Victoria. The research was carried out at the University of Dortmund. The solar gains of the permanently ventilate facade saved approximately 15–18 % of the heating load in winter [6]. The average temperature in the façade was 10–15° higher than the outside temperature. One of the drawbacks of this system is that wind speed and wind direction have a significant influence on the ventilation in the façade gap [6]. The use of double skin facade (DSF) has also been investigated [7, 8]. Additional cost of the DSF above typical static façade system has ranged significantly from 20 % to about 300 % [9].

The Experimental Setup

The experimental apparatus used to carry out the present study is shown in Fig. 80.2. The apparatus was designed to investigate the effect of the TBZ gap aspect ratio, B/H and the radiation intensity on the effectiveness of the TBZ. Only the effect of B/H is reported in this paper. The optical properties of the system can also be changed by changing the type of glass.

The heat flux was varied by changing the distance between the cavity and the solar radiation simulator source, L. The constant heat flux used in this paper corresponds to the incident solar radiation on a south-facing window in Ottawa,
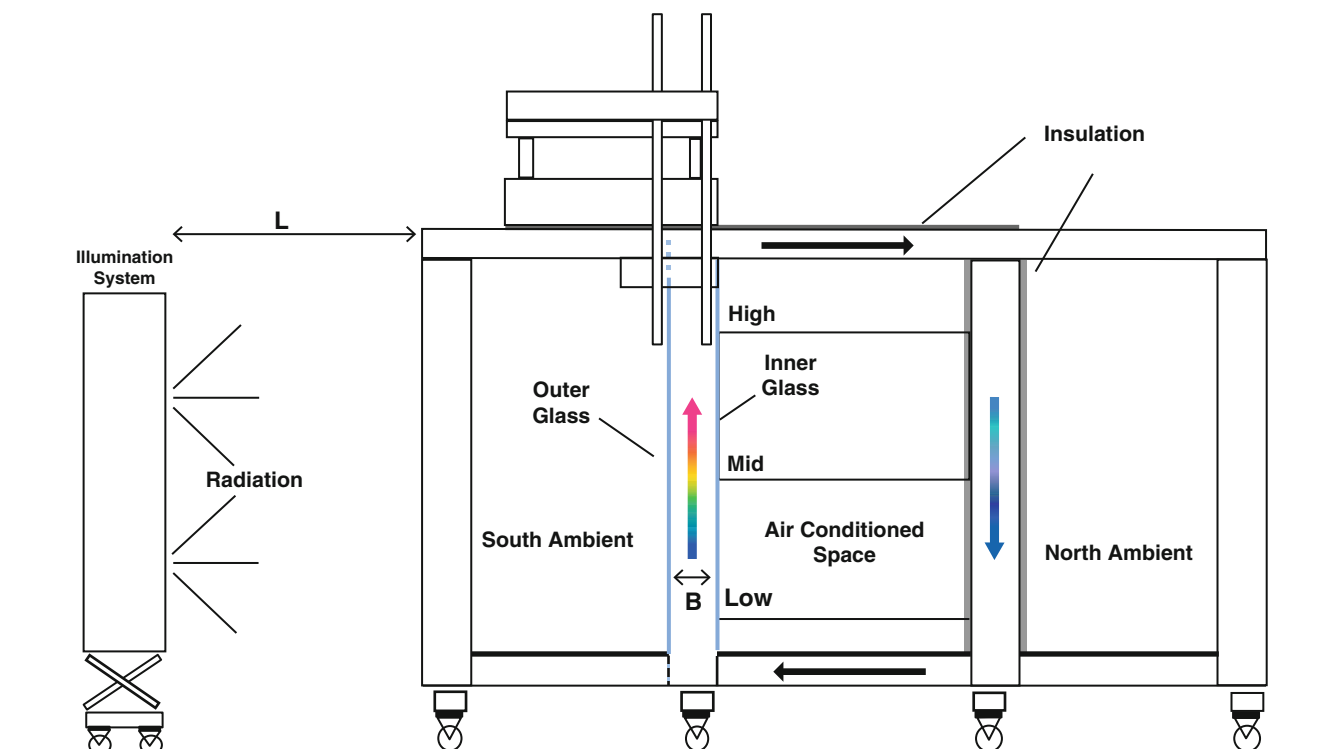
Fig. 80.2 Experimental setup

Fig. 80.3 Locations of
temperature measurements
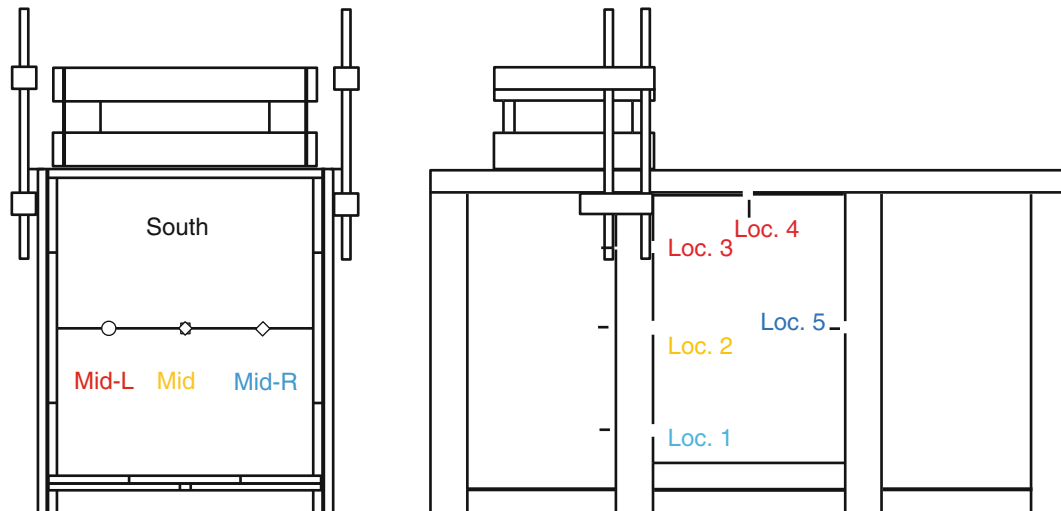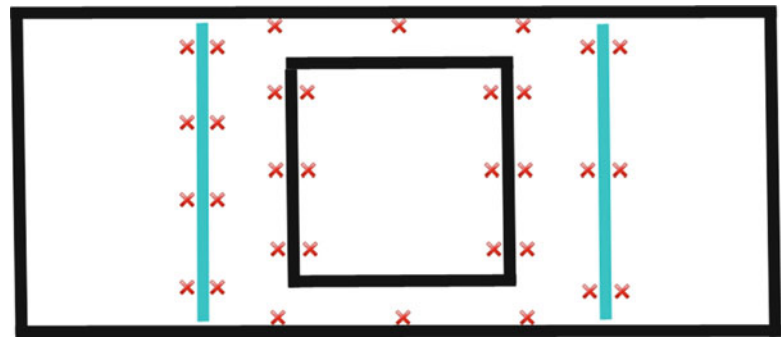
Fig. 80.4 Locations of air velocity and temperature measurements

Canada, during the month of January. The daily average heat flux is about 380 W/m^2 calculated based on the standard solar resource calculations, Duffie and Beckman (1974). This value of the heat flux was achieved with L = 1.38 m. The illumination system could cover a 1 m^2 area with a maximum average radiation intensity of 1,000 W/m^2. The light source consisted of four Quarts Tungsten Halogen (QTH) light bulbs, which give a black-body spectral properties of 3,000–3,300 °K.

A custom structural frame made of softwood lumber was used to hold the various components in place to replicate a solar TBZ. A 38.1 mm thick Expanded Polystyrene board, R-7.75, with reflective radiant barrier facing the outside of the setup was used as insulation to reduce heat losses from the surfaces exposed to the ambient. The air conditioned space was a 1 × 1 × 1 m cube. The height of the upper, lower and right gaps was kept constant at 0.1 m. The south-faced gap width, B, was varied between 0.1 and 0.7 m, which gave an aspect ratio, B/H, of 0.1–0.7.

In order to better collect the incident solar radiation from the heat source, it was necessary for the glass used in the physical prototype to have high absorbance ratio. The outer glass was a standard 6 mm thick clear window glass, which has a high solar absorbance ratio of 0.83. A solar shield grey glass was used for the inner glass surface, which has lower absorbance coefficient of 0.54. Holes were drilled through the inner glass to insert the velocity probe into the air gap at the three locations indicated by high, mid and low in Fig. 80.2.

Radiation intensity was measured using a Hukseflux LP02, ISO second class, pyrometer. The unit's accurate operational wave length range is 305–2,800 nm, which contains the majority of the energy for the solar spectrum. The average incident radiation was calculated from measurements taken over a two-dimensional, 1 × 1 m, square grid with 9 cm spacing between measurement locations.

Temperatures were measured using a number of 0.5 mm, Type-T, thermocouples placed at various locations, shown in Fig. 80.3. Thermocouples were attached to surfaces using a clear tape and shielded from direct radiation using tin foil. The laboratory air temperature was measured using five thermocouples.

Air velocity and temperature were measured at various locations as shown in Fig. 80.4, using a ComfortSense hot wire anemometer.

Numerical Investigation

The commercial CFD software program ANSYS-CFX was used to model the flow and heat transfer in a two-dimensional model of the TBZ. The computational domain is shown in Fig. 80.4.

Turbulence has been modelled using the Shear Stress Transport (SST) model developed by Menter (1994).

Results and Discussion

The effect of the gap aspect ratio, B/H, on the air velocity inside the south-facing gap measured at location 3 (see Fig. 80.5) is shown in Fig. 80.6. The air velocity has been non-dimensionalized using the average mass flow velocity inside the gap. Experiments 1, 2, 3 and 4 have been carried out using B/H values of 0.089, 0.18, 0.25 and 0.34, respectively.

The variation of the mass flow rate as a function of B/H is shown in Fig. 80.7. Following the expected trend, the mass flow rate increased with increasing the aspect ratio up to B/H = 0.25. Increasing B/H to 0.34, experiment 4, resulted in a sharp decrease in the mass flow rate. The mass flow rate calculated in the north-facing gap showed a similar trend; however it had
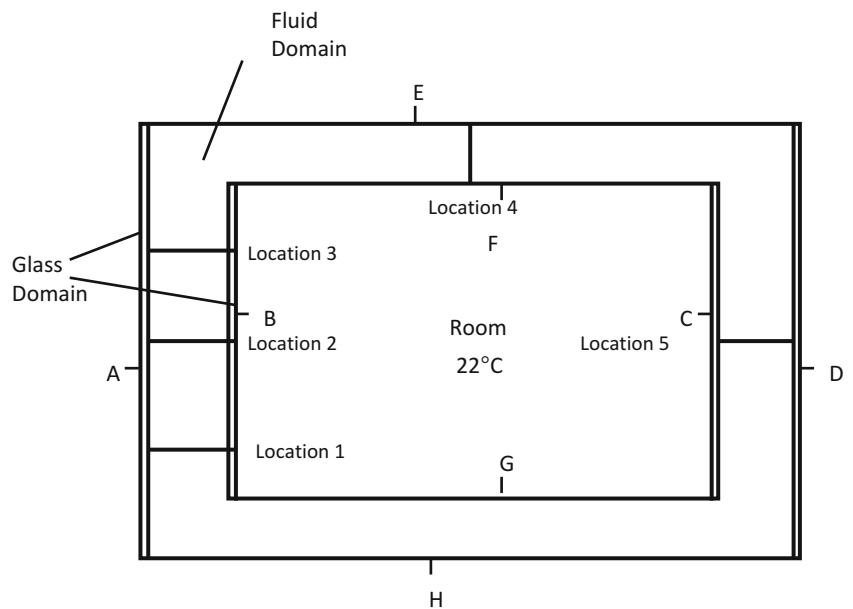
Fig. 80.5 Numerical computational domain with labelling of boundaries and locations of measurements
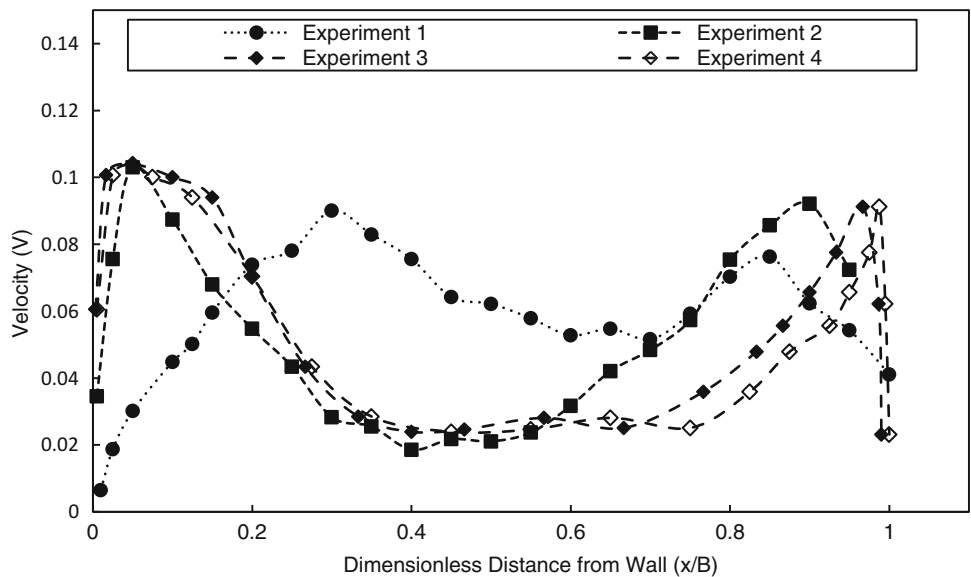
Fig. 80.6 Variation of dimensionless velocity inside south-facing gap as function of gap aspect ratio, B/H. Measurements taken at Location 3 (see Fig. 80.5)

Fig. 80.7 Mass flow rate per
meter width vs. B/H aspect ratio
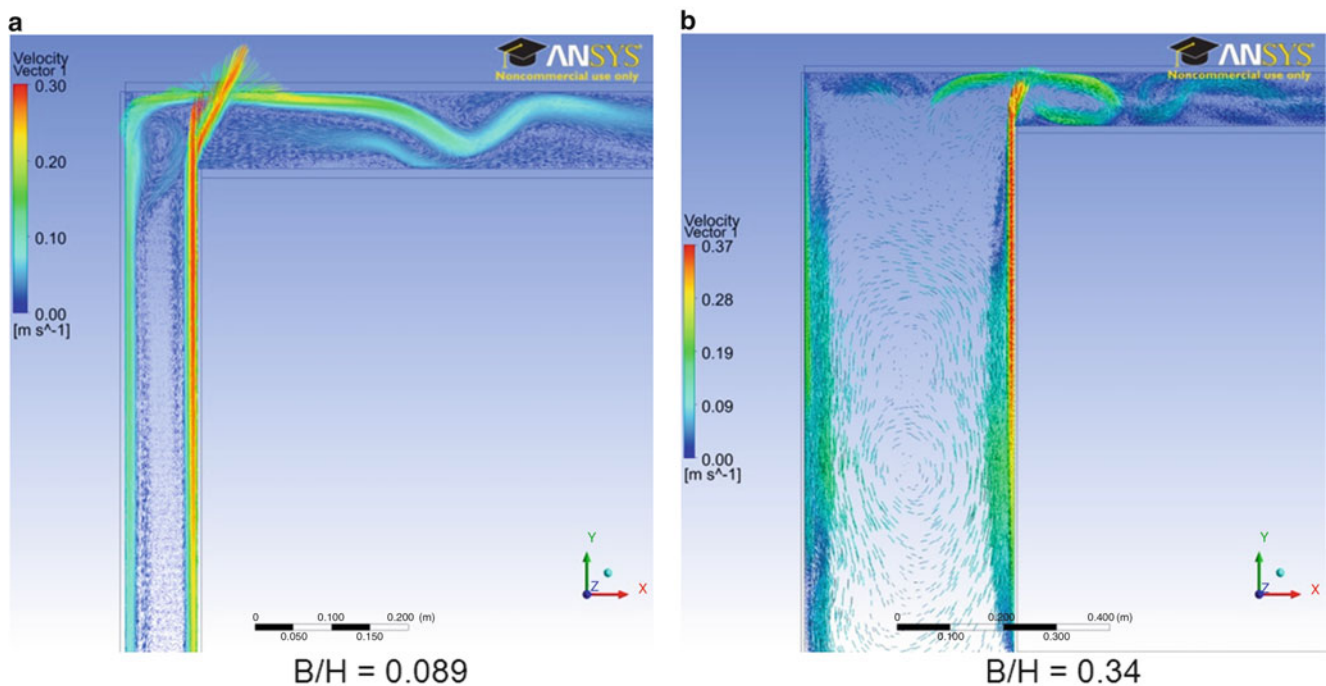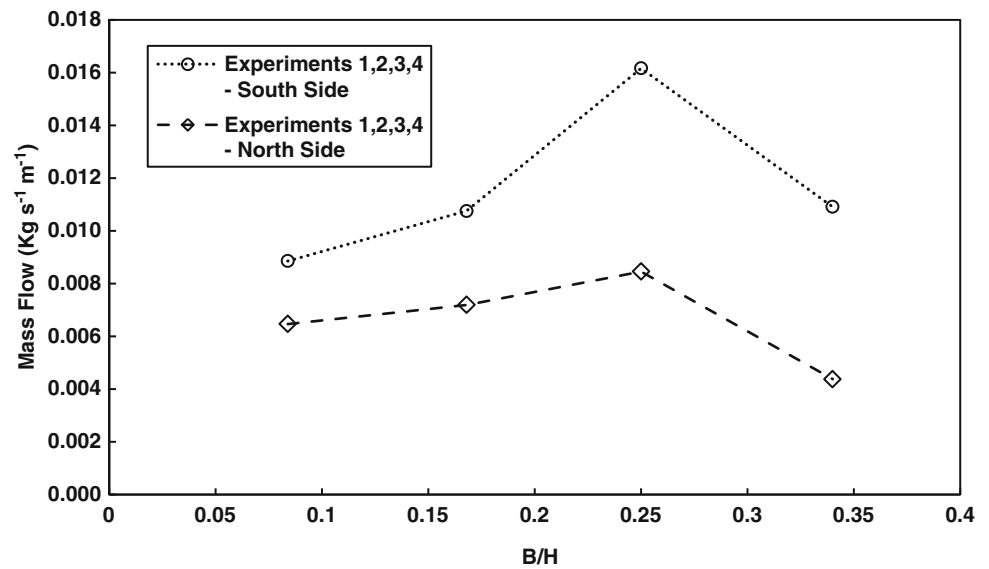
Fig. 80.8 Numerical velocity fields obtained for experiments 1 and 4, B/H = 0.089 and 0.34

lower values, due to leakage and measurements uncertainty. The significant decrease in the mass flow rate observed in experiment 4 was attributed to high recirculation developed inside the south-facing gap whereby most of the hot air stayed in the south side and did not make it to the north side of the TBZ. Such recirculation is evident from the numerically obtained velocity fields for B/H = 0.089 and 0.34 shown in Fig. 80.8.

Case Study

In order to assess the effect of using the TBZ on the energy usage of a typical building, a case study of two offices was considered; one office is located on the south side of the building and the other office is located on the north side, see Fig. 80.9. Each office is represented by a square room, having an area of 1 m². The cooling and heating load of each room

Fig. 80.9 A floor in a building with offices on south and north side
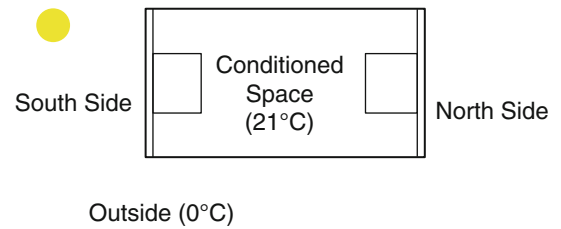
Table 80.2 Cooling and heating loads estimated with and without a TBZ

South side	No TBZ Cooling (W/m^2)	TBZ Cooling (W/m^2)
Single glazing	203	46
Double glazing	195	42
Double glazing, low e coating	184	
Triple glazing	204	
Triple glazing, low e coating	184	

North side	No TBZ Heating (W/m^2)	TBZ Heating (W/m^2)
Single glazing	105	72
Double glazing	72	54
Double glazing, low e coating	63	
Triple glazing	55	
Triple glazing, low e coating	44	

was estimated using temperatures obtained from the present experimental results and the optical properties from the 2009 ASHARE Handbook.

The representative day for the case study was chosen to be in January. As per ASHARE Fundamentals Handbook (2009), the average temperature in Ottawa in the month of January is 0 °C. Assuming no humidity, the conditioned space was kept at 21 °C, and an average daily heat flux of 380 W/m^2 was applied on the south-facing side. In order to show the benefits of the TBZ, calculations must be compared with the conventional building without a TBZ. For a building with no TBZ, all the calculations were based on the optical properties obtained from the 2009 ASHRAE handbook.

The optimum B/H aspect ratio of 0.25, as determined experimentally, was chosen for this case study. Table 80.2 shows the benefit of the TBZ. Having a TBZ reduced the cooling load of the south-facing office by 70 %. Similarly, the TBZ reduced the heating load of the north-facing office by about 30 %.

Summary and Conclusion

An investigation of the benefits of using the TBZ in buildings has been carried out. From the literature review, it was found that there were no comprehensive correlations accounting for the various parameters that affect the performance of the TBZ. These correlations are needed for performing a year-round building energy simulation that would estimate the benefits of the TBZ. The effect of the gap aspect ratio has been investigated. Four aspect ratios were investigated experimentally. Results showed that the aspect ratio of 0.25 gave the maximum mass flow rate. The experimental results were used in a case study considering cooling and heating loads of an office building located in Ottawa. Results obtained for the case study showed significant potential of the TBZ in reducing building loads.

Nomenclature

C_p	Specific heat capacity (J/kg °C)	Pr	Prandtl number
B	Spacing between glass and absorbing wall (m)	q	Heat flux (W/m^2)
e	Measured voltage (V)	Ra_H	Rayleigh number based on height
g	Gravitational acceleration (m/s^2)	Re	Reynolds number
Gr_H	Grashof number based on wall heating	T_w	Uniform temperature of wall (°C)
Gr_A	Grashof number based on air temperature	T_∞	Temperature of fluid far from wall (°C)
h	Convection heat transfer coefficient (W/m^2 °C)	V	Velocity (m/s)
H	Total cavity height (m)	$\overline{V}$	Area averaged velocity (m/s)
k	Thermal conductivity (W/m °C)	α	Thermal diffusivity (m^2/s)
L	Spacing between glass and illumination system (m)	β	Thermal expansion coefficient (1/°C)
$\dot{m}$	Mass flow rate (kg/s)	ν	Kinematic viscosity (m^2/s)
Nu_H	Nusselt number based on height	μ	Dynamic viscosity (kg/ms)
p	Measured atmospheric pressure (kPa)	ρ	Density (kg/m^3)

References

1. Natural Resources Canada (2009, April 1) Comprehensive energy use database. Retrieved October 20, 2011, from Natural Resources Canada: http://oee.nrcan.gc.ca/corporate/statistics/neud/dpa/comprehensive_tables/index.cfm?fuseaction=Selector.showTree
2. Gan GH (1998) A parametric study of Trombe walls for passive cooling of buildings. Energy Build 27:37–43
3. Richman R, Pressnail K (2010). Quantifying and predicting performance of the solar dynamic buffer zone (SDBZ) curtain wall through experimentation and numerical modeling. Energy and Build 522–533
4. Richman RC, Pressnail KD (2009) A more sustainable curtain wall system: analytical modeling of the solar dynamic buffer zone (SDBZ) curtain wall. Build Environ 44:1–10
5. Shameri MA, Alghoul MA, Sopian K, Zain MFM, Elayeb O (2011) Perspectives of double skin facade systems in buildings and energy savings. Renew Sustain Rev 15:1468–1475
6. Pasquay T (2004) Natural ventilation in high-rise buildings with double facades, saving or wasting of energy. Energy Build 381–389
7. DeHerde C a (2004) Double skin facades for office buildings. Lund University
8. Saelens D (2002) Energy performance assessment of single story multiple-skin facades
9. Arons D (2000) Properties and applications of double-skin building. Massachusetts Institute of Technology
10. Friedrich K (2011) Experimental and numerical investigation of solar air flow window. Masters Thesis, McMaster University

Determination of a Geothermal Energy Field with Audio-Magnetotelluric (AMT) Data at the South of Manisa, Turkey

Hatice Karakilcik

Abstract

In this study, we present an investigation of the geothermal energy field and its energy potential at the south of Manisa in Turkey. The resistivities of the geothermal energy field have a key role in determining geothermal energy reservoir and potential in the field. This work focuses on low-resistivity zones in order to determine the geometry and extension of the geothermal system by using the Audio-Magnetotelluric (AMT) method that is to image rock units below the shallow subsurface and determine deeper structure that might represent permeability in a geothermal system. Therefore, AMT stations were arranged with an interval of about 1 km array and its measurements were carried out at 40 sites, which were located on approximately 9.5 km long profiles at the south of Manisa. The resistivity model was obtained from the 2D inversion of AMT data to show subsurface specific conductive and resistive features in the field. As a result, two geothermal anomalies were defined at the study area by using AMT data and the resistivity of soft rock is found generally quite low ($<200\ \Omega$m), however, hard rock displayed higher resistivity. But, low resistivities can also evaluate in the fault zones because of water content and rock softening.

Keywords

AMT method • Geothermal energy • Low resistivity • Magnetotellurics

Introduction

Applied electromagnetic research in recent years has been influenced by the growing importance of geothermal energy. Geothermal energy is a major resource and potential source of low emissions renewable energy suitable for base-load electricity generation and direct-use applications. It is the natural heat of the earth stored in rocks and in the fluids within them. Significant geothermal resources can also be associated with basement rocks heated by natural radioactive decay of elements (e.g., uranium, thorium, and potassium) and in naturally circulating waters deep in sedimentary basins.

Electromagnetic methods have become powerful geophysical tools in mapping subsurface conductivity variations. The method is widely used in the exploration of geothermal resources [1]. It mainly involves the propagation of continuous wave or transient electromagnetic fields in the earth. The source may be natural or artificial. In a natural source method like magnetotellurics (MT), the fluctuation in the earth's natural magnetic field induces an electric field. By measuring the electrical and magnetic field at the surface of the earth, inferences are made about the conductivity distribution in the subsurface.

MT/audio-magnetotelluric (AMT) survey, targeted at defining the main characteristics of the geothermal reservoir at study area, can also be supplemented with other types of geophysical surveys that assist us in understanding the regional geology and the local geological structure in a geothermal prospect.

H. Karakilcik (✉)

Department of Geology Engineering, Faculty of Engineering and Architecture, University of Cukurova, Adana 01330, Turkey
e-mail: hkilcik@cu.edu.tr

AMT method has found an application in geothermal exploration primarily because of its ability to detect the depth at which rocks become conductive because of thermal excitation.

Turkey has a unique geographic position at the cross roads between Europe and Asia. It is located on an active tectonic, orogenetic belt, the Alpine-Himalaya Orogen, with young faults, and active volcanism. Turkey is rich in geothermal energy resources. Geothermal exploration in Turkey started in the early 1960s. The first geothermal well for power generation was drilled in 1968 on high enthalpy fields for potential power production. The well has a depth of 540 m and a temperature of 198 °C [2]. Turkey has significant potential geothermal resources associated with buried high heat-producing granites and lower temperature geothermal resources associated with naturally circulating waters in aquifers deep in sedimentary basins. Total geothermal potential of Turkey is estimated around 30,000 MW. In geothermal, Turkey has a proven 4,000 MW of resources over 20 °C of which 600–1,000 MW are high temperature fields able to produce electricity.

Geology

The study area is located within the northern Menderes Massif in western Turkey. Western Turkey, a region characterized by the widespread exposures of metamorphic rocks (known as the Menderes Massif—one of the largest metamorphic core complexes in the world) dissected by approximately E–W trending grabens, forms a very good example for three modes of extension in the world (Fig. 81.1).

Within the study area, four groups of rocks are recognized: (a) the metamorphic rocks—orthogneisses and metasediments; (b) pegmatoids; (c) Neogene sedimentary rocks; and (d) quaternary alluvial sediments. The structural framework of the study area is characterized by gently to moderately tilted (5–40°) Neogene sedimentary rocks cut by ~E-striking gently to steeply dipping normal faults and northerly (NNW to NNE) striking oblique-slip cross (or transverse) faults. The predominant E–W strike of normal faults and tilting reflects regional north–south extension. The strata are also deformed into multiple, discontinuous WNW to E-trending folds. This folds are extensional in origin, resulting primarily from local reversals in the predominant dip direction of normal fault systems [3].

In geothermal prospect the required information includes low-resistivity bodies, dikes, faults, irregular shaped bodies, and volcanic plugs. The two largest faults in the area are the moderately N-dipping Alaşehir frontal fault zone and gently (~10–30°) N-dipping Gediz detachment fault. Menderes metamorphic complex is typically marked by a thick zone of cataclasis that overprints an earlier mylonitic fabric, but is currently inactive, with no evidence for quaternary displacement.

Methods

The magnetotelluric (MT) method [4, 5], which operates in the frequency range 0.001 to several Hertz (Hz) is a well-established technique for imaging the conductivity structure of the Earth's crust. Its depth of investigation is typically from several hundred meters below ground surface to several kilometers or even deeper. The depth of investigation in MT is a function of subsurface resistivity and frequency (or the inverse of the period) of the electromagnetic signals. The penetration depth can be roughly related to the period by the use of the skin depth (δ meter).

An AMT sounding system appears to be an effective technique for reconnaissance exploration to detect shallow resistivity anomalies associated with geothermal reservoirs. Data acquisition for a single AMT station (Fig. 81.2) is done by measuring the input fields, two horizontal magnetic components H_x and H_y and the resulting earth response, two horizontal electrical fields, E_x and E_y, and the vertical magnetic field, H_z. The recorded time-series data were converted to the frequency domain and processed to determine the impedance tensors, which is used to derive apparent resistivities and phases at each site [6].

AMT method has proved very useful for subsurface mapping purpose by determining the low-resistivity area. Forty AMT soundings were collected in study area (Fig. 81.2). Seven profiles AMT measurements were carried out at this part of the study area using the short-period automatic magnetotelluric system with a frequency range of 128–0.16 Hz and a maximum depth penetration of about 5 km.

Fig. 81.1 (**a**) Study area. (**b**) Geology and tectonics map of the study area [3]
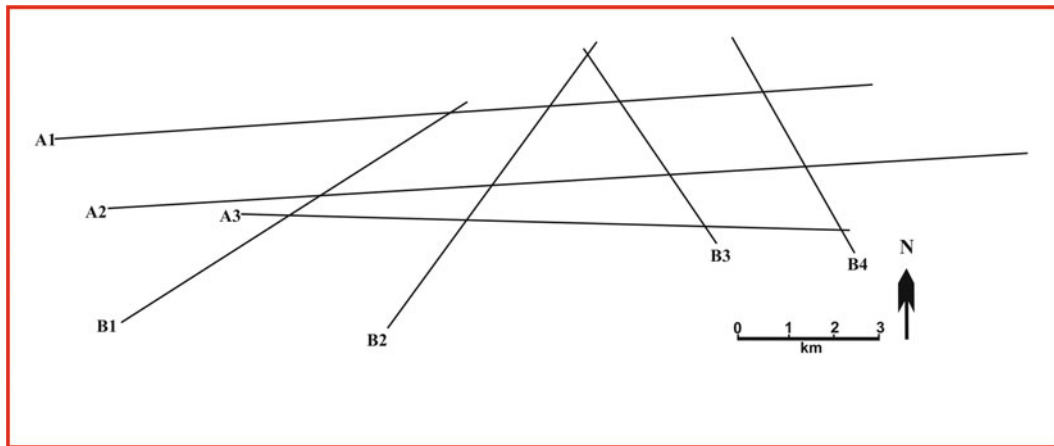
Fig. 81.2 Location map (the profiles consist of AMT data stations at the study area)

Results and Discussion

Geothermal research in the vicinity of Manisa that make up the study area dates back to the beginning in 1976 up to the present by working geological and geophysical studies at Salihli, Alaşehir, Kula, Turgutlu, and Sarıgöl geothermal fields, and appropriate drilling locations have been identified. To date, the license area of 18 at a depth of 16,648 m has been 22 geothermal drilling activity and 1,978 MWt heat energy was obtained. The results of the drilling operations are given in Table 81.1.

In general, the data quality was very good for all AMT measurement points. AMT data were analyzed and modeled using a 1D inversion scheme. 1D and 2D inversions are conducted to resolve the conductive structures. Then corresponding data on seven profiles (A1, A2, A3, B1, B2, B3, and B4) were inverted using 2D inversion schemes (Fig. 81.2).

AMT data results reveal the presence of three major conducting zones beneath the surface in the basement (Figs. 81.3, 81.4 and 81.5). Since these resources may be found in fractured, tectonically stressed areas, their presence is often marked by microseismic events that also serve as a guide to drilling into the fractured rocks once other favorable geothermal conditions are established. Since low resistivity usually indicates low permeability conductive clays, AMT surveys may be used to locate the base of a geothermal caprock and, indirectly, its high thermal gradient. The dimensions of the reservoir can then be mapped and used to identify drilling targets and prospective locations of production and injection wells. As it is seen in Fig. 81.3, at A1 profile, there are two low-resistivity zones. Resistivity value is lower than 20 Ωm.

As it is seen in Fig. 81.3, depth in the areas with low-resistivity values varies between 900 and 2,500 m. As the rock electric conductivity depends on the rock type, the minerals present the fluid temperature and the fluid salinity. These surveys can provide excellent imaging of subsurface by delineating rock types, locating deep fault zones, and mapping subsurface hydrothermal zones which are characterized by extremely low-electric conductivity. The AMT method has found an application in geothermal exploration primarily because of its ability to detect the depth at which rocks become conductive because of thermal excitation.

As shown in Fig. 81.4, at B2 profile, between 301–302, and 311 AMT stations are also zones with low-resistivity values. This field with low-resistivity values can be considered as potential geothermal reservoir. Conductive units are clear specifications of areas which are affected by geothermal fluid circulations and resolving of conductors at deep levels by AMT directly depends on their scale. Generally, geothermal anomalies in the study area first occur along ~E–W-striking normal faults, but generally not near the maximum displacement on these fault zones [3]. In cases analyzed to date, the structural settings favoring geothermal activity generate conduits of highly fractured rock along ~E–W-striking fault zones oriented approximately perpendicular to the least principal stress.

The geothermal fields in the study area occur along the active southern margin of the Gediz graben. Fractured rocks of the Menderes Massif, such as mica-schist, gneiss, and especially marbles, are the reservoir rocks. Cap rocks for the geothermal fluids include clay-rich intervals within the Neogene sedimentary units [8]. Most hot springs and hot wells with good flow rates lie near the gently N-dipping Gediz detachment fault (Fig. 81.1), where it intersects and is cut by ~N–S-striking transverse faults. Karstic marble and breccia along and near the detachment fault provide good channel ways for flow,

Table 81.1 The results of the geothermal drilling operations in and around Manisa from 1976 until 2012 [7]

City	Town	Village	Code	Year	Depth (m)	Temperature (°C)	l/s compressor	Potential (MWt)
Manisa	Salihli	Kurşunlu	K-1	1976	42.50	90	20	4.60
Manisa	Salihli	Caferbeyli	SC-1	1989	1,189	150	2	0.96
Manisa	Salihli	Kurşunlu	K-2	1992	70	94	45	11.11
Manisa	Salihli	Kurşunlu	K-3	1992	114.3	94	80	19.762
Manisa	Köprübaşı	Saraycık	S-1	1992	386	64.5	22	2.72
Manisa	Köprübaşı	Demirci	S-3	1992	135.2	74	45	7.35
Manisa	Köprübaşı	Demirci	AS-1	1994	122	43	23	0.77
Manisa	Köprübaşı	Demirci	AS-2	1994	270	29	15	0
Manisa		Kavaklıdere	AK-1	1996	750	63	3	0.35
Manisa		Kurşunlu	K-4	1996	262	58.6	45	4.45
Manisa	Alaşehir	Demirci		1997	300	36	25	0.1
Manisa	Salihli	Kurşunlu	K-5	1997	120	83	40	8.04
Manisa	Kula	Emir	E-1	1998	33	65	40	5.02
Manisa	Kula	Emir	E-2	1999	162.5	63	100	11.72
Manisa	Turgutlu	Urganlı	U-1	2001	440.6	61	22	2.39
Manisa	Alaşehir	Kavaklıdere	KG-1	2002	1,447.1	182	15	9.23
Manisa	Köprübaşı	Demirci		2003	116	42	5	0.15
Manisa	Alaşehir	Kurudere	AK-2	2004	1,507	213.43	6.74	5.03
Manisa	Alaşehir	Kavaklıdere	2010/14	2011	2,750	287.5	35	36.99
Manisa	Alaşehir	Kavaklıdere	2010/15	2011	1,750	159.53	2	2.61
Manisa	Alaşehir	Kavaklıdere	2011/3	2011	2,250	88	90	57.64
Manisa	Sarıgöl	Alemşahlı	2011/17	2012	2,672	125.21	18	6.8
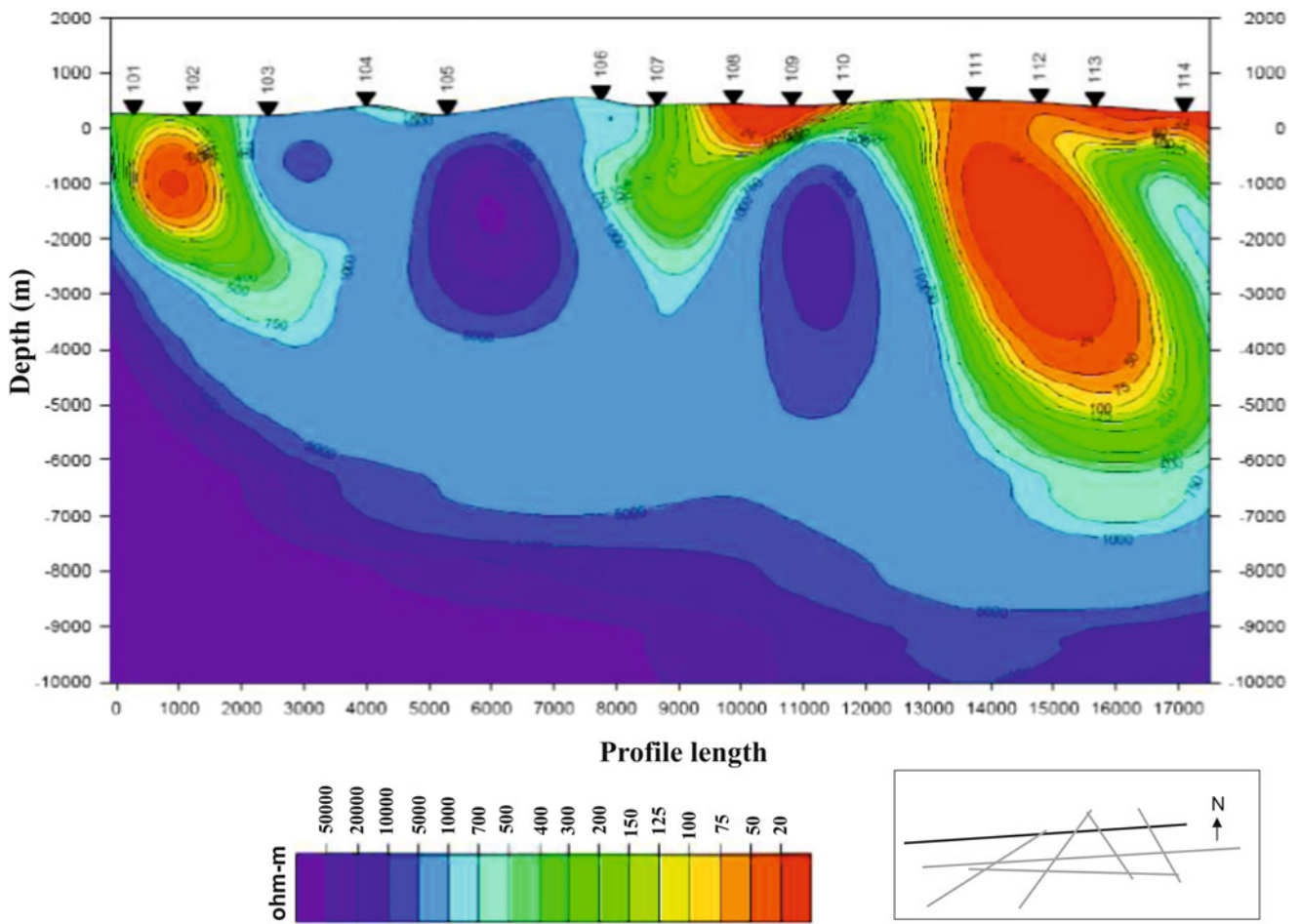
Fig. 81.3 AMT measuring points at A1 profile (between 101–102 and 111–113 AMT stations observed low-resistivity value)
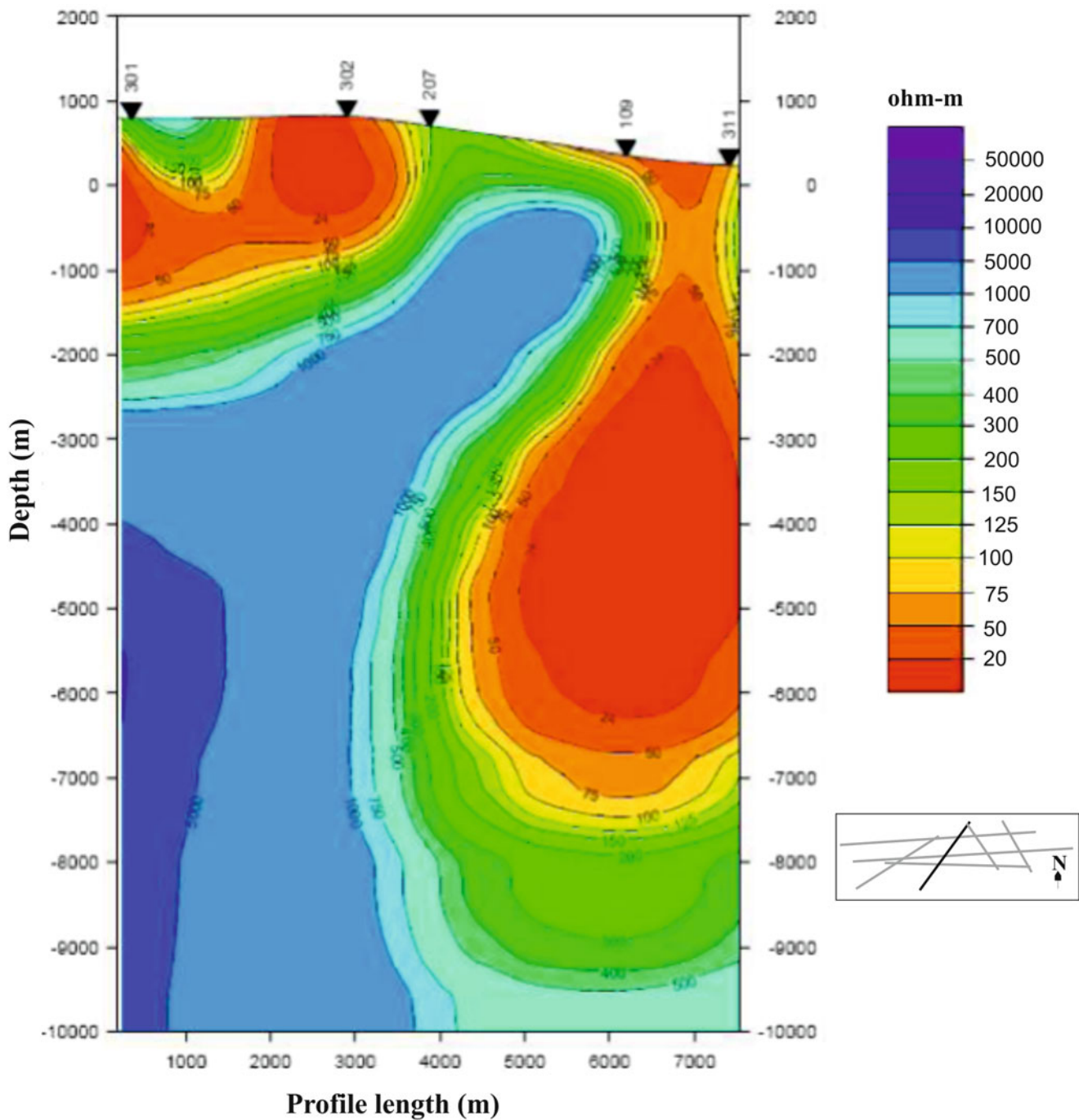
Fig. 81.4 B2 profile consists of five AMT stations and low-resistivity values

possibly somewhat distal to the main upwelling zone. The reservoir for the Kurşunlu field varies between 10 and 200 m in depth and resides in highly fractured, commonly karstified zones along the detachment fault. Temperatures at the Kurşunlu field range from 57 to 120 °C. Empirical chemical geothermometers applied to the thermo-mineral waters tentatively suggest that reservoir temperatures at Kurşunlu vary between 150 and 230 °C [8].

Thermal-mineral waters from both systems are used for bathing and medicinal purposes, but those from Kurşunlu are also utilized in a district heating system for 5,000 homes in the city of Salihli. The total discharge rate for the main producing wells at Kurşunlu is 145 l/s. The discharge rates are the highest where the reservoir is predominantly formed by marbles (versus schist). Average production temperatures are ~90 °C for the district heating.

ohm-m

50000
20000
10000
5000
1000
700
500
400
300
200
150
125
100
75
50
20
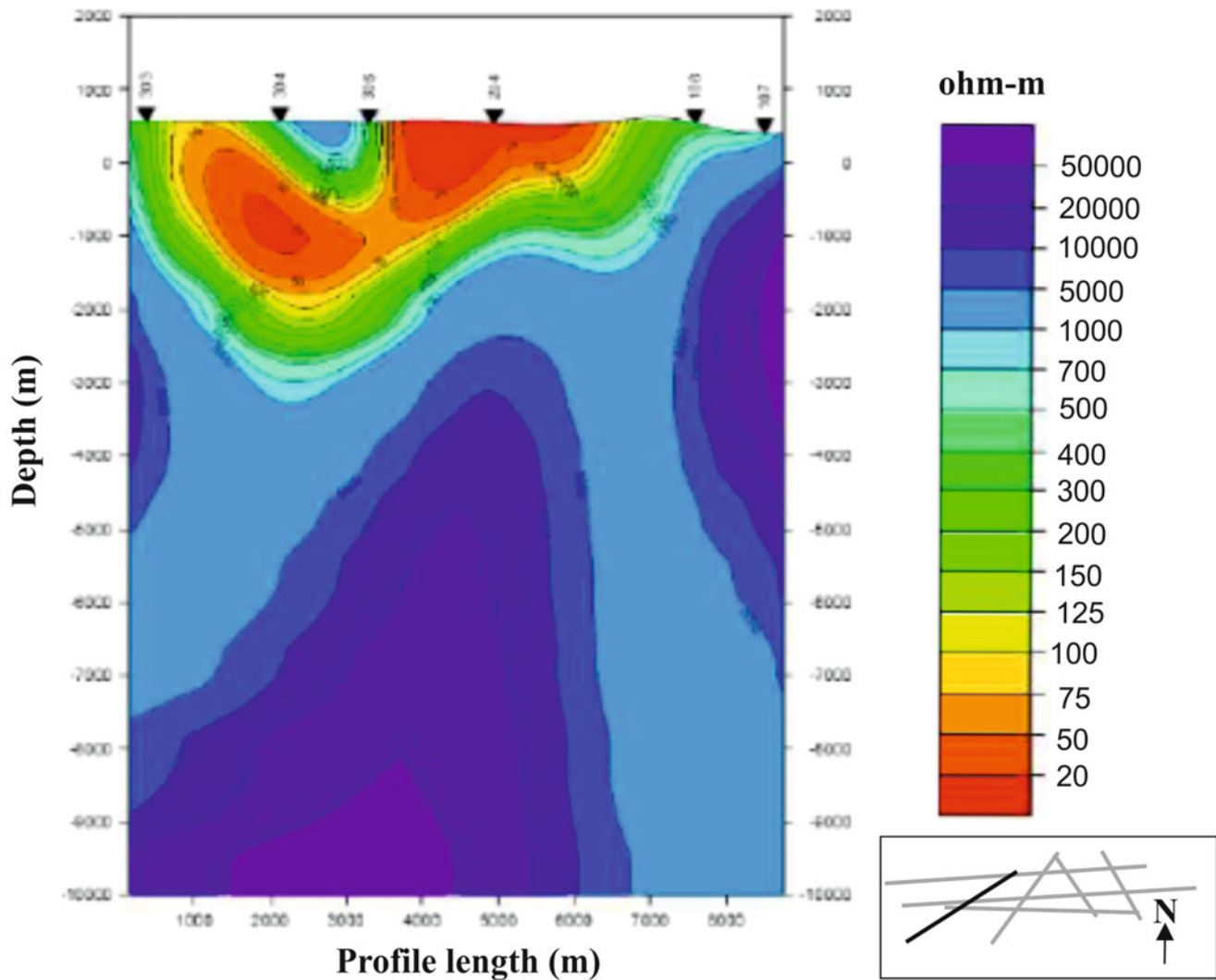
Fig. 81.5 It is seen in the AMT stations at B1 profile (red color corresponds to a value with lower resistivity)

Key Ingredients of Geothermal Energy Production

Geothermal exploration aims at identifying the geothermal resource, in terms of surface extent, volume, rock, and fluid properties and collects all necessary information for taking decisions on investing toward a geothermal power plant. Geothermal energy can simply be described as heat extracted from the earth. The extraction of this energy relies on the transport of heat from a geothermal reservoir to the surface via a fluid. This fluid is in direct contact with reservoir rocks and may naturally occur in the reservoir or may have to be introduced into the system. To understand the key ingredients for a viable geothermal system, it is useful to look at the net amount of energy produced by a single well. So, the key ingredients for geothermal energy production can be given as;

$$MW \approx c_p F(\Delta T)\,\eta - P \tag{81.1}$$

where c_p is the specific heat of the working fluid, F is the flow rate from the production well. η is the efficiency with which the heat energy can be used, P is the parasitic losses. ΔT is the sensible heat that can be extracted from the fluid produced by the production hole. The ΔT $(T_{rs} - T_{rj})$ is dependent on the reservoir temperature (T_{rs}) and the rejection temperature (T_{rj}) of the energy conversion system. Maximizing T_{rs} requires locating anomalously high thermal gradients and drilling as deep

as possible and T_{rj} requires cooling and minimization of scaling in plant and pipelines due to mineral precipitation as the fluid cools. Parasitic losses are due to pumping of the working fluid out of production wells and then pumping the fluid back in to the reservoir via injection wells. These losses are likely to be high due to pumping and cooling requirements. Using the current global experience in power generation from convective hydrothermal resources, the minimum amount of net energy produced by a well in a geothermal power system is around 4 MW [9].

Conclusions

Resistivity modeling of the AMT (high frequency MT) data can be used to help resolve the size and resistivity of the geothermal field. Analysis of the AMT dataset suggests likely signatures of hot water reservoirs in the area which are distinguished positive to contain low-resistivity values. The low-resistivity zone is called conductive zone, a deep geothermal reservoir in the study area. The conductive zones identified in the resistive basement at the AMT measurement sites can clearly be interpreted as the flow of the fluids in the faults and fractures of the metamorphic rocks. Geothermal activity may be at these zones of the study area. Numerous geothermal systems probably still remain to be discovered, since many systems have no surface activity.

Nomenclature

MT	Magnetotelluric	c_p	Specific heat (J/kg °C)
AMT	Audio-magnetotelluric	F	Flow rate (l/s)
E	East	P	Parasitic losses (J)
W	West	ΔT	Temperature difference (°C)
N	North	T	Temperature (°C)
S	South		

Greek Letter

η   Thermal energy efficiency

Subscripts

rs	Reservoir	rj	Rejection

References

1. Árnason K, Eysteinsson H, Hersir GP (2010) Joint 1D inversion of TEM and MT data and 3D inversion of MT data in the Hengill area, SW Iceland. Geothermics 39:13–34
2. Kaya T (2012) An overview on drilling and geothermal energy projects in Turkey. In: 36th GRC annual meeting international, September 30-October 3, 2012, Luncheon Reno, NV, US
3. Faulds JE, Bouchot V, Moeck I, Oguz K (2009) Structural controls on geothermal systems in western Turkey: a preliminary report. Geothermal Resources Council Transactions 33:375–381
4. Cagniard L (1953) Basic theory of the magneto-telluric method of geophysical prospecting. Geophysics 18:605–635
5. Chave AD, Jones AG (eds) (2012) The magnetotelluric method: theory and practice. Cambridge University Press, Cambridge, 552 p
6. Fantaye T (2010) Magnetotelluric and transient electromagnetic methods in geothermal exploration with examples from the Krysuvik area, SW-Iceland. United Nations University 'Geothermal Training Programme' reports 2010, number 12. Orkustofnun, Grensásvegur 9, IS-108, Reykjavík, pp 151–182
7. Republic of Turkey Ministry of Energy and Natural Resources (2013) Ankara, Turkey
8. Tarcan G, Filiz S, Gemici U (2000) Geology and geochemistry of the Salihli geothermal fields, Turkey. In: Proceedings of the world geothermal congress, Kyushu-Tohoku, 28 May–10 June 2000, pp 1829–1834
9. Huddlestone HC, Hayward J (2011) The potential of geothermal energy. Australia. www.csiro.au

Energy Production from Municipal Solid Waste Using Plasma Gasification

Hüseyin Topal

Abstract

The increasing quantity of Municipal Solid Waste (MSW) is one of the most serious environmental problems in Turkey. In order to solve this problem the government has failed to introduce any sustainable and environmental-friendly remedies. However, among several MSW treatment technologies, plasma gasification may be an alternative and reliable solution. Plasma gasification is a novel technology which does not fire the MSW as Conventional combustors do. It converts organic ingredients of the waste into a combustible gas (syngas). This paper deals with the feasibility study of utilizing plasma gasification and also co-gasification (i.e., gasification of waste with coal) for energy production from MSW. For this purpose, two methods were used; first determining the contents of the released syngas by mathematical modeling of the gasification process, and second, simulating the same process with the help of a simulation software (VMGSim). Finally, the results obtained by both methods are compared. Comparing the results revealed that calculation results from mathematical model were consistent with those outlined from simulation software.

Keywords

Plasma gasification • Municipal solid waste • Energy • Disposal

Introduction

Wastes can be defined as: "The unused or disposed part of the materials that we use to meet our needs." In industries, transportation, agriculture, tourism, and construction an enormous amount of materials change form. As we provide and consume energy for these activities, we produce gas, liquid, and solid wastes while a portion of these wastes is disposed and the remaining can be recycled to be reused (www.aso.gov.tr) [1].

The plasma reactor is an enclosed chamber into which the waste is fed. Plasma torches provide the heat, 3,000 °C or higher, in the chamber which converts organic material to a gas and inorganic material into a glassy slag. The plasma facility may generate electric power, using the fuel gases produced in the reactor. These fuel gases may be combusted in a waste-heat boiler, or cleaned and fed into a combustion turbine or other combustion device. However, the plasma facility must be large enough, in terms of waste throughput, to justify the cost of a power generation unit. The environmental controls on a plasma facility will be located downstream of the reactor and may include scrubbers, a carbon injection system, or a baghouse, whether or not the facility is generating electricity [2].

Thermal plasmas have the potential to play an important role in a variety of chemical processes. They are characterized by high-electron density and low-electron energy. Compared to most gases even at elevated temperatures and pressures, the chemical reactivity and quenching rates that are characteristic of these plasmas are far greater. Plasma technology is very drastic due to the presence of highly reactive atomic and ionic species and the achievement of higher temperatures in

H. Topal (✉)

Engineering Faculty, Department of Mechanical Engineering, Gazi University, Ankara, Turkey
e-mail: htopal@gazi.edu.tr

comparison with other thermal methods. In fact, the extremely high temperatures (several thousand degrees in Celsius scale) occur only in the core of the plasma, while the temperature decreases substantially in the marginal zones [3].

Overview of Combustion Technology

We can list the incineration methods used for waste disposal as follows [4]:

Grate Firing Systems
1. Fluidized bed furnaces,
2. Rotary kilns,
3. Alternative systems,
   - Wet oxidation,
   - Pyrolysis,
   - Gasification and combined systems,
4. Plasma technologies.

Thermal Plasma Waste Disposal

The application of plasma torches for environmental purposes is a relatively new process. Plasma torches operate simultaneously as a plasma-chemical and a thermal apparatus. The electrical energy of the torches goes into the plasma which transfers its energy to the substances to be treated, thereby triggering a dual simultaneous reaction process in the plasma-chemical reactor: the organic compounds are thermally decomposed into their constituent elements (syngas with more complete conversion of C into gas than in incinerators), and the inorganic materials are melted and converted into a dense, inert, nonleachable vitrified slag, that does not require controlled disposal. Therefore, it can be viewed as a totally closed treatment system [5].

The biggest disadvantage of thermal plasma process is its making use of electricity which is a costly energy type. However when it is considered as a long-term investment to provide a sustainable waste management system it is also promising from economical point of view. Despite the high costs of electricity, by using transferred arch equipment the energy will be used efficiently and there will be no extra load to heat the nitrogen-containing air [6]. Volatile metal substances will be gasified and along with the off-gas, halogenes and other sour gases will be carried out of apparatus. Also for degassing purposes several equipments including dust precipitator filters and absorbers have been installed to the system.

The Advantages of Plasma Compared to the Other Disposal Methods

Some of the advantages of plasma technologies over traditional combustion technologies are given in Table 82.1 [7].

Table 82.1 The advantages of plasma technologies in comparison to combustion methods

Plasma gasification	Combustion
Does not release air during the production of synthetic gas	Emissions include high level of greenhouse gas emissions, other air pollutants, dioxins, and furans
Fumes stack does not occur	High-dose fumes stack reveals
In order to void the commercially valuable slags, solids are reduced to the level of 1/150	Thirty percentage of solid wastes and potentially hazardous solid waste which is remained as ash
Takes place in a deoxygenated channel changer	More air is added to the incinerator
Plasma generator provides all the energy needed for operation	Additional fuel is required to sustain the process
Energy-rich waste is separated as a fuel	All the energy is converted into heat

Plasma Gasification Unit

The process where wastes are treated in a plasma solid waste disposal unit is shown in Fig. 82.1. After the excess humidity is taken away in the dryer, wastes are converted to syngas by means of plasma torch in the gasification reactor. In order to purify the dust that contains syngas from particles like heavy metals, it is directed to dust collectors and absorber/scrubbers. Next it is led to the second combustion chamber to be transformed to thermal energy (heat) and combustion gases leave the system through stack.

Kinetic Parameters

Gasification process is the result of carbon-based kinetic reactions inside the gasification boiler. Reaction balance is associated with A, E, Alpha (a), and Beta (b) parameters [8].

Basic reactions which are formed in the boiler:

$$\text{Carbon monoxide from, carbon } (1): \quad 2C + O_2 = 2CO \tag{82.1}$$

$$\text{Carbon monoxide from, carbon } (2): \quad C + CO_2 = 2CO \tag{82.2}$$

$$\text{Carbon monoxide from, carbon } (3): \quad C + H_2O = CO + H_2 \tag{82.3}$$

$$\text{Carbon monoxide from, carbon}: \quad C + O_2 = CO_2 \tag{82.4}$$

$$\text{Carbon dioxide, from carbon monoxide}: \quad CO + H_2O = CO_2 + H_2 \tag{82.5}$$
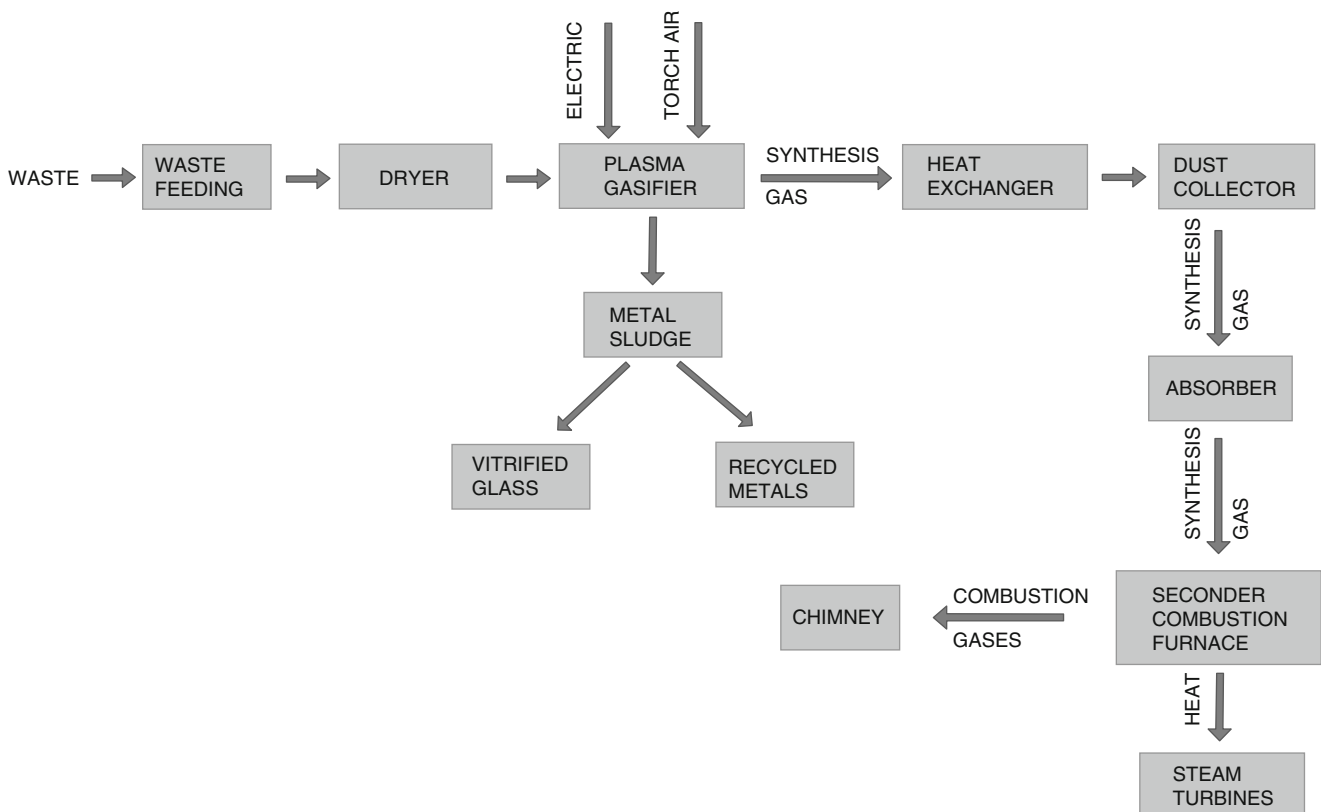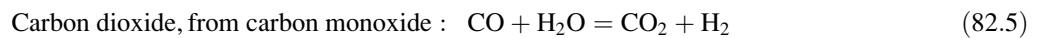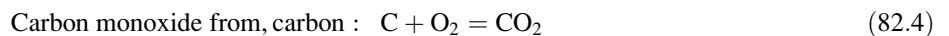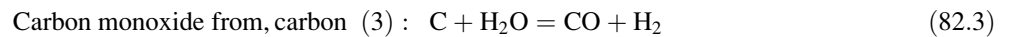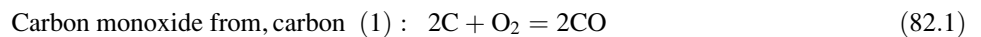
Fig. 82.1 Plasma gasification plant flowsheet

$$\text{From carbon to, hydrocarbons}: \quad C + 2H_2 = CH_4 \tag{82.6}$$

$$\text{From carbon monoxide to hydrocarbons}: \quad CO + 3H_2 = CH_4 + H_2O \tag{82.7}$$

$$C + \frac{1}{2}O_2 \rightarrow CO$$
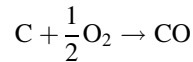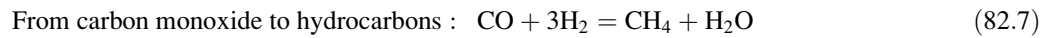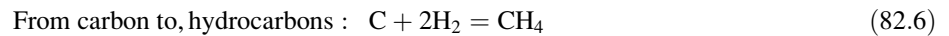
$$r_{CO_1} = A_{CO_1}P_C{P_{O_2}}^{0.5}\left(1 - \frac{1}{K_{CO_1}}\frac{P_{CO}}{P_C P_{O_2\ 0.5}}\right)\exp\left(\frac{-E_{CO_1}}{T}\right) \quad \log_{10}K_{CO_1} = \frac{\alpha}{T} + \beta \tag{82.8}$$

$$C + CO_2 \rightarrow 2CO$$
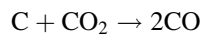
$$r_{CO_2} = A_{CO_2}P_C P_{CO_2}\left(1 - \frac{1}{K_{CO_2}}\frac{P_{CO}}{P_C P_{CO_2}}\right)\exp\left(\frac{-E_{CO_2}}{T}\right) \quad \log_{10}K_{CO_2} = \frac{\alpha}{T} + \beta \tag{82.9}$$

$$C + H_2O \rightarrow CO + H_2$$
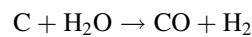
$$r_{CO_3} = A_{CO_3}P_C P_{H_2O}\left(1 - \frac{1}{K_{CO_3}}\frac{P_{CO}P_{H_2}}{P_C P_{H_2O}}\right)\exp\left(\frac{-E_{CO_3}}{T}\right) \quad \log_{10}K_{CO_3} = \frac{\alpha}{T} + \beta \tag{82.10}$$

$$C + O_2 \rightarrow CO_2$$
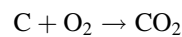
$$r_{CO_21} = A_{CO_21}P_C P_{O_2}\left(1 - \frac{1}{K_{CO_{21}}}\frac{P_{CO_2}}{P_C P_{O_2}}\right)\exp\left(\frac{-E_{CO_21}}{T}\right) \quad \log_{10}K_{CO_21} = \frac{\alpha}{T} + \beta \tag{82.11}$$

$$CO + H_2O \leftrightarrow CO_2 + H_2$$
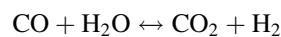
$$r_{CO_22} = A_{CO_22}P_{CO}P_{H_2O}\left(1 - \frac{1}{K_{CO_{22}}}\frac{P_{CO_2 P_{H_2}}}{P_{CO}P_{H_2O}}\right)\exp\left(\frac{-E_{CO_22}}{T}\right) \quad \log_{10}K_{CO_22} = \frac{\alpha}{T} + \beta \tag{82.12}$$

$$C + 2H_2 \rightarrow CH_4$$
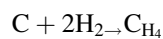
$$r_{CH_41} = A_{CH_41}P_C P_{H_2}2\left(1 - \frac{1}{K_{CH_{41}}}\frac{P_{CH_4}}{P_C (P_{H_2})^2}\right)\exp\left(\frac{-E_{CH_41}}{T}\right) \quad \log_{10}K_{CH_41} = \frac{\alpha}{T} + \beta \tag{82.13}$$

$$CO + 3H_2 \leftrightarrow CH_4 + H_2O$$
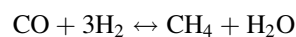
$$r_{CH_4\ (2)} = A_{CH4\ (2)}P_{CO}{P_{H_2}}^3\left(1 - \frac{1}{K_{CH_4}2}\frac{P_{CH_4}\ P_{H_2O}}{P_{CO}P_{H_2}\ 3}\right)\exp\left(\frac{-E_{CH_42}}{T}\right) \quad \log_{10}\ K_{CH_4}2 = \frac{\alpha}{T} + \beta \tag{82.14}$$

Reactions occurring in the boiler are drawn on the $\log K - 1/T$ diagram given in Fig. 82.2. As it can be seen, the reaction kinetics temperature is an influential parameter [11].

Analytical and Simulation Methods

Modeling different waste-coal mixtures with analytical methods and a simulation software
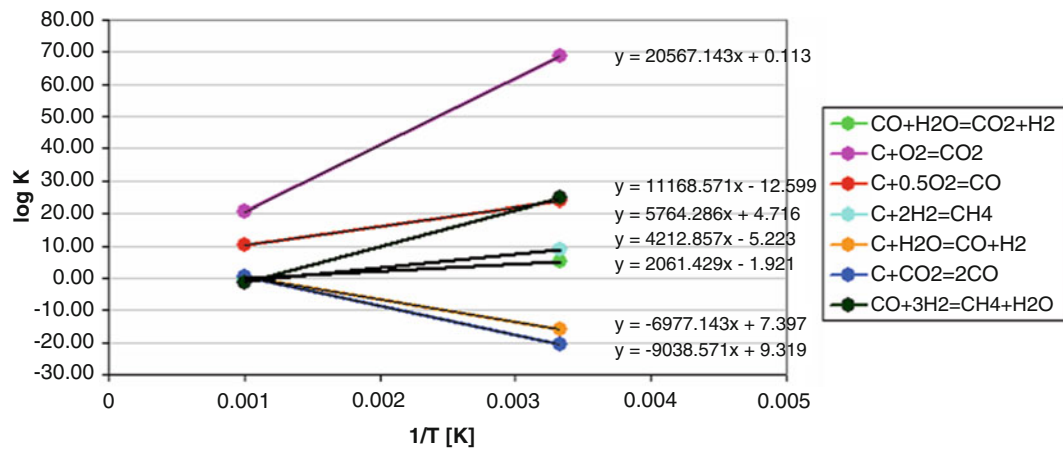
Fig. 82.2 Log K − 1/T graph

Analytical Modeling

Although several different reactions take place in the boiler, five main reactions have been observed:

$$C + H_2O = CO + H_2 \quad \text{(Endothermic gasification reactions are oxidation)} \tag{82.15}$$

$$C + CO_2 = 2CO \quad \text{(Endothermic Boudouard equivalence)} \tag{82.16}$$

$$C + 2H_2 = CH_4 \quad \text{(Exothermic formation of methane equivalent)} \tag{82.17}$$

$$CH_4 + H_2O = CO + 3H_2 \quad \text{(Endothermic decomposition of methane equivalent)} \tag{82.18}$$

$$CO + H_2O = CO_2 + H_2 \quad \text{(Exothermic conversion of gas-water balance)} \tag{82.19}$$
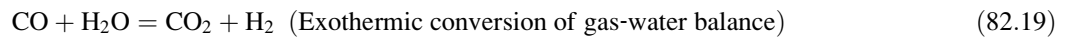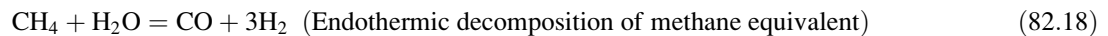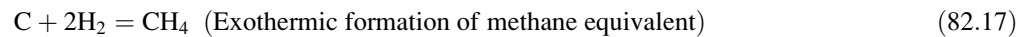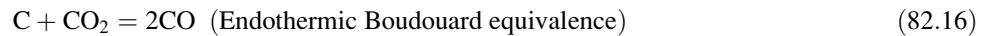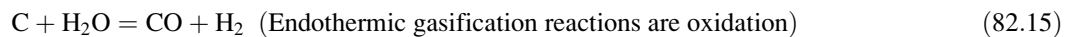
Mountouris et al. have expressed the above reactions as the following general equation [9]:

$$C_{(x)}H_{(y)}O_{(z)} + wH_2O + mO_2 + 3.76mN_2 = n_1H_2 + n_2CO + n_3CO_2 + n_4H_2O + n_5CH_4 + n_6N_2 + n_7C \tag{82.20}$$
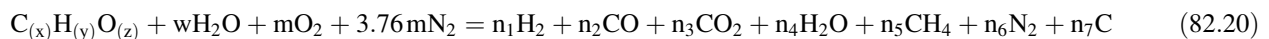
Using the above equations and assuming n_5 and n_7 values as zero, product content of gasified municipal waste, with known mass contents, and coal mixture is calculated analytically and the results are presented in Table 82.6.

Simulation Methods

Simulation of gasification process of municipal waste and imported coal mixture is carried out by means of a package software (educational version) and the contents of the produced syngas are calculated for each case (Table 82.2).

Similar to what was presented for municipal waste, the mass content of the imported coal used in the research is presented in Table 82.3.

In this study, mass content and calorific values of the syngas produced from different waste and coal mixtures are analyzed. Different combinations of coal and waste that were studied in this research are presented in Table 82.4. Calculations for each of these combinations are carried out analytically and via a simulation software. Obtained results from each of these methods are discussed and compared.

Municipal waste and coal are analyzed individually and also with waste to coal respective ratios of 25–75 %, 50–50–50 %, 75–25 %. Atomic composition for all of the combinations is given in Table 82.5.

Table 82.2 Content of municipal solid waste in Turkey (www.cevreorman.gov.tr, 2008)

Component	Percent of content	Component	Percent of content
Paper	50	C	47.9
Sawdust	3	H	6
Wood	11	N	1.2
Vegetable waste	3.7	Cl	0.1
Fabric	5.5	S	0.3
Plastic	10	O	32.9
Rubber	3.5	SiO_2	11.7
Resins	1	Lower heating value: 12,400 kJ/kg	
Electronic waste	3	Humidity: 30 %	
Construction waste	4.5		
Glass	4		
Other	0.8		

Table 82.3 Mass content of the imported coal [10]

Component	C	O	H	N	S	SiO_2	Al_2O_3	Fe_2O_3	CaO	MgO	Na_2O
% Content	61.70	13.20	4.10	1.20	0.39	11.17	4.42	1.97	1.18	0.37	0.30

Table 82.4 Models in the percentages of the waste and coal

Model 1	100 % waste	0 % coal
Model 2	75 % waste	25 % coal
Model 3	50 % waste	50 % coal
Model 4	25 % waste	75 % coal
Model 5	0 % waste	100 % coal

Table 82.5 Composition of the fuel used in the modeling

Component	Model 1 (100 % MSW)	Model 2 (75 % MSW–25 % coal)	Model 3 (50 % MSW–50 % coal)	Model 4 (25 % MSW–75 % coal)	Model 5 (100 % coal)
C	47.9	51.35	54.8	58.25	61.7
O	32,9	27.935	23.05	18.125	13.2
H	6	5.525	5.05	4.575	4.1
N	1.2	1.2	1.2	1.2	1.2
S	0.3	0.3225	0.345	0.3675	0.39
SiO_2	11.6	11.4925	11.385	11.2775	11.17
Al_2O_3	–	1.105	2.21	3.315	4.42
Fe_2O_3	–	0.4925	0.985	1.4775	1.97
CaO	–	0.295	0.59	0.885	1.18
MgO	–	0.0925	0.185	0.2775	0.37
Na_2O	–	0.075	0.15	0.225	0.3
Humidity	20	18,75	17	15,5	14
Heating value (kJ/kg)	12,400	15,058	17,715	20,373	23,030

Conclusion

In this study five simulations have been carried out for different mixtures of municipal waste, knowing its thermal capacity and mass content, and imported coal by means of a package software. The purpose of this simulation is to investigate the contents of the syngas produced by gasification of fuel feeds obtained from each of these various mixtures. It has been observed that the content of the syngas depends on the mass content of the fuel feed. If the humidity level is high enough during the gasification process it can be observed that the amount of produced hydrogen and carbon monoxide increases. As a result, enough humidity must be provided inside the fuel feed. Similarly in order to increase the amount of carbon dioxide and carbon monoxide in the contents of the syngas produced via gasification reaction, the amount oxygen being delivered to the system must be raised.

As it can be seen from Table 82.6 municipal waste, imported coal, and various combinations of these two fuels have been simulated both analytically and via a package software. The point to be considered here is that the amount of hydrogen calculated for model 1, which includes 100 % municipal waste, is considerably more than other cases in which only coal or different combinations of two fuels were used. The main reason for this is the excessive amount of humidity in the municipal waste.

Moreover, regarding Eq. (82.3) presented in the kinetic parameters section, if enough humidity is available in the setting, the rate of produced carbon monoxide will raise. As shown in Table 82.6 for model 1, which includes 100 % municipal waste, since it embodies more humidity than all other models, the rate of carbon monoxide produced during gasification is higher.

In addition, the amount of nitrogen calculated for municipal waste is far less than the cases where 100 % of coal and various combinations of two fuels were used as model. The reason for this can be explained as follows; Municipal waste contains a higher rate (32.9 % of mass content) of necessary O_2 for the production of CO and CO_2 during gasification and as a result less oxidizing air is required. While for the other models containing 100 % coal and different coal-waste mixtures, since they contain a low rate (respectively 13.2 and 23.05 % of mass content) of O_2, more oxidizing air is needed for CO and CO_2 to be formed during gasification. As a result air/waste combinations are assumed as, 0.416 mol air/mol waste for municipal waste (model 1), 1.207 mol air/mol coal for coal (model 5), 2.023 mol air/mol mixture for mixtures of municipal waste and coal. Considering that the highest rate of oxidizing air was used for gasification of coal and as a result of high nitrogen amount in the air, the syngas produced via gasification in this model will contain the highest amount of nitrogen.

In waste disposal facilities, the amount of produced heat and electric energy is an important factor but the main purpose of these facilities is to dispose hazardous wastes properly in accordance with rules and regulations. If we observe the subject from this point of view, compared to other incineration technologies, plasma technology is a cleaner and more environmental-friendly technology. Since in this method the gasification process takes place in high temperatures, formation of dioxins and furans, which is one of the major problems of incineration facilities, is avoided. Also stack effluents like heavy metals are accumulated at the bottom of the boiler as vitrified slime and can be collected safely and reused as packing material. Consequently compared to other incineration methods, disposal via plasma technology exposes less waste and plays a more environment-friendly role.

As a result of this study plasma gasification technology which is a brand new technology is simulated analytically and via computer software, amounts of obtained products are compared, and mathematical data are presented as a guidance for the industrialists who want to employ this technology in our country.

Table 82.6 Synthesis of gas released as a result of modeling compositions [11]

Synthesis gas components	100 % MSW (software)	100 % MSW (analytic)	Difference (%)	75 % MSW– 25 % coal (software)	75 % MSW– 25 % coal (analytic)	Difference (%)	50 % MSW– 50 % coal (software)	50 % MSW– 50 % coal (analytic)	Difference (%)	25 % MSW– 75 % coal (software)	25 % MSW– 75%komur (analytic)	Difference (%)	100 % coal (software)	100 % coal (analytic)	Difference (%)
Nitrogen	14.339	16.03	−10.5	27.042	27.78	−2.65	36.028	35.56	1.3	42.87	43.47	−1.38	48.585	49.101	−1.12
Hydrogen	43.078	42.178	2.07	32.626	33.32	−2.08	25.834	27.95	−7.57	20.27	21.3	−4.84	15.856	16.95	−6.45
Hydrogen dyanates	0.088	–	–	0.075	–	–	0.068	–	–	0.06	–	–	0.055	–	–
Hydrogen sulfide	0.086	–	–	0.08	–	–	0.076	–	–	0.073	–	–	0.07	–	–
Water	1.255	1.8	−30.27	2.36	0.44	81.35	1.89	1.02	46.03	2.515	0.71	71.77	2.577	0.95	63.13
Carbon monoxide	40.29	38.88	3.5	36.72	37.67	−2.52	35.023	35.18	−0.44	32.81	33.01	−0.6	31.224	30.68	1.74
Carbon dioxide	0.635	1.1	−42.27	0.89	0.77	13.48	0.906	0.27	70.2	1.24	1.52	−18.42	1.479	2.31	−35.97
Ammonia	0.22	–	–	0.19	–	–	0.169	–	–	0.151	–	–	0.137	–	–
Carbonyl sulfide	0.01	–	–	0.009	–	–	0.008	–	–	0.008	–	–	0.008	–	–

References

1. http://www.aso.org.tr/kurumsal/index.php,p.p.55 (2011)
2. Beck RW Inc. (2003) City of Honolulu review of plasma arc gasification and vitrification technology for waste disposal final report, p 4
3. Moustakas K et al (2005) J Hazard Mater B 123:120–126
4. R&R Scientific and Technical Services Ltd. Company (2007) Site and technology selection for solid waste incineration facilities (in Turkish)
5. Oost V, Hrabovsky M (2006) Pyrolysis of waste using a hybrid argon–water stabilized torch. Vacuum 80(11–12):1132–1137
6. Gomeza E, Amutha Rania D (2008) Thermal plasma technology for the treatment of wastes: a critical review. J Hazard Mater 161:614–626
7. The Northspan Group Inc. (2008) Does it make sense to move forward with a full feasibility analysis? Aitkin County Plasma Gasification Study, Duluth, p 3
8. Virtual Material Group Inc. (2010) VMGSIM ver 6.0 program tutorial, pp 1715–1736
9. Mountouris A, Voutsas E (2006) Solid waste plasma gasification: equilibrium model development and exergy analysis. Energy Convers Manag 47:1723–1737
10. Akçura F, ve Gerger M (1982) The main features of the Turkish coals. MTA Institute, Ankara (in Turkish)
11. Dereli C (2012) Solid waste disposal with plasma gasification technology. MSc Thesis, Gazi University, Ankara (in Turkish)

Prediction of Daily Average Global Solar Radiation and Parabolic Monthly Irradiation Model Parameters for Turkey

Zuhal Oktay, Can Coskun, and Mustafa Ertürk

Abstract

The amount of solar radiation falling on the surface of the earth is a very important data for engineers and scientists to model the solar energy systems and to design and carry out a performance analysis. Solar global radiation values can be estimated practically by employing parabolic monthly irradiation models (PMIMs). Following the establishing of the model parameters, average hourly global solar radiation values per month can be obtained for any given place. In this chapter, PMIM parameters are calculated for 34 cities in Turkey. Also, daily average global solar radiation values are determined by employing the measured data of 70 cities in Turkey and given in a parabolic function. The predictions are compared with the solar data available in literature for Turkey. According to annual average global solar radiation values, Turkey is divided into four regions, and a new comparison factor is introduced and called the global radiation comparison rate. This model can be applied to any specific location, where meteorological data are measured in the world. Thus, the calculation time will be reduced. It is expected that this study will be useful for designers and scientists working on solar energy systems.

Introduction

Long-term solar radiation values on an hourly and monthly basis are required in many applications of solar energy designs, such as PV/PV-T, solar heating-cooling systems, and passive solar design. The amount of the solar radiation falling on the surface of earth is primarily an important data for engineers and scientists involved in the design of solar energy systems. Different solar energy models exist for predicting the solar radiation [1]. Solar radiation models range from simple empirical relations to complex models [2–4]. Many studies have been carried out in different locations of Turkey to predict global diffuse and direct solar radiation [5–10].

In this chapter, daily average global solar radiation values are determined for 70 cities in Turkey by employing the measured data in meteorological stations first. Then the average solar radiation value is found and in accordance with this value the country is divided into four parts. A new parameter, the global radiation comparison ratio (GRCR), is defined according to the country average global solar radiation. The first and second regions have the highest solar radiation. Thus, suitable places for solar energy systems are determined and then daily global solar radiation distribution is presented.

Z. Oktay (✉) • C. Coskun
Faculty of Engineering, Energy System Engineering Department, Recep Tayyip Erdogan University, Rize, Turkey
e-mail: zuhal.oktay@gmail.com; dr.can.coskun@gmail.com

M. Ertürk
Faculty of Engineering, Mechanical Engineering Department, Balikesir University, Balikesir, Turkey
e-mail: mustafaerturk65@gmail.com

Table 83.1 Global solar radiation data recorded years for each city

Data recorded years	Cities
1975–2007 (33 years)	Samsun, Eskisehir, Rize, Van, Urfa, Hakkari, Aksaray, Diyarbakir, Malatya, Erzurum, Elazig, Kayseri, Kars, Siirt, Adana, Erzincan, Gaziantep, Adiyaman, Igdir
1975–2006 (32 years)	Balikesir, Bursa, Kastamonu, Kocaeli, Isparta, Ankara, Mugla, Cankiri, Aydin, Konya, Kirsehir, Sivas, Canakkale
1975–2005 (31 years)	Trabzon
1975–2003 (29 years)	Edirne
1977–2006 (27 years)	Antalya
1980–2006 (27 years)	Istanbul
1982–2006 (25 years)	Izmir
1984–2007 (24 years)	Karaman, Mersin, Nigde, Kilis, Ordu, Gümüshane, Tokat, Bitlis, Amasya, Antakya, Artvin, K. Maras
1984–2006 (23 years)	Afyon, Denizli, Tekirdag, Bartin, Sinop, Duzce, Corum, Bilecik, Yalova, Zonguldak, Sakarya
1985–2007 (23 years)	Batman, Mus
1986–2007 (22 years)	Bingol, Agri, Yozgat
1985–2006 (22 years)	Kutahya, Kirikkale
1975–1996 (22 years)	Usak
1987–2007 (21 years)	Tunceli
1996–2006 (11 years)	Burdur

Global Solar Radiation Data and Their Comparison with Studies in Literature

The data of global solar radiation values are taken from Turkish meteorological data stations for 70 cities in Turkey. Data recording dates are given in Table 83.1 for each city. Monthly, daily, and hourly average global solar radiation values are calculated by employing actual data. Monthly and daily average solar radiation values are compared with the data available in the literature for Turkey.

Bulut et al. [11] have proposed a new model for the determination of Turkey's daily global solar radiation. Main function is the equation given below,

$$I = I_2 + (I_1 - I_2)\left|Sin\left[\frac{\pi}{365}(d+5)\right]\right|^{1.5} \tag{83.1}$$

where d is the number of the day starting from January 1. For January 1st, $d = 1$, and for December 31st $d = 365$. By employing Eq. (83.1), the daily and annual total global solar radiation of each city can be calculated. Then these values are compared to verify our global solar radiation data. Our values are very similar for 58 cities but slightly different for 12 cities. The difference reaches as high as 10 % for Gumushane, Amasya, Yalova, Istanbul, Zonguldak, Balikesir, Tekirdag, Bartin, Sinop, Kastamonu, Kocaeli, and Edirne.

Sen et al. [12] have proposed a new model for the estimation of monthly based hourly solar radiation and tested it at a site in the northwestern part of Turkey. Our monthly and hourly based solar radiation data are compared with that study, and similar values have been achieved. Also, it is seen that our average solar data are in compliance with many studies in literature [13–16].

Estimation of Daily Average Global Solar Radiation

The daily average global radiation amount is calculated for 70 cities by employing solar data. Then daily average global radiation values are adopted as fourth order parable by employing Matlab programming. The daily average global solar radiation on a horizontal surface (I_D) in kW/m^2 can be estimated using the following equation;

$$I_D = k + l \cdot d + m \cdot d^2 + n \cdot d^3 + t \cdot d^4 \tag{83.2}$$

where d is the number of the day starting from January 1. For the January 1st, $d = 1$, and for December 31st, $d = 365$. In Eq. (83.2), k, l, m, n, and t are the model parameters. Annual and daily average global solar radiation amounts are given in Table 83.2. In this study, Turkey is classified into four groups in accordance with the annual average global solar radiation.

Table 83.2 Daily and annually average global solar radiation

Cities	Longitude (°E)	Latitude (°N)	GRCR (–)	Annually average global solar radiation (kW/m²)	Daily average global solar radiation (kW/m²) $I_D = k + l \cdot d + m \cdot d^2 + n \cdot d^3 + t \cdot d^4$				
					k	l	m	n	t
Nigde	34.40	37.59	1.30	0.532	0.231	3.56×10^{-4}	6.63×10^{-5}	-3.79×10^{-7}	5.34×10^{-10}
Van	43.41	38.28	1.22	0.496	0.214	8.60×10^{-4}	5.56×10^{-5}	-3.32×10^{-7}	4.75×10^{-10}
Antalya	30.42	36.53	1.16	0.473	0.201	6.57×10^{-4}	5.64×10^{-5}	-3.32×10^{-7}	4.73×10^{-10}
Karaman	33.14	37.11	1.16	0.473	0.188	7.30×10^{-4}	5.80×10^{-5}	-3.41×10^{-7}	4.84×10^{-10}
Mersin	34.36	36.49	1.16	0.472	0.202	1.30×10^{-3}	4.61×10^{-5}	-2.86×10^{-7}	4.11×10^{-10}
Burdur	30.17	37.43	1.15	0.468	0.173	4.43×10^{-4}	6.20×10^{-5}	-3.55×10^{-7}	4.98×10^{-10}
Diyarbakir	40.12	37.55	1.14	0.466	0.171	1.83×10^{-4}	6.67×10^{-5}	-3.76×10^{-7}	5.26×10^{-10}
Kilis	37.05	36.44	1.13	0.461	0.185	5.52×10^{-4}	5.74×10^{-5}	-3.32×10^{-7}	4.67×10^{-10}
Tunceli	39.32	39.06	1.11	0.452	0.179	-7.88×10^{-4}	7.65×10^{-5}	-4.12×10^{-7}	5.71×10^{-10}
Izmir	27.10	38.24	1.09	0.447	0.180	-1.31×10^{-4}	6.67×10^{-5}	-3.73×10^{-7}	5.24×10^{-10}
Aydin	27.50	37.51	1.08	0.442	0.175	-1.02×10^{-4}	6.49×10^{-5}	-3.62×10^{-7}	5.07×10^{-10}
K. Maras	36.56	37.36	1.08	0.440	0.148	-2.39×10^{-4}	7.27×10^{-5}	-4.02×10^{-7}	5.61×10^{-10}
Konya	32.30	37.52	1.08	0.439	0.177	6.39×10^{-4}	5.32×10^{-5}	-3.11×10^{-7}	4.40×10^{-10}
Kirsehir	34.10	39.08	1.07	0.438	0.183	5.53×10^{-4}	5.38×10^{-5}	-3.14×10^{-7}	4.45×10^{-10}
Afyon	30.32	38.45	1.07	0.437	0.159	7.39×10^{-4}	5.57×10^{-5}	-3.28×10^{-7}	4.65×10^{-10}
Urfa	38.46	37.08	1.07	0.436	0.166	9.71×10^{-5}	6.25×10^{-5}	-3.52×10^{-7}	4.93×10^{-10}
Hakkari	43.46	37.34	1.07	0.436	0.214	6.07×10^{-4}	4.69×10^{-5}	-2.79×10^{-7}	4.00×10^{-10}
Aksaray	34.03	38.23	1.06	0.435	0.184	7.66×10^{-4}	4.86×10^{-5}	-2.88×10^{-7}	4.09×10^{-10}
Bingol	40.30	38.52	1.06	0.434	0.177	-8.91×10^{-4}	7.68×10^{-5}	-4.16×10^{-7}	5.82×10^{-10}
Malatya	38.18	38.21	1.06	0.434	0.153	-1.63×10^{-4}	6.87×10^{-5}	-3.80×10^{-7}	5.29×10^{-10}
Erzurum	41.16	39.55	1.04	0.426	0.192	1.00×10^{-3}	4.25×10^{-5}	-2.61×10^{-7}	3.75×10^{-10}
Gumushane	39.27	40.27	1.04	0.426	0.128	1.18×10^{-3}	5.62×10^{-5}	-3.42×10^{-7}	4.91×10^{-10}
Siirt	41.56	37.56	1.04	0.425	0.169	1.57×10^{-4}	5.93×10^{-5}	-3.37×10^{-7}	4.75×10^{-10}
Mus	41.31	38.44	1.01	0.412	0.149	2.27×10^{-4}	5.89×10^{-5}	-3.34×10^{-7}	4.68×10^{-10}
Elazıg	39.13	38.40	1.00	0.409	0.141	-4.02×10^{-5}	6.38×10^{-5}	-3.55×10^{-7}	4.95×10^{-10}
Kayseri	35.29	38.43	1.00	0.407	0.159	-1.03×10^{-4}	5.96×10^{-5}	-3.31×10^{-7}	4.61×10^{-10}
Kars	43.05	40.36	0.99	0.406	0.198	4.25×10^{-4}	4.73×10^{-5}	-2.79×10^{-7}	4.01×10^{-10}
Bitlis	42.06	38.22	0.99	0.404	0.161	-1.82×10^{-4}	6.28×10^{-5}	-3.50×10^{-7}	4.91×10^{-10}
Adana	35.18	36.59	0.99	0.404	0.175	6.16×10^{-4}	4.67×10^{-5}	-2.76×10^{-7}	3.93×10^{-10}
Cankırı	33.37	40.36	0.99	0.404	0.134	5.50×10^{-4}	5.60×10^{-5}	-3.24×10^{-7}	4.56×10^{-10}
Kirikkale	33.30	39.50	0.98	0.402	0.138	1.36×10^{-4}	6.10×10^{-5}	-3.45×10^{-7}	4.84×10^{-10}
Kutahya	29.58	39.24	0.98	0.401	0.127	2.60×10^{-4}	6.35×10^{-5}	-3.65×10^{-7}	5.18×10^{-10}
Tokat	36.54	40.18	0.98	0.401	0.148	1.08×10^{-4}	5.94×10^{-5}	-3.36×10^{-7}	4.73×10^{-10}
Ankara	32.53	39.57	0.98	0.400	0.124	2.90×10^{-4}	5.99×10^{-5}	-3.39×10^{-7}	4.73×10^{-10}
Mugla	28.21	37.12	0.97	0.398	0.152	6.04×10^{-4}	4.89×10^{-5}	-2.86×10^{-7}	4.04×10^{-10}
Yozgat	34.49	39.50	0.97	0.397	0.145	3.60×10^{-4}	5.51×10^{-5}	-3.17×10^{-7}	4.47×10^{-10}
Gaziantep	37.22	37.05	0.97	0.397	0.133	-1.10×10^{-5}	6.04×10^{-5}	-3.36×10^{-7}	4.67×10^{-10}
Corum	34.58	40.33	0.97	0.397	0.134	4.10×10^{-4}	5.72×10^{-5}	-3.30×10^{-7}	4.66×10^{-10}
Erzincan	39.30	39.44	0.96	0.395	0.153	6.82×10^{-4}	4.84×10^{-5}	-2.87×10^{-7}	4.09×10^{-10}
Canakkale	26.24	40.08	0.95	0.387	0.122	1.90×10^{-4}	6.11×10^{-5}	-3.49×10^{-7}	4.94×10^{-10}
Usak	29.29	38.40	0.95	0.386	0.164	-2.34×10^{-4}	5.56×10^{-5}	-3.06×10^{-7}	4.26×10^{-10}
Agri	43.08	39.31	0.94	0.385	0.146	5.52×10^{-5}	5.69×10^{-5}	-3.22×10^{-7}	4.54×10^{-10}
Amasya	35.51	40.39	0.94	0.383	0.124	-2.94×10^{-4}	6.84×10^{-5}	-3.82×10^{-7}	5.39×10^{-10}
Bilecik	29.58	40.09	0.93	0.379	0.134	-3.28×10^{-4}	6.40×10^{-5}	-3.55×10^{-7}	4.99×10^{-10}
Isparta	30.33	37.45	0.92	0.375	0.152	8.44×10^{-4}	3.96×10^{-5}	-2.37×10^{-7}	3.35×10^{-10}
Adiyaman	38.17	37.45	0.91	0.373	0.130	6.97×10^{-4}	4.66×10^{-5}	-2.75×10^{-7}	3.89×10^{-10}
Igdir	44.02	39.56	0.91	0.371	0.142	6.23×10^{-4}	4.69×10^{-5}	-2.79×10^{-7}	3.99×10^{-10}
Yalova	29.16	40.39	0.91	0.370	0.098	-8.66×10^{-4}	8.04×10^{-5}	-4.39×10^{-7}	6.17×10^{-10}
Sivas	37.01	39.49	0.90	0.369	0.106	3.59×10^{-4}	5.41×10^{-5}	-3.06×10^{-7}	4.24×10^{-10}
Istanbul	29.05	40.58	0.89	0.367	0.102	-4.36×10^{-4}	7.17×10^{-5}	-3.98×10^{-7}	5.62×10^{-10}
Antakya	36.07	36.15	0.89	0.366	0.113	5.27×10^{-4}	5.15×10^{-5}	-2.99×10^{-7}	4.22×10^{-10}

(continued)

Table 83.2 (continued)

Cities	Longitude (°E)	Latitude (°N)	GRCR (–)	Annually average global solar radiation (kW/m²)	Daily average global solar radiation (kW/m²) $I_D = k + l \cdot d + m \cdot d^2 + n \cdot d^3 + t \cdot d^4$				
					k	l	m	n	t
Artvin	41.49	41.10	0.89	0.366	0.136	5.40×10^{-4}	5.09×10^{-5}	-3.03×10^{-7}	4.37×10^{-10}
Zonguldak	31.48	41.27	0.89	0.362	0.119	-1.80×10^{-3}	8.78×10^{-5}	-4.62×10^{-7}	6.43×10^{-10}
Batman	41.10	37.52	0.88	0.357	0.121	6.29×10^{-4}	4.65×10^{-5}	-2.73×10^{-7}	3.86×10^{-10}
Sakarya	30.24	40.46	0.87	0.356	0.126	-1.19×10^{-3}	7.45×10^{-5}	-3.98×10^{-7}	5.56×10^{-10}
Balikesir	27.52	39.39	0.87	0.354	0.105	-6.99×10^{-4}	6.93×10^{-5}	-3.75×10^{-7}	5.22×10^{-10}
Samsun	36.20	41.17	0.86	0.353	0.095	-2.10×10^{-4}	6.40×10^{-5}	-3.57×10^{-7}	5.02×10^{-10}
Denizli	29.05	37.47	0.86	0.352	0.112	3.05×10^{-4}	5.28×10^{-5}	-3.04×10^{-7}	4.30×10^{-10}
Tekirdag	27.29	40.59	0.86	0.351	0.083	2.41×10^{-4}	6.02×10^{-5}	-3.44×10^{-7}	4.86×10^{-10}
Bursa	29.04	40.11	0.86	0.350	0.117	-3.55×10^{-4}	6.08×10^{-5}	-3.36×10^{-7}	4.71×10^{-10}
Bartin	32.21	41.38	0.86	0.349	0.087	-4.11×10^{-5}	6.28×10^{-5}	-3.53×10^{-7}	4.96×10^{-10}
Eskisehir	30.32	39.46	0.85	0.347	0.090	6.63×10^{-4}	4.85×10^{-5}	-2.81×10^{-7}	3.92×10^{-10}
Sinop	35.10	42.02	0.84	0.344	0.087	-9.13×10^{-5}	6.42×10^{-5}	-3.62×10^{-7}	5.12×10^{-10}
Duzce			0.80	0.326	0.088	-8.77×10^{-5}	5.81×10^{-5}	-3.25×10^{-7}	4.56×10^{-10}
Kastamonu	33.46	41.22	0.80	0.326	0.098	8.34×10^{-4}	4.26×10^{-5}	-2.57×10^{-7}	3.67×10^{-10}
Ordu	37.52	40.59	0.79	0.324	0.093	5.49×10^{-4}	4.86×10^{-5}	-2.88×10^{-7}	4.13×10^{-10}
Kocaeli	29.54	40.46	0.75	0.305	0.096	-2.49×10^{-4}	5.59×10^{-5}	-3.10×10^{-7}	4.35×10^{-10}
Trabzon	39.43	41.00	0.75	0.304	0.108	9.82×10^{-4}	3.47×10^{-5}	-2.20×10^{-7}	3.22×10^{-10}
Rize	40.30	41.02	0.70	0.287	0.094	1.72×10^{-3}	2.42×10^{-5}	-1.77×10^{-7}	2.68×10^{-10}
Edirne	26.34	41.40	0.70	0.286	0.076	9.28×10^{-6}	5.12×10^{-5}	-2.91×10^{-7}	4.12×10^{-10}

Fig. 83.1 First region in Turkey

First region: Annual average global solar radiation exceeds 0.45 kW/m². There are nine cities in the first region, namely Nigde, Van, Antalya, Karaman, Mersin, Burdur, Diyarbakir, Kilis, Tunceli (see Fig. 83.1).

Second region: Annual average global solar radiation ranges between 0.40 and 0.45 kW/m². There are 25 cities in the second region, namely Izmir, Aydin, K. Maras, Konya, Kirsehir, Afyon, Urfa, Hakkari, Aksaray, Bingol, Malatya, Erzurum, Siirt, Gumushane, Mus, Elazıg, Kayseri, Kars, Bitlis, Adana, Cankırı, Kirikkale, Kutahya, Tokat, Ankara (see Fig. 83.2).

Third region: Annual average global solar radiation ranges between 0.35 and 0.40 kW/m². There are 26 cities in the third region, namely Mugla Yozgat, Gaziantep, Corum, Erzincan, Canakkale, Usak, Agri, Amasya, Bilecik, Isparta, Adiyaman, Igdir, Yalova, Sivas, Istanbul, Antakya, Artvin, Zonguldak, Batman, Sakarya, Balikesir, Samsun, Denizli, Tekirdag, Bursa (see Fig. 83.3).
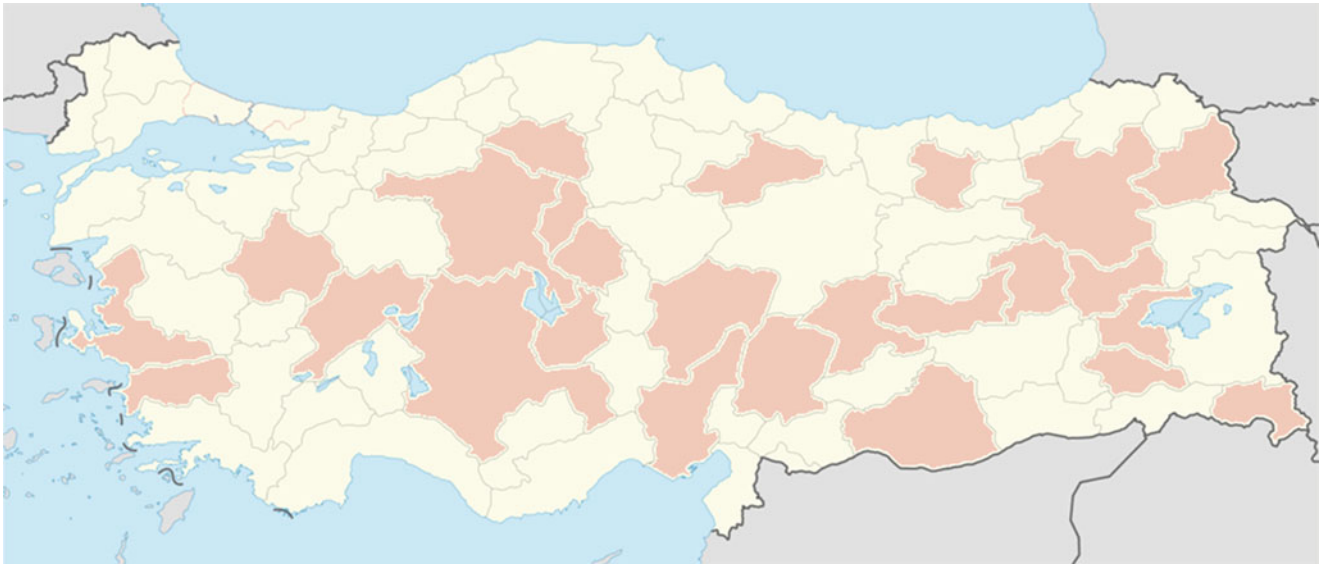
Fig. 83.2 Second region in Turkey
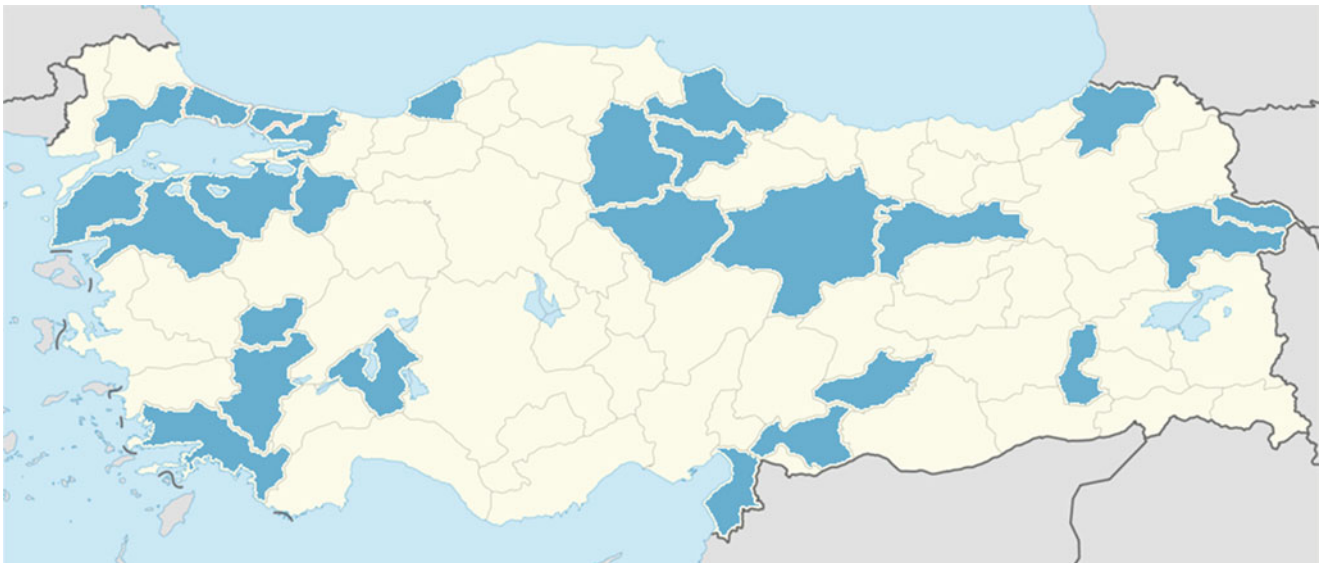
Fig. 83.3 Third region in Turkey

Fourth region: Annual average global solar radiation is lower than 0.35 kW/m^2. There are ten cities in the fourth region, namely Bartin, Eskisehir, Sinop, Duzce, Kastamonu, Ordu, Kocaeli, Trabzon, Rize, Edirne (see Fig. 83.4).

Global Radiation Comparison Ratio

Country's annual average global solar radiation is taken as a reference point for that parameter. GRCR represents the annual average solar radiation status of the city. If the GRCR is higher than 1, the city receives more annual solar radiation than the country. Each city can be compared easily by employing GRCR value. GRCR value can be found as follows (using the equations below):

$$GRCR = \frac{Annual\ average\ global\ solar\ radiation\ of\ the\ city}{Anual\ average\ global\ solar\ radiation\ of\ the\ country} = \frac{I_{Ave,City}}{I_{Ave,Country}} \qquad (83.3)$$

Fig. 83.4 Fourth region in Turkey

Annual average global solar radiation amount of any city (kW/m^2) in Turkey is given in Table 83.1. The annual average global solar radiation of the country can be found employing the equations below:

$$I_{Ave,County} = \sum_{i=1}^{i=n} \frac{I_{cty_1} \cdot area_1 + I_{cty_2} \cdot area_2 + \ldots + I_{cty_n} \cdot area_n}{area_1 + area_2 + \ldots + area_n} \tag{83.4}$$

where I_{cty} indicates annual average solar radiation of each city. "Area" represents the surface area of the city. When 70 countries are considered, annual average global solar radiation of Turkey is found as 0.408 kW/m^2. Global radiation of each city in Turkey is given in Table 83.1.

Parabolic Monthly Irradiation Model

Sen and Tan [12] noticed that after an evaluation carried out on a monthly basis, hourly solar radiation values fluctuated around a given trend. They adopted daily general trend as the second order parabola and provided a parabolic monthly irradiation model (PMIM) to evaluate the monthly based average hourly global solar radiation values of any place. Model is given in equation below:

$$I = a \cdot t^2 + b \cdot t + c \tag{83.5}$$

where I represents either monthly average hourly global or diffuse radiation amounts, and t indicates time in hours within one day. In Eq. (83.1), a, b, and c are the model parameters. In this chapter, daily general trend is adopted as the third order parabola to get more precise values.

The third order parabola is found to give better results for the model parameters and parabolic function. Our main parabolic equation is given in the equation below

$$I = a + b \cdot t + c \cdot t^2 + d \cdot t^3 \tag{83.6}$$

In Eq. (83.2), a, b, c, and d indicate the model parameters. Four model parameters and parabolic function are calculated for each month in a year. The distribution of global solar radiation for Antalya is shown in Fig. 83.5 as an example.
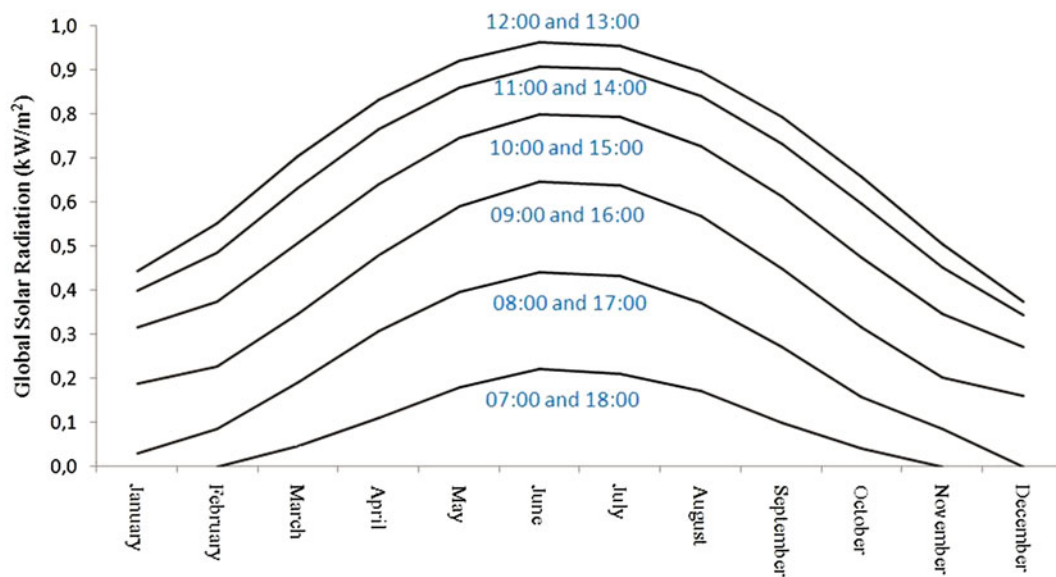
Fig. 83.5 Global solar radiation for Antalya

Conclusion

In many applications, such as in solar energy technologies, an accurate solar database is required to estimate the real trend of solar radiation in the region. In this regard, long-term hourly, daily, monthly average global solar radiations are utilized to find the accurate model parameters. In this chapter, PMIM parameters are calculated for 34 cities in Turkey. Also, daily average global solar radiation values are determined for 70 cities in Turkey by employing the data measured. According to annual average global solar radiation values, Turkey is divided into four regions and a new comparison factor is introduced and called the global radiation comparison rate.

Nomenclature

T   Hour in a day   ID   Daily average hourly global radiation (kW/m^2)

References

1. Sen Z (2008) Solar energy fundamentals and modeling techniques. Springer-Verlag, London
2. Oturanc G, Hepbasli A, Genc A (2003) Statistical analysis of solar radiation data. Energy Sources 25(11):1089–1097
3. Ulgen K, Hepbasli A (2004) Solar radiation models. Part 1: a review. Energy Sources 26(5):507–520
4. Ulgen K (2006) Optimum tilt angle for solar collectors. Energy Sources A Recov Utiliz Environ Effects 28(13):1171–1180
5. Akyuz E, Coskun C, Oktay Z, Dincer I (2012) A novel approach for estimation of photovoltaic exergy efficiency. Energy 44:1059–1066
6. Coskun C, Oktay Z, Dincer I (2011) Estimation of monthly solar radiation intensity distribution for solar energy system analysis. Energy 36(2):1319–1323
7. Yilmaz E (2010) Zonal comparison in measured and predicted global solar radiation in Turkey and Chile. Energy Sources A Recov Utiliz Environ Effects 32 (15):1454–1459
8. Bezir NC, Akkurt I, Ozek N (2010) Estimation of horizontal solar radiation in Isparta (Turkey). Energy Sources A Recov Utiliz Environ Effects 32(6):512–517
9. Oğulata RT, Oğulata SN (2002) Solar energy potential in Turkey. Energy Sources 24(12):1055–1064
10. Ulgen K, Hepbasli A (2002) Prediction of solar radiation parameters through clearness index for Izmir, Turkey. Energy Sources 24(8):773–785
11. Bulut H, Buyukalaca O (2007) Simple model for the generation of daily global solar-radiation data in Turkey. Appl Energy 84:477–491
12. Sen Z, Tan E (2001) Simple models of solar radiation data for northwestern part of Turkey. Energy Convers Manag 42:587–598
13. Kaygusuz K, Ayhan T (1999) Analysis of solar radiation data for Trabzon, Turkey. Energy Convers Manage 40(5):545–56
14. Kaygusuz K (1999) The comparison of measured and calculated solar radiations in Trabzon, Turkey. Energy Sources 21(4):347–53
15. Togrul IT, Onat E (2002) Global solar-radiation over Turkey: comparison of predicted and measured data. Renew Energy 25(1):55–67
16. Ulgen K, Hepbaslı A (2002) Comparison of solar-radiation correlations for Izmir Turkey. Int J Energy Res 26(5):413–30

Comparison of Energy Performance and Static Loads on a Building Integrated Wind, Solar, and Rainwater Harvester

84

Ali Gurbuz, Ugur Akbulut, and Mert Ozsaban

Abstract

In recent years, sustainable energy and green buildings are developed as important issues. Many helpful systems were developed to profit from advantages of different renewable energy sources. However, the research on disadvantages of sustainable energy systems is very rare and papers focus on only economic issues. In this paper, an innovative building integrated wind, solar, and rainwater harvester (WSRH) system was analyzed by nonlinear static pushover (NSP) analysis. The results are compared in terms of energy performance and its effects on the structural system.

Keywords

Innovative buildings • Hybrid system • Nonlinear static analysis

Introduction

The primary energy supply is not limitless and the energy cost is increasing day by day, which determined the reduction of the energy requirements in the residential buildings [1]. For that reason, alternative energy resources such as wind energy and solar energy have extensively invested interest by the researchers. The common drawbacks to wind and solar energy options are their unforeseeable nature and they rely on the climate changes [2]. Both wind and solar energy sources have strong relations with the environment and climate conditions. And to get a stable power output it is necessary to construct a hybrid power system [3]. But, the problems can be partially overcome by integrating two or more resources in a proper combination to form a hybrid system. For certain locations, the hybrid solar–wind power generation systems with storage banks offer a highly reliable source of power, which is suitable for electrical loads that need higher reliability.

Mostly, electricity is produced in rural power plants and transferred to urban areas. However, in developing countries, grid extension is impractical because of dispersed population, rugged terrain, or some more other reason. Thus, on-site renewable energy systems have an important role in narrowing the electricity gap in rural areas [4]. The concept of on-site renewable energy generation is to extract energy from renewable sources close to the populated area where the energy is required. The proposed wind–solar hybrid renewable energy system in this paper is a new, feasible, and compact design which can be built on the top of high-rise buildings.

On the other hand, the researches on these kinds of systems mostly focus on only energy economic issues and skip disadvantages. In this paper, an innovative building integrated wind, solar hybrid system, and rainwater harvester (WSRH) was analyzed by NSP analysis. The results are compared in terms of energy performance and its effects on the structural system.

A. Gurbuz (✉)
Faculty of Engineering, Civil Engineering Department, Recep Tayyip Erdogan University, Rize, Turkey
e-mail: ali.gurbuz@erdogan.edu.tr

U. Akbulut • M. Ozsaban
Faculty of Engineering, Mechanical Engineering Department, Recep Tayyip Erdogan University, Rize, Turkey
e-mail: ugur.akbulut@erdogan.edu.tr; mert.ozsaban@erdogan.edu.tr

As for static analyses, it is possible to use linear or nonlinear methods to determine the seismic behavior of structures. However, linear analysis uses the methods of the elastic solution; inelastic behavior includes   solution by specific coefficients. But linear analyses results are lower realistic than nonlinear analyses. It is needed to include inelastic behavior of structural elements for more realistic results. Nonlinear time history (TH) analysis where earthquake loads are applied to the building directly represents the most actual behavior of the structure. Nevertheless, TH analyses need long time period [5]. Earthquake data should be selected carefully. Past studies show that nonlinear pushover (NSP) analysis is a suitable alternative to TH analyses [6, 7]. Studies of [8] provided static pushover analyses occurrence and improvement. In addition [9–12], procedures were introduced.

Residential building's annual power consumption is approximately 37 kWh/m^2 [13] and apartment buildings are the most common residential buildings in Rize. In this study, 165 m^2 four flats and 17 stories 50 m building were analyzed. This building has 415.140 MWh annual power consumption. NSP analysis was also applied to a reinforced concrete residential building with 17 floors. Later, weight of the WSRH system was added on to the roof and analysis was repeated. Energy studies are calculated by four different forms.

Different forms are:
– Existing building integrated solar panels,
– Existing building integrated wind turbine,
– Existing building integrated rainwater harvester (RWH) system,
– Existing building with solar, wind, and rainwater harvester hybrid system.

Additionally, water storage tank of rainwater collector was placed on the roof to analyze with negative situation. Results were discussed in terms of base reactions, lateral displacements, and energy performances.

Solar, Wind, and Rainwater Harvester Systems

Solar Energy System

Based on the solar radiation data of Rize [14], the solar energy generation is estimated using Eq. (84.1).

$$E_S = G_S A_S \eta_{PS} K \qquad (84.1)$$

where G_S is the annual mean daily global irradiation, A_S is the module conversion efficiency, and K is the solar power loss. Table 84.1 lists the value for each coefficient in Eq. (84.1). Thus, the estimated daily solar energy generated is 145 kWh/day and 52.925 MWh/year.

Wind Energy System

In this study, hub height of the VAWT is assumed as 50 m. The average wind speed data of Rize for 50 m is used to calculate the wind power extraction of the VAWT. The free-stream wind speed is 4 m/s at [14].

P_W can be calculated using Eq. (84.2),

$$P_W = 0.5 C_P \eta_{TR} \eta_G \eta_{PAGV} \rho A_{WT} V^3 \qquad (84.2)$$

Table 84.1 Estimated solar energy generated in Rize

Annual mean daily global irradiation, G_s (kWh m^{-2}/day)	3.36
Solar panel area above the PAGV (m^2)	520
Estimated solar cell active area, A_s (m^2)	450
Efficiency of solar panel, η_{PS}	0.12
Estimated power loss (electric transmission), K	0.8
Estimated solar energy generated, E_{solar} (kWh/day)	145

Table 84.2 Estimated parameters (efficiency, losses, etc.) of various components in wind energy system

Generator efficiency, η_G	0.7
Efficiency due to bearing and transmission loss, η_{TR}	0.9
Efficiency due to PAGV loss, η_{PAGV}	0.8
Air density, ρ (kg/m^3)	1.225
Frontal swept surface area, A_{WT} ($= 12 \times 24$ m^2)	288
Power coefficient, C_P	0.05

Table 84.3 Summary of estimated annual energy savings

Estimated energy source	Energy generated/saved
Wind energy generated	284.5 kWh/day
Solar energy generated	145 kWh/day
Total estimated annual energy generated or saved	157 MWh/year

where C_P is the power coefficient, η_{TR} is the efficiency due to bearing and transmission loss, η_G is the generator efficiency, η_{PAGV} is the efficiency due to power-augmentation-guide-vane (PAGV) loss, ρ is the air density, A_{WT} is the swept surface area of wind turbine, and V is the wind speed [15].

With the estimated efficiency of sub-systems or components, the wind energy generation could be estimated as shown in Table 84.2. For a system with 24 m diameter and 12 m high VAWT installed on top of a building of 50 m height, the wind energy generated is approximately 103.842 MWh/year or 284.5 kWh/day (Table 84.3).

RWH System

The amount of rainwater collected (V_R) is estimated by using the Rational Equation as in Eq. (84.3)

$$V_R = A_R I C_R \tag{84.3}$$

where assumed rain catchment area (A_R) and runoff coefficient (C_R) is 720 and 0.75 m^2, respectively. Rainfall intensity (I) is 2245 mm/month.

Nonlinear Static Procedure

Seismic analyses of structures may perform by linear or nonlinear methods. Linear analysis is based on the first order linear elastic theory and inelastic behavior includes to the solution by specific coefficients. Elastic analyses results are lower realistic than inelastic analyses. It is need to include inelastic behavior of the structural elements for more realistic results.

Nonlinear Static Pushover Analysis

NSP analysis is a credible way to analyze seismic behavior of structural elements of buildings [8]. In addition [9–12], procedures were introduced NSP analyses.

Capacity curves of the structure were obtained at the end of the analysis. FEMA 356 values have been used for cracking stiffness of the structural system elements. Building materials were asummed as linear elastic. Plastic deformations were occured on the plastic hinges. On the other hand, plastic deformations are formed by bending moment in beams, and bending moment and axial forces in columns have been adopted. ATC 40 [9] values were used for plastic rotations and plastic hinge values.
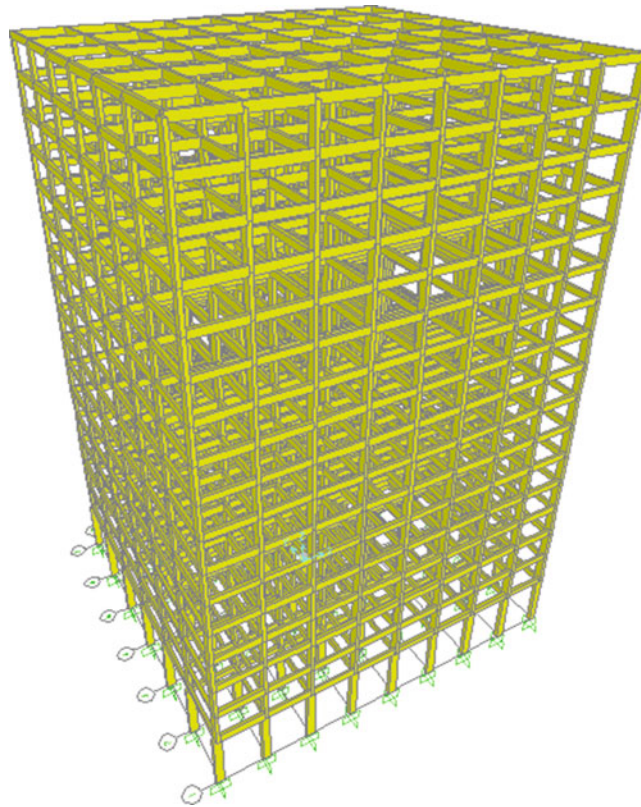
Fig. 84.1 3D view of the building for analyses

Modeling Issues

In this study, NSP analysis was performed on four different forms of 17-story RC building integrated WSRH using Sap2000 structural analyses software. Results were discussed in terms of base reactions, lateral displacements, and top displacement rates.

Nonlinear static analyses were performed by using Sap2000 nonlinear analysis program. Columns of building are defined as reinforced concrete elements which work for axial load and moment. As for beams, they are defined as reinforced concrete element which works for moment. C20 Concrete and S420 still classes were used according to Turkish Standard (TS500). Sap model of the building is shown in Fig. 84.1

Case Study

Our sample building was discussed using four different forms. These are:

Existing Building

Seventeen-storey reinforced concrete building which was designed according to the 2007 Turkish Seismic Code was selected for this study. All of the floors have the same height of 2.80 m but its base floor is 5.00 m. The building has 30 × 60 cm beams. Columns are 35 × 90 cm on base story and all of the other columns are 30 × 60 cm. The stirrups have a diameter of 8 mm with 20 cm spacing constant along the height. There is no confinement for stirrups. The mass of 17th story is calculated to be 268 tons, base story calculated to be 520 tons, and all of other stories are calculated tons. The building plan is shown in Fig. 84.2.

a

b
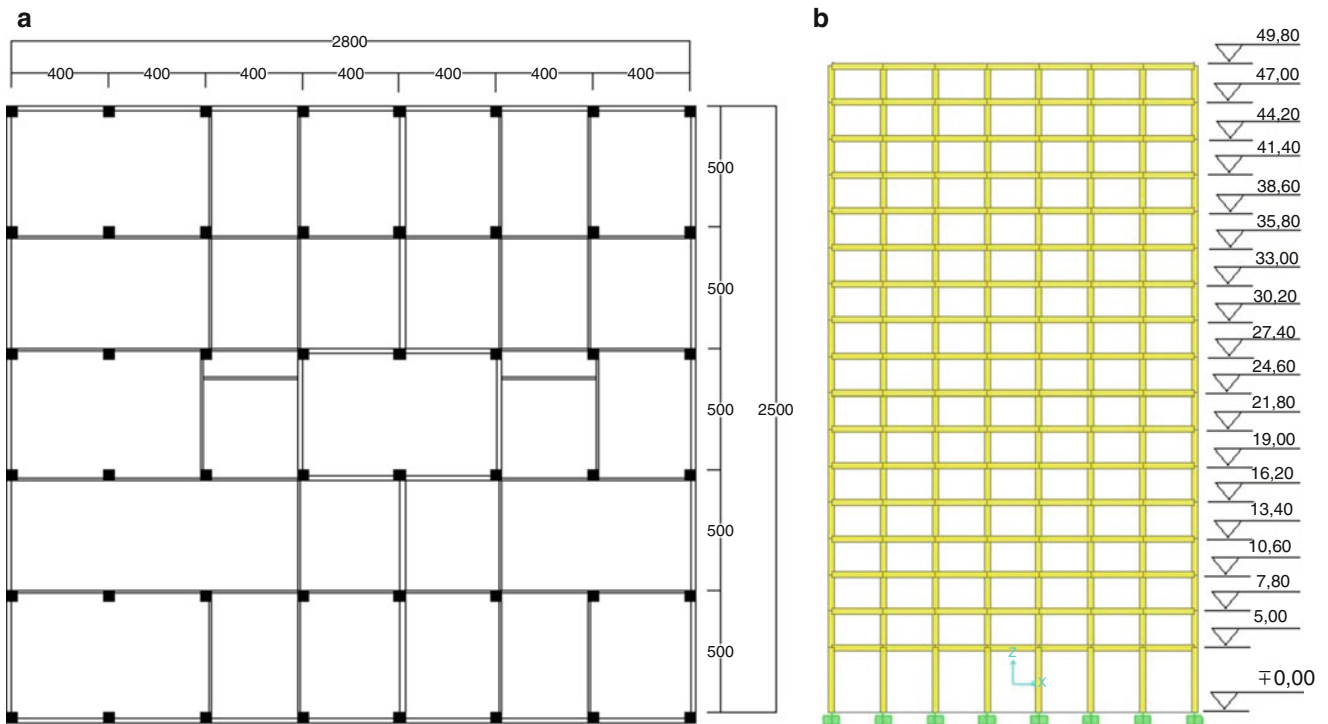
Fig. 84.2 (**a**) Plan view (cm); (**b**) lateral view (m)

Table 84.4 One hundred kilowatt wind turbine specification

Manufacturer	Astralux Wind Turbine and Power Equipment Co. Ltd. (Geneva/Switzerland)
Rotor height	12 m
Rotor diameter	24 m
Total height	22 m
Minimal working speed	1.5 m/s
Power on wind speed	4 m/s to 15 kW
Nominal working speed	9.5 m/s
Area occupied	Will be design to fit the roof
Nominal working speed	9.5 m/s
Construction materials	Aluminum, steel, concrete, and composite plastics
Total weight	35 tons

Existing Building Integrated Solar, Wind Hybrid System

A 100 kW vertical axes wind turbine (VAWT) was selected for simple building. The turbine specifications are shown in Table 84.4.

These types of wind turbines are suitable for buildings owing to slow and silent working abilities. They can be built on roof reinforced concrete buildings because they are made of safe and durable materials. Otherwise, architectural view of building is important for turbine type. VAWT can be made of same material with the roof and can be integrated to the building easily.

Cut-in wind speed 1.5 m/s and nominal working speed 9.5 m/s and the turbine rotate slowly and silently.

Additionally, 400 pieces $1,580 \times 808 \times 45$ mm solar cells were putted on the system. Five hundred and twenty square meter solar cells area was obtained totally. Solar cell specifications are shown in Table 84.5. Total weight of 400 pieces solar cells is 6.2 tons (Fig. 84.3).

Table 84.5 Solar cell specification

Material	Mono-silicon
Maximum power	180 W $\pm$ 3 %
Voltage (V)	44.4 V/5.08 A
Dimensions (H $\times$ W $\times$ D)	1,580 $\times$ 808 $\times$ 45 mm
Weight	$\approx$15.5 kg
Work Temperature	$-45 + 85$ °C

Fig. 84.3 Sample building with roof-type wind turbine

Table 84.6 Annual mean rainfalls rates in Turkey

Average rainfall period	January	February	March	April	May	June	July	August	September	October	November	December	Annual total rainfall
1970–2010	77.6	71.2	64.4	60.0	48.3	32.6	18.9	18.2	27.6	59.7	75.3	88.8	642.8

Existing Building with Solar, Wind, and Rainwater Harvester Hybrid System

RWH system was designed in two different ways in the study. Water storage tank was placed at the base floor in the first design and water was distributed by a water pump. In the second design, water storage tank was placed on the roof (Tables 84.6 and 84.7).

However, total annual mean rainfall was 642.8 mm in Turkey (Fig. 84.4). This rate increases to 2,244.9 mm for Rize City (Fig. 84.5). In this study, rain collector area is 24 $\times$ 28 m^2 on the roof. In other words, 1,508 m^3 (tons) rain falls to the roof area in a year. This proportion corresponds to over 4 tons of water per day. According to the results of Municipal Water Statistics Survey, water abstraction per capita is about 217 L per day in Turkey [16]. RWH can supply all the water demand of 19 persons of the sample building in this study. This amount is equal to 7.5 % of the whole demand for the building.

A water tank with a storage capacity of 30 tons has been placed on the roof for the first design. Then, a water tank was designed on the base floor and a water pump was added as an alternative solution.

Table 84.7 Rize, annual mean rainfall rates

Average rainfall period	January	February	March	April	May	June	July	August	September	October	November	December	Annual total rainfall
1970–2010	210.4	179.2	144.4	92.2	99.7	135.8	148.4	182.6	249.6	300.4	256.2	246	2,244.9
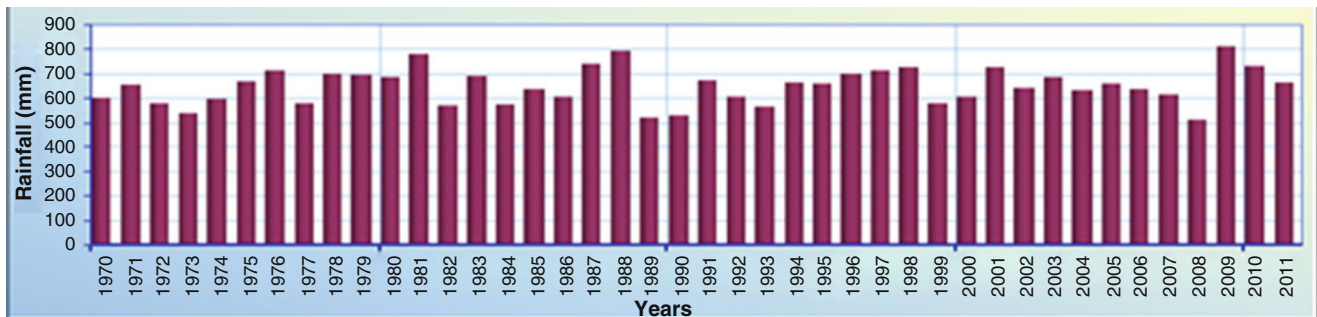
Fig. 84.4 Annual total rainfalls in Turkey (1970–2010)
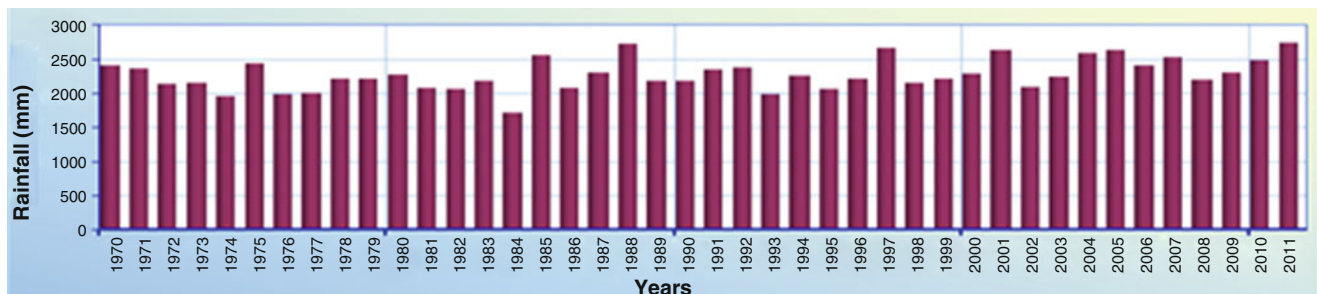
Fig. 84.5 Annual total rainfalls in Rize (1970–2010)

Results and Discussion

The results of the building are presented in terms of base reaction, lateral displacement, hinges results, and strains on the roof story. The capacity curve which obtained as a result of the NSP analysis is shown in Fig. 84.6. NSP analysis was performed in the weak direction of the building(Y direction). Building has symmetric columns and rectangular diameters. It is expected that the building is weaker in Y direction with seismic capacity.

When the three capacity curves were compared, it was observed that the Existing Building (EB) has high capacity as expected. It is shown that the differences of the results are not as high as it effects of seismic performance. WSH and WSRH results are close with EB results for inelastic part of the graphic. As for elastic part of graphic, difference of EB results with WSH and WSRH results grew a bit.

Residential buildings must be "Life Safety" (LS) or better performance to Turkish Earthquake Code 2007 (TEC). In our study, hinges results show that all forms of the building were provided "LS" level. Figures 84.7 and 84.8 show hinges results for EB—WSH and WSHR.

Even columns have larger area on the base story; the biggest damage was observed on the "A" axes columns of the base story. Because, these columns are higher than the other stories and they compensate much more moment values. Plastic hinges usually occurred on the edge of columns at the base story. Other critical elements were in middle stories. There are rarely "LS" level hinges, and mostly "IO" level hinges occurred in middle stories.

Hinges results for WSRH are shown in figure. Extra loads on the roof changed the building period and base story damages were decreased. Base stories were protected by energy absorbtion of cracs on the concrete elements. But middle stories had more damage than EB. Usually, the LS level of plastic hinges occurred on the middle story columns.
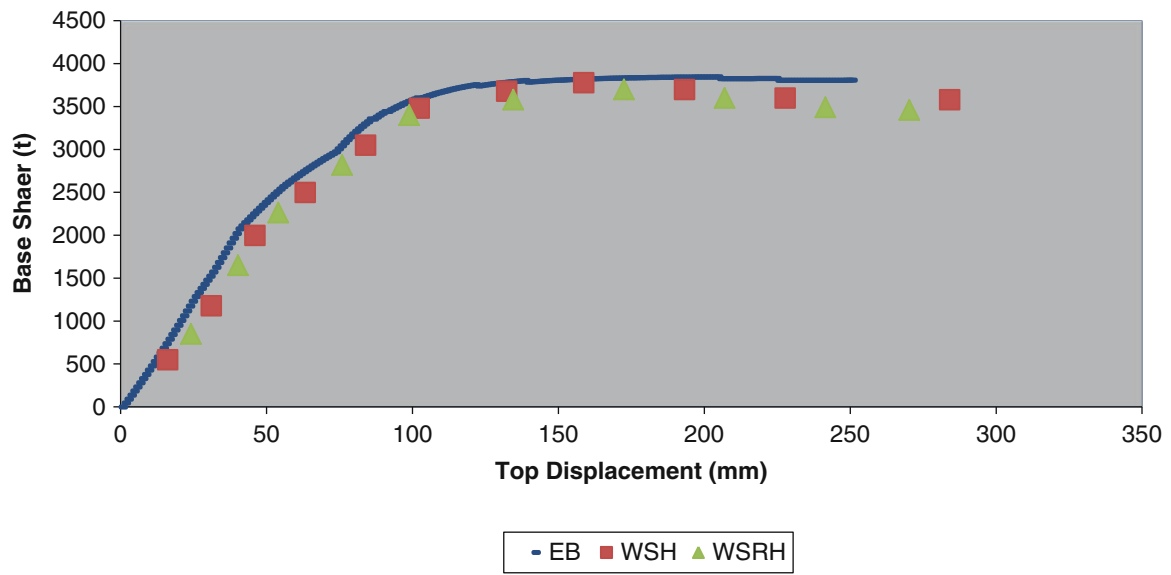
Fig. 84.6 Capacity curves for weak direction

Fig. 84.7 Hinges results for EB
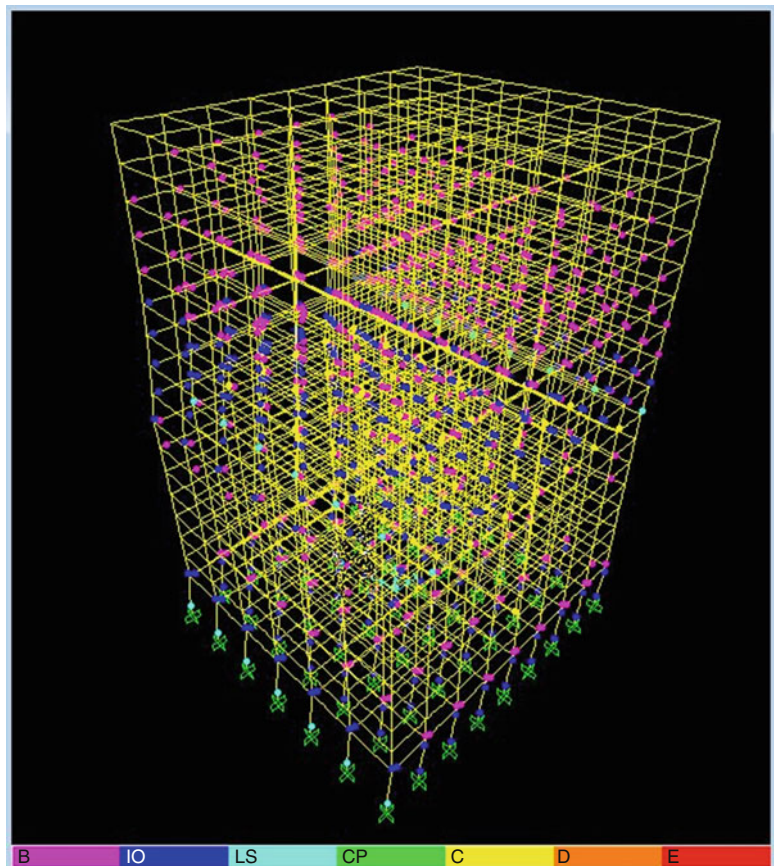
Fig. 84.8 Hinges results for WSRH
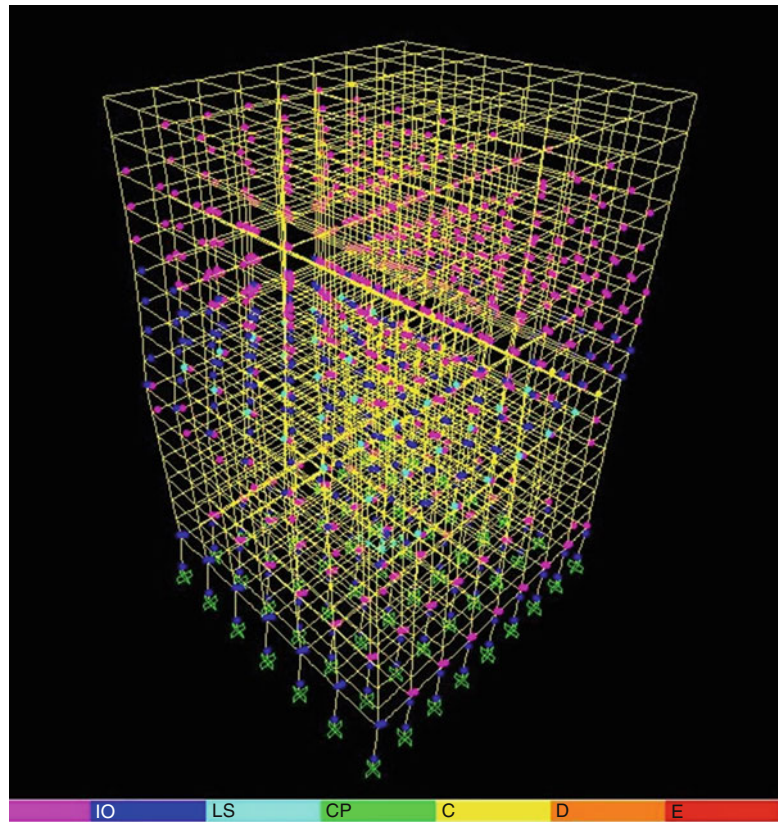
Conclusions

In this study, we presented the comparison of the energy performance and static loads on a building integrated WSRH. Databases of REPA, GEPA, and TSMS (Turkish State Meteorological Service) are used in the energetic analysis and some concluding remarks of this study are as follows:

(a) Electricity generated from wind is 104 MWh/year.
(b) Electricity from solar cell is 53 MWh/year.
(c) Total electricity from the WSRH is 157 MWh/year.
(d) Water collected by the rain harvester is 1,178 m^3/year.
(e) Annual electric consumption of the building is 415 MWh/year.
(f) Annual water consumption of the building is 12,240 m^3/year (15 m^3/month flat)
(g) Electricity compensation ratio from renewable energy is 37.8 %.
(h) Water compensation ratio from rain harvesting is 9.6 %.

References

1. Koroneos C, Kottas G (2007) Energy consumption modeling analysis and environmental impact assessment of model house in Thessaloniki—Greece. Build Environ 42:122–138
2. Kimura Y, Onai Y, Ushiyama I (1996) A demonstrative study for the wind and solar hybrid power system. Renew Energy 9:895–898
3. Yang H, Zhou W, Lou C (2009) Optimal design and techno-economic analysis of a hybrid solar–wind power generation system. Appl Energy 86:163–169
4. Saheb-Koussa D, Haddadi M, Belhamel M (2009) Economic and technical study of a hybrid system (wind-photovoltaic-diesel) for rural electrification in Algeria. Appl Energy 86:1024–1030
5. Dervişoğlu Z (2007) Comparison of performance evaluation methods of reinforced concrete buildings under earthquake effects within non linear theory framework. Master Thesis, Department of Civil Engineering, Balıkesir University, Balıkesir
6. Bhatt C, Bento R (2012) Comparison of nonlinear static methods for the seismic assessment of plan irregular frame buildings with non seismic details. J Earthq Eng 16:15–39
7. Kappos AJ, Kyriakakis P (2000) A re-evaluation of scaling techniques for natural records. Soil Dyn Earthq Eng 20:111–123

8. Saiidi M, Sozen MA (1891) Simple nonlinear seismic analysis of R/C structures. J Struct Div ASCE 107:937–951
9. ATC-40 (1996) Seismic evaluation and retrofit of concrete buildings, vols 1–2. Applied Technology Council, California
10. FEMA-356 (2000) Prestandard and commentary for seismic rehabilitation of buildings. Federal Emergency Management Agency, Washington
11. FEMA-440 (2004) Improvement of nonlinear static seismic analysis procedures. Washington
12. TSC-2007 (2007) Specifications for buildings to be built in seismic areas. Turkish Seismic Code 2007. Ministry of Public Works and Settlement, Ankara
13. Choia IY, Choa SH, Kimb JT (2012) Energy consumption characteristics of high-rise apartment buildings according to building shape and mixed-use development. Energy Build 46:123–131
14. REPA Website (2013) http://www.eie.gov.tr/YEKrepa/RIZE-REPA.pdf
15. Chong WT, Fazlizan A, Poh SC, Pan KC, Ping HW (2012) Early development of an innovative building integrated wind, solar and rain water harvester for urban high rise application. Energy Build 47:201–207
16. Municipal Water Statistics (2010) TC Turkish Statistical Institute, Press Release, No: 10753, 24/02/2012, 10:00

A Solar Energy Calculation Study for the Buildings in Bayburt in Order to Get Optimum Benefit from the Sun Directly

85

Uğur Çakır and Erol Şahin

Abstract

This study is a research made on evaluating solar energy utilization rates of the buildings and residences which are under the climatic and meteorological conditions of Bayburt. In the scope of this study, with the aim of enabling them to benefit from solar energy at the maximum level, a numerical modeling study in which we could determine the most suitable directions, shapes, and sizes of the buildings that would be built in Bayburt was carried out. Although the modeling was applied for sample buildings that have specific sizes and shapes and some results were obtained, this modeling can be used for other buildings which have different shapes and the most suitable direction and location designation that can be done. In the solar energy analysis made for the buildings, a year time was divided into four different periods. Related evaluations were made by taking into account that the building should be in shape and orientation which takes the maximum and minimum radiance in the summer and winter. Basic parameters were determined as azimuth angle, the ratio of the building length to its width, and the total periodical radiance that the building takes.

Keywords

Solar energy • Renewable energy • Solar buildings • Energy saving

Introduction

Life cycle analyses have demonstrated that the majority of energy in a building is consumed as operational energy or during the post-occupancy phase of building's life. A universally accepted method of reducing the energy demands of active or mechanical means of heating or cooling buildings is through passive solar energy. The operational energy demands of buildings can be reduced by incorporating passive solar design principles that are appropriate to the local climate in the preliminary stage [1, 2]. Passive heating or cooling by using solar energy can be used for all buildings in the world. The amount of the usable solar radiation that reaches the earth should be known firstly and then the shape, orientation, and position of building must be determined in order to get an optimum benefit from the sun. The design of collectors, the determination of the lightening loads of buildings, the evaluation of the heat energy captured from the sun, the design of the solar ovens, and the calculation of the isolation rates of greenhouses must be determined according to the amount of solar radiation or solar energy that reaches the relevant place.

As it is known, solar incidence angle of the sun differs for every day, every hour, or every second of the year because of the motion of the sun and the earth. For that reason the solar radiation energy that is gained by any place or building in the world changes continuously depending on the time. For that reason effects of solar radiation on the energy losses and gaining

U. Çakır (✉)
Engineering Faculty, Mechanical Engineering Department, Bayburt University, Bayburt, Turkey
e-mail: ucakir@bayburt.edu.tr

E. Şahin
Vocational School of Technical Sciences, Ordu University, Ordu, Turkey
e-mail: esahin1972@gmail.com

of the buildings must be taken into account in the architectural design of buildings especially in winter and summer. In summer, solar energy gaining of any building should be minimal and it should be maximal in winter.

There are some studies made on improving the architectural design of buildings to get maximum energy from the sun or use minimum energy if it uses conventional energy sources for heating or vice versa. The entire building should be considered as it is just one system. While building is being sized and positioned, the most solar energy gaining rate of the system should be put forward for cold seasons and least solar energy gaining rate of the system should be put forward for hot seasons. For optimal results the building should gain the minimum of solar energy in summer and the maximum in winter.

In a paper it is aimed to give some results of a comparative analysis of two basic sky models, isotropic: Hottel–Woertz–Liu–Jordan and anisotropic: the HDKR, Hay–Davies– Klucher–Reindl, to recommend one of these models for the determination of solar energy availability on a building envelope and to formulate the energy balance of a building. Differences between results obtained from both models increase with the slope of exposed surfaces. The biggest differences (12–15 %) are evident for vertical south surfaces, especially in summer. The simplified isotropic sky model is not recommended for the evaluation of solar radiation availability on the building envelope. Underestimation of solar gains can lead to the selection of an unsuitable concept and construction of a building and result in poor indoor thermal comfort, i.e., overheating of rooms in summer [3]. Another paper presents the results obtained from measurements and experiences gained from interviews on 12 advanced solar low-energy houses designed and built as part of the International Energy Agency (IEA) Solar Heating and Cooling Programme—Task 13. Three years after the IEA Task 13 formally ended, the results were collected by means of questionnaires sent to the former participants in Task 13. The paper gives a brief presentation of the houses and the applied energy saving measures. Measured and expected energy consumptions and indoor climate conditions are compared and differences explained. Special innovative installations and systems are described and evaluated. In general the measured energy consumption was higher than the expected values due to user influence and unforeseen technical problems but still an energy saving of 60 % compared with typical houses was achieved. Prevention of overheating requires special attention also at northern latitudes. Interviews with occupants revealed the need to explain the building's behavior thoroughly to its users and the elaboration of user manuals [4].

A building-integrated solar energy system is proposed, with the panels installed such that the overall morphology resembles that of a traditional Chinese building, i.e., roofing (eaves) at each storey, in addition to that on top of the building in another study. The panels include photovoltaic cells and solar thermal collectors, thus producing electric power as well as heating. The particular morphology provides a number of advantages, in terms of solar energy collection and shading, and their matching to temporal and locational variations in energy demand. These are in addition to the advantages of solar energy generally. Solar heating and photovoltaic power generation were calculated for a number of locations. These were compared with the space heating and air conditioning demands, respectively. The requirement for supplementary energy was calculated. Equivalent calculations for similar buildings without solar panels allowed the saving in non-solar energy to be estimated. Calculations were made for Beijing in winter, as an example of high space heating demand, for Hong Kong in summer, as an example of high air conditioning demand, and for Shanghai, as an intermediate example. These showed potential savings of up to 15 % in space heating, and up to 55 % in air conditioning energy demand [5]. The facade design is and should be considered a central issue in the design of energy-efficient buildings. That is why dynamic facade components are increasingly used to adapt to both internal and external impacts, and to cope with a reduction in energy consumption and an increase in occupant comfort. To gain a complete picture of any facade's performance and subsequently carry out a reasonable benchmarking of various facade alternatives, the total energy consumption and indoor environment need to be considered simultaneously. Nielsen et al. quantified the potential of dynamic solar shading facade components by using integrated simulations that took energy demand, the indoor air quality, the amount of daylight available, and visual comfort into consideration. Three types of facades were investigated (without solar shading, with fixed solar shading, and with dynamic solar shading), and they simulated them with various window heights and orientations. Their performance was evaluated on the basis of the building's total energy demand, its energy demand for heating, cooling, and lighting, and also its daylight factors. Simulation results comparing the three facade alternatives show potential for significant energy reduction, but greater differences and conflicting tendencies were revealed when the energy needed for heating, cooling, and artificial lighting was considered separately. Moreover, the use of dynamic solar shading dramatically improved the amount of daylight available compared to the fixed solar shading, which emphasizes the need for dynamic and integrated simulations early in the design process to facilitate informed design decisions about the facade [6].

The purpose of the study of Peippo et al. is to define a simple quantitative solar low-energy building design optimization procedure that will give the optimum design variables from a representative set of options. These include building geometry, thermal insulation, windows, solar thermal collectors, and PVs, whereas less readily quantifiable technologies such as advanced passive solar designs are not discussed. First, a set of simplified models is selected for the building energy analyses.

A numerical optimization scheme is then integrated with these models that find the optimum building design trade-off path in terms of energy and cost, in order to solve the design problems 1–3. To assess the applicability of the approach, a case study is presented for two generic building types in three different locations in Europe. Finally, the computed designs are compared with a set of realized low-energy houses [7]. Further advance of glazed, healthy building's energy efficiency and sustainability is inextricably linked to the building's envelopes/facades fundamental physics study related to the dynamic control of sunlight and optimal control of solar heat gains. Relevant mathematical models and algorithms, as well as infrastructure/hardware and software integrated performance prediction and validation are studied. Reviewed is the most recent analytical and experimental research, current state of science and art, as well as some of the on-going R&D at the edge of the new breakthroughs of the healthy buildings daylighting dynamic control's performance prediction and validation. It has been shown that, concerning the variability of the solar radiation spectra incident on the building's envelope, and also the variability of outdoor and indoor air temperature differences, it is necessary tuning control of Glazing's transmittance dependence on the solar radiation wavelength, with an aim to optimize daylighting with the reference to people needs (their health and comfort) and energy (thermal and electrical loads minimization). Finally, presented are the elements of an analytical modeling approach, as initial results of study, aimed to reach a challenging research goal—tuning control of buildings—Glazing's transmittance dependence [8].

In this paper a case study was made to determine the best orientation, type, length to width rate, and the position of residential buildings for Bayburt city which is located in the northeastern part of Anatolia in Turkey. It is a city in the Black Sea Region of Turkey. To achieve this aim most commonly used normal building types for residential applications were picked out. A mathematical model for computing the total solar energy that buildings gained from the sun every day and every month, for the latitude of Bayburt is developed for any building orientation with the help of MATLAB. Then the model was run and the solar energy gaining rates of building types are calculated according to the different floor areas for each orientation. By the way a comparison was made among the building types according to the total solar energy gained monthly, annually, and seasonally.

Case Study

Geographic and Climatic Properties of Bayburt

This case study was made for geographical and climatic conditions of Bayburt which is situated between $39^{\circ}52'$ to $40^{\circ}37'$ latitudes and $39^{\circ}37'$ to $40^{\circ}45'$ longitudes. It sits on 40.16° south and 40.15° north latitude and has an altitude of 1,556 m [2, 9].

In the region renowned for its climatic extremes, the town of Bayburt experiences comparatively mild seasonality, with an annual range of 15 °C. In summer, temperatures reach an average maximum of 27 °C, and tough figures in excess of 36–38 °C have been recorded in July or August. During the cold winter average daily maxima hover close to freezing point. Air temperature levels reach an average minimum point of −6.08 °C, and extreme variation is seen in data with absolute figures plunging to −29 °C in December and January. Generally, January is the coldest month of the year for Bayburt. Spring sees maximum temperatures jump dramatically from March to April, whilst autumn temperatures drop steadily toward the cool winter months. Diurnal temperature variation peaks during summer, when clear skies allow the escape of warm air in to the atmosphere at night. Bayburt receives high levels of solar radiation throughout the year and consequently is, on average, warmer than the surrounding slopes. Briefly, heating of the surfaces during the day creates up-slope thermal currents, which warms nearby slopes while at night, cool air drains into valleys from the surrounding mountains [10, 11].

In this study an annual period divided into two sections because of the reasons is highlighted in the previous paragraphs. First, one of them is winter section (01 November to 01 May) and second one is summer section (02 to 31 May)

The Buildings and Some Assumptions

In this study every analyzed building is thought as it is just one system. The solar energy gaining of any facade of building is not important; all amount of the solar radiation taken from the sun is our main target. We determined and selected seven types of building to make solar analysis. It is assumed that each apartment has 100 m^2 floor area and the height of every apartment is 3.5 m. Table 85.1 shows the general specifications of selected building types. Due to the fact that Bayburt is located in a cold climate region of Turkey, it is important that buildings should get more solar radiation in winter.

Table 85.1 Selected building types

Type	Number of floors	Number of apartments for each floor (100 m^2)	Total apart number	Building length (m)	Building width (m)	Basic floor area (m^2)
1	2	2	4	20	10	200
2	4	2	8	20	10	200
3	6	2	12	20	10	200
4	8	2	16	20	10	200
5	4	4	16	20	20	400
6	6	4	24	20	20	400
7	8	4	32	20	20	400
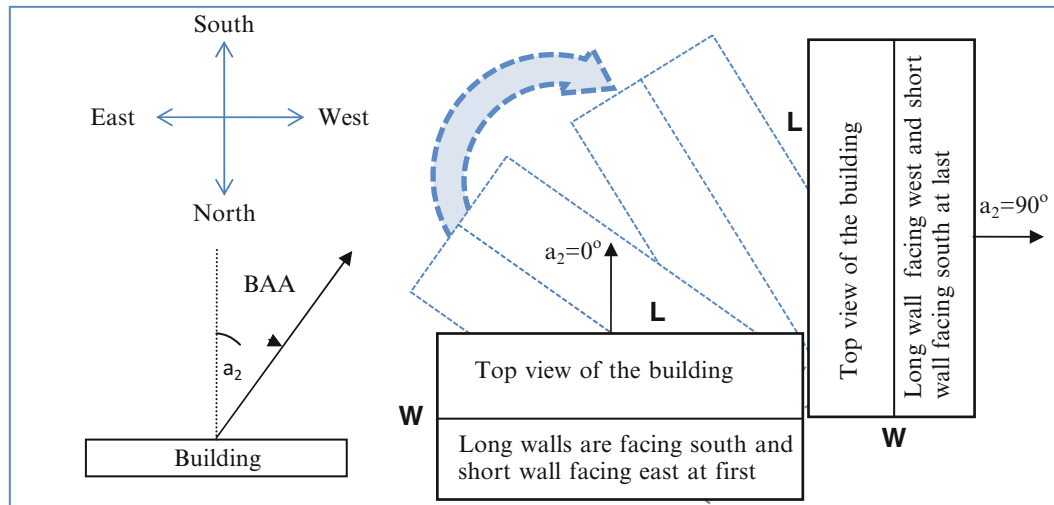
Fig. 85.1 Determining the building azimuth angle

In addition to the assumption which has been mentioned over, some other assumptions are made in order to make the investigation easy and to make the comparison more realistic. In this study only direct solar radiation was calculated, ground reflected, and diffused radiation is neglected by assuming that they will be equal for all shapes. Additionally effects of the other factors like shading, type of building material are assumed equal for all situations. These assumptions do not change the main results of this study and because of that a comparison is made in this paper.

Approach of Model

Selected types of buildings were analyzed in 89 different orientations from east–west to north–south directions by increasing the azimuth angle of the building one by one from 0° to 89°. Optimum orientation was determined to obtain the wanted total radiation energy (heat energy) in winter and summer for each type building according to different sizes. Surface azimuth is the angle on a horizontal plane between the normal to a vertical surface and the north–south direction line. A new definition was made here as building azimuth angle (BAA) and it is explained in Fig. 85.1. BAA (a$_2$) is determined according to a reference position as azimuth angle of one of the long wall is 0° as seen in Fig. 85.1. In reference position one of the long walls of the building is faced to the south. When the greenhouse (system) turns from east to the west as seen in the figure, BAA changes from 0° to 90°. When the long wall of the building is faced to the west BAA takes the value 90°.

In this study each surface of the building was analyzed separately first and then all systems were discussed. Surfaces of the building were encoded by using some abbreviations as seen in Fig. 85.2. Figure 85.2 is presented as a sample for encoding the surfaces of building.
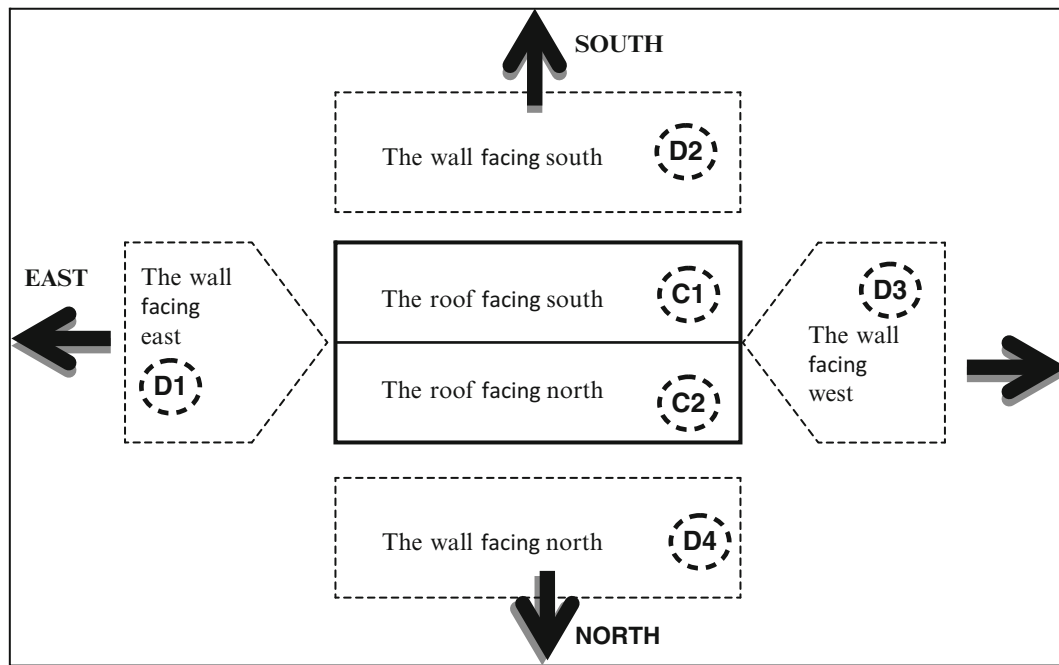
Fig. 85.2 Encoding of the building surfaces (first position)

Solar Calculations

The incident solar radiation outside the earth's atmosphere is called extraterrestrial radiation. The intensity of solar irradiation directly outside the earth's atmosphere on a horizontal surface is almost constant at around 1.367 W/m^2, so-called as solar constant. As mentioned above, since this study focuses on a comparison extraterrestrial, radiation calculations were used.

Instant and hourly incident solar radiation on an inclined surface of a building depends upon some parameters, like the time of the day, the day of the year (n), declination angle (d), solar altitude angle (z), surface azimuth angle (a) (in northern hemisphere, it is zero for south facing surfaces, 180° for north facing surfaces, −90° for east facing surfaces, and +90° for west facing surfaces), and latitude angle of the place (e).

In this study, the daily solar radiation coming onto a surface in a day between sunrise and sunset is put forward. Firstly, for a constant BAA the total daily solar radiation coming onto any surface of the building was calculated for each day of the year. This calculation was made for every surface of the building. The total daily solar radiation coming onto the building is calculated by collecting the amounts of daily total solar radiation coming onto each surface of it. The related and required values of these parameters have been computed by using (85.6)–(85.8) numbered references [12–14].

Zenith angle z is given with Eq. (85.1), where h is the hour angle, d is the declination angle, and e is the latitude angle.

$$z = \arccos(\cos d . \cos e . \cosh + \sin d . \sin e) \tag{85.1}$$

Sun rays become parallel with surface when the sun rises and sets. Solar incidence angle (H) of a surface at the time sun sets or rises can be calculated by using Eq. (85.2) and solar incidence duration (T$_g$) of any day can be calculated in time unit by using Eq. (85.3).

$$\cos H = -\frac{\sin d . \sin e}{\cos d . \cos e} = -\tan d . \tan e \tag{85.2}$$

$$T_g = \frac{2}{15} . H = \frac{2}{15} \arccos(-\tan d . \tan e) \tag{85.3}$$

Table 85.2 The algorithm which is used to evaluate the hour angles at sunrise and sunset for any inclined surface

		H_1	H_2
$\cos(g_o) > 0$ ($g_o > 90°$)	$D^2 > 0$	max $(H_{1p}, -H)$	min (H_{2p}, H)
	$D^2 < 0$	$-H$	H
$\cos(g_o) < 0$ ($g_o > 90°$)	$D^2 > 0$	max $(H_{2p}, -H)$	min (H_{1p}, H)
	$D^2 < 0$	Solar radiation does not come to the surface	

Solar incidence angle (g) of a surface at any time of the day is evaluated as;

$$\cos(g) = [\cos d.\cos e.\cosh.\cos s] + [\cos a.\cos d.\sin e.\cosh.sins] + [\sin a.\cos d.\sinh.\sin s]$$
$$+ [\sin d.\sin e.\cos s] - [\cos a.\sin d.\cos e.\sin s] \tag{85.4}$$

Here, a is defined as the azimuth angle and s is defined as the inclination angle of the surface. Terms of H_{1p} and H_{2p} are defined as the hour angles where solar incidence angle becomes zero (the sun's rays are parallel to the surface). H_{1p} and H_{2p} are calculated as;

$$H_{1p} = 2\, arctan\left(\frac{C_1 - D}{C_2 - C_3}\right) \tag{85.5}$$

$$H_{2p} = 2\, arctan\left(\frac{C_1 + D}{C_2 - C_3}\right) \tag{85.6}$$

Values of C_1, C_2, C_3, and D can be calculated by using (85.7)–(85.10) numbered equations as seen below.

$$C_1 = \sin a.\cos d.\sin s \tag{85.7}$$

$$C_2 = \cos d.[\cos e.\cos s + \cos a.\sin e.\sin s] \tag{85.8}$$

$$C_3 = \sin d.\left[\sin e.\cos s - \cos a.\cos e.sins)\right] \tag{85.9}$$

$$D = \sqrt{C_1^2 + C_2^2 - C_3^2} \tag{85.10}$$

The times that solar radiation comes parallel to the surface may be before sunrise and after sunset. For that reason if the absolute value of the hour angle at the time solar incidence comes parallel to the inclined surface greater than the hour angle at the sunrise time, the hour angle at the time that solar rays first reach to the surface is at the sunrise time. By using Eq. (85.11) the cosine of solar incidence angle (g) can be calculated when the value of h is zero (solar noon).

$$\cos g_0 = C_2 + C_3 \tag{85.11}$$

After determining the g_0 value, H_1 and H_2 values which are the hour angles at sunrise and sunset for any inclined surface can be evaluated by using the algorithm showed in Table 85.2.

It is a requirement to evaluate how many hours the solar radiation comes on an inclined surface in a day. This evaluation must be made for all days of a year. We can determine this by using the equations numbered as (85.12) and (85.13).

$$\text{for } d > 0: \quad t_{eg} = \frac{2}{15} arccos[-\tan d.\tan(e - s)] \tag{85.12}$$

$$\text{for } d < 0: \quad t_{eg} = \frac{2}{15} arccos[-\tan e.\tan d] \tag{85.13}$$

Generally extraterrestrial radiation is made use of in the calculation of the solar radiation that comes to the earth. The extraterrestrial radiation that comes on unit area of a horizontal surface instantly can be calculated by using Eq. (85.14),

where I_{gs} is the solar constant and on average it is 1,367 W/m^2. This value varies by ± 3 % as the earth orbits the sun (http://science.nasa.gov/science-news/science-at-nasa/2003/17jan_solcon/), and f is the solar constant correction coefficient and is determined by using (Eq. 85.15).

$$I_0 = I_{gs}.f.\cos z \tag{85.14}$$

$$f = 1 + 0.033\cos\left(360\frac{n}{365}\right) \tag{85.15}$$

The amount of solar radiation that comes on a horizontal surface in dt period (dQ_0) is calculated by using Eq. (85.16). This equation can be converted to Eq. (85.17) with the help of an hour angle and t $= 12/\pi$. Then we get the Eq. (85.18) by putting the Equation one which expresses the zenith angle into Eq. (85.17) and integrating it from H$_1$ to H$_2$.

Equations (85.18) and (85.19) define the amount of extraterrestrial solar radiation that comes on unit area of a horizontal surface in one day from sunrise to sunset.

$$dQ_0 = I_{gs}.f.\cos z.dt \tag{85.16}$$

$$dQ_0 = \frac{12}{\pi}.I_{gs}.f.\cos z.dh \tag{85.17}$$

$$Q_o = \frac{12}{\pi}.I_{gs}.f.\int_{H_1}^{H_2}(\cos d.\cos e.\cosh + sind.\sin e).dh \tag{85.18}$$

$$Q_o = \frac{24}{\pi}*I_{gs}*f*\left[\cos(d)\cos(e)\sin(H) + \frac{\pi}{180}H\sin(d)\sin(e)\right] \tag{85.19}$$

The amount of extraterrestrial solar radiation (Q_{oe}) that comes on the unit area of an inclined surface in one day can be calculated by using Eq. (85.20) from sunrise to sunset. s is the slope angle of the surface.

$$Q_{oe} = \frac{12}{\pi}.I_{gs}.f.\left[\begin{array}{l}\frac{\pi}{180}(H_2 - H_1).\sin d.(\sin e.\cos s - \cos e.\sin s.\cos a) + (sinH_2 - sinH_1).\\ cosd.(cose.coss + sine.sins.cosa) - (\cos H_2 - \cos H_1).cosd.sins.sina\end{array}\right] \tag{85.20}$$

Results and Discussion

Figure 85.3 shows the change of solar energy gaining of Type 1 building in winter and summer according to the BAA. As it is mentioned before, Type 1 has two floors and four apartments totally. Its length and width are 20 and 10 m. If the building is positioned with 18° BAA the solar heat energy that is gained from the sun becomes maximum for winter and if it is positioned with BAA between 75° and 90° it gets minimum solar radiation in both of the seasons. The optimum BAA is between 12° and 24°.

Figure 85.4 presents the solar energy utilization rates of the building which is selected as Type 2. This type of building has got four floors and eight apartments totally. The BAA value for Type 2 building to get maximum solar energy in winter season is 19°. But we should care about the solar radiation coming onto the building in summer. We can say that the optimum range for BAA of Type 2 is between 12° and 23°.

Figure 85.5 presents the solar energy that comes from the sun to the surfaces of building-Type 2 in winter and summer. This type of building has got 6 floors and 12 apartments totally. The best BAA value for Type 2 building to get maximum solar energy in winter season is 14°. But we should care about the solar radiation coming onto the building in summer. We can say that the optimum range for BAA of Type 2 is between 11° and 34°.

Solar energy incoming rates change of Type 4 is presented in Fig. 85.5. Type 4 has 8 floors and 16 apartments in each floor (Fig. 85.6). It has got 16 apartments totally. As seen in the figure when BAA is higher than 78°, solar energy gaining of
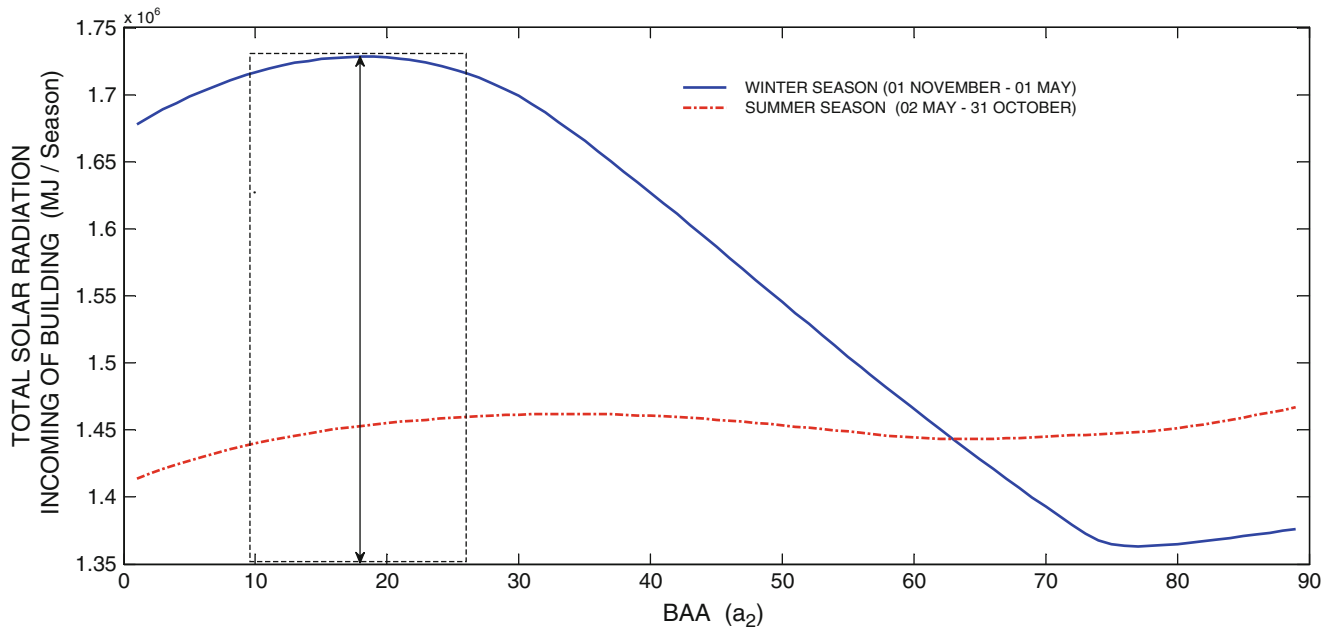
Fig. 85.3 Change of total solar energy gaining of Type 1 building according to BAA (two floors, four apartments)
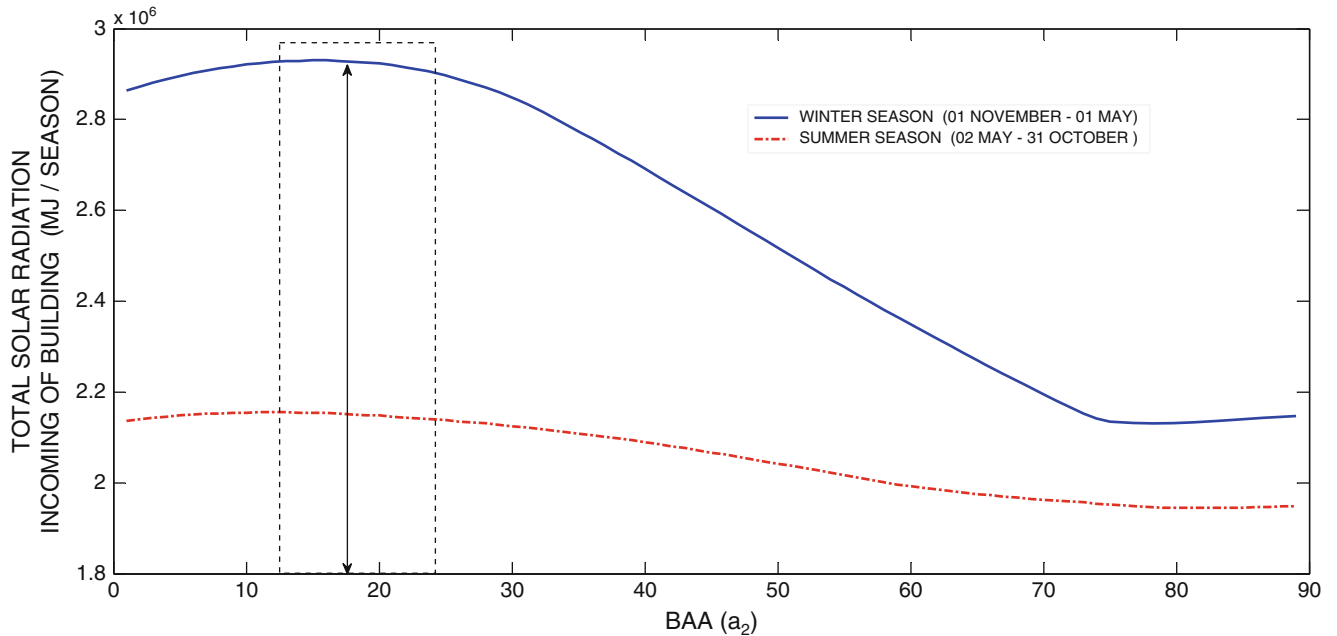
Fig. 85.4 Change of total solar energy gaining of Type 2 building according to BAA (four floors, eight apartments)

building becomes minimum in summer and winter. If the building is positioned with 15° BAA, the solar heat energy that is gained from the sun becomes maximum for winter.

Figure 85.7 presents solar energy incoming rates change of Type 5 building in two seasons depending on different BAA values. Type 5 has four floors and four apartments in each floor. It has got 16 apartments totally. As seen in the figure, when BAA is higher than 70°, solar energy gaining of building in summer becomes higher than in winter. If the building is positioned with 27° BAA, the solar heat energy that is gained from the sun becomes maximum for winter and if it is positioned with BAA between 70° and 90° it gets minimum solar radiation in winter. The optimum BAA is between 13° and 33°
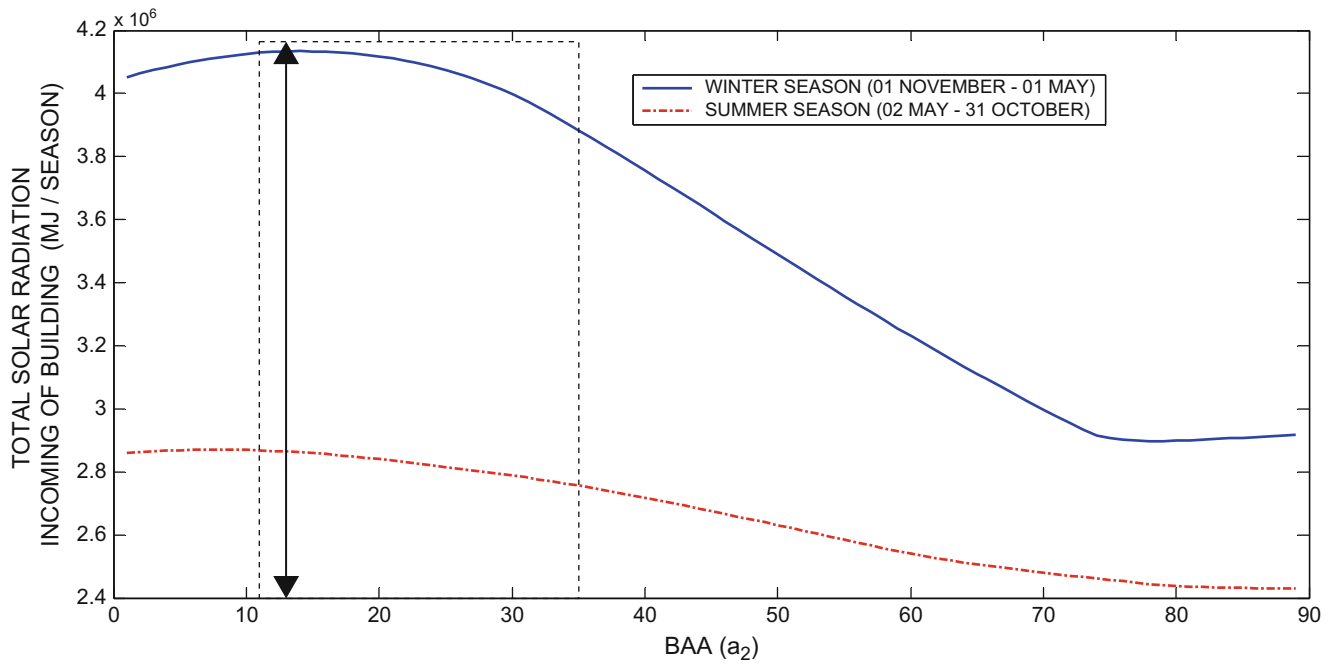
Fig. 85.5 Change of total solar energy gaining of Type 3 building according to BAA (6 floors, 12 apartments)
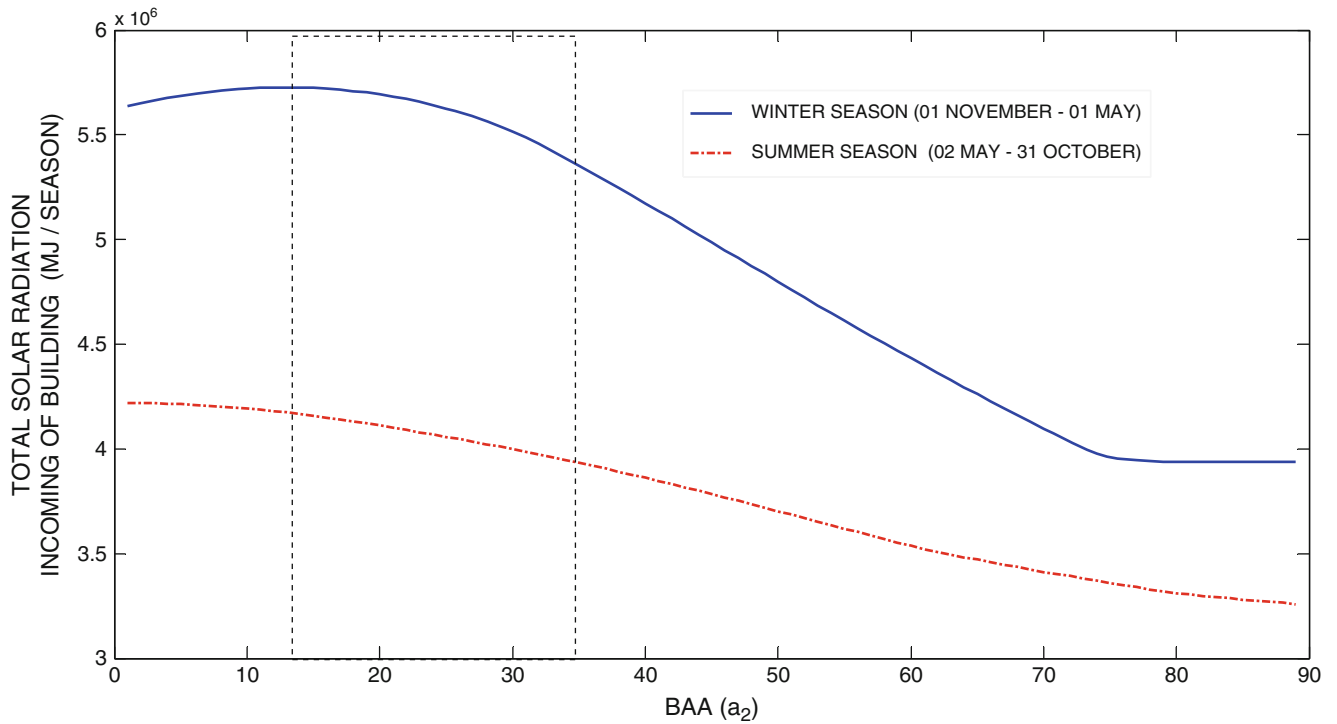
Fig. 85.6 Change of total solar energy gaining of Type 4 building according to BAA (8 floors, 16 apartments)

Change of solar radiation energy gaining of building-Type 6 according to BAA is presented in Fig. 85.8. As it is understood from Fig. 85.8 if the building is positioned with 24° BAA, the solar heat energy that is gained from the sun becomes maximum for winter and if it is positioned with BAA between 77° and 90° it gets minimum solar radiation in winter. The optimum BAA is between 20° and 40°
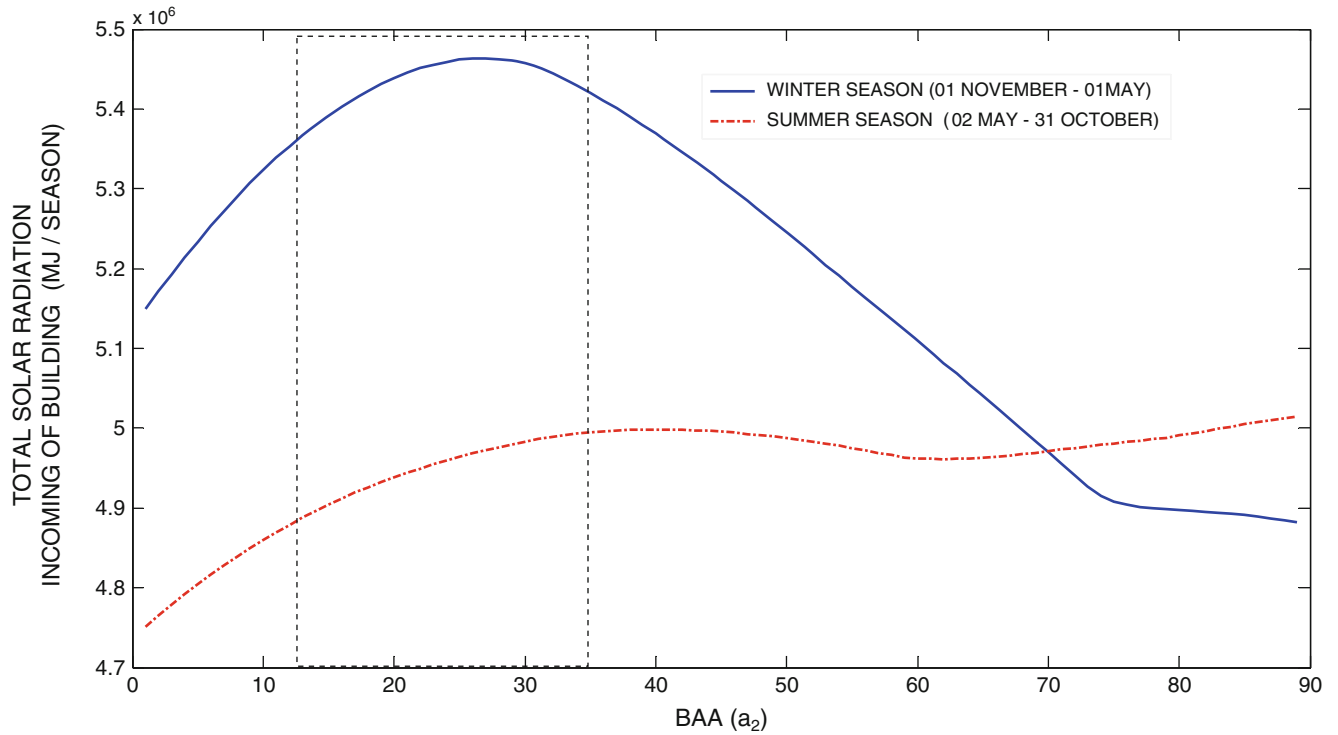
Fig. 85.7 Change of total solar energy gaining of Type 5 building according to BAA (4 floors, 16 apartments)
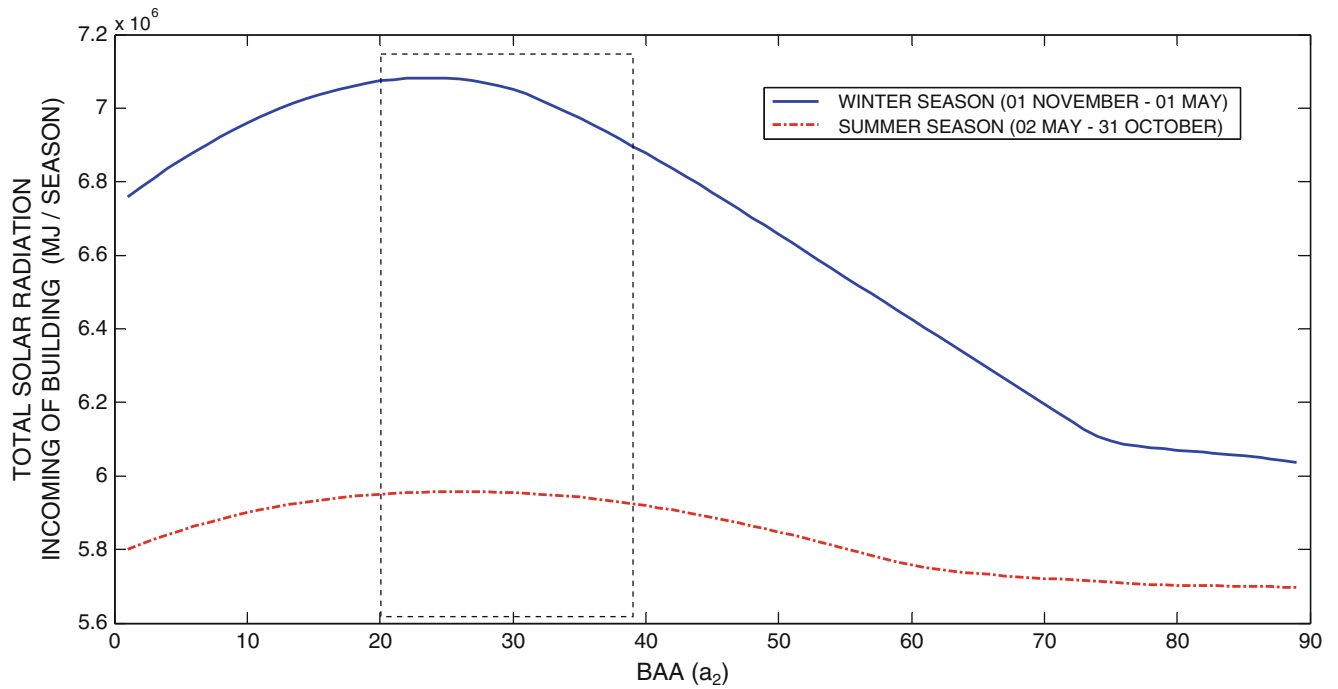
Fig. 85.8 Change of total solar energy gaining of Type 6 building according to BAA (6 floors, 24 apartments)

Figure 85.9 shows the change of solar energy gaining of Type 1 building in winter and summer according to the BAA. As it is mentioned before Type 7 has eight stores and four apartments totally. Its length and width are 20 and 20 m. If the building is positioned with 22° BAA, the solar heat energy that is gained from the sun becomes maximum for winter season and if it is positioned with BAA between 73° and 90° it gets minimum solar radiation in both of the seasons. The optimum BAA is between 16° and 32°.
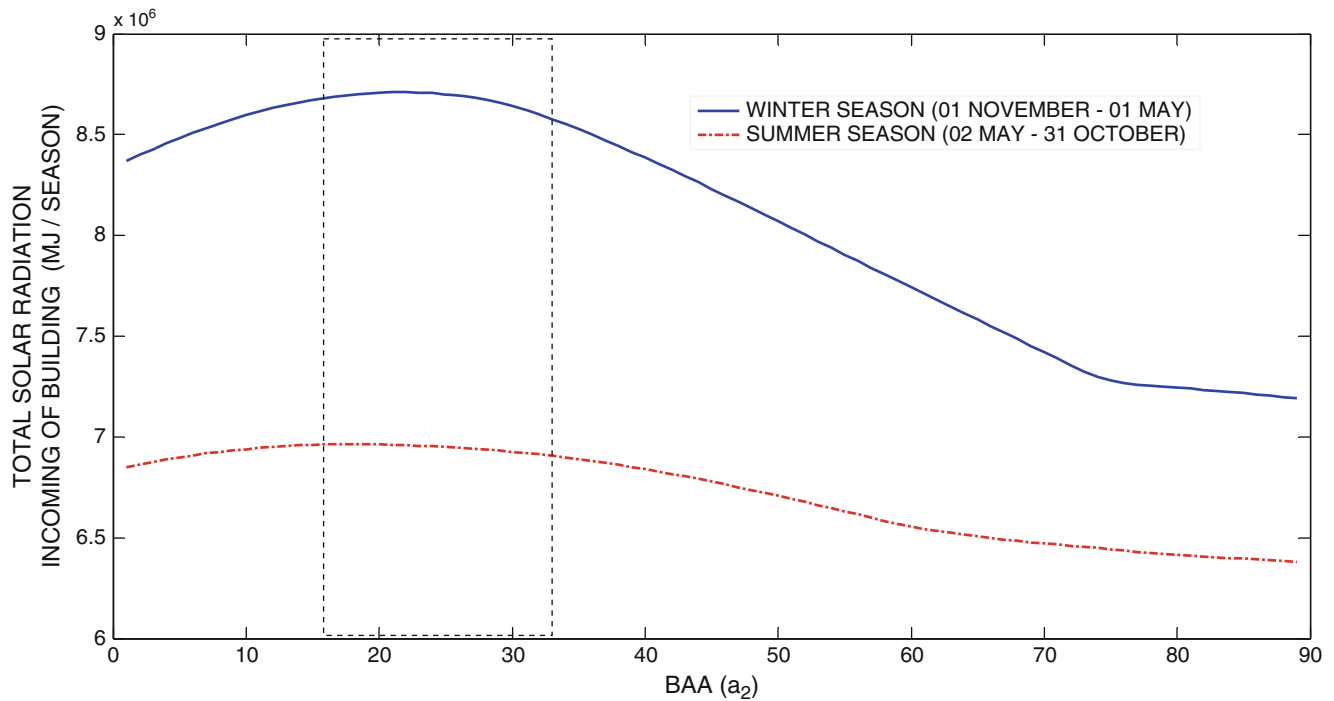
Fig. 85.9 Change of total solar energy gaining of Type 7 building according to BAA (8 floors, 32 apartments)

Table 85.3 Maximum total solar energy gaining of buildings per season

Floor	2	4		6		8	
Apartments	2	2	4	2	4	2	4
a_2 (°)	18	15	27	14	24	14	23
$Q_{o\ Summer}$	1,453,115	2,154,185	4,972,490	2,861,943	5,956,462	4,166,146	6,956,460
$Q_{o\ Winter}$	1,728,308	2,930,251	5,463,137	4,134,130	7,082,733	5,725,556	8,709,859

Fig. 85.10 Total solar energy gaining changing of buildings per season
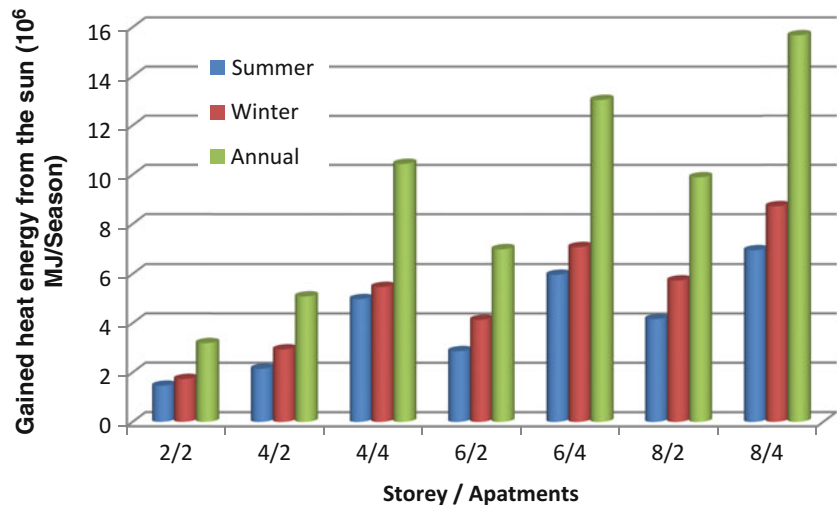
Table 85.3 shows us the optimum BAA values for buildings and the amount of heat energy gained by the sample buildings from the sun when building is positioned with optimum BAA. Additionally Fig. 85.10 presents the change of the amount of solar radiation gaining of the building when it is oriented by optimum BAA seasonally and annually. As understood from the table and figure, number of apartments per floor is more important than the height of the building to

get more benefit from the sun because the increase in total surface becomes higher when the number of apartments per floor increases. Additionally according to Fig. 85.10 and Table 85.3 the solar radiation that is gained by the building is always higher for winter and that is a desired result for Bayburt.

Conclusion

This study was made to evaluate the potential of direct solar radiation using of buildings for different types of residential buildings and different orientations of them. To achieve this aim MATLAB program was used. This modeling study and the algorithm can be used for any building in the world. Additionally this study can be used for different solar energy calculations too, for example greenhouses of solar houses. Due to the fact that winter season is too cold and summer season is cool and duration of spring/autumn seasons is very short in Bayburt, we concluded that the amount of solar radiation energy that is gained by buildings in Bayburt is more important. For that reason, the calculation and determination process of BAA is made according to the winter conditions.

It is understood from the study that solar energy calculations must be made for every building over the world, and sizes and positioning conditions of the buildings must be evaluated carefully for economic and efficient energy using issues.

References

1. A briefing for passive solar energy design, cement and concrete association of Australia (14 May 2013) http://www.concrete.net.au/publications/pdf/briefing09.pdf
2. Şahin E (2012) Determining the optimum shapes and orientations of the buildings and greenhouses in Bayburt in order to get more benefit from the sun directly. Master Thesis, Department of Mechanical Engineering, Bayburt University Graduate School of Natural and Applied Science, Turkey
3. Chwieduk DA (2009) Recommendation on modelling of solar energy incident on a building envelope. Renew Energy 34:736–741
4. Thomsen KE, Schultz JM, Poel B (2005) Measured performance of 12 demonstration projects—IEA Task 13 "advanced solar low energy buildings". Energy Build 37:111–119
5. Johnston D (2007) Solar energy systems installed on Chinese-style buildings. Energy Build 39:385–392
6. Nielsen MV, Svendsen S, Jensen LB (2011) Quantifying the potential of automated dynamic solar shading in office buildings through integrated simulations of energy and daylight. Solar Energy 85:757–768
7. Peippo K, Lund PD, Vartiainen E (1999) Multivariate optimization of design trade-offs for solar low energy buildings. Energy Build 29:189–205
8. Kima JT, Todorovica MS (2013) Tuning control of buildings Glazing's transmittance dependence on the solar radiation wavelength to optimize daylighting and building's energy efficiency. Energy Build 63:108–118
9. Comaklı K, Cakır U, Kaya M, Bakirci K (2012) The relation of collector and storage tank size in solar heating systems. Energy Convers Manag 63(2012):112–117
10. Sagona A, Sagona C (2004) An historical geography and a field survey of the Bayburt province, Archeology at the North east Anatolian frontier, Peeters 2004. ISBN: 90-429-1390-8
11. Turkish State Meteorological Service (12 March 2013)
12. Kılıç A, Öztürk A (1983) Güneş Enerjisi. Kipaş Dağıtım ve Yayıncılık (in Turkish)
13. Duffie JA, Beckman WA (1991) Solar engineering of thermal processes, 2nd edn. Wiley, New York
14. DuffieJ A, Beckman WA (1974) Solar energy thermal processes. Wiley, New York

Economic Assessment of Three Biomass-Based Hydrogen Production Systems

86

Mehmet Kursad Cohce, Ibrahim Dincer, and Marc A. Rosen

Abstract

The hydrogen economy is expected to become in the future a very significant part of the energy system for many countries, and hydrogen as a fuel will likely play an important role in the transition from fossil fuels to carbon-free and/or carbon-neutral fuels. Such a transition is directly related to hydrogen production costs. In this chapter, comprehensive economic evaluations and comparisons are reported for three simulated hydrogen production systems. The minimum hydrogen production costs are estimated for these three systems using process economic analysis software (Aspen Plus Icarus). It is found that the hydrogen production cost ranges between 1.28 and 1.78 $/kg for these three systems. The results of this investigation (1) are expected to help reduce reasonably hydrogen production costs by applying various scenarios for these three systems and (2) demonstrate hydrogen can be an economically feasible final product from biomass gasification. It is concluded that the costs of hydrogen production may be competitive in the future with the costs of the production of conventional fuels.

Keywords

Hydrogen • Energy • Biomass • Economic assessment

Introduction

Hydrogen is an attractive alternative energy carrier and this desirability is related to it being environmental friendly and available in large quantities, since hydrogen is one of the most abundant elements in the world. If hydrogen becomes widely available at low cost, it is most likely that hydrogen energy systems will be competitive with the current gasoline-supply systems. The timing the evolution towards a hydrogen economy depends on the rate of technology advances among other factors. A roadmap has been created that provides an overview of a possible evolution of hydrogen production technologies in the future [1–2], and comprehensive analyses have been reported on the feasibility of biomass derived hydrogen [3]. Such systems are often assumed to be able to supply their own power and heat by utilizing waste heat from biomass pyrolysis and further reforming [4].

An economic analysis has been conducted to investigate the effect of different parameters and variables on the cost of hydrogen produced using low to medium capacity (1.3 MW, 10 MW, and 20 MW) gasification plants [5]. It was concluded that significant cost reductions could be obtained by increasing plant size, with the cost of produced hydrogen gas found to be nearly 11–12 €/GJ with a refueling station; compression adds a cost of nearly 5 €/GJ. Therefore, the cost of hydrogen produced using biomass is estimated in this study to be 16–17 €/GJ, which is higher than the value cited in the next paragraph on hydrogen production costs. A study of the economic efficiency of hydrogen production from biomass residues in China [6] demonstrated the basic system for hydrogen production consisting of an oxygen-rich air downdraft gasifier plus

M.K. Cohce (✉) • I. Dincer • M.A. Rosen
PhD Candidate, Department of Mechanical Engineering, University of Ontario Institute of Technology (UOIT),
2000 Simcoe Street North, Oshawa, ON, Canada L1H 7K4
e-mail: mehmet.cohce@uoit.ca; ibrahim.dincer@uoit.ca; marc.rosen@uoit.ca

CO-shift reaction in a fixed bed. A cost sensitivity analysis on this system determined the cost to be 1.69 $/kg H_2 for a system capacity of 266.7 kg biomass/h (6.4 ton/day). The investigation considered ranges of hydrogen production capacity for the cost estimation varying from a cost of 2.224 $/kg H_2 for a small pilot plant of 100 kg H_2/day to 0.625 $/kg H_2 for a very large plant of 10,000,000 kg H_2/day [7].

It is important to determine the means of producing hydrogen that is the most suitable and cost-effective, as a key cost factor depends strongly on the method of hydrogen production. One assessment of hydrogen production costs determined that steam methane reforming (SMR) is currently the cheapest method of hydrogen production, and PV powered water electrolysis is the most costly; the authors also indicated that the economic analysis of different H_2 production technologies is incomplete without consideration of the environmental costs associated with the processes [8]. Although biomass can be converted through processes to generate energy, like gasification to produce hydrogen as discussed in this chapter, biomass can also be directly combusted to produce electricity.

In addition, political and social factors also affect hydrogen economics, with the utilization of renewable energy varying significantly depending on government policy and the attitudes and behaviors of relevant policy makers, the public, and industry [9].

The main objective of this study is to show from an economic point of view that gasification of oil palm shell can be used beneficially to produce hydrogen for three different hydrogen production systems. Consequently, the present work investigates the economics of hydrogen production by thermochemical biomass gasification. A parametric analysis of factors influencing the thermodynamic efficiency of biomass gasification is also carried out. The systems considered here for hydrogen production incorporate gasification, followed by steam methane reformation, and low and high temperature shift reactions. The gasification of oil palm shell, for which proximate and ultimate analyses and other data are available [10], is investigated using the Aspen Plus process simulation software and the Aspen Plus Icarus program, which is an equipment capital cost estimating software tool developed by Aspen Tech. The latter code is used to estimate system component costs. The results are expected to provide designers and researchers with an enhanced understanding of the characteristics of biomass-based hydrogen production technologies.

Economic Analysis

Three different biomass energy conversion systems are investigated in this study, including the hydrogen production and electric generation systems. This section explains the economic evaluation of these three simulated systems to estimate the minimum hydrogen production cost; explanations are also provided of the methods and sources for determining the capital cost of each piece of equipment within the plants. Once the system configurations are set up in Aspen Plus, technical data are obtained via the simulations. Some results are transferred to the Aspen Plus economic analyzer to estimate most of each component's capital cost. The majority of the costs are obtained from the literature and Icarus (an equipment capital cost estimating software tool of Aspen Tech). In order to determine the total system cost, first the purchased cost of the equipment is calculated and then cost factors are used to determine the installed equipment cost. The cost multipliers are taken from [10–11]. For the biomass-based hydrogen plants in this study, the total project investment (TPI) is evaluated as follows: TPI = (TIC) + (TINC), where TIC is the total installed cost and TINC is total indirect cost.

Total Installed Cost

To estimate the TIC, the factors considered for each piece of equipment are shown in Table 86.1. This method, which is also called technically factored estimate based on knowledge of major items of equipment, has an expected accuracy of about ± 30 % [11].

Total Indirect Cost

The indirect costs, which are the nonmanufacturing fixed-capital investment costs, are also determined using cost factors from [10]. The relevant factors are shown in Table 86.2, as percentages of the total purchased equipment cost, total installed cost, and total project investment.

Table 86.1 Cost factors in determining total installed equipment costs

	% of TPEC
Total purchased equipment cost (TPEC)	100
Purchased equipment installation	39
Instrumentation and controls	26
Piping	31
Electrical systems	10
Buildings (including services)	29
Yard improvements	12
Total installed cost (TIC)	247

Table 86.2 Cost factors for indirect costs

Indirect cost	% of TIC
Engineering	13
Construction	14
Legal and contractor fees	9
Project contingency	15
Total indirect costs (TINC)	51

Table 86.3 Feed handling, drying, gasification, and gas cleanup costs

Reference	Scaled feed handling and drying cost $K	BCL-scaled gasifier and gas cleanup cost $K
[11]	$18,840[a]	$16,392[a]
2009 (based on 3 % escalation per year)	$23,170	$20,160

[a]2,000 ton/day plant

Feed Handling, Drying, Gasification, and Gas Cleanup Capital Costs

Several reports detail the biomass handling and drying costs as well as the gasification and gas cleanup costs [12–19]. Table 86.3 summarizes the costs for feed handling and drying and for gasification and gas cleanup.

Other Capital Costs

The cost of reactors, heat exchangers, compressors, blowers, and pumps are determined using the energy and material balances from the Aspen Plus simulations along with the Aspen process economic analyzer (Icarus). The following are the sizing criteria. The surface area of each heat exchanger is calculated based on $\dot{Q} = U \times A \times \ln\Delta T$, where $\dot{Q}$ is the heat duty, U is the overall heat transfer coefficient, A is the exchanger surface area, and $\ln\Delta T$ is the log mean temperature difference. Icarus determines the appropriate heat exchanger surface area. Design information including flow rate, operating temperature, and pressure for the blowers and compressors are taken from the Aspen Plus simulation. The cost of the syngas compressor includes the cost of the interstage coolers and condenser vessels.

Operating Costs

There are two kinds of operating costs: fixed and variable. This section discusses the operating costs for the biomass gasification to hydrogen production plant including the assumptions and values for these costs.

Table 86.4 Labor costs

Worker	($) Salary	Number	($) Total cost
Plant manager	110,000	1	110,000
Plant engineer	65,000	1	65,000
Maintenance supervisor	60,000	1	60,000
Lab manager	50,000	1	50,000
Shift supervisor	45,000	5	225,000
Lab technician	35,000	2	70,000
Maintenance technician	40,000	8	320,000
Shift operators	40,000	20	800,000
Yard employees	25,000	12	300,000
Clerks and secretaries	25,000	3	75,000
Total salaries (2002)			2,080,000
Total salaries (2009) (based on 3 % escalation per year)			2,558,137

Table 86.5 Other fixed costs

Item	Factor	Cost
General overhead	95 % of total salaries	$2,430,000
Maintenance	2 % of total project investment	–
Insurance and taxes	2 % of total project investment	–

Table 86.6 Economic parameter values

Parameter	Value
Internal rate of return (after-tax)	10 %
Debt/equity	0 %/100 %
Plant life	20 years
General plant depreciation	200 % DDB
General plant recovery period	7 years
Working capital	5 % of total capital investment
Start-up time	6 months
Land	6 % of total purchased equipment cost
Construction period	2 years
Operating hours per year	8,000 h
Feedstock cost (dry basis)	$40/ton

Fixed Operating Costs

The fixed operating costs given in [17] are used as a starting point to progress fixed costs for the biomass gasification to hydrogen production plant. To determine labour costs, salaries from 2002 are used, with an assumed 3 % annual wage increase (see Table 86.4).

Also since the salaries listed in Table 86.4 are not fully loaded, a general overhead factor is used. This also covers general plant maintenance, plant security, janitorial services, communications, etc. Factors for maintenance, insurance, and taxes are obtained from [10–11] and can be seen in Table 86.5.

An excel worksheet was set up and some of the base case economic parameters used in the spreadsheet are given in Table 86.6. The depreciation amount was determined by the same method as that documented in [10, 15].

Variable Operating Costs

There are many variables affecting the variable operating costs and minor ones are neglected. The variables, information about them, and costs associated with each variable are shown in Table 86.7. This table shows in particular the assumed variable operating cost for the simulations. However, actual plants likely have different variables and costs.

Table 86.7 Variable operating costs

Variable	Information and operating cost
Tar reformer catalyst	Neglected
ZnO, steam reforming and shift catalysis	Neglected
Gasifier bed material	Neglected
Solids disposal cost	$700,000/year for 2,000 ton/day plant
Electricity (2009 values)	Price: 5.8 ¢/kWh
Natural gas (2009 values)	Pipeline composition consists of 100 % vol. CH_4, Price: $0.1/m^3
LO-CAT chemicals	Neglected
Waste water	Neglected

Source: [11]

Systems Descriptions

An economic evaluation of a complex system requires consideration of its components and their characteristics. Recently, biomass gasification in indirectly heated steam gasifiers has received much attention for the conversion of biomass to combustible gases [20]. In this section, there are some improvements, suggestions, and alterations made for the systems which are studied by [21, 22]; for instance, ways to achieve increased heat recovery or electricity production from waste heat to increase the overall system efficiency. A comparison is also presented. The aim of this section is to describe the simulated hydrogen plants and their features in detail. The hydrogen plant simulations are described with flow diagrams. The simulations are created to remain true to the original systems as described [11, 19, 23], although some minor changes are made in these simulated systems. Detailed explanations of the hydrogen production process for the three hydrogen plants are provided in this section. This stage consists of an economic evaluation for these systems to determine the minimum hydrogen production costs.

System 1

The system in Fig. 86.1 was a part of the NASA shuttle program (hydrogen production from biomass) and proposed for bagasse gasification [23]. For further study and exergy calculations, the current system was redesigned to account for missing data and information from the original proposed system. The same approach was almost followed as with the original proposed system. The planned capacity here is different than the proposed system, and the current design incorporates enhancements to increase heat recovery and reduce water consumption.

System 2

We can produce either electricity or hydrogen through gasification. However, some examples exist which produce electricity and hydrogen concurrently [19]. Figure 86.2 shows the first part of the hydrogen plant of system 2 and system 3, which is syngas production through gasification. This system reported by the FERCO SilvaGas process [24, 25] employs the low-pressure Battelle (Columbus) gasification process, which was developed by the United State Department of Energy Biomass Power Program, FERCO, Battelle Columbus Laboratory, Burlington Electric Department, Zurn Industries, OEC/Zurn, and NREL. This process consists of two physically separate reactors: a gasification reactor in which the biomass is converted to a gas mixture and residual char at a temperature of 850 to 1,000 °C and a combustion reactor that burns the residual char to provide heat for gasification.

System 3

The system in Fig. 86.3 is proposed and designed in a report using Aspen Plus by the Natural Renewable Energy Laboratory (NREL) [11]. Both energy and economic investigations are included to demonstrate that hydrogen can be an economically feasible product. In this chapter, some improvements, suggestions, and alterations are made for this system, for instance, more heat recovery or electricity production from waste heat is employed to increase the overall system efficiency.

Fig. 86.1 Block diagram of the hydrogen production plant of system 1

Fig. 86.2 Block diagram of the hydrogen production plant of system 2

Fig. 86.3 Block diagram of the hydrogen production plant of system 3

Results and Discussion

Detailed economic analyses are performed to estimate the minimum hydrogen production cost, based on the explanations, assumptions, and methods about the economic evaluations in previous sections. As can be observed in the below tables, many factors affect the minimum hydrogen production cost (MHPC). This investigation seeks to minimize the minimum hydrogen production cost and discusses how we can reduce the MHPC to make it competitive with other fuels.

Economic Results for System 1

In Table 86.8, direct capital costs, indirect capital costs, and operating costs for system 1 are presented. For this case, the tar cracking catalyst, olivine (gasifier bed material), and other catalysts' cost are not included in the operating cost. As can be seen in Table 86.8, the major parts of the operating costs are associated with the feedstock and natural gas. As a result, this system with the delivered feedstock cost at 40 $/ton exhibits a minimum hydrogen production cost of 1.78 $/kg, i.e., 14.82 $/GJ. It is also clear that some produced electricity contributes to reduce the MHPC.

Economic Results for System 2

In Table 86.9, direct capital costs, indirect capital costs, and operating costs for system 2 are presented. As can be seen for this system, the major parts of the operating costs are associated with the feedstock and natural gas. As a result, this system with the delivered feedstock cost at 40 $/ton exhibits a minimum hydrogen production cost of 1.55 $/kg, i.e., 12.8 $/GJ. This system purchases some electricity, which increases the MHPC while increasing the total operating cost.

Table 86.8 Hydrogen production economic evaluation of system 1

2000 Dry metric tonnes biomass per day, all values in 2009$			
Minimum hydrogen production cost ($/kg)	1.78	($/GJ H_2, LHV basis)	
Hydrogen production (MM kg/year)	29.76	14.82	
Delivered feedstock cost ($/dry US ton)	40.00		
Direct capital costs (M$)		*Operating costs (cents/kg H_2)*	
Feed handling and drying	$23.17	Feedstock	95.05
Gasification[a]	$12.94	Natural gas	37.05
Compression and sulfur removal	$6.41	Tar reforming catalyst	0.00
Steam methane reforming, shift, and PSA	$5.61	Other catalysts	0.00
Hydrogen compression	$0.00	Olivine	0.00
Steam system and power generation	$5.61	Other raw materials	1.68
Cooling water and other utilities	$1.27	Waste disposal	2.35
Combustor 1[a]	$1.97	Electricity	−29.96
Total installed equipment cost (TIC)	**$56.98**	Fixed costs	18.20
		Capital depreciation	14.46
Indirect costs (M$)		Average income tax	11.56
Engineering (13 % of TIC)	$7.41	Average return on investment	28.91
Construction (14 % of TIC)	$7.98	*Operating cost (M$/year)*	
Legal and contractor fees (9 % of TIC)	$5.13	Feedstock	$28.29
Project contingency (15 % of TIC)	$8.55	Natural gas	$11.03
		Tar cracking catalyst	$0.00
Total indirect costs	**$29.06**	Other catalysts	$0.00
		Olivine	$0.00
Total project investment (TPI)	**$86.04**	Other raw matl. costs	$0.50
		Waste disposal	$0.70
		Electricity	−$8.92
		Fixed costs	$5.42
		Capital depreciation	$4.30
Total plant electricity usage (kW)	26,644	Average income tax	$3.44
Electricity produced onsite (kW)	45,861	Average return on investment	$8.60
Purchased electricity (kW)	−19,217	Total operating cost	$53.36

[a]The costs estimation for the low pressure indirectly heated gasifier and combustor 1 were determined by evaluating the sources [10, 11, 17, 19].

Economic Results for System 3

In Table 86.10, direct capital costs, indirect capital costs, and operating costs for system 3 are provided. As can be seen, the major parts of operating costs are due to the feedstock and natural gas. As a result this system with the delivered feedstock cost at 40 $/ton has a minimum hydrogen production cost of 1.28 $/kg, i.e., 10 $/GJ. It is interesting to note that this system has the highest produced electricity rate, which means that for this system we can sell electricity and hydrogen at the same time to reduce operating costs which are directly linked to MHPC. Further discussion is provided in the next section in terms of economic comparisons of these three systems.

Economic Evaluations and Comparisons of the Systems

Figures 86.4 and 86.5 show the TPI and operating costs for the three cases for a plant capacity of 2,000 ton/day. The detailed capital costs for these three systems were explained previously. Once the capital and operating costs have been determined, a minimum hydrogen production cost (MHPC) can be determined using a discounted cash flow rate of return analysis. The methodology used follows that in [10, 19]. The MHPC is the production cost of hydrogen that makes the net present value of the biomass syngas to hydrogen process equal to zero with a 10 % discounted cash flow rate of return over a 20-year plant life.

Table 86.11 shows the estimated economic analysis results for a minimum hydrogen production cost for different process flows, varying between $1.28/kg and $1.78/kg with a plant capacity of 2,000 dry tonne per day. Overall, for these three

Table 86.9 Hydrogen production economic evaluation of system 2

2000 Dry metric tonnes biomass per day—all values in 2009$			
Minimum hydrogen production cost ($/kg)	1.55	($/GJ H_2, LHV basis)	
Hydrogen production at operating capacity (MM kg/year)	62.48	12.89	
Delivered feedstock cost $/dry tonne	40.00		
Direct capital costs (M$)		*Operating costs (cents/kg hydrogen)*	
Feed handling and drying	$23.17	Feedstock	45.28
Gasification	$20.16	Natural gas	46.41
Compression and sulfur removal	$12.00	Tar reforming catalyst	0.00
Steam methane reforming, shift, and PSA	$20.71	Other catalysts	0.00
Hydrogen compression	$0.00	Olivine	0.00
Steam system and power generation	$7.54	Other raw materials	0.80
Cooling water and other utilities	$5.25	Waste disposal	1.12
		Electricity	8.62
Total installed equipment cost (**TIC**)	**$88.83**	Fixed costs	11.75
		Capital depreciation	10.73
Indirect costs (M$)		Average income tax	8.59
Engineering (13 % of TIC)	$11.55	Average return on investment	21.47
Construction (14 % of TIC)	$12.44	*Operating cost (M$/year)*	
Legal and contractor fees (9 % of TIC)	$8.10	Feedstock	$28.29
Project contingency (15 % of TIC)	$13.33	Natural gas	$29.00
		Tar cracking catalyst	$0.00
Total indirect costs	**$45.31**	Other catalysts	$0.00
		Olivine	$0.00
Total project investment (**TPI**)	**$134.14**	Other raw matl. costs	$0.50
		Waste disposal	$0.70
		Electricity	$5.39
		Fixed costs	$7.34
		Capital depreciation	$6.71
Total plant electricity usage (kW)	31,904	Average income tax	$5.37
Electricity produced onsite (kW)	20,294	Average return on investment	$13.41
Purchased electricity (kW)	11,610	Total operating cost	$96.70

systems, the greater part of the operating cost is accounted for by natural gas and feedstock costs, while the capital depreciation and other costs account for only relatively small portions of the total. From references [26, 27, 28], these values vary between 1.69 and 10 $/kg, depending on plant capacity and other factors. Since there are differences with each system, the equipment required for all three systems are similar in some ways, however the needs are more basic for system 1, and more complex for system 3. The impact on capital costs are sometimes negative and at other times positive. For example, for system 1, the amount of input biomass to the gasifier is different than for systems 2 and 3. In other words, for system 1, the gasifier size will be smaller than for systems 2 and 3, and it will be cheaper than for systems 2 and 3. The hydrogen production costs in Tables 86.8, 86.9, and 86.10 depend on many factors, including feedstock cost, methane cost, electricity cost, tax, etc. Feedstock and natural gas costs alone cover a large portion of the operating cost. From this perspective the hydrogen production cost decreases drastically if the natural gas and feedstock costs are reduced. Depending on values of these parameters, we obtain the minimum hydrogen production costs seen in Table 86.11.

Another reason why the hydrogen production cost is high for these three systems is that the water in wet biomass (50 % moisture) needs to be evaporated in the drier to become dry biomass (5.7 % moisture). This process is expensive and the direct capital cost is affected in a negative way because the drier brings additional cost. If the biomass were initially dry and the need for the drier avoided, the hydrogen production cost would be reduced significantly, by approximately $0.22/kg. It can thus be an advantage to use dry biomass or to use sunlight to let the biomass dry before engaging in the process. For system 1, there is no specified hydrogen production cost available in the literature; however, the minimum hydrogen production cost is $1.78/kg which is quite reasonable. In contrast, even though the operating cost of system 1 is less than for systems 2 and 3, the hydrogen production cost is the highest because the hydrogen production capacity per year is less than for systems 2 and 3. For systems 2 and 3 the hydrogen production capacities are almost the same. The system 3 hydrogen production rate is slightly less than for system 2 due to the unpredicted losses during hydrogen production with system 3.

Table 86.10 Hydrogen production economic evaluation of system 3

2000 Dry metric tonnes biomass per day—all values in 2009$			
Minimum hydrogen production cost ($/kg)	1.28	($/GJ H$_2$, LHV basis)	
Hydrogen production at operating capacity (MM kg/year)	61.10	10.03	
Delivered feedstock cost $/dry tonne	40.00		
Direct capital costs (M$)		*Operating costs (cents/kg H$_2$)*	
Feed handling and drying	$23.17	Feedstock	46.30
Gasification	$20.16	Natural gas	53.68
Compression and sulfur removal	$15.37	Tar reforming catalyst	0.00
Steam methane reforming, shift, and PSA	$21.67	Other catalysts	0.00
Hydrogen compression	$4.99	Olivine	0.00
Steam system and power generation	$12.10	Other raw materials	0.82
Cooling water and other utilities	$5.91	Waste disposal	1.15
		Electricity	−35.66
Total installed equipment cost (TIC)	**$103.37**	Fixed costs	13.45
		Capital depreciation	12.77
Indirect costs (M$)		Average income tax	10.22
Engineering (13 % of TIC)	$7.95		
Construction (14% of TIC)	$14.47		
Legal and Contractor fees (9% of TIC)	$9.30		
Project contingency (15 % of TIC)	$15.51	*Operating cost (M$)*	
		Feedstock	$28.29
Total Indirect Costs	**$47.23**	Natural gas	$32.80
		Tar cracking catalyst	$0.00
Total project investment (TPI)	**$156.09**	Other catalysts	$0.00
		Olivine	$0.00
		Other raw matl. costs	$0.50
		Waste disposal	$0.70
		Electricity	−$21.79
		Fixed costs	$8.22
Total plant electricity usage (kW)	35,803	Capital depreciation	$7.81
Electricity produced onsite (kW)	82,760	Average income tax	$6.24
Purchased electricity (kW)	−46,957	Average return on investment	$15.61
		Total operating cost	$78.39
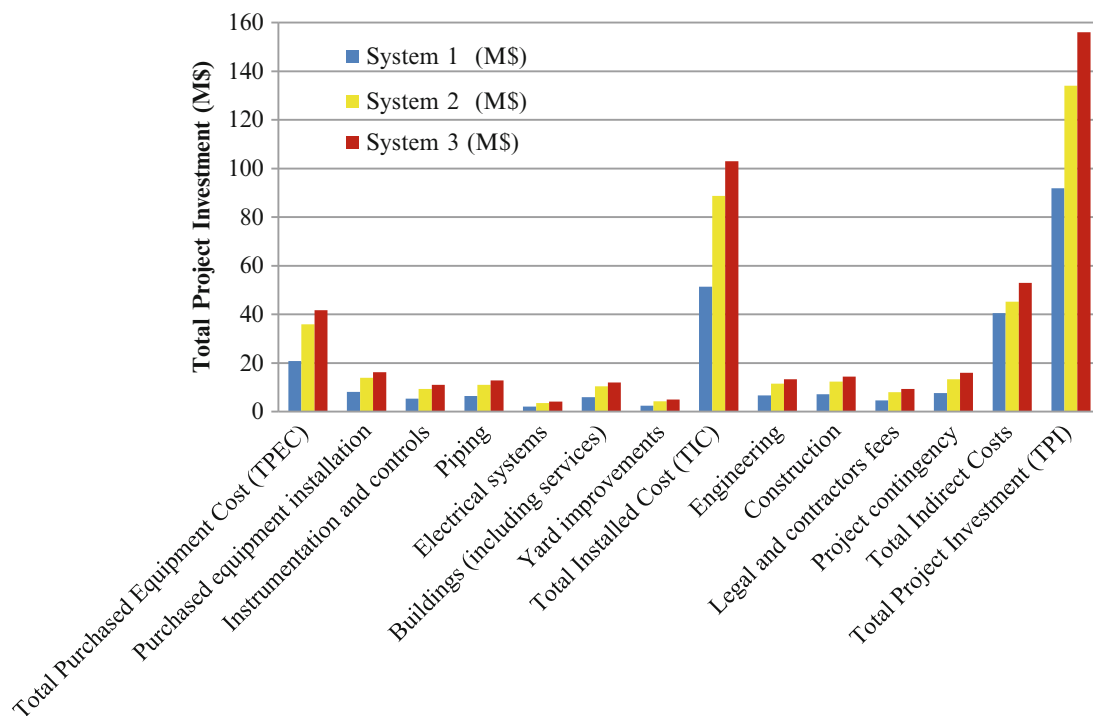
Fig. 86.4 Overview of the TPIs for the three systems
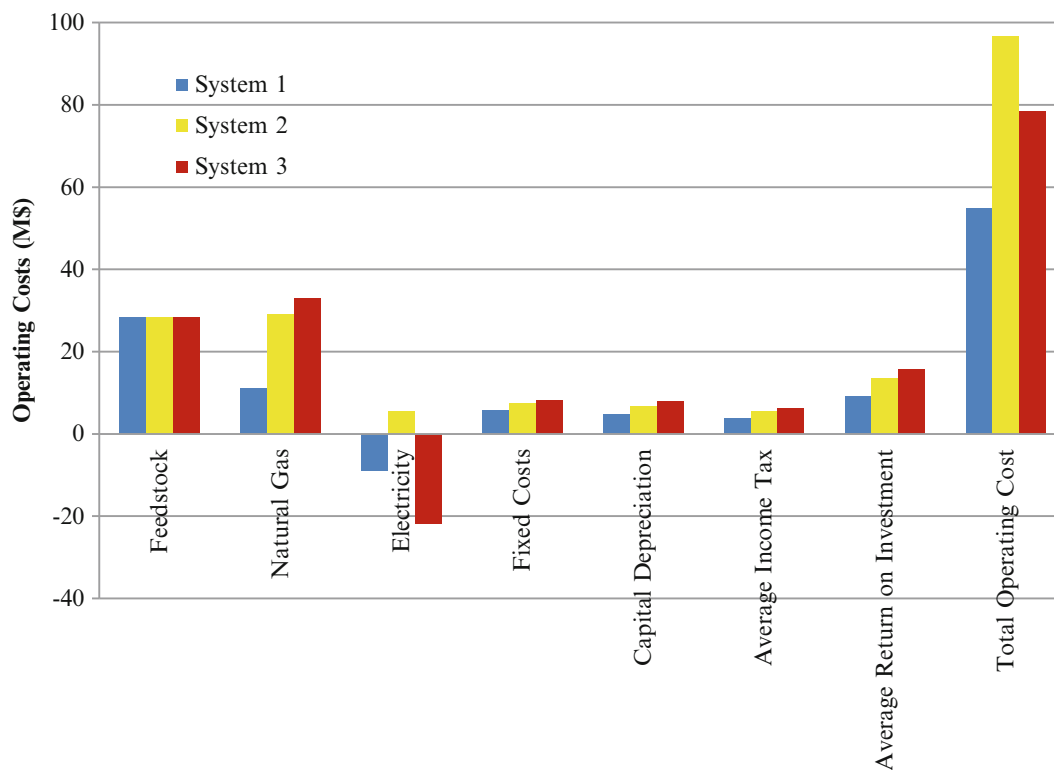
Fig. 86.5 Overview of the TOCs for the three systems

Table 86.11 Minimum hydrogen production cost (MHPC) comparisons for different processes

Formulas	System 1	System 2	System 3	Ref. [26]	[27]	[28]
$\dfrac{\text{Total operating cost (\$/year)}}{\text{Total hydrogen production (kg/year)}}$	\$1.78/kg	\$1.55/kg	\$1.28/kg	\$4.28/kg	\$10/kg	1.69/kg
$\dfrac{\text{Total operating cost (\$/year)}}{\text{Total hydrogen production (kg/year)} \times \text{LHV(GJ/kg)}}$	\$15.30/GJ	\$12.90/GJ	\$10.1/GJ			

Systems 1 and 3 have some saleable electricity, which reduces the hydrogen production cost, while system 2 purchases some electricity from outside sources, increasing the minimum hydrogen production cost. Among these systems, system 1 has the highest hydrogen production cost while it has the lowest purchased methane, implying it produces hydrogen with the highest cost and the lowest greenhouse gas emissions. Similarly, system 3 has the lowest hydrogen production cost with the highest capacity, but the highest greenhouse gas emissions (proportional to the purchase of natural gas).

Thermodynamic Comparisons of the Systems

Two of the more significant factors to be addressed following the simulation results are the overall energy and exergy efficiencies. A comparison among the simulated systems thermodynamic results is presented in this section. The energy and exergy expressions and assumptions for the simulated systems can be found [20–22]. In addition, economic evaluations and detailed explanations with the assumptions for the studied systems are presented in those references. It can be seen in Table 86.12 that the simulated systems have some shared characteristics and differences regarding simulation setup.

Table 86.12 demonstrates the differences in energy and exergy efficiencies for the three systems. In all cases, the energy and exergy efficiencies are relatively lower than the SMR or coal gasification energy and exergy results reported in the literature. The desirability of having a biomass-based hydrogen production system is motivated by environmental and

Table 86.12 Comparison of three biomass-based hydrogen plants

Parameter	System 1	System 2	System 3
Plant capacity (ton/day)	2,000	2,000	2,000
Biomass to gasifier flow rate (ton/h)	24.8	88.4	88.4
Consumed CH_4 (ton/h)	8.96	23.52	33.6
Produced H_2 flow rate (ton/h)	3.72	7.72	7.63
System energy efficiency, η_{sys} (%)	22	31	33
System exergy efficiency, ψ_{sys} (%)	19	28	29

sustainability concerns. One concern is related to releasing carbon after any process which is identified in the carbon cycle. There are many variables which can affect the overall system energy and exergy efficiencies such as the type of biomass and the amount of moisture in the biomass. In this study, all the simulated systems are placed on similar bases, for instance, the same kind of biomass is chosen, oil palm shell, and the biomass outlet temperature is set at 870 °C for these three systems so as to determine a fair comparative view of the thermodynamic efficiencies. When the simulations are developed, all variables and conditions were kept as similar as possible.

From the results, three main points are identified. First, the exergy efficiencies are noticeably lower than the corresponding energy efficiencies. Second, it can be observed that systems 2 and 3 have the same biomass flow rate to the gasifier, resulting in almost the same amount of hydrogen product. Furthermore, the amount of methane gas consumed among the systems are incorporated with the biomass directly affecting the system performance; therefore, system 3 has the highest system energy and exergy efficiencies,33 % and 29 % respectively, while system 1 has the lowest system energy and exergy efficiencies, 22 % and 19 % respectively. The energy and exergy portion of the methane included with the biomass feed can be seen in the thermodynamic evaluation section in Table 86.12 for all systems.

In system 1, energy and exergy efficiencies are relatively low due to the biomass split; this evokes less biomass entering the gasifier meaning less hydrogen production at the end. An important aspect of this system is that it consumes less CH_4 because the splitting process makes this system more sustainable even though its efficiency is the lowest with respect to the amount of the greenhouse gas released to the atmosphere, which is also the lowest, making this system more favorable environmentally. An important point is that systems 2 and 3 are similar but their energy and exergy efficiencies are different due to the fact that system 3 has more heat recovery implementation than system 2, which directly affects the produced electricity from the turbine. For instance, system 3 has separate water and steam treatment subsystems while system 2 does not. Furthermore, system 3 has more heat exchangers than system 2. In addition, system 3 has three-stage power systems consisting of a high pressure turbine, a low pressure turbine, and a vacuum turbine, while system 2 has just one turbine. System 2 produces less work output. When we compare the three simulated systems, system 3 is seen to have a more sophisticated arrangement than systems 1 and 2 making it closer to a functioning hydrogen plant by implementing water and steam treatment, and a collection unit.

It is also important to note that real world systems may have lower energy and exergy values due to the increased heat losses and lack of heat recovery. However, the simulation process enables a good understanding of the behaviours and characteristics of these systems, which can aid system developers and designers.

Conclusions

The economic investigation of three biomass-based hydrogen production systems determined that one (system 3) has a maximum energy and exergy efficiency and the lowest hydrogen production cost, which is estimated to be $1.28/kg. When we examine these three systems from energy, exergy, and economic bases, we discover that system 3 has higher energy and exergy efficiencies with a lower hydrogen production cost. System 3 also consumes the most methane gas. While system 1 consumes the least methane gas with lowest energy and exergy efficiencies, including a higher hydrogen production cost, also sustainability considerations for this energy source suggest that system 1 is more favorable than systems 2 and 3 even though it has the lowest hydrogen production rate. It can also be concluded that the gasifier is the most vital and expensive component in the simulated biomass gasification systems. To promote the use of biomass conversion in a more profitable way, an interesting strategy seems to be the use of biomass in conjunction with natural gas, in a high efficiency energy conversion system, such as a combined cycle power plant while simultaneously producing hydrogen and electricity. The hydrogen production costs decrease significantly for these three systems if natural gas and feedstock costs are reduced.

Nomenclature

A	Heat exchanger surface area, m^2		U	Heat transfer coefficient, $W/(m^2\text{-}K)$
LHV	Lower heating value, MJ/kg		T	Temperature, K
$\dot{Q}$	Heat duty, W			

Greek Symbols

¢	Cent		η	Energy efficiency, %
Δ	Difference		ψ	Energy efficiency, %

Subscript

sys System

Acronyms

COMB	Combustion		PSA	Pressure swing adsorption
COMP	Compressor		R-Equil	Equilibrium reactor
Cyc	Cyclone		R-Gibbs	Gibbs reactor
DECOMP	Decomposer		R-Yield	Yield reactor
DRY-REACT	Dry Reactor		SMR	Steam methane reformer
DRY-FLASH	Condenser		SP	Splitter
EC	Economizer		TIC	Total installed cost
HTS	High-temperature shift		TINC	Total indirect cost
HX or HE	Heat exchanger		TPI	Total project cost
LO-CAT	Liquid oxidation catalyst		TURB	Turbine
MHPC	Minimum hydrogen production cost			

References

1. Voogt MH, Uyterlinde MA, Noord M, Skytte K, Nielsen LH, Leornardi M, Whiteley M, Chapman M (2001) Renewable energy burden sharing project (REBUS): effects of burden sharing and certificate trade on the renewable electricity market in Europe. Energy Research Centre of the Netherlands (ECN), Project No: 7.7260, 113
2. Phaal R, Farrukh CJP, Probert DR (2003) Technology roadmapping – a planning framework for evolution and revolution. Technol Forecast Social Change 71:5–26
3. National Hydrogen Energy Roadmap (2002) United States Department of Energy (DOE). Washington, DC. http://www.eere.energy.gov/hydrogenandfuelcells/pdfs/national_h2_roadmap.pdf
4. Goswami DY, Mirabal ST, Goel N, Ingley HA (2003) A review of hydrogen production technologies. Fuel Cell Sci Eng Technol 1701:61–74
5. Braccio G, Matera D, Gamberale M, Addabbo V, Sharma VK (2006) Effect of different parameters and variables on the cost of hydrogen produced from biomass using gasification plants of low to medium thermal capacity. Int Energy J 7(1):43–55
6. Lv P, Wu C, Ma L, Yuan Z (2008) A study on the economic efficiency of hydrogen production from biomass residues in China. Renew Energy 33:1874–1879
7. Elnashaie S, Chen Z, Prasad P (2007) Efficient production and economics of clean-fuel hydrogen. Int J Green Energy 4:249–282
8. Thampapillai DJ (2002) Environmental economics: concepts, methods, and policies. Oxford University Press. ISBN 978-0-19-553577-8
9. Yang H, Yan R, Chen H, Lee DH, Liang DT, Zheng C (2006) Mechanism of oil palm waste pyrolysis in a packed bed. Energy Fuel 20:1321–1328
10. Peters MS, Timmerhaus KD (2003) Plant design and economics for chemical engineers, 5th edn. McGraw-Hill, New York, NY
11. Spath P, Aden A, Eggeman T, Ringer M, Wallace B, Jechura J (2005) Biomass to hydrogen production detailed design and economics utilizing the BCL indirectly heated gasifier. National Renewable Energy Laboratory, Report No. TP-510-37408
12. Breault R, Morgan D (1992) Design and economics of electricity production form an indirectly-heated biomass gasifier. Battelle Columbus Laboratory. Report No: TR4533-049-92. Columbus, OH
13. Weyerhaeuser N, Stone W (2000) Biomass gasification combined cycle. Weyerhaeuser Company, Tacoma, WA. DOE DE-FC36-96GO10173
14. Weyerhaeuser N (1992) Gasification capital cost estimation. Battelle Columbus Laboratory. Obtained from Mark Paisley, August 1994
15. Wan EI, Malcolm DF (1990) Economic assessment of advanced biomass gasification systems. In: Klass DL (ed) Energy from biomass and wastes, vol xiii. Institute of Gas Technology, Chicago, pp 791–827

16. Wright J, Feinberg D (1993) A comparison of the production of methanol and ethanol from biomass. The International Energy Agency. Contract no: 23218-1-9201/01-SQ
17. Aden A, Ruth M, Ibsen K, Jechura J, Neeves K, Sheehan J, Wallace B, Montague L, Slayton A, Lukas J (2002) Lignocellulosic biomass to ethanol process design and economics utilizing co-current dilute acid prehydrolysis and enzymatic hydrolysis for corn stover. NREL. Report No: TP-510-32438
18. Craig KR, Mann MK (1996) A report: cost and performance analysis of biomass-based integrated gasification combined-cycle (BIGCC) power systems. National Renewable Energy Laboratory. Report No: NREL/TP-430-21657
19. Corradetti A, Desideri U (2007) Should biomass be used for power generation or hydrogen production? J Eng Gas Turbines Power 129:629–634
20. Cohce MK, Dincer I, Rosen MA (2010) Thermodynamic analysis of hydrogen production from biomass gasification. Int J Hydrogen Energy 3:4970–4980
21. Cohce MK, Dincer I, Rosen MA (2011) Energy and exergy analyses of a biomass-based hydrogen production system. Bioresour Technol 102:8466–8474
22. Cohce MK, Rosen MA, Dincer I (2011) Efficiency evaluation of a biomass gasification-based hydrogen production. Int J Hydrogen Energy 36:11388–11398
23. Elbaccouch M, T-Raissi A (2004) Aspen Plus process model for the production of gaseous hydrogen via bagasse gasification. Proceedings of the 15th world hydrogen energy conference, Yokohama, Japan
24. Paisley MA, Welch MJ (2003) Biomass gasification combined cycle opportunities using the future energy silvagas gasifier coupled to Alstom's industrial gas turbines. ASME. Paper No: GT2003-38294
25. Babu SP (2002) Biomass gasification for hydrogen production-process description and research needs. Gas Technology Institute, Des Plaines, IL
26. Lv P, Yuan Z, Ma L, Wu C, Chen YZ (2007) Hydrogen rich gas production from biomass air and oxygen/steam gasification. Int J Renew Energy 33 (11):2173–2185
27. Iwasaki W (2003) A consideration of the economic efficiency of hydrogen production from biomass. Int J Hydrogen Energy 28:939–944
28. Parks GD, Curry-Nkansah M, Evan H, Sterzinger G (2011) Hydrogen production cost estimate using biomass gasification. National Renewable Energy Laboratory. Report No: NREL/BK-6A10-51726

A Dynamic Simulation Study of a Small-Scale Hydrogen Production System for a High Temperature Proton Exchange Fuel Cell

87

Atilla Ersöz

Abstract

Fuel cell-based micro-combined heat and power (micro-CHP) systems have received increasing attention recently. In this study, a small-scale hydrogen production system for 1 kW_e High Temperature Fuel Cell (HTPEM) is presented and analyzed to investigate its dynamic behavior. The simulated hydrogen production system (HPS) can be integrated with a fuel cell to produce 1 kW_e power for residential uninterruptable power supply (UPS) application. Within this frame, HPS is modeled as a steady state process and then it is operated at dynamic conditions. The system is simulated with ASPEN HYSYS process simulation software. A dynamic simulation study has been conducted to investigate the changes on temperatures, compositions, feed conditions, and electrical loads during start-up period of HPS. Hydrogen and CO have been observed in HTPEM feed stream as 34 % and 0.3 %, respectively, within these optimum ratio conditions. The results show that electrical efficiency is in the range of 26–30 %, and fuel processing efficiency is about 81–83 % at this load level.

Keywords

Fuel processing • Hydrogen • Reforming • Microcogeneration • High temperature proton exchange membrane fuel cell • Uninterruptible power supply

Introduction

Fuel cell-based micro-combined heat and power (micro-CHP) systems have received increasing attention recently. This is due to a number of reasons. First of all distributed generation minimizes transmission losses. Second, a well-developed infrastructure for distributed natural gas is already presented in several countries. Therefore, the step to produce electricity in domestic households is realistic provided that the technical and financial issues of the CHP units can be resolved. Along with the technological progress in small-scale energy conversion devices such as Stirling engines, micro-turbines, and fuel cells, small-scale applications from just a few kWs up to some tens of kWs have become available [1]. Among fuel cells, a range of different types exists including proton exchange membrane (PEM) and solid oxide fuel cells (SOFC) [2].

Stationary fuel cell-based power generation systems also offer a great market opportunity, because the technology is capable of achieving higher efficiencies, with lower emissions as compared to conventional power systems. A micro-CHP system provides electricity and heat (space heating and hot water) for a residential building demand. These systems are designed to convert the chemical energy in a hydrocarbon feedstock into both electrical power and useful heat [3, 4].

Fuel cells can be one of the ideal technologies for micro-CHP generation in terms of some characteristics such as high reliability, low environmental impact, and size flexibility. In the last decade, micro-CHP based on PEM fuel cells has been intensively developed. Most of these systems are based on low temperature PEM fuel cells which operate at less than 100 °C.

A. Ersöz (✉)
TUBITAK Marmara Research Center Energy Institute, 41470 Gebze, Kocaeli, Turkey
e-mail: atilla.ersoz@tubitak.gov.tr

Several studies about PEMFC-based CHP processes can be found in open literature. The development of PBI-based MEA seems to have introduced with some improvements as operation with natural gas in recent years. These MEAs withstand higher temperatures (up to 180 °C) and therefore tolerance to carbon monoxide (CO) is improved. As a result of these improvements, simplified purification processes in reformers are required. The fuel cells based on these MEAs are normally referred as High-Temperature Proton Exchange Membrane Fuel Cells (HTPEM) in contrast with Nafion-based Low-Temperature Proton Exchange Membrane (LTPEM) fuel cells which require high purity hydrogen. Although in the last year's attention to HTPEM fuel cells has been growing, most research activities concern with membrane modeling or experimental characterization of stacks and only few with CHP systems [5].

Currently, the fuel cell technology based on hydrogen rich reformate gas has not made the market penetration. This depends on several parameters. The current systems are too complex and have a too long start-up time for the application in the uninterruptible power supply market. Hence, only prototypes exist based on reforming of natural gas and high temperature proton exchange membrane fuel cells (HTPEMFC).

Recent progress in H_2/air PEM fuel cells has focused to develop PEM fuel cells that operate above 100 °C. There are several reasons for operating at a higher temperature: (1) Electrochemical kinetics for both electrode reactions are enhanced; (2) Water management can be simplified because only a single phase of water need to be considered; (3) The cooling system is simplified due to the increased temperature gradient between the fuel cell stack and the coolant; (4) Waste heat can be recovered as a practical energy source; (5) CO tolerance is dramatically increased thereby allowing fuel cells to use lower quality reformed hydrogen [6].

Propane, natural gas, as well as liquid hydrocarbons are currently the preferred fuels because of their high storage density for hydrogen generation in fuel cell applications. Using these fuels the existing infrastructure can be used until hydrogen is widely available.

Currently, the most promising fuel processing system design is to use the auto-thermal reforming of natural gas in combination with a high temperature fuel cell. The high temperature fuel cell can tolerate CO contents of about 3 % vol. at operation temperatures around 180 °C compared to a common PEM fuel cell [7]. Unfortunately, systems based on this technology are currently too complex in the system design. Fuel cell systems using hydrocarbons as hydrogen source are mainly combined with fuel cells working either on a very low or a very high temperature level. Fuel cells working at temperatures below 100 °C (common PEM technology) can only be operated with CO contents that are lower than 100 ppm [8]. Therefore extensive hydrogen purification steps and a very high control effort are necessary. Fuel cells which are working at very high temperatures larger than 750 °C (e.g., SOFC) don't need any hydrogen rich gas cleanup steps after the reforming process but they have problems because of thermal stress of the materials and sealing. Those fuel cells cannot be used in applications where quick start-ups or dynamic operation modes are required.

The CHP plants based on fuel cells represent an interesting alternative to traditional technologies for the combined production of electrical energy and heat; this is due to the high efficiency of the FCs in partial load, the modularity, the ability to ensure substantial autonomy of the user from the electricity transmission grid, and, last but not least, the possible reduction of environmental impact [9]. A dynamic model is essential for the fuel processor operation for the following reasons: (1) discriminating control system design for improved load rejection and (2) evaluating start-up strategies for fast start-up [10].

Dynamic Simulation

Dynamic simulation can help to create a better design, optimization, and operation of a chemical process. Chemical processes are never truly at steady state. Feed and environmental disturbances, heat exchanger fouling, and catalytic degradation continuously upset the conditions of a smooth running process. The transient behavior of the process system is the best studied using a dynamic simulation package. The design and optimization of a chemical process involves the study of both steady state and dynamic behavior. Steady state models can perform steady state energy and material balances and evaluates different plant scenarios. With dynamic simulation, it can be confirmed that the plant can produce the desired product in a manner that is safe and easy to operate [11].

In Aspen HYSYS software, the dynamic analysis of a process system can provide insight into the process system when it is not possible with steady state modeling. The following conditions can be investigated with dynamic simulation:
- Process optimization
- Controller optimization
- Safety evaluation
- Transitions between operating conditions

- Start-up/Shutdown conditions

The Aspen HYSYS dynamic model shares the same physical property packages as the steady state model. The dynamic model simulates the thermal, equilibrium, and reactive behavior of the chemical system in a similar manner as the steady state model [11].

On the other hand, the dynamic model uses a different set of conservation equations which account for changes occurring over time. The equations for material, energy, and composition balances include an additional "accumulation" term which is differentiated with respect to time. Nonlinear differential equations can be formulated to approximate the conservation principles; however, an analytical solution method does not exist [11].

Therefore, numerical integration is used to determine the process behavior at distinct time steps. The smaller the time step, the more closely the calculated solution matches the analytic solution. However, this gain in rigor is offset by the additional calculation time required to simulate the same amount of elapsed real time. A reasonable compromise is achieved by using the largest possible step size, while maintaining an acceptable degree of accuracy without becoming unstable [11].

The aim of this work is to investigate the dynamic characteristics and to realize the dynamic process simulation studies for hydrogen production system (HPS) at different loads. Dynamic process simulation studies were performed for the integration of HPS including ATR, HTS, and LTS reactors and HTPEMFC with a significant reduced start-up time. System start-up period phases envisaged for the dynamic simulation parameters are within the scope. Different operating conditions were accepted. ASPEN HYSYS process simulation software was used for the dynamic simulation studies.

Process Layout

The system is based on an auto-thermal reforming (ATR) process of natural gas and a high temperature fuel cell stack (HTPEMFC). A combination of both the processes steam reforming (SR) and partial oxidation (POX), called auto-thermal reforming (ATR), has been used for the main HPS section as shown in Fig. 87.1.

The main characteristics of ATR are as follows:
– Low energy requirement due to the complementary steam reforming (SR) and partial oxidation (POX) reactions,
– Low energy consumption,
– High Gas Space Velocity (GSV), at least one order of magnitude larger than traditional SR,
– Preset H_2/CO ratio easily regulated by inlet reactant ratios,
– CO_2 recycling.

Natural gas, steam, and air streams are introduced to ATR inlet at the beginning of the envisaged process. The auto-thermal reforming reactor is controlled at an outlet temperature around 700–800 °C which is optimized for desired hydrogen yield. Then, the outlet stream is cooled down prior to HTS inlet temperature around 350 °C. Similarly, HTS outlet is cooled down to about 250 °C for LTS inlet stream. The exothermic water gas shift reactions (HTS and LTS) convert the entire CO generated by SR and POX into CO_2, while producing the maximum yield of H_2 by utilizing the steam as a co-reactant. Finally, the syngas coming from LTS reactor cooled down again for the HTPEM inlet operating conditions around 180 °C. The following main reactions (Eqs. 87.1, 87.2, 87.3, 87.4, and 87.5) can be described in the overall reforming process:

$$CH_4 + H_2O \rightarrow CO + 3H_2 \quad \Delta H_{298°C} = 206\,kJmol^{-1} \tag{87.1}$$

$$CO + H_2O \rightarrow CO_2 + H_2 \quad \Delta H_{298°C} = -41\,kJmol^{-1} \tag{87.2}$$

$$CH_4 + 2H_2O \rightarrow CO_2 + 4H_2 \quad \Delta H_{298°C} = 165\,kJmol^{-1} \tag{87.3}$$

$$CH_4 + 1/2O_2 \rightarrow CO + 2H_2 \quad \Delta H_{298°C} = -35.7\,kJmol^{-1} \tag{87.4}$$

$$CH_4 + CO_2 \Leftrightarrow 2CO + 2H_2 \quad \Delta H_{298°C} = 247.4\,kJmol^{-1} \tag{87.5}$$

Fig. 87.1 Schematic view of the 1 kWe HTPEM FC process
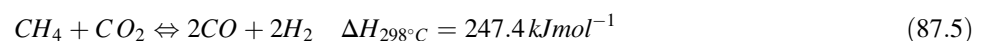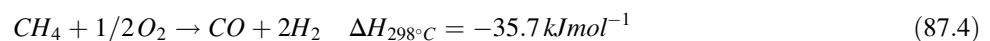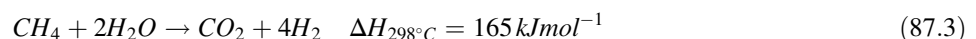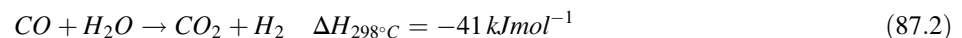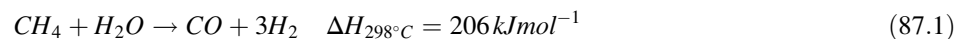
This process includes the main units implemented in the dynamic simulation study. The main units constituting the process model are as follows:

– *HTPEM fuel cell* for the production of electricity
– *Auto thermal reformer (ATR)* for the hydrogen production starting from natural gas
– *High and low temperature water gas shift reactors* (HTS & LTS) for hydrogen rich gas purification
– *Heat exchangers* to maintain desired temperature conditions
– *Control valves*
– *Control spreadsheet*
– *Flow controllers*

The main issue is a fast start-up of this HTPEMFC system. This requirement is essential for the applications of the uninterruptible power supply (UPS) unit as well as for microcogeneration (CHP) systems. One of the main issues for the UPS systems is to serve power during the electrical power outage. This challenge also has to be solved for the CHP market especially for dynamic loads and for standby modes.

Results and Discussion

Dynamic Simulation Results of the Single ATR Reactor for Start-Up Period

Simulations are based on to carry out primarily POX mode initialization of the ATR reactor. Within this assumption, only air and natural gas should be fed to first ATR reactor at the start-up phase and then the water vapor supply is fed after a period of time (Fig. 87.2).

The reactor feed stream valves are adjusted under dynamic simulation conditions. Using the simulation integrator module, the ATR exit temperature, outlet compositions, steam/carbon and oxygen/carbon ratios, natural gas, steam, and air flows is recorded versus time (Fig. 87.3). Electrical load changes (kWe) have also been observed in the light of these data.

The temperature range is determined as 700–800 °C to be appropriate at the optimum operating conditions of the ATR as can be seen from Fig. 87.4. In particular, suitable choice of operating temperature range of ATR affects the dynamic behavior, strength, and lifetime of the commercial catalyst and the reactor outlet compositions. Thus, it can be concluded that the targeted electrical load of the whole integrated process is affected by operation temperature and the reactor outlet compositions.

ATR reactor is being simulated within a dynamic equilibrium reaction model approach. Thermodynamic equilibrium takes place in the reactor considered during dynamic simulation work. ATR outlet compositions are calculated separately for each component. For the start-up period, the composition profile at ATR product stream is shown in Fig. 87.5. CO concentration is about the order of 20 % at the partial oxidation (POX) mode during initiation period. It is reduced to approximately 0.4 % after reaching steady state (approximately, 10 min later) due to the steam supply to ATR reactor. Similarly, while CO_2 is produced approximately in the range of 0.1–0.2 % during initial stage, it is increased to 0.7–0.75 % at steady state conditions.

The reactor exit stream includes about 35 % H_2O at the end of 10 min after starting feeding of water vapor approximately 100 s following the initial phase. A portion of the steam feed is consumed in the endothermic steam reforming reactions.

Hydrogen production is an extremely important step mainly through this process with the targeted fuel cell power generation. It seems that the order of 26–28 % wet basis of hydrogen is produced prior to the water gas shift reactor during start-up period.

The oxygen feed is given by the airflow which is especially consumed in POX reactions during the initiation and progression of the ATR step. The inert nitrogen which is not involved in the reaction is located in the order of approximately 26 % at reaching steady state point while the oxygen in the air is worked in the formation of exothermic reactions of partial oxidation.

Steam/carbon ratio is especially critical in terms of avoiding carbon deposition on the catalyst and the realization of endothermic steam reformer reactions. It can be said that the optimum operating ratio is about 3 during the initial start-up period, except for POX mode (Fig. 87.6). The reactor temperature increases but also the efficiency of hydrogen production reduces for the lower values of S/C ratios.

Oxygen/carbon ratio has a critical importance in the progression of the exothermic partial oxidation reactions. The efficiency of hydrogen production reduces if this rate is high. At the same time higher O_2/C ratios also causes an increase of the reactor temperature. The best data are observed between 0.6 and 0.7 at steady state condition (Fig. 87.7). In particular,
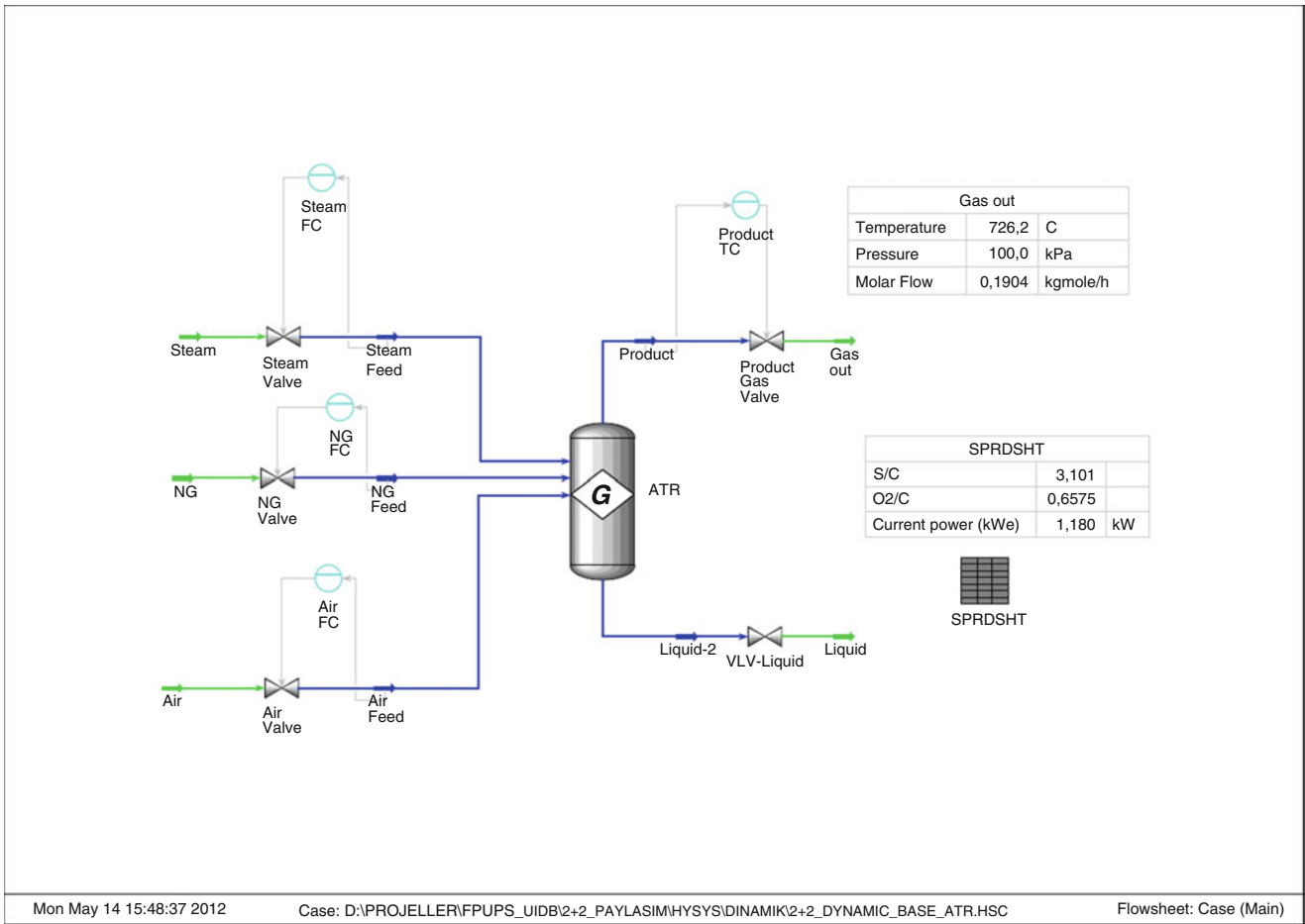
Fig. 87.2 Dynamic simulation of ATR
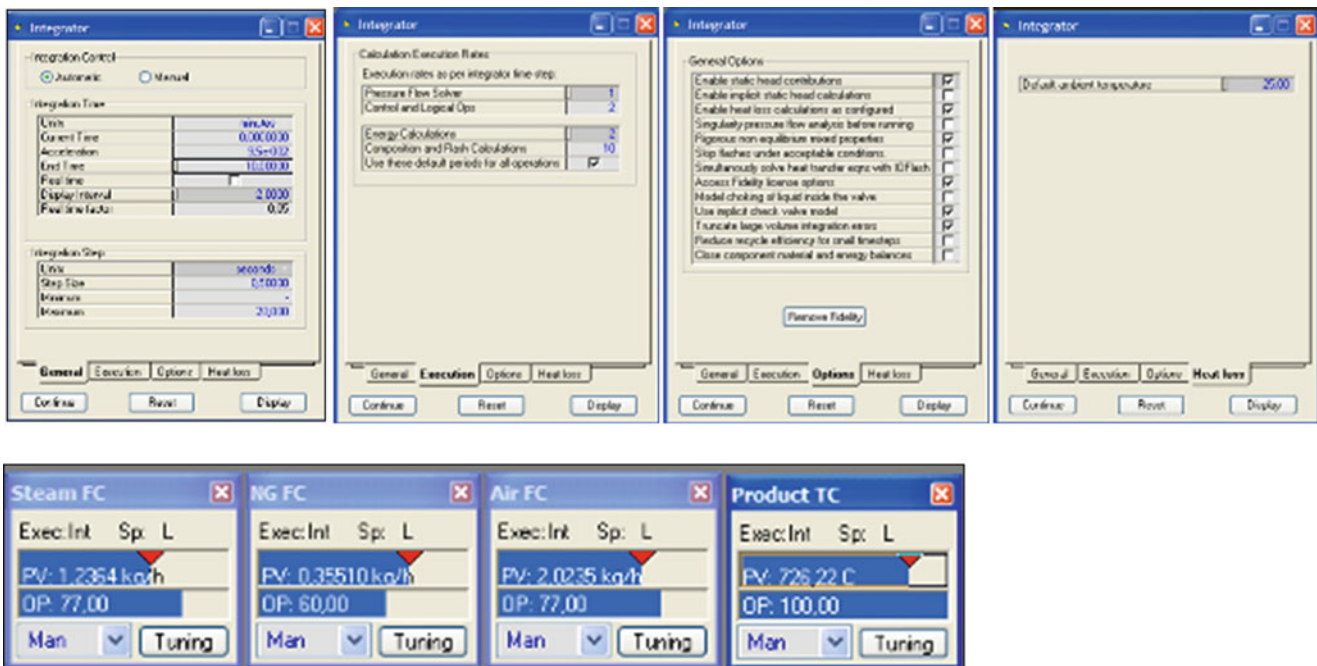
Fig. 87.3 Integrator module and flow control modules of dynamic simulation study

Fig. 87.4 ATR temperature profile during startup period
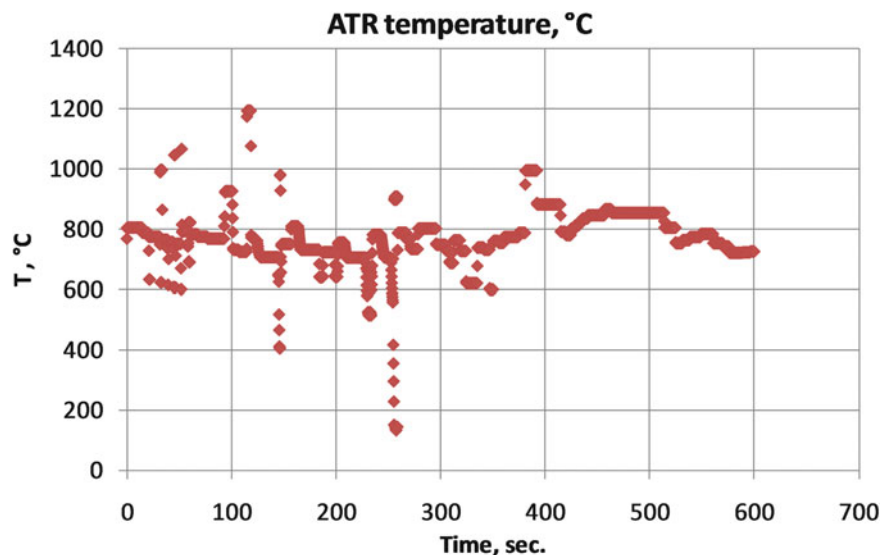
Fig. 87.5 Composition profile of ATR exit stream at startup period
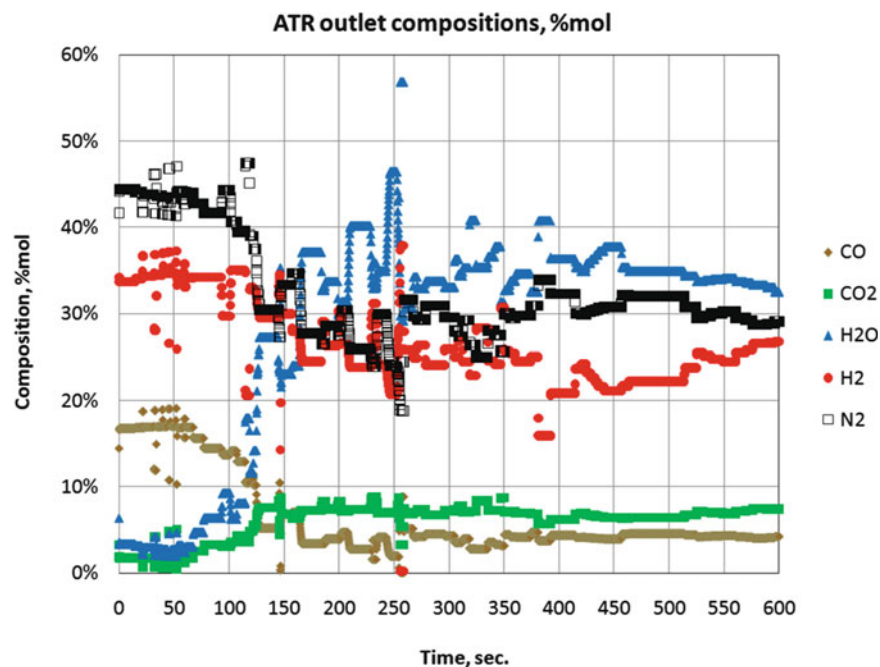
it is very important to keep this ratio at the required optimum conditions to prevent the undesirable adiabatic reaction temperature peaks or hot spots (runaway criteria). The life of the commercial catalyst used in the ATR reactor is adversely affected by unexpected temperature rises.

Natural gas feed increases up to 0.35 kg h^{-1} approximately at steady state conditions while it is about 0.05 kg h^{-1} at the beginning of the starting period. Similarly, it can be said that the value of the water vapor is approximately equal to 1.2 kg h^{-1} with a suitable S/C ratio adjustments. Air flow value is observed approximately equal to 2 kg h^{-1} at steady state conditions with a suitable O$_2$/C adjustment while it is about 0.5 % initially used in the reaction. The feed flow rates profile has been shown in Fig. 87.8 for start-up period of ATR reactor.

So far, all of the above-mentioned process variables and operating parameters are critical to achieving the target value of 1 kW$_e$ fuel cell power generation system with the application of uninterrupted power supply. The load increases from the initial value of 0.2 kW$_e$ to 1.2 kW$_e$ over the system start-up period in 10 min as can be seen from dynamic simulation study (Fig. 87.9). System start-up time is directly related to fuel cell behavior at high temperatures, heat integration, technical limitations, etc. So, it is especially targeted to reach steady state for ATR reactor conditions under a period of 10 min.

Fig. 87.6 Steam/carbon (S/C) ratio at startup of ATR
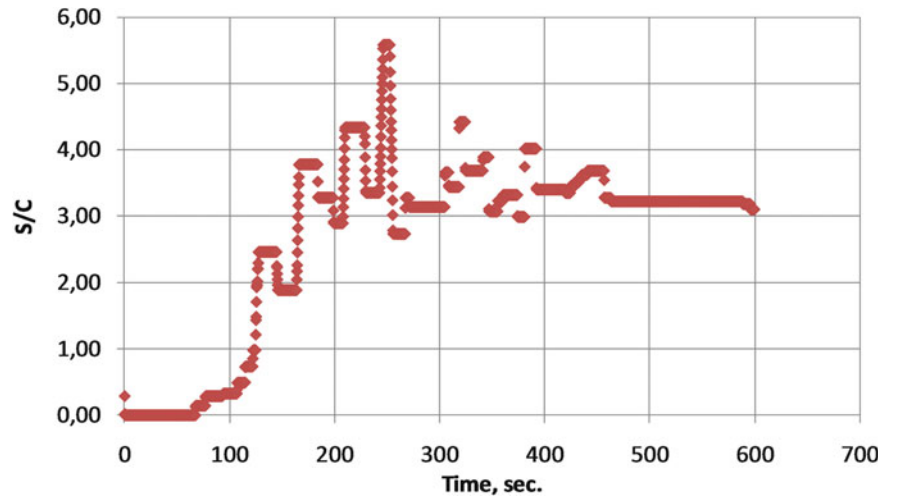
Fig. 87.7 Oxygen/carbon (O_2/C) ratio at startup of ATR
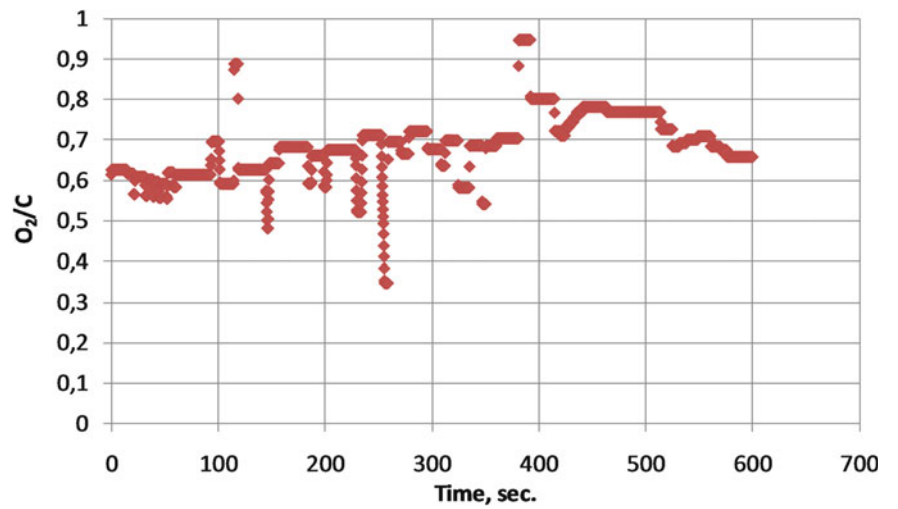
Fig. 87.8 Feed flow rates profile during startup period of ATR reactor
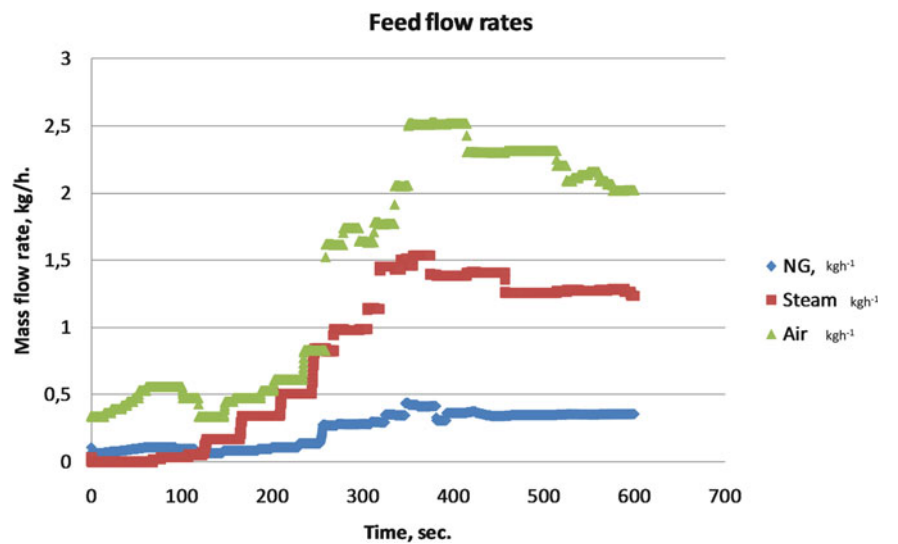
Fig. 87.9 Load change profile
at startup period of ATR
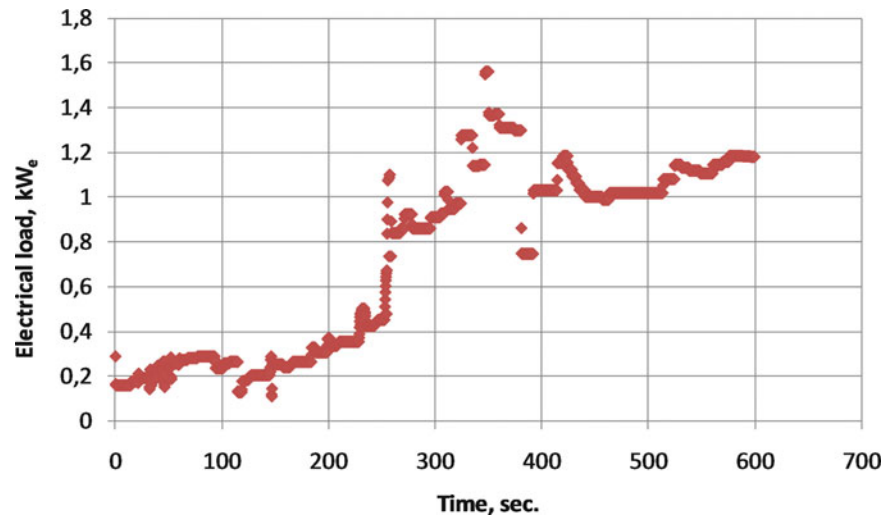
Dynamic Simulation Results for the ATR + HTS + LTS Integration at Start-up Period

The simulation of a combination of ATR-HTS-LTS reactors was carried out following the study of the singular dynamic simulation of the ATR reactor (Fig. 87.10). The above results are only given for ATR as well as to work within this integration which is carried out under the same conditions. ATR-HTS-LTS integration procedure is similar to the work of individual-simulated ATR reactor during the dynamic simulations of startup period. The ATR graphs have very similar data which are provided for the previous work for ATR reactor. Because of this, these graphs are not mentioned again in this section.

HTS and LTS reactor interactions based on the temperature and composition were investigated and are reported below.

Table 87.1 summarizes the operating conditions and the result of the efficiency calculations. The total thermal efficiency of hydrogen production system (η_{HPS}) is calculated as the ratio of the heating value of the HTPEM inlet fuel (hydrogen energy) and natural gas inlet stream. The heating value of a stream is calculated by multiplying of its lower heating value (LHV) with its mass flow rate. η_{HPS} represents the ratio of heating value of the HTPEM inlet stream to the heating value of the total fuel feed stream. The efficiency definitions are given in Eqs. (87.6) and (87.7). The net electrical efficiency of the fuel cell system, $\eta_{net\ elec}$, is the ratio of current power load and the energy content of NG feed.

The fuel processing efficiency and net electrical efficiency are calculated as

$$\eta_{HPS} = \left(m_{HTPEM\ inlet\ fuel} \times LHV_{HTPEM\ Feed}\right) / \left(m_{Fuel\ feed(NG)} \times LHV_{Fuel\ feed\ (NG)}\right) \tag{87.6}$$

$$\eta_{net\ electric} = P_{current} / LHV_{NG\ feed} \tag{87.7}$$

in which m is the mass flow rate of the feeds (kg h^{-1}), LHV is the lower heating value (kJ kg^{-1}), and P is the power load (kW$_e$). The number of cells in the fuel cell stack is one of the parameters, which affects the fuel cell's electrical efficiency and, hence, also the net electrical efficiency. The number of HTPEM cells has been taken as *50* in this study. The details of the stream data of this integrated simulation study are given in Table 87.2.

HTS is the first reactor which is integrated at the ATR optimum operating conditions. HTS input stream reduced to a value of approximately 350 °C via cooling of the ATR effluent. According to the system initialization period, the temperature of outlet stream of HTS is expected approximately to be the order of 390 °C at steady state (Fig. 87.11). An appropriate HTS operating temperature range affects the dynamic behavior and the strength of the commercial catalyst and the reactor outlet compositions. The electrical load of integrated process is influenced by the reactor outlet compositions and operating temperatures.

Water-gas shift equilibrium conversion reactions have been assumed in the reactor module during the dynamics simulations of HTS reactor. Outlet compositions have been calculated separately for each component. The composition profile at HTS product stream is shown in Fig. 87.12 for the startup period. CO concentrations at the ATR exit can be reduced to approximately 0.1 % through steady state due to supply steam while it is about the order of 14 % during the startup period.
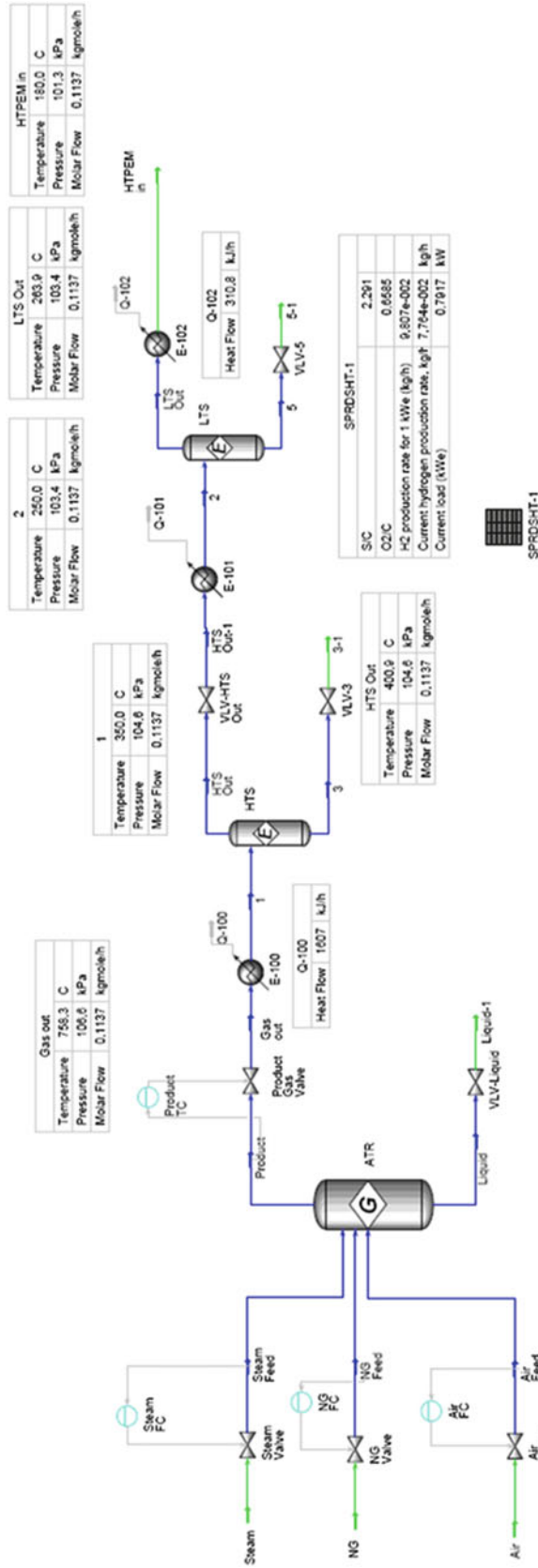
Fig. 87.10 Dynamic simulation work for ATR-HTS-LTS integration

Table 87.1 Process data for 1,097 kW$_e$ power demand

Steam feed (kmol h^{-1})	0,050	LHV of NG feed (kJ kg^{-1})	50,035
NG feed (kmol h^{-1})	0,016	Energy content of NG Feed (kW)	3,609
S/C	3,078	NG feed (kg h^{-1})	0,26
Air feed (kmol h^{-1})	0,048	NG feed (kg s^{-1})	0,0001
O$_2$/C	0,614	Energy content of H$_2$ produced (kW)	2,959
O$_2$ in air	0,208	HTPEM in H$_2$ produced (kg h^{-1})	0,089
LHV of H$_2$ (kJ kg^{-1})	120.000	Current power load (kWe)	1,097
PEM feed (kmol h^{-1})	0,124	HTPEM-feed molar flow (kmol h^{-1})	0,136
η_{HPS}	81,991	% $\eta_{net.elec}$	30,392

Table 87.2 Stream data of the integrated simulation study for ATR + HTS + LTS

Name	Steam	NG	Air	Steam feed	NG feed	Air feed	9	LTS out
Vapor fraction	1,000	1,000	1,000	1,000	1,000	1,000	0,318	1,000
Temperature (°C)	350	150	250	350	150	250	150,000	258
Pressure (kPa)	120,000	120,000	120,000	110,306	110,306	110,306	50,000	105,393
Molar flow (kmol h^{-1})	0,050	0,016	0,048	0,050	0,016	0,048	0,000	0,136
Mass flow (kg h^{-1})	0,898	0,260	1,381	0,898	0,260	1,381	0,000	2,538
Name	5	HTPEM in	5_1	4	6	7	8	Gas out
Vapor fraction	1,000	1,000	1,000	1,000	1,000	1,000	1,000	1,000
Temperature (°C)	258	180	267	180	180	180	18	672
Pressure (kPa)	105,393	102,995	68,942	101,325	102,995	102,994	102,995	108,904
Molar flow (kmol h^{-1})	0,000	0,136	0,000	−0,136	−0,136	0,000	0,000	0,136
Mass flow (kg h^{-1})	0,000	2,538	0,000	−2,538	−2,538	0,000	0,000	2,538
Name	8_1	HTS out	Product	1	3_1	HTS out-1	3	2
Vapor fraction	0,885	1,000	1,000	1,000	1,000	1,000	1,000	1,000
Temperature (°C)	25	384	673	350	407	384	384	250
Pressure (kPa)	60,000	106,820	110,306	106,821	66,859	106,459	106,821	105,393
Molar flow (kmol h^{-1})	0,000	0,136	0,136	0,136	0,000	0,136	0,000	0,136
Mass flow (kg h^{-1})	0,000	2,538	2,538	2,538	0,000	2,538	0,000	2,538

This composition is the input value for the LTS reactor which will take place in the next stage. Similarly, the initially produced CO$_2$ in the order of 4 % reaches up to about 10 % at steady state conditions. The water vapor coming from ATR exit is consumed in HTS reactions; then it reaches in the order of 30 % between 100 and 200 s. A portion of the water vapor is consumed in exothermic water gas shift reaction for the additional CO and H$_2$ production.

The amount of hydrogen produced is reached to the range of 29 % while it was in the order of 26–27 % wet based prior to the water gas shift reactor during the startup period.

Inert nitrogen which is not taking place in the reactions has been abandoned in the HTS reactor after the ATR reactions. The concentration of N$_2$ is in the order of about 30 % after reaching steady state point.

LTS inlet temperature is determined as 250 °C which is required for the normal operating range of the catalyst. The temperature of LTS input stream is reduced to 250 °C by cooling the HTS exit stream. The steady state temperatures of LTS output stream is reached to the value of 257 °C due to exothermic reaction according to the system startup period (Fig. 87.13). LTS operating temperature also affects the dynamic behavior and the strength of the catalyst and also the outlet compositions.

Similarly to HTS reactor, water-gas shift equilibrium conversion reactions have also been assumed during the dynamics simulations of LTS reactor. Outlet compositions have been calculated separately for each component. The HTS composition profile at the product stream is shown in Fig. 87.14 for the startup period.

CO concentrations at the HTS exit can be reduced to approximately 0.01 % after reaching steady state due to supply steam while it was about the order of 0.1 % at the exit of HTS during the startup period. This composition value is desired as input composition of the anode inlet fuel for the HTPEM fuel cell. The effect of CO is extremely important for PEM fuel

Fig. 87.11 HTS temperature profile at startup period
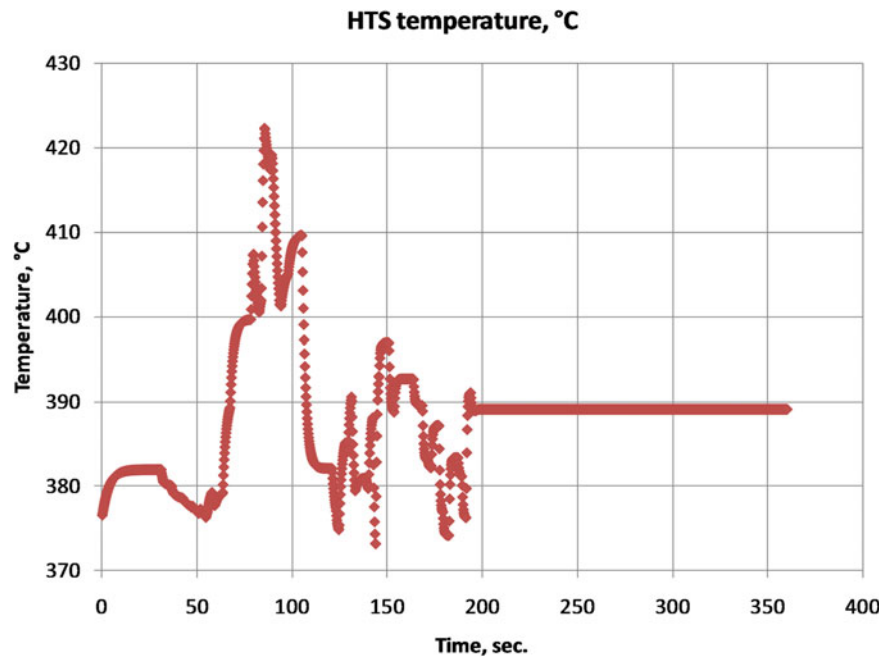
Fig. 87.12 Composition profile of HTS exit stream at startup period
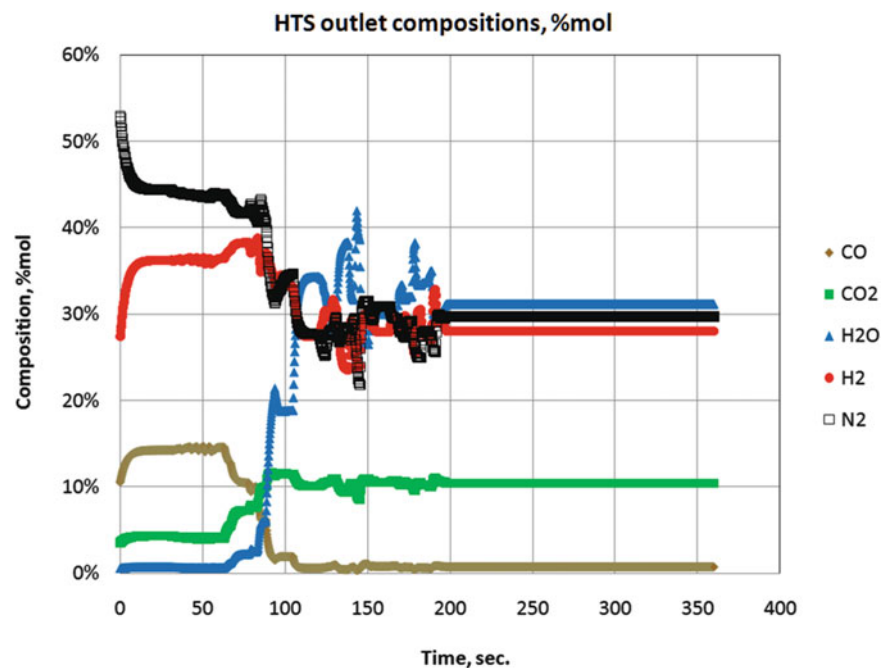
cells as it is known. The high amount of CO which can be higher than desired value reduces the effectiveness of the fuel cell catalyst and provides the loss of the activation in a short time. Similarly, the initially produced CO_2 of the order of 4 % reaches up to about 11 % at steady state.

The water vapor coming from HTS exit is consumed in LTS reactions; then it reaches in the order of 30 % between 100 and 200 s. A portion of the water vapor is consumed in exothermic water gas shift reaction for the additional CO and H_2 production. The amount of wet-based hydrogen is reached to the range of 30 % while it was in the order of 26–27 % wet based prior to the water gas shift reactors during the startup period. Inert nitrogen which is not taking place in the reactions has been abandoned in the LTS reactor after the HTS reactions. The concentration of N_2 is in the order of about 30 % after reaching steady state point.

Fig. 87.13 Temperature profile of LTS at startup period
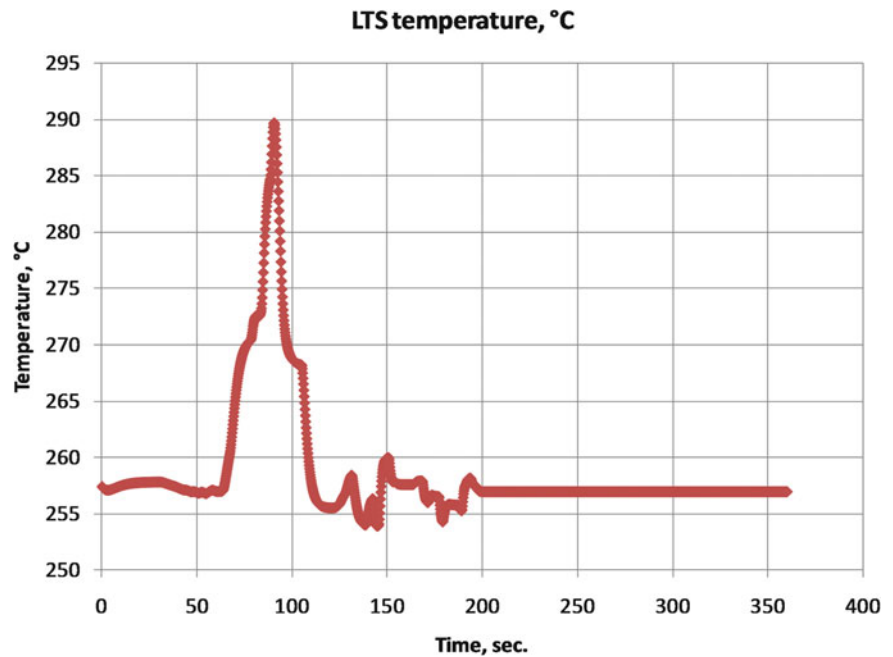
Fig. 87.14 Composition profile of LTS exit stream at startup period
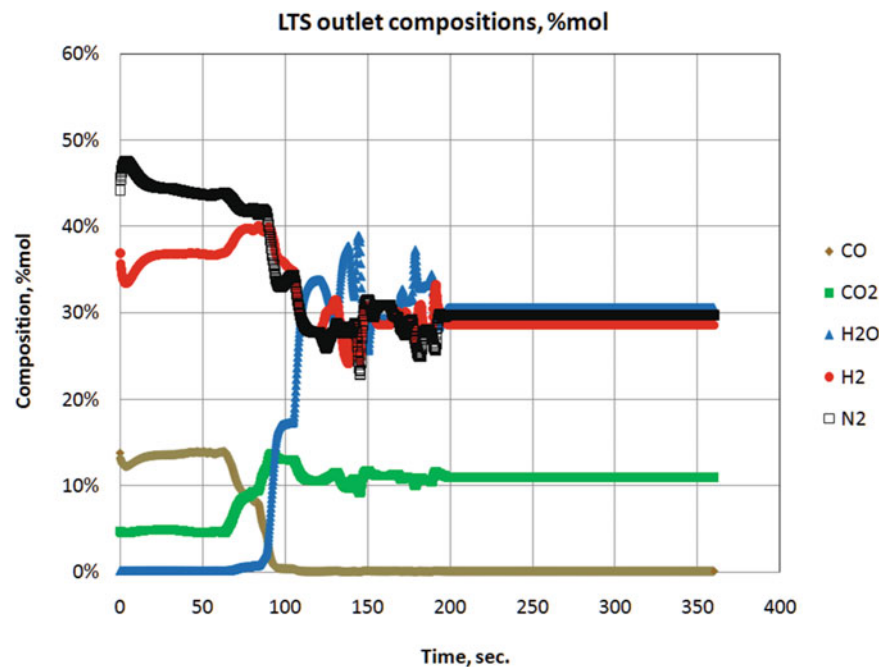
The electrical load increases from the initial value of 0.17 kWₑ up to the value of 1.02 kWₑ as can be seen from a dynamic simulation study over the period the system start up. The power variation is then fixed after 200 s (Fig. 87.15).

Concluding Remarks

In this study a process simulation model has been used to realize an analysis of a system that consists of a fuel processing system for hydrogen rich gas production using natural gas. An HTPEM fuel cell stack of 1 kWₑ has been integrated to HPS. The dynamic simulation model includes units such as HTPEM fuel cell, auto-thermal reformer (ATR), high and low temperature water gas shift reactors (HTS & LTS), heat exchangers, control valves, control spreadsheet, and flow controllers.

Optimization of the Operation Conditions in a Direct Borohydride Fuel Cell with Carbon Supported Au Anode

88

Fatma Gül Boyaci San, Osman Okur, Çiğdem Iyigün Karadağ,
Işıl Işik Gülsaç, and Emin Okumuş

Abstract

In this study, response surface methodology (RSM) based on a five variable central composite design (CCD) is employed for the optimization of the direct borohydride fuel cell (DBFC) operation conditions, where the variables are the catalyst loading, cell temperature, borohydride concentration, and flow rates of fuel and oxidant. The main effects, quadratic effects, and interactions of the five variables on the power density of fuel cell are investigated by the analysis of variance. The carbon supported Au as the anode catalyst is used to control the hydrolysis of sodium borohydride under operating conditions. The results showed that the catalyst loading is the most significant factor on the power density. Under the operation conditions of 0.52 mg/cm^2 catalyst loading, 80 °C fuel cell temperature, 3.28 L/min fuel and 0.27 L/min oxidant flow rate, and 1.5 M borohydride concentration, the maximum power density of 37.15 mW/cm^2 is obtained.

Keywords

Direct sodium borohydride • Fuel cell • Oxidation • Operation condition • Response surface methodology • Optimization

Introduction

Direct borohydride fuel cells (DBFC) are considered to be the most efficient and clean power generation devices for portable and mobile applications because of their high energy densities and theoretical working potentials. Usually, a DBFC employs an alkaline solution of sodium borohydride as fuel and oxygen or air as oxidant. Performance of a DBFC single cell depends on a large variety of factors such as materials for anode and cathode, fluid flow field, and operational parameters such as anolyte composition, flow rates of fuel and oxidant, humidity of oxidant, temperature, etc. [1–4].

The oxidation of sodium borohydride is based on a complete eight electron reaction process and provides a high theoretical specific capacity (5.67 Ah/g, based on NaBH$_4$) [5].

$$BH_4^- + 8OH^- \rightarrow BO_2^- + 6H_2O + 8e^- \quad E^0 = -1.24 \text{ V vs SHE} \tag{88.1}$$
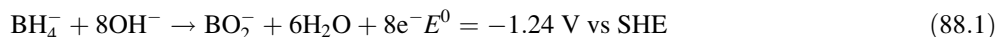
However, the actual number of electrons released is typically less than the theoretical value, due to the parallel unwanted reaction of hydrolysis, which competes with the oxidation:

$$BH_4^- + H_2O \rightarrow BO_2^- + 4H_2 \tag{88.2}$$

Unlike Pt, electrode materials such as Au and Ag showed little or no activity towards the BH$_4^-$ hydrolysis reaction [6, 7]. As a consequence, the Coulombic numbers near 8 were reported for the electro-oxidation reaction of BH$_4^-$ [8]. But these

F.G.B. San (✉) • O. Okur • Ç.I. Karadağ • I.I. Gülsaç • E. Okumuş
TÜBİTAK Marmara Research Center Energy Institute, P.O. Box 21, 41470 Gebze, Kocaeli, Turkey
e-mail: fatmagul.boyaci@tubitak.gov.tr; osman.okur@tubitak.gov.tr; cigdem.karadag@tubitak.gov.tr;
isil.gulsac@tubitak.gov.tr; emin.okumus@tubitak.gov.tr

electrode materials usually demonstrated slow electrode kinetics and low power density. Gyenge et al. suggested that alloying Ag with Ir and Pt could effectively improve the electrode kinetics [9].

One way to improve the cell performance was reported as choosing a metal with high electrocatalytic activity [8]. Kim et al. assembled the DBFCs using carbon supported Pt or unsupported Pt catalyst. It was reported that the maximum power density could only reach to 44.2 mW/cm^2 [5]. Gyenge et al. reported that Pt–Ni and Pt–Ir exhibited higher electrocatalytic activity than Pt giving a cell voltage of 0.53 V at 100 mA/cm^2 [9]. However, the maximum power density around 50 mW/cm^2 was still lower than that of the polymer electrolyte membrane fuel cell. Liu et al. studied the influence of hydrogen evolution on the cell performance. They found that the reduction of the effective reaction area caused by hydrogen evolution during the DBFC operation was a more critical problem [10]. They suggested that the addition of Nafion in anode and using a composite of Ni, metal hydride, and Pd/C as the anode catalyst improved the cell and stack performance of the DBFC by suppressing the hydrogen evolution [10, 11].

Suppression of hydrogen evolution during operation was one of the solutions to improve the cell performance. Through the anolyte flow observation in a transparent cell, we and Liu confirmed that hydrogen bubbles blocked channels and thus hindered the anolyte flow [12, 13]. They investigated the effect of the anode diffusion layer on the cell performance and stability of the DBFC. It was found that the thinner the anode diffusion layer the higher was the performance. Liu et al. tried to increase anode porosity by pasting anode ink into a piece of Ni foam. It was found the cell performance was improved from 50 to 180 mW/cm^2 [12]. Kim et al. tried to improve the stack performance by decreasing the hydrogen evolution through suitable anode design and the flow field improvement [14].

The borohydride crossover was reported as another problem influencing cathode performance [15]. It was found that the applied current during the cell operation would influence the fuel crossover. The Pt cathodes were found to have better performance stability than the Ag cathodes. The cell stability within hours was found to be greatly affected by the mass transport properties of different components. The porosities of the anode and cathode supporting materials, the membrane pretreatment, and borohydride concentration had significant influence on the performance stability [12].

To the best of our knowledge, no study was reported on the optimization of the DBFC operation conditions by a statistical approach. In this work, the carbon supported Au as the anode was used to control the hydrolysis of sodium borohydride under operating conditions. Response surface methodology (RSM) based on a five variable central composite design (CCD) was employed for the optimization of DBFC operation conditions. The five variables considered were the catalyst loading, cell temperature, borohydride concentration, flow rates of fuel, and oxygen as oxidant. The main effects, quadratic effects, and interactions of the five variables on the power density of fuel cell were investigated by the analysis of variance. The results showed that the catalyst loading was the most significant factor on the power density. The quadratic model was chosen to realize the response of borohydride concentration and interaction of catalyst loading with borohydride concentration. Predicted values from the regression equations were found to be in good agreement with observed values. According to the results, the regression equations could be used to predict and optimize the performance of DBFC. Under the operation conditions of 0.52 mg/cm^2 catalyst loading, 80 °C fuel cell temperature, 3.28 L/min fuel and 0.27 L/min oxidant flow rate, and 1.5 M borohydride concentration, the maximum power density of 37.15 mW/cm^2 is obtained.

Experimental

Materials and Chemicals

The chemical reagents, including 2-propanol, NaOH, NaBH$_4$, and 5 wt.% Nafion solution (Sigma-Aldrich), Nafion 117 membrane (DuPont, USA), and 20 wt.% Pt/C on Vulcan XC-72 carbon support (BASF Fuel Cell, Inc.) are all purchased. Homemade 10 wt.% Au/C electrocatalyst was used in the electrode preparation.

Experimental Design

A CCD with five factors at five levels was performed to ascribe the effect of factors on response surface in the region of investigation. Investigated factors that were considered to have the greatest influence on fuel cell performance in literature were cell temperature, borohydride concentrations, catalyst loading, and anode and cathode feeding rate. The CCD was

Table 88.1 Experimental data

	Factor 1	Factor 2	Factor 3	Factor 4	Factor 5	Response
Run	A: cell temperature (C)	B: anode flow rate (mL/min)	C: cathode flow rate (L/min)	D: borohydride concentration (M)	E: catalyst loading (mg/cm^2)	Power density (mW/cm^2)
1	−1	1	−1	−1	−1	14.13
2	1	−1	−1	1	1	6.34
3	0	0	0	−1	0	7.05
4	−1	−1	1	1	1	1.41
5	−1	1	1	1	−1	23.32
6	0	0	0	0	−1	26.84
7	−1	1	1	−1	1	0.7
8	0	−1	−1	0	0	7.05
9	1	1	1	−1	−1	24.72
10	−1	−1	−1	−1	1	0.7
11	1	−1	−1	−1	0	21.9
12	−1	1	1	−1	−1	12.71
13	1	0	0	0	0	14.1
14	−1	1	−1	1	1	0.7
15	−1	−1	−1	1	−1	27.42
16	0	0	0	0	1	2.12
17	1	1	−1	1	−1	36.74
18	0	0	1	0	0	7.76
19	1	−1	1	1	−1	38.16
20	−1	0	0	0	0	2.83
21	1	1	1	1	1	7.02
22	1	1	−1	−1	1	2.11
23	1	−1	1	−1	1	2.82
24	0	0	0	1	0	11.27
25	0	−1	0	0	0	7.05
26	0	1	0	0	0	7.05

applied using Design Expert 6.0 (trial version). The total number of experiments with five factors was 50 (=2^k + 2k + 6), where k is the number of factors. During our study we used ½ fraction design instead of full factorial design with 26 experiments. The first six columns of Table 88.1 show run number and experimental conditions of the runs arranged by CCD. The fuel cell performance of the process was evaluated by analyzing the response.

Fuel Cell Performance Tests

The anode electrocatalyst ink was prepared by mixing 2-propanol with 5 wt.% Nafion solution and 10 wt.% Au/C. Then, the ink was coated on a carbon cloth (Electrochem, Inc.), yielding a metal loading mass on the electrode of 0.52 mg/cm^2. The Nafion 117 membrane was cleaned by boiling in 3 wt.% H_2O_2 and 3 wt.% H_2SO_4 for 1 h, followed by boiling in ultrapure water for 2 h. The cleaned membrane was activated in 2 M NaOH solution for 1 h prior to use. The anode/membrane/cathode unit was compressed between two graphite blocks with pin type flow fields. Silicon gaskets were assembled between the electrode and the graphite block. The active area of the fuel cell was 25 cm^2. Cell performance was tested against a 1 mg/cm^2 Pt/C cathode coated on carbon paper. Peristaltic pumps were used to feed the fresh anolyte (an aqueous solution of $NaBH_4$ and 4 M NaOH) at selected flow rate. The flow rate of oxygen as an oxidant at the cathode chamber was 0.2 L/min. The oxidant was humidified by passing through a bubbler at 65 °C. Cell performance data were obtained using an electrochemical fuel cell test system (Electrochem 400 W) and a computer controlled E-load system (ECL 150).

Results and Discussion

A comparative investigation of DBFC polarization behavior was carried out relating to the cell temperature, borohydride concentration, and flow rates of fuel and oxidant. The higher and lower level values were used in a statistical analysis to determine significant parameters that are given in Table 88.2.

Polarization graph for different runs is given in Fig. 88.1. According to Fig. 88.1 the highest performance was obtained at Run 19 (80 °C, 1.5 M borohydride concentration, 1 mL/min anode, 0.4 L/min flow rates, and 0.52 mg/cm^2 catalyst loading).

The data in Table 88.1 are run through the RSM to construct an empirical model for the representation of power density in terms of independent parameters. Based on the regression analysis at 95 % of the confidence interval, the lack of fit error and p-values of parameter estimations are found to be significant. The value of $p < 0.0001$ indicates that there is only a 0.01 % chance that a "model F-value" this large could occur due to noise (Silva and Rouboa 2012). The quadratic model is used to fit the observed data by the least squares analysis.

Some of the model terms were found to be significant. The insignificant model terms can be removed and may result in an improved model. Results obtained from Analysis of variance (ANOVA) show that temperature, borohydride concentration, and catalyst loading have substantial influences on cell performance. By selecting the backward elimination procedure to automatically reduce the terms that are not significant, the resulting ANOVA tables for the reduced quadratic model is shown in Table 88.3.

Results show that the models are still significant. The predicted R^2 is in reasonable agreement with the adjusted R^2. The adjusted R^2 value is particularly useful when comparing models with different number of terms. Adequate precision compares the range of the predicted values at the design points to the average prediction error. Ratios greater than 4 indicate adequate model discrimination. The following equations are the final empirical models for the power density:

$$
\begin{aligned}
\text{Power Density} = {}& +91.64873 + 0.80192^*\text{Cell Temperature} + 31.31289^*\text{Borohydride Concentration} \\
& - 335.36728^*\text{Catalyst Loading} + 260.49383^*\text{Catalyst Loading}^2 \\
& - 0.81000^*\text{Cell Temperature}^*\text{Catalyst Loading} - 35.86667^*\text{Borohydride} \\
& \text{Concentration}^*\text{Catalyst Loading}
\end{aligned}
\tag{88.3}
$$

Table 88.2 Factors and levels of input factors for experimental design

Input factors	Low	Mean	High
Cell temperature, °C	50	65	80
Borohydride concentration, M	0.5	1.0	1.5
Anode flow rate, mL/min	1.0	3.0	5.0
Cathode flow rate, L/min	0.1	0.2	0.4
Catalyst loading, mg/cm^2	0.52	0.67	0.82
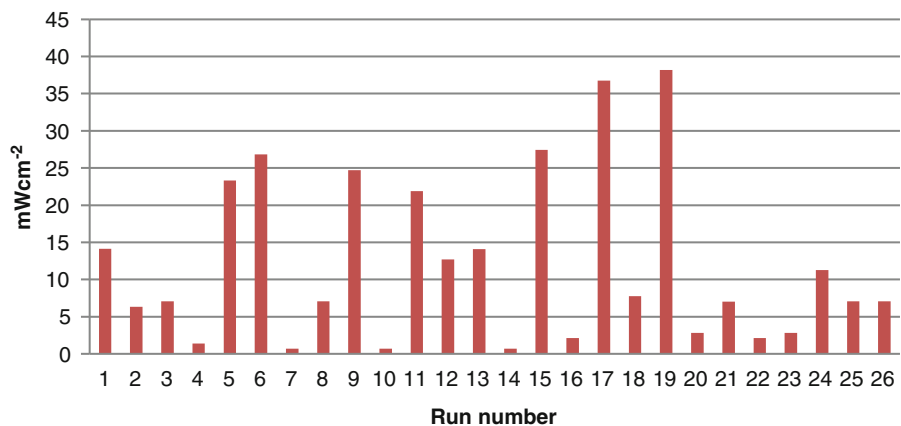
Fig. 88.1 Run number versus power density

Table 88.3 ANOVA results

Source	Sum of squares	DF	Mean square	F-value	p-Value
Model	3,137	6	522.88	212.65	<0.0001
A	272.14	1	272.14	110.68	<0.0001
D	238.64	1	238.64	97.05	<0.0001
E	2,267.34	1	2,267.34	922.09	<0.0001
E2	190.26	1	190.26	77.38	<0.0001
AE	53.14	1	53.14	21.61	0.0002
DE	115.78	1	115.78	47.08	<0.0001
Residual	46.72	19	2.46		
Cor total	3,184.02	25			
Std. dev.	1.57		R^2	0.9853	
Mean	12.08		Adj R^2	0.9807	
C.V.	12.98		Pred R^2	0.9713	
PRESS	91.24		Adeq precision	46.096	

A: cell temperature, B: anode flow rate, D: borohydride concentration, E: catalyst loading

Fig. 88.2 Predicted data versus actual data
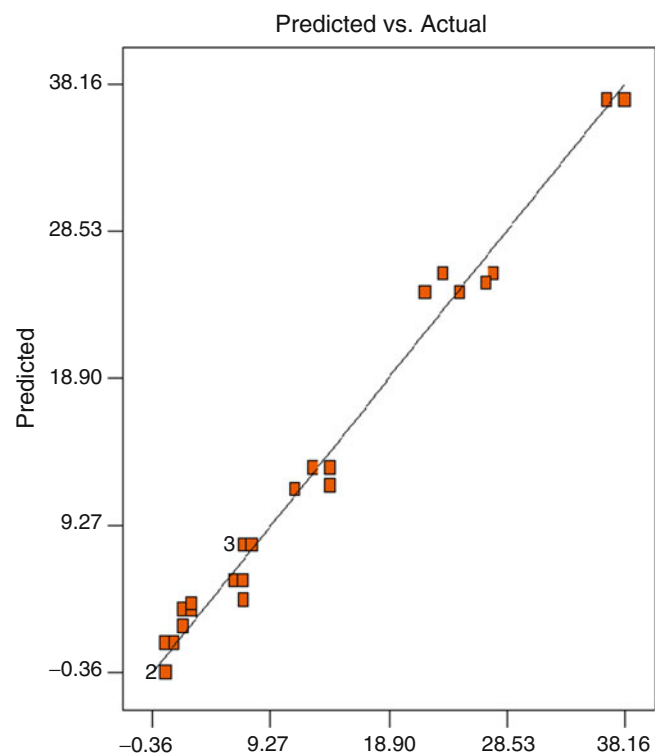
Figure 88.2 verifies that the predicted data of the response from the empirical models are in agreement with obtained ones in the range of the operating variables. The F value, model mean square divided by the error mean square, is considerably high, meaning that this model predicts fit of the experimental data. Furthermore, the high value of adjusted R^2 indicated that the model fits the observed data well.

In Fig. 88.3, it is obtained that by increasing catalyst loading of electrodes, the power density decreases linearly up to a certain value (0.7) and then it becomes constant. By increasing catalyst loading, the thickness of catalyst layer on gas diffusion layer (GDL) surface increases; hence, the active sides of catalyst particles are plugged by the other catalyst particles in upper layer. So, the reaction rate decreases and power density becomes constant. At low catalyst loading, the reaction rate and power density increase with the increase in temperature, as shown in the same figure, since the activities of

Fig. 88.3 The effect of cell temperature and catalyst loading on power density
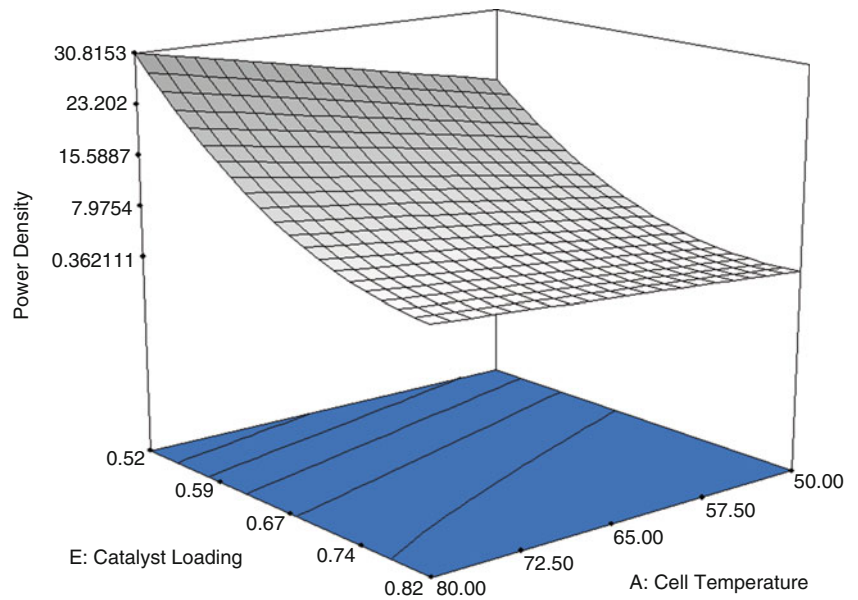
Fig. 88.4 The effect of catalyst loading and borohydride concentration on power density
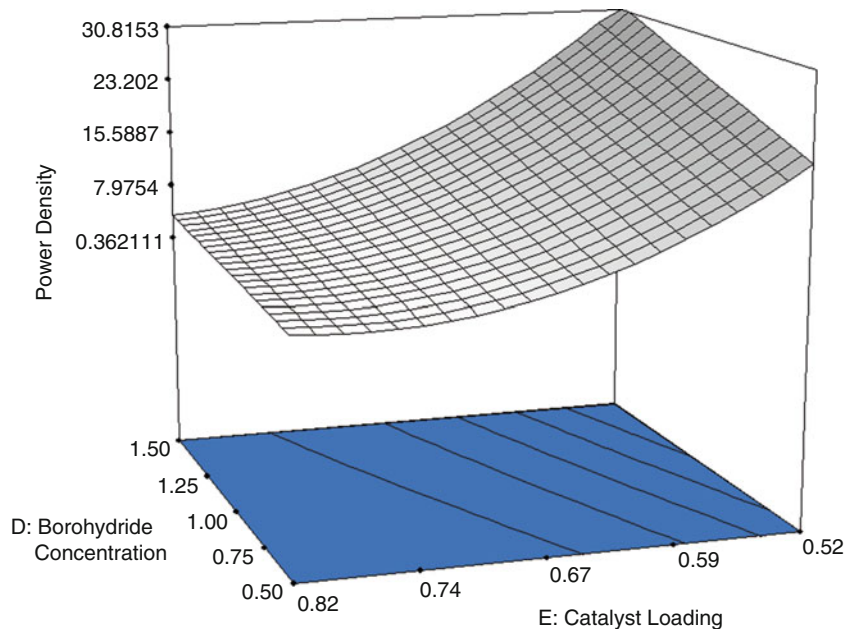
catalysts and borohydride increase at high cell temperature. However, at high catalyst loading, although the cell temperature increases the reaction rate does not change too much, because of the mass transfer limitation. At low catalyst loading, the activation of BH_4^- ion is more effective by temperature, and this effect cannot be observed significantly at high loading due to the blocked active sides.

The negative effect of catalyst loading on power density is also observed in Fig. 88.4 as in Fig. 88.3. As catalyst loading of electrodes increases, the thickness of catalyst layer increases and therefore the mass transfer limitation of ions to active sites also increase. On the other hand, as borohydride concentration increases at low loading, the power density increases. Since, the number of borohydride ions per one active side of catalyst is increased, the reaction rate increases. However, at high catalyst loading, although borohydride concentration increases, the reaction rate is not affected because of plugged active sites and high mass transfer limitations. So, if the catalyst loading in electrodes increases, the membrane electrode assembly preparation cost also increases and the cell performance decreases.

Table 88.4 Optimization study (first case)

Operation conditions	Value	Importance
Cell temperature	In range	+++
Anode flow rate	In range	+++
Cathode flow rate	In range	+++
Borohydride concentration	In range	+++
Catalyst loading	In range	+++
Power density	Maximum	+++++

Table 88.5 Five optimum points

Optimization points	Cell temperature (°C)	Anode flow rate (mL/min)	Cathode flow rate (L/min)	Borohydride concentration (M in 4 M NaOH)	Catalyst loading (mg Au/cm^2)	Power density (mW/cm^2)
1	80.00	3.45	0.38	1.50	0.52	37.1464
2	80.00	2.90	0.34	1.50	0.52	37.1464
3	80.00	1.86	0.30	1.50	0.52	37.1463
4	40.00	4.97	0.20	1.50	0.52	37.1463
5	80.00	4.67	0.21	1.50	0.52	37.1463

Fig. 88.5 The schematic representation of first optimum case
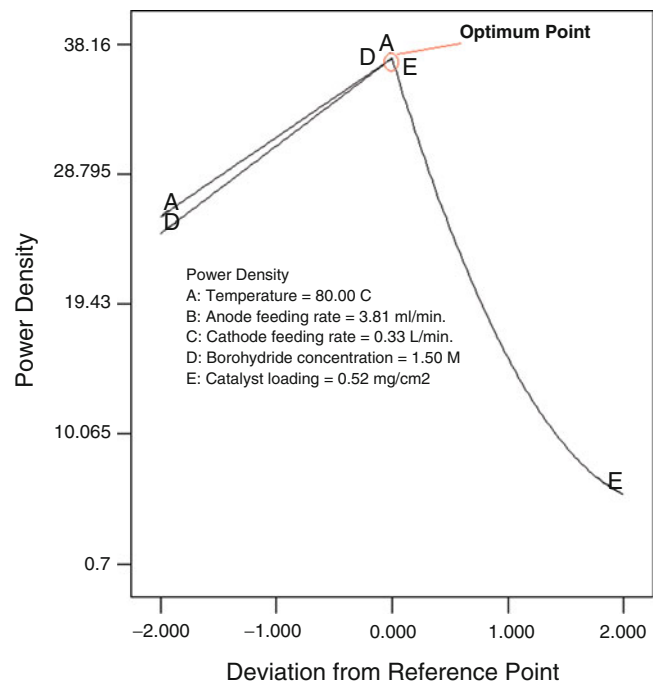
Optimization

Two cases were determined for optimization study. The first case is used to maximize the power density. As shown in Table 88.4, while temperature, anode and cathode feed flow rate, borohydride concentration, and catalyst loading were kept constant in the range, the power density was tried to maximize and its importance was accepted as maximum. By using the program, five optimum points were obtained (Table 88.5).

The maximum power density is 37.15 mW/cm^2 for five points. The operating temperature was obtained at 80 °C for four points. The main differences between one and four points were temperature and the flow rates of anode and cathode. In order to obtain the same power density value at 40 °C, the anode flow rate should be increased from 3.45 to 4.97 and the cathode feed flow rate should be decreased from 0.38 to 0.2. The schematic representation of first optimum point can be seen in Fig. 88.5.

Table 88.6 Optimization study (second case)

Operation conditions	Value	Importance
Cell temperature	Minimum	+++++
Anode flow rate	Minimum	+++++
Cathode flow rate	Minimum	+++++
Borohydride concentration	Minimum	+++++
Catalyst loading	Minimum	+++++
Power density	Maximum	+++++

Table 88.7 Maximum power density by considering minimum operating conditions

Optimization points	Cell temperature (°C)	Anode flow rate (mL/min)	Cathode flow rate (L/min)	Borohydride concentration (M in 4 M NaOH)	Catalyst loading (mg Au/cm^2)	Power density (mW/cm^2)
1	50.02	1.00	0.10	0.57	0.52	13.92
2	51.19	1.00	0.10	0.53	0.52	13.90
3	50.10	1.00	0.10	0.61	0.52	14.55
4	50.00	1.00	0.10	0.50	0.52	13.06
5	50.65	1.00	0.10	0.58	0.52	14.29

Fig. 88.6 The schematic representation of second optimization case
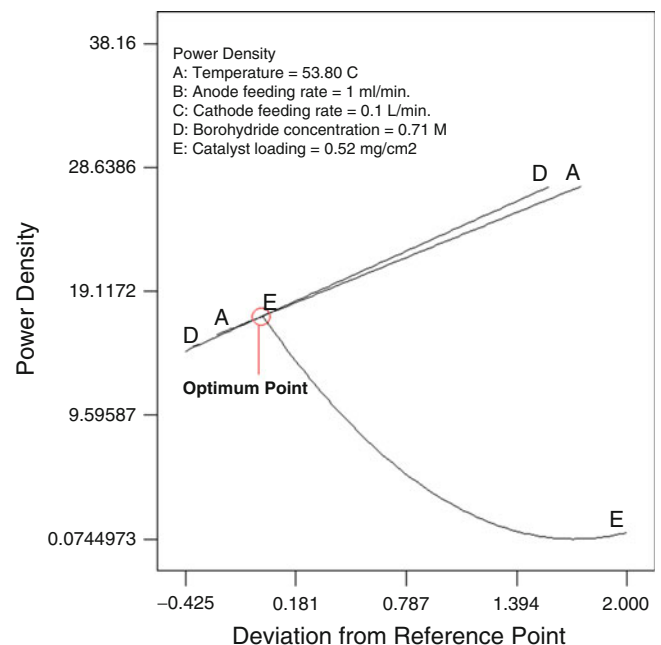
Second optimum case was obtained by minimizing operation conditions and by maximizing power density. The importance of operation conditions was given in Table 88.6.

In Table 88.7, the maximum power density was obtained as 14 mW/cm^2 by considering minimum operating conditions (cell temperature: 50 °C, anode flow rate: 1.0 mL/min, cathode flow rate: 0.1 L/min, borohydride concentration: 0.57 M in 4 M NaOH, and catalyst loading: 0.52 mg Au/cm^2). However, the power density for second case was three times lower than that of first case. The schematic representation of second optimum case was given in Fig. 88.6.

Conclusion

DBFC operation conditions were optimized with central composite method of the Design Expert software. The effects of the chosen parameters on the power density were investigated. According to the results, the most efficient parameter on the power density was determined as the catalyst loading. The other important parameters were temperature and borohydride concentration. The decrease in the performance with increasing catalyst loading can be explained as the blocking of the

active surface area at high catalyst loading and the mass transfer limitation. The maximum power density of 37.15 mW/cm^2 was obtained at the operation conditions of 0.52 mg/cm^2 catalyst loading, 80 °C fuel cell temperature, 3.28 L/min fuel and 0.27 L/min oxidant flow rates, and 1.5 M borohydride concentration. The achieved formula can be adapted to all fuel cell studies including Au catalyst, N117 membrane, and ELAT GDL.

References

1. Ma J, Choudhury NA, Sahai Y (2010) A comprehensive review of direct borohydride fuel cells. Renew Sustain Energy Rev 4:183–199
2. Celik C, Boyaci San FG, Sarac HI (2008) Effects of operation conditions on direct borohydride fuel cell performance. J Power Sources 185(1):197–201
3. Celik C, Boyaci San FG, Sarac HI (2010) Influences of sodium borohydride concentration on direct borohydride fuel cell performance. J Power Sources 195(9):2599–2603
4. Nagle LC, Rohan JF (2011) Nanoporous gold anode catalyst for direct borohydride fuel cell. Int J Hydrogen Energy 36:10319–10326
5. Kim JH, Kim HS, Kang YM, Song MS, Rajendran S, Han SC, Jung DH, Lee JY (2004) Carbon supported and unsupported Pt anodes for direct borohydride liquid fuel cells. Electrochem Soc 151:A1039–A1043
6. Lam VWS, Alfantazi A, Gyenge EL (2009) The effect of catalyst support on the performance of PtRu in direct borohydride fuel cell anodes. J Appl Electrochem 39:1763–1770
7. Pei F, Wang Y, Wang X, He P, Chen Q, Wnag X, Wnag H, Yi L, Guo J (2010) Performance of supported Au–Co alloy as the anode catalyst of direct borohydride-hydrogen peroxide fuel cell. Int J Hydrogen Energy 35:8136–8142
8. Amendola SC, Onnerud P, Kelly MT, Petillo PJ, Sharp-Goldman SL, Binder M (1999) Anovel high power density borohydride-air cell. J Power Sources 84:130–133
9. Gyenge E, Atwan M, Northwood D (2006) Electrocatalysis of borohydride oxidation on colloidal Pt and Pt-alloys (Pt-Ir, Pt-Ni, and Pt-Au) and application for direct borohydride fuel cell anodes. J Electrochem Soc 153:A150–A158
10. Liu BH, Li ZP, Zhu JK, Suda S (2008) Influences of hydrogen evolution on the cell and stack performances of the direct borohydride fuel cell. J Power Sources 183:151–156
11. Li ZP, Liu BH, Zhu JK, Suda S (2006) Depression of hydrogen evolution during operation of a direct borohydride fuel cell. J Power Sources 163:555–559
12. Liu BH, Li ZP, Suda S (2008) A study on performance stability of the passive direct borohydride fuel cell. J Power Sources 185:1257–1261
13. Park KT, Jung UH, Jeong SU, Kim SH (2006) Influence of anode diffusion layer properties on performance of direct borohydride fuel cell. J Power Sources 162:192–197
14. Kim C, Kim KJ, Ha MY (2008) Performance enhancement of a direct borohydride fuel cell in practical running conditions. J Power Sources 180:114–121
15. Liu BH, Suda S (2007) Influences of fuel crossover on cathode performance in a micro borohydride fuel cell. J Power Sources 164:100–104

A New Carbon Nanotube-Supported Pt–Ru Anodic Catalyst by Reverse Microemulsion for Direct Methanol Electro-oxidation

89

Jenshi B. Wang, Charng-Ching Yeh, and Han-Chang Gao

Abstract

A multi-walled carbon nanotube (CNT)-supported Pt–Ru nanocatalyst prepared by reverse microemulsion was studied for direct methanol electro-oxidation and compared with that made by polyol method. XRD and TEM characterization showed that the reverse micelles-synthesized alloyed particles attained a smaller average particle size and displayed a higher dispersion on the support with narrow size distribution. Results of cyclic voltammetry and chronoamperometry in 1 M methanol + 0.5 M sulfuric acid at room temperature revealed that the Pt–Ru/CNT catalyst synthesized by reverse microemulsion exhibited a much higher electro-catalytic activity than that based on polyol process.

Keywords

Methanol electro-oxidation • Microemulsion • Carbon nanotube • Anodic catalyst

Introduction

Direct methanol fuel cells (DMFC) have been attracting considerable interests in the applications of transportation and portable devices because liquid methanol as fuel is more tractable than hydrogen. Although many different catalysts have been investigated, Pt–Ru alloy system is among the most active anodic catalysts for the electro-oxidation of methanol. Several methods have been developed for the preparation of multimetallic nanoparticles [1–3]. Among these, the synthesis through microemulsion appears as one of the most promising methods since nanodroplets of water serve as nanoreactors favoring formation of monodispersed nanoparticles. The microemulsion method has advantages in that it does not require extreme conditions of temperature and pressure, while providing a convenient control of size and composition [4–6].

Carbon black such as the commercial Vulcan XC has been employed as support of the nanosized metallic particles in fuel cells. However, the presence of micropores limits its widespread applications because metallic particles may easily become trapped in the pores. In this regard, in the search for highly active catalyst electrodes, carbon nanotubes have been used recently as an alternative support, providing catalysts with better electrochemical performance due to their unique morphology and high electrical conductivity [7–9]. Although the benefit of CNT as electro-catalyst support has been recognized, still there is a dearth of works devoting to the use of microemulsions to synthesize CNT-supported Pt–Ru nanoparticles as the anodic catalysts for methanol electro-oxidation.

In this chapter, the preparation of Pt–Ru/CNT nanocatalyst using a water-in-oil reverse microemulsion of water/AOT/isooctane (AOT: sodium di-2-ethylhexyl sulfosuccinate) is reported. The structure and performance of the catalyst prepared by this method in the methanol electro-oxidation are presented and compared with those of the catalyst made by polyol process.

J.B. Wang (✉) • C.-C. Yeh • H.-C. Gao
Department of Chemical Engineering, I-Shou University, Ta-shu District, Kaohsiung 840, Taiwan
e-mail: jbwang@isu.edu.tw

Experimental

Synthesis of Nano Pt–Ru Particles and Supported Catalysts

For microemulsion-synthesized nanoparticles, the reverse micellar solutions were prepared using AOT (Sigma) as surfactant and isooctane (Mallinckrodt) as the oil phase. Aqueous solutions of H_2PtCl_6 (99.95 %, Alfa Aesar), $RuCl_3$ (99.99 %, Alfa Aesar), and N_2H_5OH (Merck) were used to form the reverse micelles. The size of the particles was controlled by fixing the molar ratio of surfactant to water ($\omega = [H_2O]/[AOT]$) at 5. All chemicals were analytically pure and used as received without further purification. Deionized water was used throughout. An appropriate amount of $RuCl_3$ was added to the solution of H_2PtCl_6 to ensure the Pt:Ru atomic ratio of 1:1 before formation of reverse micelles. Multi-walled carbon nanotube (CNT) (Sigma Aldrich AL-636509-10G) was taken as support. Before use, the CNT was ultrasonically treated in nitric acid (65 %, Fluka) at 50 °C for 4 h and dried in vacuum oven at 60 °C for 12 h. The acid pretreated CNT was added to the solution of $AOT/H_2PtCl_6 + RuCl_3$/isooctane under ultrasonic oscillation at room temperature for 1 h. Afterwards, another similar microemulsion containing hydrazine as aqueous phase, i.e., AOT/hydrazine/isooctane, was added into the CNT slurry under constant ultrasonic oscillation for 24 h. Platinum–ruthenium nanoparticles were formed upon contact between the precursor containing droplets and the hydrazine containing droplets. The concentrations of aqueous H_2PtCl_6 + $RuCl_3$ and aqueous hydrazine were 0.1 and 1.0 M, respectively. Ethanol was then employed to destabilize the microemulsion to provoke deposition of Pt–Ru nanoparticles onto the support. The mixture was filtered and washed three times with 95 % ethanol, and then the resulting supported catalyst was dried in a vacuum oven at 60 °C for 12 h. The Pt loading of all catalysts was kept at 20 wt%. The catalyst is marked as Pt–Ru/CNT (emulsion).

For polyol-based nanoparticles, appropriate amounts of H_2PtCl_6 and $RuCl_3$ with the Pt:Ru atomic ratio of 1:1 were dissolved in ethylene glycol (EG) (99 %, Panreac Quimica Sa). A glycol solution of NaOH (0.5 M) was added dropwise into the glycol solution of precursors with stirring to bring the pH of solution to 12. The temperature was then increased to 185 °C and kept constant for 2 h so that the metals were reduced adequately. Afterwards, an ultrasonically dispersed acid pretreated CNT slurry was added dropwise with constant stirring for 4 h. The mixture was separated and washed with deionized water for three times, and then the resulting filter cake was dried in a vacuum oven at 60 °C for 12 h. Likewise, the Pt loading of the catalyst was kept at 20 wt%. The catalyst prepared by this technique is designated as Pt–Ru/CNT (EG).

Experiments of transmission electron microscopy (TEM) were carried out on a Philips CM200 system to examine surface morphology of the catalysts. Samples were first ultrasonicated in ethanol for 20 min and then deposited on 200 mesh Cu grids covered with Formvar/carbon films. X-ray diffraction (XRD) patterns were obtained on a Rigaku MultiFlex diffractometer using Cu Kα radiation to study crystal structure of the supported catalysts.

Preparation of Electrodes and Electrochemical Tests

Five milligram of catalyst was added to the mixture of 1 ml of methanol and 50 μl of perfluorosulfonic acid (5 wt% Nafion, Aldrich) to formulate catalyst ink. A 25 μl ink slurry was then sampled and spread uniformly over a 3-mm glassy carbon disk electrode (with an area of 0.0707 cm^2). After methanol evaporation, the electrode was dried in oven at 75 °C for 10 min.

All of the electrochemical performance studies were conducted at room temperature on the CHI 608B potentiostat (CH Instrument) in a three-electrode cell, with SCE electrode as reference electrode and platinum wire as counter electrode. All potentials in this work are quoted against reversible hydrogen electrode (RHE). The electrolyte was a solution of 1 M CH_3OH + 0.5 M H_2SO_4, which was degassed with nitrogen for 20 min before the tests. The electrocatalytic activity studies by cyclic voltammetry (CV) for methanol oxidation were carried out in the electrolyte at 10 mV s^{-1}. To compare the long-term performance of the supported catalysts, chronoamperometrical (CA) studies were undertaken in the 1 M CH_3OH + 0.5 M H_2SO_4 electrolyte under a constant potential of 0.947 V vs. RHE for 10 min.

Results and Discussion

The Structure of Pt–Ru/CNT Catalysts

XRD patterns of the Pt–Ru/CNT catalysts prepared by the methods of polyol and microemulsion are shown in Fig. 89.1. The peak at around $2\theta = 25°$ in the XRD spectrum is ascribed to the diffraction of CNT. The peaks at about 40°, 46°, 68°, and 81° can be assigned to the Bragg reflection of Pt (111), (200), (220), and (311) plane, respectively. A shift to higher 2θ-values and an increase of peak broadening, with respect to the diffraction lines of pure Pt, were observed, suggesting Pt–Ru alloy formation with a decrease in lattice parameter and mean particle size in these two catalysts. The extensive peak broadening in the XRD patterns is attributed to the ultrafine dimensions of the crystallites formed. No diffraction lines corresponding to those of pure Ru or Ru_2O were detected, indicating that the catalysts synthesized exhibited Pt face centered cubic structure. These observations are consistent with the results of [10] for a Pt_{50}–Ru_{50} alloy and also agreed with those in the literature [11–13]. The average crystallite size of Pt–Ru/CNT (emulsion) catalyst calculated from Scherrer formula is ca. 3.54 nm.

Figure 89.2 shows the TEM image depicting the morphology of the Pt–Ru/CNT (emulsion) catalyst. The Pt–Ru particles obtained from the microemulsion method were small spherical ones which were fairly well dispersed on the CNT with a uniform particle size distribution. The spherical particle morphology might be as a result of the redox reaction between H_2PtCl_6 or $RuCl_3$ and hydrazine occurring within the dispersed aqueous droplets. Also shown in Fig. 89.2 is its size distribution histogram. Its average TEM particle size of 3.40 nm, which is very close to that calculated by the Scherrer formula, is smaller than that of 4.46 nm for Pt–Ru/CNT (EG) made by polyol process.

Electrocatalytic Activities of Electrodes

Cyclic voltammograms showing electro-catalytic activity of the electrodes prepared from Pt–Ru/CNT (emulsion) and Pt–Ru/CNT (EG) are compared in Fig. 89.3. The CV curves exhibit typical features of methanol electro-oxidation on the platinum alloy electrode. In the anodic scan, the onset of methanol oxidation occurred at ca. 0.367 V vs. RHE for Pt–Ru/CNT (emulsion), which is much lower than the onset potential of 0.67 V for Pt–Ru/CNT (EG). Furthermore, the peak current density is 17.98 mA cm^{-2} at the peak potential of 0.886 V for Pt–Ru/CNT (emulsion), while the corresponding value for Pt–Ru/CNT (EG) is 2.79 mA cm^{-2} at 0.913 V. The Pt–Ru/CNT (emulsion) catalyst prepared by microemulsion method exhibited a much higher current density than that of Pt–Ru/CNT (EG). It is also clearly observable that methanol reoxidation
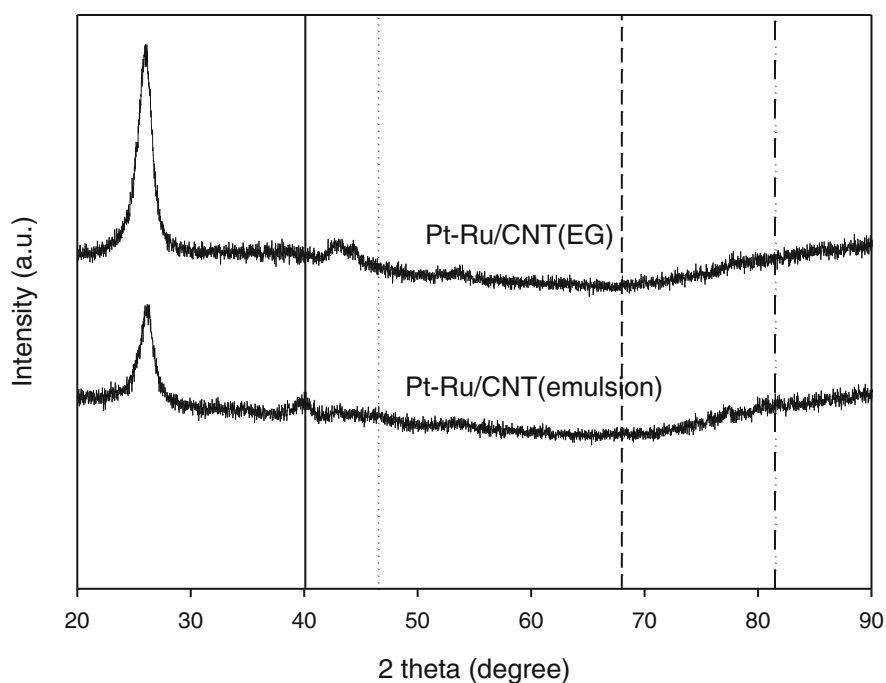
Fig. 89.1 XRD patterns of Pt–Ru/CNT (EG) and Pt–Ru/CNT (emulsion) catalysts

Fig. 89.2 (**a**) TEM micrograph
and (**b**) TEM particle size
distribution of Pt–Ru/CNT
(emulsion) catalyst
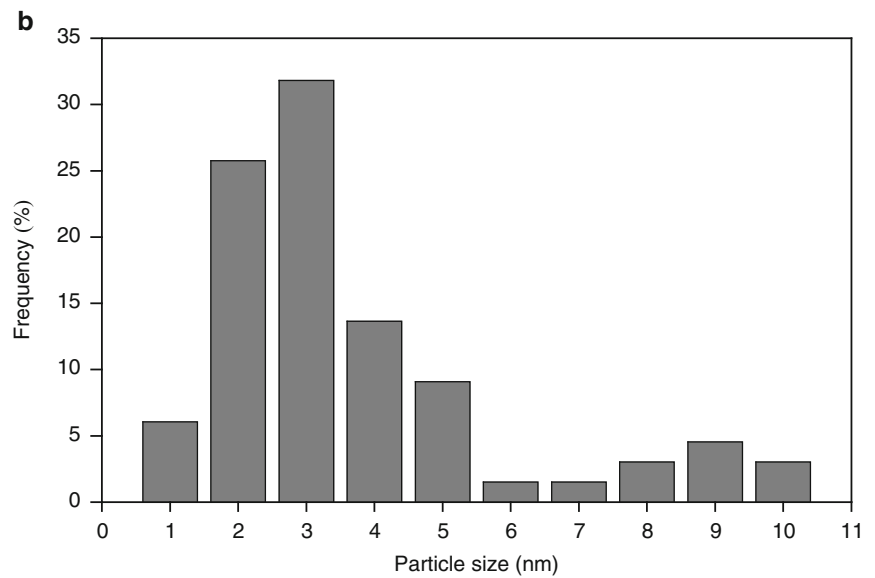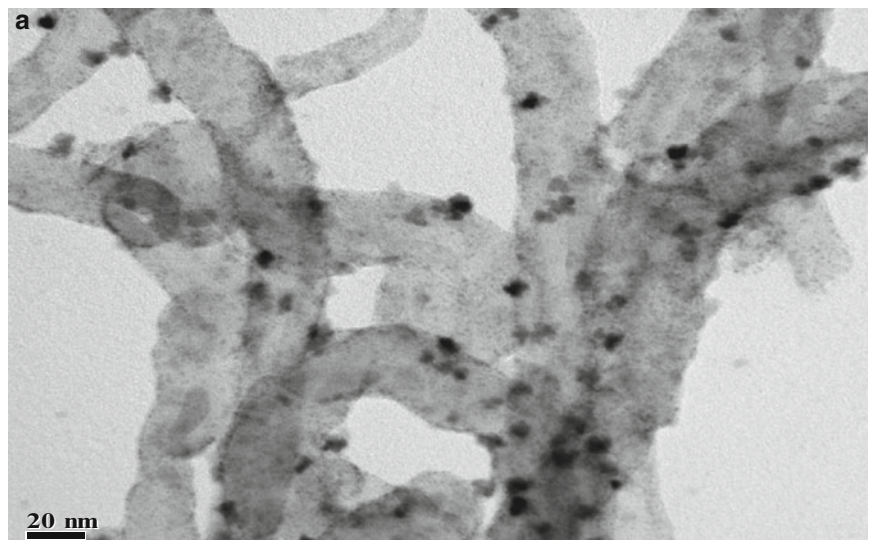
Fig. 89.3 Cyclic voltamograms
of Pt–Ru/CNT (EG) and Pt–Ru/
CNT (emulsion) in 1 M
CH_3OH + 0.5 M H_2SO_4 at
a scan rate of 10 mV s^{-1}
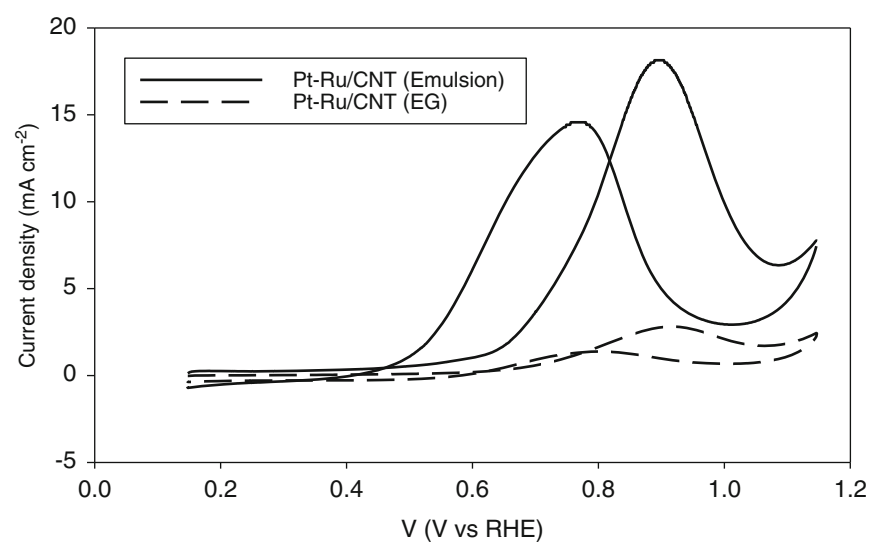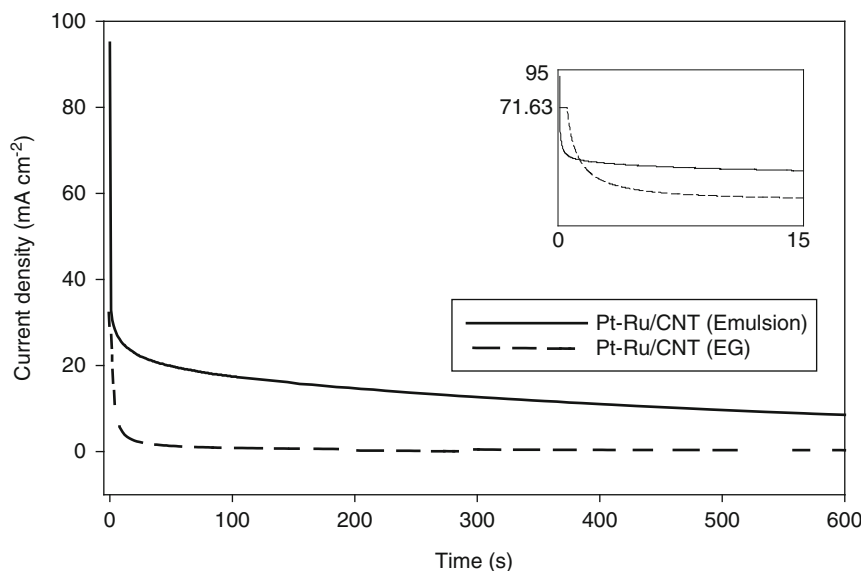
Fig. 89.4 Chronoamperometrical plot at 0.947 V vs. RHE for 10 min for Pt–Ru/CNT (EG) and Pt–Ru/CNT (emulsion) in 1 M CH$_3$OH + 0.5 M H$_2$SO$_4$, with the current magnification in the first initial 15 s shown in the inset

due to the reduction of platinum oxide occurred in the cathodic scan. These CV findings demonstrate the advantages of employing reverse micelles microemulsion to prepare Pt–Ru nanocatalysts that have high catalytic activity for methanol electro-oxidation.

Chronoamperometrical plots of current density vs. time at a constant potential of 0.947 V is displayed in Fig. 89.4. These curves reflect the activity and stability of the catalysts in catalyzing the methanol electro-oxidation. The potentiostatic currents decreased rapidly in the very initial period. This may be due to the formation of intermediate species, such as CO$_{ads}$, COOH$_{ads}$, and CHO$_{ads}$, during the methanol electro-oxidation [14]. For clarity, the inset shows the magnification of the very initial currents. Moreover, Pt–Ru/CNT (emulsion) maintained both higher initial and limiting current densities over time, which implies a much better catalytic activity and stability of methanol electro-oxidation by this catalyst. These results agree with those of CVs shown in Fig. 89.3. All these findings suggest that CNTs coupled with microemulsion technique can improve the electrochemical performance of DMFC anodes. Similar results are obtained for carbon fibers with cup-stacked-type structure [15].

Conclusions

A reverse micelles process coupled with multi-walled carbon nanotubes has been developed and proved as an excellent means for the preparation of supported Pt–Ru nanoparticles as catalysts for direct methanol electro-oxidation. The reverse microemulsion-synthesized Pt–Ru/CNT catalyst displayed a much higher electro-catalytic activity in methanol oxidation than a polyol-based one. The higher activity thus obtained by the former catalyst is attributable to the morphology of its unique nanostructure in that small spherical particles were homogeneously dispersed on the surface of carbon nanotubes with narrow particle size distribution.

References

1. Toshima N, Yonezawa T, Kushihashi K (1993) Polymer-protected palladium-platinum bimetallic clusters – preparation, catalytic properties and structural considerations. J Chem Soc Faraday Trans 89:2537–2543
2. Link S, Wang ZL, El-Sayed MA (1999) Alloy formation of gold-silver nanoparticles and the dependence of the plasmon absorption on their composition. J Phys Chem B 103:3529–3533
3. Reetz MT, Helbig W, Quaiser SA (1995) Electrochemical preparation of nanostructured bimetallic clusters. Chem Mater 7:2227–2228
4. Bagwe RP, Khilar KC (1997) Effects of the intermicellar exchange rate and cations on the size of silver chloride nanoparticles formed in reverse micelles of AOT. Langmuir 13:6432–6438
5. Bagwe RP, Khilar KC (2000) Effects of intermicellar exchange rate on the formation of silver nanoparticles in reverse microemulsions of AOT. Langmuir 16:905–910
6. Zhang P, Gao L (2003) Copper sulfide flakes and nanodisks. J Mater Chem 13:2007–2010
7. Wang C, Waje M, Wang X, Tang JM, Haddon RC, Yan YS (2004) Proton exchange membrane fuel cells with carbon nanotube based electrodes. Nano Lett 4:345–348
8. Li WZ, Liang CH, Qiu JS, Zhou WJ, Han HM, Wei ZB, Sun GQ, Xin Q (2002) Carbon nanotubes as support for cathode catalyst of a direct methanol fuel cell. Carbon 40:791–794
9. Liu ZL, Lin XH, Lee JY, Zhang W, Han M, Gan LM (2002) Preparation and characterization of platinum-based electrocatalysts on multiwalled carbon nanotubes for proton exchange membrane fuel cells. Langmuir 18:4054–4060
10. Gasteiger HA, Markovic N, Ross PN, Cairns EJ (1993) Methanol electrooxidation on well-characterized Pt-Ru alloys. J Phys Chem 97:12020–12029
11. Chu D, Gilman S (1996) Methanol electro-oxidation on unsupported Pt-Ru alloys at different temperatures. J Electrochem Soc 143:1685–1690
12. Zhou WJ, Zhou ZH, Song SQ, Li WZ, Sun GQ, Tsiakaras P, Xin Q (2003) Pt based anode catalysts for direct ethanol fuel cells. Appl Catal B Environ 46:273–285
13. Gojkovic SL, Vidakovic TR, Durovic DR (2003) Kinetic study of methanol oxidation on carbon-supported PtRu electrocatalyst. Electrochim Acta 48:3607–3614
14. Gu YJ, Wong WT (2006) Nanostructure PtRu/MWNTs as anode catalysts prepared in a vacuum for direct methanol oxidation. Langmuir 22:11447–11452
15. de Moraes IR, da Silva WJ, Tronto S, Rosolen JM (2006) Carbon fibers with cup-stacked-type structure: an advantageous support for Pt-Ru catalyst in methanol oxidation. J Power Sour 160:997–1002

Evaluation of Biohydrogen Production Potential from Sewage Sludge

İlknur Şentürk and Hanife Büyükgüngör

Abstract

Owing to limited resources and emission of pollutants, hydrogen is a promising alternative to fossil fuels. Hydrogen is a clean energy that produces water instead of greenhouse gases when combusted. Furthermore, hydrogen has a high-energy yield (about 2.75 times that of hydrocarbon fuels). Biological hydrogen production from biomass is considered one of the most promising alternatives for sustainable green energy production and important solution to a sustainable power supply and is nowadays being seen as the versatile fuel of the future, with potential to replace fossil fuels. This process is able to solve two problems: the reduction of pollution from the uncontrolled degradation of waste and the generation of a clean alternative fuel.

The treatment and disposal of sewage sludge generated in urban wastewater treatment plants are an important environmental problem. Unused, discarded biomass residues are a potential energy resource, which at present are not well managed and thus pose significant environmental problems. Recently, some studies are focusing on using the sludge to produce hydrogen by anaerobic fermentation.

Sewage sludge from a wastewater treatment plant is biomass that contains large quantities of polysaccharides and proteins and thus is a potential substrate for producing hydrogen. Limited data addressing this topic show that the biohydrogen yield using waste sludge and anaerobic fermentation is rather low. Due to low hydrogen yield from the raw sewage sludge, a number of pretreatment approaches have been investigated. Pretreatment can increase the efficiency of anaerobic stabilization of sludge by hydrolyzing the insoluble organic matter to water. This study deals with the suitability of pretreated sewage sludge as the primary substrate for microbial H_2 production and also may overcome certain important limitations of biological H_2 production.

Introduction

Over the past 50 years, the world's population has more than doubled, coupled with an expectation of a higher standard of living and an ever increasing economic output. This has resulted in a large increase in primary energy consumption, particularly the use of fossil fuel-derived energy. In 2010, world primary energy consumption grew by 5.6 %, the largest percentage growth in almost 40 years. This growth included an increase in the consumption of all major fossil fuels including oil, natural gas, and coal. This trend in increasing energy consumption is expected to continue as the world's population is projected to increase by an additional 1.4 billion people by 2030, and have an increase of 100 % of the world's real income.

İ. Şentürk (✉) • H. Büyükgüngör
Environmental Engineering Department, Ondokuz Mayis University, 55139 Atakum, Samsun, Turkey
e-mail: ilknurg@omu.edu.tr; hbuyukg@omu.edu.tr

These increases will put enormous pressure on the finite supply of fossil fuel-based energy, exacerbating global concerns over energy security, fossil fuel-based environmental impacts such as climate change, and the rising cost of energy and food. The utilization of current energy sources has been generating environmental pollution of air, water, and soil through the years. These negative effects have increased interest in the development of new technologies to obtain clean energy, mainly through the utilization of renewable energy sources. Currently, the world consumes about 15 TW of energy per year and only 7.8 % of this is derived from renewable energy sources [1, 2].

Problems of deficiencies in fossil fuel sources have become apparent in many countries. Moreover, problems of the greenhouse effect, caused by the enormous combustion of fossil fuels, have become gradually severe. Therefore, it is necessary to explore clean and renewable energy sources for use in the near future [3]. Hydrogen is a promising alternative energy to fossil fuels. It is environmental friendly renewable energy in which the by-product from its combustion with oxygen is water [4–6]. Hydrogen has a high-energy yield of 142.35 kJ/g, which is about 2.75 times greater than the hydrocarbon fuel [4, 7].

Hydrogen can be generated by thermochemical, electrochemical, or microbial fermentation (biological) processes. However, the thermochemical process requires hydrocarbon to be used as feedstocks, which mostly comes from fossil fuels while electrochemical process needs supply of electricity. Biohydrogen production from organic waste or wastewater through fermentation by anaerobic acidogenic bacteria with highly diverse fermentation characteristics and hydrogen production capabilities does not require input of external energy [5]. Recently, biohydrogen production has received an increasing attention due to a high demand of sustainable energy. Biologically, hydrogen can be produced by photo and dark fermentations [8]. Hydrogen production through photo fermentation is not favorable due to the limitations of light conversion efficiencies, photo inhibition at high solar light intensities, and the design of efficient photoreactors. Dark fermentative hydrogen production is a ubiquitous phenomenon under anoxic or anaerobic condition [5]. Dark fermentation has advantages over photo fermentation process in terms of better cost-effectiveness, higher rate of hydrogen production, and the ability to utilize various kinds of substrates [8].

Dark fermentation under anaerobic conditions can be operated without light and oxygen limits. Hydrogen production through dark fermentation has advantages over other processes due to its ability of continuous hydrogen production without an input of external energy and the stabilization of the human-derived organic wastes and biomass. Among the hydrogen production methods, the most promising, relatively economical, and also environmentally friendly one seems to be the dark fermentation of organic wastes as it solves the problems of energy production and waste disposal simultaneously [3, 5]. These human-derived organic wastes for hydrogen production mainly include milk industry wastewater, lactic acid fermentation plant wastewater, distillery wastewater, and sewage sludge as well as municipal solid waste [5]. Biomass (waste-activated sludge, plants, animals, and their organic waste products) provides approximately 14 % of the world's energy needs. In developing countries, which often have limited supplies of fossil fuels but abundant biomass resources, as much as 35 % of the energy demand is supplied by biomass. However, in developed countries with still abundant fossil fuel supplies, reliance on biomass as an energy resource is very limited, despite its huge energy potential [9].

In 2008, about 2.38 billion m^3/year of municipal and industrial wastewater was treated in wastewater treatment plants in Turkey, producing about 1,075.000 t/year of sewage sludge [10]. Landfill is one of the most common methods that are used in the final disposal of sludge worldwide [11]. The disposal of sludge generated in urban wastewater treatment plants is an important environmental problem. Unused, discarded biomass residues are a potential energy resource, which at present are not well managed and thus pose significant environmental problems [9]. Using sewage sludge as the substrate for fermentative hydrogen production offers several advantages over the use of other biomass sources. It is available at little or no cost. The supply is plentiful and can be found wherever there are human settlements [12].

The strict requirement of wastewater effluent standard and a good design for wastewater treatment process increased the quantity of waste-activated sludge (WAS), commonly known as sewage sludge. WAS is a by-product of the wastewater treatment process. Sewage sludge is mainly composed of microorganisms, and its organic substance composition is therefore different from carbohydrate-rich substrates such as glucose or starch. The sewage sludge consists of 41 % protein, 25 % lipid, 14 % carbohydrate, and 20 % unknown components on the basis of chemical oxygen demand (COD) or 32–41 % protein and 5–12 % fats on the basis of total dry solids (TDS). Thus, it represents a potential substrate for producing hydrogen [4, 7, 13]. Recently there are interests toward utilization of activated sludge as the biological material for production of renewable energy, i.e., hydrogen and methane using anaerobic digestion process [6].

But organics components in sewage sludge are mostly nonutilizable; hence pretreatment becomes essential to render them suitable for H_2 fermentation. Another credible option is co-digestion with other carbohydrate-rich biomass like food waste or molasses [14]. Kim et al. [15] have reported higher H_2 yield (122.9 mL H_2/g carbohydrate-COD) from co-digestion of 87:13 (food waste:sewage sludge). However, food waste rich in carbohydrates was the major component in that study,

not sewage sludge. In this study, it is expected to address the problems associated with waste-activated sludge disposal through simultaneous generation of clean gaseous energy in the form of hydrogen. A synchronous objective was to investigate the influence of different pretreatment on the hydrogen production using waste sludge by anaerobic fermentation.

Applicability of Biohydrogen Production from Sewage Sludge

The sewage sludge is composed of largely organic matters (59–88 %) that can decompose and produce offensive odors. These organics are mainly the microbial matters and the microorganisms include hydrogen-producing ones and hydrogen-consuming ones. The treatment and disposal of the excess sludge have become an important problem and a great challenge for many plants. Anaerobic digestion is an appropriate technique for reduction in the volume and weight of excess sludge before final disposal, and it is employed worldwide as the oldest and most important process for sludge stabilization. Additionally, anaerobic digestion can recover partly the bioenergy of sludge through producing methane. Anaerobic digestion process generally consists of four stages, i.e., hydrolysis, acidogenesis, acetogenesis, and methanogenesis (Fig. 90.1). Hydrogen is an intermediary metabolite of anaerobic digestion, which is rapidly taken up and converted to other products by the hydrogen-consuming microorganisms in the third stage of anaerobic digestion. On the other hand, the use of hydrogen is more extensive than that of methane. So, it is beneficial to get hydrogen in the anaerobic digestion of sludge. In order to harvest hydrogen, the anaerobic digestion of sludge must be blocked at the hydrogen and acetic acid formation stage, namely, the second stage of anaerobic digestion.

Sewage sludge has been used both as substrate and as source of inoculum. The major reason why sewage sludge has been focused as source of inoculum is that it is bountiful with enteric bacteria, which are potential H_2 producers. Several pure cultures and mixed microbial cultures have been successfully enriched and tested for H_2-producing potential. Nevertheless, the pursuit for ideal microbe(s) for H_2 production has thrust the researchers to screen various sources [17]. The anaerobic digestion processes using mixed cultures are shown to be more practical, because they are simpler to operate and easier to control and may
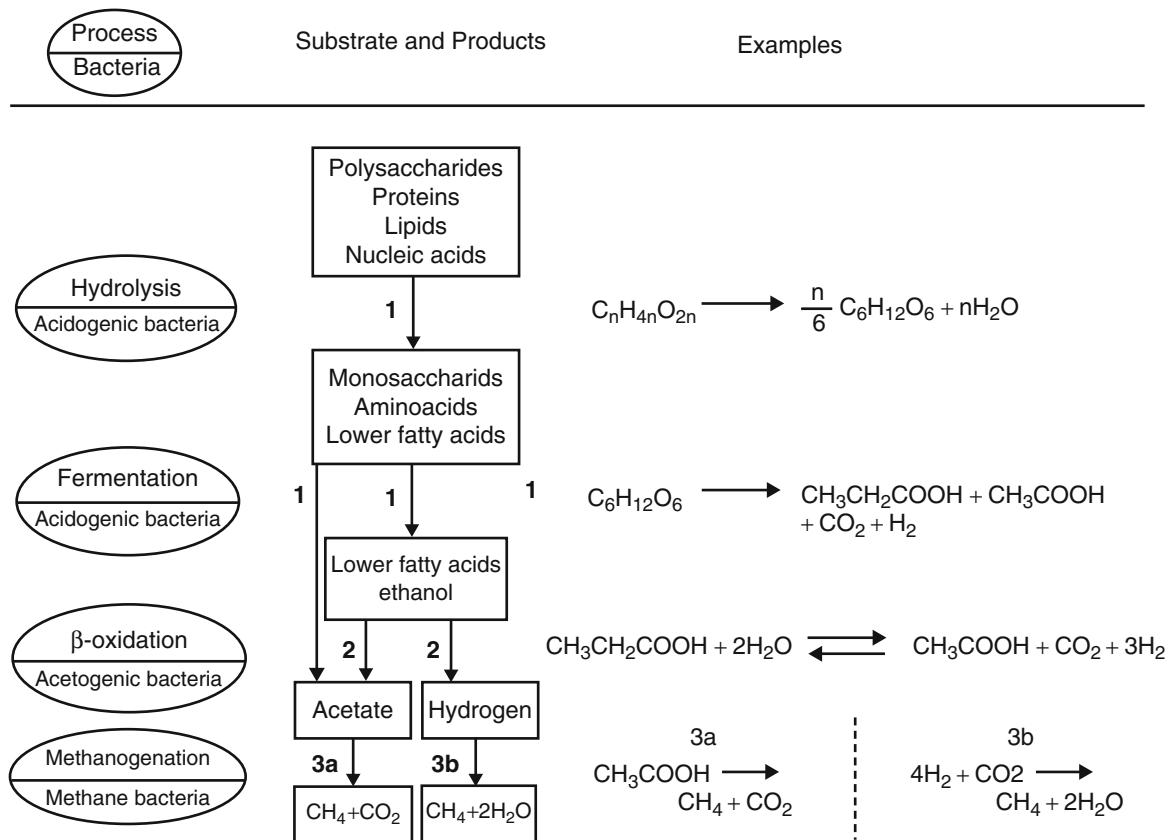
Fig. 90.1 Anaerobic metabolism [16]

have a broader choice of feedstock [18]. On these grounds, nowadays researchers are more interested in using mixed cultures, instead of pure cultures, for wastewater and waste treatment. However in mixed cultures, hydrogen produced by hydrogen-producing bacteria (such as *Clostridium sp*. and *Enterobacter*) is consumed immediately by hydrogenotrophic methanogens [19]. Thus, in order to produce hydrogen from mixed anaerobic cultures, hydrogen-consuming bacterial activity (methanogens) should be inhibited or eliminated while preserving the activity of the hydrogen-producing bacteria. Many hydrogen-producing microorganisms can form endospores, which can be considered "survival structures" developed by these organisms when unfavorable environmental conditions are encountered, e.g., high temperature, and harmful chemicals including acid and alkaline. When favorable conditions return, the spores germinate and become vegetative cells. However, most of hydrogen-consuming microorganisms, e.g., methanogens, do not have this characteristic [20]. Several methods have been reported to inhibit methanogenic activity and selectively enrich hydrogen-producing acidogenic bacteria from mixed anaerobic cultures, including heat treatment, aeration, acid and base treatment, inhibiting chemical addition such as 2-bromoethanesulfonate (BES), iodopropane, and chloroform, and acidogenic culture preparation. The physiological differences between hydrogen-producing bacteria (acidogenic bacteria) and hydrogen-consuming bacteria (methanogenic bacteria) form the fundamental basis behind the development of the various pretreatment methods proposed for preparation of hydrogen-producing seeds.

In the case of utilization of sludge as substrate for H_2 production, the pretreatment methods not only reduced the particle size but also increased the level of soluble protein. In particular, thermal and thermochemical pretreatments resulted in significant particle size reduction. The level of soluble protein increases by chemical and thermochemical pretreatment methods in particular. Proteins are principal constituents of organisms and they contain carbon, which is a common organic substance, as well as hydrogen, oxygen, and nitrogen. For this reason, it was considered that as the level of soluble protein increased, the efficiency of anaerobic digestion would be improved. The differences in the amount of biogas produced showed that the impact of the rate-limiting step could be reduced by pretreatment and digestion efficiencies of the WAS were consequently improved [21].

So far, very little work on fermentative hydrogen production from sewage sludge has been conducted. Limited data show that the biohydrogen yield using waste-activated sludge and anaerobic fermentation is rather low at 0.08 mmol H_2/g dry solid (DS) [22]. Pretreatment can increase the efficiency of anaerobic stabilization of sludge by hydrolyzing the insoluble organic matter to water (e.g., see Lee and Mueller [23] and the references cited therein). Chu et al. [24] have reported that the use of thermal boiling to hydrolyze sludge promoted the anaerobic production of methane.

Huang et al. [22] have reported yields of 0.16 g H_2/kg from waste-activated sludge, whereas Wang et al. [13, 25] reported yields equivalent to 0.9–6.3 g H_2/kg DS depending on the pretreatment applied to the sewage sludge. However, it should be noted that so far all these studies used pure cultures of bacteria as inoculum. Although this may result in higher yields it would be expensive and impractical to attempt at full scale due to the time, cost, and energy requirements of preparing and storing enough bacterial biomass to seed a digester containing thousands of liters of sewage sludge. Despite this limitation however, work published so far has demonstrated the feasibility of producing hydrogen fermentatively from sewage sludge. Wang et al. [13] also demonstrated that applying different pretreatment to sewage sludge prior to fermentation can have a significant effect on hydrogen yield. In particular, sterilization of the sewage sludge at 121 °C consistently improved hydrogen production and reduced the production of methane which can have a negative impact on hydrogen yield [12]. Hydrogen yields of 1.2 mg H_2/g COD [25] and 0.6 mol/kg COD [26] were reported when sludge was used as the raw material. However, higher hydrogen yields (15 mg H_2/g COD) were obtained from the filtrate [26]. Pretreatment of the sludge increased the soluble COD enhancing the hydrogen yield (0.9 mmol/g dried sludge) [13, 27, 28]. Consequently, in order to further increase the yield of hydrogen production, the impacts of pretreatments on hydrogen production using sewage sludge should be examined. The reason that the same sludge using different pretreatment had different hydrogen yield and lag time was demonstrated [9]. Table 90.1 lists some results from the literature. Various means of producing hydrogen using numerous substrates and seed bacteria have been reported, such as g H_2/g VSS (Volatile suspended solids), mL H_2/g COD, and others. Experimental results can almost never be compared because details for unit conversion are not available.

Impact of Ultrasonication Pretreatment on Hydrogen Production

Ultrasonic could produce cavitation in waste sludge, and cell lysis and particle size reduction would be caused by which the digestion process was enhanced [31]. It appeared from the study that the mechanical shear forces caused by ultrasonic cavitations could be a key factor for sludge disintegration and collapse of cavitation bubbles could significantly alter the sludge characteristics [32]. Tiehm et al. [33] showed that applying ultrasound (3.6 kW, 31 kHz, 64 s) to sludge disintegration can release the organic substances into the sludge, so that the soluble chemical oxygen demand (SCOD) in the supernatant increases from 630 to 2,270 mg/L. Moreover, the digestion time could be reduced to 8 days. Chu et al. [34] demonstrated that

Table 90.1 Comparison of the literature data on biohydrogen production using waste sludge

Substrate	Operating conditions				Seed	H$_2$ yield	References
	pH	T (°C)	rpm	Reactor type			
Waste-activated sludge	7.0	55	250	Batch	Anaerobic sludge (heat treated at 100 °C for 2 h)	7.81 mmol	[5]
Municipal sludge pretreatment with ultrasonic treatment	6.7–7.9	36	1,050	Batch	–	34.2–34.9 mL/g volatile solid (VS)	[29]
Aerobic thermophilic digestion sludge	5.5	55	50	Batch	–	136.9 mL H$_2$/g TS	[6]
Waste sludge sterilization for 20 min at 121 °C		35	125	Batch	*Pseudomonas sp. GZ1*	1.34 mg H$_2$/g TCOD	[4]
Wastewater sludge	~6.4	35	–	Batch	*Clostridium bifermentans*	1.5–2.1 mmol H$_2$/g COD	[13]
Sterilized sludge	7.38	35	125	Batch	*Pseudomonas sp. GZ1*	15.02 mL H$_2$/g TCOD	[9]
Sterilized sludge	–	37 ± 1	140–150	Batch	Consortiums in sterilized sludge	11.77 mL H$_2$/g DS	[20]
Alkaline treated sludge	11.0	36 ± 1	150	Batch	Alkaline treated sludge	16.59 mL H$_2$/g substrate	[7]
Sterilized sludge					Defined consortium (1:1:1)	41.23 mL H$_2$/g COD$_{reduced}$	[14]
Raw sewage sludge	11.5	37 ± 1	140–150	Batch	–	7.57 mL H$_2$/g VS	[30]
Acid pretreatment	7 ± 0.1					3.25 mL H$_2$/g VS	
Alkaline pretreatment	11.5					11.68 mL H$_2$/g VS	
Thermal pretreatment	6.8					8.62 mL H$_2$/gVS	
Ultrasonic pretreatment	6.9					3.83 mL H$_2$/g VS	

"weak" ultrasound pretreatment greatly increased both the production rate and ultimate yield of methane. Chiu et al. [35] observed simultaneous alkaline and ultrasound pretreatment was more effective in releasing SCOD.

As for the mechanisms of ultrasonic disintegration, Tiehm et al. [33] noted that hydromechanical shear forces produced by ultrasonic cavitation were predominantly responsible for sludge disintegration. However, it is still unclear about the other contributions to the ultrasonic waste-activated sludge disintegration. There are four paths, which are shown as the following, responsible for the ultrasonic activated sludge disintegration:

- Hydromechanical shear forces;
- Oxidizing effect of •OH, •H, •N, and •O produced under the ultrasonic radiation;
- Thermal decomposition of volatile hydrophobic substances in the sludge;
- Increase of temperature during ultrasonic activated sludge disintegration.

If the sludge temperature improved, the lipid on the cytoplasmic membrane can be decomposed, which results in the generation of little holes on the membrane. The intracellular substances can release through the holes, which causes the increase of SCOD in the supernatant [36].

Because the quantity of volatile hydrophobic substances in the sludge is very low, so the third path can be ignored. The increment speed in sludge temperature is slow. Wang et al. [36] have reported that the longest disintegration time is 60 min and the disintegrated sludge temperature is increased to 82 °C. According to this study on thermal sludge disintegration, improving the sludge temperature to 80 °C in 1 h produces low SCOD$_+$ and SCOD$_\%$. Therefore, the fourth can also be neglected. As for the second path, Hart [37] and Hart and Henglein [38] have demonstrated that the amount of •OH is much more than the one of •H, •N, and •O. Accordingly, the oxidizing effect of •H, •N, and •O can be ignored. From the above analysis, we know there are two main paths attributed to the ultrasonic sludge disintegration, namely, hydromechanical shear forces and the oxidizing effect of •OH [36].

Impact of Thermal Pretreatment on Hydrogen Production

Thermal treatment results in the breakdown of the gel structure of the sludge and the release of intracellular bound water. Therefore, this treatment allows a high level of solubilization, an improvement in biogas production, modification in sludge characteristics (increase in filterability and viscosity reduction), and reduction of pathogen microorganisms. The main parameter for thermal treatment is temperature; time of treatment has less influence. According to several authors, optimal temperature is around 170–200 °C. Indeed, for higher temperature, biodegradability of sludge is no more improved and can decrease. This can be due to the formation of refractory compounds linked to Maillard reactions. But a thermal treatment

around 175 °C, combined with anaerobic digestion, can highly reduce sludge production; this reduction can reach 50–70 % according to the process [39, 40].

Kim et al. [21] reported that the organic particulates in WAS were liquidized to soluble carbohydrates, lipids, and proteins or converted into lower molecular weight compounds by thermal pretreatment. Li and Noike [41] reported that the optimum pretreatment temperature and contact time for improving the anaerobic digestion of WAS were 170 °C and 60 min, respectively. Through thermal pretreatment, the gas production from WAS was greatly increased [21].

Sterilized sludge was used to produce hydrogen by anaerobic self-fermentation and raw sludge was used as control by Xiao and Liu [20]. Owing to the coexistence of hydrogen-producing microorganisms and hydrogen-consuming ones and their different growth rates, the hydrogen production and hydrogen consumption (methane production) could be detected in the anaerobic self-fermentation of the raw sludge. However, most of the organics presented in the raw sludge were of microbial cells, which were enwrapped by cell walls, and such few available organics in raw sludge for hydrogen-producing microorganisms and hydrogen-consuming ones resulted in their slow growth and metabolism. As a result, there was little hydrogen detected in the anaerobic self-fermentation of raw sludge. Apart from raw sludge, the sterilization had disrupted some microbial cells and released some intracellular organics from cell, and thus the thermally screened hydrogen-producing microorganisms in the sterilized sludge could quickly use those organics and produce hydrogen. Xiao and Liu [20] reported that the maximal hydrogen yield of the sterilized sludge (16.26 mL H_2/g VS) was much higher than that of the raw sludge (0.35 mL H_2/g VS). Guo et al. [9] also produced 1.34 mg H_2/g TCOD with sterilization pretreated sludge. This value is comparable to that of protein fermentation, but is still far lower than that of polysaccharides.

Although most hydrogen-consuming microorganisms (mainly methanogens) died during sterilization, hydrogen consumption still occurred in the later stage (after 36 h) of anaerobic self-fermentation of the sterilized sludge. Interestingly, no methane was detected in the anaerobic self-fermentation of sterilized sludge. There were three reasons for the hydrogen consumption:

(1) There are a few hydrogen-consuming microorganisms (for example, Homoacetogenic bacteria) in the sludge that can also form spores and resist autoclaving. In the initial stage of anaerobic fermentation, the hydrogen-consuming action was weak and inconspicuous because of fewer hydrogen-consuming microorganisms and their lower growth rate compared with hydrogen-producing ones. In the later stage of anaerobic fermentation, the hydrogen-consuming action became obvious along with the increase in hydrogen-consuming microorganisms.

(2) The increase of volatile fatty acids (VFA$_s$), particularly, acetic acid, could inhibit further growth of hydrogen-producing microorganisms and then result in the decrease of the hydrogen production rate.

(3) The anaerobic fermentation of proteins could not only produce hydrogen but also consume hydrogen, and high content of proteins in the sterilized sludge may also result in the consumption of hydrogen [20].

In spite of these three matters, there were some advantages of using sterilized sludge to produce hydrogen:

(1) Without any extra-seeds and any extra feeds, it is simple and convenient to produce hydrogen by anaerobic self-fermentation;

(2) Without any extra-added materials (such as alkaline and acid used in alkaline or acid pretreatment), the sterilized sludge was easy to be treated after hydrogen production;

(3) No methane was produced in the process of anaerobic self-fermentation because most of the methanogens were killed by autoclave [20].

Heat treatment temperatures range from 75 °C to 121 °C and exposure times range between 15 min and 2 h [42]. The most common condition in heat treatment is 100 °C for 15 min. Mohan et al. [43] evaluated the influence of the heat treatment of anaerobic mixed inoculum at 100 °C for 1 h on hydrogen production. Hydrogen production yield increased from 0.002 mmol H_2/g COD to 0.122 mmol H_2/g COD with heat treatment procedure. Mu et al. [44] used heat, acid, and base treatment methods to suppress methanogenesis in mixed cultures and to enrich H_2-producing inoculum. Thus, highest H_2 yield of 2.0 mol-H_2/mol-glucose was achieved with the heat-treated sludge. Ren et al. [45] studied four treatment methods including heat shock treatment, acid treatment, alkaline treatment, and repeated aeration treatment to enrich hydrogen-producing bacteria. Thus, hydrogen production increased from 180.4 mL (control) to 189.5 mL by heat treatment of sludge [46].

Impact of Acidic or Basic Pretreatment on Hydrogen Production

Hydrogen production occurs in the acidification stage, and the pH value is one of important factors affecting the biohydrogen fermentation [7]. In the conventional methanogenic process, the pH is controlled at near pH 7. At pH below 6.3 or above 7.8, methane production rate would drop sharply [47, 48]. Thus, the bioactivity of methanogens can be inhibited by adjusting the pH of anaerobic sludge away from pH 7. On the other hand, the hydrogen-producing Clostridium can resist to extreme acidity and

alkalinity by forming protective spores. Wang and Wan [49] indicated that the hydrogen production potentials of the sludge treated by acid (96.8 mL) and base (125.9 mL) were higher than hydrogen production potential of the control test (65.7 mL) during the fermentative hydrogen production using glucose as the substrate [46]. Alkaline pretreated sludge improved the hydrogen yield to 1.48 mg H_2/g DS in comparison to 0.81 mg H_2/g DS when the raw sludge was used as substrate [7].

Cai et al. [7] analyzed soluble organic matter concentrations of the raw sludge with an alkaline pretreated sludge at different initial pH values. Obviously, all concentrations of three soluble organic matters in the alkaline pretreated sludge were much higher than those in the raw sludge. The soluble protein was the major part of all three (protein, carbohydrates, and lipids) soluble organic matter. For the raw sludge, alkaline pretreatment was more effective for solubilizing organic matter than acidic pretreatment. For the alkaline pretreated sludge, the adjustment of pH had impact on soluble organic matter, and all three soluble organic matters at high initial pH of 11.0 were more than those at low initial pH of 5.0. So, alkaline pretreatment of sewage sludge could provide more soluble organic matter for biohydrogen production from sewage sludge.

Impact of Microwave Pretreatment on Hydrogen Production

The main advantages of microwave heating are the uniformity of heating and the precise control of the process temperature. Guo et al. [9] reported that the maximal hydrogen production yield obtained using microwave pretreated sludge was 14.65 mL (11.44 mL/g TCOD), and lag time was 10 h. Nakazato et al. [50] found out that microwave pretreatment improves sludge dewaterability. This effect was efficient for hydrolyzing sludge and producing hydrogen. The release of nutrient was also found in this study. Otherwise, the anaerobic digester fed with microwave irradiated sludge was more efficient in the inactivation of fecal coliforms than the other two digesters fed with raw sludge and externally heated sludge, respectively [51]. So microwave pretreated sludge could reduce the pathogen [9].

Conclusions

The major problems in biohydrogen production from wastes are the low rates and yields of hydrogen formation. Large reactor volumes are required for biohydrogen production due to low hydrogen production rates. Low yields and the rates of hydrogen formation may be overcome by selecting and using more effective organisms or mixed cultures, developing more efficient processing schemes, optimizing the environmental conditions, and developing more efficient bioreactors. Considerable research and development studies are needed to improve the "state of the art" in biohydrogen production.

Utilization of sewage sludge as substrate for H_2 production has not received much attention than what it actually deserves. The feasibility studies on fermentative H_2 production from sludge as demonstrated by few researchers suggest that lower yield is the major limitation which precludes the technology from being commercialized. However, these studies were successful in concluding certain critical findings, viz.:

1. Various pretreatments can have significant effect of on H_2 production. The main groups of the organic solids discovered in sewage sludge are proteins, carbohydrates, fats, and oils. But these organics are mostly complex and underutilized; hence pretreatment becomes essential to render them suitable for H_2 fermentation. These pretreatments include alkaline pretreatment, acidification, sterilization, ultrasonication, microwave, enzyme, and heating. Pretreatment not only released insoluble organic matter into water to increase the efficiency of fermentation, but also inactivated methanogenic bacteria in the substrate to reduce their consumption of hydrogen.
2. Nutrient formulation is necessary for amelioration of H_2 yield.
3. Mixed cultures are more efficient than pure cultures with respect to H_2 production from sewage sludge.
4. Sequential H_2 and CH_4 production system using mixed consortia can augment the total gaseous energy recovery.

From the results obtained we conclude that biohydrogen yield of sewage sludge using pretreatment methods with mixed cultures at proper bioreactor conditions can improve.

References

1. Senturk I, Buyukgungor H (2012) Evaluation of biohydrogen production potential from marine macro algae. NATO Advanced Research Workshop 984302. Black Sea: strategy for addressing its energy resources development and hydrogen energy problems, Batumi, Georgia, 7–10 October 2012
2. Senturk I, Buyukgungor H (2013) Evaluation of biohydrogen production potential from marine macro algae. In: Veziroglu A, Tsitskishvili M (eds) Black Sea energy resource development and hydrogen energy problems. NATO science for peace and security series-C: environmental security. Springer, 450 p

3. Chairattanamanokorn P, Penthamkeerati P, Reungsang A, Lo YC, Lu WB, Chang JS (2009) Production of biohydrogen from hydrolyzed bagasse with thermally preheated sludge. Int J Hydrogen Energy 34:7612–7617

4. Guo L, Li XM, Zeng GM, Zhou Y (2010) Effective hydrogen production using waste sludge and its filtrate. Energy 35:3557–3562

5. Lin YH, Zheng HX, Juan ML (2012) Biohydrogen production using waste activated sludge as a substrate from fructose-processing wastewater treatment. Process Saf Environ Prot 90:221–230

6. Sittijunda S, Reungsang A, O-thong S (2010) Biohydrogen production from dual digestion pretreatment of poultry slaughterhouse sludge by anaerobic self-fermentation. Int J Hydrogen Energy 35:13427–13434

7. Cai M, Liu J, Wei Y (2004) Enhanced biohydrogen production from sewage sludge with alkaline pretreatment. Environ Sci Technol 38:3195–3202

8. Sittijunda S, Reungsang A (2012) Biohydrogen production from waste glycerol and sludge by anaerobic mixed cultures. Int J Hydrogen Energy 37:13789–13796

9. Guo L, Li XM, Bo X, Yang Q, Zeng GM, Liao D, Liu JJ (2008) Impacts of sterilization, microwave and ultrasonication pretreatment on hydrogen producing using waste sludge. Bioresour Technol 99:3651–3658

10. Turkish Statistical Institute (2008) http://www.tuik.gov.tr

11. Ozsoy G, Dilek FB, Sanin FD (2006) An investigation of agricultural use potential of wastewater sludges in Turkey case of heavy metals. Water Sci Technol 54:155–161

12. Nicolau JM, Dinsdale R, Guwy A (2008) Hydrogen production from sewage sludge using mixed microflora inoculum: effect of pH and enzymatic pretreatment. Bioresour Technol 99:6325–6331

13. Wang CC, Chang CW, Chu CP, Lee DJ, Chang BV, Liao CS (2003) Producing hydrogen from wastewater sludge by *Clostridium bifermentans*. J Biotechnol 102 (1):83–92

14. Kotay SH, Das D (2010) Microbial hydrogen production from sewage sludge bioaugmented with a constructed microbial consortium. Int J Hydrogen Energy 35:10653–10659

15. Kim SH, Han SK, Shin HS (2004) Feasibility of biohydrogen production by anaerobic co-digestion of food waste and sewage sludge. Int J Hydrogen Energy 29:1607–1616

16. Digman B, Kim DS (2008) Review: alternative energy from food processing wastes. Environ Prog 27:524–537

17. Kotay SM, Das D (2009) Novel dark fermentation involving bioaugmentation with constructed bacterial consortium for enhanced biohydrogen production from pretreated sewage sludge. Int J Hydrogen Energy 34:7489–7496

18. Valdez-Vazquez I, Sparling R, Risbey D, Rinderknecht-Seijas N, Poggi-Varaldo HM (2005) Hydrogen generation via anaerobic fermentation of paper mill wastes. Bioresour Technol 96:1907–1913

19. Ray S, Chowdhury N, Lalman JA, Seth R, Biswas N (2008) Impact of initial pH and linoleic acid (C18:2) on hydrogen production by a mesophilic anaerobic mixed culture. J Environ Eng (ASCE) 134(2):110–117

20. Xiao B, Liu J (2009) Biological hydrogen production from sterilized sewage sludge by anaerobic self-fermentation. J Hazard Mater 168:163–167

21. Kim J, Park C, Kim TH, Lee M, Kim S, Kim SW, Lee J (2003) Effects of various pretreatments for enhanced anaerobic digestion with waste activated sludge. J Biosci Bioeng 95:271–275

22. Huang CH, Lin HY, Tsai YY, Hsie YK (2000) The preliminary studies of hydrogen production from anaerobic digestion with different substrates and cultivations. The twenty-fifth wastewater technology conference, Yunlin, Taiwan (in Chinese)

23. Lee DJ, Mueller JA (2001) Preliminary treatments. In: Spinosa L, Vesilind A (eds) Sludge into biosolids—processing, disposal, utilization. IWA, London

24. Chu CP, Lin WW, Lee DJ, Chang BV, Peng XF (2002) Thermal treatment of waste activated sludge using liquid boiling. J Environ Eng (ASCE) 128:1100–1103

25. Wang CC, Chang CW, Chu CP, Lee DJ, Chang BV, Liao CS, Tay JH (2003) Using filtrate of waste biosolids to effectively produce biohydrogen by anaerobic fermentation. Water Res 37(11):2789–2793

26. Wang CC, Chang CW, Chu CP, Lee DJ, Chang BV, Liao CS (2004) Efficient production of hydrogen from wastewater sludge. J Chem Technol Biotechnol 79:426–427

27. Kapdan IK, Kargi F (2006) Biohydrogen production from waste materials. Enzyme Microb Technol 38:569–582

28. Senturk I, Buyukgungor H (2010) An examination of used different waste materials and biohydrogen production methods. Sigma J Eng Nat Sci 28:369–395

29. Wu F, Zhou SQ, Lai YL, Zhong WJ (2009) Studies on the effects of pretreatment on production hydrogen from municipal sludge anaerobic fermentation. Nat Sci 1:10–16

30. BenYi X, JunXin L (2009) Effects of various pretreatments on biohydrogen production from sewage sludge. Chin Sci Bull 54:2038–2044

31. Clark PB, Nujjoo I (2000) Ultrasonic sludge pretreatment for enhanced sludge digestion. J Inst Water Environ Manage 14:66–71

32. Mao T, Hong SY, Show KY, Tay JH, Lee DJ (2004) A comparison of ultrasound treatment on primary and secondary sludges. Water Sci Technol 50:91–97

33. Tiehm A, Nickel K, Zellhorn M, Neis U (2001) Ultrasonic waste activated sludge disintegration for improving anaerobic stabilization. J Water Resour 35 (8):2003–2009

34. Chu CP, Lee DJ, You CS, Tay JH (2002) Weak ultrasonic pretreatment on anaerobic digestion of flocculated activated biosolids. Water Resour 36:2681–2688

35. Chiu YC, Chang CN, Lin JG, Huang SJ (1997) Alkaline and ultrasonic pretreatment of sludge before anaerobic digestion. Water Sci Technol 36(11):155–162

36. Wang F, Wang Y, Ji M (2005) Mechanisms and kinetics models for ultrasonic waste activated sludge disintegration. J Hazard Mater B123:145–150

37. Hart EJ (1986) Isotropic exchange in the sonolysis of aqueous solutions containing $^{14,14}N_2$ and $^{15,15}N_2$. J Phys Chem 90:5989–5991

38. Hart EJ, Henglein A (1986) Sonolytic decomposition of nitrous oxide in aqueous solutions. J Phys Chem 90:5992–5995

39. Bougrier C, Delgenes JP, Carrere H (2007) Impacts of thermal pre-treatments on the semicontinuous anaerobic digestion of waste activated sludge. Biochem Eng J 34:20–27

40. Genc N (2010) Biohydrogen production from waste sludge. Sigma J Eng Nat Sci 28:235–248

41. Li YY, Noike T (1992) Upgrading of anaerobic digestion of waste activated sludge by thermal pretreatment. Water Sci Technol 26:857–866

42. Li C, Fang HP (2007) Fermentative hydrogen production from wastewater and solid wastes by mixed cultures. Environ Sci Tech 37:1–39

43. Mohan VS, Babu VL, Sarma PN (2008) Effect of various pretreatment methods on anaerobic mixed microflora to enhance biohydrogen production utilizing dairy wastewater as substrate. Bioresour Technol 99:59–67

44. Mu Y, Yu H, Wang G (2007) Evaluation of three methods for enriching H_2-producing cultures from anaerobic sludge. Enzyme Microb Technol 40:947–953

45. Ren N, Guo W, Wang X, Xiang W, Liu B, Wang X, Ding J, Chen Z (2008) Effects of different pretreatment methods on fermentation types and dominant bacteria for hydrogen production. Int J Hydrogen Energy 33:4318–4324

46. Ozkan L (2009) Dark fermentative biohydrogen production from sugar-beet processing wastes. M.Sc. Thesis. The Graduate School of Natural and Applied Sciences of Middle East Technical University, 135 p

47. Chen CC, Lin CY, Lin MC (2002) Acid-base enrichment enhances anaerobic hydrogen production process. Appl Microbiol Biotechnol 58(2):224–228

48. Van Haandel AC, Lettinga G (1994) Anaerobic sewage treatment—a practical guide for regions with a hot climate. Wiley, New York, NY

49. Wang J, Wan W (2008) Comparison of different pretreatment methods for enriching hydrogen producing bacteria from digested sludge. Int J Hydrogen Energy 33:2934–2941

50. Nakazato T, Akasoka M, Tao H (2006) A rapid fractionation method for heavy metals in soil by continuous flow sequential extraction assisted by focused microwaves. Anal Bioanal Chem 386:1515–1523

51. Hong SM, Park JK, Teeradej N, Lee YO, Cho YK, Park CH (2006) Pretreatment of sludge with microwave for pathogen destruction and improved anaerobic digestion performance. Water Environ Res 78:76–83

Rajab E. Abujnah and Russell R. Chianelli

Abstract

In this study asphaltene, waste hydrocarbons, and problematic constituent present in heavy oil have been investigated for its use in dye-sensitized solar cells (DSSCs). It presents the first asphaltene (DSSCs), in which light to electricity conversion efficiency has improved from 0 % to 1.8 %. Four natural asphaltene portions were extracted and used as light absorbers in TiO_2-based dye-sensitized solar cell. The photovoltaic performance of the cells were analyzed by determining the various I–V cell parameters such as open-circuit voltage, short-circuit current, fill factor, and series resistance. The overall energy conversion efficiency was also measured to correlate the effect of the different asphaltene portions as well as concentration on the significant improvement of the solar cell parameters. The sensitization of TiO_2 electrode with H-E Asph.Fr3 asphaltene portion has resulted in a maximum energy conversion efficiency of 1.8 % of the solar cell. In particular, a maximum photocurrent density and solar conversion efficiency of 16.9 mA/cm^2 and 1.8 % have been obtained, respectively. A strategy to minimize series resistance and improve photocurrent as well as open-circuit voltage is also studied. Purifying asphaltene, using RTV mask, and employing the TiO_2 blocking layer as well as UV–O$_3$ treatment have shown to improve the performance of asphaltene DSSCs.

Keywords

Dye-sensitized solar cell • Organic solar cell • Asphaltene fractionation • Photovoltaic solar cell • Light-harvesting materials

Introduction

A photovoltaic solar cell is a proven technology to capture the solar energy and provides clean and renewable electrical energy that can reduce the world's dependency on fossil fuels and reduce Green House Gas (GHG) emission, global warming and other related environmental issues. In spite of the substantial growth over the past decades, the high cost of photovoltaic solar cells has remained a limiting factor for the implementation of the solar electricity in a large scale. Currently, the dominant photovoltaic technology is based on solid-state pn junction devices, in which semiconductor absorbers produce electron–hole pairs, and the electron–hole pairs are separated by a build-in electrical field in the pn junction to generate electricity. These types of solar cells have high power conversion efficiency; however, they suffer from high manufacturing and material cost.

Among the material systems currently of great interest for this reason are the group of molecular-based materials combinations often referred to as "organic" or "molecular" photovoltaic materials. These refer to conjugated molecular

R.E. Abujnah (✉)
Earth and Environmental Science Department, College of Science, Elmergib University, Alkhoms, Libya
e-mail: reabujnah@elmergib.edu.ly

R.R. Chianelli
Materials Research and Technology Institute, The University of Texas, at El Paso, TX, USA
e-mail: chianell@utep.edu

species, such as polymers, molecules, and dyes, which are capable of absorbing light and conducting charge and thereby acting as organic semiconductors [1]. Their attraction lies primarily in the possibility of processing such materials directly from solution, and so with bulk synthesis of the chemical materials and bulk solution processing of photovoltaic modules, the cost of the photoactive material could fall by an order of magnitude compared even with thin film inorganic semiconductors [2, 3]. Additionally, the less challenging manufacturing environment, compared, for example, with crystalline silicon wafer production, promises to reduce the capital cost for production facilities and to make the technology more widely accessible, especially in developing countries [4]. Moreover, it is also believed that if such materials are naturally synthesized and stable, the cost could be further reduced.

Dye-sensitized solar cell (DSSC) is one of the low-cost alternatives for the conventional pn junction-based solar cells and commercially promising because it can be made from low-cost materials and do not require elaborated manufacturing facilities. At the moment there are three types of dyes [5] that can produce DSSCs with AM1.5 conversion efficiencies over 10 %. However, these types of dye suffer from the drawback that they are based on the rare ruthenium transition metal.

Asphaltene is one of these materials that for sure fulfills the requirements of organic semiconductors, i.e., absorbing a broad range of visible and near-infrared light [6, 7] capable of conducting charge [22], stable, and naturally abundant. Asphaltene is an organic moiety that contains large number of structures, in particular high molecular weight-fused aromatic hydrocarbons components with heteroatoms [8]. It also contains some organic molecules that are already used in DSSC and show a promising performance, such as Porphyrin. Most of the researchers have found that the sign of asphaltene charge is positive in organic solvent such as heptane, toluene, ethanol, and nitromethane as studied by zetametry [9] and electrophoresis [10]. The origin of the electric charges is a consequence of an electron transfer between the organic solid particles and the liquid organic phase [22].

Asphaltene therefore is an excellent candidate for use in DSSC. Despite of the long-term research on this material, there was no study directed to its potential use in such purpose. This chapter introduces the first real data on using asphaltene portions as sensitizer in dye-sensitized solar cell and describes ways of improvements.

Materials and Methods

Materials

Commercial chemical agents and materials were used to prepare typical DSCs, including TiO_2 pastes, electrolytes, and the transparent conductive glass. The FTO are F-doped SnO_2 (Solaronix TCO30-8 SA, Switzerland, 8 Ω/cm^2, 3.3 mm thickness, and 500–1,000 nm transmittance). The TiO_2 paste was a highly transparent Ti-Nanoxide HT/SP and Ti-Nanoxide R/SP obtained from Solaronix Co. Switzerland. The paste contains approximately 18 % wt. of nanocrystalline titanium dioxide with 8–10 nm particle size, with terpineol and other organic binders. A layer of highly porous anatase nanocrystals is obtained after firing at 450 °C for 30 min. The obtained sintered layer is highly transparent. Three types of commercial electrolytes obtained from Solaronix company have been used in this study. They are Standard Iodolyte MPN-100. It consists of 100 mM of tri-iodide in methoxypropionitrile solution. The second one is Iodolyte TG-50. It is iodide-based redox electrolyte that consists of 50 mM of tri-iodide in tetraglyme.

Asphaltene Extraction and Purification

The crude oil sample was separated into maltenes (n-heptane soluble) and asphaltene (n-heptane insoluble) by adding n-heptane in a volume–volume ratio of n-heptane to crude oil of 40:1 followed by filtration. 50 ml of crude oil was mixed with 2,000 ml of n-heptane in a beaker; the mixture was then stirred by magnetic tip overnight at room temperature. The used solvent-to-oil ratio of 40:1 has been demonstrated to be suitable for avoiding errors in the determination of the amount of asphaltene fraction and in its characterization [11]. The mixture was filtered using a filter paper No 40 with a pore diameter of 8 μm. The obtained asphaltene contains parts of oil that does not dissolve in heptanes such as clay and sand. For this reason it was purified by dissolving it completely in toluene at room temperature and then filtered again to remove debris. The obtained solution of asphaltene and toluene was covered and kept under vacuum at room temperature for 24 h to dry out. The precipitated asphaltene was then weighted for determining asphaltene content, marked as crude asphaltene, and will be referred to as un-fractionated asphaltene.

Fractionation of Asphaltene

A sample of 3 g asphaltene was dissolved in 100 ml toluene, and 300 ml n-pentane was added into the solution and mixed by stirring with a magnetic bar at ambient temperature. After adding n-pentane, the ratio of the total volume of the n-pentane to toluene is kept at 75/25 in volume. The solution was covered and stirred for half an hour for precipitation of insoluble fraction. After filtration, the insoluble fraction was collected and dried at room temperature and left under vacuum overnight to obtain the first fraction (First precipitate. Fr.1). Another amount of 270 ml pentane was then added to the filtrate n-pentane and toluene to keep the ratio of the total volume of the n-pentane to toluene at 85/15 in volume.

The filtration and drying process was then repeated to obtain the other fractions. Fr.2 was precipitated in a solution with an n-pentane to toluene ratio of 85/15 in volume. Similarly, samples (Third precipitate. Fr.3) (n-pentane to toluene = 90/10) were precipitated in binary solutions with the increasing proportion of n-pentane. The last fraction (fourth precipitate Fr.4) was obtained by evaporating the solvents with the remaining asphaltene.

Preparation of the Photoelectrode

The blocking layer was prepared in the following manner. The (Fluorine-doped tin oxide) FTO glass was first cleaned in a detergent solution using an ultrasonic bath for 15 min, then rinsed with water and ethanol, and treated with UV–O_3 cleaner for 20 min after that the FTO glass plates were immersed into a 50 mM aqueous solution of $TiCl_4$ at 70 °C for 30 min and washed with water and ethanol. The $TiCl_4$ solution was formed by mixing 0.54 ml $TiCl_4$ in 100 ml of ultra-water in an ice path.

After applying the blocking layer, the photoelectrodes are then rinsed with d-water and ethanol and are ready for meso-layer application. The nanocrystalline TiO_2 layer was prepared by applying two layers of Ti-Nanoxide HT/SP paste by spreading (doctor blading). In the processes the FTO-coated glass was covered with two layers of parallel adhesive Scotch tape 1 cm apart to control the area and the thickness of the TiO_2 film (2.5 × 1 cm); see Fig. 91.1. Tape is used to hold the slides as well as to create the spacing required to produce the nanoparticle film. A solution of Ti-Nanoxide HT/SP paste is then applied to the top slide. A glass road is then used to draw the solution down to the slide of interest in a smooth and quick motion to coat the working electrode with nanoparticles. The film is then left to dry and the tape is removed. Films are treated at 500 °C for half an hour before soaking in a dye solution. This treatment process is used to remove any organic additives used as well as to sinter the nanoparticles together and remove any water from the active region of the cell. It is important to note that the samples should be hot (70 °C) when immersed in a dye solution to prevent H_2O adsorption. The samples were left overnight in the dark for dye adsorption. The film is then cut into the desired cell area using a glass cutter, and the titania film is scratched into 5 mm squares by using a razorblade as given in Fig. 91.1.

Preparation of the Counter Electrode

Counter electrodes were fabricated by first drilling two holes using a diamond tip drill through an FTO piece of dimensions 2.5 cm by 5 cm. Drops of water were applied during the drilling process to prevent fracture of the glass. Once the electrodes have holes in them, they are washed with d-water and detergent solution using an ultrasonic bath for 20 min to remove any organic residues, then washed in ethanol solution for 20 min and acetone for 20 min, and then cleaned with UV–O_3 cleaner for 20 min just before Pt application. Before being used in a cell, counter electrodes are coated with platinum using a 5 mM solution of hexachloroplatinic acid in ethanol. A few drops are placed on the counter electrode and left to dry for half an hour. The counter electrode is then heated at 450 °C in a furnace for half an hour. Upon cooling, the counter electrode is ready to be used in a working cell.

Assembling the Cell

Surlyn spacers are cut from a large sheet of Surlyn sandwiched between two grid paper sheets, into the desired cell active area of 10 mm by 15 mm. After soaking the working electrode in dye solution overnight, the cells were assembled. To begin, the working electrodes are removed from the dye solution and washed with ethanol for 15 s waving mildly with tweezers. The electrode is then left to dry in a vertical position. The Surlyn gasket is placed around the titania square, and the counter

Preparation of the working electrode
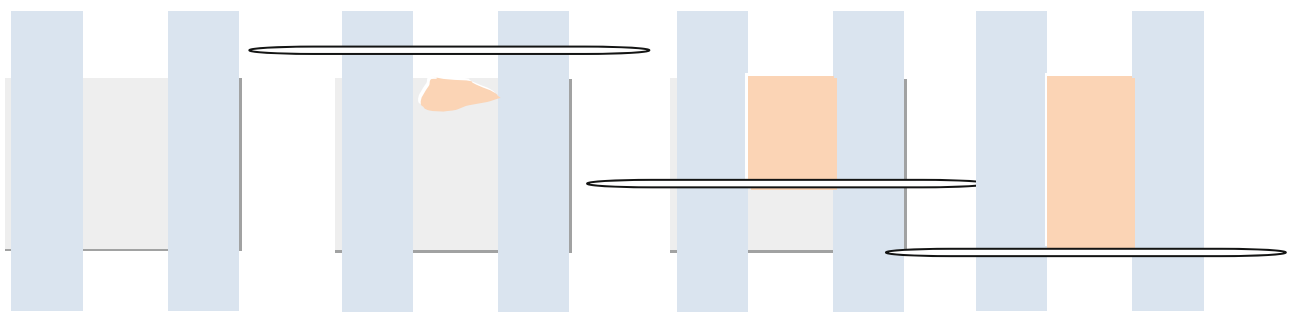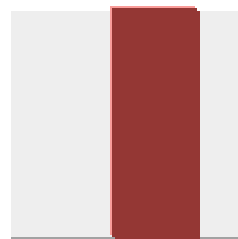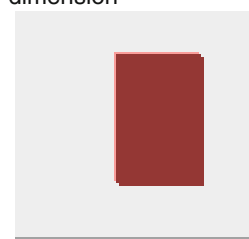
Preparation of the Counter electrode
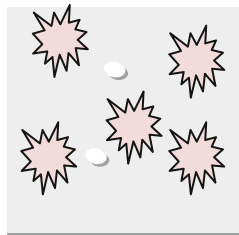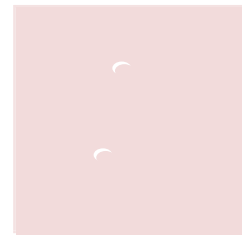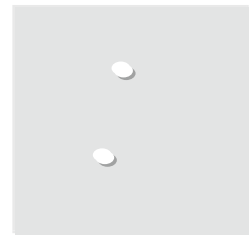
Cell building
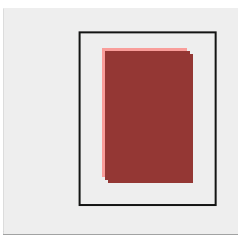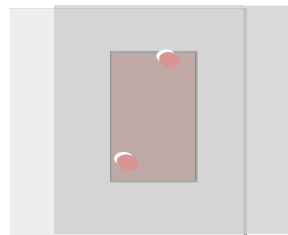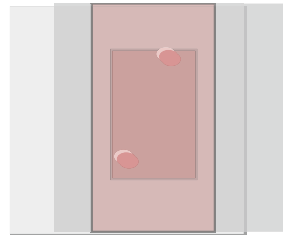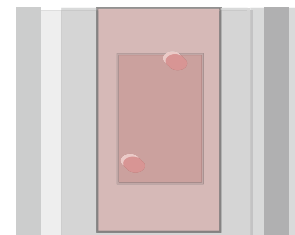
Fig. 91.1 Processes of manufacturing DSSC

electrode is then placed above the working electrode sandwiching the Surlyn gasket and placed under the hot press for 30 s. Once the Surlyn is melted (easily seen visually), the cell is left to cool in the dark. The next phase of cell assembly is to fill the solar cell with electrolyte and seal the cell. To do this, a Solaronix' Vac'n'Fill Syringe was used to fill the electrolyte and Polyimide Film Tape with Acrylic Adhesive was used to cover the holes of the counter electrode (see Fig. 91.1).

Results and Discussion

Introducing TiO$_2$ Blocking Layer

The importance of a blocking layer in organic dye-sensitized solar cells has been demonstrated in many studies [12–15]. It was shown that upon the addition of a compact layer, the light-harvesting efficiencies were more than tripled. Such a compact layer improves the adhesion of the TiO$_2$ to the TCO and provides a larger TiO$_2$/TCO contact area and more effective electron transfer from the TiO$_2$ to the TCO by preventing the electron recombination process, which occurs in the interface between the redox electrolyte and the TCO surface. The compact layer can be fabricated by various methods such as sputter deposition [12], dip coating [13], chemical vapor deposition [14], and spray pyrolysis [15]. Especially, the fabrication of the TiO$_2$ compact layer using a TiCl$_4$ aqueous solution has been widely adopted [12] and is the method used in this research.

To test the effect of the compact TiO$_2$ layer on the performance of asphaltene solar cells, we made two asphaltene solar cells both with three TiO$_2$ layers (one compact and the other is nanocrystalline layer). The used paste in these cells was the commercial highly transparent Ti-Nanoxide HT/SP paste stated above, and the TiO$_2$ compact layer was prepared using aTiCl$_4$ aqueous solution. The asphaltene was un-fractionated unpurified Hunt asphaltene obtained from Altimera crude oil with utilized concentration of 0.5 g/l. The cells were tested under solar simulator at standard condition of 1.5 sun and the results are shown in Table 91.1. It is clear that the introduction of TiO$_2$ compact layer prepared by the above-mentioned method has increased the short-circuit current, the close-circuit voltage, as well as overall cell efficiency.

Purifying Asphaltene and Using RTV Silicone Rubber Mask Layer on the Photoelectrodes

A typical DSSC usually contains three interfaces formed by FTO/TiO$_2$, TiO$_2$/dye/electrolyte, and electrolyte/Pt–FTO. Simultaneously, electrons are transferred to tri-iodide at the TiO$_2$/dye/electrolyte interface, and iodide is reduced to tri-iodide at the counter electrode. Series resistance in DSSC could arise from one of the above interfaces and has a great impact on cell performance. The values of series resistance can be raised by varying the electrical properties of TCO, increasing the thickness of the electrolyte layer and the catalytic activity of the counter electrode. Many researchers [16–18] have found that, under short circuit conditions, electron transport was predominately affected by the series resistance in TCO–dye interface, and the electrolyte/Pt–TCO interface.

The extraction of asphaltene from crude oil involves dissolving the crude oil in n-heptanes followed by filtration. Asphaltene is the part of crude oil that does not dissolve and stay on top of the filter paper. Asphaltene extracted by this method could contain inorganic impurities which may increase resistivity of the asphaltene films when applied on top of TiO$_2$. Hence, it may have an effect on charge transfer and increases the series resistance at TiO$_2$/asphaltene/electrolyte interface. For this purpose we employed the purification method described above to take off these impurities, before using it in DSSC.

In addition to that, when applying the compact layer in our previous experiments, the FTO glass was immersed completely in a TiCl$_4$ aqueous solution. Subsequently, TiO$_2$ compact layer was formed on all the TCO coating of the FTO glass used to prepare the photoelectrode. This has shown to increase the resistivity of the TCO layer; for that reason we used RTV silicone rubber paste as mask and cover the backside of glass completely and leave less than half side of conducting surface uncovered, which will be used to deposit the paste. Following these two strategies the efficiency of our cells has increased significantly when compared to previous cells from 0.07 (see Table 91.1) to 0.25 (see Table 91.2).

Table 91.1 The effect of TiO$_2$compact layer on asphaltene cell performance

Cell id	Voc (V)	Jsc (mA/cm^2)	FF (%)	IPCE (%)	Voc slope (ohms)
Without compact	0.4784	0.158	35.42	0.03	1,830
With compact	0.42	0.388	46.46	0.07	398

Table 91.2 Purified un-fractionated Hunt asphaltene cell parameters with 0.5 g/l

I-V parameter	80 mW/cm^2	100 mW/cm^2	120 mW/cm^2
Voc (V)	0.54	0.55	0.54
Jsc (mA/cm^2)	0.59	0.72	0.91
Fill factor (%)	65.4	63.2	60.6
Voc slope (ohms)	43.6	42.6	38.7
Efficiency (%)	0.26	0.25	0.25

Table 91.3 The effect of UV–O treatment on top TiO$_2$ layer

Cell id	Voc (V)	Jsc (mA/cm^2)	FF (%)	IPCE (%)
Ti HT/SP + R	0.806	8.51	15	1.03
H P25 + R	0.809	6.77	14.7	0.8

Table 91.4 The effect of ozone treatment on the asphaltene DSSC

IPCE (%)	Voc (V)	Jsc (mA/cm^2)	FF (%)	FTO UVO	CL UVO	ML UVO
1.44	0.8252	13.19	13.1	X		X
1.34	0.7818	13.55	12.9	X	X	
0.76	0.7790	7.74	12.2	X	X	X

It is clear that the enhancement of cell efficiency in this cell was a consequence of decreasing series resistance and increasing close circuit current which leads to an increase of fill factor. This is in agreement of other people findings, who found an increase of FF with decrease in series resistance [19]. To study the effect of varying light intensity on cell performance, the cell was tested under three different intensity levels 80, 100, and 120 mW/cm^2. As was expected higher light intensity produces higher current density but less fill factor and therefore lower cell efficiency. This observation is a well-known phenomenon in DSS cells [23]. This is probably due to increase in recommendation processes. The existence of the recombination process can be verified in the dark current measurement column five in the above table.

UV–Ozone Treatment of the Photoelectrode

The main components of the TiO$_2$ pastes utilized in this study as well as in most DSSC research labs more than TiO$_2$ particles are organic compounds used to disperse and link the semiconductor particles to form a network film. At high temperature sintering processes, these compounds decompose and permit the formation of porous TiO$_2$ films with high surface area. However, some carbon atoms will probably deposit on top of TiO$_2$ particles and hinder the absorption of the dye and the electron injection. UV–O$_3$ treatment is a well-known method to remove organics on transparent conducting oxides and has been widely used in organic electronic devices to clean the surface and modify the work function of ITO. Recently, UV–O$_3$ treatment was applied to synthesize porous nano-particulateTiO$_2$ films at room temperature, and remarkable improvement of photo-conversion efficiency was obtained using the treatment. It is believed that the main effect of the UV–O$_3$ treatment was reported to be the removal of residual organics and positive shift in the conduction band of the nanocrystalline titanium dioxide, which promotes electron injection from the dye [20, 21].

To see if UV–O$_3$ treatment has an effect on the performance of asphaltene solar cells, UV–O$_3$ treatment was first applied on the last TiO$_2$ layer. Two asphaltene cells were made this time, one with the commercial paste and the other is homemade paste described above. Both cells have given much better Voc and photocurrent when compared to the previous cells without UV–O$_3$ treatments (see Table 91.3).

After, our UV–O$_3$ treatment on top layer of the photoelectrode showed improvement in cell operation, we apply UV–O$_3$ in three processing steps: on bare FTO before the compact layer, before and after the compact layer, and after the meso-layer. The used asphaltene here was fr.2 asphaltene with applying concentration of 1 mg/ml. Due to difficulty of applying the previous sealing material, the sealant has changed to Polypropylene w/Rubber Medium Adhesive tape with 228.6 μm thick obtained from Grainger company item no 6JT54; the adhesive was not strong enough so some drops of crazy glue were put on top of the tape between the electrodes. So the thickness was further increased a few micrometers. The results are shown in Table 91.4.

Fig. 91.2 Absorption spectra of asphaltene thin films
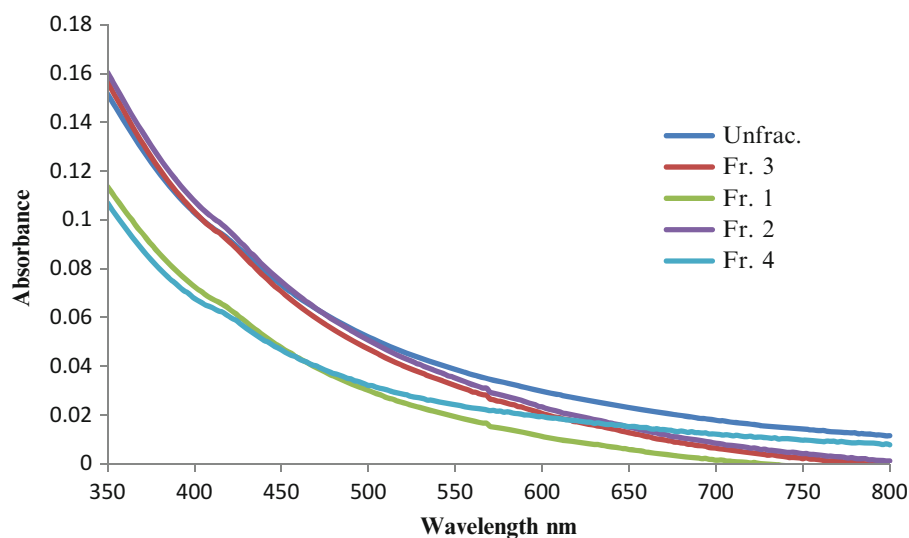
Table 91.5 Asphaltene fraction cell parameters

IPCE (%)	Voc (V)	Jsc (mA/cm^2)	FF (%)	Frac #
1.80	0.7793	13.69	16.6	3
1.38	0.7098	4.76	40.1	4
1.02	0.7724	10.52	13.0	1
1.76	0.7744	13.45	13.0	Unfrac.

The efficiency of these cells has increased four times when compared with the ones without UV–O$_3$ treatment. The improvement in efficiency was a result of a big boost in both short circuit current and open-circuit voltage. This enhancement was a result of increase in asphaltene absorption, eliminating organic contamination and therefore, higher photon capture and higher electron injection. However, these cells show very low fill factor. The decrease in the fill factor is due to increasing the electrolyte thickness as a result of increasing the sealant layer. The electrolyte ions will take longer time to reach the counter electrode before it reduced back. Similar results were observed with increasing the electrolyte thickness.

The low photocurrent in asphaltene solar cell when UV–O$_3$ treatment was done on all the three TiO$_2$ layers was probably due to electrolyte touching the counter electrode because of improper sealing. So changing the sealant is vital at this point.

Varying Asphaltene Fraction

The open-circuit voltage and short-circuit current are both dependent on the extent of light absorption. The most straightforward way to increase Jsc is to absorb a greater fraction of the incident light. The optical gap of the Ru dye in the most efficient DSSC to date is 1.8 eV, allowing it to absorb essentially all the light out to 700 nm. Increasing the photocurrent density requires decreasing the optical gap to extend the dye's absorption into the near-infrared. Our first thought of increasing short-circuit current is to try different asphaltene fraction. Fractionation of asphaltene produces slightly different absorption spectra (see Fig. 91.2).

Neglecting the fill factor at the moment, the cells made of Fr.4 which is the most toluene soluble fraction produces the less photocurrent and photo voltage when compared to the other asphaltene fractions. The less soluble asphaltene part (fraction one) generates higher photo voltage but lower photocurrent than fr.2 (see Table 91.5), fr.3, and un-fractionated asphaltene.

These results are in agreement with the absorption spectra of asphaltene thin films presented in Fig. 91.2. Both Fr.1 and Fr.4 have lower absorption in the visible part of light and therefore will have lower photocurrent. The high fill factor in Fr.4 cell is a result of changing the sealant to lower thickness and easy to process; fastelfilm 230110 with 130 μm thick film, obtained from Fastel Adhesive.

Conclusion

The essence of this research work is well encapsulated by the title of this work, namely, "Asphaltene as light-harvesting material in dye-sensitized solar cell". Despite the fact that there were considerable doubts about the suitability of these materials as sanitizer in DSSC at the start of this work, the research presented in this chapter has come a long way in removing many of these reservations. It has been proved that for at least one part of the asphaltene or asphaltene in whole can be effectively utilized. Asphaltene indeed is an excellent sanitizer in DSSC. Asphaltene, the most abundant naturally forming material and undesirable part of crude oil that causes a lot of trouble to most oil refining companies, has been shown in this study to be good sensitizer in DSSC. The results obtained show that every step in manufacturing the asphaltene cell has an effect on different cell parameters. According to results shown above, asphaltene solar cells have achieved a fill factor of 65–70 %, when series resistance was minimized, Voc of 0.7–0.8 V, and photocurrent of 10–13.69 mA/cm^2 when UV–O$_3$ treatment was employed and contaminates were eliminated. Therefore, a total overall efficiency of 4.55–7.0 % could be easily attained with good engineering design and material process. Fraction three (Fr.3) obtained at 90/10 pentane to toluene ratio has produced the best asphaltene solar cell so far with 1.8 total efficiency. Un-fractionated asphaltene produced comparable result with fraction three.

References

1. Troshin PA, Lyubovskaya RN, Razumov VF (2008) Organic solar cells: structure, materials, critical characteristics, and outlook. Nanotechnol Russia 3 (5–6):242–271
2. Shaheen SE, Ginley DS, Jabbour GE (2005) Organic-based photovoltaics: toward low-cost power generation. Mater Res Soc Bull 30(1):10–19
3. Kalowekamo J, Baker E (2009) Estimating the manufacturing cost of purely organic solar cells. Sol Energy 83(8):1224–1231
4. Brabec CJ (2004) Organic photovoltaics: technology and market. Sol Energy Mater Sol Cells 83(2–3):273–292
5. Gratzel M (2003) Dye-sensitized solar cells. J Photochem Photobiol C Photochem Rev 4:145–153
6. Ruiz-Morales Y, Mullins OC (2007) Electronic absorption edge of crude oils and asphaltenes analyzed by molecular orbital calculations with optical spectroscopy. Energy Fuels 21:944–952
7. Salmanova CK, Akhmedbekova SF, Mamedov AP, Kyazimov SM, Abdulova S (2007) Transformation of resins and asphaltene in photoirradiation. Chem Technol Fuels Oils 43(5):415–421
8. Mullins OC, Sheu EY, Hammami A, Marshall A (2007) Asphaltenes, heavy oils, and petroleomics. Springer, New York, NY
9. Siffert B, Kuczinski J, Papirer E (1990) Relationship between electrical charge and flocculation of heavy oil distillation residues in organic medium. J Colloid Interface Sci 135(1):107–117
10. Neves GBM, de Sousa MA, Travalloni-Louvisse AM, Lucas EF, Gonzalez G (2001) Characterization of asphaltene particles by light scattering and electrophoresis. Petrol Sci Technol 19(1–2):35–43
11. Ancheyta J, Centeno G, Trejo F, Marroquín G, García JA, Tenorio E, Torres A (2002) Extraction and characterization of asphaltenes from different crude oils and solvents. Energy Fuel 16(5):1121–1127
12. Ito S, Ishikawa K, Wen C-J, Yoshida S, Watanabe T (2000) Dye-sensitized photocells with meso-macroporous TiO$_2$ film electrodes. Bull Chem Soc Jpn 73 (11):2609–2614
13. Gan WY, Lam SW, Chiang K, Amal R, Zhao H, Brungs MP (2007) Novel TiO2 thin film with non-UV activated super wetting and anti fogging behaviours. J Mater Chem 17:952–954
14. Thelakkat M, Schmitz C, Schmidt H-W (2002) Fully vapor-deposited thin layer titanium dioxide solar cells. Adv Mater 14:577–581
15. Okuya M, Nakade K, Kaneko S (2002) Porous TiO$_2$ thin films synthesized by aspray pyrolysis deposition(SPD) technique and their application to dye-sensitized solar cells. Sol Energy Mater Sol Cells 70:425–435
16. Hoshikawa T, Yamada M, Kikuchi R, Eguchi K (2005) Impedance analysis for dye-sensitized solar cells with a three-electrode system. J Electroanal Chem 577:339–348
17. Anneke H, Georg A (2001) Diffusion in the electrolyte and charge-transfer reaction atthe platinum electrode in dye-sensitized solar cells. Electrochim Acta 46:3457–3466
18. Weiqing L, Linhua H, Songyuan D, Lei G, Nianquan J, Dongxing K (2010) The effect of the series resistance in dye-sensitized solar cells explored by electron transport and back reaction using electrical and optical modulation. Electrochim Acta 55:2338–2343
19. Naoki K, Islam A, Yasuo C, Han L (2006) Improvement of efficiency of dye-sensitized solar cells based on analysis of equivalent circuit. J Photochem Photobiol A Chem 182:296–305
20. Lee B-K, Kim J-J (2009) Enhanced efficiency of dye-sensitized solar cells by UV–O3 treatment of TiO2 layer. Curr Appl Phys 9:404–408
21. Zhang D, Yoshida T, Oekermann T, Furuta K, Minoura H (2006) Room-temperature synthesis of porous nanoparticulate TiO$_2$ films for flexible dye-sensitized solar cells. Adv Funct Mater 16:1228–1234
22. Jiqian W, Chuan L, Longli Z, Guohe Q, Zhaomin L (2009) The properties of asphaltenes and their interaction with amphiphiles. Energy Fuels 23(7):3625–3631
23. Lee K-M, Suryanarayanan V, Ho K-C (2009) High efficiency quasi-solid-state dye-sensitized solar cell based on polyvinyidene fluoride-co-hexafluoro propylene containing propylene carbonate and acetonitrile as plasticizers. J Photochem Photobiol A Chem 207:224–230

Plasma-Fuel Systems Utilization for Ecological and Energy Efficiency of Thermal Power Plants

V.E. Messerle and A.B. Ustimenko

Abstract

This chapter presents the results of research and application of direct-flow, vortex, and muffle plasma-fuel systems (PFS) for coal-fired boilers of thermal power plants (TPP) at Ust-Kamenogorsk, Shakhtinsk, and Almaty (TPP-2 and TPP-3) (Kazakhstan). PFS are investigated for boilers with pulverizing systems with direct injection of dust (Shakhtinsk TPP and Almaty TPP-2) and intermediate bunker (Ust-Kamenogorsk TPP and Almaty TPP-3). Also this chapter presents the results of numerical simulations of the plasma-assisted thermochemical preparation of coal for ignition and combustion in a furnace of power boiler. The calculations were performed for a low-rank bituminous coal. 1D model PLASMA-COAL was used for plasma-fuel system computation. It describes a two-phase chemically reacting flow in a plasma chamber with an internal source of heat, which can be an arc or plasma flame. The kinetic scheme describes stages of coal devolatilisation, reactions in the gas phase, and heterogeneous reactions of carbon oxidation. Data to enable a 3D numerical simulation of coal combustion in a furnace chamber were collected. The 3D numerical experiment was performed with the aid of CINAR ICE code applied to the boilers of 420 ton/h and 75 ton/h steam productivity. A comparative analysis of the coal combustion process enhanced through plasma-fuel systems and without plasma activation was carried out. As a result of the numerical experiments, the advantages of the plasma technology have been clearly demonstrated.

Keywords

Coal • Plasma • Ignition • Combustion • Plasma-fuel system • Thermal power plant

Introduction

The technology of plasma ignition of coal and its realizing PFS is electro-thermo-chemical preparation of fuel to burning (ETCPF) [1–6]. In this technology pulverized coal replaces the traditionally used fuel oil or natural gas for the boiler start-up and pulverized coal flame stabilization. Part of the coal/air mixture is fed into the PFS where the plasma flame from plasmatron, having a locally high concentration of energy, induces gasification of the coal and partial oxidation of the char carbon. As coal/air mixture is deficient in oxygen, the carbon is being mainly oxidized to carbon monoxide. As a result, a highly reactive fuel (HRF) composed of a mixture of combustible gases (at a temperature of about 1,300 K) and partially oxidized char particles is obtained at the exit of the PFS. On entry to the furnace, this HRF is easily ignited.

V.E. Messerle
Combustion Problems Institute, Almaty, Kazakhstan

Institute of Thermophysics of Russian Academy of Science, Novosibirsk, Russia

A.B. Ustimenko (✉)
NTO Plasmotechnics, Almaty, Kazakhstan

Research Institute of Experimental and Theoretical Physics, Al-Farabi Kazakh National University, Almaty, Kazakhstan
e-mail: ust@physics.kz

Fig. 92.1 PFS layout at a boiler
of 75 ton steam productivity
of Ust-Kamenogorsk TPP
(cross-sectional view
of the furnace with PFS):
1—plasmatron, 2—chamber
for plasma-assisted incineration,
3—muffle burner, 4—flame of
high reactive two-component fuel
from PFS, 5—pulverised coal
flame, 6—air–coal mixture from
the main burners, 7—furnace,
8—the main pf burners
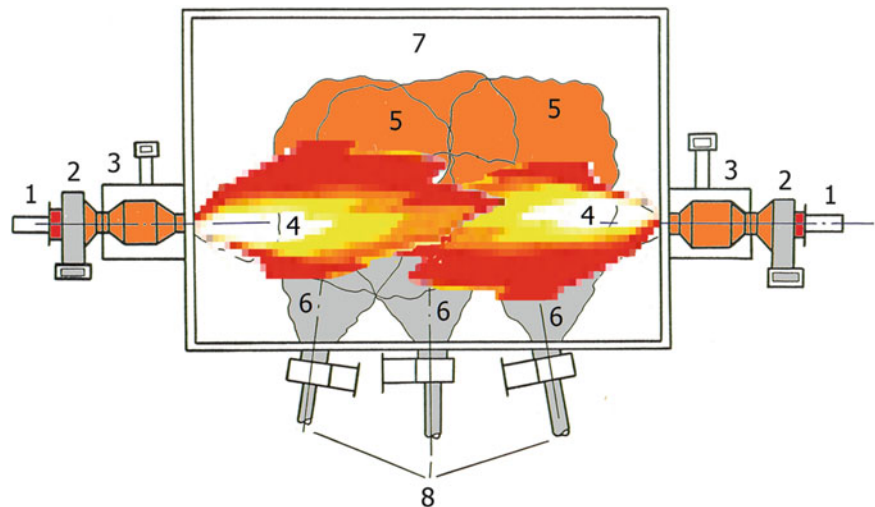
For instance, 75 ton steam productivity boiler (Fig. 92.1) of Ust-Kamenogorsk TPP has three main pulverized coal turbulent burners and two kindling muffle burners. The last two were transformed to PFS. Kuznetsk bituminous coal of 17.7 % ash content and 4,878 kcal/kg calorific value was incinerated in the boiler. During the PFS tests at this boiler, the pulverized coal flow through each PFS was 1.5 ton/h and the primary air was 2.6 ton/h. The pulverized coal flow through the main burners was 11.5 ton/h. Plasmatron power was varied from 60 to 70 kW, and its heat efficiency was 85–86 %. HRF flame temperature at the PFS exit was in the interval 1,040–1,240 °C. Plasmatron's relative power consumptions were 0.5–0.7 % of the muffle burner heat power. NOx concentration on the PFS exit was not more than 20 mg/Nm^3 and synthesis gas (CO + H$_2$) yield exceeded 60 %. In 35 min of the PFS start, stationary heat regime of the muffle burner was achieved, plasmatrons were turned off, and heated muffles went on stabilizing the flame combustion. The flames from muffle burners were 3 m in length. The boiler oil-free start-up lasted 3.25 h after which the boiler was linked up with the main steam pipeline of the TPP.

75 ton steam productivity boiler of Shakhtinsk TPP has four burners (Fig. 92.2), two on the front and rear in one layer. Bituminous coal of 30 % ash content with the flow through the burner (or PFS) 3,200 kg/h is incinerated in the boiler. Primary airflow through the burner is 6,400 kg/h, plasmatron power is 200 kW, and PFS length is 2.3 m (Fig. 92.3). Numerical modeling of the ETCPF in PFS is performed using a one-dimensional mathematical model Plasma-Coal. The calculation results allowed defining the geometric dimensions of PFS, the required power of plasmatron, temperature, velocity, and composition of the products of ETCPF. These results can be used as initial conditions for numerical simulation of HRF combustion in the boiler furnace using Cinar ICE code. 3D modeling results showed that when operating PFS ignition of pulverized coal flame starts earlier, the combustion front moves to the installation location of the PFS on the boiler, resulting in lower temperature of the exhaust gases, the concentration of nitrogen oxides in them and unburned carbon, compared with the traditional mode of coal incineration without plasma activation in PFS.

Almaty TPP-3 boiler of 160 ton/h steam productivity has four coal-fired blocks of two-layer slot burners (Fig. 92.4). Consumption of 45 % ash content and 3,800 kcal/kg calorific value Ekibastuz bituminous coal was 4 ton/h through each burner. Two PFS were installed in the lower layer of the burners diagonally. Plasmatrons were running on the power of 120–140 kW (350–450 A current and 300–350 V voltage). Ignition of the flames in the furnace was observed in 2–3 s after submitting of pulverized coal at a rate of up to 3 ton/h through each PFS. Coal-dust flame temperature at the exit of the PFS reaches 1,200–1,300 °C and is 5–6 m in length. Using these parameters, the formation of the bright yellow core flame in the center of the furnace was observed. In 3.5 h after start of the kindling parameters of the boiler reached operating values, and it was connected to the main steam pipeline, after which air/coal mixture was filed to all the burners. According to the rule one start-up of the boiler consumes 12 ton of fuel oil that by calorific value is equivalent to 30 ton of the coal. Instead, one start-up on average consumed about 16.5 ton of coal that confirms ETCPF energy efficiency. The specific power consumptions for plasmatrons were 1.2–1.4 % of the heat capacity of the pulverized coal burners.

Fig. 92.2 Layout of the furnace of BKZ-75 power boiler: 1—burner throat; 2—section of the swiveling chamber of the boiler
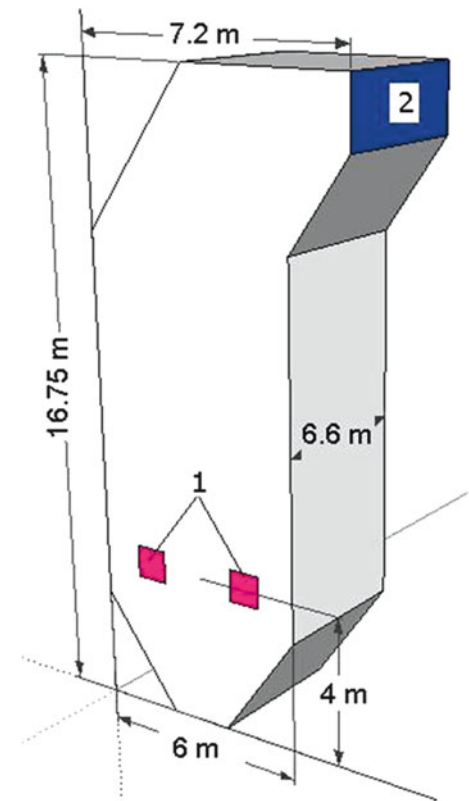
Fig. 92.3 Sketch of the PFS for replacement of the traditional burners of the boiler BKZ-75
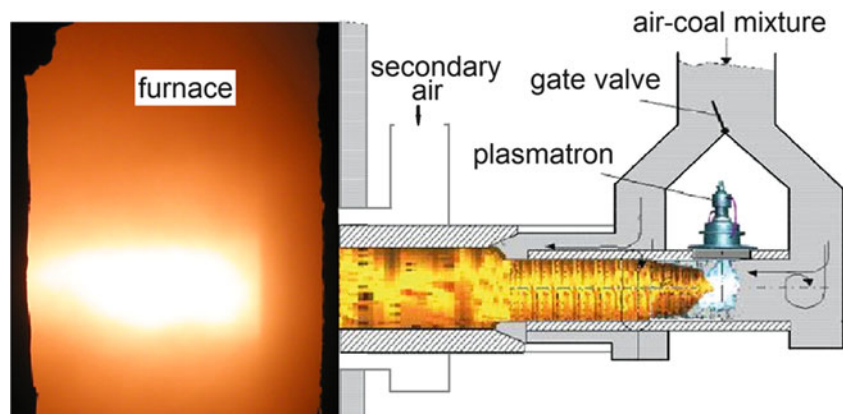
Numerical Simulation and the Comparison with Experimental Data

To understand physical mechanism of the ETCPF and combustion more completely, and to verify the software code CINAR ICE, investigations of coal incineration in the experimental furnace equipped with PFS of 3 MW thermal power have been fulfilled. Two computer codes were used for that. The first one was 1D code PLASMA-COAL [1, 2, 7, 8]. It describes a two-phase chemically reactive flow in a plasma-chamber with an internal source of heat (plasma flame). The second is 3D code CINAR ICE. It operates with real geometry of a furnace. PLASMA-COAL code has been verified using experimental data on plasma gasification and ETCPF [1, 2, 7, 8]. It was used for plasma-fuel system computation, and data to enable a 3D numerical simulation of coal combustion in a furnace equipped with PFS were collected. CINAR ICE code was used for
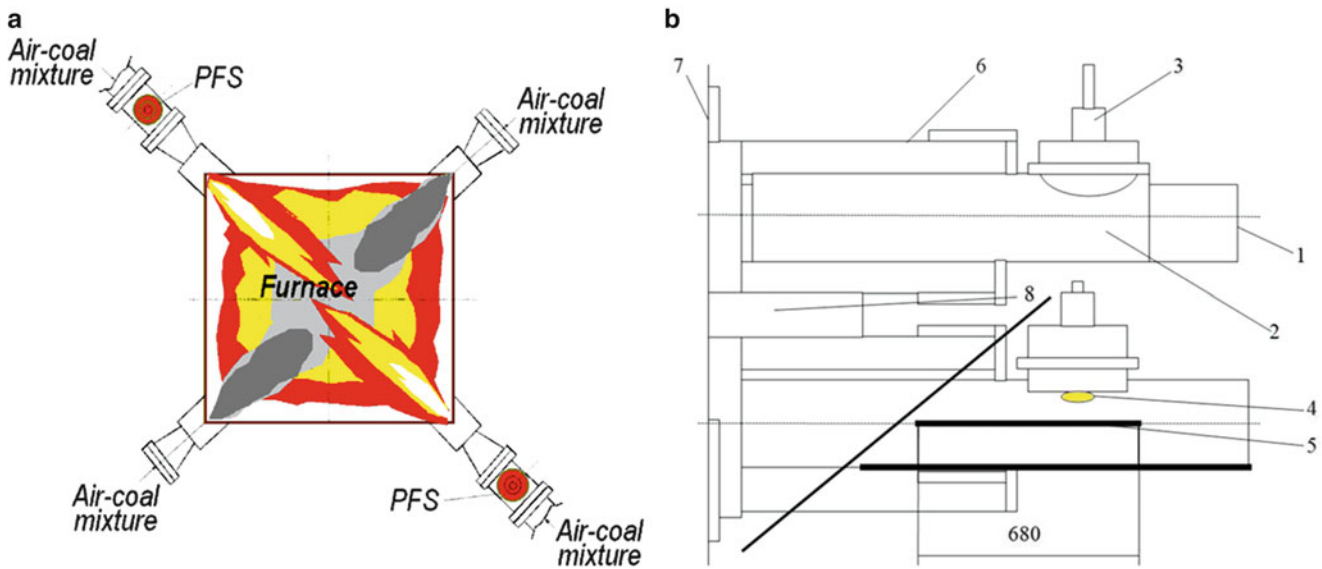
Fig. 92.4 BKZ-160 boiler furnace of 160 ton steam productivity (Almaty TPP-3) equipped with two PFS (top view) (**a**) and sketch of direct flow PFS—burner assembly with plasmatrons: 1—dust flue, 2—chamber of plasma ignition, 3—plasmatron, 4—plasma torch, 5—partition plate, 6—secondary air duct, 7—furnace border, 8—oil fuel nozzle channel (**b**)

computation of coal co-combustion with highly reactive two-component fuel in the furnace. The code has been verified for 3D simulation of traditional furnace processes [9–14]. However, to use this code for computation of coal combustion in a furnace equipped with PFS verification was required.

Following the software code CINAR ICE verification, numerical comparative simulation of ETCPF and coal combustion in a furnace of the full-scale boiler was fulfilled.

CINAR ICE code (Cinar Integrated CFD Environment) [9–14] was designed to provide computational solutions of industrial problems, especially those related to two-phase combustion. It solves the governing time-averaged Eulerian equations for the gas phase mixture combined with Lagrangian tracking of the particles [15, 16] and simulates devolatilisation, volatiles combustion (fast diffusion combustion), char combustion, and the turbulence (k-ε model). "Fast chemistry kinetics" model of chemical reactions is used in the code. The kinetic model is based on the conception of multi-fraction mixture burning [9]. Radiative heat transfer is represented by six-flow model of particles radiation and reemission [13, 14]. The Control Volume method is used for discretization of the initial equations. SIMPLE [15] algorithm is used for calculation of pressure field.

To verify CINAR ICE code, two regimes of experimental furnace were selected. The first one was conventional coal combustion, and the second regime was combustion plasma-activated coal. Plasma activation to coal combustion was provided with the plasma flame of 36 kW power. The parameters of two-component high reactive fuel produced in PFS (Fig. 92.5) were calculated using PLASMA-COAL computer code. These parameters were used as initial data for PFS equipped experimental furnace 3D simulation.

The mathematical model of ETCPF describes the two-phase (coal particles and gas-oxidiser) chemical reacting flow with an internal heat source (electric arc or flame). Generally, coal particles and gas are admitted into the PFS at ambient temperatures. Particle-to-particle, gas-to-particle transfer, and gas-to-plasma heat-mass transfers are considered. Heat and momentum transfer between the flow and the PFS wall have been calculated. The average size of the coal particles was taken as a constant and equal to the particle mineral skeleton size. In other words the particle was not resized at conversion. The particles were spherical and the temperature gradients within the particle are negligible. Also, some chemical transformations of fuel were considered. They are as follows: formation of primary volatile products from coal, conversion of evolved volatile products in the gas phase, and the char carbon gasification reactions. The coal composition was presented in the model by its organic and mineral parts. The organic mass of coal was specified by the set of the functional groups (CO, CO_2, CH_4, H_2O, C_6H_6) and carbon. An entrained flow reactor was considered and the plug flow was assumed. The resulting set of ordinary differential equations includes equations for species concentrations (chemical kinetics equations) in

Fig. 92.5 Layout drawing of plasma-fuel system: 1—plasmatron, 2—electromagnetic coil, 3—air/coal mixture, 4—ETCPF chamber, 5—air/coal mixture scroll, 6—air/coal mixture, 7—window for temperature measuring and gas sampling, 8—secondary air scroll, 9—central tube of the burner, 10—windows for temperature measuring and gas and coke residue sampling, 11—furnace, 12—secondary air, 13—plasma forming air
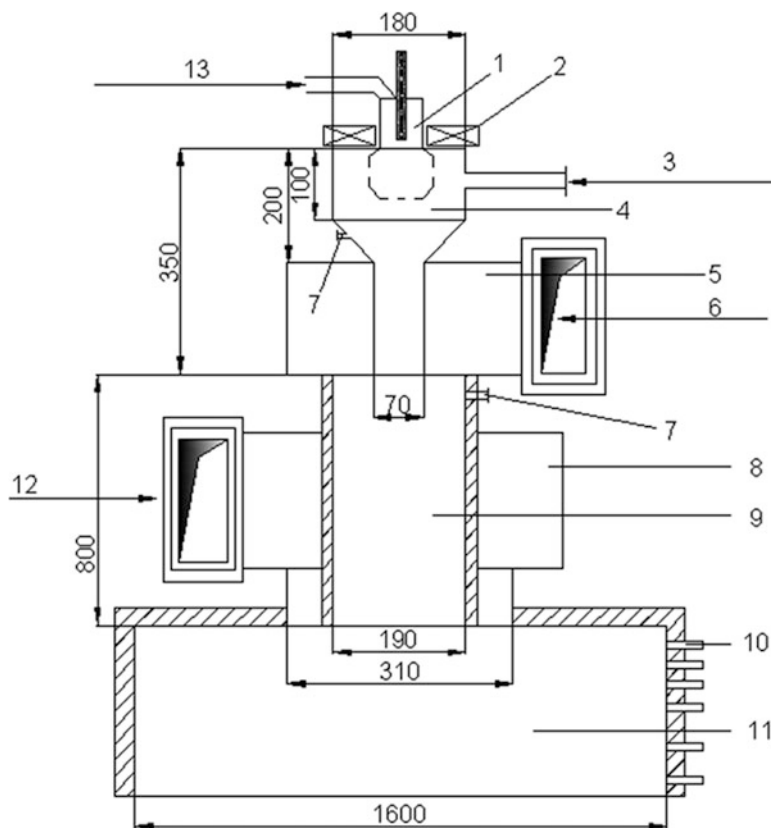
conjunction with the equations for gas and particle velocities and temperatures, respectively. The energy contribution from the plasmas had been found empirically [7] and included into the energy equation as a distribution of internal heat source. Also the model was distinguished by its detailed description of the kinetics of the chemical reactions mentioned above [6]. Kinetic scheme consists of 116 chemical reactions. The temperature dependence of rate constants is governed by the Arrhenius equation. In [2, 7, 8] the model was presented in detail.

The swirl burner was mounted axial on the furnace top (Fig. 92.5). Ekibastuz bituminous coal of 45.2 % ash content, 14.7 % devolatilization, 1.3 % two-layer slot burners humidity, and 15,960 kJ/kg heat value was incinerated in the experimental furnace [7, 13]. Grinding of coal gave the average particle size of 60 microns. PLASMA-COAL computer code has been used for calculation of ETCPF in the volume of PFS of 1.15 m length. The following initial parameters were used for calculations: plasmatron power was 36 kW, initial temperature of pulverized coal (coal/air mixture) was 300 °C, coal and air consumption through PFS were 410 and 600 kg/h, correspondingly. The air is composed of nitrogen (79 vol.%) and oxygen (21 vol.%) and neither carbon dioxide nor noble gas was taken into consideration.

As a result of calculations, temperature distribution (Fig. 92.6), gas and particles' velocities (Fig. 92.7), gas-phase components' concentrations (Fig. 92.8), gasification degree, and carbon concentrations in coke residue (Fig. 92.8) were found. Gas and coal particles' temperatures (Fig. 92.6) increase along the PFS. The heat exchange between plasma source and gas phase is prevailing at the initial section ($0 < X < 0.35$ m). Coal particles are heated from gas, and their temperature increases up to 1,121 °C in the section $0.35 \leq X < 0.8$ m due to carbon oxidation and corresponding out of heat. It exceeds the gas temperature by 264 °C. As a result of that inversion of temperature curves is observed in the section. Gas temperature reaches maximum at 1,015 °C ($X = 0.9$ m) and goes down to the outlet of PFS (T = 1,002 °C). Gas temperature is 41° higher than particles' temperature, which is related to heat emission from the particles to the wall of PFS.

Velocities of gas and particles (Fig. 92.7) equal at the PFS inlet increase with the length, achieving their maxima of 33.8 and 33.2 m/s at the PFS exit accordingly. Meanwhile gas velocity is higher one of particles along the full PFS. Note that velocity of the flow at the exit of PFS is considerably higher than one for traditional pulverized coal burner.

With coal particles' heating devolatilization and carbon gasification (Figs. 92.8 and 92.9) are observed. Concentration of combustible components (CO, H_2, H, CH_4, C_6H_6) increases along the PFS and reaches its maximum of 41.8 % at the PFS outlet. Oxidants' concentration (CO_2, H_2O, O_2) does not exceed 7.3 % at the PFS outlet. The nitrogen concentration (N_2)

Fig. 92.6 Gas (1) and particles (2) temperatures along the PFS
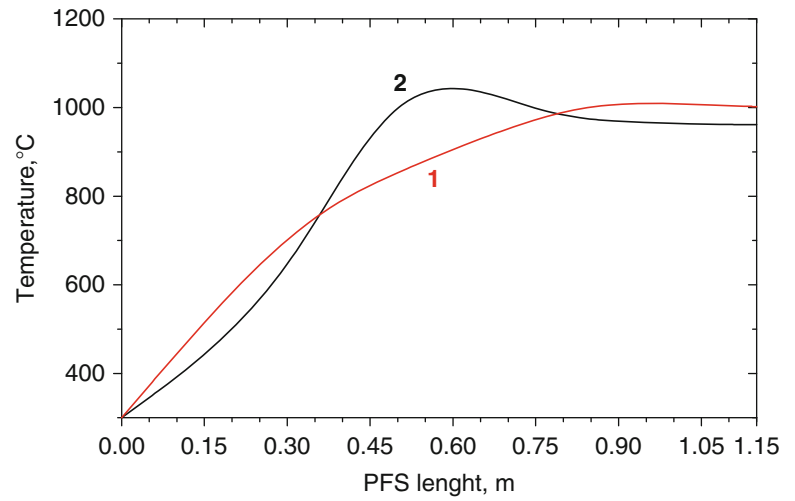
Fig. 92.7 Gas (1) and particles (2) velocities along the PFS
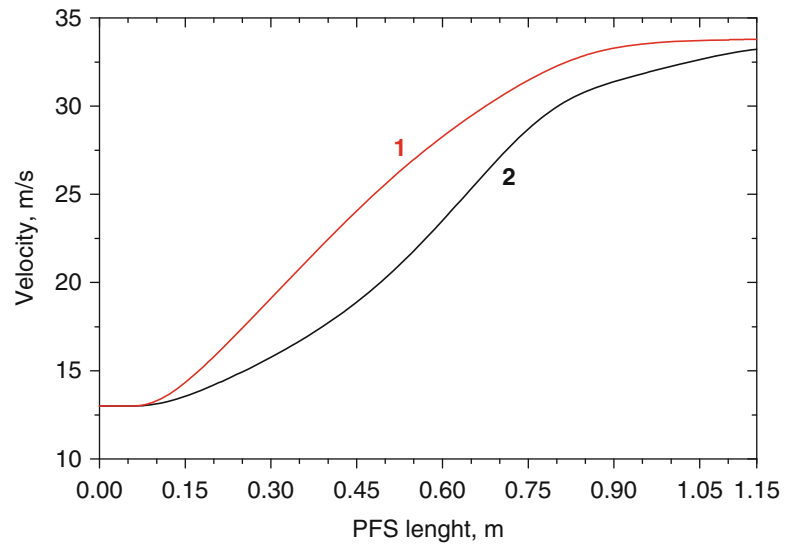
Fig. 92.8 Gas phase components concentrations along the PFS
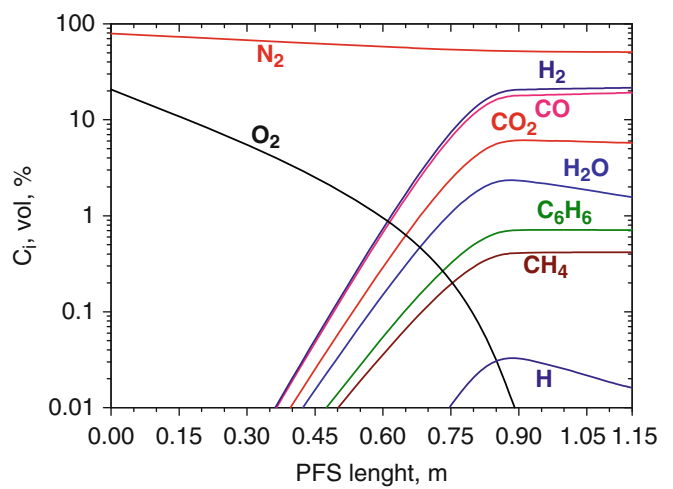
Fig. 92.9 Gasification degree (1) and carbon concentration (2) in coke residue along the PFS
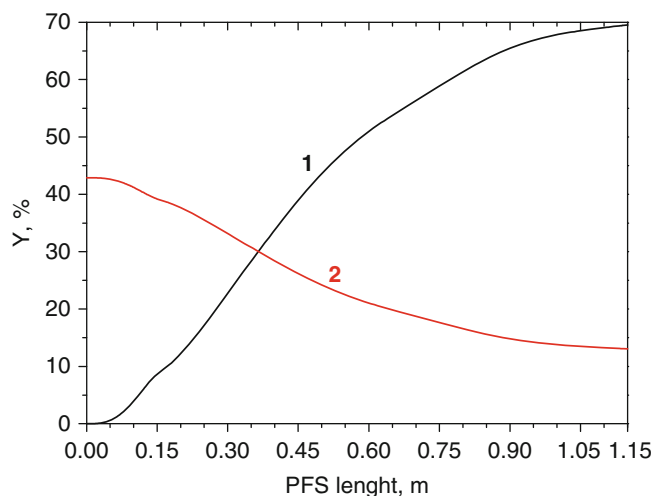
Table 92.1 Characteristics of ETCPF at the PFS exit

| Content of gas phase, vol.% and kg/h | | | | | | | | | | | |
H_2	CO	CH_4	C_6H_6	CO_2	H_2O	N_2	Ash, kg/h	Char carbon, kg/h	T_{gas}, °C	T_{solid}, °C	V_{HRF}, m/s
21.6	19.2	0.4	0.7	5.8	1.6	50.8	185.3	68.4	1,002	961	33.8
14.0	174.2	2.2	18.0	82.2	9.1	462.0					

decreases along the PFS from 79 % to 50.8 % at the outlet. The carbon concentration in the coke residue decreases, and carbon gasification degree (Fig. 92.9) increases along the PFS and achieves 69.5 % at the outlet. The two-component fuel with aforesaid characteristics is intensively ignited mixing with the secondary airflow in the furnace volume. Calorific value of the coke residue was amounted to 7,200 kJ/kg.

Integral characteristics of ETCPF at the PFS exit are gathered in Table 92.1. In the table T_{gas}, T_{solid}, and V_{HRF} are temperatures of gas and particles and velocity of the HRF correspondingly. They were taken as initial data for numerical simulation of ETCPF combustion in the experimental furnace using CINAR ICE software code. Secondary airflow rate was 2,322 kg/h. The furnace height was 7.5 m. Computing origin was the furnace top. The x, y, z grid size was, respectively, 56 × 56 × 60.

The calculations results are shown in Figs. 92.10 and 92.11. Figure 92.10 visualizes the difference between temperatures fields for the furnace in two operational regimes. The traditional mode flame, with maximum temperature of 1,580 °C, generates the common flame body with the temperature 1,300–1,580 °C. The PFS impact appears as transformation of high reactive two-component flame shape, decrease of the flame length, and increase of temperature maximum up to 2,015 °C. That can be explained by earlier ignition and more complete burning out of ETCPF.

Experimental and numerical temperature dependences on the furnace height (Fig. 92.11) are similar. The curves have typical maxima at the distance of 0.5 m from the top of the furnace. The maximal temperature level for conventional mode of the furnace operation at the distance H < 0.13 m is higher than one for plasma-activated fuel combustion. This difference is up to 164° (0.025 < H < 0.13 m). It can be explained by more intensive radiation from coal particles having higher concentration and total surface when the furnace operation is in conventional mode in comparison with plasma-activated regime of coal combustion. When PFS operates electro-thermochemically, prepared fuel (two-component high reactive fuel) is gone from it to the furnace. The fuel contains combustible gas and particles of coke residue whose mass do not exceed 30 % of the initial coal mass. That brings to triple decrease of radiative particles' total surface. In the section 0.13 ≤ H < 0.6 m, temperature at plasma-activated regime is higher than the one for conventional mode of the furnace operation. The maximum difference reaches 260° at height 0.4 m. The maximum combustion temperature of plasma-activated fuel at the experiment was 200° higher than one for conventional mode. Experimental temperature maximum was at the furnace height of 0.67 m. Higher temperature of the flame of plasma-activated fuel can be explained by more complete burnout of the fuel.

Thus, the experimental data [8, 16] were used for verification of CINAR ICE computer code. Divergence of experimental and calculated values of temperature of combustion products does not exceed 20 % along the full height of the furnace.

Fig. 92.10 Temperature fields
along the furnace height in the
central section for conventional
(**a**) and plasma-supported
(**b**) regimes
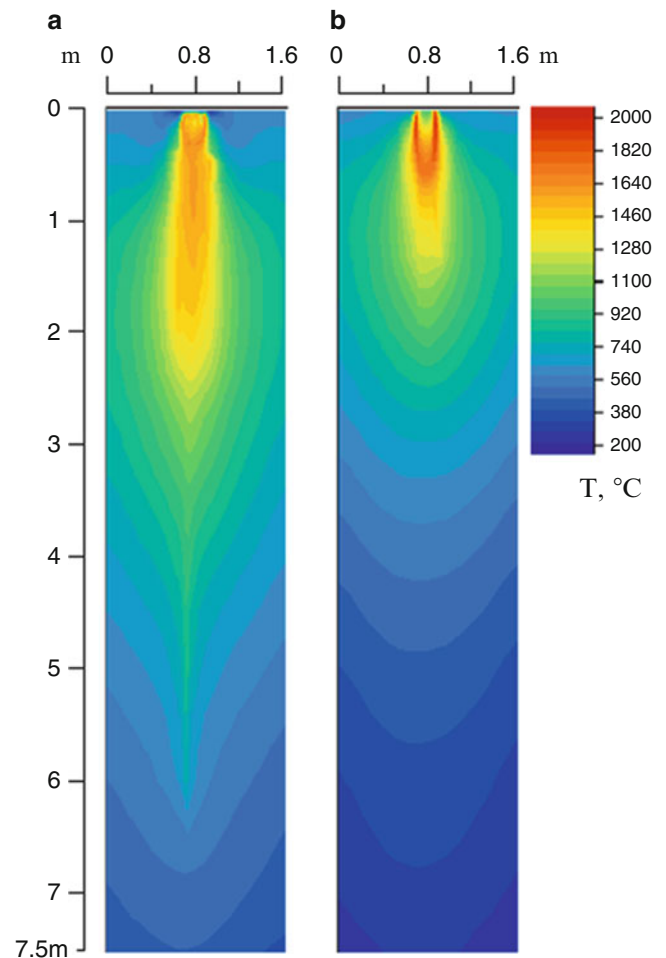
Fig. 92.11 Furnace height
distribution of the combustion
products' maximal temperature:
1—conventional incineration of
coal; 2—incineration of coal in
the furnace with PFS; *closed
circle, open circle*—experimental
data on coal incineration in the
furnace with PFS and without
PFS correspondingly
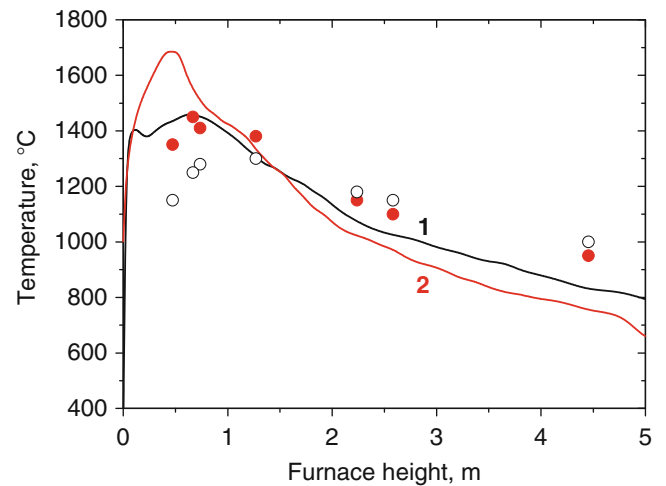
The divergence explains by imperfection of the "fast chemistry" scheme of fuel combustion used by CINAR ICE program. The concentration of unburned carbon was measured at the exit of the experimental furnace. Also divergence of the experimental and calculated values does not exceed 20 %. In experiments unburned carbon was found as 3.1 and 1.8 % for traditional and plasma-activated mode correspondingly. Computed figures were 3.72 and 1.42 % accordingly for these two modes. Concentration of nitrogen oxides at the furnace exit is significantly lower for ETCPF combustion (244.5 ppm) than

for conventional mode of coal combustion (537.9 ppm). Calculated values of NOx concentrations for these two modes were 122.1 and 228.1 ppm. However, essential quantitative difference of experimental and calculated values of NOx concentrations shows that CINAR ICE kinetic scheme of NOx formation is in need of revision.

Computation of PFS and Full-Scale Industrial Boiler's Furnace

The fulfilled verification of CINAR ICE code for plasma-assisted coal combustion in the experimental furnace of 3 MW power confirmed legitimacy of the used codes complex (PLASMA-COAL and CINAR ICE) for simulation of the furnaces equipped with PFS. Thus, in this part the numerical study was performed for a power-generating boiler with a steam productivity of 75 ton/h. The boiler's furnace (Fig. 92.2) is equipped with four swirl burners arranged in one layer, by two burners, on the boiler's front and back. Low-rank bituminous coal of 35.1 % ash content, 22 % devolatilization, and 18,550 kJ/kg heat value was incinerated in the furnace. Averaged size of the coal particles was 75 micron. All the calculations were performed in accordance to the aforecited technique.

Three modes of the boiler operation were chosen for the numerical studies. The first one was traditional regime, using four pulverized coal burners, the second one was regime with plasma activation of combustion, using the replacement of two burners onto PFS (Fig. 92.3), and the third one was regime of the boiler operation using four PFS instead of all burners.

PLASMA-COAL computer code has been used for calculation of ETCPF in the volume of PFS of 2.3 m length. The following initial parameters were used for calculations: plasmatron power was 200 kW, initial temperature of pulverized coal (coal/air mixture) was 90 °C, and coal and primary air consumptions through PFS were 3,200 and 6,400 kg/h correspondingly.

The results of numerical simulation by the PLASMA-COAL code are summarized in Table 92.2. Heat value of the coke residue was 8,580 kJ/kg. These data were taken as initial parameters for 3D computation of the furnace of the power-generating boiler equipped with PFS. This computation was performed using CINAR ICE code to demonstrate advantages of plasma-aided coal combustion technology.

Initial parameters for calculations of the furnace (Fig. 92.2) in different operational regimes were the following: temperature of the secondary air was 290 °C, coal productivity of the burner was 3,200 kg/h, and primary airflow rate through the burner was 10,260 kg/h. Secondary airflow rate to the boiler was 78,160 kg/h. The grid is defined by $85 \times 69 \times 116$ grid lines in three directions (x, y, and z).

The calculations results are shown in Figs. 92.12 and 92.13. Figure 92.12 visualizes the difference between temperature fields in three regimes of coal incineration. In the traditional regime (Fig. 92.12a), with maximum temperature of 1,852 °C, four symmetrical flames are generated. In central space of the furnace, they form overall body of flame with the temperature about 1,300 °C. In Fig. 92.12b two PFS are on top. The PFS impact appears as increase of temperature maximum up to 2,102 °C and transformation of HRF flame shape; it becomes narrow and longer. When the furnace operates with four PFS (Fig. 92.12c), the flames length increases but maximal temperature decreases to 1,930 °C.

Average characteristics of the boiler are compared in Figs. 92.13, 92.14, 92.15, and 92.16 for three modes of the boiler operation. The temperature curves have a characteristic maximum in the zone of the burners arrangement at a height of 4 m (Fig. 92.13). In the traditional mode of combustion, level of the average temperature in the furnace at a height of up to 6 m higher than that for the boiler operating with PFS. The temperature difference reaches 75° (height between 2 and 3 m), due to more intense radiation from the coal particles having a higher concentration and the total surface at the traditional combustion, compared to the operation mode with PFS. From the PFS HRF enters the combustion chamber, consisting of fuel gas and coke residue particles, whose mass does not exceed 30 % of the consumption of raw coal, which leads to a threefold reduction in the total surface of the radiating particles. Further, in the section of the furnace from 4.5 to 16.75 m, the temperature in the regime with PFS is higher than that for the traditional burning by 10° and 32° in the case of two and four PFS, respectively. This is due to more complete fuel burnout (Fig. 92.14) by ETCPF confirmed by decreased oxygen concentration in the furnace at the same location (Fig. 92.15). PFS improve the environmental characteristics of the

Table 92.2 Characteristics of ETCPF at the PFS exit

Content of gas phase, vol.% and kg/h											
H_2	CO	CH_4	C_6H_6	CO_2	H_2O	N_2	O_2	Ash, kg/h	Char carbon, kg/h	T_{HRF}, °C	V_{HRF}, m/s
14.2	18.4	0.3	0.6	6.8	2.9	56.4	0.3	1,123.2	435.0	997	189
88.5	1,599.0	14.0	133.8	931.2	162.8	4,911	31.0				
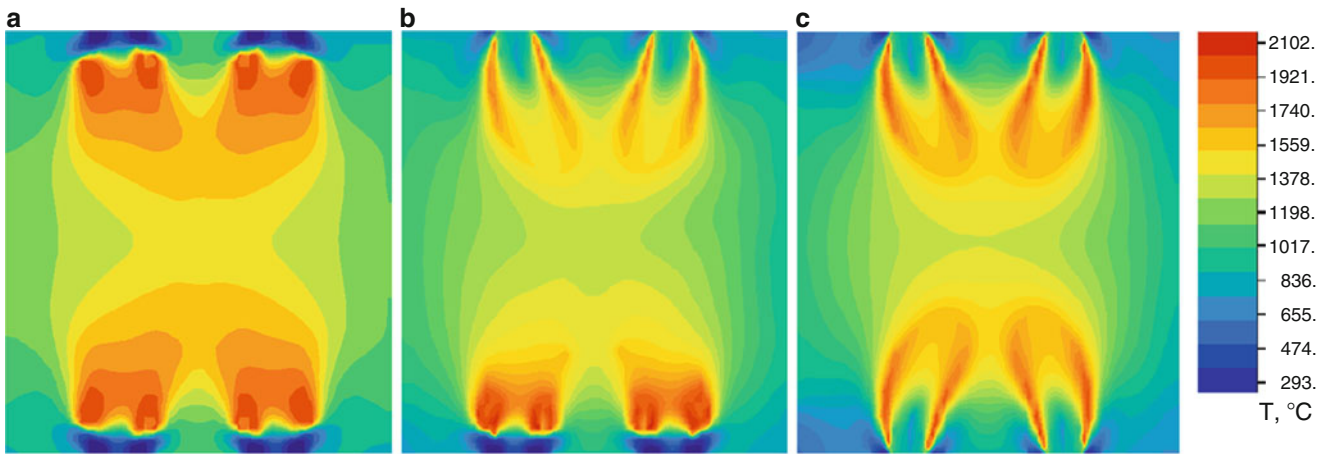
Fig. 92.12 Temperature field within the combustion chamber at the level of the pulverized coal burners: (**a**) standard operational regime; (**b**) plasma operational regime when two PFS operate; (**c**) plasma operational regime when four PFS operate

Fig. 92.13 Furnace height distribution of mass average temperature: 1—standard operational regime; 2—regime when two PFS operate; 3—regime when four PFS operate
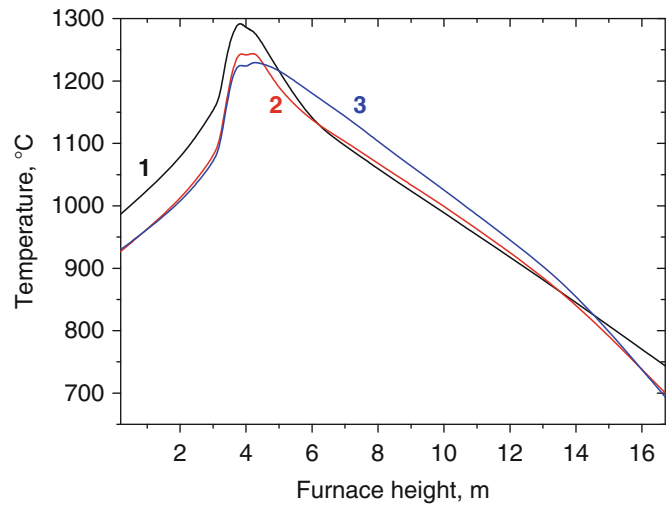
Fig. 92.14 Furnace height distribution of oxygen mean concentration: 1—standard operational regime; 2—regime when two PFS operate; 3—regime when four PFS operate
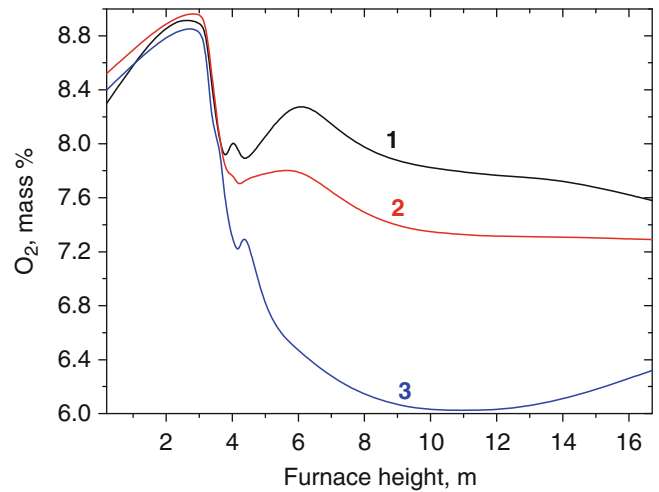
Fig. 92.15 Furnace height
distribution of carbon mean
concentrations: 1—standard
operational regime; 2—regime
when two PFS operate; 3—
regime when four PFS operate
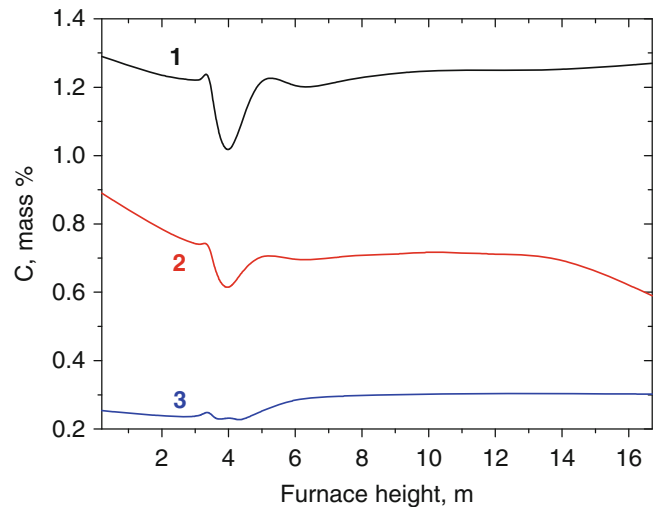
Fig. 92.16 Furnace height
distribution of NOx mean
concentration: 1—standard
operational regime; 2—regime
when two PFS operate; 3—
regime when four PFS operate
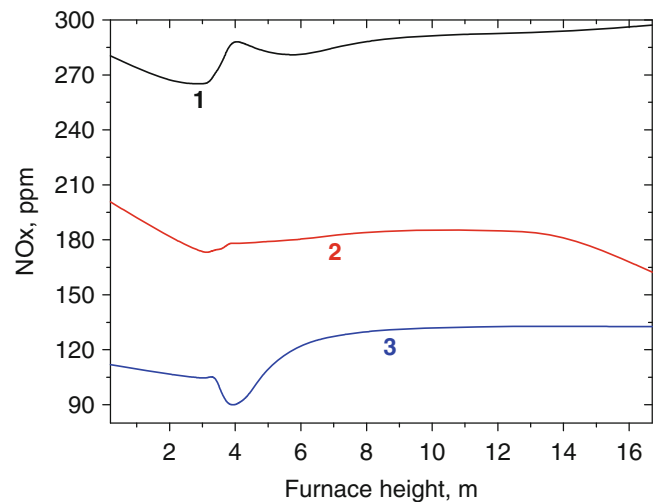
combustion of solid fuels. Compared with the traditional mode of coal incineration, use of four PFS reduces the unburned carbon at the outlet of the furnace (height of 16.75 m) four times and nitrogen oxide emissions by more than 2.2-fold (Fig. 92.16).

Computation of 420 ton/h Steam Productivity Boiler's Furnace Equipped with PFS

The fulfilled verification of CINAR ICE code for plasma-assisted coal combustion in the experimental furnace of 3 MW power confirmed legitimacy of the used codes complex (PLASMA-COAL and CINAR ICE) for simulation of the furnaces equipped with PFS. Thus, in this part the numerical study was performed for a power-generating boiler with a steam productivity of 420 ton/h. The boiler (Fig. 92.12) is equipped with six swirl burners arranged in two layers, three burners each, on faced wall of the furnace. As it is seen from the figure, three PFS are installed instead of two burners of the lower layer and one of the upper layer. Low-rank Ekibastuz bituminous coal of 40 % ash content, 24 % devolatilization, 5 % humidity, and 16,700 kJ/kg heat value was incinerated in the furnace. The coal grinding fineness is $R_{90} = 15$ %. All the calculations were performed in accordance to the aforecited technique.
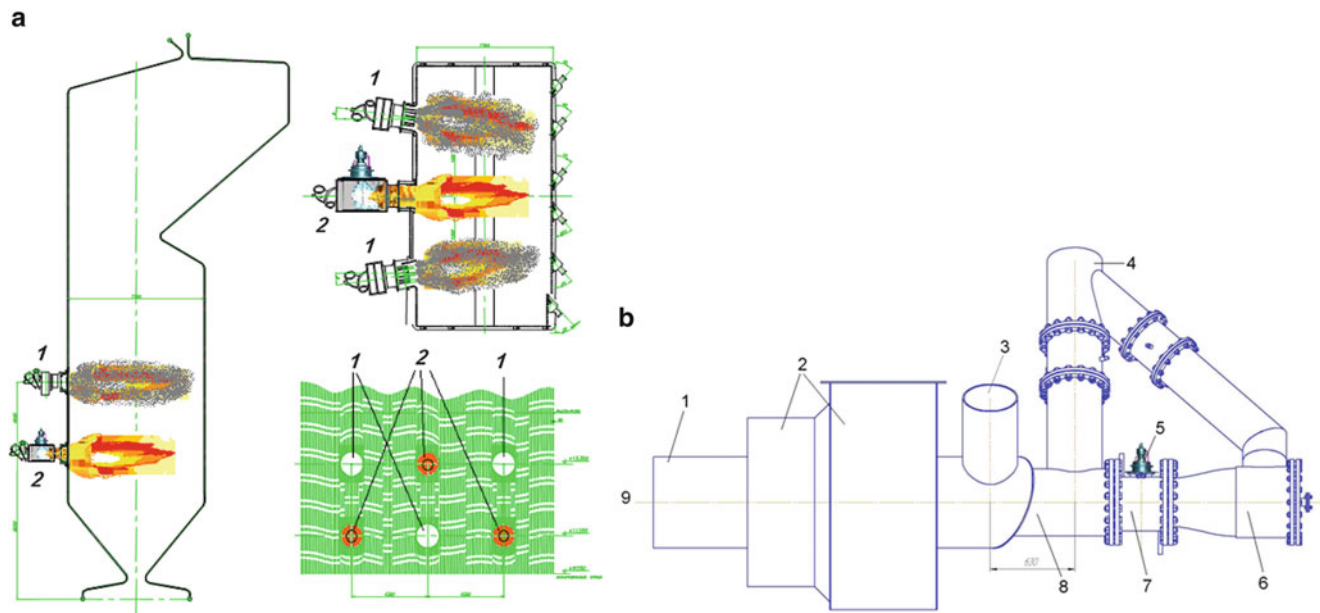
Fig. 92.17 Scheme of industrial 420 ton/h steam productivity boiler in Almaty TPP-2 (Kazakhstan) retrofitted with PFS (**a**): 1—standard pulverized coal swirl burner, 2—PFS; and layout of the PFS for the boiler (**b**): 1—channel of the external flow of pf, 2—secondary air duct, 3—inlet of pf external flow, 4—inlet of pf internal flow, 5—plasmatron, 6—chamber for pf flow turning, 7—chamber for plasma chemical preparation of fuel for combustion, 8—chamber for mixing and thermochemical preparation of fuel, 9—furnace

PLASMA-COAL computer code has been used for the calculation of ETCPF in the volume of PFS of 3.687 m length. The following initial parameters were used for calculations: plasmatron power was 200 kW, initial temperature of pulverized coal (coal/air mixture) was 90 °C, coal and air consumptions through PFS were 6,000 and 8,955 kg/h correspondingly.

The results of numerical simulation by the PLASMA-COAL code are summarized in Table 92.3. Heat value of the coke residue was 6,165 kJ/kg. These data obtained for the PFS exit were taken as initial parameters for 3D computation of the furnace of a power-generating boiler equipped with PFS. This computation was performed using CINAR ICE code to demonstrate advantages of plasma-aided coal combustion technology.

Initial parameters for calculations of the furnace (Fig. 92.17) in different operational regimes were the following: temperature of the secondary air was 280 °C, coal productivity of the burner was 12,000 kg/h, and primary airflow rate through the burner was 17,900 kg/h. Secondary airflow rate to the boiler was 446,412 kg/h. Averaged size of the coal particles was 60 micron. The furnace size is as follows: 27 m height, 7.7 m depth, and 14.5 m width. The x, y, z grid size was, respectively, $106 \times 38 \times 104$.

The model predictions are presented in the following figures which show results for the plasma-activated coal combustion in comparison with conventional coal combustion. Figures 92.18 and 92.19 show temperature fields along the furnace height in the mean cross-sectional plane for two regimes of the furnace operation, traditional (Fig. 92.18) and plasma-activated coal combustion (Fig. 92.19). The figures visually demonstrate the difference between the temperature fields for the two modes of coal combustion. When the coal combustion is in conventional mode, six symmetric pulverized coal flames are formed. Maximum temperature of these flames is 1,852 °C. In Fig. 92.19 one can see influence of PFS on to the shape of the ETCPF flame and its maximal temperature. In the presented plane PFS are upwardly. High temperature body of the flame is moved closer to the PFS exit and upper in the furnace. Its maximal temperature is 1,588 °C.

Averaged temperature curves (Fig. 92.20) have their maxima. The first one (H = 3 m) is generated by overheating of the furnace back wall by the pulverized fuel flame. The second maximum is above the level of the burners of the upper layer due to common forming of the flame body and observed moving as a result of natural convection. Averaged temperatures in the furnace operated in conventional mode are higher than those in the furnace operated in plasma-assisted regime using PFS. The difference achieves 350° at the furnace exit. The reason of this is more intensive radiation of coal particles which have higher concentration and total reacting surface when the furnace operates in conventional mode in comparison with plasma-assisted coal combustion. When PFS operate two component fuel of combustible gas and particles of coke residue

Fig. 92.18 Temperature field (°C) along the furnace height in the mean cross-sectional plane of the furnace when it works in conventional mode of coal combustion
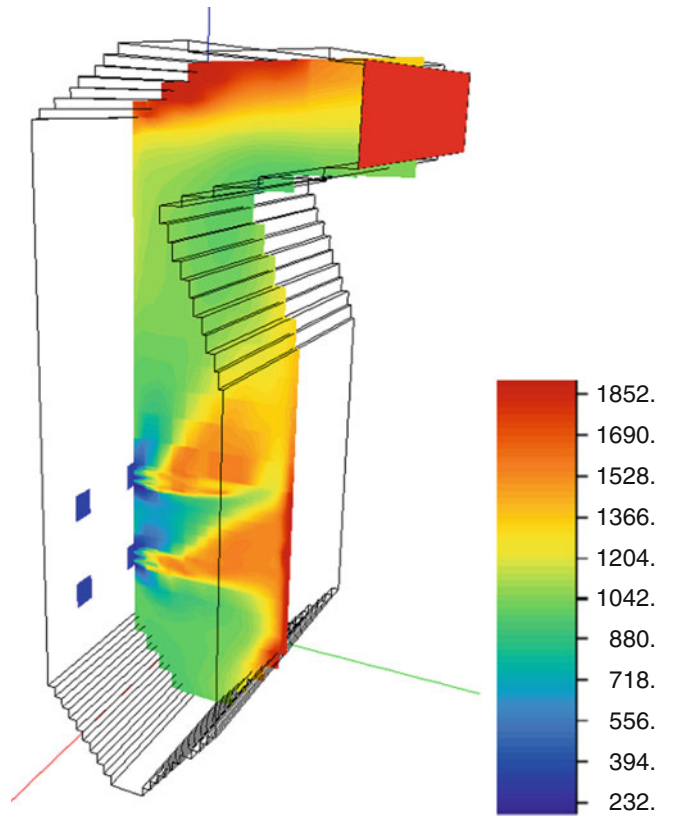
Fig. 92.19 Temperature field (°C) along the furnace height in the mean cross-sectional plane when it works in plasma-assisted mode of coal combustion using three PFS
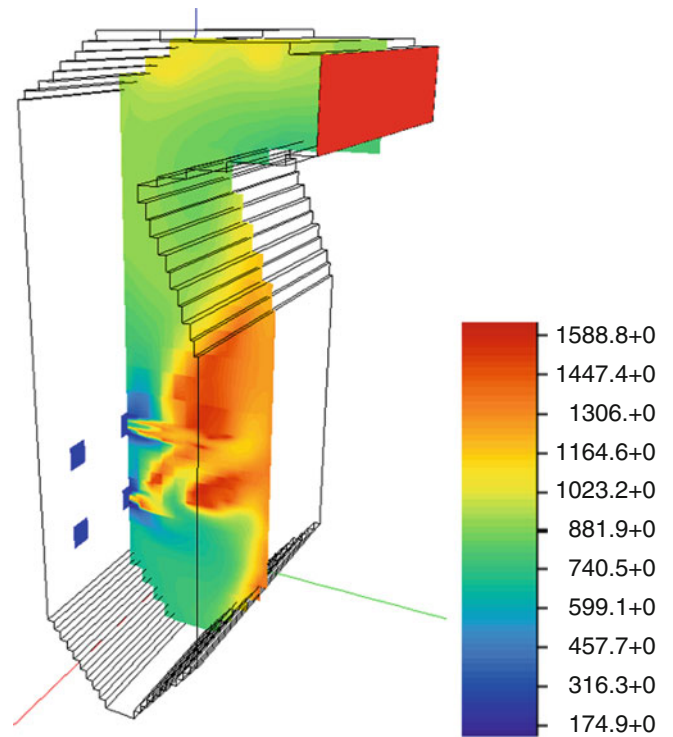
Table 92.3 Characteristics of ETCPF at the PFS exit

Content of gas phase (vol.% and kg/h)								Ash, kg/h	Char carbon, kg/h	Gas temperature, °C	Solids temperature, °C	Velocity of the flow, m/s
H_2	CO	CH_4	C_6H_6	CO_2	H_2O	N_2	O_2					
3.9	11.2	0.3	0.6	13.1	2.15	68.5	0.25	2,400	3,950	752	752	48.2
37.38	1,499	22.65	207	2,378	220.5	9,214	39.19					

Fig. 92.20 Mean concentration of temperature (T) along the furnace height (H): 1—conventional incineration of coal, 2—incineration of coal when three PFS operate
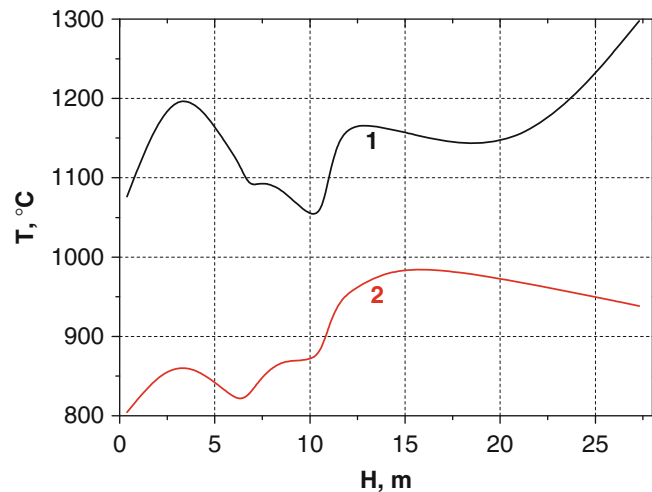
Fig. 92.21 Mean concentration of unburned carbon (C) along the furnace height: 1—conventional incineration of coal, 2—incineration of coal when three PFS operate
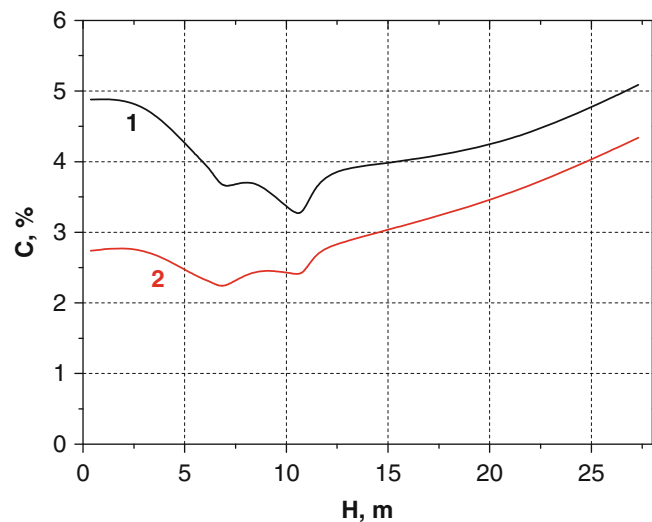
enters the furnace. Mass of this fuel does not exceed 30 % of the initial coal mass. That decreases total surface of the radiative particles.

At the furnace exit when three PFS operate, concentration of unburned carbon (Fig. 92.21) is 16 % less than that when the furnace works in traditional mode of coal combustion. Use of PFS improves ecological characteristics of the process of solid fuel combustion. Figure 92.22 demonstrates more than 33 % decrease of nitrogen oxides concentration. Evidently, decrease of unburned carbon and NOx concentrations at the furnace exit improves ecology-economic indexes of TPP.

Fig. 92.22 NO_x mean concentration along the furnace height: 1—conventional incineration of coal, 2—incineration of coal when three PFS operate
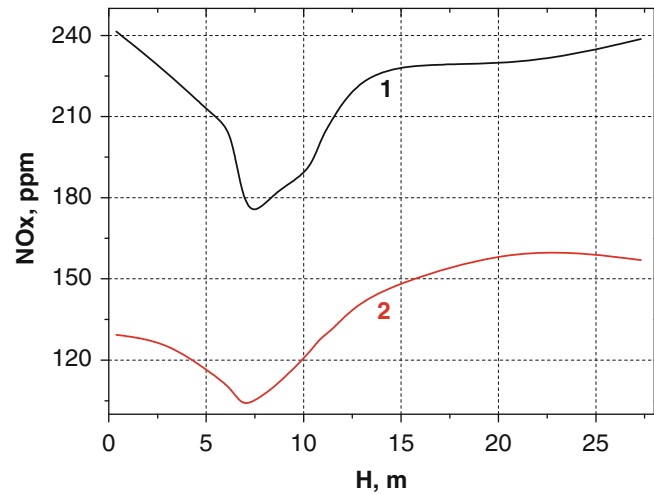
Table 92.4 Economical comparison of the PFS technology with traditional one

Conventional technology	Plasma technology
Fuel oil rate for Russian TPP	
5.1 million ton/year (cost is more than $ 2 billion)	0
Fuel oil rate for Kazakhstan TPP	
~1 million ton/year (cost is about $ 400 million)	0
Investments for TPP	
100 %	3–5 %
Operating costs	
100 %	28–30 %
Electric power consumption for TPP auxiliary	
3–5 %	0.5–1.0 %

Conclusions

Simulation and testing of PFS at existing coal-fired boilers of TPP confirmed the technical feasibility, environmental and energy efficiency of zero fuel oil start-up of the boilers, and plasma-assisted stabilization of pulverized coal flame.

PFS test at the boilers BKZ-160 and BKZ-420 of Almaty Power System in the mode of the boilers start-up from cold confirmed possibility of ignition of high-ash Ekibastuz coal.

Inculcation of PFS gives economical effect, which depends on coal/fuel oil price ratio (Table 92.4). Pay back period varies from 12 to 18 months. Economical effect for TPP of Kazakhstan is 400 million of US dollars a year.

References

1. Sakipov ZB, Messerle VE, Ibraev ShSh (1993) Electrothermochemical preparation of coal to burning. Nauka, Almaty, 259 p (in Russian)
2. Messerle VE, Ustimenko AB (2012) Plasma ignition and combustion of solid fuel. (scientific-and-technological basics). Palmarium Academic, Saarbrucken, Germany (ISBN: 978-3-8473-9845-5), 404 p (in Russian). http://ljubljuknigi.ru/
3. Gorokhovski MA, Jankoski Z, Lockwood FC, Karpenko EI, Messerle VE, Ustimenko AB (2007) Enhancement of pulverized coal combustion by plasma technology. Combust Sci Technol 179(10):2065–2090
4. Karpenko EI, Messerle VE, Ustimenko AB (2007) Plasma-aided solid fuel combustion. Proceedings of the combustion institute. Elsevier, vol 31, part II, pp 3353–3360
5. Karpenko EI, Karpenko YuE, Messerle VE, Ustimenko AB (2009) Using plasma-fuel systems at Eurasian coal-fired thermal power stations. Ther Eng 56 (6):456–461
6. Askarova AS, Karpenko EI, Lavrishcheva YI, Messerle VE, Ustimenko AB (2007) Plasma-supported coal combustion in boiler furnace. IEEE Trans Plasma Sci 35(6):1607–1616

7. Kalinenko RA, Kuznetsov AP, Levitsky AA, Messerle VE, Mirokhin YA, Polak LS, Sakipov ZB, Ustimenko AB (1993) Pulverized coal plasma gasification. Plasma Chem Plasma Process 13(1):141–167

8. Gorokhovski M, Karpenko EI, Lockwood FC, Messerle VE, Trusov BG, Ustimenko AB (2005) Plasma technologies for solid fuels: experiment and theory. J Energy Inst 78(4):157–171

9. Jankoski Z, Lockwood FC, Messerle VE, Karpenko EI, Ustimenko AB (2004) Modelling of plasma pre-treatment of powdered coal for combustion. Thermophys Aeromech 11(3):461–474

10. Lockwood FC, Salooja AP, Syed AA (1980) A prediction method for coal-fired furnaces. Combust Flame 38(1):1–15

11. Lockwood FC, Mahmud T, Yehia MA (1998) Simulation of pulverised coal test furnace performance. Fuel 77(12):1329

12. Lockwood FC, Mahmud T (1988) The prediction of swirl burner pulverised coal flames. Twenty-second symposium (international) on combustion. The Combustion Institute, Pittsburgh, PA, pp 165

13. Lockwood FC, Shan NG (1978) Evaluation of an efficient radiation flux model for furnace prediction procedures. Proceedings of the sixth international heat transfer conference, pp 1405–1413

14. Lockwood FC, Shan NG (1981) A new radiation solution method for incorporation in general combustion prediction procedures. Proceedings of the 18th international symposium on combustion. The Combustion Institute, Pittsburg, PA, pp 1405–1413

15. Launder BE, Spalding DB (1974) The numerical computation of turbulent flows. Comput Meth Appl Mech Eng 3(2):269–289

16. Messerle VE, Karpenko EI, Ustimenko AB, Lavrichshev OA (2013) Plasma preparation of coal to combustion in power boilers. Fuel Process Technol 107:93–98

Vladimir E. Messerle and Alexander B. Ustimenko

Abstract

This chapter presents review of developed plasma technologies of fuels and minerals utilization. Technical realizability, energy and ecological-economical effectiveness of these technologies are shown. Also mathematical models and realizing codes for numerical investigation of the processes of fuels and minerals processing in plasma and electromagnetic reactors, plasma-fuel systems, and power boilers are described.

Keywords

Fuel • Plasma • Gasification • Ignition • Stabilization • Processing

Introduction

Technologies of fuel and minerals utilization, which were developed and mastered in commercial or experimental-industrial scale, are discussed [1–10]. They are plasma technology of zero fuel oil (gas) boilers start-up and pulverized coal flame stabilization at coal fired thermal power plants (TPP); plasma technology of power coals processing to carbonic sorbents; plasma gasification of coal; plasma technology of pulverized coal ignition and the flame stabilization in rotary furnace for alumina agglomeration in aluminum industry and for zero fuel oil clinker calcination at cement production; plasma technology of oil refining residuum utilization; plasma-cyclone technology of bricks firing; and energy-saving electromagnetic technology for mineral materials melting. These technologies are realized with the aid of numerical modeling and plasma-fuel systems (PFS) which were developed to improve efficiency of power coals combustion to decrease share of fuel oil and natural gas in fuel balance of TPP and to decrease harmful emissions.

PFS and Plasma Technology of Oil (Gas)-Free Boilers Start-Up and Pulverized Coal Flame Stabilization at Coal Fired Thermal Power Plants

PFS are combination of pulverized fuel (pf) burners with DC arc plasma torches. Using PFS fuel oil is replaced by pulverized coal, which is a subject to plasma thermochemical preprocess to the combustion. In this technology, part of the coal/air mixture is fed into the PFS where the plasma-flame, having a locally high concentration of energy, induces gasification of the

V.E. Messerle
Combustion Problems Institute, Almaty, Kazakhstan

Institute of Thermophysics of Russian Academy of Science, Novosibirsk, Russia

A.B. Ustimenko (✉)
NTO Plasmotechnics Ltd., Almaty, Kazakhstan

Research Institute of Experimental and Theoretical Physics, Almaty, Kazakhstan
e-mail: ust@physics.kz

coal and partial oxidation of the char carbon. Since the resulting coal/air mixture is deficient in oxygen, the carbon being mainly oxidized to carbon monoxide. As a result, a highly reactive mixture of combustible gases (at a temperature of 900–1,200 K) and partially oxidized char particles are obtained at the exit of the burner. On entry to the furnace, this combustible mixture is easily ignited. This allows prompt ignition and much enhanced flame stability of the main portion of the coal flame which is not directly treated by the plasma. Activation of coal combustion by this means eliminates the need for supplementary fuel consumption (fuel oil or natural gas), traditionally used for the start-up of a coal fired furnace. Figure 93.1 illustrates the process of thermochemical preparation of coal to combustion. The figure presents scheme of the developed direct flow PFS. The process is going on at relatively low specific power consumption (SPC) of 0.05–0.4 kW h/kg of coal. It was experimentally proven that PFS use increases efficiency of coal ignition and combustion, eliminates fuel oil expenditure for start-up and flame stabilization, decreases unburned carbon, NO_x, SO_x, V_2O_5 emission, and provides ample scope for the process automation.

PFS have been tested for boilers start-up by plasma ignition of pulverized coal and flame stabilization in different countries on 30 pulverized coal boilers steam-productivity 75–670 t/h equipped with different types of pulverized coal burners (direct flow and swirl burners). When PFS were tested, power coals of all ranks (brown, bituminous, anthracite and their mixtures) were incinerated (Table 93.1). Volatile content of them was from 4 to 50 %, ash varied from 15 to 56 %, and heat of combustion was from 1,600 to 6,000 kcal/kg. The advantages of PFS technology were confirmed by 3D simulation of the boilers equipped with PFS.

For instance the schematic view of the boiler equipped with PFS and its primary dimensions are shown in Fig. 93.2. The furnace is characterized by two symmetrical combustion chambers, each having four tangentially directed main double burners in two layers. Combustion chambers are interconnected by a central section. Fuel consumption on the boiler was 121.3 t/h and total amount of air in the boiler was 553,128 Nm^3/h at temperature of the secondary air 350 °C.

Four PFS are mounted instead of four lower sections of the main double burners as it is shown in Fig. 93.2. The plasmatrons operate during the boiler warm-up period and in the case of an unstable flame. When the boiler performance is stabilized, the plasmatrons are switched off and the PFS continue to function as conventional pf burners. In the case of flame instability, the plasmatrons are restarted.

Knowledge of the SPC of a plasmatron is required to estimate PFS efficiency. This parameter is defined as a ratio of plasmatron electric power to pf consumption in the PFS. Figures 93.3 and 93.4 present experimental results for NO_x reduction and the decrease of unburned carbon during PFS operation versus SPC for the plasmatron. It is seen that the NO_x concentration is halved, and the amount of unburned carbon is reduced by a factor of 4. The NO_x decrease is caused by the
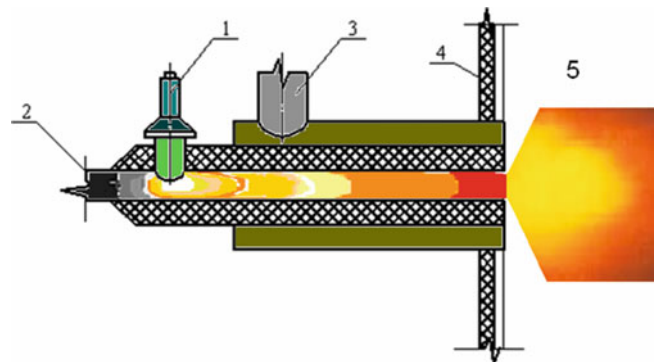
Fig. 93.1 Direct flow PFS: 1—plasmatron; 2—air/coal mixture input; 3—secondary air input; 4—side of a boiler furnace; 5—furnace

Table 93.1 Technical characteristics of coals

Coal type	W^w	A^d	V^{daf}	Q_l^w (kcal/kg)
Brown	25–35	15–20	35–50	3,000–3,800
Lignite	32–40	28–35	23–27	1,900–2,100
Shale oil	40–50	75–80	48–50	1,600–2,000
Bituminous	5–12	20–56	15–40	3,500–5,000
Anthracite	5–8	25–35	4–10	4,300–6,200
Coal mixture	10.4	48.5	38.2	3,150

W^w wet per working mass, A^d ash per dry mass, V^{daf} volatile per dry ash-free mass, Q_l^w low heat of coal combustion per working mass

Fig. 93.2 Scheme of the industrial furnace of BKZ 640-140 boiler
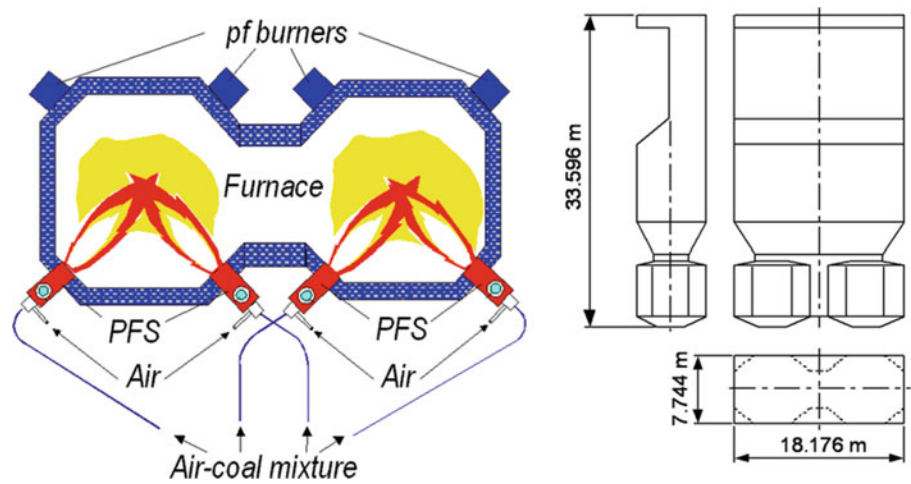
Fig. 93.3 Influence of the specific power consumption (SPC) for plasmatron on reduction of the nitrogen oxides (NO_x) concentration at plasma-assisted pf combustion
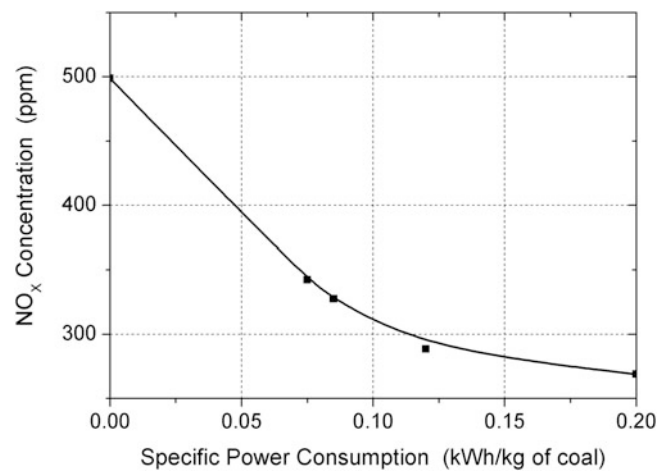
Fig. 93.4 Influence of the SPC for plasmatron on reduction of unburned carbon at plasma-assisted pf combustion
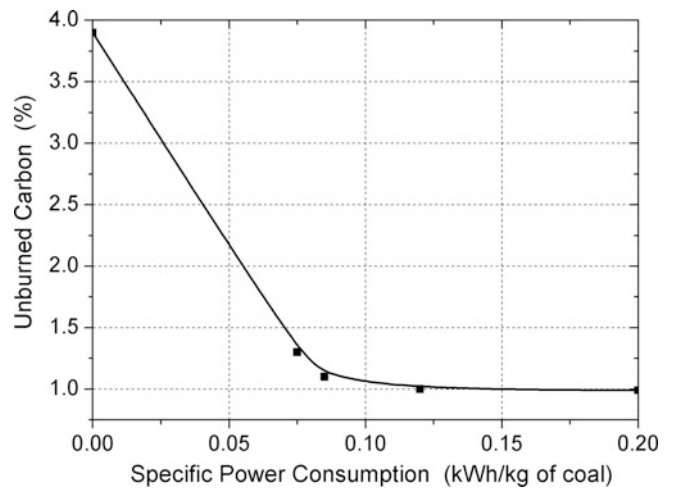
fact that the fuel nitrogen, released from the coal inside the PFS in conditions of oxygen deficiency, forms molecular nitrogen in the gas phase. Since the fuel nitrogen is evolved inside the PFS and converted to molecular nitrogen there, mainly thermal nitrogen oxides are formed within the combustor volume. However, fuel nitrogen is the main source of nitrogen oxide emission from conventionally fired pf combustors. As to unburned carbon, its decrease indicates a fuel reactivity

increase which is explained by enlargement of the coal particles reactive surface due to "heat explosion" and fragmentation as a result of their interacting with arc plasma.

Plasma-Steam Gasification and Complex Processing of Coal to Produce Synthesis Gas and Valuable Components from Ash

Plasma gasification and complex processing of coal to produce synthesis gas and valuable components from mineral mass of coal (MMC) were investigated using universal experimental setup. Plasma gasification and complex processing of low-rank coals are oriented towards the perspective of several industry branches development (power engineering, chemical industry, metallurgy). Final products are synthesis gas ($CO + H_2$), hydrogen, silicon, ferrosilicon, carbosilicon, and alumina. From an environmental point of view, these technologies are most promising. Their essence is heating of coal dust by the arc plasma, which is oxidant, to complete gasification temperature at which the coal organic matter is transformed into an environmentally friendly fuel—synthesis gas free of ash particles, nitrogen oxides, and sulfur oxides. At complex processing of coal simultaneously with gasification of organic matter in the same reaction volume coke carbon restores MMC oxides and valuable components, such as industrial silicon, ferrosilicon, aluminum, carbosilicon, and microelements of rare metals: uranium, molybdenum, vanadium, and others are formed. Figure 93.5 demonstrates experimental installation for this process realization. Coal dust with oxidant is heated by arc plasma up to the temperature of the coal complete gasification. Thus organic mass of coal is conversed into environmentally friendly fuel, synthesis gas, which is free from ash particles, nitrogen oxides, and sulfur oxides. Simultaneously reduction of the MMC oxides is taken place and valuable components like silicon, ferrosilicon, aluminum, carbosilicon, and microelements of rare metals (uranium, molybdenum, vanadium etc.) are produced.

The experimental installation is intended for work in the range of electric power 30–100 kW, mass averaged temperature 1,800–4,000 K, coal dust consumption 3–12 kg/h, and water steam flow 0.5–15 kg/h. The steam/pulverized fuel mixture entering the arc zone is heated to high temperature by the arc rotating in electromagnetic field to produce a two-phase plasma flow where the process of solid fuel gasification occurs.

Petrocoke (CP), brown (PBC), and bituminous (KBC) coals of 3, 48.1, and 44 % ash content correspondingly (Table 93.2) have been gasified in the plasma gasifier. The sieve analysis of the pulverized fuel revealed that mean sizes of the CP, PBC, and KBC dust particles were 105, 60, and 75 μm correspondingly. Thermal efficiency of the reactor was determined in the experiments as 76 %. As a result of the solid fuels gasification under steam plasma conditions concentrations of gas species, SPCs, carbon gasification degree (X_C), and weight-averaged temperatures (T_{AV}) in the reactor were revealed (Table 93.3). High quality synthesis gas was produced in the experiments on solid fuels plasma gasification. It has been found that the synthesis gas content of 85–99 vol% can be produced, and gasification degree can be reached as high as 94.2 %.

Fig. 93.5 Scheme of plasma unit for carbonaceous materials processing: 1—reactor; 2—chamber of gas and slag separation; 3—slag catcher; 4—chamber of synthesis gas removal; 5—diaphragm; 6—chamber of hydration; 7—pulverized coal feeder; 8—the cooling system; 9 and 10—electric power supply system; 11 and 12—gear for rod electrode delivery; 13—steam generator; 14—safety valve; 15—stand for slag catcher
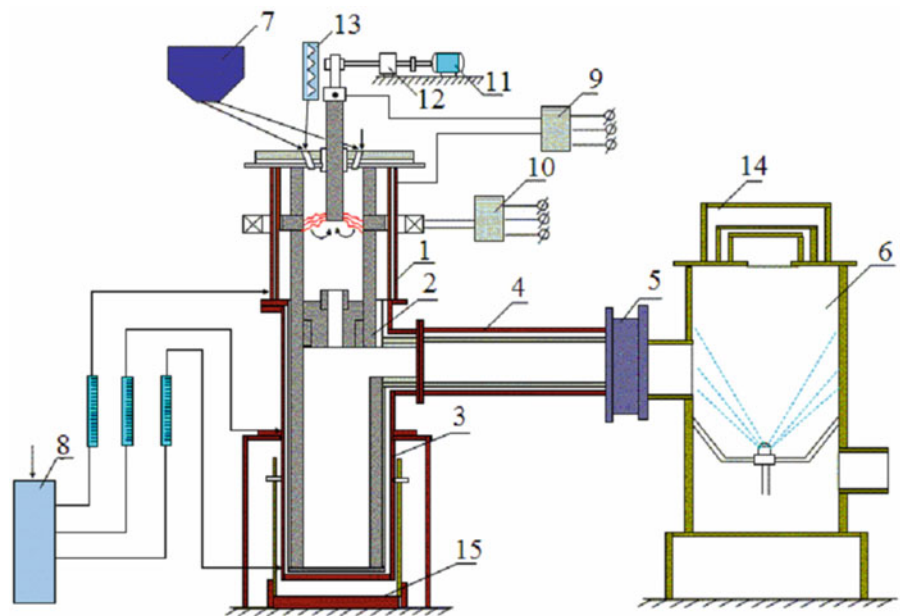
Table 93.2 Solid fuels chemical analysis, wt.%

Solid fuel	C	O	H	N	S	SiO$_2$	Fe$_2$O$_3$	CaO	MgO	K$_2$O	Na$_2$O	Al$_2$O$_3$
KBC	48.86	6.56	3.05	0.8	0.73	23.09	2.15	0.34	0.31	0.16	0.15	13.8
CP	75.0	0.88	15.53	0.01	5.63	1.31	0.6	0.1	0.05	0.07	0.04	0.78
PBC	33.60	8.52	6.50	0.88	2.40	28.52	1.73	0.41	0.46	–	–	16.98
TBC	48.58	17.85	3.64	0.78	1.14	16.64	2.13	0.88	0.67	0.01	0.01	7.67

Table 93.3 Main indexes of the solid fuels plasma gasification

N	Solid fuel	Consumption (kg/h)		P (kW)	SPC (kW h/kg)	T_{AV} (K)	CO	H$_2$	N$_2$	X_C (%)
		Fuel	Steam				vol%			
1	KBC	4.0	1.9	25	4.8	3,500	41.5	55.8	2.7	94.2
2	CP	2.5	3.0	60	9.6	3,850	36.2	63.1	0.7	78.6
3	PBC	7.6	2.7	60	5.83	2,600	34.1	51.1	14.8	92.3
4	TBC	7.1	4.5	60	5.17	3,100	45.8	49.4	4.8	93.2

Table 93.4 Degree of reduction of MMC

Place of sampling	T (K)	Θ (%)
Slag from pool of melt	2,600–2,800	8.5–44.0
Slag from the wall of the reactor	2,600–2,900	16.5–47.3
Slag from slag catcher	2,000–2,200	6.7–8.3

At complex processing of a low-rank brown coal (TBC) of 28 % ash content and 13,180 kJ/kg caloricity (Table 93.2) simultaneously with gasification of organic matter in the same reaction volume coke carbon restores MMC oxides, and valuable components are formed. Synthesis gas yield reached 95.2 %, and carbon gasification degree was 93.2 % (Table 93.3). Table 93.4 presents degree of reduction (Θ) of the samples of solid residue from different parts of the installation including special pool for melt near graphite orifice between the reactor 1 and chamber of gas and slag separation 2 (Fig. 93.5). It is seen that restored material was found in the slag in the form of ferrosilicon, silicon, and ferric carbides. The highest degree of reduction of the oxides of MMC 47 % was found in the slag from the wall of the reactor where there is a zone of maximal temperatures.

The installation (Fig. 93.5) was also used for realization some other following technologies. Technologies of plasma conversion of carbonaceous materials (coal, petroleum coke, hydrocarbon gases) are characterized by high levels of temperature and, therefore, a high degree of their thermochemical conversion to desired products. Plasmochemical technology of cracking is to heat hydrocarbon gases in the combined electric arc reactor to a temperature of pyrolysis (1,900–2,300 K) with the formation of fine carbon and hydrogen in unified technological process. Plasmochemical hydrogenation of solid fuels, which is the pyrolysis of coal in a hydrogen atmosphere, provides acetylene and other unsaturated hydrocarbons (ethylene C_2H_4, propylene, C_3H_6, C_2H_6 ethane, etc.) from cheap low-rank coals by their treatment with hydrogen plasma. Plasmochemical hydrogenation of coal is a new process of direct production of acetylene and alkenes in the gas phase, in contrast to conventional hydrogenation (liquefaction) of coal. As a result of experiments on low-rank coal hydrogenation in plasma reactor at its power of 50 kW, coal consumption of 3 kg/h, and propane–butane mixture of 150 L/h gas of the following composition is obtained, wt.%: $C_2H_6 = 50$, $C_2H_2 = 30$, $C_2H_4 = 10$.

Experiments on plasma pyrolysis (cracking) of propane–butane gas mixture were performed in the plasma reactor of 100 kW nominal power. In the experiments, propane–butane mixture flow amounted to 300 L/min, and the plasma reactor power was 60 kW. During the experiments hydrogen and carbon (soot) were obtained. Physicochemical analysis of the soot samples has shown that they are different nanocarbon structures mainly in the form of "colossal" nanotubes (Fig. 93.6) with high electrical conductivity and mechanical strength.
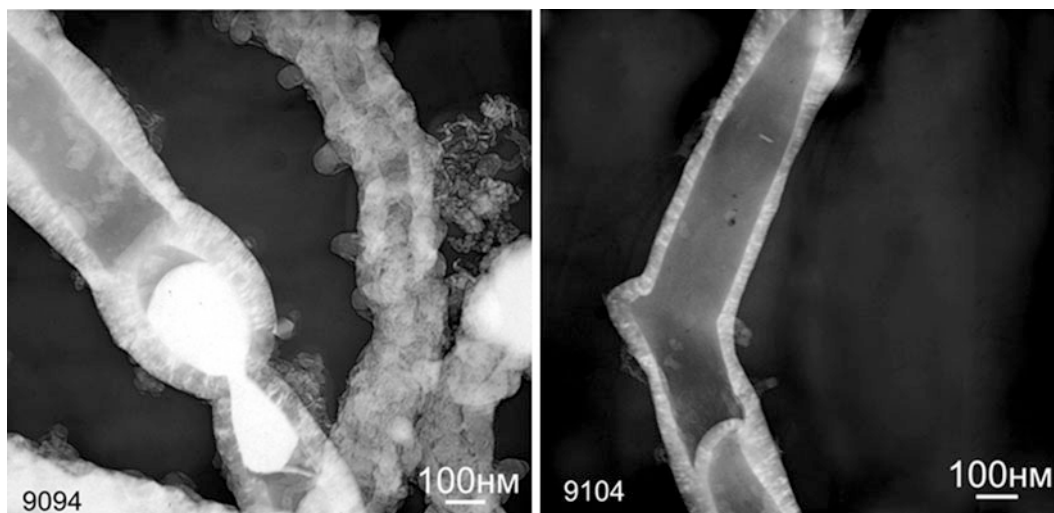
Fig. 93.6 Images of the products of propane–butane plasma pyrolisis through transmission electron microscope (TEM)—colossal carbon nanotube metal nanoparticle intercolated

Fig. 93.7 Scheme of the carbon sorbent producing: 1—PFS; 2—plasmatron; 3—coal dust hopper; 4—chamber of heating; 5—crushed coal hopper; 6—chamber of the sorbent formation
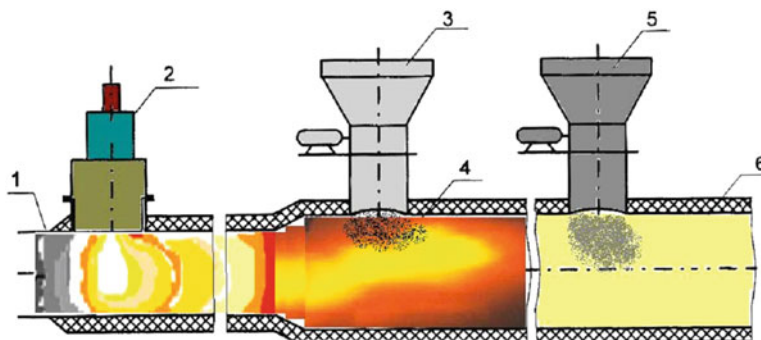
Plasma Technology of Power Coals Processing to Carbonic Sorbents

One of the newest methods of active and inexpensive sorbents production is plasma technology of power coals processing. Figure 93.7 demonstrates a pilot three plasma steps installation for carbon sorbents production from low-rank coals. The installation's productivity is 500 kg of carbonic sorbent per hour at plasmatron power of 50 kW, coal consumption through the PFS of 100 and 200 kg/h through the chamber of heating. The technology is in the following. Air/pulverized coal mixture is fed to PFS 1. Produced in PFS high reactive two component fuel inflows to the chamber of heating 4, where heat-transfer agent of coal dust is fed from coal dust hopper 3. On the heat-transfer agent achievement of specified temperature crushed coal is fed to the flow from crushed coal hopper 5. Coal particles dimension is within 5 mm. As a result of these particles pyrolysis at the exit of chamber of the sorbent formation 6 desired product, sorbent, is produced.

Cheap, active, and extended inner surface sorbent was produced from bituminous coal. Experimentally produced sorbent on this technology was tested. It confirmed the principal realizability of the technology.

Plasma Technology of Pulverized Coal Ignition and the Flame Stabilization in Rotary Furnace for Alumina Aglomeration in Aluminum Industry and for Oil-Free Clinker Firing at Cement Production

This technology is developed for the biggest in Eurasia Achinsky alumina plant, which is equipped with 11 rotary kilns of 5 m in diameter and 185 m in length. Dry alumina productivity of the kiln is 102 t/h. The kiln heat power is 108 MW. Consumption of oil for the kiln is 17,700 t/year. Traditionally to stabilize pulverized coal oil nozzle continuously operates

Fig. 93.8 Scheme of air/coal mixture ignition in a kiln (conventional installation): fuel oil flow rate is 2.5 t/h, coal consumption is 5 t/h
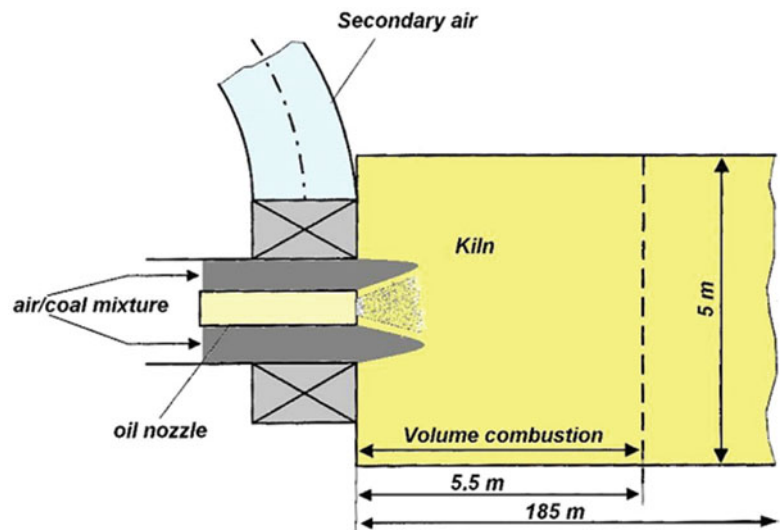
Fig. 93.9 Scheme of air/coal mixture plasma ignition in a kiln: coal consumption is 10 t/h
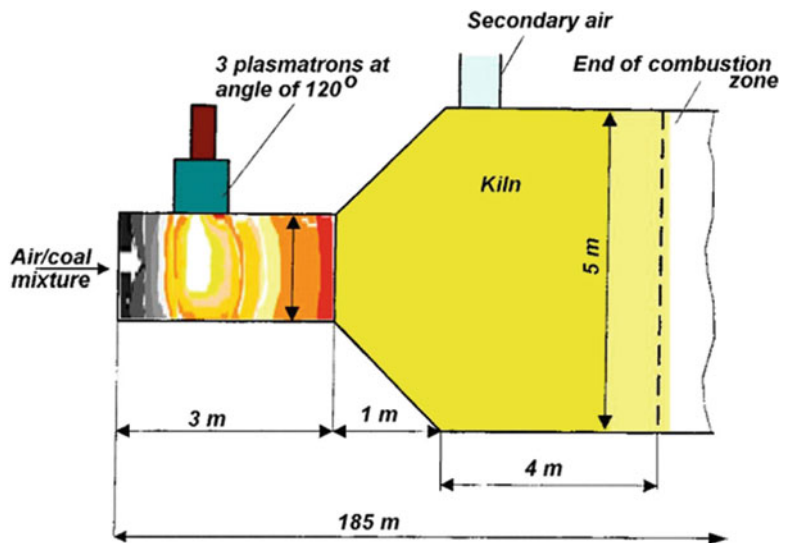
(Fig. 93.8). Fuel oil flow rate is 2.5 t/h and pulverized coal consumption is 5 t/h. To substitute fuel oil for coal and to improve ecological and economical indexes of the plant plasma technology of oil-free ignition and pulverized coal flame stabilization in inclined rotary kiln was developed. In accordance to this technology, continuously operated fuel oil nozzle is replaced with PFS. Figure 93.9 illustrates this replacement. The consumption of coal through the PFS is 10 t/h.

Without any essential modification this technology can be applied for zero fuel oil clinker calcinations to produce cement.

Plasma Technology of Oil Refining Residuum Utilization

Existing petroleum refining plants dependently on quantity of petroleum produce 4–6 % of oil refining residuum. For example processing 12 million tons of raw oil per year refinery "Neftochim" (Bourgas, Bulgaria) gets 180,000 t/year of oil refining residuum.

Traditional technology of oil refining residuum utilization is its incineration in a special rotary gas furnace. At that conversion degree of oil refining residuum does not exceed 30–40 %, and SPC for the process reaches 100–120 kW h/t of the utilizing oil refining residuum.
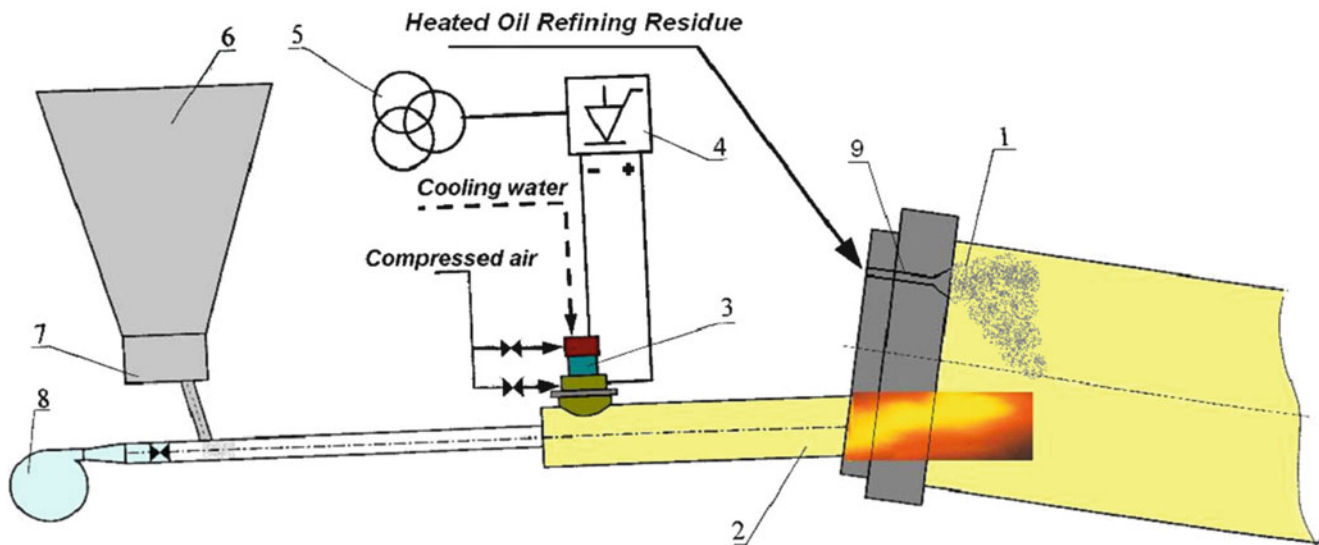
Fig. 93.10 Scheme of the installation for oil refining residue incineration using PFS: 1—rotary furnace (conventional); 2—PFS; 3—plasmatron; 4, 5—power supply source; 6—pulverized coal hopper; 7—coal dust feeder; 8—fan; 9—heated oil refining residue nozzle

To improve efficiency of the process of oil refining residuum processing the plasma technology was developed and experimentally tested. It is based on preliminary plasma thermochemical preparation of coal to burning. Instead of gas highly reactive mixture of combustible gases and partially oxidized char particles is incinerated in the furnace ensure high temperature needed for oil refining residuum processing. Figure 93.10 demonstrates the installation for oil refining residue incineration using PFS. Having oil refining residue processing productivity of 1 t/h experimental SPC amounted to 33 kW h/t. This is three to four times less than existing one.

Having 2 t/h coal consumption through the PFS and plasmatron's power of 200 kW 12 t/h of oil refining residuum can be processed. For processing of such quantity of oil refining residuum in accordance to traditional technology flow rate of natural gas amounts 1,000 m^3/h.

Plasma-Cyclone Technology of Bricks Firing

Conventionally the bricks are fired in special circular or tunnel kilns using natural gas combustion products. As it is shown in Fig. 93.11 high temperature gas can be produced by pulverized coal incineration in a plasma-cyclone chamber. Produced in PFS in the process of plasma thermochemical preparation of coal to burning two-component high reactive fuel is fed tangentially to cyclone. Under the influence of centrifugal force the molten slag formed by the combustion of coal, is thrown to the wall of the cyclone and flows down into the slag catcher. High temperature gas (1,000–1,200 K) is directed to the hot exhaust gas reservoir. From the reservoir hot gas is distributed to the kiln sections to fire the bricks. Calculated specific volume thermal intensity of plasma-cyclone chamber is 3–4 MW/m^3.

Energy-Saving Electromagnetic Technology for Mineral Materials Melting

At present natural basalt, which is a product of ancient volcanic processes, became one of the main raw material for mineral fiber production. Industrial practice shows that basalt has great perspectives. Wide assortment of high quality plate heat insulators and mats is produced from basalt wool by its mechanical and chemical processing.

Almost all firms for basalt melting mainly use gas, coke, and thermal-electric furnaces. But they are large dimensional, resource-demanding, and ecology negative. This is due to the fact that the construction industry is a large capacity.

Compact industrial installation based on the efficient plasma electromagnetic reactor is offered (Fig. 93.12). The base of the installation for heat insulators production is electromagnetic reactor. The reactor is made of stainless steel in the form of water-cooled sections. Four graphite electrodes are placed by the center and the corners of equilateral triangle in parallel
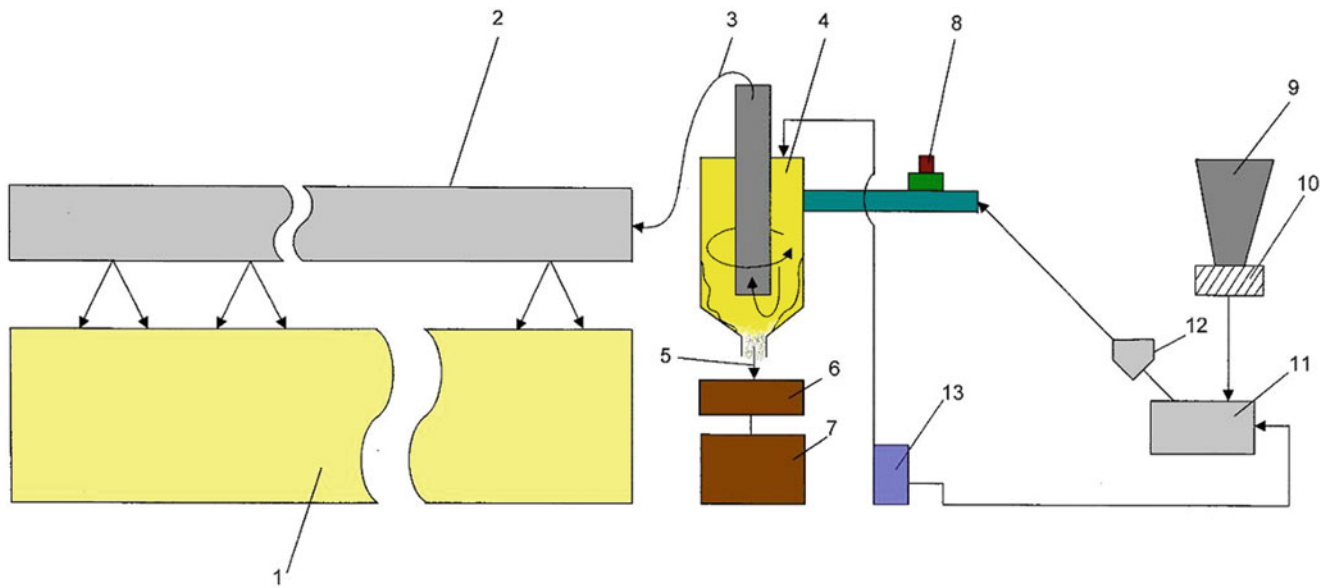
Fig. 93.11 Scheme of bricks firing in the circular kiln with plasma-cyclone chamber: 1—circular kiln for drying and firing of the bricks; 2—lined duct of hot exhaust gas supply; 3—hot exhaust gas; 4—cyclone furnace; 5—liquid slag; 6—slag catcher; 7—slag utilizer; 8—plasmatron; 9—bunker of the raw coal; 10—the coal feeder; 11—mill; 12—dust separator; 13—fan

Fig. 93.12 Four electrode plasma reactor for minerals melting and basalt flow from the reactor
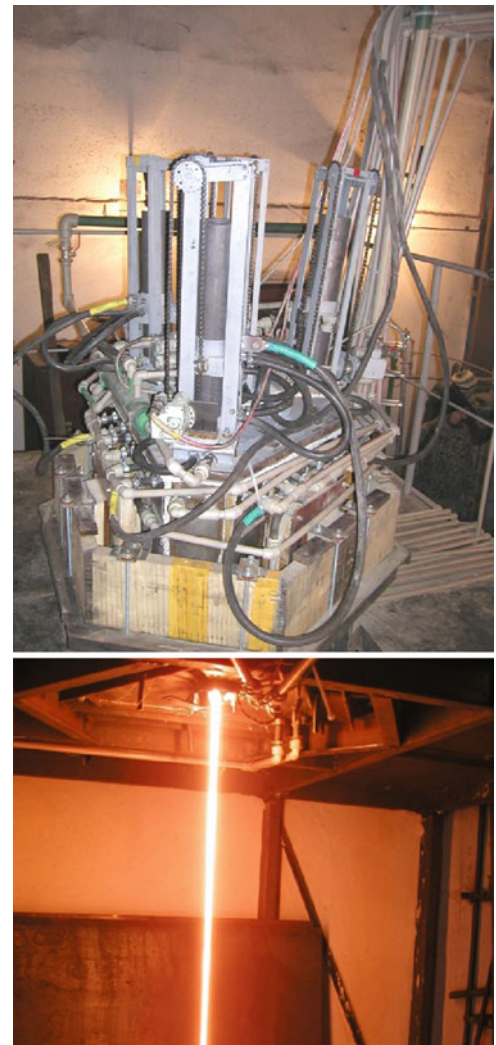
with axis of the reactor chamber. The working chamber of the reactor is enclosed into electromagnet with three poles. There are windings on the poles of electromagnet; they are inserted in a certain order, sequentially with power electrodes, and create magnetic field. The melt, produced in the reactor, is mixing as a result of interaction between the electric current, existing between the electrodes, and the magnetic field of the three-phase electromagnet. It guaranties material heating rate acceleration, its more uniform heating and homogenizing of the melt.

The melt from the reactor could be delivered either to blowing device or centrifuges for producing super thin fibers, and for manufacturing a number of new efficient heat insulating materials. It could also come to draw plates where the continuous fibers are being drawn; further the roving is produced out of them. The melt could also be directed to metallic molds and molding forms, where decorative goods, jewelry, monuments, and construction components for engineering industry are produced. External dimensions of the electrical reactor, including electromagnet, are ~1.5 × 1.5 × 1.5 m. At the reactor productivity of 200 kg/h SPC for basalt melt making came to ~0.9 kW h/kg. At that it is observed that the emission of gases polluting atmosphere is minimal. The power source is adapted to the process of three phase controlled thyristor converters. It is connected up to the power transformer having industrial frequency and voltage of 0.4–0.6 kV.

This three-phase reactor with electromagnetic mixing of the melt could be used as waste vitrification reactor or glass-melting furnace. At that, in comparison with gas glass-melting furnace SPC for the melt getting would decrease from 2.2 to 0.8–0.85 kW h/kg.

Long Life Plasmatron

The main part of the PFS is plasmatron. Its operational capability in industrial conditions depends on its electrodes long life. Direct current air arc plasmatron for which the cathode life significantly exceeded 500 hours has been developed. To ensure the electrodes long life the process of hydrocarbon gas dissociation in the electric arc discharge is used. In this method atoms and ions of carbon from near-electrode plasma deposit on the active surface of the electrodes and form electrode carbon condensate which operates as "actual" electrode [11]. To realize aforesaid the construction of electro arc generator of air plasma has been developed and tested. Figure 93.13 gives a photo of the plasmatron.

Propane–butane mixture is supplied to the zone of the arc conjunction to the copper water-cooled electrodes (cathode and anode). Linked with the arc in series, the magnetic coils guaranty stabilization of the discharge on the electrodes. During the plasmatron operation a film of the cathode condensate is formed in accordance with the processes of propane–butane molecules dissociation and carbon atoms ionization. Arisen from ionization positive carbon ions deposit onto the cathode surface under the influence of near-cathode decline in potential and form the film of the electrode condensate. It was determined the following parameters of the films. The film consists of carbon of 96.74–98.47 mass%, hydrogen of l.24–2.26 mass%, and cuprum of 0.30–1 mass%. Interplanar spacing is 0.333, 0.207, and 0.168 nm with the intensity of the X-ray picks of 100, 1, and 5 % correspondingly. Specific electrical resistance of the electrode condensate is less than 10^{-8} Ω m. Thus the film of the cathode condensate is currently installing polycrystalline graphitic material.

On the base of the microscopy and the Raman-spectroscopy investigation, it can be concluded that the electrode condensate is composite carbonic stuff made of carbon nanoclusters which consists mainly of single and multi-walled carbon nanotubes and other carbonic forms including some quantity of the copper atoms intercalated to the carbonic matrix. The electrode condensate was examined using atomic power microscope, scanning electron microscope, and transmission electron microscope (Fig. 93.14). The basic mass of the carbon sample (about 80 %) is represented as film and band graphite particles collected to aggregates of various size and density. Width of the bands varies from 40 to 160 nm. Sometimes film and band nanoparticles are collected into stratified packages which are gathered to well-ordered nanostructures.
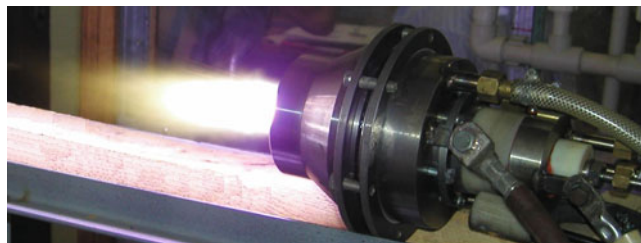
Fig. 93.13 Long life DC arc plasmatron
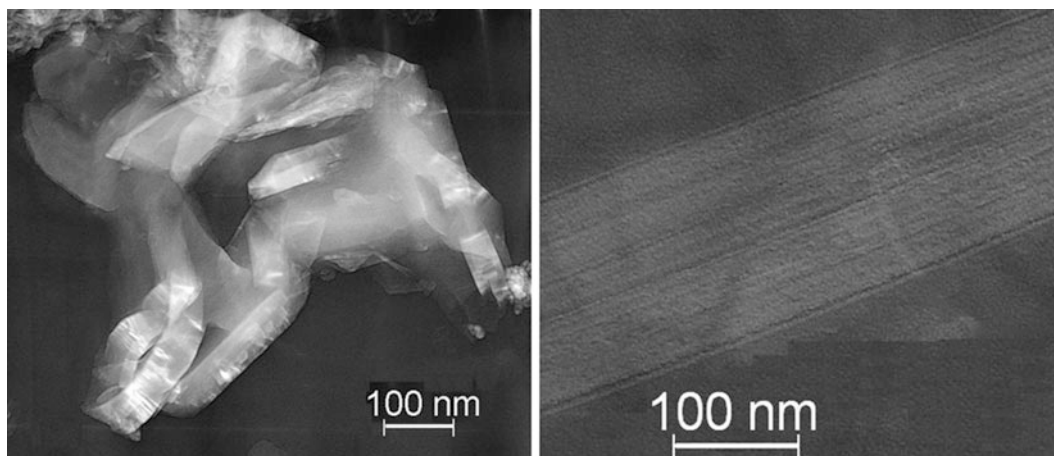
Fig. 93.14 TEM images of a sample of the electrode condensate

Created long life plasma torch was industrially tested for plasma ignition of a pulverized coal flame in Gusinoozersk thermal power plant, Russia. The tests confirmed efficiency of the plasmatron in conditions of TPP.

The Plasma Technologies Modeling

To incorporate a new technology first of all it is necessary to demonstrate its advantages in comparison with conventional technologies. Thereto mathematical modeling and numerical experiments are indispensable to life. To investigate numerically the aforenamed technologies and develop equipment for their realization the following developed and standard mathematical models and computer codes are used.

Software Code TERRA for Thermodynamic Calculations of Multicomponent Heterogeneous Systems

Software code TERRA for thermodynamic calculations of multicomponent heterogeneous systems is used to determine the conditions of thermal equilibrium of fuel and oxidant mixture at high temperatures. This software was created for high-temperature process computations and in contrast to traditional thermo chemical methods of equilibrium computation that use the Gibbs energy, equilibrium constants, and Guldberg and Vaage law of acting mass, TERRA is based on the principle of maximizing entropy for isolated thermodynamic systems in equilibrium. Fundamental lows of thermodynamics, low of conservation of mass, energy, and electric charge are methodological base of the thermodynamic computation. Code TERRA has database of thermo chemical properties for more than 3,500 chemical agents over a temperature range of 300–6,000 K. The database includes thermodynamic properties of organic and mineral components of hydrocarbon fuels. Code TERRA allows calculating products compound, SPC of plasma treated material in dependence on temperature, pressure, or any other thermodynamic parameter (Fig. 93.15).

Computer Code PLASMA-COAL for One-Dimensional Computation of the Processes in PFS or Plasma Reactor

Computer code PLASMA-COAL is designed for computation of the processes of moving, heating and kinetics of thermochemical conversion of coal-oxidant mixture in PFS or plasma reactor. In the base of this code is one-dimensional model which describes two phase (coal particles and gas-oxidizer) chemically reacting flow with an internal plasma source. The set of the ordinary differential equations includes equations for component concentrations (chemical kinetics equations) in conjunction with equations for gas and particle velocities and temperatures, respectively. The plasma source is accounted as a member of the equation of energy conservation. It is internal source of heat with empirically assigned distribution of
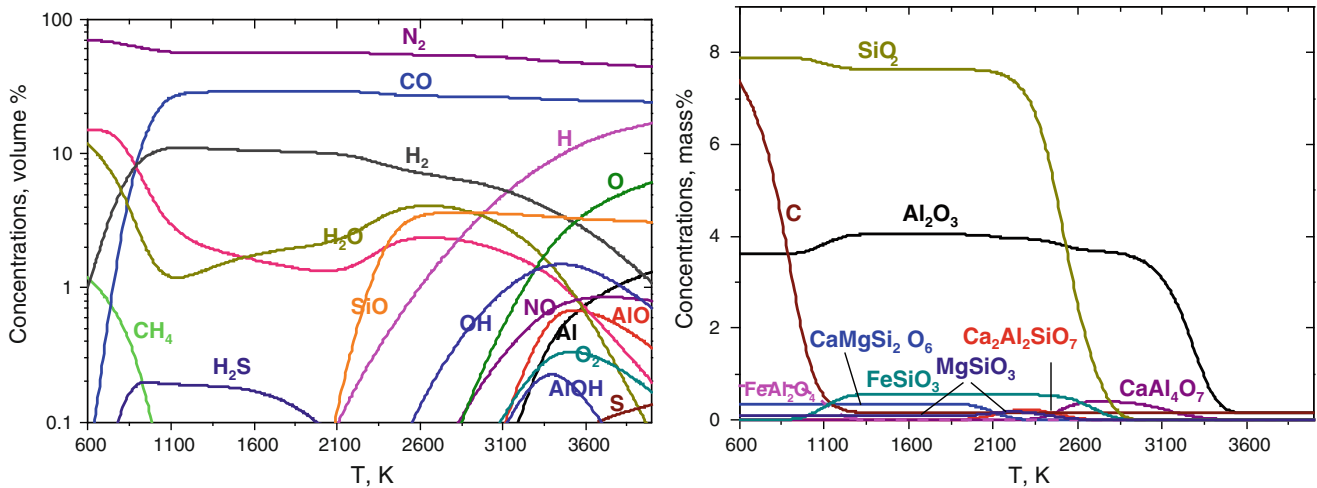
Fig. 93.15 Concentration of gas and condensed phases species dependence on temperature of coal plasma processing

Fig. 93.16 Char carbon gasification degree along a plasma-fuel system
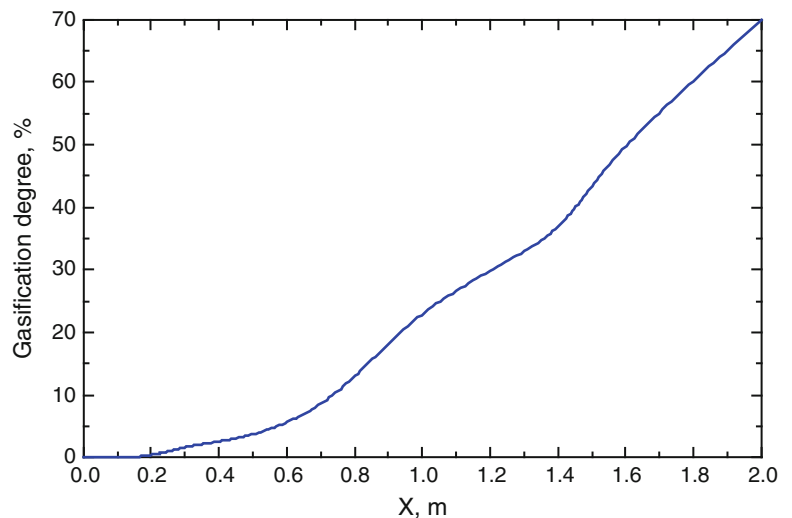
heat-evolution along the axis of chamber with plasma source. The model is also distinguished by its detailed description of the kinetics of chemical reactions of 116 reactions. The kinetic scheme includes the stages of coal volatile matter evolution, char carbon, sulfur and nitrogen gasification and conversation of evolved volatile products in the gas phase. Code PLASMA-COAL allows calculating products compound, temperature, velocities of gas and solids, gasification degree of char carbon, power of plasma source in dependence on geometrical parameters of the device for plasma-fuel processing (Fig. 93.16).

Computer Codes for Three-Dimensional Computation of the Furnaces

Computer codes FLOREAN (Institut für Wärme- und Brennstofftechnik, Braunschweig, Germany), CINAR ICE (Imperial College London, UK), and PFS-CFD the base of which is KIVA-F (Rouen University, France) are appropriated for three-dimensional computation of the furnaces of the pulverized coal fired power boilers, including the boilers equipped with PFS. These codes are based on numerical solution of the equations of energy and mass transfer taking into account chemical reactions. All three mathematical models are complicated system of nonlinear three-dimensional partial differential equations consisted of equations of continuity, gas equation, equation of two-phase medium motion, equations of heat transmission, chemical kinetics, and diffusion for components of reacting mixture with accounts of radiation and turbulent transfer by k–ε model. All these codes consider simplified kinetic model of combustion. Intermediate reactions and forming

Fig. 93.17 Temperature fields
on the level of the burners and
along a furnace in plasma
operational regime
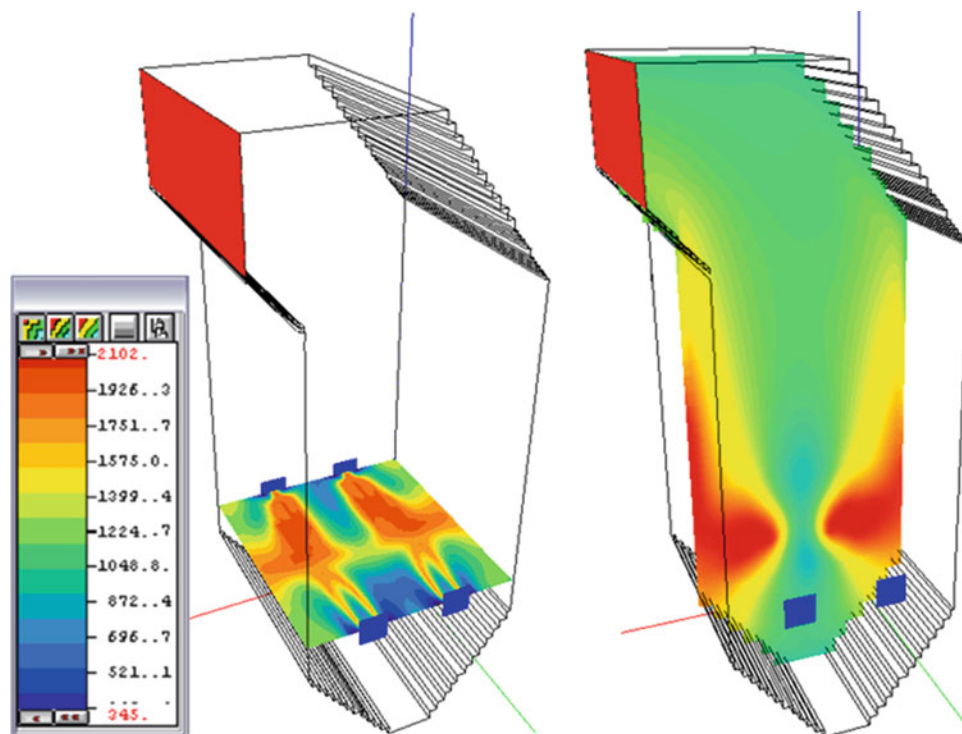
of intermediate components are not taken into account. Only coal volatile release, their oxidation to carbon oxides, and burn out of carbon are considered. Components of the velocity, fields of temperatures, pressures, concentrations of combustion products, including NO_x forming can be found using the codes (Fig. 93.17).

To simulate gas phase of two phase reactive flow codes CINAR ICE and KIVA-F use Euler approach. But to trace individual particles they use Lagrange. Code FLOREAN uses Euler approach to describe both gas phase and particles. It is supposed that velocities of particles and gas phase are equal.

All the aforesaid codes were validated comparing with experiments in laboratory and full-scale conditions. The used codes ensure competitiveness of new technologies due to decrease of expenditure onto research and experimental development and also essentially reduce the duration the last and accelerate the process of the technologies incorporation.

Conclusions

The described results of long-term studies of plasma-chemical technologies of pyrolysis, hydrogenation thermochemical preparation for combustion, gasification, and complex processing of solid fuels and cracking of hydrocarbon gases and the application of these technologies to produce desired products (hydrogen, carbon, hydrocarbon gases, synthesis gas, valuable components of the MMC, basalt melt) meets modern ecological and economic requirements of the power industry, metallurgy, and chemical industry.

Table 93.5 summarizes the results of investigation of plasma-assisted conversion of carbonaceous raw.

At complex processing of coal conversion of the mineral mass requires high temperatures (2,200–3,100 K), which leads to higher specific energy consumption up to 2–4 kW h/kg. Thus the high degree of carbon conversion (90–100 %) is achieved. Plasma-steam gasification provides a transition to the gas phase mainly organic mass of coal that does not require such high temperatures, as in the complex processing, and enables process at relatively low SPC (0.5–1.5 kW h/kg) and achieving a high degree of conversion (90–100 %). Plasma-chemical hydrogenation of coal requires high temperatures (2,800–3,200 K), which leads to high SPC for the process (6.5–8 kW h/kg), which allows achieving high conversion (70–100 %) for direct (one-step) receipt of acetylene and alkenes in the gas phase. To ensure a high degree of conversion (98–100 %) of hydrocarbon gas in the combined plasmochemical reactor there is no need in such a high temperature.

Table 93.5 The optimal range of process parameters for plasma conversion of carbonaceous raw

Fuel/plasma forming gas	T (K)	Specific power consumption (kW h/kg) of fuel	Fuel conversion degree (%)	Concentration (mg/Nm^3)	
				NO$_x$	SO$_x$
1. Plasmochemical preparation of coal for combustion (air)					
1.5–2.5	800–1,200	0.05–0.40	15–30	1–10	1–2
2. Complex processing of coal (water steam)					
1.3–2.75	2,200–3,100	2–4	90–100	1–2	1
3. Plasma gasification of coal (water steam)					
2.0–2.5	1,600–2,000	0.5–1.5	90–100	10–20	1–10
4. Plasmochemical hydrogenation of coal (hydrogen)					
10	2,800–3,200	6.5–8	70–100	0	0
5. Plasmochemical cracking of propane–butane mixture					
18 m^3/ч	1,500–2,500	2.2–3.8	98–100	0	0

That allows processing at relatively low SPC (2.2–3.8 kW h/kg). Note that all the processes of plasmochemical processing of fuels (Table 93.5) are characterized by extremely low concentrations of nitrogen oxides and sulfur emissions not exceeding 20 mg/Nm^3, which is much lower than when conventional use of fuels.

The considered computer codes have independent scientific value. They are powerful tool for investigation of modern technologies and processes of fuel and mineral processing.

References

1. Karpenko EI, Lukyachshenko VG, Messerle VE, Ustimenko AB, Yakovenko AV (2004) New technologies of fuel utilization and mineral raw processing. Combust Plasma Chem 2(2):117–145
2. Karpenko EI, Messerle VE, Ustimenko AB (2007) Plasma-aided solid fuel combustion. In: Proceedings of the combustion institute, vol 31, Part II, pp 3353–3360
3. Gorokhovski MA, Jankoski Z, Lockwood FC, Karpenko EI, Messerle VE, Ustimenko AB (2007) Enhancement of pulverized coal combustion by plasma technology. Combust Sci Technol 179(10):2065–2090
4. Messerle VE, Ustimenko AB (2007) Plasma-supported coal combustion modelling and full-scale trials. In: Syred N, Khalatov A (eds) Advanced combustion and aerothermal technologies. Springer, New York, pp 115–129
5. Messerle VE, Ustimenko AB (2007) Solid fuel plasma gasification. In: Syred N, Khalatov A (eds) Advanced combustion and aerothermal technologies. Springer, New York, pp 141–156
6. Kalinenko RA, Levitski AA, Messerle VE, Polak LS, Ustimenko AB (1993) Pulverized coal plasma gasification. Plasma Chem Plasma Process 13(1):141–167
7. Gorokhovski M, Karpenko EI, Lockwood FC, Messerle VE, Trusov BG, Ustimenko AB (2005) Plasma technologies for solid fuels: experiment and theory. J Energy Inst 78(4):157–171
8. Askarova AS, Karpenko EI, Lavrishcheva YI, Messerle VE, Ustimenko AB (2007) Plasma-supported coal combustion in boiler furnace. IEEE Trans Plasma Sci 35(6):1607–1616
9. Galvita V, Messerle VE, Ustimenko AB (2007) Hydrogen production by coal plasma gasification for fuel cell technology. Int J Hydrogen Energy 32(16):3899–3906
10. Messerle VE, Ustimenko AB (2012) Plasma ignition and combustion of solid fuel (Scientific-and-technological basics) (in Russian). Palmarium Academic Publishing, Saarbrucken, Germany, 404 p. http://ljubljuknigi.ru/ (ISBN: 978-3-8473-9845-5)
11. Golish VI, Karpenko EI, Lukyashchenko VG, Messerle VE, Ustimenko AB (2009) Nanocarbon coating of electrodes for plasma torch life prolongation. Nanotec2009.it. Nanotechnology, competitiveness and innovation for industrial growth/book of abstracts, National Research Council, Rome, Italy, 31 Mar–3 April 2009, pp 141–142

Three-Dimensional Numerical Modelling of Hydrogen, Methane, Propane and Butane Combustions in a Spherical Model Combustor

Mustafa İlbaş, Zehra Gökalp Öztürk, and Serhat Karyeyen

Abstract

In this study, combustion and emission characteristics of hydrogen, methane, propane and butane have been numerically investigated in a spherical model combustor. Predictions have been performed by using Ansys Fluent CFD code. The numerical modelling of turbulent non-premixed diffusion flames have been implemented in this combustor. Mathematical models studied in this study included the k–ε model of turbulent flow, the PDF/mixture fraction model of non-premixed combustion and P-1 radiation model. Three-dimensional modellings of the model combustor were conducted for same combustion conditions (40 kW thermal power and $\lambda = 1.0$ stoichiometric mixture ratio). According to modelling results, the maximum temperature was predicted during the hydrogen combustion as the high diffusivity, reactivity and heating value of hydrogen highly affected the flame temperature. Similarly, the minimum temperature in this model combustor was also predicted during the butane combustion. Moreover, high NO_X emissions were formed in high temperature zones because of thermal NO_X mechanism. Hence, the maximum NO_X formation was predicted for hydrogen combustion among these fuels.

Introduction

Energy is an important parameter in human life for many years and it is generally provided by fossil fuels as they comprise high energy. But, fossil fuels cause greenhouse gases formation and these gases, especially carbon dioxide, are responsible from global warming. In general, fossil fuels cannot be used directly. Its energy can be converted into heat. For this reason, combustors are necessary to convert chemical energy to heat form by combustion process. There are many kinds of combustors depending on its use and its geometry. Cylindrical combustors are the well-known combustor type and there are a lot of studies interested in cylindrical combustors in the literature.

Keramida et al. [1] investigated effects of the different radiation models on combustion modelling in natural gas-fired furnaces. Saqr et al. [2] focused on effect of free stream turbulence on NO_X and soot formation in turbulent diffusion CH_4–air flames. Yılmaz [3] modelled effect of swirl number on combustion characteristics in a natural gas diffusion flame. Khanafer and Aithal [4] performed combustion and emission profiles in swirl burners by using the finite-element commercial software FIDAP. Rangrazi et al. [5] conducted experimental study of argon dilution effects on NO_X emission in a non-premixed flame. Kamnis and Gu [6] took place numerical modelling of propane combustion in a cylindrical combustor.

M. İlbaş (✉) • S. Karyeyen
Technology Faculty, Department of Energy Systems Engineering, Gazi University, 06500 Teknikokullar, Ankara, Turkey
e-mail: ilbas@gazi.edu.tr; serhatkaryeyen@gazi.edu.tr

Z. Gökalp Öztürk
Graduate School of Natural and Applied Science, Gazi University, 06500 Teknikokullar, Ankara, Turkey
e-mail: zgokalp5263@hotmail.com

Yılmaz et al. [7] reported effect of turbulence and radiation models on combustion characteristics in propane–hydrogen diffusion flames. In an other study related with propane combustion, Large Eddy Simulation (LES) has been used to predict temperature of species concentrations by Paul et al. [8] in a cylindrical combustor. Ilbas et al. [9] numerically investigated combustion and NO_X emission characteristics of pure hydrogen and hydrogen–hydrocarbon composite fuel in a cylindrical combustor. Similarly, Tomczak et al. [10] used hydrogen–methane mixture in a gas turbine combustion system. Tabet et al. [11] conducted hydrogen–hydrocarbon turbulent non-premixed diffusion flame. Ziani et al. [12] modelled non-premixed turbulent combustion of CH_4–H_2 mixtures using the PDF approach. Combustion of hydrogen–methane-mixtured fuels was performed by Yılmaz and Ilbas [13]. Öztürk [14] modelled hydrogen combustion in a spherical combustor. Qi et al. [15] studied combustion of premixed butane–air laminar flame jet and they observed the combustion with Mach–Zehnder Interferometry.

Although there are many studies related to fuel combustions in cylindrical combustors, combustion modelling in a spherical combustor has not been performed. Because of this reason, in the present study, 3D numerical modellings of hydrogen, methane, propane and butane combustions were numerically investigated in a spherical model combustor. Many numerical modelling results will be produced with this study and these results will make important contributions to researches in combustion of different gases in different combustors.

CFD Modelling

Description of the Spherical Model Combustor

For three-dimensional CFD modelling, a spherical model combustor was developed and physical domain of this combustor is shown in Fig. 94.1. Dimensions of the combustor are: fuel inlet diameter of 10 mm, air inlet diameter of 200 mm with wall thickness of 4 mm, combustor outlet of 200 mm and combustor diameter of 600 mm. Lengths of the inlet–outlet are also equal to 50 mm. All boundary conditions are fixed at 293 K and 1 atm. The generated 3D grid for the modelling of the combustor is also shown in Fig. 94.1.
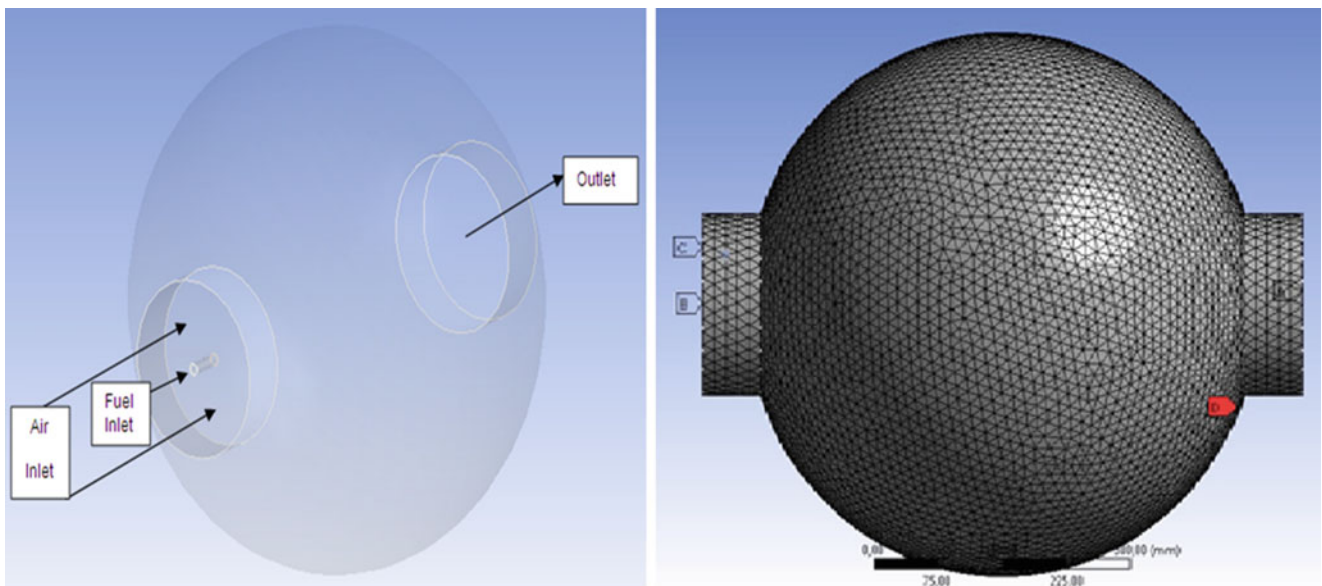
Fig. 94.1 The developed spherical model combustor and mesh structure

Mathematical and Combustion Model

The time-averaged gas phase equation for steady turbulent flow can be written as [16]:

$$\frac{\partial}{\partial x_j}(\rho u_i \Phi) = -\frac{\partial}{\partial x_i}\left(\Gamma_\Phi \frac{\partial \Phi}{\partial x_i}\right) + S_\Phi \tag{94.1}$$

where Φ is the dependent variable that can symbolize the velocity u_i. Γ_Φ is the transport coefficient of variable Φ and S_Φ is the source term of the transport equation for Φ.

This study was modelled by using the mixture fraction/PDF combustion models. This combustion model comprises the solution of transport equations for a single conserved scalar (the mixture fraction). Transport equations for individual species are not solved in this model. Individual component concentrations for species of interest are derived from the predicted mixture fraction distribution. The interaction of turbulence and chemistry is accounted for with the help of a probability density function (PDF) [17].

The PDF combustion model was specifically developed for the modelling of turbulent diffusion flames. For a fuel/oxidant system, the mixture fraction, f can be expressed in terms of the local fuel mass fraction as

$$f = \frac{m_F}{m_F + m_O} \tag{94.2}$$

where m_F and m_O are mass fractions of fuel and oxidant.

The mixture fraction, f is a conserved quantity whose value at each point in the flow domain is computed by the solution of the following conservation equation for the time-averaged value of f in the turbulent flow field [17].

$$\frac{\partial(\rho \overline{f})}{\partial t} + \frac{\partial(\rho u_i \overline{f})}{\partial x_i} = \frac{\partial}{\partial t}\left(\frac{\mu_t}{\sigma_t}\frac{\partial \overline{f}}{\partial x_i}\right) + S_m \tag{94.3}$$

where S_m is the source term.

In addition to solving the mean mixture fraction, a conservation equation is solved for the mixture fraction variance, $\overline{f'^2}$ which is used in the closure model describing turbulence–chemistry interactions [17]:

$$\frac{\partial\left(\rho \overline{f'^2}\right)}{\partial t} + \frac{\partial\left(\rho u_i \overline{f'^2}\right)}{\partial x_i} = \frac{\partial}{\partial x_i}\left(\frac{\mu_t}{\sigma_t}\frac{\partial \overline{f'^2}}{\partial x_i}\right) + C_g \mu_t \left(\frac{\partial \overline{f'^2}}{\partial x_i}\right)^2 - C_d \rho \frac{\varepsilon}{k}\overline{f'^2} \tag{94.4}$$

where σ_t, C_g and C_d are constants used in the mixture fraction/PDF model.

The radiation heat transfer occurs at high temperature levels. The gas flame temperature is generally high (1,000–1,600 °C) in combustors. Hence, the heat transfer from combustors is significant. Thus, it is essential to include the radiation model for a more accurate prediction of the temperature profile in combustors [17].

NO$_X$ Formation

Generally, NO accounts more than 95 % of the total NO$_X$ formation in most combustion processes. Because of that, it is sufficient to examine the formation of NO. In gas mixture combustion, NO formation can be attributed to three chemical kinetic processes which are thermal, prompt and fuel NO$_X$. Thermal NO$_X$ is formed by the oxidation of atmospheric nitrogen at high temperature [9]. Prompt NO$_X$ is formed by the reactions of intermediate species at the flame front. The fuel NO$_X$ mechanism defines the oxidation of the nitrogen bound in the fuel molecules [17].

Well-known Zeldovich [18] reaction determines the thermal NO:

$$O + N_2 \rightarrow N + NO \tag{94.5}$$

Table 94.1 The basic properties of the fuels [22]

	Symbol	LHV (MJ/kg)	Density (kg/m^3)	Stoichiometric air–fuel ratio
Butane	C_4H_{10}	45.37	2.5000	15.47
Propane	C_3H_8	46.34	1.8800	15.70
Methane	CH_4	50.00	0.6715	17.00
Hydrogen	H_2	120.00	0.0844	34.10

$$N + O_2 \rightarrow O + NO \tag{94.6}$$

$$N + OH \rightarrow H + NO \tag{94.7}$$

The mass transport equation is solved for the NO calculation, taking in account convection, diffusion, production and consumption of NO and related chemical species. The overall thermal NO formation rate can be calculated as [19]

$$\frac{d[NO]_T}{dt} = \frac{2[O]\left\{k_1 k_2 [O_2][N_2] - k_{-1}k_{-2}[NO]^2\right\}}{k_2[O_2] + k_{-1}[NO]} \tag{94.8}$$

The prompt NO_X formation mechanism was firstly notified by Fenimore [20]. The prompt NO_X formation is significant in most hydrocarbon fuel combustion conditions especially, low temperatures, short residence times and fuel-rich conditions. Actually, the actual prompt NO_X formation route is more complex and embodies many intermediate reactions and species. The prompt NO_X route is generally accepted as

$$CH + N_2 \rightarrow HCN + N \tag{94.9}$$

$$N + O_2 \rightarrow NO + O \tag{94.10}$$

$$HCN + OH \rightarrow CN + H_2O \tag{94.11}$$

$$CN + O_2 \rightarrow NO + CO \tag{94.12}$$
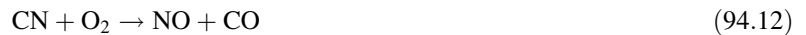
Formation rate of the prompt NO is calculated by using the De Soete [21] global model as

$$\frac{d[NO]_{pr}}{dt} = fxAx \left(\frac{RT}{P}\right)^2 [Fuel][O_2]^b [N_2] x \exp\left(\frac{E_a}{RT}\right) \tag{94.13}$$

The thermal and prompt NO_X formations are calculated by using Eqs. (94.8) and (94.13).

$$S_{NO} = M_{NO} \frac{d[NO]}{dt} \tag{94.14}$$

Basic Properties of the Fuels

In order to be modelled fuels in this combustor, the basic properties of these fuels should be known. The basic properties of butane, propane, methane and hydrogen consumed in this study are given in Table 94.1.

Results and Discussions

Model Validation

In order to validate the numerical model, the predicted axial temperature profiles for methane combustion were compared to measurements reported by Saqr et al. [2] (Fig. 94.2). This comparison is clearly seen in Fig. 94.2. Although the predicted results are in good agreement with measurements, there is a slight difference between our predictions and measurements reported by Saqr et al. This slight difference is because of the use of spherical combustor and different thermal power in predictions. However, it is mostly revealed that the predicted axial temperature profiles are in good qualitative agreement with predictions and measurements.

Temperature and NO$_X$ Distributions

In this part of the present study, hydrogen, methane, butane and propane combustions in a spherical model combustor are shown and commented. Initially, the predicted temperature distributions on y-z plane are given in Fig. 94.3a–d. According to Fig. 94.3, the predicted maximum temperature level was about 2,160 K for hydrogen combustion. Subsequent predicted maximum temperature levels were about 1,930 K for methane combustion, 1,850 K for butane combustion and 1,880 K for propane combustion. But, when it is looked at carefully, from Fig. 94.3c, d, it is clearly seen that the predicted temperature distributions are much the same in both cases. As it is seen in Table 94.1, this situation can be explained by similar heating values for butane and propane. Temperature levels for all predictions are increasing from the inlet zone towards the combustor exit. In fact, temperature levels are generally decreasing towards the combustor exit considerably in cylindrical combustors [9]. This case is expected to take place in the cylindrical and longer combustors.

Figure 94.3a shows pure hydrogen combustion. Similarly, Yilmaz and Ilbas [13] investigated hydrogen–methane-mixtured fuel combustion in a cylindrical combustor. According to this study, the maximum temperature level was determined as about 1,700 K during M30H70 fuel combustion. There is a minor difference between study of Yilmaz and Ilbas and the present studies. But, experimental and the predicted temperature levels are in good agreement. One of the reasons for some differences is different fuel gas fraction, and the basic reason is the use of different combustors (cylindrical and spherical).
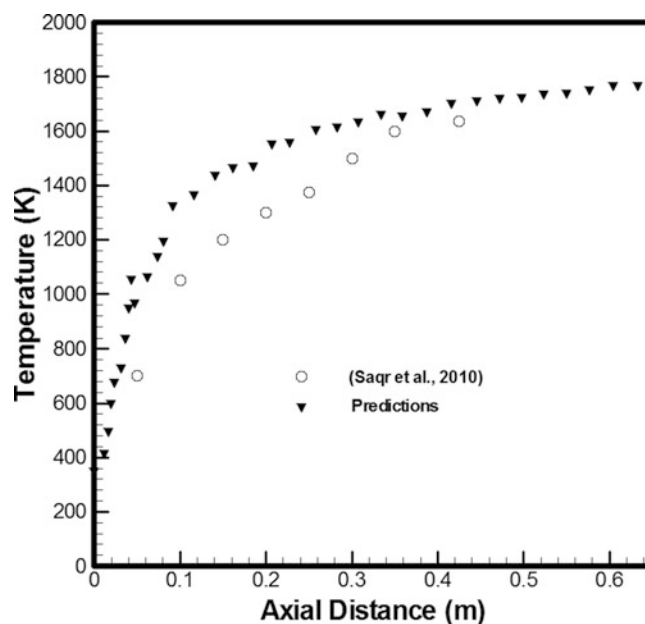
Fig. 94.2 Comparison of predicted and measured axial temperature profiles for methane combustion
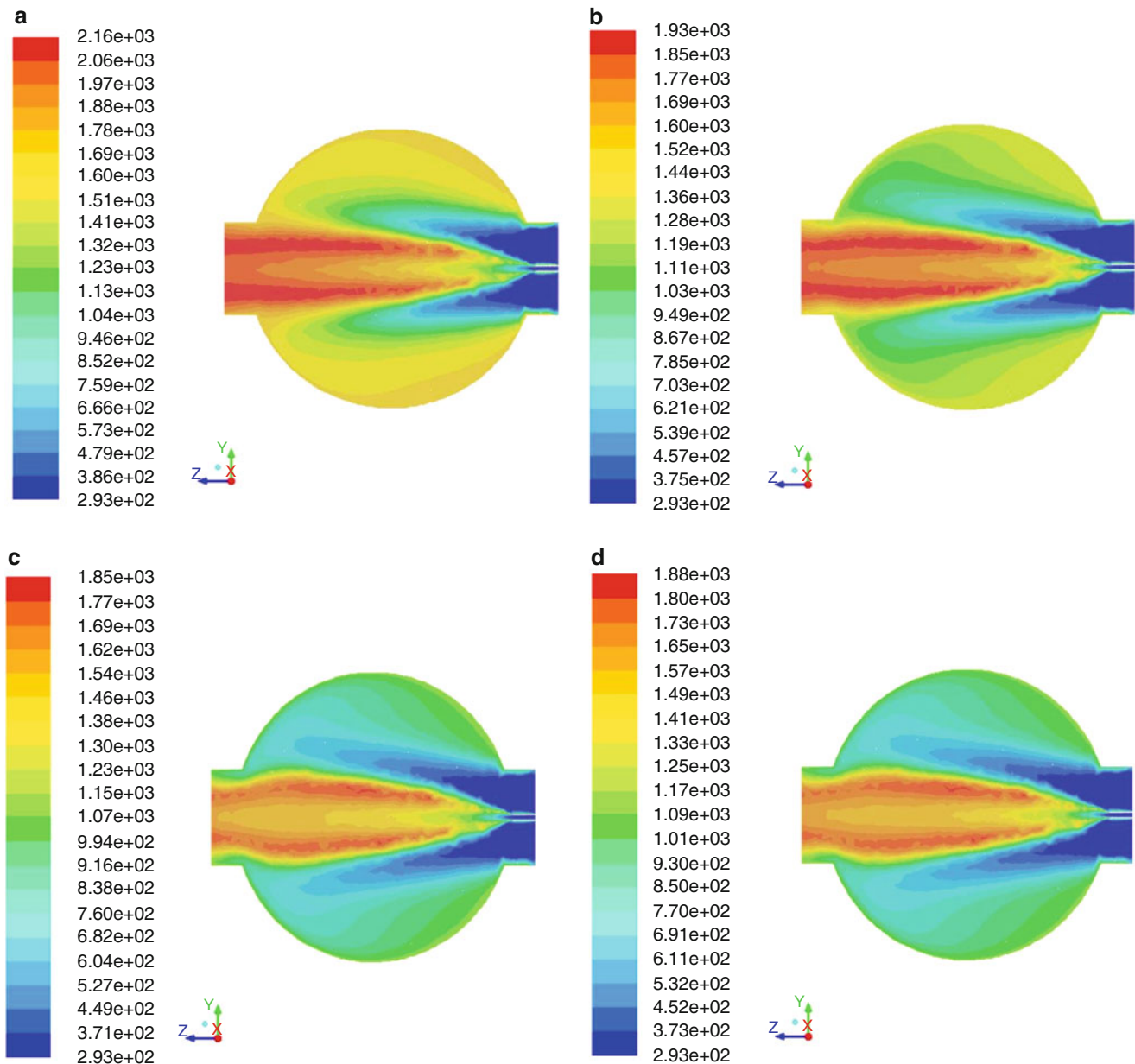
Fig. 94.3 (**a**) Temperature distributions for hydrogen combustion. (**b**) Temperature distributions for methane combustion. (**c**) Temperature distributions for butane combustion. (**d**) Temperature distributions for propane combustion

Methane combustion results are presented in Fig. 94.3b. In a study carried out in the literature, Keramida et al. [1] predicted methane combustion in a cylindrical combustor and the maximum temperature level was predicted as about 1,600 K. When our prediction compared with Keramida's study, it is seen that there is also small difference. There are two reasons for this case. Thermal powers and combustors used in those studies were different. The combustion models carried out in these studies were also different. Combustion performance was predicted by using eddy-dissipation combustion model by Keramida et al., while predictions are performed by using the mixture fraction/PDF combustion model in the present work.

The predicted temperature distributions for butane and propane combustion are illustrated in Fig. 94.3c, d. In Fig. 94.3d, temperature distribution for propane is shown, and Paul et al. [8] predicted the propane combustion by using LES method in a cylindrical combustor. According to this study, the maximum temperature value was predicted as almost 1,900 K and these results and present work results for propane combustion are very similar.

Axial temperature profiles for all fuels are shown in Fig. 94.4. As it is clearly seen in Fig. 94.4, the maximum and minimum temperature profiles are emerged during hydrogen and butane combustions throughout the combustor, respectively. As it is seen in Table 94.1, the case can be explained by different heating values.
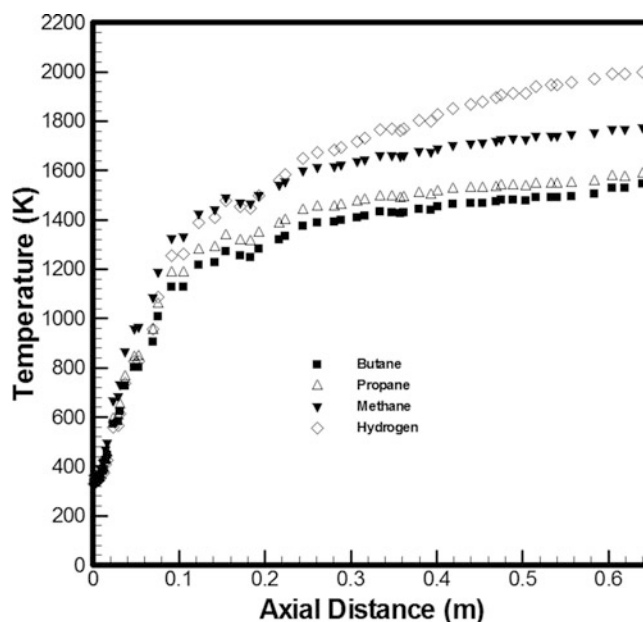
Fig. 94.4 Axial temperature profiles for all fuel combustions

In combustion modellings, temperature distributions may be shown on different planes. By this way, combustion characteristics are described in more detailed throughout the combustor. Hence, temperature distributions on x-y plane for all modellings are given in Fig. 94.5.

As it is seen in Fig. 94.5, the overall predicted flame temperature increases towards the combustor exit. In addition, the predicted wall temperature was about 1,800 K for hydrogen combustion in Fig. 94.5a. Hydrogen has the lower density in comparison with other fuels and air. Because of that, hydrogen may diffuse more effective into the spherical combustor. Moreover, it includes the highest heating value among these fuels.

NO_X distributions for hydrogen, methane, butane and propane combustions are shown in Fig. 94.6. As it is seen in Fig. 94.6, NO_X formation increases as the temperature level increases. Because, thermal NO_X formation contributes to the total NO_X formation considerably in high temperature zones. Moreover, the NO_X formation increases from the combustor inlet to the combustor exit. The maximum NO_X formation was about 1,450 ppm for hydrogen combustion. The maximum NO_X formations for the other fuels were almost 130 ppm for methane combustion, almost 60 ppm for buthane combustion and almost 90 ppm for propane combustion in combustor. In addition, Rangrazi et al. [5] obtained similar results with regard to NO_X formation at the stoichiometric condition.

Conclusions

In this study, three-dimensional CFD analyses of combustion and emission characteristics of hydrogen, methane, butane and propane were performed in a spherical combustor. Some conclusions obtained in this study are given below:

• When CFD modelling results are compared with results in the literature, it is concluded that results are in good agreement in trends and values.
• The maximum NO_X formation for hydrogen combustion and the minimum NO_X formation for butane combustion are predicted as expected.
• Although the excess NO_X formation happens during the hydrogen combustion, among the other fuels the best combustion performance is predicted for hydrogen combustion. This may be because of hydrogen containing higher heating value in proportion to the other fuels.
• As the density of air is almost 15 times higher than the density of hydrogen, the hydrogen can be a preferable fuel in the spherical combustor.
• It is revealed that the spherical combustor can be an alternative to the cylindrical combustor for hydrogen combustion.
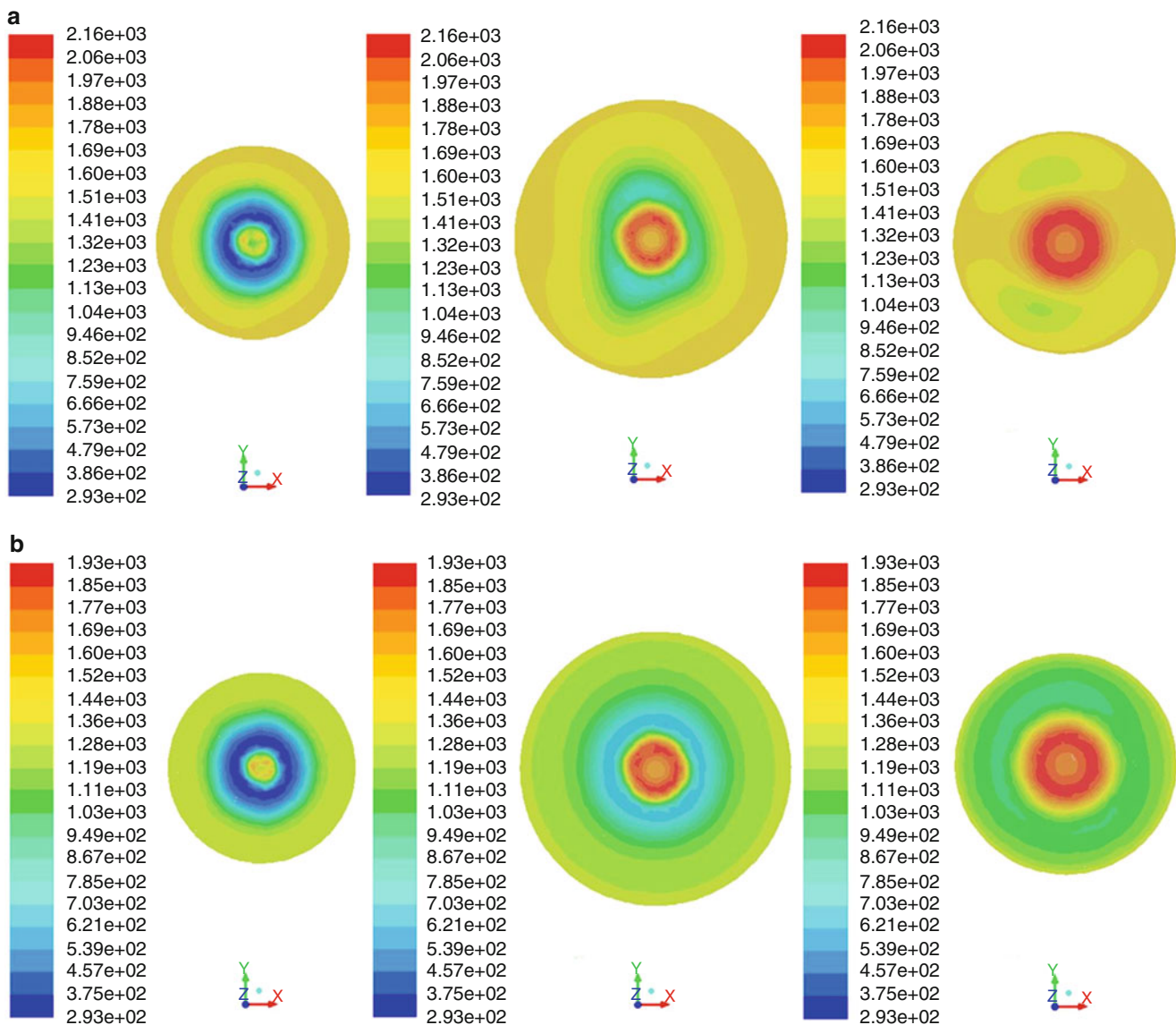
Fig. 94.5 (**a**) Temperature distributions for hydrogen combustion on x-y plane at z = 0.1 m, z = 0.3 m and z = 0.5 m (*left* to *right*). (**b**) Temperature distributions for methane combustion on x-y plane at z = 0.1 m, z = 0.3 m and z = 0.5 m (*left* to *right*). (**c**) Temperature distributions for butane combustion on x-y plane at z = 0.1 m, z = 0.3 m and z = 0.5 m (*left* to *right*). (**d**) Temperature distributions for propane combustion on x-y plane at z = 0.1 m, z = 0.3 m and z = 0.5 m (*left* to *right*)

References

1. Keramida EP, Liakos HH, Founti MA, Boudouvis AG, Markatos NC (2000) Radiative heat transfer in natural gas-fired furnaces. Int J Heat Mass Transf 43:1801–1809
2. Saqr KM, Aly HS, Sies MM, Wahid MA (2010) Effect of free stream turbulence on NO$_X$ and soot formation in turbulent diffusion CH$_4$–air flames. Int Commun Heat Mass Transf 37:611–617
3. Yılmaz İ (2013) Effect of swirl number on combustion characteristics in a natural gas diffusion flame. J Energy Resour Technol 135:042204-1
4. Khanafer K, Aithal SM (2011) Fluid-dynamic and NO$_X$ computation in swirl burners. Int J Heat Mass Transf 54:5030–5038
5. Rangrazi A, Niazmand H, Heravi HM (2013) Experimental study of argon dilution effects on NO$_X$ emission in a non-premixed flame in comparison with nitrogen. Korean J Chem Eng 30(8):1588–1593
6. Kamnis S, Gu S (2006) Numerical modelling of propane combustion in a high velocity oxygen-fuel thermal spray gun. Chem Eng Process 45:246–253
7. Yılmaz İ, Taştan M, İlbaş M, Tarhan C (2013) Effect of turbulence and radiation models on combustion characteristics in propane–hydrogen diffusion flames. Energy Convers Manage 72:179–186

c

d
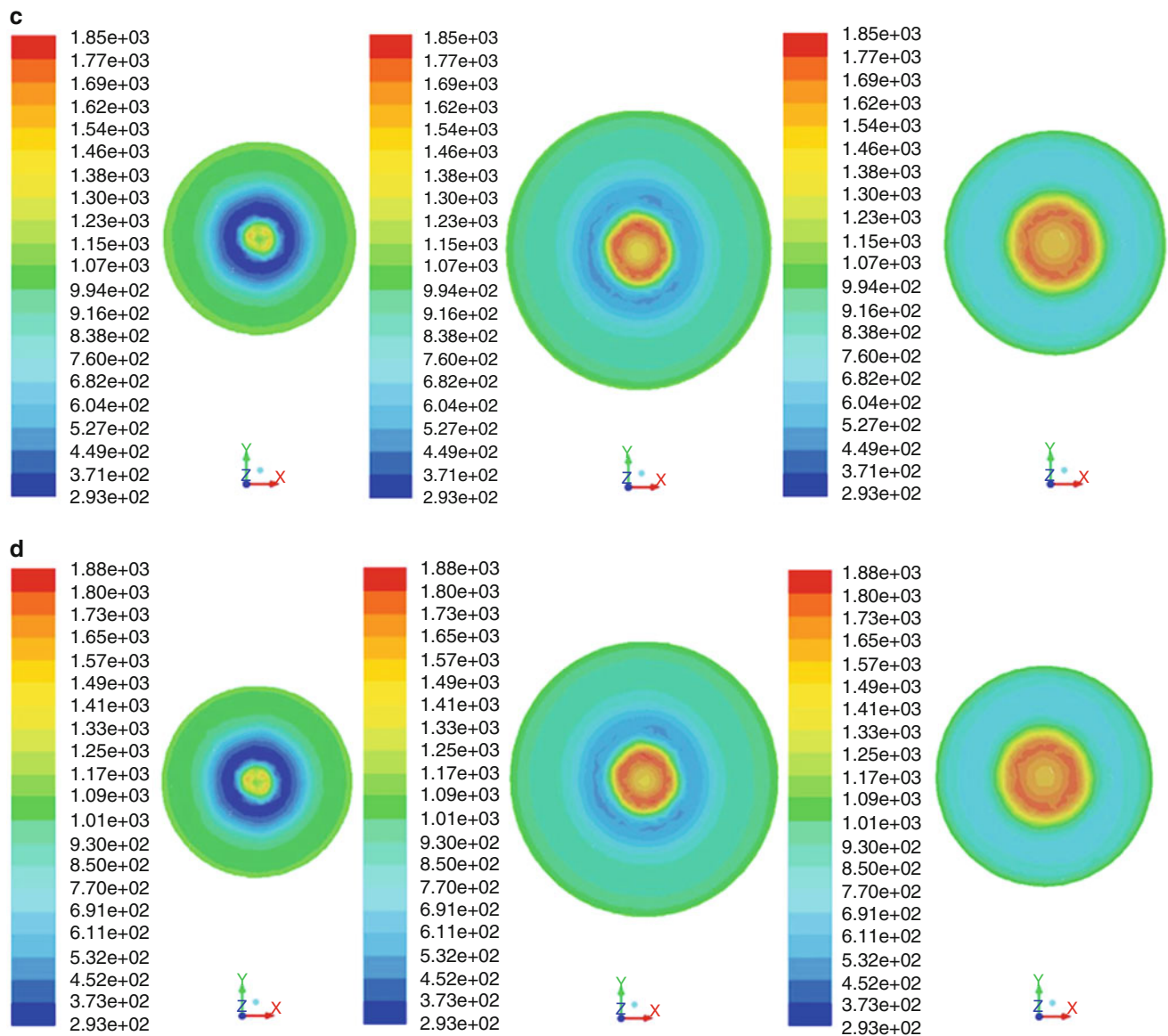
Fig. 94.5 (continued)

8. Paul SC, Paul MC, Jones WP (2010) Large eddy simulation of a turbulent non-premixed propane–air reacting flame in a cylindrical combustor. Comput Fluids 39:1832–1847

9. Ilbas M, Yılmaz İ, Kaplan Y (2005) Investigations of hydrogen and hydrogen-hydrocarbon composite fuel combustion and NO_X emission characteristics in a model combustor. Int J Hydrogen Energy 30:1139–1147

10. Tomczak HJ, Benelli G, Carrai L, Cecchini D (2002) Investigations of a gas turbine combustion system fired with mixtures of natural gas and hydrogen. IFRF Combust J Article Number 200207

11. Tabet F, Sarh B, Gökalp I (2009) Hydrogen-hydrocarbon turbulent non-premixed flame structure. Int J Hydrogen Energy 34:5040–5047

12. Ziani L, Chaker A, Chetehouna K, Malek A, Mahmah B (2013) Numerical simulations of non-premixed turbulent combustion of CH_4–H_2 mixtures using the PDF approach. Int J Hydrogen Energy 38:8597–8603

13. Yılmaz I, Ilbas M (2008) An experimental study on hydrogen–methane mixtured fuels. Int Commun Heat Mass Transf 35:178–187

14. Gökalp Öztürk Z (2013) Küresel bir yakıcıda hidrojen yanmasının hesaplamalı akışkanlar dinamiği (HAD) kullanılarak modellenmesi (in Turkish). MSc thesis. Gazi University, Institute of Science and Technology

15. Qi JA, Wong WO, Leung CW, Yuen DW (2008) Temperature field measurement of a premixed butane/air slot laminar flame jet with Mach–Zehnder interferometry. Appl Therm Eng 28:1806–1812

16. Ghenai C (2010) Combustion of syngas fuel in gas turbine can combustor. Adv Mech Eng 2010:1–13, Article ID: 342357
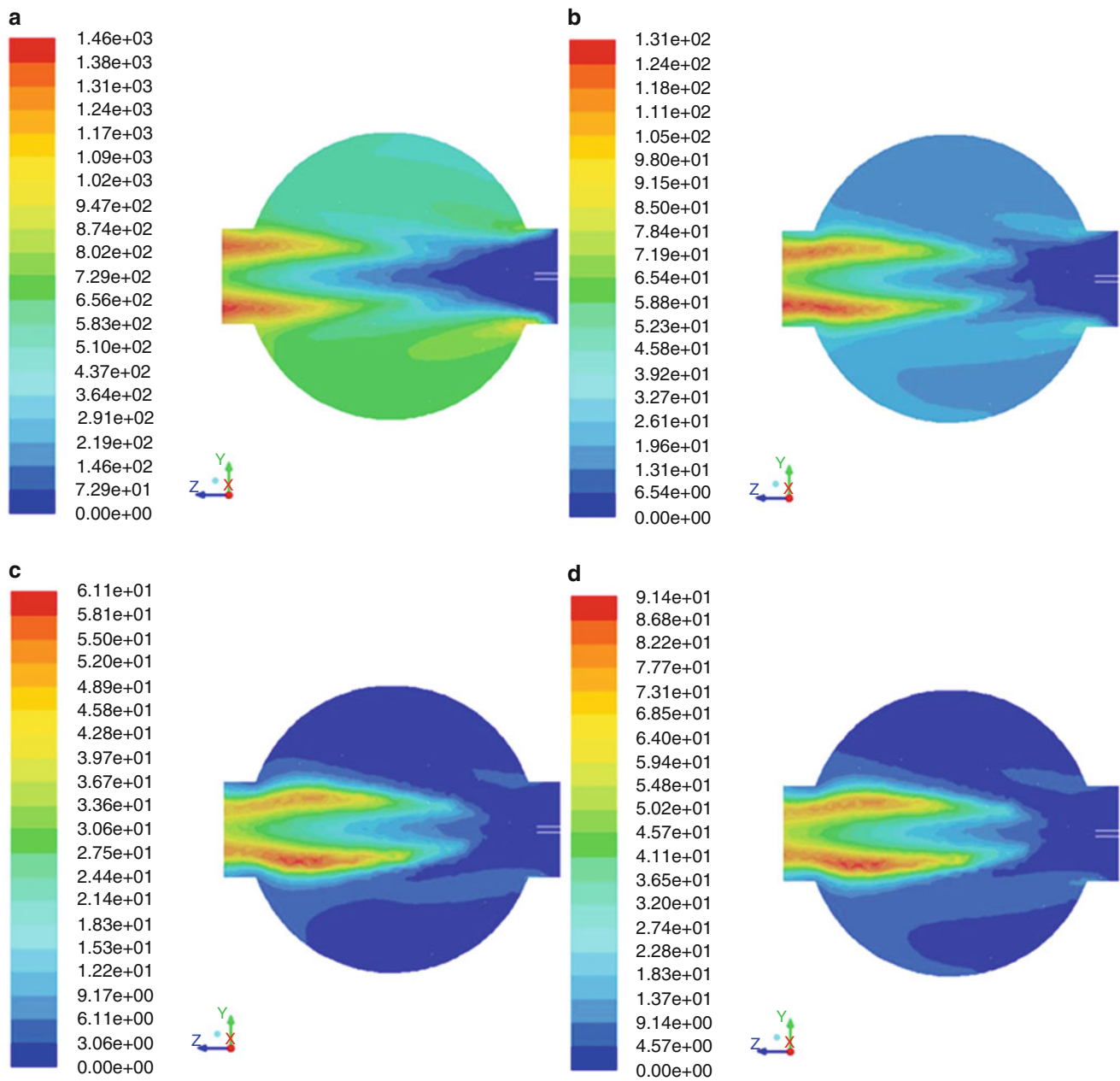
Fig. 94.6 (**a**) NO$_X$ distributions for hydrogen combustion. (**b**) NO$_X$ distributions for methane combustion. (**c**) NO$_X$ distributions for butane combustion. (**d**) NO$_X$ distributions for propane combustion

17. Ilbas M (1997) Studies of ultra low NO$_X$ burner. PhD thesis. University of Wales, College of Cardiff, UK
18. Zeldovich YAB (1947) Oxidation of nitrogen in combustion. USSR Institute of Chemical Physics: Academy of Science
19. Fluent Incorporated (2011) Fluent 13.0, User's Guide
20. Fenimore CP (1971) 13th symposium (international) on combustion, The Combustion Institute, Pittsburg, PA, USA
21. De Soete GG (1971) Overall reaction rates of NO and N$_2$ formation from fuel nitrogen. In: 15th symposium (international) on combustion, The Combustion Institute, Pittsburg, PA, USA, p 1093
22. Çengel YA, Boles MA (2002) Thermodynamics: an engineering approach, 4th edn. McGraw-Hill, New York. ISBN 007-238332-1

Development of a Reduced Mechanism for *n*-Heptane Fuel in HCCI Engines

Keyvan Bahlouli, R. Khoshbakhti Saray, and Ugur Atikol

Abstract

Due to the lack of direct control of combustion timing in the homogeneous charge compression ignition engines, the chemistry of the in-cylinder charge is responsible for the ignition. Thus, obtaining knowledge about fuel chemistry has a significant importance in engine design and optimization. Large numbers of detailed chemical kinetics mechanisms have been suggested to predict various fuels oxidation. However, employing comprehensive chemical kinetics mechanisms in predictive models results in the high demand for simulation time which makes the use of these mechanisms questionable. Consequently, reduced mechanisms of smaller sizes are needed. The objective of this study is to produce reduced mechanism of *n*-heptane fuel, to be applicable for CFD simulation, by utilizing a two-stage reduction process. This work is performed by using a validated single zone combustion model. To remove unimportant species at the first stage, the directed relation graph with error propagation (DRGEP) is applied. In the second stage, the principal component analysis (PCA) method is used to eliminate insignificant reactions and species. Peak pressure, maximum heat release, and CA50 have been selected as representative parameters for the performance of engine. For the generated reduced mechanism at each reduction step, these parameters would be calculated, and the deviations from the corresponding value obtained by applying detailed mechanism to the model will be evaluated until user-specified error tolerances violate. This combination of two methods successfully reduced the detailed Golovichev's *n*-heptane mechanism (57 species and 290 reactions) to a reduced mechanism with size of 40 species and 95 reactions, while maintaining small errors (less than 1 present) compared to the detailed mechanism.

Keywords

HCCI combustion • Reduced mechanism • DRGEP • PCA

Introduction

Reduction of transportation emissions and fuel consumption are important reasons motivating the development of alternative energy technologies for the IC engines. Homogeneous charge compression ignition (HCCI) combustion engine is a potential candidate for higher thermal efficiency and lower emissions [1–3]. However, lack of direct control for combustion timing is one of the main challenges associated with HCCI combustion engine application.

K. Bahlouli (✉) • U. Atikol
Mechanical Engineering Department, Faculty of Engineering, Eastern Mediterranean University,
North Cyprus, Via Mersin 10, Famagusta, Turkey
e-mail: Keyvan.bahlouli@emu.edu.tr; ugur.atikol@emu.edu.tr

R.K. Saray
Faculty of Mechanical Engineering, Sahand University of Technology, Tabriz, Iran
e-mail: khoshbakhti@sut.ac.ir

Accurate fuel oxidation chemistry models offer great potential for HCCI engine design and optimization. The Golovichev's mechanism [4], including 57 chemical species and 290 reactions, and more comprehensive mechanism of Curran with 560 species and 2,539 reactions [5], as examples, were introduced for *n*-heptane combustion.

However, for developing predictive combustion models, incorporating detailed chemistry into computational fluid dynamics (CFD) calculations is commonly known as essential. A large system of nonlinear stiff ordinary differential equations (ODE) is produced by using detailed chemical kinetics mechanism. The numerical solution of the large number of such systems within the CFD framework results in exceedingly long CPU times. Consequently, with most of the comprehensive kinetic mechanisms developed for hydrocarbon fuels, large-scale three-dimensional reactive flow simulations become computationally unaffordable [6]. Consequently, further reduction of the size of detailed mechanism, keeping its essential feature, is desired.

There are two main classes of reduction procedure for detailed chemical kinetic mechanisms, namely time scale analysis and skeletal reduction. Both approaches target identifying and eliminating the unnecessary species and reactions and aim at producing computationally efficient reduced mechanisms that are still able to reproduce the main features of their corresponding detailed mechanisms over the conditions of interest. Examples of time scale analysis include computational singular perturbation (CSP) [7] and intrinsic low-dimensional manifolds (ILDM) [8] methods whereas skeletal reduction contains sensitivity analysis [9], principal component analysis (PCA) [10], optimization-based techniques [11, 12], element flux-based method [13], directed relation graph (DRG) [14], and also DRG with error propagation (DRGEP) [15]. Furthermore, dynamic methods like the works of He et al. [16] and Liang et al. [6, 17] update the reduced mechanism dynamically at each time step, based on the local conditions and develop locally accurate mechanism. However, as mentioned in [16], the discontinuity in species conversion rate, when mechanisms switch during the simulation in the fly scheme, may cause species composition oscillation and the possibility of ODE solver failure. Multistage reduction schemes which are the integration of two or more reduction methods could be employed for increasing the extent of reduction such as DRGASA [18], DRGEP-PCA [19], and DRGEP-CSP-DRGEP [20]. The present work utilizes the integration of DRGEP and PCA methods. The procedure used in this work for generating the reduced mechanism is almost similar to the previous paper of the author [20] except for using PCA instead of CSP.

In this study a reduced mechanism of *n*-heptane, which is applicable for CFD simulation, is produced by utilizing two-stage reduction processes. To remove unimportant species, at the first stage, the DRG with error propagation (DRGEP) is applied. In the second stage, the PCA method is used to eliminate insignificant reactions. At each reduction step, the performance of the reduced mechanism is compared with the original one to guarantee that the generated mechanism does not exceed user-specified error tolerances.

Directed Relation Graph with Error Propagation

The DRGEP method suggests that the effect of the error established by altering the concentration of a species or by eliminating the species entirely is damped as it propagates along the graph to reach the target species, a set of species deemed of interest to the investigator. Generally speaking, the species do not have equal importance, and the species directly linked to the target is of relatively high importance than those that are farther from the targets. In order to take into account this error propagation process, a geometric damping has been introduced by Pepiot and Pitsch [15, 21] in the selection procedure as follows:

$$r_{AB,P} = \prod_{i=1}^{m-1} r_{s_i s_{i+1}} \tag{95.1}$$

$$R_{AB} = \max_{\text{All paths } P} \left[r_{AB,P} \right] \tag{95.2}$$

A new definition of the direct interaction coefficient is introduced by Pepiot and Pitsch [15] which is motivated by the shortcomings of earlier formulations, namely

$$r_{AB} = \frac{\left| \sum_{j=1}^{n} v_{A,j} \omega_j \delta_{Bj} \right|}{\max(P_A, C_A)} \tag{95.3}$$

Here

$$\delta_{Bj} = \begin{cases} 1 & \text{if the } j\text{th elementary reaction involve species B,} \\ 0 & \text{otherwise} \end{cases}$$

$$P_A = \sum_{j=1}^{n} \max\left(0, v_{A,j}\omega_j\right) \tag{95.4}$$

$$C_A = \sum_{j=1}^{n} \max\left(0, -v_{A,j}\omega_j\right) \tag{95.5}$$

Principal Component Analysis Method

In the simulation of a combustion process a set of ODE is used,

$$\frac{dc}{dt} = f(k, c) \tag{95.6}$$

Here c(t) is the concentration of any species and k is the kinetic parameter. Any change in the kinetic parameters at time t_1, where $k = k^\circ$ and $c = c^\circ$, results in a change in the solution at time t_2, where $t_1 < t_2$. Regarding this fact, Turányi et al. [10] introduced a reaction rate sensitivity gradient, which is the derivative of the deviation in the concentration of the species with respect to the rate constant as follows:

$$\widetilde{F}(k^o, c^o, t_2)_{ij} = \frac{\partial f_i(t_2)}{\partial k_j} \tag{95.7}$$

Non-dimensional sensitivity matrix Eq. (95.7) can be written as

$$\widetilde{F}(k^o, c^o, t_2)_{ij} = \frac{k_j^o}{f_1(t_2)} \frac{\partial f_i(t_2)}{\partial k_j} \tag{95.8}$$

Since f_i is given by

$$f_i(k, c) = \sum_{j=1}^{n} v_{ij}R_j = \sum_{j=1}^{n} v_{ij}k_j r_j(c) \tag{95.9}$$

The elements of the log-normalized sensitivity matrix $\widetilde{F}$ can be written as

$$\widetilde{F}_{ij} = \frac{k_j}{f_i(k, c)} \frac{\partial f_i(k, c)}{\partial f_j} = \frac{v_{ij}R_j(k, c)}{\sum_{j=1}^{n} v_{ij}R_j(k, c)} = \frac{v_{ij}R_j}{f_j} \tag{95.10}$$

in which $\widetilde{F}$ is considered as a ratio of the rate of formation or consumption of species *i* in reaction *j* and the net rate of the concentration change of species *i*. If the magnitude of $\widetilde{F}$ is equal to zero it means that species *i* does not exist in reaction *j*. As mentioned by Vajda et al. [22] the kinetic information inherent in the matrix $\widetilde{F}$ is extracted by PCA. The response function, which is the basic concept in the PCA, is reformulated for reaction rate consideration as follows:

$$Q(\alpha, c) = \sum_{j=1}^{n} \left[\frac{f_j(\alpha, c) - f_j(\alpha^\circ, c)}{f_j(\alpha^\circ, c)} \right]^2 \tag{95.11}$$

$Q(\alpha, c)$ is a measure of deviation in a reaction rate caused by a parameter perturbation, $\alpha_j = \ln k_j$ and $\alpha_j^{\circ} = \ln k_j^{\circ}$. Vajda et al. [22] suggested that Eq. (95.11) can be approximated by the simple quadratic expression:

$$\hat{Q}(\alpha) = (\Delta\alpha)^T \widetilde{F}^T \widetilde{F}(\Delta\alpha) \tag{95.12}$$

Here $(\Delta\alpha) = Q(\alpha, c)$ is in the neighborhood of α°. Kinetic information comes by performing eigenvalue-eigenvector of the matrix $\widetilde{F}^T \widetilde{F}$. The important reactions can be defined as the significant eigenvector elements of reactions which are characterized by large eigenvalues. By providing the user-specified tolerances for these parameters, unnecessary reactions can be identified.

Results and Discussion

The Golovichev's mechanism [4] consisting of 57 species and 290 reactions is chosen for the oxidation of n-heptane fuel. Five different engine-operating conditions are selected for combustion analysis of n-heptane fuel listed in Table 95.1. The reduction process which is used in the present work is based on a two-stage reduction method, which utilizes DRGEP and PCA methods successively. Also, the combustion system considered in this study is HCCI combustion modeled by a single zone combustion model. Discussion of how well the simulations reproduce experimental data is beyond the scope of this paper. More specifically, DRGEP identifies and eliminates unimportant species and reactions and then, in the second stage, the PCA method is applied to improve the process by eliminating redundant reactions. For DRGEP reduction process, like Liang et al. [6] and Shi et al. [19], fuel, HO2, and CO are selected as the target species at each sampling point. Species that are reachable from the target species are identified at each sampling point and the collection of all of these species sets constitutes the final important species set for a specific operating condition. The rest of the species are considered as unimportant species and reactions that include any of these species are eliminated from the final mechanism.

An initial tolerance value to start the DRGEP reduction process is 10^{-5} and the tolerance value for PCA reduction process that follows the DRGEP process is 10^{-3}. The selected representative parameters for investigating the validity of the reduced mechanism in this work are the predicted CA50, peak pressure, and maximum heat release. At each generation, these parameters are calculated using the HCCI engine simulation code and compared with the results obtained by using the detailed mechanism for the considered cases. The generated reduced mechanism is considered as valid one if the errors in predicted CA50, peak pressure, and maximum heat release using reduced mechanism do not exceed 1° CA, 1 %, and 1 % respectively, with those of the detailed mechanism. Therefore, for each operating conditions mentioned in Table 95.1 the developed reduced mechanisms are in different final sizes and final algorithm tolerances as can be seen in Table 95.2.

Figures 95.1 and 95.2 show the mechanism size and the interfered errors in calculation of CA50, peak pressure, and maximum heat release because of elimination of insignificant species and reactions and algorithm error tolerances at each

Table 95.1 Operating conditions for considered cases of the n-heptane-fueled HCCI engine

Case	1	2	3	4	5
Equivalence ratio (Φ)	0.68	0.41	0.43	0.38	0.26
n-Heptane mass rate (mg/s)	103.43	75.52	89.69	92.40	79.23
Air mass rate (g/s)	2.28	2.77	3.11	3.66	4.57
T_{IVC} (K)	333	333	413	413	413
P_{IVC} (bar)	1.54	1.55	1.56	1.54	1.57
% EGR	51.01	40.69	31.66	19.79	0.0
Compression ratio	11.5	11.5	11.5	11.5	11.5

Table 95.2 Comparison of n-heptane skeletal mechanisms sizes generated at each operating conditions

Case	Species	Reactions	Allowable error tolerances are exceed?
Case 1	38	65	No
Case 2	40	95	No
Case 3	36	104	No
Case 4	38	74	Yes
Case 5	38	85	No
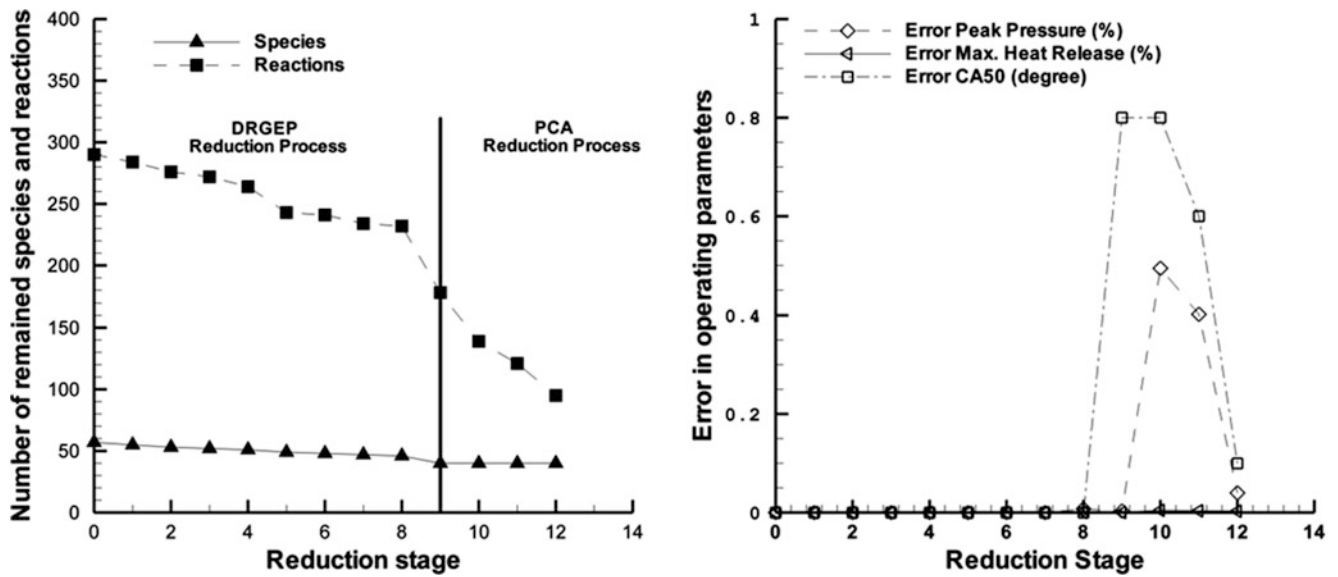
Fig. 95.1 Mechanism size and the corresponding error values at each reduction stage (case 2)

Fig. 95.2 Algorithm error tolerances for case 2 of the NG fueled HCCI engine
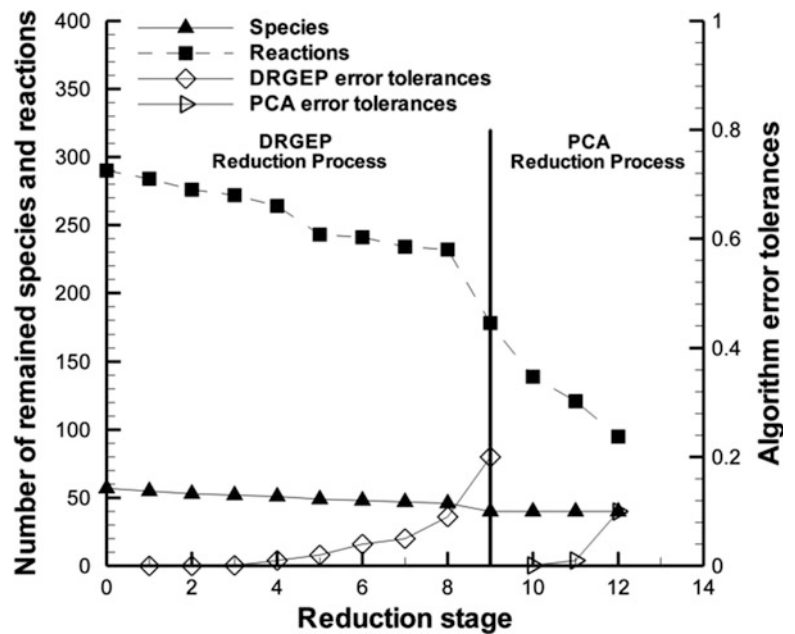
generation during DRGEP and PCA reduction processes, which are distinguished with a vertical line. The considered case in these figures is test 2. For the first reduction stage which utilizes DRGEP reduction method, insignificant species and their corresponding reactions are identified and eliminated effectively from the mechanism. Following the first stage, PCAF reduction is applied to the mechanism to remove further reactions in the second stage. By applying this two-stage reduction method, a detailed mechanism of *n*-heptane including 57 species and 290 reactions is reduced to a smaller mechanism containing 40 species and 95 reactions.

By utilizing the specified reduction processes for each of the operating conditions, the corresponding reduced mechanism is generated. However, it is required to have a single reduced mechanism. Normally, this final reduced mechanism can be developed by the combination of all the generated mechanisms of each case. Another alternative solution for this goal, as mentioned by Shi et al. [19], and also can be seen in Fig. 95.3, is to evaluate the performance of each of the reduced mechanisms at different operating conditions. It can be seen that most of the generated mechanisms can be used for all other
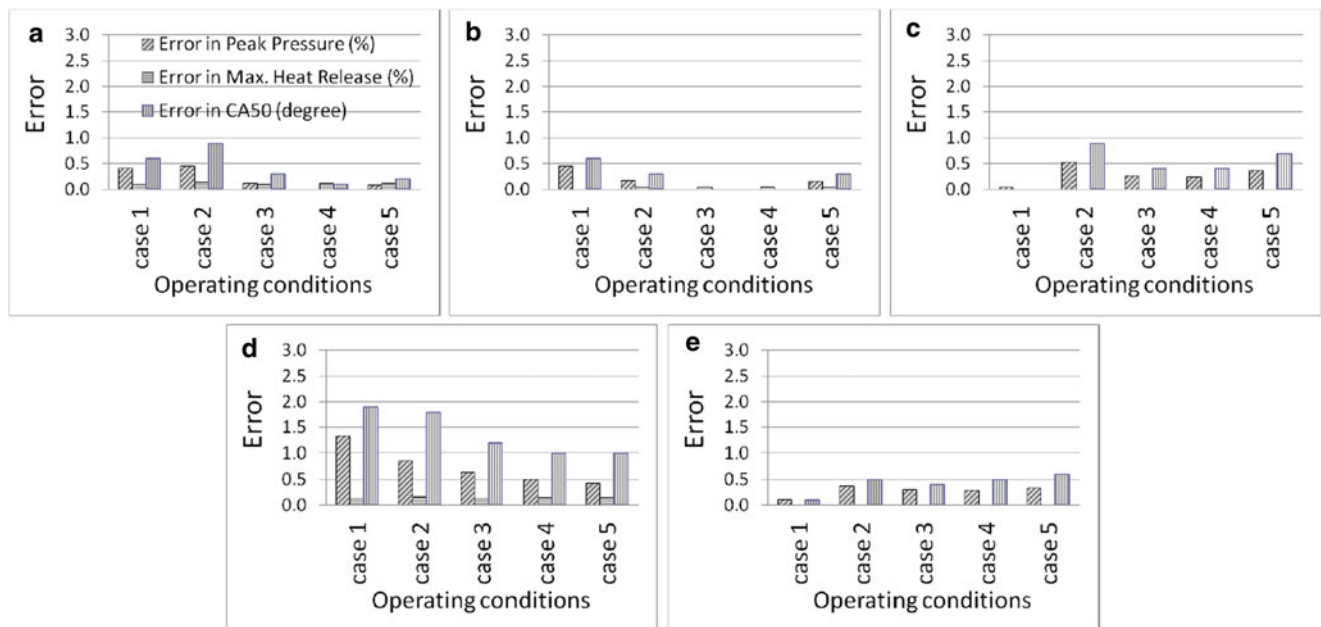
Fig. 95.3 Performance of each generated reduced mechanism for *n*-heptane fuel at different operating conditions. (**a**) Case 1. (**b**) Case 2. (**c**) Case 3. (**d**) Case 4. (**e**) Case 5
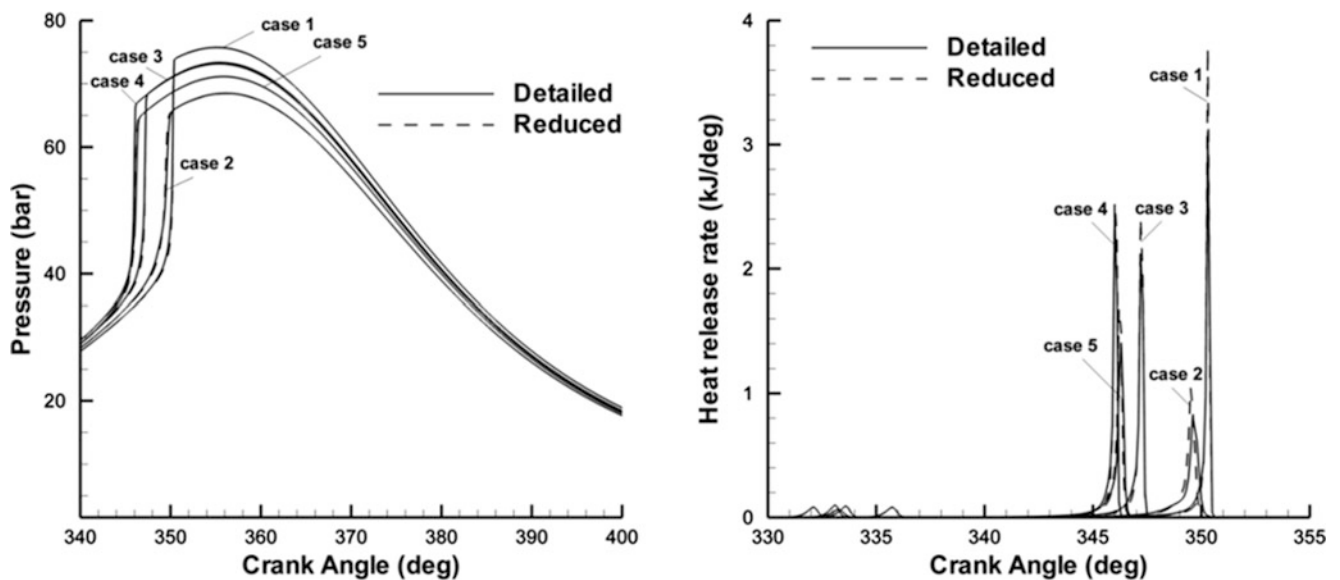
Fig. 95.4 Comparison of pressure traces and heat release rate histories by applying the detailed *n*-heptane mechanism and its reduced mechanism generated for case 2 at different operating conditions

cases while predicting the representative parameters in the error tolerance limit. For example, the generated reduced mechanism for case 1 for *n*-heptane fuel is used to simulate the combustion phase of the *n*-heptane-fueled HCCI engine in different considered cases in Table 95.1. The calculated error in predicting peak pressure, maximum heat release, and CA50 between reduced and detailed mechanisms are less than the user-specified error tolerance values. However, the developed reduced mechanism of case 4 for *n*-heptane is not able to accurately predict some of these parameters for operating conditions of case 1, case 2, and case 3; therefore, it is not considered as a valid one.

To verify the ability of the reduced mechanism in predicting the pressure trace and heat release rate histories, a comparison of these parameters between reduced and detailed mechanisms is depicted in Fig. 95.4 for different operating conditions of the *n*-heptane-fueled HCCI engine. As indicated in this figure, simulation using reduced mechanism is in good agreement with the simulation utilizing detailed mechanism.

Fig. 95.5 Error in prediction of SOC for reduced mechanism relative to the detailed one at all considered cases
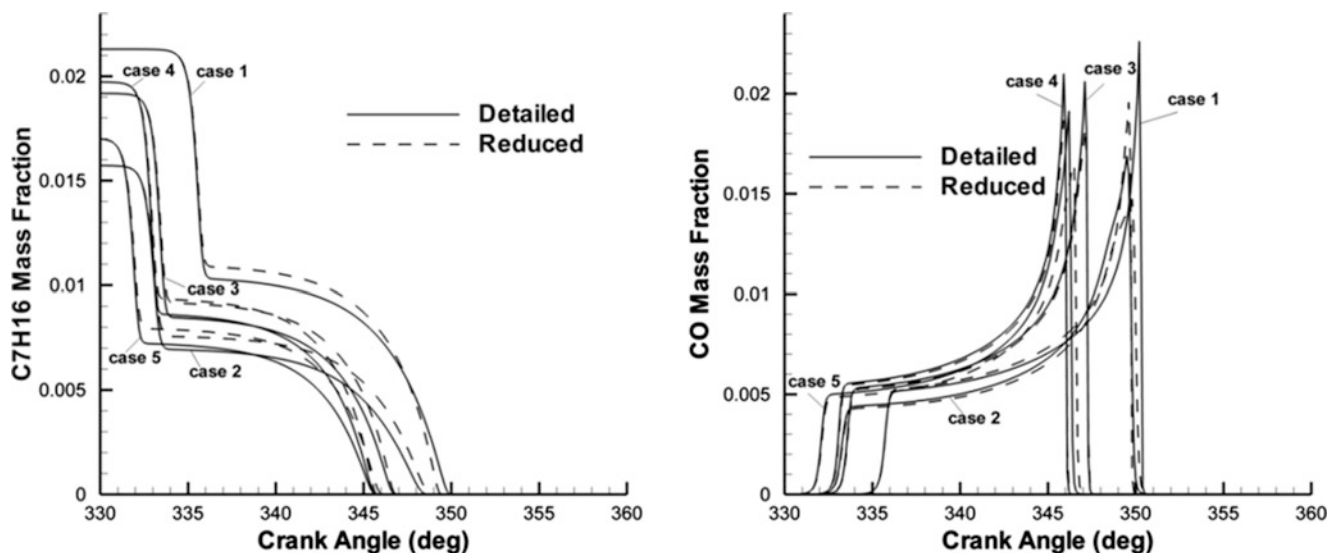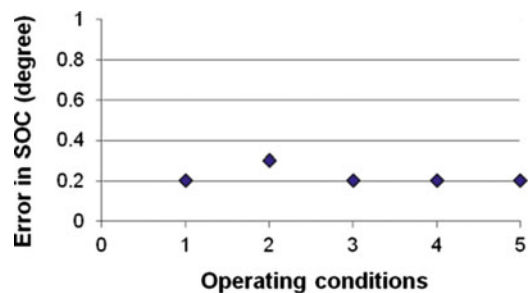
Fig. 95.6 Comparison of mass fraction for some selected species between the detailed *n*-heptane mechanism and its reduced mechanism generated for case 2

In addition to matching pressure and heat release rate traces, the start of the combustion (SOC) calculated from the reduced mechanism is compared with the corresponding detailed results. The definition of the SOC adopted here was the point at which 10 % of total heat is released. Figure 95.5 shows the difference in prediction of SOC by applying the reduced chemical kinetics mechanism and the detailed chemical kinetics mechanism in HCCI engine cycle calculations. In HCCI engines, combustion strongly depends on the chemical kinetics [1]. It is observed that the SOC is predicted accurately for all considered cases.

Finally, a comparison of the simulation results for the mass fraction profiles of some major species such as fuels and CO using the reduced mechanism and the detailed mechanism is shown in Fig. 95.6. The results show that the calculated mass fraction of these species using the reduced mechanism agrees very well with the simulation results utilizing the detailed mechanism.

The mechanism reduction achieved reduction ratios of 30 % for the number of species and also 67 % for the number of reactions.

Conclusion

In the current study, a reduced mechanism of *n*-heptane fuel based on the Golovichev's *n*-heptane mechanism was developed. Reduction procedure to develop the reduced mechanism was based on an integrated method that utilizes DRGEP and PCA reduction methods. The mechanism reduction achieved reduction ratios of 30 % for the number of species and also 67 % for the number of reactions, within tight error limits for prediction of CA50, peak pressure, and maximum heat release.

Nomenclature

c	Concentration of species	$Q\,(\alpha, c)$	Response function
C_A	Net consumption rate of species A	$r_j(c)$	Product of reactants concentration for reaction j
F	Sensitivity matrix	R_j	Reaction rate for reaction j
$\widetilde{F}$	Non-dimensional sensitivity matrix	t	Time
k	Rate constant	v	Stoichiometric coefficient
n	Total number of reactions	ω	Reaction rate
P_A	Net production rate of species A		

Greek

ϕ Total equivalence ratio

Abbreviations

EGR	Exhaust gas recirculation	SOC	Start of combustion
IVC	Inlet valve closing	SZCM	Single zone combustion model
rpm	Revolutions per minute		

References

1. Christensen M, Hultqvist A, Johansson B (1999) Demonstrating the multi fuel capability of a homogeneous charge compression ignition engine with variable compression ratio. SAE paper 1999-01-3679
2. Najt PM, Foster DE (1983) Compression-ignited homogeneous charge combustion. SAE paper 830264
3. Thring RH (1989) Homogeneous charge compression ignition (HCCI) engines. SAE paper 892068
4. Golovitchev VI Mechanisms (combustion chemistry) [Online]. http://www.tfd.chalmers.se/~valeri/MECH.html
5. Curran HJ, Gaffuri P, Pitz WJ, Westbrook CK (1998) A comprehensive modeling study of n-heptane oxidation. Combust Flame 114:149–177
6. Liang L, Stevens JG, Farrell JT (2009) A dynamic adaptive chemistry scheme for reactive flow computations. Proc Combust Inst 32I:527–534
7. Lam SH, Goussis DA (1994) CSP method for simplifying kinetics. Int J Chem Kinet 26:461–486
8. Maas U, Pope SB (1992) Simplifying chemical kinetics: intrinsic low-dimensional manifolds in composition space. Combust Flame 88:239–264
9. Hwang YT (1982) On the proper usage of sensitivities of chemical kinetics models to the uncertainties in rate coefficients. Proc Natl Sci Counc Repub China B 6:270–278
10. Turányi T, Berces T, Vajda S (1989) Reaction rate analysis of complex kinetic systems. Int J Chem Kinet 21:83–99
11. Bhattacharjee B, Schwer DA, Barton PI, Green WH (2003) Optimally-reduced kinetic models: reaction elimination in large-scale kinetic mechanisms. Combust Flame 135:191–208
12. Oluwole OO, Bhattacharjee B, Tolsma JE, Barton PI, Green WH (2006) Rigorous valid ranges for optimally reduced kinetic models. Combust Flame 146:348–365
13. Androulakis IP, Grenda JM, Bozzelli JW (2004) Time-integrated pointers for enabling the analysis of detailed reaction mechanisms. AIChE J 50:2956–2970
14. Lu T, Law CK (2005) A directed relation graph method for mechanism reduction. Proc Combust Inst 30:1333–1341
15. Pepiot-Desjardins P, Pitsch H (2008) An efficient error-propagation-based reduction method for large chemical kinetic mechanisms. Combust Flame 154:67–81
16. He K, Androulakis IP, Ierapetritou MG (2010) On-the-fly reduction of kinetic mechanisms using element flux analysis. Chem Eng Sci 65:1173–1184
17. Liang L, Stevens JG, Raman S, Farrell JT (2009) The use of dynamic adaptive chemistry in combustion simulation of gasoline surrogate fuels. Combust Flame 156:1493–1502
18. Niemeyer KE, Sung CJ, Raju MP (2010) Skeletal mechanism generation for surrogate fuels using directed relation graph with error propagation and sensitivity analysis. Combust Flame 157:1760–1770
19. Shi Y, Ge HW, Brakora JL, Reitz RD (2010) Automatic chemistry mechanism reduction of hydrocarbon fuels for HCCI engines based on DRGEP and PCA methods with error control. Energy Fuels 24:1646–1654
20. Bahlouli K, Saray RK, Atikol U (2012) Development of a reduced mechanism for n-heptane fuel in HCCI combustion engines by applying combined reduction methods. Energy Fuel 26:3244–3256
21. Pepiot-Desjardins P, Pitsch H (2005) Systematic reduction of large chemical mechanisms. Presented at the 4th joint meeting of the U.S. sections of the combustion institute. Drexel University, Philadelphia, PA
22. Vajda S, Valko P, Turanyi T (1985) Principal component analysis of kinetic-models. Int J Chem Kinet 17:55–81

Comparison of Natural Gas Fired and Induction Heating Furnaces

Umit Unver and H. Murat Unver

Abstract

Generally, in steel processing systems, steels are heated via induction or combustion furnaces. Natural gas fired furnaces have installation costs advantage while the induction furnaces have the advantages of less scale formation on the surface of the workpiece as well as less environmental pollutions. The operation cost of both systems is a vital argument to be solved. In this paper, a natural gas fired and induction heating furnaces of a forging process were studied. Thermodynamic analysis was performed for the furnaces which heat the steel workpiece up to 1,300 °C. The energy performances of both systems were analyzed and compared. It is concluded that, instead of a natural gas fired or an induction furnace, a hybrid furnace may save more energy and cost.

Keywords

Induction heating • Induction furnace • Natural gas furnace • Metal heating • Heating performance

Induction Heating

Induction heaters are used to provide alternating electric current to an electric coil (the induction coil). The induction coil becomes the electrical (heat) source that induces an electrical current into the metal part to be heated (called the workpiece). No contact is required between the workpiece and the induction coil as the heat source, and the heat is restricted to localized areas or surface zones immediately adjacent to the coil [1]. It provides faster and more precise heating of local areas, consumes less energy, and is considered environmentally friendlier than other methods. Other advantages also include lower labor cost for device operators, easy maintainability of the equipment, quality assurance, automation capability, and high reliability. Induction heating is a complex process including electromagnetic, thermal, and metallurgic phenomena. In this process an alternating electric current induces electromagnetic field, which in turn induces eddy currents in the workpiece. The induced eddy currents release energy in the form of heat, which is then distributed throughout the workpiece [2].

The principle of induction heating is mainly based on two well-known physical phenomena, electromagnetic induction, and the Joule effect [3]. The energy transfer to the object to be heated occurs by means of electromagnetic induction. It is known that an alternating current is induced in a loop of conductive material when this loop is placed in an alternating magnetic field. The formula is as follows:

$$U = d\varphi/dt \qquad (96.1)$$

U. Unver (✉)
Yalova University, Kazim Karabekir Mah. Rahmi Ustel Cad. No: 1, Yalova, Turkey
e-mail: umit.unver@yalova.edu.tr

H.M. Unver
Engineering Faculty, Kırıkkale University, Yahsihan, Kirikkle, Turkey
e-mail: unver@kku.edu.tr
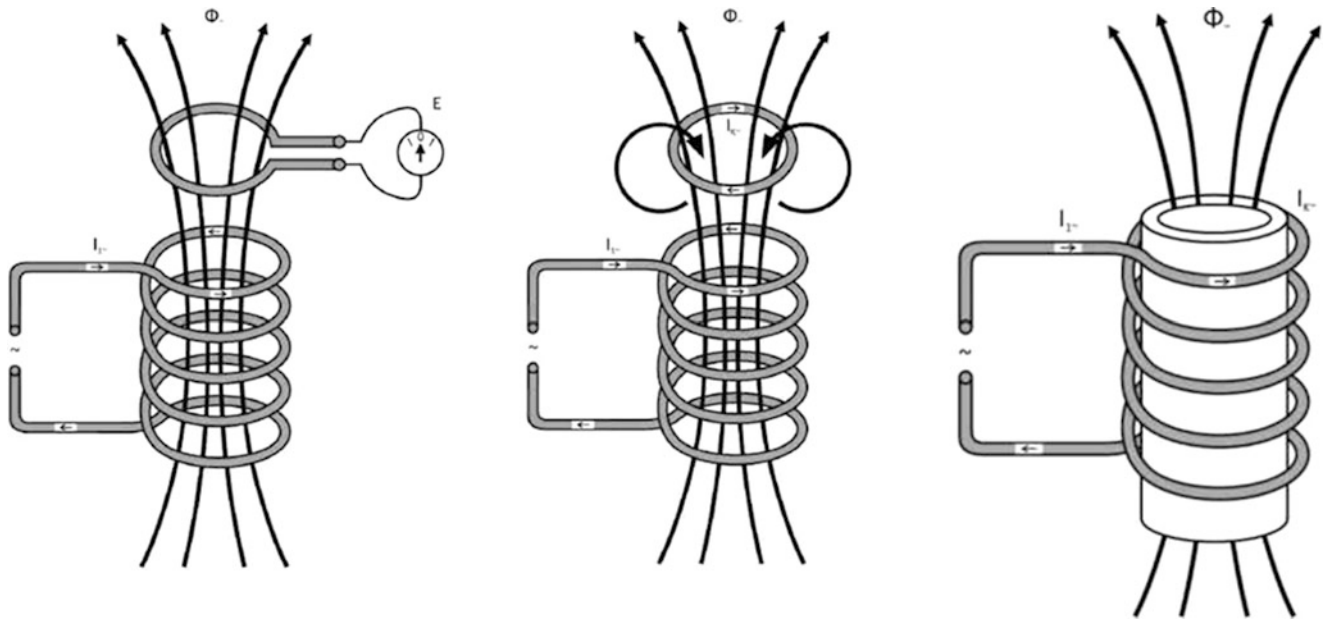
Fig. 96.1 Faraday's Induction law

where U is voltage (V), φ is magnetic flux (Wb), and t is time (s). When the loop is short-circuited, the induced voltage U will cause a current to flow that opposes its cause—the alternating magnetic field. This is the Faraday–Lenz law. If a massive conductor (e.g., a cylinder) is placed in the alternating magnetic field instead of a short-circuited loop, eddy currents (Foucault currents) will be induced (see Fig. 96.1).

The eddy currents heat up the conductor according to the Joule effect. When a current I [A] flows through a conductor with resistance R [O], the power is dissipated in the conductor. In most applications of induction heating, the determination of resistance R is not a simple matter due to the nonuniform distribution of current in the conductor.

The power requirements are related to the amount of energy required to heat a workpiece and to the induction heating system power losses. The energy or heat content required to heat the workpiece can be calculated when the material, its specific heat, and the effective weight of material to be heated per hour are known. Higher power densities provide the ability to heat surfaces more rapidly. However, there may be limitations to the amount of power that an individual induction coil can handle [1]. Power induced in the workpiece can be determined as:

$$P = U.I = R.I^2 \tag{96.2}$$

where P is the power (kW). In literature there are several studies focused on heating of metal (Tables 96.1 and 96.2).

The electrical efficiency is defined as follows [3]:

$$\eta_e = \frac{\dot{Q}_w}{\dot{Q}_e} \tag{96.3}$$

where ηe is the electrical efficiency, $\dot{Q}_w$ is the required energy for heating material (kW), and $\dot{Q}_e$ is the electric energy consumed (kW).

In Table 96.3, the efficiencies of induction systems as to frequency converters are given [3].

The data was provided from the workpiece that has widest diameter passing through the conductor. Efficiency reduces with diameter reduction, by means of the increment of air gap between the workpiece and inductor. The operating costs are compared in Table 96.4 [4]. It was indicated that heating a steel workpiece to 1,250 °C consumes 350 kWh/t. In the table, it can be seen that overall operating cost of a gas fired heating furnace is the cheapest method.

In addition, installation costs of induction and gas fired furnaces were given in Table 96.5 [5]. In the calculations, annual energy costs, scale losses, scrap losses, and labor requirements were taken into consideration. As to the results of Mortland [5], the total annual operating costs of induction furnaces are more economical than the gas fired furnaces. As it can be seen

Table 96.1 Power consumptions of various metals for hot forging heating [4]

	Steel	Aluminum	Copper	Brass (CuZn 70/30)
Forging temperature (°C)	1,250	500	900	750
Power induced (kWh/t)	240	136	105	90
Power consumed (kWh/t)	350–400	280–300	230–250	180–190
Frequency (Hz)	50–10,000	50–4,000	50–4,000	50–4,000

Table 96.2 Average power requirements for induction heat processing of common metals (kWh/t) [5]

Process	Carbon steel	Magnetic stainless steel	Nonmagnetic stainless steel	Brass
Hot forging	440.9	413.4	474.0	440.9
Hardening/aging	275.6	286.6	–	358.3
Annealing/normalizing	248.0	231.5	413.4	413.4
Warm forming	192.9	–	275.6	–
Stress relieving	165.3	55.1	220.5	220.5
Tempering	77.2	77.2	110.2	–
Curing of coatings	55.1	55.1	82.7	121.3

Table 96.3 Induction installations general aspects with various frequency converters

	Thyristors	Transistors	Tubes
Efficiency	90–97 %	75–90 %	55–70 %
Frequency range	100 Hz–10 kHz	Up to 500 kHz	Up to 3,000 kHz
Power range	Up to 10 MW	Up to 500 kW	Up to 1,200 kW

Table 96.4 Actual heating costs of various processes (euro/t) [4]

	Induction	Gas	LPG
Labor	3.85	7.7	7.7
Fuel	28.02	13.27	56.04
M&O	2.98	5.95	5.95
Scale losses	2.23	11.15	11.15
Amortization costs	15.37	7.68	7.68
Total	52.45	45.75	88.52

Table 96.5 Installation costs of induction and gas fired furnaces [5]

Item	Induction furnace	Gas fired furnace
Installed cost	$600,000	$200,000
Heating efficiency	60 %	15 %
Annual energy cost	$720,000	$540,000
Scale loss	1/2 %	2 %
Scrap loss	1/4 %	1 %
Annual scrap and scale loss cost	$150,000	$600,000
Labor requirement	1 operator 1/4 maintenance	2 operators 1/2 maintenance
Annual labor cost	$60,000	$120,000
Total annual operating cost	$930,000	$1,230,000

from Tables 96.4 and 96.5, the results are not coherent. Thus, it must be noted that these calculated costs vary as to the place, plant, and the operation.

The advantages of induction furnaces are aligned as follows [3–6]

Technical process

- Maintenance costs and spare parts costs are fair.
- High power density provides a compact installation and realizes a quick heating.
- Floor space requirements are less.
- Induction offers the possibility of reaching very high temperatures.
- Induction heating can be applied to specific area of workpiece.
- Induction installations are suited for automation.
- Recovers time and heat losses during feeding and receiving of workpiece.
- No need to stock fuel.
- A significant portion of the heat losses can be recuperated.
- Extreme purity is possible by working in a vacuum or in inert atmospheres.
- The precise location of heating can be determined accurately.
- The heating can be regulated precisely.
- Environment and working conditions.
- No production of flue gasses.
- Induction installations generally have good efficiency although this efficiency also depends upon the characteristics of the material to be heated.

Stefan and Günter recommended a hybrid furnace system that includes both with natural gas fired and induction furnaces. They advised that the material would be heated up to 700–800 °C via the gas fired furnace and to 1,200–1,300 °C via induction furnace to avoid scale formation [7].

Natural Gas Fired Furnaces

Natural gas fired furnaces (NGF) are somewhat simpler than the induction furnaces. The process can be seen and heard in the furnace. The elements are familiar and known. These furnaces can be assumed as larger scale of domestic furnaces. Therefore, most of the systems which are used in NGF are conventional, e.g., loading system, walls, and gas systems.

In NGF, main energy input is the combustion of natural gas. The electric current, which is used to run the burners and air fans, may be considered as auxiliary energy. The total energy input via natural gas combustion can be calculated as

$$\dot{Q}_f = \dot{m}_f . \, LHV \, (\text{kW}) \tag{96.4}$$

where $\dot{m}_f$ is the mass flow rate of natural gas (kg/s) and LHV is the lowest heating value. Energy of flue gases may be calculated as

$$\dot{Q}_{ex} = \dot{m}_{ex}. \; C_{ex}.(T_{ex} - T_o) \, (\text{kW}) \tag{96.5}$$

The workpiece that is loaded to furnace may be at environment temperature or any preheat temperature. The temperature difference can be calculated as the difference between inlet and exit temperatures. Thus, the total energy transferred to the workpiece in the furnace can be calculated from

$$\dot{Q}_w = \dot{m}_w.C_w.(T_w - T_o) \, (\text{kW}) \tag{96.6}$$

where $\dot{m}_w$ is the mass of workpiece loaded in 1 h (kg/h), C_w is the specific heat of workpiece in (kJ/kg °C), and T_w is the final temperature of the workpiece (K). The radiation heat transferred from the hot surfaces simply can be calculated from

$$\dot{Q}_r = \sigma. \; \varepsilon. \; A.\left(T_s^4 - T_o^4\right) (\text{kW}) \tag{96.7}$$

The heat transfer via turbulent flow natural convection from the hot surfaces can be calculated from

$$\dot{Q}_{nc} = \left[1,32 \; . \; \sqrt[3]{T_y - T_o}\right]. \; A.\left(T_y - T_o\right)(\text{kW}) \tag{96.8}$$

The efficiency of a NGF can be obtained via direct and indirect methods. In the indirect method, percentage of all losses through the total energy input must be calculated. In the direct method, proportion of the heat transferred to the workpiece to the total energy input via natural gas combustion can be calculated via the following equation:

$$\eta_\Sigma = \frac{\dot{Q}_w}{\dot{Q}_f} \tag{96.9}$$

Results and Discussion

The NGF considered in this study was installed 35 years ago, which has an old technology (Fig. 96.2). The furnace has no exhaust system and naturally has no recuperator or regenerator. The flame was blown out from the openings of the hatches. Thus, the thermal losses from the NFG were not based on only the radiation from the hot surfaces and exhaust gases. The leakage losses were highly effective because of more than 1,300 °C flame leakage. That means the energy of flame with its radiation potential is inconsumable.

In NGF systems, burners provide a stable combustion. By this means, it is easy to evaluate the volumetric or mass flow rate of natural gas. When natural gas flow rate is read, total energy consumption can be calculated via Eq. (96.4). In this study, lowest heating value (LHV) of natural gas was taken from IZGAZ (Official Gas Distribution Company).

The results of the calculations and design data of the system, which was handled with in this study, were given in Table 96.6. The exhaust losses were obtained via Eq. (96.5). It was considered that all the 1,300 °C hot stack gases were lost with their energy potential, since the NGF system has no exhaust, recuperator, or regenerator. In the system, even some of the flame was thrown out from the openings of the furnace. In most of the applications, the opening losses obtained 5 % of the total energy input. However, in this study it was calculated about 26 % of total energy input. The main reason of this is not only the loss of high temperature energy potential of the exhaust gases but also the energy potential of very high temperature flame and flames radiation potential. In this type of heating systems, the flame is wanted to be kept inside the heating zone because of its very high temperature, which is useful for convection and radiation. It is desired to finish the burning of natural gas inside the heating zone, but never outside. Because of this, the opening losses had a high percentage through the total energy input.

Hot surface radiation losses were calculated via Eq. (96.7). The mean temperatures of surfaces of the NGF were achieved via thermal camera (see Fig. 96.3). In the system, the insulations were also not optimum. At some points on the furnace, the wall temperature was reached to 200 °C. This wall temperature is definitely not allowable temperature, because it means we are using the wall as a resistant heater to heat environment. Comparing to opening losses, hot surface losses are not seem to be serious. Nevertheless, the wall temperature should still be reduced to To +40 °C.

Fig. 96.2 An operating natural gas fired furnace

Table 96.6 Design data and energy analysis of NGF

Fuel consumption per unit time (Sm^3/h)	49.5
Lowest heating value of natural gas (kWh/Sm^3)	10.64
Energy consumption per unit time (kWh/h)	527
Combustion time to attain steady state (h)	3
Natural gas consumption until steady state (Sm^3/h)	149
Total energy consumption until steady state (kW)	1,580
Energy requirement of 1 t of steel (design capacity) (kW/h)	181
Energy requirement of steel forged in unit time (actual data) (kW/h)	30
Q_{ex} exhaust losses (kW)	162
Q_{hs} radiation losses (kW)	25
Q_n natural convection losses (kW)	19
Q_o opening losses (kW)	140
Q_T total heat losses (kW)	205
Efficiency (design data) (%)	34.44
Efficiency (actual data) (%)	5.74
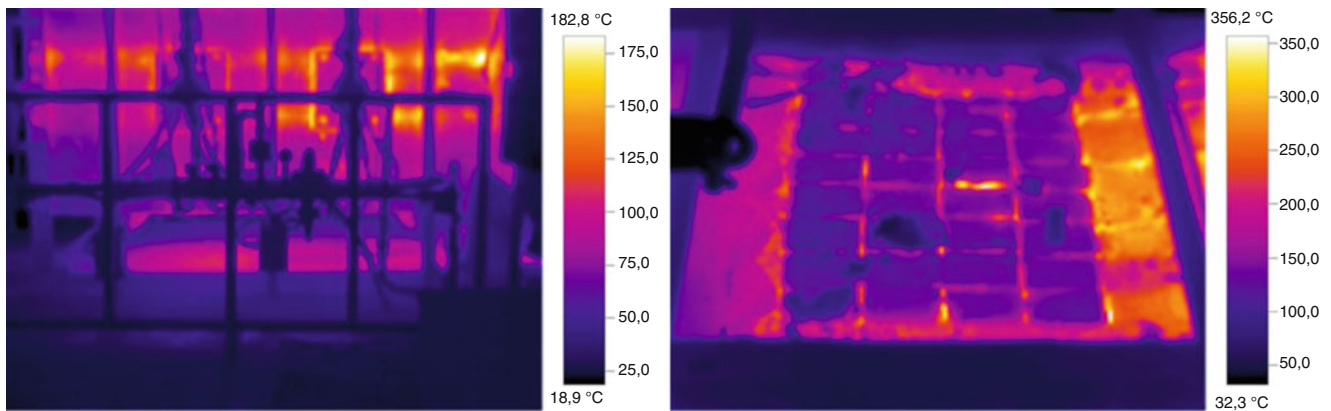
Fig. 96.3 Thermal camera view of the side wall and the top of the NGF furnace

Natural convection losses were calculated with Eq. (96.8) [8]. At first glance, the natural convection may not seem to be high in proportion to other losses. However, if the dimensions of the furnace are considered, we can conclude that it has to be reduced also. The high wall temperature causes high natural convection losses as well as radiation losses.

Finally, the efficiency of both induction and NGF systems were calculated via Eq. (96.9). The data were collected from meters for natural gas and electric. It must be noted that the NGF system starts up 3 h before shifts. Because of this, additional operating hours of combustion system were taken into account. However, the effect of pre-operating to attain steady state is various. It depends on many parameters such as the difficulty of the workpiece, operating time, production quantity, and diameter of the workpiece.

In Table 96.7, validation of the analysis results and comparison of the subject furnaces of this study were given. In the analysis, the result obtained from the induction furnace is in good agreement with [4, 5]. Mainly efficiency agrees with the literature. A slight difference may cause from Cos φ of the induction systems, but NGF system has a dramatic difference between induction furnace as well as the other NGF given in literature. The most important and basic reason is that the analyzed heating system has no exhaust. If there were, we could have a chance to measure the combustion and to recover the waste energy. The efficiency, which is given in Table 96.7, is the mean value of calculation results. A detailed analysis results of efficiency of NFG is given in Fig. 96.4. As it is mentioned, the efficiency of NGF depends on many parameters. If the order can be produced in 3 h, then the efficiency differs between 2.4 and 9.5 % as to the production mass in one shift. If the mass of the production in one shift increases, efficiency of the system also increases. Let's consider that 500 kg will be

Table 96.7 Validation of analysis and comparison

	Induction [4]	Induction [5]	Induction analyzed	NGF analyzed
Total consumption (kWh/t)	375	441	755	527
Energy requirement (kWh)	188	188	299	30
Losses (kW)	187	253	361	722
Efficiency (%)	50.23	42.72	52.19	5.74
Heating cost ($/t)	52.08	61.24	69.91	158.94

Fig. 96.4 Efficiency of natural gas fired furnace considering load-per-shift and operating hours
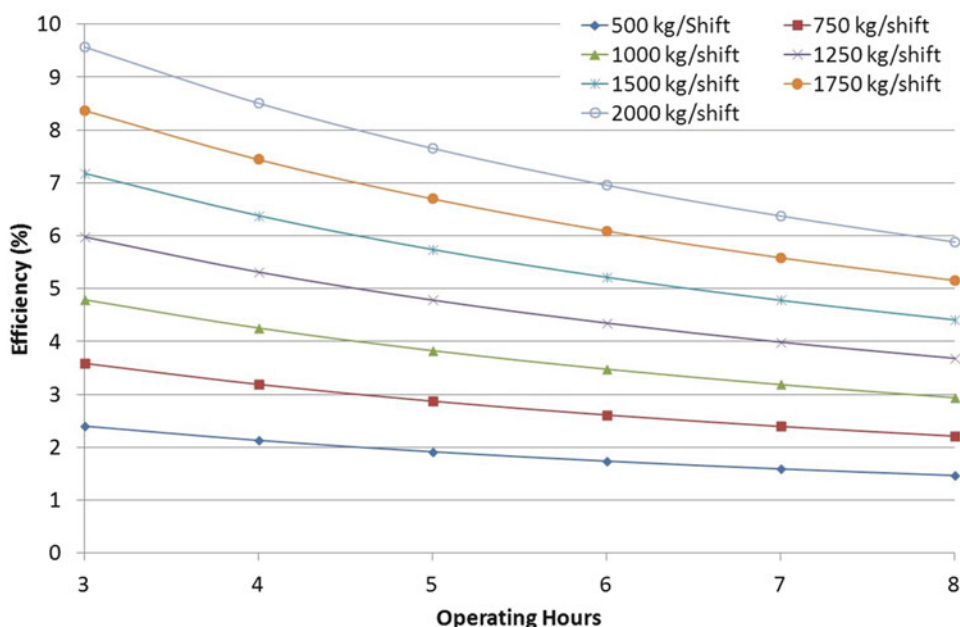
forged, when it is forged in 3 h the efficiency of the system calculated is 2.4 %. However, when production time extends to 8 h, the efficiency of the system decreases to 1.5 %.

The efficiencies given in Fig. 96.4 are all very low. The system is old and ineffective. Because of this, a project proposal was given to East Marmara Development Agency to develop the NGF system and it is accepted. In the scope of the project, the system replacement of the old system with a modern NGF system was proposed. Taking into account that the most efficiency detractive topics are exhaust losses and opening losses, the projected system will have regenerators, economizers, and tight lids. Since the most energy destructing section of the existing NGF are lids, to avoid the opening losses and leakage of the flame, a leak-proof lid system is designed. In the designed NGF, loading system will minimize the load/unload losses as well as leakage. The wall insulation is considered to stabilize the wall temperature at To +40 °C, so the radiation and natural convection losses will also decrease. With the projected NGF, efficiency is supposed to increase up to 40 %.

It is also decided that the next project will be about hybrid system that heats the workpiece up to 900 °C by NGF and to 1,300 °C by induction furnace.

Conclusion

In this study, a thermodynamic analysis has performed for two types of furnaces of a forging facility. The data are collected from an induction furnace and a NGF. It is seen that the efficiency of induction furnace is about 52 %, which agrees with the literature. However, the NGF is very ineffective since the losses of the system are very high. Depending on the lot size and

operating hours, the NGF efficiency was calculated max. 9.5 % and minimum 1.4 %. It is identified that the highest energy losses are exhaust (162 kW) and opening losses (140 kW) in order. In the current situation, heating the material with induction furnace is clearly profitable. Finally, the inefficient NGF should be remade with current technology.

Nomenclature

A	Area (m^2)	$\dot{Q}_{ex}$	Exhaust losses (kW)
C_{ex}	Specific heat of exhaust gasses (kJ/kg K)	$\dot{Q}_f$	Total energy input via combustion of natural gas (kW)
C_w	Specific heat of workpiece (kJ/kg K)	$\dot{Q}_{nc}$	Heat transfer due to natural convection (kW)
ε	Emmisivity	$\dot{Q}_r$	Radiation heat transferred from the hot surfaces (kW)
I	Current (A)	$\dot{Q}_w$	Required energy for heating workpiece (kW)
LHV	Lowest heating value (kW/kg)	R	Resistance (Ω)
$\dot{m}_{ex}$	Exhaust flow rate (kg/s)	σ	Stefan Boltzmann constant (kW/m^{2}K)
$\dot{m}_f$	Mass flow rate (kg/s)	t	Time (s)
$\dot{m}_w$	Mass heated per unit time (kg/s)	T_{ex}	Exhaust temperature (°C)
NGF	Natural gas fired furnace	T_o	Atmospheric temperature (°C)
ηe	Electrical efficiency	T_s	Surface temperature (°C)
η_Σ	Overall efficiency	T_w	Temperature of the workpiece (°C)
P	Power (kW)	U	Voltage (V)
$\dot{Q}_e$	Electric energy consumed (kW)	φ	Magnetic flux (Wb)

References

1. Haimbaugh RE (2001) Practical ınduction heat treating. ASM International, ISBN: 978-0-87170-743-7
2. Kranjc M (2010) Numerical analysis and thermographic investigation of induction heating. Int J Heat Mass Transf 53:3585–3591
3. Laborelec JC (2011) Induction heating, leonardo energy application note. Publication No. 0123, Dec 2011. ECI. www.leonardo-energy.org/drupal/node/1693
4. Poncin R (2004) İndüksiyonla takoz ısıtma. TMMOB Metalürji Mühendisleri Odası Dergisi 138:49–52 (Translator: Özen S)
5. Mortland J (1993) A cost-effective and energy-efficient method for process heating. Tech. Commentary 2(1). EPRİ Center for Materials Fabrication
6. DaWei Induction Heating Machine Co., Ltd electronic publication. http://www.induction-heating.com.cn/uploadfile/20121008/20121008214904637.pdf
7. Beer S, Günter U (2012) Combined log heating furnace inlineconcept for aluminyum extruders. Ind Technol Rep Heat Process 2:77–80
8. Tütünoğlu Y, Güven A, Öztürk İT (2012) Cam Temperleme Fırınında Enerji Analizi. TMMOB MMO Mühendis Makina Derg 53(629):s.55–s.55

Chemical Thermodynamics of Hydrocarbon Compositions in Natural Gas Field, Northeast of Thailand

Sarunya Promkotra and Tawiwan Kangsadan

Abstract

The phase envelope of hydrocarbon species in natural gas can be predicted by using thermodynamic simulation. Conceptual thermodynamics depends on physical and chemical characteristics in equilibrium condition. The API gravity of condensate is expressed in a range of 55–63°. Its average density is similar to the specific gravity of 0.74. Pressures in each gas processing process are decreased from the gas well (74.754 bar g) to the condensate tank (0.02 bar g). Mostly methane is discovered approximately 96 mol%. Due to physical and chemical properties, this petroleum reservoir indicates the dry gas reservoir. Chemical reactions depending on hydrocarbon compositions can be valuable for evaluating phase equilibrium. These chemical reactions based on hydrocarbon species are fabricated by chemical species as reactants and products. For creating them, all compositions related to the genesis of petroleum in the same environment are combined as a reactant. They are possibly defined as phase related to Gibbs free energy. Carbon dioxide, hydrogen, and nitrogen gas in petroleum reservoir are 10, 8, and 2 mol%, respectively. The chemical thermodynamics is simulated by using Prode Properties, a computer software program, in which Peng–Robinson equation of state is used as the chemical thermodynamic model. Characteristics of phase envelope consist of the critical temperature and pressure at phase transformation between liquid and gas. Two types of conceptual schemes are varying the invariable and variable mole fraction to evaluate the phase envelope. For their invariable mole fraction, the carbon ratio is defined at 60:20 percentages. Temperatures of natural gas from the phase envelope are inversely proportional to equilibrium constant. High temperature at low equilibrium constant specifies the forward chemical reaction. For their variable mole fraction, the increased carbon atoms affect to gradually intensify the temperature and pressure. Hydrocarbon types and mole fraction of these components concern to the possibility of phase envelope at suitable phase.

Keywords

Thermodynamics • Hydrocarbon • Natural gas • Phase envelope

Introduction

Natural gas systems are generally analyzed by using hydrocarbon thermodynamics to understanding the interaction between natural gas fluids and assorted environments. The outcomes lead to conception in engineering practice mainly in the reservoir, pipeline, and production process. Fluid thermodynamic behavior can be assessed behaviors of any feasible fluid

S. Promkotra (✉)
Department of Geotechnology, Faculty of Technology, Khon Kaen University, Khon Kaen 40002, Thailand
e-mail: sarunya@kku.ac.th

T. Kangsadan
Chemical and Process Engineering Program, Department of Mechanical and Process Engineering, The Sirindhorn International Thai-German Graduate School of Engineering (TGGS), King Mongkut's University of Technology North Bangkok (KMUTNB), Bangsue, Bangkok 10800, Thailand
e-mail: tawiwan.k.cpe@tggs-bangkok.org

phases as a function of temperature, pressure, and hydrocarbon components. The phase envelope of hydrocarbon species in natural gas field is essential information in order to optimize the process in the gas processing plant (GPP). By using the chemical thermodynamic concept, the phase behavior of hydrocarbon reservoir fluids will be fabricated under a series of two-phase equilibrium over the pressure–temperature range. This inquiry is a worthy research to comprehend the phase equilibria of petroleum fluid.

Reservoir fluids include a wide variety of matters of chemical nature that comprise of hydrocarbons and non-hydrocarbons. Hydrocarbon fluids in petroleum reservoir are very complex substances. Although, the complexity of hydrocarbon fluids generates in underground reservoirs, equations of state (EOS) can express the phase-behavior computations of these complex fluids. An equation of state is a methodical representation concerning pressure to temperature and volume. The appearance is used to reveal the vapor–liquid equilibrium (VLE) and the thermal properties of pure materials and mixtures. Chemical thermodynamic model depends on the category of the phases in equilibrium using the Peng–Robinson cubic equation of state for the vapor–liquid phase [1, 2]. Chemical thermodynamics of natural gas and condensate is the useful research to understand phase behaviors of different hydrocarbon criteria [3]. Normally, heavy hydrocarbon compositions affect the thermophysical properties of the gas, and the range is characteristically undefined. Most EOS is important to describe the phase equilibria of natural gas, however cannot correspond the phase loops for pressures in VLE, especially at high pressure density. The developed prediction will be utilized by the specific EOS for the performance of gas processing facilities [4].

The complete vapor–liquid phase envelope can precisely provide critical points which indicate the maximum temperature and pressure by an algorithm [5]. Currently improved methods for absolute computation of critical points are essentially considered and a thermodynamic simulation suggesting a more convenient creation. Cubic EOS, for example, the Peng–Robinson EOS, is regularly functioned by the petroleum industry for the intention of recovery and processing operations of gases at high pressures. Alfradique and Castier [6] selected the Peng–Robinson EOS in the calculation of dew points, bubble points, and critical points of natural gases. For this reason, the Peng–Robinson EOS is possibly to complete this aim with widest acceptance. Thus, the goals of this research are to identify chemical compositions of natural gas in equilibrium condition and to evaluate phase envelope of natural gas and condensate by thermodynamic simulation.

Study Area

Study area is located in the natural gas field in Udon Thani province, Thailand, where is situated a production well of the gas field. The distance from production wells to the GPP in Khon Kaen province is approximately 62 km. Natural gas and condensate are collected from GPP in Num Phong District, Khon Kaen province, located in the northeastern part of Thailand. Generally, petroleum regions in Thailand are geographically divided into Northern and Central Plains, Northeastern, Southern, Andaman Sea, and Gulf of Thailand [7]. Major produced reservoirs are supplied in different parts of the country. Commercial hydrocarbon potentials were found in the Northeast and one of them can produce petroleum gas from Permian carbonates. Exploration data reveals that Permian carbonates are considerable primary reservoirs. High-potential expectations are situated in the surroundings of Nam Phong and Sin Phu Horm Gas Field, including Phu Khieo Prospect. Dry gas is expected to be the petroleum resource in a profitable scale. Exploitation of the natural gas can be supported for the power plant [8].

Methodology

Gas Processing Plant

Petroleum fluid is transported from a petroleum reservoir to the ground surface (160 bar g pressure, 60 °C temperature) and flows to the GPP in Khon Kaen province. In the first part of GPP, petroleum fluid flows to the slug catcher (74.54 bar g pressure, 31.67 °C temperature). Fluid in this location is separated from natural gas. For the natural gas line, gas flows to the inlet coalescing filter and mercury absorber in order to eliminate dust and mercury, whereas water in natural gas is separated by triethylene glycol at the glycol contactor with the pressure of 45.01 bar g and temperature of 38.99 °C. Then, gas flows to the gas/gas exchanger and passes to the low temperature separator to decrease temperature and send to the sale gas system (27.83 bar g pressure, 41.20 °C temperature).

For the liquid line, liquid petroleum consists of condensate and water. Petroleum liquid flows to the high pressure flash vessel (6.49 bar of pressure, 24.28 °C of temperature) which condensate is separated from water. Water flows to the produced water separator and boiled at a boil-off tank, and subsequently this water is destroyed in the thermal oxidizer (700 °C). Moreover, condensate flows to the low pressure flash vessel and evaporates. Finally, condensate runs to a condensate tank to storage. Temperature and pressure in each location in GPP are useful for correlating to the conceptual model for thermodynamic simulation.

Sample Collection

Condensate samples are collected two times in August and October in 2012. These samples are taking from the inlet slug catcher, where the natural gas and other fluid mixtures (condensate and water) are separated out. Thus, petroleum-field water must be removed first from condensate. Besides, natural gas, entirely methane is also withdrawn from this process. The natural gas is collected at this point.

Natural Gas and Condensate Analysis

Natural gas and condensate compositions are obtained by the gas chromatography (GC), GC-2010 Plus (Shimadzu), based on ASTM D1945. Two varieties of solvents for carrier phase are n-heptane and n-hexane, and methyl heptadecanoate ($C_{18}H_{36}O_2$) is a standard solution to define the hydrocarbon series on chromatograms. Physical properties of condensate are examined in the chemical laboratory, such as density, specific gravity, API gravity, Reid vapor pressure (RVP), and true vapor pressure (TVP), according to ASTM D5191. In addition, these parameters are daily measured to maintain the quality of condensate.

Chemical Thermodynamic Simulation

The phase behavior in the reservoir is studied over the pressure–temperature range where the fluid as a single phase and petroleum oil and gas as a two-phase equilibrium can be observed. Possibility of chemical reaction in petroleum reservoir can create phase depending on hydrocarbon composition. This reservoir of the study area is a dry gas reservoir, abundant with methane gas [9]. The advent of highly methane found by analytical results of the natural gas can prove this assumption. Chemical reactions based on hydrocarbon types are fabricated by chemical species as reactants and products. The Peng–Robinson equation of state is suitable for simulating the chemical thermodynamic model [10]. Thus, phase equilibrium obtains the occurrence of condensate and natural gas under chemical equilibrium at any temperature and pressure change. The Prode Properties, a computer software program, provide the thermodynamic framework designed to afford phase envelope in process simulation. This program is used in direct integration with Excel software program. The calculated equilibrium points including critical points, cricondentherm, and cricondenbar are displayed in Excel page. Thus, phase diagram and phase envelope of natural gas mixtures are obtained by the Prode Properties [11].

Prediction of hydrocarbon parameters is mainly temperature and pressure. Hydrocarbon component such as methane is dominantly a precursor in every chemical reaction. Moreover, other gases related to the genesis within reservoir and exist in the same environment are combined as a reactant. Results from the gas analyzer show that carbon dioxide, hydrogen gas, and nitrogen in the reservoir are 10, 8, and 2 mol%, respectively. Chemical reactions are conducted by using petroleum components from condensate which is collected in GPP. Two important conditions to control phase behavior consist of pressure and temperature. General scheme for these two variables, pressure and temperature, are defined as 200 bar.g and 200 °C, respectively. Not only these conditions are concerned but geological specifications are also considerable as well. Relationship between chemical equilibrium involved in thermodynamics indicates that they lead to the phase change. All chemical species are representative for evaluating the possibility of phase envelope. Thus, five chemical reactions are created totally, based on these criteria, as follows:

Condition: Pressure = 200 bar.g, Temperature = 200 °C.

Variable chemical species depending on reactant, as indicated in each chemical reaction:

1. Chemical Reaction-1
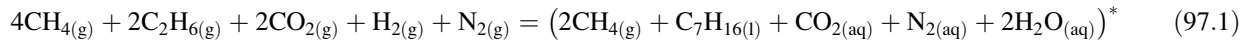
$$4CH_{4(g)} + 2C_2H_{6(g)} + 2CO_{2(g)} + H_{2(g)} + N_{2(g)} = \left(2CH_{4(g)} + C_7H_{16(l)} + CO_{2(aq)} + N_{2(aq)} + 2H_2O_{(aq)}\right)^* \tag{97.1}$$

2. Chemical Reaction-2

$$3CH_{4(g)} + C_3H_{8(g)} + 3CO_{2(g)} + 4H_{2(g)} + N_{2(g)} = \left(CH_{4(g)} + C_7H_{16(l)} + CO_{2(aq)} + N_{2(aq)} + 4H_2O_{(aq)}\right)^* \tag{97.2}$$

3. Chemical Reaction-3

$$2CH_{4(g)} + C_4H_{10(g)} + 3CO_{2(g)} + 4H_{2(g)} + N_{2(g)} = \left(CH_{4(g)} + C_7H_{16(l)} + CO_{2(aq)} + N_{2(aq)} + 4H_2O_{(aq)}\right)^* \tag{97.3}$$

4. Chemical Reaction-4

$$CH_{4(g)} + C_5H_{12(g)} + 3CO_{2(g)} + 4H_{2(g)} + N_{2(g)} = \left(CH_{4(g)} + C_7H_{16(l)} + CO_{2(aq)} + N_{2(aq)} + 4H_2O_{(aq)}\right)^* \tag{97.4}$$
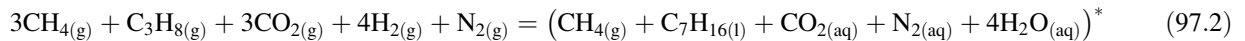
5. Chemical Reaction-5
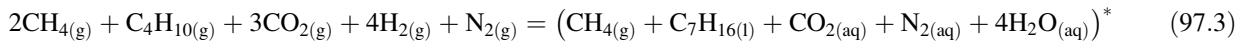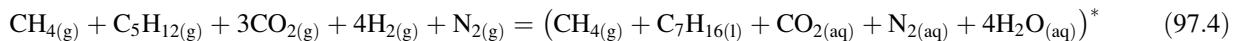
$$CH_{4(g)} + C_6H_{12(g)} + 2CO_{2(g)} + 3H_{2(g)} + N_{2(g)} = \left(CH_{4(g)} + C_7H_{16(l)} + CO_{2(aq)} + N_{2(aq)} + 2H_2O_{(aq)}\right).^* \tag{97.5}$$
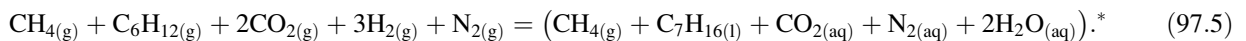
Remark: "*" = Optional.

Results and Discussion

Natural Gas and Condensate

Natural gas (and other liquid) flows from the gas well to the GPP and meets the first location at the inlet slug catcher to separate fluid mixture. Liquid (condensate and water) is isolated from natural gas before flowing to the high pressure flash vessel. Gas chromatography is a technique to detect hydrocarbon composition of the natural gas in the gas line. Its chemical composition in mole fraction is indicated in Table 97.1.

Some parameters of condensate, for example, density, specific gravity, API gravity, RVP, and TVP are determined in the chemical laboratory and indicated in Table 97.2. According to the results in these two tables, the number 1 and 2 are the sampling dates on August 18th, 2012 and October 2nd, 2012, respectively. Each location, inlet slug catcher, high pressure flash vessel, low pressure flash vessel, produced water separator, condensate tank shows the comparison of their properties among them. Condensate samples are also examined by the gas chromatography. Hydrocarbon compositions in mole percent are indicated in Table 97.1. Chromatogram of condensate at the inlet slug catcher is depicted in Fig. 97.1. Information from GPP consists of temperature and pressure, combination with physical properties and chemical properties measured in chemical laboratory. All results are appraised to determine the chemical thermodynamic concept.

Invariable Mole Fraction

The results of the thermodynamic simulations display the relationship of pressure as a function of temperature. These correlations depend on chemical reaction from Eq. (97.1), as indicated in Fig. 97.2. Mole fraction of hydrocarbon is defined only 80 mol% due to the result of GC indicating sum of other gases at 20 mol%. Methane is mainly fraction of hydrocarbon (60 mol%). According to each chemical reaction as shown in Table 97.3, another hydrocarbon gas either ethane, propane, butane, pentane, or hexane is considered to be 20 mol%. Every hydrocarbon equals to 60 mol% of methane and 20 mol% of other gases.

The relationship of pressure as a function of temperature displays the critical point (red triangle, as shown in Fig. 97.2) which occurs under specific conditions, such as temperature, pressure, or composition of hydrocarbon at which no phase boundaries exist. Dew line (dark blue line) is a saturation line appearing in gas phase, but liquid fraction line (bright blue line)

Table 97.1 Chemical compositions of natural gas and condensate

Components (mol%)	Natural gas	Condensate (1) August 18th 2012	Condensate (2) October 2nd 2012
Methane	96.6428	–	–
Ethane	0.8981	–	–
Propane	0.1095	–	–
i-Butane	0.0178	–	–
n-Butane	0.0356	–	–
i-Pentane	0.0151	–	–
n-Pentane	0.0232	–	–
Hexane	0.1018	–	–
Heptane	–	20.168	21.424
Octane	–	24.259	23.745
Nonane	–	18.236	19.681
Decane	–	14.418	13.779
Undecane	–	10.573	10.155
Dodecane	–	6.147	5.772
Tridecane	–	3.218	2.899
Tetradecane	–	1.736	1.495
Pentadecane	–	0.859	0.716
Hexadecane	–	0.386	0.333
CO_2	0.5021	–	–
N_2	1.6537	–	–
Water	–	0.012	0.009

Table 97.2 Physical properties of condensate

Sampling location	Sampling time	Density (g/cm^3)	API gravity	Specific gravity	RVP (psi)	TVP (psi)
Inlet slug catcher	1	0.76	55.77	0.7556	0.91	1.51
	2	0.75	55.52	0.7566	0.75	1.35
High pressure flash vessel	1	0.72	57.50	0.7487	0.99	1.60
	2	0.76	58.20	0.7459	0.97	1.58
Low pressure flash vessel	1	0.75	59.83	0.7396	1.42	1.52
	2	0.74	60.03	0.7362	1.68	1.95
Produced water separator	1	0.73	62.84	0.7281	3.03	3.70
	2	0.73	61.28	0.7340	1.99	2.51
Condensate tank	1	0.75	57.50	0.7487	1.33	1.96
	2	0.73	61.59	0.7328	1.64	2.16

is a saturation line taking place in liquid phase. Moreover, cricondenbar (CriP) point is the maximum pressure and cricondentherm (CriT) is the maximum temperature at which liquid and vapor may coexist in equilibrium. Unit of pressure is bar g, which is abbreviated from bar gauge, which actually measures the difference between the fluid pressure and the atmospheric pressure.

Variable Mole Fraction

According to chemical reaction for thermodynamic assumption, hydrocarbon types and their concentrations (mole fraction) are varied, as shown in Table 97.4. The outcomes from thermodynamic simulation show phase envelopes (Figs. 97.3, 97.4, and 97.5), where a dew line (solid line) is a saturation line appearing in gas phase, but bubble line (dash line) is a saturation line taking place in liquid phase. Each phase diagram reveals the critical point of temperature (T_c) and pressure (P_c). At this point, there is no phase boundaries between the liquid and gaseous phases. Moreover, cricodentherm (CriT) and cricodenbar (CriP) come from their phases. These variables can be extracted from the plot of temperature as a function of pressure.
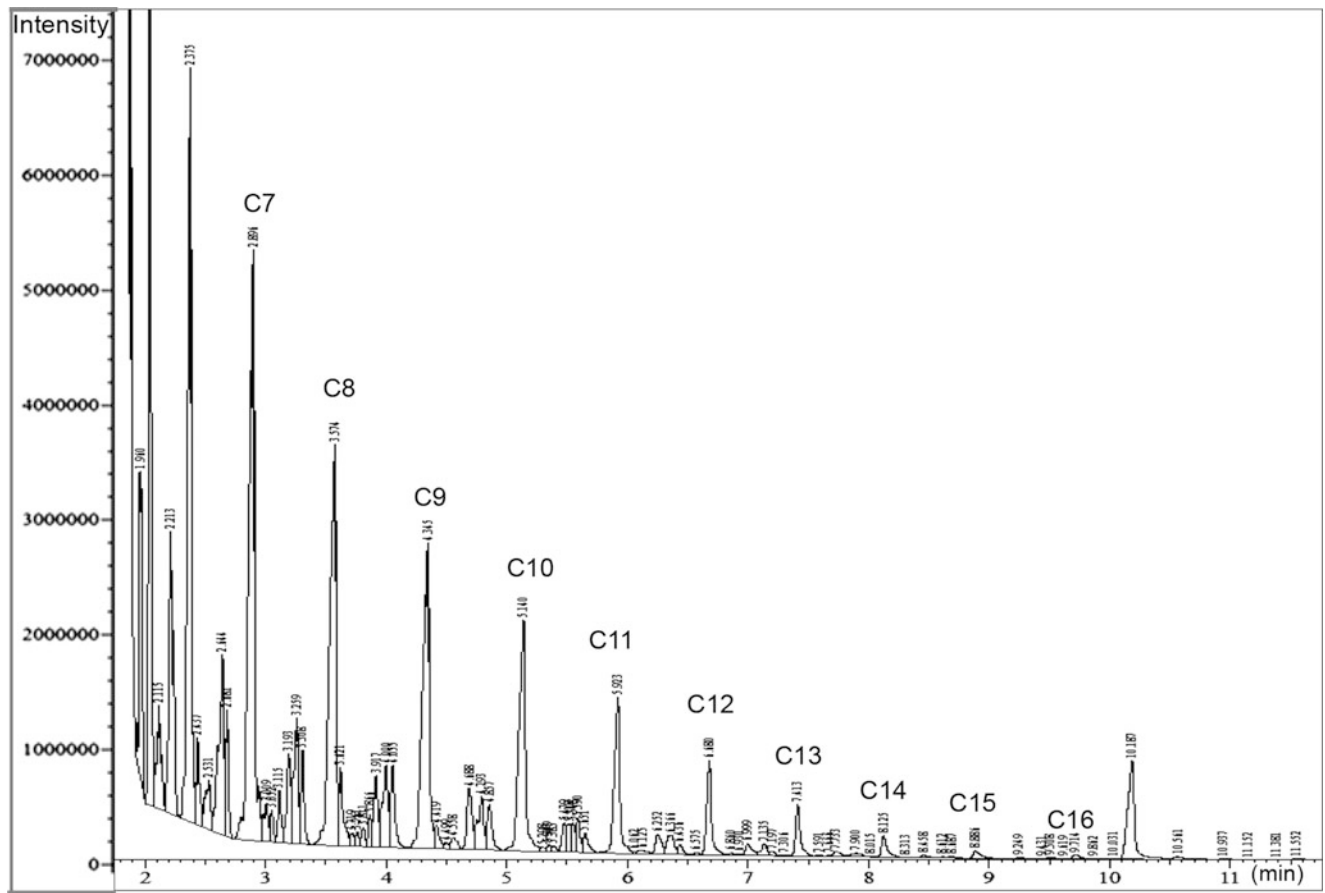
Fig. 97.1 Chromatogram of condensate (inlet slug catcher)

Fig. 97.2 Pressure as a function of temperature for methane and ethane, and parameters at critical point

Parameters at Critical Point	
Pressure	90.62 bar.g
Temperature	-35.22°C
Cricodentherm	-27.17°C
Cricodenbar	92.72 bar.g
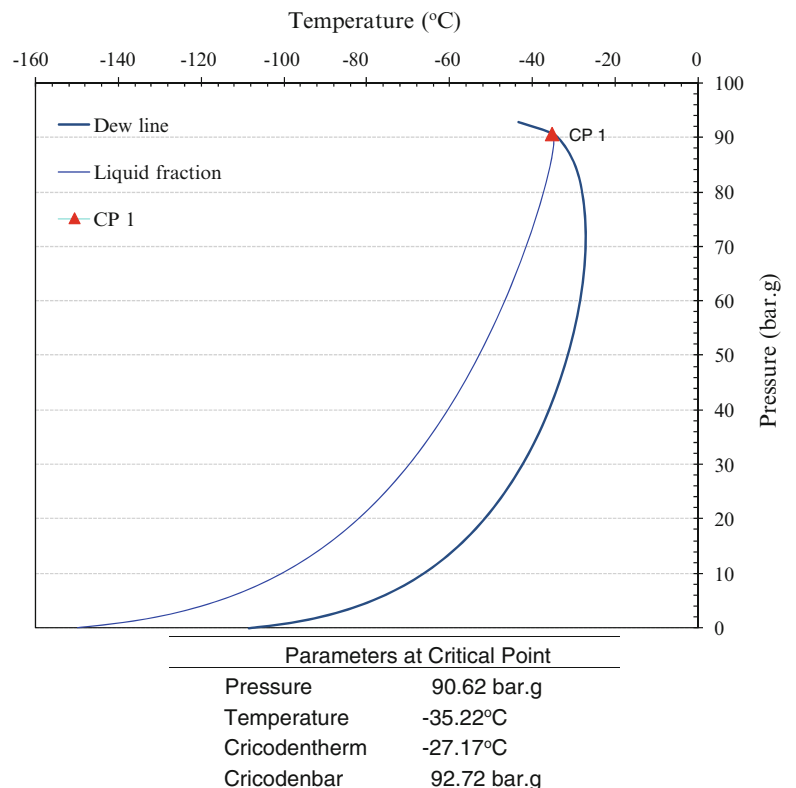
Table 97.3 Carbon ratio and mole fraction of each chemical reaction

Chemical reaction	Carbon ratio	Mole fraction (%)
Eq. (97.1)	$C_1:C_2$	60:20
Eq. (97.2)	$C_1:C_3$	60:20
Eq. (97.3)	$C_1:C_4$	60:20
Eq. (97.4)	$C_1:C_5$	60:20
Eq. (97.5)	$C_1:C_6$	60:20

Table 97.4 Pressure and temperature of each chemical reaction

Reaction	Carbon ratio	Concentration (mol%)	P_c (bar g)	T_c (°C)	CriP (bar g)	CriT (°C)
Eq. (97.1)	$C_1:C_2$	60:20	90.62	−35.23	92.72	−27.18
		50:30	90.89	−20.92	95.39	−14.71
		40:40	88.11	−8.460	−1.103	−4.150
		30:50	83.61	2.360	−1.103	5.080
		20:60	78.25	11.76	−1.103	13.27
Eq. (97.2)	$C_1:C_3$	60:20	121.56	−5.340	124.18	16.91
		50:30	116.98	20.15	126.20	35.21
		40:40	106.48	40.17	121.95	49.57
		30:50	94.49	55.60	1.013	61.41
		20:60	82.76	68.70	−1.013	71.49
Eq. (97.3)	$C_1:C_4$	60:20	142.01	18.20	146.20	50.61
		50:30	129.44	50.70	143.93	70.92
		40:40	111.91	56.00	134.24	61.41
		30:50	94.99	74.40	−1.013	86.32
		20:60	79.92	106.67	−1.013	109.00
Eq. (97.4)	$C_1:C_5$	60:20	181.44	51.83	190.55	98.63
		50:30	154.49	94.27	182.24	120.97
		40:40	126.34	122.55	165.23	137.44
		30:50	102.50	142.43	145.32	150.38
		20:60	83.12	157.03	−1.013	160.96
Eq. (97.5)	$C_1:C_6$	60:20	215.87	92.19	238.10	147.22
		50:30	185.36	120.45	201.30	167.21
		40:40	131.75	171.32	193.01	186.69
		30:50	102.98	191.37	164.89	199.34
		20:60	80.50	205.91	−1.013	209.48

Fig. 97.3 Effect of composition on phase envelope, methane–ethane binary according to the chemical reaction Eq. (97.1)
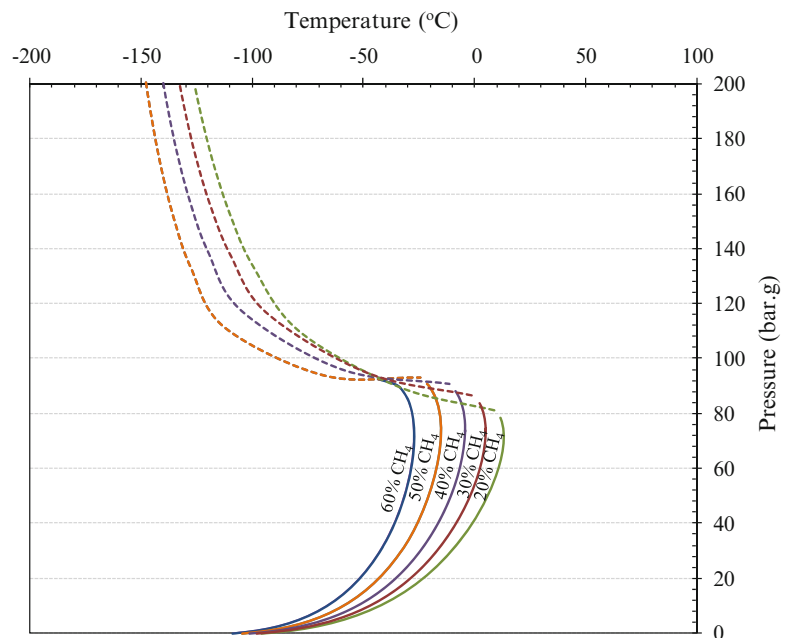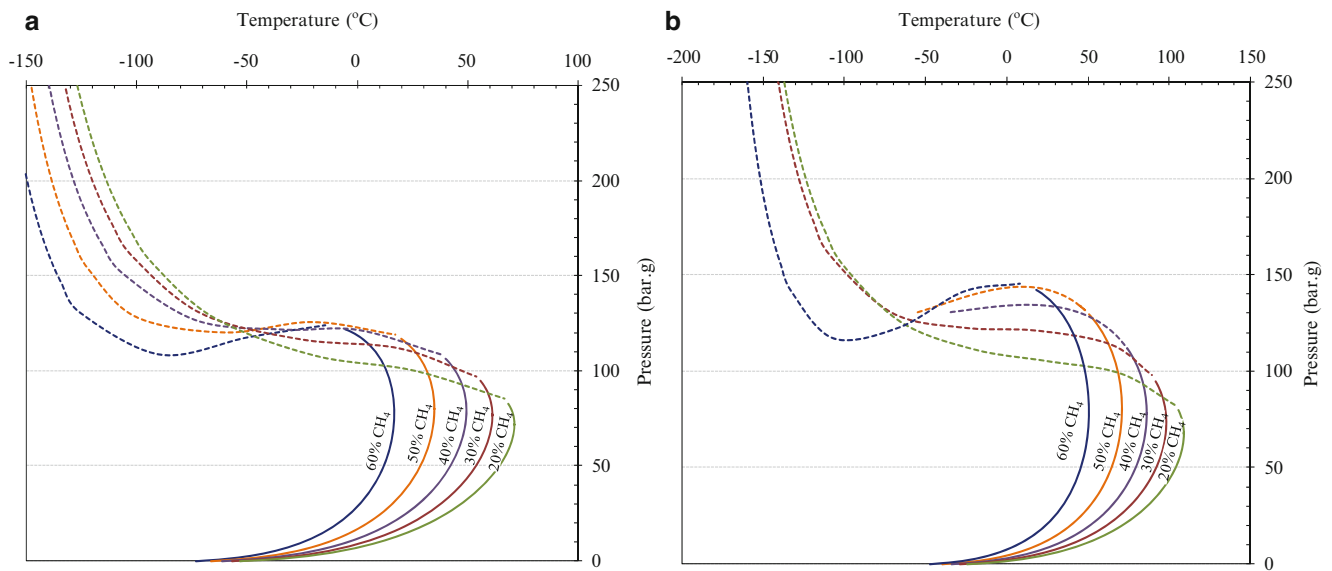
Fig. 97.4 Effect of composition on phase envelope of binary compositions of (**a**) methane–propane for the chemical reaction Eq. (97.2), and (**b**) methane–butane for the chemical reaction Eq. (97.3)
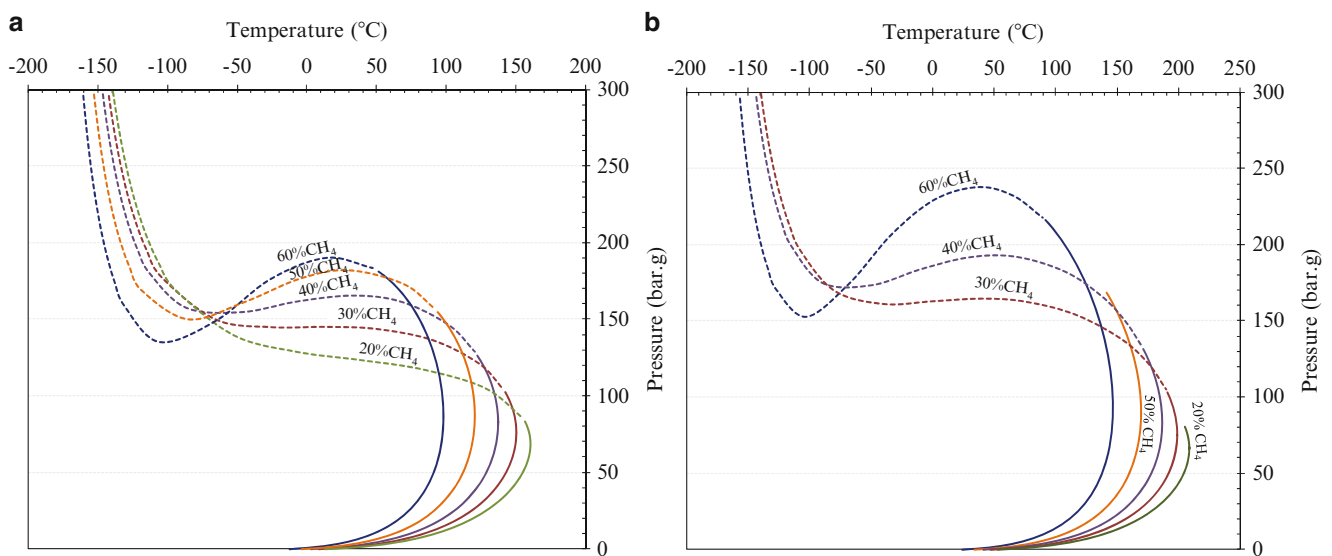
Fig. 97.5 Effect of composition on phase envelope of (**a**) methane–pentane binary for the chemical reaction Eq. (97.4) and (**b**) methane–hexane binary for the chemical reaction Eq. (97.5)

Equilibrium Constant of Chemical Reaction

The van't Hoff equation in chemical thermodynamics relates to the change of temperature and equilibrium constant, given the standard enthalpy change ($\Delta H°$) for calculation. The energy associated with a chemical reaction, in terms of standard enthalpy change or Gibbs free energy, can determine the possibility of chemical reaction under this circumstance. Gibbs free energy (referred to $\Delta G°$) is also the chemical potential that is minimized when a system reaches to equilibrium at constant pressure and temperature. Its derivative with respect to the reaction complement of the system disappears at the equilibrium state. Thus, the free energy is a suitable criterion of spontaneity for the genesis of the chemical reaction with constant pressure and temperature. The free energy of a chemical reaction is calculated by the sum of its enthalpy (H) along with the temperature (T) and entropy (S). Gibbs free energy, enthalpy, and equilibrium constant (K_{eq}) of each chemical reaction are

Table 97.5 Gibbs free energy, enthalpy, and equilibrium constant of each chemical reaction

Reaction	Gibbs free energy (kJ/mol)	Enthalpy (kJ/mol)	Equilibrium constant (K_{eq})			
			0 °C	15 °C	25 °C	200 °C
Eq. (97.1)	32.555	−217.900	0.93073	0.92838	0.92695	0.91184
Eq. (97.2)	−17.94	−310.228	1.01537	1.01033	1.00726	0.97514
Eq. (97.3)	−75.99	−363.084	1.03752	1.03355	1.03113	1.00571
Eq. (97.4)	−134.565	−417.015	1.0615	1.05795	1.05578	1.03297
Eq. (97.5)	−193.837	−471.633	1.08577	1.08301	1.08133	1.06359
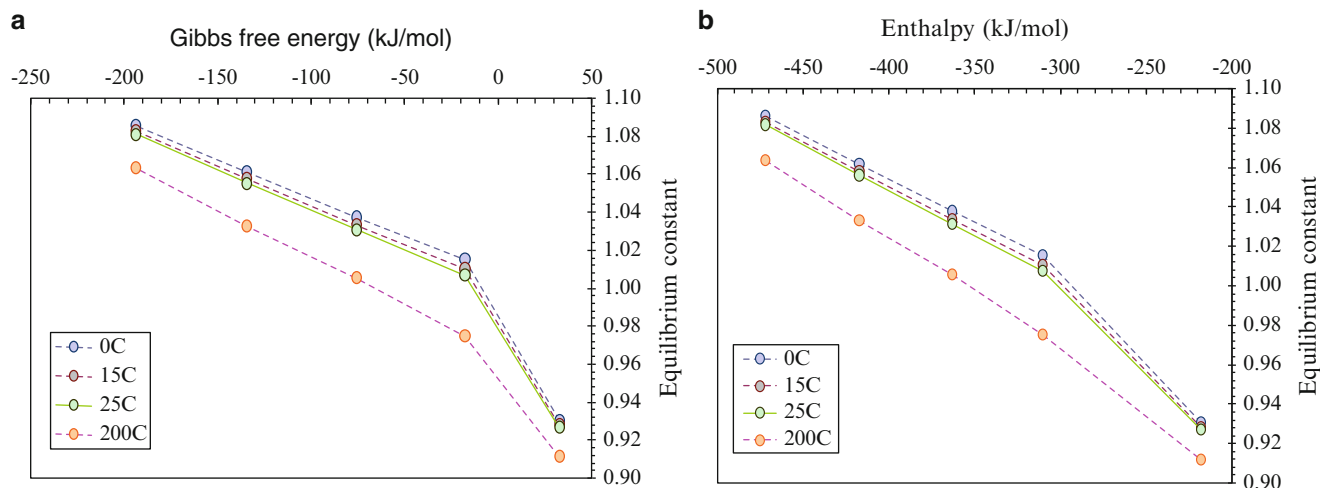
Fig. 97.6 Equilibrium constant as a function of temperature at 0, 15, 25, and 200 °C of (**a**) Gibbs free energy and (**b**) enthalpy

calculated at temperatures of 0, 15, 25, and 200 °C, as shown in Table 97.5 and corresponding to Fig. 97.6. According to Gibbs free energy, the chemical reaction Eq. (97.1) is a non-spontaneous process because of the positive energy, which implies the reverse reaction. This chemical reaction is not capable of proceeding in a given direction, as written. It needs to be driven by an outside source of energy. However, others are the spontaneous reactions and relevant to the assumptions based on conceptual chemical thermodynamics. Moreover, enthalpy of reaction indicates all negative numbers as an exothermic reaction. Therefore, these chemical reactions do not need to add more heat to the system.

For invariable mole fraction of hydrocarbon, methane and another gas are controlled in the ratio of 60:20. Temperature as a function of pressure presents the linear correlation, as shown in Fig. 97.7. Increasing the number of carbon atoms will gradually intensify the temperature and pressure. Linear relationship of the critical point and CriT–CriP line is similar to each other (Fig. 97.8). However, at high temperature and pressure, these two lines are obviously separated. Equilibrium at critical point expresses the different phases between liquid and gas. On the other hand, for variable mole fraction of hydrocarbon, the difference of methane affects the relationship between temperature and pressure. No linear correlation is found all over the plot. The interval between temperature and pressure is obtained from reducing methane concentration. Moreover, hydrocarbon gas change, from ethane to hexane, can cause different consequences. The lowest value of pressure is −1.013 bar g which is hardly realistic. The results of these chemical thermodynamic simulations can predict the possibility of phase equilibria. Hydrocarbon types and mole fraction of these components influence the occurrence of phase envelope.

For equilibrium condition of thermodynamic simulation, thermodynamic calculations based on the chemical reaction are pursued under exothermic reaction which reveal by enthalpy computation. These enthalpies relate to the equilibrium constant at different temperatures: 0, 15, 25, and 200 °C. The higher temperature can cause the lower equilibrium constant. This condition indicates that chemical reaction tends to be depleted. Creation of the chemical reaction depends on the estimation of hydrocarbon type. Reactants and products define the possible of phase equilibrium in which is correlated to Gibbs free energy.

Fig. 97.7 Pressure as a function of temperature for each chemical reaction at critical point
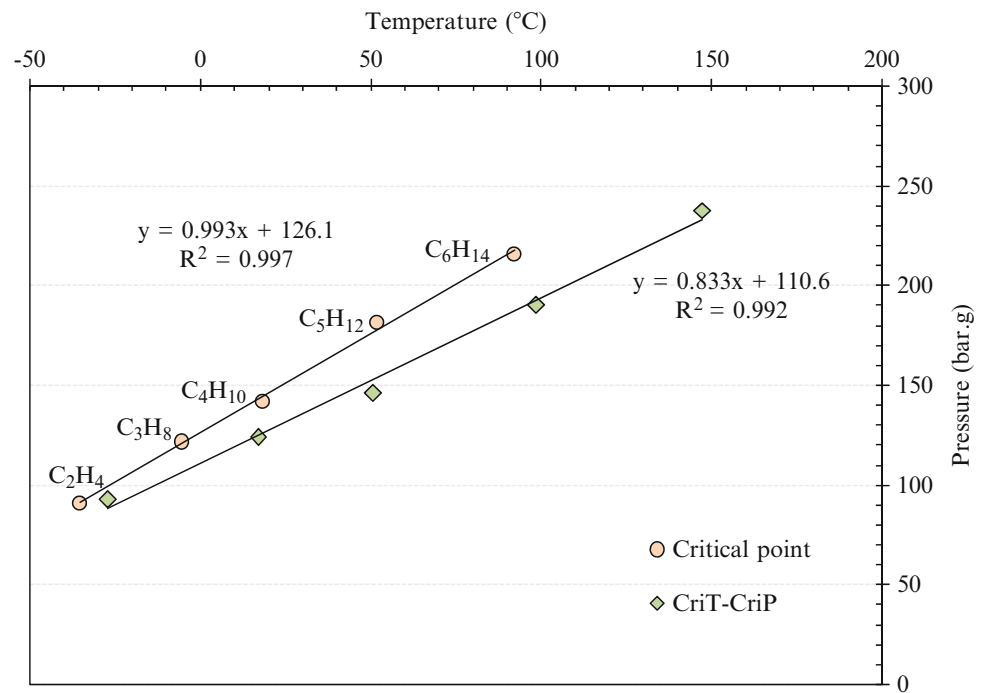
Fig. 97.8 Pressure as a function of temperature at critical point and indicating cricondenbar (CriP) and cricodentherm (CriT) of overall data corresponding to Fig. 97.7
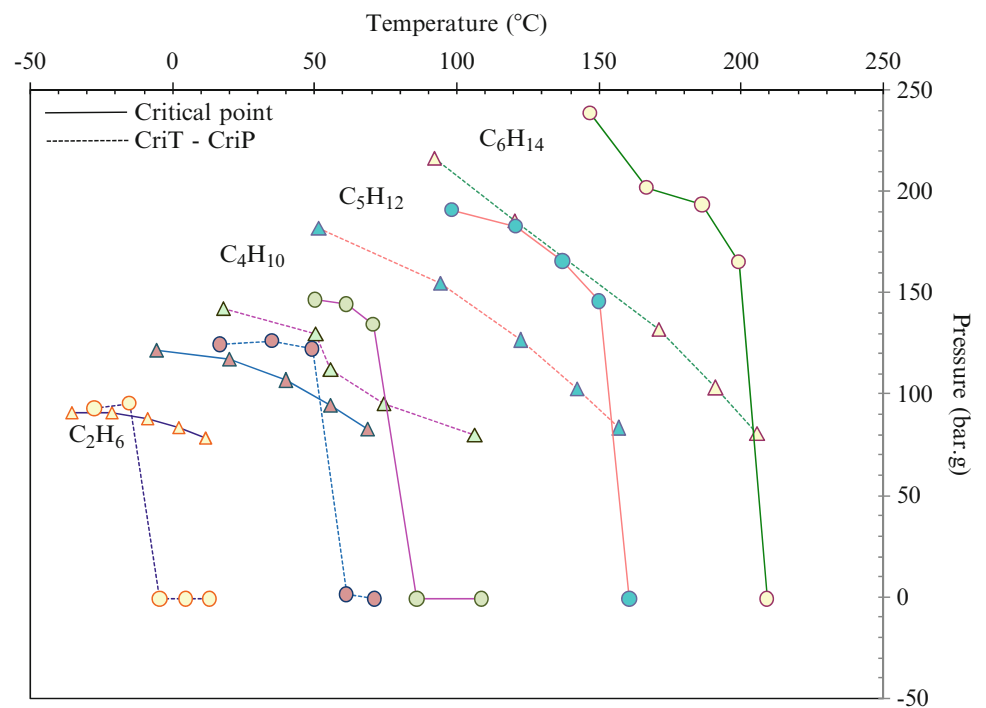
Phase Behavior of Dry Gas Reservoir Fluid

The thermodynamic simulation indicates that the phase diagram on the pressure–temperature construction typifies the behavior of a dry gas reservoir. If the pressure and temperature are reduced from the original reservoir conditions to standard stock tank conditions (condensate tank), there is no liquid recovery, and the reservoir fluid remains completely in the gaseous phase during the process. The pressure–temperature curve for hydrocarbon reservoir can be classified in terms of its phase envelope. The typical components of gas production from petroleum reservoirs can be explained in their phase envelopes.

Conclusions

The phase envelope of hydrocarbon species in natural gas field predicted by using thermodynamic simulation is studied. This inquiry is valuable research to comprehend the phase equilibria of natural gas and condensate. Their thermodynamic concepts are based on physical and chemical characteristics in equilibrium condition. Phase envelope can be evaluated at suitable phase. The condensate samples are collected from the GPP, where sampling is on August 18th and October 2nd 2012.

The series of sample collection are followed based on inlet slug catcher, inlet high pressure flash vessel, outlet high pressure flash vessel, inlet produced water separator, outlet produced water separator, low pressure flash vessel condensate tank A and condensate tank B. Their physical properties and chemical composition of natural gas and condensate are examined. The physical properties of condensate are analyzed on the basis of API gravity, density, RVP, TVP, pressure, and temperature. The API gravity of condensate in each process is presented in the range of 55–63°. Pressures in each process are decreased from inlet slug catcher to the condensate tank, where the maximum pressure is 747.54 bar g of the inlet slug catcher. Methane is discovered approximately 96 mol% and other hydrocarbon gases 0.1–1%.

Possibility of chemical reaction depending on chemical species is assumed by equilibrium condition between natural gas and condensate. Five variable chemical reactions are selected by mainly methane. The interest reactants are paired between methane and another hydrocarbon combined to carbon dioxide gas, hydrogen gas, and nitrogen gas. The results from experiment can be beneficial for evaluating an assumption to predict the phase equilibrium depending on the chemical reaction. The Prode Properties is a computer simulation program which shows characteristics of phase equilibrium of each component. Phase envelope of natural gas shows that temperature is inversely proportional to equilibrium constant. Low equilibrium constant at high temperature indicates that chemical reaction tends to be moved further slowly. If the number of carbon atoms increases from 1 to 6, the temperature and pressure will increase gradually. Hydrocarbon types and its compositions can affect the phase envelope.

References

1. Freze R, Chevalier JL, Peneloux A, Rauzy E (1983) Vapour–liquid equilibria calculations for normal fluid systems using a new cubic equation of state. Fluid Phase Equilib SPE J 3:65–80
2. Gabitto JF, Tsouris C (2010) Physical properties of natural gas. J Thermodyn 1:1–12
3. Ayala LH (2006) The role of fluid thermodynamic behavior in natural gas handling and transportation. Business Briefing: Hydrocarbon World 2006. Touch Briefings Ltd., London, UK
4. Atilhana M, Aparicio-Martinezb S, Hallc KR, El-Halwagic M, Iglesias-Silva GA (2010) On the PρT, PηT and phase envelope behavior characterization of Qatari type natural gas mixtures. Proceedings of the 2nd annual gas processing symposium, Qatar, 10–14 Jan 2010, pp 399–407
5. Michelsen ML (1980) Calculation of phase envelopes and critical points for multicomponent mixtures. Fluid Phase Equilib 4:1–10
6. Alfradique MF, Castier M (2007) Calculation of phase equilibrium of natural gases with the Peng–Robinson and PC-SAFT equations of state. Oil Gas Sci Technol 62:707–714
7. Ministry of Energy (2007) Petroleum field in Thailand. http://www.dmf.go.th/
8. Sattayarak N (2005) Petroleum potential of northeast Thailand. International conference on geology, geotechnology and mineral resources of Indochina (GEOINDO'2005), Khon Kaen University, Khon Kaen, Thailand, pp 21–30
9. Campbell JM (1994) Gas Conditioning and Processing (Campbell Petroleum Series), 17th edn. Campbell Petroleum, United States of America
10. USGS (2006) http://pubs.usgs.gov/of/2005/1451/equation.html
11. Prode Properties (2010) Phase envelope. http://www.prode.com

Use of Hazelnut Oil Ethyl Ester as a Fuel in Pre-chamber Diesel Engine

Murat Cetin and Ahmet Tandiroglu

Abstract

This study briefly reviews the use of hazelnut oil ethyl ester which was produced by hazelnut oil as an alternative fuel in pre-chamber diesel engines, and compares it with pure hazelnut oil and diesel fuel. In the experiments, a naturally aspirated, pre-chamber indirect injection, four cylinders, four-stroke diesel engine was used. During the test, power, torque, emissions values, and fuel consumption were measured with respect to the engine speed. As a viscosity and density of hazelnut oil ethyl ester was found to closely similar to those of diesel fuels. Test results obtained from hazelnut oil ethyl ester were compared to hazelnut oil and standard diesel fuel test results. CO, NOx, smoke density of hazelnut fuel, and exhaust temperatures were lower than of diesel fuel. The biodiesel NOx emissions higher than diesel fuel all engine rpm and NOx emission was measured 15 % higher from the diesel fuel. The specific fuel consumption is increased: at low-speed 6 %, medium speed 9 %, and high-speed 12 %. The average increase in specific fuel consumption 9.7 % is determined. As a result of this study, it is concluded that hazelnut oil biodiesel could be used as an alternative fuel in diesel engines.

Keywords

Hazelnut oil • Hazelnut oil ethyl ester • Alternative fuel • Combustion • Diesel engine

Introduction

Diesel fuel is largely consumed by the transportation sector. Diesel engines are usually employed by heavy duty vehicles used for transportation in the world and contribute to the prosperity of the worldwide economy. Due to increased environmental problems and fast depletion of fossil fuel resources is demanding an urgent need to carry out research work to find out the viable alternative fuels and sustainable energy systems. Studies on internal combustion engines have been recently concentrated on alternative fuels. In general, they agree that plenty of oil will be used as an energy carrier. Over the past decades, since the invention of internal combustion engines, the development of integral combustion engines has been based on the availability of petroleum-derived fuel, which in turn has been tailored to meet the needs of current engines. However, alternative fuels for diesel engines have become increasingly important due to the gradual depletion of world petroleum reserves, increasing fuel prices, and the impact of environmental pollution due to increasing exhaust emissions and several socioeconomic aspects. As the public concern about environmental pollution and energy security increases, alternative diesel fuels, such as biodiesel, diesel, and ethanol–diesel fuel blends, are receiving more attention. The increase in alternative fuel investigations is caused by two main factors: a rapid decrease in world petroleum reserves and

M. Cetin (✉)
Department of Engine Vehicles and Transportation Technologies, Vocational High School, Erzincan University, 24100 Erzincan, Turkey
e-mail: mcetin@erzincan.edu.tr

A. Tandiroglu
Department of Mechanical Engineering Technology, Vocational High School, Erzincan University, 24100 Erzincan, Turkey
e-mail: atandiroglu@erzincan.edu.tr

important environmental concerns originating from exhaust emissions. Besides them, some other aspects such as increasing fuel price, the idea of supplying the fuel demand from local sources, for reducing the import of the crude oil, and creating new employments have promoted these investigations. A number of researchers have investigated the effect of using different kinds of biodiesel and biodiesel blended with ethanol or methanol in diesel engines [1, 2]. The fuels produced by transesterification of the oils are called biodiesel. The advantages of biodiesels as diesel fuel are as follows: the minimal sulfur and aromatic hydrocarbons content, higher flash point, lubricity, cetane number, biodegradability, and not containing any metals or crude oil residues and nontoxicity. Although biodiesel cannot entirely replace petroleum-based fuels, biofuels and diesel fuel blends can be used on existing engines to achieve both environmental and energy benefits. Biodiesel has properties similar to those of traditional fossil diesel fuel such that it can be substituted for diesel fuel with little or no engine modification. Studies clearly indicate that the use of biodiesel may potentially reduce the dependence on petroleum diesel fuel and improve air quality. Substantial reduction in particulate emissions can be obtained through the addition of biodiesel to diesel fuel. Vegetable oils, the main source of biodiesel, have considerably higher viscosity and density compared to diesel fuel. Despite transesterification process, which has a decreasing effect on the viscosity of vegetable oil, it is known that biodiesel still has some higher viscosity and density when compared to diesel fuel [3, 4]. The viscosities of fuels have important effects on fuel droplet formation, atomization, vaporization, and fuel/air mixing process, thus influencing the exhaust emissions and performance parameters of the engine. The vegetable oil ester-based biodiesel has long been used as fuel for diesel engines. Many studies about the use of biodiesel fuels in diesel engines have been done and some of them have been reviewed. Studies clearly indicate that the use of biodiesel may potentially reduce the dependence on diesel fuel and improve air quality. Substantial reduction in particulate emissions can be obtained through the addition of biodiesel to diesel fuel. B20 (a mixture of 20 % biodiesel and 80 % diesel) has become the most popularly used biodiesel fuel blend and this blend level has been studied in different countries. Biodiesel blended with ethanol the performance and emissions on and it found reduction of CO and NOx emissions using 20 % blended fuel but an increase in HC emission. Compared the emissions of biodiesel and biodiesel with emulsified and fumigated methanol and found that the disadvantage of increased NOx emission of biodiesel. Compared to fossil diesel fuel, biodiesel has several superior combustion characteristics. Biodiesel fuel can effectively reduce engine-out emissions of particulate matter, CO, and hydrocarbons in modern four-stroke compression-ignition engines. The exhaust emissions of diesel engines fuelled with biodiesel or its blends with diesel fuel have been studied by many investigators. It has been usually reported that there are reductions in CO, HC, and smoke emissions while NOx emissions increase. It has been shown that the oxygen content in biodiesel is the main factor for reducing pollutant emissions and increasing NOx as a result of better combustion [5–8].

Turkey's energy demand has risen rapidly as a result of economic and social development over the past 2 decades. As in many other countries, Turkey is dependent on fossil fuels to meet its energy requirements. Fossil fuels account for approximately 88 % of the country's total primary energy consumption. Turkey imports three major sources of energy, and its dependence on imported fossil fuels is expected to increase even further. At present, Turkey's oil production met only 10 % of demand; the remaining 90 % is being imported every year. In spite of Turkey's heavy dependence on fossil fuels for energy demand, the country has a large potential for development of renewable resources of every type. Biofuels can provide an opportunity for Turkey to decrease its dependence on foreign oil, eliminate irregularities in agriculture, create new employment opportunities, and decrease rural depopulation and sustainable energy development. In the 2020s, it is estimated that gasoline consumption will remain at its current levels of around 2.5 million tones. However, it is likely that diesel consumption will rise from 13.9 million tons (in 2010) to 18.3 million tons [9]. Turkey has a large area of suitable agricultural land for the production of biofuel crops. Turkey's biodiesel production is only around 60,000 t/year. In this study, this main idea has been taken as the research aim and the evaluation of the direct use of hazelnut oil and hazelnut oil biodiesel as a diesel fuel has been investigated and compared with that of diesel fuel. Hazelnut is especially important in Turkey, because Turkey is the biggest hazelnut producer country in the world, and hazelnut oil was selected for the study because of its wide use in Turkey. Yields of 2,200 kg/ha annually are common with good cultural practice, or 20 barrels of petroleum equivalent per hectare-year [1]. In Turkey, studies about the use of hazelnut oil biodiesel fuels in diesel engines have been done. The hazelnut oil methyl ester was tested in a four cylinder, turbocharged, direct injection diesel engine, and test results compared to standard diesel fuel test results. As a test results, hazelnut oil methyl ester are very close to diesel fuel and CO, NOx, smoke density of hazelnut oil methyl ester and exhaust temperatures were lower than of diesel fuel [10]. Biodiesel from a hazelnut soapstock/waste sunflower oil mixture was investigated the effects of the methyl ester addition in different proportions to Diesel No. 2. The CO emissions of the blend were higher at low speed and lower at high speeds, and higher CO_2 emissions in the experimental speed range and NOx emissions slightly increased due to the higher combustion temperature and the presence of fuel oxygen with the blend at full load were observed [11].

Obtaining of Hazelnut Oil Ethyl Ester

The transesterification is a widely applied, convenient, and most promising method for reduction of viscosity and density of vegetable oils. A detailed description of the transesterification process can be found in the literature. Although neighbor and boundary to Europe a limited amount of biodiesel is produced from rapeseed oil in Turkey, cottonseed oil offers a great potential as the source of biodiesel because cotton is the second produced seed plant after sunflower in terms of the cultivated area [2, 11]. At the beginning of the study, the natural hazelnut oil used as a fuel and it was produced by The Union of Hazelnut Sales Cooperative. Transesterification is an efficient method to decrease and convert high viscosity vegetable oil into a fuel with chemical properties similar to those of diesel fuel. In the present study, base catalyzed transesterification NaOH is used to prepare biodiesel from hazelnut oil. The production of hazelnut oil ethyl ester was made in Erzincan University Vocational High School, Department of Engine Vehicles and Transportation Technologies, Automotive Technology Program of diesel engines laboratory by using biodiesel production system. The transesterification process of hazelnut oil was performed using 1.25 L ethyl alcohol and 50 g sodium hydroxide as catalyst per 5 L pure refined hazelnut oil. Biodiesel production process, purity of 99.8 % sodium hydroxide, 0.910 kg/L density of pure refined hazelnut oil, purity 99.5 %, and 99.8 % purity, 0.79 kg/L density of ethanol was used. First, hazelnut oil was heated to about 65 °C in a reactor with a capacity of about 8 L. Ethanol and catalyst were mixed in a separate glass containers. Then, the catalyst and ethanol mixture were to dissolve and added to the heated hazelnut oil in the reactor. The mixture was stirred for 1 h at a fixed temperature of about 65 °C to esterification reaction. After esterification process, the glycerol layer was settled down, the ester layer formed at the upper part of the container and the products which are divided in separate containers. A temperature of 65 ± 1 °C was maintained for 4 h, and the reaction products were allowed to settle under gravity for 6 h in a separating funnel. After the production; washing of the biodiesel thus produced is essential for removal of the impurities, water, and the residual catalyst, which may be harmful for combustion engines. Produced biodiesel was heated at 100 °C, for removing water contained in the esterified hazelnut oil. The mixture was again allowed to settle under gravity for 6 h, and the lower layer of water containing impurities was drained out. Finally, the produced hazelnut oil biodiesel was left to cool down. The production process is presented schematically in Fig. 98.1, and the overall reaction is represented in Fig. 98.2.

Produced hazelnut oil biodiesel and hazelnut oil were analyzed at the laboratory of chemical and used fuels properties are given as a comparison of in Table 98.1. As shown in Table 98.1, there is significant difference for specific gravity and heating value between vegetable oils and diesel fuel. Viscosity of hazelnut oil is more than 11 times than that of diesel fuel and hazelnut oil has about 27 % lower heating value. Viscosity of hazelnut oil biodiesel is more than 1.75 times than that of diesel fuel and hazelnut oil biodiesel has about 14 % lower heating value. From the technological point of view, the fuel
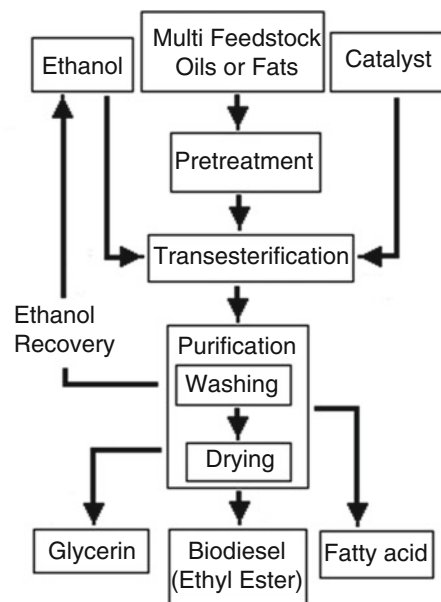
Fig. 98.1 The flow chart of the biodiesel production process

Fig. 98.2 The transesterification of triolein (glycerol trioleate) to C_{18} ethyl esters [12]

$$C_{17}H_{33}COOCH_2 \qquad\qquad HOCH_2$$

$$C_{17}H_{33}COOCH \ + \ 3C_2H_5OH \ \underset{\longrightarrow}{\overset{Catalyst}{\longleftarrow}} \ HOCH + 3C_{17}H_{33}COOC_2H_5$$

$$C_{17}H_{33}COOCH_2 \qquad\qquad HOCH_2$$

Triolein ___ Ethanol ___ Glycerol ___ C_{18} Ethylester (Biodiesel)
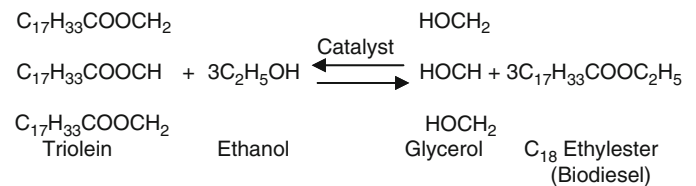
Table 98.1 Property of hazelnut oil biodiesel, hazelnut oil, and diesel fuel

Property	Hazelnut oil biodiesel	Hazelnut oil	Diesel oil
Density (kg/L)	0.82	0.91	0.86
Flash point (°C)	50–170	245	60
Cetane	45–50	41–43	50 min
Sulfur (%)	0.00–0.0024	0.030	0.050
Heating value (kJ/kg)	38,724	33,028	45,390
Color	Light green	Amber yellow	–
Kinematic viscosity (mm^2/s)	1.9–5.6	30.97	2.9
Water and sediments (%)	0	0	Trace
Ash (%)	0.01–0.02	0.004	0.001
Density (kg/L)	0.82	0.91	0.86
Flash point (°C)	50–170	245	60
Cetane	45–50	41–43	50 min

property of hazelnut oil and hazelnut oil biodiesel seems to meet the fundamental requirements of a diesel engine. Therefore, use of hazelnut oil and hazelnut oil biodiesel as a fuel substitute for conventional diesel fuel in a diesel engine is reasonable and prospective.

Experimental Study

The layout of the experimental setup is shown in Fig. 98.3. The experimental setup consists of a naturally aspirated IDI diesel engine, an engine test bed, a gas analyzers, and thermocouples. The experiments were performed with a 2,403 cm^3 displacement, four cylinders, four-stroke, water cooled, 21:1 compression ratio pre-chamber diesel engine of Mercedes-Benz OM 616. The maximum torque was 138 Nm at 2,400 rpm, and the maximum engine power was 44 kW at 4,200 rpm. For such a proposal, at the conventional diesel engine not modification of structure is unnecessary as has been confirmed. A hydrokinetic dynamometer was coupled to the engine and the engine's power was measured. A simple mechanism has been attached to the engine speed by controlling the throttle position, and the engine was examined at partial and full loads. In order to satisfy the standard conditions for each fuel at the experimental engine, it was possible to keep constant test process operating parameters of the engine circuits, the oil and cooling water temperatures, which can influence mainly the exhaust emission levels, thus increasing the credibility for comparing the measured values. The same procedure was repeated for three type fuels by keeping the same engine operating conditions. The differences in the measured performance and exhaust emission parameters from the baseline operation of the engine, when working with conventional diesel fuel, hazelnut oil and hazelnut oil biodiesel were determined and compared. The series of tests were conducted by using three different type fuels, with the engine working at a different speeds, and the static injection timing was kept at 24° crank angle before top dead center. The fuel piping system allows three separate pipe lines for diesel fuel; hazelnut oil and hazelnut oil biodiesel in order to avoid mixing between the tested fuels and the engine was run for about 20 min to stabilize at its new condition in each fuel change. At the beginning of the study, the investigation effort was directed to study the engine performance, emission characteristics of diesel engine using diesel fuel. In the second and third phases of the study, the investigation effort was directed to study the engine performance, emission characteristics of diesel engine using diesel fuel and 100 % refined hazelnut oil and hazelnut oil biodiesel. K type thermocouples and sensors are installed in the system in order to measure the parameters: pressure and temperature of lubricant oil, fuel consumption, fuel temperature, temperature of cooling water, pressure, speed, and temperature of intake air, exhaust gas temperature, ambient temperature, atmospheric pressure, and humidity. A Bosch ETT008.55EU model and Bosch BEA370 gas analyzer were used to measure the CO, CO_2 in percentages
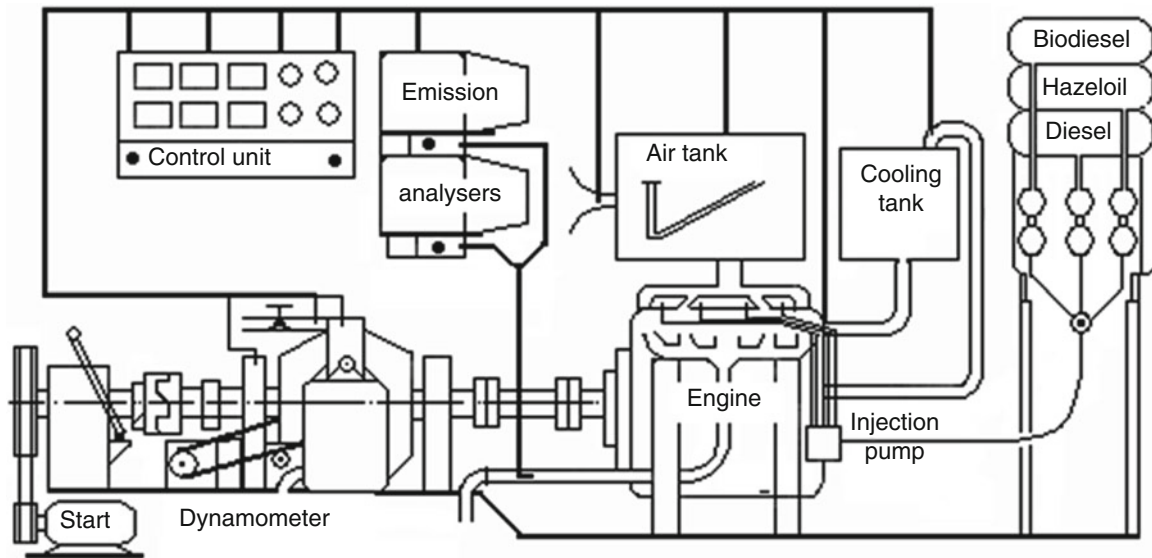
Fig. 98.3 The experimental apparatus

by volume and NOx and HC ppm by volume. Smoke was measured with Bosch 3.011 exhaust-gas measuring module for diesel engine emissions. The initial data were taken after the stabilization of the engine during running. The results of this study that has been performed with precombustion chamber diesel engine have indicated that hazelnut oil and hazelnut oil biodiesel are employed as substitutes for diesel fuel.

Calculation of the Engine Performance Parameters

The experiments were performed without any modification on the engine. For each fuel testing, the volumetric flow rates of air and fuels were measured and based on which the mass consumption rates of the fuel were calculated. The air/fuel ratio was calculated, based on the stoichiometric air/fuel ratio and the actual air/fuel ratio. During the experimental study, indicated performance parameters, such as the brake power (Pe), the brake specific fuel consumption (be), the brake thermal efficiency (bte), and the brake mean effective pressure (bmep) can be determined by using the following equations respectively, according to the engine torque (Me), the engine speed (ne), and the mass consumption rate ($\dot{m}$f) of the fuel. The brake power, Pe (in kW)

$$P_e = \frac{Me \times ne}{9549} \tag{98.1}$$

The brake mean effective pressure, bmep (in bar),

$$bmep = (4\pi Me/VH) \times 10^{-5} \tag{98.2}$$

As known, VH (in m^3) is the engine total (i.e., of all four cylinders) displacement volume. The brake specific fuel consumption (be) (in g/kWh):

$$B_f = \dot{m}_f . \rho_f . 10^{-3.} 3600/Pe \tag{98.3}$$

$$b_e = \frac{3600}{H_u . \eta_e} \tag{98.4}$$

where be is the $\dot{m}$f is the mass consumption rate of the fuels in kg/s, Hu is the lower heating value of the fuels in kJ/kg and is a constant which depends on the kind of the fuel. The primary evaluation calculated for pre-chamber diesel engine burning of
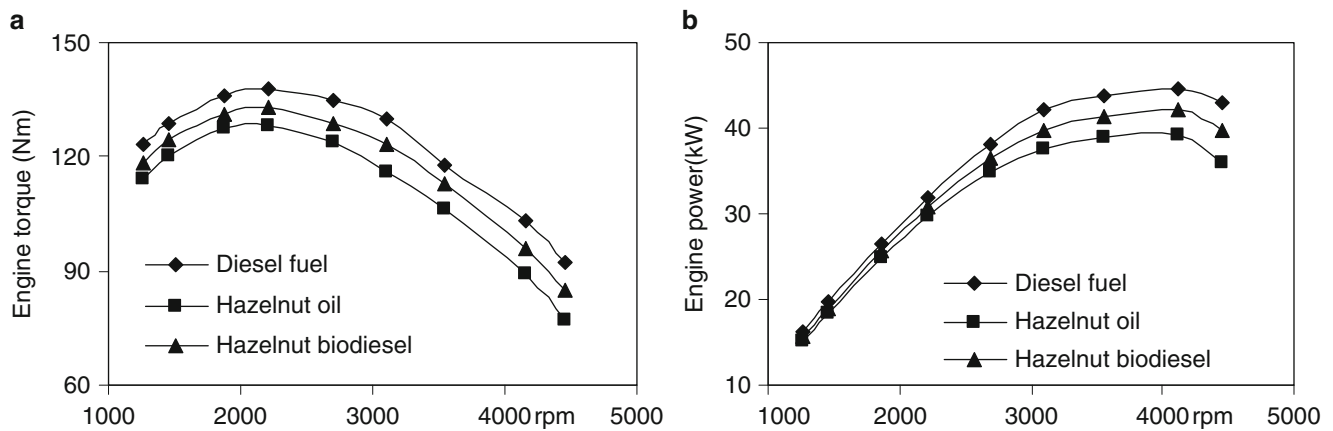
Fig. 98.4 (**a**) Variation of engine torque and (**b**) engine power parameters versus engine speed for fuels

diesel fuel, hazelnut oil, and hazelnut oil biodiesel is its thermal efficiency (η_e). The relationship between thermal efficiency (η_e) and specific fuel consumption (be) is represented by Eqs. (98.3) and (98.4). For making easy to understand, we used the specific fuel consumption as an estimate of the thermal efficiency and, on account of the inverse relationship between them, a decrease in specific fuel consumption would reflect an increase in thermal efficiency. Thus, in the following tests, specific fuel consumption will be taken as the main evaluation parameter.

Results and Discussion

The engine performance at various loads using diesel fuel, hazelnut oil, and hazelnut oil biodiesel was observed in terms of brake power (Pe), brake specific fuel consumption (bsfc), and exhaust emissions (CO, CO_2, HC, NOx, and O_2). The viscosities of biodiesel fuels have important effects on fuel droplet formation, atomization, vaporization, and fuel/air mixing process, thus influencing the exhaust emissions and performance parameters of the engine.

Engine Performance

The results have been compared with the basic engine performance using 100 % diesel fuel at different load conditions over the engine speed range. For three test fuels, the torque variations with engine speed were shown in Fig. 98.4a, the maximum torque values were observed around 2,250 rpm of engine; for all test fuels similar to the torque values, the torque for diesel fuel was higher than hazelnut oil and hazelnut oil biodiesel fuels. Figure 98.4b shows that the values of brake power variations of the test engine for three test fuels. It is clear from Fig. 98.4b that the power of diesel fuel was found higher than hazelnut oil and hazelnut oil biodiesel fuels. It can be observed that the engine torque and power increase with increase in engine speed. Using 100 % hazelnut oil and hazelnut oil biodiesel, for all of engine load and speed conditions, the engine power and torque are generally slightly lower than the corresponding values using diesel fuel. There are two reasons for taking this result: first, the higher calorific value of diesel fuel is higher than hazelnut oil and hazelnut oil biodiesel. Second, the viscosity of hazelnut oil and hazelnut oil biodiesel is higher than diesel fuel, and combustion has been affected and deteriorated from the viscosity of hazelnut oil and hazelnut oil biodiesel. The maximum torque values for diesel fuel 138 Nm, for hazelnut oil 128 Nm, and for hazelnut oil biodiesel 133 Nm were measured respectively at 2,155 rpm. The lowest torque value was obtained for hazelnut oil fuel for all speeds of engine. The maximum engine power values for diesel fuel 43 kW, for hazelnut oil 37.4 kW, and for hazelnut oil biodiesel 41 kW were measured respectively at 4,200 rpm. The lowest power value was obtained for hazelnut oil fuel for all speeds of engine.

Fig. 98.5 Variations of specific fuel consumption parameters versus engine speed for fuels
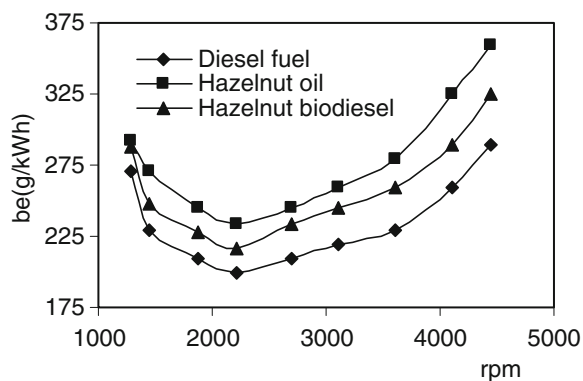
Fig. 98.6 Variations of CO emissions parameters versus engine speed for fuels
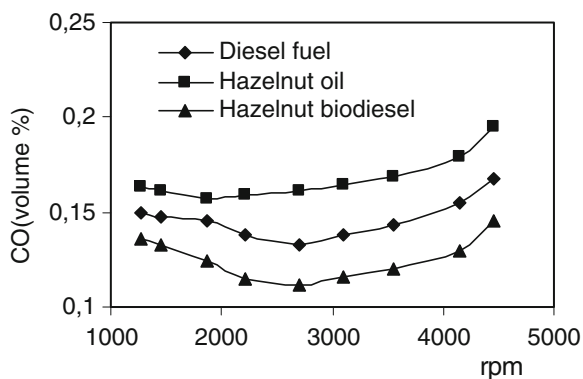
Specific Fuel Consumption

Figure 98.5 shows that the fuel consumption rates out of the three fuels, the specific fuel consumption (be) curves were optioned for best torque all engine speeds. As shown the curves, the specific fuel consumption (be) for the three fuels decreased slightly with the increase in medium engine speed and increase in engine torque. Hazelnut oil and hazelnut oil biodiesel consumption increased roughly in proportion with engine speed under engine loads conditions. This is primarily due to the fact that diesel has the highest heating value from than other two fuels, and needed the lowest fuel consumption rate for achieving the same engine brake horsepower output as the other fuels. Hazelnut oil biodiesel consumed less than hazelnut oil in attaining the same engine horsepower output, for that its heating value was higher than hazelnut oil. Depending on the high engine speeds, the friction power increased according to the mechanical efficiency dropped and the engine torque output decreased, this situation leading to an increase in the fuel consumption rate for all fuels. Results from the tests of the engine fuelled by diesel fuel, hazelnut oil, and hazelnut oil biodiesel indicated that specific fuel consumption of the engine fuelled by hazelnut oil is approximately 15 % higher and hazelnut oil biodiesel is approximately 10 % than that of diesel fuel. The increase of the specific fuel consumption (be) can be explained by the lower heat values of hazelnut oil and hazelnut oil biodiesel compared with that of diesel fuel. For the lower heat values of hazelnut oil and hazelnut oil biodiesel, more fuel has to be injected to obtain the same power output.

Exhaust Gas Emissions

Figure 98.6 shows the CO emissions for the two alternative fuels under different engine speeds. The minimum CO emissions were obtained with hazelnut oil biodiesel and the maximum CO emissions were obtained with hazelnut oil. The diesel fuel CO emission is between hazelnut oil biodiesel and hazelnut oil. Due to the high viscosity, the air/fuel mixing process is affected by the difficulty in atomization of the hazelnut oil. The higher the load, the richer the fuel mixture burned, and thus, more CO is produced. This situation is typical of behavior for a homogenous charge engine as CO emission is usually

Fig. 98.7 Variations of HC emissions versus engine speed for fuels
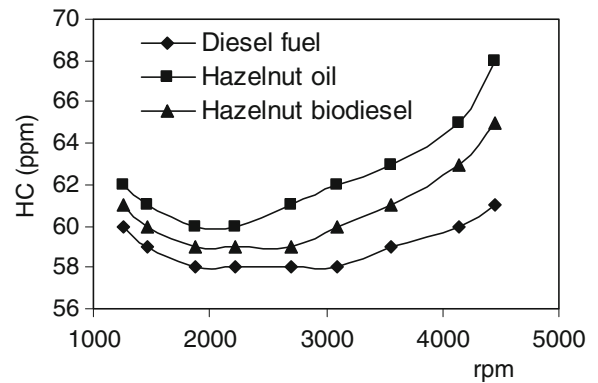
Fig. 98.8 Variations of O$_2$ concentrations parameters versus engine speed for fuels
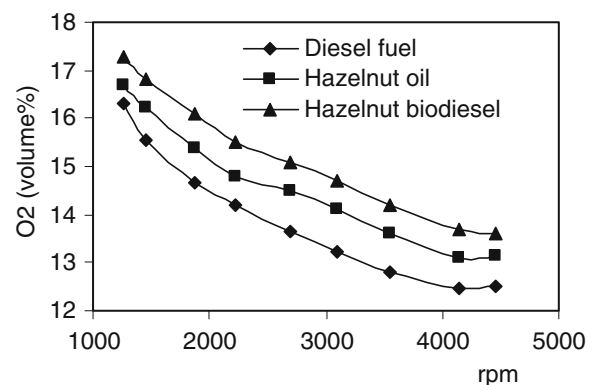
affected by fuel viscosity and combustion quality. The increase in the CO levels is same for the same increase of the supplied hazelnut oil biodiesel, diesel fuel, and hazelnut oil at maximum engine rpm region. In addition, hazelnut oil biodiesel was found to emit significantly lower CO concentrations compared to diesel fuel and hazelnut oil. The hazelnut oil and hazelnut oil biodiesel contain 10 % oxygen on a mass base and have lower carbon content than the diesel fuel. Because of the oxygen content in the biodiesel enhances, it thereby reduces the formation of CO emission in combustion process. Therefore, the hazelnut oil biodiesel can be used as a clean, lower carbon alternative fuel to replace fossil fuel for diesel engines. As it is clear from the figure that the curves of CO emissions for hazelnut oil biodiesel remain under the curve of pure diesel but increase on use of the hazelnut oil all engine speeds.

Figure 98.7 shows that the HC emissions for all fuels are lower in partial load and decreases at medium engine speed but tend to increase at higher engine speed and engine loads. The emissions of unburned hydrocarbons HC for hazelnut oil biodiesel are higher than diesel fuel at all engine speeds. HC emissions in hazelnut oil and hazelnut oil biodiesel are higher than the diesel fuel. The high viscosity of hazelnut oil and hazelnut oil biodiesel were caused to deteriorate, the combustion tends to generate high levels of unburned hydrocarbons. Factors causing combustion deterioration (such as high latent heats of vaporization) could be responsible for the increased HC production. Although the CO and HC emission of hazelnut oil was higher than diesel fuel, the HC emission of hazelnut oil biodiesel was higher and the CO emission was lower than diesel fuel. This is because of better combustion of hazelnut oil biodiesel inside the combustion chamber due to oxygen content in biodiesel.

Figure 98.8 shows O$_2$ concentrations for diesel fuel, hazelnut oil, and hazelnut oil biodiesel, respectively. The hazelnut oil and hazelnut oil biodiesel O$_2$ emissions values are show that almost the same when operating with diesel fuel. It can be seen that oxygen concentration available for reactions decreases the engine speed, and O$_2$ emissions are higher than diesel at all speed range. It can be said that O$_2$ concentration was high in the exhaust gases and similar for fuels. This high oxygen concentration could be explained as due to the oxygen content of hazelnut oil biodiesel and hazelnut oil and excessive air in the combustion. This is due to the lack of oxygen resulting from the operation at higher air/fuel ratios. O$_2$ emissions and CO$_2$ emissions are opposite situation to as shown in Figs. 98.8 and 98.9. This situation can be explained by the detailed chemical structures of hazelnut oil, hazelnut oil ester, and combustion reactions.

Fig. 98.9 Variations of CO_2 emissions versus engine speed for fuels
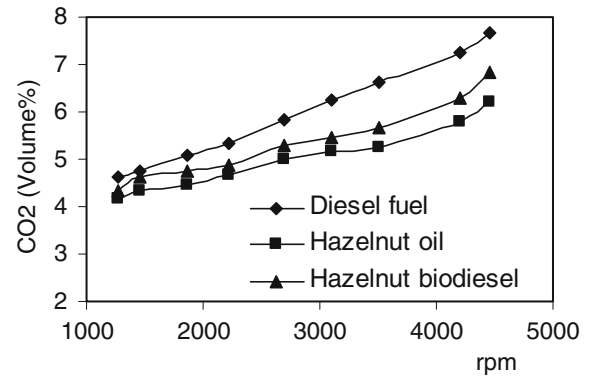
Fig. 98.10 Variations of smoke concentrations versus engine speed for fuels
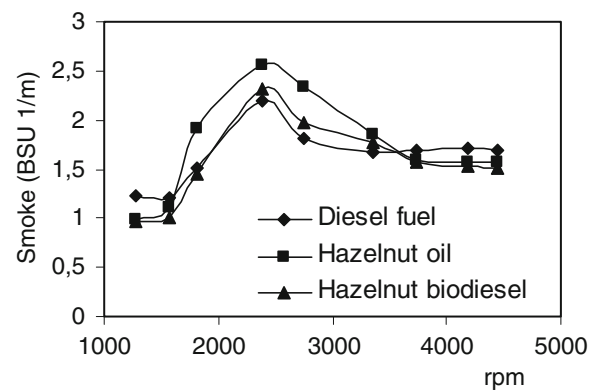
Figure 98.9 shows CO_2 emissions, respectively, for all test fuels under varied engine speeds. The CO_2 emission is increased with increasing engine speed for three fuels. Diesel fuel produced the highest amount of CO_2 than the hazelnut oil and hazelnut oil biodiesel fuels for all engine speeds. The hazelnut oil, hazelnut oil biodiesel are lower CO_2 emission values indices than diesel fuel. The reason for this, the fact that hazelnut oil and hazelnut biodiesel are a low carbon fuel and have a lower carbon/hydrogen ratio than diesel fuel. This is probably due to the fact that this hazelnut oil, hazelnut oil biodiesel has the lowest air/fuel ratio and also the fact that CO_2 emission concentration decreases with the decrease of the air/fuel ratio. In addition, the carbon contents of diesel fuel are higher than hazelnut oil and hazelnut oil biodiesel. The burning of the hazelnut oil and hazelnut oil biodiesel appeared to emit the lowest CO_2 emission, primarily owing to its having the lowest carbon content from diesel fuel. Generally, the amount of carbon dioxide is proportional to the amount of fuel burned, and the CO_2 emissions increase with increasing engine speed and the mass of fuel injected using the fuel. It is an indication of efficient combustion of biodiesel due to its oxygenated nature which helps for more complete combustion.

Figure 98.10 shows the smoke values versus to engine rpm for all the used fuels. According to Fig. 98.10, the hazelnut oil and hazelnut oil biodiesel produce less smoke than the diesel fuel at 2,000 rpm engine speeds approximately. The smokes for hazelnut oil and hazelnut oil biodiesel are lower than that of the diesel fuel under 2,000 rpm engine speed, and lesser amount of unburned hydrocarbons are measured in the engine exhaust gases. But in higher speed, hazelnut oil and hazelnut oil biodiesel produced significantly higher smoke than diesel fuel. It is explained that the hazelnut oil viscosity and the hazelnut oil biodiesel viscosity are higher than diesel fuel, and this situation causes deterioration of combustion and incomplete combustion.

Figure 98.11 shows the NOx emissions for the all fuels under varied engine speeds and engine torques. The hazelnut oil biodiesel and hazelnut oil were produced a higher amount of NOx, while diesel fuel produced the low amount of NOx emissions at these engine speeds. The NOx emission values were observed to decrease with the increase in engine speed for all fuels. The formation of NOx depends to a large extent on the flame temperature and high compression ratio. The NOx emission decreases with the decrease in the fuel to air ratio under fuel-lean burning conditions of high engine speed. The NOx emissions with hazelnut oil biodiesel increase approximately 12–18 % as compared to diesel fuel for all engine speed.

Fig. 98.11 Variations of NOx emissions versus engine speed for fuels
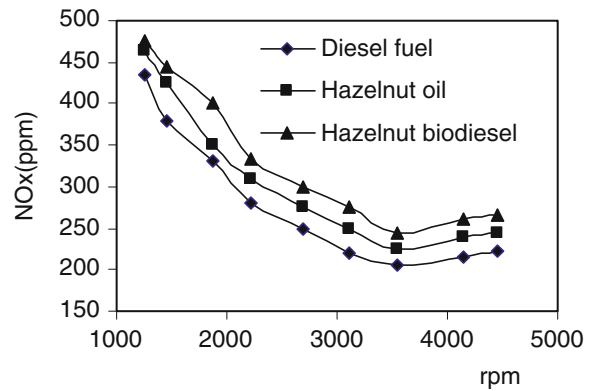
Fig. 98.12 Variations of the exhaust gas temperature versus engine speed for fuels
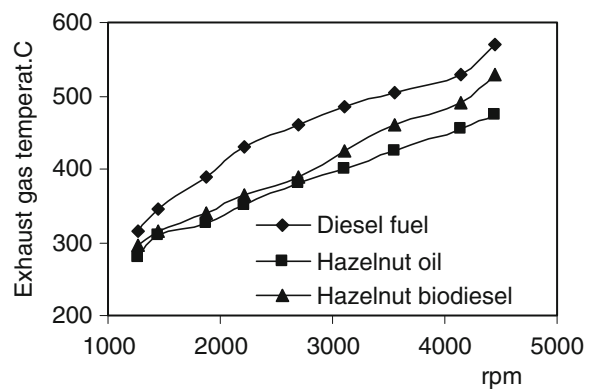
The NOx emissions with hazelnut oil biodiesel are higher approximately 8–10 % as compared to hazelnut oil, and the NOx emissions with hazelnut oil are higher approximately 10–14 % as compared to diesel fuel. This situation is probably the relatively higher oxygen content of hazelnut oil biodiesel, which produced a higher NOx formation from pure hazelnut oil and diesel fuel. The increase in NOx emissions may be attributed to various reasons, such as improved fuel spray characteristics, high viscosity, and better combustion of biodiesel due to its high oxygen content and higher. Finally, it is seen that the hazelnut oil biodiesel and hazelnut oil operations usually yield higher NOx emissions at all engine test speeds compared to that of diesel fuel operations.

Figure 98.12 shows the exhaust gas temperatures change depending on engine rpm for different fuels. It can be seen that hazelnut oil biodiesel and hazelnut oil exhaust gas temperatures lower than diesel fuel for all of the engine speeds. The highest value of exhaust gas temperature was observed at 4,350 rpm with diesel fuel (555 °C) at full load, whereas the corresponding value with the hazelnut oil biodiesel was measured at 515 °C. The increase in exhaust gas temperature using hazelnut oil reached maximum at 465 °C. The reason for this change in the exhaust gas temperature, hazelnut oil and hazelnut oil biodiesel are low calorific value than diesel fuel and the differences of the cetane number. It can be said that depends on the high cetane number of biodiesel, the ignition delay shortening and as a result of the final temperature of combustion temperature is lower than diesel fuel combustion.

Conclusions

The experiments are conducted for diesel fuel, pure hazelnut oil, and hazelnut oil biodiesel (hazelnut oil ethyl ester) for different fuels at various loads. The following conclusions may be drawn from the present study:

– It was shown that hazelnut oil biodiesel as an alternative fuel can be used successfully to run pre-chamber diesel engine without modifications to the engine and subsystems.

– Specific fuel consumption with hazelnut oil biodiesel is higher than diesel fuel. This is attributed to the lower heating value of the hazelnut oil biodiesel.
– Hazelnut oil biodiesel emissions are higher (HC, NOx, and smoke) except for CO and CO_2 when compared with diesel fuel emissions.
– The increase in NOx emissions was proportional to the amount of biodiesel. In the case of biodiesel, the increase in NOx emission was 15 % compared to the diesel fuel, respectively.
– Hazelnut oil biodiesel physical and chemical properties are similar, and hazelnut oil biodiesel heat value close to diesel fuel, but it is lower.
– In the specific fuel consumption increased, at low-speed 6 %, medium speed 9 %, high-speed 12 %. Specific fuel consumption increased by an average rate of 9.7 % was determined.
– At present, hazelnut oil biodiesel is more expensive than diesel fuel. If hazelnut is not used as a food, with local availability of the fuel it is favorable to adopt in the economic point of view.

Based on these results and the local availability of hazelnut oil biodiesel, it may be concluded that the fuel derived from hazelnut is a potential candidate for internal combustion engines.

Nomenclature

be	Specific fuel consumption, kg/kWh	L	Liter
bmep	Brake mean effective pressure	Me	Effective torque, Nm
BSU	Bosch smoke unit	$\dot{m}f$	Mass flow of fuel, kg
BSU	L/m	NaOH	Sodium hydroxide
bte	Brake thermal efficiency, %	ne	Engine, rpm
°C	Degree centigrade	Nm	Newton meter
CO	Carbon monoxide	NOx	Nitrogen oxides
CO_2	Carbon dioxide	O_2	Oxygen
η_e	Thermal efficiency, %	Pe	Brake power, kW
HC	Hydrocarbon	PPM	Parts per million
Hu	Lower heating value, kJ/kg	rpm	Revolution per minutes
IDI	Indirect diesel injection	ρ	Density, kg/m^3
kg	Kilogram	% vol.	Percentages of volume
kW	Kilowatt		

References

1. Cetin M, Yuksel F (2007) The use of hazelnut oil as a fuel in pre-chamber diesel engine. Appl Therm Eng 27:63–67
2. Karaosmanoglu F, Kurt G, Ozaktas T (2000) Long term CI engine test of sunflower oil. Renew Energy 19:219–221
3. Huzayyin AS, Bawady AH, Rady MA, Dawood A (2004) Experimental evaluation of diesel engine performance and emission using blends of jojoba oil and diesel fuel. Energy Convers Manage 45:2093–2112
4. Kalam MA, Husnawan M, Masjuki HH (2003) Exhaust emissions and combustion evaluation of coconut oil-powered indirect injection diesel engine. Renew Energy 28:2405–2415
5. Buyukkaya E (2010) Effects of biodiesel on a DI diesel engine performance, emission and combustion characteristics. Fuel 89:3099–3105
6. Karabektas M, Ergen G, Hosoz M (2008) The effects of preheated cottonseed oil methyl ester on the performance and exhaust emissions of a diesel engine. Appl Therm Eng 28:2136–2143
7. Mbarawa M (2010) The effect of clove oil and diesel fuel blends on the engine performance and exhaust emissions of a compression-ignition engine. Biomass Bioenergy 34:1555–1561
8. Murugesan A, Umarani C, Subramanian R, Nedunchezhian N (2009) Bio-diesel as an alternative fuel for diesel engines—a review. Renew Sustain Energy Rev 13:653–662
9. Erkut Y (2010) TÜPRAŞ to invest $2 billion to increase diesel production. The Turkish Petroleum Refineries Corporation (TÜPRAŞ)
10. İçingür Y, Koçak MS (2006) A study on the performance and emission parameters of hazelnut oil methyl ester as an alternative diesel fuel. J Polytech 9:119–124
11. Usta N, Ozturk E, Can O, Conkur ES, Nas S, Con AH, Can AC, Topcu M (2005) Combustion of biodiesel fuel produced from hazelnut soapstock/waste sunflower oil mixture in a diesel engine. Energy Convers Manage 46:741–755
12. Li E, Zhi Ping X, Rudolph V (2009) MgCoAl–LDH derived heterogeneous catalysts for the ethanol transesterification of canola oil to biodiesel. Appl Catal B Environ 88(1–2):42–49

Sarunya Promkotra and Tawiwan Kangsadan

Abstract

Petroleum transport from a gas well to the gas production plant is relevant to the petroleum production of the natural gas field. This migration affects movement direction on distance and chemical components under the emphasis upon the relationship between condensate and other fluid hydrocarbons. The physical properties of condensate are analyzed on the basis of API gravity (55.52–62.84°), density (0.73–0.76 g/cm^3), specific gravity (0.7362–0.7566), Reid vapor pressure, and true vapor pressure. The highest hydrocarbon composition is methane, 96.70 %. Hydrocarbon concentrations from the gas processing plant are found overall C_7+ (heptane, C_7H_{16}) to C_{16} (hexadecane, $C_{16}H_{34}$), and found most octane (C_8H_{18}). Petroleum dynamics is evaluated in the criteria of petroleum transport in closed conduit. Mathematical model of petroleum dynamics is defined by the diffusion coefficient of the specific chemical reactions depending on methane–ethane and methane–propane which are 15.71 and 9.20 cm^2/s, respectively. The quantities of molar fluxes gradually increase from one location to another location when phases change from gas to liquid, and decrease to the condensate storage tank due to the completion of liquid. The liquid phase preferably occurs because propane is slightly heavier than ethane. Their physical properties have been less affected to molar flux in the chemical reaction of propane. According to methane–ethane combination, molar fluxes as a function of sampling distances of methane in reactants are higher than methane in products. Besides, the molar fluxes of other components are expressed in the systematic trend.

Introduction

Condensate is a liquid hydrocarbon phase with low density and high API gravity which usually takes place in correlation with natural gas. Its occurrence as a liquid phase relies on temperature and pressure states in petroleum reservoir permitting condensation of liquid from vapor. Productivity of condensate from petroleum reservoirs is complex due to the pressure sensitivity. Condensate becomes increasingly essential due to the growing world dependence on the soaring of petroleum products in the marketplace. The recent comprehension of gas-condensate flow behavior within reservoir rocks is inadequate because of the limited data accessible. Besides, this fluid withdrawal from reservoir rocks to the gas well is required of accurate relative data for petroleum dynamics in both gas-condensate reservoirs and the gas well. During condensate production, fluid transportation from the well and the gas processing plant has to maintain pressure difference. If the controlled pressure drops below the dew point during production, the condensate will condense from gas to liquid. According to the operation within the gas processing plant in Num Phong District, Khon Kaen Province, the northeast of

S. Promkotra (✉)
Department of Geotechnology, Faculty of Technology, Khon Kaen University, Khon Kaen 40002, Thailand
e-mail: sarunya@kku.ac.th

T. Kangsadan
Chemical and Process Engineering Program, Department of Mechanical and Process Engineering, The Sirindhorn International Thai-German Graduate School of Engineering (TGGS), King Mongkut's University of Technology North Bangkok (KMUTNB), Bangsue, Bangkok 10800, Thailand
e-mail: tawiwan.k.cpe@tggs-bangkok.org

Thailand, mostly methane gas is discovered approximately 96 mol% [1]. Due to physical and chemical properties, this petroleum reservoir indicates the dry gas reservoir [2]. The pressure and temperature from a petroleum reservoir to the ground surface change from 160 bar g and 60 °C to 74.54 bar g and 31.67 °C. While petroleum fluid flows to the slug catcher, condensate mixture in this location is separated from natural gas. For the liquid processing, liquid petroleum mixture consists of condensate and water. This mixture flows to the high pressure flash vessel (pressure 6.49 bar, temperature 24.28 °C) which condensate is separated from water. Besides, condensate flows to the low pressure flash vessel and evaporates. At last, it is kept in a storage tank (a condensate tank). Having a high liquid hydrocarbon yield is often utilized for liquid petroleum reserves. Temperature and pressure in each location of the gas processing plant are effective to create the chemical thermodynamic simulation and also its fluid dynamics [3].

Petroleum dynamics is the main study of this research. This foremost scheme is aimed to identify the petroleum flow in the closed conduit from the gas well to the gas processing plant. To investigate petroleum migration with emphasis upon the relationship between condensate and other fluid hydrocarbons, mathematical fluid dynamics of petroleum mixture in one direction is evaluated to the petroleum production in the gas production plant. This study will provide more understanding in petroleum migration from the gas well to cylindrical pipe and finally to process production plant. The distance from the wells to the gas plant is approximately 62 km. High efficiency well for producing the natural gas can produce the natural gas about 60–140 MMscfd. Samples of natural gas and condensate from the gas field are collected from the gas processing plant at this point. At present, petroleum dynamics depended on petroleum migration has been studied by simulation, and not by mathematical modeling. For the simplicity, the specific location within the gas plant is selected in this modeling. Thus, these studied results will explicit the relationship of petroleum dynamics in specific direction and areas.

Methodology

Condensate and natural gas are collected during August to October 2012 from the gas processing plant at the inlet slug catcher, high pressure flash vessel, and condensate tank, as shown in Fig. 99.1. Collecting sample is covered during rainy season which affects on deeply groundwater. Generally, condensate, water, and natural gas mix together by ultimate condition. Thus, water from fluid mixture has to be removed from condensate at the outlet slug catcher, where condensate and water are unblended. Analytical results of this water indicate remarkably fresh water, confirmed by the total dissolved solids (TDS) with a value below 200 mg/L. Moreover, condensate sample from the inlet slug catcher (upstream) has approximately the same composition likewise the natural hydrocarbon from the petroleum reservoir. Therefore, this state is assumed as the representative of liquid petroleum from the petroleum well. Expectation of the geochemical relation of
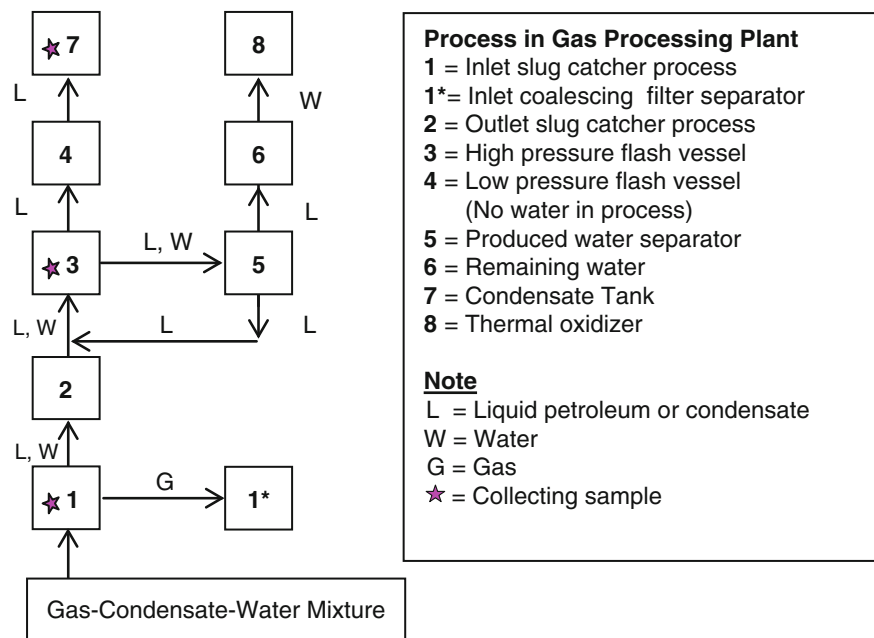
Fig. 99.1 Flow chart of gas-condensate-water processes of the gas processing plant

Fig. 99.2 Schematic diagram of cylindrical pipe where hydrocarbon migrated from the gas well to the gas processing plant
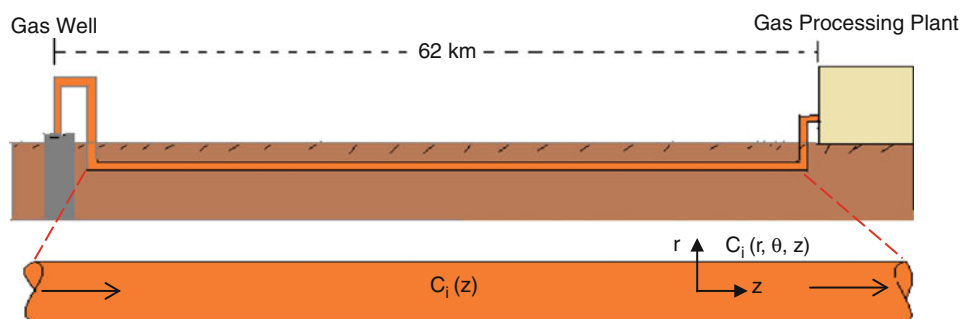
condensate and natural gas would gain: (1) physical properties of condensate and natural gas, (2) geochemical compositions related to physical properties, and (3) conceptual stability condition corresponding to condensate and natural gas.

Condensate and Natural Gas

Physical properties of condensate are examined for density, specific gravity, API gravity, followed by ASTM D5191. Reid vapor pressure (RVP) and true vapor pressure (TVP) are followed by the analytical methods of the vapor pressure of petroleum products (Mini Method). These parameters are always measured daily for maintaining the quality of condensate. Hydrocarbon compositions of both condensate and natural gas are determined by the gas chromatography (GC), GC-2010 Plus (Shimadzu), based on ASTM D1945. Its capillary column is HT-5 type with 25 m in length and a 0.10 μm film thickness. Hydrogen gas is used as a carrier gas with the flow rate of 47 mL/min. The column over temperatures set at 170, 270, and 380 °C, with a temperature ramp of 15, 8, and 15 °C/min. Detection of the analyses is performed using the flame ionization detector (FID). Internal standard is principally methyl haptadecanoate ($C_{18}H_{36}O_2$). It will be referenced in the calibration standard and used to calculate concentrations as a marker of analytical chromatograms.

Hydrocarbon Transport in Conduit

Fluid hydrocarbon will be withdrawn from the reservoir and migrated from the gas well to the gas processing plant. The distance between two locations is approximately 62 km through cylindrical pipe. This pipe is lined down under the surface around 2 m, as shown in Fig. 99.2. The hydrocarbon components are assumable the same compositions as situated in the reservoir rocks. This mathematical dynamics focuses on the migration of hydrocarbon masses in one direction. Furthermore, the hydrocarbon transport is considered to be in the laminar flow regime, without any angle in the cylindrical pipe.

Cylindrical Coordinate System

Three-dimensional coordinate system is designed by the cylindrical coordinate system in specific point based on the position or distance from a selected reference axis. The direction from the axis relates to the reference direction and distance from a selected reference perpendicular to the axis. The radial distance or the distance from the axis refers to the angular position or as the azimuth. Two-dimensional polar coordinate system (both combination of the radius and the azimuth) correspond to A in the plane through the point, analogous to the reference plane. Longitudinal position (or axial position) is defined as the altitude as the third coordinate, if the reference plane is considered horizontal. Cylindrical coordinates are practical in association to purposes and occurrences that have some gyratory symmetry concerning the longitudinal axis, for example water flow in a conduit or closed canal for circular cross-section. The following mathematical summary of cylindrical coordinate system is derived by Kangsadan [4].

$$C_i(t, r, \theta, z) = C_i(z) \tag{99.1}$$

Assumption
1. At steady state, C_i is not a function of time (t).
2. No concentration distribution in radial direction; C_i is not a function of radius (r).

3. No concentration distribution in radial direction; C_i is not a function of angular (θ).
   In which, C_i = molar concentration of component i
   z = distance (m).

Mechanism of Mass Transport

Mass transport is the transport of the one constituent from a region of higher concentration to that of a lower concentration. The net flow of each molecular species occurs in the direction of the negative concentration gradient. Since mass transfer or diffusion occurs only in mixture, its evaluation must involve the examination of the effect of each component.

Molecular Mass Transfer or Diffusion

Molecular of mass transfer, sometimes called diffusion mass, can be transferred by random molecular motion in quiescent fluids independent of any convection within system. Convection mass transfer mass can be transferred from surface into a moving fluid as follows:

$$\text{Mass or molar fluxes : Flux} = \frac{\text{Mass or Molar Rate}}{\text{Surface Area}} \qquad (99.2)$$

Mass or molar flux of a given species is a vector quantity denoting the amount of the particular species, in either mass or molar units, that passes per given increment of time through a unit area normal to the vector. Flux must be defined a reference to the following condition:

Stationary reference: coordinates are fixed in space; N_{az} = molar flux of component A relative to a stationary.

$$\text{Equation of continuity : } \nabla \cdot N_A + \frac{\partial C_A}{\partial t} - R_A = 0 \qquad (99.3)$$

in which ∇ = del or gradient operator, the vector derivative of a scalar
$\frac{\partial C_A}{\partial t}$ = molar concentration of component A gradient in time-direction
R_A = rate of component A

Generalize expression for fluxes; defined no reaction $R_A = 0$ and at steady state: $\frac{\partial C_A}{\partial t} = 0$.

$$\text{Thus, } \frac{dN_{AZ}}{dz} = 0$$

$$N_{AZ} = -D_{AB}\frac{dC_A}{dz} + X_A(N_{AX} + N_{BX}) \qquad (99.4)$$

in which X_A = mole fraction (mole of A divided by total mole)
D_{AB} = mass diffusivity or diffusion coefficient for component A diffusing through component B (cm^2/s).

Diffusion Coefficient

The Fuller correlation is estimating the diffusion coefficient for nonpolar, binary at low pressure [5]. Empirical correlation recommended by

$$D_{AB} = \frac{10^{-3}\, T^{1.75} \left(\frac{1}{M_A} + \frac{1}{M_B}\right)^{\frac{1}{2}}}{P\left[(\sum v)_A^{\frac{1}{3}} + (\sum v)_B^{\frac{1}{3}}\right]^2}. \qquad (99.5)$$

in which T = absolute temperature (K)

M_A = molecular weight of diffusing species A (g/mol)

M_B = molecular weight of diffusing species B (g/mol)

P = pressure (atm)

$\Sigma v_{A,B}$ = sum of the diffusion volume for components A and B.

Results and Discussion

These research studies are to exemplify parameters which are important for gas processing control in the gas processing plant. Experimental results of condensate and natural gas obtain physical properties and chemical compositions which are useful for the basic information of fabricating mathematical modeling. Mathematical fluid dynamics applies to identify petroleum in a closed conduit related to the petroleum production. Parameters of condensate, such as temperature and pressure are recorded in the production plant in each process. Both parameters are automatically monitored by time. Detailed data are compared in Table 99.1. Besides, concentration of all components (in mol%) of the natural gas and condensate are plotted all together, as illustrated in Fig. 99.3. Different temperatures and pressures depend upon various processes in the gas processing plant. Maximum and minimum pressures are found approximately to be 70 and 0.02 bar in the inlet slug catcher and condensate tank, respectively. Reduced pressure is subjected to control the condensate condition in liquid and to separate the natural gas. These pressures related to the processes in the gas production plant will gradually be decreased in

Table 99.1 Measuring parameters (average) in each location

Parameters	Inlet slug catcher	Outlet slug catcher	High pressure flash vessel	Low pressure flash vessel	Condensate tank
Pressure (bar)	65.55	65.55	6.95	0.265	0.02
Temperature (°C)	29.03	29.03	42.78	54.65	29.5
Density (g/cm^3)	0.7550	0.7400	0.7450	0.7300	0.7400
Specific gravity	0.7561	0.7473	0.7379	0.7311	0.7414
API gravity (°)	55.65	57.85	59.93	62.06	59.36
RVP (psi)	0.83	0.98	1.55	2.51	1.42
TVP (psi)	1.43	1.59	1.735	3.105	2.05
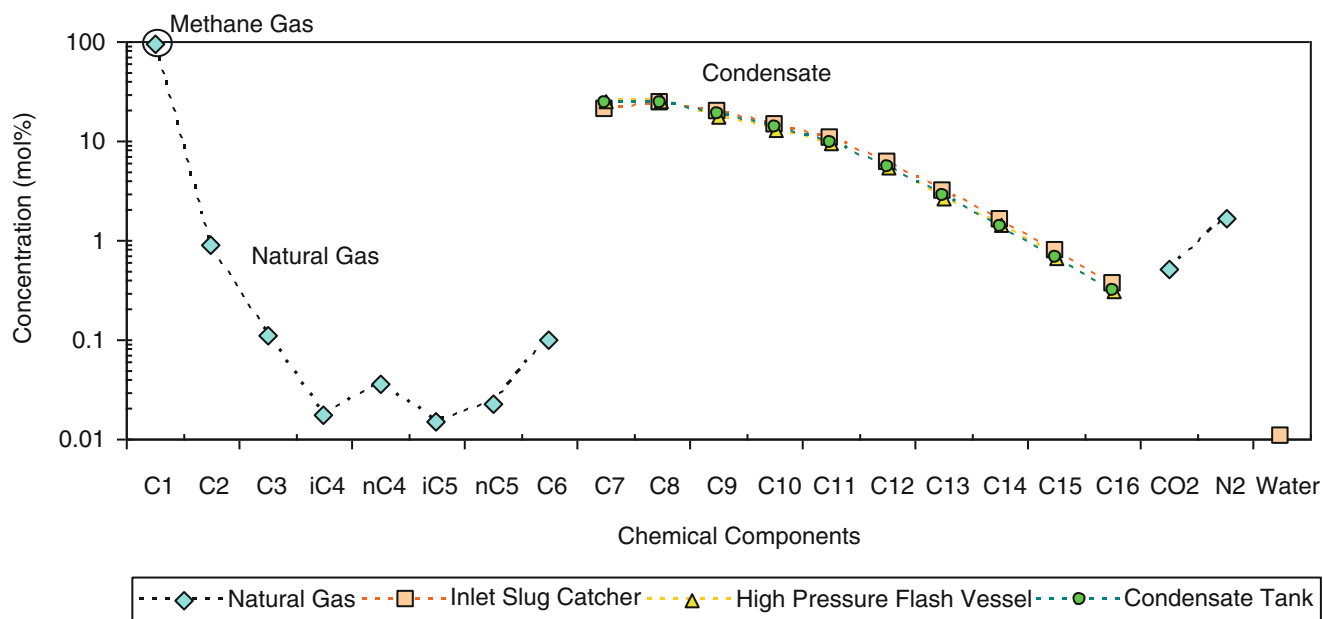
Fig. 99.3 Relationship of concentration (in mol%) and chemical components compared to natural gas and condensate

Table 99.2 Physical properties of petroleum-field waters

Parameters	Inlet slug catcher	Outlet slug catcher	High pressure flash vessel	Low pressure flash vessel	Produced water separator	Condensate tank
pH	7.09	6.32	6.42	5.81	7.28	6.38
Temperature (°C)	41.10	27.90	27.65	33.50	28.95	26.30
EC (μS/cm)	–	334.0	239.0	–	411.4	–
TDS (mg/L)	–	149.9	105.0	–	186.7	–

Table 99.3 All compositions and criteria depending on Eqs. (99.1) and (99.2)

Symbol and components	Concentration (C_A)	Diffusion coefficient (cm^2/s)	References for diffusion coefficient
H = H_2	C_H = concentration of H_2	1.60	http://www.thermopedia.com/content/
C = CO_2	C_C = concentration of CO_2	0.11	http://www.thermopedia.com/content/
N = N_2	C_N = concentration of N_2	0.19	http://www.thermopedia.com/content/
W = H_2O	C_W = concentration of H_2O	0.28	http://www.thermopedia.com/content/
1 = CH_4	C_1 = concentration of CH_4	0.18	http://www.thermopedia.com/content/
2 = C_2H_6	C_2 = concentration of C_2H_6	1.52×10^{-16}	Witherspoon and Saraf [8]
3 = C_3H_8	C_3 = concentration of C_3H_8	1.21×10^{-16}	Witherspoon and Saraf [8]
7 = C_7H_{16}	C_7 = concentration of C_7H_{16}	3.67×10^{-16}	Leahy-Dios et al. [9]

each location from the inlet to condensate tank. Temperature gradients are more dominant than pressure which are concerning by the controlling process. Both temperature and pressure play a critical role for phase change and phase equilibria from the petroleum reservoir, gas well, and gas plant. Thus, chemical thermodynamics and petroleum dynamics are the nutshell for conceptual correlation.

Physical properties of petroleum-field waters are determined on site during sample collection, as indicated in Table 99.2. Water samples obtain from fluid samples which consist of condensate and also petroleum-field waters. Some parameters are not available for measurement, such as electrical conductivity (EC) and TDS. At this present, water combined in the hydrocarbon system is found less and not enough for further collection. The measurements of both EC and TDS indicate that these petroleum-field waters are in the condition of fresh water. In general, water in any deep aquifers will present itself as brackish water (or saline). However, these water samples at this time are not affected at all. This phenomenon are totally shown distinguished results of petroleum-field water in 2009 and 2011 [6, 7].

Hydrocarbon Transport in Closed Conduit

Due to the chemical thermodynamics of fluid hydrocarbons, natural gas and condensate, the conceptual model for mass transport is constructed by concentrations of hydrocarbon components. These fluid movements can present the migration of hydrocarbon in closed conduit. Distance from petroleum reservoir to the gas well and transport to the processing plant is very complex computation in mathematic scheme. Thus, this hydrocarbon transport is indicated only for the gas well to the gas processing plant. Assumption for this transport depends on the chemical reaction in equilibrium condition and one direction from the well to the gas plant. Prediction of parameters generates mainly from temperature and pressure. Methane is dominantly a precursor in every chemical reaction. Moreover, other gases related to the genesis within reservoir and exist in the same environment are combined as a reactant. The results of GC from chemical laboratory indicate carbon dioxide, hydrogen gas, and nitrogen in which reservoir are 10, 8, and 2 mol%, respectively. Chemical equations are conducted by using petroleum components from condensate which is collected in the gas processing plant. There are simply two chemical reactions creating based on following criteria.

Computational Criteria

Variable chemical species depend on reactants and products, as indicated in two chemical reactions, number 1 and 2. Diffusion coefficients are indicated in Table 99.3 for calculation of multicomponent gas mixtures and binary diffusion coefficients (cm^2/s) at STP (temperature (273 K), pressure (1 atm)).

$$\text{Reaction No.1}: 4CH_{4(g)} + 2C_2H_{6(g)} + 2CO_{2(g)} + H_{2(g)} + N_{2(g)}$$
$$\rightarrow 2CH_{4(g)} + C_7H_{16(l)} + CO_{2(aq)} + N_{2(aq)} + 2H_2O_{(aq)} + H_{2(aq)} \tag{99.6}$$

$$\text{Reaction No.2}: 3CH_{4(g)} + C_3H_{8(g)} + 3CO_{2(g)} + 4H_{2(g)} + N_{2(g)}$$
$$\rightarrow CH_{4(g)} + C_7H_{16(l)} + CO_{2(aq)} + N_{2(aq)} + 4H_2O_{(aq)} \tag{99.7}$$
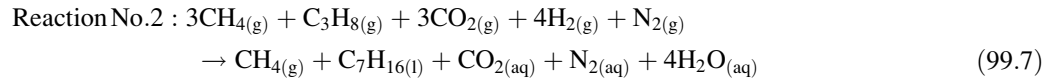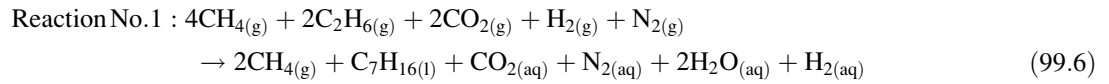
Calculation Outlines for Chemical Reaction 1

Mass (or chemical species) transports (N_{Az}) can be calculated by Eq. (99.4). The minus sign of this diffusion equation refers to the direction of mass from high to low concentration. The different concentrations have to be defined as the direction, based on the Fick's first law of diffusion. Also, diffusion coefficient (D_{AB}) is calculated by using Eq. (99.5). The subscript numbers refer to each hydrocarbon type and also their components indicating on the chemical reaction (Reaction No. 1), $D_{1-2-C-H-N-1^*-7^*-C^*-N^*-W^*-H^*}$. Substitute the diffusion coefficient (v) of each species from Table 99.3 into Eq. (99.8). Then,

$$D_{1-2-C-H-N-1^*-7^*-C^*-N^*-W^*-H^*} = D_{AB}$$

$$= \frac{10^{-3}(T)^{1.75}\left(\frac{1}{M_1}+\frac{1}{M_2}+\frac{1}{M_C}+\frac{1}{M_H}+\frac{1}{M_N}+\frac{1}{M_{1^*}}+\frac{1}{M_{7^*}}+\frac{1}{M_{C^*}}+\frac{1}{M_{N^*}}+\frac{1}{M_{W^*}}+\frac{1}{M_{H^*}}\right)^{\frac{1}{2}}}{P\left[(\sum v)_1^{\frac{1}{3}}+(\sum v)_2^{\frac{1}{3}}+(\sum v)_C^{\frac{1}{3}}+(\sum v)_H^{\frac{1}{3}}+(\sum v)_N^{\frac{1}{3}}+(\sum v)_{1^*}^{\frac{1}{3}}+(\sum v)_{7^*}^{\frac{1}{3}}+(\sum v)_{C^*}^{\frac{1}{3}}+(\sum v)_{N^*}^{\frac{1}{3}}+(\sum v)_{W^*}^{\frac{1}{3}}+(\sum v)_{H^*}^{\frac{1}{3}}\right]^2}$$

$$= \frac{10^{-3}(273\,K)^{1.75}\left(\frac{1}{4(16)}+\frac{1}{2(30)}+\frac{1}{2(44)}+\frac{1}{2}+\frac{1}{28}+\frac{1}{2(16)}+\frac{1}{100}+\frac{1}{44}+\frac{1}{28}+\frac{1}{2(18)}+\frac{1}{2}\right)^{\frac{1}{2}}}{(1\ atm)\left[(0.18)_1^{\frac{1}{3}}+(1.52)_2^{\frac{1}{3}}+(0.11)_C^{\frac{1}{3}}+(1.60)_H^{\frac{1}{3}}+(0.19)_N^{\frac{1}{3}}+(0.18)_{1^*}^{\frac{1}{3}}+(3.67)_{7^*}^{\frac{1}{3}}+(0.11)_{C^*}^{\frac{1}{3}}+(0.19)_{N^*}^{\frac{1}{3}}+(0.28)_{W^*}^{\frac{1}{3}}+(1.60)_{H^*}^{\frac{1}{3}}\right]^2}$$

$$= \frac{20.1420}{1.2820} = 15.71\,cm^2/s. \tag{99.8}$$

Thus, diffusion coefficient (D_{AB}) of this chemical reaction is 15.71 cm^2/s. This value will be used for Eq. (99.4). The term of N_{1Z} in this equation is a molar flux of the methane reactant ($CH_{4\ (g)}$). Define $\frac{dN_{1z}}{dz} = 0$, then

$$N_{1Z} = -D_{AB}\frac{dC_1}{dz} + \frac{C_1}{C_T}\left(N_{2Z} + N_{CZ} + N_{HZ} + N_{NZ} + N_{1Z}^* + N_{7Z}^* + N_{CZ}^* + N_{NZ}^* + N_{WZ}^* + N_{HZ}^*\right). \tag{99.9}$$

From the chemical reaction, the molar flux of N_{1Z} from Eq. (99.9) is rearranged to other side in terms of reactants and products. For example, methane is expressed as the N_{1Z} in this reaction. The results of each term in Table 99.4 will be replaced back in Eq. (99.9). Table 99.4 presents the relationship of the methane and other species in the chemical equation. According to Eq. (99.9), the molar flux of methane can be completed as follows:

$$N_{1Z} = -(15.71)\frac{d(2,903.991)}{dz} + \frac{2,903.991}{3,531.467}$$
$$\times (0.5\,N_{1Z} + 0.5\,N_{1Z} + 0.25\,N_{1Z} + 0.25\,N_{1Z} - 0.5\,N_{1Z} - 0.25\,N_{1Z} - 0.25\,N_{1Z} - 0.25\,N_{1Z} - 0.5\,N_{1Z} - 0.25\,N_{1Z})$$

$$N_{1Z} = -15.71\left(cm^2/s\right)\frac{(2,903.991-0)\,(mol\%/m^3.\,sec)}{(62-0)\,km} + (0.822)(-0.5\,N_{1Z}) = -5,214.393\,(mol\%/m^2s).$$

Table 99.4 Defined terms for calculation of molar flux of the methane reactant (N_{1Z}) in chemical reaction number 1

Reactants	Products (*)
$N_{1Z} = \frac{4\,N_{2Z}}{2}$, then $N_{2Z} = 0.5\,N_{1Z}$	$N_{1Z} = -\frac{4\,N_{1Z}^*}{2}$, then $N_{1Z}^* = -0.5\,N_{1Z}$
$N_{1Z} = \frac{4\,N_{CZ}}{2}$, then $N_{CZ} = 0.5\,N_{1Z}$	$N_{1Z} = -\frac{4\,N_{7Z}^*}{1}$, then $N_{7Z}^* = -0.25\,N_{1Z}$
$N_{1Z} = \frac{4\,N_{HZ}}{1}$, then $N_{HZ} = 0.25\,N_{1Z}$	$N_{1Z} = -\frac{4\,N_{CZ}^*}{1}$, then $N_{CZ}^* = -0.25\,N_{1Z}$
$N_{1Z} = \frac{4\,N_{NZ}}{1}$, then $N_{NZ} = 0.25\,N_{1Z}$	$N_{1Z} = -\frac{4\,N_{NZ}^*}{1}$, then $N_{NZ}^* = -0.25\,N_{1Z}$
–	$N_{1Z} = -\frac{4\,N_{WZ}^*}{2}$, then $N_{WZ}^* = -0.5\,N_{1Z}$
	$N_{1Z} = -\frac{4\,N_{HZ}^*}{1}$, then $N_{HZ}^* = -0.25\,N_{1Z}$

Table 99.5 Defined terms for calculation of molar flux

Chemical species		CH_4	C_2H_6	CO_2	H_2	N_2	CH_4	C_7H_{16}	CO_2	N_2	H_2O	H_2	Sum of each species
Reactants													
Methane	N_{1Z}	0	0.5	0.5	0.3	0.3	−0.5	−0.3	−0.3	−0.3	−0.5	−0.3	−0.5
Ethane	N_{2Z}	2	0	1	0.5	0.5	−1	−0.5	−0.5	−0.5	−1	−0.5	0
Carbon dioxide	N_{CZ}	2	1	0	0.5	0.5	−1	−0.5	−0.5	−0.5	−1	−0.5	0
Hydrogen gas	N_{HZ}	4	2	2	0	1	−2	−1	−1	−1	−2	−1	1
Nitrogen gas	N_{NZ}	4	2	2	1	0	−2	−1	−1	−1	−2	−1	1
Products													
Methane	N_{1Z}	−2	−1	−1	−0.5	−0.5	0	0.5	0.5	0.5	1	0.5	−2
Heptane	N_{2Z}	−4	−2	−2	−1	−1	2	0	1	1	2	1	−3
Carbon dioxide	N_{CZ}	−4	−2	−2	−1	−1	2	1	0	1	2	1	−3
Nitrogen	N_{HZ}	−4	−2	−2	−1	−1	2	1	1	0	2	1	−3
Water	N_{WZ}	−2	−1	−1	−0.5	−0.5	1	0.5	0.5	0.5	0	0.5	−2
Hydrogen	N_{HZ}	−4	−2	−2	−1	−1	2	1	1	1	2	0	−3

Table 99.6 Criteria for molar flux calculation (Reaction No. 1) of the inlet slug catcher

Reactants	Diffusion flux ($mol\%/ft^3$)	(in 100 %)	($mol\%/m^3$)	Products	Diffusion flux ($mol\%/ft^3$)	(in 100 %)	($mol\%/m^3$)
Methane	96.72	82.236	2,904.12	Methane	96.72	76.128	2,688.432
Ethane	0.893	0.760	26.825	Heptane	20.168	15.874	560.590
Carbon dioxide	10	8.502	300.261	Carbon dioxide	0.503	0.396	13.973
Hydrogen gas	8	6.802	240.208	Nitrogen	1.659	1.305	46.103
Nitrogen gas	2	1.7	60.052	Hydrogen	8	6.297	222.368
Total	117.613	100	3,531.467	Total	127.049	100	3,531.467

Then, the diffusion coefficient of the methane reactant is finally revealed as 5,214.393 $mol\%/m^2\,s$. The minus sign of this diffusion of molar flux (N_{1Z}) refers to the direction of methane from the gas well to the gas plant. The concentration and condition for calculating the molar flux in the inlet slug catcher are shown in Tables 99.5, 99.6, and 99.7. According to the gas processing plant, flow rate of petroleum fluid per day is 7,000,000 scf or 1,982,179.261 m^3. The diffusion coefficient of the chemical reaction (Reaction No. 1) is 15.71 cm^2/s. The distance from the gas well to the production plant is 62 km, the distance from the inlet slug catcher to the high pressure flash vessel is 0.05 km, and the distance from the high pressure flash vessel to the condensate tank is 0.10 km, respectively. Computational results of molar fluxes of the inlet slug catcher, high pressure flash vessel, and condensate tank based on the chemical reaction (Reaction No. 1) are presented in Table 99.8.

Table 99.7 Results of molar flux calculation (Reaction No. 1) of the inlet slug catcher

		Concentration gradient ($mol\%/m^3$ km)	Diffusion flux ($mol\%/m^2$ s)	Mole fraction (X_A)	Molar flux constant	Parameter of bulk motion contribution		Molar flux ($mole\%/m^2$ s)
						Any species (N_z)	Specific species (N_{iz})	
Reactants								
$CH_{4\ (g)}$	N_{1Z}	46.841	7,358.666	0.822	−0.5	−0.411	1.411	5,214.557
$C_2H_{6\ (g)}$	N_{2Z}	0.433	67.972	0.008	0	0	1	67.972
$CO_{2\ (g)}$	N_{CZ}	4.843	760.822	0.085	0	0	1	760.822
$H_{2\ (g)}$	N_{HZ}	3.874	608.657	0.068	1	0.068	0.932	653.079
$N_{2\ (g)}$	N_{NZ}	0.969	152.164	0.017	1	0.017	0.983	154.797
Products								
$CH_{4\ (g)}$	N_{1Z}	43.362	6,812.141	0.761	−2	−1.523	2.523	2,700.489
$C_7H_{16\ (l)}$	N_{2Z}	9.042	1,420.464	0.159	−3	−0.476	1.476	962.227
$CO_{2\ (aq)}$	N_{CZ}	0.225	35.406	0.004	−3	−0.012	1.012	34.991
$N_{2\ (aq)}$	N_{NZ}	0.744	116.818	0.013	−3	−0.039	1.039	112.415
$H_{2\ (aq)}$	N_{HZ}	3.587	563.453	0.063	−3	−0.189	1.189	473.926

Table 99.8 Results of molar flux calculation (Reaction No. 1) of the inlet slug catcher, high pressure flash vessel, and condensate tank

Chemical Reaction No. 1	Chemical species		Inlet slug catcher	High pressure flash vessel	Condensate tank
			Molar fluxes ($mol\%/m^2 \cdot s$)		
Reactant	$CH_{4\ (g)}$	N_{1Z}	5,214.56	6,466,050.47	3,233,025.23
Reactant	$C_2H_{6\ (g)}$	N_{2Z}	67.972	84,285.03	42,142.51
Reactant	$CO_{2\ (g)}$	N_{CZ}	760.822	943,418.72	471,709.36
Reactant	$H_{2\ (g)}$	N_{HZ}	653.079	809,818.38	404,909.19
Reactant	$N_{2\ (g)}$	N_{NZ}	154.797	191,947.79	95,973.90
Total reactants			6,851.23	8,495.520.382	4,247,760.19
Product	$CH_{4\ (g)}$	N^*_{1Z}	2,700.49	3,387,113.32	1,688,807.91
Product	$C_7H_{16\ (l)}$	N^*_{7Z}	962.227	1,295,731.22	635,374.58
Product	$CO_{2\ (aq)}$	N^*_{CZ}	34.991	43,397.94	21,697.80
Product	$N_{2\ (aq)}$	N^*_{NZ}	112.415	139,493.79	69,734.78
Product	$H_{2\ (aq)}$	N^*_{HZ}	473.926	589,432.74	294,500.21
Product	$H_2O_{(aq)}$	N^*_{WZ}	–	–	–
Total products			4,284.05	5,455,169.01	2,710,115.27
Total of chemical reaction			2,567.18	3,040,351.38	1,537,644.92

Calculation Outlines for Chemical Reaction 2

For the chemical reaction number 2, mass (or chemical species) transport can also be calculated by Eq. (99.4) and the diffusion coefficient (D_{AB}) is calculated by Eq. (99.5). The subscript numbers refer to each hydrocarbon type and also their components indicating on the chemical reaction (Reaction No. 2), $D_{1-3-C-H-N-1^*-7^*-C^*-N^*-W^*}$. Substitute the diffusion coefficient (v) of each species from Table 99.3 into Eq. (99.8). Then, $D_{1-3-C-H-N-1^*-7^*-C^*-N^*-W^*} = D_{XY}$

$$D_{1-3-C-H-N-1^*-7^*-C^*-N^*-W^*} = D_{XY}$$

$$= \frac{10^{-3}(273\ K)^{1.75}\left(\frac{1}{3(16)} + \frac{1}{44} + \frac{1}{3(44)} + \frac{1}{4(2)} + \frac{1}{28} + \frac{1}{16} + \frac{1}{100} + \frac{1}{44} + \frac{1}{28} + \frac{1}{4(18)}\right)^{\frac{1}{2}}}{(1\ atm)\left[(0.18)_1^{\frac{1}{3}} + \left(1.21 \times 10^{-16}\right)_2^{\frac{1}{3}} + (0.11)_C^{\frac{1}{3}} + (1.60)_H^{\frac{1}{3}} + (0.19)_N^{\frac{1}{3}} + (0.18)_{1^*}^{\frac{1}{3}} + \left(3.67 \times 10^{-16}\right)_{7^*}^{\frac{1}{3}} + (0.11)_{C^*}^{\frac{1}{3}} + (0.19)_{N^*}^{\frac{1}{3}} + (0.28)_{W^*}^{\frac{1}{3}}\right]^2}$$

$$= 9.20\ cm^2/s.$$

Thus, diffusion coefficient (D_{AB}) of this chemical reaction equals to 9.20 cm^2/s. This value will be used for Eq. (99.4). The term of N_{1Z} for this reaction is a molar flux of methane reactant ($CH_{4\ (g)}$). Define $\frac{dN_{1z}}{dz} = 0$, then

Table 99.9 Results of molar flux calculation (Reaction No. 2) of the inlet slug catcher, high pressure flash vessel, and condensate tank

Chemical Reaction No. 2	Chemical species		Inlet slug catcher	High pressure flash vessel	Condensate tank
			Molar fluxes (mol%/m$^2 \cdot$ s)		
Reactant	CH_4 (g)	N_{1Z}	5,981.88	7,417,527.97	3,908,956.59
Reactant	C_3H_8 (g)	N_{3Z}	40.733	50,509.54	26,793.23
Reactant	CO_2 (g)	N_{CZ}	458.811	568,926.12	335,446.69
Reactant	H_2 (g)	N_{HZ}	356.438	441,983.56	259,915.95
Reactant	N_2 (g)	N_{NZ}	93.9	116,435.82	68,797.98
Total reactants			6,931.76	8,595,383.00	4,599,910.44
Product	CH_4 (g)	N^*_{1Z}	841.013	1,059,932.18	527,854.69
Product	C_7H_{16} (l)	N^*_{7Z}	480.629	639,201.05	314,364.31
Product	CO_2 (aq)	N^*_{CZ}	21.67	26,881.99	13,439.63
Product	N_2 (aq)	N^*_{NZ}	68.253	84,744.22	42,358.56
Product	H_2O (aq)	N^*_{WZ}	–	–	–
Total products			1,411.57	1,810,759.44	898,017.19
Total of chemical reaction			5,520.20	6,784,623.56	3,701,893.25

$$N_{1Z} = -D_{AB} \frac{dC_1}{dz} + \frac{C_1}{C_T} \left(N_{3Z} + N_{CZ} + N_{HZ} + N_{NZ} + N^*_{1Z} + N^*_{7Z} + N^*_{CZ} + N^*_{NZ} + N^*_{WZ} \right). \tag{99.10}$$

From the chemical reaction (Reaction No. 2), the molar flux of N_{1Z} from Eq. (99.10) is rearranged in terms of reactants and products. For example, methane is expressed as the N_{1Z} in this reaction. The diffusion coefficient of the methane reactant is finally revealed as 5,981.509 mol%/m$^2 \cdot$ s. Computational results of molar fluxes of the inlet slug catcher, high pressure flash vessel, and condensate tank of this chemical reaction are presented in Table 99.9.

Petroleum Dynamics for Chemical Reaction 1

Assumption for this mathematical concept for hydrocarbon dynamics is defined for one direction from the gas well to the gas plant. Both chemical reactions consist of dominantly methane gas and other hydrocarbons, such as ethane and i-propane, as the reactants. The diffusion coefficient of chemical reaction (No. 1) is 15.71 cm^2/s. Molar fluxes of the inlet slug catcher, high pressure flash vessel, and condensate tank for the reactants and products are plotted as a function of the sampling distances (Fig. 99.4). Starting from the inlet slug catcher, the quantities of all molar fluxes are gradually increasing in the high pressure flash vessel because of phase change from gas to liquid and decreasing to the condensate tank due to the completion of liquid phase. These effects on molar fluxes depend on chemical species under thermodynamic equilibrium and controlling system in the gas processing plant. The relationship of molar fluxes as a function of sampling distance is especially expressed in systematic trend for reactants (Fig. 99.4a), but complicated for products (Fig. 99.4b). Overall for the reactants, the molar fluxes of methane are found most which relevant to concentrations defined at the beginning. The intervals of each molar flux are obviously evident, except carbon dioxide and nitrogen gas. Obviously distinction of molar fluxes occurs in the products at the high pressure flash vessel and condensate tank. Relationship of molar fluxes as a function of the sampling distance presents the different phase at the high pressure flash vessel. Methane and heptanes are found in most amounts. In contrast, the different molar fluxes in high pressure flash vessel compared to the inlet slug catcher and condensate tank do not have systematic trends because of miscible phase between gas and liquid. According to the physical properties of condensate in deferent locations, the API gravity, density, specific gravity, and vapor pressure are found low to high. However, pressures in the controlling system decrease rapidly. Molar fluxes of hydrogen gas (very light gas) and heptanes (pure liquid) thus increase in the condensate tank, as illustrated in Fig. 99.4b.
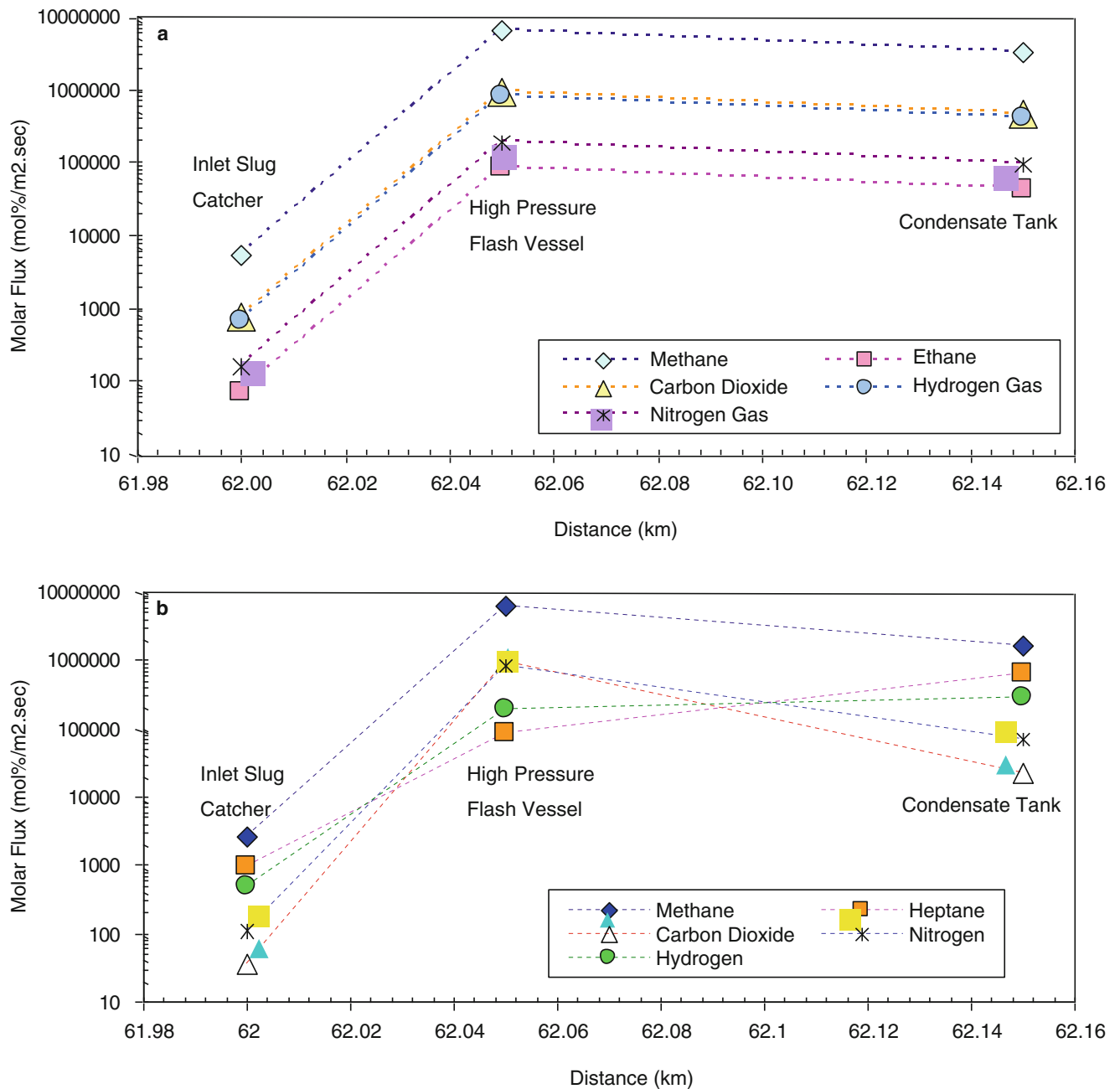
Fig. 99.4 Molar fluxes as a function of distances (sampling location) of (**a**) reactants and (**b**) products for the chemical reaction number 1

Petroleum Dynamics for Chemical Reaction 2

Chemical equilibrium involved in thermodynamics of this chemical reaction indicates the spontaneous reaction. All chemical species are representative for evaluation the possibility of phase envelope and applicable to the assumptions depending on theoretical chemical thermodynamics. The diffusion coefficient of this reaction is 9.20 cm^2/s. Relationship of molar fluxes as a function of sampling distances of the reactants and products is entirely in the systematic trend. Volatile matters are vanished. For the molar fluxes of reactants (Fig. 99.5a), the characteristic trend is similar to the products, as shown in Fig. 99.5b. The difference of the chemical reactions 1 and 2 is the hydrocarbon mixture, methane, and another gas (ethane, or propane). Propane is slightly heavier than ethane. Thus, the liquid phase prefers to occur. The physical properties will be affected less in the chemical reaction no. 2. Gibbs free energy (ΔG), enthalpy (ΔH), and equilibrium constant (K_{eq}) at
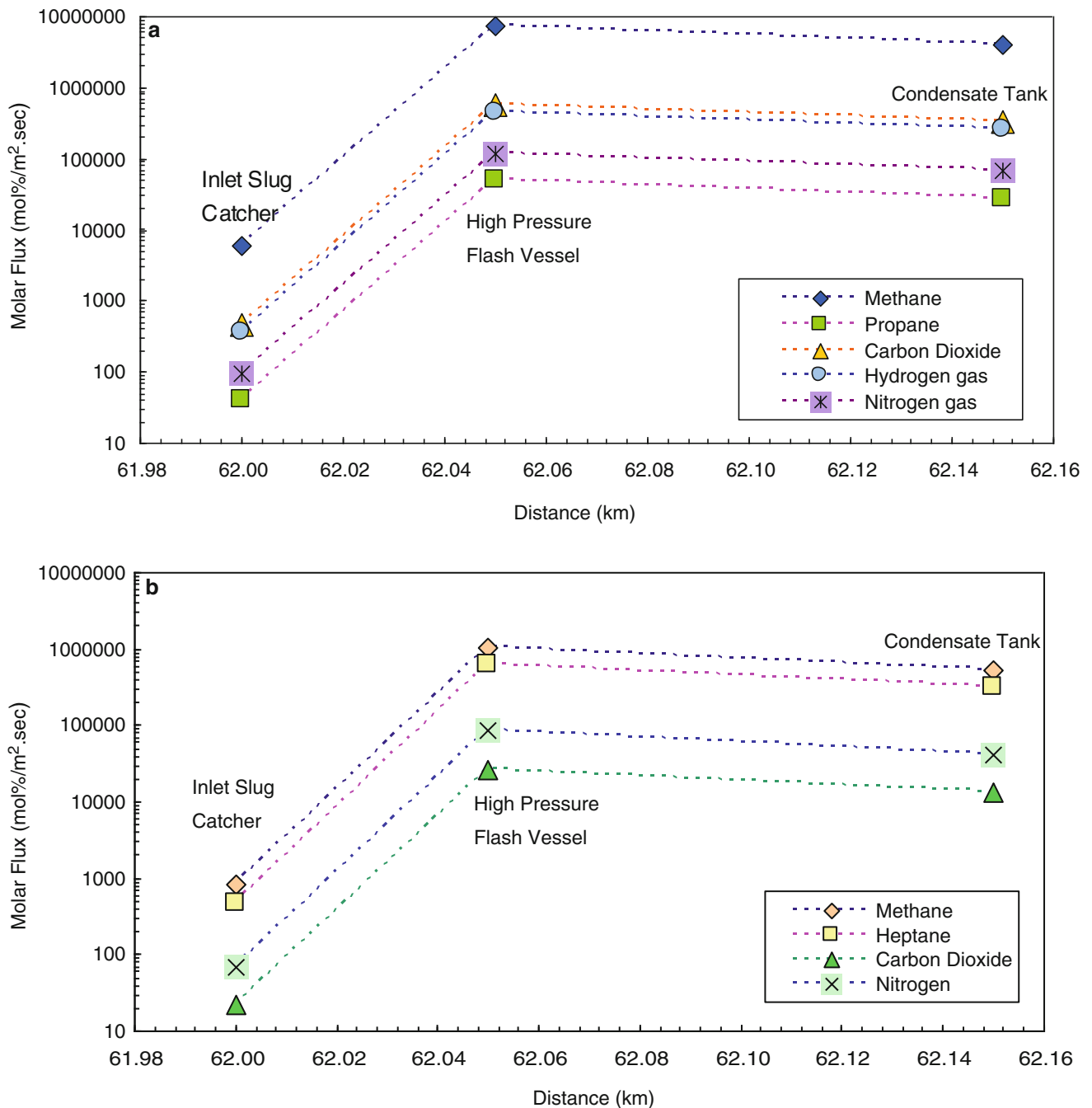
Fig. 99.5 Molar fluxes as a function of distance (sampling location) of (**a**) reactants and (**b**) products for the chemical reaction number 2

temperature of 0, 15, 25, and 200 °C are calculated, as shown in Table 99.10. This chemical reaction is a spontaneous process and relevant to the assumptions based on conceptual chemical thermodynamics.

For the chemical reaction no. 2, the relationship of methane molar fluxes between reactants and products presents the large interval between the reactants and products than the chemical reaction no. 1 because of different hydrocarbon types. Phase separation easily occurs in the reaction no. 2. Unconformity of relationship of methane molar fluxes between reactants and products depending on the physical properties in the chemical reaction no. 1 causes closely molar fluxes at the high pressure flash vessel.

Table 99.10 Gibbs free energy, enthalpy, and equilibrium constant of each chemical reaction

Reaction number	Gibbs free energy (ΔG) (kJ/mol)	Enthalpy (ΔH) (kJ/mol)	Equilibrium constant (K_{eq})			
			0 °C	15 °C	25 °C	200 °C
1	32.555	−217.900	0.93073	0.92838	0.92695	0.91184
2	−17.94	−310.228	1.01537	1.01033	1.00726	0.97514

Conclusions

This fluid within the reservoir will be brought from underground to a gas processing plant. Methane gas is found most approximately more than 96 mol%. Hydrocarbon transport is defined only from the gas well to the gas production plant. Criteria for this transport depend only on two chemical reactions in equilibrium condition. Their physical properties and chemical composition of natural gas and condensate are examined. Pressures in each process are decreased staring from the inlet slug catcher to condensate tank. Petroleum-field water indicates fresh water. Hydrocarbon concentrations of condensate are found C_7+ to C_{16}. Dynamic migration of petroleum is pursued in the closed conduit, cylindrical pipe, from the gas well to the gas processing plant. The diffusion coefficient of chemical reaction nos. 1 and 2 are 15.71 and 9.20 cm²/s, respectively. Distinction of molar fluxes occurs in the products of the chemical reaction no. 1. The molar fluxes of the high pressure flash vessel are generally the highest content because of phase change from gas to liquid, and decrease to the condensate due to the completion of liquid phase. These effects on molar fluxes depend on chemical species based on thermodynamic equilibrium and controlling system in the gas processing plant. In general, inclusive the reactants, the molar fluxes of methane are found most which relevant to concentrations defined at the beginning. The intervals of each molar flux are obviously evident, except carbon dioxide and nitrogen gas. Hydrocarbon mixture in the chemical reaction nos. 1 and 2 plays a critical role for phase changes and affected to the molar fluxes of each chemical species. Moreover, the miscible phase of methane can cause the variation of their molar fluxes which are affected by temperature controlling during natural gas and condensate separation.

References

1. Sattayarak N (2005) Petroleum potential of the Northeast, Thailand. In: Proceedings of international conference on geology, geotechnology and mineral resources of Indochina (GEOINDO 2005), Khon Kaen, Thailand, 28–30 Nov 2005, pp 21–30
2. PTT Exploration and Production Public Company Limited (2006) Phu Horm gas field comes to stream adding energy security to the northeastern part of Thailand. Retrieved 1 Nov 2012 from http://www.pttep.com/en/
3. Fan L, Harris BW, Jamaluddin A (J), Kamath J, Mott R, Pope GA, Shandrygin A, Whitson CH (2005/2006) Understanding gas-condensate reservoirs. Oilfield Rev 17:14–27
4. Kangsadan T (2012) Fundamental concepts of mass transport. Lecture Manuscript in Interfacial Transport Phenomena. The Sirindhorn International Thai–German Graduate School (TGGS) of Engineering, King Mongkut's University of Technology North Bangkok
5. Fuller EN, Schettler PD, Giddings JC (1966) Prediction of binary gas diffusivities. Retrieved 15 Nov 2012 from http://www.engin.umich.edu/~cre/course/lectures/eleven/exam4.htm
6. Buaphai P (2011) Experimental study on clathrate hydrate phase equilibria. B.Sc.'s thesis in geotechnology, Faculty of Technology, Khon Kaen University, Thailand
7. Kumchawong W (2009) Phase equilibria of condensate and natural gas corresponding to petroleum-field water in Sin Phu Horm gas field. B.Sc.'s thesis in geotechnology, Faculty of Technology, Khonkaen University, Khon Kaen, Thailand
8. Witherspoon PA, Saraf DN (1965) Diffusion of methane, ethane, propane and *n*-butane in water from 25° – 43°. J Phys Chem 69:3752–3755, http://www.thermopedia.com/content/696/#DIFFUSION_COEFFICIENT_TABLE1
9. Leahy-Dios A, Zhuo L, Firoozabadi A (2008) New thermal diffusion coefficient measurements for hydrocarbon binary mixtures: viscosity and composition dependency. J Phys Chem 112:6442–6447

Asok K. Sen, M. Akif Ceviz, and Erdogan Guner

Abstract

A gasoline engine may misfire when operating under lean-burn conditions. This study investigates the effect of adding hydrogen to the gasoline–air mixture on the misfire phenomenon. The effect of hydrogen addition is characterized by performing a statistical analysis of the indicated mean effective pressure (IMEP) time series over 1,000 engine cycles. Using the coefficient of variation (COV) of the IMEP time series, it is shown that hydrogen addition can suppress the misfires. In addition, it is demonstrated that the IMEP time series exhibiting misfire cycles are best modeled by a non-Gaussian probability distribution such as the generalized logistic distribution, whereas those with no or very little misfire can be modeled by a normal (Gaussian) distribution.

Keywords

Gasoline engine • Misfire • Hydrogen addition • Indicated mean effective pressure • Statistical analysis

Introduction

It has long been recognized that the process variables such as pressure in an internal combustion engine undergo cycle-to-cycle variations (CCV). These variations may become severe under lean-burn conditions, and for highly dilute mixtures with exhaust gas recirculation [1–3]. A small amount of CCV (slow burns) leads to unwanted engine vibration and noise, whereas large CCV (incomplete burns) result in increased hydrocarbon emissions. Incomplete burns are otherwise referred to as misfires. Lean misfires may occur due to an imbalance in air–fuel ratio with too much air but too little fuel [4]. Since an engine needs a richer mixture for a smooth idle, lean misfires may be more noticeable when the engine is idling. An undesirable consequence of a misfire is that the unburned fuel or flammable hydrocarbons are delivered to the exhaust manifold where they may ignite unpredictably. The purpose of this paper is to examine the lean misfire phenomenon in a gasoline engine and study the effect of adding hydrogen to the gasoline–air mixture on the misfires.

Several researchers have investigated the effect of hydrogen addition on engine performance and exhaust emissions in gasoline engines under lean operating conditions. In their experiments, [5] the effect of adding small amounts of hydrogen to hydrocarbon–air mixtures is examined. They observed that hydrogen addition can lead to an increase in brake thermal efficiency and a reduction in HC emissions. More recently, Tahtouh et al. [6] also showed that high values of indicated engine efficiency with low values of HC, NO_x, and CO emissions can be achieved by combining hydrogen addition with lean and/or diluted conditions. Among others, D'Andrea et al. [7] performed an experimental study of a spark ignition engine

A.K. Sen (✉)
Richard G. Lugar Center for Renewable Energy, Department of Mathematical Sciences, Indiana University, 402 North Blackford Street, Indianapolis, IN 46202, USA
e-mail: asen@iupui.edu

M.A. Ceviz • E. Guner
Department of Mechanical Engineering, Faculty of Engineering, University of Atatürk, Erzurum 25240, Turkey
e-mail: aceviz@atauni.edu.tr; erdoganguner@atauni.edu.tr

fueled by gasoline–hydrogen blends and revealed that hydrogen addition improves the work output and decreases the burn duration under lean conditions. Verhlest et al. [8] presented the variations in thermal efficiency of a spark ignition engine fueled by gasoline–hydrogen blends at several engine speeds and loads. They found that hydrogen offered the possibility of a more flexible load control strategy. At low loads, important in everyday driving, the efficiency gain from hydrogen addition was significantly high, achieving up to 60 % increase in thermal efficiency. A similar investigation on combustion and emissions of a hydrogen-gasoline engine was carried out by Ji et al. [9] at various loads under lean-burn conditions.

There have been numerous studies investigating the CCV in spark ignition engines [10–14]. In these studies, the CCV were analyzed using the coefficient of variation (COV) of the time series of the indicated mean effective pressure (IMEP) or heat release. More recent efforts have used a wavelet-based approach to analyze the CCV [15–17]. In this paper, we perform a statistical analysis of the CCV of the IMEP time series in a gasoline engine using their COV, skewness, and kurtosis, and investigate the effect hydrogen addition on the misfire phenomenon. In particular, we show that hydrogen addition can suppress the misfires. In addition, we demonstrate that the IMEP time series exhibiting misfire cycles are best modeled by a non-Gaussian probability distribution such as the three-parameter generalized logistic (GLO) distribution, whereas those with almost no misfires can be modeled by a normal (Gaussian) distribution.

Experimental Procedure

The experiments were performed on a FORD MVH-418 spark ignition engine with electronically controlled fuel injectors. A schematic layout of the experimental set up and the engine specifications can be found in an earlier paper [18]. The engine was coupled to a hydraulic dynamometer. A lean combustible mixture with air–fuel ratio of 1.26 was used, and hydrogen was added to the gasoline–air mixture in the amounts 2.14, 5.28, and 7.74 % by volume. The engine was operated at 2,000 rpm. The engine speed was measured using a 60-tooth sprocket and a magnetic pickup. The in-cylinder pressure measurements were made with a KISTLER 6117BFD17 quartz pressure transducer connected to a charge amplifier. The crank angle was measured by an optical shaft encoder. The optical shaft encoder was rigidly mounted on the front of the engine and connected to the crankshaft with a flexible coupler. The in-cylinder pressure data from the charge amplifier and crank angle data from the encoder were recorded by National Instruments Corporation's high speed M-series, 6250 model, 1.25 MS/s DAQ Card in an Intel 4 CPU 2.00 GHz personal computer. The software package NI-DAQmx from the National Instruments Corporation was used for data collection. The pressure data were recorded over 1,000 consecutive engine cycles. From the pressure measurements, the IMEP values were calculated as follows. The IMEP is defined as the average pressure in the cylinder over one engine cycle, and is given by $IMEP = W_c/V_d$, where V_d is the engine displacement volume, and W_c is the amount of work done per cycle: $W_c = \oint PdV$. Here P represents the actual (i.e., measured) pressure inside the engine cylinder.

Statistical Methodology

As mentioned in Sect. 100.1, we investigated the misfire phenomenon by performing a statistical analysis of the IMEP time series. Consider a time series $\{x_i\}$, $i = 1, 2, 3, \ldots, N$. For this time series, the various statistical parameters, namely, mean (μ), standard deviation (σ), COV, skewness (S), and kurtosis (K) are defined by

$$\mu = \frac{1}{N} \sum_{i=1}^{N} x_i, \quad \sigma^2 = \frac{1}{N} \sum_{i=1}^{N} (x_i - \mu)^2, \quad COV = \frac{\sigma}{\mu} x\,100, \tag{100.1a}$$

$$S = \frac{\frac{1}{N} \sum_{i=1}^{N} (x_i - \mu)^3}{\sigma^3}, \quad K = \frac{\frac{1}{N} \sum_{i=1}^{N} (x_i - \mu)^4}{\sigma^4} \tag{100.1b}$$

Note that the COV is usually expressed in percent form. The COV is a useful statistic for comparing the degree of variation between two time series even when their mean values are quite different from each other. The skewness (S) is a measure of asymmetry in the distribution of data in the time series. A distribution with zero skewness, such as a normal distribution, is symmetric, i.e., it looks the same to the left and right of the center point or the mean value. A distribution with

a negative skewness has a longer tail to the left indicating the presence of small values in the time series. On the other hand, a distribution with a positive skewness has a longer right tail. The kurtosis (K) is a statistical measure that indicates whether the data distribution is peaked or flat relative to a normal distribution. A normal distribution has a kurtosis of 3. Distributions with high kurtosis ($K > 3$) tend to be peaked around the mean, decrease rapidly, and have heavy tails, whereas those with low kurtosis ($K < 3$) tend to have a flat top around the mean. Note that since a normal distribution is symmetric about the mean, the probability of seeing a normally distributed value that is far (i.e., more than a few standard deviations) from the mean is very low. In other words, a normal distribution does not exhibit tail behavior. We will use the skewness and kurtosis values of the IMEP time series to describe the misfires that may occur in a spark ignition engine under lean-burn conditions.

Results and Discussion

The various IMEP time series analyzed here are depicted in Fig. 100.1, and the statistical parameters of these time series are listed in Table 100.1. Consider first Fig. 100.1a which shows the IMEP time series for the gasoline engine (with no hydrogen added). In this figure, the misfire cycles are identified as those with low IMEP values. The histogram of this time series is shown in Fig. 100.2a, along with the values of skewness $= -2.61$ and kurtosis $= 15.8$ from Table 100.1. Note that the histogram is skewed to the left, i.e., it has a long left tail representing the low IMEP values. Since a normal or Gaussian distribution has zero skewness and kurtosis equal to 3, clearly, the above time series cannot be adequately characterized by a normal distribution. The negative skewness is consistent with the long left tail in the histogram, and the high value of kurtosis indicates that the distribution of this IMEP time series is more peaked than a normal distribution. We have fitted several three-parameter non-Gaussian distributions to this time series. The distribution with the best fit is found to be the GLO distribution [19]. A brief description of the GLO distribution is given in Appendix. The goodness of fit of the GLO distribution was assessed using the Kolmogorov–Smirnov statistic [20]. The GLO distribution has been used to model the
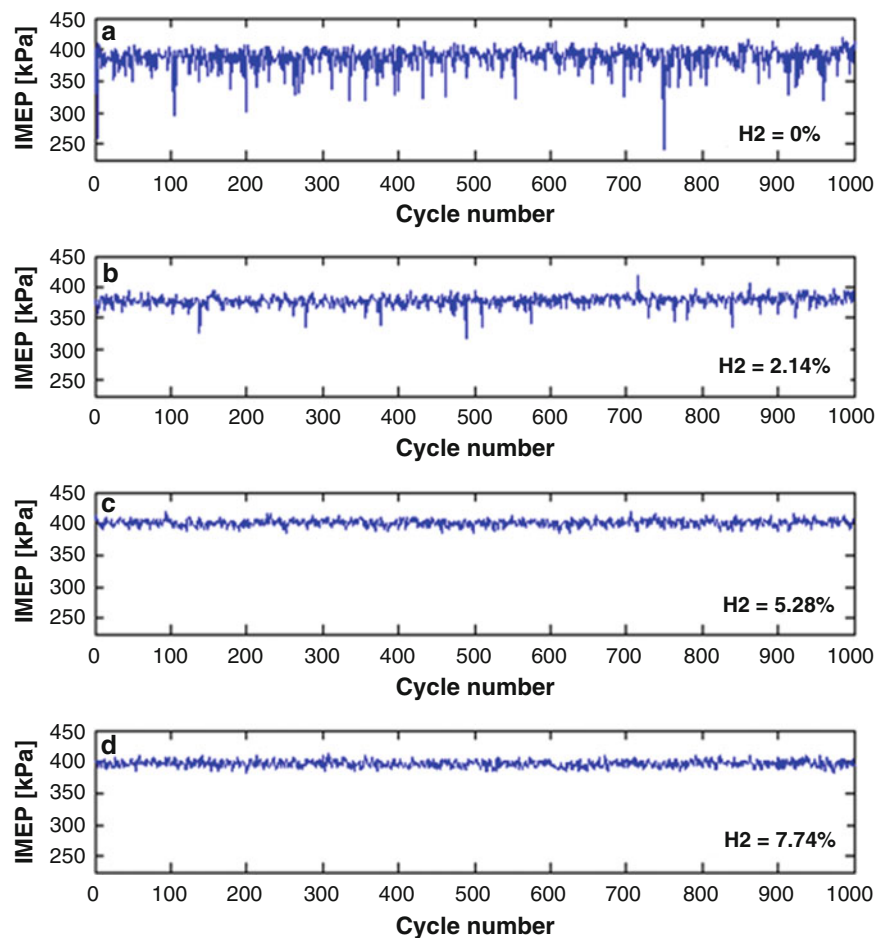
Fig. 100.1 Indicated mean effective pressure (IMEP) time series of the gasoline engine with (**a**) no hydrogen added, (**b**) 2.14 % hydrogen added, (**c**) 5.28 % hydrogen added, and (**d**) 7.74 % hydrogen added

Table 100.1 Statistical parameters of the IMEP time series for different hydrogen fractions

H_2 (%)	Mean	SD	COV	Skewness	Kurtosis
0.00	387.8	16.59	4.28	−2.61	15.8
2.14	378.4	8.14	2.15	−1.54	11.2
5.28	401.3	4.96	1.25	−0.26	3.56
7.74	396.9	4.84	1.22	−0.02	2.77

SD standard deviation, *COV* coefficient of variation
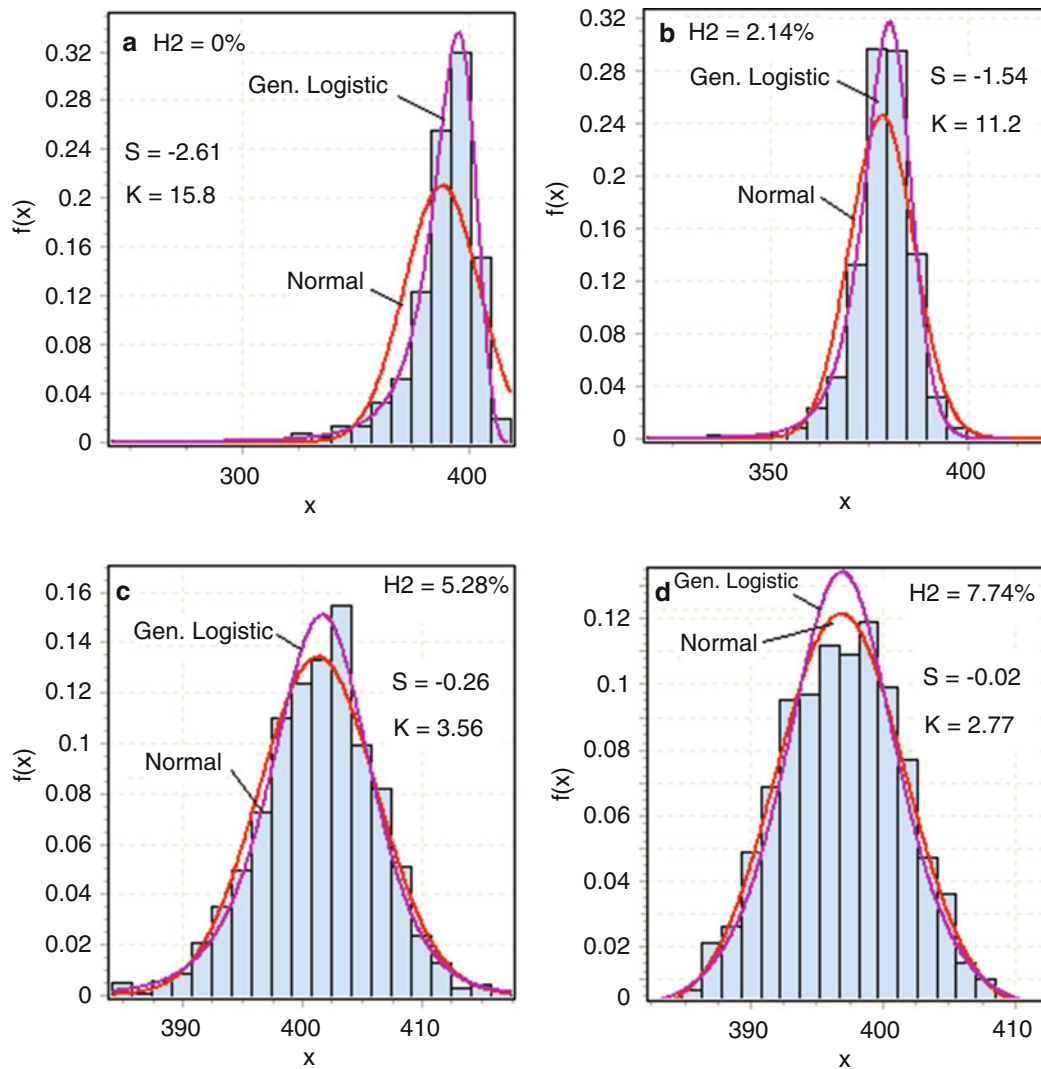
Fig. 100.2 Histograms of the various IMEP time series shown in Fig. 100.1, and the probability density functions [f(x)] of the fitted distributions. Here *x* represents the IMEP variable

occurrence of extreme events in many applications including analysis of bioassays [21], financial time series analysis [22, 23], and flood frequency analysis [24, 25].

For the IMEP time series of the gasoline engine shown in Fig. 100.1a, the GLO distribution given by Eq. (100.2) in Appendix provides the best fit with the following parameter values: $\mu = 391.34$, $\sigma = 7.045$, and $k = -0.278$. The probability density function (pdf) of this distribution is drawn in Fig. 100.2a overlapping the histogram. For comparison, the fitted normal distribution is also shown in this figure.

Next we consider the IMEP time series of the engine fueled by gasoline–hydrogen–air mixtures. Figure 100.1b–d depicts the IMEP time series for the mixtures containing 2.14 %, 5.28 %, and 7.74 % hydrogen fractions, respectively. Note that in

Fig. 100.1c and d, the IMEP values are more or less symmetrically distributed about their mean. In other words, there are very few misfire cycles present. The histograms of the three time series are shown in Fig. 100.2b–d, and their statistical parameters are listed in Table 100.1. Consider the IMEP time series shown in Fig. 100.1b which applies to the gasoline–hydrogen blend containing 2.14 % hydrogen. The skewness and kurtosis of this time series are -1.54 and 11.2, respectively. Clearly, this time series also cannot be modeled by a normal distribution. In fact, the three-parameter GLO distribution with $\mu = 379.23$, $\sigma = 4.024$, and $k = -0.129$ is found to provide the best fit to this time series. As in Fig. 100.2a, the fitted GLO distribution and the normal distribution are shown in this figure overlapping the histogram. The histogram of the IMEP time series for the gasoline–hydrogen blend with 5.28 % hydrogen is presented in Fig. 100.2c. From the shape of this histogram and the skewness and kurtosis values, it is apparent that the distribution of this time series is close to a normal distribution. We have fitted a normal distribution and a GLO distribution to this dataset, and drawn them overlapping the histogram. Finally, consider the gasoline–hydrogen blend with 7.74 % hydrogen. Figure 100.2d shows the histogram of the IMEP time series for this case. Because the skewness and kurtosis values of this time series are very close to those of a normal distribution, we have fitted a normal distribution to this time series. The fitted normal distribution is shown overlapping the histogram in Fig. 100.2d. For comparison, the fitted GLO distribution is also shown in this figure.

It is appropriate to note from Table 100.1 that the COV is highest for the IMEP time series of the gasoline engine (with no hydrogen added). The COV values continually decrease as the amount of hydrogen added increases, indicating that the cyclic variations of IMEP are reduced with hydrogen addition. While the cyclic variations can, in general, be adequately described on the basis of the COV of the IMEP time series, the misfire cycles can be more appropriately identified on the basis of their skewness and kurtosis.

Conclusions

We have examined the lean misfire phenomenon in a gasoline engine. Using the COV of the IMEP time series, it is shown that by adding a small amount of hydrogen to the gasoline–air mixture, the misfires can be suppressed. We have also demonstrated that the IMEP time series associates with misfires can be modeled by a non-Gaussian probability distribution such as the GLO distribution, whereas those with almost no misfires can be modeled by a normal distribution. The large amount of data collected over 1,000 consecutive engine cycles enables us to clearly observe the many misfire cycles that can occur in a spark ignition engine under lean-burn conditions.

Appendix

The Generalized Logistic Distribution

The three-parameter generalized logistic (GLO) distribution is a generalization of the two-parameter logistic distribution. The probability density function (pdf) of the GLO distribution is given by [19]

$$f(x) = \frac{\left[1 + k\frac{x-\mu}{\sigma}\right]^{-1-1/k}}{\sigma\left[1 + \left(1 + k\frac{x-\mu}{\sigma}\right)^{-1/k}\right]^2} \quad k \neq 0, \tag{100.2}$$

$$f(x) = \frac{\exp\left(-\frac{x-\mu}{\sigma}\right)}{\sigma\left[1 + \exp\left(-\frac{x-\mu}{\sigma}\right)\right]^2} \quad k = 0. \tag{100.3}$$

Here the symbols μ, σ, and k represent the location parameter, scale parameter, and shape parameter, respectively. A positive value of k corresponds to a positively skewed distribution, i.e., with a longer right tail, whereas a negative value of k represents a negative skewed distribution with a longer left tail. When $k = 0$, the GLO distribution becomes the logistic distribution which is symmetric.

References

1. Heywood JB (1988) Internal combustion engine fundamentals. McGraw-Hill, New York
2. Wagner RM, Drallmeier JA, Daw CS (1998) Prior-cycle effects in lean spark ignition combustion—fuel/air charge considerations. SAE paper no: 981047
3. Young MB (1981) Cyclic dispersion in a homogeneous charge spark ignition engine: a literature survey. SAE paper no: 810020
4. Scholl D, Russ S (1999) Air-fuel ratio dependence of random and deterministic cyclic variability in a spark-ignited engine. SAE paper no: 1999-01-3513
5. Apostolescu N, Chiriac R (1996) A study of combustion of hydrogen-enriched gasoline in a spark ignition engine. SAE paper no: 960603
6. Tahtouh T, Halter F, Samson E, Mounaim-Rousselle C (2011) Effects of hydrogen addition under lean and diluted conditions on combustion characteristics and emissions in a spark-ignition engine. Int J Engine Res 35:466–483
7. D'Andrea T, Henshaw PF, Ting DSK (2004) The addition of hydrogen to a gasoline-fueled SI engine. Int J Hydrogen Energy 29:1541–1552
8. Verhlest S, Maesschalck SP, Rombaut H, Sierens R (2009) Efficiency comparison between hydrogen and gasoline on a bi-fuel hydrogen/gasoline engine. Int J Hydrogen Energy 34:2504–2510
9. Ji C, Wang S, Zhang B (2010) Combustion and emissions characteristics of a hybrid hydrogen-gasoline engine under various loads and lean conditions. Int J Hydrogen Energy 35:5714–5722
10. Fujikawa T, Nomura Y, Hatton Y, Kobayashi T, Kanda M (2003) Analysis of cycle-by-cycle variations in a direct-injection spark-ignition engine using a laser-induced fluorescence technique. Int J Engine Res 4:143–153
11. Galloni T (2009) Analysis about parameters that affect cyclic variation in a spark ignition engine. Appl Therm Eng 28:1131–1137
12. Ishii K, Sasaki T, Urata Y, Yoshida K, Ohno T (1997) Investigation of cyclic variation of heat release under lean burn operation in a spark ignition engine. SAE paper no: 972830
13. Ozdor N, Dulger M, Sher E (1994) Cyclic variability in spark ignition engines: a literature survey. SAE paper no: 940987
14. Zervas E (2004) Correlations between cycle-to-cycle variations and combustion parameters of a spark ignition engine. Appl Therm Eng 24:2075–2081
15. Ceviz MA, Sen AK, Kuleri AK, Oner IV (2012) Engine performance, exhaust emissions and in a lean burn gasoline engine fueled by gasoline–hydrogen blends. Appl Therm Eng 34:314–324
16. Sen AK, Litak G, Edwards KD, Finney CEA, Daw CS, Wagner RM (2011) Characteristics of cyclic heat release variability in the transition from spark ignition to HCCI in a gasoline engine. Appl Energy 88:1649–1655
17. Sen AK, Wang J, Huang Z (2012) Investigating the dynamics of cyclic variability in a natural gas spark ignition engine: wavelet-based multiresolution analysis. Appl Energy 88:4860–4866
18. Ceviz MA, Çavuşoğlu B, Kaya F, Öner İV (2011) Determination of cycle number for real in-cylinder pressure cycle analysis in internal combustion engines. Energy 36:2465–2472
19. Johnson NL, Kotz S, Balakrishnan N (1995) Continuous univariate distributions, vol 2. Wiley, New York
20. Sheskin D (2007) Handbook of parametric and nonparametric statistical procedures, 4th edn. CRC, Boca Raton, FL
21. El-Saidi MA, George EO (1990) A generalized logistic model for quantal response bioassay. Biom J 32:943–954
22. Gettinby GD, Sinclair CD, Power DM, Brown RA (2004) An analysis of the extreme share returns in the UK from 1975 to 2000. J Bus Finance Account 31:607–646
23. Tolika K, Gettinby GD (2009) Modeling the distribution of extreme share returns in Singapore. J Empir Finance 16:252–263
24. Ali S, Davar M (2008) Comprehensive evaluation of regional flood frequency analysis by L- and LH moments: development of LH moments parameters for the generalized Pareto and generalized logistic distributions. Stoch Environ Res Risk Assess 23:137–152
25. Kjeldsen TR, Jones DA (2004) Sampling variance of flood quantiles from the generalized logistic distribution estimated using the method of L-moments. Hydrol Earth Syst Sci 8:183–190

Index

A